THE INTERNATIONAL LINEAR COLLIDER

Technical Design Report | Volume 1: Executive Summary

The International Linear Collider

Technical Design Report

2013

Volume 1: Executive Summary

Volume 2: Physics

Volume 3: Accelerator

Part I: R&D in the Technical Design Phase

Volume 3: Accelerator

Part II: Baseline Design

Volume 4: Detectors

Volume 1

Executive Summary

Editors

Ties Behnke, James E. Brau, Brian Foster, Juan Fuster, Mike Harrison, James McEwan Paterson, Michael Peskin, Marcel Stanitzki, Nicholas Walker, Hitoshi Yamamoto

Acknowledgements

We acknowledge the support of BMWF, Austria; MinObr, Belarus; FNRS and FWO, Belgium; NSERC, Canada; NSFC, China; MPO CR and VSC CR, Czech Republic; Commission of the European Communities; HIP, Finland; IN2P3/CNRS, CEA-DSM/IRFU, France; BMBF, DFG, Helmholtz Association, MPG and AvH Foundation, Germany; DAE and DST, India; ISF, Israel; INFN, Italy; MEXT and JSPS, Japan; CRI(MST) and MOST/KOSEF, Korea; FOM and NWO, The Netherlands; NFR, Norway; MNSW, Poland; ANCS, Romania; MES of Russia and ROSATOM, Russian Federation; MON, Serbia and Montenegro; MSSR, Slovakia; MICINN-MINECO and CPAN, Spain; SRC, Sweden; STFC, United Kingdom; DOE and NSF, United States of America.

Contents

1 Introduction **1**

2 Physics at the International Linear Collider **3**

3 The International Linear Collider Accelerator **9**

3.1 The ILC Technical Design . . . 9

3.1.1 Overview . . . 9

3.1.2 Machine parameters . . . 10

3.2 Accelerator Layout & Design . . . 12

3.2.1 Superconducting RF Main Linacs . . . 12

3.2.2 Electron source . . . 14

3.2.3 Positron source . . . 14

3.2.4 Damping rings . . . 15

3.2.5 Ring to Main Linac (RTML) . . . 16

3.2.6 Beam Delivery System (BDS) . . . 16

3.2.7 Conventional facilities and site-dependent designs . . . 17

3.2.8 Special considerations for running at low centre-of-mass energy . . . 18

3.2.9 Luminosity and energy upgrade options . . . 19

3.2.10 Value estimate and methodology . . . 19

3.3 ILC R&D during the technical design phase . . . 22

3.3.1 Main achievements of the SCRF R&D effort . . . 23

3.3.2 R&D on RF power generation and distribution . . . 24

3.3.3 Beam test facilities . . . 25

3.3.4 Future engineering and R&D . . . 26

4 ILC Detectors **27**

4.1 Introduction and Physics Performance Requirements . . . 27

4.2 Backgrounds . . . 28

4.3 Beam Instrumentation . . . 28

4.4 Two Detectors . . . 28

4.5 Detector R&D . . . 30

4.6 SiD . . . 30

4.6.1 The SiD detector . . . 30

4.6.2 SiD detector performance . . . 32

4.6.3 SiD costing . . . 33

4.7 ILD . . . 33

4.7.1 The ILD detector . . . 34

4.7.2 ILD detector performance . . . 35

4.7.3 ILD costing . . . 36

5 Conclusion **39**

Contributing Institutes **41**

Chapter 1
Introduction

The International Linear Collider (ILC) is a 200–500 GeV (extendable to 1 TeV) centre-of-mass high-luminosity linear electron-positron collider, based on 1.3 GHz superconducting radio-frequency (SCRF) accelerating technology. Its parameters have been set by physics requirements first outlined in 2003, updated in 2006, and thoroughly discussed over many years with the physics user community. The physics parameters have been reviewed continuously and found to be robust to advances in the science, including the recent discovery of a Higgs boson at the Large Hadron Collider at CERN.

The collider design is the result of nearly twenty years of R&D. The heart of the ILC, the superconducting cavities, is based on over a decade of pioneering work by the TESLA collaboration in the 1990s. Some other aspects were based on the R&D carried out for the JLC/GLC and NLC projects, which were based on room-temperature accelerating structures. Since 2005, the design of the ILC accelerator has continued as a worldwide international collaboration coordinated by the Global Design Effort (GDE) under a mandate from the International Committee for Future Accelerators (ICFA). Drawing on the resources of over 300 national laboratories, universities and institutes worldwide, the GDE produced the ILC *Reference Design Report* (RDR) in August 2007. The work done by the GDE during the RDR phase identified several high-risk challenges that required R&D, which have since been the focus of the worldwide activity during the Technical Design Phase. In parallel with the accelerator effort, detailed baseline designs of two detectors have been developed by large international teams as a result of intense detector R&D under the coordination of the Research Directorate, also established by a mandate of ICFA.

These efforts have now successfully culminated in the publication of this *Technical Design Report*, completing the mandates of both the GDE and the Research Directorate. The report describes a conceptual design for the ILC project that reflects an international consensus.

This Executive Summary first discusses the physics goals of the ILC. It then addresses the design and the associated value cost estimate of the accelerator, followed by the R&D results which underpin its technical design. It concludes with a discussion of the ILC detector design and development outcomes and their cost estimates.

Chapter 2
Physics at the International Linear Collider

Today the search for new particles and forces at energies of hundreds or thousands of GeV plays a central role in the field of elementary particle physics. Particle physicists have established a "Standard Model" for the strong, weak, and electromagnetic interactions that passes tests at both low and high energies. The model is extremely successful, and yet it is incomplete in many important respects. New particles and interactions are needed to fill the gaps.

Some of the difficulties of the Standard Model are deep and abstract; their explanations may be found only in the distant future. The Standard Model does not explain how gravity is connected to the other forces of nature. It does not explain why the basic particles of matter are the quarks and leptons, or how many of these there should be.

However, the Standard Model also fails to explain three phenomena that, by rights, should be accounted for at the energies now being probed with particle accelerators. Astronomers believe that the dominant form of matter in the universe is a neutral, weakly interacting species called "dark matter" that cannot be composed of any particle present in the Standard Model. The Standard Model cannot explain why the universe contains atomic matter made of electrons, protons and neutrons but no comparable amount of antimatter.

Behind these two striking problems, there is a third. The equations of the Standard Model are based on a symmetry principle, electroweak symmetry, that forbids the generation of mass for any of its fundamental particles. The universe contains an element that chooses a direction with respect to this symmetry. This asymmetrical force creates the masses of the quarks, leptons, and bosons of the Standard Model and also drives many other essential properties of the laws of nature. The Standard Model postulates a field, called the *Higgs field*, that gives rise to this force. However, it does not explain the properties of this field. The idea that the asymmetry comes from a single Higgs field is just a guess among many other possibilities.

The problem of the Higgs field is likely to be connected to the earlier questions about the matter content of the universe. Explanatory models of the Higgs field often contain particles with the correct properties to make up the dark matter. There are also strong, independent, arguments that the mass of the dark-matter particle is comparable to the masses—of the order of 100 GeV—of the heaviest particles that receive mass from the Higgs field. The excess of baryons over antibaryons in the universe could arise from interactions among Higgs fields that violate the space-time symmetry CP. More generally, any model of fundamental physics at energies above 100 GeV must contain the Higgs field or some generalisation and must account for the place of this field within its structure.

A way to prove the existence of the Higgs field and to study its interactions is to find and study the quantum of this field, called the *Higgs boson*. The International Linear Collider was designed to study this particle and other new particles that might be associated with it. It provides an ideal

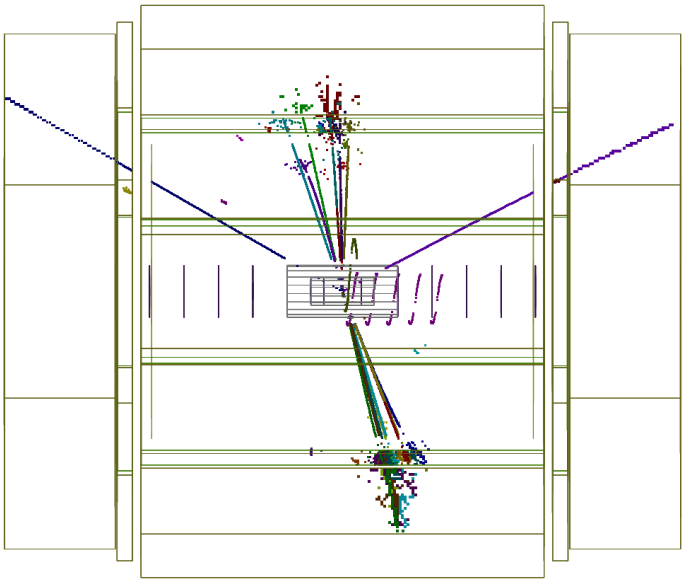

Figure 2.1
An event of reaction $e^+e^- \to Zh$, with $Z \to \mu^+\mu^-$, $h \to b\bar{b}$, as it would be observed in the ILD detector at the ILC.

setting for detailed exploration of the origin and nature of the Higgs field. The physics program of the ILC is described in detail in the Physics Volume, Volume 2 of this report.

In July, 2012, the ATLAS and CMS experiments at the CERN Large Hadron Collider announced the discovery of a new particle with a mass of 125 GeV and many properties of the Higgs boson as postulated in the Standard Model. The LHC experiments also exclude the possibility that the Higgs boson has higher mass, up to masses beyond 600 GeV and close to the theoretical upper bound. The ILC is an ideal machine to study this Higgs particle at 125 GeV. If this particle is one of several Higgs bosons and a different boson is the one that makes the main contributions to the W and Z boson masses, that particle must also appear at the ILC. Thus, the ILC definitely offers a direct path to the study of the Higgs field and its implications for particle physics.

The initial program of the ILC for a 125 GeV Higgs boson will be centred at an energy of 250 GeV, which gives the peak cross section for the reaction $e^+e^- \to Zh$. In this reaction, the identification of a Z boson at the energy appropriate to recoil against the Higgs boson tags the presence of the Higgs boson. In this setting, it is possible to measure the rates for all decays of the Higgs boson—even decays to invisible or unusual final states—with high precision. An example of an event with a Higgs boson decay to quarks is shown in Fig. 2.1. Such decays are very difficult to separate from Standard Model background events at the LHC. The precision measurement of the rates of decay of the Higgs boson to the various types of quarks, leptons, and bosons will give evidence on whether the Higgs field operates alone to create the masses of these particles, or whether it has partners that are additional new particles addressing the other questions raised above.

The study of the Higgs boson will continue, with additional essential elements, at higher energies. At 500 GeV, the full design energy of the ILC, measurement of the process $e^+e^- \to \nu\bar{\nu}h$ will give the absolute normalisation of the underlying Higgs coupling strengths, needed to determine the individual couplings to the percent level of accuracy. Raising the energy further allows the ILC experiments to make precise measurements of the Higgs boson coupling to top quarks and to determine the strength of the Higgs boson's nonlinear self-interaction.

The ILC also will make important contributions to the search for new particles associated with the Higgs field, dark matter, and other questions of particle physics. For many such particles with only electroweak interactions, searches at the LHC will be limited by low rates relative to strong-interaction induced processes, and by large backgrounds. The ILC will identify or exclude these particles unambiguously up to masses at least as high as the ILC beam energy. The Physics Volume

discusses a variety of models for new physics in which such particles are required and illustrates the crucial role of the ILC for these models. For example, many models contain partners of the Higgs boson. The very attractive theory of supersymmetry, a symmetry between matter and force-carrying particles, requires matter-type Higgs particles. These particles are difficult to detect at the LHC because of their expected low energy release and low production rate. The ILC, however, can search for these particles in a direct and definitive way. If new particles are discovered, either at the LHC or at the ILC, the ILC will be able to measured their quantum numbers unambiguously and determine their couplings to the percent level. The motivations for this study include exploration of the question of whether a new neutral, weakly interacting particle discovered at particle accelerators actually might be the constituent of the dark matter of the universe.

The ILC will also constrain or discover new interactions at higher mass scales through pair-production of quarks and leptons, W and Z bosons, and top quarks. Much of our detailed knowledge of the current Standard Model comes from the precision measurement of the properties of the Z boson at e^+e^- colliders. The ILC will extend this level of precision to the W boson and the top quark. The ILC will measure the mass of the top quark in a direct way that is not possible at hadron colliders, fixing a crucial input to particle physics calculations. The top quark is the heaviest particle of the Standard Model, and, as such, must have especially strong coupling to the Higgs field. The precision study of the electroweak couplings of the top quark can reveal the presence of composite structure in the Higgs particle. Characteristic effects are expected in models with strong interactions among the Higgs fields, and in models where the asymmetrical forces associated with the Higgs fields are signs of extra, hidden dimensions of space.

Table 2.1
Major physics processes to be studied by the ILC at various energies. The table indicates the various Standard Model reactions that will be accessed at increasing collider energies, and the major physics goals of the study of these reactions. A reaction listed at a given energy will of course be studied at all higher energies.

Energy	Reaction	Physics Goal
91 GeV	$e^+e^- \to Z$	ultra-precision electroweak
160 GeV	$e^+e^- \to WW$	ultra-precision W mass
250 GeV	$e^+e^- \to Zh$	precision Higgs couplings
350–400 GeV	$e^+e^- \to t\bar{t}$	top quark mass and couplings
	$e^+e^- \to WW$	precision W couplings
	$e^+e^- \to \nu\bar{\nu}h$	precision Higgs couplings
500 GeV	$e^+e^- \to f\bar{f}$	precision search for Z'
	$e^+e^- \to t\bar{t}h$	Higgs coupling to top
	$e^+e^- \to Zhh$	Higgs self-coupling
	$e^+e^- \to \tilde{\chi}\tilde{\chi}$	search for supersymmetry
	$e^+e^- \to AH, H^+H^-$	search for extended Higgs states
700–1000 GeV	$e^+e^- \to \nu\bar{\nu}hh$	Higgs self-coupling
	$e^+e^- \to \nu\bar{\nu}VV$	composite Higgs sector
	$e^+e^- \to \nu\bar{\nu}t\bar{t}$	composite Higgs and top
	$e^+e^- \to \tilde{t}\tilde{t}^*$	search for supersymmetry

One of the advantages of a linear collider is its ability to operate, with minimal modification, at any energy within a wide range that its technology makes available. Table 2.1 lists the major reactions that will be studied at the ILC in the various stages of its program, with collider energies from 90 GeV to 1000 GeV. These include Higgs boson reactions, studies of pair production, and searches for new particles, as described in the previous paragraphs. A linear collider also makes it possible to collide electron and positron beams with high spin polarisation. This makes available many new observables that cannot be measured at colliders of other types. Because the Standard Model violates parity in a maximal way, the quantum numbers of new particles and the full set of couplings for W, t, and other known particles can only be measured unambiguously through the use of these spin observables. In the Physics Volume, the key role of beam polarisation in the ILC measurements is explained for each of the topics discussed.

There is another advantage of a linear electron-positron collider over a proton-proton collider such as the LHC. The total rate of high-energy collisions and the complexity of these collisions are both much lower at the electron-positron accelerator. This allows the design of particle detectors with higher intrinsic resolution than those at proton colliders, and with less obscuring material between the particle collision point and the sensitive elements. At an electron-positron collider, silicon sensors can be brought within 2 cm of the interaction point to produce a high-precision image of the particle tracks emerging from the collision. This enables very efficient identification of short-lived particles such as the heavy quarks and leptons b, c, and τ. The proposed designs of the detectors for the ILC, and the evaluation of the capabilities of these detectors in relation to the goals of the ILC physics program, is described in the Detector Volume, Volume 4 of this report.

Table 2.2. Key precision Standard Model measurements that will be achieved with the ILC. Estimates for Higgs assume $m_{\rm h} = 125$ GeV. These analyses require no significant model-dependent assumptions. ILC will also search systematically for all particles with electroweak couplings up to the masses close to the $\rm e^+$ and $\rm e^-$ beam energies. The last section of the table shows the precision that the ILC can achieve in measuring properties of some illustrative new particles that might be discovered at the ILC. Measurement accuracies are quoted for ILC event samples of 250 fb^{-1} at 250 GeV, 500 fb^{-1} at 500 GeV, and 1000 fb^{-1} at 1000 GeV, with electron/positron polarization of 80%/30% in the first two cases and 80%/20% in the third case. Dedicated threshold scans require less luminosity at energies specifically chosen for the task.

Topic	Parameter	Accuracy $\Delta X/X$	
Higgs	$m_{\rm h}$	0.03%	$\Delta m_{\rm h} = 35$ MeV, 250 GeV
	$\Gamma_{\rm h}$	1.6%	250 GeV and 500 GeV
	$g(hWW)$	0.24%	
	$g(hZZ)$	0.30%	
	$g(hb\bar{b})$	0.94%	
	$g(hc\bar{c})$	2.5%	
	$g(hgg)$	2.0%	
	$g(h\tau^+\tau^-)$	1.9%	
	$BR(h \to \text{invis.})$	$< 0.30\%$ (95% conf.)	
	$g(ht\bar{t})$	3.7%	1000 GeV
	$g(hhh)$	26%	
	$g(h\mu^+\mu^-)$	16%	
Top	$m_{\rm t}$	0.02%	$\Delta m_{\rm t} = 34$ MeV, threshold scan
	$\Gamma_{\rm t}$	2.4%	
	$\tilde{F}^{\gamma}_{1\rm V}$	0.2%	500 GeV
	$\tilde{F}^{Z}_{1\rm V}$	0.3%	
	$\tilde{F}^{Z}_{1\rm A}$	0.5%	
	$\tilde{F}^{\gamma}_{2\rm V}$	0.3%	
	$\tilde{F}^{Z}_{2\rm V}$	0.6%	
W	$m_{\rm W}$	0.004%	$\Delta m_{\rm W} = 3$ MeV, threshold scan
	g_1	0.16%	500 GeV
	κ_γ	0.03%	
	$\kappa_{\rm Z}$	0.03%	
	λ_γ	0.06%	
	$\lambda_{\rm Z}$	0.07%	
H^0, A^0	$m_{\rm H}$, $m_{\rm A}$	1.5%	
	$\tan\beta$	20%	
$\widetilde{\chi}^+$	$m(\widetilde{\chi}^+)$	1%	
	$m(\widetilde{\chi}^0)$	1%	
$\widetilde{t}$	$m(\widetilde{t})$	1%	
	$\cos\theta_{\rm t}$	0.4%	

Table 2.2 gives an illustrative list of quantities that can be measured at ILC, and the measurement accuracies that the ILC experiments expect to achieve. Any unfamiliar terminology in this table is defined in the appropriate chapter of the Physics Volume. The ILC study of the Higgs boson gives the complete profile of Higgs boson couplings. The ILC studies of the top quark and the W boson probe the electroweak couplings of these heavy elementary particles with measurement accuracies qualitatively superior to those expected from the LHC. As shown in the Physics Volume, measurements at this level probe the effects expected from the coupling of top quarks and W bosons to composite

and strongly interacting Higgs fields.

The final elements of the table give some examples of the ability of the ILC to follow up the discovery of new particles with precision measurements of their properties. In experiments at hadron colliders, mixing angles, such as $\tan\beta$ for Higgs bosons and $\cos\theta_{\rm t}$ for supersymmetric partners of top quarks, are measured indirectly through multi-variable fits that depend on detailed properties of the model under study. In contrast, the ILC measurements are unambiguously interpreted and lead to model-independent determinations of the parameters. These mixing angles appear ubiquitously in the predictions of extended Higgs and supersymmetry models. Through these measurements, the ILC will not only produce its own discoveries but also will enable sharper and more informative analysis of the data collected at the LHC.

The ILC then offers many opportunities for measurements that will address the most important current problems of particle physics. It will give unique views of the Higgs boson, the top quark, and possible new particles relevant to the mysteries of the matter content of the universe. The collider enables incisive measurements of very high precision. The ILC is thus an essential tool that will advance our understanding of the basic laws of nature.

Chapter 3
The International Linear Collider Accelerator

3.1 The ILC Technical Design

3.1.1 Overview

The International Linear Collider (ILC) is a high-luminosity linear electron-positron collider based on 1.3 GHz superconducting radio-frequency (SCRF) accelerating technology. Its centre-of-mass-energy range is 200–500 GeV (extendable to 1 TeV). A schematic view of the accelerator complex, indicating the location of the major sub-systems, is shown in Fig. 3.1:

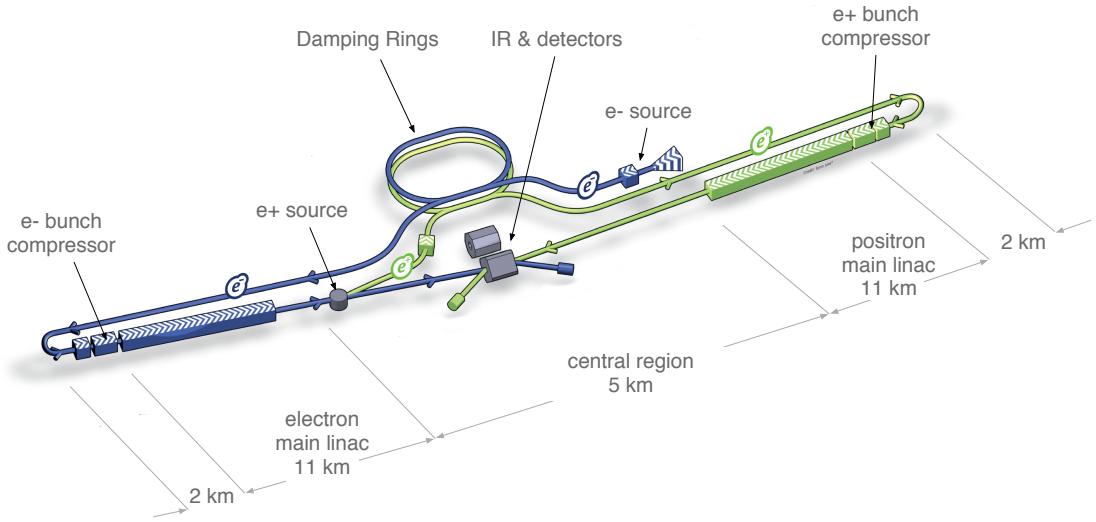

Figure 3.1. Schematic layout of the ILC, indicating all the major subsystems (not to scale).

- a polarised electron source based on a photocathode DC gun;
- a polarised positron source in which positrons are obtained from electron-positron pairs by converting high-energy photons produced by passing the high-energy main electron beam through an undulator;
- 5 GeV electron and positron damping rings (DR) with a circumference of 3.2 km, housed in a common tunnel;
- beam transport from the damping rings to the main linacs, followed by a two-stage bunch-compressor system prior to injection into the main linac;
- two 11 km main linacs, utilising 1.3 GHz SCRF cavities operating at an average gradient of 31.5 MV/m, with a pulse length of 1.6 ms;

- two beam-delivery systems, each 2.2 km long, which bring the beams into collision with a 14 mrad crossing angle, at a single interaction point which can be occupied by two detectors in a so-called "push-pull" configuration.

The total footprint of the ILC complex is $\sim$ 31 km long. The electron source, positron source (including an independent low-powered auxiliary source), and the electron and positron damping rings are centrally located around the interaction region (IR) in the Central Region. The damping-ring complex is displaced laterally to avoid interference with the detector hall. The electron and positron sources themselves are housed in the same (main accelerator) tunnels as the beam-delivery systems, which reduces the overall cost and size of the central-region underground construction.

3.1.2 Machine parameters

The top-level parameters for the baseline operational range of centre-of-mass energies from 250 to 1000 GeV were set in close discussion with the physics community that will exploit the ILC. The baseline performance requirements thus obtained have been optimised with respect to cost, physics performance and risk. All have been either directly demonstrated, or represent justifiable extrapolations from the current state of the art. Table 3.1 shows the parameters for several centre-of-mass energies, including possible upgrades and staging.

The parameters in Table 3.1 represent relatively conservative operating points resulting from optimisation subject to the constraints imposed by the various accelerator sub-systems. For example, the bunch charge, bunch spacing and the total number of bunches in the damping rings are limited by various instability thresholds (most notably the electron cloud in the positron ring), realistic rise-times for the injection and extraction kickers, and the desire to minimise the circumference of the rings. Secondly, the maximum length of the beam pulse is constrained to $\sim$ 1.6 ms, which is routinely achieved in the available 1.3 GHz 10 MW multi-beam klystrons and modulators. The beam current is further constrained by the need to minimise the number of klystrons (peak power) and higher-order modes (cryogenic load and beam dynamics). Dynamic cryogenic load (refrigeration) is also a cost driver, which limits the repetition rate of the machine. Thirdly, both the electron and positron sources constrain the achievable beam current and total charge: For the laser-driven photocathode polarised electron source, the limits are set by the laser; for the undulator-based positron source, the limits are set by the power deposition in the photon target. The beam pulse length is further constrained by the achievable performance of the warm RF capture sections (both sources). Finally, at the interaction point, single-bunch parameters are limited by the strong beam-beam effects and requirements on both the beam-beam backgrounds and beam stability.

Table 3.1. Summary table of the 250–500 GeV baseline and luminosity and energy upgrade parameters. Also included is a possible 1st stage 250 GeV parameter set (half the original main linac length)

			Baseline 500 GeV Machine			1st Stage	L Upgrade	$E_{\rm CM}$ Upgrade	
Centre-of-mass energy	$E_{\rm CM}$	GeV	250	350	500	250	500	A 1000	B 1000
Collision rate	$f_{\rm rep}$	Hz	5	5	5	5	5	4	4
Electron linac rate	$f_{\rm linac}$	Hz	10	5	5	10	5	4	4
Number of bunches	$n_{\rm b}$		1312	1312	1312	1312	2625	2450	2450
Bunch population	N	$\times 10^{10}$	2.0	2.0	2.0	2.0	2.0	1.74	1.74
Bunch separation	$\Delta t_{\rm b}$	ns	554	554	554	554	366	366	366
Pulse current	$I_{\rm beam}$	mA	5.8	5.8	5.8	5.8	8.8	7.6	7.6
Main linac average gradient	$G_{\rm a}$	MV m^{-1}	14.7	21.4	31.5	31.5	31.5	38.2	39.2
Average total beam power	$P_{\rm beam}$	MW	5.9	7.3	10.5	5.9	21.0	27.2	27.2
Estimated AC power	$P_{\rm AC}$	MW	122	121	163	129	204	300	300
RMS bunch length	$\sigma_{\rm z}$	mm	0.3	0.3	0.3	0.3	0.3	0.250	0.225
Electron RMS energy spread	$\Delta p/p$	%	0.190	0.158	0.124	0.190	0.124	0.083	0.085
Positron RMS energy spread	$\Delta p/p$	%	0.152	0.100	0.070	0.152	0.070	0.043	0.047
Electron polarisation	P_-	%	80	80	80	80	80	80	80
Positron polarisation	P_+	%	30	30	30	30	30	20	20
Horizontal emittance	$\gamma\epsilon_{\rm x}$	µm	10	10	10	10	10	10	10
Vertical emittance	$\gamma\epsilon_{\rm y}$	nm	35	35	35	35	35	30	30
IP horizontal beta function	$\beta^*_{\rm x}$	mm	13.0	16.0	11.0	13.0	11.0	22.6	11.0
IP vertical beta function	$\beta^*_{\rm y}$	mm	0.41	0.34	0.48	0.41	0.48	0.25	0.23
IP RMS horizontal beam size	$\sigma^*_{\rm x}$	nm	729.0	683.5	474	729	474	481	335
IP RMS veritcal beam size	$\sigma^*_{\rm y}$	nm	7.7	5.9	5.9	7.7	5.9	2.8	2.7
Luminosity	L	$\times 10^{34}$ cm^{-2}s^{-1}	0.75	1.0	1.8	0.75	3.6	3.6	4.9
Fraction of luminosity in top 1%	$L_{0.01}/L$		87.1%	77.4%	58.3%	87.1%	58.3%	59.2%	44.5%
Average energy loss	$\delta_{\rm BS}$		0.97%	1.9%	4.5%	0.97%	4.5%	5.6%	10.5%
Number of pairs per bunch crossing	$N_{\rm pairs}$	$\times 10^3$	62.4	93.6	139.0	62.4	139.0	200.5	382.6
Total pair energy per bunch crossing	$E_{\rm pairs}$	TeV	46.5	115.0	344.1	46.5	344.1	1338.0	3441.0

3.2 Accelerator Layout & Design

3.2.1 Superconducting RF Main Linacs

The ILC Main Linacs accelerate the beam from 15 GeV (after acceleration in the upstream bunch compressors) to a maximum energy of 250 GeV. Beam acceleration in each linac is provided by approximately 7,400 1 m-long superconducting nine-cell niobium cavities (see Fig. 3.2) operating at 2 K, assembled into $\sim$ 850 cryomodules. The average accelerating gradient of the cavities is 31.5 MV/m (for 500 GeV centre-of-mass beam energy), with a corresponding quality factor $Q_0 \geq 10^{10}$. A random cavity-to-cavity gradient spread of $\pm$20% is tolerated to accommodate expected mass-production variations in the maximum achievable gradient. The choice of these key parameters is the result of over a decade of extensive R&D. The GDE recognised the need to establish expertise in this technology in all three regions of the world and established the high-gradient programme as its highest priority during the Technical Design Phase. As a result, extensive worldwide experience both in the labs and in industry now gives high confidence that these requirements can be routinely achieved. (See Section 3.3.1 for details.)

Figure 3.2
A 1.3 GHz superconducting niobium nine-cell cavity.

For an average of 31.5 MV/m operation with the nominal beam current of 5.8 mA, the optimal matched $Q_{\rm L}$ is $\sim 5.4\times10^6$. This corresponds to a cavity fill time of 925 µs, which, added to the nominal beam pulse width of 727 µs, gives a total RF pulse length of 1.65 ms.

The cavity package includes the cavity mechanical tuner, which is integrated into the titanium helium vessel of the cavity, and an adjustable high-power coupler. In addition to a slow mechanical tuner (used for initial tuning and slow drift compensation), a fast piezo-driven tuner is also included to compensate dynamically for the mechanical deformation of the cavity caused by the RF pulse, known as "Lorentz-force detuning".

The cryomodules (Fig. 3.3) that make up the Main Linacs are 12.65 m long. There are two types: a Type A module with nine 1.3 GHz nine-cell cavities and Type B with eight nine-cell cavities and one superconducting quadrupole package located at the centre of the module.

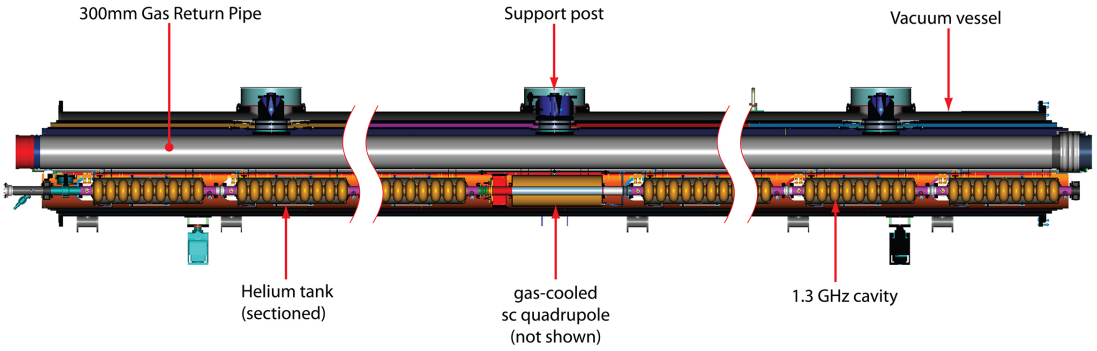

Figure 3.3. Longitudinal cross section of an ILC cryomodule (Type B).

The cryomodule design is a modification of the Type-3 version developed and used at DESY in the FLASH accelerator as well as the 100 cryomodules currently being produced by industry for

the European X-Ray FEL (XFEL), also based at DESY. A 300 mm-diameter helium-gas return pipe serves as the primary support for the nine cavities and other beamline components in the Type A module. For Type B, the central cavity package is replaced by a superconducting quadrupole package that includes the quadrupole itself, a cavity BPM, and superconducting horizontal- and vertical-corrector dipole magnets. The quadrupoles establish the magnetic lattice for the Main Linac, which is a weak-focusing FODO optics with an average beta function of ~ 80 m. Every cryomodule also contains a 300 mm-long assembly that removes energy from beam-induced higher-order modes above the cavity cut-off frequency through the 40–80 K cooling system.

To operate the cavities at 2 K, they are immersed in a saturated He-II bath. Shields cooled with Helium gas intercept thermal radiation and provide a heat sink for conduction at 5–8 K and at 40–80 K. Each cryomodule has an estimated 2 K static cryogenic heat load of 1.3 W while the 2 K dynamic heat load is approximately 9.8 W. Liquid helium for the main linacs and the bunch compressor RF is supplied from a total of 10-12 large cryogenic plants, each of which has an installed equivalent cooling power of ~ 20 kW at 4.5 K. The plants are located in pairs separated by 5 km along the linacs, with each plant cooling ~ 2.5 km of continuous linac. The main linacs follow the Earth's average curvature to simplify the liquid-helium transport and tunnel construction.

The RF power is provided by 10 MW multi-beam klystrons (MBK) each driven by a 120 kV Marx modulator. The 10 MW MBK has achieved the ILC specifications and is now a well established technology with several vendors worldwide. The 120 kV Marx-modulator prototypes have achieved the required specifications and are now undergoing design optimisation for transfer to industrial vendors. (See Section 3.3.2.)

Two alternative methods of transporting the RF microwave power to the accelerating structures are considered in the baseline. The first is a Distributed Klystron Scheme (DKS), where each klystron drives 39 cavities; the klystrons and modulators are distributed along the entire length of the SCRF linacs, in the same tunnel but shielded from the accelerator itself, which allows personnel access to make repairs as necessary while beam is on. The second is a novel Klystron Cluster Scheme (KCS), where all the klystrons are located in 'clusters' in surface buildings located periodically along the linacs. The power from a single cluster of 19 klystrons (~ 190 MW) is combined into an over-moded waveguide, which then transports the power down into the tunnel and along an approximately 1 km section of linac. A Coaxial Tap-Off extracts ~ 6.7 MW of power to a local power-distribution system feeding three cryomodules containing 26 cavities.

The advantages of KCS are primarily that most of the heat load is on the surface, where it can be more cost-effectively removed, at the same time as reducing the required underground volume. The disadvantages are the need for additional surface buildings and shafts (one every 2 km of linac), and additional losses in the long waveguide distribution systems. In addition significant R&D is still required compared to the mature and tested distributed system (see Section 3.3.2). Nonetheless, the estimated cost savings associated with KCS make it an attractive solution for flatter terrains with sufficient space for the required surface infrastructure. For more mountainous terrains or sites where surface access is at a premium, DKS is the preferred solution.

For both KCS and DKS, the in-tunnel power-distribution system to the cavities themselves is essentially identical. A key requirement is the ability to tune both the phase and forward power to each cavity remotely, in order to support the allowed $\pm 20\%$ gradient spread among the cavities, thus maximising the accelerating gradient.

3.2.2 Electron source

The polarised electron source shares the central region accelerator tunnel with the positron Beam Delivery System. The beam is produced by a laser illuminating a strained GaAs photocathode in a DC gun, providing the necessary bunch train with 90% polarisation. Two independent laser and gun systems provide redundancy. Normal-conducting structures are used for bunching and pre-acceleration to 76 MeV, after which the beam is accelerated to 5 GeV in a superconducting linac. Before injection into the damping ring, superconducting solenoids rotate the spin vector into the vertical, and a separate Type-A superconducting RF cryomodule is used for energy compression.

3.2.3 Positron source

The major elements of the ILC positron source are shown in Fig. 3.4. After acceleration in the main linac, the primary electron beam is transported through a 147 m superconducting helical undulator that generates photons with maximum energies from $\sim$ 10 MeV up to $\sim$ 30 MeV depending on the electron beam energy. The electron beam is then separated from the photon beam and displaced horizontally by 1.5 m using a low-emittance-preserving chicane. The photons from the undulator are directed onto a rotating 0.4 radiation-length Ti-alloy target $\sim$ 500 m downstream, producing a beam of electron-positron pairs. This beam is then matched using an optical-matching device (a pulsed flux concentrator) into a normal conducting (NC) L-band RF and solenoidal-focusing capture system and accelerated to 125 MeV. The electrons and remaining photons are separated from the positrons and dumped. The positrons are accelerated to 400 MeV in a NC L-band linac with solenoidal focusing. Similar to the electron beam, the positron beam is then accelerated to 5 GeV in a superconducting linac which uses modified Main Linac cryomodules, the spin is rotated into the vertical, and the energy spread compressed before injection into the positron damping ring.

The target and capture sections are high-radiation areas which will require shielding and remote-handling facilities.

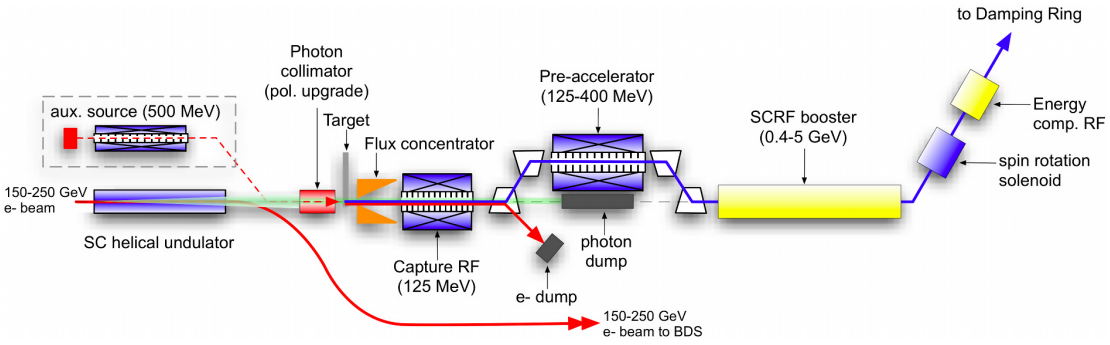

Figure 3.4. Overall Layout of the Positron Source, located at the end of the electron Main Linac.

The baseline design provides a polarisation of 30%. Space for a $\sim$ 220 m undulator has been reserved for an eventual upgrade to 60% polarisation, which would also require a photon collimator upstream of the target.

A low-intensity auxiliary positron source supports commissioning and tuning of the positron and downstream systems when the high-energy electron beam is not available. This is effectively a conventional positron source, which uses a 500 MeV NC linac to provide an electron beam that is directed onto the photon target, providing a few percent of the nominal positron current.

To accommodate the 10 Hz operation required to produce the required number of positrons at centre-of-mass energies below 300 GeV (see Section 3.2.8), a separate pulsed extraction line is required immediately after the undulator, to transport the 150 GeV electron pulse for positron-production to the high-powered tune-up dump, located downstream in the Beam Delivery System.

3.2.4 Damping rings

The ILC damping rings must accept e^- and e^+ beams with large transverse and longitudinal emittances and damp them to the low emittances required for luminosity production. The specification for the extracted normalised vertical emittance of 20 nm represents a reduction of five orders of magnitude for the positron bunch. This reduction must be achieved within the 200 ms between machine pulses (100 ms for 10-Hz mode). In addition, the $\sim$ 1 ms beam pulse must be compressed on injection by roughly a factor of 90 to fit into the ring circumference of 3.2 km; a corresponding decompression is required on extraction. For the baseline parameters, the bunch spacing within trains is approximately 8 ns, which determines the rise and fall time of the injection and extraction kicker systems. (For the luminosity upgrade this number reduces to $\sim$ 4 ns.) Individual bunch injection and extraction is accomplished in the horizontal plane using a total of 42 fast kickers switching 10 kV pulses with rise/fall times of $\sim$ 3 ns.

One electron and one positron ring are included in the baseline, operating at a beam energy of 5 GeV. Both rings are housed in a single tunnel with one ring positioned directly above the other. The damping ring complex is located in the central region, horizontally offset from the interaction region by approximately 100 m to avoid the detector hall. The damping rings are connected to the electron and positron main accelerators by transfer lines.

The damping-ring lattice follows a race-track design. The two arc sections are constructed from 75 Theoretical Minimum Emittance (TME) cells. One of the two 712 m-long straight sections accommodates the RF cavities, damping wigglers, and a variable path length to accommodate changes in phase (phase trombone), while the other contains the injection and extraction systems, and a circumference-adjustment chicane.

Damping is accomplished by approximately 113 m of superferric wigglers (54 units $\times$ 2.1 m) in each damping ring. The wigglers operate at 4.5 K, with a peak-field requirement of 2.16 T.

The superconducting RF system is operated in continuous-wave (CW) mode at 650 MHz, and provides a maximum of 20 MV for each ring, required for the positron ring in 10 Hz mode (nominal 5 Hz operation requires 14 MV for both electron and positron). The frequency is chosen to be half the linac RF frequency to maximise the flexibility for different bunch patterns. The single-cell cavities operate at 4.5 K and are housed in twelve 3.5 m-long cryomodules. The RF section of the lattice can accommodate up to 16 cavities, of which 12 are assumed to be installed for the baseline.

The momentum compaction of the lattice is relatively large, which helps to maintain single-bunch stability, but requires a relatively high RF voltage to achieve the design RMS bunch length (6 mm). The dynamic aperture of the lattice is sufficient to allow the large-emittance injected beam to be captured with minimal loss.

Mitigation of the fast ion instability in the electron damping ring is achieved by limiting the pressure in the ring to below 1 nTorr and by the use of short gaps in the ring fill pattern and a fast transverse feedback system, similar to those used in B-factories.

The performance of the damping rings was noted as one of the biggest challenges facing the post-RDR R&D programme. In particular, intensive studies were carried out on the electron-cloud effect, in which electrons emitted from the vacuum-pipe walls by synchrotron-radiation photons are attracted to the positron beam, resulting in a perturbing electromagnetic field that increases the beam emittance. These studies have resulted in mitigation methods that have been included in a major redesign of the vacuum systems for the baseline damping rings (see Section 3.3.3).

3.2.5 Ring to Main Linac (RTML)

The electron and positron Ring to Main Linac (RTML) systems are the longest continuous beamlines in the ILC. The layout of the RTML is identical for both electrons and positrons. The RTML consists of five subsystems, representing the various functions that it must perform: a $\sim$ 15 km long 5 GeV transport line; betatron and energy collimation systems; a 180° turn-around, which enables feed-forward beam stabilisation; spin rotators to orient the beam polarisation to the desired direction; and a two-stage bunch compressor to compress the beam bunch length from several millimetres to a few hundred microns, as required at the IP.

The two-stage bunch compressor includes acceleration from 5 GeV to 15 GeV in order to keep the increase in relative energy spread associated with bunch compression small. The acceleration is provided by sections of SCRF main-linac technology. A primary challenge for the RTML systems is the preservation of the damped emittance extracted from the damping rings; the combination of the long uncompressed bunch from the damping ring and large energy spread (after compression) make the tuning and tolerances particularly demanding. However, tuning techniques developed through detailed simulations have demonstrated acceptable emittance growth.

In addition to the beam-dynamics challenges, acceptable jitter in bunch arrival time at the IP requires an RMS phase jitter of $\leq 0.24°$ between the electron and positron bunch-compressor RF systems. Beam-based feedback systems integrated into the bunch-compressor low-level RF system should be able to limit the phase jitter to this level.

3.2.6 Beam Delivery System (BDS)

The ILC BDS is responsible for transporting the $\mathrm{e^+e^-}$ beams from the exit of the high-energy linacs, focusing them to the sizes required to meet the ILC luminosity goals, bringing them into collision, and then transporting the spent beams to the main beam dumps. In addition, the BDS must perform several other critical functions, including characterising the incoming (transverse) beam phase-space and matching it into the final focus; removing any beam halo from the linac to minimise background in the detectors; and measuring and monitoring the key physics parameters such as energy and polarisation before and after the collisions.

There is a single collision point with a 14 mrad total crossing angle. The 14 mrad geometry provides space for separate extraction lines but requires crab cavities to rotate the bunches in the horizontal plane for effective head-on collisions. There are two detectors in a common interaction region (IR) hall in a so-called 'push-pull' configuration.

The geometry of the BDS has been designed to accommodate the upgrade to 1 TeV centre-of-mass energy, in particular to minimise the emittance growth due to synchrotron radiation to less than 10%. The baseline lattice uses fewer magnets (predominantly dipoles) for the lower-energy operation.

There are five main subsystems of the BDS. First, in the direction of the beam, is a section containing emittance measurement and matching (correction), trajectory feedback, polarimetry and energy diagnostics; secondly, a collimation section removes beam-halo particles that would otherwise generate unacceptable background in the detector and also contains magnetised iron shielding to deflect muons generated in the collimation process; thirdly, the final focus (FF) uses strong compact superconducting quadrupoles to focus the beam at the IP, with sextupoles providing local chromaticity correction; the final pair of quadrupoles closest to the IP is integrated into each particle physics detector to facilitate rapid exchanges of the detectors in 'push-pull'; fourthly, the interaction region contains the detectors; finally, the extraction line has a large-enough bandwidth to cleanly transport the heavily disrupted beam to a high-powered water-cooled dump, and also contains important polarisation and energy diagnostics.

The beam-delivery optics provides a demagnification factor of typically several hundreds in the

beam size, resulting in very large beta functions (several thousand kilometres) at critical locations, leading to the tightest alignment tolerances in the entire machine. In addition, correction of the strong chromaticity and geometric aberrations requires a delicate balance of higher-order optical terms. The tight tolerances on magnet motion (tens of nanometres), makes continuous trajectory correction and the use of fast beam-based feedback systems mandatory. Furthermore, several critical components (e.g. the final-focusing doublet) may well require mechanical stabilisation. Beam-based alignment and beam phase-space tuning algorithms are necessary to adjust and tune the optical aberrations that would otherwise significantly degrade the luminosity. The ability to tune the beams to the required levels relies extensively on precision remote mechanical adjustment of the magnets and diagnostics with matching precision. Many of the techniques and instrumentation were successfully developed at the Final Focus Test Beam experiment at SLAC, and currently at the ATF2 facility at KEK (see Section 3.3.3).

The tight tolerance on the relative uncorrelated phase jitter between the electron and positron superconducting crab-cavity systems requires timing precisions to the level of tens of femtoseconds. Although this tolerance is tight, it is comparable to that achieved at modern linac-driven FELs.

Control of machine-generated backgrounds is performed by careful optics control and tuning of an extensive collimation system, as well as by the use of non-linear elements ('tail-folding' octupoles). Wakefield effects at the small apertures are taken into account in the design of the mechanical collimators.

The main beam dumps, which use a high-pressure high-velocity water design, are a major installation. Since the dumps will be significantly activated during operation, they are designed and rated for the full upgrade average beam power of 14 MW, in order to avoid having to replace them during the energy upgrade to 1 TeV.

3.2.7 Conventional facilities and site-dependent designs

Together with the Main Linac systems, conventional facilities and siting (CFS) represent the two largest elements of the total project cost. The CFS design and costs can be broken down into three main areas: civil construction, including underground and surface structures, shafts and access tunnels; electrical systems (AC power distribution etc.); and mechanical systems (water cooling and air handling etc.).

The CFS solutions and associated cost are developed based on the requirements defined by the accelerator layout and parameters outlined in the previous sections. Minimisation of the total CFS cost requires an understanding of how it depends on the accelerator design, and if necessary modifying and iterating that design. Reduction of the scope of the underground civil construction (for example) was considered a primary design goal during the Technical Design Phase and resulted in significant modifications to the accelerator design and parameter space. In addition, the criteria for the electrical and mechanical systems, access shafts and tunnels have been scrutinised to reduce costs.

The solutions to implement the accelerator functionality are heavily influenced by regional considerations of site topography and geology, as well as local legislation (such as safety requirements). Geology will determine the most cost-effective approach to tunnelling method, while topography can influence the surface structures, access tunnels and shafts. All of these factors can shift the balance of the cost-optimisation and influence the accelerator design. As a result, the final machine will be influenced by the choice of site.

In the absence of a definitive site for the ILC, it was necessary to evaluate different sites with different characteristics. To this end, several sample sites have been developed. As noted in Section 3.2.1, two site-specific design variants emerged: one suitable for a flatter terrain (flat topography) using the Klystron Cluster Scheme (KCS); and one for a more mountainous terrain

(mountainous topography) using the Distributed Klystron Scheme (DKS).

The Americas site in Northern Illinois near Fermilab is essentially flat and provides a range of locations to position the ILC in a north-south orientation; that chosen has approximately one-quarter of the machine on the Fermilab site with the tunnels bored in a contiguous dolomite rock strata ('Galena Platteville'), at a typical depth of 30–100 m below the surface. For Asia, two possible ILC candidate sites have been identified: Kitakami in the Tohoku district in northern Japan; and Sefuri in the Kyushu district in the south. Both provide a uniform terrain located along a mountain range, with a tunnel depth ranging from 40 m to 600 m in uniform granite geology highly suited to modern tunnelling methods. The European site is located at CERN, Geneva, Switzerland, and runs parallel to the Jura mountain range, close to the CERN site, mostly in the 'Molasse' (a local impermeable sedimentary rock), at a typical depth of 370 m.

The Americas and European sample sites are relatively similar and are examples of 'flat topography' sites using KCS. The geology lends itself well to the use of Tunnel Boring Machines (TBM) which provide a round tunnel cross section. The Japanese sites are examples of mountainous topology using DKS, where available space for surface infrastructure is severely limited, requiring most of the accelerator infrastructure to be housed underground. The most cost-effective tunnelling solution in this geology and topography is "drill and blast" as exemplified by the New Austrian Tunnelling Method.

3.2.8 Special considerations for running at low centre-of-mass energy

While performance requirements at the maximum energy dictate many of the key parameters and the overall geometry and cost of the machine, running at lower energies is also an important part of the physics potential of the ILC. This is especially true given the recent discovery of a Higgs boson at the LHC. Sufficient luminosity needs to be produced to enable the study of important physics quantities at the threshold for producing it in association with a Z^0, around 220 GeV. Two issues limit the possible performance at these lower energies: first, the undulator-based positron source must have an electron-beam energy of at least 150 GeV to produce the requisite positron intensity; secondly, the beam divergence at the interaction point is constrained by the allowable synchrotron radiation fan generated by the final doublet. This results in luminosity falling off more rapidly than the normal scaling as the inverse of the beam energy.

The solution adopted for the first issue for the current baseline is to interleave the normal "physics" pulse (which at low energies cannot produce the required number of positrons) with an additional electron pulse at 150 GeV. Having produced the positrons, this "extra" pulse is extracted to the beam dump. This scheme doubles the frequency of electron (but not positron) beam pulses to 10 Hz. This so-called "10 Hz" operation mode implies several design criteria for the baseline. First, both electron and positron damping rings must now damp the beam in 100 ms instead of the nominal 200 ms. This requires additional wigglers and RF in the ring. Secondly, the positron damping ring is 'empty' for 100 ms, after which the current is ramped up in $\sim$ 1 ms (and similarly ramped down during extraction). Dealing with transient beam loading requires an additional RF power overhead of approximately 15%. Thirdly, all the machine elements of the electron machine before the positron source must run at 10 Hz. Fourthly, the positron-production pulse (150 GeV beam) must be safely extracted after the undulator and dumped, requiring an additional pulsed magnet and extraction beamline system. Finally, a pulsed-magnet steering system is required upstream of the source undulator (downstream of the main electron linac) to compensate for the difference in trajectory between the 150 GeV positron production and 150 GeV luminosity pulses. The 10 Hz mode is cost effective because the total RF power and cryoload for the main (electron) linac do not exceed that at 250 GeV beam energy at 5 Hz when the beam energy (and therefore the main linac gradient) is reduced below 150 GeV. However,

for the electron bunch compressor and source linacs, the AC power requirement effectively doubles for the 10 Hz operation mode, which also drives the design criteria and power requirements for the damping rings.

To mitigate the second problem related to the beam-divergence constraint at the IP, a shorter final-doublet (FD) arrangement can be used for energies less than 300 GeV. This increases the collimation depth and the allowed IP beam divergence (by up to 30% in the horizontal plane), thus increasing the luminosity. The FD will be implemented in a modular design to accommodate both high- and low-energy running configurations, thus avoiding the need to exchange the magnet cryostat.

There are no issues with running the main SCRF linacs at reduced gradient for the low centre-of-mass running. The lower average gradient results in a shorter fill time and overall higher RF-to-beam power efficiency. Simulations of the beam dynamics have indicated no significant additional degradation of vertical emittance.

3.2.9 Luminosity and energy upgrade options

This TDR has been optimised for the 500 GeV baseline scenario. Although considered in significantly less detail, two upgrade scenarios are foreseen.

The first upgrade is in luminosity, by up to a factor of two, accomplished by doubling the number of bunches per beam pulse (doubling the beam power). This requires increasing the number of klystrons and modulators by approximately 50%. A second positron damping ring can be installed in the same tunnel should electron-cloud effects at these higher currents prove problematic. All other accelerator systems are already rated for the higher beam power. Basic (minimum) provisions for the required conventional facilities are included in the baseline design to support the luminosity upgrade, although modifications to the cooling systems would be required.

Secondly, an upgrade of the centre-of-mass energy up to 1 TeV is foreseen, by approximately doubling the length of the main linacs. The current preferred concept is to retain the original linacs and use them to accelerate a higher energy beam (265–500 GeV), while the new upgrade linac extensions would then provide acceleration from the bunch compressor energy of 15 GeV up to 265 GeV. In addition to the major construction required for the linac extensions, a relocation of the bunch compressors and 180-degree turn-around is required, as well as an extension of the RTML long transport line. The upgrade to the main linacs themselves is based on a forward-looking SCRF technology compatible with the original linac installation (RF pulse length etc.), but with higher-performance specifications (45 MV/m with $Q_0 = 2 \times 10^{10}$). These ambitious goals will require extensive R&D, which is assumed to continue in parallel with the construction and operation of the baseline accelerator. The overall site requirement for the TeV machine is approximately 50 km, with a site power requirement of approximately 300 MW. In order to minimise the impact on the existing machine during the upgrade construction, the baseline BDS geometry and high-power beam dumps are already compatible with 500 GeV beam operation. All of the candidate sites can accommodate such an upgrade.

3.2.10 Value estimate and methodology

The new baseline design for the ILC given in the TDR provides the basis for an updated cost estimate. A value estimate approach has been adopted, which is independent of any particular national accounting system but compatible with them all and thus is suitable for a collaborative venture. It has been used by both ITER and the LHC.

The value estimate covers the construction cost for a machine of 500 GeV centre-of-mass energy. It includes a small number of items rated for 1 TeV to enable a later upgrade. Typically these elements are in places difficult to retrofit, such as beam dumps. The value estimate omits a number of items

such as pre-construction, taxes, contingency, escalation, spare equipment, beam commissioning, etc. that would be included in some regionally specific estimates.

The value estimate has two parts: component value and explicit labour. The value of a component is defined as the lowest reasonable estimate of the procurement cost of an item that meets the technical specifications in the required quantity in a major industrial nation. It includes the material costs and the implicit labour required to fabricate the component.

Explicit labour, which is accounted for in person-hours, is required manpower which could be provided by collaborating institution or the host laboratory, or could be purchased from industrial vendors.

The estimate should allow funding agencies that are considering contributions to the project to assess the nature and scope of the required resources. It also provides detailed information on cost drivers which can be used during the pre-construction phase for further cost optimisation through either value engineering or additional R&D.

In order to minimise regional price distortions related to exchange rates, currency conversions were based on purchasing-power-parity (PPP) indices as published by the Organization for Economic Co-operation and Development (OECD). The currency unit for the value estimate was the ILCU, defined as a 2012 US dollar. Estimates performed at dates different from the TDR reference date of January 2012 were escalated using regional indices for either civil engineering or equipment. Volume 3 Part-II contains a detailed discussion on the use of PPP indices.

The estimates for each cost element are median estimates that correspond to the 50% probability point in the cost-distribution curve. All major procurements are estimated assuming a minimum of two vendors with specifications and quantities as given in the TDR.

Uncertainty estimates have been made for each cost element in the TDR. The uncertainties are based on the design maturity of the item, the level of technical risk, the source or quality of the cost or labour information, and the extent, if any, of the scaling to large quantities. Based on this information, the fractional cost increase required to reach an 84% confidence level has been computed. This cost increase is called the "cost premium", and it is provided as part of the value estimate.

To account for the economies of scale when the cost basis explicitly corresponds to a significantly smaller number of units than that required for the ILC, the unit estimate has been obtained by applying a discount derived from a learning curve. Based on previous HEP projects, learning curves in the range of 85-95% would be expected. In the absence of any additional vendor information a relatively conservative 95% was typically adopted.

Approximately 75% of the TDR estimate has a new cost basis compared to the previous costing exercise in 2006. This includes the major project cost drivers, conventional facilities and the SCRF systems and components. Significant information was accumulated during the GDE R&D program related to SCRF cavity costs in addition to recent data obtained from European XFEL contracts. The other 25% was based on estimates made during the 2007 Reference Design study, adjusted for both inflation at the component level and the unit counts reflecting the updated TDR design. The breakdown of the cost basis is shown in Fig. 3.5.

The majority of the cost basis involves industrial estimates of various types. The labour estimate is principally based on prior experience of national laboratory staff.

The value estimate for the TDR design, averaged over three regional sites, is 7.8 billion ILCU. This is dominated by the SCRF components and related systems, together with the conventional facilities. These two elements account for 73% of the total. The main linac itself corresponds to 67% of the total project. **The total explicit labour estimate is 22.6 million person-hours.** Installation and laboratory management/administration are the biggest single elements. The cost premiums for both value and labour are approximately 25%. The sub-system value breakdown is shown in Fig. 3.6.

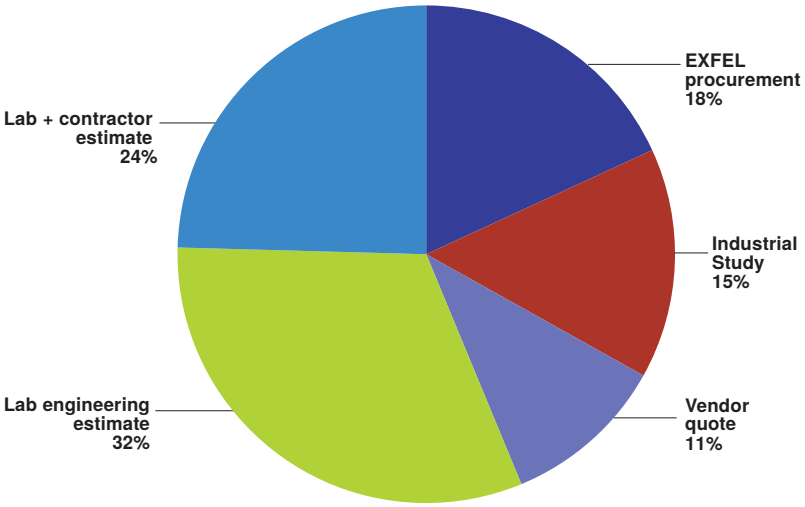

Figure 3.5
ILC TDR Value estimate cost basis.

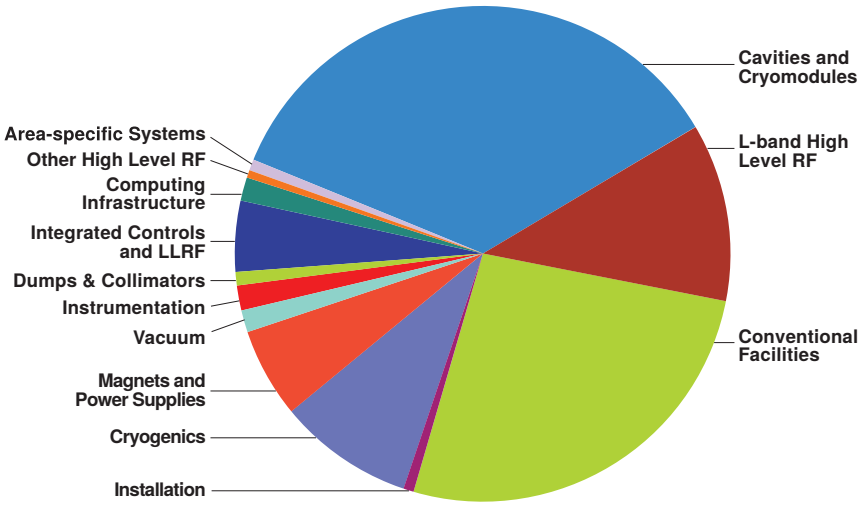

Figure 3.6
Distribution of cost by sub-system.

These totals represent an increase of 7% in value and a reduction of 8% in explicit labour relative to the estimates made for the 2007 *Reference Design Report* (after adjustment for inflation from 2007 to 2012). The major contribution to the increase was the cryomodule cost which was based on current industrial studies and actual European XFEL contracts extrapolated to ILC quantities, rather than older industrial studies and engineering estimates. This increase was offset in several areas due in large part to the more efficient TDR design.

Any schedule for a project such as the ILC is determined by the availability of resources and the ability to utilise them efficiently. Without knowledge of the chosen Governance and Project Management structure and funding profiles, a more accurate schedule cannot be formulated. Nonetheless, making some reasonable assumptions in these areas, it appears that the overall construction schedule is determined by the civil construction activities in the central campus region covering the detector halls, the damping rings, and the injectors. These elements are site dependent. The Main Linac schedule is determined by the delivery of the SCRF cryomodules, which are the technical components with the longest lead time. A funding profile which peaks at 15% of the total project cost in year four is consistent with a nine-year period between ground breaking and the start of beam commissioning. Machine installation starts in year seven. A representative schedule for a mountainous site is shown in Fig. 3.7.

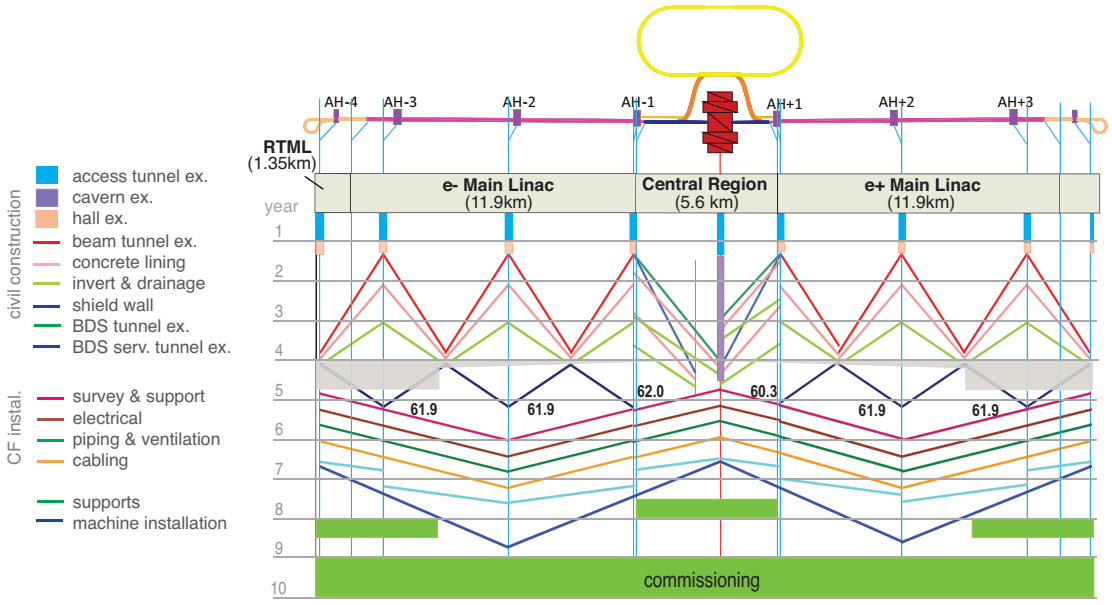

Figure 3.7. A possible ILC project construction schedule. Years from construction start are represented vertically, while progress along the machine footprint is shown horizontally (not to scale). Vertical lines represent access tunnel locations.

3.3 ILC R&D during the technical design phase

The ILC technical design, layout and parameters presented in Section 3.1 reflect the results of the significant R&D that has been performed during the technical design phase. The global R&D programme itself was prioritised based on an evaluation of the remaining technical risks in the published 2007 Reference Design. At that time, the five highest identified priority items were:

1. SCRF cavities capable of reproducibly achieving at least 35 MV/m;
2. a cryomodule consisting of nine cavities, operating at an average of gradient of 31.5 MV/m;
3. linac string test (or integration test) of more than one cryomodule with beam;
4. development of models and mitigation techniques for electron-cloud effects in the positron damping ring;
5. demonstration of the small spot size and stability produced using the final focus optics that is used in the baseline design of the beam delivery system.

Other R&D areas (for example the sources) were also identified. The first three priority R&D items all relate to the SCRF linear-accelerator technology, the primary cost driver of the machine. Although it was noted by the International Technology Review Panel that TESLA SRF technology was 'mature', the ILC gradient goal had only been achieved in a handful of cavities (one of which had accelerated beam at 35 MV/m in the TESLA Test Facility at DESY – a proof of principle). One of the major technical aims has been the demonstration of large-scale production of reproducible high-gradient SCRF cavities, which required a detailed fundamental understanding of the physics involved in the technology. During the R&D programme from 2007–2012, more than 200 cavities have been successfully manufactured and processed.

The successful development of industrial capacity in each of the three regions (Asia, the Americas and Europe) resulted in multiple vendors capable of producing high-performance ILC cavities. In the USA, these were tested at Fermilab, Argonne National Laboratory and Jefferson Lab; in Japan at KEK; and in Europe at DESY, where development has been driven by the design and construction of the European X-ray free-electron laser (XFEL). The 17.5 GeV SCRF linac of the European XFEL

represents the largest deployment of the technology to date. In many ways it provides an excellent large-scale prototype for the ILC.

Cryomodule development and integrated systems testing is being pursued at all the primary SCRF sites. The FLASH FEL facility at DESY has successfully accelerated an ILC-like electron beam through high-gradient cryomodules, and has demonstrated many of the tuning techniques required by the ILC. Further system-test accelerators at Fermilab (NML) and at KEK (STF) have been under development and will see beam operation in 2013. The global cryomodule integration (S1-Global) programme at KEK successfully integrated cavities and auxiliary components delivered from DESY, FNAL, INFN and KEK into a single cryomodule, allowing direct comparative tests of different technologies as well as demonstrating the key concept of "plug compatibility", simplifying integration of parallel design-efforts worldwide. Other main-linac components developed by the R&D program include a tuneable high-power RF delivery system and associated low-level RF controls, and a next generation solid-state modulator.

During development of the 2007 *Reference Design Report*, emittance dilution in the positron damping ring arising from the electron-cloud effect was identified as one of the primary major technical risks to the design luminosity. As a result, a multi-year study was launched at the CESR accelerator at Cornell, later named the Cornell Electron-Positron Storage Ring Test Accelerator (CesrTA). The well understood machine characteristics and highly flexible operating parameters of the CesrTA facility supported an R&D program that has culminated in a definitive report on the physics of high-intensity, positively charged beams. The study also developed and identified techniques to reduce the electron-cloud effect to an acceptable level that are now included in the TDR.

Some highlights of the R&D programmes whose success is the foundation of the TDR baseline design are given below.

3.3.1 Main achievements of the SCRF R&D effort

The performance of superconducting cavities is primarily limited by two effects: field emission and quench-causing surface defects. Improvements in surface treatments have essentially mitigated the onset of field emission at gradients below 35 MV/m. The invention and deployment of tools to identify and repair quench-causing defects at low cavity gradient has led to the establishment of a baseline set of procedures for cavity fabrication and surface preparation which minimise surface defects. These techniques were fully implemented during the final phase of the R&D program giving the results shown in Fig. 3.8 a two-pass production yield of 94% for cavities satisfying 35 MV/m ± 20%, with an average gradient of 37.1 MV/m. These results exceed the 2006 GDE R&D goal of 90% yield and 35 MV/m average gradient.

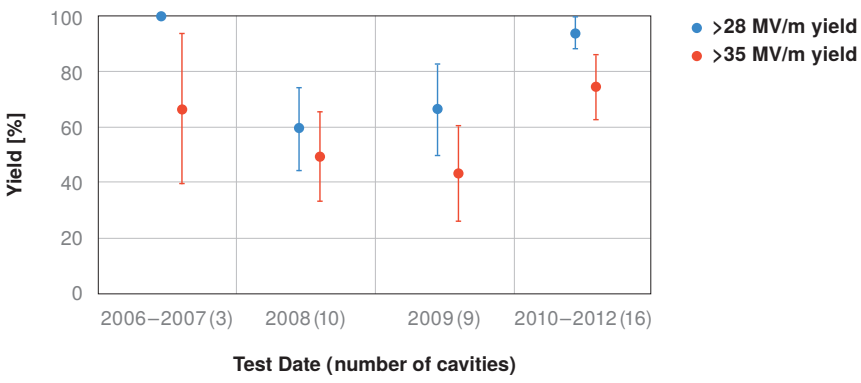

Figure 3.8 Cavity yield for the years indicated during the GDE R&D programme. The results include cavities having had up to two surface chemistry treatment.

In addition to the performance of individual cavities an average field gradient of 32 MV/m has been achieved in a prototype cryomodule for the European XFEL program (pictured in Fig. 3.9a).

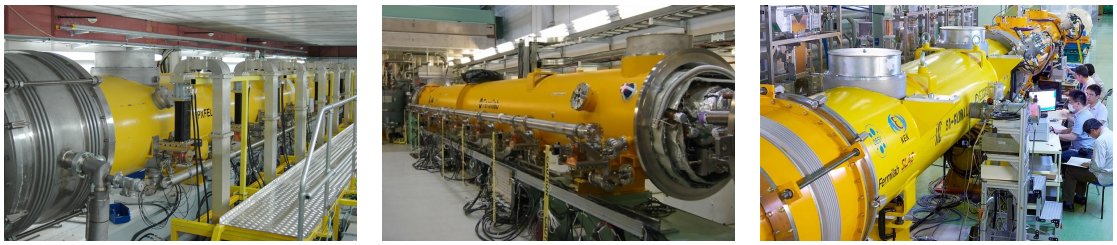

(a) PXFEL1 at DESY **(b)** CM2 at FNAL **(c)** S1-Global at KEK

Figure 3.9. Cryomodules assembled in all three regions.

The S1-Global programme (see Fig. 3.10) successfully demonstrated "plug compatibility" by building one cryomodule from cavities and couplers supplied from several different national laboratories. Specifically the half-size cryomodule-C was built from an INFN cryostat, DESY cavities and couplers, and FNAL cavities and couplers in cooperation with SLAC. The cryomodule power system is another good example of plug compatibility. The ability to incorporate and test several different component designs within a single integrated test setup was another important aspect of the S1-Global programme, providing input to many of the baseline technology decisions for the TDR.

Figure 3.10
Fish-eye view of the S1-Global cryomodule at KEK.

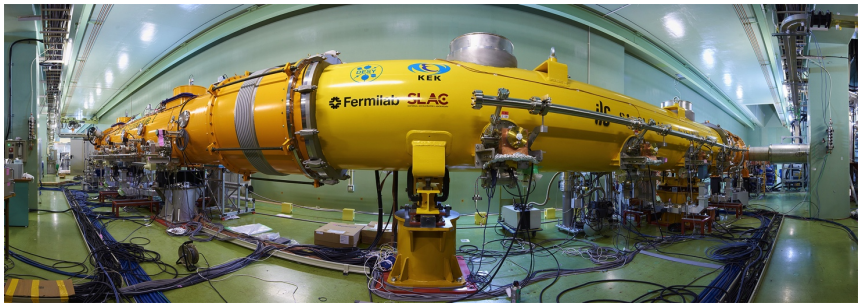

3.3.2 R&D on RF power generation and distribution

Klystron and modulators The RF system features a 10 MW, high-efficiency (65%), Multiple-Beam Klystron (MBK) that produces 1.6 ms pulses at a rate up to 10 Hz. For this application, three vendors developed tubes of somewhat different designs, of which two were successful to the extent that they have been adopted for use in the European XFEL linac where they will run nominally at 5 MW but have 10 MW capabilities.

The klystron modulator is another large component in the linac RF power system. A new type of modulator, the all-solid-state Marx modulator, was proposed and developed at SLAC National Accelerator Laboratory and with industry. This type of modulator has many advantages over the 'traditional' kind: compactness, lower cost, operational flexibility and lack of oil-filled transformers inside tunnel enclosures. The Marx modulator design has been adopted as baseline for all ILC RF power systems.

RF distribution The ILC baseline linac will need to accelerate a nominal 6 mA of beam current, but needs to be capable of accelerating up to 9 mA to allow scope for future upgrades. Multiple cavities (26 or 39 depending on the configuration and beam current) are effectively driven by one 10 MW power source. A $\pm$20% spread in cavity-to-cavity performance is expected. The power-distribution system driving the cavities has therefore been developed to provide remotely adjustable power ratios, allowing each cavity to be driven at its maximum gradient while minimising the power losses in the waveguide components.

For the flat-topography single-tunnel design, a new high-power distribution system was proposed and developed. The Klystron Cluster System (KCS) has all klystrons and associated power supplies

located in a series of ten surface buildings along the Main Linacs. In each building there are two sets of typically 19 klystrons (for the 5 mA baseline) or 29 klystrons (for the 9 mA upgrade) whose power is combined and then transported in a 0.5 m diameter, pressurised aluminum over-moded circular waveguide. Up to 10 MW of power is tapped off periodically to feed each group of 26 cavities (3 cryomodules). This required the development of several waveguide components, such as combiners, bends, adjustable tap-offs and the long circular over-moded waveguides. Development and testing of these components will continue as required.

3.3.3 Beam test facilities

Beam test facilities are required for critical technical demonstrations, including accelerating gradient, beam dynamics, and precision beam handling. The scope of test-facility activity needed to mitigate technical risks was assessed during the development of the 2007 Reference Design Report. Purpose-built test facilities were then either constructed by collaborative teams or provided through adaptation of existing facilities. The primary goals of these beam test facilities were: the demonstration of ILC linac performance and evaluation of realistic cavity performance with beam acceleration; demonstration of a number of cavities operated in an accelerator showing repeatable performance and providing an estimate of reliability; studies of instabilities in the damping rings, such as electron cloud, and mitigation techniques; and demonstrations of the generation and handling of low-emittance beams using precision optics and stabilisation tools.

The 9 mA Experiment at FLASH The FLASH (Free electron LASer in Hamburg) accelerator became a user facility operating as a soft X-ray free-electron laser in 2005. The FLASH linac is a 1.25 GeV linac based on Tesla-type technology and operates 5000 hours per year on average. The '9-mA' program was proposed by the GDE in 2008 with the goals of demonstrating reliable operation of the linac with ILC-like bunch trains and to characterise the limits of operation of gradient and RF power. Typical beam properties for FEL user operation (charge, number of bunches, average beam power) are less challenging than those required for the 9 mA studies. For DESY, however, these studies have been important for integration and operational issues associated with running long bunch trains and high bunch charge, both for FLASH itself and for the European XFEL.

Much can be learnt from FLASH but the European XFEL, currently under construction, offers an even greater opportunity for gaining invaluable experience with constructing, commissioning, and operating a large-scale superconducting high-power linac. The superconducting linac facilities at KEK and FNAL (see Fig. 3.9) are in the early stages of commissioning and they will further expand operating experience around the world.

CesrTA (Cornell) and electron-cloud R&D One of the principal R&D issues for the positron damping ring of the ILC was to ensure that the build-up of the electron cloud (EC) in the vacuum chambers can be kept below the levels at which EC-induced emittance growth and beam instabilities occur. During Phase I (2008-2010), a focused effort to study methods of suppressing the EC as well as measuring its impact on ultra-low emittance beams was undertaken at CesrTA. In addition, a complementary R&D program has continued at various laboratories around the world to develop better techniques to mitigate the build-up of the electron cloud. As part of this coordinated global programme, a major emphasis was placed on developing and benchmarking simulation tools and measurement techniques.

The results from the first three years (Phase I) of the CesrTA R&D programme have been incorporated into the design of the ILC damping-ring vacuum chamber; the findings of the programme are documented in the CesrTA Phase I Report. In particular, the observed efficacy of grooved chamber surfaces in the dipoles as well as that of the clearing electrode in the high-field wigglers provide confidence that practical electron-cloud mitigation measures can be prepared for the arc and wiggler straight regions of the ILC positron damping ring. The importance of cloud mitigation in the damping

ring quadrupole chambers has also been demonstrated. New coating technologies to suppress the secondary-electron yield show great promise. However, there is still the issue of studying the long-term performance and durability of these coatings. This will be a subject of study during Phase II of the CesrTA programme. Perhaps most importantly, the flexibility of CESR operations has enabled a systematic programme of electron-cloud build-up and electron-cloud-induced beam-dynamics studies. By benchmarking physics models and simulations against these studies, confidence in being able to make valid projections of the expected ILC positron-damping performance has been significantly enhanced.

ATF2 final-focus experiment The challenge of colliding nanometre-sized beams at the interaction point (IP) involves three distinct issues: creating small emittance beams; preserving emittance during acceleration and transport; and focusing the beams to nanometre sizes before colliding them.

The Accelerator Test Facility (ATF) at KEK is a prototype damping ring to deal with the first issue and has succeeded in obtaining the emittances that almost satisfy ILC requirements; these have also already been achieved in two third-generation light sources. The ATF is now used as an injector for the ATF2 final-focus test beam line, which was constructed in 2008 to study the third issue. The ATF2 beam line stretches about 90 meters from the beam-extraction point in the ATF damping ring to the focal point. Anticipating gradual movements of supports and magnets due to thermal variations or slow ground motion, quadrupoles and sextupoles were mounted on remote-controlled three-axis movers. Overall alignment precisions of 0.1 mm (displacement) and 0.1 mrad (rotations) have been achieved using conventional alignment/metrology techniques. The final alignment of the magnets is achieved via beam-based alignment (BBA) techniques.

ATF2 is a follow-up to the Final-Focus Test Beam (FFTB) experiment at SLAC, but with different beam-line optics based on a scheme of local chromaticity correction, which facilitates a shorter design and a larger energy bandwidth. As with FFTB, the vertical beam size at the focal point has been chosen to have the same demagnification as the ILC and similar levels of chromatic aberration. The primary goals for ATF2 are to achieve a 37 nm vertical beam size at the IP, stabilise it at the nanometre level, and then maintain the beam size and stability over a period of time. In December 2012, ATF2 achieved a beam size within a factor 2 of the first goal. The R&D towards successful completion of the goals will continue following many months of delay after recovery from the Great East Japan Earthquake.

3.3.4 Future engineering and R&D

The successful conclusion of the GDE R&D programme establishes technical viability but there are many other aspects of the ILC that will require additional work. Cost containment through value engineering of the cryomodule remains to be performed prior to production. Couplers, tuners, and other components would benefit from further detailed engineering studies. Minimising the loss of gradient performance from individual cavities in vertical tests to cavity strings in cryomodules is an important goal. The RF power systems are also good candidates for additional cost engineering. At some point an actual site will be proposed and adapting the TDR baseline to a site-specific design will be necessary. Continued operation of the test beam facilities is envisaged for the next several years. The transport and stabilisation of high brightness beams at the ATF, developing high brightness techniques at CESR-TA, and beam acceleration tests at FLASH will all continue. The XFEL project at DESY will provide a unique opportunity to monitor high-volume cryomodule production. When this facility is operational in 2015, it will also test ILC beam-control techniques.

Chapter 4
ILC Detectors

4.1 Introduction and Physics Performance Requirements

In order to realise the physics program, the ILC detectors face challenges requiring significant advances in collider detector performance. The machine environment is benign by LHC standards, enabling designs and technologies that are unthinkable at the LHC. However, the ILC environment poses its own set of background issues that must be overcome. The "Detailed Baseline Design" of the SiD and ILD detectors have been developed to achieve the requirements for all considered physics programs, over the full range of centre-of-mass energies from 200 GeV up to 1 TeV, as well as the possibility of special running at the Z-pole.

The ILC physics opportunities place a premium on high-resolution jet energy reconstruction and di-jet mass performance. Event reconstruction techniques based on the Particle Flow Algorithm (PFA) have been developed to meet this challenge. This motivates highly granular electromagnetic and hadron calorimeters and highly efficient tracking systems. New detector technologies and new reconstruction algorithms based on the PFA approach achieve the needed precision in the reconstruction of jets of 3 to 4 percent for 100 GeV jets, set by the requirement to separate W and Z di-jet final states. The requirements on momentum resolution for charged tracks ($\Delta p/p^2$ of $5 \times 10^{-5}\,(\mathrm{GeV/c})^{-1}$) are driven by reconstruction of a Higgs boson recoiling from the associated Z boson decaying to a lepton pair in the Higgs-strahlung process. Flavour and quark-charge tagging will be available at an unprecedented level of performance as a result of the development of a new generation of vertex detectors. Particle identification is achieved by the highly granular calorimeters and muon identification is aided by the instrumented iron return yoke.

A very important element of the detector design work has been the common effort to develop and apply simulation tools to realise realistic detector-performance estimates. A small group of experts from both SiD and ILD have cooperated closely on this critical work.

To preserve this unprecedented performance, the inner detectors must accommodate very low-mass detectors and supports. This is a significant challenge. The detector designs have achieved the required light-weight support structures with minimal dead spaces. This was greatly simplified by the ILC time structure of 1 millisecond bunch trains at 5 Hertz. This very sparse filling allows power for many of the detector subsystems to be switched off between bunch trains (so-called power pulsing), reducing the heat load and the need for cooling. The design of these power-pulsed systems presents a significant challenge, including the need for quiescent currents.

4.2 Backgrounds

While benign by LHC standards, ILC machine backgrounds must be understood and taken into account to give optimal performance of the detectors. A variety of processes create beam-induced backgrounds in the detectors. The main sources are beamstrahlung, which is induced by the interaction of one beam with the bunch with which it collides, synchrotron radiation, muons, and neutrons. Significant numbers of low-energy e^+e^- pairs are produced at the interaction point from beamstrahlung; the interaction region layout has been designed to guide these background charged particles out of the detector by adding a dipole field to the conventional solenoidal field (so-called *anti-DID*). These background pairs must be dealt with in the vertex detector design, but they primarily affect the very forward detectors, which need to be able to withstand the significant radiation loads, and at the same time maintain sensitivity to single high-energy particles. An optimised collimation system is used to control the synchrotron radiation generated upstream. Various schemes are employed to minimise the impact of muons and neutrons.

Another important background comes from photon-photon collisions. These events produce high-transverse-momentum particles that overlap with the particles from the less-common hard-scattering events. Time stamping at the single-bunch level can help in reducing the number of overlapping events. In addition sophisticated algorithms have been developed to identify and subtract these events based on topology and detailed properties.

4.3 Beam Instrumentation

Precise knowledge of beam parameters is critical to the ILC physics program. Luminosity, beam energy, and polarisation are measured by instrumentation close to the main detectors. Low-angle Bhabha scattering detected by dedicated calorimeters can provide the necessary precision for the integrated luminosity. Acollinearity and energy measurements of Bhabha events in the polar-angle region from 120–400 mrad can be used to extract the luminosity as a function of energy, $\mathrm{d}L/\mathrm{d}E$. Beam-energy measurements with an accuracy of (100–200) parts per million are done both upstream and downstream of the collision point to provide redundancy and reliability of the results. Precise measurements of parity-violating asymmetries require polarisation measurements with a precision of 0.25% or better. High statistics Giga-Z running requires polarimetry at the 0.1% level. The primary polarisation measurement comes from dedicated Compton polarimeters detecting backscattered electrons and positrons. The best accuracy is achieved by implementing polarimeters both upstream and downstream of the interaction region (IR).

4.4 Two Detectors

The ILC has been designed to enable two experiments (SiD and ILD) sharing one interaction region using a push-pull approach. This two-detector design is motivated by the enhanced scientific productivity of past collider facilities which benefited from independent operation of multiple experiments, providing complementary strengths, cross-checking and confirmation of results, reliability, insurance against mishaps, competition between collaborations, as well as increased number of involved scientific personnel. Figure 4.1 shows the arrangement of the two detectors in the detector hall.

Both detector designs are conceived as multi-purpose detectors, optimised for the broad range of physics opportunities at the ILC. SiD is a compact, cost-constrained detector made possible with a 5 Tesla magnetic field and silicon tracking. Silicon enables time-stamping on single bunch crossings to provide robust performance, derived from immunity to spurious background bursts. The highly granular calorimeter is optimised for particle-flow analysis. The ILD group has designed a large detector with robust and stable performance over a wide range of energies. The concept uses a tracking system based on a continuous-readout time-projection chamber combined with silicon

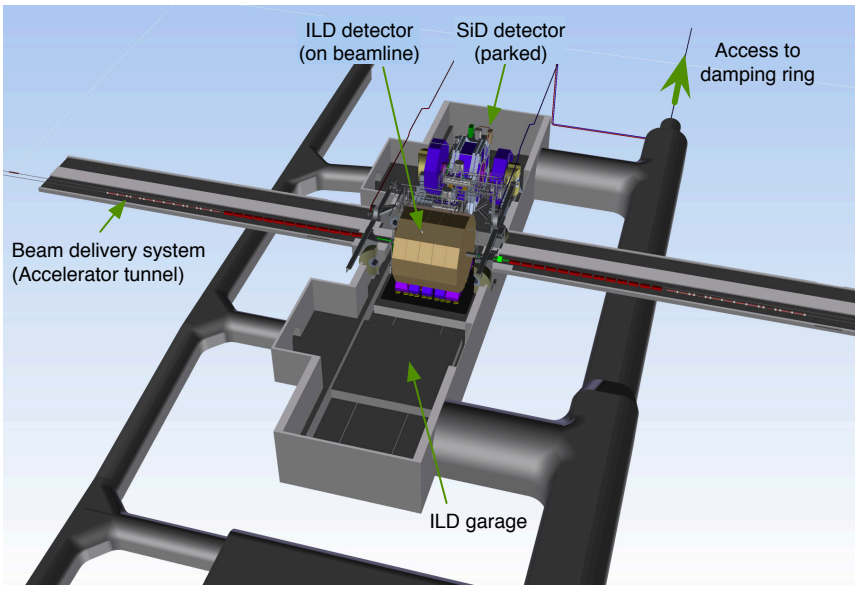

Figure 4.1
Example layout of the detector hall for the Mountain Topography site, showing the location of the two detectors in a push-pull arrangement.

tracking for excellent efficiency and robust pattern-recognition performance. A granular calorimeter system contained inside a 3.5 T magnetic field provides very good particle-flow reconstruction. Both detectors provide flexibility for operation at energies up to the TeV range.

The push-pull operation scheme calls for one detector taking data while the other is out of the beam in a close-by maintenance position. At regular intervals, the data-taking detector is pushed laterally out of the interaction region, while the other detector is being pulled in. These intervals are short enough to ensure both acquire data on any potential discovery. The time for transition must be on the order of one day to maximise ILC integrated luminosity.

A time-efficient implementation of the push-pull operation sets specific requirements and challenges for many detector and machine systems, in particular the IR magnets, the cryogenics, the alignment system, the beamline shielding, the detector design, and the overall integration. The functional requirements and interface specifications for the push-pull IR have been developed, with a detailed design of technical systems and the experimental area from detailed engineering specifications.

The detector motion and support system has to ensure reliable push-pull operation for roughly one hundred moves over the life of the experiment, while preserving alignment of the detector's internal components and ensuring accuracy of detector positioning. The motion system must preserve structural integrity of the collider hall floor and walls, be compatible with vibration stability of the detector at the level of tens of nanometers and be compatible with earthquake-safety standards.

The detectors will be placed on platforms that preserve the detector alignment and distribute the load evenly onto the floor. Details of the design of such platforms and the interfaces between the platform and the detectors have been developed. The ILC detectors are self-shielding with respect to ionising radiation from maximum credible beam-loss scenarios. Additional shielding must fill the gap between the detector and the wall in the beam position.

The stray magnetic fields outside the iron return yokes of each detector must be small enough not to disturb the other detector during operation or maintenance. A limit for the magnetic fields is 5 mT at a lateral distance of 15 m from the beam line. Fringe fields from the detector return yokes have been carefully simulated and designs for both SiD and ILD have been developed to meet these requirements.

The installation schemes for the detectors and the layout of the experimental areas on the surface and underground depend on the geographical situation of the possible ILC sites. While the European and American sample sites assume a flat surface area, the Asian sample sites in Japan are located in

mountains where the requirements for the conventional facilities and buildings are different.

4.5 Detector R&D

The high levels of performance in the ILC detector designs result from more than a decade of R&D conducted in the Americas, Asia, and Europe, by a number of R&D collaborations. Technological solutions for the key systems of the SiD and ILD designs have been developed and have been validated in extensive test-beam campaigns. Through internationally coordinated R&D groups, a successful, well-focused programme of innovative instrumentation development has been performed even with rather limited resources. A notable achievement has been the combined work of simulation and beam tests to verify the understanding and precision of the PFA calorimetry technique. These efforts have achieved the critical goals on all subsystems, and continue to advance the technology, further optimising the performance.

4.6 SiD

SiD is a general-purpose detector designed to perform precision measurements at a Linear Collider. It satisfies the challenging detector requirements for physics at the ILC. SiD is the result of many years of creative design by physicists and engineers, backed up by a substantial body of past and ongoing detector research and development. While each component has benefitted from continual development, the SiD design integrates these components into a complete system for excellent measurements of jet energies, based on the Particle Flow Algorithm (PFA) approach, as well as of charged leptons, photons and missing energy. The use of robust silicon vertexing and tracking makes SiD applicable to a wide range of energies from a Higgs factory to beyond 1 TeV. SiD has been designed in a cost-conscious manner, with the compact design that minimises the volumes of high-performing, high-value, components, while maintaining critical levels of performance. The restriction on dimensions is offset by the relatively high central magnetic field from a superconducting solenoid.

4.6.1 The SiD detector

SiD is a compact detector based on a powerful silicon pixel vertex detector, silicon tracking, silicon-tungsten electromagnetic calorimetry (ECAL) and highly segmented hadronic calorimetry (HCAL). SiD also incorporates a high-field solenoid, iron flux return, and a muon identification system (see Fig. 4.2).

The choice of silicon detectors for tracking and vertexing ensures that SiD is robust with respect to beam backgrounds or beam loss, provides superior charged-particle momentum resolution, and eliminates out-of-time tracks and backgrounds. The main tracking detector and calorimeters are "live" only during each single bunch crossing, so beam-related backgrounds and low-p_{T} backgrounds from $\gamma\gamma \to \mathrm{hadrons}$ processes will be reduced to the minimum possible levels. The SiD calorimetry is optimised for excellent jet-energy measurement using the PFA technique. The complete tracking and calorimeter systems are contained within a superconducting solenoid, which has a 5 T field strength, enabling the overall compact design. The coil is located within a layered iron structure that returns the magnetic flux and is instrumented to allow the identification of muons.

The tracking system is a key element as the particle-flow algorithm requires excellent tracking with superb efficiency and good two-particle separation. The requirements for precision measurements, in particular in the Higgs sector, place high demands on the momentum resolution at the level of $\delta(1/p_{\mathrm{T}}) \sim 2\text{–}5 \times 10^{-5}\,(\mathrm{GeV/c})^{-1}$ and the material budget of the tracking system. Highly efficient tracking is achieved using the pixel detector and main tracker to recognise and measure prompt tracks.

The SiD vertex detector uses a barrel and disk layout. The barrel section consists of five silicon pixel layers with a pixel size of $20\times20\,\mu\mathrm{m}^2$. The forward and backward regions each have four silicon

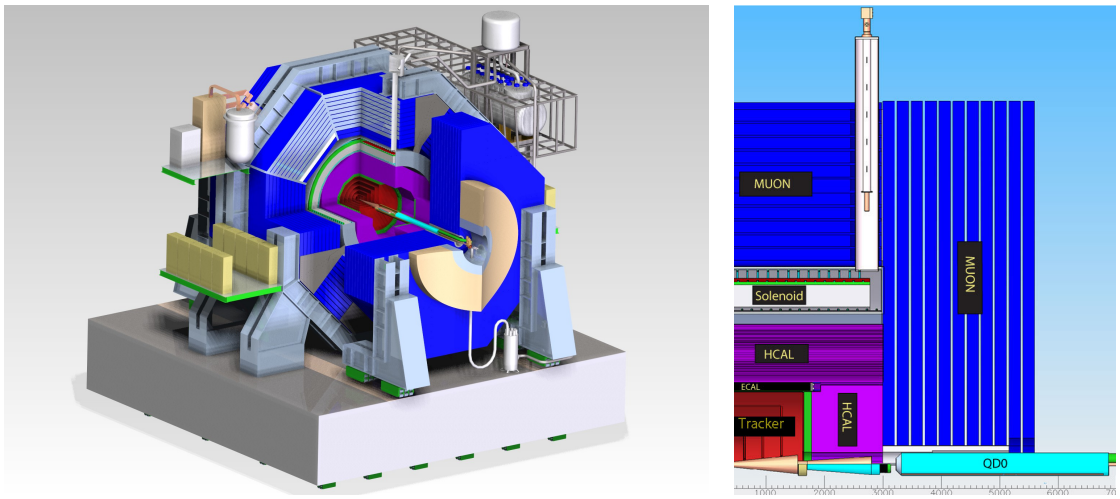

Figure 4.2. The SiD detector, showing (left) an isometric view on the platform, and (right) a quadrant section. Colour coding: tracking (red), ECAL (green), HCAL (violet) and the flux return (blue).

pixel disks. In addition, there are three silicon pixel disks at a larger distance from the interaction point to provide uniform coverage for the transition region between the vertex detector and the outer tracker. This configuration provides for very good hermeticity with uniform coverage and guarantees excellent charged-track pattern-recognition capability and impact-parameter resolution over the full solid angle. The vertex detector design relies on power pulsing during bunch trains to minimise heating and uses forced air for its cooling. The main tracker technology of choice is silicon-strip sensors arrayed in five nested cylinders in the central region with an outer cylinder radius of 1.25 m and four disks in each of the endcap regions. The geometry of the endcaps minimises the material budget to enhance forward tracking. The detectors are single-sided silicon sensors with a readout pitch of 50 µm.

The choice of PFA imposes a number of basic requirements on the calorimetry. The central calorimeter system must be contained within the solenoid in order to reliably associate tracks to energy deposits. The electromagnetic and hadronic sections must have imaging capabilities that allow both efficient track-following and correct assignment of energy clusters to tracks. These requirements imply that the calorimeters must be finely segmented both longitudinally and transversely.

The combined ECAL and HCAL systems consist of a central barrel part and two endcaps, nested inside the barrel. The entire barrel system is contained within the volume of the cylindrical superconducting solenoid. The electromagnetic calorimeter has silicon active layers between tungsten absorber layers. The active layers use $3.5\times3.5\,\mathrm{mm}^2$ hexagonal silicon pixels, which provide excellent spatial resolution. The structure has 30 layers in total, the first 20 layers having a thinner absorber than the last ten layers. This configuration is a compromise between cost, electromagnetic shower radius, sampling frequency, and shower containment. The total depth of the electromagnetic calorimeter is 26 radiation lengths (X_0) and one nuclear interaction length. The hadronic calorimeter has a depth of 4.5 nuclear interaction lengths, consisting of alternating steel plates and active layers. The baseline choice for the active layers is the glass resistive-plate chamber with an individual readout segmentation of $10\times10\,\mathrm{mm}^2$. Two special calorimeters are foreseen in the very forward region: LumiCal for precise measurement, and BeamCal for fast estimation, of the luminosity.

The SiD superconducting solenoid is based on the CMS solenoid design philosophy and construction techniques, using a slightly modified CMS conductor as its baseline design. Superconducting strand count in the coextruded Rutherford cable was increased from 32 to 40 to accommodate the higher 5 T central field. The flux-return yoke is instrumented with position sensitive detectors to serve as both a muon filter and a tail catcher. The SiD Muon System baseline design is based on

scintillator technology, using extruded scintillator readout with wavelength-shifting fibre and SiPMs. Simulation studies have shown that nine or more layers of sensitive detectors yield adequate energy measurements and good muon-detection efficiency and purity.

4.6.2 SiD detector performance

A large fraction of the software for the generation, simulation and reconstruction is shared between the detector concepts. The SiD detector is fully implemented and simulated using SLIC, which is based on GEANT4. The background originating from incoherent pair interactions and from $\gamma\gamma \to \text{hadrons}$ for one bunch crossing is fully taken into account by the simulation. The events are then passed through the reconstruction software suite, which encompasses digitisation, tracking, vertexing and the Pandora PFA algorithm. The material budget of the simulated tracker and the simulated tracking performance for single particles are shown in Fig. 4.3.

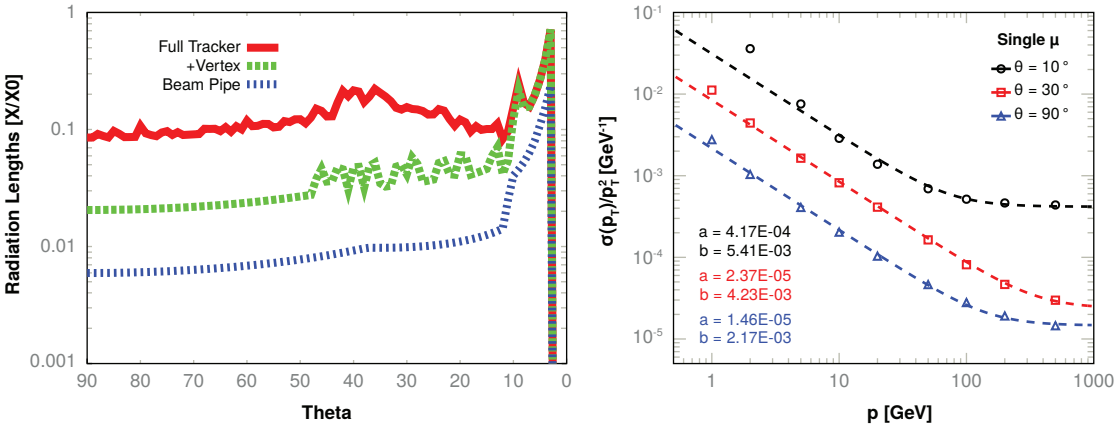

Figure 4.3. Left: SiD Tracker Material budget in terms of X_0. Right: the normalised transverse momentum resolution for single-muon events.

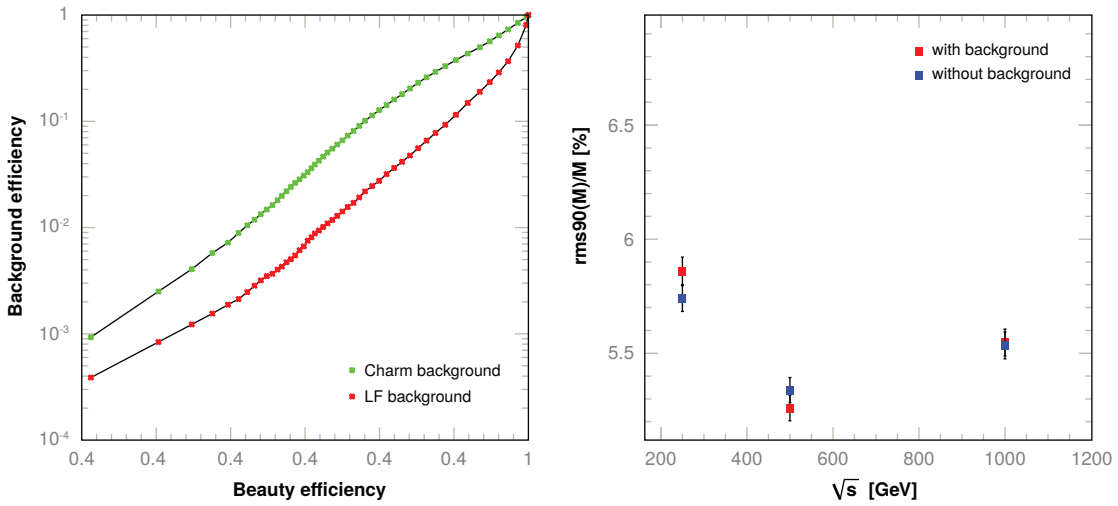

Figure 4.4. Left: Mis-identification efficiency of light quark (red points) and c quark events (green points) as b quark jets versus the b identification efficiency in di-jet events at $\sqrt{s} = 91\,\text{GeV}$ including background from $\gamma\gamma \to \text{hadrons}$ and incoherent pairs. Right: Mass resolution of reconstructed ZZ events with and without the backgrounds from $\gamma\gamma \to \text{hadrons}$ and incoherent pairs at different values of $\sqrt{s}$.

The material budget of the entire tracking system is less than 0.2 X_0 down to very low angles. The current design achieves an asymptotic momentum resolution of $\delta(1/p_T) = 1.46 \times 10^{-5}\,(\text{GeV/c})^{-1}$ and an transverse impact parameter resolution better than 2 μm. The ability to tag bottom and charm decays with high purity has been a driving factor in the design of the vertex detector. Figure 4.4 (left)

illustrates the capability of the SiD to separate b-quarks also in the presence of the full beam background.

Besides the detector performance, sophisticated reconstruction algorithms are necessary to obtain a jet-energy resolution that allows the separation of hadronic W and Z decays. To avoid a bias from possible tails, the rms_{90} value is computed to describe the energy or mass resolution of a particle-flow algorithm. It is defined as the standard deviation of the distribution in the smallest range that contains 90% of the events. Figure 4.4 (right) shows the mass resolution of reconstructed Z bosons in $e^+e^- \to \mathrm{ZZ}$ events at different collision energies, where one Z decays to neutrinos, the other to two light quarks that give rise to two jets.

4.6.3 SiD costing

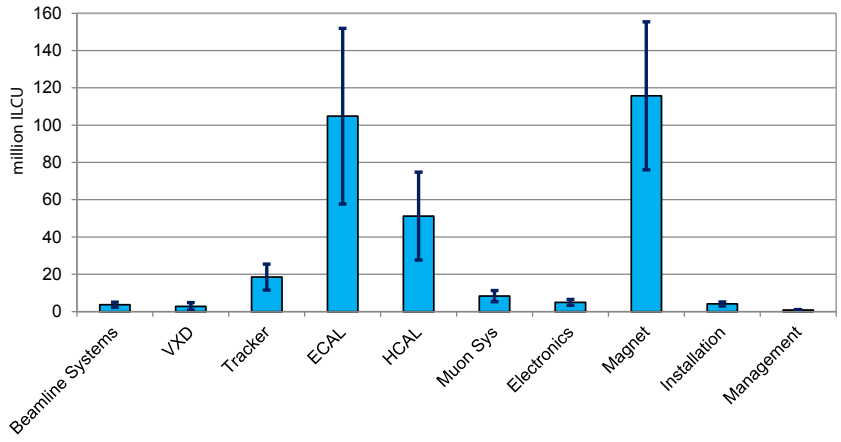

Figure 4.5
Subsystem M&S Costs in million ILCU. The error bars indicate the subsystem contingency.

The SiD cost estimate is a construction cost estimate; it does not include R&D, commissioning, operating costs, or physicist salaries. The parametric model of the detector maintains a self-consistent model of SiD. It is also straightforward to vary the SiD detector parameters. For each system, the cost-driving component count is calculated. The model then estimates both M&S and labour costs that are associated with the actual scale of SiD. Contingency is estimated for each quantity to estimate the uncertainties in the costs of the detector components (see Fig. 4.5). A set of unit costs for some basic commodity items, which has been agreed upon for ILC and CLIC detector cost estimates, is used in the SiD and ILD cost estimates.

The SiD cost is 315 million ILCU for M&S, 316 thousand person-hours engineering, 904 thousand person-hours technical, and 51 thousand person-hours administrative labour. The estimated M&S contingency, reflecting uncertainty in unit costs and some estimate of the maturity of this study, is 127 million ILCU.

4.7 ILD

The ILD concept has been designed as a multi-purpose detector. It has been designed for optimal particle-flow (PFA) performance. A high-precision vertex detector is followed by a hybrid tracking system, realised as a combination of silicon tracking with a time-projection chamber, and a calorimeter system. The complete system is located inside a 3.5 T solenoid. The inner-detector system is highly granular, and provides a robust and detailed three-dimensional imaging capability of the events. On the outside of the coil, the iron return yoke is instrumented as a muon system and as a tail-catcher calorimeter. The detector is shown in Fig. 4.6

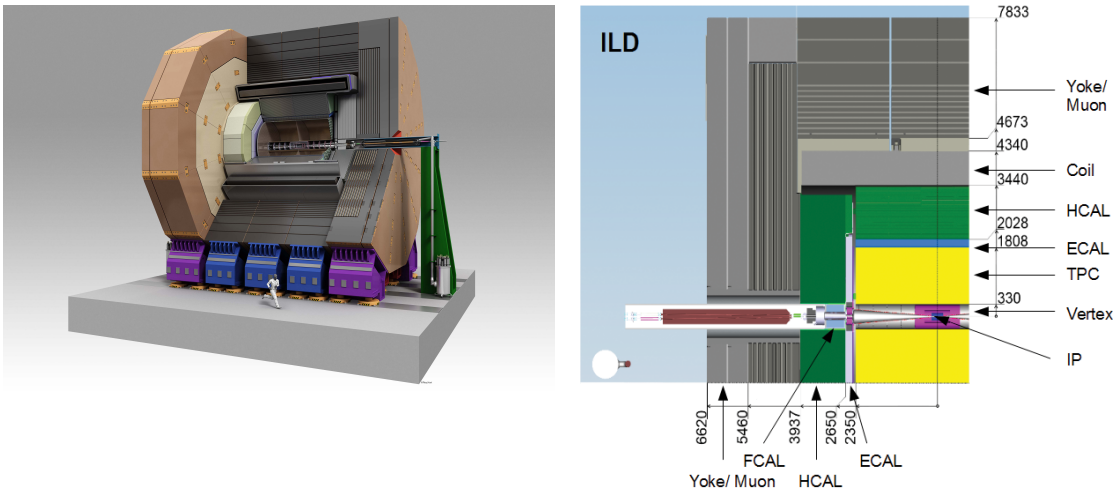

Figure 4.6. Views of the ILD detector concept. The interaction point in the quadrant view (right) is in the lower right corner of the picture. Dimensions are in mm.

4.7.1 The ILD detector

The vertex detector is realised as a multi-layer pixel vertex detector (VTX), with three superlayers each comprising two layers, or as a 5 layer geometry. In either case the detector has a pure barrel geometry. To minimise the occupancy from background hits, the first superlayer is only half as long as the outer two. Whilst the underlying detector technology has not yet been decided, the VTX is optimised for point resolution and minimum material thickness.

A system of silicon strip and pixel detectors surrounds the VTX detector. In the barrel, two layers of silicon strip detectors (SIT) are arranged to bridge the gap between the VTX and the TPC. In the forward region, a system of two silicon-pixel disks and five silicon-strip disks (FTD) provides low angle tracking coverage.

A distinct feature of ILD is a large-volume time-projection chamber (TPC) with up to 224 points per track. The TPC is optimised for 3-dimensional point resolution and minimum material in the field cage and in the end-plate. It also allows $\mathrm{d}E/\mathrm{d}x$-based particle identification.

Outside the TPC a system of Si-strip detectors, one behind the end-plate of the TPC (ETD) and one in between the TPC and the ECAL (SET), provide additional high-precision space points which improve the tracking performance and provide additional redundancy in the regions between the main tracking volume and the calorimeters.

A highly segmented electromagnetic calorimeter (ECAL) provides up to 30 samples in depth and small transverse cell size, split into a barrel and an end-cap system. Tungsten has been chosen as absorber; for the sensitive area, silicon diodes, scintillator strips or a combination are considered.

The ECAL is followed by a highly segmented hadronic calorimeter (HCAL) with up to 48 longitudinal samples and small transverse cell sizes. Two options are considered, both based on a steel-absorber structure. One option uses scintillator tiles of $3\times3\,\mathrm{cm}^2$, which are read out with an analogue system. The second uses a gas-based readout which allows a $1\times1\,\mathrm{cm}^2$ cell geometry with a binary or semi-digital readout of each cell.

At very forward angles, below the coverage provided by the ECAL and the HCAL, a system of high-precision and radiation-hard calorimetric detectors (LumiCAL, BeamCAL, LHCAL) is foreseen. These extend the calorimetric solid-angle coverage to almost 4π, measure the luminosity, and monitor the quality of the colliding beams.

A large volume superconducting coil surrounds the calorimeters, creating an axial B-field of nominally 3.5 Tesla. An iron yoke, instrumented with scintillator strips or resistive plate chambers

(RPCs), returns the magnetic flux of the solenoid, and, at the same time, serves as a muon filter, muon detector and tail-catcher calorimeter.

To maximise the sensitivity of the detector to the physics at the ILC, the detector will be operated in a continuous readout mode, without a traditional hardware based trigger.

In close collaboration with the detector R&D groups, all key components of the ILD proposal have been evaluated and the key performance criteria have been demonstrated in test-beam experiments. This is of particular importance for the very ambitious calorimeter proposal.

A first engineering study of the integration of the ILD detector has been performed. This study has included a detailed review of the detector components, their sizes, and in particular the support structures needed to mount the detector. Assembly and maintenance procedures have been simulated to validate the integration concept. Estimates of services needed have been included as far as possible, and realistic tolerances have been inserted into the designs. A detailed model of the complete detector has been built using modern CAD tools, and compared to the simulation model used for the performance evaluation.

4.7.2 ILD detector performance

The performance of the ILD concept has been extensively studied using a detailed GEANT4 based simulation model and sophisticated reconstruction tools. Backgrounds have been taken into account to the best of current knowledge.

A key characteristic of the detector is the amount of material within it. Particle flow requires a thin tracker, to minimise interactions before the calorimeters, and thick calorimeters, to fully absorb the showers. Figure 4.7 (left) shows the material in the detector in radiation lengths, for the different parts of the tracking system. The amount of material up to the end of the tracking is mostly below 10% for the full solid angle. The right-hand plot shows the total interaction length including the calorimeter system. Clearly visible is the increase of material in the end-cap due to the support structure for the readout in the TPC. Since this material however is located very close to the end-cap calorimeter it has only a very small negative impact on the performance, as can be seen from the top curve in the left plot, the total number of radiation length until the first active layer inside the ECAL.

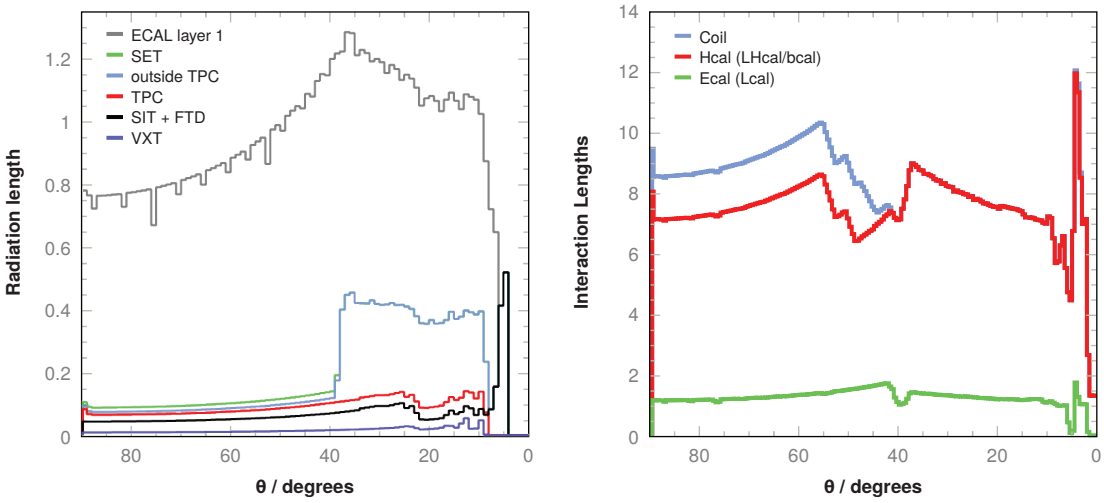

Figure 4.7. Left: Average total radiation length of the material in the tracking detectors as a function of polar angle. The red curve shows the material in the tracking system without the outer material in field cage or endplate, the grey line the total material up to the first active layer inside the ECAL is reached. Right: Total interaction length in the detector, up to the end of the calorimeter system (red line), and including the coil of the detector (light-blue line).

The performance of the tracking system can be summarised by its combined momentum resolution, shown in Fig. 4.8 (left). A resolution of $\sigma_{1/p_T} = 2 \times 10^{-5}\,\mathrm{GeV}^{-1}$ has been achieved for high momenta.

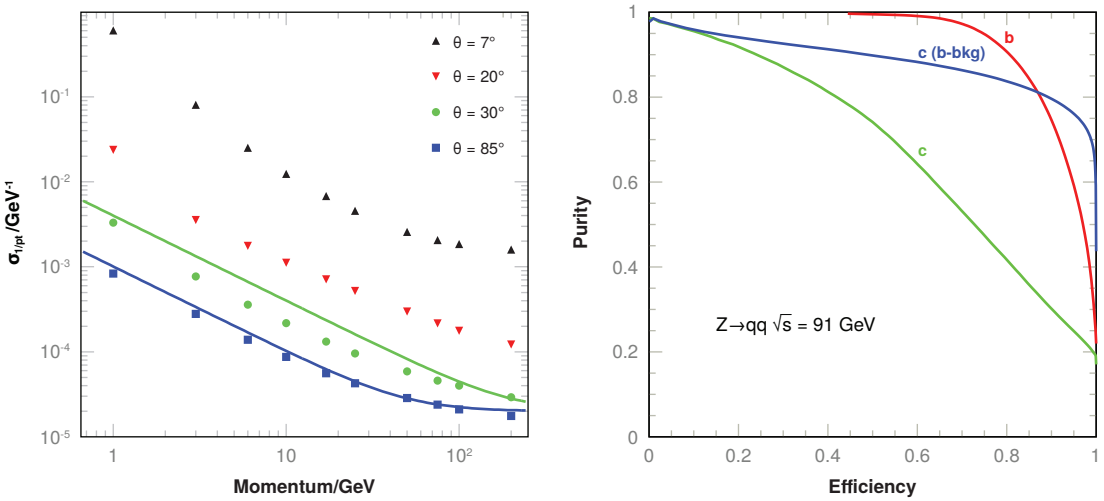

Figure 4.8. Left: Momentum resolution as a function of the transverse momentum of particles, for tracks with different polar angles. Also shown is the theoretical expectation. Right: Flavour tagging performance for $Z \to q\bar{q}$ samples at 91 GeV.

For many physics studies the tagging of long-lived particles is of key importance. The ability of ILD to reconstruct displaced vertices is shown in Fig. 4.8 (right).

Calorimeter system and tracking system enter into the particle flow performance together. The performance of the ILD detector for different energies and as a function of the polar angle is shown in Fig. 4.9. The jet-energy resolution stays below 4% for nearly the full solid angle, and is nearly independent of the centre-of-mass energy.

Figure 4.9
Fractional jet-energy resolution plotted against $|\cos\theta|$ where θ is the polar angle of the thrust axis of the event.

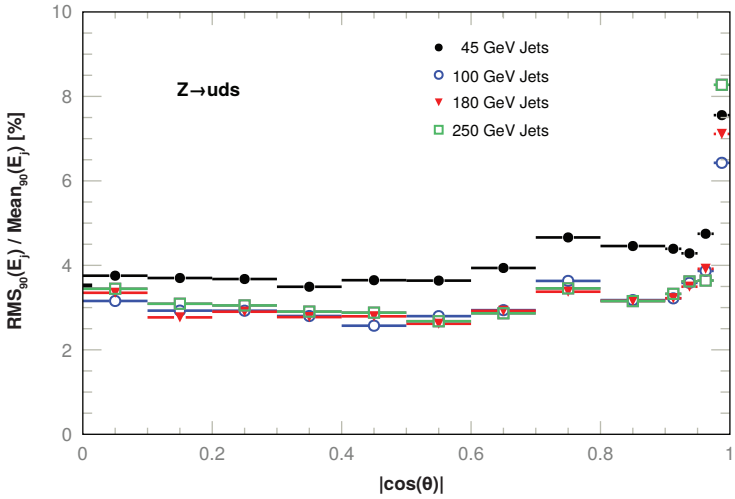

4.7.3 ILD costing

A significant effort has been undertaken to evaluate the cost of the ILD concept. In most cases the prototypes constructed over the past few years have given important input to validate the costs, and to provide guidance towards large-scale production of detector components. For the most relevant items the estimates are based on quotes from manufactures, and are often based on extensive discussions.

Depending on the option chosen, the cost of the ILD concept varies between 350 and 440 million ILCU. This cost does not include labour, or any contingency.

The distribution of costs among the different ILD systems is shown in Fig. 4.10 as a fraction of the total cost of the detector. As basis for this plot an average cost of the ILD concept of 392 million ILCU was used.

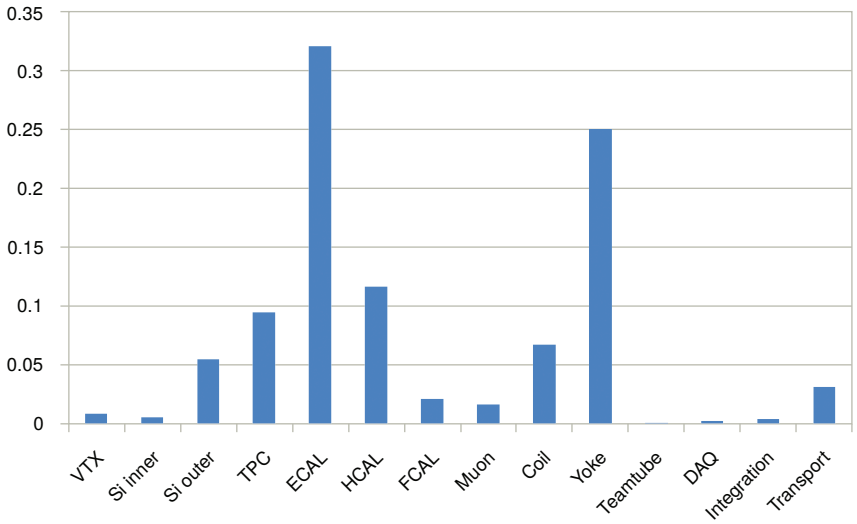

Figure 4.10
Costs distribution of ILD (shown as a fraction of the total cost).

The costs are dominated by the coil/yoke system, and by the calorimeter system, in particular the electromagnetic calorimeter. While the scope for the reduction of the costs for the coil/yoke are limited and largely depend on the requirement of a very small magnetic stray field outside the detector, large efforts are ongoing to optimise the cost of the active detector elements. A large part of the cost of the electromagnetic calorimeter come from the sensors. Significant technological progress over the past years has already resulted in significantly reduced costs, and more progress might be expected in the future. The subdetector technology itself is also undergoing a vigorous optimisation, including the exploration of hybrid solutions from silicon- and scintillator-based systems. Re-optimisation of the ILD detector for the anticipated physics program, in view of the much improved understanding of technologies and costs, will be one of the challenges in the near future.

Chapter 5
Conclusion

The ILC accelerator project described in this Executive Summary and in the volumes of the *Technical Design Report* is technically mature and ready for construction. The elements of the project have been carefully costed and reviewed by teams of experts. The scientific case for constructing the ILC is extraordinarily strong; the discovery at the LHC of a 125 GeV boson displaying many of the properties expected of the Higgs boson provides a compelling scientific target for the ILC. In addition to studies of this new Higgs boson candidate, operating the ILC at top threshold at 350 GeV provides crucial precision in the study of top quark properties, surpassing LHC precision. Above 500 GeV the Higgs self-coupling, the top Yukawa coupling and longitudinal W scattering can be investigated with very high accuracy. Finally, the ILC provides new physics discovery potential through a variety of channels, including dark-matter searches and searches for new interactions at higher mass scales through precision studies of pair-production of quarks, leptons, and W and Z bosons. Detector designs have been developed, simulated, prototyped and validated to demonstrate the required high level detector performance is achievable.

The decades spent to prove that the ILC can be built and optimally exploited have now reached a culmination in the production of this *Technical Design Report*. The next steps are to choose a suitable site, allowing necessary site-dependent design details to be determined, while establishing a world-wide consensus to construct the project and setting up an appropriate international organisation. One of the most exciting scientific projects ever conceived is poised to begin.

Contributing Institutes

Academia Sinica - 128 Sec. 2, Institute of Physics, Academia Rd., Nankang, Taipei 11529, Taiwan, R.O.C.
AGH University of Science and Technology, Akademia Gorniczo-Hutnicza im. Stanislawa Staszica w Krakowie, Al. Mickiewicza 30 PL-30-059 Cracow, Poland
Aichi Medical University, Nagakute, Aichi, 480-1195, Japan
Akita International University, Yuwa, Akita City, 010-1292, Japan
Albert-Ludwigs Universität Freiburg, Physikalisches Institut, Hermann-Herder Str. 3, D-79104 Freiburg, Germany
Ankara Üniversitesi Fen Fakültesi, Fizik Bölümü, Dögol Caddesi, 06100 Tandoğan Ankara, Turkey
Argonne National Laboratory (ANL), 9700 S. Cass Avenue, Argonne, IL 60439, USA
Baylor University, Department of Physics, 101 Bagby Avenue, Waco, TX 76706, USA
Beijing University, Department of Physics, Beijing, China 100871
Benares Hindu University, Benares, Varanasi 221005, India
Borough of Manhattan Community College, The City University of New York, Department of Science, 199 Chambers Street, New York, NY 10007, USA
Brandenburg University of Technology, Postfach 101344, D-03013 Cottbus, Germany
Brookhaven National Laboratory (BNL), P.O.Box 5000, Upton, NY 11973-5000, USA
Brown University, Department of Physics, Box 1843, Providence, RI 02912, USA
Budker Institute for Nuclear Physics (BINP), 630090 Novosibirsk, Russia
Calcutta University, Department of Physics, 92 A.P.C. Road, Kolkata 700009, India
California Institute of Technology, Physics, Mathematics and Astronomy (PMA), 1200 East California Blvd, Pasadena, CA 91125, USA
California State University, Los Angeles, Dept. of Physics and Astronomy, 5151 State University Dr., Los Angeles, CA 90032, USA
Carleton University, Department of Physics, 1125 Colonel By Drive, Ottawa, Ontario, Canada K1S 5B6
Carnegie Mellon University, Department of Physics, Wean Hall 7235, Pittsburgh, PA 15213, USA
CEA Saclay, IRFU, F-91191 Gif-sur-Yvette, France
CEA Saclay, Service de Physique Théorique, CEA/DSM/SPhT, F-91191 Gif-sur-Yvette Cedex, France
Center for High Energy Physics (CHEP) / Kyungpook National University, 1370 Sankyuk-dong, Buk-gu, Daegu 702-701, Republic of Korea
Center for High Energy Physics (TUHEP), Tsinghua University, Beijing, China 100084
Center For Quantum Spacetime (CQUeST), Sogang University, 35 Baekbeom-ro, Mapo-gu, Seoul 121-742, Republic of Korea
Centre de Physique des Particules de Marseille (CPPM), Aix-Marseille Université, CNRS/IN2P3, 163, Avenue de Luminy, Case 902, 13288 Marseille Cedex 09, France
Centre de Physique Theorique, CNRS - Luminy, Universiti d"Aix - Marseille II, Campus of Luminy, Case 907, 13288 Marseille Cedex 9, France
Centre Lasers Intenses et Applications (CELIA), Université Bordeaux 1 - CNRS - CEA, 351 Cours de la Libération, 33405 Talence Cedex, France
Centro Brasileiro de Pesquisas Físicas (CBPF), Rua Dr. Xavier Sigaud, n.150 22290-180, Urca - Rio de Janeiro, RJ, Brazil
Centro de Investigaciones Energéticas, Medioambientales y Tecnológicas, CIEMAT, Avenida Complutense 22, E-28040 Madrid, Spain
Centro Nacional de Microelectrónica (CNM), Instituto de Microelectrónica de Barcelona (IMB), Campus UAB, 08193 Cerdanyola del Vallès (Bellaterra), Barcelona, Spain
CERN, CH-1211 Genève 23, Switzerland
Charles University, Institute of Particle & Nuclear Physics, Faculty of Mathematics and Physics, V Holesovickach 2, CZ-18000 Prague 8, Czech Republic
Chiba University of Commerce, 1-3-1 Konodai, Ichikawa-shi, Chiba, 272-8512, Japan
Chonbuk National University, Division of Science Education, Jeonju 561-756, Republic of Korea
Chonbuk National University, Physics Department, Jeonju 561-756, Republic of Korea
Chubu University, 1200 Matsumoto-cho, Kasugai-shi, Aichi, 487-8501, Japan
Chung Yuan Christian University, Department of Physics, 200 Chung Pei Rd., Chung Li 32023 Taiwan, R.O.C
Cockcroft Institute, Daresbury, Warrington WA4 4AD, UK
College of William and Mary, Department of Physics, Williamsburg, VA, 23187, USA
Columbia University, Department of Physics, New York, NY 10027-6902, USA
Cornell University, Laboratory for Elementary-Particle Physics (LEPP), Ithaca, NY 14853, USA
Czech Technical University in Prague, Institute of Experimental and Applied Physics (IEAP), Horska 3a/22, 12800 Prague 2, Czech Republic
Czech Technical University, Faculty of Nuclear Science and Physical Engineering, Brehova 7, CZ-11519 Prague 1, Czech Republic
Departamento de Física Teórica, Facultad de Ciencias, Módulo 15 (antiguo C-XI) y Módulo 8, Universidad Autónoma de Madrid, Campus de Cantoblanco, 28049 Madrid, Spain
Deutsches Elektronen-Synchrotron DESY, A Research Centre of the Helmholtz Association, Notkestrasse 85, 22607 Hamburg, Germany (Hamburg site)
Deutsches Elektronen-Synchrotron DESY, A Research Centre of the Helmholtz Association, Platanenallee 6, 15738 Zeuthen, Germany (Zeuthen site)
Durham University, Department of Physics, Ogen Center for Fundamental Physics, South Rd., Durham DH1 3LE, UK
École Normale Supérieure de Lyon, 46 allée d'Italie, 69364 Lyon Cedex 07, France
Ege University, Department of Physics, Faculty of Science, 35100 Izmir, Turkey
Enrico Fermi Institute, University of Chicago, 5640 S. Ellis Avenue, RI-183, Chicago, IL 60637, USA
ETH Zürich, Institute for Particle Physics (IPP), Schafmattstrasse 20, CH-8093 Zürich, Switzerland
ETH Zürich, Institute for Theoretical Physics (ITP), Wolfgang-Pauli-Str. 27, Zürich, Switzerland
European Spallation Source ESS AB, Box 176, 221 00 Lund, Sweden
Ewha Womans University, 11-1 Daehyun-Dong, Seodaemun-Gu, Seoul, 120-750, Republic of Korea
Excellence Cluster Universe, Technische Universität München, Boltzmannstr. 2, 85748 Garching, Germany
Fermi National Accelerator Laboratory (FNAL), P.O.Box 500, Batavia, IL 60510-0500, USA
Florida State University, Department of Physics, 77 Chieftan Way, Tallahassee, FL 32306-4350, USA

Fujita Gakuen Health University, Department of Physics, Toyoake, Aichi 470-1192, Japan
Fukui University of Technology, 3-6-1 Gakuen, Fukui-shi, Fukui 910-8505, Japan
Fukui University, Department of Physics, 3-9-1 Bunkyo, Fukui-shi, Fukui 910-8507, Japan
Gangneung-Wonju National University, 210-702 Gangneung Daehangno, Gangneung City, Gangwon Province, Republic of Korea
Georg-August-Universität Göttingen, II. Physikalisches Institut, Friedrich-Hund-Platz 1, 37077 Göttingen, Germany
Global Design Effort
Hanyang University, Department of Physics, Seoul 133-791, Republic of Korea
Harish-Chandra Research Institute, Chhatnag Road, Jhusi, Allahabad 211019, India
Helmholtz-Zentrum Berlin für Materialien und Energie (HZB), Wilhelm-Conrad-Röntgen Campus, BESSY II, Albert-Einstein-Str. 15, 12489 Berlin, Germany
Helsinki Institute of Physics (HIP), P.O. Box 64, FIN-00014 University of Helsinki, Finland
Henan Normal University, College of Physics and Information Engineering, Xinxiang, China 453007
High Energy Accelerator Research Organization, KEK, 1-1 Oho, Tsukuba, Ibaraki 305-0801, Japan
Hiroshima University, Department of Physics, 1-3-1 Kagamiyama, Higashi-Hiroshima, Hiroshima 739-8526, Japan
Hiroshima University, Graduate School of Advanced Sciences of Matter, 1-3-1 Kagamiyama, Higashi-Hiroshima, Hiroshima 739-8530, Japan
Hokkai-Gakuen University, 4-1-40 Asahimachi, Toyohira-ku, Sapporo 062-8605, Japan
Hokkaido University, Department of Physics, Faculty of Science, Kita, Kita-ku, Sapporo-shi, Hokkaido 060-0810, Japan
Humboldt Universität zu Berlin, Fachbereich Physik, Institut für Elementarteilchenphysik, Newtonstr. 15, D-12489 Berlin, Germany
Hyogo University of Teacher Education, 942-1 Shimokume, Kato-city, Hyogo 673-1494, Japan
Ibaraki National College of Technology, 866 Nakane, Hitachinaka, Ibaraki 312-8508, Japan
Ibaraki University, College of Technology, Department of Physics, Nakanarusawa 4-12-1, Hitachi, Ibaraki 316-8511, Japan
Imperial College, Blackett Laboratory, Department of Physics, Prince Consort Road, London, SW7 2BW, UK
Indian Association for the Cultivation of Science, Department of Theoretical Physics and Centre for Theoretical Sciences, Kolkata 700032, India
Indian Institute of Science Education and Research (IISER) Kolkata, Department of Physical Sciences, Mohanpur Campus, PO Krishi Viswavidyalaya, Mohanpur 741252, Nadia, West Bengal, India
Indian Institute of Science, Centre for High Energy Physics, Bangalore 560012, Karnataka, India
Indian Institute of Technology Indore, IET Campus, M-Block, Institute of Engineering and Technology (IET), Devi Ahilya Vishwavidyalaya Campus, Khandwa Road, Indore - 452017, Madhya Pradesh, India
Indian Institute of Technology, Bombay, Powai, Mumbai 400076, India
Indian Institute of Technology, Guwahati, Guwahati, Assam 781039, India
Indiana University, Department of Physics, Swain Hall West 117, 727 E. 3rd St., Bloomington, IN 47405-7105, USA
Institucio Catalana de Recerca i Estudis, ICREA, Passeig Lluis Companys, 23, Barcelona 08010, Spain
Institut de Physique Nucléaire de Lyon (IPNL), Domaine scientifique de la Doua, Bâtiment Paul Dirac 4, rue Enrico Fermi, 69622 Villeurbanne, Cedex, France
Institut für Experimentelle Kernphysik, KIT,Universität Karlsruhe (TH), Wolfgang-Gaede-Str. 1, Postfach 6980, 76128 Karlsruhe, Germany
Institut für Theoretische Physik (ITP), Karlsruher Institut für Technologie (KIT), Fakultät für Physik, Postfach 6980, 76049 Karlsruhe, Germany
Institut für Theoretische Teilchenphysik, Campus Süd, Karlsruher Institut für Technologie (KIT), 76128 Karlsruhe, Germany
Institut National de Physique Nucleaire et de Physique des Particules, 3, Rue Michel- Ange, 75794 Paris Cedex 16, France
Institut Pluridisciplinaire Hubert Curien, 23 Rue du Loess - BP28, 67037 Strasbourg Cedex 2, France
Institute for Chemical Research, Kyoto University, Gokasho, Uji, Kyoto 611-0011, Japan
Institute for Cosmic Ray Research, University of Tokyo, 5-1-5 Kashiwa-no-Ha, Kashiwa, Chiba 277-8582, Japan
Institute for Mathematics, Astrophysics and Particle Physics (IMAPP), P.O. Box 9010, 6500 GL Nijmegen, Netherlands
Institute for Nuclear Research, Russian Academy of Sciences (INR RAS), 60-th October Anniversary Prospect 7a, 117312, Moscow, Russia
Institute for Scintillation Materials (ISMA), 60 Lenina Ave, 61001, Kharkiv, Ukraine
Institute for studies in fundamental sciences (IPM), Niavaran Square, P.O. Box 19395-5746, Tehran, Iran
Institute of High Energy Physics - IHEP, Chinese Academy of Sciences, P.O. Box 918, Beijing, China 100049
Institute of Mathematical Sciences, Taramani, C.I.T. Campus, Chennai 600113, India
Institute of Particle Physics, Canada
Institute of Physics, ASCR, Academy of Science of the Czech Republic, Division of Elementary Particle Physics, Na Slovance 2, CZ-18221 Prague 8, Czech Republic
Institute of Physics, Vietnam Academy of Science and Technology (VAST), 10 Dao-Tan, Ba-Dinh, Hanoi 10000, Vietnam
Institute of Theoretical and Experimetal Physics, B. Cheremushkinskawa, 25, RU-117259, Moscow, Russia
Instituto de Fisica Corpuscular (IFIC), Centro Mixto CSIC-UVEG, Edificio Investigacion Paterna, Apartado 22085, 46071 Valencia, Spain
Instituto de Física da Universidade Federal do Rio Grande do Sul (UFRGS), Av. Bento Gonçalves 9500, Caixa Postal 15051, CEP 91501-970, Porto Alegre, RS, Brazil
Instituto de Fisica de Cantabria, (IFCA, CSIC-UC), Facultad de Ciencias, Avda. Los Castros s/n, 39005 Santander, Spain
Instituto de Física Teórica UAM/CSIC, C/ Nicolás Cabrera 13-15, Universidad Autónoma de Madrid, Cantoblanco, 28049 Madrid, Spain
Instituto Galego de Fisica de Altas Enerxias (IGFAE,USC) Facultad de Fisica, Campus Sur E-15782 Santiago de Compostela, Spain
Instituto Tecnológico de Aragón (ITA), C/ María de Luna 7-8, 50018 Zaragoza, Spain
Instituto Universitario de Física Fundamental y Matemáticas de la Universidad de Salamanca (IUFFyM), Casas del Parque, 37008 Salamanca, Spain
Inter-University Accelerator Centre, Aruna Asaf Ali Marg, Post Box 10502, New Delhi 110067, India
International Center for Elementary Particle Physics, University of Tokyo, Hongo 7-3-1, Bunkyo District, Tokyo 113-0033, Japan
International Institute of Physics, Federal University of Rio Grande do Norte, Av. Odilon Gomes de Lima, 1722 - Capim Macio - 59078-400 - Natal-RN, Brazil
Iowa State University, Department of Physics, High Energy Physics Group, Ames, IA 50011, USA
Istituto Nazionale di Fisica Nucleare (INFN), Laboratorio LASA, Via Fratelli Cervi 201, 20090 Segrate, Italy
Istituto Nazionale di Fisica Nucleare (INFN), Sezione di Firenze, Via G. Sansone 1, I-50019 Sesto Fiorentino (Firenze), Italy
Istituto Nazionale di Fisica Nucleare (INFN), Sezione di Milano Bicocca, Piazza della Scienza 3, I-20126 Milano, Italy
Istituto Nazionale di Fisica Nucleare (INFN), Sezione di Milano, Via Celoria 16, I-20133 Milano, Italy
Istituto Nazionale di Fisica Nucleare (INFN), Sezione di Napoli, Complesso Università di Monte Sant'Angelo,via, I-80126 Napoli, Italy
Istituto Nazionale di Fisica Nucleare (INFN), Sezione di Pavia, Via Bassi 6, I-27100 Pavia, Italy
Istituto Nazionale di Fisica Nucleare (INFN), Sezione di Perugia, Via A. Pascoli, 06123 Perugia, Italy
Istituto Nazionale di Fisica Nucleare (INFN), Sezione di Pisa, Edificio C - Polo Fibonacci Largo B. Pontecorvo, 3, I-56127 Pisa, Italy
Istituto Nazionale di Fisica Nucleare (INFN), Sezione di Roma, c/o Dipartimento di Fisica - Università degli Studi di Roma "La Sapienza", P.le Aldo Moro 2, I-00185 Roma, Italy
Istituto Nazionale di Fisica Nucleare (INFN), Sezione di Torino, c/o Università di Torino, facoltà di Fisica, via P Giuria 1, 10125 Torino, Italy
Istituto Nazionale di Fisica Nucleare (INFN), Sezione di Trieste, Padriciano 99, I-34012 Trieste (Padriciano), Italy
ITER Organization, Route de Vinon-sur-Verdon, 13115 St. Paul-lez-Durance, France
Iwate University, 4-3-5 Ueda, Morioka, Iwate, 020-8551, Japan

Jagiellonian University, Institute of Physics, Ul. Reymonta 4, PL-30-059 Cracow, Poland
Jamia Millia Islamia, Department of Physics, Jamia Nagar, New Delhi 110025, India
Japan Aerospace Exploration Agency, Sagamihara Campus, 3-1-1 Yoshinodai, Sagamihara, Kanagawa 220-8510 , Japan
Japan Atomic Energy Agency, 4-49 Muramatsu, Tokai-mura, Naka-gun, Ibaraki 319-1184, Japan
Japan Synchrotron Radiation Research Institute (JASRI), 1-1-1, Kouto, Sayo-cho, Sayo-gun, Hyogo 679-5198, Japan
Johannes Gutenberg Universität Mainz, Institut für Physik, 55099 Mainz, Germany
John Adams Institute for Accelerator Science at Royal Holloway University of London, Egham Hill, Egham, Surrey TW20 0EX, UK
John Adams Institute for Accelerator Science at University of Oxford, Denys Wilkinson Building, Keble Road, Oxford OX1 3RH, UK
Johns Hopkins University - Henry A. Rowland Department of Physics & Astronomy 3701 San Martin Drive, Baltimore, Maryland (MD) 21218, USA
Joint Institute for Nuclear Research (JINR), Joliot-Curie 6, 141980, Dubna, Moscow Region, Russia
Joint Institute for Power and Nuclear Research "Sosny" at National Academy of Sciences of Belarus, 99 Academician A.K.Krasin Str., Minsk BY-220109, Belarus
Jozef Stefan Institute, Jamova cesta 39, 1000 Ljubljana, Slovenia
Julius-Maximilians-Universität Würzburg, Fakultät für Physik und Astronomie, Am Hubland, 97074 Würzburg, Germany
Juntendo University, School of Medicine, Dept. of Physics, Hiraga-gakuendai 1-1, Inzai-shi, Chiba 270-1695, Japan
Justus-Liebig-Universität Gießen, II. Physikalisches Institut, Heinrich-Buff-Ring 16, 35392 Gießen, Germany
Kanazawa University, Institute for Theoretical Physics (KITP), School of Mathematics and Physics, College of Science and Engineering, Kakuma-machi, Kanazawa city, Ishikawa 920-1192, Japan
Kansas State University, Department of Physics, 116 Cardwell Hall, Manhattan, KS 66506, USA
Kavli Institute for the Physics and Mathematics of the Universe (Kavli IPMU), University of Tokyo, 5-1-5 Kashiwanoha, Kashiwa, 277-8583, Japan
King Saud University (KSU), Dept. of Physics, P.O. Box 2454, Riyadh 11451, Saudi Arabia
King's College London - Department of physics, Strand, London WC2R 2LS, London, UK
Kinki University, Department of Physics, 3-4-1 Kowakae, Higashi-Osaka, Osaka 577-8502, Japan
Kobe University, Department of Physics, 1-1 Rokkodai-cho, Nada-ku, Kobe, Hyogo 657-8501, Japan
Kogakuin University, Department of Physics, Shinjuku Campus, 1-24-2 Nishi-Shinjuku, Shinjuku-ku, Tokyo 163-8677, Japan
Konkuk University, 93-1 Mojin-dong, Kwanglin-gu, Seoul 143-701, Republic of Korea
Korea Advanced Institute of Science & Technology, Department of Physics, 373-1 Kusong-dong, Yusong-gu, Taejon 305-701, Republic of Korea
Korea Institute for Advanced Study (KIAS), School of Physics, 207-43 Cheongryangri-dong, Dongdaemun-gu, Seoul 130-012, Republic of Korea
Kyoto University, Department of Physics, Kitashirakawa-Oiwakecho, Sakyo-ku, Kyoto 606-8502, Japan
Kyoto University, Yukawa Institute for Theoretical Physics, Kitashirakawa-Oiwakecho, Sakyo-Ku, Kyoto 606-8502, Japan
Kyushu University, Department of Physics, 6-10-1 Hakozaki, Higashi-ku, Fukuoka 812-8581, Japan
L.P.T.A., UMR 5207 CNRS-UM2, Université Montpellier II, Case Courrier 070, Bât. 13, place Eugène Bataillon, 34095 Montpellier Cedex 5, France
Laboratoire Charles Coulomb UMR 5221 CNRS-UM2, Université Montpellier 2, Place Eugène Bataillon - CC069, 34095 Montpellier Cedex 5, France
Laboratoire d'Annecy-le-Vieux de Physique des Particules (LAPP) , Université de Savoie, CNRS/IN2P3, 9 Chemin de Bellevue, BP 110, F-74941 Annecy-Le-Vieux Cedex, France
Laboratoire d'Annecy-le-Vieux de Physique Theorique (LAPTH), Chemin de Bellevue, BP 110, F-74941 Annecy-le-Vieux Cedex, France
Laboratoire d'AstroParticules et Cosmologie (APC), Université Paris Diderot-Paris 7 - CNRS/IN2P3, Bâtiment Condorcet, Case 7020, 75205 Paris Cedex 13, France
Laboratoire de l'Accélérateur Linéaire (LAL), Université Paris-Sud 11, Bâtiment 200, 91898 Orsay, France
Laboratoire de Physique Corpusculaire de Clermont-Ferrand (LPC), Université Blaise Pascal, I.N.2.P.3./C.N.R.S., 24 avenue des Landais, 63177 Aubière Cedex, France
Laboratoire de Physique Nucléaire et des Hautes Energies (LPNHE), UPMC, UPD, IN2P3/CNRS, 4 Place Jussieu, 75005, Paris Cedex 05, France
Laboratoire de Physique Subatomique et de Cosmologie (LPSC), Université Joseph Fourier (Grenoble 1), CNRS/IN2P3, Institut Polytechnique de Grenoble, 53 rue des Martyrs, F-38026 Grenoble Cedex, France
Laboratoire de Physique Theorique, Université de Paris-Sud XI, Batiment 210, F-91405 Orsay Cedex, France
Laboratoire Leprince-Ringuet (LLR), École polytechnique – CNRS/IN2P3, Route de Saclay, F-91128 Palaiseau Cedex, France
Laboratoire Univers et Particules de Montpellier (LUPM) - UMR5299, Université de Montpellier II, Place Eugène Bataillon - Case courrier 72, 34095 Montpellier Cedex 05, France
Laboratori Nazionali di Frascati, via E. Fermi, 40, C.P. 13, I-00044 Frascati, Italy
Laboratório de Instrumentação e Física Experimental de Partículas (LIP LISBOA), Av. Elias Garcia 14 - 1°, 1000-149 Lisbon, Portugal
Lancaster University, Physics Department, Lancaster LA1 4YB, UK
Lawrence Berkeley National Laboratory (LBNL), 1 Cyclotron Rd, Berkeley, CA 94720, USA
Lawrence Livermore National Laboratory (LLNL), Livermore, CA 94551, USA
Lebedev Physical Institute, Leninsky Prospect 53, RU-117924 Moscow, Russia
Lomonosov Moscow State University, Skobeltsyn Institute of Nuclear Physics (MSU SINP), 1(2), Leninskie gory, GSP-1, Moscow 119991, Russia
Louisiana Tech University, Department of Physics, Ruston, LA 71272, USA
Ludwig-Maximilians-Universität München, Fakultät für Physik, Am Coulombwall 1, D - 85748 Garching, Germany
Lunds Universitet, Fysiska Institutionen, Avdelningen för Experimentell Högenergifysik, Box 118, 221 00 Lund, Sweden
L'Université Hassan II, Aïn Chock, "Réseau Universitaire de Physique des Hautes Energies" (RUPHE), Département de Physique, Faculté des Sciences Aïn Chock, B.P 5366 Maarif, Casablanca 20100, Morocco
Massachusetts Institute of Technology (MIT), Laboratory for Nuclear Science, 77 Massachusetts Avenue, Cambridge, MA 02139, USA
Max-Planck-Institut für Physik (Werner-Heisenberg-Institut), Föhringer Ring 6, 80805 München, Germany
McGill University, Department of Physics, Ernest Rutherford Physics Bldg., 3600 University Street, Montreal, Quebec, H3A 2T8 Canada
McMaster University, Department of Physics & Astronomy, 1280 Main Street West, Hamilton, ON, L8S 4M1, Canada
Meiji Gakuin University, Department of Physics, 2-37 Shirokanedai 1-chome, Minato-ku, Tokyo 244-8539, Japan
Michigan State University, Department of Chemical Engineering & Materials Science, 2527 Engineering Building East Lansing, MI 48824-1226, USA
Michigan State University, Department of Physics and Astronomy, East Lansing, MI 48824, USA
Middle East Technical University, Department of Physics, TR-06531 Ankara, Turkey
Miyagi Gakuin Women's University, Faculty of Liberal Arts, 9-1-1 Sakuragaoka, Aoba District, Sendai, Miyagi 981-8557, Japan
MSU-Iligan Institute of Technology, Department of Physics, Andres Bonifacio Avenue, 9200 Iligan City, Phillipines
Nagasaki Institute of Applied Science, 536 Abamachi, Nagasaki-Shi, Nagasaki 851-0193, Japan
Nagoya University, Department of Materials Science and Engineering, Furo-cho, Chikusa-ku, Nagoya, 464-8603, Japan
Nagoya University, Department of Physics, School of Science, Furo-cho, Chikusa-ku, Nagoya, Aichi 464-8602, Japan
Nagoya University, Kobayashi-Maskawa Institute for the Origin of Particles and the Universe (KMI), Furo-cho, Chikusa-ku, Nagoya Aichi 464-8602, Japan
Nanjing University, Department of Physics, Nanjing, China 210093
Nara Women's University, High Energy Physics Group, Kitauoya-Nishimachi, Nara 630-8506, Japan

National Central University, High Energy Group, Department of Physics, Chung-li, Taiwan 32001, R.O.C
National Centre of Nuclear Research (NCBJ), ul. Andrzeja Soltana 7, 05-400 Otwock-Swierk, Poland
National Cheng Kung University, Physics Department, 1 Ta-Hsueh Road, Tainan, Taiwan 70101, R.O.C
National Chiao-Tung University, Institute of Physics, 1001 Ta Hsueh Rd, Hsinchu, Taiwan 300, R.O.C.
National Institute of Chemical Physics and Biophysics (NICPB), Ravala pst 10, 10143 Tallinn, Estonia
National Institute of Physics and Nuclear Engineering "Horia Hulubei" (IFIN-HH), Str. Reactorului no.30, P.O. Box MG-6, R-76900 Bucharest - Magurele, Romania
National Research Centre "Kurchatov Institute", 1 Akademika Kurchatova pl., Moscow, 123182, Russia
National Science Center - Kharkov Institute of Physics and Technology (NSC KIPT), Akademicheskaya St. 1, Kharkov, 61108, Ukraine
National Scientific & Educational Centre of Particle & High Energy Physics (NCPHEP), Belarusian State University, M.Bogdanovich street 153, 220040 Minsk, Belarus
National Taiwan University, Physics Department, Taipei, Taiwan 106, R.O.C
Niels Bohr Institute (NBI), University of Copenhagen, Blegdamsvej 17, DK-2100 Copenhagen, Denmark
Niigata University, Department of Physics, Ikarashi, Niigata 950-218, Japan
Nikhef, National Institute for Subatomic Physics, P.O. Box 41882, 1009 DB Amsterdam, Netherlands
Nippon Dental University School of Life Dentistry at Niigata, 1-8 Hamaura-cho, Chuo-ku, Niigata 951-1500, Japan
North Carolina A&T State University, 1601 E. Market Street, Greensboro, NC 27411, USA
Northeastern University, Physics Department, 360 Huntington Ave, 111 Dana Research Center, Boston, MA 02115, USA
Northern Illinois University, Department of Physics, DeKalb, Illinois 60115-2825, USA
Northwestern University, Department of Physics and Astronomy, 2145 Sheridan Road., Evanston, IL 60208, USA
Novosibirsk State University (NGU), Department of Physics, Pirogov st. 2, 630090 Novosibirsk, Russia
Ochanomizu University, Department of Physics, Faculty of Science, 1-1 Otsuka 2, Bunkyo-ku, Tokyo 112-8610, Japan
Orissa University of Agriculture & Technology, Bhubaneswar 751003, Orissa, India
Osaka City University, Department of Physics, Faculty of Science, 3-3-138 Sugimoto, Sumiyoshi-ku, Osaka 558-8585, Japan
Osaka University, Department of Physics, 1-1 Machikaneyama, Toyonaka, Osaka 560-0043, Japan
Österreichische Akademie der Wissenschaften, Institut für Hochenergiephysik, Nikolsdorfergasse 18, A-1050 Vienna, Austria
Pacific Northwest National Laboratory, (PNNL), PO Box 999, Richland, WA 99352, USA
Panjab University, Chandigarh 160014, India
Pavel Sukhoi Gomel State Technical University, ICTP Affiliated Centre & Laboratory for Physical Studies, October Avenue, 48, 246746, Gomel, Belarus
Perimeter Institute for Theoretical Physics, 31 Caroline Street North, Waterloo, Ontario N2L 2Y5, Canada
Physical Research Laboratory, Navrangpura, Ahmedabad 380 009, Gujarat, India
Pohang Accelerator Laboratory (PAL), San-31 Hyoja-dong, Nam-gu, Pohang, Gyeongbuk 790-784, Republic of Korea
Pontificia Universidad Católica de Chile, Avda. Libertador Bernardo OHiggins 340, Santiago, Chile
Princeton University, Department of Physics, P.O. Box 708, Princeton, NJ 08542-0708, USA
Purdue University, Department of Physics, West Lafayette, IN 47907, USA
Queen Mary, University of London, Mile End Road, London, E1 4NS, United Kingdom
Rheinisch-Westfälische Technische Hochschule (RWTH), Physikalisches Institut, Physikzentrum, Otto-Blumenthal-Straße, 52056 Aachen
RIKEN, 2-1 Hirosawa, Wako, Saitama 351-0198, Japan
Royal Holloway, University of London (RHUL), Department of Physics, Egham, Surrey TW20 0EX, UK
Russian Academy of Science, Keldysh Institute of Applied Mathematics, Muiskaya pl. 4, 125047 Moscow, Russia
Rutgers, The State University of New Jersey, Department of Physics & Astronomy, 136 Frelinghuysen Rd, Piscataway, NJ 08854, USA
Saga University, Department of Physics, 1 Honjo-machi, Saga-shi, Saga 840-8502, Japan
Saha Institute of Nuclear Physics, 1/AF Bidhan Nagar, Kolkata 700064, India
Salalah College of Technology (SCOT), Engineering Department, Post Box No. 608, Postal Code 211, Salalah, Sultanate of Oman
Saudi Center for Theoretical Physics, King Fahd University of Petroleum and Minerals (KFUPM), Dhahran 31261, Saudi Arabia
Seikei University, Faculty of Science and Technology, 3-3-1 Kichijoji-Kitamachi, Musashino-shi, Tokyo 180-8633, Japan
Seoul National University, San 56-1, Shinrim-dong, Kwanak-gu, Seoul 151-742, Republic of Korea
Setsunan University, Institute for Fundamental Sciences, 17-8 Ikeda Nakamachi, Neyagawa, Osaka, 572-8508, Japan
Shanghai Jiao Tong University, Department of Physics, 800 Dongchuan Road, Shanghai, China 200240
Shinshu University, 3-1-1, Asahi, Matsumoto, Nagano 390-8621, Japan
Shiv Nadar University, Village Chithera, Tehsil Dadri, District Gautam Budh Nagar, 203207 Uttar Pradesh, India
Shizuoka University, Department of Physics, 836 Ohya, Suruga-ku, Shizuoka 422-8529, Japan
SLAC National Accelerator Laboratory, 2575 Sand Hill Road, Menlo Park, CA 94025, USA
Society for Applied Microwave Electronics Engineering and Research (SAMEER), I.I.T. Campus, Powai, Post Box 8448, Mumbai 400076, India
Sokendai, The Graduate University for Advanced Studies, Shonan Village, Hayama, Kanagawa 240-0193, Japan
Spallation Neutron Source (SNS), Oak Ridge National Laboratory (ORNL), P.O. Box 2008 MS-6477, Oak Ridge, TN 37831-6477, USA
State University of New York at Binghamton, Department of Physics, PO Box 6016, Binghamton, NY 13902, USA
State University of New York at Buffalo, Department of Physics & Astronomy, 239 Franczak Hall, Buffalo, NY 14260, USA
State University of New York at Stony Brook, Department of Physics and Astronomy, Stony Brook, NY 11794-3800, USA
STFC Daresbury Laboratory, Daresbury, Warrington, Cheshire WA4 4AD, UK
STFC Rutherford Appleton Laboratory, Chilton, Didcot, Oxon OX11 0QX, UK
Sungkyunkwan University (SKKU), Natural Science Campus 300, Physics Research Division, Chunchun-dong, Jangan-gu, Suwon, Kyunggi-do 440-746, Republic of Korea
Swiss Light Source (SLS), Paul Scherrer Institut (PSI), PSI West, CH-5232 Villigen PSI, Switzerland
Tata Institute of Fundamental Research, School of Natural Sciences, Homi Bhabha Rd., Mumbai 400005, India
Technical University of Lodz, Department of Microelectronics and Computer Science, al. Politechniki 11, 90-924 Lodz, Poland
Technische Universität Dresden, Institut für Kern- und Teilchenphysik, D-01069 Dresden, Germany
Tel-Aviv University, School of Physics and Astronomy, Ramat Aviv, Tel Aviv 69978, Israel
Texas A&M University, Physics Department, College Station, 77843-4242 TX, USA
The Henryk Niewodniczanski Institute of Nuclear Physics, Polish Academy of Sciences (IFJ PAN), ul. Radzikowskiego 152, PL-31342 Cracow, Poland
Thomas Jefferson National Accelerator Facility (TJNAF), 12000 Jefferson Avenue, Newport News, VA 23606, USA
Tohoku Gakuin University, Department of Business Administration, 1-3-1 Tsuchitoi, Aoba-ku Sendai, Miyagi 980-8511, Japan
Tohoku Gakuin University, Faculty of Technology, 1-13-1 Chuo, Tagajo, Miyagi 985-8537, Japan
Tohoku University, Department of Physics, Aoba District, Sendai, Miyagi 980-8578, Japan
Tohoku University, Research Center for Electron Photon Science, Taihaku District, Sendai, Miyagi 982-0826, Japan
Tohoku University, Research Center for Neutrino Science, Aoba District, Sendai, Miyagi 980-8578, Japan
Tokyo Institute of Technology, Department of Physics, 2-12-1 O-Okayama, Meguro, Tokyo 152-8551, Japan
Tokyo Metropolitan University, Faculty of Science and Engineering, Department of Physics, 1-1 Minami-Osawa, Hachioji-shi, Tokyo 192-0397, Japan
Tokyo University of Agriculture Technology, Department of Applied Physics, Naka-machi, Koganei, Tokyo 183-8488, Japan
Toyama Prefectural University, Department of Mathematical Physics, 5180 Kurokawa Imizu-shi, Toyama, 939-0398, Japan
TRIUMF, 4004 Wesbrook Mall, Vancouver, BC V6T 2A3, Canada

Universidad Autónoma de San Luis Potosí, Alvaro Obregon 64, Col. Centro, San Luis Potosí, S.L.P. 78000, México
Universidad de Granada, Departamento de Física Teórica y del Cosmos, Campus de Fuentenueva, E-18071 Granada, Spain
Universidad de los Andes, Faculty of Science, Department of Physics, Carrera 1 18A-10, Bloque Ip. Bogotá, Colombia
Universidad de Oviedo, Departamento de Física, Campus de Llamaquique. C/ Calvo Sotelo, s/n 33005 Oviedo, Spain
Universidad de Salamanca, Departamento de Física Fundamental, Plaza de la Merced, s/n., 37008 Salamanca, Spain
Universidad de Sevilla, Escuela Técnica Superior de Ingeniería, Departamento Ingeniería Electrónica, Camino de los Descubrimientos s/n, 41092 Sevilla, Spain
Universidad de Zaragoza - Departamento de Física Teórica, Pedro Cerbuna 12, E-50009 Zaragoza, Spain
Universidad Nacional Autónoma de México, Instituto de Física, Circuito de la Investigación Cientifica s/n, Ciudad Universitaria, CP 04510 México D.F., Mexico
Universidad Nacional de La Plata, Departamento de Física, Facultad de Ciencias Exactas, C.C. N 67, 1900 La Plata, Argentina
Universidade do Estado do Rio de Janeiro (UERJ), Rio de Janeiro, RJ - Brasil 20550-900, Brazil
Universidade Federal de Pelotas, Instituto de Física e Matemática, Campus Universitário, Caixa Postal 354, 96010-900 Pelotas, RS, Brazil
Universidade Federal do Rio de Janeiro (UFRJ), Instituto de Física, Av. Athos da Silveira Ramos 149, Centro de Tecnologia - Bloco A, Cidade Universitária, Ilha do Fundão, Rio de Janeiro, RJ, Brazil
Universitá degli Studi di Napoli "Federico II", Dipartimento di Fisica, Via Cintia, 80126 Napoli, Italy
Universitat Autònoma de Barcelona, Departament de Física, Edifici C, 08193 Bellaterra, Barcelona, Spain
Universitat Autònoma de Barcelona, Institut de Fisica d'Altes Energies (IFAE), Campus UAB, Edifici Cn, E-08193 Bellaterra, Barcelona, Spain
Universität Bonn, Physikalisches Institut, Nußallee 12, 53115 Bonn, Germany
Universität Heidelberg, Institut für Theoretische Physik, Philosophenweg 16, 69120 Heidelberg, Germany
Universität Heidelberg, Kirchhoff-Institut für Physik, Im Neuenheimer Feld 227, 69120 Heidelberg, Germany
Universitat Politècnica de Catalunya, Institut de Tècniques Energètiques, Campus Diagonal Sud, Edifici PC (Pavelló C). Av. Diagonal, 647 08028 Barcelona, Spain
Universitat Ramon Llull, La Salle, C/ Quatre Camins 2, 08022 Barcelona, Spain
Universität Rostock, 18051 Rostock, Germany
Universität Siegen, Naturwissenschaftlich-Technische Fakultät, Department Physik, Emmy Noether Campus, Walter-Flex-Str.3, 57068 Siegen, Germany
Universität Wien - Theoretische Physik Boltzmanngasse 5, A-1090 Vienna, Austria
Université catholique de Louvain, Centre for Cosmology, Particle Physics and Phenomenology (CP3), Institute of Mathematics and Physics, 2 Chemin du Cyclotron, 1348 Louvain-la-Neuve, Belgium
Université de Montréal, Département de Physique, Groupe de Physique des Particules, C.P. 6128, Succ. Centre-ville, Montréal, Qc H3C 3J7, Canada
Université de Strasbourg, UFR de Sciences Physiques, 3-5 Rue de l'Université, F-67084 Strasbourg Cedex, France
Université Libre de Bruxelles, Boulevard du Triomphe, 1050 Bruxelles, Belgium
Universittà di Catania, Dipartimento di Fisica e Astronomia, Via Santa Sofia 64, 95123 Catania, Italy
University College London (UCL), High Energy Physics Group, Physics and Astronomy Department, Gower Street, London WC1E 6BT, UK
University College, National University of Ireland (Dublin), Department of Experimental Physics, Science Buildings, Belfield, Dublin 4, Ireland
University de Barcelona, Facultat de Física, Av. Diagonal, 647, Barcelona 08028, Spain
University of Alberta - Faculty of Science, Department of Physics, 4-181 CCIS, Edmonton AB T6G 2E1, Canada
University of Arizona, Department of Physics, 1118 E. Fourth Street, PO Box 210081, Tucson, AZ 85721, USA
University of Bergen, Institute of Physics, Allegaten 55, N-5007 Bergen, Norway
University of Birmingham, School of Physics and Astronomy, Particle Physics Group, Edgbaston, Birmingham B15 2TT, UK
University of Bristol, H. H. Wills Physics Lab, Tyndall Ave., Bristol BS8 1TL, UK
University of British Columbia, Department of Physics and Astronomy, 6224 Agricultural Rd., Vancouver, BC V6T 1Z1, Canada
University of California (UCLA), Los Angleles, CA 90095, US
University of California Berkeley, Department of Physics, 366 Le Conte Hall, #7300, Berkeley, CA 94720, USA
University of California Davis, Department of Physics, One Shields Avenue, Davis, CA 95616-8677, USA
University of California Irvine, Department of Physics and Astronomy, High Energy Group, 4129 Frederick Reines Hall, Irvine, CA 92697-4575 USA
University of California Santa Cruz, Institute for Particle Physics, 1156 High Street, Santa Cruz, CA 95064, USA
University of Cambridge, Cavendish Laboratory, J J Thomson Avenue, Cambridge CB3 0HE, UK
University of Colorado at Boulder, Department of Physics, 390 UCB, University of Colorado, Boulder, CO 80309-0390, USA
University of Cyprus, Department of Physics, P.O.Box 20537, 1678 Nicosia, Cyprus
University of Delhi, Department of Physics and Astrophysics, Delhi 110007, India
University of Delhi, S.G.T.B. Khalsa College, Delhi 110007, India
University of Dundee, Department of Physics, Nethergate, Dundee, DD1 4HN, Scotland, UK
University of Edinburgh, School of Physics, James Clerk Maxwell Building, The King's Buildings, Mayfield Road, Edinburgh EH9 3JZ, UK
University of Florida, Department of Physics, Gainesville, FL 32611, USA
University of Ghent, Department of Subatomic and Radiation Physics, Proeftuinstraat 86, 9000 Gent, Belgium
University of Glasgow, SUPA, School of Physics & Astronomy, University Avenue, Glasgow G12 8QQ, Scotland, UK
University of Hamburg, Physics Department, Luruper Chaussee 149, 22761 Hamburg, Germany
University of Hawaii, Department of Physics and Astronomy, HEP, 2505 Correa Rd., WAT 232, Honolulu, HI 96822-2219, USA
University of Helsinki, Department of Physical Sciences, P.O. Box 64 (Vaino Auerin katu 11), FIN-00014, Helsinki, Finland
University of Illinois at Chicago, Department Of Physics, 845 W Taylor St., Chicago IL 60607, USA
University of Iowa, Department of Physics and Astronomy, 203 Van Allen Hall, Iowa City, IA 52242-1479, USA
University of Kansas, Department of Physics and Astronomy, Malott Hall, 1251 Wescoe Hall Drive, Room 1082, Lawrence, KS 66045-7582, USA
University of Liverpool, Department of Physics, Oliver Lodge Lab, Oxford St., Liverpool L69 7ZE, UK
University of Liverpool, Division of Theoretical Physics, Department of Mathematical Sciences, Chadwick Building, Liverpool L69 3BX, UK
University of Ljubljana, Faculty of Mathematics and Physics, Jadranska ulica 19, 1000 Ljubljana, Slovenia
University of Lodz, Faculty of Physics and Applied Informatics, Pomorska 149/153, PL-90-236 Lodz, Poland
University of Malaya, Faculty of Science, Department of Physics, 50603 Kuala Lumpur, Malaysia
University of Manchester, School of Physics and Astronomy, Schuster Lab, Manchester M13 9PL, UK
University of Maribor, Faculty of Chemistry and Chemical Engineering (FKKT), Smetanova ulica 17, 2000 Maribor, Slovenia
University of Maryland, Department of Physics and Astronomy, Physics Building (Bldg. 082), College Park, MD 20742, USA
University of Massachusetts - Amherst, Department of Physics, 1126 Lederle Graduate Research Tower (LGRT), Amherst, MA 01003-9337, USA
University of Melbourne, School of Physics, Victoria 3010, Australia
University of Michigan, Department of Physics, 500 E. University Ave., Ann Arbor, MI 48109-1120, USA
University of Minnesota, 148 Tate Laboratory Of Physics, 116 Church St. S.E., Minneapolis, MN 55455, USA
University of Mississippi, Department of Physics and Astronomy, 108 Lewis Hall, PO Box 1848, Oxford, Mississippi 38677-1848, USA

University of Missouri – St. Louis, Department of Physics and Astronomy, 503 Benton Hall One University Blvd., St. Louis Mo 63121, USA
University of New Mexico, New Mexico Center for Particle Physics, Department of Physics and Astronomy, 800 Yale Boulevard N.E., Albuquerque, NM 87131, USA
University of North Carolina at Chapel Hill, Department of Physics and Astronomy, Phillips Hall, CB #3255, 120 E. Cameron Ave., Chapel Hill, NC 27599-3255, USA
University of Notre Dame, Department of Physics, 225 Nieuwland Science Hall, Notre Dame, IN 46556, USA
University of Oklahoma, Department of Physics and Astronomy, Norman, OK 73071, USA
University of Oregon, Department of Physics, 1371 E. 13th Ave., Eugene, OR 97403, USA
University of Oxford, Particle Physics Department, Denys Wilkinson Bldg., Keble Road, Oxford OX1 3RH England, UK
University of Pavia, Department of Physics, via Bassi 6, I-27100 Pavia, Italy
University of Pennsylvania, Department of Physics and Astronomy, 209 South 33rd Street, Philadelphia, PA 19104-6396, USA
University of Pittsburgh, Department of Physics and Astronomy, 100 Allen Hall, 3941 O'Hara St, Pittsburgh PA 15260, USA
University of Regina, Department of Physics, Regina, Saskatchewan, S4S 0A2 Canada
University of Rochester, Department of Physics and Astronomy, Bausch & Lomb Hall, P.O. Box 270171, 600 Wilson Boulevard, Rochester, NY 14627-0171 USA
University of Science and Technology of China, Department of Modern Physics (DMP), Jin Zhai Road 96, Hefei, China 230026
University of Silesia, Institute of Physics, Ul. Uniwersytecka 4, PL-40007 Katowice, Poland
University of South Carolina, Department of Physics and Astronomy, 712 Main Street, Columbia, SC 29208, USA
University of Southampton, School of Physics and Astronomy, Highfield, Southampton S017 1BJ, England, UK
University of Southern California, Department of Physics & Astronomy, 3620 McClintock Ave., SGM 408, Los Angeles, CA 90089-0484, USA
University of Sydney, Falkiner High Energy Physics Group, School of Physics, A28, Sydney, NSW 2006, Australia
University of Tartu, Institute of Physics, Riia 142, 51014 Tartu, Estonia
University of Texas at Austin, Department of Physics, 1 University Station C1600, Austin, Texas 78712, USA
University of Texas at Dallas, Department of Physics, 800 West Campbell Road, Richardson, Texas 75080, USA
University of Texas, Center for Accelerator Science and Technology, Arlington, TX 76019, USA
University of Tokushima, Institute of Theoretical Physics, Tokushima-shi 770-8502, Japan
University of Tokyo, Department of Physics, 7-3-1 Hongo, Bunkyo District, Tokyo 113-0033, Japan
University of Toronto, Department of Physics, 60 St. George St., Toronto M5S 1A7, Ontario, Canada
University of Toyama, Department of Physics, 3190 Gofuku, Toyama 930-8555, Japan
University of Tsukuba, Faculty of Pure and Applied Sciences, 1-1-1 Ten'nodai, Tsukuba, Ibaraki 305-8571, Japan
University of Victoria, Department of Physics and Astronomy, P.O.Box 3055 Stn Csc, Victoria, BC V8W 3P6, Canada
University of Virginia, Department of Physics, 382 McCormick Rd., PO Box 400714, Charlottesville, VA
University of Warsaw, Institute of Experimental Physics, Ul. Hoza 69, PL-00 681 Warsaw, Poland
University of Warsaw, Institute of Theoretical Physics, Ul. Hoza 69, PL-00 681 Warsaw, Poland
University of Washington, Department of Physics, PO Box 351560, Seattle, WA 98195-1560, USA
University of Wisconsin, Physics Department, Madison, WI 53706-1390, USA
University of Wuppertal, Gaußstraße 20, D-42119 Wuppertal, Germany
Università degli Studi di Milano, Dipartimento di Fisica, Via Celoria 16, 20133 Milano, Italy
Università degli Studi di Roma "La Sapienza", Dipartimento di Fisica, Piazzale Aldo Moro 5, 00185 Roma, Italy
Università degli Studi di Trieste, Dipartimento di Fisica, via A. Valerio 2, I-34127 Trieste, Italy
Università dell'Insubria in Como, Dipartimento di Scienze CC.FF.MM., via Vallegio 11, I-22100 Como, Italy
Università di Milano-Bicocca, Dipartimento di Fisica"G. Occhialin", Piazza della Scienza 3, 20126 Milano, Italy
Università di Pisa, Departimento di Fisica "Enrico Fermi", Largo Bruno Pontecorvo 3, I-56127 Pisa, Italy
Universiy of Huddersfield, International Institute for Accelerator Applications, Queensgate Campus, Huddersfield HD1 3DH, UK
UPMC Univ. Paris 06, Faculté de Physique (UFR 925), 4 Place Jussieu, 75252 Paris Cedex 05, France
Vietnam National University, Laboratory of High Energy Physics and Cosmology, Faculty of Physics, College of Science, 334 Nguyen Trai, Hanoi, Vietnam
Vietnam National University, University of Natural Sciences, 227 Nguyen Van Cu street, District 5, Ho Chi Minh City, Vietnam
VINCA Institute of Nuclear Sciences, Laboratory of Physics, PO Box 522, YU-11001 Belgrade, Serbia
Virginia Commonwealth University, Department of Physics, P.O. Box 842000, 701 W. Grace St.,Richmond, VA. 23284-2000, USA
Virginia Polytechnic Institute and State University, Physics Department, Blacksburg, VA 2406, USA
Vrije Universiteit Brussel, Pleinlaan 2, 1050 Brussels, Belgium
Vrije Universiteit, Department of Physics, Faculty of Sciences, De Boelelaan 1081, 1081 HV Amsterdam, Netherlands
Warsaw University of Technology, The Faculty of Electronics and Information Technology, ul. Nowowiejska 15-19, 00-665 Warsaw, Poland
Waseda University, Advanced Research Institute for Science and Engineering, Shinjuku, Tokyo 169-8555, Japan
Wayne State University, Department of Physics, Detroit, MI 48202, USA
Weizmann Institute of Science, Department of Particle Physics, P.O. Box 26, Rehovot 76100, Israel
Yale University, Department of Physics, New Haven, CT 06520, USA
Yamagata University, 1-4-12 Kojirakawa-cho, Yamagata-shi, Yamagata, 990-8560, Japan
Yerevan Physics Institute, 2 Alikhanyan Brothers St., Yerevan 375036, Armenia
Yonsei University, Department of Physics, 134 Sinchon-dong, Sudaemoon-gu, Seoul 120-749, Republic of Korea

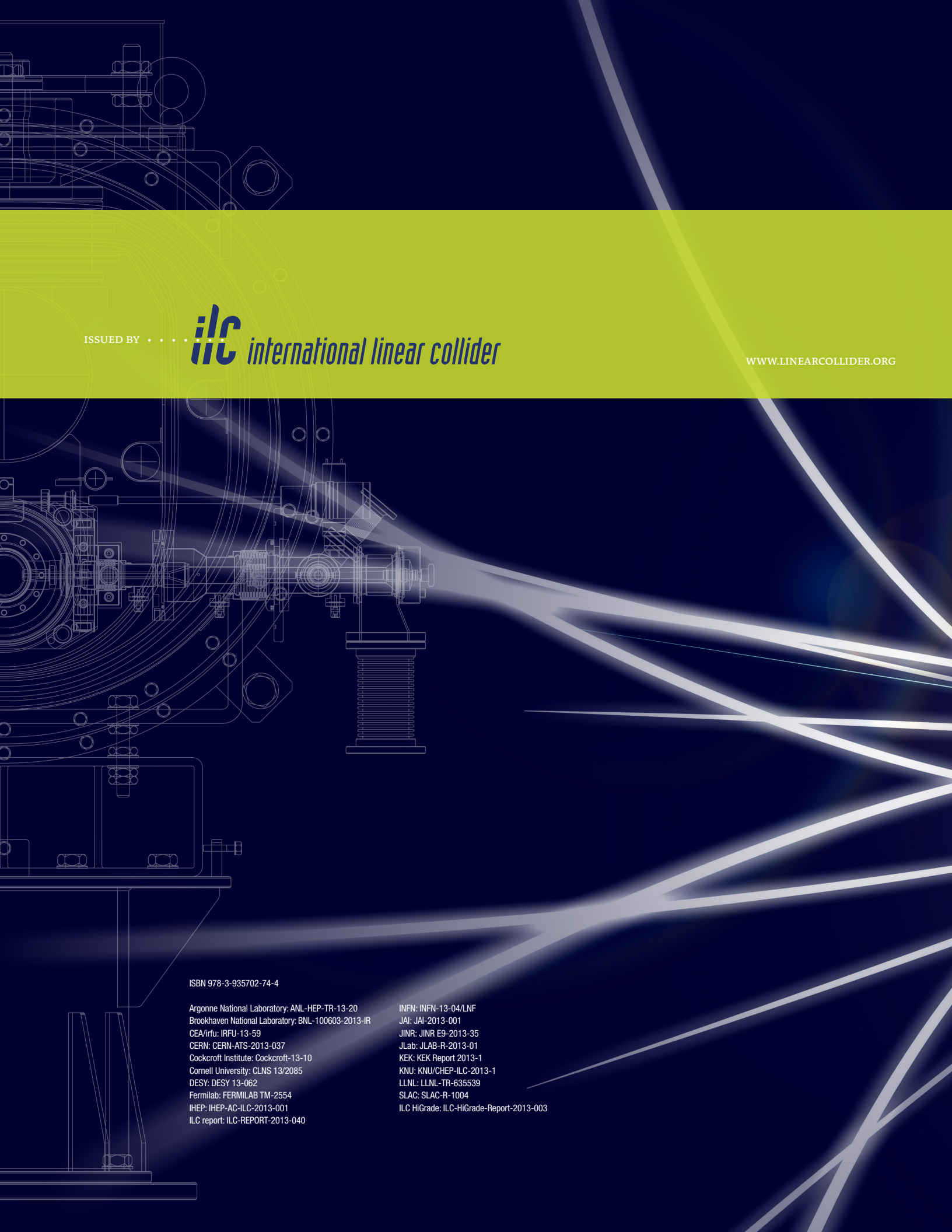

ISSUED BY • • • • • • • • ilc international linear collider

WWW.LINEARCOLLIDER.ORG

ISBN 978-3-935702-74-4

Argonne National Laboratory: ANL-HEP-TR-13-20
Brookhaven National Laboratory: BNL-100603-2013-IR
CEA/irfu: IRFU-13-59
CERN: CERN-ATS-2013-037
Cockcroft Institute: Cockcroft-13-10
Cornell University: CLNS 13/2085
DESY: DESY 13-062
Fermilab: FERMILAB TM-2554
IHEP: IHEP-AC-ILC-2013-001
ILC report: ILC-REPORT-2013-040
INFN: INFN-13-04/LNF
JAI: JAI-2013-001
JINR: JINR E9-2013-35
JLab: JLAB-R-2013-01
KEK: KEK Report 2013-1
KNU: KNU/CHEP-ILC-2013-1
LLNL: LLNL-TR-635539
SLAC: SLAC-R-1004
ILC HiGrade: ILC-HiGrade-Report-2013-003

THE INTERNATIONAL LINEAR COLLIDER

Technical Design Report | Volume 2: Physics

The International Linear Collider

Technical Design Report

2013

Volume 1: Executive Summary

Volume 2: Physics

Volume 3: Accelerator

Part I: R&D in the Technical Design Phase

Volume 3: Accelerator

Part II: Baseline Design

Volume 4: Detectors

Volume 2

Physics

Editors

Howard Baer, Tim Barklow, Keisuke Fujii, Yuanning Gao, Andre Hoang, Shinya Kanemura, Jenny List, Heather E. Logan, Andrei Nomerotski, Maxim Perelstein, Michael E. Peskin, Roman Pöschl, Jürgen Reuter, Sabine Riemann, Aurore Savoy-Navarro, Geraldine Servant, Tim M. P. Tait, Jaehoon Yu

Acknowledgements

We acknowledge the support of BMWF, Austria; MinObr, Belarus; FNRS and FWO, Belgium; NSERC, Canada; NSFC, China; MPO CR and VSC CR, Czech Republic; Commission of the European Communities; HIP, Finland; IN2P3/CNRS, CEA-DSM/IRFU, France; BMBF, DFG, Helmholtz Association, MPG and AvH Foundation, Germany; DAE and DST, India; ISF, Israel; INFN, Italy; MEXT and JSPS, Japan; CRI(MST) and MOST/KOSEF, Korea; FOM and NWO, The Netherlands; NFR, Norway; MNSW, Poland; ANCS, Romania; MES of Russia and ROSATOM, Russian Federation; MON, Serbia and Montenegro; MSSR, Slovakia; MICINN-MINECO and CPAN, Spain; SRC, Sweden; STFC, United Kingdom; DOE and NSF, United States of America.

Contents

1 Introduction **1**

1.1 Physics at the ILC . . . 1

1.2 Advantages of e^+e^- colliders . . . 2

1.2.1 Cleanliness . . . 2

1.2.2 Democracy . . . 3

1.2.3 Calculability . . . 4

1.2.4 Detail . . . 5

1.3 Modes of operation of the ILC . . . 6

1.4 Key physics explorations at the ILC . . . 8

2 Higgs Boson **13**

2.1 The Higgs mechanism in the Standard Model . . . 14

2.2 Higgs coupling deviations from new physics . . . 17

2.2.1 The Decoupling Limit . . . 17

2.2.2 Additional Higgs bosons . . . 18

2.2.3 New states to solve the gauge hierarchy problem . . . 19

2.2.4 Composite Higgs . . . 20

2.2.5 Mixing of the Higgs with an electroweak-singlet scalar . . . 20

2.2.6 The case of supersymmetry . . . 21

2.2.7 Conclusions . . . 23

2.3 Status and prospects for Higgs measurements at LHC . . . 23

2.3.1 The LHC Higgs discovery . . . 23

2.3.2 Prospects for measuring the Higgs mass and quantum numbers at LHC . . . 24

2.3.3 Prospects for determining the Higgs couplings from LHC data . . . 24

2.3.4 Prospects for measurement of the triple Higgs coupling at the LHC . . . 27

2.4 Higgs measurements at ILC at 250 GeV . . . 28

2.4.1 Mass and quantum numbers . . . 29

2.4.2 Inclusive cross section . . . 31

2.4.3 Branching ratios and couplings . . . 32

2.5 Higgs measurements at ILC at 500 GeV . . . 36

2.5.1 Top quark Yukawa coupling . . . 36

2.5.2 Higgs self-coupling . . . 37

2.5.3 WW fusion and the hWW coupling . . . 38

2.5.4 Expected improvements of branching ratio measurements . . . 38

2.6 Higgs measurements at ILC at 1000 GeV . . . 39

2.6.1 Measurement of $h \to \mu^+\mu^-$ decay using $e^+e^- \to \nu\overline{\nu}h$ . . . 39

2.6.2 Top quark Yukawa coupling . . . 40

2.6.3 Higgs self-coupling in the $e^+e^- \to \nu_e\overline{\nu}_e hh$ process . . . 41

2.7 Summary of measurement precisions expected at ILC . . . 42
2.8 Conclusion . . . 43

3 Two-Fermion Processes 53
3.1 Systematics of $e^+e^- \to f\overline{f}$ . . . 53
3.2 Z' physics . . . 54
3.2.1 Benchmark Z' models . . . 55
3.2.2 Current limits on Z' and the ILC reach . . . 56
3.2.3 Measurement of Z' couplings . . . 56
3.2.4 Z' model discrimination . . . 57
3.3 Quark and lepton compositeness . . . 57
3.4 Extra dimensions . . . 58
3.4.1 Flat, TeV-sized extra dimensions . . . 58
3.4.2 Large extra dimensions . . . 59
3.4.3 Randall-Sundrum warped extra dimensions . . . 60

4 W and Z Boson Physics 63
4.1 Beyond the SM W/Z sector: the EW chiral Lagrangian . . . 64
4.1.1 Formalism of the EW chiral Lagrangian . . . 64
4.1.2 EW chiral Lagrangian and Higgs sector resonances . . . 66
4.2 Vector boson pair production . . . 69
4.2.1 $e^+e^- \to W^+W^-$ . . . 70
4.2.2 $e^+e^- \to ZZ$ . . . 73
4.2.3 $\gamma\gamma \to W^+W^-$ . . . 73
4.3 Triple vector boson production . . . 74
4.4 WW, ZZ scattering at high energy . . . 76
4.5 Giga-Z . . . 79
4.5.1 Precision measurement program at the Z . . . 80
4.5.2 Precision measurement of the W boson mass . . . 82

5 Top Quark 89
5.1 Top quark properties from hadron colliders . . . 90
5.1.1 Top quark hadronic cross section . . . 90
5.1.2 Top quark mass and width . . . 90
5.1.3 Helicity of the W boson . . . 91
5.1.4 Top coupling to Z^0 and γ . . . 92
5.1.5 Asymmetries at hadron colliders . . . 92
5.2 $e^+e^- \to t\bar{t}$ at threshold . . . 93
5.2.1 Status of QCD theory . . . 93
5.2.2 Simulations and measurements . . . 94
5.3 Probing the top quark vertices at the ILC . . . 95
5.3.1 Models with top and Higgs compositeness . . . 96
5.3.2 ILC measurements . . . 97
5.3.3 An example: the Randall-Sundrum scenario . . . 99
5.3.4 Remarks on $(g-2)_t$ . . . 100
5.4 Concluding remarks . . . 101

6 Extended Higgs Sectors **107**
6.1 General description of extended Higgs sectors . . . 108
6.1.1 The Two Higgs Doublet Model . . . 108
6.1.2 Models with Higgs singlets . . . 110
6.1.3 Models with Higgs triplets . . . 111
6.2 Extended Higgs bosons searches at the ILC . . . 113
6.2.1 Constraints from the LHC experiments . . . 113
6.2.2 Neutral Higgs pair production at ILC . . . 115
6.2.3 Charged Higgs boson production . . . 116
6.2.4 Measurement of $\tan\beta$ . . . 119
6.3 Exotic Higgs bosons . . . 120
6.4 Summary . . . 122

7 Supersymmetry **127**
7.1 Introduction . . . 128
7.2 Setting the scene . . . 128
7.3 Direct and indirect experimental constraints . . . 130
7.3.1 Particle sectors of a supersymmetric model . . . 130
7.3.2 Indirect constraints on SUSY models . . . 130
7.3.3 Impact of Higgs searches . . . 131
7.3.4 Direct searches for supersymmetric particles . . . 132
7.3.5 Impact of the constraints on the SUSY particle sectors . . . 133
7.4 Two benchmark points for the ILC . . . 134
7.4.1 Natural SUSY and light higgsinos . . . 134
7.4.2 An MSSM model with light sleptons . . . 135
7.5 Experimental capabilities and parameter determination . . . 135
7.5.1 Neutralino and chargino sector . . . 136
7.5.2 Gravitinos . . . 137
7.5.3 Third generation squarks . . . 138
7.5.4 Scalar charged leptons . . . 139
7.5.5 Sneutrinos . . . 141
7.5.6 Beyond the CP and RP conserving MSSM . . . 142
7.5.7 Parameter determination and model discrimination . . . 143
7.6 Conclusions . . . 145

8 Cosmological Connections **153**
8.1 Baryogenesis at the Electroweak Scale . . . 154
8.1.1 Electroweak baryogenesis in supersymmetry . . . 154
8.1.2 Electroweak baryogenesis in composite Higgs models . . . 156
8.1.3 Effective field theory approach to the EW phase transition . . . 159
8.2 Dark matter . . . 160
8.2.1 Dark matter and the WIMP paradigm . . . 160
8.2.2 Theories of WIMPs . . . 161
8.2.3 Determination of dark matter parameters . . . 162
8.2.4 ILC studies of dark matter parameter determination . . . 163
8.3 Conclusions . . . 166

9 Conclusion **171**

List of Signatories **173**

Chapter 1
Introduction

1.1 Physics at the ILC

For more than twenty years, an advanced electron-positron collider has been put forward as a key component of the future program of elementary particle physics. We have a well-established Standard Model of particle physics, but it is known to be incomplete. Among the many questions that this model leaves open, there are two — the origin of the masses of elementary particles and the particle identity of cosmic dark matter – that should be addressed at energy scales below 1 TeV. It has been appreciated for a long time that a next-generation electron-positron collider would give us the ability to make precision measurements that would shed light on these mysteries.

Now the technology to build this electron-positron collider has come of age. This report is a volume of the Technical Design Report for the International Linear Collider (ILC). The accompanying volumes of this report lay out the technical design of a high-luminosity e^+e^- collider at 500 GeV in the center of mass and of detectors that could make use of the collisions to perform high-precision measurements. In this volume, we summarize the physics arguments for building this collider and their appropriate relation to the situation of particle physics as of the fall of 2012. The discussion in this volume supplements the presentation of the physics opportunities for a 500 GeV e^+e^- collider given in the review articles [1–3], the 2001 regional study reports [4–6], the 2006 study of ILC/LHC complementarity [7], and the 2007 ILC Reference Design Report [8].

There are two important reasons to review the physics arguments for the ILC now. First, the Large Hadron Collider (LHC) has now begun to explore the energy region up to 1 TeV in proton-proton collisions. The LHC experiments have discovered a resonance that is a strong candidate for a Higgs boson similar to that of the Standard Model and have measured the mass of this resonance to be about 125 GeV [9, 10] It has been understood for a long time that there are intrinsic limitations to the ability of hadron colliders to study color-singlet scalar particles, and that precision measurements, to the few percent level, are needed to place a new scalar particle correctly within our model of particle physics. The ILC is an ideal machine to address this question. In this report, we will describe the system of measurements that will be needed to probe the identity of the Higgs boson and present new estimates of the capability of the ILC to make those measurements.

We will also describe many other opportunities that the ILC provides to probe for and study new physics, both through the production of new particle predicted by models of physics beyond the Standard Model and through the study of indirect effects of new physics on the W and Z bosons, the top quark, and other systems that can be studied with precision at the ILC. It is important to re-evaluate the merits of these experiments in view of new constraints from the LHC, and we will do that in this report.

The experience of operating the LHC and its detectors also allows us to make more concrete projections of the long-term capabilities of the LHC experiments and the complementarity of the measurements from the ILC experiments. We have tried to incorporate the best available information

into this report.

A second reason to revisit to physics case for the ILC is that the studies for the technical design and benchmarking of the ILC detectors have given us a more precise understanding of their eventual capabilities. In many cases, the performance of the detectors found in full-simulation studies exceeds the capabilities claimed from studies done at earlier stages of the conceptual detector design process. Our estimates here will be based on these new results.

To support a major accelerator project such as the ILC, it should be a criterion that this project will advance our knowledge of particle physics *qualitatively* beyond the information that will be available from currently operating accelerators, including the results expected from the future stages of the LHC. In this report, we will address this question. We will demonstrate the profound advances that the ILC will make in our understanding of fundamental physics.

1.2 Advantages of e^+e^- colliders

Over the past forty years, experiments at proton and electron colliders have played complementary roles in illuminating the properties of elementary particles. For example, the bottom quark was first discovered in 1977 through the observation of the Υ resonances in proton-proton collisions. However, many of the most revealing properties of the b quark, from its unexpectedly long lifetime to its decays with time-dependent CP violation, were discovered at e^+e^- colliders.

Today, the LHC offers obvious advantages for experimenters in providing very high energy and very high rates in typical reactions. The advantages of the ILC are different and perhaps more subtle to appreciate. In this section, we will review these advantages in general terms. We will revisit these points again and again in our discussions of specific processes that will be studied at the ILC.

1.2.1 Cleanliness

An elementary difference between hadron and electron collisions is apparent in the design of detectors: The environment for electron-positron collisions is much more benign. At LHC energies, the proton-proton total cross section is roughly 100 mb. In the current scheme for running the LHC, proton-proton bunch collisions occur every 50 nsec, each bunch crossing leads to about 30 proton-proton collisions, and each of these produces hundreds of energetic particles. At the ILC, the most important chronic background source comes from photon-photon collisions, for which the cross section is hundreds of nb. Bunch crossings are spaced by about 300 nsec; at each bunch crossing we expect about 1 photon-photon collision, producing a few hadrons in the final state. Each e^+e^- bunch crossing does produce a large number of secondary electron-positron pairs, but these are mainly confined to a small volume within 1 cm of the beam.

The difference between hadron-hadron and e^+e^- collisions has profound implications for the detectors and for experimentation. The LHC detectors must be made of radiation-hard materials to handle a high occupancy rate. They must have thick calorimeters to contain particles with a wide range of energies, requiring also the placement of solenoids inside the calorimeter volume. They must have complex trigger systems that cut down rates to focus on the most interesting events. At the ILC, tracking detectors can be made as thin as technically feasible. All elements, from the vertex detector to the calorimeter, can be brought much closer to the interaction point and contained inside the solenoid. The ILC detectors are projected to improve the momentum resolution from tracking by a factor of 10 and the jet energy resolution of the detector by a factor of 3 or better. The very close placement of the innermost pixel vertex detector layer leads to excellent b, charm and τ tagging capabilities. In addition, the complications in analyzing LHC events due to hadrons from the underlying-event and pileup from multiple collisions in each beam crossing are essentially removed at the ILC. The e^+e^- environment thus provides a setting in which the basic high-energy collision can

be measured with high precision.

1.2.2 Democracy

The elementary coupling e of the photon is the same for all species of quarks and leptons, and the same also for new particles from beyond the Standard Model. Thus, e^+e^- annihilation produces pairs of all species, new and exotic, at similar rates.

At the LHC, the gluon couples equally to all quarks and to new colored particles. However, here, this democracy is hardly evident experimentally. Soft, non-perturbative strong interactions are the dominant mechanism for particle production and involve only the light quarks and gluons. Further, because the proton is a composite object with parton distributions that fall steeply, the production cross sections are much lower for heavy particles than for light ones. At the LHC, the cross section for producing bottom quarks is of the order of 1 mb, already much lower than the total inelastic cross section. The cross section for top quark pair production at the 14 TeV LHC is expected to be about 1 nb. Production cross sections for new particles will be 1 pb or smaller. Thus, interesting events occur at rates of 10^{-7} to 10^{-13} of the total event rate. This implies, first, that a trigger system is needed to exclude all events but 1 in 10^6 before any data analysis is possible. Beyond this, only events with unusual and striking properties can be recognized in the much larger sample of background QCD events. A new particle or process can be studied only if its signals can be clearly discriminated from those of QCD reactions.

At the ILC, the cross sections for light quark and lepton pair production are much smaller, but also more comparable to the cross sections for interesting new physics processes. The main Standard Model processes in e^+e^- annihilation — annihilation to quark and lepton pairs, annihilation to W^+W^-, and single W and Z production – all have cross sections at the pb level at 500 GeV. New particle production processes typically have cross sections of order 10–100 fb and result in events clearly distinguishable from the basic Standard Model reactions.

This has a number of important implications for e^+e^- experimentation. First, no trigger is needed. The ILC detectors can record all bunch crossings and performed any needed event reduction offline. Second, no special selection is needed in classifying events. That is, all final states of a decaying particle, not only the most characteristic ones, can be used for physics analyses. At the LHC, it is not possible to measure absolute branching ratios or total widths; at the ILC, these quantitites are directly accessible. Third and perhaps most importantly, at the ILC, it is much easier to recognize W and Z bosons in their hadronic decay modes than at the LHC. Since most W and Z decays are to hadronic modes, this is a tremendous advantage in the systematic study of heavy particles whose decay products typically include the weak bosons. We will see that this advantage applies not only to exotic particles but also in the study of the top quark and the Higgs boson.

The Higgs boson is produced in roughly one in one billion pp collisions at LHC energies. The modes actually used in the Higgs discovery occur at the rate of one in a trillion pp collisions. At the ILC, Higgs events occur at about 1% of all e^+e^- annihilations, and the resulting events are quite characteristic. They can be picked out and analyzed by eye. Figure 1.1 shows typical simulated events of $e^+e^- \to Zh$.

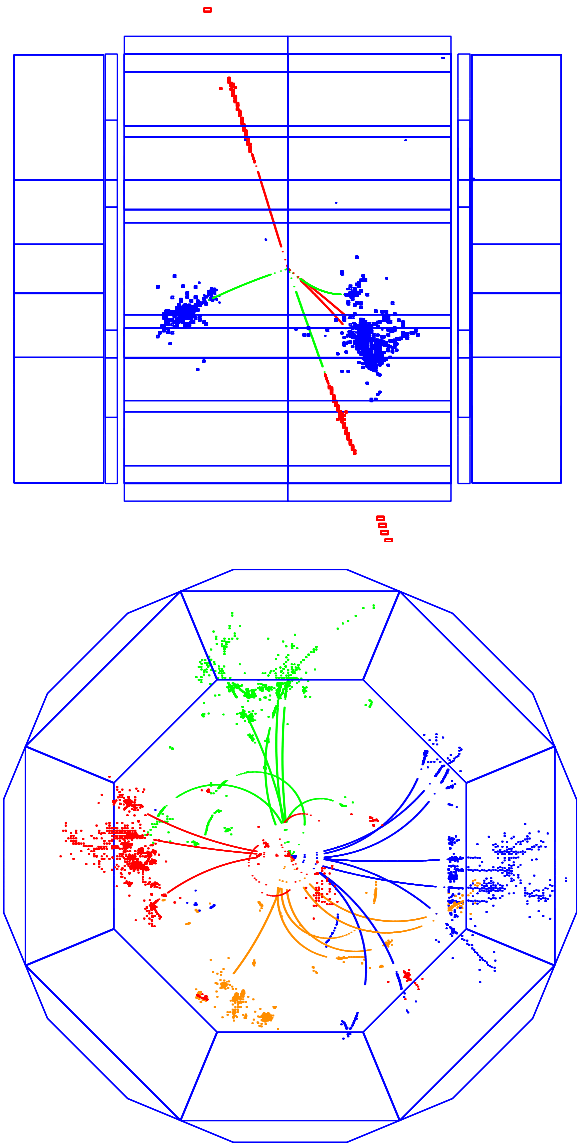

Figure 1.1
Simulated $e^+e^- \to Zh$ events: Top: $e^+e^- \to Zh \to \mu^-\mu^-\tau^+\tau^-$; Bottom: $e^+e^- \to Zh \to b\bar{b}\,b\bar{b}$ [11].

1.2.3 Calculability

At the LHC, all cross section calculations rely on QCD. Any theoretical calculation of signal or background has systematic uncertainties from the proton structure functions, from unknown higher-order perturbative QCD corrections, and from nonperturbative QCD effects. NLO QCD corrections to cross section calculations are typically at the 30-50% level. For the Higgs boson cross section, the first correction is +100%. To achieve theoretical errors smaller than 10% requires computations to NNLO or beyond, a level that is not feasible now except for the simplest reactions.

At the ILC, the initial-state e^- and e^+ are pointlike elementary particles, coupling only to the electroweak interactions. The first radiative corrections to cross sections are at the few-percent level. With effort, one can reach the part-per-mil level of theoretical precision, a level already achieved in the theoretical calculations for the LEP program.

Thus, it is possible to study heavy particles through their effects in perturbing the Standard Model at lower energies. For example, the LHC will be able to detect Z' bosons up to 4-5 TeV by searches for production of high-mass $\mu^+\mu^-$ pairs. The ILC at 500 GeV is sensitive to the presence of bosons with comparably high masses by searching for deviations from the precise Standard Model predictions for $e^+e^- \to f\overline{f}$ cross sections. By studying the dependence of these deviations on flavor and polarization, the ILC experiments can reconstruct the complete phenomenological profile of the

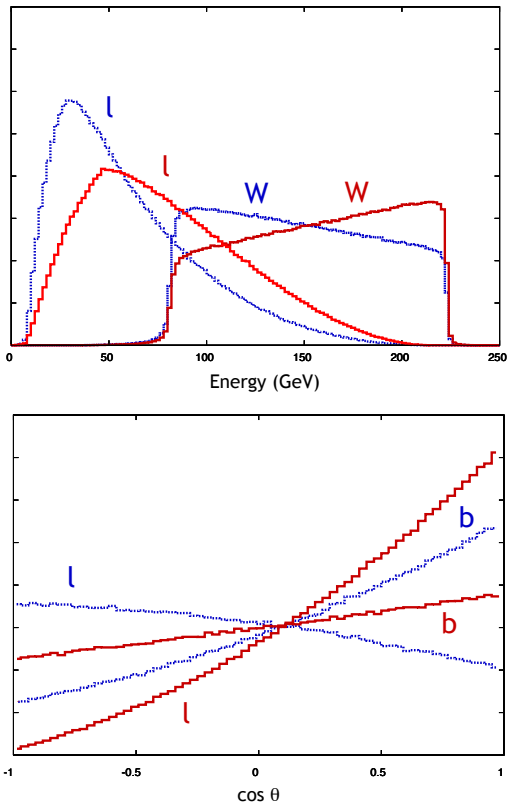

Figure 1.2 Spin asymmetries in $e^+e^- \to t\bar{t}$: For the two fully polarized beam initial state ($e^-_R e^+_L$ - red, solid, $e^-_L e^+_R$ - blue, dotted), the figures show: Top: the energy distributions of the W and ℓ (or d, s quark). Bottom: the $\cos\theta$ distributions of the b and ℓ.

heavy boson. Similar precision measurements can give new information about heavy particles that couple to the top quark and the Higgs boson.

Beyond this, the high precision theoretical understanding of Standard Model signal and background processes available at the ILC can make it possible to find elusive new physics interactions, and to characterize these interactions fully.

1.2.4 Detail

Because of the simplicity of event selections at the ILC and the absence of a complicating underlying event, physics analyses at the ILC can be done by reconstructing complete events and determining quark and lepton momenta by kinematic fitting. Such an analysis reveals the spin-dependence of production and decay processes. The ILC will also provide polarized electron and positron beams, and so the processes studied there can be completely characterized for each initial and final polarization state.

We are used to thinking of quarks and leptons at low energy as single massive objects. However, at energies above the Z^0 mass, the left- and right-handed components of quarks and leptons behave as distinct particles with different $SU(2) \times U(1)$ quantum numbers. The weak-interaction decays of heavy particles, including the top quark and the W and Z bosons, have order-1 spin asymmetries. These spin effects are difficult to observe at hadron colliders. Most typically, they are used as inputs to perform signal/background discrimination using the matrix element method of multivariate event selection. At the ILC, they are obvious aspects of the physics. That is, we do not rely on the correctness of the predicted Standard Model distribution but instead observe these distributions in full detail. In Fig. 1.2, we present an array of nontrivial energy and angular distributions generated by the spin asymmetries in the process $e^+e^- \to t\bar{t}$. In every process studied at the ILC, spin effects provide a crucial new handle on the physics, allowing us to make interpretations at the basic level of the underlying weak-interaction quantum numbers.

Table 1.1. Major physics processes to be studied by the ILC at various energies. The table indicates the various Standard Model reactions that will be accessed at increasing collider energies, and the major physics goals of the study of these reactions. A reaction listed at a given energy will of course be studied at all higher energies. The last column gives the motivation for the use of polarized beams. Polarization is always an important component of the ILC program, but for different reasons in different reactions. The codes **A**, **H**, **L**, and **B** are explained in the text.

Energy	Reaction	Physics Goal	Polarization
91 GeV	$e^+e^- \to Z$	ultra-precision electroweak	**A**
160 GeV	$e^+e^- \to WW$	ultra-precision W mass	**H**
250 GeV	$e^+e^- \to Zh$	precision Higgs couplings	**H**
350–400 GeV	$e^+e^- \to t\bar{t}$	top quark mass and couplings	**A**
	$e^+e^- \to WW$	precision W couplings	**H**
	$e^+e^- \to \nu\bar{\nu}h$	precision Higgs couplings	**L**
500 GeV	$e^+e^- \to f\bar{f}$	precision search for Z'	**A**
	$e^+e^- \to t\bar{t}h$	Higgs coupling to top	**H**
	$e^+e^- \to Zhh$	Higgs self-coupling	**H**
	$e^+e^- \to \tilde{\chi}\tilde{\chi}$	search for supersymmetry	**B**
	$e^+e^- \to AH, H^+H^-$	search for extended Higgs states	**B**
700–1000 GeV	$e^+e^- \to \nu\bar{\nu}hh$	Higgs self-coupling	**L**
	$e^+e^- \to \nu\bar{\nu}VV$	composite Higgs sector	**L**
	$e^+e^- \to \nu\bar{\nu}t\bar{t}$	composite Higgs and top	**L**
	$e^+e^- \to \tilde{t}\tilde{t}^*$	search for supersymmetry	**B**

1.3 Modes of operation of the ILC

At a proton-proton collider, one creates collisions at a fixed center of mass energy, relying on the energy distribution of partons in the proton to sample a range of collisions energies for elementary processes. At a circular e^+e^- collider, the maximum energy is preset by the size of the ring, and typically the performance of the accelerator is best just near this maximum energy. An e^+e^- linear collider is more forgiving in terms of operating at different energies and in different running conditions. In principle, it is possible to run at any energy up to the energy set by the length of the machine, with a penalty in luminosity roughly proportional to the reduction in the energy. Increasing the length of the machine of course requires the purchase of more components, but in principle a linear collider can also be lengthened to smoothly raise its maximum collision energy if physics discoveries call for this.

This flexibility has let the designers of the ILC to envision an experimental programs at series of energies well adapted to individual physics goals. In Table 1.1, we list possible center of mass energies at which the ILC could be run. These encompass the following:

- **91 GeV and 160 GeV**: These energies correspond to the Z resonance and the threshold for $e^+e^- \to W^+W^-$. The ILC is capable of achieving a luminosity much higher than that of the LEP program of the 1990's. This motivates a *Giga-Z* program, to improve the precision electroweak measurements of Z asymmetries and couplings by an order of magnitude, and a *Mega-W* program to measure the W mass with MeV precision.
- **250 GeV**: This energy is the peak of the cross section for the reaction $e^+e^- \to Zh$, for h the new boson resonance discovered near 125 GeV. Whether or not h is a Higgs boson, these experiments will begin the precision study of the nature and couplings of this particle. The h production events are tagged, allowing study of invisible and unexpected decay modes.
- **350-400 GeV**: Within a few GeV of 350 GeV, the e^+e^- annihilation cross section is expected to show a prominent rise associated with the threshold for top quark pair production. Because of its short lifetime, the top quark has no stable bound states. Instead, it has a threshold structure whose shape is precisely predicted by *perturbative* QCD. Measurement of this threshold shape will yield the top quark mass to an accuracy of 100 MeV for input to grand unification and other fundamental physics predictions. Measurements of the full details of the $t\bar{t}$ final states near threshold and in the continuum will provide a new program of precision measurements constraining electroweak symmetry breaking.

The Higgs boson reaction $e^+e^- \to \nu\overline{\nu}h$ turns on in this energy region. The study of this reaction gives a measurement of the hWW coupling, an essential ingredient in a program of precision Higgs boson studies. The cross section for this reaction grows at higher energies roughly as $\log(E_{\rm CM}/m_h)$, providing large statistics for the study of rare Higgs decays.

Finally, the reaction $e^+e^- \to W^+W^-$ becomes exceptionally sensitive to possible modification of the Standard Model couplings at high energy, with the effect of modified couplings growing as $(E/m_w)^2$. In this energy region and above, precision W coupling measurements provide a third powerful probe for new physics.

- **500 GeV**: Running at the full energy and highest luminosity of the ILC increases the power of the precision experiments just described. In addition, precision studies of two-fermion reactions $e^+e^- \to f\overline{f}$ can probe sensitively for vector resonances at high energy, new fermion interactions, and quark and lepton compositeness. This program also allows us to search for new particles such as color-singlet supersymmetry particles and states of an extended Higgs sector in parameter regions that are very difficult for the LHC experiments to explore.
- **up to 1000 GeV**: Running at even high energies, which is envisioned in upgrades of the ILC, allows a number of new measurements sensitive to the Higgs boson coupling to the top quark and the Higgs boson self-coupling, to additional probes of strongly-interacting or composite models of the Higgs boson, and to searches for new exotic particles.

The exact run plan that will be carried out at the ILC will depend on the situation in particle physics at the time of the ILC operation, taking into account new discoveries and measurements from the LHC in its running at 14 TeV. For definiteness in our projections for the ILC capabilities for Higgs boson couplings, we will discuss here a canonical program with stages at 250 GeV, 500 GeV, and 1000 GeV, with integrated luminosity 250 fb^{-1}, 500 fb^{-1}, and 1000 fb^{-1}, respectively, at these stages.

Both the electron and the positron beams at the ILC will be polarized. As we have emphasized already in the previous section, ILC cross sections depend on beam polarization in order 1. Thus, polarization is an essential ingredient in the experimental program.

In Table 1.1, we have devoted the last column to the role of polarization in the study of each of the major physics reactions. Beam polarization always plays an important role, but this role differs from one reaction to the next [12]. Going down the Table, we see four distinct modes in which beam polarization is used. These are:

A: At the Z resonance, in the precision measurement of the electroweak couplings of the top quark, and in precision measurement of $e^+e^- \to f\overline{f}$, the beam polarization asymmetry is a crucially informative observable.

H: In e^+e^- annihilation, an electron annihilates a positron of the opposite helicity. Thus, opposite polarization of electrons and positrons ($e^-_Le^+_R$ and $e^-_Re^+_L$) enhances the luminosity.

L: Certain Standard Model processes, especially at high energy, occur dominantly from the $e^-_Le^+_R$ polarization state. Polarizing to this state greatly enhances the rates and suppresses background.

B: Conversely, new physics searches at high energy benefit from use of the polarization state $e^-_Re^+_L$ to suppress Standard Model background.

In this volume, we will discuss only e^+e^- experiments, but the ILC also has the possibility of hosting experimental programs with $\gamma\gamma$ and e^-e^- collisions. A review of these options and more detailed discussion of the role of polarization can be found in Part 4 of [4].

1.4 Key physics explorations at the ILC

In the following sections of this volume, we will present the major aspects of the physics program of the ILC in detail. We will see explicitly how the features of e^+e^- experimentation and the specific reactions outlined above translate into measurements with direct and illuminating physical interpretation.

We begin by discussing the ILC program on the Higgs boson. There is now great excitement over the discovery of a bosonic resonance at the LHC whose properties are consistent with those of the Higgs boson [9, 10]. This particle might indeed be the Higgs boson predicted by the Standard Model, a similar particle arising from a different model of electroweak symmetry breaking, or a particle of totally different origin that happens to be a scalar resonance. To choose among these options, detailed precision measurements of this particle are needed.

In Section 2, we will present the program of precision measurements of the properties of this new boson that would be made by the ILC experiments. Since the new boson is observed to decay to WW and ZZ at rates comparable to the predictions for the Standard Model Higgs boson, we already know that its production cross section at the ILC will be sufficient to carry out this program. We will first set out the requirements for an experimental program that has sufficient sensitivity to distinguish the various hypotheses for the nature of the new scalar. Very high precision—at the level of percent accuracy in the new coupling constants—is needed. It is unlikely that the LHC experiments will reach this level of performance. We will then describe the variety of measurements that the ILC experiment would be expected to carry out for this particle at the various stage of ILC operation. As we have already emphasized, the ILC program on the Higgs boson includes experiments at 250 GeV, the peak of the cross section for $e^+e^- \to Zh$, and at higher energies to access the process $e^+e^- \to \nu\bar{\nu}h$ with WW fusion production of the Higgs boson. We will show that these measurements will be extremely powerful probes. They will definitively settle the question of the nature of the new boson and will give insight into any larger theory of which it might be a part.

The LHC has not yet provided evidence for signals of new physics beyond the Standard Model from its early running at 7 and 8 TeV. There are two distinct attitudes to take toward the current situation. The first is that it is premature to draw any conclusions at the present time. The LHC experimental program is still in its early stages. The accelerator has not yet reached its design energy and has so far accumulated only 1% of its eventual data set. The second is that the discovery of the new scalar boson—especially if turns out to have the properties similar to the Standard Model Higgs boson—and the deep exclusions already made for supersymmetry and other new physics models have already changed our ideas about new physics at the TeV energy scale. Our information from the LHC is certainly incomplete. We look forward to new information and new discoveries in the LHC run at 14 TeV that will take place in the latter years of this decade. And, yet, we must take seriously the implications of what we have already learned.

Though the Standard Model of particle physics is internally consistent and, so far, is not significantly challenged experimentally, it is incomplete in many respects. Most challenging is the lack, in the Standard Model, of any explanation for the spontaneous breaking of electroweak symmetry that leads to the masses of all quarks, leptons, and gauge bosons and provides the qualitative structure of their fundamental interactions.

The problem of electroweak symmetric breaking has motivated a large number of proposals for new physics at the TeV energy scale. These proposals fall into three classes. The first postulates that electroweak symmetry is broken by new strong interactions at the TeV energy scale. In these models, the key observables are the parameters of weak vector boson scattering at TeV energies. The discovery of a new light scalar, especially if its couplings to W and Z are seen to be those characteristic of a Higgs boson with a nonzero vacuum expectation value, deals a signficant blow to this whole set of

models.

The second class of models posulates that electroweak symmetry breaking is due to the expectation value of an effective Higgs field that is composite at a higher mass scale. Little Higgs models, in which the Higgs boson is a Goldstone boson of a higher energy theory, and Randall-Sundrum models and other theories with new dimensions of space, are examples of theories in this class. These theories predict new particles with the quantum numbers of the top quark and the W and Z bosons, with TeV masses. These particles should eventually be discovered at the LHC in its 14 TeV program. The other crucial predictions of these models are modifications of the couplings of the heaviest particles of the Standard Model, the W, Z, and top quark. The ILC is ideally suited to observe these effects through precision measurement of the properties of W, Z, and t. Extreme energies are not required; the ILC design center of mass energy of 500 GeV is quite sufficient.

The third class of models postulates the Higgs field as an elementary scalar field, requiring supersymmetry to tame its ultraviolet divergences. The LHC has now excluded the constrained supersymmetric models that were considered paradigmatic in the period up to 2009 for masses low enough that supersymmetry dynamics naturally drives electroweak symmetry breaking. However, supersymmetry has a large parameter space, and compelling regions are still consistent with the LHC exclusions. The typical property of these regions is that the lightest supersymmetric particles are the fermionic partners of the Higgs bosons. These particles are very difficult to discover or study at the LHC but are expected to be readily accessible to the ILC at 500 GeV. Models of this type are also likely to contain additional Higgs bosons at relatively low masses that would be targets of study at the ILC.

Thus, we argue, the exclusion of new physics at this early stage of the LHC program, combined with the observation of a new boson resembling the Standard Model Higgs boson, strengthens the case for the ILC as probe of new physics beyond the Standard Model.

In Sections 3–7 of this report, we will explain this viewpoint in full detail. We will begin in Section 3 with a review of the ILC program on $e^+e^- \to f\overline{f}$ processes, where f is a light quark or lepton. The precision study of these processes is sensitive to new heavy gauge bosons. These reactions also probe models with extra space dimensions, and models in which the electron is composite with a very small size. We will explain how experiments at 500 GeV can reveal the nature of any such boson or composite structure, qualitatively improving on the information that we will obtain from the LHC.

In Sections 4–5, we will describe the ILC program relevant to models with a light Higgs boson that is composite at a higher energy scale. In Section 4, we will review the ILC program on the W and Z bosons. We will describe the capabilities of the ILC for the measurement of W boson couplings and W boson scattering. We will show that how these measurements are capable of revealing new terms in the couplings of W and Z induced by Higgs composite structure.

In Section 5, we will review the ILC program on the top quark. We will describe the study of top quark production at threshold and at higher energies near the maximum of the cross section for $e^+e^- \to t\bar{t}$. This study gives new, nontrivial, tests of QCD and also gives access to couplings of the top quark that are extremely difficult to study at the LHC. In models in which the top quark couples to a composite Higgs boson or a strongly interacting Higgs sector, the couplings of the top quark to the Z boson provide crucial tests not available at the LHC. We will describe the beautiful probes of these couplings availabe at the 500 GeV ILC.

In Sections 6–7, we will discuss the ILC program in searching for and measuring the properties of new particles predicted by supersymmetry and other models in which the Higgs boson is an elementary scalar field. We will discuss particles that, although they are within the energy range of the ILC, they would not be expected to be found at the LHC at the current stage of its program. These particles might be discovered at the LHC with higher energy or luminosity, or their discovery might have to

wait for the ILC. In either case, the ILC will make measurements that will be key to understanding their role in models of new physics.

In Section 6, we will review ILC measurements on new bosons associated with the Higgs boson within a larger theory of electroweak symmetry breaking. We will note many aspects of these more complex theories that the ILC will be able to clarify, beyond the results anticipated from the LHC.

In Section 7, we will review the program of ILC measurements on supersymmetric particles that might be present in the ILC mass range. In this discussion, we will review the current constraints on supersymmetry. We will observe that many scenarios are still open in which new particles can found at the 500 GeV ILC. We will present the detailed program of measurements that the ILC can carry out on these particles. This discussion will also illustrate that broad capabilities that the ILC experiments provide to understand the nature of new particles discovered at the LHC, whatever their origin in terms of an underlying model.

As we have already noted, the current exclusions of new particles by the LHC experiments drive us, in models of supersymmetry, to models in which the lightest supersymmetric particles are the charged and neutral Higgsinos, which would naturally lie in the 100–200 GeV mass range. These particles are very difficult to identify at the LHC but would be easily seen and studied at the ILC. More generally, if supersymmetry is indeed realized in nature, the ILC can be expected to directly probe those parameters of supersymmetry most intimately connected to the mechanism of electroweak symmetry breaking. We will explain this point of view in detail in Section 7.

Finally, in Section 8, we will discuss the role of the ILC in understanding cosmology and, in particular, the unique experiments possible at the ILC that will shed light on the nature of the dark matter of the universe. Section 9 will give some general conclusions.

Bibliography

[1] H. Murayama and M. E. Peskin, Ann. Rev. Nucl. Part. Sci. **46**, 533 (1996) [hep-ex/9606003].

[2] E. Accomando *et al.* [ECFA/DESY LC Physics Working Group Collaboration], Phys. Rept. **299**, 1 (1998) [hep-ph/9705442].

[3] S. Dawson and M. Oreglia, Ann. Rev. Nucl. Part. Sci. **54**, 269 (2004) [hep-ph/0403015].

[4] T. Abe *et al.* [American Linear Collider Working Group Collaboration], "Linear collider physics resource book for Snowmass 2001." hep-ex/0106055,0106056,0106057,0106058.

[5] J. A. Aguilar-Saavedra *et al.* [ECFA/DESY LC Physics Working Group Collaboration], "Physics at an e+ e- linear collider," hep-ph/0106315.

[6] K. Abe *et al.* [ACFA Linear Collider Working Group Collaboration], "Particle physics experiments at JLC," hep-ph/0109166.

[7] G. Weiglein *et al.* [LHC/LC Study Group Collaboration], Phys. Rept. **426**, 47 (2006) [hep-ph/0410364].

[8] G. Aarons *et al.* [ILC Collaboration], "International Linear Collider Reference Design Report Volume 2: Physics At The ILC," Volume 2, (2007). http://www.linearcollider.org/about/Publications/Reference-Design-Report, arXiv:0709.1893 [hep-ph].

[9] G. Aad *et al.* [ATLAS Collaboration], Phys. Lett. B **716**, 1 (2012) [arXiv:1207.7214 [hep-ex]].

[10] S. Chatrchyan *et al.* [CMS Collaboration], Phys. Lett. B **716**, 30 (2012) [arXiv:1207.7235 [hep-ex]].

[11] M. Ruan, J. Phys. Conf. Ser. **368**, 012040 (2012).

[12] G. Moortgat-Pick, T. Abe, G. Alexander, B. Ananthanarayan, A. A. Babich, V. Bharadwaj, D. Barber and A. Bartl *et al.*, Phys. Rept. **460**, 131 (2008) [hep-ph/0507011].

Chapter 2
Higgs Boson

Precision studies of the weak interactions at LEP, SLC, Tevatron, and LHC have shown that they are described by a spontaneously broken $\mathrm{SU}(2)_L \times \mathrm{U}(1)_Y$ gauge theory. The quantum numbers of all fermions are verified experimentally, and the properties of the heavy vector bosons W and Z predicted by the theory are in excellent accord with the theory at the level of one-loop electroweak corrections [1]. However, the basic $SU(2) \times U(1)$ symmetry of the model forbids the generation of mass for all quarks, leptons, and vector bosons. Thus, this symmetry must be spontaneously broken. The theory of weak interactions then requires a vacuum condensate that carries charge under the $\mathrm{SU}(2)_L \times \mathrm{U}(1)_Y$ gauge groups.

In local quantum field theory, it is not possible to simply postulate the existence of a uniform vacuum condensate. This condensate must be associated with a field that has dynamics and quantum excitations. To prove the correctness of our theory of weak interactions, it is essential to study this field directly and to prove through experiments that the field and its quantum excitations have the properties required to generate mass for all particles. We have little direct or indirect information about the nature of this field. The Standard Model postulates the simplest possibility, that the needed spontaneous symmetry breaking is generated by one $SU(2)$ doublet scalar field, the Higgs field, with one new physical particle, the Higgs boson. The true story of electroweak spontaneous symmetry breaking could be much more complex.

The Higgs field, or a more general Higgs sector, couples to every type of particle. It likely plays an important role in all of the unanswered questions of elementary particle physics, including the nature of new forces and underlying symmetries, CP violation and baryogenesis, and the nature and relation of quark and lepton flavors. To make progress on these problems, we must understand the Higgs sector in detail.

In July 2012, the ATLAS and CMS experiments presented very strong evidence for a new particle whose properties are consistent with those of the Standard Model Higgs boson [2, 3]. Additional evidence for this particle was provided by the CDF and DO experiments [4]. This gives us a definite point of entry into the exploration of the Higgs sector. It would be ideal to produce this particle in a well-controlled setting and measure its mass, quantum numbers, and couplings with high precision. The particle is at a mass, 125 GeV, that is readily accessible to a next-generation e^+e^- collider. It has been observed to couple to ZZ and WW, insuring that the major production reactions in e^+e^- collisions are present. The ILC is precisely the right accelerator to make these experiments available.

Though there is no reason to believe that the simple picture given by the Standard Model is correct, the minimal theory of electroweak symmetry breaking given by the Standard Model is a convenient place to begin in describing the capabilities of any experimental facility. This is especially true because, as we will discuss in Section 2.2, most models with larger and more complex Higgs sectors contain a particle that strongly resembles the Standard Model Higgs boson.

In this chapter, then, we will describe the capabilities of the ILC to obtain a comprehensive

understanding of the Standard Model Higgs boson. In Section 2.1, we will review the Higgs mechanism and write its basic formulae. In Section 2.2, we will discuss the relation of the Standard Model Higgs boson to similar particles in more general theories of elementary particles. We will review the Decoupling Theorem that requires a boson similar to the Standard Model Higgs boson in a wide variety of models, and we will review the expected sizes of deviations from the simplest Standard Model expectations. In Section 2.3, we will review the prospects for measurements on the Higgs boson at the LHC. In Sections 2.4–2.6, we will discuss the capabilities of the ILC to measure properties of the Higgs boson in stages of center of mass energy—250 GeV, 500 GeV, and 1 TeV.

The prospects for the ILC to investigate other possible states of the Higgs sector will be discussed separately in Chapter 6 of this report.

2.1 The Higgs mechanism in the Standard Model

We begin by briefly reviewing the Higgs mechanism in the Standard Model (SM). In the SM, electroweak symmetry is broken by an SU(2)-doublet scalar field,

$$\Phi = \begin{pmatrix} G^+ \\ (h+v)/\sqrt{2} + iG^0/\sqrt{2} \end{pmatrix}. \tag{2.1}$$

Here h is the physical SM Higgs boson and G^+ and G^0 are the Goldstone bosons eaten by the W^+ and Z. Electroweak symmetry breaking is caused by the Higgs potential, the most general gauge-invariant renormalizable form of which is,

$$V = \mu^2 \Phi^\dagger \Phi + \lambda \left(\Phi^\dagger \Phi\right)^2. \tag{2.2}$$

A negative value of μ^2 leads to a minimum away from zero field value, causing electroweak symmetry breaking. Minimizing the potential, the Higgs vacuum expectation value (vev) and the physical Higgs mass are

$$v^2 = -\mu^2/\lambda \simeq (246\ \mathrm{GeV})^2, \quad m_h^2 = 2\lambda v^2 = 2|\mu^2|. \tag{2.3}$$

For $m_h \sim 125\,\mathrm{GeV}$, we have a weakly coupled theory with $\lambda \sim 1/8$ and $|\mu^2| \sim m_W^2$. The potential also gives rise to triple and quartic interactions of h, with Feynman rules given by

$$hhh: \ -6i\lambda v = -3i\frac{m_h^2}{v}, \quad hhhh: \ -6i\lambda = -3i\frac{m_h^2}{v^2}. \tag{2.4}$$

The couplings of the physical Higgs boson to other SM particles are predicted entirely in terms of v and the known particle masses via the SM Higgs mass generation mechanism. The couplings of the W and Z bosons to the Higgs arise from the gauge-kinetic terms,

$$\mathcal{L} \supset (\mathcal{D}^\mu \Phi)^\dagger (\mathcal{D}_\mu \Phi), \quad \mathcal{D}_\mu = \partial_\mu - igA_\mu^a T^a - ig' B_\mu Y, \tag{2.5}$$

where g and g' are the $\mathrm{SU}(2)_L$ and $\mathrm{U}(1)_Y$ gauge couplings, respectively, and the hypercharge of the Higgs doublet is $Y = 1/2$. This gives rise to the W and Z masses,

$$m_W = g\,\frac{v}{2}, \quad m_Z = \sqrt{g^2 + g'^2}\,\frac{v}{2}, \tag{2.6}$$

and couplings to the Higgs given by

$$\begin{aligned} W_\mu^+ W_\nu^- h: \ & i\frac{g^2 v}{2} g_{\mu\nu} = 2i\frac{M_W^2}{v} g_{\mu\nu}, & W_\mu^+ W_\nu^- hh: \ & i\frac{g^2}{2} g_{\mu\nu} = 2i\frac{M_W^2}{v^2} g_{\mu\nu}, \\ Z_\mu Z_\nu h: \ & i\frac{(g^2+g'^2)v}{2} g_{\mu\nu} = 2i\frac{M_Z^2}{v} g_{\mu\nu}, & Z_\mu Z_\nu hh: \ & i\frac{(g^2+g'^2)}{2} g_{\mu\nu} = 2i\frac{M_Z^2}{v^2} g_{\mu\nu}. \end{aligned} \tag{2.7}$$

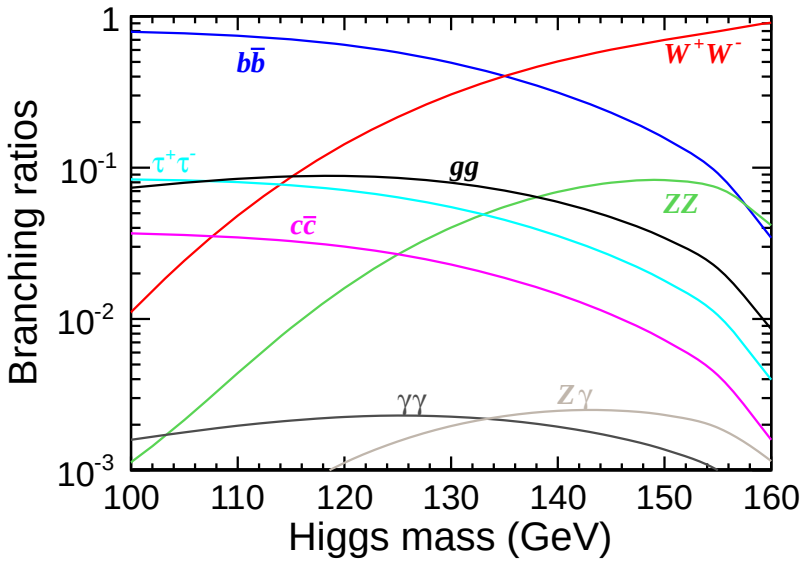

Figure 2.1
Branching fractions of the Standard Model Higgs as a function of the Higgs mass.

The photon remains massless and has no tree-level coupling to the Higgs.

The couplings of the quarks and charged leptons to the Higgs arise from the Yukawa terms,

$$\mathcal{L} \supset -y^u_{ij}\overline{u}_{Ri}\tilde{\Phi}^\dagger Q_{Lj} - y^d_{ij}\overline{d}_{Ri}\Phi^\dagger Q_{Lj} - y^\ell_{ij}\overline{\ell}_{Ri}\Phi^\dagger L_{Lj} + \text{h.c.}, \tag{2.8}$$

where $Q_L = (u_L, d_L)^T$, $L_L = (\nu_L, e_L)^T$, $\tilde{\Phi} = i\sigma^2\Phi^*$ is the conjugate Higgs doublet, and y^u, y^d, and y^ℓ are 3×3 Yukawa coupling matrices for the up-type quarks, down-type quarks, and charged leptons, respectively. The Yukawa matrices can be eliminated in favor of the fermion masses, yielding Higgs couplings to fermions proportional to the fermion mass,

$$h\overline{f}f: \; -i\,\frac{y_f}{\sqrt{2}} = -i\,\frac{m_f}{v}, \tag{2.9}$$

where $y_f v/\sqrt{2} = m_f$ is the relevant fermion mass eigenvalue.

Thus we see that, in the SM, all the couplings of the Higgs are predicted with no free parameters once the Higgs mass is known. This allows the Higgs production cross sections and decay branching ratios to be unambiguously predicted. The key regularity is that each Higgs coupling is proportional to the mass of the corresponding particle. One-loop diagrams provide additional couplings and decay modes to gg, $\gamma\gamma$, and γZ. In the SM, the Higgs coupling to gg arises mainly from the one-loop diagram involving a top quark. The Higgs couplings to $\gamma\gamma$ and γZ arise at the one-loop level mainly from diagrams with W bosons and top quarks in the loop.

The Higgs boson branching fractions in the Standard Model are currently predicted with relatively small errors, of the order of 5% in most cases. A current assessment is given in [5]. These errors may be improved to below the 1% level in the era in which the ILC experiments will run. A case of particular interest is the partial width for $h \to b\bar{b}$ The uncertainty estimated in [5] is 3%. The estimate is dominated by errors of order 1% on the measured values of m_b and α_s and by errors from missing electroweak radiative corrections at NLO. The uncertainty from truncation of the QCD perturbation series is much smaller, 0.2%, since this series is known to N^{4}LO from a heroic calculation by Baikov, Chetyrkin, and Kühn [6]. The $\overline{MS}$ bottom quark mass is already known better than the estimate used in [5]. QCD sum rules [7] and lattice gauge theory calculations [8] give consistent estimates with errors below 0.6%. The same papers also give consistent estimates of the $\overline{MS}$ charm quark mass at 3 GeV, with an error on the lattice side of 0.6%. The lattice results, based on our

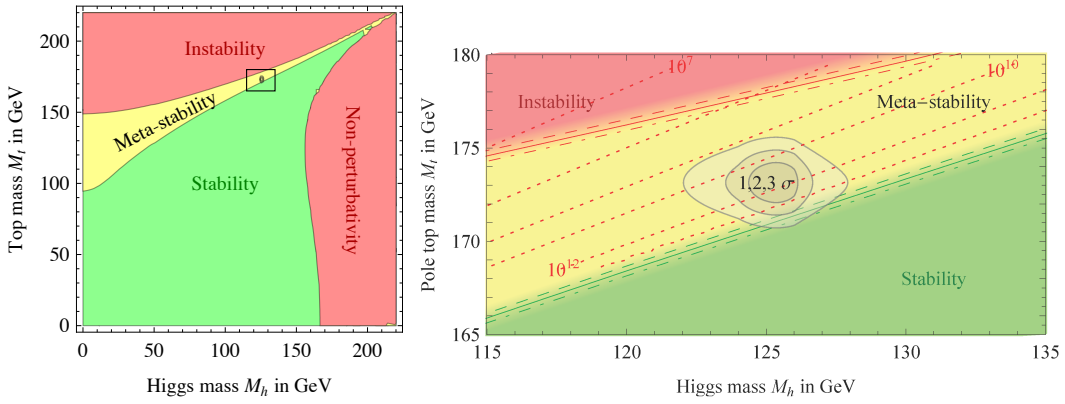

Figure 2.2. Regions of stability and instability for the Higgs potential of the Standard Model, in the plane of m_h vs. m_t, from [14]. The right-hand figure show the 1, 2, and 3 σ contours corresponding to the currently preferred values of the Higgs boson and top quark masses.

precise knowledge of the heavy quark meson masses, are improvable. Electroweak radiative correction calculations to NNLO are within the state of the art. The value of α_s will be known with an error well below 1% from event shape measurments at the ILC. In all, we expect that the theoretical error on $\Gamma(h \to b\bar{b})$ will be below 1% in the era when the ILC measurements on the Higgs boson are ready for interpretation. Most of the considerations of this paragraph apply also to the partial width for $\Gamma(h \to c\bar{c})$. In particular, the same papers cited above also give consistent estimates of the $\overline{MS}$ charm quark mass at 3 GeV, with an error on the lattice side of 0.6%. We expect that the total theoretical error on this quantity can be brought down close to 1%.

Figure 2.1 plots the branching fraction of the Standard Model Higgs boson as a function of the Higgs mass. The figure tells us that the Higgs boson mass $m_h \simeq 125$ GeV provides a very favorable situation in which a large number of decay modes have similar sizes and are accessible to experiments that provide a large Higgs event sample. The ILC, including its eventual 1 TeV stage, will allow measurement of the Higgs boson couplings to W, Z, b, c, τ, and μ, plus the loop-induced couplings to gg, $\gamma\gamma$, and γZ. The regularity of the SM that the Higgs couplings are precisely proportional to mass can thus be verified or refuted through measurements of many couplings spanning a large dynamic range.

A deviation of any of the tree-level Higgs boson couplings to WW, ZZ, or SM fermions indicates that additional new physics—either additional Higgs bosons or electroweak symmetry-breaking strong dynamics—is needed to generate the full masses of these particles and to assure good behavior of the associated scattering amplitudes in the high-energy limit [9, 10].

The Higgs potential in the Standard Model has another very unusual feature to which we call attention. These remarks apply specifically to the situation in which there is no new physics close to the TeV energy scale. In that case, for large values of the top quark Yukawa coupling y_t, renormalization group running to small distance scales drives the Higgs coupling λ negative and creates an instability of the Higgs potential [11]. If the low-energy value of λ is large enough, the Higgs potential is stable for all values of $\langle\Phi\rangle$ below the Planck scale. However, it turns out that the currently measured value of the top mass is too high to guarantee stability for a Higgs boson mass value of 125 GeV. The minimum of the Higgs boson potential corresponding to the Standard Model might still be metastable for times longer than the age of the universe [12].

The stability region of the Standard Model, in relation to the current value of the top quark mass and the value near 125 GeV for the Higgs boson mass, is shown in Fig. 2.2 [13, 14]. There is a small sliver of the (m_h, m_t) plane in which the Higgs potential is metastable, and the currently preferred values lie in that region. However, as shown in the inset, these values are plausibly consistent with

eternal stability of the Standard Model. If the Standard Model turns out to be correct, we will need to know the value of the top quark mass very precisely to understand its eventual fate. As we will discuss in Section 5.1, it is not clear that hadron collider experiments will provide a substantially improved measurement of the top quark mass. Only the ILC, which will measure the top quark mass to an accuracy of about 100 MeV, will have the power to resolve the question of the ultimate fate of the Standard Model vacuum.

2.2 Higgs coupling deviations from new physics

2.2.1 The Decoupling Limit

In this section, we will discuss possible modifications of the Higgs boson couplings that might be searched for in precision Higgs experiments. It is a general property in many class of models of new physics beyond the Standard Model that they contain a light scalar field, elementary or effective, whose vacuum expectation value is the main source of electroweak symmetry breaking. It is possible that this particle can look very different from the Standard Model Higgs boson. At the moment, there is much interest in this question, stimulated by the values of the first measured Higgs production rates. Models predicting such large deviations can be found in [15–18] and other recent theoretical papers. If it turns out that the new boson has couplings very different from the Standard Model predictions, it will of course be important to measure those couplings as accurately as possible.

However, it is much more common that the lightest Higgs boson of new physics models has coupling that differ at most at the 5-10% level from the Standard Model expectations. This point was made recently through the study of a number of examples by Gupta, Rzehak, and Wells [19]; we will provide some additional examples here. A future program of Higgs physics must acknowledge this point and strive for the level of accuracy that is actually called for in these models.

The logic of this prediction is expressed by the Decoupling Limit of Higgs models described by Haber in [20]. Consider a model with many new particles, in which all of these new particles are heavy while an $SU(2)$ doublet of scalars has a relatively small mass parameter. There are many reasons why the mass parameter of the doublet might be smaller than the typical mass scale of new particles. It might be driven small by renormalization group running, as happens in supersymmetry; it might be suppressed because the scalar is a pseudo-Goldstone boson, as happens in Little Higgs models. In any event, if there is separation between the masses of other new particles and the mass parameter of the scalar doublet, we can integrate out the heavy particles and write an effective Lagrangian for the light doublet. The resulting effective theory is precisely the Standard Model, plus possible higher-dimension operators. If the light doublet acquires a vev, its physical degree of freedom is an effective Higgs particle, with precisely the properties of the Standard Model Higgs up to the effects of the higher-dimension operators. These effects are then required to be of the order of

$$m_h^2/M^2 \quad \text{or} \quad m_t^2/M^2 \ , \tag{2.10}$$

where M is the mass scale of the new particles. The following sections will give quantitative examples of Higgs coupling deviations that follow this systematic dependence.

2.2.2 Additional Higgs bosons

If there is one doublet of Higgs field that breaks the electroweak gauge symmetry, there could well be more. Models that give mechanisms of electroweak symmetry breaking often require more than one Higgs field doublet. A prominent example is supersymmetry, which requires one Higgs doublet to give mass to the up-type fermions and a different Higgs doublet to give mass to the down-type fermions. Any enlargement of the Higgs sector has visible effects on the couplings of the lightest Higgs boson.

We can explore this in the case of the model with two Higgs doublets. Both doublets contribute to the W and Z masses. If fermions acquire masses from one or the other doublet, their couplings to the lightest Higgs boson are modified according to the Higgs sector mixing angles α and β. For the Higgs structure of the Minimal Supersymmetric Standard Model (MSSM), the couplings of the light SM-like Higgs boson h are modified at tree level to

$$\begin{aligned} \frac{g_{hVV}}{g_{h_{\rm SM}VV}} &= \sin(\beta-\alpha) \\ \frac{g_{htt}}{g_{h_{\rm SM}tt}} = \frac{g_{hcc}}{g_{h_{\rm SM}cc}} &= \sin(\beta-\alpha) + \cot\beta\cos(\beta-\alpha) \\ \frac{g_{hbb}}{g_{h_{\rm SM}bb}} = \frac{g_{h\tau\tau}}{g_{h_{\rm SM}\tau\tau}} &= \sin(\beta-\alpha) - \tan\beta\cos(\beta-\alpha). \end{aligned} \tag{2.11}$$

The constrained form of the MSSM Higgs potential lets us express the couplings in terms of the mass M_A of the CP-odd Higgs boson A^0 (for large M_A, the other Higgs states H^0 and $H^\pm$ are nearly degenerate with A^0). For $\tan\beta$ larger than a few, this yields [29]

$$\begin{aligned} \frac{g_{hVV}}{g_{h_{\rm SM}VV}} &\simeq 1 - \frac{2c^2 m_Z^4 \cot^2\beta}{m_A^4} \\ \frac{g_{htt}}{g_{h_{\rm SM}tt}} = \frac{g_{hcc}}{g_{h_{\rm SM}cc}} &\simeq 1 - \frac{2cm_Z^2 \cot^2\beta}{m_A^2} \\ \frac{g_{hbb}}{g_{h_{\rm SM}bb}} = \frac{g_{h\tau\tau}}{g_{h_{\rm SM}\tau\tau}} &\simeq 1 + \frac{2cm_Z^2}{m_A^2}, \end{aligned} \tag{2.12}$$

where the coefficient c denotes the SUSY radiative corrections to the CP-even Higgs mass matrix.

We will review the LHC capabilities for detecting the heavy Higgs states in Section 6. The reach depends strongly on $\tan\beta$, but for moderate values of $\tan\beta$ it will be very difficult for the LHC to observe these states if their masses are 200 GeV. If we choose this value as a reference point, then, for $\tan\beta = 5$ and taking $c \simeq 1$, the h^0 couplings are approximately given by

$$\begin{aligned} \frac{g_{hVV}}{g_{h_{\rm SM}VV}} &\simeq 1 - 0.3\% \left(\frac{200\ \text{GeV}}{m_A}\right)^4 \\ \frac{g_{htt}}{g_{h_{\rm SM}tt}} = \frac{g_{hcc}}{g_{h_{\rm SM}cc}} &\simeq 1 - 1.7\% \left(\frac{200\ \text{GeV}}{m_A}\right)^2 \\ \frac{g_{hbb}}{g_{h_{\rm SM}bb}} = \frac{g_{h\tau\tau}}{g_{h_{\rm SM}\tau\tau}} &\simeq 1 + 40\% \left(\frac{200\ \text{GeV}}{m_A}\right)^2. \end{aligned} \tag{2.13}$$

At the lower end of the range, the LHC experiments should see the deviation in the hbb or $h\tau\tau$ coupling. However, the heavy MSSM Higgs bosons can easily be as heavy as 1 TeV without fine tuning of parameters. In this case, the deviations of the gauge and up-type fermion couplings are well below the percent level, while those of the Higgs couplings to b and τ are at the percent level,

$$\frac{g_{hbb}}{g_{h_{\rm SM}bb}} = \frac{g_{h\tau\tau}}{g_{h_{\rm SM}\tau\tau}} \simeq 1 + 1.7\% \left(\frac{1\ \text{TeV}}{m_A}\right)^2. \tag{2.14}$$

In this large-m_A region of parameter space, vertex corrections from SUSY particles are typically also at the percent level.

More general two-Higgs-doublet models follow a similar pattern, with the largest deviation appearing in the Higgs coupling to fermions that get their mass from the Higgs doublet with the smaller vev. The decoupling with m_A in fact follows the same quantitative pattern so long as the dimensionless couplings in the Higgs potential are not larger than $\mathcal{O}(g^2)$, where g is the weak gauge coupling.

2.2.3 New states to solve the gauge hierarchy problem

Many models of new physics are proposed to solve the *gauge hierarchy problem* by removing the quadratic divergences in the loop corrections to the Higgs field mass term μ^2. Supersymmetry and Little Higgs models provide examples. Such models require new scalar or fermionic particles with masses below a few TeV that cancel the divergent loop contributions to μ^2 from the top quark. For this to work, the couplings of the new states to the Higgs must be tightly constrained in terms of the top quark Yukawa coupling. Usually the new states have the same electric and color charge as the top quark, which implies that they will contribute to the loop-induced hgg and $h\gamma\gamma$ couplings. The new loop corrections contribute coherently with the Standard Model loop diagrams.

For new scalar particles (*e.g.*, the two top squarks in the MSSM), the resulting effective hgg and $h\gamma\gamma$ couplings are given by

$$\begin{aligned} g_{hgg} &\propto \left| F_{1/2}(m_t) + \frac{2m_t^2}{m_T^2} F_0(m_T) \right|, \\ g_{h\gamma\gamma} &\propto \left| F_1(m_W) + \frac{4}{3} F_{1/2}(m_t) + \frac{4}{3}\frac{2m_t^2}{m_T^2} F_0(m_T) \right|. \end{aligned} \tag{2.15}$$

Here F_1, $F_{1/2}$, and F_0 are the loop factors defined in [21] for spin 1, spin 1/2, and spin 0 particles in the loop, and m_T is the mass of the new particle(s) that cancels the top loop divergence. For application to the MSSM, we have set the two top squark masses equal for simplicity. For new fermionic particles (*e.g.*, the top-partner in Little Higgs models), the resulting effective couplings are

$$\begin{aligned} g_{hgg} &\propto \left| F_{1/2}(m_t) + \frac{m_t^2}{m_T^2} F_{1/2}(m_T) \right|, \\ g_{h\gamma\gamma} &\propto \left| F_1(m_W) + \frac{4}{3} F_{1/2}(m_t) + \frac{4}{3}\frac{m_t^2}{m_T^2} F_{1/2}(m_T) \right|. \end{aligned} \tag{2.16}$$

For simplicity, we have ignored the mixing between the top quark and its partner. For $m_h = 120$–130 GeV, the loop factors are given numerically by $F_1(m_W) = 8.2$–8.5 and $F_{1/2}(m_t) = -1.4$. For $m_T \gg m_h$, the loop factors tend to constant values, $F_{1/2}(m_T) \to -4/3$ and $F_0(m_T) \to -1/3$.

Very generally, then, such models predict deviations of the loop-induced Higgs couplings from top-partners of the decoupling form. Numerically, for a scalar top-partner,

$$\frac{g_{hgg}}{g_{h_{\rm SM}gg}} \simeq 1 + 1.4\% \left(\frac{1\ \text{TeV}}{m_T}\right)^2, \qquad \frac{g_{h\gamma\gamma}}{g_{h_{\rm SM}\gamma\gamma}} \simeq 1 - 0.4\% \left(\frac{1\ \text{TeV}}{m_T}\right)^2, \tag{2.17}$$

and for a fermionic top-partner,

$$\frac{g_{hgg}}{g_{h_{\rm SM}gg}} \simeq 1 + 2.9\% \left(\frac{1\ \text{TeV}}{m_T}\right)^2, \qquad \frac{g_{h\gamma\gamma}}{g_{h_{\rm SM}\gamma\gamma}} \simeq 1 - 0.8\% \left(\frac{1\ \text{TeV}}{m_T}\right)^2. \tag{2.18}$$

A "natural" solution to the hierarchy problem that avoids fine tuning of the Higgs mass parameter thus generically predicts deviations in the hgg and $h\gamma\gamma$ couplings at the few percent level due solely

to loop contributions from the top-partners. These effective couplings are typically also modified by shifts in the tree-level couplings of h to $t\bar{t}$ and WW.

The Littlest Higgs model [22, 23] gives a concrete example. In this model, the one-loop Higgs mass quadratic divergences from top, gauge, and Higgs loops are cancelled by loop diagrams involving a new vector-like fermionic top-partner, new W' and Z' gauge bosons, and a triplet scalar. For a top-partner mass of 1 TeV, the new particles in the loop together with tree-level coupling modifications combine to give [24]

$$\begin{aligned} \frac{g_{hgg}}{g_{h_{\rm SM}gg}} &= 1-(5\%\sim 9\%) \\ \frac{g_{h\gamma\gamma}}{g_{h_{\rm SM}\gamma\gamma}} &= 1-(5\%\sim 6\%), \end{aligned} \tag{2.19}$$

where the ranges correspond to varying the gauge- and Higgs-sector model parameters. Note that the Higgs coupling to $\gamma\gamma$ is also affected by the heavy W' and triplet scalars running in the loop. The tree-level Higgs couplings to $t\bar{t}$ and WW are also modified by the higher-dimension operators arising from the nonlinear sigma model structure of the theory.

2.2.4 Composite Higgs

Another approach to solve the hierarchy problem makes the Higgs a composite bound state of fundamental fermions with a compositeness scale around the TeV scale. Such models generically predict deviations in the Higgs couplings compared to the SM due to higher-dimension operators involving the Higgs suppressed by the compositeness scale. This leads to Higgs couplings to gauge bosons and fermions of order

$$\frac{g_{hxx}}{g_{h_{\rm SM}xx}} \simeq 1 \pm \mathcal{O}(v^2/f^2), \tag{2.20}$$

where f is the compositeness scale.

As an example, the Minimal Composite Higgs model [25] predicts [26]

$$\begin{aligned} a \equiv \frac{g_{hVV}}{g_{h_{\rm SM}VV}} &= \sqrt{1-\xi} \\ c \equiv \frac{g_{hff}}{g_{h_{\rm SM}ff}} &= \begin{cases} \sqrt{1-\xi} & ({\rm MCHM4}) \\ (1-2\xi)/\sqrt{1-\xi} & ({\rm MCHM5}), \end{cases} \end{aligned} \tag{2.21}$$

with $\xi = v^2/f^2$. Here MCHM4 refers to the fermion content of the original model of Ref. [25], while MCHM5 refers to an alternate fermion embedding [27]. Again, naturalness favors $f \sim$ TeV, leading to

$$\begin{aligned} \frac{g_{hVV}}{g_{h_{\rm SM}VV}} &\simeq 1-3\%(1\ {\rm TeV}/f)^2 \\ \frac{g_{hff}}{g_{h_{\rm SM}ff}} &\simeq \begin{cases} 1-3\%(1\ {\rm TeV}/f)^2 & ({\rm MCHM4}) \\ 1-9\%(1\ {\rm TeV}/f)^2 & ({\rm MCHM5}). \end{cases} \end{aligned} \tag{2.22}$$

2.2.5 Mixing of the Higgs with an electroweak-singlet scalar

If the SM Higgs mixes with an electroweak-singlet scalar, all Higgs couplings become modified by the same factor,

$$\frac{g_{hVV}}{g_{h_{\rm SM}VV}} = \frac{g_{hff}}{g_{h_{\rm SM}ff}} = \cos\theta \simeq 1-\frac{\delta^2}{2}, \tag{2.23}$$

where $h = h_{\rm SM}\cos\theta + S\sin\theta$, S is the singlet, and the last approximation holds when $\delta \equiv \sin\theta \ll 1$. The orthogonal state, $H = -H_{\rm SM}\sin\theta + S\cos\theta$, has couplings to SM particles proportional to $-\sin\theta$.

When H is heavy, the size of $\sin\theta$ is constrained by precision electroweak data (assuming no

cancellations due to other BSM physics). At one loop, the contributions to the T parameter from h and H are given by [19]

$$T = T_{\rm SM}(m_h)\cos^2\theta + T_{\rm SM}(m_H)\sin^2\theta, \tag{2.24}$$

where $T_{\rm SM}(m)$ refers to the SM T parameter evaluated at a Higgs mass m. The same form holds for the S parameter. Large m_H is therefore only consistent with precision electroweak constraints for small $\sin\theta$; for example, for $m_H = 1$ TeV, Ref. [19] finds $\sin^2\theta \leq 0.12$, corresponding to $g_{hxx}/g_{H_{\rm SM}xx} \simeq 1 - 6\%$.

Similar effects follow from mixing of the SM Higgs with a radion in Randall-Sundrum models or a dilaton in models with conformally-invariant strong dynamics. The couplings of a radion or dilaton to SM particles are suppressed by a factor v/f compared to those of the SM Higgs, where f is the scale of the warped or conformal dynamics. The couplings of the mass eigenstate $h = H_{\rm SM}\cos\theta + \chi\sin\theta$ are modified according to

$$\frac{g_{hVV}}{g_{H_{\rm SM}VV}} = \frac{g_{hff}}{g_{H_{\rm SM}ff}} = \cos\theta + \frac{v}{f}\sin\theta \simeq 1 - \frac{\delta^2}{2} + \frac{v}{f}\delta. \tag{2.25}$$

For $f \simeq 1$ TeV and $\sin^2\theta$ as above, this corresponds to $g_{hxx}/g_{H_{\rm SM}xx} \simeq 1 - 6\% \pm 8.5\%$, where we allow for either sign of δ.

2.2.6 The case of supersymmetry

The MSSM contains a mixture of effects discussed in the previous sections. It has an extended Higgs sector, affecting the tree level couplings to the lightest Higgs boson h, and it also introduces new particles, the top squarks, gauginos, and Higgsinos, whose loops cancel the quadratic divergences in the Higgs field mass term.

Supersymmetry is described by a large parameter space with many options for the form of the new particle spectrum. We will discuss this parameter space in some detail in Chapter 7. Here, we will give some examples of the effects that might be expected in the Higgs boson couplings.

We have already pointed out that the parameter space of the MSSM contains scenarios that give order 1 corrections to the Higgs boson couplings; examples are given in [15]. A more typical situation with heavy superparticle masses is given by the $m_h^{\rm max}$ benchmark scenario studied in [28, 29], with $m_A = 1$ TeV, $\tan\beta = 5$. This parameter set yields masses for the two top squarks of 857 GeV and 1200 GeV. We compute the Higgs couplings using `HDECAY4.43` [30]. The Higgs couplings to gg and $\gamma\gamma$ are modified mainly by the loop effects from the new particles, to give

$$\begin{aligned} \frac{g_{hgg}}{g_{h_{\rm SM}gg}} &= 1 - 2.7\% \\ \frac{g_{h\gamma\gamma}}{g_{h_{\rm SM}\gamma\gamma}} &= 1 + 0.2\%, \end{aligned} \tag{2.26}$$

These estimates include the effect on the $\gamma\gamma$ coupling of charginos in the loop, since the lightest chargino mass is 201 GeV in this benchmark scenario, and the modification of the tree-level $ht\bar{t}$ coupling due to the presence of the second Higgs doublet. The couplings to massive vector bosons and to $c\bar{c}$ and $\tau^+\tau^-$ come mainly from the modification of the tree-level couplings. One finds

$$\begin{aligned} \frac{g_{hVV}}{g_{h_{\rm SM}VV}} &= 1 - \mathcal{O}(10^{-4}), \qquad \frac{g_{hcc}}{g_{h_{\rm SM}cc}} = 1 - 0.3\% \\ & \frac{g_{h\tau\tau}}{g_{h_{\rm SM}\tau\tau}} = 1 + 2.5\%. \end{aligned} \tag{2.27}$$

Finally, the $hb\bar{b}$ coupling receives corrections both from this source and from a loop effect involving

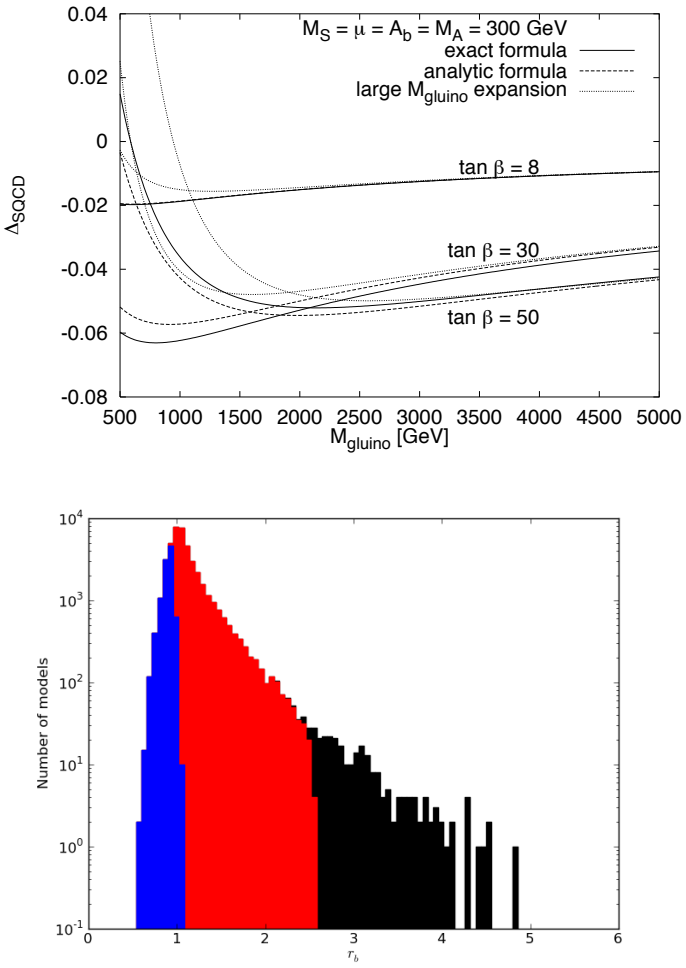

Figure 2.3
(a) Fractional correction to the $hb\bar{b}$ coupling due to loop diagrams with supersymmetric particles in the MSSM, from [31], as a function of the mass of the gluino. (b) Values of r_b, the ratio of $\Gamma(h \to b\bar{b})$ to its Standard Model value, in a large set of MSSM models randomly generated in a 19-dimensional model space and then selected to satisfy all current experimental constraints, from [32].

the supersymmetry partners of the b and t quarks

$$\frac{g_{hbb}}{g_{h_{\rm SM}bb}} = 1 + 3.5\%. \tag{2.28}$$

It is dangerous, though, to view any particular model as typical in a model space as diverse as that of supersymmetry. As was shown already in [31], the loop corrections to the $hb\bar{b}$ vertex, though they formally follow the decoupling law, can be numerically large, especially for large values of $\tan\beta$. Fig. 2.3(a) illustrates this by showing the fractional correction to the $hb\bar{b}$ vertex for three values of $\tan\beta$. Fig. 2.3(b) shows the distribution of

$$r_b = \frac{g^2_{hbb}}{g^2_{h_{\rm SM}bb}} \tag{2.29}$$

in a very large sample of MSSM models satisfying current experimental constraints—including $m_h = 125.0 \pm 2.0$—generated in a 19-parameter supersymmetry parameter space [32]. Decoupling gives many models where r_b is very close to 1, but there are also models with deviations from 1 of all magnitudes that are found as we explore the parameter space. The figure makes clear that r_b is a useful discriminator of new physics models, both at the accuracy of a order-1 measurement and at any successive level of accuracy down to the percent level. Similar conclusions hold for all other coupling deviations, though it is the deviation in the $hb\bar{b}$ coupling that is most sensitive as the superpartner masses become large.

2.2.7 Conclusions

Though large deviations are possible in some models, the more general expectation in models of new physics is that a light Higgs boson has couplings to vector bosons, fermions, gg, and $\gamma\gamma$ similar to those of the Higgs boson of the Standard Model. Thus, the study of the Higgs boson couplings is likely to require precision measurements. Nevertheless, there are many models in which some of the Higgs couplings have 5-10% discrepancies from their Standard Model values. Discovery of these discrepancies would be an important clue to the nature of new physics at higher mass scales. To recognize these effects, it is important to be able to measure the Higgs boson couplings comprehensively and with high accuracy. We will now discuss how that can be done.

2.3 Status and prospects for Higgs measurements at LHC

The ATLAS and CMS experiments have now demonstrated that they have the capability to study the Standard Model Higgs boson. They have presented strong evidence for a scalar particle of mass about 125 GeV that is consistent with the profile of the Standard Model Higgs. The isolation of this signal in the LHC environment is extremely challenging. The strongest signal of the Higgs boson so far observed at the LHC comes in the Higgs decay to $\gamma\gamma$, a process that occurs less than once in 10^{12} proton-proton collisions. However, the Tevatron and LHC experiments have proven that they can make measurements of such rare events in the high background conditions of hadron colliders. In this section, we will review how far the LHC experiments are expected to go toward a comprehensive understanding of the Higgs boson in the case in which this particle has the couplings expected in the Standard Model.

2.3.1 The LHC Higgs discovery

As of July 2012, ATLAS and CMS presented Higgs results based on integrated luminosities up to 5.1 fb^{-1} at 7 TeV plus 5.9 fb^{-1} at 8 TeV [33,34]. Each experiment observed an excess in $\gamma\gamma$ with local significance of 4.1–4.5σ and an excess in 4ℓ (consistent with being from ZZ^*) with local significance of 3.2–3.4σ. The signal strengths in these channels are consistent with SM expectations. The LHC experiments made a measurement of the resonance mass in these two final states with the result $125.3 \pm 0.4\ (\mathrm{stat}) \pm 0.5\ (\mathrm{syst})$ GeV (CMS) and $126.0 \pm 0.4\ (\mathrm{stat}) \pm 0.4\ (\mathrm{syst})$ GeV (ATLAS).

CMS also presented results including 8 TeV data for the final states bb, $\tau\tau$, and WW [34]. ATLAS has presented results including 8 TeV data for the WW final state [35]; results for the other channels are expected soon. These final states have poorer mass resolution than $\gamma\gamma$ and $ZZ^* \to 4\ell$. ATLAS observed an excess in the WW channel at the 3.2σ level. CMS saw a modest excess in WW at the 1.5σ level and no excess in the bb and $\tau\tau$ channels. The rates in these channels are also broadly consistent with SM expectations.

A summary of the ATLAS and CMS results as of August 2012 have been published in [2, 3].

In addition to inclusive Higgs production, which is dominated in the SM by gluon fusion, the ATLAS and CMS analyses include event selections with enhanced sensitivity to vector boson fusion (VBF) and Higgs production in association with W, Z, or $t\bar{t}$. As of the fall of 2012, these subdominant production modes have not been conclusively observed.

The Tevatron experiments CDF and DO have also presented evidence for the presence of this particle [4]. The Tevatron search specifically targets the production reactions $q\bar{q} \to h + W, Z$ with the decay $h \to b\bar{b}$. The significance is 2.7 σ assuming the resonance mass given by the LHC experiments.

Observation of the Higgs candidate in $\gamma\gamma$ excludes the possibility of the resonance being a spin-1 particle via the Landau-Yang theorem [36]. Observation of a signal in the ZZ^* final state strongly disfavors the possibility that it is a pseudoscalar because in this case the ZZ coupling must be loop-induced; most pseudoscalar models predict a ratio of rates in ZZ^* versus $\gamma\gamma$ much smaller

than observed. Prospects for direct LHC measurements of the spin and CP quantum numbers will be discussed below.

2.3.2 Prospects for measuring the Higgs mass and quantum numbers at LHC

The mass of the Higgs boson is an intrinsically important parameter of the Standard Model. Moreover, the Higgs mass must be known accurately in order to interpret other measurements in precision Higgs physics. In particular, because the Higgs decay widths to WW and ZZ depends sensitively on m_h below the WW threshold, a precise measurement of the Higgs mass is necessary in order to extract the Higgs couplings from branching ratio measurements. For $m_h = 115$–130 GeV, each 100 MeV of uncertainty in m_h introduces 0.6–0.5% uncertainty in the ratio of the $hb\bar{b}$ and hWW couplings, g_b/g_W.

The LHC is expected to make a precision measurement of the mass of the Higgs boson. As of this writing, the LHC experiments have already measured the Higgs mass with an uncertainty of 0.4 GeV (statistical) and 0.4–0.5 GeV (systematic) [33, 34]. Most of the sensitivity to the Higgs mass around 125 GeV comes from the $\gamma\gamma$ channel, with a subleading contribution from the $ZZ^* \to 4\ell$ channel. The ATLAS and CMS experiments estimate that, with large data samples ~ 300 fb^{-1}, they can determine the Higgs mass in absolute terms to an accuracy of 0.1 GeV [37–39]. Interference of the continuum $gg \to \gamma\gamma$ background with the diphoton signal shifts the peak downward by ~ 150 MeV or more [40] and must be taken into account at this level of precision.

The LHC also has excellent prospects to answer the question of the spin and parity of the Higgs boson. The SM Higgs coupling has the special form $hV_\mu V^\mu$, which arises specifically from the kinetic term of a scalar field with a vacumm expectation value that breaks $SU(2) \times U(1)$ symmetry. In contrast, generic loop-induced couplings for a neutral scalar take the form $\phi V_{\mu\nu} V^{\mu\nu}$ for a CP-even scalar, or $\phi V_{\mu\nu} \widetilde{V}^{\mu\nu}$ for a CP-odd scalar, with $\widetilde{V}^{\mu\nu} = \epsilon^{\mu\nu\rho\sigma} V_{\rho\sigma}$. These loop-induced couplings are typically suppressed in size by a factor $\alpha/4\pi$. So, already, the fact that the boson found by ATLAS and CMS is seen in its decay to ZZ^* provides *prima facie* evidence that this boson is a CP even scalar with a vacuum expectation value. The true test of this hypothesis will come in the study of angular correlations in the boson's decays. The study of $h \to ZZ^* \to 4$ leptons is especially powerful [41–43]. The possible structures of couplings can also be distinguished experimentally using angular correlations of the forward tagging jets in weak boson fusion Higgs production or the four final-state fermions in $h \to VV$ decays. For example, the azimuthal angle $\Delta\phi_{jj}$ of the forward tagging jets in weak boson fusion has a fairly flat distribution for the SM $hV_\mu V^\mu$ coupling, while for the CP-even loop-induced vertex the distribution peaks at $\Delta\phi_{jj} \sim 0$, π and for the CP-odd vertex it peaks at $\pi/2$, $3\pi/2$ [44–46]. Tests of the Higgs spin from $h \to \gamma\gamma$ decays are discussed in [47, 48].

2.3.3 Prospects for determining the Higgs couplings from LHC data

The LHC experiments are in principle sensitive to almost the full range of SM Higgs couplings. The decays to $\gamma\gamma$, ZZ and WW are already seen. The decay to $\tau^+\tau^-$ is expected to be straightforward to observe with luminosity samples of 30 fb^{-1} at 14 TeV. The decay to $b\bar{b}$ and the process $pp \to t\bar{t}h$ should also be observed with similar luminosity samples, although that observation is much less straightfoward. We will discuss the observation of $h \to b\bar{b}$ further below. The LHC observations are sensitive to the hgg coupling because $gg \to h$ is a primary channel for the production of the Higgs boson at the LHC. The only significant decay mode of the SM Higgs boson omitted from this list is $h \to c\bar{c}$, for which there is currently no strategy proposed. However, this is a relatively minor mode, with a branching ratio of about 3% for a Higgs boson of mass 125 GeV. In addition, it is possible to discover or bound invisible modes of Higgs decay by observing the WW fusion production of a Higgs with two forward tagging jets [49].

The large number of measurements of $\sigma \cdot BR$ for the various modes of Higgs production and decay that are available at the LHC brings us very close to the situation in which LHC data can determine the Higgs couplings in a model-independent way. However, some problems remain. One is a genuine gap in the logic that needs to be filled by a model assumption. An observable $\sigma(A\overline{A} \to h) \cdot BR(h \to B\overline{B})$ depends on the Higgs boson couplings through the factor

$$\frac{g^2(hAA)g^2(hBB)}{\Gamma_T} \ . \tag{2.30}$$

where Γ_T is the total width of the Higgs. For a Higgs boson of mass 125 GeV, the total width is expected to be about 4 MeV. Such a small value cannot be measured directly at either hadron-hadron or e^+e^- colliders, so it must be determined by the fit to the collection of $\sigma \cdot BR$ measurements. However, there might always be decay modes of the Higgs boson that are unobservable in the LHC experimental environment. The presence of such modes would increase Γ_T. Thus, we need to impose a constraint that puts an upper limit on Γ_T.

A useful constraint comes from the fact that, under rather general conditions [50], that each scalar with a vev makes a positive contribution to the masses of the W and Z. Since the Higgs couplings to the W and Z also arise from the vev, this implies that the coupling of any single Higgs field is bounded above by the coupling that would give the full mass of the vector bosons. This implies

$$g^2(hWW) \leq g^2(hWW)|_{SM} \quad \text{and } g^2(hZZ) \leq g^2(hZZ)|_{SM} \tag{2.31}$$

Then the measurement of the $\sigma \cdot BR$ for a process such as WW fusion to h with decay to WW^*, which is proportional to $g^4(hWW)/\Gamma_T$, puts an upper limit on Γ_T. This constraint was first applied to Higgs coupling fitting by Dührssen *et al.* [51]. In the literature, this constraint is sometimes applied together with the relation

$$g^2(hWW)/g^2(hZZ) = \cos^2\theta_w \ . \tag{2.32}$$

The relation (2.32), however, requires models in which the Higgs is a mixture of $SU(2)$ singlet and doublet fields only, while (2.31) is more general [52].

The application of this constraint solves the problem of principle for the determination of the the absolute strengths of Higgs boson couplings from LHC data. In practice, however, there is another important source of difficulty. A SM Higgs boson of mass 125 GeV has a 60% branching fraction to the final state $b\bar{b}$. Thus, measurements that involve the $b\bar{b}$ final state play a large role in determining the Higgs total width, and any errors in that determination feed back into all Higgs couplings. Unfortunately, it is very difficult to observe decays $h^0 \to b\bar{b}$ at the LHC. The simple argument for this is that the cross section for producing $h^0 \to b\bar{b}$ is of the order of pb while the cross section for producing a pair of b jets at the Higgs boson mass is of the order of μb. The literature on Higgs boson measurements at the LHC has gone through cycles of optimism and pessimism about the possibility of overcoming this problem. Currently, we are in a state of optimism, due to the observation of Butterworth, Davison, Rubin, and Salam that highly boosted Higgs bosons can be distinguished by recognizing the Higgs as an exotic jet with special internal structure [53]. The Butterworth *et al.* paper discussed the observation of $h \to b\bar{b}$ in the reactions $pp \to W, Z + h$. Plehn, Salam, and Spannowsky have argued that an extension of this technique also allows the study of $pp \to t\bar{t} + h$ with $h \to b\bar{b}$ at the LHC [54]. However, it is one thing to observe these processes and quite another to use them to measure Higgs couplings with high precision. It is not yet understood how to calibrate these methods or what their ultimate systematic errors might be. Further, the selection of particular jet configurations potentially introduces large theoretical errors into the calculation of the relevant cross sections. The uncertainty in the extraction of couplings from these channels propagates back

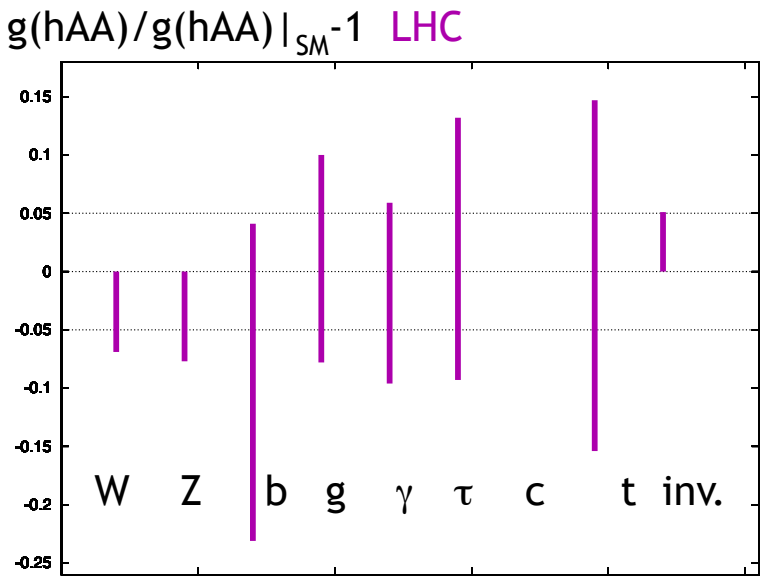

Figure 2.4. Estimate of the sensitivity of the LHC experiments to Higgs boson couplings in a model-independent analysis. The plot shows the 1 σ confidence intervals for LHC at 14 TeV with 300 fb^{-1} as they emerge from the fit described in the text. Deviation of the central values from zero indicates a bias, which can be corrected for. The upper limit on the WW and ZZ couplings arises from the constraints (2.31). No error is estimated for $g(hcc)$. The bar for the invisible channel gives the 1 σ upper limit on the *branching ratio*. The analysis assumes a data set of 300 fb^{-1} with one detector. The methodology leading to this figure is explained in [65].

Table 2.1. Expected Higgs self-coupling 1σ sensitivity limits for $m_h = 120$ GeV, from Refs. [71, 73]. Sensitivity is expressed in terms of $\Delta\lambda_{hhh} \equiv \lambda/\lambda_{\rm SM} - 1$. The $bb\tau\tau$ final state signal cross section is too small to be observed at the 300 fb^{-1} LHC [71].

	LHC (300 fb^{-1})	SLHC (3000 fb^{-1})
$4b$ [71]	$-6.8 < \Delta\lambda_{hhh} < 10.1$	$-3.1 < \Delta\lambda_{hhh} < 6.0$
$bb\tau\tau$ [71]	–	$-1.6 < \Delta\lambda_{hhh} < 3.1$
	LHC (600 fb^{-1})	SLHC (6000 fb^{-1})
$bb\gamma\gamma$ [73]	$-0.74 < \Delta\lambda_{hhh} < +0.94$	$-0.46 < \Delta\lambda_{hhh} < +0.52$

into the whole system of couplings determined from LHC data.

Over the years, there have been many attempts to estimate the ultimate sensitivity of the LHC experiments to the Higgs boson couplings. The most complete work on this subject to date is the 2003 Ph.D. thesis of Dührssen [55] and the subsequent analysis of this work with Heinemeyer, Logan, Rainwater, Weiglein, and Zeppenfeld [56]. This work has been updated by the SFitter group in [57, 58] and in the recent paper [59]. Other analysis using stronger model assumptions have been given in [60] and [61]. It is clear from the explanation given in the previous paragraph that any such analysis from before 2010 is excessively optimistic.

We have tried to make our own analysis of the model-independent LHC sensitivity to Higgs couplings, also bringing up to date the estimates in [55] and taking into account new results on the LHC capabilities for Higgs couplings presented by the ATLAS and CMS collaborations in [62–64]. The results are shown in Fig. 2.4. The details of the analysis are given in [65]. For comparison, the most recent estimates from the Sfitter group are shown in Fig. 2.5. The results differ in some details, but they are qualitatively similar. In [64], the CMS collaboration has presented a second scenario with more optimistic projections; however, these are based on the assumption, so far unsupported by simulation work, that systematic errors can be decreased with increasing data sets as $1/\sqrt{N}$, even in the high-luminosity LHC era.

This estimate leads to a quite definite conclusion. The LHC experiments will be able to

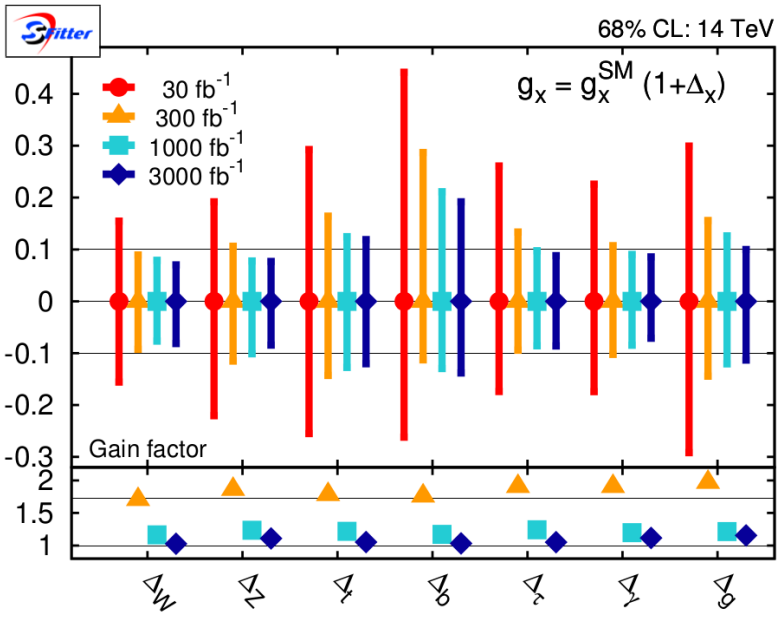

Figure 2.5. Estimate of the sensitivity of the LHC experiments to Higgs boson couplings in a model-independent analysis with one detector and varying luminosity sample, from the SFitter group [59].

simultaneously determine the Higgs couplings to Standard Model particle in a way that is, if not completely model-independent, at least relies onlly on the minimal theoretical assumptions described above. These determinations should be accurate enough to confirm or refute the hypothesis that the particle recently observed has the profile of the Standard Model Higgs boson. However, these experiments will not provide sufficient accuracy in the Higgs couplings to test for the deviations expected in new physics models in the Decoupling Limit. That is, they will not be able to access the deviation of Higgs couplings from the Standard Model for most of the effects described in Section 2.2. To reach the level required for this, a stronger tool is needed.

2.3.4 Prospects for measurement of the triple Higgs coupling at the LHC

Measurement of the Higgs quartic coupling parameter λ provides a test of the electroweak symmetry breaking mechanism through the structure of the Higgs potential. This coupling can be probed via a measurement of the triple-Higgs vertex, which contributes along with other diagrams to Higgs pair production. This coupling can be significantly modified in models with extended Higgs sectors, in particular in models that increase the strength of the electroweak phase transition to provide viable baryogenesis [66]. For Higgs pair production via $gg \to hh$, low-mass new physics in the loops can rather significantly affect the cross section even if it does not have a large effect on the $gg \to h$ cross section [67, 68].

Measuring the triple Higgs coupling at the LHC is very challenging for a 125 GeV Higgs boson. The largest production cross section is $gg \to hh$, with other potential production modes (VBF $qq \to qqhh$, $q\bar{q} \to Vhh$, and $gg, q\bar{q} \to t\bar{t}hh$) being severely rate-limited. The $4W$ final state has been studied for $m_h > 150$ GeV [69] and was found to be promising for $m_h \simeq 170$–200 GeV at the high-luminosity (10^{35} cm^{-2}s^{-1}) LHC [70]; however, this final state is suppressed by the falling $h \to WW$ branching ratio at lower masses (a factor of $(0.22)^2 = 0.048$ at $m_h = 125$ GeV, compared to 0.92 (0.55) at $m_h = 170$ (200) GeV). This suppression will be compensated somewhat by an enhanced production cross section at lower masses, but no LHC study has been done in the $4W$ final state for a low-mass Higgs.

The $4b$ and $bb\tau\tau$ final states were studied for a 120 GeV Higgs in Ref. [71, 72] and the more

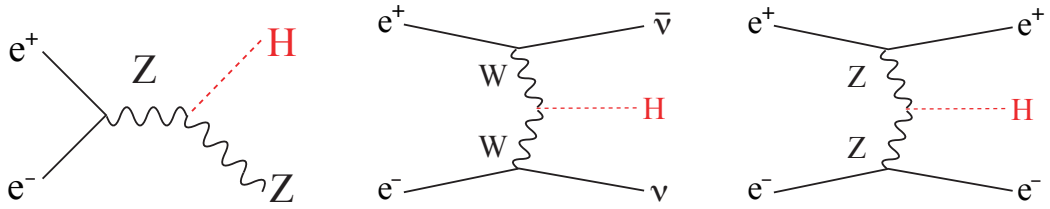

Figure 2.6. Feynman diagrams for the three major Higgs production processes at the ILC: $e^+e^- \to Zh$ (left), $e^+e^- \to \nu\bar{\nu}H$ (center), and $e^+e^- \to e^+e^-H$ (right).

promising $bb\gamma\gamma$ final state was studied in Ref. [73]. The expected triple-Higgs coupling sensitivity can be expressed as $\Delta\lambda_{hhh} \equiv \lambda/\lambda_{\rm SM} - 1$, assuming no new particles contribute to the $gg \to h$ and $gg \to hh$ loops. The results, summarized in Table 2.1, indicate that only order-1 sensitivity will be possible.

The ATLAS submission to the European Strategy Study [62], gives some new results on the measurement of the triple Higgs coupling. The report estimates that, with 3000 fb^{-1} and combining both LHC experiments, "a $\sim$ 30% measurement of λ_{HHH} may be achieved". We look forward to the studies, not yet reported, that will support this conclusion.

2.4 Higgs measurements at ILC at 250 GeV

The physics program of the LHC should be contrasted with the physics program that becomes available at the ILC. The ILC, being an e^+e^- collider, inherits traditional virtues of past e^+e^- colliders such as LEP and SLC. We have described these in Chapter 1. The ILC offers well defined initial states, a clean environment, and reasonable signal-to-noise ratios even before any selection cuts. Thanks to the clean environment, it can be equipped with very high precision detectors. The experimental technique of Particle Flow Analysis (PFA), described in Volume 4 of this report, offers a qualitative improvement in calorimetry over the detectors of the LEP era and sufficient jet mass resolution to identify W and Z bosons in their hadronic decay modes. Thus, at the ILC, we can effectively reconstruct events in terms of fundamental particles — quarks, leptons, and gauge bosons. Essentially, we will be able to analyze events as viewing Feynman diagrams. By controlling beam polarization, we can even select the Feynman diagrams that participate a particular reaction under study. The Higgs boson can be observed in all important modes, including those with decay to hadronic jets. This is a great advantage over the experiments at the LHC and provides the opportunity to carry out a truly complete set of precision measurements of the properties of the Standard-Model-like Higgs boson candidate found at the LHC.

The precision Higgs program will start at $\sqrt{s} = 250\,$GeV with the Higgs-strahlung process, $e^+e^- \to Zh$ (Fig. 2.6 (left)).The production cross section for this process is plotted in Fig. 2.7 as a function of $\sqrt{s}$ together with that for the weak boson fusion processes (Figs. 2.6-(center and right)). We can see that the Higgs-strahlung process attains its maximum at around $\sqrt{s} = 250\,$GeV and dominates the fusion processes there. The cross section for the fusion processes increases with the energy and takes over that of the Higgs-strahlung process above $\sqrt{s} \gtrsim 400\,$GeV.

The production cross section of the Higgs-strahlung process at $\sqrt{s} \simeq 250\,$GeV is substantial for the low mass Standard-Model-like Higgs boson. Its discovery would require only a few fb^{-1} of integrated luminosity. With 250 fb^{-1}, about $8. \times 10^4$ Higgs boson events can be collected. Note that, here and in the rest of our discussion, we take advantage of the ILC's positron polarization to increase the Higgs production rate over that expected for unpolarized beams.

The precise determination of the properties of the Higgs boson is one of the main goals of the ILC. Only after this study is completed can we settle the question of whether the new resonance is

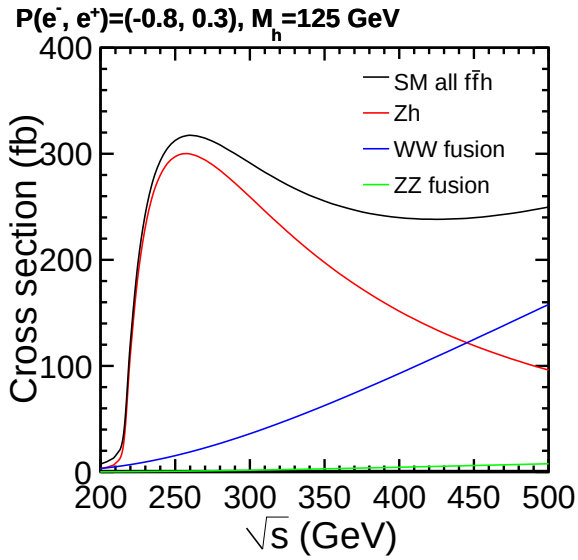

Figure 2.7 Production cross section for the $e^+e^- \to Zh$ process as a function of the center of mass energy for $m_h = 125\,\text{GeV}$, plotted together with those for the WW and ZZ fusion processes: $e^+e^- \to \nu\bar{\nu}H$ and $e^+e^- \to e^+e^-H$.

the Standard Model Higgs boson, a Higgs boson of a more general theory, or a particle of a different origin. Particular important for this question are the values of the Higgs boson mass, m_h, and the Higgs production cross sections and branching ratios.

In this section and the following ones, we will present the measurement accuracies for the Higgs boson properties expected from the ILC experiments. These measurement accuracies are estimated from full simulation studies with the ILD and SiD detectors described in the Detector Volume, Volume 4 of this report. Because these full-simulation studies are complex and were begun long before the LHC discovery, the analyses assumed a Higgs boson of mass 120 GeV. In this section and the next two sections, then, all error estimates refer to 120 GeV Higgs boson. In Section 2.7, we will present a table in which our results are extrapolated to measurement accuracies for a 125 GeV Higgs boson, taking into appropriate account the changes in the signal and background levels in these measurements.

2.4.1 Mass and quantum numbers

We first turn our attention to the measurements of the mass and spin of the Higgs boson, which are necessary to confirm that the Higgs-like object found at the LHC has the properties expected for the Higgs boson. We have discussed in the previous section that the LHC already offers excellent capabilities to measure the mass and quantum numbers of the Higgs boson. However, the ILC offers new probes of these quantities that are very attractive experimentally. We will review them here.

We first discuss the precision mass measurement of the Higgs boson at the ILC. This measurement can be made particularly cleanly in the process $e^+e^- \to Zh$, with $Z \to \mu^+\mu^-$ and $Z \to e^+e^-$ decays. Here the distribution of the invariant mass recoiling against the reconstructed Z provides a precise measurement of m_h, independently of the Higgs decay mode. In particular, the $\mu^+\mu^-X$ final state provides a particularly precise measurement as the e^+e^-X channel suffers from larger experimental uncertainties due to bremsstrahlung. It should be noted that it is the capability to precisely reconstruct the recoil mass distribution from $Z \to \mu^+\mu^-$ that defines the momentum resolution requirement for an ILC detector.

The reconstructed recoil mass distributions, calculated assuming the Zh is produced with four-momentum $(\sqrt{s}, 0)$, are shown in Fig.2.8. In the e^+e^-X channel FSR and bremsstrahlung photons are identified and used in the calculation of the $e^+e^-(n\gamma)$ recoil mass. Fits to signal and background components are used to extract m_h. Based on this model-independent analysis of Higgs production in the ILD detector, it is shown that m_h can be determined with a statistical precision of 40 MeV (80 MeV) from the $\mu^+\mu^-X$ (e^+e^-X) channel. When the two channels are combined an uncertainty

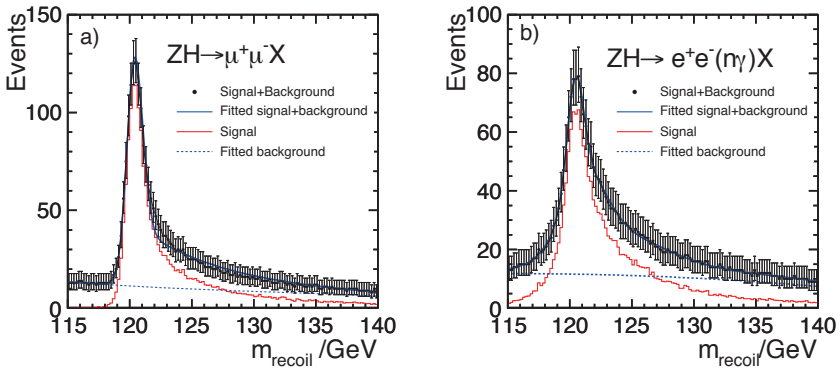

Figure 2.8
Higgs recoil mass distribution in the Higgs-strahlung process $e^+e^- \to Zh$, with (a) $Z \to \mu^+\mu^-$ and (b) $Z \to e^+e^-(n\gamma)$. The results are shown for $P(e^+, e^-) = (+30\%, -80\%)$ beam polarization.

of 32 MeV is obtained [74, 75]. The corresponding model independent uncertainty on the Higgs production cross section is 2.5%. Similar results were obtained from SiD [76]. It should be emphasized that these measurements only used the information from the leptonic decay products of the Z and are independent of the Higgs decay mode. As such this analysis technique could be applied even if the Higgs decayed invisibly and hence allows us to determine the absolute branching ratios including that of invisible Higgs decays. By combining the branching ratio to ZZ with the production cross section, which involves the same g_{hZZ} coupling, one can determine the total width and the absolute scale of partial widths with no need for the theoretical assumptions needed for the LHC case. We will return to this point later.

It is worth noting that, for the $\mu^+\mu^- X$ channel, the width of the recoil mass peak is dominated by the beam energy spread. In the above study Gaussian beam energy spreads of $0.28\,\%$ and $0.18\,\%$ are assumed for the incoming electron and positron beams respectively. For ILD the detector response leads to the broadening of the recoil mass peak from 560 MeV to 650 MeV. The contribution from momentum resolution is therefore estimated to be 330 MeV. Although the effect of the detector resolution is not negligible, the dominant contribution to the observed width arises from the incoming beam energy spread rather than the detector response. This is no coincidence; the measurement of m_h from the $\mu^+\mu^- X$ recoil mass distribution was one of the benchmarks used to determine the momentum resolution requirement for a detector at the ILC.

If there are additional Higgs fields with vacuum expectation values that contribute to the mass of the Z, the corresponding Higgs particles will also appear in reactions $e^+e^- \to Zh'$, and their masses can be determined in the same way.

We now turn to the determination of the spin and CP properties of the Higgs boson. The $h \to \gamma\gamma$ decay observed at the LHC rules out the possibility of spin 1 and restricts the charge conjugation C to be positive. We have already noted that the discrete choice between the CP even and CP odd charge assignments can be settled by the study of Higgs decay to ZZ^* to 4 leptons at the LHC.

The ILC offers an additional, orthogonal, test of these assignments. The threshold behavior of the Zh cross section has a characteristic shape for each spin and each possible CP parity. For spin 0, the cross section rises as β near the threshold for a CP even state and as β^3 for a CP odd state. For spin 2, for the canonical form of the coupling to the energy-momentum tensor, the rise is also β^3. If the spin is higher than 2, the cross section will grow as a higher power of β. With a three-$20\,\mathrm{fb}^{-1}$-point threshold scan of the $e^+e^- \to Zh$ production cross section we can separate these possibilities as shown in Fig. 2.9 (left) [77]. The discrimination of more general forms of the coupling is possible by the use of angular correlations in the boson decay; this is discussed in detail in [78].

At energies well above the Zh threshold, the Zh process will be dominated by longitudinal Z production as implied by the equivalence theorem. The reaction will then behave like a scalar pair production, showing the characteristic $\sim \sin^2\theta$ dependence if the h particle's spin is zero. The

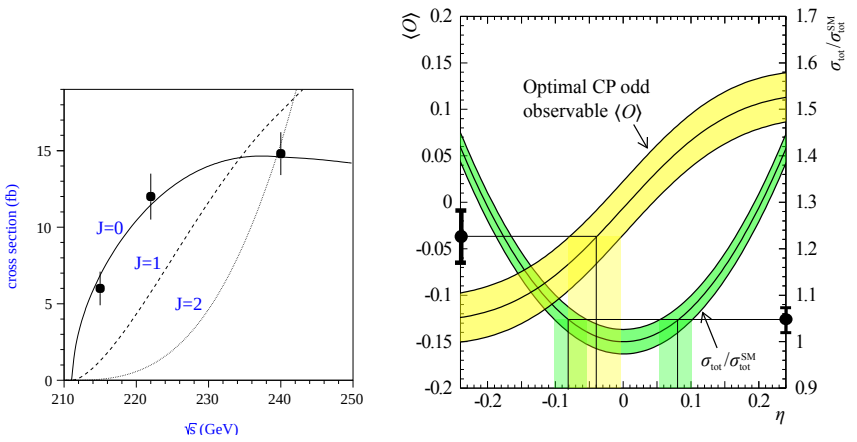

Figure 2.9
Left: Threshold scan of the $e^+e^- \to Zh$ process for $m_h = 120\,\text{GeV}$, compared with theoretical predictions for $J^P = 0^+$, 1^-, and 2^+ [77]. Right: Determination of CP-mixing with 1-σ bands expected at $\sqrt{s} = 350\,\text{GeV}$ and $500\,\text{fb}^{-1}$ [79].

measurement of the angular distribution will hence strongly corroborate that the h is indeed a scalar particle.

The analytic power of the ILC is emphasized when we consider more detailed questions. It is possible that the h is not a CP eigenstate but rather a mixture of CP even and CP odd components. This occurs if there is CP violation in the Higgs sector. It is known that CP violation from the CKM matrix cannot explain the cosmological excess of baryons over antibaryons; thus, a second source of CP violation in nature is needed. One possibility is that this new CP violation comes from the Higgs sector and gives rise to net baryon number at the electroweak phase transitions, through mechanisms that we will discuss in Section 9.1 of this report. For these models, the h mass eigenstates can be mainly CP even but contain a small admixture of a CP odd component.

A small CP odd contribution to the hZZ coupling can affect the threshold behavior. The right-hand side of Fig. 2.9 shows the determination of this angle at a center of mass energy of 350 GeV from the value of the total cross section and from an appropriately defined optimal observable [79].

Tests of mixed CP property using the hZZ coupling may not be the most effective ones, since the CP odd hZZ coupling is of higher dimension and may be generated only through loops. It is more effective to use a coupling for which the CP even and CP odd components are on the same footing. An example is the h coupling to $\tau^+\tau^-$, given by

$$\Delta\mathcal{L} = -\frac{m_\tau}{v} h\, \overline{\tau}(\cos\alpha + i \sin\alpha\gamma^5)\tau \tag{2.33}$$

for a Higgs boson with a CP odd component. The polarizations of the final state τs can be determined from the kinematic distributions of their decay products; the CP even and odd components interfere in these distributions [80, 81]. In [82], it is estimated that the angle α can be determined at the ILC to an accuracy of 6°.

2.4.2 Inclusive cross section

Whereas all Higgs boson measurements at the LHC are measurements of $\sigma \cdot BR$, the ILC allows us to measure the absolute size of a Higgs inclusive cross section. This can be done by applying the recoil technique discussed above to the measurement of (σ_{Zh}) for the $e^+e^- \to Zh$ process. The measurement gives the cross section to a relative accuracy of $2.5\,\%$ at $250\,\text{fb}^{-1}$ without looking at the h decay at all. This cross section is indispensable for extracting branching ratio (BR) from the event rate, which is proportional to $\sigma_{Zh} \cdot BR$, and limits its precision.

It is worth noting that the inclusive cross section is a direct measure of the h to ZZ coupling (g_{hZZ}). This single measurement at the ILC is capable of determining this coupling to $1.3\,\%$. If the h particle is a scalar particle, this coupling must originate from a gauge-kinetic term of the form

given by Eq.(2.5) with one Φ leg replaced by the vacuum expectation value associated with the h particle. The observation of this coupling is, therefore, a strong evidence of the existence of a vacuum condensate associated with the h particle. Moreover, the vacuum expectation value here has no solid reason to saturate the standard model value, $v = 246\,\text{GeV}$. The g_{hZZ} coupling hence measures to what extent the vacuum expectation value associated with the multiplet to which the h particle belongs explains the mass of the Z boson. This measurement, even considered alone, has extraordinary power to address the most basic issues in the breaking of electroweak symmetry.

As noted above, the ILC will not be capable of directly observing the width of the Higgs boson if it is as small as the Standard Model prediction of 4 MeV. However, because the ILC experiments can make this inclusive cross section measurement, they can also determine the width of the Higgs boson in a completely model-independent way. As a first step, note that the recoil technique gives Higgs boson branching ratios directly. We identify a Z boson at the correct lab energy to be in recoil against the Higgs and count events on the opposite side in every final state. Then the total width of the Higgs is given by the formula

$$\Gamma_{\text{tot}} = \frac{\Gamma(h \to ZZ)}{BR(h \to ZZ)} \ , \tag{2.34}$$

The quantity $\Gamma(h \to ZZ)$ is directly proportional to the inclusive cross section. The Higgs branching ratio to ZZ is unfortunately quite small, so the direct measurement of this quantity at 250 GeV is statistics limited. In Section 2.5, we will explain how this quantity can be determined more accurately from data at higher energy. We will demonstrate there that, with 500 GeV data, the ILC should achieve an unambiguous measurement of the Higgs boson width to 6% accuracy.

2.4.3 Branching ratios and couplings

As we have just explained, the measurement of the inclusive cross section of the $e^+e^- \to Zh$ process allows us to directly extract the h particle's branching fractions. A precise measurement of the absolute branching ratios of the Higgs bosons is an important test of the mass generation mechanism and provides a window into effects beyond the SM. For the branching ratio measurements we again use the $e^+e^- \to Zh$ process, but this time exploiting all the decay modes of the Z boson including the $Z \to q\bar{q}$ and $Z \to \nu\bar{\nu}$ decays. The use of fully hadronic final states is possible only in a very clean environment of an e^+e^- collider. In the clean environment of the ILC we can also use a high performance micro-vertex detector, placed very close to the interaction point, which makes it possible to identify not only $h \to b\bar{b}$ but also $h \to c\bar{c}$ decays. Figure 2.10 shows a lego plot of the multivariate estimate of b-likeness vs. c-likeness for the template samples of the signal and the SM background events. We can see the clear differences between the different decay modes of the Higgs boson. Thanks to these clear differences, a fit using these templates hence provides separate measurements of the cross section times branching fraction for the Higgs decays to $b\bar{b}$, $c\bar{c}$, and gg with negligible mutual correlation. Together with the measurement of the $h \to \tau^+\tau^-$ decays, we can access the Yukawa couplings of both up-type and down-type fermions and test the coupling-mass proportionality. The loop-induced $h \to gg$ decay is indirectly sensitive to the top Yukawa coupling and possibly other new strongly interacting particles that couple to the Higgs particle but are too heavy to produce directly. By the same token, the $h \to \gamma\gamma$ and the $h \to Z\gamma$ decays are also important as tools to probe heavy particles with electroweak charges. The expected accuracies on the branching ratios are summarized in Table 2.2. It is worth noting that these full simulation results are consistent with the past fast simulation results [87–91].

The h decay to invisible final states, if any, can be measured by looking at the recoil mass under the condition that nothing observable is recoiling against the Z boson. Higgs portal models

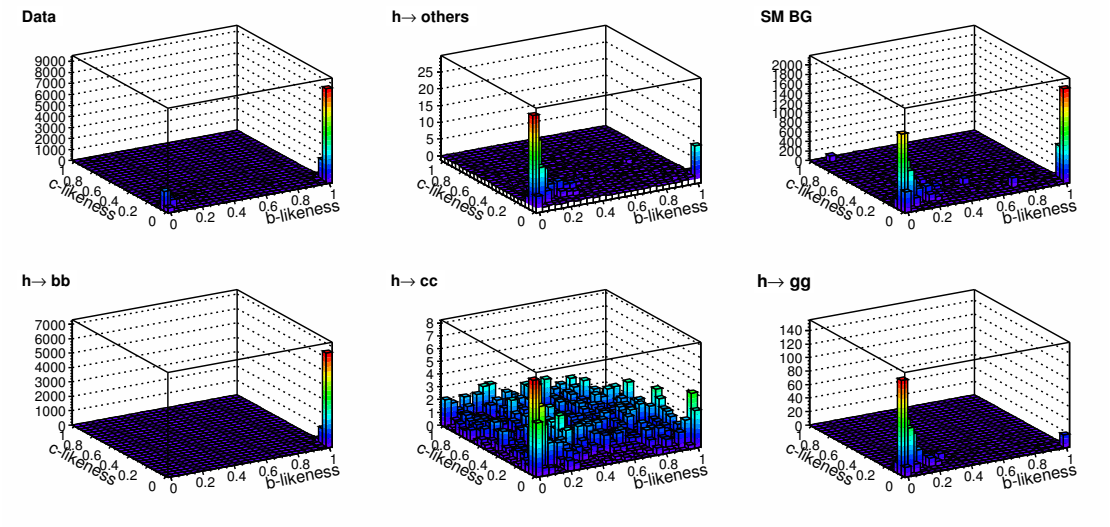

Figure 2.10. Two-dimensional images of the three-dimensional template samples as a function of b-likeness v.s. c-likeness. The bottom row shows Higgs decays, left to right, to $b\bar{b}$, $c\bar{c}$, and gg. The top row shows, left to right, the full Monte Carlo Higgs sample after event selection, the Higgs decays to non-2-jet modes, and the Standard Model background. From [83].

Table 2.2. Expected accuracies for the h boson branching ratios for $m_h = 120$ GeV, obtained with full detector simulations at the $\sqrt{s} = 250$ GeV assuming $\mathcal{L} = 250$ fb^{-1} and $(e^-, e^+) = (-0.8, +0.3)$ beam polarization [83–86]. The errors on BR include the error on σ of 2.5% from the recoil mass measurement.

mode	BR	$\sigma \cdot BR$ (fb)	$N_{evt}/250\,\text{fb}^{-1}$	$\Delta(\sigma\,BR)/(\sigma\,BR)$	$\Delta BR/BR$
$h \to b\bar{b}$	65.7%	232.8	58199	1.0%	2.7%
$h \to c\bar{c}$	3.6%	12.7	3187	6.9%	7.3%
$h \to gg$	5.5%	19.5	4864	8.5%	8.9%
$h \to WW^*$	15.0%	53.1	13281	8.1%	8.5%
$h \to \tau^+\tau^-$	8.0%	28.2	7050	3.6%	4.4%
$h \to ZZ^*$	1.7%	6.1	1523	26%	26%
$h \to \gamma\gamma$	0.29%	1.02	255	23-30%	23-30%

predict such decays and provide a unique opportunity to access dark matter particles [92]. The main background is $e^+e^- \to ZZ$ followed by one Z decaying into a lepton pair and the other into a neutrino pair. With an integrated luminosity of 250 fb^{-1} at $\sqrt{s} = 250$ GeV, the ILC can set a 95% CL limit on the invisible branching ratio to 4.8% using the golden $Z \to \mu^+\mu^-$ mode alone [93]. Using other modes including $Z \to q\bar{q}$, we could improve this significantly to 0.8% [94].

The branching fraction measurements discussed so far are still statistics limited. If we are to improve the measurement precisions by increasing the integrated luminosity by doubling the number of bunches or by running longer, etc., we will need to estimate the systematic errors that may limit the measurement in particular for $h \to b\bar{b}$. The systematic error from the uncertainty in luminosity measurement should be less than 0.1% and thus negligible. The dominant source of systematic errors is probably that from flavor identification and the separation of Z plus jet signal from Standard Model backgrounds using the multivariate analysis described above. We are still in the process of optimizing this analysis, but we expect the systematic error due to flavor-tagging can be controlled by using the calibration processes ZZ, $Z\gamma$, and WW, all of which have large cross sections. These calibration samples will also allow us to calibrate and normalize the background estimate.

To determine the absolute normalization of Higgs boson partial widths from the measurements of branching ratios, we need to combine these with an accurate value of one partial width or cross section. As described above, the 250 GeV running of the ILC for 250 fb^{-1} will determine the cross section for $e^+e^- \to Zh$ very accurately, to 2.5%. The value can be directly converted to g_{hZZ} or to

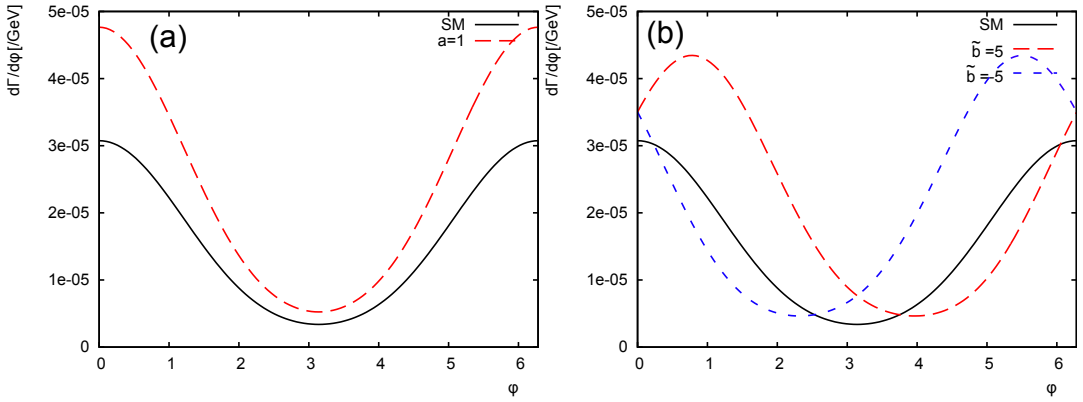

Figure 2.11. Distribution of the angle ϕ between two decay planes of W and W^* from the decay $H \to WW^* \to 4j$ with the inclusion of anomalous couplings [97]. (a) The SM curve along with that for $a = 1$, $b = \tilde{b} = 0$, $\Lambda = 1$ TeV; the position of the minimum is the same for both distributions. (b) The SM result with the cases $\tilde{b} = \pm 5$, $a = b = 0$, $\Lambda = 1$ TeV; the position of the minimum is now shifted as discussed in the text. From [97].

the absolute partial width $\Gamma(ZZ)$. However, to use this value to normalize the other Higgs partial widths in a completely model-independent analysis, we would need to use the formula similar to (2.34)

$$\Gamma(A) = \Gamma(ZZ) \cdot \frac{BR(A)}{BR(ZZ)}, \tag{2.35}$$

and so we again need to measure the branching ratio for $h \to ZZ^*$. This is not easy to do at the ILC because it is a rare mode giving low statistics for a Higgs boson with $m_h \simeq 120$ GeV. No full simulation study of the $h \to ZZ^*$ branching ratio in $e^+e^- \to Zh$ is currently available. We will therefore use the result of the $h \to WW^*$ study [85] and scale accordingly. The error for the $h \to WW^*$ decay implies a 26% relative error for the $h \to ZZ^*$ branching ratio. The use of the formula (2.35) then implies that the uncertainties in absolute partial widths or Higgs couplings are those listed convolved with $2.5 \oplus 26\%$. This significantly degrades the precision information obtained at the ILC.

An alternative is to use the theoretical assumption

$$g(hWW)/g(hZZ) = \cos^2\theta_W \tag{2.36}$$

to tie together the hZZ and hWW couplings. Now $BR(WW^*)$ can be used in the denominator of Eq.(2.35). The error added in converting from branching ratios to partial widths is $2.5 \oplus 8.6\% = 9.0\%$.

A better way is to use the WW fusion process, $e^+e^- \to \nu\bar{\nu}h$. The cross section for this process is proportional to $g^2(hWW)$ and thus to the $h \to WW^*$ partial width [95]. Although the WW fusion cross section is small at $\sqrt{s} = 250$ GeV, 18 fb for $m_h = 120$ GeV and the standard left-hand beam combination, $(P_{e^-}, P_{e^+}) = (-0.8, +0.3)$, the expected yield exceeds 4k events and allows the measurement of the WW fusion cross section to $\Delta\sigma(WW)/\sigma(WW) = 7.2\%$ for the $250\,\mathrm{fb}^{-1}$. Combining the $BR(WW^*)$ measurement, this implies that the total width can be determined to 11% in a completely model-independent way from 250 GeV data alone [96]. As we will see below, the determination of the absolute strength of the Higgs coupling to WW is expected to be further improved by a measurement of the WW fusion cross section at $\sqrt{s} = 500$ GeV. The 500 GeV data can also be used to improve the accuracy on the $BR(WW^*)$.

So far we have been dealing with the branching ratios and partial widths after phase space integration. The $h \to WW^*$ decay provides an interesting opportunity to study its differential width and probe the Lorentz structure of the hWW coupling through angular analyses of the decay products. The relevant part of the general interaction Lagrangian, which couples the Higgs boson to W bosons

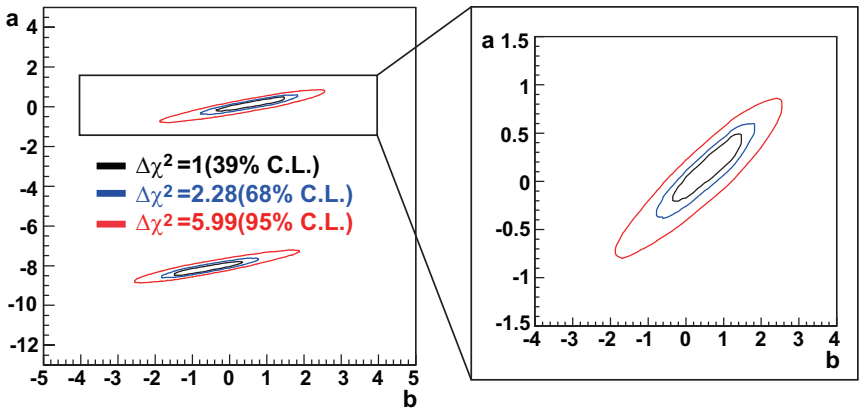

Figure 2.12
Probability contours for $\Delta\chi^2 = 1$, 2.28, and 5.99 in the a-b plane, which correspond to 39%, 68%, and 95% C.L., respectively.

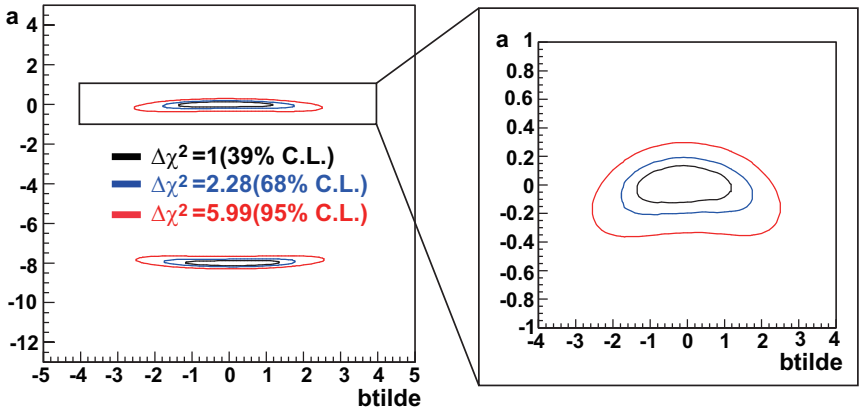

Figure 2.13
Contours similar to Fig. 2.12 plotted in the a-$\tilde{b}$ plane.

in a both Lorentz- and gauge-symmetric fashion, can be parameterized as

$$\mathcal{L}_{\mathrm{hWW}} = 2m_W^2 \left(\frac{1}{v} + \frac{a}{\Lambda}\right) h\, W_\mu^+ W^{-\mu} + \frac{b}{\Lambda} h\, W_{\mu\nu}^+ W^{-\mu\nu} + \frac{\tilde{b}}{\Lambda} h\, \epsilon^{\mu\nu\sigma\tau} W_{\mu\nu}^+ W_{\sigma\tau}^- \,, \tag{2.37}$$

where $W_{\mu\nu}^{\pm}$ is the usual gauge field strength tensor, $\epsilon^{\mu\nu\sigma\tau}$ is the Levi-Civita tensor, v is the VEV of the Higgs field, and Λ is a cutoff scale[1]. The real dimensionless coefficients, a, b, and $\tilde{b}$, are all zero in the Standard Model and measure the anomaly in the hWW coupling, which arise from some new physics at the scale Λ. The coefficient a stands for the correction to the Standard Model coupling. The coefficients b and $\tilde{b}$ parametrize the leading dimension-five non-renormalizable interactions and corresponding to $(\boldsymbol{E}\cdot\boldsymbol{E} - \boldsymbol{B}\cdot\boldsymbol{B})$-type CP-even and $(\boldsymbol{E}\cdot\boldsymbol{B})$-type CP-odd contributions. The a coefficient, if nonzero, would modify just the normalization of the Standard Model coupling, while the b and $\tilde{b}$ coefficients would change the angular correlations of the decay planes. This effect is shown in Fig. 2.11 [97]. Nonzero b and $\tilde{b}$ would also modify the momentum distribution of the W boson in the Higgs rest frame. Simultaneous fits to p_W and ϕ_{plane} result in the contour plots in Figs.2.12 and 2.13.

[1] The Lagrangian (2.37) is not by itself gauge invariant; to restore explicit gauge invariance we must also include the corresponding anomalous couplings of the Higgs boson to Z bosons and photons.

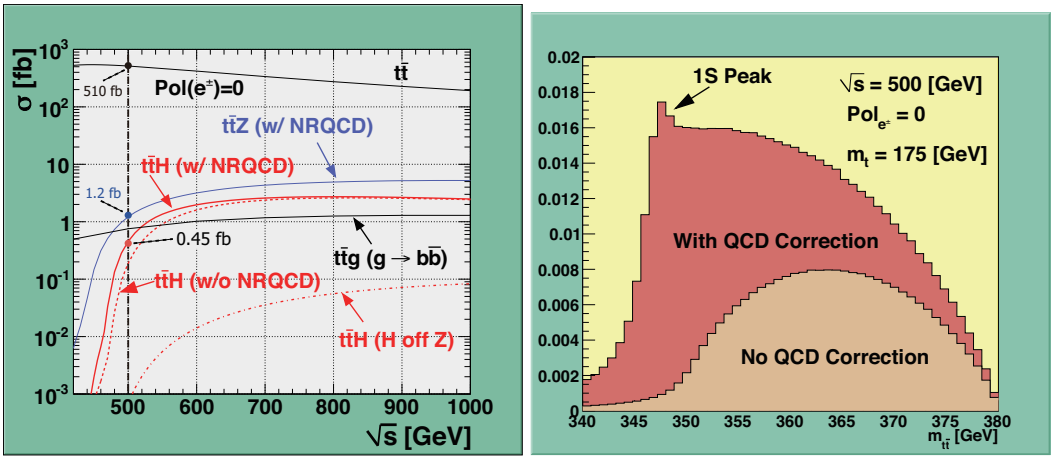

Figure 2.14. Left: Cross section for the $e^+e^- \to t\bar{t}h$ process as a function of $\sqrt{s}$, together with those of background processes, $e^+e^- \to t\bar{t}Z$, $\to t\bar{t}g^*$, and $\to t\bar{t}$. Right: The invariant mass distribution of the $t\bar{t}$ system from the $e^+e^- \to t\bar{t}h$ process with and without the non-relativistic QCD correction.

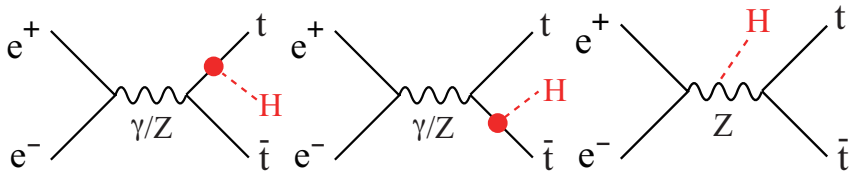

Figure 2.15. Three diagrams contributing to the $e^+e^- \to t\bar{t}h$ process. The h-off-t or $\bar{t}$ diagrams, (a) and (b), contain the top Yukawa coupling while the h-off-Z diagram (c) does not.

2.5 Higgs measurements at ILC at 500 GeV

The two very important processes will become accessible for the first time at $\sqrt{s} = 500\,\text{GeV}$. The first is the $e^+e^- \to t\bar{t}h$ process [98, 99], in which the top Yukawa coupling will appear in the tree level for the first time at the ILC. The top quark, being the heaviest matter fermion in the Standard Model, would be crucial to understand the fermion mass generation mechanism. The second is the $e^+e^- \to Zhh$ process, to which the triple Higgs coupling contributes in the tree level. The self-coupling is the key ingredient of the Higgs potential and its measurement is indispensable for understanding the electroweak symmetry breaking.

2.5.1 Top quark Yukawa coupling

Past simulation studies for the $e^+e^- \to t\bar{t}h$ process were mostly made at around $\sqrt{s} = 800\,\text{GeV}$, since the cross section attains its maximum there for $m_h \simeq 120\,\text{GeV}$ [100–102]. It was pointed out, however, that the cross section would be significantly enhanced near the threshold due to the bound-state effects between t and $\bar{t}$ [103–109]. The effect is made obvious in the right-hand plot of Fig. 2.14. This enhancement implies that the measurement of the top Yukawa coupling might be possible already at $\sqrt{s} = 500$ GeV [110]. A serious simulation study at $\sqrt{s} = 500$ GeV was performed for the first time, with the QCD bound-state effects consistently taken into account for both signal and background cross sections, in [111].

The $e^+e^- \to t\bar{t}h$ reaction takes place through the three diagrams shown in Fig. 2.15 As shown in Fig. 2.14 (left), the contribution from the irrelevant h-off-Z diagram is negligible at $\sqrt{s} = 500\,\text{GeV}$, thereby allowing us to extract the top Yukawa coupling g_t by just counting the number of signal events. By combining the 8-jet and 6-jet-plus-lepton modes of $e^+e^- \to t\bar{t}h$ followed by $h \to b\bar{b}$, the analysis of [111] showed that a measurement of the top Yukawa coupling to $\Delta g_t/g_t = 10\%$ is possible

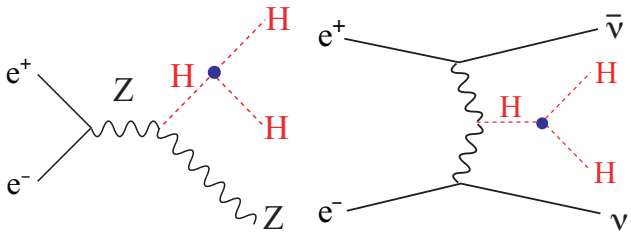

Figure 2.16
Relevant diagrams containing the triple Higgs coupling for the two processes: $e^+e^- \to Zhh$ (left) and $e^+e^- \to \nu_e\overline{\nu}_e hh$.

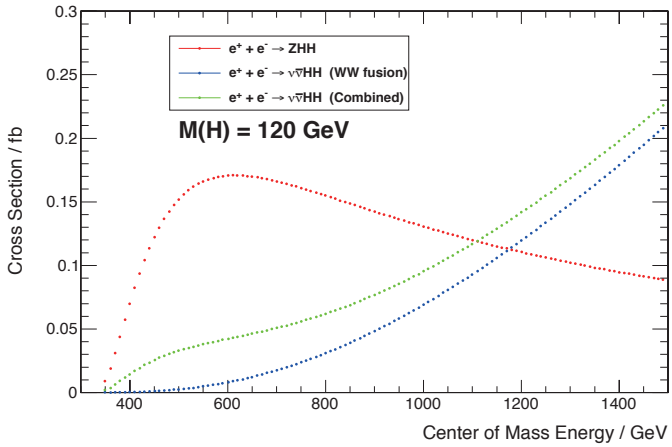

Figure 2.17
Cross sections for the two processes $e^+e^- \to Zhh$ (left) and $e^+e^- \to \nu_e\overline{\nu}_e hh$ as a function of $\sqrt{s}$ for $m_h = 120$ GeV.

for $m_h = 120$ GeV with polarized electron and positron beams of $(P_{e^-}, P_{e^+}) = (-0,8, +0.3)$ and an integrated luminosity of 1 ab^{-1}. This result obtained with a fast Monte Carlo simulation has just recently been corroborated by a full simulation [112, 113].

2.5.2 Higgs self-coupling

The triple Higgs boson coupling can be studied at the ILC through the processes $e^+e^- \to Zhh$ and $e^+e^- \to \nu_e\overline{\nu}_e hh$. The relevant Feynman diagrams are shown in Fig. 2.16 [114]. The cross sections for the two processes are plotted as a function of $\sqrt{s}$ for $m_h = 120$ GeV in Fig. 2.17. The cross section reaches its maximum of about 0.18 fb at around $\sqrt{s} = 500$ GeV, which is dominated by the former process. A full simulation study of the process $e^+e^- \to Zhh$ followed by $h \to b\bar{b}$ has recently been carried out in [115], making use of a new flavor tagging package (LCFIplus) [116] together with the conventional Durham jet clustering algorithm.

From the combined result of the three channels corresponding to different Z decay modes, $Z \to l^+l^-$, $\nu\overline{\nu}$, and $q\bar{q}$, it was found that the process can be detected with an excess significance of 5-σ and the cross section can be measured to $\Delta\sigma/\sigma = 0.27$ for an integrated luminosity of 2 ab^{-1} with beam polarization $(P_{e^-}, P_{e^+}) = (-0,8, +0.3)$. Unlike the $e^+e^- \to t\bar{t}h$ case, however, the contribution from the background diagrams without the self-coupling is significant and the relative error on the self-coupling λ is $\Delta\lambda/\lambda = 0.44$ with a proper event weighting to enhance the contribution from the self-coupling diagram. The result is not yet very satisfactory compared to the results from earlier fast simulation studies [117–121]. The major problem in the analysis is mis-clustering of color-singlet groups. Figure 2.18 compares the reconstructed invariant masses for the two Higgs candidates with Durham jet clustering (a) and with perfect jet clustering using Monte Carlo truth (b). We can see that the separation between the signal and the background is significantly improved if there is no mis-jet-clustering. A new jet clustering algorithm is now being developed.

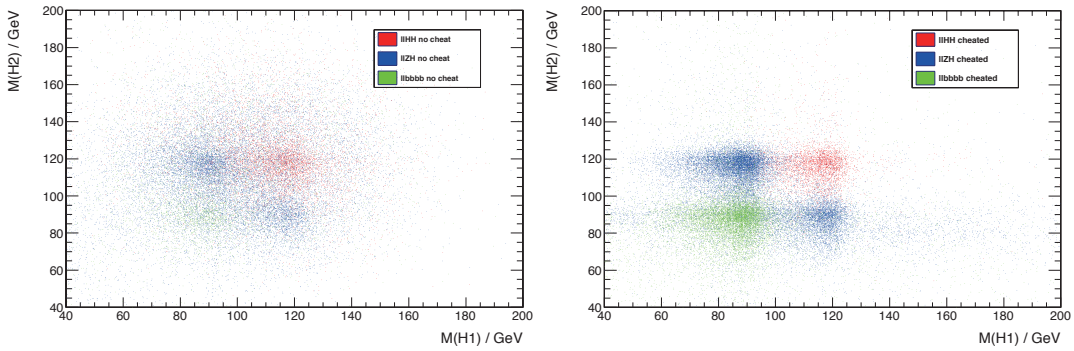

Figure 2.18. Scatter plot of the invariant masses of the two Higgs candidates. Left: with Durham jet clustering. Right: with perfect jet clustering using Monte Carlo truth on the color flow.

2.5.3 WW fusion and the hWW coupling

As shown in Fig.2.7, the WW fusion process takes over the Higgs-strahlung process at around $\sqrt{s} = 450\,\text{GeV}$. The cross section for the fusion process is about 160 fb at $\sqrt{s} = 500$ GeV for $m_h = 120\,\text{GeV}$. Thanks to this large cross section and the larger luminosity expected at this energy, the fusion process provides a unique opportunity to directly measure the hWW coupling with high precision. With an integrated luminosity of $500\,\text{fb}^{-1}$, we can measure this cross section times the branching fraction to $b\bar{b}$ to a statistical accuracy of 0.60%. In terms of Higgs cross sections and branching ratios, the quantity measured is

$$\sigma(\nu\bar{\nu}h) \cdot BR(h \to b\bar{b}) \sim \Gamma(h \to WW^*) \cdot BR(h \to b\bar{b}) \ . \tag{2.38}$$

By combining this with the direct branching ration measurements at $\sqrt{s} = 250\,\text{GeV}$, we will be able to determine the cross section $\sigma(\nu\bar{\nu}h)$ to an accuracy of 2.7%, which translates to an expected error on the hWW coupling of $\Delta g_{hWW}/g_{hWW} = 1.4\%$. The large data sample of the fusion process is also useful to improve the precision of the $h \to WW^*$ branching ratio. It is noteworthy that the background separation is easier at $\sqrt{s} = 500$ GeV than at $\sqrt{s} = 250$ GeV, enabling us to determine the cross section times branching ratio for $\sigma(\nu\bar{\nu}h) \cdot BR(WW^*)$ to 3.0% acccuracy. Applying Eq.(2.34) with ZZ replaced by WW, we can determine the Higgs total width to $\Delta\Gamma_{\text{tot}}/\Gamma_{\text{tot}} \simeq 6\%$. The clean sample of WW^* decays can be also used to investigate the Lorentz structure of the hWW coupling as we discussed in the angular analysis of the $h \to WW^*$ decays in the $e^+e^- \to Zh$ process at $\sqrt{s} = 250$ GeV.

The measurement of the Higgs boson width can be further improved by using the full set of Higgs rate measurements and insisting that the observed branching ratios should sum to 1. Since *all* Higgs boson decay modes are observed in recoil against the Z, this assumption is justified at an e^+e^- collider. At the end of this chapter, we will report on a global fit to the full set of Higgs couplings of a 125 GeV Higgs bosons. In that fit, the Higgs boson width is determined to an accuracy of 1.6%.

2.5.4 Expected improvements of branching ratio measurements

The Higgs sample from the WW fusion and the Higgs-strahlung processes at $\sqrt{s} = 500\,\text{GeV}$ will enable us to significantly improve the branching ratio measurements described above for the $\sqrt{s} = 250$ GeV run. In particular we can do a template fitting similar to that employed for the $e^+e^- \to Zh$ sample at $\sqrt{s} = 250\,\text{GeV}$. The flavor-tagging performance at $\sqrt{s} = 500\,\text{GeV}$ will be similar, too. The expected relative errors on the cross section times branching ratios are summarized in Table 2.3. The table shows that the WW fusion process contributes significantly, while the relative error on $\Delta BR(b\bar{b})/BR(b\bar{b})$

Table 2.3. Expected accuracies for the h boson branching ratios for $m_h = 120$ GeV when the 250 GeV measurements assuming $\mathcal{L} = 250\,\text{fb}^{-1}$ in Table 2.2 are combined with those at $\sqrt{s} = 500$ GeV assuming $\mathcal{L} = 500\,\text{fb}^{-1}$ and $(e^-, e^+) = (-0.8, +0.3)$ beam polarization. The errors on BRs include the error on σ of 2.5% from the recoil mass measurement at $\sqrt{s} = 250\,\text{GeV}$.

	$\Delta(\sigma \cdot BR)/(\sigma \cdot BR)$			$\Delta BR/BR$
mode	Zh @ 250 GeV	Zh @ 500 GeV	$\nu\bar{\nu}h$ @ 500 GeV	combined
$h \to b\bar{b}$	1.0%	1.6%	0.60%	2.6%
$h \to c\bar{c}$	6.9%	11%	5.2%	4.6%
$h \to gg$	8.5%	13%	5.0%	4.8%
$h \to WW^*$	8.1%	12.5%	3.0%	3.8%
$h \to \tau^+\tau^-$	3.6%	4.6%	11%	3.6%
$h \to ZZ^*$	26%	34%	10%	9.3%
$h \to \gamma\gamma$	23-30%	29-38%	19-25%	13-17%

is limited by the error on the Zh production cross section at $\sqrt{s} = 250\,\text{GeV}$ from the recoil mass measurement. If we need higher accuracy for $\Delta BR(b\bar{b})/BR(b\bar{b})$, we will need to run longer at $\sqrt{s} = 250\,\text{GeV}$, though slight improvement is also expected from the recoil mass measurement at $\sqrt{s} = 500\,\text{GeV}$.

2.6 Higgs measurements at ILC at 1000 GeV

Two out of the three processes selected as the DBD benchmark reactions at $\sqrt{s} = 1000$ GeV involve Higgs boson production: $e^+e^- \to t\bar{t}h$ and $e^+e^- \to \nu\bar{\nu}h$. We showed above that we would be able determine the top Yukawa coupling to an accuracy of about 10 % at $\sqrt{s} = 500\,\text{GeV}$ for $m_h = 120\,\text{GeV}$, using the former process. The signal cross section grows to its maximum at around $\sqrt{s} = 700$ and only slowly decreases toward $\sqrt{s} = 1000\,\text{GeV}$, while the $e^+e^- \to t\bar{t}$ background decreases much more rapidly. Thus, a more precise measurement of the top Yukawa coupling will be possible at this higher energy.

At the same time, the WW fusion process $e^+e^- \to \nu\bar{\nu}h$ dominates the s-channel Higgs-sthrahlung process. Taking advantage of electron and positron beam polarization, the cross section for the WW fusion process at 1000 GeV will be as large as $400\,\text{fb}$ for $(P_{e^-}, P_{e^+}) = (-0.8, +0.2)$ and $m_h = 125\,\text{GeV}$, as shown in Fig. 2.19. Taking into account the higher luminosity expected at $\sqrt{s} = 1000\,\text{GeV}$, this process will give us a high statistics Higgs boson sample: 4×10^5 events for $1\,\text{ab}^{-1}$. This will allow us to improve the branching ratios to the various modes discussed above as well as to access the rare mode $h \to \mu^+\mu^-$. It is also noteworthy that one more process, $e^+e^- \to \nu\bar{\nu}hh$ process, will become sizable at $\sqrt{s} = 1000$ GeV. This reaction can be used together with the $e^+e^- \to Zhh$ process to improve the measurement of the Higgs self-coupling.

The WW fusion processes occur only from the initial state $e^-_L e^+_R$, and the top quark production cross section is also much larger from this initial state. Thus, it is advantageous to spend most of the running time at 1000 GeV using the beam polarizations that favor $e^-_L e^+_R$. The accuracies estimated for ILC in this section will thus be based on 1000 fb^{-1} taken *entirely* with the beam polarizations $(P_{e^-}, P_{e^+}) = (-0.8, +0.2)$.

2.6.1 Measurement of $h \to \mu^+\mu^-$ decay using $e^+e^- \to \nu\bar{\nu}h$

The branching fraction of the $h \to \mu^+\mu^-$ decay is as small as 0.03 % for the 120 GeV Standard Model Higgs boson. Its measurement thus requires a very good invariant mass resolution for the $\mu^+\mu^-$ pair. The measurement of this rare mode is a challenge to the tracking detectors and hence was chosen as one of the benchmark processes. The SiD group performed a full simulation study of the $h \to \mu^+\mu^-$ decay at $\sqrt{s} = 250\,\text{GeV}$ with $250\,\text{fb}^{-1}$ for $m_h = 120\,\text{GeV}$ as one of its LOI studies [76]. The expected number of signal events was only 26 before any cuts. After a simple cut-and-count analysis, the expected number of signal events became 8 with 39 background events in the final sample

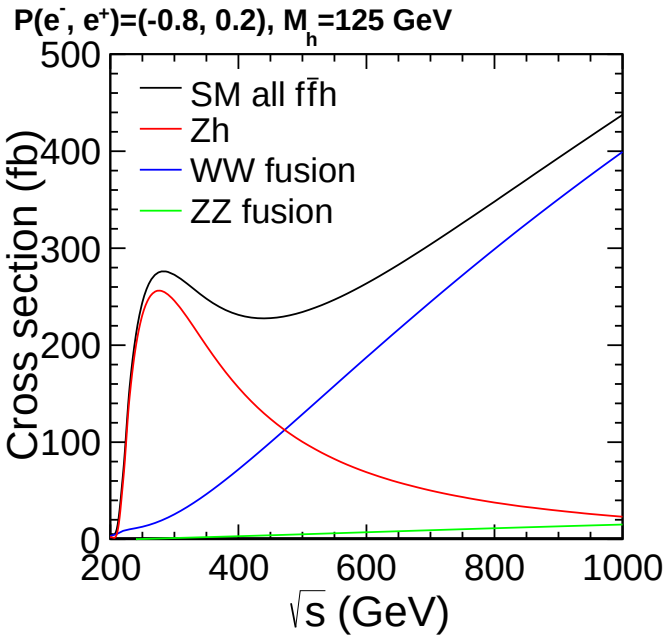

Figure 2.19 Production cross sections for the Higgs-strahlung, $e^+e^- \to Zh$, the WW fusion, $e^+e^- \to \nu\bar{\nu}H$, and ZZ fusion processes as a function of the center of mass energy for $m_h = 125\,\text{GeV}$ and beam polarization $(P_{e^-}, P_{e^+}) = (-0.8, +0.2)$.

of $e^+e^- \to Zh$ followed by $Z- > q\overline{q}$ and $h \to \mu^+\mu^-$. This corresponds to a statistical significance of $1.1\ \sigma$. The WW fusion process at $\sqrt{s} = 1000\,\text{GeV}$ will provide a higher statistics sample of Higgs bosons, as discussed above. We thus expect about 100 events for the $h \to \mu^+\mu^-$ mode. Since the cross sections for the $e^+e^- \to W^+W^- \to \mu^+\nu_\mu\mu^-\overline{\nu}_\mu$ and $e^+e^- \to ZZ \to \mu^+\mu^- f\overline{f}$ backgrounds will decrease, while the signal cross section will increase at higher energies, we would expect a meaningful measurement of the muon Yukawa coupling. An earlier fast simulation result showed that a $5\ \sigma$ signal peak would be observed with a $1\,\text{ab}^{-1}$ sample for $m_h = 120\,\text{GeV}$ [122, 123]. More recent full simulations by SiD and ILD showed that indeed we would be able to measure $\sigma \times BR(h \to \mu^+\mu^-)$ to 32% for $m_h = 125\,\text{GeV}$ even with the full beam-induced backgrounds. Together with the tau Yukawa coupling from the $h \to \tau^+\tau^-$ branching ratio, this measurement will provide an insight into the physics of lepton mass generation. With the charm Yukawa coupling from the $h \to c\bar{c}$ branching fraction, this also will allow us to probe the mass generation mechanism for the second generation matter fermions.

The new high-statistics sample of Higgs boson allows branching ratio measurements for the other decay modes to be improved. For example, we can achieve $\Delta BR(h \to \gamma\gamma)/BR((h \to \gamma\gamma) \simeq 5\,\%$ for $m_h = 120\,\text{GeV}$ with $1\,\text{ab}^{-1}$ taken at $(P_{e^-}, P_{e^+}) = (-0.8, +0.5)$ [124].

2.6.2 Top quark Yukawa coupling

The 10% accuracy on the top quark Yukawa coupling expected at $\sqrt{s} = 500\,\text{GeV}$ can be significantly improved by the data taken at 1000 GeV, thanks to the larger cross section and the less background from $e^+e^- \to t\bar{t}$. Fast simulations at $\sqrt{s} = 800\,\text{GeV}$ showed that we would be able to determine the top Yukawa coupling to 6% for $m_h = 120\,\text{GeV}$, given an integrated luminosity of $1\,\text{ab}^{-1}$ and residual background uncertainty of 5% [100, 101]. As described in the Detector Volume, Volume 4 of this report, full simulations just recently completed by SiD and ILD showed that the top Yukawa coupling could indeed be measured to a statistical precision of 4.0% for $m_h = 125\,\text{GeV}$ with $1\,\text{ab}^{-1}$.

Table 2.4. Expected accuracies for cross section times branching ratio measurements for the $125\,\text{GeV}$ h boson.

	$\Delta(\sigma \cdot BR)/(\sigma \cdot BR)$				
$\sqrt{s}$ and $\mathcal{L}$ (P_{e^-}, P_{e^+})	250 fb^{-1} at 250 GeV (-0.8,+0.3)		500 fb^{-1} at 500 GeV (-0.8,+0.3)		1 ab^{-1} at 1 TeV (-0.8,+0.2)
mode	Zh	$\nu\bar{\nu}h$	Zh	$\nu\bar{\nu}h$	$\nu\bar{\nu}h$
$h \to b\bar{b}$	1.1%	10.5%	1.8%	0.66%	0.47%
$h \to c\bar{c}$	7.4%	-	12%	6.2%	7.6%
$h \to gg$	9.1%	-	14%	4.1%	3.1%
$h \to WW^*$	6.4%	-	9.2%	2.6%	3.3%
$h \to \tau^+\tau^-$	4.2%	-	5.4%	14%	3.5%
$h \to ZZ^*$	19%	-	25%	8.2%	4.4%
$h \to \gamma\gamma$	29-38%	-	29-38%	20-26%	7-10%
$h \to \mu^+\mu^-$	100%	-	-	-	32%

2.6.3 Higgs self-coupling in the $e^+e^- \to \nu_e\bar{\nu}_e hh$ process

At $\sqrt{s} = 1000\,\text{GeV}$, the $e^+e^- \to \nu\bar{\nu}hh$ process will become significant and open up the possibility of measuring the triple Higgs coupling in the WW channel [120]. The cross section for this process is only about $0.07\,\text{fb}^{-1}$, but the sensitivity to the self-coupling is potentially higher since the contribution from the background diagrams is smaller, leading to the relation $\Delta\lambda/\lambda \simeq 0.85 \times (\Delta\sigma_{\nu\bar{\nu}hh}/\sigma_{\nu\bar{\nu}hh})$, as compared to $\Delta\lambda/\lambda \simeq 1.8 \times (\Delta\sigma_{Zhh}/\sigma_{Zhh})$ for the $e^+e^- \to Zhh$ process at 500 GeV. An early fast simulation study of $e^+e^- \to \nu\bar{\nu}hh$ showed that one could determine the triple Higgs coupling to an accuracy of $\Delta\lambda/\lambda \simeq 0.12$ [121], assuming $1\,\text{ab}^{-1}$ luminosity and 80% left-handed electron polarization. A more recent fast simulation study indicated an accuracy $\Delta\lambda/\lambda \simeq 0.17$ for $2\,\text{ab}^{-1}$ with $(P_{e^-}, P_{e^+}) = (-0.8, +0.2)$. The difference could be attributed to the more realistic analysis based on jet-clustering after parton showering and hadronization, as well as more background processes considered in the latter study. Finally, the measurement of the self-coupling has now been studied at 1 TeV will full simulation. That analysis is described in the Detector Volume, Volume 4 of this report. The result, for for $2\,\text{ab}^{-1}$ with $(P_{e^-}, P_{e^+}) = (-0.8, +0.2)$, is $\Delta\lambda/\lambda \simeq 0.21$.

In addition to the fusion process, we also can use the $e^+e- \to Zhh$ process at $\sqrt{s} = 1000$ GeV. This process has somewhat less sensitivity, $\Delta\lambda/\lambda \simeq 2.8 \times (\Delta\sigma_{Zhh}/\sigma_{Zhh})$. The analysis gives $\Delta\lambda/\lambda \simeq 0.53$. Combining all of the measurements, assuming the nominal integrated luminosities of $500\,\text{fb}^{-1}$ at $\sqrt{s} = 500\,\text{GeV}$ and $2000\,\text{fb}^{-1}$ at $\sqrt{s} = 1000\,\text{GeV}$ with the left-handed beam combination: $(P_{e^-}, P_{e^+}) = (-0.8, +0.2)$, we expect that the Higgs self-coupling could be measured to $\Delta\lambda/\lambda \simeq 20.\%$.

Table 2.5. Expected accuracies for top Yukawa and self-coupling measurements of the 125 GeV h boson, with the specified energies and luminosity samples. The current analyses use the $h \to b\bar{b}$ mode only.

process	$\sqrt{s}$ [GeV]	$\mathcal{L}$ [fb^{-1}]	(P_{e^-}, P_{e^+})	$\Delta(\sigma \cdot BR)/(\sigma \cdot BR)$	$\Delta g/g$
$t\bar{t}h$	500	500	(-0.8,+0.3)	35%	18%
Zhh	500	500	(-0.8,+0.3)	64%	104%
$t\bar{t}h$	1000	1000	(-0.8,+0.2)	8.7%	4.0%
$\nu\bar{\nu}hh$	1000	1000	(-0.8,+0.2)	38%	28%

Table 2.6. Expected accuracies for Higgs boson couplings derived from the accuracy estimates for measured rates given in Tables 2.4 and 2.5. For the invisible branching ratio, the numbers quoted are 95% confidence upper limits. The four columns refer to: LHC, 300 fb^{-1}, 1 detector; ILC at 250 GeV, with 250 fb^{-1}; ILC at 500 GeV, with 500 fb^{-1}; ILC at 1000 GeV, with 1000 fb^{-1}. Each column includes the stated data set and all previous ones [65].

Mode	LHC	ILC(250)	ILC500	ILC(1000)
WW	4.1 %	1.9 %	0.24 %	0.17 %
ZZ	4.5 %	0.44 %	0.30 %	0.27 %
$b\bar{b}$	13.6 %	2.7 %	0.94 %	0.69 %
gg	8.9 %	4.0 %	2.0 %	1.4 %
$\gamma\gamma$	7.8 %	4.9 %	4.3 %	3.3 %
$\tau^+\tau^-$	11.4 %	3.3 %	1.9 %	1.4 %
$c\bar{c}$	–	4.7 %	2.5 %	2.1 %
$t\bar{t}$	15.6 %	14.2 %	9.3 %	3.7 %
$\mu^+\mu^-$	–	–	–	16 %
self	–	–	104%	26 %
BR(invis.)	$< 9\%$	< 0.44 %	< 0.30 %	< 0.26 %
$\Gamma_T(h)$	20.3%	4.8 %	1.6 %	1.2 %

2.7 Summary of measurement precisions expected at ILC

For historical reasons, most of the full simulation studies we discussed above were done for $m_h = 120$ GeV. Given the likelihood that the new particle discovered at the LHC is a Higgs boson, we would like to know the ILC capabilities for a Higgs boson of mass 125 GeV. These can be obtained by extrapolation of the full-simulation results, taking into account the changes in the signal and background as well as the changes in the pattern of Higgs boson branching ratios as the assumed mass is changed. The extrapolated results for the $\sigma \cdot BR$ measurements at different energies are summarized in Table 2.4. In the extrapolation, we scaled the signal and the background with the effective cross sections calculated with the new TDR beam parameters and, for the signal, applied the LHC-recommended branching ratios for $m_h = 125$ GeV. For the 1 TeV results, there are some differences between ILD and SiD as seen in the benchmark results described in the corresponding DBD chapters. We listed the SiD values here to be conservative.

We performed a similar exercise for the top Yukawa coupling and the self-coupling measurements and tabulated the results of the extrapolation in Table 2.5, where we just scaled the signal with the background unchanged. Since the mass separation from W and Z bosons should be better for $m_h = 125$ GeV than for $m_h = 120$ GeV, these estimates should be conservative.

The measurements in Tables 2.4 and 2.5 imply a very high level of precision for the various Higgs boson couplings. To quantify this, we have carried out a global fit to these measurements, assuming the errors given in these tables with the Standard Model as the central value in all cases. The fit is done in parallel to the analysis reported above for the LHC in Fig. 2.4, with 9 parameters representing independent Higgs boson couplings to WW, ZZ, $b\bar{b}$, gg, $\gamma\gamma$, $\tau^+\tau^-$, $c\bar{c}$, $t\bar{t}$, and invisible final states. The results for the errors on Higgs couplings are shown in Table 2.6. The four columns represent the errors from LHC (300 fb^{-1}, 1 detector) only, and then, cumulatively, ILC at 250 GeV, ILC at 500 GeV, and ILC at 1000 GeV [65]. The result of this fit are shown graphically in Fig. 2.20.

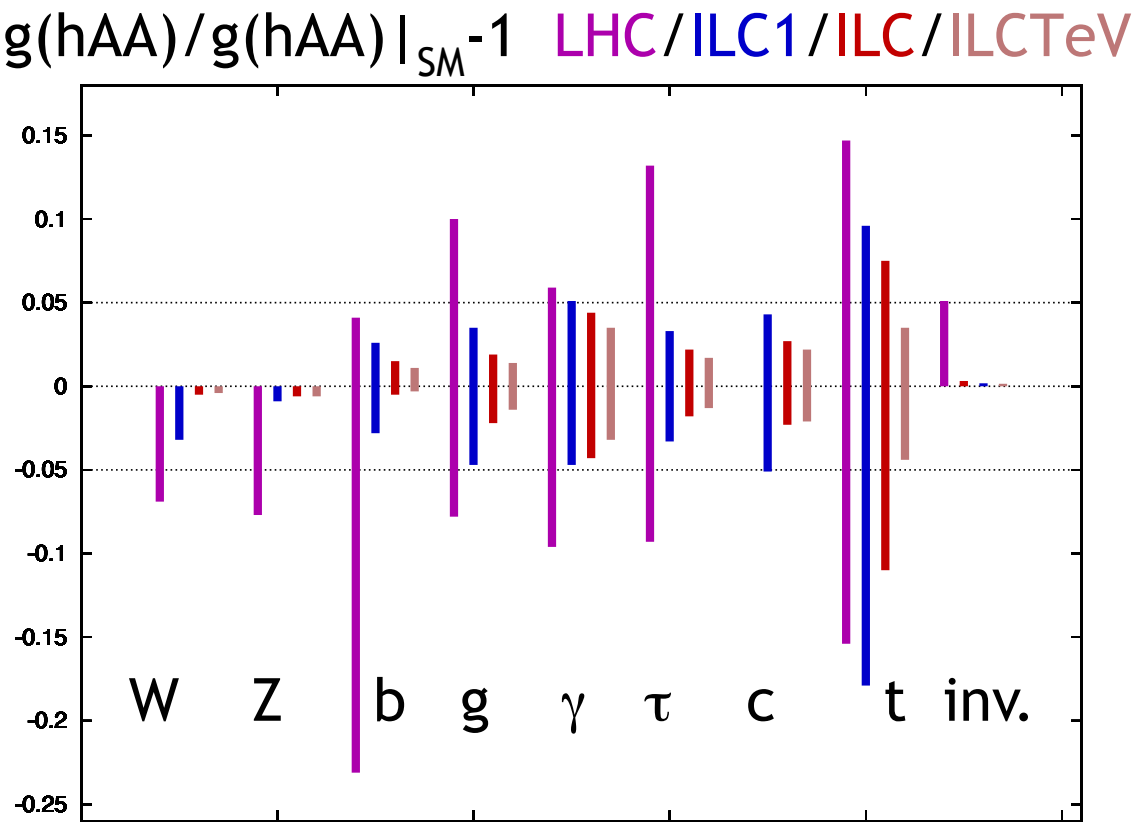

Figure 2.20. Estimate of the sensitivity of the ILC experiments to Higgs boson couplings in a model-independent analysis. The plot shows the 1 σ confidence intervals as they emerge from the fit described in the text. Deviation of the central values from zero indicates a bias, which can be corrected for. The upper limit on the WW and ZZ couplings arises from the constraints (2.31). The bar for the invisible channel gives the 1 σ upper limit on the *branching ratio*. The four sets of errors for each Higgs coupling represent the results for LHC (300 fb^{-1}, 1 detector), the threshold ILC Higgs program at 250 GeV, the full ILC program up to 500 GeV, and the extension of the ILC program to 1 TeV. The methodology leading to this figure is explained in [65].

2.8 Conclusion

The landscape of elementary particle physics has been altered by the discovery by the ATLAS and CMS experiments of a new boson that decays to $\gamma\gamma$, ZZ, and WW final states [2, 3]. The question of the identity of this bosons and its connection to the Standard Model of particle physics has become the number one question for our field. In this section, we have presented the capabilities of the ILC to study this particle in detail. The ILC can access the new boson through the reactions $e^+e^- \to Zh$ and through the WW fusion reaction $e^+e^- \to \nu\bar{\nu}h$. Though our current knowledge of this particle is still limited, we already know that these reactions are available at rates close to those predicted for the Higgs boson in the Standard Model. The ILC is ideally situated to give us a full understanding of this particle, whatever its nature.

The leading hypothesis for the identity of the new particle is that it is the Higgs boson of the Standard Model, or a similar particle responsible for electroweak symmetry breaking in a model that includes new physics at the TeV energy scale. We have argued that, if this identification proves correct, the requirements for experiments on the nature of this boson are extremely challenging. Though there are new physics models that predict large deviations of the boson couplings from the Standard Model predictions, the typical expectation in new physics models is that the largest deviations from the Standard Model are at the 5–10% level. Depending on the model, these deviations can occur in any of the boson's couplings. Thus, a comprehensive program of measurements is needed, one capable of being interpreted in a model-independent way. Our estimate of the eventual LHC capabilities, given

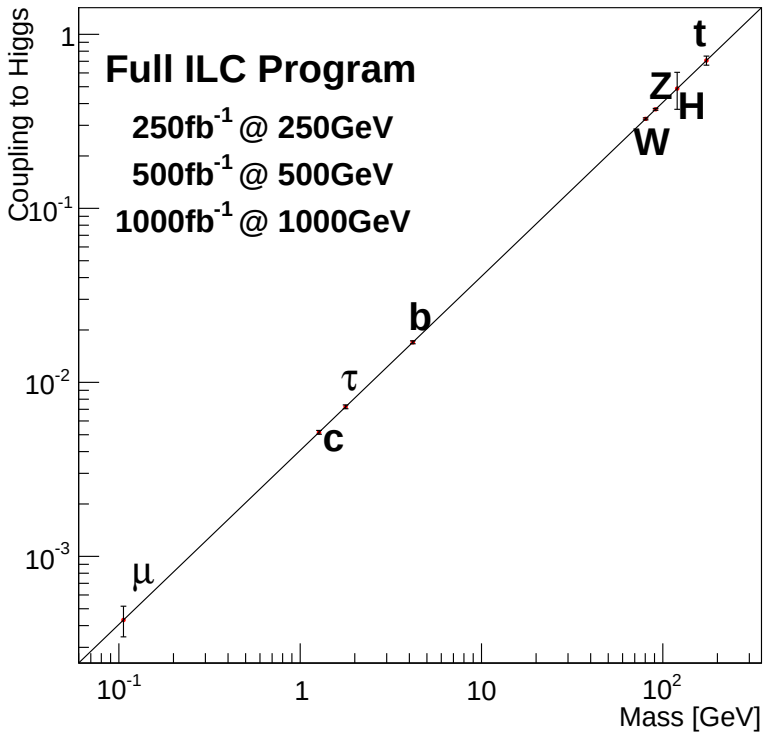

Figure 2.21
Expected precision from the full ILC program of tests of the Standard Model prediction that the Higgs coupling to each particle is proportional to its mass.

in Fig. 2.4, falls short of that goal.

We then presented the capabilities of the ILC for precision measurements of the Higgs boson couplings. The ILC program for Higgs couplings can begin at a center of mass energy of 250 GeV, near the peak of the cross section for $e^+e^- \to Z^0h^0$. This program allows a direct measurement of the cross section, rather than measurement that includes branching ratios, already eliminating an important source of ambiguity from the LHC data. The program also allows the measurement of individual branching channels, observed in recoil against the Z^0 boson. The excellent flavor tagging capabilities of the ILC experiments allow access to the $c\bar{c}$ decay mode of the Higgs boson and sharpen the observation of many other modes. The ILC experiments are highly sensitive to possible invisible or other unexpected decay modes of the Higgs boson, with sensitivity at the percent level.

A later stage of ILC running at the full energy of 500 GeV will enhance these capabilities. At 500 GeV, the W fusion reaction $e^+e^- \to \nu\bar{\nu}h$ turns on fully, giving a very precise constraint on the Higgs boson coupling to WW. The increased statistics sharpens the measurement of rare branching channels such as $\gamma\gamma$. Higher energy also gives improved $g/c/b$ separation in the hadronic decay models. Running at 500 GeV allows the first direct measurements of the Higgs coupling to $t\bar{t}$ and the Higgs self-coupling.

The technology of the ILC will eventually allow extended running at higher energies, up to 1 TeV in the center of mass. A 1 TeV program will add further statistics to the branching ratio measurements in all channels, using the increasing $e^+e^- \to \nu\bar{\nu}h$ cross section. It also very much increases the sensitivity of the determinations of the Higgs coupling to $t\bar{t}$ and the Higgs self-coupling.

The progression of this program is shown graphically in Fig. 2.20. For each Higgs boson coupling, four sets of error bars are shown, always assuming that the underlying value of the coupling is that of the Standard Model. The first is the estimate of the LHC capability, from Fig. 2.4. The second is the error that would be obtained by adding the data from a 250 fb^{-1} run of the ILC at 250 GeV. The third is the error that would be obtained by adding to this the data from a 500 fb^{-1} run of the ILC

at 500 GeV. The final error bar would be the result of adding a 1 ab^{-1} data set at 1 TeV. Not shown, but also relevant, are the capabilities of the ILC to measure the Higgs self-coupling to about 24% accuracy and the Higgs coupling to $\mu^+\mu^-$ to about 20% accuracy in the 1 TeV program.

The results of this program can also be represented as precision tests of the Standard Model relation that the Higgs coupling to each particle is exactly proportional to the mass of that particle. The expected uncertainties in those tests from the measurements described above are shown in Fig. 2.21.

This is the program that is needed to fully understand the nature of the newly discovered boson and its implications for the puzzle of electroweak symmetry breaking. The ILC can provide it.

Bibliography

[1] [ALEPH and DELPHI and L3 and OPAL and SLD and LEP Electroweak Working Group and SLD Electroweak Group and SLD Heavy Flavour Group Collaborations], Phys. Rept. **427**, 257 (2006) [hep-ex/0509008].

[2] G. Aad *et al.* [ATLAS Collaboration], Phys. Lett. B **716**, 1 (2012) [arXiv:1207.7214 [hep-ex]].

[3] S. Chatrchyan *et al.* [CMS Collaboration], Phys. Lett. B **716**, 30 (2012) [arXiv:1207.7235 [hep-ex]].

[4] T. Aaltonen *et al.* [CDF and D0 Collaborations], Phys. Rev. Lett. **109**, 071804 (2012) [arXiv:1207.6436 [hep-ex]].

[5] A. Denner, S. Heinemeyer, I. Puljak, D. Rebuzzi and M. Spira, Eur. Phys. J. C **71**, 1753 (2011) [arXiv:1107.5909 [hep-ph]].

[6] P. A. Baikov, K. G. Chetyrkin and J. H. Kuhn, Phys. Rev. Lett. **96**, 012003 (2006) [hep-ph/0511063].

[7] K. Chetyrkin, J. H. Kuhn, A. Maier, P. Maierhofer, P. Marquard, M. Steinhauser and C. Sturm, Theor. Math. Phys. **170**, 217 (2012) [arXiv:1010.6157 [hep-ph]].

[8] C. McNeile, C. T. H. Davies, E. Follana, K. Hornbostel and G. P. Lepage, Phys. Rev. D **82**, 034512 (2010) [arXiv:1004.4285 [hep-lat]].

[9] B. W. Lee, C. Quigg and H. B. Thacker, Phys. Rev. Lett. **38**, 883 (1977); Phys. Rev. D **16**, 1519 (1977).

[10] T. Appelquist and M. S. Chanowitz, Phys. Rev. Lett. **59**, 2405 (1987) [Erratum-ibid. **60**, 1589 (1988)].

[11] H. D. Politzer and S. Wolfram, Phys. Lett. B **82**, 242 (1979) [Erratum-ibid. **83B**, 421 (1979)].

[12] G. Isidori, G. Ridolfi and A. Strumia, Nucl. Phys. B **609**, 387 (2001) [hep-ph/0104016].

[13] F. Bezrukov, M. Y. Kalmykov, B. A. Kniehl and M. Shaposhnikov, JHEP **1210**, 140 (2012) [arXiv:1205.2893 [hep-ph]].

[14] G. Degrassi, S. Di Vita, J. Elias-Miro, J. R. Espinosa, G. F. Giudice, G. Isidori and A. Strumia, JHEP **1208**, 098 (2012) [arXiv:1205.6497 [hep-ph]].

[15] M. Carena, S. Gori, N. R. Shah, C. E. M. Wagner and L. -T. Wang, arXiv:1205.5842 [hep-ph].

[16] J. R. Espinosa, C. Grojean and M. Muhlleitner, EPJ Web Conf. **28**, 08004 (2012) [arXiv:1202.1286 [hep-ph]].

[17] F. Goertz, U. Haisch and M. Neubert, Phys. Lett. B **713**, 23 (2012) [arXiv:1112.5099 [hep-ph]].

[18] J. F. Gunion, Y. Jiang and S. Kraml, arXiv:1207.1545 [hep-ph].

[19] R. S. Gupta, H. Rzehak and J. D. Wells, arXiv:1206.3560 [hep-ph].

[20] H. E. Haber, in *From the Planck Scale to the Weak Scale (SUSY 94)*, P. Nath, T. Taylor, and S. Pokorski, eds. (World Scientific, 1995) [hep-ph/9501320].

[21] J. F. Gunion, H. E. Haber, G. L. Kane and S. Dawson, "The Higgs Hunter's Guide" (Addison-Wesley, Reading, MA, 1990).

[22] N. Arkani-Hamed, A. G. Cohen, E. Katz and A. E. Nelson, JHEP **0207**, 034 (2002) [hep-ph/0206021].

[23] T. Han, H. E. Logan, B. McElrath and L. -T. Wang, Phys. Rev. D **67**, 095004 (2003) [hep-ph/0301040].

[24] T. Han, H. E. Logan, B. McElrath and L. -T. Wang, Phys. Lett. B **563**, 191 (2003) [Erratum-ibid. B **603**, 257 (2004)] [hep-ph/0302188].

[25] K. Agashe, R. Contino and A. Pomarol, Nucl. Phys. B **719**, 165 (2005) [hep-ph/0412089].

[26] J. R. Espinosa, C. Grojean and M. Muhlleitner, JHEP **1005**, 065 (2010) [arXiv:1003.3251 [hep-ph]].

[27] R. Contino, L. Da Rold and A. Pomarol, Phys. Rev. D **75**, 055014 (2007) [hep-ph/0612048].

[28] M. S. Carena, S. Heinemeyer, C. E. M. Wagner and G. Weiglein, hep-ph/9912223.

[29] M. S. Carena, H. E. Haber, H. E. Logan and S. Mrenna, Phys. Rev. D **65**, 055005 (2002) [Erratum-ibid. D **65**, 099902 (2002)] [hep-ph/0106116].

[30] A. Djouadi, J. Kalinowski and M. Spira, Comput. Phys. Commun. **108**, 56 (1998) [hep-ph/9704448].

[31] H. E. Haber, M. J. Herrero, H. E. Logan, S. Penaranda, S. Rigolin and D. Temes, Phys. Rev. D **63**, 055004 (2001) [hep-ph/0007006].

[32] M. W. Cahill-Rowley, J. L. Hewett, A. Ismail and T. G. Rizzo, Phys. Rev. D **86**, 075015 (2012) [arXiv:1206.5800 [hep-ph]].

[33] ATLAS Collaboration, ATLAS-CONF-2012-093.

[34] CMS Collaboration, Physics Analysis Summary CMS-PAS-HIG-12-020.

[35] ATLAS Collaboration, ATLAS-CONF-2012-098.

[36] L. D. Landau, Dokl. Akad. Nauk. USSR **60**, 207 (1948); C.-N. Yang, Phys. Rev. **77**, 242 (1950).

[37] ATLAS Collaboration, "ATLAS Detector and Physics Performance Technical Design Report," CERN-LHCC-99-15.

[38] CMS Collaboration, "CMS Physics Technical Design Report. Volume II: Physics Performance," CERN-LHCC-2006-001.

[39] F. Gianotti and M. Pepe-Altarelli, Nucl. Phys. Proc. Suppl. **89**, 177 (2000) [hep-ex/0006016].

[40] S. P. Martin, arXiv:1208.1533 [hep-ph].

[41] S. Y. Choi, D. J. Miller, 2, M. M. Muhlleitner and P. M. Zerwas, Phys. Lett. B **553** (2003) 61 [hep-ph/0210077].

[42] Y. Gao, A. V. Gritsan, Z. Guo, K. Melnikov, M. Schulze and N. V. Tran, Phys. Rev. D **81**, 075022 (2010) [arXiv:1001.3396 [hep-ph]].

[43] A. De Rujula, J. Lykken, M. Pierini, C. Rogan and M. Spiropulu, Phys. Rev. D **82**, 013003 (2010) [arXiv:1001.5300 [hep-ph]].

[44] T. Plehn, D. L. Rainwater and D. Zeppenfeld, Phys. Rev. Lett. **88**, 051801 (2002) [hep-ph/0105325].

[45] V. Hankele, G. Klamke, D. Zeppenfeld and T. Figy, Phys. Rev. **D74**, 095001 (2006).

[46] C. Englert, D. Goncalves-Netto, K. Mawatari and T. Plehn, JHEP **1301**, 148 (2013) [arXiv:1212.0843 [hep-ph]].

[47] J. Ellis and D. S. Hwang, JHEP **1209** (2012) 071 [arXiv:1202.6660 [hep-ph]].

[48] S. Y. Choi, M. M. Muhlleitner and P. M. Zerwas, Phys. Lett. B **718**, 1031 (2013) [arXiv:1209.5268 [hep-ph]].

[49] O. J. P. Eboli and D. Zeppenfeld, Phys. Lett. B **495**, 147 (2000) [hep-ph/0009158].

[50] J. F. Gunion, H. E. Haber and J. Wudka, Phys. Rev. D **43**, 904 (1991).

[51] M. Dührssen, S. Heinemeyer, H. Logan, D. Rainwater, G. Weiglein and D. Zeppenfeld, Phys. Rev. **D70**, 113009 (2004).

[52] I. Low and J. Lykken, JHEP **1010**, 053 (2010) [arXiv:1005.0872 [hep-ph]].

[53] J. M. Butterworth, A. R. Davison, M. Rubin and G. P. Salam, Phys. Rev. Lett. **100**, 242001 (2008) [arXiv:0802.2470 [hep-ph]].

[54] T. Plehn, G. P. Salam and M. Spannowsky, Phys. Rev. Lett. **104**, 111801 (2010) [arXiv:0910.5472 [hep-ph]].

[55] M. Dührssen, ATLAS report ATL-PHYS-2003-030 (2003).

[56] M. Dührssen, S. Heinemeyer, H. Logan, D. Rainwater, G. Weiglein and D. Zeppenfeld, Phys. Rev. D **70**, 113009 (2004) [hep-ph/0406323], hep-ph/0407190.

[57] R. Lafaye, T. Plehn, M. Rauch, D. Zerwas and M. Dührssen, JHEP **08** (2009) 009.

[58] M. Klute, R. Lafaye, T. Plehn, M. Rauch and D. Zerwas, Phys. Rev. Lett. **109**, 101801 (2012) [arXiv:1205.2699 [hep-ph]].

[59] M. Klute, R. Lafaye, T. Plehn, M. Rauch and D. Zerwas, arXiv:1301.1322 [hep-ph]; D. Zerwas, presentation at the LCWS 2012 Workshop, October 2012.

[60] D. Zeppenfeld, R. Kinnunen, A. Nikitenko and E. Richter-Was, Phys. Rev. D **62**, 013009 (2000); A. Djouadi *et al.*, arXiv:hep-ph/0002258; D. Zeppenfeld, hep-ph/0203123.

[61] A. Belyaev and L. Reina, JHEP **08** (2002) 041.

[62] ATLAS Collaboration, submission to the European Strategy Preparatory Group, https://indico.cern.ch/contributionDisplay.py?contribId=141&confId=175067

[63] CMS Collaboration, submission to the European Strategy Preparatory Group, https://indico.cern.ch/contributionDisplay.py?contribId=144&confId=175067

[64] CMS Collaboration, CMS Note-2012/006 (2012).

[65] M. E. Peskin, arXiv:1207.2516 [hep-ph].

[66] S. Kanemura, Y. Okada and E. Senaha, Phys. Lett. B **606**, 361 (2005) [hep-ph/0411354].

[67] E. Asakawa, D. Harada, S. Kanemura, Y. Okada and K. Tsumura, Phys. Rev. D **82**, 115002 (2010) [arXiv:1009.4670 [hep-ph]].

[68] G. D. Kribs and A. Martin, arXiv:1207.4496 [hep-ph].

[69] U. Baur, T. Plehn and D. L. Rainwater, Phys. Rev. Lett. **89**, 151801 (2002) [hep-ph/0206024]; Phys. Rev. D **67**, 033003 (2003) [hep-ph/0211224].

[70] F. Gianotti, M. L. Mangano, T. Virdee, S. Abdullin, G. Azuelos, A. Ball, D. Barberis and A. Belyaev *et al.*, Eur. Phys. J. C **39**, 293 (2005) [hep-ph/0204087].

[71] U. Baur, T. Plehn and D. L. Rainwater, Phys. Rev. D **68**, 033001 (2003) [hep-ph/0304015].

[72] M. J. Dolan, C. Englert and M. Spannowsky, JHEP **1210**, 112 (2012) [arXiv:1206.5001 [hep-ph]].

[73] U. Baur, T. Plehn and D. L. Rainwater, Phys. Rev. D **69**, 053004 (2004) [hep-ph/0310056].

[74] ILD Concept Team, T. Abe *et al.* [ILD Concept Group - Linear Collider Collaboration], arXiv:1006.3396 [hep-ex].

[75] H. Li, Orsay Ph.D. thesis, LAL-09-118 (2009); H. Li *et al.* [ILD Design Study Group Collaboration], arXiv:1202.1439 [hep-ex];

[76] SiD Concept Team, H. Aihara, (Ed.), P. Burrows, (Ed.), M. Oreglia, (Ed.), E. L. Berger, V. Guarino, J. Repond, H. Weerts and L. Xia *et al.*, arXiv:0911.0006 [physics.ins-det].

[77] M. T. Dova, P. Garcia-Abia, and W. Lohmann, hep-ph/0302113.

[78] D. J. Miller, S. Y. Choi, B. Eberle, M. M. Muhlleitner and P. M. Zerwas, Phys. Lett. B **505** 149 (2001) [hep-ph/0102023].

[79] M. Schumacher, LC Note LC-PHSM-2001-003 (2001).

[80] M. Kramer, J. H. Kuhn, M. L. Stong and P. M. Zerwas, Z. Phys. C **64**, 21 (1994) [hep-ph/9404280].

[81] S. Berge, W. Bernreuther and H. Spiesberger, arXiv:1208.1507 [hep-ph].

[82] K. Desch, A. Imhof, Z. Was and M. Worek, Phys. Lett. B **579**, 157 (2004) [hep-ph/0307331].

[83] H. Ono and A. Miyamoto, arXiv:hep-ex/1207.0300

[84] Y. Banda, T. Lasťovicka, and Andrei Nomerotski, Phys. Rev. **D82**, 033013 (2010)

[85] H. Ono, presentation at the KILC2012 workshop, April 2012.

[86] S.Kawada, K.Fujii, T.Suehara, T.Takahashi, and T.Tanabe, LC Note LC-REP-2013-001 (2013).

[87] ACFA Linear Collider Working Group, K. Abe et al., hep-ph/0109166.

[88] M. Battaglia, hep-ph/9910271.

[89] T. Kuhl and K. Desch, LC-PHSM-2007-2.

[90] G. Borisov and F. Richard, hep-ph/9905413.

[91] E. Boos, J. C. Brient, D. W. Reid, H. J. Schreiber and R. Shanidze, Eur. Phys. J. C **19**, 455 (2001) [hep-ph/0011366].

[92] C. Englert, T. Plehn, D. Zerwas and P. M. Zerwas, Phys. Lett. B **703**, 298 (2011) [arXiv:1106.3097 [hep-ph]].

[93] H. Ono, presentation at the Asian Physics and Software Meeting, June, 2012.

[94] A. Yamamoto, presentation at the Asian Physics and Software Meeting, June, 2012.

[95] K. Desch and N. Meyer, LC Note LC-PHSM-2001-025 (2001).

[96] C.F. Dürig, presentation at LCWS12, Arlington, Texas, Oct. 2012..

[97] Y. Takubo, R. N. Hodgkinson, K. Ikematsu, K. Fujii, N. Okada and H. Yamamoto, arXiv:1011.5805 [hep-ph].

[98] K. Hagiwara, H. Murayama and I. Watanabe, Nucl. Phys. B **367**, 257 (1991).

[99] A. Djouadi, J. Kalinowski and P. M. Zerwas, Z. Phys. C **54**, 255 (1992).

[100] A. Juste and G. Merino, hep-ph/9910301.

[101] A. Gay, Eur. Phys. J. C **49**, 489 (2007) [hep-ph/0604034].

[102] H. Baer, S. Dawson and L. Reina, Phys. Rev. D **61**, 013002 (2000) [hep-ph/9906419].

[103] S. Dittmaier, M. Kramer, Y. Liao, M. Spira and P. M. Zerwas, Phys. Lett. B **441**, 383 (1998) [hep-ph/9808433].

[104] S. Dawson and L. Reina, Phys. Rev. D **59**, 054012 (1999) [hep-ph/9808443].

[105] G. Belanger, F. Boudjema, J. Fujimoto, T. Ishikawa, T. Kaneko, K. Kato, Y. Shimizu and Y. Yasui, Phys. Lett. B **571**, 163 (2003) [hep-ph/0307029].

[106] A. Denner, S. Dittmaier, M. Roth and M. M. Weber, Nucl. Phys. B **680**, 85 (2004) [hep-ph/0309274].

[107] Y. You, W. -G. Ma, H. Chen, R. -Y. Zhang, S. Yan-Bin and H. -S. Hou, Phys. Lett. B **571**, 85 (2003) [hep-ph/0306036].

[108] C. Farrell and A. H. Hoang, Phys. Rev. D **72**, 014007 (2005) [hep-ph/0504220].

[109] C. Farrell and A. H. Hoang, Phys. Rev. D **74**, 014008 (2006) [hep-ph/0604166].

[110] A. Juste et al., "Report of the 2005 Snowmass Top/QCD Working Group", econf/C0508141:PLEN0043 (2005), arXiv:hep-ph/0601112.

[111] R. Yonamine, K. Ikematsu, T. Tanabe, K. Fujii, Y. Kiyo, Y. Sumino and H. Yokoya, Phys. Rev. D **84**, 014033 (2011) [arXiv:1104.5132 [hep-ph]].

[112] T. Tanabe, et al, presentation at the ILD Workshop, Kyushu, May, 2012.

[113] H. Tabassam and V. Martin, arXiv:1202.6013 [hep-ex].

[114] A. Djouadi, W. Kilian, M. Muhlleitner and P. M. Zerwas, Eur. Phys. J. C **10**, 27 (1999) [hep-ph/9903229].

[115] J. Tian, et al, private communication.

[116] T. Suehara and T. Tanabe, presentation at the KILC12 workshop, April 2012.

[117] C. Castanier, P. Gay, P. Lutz and J. Orloff, hep-ex/0101028.

[118] U. Baur, T. Plehn, and D. Rainwater in G. Weiglein *et al.* [LHC/LC Study Group Collaboration], Phys. Rept. **426**, 47 (2006) [hep-ph/0410364].

[119] M. Battaglia, E. Boos and W. -M. Yao, eConf C **010630**, E3016 (2001) [hep-ph/0111276].

[120] Y. Yasui, S. Kanemura, S. Kiyoura, K. Odagiri, Y. Okada, E. Senaha and S. Yamashita, hep-ph/0211047.

[121] S. Yamashita, presentation at the LCWS04 workshop, April, 2004.

[122] M. Battaglia and A. De Roeck, eConf C **010630**, E3066 (2001) [hep-ph/0111307].

[123] M. Battaglia and A. De Roeck, hep-ph/0211207.

[124] T. L. Barklow, hep-ph/0312268.

[125] J. Tian, KEK Ph.D. Thesis (2012).

Chapter 3
Two-Fermion Processes

The reactions $e^+e^- \to f\overline{f}$, where f could be leptons or quarks, provide a powerful tool to search for and characterize physics beyond the Standard Model at the ILC. These processes are distinguished by clean, simple final states, and precise perturbative predictions of the SM contributions are available. As a result, ILC experiments will be sensitive to even small deviations from the SM predictions in these channels, enabling them to study new physics at energy scales far above the center-of-mass energy of the collider.

3.1 Systematics of $e^+e^- \to f\overline{f}$

Despite the simplicity of the two-fermion final state, the process $e^+e^- \to f\overline{f}$ offers a large number of methods with which to probe for deviations from the Standard Model. In this section, we will review the observables that the ILC will make available. In the following sections, we will review how these observables can be applied to discover and then to analyze many signals of new physics that can appear in these reactions.

For all channels except $e^+e^- \to e^+e^-$, helicity conservation implies that the process $e^+e^- \to f\overline{f}$ is dominated by s-channel spin 1 exchange. This assumption applies whenever fermion mass effects can be neglected, and this is an excellent approximation at 500 GeV for pair-production of all Standard Model fermions except the top quark. In this case, the angular distribution of $e^+e^- \to f\overline{f}$ is simply written as

$$\frac{d\sigma}{d\cos\theta} = \frac{\pi\alpha^2}{2s}[A_+(1+\cos\theta)^2 + A_-(1-\cos\theta)^2] \ . \tag{3.1}$$

The coefficients A_+, A_- depend on the electron polarization. Models with gravitational effects at the TeV scale (for example, Randall-Sundrum models [1]) will add terms from s-channel spin 2 exchange that are higher polynomials in $\cos\theta$.

In (3.1), the term multiplying A_+ is generated by the polarized reactions $e^-_L e^+_R \to f_L \overline{f}_R$ and $e^-_R e^+_L \to f_R \overline{f}_L$, the term multiplying A_- is generated by $e^-_L e^+_R \to f_R \overline{f}_L$ and $e^-_R e^+_L \to f_L \overline{f}_R$. All other polarized cross sections are zero in the absence of mass corrections. This means that by measuring the cross sections and forward backward asymmetries with highly polarized e^-_L and e^-_R, we obtain 4 independent pieces of information on the s-channel amplitudes. In principle, only the electron beam needs to be polarized. However, even a small polarization of the positron beam improves the effective initial-state polarization according to

$$P_{eff} = \frac{P(e^-) + P(e^+)}{1 + P(e^-)P(e^+)} \ . \tag{3.2}$$

Thus, a measurement with 80% polarization in the electron beam and 30% polarization in the positron beam yields an effective initial-state polarization of almost 90%. At the ILC, polarization is monitored externally, but in addition the actual polarization in collisions can be determined from the high-rate processes of Bhabha scattering and forward W^-W^+ production. Theoretical calculations of the

2-fermion cross sections are controlled to below the part-per-mil level.

The four observables described in the previous paragraph are available for any final state that can be distinguished at the ILC. That is, these quantities can be measured separately for light quarks, c quarks, b quarks, e, μ, and τ. The typical c, τ and b identification efficiencies expected at the ILC are 35%, 60%, and over 96%, respectively [2]. In addition, the final state τ lepton polarization can be determined as a cross-check on the leptonic coupling measurements [3, 4].

The dominant contributions to $e^+e^- \to f\overline{f}$ at 500 GeV will probably come from Standard Model s-channel γ and Z^0 exchange. However, additional effects may arise from new gauge bosons, from contact interactions associated with fermion compositeness, or from effects of extra dimensions. These terms can be seen at the ILC as corrections to the $e^+e^- \to f\overline{f}$ cross sections and asymmetries, arising from interference of new physics with the Standard Model amplitudes. In addition, for example in the case of extra dimensions, these effects can add additional dependence on $\cos\theta$ related to the spin-2 graviton exchange. We will now review the expected sensitivity of the ILC experiments to these effects.

3.2 Z' physics

A canonical, well-motivated example of new physics that can be discovered and studied in $e^+e^- \to f\overline{f}$ is a new, heavy, electrically neutral gauge boson, commonly denoted by Z'. There are many extensions of the SM that predict one or more such particles (for reviews and references, see [5, 6]). For example, Grand Unified Theories (GUTs) based on groups such as $SO(10)$ or E_6 contain extra $U(1)$ factors in addition to the SM gauge group, and hence Z' bosons. Similarly, superstring constructions often involve large gauge symmetries that contain extra $U(1)$ factors. Since the Z' couplings conserve baryon and lepton numbers, the mass of the Z' may be well below the GUT or string scale, as low as the TeV, without conflict with experiment. In fact, in many supersymmetric GUT and string models, the Z' mass is tied to the soft supersymmetry breaking scale, expected to be at the TeV scale. The motivation for a TeV-scale Z' is particularly strong in supersymmetric models with additional particles that are singlets of the SM $SU(2) \times U(1)$. One of these models, the next-to-minimal supersymmetric standard model (NMSSM), has recently attracted much interest, since it provides a simple way to reduce the fine-tuning associated with a 125 GeV Higgs [7]. The weak-scale mass of the SM singlet field can be naturally explained if this field is charged under a new $U(1)$ symmetry broken at TeV energies; in addition, the domain-wall problem of the NMSSM is avoided in this case. Among non-supersymmetric possibilities, a very interesting example of a model containing a Z' is the Little Higgs model, where extra gauge bosons are introduced to cancel quadratic divergences in the Higgs mass renormalization by the SM gauge bosons (for reviews and references, see [8]). Naturalness of electroweak symmetry breaking requires that these new gauge bosons appear at the TeV scale.

Searches for Z' have been conducted, most recently, at LEP and the Tevatron, and are currently in progress at the LHC. The negative results of these searches preclude the possibility of on-shell Z' production at the ILC. Indeed, the LHC now excludes the appearance of large Z' resonances over most of the range of proposed 3 TeV lepton colliders. This makes it likely that our most important tool for the characterization of any Z' discovered at the LHC will be through indirect effects uncovered through the precision measurement of $e^+e^- \to f\overline{f}$ processes. The dominant effects of new physics in this case come from the interference between the diagrams involving the SM γ/Z^0 and those involving the Z'. Thanks to the high precision of the ILC, its capabilities to discover the Z' and measure its couplings actually exceed those of the LHC in most cases.

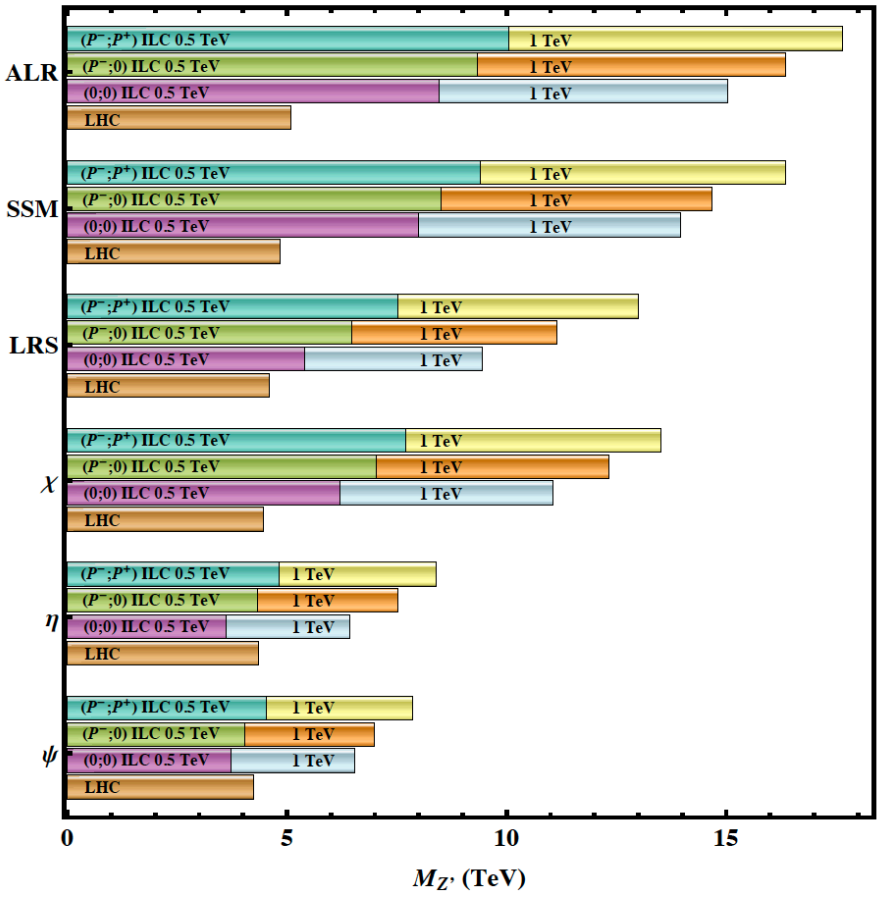

Figure 3.1. Sensitivity of the ILC to various candidate Z' bosons (quoted as 95% confidence limits for exclusion), with $\sqrt{s} = 0.5$ (1.0) TeV and $\mathcal{L}_{\rm int} = 500$ (1000) fb^{-1}. The sensitivity of the LHC-14 via Drell-Yan process $pp \to \ell^+\ell^- + X$ with 100 fb^{-1} of data are shown for comparison. For details, see [14].

3.2.1 Benchmark Z' models

Predictions for the contribution of a Z' to any observable depend on the boson's mass $M_{Z'}$ and its couplings to the SM fermions, which are model-dependent. While a very large variety of models have been proposed, a few canonical benchmark cases have been extensively studied and provide a set of reference points for comparisons between experiments. The Sequential Standard Model (SSM) assumes that all Z' couplings are the same as for the SM Z. The left-right symmetric (LRS) model extends the SM electroweak gauge group to $SU(2)_L \times SU(2)_R \times U(1)_{B-L}$, with the $SU(2)_R \times U(1)_{B-L} \to U(1)_Y$ breaking at the TeV scale. The Z' couples to the linear combination of T_{3R} and $B - L$ currents orthogonal to the SM hypercharge. Another set of popular benchmark models is based on the E_6 GUT, where the TeV-scale Z' is generally a linear combination of the two extra $U(1)$ gauge bosons Z_ψ and Z_χ: $Z' = Z_\chi \cos\beta + Z_\psi \sin\beta$. Some well-motivated possibilities are $\beta = 0$ (the "χ-model"), $\beta = \pi/2$ (the "ψ-model"), and $\beta = \pi - \arctan\sqrt{5/3}$ (the "η-model", which occurs in Calabi-Yau compactification of the heterotic string if E_6 breaks directly to a rank-5 group). It is also possible to embed a left-right symmetric model in E_6, leading to the so-called "alternative" left-right (ALR) model. The Z' couplings to the SM fermions in each of these models can be found, for example, in Table 1 of [9]. Well-studied Little Higgs models that contain Z' candidates include the original "Littlest Higgs" (LH) [10], as well as the Simplest Little Higgs (SLH) [11].

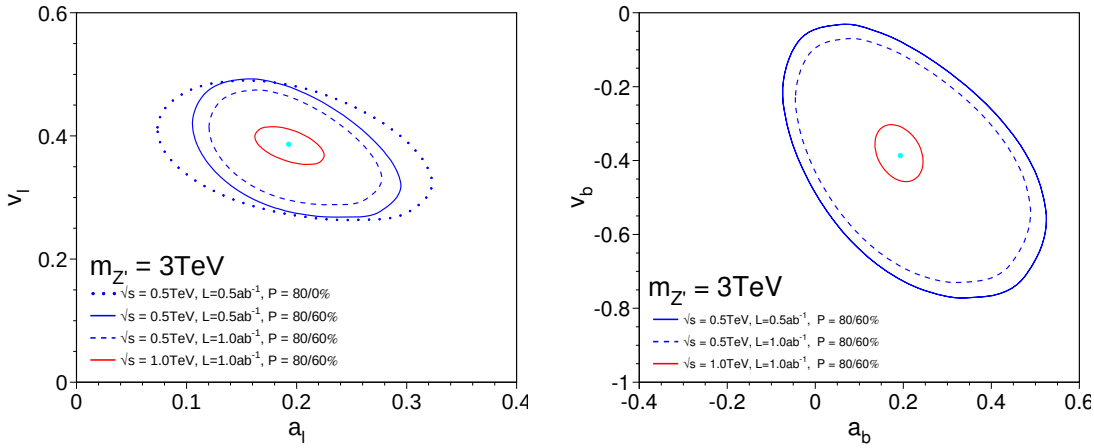

Figure 3.2. Derived coupling of a $SO(10)$ Z' boson with $m_{Z'} = 3$ TeV to leptons (left) and b-quarks (right). Only the results for positive values of the vector leptonic coupling v_l are shown; there is a reflection with all Z' couplings reversed. The two solid curves correspond to ILC at 500 (1000) GeV with 500 (1000) fb^{-1} and $P_{eff} = 95\%$.

3.2.2 Current limits on Z' and the ILC reach

The most restrictive bounds on most Z' models currently come from the LHC experiments. Both ATLAS and CMS published bounds using the 20 fb^{-1} dataset at $\sqrt{s} = 8$ TeV, with dielectron and dimuon final states [12, 13]. For the SSM, the current bound on the Z' mass is 2.9 TeV, stronger than the indirect LEP-2 bound. A wide range of E_6 models have been excluded for Z' masses below $2.4 - 2.6$ TeV, indicating that the model-dependence is rather weak.

The current LHC bounds rule out the possibility of on-shell production of a Z' at the ILC. However, the ILC will be sensitive to Z' even at $\sqrt{s} \ll M_{Z'}$, via contact-interaction corrections to 2-fermion processes. A recent estimate of the ILC reach in various Z' models [14], compared to the LHC reach at 14 TeV [9], is shown in Fig. 3.1. The reach of a 500 GeV ILC exceeds the LHC reach in most models, while a 1 TeV ILC will significantly improve on the LHC performance in all cases, with sensitivity well above 10 TeV in many models.

3.2.3 Measurement of Z' couplings

If a Z' is discovered, the next task would be to measure its couplings to SM fermions. In this section, we present a case study illustrating the capabilities of the ILC to perform this measurement. We assume that the Z' arises from $SO(10) \to SU(5)$ gauge symmetry breaking (the χ-model), and has a mass of 3 TeV. Such a Z' would be discovered at the LHC, and its mass and spin can be measured there. The ILC's role would be to complete the characterization of this particle by a precise measurement of its couplings.

The values of the Z' vector and axial-vector couplings v_f and a_f are primarily determined by the measurement of the cross section of the process $e^+e^- \to f\bar{f}$. Measurements of the forward-backward charge asymmetry and of the left-right asymmetry shrink the range for axial-vector coupling and the left- and right-handed couplings, respectively. More details can be found in [5, 15]. Assuming lepton universality, the combination of all leptonic final states allows a precise measurement of the leptonic Z' couplings. Here, the role of beam polarization is important. Without polarized beams, a 4-fold sign ambiguity for the couplings a_l and v_l is obtained. With a polarized electron beam, only a twofold ambiguity remains, and the Z' couplings are determined with higher precision. Having both beams polarized improves the results further: the effective luminosity is increased and the error on the A_{LR} measurement can be decreased due to the reduced uncertainty of the effective polarization. Once the leptonic couplings are measured, the Z' couplings to quarks can be obtained from hadronic final states. Excellent flavor tagging at the ILC with high efficiency and purity is essential to achieve high

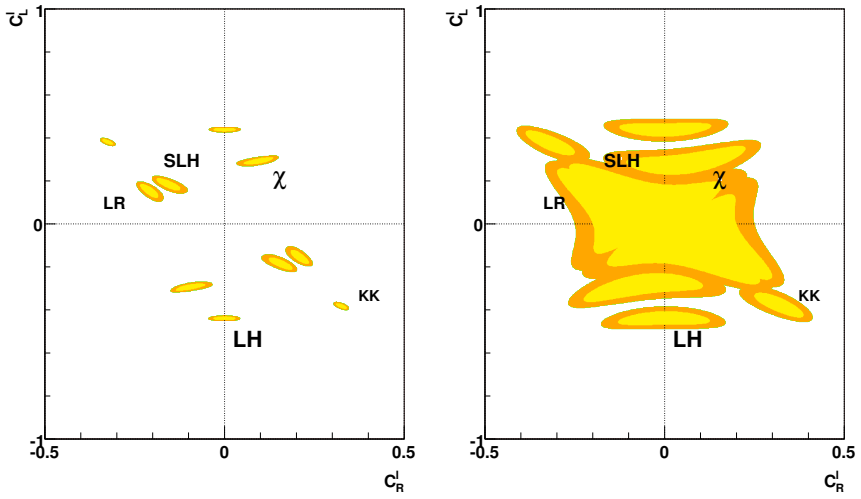

Figure 3.3 95% confidence regions in the plane of the couplings of left- and right-handed leptons to a Z' boson, for the ILC with $\sqrt{s} = 500$ GeV and 1000 fb^{-1} and 80%/60% electron and positron polarization, for $M_{Z'} = 2$ TeV (left panel) and 4 TeV (right panel). For further details, see [16].

precision measurements.

The results for the measurement of leptonic Z' couplings are presented in Fig. 3.2. Systematic uncertainties of 0.2% for the leptonic observables and the luminosity are taken into account; a 0.25% error on beam polarization measurement is assumed. The Z' coupling to b-quarks resulting from a simultaneous fit to lepton and $b\bar{b}$ final states is shown in Fig. 3.2, where a systematic uncertainty of 0.5% is assumed for b-quark observables.

It is evident that increasing the center-of-mass energy is more efficient than collecting more luminosity. At high luminosities systematic uncertainties limit the sensitivity, and even in case of negligible systematic errors doubling the luminosity would improve the range for the Z' couplings only by a factor 0.84. A rough scaling for Z' couplings and mass with energy and luminosity is given by the relation $g/m_{Z'} \propto (s \cdot L_{int})^{-1/4}$.

3.2.4 Z' model discrimination

Since every model predicts a particular pattern of Z' couplings to SM fermions, a measurement of these couplings makes it possible to distinguish between models. For example, expected accuracy of the measurement of the Z' couplings to charged leptons, in a variety of popular Z' models, is shown in Fig. 3.3 (from [16]). The predictions of the benchmark models are quite distinct. Most models can be readily distinguished even for a Z' as heavy as 4 TeV, at a 500 GeV ILC. It should be emphasized that beam polarization plays a crucial role in this analysis.

3.3 Quark and lepton compositeness

In many extensions of the SM, quarks and leptons themselves are composite particles, resolved into more fundamental constituents at an energy scale Λ. The effect of such compositness in $2 \to 2$ fermion scattering processes at energies well below Λ is to induce contact-interaction type corrections, similar to the corrections due to a heavy resonance discussed above. The effects can be parametrized by adding four-fermion operators to the Lagrangian with coefficients proportional to inverse powers of Λ [17]. Currently, the strongest bounds on four-lepton and $eeqq$ operators are $\Lambda \gtrsim 10$ TeV [18, 19]. These bounds come from experiments at LEP. The LHC is unlikely to improve these limits, since at the LHC we have only limited polarization observables in 4-fermion reactions and we do not know the flavor of initial state quarks. The ILC can dramatically increase the reach, with sensitivity to scales as high as $50 - 100$ TeV depending on the helicity structure of the operators (see Fig. 3.4.)

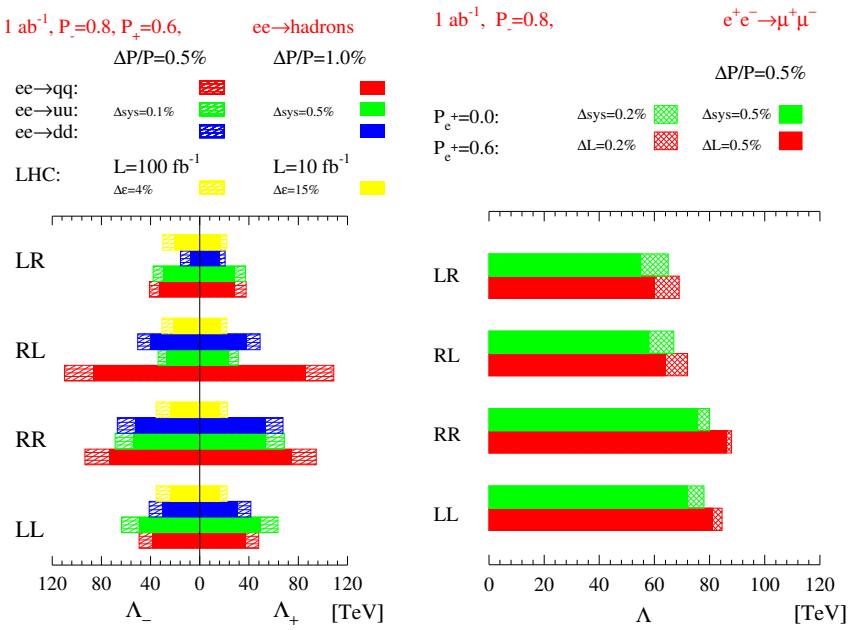

Figure 3.4 Sensitivities (95% c.l.) of a 500 GeV ILC to contact interaction scales Λ for different initial helicities, from [20]. Left: $e^+e^- \to$ hadrons. Right: $e^+e^- \to \mu^+\mu^-$.

3.4 Extra dimensions

Many interesting extensions of the SM postulate the existence of extra spatial dimensions, beyond the familiar three, which are usually assumed to be compact. Motivation for extra dimensions comes from two sides. From the top-down point of view, consistency of string theory requires that the full space-time be 10-dimensional, and additional dimensions must be compactified. From the bottom-up perspective, models with extra dimensions can address some of the theoretical shortcomings of the SM, such as the gauge hierarchy problem. While the extra dimensions of string theory can have any size, in all phenomenologically interesting models the extra dimensions become experimentally manifest at the TeV scale, within the range of the ILC experiments.

Phenomenologically, the most important feature of models with extra dimensions is the appearance of Kaluza-Klein (KK) resonances. Each SM particle (including the graviton) that is allowed to propagate beyond 4D is accompanied by a tower of KK excitations, particles of the same spin and progressively higher masses. In the simplest case of toroidal compactification of radius R, the n-th KK mode has mass $m_n = n/R$. The effect of the KK modes on $e^+e^- \to f\overline{f}$ are similar to that of a Z'. They produce contact interactions, or, if collision energy is sufficient, resonances.

3.4.1 Flat, TeV-sized extra dimensions

The simplest extension is to add k extra dimensions compactified on a torus T^k, and allow all SM fields to propagate in the full space. The most popular model of this type is the "universal extra dimension" (UED) model [21], with $k = 1$ and radius $R \sim 1/\text{TeV}$. This model assumes a $\mathcal{Z}_2$ symmetry under which the n-th KK mode has KK-parity $(-1)^n$. As a result, production of a single first-level KK partner in SM collisions is not possible, and the phenomenology of the first-level KK states is similar to that of supersymmetric models with R-parity. The even-level KK states, on the other hand, may be singly produced via KK-number violating interactions, induced by loops [22]. This leads to resonances or contact-interaction corrections in $e^+e^- \to f\overline{f}$ [23, 24]. An estimated sensitivity of the ILC to the UED model is shown in Fig. 3.5; values of $1/R \sim 1$ TeV can be probed. The reach is significantly lower than for a conventional Z', due to loop-suppressed couplings. However, it should be noted that the same suppression severely limits the ability of the LHC to search for the single KK-mode production. Any resonance for which the coupling to quarks is suppressed by a factor of 10 would contribute a fluctuation below 1% in the Drell-Yan mass spectrum, and this will be indistinguishable

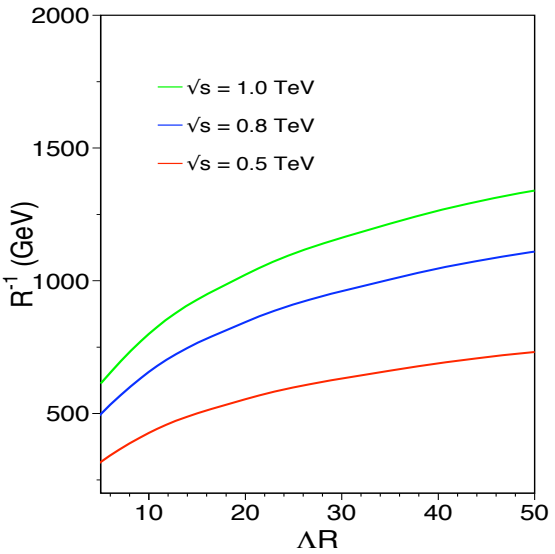

Figure 3.5
Discovery reach of the ILC, with $\mathcal{L}_{\rm int} = 1000$ fb^{-1} and energy indicated on the plot, for the UED model in the 2-fermion channel. Polarization of 80%/60% for electrons/positrons is assumed. Leptonic and hadronic final states are combined. The scale Λ is the cutoff of the theory. From [23].

even for rather light KK masses. Small mass splittings among the KK states at the first level make the LHC searches for pair-production very difficult as well.

3.4.2 Large extra dimensions

The extra dimensions may have sizes much larger than TeV^{-1}, if *only* gravity can propagate in them, while the SM fields are confined on a 4D "brane" inside the full space. Arkani-Hamed, Dimopoulos and Dvali (ADD) [25] proposed that such models can provide an alternative solution to the gauge hierarchy problem: gravity is weaker than other forces due to the larger space in which it propagates. The ADD model is characterized by the fundamental Planck scale M_D (required to be ∼TeV to solve the hierarchy problem); and the number of extra dimensions k. Constraints on macroscopic modifications of Newtonian gravity imply that only cases $k \geq 2$ are phenomenologically relevant.

The model predicts a tower of KK gravitons G_{KK}, with very small spacing in mass, of order $1/R$. While each of the G_{KK} couples to the SM with gravitational strength, their large multiplicity may yield observable effects in $e^+e^- \to G_{KK} \to f\bar{f}$, although no individual resonances can be observed. Instead, the effect is a contact-interaction correction, parametrized as a dimension-8 operator [26]

$$\mathcal{L} = \frac{4\lambda}{\Lambda_H^4} T_{\mu\nu} T^{\mu\nu} \,, \tag{3.3}$$

where $T_{\mu\nu}$ is the SM fermion energy-momentum tensor, $\lambda = \pm 1$, and $\Lambda_H \sim M_D$ is the effective Planck scale.

The strongest bounds on the ADD model currently come from the LHC. A search for anomalous jet+$\not{E}_T$ events at CMS with 20 fb^{-1} at 8 TeV [27] constrains $M_D > 3.0 - 5.0$ TeV for $k = 2 \ldots 6$ (with lower bounds for higher k). In addition, searches for operators of the form (3.3) in $\ell^+\ell^-$ final states [28] provide a bound $\Lambda_H \gtrsim 4.0$ GeV, approximately independent of k. The estimate of the discovery reach of the 500 GeV ILC is $\Lambda_H \approx 5.0 - 5.5$ TeV [29]. Since the KK graviton is a spin-2 object, the angular distribution of the final-state fermions in the ADD model is quite distinct from the case of a spin-1 Z' or KK gauge boson. A unique identification of the spin-2 origin of the contact-interaction correction at a 500 GeV ILC is possible for Λ_H up to about 3.0 TeV [30]; however, the LHC is likely to have an even higher reach using the dilepton final states [31]. Another crucial test of the gravitational nature of the contact interaction would be an independent determination of the size of the effect in a variety of four-fermion channels. Gravity couples to the total energy-momentum tensor, resulting in a set of four-fermion operators independent of the fermion type. Alternative

models for spin-2 contact interactions, such as the exchange of string-Regge excitations of the SM gauge bosons [32], predict effects of different sizes for up-type and down-type quarks and leptons. The ILC will provide an ideal environment to perform this test.

3.4.3 Randall-Sundrum warped extra dimensions

While the ADD model eliminates the usual gauge hierarchy, it faces its own hierarchy problem: the large ratio of the size of the extra dimensions and their natural scale, TeV^{-1}, must be explained. This difficulty is avoided in the Randall-Sundrum (RS) model [1], which extends the space by a single extra dimension, compactified on an orbifold $S_1/\mathcal{Z}_2$, effectively an interval. The characteristic feature of this model is the non-flat "warped" metric, which can be used to generate the observed large hierarchy between the Planck and the weak scale without assuming any hierarchies among the input parameters. Interestingly, AdS/CFT duality has been used to argue that the RS model is simply a weakly-coupled description of a strongly-coupled four-dimensional model with a composite Higgs boson.

In the original RS model, only gravity was assumed to propagate in the full 5D space, while all SM fields were confined on the 4D boundary. As in ADD, potentially observable KK modes of the graviton are predicted; however, their masses are spaced by $\mathcal{O}$(TeV), and their couplings to the SM are suppressed by a scale of $\mathcal{O}$(TeV) and not the Planck scale. The LHC experiments search for RS KK graviton resonances in the $\ell^+\ell^-$ and $\gamma\gamma$ final states. The graviton couplings to the SM depend on the curvature of the extra dimension k. The dimensionless ratio $k/\overline{M}_{\rm Pl}$ is expected to be in a range between 0.01 and 0.1 on naturalness grounds. The current LHC bounds on the KK graviton mass vary from 2.1 TeV for $k/\overline{M}_{\rm Pl} = 0.1$ to 0.9 TeV for $k/\overline{M}_{\rm Pl} = 0.01$ [12, 13]. The LHC reach with $\sqrt{s} = 14$ TeV, $L_{\rm int} = 100$ fb^{-1} is expected to be $2.5 - 4.5$ TeV, for the same range of $k/\overline{M}_{\rm Pl}$ [33]. At the ILC, these resonances appear as interference effects both in e^+e^- and in $\gamma\gamma$ annihilation processes. As with Z' resonances, the sensitivity is comparable to that for direct resonance searches at the LHC.

Bibliography

[1] L. Randall and R. Sundrum, Phys. Rev. Lett. **83**, 3370 (1999) [hep-ph/9905221].

[2] J. Brau, (Ed.) *et al.* [ILC Collaboration], *"ILC Reference Design Report: ILC Global Design Effort and World Wide Study,"* arXiv:0712.1950 [physics.acc-ph];
G. Aarons *et al.* [ILC Collaboration], *"International Linear Collider Reference Design Report Volume 2: Physics At The ILC,"* arXiv:0709.1893 [hep-ph].

[3] H. Aihara, (Ed.), P. Burrows, (Ed.), M. Oreglia, (Ed.), E. L. Berger, V. Guarino, J. Repond, H. Weerts and L. Xia *et al.*, arXiv:0911.0006 [physics.ins-det].

[4] T. Abe *et al.* [ILD Concept Group - Linear Collider Collaboration], arXiv:1006.3396 [hep-ex].

[5] A. Leike, Phys. Rept. **317**, 143 (1999) [hep-ph/9805494].

[6] P. Langacker, Rev. Mod. Phys. **81**, 1199 (2009) [arXiv:0801.1345 [hep-ph]].

[7] L. J. Hall, D. Pinner and J. T. Ruderman, JHEP **1204**, 131 (2012) [arXiv:1112.2703 [hep-ph]].

[8] M. Schmaltz and D. Tucker-Smith, Ann. Rev. Nucl. Part. Sci. **55**, 229 (2005) [hep-ph/0502182];
M. Perelstein, Prog. Part. Nucl. Phys. **58**, 247 (2007) [hep-ph/0512128].

[9] P. Osland, A. A. Pankov, A. V. Tsytrinov and N. Paver, Phys. Rev. D **79**, 115021 (2009) [arXiv:0904.4857 [hep-ph]].

[10] N. Arkani-Hamed, A. G. Cohen, E. Katz and A. E. Nelson, JHEP **0207**, 034 (2002) [hep-ph/0206021].

[11] M. Schmaltz, JHEP **0408**, 056 (2004) [hep-ph/0407143].

[12] CMS Collaboration, Physics Analysis Summary CMS PAS EXO-12-061.

[13] G. Aad *et al.* [ATLAS Collaboration], ATLAS-CONF-2013-017.

[14] P. Osland, A. A. Pankov and A. V. Tsytrinov, Eur. Phys. J. C **67**, 191 (2010) [arXiv:0912.2806 [hep-ph]].

[15] A. Leike and S. Riemann, Z. Phys. C **75**, 341 (1997) [hep-ph/9607306].

[16] S. Godfrey, P. Kalyniak and A. Tomkins, hep-ph/0511335.

[17] E. Eichten, K. D. Lane and M. E. Peskin, Phys. Rev. Lett. **50**, 811 (1983).

[18] K. Nakamura *et al.* [Particle Data Group Collaboration], J. Phys. G G **37**, 075021 (2010).

[19] S. Chatrchyan *et al.* [CMS Collaboration], arXiv:1212.4563 [hep-ex].

[20] S. Riemann, LC-TH-2001-007.

[21] T. Appelquist, H. -C. Cheng and B. A. Dobrescu, Phys. Rev. D **64**, 035002 (2001) [hep-ph/0012100].

[22] H. -C. Cheng, K. T. Matchev and M. Schmaltz, Phys. Rev. D **66**, 056006 (2002) [hep-ph/0205314].

[23] S. Riemann, eConf C **050318**, 0303 (2005) [hep-ph/0508136].

[24] B. Bhattacherjee and A. Kundu, Phys. Lett. B **627**, 137 (2005) [hep-ph/0508170];
B. Bhattacherjee, Pramana **69**, 855 (2007) [hep-ph/0608227].

[25] N. Arkani-Hamed, S. Dimopoulos and G. R. Dvali, Phys. Lett. B **429**, 263 (1998) [hep-ph/9803315].

[26] J. L. Hewett, Phys. Rev. Lett. **82**, 4765 (1999) [hep-ph/9811356].

[27] CMS Collaboration, Physics Analysis Summary CMS PAS EXO-12-048.

[28] CMS Collaboration, Physics Analysis Summary CMS PAS EXO-12-027, Physics Analysis Summary CMS PAS EXO-12-031.

[29] T. G. Rizzo, AIP Conf. Proc. **1256**, 27 (2010) [arXiv:1003.1698 [hep-ph]].

[30] T. G. Rizzo, JHEP **0210**, 013 (2002) [hep-ph/0208027].

[31] E. W. Dvergsnes, P. Osland, A. A. Pankov and N. Paver, Phys. Rev. D **69**, 115001 (2004) [hep-ph/0401199].

[32] S. Cullen, M. Perelstein and M. E. Peskin, Phys. Rev. D **62**, 055012 (2000) [hep-ph/0001166].

[33] H. Davoudiasl, J. L. Hewett and T. G. Rizzo, Phys. Rev. D **63**, 075004 (2001) [hep-ph/0006041].

Chapter 4
W and Z Boson Physics

The ILC will yield a new level of precision in measurements of the W and Z boson masses, widths, and couplings. Several different ILC processes contribute to these measurements. These include the continuum production of two vector bosons, $e^+e^- \to W^+W^-$ and $e^+e^- \to ZZ$, production of weak bosons in 2-photon reactions, and triple boson production $e^+e^- \to VVV$, where the final state can be WWZ, ZZZ, or $WW\gamma$. In addition, the ILC can study vector boson scattering at high energy. Furthermore, the ILC offers the possibility of dedicated low-energy runs at the Z and at the WW threshold. In all cases, these measurements will supersede the precision of existing measurements from the previous colliders, including SLC, LEP and the Tevatron, and are expected also to surpass the accuracies that will be available from the LHC.

As we will explain in detail in this section, these measurements will allow us to go beyond simple tests of the description of the W and Z bosons in the Standard Model. Through the Higgs mechanism of mass generation, massive W and Z bosons contain states that belong to the Higgs boson sector and exhibit possible new couplings associated with Higgs boson compositeness or strong interactions. Precise measurements of the W and Z properties can reveal these effects.

Many models of new physics beyond the Standard Model predict new couplings of the W and Z bosons. These include models with additional heavy vector bosons such as technicolor and topcolor, Little Higgs models, extra-dimensional models with Kaluza-Klein recurrences of the W and Z boson, and Twin Higgs models. In many of these cases, the additional gauge bosons would be fermiophobic and would thus evade direct searches at the LHC. The new bosons must then be found through their mixing with the W and Z bosons. Such mixing effects could be detected by the precision measurements described in this section.

4.1 Beyond the SM W/Z sector: the EW chiral Lagrangian

To interpret the results of precision measurements of the various W and Z processes that will be studied at the ILC, it is useful to have a common theoretical framework to which all of these measurements can be related. Frameworks of two different types are commonly used. The first is based on an effective field theory (EFT) that includes the most general modifications of the W and Z couplings that might be induced by adding higher-dimension operators to the Standard Model Lagrangian. Such effective field theories are presented in the literature in [1, 2]. A complementary approach is to postulate resonances with various quantum numbers and couple these to the W, Z, and Higgs bosons [3]. It is rather easy to switch between the two descriptions. Then limits on anomalous W and Z couplings parametrized in the EFT language can be expressed in terms of limits on the mass and width parameters of physical resonances.

In this section, we will summarize the description of the electroweak (EW) effective Lagrangian and its parameters from these two points of view and define the parameters of this Lagrangian that can be constrained by experiment. In the remainder of this chapter, we will quote constraints on this effective Lagrangian that can be obtained from the ILC experiments.

4.1.1 Formalism of the EW chiral Lagrangian

The EW effective chiral Lagrangian consists basically of the $SU(2)_L \times U(1)_Y$-invariant SM Lagrangian (without the Higgs field) and a non-linear sigma model describing the Goldstone bosons (which provide the longitudinal degrees of freedom of W and Z). Though this formulation of the electroweak Lagrangian was originally constructed for models containing very heavy, composite, or no Higgs bosons, it can be easily extended to include a 125 GeV Higgs boson as indicated by the 2012 LHC discovery [4]. The lowest-order EW chiral Lagrangian contains the kinetic terms for the weak and hypercharge bosons as well as the kinetic term for their longitudinal degrees of freedom, which also yields the gauge boson mass terms. There is one additional possible dimension 2 operator, $\mathcal{L}_0'$. At the next order in mass dimension, there are ten possible dimension 4 operators (assuming C and CP conservation), $\mathcal{L}_{i=1,\ldots,10}$, with corresponding operator coefficients, $\alpha_{i=1,\ldots,10}$. The operators give all possible Lorentz- and gauge-invariant combinations of the transverse and longitudinal electroweak gauge fields. The detailed form of the Lagrangian can be found in [1–3, 5].

All of these operators modify the 2-, 3- and 4-point functions of the EW gauge bosons: $\mathcal{L}_0', \mathcal{L}_1, \mathcal{L}_8$ give the oblique corrections which modify the gauge-boson propagators, while $\mathcal{L}_2, \mathcal{L}_3, \mathcal{L}_9$ induce anomalous triple gauge couplings (TGCs). The remaining five operators ($\mathcal{L}_4$–$\mathcal{L}_7$ and $\mathcal{L}_{10}$) only affect the quartic gauge couplings (QGCs). The coefficient of the extra dimension-2 operator, the parameter β_1, is directly related to the ρ or T parameter, and thus is rather special. Experimentally it is well-known that the deviation from $\rho = 1$ is quite small, such that the leading-order Lagrangian possesses a custodial isospin symmetry which is broken only at next-to-leading order by the non-vanishing EW mixing angle and the mass splittings inside the fermionic isospin doublets. Sometimes such custodial isospin conservation is assumed. This would then eliminate the operators $\mathcal{L}_6$–$\mathcal{L}_{10}$.

At the next order in mass dimension, there are five dimension-6 operators, $\mathcal{L}^{\lambda}_{1,\ldots,5}$, with coefficients $\alpha^{\lambda}_{i=1,\ldots,5}$ [1–3, 5]. These operators, which can be interpreted as contributions to anomalous magnetic moments of the EW gauge bosons, appear in the same order in the power counting of the perturbative expansion as the operators listed above. The first two, containing three field-strength tensors, induce also anomalous TGCs, while the last three, containing two field-strengths and two longitudinal bosons, only contribute to the QGCs. Including a light Higgs boson leads to more operators containing the Higgs field, some of which are however redundant and can be eliminated via equations of motion [6].

As we have discussed already, all of these ten plus five operators can be generated when integrating out one or more heavy particles beyond the SM. It is not unlikely that heavy particles that could

contribute to the EW effective Lagrangian in this way would be discovered at the LHC in its run at 14 TeV.

We will see in subsequent sections that the ILC experiments can make precise statements about the values of the α_i parameters. Though the ILC measurements are done on the electroweak gauge bosons, the Equivalence Theorem [7] implies that the longitudinal polarization states of massive gauge bosons have couplings associated with the Higgs sector responsible for their mass generation. Thus, measurements of the W and Z couplings, codified by the α_i parameters, have a direct interpretation as Higgs sector interactions and can be used to constrain models of Higgs dynamics. For example, the values of the α_i constrain the existence of possible resonances, associated with composite Higgs sectors, strong weak interactions or similar models. We will describe this connection below.

First, however, it will be useful to explain how the formalism presented in the previous section is connected to the trilinear and quartic vector boson couplings. Within the SM, the trilinear and quartic couplings are specified by the constraints of gauge invariance. Beyond the SM, additional couplings may appear. Often, these are represented by effective Lagrangians with many parameters. The systematic effective Lagrangian approach of the previous section organizes these parameters in a useful way.

The EW chiral Lagrangian provides an off-shell formulation for a general electroweak sector combining all possible operators up to dimension 4. Complete (fermionic) matrix elements for $2 \to 6$ processes can be computed using the Feynman rules derived from this Lagrangian. These Feynman rules include EW boson interactions with anomalous couplings. In the next few paragraphs, we will give the relation between a general parametrization of the anomalous couplings and the effective Lagrangian parameters α_i.

In unitarity gauge, the trilinear gauge interactions are conventionally written

$$\begin{aligned} L_{\mathrm{WWV}} \;=\; & g_{\mathrm{WWV}}[\\ & \mathrm{i}g_1^{\mathrm{V}} V_\mu \left(W_\nu^- W_{\mu\nu}^+ - W_{\mu\nu}^- W_\nu^+\right) + \mathrm{i}\kappa_{\mathrm{V}} W_\mu^- W_\nu^+ V_{\mu\nu} + \mathrm{i}\frac{\lambda^{\mathrm{V}}}{m_{\mathrm{W}}^2} W_{\lambda\mu}^- W_{\mu\nu}^+ V_{\nu\lambda} \\ & + g_4^{\mathrm{V}} W_\mu^- W_\nu^+ \left(\partial_\mu V_\nu + \partial_\nu V_\mu\right) + g_5^{\mathrm{V}} \epsilon_{\mu\nu\lambda\rho} \left(W_\mu^- \partial_\lambda W_\nu^+ - \partial_\lambda W_\mu^- W_\nu^+\right) V_\rho \\ & + \mathrm{i}\tilde{\kappa}^{\mathrm{V}} W_\mu^- W_\nu^+ \tilde{V}_{\mu\nu} + \mathrm{i}\frac{\tilde{\lambda}^{\mathrm{V}}}{m_{\mathrm{W}}^2} W_{\lambda\mu}^- W_{\mu\nu}^+ \tilde{V}_{\nu\lambda}] \,, \end{aligned} \tag{4.1}$$

Similarly, the quartic gauge interactions are expressed as

$$\begin{aligned} \mathcal{L}_{QGC} = & e^2 \left[g_1^{\gamma\gamma} A^\mu A^\nu W_\mu^- W_\nu^+ - g_2^{\gamma\gamma} A^\mu A_\mu W^{-\nu} W_\nu^+\right] \\ & + e^2 \frac{c_w}{s_w} \left[g_1^{\gamma Z} A^\mu Z^\nu \left(W_\mu^- W_\nu^+ + W_\mu^+ W_\nu^-\right) - 2 g_2^{\gamma Z} A^\mu Z_\mu W^{-\nu} W_\nu^+\right] \\ & + e^2 \frac{c_w^2}{s_w^2} \left[g_1^{ZZ} Z^\mu Z^\nu W_\mu^- W_\nu^+ - g_2^{ZZ} Z^\mu Z_\mu W^{-\nu} W_\nu^+\right] \\ & + \frac{e^2}{2 s_w^2} \left[g_1^{WW} W^{-\mu} W^{+\nu} W_\mu^- W_\nu^+ - g_2^{WW} \left(W^{-\mu} W_\mu^+\right)^2\right] + \frac{e^2}{4 s_w^2 c_w^4} h^{ZZ} (Z^\mu Z_\mu)^2 \quad . \end{aligned} \tag{4.2}$$

The overall prefactors are $g_{WW\gamma} = e$ and $g_{WWZ} = e\cos\theta_W / \sin\theta_W$. The symbols $V_{\mu\nu}$ and $\tilde{V}_{\mu\nu}$ are defined as:

$$V_{\mu\nu} = \partial_\mu V_\nu - \partial_\nu V_\mu \qquad \tilde{V}_{\mu\nu} = \epsilon_{\mu\nu\rho\sigma} V^{\rho\sigma}/2 \,. \tag{4.3}$$

The SM values of the trilinear couplings in (4.1) are given by

$$g_1^{\gamma,Z} = \kappa^{\gamma,Z} = 1, \quad g_4^{\gamma,Z} = g_5^{\gamma,Z} = \tilde{\kappa}^{\gamma,Z} = 0 \quad \text{and} \quad \lambda^{\gamma,Z} = \tilde{\lambda}^{\gamma,Z} = 0 \qquad , \tag{4.4}$$

The deviations of the couplings from the SM values are expressed in terms of the α_i parameters as

$$\Delta g_1^\gamma = 0 \qquad \Delta\kappa^\gamma = g^2(\alpha_2 - \alpha_1) + g^2\alpha_3 + g^2(\alpha_9 - \alpha_8) \tag{4.5}$$

$$\Delta g_1^Z = \delta_Z + \frac{g^2}{c_w^2}\alpha_3 \qquad \Delta\kappa^Z = \delta_Z - g^2(\alpha_2 - \alpha_1) + g^2\alpha_3 + g^2(\alpha_9 - \alpha_8) \tag{4.6}$$

and

$$\lambda^\gamma = -\frac{g^2}{2}\left(\alpha_1^\lambda + \alpha_2^\lambda\right) \qquad \lambda^Z = -\frac{g^2}{2}\left(\alpha_1^\lambda - \frac{s_w^2}{c_w^2}\alpha_2^\lambda\right) \tag{4.7}$$

where δ_Z is determined by the precision electroweak corrections. Note that in this setup only the C- and P-conserving parameters g_1, κ and λ can be generated. The parameters g_5, which violate C and P separately but leaves CP intact, and g_4, $\tilde{\kappa}$ and $\tilde{\lambda}$, which violate CP, are not shifted.

The SM values of the quartic couplings in (4.2) are given by

$$g_1^{VV'} = g_2^{VV'} = 1 \quad (VV' = \gamma\gamma, \gamma Z, ZZ, WW), \qquad h^{ZZ} = 0. \tag{4.8}$$

Deviations from these SM values in the quartic couplings are introduced through the corrections induced by the α_i to the couplings that preserve custodial $SU(2)$ symmetry,

$$\Delta g_1^{\gamma\gamma} = \Delta g_2^{\gamma\gamma} = 0 \qquad \Delta g_1^{\gamma Z} = \Delta g_2^{\gamma Z} = \frac{g^p p}{c_w^2 - s_w^2}\alpha_1 + \frac{g^2}{c_w^2}\alpha_3 \tag{4.9a}$$

$$\Delta g_1^{ZZ} = 2\Delta g_1^{\gamma Z} + \frac{g^2}{c_w^4}\alpha_4 \qquad \Delta g_2^{ZZ} = 2\Delta g_1^{\gamma Z} - \frac{g^2}{c_w^4}\alpha_5 \tag{4.9b}$$

$$\Delta g_1^{WW} = 2c_w^2\Delta g_1^{\gamma Z} + g^2\alpha_4 \qquad \Delta g_2^{WW} = 2c_w^2\Delta g_1^{\gamma Z} - g^2\left(\alpha_4 + 2\alpha_5\right) \tag{4.9c}$$

$$h^{ZZ} = g^2\left(\alpha_4 + \alpha_5\right). \tag{4.9d}$$

Since we have consistently generated the trilinear and quartic couplings from a theory with exact but spontaneously broken $SU(2) \times U(1)$ symmetry, the vertices described in this section fit together into a unified formalism that can be used to compute the scattering amplitudes for complete electroweak processes. In particular, this formalism gives a consistent definition to off-shell propagators and vertices that appear in processes containing the quartic gauge boson vertices. The results of all experiments are expressed in terms of the parameters α_i.

4.1.2 EW chiral Lagrangian and Higgs sector resonances

We now return to the question of the interpretation of the α_i parameters in terms of possible resonances in the electroweak sector. A formalism complementary to the chiral Lagrangian approach summarized above, based on adding resonances to the SM Lagrangian has been described in [3]. Note that this formalism can easily include a light Higgs boson as one of the resonances included. We review this formalism briefly here.

There are three different combinations of spin and isospin for which resonances can couple to the EW gauge boson system. The spin of these resonances can be 0, 1, or 2 (scalar, vector, or tensor), and, similarly, the value of the isospin, under the custodial isospin symmetry, can be 0, 1, or 2 (in this context, labeled singlet, triplet, and quintet). To couple invariantly to a pair of weak bosons, the parity in spin and isospin must be equal; hence we consider resonances with the quantum numbers:

- scalar singlet σ, scalar quintet ϕ,
- vector triplet ρ,
- tensor singlet f, tensor quintet a.

Table 4.1. Coefficients ξ appearing in the formula (4.10) for the partial widths for resonances with various quantum numbers to decay into longitudinally polarized vector bosons.

Resonance	σ	ϕ	ρ	f	a
Γ	6	1	$4v^2/3M^2$	1/5	1/30

In the model, these resonances are allowed to have arbitrary masses and widths, including both extreme cases of extremely heavy ($M \to \infty$) or extremely broad ($\Gamma \sim M \to \infty$) resonances. We might also list π (scalar triplet) and ω (vector singlet), but their couplings to pairs of weak bosons violate custodial isospin. Then either their couplings are small, so that we can ignore them, or they require unnatural cancellations to preserve the SM value of the ρ parameter.

An example of such a resonance of the type σ is the SM Higgs boson itself. The techni-rho resonance of technicolor models is an example of the vector triplet ρ. This set of quantum numbers also appears in an extra-dimensional context as a Kaluza-Klein W' or Z' [8]. An example of the tensor f is the graviton resonance in Randall-Sundrum models [9].

For the purposes of this section, we will assume that resonances in the EW sector have fermionic couplings very suppressed compared to the couplings to the EW sector. The opposite case has been discussed already in Chapter 3. For resonances that do not couple strongly to fermions, the dominant decays are to longitudinal EW gauge bosons. The widths are given by formulae

$$\Gamma_i = \frac{g_i^2}{64\pi} \frac{M^3}{v^2} \cdot \xi \ , \tag{4.10}$$

where the coefficients ξ are displayed in Table 4.1. The couplings g_i are the elementary couplings appearing in the resonance Lagrangian. With increasing number of spin and isospin components, the resonance width decreases. Note that, with our normalization convention for the dimensionless couplings g_i, the width of a vector resonance has a scaling behavior different from that of the other cases. If we want to work in a purely phenomenological approach, it is useful to eliminate the couplings g_i in terms of the resonance widths using (4.10).

At the ILC, we are mainly concerned with (precision) measurements of electroweak processes at energies below the first resonance in an extended electroweak/Higgs sector. Any deviations observed from the Standard Model predictions can be interpreted in terms of the α_i parameters. To understand the relation of these parameters to the system of resonances, we can integrate out the resonances and expand the resulting effective Lagrangian in powers of E/M. The terms resulting from this integration out shift the parameters of the Standard Model Lagrangian, shift the parameters β_1 and α_2, and shift the other α_i parameters. The shifts of the Standard Model couplings are absorbed into the renormalized electroweak parameters. The shifts of α_2 and β_1 appear in the S and T parameters of electroweak interactions. The remaining shifts of the α_i provide new information. The most important effects appear as shifts of α_4 and α_5. The translation from the resonance masses to α_4 and α_5 is given by the relation

$$\Delta\alpha_i = \frac{16\pi\Gamma}{M} \frac{v^4}{M^4} \cdot \zeta \tag{4.11}$$

where the coefficients ζ are displayed for each type of resonance in Table 4.2.

Figure 4.1 shows the shifts in α_4 and α_5 induced by each particular type of Higgs sector resonance. There is an ambiguity in the values of the α_i associated with a change in the renormalization scale of

Table 4.2. Coefficients ζ in the relation (4.11) between the parameters of a Higgs sector resonance and the chiral Lagrangian coefficients α_4 and α_5 that result from integrating out that heavy resonance.

Resonance	σ	ϕ	ρ	f	a
$\Delta\alpha_4$	0	$\frac{1}{4}$	$\frac{3}{4}$	$\frac{5}{2}$	$-\frac{5}{8}$
$\Delta\alpha_5$	$\frac{1}{12}$	$-\frac{1}{12}$	$-\frac{3}{4}$	$-\frac{5}{8}$	$\frac{35}{8}$

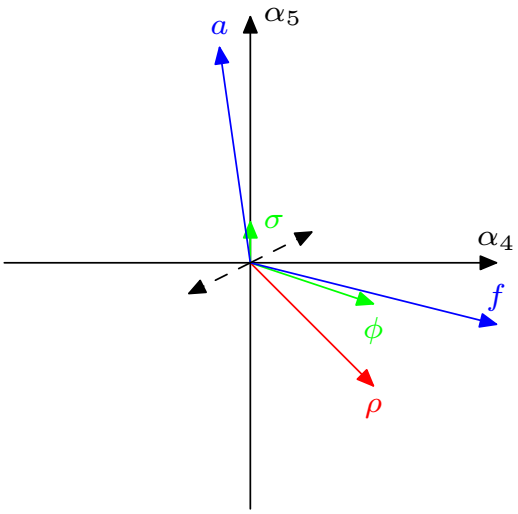

Figure 4.1 Anomalous couplings $\alpha_{4/5}$ in the low-energy effective theory coming from the different resonances under the assumption of equal masses and widths, $M \sim \Gamma$ (Table 4.2). The dashed arrow indicates the shift due to renormalization scale variation.

the effective low-energy Lagrangian

$$\alpha_4(\mu) = \alpha_4(\mu_0) - \frac{1}{12}\,\frac{1}{16\pi^2}\,\ln\frac{\mu^2}{\mu_0^2}$$
$$\alpha_5(\mu) = \alpha_5(\mu_0) - \frac{1}{24}\,\frac{1}{16\pi^2}\,\ln\frac{\mu^2}{\mu_0^2}\,, \tag{4.12}$$

where μ_0 is a reference scale. This shift is plotted as a dashed arrow in Fig. 4.1. Fortunately, this small shift is almost orthogonal, in the (α_4, α_5) plane, to the direction of the shift induced by a resonance. It should be interpreted as a theory uncertainty in the prediction for these shifts.

In the case that there is only one dominant resonance present, a combined fit to both α parameters allows us to disentangle isosinglet from isotriplet or isoquintet resonances. A worked example is given in [10]. The angular distributions of final vector bosons provide further information on the nature of a resonance. For example, a ρ resonance multiplet would have the characteristic feature that the ZZ decay channel is absent, by virtue of the Landau-Yang theorem

There is one more important issue to discuss in setting up the theory of strong interaction corrections to the electroweak sector. This is the question of high-energy behavior and unitarity. At the ILC, experiments on trilinear and quartic couplings in $e^+e^- \to VV$ and related processes can be analyzed by using the low energy effective Lagrangian directly. This is even correct in the study of vector boson scattering, $VV \to VV$, where corrections to the effective Lagrangian description come in only at the highest subprocess energies near 1 TeV. Measurements of these effects at hadron colliders probe a region of higher energies in which expressions derived from the effective Lagrangian must be greatly modified. The reason for this is that vertices due to higher-dimension operators grow dramatically at high energy and, if left unmodified, violate unitarity. In reality, unitarity can never be violated, but the restoration of unitarity requires additional higher-order effects or a proper UV completion of the theory. This introduces new parameters into the description. Even at the Tevatron, the analysis of measurements of the trilinear couplings must include form factors or other modifications so that the theory used to fit the data is internally consistent and avoids violation of

unitarity. This is the flip side of the observation that, because it accesses higher energies, the LHC offers the opportunity to discover new states of an extended electroweak/Higgs sector as resonances. If resonances are not observed, or are not prominent, or if there are additional resonances beyond the reach of the LHC, there is no definite theoretical framework, and so results from the LHC will have ambiguity or model-dependence.

Thus, some heuristics are needed to define a complete formalism in which EFT descriptions like the EW chiral Lagrangian can be used as the basis of a formalism that can produce simulations to be compared to collider data and translate search limits between LHC and ILC experiments. In setting up this formalism, it would be advantageous to include possible first resonances explicitly, since these might be within the kinematical reach of the LHC. Such resonances would appear in strongly interacting Higgs sector models or in extra-dimensional models. On the other hand, the formalism must give amplitudes that preserve unitary. This second task can be achieved either by introducing momentum-dependent form factors for the low-energy scattering amplitudes and regularizing them, or using unitarization methods like the K matrix [11]. Details of a formalism that accomplishes this, and the translation between LHC and ILC results within this formalism, can be found in [3]. This method of unitarization can be combined with the generic off-shell parameterization of EW boson scattering given in (4.1) and (4.2) to give a complete description of Goldstone boson scattering amplitudes. For that purpose, the constant parameters $\alpha_{4/5}$ are replaced by energy-dependent (i.e., s-dependent) form factors. The technical details of that implementation can be found in [3]. This prescription does break crossing symmetry, but in fact that is broken already by the K-matrix prescription for unitarization. In principle, anomalous couplings for resonances might also be included. Such couplings are not considered here. We assume that they are subleading in the high-energy regime of a 1 TeV ILC or at LHC.

With this formalism in hand one can easily switch between the high-energy measurements on VV scattering in the LHC environment and the much more precise measurements possible at the ILC and consider at the same time the parallel information from di- or triboson production. In the following sections we describe diboson production in the channels WW and ZZ, the corresponding photon-induced processes, triboson production, EW boson scattering. We also discuss low-energy precision measurements at the Z and at the WW threshold.

4.2 Vector boson pair production

The major weak processes to be studied at an ILC are pair production of electroweak gauge bosons, $e^+e^- \to W^+W^-$ and $e^+e^- \to ZZ$. The ILC will be the first collider to provide W pair production in lepton collisions with polarized beams. Due to the $V-A$ structure of the W boson interactions, polarization of the beams radiating the electroweak boson can substantially enhance or suppress their production. Note, that there is also as a competing process, single W production, originating mostly from photon-W fusion (cf. Fig. 4.2). Since pair production is dominated by the s-channel pole, its cross section falls off linearly with energy. ILC will be the first lepton collider to enter that regime. On the other hand, single production is kinematically enhanced through the t-channel propagators and rises logarithmically with energy. 1 TeV is roughly the energy where the cross section for single production starts to exceed that of pair production.

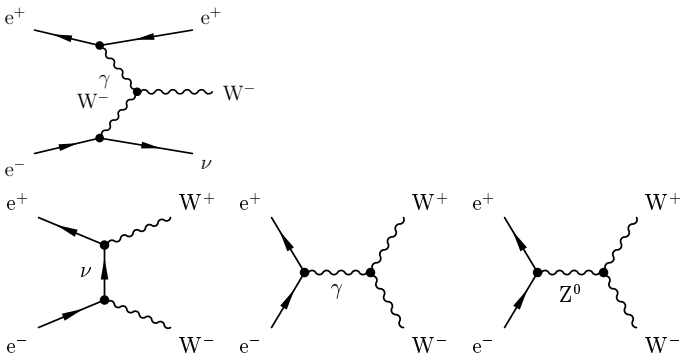

Figure 4.2 Dominant Feynman diagrams for W boson production at the ILC. Top: single W production. Bottom: W^+W^- pair production.

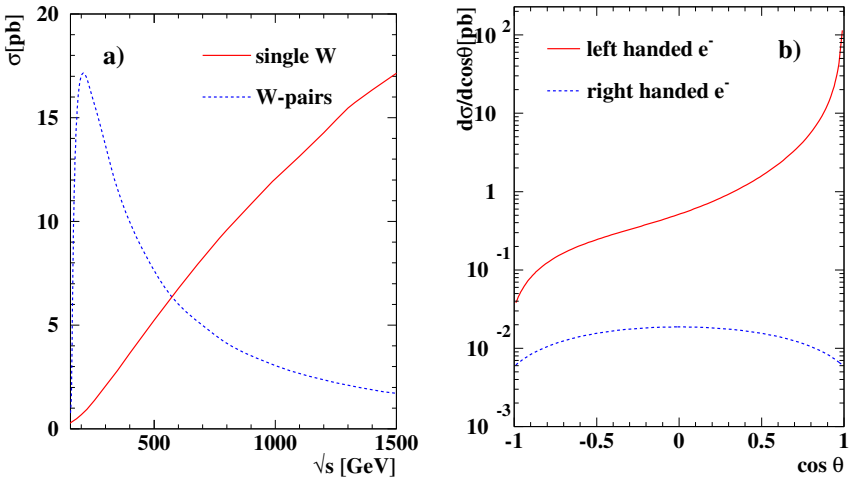

Figure 4.3 Left: Total cross section for single W [20–22] and W pair production [12] as a function of the center of mass energy. Right: Differential cross section for W pair production as a function of the W polar angle for different beam polarizations.

4.2.1 $e^+e^- \to W^+W^-$

WW production at a lepton collider is a theoretically well-studied process for which full next-to-leading (NLO) electroweak corrections are available, including the W decays both in the double-pole approximation [12] and in a full $2 \to 4$ calculation [13]. These results have been cast into dedicated NLO Monte-Carlo programs, YFSWW3 [14] and RacoonWW [15]. The effects of finite fermion masses and different cuts on the cross section and distributions have also been studied in [16]. Furthermore, by means of effective field theory methods, the precise line-shape of W pairs close to the thresholds have been investigated [17]. The leading NNLO corrections have recently been calculated in this framework [18]. The single W production at a lepton collider is also available at NLO [19].

Fig. 4.3 shows, on the left, the cross sections for single W and W pair production at the ILC as a function of the center of mass energy. The right hand side of the figure shows the power of polarized beams at the ILC to enrich different helicity modes of the Ws and hence their angular correlations.

The process of WW production at the ILC allows for a sensitive measurement of triple gauge boson couplings, defined in (4.1). If one replaces the constant parameters by momentum-dependent form factors, (4.1) is in fact the most general parameterization. However, restricting again to the two lowest orders in the expansion of the EW chiral Lagrangian takes one back to constant coupling parameters. Note that there are some constraints to be fulfilled due to the unbroken electromagnetic gauge invariance, namely $g_1^\gamma(q^2=0)=1$ and $g_5^\gamma(q^2=0)=0$ at zero momentum transfer.

Measurements of W pair production disentangle the various gauge structures contributing to the production amplitudes. The amplitudes depend on both sets of trilinear couplings, $WW\gamma$ and WWZ. The differential cross section with respect to the angle of the W boson to the beam itself is sensitive to deviations from the SM values of the triple gauges couplings at the sub-percent level. The left-right asymmetry as function of the W production angle adds to this information and enables one to discriminate between contributions to the anomalous $WW\gamma$ and WWZ coupling. This can

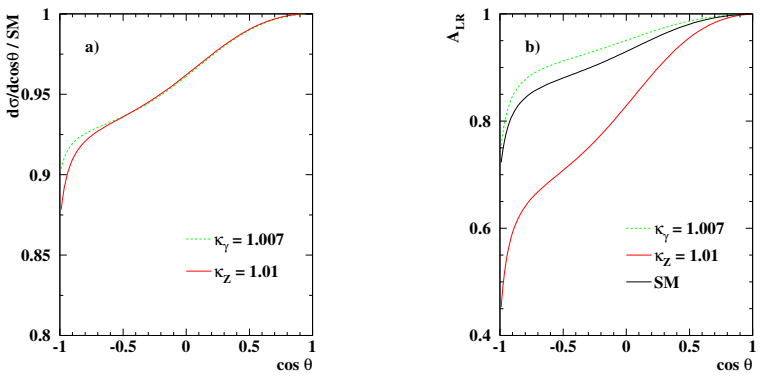

Figure 4.4
The effect of anomalous triple gauge couplings on the W pair cross section, as a ratio to the SM prediction, as a function of the W polar angle. Left: for the differential cross section. Right: for the left-right polarization asymmetry.

be seen from Fig. 4.4.

Analyses of WW production to measure triple gauge couplings rely on a set of five different observables. We have already discussed the dependence on the polar angle θ_W of the outgoing W^- with respect to the beam direction. This is the variable whose dependence is shown in Figs. 4.3 and 4.4. In addition, we can measure the polar angle θ^* of the decay fermion, with respect to the flight direction of the W boson in the rest frame of the W boson, for each of the two W bosons. These variables are sensitive to the longitudinal polarization of the W bosons. Finally, the transverse polarization of the W bosons can be accessed via the azimuthal angles ϕ^* of the fermions in the plane constructed from the beam and the W flight direction.

The most frequent decay mode of a WW pair is the semileptonic one, which constitutes 44 % of all WW decays. In semileptonic events, the polar angle of the negatively charged W^- can be unambiguously reconstructed from the jet momenta and the lepton charge. Furthermore, the fermionic decay angles can be uniquely determined in case of the leptonically decaying W. For the hadronically decaying W there is a twofold ambiguity, $(\cos\theta^*, \phi^*) \longleftrightarrow (-\cos\theta^*, \phi^* + \pi)$, arising from the fact that quarks and antiquarks cannot be distinguished, except possibly in $W \to c$ decays. While the semileptonic event sample is by far the most sensitive to triple gauge couplings, the largest sample is the fully hadronic one, which constitutes 46% of all decays. Here the sign ambiguity for the production angle of the Ws cannot be resolved, since there is no means to determine the W charges from the jet measurements. Even with sophisticated existing methods to get the correct pairing of jets, the sensitivity to the triple gauge couplings is smaller than from the semileptionic sample. The fully leptonic samples are smaller and more difficult to analyze. In roughly the half of these events, one lepton is a τ, so a complete kinematic reconstruction is not completely possible. For the rest, there is a twofold ambiguity because of the missing information from the two neutrinos, and measurements from those samples are also limited by statistics.

Mixed leptonic and hadronic decays from W pairs at the ILC can be selected very efficiently, and they also profit from a rather low background. As can be seen from Fig. 4.4, the cross section exhibits a large forward peak stemming from the t-channel neutrino exchange. This peak cross section events are not sensitive to triple gauge couplings at all, and are even partially lost in the beam pipe. Because the boost is much larger than at LEP, the W production angle can be measured with much higher accuracy than in the LEP experiments. The detector resolution in those measurements is expected to be sufficiently good that there are almost no detector effects on the measurements; this is shown in [23]).

In most studies one marginalizes over some of the variables, since it is cumbersome to work with five independent variables. Many of the studies up to now have made use of the spin density matrix formalism [24]. It has been shown that this formalism leads to close to optimal results. In that formalism, it is possible to clearly separate signals from C, P, or CP-violating couplings from

Table 4.3
Accuracies, quoted as 1 σ errors, from single parameter fits for the different triple gauge couplings, $\sqrt{s} = 500$ GeV with $\mathcal{L} = 500$ fb^{-1} and for $\sqrt{s} = 800$GeV with $\mathcal{L} = 1000$ fb^{-1}. For both energies, $\mathcal{P}_{e^-} = 80\%$ and $\mathcal{P}_{e^+} = 60\%$ has been used.

coupling	error $\times 10^{-4}$	
	$\sqrt{s} = 500$ GeV	$\sqrt{s} = 800$ GeV
C,P-conserving, $\mathrm{SU(2)} \times \mathrm{U(1)}$ relations:		
Δg_1^Z	2.8	1.8
$\Delta\kappa_\gamma$	3.1	1.9
λ_γ	4.3	2.6
C,P-conserving, no relations:		
Δg_1^Z	15.5	12.6
$\Delta\kappa_\gamma$	3.3	1.9
λ_γ	5.9	3.3
$\Delta\kappa_Z$	3.2	1.9
λ_Z	6.7	3.0
not C or P conserving:		
g_5^Z	16.5	14.4
g_4^Z	45.9	18.3
$\tilde{\kappa}_Z$	39.0	14.3
$\tilde{\lambda}_Z$	7.5	3.0

the corresponding C- or P-conserving ones. As one example to illustrate how this works, note that imaginary parts of off-diagonal elements of the spin-density matrix are only populated if there are nonzero CP-violating couplings. It has been shown that there are only negligible correlations between the different sets of couplings, hence, the fits can be done separately. These single parameter fits are quite useful to test models beyond the SM, though in principle a multi-variate analysis allows one to determine all five different C- and P-conserving couplings separately with the data from different beam polarization settings. Usually, one assumes full electroweak $SU(2) \times U(1)$ gauge invariance among the parameters, which leads to the following relations among the different parameters:

$$\begin{aligned} \Delta\kappa_\gamma &= -\cot^2\theta_W(\Delta\kappa_Z - g_1^Z) \\ \lambda_\gamma &= \lambda_Z \, . \end{aligned} \tag{4.13}$$

Table 4.3 shows the results from [5] for the sensitivity of the WW measurement on the different anomalous triple gauge couplings, using integrated luminosities of 0.5 ab^{-1} for 500 GeV CM energy and 1 ab^{-1} for 800 GeV. This analysis assumed 80% polarization of the electron beam and 60% polarization for the positron beam. This corresponds to an effective polarization $P_{eff} = 95\%$, while $P_{eff} = 89\%$ is more appropriate for the current ILC design; the change has only a minor effect on the final results. For the case of 800 GeV center of mass energy, the parameter fits which exhibit the largest correlations are illustrated in Fig. 4.5.

Note that these measurements are very precise and do not suffer from any significant systematic uncertainties, since detector effects, backgrounds, and smearing from beamstrahlung are almost negligible. The beam polarization can be determined in situ using the so-called Blondel scheme [25, 26]. Consequently, one can neglect additional systematic uncertainties from beam polarization. If there is no positron polarization at all, the statistical errors grow by about 50%. However, uncertainties are still completely under control. The forward peak is exclusively given by neutrino t-channel exchange, which only couples to left-handed electrons. Then the effective polarization P_{eff} can still be determined from data alone [26].

To match the experimental precision, the theoretical errors need to be smaller than 0.5-1.0%. This is achieved in the predictions from the dedicated NLO programs RacoonWW and YFSWW3 [12]. In fact, the measurement at the ILC is so precise that it is smaller than the size of SM loop corrections. The errors are also smaller than some of the BSM loop corrections, for example, those from supersymmetry, as computed, for example, in [27]. With such precision it is possible to overconstrain the SM, and also to use the ILC measurements to search for deviations from the SM in virtual effects by new heavy particles. While the sensitivity to the dipole moment-like couplings $\Delta\lambda_\gamma$ are of the same order for the LHC and the ILC, estimates for the precision for different colliders for

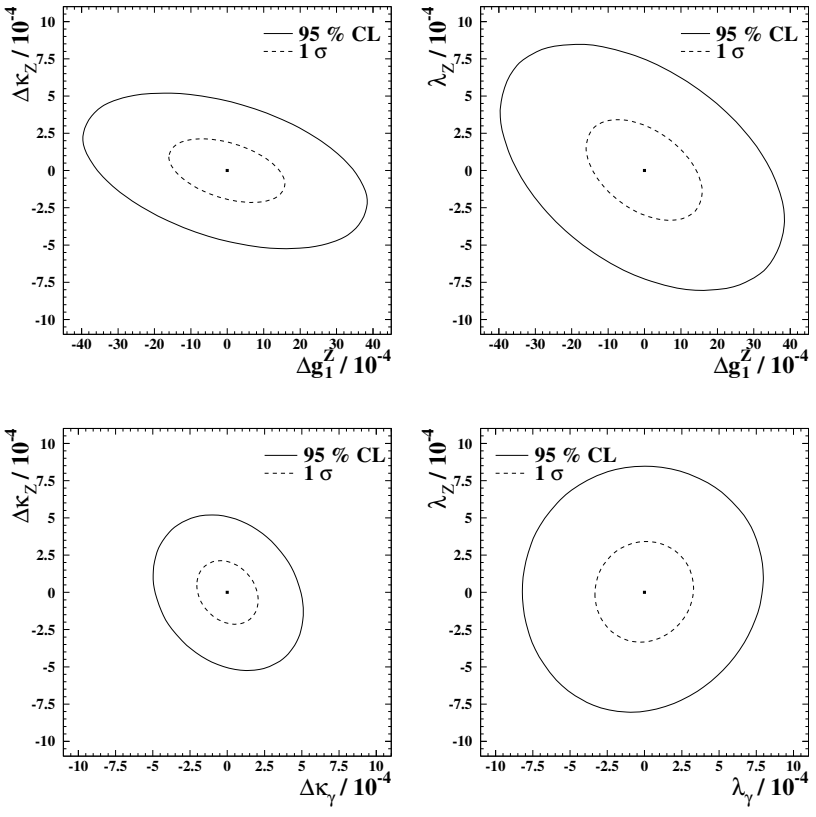

Figure 4.5
Two-dimensional sensitivity contours at 1σ and 95 % significance for several combinations of trilinear gauge couplings at a c.m. energy of 800 GeV for an integrated luminosity of 1 ab^{-1}, with 80 % electron and 60 % positron polarization. For all other variables the correlations are small.

the trilinear coupling $\Delta\kappa_\gamma$ show that a 500 GeV ILC will supersede the LHC by roughly a factor of 10, increasing to a factor of 30 for 1 TeV running [5].

Some more details about measurements from the photon-induced channel as well as the precision measurement of the W boson mass will be described in the following sections.

4.2.2 $e^+e^- \to ZZ$

This process is not used to do precision measurements at the ILC, since it is not sensitive the the leading EFT corrections. The measurement of this process mainly serves as a data-driven estimate of the background to the WW production process. Many algorithms and details about how to separate the two processes can be found in [28].

4.2.3 $\gamma\gamma \to W^+W^-$

Though there is the specific option to construct a high-energy photon-photon collider by means of Compton backscattering, we do not discuss such measurements here. However, γ-induced processes also occur through photons from initial state radiation and beamstrahlung. These processes give a severe background for many new-physics searches, as discussed, for example, in [29]. But, on the other hand, they provide an opportunity to measure the γ-induced pair production of W pairs, which has a large cross section of about 80 pb at 500 GeV. The physics of this process is similar to the single-W production in $W\gamma$ fusion, whose cross section is roughly 30 pb at 500 GeV. The pair production process has been studied with the focus on the determination of possible anomalous gauge boson couplings, and its NLO corrections have been calculated in the double-pole approximation [30].

Using single W and W pair production from the photon substructure inside the electron beams adds an event sample of roughly the same order of magnitude to the sample from the e^+e^- direct production mode. There are no studies on these modes using high luminosity from the point of view of anomalous coupling measurements. Low luminosity studies of the W modes have focused on the

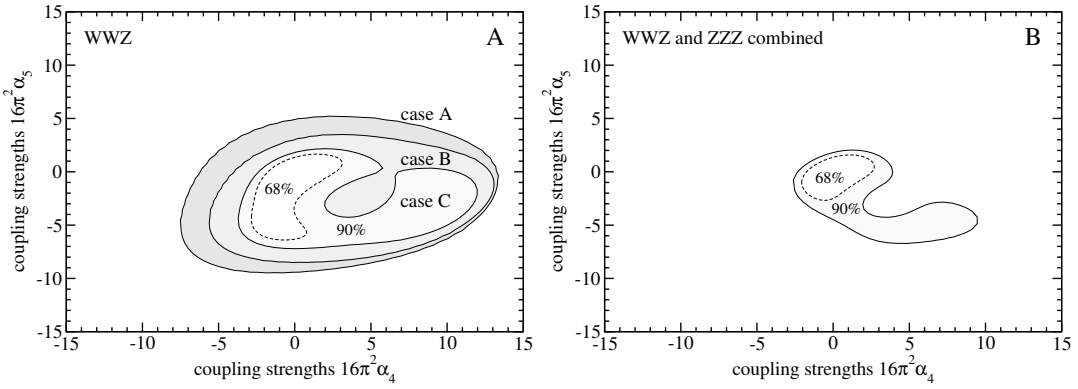

Figure 4.6. Expected sensitivity of a 1 TeV ILC for anomalous quartic gauge coupling parameters α_4/α_5, assuming an integrated luminosity of 1 ab^{-1}. Left: WWZ alone. Right: WWZ and ZZZ combined. The solid lines show the 90% CLs. Cases A, B, and C refer, respectively, to the unpolarized case, the case with 80% electron polarization and the case with 80% electron plus 60% positron polarization. From [10].

total cross section measurement in the central part of the detector; this yields an order of magnitude less sensitivity than the direct production from the e^+e^- mode. Adding angular correlations and the other observables mentioned in section 4.2 could possibly result in almost the same sensitivity as the e^+e^- mode, thereby doubling the total statistics of the event samples.

4.3 Triple vector boson production

The production of three electroweak gauge bosons, mainly $e^+e^- \to W^+W^-Z$ and $e^+e^- \to ZZZ$, is an important precision test for the structure of the electroweak interactions. It has not been kinematically accessible at LEP. The measurement of these processes at the ILC allows a very clean and precise measurement of the triple and quartic gauge couplings and is complimentary to the corresponding observables in vector boson scattering processes. Though triboson production has already been measured at Tevatron and has and will be measured at the LHC, the process is much cleaner and offers a much higher precision at the ILC. For the ILC, the best dataset is that using the fully hadronic final state, which constitutes 32% of all WWZ and ZZZ events. Although, in principle, new-physics parameters that enter oblique corrections and triple gauge couplings can be determined in triple boson production, it is reasonable to assume that these have already been fixed by measurements of WW production (or VV scattering). Hence, they will be ignored in this section. In contrast to vector boson scattering, the different α parameters from the electroweak chiral Lagrangian cannot be completely disentangled in this measurement: the process $e^+e^- \to W^+W^-Z$ depends on the two linear combinations $\alpha_4 + \alpha_6$ and $\alpha_5 + \alpha_7$, while $e^+e^- \to ZZZ$ depends on the linear combination $\alpha_4 + \alpha_5 + 2(\alpha_6 + \alpha_7 + \alpha_{10})$.

The main SM background is rather large for the channel W^+W^-Z, coming from $t\bar{t}$ production with hadronically decaying Ws. This background can be substantially reduced using right-handed electron polarization, which populates the longitudinal modes of the EW gauge bosons. For a 1 TeV ILC without polarization, the cross sections are 59 fb for WWZ and 0.8 fb for ZZZ production, respectively. Switching on electron polarization reduces the WWZ cross section to 12 fb, for 80% right-handed electrons. For the neutral process, ZZZ, the SM background is negligible. Simulations of both processes are available at next-to-leading order [31–33]; in addition, most of the corrections are available in a dedicated Monte-Carlo program, LUSIFER [34].

The phenomenological analysis of these processes has been carried out in [10]. For the WWZ process, three independent kinematical variables that are used, the invariant masses M_{WZ} and M_{WW} and the angle θ between the electron beam axis and the flight direction of the Z boson. From the angular corrections as well as the diboson invariant masses, deviations from the SM can be determined

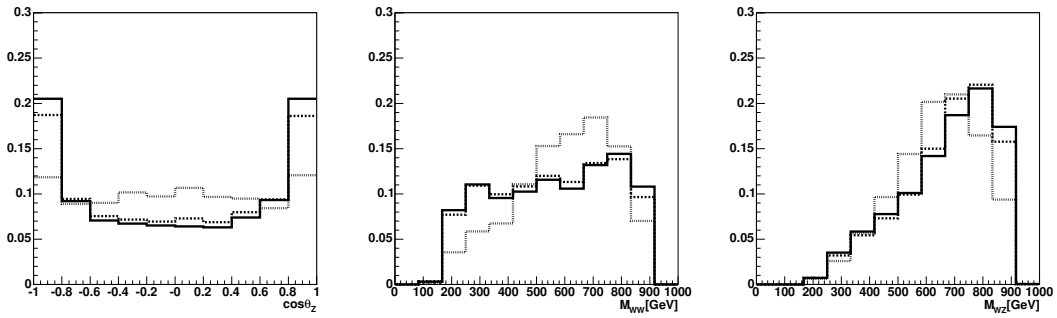

Figure 4.7. Reconstructed distributions of (left to right) $\cos\theta$, M_{WW}, and M_{WZ} for $e^+e^- \to WWZ$, at the ILC at 1 TeV with 1 ab^{-1}, with 80% electron and 60% positron polarization. To show the shape dependence, the distributions are normalized to the respective total number of events for the SM. The solid, dashed, and dotted distributions are drawn for the SM, $\alpha_4 = 1.6\pi^2 \approx 15.8$ and $\alpha_5 \approx 15.8$, respectively [10].

Table 4.4. Sensitivity of α_4 and α_5, for the ILC at 1 TeV with 1 ab^{-1}, expressed as 1σ errors. The columns correspond to: WWZ: two-parameter fit; ZZZ: one-parameter fit; 'best': best combination of both. From [10].

		WWZ			ZZZ	best
		no pol.	e^- pol.	both pol.	no pol.	
$16\pi^2\Delta\alpha_4$	σ^+	9.79	4.21	1.90	3.94	1.78
	σ^-	−4.40	−3.34	−1.71	−3.53	−1.48
$16\pi^2\Delta\alpha_5$	σ^+	3.05	2.69	1.17	3.94	1.14
	σ^-	−7.10	−6.40	−2.19	−3.53	−1.64

(see Fig. 4.7), which then enable one to set limits on the anomalous couplings. Fig. 4.6 shows the expected sensitivity for the parameters α_4 and α_5 at the 90 and 68 per cent confidence level. The detailed values are give in Table 4.4.

Further information comes from the process $e^+e^- \to W^+W^-\gamma$, which is complimentary to the WWZ channel mentioned above. This channel is particularly interesting in the search for possible parity-violating operators. Because one does not have to pay the price for an additional weak boson, a considerable sensitivity could already be achieved at 500 GeV (or even 200 GeV) center-of-mass energy [35].

4.4 WW, ZZ scattering at high energy

The process of WW/ZZ scattering is at the heart of the study of the electroweak symmetry breaking mechanism because it reveals the self-interaction of both transversely and longitudinally polarized electroweak gauge bosons. The scattering of transversely polarized vector bosons is the equivalent of gluon-gluon scattering in QCD. The scattering of longitudinally polarized bosons is in fact the scattering of the Goldstone boson modes inside the electroweak gauge bosons, whose tree-level unitarity has been one of the most profound motivations for the existence of a Higgs boson [36]. In most studies, the scattering of weak gauge bosons has been seen specifically as a means to study the EW sector in the absence of a light Higgs boson, or, alternatively, to search for the presence of strong EW interactions. For an overview, see [37]. But even after the discovery of a light Higgs-like boson around 125 GeV [4], the scattering of EW gauge bosons remains one of the most important physical observables in the EW sector. Together with the precise measurements of the properties of the Higgs boson at the LHC and the ILC, VV scattering allows us to overconstrain the EW sector and search for deviations from the EW structure of the Standard Model. Further, it offers by itself the possibility of searching for new physics in the EW sector beyond the Standard Model in a rather model-independent way. Any type of new physics that has considerable couplings to the SM fermions is very likely to show up earlier in Drell-Yan like processes at LHC or directly in electroproduction at the ILC. However, for new particles that couple only to the electroweak gauge sector (or have highly suppressed fermionic couplings), VV scattering will be the primary production process. Furthermore, there are models, such as the strongly interacting light Higgs (SILH) [38], that give rise to a more or less SM-like Higgs boson, but nevertheless feature different physics at higher energies. For all of these reasons, the precision study of vector boson scattering has special importance.

The LHC will measure VV scattering in the upcoming years; there are possibly even events in the final 2012 data set. On the other hand, the ILC offers the opportunity to use all vector boson final states, including the hadronic ones which cannot be used at the LHC because of trigger and background considerations. Furthermore, at the ILC, beam polarization allows the experiments to enrich longitudinal polarizations of the SM gauge bosons and to improve the ratio of longitudinal boson signal over transversely polarized boson background.

In order not to deal with a plethora of models, we will discuss the physics of VV scattering in an approach as model-independent as possible. Most of our discussion is based on the approach of the EW chiral Lagrangian [1, 2]. In the original approach, this is understood formally as taking the limit of an infinitely heavy Higgs boson and removing it from the SM. The interactions left over give a nonlinear sigma model containing higher-dimensional operators coupling the transversal and longitudinal EW gauge bosons to each other. Such an approach was invented as a low-energy effective theory (LET) for the case of a heavy SM Higgs boson, for technicolor models featuring several strongly interacting resonances in the EW sector, or for Higgsless models (which are in some sense dual to the former class of models). In the light of the discovery of a light scalar boson at LHC, these specific models are now disfavored. However, such an electroweak chiral Lagrangian can be enlarged by the presence of possible resonances in the EW sector that could possibly couple to the EW sector. Such resonances can be classified to their spin and isospin quantum numbers. This classification has been performed in [3] including isoscalar, -vector, or -tensor resonances of spin 0, 1 and 2 that couple to a system of two weak gauge bosons. A light SM Higgs boson is just the isoscalar spin 0 case with particular couplings and is hence easily incorporated in that approach. The details have been summarized in the introductory Section 4.1.

The performance of a 1 TeV ILC for determining deviations from the triple and quartic gauge couplings of the SM has been studied in [10], extending an earlier analysis in [39]. These studies have been performed with full six-fermion matrix elements; hence, no simplifications such as the

Table 4.5
Processes generated for the study of vector boson scattering in [10], giving the cross sections for signal and background for $\sqrt{s} = 1$ TeV, 80% left-handed polarization 80% for the electron beam 40% right-handed polarization for the positron beam. For each process, those final-state flavor combinations are included that correspond to the indicated signal or background subprocess.

Process	Subprocess	σ [fb]
$e^+e^- \to \nu_e\overline{\nu}_e q\bar{q}q\bar{q}$	$W^+W^- \to W^+W^-$	23.19
$e^+e^- \to \nu_e\overline{\nu}_e q\bar{q}q\bar{q}$	$W^+W^- \to ZZ$	7.624
$e^+e^- \to \nu\overline{\nu}q\bar{q}q\bar{q}$	$V \to VVV$	9.344
$e^+e^- \to \nu e q\bar{q}q\bar{q}$	$WZ \to WZ$	132.3
$e^+e^- \to e^+e^- q\bar{q}q\bar{q}$	$ZZ \to ZZ$	2.09
$e^+e^- \to e^+e^- q\bar{q}q\bar{q}$	$ZZ \to W^+W^-$	414.
$e^+e^- \to b\bar{b}X$	$e^+e^- \to t\bar{t}$	331.768
$e^+e^- \to q\bar{q}q\bar{q}$	$e^+e^- \to W^+W^-$	3560.108
$e^+e^- \to q\bar{q}q\bar{q}$	$e^+e^- \to ZZ$	173.221
$e^+e^- \to e\nu q\bar{q}$	$e^+e^- \to e\nu W$	279.588
$e^+e^- \to e^+e^- q\bar{q}$	$e^+e^- \to e^+e^- Z$	134.935
$e^+e^- \to X$	$e^+e^- \to q\bar{q}$	1637.405

Table 4.6
Sensitivity to quartic anomalous couplings in the various quasi-elastic weak-boson scattering processes accessible at the ILC.

$e^+e^- \to$	α_4	α_5	α_6	α_7	α_{10}
$W^+W^- \to W^+W^-$	+	+	-	-	-
$W^+W^- \to ZZ$	+	+	+	+	-
$W^\pm Z \to W^\pm Z$	+	+	+	+	-
$ZZ \to ZZ$	+	+	+	+	+

effective W approximation (EWA), the Goldstone-boson equivalence theorem or the narrow-width approximation have been made. Note that a clear distinction of signal and backgrounds is rather intricate, since many EW processes (for example, triboson production) are intermingled with the pure VV scattering process.

For the simulation we assume a center of mass energy of 1 TeV and a total luminosity of 1000 fb^{-1}. Beam polarization of 80% for electrons and 40% for positrons is also assumed. Since the six-fermion processes under consideration contain contributions from the triple weak-boson production processes considered in the previous section (ZZ or W^+W^- with neutrinos of second and third generation as well as a part of $\nu_e\overline{\nu}_e WW(ZZ)$, $e\nu_e WZ$ and $e^+e^-W^+W^-$ final states), there is no distinct separation of signal and background. Signal processes are thus affected by all other vector boson processes as well as by pure background. The studies have been performed with event samples generated with `WHIZARD` [22], the shower and hadronization with `Pythia` [40] and the ILC detector response with `SimDet` [41]. Initial-state radiation (ISR) from the lepton beams is explicitly included. The processes studied and their cross sections are given in Table 4.5.

Possible observables sensitive to modifications in the (triple and quartic) couplings of longitudinal EW bosons are the total cross section as well as cross sections differential in the EW boson production and decay angles. In measuring properties of longitudinal gauge bosons, it is highly non-trivial if not impossible to measure observables like transverse momentum, since a cut has to be used to suppress the background from transverse gauge bosons, which drops off less fast than the contribution from longitudinal bosons. The general steps of this cut-based analysis use electron/positron tagging to identify background, with cuts on transverse momentum, missing mass and missing energy, as well as cuts around the EW boson masses to veto against events that are not tightly reconstructed. For the extraction of parameters like the triple and quartic gauge coupling, a binned likelihood fit has been used, in which events are described by a total of four kinematical variables.

We summarize the combined results for the measurements of anomalous EW couplings in Table 4.7 and Table 4.8. Both $SU(2)_c$ conserving and $SU(2)_c$ violating couplings are taken into account. The results are shown in Fig. 4.8 in graphical form, where projections of the multi-dimensional exclusion region in all αs around the reference point $\alpha_i \equiv 0$ onto the two-dimensional subspaces (α_4, α_5) and (α_6, α_7) have been made. In order to transform these bounds on α_i parameters into more physical terms, and also in order to compare the capabilities of the ILC with direct resonance searches at the LHC, one can use the formalism described in the introductory section of this chapter to trade the anomalous couplings for parameters of physical resonances. These results for quartic gauge couplings in vector boson scattering can be combined with the ILC measurement results for

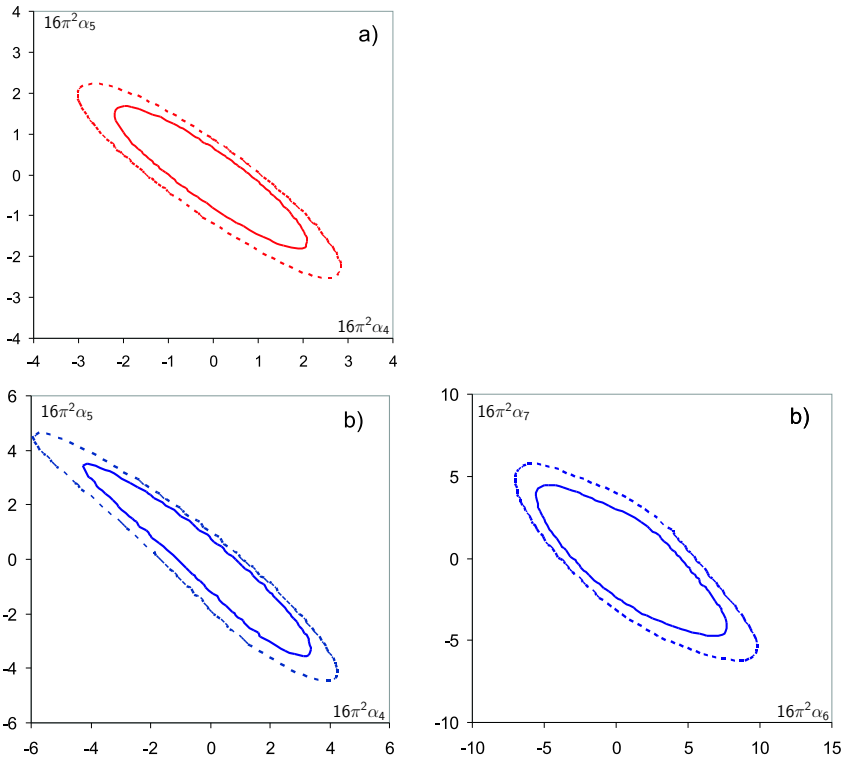

Figure 4.8 The expected sensitivity to quartic anomalous couplings of a 1 TeV ILC with 1 ab^{-1}, in a combined fit for all sensitive processes. The dotted and solid lines show the 60% and 90% confidence regions. Top: (α_4, α_5) in the case with $SU(2)_c$ conservation. Bottom: (α_4, α_5) and (α_6, α_7) in the case with broken $SU(2)_c$. From [10].

Table 4.7. The expected sensitivity to quartic anomalous couplings from the ILC with 1 TeV and 1 ab^{-1} under the assumption of custodial $SU(2)_c$ conservation. The positive and negative 1 sigma errors are given separately. From [10].

coupling	$\sigma-$	$\sigma+$
α_4	-1.41	1.38
α_5	-1.16	1.09

triple gauge couplings and oblique corrections. Taking a single one of the resonances into account at each time, one could from the measured value of the α parameters reconstruct the properties and parameters of the resonance producing that particular value. From this, the sensitivity to new physics showing up as resonances in the high-energy region of EW boson scattering can be determined.

The dependence of the different resonances on the α parameters as well as the correlation of the parameters and the technical points of the fit can be found in [10]. Here, we just give the scalar singlet as an example: in that case, α_4 and α_6 are zero, and, for the isospin-conserving case, in addition α_7 and α_{10} are zero. If one uses the relation from integrating out the resonance, $\alpha_5 = g_\sigma^2 v^2/8M_\sigma^2$ and introduces the ratio between the width and the mass of the resonance, $f_\sigma = \Gamma_\sigma/M_\sigma$ one can solve for the mass of the resonance: $M_\sigma = v\,[4\pi f_\sigma/(3\alpha_5)]^{\frac{1}{4}}$. From the fit one can deduce the mass reach for scalar resonances at the ILC depending on scenarios with different widths. The results for the different masses for all cases are shown in Table 4.9. They can be summarized in the following numbers which hold for the $SU(2)_c$-conserving case: for spin-0 particles, the accessible reach is 1.39, 1.55, and 1.95 TeV for the isospin channels $I = 0$, $I = 1$, and $I = 2$, respectively, assuming a single resonance with optimal width to mass ratio that exclusively couples to the EW boson sector. For a vector resonance, the reach is 1.74 TeV for isosinglet and 2.67 TeV for isotriplets, respectively. Tensors provide the best reach because of the higher number of degrees of freedom participating. Here the ILC is sensitive to resonances of mass 3.00, 3.01, and 5.84 TeV for the isospin channels $I = 0$, $I = 1$, and $I = 2$, respectively. In the case of $SU(2)_c$ violation the effects on EW boson scattering are larger or more significant. In this sense, the $SU(2)_c$-conserving limit is a conservative estimate, though it is also favored by the EW measurements from SLC, LEP, Tevatron, and LHC.

Table 4.8. The expected sensitivity to quartic anomalous couplings from the ILC with 1 TeV and 1 ab^{-1} for the case of broken $SU(2)_c$. The positive and negative 1 sigma errors are given separately. From [10].

coupling	$\sigma-$	$\sigma+$
α_4	-2.72	2.37
α_5	-2.46	2.35
α_6	-3.93	5.53
α_7	-3.22	3.31
α_{10}	-5.55	4.55

Table 4.9 Mass reach at a 1 TeV ILC in VV scattering, assuming a data set of 1 ab^{-1}, for four different values of the ratio of width over mass for the resonances.

$f_{\text{Res.}} = \Gamma_{\text{Res.}}/M_{\text{Res.}}$	1.0	0.8	0.6	0.3
scalar singlet, M_σ [TeV], $SU(2)_c$ cons.	1.55	1.46	1.36	1.15
scalar singlet, M_σ [TeV], $SU(2)_c$ broken	1.39	1.32	1.23	—
scalar triplet, M_{π^0} [TeV]	1.39	1.32	1.23	—
scalar triplet, $M_{\pi^\pm}$ [TeV]	1.55	1.47	1.37	1.15
scalar quintet, M_ϕ [TeV], $SU(2)_c$ cons.	1.95	1.85	1.72	1.45
scalar quintet, $M_{\phi^{\pm\pm}}$ [TeV], $SU(2)_c$ broken	1.95	1.85	1.72	1.45
scalar quintet, $M_{\phi^\pm}$ [TeV], $SU(2)_c$ broken	1.64	1.55	1.44	1.21
scalar quintet, M_{ϕ^0} [TeV], $SU(2)_c$ broken	1.55	1.46	1.35	1.14
vector singlet, M_ω [TeV], gen. case	2.22	2.10	1.95	1.63
vector triplet, M_ρ [TeV], $SU(2)_c$ cons.	2.49	2.36	2.19	1.84
vector triplet, $M_{\rho^\pm}$ [TeV], no $SU(2)_c$, no mag. mom.	2.67	2.53	2.35	1.98
vector triplet, M_{ρ^0} [TeV], no $SU(2)_c$, no mag. mom.	1.74	1.65	1.53	1.29
vector triplet, $M_{\rho^\pm}$ [TeV], special $SU(2)_c$ viol.	3.09	2.92	2.72	2.29
vector triplet, M_{ρ^0} [TeV], special $SU(2)_c$ viol.	1.78	1.69	1.57	1.32
vector triplet, $M_{\rho^\pm}$ [TeV], gen. case	2.54	2.41	2.34	1.88
vector triplet, M_{ρ^0} [TeV], gen. case	1.71	1.62	1.51	1.27
tensor singlet, M_f [TeV], $SU(2)_c$ cons.	3.29	3.11	2.89	2.43
tensor singlet, M_f [TeV], $SU(2)_c$ viol.	3.00	2.84	2.64	2.22
tensor triplet, M_{a^0} [TeV]	3.01	2.85	2.65	2.23
tensor triplet, $M_{a^\pm}$ [TeV]	2.81	2.66	2.47	2.08
tensor quintet, M_t [TeV], $SU(2)_c$ cons.	4.30	4.06	3.78	3.18
tensor quintet, M_{t^c} [TeV], special $SU(2)_c$ viol.	6.76	6.39	5.95	5.00
tensor quintet, M_{t^0} [TeV], special $SU(2)_c$ viol.	4.53	4.28	3.98	3.35
tensor quintet, $M_{t^{\pm\pm}}$ [TeV], gen. case	5.17	4.89	4.55	3.83
tensor quintet, $M_{t^\pm}$ [TeV], gen. case	3.64	3.44	3.20	2.69
tensor quintet, M_{t^0} [TeV], gen. case	5.84	5.52	5.14	4.32

4.5 Giga-Z

One of the main advantages of the ILC is its staged operation at almost arbitrary CM energies. This offers the opportunity to run the collider at rather low energies on the Z resonance or at the WW threshold to gather large amounts of data and perform precision measurements of the electroweak sector of the SM.

4.5.1 Precision measurement program at the Z

Running at a luminosity value of $\mathcal{L} = 10^{34}$ cm^{-2} s^{-1} allows to revisit the physics at LEP1 and SLC within a couple of days and study several billion Z bosons within 1-2 months [42]. This is a especially important because two measurements at LEP1 and SLC constitute (together with the muon $g-2$) presently give the largest deviation from SM predictions. With the Giga-Z option the tension between the two data sets from LEP1 and SLC could be resolved. Since these measurements are at the heart of the electroweak sector of the SM we describe them in detail.

The first of these measurements to be studied at the Z pole is the left-right asymmetry

$$A_{LR} = \frac{1}{\mathcal{P}} \frac{\sigma_L - \sigma_R}{\sigma_L + \sigma_R} \,, \tag{4.14}$$

where $\sigma_{L/R}$ are the total cross sections for left- and right-handed polarized electrons and $\mathcal{P}$ is the longitudinal electron polarization. The measurement of the left-right asymmetry directly accesses the effective weak mixing angle, $\sin^2\theta^\ell_{eff}$, which in the case of a pure Z exchange is given by

$$A_{LR} = \mathcal{A}_e = \frac{2 v_e a_e}{v_e^2 + a_e^2} \,, \tag{4.15}$$

where v_e and a_e are the vector and axial vector coupling of the Z boson to electrons. Their ratio is given by $v_e/a_e = 1 - 4\sin^2\theta^\ell_{eff}$. At the ILC in the Giga-Z option the left-right asymmetry A_{LR} can be measured using the hadronic Z decays on the Z poles; this has a very high efficiency and almost no background. The technical details about this measurement and the other Z pole observables can be found in [43]. Using a few billion events on the Z pole translates into a statistical error of the order $\Delta A_{LR} = 10^{-5}$, with systematic uncertainties also under control at this level. The relative uncertainty on the polarization needs to be smaller than the corresponding uncertainty of the left-right asymmetry, $\Delta\mathcal{P}/\mathcal{P} < \Delta A_{LR}/A_{LR} = 10^{-4}$, which is only possible if both polarized electrons and positrons are available. In that case an in-situ polarization measurement is possible by means of the Blondel scheme [25]. Using the cross section with unpolarized beams, σ_0, and the polarization $\mathcal{P}_{e^-}$ and $\mathcal{P}_{e^+}$ for electrons and positrons, respectively, the polarized beam cross section can be expressed via the formula

$$\sigma = \sigma_0 \left\{ 1 - \mathcal{P}_{e^-}\mathcal{P}_{e^+} + A_{LR} \cdot (\mathcal{P}_{e^+} - \mathcal{P}_{e^-}) \right\} \,. \tag{4.16}$$

If a method is used to externally determine all the four different combinations of beam polarizations, then the left-right asymmetry can be directly determined via

$$A_{LR} = \sqrt{\frac{(\sigma_{++} + \sigma_{-+} - \sigma_{+-} - \sigma_{--})(-\sigma_{++} + \sigma_{-+} - \sigma_{+-} + \sigma_{--})}{(\sigma_{++} + \sigma_{-+} + \sigma_{+-} + \sigma_{--})(-\sigma_{++} + \sigma_{-+} + \sigma_{+-} - \sigma_{--})}} \,. \tag{4.17}$$

Here σ_{ij} is the cross section where the electron beam has the polarization i and the positron beam the polarization j. In deriving this formula one has to assume that the absolute polarization values of the bunches with opposing helicity states are equal. Either to assure that this assumption is correct or in order to determine the corresponding corrections one needs polarimeters. Most systematics cancel out of this measurement since within each beam only relative measurements are necessary. Hence, this scheme allows one to achieve the desired accuracy in the polarization measurement. Note that because of helicity selection rules the cross sections for the combinations $(++)$ and $(--)$ are tiny, so that the collider needs to run only for one tenth of its luminosity on these helicity configurations in order to already reach optimal statistical precision. The in-situ polarization measurement with the Blondel scheme, on the other hand, yields a statistical error that is only slightly bigger than the one with the external polarimeter, if the degree of positron polarization exceeds $\mathcal{P}_{e^+} > 0.5$. If that

Table 4.10
Precision of several SM observables that can be achieved at the ILC from a high-luminosity low-energy run (GigaZ option). The left column gives the present status together with possible expectations from the LHC experiments; the right column gives the Giga-Z expectation. The values given for the $\Delta\rho$ parameter and for the determination of the strong coupling constant assume $N_\nu = 3$.

	LEP/SLC/Tev/world av. [49]	ILC
$\sin^2\theta^\ell_{\text{eff}}$	0.23146 ± 0.00017	$\leq \pm 0.00001$
M_Z	91.1876 ± 0.0021 GeV	± 0.0016 GeV
Γ_Z	2.4952 ± 0.0023 GeV	± 0.0008 GeV
$\alpha_s(m_Z^2)$	0.1184 ± 0.0007	± 0.0005
$\Delta\rho$	$(0.55 \pm 0.10) \cdot 10^{-2}$	$\pm 0.05 \cdot 10^{-2}$
N_ν	2.984 ± 0.008	± 0.004
$\mathcal{A}_b$	0.923 ± 0.020	± 0.001
R^0_{b}	0.21653 ± 0.00069	± 0.00014
M_W	80.385 ± 0.015 GeV	± 0.006 GeV

value goes down to 20% the statistical error for 10^9 Z bosons on the peak reaches $\Delta A_{LR} = 8 \cdot 10^{-5}$. Another crucial ingredient for the precision of this measurement is the simultaneous knowledge of both the c.m. energy and the mass of the Z boson, M_Z. This is because the $\gamma - Z$ interference generates a slope in the peak cross section of roughly $dA_{LR}/d\sqrt{s} = 2 \cdot 10^{-2}/\text{GeV}$. To suppress the dominance of the parametric uncertainty on the beam energy within the systematics one needs to calibrate the beam energy with the help of a spectrometer relative to the Z mass with a precision of 1 MeV and allow for a scan around the vicinity of the Z resonance peak. The second biggest systematics effect comes from the influence of the beamstrahlung which induces a shift in the value of A_{LR} by $\Delta A_{LR} = 9 \cdot 10^{-4}$. For that scope the beamstrahlung spectrum needs to be known at a precision at the order of one per cent or even below, and studies show that this achievable [44–46]. All other systematic errors are very small, such that a quite conservative error estimate results in a final uncertainty of $\Delta A_{LR} = 10^{-4}$. That systematic uncertainty translates into an error of the weak mixing angle of $\Delta \sin^2\theta^\ell_{eff} = 1.3 \cdot 10^{-5}$. However, in principle, the beamstrahlung spectrum should be the same both in the A_{LR} measurement in the scan for the calibration. In that case the whole effect of beamstrahlung results in an obvious shift of the center of mass energy that cancels out in the uncertainties. Then, a precision in the measurement of the effective weak angle well below 10^{-5} could be achieved.

As mentioned above, there is a discrepancy between the measured value of A_{LR} and the value measured for a related quantity, the forward-backward asymmetry for bottom quarks $\mathcal{A}_b$. Since the ILC detectors will have b-tagging capabilities of an unprecedented excellence, the ILC can improve the precision of the $\mathcal{A}_b$ measurement by a factor of almost a factor of 20 [47]. A resolution of this discrepancy itself might allow improvement of the whole consistency and quality of the electroweak fit and open a door to precision searches for deviations from the SM.

The other observables that can be determined from the measurement of the Z lineshape are the partial and the total width of the Z boson, the Z mass M_Z, the strong coupling constant at the scale of M_Z ($\alpha_s(M_Z)$), the ρ parameter, which is a measure of the modification of the strength of the fermionic Z couplings due to radiative corrections, and the number of light, weakly-interacting neutrino species, N_ν.

Concerning the partial widths and the total width of the Z boson, there is still a considerable effect to the improved ILC measurements; however, it is less spectacular than the improvement for the weak mixing angle. The measurement of the total Z width by the lineshape determination depends on the precision of the beam spectrometer and the calibration measurement of the beamstrahlung. This means that a total precision of the order $\Delta\Gamma_Z \approx 1$ MeV or better is possible. At the ILC, there will be a factor of up to three improvement for the selection efficiencies for hadrons, muons, and tau leptons compared to the LEP experiments [23, 48]. There will also be considerable improvement in the experimental systematics of the luminosity compared to LEP, such that the errors can be further reduced. Note that this has been accompanied by matching improvements in the theoretical predictions for the electroweak precision observables, which are now mostly at the two- or even three-loop level [50].

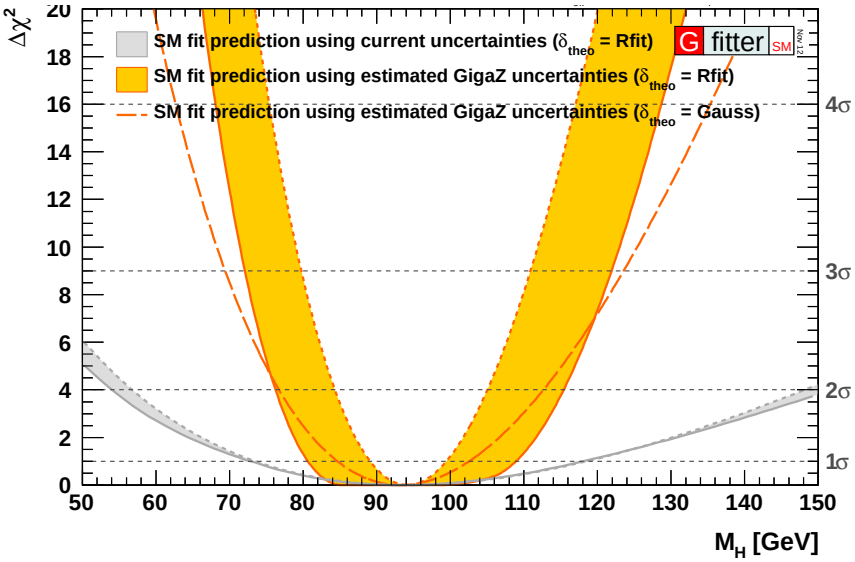

Figure 4.9 Contour of χ^2 in the precision electroweak fit as a function of the Higgs boson mass for the current values (grey band) and for improved uncertainties expected from the Giga-Z program (orange band) [51]. The figure assumes that the current central value remains unchanged.

For almost all of these variables the ILC can considerably improve on the present-day precision. These improvements are summarized in Table 4.10. Taking into account the excellent b-tagging performance at the ILC detectors, even the ratio R_b of the partial Z width to bottom quarks to the full hadronic width can be improved at least by a factor of five.

A measure of the increased analytical power available from the Giga-Z program is shown in Fig. 4.9. The figure shows the χ^2 of the current electroweak fit as a function of the Higgs boson mass, and the χ^2 curve that would result for the same central value and the measurement uncertainties that would result from Giga-Z. With these assumptions, the fit would give a Higgs boson mass of $m_h = 92.3^{+16.6}_{-11.6}$ GeV, with current theory errors, or $^{+5.3}_{-5.0}$ GeV, with negligible theory errors. Even in the former case, a mass of 126 GeV for the Higgs boson would be excluded at almost the 4 σ level in a pure Standard Model fit, requiring additional contributions from new particles at the TeV mass scale [51, 52].

4.5.2 Precision measurement of the W boson mass

The final physics point to be discussed here is the measurement of the W boson mass from a threshold scan at the W pair production threshold. The overall WW cross section is proportional near threshold to the the (non-relativistic) velocity β of the W boson. Thus, the cross section around the threshold is highly sensitive to the exact value of the W mass. It is important that the s-channel and t-channel diagrams contribute differently in this region. The s-channel contribution is suppressed by β^3, while the t-channel only by one power of β. The t-channel contribution depends only on the $We\nu_e$ coupling, which is well-known. Hence, the predictions for the threshold cross section are free from any possible contamination from unknown physics. Any new physics effects from the triple gauge couplings enter in the s-channel diagrams and are thus suppressed relative to the leading cross section by β^2. This guarantees a clean measurement of the W mass from the threshold scan. This experimental setup is underlined by theoretical calculations in the last decade which provide full $2 \to 4$ calculations at next-to-leading order [13] and leading NNLO corrections to the total cross section [18], which allows to reduce the theory uncertainties to the same level as the experimental error estimates. Note that by using different polarization states an enhancement or suppression of the signal is possible such that the background can be directly estimated from the run by switching polarizations.

In an early study on such a scan [53], a scan in five steps between 160.4 and 162 GeV and an additional data point at $\sqrt{s} = 170$ GeV has been investigated. The analysis assumed an integrated luminosity of 100 fb^{-1} and the same efficiency and purity values as obtained at LEP. With a total

error of 0.25% on the luminosity and the selection efficiencies in that setup, M_W can be determined with an error of $6 - 7$ MeV. The upper value comes from a fit where the efficiencies are not fixed but left free to float which shows the experimental stability of that method. If the detector performs much better than in the original study as would be expected for the ILC detectors [23], a precision of a few MeV can be achieved.

Bibliography

[1] S. Weinberg, Phys. Rev. **166**, 1568 (1968); C. G. Callan, Jr., S. R. Coleman, J. Wess and B. Zumino, Phys. Rev. **177**, 2239 (1969); Phys. Rev. **177**, 2247 (1969); J. Gasser and H. Leutwyler, Annals Phys. **158**, 142 (1984); Nucl. Phys. B **250**, 465 (1985); T. Appelquist and C. W. Bernard, Phys. Rev. D **22**, 200 (1980); A. C. Longhitano, Phys. Rev. D **22**, 1166 (1980); Nucl. Phys. B **188**, 118 (1981); T. Appelquist and G. -H. Wu, Phys. Rev. D **48**, 3235 (1993) [hep-ph/9304240].

[2] For reviews, see [37]; W. Kilian and P. M. Zerwas, hep-ph/0601217; A. Dobado, A. Gomez-Nicola, A. L. Maroto and J. R. Pelaez, N.Y., Springer-Verlag, 1997. (Texts and Monographs in Physics); W. Kilian, Springer Tracts Mod. Phys. **198**, 1 (2003).

[3] A. Alboteanu, W. Kilian and J. Reuter, JHEP **0811**, 010 (2008) [arXiv:0806.4145 [hep-ph]].

[4] G. Aad *et al.* [ATLAS Collaboration], Phys. Lett. B **716**, 1 (2012) [arXiv:1207.7214 [hep-ex]]; S. Chatrchyan *et al.* [CMS Collaboration], Phys. Lett. B **716**, 30 (2012) [arXiv:1207.7235 [hep-ex]].

[5] J. A. Aguilar-Saavedra *et al.* [ECFA/DESY LC Physics Working Group Collaboration], hep-ph/0106315.

[6] W. Kilian and J. Reuter, Phys. Rev. D **70**, 015004 (2004) [hep-ph/0311095].

[7] C. E. Vayonakis, Lett. Nuovo Cim. **17**, 383 (1976); M. S. Chanowitz and M. K. Gaillard, Nucl. Phys. B **261**, 379 (1985); G. J. Gounaris, R. Kogerler and H. Neufeld, Phys. Rev. D **34**, 3257 (1986); Y. -P. Yao and C. P. Yuan, Phys. Rev. D **38**, 2237 (1988); J. Bagger and C. Schmidt, Phys. Rev. D **41**, 264 (1990).

[8] C. Csaki, C. Grojean, H. Murayama, L. Pilo and J. Terning, Phys. Rev. D **69** (2004) 055006 [arXiv:hep-ph/0305237]; C. Csaki, C. Grojean, L. Pilo and J. Terning, Phys. Rev. Lett. **92** (2004) 101802 [arXiv:hep-ph/0308038]; Y. Nomura, JHEP **0311** (2003) 050 [arXiv:hep-ph/0309189]; G. Burdman and Y. Nomura, Phys. Rev. D **69** (2004) 115013 [arXiv:hep-ph/0312247].

[9] L. Randall and R. Sundrum, Phys. Rev. Lett. **83** (1999) 3370 [arXiv:hep-ph/9905221].

[10] M. Beyer, W. Kilian, P. Krstonosic, K. Monig, J. Reuter, E. Schmidt and H. Schroder, Eur. Phys. J. C **48**, 353 (2006) [hep-ph/0604048].

[11] S.N. Gupta, *Quantum Electrodynamics*, Gordon and Breach, 1981; M. S. Chanowitz, Phys. Rept. **320**, 139 (1999)

[12] A. Denner, S. Dittmaier, M. Roth and D. Wackeroth, Nucl. Phys. B **587**, 67 (2000) [hep-ph/0006307]; Phys. Lett. B **475**, 127 (2000) [hep-ph/9912261]; Eur. Phys. J. direct C **2**, 4 (2000) [hep-ph/9912447]; S. Jadach, W. Placzek, M. Skrzypek, B. F. L. Ward and Z. Was, Phys. Rev. D **65**, 093010 (2002) [hep-ph/0007012].

[13] A. Denner, S. Dittmaier, M. Roth and L. H. Wieders, Phys. Lett. B **612**, 223 (2005) [Erratum-ibid. B **704**, 667 (2011)] [hep-ph/0502063]; Nucl. Phys. B **724**, 247 (2005) [Erratum-ibid. B **854**, 504 (2012)] [hep-ph/0505042].

[14] S. Jadach, W. Placzek, M. Skrzypek, B. F. L. Ward and Z. Was, Comput. Phys. Commun. **140**, 475 (2001) [hep-ph/0104049].

[15] A. Denner, S. Dittmaier, M. Roth and D. Wackeroth, Comput. Phys. Commun. **153**, 462 (2003) [hep-ph/0209330].

[16] F. Jegerlehner and K. Kolodziej, Eur. Phys. J. C **20**, 227 (2001) [hep-ph/0012250].

[17] M. Beneke, P. Falgari, C. Schwinn, A. Signer and G. Zanderighi, Nucl. Phys. B **792**, 89 (2008) [arXiv:0707.0773 [hep-ph]].

[18] S. Actis, M. Beneke, P. Falgari and C. Schwinn, Nucl. Phys. B **807**, 1 (2009) [arXiv:0807.0102 [hep-ph]].

[19] G. Passarino, Nucl. Phys. B **578**, 3 (2000) [hep-ph/0001212].

[20] A. Pukhov, E. Boos, M. Dubinin, V. Edneral, V. Ilyin, D. Kovalenko, A. Kryukov and V. Savrin *et al.*, hep-ph/9908288.

[21] E. E. Boos and M. N. Dubinin, hep-ph/9909214.

[22] W. Kilian, T. Ohl and J. Reuter, Eur. Phys. J. C **71**, 1742 (2011) [arXiv:0708.4233 [hep-ph]]; M. Moretti, T. Ohl and J. Reuter, LC Notes LC-TOOL-2001-040, hep-ph/0102195.

[23] H. Aihara, *et al.* [SiD Concept Group - Linear Collider Collaboration], arXiv:0911.0006 [physics.ins-det]; T. Abe *et al.* [ILD Concept Group - Linear Collider Collaboration], arXiv:1006.3396 [hep-ex].

[24] W. Menges, LC Notes LC-PHSM-2001-022 (2001).

[25] A. Blondel, Phys. Lett. B **202**, 145 (1988) [Erratum-ibid. **208**, 531 (1988)].

[26] K. Monig, LC Notes LC-PHSM-2000-059 (2000).

[27] S. Alam, Phys. Rev. D **50**, 124 (1994); Phys. Rev. D **50**, 148 (1994); Phys. Rev. D **50**, 148 (1994).

[28] M. Beckmann, DESY-THESIS-2010-014 (2010).

[29] J. Kalinowski, W. Kilian, J. Reuter, T. Robens and K. Rolbiecki, JHEP **0810**, 090 (2008) [arXiv:0809.3997 [hep-ph]].

[30] A. Bredenstein, S. Dittmaier and M. Roth, Eur. Phys. J. C **36**, 341 (2004) [hep-ph/0405169]; Eur. Phys. J. C **44**, 27 (2005) [hep-ph/0506005].

[31] F. Boudjema, L. D. Ninh, S. Hao and M. M. Weber, Phys. Rev. D **81**, 073007 (2010) [arXiv:0912.4234 [hep-ph]].

[32] S. Ji-Juan, M. Wen-Gan, Z. Ren-You, W. Shao-Ming and G. Lei, Phys. Rev. D **78**, 016007 (2008) [arXiv:0807.0669 [hep-ph]].

[33] S. Wei, M. Wen-Gan, Z. Ren-You, G. Lei and S. Mao, Phys. Lett. B **680**, 321 (2009) [Erratum-ibid. **684**, 281 (2010)] [arXiv:0909.1064 [hep-ph]].

[34] S. Dittmaier and M. Roth, Nucl. Phys. B **642**, 307 (2002) [hep-ph/0206070].

[35] A. Denner, S. Dittmaier, M. Roth and D. Wackeroth, Eur. Phys. J. C **20**, 201 (2001) [hep-ph/0104057].

[36] B. W. Lee, C. Quigg and H. B. Thacker, Phys. Rev. Lett. **38**, 883 (1977); Phys. Rev. D **16**, 1519 (1977).

[37] C. T. Hill and E. H. Simmons, Phys. Rept. **381**, 235 (2003) [Erratum-ibid. **390**, 553 (2004)] [hep-ph/0203079].

[38] G. F. Giudice, C. Grojean, A. Pomarol and R. Rattazzi, JHEP **0706**, 045 (2007) [hep-ph/0703164].

[39] R. Chierici, S. Rosati and M. Kobel, LC NOtes LC-PHSM-2001-038 (2001).

[40] T. Sjöstrand, L. Lönnblad and S. Mrenna, *PYTHIA 6.2: Physics and manual*, hep-ph/0108264; T. Sjöstrand, P. Eden, C. Friberg, L. Lönnblad, G. Miu, S. Mrenna and E. Norrbin, PYTHIA V6.221, Comp. Phys. Commun. 135 (2001) 238.

[41] M. Pohl and H. J. Schreiber, *SIMDET - Version 4: A parametric Monte Carlo for a TESLA detector*, hep-ex/0206009.

[42] J. Erler, S. Heinemeyer, W. Hollik, G. Weiglein and P. M. Zerwas, Phys. Lett. B **486** (2000) 125 [hep-ph/0005024].

[43] R. Hawkings and K. Monig, Eur. Phys. J. direct C **1**, 8 (1999) [hep-ex/9910022];

[44] K. Monig, LC Notes LC-PHSM-2000-060 (2000).

[45] G. White, Conf. Proc. C **0505161**, 1446 (2005).

[46] G. Bonvicini and N. Powell, physics/0503033 [physics.acc-ph].

[47] A. Gurtu, presentation at the ICHEP 2000 conference, July, 2000.

[48] M. Winter, LC Notes LC-PHSM-2001-016 (2001).

[49] J. Beringer *et al.* [Particle Data Group Collaboration], *Review of Particle Physics (RPP)*, Phys. Rev. D **86**, 010001 (2012).

[50] M. Awramik, M. Czakon, A. Freitas and G. Weiglein, Phys. Rev. Lett. **93**, 201805 (2004) [hep-ph/0407317]; M. Awramik, M. Czakon and A. Freitas, JHEP **0611**, 048 (2006) [hep-ph/0608099]; M. Awramik, M. Czakon, A. Freitas and B. A. Kniehl, Nucl. Phys. B **813**, 174 (2009) [arXiv:0811.1364 [hep-ph]]; S. Actis, M. Czakon, J. Gluza and T. Riemann, Nucl. Phys. B **786**, 26 (2007) [arXiv:0704.2400 [hep-ph]].

[51] A. Hoecker and R. Kogler, personal communication; updated from [52].

[52] H. Flacher, M. Goebel, J. Haller, A. Hocker, K. Monig and J. Stelzer, Eur. Phys. J. C **60**, 543 (2009) [Erratum-ibid. C **71**, 1718 (2011)] [arXiv:0811.0009 [hep-ph]]; A. B. Arbuzov, M. Awramik, M. Czakon, A. Freitas, M. W. Grunewald, K. Monig, S. Riemann and T. Riemann, Comput. Phys. Commun. **174**, 728 (2006) [hep-ph/0507146]; D. Y. .Bardin, P. Christova, M. Jack, L. Kalinovskaya, A. Olchevski, S. Riemann and T. Riemann, Comput. Phys. Commun. **133**, 229 (2001) [hep-ph/9908433].

[53] G. Wilson, LC Notes LC-PHSM-2001-009 (2001).

Chapter 5
Top Quark

The top quark is by far the heaviest particle of the Standard Model. Its large mass implies that the top quark is the Standard Model particle most strongly coupled to the mechanism of electroweak symmetry breaking. For this and other reasons, the top quark is expected to be a window to any new physics at the TeV energy scale. In this section, we will review the ways that new physics might appear in the precision study of the top quark and the capabilities of the ILC to discover these effects.

The top quark was discovered at the Tevatron proton-antiproton collider by the D0 and CDF experiments [1, 2]. Up to now, the top quark has only been studied at hadron colliders, at the Tevatron and, only in past three years, at the LHC. The Tevatron experiments accumulated a data sample of about $12\,\text{fb}^{-1}$ in Run I and Run II, at center of mass energies of $1.8\,\text{TeV}$ and $1.96\,\text{TeV}$, respectively. About half of this data is fully analyzed. At the LHC, a data sample of about $5\,\text{fb}^{-1}$ has been recorded at a center-of-mass energy of $7\,\text{TeV}$ up to the end of 2011. In 2012, the machine has operated at a center of mass energy of $8\,\text{TeV}$. In the following section, we will review the properties of the top quark determined so far at hadron colliders, based on the currently analyzed data sets. We will also discuss the eventual accuracies that will be reached in this program over the long term.

The ILC would be the first machine at which the top quark is studied using a precisely defined leptonic initial state. This brings the top quark into an evironment in which individual events can be analyzed in more detail, as we have explained in the Introduction. It also changes the production mechanism for top quark pairs from the strong to the electroweak interactions, which are a step closer to the phenomena of electroweak symmetry breaking that we aim to explore. Finally, this change brings into play new experimental observables—weak interaction polarization and parity asymmetries—that are very sensitive to the coupling of the top quark to possible new interactions. It is very possible that, while the top quark might respect Standard Model expectations at the LHC, it will break those expectations when studied at the ILC.

5.1 Top quark properties from hadron colliders

In this section, we will review the present and future capabilities of hadron colliders to study the top quark. This section is based largely on the review published in [3]. Where applicable, the information has been updated.

5.1.1 Top quark hadronic cross section

A central measurement for the top quark at hadron colliders is the $t\bar{t}$ production cross-section. At hadron colliders the following channels are typically measured: (1) lepton+jets channels, (2) dilepton channels, (3) fully hadronic channels, (4) channels with jets and missing transverse momentum (MET).For these channels the Tevatron experiments have published values between $7.2\,\mathrm{pb}$ and $7.99\,\mathrm{pb}$ [3]. The error on these values is typically 6–7%. The LHC experiments report values at 7 TeV [4, 5]

$$\begin{aligned}\sigma_{t\bar{t}} &= 177 \pm 3\,(\mathrm{stat.})^{+8}_{-7}\,(\mathrm{syst.}) \pm 7\,(\mathrm{lumi.})\,\mathrm{pb} \quad \text{ATLAS} \\ \sigma_{t\bar{t}} &= 166 \pm 2\,(\mathrm{stat.}) \pm 11\,(\mathrm{syst.}) \pm 8\,(\mathrm{lumi.})\,\mathrm{pb} \qquad \text{CMS}\end{aligned} \tag{5.1}$$

This is to be compared with theoretical estimates from 'approximate NNLO' QCD predictions, for example, [6, 7]

$$\sigma_{t\bar{t}} = 163^{+7}_{-5}\,(\mathrm{scale}) \pm 9\,(\mathrm{PDF})\,\mathrm{pb}. \tag{5.2}$$

A full NNLO QCD calculation should decrease the first error significantly. The agreement between theory and experiment is excellent at the present stage, both for the LHC and for the Tevatron results. Already at this early stage of data taking the LHC experiments are limited by the systematic uncertainty. For ATLAS, the dominant sources of the systematic error are those from predictions of different event generators together with the uncertainties of the parton distribution function of the proton. On the experimental side, the jet energy resolution constitutes an important source of systematic error. However, there are other sources of comparable influence, from the electron and muon identification. The quoted sources contribute roughly equally to the systematic error.

5.1.2 Top quark mass and width

The mass of the top quark is a fundamental parameter of the electroweak theory. In discussions of physics beyond the Standard Model, the top quark appears ubiquitously. To interpret particle physics measurements in terms of new physics effects, the top quark mass must be known very accurately. Two well known examples are the precision electroweak corrections, where the top quark contributions must be fixed to allow Higgs and other new particle corrections to be determined, and the theory of the Higgs boson mass in supersymmetry, in which the loop corrections are proportional to $(m_t/m_W)^4$.

Care must be taken in relating the measured top quark mass to the value of the top quark mass that is used as input in these calculations. Loop effects typically take as input a short-distance definition of the top quark mass such as the $\overline{MS}$ mass parameter. We will explain below that the determination of the top quark mass from the threshold cross section in e^+e^- annhilation uses a precise short-distance definition of the top quark mass, though a different one from the $\overline{MS}$ mass.

Another frequently used definition of the top quark mass is provided by the position of the pole in the top quark propagator computed in perturbation theory. This top quark mass is greater than the $\overline{MS}$ mass by about 10 GeV. This difference contains a parametric ambiguity of order the QCD hadronization scale due to the asymptotic character of the perturbative series caused by the infrared sensitivity of the pole mass.

Current determinations of the top quark mass from kinematic distributions do not use either of these, in principle, well defined top quark mass definitions. Instead, they define the top quark

mass as the input mass parameter of a Monte Carlo event generator, which is then constrained by measurements of the kinematics of the $t\bar{t}$ final state. At this time, there is no concrete analysis that relates this mass to either the short distance or the pole value of the top quark mass. For the case of e^+e^- production of top quark pairs, it was shown in [8] how to relate event-shape variables that depend strongly on the top quark mass to an underlying short-distance mass parameter. The analysis requires center of mass energies much larger than $2m_t$. For hadron colliders, the corresponding analysis is much more difficult and has not yet been done.

Within the framework that is available now, the Tevatron and LHC experiments have achieved quite a precise determination of the top quark mass from kinematic observables. The value of the top quark mass m_t as published by the Tevatron Electroweak Working Group is given to be $m_t = 173.2 \pm 0.9\,\text{GeV}$ [9]. This value has been obtained from the combined measurements of the Tevatron experiments. The LHC experiments report values of $m_t = 174.5 \pm 0.6 \pm 2.3\,\text{GeV}$ for the ATLAS collaboration [10] and $m_t = 172.6 \pm 0.4 \pm 1.2\,\text{GeV}$ for the CMS collaboration [11], where, in each case, the first error is statistical and the second is systematic. The dominant systematic errors come from jet energy resolution. In both cases, the mass definition used is that of the Monte Carlo event generator. Reduction of the error well below 1 GeV will require a more careful theoretical analysis giving the relation of the mass parameter used in these measurements to a more precise top quark mass definition.

Within the Standard Model the total decay width Γ_t of the top quark is dominated by the partial decay width $\Gamma(t \to Wb)$. The top quark width is predicted to be approximately 1.5 GeV, which is substantially larger than the hadronization scale Λ_{QCD}. On the other hand, this value is small enough that it is not expected to be directly measured at the LHC.

At hadron colliders, the decay width can be determined via

$$\Gamma_t = \Gamma(t \to Wb)/BR(t \to Wb)\ . \tag{5.3}$$

The partial width $\Gamma(t \to Wb)$ is determined from the cross section for single top events while the branching ratio $BR(t \to Wb)$ is derived from top pair events. D0 gives a value of $\Gamma_t = 1.99^{+0.69}_{-0.55}$ [12]. CDF uses only the top quark mass spectrum and reports the 68% confidence interval to be $0.3 < \Gamma_t < 4.4\,\text{GeV}$ [13]. It is interesting to note here that D0 has published for the ratio of branching ratios $BR(t \to Wb)/BR(t \to Wq)$ a value of 0.9 ± 0.04 [14], which is about 2.5σ away from the Standard Model expectation.

5.1.3 Helicity of the W boson

The top quark has a very short lifetime of about $10^{-25}\,\text{s}$. Since this is about 10 times shorter than typical scales for long range QCD processes, the top quark decays long before hadronization can affect it. Therefore, the structure of the top quark decay is very close to that of a bare quark. Within the Standard Model, the top quark decays almost exclusively via $t \to W^+b$. The V-A nature of the weak decay dictates that the resulting b quark is almost completely left handed polarized. It also dictates the polarization of the W boson, which in turn can be measured by observing the W decay. The prediction is that the W is produced only in the left-handed and longitudinal polarization states, with the fraction of longitudinal W bosons predicted to be

$$f_0 = \frac{m_t^2}{2m_W^2 + m_t^2}\ . \tag{5.4}$$

The Standard Model predicts a value of $f_0 = 0.703$. The CDF experiment measures this value to be $f_0 = 0.78^{+0.19}_{-0.20}(\text{stat.}) \pm 0.06(\text{syst.})$ [15], in agreement with the Standard Model. The most precise measurements of this value have been achieved with events in which both the W boson from the t

and the one from the $\bar{t}$ decay into leptons.

5.1.4 Top coupling to Z^0 and γ

It is particularly interesting to study the coupling of the top quark to the photon and the Z^0 boson to search for effects of new physics. Both of these couplings are subdominant effects at hadron colliders. The electroweak production of $t\bar{t}$ is suppressed with respect to QCD production, and this is especially true at the LHC where most of the $t\bar{t}$ production comes from gluon-gluon fusion. Radiation of photons from $t\bar{t}$ has been observed at the Tevatron. So far no precision measurements on the coupling of top quarks to the Z^0 boson have been reported.

Constraints on the top quark couplings to γ and Z^0 have been reported using the expression for the couplings [16]

$$\Gamma_{\mu}^{ttX}(k^2,\, q,\, \overline{q}) = ie\left\{\gamma_{\mu}\left(\widetilde{F}_{1V}^{X}(k^2) + \gamma_5\widetilde{F}_{1A}^{X}(k^2)\right) + \frac{(q-\overline{q})_{\mu}}{2m_t}\left(\widetilde{F}_{2V}^{X}(k^2) + \gamma_5\widetilde{F}_{2A}^{X}(k^2)\right)\right\}. \quad (5.5)$$

where $X = \gamma, Z$ and the $\widetilde{F}$ are related to the usual form factors F_1, F_2 by

$$\widetilde{F}_{1V}^{X} = -\left(F_{1V}^{X} + F_{2V}^{X}\right), \qquad \widetilde{F}_{2V}^{X} = F_{2V}^{X}, \qquad \widetilde{F}_{1A}^{X} = -F_{1A}^{X}, \qquad \widetilde{F}_{2A}^{X} = -iF_{2A}^{X}. \quad (5.6)$$

In the Standard Model the only form factors which are different from zero are $F_{1V}^{\gamma}(k^2)$, $F_{1V}^{Z}(k^2)$ and $F_{1A}^{Z}(k^2)$. The quantities $F_{2V}^{\gamma,Z}(k^2)$ are the electric and weak magnetic dipole moment (EDM and MDM) form factors.

$F_{2A}^{\gamma}(k^2)$ is the CP-violating electric dipole moment form factor of the top quark, and $F_{2A}^{Z}(k^2)$ is the weak electric dipole moment (WDM). These two form factors violate CP. In the Standard Model they receive contributions only from the three loop level and beyond.

In the case of the $t\bar{t}Z^0$ final state, relatively clean measurements are expected at the LHC when the Z^0 decays leptonically. However, the cross section is quite small, so that meaningful results with precision of about 10% for $F_{1A}^{Z^0}$ and 40% for $F_{2V,A}^{Z^0}$ can only be expected after a few 100 fb^{-1}. At the HL-LHC, with an integrated luminosity of about 3000 fb^{-1}, the precision of this measurement is expected to improve by factors between 1.6 for $F_{2V,A}^{Z^0}$ and 3 for $F_{1A}^{Z^0}$. The situation is considerably better for measurements of the $t\bar{t}\gamma$ vertex. Already for 30 fb^{-1} at the LHC, measurements with a precision of about 20% to 35% can be expected. These measurements may improve at the HL-LHC to values between 2% and 10%

For the related question of the coupling of the top quark to the Higgs boson, both the LHC expectations and the projections for the ILC are discussed in Chapter 2 of this report.

5.1.5 Asymmetries at hadron colliders

The last few years were marked by a number of publications from the Tevatron experiments which reported on tensions with Standard Model predictions in the measurement of forward backward asymmetries A_{FB}. This observable counts the difference in the number of events in the two hemispheres of the detector. In hadronic collisions, the polar angle is typically reported in terms of the rapidity y, which is invariant under longitudinal boosts and more descriptive at very forward and backward angles. For the analyses here and at the LHC, at least one member of the $t\bar{t}$ pair is required to decay leptonically to assure the particle identification. The average asymmetry reported by CDF is $0.201 \pm 0.065\,(\text{stat.}) \pm 0.018\,(\text{syst.})$ [17] which agrees with $0.196 \pm 0.060\,(\text{stat.})^{+0.018}_{-0.026}\,(\text{syst.})$ as reported by DO [18]. These values can be compared with an asymmetry of about 0.07 predicted by the to Standard Model from NLO QCD and electroweak effects. This result is difficult to verify at the LHC. The LHC is a proton-proton collider, so the two hemispheres are intrinsically symmetric. Further, at the LHC at 7 TeV, only 15% of the interactions arise from $q\bar{q}$ collisions; the 85% from

gg collisions can have no intrinsic asymmetry. Still, in $q\bar{q}$ collisions at the LHC, it is likely that the q is a valence quark while the $\bar{q}$ is pulled from the sea. This implies that $t\bar{t}$ pairs produced from $q\bar{q}$ are typically boosted in the direction of the q. This offers methods to observe a forward backward asymmetry in $q\bar{q} \to t\bar{t}$. For example, a forward-backward asymmetry in the $q\bar{q}$ reaction translates into a smaller asymmetry A_C in the variable $\Delta|y| = |y_t| - |y_{\bar{t}}|$. For this observable, CMS measures $A_C = 0.004 \pm 0.010\,(\text{stat.}) \pm 0.012\,(\text{syst.})$ [19], which agrees with the Standard Model predictions within the relatively large uncertainties. So far, the LHC experiments have not provided any independent evidence for asymmetries outside the Standard Model predictions [3, 20]. The theoretical interpretation of these asymmetries is also very uncertain. Many plausible models of the $t\bar{t}$ asymmetry predict effects in top quark physics at high energy that are excluded at the LHC. For a review of the current situation, see [21, 22]. It is possible that the tension between theory and experiment can be resolved by more accurate QCD calculation. For example, a lower choice of the QCD renormalization scale, argued for in [23], would increase the Standard Model prediction.

5.2 $e^+e^- \to t\bar{t}$ at threshold

One of the unique capabilities of an e^+e^- linear collider is the ability to carry out cross section measurements at particle production thresholds. The accurately known and readily variable beam energy of the ILC makes it possible to measure the shape of the cross section at any pair-production threshold within its range. Because of the leptonic initial state, it is also possible to tune the initial spin state, giving additional options for precision threshold measurements. The $t\bar{t}$ pair production threshold, located at a center of mass energy energy $\sqrt{s} \approx 2m_t$, allows for precise measurements of the top quark mass m_t as well as the top quark total width Γ_t and the QCD coupling α_s. Because the top is a spin-$\frac{1}{2}$ fermion, the $t\bar{t}$ pair is produced in an angular S-wave state. This leads to a clearly visible rise of the cross section even when folded with the ILC luminosity spectrum. Moreover, because the top quark pair is produced in a color singlet state and because the finite top lifetime provides an effective infrared cutoff for QCD corrections, the experimental measurements can be compared with very accurate and unambiguous analytic theoretical predictions of the cross section with negligible hadronization effects. The dependence of the top quark cross section shape on the top quark mass and interactions is computable to high precision with full control over the renormalization scheme dependence of the top mass parameter. In this section, we will review the expectations for the theory and ILC measurements of the top quark threshold cross section shape. The case of the top quark threshold is not only important in its own right but also serves as a prototype case for other particle thresholds that might be accessible at the ILC.

5.2.1 Status of QCD theory

The calculation of the total top pair production cross section makes use of the method of non-relativistic effective theories. The top quark mass parameter used in this calculation is defined at the scale of about 10 GeV corresponding to the typical physical separation of the t and $\bar{t}$. This mass parameter can be converted to the $\overline{MS}$ mass in a controlled way. The summation of QCD Coulomb singularities, treated by a non-relativistic fixed-order expansion, is well known up to NNLO [24] and has recently been extended accounting also for NNNLO corrections [25]. Large velocity QCD logarithms have been determined using renormalization-group-improved non-relativistic perturbation theory up to NLL order, with a partial treatment of NNLL effects [26, 27]. Recently the dominant ultrasoft NNLL corrections have been completed [28]. The accuracy in this calculation is illustrated in Fig. 5.1.

Since the top quark kinetic energy is of the order of the top quark width, electroweak effects, which also include finite-lifetime and interference contributions, are crucial as well. This makes

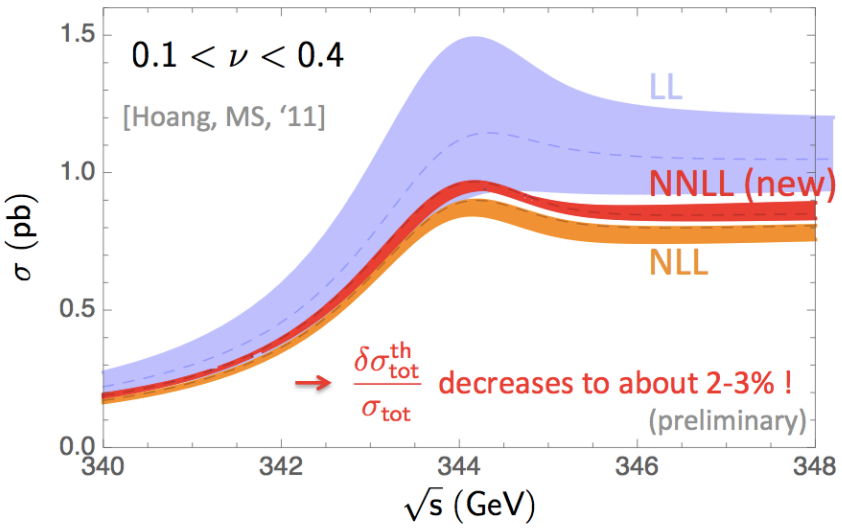

Figure 5.1
Accuracy of the prediction of the top pair production cross section at the $t\bar{t}$ threshold at the ILC, in the 1S mass scheme, as achieved by QCD calculations with resummation of logarithmic corrections to leading (LL), next-to-leading (NLL), and next-to-next-to-leading (NNLL) order. From [31].

the cross section dependent on the experimental prescription concerning the reconstructed final state. Recently a number of partial results have been obtained [29, 30] which put approximate NNLL order predictions within reach. Theoretical predictions for differential cross sections such as the top momentum distribution and forward-backward asymmetries are only known at the NNLO level and thus are much less developed.

5.2.2 Simulations and measurements

The most thorough experimental study of the top quark threshold has been carried out by Martinez and Miquel in [32]. These authors assumed a total integrated luminosity of 300 fb^{-1}, distributed over 10 equidistant energy points in a 10 GeV range around the threshold, using the TELSA beam parameters. To treat the strong correlation of the input theory parameters, simultaneous fits were carried out for the top quark mass, the QCD coupling and the top quark width from measurments of the total cross section, the top momentum distributions and the forward-backward asymmetry. These were simulated based on the code TOPPIK with NNLO corrections [33]. The study obtained the uncertainties $\Delta m_t = 19$ MeV, $\Delta\alpha_s(m_Z) = 0.0012$ and $\Delta\Gamma_t = 32$ MeV, when all observables were accounted for Using just the total cross section measurements, the results were $\Delta m_t = 34$ MeV, $\Delta\alpha_s(m_Z) = 0.0023$ and $\Delta\Gamma_t = 42$ MeV. The difference shows the discriminating power of additional observables of the threshold region. The analysis included a theory uncertainty in the cross section codes of 3%, which at this time is only approached for total cross section computations. Although the analysis was only based on fixed order NNLO predictions, the quoted uncertainties should be realistic.

The analysis in [32] did not yet include a complete study of experimental systematic uncertainties, including, in particular, uncertainties in the knowledge of the luminosity spectrum. This last point is addressed in a more recent study by Seidel, Simon, and Tesar, for which the results are shown in Fig. 5.2 [34]. That study was carried with a full detector simulation using the ILD detector. It takes the initial state radiation and beamstrahlung of the colliding beams into account. The figure underlines the high sensitivity of the threshold region to the actual value of the top quark mass. The statistical precision obtained on the top quark mass in this study is of the order of 30 MeV. Due to the QCD corrections relevant for a precise calculation of the top quark mass, the threshold scan is sensitive to the value of α_s. The error ellipse as obtained in a combined determination of α_s and m_t is shown in the right-hand panel of Fig. 5.2.

The threshold top quark mass determined in this study must still be converted to the standard top quark $\overline{MS}$ mass. The conversion formula, to three-loop order, is given in [33]. The conversion adds an error of about 100 MeV from truncation of the QCD perturbation series and an error of

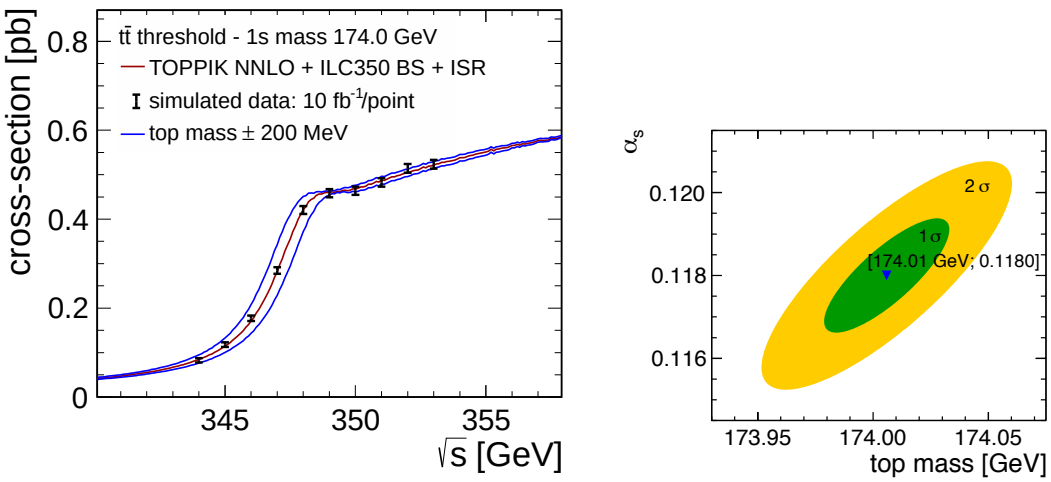

Figure 5.2. Illustration of a top quark threshold meausurement at the ILC. In the simulation, the top quark mass has been chosen to be 174. GeV. The blue lines show the effect of varying this mass by 200 MeV. The study is based on full detector simulation and takes initial state radiation (ISR) and beamstrahlung (BS) and other relevant machine effects into account: (left) the simulated threshold scan. (right) error ellipse for the determination of m_t and α_s. From [34].

70 MeV for each uncertainty of 0.001 in the value of α_s. Both sources of uncertainty should be reduced by the time of the ILC running. In particular, the study of event shapes in $e^+e^- \to q\bar{q}$ at the high energies available at ILC should resolve current questions concerning tensions between precision determinations of α_s. It is important to note that these estimates of the accuracy of mass values are derived from a precision theory of the relation between the threshold mass and the top quark $\overline{MS}$ mass. A comparable theory simply does not exist for the conversion of the top quark mass measured in hadronic collisions to the $\overline{MS}$ value.

The precise determination of the top quark mass is likely to have important implications for fundamental theory. We have given one example at the end of Section 2.1. In that case, the value of the top quark mass, accurate at the level that ILC will provide, literally decides the fate of the universe.

In principle, the contribution of the Higgs exchange potential to the $t\bar{t}$ threshold makes it possible to measure that Higgs coupling to $t\bar{t}$. However, the precision of this measurement is strongly limited by the fact that the Higgs corrections are suppressed by the inverse square of the Higgs mass. For a Higgs mass of $m_H = 120$ GeV the study in [32] found that uncertainties of at least several 10% should be expected in a measurement of the top quark Higgs Yukawa coupling. This coupling can be measured more accurately from the cross section for $e^+e^- \to t\bar{t}h$, as is explained in Section 2.6 and 2.7 of this report.

5.3 Probing the top quark vertices at the ILC

At higher energy, the study of $t\bar{t}$ pair production at the ILC is the ideal setting in which to make precise measurements of the the coupling of the top quark to the Z^0 boson and the photon. In contrast to the situation at hadron colliders, the leading-order pair production process $e^+e^- \to t\bar{t}$ goes directly through the $t\bar{t}Z^0$ and $t\bar{t}\gamma$ vertices. There is no concurrent QCD production of top pairs, which increases greatly the potential for a clean measurement. In the following section, we will review the importance of measuring these couplings precisely. Then we will describe studies of the experimental capabilities of the ILC to perform these measurements.

5.3.1 Models with top and Higgs compositeness

There are several classes of models that seek to answer the question of where the Higgs boson comes from and why it acquires a symmetry-breaking vaccum expectation value. Among these is supersymmetry, which will have its own discussion in Chapter 7 of this report. An alternative point of view is that the Higgs boson is a composite state within a larger, strongly interacting theory at the TeV scale. Though the first models of this type contained no light Higgs bosons, there are now many models that naturally contain a light Higgs boson very similar to the Higgs boson of the Standard Model coupling to new heavy particles at the TeV mass scale. In Chapters 2–4, we have described tests of models of this type at the ILC in Higgs boson, two-fermion, and W boson measurements.

The top quark is the heaviest known particle that derives its mass entirely from electroweak symmetry breaking. Due to its high mass the top quark couples to the Higgs with a Yukawa coupling of strength $\lambda_t \approx 1$. It is therefore likely that any composite structure of the Higgs boson must be reflected in composite structure or non-Standard interactions of the top quark. While such interactions may exist, they may not be easy to find. The coupling of the top quark to the gluon and the photon are constrained at $Q^2 = 0$ by requirements from exact QCD and QED gauge invariance. However, the low-energy $t\bar{t}Z$ vertex is much less constrained. It is then likely that this is the crucial place to look for deviations from the Standard Model induced by a strongly interacting Higgs sector.

Models of composite Higgs bosons can be constructed in three ways that seem at first sight to be distinctly different. The Higgs bosons may be Goldstone bosons associated with strong-interaction symmetry breaking at the 10 TeV energy scale, as in Little Higgs models. They may arise as partners of gauge bosons in theories with an extra space dimension, as in Gauge-Higgs Unification. Or, they may arise in extra-dimensional theories as states confined to a lower-dimensional subspace or 'brane'. Randall and Sundrum constructed a model of the last type [35] but also argued that all three classes of models are related by strong coupling-weak coupling duality [36]. That is, it is possible to view the extra-dimensional models as tools that allow weak coupling calculations of effects that are intrinsically manifestations of strong coupling and composite state dynamics.

The Randall-Sundrum approach also includes a model explanation of the hierarchy of Higgs-fermion Yukawa couplings. This is one of the most mysterious aspects of the Standard Model, reflected in the fact that the top quark and the up quark have exactly the same quantum numbers but differ in mass by a factor of 10^5. The extra dimension offers the possibility that the different flavors of fermion have wavefunction of different shape in the full space, and therefore different overlap with the wavefunction of the Higgs boson. In general, also, the right and left chiral components of each quark and lepton may have wavefunctions with different dependence on the extra dimensions. It is a typical prediction of Randall-Sundrum theories that the chiral components of the top quark have wavefunctions in the fifth dimension significantly different from those of the other quarks and from one another. The wavefunction of the right-handed top quark is shifted toward the low-energy boundary of the space, called the 'TeV brane', where the Higgs field is located. These differences of the wavefunctions are reflected directly in couplings of the top quark to the Z^0. These couplings are shifted from the values predicted in the Standard Model, with larger shifts specifically for the right-handed top quark. Figure 5.3 collects a number of predictions of the fractional shifts in the t_L and t_R couplings to the Z^0 in a variety of models proposed in the literature.

Models with extra dimensions may also be suited to explain the tensions observed at the Tevatron discussed in Section 5.1.5. The top forward-backward asymmetry may, for example, be explained by a new color octet vector boson G_μ, which couples weakly to light quarks but strongly to the top quark. This difference is required in order to suppress ordinary dijet production from the new colour-octet state. The difference in the coupling can be realized by the arrangement of the top quark wavefunction along the extra-dimension [22].

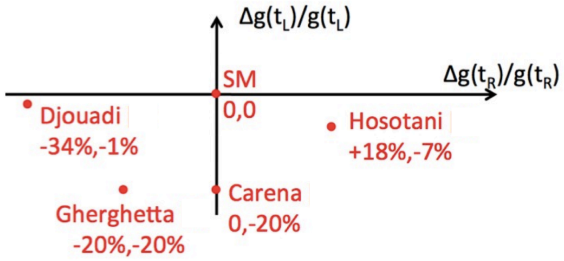

Figure 5.3 Predictions of Randall-Sundrum extra dimensional models from various groups [37–40] for deviations from Standard Model couplings of the t quark to the Z boson, from [44].

5.3.2 ILC measurements

In the previous section, we have described theories in which the top quark and Higgs boson are composite, with this compositeness being an essential element of the physics of electroweak symmetry breaking. A key test of this idea would come from the measurement of the $t\bar{t}Z$ couplings. Significant deviations from the predictions of the Standard Model would be expected. The ILC provides an ideal environment to measure these couplings. At the ILC, $t\bar{t}$ pairs would be copiously produced, with several 100,000 events for an integrated luminosity of $500\,\mathrm{fb}^{-1}$. The production is by s-channel γ and Z exchange, so the Z couplings enter the cross section in order 1. It is possible to almost entirely eliminate the background from other Standard Model processes. The ILC will allow for polarized electron and positron beams. This allows us to measure not only the total cross section for $t\bar{t}$ production but also the left-right asymmetry A_{LR}, the change in cross-section for different beam polarizations. For the b quark, The most precise measurements for the b quark of A_{LR} at SLC and the forward-backward asymmetry at LEP result in a 3 σ discrepancy of the effective electroweak mixing angle $\sin^2\theta_{eff}$ that has yet to be resolved [41]. If this effect is real, it is likely to be larger for the heavy top quark.

With the use of polarized beams, t and $\bar{t}$ quarks oriented toward different angular regions in the detector are enriched in left-handed or right-handed top quark polarization [42]. This means that the experiments can independently access the couplings of left- and right-handed polarized quarks to the Z boson. In principle, measurement of the cross sections and forward-backward asymmetries for two different polarization settings measures both the photon and Z couplings of the top quark for each handedness. New probes of the top quark decay vertices are also available, although we expect that these will already be highly constrained by the LHC measurements of the W polarization in top decay.

Recent studies based on full simulation of ILC detectors for a center of mass energy of $\sqrt{s} = 500\,\mathrm{GeV}$ demonstrate that a precision on the determination of the couplings the left and the right chiral parts of the top quark wave function to the Z^0 to better than 1% can be achieved [44–46]. The most recent example of such a study, with full detector simulation, is shown in Figure 5.4. The figure demonstrates the clean reconstruction of the top quark direction, which allows for the precise determination of the forward-backward asymmetry. It has to be noted, however, that the final state gives rise to ambiguities in the correct association of the b quarks to the W bosons, see [46] for an explanation. These ambiguities can be nearly eliminated by requiring a high quality of the event reconstruction. The control of the ambiguities requires an excellent detector performance and event reconstruction. Another solution is the use of the vertex charge to separate the t and $\bar{t}$ decays. It is shown in [45] that the high efficiency of vertex tagging in the ILC detectors will make this strategy available. The expected percent level independent measurements of the left- and right-handed top quark couplings will clearly discriminate the models shown in Fig. 5.3.

Even more incisive measurements than presented using optimised observables are investigated in [43]. These observables are the top pair production cross-section for left- and right-handed polarised beams and the fraction of right-handed (t_R) and left handed top quarks (t_L). Following a suggestion

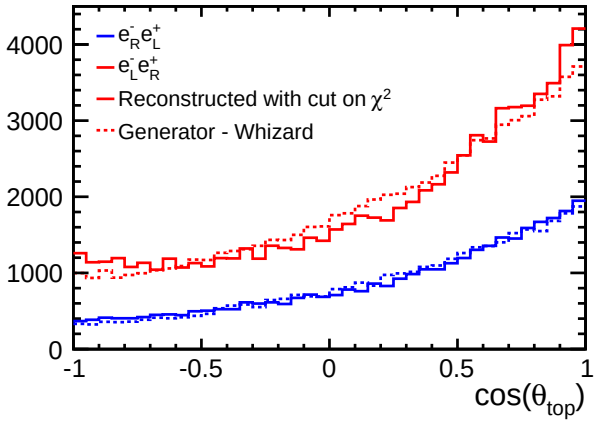

Figure 5.4
Reconstruction of the direction of the top quark in $t\bar{t}$ pair production for two different beam polarization [43]. It is known from [44] that the background is negligible.

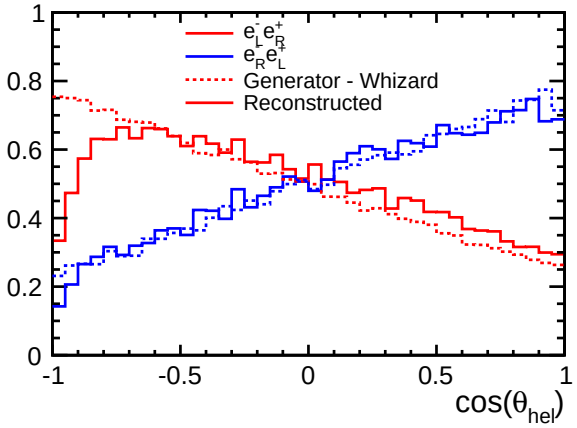

Figure 5.5
Top: Generated and reconstructed distributions of the top quark helicity angle $\cos\theta_{hel}$ in $e^+e^- \to t\bar{t}$ at the ILC at 500 GeV, from [43].

by [47] for the Tevatron, the fraction of t_L and t_R in a given sample can be determined with the helicity asymmetry. In the top quark rest frame the distribution of the polar angle θ_{hel} of a decay lepton is

$$\frac{1}{\Gamma}\frac{d\Gamma}{d\cos\theta_{hel}} = \frac{1 + a_t \cos\theta_{hel}}{2} \tag{5.7}$$

where a_t varies between $+1$ and -1 depending on the fraction of right-handed (t_R) and left handed top quarks (t_L). The observable $\cos\theta_{hel}$ can easily be measured at the ILC. This observable is much less sensitive to ambiguities in the event reconstruction than the forward backward asymmetry. The slope of the resulting linear distribution provides a very robust measure of the net polarisation of a top quark sample. This net polarization is sensitive to new physics. The result of a full simulation study is shown in Fig. 5.5. It is demonstrated that over a range in $\cos\theta_{hel}$ the generated distribution is retained after event reconstruction. The reconstruction is nearly perfect for initial right handed electron beams. Remaining discrepancies in case of left handed electron beams can be explained by reconstruction inefficiencies for low final state lepton energies.

The observables A_{FB}, cross sections and helicity asymmetries are used to disentangle the coupling of the top quark to the photon and to the Z. Figure 5.6 compares the precision on the form factors expected from the LHC with that from the ILC.

Numerical values for the expected accuracies at linear e^+e^- colliders, ILC and earlier on TESLA [49], on seven top quark form factors (due to QED gauge invariance the coupling $\widetilde{F}^{\gamma}_{1A}$ is fixed to 0), taken from the studies [43, 48, 49], are given in Tables 5.1 and 5.2, along with comparisons to the expectations from the LHC experiments.

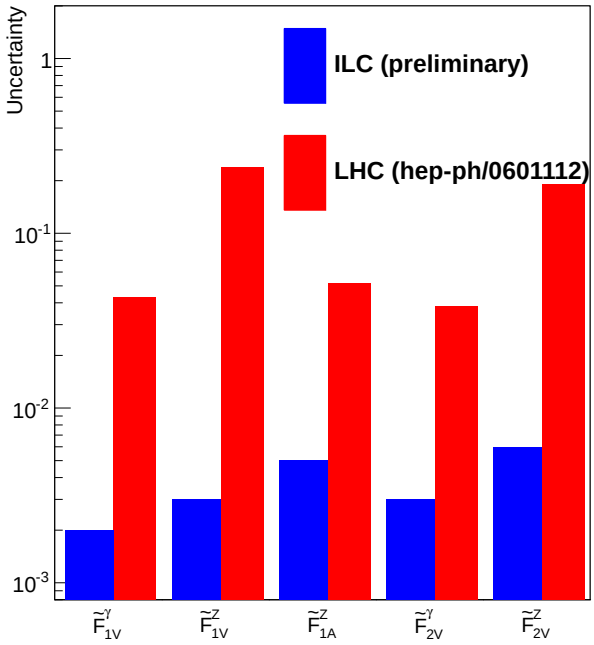

Figure 5.6
Comparison of precisions for CP conserving form factors of the top quark coupling to γ and Z, $\widetilde{F}^{\gamma,Z}_{1V,A}$, expected at the LHC, taken from [16], and at the ILC. The LHC results assume an integrated luminosity of $\mathcal{L} = 300$ fb^{-1}. The results for ILC [43] assume an integrated luminosity of $\mathcal{L} = 500$ fb^{-1} at $\sqrt{s} = 500$ GeV and 80% electron and 30% positron polarization.

Table 5.1. Sensitivities achievable at 68% CL for the CP-conserving top quark form factors $\widetilde{F}^{X}_{1V,A}$ and $\widetilde{F}^{X}_{2V}$ defined in (5.5), at LHC and at the ILC. The assumed luminosity samples and, for ILC, beam polarization, are indicated. In the LHC studies and in the study [48], only one form factor at a time is allowed to deviate from its SM value. In the study [43], the form factors are allowed to vary independently.

Coupling	LHC [16] $\mathcal{L} = 300$ fb^{-1}	e^+e^- [48] $P_{e^-} = \pm 0.8$	e^+e^- [43] $\mathcal{L} = 500$ fb^{-1}, $P_{e^-,+} = \pm 0.8, \mp 0.3$
$\Delta\widetilde{F}^{\gamma}_{1V}$	$^{+0.043}_{-0.041}$	$^{+0.047}_{-0.047}$, $\mathcal{L} = 200$ fb^{-1}	$^{+0.002}_{-0.002}$
$\Delta\widetilde{F}^{Z}_{1V}$	$^{+0.24}_{-0.62}$	$^{+0.012}_{-0.012}$, $\mathcal{L} = 200$ fb^{-1}	$^{+0.003}_{-0.003}$
$\Delta\widetilde{F}^{Z}_{1A}$	$^{+0.052}_{-0.060}$	$^{+0.013}_{-0.013}$, $\mathcal{L} = 100$ fb^{-1}	$^{+0.005}_{-0.005}$
$\Delta\widetilde{F}^{\gamma}_{2V}$	$^{+0.038}_{-0.035}$	$^{+0.038}_{-0.038}$, $\mathcal{L} = 200$ fb^{-1}	$^{+0.003}_{-0.003}$
$\Delta\widetilde{F}^{Z}_{2V}$	$^{+0.27}_{-0.19}$	$^{+0.009}_{-0.009}$, $\mathcal{L} = 200$ fb^{-1}	$^{+0.006}_{-0.006}$

5.3.3 An example: the Randall-Sundrum scenario

The sensitivity of the top quark couplings to new physics can be paramerised by general dimension six operators contributing to the $t\bar{t}\gamma$ and $t\bar{t}Z$ vertex [50]. However, the potential of the ILC might be demonstrated more clearly by presenting a concrete example with one particular model. In the original model of Randall and Sundrum [35] there are additional massive gauge bosons in an assumed extra dimension. The model predicts increased couplings of the top quark, and perhaps also the b quark, to these Kaluza Klein particles. Following the analysis in [37, 51], one can fix the parameters of the model so that these enhancements fit the two anomalies observed in the forward-backward asymmetry for b quarks $A_{FB,b}$ at LEP1 and for top quarks $A_{FB,t}$ at the Tevatron. This gives a viable model of top quark interactions associated with top and Higgs compositeness. Figure 5.7 shows the expected modifications of the helicity angle distributions within this scenario.

Both the slopes and total cross sections are deeply modified in this scenario for the two polarizations. As explained previously, these observables are directly measured at the ILC, and the measurements allow one to fully disentangle the individual modifications of the Z and photon couplings to top quarks. It can also be shown that by running at two energies, for instance 500 GeV and 1 TeV,

Table 5.2. Sensitivities achievable at 68.3% CL for the top quark CP-violating magnetic and electric dipole form factors $\widetilde{F}_{2A}^{X}$ defined in (5.5), at the LHC and at linear e^+e^- colliders as published in the TESLA TDR. The assumed luminosity samples and, for TESLA, the beam polarization, are indicated. In the LHC studies and in the TESLA studies, only one form factor at a time is allowed to deviate from its SM value.

Coupling	LHC [16] $\mathcal{L} = 300$ fb^{-1}	e^+e^- [49] $\mathcal{L} = 300$ fb^{-1}, $P_{e^-,+} = -0.8$
$\Delta\mathrm{Re}\,\widetilde{F}_{2A}^{\gamma}$	$^{+0.17}_{-0.17}$	$^{+0.007}_{-0.007}$
$\Delta\mathrm{Re}\,\widetilde{F}_{2A}^{Z}$	$^{+0.35}_{-0.35}$	$^{+0.008}_{-0.008}$
$\Delta\mathrm{Im}\,\widetilde{F}_{2A}^{\gamma}$	$^{+0.17}_{-0.17}$	$^{+0.008}_{-0.008}$
$\Delta\mathrm{Im}\,\widetilde{F}_{2A}^{Z}$	$^{+0.035}_{-0.035}$	$^{+0.015}_{-0.015}$

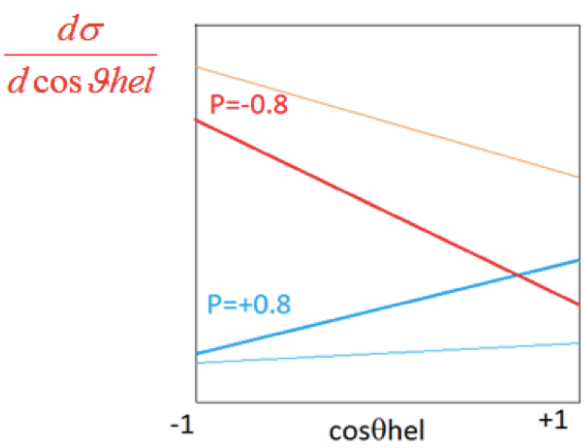

Figure 5.7 Distributions of the helicity angle $\cos\theta_{hel}$ expected from the Standard Model (thick lines) and their modifications by the Randall-Sundrum model presented in [51]. The results are shown for electron and positron beam polarization equal to -80%/+30% and +80%/-30%.

one can fully extract the parameters of the model, for instance, the Kaluza Klein boson masses, which can be measured with about 1% precision.

When the Kaluza Klein particles become very heavy, ILC at 500 GeV can observe deviations in top couplings at greater than 3 σ for masses which, depending on the details of the model, typically range between 4 and 48 TeV

5.3.4 Remarks on $(g-2)_t$

The determination of $\widetilde{F}_{2V}^{\gamma}$ gives access to the anomalous magnetic moment $(g-2)_t$ through the relation $\widetilde{F}_{2V}^{\gamma} = Q_t(g-2)_t/2$. The top quark $(g-2)$ receives Standard Model contributions from QED, QCD and EW [52]. One sees that this quantity will be measured to about 0.1% accuracy.

What is known about $(g-2)_t$? Limits from the reaction $b \to s\gamma$ giving a very crude constraint [53] :

$$-3.5 < g_t < 3.6 \tag{5.8}$$

In [54], it is argued that $(g-2)_t$ is a very sensitive measurement for compositeness. For leptons, this measure constrains compositeness at the 10000 TeV ($10^{-18}\,\mathrm{cm}$) level. In other words, e and μ are almost precisely elementary objects. But this need not be true for the top quark. The value of $(g-2)_t/2$ is proportional to m_t/M, where M is the scale of top quark compositeness. It follows that, with the 0.1% accuracy expected at the ILC, the compositeness of the top quark can be tested up to about 100 TeV.

5.4 Concluding remarks

The top quark could be a window to new physics associated with light composite Higgs bosons and strong coupling in the Higgs sector. The key parameters here are the electroweak couplings of the top quark. We have demonstrated that the ILC offers unique capabilities to access these couplings and measure them to the required high level of precision. The mass of the top quark, which is a most important quantitiy in many theories can be measured in a model independent fashion to a precision of better than 100 MeV. It has however to be pointed out that all of these precision measurements require a superb detector performance and event reconstruction. The key requirements are the tagging of final state b quarks with and efficiency and purity of better than 90% and jet energy reconstruction using particle flow of about 4% in the entire accessible energy range. These requirements are met for the ILC detectors described in the Volume 4 of this report.

Bibliography

[1] F. Abe *et al.* [CDF Collaboration], Phys. Rev. Lett. **74**, 2626 (1995) [hep-ex/9503002].

[2] S. Abachi *et al.* [D0 Collaboration], Phys. Rev. Lett. **74**, 2632 (1995) [hep-ex/9503003].

[3] K. Lannon, F. Margaroli and C. Neu, arXiv:1201.5873v1 [hep-ex].

[4] ATLAS Collaboration, ATLAS-CONF-2012-024.

[5] CMS collaboration, CMS-PAS-TOP-11-024.

[6] N. Kidonakis, Phys. Rev. D **82**, 114030 (2010) [arXiv:1009.4935 [hep-ph]].

[7] The current predictions, which have a range of about 8 pb, are reviewed in N. Kidonakis and B. D. Pecjak, arXiv:1108.6063 [hep-ph].

[8] S. Fleming, A. H. Hoang, S. Mantry and I. W. Stewart, Phys. Rev. D **77**, 114003 (2008) [arXiv:0711.2079 [hep-ph]].

[9] Tevatron Electroweak Working Group and CDF and DO Collaborations, FERMILAB-TM-2504-E, CDF-NOTE-10549, D0-NOTE-6222, arXiv:1107.5255v3 [hep-ex].

[10] G. Aad *et al.* [ATLAS Collaboration], Eur. Phys. J. C **72**, 2046 (2012) [arXiv:1203.5755 [hep-ex]].

[11] CMS COllaboration, Physics Analysis Summary CMS-PAS-TOP-11-018 (2011).

[12] V. M. Abazov *et al.* [D0 Collaboration], Phys. Rev. Lett. **106**, 022001 (2011) [arXiv:1009.5686 [hep-ex]].

[13] T. Aaltonen *et al.* [CDF Collaboration], Phys. Rev. Lett. **105**, 232003 (2010) [arXiv:1008.3891 [hep-ex]].

[14] V. M. Abazov *et al.* [D0 Collaboration], Phys. Rev. Lett. **107**, 121802 (2011) [arXiv:1106.5436 [hep-ex]].

[15] CDF Collaboration, CDF Note 10333 (2010).

[16] A. Juste et al., "Report of the 2005 Snowmass Top/QCD Working Group", econf/C0508141:PLEN0043 (2005), arXiv:hep-ph/0601112.

[17] T. Schwarz *et al.*, [CDF Collaboration], CDF-Note 10584 (2011).

[18] V. M. Abazov *et al.* [D0 Collaboration], Phys. Rev. D **84**, 112005 (2011) [arXiv:1107.4995 [hep-ex]].

[19] CMS Collaboration, Physics Analysis Summary CMS-PAS-TOP-11-30 (2011).

[20] ATLAS Collaboration, ATLAS-CONF-2011-106 (2011).

[21] M. I. Gresham, I. -W. Kim and K. M. Zurek, Phys. Rev. D **85**, 014022 (2012) [arXiv:1107.4364 [hep-ph]].

[22] J. A. Aguilar-Saavedra, arXiv:1202.2382v1 [hep-ph].

[23] S. J. Brodsky and X. -G. Wu, Phys. Rev. Lett. **109**, 042002 (2012) [arXiv:1203.5312 [hep-ph]].

[24] A. H. Hoang, M. Beneke, K. Melnikov, T. Nagano, A. Ota, A. A. Penin, A. A. Pivovarov and A. Signer *et al.*, Eur. Phys. J. direct C **2**, 1 (2000) [hep-ph/0001286].

[25] M. Beneke and Y. Kiyo, Phys. Lett. B **668**, 143 (2008) [arXiv:0804.4004 [hep-ph]].

[26] A. H. Hoang, A. V. Manohar, I. W. Stewart and T. Teubner, Phys. Rev. D **65**, 014014 (2002) [hep-ph/0107144].

[27] A. Pineda and A. Signer, Nucl. Phys. B **762**, 67 (2007) [hep-ph/0607239].

[28] A. H. Hoang and M. Stahlhofen, JHEP **1106**, 088 (2011) [arXiv:1102.0269 [hep-ph]].

[29] A. H. Hoang, C. J. Reisser and P. Ruiz-Femenia, Phys. Rev. D **82**, 014005 (2010) [arXiv:1002.3223 [hep-ph]].

[30] A. A. Penin and J. H. Piclum, JHEP **1201**, 034 (2012) [arXiv:1110.1970 [hep-ph]].

[31] M. Stahlhofen, Talk at the Top Physics Workshop, Paris, May 2012.

[32] M. Martinez and R. Miquel, Eur. Phys. J. C **27**, 49 (2003) [hep-ph/0207315].

[33] A. H. Hoang and T. Teubner, Phys. Rev. D **60**, 114027 (1999) [hep-ph/9904468].

[34] K. Seidel, F. Simon, and M. Tesar, CERN LCD-Note-2012-013 (2012).

[35] L. Randall and R. Sundrum, Phys. Rev. Lett. **83** (1999) 3370; M. Gogberashvili, Int. J. Mod. Phys. D **11** (2002) 1635.

[36] N. Arkani-Hamed, M. Porrati and L. Randall, JHEP **0108**, 017 (2001) [hep-th/0012148].

[37] A. Djouadi, G. Moreau, and F. Richard., Nucl. Phys. B, **773** (1-2):43 (2007), arXiv:hep-ph/0610173v1.

[38] Y. Hosotani and M. Mabe, Phys. Lett. B **615**, 257 (2005) [hep-ph/0503020].

[39] Y. Cui, T. Gherghetta and J. Stokes, JHEP **1012**, 075 (2010) [arXiv:1006.3322 [hep-ph]].

[40] M. S. Carena, E. Ponton, J. Santiago and C. E. M. Wagner, Nucl. Phys. B **759**, 202 (2006) [hep-ph/0607106].

[41] S. Schael *et al.* [ALEPH and DELPHI and L3 and OPAL and SLD and LEP Electroweak Working Group and SLD Electroweak Group and SLD Heavy Flavour Group Collaborations], Phys. Rept. **427**, 257 (2006) [hep-ex/0509008], updated in [hep-ex/0911.2604].

[42] S. J. Parke and Y. Shadmi, Phys. Lett. B **387**, 199 (1996) [hep-ph/9606419].

[43] M.S. Amjad *et al.*, LC Report LC-REP-2013-007 (2013).

[44] P. Doublet, PhD-Thesis Université de Paris XI and LAL, LAL 11-222 (2011).

[45] E. Devetak, A. Nomerotski and M. Peskin, Phys. Rev. D **84**, 034029 (2011) [arXiv:1005.1756 [hep-ex]].

[46] P. Doublet, F. Richard, R. Poschl, T. Frisson and J. Rouene, arXiv:1202.6659 [hep-ex].

[47] E. L. Berger, Q. -H. Cao, C. -R. Chen, J. -H. Yu and H. Zhang, Phys. Rev. Lett. **108**, 072002 (2012) [arXiv:1201.1790 [hep-ph]].

[48] T. Abe *et al.* [American Linear Collider Working Group Collaboration], *Linear Collider Physics Resource Book for Snowmass 2001*, Part 3, hep-ex/0106057.

[49] J. A. Aguilar-Saavedra *et al.* [ECFA/DESY LC Physics Working Group Collaboration], "Physics at an e+ e- linear collider," hep-ph/0106315.

[50] J. A. Aguilar-Saavedra, M. C. N. Fiolhais and A. Onofre, JHEP **1207**, 180 (2012) [arXiv:1206.1033 [hep-ph]].

[51] A. Djouadi, G. Moreau, F. Richard and R. K. Singh, Phys. Rev. D **82**, 071702 (2010) [arXiv:0906.0604 [hep-ph]]; A. Djouadi, G. Moreau and F. Richard, Phys. Lett. B **701**, 458 (2011) [arXiv:1105.3158 [hep-ph]].

[52] A.G. Grozin, P. Marquard, J.H. Piclum, M Steinhauser, Nucl. Phys. B **789** 277 (2008), arXiv:0707.1388 [hep-ph].

[53] L. Labun, J. Rafelski, arXiv:1209.1046 [hep-ph].

[54] S. Brodsky and S. Drell, Phys. Rev. D **22** 2236 (1980).

Chapter 6
Extended Higgs Sectors

The Higgs sector in the Standard Model is of the simplest and most minimal form, containing one isospin doublet of scalar fields and one physical particle, the Higgs boson [1]. In Chapter 2, we have described the phenomenology of this minimal Higgs boson in some detail. However, it must always be kept in mind that the minimal model might not be the correct one. There is no principle that requires the Higgs sector to be of the minimal form. There are many possibilities for extension of the Higgs sector, corresponding to adding further multiplets of scalar fields, which might be singlets, doublets, or higher representations of $SU(2) \times U(1)$.

In fact, many new physics models, proposed to solve problems with the Standard Model or provide missing elements such as dark matter, naturally contain extended Higgs sectors. Among the models proposed to solve the gauge hierarchy problem and provide mechanism for electroweak symmetry breaking are supersymmetry, Little Higgs models, and models such as Gauge-Higgs unification that require new dimensions of space. Each of these models predicts a light Higgs boson similar to the Higgs boson of the Standard Model. In each case, however, this boson is a part of a larger Higgs sector with multiple scalar fields and, in the three cases, the details of the extension are different. Extended Higgs sectors are also introduced to build models for specific phenomena that cannot be explained in the SM, such as baryogenesis, dark matter, and neutrino masses.

Extended Higgs sectors can be searched for at hadron colliders, but often they are difficult to find. Higgs bosons have subdominant, electroweak-scale production cross sections. Their most prominent decay modes can be mimicked by background reactions from top and bottom quarks and other sources. At an e^+e^- collider, on the other hand, extended Higgs bosons have pair-production cross sections that are as substantial as those for other particles with electroweak charges. The comprehensive search for extended Higgs bosons and the precision measurement of the properties of all accessible Higgs particles is thus an important goal for the ILC.

In Section 6.1 below, we give an orientation for models with extended Higgs sectors, defining the sometimes complex notation and clarifying the spectrum of physical Higgs states in various scenarios. In Section 6.2, we summarize the current constraints on these extended Higgs sectors, and the direct searches for extended Higgs bosons that can be carried out at the ILC. In Section 6.3, we discuss the ILC phenomenology of various exotic scenarios for neutrino mass, baryogenesis and dark matter which are relevant to extended Higgs sectors. Conclusions are given in Section. 6.4.

6.1 General description of extended Higgs sectors

The simplest examples of an extended Higgs sector are built by the addition of one $SU(2) \times U(1)$ singlet or one additional $SU(2) \times U(1)$ doublet scalar field. The case of an additional doublet is especially important. Supersymmetry requires distinct Higgs doublets to give mass to the u- and d-type quarks, and so the Minimal Supersymmetric Standard Model (MSSM) contains an extended Higgs sector [2]. In this section, we will describe the structure of these and more complicated Higgs sectors and define the parameters needed for a discussion of the phenomenology of these models.

6.1.1 The Two Higgs Doublet Model

The Two Higgs Doublet Model (THDM) includes two $SU(2) \times U(1)$ scalar doublets with $Y = 1$ [3]. The Higgs doublets can be parameterized as

$$\Phi_i = \begin{bmatrix} w_i^+ \\ \frac{1}{\sqrt{2}}(v_i + h_i + iz_i) \end{bmatrix}, \quad (i = 1, 2). \tag{6.1}$$

The most general Higgs potential is parametrized by three mass parameters and 7 independent quartic coupling constants.

$$\begin{aligned} V = {} & m_1^2|\Phi_1|^2 + m_2^2|\Phi_2|^2 - (m_3^2\Phi_1^\dagger\Phi_2 + h.c.) + \tfrac{1}{2}\lambda_1|\Phi_1|^4 + \tfrac{1}{2}\lambda_2|\Phi_2|^4 + \lambda_3|\Phi_1|^2|\Phi_2|^2 \\ & + \lambda_4|\Phi_1^\dagger\Phi_2|^2 + \tfrac{1}{2}[\lambda_5(\Phi_1^\dagger\Phi_2)^2 + \lambda_6|\Phi_1|^2\Phi_1^\dagger\Phi_2 + \lambda_7|\Phi_2|^2\Phi_1^\dagger\Phi_2 + h.c.]. \end{aligned} \tag{6.2}$$

The Higgs potential in the MSSM is a special case of this potential in which the quartic couplings are related to the $SU(2)$ and $U(1)$ gauge couplings by supersymmetry. The model contains 3 degrees of freedom that are eaten by the $W^\pm$ and Z^0 when their masses are generated through the Higgs mechanism. This leaves over 5 physical Higgs bosons, two CP-even scalars h and H, one CP-odd scalar A, and one pair of charged scalars $H^\pm$. The mass eigenstates are related to the fields in (6.1) by mixng angles α and β according to

$$\begin{aligned} h &= -h_1 \sin\alpha + h_2 \cos\alpha, & H &= h_1 \cos\alpha + h_2 \sin\alpha \\ H^\pm &= w_1^\pm \cos\beta + w_2^\pm \cos\alpha, & A &= z_1 \cos\beta + z_2 \sin\beta, \end{aligned} \tag{6.3}$$

We define h to be the lighter CP-even boson. The angle β yields the parameter $\tan\beta = v_2/v_1$.

The two vacuum expectation values v_1 and v_2 satisfy

$$v_1^2 + v_2^2 = v^2 = (246 \text{ GeV})^2 \ . \tag{6.4}$$

The vector boson coupling constants for the lighter Higgs boson, hZZ and hWW, are given by that of the SM Higgs boson times $\sin(\beta - \alpha)$, while those for HZZ and HWW are proportional to $\cos(\beta - \alpha)$. The scalars h and H thus share the Higgs field vacuum expectation value and share the strength of the coupling of WW and ZZ to scalar fields. The trilinear couplings $H^\pm W^\mp Z$, $H^\pm W^\mp \gamma$, AW^+W^-, AZZ are zero at tree level.

Of the two mass parameters in (6.2), m_1 and m_2 are directly related to v_1 and v_2. The third parameter m_3 does not drive electroweak symmetry breaking and can potentially be much larger. When

$$M^2 \equiv m_3^2/\sin\beta\cos\beta \gg v^2 \ , \tag{6.5}$$

then we approach to the *decoupling limit* where the masses of the added scalar states H, A, and $H^\pm$

Table 6.1. Four possible Z_2 charge assignments that forbid dangerous flavor-changing neutral current effects in the THDM. [5].

	Φ_1	Φ_2	u_R	d_R	ℓ_R	Q_L, L_L
Type I	+	−	−	−	−	+
Type II (MSSM like)	+	−	−	+	+	+
Type X (lepton specific)	+	−	−	−	+	+
Type Y (flipped)	+	−	−	+	−	+

Table 6.2. The mixing factors ξ_X^f in the THDM Higgs interactions given in (6.7) [6].

	ξ_h^u	ξ_h^d	ξ_h^ℓ	ξ_H^u	ξ_H^d	ξ_H^ℓ	ξ_A^u	ξ_A^d	ξ_A^ℓ
Type I	$\frac{\cos\alpha}{\sin\beta}$	$\frac{\cos\alpha}{\sin\beta}$	$\frac{\cos\alpha}{\sin\beta}$	$\frac{\sin\alpha}{\sin\beta}$	$\frac{\sin\alpha}{\sin\beta}$	$\frac{\sin\alpha}{\sin\beta}$	$-\cot\beta$	$\cot\beta$	$\cot\beta$
Type II	$\frac{\cos\alpha}{\sin\beta}$	$-\frac{\sin\alpha}{\cos\beta}$	$-\frac{\sin\alpha}{\cos\beta}$	$\frac{\sin\alpha}{\sin\beta}$	$\frac{\cos\alpha}{\cos\beta}$	$\frac{\cos\alpha}{\cos\beta}$	$-\cot\beta$	$-\tan\beta$	$-\tan\beta$
Type X	$\frac{\cos\alpha}{\sin\beta}$	$\frac{\cos\alpha}{\sin\beta}$	$-\frac{\sin\alpha}{\cos\beta}$	$\frac{\sin\alpha}{\sin\beta}$	$\frac{\sin\alpha}{\sin\beta}$	$\frac{\cos\alpha}{\cos\beta}$	$-\cot\beta$	$\cot\beta$	$-\tan\beta$
Type Y	$\frac{\cos\alpha}{\sin\beta}$	$-\frac{\sin\alpha}{\cos\beta}$	$\frac{\cos\alpha}{\sin\beta}$	$\frac{\sin\alpha}{\sin\beta}$	$\frac{\cos\alpha}{\cos\beta}$	$\frac{\sin\alpha}{\sin\beta}$	$-\cot\beta$	$-\tan\beta$	$\cot\beta$

become much larger than the mass of h:

$$m_h^2 \simeq \lambda_i v^2 \text{ (SM like)}, \qquad m_\phi^2 \sim \lambda_i v^2 + M^2, \text{where } \phi = H, A, \text{and } H^\pm, \tag{6.6}$$

with $\sin(\beta-\alpha) \simeq 1$ [4] . In this case, the phenomenology of h is similar to that of the SM Higgs boson except for small deviations in the Higgs boson couplings. However, it is not necessary that the additional bosons be heavy, and, in this case, there is room for substantial mixing between h and H.

In the THDM, both of the doublets can in principle couple to fermions, and this can lead to dangerous flavor-changing neutral current couplings. A well-known way to suppress these couplings is to impose a softly broken Z_2 symmetry so that only one of the two Higgs doublets gives mass to the u-type quarks, to the d-type quarks, and to the leptons. The various possible assignments lead to four distinct models, displayed in Table 6.1 [5–7]. In the MSSM, supersymmetry requires the Type II assignment, with one doublet giving mass to the u quarks and the other to the d quarks and the charged leptons. In more general models, though, all four possibilities are open. The Yukawa interactions for these models are expressed as

$$\begin{aligned}\mathcal{L}_{THDM}^Y = & -\textstyle\sum_{f=u,d,e}\left(\frac{m_f}{v}\xi_h^f \overline{f} f h + \frac{m_f}{v}\xi_H^f \overline{f} f H + i\frac{m_f}{v}\xi_A^f \overline{f}\gamma_5 f A\right) \\ & - \left[\sqrt{2}V_{ud}\overline{u}\left(\tfrac{m_u}{v}\xi_A^u P_L + \tfrac{m_d}{v}\xi_A^d P_R\right) d\, H^+ + \tfrac{\sqrt{2}m_\ell \xi_A^\ell}{v}\overline{\nu_L} e_R H^+ + h.c.\right],\end{aligned} \tag{6.7}$$

where $P_{L/R}$ are projection operators for left-/right-handed fermions, and the factors ξ_φ^f are listed in Table 6.2.

The decays of the Higgs bosons in the THDM depend on the model chosen for the Yukawa interactions. When $\sin(\beta-\alpha) = 1$ [4], the decay pattern of h is almost the same as that in the Standard Model. However, the decay patterns of H, A, and $H^\pm$ can vary over a large range. Figure 6.1 shows the decay branching ratios of H, A and $H^\pm$ as a function of $\tan\beta$ for the four models, for boson masses of 150 GeV and $\sin(\beta-\alpha) = 1$. The decay pattern of H is typically similar to that of A, but with some important exceptions. In the type I THDM, all fermionic decays, and the gg decay mode, are suppressed at large $\tan\beta$. However, H, but not A, couples to H^+H^-, and this allows for H a significant decay through a scalar loop to $\gamma\gamma$.

In general, the complexity of the H, A, $H^\pm$ decay schemes and in the four possible models make it difficult to determine the underlying model unless these bosons are created through a simple and well-characterized pair-production reaction. Thus, even if these bosons are discovered at the LHC, it

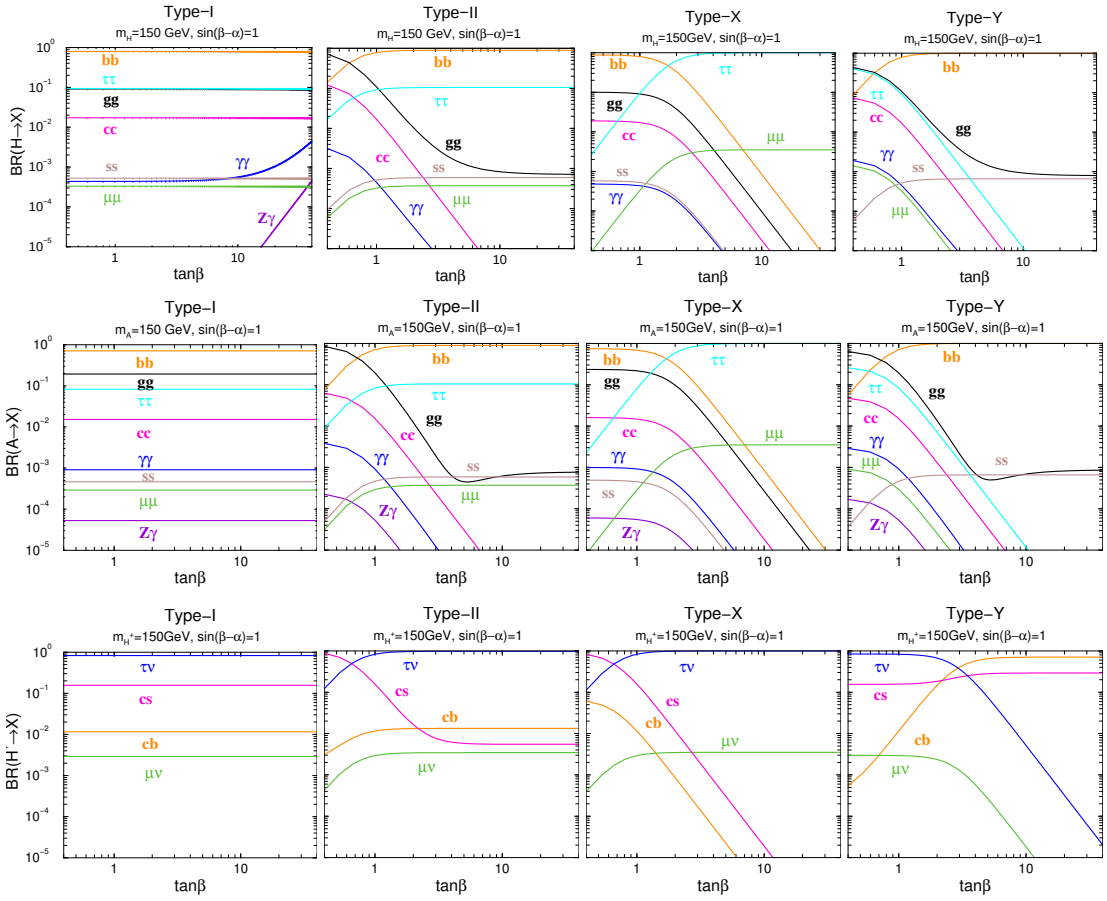

Figure 6.1. Decay branching ratios of H, A and $H^{\pm}$ in the four different types of THDM as a function of $\tan\beta$ for $m_H = m_A = m_{H^{\pm}} = 150$ GeV. The SM-like limit $\sin(\beta-\alpha) = 1$ is taken.

will be important to study them in e^+e^- pair-production at the ILC.

6.1.2 Models with Higgs singlets

Another simple extension of the SM Higgs sector is the addition of a singlet scalar field S with $Y = 0$. Such a singlet field is introduced in new physics models with an extra $U(1)$ gauge symmetry [8], for example, a theory with a $U(1)$ boson coupling to $B - L$ [9]. A neutral singlet scalar field is also introduced in the Next-to-Minimal SUSY Standard Model (NMSSM), along with the second Higgs doublet required in SUSY [10]. Singlet Higgs fields do not couple directly to quarks, leptons or gauge bosons of the SM.

In the model with only one additional neutral singlet scalar field to the SM, we parameterize the SM doublet Φ and S as

$$\Phi = \begin{bmatrix} \varphi^+ \\ \frac{1}{\sqrt{2}}(v + \varphi + i\chi) \end{bmatrix}, \qquad S = \frac{1}{\sqrt{2}}(v_S + \varphi_S + i\chi_S), \tag{6.8}$$

where $v = 246$ GeV, and v_S is the vacuum expectation value of the singlet. The two CP-even mass eigenstates h and H are mixtures of φ and φ_S,

$$h = \varphi\cos\theta - \varphi_S\sin\theta, \qquad H = \varphi\sin\theta + \varphi_S\cos\theta. \tag{6.9}$$

In models with an extra $U(1)$ gauge boson, this boson absorbs the CP-odd component field χ_S. Then the difference from the SM is just one additional CP-even scalar boson H. Models with only added

Higgs singlets contain no physical charged Higgs bosons. All of the SM fields obtain mass from the VEV of the doublet v. Their coupling constants with h and H are obtained by the replacement $\phi_{\rm SM} \to h\cos\theta + H\sin\theta$.

In the decoupling regime $\theta \sim 0$. Then h is SM-like with couplings reduced from their SM values by $\cos\theta \approx 1 - \theta^2/2$. On the other hand, when $\tan\theta \sim \mathcal{O}(1)$, both the h and H behave as SM-like Higgs bosons, sharing the SM couplings to gauge bosons and fermions. If h and H are almost degenerate in mass, the two bosons might appear as a single SM Higgs boson in the LHC experiments. At the ILC, the tagging of the Higgs mass by the Z energy in $e^+e^- \to Z + (h, H)$ could allow the two Higgs bosons to be better separated.

The reduced couplings of h and H result in smaller production cross sections as compared to the SM predictions. Therefore, the mass bounds from the collider experiment can be milder. For example, the LEP experiments exclude the h only to about 110 GeV for $\sin\theta = 1/\sqrt{2}$ while the exclusion in the SM is about 114 GeV [11]. Basso, Moretti and Pruna have surveyed the ILC phenomenology of the Higgs sector in the minimal $B - L$ model [12].

6.1.3 Models with Higgs triplets

We can go on to consider models that add scalar fields in higher representations of $SU(2)$, models with fields with $I = 1, \frac{3}{2}, \ldots$. There are many such models. However, these models are constrained by the requirement that they do not give sizable tree level corrections to the Standard Model relation

$$\rho = \frac{m_W^2}{m_Z^2 \cos^2\theta} = 1 \ . \tag{6.10}$$

When electroweak radiative corrections are included, (6.10) is in excellent agreement with the data, so it is dangerous to add to the model with fields that can modify it. In a general $SU(2) \times U(1)$ model with n scalar multiplets ϕ_i with isospin T_i and hypercharge Y_i, the ρ parameter is given at the tree level by

$$\rho = \frac{\sum_{i=1}^n [T_i(T_i+1) - \frac{1}{4}Y_i^2]v_i^2}{\sum_{i=1}^n \frac{1}{2}Y_i^2 v_i^2}, \tag{6.11}$$

where v_i are vacuum expectation values of ϕ_i. So, singlets and doublets with $Y_i = \pm\frac{1}{2}$ preserve $\rho = 1$, while adding higher representation generally modifies this relation, unless those fields have very small vacuum expectation values [13].

As an example of a model that adds an isospin triplet, we review the case of a Higgs representation with $I = 1$ and $Y = 2$. A vacuum expectation value of this field can produce a Majorana neutrino mass [14].

A model with this triplet field will contain a Higgs doublet Φ in addition to the triplet Δ. The component fields are

$$\Phi = \begin{bmatrix} \varphi^+ \\ \frac{1}{\sqrt{2}}(v_\varphi + \varphi + i\chi) \end{bmatrix}, \qquad \Delta = \begin{bmatrix} \Delta^+/\sqrt{2} & \Delta^{++} \\ \frac{1}{\sqrt{2}}(v_\Delta + \delta + i\eta) & -\Delta^+/\sqrt{2} \end{bmatrix}, \tag{6.12}$$

where v_φ and v_Δ are the vacuum expectation values. The physical scalar states are two CP-even bosons (h and H), a CP-odd boson (A), singly charged pair ($H^\pm$), and a doubly charged pair ($H^{\pm\pm}$). These are related to the original component fields by mixing angles α, β_0 and $\beta_\pm$,

$$\begin{aligned} &h = \varphi\cos\alpha + \delta\sin\alpha, \quad H = -\varphi\sin\alpha + \delta\cos\alpha, \\ &A = -\chi\sin\beta_0 + \eta\cos\beta_0, \quad H^\pm = -\varphi^\pm\sin\beta_\pm + \Delta^\pm\cos\beta_\pm, \quad H^{\pm\pm} = \Delta^{\pm\pm}. \end{aligned} \tag{6.13}$$

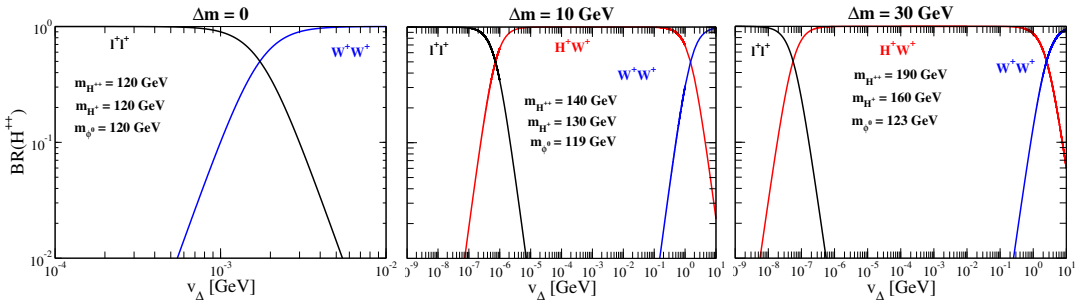

Figure 6.2. Decay branching ratio of H^{++} as a function of v_Δ. Left: $m_{H^{++}}$ is set to be 120 GeV, $\Delta m = 0$. Center: $m_{H^{++}}$ is 140 GeV, $\Delta m = 10$ GeV. Right: $m_{H^{++}}$ is 190 GeV, $\Delta m = 30$ GeV.

We must arrange $v_\Delta \ll v_\varphi$ to preserve $\rho \simeq 1$. This constraint implies the mass relations

$$m_h^2 \simeq 2\lambda_1 v^2, \quad m_{H^{++}}^2 - m_{H^+}^2 \simeq m_{H^+}^2 - m_A^2 \ , \quad \text{and} \quad m_H^2 \simeq m_A^2, \tag{6.14}$$

with $\alpha \ll 1$, $\beta_0 \ll 1$ and $\beta_\pm \ll 1$. Therefore, the model has a Standard Model-like Higgs boson h and additional triplet-like scalar states whose masses become approximately equal in the decoupling limit.

The doubly charged Higgs bosons H^{++} are the most characteristic feature of the model. The requirement that the vacuum expectation value of Δ gives a Majorana neutrino mass requires that this field must be assigned lepton number $L = 2$. Then, if the new Higgs bosons are degenerate, the dominant decays would be to lepton and neutrino pairs. In particular, H^{++} would be expected to decay to $\ell^+\ell^+$. At the LHC, the search for $H^{\pm\pm}$ is underway using this decay mode. The exclusion of the signal implies a lower bound on the mass of H^{++}, $m_{H^{++}} \gtrsim 400$ GeV [15], assuming a 100% branching ratio.

However, this analysis is correct only for a limited parameter region in which the vacuum expectation value of Δ is extremely small, $v_\Delta < 10^{-3}$ GeV. For larger, but still small, values of v_Δ, a small mass splittings between H^+ and H^{++} opens up that allows the decay to take advantage of the much larger coupling to H^+W^+ [16]. In Fig. 6.2, the decay branching ratios for $H^{\pm\pm}$ are shown as a function of v_Δ [17]. For $v_\Delta \sim 1$ GeV, corresponding to mass difference $\Delta m \sim 10$ GeV, the decay into H^+W^+ is dominant for a wide range of v_Δ when $m_{H^{++}} > m_{H^+} > m_{A,H}$. In this case, H^{++} could be identified through its cascade decay. It is also possible to realize the opposite sign of the mass difference. In this case, the H^{++} decays into W^+W^+.

This model gives another illustration that the properties of an extended Higgs boson can be highly sensitive to the parameter choices. In the most favorable cases, discovery is straightforward; other parameter choices, which might be equally or more likely, are more challenging. To work backwards from the data to the underlying parameters, we require a well-understood production mechanism and broad sensitivity to a wide range of final states.

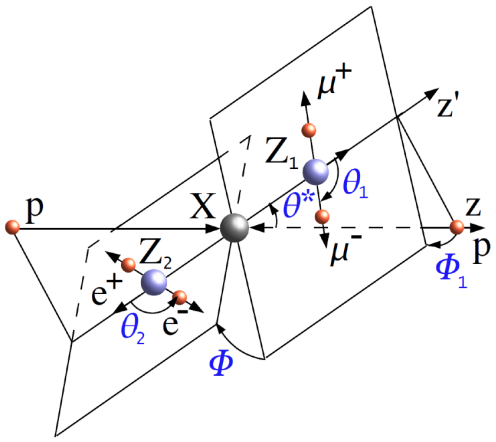

Figure 6.3
Schema of the angular analysis of the the Higgs decay into a pair of Z bosons that decay then into 4 leptons, as used by the CMS experiment [20].

6.2 Extended Higgs bosons searches at the ILC

The discovery of additional Higgs bosons such as H, A, $H^{\pm}$ and $H^{\pm\pm}$ would give direct evidence for extended Higgs sector. As already discussed, there are many possibilities for the decay branching ratios of these particles, illustrated by the various schemes presented in Section 6.2. The ongoing searches at LHC rely on specific production and decay mechanisms that occupy only a part of the complete model parameter space. At the ILC, the extended Higgs bosons are produced in electroweak pair production through cross sections that depend only on the $SU(2) \times U(1)$ quantum numbers and the mixing angles. Thus, the reach of the ILC is typically limited to masses less than $\sqrt{s}/2$, but it is otherwise almost uniform over the parameter space.

6.2.1 Constraints from the LHC experiments

The LHC is imposing several types of constraints in the exploration of the Higgs sector, but certainly the main constraint comes from the discovery of the resonance at 125 GeV by ATLAS [18] and CMS [19]. The resonance appears with particular significance in the decay channels into two γ's and two Z^0 bosons. The exact nature of this new resonance has still to be confirmed. However there are some indications that it could well be the light Higgs neutral boson we have been so long looking for.

CMS has already performed an angular analysis of the channel $pp \to ZZ \to 4$ charged leptons (see Fig. 6.3). This analysis can potentially discriminate between a boson that decays mainly to longitudinally polarized Z bosons, as expected if the boson is a scalar field with a vacuum expectation value, and a boson that decays only to transversely polarized Z bosons, as expected for a 0^- boson and for other non-Higgs hypotheses. At present, the CMS analysis favors the 0^+ SM hypothesis over the 0^- hypothesis by 2.5 σ [20]. This gives hope that, with the full 2012 data set, we might have strong evidence that the resonance is a "Higgs boson".

In the context of extended Higgs models, this resonance might be interpreted as the h or the H, or, if these bosons are within a few GeV of one another, both [21, 22]. The discrimination of these possibilities from the Standard Model will require much better measurements of the relative rates and, eventually, absolute branching ratios, into $\gamma\gamma$, WW, ZZ, $b\bar{b}$ and $\tau^+\tau^-$. The decay mode into τ lepton pairs, in particular, is quite important for many BSM cases [23, 24]. The current situation is consistent with the Standard Model, but the errors leave much room for other possibilities. The resolution of these questions will probably need to wait for the 14 TeV era at the LHC, or for measurements of even higher precision.

Beyond the search channels for a Standard Model Higgs boson, the LHC experiments are exploring additional channels that are specific to extended Higgs bosons. ATLAS and CMS have already performed a number of extended Higgs searches. The published results are only based on the

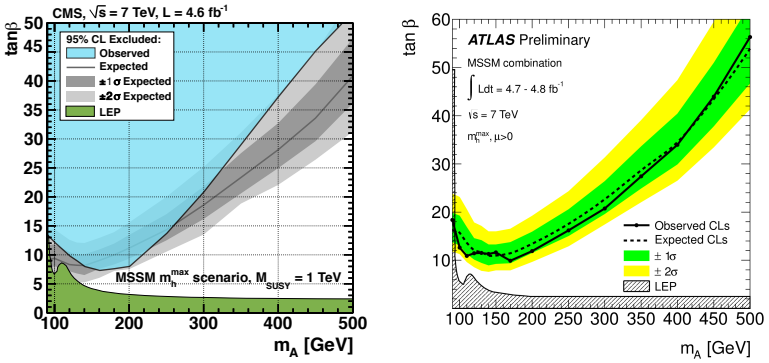

Figure 6.4
Limits on the signature with of extended Higgs particles decaying to two τ leptons, obtained by scanning $\tan\beta$ for each M_A mass hypothesis and taking into account the dependence of M_h and M_H on $\tan\beta$, from Left: from CMS. Right: from ATLAS.

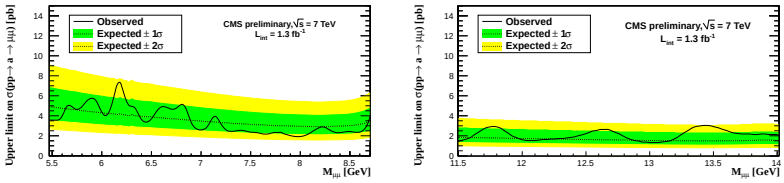

Figure 6.5
CMS search for a low mass Higgs decaying into two muons in a NMSSM scenario with the first 1.3 fb^{-1} of data, from [25].

2011 data. Much more will become soon available by adding the first $5fb^{-1}$ data that are already recorded in 2012. The experiments have scanned a mass range up to 350-400 GeV/c^2 in a variety of interesting processes and BSM scenarios. There is presently no evidence for such new BSM heavy Higgs signals. The current results from the charged Higgs searches at hadron colliders are reported in section 6.2.3.

In the context of MSSM, the neutral Higgs bosons h, H and A are searched for in their decay into two b quarks, two muons or two τ leptons. Doubly charged Higgs boson and Higgs boson in the SM reinterpreted with 4th generation of fermions are also investigated. The resonance at 126 GeV decaying into 2 photons is further reinterpreted in terms of a fermiophobic Higgs scenario. Some of the main present results at LHC on these searches are shown in Fig. 6.4. No significant excess is observed, and limits are set as low as $\tan\beta$ equal to 10. This is already a dramatic improvement compared to the Tevatron results.

The Next-to-Minimal Supersymmetric Standard Model (NMSSM) gives the possibility of a very light CP odd scalar boson that would decay to two muons. Both ATLAS and CMS have searched for a light extended Higgs boson of this type, but so far no signficant excess has been found. Figure 6.5 shows the results obtained by CMS based on 1.3 fb^{-1} of data taken in 2011 [25]. This study demonstrates the potential of the LHC detectors to look for relatively low mass bosons produced as the result of high energy processes.

Other important constraints on extended Higgs bosons come from heavy flavor experiments, notably, meaurements of $b \to s\gamma$ and the process $B_s \to \mu^+\mu^-$ recently observed by LHCb [26]. Unfortunately, though deviations from the Standard Model predictions can clearly indicate a need for new physics, consistency of the Standard Model can result from cancellations among different contributions to loop-induced processes.

These examples, taken from the current early stages of the LHC program, demonstrate the great power that will eventually be available from the LHC in exploring for specific, even quite subtle, signatures of extended Higgs particles. We have argued, though, that this capability needs to be complemented by a broad program of searches based on a precisely understood production mechanism. We wil now describe how that such a program can be carried out at the ILC.

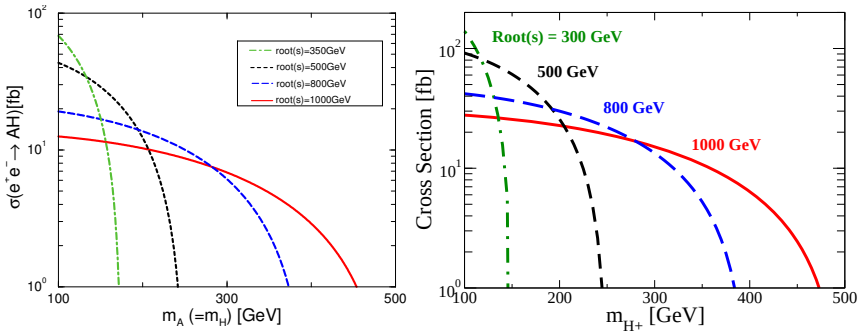

Figure 6.6 Extended Higgs boson production cross sections as a function of the produced boson mass, at CM energies of 350, 500, 800, and 1000 GeV. Left: $e^+e^- \to AH$. Right: $e^+e^- \to H^+H^-$.

6.2.2 Neutral Higgs pair production at ILC

At the ILC, the pair production of extended Higgs bosons $e^+e^- \to AH$ in the THDM case, depends only on the boson masses in the decoupling limit. The production cross sections are shown in Fig. 6.6 for $\sqrt{s} = 350, 500,\ 800$, and 1000 GeV as a function of m_A [27]. The decays of the extended Higgs state are mainly to fermion pairs. Thus, the observation of pair-produced Higgs bosons in various decay channels allows us to determine the type of Yukawa interaction, in the sense of Section 6.1.1, through the measurement of the corresponding branching ratios. For example, in the MSSM, which requires a Type II Higgs structure, the dominant final states for HA production should be $bbbb$ and $bb\tau\tau$, while in the Type X (lepton specific) structure the dominant final state should be $\tau\tau\tau\tau$ for $\tan\beta > 2$. In a Type I Higgs model, the $bbjj$ final states signature is also important in addition to the $bbbb$ and $bb\tau\tau$ signatures, over a wide range of $\tan\beta$ values, while in Type Y (flipped) the $bbbb$ states dominate and the $bb\tau\tau$ and $bbjj$ states are suppressed for $\tan\beta > 2$.

The signals from HA production in the $bbbb$ and $bb\tau\tau$ channels, in the context of the MSSM (Type-II THDM), was carried out in the studies of [28, 29]. A rather detailed detector simulation was performed in [29], including all the SM backgrounds at $\sqrt{s} = 500$, 800 and 1000 GeV. Using a kinematical fit which imposes energy momentum conservation and under the assumed experimental conditions, a statistical accuracy on the Higgs boson mass from 0.1 to 1 GeV is found to be achievable. The topological cross section of $e^+e^- \to HA \to bbbb$ ($e^+e^- \to HA \to \tau\tau bb$) could be determined with a relative precision of 1.5% to 7% (4% to 30%). The width of H and A could also be determined with an accuracy of 20% to 40%, depending on the mass of the Higgs bosons. Figure 6.7 shows, on the left, the $\tau^+\tau^-$ invariant mass obtained by a kinematic fit in $e^+e^- \to HA \to b\bar{b}\tau^+\tau^-$ for $m_A = 140$ GeV and $m_H = 150$ GeV, for $\sqrt{s} = 500$ GeV and 500 fb^{-1} [29].

The $\tau^+\tau^-\tau^+\tau^-$ and $\mu^+\mu^-\tau^+\tau^-$ final states would be dominant for the type X (lepton specific) THDM. When $\sqrt{s} = 500$ GeV, assuming an integrated luminosity of 500 fb^{-1}, one expects to collect 16,000 (18,000) $\tau^+\tau^-\tau^+\tau^-$ events in the type X (type II) THDM, and 110 (60) $\mu^+\mu^-\tau^+\tau^-$ events in the same models, assuming $m_H = m_A = m_{H^\pm} = 130$ GeV, $\sin(\beta-\alpha) = 1$ and $\tan\beta = 10$. These numbers do not change much for $\tan\beta \gtrsim 3$. It is important to recognize that the four-momenta of the τ leptons can be solved by a kinematic fit based on the known center of mass energy and momentum, by applying the collinear approximation to each set of τ lepton decay products [30, 31]. Figure 6.7 shows, on the right, the two dimensional invariant mass distribution of the τ lepton pairs from the neutral Higgs boson decays as obtained with a simulation at 500 GeV in which the masses of the neutral Higgs bosons are taken to be 130 GeV and 170 GeV [32].

Although the associated Higgs production process $e^+e^- \to HA$ is a promising one for testing the properties of the extended Higgs sectors, the kinematic reach is restricted by $m_H + m_A < \sqrt{s}$ and is not available beyond this limit. Above the threshold of the HA production, the associated production processes $t\bar{t}\Phi$, $b\bar{b}\Phi$ and $\tau^+\tau^-\Phi$ ($\Phi = h, H, A$) could be used [33]. In particular, for $b\bar{b}\Phi$

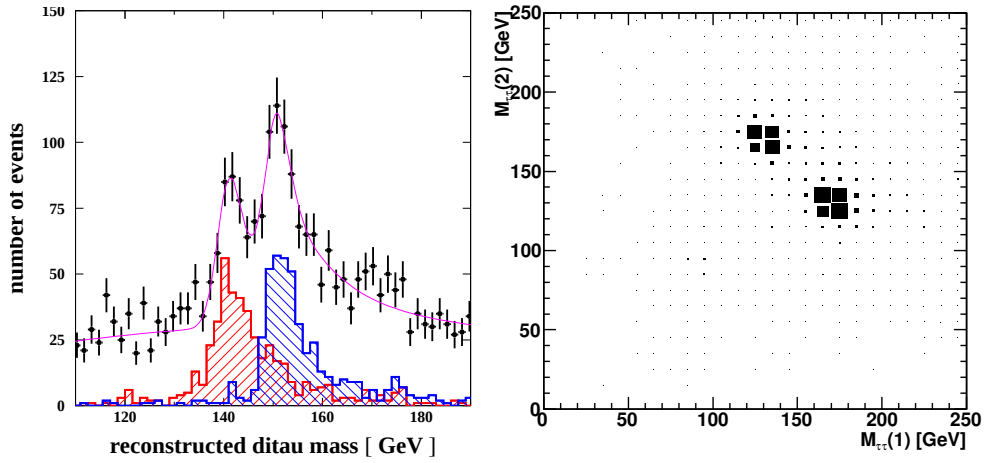

Figure 6.7. Left: Invariant mass reconstruction from the kinematical fit in the process $e^+e^- \to HA \to b\bar{b}\tau^+\tau^-$ in the Type-II (MSSM like) THDM for $m_A = 140$ GeV and $m_H = 150$ GeV at $\sqrt{s} = 500$ GeV and 500 fb^{-1} [29] Right: Two dimensional distribution of ditau invariant mass in $e^+e^- \to HA \to \tau^+\tau^-\tau^+\tau^-$ in the Type X (lepton specific) THDM for $m_A = 170$ GeV and $m_H = 130$ GeV for $\sqrt{s} = 500$ GeV and 500 fb^{-1} [32].

and $\tau^+\tau^-\Phi$, the mass reach is extended almost up to the collision energy. The cross sections for these processes are proportional to the Yukawa interaction, so they directly depend on the type of Yukawa coupling in the THDM structure. In MSSM or the Type II THDM (Type I THDM), these processes are enhanced (suppressed) for large $\tan\beta$ values. In Type X THDM, only the $\tau^+\tau^-H/A$ channels could be significant while only $b\bar{b}H/A$ channels would be important in Type I and Type Y THDMs. These reactions can then be used to discriminate the type of the Yukawa interaction.

6.2.3 Charged Higgs boson production

The charged Higgs bosons $H^\pm$ are a clear signature for the extended Higgs sectors. They appear in most of the models except for those with only additional neutral singlets. Particular models imply constraints between the charged and neutral Higgs boson masses. In particular, in the MSSM, the mass $m_{H^\pm}$ is related to m_A by $m_{H^\pm} = (m_A^2 + m_W^2)^{1/2}$ at the leading order. The precise measurement of the mass is very important in order to distinguish the MSSM from the other models, especially if the SUSY particles are rather heavy.

The direct lower bounds on $m_{H^\pm}$ come from LEP. The absolute lower bound is obtained as 79.3 GeV by ALEPH, and assuming the type II THDM, the bounds are 87.8 GeV for $\tan\beta \gg 1$ using the decay $\tau\nu$ mode, and 80.4 for relatively low $\tan\beta$ values. Using the characteristic relation in the MSSM, $m_{H^\pm} = (m_A^2 + m_W^2)^{1/2}$ with the absolute bounds $m_A > 92$ GeV, one obtains $m_{H^\pm} > 122$ GeV.

It is well known that $m_{H^\pm}$ in the Type II (and Type Y) THDM is stringently constrained by the precision measurements of the radiative decay of $B \to X_s\gamma$ by Belle, BABAR and CLEO. In these types of THDMs the loop contributions of $W^\pm$ and $H^\pm$ are always constructive, while this it not the case in the Type I and Type X. Consequently, a stringent lower bound on $m_{H^\pm}$ is obtained in the Type II (and Type Y); i.e., 295 GeV $< m_{H^\pm}$ [34], while $m_{H^\pm} \sim 100$ GeV is not excluded unless $\tan\beta < 2$ in Type Y (Type X). The decay $B \to \tau\nu$ also can be used to constrain the charged Higgs parameters, being sensitive to $\tan\beta^2/m_{H^\pm}^2$ in the Type II THDM. The data already exclude $m_{H^\pm} < 300$ (1100) GeV for $\tan\beta > 40$ (100) at the 95% CL [35]. Similar but milder constraint on $m_{H^\pm}$ comes from tau leptonic decays in the Type II and Type X THDM: $m_{H^\pm} \sim 100$ GeV is excluded for $\tan\beta > 60$ in both models. These bounds can be relaxed in the MSSM through cancellation with loop diagrams involving supersymmetric partners.

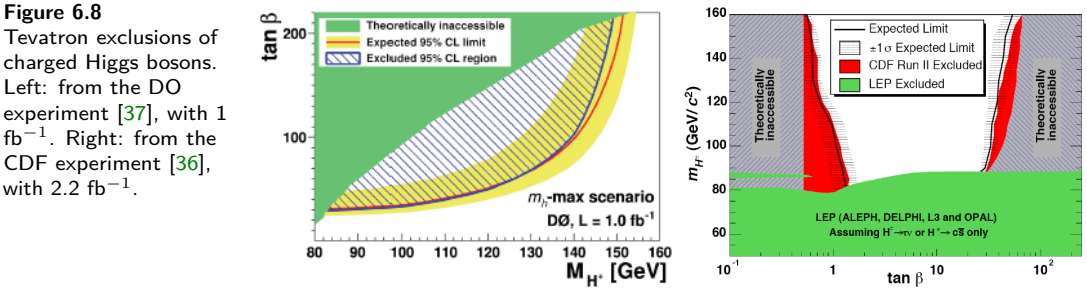

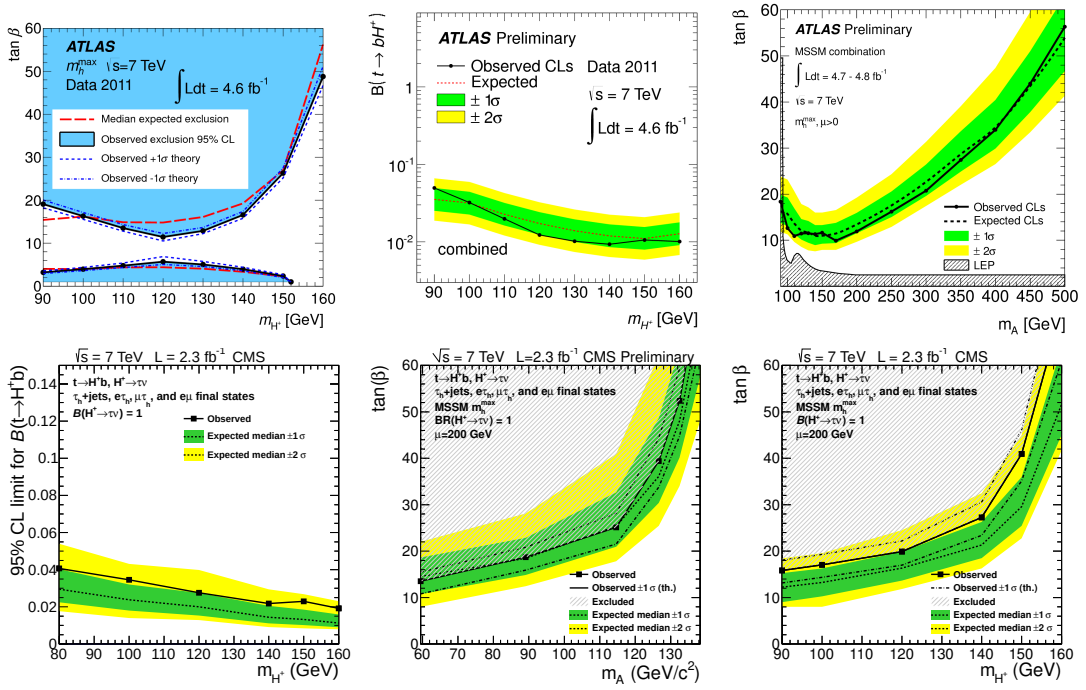

Figure 6.8
Tevatron exclusions of charged Higgs bosons. Left: from the DO experiment [37], with 1 fb^{-1}. Right: from the CDF experiment [36], with 2.2 fb^{-1}.

Figure 6.9. Top: Charged Higgs searches results from the ATLAS experiment at the LHC, based on only 4.6 fb^{-1} of data [38]. Bottom: Charged Higgs searches results from the CMS experiment at the LHC, based on only 2.3 fb^{-1} of data [39].

If a charged Higgs boson is lighter than the top quark, the decay $t \to H^+b$ can compete with the SM decay $t \to W^+b$. Both the Tevatron and the LHC experiments have searched for this process.

The Tevatron analyses look for top quark decays to H^+b in which the charged Higgs decays to $c\bar{s}$ or $\tau\nu$ [36, 37]. The results of these searches are shown in Fig. 6.8 as a function of $\tan\beta$ over a charged Higgs mass range between 90 and 160 GeV. In the case of the charged Higgs decay into a τ lepton, the search is carried out by measuring the branching ratio of the top into a τ lepton and by looking for a τ excess with respect to lepton universality. This measurement is effective for $\tan\beta > 1$. The search for the decay into $c\bar{s}$ is carried out by looking for a second bump in the two jet mass distribution of the events. This is effective for $\tan\beta < 1$.

The LHC experiments look for three possible final state signatures of a top pair production with a charged Higgs decay on one side and a standard Wb decay on the other side. The three modes are lepton + jets, with the lepton coming from τ decay, τ + lepton, with the lepton coming from W decay, and τ + jets, with the standard top decay purely hadronic. The results obtained by ATLAS, based only on the 2011 data [38], are shown in the top line of Fig. 6.9. No significant excess is observed, thus leaving very little room for a light charged Higgs with a mass below the top mass. Similarly, CMS, in an analysis with 2011 data corresponding to only to 2.3 fb^{-1} of the recorded 2011 luminosity [39], obtains an upper limit on BR($t \to H^+b$) that excludes a wide region of large $\tan\beta$ in

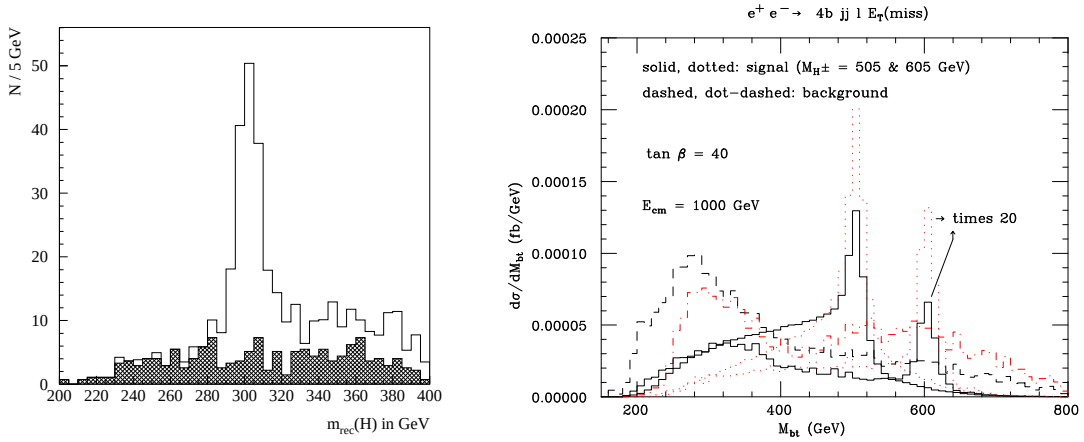

Figure 6.10. Left: Fitted charged Higgs boson mass in $H^+H^- \to (t\bar{b})(\bar{t}b)$ in the MSSM, with $m_{H^\pm} = 300$ GeV, measured at the ILC at CM energy 800 GeV with 1 ab^{-1} of data. The background is shown by the dark histogram [41]. Right: Differential distribution of the reconstructed Higgs mass for the signal $e^+e^- \to b\bar{t}H^+ + t\bar{b}H^- \to t\bar{t}b\bar{b}$ and the background $e^+e^- \to t\bar{t}g^* \to t\bar{t}b\bar{b}$ in the MSSM or the Type II THDM [42].

the MSSM parameter space for $M_{H^+}/M_A > M_{\rm top}$. This is shown in the second line of Fig. 6.9.

At the ILC, charged Higgs bosons are produced in pairs in $e^+e^- \to H^+H^-$ [40]. The cross section is a function only of $m_{H^\pm}$ and is independent of the type of Yukawa interaction in the THDM. Therefore, as in the case of the HA production, the study of the final state channels can be used to determine the type of Yukawa interaction. When $m_{H^\pm} > m_t + m_b$, the main decay mode is tb in Type I, II and Y, while in Type X the main decay mode is $\tau\nu$ for $\tan\beta > 2$. When $H^\pm$ cannot decay into tb, the main decay mode is $\tau\nu$ except in Type Y for large $\tan\beta$ values. For $m_{H^\pm} < m_t - m_b$, the charged Higgs boson can also be studied via the decay of top quarks $t \to bH^\pm$ in THDMs except in Type X THDM case with $\tan\beta > 2$.

In the MSSM, a detailed simulation study of this reaction has been performed for the final state $e^+e^- \to H^+H^- \to t\bar{b}\bar{t}b$ for $m_{H^\pm} = 300$ GeV at $\sqrt{s} = 800$ GeV [41]. The final states is 4 b-jets with 4 non-b-tagged jets. Assuming an integrated luminosity of 1 ab^{-1}, a mass resolution of approximately 1.5% can be achieved (Figure 6.10 (left)). The decay mode $tbtb$ can also be used to determine $\tan\beta$, especially for relatively small values, $\tan\beta < 5$), where the production rate of the signal strongly depends on this parameter.

The pair production is kinematically limited to relatively light charged Higgs bosons with $m_{H^\pm} < \sqrt{s}/2$. When $m_{H^\pm} > \sqrt{s}/2$, one can make use of the single production processes $e^+e^- \to t\bar{b}H^+$, $e^+e^- \to \tau\bar{\nu}H^+$, $e^+e^- \to W^-H^+$, $e^+e^- \to H^+e^-\nu$ and their charge conjugates. The cross sections for the first two of these processes are directly proportional to the square of the Yukawa coupling constants. The others are one-loop induced. Apart from the pair production rate, these single production processes strongly depend on the type of Yukawa interaction in the THDM structure. In general, their rates are small and quickly suppressed for larger values of $m_{H^\pm}$. They can be used only for limited parameter regions where $m_H^\pm$ is just above the threshold for the pair production with very large or low $\tan\beta$ values.

In [42], a simulation study for the process $e^+e^- \to t\bar{b}H^- + b\bar{t}H^+ \to 4b + jj + \ell + p_T^{\rm miss}$ ($\ell = e$, μ) has been done for $m_{H^\pm}$ just above the pair production threshold $m_{H^\pm} \simeq \sqrt{s}/2$. It is shown that this process provides a significant signal of $H^\pm$ in a relatively small region just above $\sqrt{s}/2$, for very large or very small values of $\tan\beta$, assuming a high b-tagging efficiency. The reconstructed H^+ mass distribution is shown in the right-hand side of Fig. 6.10.

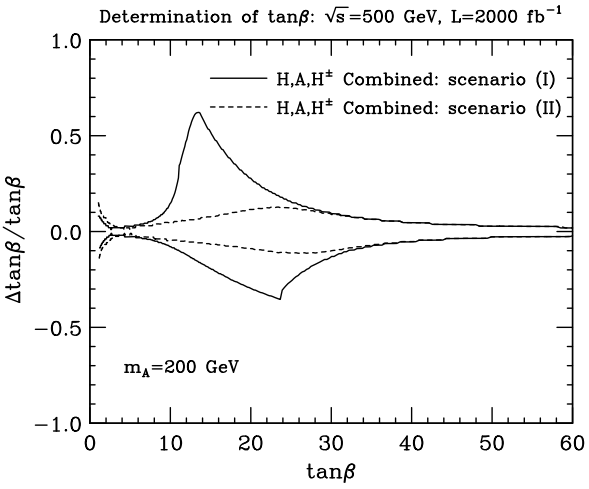

Figure 6.11
Estimates of the 1 σ statistical upper and lower bounds on $\tan\beta$ from ILC measurements, for an MSSM model with $m_{H^\pm} \sim m_A = 200$ GeV, assuming $\sqrt{s} = 500$ GeV and 2000 fb^{-1} of data, from [43]. The quantity plotted is the relative error, $\Delta\tan\beta/\tan\beta$.

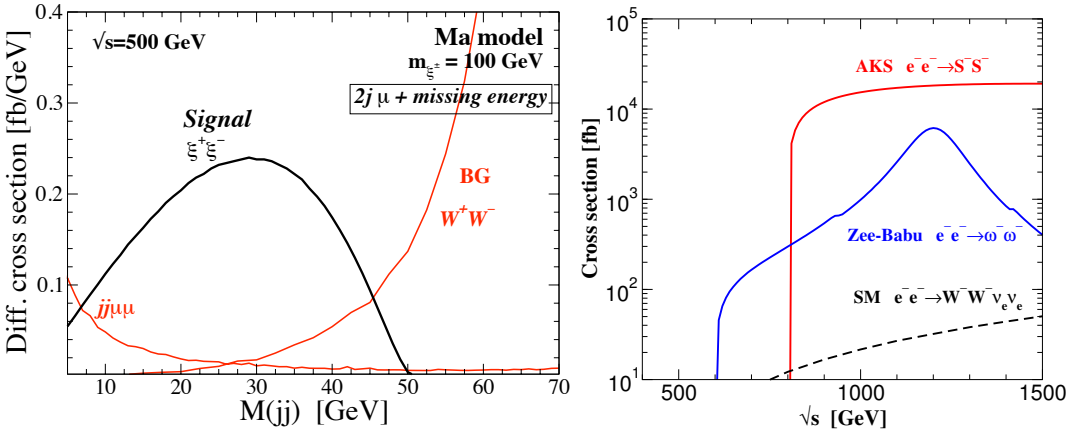

Figure 6.12. Left: The jet invariant mass distributions of the signal and background in the Ma model at $\sqrt{s} = 500$ GeV. The signal process is $e^+e^- \to \xi^+\xi^- \to jj\mu\nu\xi_r^0\xi_r^0$, with $m_{\xi^\pm} = 100$ GeV. Right: The cross sections of like-sign charged Higgs pair productions in the Zee-Babu model ($\omega^-\omega^-$) and in the AKS model (S^-S^-), shown as a function of the collision energy $\sqrt{s}$ [44].

6.2.4 Measurement of $\tan\beta$

The ILC measurements on charged and neutral extended Higgs bosons would be able to precisely determine $\tan\beta$, the most important parameter in the extended Higgs sector with two Higgs doublet fields. In Ref. [43], the sensitivity to $\tan\beta$ is studied by combining the measurements of production processes, branching ratios and decay widths of heavy Higgs bosons H, A and $H^\pm$. The study is done in the context of the MSSM Type II scenario. In the case of $m_A = 200$ GeV with $\sqrt{s} = 500$ GeV and 2 ab^{-1}, the sensitivity is evaluated by using a large variety of complementary methods such as the production rates of $e^+e^- \to HA \to b\bar{b}b\bar{b}$ and $e^+e^- \to H^+H^- \to t\bar{b}\bar{t}b$, which provide a good sensitivity to $\tan\beta$ for relatively low $\tan\beta$, and the rate of $e^+e^- \to b\bar{b}A$, $b\bar{b}H \to b\bar{b}b\bar{b}$ and the measurement of the total widths of H, A and $H^\pm$, which become important for large $\tan\beta$ values. For intermediate $\tan\beta$ values, the sensitivity is rather worse for the scenario (I) where heavy Higgs bosons only decay into the SM particles but it is much better for the scenario (II) where they can decay into superpartner particles via $H^\pm \to \tilde{\chi}^\pm\tilde{\chi}^0$ and similar processes. For $3 < \tan\beta < 5$, where the LHC does not have good sensitivity to extended Higgs bosons, the ILC can measure $\tan\beta$ quite accurately. The combined expected errors on $\tan\beta$ is shown in Figure 6.11. For low $\tan\beta$ regime, a good sensitivity (a few %) to $\Delta\tan\beta/\tan\beta$ can be achieved, while for $10 < \tan\beta < 30$ the accuracy would be 10–30%.

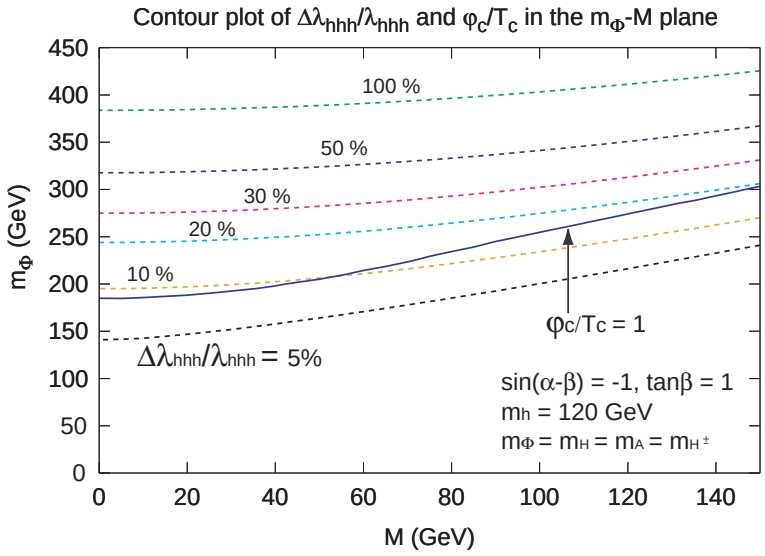

Figure 6.13. The region of strong first order phase transition ($\varphi_c/T_c > 1$) required for successful electroweak baryogenesis, shown as a contour plot of the deviation in the triple Higgs boson coupling from the SM prediction [51]. In this plot, m_Φ represents the degenerate mass of H, A and $H^\pm$. The quantity M is defined in (6.5).

6.3 Exotic Higgs bosons

Various exotic possibilities for the extended Higgs sector are motivated by other challenging problems of particle physics. We have little direct insight from experiment into the mechanisms that lead to neutrino masses, baryogenesis, and dark matter. The answers to each of these questions might arise in an extended Higgs boson sector. Models that address these questions have striking implications for extended Higgs processes that might be observed at the ILC.

We have already pointed out that neutrino masses might be associated with the addition to the Standard Model of a triplet Higgs boson multiplet. These models, described in Section 6.1.3, lead to novel reactions at the ILC, including H^{++} pair production to modes that are very difficult to discover at the LHC. For example, for $m_{H^{++}} > m_{H^+} > m_{A,H}$ with the mass difference of $O(10)$ GeV and $v_\Delta \sim 10^{-5}$-10^{-3} GeV, the main decay modes are $H^{\pm\pm} \to H^\pm W^\pm$, $H^\pm \to W^+ H$ and $W^\pm A$, and $H, A \to \nu\,\overline{\nu}$ [16]. In this case, it is challenging to measure the signal at the LHC [17], but the ILC may be able to study it via $e^+e^- \to H^{++}H^{--} \to \ell^+\ell^+ jjjj\nu\nu\nu\nu$ if the background is reduced sufficiently. The cross section of $H^{++}H^{--}$ is about 100 fb for $m_{H^\pm\pm} = 200$ GeV, which implies that of the final state with a same sign dilepton signature with jets and missing energies can be around 10 fb, including the charge conjugated final state.

An alternative scenario for neutrino masses is based on radiative generation of neutrino masses by an extension of the Higgs sector [45–47]. The source of lepton number violation in these models is a coupling in the extended Higgs sector or the Majorana masses of Z_2-odd right-handed neutrinos. The ILC can test these models by measuring characteristic extra scalars. For example, in the Ma model [46], where neutrino masses are generated at the one-loop level by the Z_2 odd scalars and right handed neutrinos, the Z_2 odd scalar doublets $(\xi^+, \xi^0)^T$ would be observed at the ILC in a jets plus leptons final state, $e^+e^- \to \xi^+\xi^- \to jj\mu\nu\xi_r^0\xi_r^0$. The left side of Figure 6.12 shows the characteristic 2-jet mass distribution in this reaction. A striking test of these models would be the observation of double like-sign Higgs production in e^-e^- collisions. The cross sections for this process in the Zee-Babu model [45] and the Aoki-Kanemura-Seto model [47] are shown in the right side Fig. 6.12.

Among the various scenarios for baryogenesis, electroweak baryogenesis [48] is attractive because of its testability in collider experiments. The parameter region for electroweak baryogenesis in the

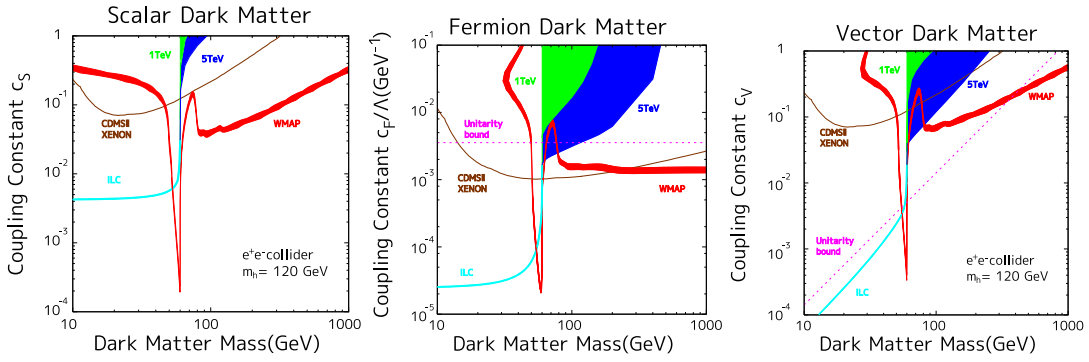

Figure 6.14. Sensitivities to detect the signal of scalar, fermionic, and vector dark matter signal at the ILC and CLIC, from [55]. The parameter regions with $N_S/\sqrt{N_S+N_B} > 5$ are shown in green for an e^+e^- collider with CM energy 1 TeV and in blue for an e^+e^- collider with CM energy and 5 TeV. In both cases, 1 ab^{-1} of data is assumed, with $m_h = 120$ GeV. Constraints on direct detection experiments and the tree level unitarity limit for dark matter are also shown.

SM is already excluded. However, electroweak baryogenesis is possible within the THDM [49], which allows additional CP violating phases and a sufficiently strong 1st order electroweak phase transition. This scenario is compatible with a mass of 125 GeV for the h boson by making use of loop effects of extra Higgs bosons. One of the interesting phenomenological predictions for such a scenario is a large quantum effect on the triple Higgs boson coupling [50, 51]. The requirement of sufficiently strong 1st order phase transition results in a large deviation in the triple Higgs boson coupling as seen in Fig. 6.13. The predicted effect would be clearly seen in the triple Higgs boson measurements described in Section 2.6.3. Electroweak baryogenesis will be discussed further in Section 8.1.

Dark matter requires a new stable particle with mass at the weak interaction scale. Though models involving supersymmetry and extra dimensions are more fashionable, there is no reason why this particle cannot come from an extended Higgs sector. The dark matter particle can be made stable by a Z_2 or higher discrete symmetry of this sector. Models realizing this scenario are given in [52–54].

An important phenomenological prediction of these scenarios is the invisible decay $h \to DD$ of the SM like Higgs boson in to a dark matter pair, if this decay is kinematically allowed. At the linear collider, these invisible decays can be well measured via $e^+e^- \to Zh$, as we have discussed in Section 2.4.3. The case $m_h < 2m_D$, where the above decay mode is not open, can be studied in the ZZ fusion process. Nabeshima has analyzed the LHC and linear collider prospects for the study of this reaction as shown in Fig. 6.14. The dark matter consistent with the WMAP data would be tested at the ILC [55].

6.4 Summary

The Higgs sector is the window for new physics beyond the Standard Model. There is no reason to restrict this sector to the SM Higgs. There are several important theoretical frameworks that predict an enriched Higgs sector. These extended Higgs sector possibilities are very important to explore not only for clarifying the nature of the electroweak symmetry breaking but also for investigating more general schemes for physics beyond the Standard Model. The ILC brings important capabilities to this study.

First, the ILC offers increased potential for discovery. The LHC experiments have a strong potential for discovery if an extended Higgs sector; they will be able to cover a wide region in the parameter space including the possibility to reach relatively high masses. But the ILC covers all possibilities for pair-production of extended Higgs bosons uniformly up to the kinematic limit. This adds important capability for charged Higgs bosons and in the low $\tan\beta$ region that hadron colliders have difficulty in reaching.

Second, the ILC offers a program of comprehensive precision measurements. To understand the coupling scheme of extended Higgs bosons, we need measurements of rates to a variety of channels with a production cross section that is precisely known as a function of the boson masses. Electroweak pair production at the ILC provides just this setting.

Finally, the ILC has great power to discriminate between possible theoretical frameworks. We have emphasized that the phenomenology of extended Higgs models can be complex, with several new parameters and mixing angles, in each of many possible theoretical schemes. The experiments offered by the ILC provide a level of definiteness of interpretation that are not provided by hadron collider measurements of individual reaction rates.

The possibility of an extended Higgs sector is a key topic for models of physics beyond the Standard Model. In order to advance into this unknown field and to disentangle the many present proposed theoretical frameworks, it is essential to have complementary machines for comparing and combining their results. ILC is essential to LHC and vice and versa.

Bibliography

[1] A. Djouadi, Phys. Rept. **457**, 1 (2008) [hep-ph/0503172].

[2] A. Djouadi, Phys. Rept. **459**, 1 (2008) [hep-ph/0503173].

[3] G. C. Branco, P. M. Ferreira, L. Lavoura, M. N. Rebelo, M. Sher and J. P. Silva, Phys. Rept. **516**, 1 (2012) [arXiv:1106.0034 [hep-ph]].

[4] J. F. Gunion and H. E. Haber, Phys. Rev. D **67**, 075019 (2003) [hep-ph/0207010].

[5] V. D. Barger, J. L. Hewett and R. J. N. Phillips, Phys. Rev. D **41**, 3421 (1990).

[6] M. Aoki, S. Kanemura, K. Tsumura and K. Yagyu, Phys. Rev. D **80**, 015017 (2009) [arXiv:0902.4665 [hep-ph]].

[7] S. Su and B. Thomas, Phys. Rev. D **79**, 095014 (2009) [arXiv:0903.0667 [hep-ph]]; H. E. Logan and D. MacLennan, Phys. Rev. D **79**, 115022 (2009) [arXiv:0903.2246 [hep-ph]].

[8] R. Schabinger and J. D. Wells, Phys. Rev. D **72**, 093007 (2005) [hep-ph/0509209].

[9] S. Khalil, J. Phys. G G **35**, 055001 (2008) [hep-ph/0611205].

[10] U. Ellwanger, C. Hugonie and A. M. Teixeira, Phys. Rept. **496**, 1 (2010) [arXiv:0910.1785 [hep-ph]].

[11] R. Barate *et al.* [LEP Working Group for Higgs boson searches and ALEPH and DELPHI and L3 and OPAL Collaborations], Phys. Lett. B **565**, 61 (2003) [hep-ex/0306033].

[12] L. Basso, S. Moretti and G. M. Pruna, Eur. Phys. J. C **71**, 1724 (2011) [arXiv:1012.0167 [hep-ph]].

[13] Specific exceptions are known; these are reviewed in I. Low and J. Lykken, JHEP **1010**, 053 (2010) [arXiv:1005.0872 [hep-ph]].

[14] R. N. Mohapatra and G. Senjanovic, Phys. Rev. D **23**. 165 (1981).

[15] G. Aad et. al, [ATLAS Collaboration], Phys. Rev. D **85**, 032004 (2012); CMS Collaboration, *Report Number* CMS-PAS-HIG-12-005.

[16] P. Fileviez Perez, T. Han, G. -y. Huang, T. Li and K. Wang, Phys. Rev. D **78**, 015018 (2008) [arXiv:0805.3536 [hep-ph]].

[17] M. Aoki, S. Kanemura and K. Yagyu, Phys. Rev. D **85**, 055007 (2012) [arXiv:1110.4625 [hep-ph]].

[18] G. Aad *et al.* [ATLAS Collaboration], Phys. Lett. B **716**, 1 (2012) [arXiv:1207.7214 [hep-ex]].

[19] S. Chatrchyan *et al.* [CMS Collaboration], Phys. Lett. B **716**, 30 (2012) [arXiv:1207.7235 [hep-ex]].

[20] CMS Collaboration, Physics Analysis Summary CMS-PAS-HIG-12-041 (2012).

[21] J. F. Gunion, Y. Jiang and S. Kraml, Phys. Rev. D **86**, 071702 (2012) [arXiv:1207.1545 [hep-ph]].

[22] P. M. Ferreira, H. E. Haber, R. Santos and J. P. Silva, arXiv:1211.3131 [hep-ph].

[23] ATLAS Collaboration, ATLAS-CONF-2012-160 (2012).

[24] CMS Collaboration, Physics Analysis Summary CMS-PAS-HIG-12-043 (2012).

[25] The CMS Collaboration, CERN-PH-EP-2012-176; HEP-EX 1206.6326.

[26] R. Aaij *et al.* [LHCb Collaboration], arXiv:1211.2674 [hep-ex].

[27] J. F. Gunion, et al., Phys. Rev. D **38**, 3444 (1988); A. Djouadi, J. Kalinowski and P. M. Zerwas, Z. Phys. C **57**, 569 (1993).

[28] J. A. Aguilar-Saavedra *et al.* [ECFA/DESY LC Physics Working Group Collaboration], hep-ph/0106315.

[29] K. Desch, T. Klimkovich, T. Kuhl and A. Raspereza, hep-ph/0406229.

[30] S. Schael *et al.* [LEP Working Group for Higgs boson searches and ALEPH and DELPHI and L3 and OPAL Collaborations], Eur. Phys. J. C **47**, 547 (2006). [arXiv:hep-ex/0602042].

[31] J. Abdallah *et al.* [DELPHI Collaboration], Phys. Lett. B **552**, 127 (2003). [hep-ex/0303026].

[32] K. Tsumura, presentation at the KILC12 workshop (2012).

[33] A. Djouadi, K. Kalinowski, P. M. Zerwas, Modern Phys. Lett. A **7**, 1765 (1992); A. Djouadi, K. Kalinowski, P. M. Zerwas, Z. Phys. C **54**, 255 (1992).

[34] M. Misiak, H. M. Asatrian, K. Bieri, M. Czakon, A. Czarnecki, T. Ewerth, A. Ferroglia and P. Gambino *et al.*, Phys. Rev. Lett. **98**, 022002 (2007) [hep-ph/0609232].

[35] M. Rozanska, PoS CHARGED **2010**, 005 (2010).

[36] A. Abulencia *et al.* [CDF Collaboration], Phys. Rev. Lett. **96**, 042003 (2006) [hep-ex/0510065].

[37] V. M. Abazov *et al.* [D0 Collaboration], Phys. Lett. B **682**, 278 (2009) [arXiv:0908.1811 [hep-ex]].

[38] G. Aad *et al.* [ATLAS Collaboration], JHEP **1206**, 039 (2012) [arXiv:1204.2760 [hep-ex]].

[39] S. Chatrchyan *et al.* [CMS Collaboration], JHEP **1207**, 143 (2012) [arXiv:1205.5736 [hep-ex]].

[40] S. Komamiya, Phys. Rev. D **38**, 2158 (1988).

[41] M. Battaglia, A. Ferrari, A. Kiiskinen and T. Maki, eConf C **010630**, E3017 (2001) [hep-ex/0112015].

[42] S. Moretti, Eur. Phys. J. C **34**, 157 (2004) [hep-ph/0306297].

[43] J. F. Gunion, T. Han, J. Jiang and A. Sopczak, Phys. Lett. B **565**, 42 (2003) [hep-ph/0212151].

[44] M. Aoki and S. Kanemura, Phys. Lett. B **689**, 28 (2010) [arXiv:1001.0092 [hep-ph]].

[45] A. Zee, Nucl. Phys. B **264**, 99 (1986); K. S. Babu, Phys. Lett. B **203**, 132 (1988).

[46] E. Ma, Phys. Rev. D **73**, 077301 (2006) [hep-ph/0601225].

[47] M. Aoki, S. Kanemura and O. Seto, Phys. Rev. Lett. **102**, 051805 (2009) [arXiv:0807.0361 [hep-ph]].

[48] V. A. Kuzmin, V. A. Rubakov, M. E. Shaposhnikov, Phys. Lett. **B155** (1985) 36.

[49] L. Fromme, S. J. Huber and M. Seniuch, JHEP **0611** (2006) 038; A. Kozhushko, V. Skalozub, Ukr. J. Phys. **56** (2011) 431-442.

[50] C. Grojean, G. Servant and J. D. Wells, Phys. Rev. D **71**, 036001 (2005) [hep-ph/0407019].

[51] S. Kanemura, Y. Okada and E. Senaha, Phys. Lett. B **606** (2005) 361.

[52] J. McDonald, Phys. Rev. D **50**, 3637 (1994); C. P. Burgess, M. Pospelov and T. ter Veldhuis, Nucl. Phys. B **619**, 709 (2001).

[53] For a review, see the following and the references therein: G. Jungman, M. Kamionkowski and K. Griest, Phys. Rept. **267**, 195 (1996); G. Bertone, D. Hooper and J. Silk, Phys. Rept. **405**, 279 (2005).

[54] For a revew, see: M. Perelstein, Prog. Part. Nucl. Phys. **58**, 247 (2007).

[55] T. Nabeshima, arXiv:1202.2673 [hep-ph].

Chapter 7
Supersymmetry

In this Chapter, we discuss the opportunities the ILC provides for the detailed analysis of new sectors of particles by direct spectroscopy, taking Supersymmetry as perhaps the best studied example. The key assets of a Linear Collider, namely its clean environment, the flavour democracy of the electroweak interaction, the tunable center-of-mass energy and the adjustable beam polarisation offer unique potential which is in every sense complementary to the LHC. These unique features of a linear e^+e^- collider allow for high precision studies of any new particles which might be discovered by the LHC. Perhaps more importantly, they allow for discovery of a variety of new matter states which can be produced at LHC, but which would lie hopelessly buried beneath formidable QCD backgrounds, and inaccessible to discovery.

Supersymmetry has long been considered a strong point of the case for the ILC. It has been known for a long time that the ILC has the ability to make precise measurements, not only of supersymmetry particle masses, but also of the underlying fundamental parameters of the model [1]. The precision measurement of masses is not degraded even in the presence of cascade decays of sparticles which are the norm in many models [2]. The ability of ILC measurements to complement and extend the information we will obtain on supersymmetric particles from the LHC has been studied explicitly in many examples [3, 4]. However, the first results from the LHC have shifted the ground under the theory of supersymmetry, ruling out many of the benchmark models and changing our perspective on what regions of the model space are the most relevant. In this Chapter, we present a new discussion of supersymmetry at the ILC relevant to the current LHC era. We will review the continued importance of supersymmetry as a principle for physics beyond the Standard Model. We will then discuss the classes of supersymmetry models that remain consistent with the LHC data and the particular role that the ILC will have in the exploration of new particles in these models.

Following an introduction, in 7.2 we will lay the basis for our discussion of the experimental capabilities of the ILC by summarizing the *recent change of paradigm* from very constrained models to considerations of naturalness and phenomenological approaches. In section 7.3 we continue with a brief dicussion of the state of direct and indirect constraints on SUSY (circa summer 2012) and it's implications for the ILC. As an illustration of these ideas and as guideline for the experimental discussion, we continue in section 7.4 by introducing two example scenarios compatible with current knowledge, but featuring very different phenomenology. The main part of this section, section 7.5 finally highlights possible key measurements for a variety of new particles, including remarks on model discrimination and parameter determination.

7.1 Introduction

While no direct evidence for the existence of non-Standard Model particles has emerged so far, there are many indications that the Standard Model (SM) is not valid up to the Planck scale. Among these, the most well-known is the gauge hierarchy problem, the instability of the weak scale against quantum corrections to fundamental scalar fields. Solutions to this problem require new particles to appear at or around the weak scale. Additional problems arise from cosmology. The SM does not contain any candidate particles to constitute the needed cold dark matter (CDM). It also lacks a sufficient source of CP violation needed to explain baryogenesis. The SM is not sufficient as a part of a complete theory of nature at very small distance scales because the SM gauge couplings do not unify when extrapolated to high energies, and because the SM has no clear way to incorporate quantum gravity.

One approach which has the potential to address all these problems is Supersymmetry (SUSY), a quantum spacetime symmetry which predicts a correspondence between bosonic and fermionic fields [5–8]. SUSY removes the quadratic divergences of scalar field theory and thus offers a solution to the aforementioned gauge hierarchy problem. This allows for stable extrapolation of the Standard Model couplings into the far ultraviolet ($E \gg M_{weak}$) regime [9, 10], with the suggestion of gauge unification. SUSY provides an avenue for connecting the Standard Model to ideas of grand unification (GUTs) and/or string theory, and provides a route to unification with gravity via local SUSY, or supergravity theories [11–13]. SUSY theories offer several candidates [14] for dark matter, including the neutralino, the gravitino or a singlet sneutrino. In SUSY theories where the strong CP problem is solved via the Peccei-Quinn mechanism, there is the added possibility of mixed axion-neutralino [15–17], axion-axino [18–20] or axion-gravitino cold dark matter. In order to explain the measured baryon to photon ratio $\eta \sim 10^{-10}$, SUSY offers at least three prominent possibilities including electroweak baryogenesis (now nearly excluded in the minimal theory by limits on $m_{\tilde{t}_1}$ and a light Higgs scalar with $m_h \sim 125$ GeV [21]), thermal and non-thermal leptogenesis [22], and Affleck-Dine baryo- or leptogenesis [23, 24].

There is good reason, then, to adopt SUSY as a well-motivated example of an extension of the Standard Model in order to discuss the potential of the ILC to solve the current puzzles of electroweak symmetry breaking, cosmology and grand unification. In this section, we will describe the capabilities offered by the ILC for the discovery of supersymmetric particles and the precision measurement of their properties. It should be stressed that the experimental capabilities of the ILC presented here apply to new particles with similar signatures whatever the nature of the high scale model.

7.2 Setting the scene

The simplest supersymmetric theory which contains the SM is known as the Minimal Supersymmetric Standard Model, or MSSM. To construct the MSSM, one adopts the gauge symmetry of the SM and promotes all SM fields to superfields. There is a unique generalization of the SM if one imposes the requirements of gauge symmetry, renormalizability, and R-parity conservation. This model requires two Higgs doublet superfields, and thus includes an extended Higgs sector as described in Section 6 as well as corresponding higgsino particles. To be phenomenologically viable, supersymmetry must be broken. SUSY breaking is implemented explicitly in the MSSM by adding all allowed *soft* SUSY breaking terms. The resulting model contains 178 parameters, many of which lead to flavor violation (FV) or CP violation (CPV). The pMSSM ignores the FV and CPV terms, and then contains just 19 or 24 weak scale parameters, depending on whether one does or does not assume universality between the masses of the first and second generation scalar superpartners [25, 26].

Because of the large number of parameters in the general MSSM, the phenomenology of SUSY has often been discussed in terms of a subspace of the more general theory with a reduced parameter set. For many years, the phenomenology of SUSY was described using the parameter space of a

set of models called "minimal supergravity" [27], also known as mSUGRA or the cMSSM. These models assumed that the soft supersymmetry breaking parameters unified at the GUT scale, so that the model could be described by four parameters, a weak scale gravitino mass $m_{3/2}$ and universal scalar masses m_0, gaugino masses $m_{1/2}$ and trilinear terms A_0 at the GUT scale. Other similarly specific choices are given by the minimal gauge mediated SUSY breaking model [28] and the minimal anomaly-mediated SUSY breaking model [29, 30]. In all of these schemes, the unification assumption ties together the mass scales of the supersymmetric partners of quarks, gluons, gauge bosons, and Higgs bosons.

In fact, it was realized a long time ago that the constraints linking these scales are not necessary and might not yield the most attractive models. In 1996, Cohen, Kaplan, and Nelson discussed the "more minimal supersymmetric Standard Model" in which only the partners of the third generation particles are light [31]. Over the years, other authors have discussed models in which some or all of the squarks are very heavy with respect to the electroweak scale without disturbing the naturalness of electroweak symmetry breaking [32–34].

Now the first data from the LHC have weighed in on this issue. Searches at ATLAS and CMS have excluded minimal supergravity or the cMSSM for all models in which the squark and gluino masses are below 1 TeV [35, 36]. These powerful exclusions have, to our knowledge, not caused any theorists to abandon SUSY. However, they have led to a dramatic change in thinking about the parameter space of the MSSM.

Specifically, these exclusions have led theorists to rethink the expectations for the masses of supersymmetric particles that come from the idea that supersymmetry should naturally produce the scale of electroweak symmetry breaking. It is easy to arrange in a supersymmetric model that the Higgs bosons have a potential with a symmetry-breaking minimum. The condition for minimizing this potential can be written

$$\frac{1}{2}m_Z^2 = \frac{(m_{H_d}^2 + \Sigma_d) - (m_{H_u}^2 + \Sigma_u)\tan^2\beta}{(\tan^2\beta - 1)} - \mu^2 \ . \tag{7.1}$$

where, Σ_u and Σ_d arise from radiative corrections [37]. The largest contribution to Σ_u comes from the mass of the top squarks $\tilde{t}_i$, $i = 1, 2$,

$$\Sigma_u(\tilde{t}_i) \sim -\frac{3y_t^2}{16\pi^2} \times m_{\tilde{t}_i}^2 \log(m_{\tilde{t}_i}^2/Q^2), \tag{7.2}$$

where y_t is the top quark Yukawa coupling and $Q = \sqrt{m_{\tilde{t}_1} m_{\tilde{t}_2}}$. The negative sign of this radiative correction is typically the force that drives the Higgs mass term negative.

The MSSM is said to generate the electroweak scale "naturally" if the terms in (7.1) are all of roughly the same size, without large cancellations between the two terms on the right-hand side. By this criterion, the primary implication of the naturalness of the electroweak scale is that the parameter μ, the higgsino mass parameter, should be of the order of 100 GeV [38, 39]. Other supersymmetric partners are required to be light only to the extent that they contribute to the parameters of (7.1) through radiative corrections. The particles primarily constrained by this criterion are the higgsinos themselves, the top squarks, which enter through (7.2), and the gluino, whose mass enters the radiative corrections to the top squark masses.

Imposing this criterion strictly leads to a very different spectrum from that of the cMSSM. In the cMSSM, μ is an output parameter and the values typically output are larger than the squark and gluino masses. Direct argumentation from (7.1), on the other hand, leads to a spectrum in which $|\mu| \sim 100 - 200$ GeV, so that the lightest neutralino is likely higgsino-like. The third generation squarks should have masses that are relatively small, though these masses might be as high as $\lesssim 1 - 1.5$

TeV [40]. The gluino could be heavier, up to a few TeV [41]. The superpartners of electroweak gauge bosons would be found at masses of 1-2 TeV, while the first and second generation scalar partners could be much heavier, possibly in the multi-TeV regime. This last condition is actually beneficial, giving at least a partial solution to the SUSY flavor, CP, proton decay, and gravitino problems. This region of the MSSM parameter space has been dubbed "natural SUSY" [42]. The extreme limit of this schema, in which only the higgsinos are light, has been studied in [43, 44]. A more general exploration of the parameter space of natural SUSY can be found in [45].

The push from the LHC results toward natural SUSY has motivated many theorists to find model-building explanations for this choice of SUSY parameters. Some interesting proposals can be found in [46–49]. Not only have the LHC results on SUSY not damped theorists' enthusiasm, but they have pushed theorists increasingly toward models with higgsino-like charginos and neutralinos with masses below 250 GeV that are ideal targets for the ILC experiments.

7.3 Direct and indirect experimental constraints

7.3.1 Particle sectors of a supersymmetric model

In this section, we present the current direct and indirect experimental constraints on SUSY models. We have emphasized in the previous section that a SUSY model consistent with the experimental constraints from the LHC probably does not belong to the subspace of artificially unified models such as the cMSSM. We find it most useful to analyze an MSSM model in terms of distinct particle sectors with different properties and influence. At generic points in the MSSM parameter space, these sectors can have masses very different from one another. It is important to keep track of which experimental constraints apply to which sector.

The new particle sectors of an MSSM model are:

1. The first and second generation squarks.
2. The first and second generation sleptons.
3. The third generation squarks and sleptons.
4. The gauginos.
5. The higgsinos.

We have already described the constraints on the masses of these particles from the theoretical consideration of naturalness. We now review the constraints from experiment.

7.3.2 Indirect constraints on SUSY models

The magnetic moment of the muon $a_\mu \equiv \frac{(g-2)_\mu}{2}$ was measured by the Muon $g-2$ Collaboration [50] and has been found to give a 3.6σ discrepancy with SM calculations based on e^+e^- data [51]: $\Delta a_\mu = a_\mu^{meas} - a_\mu^{SM}[e^+e^-] = (28.7 \pm 8.0) \times 10^{-10}$. When τ-decay data are used to estimate the hadronic vacuum polarization contribution rather than low energy e^+e^- annihilation data, the discrepancy reduces to 2.4σ, corresponding to $\Delta a_\mu = a_\mu^{meas} - a_\mu^{SM}[\tau] = (19.5 \pm 8.3) \times 10^{-10}$. The SUSY contribution to the muon magnetic moment is [52]

$$\Delta a_\mu^{SUSY} \sim \frac{m_\mu^2 \mu M_i \tan\beta}{m_{SUSY}^4} \ , \tag{7.3}$$

where $i = 1, 2$ labels the electroweak gaugino masses and m_{SUSY} is the characteristic sparticle mass circulating in the muon-muon-photon vertex correction, one of: $m_{\tilde{\mu}_{L,R}}$, $m_{\tilde{\nu}_\mu}$, $m_{\tilde{\chi}_i^+}$ and $m_{\tilde{\chi}_j^0}$. Attempts to explain the muon $g-2$ anomaly using supersymmetry usually invoke sparticle mass spectra with relatively light smuons and/or large $\tan\beta$ (see *e.g.* Ref. [53]). Some SUSY models where $m_{\tilde{\mu}_{L,R}}$ is correlated with squark masses (such as mSUGRA) are now highly stressed to explain the

$(g-2)_\mu$ anomaly. In addition, since naturalness favors a low value of $|\mu|$, tension again arises between a large contribution to Δa_μ^{SUSY} and naturalness conditions. These tensions motivate scenarios with non-universal scalar masses [54].

The combination of several measurements of the $b \to s\gamma$ branching fraction finds that $BF(b \to s\gamma) = (3.55 \pm 0.26) \times 10^{-4}$ [55]. This is somewhat higher than the SM prediction [56] of $BF^{SM}(b \to s\gamma) = (3.15 \pm 0.23) \times 10^{-4}$. SUSY contributions to the $b \to s\gamma$ decay rate come mainly from chargino-top squark loops and loops containing charged Higgs bosons. They are large when these particles are light and when $\tan\beta$ is large [57].

The decay $B_s \to \mu^+\mu^-$ occurs in the SM at a calculated branching ratio value of $(3.2 \pm 0.2) \times 10^{-9}$. The CMS experiment [58] has provided an upper limit on this branching fraction of $BF(B_s \to \mu^+\mu^-) < 1.9 \times 10^{-8}$ at 95% CL. The CDF experiment [59] claims a signal in this channel at $BF(B_s \to \mu^+\mu^-) = (1.8 \pm 1.0) \times 10^{-8}$ at 95% CL, which is in some discord with the CMS result. Finally, the LHCb experiment has reported a strong new bound of $BF(B_s \to \mu^+\mu^-) < 4.5 \times 10^{-9}$ [60]. In supersymmetric models, this flavor-changing decay occurs through exchange of the pseudoscalar Higgs A [61,62]. The contribution to the branching fraction from SUSY is proportional to $\tan^6\beta/m_A^4$.

The branching fraction for $B_u \to \tau^+\nu_\tau$ decay is calculated [63] in the SM to be $BF(B_u \to \tau^+\nu_\tau) = (1.10 \pm 0.29) \times 10^{-4}$. This is to be compared to the value from the Heavy Flavor Averaging group [64], which finds a measured value of $BF(B_u \to \tau^+\nu_\tau) = (1.41 \pm 0.43) \times 10^{-4}$, in agreement with the SM prediction, but leaving room for additional contributions. The main contribution from SUSY comes from tree-level charged Higgs exchange, and is large at large $\tan\beta$ and low m_{H^+}.

Finally, measurements of the cold dark matter (CDM) abundance in the universe find $\Omega_{CDM}h^2 \sim 0.11$, where Ω_{CDM} is the dark matter relic density scaled in terms of the critical density. Simple explanations for the CDM abundance in terms of thermally produced neutralino LSPs are now highly stressed by LHC SUSY searches, and are even further constrained if the light SUSY Higgs h turns out to have mass ~ 125 GeV [65]. A higgsino LSP is not a good dark matter candidate, since it has too large an annihilation rate to vector boson pairs, leading to too small a thermal relic density. However, this deficit can be repaired in well-motivated extensions of the MSSM, including mixed axion-LSP dark matter and models with late decaying moduli fields. For purposes of considering ILC or LHC physics, it seems prudent not to take dark matter abundance constraints on SUSY theories too seriously at this point in time.

7.3.3 Impact of Higgs searches

The ATLAS and CMS experiments have reported the discovery of a narrow resonance with mass near 125 GeV [66,67]. At the same time, they exclude a Standard Model-like Higgs boson in the mass ranges $110-123$ and $130-558$ GeV at 95% CL. The discovery is based on an excess of events mainly in the $\gamma\gamma$, $ZZ^* \to 4\ell$ and WW^* decay channels. These excesses are also corroborated by recent reports from CDF and D0 at the Fermilab Tevatron of excess events in the $Wb\bar{b}$ and other channels over the mass range 115-130 GeV [68].

Searches by ATLAS and CMS for $H,\ A \to \tau^+\tau^-$ now exclude a large portion of the m_A vs. $\tan\beta$ plane [69,70]. In particular, the region around $\tan\beta \sim 50$, which is favored by Yukawa-unified SUSY GUT theories, now excludes $m_A < 500$ GeV. For $\tan\beta = 10$, only the range $120\ \text{GeV} < m_A < 220$ GeV is excluded. ATLAS excludes charged Higgs bosons produced in association with a $t\bar{t}$ pair for $m_{H^\pm} < 150$ GeV for $\tan\beta \sim 20$ [71].

A Higgs mass of $m_h = 125 \pm 3$ GeV lies within the narrow mass range $m_h \sim 115-135$ GeV which is allowed between LEP searches for a SM-like Higgs boson and calculations of an upper limit to m_h within the MSSM. However, such a large value of m_h requires large radiative corrections and large mixing in the top squark sector. In models such as mSUGRA, trilinear soft parameters $A_0 \sim \pm 2m_0$

are thus preferred, and values of $A_0 \sim 0$ would be ruled out [72–74]. In other constrained models such as the minimal versions of GMSB or AMSB, Higgs masses of 125 GeV require even the lightest of sparticles to be in the multi-TeV range [65], leading to enormous electroweak fine-tuning. In the mSUGRA/cMSSM model, requiring a Higgs mass of about 125 GeV pushes the best fit point in m_0 and $m_{1/2}$ space into the multi-TeV range [72] and makes global fits of the model to data increasingly difficult [75]. This already motivates us to consider the prospects for precision measurements of new particles at the ILC in a more general context than the cMSSM.

7.3.4 Direct searches for supersymmetric particles

The most model-independent limits on SUSY particles, especially the uncoloured ones, have been set by the LEP experiments [76–80] on *sleptons, charginos and neutralinos*. The fact that these limits have not been superseded in the general case by LHC data illustrates the complementarity of e^+e^- and pp colliders as well as the fact that the interpretation of e^+e^- data requires significantly fewer model assumptions.

The ATLAS and CMS collaborations have searched for multi-jet$+E_T^{\rm miss}$ events arising from gluino and squark pair production in 4.4 fb^{-1} of 2011 data taken at $\sqrt{s} = 7$ TeV [81, 82] and in up to 5.8 fb^{-1} of 2012 data taken at $\sqrt{s} = 8$ TeV [83]. In the limit of very heavy squark masses, they exclude $m_{\tilde{g}} \lesssim 1.1$ TeV, while for $m_{\tilde{q}} \simeq m_{\tilde{g}}$ then $m_{\tilde{g}} \lesssim 1.5$ TeV is excluded, assuming $m_{\tilde{\chi}_1^0} = 0$ GeV in both cases. $m_{\tilde{q}}$ refers to a generic first generation squark mass scale, since these are the ones whose production rates depend strongly on valence quark PDFs in the proton.

A recent ATLAS search for direct bottom squark pair production followed by $\tilde{b}_1 \to b\tilde{\chi}_1^0$ decay ($pp \to \tilde{b}_1\bar{\tilde{b}}_1 \to b\bar{b} + E_T^{\rm miss}$) based on 2 fb^{-1} of data at $\sqrt{s} = 7$ TeV now excludes $m_{\tilde{b}_1} \lesssim 350$ GeV for $m_{\tilde{\chi}_1^0}$ as high as 120 GeV. For larger values of $m_{\tilde{\chi}_1^0}$, there is no limit at present [84]. These constraints also apply to top squark pair production where $\tilde{t}_1 \to b\tilde{\chi}^+$ decay and the $\tilde{\chi}^+$ decays to soft, nearly invisible particles, as would be expected in natural SUSY.

In models with gaugino mass unification and heavy squarks (such as mSUGRA with large m_0), electroweak gaugino pair production $pp \to \tilde{\chi}_1^\pm\tilde{\chi}_2^0$ is the dominant SUSY particle production cross section at LHC7 for $m_{\tilde{g}} > 0.5$ TeV [85]. Two searches by ATLAS in the 3 lepton final state using 2.1 fb^{-1} of 7 TeV data [86] and in the 2 lepton final state using 4.7 fb^{-1} of 8 TeV data [87] give results in the pMSSM and in a simplified model. Both cases assume that chargino and neutralino decay to intermediate sleptons, which enhances the leptonic branching fractions. The theoretically more interesting case of chargino and neutralino three-body decay through W^* and Z^* leading to a clean trilepton signature [88, 89] awaits further data and analysis.

The opposite-sign/same flavor dilepton final state [87] can also originate from direct production of slepton pairs. The resulting exclusion in the slepton-LSP mass plane is rather model-independent and extends the LEP2 limit to higher slepton masses of up to 200 GeV for an LSP mass of 30 GeV. For LSP masses larger than 80 GeV, no slepton masses can be excluded beyond the LEP2 limit.

In addition, a wide variety of other searches for SUSY have been made – including searches for long-lived quasi-stable particles, electroweakinos with small mass difference, RPV SUSY, minimal gauge mediated SUSY etc. After 5 fb^{-1} of data at LHC7 and a first glimpse into another 5 fb^{-1} of data at LHC8, it is safe to say that no compelling signal for SUSY has yet emerged at LHC.

7.3.5 Impact of the constraints on the SUSY particle sectors

We can summarize the results of this section as constraints on the various sectors of an MSSM model set out in Section 7.3.1:

1. The first and second generation squarks: The particles in this sector are highly constrained by flavour and CP violation limits and by LHC squark searches. Typically we expect $m_{\tilde{q}} \gtrsim 1.5$ TeV. This sector has little connection to the EW scale: indeed, in split SUSY models [90] the squark (and slepton) masses are sometimes pushed to the 10^{10} GeV level.

2. The first and second generation sleptons: The particles in this sector are favored by $(g-2)_\mu$ to have masses below 1 TeV. However, the absence of leptonic flavour violating processes (*e.g* $\mu \to e\gamma$ decay) push this sector to be much heavier.

3. The third generation squarks and sleptons: The particles in this sector are influenced by large Yukawa couplings. Naturalness favors their masses to be below a few TeV. B-meson decay data prefer top squarks with mass at or above the TeV scale.

4. The gauginos: The particles in this sector are in principle independent of the squark mass scale and might also be independent of one another. Simple SUSY GUT models favor gaugino mass unification $M_1 = M_2 = M_3 \equiv m_{1/2}$ at M_{GUT}, giving a $1:2:7$ ratio of masses at the weak scale. More general models allow for essentially independent gauginos masses. Electroweak fine-tuning prefers gaugino masses not too far above the TeV scale. As of today, M_1 and M_2 are not substantially constrained beyond the LEP limits, but M_3, the gluino mass, probably must be above 1 TeV.

5. The higgsinos: The masses of the particles in this sector are determined by the superpotential μ term, which is not a soft SUSY breaking term. In the context of the MSSM alone, it could be expected to occur at the M_{GUT} or M_{string} scale. This however would require immense fine-tuning in the corrections to the Z mass: *c.f.* Eq'n 7.1. Naturalness arguments prefer a value of $|\mu|$ not far above ~ 100 GeV, close to but somewhat beyond the limits from LEP2 chargino searches.

Ironically, the LHC has its greatest capability—in terms of mass reach—to detect the first generation squarks and the gluinos. These are particles with indirect or no connection to the Z mass scale. On the other hand, the ILC has an excellent capability to detect electroweakinos. In the case where the light electroweakinos are higgsinos, the ILC would be directly probing that sector which is most directly connected to the Z-mass scale via electroweak fine-tuning. The ILC also has excellent capabilities to study the sleptons, probing a sector that is very difficult to study at the LHC. It is possible that the third generation squarks and sleptons lie within the mass range of the ILC. In that case, the ILC would greatly enhance the knowledge of these sparticles gained from the LHC, since the ILC has the capability to precisely measure not only the masses but also the quantum numbers and mixing angles of these particles. We will present examples of these ILC capabilities in the next several sections.

7.4 Two benchmark points for the ILC

In Ref. [91], a variety of post LHC7 benchmark points for ILC physics were proposed. Here, we include two of these for reference in the discussion of supersymmetric particle discovery and measurement capabilities at the ILC. These models are completely viable in the face of the LHC supersymmetry searches and they address important questions in physics beyond the Standard Model. Many of the more specific scenarios discussed in Section 7.5 can be identified within their particle spectra. A very large number of additional viable supersymmetry models, illustrating models with both neutralino and gravitino LSPs, are presented in [92],

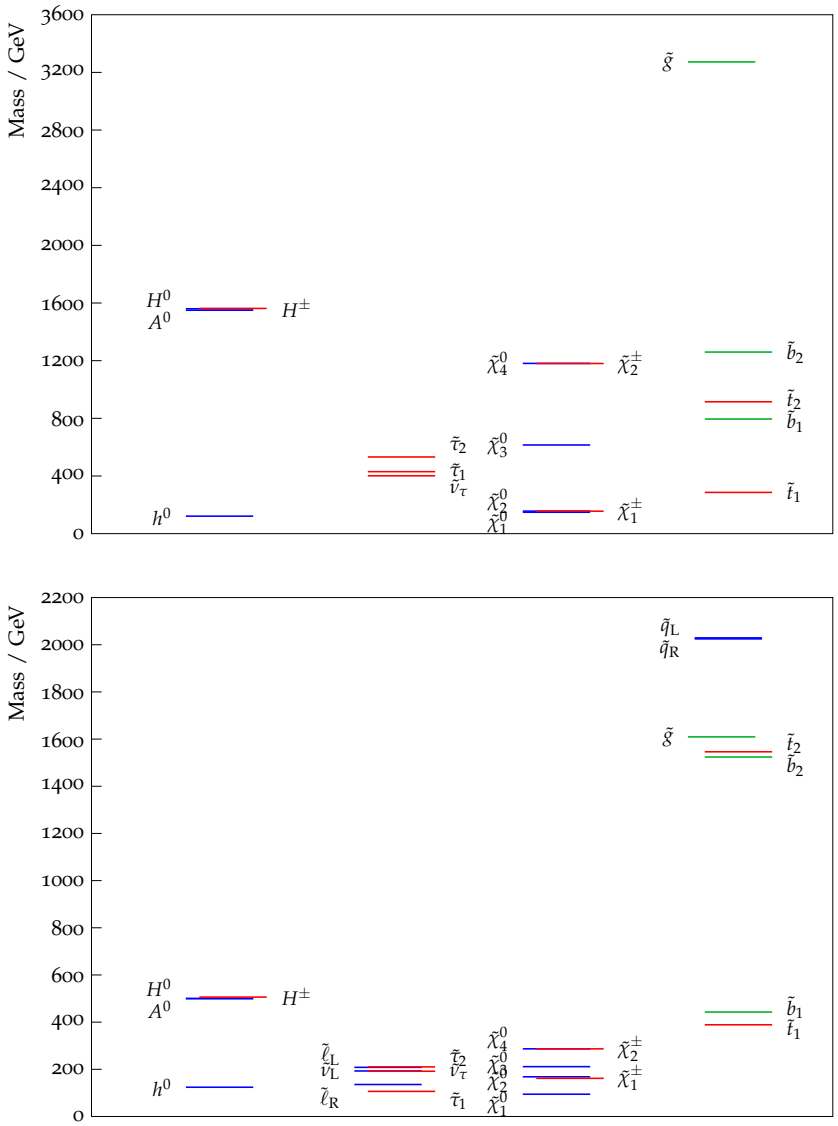

Figure 7.1 SUSY particle spectrum of the two benchmark scenarios discussed in Section 7.4: Top: Natural SUSY model; Bottom: $\delta M\tilde{\tau}$ model.

7.4.1 Natural SUSY and light higgsinos

For natural SUSY (NS), we adopt a benchmark point using input parameters $m_0(1,2) = 13500$ GeV, $m_0(3) = 760$ GeV, $m_{1/2} = 1380$ GeV, $A_0 = -167$ GeV, $\tan\beta = 23$ GeV, $\mu = 150$ GeV and $m_A = 1550$ TeV. The resulting mass spectrum is listed in Table 1 of Ref. [91] and shown in Figure 7.1.

The point contains higgsino-like $\tilde{\chi}_1^0$, $\tilde{\chi}_2^0$ and $\tilde{\chi}_1^\pm$ with masses $\sim \mu = 150$ GeV, where $m_{\tilde{\chi}_1} - m_{\tilde{\chi}_1^0} = 7.4$ GeV and $m_{\tilde{\chi}_2^0} - m_{\tilde{\chi}_1^0} = 7.8$ GeV. Due to the small energy release in their three body decays, the $\tilde{\chi}_1^\pm$ and $\tilde{\chi}_2^0$ will be difficult to detect at LHC [44]. Third generation squark masses are at $m_{\tilde{t}_1} = 286.1$ GeV, $m_{\tilde{t}_2} = 914.9$ GeV and $m_{\tilde{b}_1} = 795.1$ GeV. Since the mass difference $m_{\tilde{t}_1} - m_{\tilde{\chi}_1^0}$ is less than the

top mass, the decay $\tilde{t}_1 \to b\tilde{\chi}_1^{\pm}$ dominates, thus yielding a signature for $\tilde{t}_1$ pair production of two acollinear b-jets plus missing transverse energy. It is likely that the LHC experiments will eventually find the $\tilde{t}_1$, though at the moment the searches are not sensitive. Resolving the $\tilde{\chi}_1^{\pm}$, $\tilde{\chi}_1^0$ (and $\tilde{\chi}_2^0$) as distinct states will be extremely difficult at the LHC. Most other sparticles lie well beyond LHC reach.

For ILC, the spectrum of higgsino-like $\tilde{\chi}_1^{\pm}$, $\tilde{\chi}_1^0$ and $\tilde{\chi}_2^0$ would be accessible for $\sqrt{s} \gtrsim 320$ GeV via $\tilde{\chi}^+\tilde{\chi}^-$ and $\tilde{\chi}_2^0\tilde{\chi}_2^0$ pair production and $\tilde{\chi}_1^0\tilde{\chi}_2^0$ mixed production. although the energy release from decays will be small at beam energies near the threshold. Top squark pair production would become accessible when $\sqrt{s}$ exceeds about 575 GeV.

7.4.2 An MSSM model with light sleptons

Using the freedom in the MSSM to decouple the masses of squarks and sleptons, we generated a model in the 13-parameter pMSSM that gives a spectrum of color singlet particles close to that of the well-studied SPS1a′ point [93]. The SPA1a′ point is phenomenologically well-motivated in that it naturally reconciles the measured $(g-2)_\mu$ anomaly (which favors light smuons) with the measured $b \to s\gamma$ branching fraction (which favors rather heavy third generation squarks). It furthermore predicts a neutralino relic density compatible with cosmological observations, making use of stau coannihilation. The SPA1a′ point belongs to the cMSSM and so is now excluded by LHC searches for squarks and sleptons. But it is easy to find a more general MSSM point that shares its virtues and is not yet tested by LHC searches. We call this the $\delta M\tilde{\tau}$ model. The particle masses of this model are listed in Table 2 of Ref. [91] and displayed in Figure 7.1.

With gluino and first/second generation squark masses around 2 TeV, the model lies beyond current LHC limits, especially since the gluino decays dominantly via $\tilde{t}_1 t$ or $\tilde{b}_1 b$. The tau sleptons $\tilde{\tau}_1$ have masses of 104 GeV, so stau pair production would be accessible even at the first stage of ILC running. Right-selectrons and smuons with mass 135 GeV would also be produced at the ILC during the early runs, while left-sleptons and sneutrinos, with mass about 200 GeV, would be accessible when $\sqrt{s}$ exceeds 400 GeV. The $\tilde{\chi}_1^0\tilde{\chi}_2^0$ reaction opens up at $\sqrt{s} > 250$ GeV, and $\tilde{\chi}_1^+\tilde{\chi}_1^-$ pair production is accessible for $\sqrt{s} \gtrsim 310$ GeV. In addition, with $m_{A,H} \sim 400$ GeV, hA production opens at 525 GeV, stop pair production at 600 GeV, sbottom pair production at 680 GeV and finally charged Higgses and HA appear at 800 GeV.

7.5 Experimental capabilities and parameter determination

In this section, we will review the ILC's experimental capabilities for precision measurements of SUSY particle properties. These measurements allow to determine the parameters of the underlying theory and to test its consistency at the quantum loop level.

As discussed above, the highly constrained cMSSM/mSUGRA models of supersymmetry are under tension from several different types of LHC observations. Therefore, we will discuss SUSY measurements in the more general context of the CP and R-parity conserving MSSM. At the ILC, we will study the lightest particles of the SUSY spectrum, so the measurements that we will discuss involve simple reactions without complex cascade decay chains [94]. Thus, these measurements involve only a few of the MSSM parameters and, typically, those parameters can be determined with high precision.

We start with the minimal case in which only the lighter neutralinos and charginos are kinematically accessible. We then proceed to discuss sleptons and squarks, especially those of the third generation. Finally, we discuss possible extensions of the theory, encompassing R-parity violation, CP violation, the NMSSM and the MSSM with an additional gauge group. We close with comments on model discrimination and parameter determination.

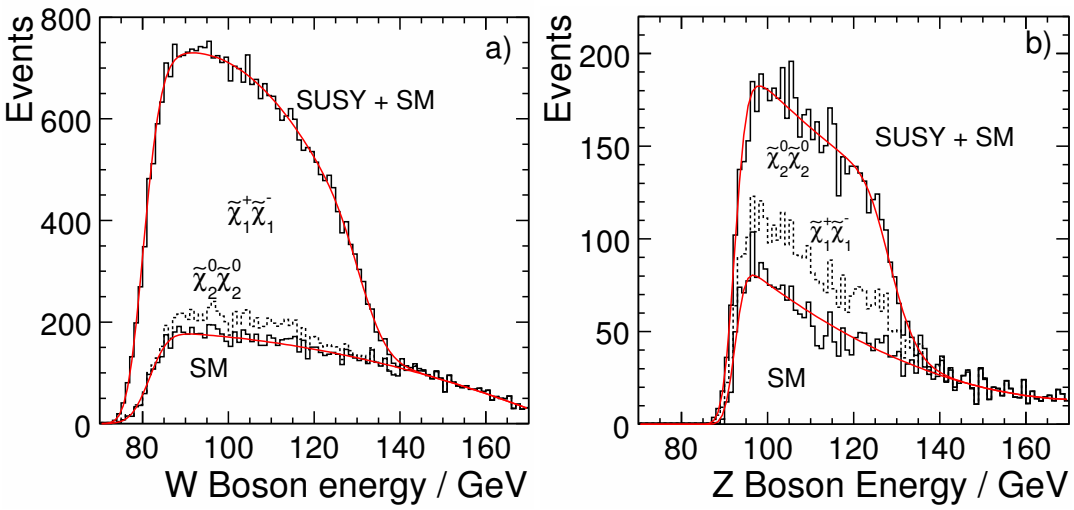

Figure 7.2. ILC measurements in chargino and neutralino pair production at 500 GeV. Top: Energy spectrum of the $W^{\pm}$ candidates reconstructed from events selected as $\tilde{\chi}_1^{\pm}$ pair production. Bottom: Energy spectrum of the Z^0 candidates reconstructed from events selected as $\tilde{\chi}_2^0$ pairs. From [103].

Figure 7.3 Measurement of the chargino mixing angles at the ILC at 500 GeV from the production cross-sections using $e^-_L e^+_R$ and $e^-_R e^+_L$ polarized beams. From [104].

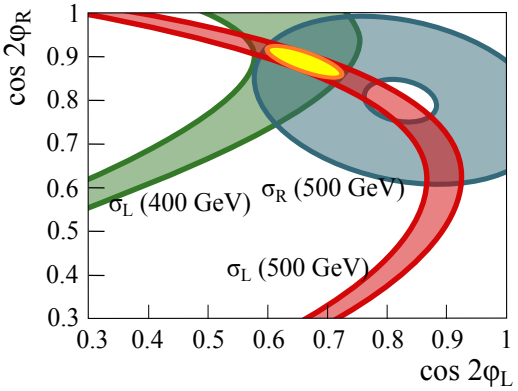

7.5.1 Neutralino and chargino sector

At the ILC, the electroweak gaugino sector can be probed in a model independent way up to masses of $\sqrt{s}/2$. Associated pair production can access masses above this value. The masses and couplings of the electroweak gauginos can be measured with high precision [95, 96]. Especially accurate values of the masses can be obtained through threshold scans, which have a precision below the per mil level [97, 98]. The relatively simple dynamics of pair production in e^+e^- gives powerful methods for spin and quantum number determination [99].

Most of the SUSY models consistent with all experimental data feature light electroweakinos. These can either have dominant Bino/Wino components, or—as motivated by naturalness—dominant higgsino components. Examples of the latter case include the Natural SUSY benchmark introduced in section 7.4.1, as well as models with mixed gauge-gravity mediation [100], and the remaining points in the cMSSM parameter space. A more detailed overview of the light higgsino case is given in [91]. A characteristic pattern in all cases is a very small mass splitting between the χ_1^0 and $\chi_1^{\pm}$ / χ_2^0 of typically a few GeV or smaller. This small splitting is very difficult to resolve at the LHC. However, these states can be discovered and disentangled at the ILC by using ISR recoil techniques to overcome the background from 2-photon processes, and taking advantage of the capability of the detectors to observe the very soft visible decay products of the $\chi_1^{\pm}$ / χ_2^0. These models can also lead to short displaced vertices that can be resolved thanks to the excellent vertex resolution at the ILC.

In the past, the case of small mass splitting between $\chi_1^{\pm}$ and χ_1^0 has been studied in the context

of AMSB models [101], where it has been shown that mass differences down to 50 MeV can be resolved. For a 400 MeV mass difference, it has been shown that the $\chi_1^\pm$ mass can be determined to 1.8 GeV from the recoil against an ISR photon. Observing the energy of the single soft pion from the $\chi_1^\pm$ decay, the $\chi_1^\pm$–χ_1^0 mass difference can be determined to 7 MeV [102]. Although the minimal version of the AMSB is currently disfavoured due to its incompatibility with a Higgs mass of 125 GeV, the fact that such small mass differences can be precisely measured at the ILC remains unchanged. In the Natural SUSY example discussed above, it is also true that the χ_2^0 is nearly mass degenerate with the $\chi_1^\pm$. This creates an additional experimental complication, but on the other hand offers an additional handle for parameter determination. While a detailed experimental study is underway, the χ_2^0 / $\chi_1^\pm$ separation should be possible when the various exclusive decay modes are exploited, which is feasible due to the clean environment and excellent detector resolutions available at the ILC. The measurement of the polarization and beam energy dependence of the cross-sections of these processes then allows us to establish the higgsino character of the particles and to precisely determine μ.

If the mass difference between $\chi_1^\pm$ or χ_2^0 and χ_1^0 is larger than about 80 GeV without sleptons in between, the decays of these particles will proceed via real $W^\pm$ or Z bosons. In the challenging case where $\chi_1^\pm$ and χ_2^0 are nearly mass degenerate, their decays can be disentangled even in the fully hadronic decay mode. This case has been studied both by SiD and ILD in full detector simulation. Figure 7.2 shows the energy spectra of the reconstructed gauge boson candidates from signal, SUSY and SM background for the chargino and neutralino event selection [103]. Assuming an integrated luminosity of 500 fb^{-1} at $\sqrt{s} = 500$ GeV and a beam polarization of $P(e^+, e^-) = (30\%, -80\%)$, the edge positions can be determined to a few hundred MeV. Due to sizable correlations, this translates into uncertainties of 2.9, 1.7 and 1.0 GeV for the χ_2^0, $\chi_1^\pm$ and the χ_1^0 masses, respectively. The cross-sections can be measured to 0.8% (2.8%) in the $\chi_1^\pm$ (χ_2^0) case from the hadronic channel alone.

Independently of the mass splitting, the polarized cross-section measurements at different center-of-mass energies can be employed to determine the mixing angles in the chargino sector, as illustrated in Figure 7.3 [104]. This example is based on simulations performed in the SPS1a scenario; the results also apply to the $\delta M\tilde{\tau}$ scenario introduced above. The bands include both statistical and systematical uncertainties, where the limiting contribution is the precision of the chargino mass.

More recently, it has been shown that the achievable experimental precision allows us also to determine the top squark masses and mixing angle via loop contributions to the polarized chargino cross-sections and the forward-backward asymmetries [105]. This allows us to predict and to constrain the heavier states of the SUSY model and to test its structure directly independently of the SUSY breaking scheme.

7.5.2 Gravitinos

If the gravitino is lighter than the lightest neutralino, the neutralino could decay into a photon plus a gravitino. In such a case, the lifetime of the neutralino is related to the mass of the gravitino: $\tau_\chi \sim m_{3/2}^2 M_{Pl}^2/m_\chi^5$. Therefore the measurement of the neutralino lifetime gives access to $m_{3/2}$ and the SUSY breaking scale. A similar statement applies to models in which a different particle is the lightest Standard Model superpartner, decaying to the gravitino. A well-studied example is that of the $\tilde{\tau}$ NLSP. The experimental capabilities of a Linear Collider in scenarios with a gravitino LSP have been evaluated comprehensively many years ago [106], where it has been demonstrated that with the permille level mass determinations from threshold scans, the clean environment and the excellent detector capabilities, especially in tracking and highly granular calorimetry, fundamental SUSY parameters can be determined to 10% or better.

Although this study was based on minimal GMSB models, which are currently disfavoured by their prediction of too low masses for the Higgs boson and the gluino, the signatures and experimental

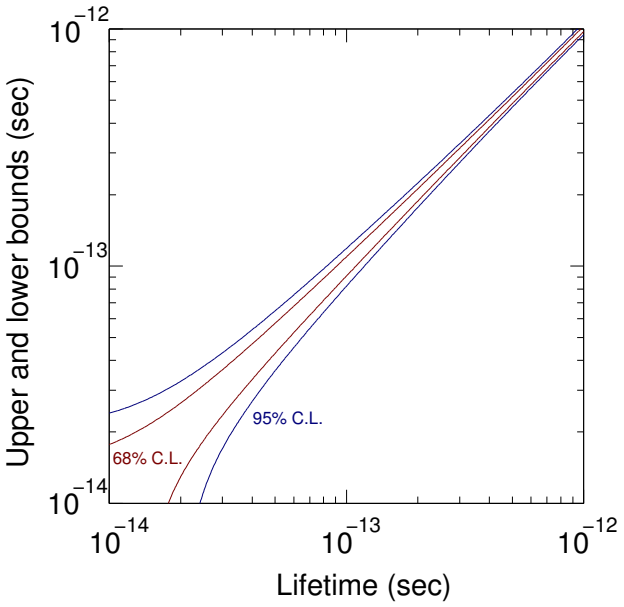

Figure 7.4
ILC measurement of the lifetime of the gravitino in a GMSB scenario, from [108]. The 1σ and 2σ uncertainty bands are shown as a function of the lifetime of a $\tilde{\tau}$ with a mass of 120 GeV.

techniques remain perfectly valid. They could apply to other non-minimal scenarios including general gauge mediation. Aspects of the detector performance which were still speculative when the studies in [106] were performed have been established in the intervening time with testbeam data from prototype detectors. For instance, the performance of neutralino lifetime determination from non-pointing clusters in the electromagnetic calorimeter has recently been reevaluated based on full detector simulation gauged against Calice testbeam data. These confirm the estimates from [106] that lifetimes between 0.1 and 10 ns can be reconstructed with a few percent accuracy, although a calibration of the lifetime reconstruction is needed [107]. Similarly it has been shown in [108], that, in the case of a $\tilde{\tau}$ NLSP, the lifetime can be measured down to 10^{-5} ns, corresponding to gravitino masses of a few eV. Figure 7.4 shows the 1σ and 2σ uncertainty bands as a function of the lifetime of a $\tilde{\tau}$ with a mass of 120 GeV.

Scenarios with very long-lived $\tilde{\tau}$ NLSPs which get trapped in the calorimeter and decay much later have been studied in [109]. It has been shown there that, with a suitable read-out of the ILC detectors, the gravitino mass and the SUSY breaking scale can also be determined in such cases. The first signs of these heavy, detector-stable charged particles would their large ionization losses in the tracking volume. This is a nearly background-free signature even at the LHC, so it is also possible there to discover electroweak production of very long-lived $\tilde{\tau}$ NLSPs or $\tilde{\chi}_1^{\pm}$ NLSPs. If this discovery were made, it would be important and fascinating to measure the polarized electroweak cross sections of these particles with high precision at the ILC.

7.5.3 Third generation squarks

At the ILC, the stop $\tilde{t}_1$ can be probed up to $m_{\tilde{t}_1} = \sqrt{s}/2$ regardless of its decay mode and the masses of other new particles. At $\sqrt{s} = 500$ GeV, the $\tilde{t}_1$ mass can be determined to 1 GeV in the $\tilde{t}_1 \to c\tilde{\chi}_1^0$ decay mode, which dominates for small mass differences, and to 0.5 GeV in the $\tilde{t}_1 \to b\tilde{\chi}_1$ mode [110]. At the same time, the stop mixing angle can be determined to $\Delta \cos\theta_t = 0.009$ and 0.004 in the neutralino and chargino modes, respectively. A more recent study improved the mass resolution in the $\tilde{t}_1 \to c\tilde{\chi}_1^0$ decay to 0.42 GeV, including systematic uncertainties estimated based on LEP experience by assuming data from two different center-of-mass energies [111]. In a top-squark co-annihilation scenario, the predicted dark matter relic density depends strongly on the stop-neutralino mass difference. The precise ILC mass measurenents give an uncertainty on the calculated dark matter relic density of $\Delta\Omega_{\rm CDM}h^2 = 0.015$, comparable to the current WMAP precision. Figure 7.5 shows

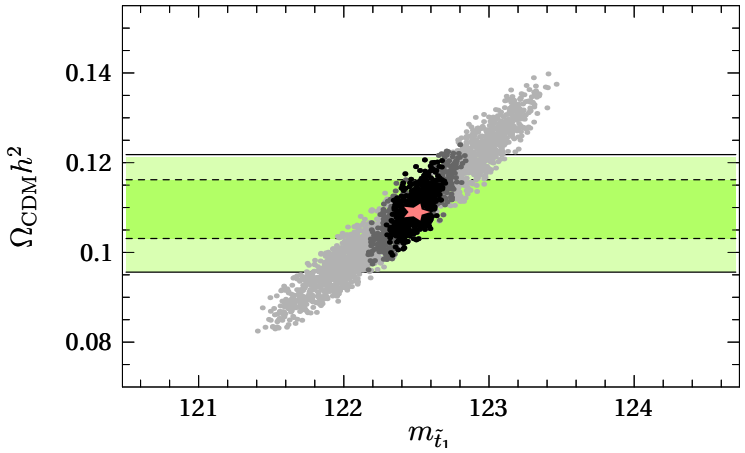

Figure 7.5. Predicted dark matter density Ω_{DM} in a stop coannihilation model. The scatter plot shows the values of Ω_{DM} and $m_{\tilde{t}_1}$ for models consistent with ILC observations within 1σ experimental precision, assuming a meaurement error on the mass splitting in the decay, $\delta\tilde{t}_1$, of 1.2 GeV (light gray), 0.42 GeV (dark gray) and 0.24 GeV (black). The bands show the current WMAP precision on Ω_{DM}. The input value is marked with a star. From [111].

the correlation between the stop mass and $\Omega_{\rm CDM}h^2$ and the respective precisions. This clearly shows that sub-GeV precision on the stop mass is mandatory to establish the $\tilde{\chi}_1^0$ as a cosmic relic. Although these studies were performed with slightly lower stop masses, one can expect similar precisions in the two scenarios introduced in section 7.4 if on the way to a 1 TeV upgrade the ILC is operated at a center-of-mass energy of 600 GeV or above. And, indeed, there is still much room for the $\tilde{t}_1$ to be found at the LHC at a mass below 250 GeV.

The polarized cross sections $\sigma(e_L^-e_R^+ \to \tilde{t}_1\bar{\tilde{t}}_1)$ and $\sigma(e_R^-e_L^+ \to \tilde{t}_1\bar{\tilde{t}}_1)$ allows a direct determination of the $(\tilde{t}_L, \tilde{t}_R)$ mixing angle with an accuracy of a few degrees. This is crucial information for the theory of electroweak symmetry breaking in SUSY and for the explanation for the Higgs boson mass at 125 GeV.

In sbottom-co-annihilation scenarios, which typically exhibit a sbottom-LSP mass difference of about 10% of the LSP mass, the process $\tilde{b}_1 \to b\tilde{\chi}_1^0$ can be discovered for sbottom masses up to about 10 GeV below the kinematic limit and for mass differences down to only 5 GeV larger than the kinematic limit [112]. It will be extremely difficult to cover such small mass differences comprehensively at the LHC.

Additional interesting reactions arise if the stop and sbottom decay to Higgsinos. We have argued that, because of naturalness, this is the expected situation. Then the charginos are close in mass to the neutralinos, allowing the decay $\tilde{t} \to \widetilde{\chi}^+ b$, with a subsequent decay of the $\widetilde{\chi}^+$ with small missing energy release. The ability of the ILC to study decay chains with small energy differences will be important if this is a dominant mode.

7.5.4 Scalar charged leptons

For slepton masses below $\sqrt{s}/2$, sleptons could be produced copiously at the ILC without relying on cascades from heavier sparticles. The lighter sleptons typically decay directly into the corresponding lepton and the lightest neutralino, giving a very clear signature of two isolated same flavor opposite sign leptons and missing four-momentum. The lepton energy spectrum has a box-like shape, and its lower and upper edge give direct access to the slepton and neutralino mass. In practice, the box is slightly smeared by the beam energy spectrum, ISR, detector resolution and, in case of τ leptons, by the unmeasured neutrinos from the τ decay. Nevertheless, this technique works reliably down to very small mass differences of a few GeV. For mass differences below ~ 10 GeV, the lower edge is buried in background from 2-photon processes. Then an additional observable is needed to determine the

lightest neutralino mass. The adjustable center-of-mass energy of the ILC allows us to achieve even higher precision by scanning the production thresholds.

In SUSY, the superpartners of the left- and right-handed leptons are distinct scalar particles with different electroweak quantum numbers. These particles can be distinguished at the ILC in a model-independent way by the measurement of their production cross sections from left- and right-polarized beams in e^+e^- annihilation [113]. It is not expected that the left- and right-sleptons should be mass degenerate, but, even in this case, the two particles can be studied separately, since each has enhanced production in cases with electron beams of the same handedness. For the case of τ sleptons, the polarization of the τ leptons produced in the decay can be analyzed to provide another powerful probe of the slepton quantum numbers and couplings [114].

The heavier sleptons typically decay via intermediate charginos, neutralinos or sneutrinos, depending on the details of the spectrum [94]. By choosing an intermediate center-of-mass energy, the production of heavier superpartners and thus the background from their cascades can be switched off. This allows the ILC experiments to disentangle even rich spectra similar to the $\delta M\tilde{\tau}$ scenario discussed above.

The $\tilde{\tau}$ sector of a scenario very similar to $\delta M\tilde{\tau}$ has recently been studied in full simulation with the ILD detector [115], since the small $\tilde{\tau}$-$\tilde{\chi}^0_1$ mass difference provides an interesting challenge for the detector and the accelerator conditions. In this case, the beam energy spectrum was accounted for and also accelerator background from e^+e^- pairs created from beamstrahlung was overlayed in order to verify the robustness of the reconstruction even of fragile final states such as soft τ leptons against spurious tracks and clusters from beam background.

With an integrated luminosity of 500 fb^{-1} at a center-of-mass energy of $\sqrt{s} = 500$ GeV and with $P(e^+, e^-) = (-30\%, +80\%)$, the following results were achieved for the $\tilde{\tau}$ masses using pair production cross-sections and the τ polarisation $\mathcal{P}_\tau$ from $\tilde{\tau}$ decays. Both of these quantities depend on the $\tilde{\tau}$ mixing angle, the higgsino component of the $\tilde{\chi}^0_1$ and $\tan\beta$ in a well-understood way.

$$
\begin{aligned}
\delta M(\tilde{\tau}_1) &= {}^{+0.03}_{-0.05} \pm 1.1 \cdot \delta M(\tilde{\chi}^0_1)\ \text{GeV (endpoint)} \\
\delta M(\tilde{\tau}_2) &= {}^{+11}_{-5} \pm 18 \cdot \delta M(\tilde{\chi}^0_1)\ \text{GeV (endpoint)} \\
\frac{\delta\sigma}{\sigma}(\tilde{\tau}_1) &= 3.1\ \% \\
\frac{\delta\sigma}{\sigma}(\tilde{\tau}_2) &= 4.2\ \% \\
\mathcal{P}_\tau &= 91 \pm 6 \pm 5\ (\text{bkg}) \pm 3\ (\text{SUSY masses})\ \%\ (\pi\ \text{channel}) \\
\mathcal{P}_\tau &= 86 \pm 5\ \%\ (\rho\ \text{channel}).
\end{aligned}
$$

The measurement of the endpoint of the τ jet energy spectrum from $\tilde{\tau}_1$ decays is shown in Figure 7.6. The $\tilde{\tau}$ mixing angle can be determined independently of the τ polarisation from $\tilde{\tau}_1\tilde{\tau}_2$ associated production below the $\tilde{\tau}_2$ pair production threshold. With a dedicated threshold scan, the $\tilde{\tau}_2$ mass measurement can be improved to $\delta M(\tilde{\tau}_2) \approx 0.86$ GeV [116]. Even smaller mass differences have been studied in an earlier fast simulation analysis [117], which found $\delta M(\tilde{\tau}_1) \approx 0.15 - 0.3$ GeV depending on $\tilde{\tau}_1$ mass and the $\tilde{\tau}_1$-$\tilde{\chi}^0_1$ mass difference.

Since the measurement of isolated electrons and muons is straightforward for the ILC detectors, scalar electron and muon production have mainly been studied in fast detector simulations. In [117, 118], a scenario similar to $\delta M\tilde{\tau}$ has been studied assuming an integrated luminosity of 200 fb^{-1} and beam polarisations of $P(e^+, e^-) = (-60\%, +80\%)$ at a center-of-mass energy of $\sqrt{s} = 400$ GeV. The study found precisions of $\delta M(\tilde{\mu}_R) \approx 170$ MeV and $\delta M(\tilde{e}_R) \approx 90$ MeV. Comparable values were found in [116], where in addition a precision of 20 MeV was achieved for $M(\tilde{e}_R)$ from a threshold scan. This

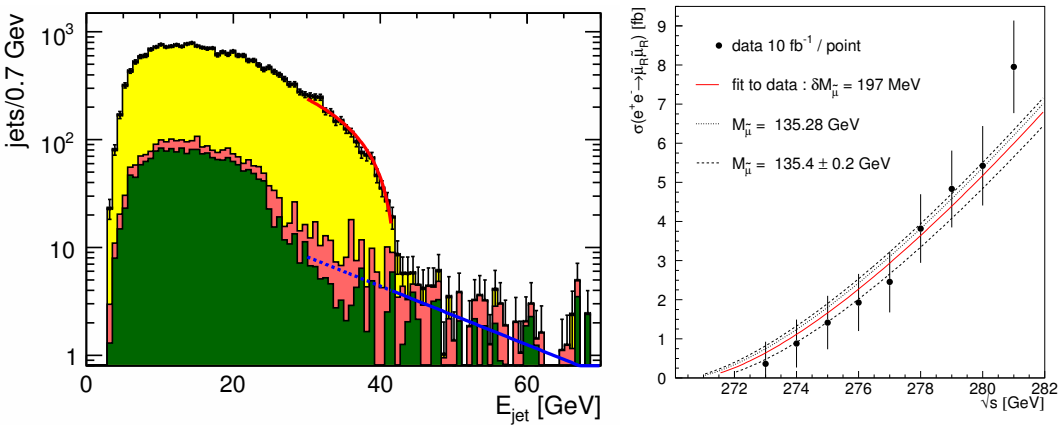

Figure 7.6. Left: Measurement of the $\tilde{\tau}_1$ mass from the endpoint of the τ jet energy spectrum in a scenario with small $\tilde{\tau}_1$-χ_1^0 mass difference very similar to the $\delta M\tilde{\tau}$ scenario introduced in Section 7.4.2. The stacked histogram contains (from the bottom), SUSY background, SM background, signal. The background is fitted in the signal-free region to the right (solid portion of the line), and extrapolated into the signal region (dashed). From [115]. Right: Measurement of the $\tilde{\mu}_R$ mass from a threshold scan with a total integrated luminosity of 100 fb^{-1}. The precision of about 200 MeV obtained in this study is limited by the assumed integrated luminosity [120].

kind of precision below 100 MeV can typically be obtained when no irreducible SUSY background from other cascades is present.

The $\delta M\tilde{\tau}$ scenario is actually challenging in this respect, since substantial background from neutralino decays into muons is present at the $\tilde{\mu}_R$ pair production threshold. This case has recently been studied using the fast simulator SGV [119] tuned to the detector performance found in full simulation of the ILD detector concept. All relevant SM backgrounds, especially $W^+W^- \to l^+\nu l^-\overline{\nu}$, $ZZ \to$ 4 leptons, and μ and τ pairs, as well as all open SUSY channels were generated with Pythia 6.422 at 9 center of mass energies near the $\tilde{\mu}_R$ threshold. The simulations included beamstrahlung based on Circe 1 and the incoming beam energy spectrum according to the TDR design of the ILC. The measured cross-section as a function of the center of mass energy is shown in Figure 7.6 assuming 10 fb^{-1} per point with $P(e^+,e^-) = (-30\%,+80\%)$. A fit to the threshold yields a statistically limited uncertainty of about 200 MeV on the $\tilde{\mu}_R$ mass [120].

In case of the heavier smuon $\tilde{\mu}_L$, a mass resolution of 100 MeV has been achieved in full simulation for the ILD Letter of Intent assuming 500 fb^{-1} with $P(e^+,e^-) = (+30\%,-80\%)$ at $\sqrt{s} = 500$ GeV [121]. This is consistent with earlier fast simulation studies [98, 116].

All resolutions here are by far statistically limited. Masses or cross-sections critical for SUSY parameter determination in a certain scenario could therefore be measured with even better precision when more integrated luminosity is accumulated in the corresponding running configuration of the machine.

7.5.5 Sneutrinos

Depending on the properties of the sparticle spectrum, sneutrinos may decay visibly into modes such as $\tilde{\nu}_\ell \to \ell\tilde{\chi}_1^+$ [2], or they may decay invisibly via $\tilde{\nu}_\ell \to \nu_\ell\tilde{\chi}_1^0$. Even in this latter case, the sneutrino mass can be measured from cascade decays of other sparticles. For instance, in the $\delta M\tilde{\tau}$ scenario, the chargino has a 13% branching fraction into a sneutrino and the corresponding charged lepton. From these decays, the sneutrino mass can be reconstructed to $\delta M(\tilde{\nu}) \approx 0.5$ GeV [122, 123].

Sneutrinos which are too heavy to be produced directly still influence the cross section for chargino production and the forward-backward asymmetry of three-body chargino decays. The latter yields $\delta M(\tilde{\nu}) \approx 10$ GeV for sneutrino masses up to 1 TeV at $\sqrt{s} = 500$ GeV [98]. The chargino pair

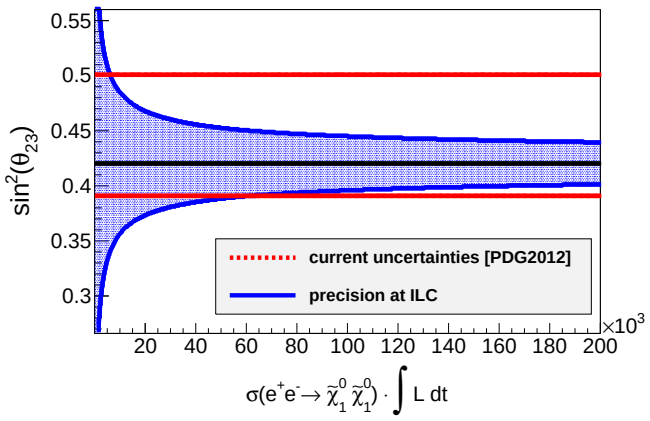

Figure 7.7. The precision expected from ILC measurements on the neutrino mixing angle $\sin^2\theta_{23}$ from RPV decays of the χ_1^0, shown as a function of the number of neutralino pairs produced [129]. The dotted lines give the current precision from neutrino oscillation measurements. Over a large part of the m_0 vs. $m_{1/2}$ plane, the neutralino pair production cross-section is of order 100 fb.

production cross-section is sensitive to sneutrino masses of up to 12 TeV at center-of-mass energies $\sqrt{s} \sim 1$ TeV [124].

7.5.6 Beyond the CP and RP conserving MSSM

R-Parity Violation:

R-parity violation (RPV) has two important experimental consequences at colliders: it allows for single production of SUSY particles, and it allows the LSP to decay to purely SM particles. The latter aspect makes RPV SUSY much harder to detect at the LHC due to the absence of missing transverse energy, so that the currently explored region is significantly smaller than in the R-parity conserving case, even when assuming mass unification at the GUT scale as in the cMSSM [125].

Bilinear R-parity violation (bRPV) has phenomenological motivations in neutrino mixing [126] as well as in leptogenesis [127, 128]. In this case, the characteristic decay $\tilde{\chi}_1^0 \to W^{\pm} l^{\mp}$ will lead to background-free signatures at the ILC, possibly with a detectable lifetime of the $\tilde{\chi}_1^0$ depending on the strength of the RPV couplings. In the hadronic decay mode of the $W^{\pm}$, these events can be fully reconstructed and the $\tilde{\chi}_1^0$ mass can be measured to $\mathcal{O}(100)$ MeV depending on the assumed cross-section [129]. By measuring the ratio of the branching ratios for $\tilde{\chi}_1^0 \to W^{\pm}\mu^{\mp}$ and $\tilde{\chi}_1^0 \to W^{\pm}\tau^{\mp}$, the neutrino mixing angle $\sin^2\theta_{23}$ can be determined to percent-level precision, as illustrated in Figure 7.7. Agreement with measurements from neutrino oscillation experiments would then prove that RPV SUSY is the origin of the structure of mixing in the neutrino sector.

In the case of trilinear R-parity violation, s-channel sneutrino-exchange can interfere with SM Bhabha scattering. For $m_{\tilde{\nu}} < \sqrt{s}$, sharp resonances are expected. In addition, heavier sneutrinos could be detected via contact interactions, for example up to $m_{\tilde{\nu}} = 1.8$ TeV for $\lambda_{1j1} = 0.1$ at $\sqrt{s} = 800$ GeV [101].

CP violation:

An attractive feature of supersymmetry is that it allows for new sources of CP violation which are needed in order to explain the baryon-antibaryon asymmetry observed in the universe. The neutralino and chargino sector can accommodate two independent CP phases, for instance on M_1 and μ when rotating away the phase of M_2 by a suitable redefinition of the fields. While the phase of μ is strongly constrained by EDM bounds, the phase of M_1 could lead to CP sensitive triple product asymmetries up to 10%. These can be measured from neutralino two-body decays into slepton and lepton to $\pm 1\%$. From a fit to the measured neutralino cross-sections, masses and CP-asymmetries, $|M_1|$ and

$|\mu|$ can be determined to a few permille, M_2 to a few percent, Φ_1 to 10% as well as $\tan\beta$ and Φ_μ to 16% and 20%, respectively [130]. Other models of baryogenesis accessible to study at the ILC are discussed in Section 8.1.

NMSSM:

If indeed the higgsino is the LSP, as motivated by naturalness, then all by itself it is not a good dark matter candidate, since higgsino pairs annihilate rapidly into WW and ZZ. However, if we invoke an extended Higgs sector (the NMSSM) to explain the value of the Higgs boson mass, this extension adds a new SUSY partner, the singlino, which might have mass below that of the higgsino. The decay width of the higgsino to the singlino is of order 100 MeV. The pattern of decay final states is rich, and the measurement of branching ratios will illuminate the Higgs sector [131]. These decay products are quite soft, however, and are invisible under the standard LHC trigger constraints. Whether or not these particles can be seen at the LHC, the ILC would again be needed for a complete study. The annihilation cross section of singlinos, which determines the singlino thermal dark matter density, depends on the singlino-higgsino mixing angle. This could be measured at the ILC by measurement of the higgsino width using a threshold scan or by precision measurments of the NMSSM mass eigenvalues.

The capabilities of the ILC to distinguish between the NMSSM and the MSSM when the observable particle spectrum and the corresponding decay chains are very similar has been studied for instance in [132] based on analytical calculations. The study showed that with data taken at three different center-of-mass energies the distinction is possible. When exploiting the available information even more efficiently by applying a global fit, even two center-of-mass energies can be sufficient [133]. If the full neutralino/chargino spectrum is accessible, sum rules for the production cross sections can be exploited that show a different energy behaviour in the two models.

In scenarios where the lightest SUSY particle is nearly a pure singlino, the higgino lifetimes are long, leading to a displaced vertex signature. The lifetimes can be precisely resolved thanks to the excellent vertex resolution of the ILC detectors.

7.5.7 Parameter determination and model discrimination

Beyond simply measuring the properties of new particles, a further goal of ILC is to fully uncover the underlying theory. This involves, among other issues, the measurement of the statistics of the new particles and the verification of symmetry predictions of the model. In this, we review some examples of such studies.

For example, if only the minimal particle content of a weakly interacting new particle χ^0 and an electrically charged partner $\chi^\pm$ is observed, the behaviour of the production cross-section at threshold and the production angle distribution of $\chi^+\chi^-$ pair production can be employed to distinguish between SUSY, where the χ's are fermions, Littlest Higgs models, where they are vector bosons, and Inert Higgs models, where they are scalar bosons [134].

If the model is indeed SUSY, we would like to establish the basic symmetry relation of supersymmety experimentally. This can be done by examining whether the gauge couplings $g(Vff)$ and $\overline{g}(V\tilde{f}\tilde{f})$ of a vector boson V and the Yukawa coupling $\tilde{g}(\tilde{V}f\tilde{f})$ for corresponding gauginos are equal [135]. From the various cross-section measurements in the slepton and gaugino sector, these couplings can be extracted and their equality checked with sub-percent precision [1, 2, 98].

In addition to the couplings, the mass measurements at ILC, at the per mille level, allow one to extract the weak scale MSSM parameters. Here the polarized beams play a crucial role since they allow us to determine the mixing character both in the gaugino and in the slepton sector, especially if left- and right-handed superpartners are close in mass and thus difficult to separate kinematically. These parameters can then be extrapolated to higher energy using the renormalization group equations [136].

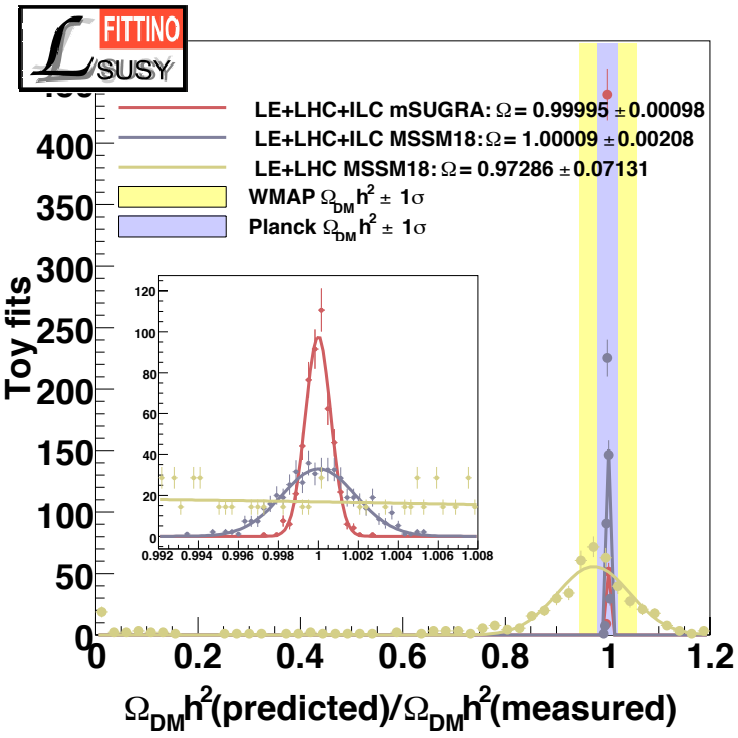

Figure 7.8
Ratio of the predicted value of the dark matter density $\Omega_{\rm pred}h^2$ to the nominal value of $\Omega_{\rm SPS1a}h^2$ in the SPS1a scenario, for a variety of Fittino Toy Fits without using $\Omega_{\rm CDM}h^2$ as an observable, from [142]. The anticipated predictions for LHC and ILC measurements on this model are compared to current and projected cosmological observations.

This might reveal that groups of these parameters unify, for example, at the GUT scale. The impact of ILC precision on this procedure has been studied in detail in [137], based on a scenario in which the color singlet sector is nearly identical to that of the $\delta M\tilde{\tau}$ scenario. They found that the weak scale parameters can be determined to percent level precision, some even to the per mille level. They further showed that ILC precision, beyond that achievable at the LHC, is needed to establish whether the weak scale parameters are consistent with a certain SUSY breaking scheme (in this case mSUGRA) or not. MSSM parameter determinations, both analytically and employing global fits, have been studied also in various other scenarios in [93, 138–140].

Another crucial question to be answered is that of whether the lightest SUSY particle can account for some or all of the cosmological dark matter. Assuming that lightest SUSY particle was produced thermally in the early universe, its relic density can be computed from the Lagrangian parameters obtained from collider data and the result can be compared to the observed value of the dark matter density [141]. The Fittino collaboration has studied the prediction of the dark matter density from ILC data at the reference point $SPS1a'$, which, for this analysis, is very similar to the $\delta M\tilde{\tau}$ scenario [142]. Figure 7.8 shows the result of this comparison without assuming a specific SUSY breaking scenario, *i.e.* based on weak scale parameters. In this scenario, the ILC precision is needed to match the precision of the prediction to that expected from cosmological observations.

The $SPS1a'/\delta M\tilde{\tau}$ point is a rather special case in which $\Omega_{\rm CDM}h^2$ can be predicted with part per mille accuracy. More typically, the mechanisms that establish the dark matter relic density are more complex, and the accuracy of the prediction from collider data is less. We have seen an example already in Section 4.5.3 in our discussion of the stop coannihilation scenario. However, the more complex the physics of the dark matter density, the more important it is to make high precision measurements of the SUSY parameters. This important question will be discussed further in Section 8.2.

7.6 Conclusions

In this section, we have discussed the ILC capabilities for supersymmetry measurements in the light of the new information that we have gained from the LHC experiments. The discovery of a new boson at 125 GeV points to a mechanism of electroweak symmetry breaking that involves weakly coupled scalar fields. Supersymmetry is one of, if not the leading candidate, for such a model.

So far, the ATLAS and CMS experiments have found no evidence for supersymmetric particles. They have presented impressive limits on the masses of squarks and gluinos. However, these limits do not exclude the possibility of SUSY at the TeV scale. Rather, they push us to explore SUSY models in different parameter regions of the MSSM than those that have been given most attention in the past.

In particular, the LHC exclusions have focused much attention on models in which the first- and second-generation squarks are heavy while the naturalness of the electroweak symmetry breaking scale keeps color singlet particles light. Naturalness arguments, in particular, favor a low value of $\mu \sim M_Z$, with μ ranging perhaps as high as 200–300 GeV. This then leads to a spectrum including several light higgsino-like charginos and neutralinos. The lightest neutralino, which is a possible WIMP candidate, would be predominantly higgsino-like. The light higgsinos are automatically mass-degenerate with typical mass gaps of 10-20 GeV. The small energy release from higgsino decay would be very difficult to detect at LHC. In contrast, an ILC with $\sqrt{s} = 0.25 - 1$ TeV would be a *higgsino factory*, in addition to being a Higgs factory! These arguments, and also possibly the muon $g-2$ anomaly, predict a rich array of new matter states likely accessible to the ILC.

In our review of the experiments at the ILC that would discover and measure the properties of these particles, we have emphasize the many tools that the ILC detectors will provide for exploring the nature of these new states of matter. These include the tunable beam energy, the use of beam polarization, precision tracking, vertex finding and calorimetry, which provide the ability to detect very low energetic particles as well as to observe and separate W and Z in hadronic modes. We have shown with many examples that all of these capabilities find new uses in the exploration of a new sector of particles.

The precision measurements available at the ILC will provide a window to physics at much higher energy scales, possibly those associated with grand unification and string theory. The ILC will also provide a key connection between particle physics and cosmology, especially in identifying the nature of dark matter and shedding light on possible mechanisms for baryogenesis.

Supersymmetry is challenged by the new results from the LHC, but this theory is still very attractive for the answers that it gives to the pressing theoretical problems of the Standard Model. The constraints from the LHC guide us to new regions of the large parameter space of supersymmetry. The ILC will explore these regions definitively and make precise measurements of new particles that may be found there. From this perspective, the construction of an ILC is more highly motivated now than ever before.

Bibliography

[1] T. Tsukamoto, K. Fujii, H. Murayama, M. Yamaguchi and Y. Okada, Phys. Rev. D **51**, 3153 (1995).

[2] H. Baer, R. B. Munroe and X. Tata, Phys. Rev. D **54**, 6735 (1996) [Erratum-ibid. D **56**, 4424 (1997)] [hep-ph/9606325].

[3] G. Weiglein *et al.* [LHC/LC Study Group Collaboration], Phys. Rept. **426**, 47 (2006) [hep-ph/0410364].

[4] S. Y. Choi, Eur. Phys. J. C **59**, 543 (2009) [arXiv:0809.1707 [hep-ph]].

[5] J. Wess and B. Zumino, Phys. Lett. B **49**, 52 (1974).

[6] A. Salam and J. A. Strathdee, Phys. Rev. D **11**, 1521 (1975).

[7] A. Salam and J. A. Strathdee, Phys. Lett. B **51**, 353 (1974).

[8] For a review, see *e.g. Weak scale supersymmetry: From superfields to scattering events*, by H. Baer and X. Tata, Cambridge, UK: Univ. Pr. (2006), 537 p.

[9] E. Witten, Nucl. Phys. B **188**, 513 (1981).

[10] R. K. Kaul, Phys. Lett. B **109**, 19 (1982).

[11] S. Ferrara *et al.*, Phys. Rev. D **15**, 1013 (1977).

[12] E. Cremmer, S. Ferrara, L. Girardello and A. Van Proeyen, Nucl. Phys. B **212**, 413 (1983).

[13] For a review, see *e.g.* H. P. Nilles, Phys. Rept. **110**, 1 (1984).

[14] F. D. Steffen, Eur. Phys. J. C **59**, 557 (2009) [arXiv:0811.3347 [hep-ph]].

[15] K. -Y. Choi, J. E. Kim, H. M. Lee and O. Seto, Phys. Rev. D **77**, 123501 (2008) [arXiv:0801.0491 [hep-ph]].

[16] H. Baer, A. Lessa, S. Rajagopalan and W. Sreethawong, JCAP **1106**, 031 (2011) [arXiv:1103.5413 [hep-ph]].

[17] H. Baer, A. Lessa and W. Sreethawong, JCAP **1201**, 036 (2012) [arXiv:1110.2491 [hep-ph]].

[18] K. Rajagopal, M. S. Turner and F. Wilczek, Nucl. Phys. B **358**, 447 (1991).

[19] L. Covi, H. -B. Kim, J. E. Kim and L. Roszkowski, JHEP **0105**, 033 (2001) [hep-ph/0101009].

[20] H. Baer, A. D. Box and H. Summy, JHEP **0908**, 080 (2009) [arXiv:0906.2595 [hep-ph]].

[21] D. Curtin, P. Jaiswal and P. Meade, arXiv:1203.2932 [hep-ph].

[22] W. Buchmüller, R. D. Peccei and T. Yanagida, Ann. Rev. Nucl. Part. Sci. **55**, 311 (2005) [hep-ph/0502169].

[23] I. Affleck and M. Dine, Nucl. Phys. B **249**, 361 (1985).

[24] M. Dine, L. Randall and S. D. Thomas, Nucl. Phys. B **458**, 291 (1996) [hep-ph/9507453].

[25] H. Baer, F. E. Paige, S. D. Protopopescu and X. Tata, hep-ph/9305342.

[26] A. Djouadi, J. -L. Kneur and G. Moultaka, Comput. Phys. Commun. **176**, 426 (2007) [hep-ph/0211331].

[27] R. Arnowitt and P. Nath, "Perspectives on Supersymmetry II," G. L. Kane, ed. (World Scientific, 2010). [arXiv:0912.2273 [hep-ph]].

[28] G. F. Giudice and R. Rattazzi, Phys. Rept. **322**, 419 (1999) [hep-ph/9801271].

[29] L. Randall and R. Sundrum, Nucl. Phys. B **557**, 79 (1999) [hep-th/9810155].

[30] G. F. Giudice, M. A. Luty, H. Murayama and R. Rattazzi, JHEP **9812**, 027 (1998) [hep-ph/9810442].

[31] A. G. Cohen, D. B. Kaplan and A. E. Nelson, Phys. Lett. B **388**, 588 (1996) [hep-ph/9607394].

[32] J. L. Feng, K. T. Matchev and T. Moroi, Phys. Rev. Lett. **84**, 2322 (2000) [hep-ph/9908309].

[33] S. Dimopoulos and G. F. Giudice, Phys. Lett. B **357**, 573 (1995) [hep-ph/9507282].

[34] M. Perelstein and C. Spethmann, JHEP **0704**, 070 (2007) [hep-ph/0702038].

[35] G. Aad *et al.* [ATLAS Collaboration], Phys. Lett. B **710**, 67 (2012) [arXiv:1109.6572 [hep-ex]].

[36] S. Chatrchyan *et al.* [CMS Collaboration], Phys. Rev. Lett. **107**, 221804 (2011) [arXiv:1109.2352 [hep-ex]].

[37] R. L. Arnowitt and P. Nath, Phys. Rev. D **46**, 3981 (1992).

[38] K. L. Chan, U. Chattopadhyay and P. Nath, Phys. Rev. D **58**, 096004 (1998) [hep-ph/9710473].

[39] R. Kitano and Y. Nomura, Phys. Lett. B **631**, 58 (2005) [hep-ph/0509039]; Phys. Rev. D **73**, 095004 (2006) [hep-ph/0602096].

[40] H. Baer, V. Barger, P. Huang, A. Mustafayev and X. Tata, arXiv:1207.3343 [hep-ph].

[41] C. Brust, A. Katz, S. Lawrence and R. Sundrum, JHEP **1203**, 103 (2012) [arXiv:1110.6670 [hep-ph]].

[42] M. Papucci, J. T. Ruderman and A. Weiler, arXiv:1110.6926 [hep-ph].

[43] K. Cheung, C. -W. Chiang and J. Song, JHEP **0604**, 047 (2006) [hep-ph/0512192].

[44] H. Baer, V. Barger and P. Huang, JHEP **1111**, 031 (2011) [arXiv:1107.5581 [hep-ph]].

[45] H. Baer, V. Barger, P. Huang and X. Tata, JHEP **1205**, 109 (2012) [arXiv:1203.5539 [hep-ph]].

[46] C. Csaki, L. Randall and J. Terning, arXiv:1201.1293 [hep-ph].

[47] T. Cohen, A. Hook and G. Torroba, arXiv:1204.1337 [hep-ph].

[48] N. Craig, M. McCullough and J. Thaler, JHEP **1206**, 046 (2012) [arXiv:1203.1622 [hep-ph]].

[49] L. Randall and M. Reece, arXiv:1206.6540 [hep-ph].

[50] G. W. Bennett *et al.* [Muon G-2 Collaboration], Phys. Rev. D **73**, 072003 (2006) [arXiv:hep-ex/0602035].

[51] M. Davier, A. Hoecker, B. Malaescu and Z. Zhang, Eur. Phys. J. C **71**, 1515 (2011) [Erratum-ibid. C **72**, 1874 (2012)] [arXiv:1010.4180 [hep-ph]].

[52] T. Moroi, Phys. Rev. D **53**, 6565 (1996) [Erratum-ibid. D **56**, 4424 (1997)] [hep-ph/9512396].

[53] J. L. Feng and K. T. Matchev, Phys. Rev. Lett. **86**, 3480 (2001) [hep-ph/0102146].

[54] H. Baer, A. Belyaev, T. Krupovnickas and A. Mustafayev, JHEP **0406**, 044 (2004) [hep-ph/0403214].

[55] D. Asner *et al.* [Heavy Flavor Averaging Group], arXiv:1010.1589 [hep-ex].

[56] M. Misiak *et al.*, Phys. Rev. Lett. **98**, 022002 (2007) [hep-ph/0609232].

[57] H. Baer and M. Brhlik, Phys. Rev. D **55**, 3201 (1997) [hep-ph/9610224].

[58] S. Chatrchyan *et al.* [CMS Collaboration], Phys. Rev. Lett. **107** (2011) 191802 [arXiv:1107.5834 [hep-ex]].

[59] T. Aaltonen *et al.* [CDF Collaboration], Phys. Rev. Lett. **107** (2011) 191801 [Erratum-ibid. **107** (2011) 239903] [arXiv:1107.2304 [hep-ex]].

[60] R. Aaij *et al.* [LHCb Collaboration], arXiv:1203.4493 [hep-ex].

[61] K. S. Babu and C. F. Kolda, Phys. Rev. Lett. **84**, 228 (2000) [hep-ph/9909476].

[62] J. K. Mizukoshi, X. Tata and Y. Wang, Phys. Rev. D **66**, 115003 (2002) [hep-ph/0208078].

[63] D. Eriksson, F. Mahmoudi and O. Stal, JHEP **0811**, 035 (2008) [arXiv:0808.3551 [hep-ph]].

[64] E. Barberio *et al.* [Heavy Flavor Averaging Group], arXiv:0808.1297 [hep-ex].

[65] H. Baer, V. Barger and A. Mustafayev, JHEP **1205**, 091 (2012) [arXiv:1202.4038 [hep-ph]].

[66] S. Chatrchyan *et al.* [CMS Collaboration], Phys. Lett. B **716**, 30 (2012) [arXiv:1207.7235 [hep-ex]].

[67] G. Aad *et al.* [ATLAS Collaboration], Phys. Lett. B **716**, 1 (2012) [arXiv:1207.7214 [hep-ex]].

[68] T. Aaltonen *et al.* [CDF and D0 Collaborations], Phys. Rev. Lett. **109**, 071804 (2012) [arXiv:1207.6436 [hep-ex]].

[69] S. Chatrchyan *et al.* [CMS Collaboration], Phys. Lett. B **713**, 68 (2012) [arXiv:1202.4083 [hep-ex]].

[70] ATLAS collaboration, ATLAS-CONF-2012-094.

[71] G. Aad *et al.* [ATLAS Collaboration], JHEP **1206**, 039 (2012) [arXiv:1204.2760 [hep-ex]].

[72] H. Baer, V. Barger and A. Mustafayev, Phys. Rev. D **85**, 075010 (2012) [arXiv:1112.3017 [hep-ph]].

[73] A. Arbey, M. Battaglia, A. Djouadi, F. Mahmoudi and J. Quevillon, Phys. Lett. B **708**, 162 (2012) [arXiv:1112.3028 [hep-ph]].

[74] S. Heinemeyer, O. Stal and G. Weiglein, Phys. Lett. B **710**, 201 (2012) [arXiv:1112.3026 [hep-ph]].

[75] O. Buchmueller, R. Cavanaugh, A. De Roeck, M. J. Dolan, J. R. Ellis, H. Flacher, S. Heinemeyer and G. Isidori *et al.*, Eur. Phys. J. C **72**, 2020 (2012) [arXiv:1112.3564 [hep-ph]].

[76] A. Heister *et al.* [ALEPH Collaboration], Phys. Lett. B **526**, 206 (2002) [hep-ex/0112011].

[77] A. Heister *et al.* [ALEPH Collaboration], Phys. Lett. B **583**, 247 (2004).

[78] J. Abdallah *et al.* [DELPHI Collaboration], Eur. Phys. J. C **31**, 421 (2003) [hep-ex/0311019].

[79] P. Achard *et al.* [L3 Collaboration], Phys. Lett. B **580**, 37 (2004) [hep-ex/0310007].

[80] G. Abbiendi *et al.* [OPAL Collaboration], Eur. Phys. J. C **32**, 453 (2004) [hep-ex/0309014].

[81] G. Aad *et al.* [ATLAS Collaboration], arXiv:1208.0949 [hep-ex].

[82] CMS collaboration, Physics Analysis Summary CMS-PAS-SUS-12-005 (2012).

[83] ATLAS collaboration, ATLAS-CONF-2012-109 (2012).

[84] G. Aad *et al.* [ATLAS Collaboration], Phys. Rev. Lett. **108**, 181802 (2012) [arXiv:1112.3832 [hep-ex]].

[85] H. Baer, V. Barger, S. Kraml, A. Lessa, W. Sreethawong and X. Tata, JHEP **1203**, 092 (2012) [arXiv:1201.5382 [hep-ph]].

[86] G. Aad *et al.* [ATLAS Collaboration], Phys. Rev. Lett. **108**, 261804 (2012) [arXiv:1204.5638 [hep-ex]].

[87] G. Aad *et al.* [ATLAS Collaboration], arXiv:1208.2884 [hep-ex].

[88] H. Baer and X. Tata, Phys. Lett. B **155**, 278 (1985).

[89] H. Baer, C. -h. Chen, F. Paige and X. Tata, Phys. Rev. D **50**, 4508 (1994) [hep-ph/9404212].

[90] N. Arkani-Hamed, S. Dimopoulos, G. F. Giudice and A. Romanino, Nucl. Phys. B **709**, 3 (2005) [hep-ph/0409232].

[91] H. Baer and J. List, arXiv:1205.6929 [hep-ph].

[92] M. W. Cahill-Rowley, J. L. Hewett, S. Hoeche, A. Ismail and T. G. Rizzo, Eur. Phys. J. C **72**, 2156 (2012) [arXiv:1206.4321 [hep-ph]].

[93] J. A. Aguilar-Saavedra *et al.*, Eur. Phys. J. C **46**, 43 (2006) [hep-ph/0511344].

[94] H. Baer, A. Bartl, D. Karatas, W. Majerotto and X. Tata, Int. J. Mod. Phys. A **4**, 4111 (1989).

[95] S. Y. Choi, A. Djouadi, M. Guchait, J. Kalinowski, H. S. Song and P. M. Zerwas, Eur. Phys. J. C **14**, 535 (2000) [hep-ph/0002033].

[96] S. Y. Choi, J. Kalinowski, G. A. Moortgat-Pick and P. M. Zerwas, Eur. Phys. J. C **22**, 563 (2001) [Addendum-ibid. C **23**, 769 (2002)] [hep-ph/0108117].

[97] J. L. Feng and M. E. Peskin, Phys. Rev. D **64**, 115002 (2001) [hep-ph/0105100].

[98] H.-U. Martyn, hep-ph/0302024.

[99] S. Y. Choi, K. Hagiwara, H. -U. Martyn, K. Mawatari and P. M. Zerwas, Eur. Phys. J. C **51** (2007) 753 [hep-ph/0612301].

[100] F. Brummer and W. Buchmuller, JHEP **1107**, 010 (2011) [arXiv:1105.0802 [hep-ph]].

[101] J. A. Aguilar-Saavedra *et al.* [ECFA/DESY LC Physics Working Group Collaboration], hep-ph/0106315.

[102] C. Hensel, PhD Thesis, University of Hamburg, 2002, http://www-flc.desy.de/thesis/doctor.2002.hensel.ps.gz.

[103] T. Suehara and J. List, arXiv:0906.5508 [hep-ex].

[104] K. Desch, J. Kalinowski,G. Moortget-Pick, M. M. Nojiri and G. Polesello, arXiv:hep-ph/0312069.

[105] A. Bharucha, arXiv:1202.6284 [hep-ph], updated including parameter determination in his talk at ICHEP 2012, Melbourne (2012).

[106] S. Ambrosanio and G. A. Blair, Eur. Phys. J. C **12**, 287 (2000) [hep-ph/9905403].

[107] N. Wattimena, PhD Thesis, University of Hamburg, 2009. http://www-library.desy.de/cgi-bin/showprep.pl?desy-thesis-10-006.

[108] S. Matsumoto and T. Moroi, Phys. Lett. B **701**, 422 (2011) [arXiv:1104.3624 [hep-ph]].

[109] H.-U. Martyn, Eur. Phys. J. C **48**, 15 (2006) [hep-ph/0605257].

[110] R. Keranen, A. Sopczak, H. Kluge and M. Berggren, Eur. Phys. J. direct C **2**, 7 (2000).

[111] A. Freitas, C. Milstene, M. Schmitt and A. Sopczak, JHEP **09**, 076 (2008)

[112] A. Belyaev, T. Lastovicka, A. Nomerotski and G. Lastovicka-Medin, Phys. Rev. D **81**, 035011 (2010) [arXiv:0912.2411 [hep-ph]].

[113] M. M. Nojiri, K. Fujii and T. Tsukamoto, Phys. Rev. D **54**, 6756 (1996) [hep-ph/9606370].

[114] M. M. Nojiri, Phys. Rev. D **51**, 6281 (1995) [hep-ph/9412374].

[115] P. Bechtle, M. Berggren, J. List, P. Schade and O. Stempel, Phys. Rev. D **82**, 055016 (2010) [arXiv:0908.0876 [hep-ex]].

[116] P. D. Grannis, hep-ex/0211002.

[117] H.-U. Martyn, hep-ph/0408226.

[118] A. Freitas, H. -U. Martyn, U. Nauenberg and P. M. Zerwas, hep-ph/0409129.

[119] M. Berggren, arXiv:1203.0217 [physics.ins-det].

[120] M. Berggren, private communication.

[121] M. Berggren, N. d'Ascenzo, P. Schade and O. Stempel, arXiv:0902.2434 [hep-ex].

[122] J. Kalinowski, W. Kilian, J. Reuter, T. Robens and K. Rolbiecki, JHEP **0810**, 090 (2008) [arXiv:0809.3997 [hep-ph]].

[123] A. Freitas, W. Porod and P. M. Zerwas, Phys. Rev. D **72**, 115002 (2005) [hep-ph/0509056].

[124] M. Berggren, F. Richard and Z. Zhang, hep-ph/0510088.

[125] H. Baer, C. -H. Chen and X. Tata, Phys. Rev. D **55**, 1466 (1997) [hep-ph/9608221].

[126] W. Porod, M. Hirsch, J. Romao and J. W. F. Valle, Phys. Rev. D **63**, 115004 (2001) [hep-ph/0011248].

[127] S. Bobrovskyi, W. Buchmuller, J. Hajer and J. Schmidt, JHEP **1010**, 061 (2010) [arXiv:1007.5007 [hep-ph]].

[128] S. Bobrovskyi, W. Buchmuller, J. Hajer and J. Schmidt, JHEP **1109**, 119 (2011) [arXiv:1107.0926 [hep-ph]].

[129] B. Vormwald, presentation at the KILC12 workshop, April, 2012.

[130] O. Kittel, G. Moortgat-Pick, K. Rolbiecki, P. Schade and M. Terwort, Eur. Phys. J. C **72**, 1854 (2012) [arXiv:1108.3220 [hep-ph]].

[131] D. Das, U. Ellwanger and A. M. Teixeira, JHEP **1204**, 067 (2012) [arXiv:1202.5244 [hep-ph]].

[132] G. A. Moortgat-Pick, S. Hesselbach, F. Franke and H. Fraas, JHEP **0506**, 048 (2005) [hep-ph/0502036].

[133] A. Hartin, talk at the LCWS 2010 Workshop, Beijing (2010).

[134] M. Asano, T. Saito, T. Suehara, K. Fujii, R. S. Hundi, H. Itoh, S. Matsumoto and N. Okada *et al.*, Phys. Rev. D **84**, 115003 (2011) [arXiv:1106.1932 [hep-ph]].

[135] J. L. Feng, M. E. Peskin, H. Murayama and X. R. Tata, Phys. Rev. D **52**, 1418 (1995) [hep-ph/9502260].

[136] G. A. Blair, W. Porod and P. M. Zerwas, Phys. Rev. D **63**, 017703 (2001) [hep-ph/0007107].

[137] P. Bechtle, K. Desch, W. Porod and P. Wienemann, Eur. Phys. J. C **46**, 533 (2006) [hep-ph/0511006].

[138] E. Boos, H. U. Martyn, G. A. Moortgat-Pick, M. Sachwitz, A. Sherstnev and P. M. Zerwas, Eur. Phys. J. C **30**, 395 (2003) [hep-ph/0303110].

[139] G. A. Blair, A. Freitas, H. -U. Martyn, G. Polesello, W. Porod and P. M. Zerwas, Acta Phys. Polon. B **36**, 3445 (2005) [hep-ph/0512084].

[140] D. Zerwas, AIP Conf. Proc. **1078**, 90 (2009) [arXiv:0808.3506 [hep-ph]].

[141] E. A. Baltz, M. Battaglia, M. E. Peskin and T. Wizansky, Phys. Rev. D **74**, 103521 (2006) [hep-ph/0602187].

[142] P. Bechtle, K. Desch, M. Uhlenbrock and P. Wienemann, Eur. Phys. J. C **66**, 215 (2010) [arXiv:0907.2589 [hep-ph]].

Chapter 8
Cosmological Connections

Two of the major puzzles of cosmology can be explained with new physics at the electroweak scale. These are the matter-antimatter asymmetry, which might be due to baryogenesis at the electroweak phase transition, and the dark matter of the universe, which might be composed of a stable weakly-interacting massive particle (WIMP) with a mass at the hundred GeV scale. We have seen references to both of these mechanisms that might act in the early universe in our discussions of the top quark, extended Higgs sectors, and supersymmetry. In this chapter, we review these topics in a more unified way.

Both electroweak baryogenesis mechanisms and WIMP candidates naturally arise within the two major paradigms for explaining electroweak symmetry breaking, supersymmetry and Higgs compositeness. To work correctly, these phenomena require quite specific details of the spectrum and parameter choices. These details must be verified if we are to understand whether the particles observed at the TeV scale indeed suffice to explain these major cosmological mysteries. The details that we must learn concern aspects of the TeV scale physics that are especially difficult to access at hadron colliders—knowledge of the Higgs spectrum and couplings and the properties of other color-singlet particles, and understanding of the more general new particle spectrum in situations with compressed spectra and small energy release in decays.

The capabilities of the ILC that we have described in earlier chapters are sufficient to meet these challenges. This might be the strongest motivation for the construction of the ILC, that it provides unique opportunities to understand the basic mechanism that form the universe we see around us.

8.1 Baryogenesis at the Electroweak Scale

Among the mechanism for creating the baryon number of the universe, an especially attractive one is the idea that this asymmetry was created as a result of the electroweak phase transition [1]. The high temperature phase of the Standard Model contains a mechanism for baryon number violation, the thermally activated sphaleron solution of the $SU(2)$ gauge theory, which has the ability to simultaneously violate baryon and lepton number. A net baryon asymmetry can be produced if the two other Sakharov conditions are satisfied, that is, if the theory has sufficient appropriate CP violation and if the electroweak phase transition is first-order [2]. The process is non-local, relying on the dynamics in the vicinity of expanding bubbles that grow the broken symmetry phase out of the supercooled high-temperature symmetric phase of the electroweak theory. The walles of these bubbles carry the CP violating interactions [3]. Because it involves electroweak scale physics only, this mechanism is particularly appealing and amenable to experimental test and verification.

EW baryogenesis has been investigated in detail in the Standard Model [4] and its supersymmetric extension [5–9]. Within the SM parametrization of the Higgs potential, the one loop effective potential at high temperature roughly reads

$$V(\phi, T) \approx \frac{1}{2}(\mu^2 + cT^2)\phi^2 + \frac{\lambda}{4}\phi^4 - ET\phi^3 \ , \tag{8.1}$$

where

$$-ET\phi^3 \subset -\frac{T}{12\pi}\sum_{i=W,Z,h} m_i^3(\phi) \tag{8.2}$$

The last term is responsible for a barrier separating the symmetric and broken EW vacua; this barrier gives the possibility of a first-order EW phase transition. The coefficient E is due to *bosonic* degrees of freedom coupling to the Higgs. In the SM, E is too small and the phase transition can be first-order only for a very light Higgs, a possibility that is excluded experimentally [10]. In the MSSM, new bosonic degrees of freedom with large couplings to the Higgs—in particular, the stop $\tilde{t}$—can enhance the value of E and guarantee that ϕ/T can be large enough at the time of the transition to suppress sphaleron washout. This has led to the so-called light stop scenario for EW baryogenesis. Possible extensions of the Higgs sector, without or outside the MSSM, offer other possibilities to realize this mechanism.

8.1.1 Electroweak baryogenesis in supersymmetry

The correlation between the strength of the EW phase transition and the collider signatures of the Higgs boson were recently studied in [11] in the case of a simplified model including a new scalar field X that couples to H according to:

$$-\mathcal{L} = M_X^2|X|^2 + \frac{K}{6}|X|^4 + Q|X|^2|H|^2 = M_X^2|X|^2 + \frac{K}{6}|X|^4 + \frac{1}{2}Q(v^2 + 2vh + h^2)|X|^2 \tag{8.3}$$

These basic interactions describe a broad range of theories. In particular, they apply to the MSSM, where X corresponds to a light, mostly right-handed scalar top quark responsible for one-loop thermally generated cubic Higgs interactions. However, it doe not apply to models where the strength of the EW phase transition is affected by other scalars. The quantity Q parametrizes the strength of the X coupling to the H which will induce the potential barrier.

Analysis of the Higgs potential using this approach or more specific calculations indicates that there is a fine-tuned window of parameter space in the MSSM where EW baryogenesis is viable [12, 13]. It corresponds to a stop-split supersymmetric spectrum illustrated in Fig. 8.1. A light Higgs boson and a light $\tilde{t}_R$, with mass less than 115 GeV, are needed for the EW phase transition to be sufficiently

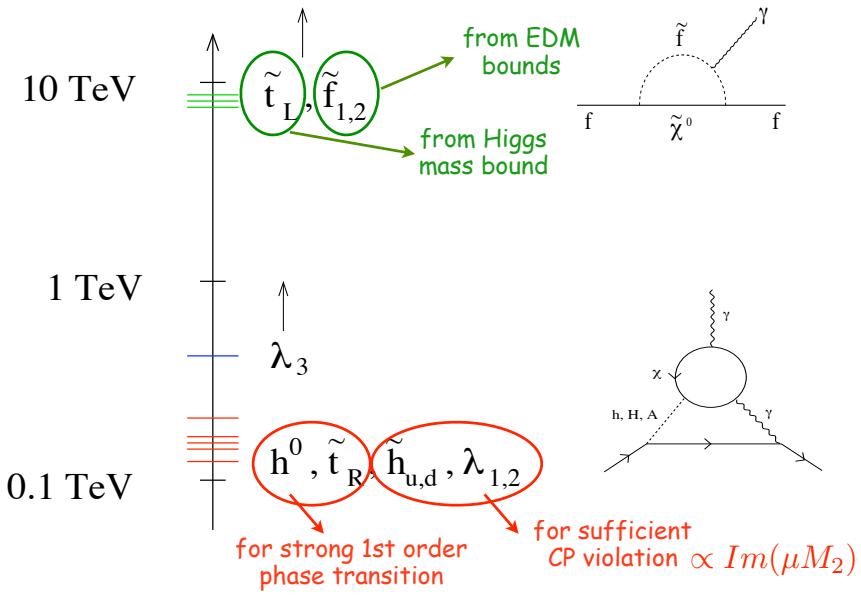

Figure 8.1
The stop-split supersymmetric spectrum of MSSM EW baryogenesis.

first-order. At the same time, the $\tilde{t}_L$ should be heavy to produce a sufficiently heavy Higgs boson to agree with experimental observation. A generic difficulty of EW baryogenesis is that it requires large new sources of CP violation [14] which are typically at odds with experimental constraints from electric dipole moments. To evade these constraints the other sfermions should be also heavy. The mechanism does require a light higgsino and a light chargino to supply CP-violating scattering processes within the expanding bubble walls during the phase transition.

The Higgs boson mass value of about 125 GeV is consistent with this scenario but narrows the parameter space. Additional constraints on the model will be derived once the Higgs branching ratios are measured with higher precision, since new fields that couple to the Higgs can lead to significant modifications of the rates for Higgs boson production and decay. The light stop or, more generally, the X particle, appears in the loop diagrams that are responsible for the Higgs decays to gg and $\gamma\gamma$ (discussed in Section 2.2.3) and can modify these rates by effects of order 1. A new scalar will typically interfere constructively with the top quark contribution to these loops, increasing the partial width to gg but decreasing the width to $\gamma\gamma$. The effect on the rate for $gg \to h \to \gamma\gamma$ is plotted in Fig. 8.2 for the case of the scalar with the quantum numbers of the MSSM stop. From this plot, it is clear that, in the region where the phase transition is sufficiently strongly first-order ($\phi_c/T_c > 0.9$), large deviations are expected with respect to the SM Higgs properties. Actually, it was concluded in [15] that EW baryogenesis in the MSSM can already be excluded using 2011 LHC data, see Fig. 8.3.

However, the MSSM, using only the stop and making no extension of the Higgs sector, may well be too restrictive a context. If the rate for Higgs production and decay to $\gamma\gamma$ remains high compared to the Standard Model, this scenario could remain in play due to new light Higgs particles discoverable at the ILC.

A difficulty with implementing electroweak baryogenesis within the MSSM is that the first-order phase transition appears only as a one-loop effect. It is much easier to obtain a strong first-order phase transition by modifying the Higgs potential at tree level. One straightforward example is to add a scalar singlet. There is an extensive literature on this possibility. A recent and complete study of this scenario was provided in [16]. Interestingly, such a scenario can be theoretically well-motivated in composite models where the Higgs arises as a pseudo-Nambu Goldstone boson of a new strongly interacting sector, as we discuss next.

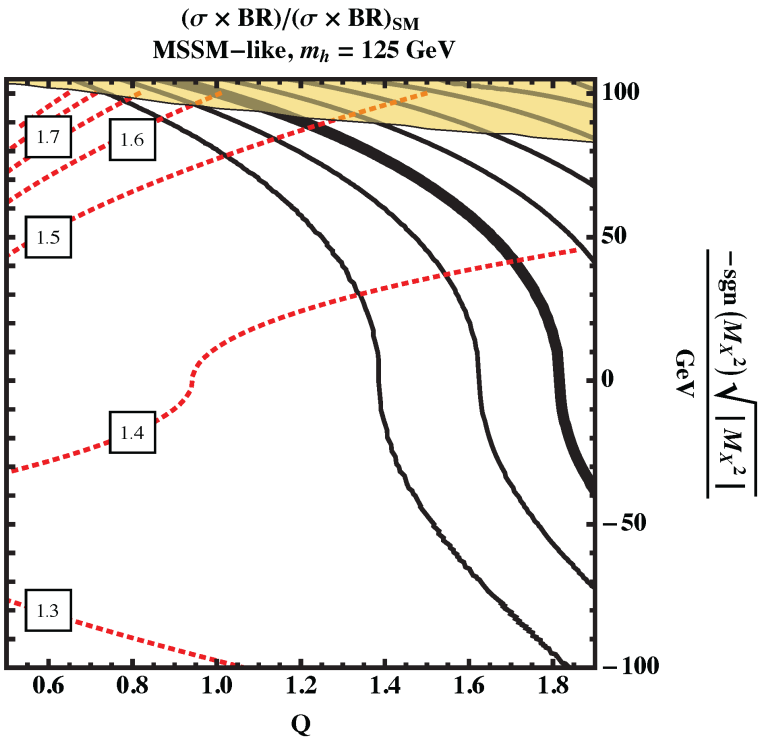

Figure 8.2. Contours of the ratio ϕ_c/T_c of the Higgs field value to the temperature of a first-order electroweak phase transition, for a new boson with the quantum numbers of $\tilde{t}_R$. The bold line denotes $\phi_c/T_c = 0.9$, and the adjacent solid lines delineate steps of $\Delta(\phi_c/T_c) = 0.2$. The yellow shaded region is excluded by the existence of a charge-color minimum. The red dotted lines show contours of the rate for $gg \to h \to \gamma\gamma$ from the Standard Model value, from [11]. The parameters M_X and Q are defined in (8.3).

8.1.2 Electroweak baryogenesis in composite Higgs models

The idea of Higgs compositeness has received a revival of interest in the last few years [17, 18], boosted by the dual description in terms of warped extra dimensional models. In composite Higgs models, the hierarchy between the Planck and TeV scale is due to the slow logarithmic running of an asymtotically free hypercolor interaction that becomes strong and confines close to the EW scale. In analogy with QCD, as the strong interaction confines, the global symmetry acting on the hyperquarks is broken down to a subgroup, delivering Goldstone bosons which are the analogs of the pions in QCD and may be identified as the degrees of freedom belonging to the Higgs doublet. The spectrum of composite Higgs bosons is determined by the structure of this symmetry breaking. The bosons are organized according to a coset space G/H, where G is the symmetry group of the unbroken model and H is the residual symmetry unbroken by the action of the new strong interactions. In these models, the top quark is also composite, since the hierarchy of Yukawa couplings is explained by partial fermion compositeness.

To preserve the custodial symmetry required in the electroweak theory, G should contain an $SO(4)$ subgroup, with the Higgs multiplet transforming in the $(2,2)$ representation. This restricts the possible choices of G and H. In the minimal composite Higgs model, G is the group $SO(5)$, spontaneously broken to $SO(4)$. The full symmetry G is broken by loops of fermions or gauge bosons, which generate mass for the bosons and eventually generate the potential responsible for electroweak symmetry breaking.

To preserve the custodial $SO(4)$ symmetry of the SM, the Higgs should transform as a $(2,2)$ of $SU(2)_L \times SU(2)_R \sim SO(4)$. In the minimal composite Higgs model SO(5) breaks to SO(4),

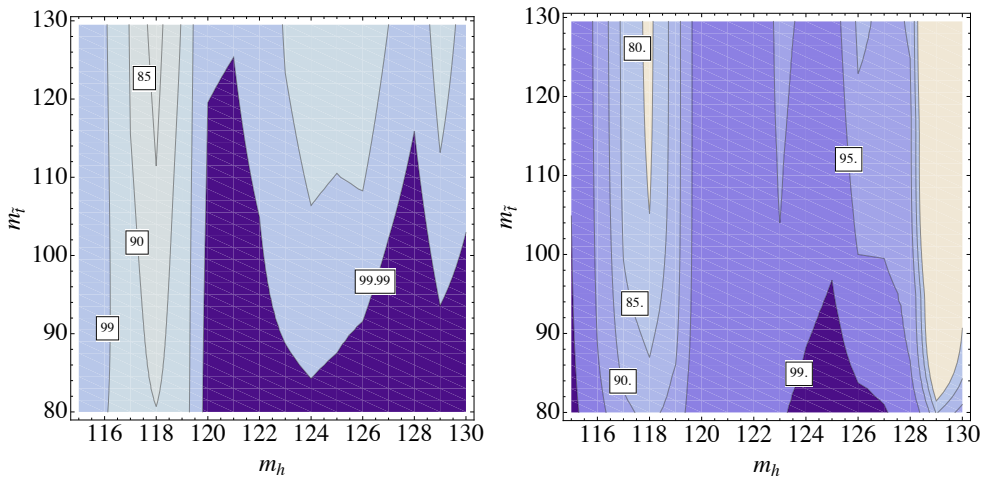

Figure 8.3. Confidence levels of exclusion of a general Light Stop scenario in the $(m_h, m_{\tilde{t}_R})$ plane. $\tilde{t_L}$ is taken very heavy while m_A and $\tan\beta$ are varied in the range (1500, 2000) GeV and (5,15). From [15].

Figure 8.4
Diagram illustrating the largest contribution to the electron EDM due to the Higgs-singlet mixing where the new singlet s couples only to the top quark, as needed for EW baryogenesis and as motivated by the scenario of partial compositeness. From [21].

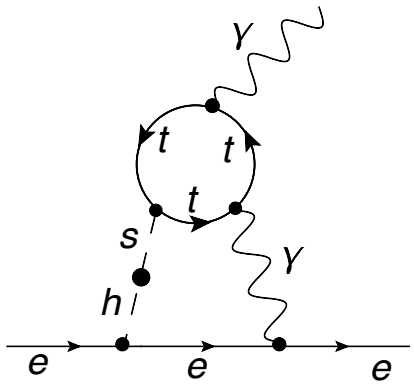

delivering 4 goldstone bosons which are identified as the Higgs degrees of freedom. The $SO(5)$ symmetry is broken explicitly both by the fermions which do not come in complete representations of SO(5) and by the gauging of $SU(2)_L \in SO(5)$. A catalog of possible choices for G and H is presented in [19]. Loops of SM fermions or gauge bosons communicate the explicit breaking to the Goldstone bosons and generate a potential for the Higgs.

These composite Higgs models offer new possibilities for EW baryogenesis. Naturalness in these scenario implies modifications in the Higgs and top sectors, which are precisely the ones believed to be responsible for EW baryogenesis. Specific choices of G and H imply the presence of additional light scalars that can make the electroweak transition first-order. For instance, if the coset is $SO(6)/SO(5)$, we expect an additional singlet [20]. Another possibility is $SO(6)/SO(4) \times SO(2)$, which gives two Higgs doublets.

For the choice $SO(6)/SO(5)$, the extra singlet has a dimension-five pseudoscalar couplings to the top quarks that can break CP. EW baryogenesis in this context has been studied in [21]. The extra singlet is responsible for making the EW phase transition first order. Secondly, if that scalar couples to the top quark it can lead to a non-trivial CP-violating phase along the bubbles of the EW phase transition creating the seed for the sphaleron to generate a non-zero baryon asymmetry. It was shown that the correct amount of asymmetry can be produced in a large region of parameter space. The new complex phases and the mixing between the Higgs and the singlet lead to new contributions to the EDMs of neutron and electron not far from the reach of current and future experiments (see Fig. 8.4). The new singlet and the new CP-violating top couplings will be visible at the ILC as direct

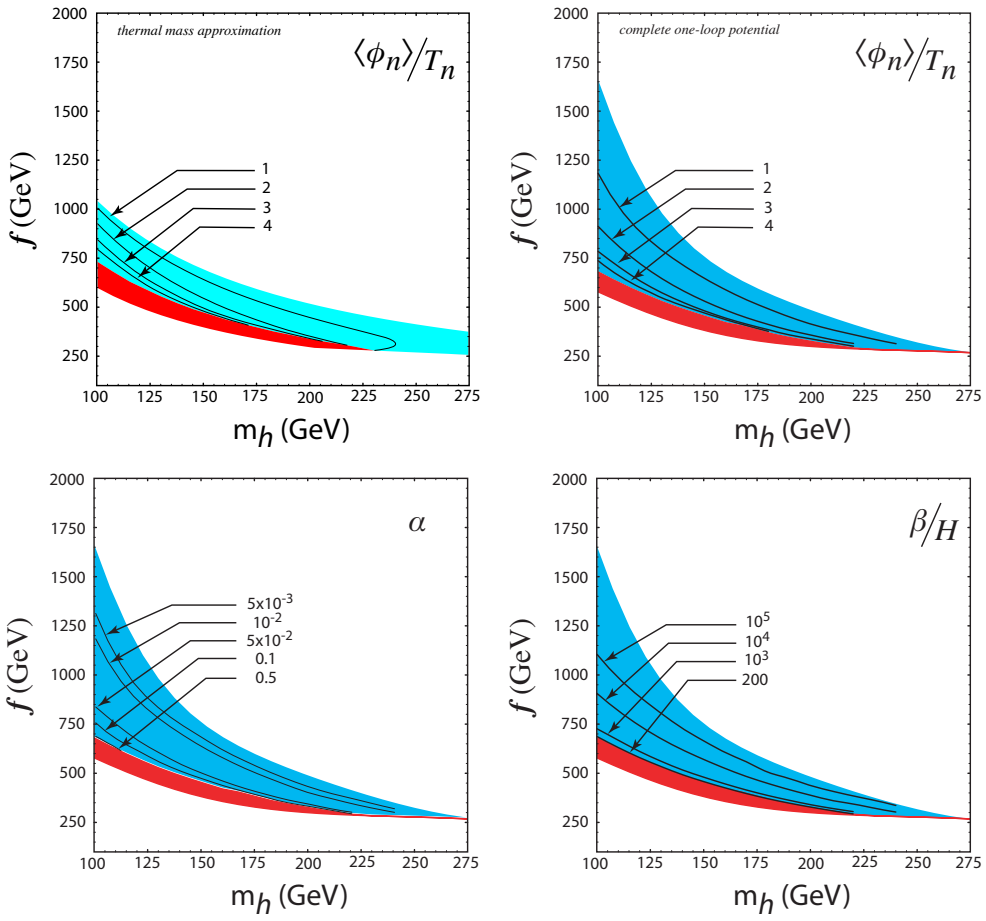

Figure 8.5. Phenomenology of the electroweak phase transition in the effective description (8.4). Upper panel: Contours of the ratio $\langle\phi\rangle/T$ evaluated at the nucleation temperature in the blue region that allows for a first-order EW phase transition. The left plot uses the thermal mass approximation [30] while the right plot uses the full one-loop potential [31]. Below the red lower bound, the EW symmetry remains intact in the vacuum while above the blue upper one, the phase transition is second order or not even occurs. Within the red band, the universe is trapped in a metastable vacuum and the transition never proceeds. The lower panel shows contours of α, the ratio of latent heat to thermal energy density, and $\beta/H = T_n d(S_3/T)/dT$, approximately equal to the number of bubbles per horizon volume, from [31]. These quantities measure the amount of supercooling.

tests of this scenario.

The nature of the EW phase transition has also been studied in a number of contexts that give more specific models of the new strong interactions associated with composite Higgs bosons. These include models of technicolor [22], models with flat extra dimensions [23], and Randall-Sundrum models [24–28]. However, no full calculation of the baryon asymmetry has been carried out in these contexts. In some of these constructions, the EW phase transition can be too strongly first-order, leading to supersonic bubble growth which suppresses diffusion of CP violating densities in front of the bubble walls, thus preventing the mechanism of EW baryogenesis [29].

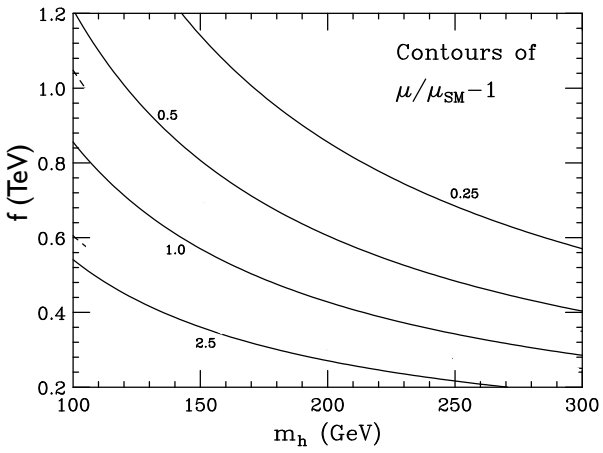

Figure 8.6
Contours of $\mu/\mu_{SM} - 1$ in the (m_h, f) plane.

8.1.3 Effective field theory approach to the EW phase transition

The influence of tree-level modifications of the Higgs potential in making the EW phase transition strongly first order can be analyzed more generally using an effective field theory approach. For example, one can add dimension-6 operators to the Higgs potential, allowing a negative value for the quartic coupling [30, 31]:

$$V(\phi) = \mu^2|\phi|^2 - \lambda|\phi|^4 + \frac{|\phi|^6}{f^2} \tag{8.4}$$

The phenomenology of this effective theory is illustrated in Fig. 8.5, which shows contours of quantities characterizing the strength of the phase transition and the amount of supercooling in the (m_h, f) plane. From these plots, it is clear that a phase transition that is strong enough for EW baryogenesis arises in a sizable region of parameter space.

In the parameter region of interest, a potential such as (8.4) leads to deviations of order 1 in the Higgs self-couplings. We can write the potential for the Higgs field h, the fluctuation from the vacuum expectation value, as

$$\mathcal{L} = m_H^2 h^2/2 + \mu h^3/3! + \eta h^4/4! + \cdots \tag{8.5}$$

when, from the effective theory (8.4),

$$\mu = 3\frac{m_H^2}{v} + 6\frac{v^3}{f^2} \qquad \eta = 3\frac{m_H^2}{v^2} + 36\frac{v^2}{f^2}. \tag{8.6}$$

The SM couplings are recovered as $f \to \infty$ [30]. Figure 8.6 shows contours of $\mu/\mu_{\rm SM} - 1$ in the f vs. m_H plane. Therefore, non-trivial probes of the Higgs potential may be obtained from precise measurements of the trilinear Higgs coupling. See [32] for other examples. As we have emphasized in Section 2.6.3, this is a difficult quantity to measure at any collider, but it is expected to be accessible at the ILC with an accuracy that clearly distinguishes the curves in the figure.

The bubble wall velocity is a key quantity entering the calculation of the baryon asymmetry. A model-independent and unified description of the different regimes (detonation, deflagration, hybrid, runaway) characterizing bubble growth was presented in [29]. The results are summarized in Fig. 8.7,, which shows contours for the bubble wall velocity in the plane (η, α_N) where η and α_N are dimensionless parameters characterizing the strength of the phase transition (roughly the ratio of latent heat to thermal energy density) and the amount of friction. In the SM, $\eta \sim 1/1000$, while in the MSSM, $\eta \sim 1/30$. Eventually, one would have to calculate these quantities from measured parameters of the Higgs potential and the new particle spectrum for a reliable computation of the baryon asymmetry.

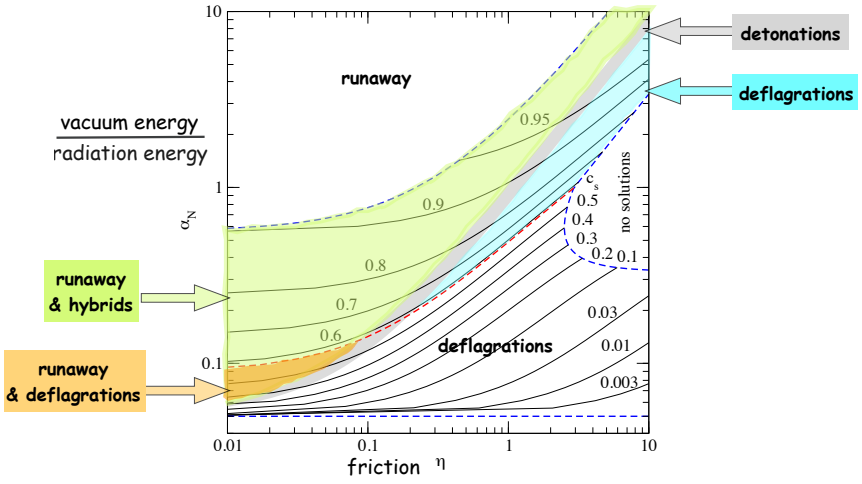

Figure 8.7
Contours of the bubble wall velocity in a first-order cosmic phase transition in the (η, α_N) plane, from [29].

8.2 Dark matter

The existence and central role of dark matter is now one of the pillars of the standard model of cosmology. There are many pieces of evidence, from galactic length scales, cluster lengths scales, and the largest observable scales in the universe, that roughly 20% of the energy and 80% of the mass in the Universe is in the form of massive, non-baryonic particles with relatively weak interactions with ordinary matter [33, 34]. There are many proposals for the nature of this dark matter. The proposed particles span an enormous range in mass, from 10^{-5} eV to macroscopic and even planetary-scale masses. However, the most attractive proposal, and the one that we will concentrate on here, is that the particle that makes up dark matter is a 'weakly-interacting massive particle' (WIMP).

8.2.1 Dark matter and the WIMP paradigm

A WIMP is defined as a weakly interacting neutral particle that is stable over the lifetime of the universe. WIMPs can be created or destroyed only in pairs. The WIMP model further assumes that the WIMPs were in thermal equilibrium with the hot plasma of Standard Model particles early in the history of the universe. This initial condition allows us to predict the current density of WIMPs. In the model, when the temperature of the universe decreased below the WIMP mass, WIMPs began to annihilate, but, because the anninhilation requires a pair of WIMPs, the annihilation cut off when the density of WIMPs reached a well-defined small value. The density of WIMPs decreased further due to the expansion of the universe. However, as the Universe cooled, this small density of massive WIMPs eventually came to dominate the energy in radiation. By this logic, it is possible to derive an expression for Ω, the current energy density of the universe in WIMPs, in the form

$$\Omega \sim \frac{x_F T_0^3}{\rho_c M_{Pl}} \frac{1}{\langle \sigma_{ann} v \rangle} \ . \tag{8.7}$$

In this expression, $x_F = m/T_F$, with m the WIMP mass and T_F is the freeze-out temperature at which annihilation turns off, T_0 is the temperature of photons today, ρ_c is the critical energy density, M_{Pl} is the Planck scale, and $\langle \sigma_{ann} v \rangle$ is the inclusive cross section for WIMP pair annihilation into SM particles, averaged over the WIMP thermal velocity distribution at freeze-out. Typically $x_F \approx 25$, with weak dependence on the WIMP mass, and the other parameters in the equation, including Ω, are well measured. The expression (8.7) then determines the value of the annihilation cross section needed for the entire dark matter relic density to be composed of a single WIMP species. The result

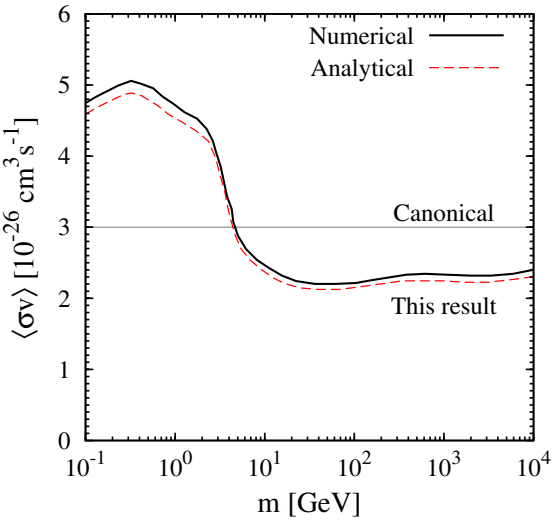

Figure 8.8
Desired annihilation cross section $\langle\sigma v\rangle$ to obtain the measured thermal relic density, as a function of the WIMP mass m (from [35]). The line marked "canonical" shows the often-quoted value 3×10^{26} cm^3/s.

is shown in Fig. 8.8 [35]. The required value is roughly

$$\langle\sigma_{ann} v\rangle \approx (1 \text{ pb}) \cdot c \,, \tag{8.8}$$

indicating that a WIMP with mass and interactions at the electroweak scale naturally leads to the required density of dark matter.

This observation motivates searches for WIMPs with masses of the order of 100 GeV, making use of techniques from particle physics. The three pillars of WIMP searches are: indirect detection of residual annihilation of WIMPs in the galactic neighborhood, direct detection of ambient WIMPs scattering in sensitive detectors on Earth, and artificial production of of WIMPs at high energy accelerators.

If a candidate particle for WIMP dark matter can be produced at the ILC, the precision study of its mass and properties available through the ILC measurements might make it possible to predict its pair annihilation cross section and thus its thermal relic density. This prediction could then be compared to the density of dark matter measured by astrophysical observations. This possibility of a direct connection between physics at the smallest and largest length scales is extremely enticing. Later in this section, we will discuss a number of scenarios in which the ILC makes such a comparison possible.

8.2.2 Theories of WIMPs

By far the most popular vision of WIMP dark matter is the neutralino found in supersymmetric theories. Supersymmetric theories are particularly amenable to searches at the LHC, because they contain a wealth of new colored states (squarks and gluons) with large hadroproduction cross sections. Such particles can decay into the dark matter plus jets of hadrons, leading to events characterized by hadronic activity together with a large imbalance of transverse momentum. As of this writing, the absence of a signal places limits on the masses of squarks and gluons to be substantially in excess of 1 TeV, depending on the fine details of the mass spectrum [36, 37]. The null results of these searches, especially when combined with the identification of the resonance near 125 GeV as the Higgs boson, have led some to propose that, if supersymmetry is realized in nature, it may not be minimal [38]. Nonetheless, viable points with modest fine-tuning still exist [39], and for the purposes of this discussion we will stay within the minimal supersymmetric extension of the SM. We have given a more detailed overview of the possibilities for supersymmetry consistent with the LHC constraints in Chapter 7.

Searches for supersymmetry based on the 2011 LHC data have focused on searches for the colored superpartners [40]. Such searches are important in terms of characterizing the overall scale of superpartner masses, but offer only limited information on the properties of supersymmetric dark matter. As the LHC collects more data and at higher energies, it becomes more sensitive to direct production of electroweak superpartners, and thus has more directly to say about the properties of dark matter. However, as we have stressed in Section 7.3, some spectra for electroweak SUSY spectra will continue to be very difficult to explore at the LHC.

Beyond supersymmetric theories, the most studied candidates for WIMP dark matter include the lightest Kaluza-Klein particle in 5-dimensional [41, 42] or 6-dimensional [43, 44] theories with Universal Extra Dimensions [45], and a light neutral vector boson in little Higgs theories [46, 47] incorporating T-parity [48]. All of these theories are primarily distinguished from supersymmetric theories in that the WIMP is a boson rather than a Majorana fermion. One other nonsupersymmetric theory which affords some contrast is based on a warped extra dimension [49] and has a dark matter particle which is a Dirac fermion [50–53].

Recently, there has also been activity aimed at capturing features of WIMP dark matter in cases where the particles mediating the interactions are heavy compared to the energy transfer of the processes of interest, by making use of effective field theory (EFT) descriptions of WIMPs [54–57] Such effective field theories allow for one to capture the low energy properties of any theory which is amenable to an EFT description, and facilitates comparisons between the different types of searches for dark matter. The picture which emerges from such studies is that there is a large degree of complementarity between direct, indirect, and collider searches. Direct and indirect detection constraints are typically stronger than collider bounds, but also subject to relatively large astrophysical uncertainties, and only apply to interactions which do not vanish in the limit in which WIMPs are non-relativistic. Instead, collider bounds apply roughly uniformly to any type of interaction involving the particles available in the initial state, but are limited for heavy WIMP masses by the finite energy available in the collision.

Another feature which is easily discerned from effective theory descriptions is that bounds from the Tevatron and LHC typically apply to WIMP couplings to quarks and gluons, whereas the couplings most relevant at a high energy e^+e^- collider are the couplings to electrons and photons. While the most popular models of dark matter predict that couplings to quarks and leptons are comparable, it is possible to construct leptophilic models [58–60], motivated in part by the observation of an anomalous positron flux by the PAMELA and Fermi LAT collaborations [61, 62].

Beyond the straightforward freeze-out paradigm, there are other models of dark matter for which dark matter particles at the electroweak scale are relevant. The universe energy density stored in WIMPs may exhibit an explicit dependence on extra parameters, in particular the dark matter mass, for instance in models of asymmetric dark matter, *e.g.* [63]. Dark matter may also be produced by 'freeze-in' scenarios such as that in [64] or in scenarios where DM is is produced through decays [65].

8.2.3 Determination of dark matter parameters

Once dark matter is detected through a non-gravitational interaction, and is thus confirmed to be some kind of weakly interacting particle, the primary question will be whether or not its annihilation cross section is of the correct size for it to explain the cosmic dark matter as a thermal relic. If the annihilation cross section reconstructed from measurements on the particle is consistent with the determinations of the dark matter density, it will provide evidence that the thermal history of the Universe was (at least approximately) standard back to the time that the dark matter froze out—about 1 nsec after the Big Bang. This would parallel the argument the successful predictions of Big Bang nucleosynthesis based on measurements in nuclear physics lead to a compelling picture of

the history of the Universe back to temperatures of order MeV [66] and times of order 1 second.

In principle, the most direct determination of the dark matter annihilation cross section would come from an observation by indirect detection experiments which look for annihilation of WIMPs in the galaxy. In practice, this is a daunting task, because of large uncertainties in astrophysical backgrounds, which can mask or pollute the signal, and in the distribution of dark matter itself, which enters into the observed photon flux as the density squared integrated along the line of sight of the observation. In addition, a relatively few final states are expected to be observable on the Earth, necessarily leading to an incomplete picture. In addition, the annihilation cross section observed in indirect detection might be very different from the one that determined the dark matter cross section in the early universe. If the cross section is strongly velocity-dependent, as happens, for example, in some SUSY models, annihilation channels which were important at the time of freeze-out ($v \sim 0.1$) may be subdominant in the galaxy today ($v \sim 10^{-3}$).

Direct detection experimentscan be used to estimate the annihilation cross section only if analyzed in an effective-interaction picture. In this context, they are sensitive only to couplings of dark matter to colored SM particles, which could turn out to represent a relatively unimportant fraction of the totality of WIMP annihilation. Direct detection also loses track of some types of interactions which may be important for WIMP annihilation, but are suppressed in the non-relativistic limit of elastic scattering.

Because of these limitations, colliders are likely to play the central role in providing the data from which to compute a WIMP relic density that can be compared with cosmological observations. We emphasize that this requires a complete picture of dark matter interactions with all SM species. Hadron colliders such as the LHC have large rates of production for exotic colored particles (and also typically higher energies, allowing searches for more massive particles), but also larger backgrounds that can hide many possible decay channels. In a typical theory of WIMPs such as the MSSM or UED models, the relic density is controlled by a a complicated interplay between annihilations into colored and uncolored states. For all of these reasons, input from an e^+e^- collider such as ILC is likely to be essential.

8.2.4 ILC studies of dark matter parameter determination

In this section, we will review studies that have been done on the determination of dark matter parameters from collider data. Our discussion is based mainly on a few of the most detailed studies of the MSSM [67, 68]. These studies assume LHC running at $\sqrt{s} = 14$ TeV with data sets of hundreds of fb^{-1}. Under such conditions, many of the measurements will be systematics limited and thus the precise assumptions for collected data sample are less important than the assumed collision energy. The specific models analyzed in these papers are now excluded by LHC searches; however, as we have discussed in Section 7.4, very similar models with heavier squarks and gluinos are still viable and even attractive. Other examples of dark matter density determination are given in Section 7.5 and in [70–79].

In [68, 69], two mSUGRA-inspired models are investigated in terms of the ability of the LHC and 500 GeV ILC to reconstruct the spectrum and couplings of the neutralino. Model B′ is characterized by low sparticle masses and large mass splittings, resulting in a model that is particularly amenable to reconstruction using LHC measurements alone. In Figure 8.9, we show the sparticle spectrum and the range of reconstructed relic densities for model B′. The color-singlet sector of this model is similar to that of the benchmark model presented in Section 7.4.2. The derived relic density indicates that for this case, LHC data alone can predict the WIMP relic density to order 1 in Ω. Adding data from the ILC, which would be very rich given the low values of the superparticle masses, the prediction for Ω is given to 20% accuracy. This model is very similar to model LCC1 studied in [67]. In that study,

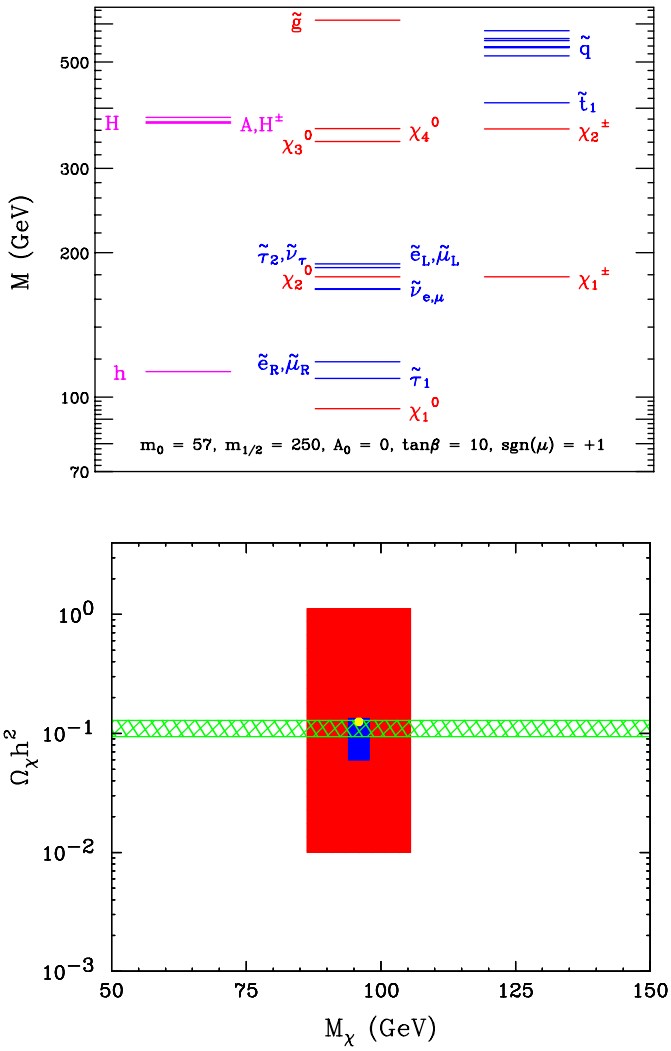

Figure 8.9
Projections for the estimation of the dark matter relic density from colliders in the supersymmetric B′ model described in [68, 69]. Top: Spectrum of the model. Bottom: Projections for determination of the WIMP mass and inferred relic density based on measurements at the LHC (red rectangle) and ILC (blue rectangle). The measurement of the relic density from cosmology is indicated by the green hatched region. The actual model prediction is shown as the yellow dot.

including information from a wider range of ILC observables, it is possible to predict the relic density to lie within a few percent of the underlying value.

In [67], three additional MSSM parameter choices (LCC2-4) are investigated from the point of view of indirect and direct searches for dark matter, LHC searches, and an ILC at $\sqrt{s} = 500$ GeV and 1000 GeV, in order to see how many relevant dark matter properties can be reconstructed. In Model LCC3, the relic density is largely controlled by late coannihilation of the lightest neutralino with a stau. The small mass splitting renders the stau particularly challenging to reconstruct at the LHC. In Fig. 8.10, we show the sparticle spectrum and the range of reconstructed relic densities for model LCC3. As shown, the LHC has essentially no ability to reconstruct the relic density, because it is unable to obtain precise enough measurements of the neutralino and stau masses and the important parameter $\tan\beta$. In addition, and the neutralino and tau compositions leave large uncertainties in the coannhilation cross section. At the 500 GeV ILC, the situation clarifies, but remains rather uncertain, because while the neutralino and stau masses become much better measured, the neutralino composition remains uncertain. A 1 TeV ILC can fill in this remaining information, and results in a reasonably precise measurement of Ωh^2 to within a factor of two.

In LCC4, the relic density is driven by neutralinos which annihilate through a heavy Higgs resonance that is approximately on-shell because the SUSY Higgses have masses $\sim 2m_{\chi_1^0}$. The colored sparticles are heavy (roughly at the current LHC exclusion limits for the gluino and first two generations of squarks and well above the current limits on third generation squarks). This point is a

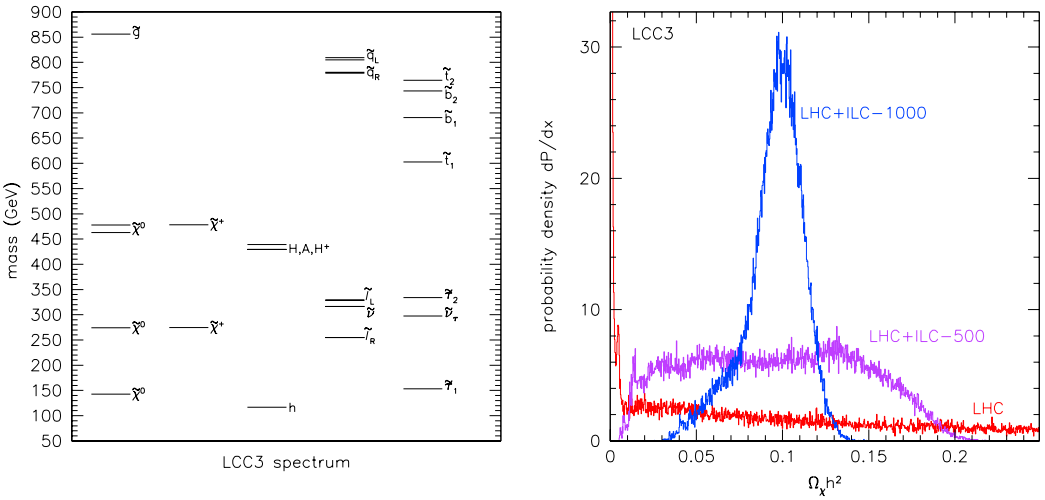

Figure 8.10. Projections of the estimation of the dark matter relic density from colliders, at the MSSM point LCC3, from [67]. Left: Mass spectrum of the model. Right: Probability distribution of the predicted relic density based on measurements at the LHC alone (red histogram), LHC + a 500 GeV ILC (magenta histogram) and LHC + a 1000 GeV ILC (blue histogram).

particular challenge for the LHC (despite the fact that it is able to observe much of the spectrum of particles) to reconstruct, because it requires very high precision measurements of the mass of the lightest neutralino and the mass and width of the pseudo-scalar Higgs boson A^0, as well as reasonably precise knowledge of the lightest neutralino composition; see Fig. 8.11. The resulting relic density prediction is peaked at very low values, with a substantial tail that extends past the WMAP measurement. At the 500 GeV ILC, the situation remains somewhat fuzzy, because the pseudo-scalar Higgs remains out of kinematic reach, though the composition of the neutralino becomes much-better understood. At the 1000 GeV ILC, the pair-production process $e^+e^- \to HA$ opens up, and the picture becomes reasonably clear.

Over-all, the picture that emerges is one in which the ILC is often necessary to provide the crucial information allowing one to reconstruct the relic density of neutralinos. Whether it is effective in accomplishing this goal is largely dependent on whether or not it has enough energy to access the important states. In the case studies shown here, the LHC data will be able to identify the relevant mass scales for new particles, but after the LHC program it still remains unclear which particles exactly are crucial to determining the neutralino annihilation rate and the relic density. That can be determined only by more detailed studies of the neutralino which are made possible at the ILC.

As a final example, we consider a leptophilic model of dark matter. If interactions between a generic Dirac WIMP χ and the SM leptons are mediated by a heavy vector particle, they may be described by the effective vertex,

$$\frac{1}{M_*^2}\,\overline{\chi}\gamma^\nu\chi \sum_{\ell=e,\mu,\tau} \overline{\ell}\gamma_\nu\ell \tag{8.9}$$

We assume that there are no couplings to quarks at tree level. The parameter M_* is a dimensionful coupling constant which maps on to the description of Z' exchange through $1/M_*^2 \leftrightarrow g_\ell g_\chi/M_{Z'}^2$. If this interaction is the only way dark matter can interact with the SM, the observed relic density will be obtained for $M_* \sim 1$ TeV for a WIMP mass around 100 GeV [58]. A dark matter model of this type is constrained by LEP II through the L3 [80] and DELPHI [81] measurements of the process $e^+e^- \to \nu\overline{\nu}\gamma$ to $M_* \geq 480$ GeV [82]. While in principle the LHC could hope to observe processes such as $pp \to e^+e^-\chi\overline{\chi}$, these processes are very rare and unlikely to provide better bounds than the

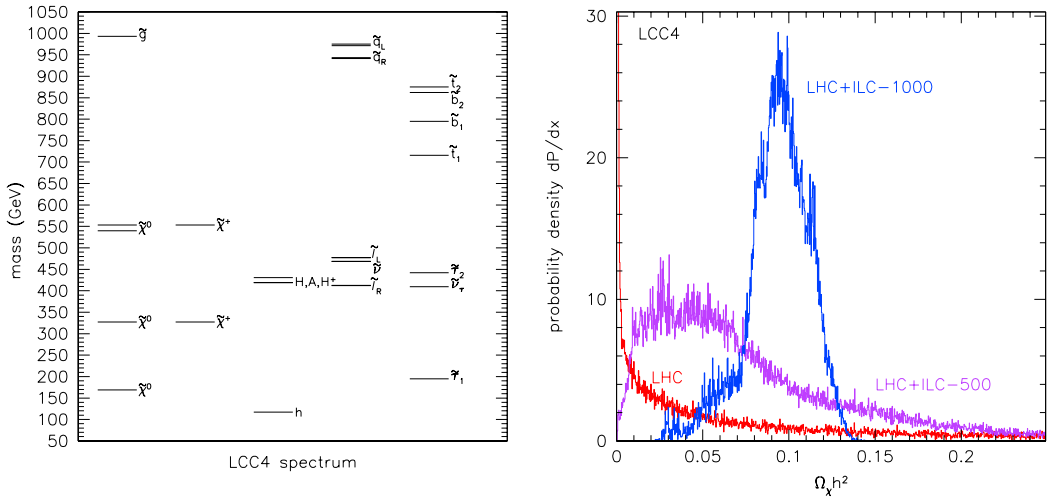

Figure 8.11. Projetions of the estimation of the dark matter relic density from colliders, at the MSSM point LCC4, from [67]. Left: Mass spectrum of the model. Right: Probability distribution of the predicted relic density based on measurements at the LHC alone (red histogram), LHC + a 500 GeV ILC (magenta histogram) and LHC + a 1000 GeV ILC (blue histogram).

LEP searches. A recent 500 GeV ILC study of the process $e^+e^- \to \chi\overline{\chi}\gamma$ reveals the ability to place much more stringent limits on the cross section, particularly if the beams are polarized, which allows one to reduce the SM background [83]. The limits on the cross section translate into limits on M_* of about 1.7 TeV for 100 GeV mass WIMPs. Then the ILC will be able to discover or rule out this class of leptophobic dark matter, and confirm its nature as a thermal relic.

8.3 Conclusions

In this section, we have reviewed in some detail models of baryogenesis and dark matter associated with new physics at the TeV energy scale. The discussion of models rapidly becomes complex and technical, because the predictions of the models for the baryon asymmetry and dark matter depend on detailed properties of the model. The most crucial aspects of the models come in the Higgs sector and in the superpartners or more general partners of Higgs and gauge bosons. At hadron colliders, it is very difficult even to discover these particles. In all but the simplest models, reaching the level of detail that is required to make predictions relevant to cosmology is quite beyond the capabilities of hadron collider experiments.

Experiments at the ILC also must be lucky. The relevant new particles—extended Higgs bosons, neutralinos, sleptons—must be light enough to be observed at the ILC in pair production. But, given this possibility, the ILC experiments will have the power to test theories of the type that we have discussed. Thus, the ILC offers unique opportunities to connect detailed aspects of particle physics to grand questions about the composition of the universe.

Bibliography

[1] V. A. Kuzmin, V. A. Rubakov and M. E. Shaposhnikov, Phys. Lett. B **155**, (1985) 36.

[2] A. D. Sakharov, Pisma Zh. Eksp. Teor. Fiz. **5**, 32 (1967) [JETP Lett. **5**, 24 (1967)] [Sov. Phys. Usp. **34**, 392 (1991)] [Usp. Fiz. Nauk **161**, 61 (1991)].

[3] A. G. Cohen, D. B. Kaplan and A. E. Nelson, Phys. Lett. B **245** (1990) 561; Nucl. Phys. B **349** (1991) 727; Nucl. Phys. B **373** (1992) 453; Phys. Lett. B **336** (1994) 41 [hep-ph/9406345]. For a review see e.g J. M. Cline, [hep-ph/0609145].

[4] M. Joyce, T. Prokopec and N. Turok, Phys. Rev. D **53** (1996) 2930 [arXiv:hep-ph/9410281]. M. Joyce, T. Prokopec and N. Turok, Phys. Rev. D **53** (1996) 2958 [arXiv:hep-ph/9410282].

[5] P. Huet and A. E. Nelson, Phys. Rev. D **53** (1996) 4578 [arXiv:hep-ph/9506477].

[6] J. M. Cline, M. Joyce and K. Kainulainen, JHEP **0007** (2000) 018 [arXiv:hep-ph/0006119].

[7] M. S. Carena, M. Quiros, M. Seco and C. E. M. Wagner, Nucl. Phys. B **650**, 24 (2003) [arXiv:hep-ph/0208043].

[8] T. Konstandin, T. Prokopec, M. G. Schmidt and M. Seco, Nucl. Phys. B **738**, 1 (2006) [arXiv:hep-ph/0505103].

[9] V. Cirigliano, S. Profumo and M. J. Ramsey-Musolf, JHEP **0607** (2006) 002 [arXiv:hep-ph/0603246].

[10] F. Csikor, Z. Fodor, J. Heitger, Phys. Rev. Lett. **82** (1999) 21-24. [hep-ph/9809291].

[11] T. Cohen, D. E. Morrissey and A. Pierce, arXiv:1203.2924 [hep-ph].

[12] M. Carena, G. Nardini, M. Quiros and C. E. M. Wagner, Nucl. Phys. B **812**, 243 (2009) [arXiv:0809.3760 [hep-ph]].

[13] A. Delgado, G. Nardini and M. Quiros, JHEP **1204**, 137 (2012) [arXiv:1201.5164 [hep-ph]].

[14] M. B. Gavela, P. Hernandez, J. Orloff, O. Pene, Mod. Phys. Lett. **A9**, 795-810 (1994). [hep-ph/9312215, hep-ph/9312215].

[15] D. Curtin, P. Jaiswal and P. Meade, arXiv:1203.2932 [hep-ph].

[16] J. R. Espinosa, T. Konstandin and F. Riva, Nucl. Phys. B **854**, 592 (2012) [arXiv:1107.5441 [hep-ph]].

[17] K. Agashe, R. Contino and A. Pomarol, Nucl. Phys. B **719**, 165 (2005) [hep-ph/0412089].

[18] R. Contino, arXiv:1005.4269 [hep-ph].

[19] J. Mrazek, A. Pomarol, R. Rattazzi, M. Redi, J. Serra and A. Wulzer, Nucl. Phys. B **853**, 1 (2011) [arXiv:1105.5403 [hep-ph]].

[20] B. Gripaios, A. Pomarol, F. Riva and J. Serra, JHEP **0904**, 070 (2009) [arXiv:0902.1483 [hep-ph]].

[21] J. R. Espinosa, B. Gripaios, T. Konstandin and F. Riva, JCAP **1201**, 012 (2012) [arXiv:1110.2876 [hep-ph]].

[22] J. M. Cline, M. Jarvinen, F. Sannino, Phys. Rev. **D78**, 075027 (2008). [arXiv:0808.1512 [hep-ph]]. M. Jarvinen, T. A. Ryttov, F. Sannino, Phys. Rev. **D79**, 095008 (2009). [arXiv:0903.3115 [hep-ph]].

[23] G. Panico and M. Serone, JHEP **0505**, 024 (2005) [hep-ph/0502255].

[24] P. Creminelli, A. Nicolis and R. Rattazzi, JHEP **0203** (2002) 051 [arXiv:hep-th/0107141].

[25] L. Randall and G. Servant, JHEP **0705** (2007) 054 [arXiv:hep-ph/0607158].

[26] G. Nardini, M. Quiros and A. Wulzer, JHEP **0709** (2007) 077 [arXiv:0706.3388 [hep-ph]].

[27] T. Konstandin, G. Nardini and M. Quiros, arXiv:1007.1468 [hep-ph].

[28] T. Konstandin and G. Servant, JCAP **1112**, 009 (2011) [arXiv:1104.4791 [hep-ph]].

[29] J. R. Espinosa, T. Konstandin, J. M. No and G. Servant, JCAP **1006** (2010) 028 [arXiv:1004.4187 [hep-ph]].

[30] C. Grojean, G. Servant and J. D. Wells, Phys. Rev. D **71**, 036001 (2005) [hep-ph/0407019].

[31] C. Delaunay, C. Grojean and J. D. Wells, JHEP **0804**, 029 (2008) [arXiv:0711.2511 [hep-ph]].

[32] A. Noble and M. Perelstein, Phys. Rev. D **78**, 063518 (2008) [arXiv:0711.3018 [hep-ph]].

[33] G. Bertone, D. Hooper and J. Silk, Phys. Rept. **405**, 279 (2005) [hep-ph/0404175].

[34] J. L. Feng, Ann. Rev. Astron. Astrophys. **48**, 495 (2010) [arXiv:1003.0904 [astro-ph.CO]].

[35] G. Steigman, B. Dasgupta and J. F. Beacom, arXiv:1204.3622 [hep-ph].

[36] ATLAS Collaboration, ATLAS-CONF-2012-033 (2012).

[37] CMS Collaboration, CMS-SUS-12-011 (2012).

[38] L. J. Hall, D. Pinner and J. T. Ruderman, JHEP **1204**, 131 (2012) [arXiv:1112.2703 [hep-ph]].

[39] M. W. Cahill-Rowley, J. L. Hewett, A. Ismail and T. G. Rizzo, arXiv:1206.5800 [hep-ph].

[40] For a recent status report with theoretical perspective, see: S. Kraml, arXiv:1206.6618 [hep-ph].

[41] G. Servant and T. M. P. Tait, Nucl. Phys. B **650**, 391 (2003) [hep-ph/0206071].

[42] H. -C. Cheng, J. L. Feng and K. T. Matchev, Phys. Rev. Lett. **89**, 211301 (2002) [hep-ph/0207125].

[43] G. Burdman, B. A. Dobrescu and E. Ponton, JHEP **0602**, 033 (2006) [hep-ph/0506334].

[44] B. A. Dobrescu, D. Hooper, K. Kong and R. Mahbubani, JCAP **0710**, 012 (2007) [arXiv:0706.3409 [hep-ph]].

[45] T. Appelquist, H. -C. Cheng and B. A. Dobrescu, Phys. Rev. D **64**, 035002 (2001) [hep-ph/0012100].

[46] J. Hubisz and P. Meade, Phys. Rev. D **71**, 035016 (2005) [hep-ph/0411264].

[47] A. Birkedal, A. Noble, M. Perelstein and A. Spray, Phys. Rev. D **74**, 035002 (2006) [hep-ph/0603077].

[48] H. -C. Cheng and I. Low, JHEP **0309**, 051 (2003) [hep-ph/0308199].

[49] L. Randall and R. Sundrum, Phys. Rev. Lett. **83**, 3370 (1999) [hep-ph/9905221].

[50] K. Agashe and G. Servant, Phys. Rev. Lett. **93**, 231805 (2004) [hep-ph/0403143].

[51] K. Agashe and G. Servant, JCAP **0502**, 002 (2005) [hep-ph/0411254].

[52] C. B. Jackson, G. Servant, G. Shaughnessy, T. M. P. Tait and M. Taoso, JCAP **1004**, 004 (2010) [arXiv:0912.0004 [hep-ph]].

[53] G. Belanger, A. Pukhov and G. Servant, JCAP **0801**, 009 (2008) [arXiv:0706.0526 [hep-ph]].

[54] A. Birkedal, K. Matchev and M. Perelstein, Phys. Rev. D **70**, 077701 (2004) [hep-ph/0403004].

[55] Q. -H. Cao, C. -R. Chen, C. S. Li and H. Zhang, JHEP **1108**, 018 (2011) [arXiv:0912.4511 [hep-ph]].

[56] M. Beltran, D. Hooper, E. W. Kolb and Z. C. Krusberg, Phys. Rev. D **80**, 043509 (2009) [arXiv:0808.3384 [hep-ph]].

[57] W. Shepherd, T. M. P. Tait and G. Zaharijas, Phys. Rev. D **79**, 055022 (2009) [arXiv:0901.2125 [hep-ph]].

[58] R. Harnik and G. D. Kribs, Phys. Rev. D **79**, 095007 (2009) [arXiv:0810.5557 [hep-ph]].

[59] P. J. Fox and E. Poppitz, Phys. Rev. D **79**, 083528 (2009) [arXiv:0811.0399 [hep-ph]].

[60] Q. -H. Cao, E. Ma and G. Shaughnessy, Phys. Lett. B **673**, 152 (2009) [arXiv:0901.1334 [hep-ph]].

[61] O. Adriani *et al.* [PAMELA Collaboration], Nature **458**, 607 (2009)

[62] M. Ackermann *et al.* [Fermi LAT Collaboration], Phys. Rev. Lett. **108**, 011103 (2012) [arXiv:1109.0521 [astro-ph.HE]].

[63] M. Cirelli, P. Panci, G. Servant and G. Zaharijas, JCAP **1203**, 015 (2012) [arXiv:1110.3809 [hep-ph]].

[64] X. Chu, T. Hambye and M. H. G. Tytgat, JCAP **1205**, 034 (2012) [arXiv:1112.0493 [hep-ph]].

[65] W. Buchmuller, V. Domcke and K. Schmitz, Phys. Lett. B **713**, 63 (2012) [arXiv:1203.0285 [hep-ph]].

[66] K. A. Olive, G. Steigman and T. P. Walker, Phys. Rept. **333**, 389 (2000) [astro-ph/9905320].

[67] E. A. Baltz, M. Battaglia, M. E. Peskin and T. Wizansky, Phys. Rev. D **74**, 103521 (2006) [hep-ph/0602187].

[68] A. Birkedal, K. Matchev, J. Alexander, K. Ecklund, L. Fields, R. C. Gray, D. Hertz and C. D. Jones *et al.*, eConf C **050318**, 0708 (2005) [hep-ph/0507214].

[69] A. Birkedal, AIP Conf. Proc. **805**, 55 (2006) [hep-ph/0509199].

[70] J. L. Feng, M. E. Peskin, H. Murayama and X. R. Tata, Phys. Rev. D **52**, 1418 (1995) [hep-ph/9502260].

[71] B. C. Allanach, G. Belanger, F. Boudjema and A. Pukhov, JHEP **0412**, 020 (2004) [hep-ph/0410091].

[72] M. M. Nojiri, G. Polesello and D. R. Tovey, JHEP **0603**, 063 (2006) [hep-ph/0512204].

[73] S. Matsumoto, M. Asano, K. Fujii, T. Honda, R. S. Hundi, H. Ito, S. Kanemura and T. Nabeshima *et al.*, Nuovo Cim. **034C**, 93 (2011).

[74] J. A. Conley, H. K. Dreiner and P. Wienemann, Phys. Rev. D **83** (2011) 055018 [arXiv:1012.1035 [hep-ph]].

[75] H. Baer, V. Barger, P. Huang and X. Tata, JHEP **1205**, 109 (2012) [arXiv:1203.5539 [hep-ph]].

[76] T. Moroi, Y. Shimizu and A. Yotsuyanagi, Phys. Lett. B **625**, 79 (2005) [hep-ph/0505252].

[77] T. Moroi and Y. Shimizu, Phys. Rev. D **72**, 115012 (2005) [hep-ph/0509196].

[78] S. Kanemura, S. Matsumoto, T. Nabeshima and H. Taniguchi, Phys. Lett. B **701**, 591 (2011) [arXiv:1102.5147 [hep-ph]].

[79] E. Kato, M. Asano, K. Fujii, S. Matsumoto, Y. Takubo and H. Yamamoto, arXiv:1203.0762 [hep-ph].

[80] P. Achard *et al.* [L3 Collaboration], Phys. Lett. B **587**, 16 (2004) [hep-ex/0402002].

[81] J. Abdallah *et al.* [DELPHI Collaboration], Eur. Phys. J. C **38**, 395 (2005) [hep-ex/0406019].

[82] P. J. Fox, R. Harnik, J. Kopp and Y. Tsai, Phys. Rev. D **84**, 014028 (2011) [arXiv:1103.0240 [hep-ph]].

[83] C. Bartels, M. Berggren and J. List, arXiv:1206.6639 [hep-ex].

Chapter 9
Conclusion

In this report, we have surveyed the range of physics topics that will be addressed by the ILC.

Our primary emphasis has been on the study of a Standard Model-like Higgs boson. The discovery of a new boson by the ATLAS and CMS experiments has vaulted the question of its properties of the top of the list of questions in high energy physics. We have argued that the ILC is perfectly matched to this problem. The ILC will be able to deliver a precise description of the properties of this new particle.

The ability of the ILC to operate at several different energies plays an important role in its ability to study the Higgs boson. We have described three phases of the Higgs boson program. First, at $\sqrt{s} = 250$ GeV, one may expect the precision measurement of the Higgs mass and its major branching fractions and the search for invisible and exotic modes. Second, at $\sqrt{s} = 500$ GeV, we anticipate precision measurements of the Higgs coupling to the W boson and the higher statistics study of modes with small branching fractions. Finally, at $\sqrt{s} = 1$ TeV, for the measurement of the Higgs couplings to the top quark and the muon, and the Higgs self-coupling can be made. The suite of measurements at these three energies combines to provide a complete picture of the interactions of the Higgs particle and an incisive test of its role in the generation of mass for all elementary particles.

We have also emphasized the ability of the ILC to carry out precision measurements of the properties of the W and Z bosons and the top quark, and of elementary $e^+e^- \to 2$ fermion reactions. In addition, we have shown that the ILC has excellent capabilities to study new color-singlet particles that might be present in the mass range of a few hundred GeV.

The nature of the Higgs boson and the origin of electroweak symmetry breaking remains a central and puzzling problem. The traditional approaches to this problem either involve strong coupling in the Higgs sector, building the Higgs boson as a composite state, or weak coupling in the Higgs sector, realizing the Higgs as one member of a new multiplet of particles. Both types of models have been reshaped by the discoveries and exclusions from the LHC.

If the Higgs sector is strongly coupled, the model must be one with a light composite Higgs boson and additional vectorlike particles at the TeV scale. We have shown how the precision measurement capabilities of the ILC will give important clues to the properties of these models that will not be available from the LHC.

If the Higgs sector is weakly coupled, it is very likely that there are new color-singlet particles that are extremely difficult to study at the LHC. We have argued, in particular, that the LHC results motivate models of supersymmetry that have a spectrum of this type. The colored states of the supersymmetry spectrum may well be discovered in the 14 TeV program of the LHC. The lightest particles of supersymmetry, with their possible connection to the dark matter of the universe, will require the ILC for their proper understanding. For the highly motivated case of natural supersymmetry, the ILC could make the definitive test of this class of models, since charged higgsinos are expected to be present with mass below about 200 GeV. If these light higgsinos do indeed exist, then ILC would

be a higgsino factory in addition to a Higgs factory.

For both types of models, the precision study of the Higgs boson will provide essential clues. To obtain these clues, we have shown that it will be necessary to measure the couplings of the Higgs boson at the few percent level. The ILC will give us that capability.

For all of these reasons, the physics questions that are before us now call for the ILC as the next major facility in high energy physics.

List of Signatories

The following list of signatories represents a comprehensive list of those people who have contributed to the R&D and design work, for both the accelerator and the detectors, which is summarised in this report. The list also includes those people who wish to indicate their support for the next phases of the worldwide ILC effort.

It should be noted that inclusion in this list does not indicate any formal commitment by the signatories. It does not indicate commitment to the specific detector designs presented, nor exclusive support for ILC over other collider programs.

A. Abada[171], T. Abe[24], T. Abe[236], J. M. Abernathy[379], H. Abramowicz[265], A. Abusleme[231], S. Aderhold[47], O. Adeyemi[333], E. Adli[357,251], C. Adloff[164], C. Adolphsen[251], K. Afanaciev[209], M. Aguilar[31], S. Ahmad[93], A. Ahmed[382], H. Aihara[375], R. Ainsworth[237,139], S. Airi[154], M. Aizatskyi[208], T. Akagi[73], M. Akemoto[71], A. Akeroyd[367], J. Alabau-Gonzalvo[108], C. Albajar[46], J. E. Albert[379], C. Albertus[281], J. Alcaraz Maestre[31], D. Alesini[174], B. Alessandro[128], G. Alexander[265], J. P. Alexander[43], A. Alhaidari[243], N. Alipour Tehrani[33], B. C. Allanach[323], O. Alonso[311], J. Alwall[210], J. W. Amann[251], Y. Amhis[167], M. S. Amjad[167], B. Ananthanarayan[83], A. Andreazza[386,122], N. Andreev[58], L. Andricek[186], M. Anduze[172], D. Angal-Kalinin[258], N. Anh Ky[106,394], K. A. Aniol[18], K. I. Aoki[148], M. Aoki[148], H. Aoyagi[137], S. Aoyama[250], S. J. Aplin[47], R. B. Appleby[343,40], J. Arafune[96], Y. Arai[71], S. Araki[71], L. Arazi[404], A. Arbey[50], D. Ariza[47], T. Arkan[58], N. D. Arnold[7], D. Arogancia[194], F. Arteche[113], A. Aryshev[71], S. Asai[375], T. Asaka[137], T. Asaka[212], E. Asakawa[220], M. Asano[333], F. B. Asiri[58], D. Asner[225], M. Asorey[286], D. Attié[21], J. E. Augustin[169], D. B. Augustine[58], C. S. Aulakh[226], E. Avetisyan[47], V. Ayvazyan[47], N. Azaryan[142], F. Azfar[358], T. Azuma[246], O. Bachynska[47], H. Baer[355], J. Bagger[141], A. Baghdasaryan[407], S. Bai[102], Y. Bai[384], I. Bailey[40,176], V. Balagura[172,107], R. D. Ball[329], C. Baltay[405], K. Bamba[198], P. S. Bambade[167], Y. Ban[9], E. Banas[268], H. Band[384], K. Bane[251], M. Barbi[362], V. Barger[384], B. Barish[17,65], T. Barklow[251], R. J. Barlow[392], M. Barone[58,65], I. Bars[368], S. Barsuk[167], P. Bartalini[210], R. Bartoldus[251], R. Bates[332], M. Battaglia[322,33], J. Baudot[94], M. Baylac[170], P. Bechtle[295], U. Becker[185,33], M. Beckmann[47], F. Bedeschi[126], C. F. Bedoya[31], S. Behari[58], O. Behnke[47], T. Behnke[47], G. Belanger[165], S. Belforte[129], I. Belikov[94], K. Belkadhi[172], A. Bellerive[19], C. Belver Aguilar[108], A. Belyaev[367,259], D. Benchekroun[184], M. Beneke[57], M. Benoit[33], A. Benot-Morell[33,108], S. Bentvelsen[213], L. Benucci[331], J. Berenguer[31], T. Bergauer[224], S. Berge[138], E. Berger[7], J. Berger[251], C. M. U. Berggren[47], Z. Bern[318], J. Bernabeu[108], N. Bernal[295], G. Bernardi[169], W. Bernreuther[235], M. Bertucci[119], M. Besancon[21], M. Bessner[47], A. Besson[94,306], D. R. Bett[358,140], A. J. Bevan[234], A. Bhardwaj[326], A. Bharucha[333], G. Bhattacharyya[241], B. Bhattacherjee[150], B. Bhuyan[86], M. E. Biagini[174], L. Bian[102], F. Bianchi[128], O. Biebel[182], T. R. Bieler[190], C. Biino[128], B. Bilki[7,337], S. S. Biswal[221], V. Blackmore[358,140], J. J. Blaising[164], N. Blaskovic Kraljevic[358,140], G. Blazey[217], I. Bloch[48], J. Bluemlein[48], B. Bobchenko[107], T. Boccali[126], J. R. Bogart[251], V. Boisvert[237], M. Bonesini[121], R. Boni[174], J. Bonnard[168], G. Bonneaud[169], S. T. Boogert[237,139], L. Boon[233,7],

G. Boorman[237,139], E. Boos[180], M. Boronat[108], K. Borras[47], L. Bortko[48], F. Borzumati[272], M. Bosman[294], A. Bosotti[119], F. J. Botella[108], S. Bou Habib[401], P. Boucaud[171], J. Boudagov[142], G. Boudoul[89], V. Boudry[172], D. Boumediene[168], C. Bourgeois[167], A. Boveia[52], A. Brachmann[251], J. Bracinik[315], J. Branlard[47,58], B. Brau[346], J. E. Brau[356], R. Breedon[320], M. Breidenbach[251], A. Breskin[404], S. Bressler[404], V. Breton[168], H. Breuker[33], C. Brezina[295], C. Briegel[58], J. C. Brient[172], T. M. Bristow[329], D. Britton[332], I. C. Brock[295], S. J. Brodsky[251], F. Broggi[119], G. Brooijmans[42], J. Brooke[316], E. Brost[356], T. E. Browder[334], E. Brücken[69], G. Buchalla[182], P. Buchholz[301], W. Buchmuller[47], P. Bueno[111], V. Buescher[138], K. Buesser[47], E. Bulyak[208], D. L. Burke[251], C. Burkhart[251], P. N. Burrows[358,140], G. Burt[40], E. Busato[168], L. Butkowski[47], S. Cabrera[108], E. Cabruja[32], M. Caccia[389,122], Y. Cai[251], S. S. Caiazza[47,333], O. Cakir[6], P. Calabria[89], C. Calancha[71], G. Calderini[169], A. Calderon Tazon[110], S. Callier[93], L. Calligaris[47], D. Calvet[168], E. Calvo Alamillo[31], A. Campbell[47], G. I. E. Cancelo[58], J. Cao[102], L. Caponetto[89], R. Carcagno[58], M. Cardaci[201], C. Carloganu[168], S. Caron[97,213], C. A. Carrillo Montoya[123], K. Carvalho Akiba[291], J. Carwardine[7], R. Casanova Mohr[311], M. V. Castillo Gimenez[108], N. Castro[175], A. Cattai[33], M. Cavalli-Sforza[294], D. G. Cerdeno[111], L. Cerrito[234], G. Chachamis[108], M. Chadeeva[107], J. S. Chai[260], D. Chakraborty[217], M. Champion[254], C. P. Chang[201], A. Chao[251], Y. Chao[210], J. Charles[28], M. Charles[358], B. E. Chase[58], U. Chattopadhyay[81], J. Chauveau[169], M. Chefdeville[164], R. Chehab[89], A. Chen[201], C. H. Chen[203], J. Chen[102], J. W. Chen[210], K. F. Chen[210], M. Chen[330,102], S. Chen[199], Y. Chen[1], Y. Chen[102], J. Cheng[102], T. P. Cheng[351], B. Cheon[66], M. Chera[47], Y. Chi[102], P. Chiappetta[28], M. Chiba[276], T. Chikamatsu[193], I. H. Chiu[210,210], G. C. Cho[220], V. Chobanova[186], J. B. Choi[36,36], K. Choi[157], S. Y. Choi[37], W. Choi[375,248], Y. I. Choi[260], S. Choroba[47], D. Choudhury[326], D. Chowdhury[83], G. Christian[358,140], M. Church[58], J. Chyla[105], W. Cichalewski[263,47], R. Cimino[174], D. Cinca[337], J. Clark[58], J. Clarke[258,40], G. Claus[94], E. Clement[316,259], C. Clerc[172], J. Cline[187], C. Coca[206], T. Cohen[251], P. Colas[21], A. Colijn[213], N. Colino[31], C. Collard[94], C. Colledani[94], N. Collomb[258], J. Collot[170], C. Combaret[89], B. Constance[33], C. A. Cooper[58], W. E. Cooper[58], G. Corcella[174], E. Cormier[29], R. Cornat[172], P. Cornebise[167], F. Cornet[281], G. Corrado[123], F. Corriveau[187], J. Cortes[286], E. Cortina Gil[303], S. Costa[308], F. Couchot[167], F. Couderc[21], L. Cousin[94], R. Cowan[185], W. Craddock[251], A. C. Crawford[58], J. A. Crittenden[43], J. Cuevas[283], D. Cuisy[167], F. Cullinan[237], B. Cure[33], E. Currás Rivera[110], D. Cussans[316], J. Cvach[105], M. Czakon[235], K. Czuba[401], H. Czyz[365], J. D'Hondt[399], W. Da Silva[169], O. Dadoun[167], M. Dahiya[327], J. Dai[102], C. Dallapiccola[346], C. Damerell[259], M. Danilov[107], D. Dannheim[33], N. Dascenzo[47,238], S. Dasu[384], A. K. Datta[67], T. S. Datta[115], P. Dauncey[80], T. Davenne[259], J. David[169], M. Davier[167], W. De Boer[90], S. De Cecco[169], S. De Curtis[120], N. De Groot[97,213], P. De Jong[213], S. De Jong[97,213], C. De La Taille[93], G. De Lentdecker[307], S. De Santis[177], J. B. De Vivie De Regie[167], A. Deandrea[89], P. P. Dechant[49], D. Decotigny[172], K. Dehmelt[257], J. P. Delahaye[251,33], N. Delerue[167], O. Delferriere[21], F. Deliot[21], G. Della Ricca[388], P. A. Delsart[170], M. Demarteau[7], D. Demin[142], R. Dermisek[87], F. Derue[169], K. Desch[295], S. Descotes-Genon[171], A. Deshpande[252], A. Dexter[40], A. Dey[81], S. Dhawan[405], N. Dhingra[226], V. Di Benedetto[58,123], B. Di Girolamo[33], M. A. Diaz[231], A. Dieguez[311], M. Diehl[47], R. Diener[47], S. Dildick[331], M. O. Dima[206], P. Dinaucourt[167,93], M. S. Dixit[19], T. Dixit[252], L. Dixon[251], A. Djouadi[171], S. Doebert[33], M. Dohlus[47], Z. Dolezal[34], H. Dong[102], L. Dong[102], A. Dorokhov[94], A. Dosil[112], A. Dovbnya[208], T. Doyle[332], G. Doziere[94], M. Dragicevic[224], A. Drago[174], A. J. Dragt[345], Z. Drasal[34], I. Dremin[179], V. Drugakov[209], J. Duarte Campderros[110], F. Duarte Ramos[33], A. Dubey[272], A. Dudarev[142], E. Dudas[171,171], L. Dudko[180], C. Duerig[47], G. Dugan[43], W. Dulinski[94], F. Dulucq[93], L. Dumitru[206], P. J. Dunne[80], A. Duperrin[27], M. Düren[147], D. Dzahini[170], H. Eberl[224], G. Eckerlin[47], P. Eckert[297], N. R. Eddy[58],

W. Ehrenfeld[295], G. Eigen[314], S. Eisenhardt[329], L. Eklund[332], L. Elementi[58], U. Ellwanger[171], E. Elsen[47], I. Emeliantchik[209], L. Emery[7], K. Enami[71], K. Endo[71], M. Endo[375], J. Engels[47], C. Englert[49], S. Eno[345], A. Enomoto[71], S. Enomoto[197], F. Eozenou[21], R. Erbacher[320], G. Eremeev[269], J. Erler[287], R. Escribano[294], D. Esperante Pereira[108], D. Espriu[311], E. Etzion[265,33], S. Eucker[47], A. Evdokimov[336,107], E. Ezura[71], B. Faatz[47], G. Faisel[201], L. Fano[125], A. Faraggi[340], A. Fasso[251], A. Faus-Golfe[108], L. Favart[307], N. Feege[257], J. L. Feng[321], T. Ferber[47], J. Ferguson[33], J. Fernández[283], P. Fernández Martínez[108], E. Fernandez[294,293], M. Fernandez Garcia[110], J. L. Fernandez-Hernando[130], P. Fernandez-Martinez[32], J. Fernandez-Melgarejo[33], A. Ferrer[108], F. Ferri[21], S. Fichet[117], T. Fifield[347], L. Filkov[179], F. Filthaut[97,213], A. Finch[176], H. E. Fisk[58], T. Fiutowski[2], H. Flaecher[316], J. W. Flanagan[71], I. Fleck[301], M. Fleischer[47], C. Fleta[32], J. Fleury[93], D. Flores[32], M. Foley[58], M. Fontannaz[171], K. Foraz[33], N. Fornengo[128], F. Forti[126,391], B. Foster[47,140], M. C. Fouz[31], P. H. Frampton[353], K. Francis[7], S. Frank[224], A. Freitas[361], A. Frey[64], R. Frey[356], M. Friedl[224], C. Friedrich[48], M. Frigerio[163], T. Frisson[167], M. Frotin[172], R. Frühwirth[224], R. Fuchi[378], E. Fuchs[47], K. Fujii[71], J. Fujimoto[71], H. Fuke[134], B. Fuks[94,33], M. Fukuda[71], S. Fukuda[71], K. Furukawa[71], T. Furuya[71], T. Fusayasu[195], J. Fuster[108], N. Fuster[108], Y. Fuwa[95,159], A. Gaddi[33], K. Gadow[47], F. Gaede[47], R. Gaglione[164], S. Galeotti[126], C. Gallagher[356], A. A. Gallas Torreira[112], L. Gallin-Martel[170], A. Gallo[174], D. Gamba[140,33], D. Gamba[128], J. Gao[102], Y. Gao[24], P. H. Garbincius[58], F. Garcia[69], C. Garcia Canal[288], J. E. Garcia Navarro[108], P. Garcia-Abia[31], J. J. Garcia-Garrigos[108], L. Garcia-Tabares[31], C. García[108], J. V. García Esteve[286], I. García García[108], S. K. Garg[408], L. Garrido[311], E. Garutti[333], T. Garvey[167,261], M. Gastal[33], F. Gastaldi[172], C. Gatto[58,123], N. Gaur[326], D. Gavela Pérez[31], P. Gay[168], M. B. Gay Ducati[109], L. Ge[251], R. Ge[102], A. Geiser[47], A. Gektin[100], A. Gellrich[47], M. H. Genest[170], R. L. Geng[269], S. Gentile[387,127], A. Gerbershagen[33,358], R. Gerig[7], S. German[111], H. Gerwig[33], S. Ghazaryan[47], P. Ghislain[169], D. K. Ghosh[81], S. Ghosh[115], S. Giagu[387,127], L. Gibbons[43], S. Gibson[139,33], V. Gilewsky[143], A. Gillespie[328], F. Gilman[20], B. Gimeno Martínez[108], D. M. Gingrich[312,279], C. M. Ginsburg[58], D. Girard[164], J. Giraud[170], G. F. Giudice[33], L. Gladilin[180], P. Gladkikh[208], C. J. Glasman[343,40], R. Glattauer[224], N. Glover[49], J. Gluza[365], K. Gnidzinska[263], R. Godbole[83], S. Godfrey[19], F. Goertz[54], M. Goffe[94], N. Gogitidze[179,47], J. Goldstein[316], B. Golob[144,341], G. Gomez[110], V. Goncalves[290], R. J. Gonsalves[256], I. González[283], S. González De La Hoz[108], F. J. González Sánchez[110], G. Gonzalez Parra[294], S. Gopalakrishna[103], I. Gorelov[352], D. Goswami[86], S. Goswami[229], T. Goto[71], K. Gotow[398], P. Göttlicher[47], M. Götze[385], A. Goudelis[165], P. Goudket[258], S. Gowdy[33], O. A. Grachov[309], N. A. Graf[251], M. Graham[251], A. Gramolin[15], R. Granier De Cassagnac[172], P. Grannis[257], P. Gras[21], M. Grecki[47], T. Greenshaw[339], D. Greenwood[181], C. Grefe[33], M. Grefe[111], I. M. Gregor[47], D. Grellscheid[49], G. Grenier[89], M. Grimes[316], C. Grimm[58], O. Grimm[53], B. Grinyov[100], B. Gripaios[323], K. Grizzard[141], A. Grohsjean[47], C. Grojean[294,33], J. Gronberg[178], D. Grondin[170], S. Groote[370], P. Gros[240], M. Grunewald[310], B. Grzadkowski[382], J. Gu[102], M. Guchait[262], S. Guiducci[174], E. Guliyev[172], J. Gunion[320], C. Günter[47], C. Gwilliam[339], N. Haba[75], H. Haber[322], M. Hachimine[197], Y. Haddad[172], L. Hagge[47], M. Hagihara[378], K. Hagiwara[71,158], J. Haley[216], G. Haller[251], J. Haller[333], K. Hamaguchi[375], R. Hamatsu[276], G. Hamel De Monchenault[21], L. L. Hammond[58], P. Hamnett[47], L. Han[364], T. Han[361], K. Hanagaki[223], J. D. Hansen[211], K. Hansen[47], P. H. Hansen[211], X. Q. Hao[70], K. Hara[71], K. Hara[378], T. Hara[71], D. Harada[83], K. Harada[161], K. Harder[259], T. Harion[297], R. V. Harlander[385], E. Harms[58], M. Harrison[13], O. Hartbrich[47,385], A. Hartin[47], T. Hartmann[300], J. Harz[47], S. Hasegawa[197], T. Hasegawa[71], Y. Hasegawa[248], M. Hashimoto[38], T. Hashimoto[62], C. Hast[251], S. Hatakeyama[135], J. M. Hauptman[118], M. Hauschild[33], M. Havranek[105], C. Hawkes[315], T. Hayakawa[197], H. Hayano[71], K. Hayasaka[198], M. Hazumi[71,253], H. J. He[24], C. Hearty[317,104], H. F. Heath[316],

T. Hebbeker[235], M. Heck[90], V. Hedberg[183], D. Hedin[217], S. M. Heindl[90], S. Heinemeyer[110], I. Heinze[47], A. Hektor[205], S. Henrot-Versille[167], O. Hensler[47], A. Heo[23], J. Herbert[258], G. Herdoiza[138], B. Hermberg[47], J. J. Hernández-Rey[108], M. J. Herrero[111], B. Herrmann[165], A. Hervé[384], J. Hewett[251], S. Hidalgo[32], B. Hidding[333,318], N. Higashi[375], N. Higashi[71], T. Higo[71], E. Higón Rodríguez[108], T. Higuchi[150], M. Hildreth[354], C. T. Hill[58], S. Hillert[295], S. Hillier[315], T. Himel[251], A. Himmi[94], S. Himori[272], Z. Hioki[374], B. Hippolyte[94], T. Hiraki[159], K. Hirano[136], S. Hirano[197], K. Hirata[71], T. Hirose[276], M. Hirsch[108], J. Hisano[197], P. M. Ho[210], A. Hoang[302], A. Hocker[58], A. Hoecker[33], M. Hoeferkamp[352], M. Hoffmann[47], W. Hollik[186], K. Homma[72], Y. Homma[154], S. Honda[378], T. Honda[71], Y. Honda[71], N. T. Hong Van[106], K. Honkavaara[47], T. Honma[71], T. Hori[236], T. Horiguchi[272], Y. Horii[197], A. Horio[196], R. Hosaka[377], Y. Hoshi[271], H. Hoshino[197], K. Hosoyama[71], J. Y. Hostachy[170], G. W. Hou[210], M. Hou[102], A. Hoummada[184], M. S. Hronek[58], T. Hu[102], C. Hu-Guo[94], M. Huang[24], T. Huang[102], E. Huedem[58], F. Hügging[295], J. L. Hugon[330], C. Hugonie[173], K. Huitu[335], P. Q. Hung[380], C. Hunt[80], U. Husemann[90], G. Hussain[24], D. Hutchcroft[339], Y. Hyakutake[79], J. C. Ianigro[89], L. E. Ibanez[111], M. Ibe[96], M. Idzik[2], H. Igarashi[78], Y. Igarashi[71], K. Igi[236], A. Ignatenko[209], O. Igonkina[213], T. Iijima[198,197], M. Iinuma[73], Y. Iiyama[20], H. Ikeda[134], K. Ikeda[71], K. Ikematsu[301], J. I. Illana[281], V. A. Ilyin[207,180], A. Imhof[333], T. Inagaki[236], T. Inagaki[197], K. Inami[197], S. Inayoshi[248], K. Inoue[161], A. Irles[108], S. Isagawa[71], N. Ishibashi[378], A. Ishida[375], K. Ishida[212], N. Ishihara[71], S. Ishihara[77], K. Ishii[71], A. Ishikawa[272], K. Ishikawa[375], K. I. Ishikawa[72], K. Ishikawa[75], T. Ishikawa[71], M. Ishitsuka[275], K. Ishiwata[17], G. Isidori[174], A. Ismail[251], S. Iso[71], T. Isogai[197], C. Issever[358], K. Itagaki[272], T. Itahashi[223], A. Ito[275], F. Ito[378], S. Ito[272], R. Itoh[71], E. Itou[71], M. I. Ivanyan[26], G. Iwai[71], S. Iwamoto[375], T. Iwamoto[116], H. Iwasaki[71], M. Iwasaki[71], Y. Iwashita[95], S. Iwata[71], S. Iwata[276], T. Izubuchi[13,236], Y. Izumiya[272], S. Jablonski[401], F. Jackson[258], J. A. Jacob[316], M. Jacquet[167], P. Jain[40], P. Jaiswal[59], W. Jalmuzna[263], E. Janas[401], R. Jaramillo Echeverría[110], J. Jaros[251], D. Jatkar[67], D. Jeans[375], R. Jedziniak[58], M. J. Jenkins[176,40], K. Jensch[47], C. P. Jessop[354], T. Jezynski[47], M. Jimbo[35], S. Jin[102], O. Jinnouchi[275], M. D. Joergensen[211], A. S. Johnson[251], S. Jolly[309], D. T. Jones[340], J. Jones[258,40], R. M. Jones[343,40], L. Jönsson[183], N. Joshi[237], C. K. Jung[257,150], N. Juntong[343,40], A. Juste[88,294], W. Kaabi[167], M. Kadastik[205], M. Kado[167,33], K. Kadota[197], E. Kajfasz[27], R. Kajikawa[197], Y. Kajiura[197], M. Kakizaki[377], E. Kako[71], H. Kakuhata[377], H. Kakuno[276], A. Kalinin[258], J. Kalinowski[382], G. E. Kalmus[259], K. Kamada[47], J. Kaminski[295], T. Kamitani[71], Y. Kamiya[116], Y. Kamiya[71], R. Kammering[47], T. Kamon[266], J. I. Kamoshita[60], T. Kanai[275], S. Kananov[265], K. Kanaya[378], M. Kaneda[33], T. Kaneko[71,253], S. Kanemura[377], K. Kaneta[75], W. Kang[102], D. Kanjilal[115], K. Kannike[205], F. Kapusta[169], D. Kar[332], P. Karataev[237,139], P. E. Karchin[403], D. Karlen[379,279], S. Karstensen[47], Y. Karyotakis[164], M. Kasemann[47], V. S. Kashikhin[58], S. Kashiwagi[273], A. Kataev[98], V. Katalev[48], Y. Kataoka[116], N. Katayama[150], R. Katayama[375], E. Kato[272], K. Kato[155], S. Kato[71], Y. Kato[153], T. Katoh[71], A. Kaukher[47], S. Kawabata[71], S. I. Kawada[73], K. Kawagoe[161], M. Kawai[71], T. Kawamoto[116], H. Kawamura[71], M. Kawamura[71], Y. Kawamura[248], S. Kawasaki[71], T. Kawasaki[212], H. Kay[47], S. Kazama[375], L. Keegan[111], J. Kehayias[150], L. Keller[251], M. A. Kemp[251], J. J. Kempster[237], C. Kenney[251], I. Kenyon[315], R. Kephart[58], J. Kerby[7], K. Kershaw[33], J. Kersten[333], K. Kezzar[151], V. G. Khachatryan[26], M. A. Khan[23], S. A. Khan[242], Y. Khoulaki[184], V. Khoze[49], H. Kichimi[71], R. Kieffer[33], C. Kiesling[186], M. Kikuchi[377], Y. Kikuta[71], M. Killenberg[47], C. S. Kim[408], D. W. Kim[63], D. Kim[23], E. J. Kim[36,36], E. S. Kim[23], G. Kim[23], H. S. Kim[23], H. D. Kim[245], J. Kim[63], S. H. Kim[378], S. K. Kim[245], S. G. Kim[87], Y. I. Kim[358,140], Y. Kimura[71], R. E. Kirby[251], F. Kircher[21], Y. Kishimoto[96], L. Kisslinger[20], T. Kitahara[375], R. Kitano[272], Y. Kiyo[146,71], C. Kleinwort[47], W. Klempt[33], P. M. Kluit[213], V. Klyukhin[180,33], M. Knecht[28], J. L. Kneur[163], B. A. Kniehl[333], K. Ko[251], P. Ko[158], D. Kobayashi[275], M. Kobayashi[71], N. Kobayashi[71],

T. Kobayashi[116], M. Koch[295], P. Kodys[34], U. Koetz[47], E. N. Koffeman[213], M. Kohda[210], S. Koike[71], Y. Kojima[71], K. Kolodziej[365], Y. Kolomensky[319,177], S. Komamiya[375], T. Kon[244], P. Konar[229], Y. Kondou[71], D. Kong[23], K. Kong[338], O. C. Kong[201], T. Konno[275,275], V. Korbel[47], J. G. Körner[138], S. Korpar[344,144], S. R. Koscielniak[279], D. Kostin[47], K. Kotera[248], W. Kotlarski[382], J. Kotula[268], E. Kou[167], V. Kovalenko[333], S. V. H. Kox[170], K. Koyama[75], M. Krämer[235], S. Kraml[170], M. Krammer[224], M. W. Krasny[169], F. Krauss[49], T. Krautscheid[295], M. Krawczyk[382], K. Krempetz[58], P. Križan[341,144], B. E. Krikler[80], A. Kronfeld[58], K. Kruchinin[237,139], D. Krücker[47], K. Krüger[47], B. Krupa[268], Y. P. Kuang[24], K. Kubo[71], T. Kubo[71], T. Kubota[347], T. Kubota[275], Y. Kubyshin[298,180], V. Kuchler[58], I. M. Kudla[202], D. Kuehn[47], J. H. Kuehn[92], C. Kuhn[94], S. Kulis[2], S. Kulkarni[170], A. Kumar[10], S. Kumar[86], T. Kumita[276], A. Kundu[16], Y. Kuno[223], C. M. Kuo[201], M. Kurachi[198], A. Kuramoto[253], M. Kurata[375], Y. Kurihara[71], M. Kuriki[73,71], T. Kurimoto[377], S. Kuroda[71], K. Kurokawa[71], S. I. Kurokawa[71], H. Kuwabara[276], M. Kuze[275], J. Kvasnicka[105], P. Kvasnicka[34], Y. Kwon[408], L. Labun[210], C. Lacasta[108], T. Lackowski[58], D. Lacour[169], V. Lacuesta[108], R. Lafaye[164], G. Lafferty[343], B. Laforge[169], I. Laktineh[89], R. L. Lander[320], K. Landsteiner[111], S. Laplace[169], K. J. Larsen[213], R. S. Larsen[251], T. Lastovicka[105], J. I. Latorre[311], S. Laurien[333], L. Lavergne[169], S. Lavignac[22], R. E. Laxdal[279], A. C. Le Bihan[94], F. R. Le Diberder[167], A. Le-Yaouanc[171], A. Lebedev[13], P. Lebrun[33], T. Lecompte[7], T. Leddig[300], F. Ledroit[170], B. Lee[25], K. Lee[158], M. Lee[177], S. H. Lee[260], S. W. Lee[267], Y. H. Lee[210], J. Leibfritz[58], K. Lekomtsev[71], L. Lellouch[28], M. Lemke[47], F. R. Lenkszus[7], A. Lenz[49,33], O. Leroy[27], C. Lester[323], L. Levchuk[208], J. Leveque[164], E. Levichev[15], A. Levy[265], I. Levy[265], J. R. Lewandowski[251], B. Li[24], C. Li[364], C. Li[102], D. Li[102], H. Li[380], L. Li[195], L. Li[247], L. Li[364], S. Li[102], W. Li[102], X. Li[102], Y. Li[24], Y. Li[24], Y. Li[24], Z. Li[251], Z. Li[102], J. J. Liau[210], V. Libov[47], L. Lilje[47], J. G. Lima[217], C. J. D. Lin[204], C. M. Lin[154], C. Y. Lin[201], H. Lin[102], H. H. Lin[210], F. L. Linde[213], R. A. Lineros[108], L. Linssen[33], R. Lipton[58], M. Lisovyi[47], B. List[47], J. List[47], B. Liu[24], J. Liu[364], R. Liu[102], S. Liu[167], S. Liu[247], W. Liu[7], Y. Liu[102], Y. Liu[337,58], Z. Liu[361], Z. Liu[102], Z. Liu[102], A. Lleres[170], N. S. Lockyer[279,317], W. Lohmann[48,12], E. Lohrmann[333], T. Lohse[76], F. Long[102], D. Lontkovskyi[47], M. A. Lopez Virto[110], X. Lou[102,372], A. Lounis[167], M. Lozano Fantoba[32], J. Lozano-Bahilo[281], C. Lu[232], R. S. Lu[210], S. Lu[47], A. Lucotte[170], F. Ludwig[47], S. Lukic[396], O. Lukina[180], N. Lumb[89], B. Lundberg[183], A. Lunin[58], M. Lupberger[295], B. Lutz[47], P. Lutz[21], T. Lux[294], K. Lv[102], M. Lyablin[142], A. Lyapin[237,139], J. Lykken[58], A. T. Lytle[262], L. Ma[258], Q. Ma[102], R. Ma[312], X. Ma[102], F. Machefert[167], N. Machida[377], J. Maeda[276], Y. Maeda[159], K. Maeshima[58], F. Magniette[172], N. Mahajan[229], F. Mahmoudi[168,33], S. H. Mai[201], C. Maiano[119], H. Mainaud Durand[33], S. Majewski[356], S. K. Majhi[81], N. Majumdar[241], G. Majumder[262], I. Makarenko[47], V. Makarenko[209], A. Maki[71], Y. Makida[71], D. Makowski[263], B. Malaescu[169], J. Malcles[21], U. Mallik[337], S. Malvezzi[121], O. B. Malyshev[258,40], Y. Mambrini[171], A. Manabe[71], G. Mancinelli[27], S. K. Mandal[150], S. Mandry[309,186], S. Manen[168], R. Mankel[47], S. Manly[363], S. Mannai[303], Y. Maravin[149], G. Marchiori[169], M. Marcisovsky[105,45], J. Marco[110], D. Marfatia[338], J. Marin[31], E. Marin Lacoma[251], C. Marinas[295], T. W. Markiewicz[251], O. Markin[107], J. Marshall[323], S. Martí-García[108], A. D. Martin[49], V. J. Martin[329], G. Martin-Chassard[93], T. Martinez De Alvaro[31], C. Martinez Rivero[110], F. Martinez-Vidal[108], H. U. Martyn[235,47], T. Maruyama[251], A. Masaike[159], T. Mashimo[116], T. Masubuchi[116], T. Masuda[159], M. Masuzawa[71], Z. Mateusz[401], A. Matheisen[47], H. Mathez[89], J. Matias[293], H. Matis[177], T. Matsubara[276], T. Matsuda[71], T. Matsui[377], S. Matsumoto[161], S. Matsumoto[150], Y. Matsumoto[220], H. Matsunaga[71], T. Matsushita[154], T. S. Mattison[317], V. A. Matveev[142], U. Mavric[47], G. Mavromanolakis[33], K. Mawatari[399], S. J. Maxfield[339], K. Mazumdar[262], A. Mazzacane[58,123], R. L. Mccarthy[257], D. J. Mccormick[251], J. Mccormick[251], K. T. Mcdonald[232], R. Mcduffee[324], P. Mcintosh[258], B. Mckee[251], M. Medinnis[47], S. Mehlhase[211], T. Mehrling[47,333],

A. Mehta[339], B. Mele[127], R. E. Meller[43], I. A. Melzer-Pellmann[47], L. Men[102], G. Mendiratta[83], Z. Meng[316], M. H. Merk[213,400], M. Merkin[180], A. Merlos[32], L. Merminga[279], A. B. Meyer[47], A. Meyer[235], N. Meyners[47], Z. Mi[102], P. Michelato[119], S. Michizono[71], S. Mihara[71], A. Mikhailichenko[43], D. J. Miller[309], C. Milstene[403], Y. Mimura[210], D. Minic[398], L. Mirabito[89], S. Mishima[387], T. Misumi[13], W. A. Mitaroff[224], T. Mitsuhashi[71], S. Mitsuru[71], K. Miuchi[154], K. Miyabayashi[200], A. Miyamoto[71], H. Miyata[212], Y. Miyazaki[161], T. Miyoshi[71], R. Mizuk[107], K. Mizuno[3], U. Mjörnmark[183], J. Mnich[47], G. Moeller[47], W. D. Moeller[47], K. Moenig[48], K. C. Moffeit[251], P. Mohanmurthy[269], G. Mohanty[262], L. Monaco[119], S. Mondal[81], C. Monini[170], H. Monjushiro[71], G. Montagna[359,124], S. Monteil[168], G. Montoro[298], I. Montvay[47], F. Moortgat[53], G. Moortgat-Pick[333,47], P. Mora De Freitas[172], C. Mora Herrera[30], G. Moreau[171], F. Morel[94], A. Morelos-Pineda[280], M. Moreno Llacer[108], S. Moretti[367,259], V. Morgunov[47,107], T. Mori[71], T. Mori[272], T. Mori[116], Y. Morita[71], S. Moriyama[96,150], L. Moroni[121], Y. Morozumi[71], H. G. Moser[186], A. Moszczynski[268], K. Motohashi[275], T. Moulik[249], G. Moultaka[163], D. Moya Martin[110], S. K. Mtingwa[215], G. S. Muanza[27], M. Mühlleitner[91], A. Mukherjee[85], S. Mukhopadhyay[241], M. Mulders[33], D. Muller[251], F. Müller[47], T. Müller[90], V. S. Mummidi[83], A. Münnich[47], C. Munoz[111], F. J. Muñoz Sánchez[110], H. Murayama[375,319], R. Murphy[7], G. Musat[172], A. Mussgiller[47], R. Muto[71], T. Nabeshima[377], K. Nagai[71], K. Nagai[378], S. Nagaitsev[58], T. Nagamine[272], K. Nagano[71], K. Nagao[71], Y. Nagashima[223], S. C. Nahn[185], P. Naik[316], D. Naito[159], T. Naito[71], H. Nakai[71], K. Nakai[71,223], Y. Nakai[161], Y. Nakajima[177], E. Nakamura[71], H. Nakamura[71], I. Nakamura[71], S. Nakamura[159], S. Nakamura[71], T. Nakamura[116], K. Nakanishi[71], E. Nakano[222], H. Nakano[212], H. Nakano[272], Y. Namito[71], W. Namkung[230], H. Nanjo[159], C. D. Nantista[251], O. Napoly[21], Y. Nara[4], T. Narazaki[272], S. Narita[131], U. Nauenberg[324], T. Naumann[48], S. Naumann-Emme[47], J. Navarro[108], A. Navitski[47], H. Neal[251], K. Negishi[272], K. Neichi[270], C. A. Nelson[255], T. K. Nelson[251], S. Nemecek[105], M. Neubert[138], R. Neuhaus[218], L. J. Nevay[237], D. M. Newbold[316,259], O. Nezhevenko[58], F. Nguyen[175], M. Nguyen[172], M. N. Nguyen[251], T. T. Nguyen[106], R. B. Nickerson[358], O. Nicrosini[124], C. Niebuhr[47], J. Niehoff[58], M. Niemack[43], U. Nierste[92], H. Niinomi[159], I. Nikolic[169], H. P. Nilles[295], S. Nishida[71], H. Nishiguchi[71], K. Nishiwaki[67], O. Nitoh[277], L. Niu[24], R. Noble[251], M. Noji[71], M. Nojiri[71,150], S. Nojiri[197,198], D. Nölle[47], A. Nomerotski[358], M. Nomura[135], T. Nomura[201], Y. Nomura[319,177], C. Nonaka[198], J. Noonan[7], E. Norbeck[337], Y. Nosochkov[251], D. Notz[47], O. Novgorodova[48,12], A. Novokhatski[251], J. A. Nowak[349], M. Nozaki[71], K. Ocalan[192], J. Ocariz[169], S. Oda[161], A. Ogata[71], T. Ogawa[248], T. Ogura[248], A. Oh[343], S. K. Oh[156], Y. Oh[23], K. Ohkuma[61], T. Ohl[145], Y. Ohnishi[71], K. Ohta[189], M. Ohta[71,253], S. Ohta[71,253], N. Ohuchi[71], K. Oishi[161], R. Okada[71], Y. Okada[71,253], T. Okamura[71], H. Okawa[13], T. Okugi[71], T. Okui[59], K. I. Okumura[161], Y. Okumura[52,58], L. Okun[107], H. Okuno[236], C. Oleari[390], C. Oliver[31], B. Olivier[186], S. L. Olsen[245], M. Omet[253,71], T. Omori[71], Y. Onel[337], H. Ono[214], Y. Ono[272], D. Onoprienko[251], Y. Onuki[116,150], P. Onyisi[371], T. Oogoe[71], Y. Ookouchi[159], W. Ootani[116], M. Oreglia[52], M. Oriunno[251], M. C. Orlandea[206], J. Orloff[168], M. Oroku[375,71], R. S. Orr[376], J. Osborne[33], A. Oskarsson[183], P. Osland[314], A. Osorio Oliveros[282], L. Österman[183], H. Otono[223], M. Owen[343], Y. Oyama[71], A. Oyanguren[108], K. Ozawa[71,375], J. P. Ozelis[58,191], D. Ozerov[47], G. Pásztor[304,99], H. Padamsee[43], C. Padilla[294], C. Pagani[119,386], R. Page[316], R. Pain[169], S. Paktinat Mehdiabadi[101], A. D. Palczewski[269], S. Palestini[33], F. Palla[126], M. Palmer[58], F. Palomo Pinto[285], W. Pan[102], G. Pancheri[174], M. Pandurovic[396], O. Panella[125], A. Pankov[227], Y. Papaphilippou[33], R. Paparella[119], A. Paramonov[7], E. K. Park[75], H. Park[23], S. I. Park[23], S. Park[260], S. Park[373], W. Park[23], A. Parker[323], B. Parker[13], C. Parkes[343], V. Parma[33], Z. Parsa[13], R. Partridge[251], S. Pastor[108], E. Paterson[251], M. Patra[83], J. R. Patterson[43], M. Paulini[20], N. Paver[129], S. Pavy-Bernard[167],

B. Pawlik[268], A. Pérez Vega-Leal[285], B. Pearson[355], J. S. Pedersen[211], A. Pedicini[397], S. Pedraza López[108], G. Pei[102], S. Pei[102], G. Pellegrini[32], A. Pellegrino[213], S. Penaranda[286], H. Peng[364], X. Peng[102], M. Perelstein[43], E. Perez[112], M. A. Perez-Garcia[284,114], M. Perez-Victoria[281], S. Peris[293], D. Perret-Gallix[164], H. Perrey[47], T. M. Perry[384], M. E. Peskin[251], P. Petagna[33], R. Y. Peters[64,47], T. C. Petersen[211], D. P. Peterson[43], T. Peterson[58], E. Petrakou[210], A. A. Petrov[403], A. Petrukhin[89,107], S. Pfeiffer[47], H. Pham[94], K. H. Phan[395,71], N. Phinney[251], F. Piccinini[124], A. Pich[108], R. Pichai[85], J. Piedra[283], J. Piekarski[401], A. Pierce[348], P. Pierini[119], N. Pietsch[333,47], A. Pineda[293], J. Pinfold[312,152], A. Piotrowski[263], Y. Pischalnikov[58], R. Pittau[281], M. Pivi[251], W. Placzek[132], T. Plehn[296], M. A. Pleier[13], M. Poelker[269], L. Poggioli[167], I. Pogorelsky[13], V. Poireau[164], M. E. Pol[30], I. Polak[105], F. Polci[169], M. Polikarpov[107], T. Poll[316,259], M. W. Poole[258,40], W. Porod[145], F. C. Porter[17], S. Porto[333], J. Portolés[108], R. Pöschl[167], S. Poss[33], C. T. Potter[356], P. Poulose[86], K. T. Pozniak[401], V. Prahl[47], R. Prepost[384], C. Prescott[251], D. Price[87], T. Price[315], P. S. Prieto[58], D. Protopopescu[332], D. Przyborowski[2], K. Przygoda[263], H. Przysiezniak[164], F. Ptochos[325], J. Puerta-Pelayo[31], C. Pulvermacher[90], M. Purohit[366], Q. Qin[102], F. Qiu[102], H. Qu[102], A. Quadt[64], G. Quast[90], D. Quirion[32], M. Quiros[88], J. Rademacker[316], R. Rahmat[350], S. Rai[67], M. Raidal[205], S. Rakshit[84], M. Ramilli[333], F. Rarbi[170], P. Ratoff[176], T. Raubenheimer[251], M. Rauch[91], L. Raux[93], G. Raven[400,213], P. Razis[325], V. Re[124], S. Redford[33], C. E. Reece[269], I. Reichel[177], A. Reichold[358,140], P. Reimer[105], M. Reinecke[47], A. Rekalo[100], J. Repond[7], J. Resta-Lopez[108], J. Reuter[47], J. T. Rhee[156], P. M. Ribeiro Cipriano[47], A. Ribon[33], G. Ricciardi[292,123], F. Richard[167], E. Richter-Was[132], G. Riddone[33], S. Riemann[48], T. Riemann[48], M. Rijssenbeek[257], K. Riles[348], C. Rimbault[167], R. Rimmer[269], S. D. Rindani[229], A. Ringwald[47], L. Rinolfi[33], I. Ripp-Baudot[94], I. Riu[294], T. G. Rizzo[251], P. Robbe[167], J. Roberts[140,33], A. Robson[332], G. Rodrigo[108], P. Rodriguez[251], P. Rodriguez Perez[112], K. Rolbiecki[111], P. Roloff[33], R. S. Romaniuk[401], E. Romero Adam[108], A. Ronzhin[58], L. Roos[169], E. Ros[108], A. Rosca[47], C. Rosemann[47], J. Rosiek[382], M. C. Ross[251], R. Rossmanith[90], S. Roth[235], J. Rouënè[167], A. Rowe[58], P. Rowson[251], A. Roy[115], L. Royer[168], P. Royole-Degieux[93], C. Royon[21], A. Rozanov[27], M. Ruan[172], D. L. Rubin[43], I. Rubinskiy[47], R. Rückl[145], R. Ruiz[361], R. Ruiz De Austri[108], P. Ruiz Valls[108], P. Ruiz-Femenía[108], A. Ruiz-Jimeno[110], R. Ruland[251], V. Rusinov[107], J. J. Russell[251], I. Rutkowski[401], V. Rybnikov[47], A. Ryd[43], A. Sabio Vera[111], B. Sabirov[142], J. J. Saborido Silva[112], H. F. W. Sadrozinski[322], T. Saeki[71], B. Safarzadeh[101], P. Saha[305], H. Sahoo[7], A. Sailer[33], N. Saito[71], T. Saito[272], T. Sakaguchi[13], H. Sakai[71], K. Sakai[71], K. Sakaue[402], K. Sakurai[47], R. Salerno[172], J. Salfeld-Nebgen[47], J. Salt[108], L. Sanchez[31], M. A. Sanchis Lozano[108], J. Sandweiss[405], A. Santa[377], A. Santagata[286], A. Santamaria[108], P. Santorelli[292], T. Sanuki[272], A. A. Sapronov[142], M. Sasaki[96], H. Sato[248], N. Sato[71], Y. Sato[272], M. Satoh[71], E. Sauvan[164], V. Saveliev[238,47], A. Savoy-Navarro[166,126], M. Sawabe[71], R. Sawada[116], H. Sawamura[402], L. Sawyer[181], O. Schäfer[300,47], R. Schäfer[47], J. Schaffran[47], T. Schalk[322,251], R. D. Schamberger[257], J. Scheirich[34], G. Schierholz[47], F. P. Schilling[90], F. Schirra[89], F. Schlander[47], H. Schlarb[47], D. Schlatter[33], P. Schleper[333], J. L. Schlereth[7], R. D. Schlueter[177], C. Schmidt[47], U. Schneekloth[47], S. Schnetzer[239], T. Schoerner-Sadenius[47], M. Schram[225], H. J. Schreiber[48], S. Schreiber[47], K. P. Schüler[47], D. Schulte[33], H. C. Schultz-Coulon[297], M. Schumacher[5], S. Schumann[64], B. A. Schumm[322], M. H. Schune[167], S. Schuwalow[333,48], C. Schwanda[224], C. Schwanenberger[343], F. Schwartzkopff[295], D. J. Scott[258,58], F. Sefkow[47,33], A. Segui[286], N. Seguin-Moreau[93], S. Seidel[352], Y. Seiya[222], J. Sekaric[338], K. Seki[197], S. Sekmen[33], S. Seletskiy[13], S. Sen[337], E. Senaha[158], K. Senyo[406], S. Senyukov[94], I. Serenkova[227], D. A. Sergatskov[58], H. Sert[47,333], D. Sertore[119], A. Seryi[358,140], O. Seto[74], R. Settles[186], P. Sha[102], S. Shahid[301], A. Sharma[33], G. Shelkov[142], W. Shen[297], J. C. Sheppard[251], M. Sher[41], C. Shi[102], H. Shi[102], T. Shidara[71], W. Shields[237,139], M. Shimada[71], H. Shimizu[71], Y. Shimizu[272],

M. Shimojima[195], S. Shimojima[276], T. Shindou[155], N. Shinoda[272], Y. Shinzaki[272], M. Shioden[78,71], I. Shipsey[233], S. Shirabe[161], M. J. Shirakata[71], T. Shirakata[71], G. Shirkov[142], T. Shishido[71], T. Shishido[71], J. G. Shiu[210], R. Shivpuri[326], R. Shrock[257], T. Shuji[71], N. Shumeiko[209], B. Shuve[228,188], P. Sicho[105], A. M. Siddiqui[133], P. Sievers[33], D. Sikora[401], D. A. Sil[86], F. Simon[186], N. B. Sinev[356], W. Singer[47], X. Singer[47], B. K. Singh[10], R. K. Singh[82], N. Sinha[103], R. Sinha[103], K. Sinram[47], T. Sinthuprasith[14], P. Skubic[355], R. Sliwa[167], I. Smiljanic[396], J. R. Smith[373,7], J. C. Smith[251,43], S. R. Smith[251], J. Smolík[105,45], J. Snuverink[237,139], B. Sobloher[47], J. Sola[311], C. Soldner[186,57], S. Soldner-Rembold[343], D. Son[23], H. S. Song[260], N. Sonmez[51], A. Sopczak[44], D. E. Soper[356], P. Spagnolo[126], S. Spannagel[47], M. Spannowsky[49], A. Sparkes[329], C. M. Spencer[251], H. Spiesberger[138], M. Spira[261], M. Stahlhofen[47], M. Stanescu-Bellu[48], M. Stanitzki[47], S. Stapnes[33], P. Starovoitov[209], F. Staufenbiel[48], L. Steder[47], M. Steder[47], A. Steen[89], G. Steinbrueck[333], M. Steinhauser[92], F. Stephan[48], W. Stephen[237], S. Stevenson[358], I. Stewart[185], D. Stöckinger[264], H. Stoeck[369], M. Strauss[355], S. Striganov[58], D. M. Strom[356], R. Stromhagen[47], J. Strube[33], A. Strumia[205], G. Stupakov[251], N. Styles[47], D. Su[251], F. Su[102], S. Su[313], J. Suarez Gonzalez[209], Y. Sudo[161], T. Suehara[116], F. Suekane[274], Y. Suetsugu[71], R. Sugahara[71], A. Sugamoto[220], H. Sugawara[71], Y. Sugimoto[71], A. Sugiyama[240], H. Sugiyama[377], M. K. Sullivan[251], Y. Sumino[272], T. Sumiyoshi[276,71], H. Sun[102], M. Sun[20], X. Sun[170], Y. Sun[102], Y. Susaki[197], T. Suwada[71], A. Suzuki[71], S. Suzuki[240], Y. Suzuki[71], Y. Suzuki[73], Z. Suzuki[272], K. Swientek[2], C. Swinson[13], Z. M. Szalata[251], B. Szczepanski[47], M. Szelezniak[94], J. Szewinski[202], A. Sznajder[289], L. Szymanowski[202], H. Tabassam[329], K. Tackmann[47], M. Taira[71], H. Tajima[197,251], F. Takahashi[272], R. Takahashi[71], R. Takahashi[75], T. Takahashi[73], Y. Takahashi[197], K. Takata[71], F. Takayama[160], Y. Takayasu[75], H. Takeda[154], S. Takeda[71], T. Takeshita[248], A. Taketani[236], Y. Takeuchi[378], T. Takimi[262], Y. Takubo[71], Y. Tamashevich[47], M. Tamsett[181], M. Tanabashi[198,197], T. Tanabe[116], G. Tanaka[161], M. M. Tanaka[71], M. Tanaka[223], R. Tanaka[73], H. Taniuchi[377], S. Tapprogge[138], E. Tarkovsky[107], M. A. Tartaglia[58], X. R. Tata[334], T. Tauchi[71], M. Tawada[71], G. Taylor[347], A. M. Teixeira[168], V. I. Telnov[15,219], P. Tenenbaum[251], E. Teodorescu[206], S. Terada[71], Y. Teramoto[222], H. Terao[200], A. Terashima[71], S. Terui[71], N. Terunuma[71], M. Terwort[47], M. Tesar[186], F. Teubert[33], T. Teubner[340], R. Teuscher[376], T. Theveneaux-Pelzer[168], D. Thienpont[93,172], J. Thom-Levy[43], M. Thomson[323], J. Tian[71], X. Tian[366], M. Tigner[43], J. Timmermans[213], V. Tisserand[164], M. Titov[21], S. Tjampens[164], K. Tobe[197], K. Tobioka[150,319], K. Toda[278], M. Toda[71], N. Toge[71], J. Tojo[161], K. Tokushuku[71], T. Toma[49], R. Tomas[33], T. Tomita[161], A. Tomiya[223], M. Tomoto[197,198], K. Toms[352], M. Tonini[47], F. Toral[31], E. Torrence[356], E. Torrente-Lujan[33], N. Toumbas[325], C. Touramanis[339], F. Toyoda[161], K. Toyomura[71], G. Trahern[55], T. H. Tran[172], W. Treberspurg[224], J. Trenado[311], M. Trimpl[58], S. Trincaz-Duvoid[169], M. Tripathi[320], W. Trischuk[376], M. Trodden[360], G. Trubnikov[142], H. C. Tsai[39], J. F. Tsai[210], K. H. Tsao[336], R. Tschirhart[58], E. Tsedenbaljir[210], S. Y. Tseng[201], T. Tsuboyama[71], A. Tsuchiya[250], K. Tsuchiya[71], T. Tsukamoto[71], K. Tsumura[197], S. Tsuno[71], T. Tsurugai[189], T. Tsuyuki[96], B. Tuchming[21], P. V. Tyagi[68,254], I. Tyapkin[142], M. Tytgat[331], K. Uchida[295], F. Uchiyama[71], Y. Uchiyama[116], S. Uehara[71], H. Ueno[161], K. Ueno[71], K. Ueno[71], K. Ueshima[274], Y. Uesugi[73], N. Ujiie[71], F. Ukegawa[378], N. Ukita[378], M. Ullán[32], H. Umeeda[72], K. Umemori[71], Y. Unno[66], S. Uozumi[23], J. Urakawa[71], A. M. Uranga[111], J. Urresti[32], A. Ushakov[333], I. Ushiki[272], Y. Ushiroda[71], A. V[83], P. Vázquez Regueiro[112], L. Vacavant[27], G. Valencia[118], L. Valery[168], I. Valin[94], J. W. Valle[108], C. Vallee[27], N. Van Bakel[213], H. Van Der Graaf[213], N. Van Der Kolk[167], E. Van Der Kraaij[33], B. Van Doren[338], B. Van Eijk[213], R. Van Kooten[87], W. T. Van Oers[279], D. Vanegas[108], P. Vanhoefer[186], P. Vankov[47], P. Varghese[58], A. Variola[167], R. Varma[85], G. Varner[334], G. Vasileiadis[162], A. Vauth[47], J. Velthuis[316], S. K. Vempati[83], V. Vento[108], M. Venturini[177], M. Verderi[172], P. Verdier[89], A. Verdugo[31],

A. Vicente[171], J. Vidal-Perona[108], H. L. R. Videau[172], I. Vila[110], X. Vilasis-Cardona[299], E. Vilella[311], A. Villamor[32], E. G. Villani[259], J. A. Villar[286], M. A. Villarejo Bermúdez[108], D. Vincent[169], P. Vincent[169], J. M. Virey[28], A. Vivoli[58], V. Vogel[47], R. Volkenborn[47], O. Volynets[47], F. Von Der Pahlen[110], E. Von Toerne[295], B. Vormwald[47], A. Voronin[180], M. Vos[108], J. H. Vossebeld[339], G. Vouters[164], Y. Voutsinas[94,47], V. Vrba[105,45], M. Vysotsky[107], D. Wackeroth[256], A. Wagner[47], C. E. Wagner[7,52], R. Wagner[7], S. R. Wagner[324], W. Wagner[385], J. Wagner-Kuhr[90], A. P. Waite[251], M. Wakayama[197], Y. Wakimoto[276], R. Walczak[358,140], R. Waldi[300], D. G. E. Walker[251], N. J. Walker[47], M. Walla[47], C. J. Wallace[49], S. Wallon[171,393], D. Walsh[328], S. Walston[178], W. A. T. Wan Abdullah[342], D. Wang[102], G. Wang[102], J. Wang[251], L. Wang[251], L. Wang[52], M. H. Wang[251], M. Z. Wang[210], Q. Wang[102], Y. Wang[102], Z. Wang[24], R. Wanke[138], C. Wanotayaroj[356], B. Ward[8], D. Ward[323], B. Warmbein[47], M. Washio[402], K. Watanabe[71], M. Watanabe[212], N. Watanabe[71], T. Watanabe[155], Y. Watanabe[71], S. Watanuki[272], Y. Watase[71], N. K. Watson[315], G. Watts[383], M. M. Weber[90], H. C. Weddig[47], H. Weerts[7], A. W. Weidemann[251], G. Weiglein[47], A. Weiler[47], S. Weinzierl[138], H. Weise[47], A. Welker[138], N. Welle[47], J. D. Wells[33,348], M. Wendt[58,33], M. Wenskat[47], H. Wenzel[58], N. Wermes[295], U. Werthenbach[301], W. Wester[58], L. Weuste[186,57], A. White[373], G. White[251], K. H. Wichmann[47], M. Wielers[183], R. Wielgos[58], W. Wierba[202], T. Wilksen[47], S. Willocq[346], F. F. Wilson[259], G. W. Wilson[338], P. B. Wilson[251], M. Wing[309], M. Winter[94], K. Wittenburg[47], P. Wittich[43], M. Wobisch[181], A. Wolski[339,40], M. D. Woodley[251], M. B. Woods[251], M. Worek[385], S. Worm[33,259], G. Wormser[167], D. Wright[178], Z. Wu[251], C. E. Wulz[224], S. Xella[211], G. Xia[40,343], L. Xia[7], A. Xiao[7], L. Xiao[251], M. Xiao[102], Q. Xiao[102], J. Xie[7], C. Xu[102], F. Xu[210], G. Xu[102], K. Yagyu[201], U. A. Yajnik[85], V. Yakimenko[251], S. Yamada[71,116], S. Yamada[71], Y. Yamada[272], Y. Yamada[402], A. Yamaguchi[274], D. Yamaguchi[275], M. Yamaguchi[272], S. Yamaguchi[272], Y. Yamaguchi[375], Y. Yamaguchi[75], A. Yamamoto[71,375], H. Yamamoto[272], K. Yamamoto[222], K. Yamamoto[118], M. Yamamoto[71], N. Yamamoto[197], N. Yamamoto[71], Y. Yamamoto[71], Y. Yamamoto[375], T. Yamamura[375], T. Yamanaka[116], S. Yamashita[116], T. Yamashita[3], Y. Yamashita[214], K. Yamauchi[197], M. Yamauchi[71], T. Yamazaki[375], Y. Yamazaki[154], J. Yan[375,71], W. Yan[364], C. Yanagisawa[257,11], H. Yang[247], J. Yang[56], U. K. Yang[245,343], Z. Yang[24], W. Yao[177], S. Yashiro[71], F. Yasuda[375], O. Yasuda[276], I. Yavin[188,228], E. Yazgan[331], H. Yokoya[377], K. Yokoya[71], H. Yokoyama[375], S. Yokoyama[275], R. Yonamine[71], H. Yoneyama[240], M. Yoshida[71], T. Yoshida[62], K. Yoshihara[116,33], S. Yoshihara[116,33], M. Yoshioka[71,272], T. Yoshioka[161], H. Yoshitama[73], C. C. Young[251], H. B. Yu[348], J. Yu[373], C. Z. Yuan[102], F. Yuasa[71], J. Yue[102], A. Zabi[172], W. Zabolotny[401], J. Zacek[34], I. Zagorodnov[47], J. Zalesak[105,58], A. F. Zarnecki[381], L. Zawiejski[268], M. Zeinali[101], C. Zeitnitz[385], L. Zembala[401], K. Zenker[47], D. Zeppenfeld[91], D. Zerwas[167], P. Zerwas[47], M. Zeyrek[192], A. Zghiche[164], J. Zhai[102], C. Zhang[102], J. Zhang[102], J. Zhang[7], Y. Zhang[24,33], Z. Zhang[167], F. Zhao[102], F. Zhao[102], T. Zhao[102], Y. Zhao[251], H. Zheng[102], Z. Zhengguo[364], L. Zhong[24], F. Zhou[251], X. Zhou[364,102], Z. Zhou[102], R. Y. Zhu[17], X. Zhu[24], X. Zhu[102], M. Zimmer[47], F. Zomer[167], T. Zoufal[47], R. Zwicky[329]

1 Academia Sinica - 128 Sec. 2, Institute of Physics, Academia Rd., Nankang, Taipei 11529, Taiwan, R.O.C.
2 AGH University of Science and Technology, Akademia Gorniczo-Hutnicza im. Stanislawa Staszica w Krakowie, Al. Mickiewicza 30 PL-30-059 Cracow, Poland
3 Aichi Medical University, Nagakute, Aichi, 480-1195, Japan
4 Akita International University, Yuwa, Akita City, 010-1292, Japan
5 Albert-Ludwigs Universität Freiburg, Physikalisches Institut, Hermann-Herder Str. 3, D-79104 Freiburg, Germany
6 Ankara Üniversitesi Fen Fakültesi, Fizik Bölümü, Dögol Caddesi, 06100 Tandoğan Ankara, Turkey
7 Argonne National Laboratory (ANL), 9700 S. Cass Avenue, Argonne, IL 60439, USA
8 Baylor University, Department of Physics, 101 Bagby Avenue, Waco, TX 76706, USA
9 Beijing University, Department of Physics, Beijing, China 100871
10 Benares Hindu University, Benares, Varanasi 221005, India
11 Borough of Manhattan Community College, The City University of New York, Department of Science, 199 Chambers Street, New York, NY 10007, USA
12 Brandenburg University of Technology, Postfach 101344, D-03013 Cottbus, Germany
13 Brookhaven National Laboratory (BNL), P.O.Box 5000, Upton, NY 11973-5000, USA
14 Brown University, Department of Physics, Box 1843, Providence, RI 02912, USA
15 Budker Institute for Nuclear Physics (BINP), 630090 Novosibirsk, Russia
16 Calcutta University, Department of Physics, 92 A.P.C. Road, Kolkata 700009, India
17 California Institute of Technology, Physics, Mathematics and Astronomy (PMA), 1200 East California Blvd, Pasadena, CA 91125, USA
18 California State University, Los Angeles, Dept. of Physics and Astronomy, 5151 State University Dr., Los Angeles, CA 90032, USA
19 Carleton University, Department of Physics, 1125 Colonel By Drive, Ottawa, Ontario, Canada K1S 5B6
20 Carnegie Mellon University, Department of Physics, Wean Hall 7235, Pittsburgh, PA 15213, USA
21 CEA Saclay, IRFU, F-91191 Gif-sur-Yvette, France
22 CEA Saclay, Service de Physique Théorique, CEA/DSM/SPhT, F-91191 Gif-sur-Yvette Cedex, France
23 Center for High Energy Physics (CHEP) / Kyungpook National University, 1370 Sankyuk-dong, Buk-gu, Daegu 702-701, Republic of Korea
24 Center for High Energy Physics (TUHEP), Tsinghua University, Beijing, China 100084
25 Center For Quantum Spacetime (CQUeST), Sogang University, 35 Baekbeom-ro, Mapo-gu, Seoul 121-742, Republic of Korea
26 Center for the Advancement of Natural Discoveries using Light Emission (CANDLE), Acharyan 31, 0040, Yerevan, Armenia
27 Centre de Physique des Particules de Marseille (CPPM), Aix-Marseille Université, CNRS/IN2P3, 163, Avenue de Luminy, Case 902, 13288 Marseille Cedex 09, France
28 Centre de Physique Theorique, CNRS - Luminy, Universiti d"Aix - Marseille II, Campus of Luminy, Case 907, 13288 Marseille Cedex 9, France
29 Centre Lasers Intenses et Applications (CELIA), Université Bordeaux 1 - CNRS - CEA, 351 Cours de la Libération, 33405 Talence Cedex, France
30 Centro Brasileiro de Pesquisas Físicas (CBPF), Rua Dr. Xavier Sigaud, n.150 22290-180, Urca - Rio de Janeiro, RJ, Brazil
31 Centro de Investigaciones Energéticas, Medioambientales y Tecnológicas, CIEMAT, Avenida Complutense 22, E-28040 Madrid, Spain
32 Centro Nacional de Microelectrónica (CNM), Instituto de Microelectrónica de Barcelona (IMB), Campus UAB, 08193 Cerdanyola del Vallès (Bellaterra), Barcelona, Spain
33 CERN, CH-1211 Genève 23, Switzerland
34 Charles University, Institute of Particle & Nuclear Physics, Faculty of Mathematics and Physics, V Holesovickach 2, CZ-18000 Prague 8, Czech Republic
35 Chiba University of Commerce, 1-3-1 Konodai, Ichikawa-shi, Chiba, 272-8512, Japan
36 Chonbuk National University, Division of Science Education, Jeonju 561-756, Republic of Korea
37 Chonbuk National University, Physics Department, Jeonju 561-756, Republic of Korea
38 Chubu University, 1200 Matsumoto-cho, Kasugai-shi, Aichi, 487-8501, Japan
39 Chung Yuan Christian University, Department of Physics, 200 Chung Pei Rd., Chung Li 32023 Taiwan, R.O.C
40 Cockcroft Institute, Daresbury, Warrington WA4 4AD, UK
41 College of William and Mary, Department of Physics, Williamsburg, VA, 23187, USA
42 Columbia University, Department of Physics, New York, NY 10027-6902, USA
43 Cornell University, Laboratory for Elementary-Particle Physics (LEPP), Ithaca, NY 14853, USA
44 Czech Technical University in Prague, Institute of Experimental and Applied Physics (IEAP), Horska 3a/22, 12800 Prague 2, Czech Republic
45 Czech Technical University, Faculty of Nuclear Science and Physical Engineering, Brehova 7, CZ-11519 Prague 1, Czech Republic
46 Departamento de Física Teórica, Facultad de Ciencias, Módulo 15 (antiguo C-XI) y Módulo 8, Universidad Autónoma de Madrid, Campus de Cantoblanco, 28049 Madrid, Spain
47 Deutsches Elektronen-Synchrotron DESY, A Research Centre of the Helmholtz Association, Notkestrasse 85, 22607 Hamburg, Germany (Hamburg site)
48 Deutsches Elektronen-Synchrotron DESY, A Research Centre of the Helmholtz Association, Platanenallee 6, 15738 Zeuthen, Germany (Zeuthen site)
49 Durham University, Department of Physics, Ogen Center for Fundamental Physics, South Rd., Durham DH1 3LE, UK
50 École Normale Supérieure de Lyon, 46 allée d'Italie, 69364 Lyon Cedex 07, France
51 Ege University, Department of Physics, Faculty of Science, 35100 Izmir, Turkey

52 Enrico Fermi Institute, University of Chicago, 5640 S. Ellis Avenue, RI-183, Chicago, IL 60637, USA
53 ETH Zürich, Institute for Particle Physics (IPP), Schafmattstrasse 20, CH-8093 Zürich, Switzerland
54 ETH Zürich, Institute for Theoretical Physics (ITP), Wolfgang-Pauli-Str. 27, Zürich, Switzerland
55 European Spallation Source ESS AB, Box 176, 221 00 Lund, Sweden
56 Ewha Womans University, 11-1 Daehyun-Dong, Seodaemun-Gu, Seoul, 120-750, Republic of Korea
57 Excellence Cluster Universe, Technische Universität München, Boltzmannstr. 2, 85748 Garching, Germany
58 Fermi National Accelerator Laboratory (FNAL), P.O.Box 500, Batavia, IL 60510-0500, USA
59 Florida State University, Department of Physics, 77 Chieftan Way, Tallahassee, FL 32306-4350, USA
60 Fujita Gakuen Health University, Department of Physics, Toyoake, Aichi 470-1192, Japan
61 Fukui University of Technology, 3-6-1 Gakuen, Fukui-shi, Fukui 910-8505, Japan
62 Fukui University, Department of Physics, 3-9-1 Bunkyo, Fukui-shi, Fukui 910-8507, Japan
63 Gangneung-Wonju National University, 210-702 Gangneung Daehangno, Gangneung City, Gangwon Province, Republic of Korea
64 Georg-August-Universität Göttingen, II. Physikalisches Institut, Friedrich-Hund-Platz 1, 37077 Göttingen, Germany
65 Global Design Effort
66 Hanyang University, Department of Physics, Seoul 133-791, Republic of Korea
67 Harish-Chandra Research Institute, Chhatnag Road, Jhusi, Allahabad 211019, India
68 Helmholtz-Zentrum Berlin für Materialien und Energie (HZB), Wilhelm-Conrad-Röntgen Campus, BESSY II, Albert-Einstein-Str. 15, 12489 Berlin, Germany
69 Helsinki Institute of Physics (HIP), P.O. Box 64, FIN-00014 University of Helsinki, Finland
70 Henan Normal University, College of Physics and Information Engineering, Xinxiang, China 453007
71 High Energy Accelerator Research Organization, KEK, 1-1 Oho, Tsukuba, Ibaraki 305-0801, Japan
72 Hiroshima University, Department of Physics, 1-3-1 Kagamiyama, Higashi-Hiroshima, Hiroshima 739-8526, Japan
73 Hiroshima University, Graduate School of Advanced Sciences of Matter, 1-3-1 Kagamiyama, Higashi-Hiroshima, Hiroshima 739-8530, Japan
74 Hokkai-Gakuen University, 4-1-40 Asahimachi, Toyohira-ku, Sapporo 062-8605, Japan
75 Hokkaido University, Department of Physics, Faculty of Science, Kita, Kita-ku, Sapporo-shi, Hokkaido 060-0810, Japan
76 Humboldt Universität zu Berlin, Fachbereich Physik, Institut für Elementarteilchenphysik, Newtonstr. 15, D-12489 Berlin, Germany
77 Hyogo University of Teacher Education, 942-1 Shimokume, Kato-city, Hyogo 673-1494, Japan
78 Ibaraki National College of Technology, 866 Nakane, Hitachinaka, Ibaraki 312-8508, Japan
79 Ibaraki University, College of Technology, Department of Physics, Nakanarusawa 4-12-1, Hitachi, Ibaraki 316-8511, Japan
80 Imperial College, Blackett Laboratory, Department of Physics, Prince Consort Road, London, SW7 2BW, UK
81 Indian Association for the Cultivation of Science, Department of Theoretical Physics and Centre for Theoretical Sciences, Kolkata 700032, India
82 Indian Institute of Science Education and Research (IISER) Kolkata, Department of Physical Sciences, Mohanpur Campus, PO Krishi Viswavidyalaya, Mohanpur 741252, Nadia, West Bengal, India
83 Indian Institute of Science, Centre for High Energy Physics, Bangalore 560012, Karnataka, India
84 Indian Institute of Technology Indore, IET Campus, M-Block, Institute of Engineering and Technology (IET), Devi Ahilya Vishwavidyalaya Campus, Khandwa Road, Indore - 452017, Madhya Pradesh, India
85 Indian Institute of Technology, Bombay, Powai, Mumbai 400076, India
86 Indian Institute of Technology, Guwahati, Guwahati, Assam 781039, India
87 Indiana University, Department of Physics, Swain Hall West 117, 727 E. 3rd St., Bloomington, IN 47405-7105, USA
88 Institucio Catalana de Recerca i Estudis, ICREA, Passeig Lluis Companys, 23, Barcelona 08010, Spain
89 Institut de Physique Nucléaire de Lyon (IPNL), Domaine scientifique de la Doua, Bâtiment Paul Dirac 4, rue Enrico Fermi, 69622 Villeurbanne, Cedex, France
90 Institut für Experimentelle Kernphysik, KIT,Universität Karlsruhe (TH), Wolfgang-Gaede-Str. 1, Postfach 6980, 76128 Karlsruhe, Germany
91 Institut für Theoretische Physik (ITP), Karlsruher Institut für Technologie (KIT), Fakultät für Physik, Postfach 6980, 76049 Karlsruhe, Germany
92 Institut für Theoretische Teilchenphysik, Campus Süd, Karlsruher Institut für Technologie (KIT), 76128 Karlsruhe, Germany
93 Institut National de Physique Nucleaire et de Physique des Particules, 3, Rue Michel- Ange, 75794 Paris Cedex 16, France
94 Institut Pluridisciplinaire Hubert Curien, 23 Rue du Loess - BP28, 67037 Strasbourg Cedex 2, France
95 Institute for Chemical Research, Kyoto University, Gokasho, Uji, Kyoto 611-0011, Japan
96 Institute for Cosmic Ray Research, University of Tokyo, 5-1-5 Kashiwa-no-Ha, Kashiwa, Chiba 277-8582, Japan
97 Institute for Mathematics, Astrophysics and Particle Physics (IMAPP), P.O. Box 9010, 6500 GL Nijmegen, Netherlands
98 Institute for Nuclear Research, Russian Academy of Sciences (INR RAS), 60-th October Anniversary Prospect 7a, 117312, Moscow, Russia
99 Institute for Particle and Nuclear Physics, Wigner Research Centre for Physics, Hungarian Academy of Sciences, P.O. Box 49, 1525 Budapest, Hungary
100 Institute for Scintillation Materials (ISMA), 60 Lenina Ave, 61001, Kharkiv, Ukraine
101 Institute for studies in fundamental sciences (IPM), Niavaran Square, P.O. Box 19395-5746, Tehran, Iran
102 Institute of High Energy Physics - IHEP, Chinese Academy of Sciences, P.O. Box 918, Beijing, China 100049
103 Institute of Mathematical Sciences, Taramani, C.I.T. Campus, Chennai 600113, India
104 Institute of Particle Physics, Canada

105 Institute of Physics, ASCR, Academy of Science of the Czech Republic, Division of Elementary Particle Physics, Na Slovance 2, CZ-18221 Prague 8, Czech Republic
106 Institute of Physics, Vietnam Academy of Science and Technology (VAST), 10 Dao-Tan, Ba-Dinh, Hanoi 10000, Vietnam
107 Institute of Theoretical and Experimetal Physics, B. Cheremushkinskawa, 25, RU-117259, Moscow, Russia
108 Instituto de Fisica Corpuscular (IFIC), Centro Mixto CSIC-UVEG, Edificio Investigacion Paterna, Apartado 22085, 46071 Valencia, Spain
109 Instituto de Física da Universidade Federal do Rio Grande do Sul (UFRGS), Av. Bento Gonçalves 9500, Caixa Postal 15051, CEP 91501-970, Porto Alegre, RS, Brazil
110 Instituto de Fisica de Cantabria, (IFCA, CSIC-UC), Facultad de Ciencias, Avda. Los Castros s/n, 39005 Santander, Spain
111 Instituto de Física Teórica UAM/CSIC, C/ Nicolás Cabrera 13-15, Universidad Autónoma de Madrid, Cantoblanco, 28049 Madrid, Spain
112 Instituto Galego de Fisica de Altas Enerxias (IGFAE,USC) Facultad de Fisica, Campus Sur E-15782 Santiago de Compostela, Spain
113 Instituto Tecnológico de Aragón (ITA), C/ María de Luna 7-8, 50018 Zaragoza, Spain
114 Instituto Universitario de Física Fundamental y Matemáticas de la Universidad de Salamanca (IUFFyM), Casas del Parque, 37008 Salamanca, Spain
115 Inter-University Accelerator Centre, Aruna Asaf Ali Marg, Post Box 10502, New Delhi 110067, India
116 International Center for Elementary Particle Physics, University of Tokyo, Hongo 7-3-1, Bunkyo District, Tokyo 113-0033, Japan
117 International Institute of Physics, Federal University of Rio Grande do Norte, Av. Odilon Gomes de Lima, 1722 - Capim Macio - 59078-400 - Natal-RN, Brazil
118 Iowa State University, Department of Physics, High Energy Physics Group, Ames, IA 50011, USA
119 Istituto Nazionale di Fisica Nucleare (INFN), Laboratorio LASA, Via Fratelli Cervi 201, 20090 Segrate, Italy
120 Istituto Nazionale di Fisica Nucleare (INFN), Sezione di Firenze, Via G. Sansone 1, I-50019 Sesto Fiorentino (Firenze), Italy
121 Istituto Nazionale di Fisica Nucleare (INFN), Sezione di Milano Bicocca, Piazza della Scienza 3, I-20126 Milano, Italy
122 Istituto Nazionale di Fisica Nucleare (INFN), Sezione di Milano, Via Celoria 16, I-20133 Milano, Italy
123 Istituto Nazionale di Fisica Nucleare (INFN), Sezione di Napoli, Complesso Universitá di Monte Sant'Angelo,via, I-80126 Naples, Italy
124 Istituto Nazionale di Fisica Nucleare (INFN), Sezione di Pavia, Via Bassi 6, I-27100 Pavia, Italy
125 Istituto Nazionale di Fisica Nucleare (INFN), Sezione di Perugia, Via A. Pascoli, 06123 Perugia, Italy
126 Istituto Nazionale di Fisica Nucleare (INFN), Sezione di Pisa, Edificio C - Polo Fibonacci Largo B. Pontecorvo, 3, I-56127 Pisa, Italy
127 Istituto Nazionale di Fisica Nucleare (INFN), Sezione di Roma, c/o Dipartimento di Fisica - Università degli Studi di Roma "La Sapienza", P.le Aldo Moro 2, I-00185 Roma, Italy
128 Istituto Nazionale di Fisica Nucleare (INFN), Sezione di Torino, c/o Universitá di Torino, facoltá di Fisica, via P Giuria 1, 10125 Torino, Italy
129 Istituto Nazionale di Fisica Nucleare (INFN), Sezione di Trieste, Padriciano 99, I-34012 Trieste (Padriciano), Italy
130 ITER Organization, Route de Vinon-sur-Verdon, 13115 St. Paul-lez-Durance, France
131 Iwate University, 4-3-5 Ueda, Morioka, Iwate, 020-8551, Japan
132 Jagiellonian University, Institute of Physics, Ul. Reymonta 4, PL-30-059 Cracow, Poland
133 Jamia Millia Islamia, Department of Physics, Jamia Nagar, New Delhi 110025, India
134 Japan Aerospace Exploration Agency, Sagamihara Campus, 3-1-1 Yoshinodai, Sagamihara, Kanagawa 220-8510 , Japan
135 Japan Atomic Energy Agency, 4-49 Muramatsu, Tokai-mura, Naka-gun, Ibaraki 319-1184, Japan
136 Japan Atomic Energy Agency, Tokai Research and Development Center, 2-4 Shirane Shirakata, Tokai-mura, Naka-gun, Ibaraki 319-1195, Japan
137 Japan Synchrotron Radiation Research Institute (JASRI), 1-1-1, Kouto, Sayo-cho, Sayo-gun, Hyogo 679-5198, Japan
138 Johannes Gutenberg Universität Mainz, Institut für Physik, 55099 Mainz, Germany
139 John Adams Institute for Accelerator Science at Royal Holloway University of London, Egham Hill, Egham, Surrey TW20 0EX, UK
140 John Adams Institute for Accelerator Science at University of Oxford, Denys Wilkinson Building, Keble Road, Oxford OX1 3RH, UK
141 Johns Hopkins University - Henry A. Rowland Department of Physics & Astronomy 3701 San Martin Drive, Baltimore, Maryland (MD) 21218, USA
142 Joint Institute for Nuclear Research (JINR), Joliot-Curie 6, 141980, Dubna, Moscow Region, Russia
143 Joint Institute for Power and Nuclear Research "Sosny" at National Academy of Sciences of Belarus, 99 Academician A.K.Krasin Str., Minsk BY-220109, Belarus
144 Jozef Stefan Institute, Jamova cesta 39, 1000 Ljubljana, Slovenia
145 Julius-Maximilians-Universität Würzburg, Fakultät für Physik und Astronomie, Am Hubland, 97074 Würzburg, Germany
146 Juntendo University, School of Medicine, Dept. of Physics, Hiraga-gakuendai 1-1, Inzai-shi, Chiba 270-1695, Japan
147 Justus-Liebig-Universität Gießen, II. Physikalisches Institut, Heinrich-Buff-Ring 16, 35392 Gießen, Germany
148 Kanazawa University, Institute for Theoretical Physics (KITP), School of Mathematics and Physics, College of Science and Engineering, Kakuma-machi, Kanazawa city, Ishikawa 920-1192, Japan
149 Kansas State University, Department of Physics, 116 Cardwell Hall, Manhattan, KS 66506, USA
150 Kavli Institute for the Physics and Mathematics of the Universe (Kavli IPMU), University of Tokyo, 5-1-5 Kashiwanoha, Kashiwa, 277-8583, Japan
151 King Saud University (KSU), Dept. of Physics, P.O. Box 2454, Riyadh 11451, Saudi Arabia
152 King's College London - Department of physics, Strand, London WC2R 2LS, London, UK
153 Kinki University, Department of Physics, 3-4-1 Kowakae, Higashi-Osaka, Osaka 577-8502, Japan
154 Kobe University, Department of Physics, 1-1 Rokkodai-cho, Nada-ku, Kobe, Hyogo 657-8501, Japan

155 Kogakuin University, Department of Physics, Shinjuku Campus, 1-24-2 Nishi-Shinjuku, Shinjuku-ku, Tokyo 163-8677, Japan

156 Konkuk University, 93-1 Mojin-dong, Kwanglin-gu, Seoul 143-701, Republic of Korea

157 Korea Advanced Institute of Science & Technology, Department of Physics, 373-1 Kusong-dong, Yusong-gu, Taejon 305-701, Republic of Korea

158 Korea Institute for Advanced Study (KIAS), School of Physics, 207-43 Cheongryangri-dong, Dongdaemun-gu, Seoul 130-012, Republic of Korea

159 Kyoto University, Department of Physics, Kitashirakawa-Oiwakecho, Sakyo-ku, Kyoto 606-8502, Japan

160 Kyoto University, Yukawa Institute for Theoretical Physics, Kitashirakawa-Oiwakecho, Sakyo-Ku, Kyoto 606-8502, Japan

161 Kyushu University, Department of Physics, 6-10-1 Hakozaki, Higashi-ku, Fukuoka 812-8581, Japan

162 L.P.T.A., UMR 5207 CNRS-UM2, Université Montpellier II, Case Courrier 070, Bât. 13, place Eugène Bataillon, 34095 Montpellier Cedex 5, France

163 Laboratoire Charles Coulomb UMR 5221 CNRS-UM2, Université Montpellier 2, Place Eugène Bataillon - CC069, 34095 Montpellier Cedex 5, France

164 Laboratoire d'Annecy-le-Vieux de Physique des Particules (LAPP) , Université de Savoie, CNRS/IN2P3, 9 Chemin de Bellevue, BP 110, F-74941 Annecy-Le-Vieux Cedex, France

165 Laboratoire d'Annecy-le-Vieux de Physique Theorique (LAPTH), Chemin de Bellevue, BP 110, F-74941 Annecy-le-Vieux Cedex, France

166 Laboratoire d'AstroParticules et Cosmologie (APC), Université Paris Diderot-Paris 7 - CNRS/IN2P3, Bâtiment Condorcet, Case 7020, 75205 Paris Cedex 13, France

167 Laboratoire de l'Accélérateur Linéaire (LAL), Université Paris-Sud 11, Bâtiment 200, 91898 Orsay, France

168 Laboratoire de Physique Corpusculaire de Clermont-Ferrand (LPC), Université Blaise Pascal, I.N.2.P.3./C.N.R.S., 24 avenue des Landais, 63177 Aubière Cedex, France

169 Laboratoire de Physique Nucléaire et des Hautes Energies (LPNHE), UPMC, UPD, IN2P3/CNRS, 4 Place Jussieu, 75005, Paris Cedex 05, France

170 Laboratoire de Physique Subatomique et de Cosmologie (LPSC), Université Joseph Fourier (Grenoble 1), CNRS/IN2P3, Institut Polytechnique de Grenoble, 53 rue des Martyrs, F-38026 Grenoble Cedex, France

171 Laboratoire de Physique Theorique, Université de Paris-Sud XI, Batiment 210, F-91405 Orsay Cedex, France

172 Laboratoire Leprince-Ringuet (LLR), École polytechnique – CNRS/IN2P3, Route de Saclay, F-91128 Palaiseau Cedex, France

173 Laboratoire Univers et Particules de Montpellier (LUPM) - UMR5299, Université de Montpellier II, Place Eugène Bataillon - Case courrier 72, 34095 Montpellier Cedex 05, France

174 Laboratori Nazionali di Frascati, via E. Fermi, 40, C.P. 13, I-00044 Frascati, Italy

175 Laboratório de Instrumentação e Física Experimental de Partículas (LIP LISBOA), Av. Elias Garcia 14 - 1°, 1000-149 Lisbon, Portugal

176 Lancaster University, Physics Department, Lancaster LA1 4YB, UK

177 Lawrence Berkeley National Laboratory (LBNL), 1 Cyclotron Rd, Berkeley, CA 94720, USA

178 Lawrence Livermore National Laboratory (LLNL), Livermore, CA 94551, USA

179 Lebedev Physical Institute, Leninsky Prospect 53, RU-117924 Moscow, Russia

180 Lomonosov Moscow State University, Skobeltsyn Institute of Nuclear Physics (MSU SINP), 1(2), Leninskie gory, GSP-1, Moscow 119991, Russia

181 Louisiana Tech University, Department of Physics, Ruston, LA 71272, USA

182 Ludwig-Maximilians-Universität München, Fakultät für Physik, Am Coulombwall 1, D - 85748 Garching, Germany

183 Lunds Universitet, Fysiska Institutionen, Avdelningen för Experimentell Högenergifysik, Box 118, 221 00 Lund, Sweden

184 L'Université Hassan II, Aïn Chock, "Réseau Universitaire de Physique des Hautes Energies" (RUPHE), Département de Physique, Faculté des Sciences Aïn Chock, B.P 5366 Maarif, Casablanca 20100, Morocco

185 Massachusetts Institute of Technology (MIT), Laboratory for Nuclear Science, 77 Massachusetts Avenue, Cambridge, MA 02139, USA

186 Max-Planck-Institut für Physik (Werner-Heisenberg-Institut), Föhringer Ring 6, 80805 München, Germany

187 McGill University, Department of Physics, Ernest Rutherford Physics Bldg., 3600 University Street, Montreal, Quebec, H3A 2T8 Canada

188 McMaster University, Department of Physics & Astronomy, 1280 Main Street West, Hamilton, ON, L8S 4M1, Canada

189 Meiji Gakuin University, Department of Physics, 2-37 Shirokanedai 1-chome, Minato-ku, Tokyo 244-8539, Japan

190 Michigan State University, Department of Chemical Engineering & Materials Science, 2527 Engineering Building East Lansing, MI 48824-1226, USA

191 Michigan State University, Department of Physics and Astronomy, East Lansing, MI 48824, USA

192 Middle East Technical University, Department of Physics, TR-06531 Ankara, Turkey

193 Miyagi Gakuin Women's University, Faculty of Liberal Arts, 9-1-1 Sakuragaoka, Aoba District, Sendai, Miyagi 981-8557, Japan

194 MSU-Iligan Institute of Technology, Department of Physics, Andres Bonifacio Avenue, 9200 Iligan City, Phillipines

195 Nagasaki Institute of Applied Science, 536 Abamachi, Nagasaki-Shi, Nagasaki 851-0193, Japan

196 Nagoya University, Department of Materials Science and Engineering, Furo-cho, Chikusa-ku, Nagoya, 464-8603, Japan

197 Nagoya University, Department of Physics, School of Science, Furo-cho, Chikusa-ku, Nagoya, Aichi 464-8602, Japan

198 Nagoya University, Kobayashi-Maskawa Institute for the Origin of Particles and the Universe (KMI), Furo-cho, Chikusa-ku, Nagoya Aichi 464-8602, Japan

199 Nanjing University, Department of Physics, Nanjing, China 210093

200 Nara Women's University, High Energy Physics Group, Kitauoya-Nishimachi, Nara 630-8506, Japan

201 National Central University, High Energy Group, Department of Physics, Chung-li, Taiwan 32001, R.O.C

202 National Centre of Nuclear Research (NCBJ), ul. Andrzeja Soltana 7, 05-400 Otwock-Swierk, Poland

203 National Cheng Kung University, Physics Department, 1 Ta-Hsueh Road, Tainan, Taiwan 70101, R.O.C

204 National Chiao-Tung University, Institute of Physics, 1001 Ta Hsueh Rd, Hsinchu, Taiwan 300, R.O.C.
205 National Institute of Chemical Physics and Biophysics (NICPB), Ravala pst 10, 10143 Tallinn, Estonia
206 National Institute of Physics and Nuclear Engineering "Horia Hulubei" (IFIN-HH), Str. Reactorului no.30, P.O. Box MG-6, R-76900 Bucharest - Magurele, Romania
207 National Research Centre "Kurchatov Institute", 1 Akademika Kurchatova pl., Moscow, 123182, Russia
208 National Science Center - Kharkov Institute of Physics and Technology (NSC KIPT), Akademicheskaya St. 1, Kharkov, 61108, Ukraine
209 National Scientific & Educational Centre of Particle & High Energy Physics (NCPHEP), Belarusian State University, M.Bogdanovich street 153, 220040 Minsk, Belarus
210 National Taiwan University, Physics Department, Taipei, Taiwan 106, R.O.C
211 Niels Bohr Institute (NBI), University of Copenhagen, Blegdamsvej 17, DK-2100 Copenhagen, Denmark
212 Niigata University, Department of Physics, Ikarashi, Niigata 950-218, Japan
213 Nikhef, National Institute for Subatomic Physics, P.O. Box 41882, 1009 DB Amsterdam, Netherlands
214 Nippon Dental University School of Life Dentistry at Niigata, 1-8 Hamaura-cho, Chuo-ku, Niigata 951-1500, Japan
215 North Carolina A&T State University, 1601 E. Market Street, Greensboro, NC 27411, USA
216 Northeastern University, Physics Department, 360 Huntington Ave, 111 Dana Research Center, Boston, MA 02115, USA
217 Northern Illinois University, Department of Physics, DeKalb, Illinois 60115-2825, USA
218 Northwestern University, Department of Physics and Astronomy, 2145 Sheridan Road., Evanston, IL 60208, USA
219 Novosibirsk State University (NGU), Department of Physics, Pirogov st. 2, 630090 Novosibirsk, Russia
220 Ochanomizu University, Department of Physics, Faculty of Science, 1-1 Otsuka 2, Bunkyo-ku, Tokyo 112-8610, Japan
221 Orissa University of Agriculture & Technology, Bhubaneswar 751003, Orissa, India
222 Osaka City University, Department of Physics, Faculty of Science, 3-3-138 Sugimoto, Sumiyoshi-ku, Osaka 558-8585, Japan
223 Osaka University, Department of Physics, 1-1 Machikaneyama, Toyonaka, Osaka 560-0043, Japan
224 Österreichische Akademie der Wissenschaften, Institut für Hochenergiephysik, Nikolsdorfergasse 18, A-1050 Vienna, Austria
225 Pacific Northwest National Laboratory, (PNNL), PO Box 999, Richland, WA 99352, USA
226 Panjab University, Chandigarh 160014, India
227 Pavel Sukhoi Gomel State Technical University, ICTP Affiliated Centre & Laboratory for Physical Studies, October Avenue, 48, 246746, Gomel, Belarus
228 Perimeter Institute for Theoretical Physics, 31 Caroline Street North, Waterloo, Ontario N2L 2Y5, Canada
229 Physical Research Laboratory, Navrangpura, Ahmedabad 380 009, Gujarat, India
230 Pohang Accelerator Laboratory (PAL), San-31 Hyoja-dong, Nam-gu, Pohang, Gyeongbuk 790-784, Republic of Korea
231 Pontificia Universidad Católica de Chile, Avda. Libertador Bernardo OHiggins 340, Santiago, Chile
232 Princeton University, Department of Physics, P.O. Box 708, Princeton, NJ 08542-0708, USA
233 Purdue University, Department of Physics, West Lafayette, IN 47907, USA
234 Queen Mary, University of London, Mile End Road, London, E1 4NS, United Kingdom
235 Rheinisch-Westfälische Technische Hochschule (RWTH), Physikalisches Institut, Physikzentrum, Otto-Blumenthal-Straße, 52056 Aachen
236 RIKEN, 2-1 Hirosawa, Wako, Saitama 351-0198, Japan
237 Royal Holloway, University of London (RHUL), Department of Physics, Egham, Surrey TW20 0EX, UK
238 Russian Academy of Science, Keldysh Institute of Applied Mathematics, Muiskaya pl. 4, 125047 Moscow, Russia
239 Rutgers, The State University of New Jersey, Department of Physics & Astronomy, 136 Frelinghuysen Rd, Piscataway, NJ 08854, USA
240 Saga University, Department of Physics, 1 Honjo-machi, Saga-shi, Saga 840-8502, Japan
241 Saha Institute of Nuclear Physics, 1/AF Bidhan Nagar, Kolkata 700064, India
242 Salalah College of Technology (SCOT), Engineering Department, Post Box No. 608, Postal Code 211, Salalah, Sultanate of Oman
243 Saudi Center for Theoretical Physics, King Fahd University of Petroleum and Minerals (KFUPM), Dhahran 31261, Saudi Arabia
244 Seikei University, Faculty of Science and Technology, 3-3-1 Kichijoji-Kitamachi, Musashino-shi, Tokyo 180-8633, Japan
245 Seoul National University, San 56-1, Shinrim-dong, Kwanak-gu, Seoul 151-742, Republic of Korea
246 Setsunan University, Institute for Fundamental Sciences, 17-8 Ikeda Nakamachi, Neyagawa, Osaka, 572-8508, Japan
247 Shanghai Jiao Tong University, Department of Physics, 800 Dongchuan Road, Shanghai, China 200240
248 Shinshu University, 3-1-1, Asahi, Matsumoto, Nagano 390-8621, Japan
249 Shiv Nadar University, Village Chithera, Tehsil Dadri, District Gautam Budh Nagar, 203207 Uttar Pradesh, India
250 Shizuoka University, Department of Physics, 836 Ohya, Suruga-ku, Shizuoka 422-8529, Japan
251 SLAC National Accelerator Laboratory, 2575 Sand Hill Road, Menlo Park, CA 94025, USA
252 Society for Applied Microwave Electronics Engineering and Research (SAMEER), I.I.T. Campus, Powai, Post Box 8448, Mumbai 400076, India
253 Sokendai, The Graduate University for Advanced Studies, Shonan Village, Hayama, Kanagawa 240-0193, Japan
254 Spallation Neutron Source (SNS), Oak Ridge National Laboratory (ORNL), P.O. Box 2008 MS-6477, Oak Ridge, TN 37831-6477, USA
255 State University of New York at Binghamton, Department of Physics, PO Box 6016, Binghamton, NY 13902, USA
256 State University of New York at Buffalo, Department of Physics & Astronomy, 239 Franczak Hall, Buffalo, NY 14260, USA
257 State University of New York at Stony Brook, Department of Physics and Astronomy, Stony Brook, NY 11794-3800, USA
258 STFC Daresbury Laboratory, Daresbury, Warrington, Cheshire WA4 4AD, UK

259 STFC Rutherford Appleton Laboratory, Chilton, Didcot, Oxon OX11 0QX, UK

260 Sungkyunkwan University (SKKU), Natural Science Campus 300, Physics Research Division, Chunchun-dong, Jangan-gu, Suwon, Kyunggi-do 440-746, Republic of Korea

261 Swiss Light Source (SLS), Paul Scherrer Institut (PSI), PSI West, CH-5232 Villigen PSI, Switzerland

262 Tata Institute of Fundamental Research, School of Natural Sciences, Homi Bhabha Rd., Mumbai 400005, India

263 Technical University of Lodz, Department of Microelectronics and Computer Science, al. Politechniki 11, 90-924 Lodz, Poland

264 Technische Universität Dresden, Institut für Kern- und Teilchenphysik, D-01069 Dresden, Germany

265 Tel-Aviv University, School of Physics and Astronomy, Ramat Aviv, Tel Aviv 69978, Israel

266 Texas A&M University, Physics Department, College Station, 77843-4242 TX, USA

267 Texas Tech University, Department of Physics, Campus Box 41051, Lubbock, TX 79409-1051, USA

268 The Henryk Niewodniczanski Institute of Nuclear Physics, Polish Academy of Sciences (IFJ PAN), ul. Radzikowskiego 152, PL-31342 Cracow, Poland

269 Thomas Jefferson National Accelerator Facility (TJNAF), 12000 Jefferson Avenue, Newport News, VA 23606, USA

270 Tohoku Gakuin University, Department of Business Administration, 1-3-1 Tsuchitoi, Aoba-ku Sendai, Miyagi 980-8511, Japan

271 Tohoku Gakuin University, Faculty of Technology, 1-13-1 Chuo, Tagajo, Miyagi 985-8537, Japan

272 Tohoku University, Department of Physics, Aoba District, Sendai, Miyagi 980-8578, Japan

273 Tohoku University, Research Center for Electron Photon Science, Taihaku District, Sendai, Miyagi 982-0826, Japan

274 Tohoku University, Research Center for Neutrino Science, Aoba District, Sendai, Miyagi 980-8578, Japan

275 Tokyo Institute of Technology, Department of Physics, 2-12-1 O-Okayama, Meguro, Tokyo 152-8551, Japan

276 Tokyo Metropolitan University, Faculty of Science and Engineering, Department of Physics, 1-1 Minami-Osawa, Hachioji-shi, Tokyo 192-0397, Japan

277 Tokyo University of Agriculture Technology, Department of Applied Physics, Naka-machi, Koganei, Tokyo 183-8488, Japan

278 Toyama Prefectural University, Department of Mathematical Physics, 5180 Kurokawa Imizu-shi, Toyama, 939-0398, Japan

279 TRIUMF, 4004 Wesbrook Mall, Vancouver, BC V6T 2A3, Canada

280 Universidad Autónoma de San Luis Potosí, Alvaro Obregon 64, Col. Centro, San Luis Potosí, S.L.P. 78000, México

281 Universidad de Granada, Departamento de Física Teórica y del Cosmos, Campus de Fuentenueva, E-18071 Granada, Spain

282 Universidad de los Andes, Faculty of Science, Department of Physics, Carrera 1 18A-10, Bloque Ip. Bogotá, Colombia

283 Universidad de Oviedo, Departamento de Física, Campus de Llamaquique. C/ Calvo Sotelo, s/n 33005 Oviedo, Spain

284 Universidad de Salamanca, Departamento de Física Fundamental, Plaza de la Merced, s/n., 37008 Salamanca, Spain

285 Universidad de Sevilla, Escuela Técnica Superior de Ingeniería, Departamento Ingeniería Electrónica, Camino de los Descubrimientos s/n, 41092 Sevilla, Spain

286 Universidad de Zaragoza - Departamento de Física Teórica, Pedro Cerbuna 12, E-50009 Zaragoza, Spain

287 Universidad Nacional Autónoma de México, Instituto de Física, Circuito de la Investigación Cientifica s/n, Ciudad Universitaria, CP 04510 México D.F., Mexico

288 Universidad Nacional de La Plata, Departamento de Física, Facultad de Ciencias Exactas, C.C. N 67, 1900 La Plata, Argentina

289 Universidade do Estado do Rio de Janeiro (UERJ), Rio de Janeiro, RJ - Brasil 20550-900, Brazil

290 Universidade Federal de Pelotas, Instituto de Física e Matemática, Campus Universitário, Caixa Postal 354, 96010-900 Pelotas, RS, Brazil

291 Universidade Federal do Rio de Janeiro (UFRJ), Instituto de Física, Av. Athos da Silveira Ramos 149, Centro de Tecnologia - Bloco A, Cidade Universitária, Ilha do Fundão, Rio de Janeiro, RJ, Brazil

292 Universitá degli Studi di Napoli "Federico II", Dipartimento di Fisica, Via Cintia, 80126 Napoli, Italy

293 Universitat Autònoma de Barcelona, Departament de Física, Edifici C, 08193 Bellaterra, Barcelona, Spain

294 Universitat Autònoma de Barcelona, Institut de Fisica d'Altes Energies (IFAE), Campus UAB, Edifici Cn, E-08193 Bellaterra, Barcelona, Spain

295 Universität Bonn, Physikalisches Institut, Nußallee 12, 53115 Bonn, Germany

296 Universität Heidelberg, Institut für Theoretische Physik, Philosophenweg 16, 69120 Heidelberg, Germany

297 Universität Heidelberg, Kirchhoff-Institut für Physik, Im Neuenheimer Feld 227, 69120 Heidelberg, Germany

298 Universitat Politècnica de Catalunya, Institut de Tècniques Energètiques, Campus Diagonal Sud, Edifici PC (Pavelló C). Av. Diagonal, 647 08028 Barcelona, Spain

299 Universitat Ramon Llull, La Salle, C/ Quatre Camins 2, 08022 Barcelona, Spain

300 Universität Rostock, 18051 Rostock, Germany

301 Universität Siegen, Naturwissenschaftlich-Technische Fakultät, Department Physik, Emmy Noether Campus, Walter-Flex-Str.3, 57068 Siegen, Germany

302 Universität Wien - Theoretische Physik Boltzmanngasse 5, A-1090 Vienna, Austria

303 Université catholique de Louvain, Centre for Cosmology, Particle Physics and Phenomenology (CP3), Institute of Mathematics and Physics, 2 Chemin du Cyclotron, 1348 Louvain-la-Neuve, Belgium

304 Université de Genève, Section de Physique, 24, quai E. Ansermet, 1211 Genève 4, Switzerland

305 Université de Montréal, Département de Physique, Groupe de Physique des Particules, C.P. 6128, Succ. Centre-ville, Montréal, Qc H3C 3J7, Canada

306 Université de Strasbourg, UFR de Sciences Physiques, 3-5 Rue de l'Université, F-67084 Strasbourg Cedex, France

307 Université Libre de Bruxelles, Boulevard du Triomphe, 1050 Bruxelles, Belgium

308 Universittà di Catania, Dipartimento di Fisica e Astronomia, Via Santa Sofia 64, 95123 Catania, Italy

309 University College London (UCL), High Energy Physics Group, Physics and Astronomy Department, Gower Street, London WC1E 6BT, UK

310 University College, National University of Ireland (Dublin), Department of Experimental Physics, Science Buildings, Belfield, Dublin 4, Ireland
311 University de Barcelona, Facultat de Física, Av. Diagonal, 647, Barcelona 08028, Spain
312 University of Alberta - Faculty of Science, Department of Physics, 4-181 CCIS, Edmonton AB T6G 2E1, Canada
313 University of Arizona, Department of Physics, 1118 E. Fourth Street, PO Box 210081, Tucson, AZ 85721, USA
314 University of Bergen, Institute of Physics, Allegaten 55, N-5007 Bergen, Norway
315 University of Birmingham, School of Physics and Astronomy, Particle Physics Group, Edgbaston, Birmingham B15 2TT, UK
316 University of Bristol, H. H. Wills Physics Lab, Tyndall Ave., Bristol BS8 1TL, UK
317 University of British Columbia, Department of Physics and Astronomy, 6224 Agricultural Rd., Vancouver, BC V6T 1Z1, Canada
318 University of California (UCLA), Los Angleles, CA 90095, US
319 University of California Berkeley, Department of Physics, 366 Le Conte Hall, #7300, Berkeley, CA 94720, USA
320 University of California Davis, Department of Physics, One Shields Avenue, Davis, CA 95616-8677, USA
321 University of California Irvine, Department of Physics and Astronomy, High Energy Group, 4129 Frederick Reines Hall, Irvine, CA 92697-4575 USA
322 University of California Santa Cruz, Institute for Particle Physics, 1156 High Street, Santa Cruz, CA 95064, USA
323 University of Cambridge, Cavendish Laboratory, J J Thomson Avenue, Cambridge CB3 0HE, UK
324 University of Colorado at Boulder, Department of Physics, 390 UCB, University of Colorado, Boulder, CO 80309-0390, USA
325 University of Cyprus, Department of Physics, P.O.Box 20537, 1678 Nicosia, Cyprus
326 University of Delhi, Department of Physics and Astrophysics, Delhi 110007, India
327 University of Delhi, S.G.T.B. Khalsa College, Delhi 110007, India
328 University of Dundee, Department of Physics, Nethergate, Dundee, DD1 4HN, Scotland, UK
329 University of Edinburgh, School of Physics, James Clerk Maxwell Building, The King's Buildings, Mayfield Road, Edinburgh EH9 3JZ, UK
330 University of Florida, Department of Physics, Gainesville, FL 32611, USA
331 University of Ghent, Department of Subatomic and Radiation Physics, Proeftuinstraat 86, 9000 Gent, Belgium
332 University of Glasgow, SUPA, School of Physics & Astronomy, University Avenue, Glasgow G12 8QQ, Scotland, UK
333 University of Hamburg, Physics Department, Luruper Chaussee 149, 22761 Hamburg, Germany
334 University of Hawaii, Department of Physics and Astronomy, HEP, 2505 Correa Rd., WAT 232, Honolulu, HI 96822-2219, USA
335 University of Helsinki, Department of Physical Sciences, P.O. Box 64 (Vaino Auerin katu 11), FIN-00014, Helsinki, Finland
336 University of Illinois at Chicago, Department Of Physics, 845 W Taylor St., Chicago IL 60607, USA
337 University of Iowa, Department of Physics and Astronomy, 203 Van Allen Hall, Iowa City, IA 52242-1479, USA
338 University of Kansas, Department of Physics and Astronomy, Malott Hall, 1251 Wescoe Hall Drive, Room 1082, Lawrence, KS 66045-7582, USA
339 University of Liverpool, Department of Physics, Oliver Lodge Lab, Oxford St., Liverpool L69 7ZE, UK
340 University of Liverpool, Division of Theoretical Physics, Department of Mathematical Sciences, Chadwick Building, Liverpool L69 3BX, UK
341 University of Ljubljana, Faculty of Mathematics and Physics, Jadranska ulica 19, 1000 Ljubljana, Slovenia
342 University of Malaya, Faculty of Science, Department of Physics, 50603 Kuala Lumpur, Malaysia
343 University of Manchester, School of Physics and Astronomy, Schuster Lab, Manchester M13 9PL, UK
344 University of Maribor, Faculty of Chemistry and Chemical Engineering (FKKT), Smetanova ulica 17, 2000 Maribor, Slovenia
345 University of Maryland, Department of Physics and Astronomy, Physics Building (Bldg. 082), College Park, MD 20742, USA
346 University of Massachusetts - Amherst, Department of Physics, 1126 Lederle Graduate Research Tower (LGRT), Amherst, MA 01003-9337, USA
347 University of Melbourne, School of Physics, Victoria 3010, Australia
348 University of Michigan, Department of Physics, 500 E. University Ave., Ann Arbor, MI 48109-1120, USA
349 University of Minnesota, 148 Tate Laboratory Of Physics, 116 Church St. S.E., Minneapolis, MN 55455, USA
350 University of Mississippi, Department of Physics and Astronomy, 108 Lewis Hall, PO Box 1848, Oxford, Mississippi 38677-1848, USA
351 University of Missouri – St. Louis, Department of Physics and Astronomy, 503 Benton Hall One University Blvd., St. Louis Mo 63121, USA
352 University of New Mexico, New Mexico Center for Particle Physics, Department of Physics and Astronomy, 800 Yale Boulevard N.E., Albuquerque, NM 87131, USA
353 University of North Carolina at Chapel Hill, Department of Physics and Astronomy, Phillips Hall, CB #3255, 120 E. Cameron Ave., Chapel Hill, NC 27599-3255, USA
354 University of Notre Dame, Department of Physics, 225 Nieuwland Science Hall, Notre Dame, IN 46556, USA
355 University of Oklahoma, Department of Physics and Astronomy, Norman, OK 73071, USA
356 University of Oregon, Department of Physics, 1371 E. 13th Ave., Eugene, OR 97403, USA
357 University of Oslo, Department of Physics, P.O box 1048, Blindern, 0316 Oslo, Norway
358 University of Oxford, Particle Physics Department, Denys Wilkinson Bldg., Keble Road, Oxford OX1 3RH England, UK
359 University of Pavia, Department of Physics, via Bassi 6, I-27100 Pavia, Italy
360 University of Pennsylvania, Department of Physics and Astronomy, 209 South 33rd Street, Philadelphia, PA 19104-6396, USA
361 University of Pittsburgh, Department of Physics and Astronomy, 100 Allen Hall, 3941 O'Hara St, Pittsburgh PA 15260, USA
362 University of Regina, Department of Physics, Regina, Saskatchewan, S4S 0A2 Canada

363 University of Rochester, Department of Physics and Astronomy, Bausch & Lomb Hall, P.O. Box 270171, 600 Wilson Boulevard, Rochester, NY 14627-0171 USA
364 University of Science and Technology of China, Department of Modern Physics (DMP), Jin Zhai Road 96, Hefei, China 230026
365 University of Silesia, Institute of Physics, Ul. Uniwersytecka 4, PL-40007 Katowice, Poland
366 University of South Carolina, Department of Physics and Astronomy, 712 Main Street, Columbia, SC 29208, USA
367 University of Southampton, School of Physics and Astronomy, Highfield, Southampton S017 1BJ, England, UK
368 University of Southern California, Department of Physics & Astronomy, 3620 McClintock Ave., SGM 408, Los Angeles, CA 90089-0484, USA
369 University of Sydney, Falkiner High Energy Physics Group, School of Physics, A28, Sydney, NSW 2006, Australia
370 University of Tartu, Institute of Physics, Riia 142, 51014 Tartu, Estonia
371 University of Texas at Austin, Department of Physics, 1 University Station C1600, Austin, Texas 78712, USA
372 University of Texas at Dallas, Department of Physics, 800 West Campbell Road, Richardson, Texas 75080, USA
373 University of Texas, Center for Accelerator Science and Technology, Arlington, TX 76019, USA
374 University of Tokushima, Institute of Theoretical Physics, Tokushima-shi 770-8502, Japan
375 University of Tokyo, Department of Physics, 7-3-1 Hongo, Bunkyo District, Tokyo 113-0033, Japan
376 University of Toronto, Department of Physics, 60 St. George St., Toronto M5S 1A7, Ontario, Canada
377 University of Toyama, Department of Physics, 3190 Gofuku, Toyama 930-8555, Japan
378 University of Tsukuba, Faculty of Pure and Applied Sciences, 1-1-1 Ten'nodai, Tsukuba, Ibaraki 305-8571, Japan
379 University of Victoria, Department of Physics and Astronomy, P.O.Box 3055 Stn Csc, Victoria, BC V8W 3P6, Canada
380 University of Virginia, Department of Physics, 382 McCormick Rd., PO Box 400714, Charlottesville, VA
381 University of Warsaw, Institute of Experimental Physics, Ul. Hoza 69, PL-00 681 Warsaw, Poland
382 University of Warsaw, Institute of Theoretical Physics, Ul. Hoza 69, PL-00 681 Warsaw, Poland
383 University of Washington, Department of Physics, PO Box 351560, Seattle, WA 98195-1560, USA
384 University of Wisconsin, Physics Department, Madison, WI 53706-1390, USA
385 University of Wuppertal, Gaußstraße 20, D-42119 Wuppertal, Germany
386 Università degli Studi di Milano, Dipartimento di Fisica, Via Celoria 16, 20133 Milano, Italy
387 Università degli Studi di Roma "La Sapienza", Dipartimento di Fisica, Piazzale Aldo Moro 5, 00185 Roma, Italy
388 Università degli Studi di Trieste, Dipartimento di Fisica, via A. Valerio 2, I-34127 Trieste, Italy
389 Università dell'Insubria in Como, Dipartimento di Scienze CC.FF.MM., via Vallegio 11, I-22100 Como, Italy
390 Università di Milano-Bicocca, Dipartimento di Fisica"G. Occhialin", Piazza della Scienza 3, 20126 Milano, Italy
391 Università di Pisa, Departimento di Fisica "Enrico Fermi", Largo Bruno Pontecorvo 3, I-56127 Pisa, Italy
392 Universiy of Huddersfield, International Institute for Accelerator Applications, Queensgate Campus, Huddersfield HD1 3DH, UK
393 UPMC Univ. Paris 06, Faculté de Physique (UFR 925), 4 Place Jussieu, 75252 Paris Cedex 05, France
394 Vietnam National University, Laboratory of High Energy Physics and Cosmology, Faculty of Physics, College of Science, 334 Nguyen Trai, Hanoi, Vietnam
395 Vietnam National University, University of Natural Sciences, 227 Nguyen Van Cu street, District 5, Ho Chi Minh City, Vietnam
396 VINCA Institute of Nuclear Sciences, Laboratory of Physics, PO Box 522, YU-11001 Belgrade, Serbia
397 Virginia Commonwealth University, Department of Physics, P.O. Box 842000, 701 W. Grace St.,Richmond, VA. 23284-2000, USA
398 Virginia Polytechnic Institute and State University, Physics Department, Blacksburg, VA 2406, USA
399 Vrije Universiteit Brussel, Pleinlaan 2, 1050 Brussels, Belgium
400 Vrije Universiteit, Department of Physics, Faculty of Sciences, De Boelelaan 1081, 1081 HV Amsterdam, Netherlands
401 Warsaw University of Technology, The Faculty of Electronics and Information Technology, ul. Nowowiejska 15-19, 00-665 Warsaw, Poland
402 Waseda University, Advanced Research Institute for Science and Engineering, Shinjuku, Tokyo 169-8555, Japan
403 Wayne State University, Department of Physics, Detroit, MI 48202, USA
404 Weizmann Institute of Science, Department of Particle Physics, P.O. Box 26, Rehovot 76100, Israel
405 Yale University, Department of Physics, New Haven, CT 06520, USA
406 Yamagata University, 1-4-12 Kojirakawa-cho, Yamagata-shi, Yamagata, 990-8560, Japan
407 Yerevan Physics Institute, 2 Alikhanyan Brothers St., Yerevan 375036, Armenia
408 Yonsei University, Department of Physics, 134 Sinchon-dong, Sudaemoon-gu, Seoul 120-749, Republic of Korea

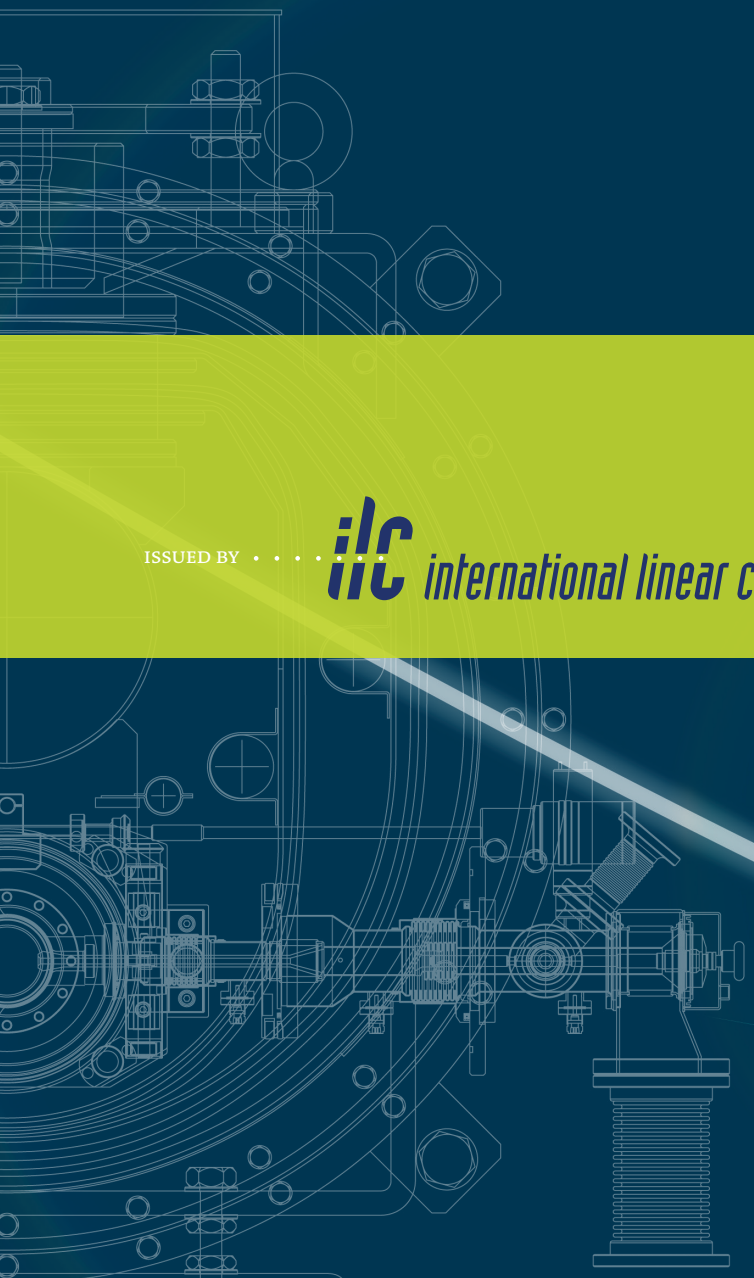

ISSUED BY • • • • • • • • • ilc international linear collider

WWW.LINEARCOLLIDER.ORG

ISBN 978-3-935702-75-1

Argonne National Laboratory: ANL-HEP-TR-13-20
Brookhaven National Laboratory: BNL-100603-2013-IR
CEA/irfu: IRFU-13-59
CERN: CERN-ATS-2013-037
Cockcroft Institute: Cockcroft-13-10
Cornell University: CLNS 13/2085
DESY: DESY 13-062
Fermilab: FERMILAB TM-2554
IHEP: IHEP-AC-ILC-2013-001
ILC report: ILC-REPORT-2013-040
INFN: INFN-13-04/LNF
JAI: JAI-2013-001
JINR: JINR E9-2013-35
JLab: JLAB-R-2013-01
KEK: KEK Report 2013-1
KNU: KNU/CHEP-ILC-2013-1
LLNL: LLNL-TR-635539
SLAC: SLAC-R-1004
ILC HiGrade: ILC-HiGrade-Report-2013-003

THE INTERNATIONAL LINEAR COLLIDER

Technical Design Report | Volume 3.1: Accelerator R&D

The International Linear Collider

Technical Design Report

2013

Volume 1: Executive Summary

Volume 2: Physics

Volume 3: Accelerator

Part I: R&D in the Technical Design Phase

Volume 3: Accelerator

Part II: Baseline Design

Volume 4: Detectors

Volume 3

Accelerator

Part I

R&D in the Technical Design Phase

Editors

Chris Adolphsen, Maura Barone, Barry Barish, Karsten Buesser, Phil Burrows, John Carwardine (Editorial Board Chair), Jeffrey Clark, Hélène Mainaud Durand, Gerry Dugan, Eckhard Elsen, Atsuto Enomoto, Brian Foster, Shigeki Fukuda, Wei Gai, Martin Gastal, Rongli Geng, Camille Ginsburg, Susanna Guiducci, Mike Harrison, Hitoshi Hayano, Keith Kershaw, Kiyoshi Kubo, Vic Kuchler, Benno List, Wanming Liu, Shinichiro Michizono, Christopher Nantista, John Osborne, Mark Palmer, James McEwan Paterson, Thomas Peterson, Nan Phinney, Paolo Pierini, Marc Ross, David Rubin, Andrei Seryi, John Sheppard, Nikolay Solyak, Steinar Stapnes, Toshiaki Tauchi, Nobu Toge, Nicholas Walker, Akira Yamamoto, Kaoru Yokoya

Acknowledgements

We acknowledge the support of BMWF, Austria; MinObr, Belarus; FNRS and FWO, Belgium; NSERC, Canada; NSFC, China; MPO CR and VSC CR, Czech Republic; Commission of the European Communities; HIP, Finland; IN2P3/CNRS, CEA-DSM/IRFU, France; BMBF, DFG, Helmholtz Association, MPG and AvH Foundation, Germany; DAE and DST, India; ISF, Israel; INFN, Italy; MEXT and JSPS, Japan; CRI(MST) and MOST/KOSEF, Korea; FOM and NWO, The Netherlands; NFR, Norway; MNSW, Poland; ANCS, Romania; MES of Russia and ROSATOM, Russian Federation; MON, Serbia and Montenegro; MSSR, Slovakia; MICINN-MINECO and CPAN, Spain; SRC, Sweden; STFC, United Kingdom; DOE and NSF, United States of America.

Contents

Common preamble to Parts I and II 1

1 Introduction 3

2 Superconducting RF technology 5

2.1 Overview . . . 5
2.2 Development of Cavity Infrastructure and R&D . . . 7
2.2.1 Production and Test Facilities . . . 8
2.2.2 Inspection Infrastructure and Capabilities . . . 10
2.2.3 Cavity-Tuning Facilities . . . 11
2.2.4 Quench Detection . . . 12
2.2.5 Test Infrastructure and Measurement Techniques . . . 12
2.2.6 Diagnostics for Field Emission . . . 13
2.2.7 Remediation Techniques . . . 14
2.2.8 Infrastructure for High-power Couplers . . . 14
2.3 High-gradient SCRF Cavity Yield . . . 15
2.3.1 Baseline Cavity . . . 15
2.3.2 R&D on ILC High-gradient-cavity Processing . . . 19
2.3.3 Yield and cavity selection criterion . . . 25
2.3.4 ILC Cavities for the 1 TeV Upgrade . . . 28
2.4 Cavity Integration . . . 32
2.4.1 Frequency Tuners . . . 32
2.4.2 Input power couplers . . . 35
2.4.3 Magnetic shields . . . 38
2.4.4 Summary of Cavity Integration R&D . . . 40
2.5 Anticipated Benefits from the European XFEL . . . 40
2.5.1 Cavities . . . 42
2.5.2 Cryomodule . . . 43
2.5.3 RF Power System . . . 44
2.5.4 Accelerator Module Test Facility . . . 45
2.5.5 Electronic Documentation System . . . 45
2.5.6 European XFEL as a Beam Test Linac for ILC . . . 45
2.6 The S1-Global Experiment . . . 46
2.6.1 Cryomodules and Cryogenics . . . 47
2.6.2 High-level and Low-level RF . . . 48
2.6.3 Performance Test of Individual Cavities . . . 49
2.6.4 Cavity Performance in the S1-Global Experiment . . . 50
2.6.5 Power-coupler Conditioning . . . 50

2.6.6 Lorentz-force Detuning . . . 51
2.6.7 Operation of Seven Cavities with Vector-sum Feedback Control . . . 53
2.6.8 Summary of S1-Global Experiment . . . 53
2.7 Cryomodule and Quadrupole R&D . . . 54
2.7.1 Thermal Performance of the S1-Global Modules . . . 55
2.7.2 Thermal Performance of the European XFEL Prototype Module . . . 57
2.7.3 Cryogenic Thermal Balance . . . 59
2.7.4 R&D on the Split Quadrupole . . . 59
2.8 RF Power Generation and Distribution . . . 61
2.8.1 Overview of HLRF R&D . . . 61
2.8.2 European XFEL RF-System Evolution . . . 62
2.8.3 Radiofrequency System R&D for the ILC . . . 63
2.8.4 Waveguide Components R&D . . . 67
2.8.5 R&D of the Distributed RF Scheme (DRFS) . . . 72
2.8.6 R&D of the Klystron Cluster RF Scheme (KCS) . . . 73
2.9 R&D towards Mass-production and Design for Manufacture . . . 76
2.9.1 R&D and Studies towards Cavity Industrialisation . . . 76
2.9.2 R&D and Studies towards Cryomodule Industrialisation . . . 77

3 Beam Test Facilities 79
3.1 Overview . . . 79
3.2 FLASH 9 mA experiment . . . 80
3.2.1 Introduction . . . 80
3.2.2 FLASH Main Linac . . . 81
3.2.3 Low-Level RF Control . . . 82
3.2.4 FLASH Control System . . . 83
3.2.5 High-power long-pulse studies . . . 83
3.2.6 RF-power overhead studies . . . 84
3.2.7 Compensation Studies for Lorentz-force detuning . . . 86
3.2.8 Gradient Studies: Beam Operation close to Quench . . . 87
3.2.9 Ramp-up to Full Beam Power and Maximum Gradients . . . 89
3.2.10 Management of Operational Gradient Limits . . . 90
3.2.11 Energy Stability . . . 91
3.2.12 Automation . . . 92
3.2.13 Conclusions . . . 93
3.3 STF beam test facility at KEK . . . 94
3.3.1 Introduction . . . 94
3.3.2 Quantum-Beam Accelerator as an injector for STF-2 . . . 94
3.3.3 The STF-2 accelerator . . . 97
3.4 Fermilab Cryomodule 1 Test . . . 97
3.4.1 Introduction/Goals . . . 97
3.4.2 Commissioning & Testing Protocol . . . 98
3.4.3 Cold-Coupler Conditioning and Performance . . . 98
3.4.4 Ancillary Systems and Findings . . . 102
3.4.5 9-millisecond-Pulse Tests . . . 102
3.4.6 Future Prospects . . . 103
3.4.7 Summary . . . 103

3.5 CesrTA and Electron-cloud R&D . . . 103
3.5.1 Introduction to the Electron-cloud R&D Program . . . 103
3.5.2 The CesrTA R&D Programme . . . 104
3.5.3 Electron-cloud R&D at Other Laboratories . . . 111
3.5.4 Recommendations for Electron-cloud Mitigation . . . 112
3.5.5 CesrTA Phase II Plans . . . 112
3.6 ATF2 Final-Focus Experiment . . . 113
3.6.1 Introduction . . . 113
3.6.2 Status of ATF2 Systems . . . 115
3.6.3 Tuning Status Towards Achievement of Goal 1 . . . 117
3.6.4 Stability . . . 121

4 Accelerator Systems R&D 123
4.1 Overview . . . 123
4.2 Polarised electron source . . . 125
4.2.1 Beam Parameters . . . 125
4.2.2 System Description . . . 125
4.3 Positron Source . . . 128
4.3.1 Overview . . . 128
4.3.2 Undulator . . . 128
4.3.3 Conversion target . . . 130
4.3.4 Optical Matching Device . . . 131
4.3.5 Photon collimator . . . 131
4.3.6 Prototyping of normal-conducting RF accelerating structures and RF breakdown Study . . . 133
4.3.7 Performance simulation . . . 134
4.3.8 Lattice design . . . 135
4.3.9 Spin flipper . . . 135
4.3.10 Remote handling and radiation shielding . . . 135
4.3.11 Alternative source . . . 136
4.4 Damping ring . . . 139
4.4.1 Electron-cloud mitigation . . . 139
4.4.2 Ultra-low-emittance operation . . . 139
4.4.3 Performance of fast injection/extraction kickers . . . 140
4.5 Beam Delivery System and MDI . . . 143
4.5.1 Introduction . . . 143
4.5.2 Cold QD0 Design . . . 143
4.5.3 Permanent QD0 design . . . 146
4.5.4 Intra-train Feedback System . . . 148
4.5.5 Push-pull system . . . 150
4.5.6 Alignment systems . . . 152
4.6 Beam dynamics (simulations) . . . 154
4.6.1 Overview . . . 154
4.6.2 Sources of Luminosity Degradation . . . 154
4.6.3 Impact of Static Imperfections . . . 155
4.6.4 Dynamic Effects . . . 159
4.6.5 Optics for the Upgrade to 1 TeV . . . 163

5 Conventional Facilities and Siting Studies **165**
5.1 CFS design considerations . . . 165
5.1.1 Central Region integration . . . 165
5.1.2 Main Linac underground enclosures . . . 166
5.1.3 Detector hall and detector assembly . . . 167
5.1.4 Life-safety and egress . . . 168
5.1.5 Electrical and mechanical utilities . . . 169
5.2 Descriptions of studies . . . 169
5.2.1 Americas Region . . . 169
5.2.2 Asian Region . . . 171
5.2.3 European Region . . . 171

6 Post-TDR R&D **173**
6.1 The R&D Program . . . 173
6.2 Accelerator Design and Integration . . . 174
6.2.1 Physics Requirements . . . 174
6.2.2 Programmatic Synergies . . . 174
6.2.3 Site Studies . . . 175
6.3 Main-Linac Technical Components . . . 175
6.3.1 Test Facilities – Superconducting Linac Technology . . . 175
6.3.2 Cavity gradient . . . 176
6.3.3 Cryomodule . . . 176
6.3.4 Industrialisation . . . 176
6.4 Beam-Test Facilities . . . 177
6.4.1 Main Linac Technology - FLASH, XFEL, STF, NML . . . 177
6.4.2 Electron Cloud – Cesr Test Accelerator (CesrTA) . . . 177
6.4.3 Beam Delivery – Accelerator Test Facility (ATF / ATF2) . . . 178
6.5 Remaining R&D at other facilities . . . 179
6.5.1 Positron source . . . 179
6.5.2 Beam-Delivery System (BDS) and Machine-Detector Interface (MDI) . . . 179

Bibliography **181**

List of Signatories **201**

Common preamble to Parts I and II

The International Linear Collider (ILC) is a linear electron-positron collider based on 1.3 GHz superconducting radio-frequency (SCRF) accelerating technology. It is designed to reach 200-500 GeV (extendable to 1 TeV) centre-of-mass energy with high luminosity. The design is the result of over twenty years of linear collider R&D, beginning in earnest with the construction and operation of the SLC at SLAC. This was followed by extensive development work on warm X-band solutions (NLC/JLC) and the pioneering work by the TESLA collaboration in the 1990s on superconducting L-band RF. In 2004, the International Technology Review Panel, set up by the International Committee for Future Accelerators, ICFA, selected superconducting technology for ILC construction. The Global Design Effort (GDE) was set up by ICFA in 2005 to coordinate the development of this technology as a worldwide international collaboration. Drawing on the resources of over 300 national laboratories, universities and institutes worldwide, the GDE produced the ILC *Reference Design Report* (RDR) [1–4] in August 2007. The report describes a conceptual design for the ILC and gives an estimated cost and the required personnel from collaborating institutions.

The work done by the GDE during the RDR phase identified many high-risk challenges that required R&D, which have subsequently been the focus of the worldwide activity during the Technical Design Phase. This phase has achieved a significant increase in the achievable gradient of SCRF cavities through a much better understanding of the factors that affect it. This improved understanding has permitted the industrialisation of the superconducting RF technology to more than one company in all three regions, achieving the TDP goal of 90 % of industrially produced cavities reaching an accelerating gradient of 31.5 MV/m. A further consequence is an improved costing and construction schedule than was possible in the RDR. Other important R&D milestones have included the detailed understanding of the effects of, and effective mitigation strategies for, the "electron-cloud" effects that tend to deteriorate the quality of the positron beam, particularly in the ILC damping rings. The achievement of the R&D goals of the TDR has culminated in the publication of this report, which represents the completion of the GDE's mandate; as such, it forms a detailed solution to the technical implementation of the ILC, requiring only engineering design related to a site-specific solution to allow the start of construction.

Volume 3 (Accelerator) of the *Technical Design Report* is divided into two separate parts reflecting the GDE's primary goals during the Technical Design Phase period (2007–2012):

Part I: R&D in the Technical Design Phase summarises the programmes and primary results of the risk-mitigating worldwide R&D including industrialisation activities.

Part II: Baseline Design provides a comprehensive summary of the reference layout, parameters and technical design of the accelerator, including an updated cost and construction schedule estimate.

The R&D results and studies of cost-effective solutions for the collider presented in Part I directly support the design presented in Part II, which is structured as a technical reference.

Chapter 1
Introduction

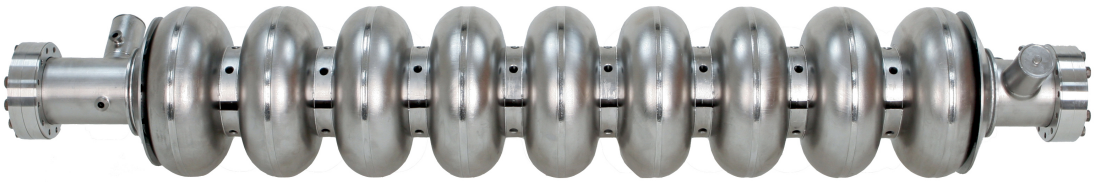

Figure 1.1. A superconducting nine-cell 1.3 GHz resonator (cavity).

The ILC *Reference Design Report* [3] published in 2007 documented a baseline design for the ILC that was by intention conservative. Several areas were identified as requiring further R&D both to reduce risk and to contain possible cost increases. This volume of the TDR concentrates on these R&D areas, the four highest priority items being:

1. SRF cavities capable of reproducibly achieving at least 35 MV/m.
2. A cryomodule consisting of eight or more cavities, operating at a gradient of 31.5 MV/m.
3. Linac string test (or integration test) of more than one cryomodule linac with beam.
4. Development of models and mitigation techniques for electron-cloud effects in the positron damping ring.

Other R&D areas (for example in the beam-delivery system and the sources) were also identified.

The first three priority R&D items all relate to the SCRF linear-accelerator technology, the primary cost driver of the machine. Although it was noted by the International Technology Review Panel [5] that TESLA SRF technology was 'mature', the ILC gradient goal had only been achieved in a handful of cavities (one of which had accelerated beam at 35 MV/m in the TESLA Test Facility at DESY – a proof of principle). One of the major technical aims has been the demonstration of large-scale production of reproducible high-gradient SCRF cavities, which required a detailed fundamental understanding of physics involved in the technology. During the five-year R&D programme, more than 200 cavities have been successfully manufactured and processed (Section 2.3). This required the development of the necessary fabrication and test infrastructure in all three regions (Section 2.2). In the USA, the sites were Fermilab, Argonne National Laboratory and Jefferson Lab. The Japanese site was KEK. In Europe, development has been driven by the design and construction of the European X-ray free-electron laser at DESY [6]. This major project uses technology very similar to that used in the ILC and therefore can be considered a large prototype.

An equally important programme has been the development of industrial capacity in each region, which has successfully resulted in multiple vendors in Asia, the Americas and Europe, each capable of producing high-performance ILC cavities. Cryomodule development and integrated systems testing is being pursued at all the primary SCRF sites: The FLASH FEL facility at DESY (Section 3.2) has successfully accelerated an ILC-like electron beam through high-gradient cryomodules, and has demonstrated many of the demanding tuning techniques required by the ILC; further system-test accelerators at Fermilab (NML) (Section 3.4) and at KEK (STF) Section 3.3) have been under development and will see beam operation in 2013. The S1-Global programme at KEK [7] successfully integrated cavities and auxiliary components delivered from DESY, FNAL, INFN and KEK into a single cryomodule, allowing direct comparative tests of different technologies as well as demonstrating the key concept of "plug compatibility", simplifying integration of parallel design efforts worldwide.

Other main-linac components developed by the R&D program include a tuneable high-power RF delivery system and associated low-level RF controls, and a next-generation solid-state modulator (Section 2.8).

During the ILC reference design phase, electron-cloud issues were identified as the major technical risk to the design luminosity. A multi-year study was therefore launched at the CESR accelerator at Cornell [8]. The well understood machine characteristics and highly flexible operating parameters of this facility facilitated an R&D program that has culminated in a definitive report on the physics of high-intensity, positively charged beams. The study also developed and identified acceptable mitigation techniques that are now included in the baseline design (Section 3.5).

The Accelerator Test Facilities (ATF, and ATF-2) at KEK have been successfully constructed and commissioned to demonstrate stable collisions of very small beams (Section 3.6). Other R&D which focuses on specific critical components (for example: polarised electron source; undulator, target and capture device for the positron source; fast kicker systems for the damping rings; high-powered beam dumps for the BDS), have also made significant progress and have demonstrated all key ILC parameters, either directly or via low-risk extrapolation (Chapter 4).

The remainder of this document focuses on describing the R&D programmes whose success is the foundation of the TDR reference design.

Chapter 2
Superconducting RF technology

2.1 Overview

The R&D for superconducting radiofrequency (SCRF) technology has been a high-priority and prominent global activity for the ILC in the Technical Design Phase (TDP) [9]. This activity builds on and extends the pioneering work accomplished in the decade leading up to the International Technology Review Panel's (ITRP) choice of SCRF technology in 2004 [10]. In that decade, R&D on 1.3 GHz technology carried out by the TESLA Collaboration[1] succeeded in reducing the cost per MeV/m by a large factor over the early 1990s state-of-the-art SCRF [11].

Four critical R&D topics were identified [12,13] by the ILC Program Advisory Committee and were adopted as the technical goals for the TDP. They are summarised in Table 2.1. (The notation *S0-S2* refers to the shorthand for the individual goals set at the beginning of the TDP). The goals include high-gradient operation in individual cavities (S0), assembly of a string of cavities in a cryomodule (S1), the test of a cryomodule with beam acceleration (S2), and to increase the involvement of industries in this development so that eventually major parts of the production can be carried out in industry.

Table 2.1 The main goals and timeline for SCRF R&D established at the beginning of the Technical Design Phase

Year	2007	2008	2009	2010	2011	2012
S0: Cavity gradient at 35 MV/m in vertical test	→ yield 50%			→ yield 90%		
S1: Cavity string at average gradient of 31.5 MV/m in cryomodule		Global effort for string assembly and test				
S2: System test with beam acceleration including high- and low-level RF		FLASH at DESY, ASTA/NML at FNAL, STF2 at KEK				
Industrialisation: Study and preparation for industrial production of SCRF cavities and cryomodules			Production technology R&D			

This chapter describes the major technical progress of the GDE program in pursuit of these goals. Highlights of the R&D are summarised in Table 2.2.

One of the immediate challenges of the SCRF R&D was to identify the technical causes for gradient limitations and to find means of eliminating such effects. The development of such remediation methods thus allows a baseline process for consistent production of 35 MV/m cavities to be defined. This process is needed to achieve both the high-gradient goal and to demonstrate a *production yield* of 90 % worldwide. This goal has been met in the TDP-phase 2 program: a yield of 94 % for cavity production above 28 MV/m and an average gradient of 37.1 MV/m has been achieved. The yield thus corresponds to 94 % for a cavity ensemble with an average gradient above 35 MV/m and complies

[1] now known as TESLA Technology Collaboration (TTC), see http://tesla.desy.de

Table 2.2
Main achievements of the SCRF R&D effort.

Achievements
▪ Understanding and mitigation of field emission at low gradient. ▪ Deployment of tools to identify and repair quench-causing defects in low gradient cavities. ▪ Establishment of a baseline sequence of cavity fabrication and surface preparation for ILC. ▪ Achievement of a production yield of 94 % for cavities with an average gradient of 37.1 MV/m. The ensemble comprises of cavities with fields satisfying 35 MV/m ± 20 %. The yield for cavities with gradient above 28 MV/m (35 MV/m) is 94 % (75 %). ▪ Achievement of an average field gradient of 32 MV/m in a prototype cryomodule for the European XFEL program. ▪ Demonstration of the technical feasibility of assembling ILC cryomodules with global in-kind contributions.

with the allowable gradient-spread specification of ±20 %. The yield for cavities with gradient above is 35 MV/m is 75 %. Larger statistics on the yield will soon be obtained from the European XFEL cavity production program, for which at least the first-pass processing is very similar to that of the ILC.

Associated systems such as high- and low-level RF, the cryomodule including quadrupoles and beam-position monitors, and cryogenics have to match these demands. Demonstrating these additional requirements has necessitated extending the SCRF infrastructure which was successfully constructed and commissioned at FNAL, ANL, JLab and KEK in addition to the existing infrastructure at DESY.

There were several noteworthy achievements in the HLRF R&D program. The modulator adopted for the baseline design was developed based on a Marx topology using solid-state switching in a modular design, which has many advantages including high availability, no need for a pulse transformer, vernier control and cost. The local power-distribution system evolved from the RDR to allow for a ± 20 % spread in cavity gradients. For the flat-site single-tunnel design the klystrons are moved to the surface and the RF outputs of clusters of klystrons are combined and transporting to the tunnel via low-loss waveguide for feeding long strings of cryomodules. R&D on this approach was based at SLAC, with primary goals of testing the feasibility of using over-moded waveguides for transporting the very high RF power levels and the ability to incrementally tap-off the power for the cryomodules. The LLRF controls were developed as part of the FLASH program and have exceeded the requirements for beam control.

Given the large number of institutions spread across the world that contribute to ILC SCRF R&D, it was considered important to establish the concept of *plug-compatibility*. This allows the R&D efforts in the collaborating institutes the flexibility to have variants of cavities, flanges etc. as long as they meet agreed interface definitions. A large number of technical interfaces have been defined to enable more efficient R&D. This international effort is exemplified in the construction of a cryomodule, *S1-Global* [14, 15] hosted at KEK, which facilitated the exploration of the plug-compatible design philosophies and comparisons of technologies.

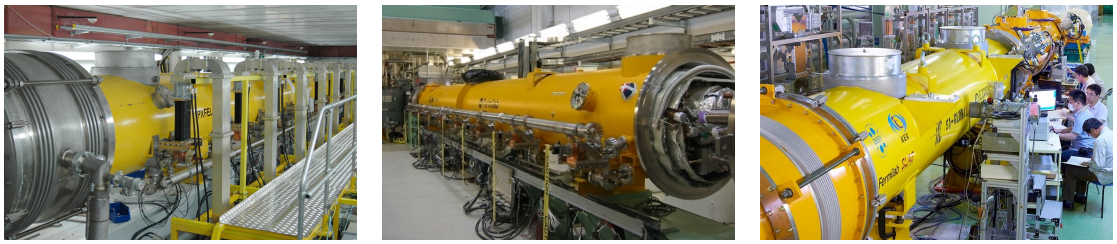

(a) PXFEL1 at DESY **(b)** CM2 at FNAL **(c)** S1-Global at KEK

Figure 2.1. Cryomodules assembled in all three regions.

The FLASH facility at DESY has been used to demonstrate the S2 goal of controlled beam

acceleration in a multi-year series of dedicated beam study periods. More recently beam acceleration has also been achieved in the STF facility in KEK.

An impression of the widespread activities necessary to address the SCRF R&D goals can be obtained from the completion of cryomodules at DESY, FNAL and KEK (see Fig. 2.1). The cryomodule assembly at KEK stands out for its truly global nature. The cavity production facility at KEK is a one-stop facility for cavity production open to users and industry (Fig. 2.2).

Figure 2.2
The Cavity Fabrication Facility at KEK showing the electron-beam-welding setup.

In parallel with the efforts in the laboratories, a technology-transfer program was launched with the goal of increasing the number of qualified vendors in the Americas and Asia regions. Several manufacturers are now engaged in the production of cavities. While originally only two companies could provide cavities meeting the ILC criteria, companies in all three regions are now successfully manufacturing high-gradient cavities. The number of successfully tested cavities achieving the ILC specification has now reached several dozen.

Several studies of SCRF mass-production models were commissioned from industry. These also included R&D for cost-effective industrialisation as an additional development towards a realistic proposal of the machine.

Overall the GDE SCRF R&D program has been very successful. It has achieved its technical goals and moreover demonstrated that tremendous progress can be made with an international effort in which all partners co-ordinate their respective programmes in order to achieve a common goal.

2.2 Development of Cavity Infrastructure and R&D

An important component of the worldwide ILC SCRF R&D program has been the design, fabrication, dissemination and utilisation of the best SCRF technologies across the world, such that not only are the best tools available at the originating laboratory or industry, but these best tools are available at all locations. It has only been through the close and cooperative interaction of SCRF researchers worldwide that the outstanding progress in cavity fabrication and performance has been realised in the past five years.

The following sections give an account of the installed infrastructure at the various laboratories participating in SCRF R&D worldwide, demonstrating how new tools or the systematic application of existing tools have produced the progress detailed in the subsequent sections.

2.2.1 Production and Test Facilities

Following the development of a standard processing scheme (Section 2.3), cavity-production infrastructure based on the best practices has been created and implemented in all regions. This has allowed for uniformity of treatment practices across the three regions, as well as the exchange of cavities between laboratories for tests and R&D. In addition, as processes became stable and a de facto standard, efforts have been made worldwide to move those manufacturing steps out to industrial partners. In the Americas and Europe this has led to the installation and commissioning of equipment directly at industrial partners; in Asia, this is accomplished through creation of a pilot plant at KEK that is available for industrial partners to use.

In Europe, the mass production of 800 cavities for the European XFEL at DESY has started and begins to provide important information regarding the control of processes in an industrial environment (Section 2.5). This development marks an important milestone since the cavity-treatment process outlined in Section 2.3 was agreed as suitable for mass production. In addition to the European XFEL order, the contracts include 24 cavities that will be available for additional treatment for highest gradients and will be supplemented with couplers and tuners. These cavities are part of the ILC-HiGrade project [16] that addresses the high gradient in the context of cavity mass production.

In the Americas, new chemical-processing facilities have been created at several labs. A joint Argonne/Fermilab facility (see Fig. 2.3) was based on the existing faciliities at JLab. In the Americas, approximately 100 9-cell cavities sourced from industries in both Europe and the United States are being used to verify, improve and simplify the production formula and improve infrastructure at the laboratories and capabilities in industry. The typical process for developing a vendor includes production and test of several single-cell prototypes and, after successful testing of these, progression to production of full 9-cell cavities. To give one example, in 2007 there was one vendor in the Americas qualified to build 9-cell cavities; this vendor has now not only tuned-up their production process to successfully make multiple nine-cell cavities, but a second vendor has recently had its first nine-cell cavity tested, reaching a gradient of 29 MV/m with no field emission. The progress in cavity-production capability in industry worldwide is shown in Table 2.3. In the six years since the launch of the programme, the number of qualified vendors has increased from two to five[2], while the number of laboratories capable of achieving ILC gradients has gone from one to five.

Figure 2.3
The joint ANL/FNAL chemical-processing facility.

The creation of more production facilities has included, beyond electro-polishing (EP) facilities, the creation of high-pressure rinsing systems and associated cleanrooms at ANL, and the commissioning of furnaces at Fermilab and Cornell to remove the last large bottleneck in the production of cavities. The engineering of this processing facility, and the standardisation of the chemical-processing steps, has now led to a chemical-polishing facility being assembled in industry, where it is currently being

[2] Advanced Energy Systems (AES), USA; ACCEL – now Research Instruments (RI), Germany; Zanon, Italy; Mitsubishi Heavy Industries (MHI) and Hitachi, Japan.

Table 2.3
The progress in qualifying vendors and their success in achieving the 35 MV/m gradient goal in fabrication.

year	# 9-cell cavities qualified	Labs achieving 35 MV/m processing	Companies achieving 35 MV/m fabrication
2006	10	DESY	ACCEL, ZANON
2011	41	DESY, JLAB, FNAL, KEK	RI, ZANON, AES, MHI
2012	(45)	DESY, JLAB, FNAL, KEK, Cornell	RI, ZANON, AES, MHI, Hitachi

commissioned with the processing of nine-cell cavities.

In Asia a new EP facility was constructed and became operational in 2008 (Fig. 2.4) for the cavity process and treatment at STF. In addition to the EP system, the STF infrastructure includes a buffered chemical-polishing utility for small parts and flange-surface etching, ultrasonic rinsing, a high-pressure rinsing system and a cleanroom for cavity assembly. Various diagnostics are provided, and are extensive enough to carry out systematic studies of the EP parameters.

Figure 2.4
EP facility at KEK

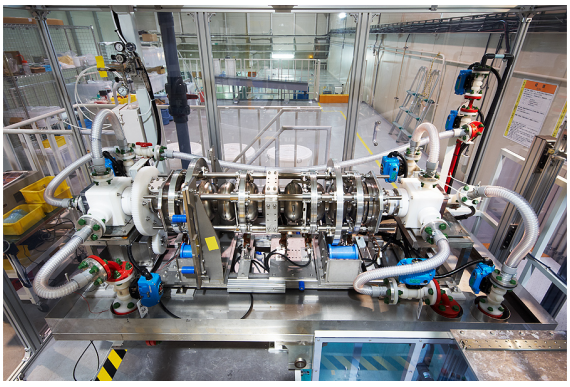

At KEK, a pilot-plant fabrication facility has been created to study potential improvements to cavity fabrication. Although located at KEK, the facility is open to industries who wish to use its capabilities, including an electron-beam welder, a trimming machine, a press machine and a chemical pre-processing facility. Figure 2.5 shows the general layout. The cavities to be fabricated by using the facility are expected to be installed in cryomodules and tested at STF between 2013 and 2014 (Section 3.3).

Figure 2.5
Layout of the KEK Fabrication Facility for cavities.

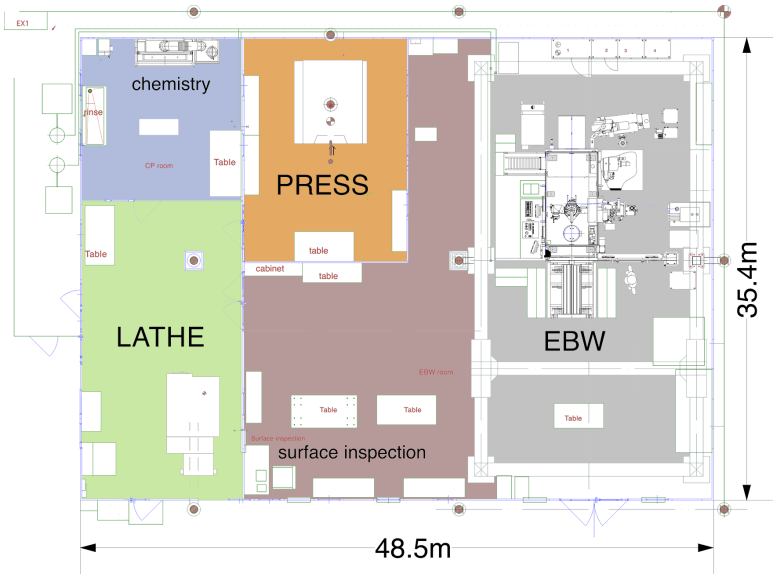

At IHEP, Beijing, an R&D program of 1.3 GHz SCRF technology has resulted in the completion of the first large-grain low-loss 9-cell cavity and installation of several key SCRF facilities including a mechanical-polishing machine, a chemical-etching tool, a high-pressure rinsing machine, and a

cavity-inspection camera [17]. Beijing University (BKU) has proceeded to develop 1.3 GHz cavities with the primary objective of applications in photon science using facilities in Chinese industry.

At CEA-Saclay a system for vertical EP of cavities is being developed, based on the original Cornell system [18]. The system will simplify the critical surface-treatment process of electropolishing for superconducting niobium cavities. So far, most systems rely on a *horizontal* EP, which necessitates a mechanical rotation of the cavity, which can be avoided in the vertical system making it mechanically simpler. In addition a vertical system allows for easier draining of the processing acids. An initial design has been produced at Saclay/IRFU and is under test (see Fig. 2.6).

Figure 2.6
A photograph of the facility for vertical electropolishing at Saclay/IRFU.

In addition to the standard EP infrastructure that now exists in all three regions, Fermilab has successfully set up a centrifugal mechanical or barrel polishing (CBP) facility, based on the concept originally proposed and tested at KEK in the 1990's [19]. Originally proposed as a remedial technique for low-performance cavities, the recent studies with the new infrastructure have demonstrated excellent performance, pointing the way to the possible use of CBP instead of bulk EP (see Section 2.3.3).

2.2.2 Inspection Infrastructure and Capabilities

One of the most important developments has been in the area of optical inspection techniques, both before and after cavity test. A leading cause of quench limits in cavities is the existence of surface defects near the weld equators, developing a high resolution, automated camera system was one of the priorities.

Figure 2.7
The setup for use of the Kyoto-KEK camera and an example image.

(a) Kyoto-KEK optical-inspection camera system.

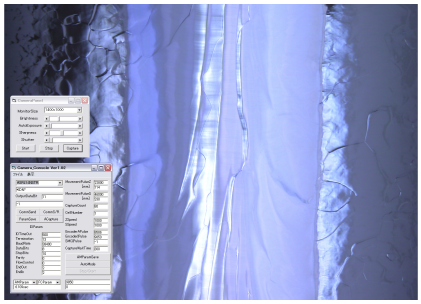

(b) Example of automated image-capture software displaying the area of the welding seam.

Two types of high-resolution cavity-inspection tools have been developed in recent years under the globally coordinated ILC gradient R&D effort. The most utilised camera system was developed in a collaboration of KEK and Kyoto University [20]. The camera can resolve surface features down to 10 µm. Some depth profile information can also be obtained. A newly developed high-performance

CMOS camera, when combined with an LED illumination system, resulted in a ten-times increase in brightness and much improved resolution. The other type is based on imaging by a combination of a long-distance microscope and a tiltable mirror inserted into the cavity [21]. Automated image-capturing instruments have been put in place at Cornell, DESY, FNAL, JLab and KEK and defect-finding and surface-characterisation software is being further optimised. Figure 2.7 shows one implementation of the camera system for cavity-surface inspection, together with an example of a high-resolution image of the electron-beam weld.

The Kyoto-KEK camera system is used now for inspection of the interior of most cavities available for research and optimisation. It also plays a vital role in qualifying production lines in industry for the European XFEL. Additionally, in conjunction with measurements taken during tests, the system is used to correlate quench positions with surface irregularities. These correlations allow the use of local remediation techniques to repair the surface and mechanically remove the performance limitation. An ongoing effort [22] is to correlate the irregularities seen before test with the test results, such that the camera can be used in a predictive, rather than reactive, manner.

The camera system is also used to characterise the surface properties in a quantitative manner [22]. Estimators for surface roughness, typical feature size etc. derived from image processing serve to enable the objective comparison of surface-treatment methods.

In addition to the optical inspection camera systems, several labs have developed infrastructure and techniques to examine cavity surface irregularities the surface chemical characteristics. These include (among others) the replica moulding technique [23, 24], and techniques for microscopically analysing samples cut from sacrificed cavities (see for example [25]).

Finally, Fermilab and Kyoto-KEK are investigating in X-ray tomography to identify voids in the cavity material. Tomography has the advantage over the camera system that it finds defects buried below the surface; as some of the limiting surface features are believed to be due to diffusion of sub-surface defects during welding, or voids revealed during processing, tomography is a promising technique for the quality assessment of incoming half-cells before welding in the cavity-manufacturing process.

2.2.3 Cavity-Tuning Facilities

Figure 2.8 The tools in place for the European XFEL for the mechanical adjustment of cavities.

(a) HaZeMeMa, the tool for room-temperature RF measurement of half cells

(b) The tool for field-flatness tuning and geometric adjustment of 9-cell cavities.

Automatic cavity-tuning machines are also now operational worldwide. Originally designed at DESY [26], the current versions have been created in collaboration by DESY, KEK and Fermilab [27]. The machine has the capability of tuning field flatness and correcting cell-to-cell alignment through linked operation between the automated software, bead-pull, six-jaw cell deforming, and the system to measure cavity eccentricity. In conjunction with the European XFEL production, two European manufacturers have been supplied with tools certified to European standards to perform the tuning.

These automated tools can be operated by non-RF experts and will simultaneously provide a standardised log of the recorded data. Figure 2.8 shows the automated room-temperature RF measurement of half cells ("HaZeMeMa") and the tuning machines in use in the production for the European XFEL.

2.2.4 Quench Detection

Two possible approaches have been developed to detect localised quenches in a cavity. A second-sound system, originally conceived and developed at Cornell [28, 29], uses oscillating super leak transducers (OST) and the signal of the phase transition of superfluid helium propagating in the helium to triangulate the quench location at the cavity outer surface during vertical test. The system is relatively simple and locates the quench location to a precision of a couple of centimetres. Presently, Cornell OSTs are implemented in many laboratories such as DESY, FNAL, JLab and KEK.

Alternatively, extensive *temperature mapping* systems [30–35] have been developed and are in widespread use in various implementations. In all cases, carbon resistors are placed on the outer surface of a cavity and register heat fluxes due to localised RF heating at the quench location on the inner surface of the cavity. Mapping is made either by fixing a net of resistors in place on the cavity [30], or by rotating a linear array of thermometers azimuthally around the profile of the cavity [31]. Depending on the origin of the quench and the density of resistors, the system identifies the location of the hot spot to within a few millimetres.

Both the second-sound and temperature-mapping techniques, used in conjunction with the Kyoto-KEK camera, have had great success in identifying surface flaws that have caused the quench (see Section 2.3.3).

2.2.5 Test Infrastructure and Measurement Techniques

The first 2 K cold test of a cavity is usually carried out in a cryostat housed vertically in a cylindrical dewar. Such vertical test facilities are now in place at multiple laboratories worldwide. For the European XFEL, the first cold test of the incoming 9-cell cavities will be made at the Accelerator Module Test Facility (AMTF), shown in Fig. 2.9. The cavities (including helium tank) will be lowered into the vertical cryostat in sets of four as shown in Fig. 2.10a to minimise the mounting effort and the number of cooling cycles.

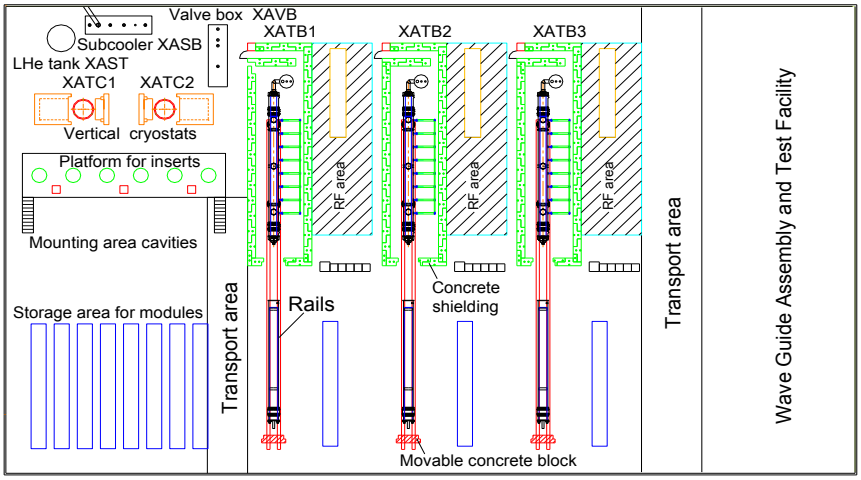

Figure 2.9 Layout of the Accelerator Module Test Facility hall at DESY.

The facility has been planned for minimal physical handling of the cavities to guarantee high throughput and reproducibility. The test procedure was standardised and aims for rapid characterisation of the cavity performance. Cavities failing the standard test (π-mode) will be further examined in the vertical test stands where additional RF-modes can be excited for detailed investigations of the cavity.

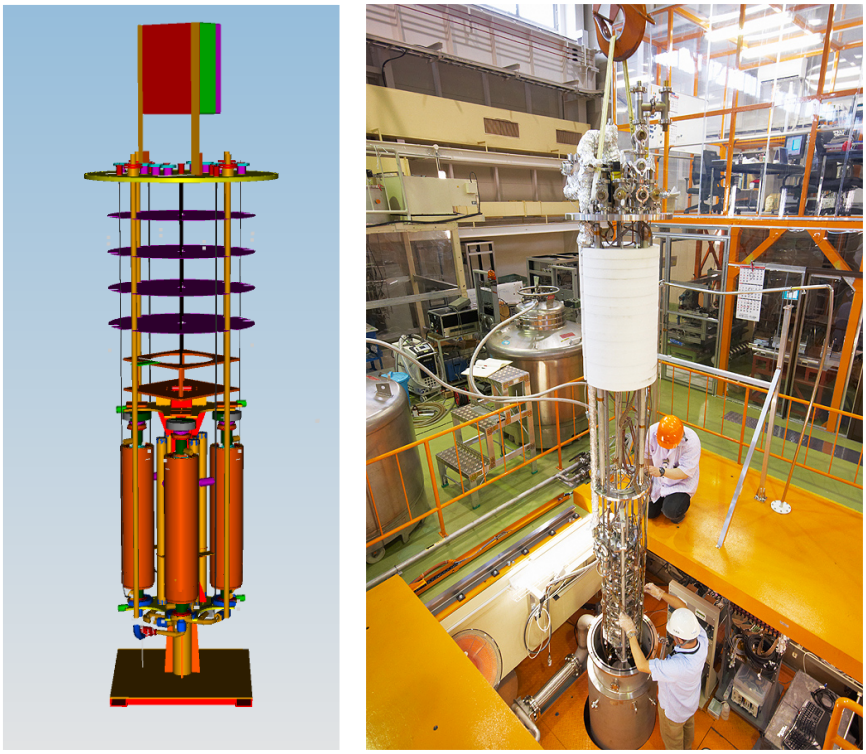

(a) (b)

Figure 2.10
(a) Four cavities, with their He vessels, ready to be lowered into the vertical cryostat. (b) The vertical test stand established at KEK-STF

The latter vertical cryostat has been equipped with OST sensors for quench detection.

The first vertical test system at Fermilab was commissioned in 2007. The Fermilab facility is now capable of two cool-downs per week for either 9-cell or single-cell tests [36]. This single dewar has averaged 80 test cycles in the past 2 years, and in 2013 two new, larger dewars will be brought online.

At STF, the vertical test stand for low-power cavity-field testing was commissioned in 2008. For the vertical test, the first 4 m-deep cryostat was assembled together with radiation shielding and a helium-pumping system. The test stand is now routinely operated once per week. Figure 2.10b shows the vertical test facility at KEK-STF.

The Horizontal Test Facility (HTF) at Fermilab was brought online in 2008 and has been used at a rate of approximately one test per month for qualifying the cavity-dressing process before assembly into an ILC-style cryomodule, known as CM-2 [37]. HTF allows for an intermediate system test of the jacketed cavity and coupler system, before string assembly.

2.2.6 Diagnostics for Field Emission

It is expected that field emission will continue to be a limiting factor in high gradient cavities. Furthermore, limits on dark current in the linacs will effectively set acceptance criteria for field emission during production of the cavities. Monitoring systems for field-emission remain relatively immature across the various test infrastructures worldwide; developing a reliable measurement system as well as techniques for cross-calibration of infrastructure remains an important on-going R&D item. The most common diagnostic for field emission is the detection of Bremsstrahlung X-rays by radiation sensors placed above the top plate of the cavity-testing dewar. This convenient diagnostic provides information about the onset of field emission and the strength of field emitters. Alternatively, radiation sensors such as silicon diodes are placed adjacent to the cavity (hence immersed in liquid helium). These can be implemented as an X-ray mapping system, either fixed [33] or rotating [35]. The energy spectrum of Bremsstrahlung X-rays is sometimes measured by using scintillators and associated electronics. The end-point energy corresponds to the highest impact energy of field-emitted

electrons. Since impacting electrons also deposit heat into the cavity wall, linear heating patterns will appear on the temperature map. The information from X-ray diagnostics, when combined with numerical simulations of electron trajectories, provides insights into the location of field emitters.

2.2.7 Remediation Techniques

The ability to mechanical repair the identified cavity surface defects which can limit the performance of a cavity is important in achieving the required production yields at high gradients. Several methods have been developed and applied in various locations worldwide.

Local mechanical grinding has proven very successful in remediating defects which cause cavities to quench (Section 2.3.3) . A miniature grinding mechanism with a very small CCD camera that fits in the cavity has been developed for the purpose as shown (Fig. 2.11).

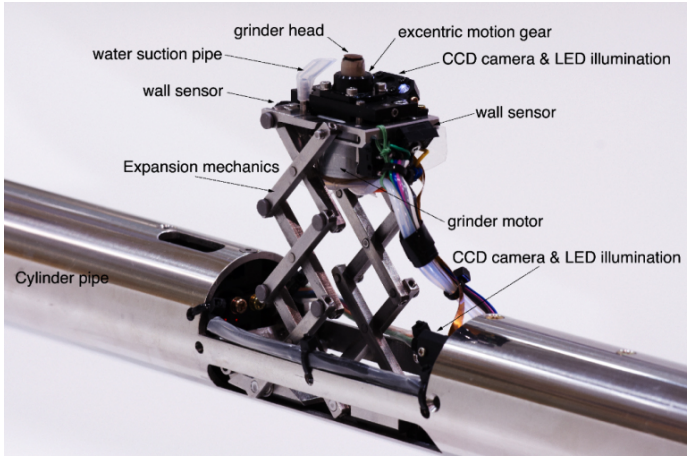

Figure 2.11
Local grinding tool with an expandable motor stage installed in a 50 mm-diameter cylindrical housing.

CBP also started as a remediation technique, although it was known that this implies a reset of the whole cavity surface, not just a local area. Consequently new problematic surface features may become uncovered. After several cavities of relatively low performance were treated with the tumbling technique, many of the imperfections, or pits disappeared. The technique has therefore been used for proactive repair before the first processing and test of a cavity at FNAL.

2.2.8 Infrastructure for High-power Couplers

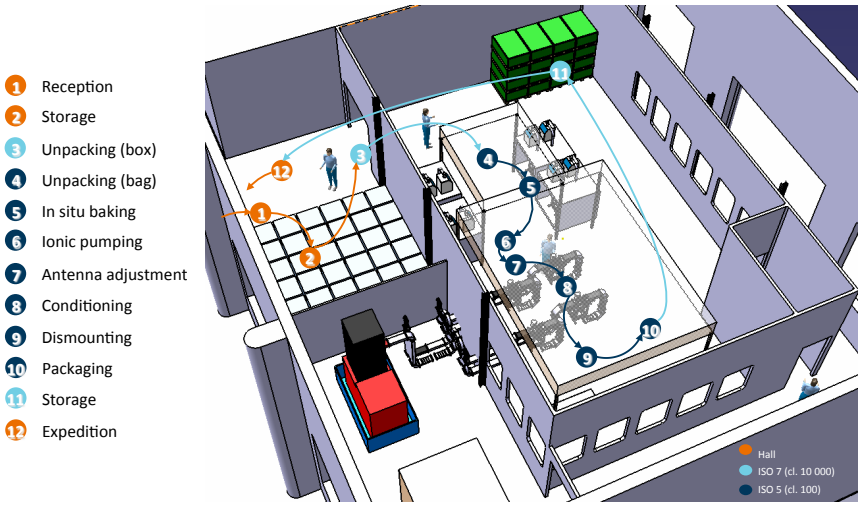

Figure 2.12
Layout of the coupler-conditioning facility at CNRS/LAL.

The high-power input couplers for the cavities transfer the RF-power from the waveguide system into the cavity. They provide the power transition between warm exterior and cold interior of the cavity. Since the power loads vary through the couplers of a cryomodule they have to be adjustable

and hence constitute a delicate and costly piece of the SCRF equipment. The couplers are now produced in industry.

The assembled couplers have to undergo a careful and time consuming burn-in procedure, during which they are slowly conditioned. Tests at LAL had shown that the procedure could be dramatically shortened in an automatic set-up. The installed infrastructure enabling the test of the mass-produced couplers is shown in Fig. 2.12. An overall speed-up of the conditioning by a factor of four has been achieved by driving several cavities in parallel from the same RF source. Such a setup necessitates an elaborate RF network so that each coupler can be conditioned up to 5 MW. The capacity is expandable: instead of the currently foreseen four coupler pairs that will be tested in parallel, the system could be extended to process eight pairs. The processing time of a single coupler is typically a week.

As a contribution to the US SCRF cryomodule programme centred at FNAL, SLAC has been responsible for inspection, cleaning, assembly and high-power RF processing of industry-produced TTF-III-style fundamental power couplers [38]. Couplers were mounted in pairs side-by-side on a disk-shaped circular TM_{11}-mode coupler-processing cavity developed at SLAC [39], as shown in Fig. 2.13.

Figure 2.13
A pair of TTF-III-type couplers mounted on a coupler-processing cavity and installed for high-power processing.

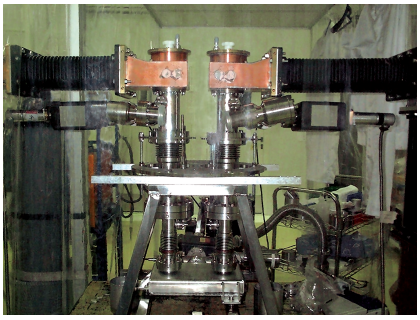

2.3 High-gradient SCRF Cavity Yield

2.3.1 Baseline Cavity

The TESLA 9-cell superconducting cavity [40] is the baseline design for the ILC. It has been developed over the past 15 years and achieved the highest gradients to date for multi-cell cavities. The cavities are to be qualified for ILC at an average gradient of 35 MV/m, with a permissible spread of up to $\pm$20%, in a vertical test and operated at an average gradient of 31.5 MV/m in cryomodules.

2.3.1.1 Cavity-Shape Design

Figure 2.14
TESLA-style 9-cell niobium cavity.

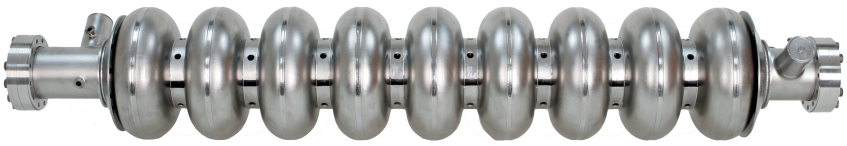

Numerous cavities of TESLA-style (or TESLA-like-style) 9-cell cavities (see Fig. 2.14) manufactured by different vendors and processed at various facilities in the three regions (Asia, Americas and Europe) have demonstrated vertical-test results which meet the gradient and Q_0 required for ILC [14, 41, 42]. There is significant operational experience with these cavities and it has been demonstrated with beam that accelerating gradients of greater than 35 MV/m are possible after installation in a cryomodule.

The ILC 9-cells cavity works in RF π-mode at a resonant frequency of 1.3 GHz. Each cavity consists of nine accelerating cells and two end-group sections. One end group has a port for coupling

RF power from the power source into the structure, and the other end has a port for a field-sampling probe used to determine and control the accelerating gradient. Each end group also has a resonant higher-order-mode (HOM) coupler structure with a probe port that is connected to a small electric-field antenna for extracting HOM power and for diagnostics.

Among other factors, the cell shape is optimised for a small ratio of the surface electric field E_{peak} to the acceleration gradient E_{acc} i.e. E_{peak}/E_{acc}. At the time of the TESLA cavity shape design, field emission was a principal gradient limitation issue. Hence a logical design optimisation goal is to reduce E_{peak}/E_{acc}.

With the recent development of advanced surface processing and cleaning procedures, field emission has been significantly reduced during the vertical test of 9-cell cavities. However, as the ILC gradient goal of 35 MV/m is considerably higher than the original TESLA gradient goal of 25 MV/m, a reduced E_{peak}/E_{acc} remains an attractive feature. This argument becomes more compelling in view of the allowable gradient scatter. To meet the average goal, the gradient of individual cavities may need to go as high as 42 MV/m during the vertical qualification test, which presents a significantly increased risk of field emission.

Table 2.4
Parameters of the 9-cell SCRF cavities.

Parameter	Value
Type of accelerating structure	Standing wave
Accelerating mode	TM_{010}, π-mode
Type of cavity-cell shape	Tesla (or Tesla-like)
Fundamental frequency	1.300 GHz
Operation:	
– Average gradient (range allowed)	31.5 MV/m ($\pm$20%)
– Quality factor (at 31.5 MV/m)	$\geq 1 \times 10^{10}$
Qualification:	
– Average gradient (range allowed)	35.0 MV/m ($\pm$20%)
– Quality factor (at 35 MV/m)	$\geq 0.8 \times 10^{10}$
– Field flatness	$\geq$ 95 %
– Acceptable radiation (at 35 MV/m)	$\leq 10^{-2}$ mGy/min
Active length	1038.5 mm
Total length (beam flanges, face-to-face)	1247.4(30) mm
Input-coupler pitch distance, including inter-connection	1326.7 mm
Number of cells	9
Cell-to-cell coupling	1.87%
Iris aperture diameter (inner/end cell)	70/78 mm
Equator inner diameter	$\sim$210 mm
R/Q	1036 Ω
E_{peak}/E_{acc}	2.0
B_{peak}/E_{acc}	4.26 mT/(MV/m)
Tunable range	$\pm$300 kHz
$\Delta f/\Delta L$	315 kHz/mm
Number of HOM couplers	2
Q_{ext} for high-impedance HOM	$< 1.0 \times 10^5$
Nb material for cavity (incl. HOM coupler and beam pipe):	
– RRR	$\geq$300
– Mechanical yield strength (annealed)	$\geq$39 MPa
Material for helium tank	Nb-Ti Alloy
Max design pressure (high-pressure safety code)	0.2 MPa
Max hydraulic-test pressure	0.3 MPa

There are alternative cavity-shape designs (see Section 2.3.4.2) that have a reduced ratio of the peak surface magnetic field H_{peak} to the accelerating gradient, H_{peak}/E_{acc}, at the cost of increased E_{peak}/E_{acc}. The reduced H_{peak}/E_{acc} makes the alternative shape cavities a preferred choice for reaching the ultimate gradient, because of the higher fundamental theoretical limit to the surface magnetic field. This expected benefit has been successfully demonstrated with many 1-cell cavities [43, 44]. However, the ILC cavity-gradient R&D results in recent years have shown that the gradient in practical 9-cell cavities is predominantly limited by highly localised defects. The full potential of alternative-shape cavities to approach the ultimate gradient is yet to be demonstrated in 9-cell cavities through extended R&D. Initial experience has shown that the alternate-shape 9-cell

cavities do indeed have increased field emission due to the higher E_{peak}/E_{acc}.

Considering the global experience with 9-cell niobium cavities, the TESLA shape was confirmed as the baseline cavity shape for ILC. Table 2.4 gives a summary of the major RF parameters of the TESLA-shape cavity.

2.3.1.2 Cavity material, Fabrication, Processing and Cryogenic RF Testing

The basic acceleration cells in a baseline cavity are fabricated by using high-purity sheet niobium with a typical RRR (Resistive Resistance Ratio) of 300 or better. These raw materials are commercially produced and are available from vendors in all three regions. By multiple steps of electron-beam melting under vacuum, the purity of a niobium ingot is improved with the reduction of interstitial impurities such as C, N, O. After a series of forging, rolling, annealing and etching processes, the niobium ingot is reduced to fine-grain niobium sheets suitable for forming into half-cells through deep drawing. Table 2.5 gives typical properties of high-purity niobium for use in ILC cavities.

Table 2.5
Typical properties of high-purity niobium for use in ILC cavities

Element	Impurity content in ppm (wt)	Property	Value
Ta	$\leq$500	RRR	$\geq$300
W	$\leq$70	Grain size	$\approx$ 50 µm
Ti	$\leq$50	Yield strength	$>$ 50 MPa
Fe	$\leq$30	Tensile strength	$>$100 MPa
Mo	$\leq$50	Elongation at break	30%
Ni	$\leq$30	Vickers hardness	
H	$\leq$2	HV 10	$\leq$50
N	$\leq$10		
O	$\leq$10		
C	$\leq$10		

As a quality assurance check prior to use, the cell material is eddy-current scanned to a depth of 0.5 mm into the surface of the sheet material. Over decades, the effort of SCRF cavity development has been marked by close information feedback between laboratories and industries, which allowed steady improvement of the quality of niobium sheets in recent years. The niobium-material vendors have accumulated additional experience due to the global ramp-up of the effort in developing the SCRF technology for the ILC, leading to increased consistency in delivered niobium sheets. Although all niobium sheets for the European XFEL cavity production will be eddy-current scanned, it is likely that for ILC production only random spot-checking of sheet niobium will be required as a QA/QC step.

Niobium sheets are formed into cups through deep drawing. The dies are usually made from a high-yield-strength aluminium alloy. The half-cells are machined at the iris and the equator. At the iris, the half-cells are cut to the specified length (allowing for weld shrinkage) while at the equator an extra length of $\sim$ 1 mm is left to retain the possibility of a precise length trimming of the dumbbell after frequency measurements. The half-cells are thoroughly cleaned by ultrasonic degreasing and chemical etching. Two half-cells are then joined at the iris with electron-beam welding (EBW) to form a *dumbbell*. The EBW at the iris is usually done from the inside to ensure a smooth weld seam at the location of the highest electric field in the resonator. Since niobium is a strong Getter material for oxygen, it is important to carry out the EBW in sufficiently good vacuum. Tests have shown that RRR 300 niobium is not degraded by welding at a pressure below 6.7 mPa.

The next step is the EBW of the stiffening ring between cells. Here the welding shrinkage may lead to a significant distortion of the cell shape, which needs to be corrected. Afterwards, frequency measurements are made on the dumbbells to determine the correct amount of trimming at the equators. Then the equator weld is prepared followed by additional chemical etching. Next, the dumbbell RF surface QA/QC is performed through visual inspection; sometimes overnight soaking in de-ionized water is used to disclose iron inclusion originating from the sheet-rolling process. Defects

and foreign-material imprints from raw material or previous fabrication steps are removed by mechanical grinding. After the inspection and cleaning (a light etching followed by de-ionized water rinsing and clean-room drying), eight dumbbells and two end-group sub-assemblies are stacked in a fixture to carry out the equator EBWs, which are done from the outside. The weld parameters are chosen to achieve full penetration. A reliable method for obtaining a smooth weld seam of a few mm width at the inner surface is to raster a slightly defocused beam in an elliptic pattern and to apply 50 % of beam power during the first weld pass and 100 % beam power in the second pass.

Figure 2.15 shows the flow diagram of the fabrication steps for the complete 9-cell cavity.

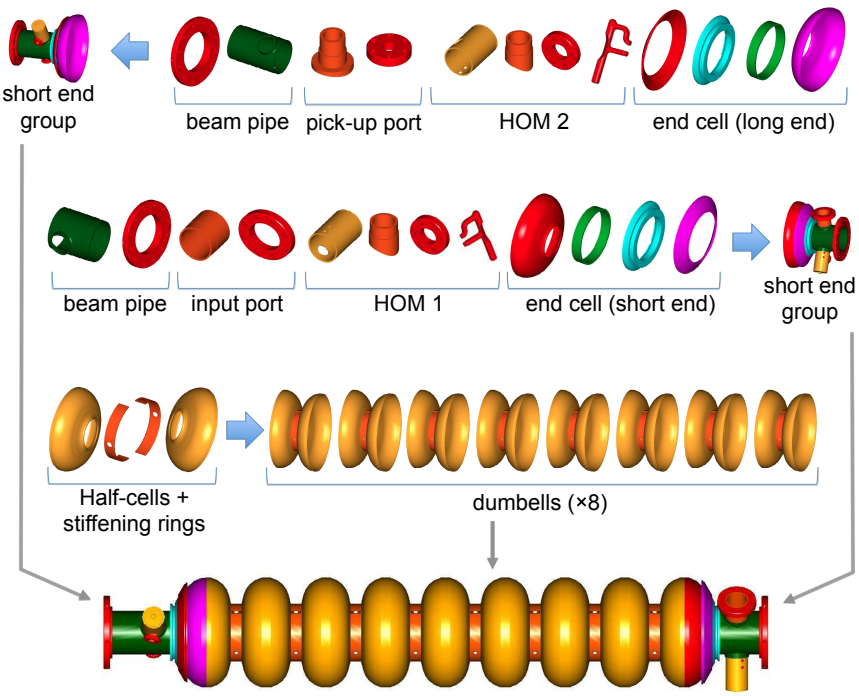

Figure 2.15
ILC 9-cell-cavity fabrication flow diagram.

As a quality-assurance check prior to cavity processing and testing, the RF surface of a completed 9-cell cavity is optically inspected for irregularities in the EBW regions. It has been shown that defects that cause the most quenches are located in the fusion zone or the heat-affected zone of the equator weld. Many of these defects can be traced back to the fabrication process. Typically, the fusion zone is a few mm in width. The heat-affected zone is a narrow region outside the fusion zone, where grain-growth is apparent due to heat deposited during the welding. The two heat-affected zones (one each on both sides of the weld) plus the fusion zone covers a total zone typically 40–50 mm in width. Due to the high surface magnetic field in this region, quenches can be initiated either through a thermal process (such as strong resistive heating of a normal-conducting inclusion) or a magneto-thermal process (such as strong magnetic field enhancement at sharp edges of pure geometric defects). There is a growing database on the optically identifiable defects, which are correlated to quench during the final cavity-qualification test [45–47]. The optical inspection is very effective in identifying sub-mm sized geometrical defects in the equator region, such as sharp edges, exposed welding pores/holes, unclosed weld prep, rough under-bead and weld spatters etc. This not only provides rapid feedback for production but also allows informed decisions for defect removal by suitable methods, such as local grinding at a distinctive defect area [48] and mechanical polishing over the entire RF surface of a completed cavity [49]. Overall, the QA/QC of the completed cavity by optical inspection is an important step for improved production yield. Ultimately, this leads to cost-effective mass production of niobium cavities.

Prior to the cavity surface processing, a series of mechanical, vacuum and RF inspections are carried out. The cavity is mechanically measured with a coordinate measuring machine to compare

dimensional measurements against mechanical tolerances identified on design drawings. All the welding joints are leak checked. The cavity fundamental mode frequency is measured. The frequency of other pass-band modes may be also measured. The field flatness of the fundamental mode may be measured, which is done by pulling a bead through the beam axis of the cavity. This determines the stored energy of each cell and provides an indication of uniformity of the electric field on the beam axis. In case of a severely non-uniform field distribution, a rough tuning is done by mechanically squeezing or stretching the cells in order to reach the fundamental-mode frequency and a total length within the specified tolerances.

Cavity surface processing consists of a series of steps. This has been the focus of the globally coordinated cavity gradient R&D program in the past years [50]. The ILC baseline surface processing is described in detail in Section 2.3.2.

After the completion of the cavity processing steps, the cavity proceeds for qualification RF testing[3]. The cavity is mounted vertically in a cryogenic test stand. RF cables are connected to the cavity probes and the stand is inserted into a cryogenic dewar. The dewar is cooled to 2 K with the entire cavity immersed in superfluid liquid helium. The cavity is tested to determine its gradient, quality factor and limitations. In case of sub-standard performance limited by quench, the pass-band excitation measurement technique may be used during vertical testing for identifying the weakest cell. Additional instrumentation such as Cornell OST's [28] may be used for identification of quench sources with spatial resolution of a few cm for the fundamental mode or other pass-band modes. An important diagnostic associated with cavity testing for field-emission monitoring is X-ray detection. It is customary to place gamma probes outside the dewar. Some radiation sensors such as silicon diodes can be placed on the cavity and immersed in liquid helium. The cryogenic radiation sensors may be permanently attached to a cavity, allowing tracking of the field-emission performance of the cavity from its vertical qualification testing to horizontal testing in the final cryomodule.

Experience has shown that some cavities will not pass the ILC specification during the first qualification test but a second-pass reprocessing can often raise its performance effectively. By allowing the second-pass reprocessing, the overall yield of acceptable cavities is improved in a cost-effective manner. The average gradient also tends to improve. A detailed description of the criterion for the second-pass processing is given in Section 2.3.3.

2.3.2 R&D on ILC High-gradient-cavity Processing

The baseline procedure [51] of ILC 9-cell niobium cavity processing and handling is summarised in Table 2.6. A detailed description of the key processing steps is given in the following sections.

Table 2.6
Processing and handling of high-purity niobium cavities

Light BCP etching (10 µm)
Heavy EP (100-120 µm)
Post-heavy-EP cleaning
Vacuum-furnace outgassing (800 °C for 2 h)
RF tuning by no-touch bead-pull
Light EP (25 µm)
Post-light-EP cleaning
First HPR 3 passes ($\sim$ 6 h)
First clean room assembly
Final HPR 3 passes ($\sim$ 6 h)
Final clean-room assembly
Leak checking
In-situ baking at 120 °C for 48 h

[3] For the mass production of ILC cavities, the helium vessel will be welded to the cavity and the HOM couplers will be tuned and attached before the cavity qualification test, following the current European XFEL approach.

2.3.2.1 Electrolyte Mixing

Electrolytes for the electropolishing have to be mixed in a suitable molar ratio of HF:H_2O:H_2SO_4 which is compatible with the original Siemens recipe [52]. As the weight concentration of commercial acids varies across regions, the volume ratio needs to be tailored to the suitable molar ratio. For example, a volume ratio of 1:10 HF(48%):H_2SO_4(96%) is used at JLab. Prior to mixing, the electrolyte storage tank and acid piping are flushed with sulphuric acid (96 % concentration) to eliminate water residues. Then 210 l of sulphuric acid (96 %) are transferred into the electrolyte storage tank and chilled while keeping the acid in circulation. (This is done by connecting the cavity acid inlet hose with the cavity acid outlet hose). The first 5 l of hydrofluoric acid (48 %) are added when the electrolyte temperature in the storage tank reaches 15 °C or lower. The acid continues to be circulated until the electrolyte temperature recovers to 15 °C, at which point the second 5 l of hydrofluoric acid are added. The process is repeated till 21 l of hydrofluoric acid have been added.

2.3.2.2 Electropolishing

A horizontally placed EP [53] machine is used for the baseline EP processing in all regions. Three key EP parameters have been established and are monitored during processing, as shown in Table 2.7.

Table 2.7
Details of the electropolishing procedure

Parameter	Explanation
Voltage	Nominal at 14.5 V as measured across the body of cavity and the cathode, allowable range 13–17 V
Cavity cell temperature	Nominal at 25 °C as measured at the cavity outer surface near the equator region, allowable range 20–30 °C for final light EP and nominal at 30 °C, allowable range up to 35 °C for heavy EP.
Acid flow rate	Nominal at 3–4 l/min

In addition to these key parameters, it is important to keep the purging nitrogen gas flow at the minimum level. The acid supplying holes in the cathode tube face upward. This reduces the disturbance of the viscous layer across the acid-niobium interface.

Several provisions are available for control of the cavity-cell temperature: by steering the chilled water set-point; by duty-cycling the voltage; by irrigating the hot spot on the cavity outer surface with chilled water. Typically, by using one or more of these methods, a standard fine-grain 9-cell cavity EP can be operated within the allowable temperature ranges. A setup to provide water irrigation for the outer surface of the cavity is useful for temperature control in extended ranges. This scheme was first successfully demonstrated at the Cornell vertical EP machine [54]. Figure 2.16 shows an example as used in the JLab horizontal EP machine. An array of nozzles sprays chilled water at the iris and equator regions from the bottom of the cavity. Cavity rotation achieves uniform whole-cavity cooling. This chilled-water irrigation system has been used routinely for electropolishing of 86 7-cell cavities for the CEBAF upgrade, for which a lower cell temperature (20 °C) was desired.

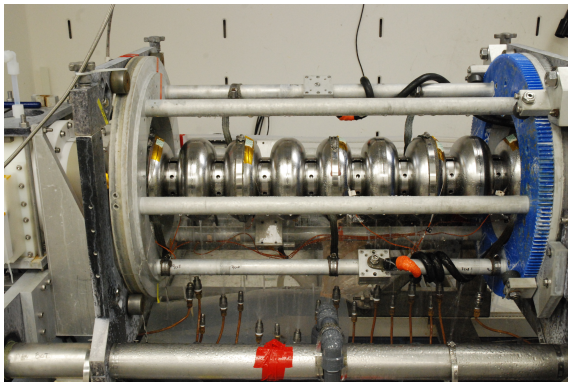

Figure 2.16
Cavity outer surface water irrigation setup as implemented in the JLab EP machine. An array of nozzles spray chilled water at selected iris or equator regions.

The best EP result is obtained in the continuous-current-oscillation mode. The appearance of current oscillation also serves as a sensitive in-situ process QA/QC indicator. The disappearance of current oscillation is correlated to excessive loss of HF or excessive H_2O in the electrolyte.

An *HF Auto Rinse* procedure has been found to be beneficial: the acid flow and the cavity rotation continues after the EP voltage is shut off. Under this condition, HF continues to react with the top layer of the cavity inner surface while the anodisation process is stopped. An effect similar to that achieved by HF rinsing has been observed, in which the sulphur-bearing niobium-oxide granules, an inherent contaminant on the finished niobium surface due to the EP process itself [55], are effectively removed from the cavity surface.

2.3.2.3 Post Cleaning after Heavy EP

The cleaning steps applied after heavy EP are summarised in Table 2.8.

Table 2.8 Processing and handling after initial heavy EP processing

Low-pressure water rinsing	Immediately after the cavity is dismounted from the EP machine, the cavity inner surface is copiously irrigated with de-ionized water.
Brushing & wiping	The HOM can and cavity end group are brushed and wiped with soapy water. This procedure cleans the inner surface areas that lack direct line-of-sight access by the high-pressure water jets.
Ultrasonic cleaning for 1 h	The entire cavity is immersed in a bath of hot (50 °C) de-ionized water with 2 % Liquinox mixed.
Ethanol rinsing	About 5 l of high-purity ethanol is transferred into th sealed cavity. The cavity is tilted and flipped for 10 min.
Rinsing	High-pressure water rinsing for two passes, each for about 2 h.

2.3.2.4 Vacuum-Furnace Heat Treatment

Following post-heavy-EP cleaning, the cavity is heat treated in a vacuum furnace for hydrogen degassing. The baseline furnace vacuum is typically in the mid-10^{-6} Pa range after over-night pumping. The furnace temperature ramps up at a rate of 5 °C/min, remains at 800 °C for 2 h, then ramps down naturally by turning off the heating elements.

2.3.2.5 RF Tuning by No-Touch Bead-Pull

It is necessary to tune the cavity π-mode field flatness following the heavy EP and vacuum-furnace outgassing. A no-touch bead-pull procedure has been developed for the final tuning prior to the final EP [51].

2.3.2.6 Post Cleaning and Handling after Final EP

The cavity handling steps completing and following the final EP are described in Table 2.9.

2.3.2.7 Results on field emission and quench limitations

The initial S0 effort focused on the issue of field emission, which was identified to be the main cause of gradient variability at the beginning of the ILC Technical Design Phase. The R&D priority was given to improved post-EP cleaning procedures. Three methods are now established for effective field-emission reduction: (1) Ethanol rising was successfully developed and applied at DESY [56]; (2) Ultrasonic cleaning was introduced and optimised at JLab [57]; (3) EP with a fresh acid mixture was found effective for field-emission reduction at KEK [58]. Some of the methods have been successfully transferred across facilities at different labs.

The source of field emission is now better understood. Besides the traditional particulate field emitters, niobium oxide granules are found to be a major field emitter introduced by the

Table 2.9
Post cleaning and handling after Final EP

Low-pressure water rinsing	Immediately after the cavity is dismounted from the EP machine, the cavity inner surface is copiously irrigated with de-ionized water.
Brushing & wiping	The HOM-can and cavity end group are brushed and wiped with soapy water. This procedure cleans the inner surface areas that lack direct line-of-sight access by the high-pressure water jets.
Ultrasonic cleaning for 1 h	The entire cavity is immersed in a bath of hot (50 °C) de-ionized water with 2 % Liquinox.
Rinsing	First high-pressure water rinsing. 3 passes, each for about 2 h.
Assembly	First clean-room assembly of all (except the bottom flange sub-assembly) auxiliary hardware components including RF probes.
Rinsing	Final high-pressure water rising. 3 passes, each for about 2 h.
Final Assembly	Final clean-room assembly of the bottom flange sub-assembly.
Pump down	Slow pump down. The speed of pump down is controlled to avoid turbulent flow. This prevents transfer of agitated particulates in the vacuum pluming into the cavity.
Leak checking	–
Baking	Baking at 120 °C for 48 h. The cavity under vacuum is enclosed in an insulated baking box. Hot nitrogen is blown into the box. The temperature of the centre cell is used for process control.

electropolishing process itself [59, 60]. Wiping and brushing of end-group components immediately after EP processing reduces niobium-oxide granules (often accompanied by increased sulphur-bearing compounds) in the hidden areas where HPR cleaning is less effective due to lack of direct water-jet bombardment [44]. Streamlined clean-room assembly procedures are now routinely used, resulting in minimum re-contamination by particulates generated by the assembly process itself. *Field-emission-free* performance up to 40 MV/m has been demonstrated in several electropolished 9-cell cavities. Efforts are continuing to develop new and improved cleaning techniques with a view to complete eradication of field emission up to the theoretical quench limit of a niobium cavity.

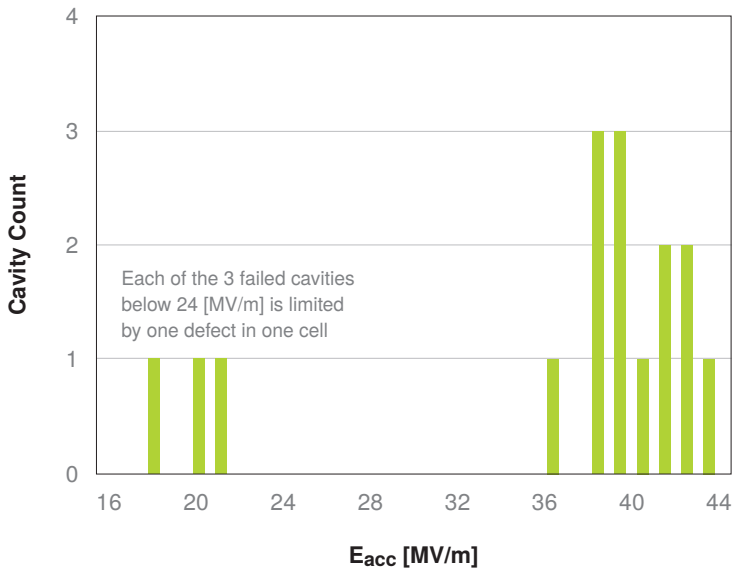

Figure 2.17
Two classes of quench limit in the state-of-the-art 9-cell niobium cavities. Shown are 16 9-cell cavities (10 built by ACCEL/RI ad 6 by AES), processed and tested at JLab since July 2008.

The understanding of the source of quenches is much improved thanks to the routine applications of various diagnostic systems described in Section 2.2.2. Generally speaking, there are two classes of quenches (see Fig. 2.17). Quenches at < 25 MV/m are found to be caused predominantly by highly localised geometrical defects near the electron-beam-welded joint at the cavity equator. These defects, referred to as type-I defects, can be roughly categorised as circular pits or bumps with a

typical diameter in the range of 200–800 µm. The detailed morphology of type-I defects can be quite complicated, as revealed by replica measurements and by microscopic inspection of small samples cut out from real cavities [25]. There is experimental evidence to show that the effect of local magnetic-field enhancement at sharp edges is responsible for initiation of quenches at geometrical defects [61, 62]. The magnetic-field enhancement factors have been calculated for simple geometrical features [63]. The quench limit at < 25 MV/m due to geometrical defects is insensitive to EP even when applied repeatedly. Sometimes, pre-cursor defects are already evident prior to any chemical processing of the cavity surface. Therefore, the most likely cause of these defects lies in the cavity fabrication, in particular the electron-beam welding process where bulk defects such as voids and surface irregularities are possible under certain conditions. It is now recognised that, in order to prevent quenching below 25 MV/m, improved QA/QC in material and fabrication are important. Experience has shown that the performance of cavities limited by type-I defects can be significantly improved by removing the known limiting defects. Several methods have been explored including local grinding [48], targeted mechanical polishing [64], whole-surface mechanical polishing [49], local re-melting by an electron beam [65] and local re-melting by a laser beam [66]. These methods have all shown promising results with 1-cell cavities. However, up to now, only the local grinding and mechanical polishing (targeted or whole-surface) have been successfully applied to 9-cell cavities, as discussed in Section 2.2.7.

Further studies are still needed to understand the source of quenches at higher gradients in the nominal range of > 30 MV/m. It is clear that the quenches above 30 MV/m are also caused by highly localised defects near the equator electron-beam weld (like quenches caused by type-I defects). These defects are categorised as type-II defects. Unlike the type-I defects, it appears that there is no observable feature (down to the spatial limit of the present optical-inspection technique, typically a few µm) at the site of the quench-causing defect. This suggests the subtle nature of the source of type-II defects. It has been suggested that the locally suppressed superconductivity due to compositional irregularities or lattice irregularities may be responsible. Additional capabilities of compositional analysis "in-situ" at the predicted quench location are expected to shed light on this issue. Off-line, the microscopic analysis of small samples cut out at the predicted quench location will provide important information for further gradient improvement. It has been also found by experience that the performance of a cavity quench-limited at > 30 MV/m is often improved by an additional light EP processing followed by low-temperature baking (120 °C).

2.3.2.8 Progress in raising the quality factor

The unloaded quality factor Q_0 of the ILC 9-cell niobium cavity is required to exceed 10^{10} at the average ILC beam operation gradient of 31.5 MV/m. There are three known mechanisms that may cause Q_0 degradation due to surface-field effects, namely Q-disease, field emission and the so-called high-field Q-slope. At 31.5 MV/m accelerating gradient, the peak surface electric and magnetic field for a TESLA-shape cavity are 63 MV/m and 134 mT, respectively. Successful improvement in post-EP cleaning and handling has significantly reduced the field-emission problem during cavity vertical testing (see Section 2.3.2.7). Heat treatment at 800 °C in a vacuum furnace prior to the final surface processing outgases hydrogen and hence removes the Q-disease problem. Surface processing by EP followed by in-situ low-temperature bake at 120 °C for 48 h effectively corrects the high-field Q-slope problem for the peak surface electric-field regime up to 180 mT [51].

With the application of the above cavity treatment and processing procedures, the Q_0 of a 9-cell ILC cavity during vertical test is likely to exceed 10^{10} at 31.5 MV/m accelerating gradient (Fig. 2.18). However, since additional handling is necessary to assemble qualified cavities into a cavity string for cryomodule inclusion, great care must be exercised to prevent re-contamination of the cavity surface.

Experience has shown that field emitters introduced by re-contamination may cause significant loss of quality factor from vertical qualification tests to the beam operation of cavities.

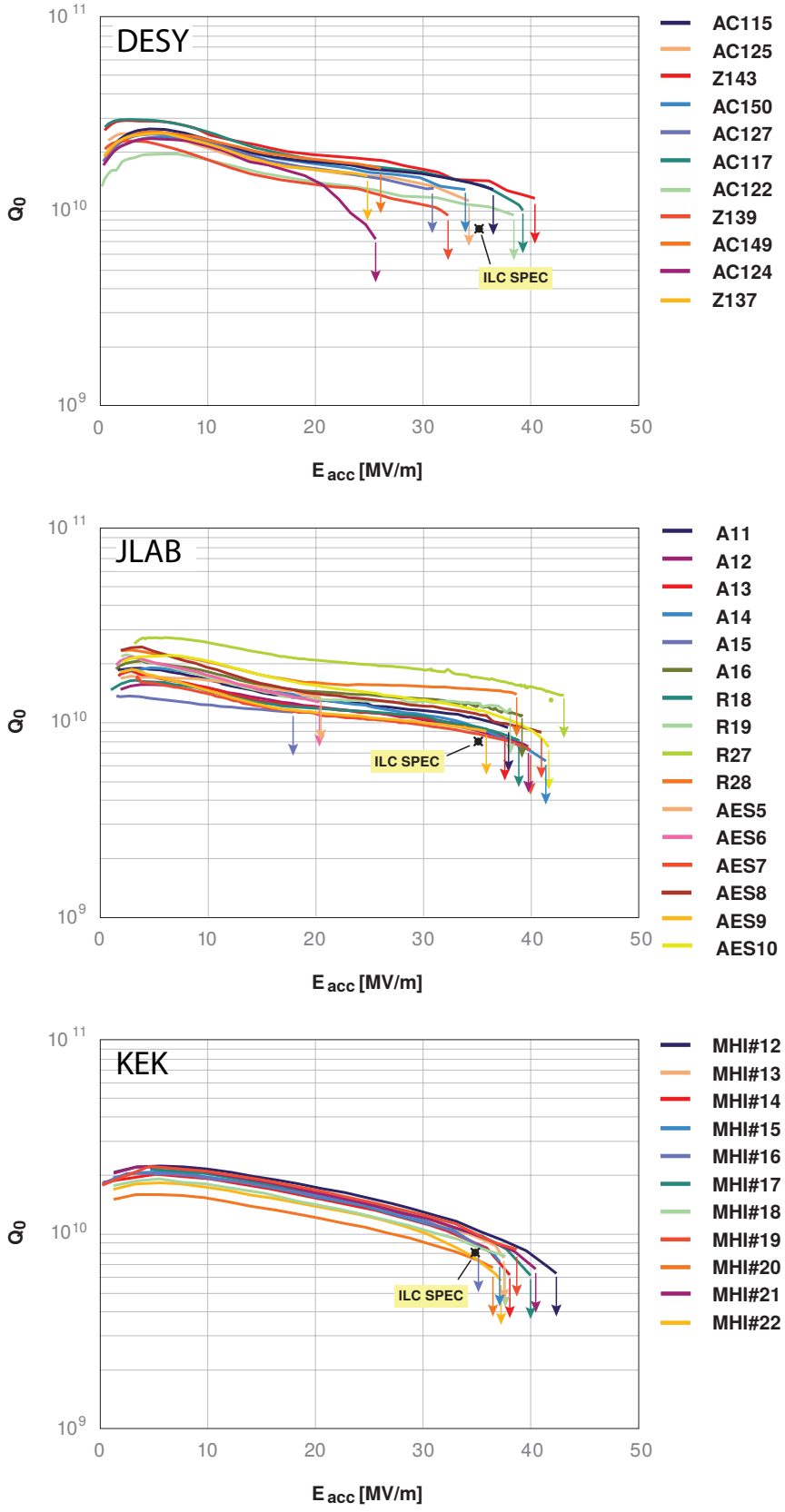

Figure 2.18
Examples of Q(E_{acc}) for 9-cell cavities processed following the baseline ILC cavity surface processing in the regions.

2.3.3 Yield and cavity selection criterion

A global R&D program was established in 2006 to address the challenge of reaching the ILC gradient specification. The *S0* program, coordinated by the GDE Cavity Group, attracted global participation from ANL, Cornell, DESY, FNAL, JLab, KEK and other labs such as IHEP (Beijing), Peking University, Saclay and TRIUMF. Significant progress in understanding the gradient limit and gradient variation has been made by instrumented cavity testing at cryogenic temperatures and high-resolution optical inspection of the cavity surface. This has been accompanied by steady progress in reproducibility at 35 MV/m and in improved practical gradient limit in 9-cell cavities. At the beginning of the technical design phase, Europe was the only region having demonstrated 35 MV/m cavity fabrication and processing. Today, 35 MV/m cavity fabrication and processing have been demonstrated also in the Asia and Americas regions (Fig. 2.18). A solid SCRF technical base for the ILC on a global scale is now in place.

The global efforts in ILC gradient R&D are rewarded not only by improved gradient yield and reproducibility but also an extended gradient envelope. By mid 2010, a major SCRF gradient R&D milestone of 50 % yield at 35 MV/m has been achieved. The average gradient in state-of-the-art 9-cell cavities has now been raised to $\sim$ 40 MV/m, a steady increase in comparison to the value of 35 MV/m in 2005.

At the start of the GDE cavity R&D programme, goals of a 50 % process yield by 2010 (phase I of the R&D program) and a 90 % production yield were established at 35 MV/m with $Q_0 \geq 8 \times 10^9$ by 2012 (phase II of the program). Since the cavity gradients are given by a distribution rather than a single number, as the Technical Design Phase of the ILC progressed, the need for a clearer definition of the gradient yield was recognised. In order to accomplish this, a globally consistent and up-to-date database for recording test results was established [67]. In 2009, the GDE ILC Cavity Group proposed a clear definition for the gradient yield, which adopted the concept of the first-pass and second-pass yield. The rule for cavity selection was also established. In the meantime, the ILC Global Cavity Database Team was created as a part of the S0 effort. The team included members from Fermilab, DESY, JLab, Cornell, and KEK, and took on the task of creating the database, updating and presenting the data. The results of this effort are a clear, objective, and publicly accessible database where the progress of cavity R&D can be tracked. At the time of this TDR the database contains information on 134 cavities. This includes both cavities produced purely for gradient R&D and ones produced for development purposes.

Great progress has been made during the GDE program in essentially all aspects of high-gradient cavity production. A strong technology transfer program from the various national labs to their respective vendors dramatically improved the cavity production techniques and associated QA programs. Diagnostic improvements have resulted in an enhanced understanding of the reasons for gradient performances that failed to meet the desired goals and help guide additional processing. The growing success of the R&D program has resulted in the cavity gradient performance being time dependent. It has improved, within the statistical scatter, throughout the 5-year program.

The most recent data for first-pass and second-pass results [68] are shown in Fig. 2.19. By way of definition, the plots only include results from a vendor/laboratory combination who have previously demonstrated the ability to fabricate and process a cavity that achieves at least 35 MV/m in a vertical test. The plots only include cavities that were processed according to the baseline processing cycle, which includes electropolishing. These criteria were imposed in order to facilitate an *apples to apples* comparison of the gradient results. The first-pass test results drive the second-pass re-processing. If the gradient $\geq$ 35 MV/m and $Q_0 \geq 8 \times 10^9$, the cavity is accepted. If the gradient is below 35 MV/m, the cavity will be given a second-pass reprocessing. The choice of second-pass process is made by the test laboratory based on first-pass test results, but must be one of two standard second-pass

processes, i.e. a high-pressure rinse or a second standard EP.

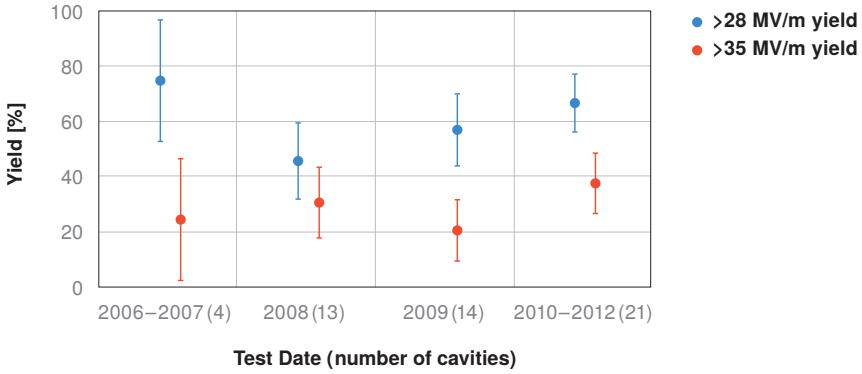

(a) First-pass yield

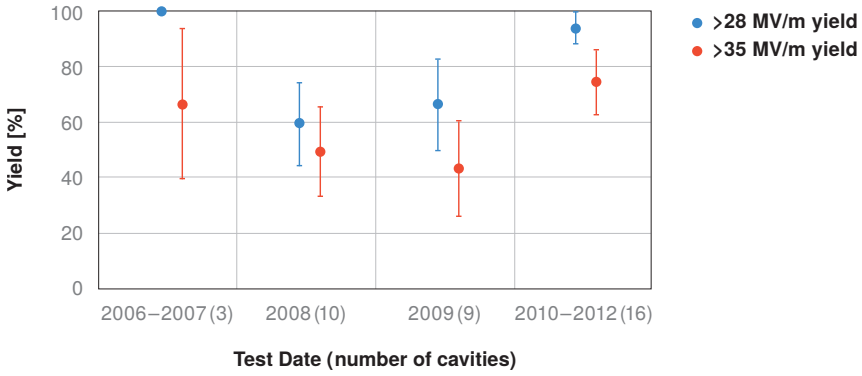

(b) Second-pass yield

Figure 2.19 Cavity yield for two gradient thresholds as a function of years, based on the global ILC cavity database updated as of October 2012 [67, 68]. Numbers in parentheses refer to cavity sample size. The cavities received standard treatment and were provided by established vendors.

It is apparent from the graphs that yields are improving with time, particularly for second-pass results. The latest second-pass test results from 2010-2012 show that a (75±11)% yield has been achieved at 35 MV/m and (94±6)% for >28 MV/m on a global basis of 16 cavities. This improvement is attributable to improved diagnostic tools that have been developed during the GDE global R&D program, to direct the second-pass process more accurately. Repeatability in EP processing, which was demonstrated in the past two years, also plays an important role in improving the second-pass yield by raising the gradient performance of cavities quench limited in the range 25–35 MV/m. It should be noted that the distribution of first-pass gradients from cavities which did not yet receive a second-pass process is statistically equivalent to those from cavities which did receive a second-pass process and appear in the plot; no bias has been introduced into the second-pass distribution based on first-pass results.

By allowing a targeted second-pass re-treatment or re-processing, a significant cost-saving benefit can be expected over simply rejecting cavities. Another important benefit is that a higher average gradient can be expected by allowing the second-pass processing, providing valuable gradient margins.

After it was decided to implement a RF power distribution system in the linac that could operate with a cavity-gradient spread of ±20%, acceptance is based on cavities exceeding 28 MV/m. This then introduces the concept of average gradient of the ensembles as another important figure of merit. A 100 % yield of cavities operating at exactly 28 MV/m would exceed the yield criteria but fail to meet the operational goal of an average gradient of 35 MV/m. The average gradient for the ensemble of second-pass cavities in Fig. 2.19 meeting the >28 MV/m criteria is 37.1 MV/m. Thus the standard processing cycle has resulted in an average yield and gradient which meet the desired ILC goals.

As of today a small fraction (∼6%) of cavities will be rejected according to this criterion. These rejected cavities may still have high enough gradient to be used for the positron source or polarised

electron source.

There are two repair techniques, developed during the last few years and now in use at the national labs, which both promise to have an impact on the cavity yield: localised grinding and centrifugal barrel polishing (tumbling). The results of these repair attempts have been impressive for cavities in this category and are shown in Table 2.10. For this proof-of-principle, all fine-grain ILC-shape cavities are included, independent of whether they were fabricated by an established vendor or not; however, it should be noted that the cavities have had a wide range of surface processes before the attempted repair of recognised defects. Localised grinding, a technique implemented at KEK, is based on finding defects using an optical inspection of a cavity as described in Section 2.2.2; defects are subsequently removed with a miniature grinding tool. This inspection can take place on either a tested cavity, where the grinding may be guided to performance-limiting defects, or on an incoming cavity, for which all observed localised defects are removed. With the tumbling technique, up to four cavities may be processed in parallel in a single week-long cycle using a progressively finer abrasive until at the end a mirror-like finish is achieved. As part of the tumbling process, light electropolishing is performed. To date, two 9-cell cavities with known limiting surface defects have been tumbled to remove their defects [69]. Both procedures are being optimised. Thirteen cavities have been repaired to date for which test results are known. Substantial performance improvement is achieved in most cases, and indeed for these cases, additional repair is likely to result in further improvement. These may be viable procedures which could be incorporated into standard processing cycles.

Table 2.10
All fine-grain ILC cavity repairs of localised defects by local grinding or tumbling.

cavity	repair	gradient MV/m before	after	comment
MHI-08	grinding	16	27	achieved 38 MV/m in 4th test (1 repair cycle)
MHI-10	grinding	26	27	1 repair cycle
MHI-14	grinding	13	37	achieved 37 MV/m in 3rd test (1 repair cycle)
MHI-15	grinding	23	36	achieved 36 MV/m in 4th test (3 repair cycles)
MHI-16	grinding	21	34	1 repair cycle
MHI-18	grinding	31	30	2 repair cycles; additional repair/test cycle in progress
MHI-19	grinding	26	37	achieved 37 MV/m in 2nd test (1 repair cycle)
MHI-20	grinding	9	35	achieved 35 MV/m in 3rd test (2 repair cycles)
MHI-22	grinding	32	36	achieved 36 MV/m in 2nd test (1 repair cycle)
AES003	grinding	11	30	had been quench-limited below 20 MV/m after repeated EP; results shown after 1 repair cycle; 37 MV/m was reached with additional HPR
TB9RI026	grinding	20	36	achieved 35 MV/m in 2nd test (1 repair cycle)
HIT-02	grinding	35	41	FE reduction in 2nd test (1 repair cycle)
TOS-2	grinding	31	33	achieved 33 MV/m in 2nd test (1 repair cycle)
TB9ACC015	tumbling	18	35	tumbling proceeded until limiting defect removed (1 repair/test cycle)
TB9AES006	tumbling	21	36	tumbling proceeded until limiting defect removed (1 repair/test cycle)

2.3.3.1 Increasing Production Yield

Increasing the yield beyond the ILC goal of 90% (or ensuring the 90% target) will be most easily accomplished by incorporating a repair step into the processing cycle. As mentioned in the last section, cavity repairs (grinding and tumbling together) were successful in most cases in the 2011/12 time period. Since the standard processing cycle does not include a repair step, none of these data are reflected in the yield plots of Fig. 2.19. Indeed at this time it appears that essentially all cavities which fulfill the manufacturing specifications will meet, or can be made to meet, the gradient acceptance requirements. The decision of whether to repair or reject under-performing cavities will depend on whether a repair is cost effective. In this regard the repair scenario looks promising. Localised grinding can be performed by trained technicians at cavity vendors in about one day. A tumbling cycle at Fermilab can process four cavities in parallel in one week, and studies are ongoing to reduce or remove the chemistry steps, which may result in both reduction of acid use and touch labor. A cavity optical inspection is part of the normal acceptance process. After this optical inspection, targeted repair can proceed.

2.3.3.2 Summary on cavity yield

Based on the cavity data for phase II of the R&D programme, the 90 % second-pass yield goal has been met for gradients >28 MV/m. This ensemble of cavities has an average gradient of 37.1 MV/m, slightly exceeding the 35 MV/m goal. Cavity repair appears to be a viable option to ensure or raise the yield should that prove cost effective.

2.3.4 ILC Cavities for the 1 TeV Upgrade

Long-term R&D addresses both the gradient and Q_0 need for the ILC 1 TeV-upgrade. With an improved cavity cell shape and optimised material properties, 9-cell niobium cavities should be able to reach gradients in the range of 40–60 MV/m, as indicated below.

2.3.4.1 Cavity Performance Goal: Gradient and Quality Factor

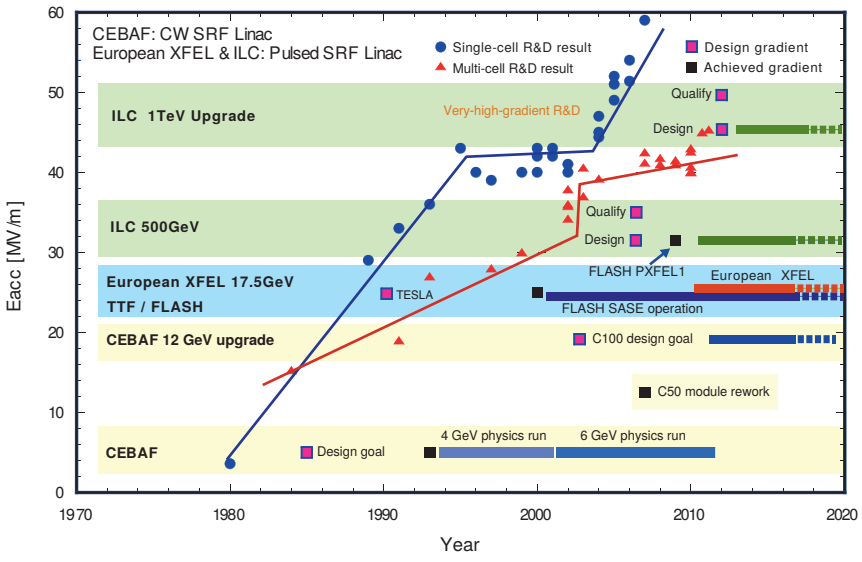

Figure 2.20
L-band SCRF niobium-cavity-gradient envelope and gradient R&D impact on SCRF linacs.

The cavity performance goal for the 1 TeV upgrade of ILC is 45 MV/m at Q_0 of 2×10^{10}. A higher Q_0 is necessary to keep the cryogenic load at a manageable level as the cavity gradient is raised. Many 1-cell cavities have demonstrated a gradient of more than 50 MV/m in alternate-shape cavities. A 9-cell large-grain niobium cavity has achieved a record gradient of 45 MV/m [70]. Figure 2.20 illustrates the gradient envelopes of L-band SCRF niobium cavities and gradient R&D impact on

SCRF linacs. Based on these results, it is believed that the SCRF cavity-gradient goal for 1 TeV ILC upgrade is reachable. The most promising path is the alternate-shape cavities processed by the current baseline recipe for the final surface processing.

In the long term, thin-film-coated cavities (such as Nb_3Sn) or multi-layer coated cavities offer potential of significantly increased cavity performance over the present state of the art.

2.3.4.2 Alternate-shape cavities

Alternative cavity shapes have a reduced ratio of the peak surface magnetic field to the acceleration gradient. There are three major alternate cavity-shape designs, namely re-entrant [71], low loss [72] and low surface field [73]. An effective increase of gradient up to 15 % can be expected as compared to the baseline shape. This is very attractive as this gain can be expected readily from the established baseline cavity processing that has been proven with the baseline cavity. In addition, these alternative shapes are more energy efficient. A reduction of dynamic heat loss of up to 25 % can be expected. There are some disadvantages to alternative shapes, for example reduced cell-to-cell coupling and increased HOM loss factors. These issues need to be further investigated in future ILC high-gradient cavity R&D.

Many 1-cell cavities have demonstrated a gradient of > 50 MV/m [74]. The current record gradient is 59 MV/m achieved by a 1-cell re-entrant-shape cavity [43].

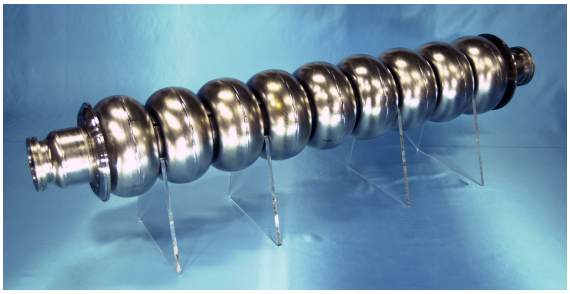

Figure 2.21
A 9-cell low-loss "ICHIRO" niobium cavity developed at KEK

The excellent 1-cell cavity results validate the rationale of lowering the peak surface-magnetic-field ratio to give higher acceleration gradient. However, the cleaning of the electropolished cavity surface must be improved, as the peak surface field in the real 9-cell cavities of alternate shapes are significantly (20%) higher than that in the baseline cavity. So far, most experience in alternate-shape 9-cell cavities is obtained with the ICHIRO shape developed at KEK (Fig. 2.21). The best ICHIRO 9-cell cavity has reached an accelerating gradient of 40 MV/m, limited by strong field emission [75]. Cornell University is continuing the development of 9-cell re-entrant shape cavities. JLab is developing the first prototype 9-cell cavity of the Low-surface-field (LSF) shape. The LSF shape, designed by SLAC, achieves 11% improvement in the peak surface-magnetic-field ratio without raising the peak surface electric field [73]. Table 2.11 gives a comparison of RF parameters of alternate shape cavity with the baseline cavity.

Table 2.11
Comparison of RF parameters of alternate-shape cavities with the baseline

		TESLA	Low-loss/ ICHIRO	Re-entrant	Low-surface field
frequency	GHz	1.3	1.3	1.3	1.3
Aperture	mm	70	60	60	60
E_{peak}/E_{acc}	–	1.98	2.36	2.28	1.98
H_{peak}/E_{acc}	mT/(MV/m)	4.15	3.61	3.54	3.71
Cell-cell coupling	%	1.90	1.52	1.57	1.27
G*R/Q	Ω^2	30840	37970	41208	36995

2.3.4.3 Large-grain niobium cavities

The large-grain material is sliced directly from the high-purity niobium ingot. Many processing and handling steps for producing sheet niobium can be avoided. Therefore the large-grain material has potential for material cost saving. The forming and welding of large-grain half-cells are somewhat trickier. Due to considerable progress in the past few years, about twenty 9-cell large-grain niobium cavities have been fabricated and tested. Quite a number of 1-cell large-grain cavities have achieved a high gradient of $> 35\,\mathrm{MV/m}$ with buffered chemical processing [76]. Eight industrially fabricated 9-cell large-grain niobium cavities have been processed and tested at DESY. Many of them reached a high gradient, with one of them reaching a remarkable 45 MV/m (Fig. 2.22), a record in 9-cell niobium cavities [70]. DESY's experience has shown that EP is still a necessary surface-processing step to reach high gradient in such 9-cell cavities. KEK and IHEP are also developing large-grain cavities [77, 78]

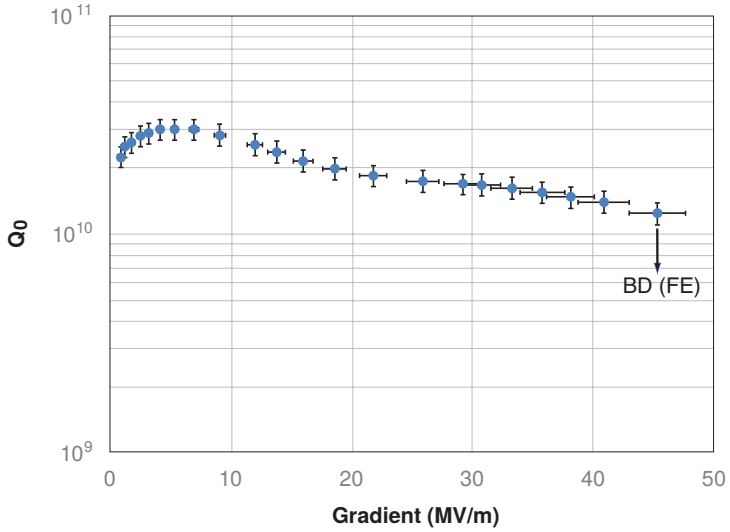

Figure 2.22
Demonstration of 45 MV/m by a 9-cell large-grain niobium TESLA shape cavity (AC155) at DESY.

An interesting observation is that the Q_0 value of a large-grain niobium cavity is higher as compared to that of a baseline fine-grain niobium cavity [79, 80]. Therefore, the large-grain material offers the added benefit of achieving higher Q_0 while the gradient is further pushed towards the 50 MV/m range. It is expected that large-grain material will be further evaluated for future high-gradient SCRF cavity R&D toward the 1 TeV upgrade of ILC.

2.3.4.4 Seamless cavities

The seamless cavity technology eliminates electron-beam welding at the equator region, where the peak surface magnetic field is high. It offers not only a possibility of cost saving in cavity fabrication but also a possibility of improved gradient yield. There are different approaches for making seamless cavities. Significant experience has been accumulated with the hydro-forming approach [81]. Many 1-cell, 2-cell and 3-cell hydro-formed seamless units have been produced and tested, showing gradients in the range comparable to that of welded cavities. More recently, several 9-cell seamless cavities have been fabricated by welding three 3-cell units together at the iris. The best result achieved so far is 34 MV/m, limited by quench [82].

To facilitate seamless-cavity fabrication, improved seamless tubes have been recently developed [83]. The first 9-cell cavity using these tubes (made by joining three 3-cell units through electron beam welding at iris) has been completed and is in the process of processing at testing at JLab [84].

The seamless-cavity fabrication technique is most suitable for building 9-cell cavities by using niobium-copper (Nb-Cu)-clad material [85, 86]. Due to the reduced use of niobium, the Nb-Cu clad

material cavity has the potential for cost saving. The excellent thermal conductivity of copper at cryogenic temperatures provides good thermal stabilisation against local heating due to the presence of defects and hence is expected to improve gradient yield.

2.3.4.5 Mechanical polishing

Mechanical polishing has been developed for a long time at KEK [87, 88]. It effectively eliminates surface defects originated from cavity fabrication steps. Therefore, the tolerance for fabrication flaws can be expected to increase. The mechanical removal of the damaged layer also reduces the amount of bulk surface removal by EP. These lead to improved fabrication yield and possibly some cost saving in fabrication and processing of ILC cavities. More recently, the mechanical polishing has been further optimised at FNAL and a mirror-finish inner surface has been achieved [49]. The FNAL efforts demonstrated effective cavity-performance improvement by using mechanical polishing to remove known quench-causing defects (see Fig. 2.23) [69]. Work is continuing at FNAL in assessing the suitability of implementing the mechanical polishing into the baseline cavity-processing steps.

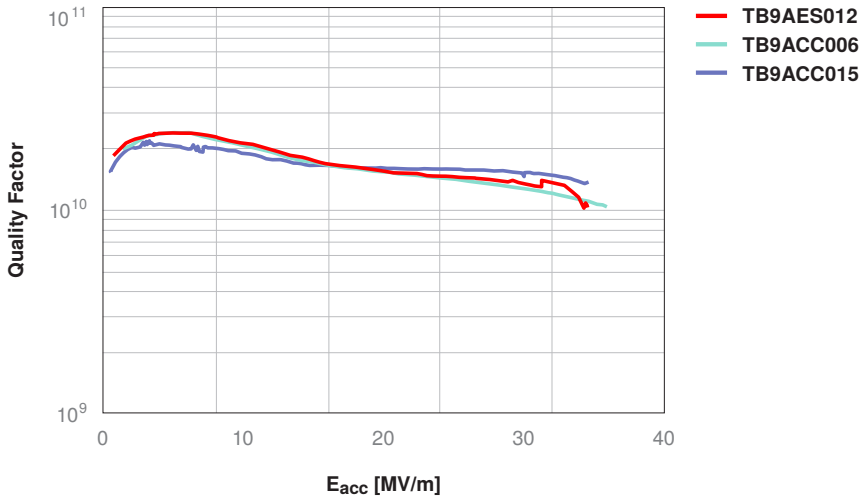

Figure 2.23
Q(E_{acc}) of 9-cell niobium cavities mechanically polished at FNAL followed by standard ILC final surface processing.

2.3.4.6 Challenges and Perspectives

There are two major challenges toward the realisation of the SCRF cavity performance goal for the 1 TeV upgrade of ILC. The first one is to reduce field emission in the regime of very high surface field (100–120 MV/m). Although there is no known intrinsic limit to the sustainable electric field on the superconducting niobium, there is no experience yet with 9-cell cavities at this peak surface field. Fundamental studies of the nature of field emitters on a niobium surface are necessary. Advanced surface cleaning and in-situ processing procedures need to be developed. A quality factor of 2×10^{10} at 45 MV/m has not been demonstrated even in a 1-cell cavity. Fundamental studies of medium-field Q-slope and high-field Q-slope are essential. Optimised heat treatment and surface coating need to be explored. A strong material R&D including RF characterisation (surface resistance and RF critical field) of small samples must be an integral part of the post-TDR SCRF R&D portfolio.

2.4 Cavity Integration

The cavity package in the cryomodule is an integrated system which consists of the niobium cavity proper, the input-power coupler, the titanium helium vessel, the frequency tuner, and the magnetic shield. The R&D performed on the frequency tuners, the input-power couplers, and the magnetic shields is summarised in this section.

2.4.1 Frequency Tuners

The frequency tuners play an important role in the efficient operation of a cavity. Both the fundamental frequency of the cavity can be adjusted and the detuning of the cavity under the Lorentz force (LFD) in a long RF pulse can be counteracted. All tuners apply a longitudinal force to change the length of the cavity. Typically a motor-driven adjustment applies the force to adjust the length of the cavity to the fundamental mode. A piezo-driven fine-adjustment applies a force to counteract the effect of the Lorentz force. Sophisticated feedback systems are required to control the action of the tuners during pulse operation. Achieving high reliability of the tuners (both mechanical and piezo) is a key requirement, and careful design of the stepper-motor drivers and associated gearing is crucial in this respect. This is particularly important for those designs that have the motor drive mounted directly at the tuner (in the cold) and which are not accessible outside the module.

The so-called Saclay/DESY tuner (Section 2.4.1.2) is the latest version of the tuner in operation at the TTF/FLASH facility, where 56 such tuners are routinely operated in the 7 installed cryomodules. (The same tuner will be used for the 800 cavities in the European XFEL). However, the Saclay tuner is mounted at the end of the cavity, extending the beam pipe on that end by 3.5 cm. To save this distance and increase the packing factor of the cavities in the ILC modules, it was considered attractive to include the tuner directly into the cavity helium tank, thus increasing the effective accelerating gradient. This has resulted in the design of the blade tuner which has been adopted as the baseline solution.

2.4.1.1 Blade Tuner

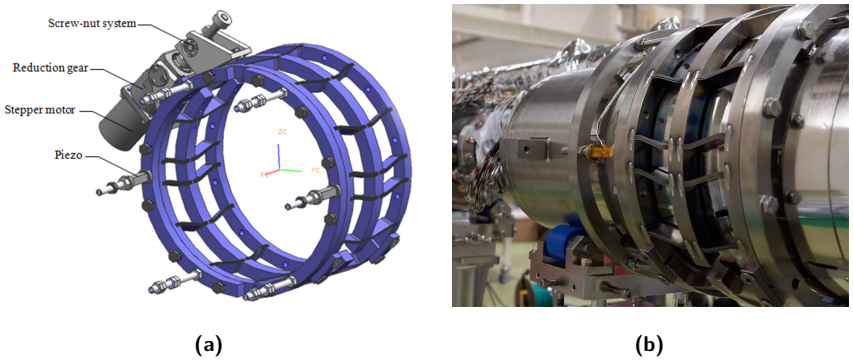

(a) **(b)**

Figure 2.24 Blade tuner. (a) Drawing. (b) One of the two mid-plane mounted piezoelectric actuators is shown.

The blade tuner has been developed by INFN Milan as a coaxial and light-weight tuning solution for TESLA-type cavities, starting from the original model built for DESY. As shown in Fig. 2.24a and Fig. 2.24b, it features the concept of elastic blades capable of transforming a rotational movement of the central ring into a longitudinal cavity strain with zero backlash. The tuner mechanics as well as the blades are made from titanium, utilising its mechanical strength and also in order to minimise the effect of differential thermal contraction. The slow-tuning action is generated by a cold drive unit based on a stepper motor and coupled to a mechanical reduction gear. A CuBe-threaded shaft is used as a screw-nut system that generates the azimuthal motion of the central rings. The fast-tuning action is carried out by two piezoelectric ceramic actuators that are installed on the longitudinal plane on opposite sides of the helium jacket; their action is in series to that of the tuner in order to achieve

the highest possible efficiency in transferring their stroke to the cavity. The entire mechanical load acting on the tuning system is generated by the cavity elasticity. Upon installation, an initial pre-load is set via a calibrated stretching of the cavity in order to achieve the optimal working condition for the piezo actuators. The cavity tension is large enough to accommodate the mechanical tuner range, thus guaranteeing that the piezos are always operated under compression. Details of the tuner and the actuators installed are also reported in Table 2.12. The blade-tuner cavity unit has been produced by a joint collaboration between FNAL and INFN in order to produce CM-2 for the NML/ASTA facility at Fermilab (see Section 3.4). The coaxial tuner is installed on the outside of the helium vessel that itself is split in two halves by a bellows to allow longitudinal adjustability. Moving the tuning bellow to the central position allowed for a simplification of the end cones region compared to the original TTF design.

Table 2.12
Various tuners investigated in the Technical Design Phase.

	Blade tuner	Saclay/DESY tuner	Slide-jack tuner
Type	Coaxial	Lateral-Pick-up side	Coaxial and lateral coupler side
Tuner stiffness (design)	30 kN/mm	40 kN/mm	290 kN/mm
Drive unit	Inside vessel, Stepper motor + Harmonic Drive	Inside vessel, Stepper motor + Harmonic Drive	Outside vessel, both manual or stepper motor actuation
Nominal frequency	1.3 GHz	1.3 GHz	1.3 GHz
Nominal tunable range	600 kHz	500 kHz	900 kHz
Nominal sensitivity	1.5 Hz/step	1 Hz/step	3 Hz/step
Piezo	2, thin-layer (0.1 mm), dim. $10\times10\times40\,mm^3$	2, thin-layer (0.1 mm), dim. $10\times10\times40\,mm^3$	1, thick-layer (2 mm), dim. diameter $35\times78\,mm^2$
Piezo Voltage	200 V	200 V	1000 V, operated at 500 V
Nominal piezo stroke at R.T.	55 µm	55 µm	40 µm
Nominal piezo capacitance at R.T.	8 µF	8 µF	0.9 µF

2.4.1.2 Saclay/DESY tuner

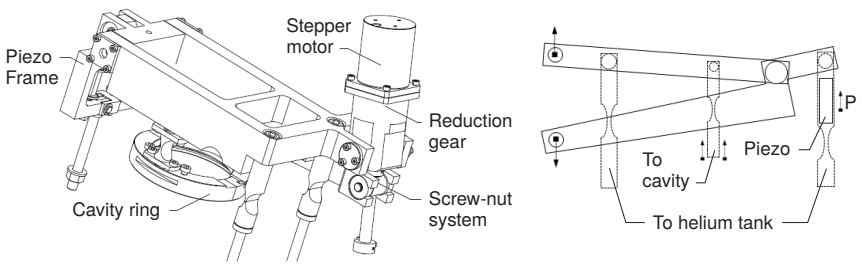

Figure 2.25
Saclay/DESY tuner pictorial view

(a) Tuner assembly

(b) Lever system for stepper-motor and piezos

The Saclay/DESY tuner has been further developed at DESY based on long operational experience. The Saclay/DESY tuning mechanics, shown in Fig. 2.25 and Fig. 2.26, is composed of a compact double lever installed at the pick-up side of the helium jacket made of stainless steel. The lever is

Figure 2.26
Saclay/DESY Tuner

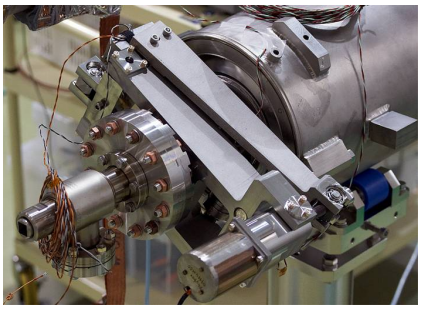

(a) Saclay/DESY tuner mounted on the cavity jacket

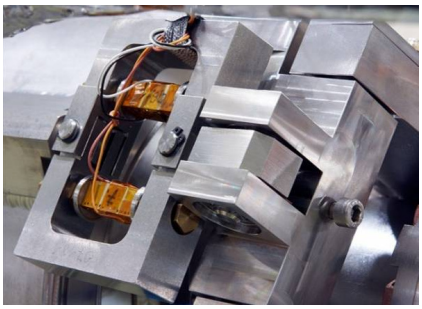

(b) Piezo pre-loading frame of the Saclay/DESY tuner

designed for a 1:25 reduction ratio and transfers to the cavity ring the tuning action generated by a cold drive unit based on a stepper motor equipped with a reduction gear and a screw-nut system. Two piezo actuators are installed to provide dynamic fast-tuning capabilities; they are both contained in a single preloading frame mounted at one side that acts on the cavity through the same lever mechanics. The piezo frame provides the required mechanical load on the actuators (almost independently of the load supplied by the tensioned cavity). The entire tuning system is installed outside of the helium tank (the tank itself can then be a relatively simply cylindrical design). A bellow with reduced radius is provided at the end opposite the power coupler, and fits in between the tuner joints, in order to accommodate the tuning strain. The double piezo configuration is, in this case, mainly chosen for redundancy reasons and the parallel action of the two actuators is not leading to a net doubling of the force. Moreover, the double piezo configuration, as in both blade and Saclay/DESY tuners, allows for the possibility of using the spare actuator as a passive sensing element. The salient characteristics of the Saclay/DESY tuner are summarised in Table 2.12.

2.4.1.3 Slide-jack Tuner

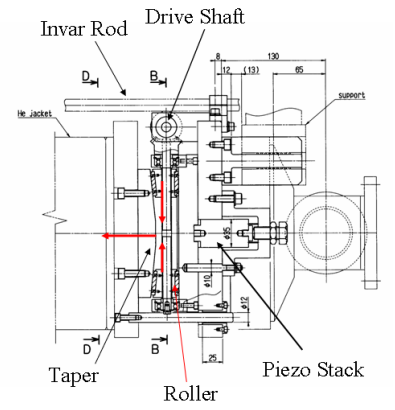

(a) Schematic drawing

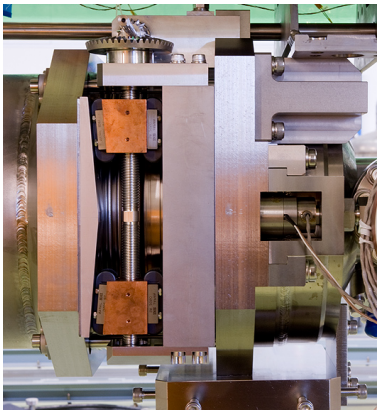

(b) Photograph

(c) Driver

Figure 2.27. Slide-jack tuner

The slide-jack tuner has been specifically designed for the TESLA-like cavities developed at KEK for the STF project. Here the strategy of minimising the Lorentz force detuning has been pursued from the start. The design thus corresponds to a stiffer layout of the cavity and its constraints. The geometry of the resonator and the end cone regions have been optimised, which resulted in a longitudinal spring constant significantly higher than the original TESLA-type system. The coaxial tuning mechanism has been designed accordingly and is shown in Fig. 2.27.

The slow-tuning action is generated through rolling elements sliding on a sloping surface; this mechanism transforms the rotation of a driving shaft into a longitudinal cavity strain. In order to

maximise reliability and ease of maintenance, no cold drive unit is foreseen in the design; the main driving shaft passes through the cryomodule vacuum vessel and the actual drive unit is placed outside. Either a stepper motor or a manual driver can be used. A single high-voltage, multiple thick-layer piezo actuator is installed at the coupler side of the jacket to provide fast-tuning capabilities. In the baseline design of this coaxial tuner, the slide-jack mechanics is installed between the pads, thus acting as a middle tuner. Similarly to the blade-tuner design, the helium jacket is split into two halves separated by a bellow. This slide-jack-tuner geometry will be referred to as *central* slide-jack. In order to compare the effects of different geometries for the tuning system, an additional cavity package has been developed which places the same slide-jack coaxial mechanical system outside the brackets on the helium tank on the coupler side, thus effectively acting as a *lateral* slide-jack tuner. The individual characteristics of the slide-jack tuners are summarised in Table 2.12.

2.4.1.4 Measurement of Tuning Action

Comparative tests of the four tuner variants were performed at KEK as part of the S1-Global study program (Section 2.6). The full tuning ranges were successfully made on all four tuner variants in the cooled state: 300 kHz for the blade tuners, 400 kHz for the Saclay/DESY tuners, and 800 kHz for both KEK tuner variants. The resolution of the frequency control was also measured. Tuner performance using the piezo actuators was also measured: both DC and transient responses where successfully measured on each tuner type. Further details of the test results can be found in Section 2.6 and in the S1-Global report [7]. A key outcome from these tests was the successful validation of the technical performance of all four tuner design variants.

2.4.2 Input power couplers

Two types of input couplers were explicitly examined and evaluated in the Technical Design Phase, at the S1-Global experiment (see Section 2.6). Their key parameters are summarised in Table 2.13.

Table 2.13
Main characteristics of input couplers

	TTF-III coupler	STF-2 coupler
Frequency	1.3 GHz	1.3 GHz
Pulse width	1.5 ms	1.5 ms
Repetition rate	5 Hz	5 Hz
Beam current	9 mA	9 mA
Required RF power	350 kW	350 kW
Range of external Q value	1×10^6–10×10^6	2×10^6–4×10^6

While the power requirements are fulfilled by both couplers it should be noted that the range of supported external Q-values is not yet sufficient for the STF-2 coupler.

2.4.2.1 TTF-III power couplers

Figure 2.28
TTF-III input coupler.

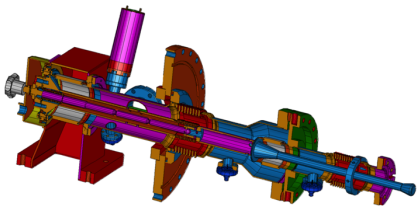

(a) Drawing

(b) Assembly components

The TTF-III input power coupler is a mature design having now over a decade of R&D, and has been used extensively for the cryomodules developed at DESY for FLASH (56 couplers total), as

well as a slightly modified design for the required 800 couplers for the European XFEL. The TTF-III coupler uses a double window design (warm and cold). Both the warm and cold RF windows consist of cylindrical ceramics made of Al_2O_3. The vacuum surface of the ceramic windows is coated with titanium-nitride (few nm) in order to prevent multipacting. The presence of bellows in the outer conductor allows the antenna protrusion into the cavity beam tube to be adjusted for variable power coupling. The inner conductor of the coupler can be DC biased in order to suppress multipacting. The input coupler has three electron current pick-up probes in order to measure electronic activity inside the coupler. The coupler and some of its components are shown in Fig. 2.28.

Figure 2.29
Set-up of high-power test stand at LAL.

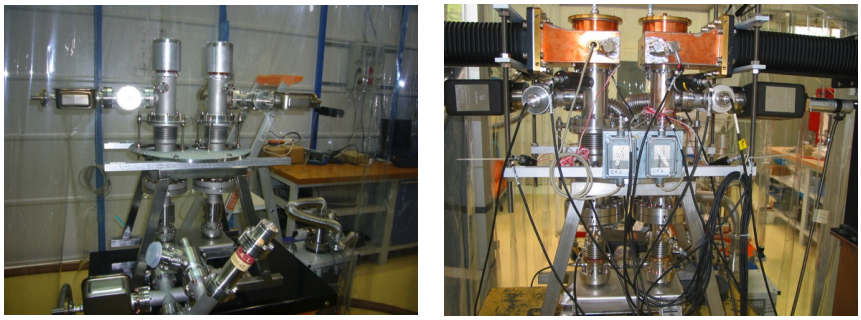

(a) Two couplers being conditioned

(b) Coupler test infrastructure

Four Type-III couplers were used for the S1-Global experiment (see Section 2.6). The two couplers for the DESY cavities were successfully conditioned at DESY and LAL respectively, while the remaining two couplers for the FNAL cavities were conditioned by SLAC. Figure 2.29 shows the processing set-up at LAL, and a similar system is installed at SLAC.

The RF conditioning of four TTF-III input couplers in the S1-global cryomodule was carried out with a high-power RF source connected to a 5 MW pulsed klystron. A monitoring system for electron activity using electron pick-up probes, and the interlock system for coupler protection, was supplied from DESY; both were attached to the TTF-III input couplers. The conditioning of the input couplers at room temperature before cooling had been carried out at up to 500 kW with pulse width of 0.5 ms and up to 200 kW with pulse width of 1.5 ms under total-reflection condition. The average conditioning time in four TTF-III input couplers was about 21 h. The vacuum interlock level was set at 2×10^{-4} Pa.

2.4.2.2 STF-2 power couplers

The input coupler, which consists of cold and warm sections, has two TRISTAN-type coaxial-disk RF windows as shown in Fig. 2.30. A bellow at the outer conductor in the 5 K part was eliminated to facilitate cavity assembly. The STF-1 input couplers used for the STF phase-1.0 had a simple structure with no variable coupling. Several improvements were made in the STF-2 input couplers for the S1-Global cryomodule. The schematic drawing and the completed STF-2 input couplers are shown in Fig. 2.31. The main features of the STF-2 coupler are summarised as follows:

1. Bellows were attached at the antenna tip of the inner conductor, so that a variable coupling of $\pm 30\%$ can be achieved.
2. The characteristic RF impedance is 41.5 Ω after enlarging the diameter of the inner conductor to insert a mechanism for variable coupling inside the inner conductor.
3. Thermal anchors at 5 K and 80 K were improved to suppress heat losses efficiently.
4. The design of the doorknob transition was modified to reduce the total length of the connection to the waveguide system.

Figure 2.30
Ceramics windows for the STF coupler.

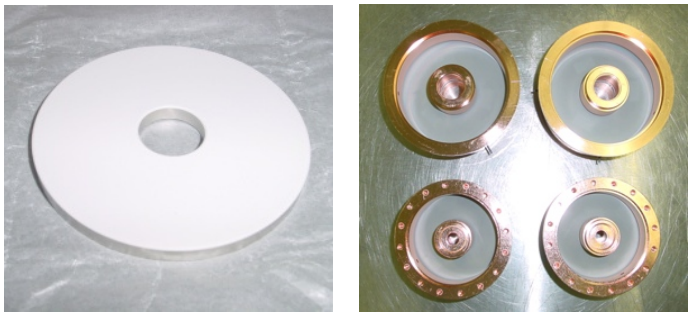

(a) Tristan-type coaxial ceramic disks

(b) RF windows after first brazing

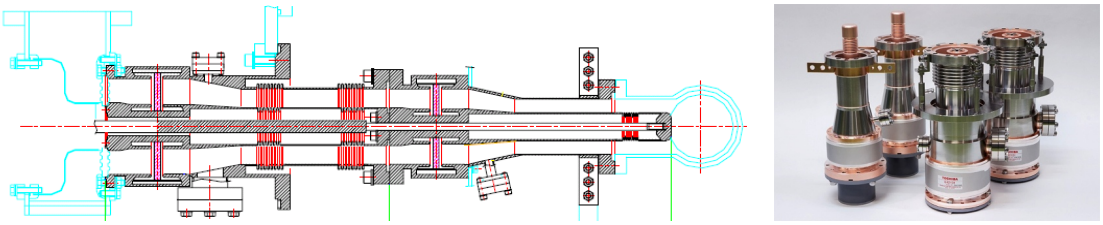

(a) Schematic drawing of the STF-2 input coupler

(b) Two sets of completed STF-2 input couplers

Figure 2.31. STF-2 input coupler

The static loss of 1.1 W at 5 K is five times larger than the dynamic loss of 0.2 W at an input RF power of 350 kW. The elimination of the thin bellows at the outer conductor in the 5 K part might be one of the causes for the high static loss at 5 K.

Prior to the assembly of the 9-cell cavities, the input couplers were conditioned using a high-power test stand, as shown in Fig. 2.32. The RF input power required for the conditioning in the travelling-wave mode at the test stand was determined to be four times higher than that in the standing-wave mode in the cryomodule. The conditioning was initially started using short pulses of 0.01 or 0.1 ms and the RF power level was increased very carefully. Finally, conditioning up to 1.0 MW in pulsed operation with 1.5 ms pulse width at 5 Hz was successfully performed on the four input couplers. The conditioning time at the test stand was approximately 60-120 h, as shown in Table 2.14.

Figure 2.32
Couplers in high-power test stand at KEK.

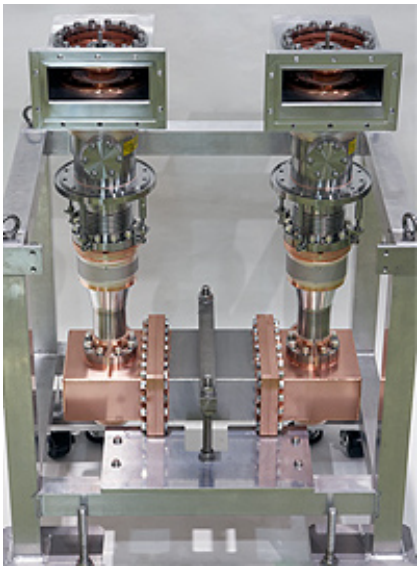

Table 2.14
RF conditioning of STF-II input couplers

Pulsed operation	Couplers #1 and #2 max. P_{rf}, time	Couplers #3 and #4 max. P_{rf}, time
5 ms, 1-5 Hz	1500 kW, 33 h	–
10 ms, 1-5 Hz	1230 kW, 47 h	1080 kW, 33 h
20 ms, 5 Hz	–	1140 kW, 1 h
30 ms, 5 Hz	1010 kW, 5 h	1120 kW, 2 h
60 ms, 5 Hz	1060 kW, 4 h	–
0.1 ms, 5 Hz	950 kW, 6 h	1050 kW, 7 h
0.2 ms, 5 Hz	880 kW, 6 h	–
0.5 ms, 5 Hz	820 kW, 4 h	800 kW, 14 h
1.0 ms, 5 Hz	810 kW, 6 h	–
1.5 ms, 5 Hz	750 kW, 8 h	270 kW, 6 h
Total time	119 hours	63 hours

After installation of the cryomodule in the STF tunnel, the warm and cold parts of the coupler were joined inside a special booth to maintain a clean environment. In-situ baking of cold RF windows inside the cryomodule was carried out at 85 °C for 15 h. The baking of cold RF windows prior to conditioning is very effective for reducing the conditioning time. The conditioning of the input couplers at room temperature before cooling was carried out at up to 500 kW with a pulse width of 0.5 ms and up to 200 kW for pulse widths of 1.5 ms under total-reflection conditions. The average conditioning time of the four STF-2 input couplers was about 15 h - shorter than for the TTF-III input couplers.

2.4.3 Magnetic shields

The magnetic shield for the TESLA-style cavities is well established; no further R&D has been carried out recently. The shield design however had to accommodate the blade tuner.

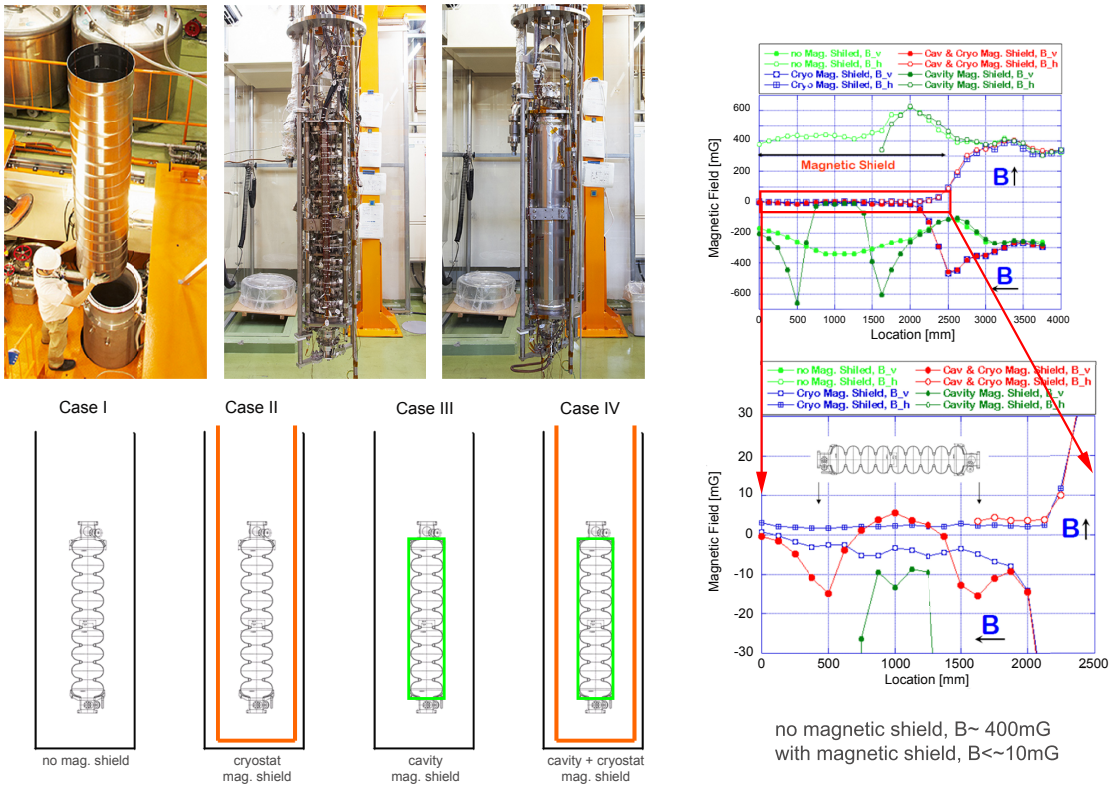

Figure 2.33. Four setups for the magnetic shield study in the vertical cryostat test and residual magnetic field inside the vertical cryostat.

In contrast, it was decided to test the design of the magnetic shield for the KEK cavities from the ground up. The design comprises the assembly of the cylindrical magnetic shield inside the titanium helium vessel with two conical shields between the end plates and the end cells. This configuration of

the magnetic shield inside the vessel simplifies the cavity package installation into the cryomodule. The effectiveness of the magnetic shielding could be systematically studied in four configurations in the vertical test setup in STF (see Fig. 2.33); the configurations range from no shielding at all via shielding of cryostat or cavity to shielding of both cryostat and cavity. The configurations are detailed in Table 2.15, which includes the measurement of the residual resistance derived from the Q_0-measurement of the cavity in each configuration (Fig. 2.34).

Table 2.15
Magnetic shielding configurations in the vertical test

Case	Shielding of		R_{res}
	Cryostat	Cavity	
1	–	–	126.0 nΩ
2	yes	–	10.3 nΩ
3	–	yes	13.2 nΩ
4	yes	yes	8.3 nΩ

The measurements show that the cavity shielding (case 3) is almost as effective as the full cryostat shielding (case 2). The difference of 3 nΩ is small and has to account for the contribution from the beam-pipe port. That contribution will be further reduced once the cavity is mounted in the steel cryostat of the cryomodule, which provides extra shielding.

The magnetic shielding for the KEK developed cavities has thus been qualified and is adequate. The magnetic shield could be placed inside LHe tank allowing for a simplified the shield design with a single cylinder and the added convenience of unobscured mounting of the blade tuner outside the LHe tank.

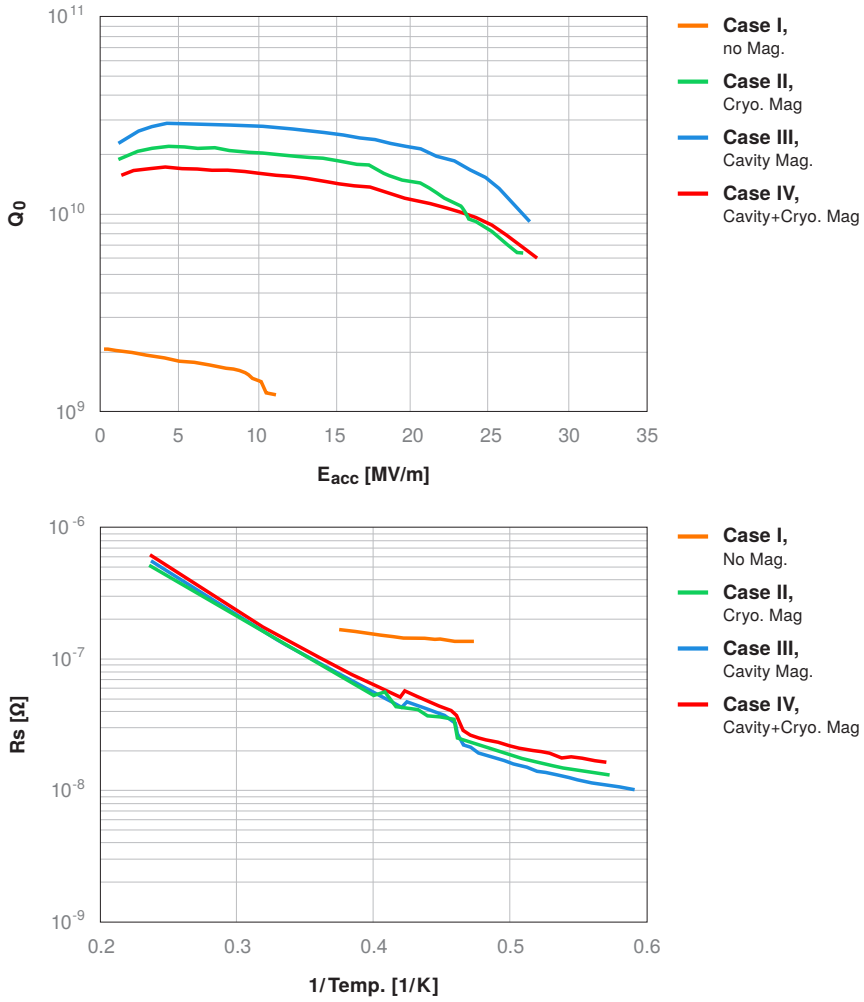

Figure 2.34
The vertical-test results for the four setups of the magnetic-shield study.

2.4.4 Summary of Cavity Integration R&D

Three frequency tuner designs have been successfully evaluated: blade tuner, DESY/Saclay tuner; and slide-jack tuner. All three designs met the ILC requirements under the same cryomodule-operation conditions, both in low-power and high-RF-power tests.

The two coupler types (TTF Type-III and STF2-coupler) have been compared with respect to installation procedure, RF processing, power capabilities and thermal performance. The Type-III coupler is by far the most mature design (with several years of operational experience), and has repeatedly achieved all necessary specifications for the ILC. However, the STF-2 coupler allows for a simpler installation procedure since it has no flexible bellows on the outer cylinder of the cold coupler part, and has a simpler design overall. The power capability is within requirements and the conditioning time was similar for both coupler types. The STF-2 coupler showed excess heat load around the cold part, with the first model installed in the S1-Global cryomodule. It has since been improved and is now consistent with the required design value after a test in the Quantum Beam program at KEK. In all, it is hoped that with further R&D, the STF coupler design can be made to be a more cost-effective alternative to the current TTF Type-III baseline design.

Finally, two approaches to the magnetic shield for the cavity have been evaluated, namely one external to and one internal to the helium tank, the former being the more common approach adopted by DESY and the European XFEL. The advantages of the internal tank are a simpler design (simple cylindrical shield with conical end parts), and easier assembly of the tuner during module assembly (cost factor). The internal design tested at S1-Global showed a tolerable 3 nΩ increase of the residual resistance compared to the external design. Although the internal design is currently the ILC baseline, the final design of the shield compatible with a cost-effective approach for the helium tank and tuner still needs to be made.

2.5 Anticipated Benefits from the European XFEL

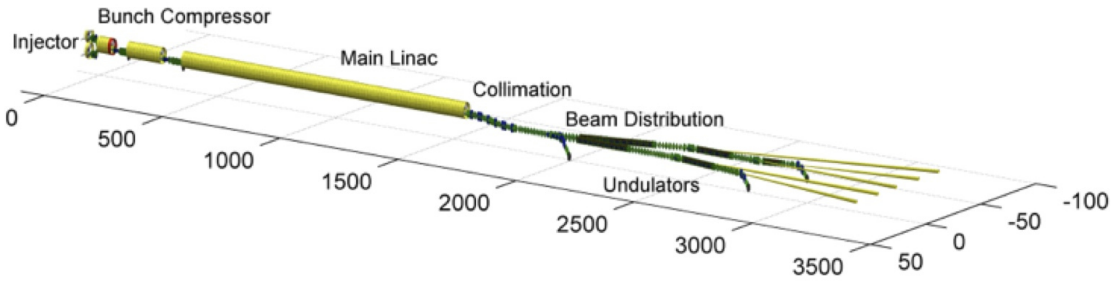

Figure 2.35. The layout of the European XFEL

The internationally organised European X-ray Free Electron Laser is currently under construction at the DESY and will begin operation in 2015 [6]. The layout is shown schematically in Fig. 2.35. Both the European XFEL and ILC use fundamentally the same pulsed SCRF technology originally developed for the TESLA linear collider [11]; both projects have shared in the worldwide R&D over the last twenty years. With 100 cryomodules containing 800 1.3 GHz superconducting cavities, the European XFEL is the first large-scale deployment of this technology. The strong synergy between the two projects provides unique and critically important benefits for the ILC development, ranging from fundamental R&D, through to integration and mass production and ultimately cost. As an international collaboration based on in-kind contributions, the European XFEL has also provided invaluable insights for the governance aspects of any future large-scale internationally funded project. Once operational, the European XFEL will provide unique operations and commissioning experience of a large-scale linac (7 % of an ILC linac). Table 2.16 lists the key parameters for the European

XFEL compared to the current ILC baseline.

Table 2.16 Comparison of some key parameters for the European XFEL and ILC Main Linac. For the ILC, the positron linac has been taken as an example. Where there is a difference between the regional variants, the values for mountainous/flat topographies are given. (The explicit numbers for the flat-topography design using KCS are average values.)

		European XFEL	ILC
Maximum beam energy	GeV	17.5	250
Accelerating gradient	MV/m	23.6	31.5
Charge per bunch	nC	1	3.2
Number of bunches per pulse		3250	1312
Repetition rate	Hz	10	5
Bunch spacing	ns	200	554
Beam current	mA	5	5.8
Beam pulse length	μs	650	727
Matched loaded Q		4.7×10^6	5.5×10^6
Fill time	μs	803	927
RF pulse length	ms	1.45	1.65
Number of klystrons		29	188/205
Number of cavities		800	7332
Number of cryomodules		100	846
Cavities per klystron		32	39/36
Average beam power per klystron	MW	3.92	7.37/6.80
Normalised Emittance (linac exit)	$\times 10^{-6}$m	1.4	0.003
BPM resolution	μm	50	1
Quadrupole lattice spacing	m	12	38

The 800 superconducting cavities will be operated at an average gradient of 23.6 MV/m to accelerate the electron beam to an energy of up to 17.5 GeV. The 800 cavities — complete with input couplers, HOM couplers and mechanical tuners —will be installed into 100 cryomodules, each containing a string of eight cavities plus one superconducting quadrupole package (including dipole correctors and a beam position monitor). A total of 29 RF stations will supply the necessary RF power of typically 4 MW of beam power per four accelerator modules. The relatively low gradient (as compared to ILC) is considered conservative. However, it is important to note that the approach to cavity production for the European XFEL follows the same basic recipe that has essentially demonstrated the ILC yield (see Section 2.3.1.2), and there is every expectation that the average achievable gradient will exceed the specification, facilitating the possibility to upgrade to shorter wavelengths (higher beam energy). For this reason, the beam-line sections downstream of the linac are designed to accommodate a maximum beam energy of 20 GeV, corresponding to an average gradient of 28 MV/m.The construction of the cold linac is a common effort of many institutes. The overall coordination is with DESY as chair of the European XFEL Accelerator Consortium. Table 2.17 summarises the major contributions.

Table 2.17 Contributions to the European XFEL Cold Linac

Institute	Component 7 Task
CEA Saclay / IRFU, France	Cavity string and module assembly; cold beam position monitors
CNRS / LAL Orsay, France	RF main input coupler incl. RF conditioning
DESY, Germany	Cavities & cryostats; contributions to string & module assembly; coupler interlock; frequency tuner; cold-vacuum system; integration of superconducting magnets; cold beam-position monitors
INFN Milano, Italy	Cavities & cryostats
Soltan Inst., Poland	Higher-order-mode coupler & absorber
CIEMAT, Spain	Superconducting magnets
IFJ PAN Cracow, Poland	RF cavity and cryomodule testing
BINP, Russia	Cold vacuum components

The following sections briefly describe the status of the major sub-systems of the SCRF linac, emphasising the synergy with the ILC.

2.5.1 Cavities

The European XFEL cavities, high-power input and HOM couplers use the same modified TESLA design on which the ILC design is based (see Section 2.3.1). The mechanical design of the cavity itself differs slightly in the length of the long-end beam pipe, which has been reduced by ∼3 cm for the ILC cavity design to increase the packing factor of the much larger machine. As with the ILC, the complete European XFEL cavity package also includes the helium tank, magnetic shield and slow mechanical tuner and a fast piezo tuner, although here the actual baseline designs differ (Section 2.4), in part to accommodate the shorter inter-cavity spacing in the ILC design.

Two European vendors have been successfully qualified for the European XFEL industrial production of the required 800 cavities over a two-year period. The vendors are responsible for both the mechanical fabrication of the cavity as well as the surface preparation. The niobium and niobium-titanium material used for the production has been procured by DESY, which provides the necessary strict quality controls before delivery to the cavity vendors. The finished complete cavities are delivered to DESY ready for performance testing in a vertical-test cryostat. No performance guarantee has been specified for the industrial production; however the mechanical fabrication and surface preparation must precisely follow detailed specifications, which include the exact definition of infrastructure to be used. These specifications developed by DESY for the cavity production process (and also used during the tendering) have since been made generally available to the SCRF community, and have been used by the GDE as the basis for the industrial quotes and studies for the mass production of the 18,000 cavities required for the ILC.

The European XFEL cavity production benefits from the ∼20 years of linear collider R&D efforts at DESY and elsewhere. The long collaboration within the TESLA Technology Collaboration led to the set-up of infrastructure at DESY, mostly for cavity preparation, assembly and testing. The European XFEL cavity contract is based on improved infrastructure, both at DESY and at the two cavity vendors. Quality control of the required Niobium material — altogether twelve different lots of sheets, tubes, and rods — is done in a new dedicated DESY infrastructure. In addition optical inspection of the mirror-like inner surface of the finished cavities has been improved. DESY has developed a fully-automated optical system based on the KEK/Kyoto University high-resolution camera system (see Section 2.2.2) which is playing an important role during qualification of the first pre-series cavities. Any change in the production process (e.g. modification of welding parameters) will require optical inspection. The specifications for the surface preparation has equally benefited from the advances due to worldwide R&D. As a result, the European XFEL treatment will follow the same steps as the ILC (see Section 2.3.1.2), with the possible exception that buffered chemical polishing (BCP) is allowed as an alternative to electro-polishing (EP) for the final 'fine' polishing step. It is expected that at least one-half of the total of 800 cavities for European XFEL will follow the ILC recipe exactly (i.e. using final EP), and will be tested to their maximum performance: hence the European XFEL production will provide a large and unparalleled data sample for ILC-like cavity production using the now standard recipe for achieving high gradients.

As with the ILC, all European XFEL cavities will be tested at 2 K in a low-power vertical cryostat. The European XFEL production rate of 8 cavities per week requires two vertical test cryostats housing four cavities each, which are then RF tested in one cool-down / warm-up cycle. Development of automated systems and procedures for these tests are directly applicable to future ILC production.

2.5.2 Cryomodule

The cryostat design for the European XFEL is based on the first cryostats developed and built by INFN Milano within the TESLA R&D effort. Although the ILC module has developed several differences, it remains very close to the European XFEL design. Figure 2.36 shows a comparison of the ILC and XFEL cryomodule designs.

From the perspective of production, the cryomodule can be separated into three parts:

- the string assembly which comprises of the eight cavities and their associated auxiliary components (high-power input coupler, HOM couplers, helium tank, mechanical tuner etc.), the superconducting quadrupole package including a beam position monitor and a HOM absorber;
- the so-called cold-mass of the cryostat, which includes the 300 mm gas-return pipe, support fixtures (for the cavity string), thermal shields, cryogenic piping etc.;
- the outer (insulating) vacuum vessel.

The original type-I cryostat design was improved for FLASH at DESY (type-II); the further improved type-III design was finally shared with the worldwide community and forms the basis of the ILC type-IV module. Only minor modifications have been made to the type-III for the European XFEL. The procurement of the 100 cryostats (cold-mass and outer vessel) is organised by DESY; in total four vendors were qualified, and two finally contracted for the series production.

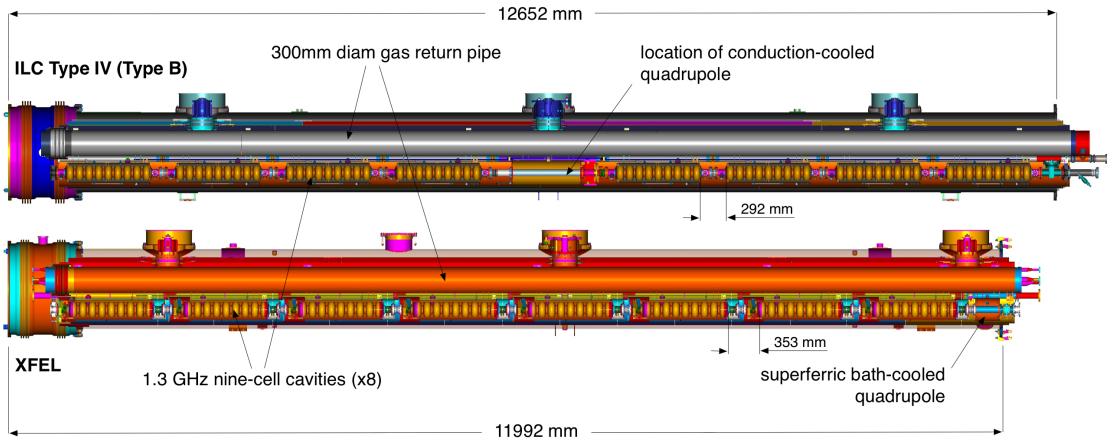

Figure 2.36. A comparison of the ILC (top) and XFEL (bottom) cryomodules. For the ILC the Type-IV module design with 8 cavities and one quadrupole package is shown. The most obvious difference is the longer length of the ILC module, driven primarily by the larger centrally located quadrupole (the longer quadrupole is required for the higher beam energy). The XFEL uses a superferric bath-cooled quadrupole located at the end of the module, while the ILC baseline locates the conduction-cooled magnet at the more stable central location. The reduced inter-cavity spacing is also indicated (ILC being 6 cm less than XFEL).

The cavity string and module assembly for the European XFEL is the responsibility of CEA Saclay / IRFU (France). A new dedicated infrastructure has been set-up for this purpose. Construction of the infrastructure started in 2009 and major parts were commissioned in 2010. An intense two-phase training period was used to transfer the assembly procedures from DESY to the IRFU supervisors and then to a sub-contracted company who will provide the approximately 30 personnel required to assemble the cryomodules at a rate of one per week. All major components required for the assembly are supplied by European XFEL collaboration partners as shown in Table 2.17. The work done at IRFU starts with the reception of already tested components (cavities, couplers, etc.) and ends with the shipping of completed accelerator modules ready for testing at DESY. As with the cavity production, the detailed specifications for the module assembly have been made available to the GDE and have been used as the basis for the industrial studies for ILC module assembly and cost estimation (see Section 2.9). Furthermore, the similarity in cryomodule designs has provided important technical information such as cryogenic heat loads, which can easily be scaled to the ILC specifications.

The first XFEL prototype module (PXFEL-1) achieved an average gradient on the module test stand of 32.5 MV/m when each cavity was driven independently (see Fig. 2.37), and represents the best performing module to date. The module average reflects a 10 % performance drop from the average of the individual cavity measurements achieved in the low-powered vertical tests (36.1 MV/m), mainly due to the large degradation observed in the last two cavities in the string (cavities No. 7 and 8). Such degradation in one or two cavities is not atypical and is an indication of contamination during string assembly. The XFEL series production will provide significantly larger statistics to help mitigate such assembly errors. PXFEL-1 is now installed in the FLASH linac, where it routinely accelerates beam, albeit at a reduced average gradient due to the limitations of the RF power distribution system. With its high-gradient cavities, it has been a focus of the ILC experimental programme at FLASH (see Section 3.2).

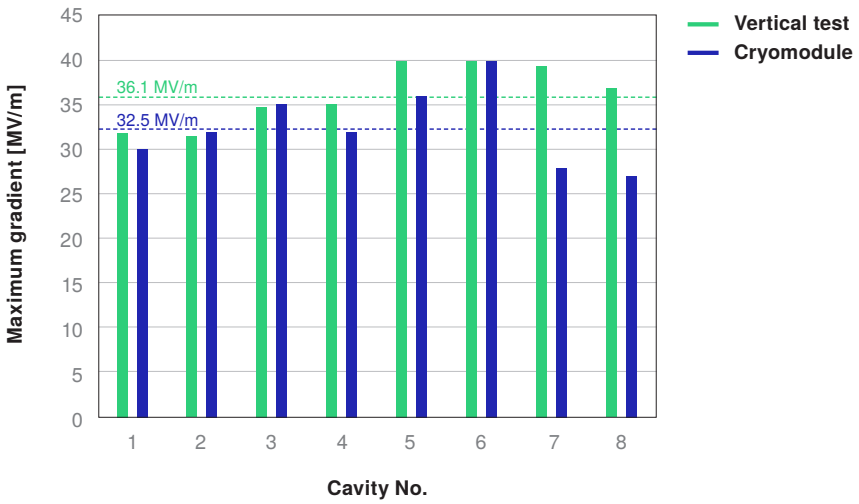

Figure 2.37 Maximum gradient results for the XFEL prototype module PXFEL-1, where an average of 32.5 MV/m was successfully demonstrated (without beam) [89]. The individual cavity performance results from the low-power vertical tests are also shown for comparison. The observed 10 % degradation is primarily due to cavities 7 and 8.

2.5.3 RF Power System

The RF system includes all components required to convert AC line power to pulsed RF power and to distribute it to the superconducting cavities of the accelerator. The main components have been developed, constructed and tested for several years since the early 1990s, when DESY started to host the TESLA test facility (later converted to FLASH). The RF power source has now had nearly two decades of operational experience at TTF/FLASH, and more recently at the RF gun test-stand PITZ at DESY, Zeuthen. The European XFEL will use altogether 29 complete RF stations. The stations are split into the modulator installed outside the accelerator tunnel, and the pulse transformer / 10 MW multi-beam-klystron units inside the tunnel, close to the accelerator modules. Pulse cables of a length up to approximately 1 km connect both parts of the RF station. The 10 MW multi-beam klystron technology is shared by the European XFEL and ILC (Section 2.8). The many years of development of this klystron have lead to a mature design and the qualification of three vendors, from which two were contracted for the production of European XFEL klystrons. Modulator development started with the Fermilab bouncer-type modulator originally provided for the TESLA Test Facility in the mid 1990ies. A second generation of bouncer-type modulator was built by a German company. After further R&D, the European XFEL has finally adopted a pulse-step modulator — a solid-state modulator not unlike the ILC baseline Marx modulator. Beyond the klystron and modulator, further development of the RF system was required for the European XFEL. Due to the limited space inside the European XFEL tunnel, a compact waveguide distribution system has been developed. The waveguide distribution is based on a binary cell which consists of two circulators connected to a shunt tee with integrated phase shifters. Four binary cells are combined by three asymmetric pre-tunable

shunt tees. The asymmetric shunt tees allow adjustment of the RF power to each pair of cavities to maximise the available cryomodule voltage. One MBK will drive 32 cavities (four cryomodules) via the distribution system. This is directly comparable to the approach adopted by ILC, although the details of the waveguide distribution systems are different; in particular the ILC distribution system can remotely adjust power to individual cavities.

2.5.4 Accelerator Module Test Facility

The primary performance testing of both cavities (vertical test) and the final complete cryomodules delivered from CEA Saclay will be made at DESY. A testing rate of 1 module and 8 cavities per week is foreseen. A new dedicated infrastructure has been set up for these tests —the Accelerator Module Test Facility (AMTF) — which offers not only the vertical tests for the cavities delivered from industry but includes also three complete test benches for assembled accelerator modules, which can be operated in parallel. AMTF also provides a test and assembly area for the waveguide distribution system, which is mounted to the module before installation in the tunnel. A test cryostat for the superconducting magnets is located in a neighbouring hall. All tests are performed by a dedicated team of some 20 people from IFJ PAN Cracow, Poland (as an in-kind contribution).

2.5.5 Electronic Documentation System

In addition to the technical specifications for the production process (from material QA/QC through to the final testing), the documentation process is also critically important. DESY has developed a set of comprehensive electronic documents which support every step of the manufacturing and testing process. Personnel at both DESY and in industry have been trained to use the central DESY engineering data-management system (EDMS), which will provide complete and traceable documentation for every component in the machine. This is particularly important for the cavity production, not least for the adherence to the pressure vessel regulations. Every single part can be tracked through the successive cavity production, testing, and ultimately installation in the accelerator tunnel. DESY is providing the same EDMS support for the GDE, facilitating a central database for the technical design documentation for the ILC baseline. The development of the EDMS system for European XFEL and ILC by the DESY team continued in parallel, to the mutual benefit of both projects.

2.5.6 European XFEL as a Beam Test Linac for ILC

As noted above, the European XFEL is due to begin operation with beam in 2015, effectively providing the ILC with a demonstration of an approximate 1 km of superconducting linac based on the same technology. Both through early commissioning and development and finally to routine user operation, the European XFEL will provide unprecedented experience in the operation of such a linac. Although much of the development work and "proof of principle" operations issues have been successfully dealt with at FLASH, the European XFEL will offer the unique advantages of understanding the issues pertaining to a much larger-scale deployment. In particular:

- operational experience with a long cryogenic string, in which half the cryogenic heat load is due to the pulsed RF;
- control system development — especially for the LLRF controls – including large-scale automation of tuning required for European XFEL (and scalable to ILC);
- Machine-protection philosophy, including trip-recovery, quench protection etc.;
- Energy management (dealing with failed RF stations);
- Short and long-term stability, including statistics on cavity detuning, calibration drifts etc.;

- Beam-dynamics issues associated with a long linac, including emittance preservation and HOM wakefield effects[4].

Until construction of the ILC, the European XFEL will represent a unique facility in the world. The direct synergy with ILC will allow much of the operations experience and control system development to be directly applicable to the larger machine. Together with FLASH and the more directly dedicated beam-test facilities at KEK and Fermilab, it is expected that the European XFEL will prove invaluable in understanding how to effectively operate a superconducting linac of the scale of the ILC.

2.6 The S1-Global Experiment

The S1-Global program was proposed in early 2008 with the aim of carrying out a string test of superconducting RF cavities during the ILC-GDE Technical Design Phase. The proposal was to coordinate a global collaboration involving various institutions around the world that would bring together eight 9-cell L-band cavities and associated hardware components, install them in common cryostat modules (cryomodules), and demonstrate their operation. This proposal by the GDE received strong support from the collaborating laboratories and was completed in a three-year period, ending in 2011 [7].

Two cavities with blade tuners were provided by Fermilab, two with Saclay/DESY-tuners were provided by DESY, and four with slide-jack tuners were provided by KEK. Information on the cavities is summarised in Table 2.18. Prior to being brought together for assembly into cryomodules, each of these cavities was processed and individually cold tested by the contributing laboratory. The cryomodules were provided by KEK (Hitachi) and INFN (Zanon). Input-power couplers for the cavities were contributed by SLAC, DESY, and KEK. The RF wave-guide components were provided by KEK and SLAC.

Table 2.18
Cavities used in the S1-Global experiment

Cryomodule position	Cavity name	Company	Institute	Tuner	Coupler
C1	TB9AES004	AES	FNAL	Blade	TTF-III
C2	TB9ACC011	ACCEL	FNAL	Blade	TTF-III
C3	Z108	Zanon	DESY	DESY	TTF-III
C4	Z109	Zanon	DESY	DESY	TTF-III
A1	MHI-05	MHI	KEK	S-J central	KEK-STF
A2	MHI-06	MHI	KEK	S-J central	KEK-STF
A3	MHI-07	MHI	KEK	S-J lateral	KEK-STF
A4	MHI-09	MHI	KEK	S-J lateral	KEK-STF

The programme successfully addressed such critical issues as plug-compatibility of hardware components (i.e. that parts must be compatible but not necessarily identical), as well as single- and multiple-cavity operation with pulsed microwave power and associated LLRF controls. While the S1-Global program did not involve beam operations, it covered all the essential steps required prior to beam acceleration in a superconducting linac.

The configuration and setup are shown in Fig. 2.38 and Fig. 2.39. The participating institutions contributed their hardware and human resources on an equal footing, and closely shared the experience of assembling a complex superconducting linac whose component designs and manufacturing were remotely coordinated. The STF site at KEK was selected as the host site, so as to take advantage of a one-year time slot that was available at the STF.

[4] while important experience can be gained from the European XFEL, the direct application to ILC is limited due to the factor of 500 difference in (vertical) emittance.

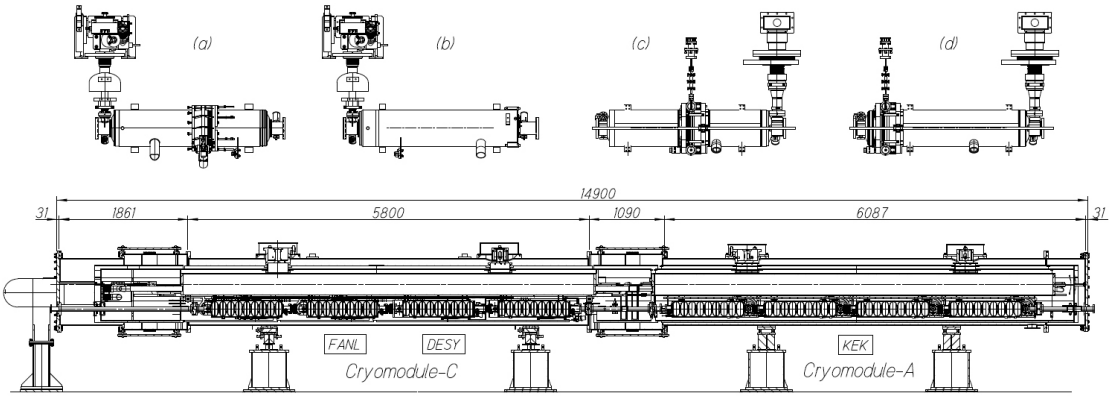

Figure 2.38. Layout of cavities in the S1-Global cryomodule string.

Figure 2.39
Fish-eye view of the S1-Global cryomodule from the side of the input coupler.

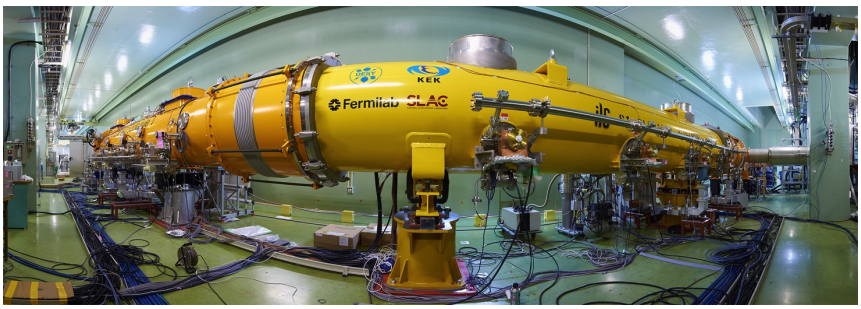

2.6.1 Cryomodules and Cryogenics

Figure 2.40
Cross section of Module-C for FNAL cavity (b) Cross section of Module-A for KEK cavity

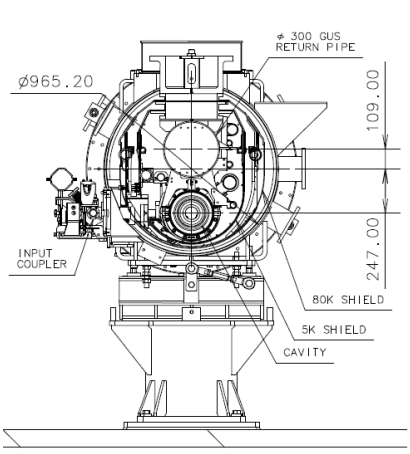

(a) Module-C for FNAL cavity

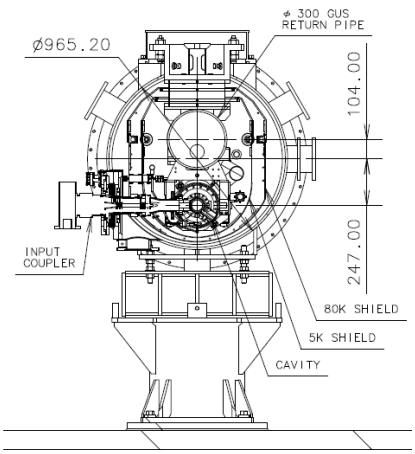

(b) Module-A for KEK cavity

Two cryomodules were used at the S1-Global experiment, cryomodules A and C. The cross section of Cryomodule-C is almost the same as the TTF-type III cryomodule, as shown in Fig. 2.40a. The cryomodule consists of the cavity packages, input couplers, the gas return pipe (GRP), magnetic shields, two sets of thermal shields, cooling pipes and the vacuum vessel. The distance between the input couplers is the same as for the TTF-type III and European XFEL design. The design of the cavity LHe jackets differs because of the different types of frequency tuners, namely the blade tuner and the Saclay/DESY-type tuner, as shown in Fig. 2.38. However, the cavity-support lugs have the same distance between two lugs along their axis, and a fixed distance from the input coupler axis, independent of the type of cavity package design and as a result, the cavity package supports to the GRP are identical, i.e. *plug compatible*. The frequency tuners of these cavities were driven by a cold motor and the piezo element. The cold motors were installed inside the 5 K shield. The DESY and

FNAL cavities were designed to be enclosed with the magnetic shields. The cold mass at 2 K was enclosed with two thermal shields at 5 K and 80 K which were cooled with LHe and LN_2, respectively.

Cryomodule-A, which was used for the cold tests at STF phase-1, has been arranged to accommodate components of different dimensions and assembly. The KEK tuners have a drive motor outside the vacuum vessel and the ports for the shafts are welded on the vacuum vessel. The frequency tuners of these cavities were driven by the warm motor, while the piezo element is on the cold side. The cryomodule parameters are summarised in Table 2.19.

Table 2.19
S1-Global Cryomodule Parameters.

	Module-A	Module-C
Vacuum-vessel length	6087 mm	5800 mm
Vacuum-vessel O.D.	965.2 mm	965.2 mm
Gas-return-pipe length	5830 mm	6000 mm
Gas-return-pipe O.D.	318.5 mm	312.0 mm
2K LHe-supply pipe O.D.	76.3 mm	76.1 mm
5K-shield pipe O.D. [F/R]	30/30 mm	60/60.3 mm
80K-shield pipe O.D. [F/R]	30/30 mm	60/60.3 mm
Cool-down pipe O.D.	27.2 mm	42.2 mm
Distance between couplers	1337.0 mm	1383.6 mm
Cavity package	KEK-a/KEK-b	FNAL/DESY
Cavity type	TESLA-like	TESLA-type
Tuner type	Slide-jack	Blade / Saclay/DESY
Input-coupler type	STF-2	TTF-III
Magnetic shield	Inside jacket	Outside jacket
Package length	1247.6 mm	1247.4/1283.4 mm

The 2 K cryogenic system consists of a helium liquefier/refrigerator, a liquefied-helium storage vessel, a 2 K refrigerator cold box, two cryomodules, a helium-gas pumping system and high-performance transfer lines. Liquid helium is produced with a helium liquefier/refrigerator and collected in a storage vessel. The 2 K refrigerator cold box contains a He I pot, a He II pot, a heat exchanger and a Joule-Thomson (J-T) valve. After filling up the He II pot and the cryomodules with liquid helium, the system was pumped down to 3.2 kPa (the saturation pressure of helium at 2 K).

A more complete description of the S1-Global hardware is included in the full S1-Global report [7].

2.6.2 High-level and Low-level RF

Two high-level RF (HLRF) systems were used for S1-Global; stations 1 and 2. A TH2104C klystron was used for station No. 1 and a newly procured TH2104A for station No. 2. Both klystrons were capable of 5 MW output power at 1.3 GHz with a pulse width of 1.5 ms and a repetition rate of 5 Hz. The modulators incorporated a bouncer circuit and pulse droop was successfully compensated. The flat-top performance of the bouncer circuit in both modulators was better than $\pm$ 0.8%. The power-distribution system (PDS) comprised of two designs; the linear PDS and the tree-type PDS using 3 dB power dividers. Both systems were evaluated in the S1-Global test, as shown in Fig. 2.41. A tree-type power-dividing scheme using variable 3 dB hybrids was used with cryomodule-C. In this system, variable power dividers, i.e. variable tap-offs (VTO) supplied by SLAC, were utilised. A linear distribution system (TESLA-type PDS) was used in cryomodule-A. In order to protect the klystron from large reflected rf power, a 5 MW circulator was installed filled with SF_6 gas. In each coupler port, a 400 kW circulator was installed to eliminate any reflected power from the cavity. In addition, a variable loaded Q system (Q_L) using a reflector and a phase shifter was introduced in each coupler port.

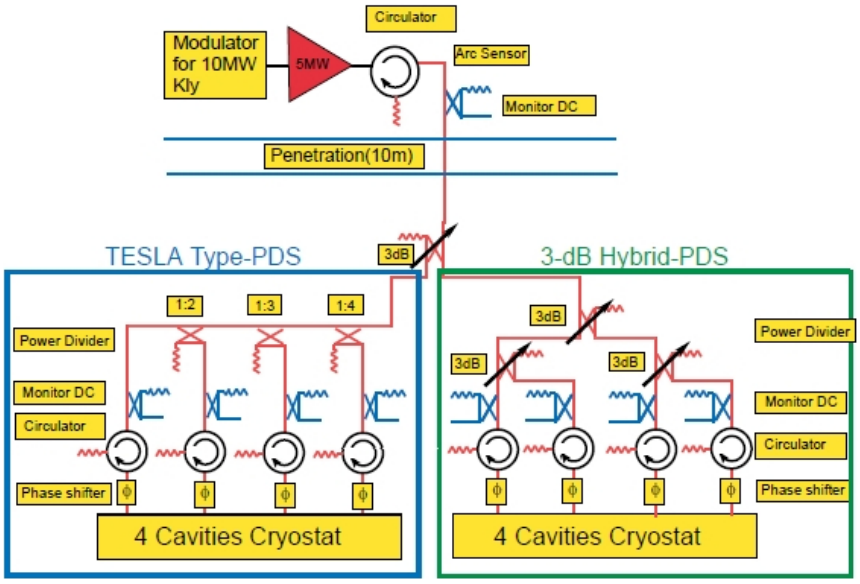

Figure 2.41 Power-distribution system used in the S1-Global test.

2.6.3 Performance Test of Individual Cavities

The cryomodules were cooled down three times in total during the period June 2010 to February 2011. The first cool-down test was carried out from June to July 2010 to measure the thermal and mechanical performance of the cryomodules, together with low-power RF tests of all cavities [90, 91]. The second test was done from September to December 2011 to verify the cavity performance, Lorentz-force detuning (LFD) measurements and compensation by piezo tuners, long-term operation, and dynamic loss measurements under high RF power. The distributed RF system (DRFS) was tested in the third cold test [92] from Jan to Feb 2011 by using two 800 kW klystrons. In the low-power RF tests [90] by the INFN/FNAL/KEK team in the first cool-down, it was found that tuners attached in TB9ACC011 and MHI-09 did not function properly. Therefore, simultaneous operation of multiple cavities was limited to 7 cavities rather than 8. All of the operating tuners provided an acceptable tuning range. The results of the low-power tuner tests are shown in Fig. 2.42.

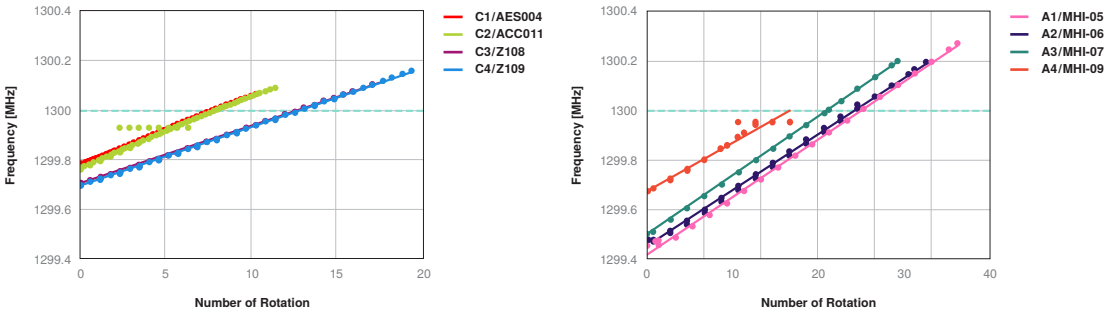

Figure 2.42. The result of the drive test for the motor tuner at low power. The tuner of TB9ACC011 did not work at 2 K, and MHI-09 could not be set to 1.3 GHz.

Adjustment of the variable coupling could be performed for all power couplers, and they were set to the optimum coupling of 2.4×10^6, resulting in a pulse rise time of 540 µs, as shown in Fig. 2.43.

The problems with the tuners and actuators were investigated and were the result of mechanical problems and are meanwhile well understood. One tuner failure was caused by the working loose of two screws in the shaft, presumably from mechanical vibrations during operation. The other failure related to a flange bending under the welding operation. The actuator failure was caused by misalignment of the brass caps holding the actuator stack and is hence related to mechanical tolerances during assembly.

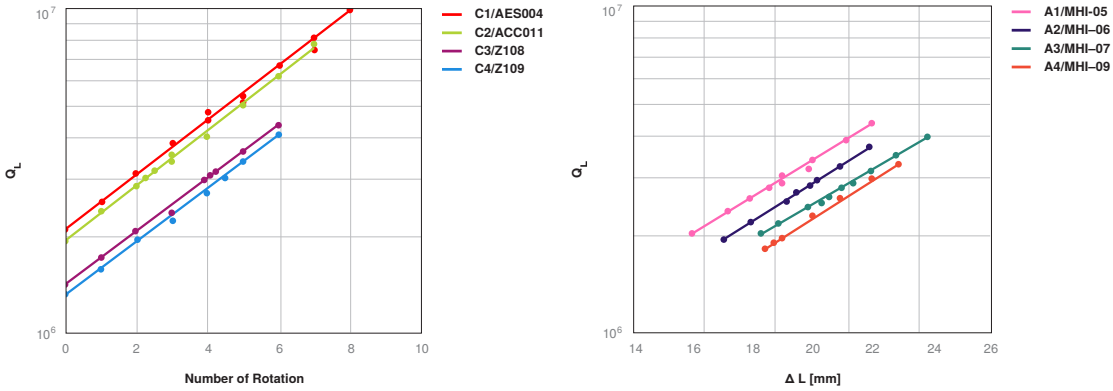

Figure 2.43. The results of the drive test for the variable coupling of the power couplers.

2.6.4 Cavity Performance in the S1-Global Experiment

After the second cool-down, the cavities were conditioned at high power. The achieved gradient values in vertical and cryomodule tests are shown in Fig. 2.44. The maximum average gradient was 30.0 MV/m in the vertical test, 27.7 MV/m for single cavity operation and 26.0 MV/m for simultaneous operation of seven cavities in the cryomodule test.

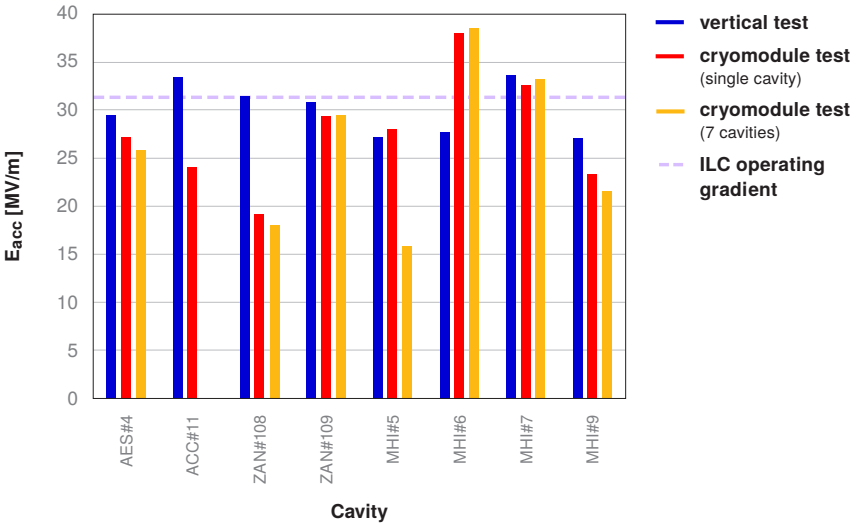

Figure 2.44 The achieved gradient values for eight cavities in vertical and cryomodule tests. The maximum average gradient is 30.0 MV/m at vertical test, 27.7 MV/m for single cavity operation and 26.0 MV/m for simultaneous operation of seven cavities at cryomodule test. The purple dotted line shows the ILC specification of 31.5 MV/m.

The performance of MHI-06 was much improved over the vertical test, reaching a gradient of 38 MV/m. On the other hand, the gradients of the two cavities (TB9ACC011 and Z108) were significantly reduced. The reasons for this are still unclear. While the assembly processes or the transport to KEK are possible candidates, the correct explanation will only come from a "post-mortem" study. The performance of MHI-05 (actually, the performance of the input coupler) also degraded following operation at high power levels.

2.6.5 Power-coupler Conditioning

All power couplers were RF conditioned at room temperature. During conditioning, the standing wave persists in the power coupler due to total reflection. The achievable power was 500 kW for a pulse width of 500 μs and 200 kW for 1500 μs at a repetition rate of 5 Hz. The average conditioning time was 21 hours for TTF-III-type couplers and 13 hours for STF-2-type, respectively. The difference can probably be attributed to the structure of the RF window. None of the RF windows had a vacuum leak during the experiments.

2.6.6 Lorentz-force Detuning

The magnitude of the Lorentz-force detuning (LFD) was measured by stepping the pulse length in the so-called *pulse-shortening* method (see Fig. 2.45). The detuning frequency for the three phases – rise, flat top, and full-pulse – was evaluated to compare the stiffness of all the cavities. The slopes of linear fitting between the detuning frequency for the three periods and the square of the gradient gives the cavity stiffness, as shown in Fig. 2.46. The MHI cavities were found to be more rigid than the others. The effect is noticeable in the flat-top period, while the difference is smaller in the rise period.

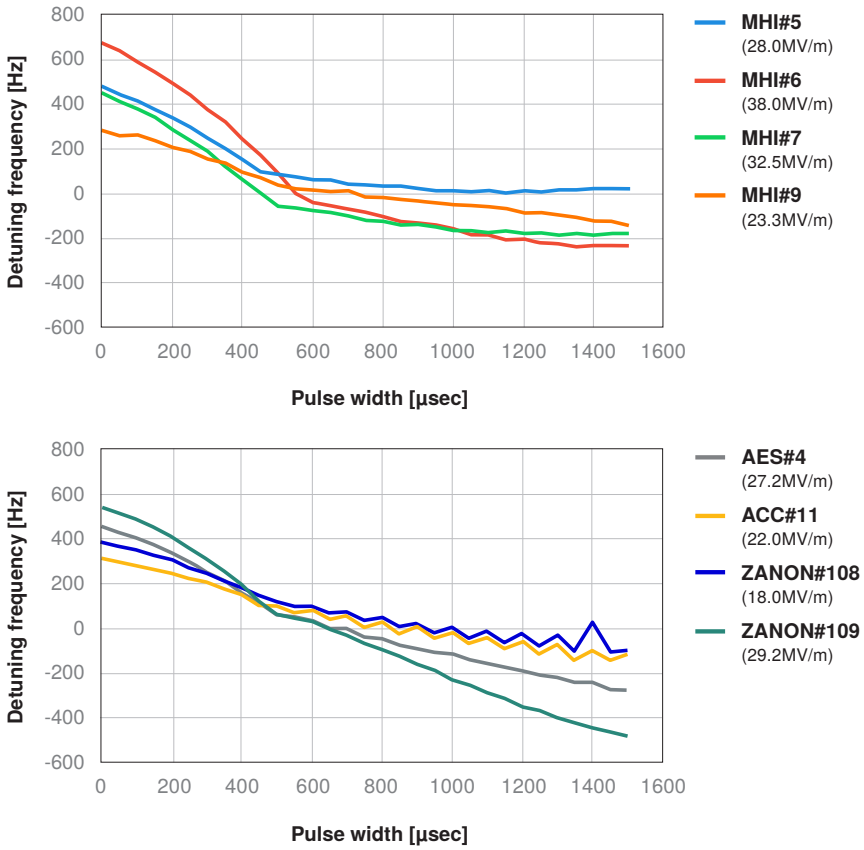

Figure 2.45
The result of LFD measurement at the maximum gradient for every cavity. (top) Cryomodule-A, (bottom) Cryomodule-C

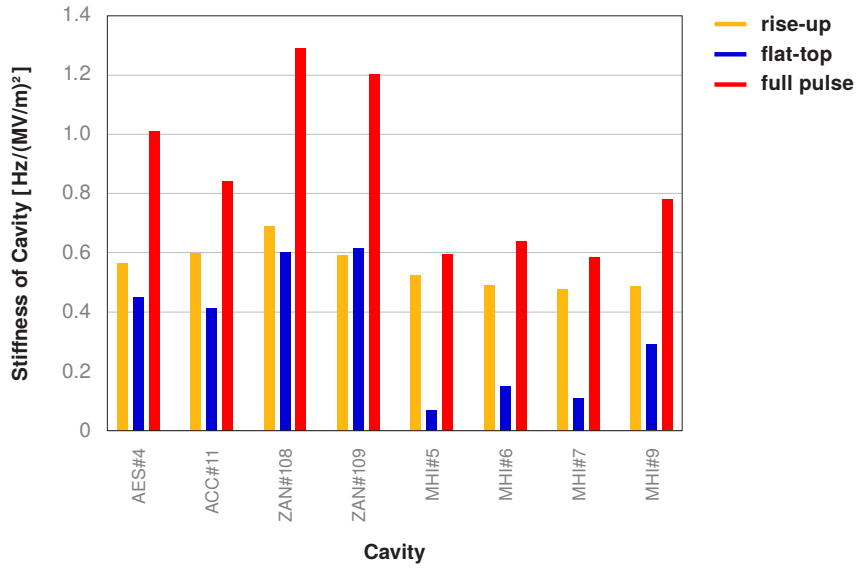

Figure 2.46
Comparison of the slopes from rise, flat top and full-pulse.

Two methods of LFD compensation were successfully tried: *single-pulse compensation* by a half-sine waveform, which was used at STF Phase-1 [93] and a new method known as *adaptive*

compensation [94].

To compensate the LFD, a pulse corresponding to a half-period sine-wave is applied to the piezo tuner before the start of the RF pulse. There are four adjustable parameters, namely drive frequency, delay time, pulse height, and pulse offset. The excursion peak-to-peak of the detuning frequency at the flat top of the pulse was introduced as a measure of the compensation [93]. Figure 2.47 shows the correlation between the peak-to-peak of the detuning frequency and the gradient for the best three results of the compensation by the pulse-shortening method. After the compensation, the MHI cavity still has a smaller peak-to-peak of the detuning frequency at the flat-top period, which is expected from the stiffer structure of the MHI cavity package.

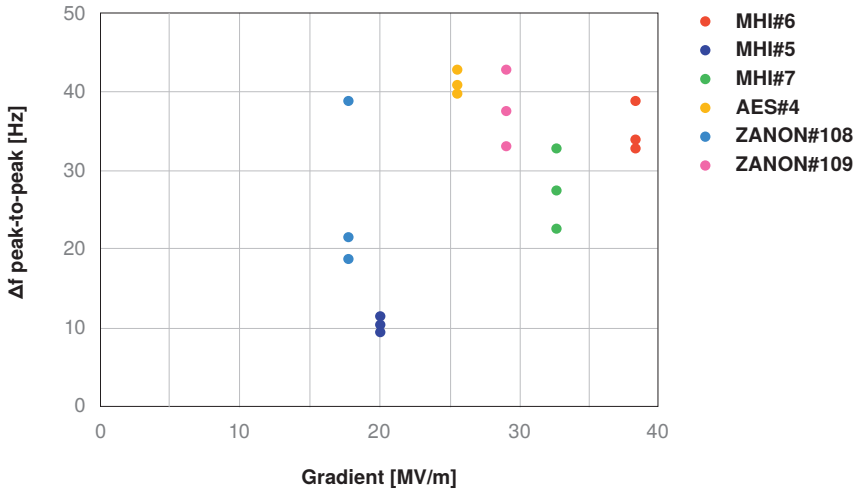

Figure 2.47
The correlation between the excursion peak-to-peak of the detuning frequency at flat top and field. The best three results are shown.

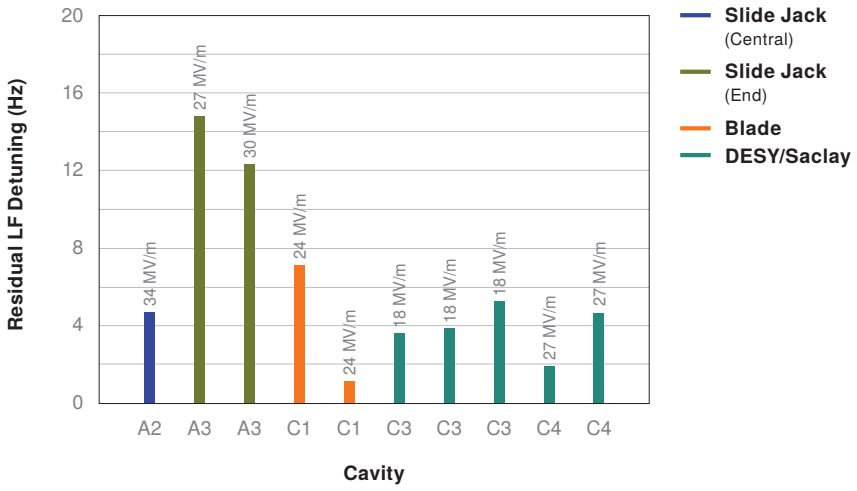

Figure 2.48
A comparison of the average residual detuning during the flat top in different S1-Global cavity designs following adaptive feed-forward compensation.

In addition to the standard method of LFD compensation, an adaptive feed-forward method developed at FNAL for CM1 was employed to compensate detuning in six of the eight S1-Global cavities [94]. The adaptive feed-forward procedure first measured the detuning response of each individual cavity to a series of small-amplitude, short-duration piezo stimulus pulses and to changes in the DC bias applied to the piezo. The matrices of stimulus and response data were then inverted using least squares to obtain the small-signal cavity detuning response for any arbitrary piezo waveform and to determine the piezo waveform required to cancel any arbitrary detuning profile. The feed-forward method allows the detuning compensation process to be fully automated; it can track changes in cavity gradient without the need for operator intervention; and it can automatically adjust the piezo bias to correct for changes in the cavity resonance frequency caused by changes in the pressure of the surrounding helium bath and any other slowly changing sources of detuning. The residual

RMS detuning following compensation was less than 15 Hz in all cavities, regardless of design or gradient, as shown in Fig. 2.48. With the exception of the end slide-jack design, which may not have received an adequate piezo drive signal, the residual detuning ranged between 2–8 Hz. At this level of compensation, residual detuning will have no significant impact on the design or operation of the ILC.

2.6.7 Operation of Seven Cavities with Vector-sum Feedback Control

In the final stage of the experiment, one 5 MW klystron fed its power to all seven cavities and the performance of operation with vector-sum feedback control was evaluated [95]. During this operation, one cavity (C-2) could not be used for the vector-sum control because of the mechanical problem with the tuner. The input power to the cavities was adjusted by the tuneable hybrids and the variable tap-offs [96] to yield the maximum gradient for each cavity. As described in the previous section, the detuning of cavities during the RF pulse flat-top (1 ms) was effectively eliminated using the piezo tuners.

The result of vector-sum feedback control operation for seven cavities is shown in Fig. 2.49. The average gradient of the seven cavities after input-power optimisation for each cavity was close to 26 MV/m. Since the average of each cavity's quench limit was 26.7 MV/m, the operation near quench limit of each cavity was achieved. The amplitude and phase stabilities were 0.005 % rms and 0.015° rms, respectively, which satisfy the ILC requirements of 0.07 % rms in amplitude and 0.24° rms in phase [3].

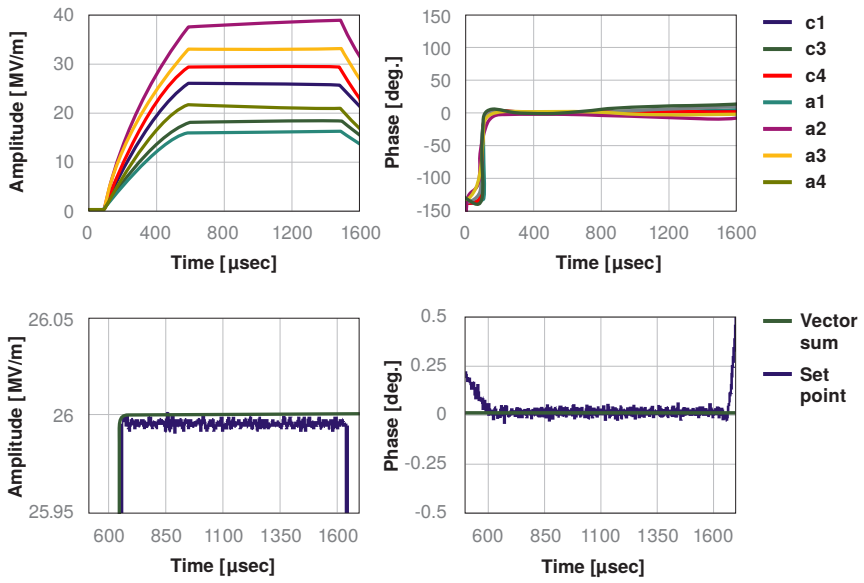

Figure 2.49 Vector-sum operation. Left: each cavity's gradient and vector-sum gradient, right: each cavity's phase and vector-sum phase.

2.6.8 Summary of S1-Global Experiment

The S1-global program successfully achieved the GDE R&D goal of the fabrication and test of a cavity string. The cavity ensemble achieved an average gradient of 30.0 MV/m before installation, 27.7 MV/m for single cavity operation after installation, and 26.0 MV/m for 7 cavity simultaneous operation in a cryomodule. The ability to operate (and control) cavities in a cryomodule close to their nominal quench thresholds with a tunable PDS was also shown. Compensation of Lorentz-force detuning maintained the cavity frequencies well within the required tolerances. Although all of the tuner designs achieved the necessary frequency range, mechanical failures in two of these tuners impacted the operation in two of the cavities. These failures are not systematic and can be attributed to the lack of maturity of the cryomodule mechanical-assembly procedures and the associated quality controls.

The *plug-compatibility concept* was verified by building one cryomodule from cavities and couplers supplied from several national laboratories. A good example is the half-size cryomodule-C which was built from an INFN cryostat, DESY cavities and couplers, and FNAL cavities and couplers in cooperation with SLAC. The cryomodule power systems is another good example. The ability to incorporate and test several different component designs within a single integrated test set-up was an important aspect of the R&D program.

A less obvious but also important aspect of this program was the fact that it was the manifestation of a global engineering effort under the GDE organisation. Distributed design and fabrication requires the adoption and utilisation of common CAD design tools and data bases together with an unprecedented level of communication among the participants. This degree of detailed collaboration has rarely, if ever, been attempted across major research laboratories. Not only did the GDE learn how to build cryomodules but also how to organise the efforts to accomplish this. This bodes well for a construction project which is envisaged to embody significant international co-operation.

2.7 Cryomodule and Quadrupole R&D

The overall ILC cryogenic scheme evolved from the TESLA proposal [11]. The TESLA cryomodule design was conceived in the late 90s to meet the project requirements of high-filling factors, moderate capital and operation costs and effective alignment and assembly procedures [97]. This module design has been employed for the realisation of the TESLA Test Facility (TTF) linac, now operating as the FLASH FEL facility in DESY, and was improved in several iterations during the deployment of the facility [98]. The successful TTF design, with minimal modifications, was later adopted for the linac of the European XFEL, which is composed of 100 modules of this type, and evolved with few variations, into the baseline for the ILC [3, 50].

The energy reach and beam requirements of the ILC require

- a *high filling factor* (the ratio between the total length of the linac and the length in which acceleration takes place) to reduce the machine footprint;
- *moderate capital and operation cost* per unit length - a simple design, based on proven and reliable technologies, readily available in the industrial contexts, will tend to minimise costs, while operational cost is reduced by a careful thermal design aimed at minimisation of all spurious static losses to the 2 K environment;
- effective *assembly and alignment procedures* for beam-line components - cost-effective module assembly procedures compatible with the cleanliness needed by high-gradient bulk-Nb cavity technology provide the former, while preservation, reproducibility and stability of beam-line components is crucial for the achievement of beam parameters.

The high filling-factor concept favours long cryomodules (containing several cavities) and their connection in long cryo-units, separated by short interconnections. This aspect, combined with the requirement for low cryogenic loss, led to the integration of the cryogenic-cooling circuits into the cryostat. Thus in this scheme the cryomodule, besides providing the usual functions of mechanical-support structure for the beam-line elements and isolation from the warm-temperature environment, becomes a substantial part of the cryogenic system, since it represents the region where nearly all losses occur and also takes care of the fluid distribution in the linac.

The TTF module has been developed in order to meet the requirements mentioned above and has been extensively characterised, thoroughly tested and operated for years in a linac driving the high-availability user facility FLASH. From this design all the DESY FLASH and European XFEL linac modules, the FNAL-type-IV modules for NML and the S1-Global modules at KEK have been derived, with small variations, and manufactured by several companies worldwide.

The ILC-module concept therefore builds on a reliable and mature technology, currently available

in different laboratories worldwide as a result of the ILC S1 and S2 efforts. The already large experience gained at FLASH and at the facilities based on this design will be soon consolidated by the large amount of information coming from the European XFEL, which will deploy a 100-module linac at a tunnel installation rate of 1 module per week. The experience so accumulated will be particularly relevant for the further evolution and the finalisation of the ILC-module concept. The following subsections briefly summarise the recent status of R&D activities worldwide in this area..

2.7.1 Thermal Performance of the S1-Global Modules

The S1-Global (Section 2.6) collaboration launched a strong effort dedicated to the experimental assessment of the thermal performance of the different cryomodule and subcomponent variants [99]. Such an activity is motivated by:

- the study of design variants for a possible cost reduction of the mass-produced cryomodules;
- the opportunity given by the experimental activities at KEK to provide a comparison for the thermal performance of the different variants integrated in the S1-Global setup;
- the need to benchmark with experimental measurements the heat-load calculations based on engineering calculations and FEM models.

2.7.1.1 Simplification Studies of the 5 K-Shield

One of the original STF modules was used to explore the feasibility and the consequences of removing the inner 5 K shield of the cryomodules, as a possible cost-reduction measure, leading to a decrease in fabrication costs and envisaged simplifications of the assembly operations. This concept has been tested at KEK by heat-load measurement with and without the shield. Heat loads were measured by means of the evaporated mass flow for the 2 K region and of the shield-temperature increase after stopping the coolant for the shield circuits [99].

In the ILC cryomodule both thermal shields provide a manifold for the thermalisation of direct conduction paths to the many penetrations reaching the 2 K environment (couplers, HOM, current leads, supports, cables etc.). Thus a thermal sinking of these conduction paths must be provided by a circuit at approximately 5 K in order to limit direct heat flow by conduction at 2 K; a complete elimination of the 5 K shield is therefore not feasible.

The possibility of partial removal of the heat shield remained. This was investigated at KEK by retaining the top shield parts while removing the bottom shield portions. Heat loads were measured in these two setups (with and without bottom shield portions) to support and validate heat-load estimates from FEM modelling. The removal of the bottom shields led to an increase of static loads to the 2 K region of approximately 0.8 W in the 6 m-long S1-Global module, as a consequence of the thermal radiation from the 70 K shield now impinging on the 2 K surfaces. This data allowed the FEM-model parameters (e.g. surface emissivities to account for multilayer insulation) to be tuned in order to explore mitigating actions by means of alternate cooling schemes. Further FEM studies originating from the analysis of these measurements showed that the radiation-load increase can be avoided by implementing an alternate scheme for cryogenic-coolant flow. The decrease of the average shield temperature obtained by reversing the coolant-flow direction allows a reduction of the thermal static load to the coldest temperature level. Thus it is in principle possible to remove the lower 5 K shield while keeping the overall static consumption of an ILC module to the same level as the nominal RDR design with a complete 5 K shield. However, the proper implementation of a reversal of the cryogenic flow would necessitate a complete redesign of the module transverse cross section, with redistribution of the cryogenic piping. A complete module redesign, even when retaining nominal heat-load performance, could severely compromise the consolidated experience gained from the evolution of these modules which will be further supported in the near future by the European

XFEL modules. It was therefore decided to retain the nominal cooling scheme as foreseen by the RDR (matching the module layout for the European XFEL) and leave the possibility for reconsidering the 5K removal/flow inversion possibility at a later engineering stage of the project, together with the finalisation and final optimisation of the temperature stages of the cryosystems.

2.7.1.2 Analytic Heat-Load Measurements

The characterisation of the thermal performance of the design variants for the components is important in order to include heat-load estimations for the plug-compatible components of the ILC cryomodules that do not exceed the overall heat-load budget available for the cryomodule unit. Such tests were carried out; details of the configuration are given in Section 2.6.

The cryomodules and STF cryogenic infrastructure have been instrumented with a large number of sensors to monitor component temperatures and cryogenic flow conditions. This allows the assessment of heat loads at the different circuit levels and a comparison with the evaluations. Experimental procedures have been devised to assess individual contributions from the components. Table 2.20 compares the static estimations and measurements. As for the case of the 5 K shield studies previously reported, the overall heat loads on the 2 K environment have been derived from the mass flows of the evaporated LHe by the cavity vessels, and the static losses on the 5 K and 80 K circuits have been derived from the temperature (i.e. enthalpy) rises of the average shield temperatures after stopping the coolant flow. A dozen temperature sensors were installed on each thermal shield of the module in order to perform these measurements. Temperature sensors were also placed at thermal sinks in order to analyse the heat-load contributions of individual conduction paths.

Table 2.20
Comparison of static S1-Global module heat-load estimations with measurements.

Temperature	Component	Module-A [W]	Module-C [W]
2 K	Thermal radiation	≈0.0	≈ 0.0
	Input couplers (4×)	0.29	0.08
	HOM RF, Piezo cables	2.1	0.71
	Tuner driving shafts (4×)	0.48	NA
	Temperature sensor wires	0.18	
	WPM, pin diodes wires	1.72	0.82
	WPM connection pipe	0.17	≈0.0
	Support posts (2×)	0.25	
	Beam Pipe	0.02	<0.01
Total Estimated 2 K load at module		5.2	2.1
Total Estimated 2 K load (both modules)		7.3 (6.8 without support posts)	
Total Measured 2 K load (both modules)		7.2	
5 K	Thermal radiation	0.66	0.68
	Input couplers (4×)	4.00	0.92
	Support posts (2×)	1.54	
	Sensor wires	0.9	
	Beam Pipe	0.1	0.05
Total Estimated 5 K load at module		7.2	4.1
Total Measured 5 K load at module		7.3	5.3
80 K	Thermal radiation	16.6	15.9
	Input couplers (4×)	9.60	7.28
	Support posts (2×)	10.78	
	RF cables	6.88	1.30
	Sensor wires	0.08	
	Beam Pipe	0.37	0.10
Total Estimated 80 K load at module		44.4	35.3
Total Measured 80 K load at module		48.7	34.4

The good agreement between estimates and measurements in the S1-Global experiment, which has been made possible by the large amount of diagnostics implemented during the test cool-downs by the KEK team, is another confirmation that the module design is well understood in terms of its thermal behaviour. Thus design options of subcomponents can be explored by means of suitably detailed FEM models in order to derive their thermal performance with a reasonable error margin.

Other studies have been performed in the past also to benchmark transient behaviour during cooldown, with similarly good agreement [100].

Table 2.20 is also a useful example to illustrate the opportunity for value engineering and overall optimisation for a complex system such as the ILC cryomodule. For example, Module-A was equipped with better-grade RF cables for the HOM and Wire Position Monitor (WPM) sensors, resulting in an increased heat leak to the 2 K environment. The use of external motor drives for the tuner action to allow replacement without dismounting the module (as a measure to reduce maintenance times) introduces additional heat loads to the cavity environment. The different coupler designs also have different thermal performance due to different design choices (e.g. the STF-2 coupler design, contrary to the TTF-III, has no bellows between the 5 K and 70 K intercepts to simplify clean-room assembly) , which should be factored in when considering plug-compatible component design.

A third important activity carried by the S1-Global collaboration has been the assessment of the cavity and coupler dynamic loads during module testing. This has been achieved by a sequence of four measurements of static and dynamic loads of each cavity on resonance and in detuning conditions, evaluated from the flow rate of evaporated LHe. All cavities were driven to high field values (25–38 MV/m) with a Q_0 estimated from this analysis in the range $\approx$ 4-9 $\times$ 10^9. These measurements were then repeated by driving all four cavities simultaneously in each of the modules, leading to the heat-load values reported in Table 2.21. The extensive temperature diagnostics implemented in the modules showed that the different behaviour in the coupler dynamic loads in the two modules was associated with a substantial temperature increase at the interconnection flange between the STF-2 couplers and the cavity port. The temperature rise originated at the 3 µm-thick Cu layer on the inner surface of the outer conductor. The measurements taken at S1-Global were instrumental in a redesign of the Quantum-Beam cryomodule couplers at KEK to use a different coating procedure and more performant thermal anchoring to reduce the static and dynamic heat losses.

Table 2.21
S1-Global RF dynamic heat-load measurements.

	Module C 4 cavities		Module A 4 cavities	
	resonant	detuned	resonant	detuned
Gradient MV/m	20.0	32.0	26.9	32.0
Total RF load, W	2.7	–	6.9	–
Coupler dynamic load, W	0.2	0.5	2.5	4.6
Cavity RF load, W	2.5	–	4.4	–

2.7.2 Thermal Performance of the European XFEL Prototype Module

The European XFEL has started the procurement of 100 cryomodules. All modules will be thoroughly tested for their RF and cryogenic performance at the Accelerator Module Test Facility (AMTF) in DESY before tunnel installation, and will yield a copious amount of data of interest to the ILC.

An update of all static heat-load evaluations for the European XFEL module design, integrating the minor changes introduced with respect to the Type-III TTF modules, has been performed at DESY [101] and compared to the thermal performance of the European XFEL prototype modules, assessed experimentally at the DESY CryoModule Test Facility (CMTB).

Table 2.22
European XFEL updated evaluation of static heat load.

Temperature level	Static heat load (W) Calculated	Measured
2 K	2.1	3.5-6
5-8 K	6-12	6-11
40/80 K	100-120	100-120

Thermal loads have been assessed and measured several times, under different operating conditions, as a function of the outer-shield temperature (which varies along the cryostring). The heat loads in

the 2 K region are evaluated from the mass-flow rate of the evaporated helium during the tests, while the loads on the 5 K and 80 K circuits are evaluated from the helium-coolant-flow conditions and cross-checked with the enthalpy response of the cold mass. A separate test with a dummy module was performed to separate the heat loads of the end/feed caps of the CMTB from that of the module.

Table 2.22 lists the updated heat-transfer evaluations (for current leads, power couplers, support posts, thermal radiation etc.) and the comparison with the measured values of the three prototypes, which are also shown in Fig. 2.50, along with the budget values foreseen by the refrigerator.

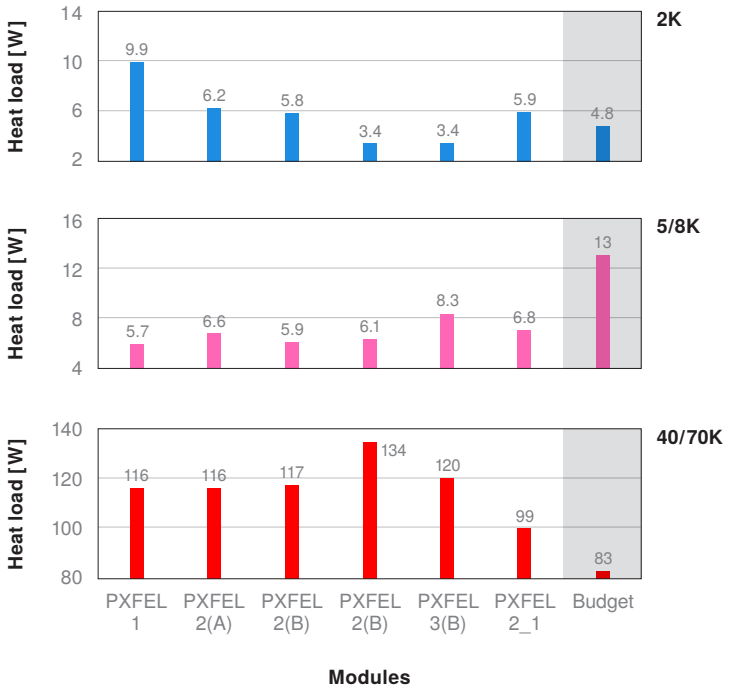

Figure 2.50
European XFEL prototype module heat-load measurements at CMTB, compared to the budget values.

Generally speaking, measured values agree with calculated values for the 5/8 K and 40/80 K circuits. The increase in heat loads in the outer shields during the PXFEL3 (A) test has been traced to an improper tuner-assembly operation, which caused a thermal contact. The lower 40/80 K heat loads shown by the PXFEL2_1 measurements seem to suggest a better performance of the new MLI blankets that have been used for this test.

The measured values for the 2 K environment deviate from the evaluations due to an underestimation of the cabling heat loads and, furthermore, varied due to inconsistencies in the installation. The high static loads of PXFEL1 have been traced to an incorrect layout of a prototype current lead.

As for the S1-Global measurements, the European XFEL experience shows that it is possible to predict thermal performance of cryomodules with reasonable error margins, but great attention needs to be paid to the details of the models, which need to include all heat-transfer mechanisms. Figure 2.50 clearly show also a training effect for the most sensitive 2 K environment, showing a decrease in time of measured heat loads. One of the crucial outcomes of the European XFEL AMTF test for ILC would be the confirmation of this trend for the testing of the series modules.

2.7.3 Cryogenic Thermal Balance

The activity in the Technical Design Phase has confirmed that the thermal behaviour of the module and its subcomponents can be reliably estimated with numerical models to explore design variants and simplifications so that design complexity and thermal performance can be balanced and to allow reliability-driven options to be explored. The European XFEL will also provide substantial experience from the AMTF operation with the series module testing in the coming years.

The baseline ILC TDR cryomodule is therefore almost unchanged from the description provided in the RDR, with a unique slot length of 12.652 m for the two main variants (nine-cavity module and eight-cavity-plus-quadrupole module) . The present baseline relies also on the use of a conduction-cooled split quadrupole, as discussed in the next section.

2.7.4 R&D on the Split Quadrupole

Superconducting linear accelerators need a number of cryomodules with superconducting quadrupole magnets for beam focusing and steering. Various superconducting magnet designs have been investigated. Nearly all are bath cooled by LHe and they need to be assembled with the string of superconducting RF (SCRF) cavities inside a clean room, leading to the risk of particle contamination of the cavity surfaces and to increased chances of cavity-performance deterioration. In contrast a splittable magnet can be assembled around the beam pipe after all SCRF cavities are installed and sealed inside the clean room. In this case the magnet will never enter the clean room and its installation will not lead to the risk of contaminating the SCRF cavity inner surfaces. The splittable quadrupole was designed and built at Fermilab and tested in a 4.4 K helium bath at the FNAL Magnet Test Facility (MTF).

Table 2.23
Specifications and parameters for the split-table quadrupole magnet.

Parameter	Value	Unit
Peak gradient	54	T/m
Integrated gradient	36	T
Peak operating quadrupole current	100	A
Magnet total length	680	mm
SC-wire diameter	0.5	mm
NbTi-filament size (vendor value)	3.7	μm
Cu:SC volume ratio	1.5	
Superconductor Critical current (5 T and 4.2 K)	200	A
Coil maximum field at 100 A current	3.3	T
Magnetic-field stored energy	40	kJ
Quadrupole inductance	3.9	H
Number of turns/pole in quadrupole coil	900	
Yoke outer diameter	280	mm

The main issue for the ILC quadrupole is to provide magnetic axis stability of 5 μm over a ± 20% field range. This requirement arises from the Beam-Based Alignment (BBA) technique. The magnetic and mechanical effects which correlate with the magnetic axis stability must be minimised.

Table 2.23 shows the specification and design parameters for the splittable quadrupole shown in Fig. 2.51a. The quadrupole has a vertical split plane and is assembled from two half cores having racetrack superconducting coils on magnet poles. The magnet halves are tightened to each other by stainless-steel bandage rings. This assembly is surrounded by Al thermal leads which have a good thermal contact with the cryomodule LHe supply line. The LHe line provides the cooling by conduction to this cryogen-free magnet [102].

The fabrication and test of a splittable quadrupole confirmed the design concept. Figure 2.51b shows the quadrupole on the vertical test insert ready for measurement in pool-bath mode at FNAL.

After training up to 110 A, the magnet reached 20% current margin, as shown in Fig. 2.52a; the specified peak gradient of 54 T/m was reached at 90 A [103].

Figure 2.51
Split quadrupole.

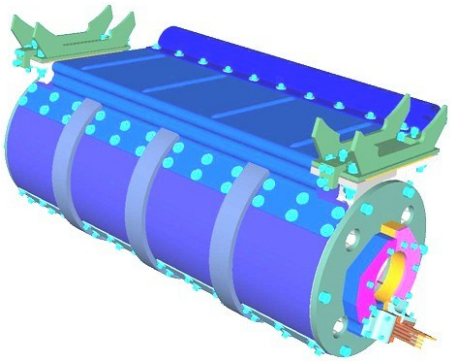

(a) Final assembly of the split quadrupole.

(b) The split quadrupole mounted on the insert of the cryostat.

Figure 2.52
Tests of the quadrupole.

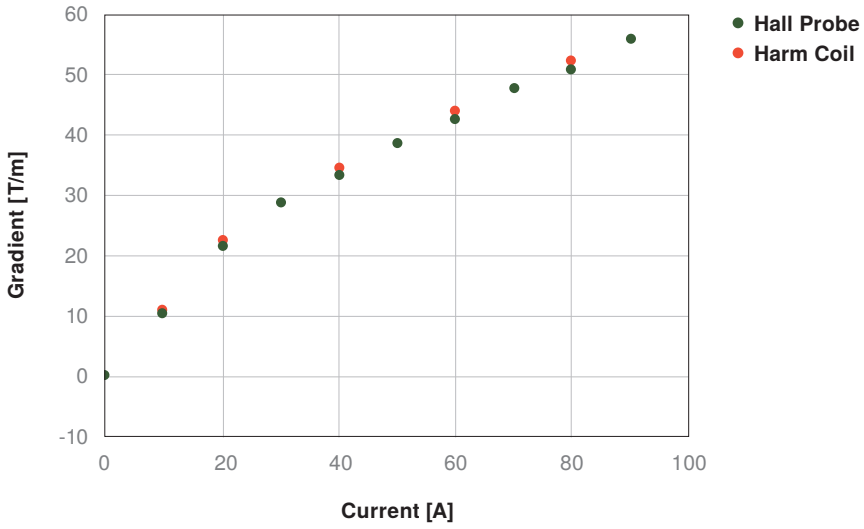

(a) The quadrupole gradient as a function of current.

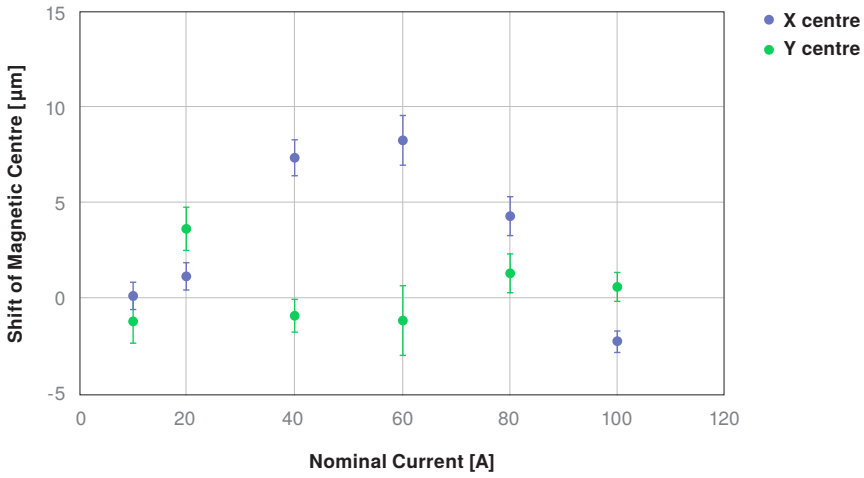

(b) The shift of the magnetic centre as a function of current.

The shift in the centre position of the quadrupole over a 20 % gradient change is shown in Fig. 2.52b as a function of the nominal operating current; it only slightly exceeds the specifications of 5 µm on the horizontal plane at currents in the 30–70 A range. More careful control of the yoke gap

size and uniformity may improve this. Future plans are to improve the magnet split-plane flatness to eliminate small gaps, and test again in a conduction-cooling mode.

2.8 RF Power Generation and Distribution

2.8.1 Overview of HLRF R&D

2.8.1.1 RDR RF System Design and TESLA R&D

The High Level RF (HLRF) system as described in the 2006 ILC RDR [3] is very similar to that developed for the TESLA linear collider design that was tested starting in 1997 at the DESY TESLA Test Facility (TTF), which is now called FLASH. The RF system features a 10 MW, high efficiency (65%), Multiple-Beam Klystron (MBK) that produces 1.6 ms pulses at a rate up to 10 Hz. For this application, three vendors developed tubes of somewhat different designs, of which two were successful to the extent that they have been adopted for use in the European XFEL Linac where they will run nominally at 5 MW but have 10 MW capability. Two horizontal-oriented MBKs are shown in Fig. 2.53. At TTF, the klystrons (both single and multiple beam) were powered with Pulse-Transformer style, 120 kV modulators with solid-state switches and 'bouncer' circuits for droop compensation (i.e., to offset the voltage decrease as the storage capacitors discharge). Finally, for the distribution of the RF power to the cavities at TTF, the waveguide components (e.g. power dividers, isolators and loads) were developed with industry [11].

Figure 2.53
Horizontally mounted MBKs; (left) Toshiba E3736, (right) ThalesTH1801.

2.8.1.2 ILC RF System Evolution

After the ITRP decision in 2004, KEK and SLAC/FNAL embarked on setting up their own HLRF test stations to support the SCRF infrastructure for STF at KEK and for NML at FNAL, respectively. SLAC also started a program to improve the modulator, klystron and RF-distribution designs to make them more versatile, more efficient and less costly.

During the Technical Design Phase after the RDR completion, two RF-system layouts in a single tunnel for the Main Linacs were proposed as cost-saving measures and presented in SB2009 [104]. The evolution and development of these proposals up to 2011 is described in the Interim Report on the ILC R&D Program [50]; the basic concepts are summarised below.

The Distributed RF System (DRFS) has all RF-system components located in a single tunnel, which has advantages for a mountainous site. Instead of trying to fit the RDR RF system in a single tunnel along with the cryomodules, smaller, lower power (800 kW) klystrons are used to feed two (for high-power upgrade) or four cavities (for low-power baseline) locally. The lower-power tubes should have a higher reliability to offset the much longer time to repair resulting from access to the tunnel now being limited to periods when the beams were off. The DRFS klystron features an

anode electrode that is voltage modulated to switch the tube to a 70 kV, droop-compensated supply. Assessment of availability, operability and maintainability were based on performance of similar types of tubes. The DRFS design and related R&D are described in more detail in Section 2.8.5. Though DRFS has many advantages for use in mountainous regions, it was estimated to cost more than the RDR solution. After the introduction of the large Kamaboko-style tunnel for a mountainous site, DRFS was abandoned, as this tunnel includes a thick partition wall that allows access for repair to the RF system during operation. Instead, the Distributed Klystron System (DKS) was adopted, which is similar to the RDR RF-system layout (i.e. with 10 MW MBKs locally driving multiple cavities), as described in Section 3.8.

The Klystron Cluster System (KCS) has all klystrons and associated power supplies located in a series of ten surface buildings along the Main Linacs. In each building there are two sets of typically 19 klystrons (for the low-power baseline) or 29 klystrons (for the high-power upgrade) whose power is combined in a 0.5 m diameter, pressurised aluminum circular waveguide. These two waveguides extend down and along the accelerator tunnel (one upstream and one downstream) where power is tapped off periodically to feed groups of 26 cavities (3 cryomodules). KCS is particularly suitable for a flat site. The KCS concept and related R&D are described in Section 2.8.6.

2.8.2 European XFEL RF-System Evolution

The RF system for the European XFEL has also evolved since the original version that was to be part of the TESLA Linear Collider. A single tunnel was always assumed for the European XFEL with the RF system split between the tunnel and surface buildings. That is, 10 kV pulse generators and droop compensation circuits for the modulators are located in clusters in surface buildings, which allows easy access for repair. They connect through cables (four per unit) that extend along the linac tunnel to 1:12 pulse transformers that drive 10 MW MBKs. The RF power from each klystron is then distributed to 32 cavities.

After the ITRP decision, DESY and collaborators continued to develop the pulsed transformer modulators, multi-beam klystrons and power-distribution components with both the European XFEL and ILC in mind. In particular, the Modulator Test Facility (MTF) was constructed at PITZ and RF system testing has been on-going there since 2006. However, two major changes have since been incorporated in the European XFEL RF-system design. One was to use a Pulse Step Modulator in which several switching modules are connected in series to generate the 10 kV pulses that drive the transformers in the tunnel. This design allows better control of the HV waveform shape and costs less than the Pulse-Transformer approach. Figure 2.54 shows photos of both types of modulators.

Figure 2.54
Modulator development for the European XFEL.

(a) Bouncer-type modulator

(b) Thomson pulse-step modulator in the MTF hall

The other change addresses the power distribution to the cavities. For TTF/ FLASH, the power-distribution system includes back-terminated power splitters and 3-stub tuners to control the cavity phase and loaded Q. As this system is fairly bulky, has no provisions for changing the power split to the cavities and the cavity phase is hard to tune, a more versatile and streamlined waveguide distribution system that can come attached to the cryomodules during installationwas adopted for

the European XFEL. It features Asymmetric Shunt Tee (ASTs) which are non-back-terminated power dividers that can be readily customised before installation to achieve the desired power division based on the cavity performance measured in the test stands. Compact phase shifters are also used instead of the 3-stub tuners (the loaded Q can still be controlled through the coupler antenna position). Figure 2.55 shows such a distribution system attached to a cryomodule [105]. Commissioning of the European XFEL linac is expected to start in 2015.

Figure 2.55 European XFEL-type waveguide distribution tested on the cryomodule ACC7 at FLASH.

2.8.3 Radiofrequency System R&D for the ILC

This section describes the various RF-system R&D that has been carried out during the past eight years for the ILC, and the facilities where the RF systems have been used as part of a larger SCRF linac R&D program. These efforts include the development of 120 kV Marx modulators, 10 MW sheet-beam klystrons, 800 kW, high-availability klystrons, a variety of variable power dividers and a clustered klystron scheme for delivering RF power from surface buildings to the tunnel below. Overall, the programme has gone a long way to demonstrating that the RF system requirements for the ILC are achievable.

2.8.3.1 RF Systems at ILC Test Facilities

At KEK, the Superconducting Test Facility (STF) was started in 2005 to test SCRF technology including RF systems for the ILC. It has seen various successful development stages, namely STF-0, STF-1 and the S1-Global experiment; the Quantum-Beam project and STF-II will follow and include beam acceleration. Three RF stations were developed at STF that all use the Pulse-Transformer-style modulators. Two klystrons, a 5 MW Thales TH2104A/C, and a horizontally mounted 10 MW Toshiba Multi-Beam Klystron (MBK), were procured and tested in this station [106], see Fig. 2.56.

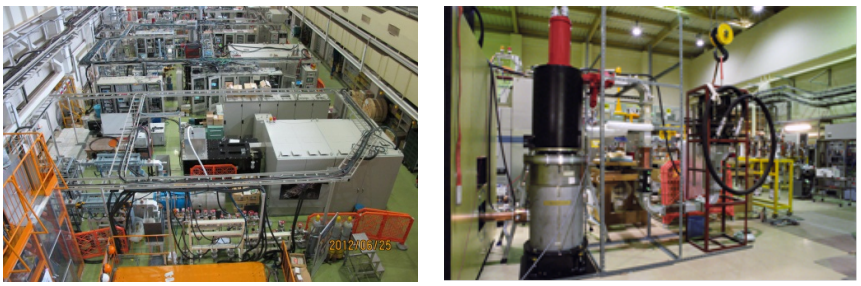

(a) Hall **(b)** Klystron

Figure 2.56 STF test station in KEK.

At the New Muon Lab (NML) at FNAL, a SCRF test area was also constructed for a similar purpose. It includes older style RF-system components (Pulse-Transformer modulators and commercial

5 MW klystrons and waveguide components) and R&D components provided by SLAC (8-cavity cryomodule RF-distribution systems and eventually a Marx Modulator). Recently, FNAL also acquired a horizontally mounted 10 MW Multi-Beam Klystron from CPI.

At SLAC, two L-band RF stations were built in End Station B for the ILC RF system program. The first uses a SNS High-Voltage-Converter Modulator to drive a 5 MW Thales TH2104C klystron. It has been used for various components tests (waveguides, couplers, windows, a 5-cell cavity, RF distribution systems and initial tests of the klystron cluster scheme). The second system is meant to be as ILC-like as possible and includes a state-of-the art control system. As discussed below, it is currently configured with the P1 Marx Modulator driving a vertically mounted 10 MW Toshiba Multi-Beam Klystron. Recently, the power from one arm of the MBK has been used to test a 40 m-long circulator waveguide and bend for the KCS program. It will be upgraded with the P2 Marx modulator during 2013 and another MBK will be delivered.

2.8.3.2 Marx-Modulator R&D

To drive the 10 MW klystrons that had been developed for the TESLA linear-collider design, a Pulse-Transformer-style modulator was developed by FNAL and industrialised by DESY. They are specified to produce 120 kV, 140 A, 1.6 ms pulses at up to 10 Hz. For these modulators, storage capacitors are charged to 11 kV between pulses and then connected to the primary of a 12:1 transformer via solid state switches (IGCTs initially and later IGBTs) to produce the HV that drives the klystron. A 1 kV resonant 'bouncer' circuit was included in series in the primary circuit to offset the voltage droop of the storage capacitors as they discharge. While this design had proven robust (10 had been built by 2005), they required a large oil-filled transformer and the pulse shape could not be finely controlled.

With the emergence of affordable, low-loss, high-power (MW) transistor (IBGT) switches in the late 1990's and early 2000's, various adder-modulator topologies became viable that eliminated the need for traditional transformers. During this period, SLAC developed inductive adder modulators for the NLC klystrons that consisted of stacks of ferrite cores that were each driven in parallel via IGBT switches. A common, multi-turn secondary then added the induced voltages to drive high-voltage (500 kV), short-pulse (1.5 µs) klystrons. A capacitive adder (aka Marx Modulator) program was started at SLAC as well for the NLC, and with the ITRP decision in 2004, the program was redirected to designing modulators for the ILC where the inductive approach is not feasible given the long (1.6 ms) pulses required.

The operational modes and basic Marx circuit without droop compensation are illustrated in Fig. 2.57. One advantage of this scheme is the modular design, which both simplifies fabrication and improves reliability as spare modules are included that automatically turn on if others fail. Also, these modules, which are pulsed up to 120 kV, can be supported and connected in ways that does not require immersion in oil to suppress arcing. For cooling, a closed forced-air system suffices. The biggest advantage is that no large, oil-filled transformer is required (such a transformer would in any case become prohibitive in size if the pulse length needed to be significantly increased).

As part of the SLAC ILC RF program, two Marx Modulators (P1 and P2) were successfully built and tested during the past eight years, as discussed below. More recently, two Marx Modulators were funded as part the US SBIR program: one from ISA Corporation, which was never fully completed, and one from Diversified Technology Inc. (DTI), which was built, tested briefly at DTI at low average power and is currently at KEK awaiting full evaluation. The main design features of these four modulators are listed in Table 2.24.

The P1 Marx Modulator [107] consists of sixteen, 11 kV modules and a single Vernier Marx module in a cantilevered arrangement of corona-shielded circuit boards that connect to a G10 backplane, which runs along the centre (see Fig. 2.58 – the far end is grounded and a 120 kV output cable

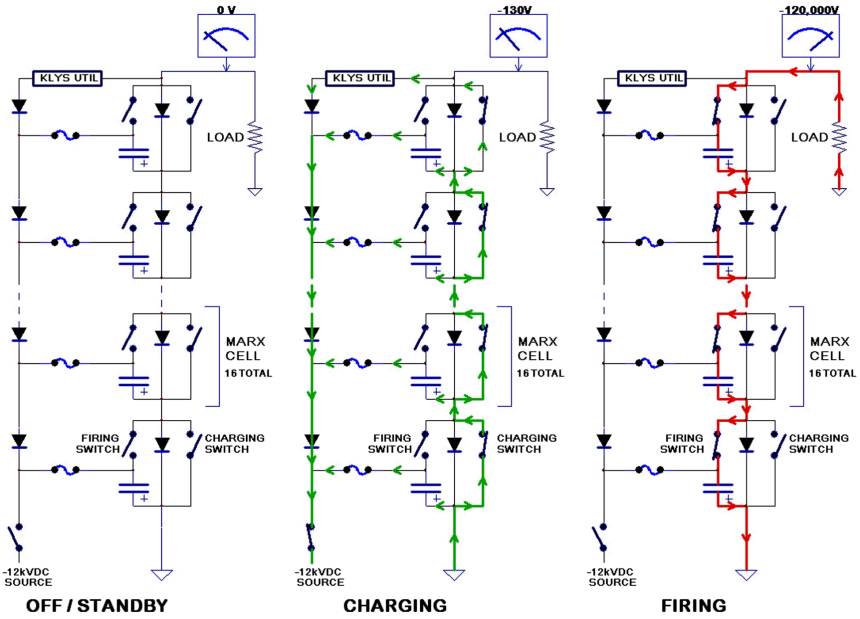

Figure 2.57 Block diagram of Marx Modulator with illustration of the basic mode of operation. The modes off/standby, charging and firing are illustrated schematically (from left to right)

Table 2.24 Variants of the US DOE SBIR-funded Marx-Modulator research

	SLAC P1	DTI	ISA Corp.	SLAC P2
Cell voltage	11 kV	6 kV	3.5 kV	3.75 kV
Number of cells	16	20	42 (7 delay)	32
Redundancy	Vernier (16) 1.2 kV + delay	Correction cells (16) 0.9 kV	Vernier (16) 0.5 kV + delay	Regulated cell (PWM correction)
Regulation	N+1	N+3	N+1	N+2
Status	full test completed	SLAC/KEK for MTBF test	Voltage test completed	full test completed

connects to the near end). The triggering sequence is designed to promptly turn-on eleven modules, then stagger turn on the remaining five modules to coarsely compensate the storage-capacitor droop. The Vernier Marx module (with sub-modules charged to 1 kV) staggers the sub-module turn-on and turn-off to further regulate the output to the specified 0.5%. The waveforms in Fig. 2.59a illustrate this droop compensation (also shown is output power versus modulator-voltage measurements over a running period of several thousand hours).

Figure 2.58 SLAC Marx Modulator and test stand in which the modulator (in a electrically shielded enclosure in the background) drives either a water load (cart in foreground in which the modulator HV is shown connected through the black cable) or a 10 MW Toshiba Multi-Beam Klystron (located in the black lead-lined 'tower' that sits on top of an oil tank).

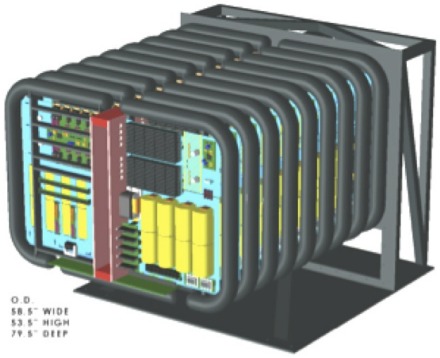

(a) SLAC P1 Marx-Modulator cell arrangement.

(b) P1 test stand

Until recently, the P1 had been undergoing lifetime testing, driving a 10 MW Multiple-Beam Klystron (MBK) as shown in Fig. 2.58. The modulator has been operated for nearly 6000 h, although about half of this time at half pulse width after it was discovered that the aluminised polyethylene

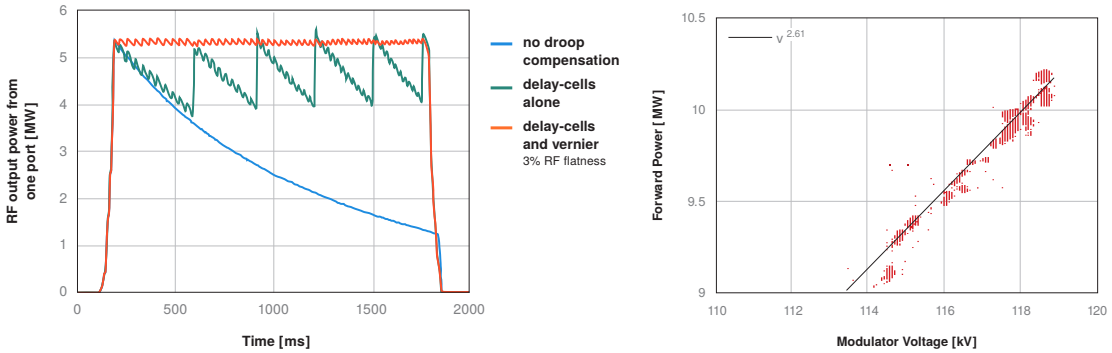

(a) Droop compensation.

(b) Output power vs voltage of the SLAC P1.

Figure 2.59. SLAC P1 Marx-Modulator tests.

storage capacitors degraded with full-pulse but not half-pulse operation. The capacitors were replaced recently with more robust zinc-based versions but they have not run long enough at full pulse width to verify that the issue has been fully resolved (bench tests were not conclusive). Damage from corona arcing on the P1 backplane was also discovered and a fix was implemented. For the klystron, there have only been a few faults (window and gun arcs) at full power (10 MW) operation.

Building upon the experience with the P1 Marx, the SLAC P2 Marx was designed to include several improvements [107]. It has 32 modules 3.75 kV where each module individually regulates its output via a buck converter, including compensating the capacitor-voltage droop. If any two modules become inoperable, they can be bypassed by increasing the applied charging voltage or turning on spare modules, allowing the modulator operation to continue. In addition, the modular design allows better utilisation of high-volume manufacturing techniques, and there is no arraying of solid-state switches within a module, simplifying the control and protection schemes. Finally, the module layout is much different (see Section 3.6.1).

The SLAC P2 Marx utilises a hierarchical control system with a system-level application manager and module-level hardware manager [108]. Communication is accomplished using Gigabit fibre-optic Ethernet through a commercial switch. The application manager coordinates the state control of the modulator, handles external interlocks, interfaces with DC chargers, archives diagnostics, processes prognostic routines, coordinates module timings and implements the regulation scheme. The module hardware managers control the state of the modules, implement module IGBT switching routines, gather and transmit diagnostics, and provide fault protection. Each hardware manager incorporates twelve 12-bit, 1 MS/s ADCs, which monitor module voltages, currents, and temperatures. A feedforward algorithm is used to generate very flat pulses – a 0.05% flatness has been achieved when operated with a water load (see Section 3.6.1).

The P2s ability to survive an arc-down at full output power without damage to components has been successfully demonstrated, along with the requirement for klystron protection, namely that less than 20 J be deposited in the load. Since its storage capacitors discharge one-half as much as those in the P1, the lack of capacitor damage seen when running the P1 at half pulse width would indicate that the P2 capacitors should not degrade. The P2 has not yet been tested at full average power but will be run long term to full specification (driving the 10 MW MBK) starting in 2013. It has been adopted for the ILC Linacs to replace the Pulse-Transformer modulator as it is less expensive, has better performance ($< 0.1\,\%$ pulse flatness) and has no large transformers.

2.8.3.3 Sheet-beam Klystron

As a plug-compatible alternative to a multi-beam klystron, the development of a L-band sheet-beam klystron (SBK) was pursued at SLAC, with the same 10 MW, 1.6 ms, 5 Hz specifications, operating at the same voltage and beam current. The goal was a less expensive and more compact RF power source with potentially greater efficiency [109]. Figure 2.60 shows the considerable progress made in the design, which uses a periodic-cusp magnet-focusing scheme and a 40-to-1 beam aspect ratio. Unfortunately, after discovery through 3-D simulations of strong trapped-mode-driven beam instabilities [110], it was realised that a stronger solenoidal focusing scheme would be needed to produce stable operation. Since this would be make the tube less competitive as an alternative to the MBK, the program was discontinued after a gun with an elliptically-shaped cathode was tested.

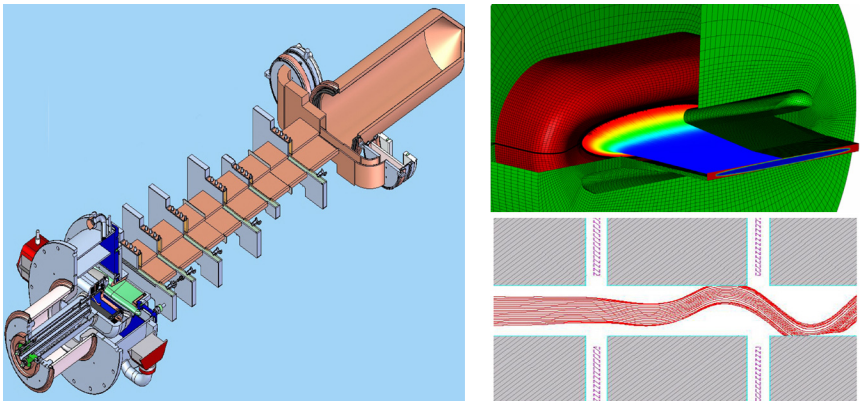

Figure 2.60 Sheet-beam Klystron design and MICHELLE tracking-code simulations

(a) Sheet-beam klystron design

(b) Simulations of the focused sheet beam leaving the cathode, and of the beam hitting the wall due to instability oscillations

2.8.4 Waveguide Components R&D

2.8.4.1 Waveguide Components

The 1.3 GHz L-band rf power needed by the cavities to accelerate the beam is delivered to their fundamental power-coupler inputs through nitrogen-filled aluminium WR650 (16.51 cm × 8.255 cm) rectangular waveguides. Simple pieces such as straights, bends, Ts and semi-flexible bellows can generally be customised by waveguide vendors. However, a number of functions need to be accomplished in the waveguide circuit that require special components. Some of these were developed for FLASH/European XFEL and could be directly used for the ILC design. These include isolators, loads, directional couplers and in-line phase shifters, all available from specific vendors. Even for these, some modifications and variations were pursued, while for other functions, particularly power division, new ILC components had to be developed.

The isolator assumed in the RDR is based on a design, still used by DESY, that can handle 400 kW peak power with full reflection at any phase and 8 kW average power, with fairly low-loss —approximately 0.1 dB [3]. In particular, a version was developed that incorporates directional coupler pickups in the input and load ports, eliminating the need for a separate component. In order to explore cost efficiency, a comparable isolator was developed by a Japanese company and tested in the S1-Global test.

In the RDR design, RF phase was adjusted via a three-stub tuner. This was superseded by a DESY phase-shifter design using a motorised movable side wall inside a short WR650 section to vary the guide wavelength. This gives a range of more than 100° with a reflection below −23 dB. At KEK, a variant phase shifter was developed that uses a movable floating pontoon to change the effective

phase length, also allowing a wide range of cavity-phase adjustment.

The klystron output windows require pressurisation, whereas the cavity-coupler input boxes are not pressurisable. Therefore a waveguide pressure window is needed somewhere in between. Although a commercial pillbox window with rubber seals is available, SLAC developed a simpler, more compact, radiation-hard version. Its main component is a block of ceramic with transverse dimensions equal to that of the waveguide and with a thickness (few centimeters) to achieve an RF match. It is electro-plated around its perimeter with a centimetre-thick layer of copper and, after machining, fits into an aluminum flange frame.

All pieces of waveguide upstream of the window, in which the power is higher, are pressurised to 300 kPa with dry nitrogen, which requires that the waveguide have thicker walls and a more robust construction. To join WR650 waveguides, whether pressurised or not, aluminium gaskets are used at SLAC and FNAL. They have partially recessed rubber rings on each side to provide a pressure seal and the inner edges have raised, dimpled surfaces to assure an RF seal. At KEK, rubber inserts are placed in flange grooves to seal pressure and the flanges are machined flat at the 25–50 µm-level to achieve good electrical contact.

2.8.4.2 Power-Split Adjustment

The one area that called for a focused R&D effort was the development of RF power dividers, which are required for distributing RF from a given source to multiple cavities. For the RDR, it was assumed that all cavities would get equal power; fixed waveguide splitters of various increasing couplings were to be used in linear distribution lines, as they had been at DESY. Also, 50 % power dividers (i.e. 3 dB splitters) were required to feed pairs of cavities in the RF distribution systems that SLAC built for FNAL, where the goal was to achieve better isolation of the output ports than that typical from commercial 3 dB splitters. For this purpose, SLAC designed and built a four-port 3 dB H-hybrid [111] via dip-brazing with highly isolated output ports, as seen in Fig. 2.61a.

Figure 2.61 Power-distribution systems developed at SLAC.

(a) A two-feed unit of PDS1, incorporating a VTO and H-hybrid, installed on a cryomodule at NML.

(b) A two-feed unit of PDS2, incorporating a VPD, ready for high-power testing at SLAC.

When it was decided to allow a range of cavity operating gradients to be accepted. increasing the cavity yield, R&D was done on tailoring the power distribution so each cavity could reach its maximum sustainable gradient. As noted above, the European XFEL project also added provisions for this purpose. For the ILC, three 4-port devices were developed, each of which operates with a load on the unused port at the input end to back terminate it. They are summarised below – the latter two have been adopted for use in the local RF-power-distribution system for the ILC.

The variable tap-off, or VTO [112], shown in Fig. 2.62, was developed first to deal with the

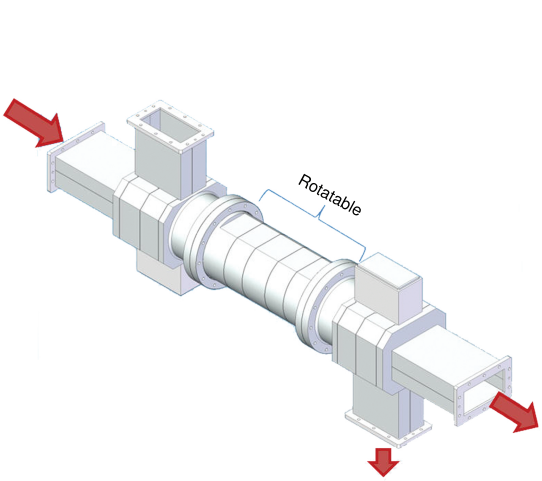

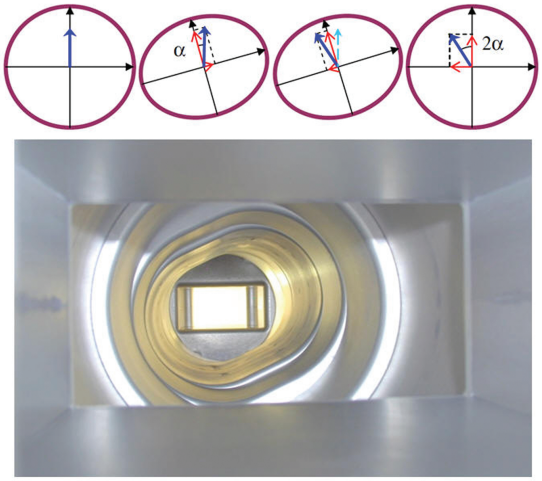

(a) VTO Assembly. The rotatable central section allows adjustment for any coupling ratio

(b) Above: polarisation rotation along the VTO; one component slips in phase by 180 degrees relative to the other by the time circular symmetry is restored. Below: photograph looking through the VTO

Figure 2.62. Variable Tap-off power divider (VTO)

gradient spreads in the FNAL cryomodules. This 4-port device has three pieces: each end consists of a 3-port section whose two orthogonal rectangular WR650 ports each couple into a different polarization of TE_{11} in the circular third port; the central section has round ends step-tapered to an oval cross-section at its centre. The latter serves basically as a mode rotator; its orientation determines how power entering a given port at one end of the VTO is divided between the ports at the other end. It can be adjusted to provide any desired split without affecting the output phases. However, since the adjustment requires opening the waveguide and rotating the centre section, it would require an access to the accelerator tunnel if used for the ILC.

Figure 2.63
a) the VPD (Variable Power Divider), composed of folded magic-Ts and U-bend phase shifters (with offset spacers), and b) the U-bend phase shifter, with motorised feed-through-supported trombone-like inner waveguide.

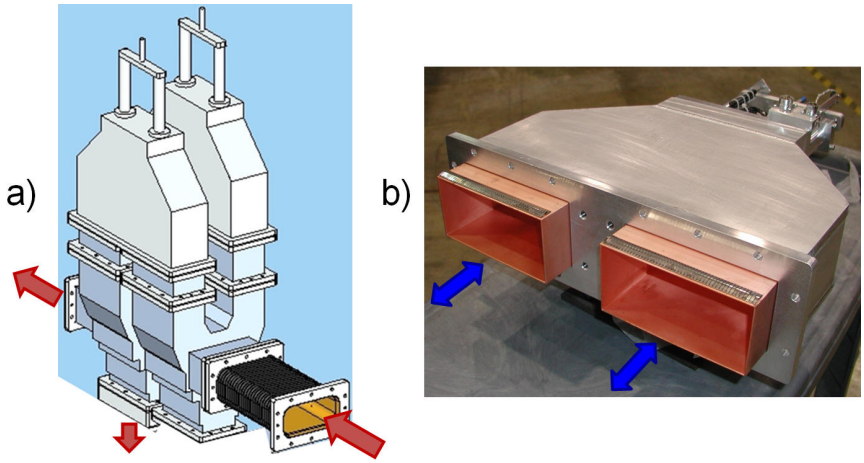

The variable power divider (VPD) was developed to provide the same functionality as the VTO but with remote adjustability. Illustrated in Fig. 2.63, it consists of a pair of folded magic-Ts connected by trombone-like U-bend phase shifters. The latter component, also pictured, was developed at SLAC for this application. It contains a thin-walled mitred H-plane U-bend in copper-plated stainless steel that fits inside WR650, with springy finger-stock on the outer broad-wall edges for electrical contact. Housed in an aluminium outer shell for pressurisation, this bend can be moved by motorised feed-throughs attached to its back. The RF phase shift through the bend is thus adjusted by a change of path length, rather than a change in guide wavelength. Tests of a prototype showed ~ 0.02 dB loss and reflections of -51–-36 dB over a phase range of 120° . Moving the two U-bend phase

shifters in opposite directions keeps the combined VPD output phases fixed, but allows a full range of amplitude variation. The VPD and VTO have been tested to power levels of 3–4 MW with 1.2 ms pulses without breakdown.

Finally, the variable H-hybrid was developed in parallel at KEK. This four-port device is based on the SLAC H-hybrid, with a pair of movable pontoons introduced in the dual-moded interaction region to provide coupling variation by affecting phase lengths, the same innovative mechanism used in the KEK phase shifter. This scheme provides a wide range of adjustment in the power division ratio, but the output phases are also affected as the amplitudes are changed. The variable H-hybrid is a relatively simple and cost-effective device. A schematic drawing and simulation results are shown in Fig. 2.64.

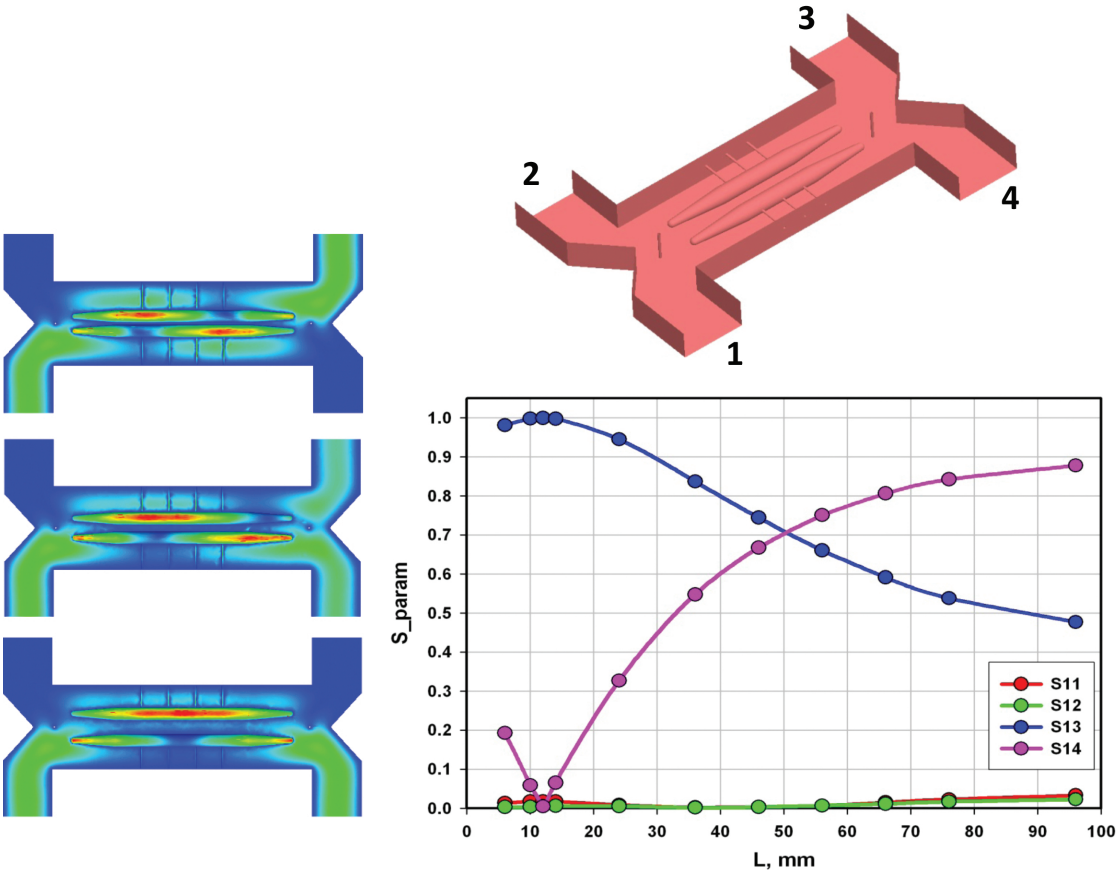

(a) Simulated electric field plots illustrating power split variation mechanism in the Variable H-Hybrid.

(b) Model and scattering parameters as functions of pontoon position for the physically shorter not-full-range design.

Figure 2.64. Variable H-hybrid.

2.8.4.3 RF Power-Distribution Systems

Two full-cryomodule (8-cavity) power-distribution systems have been built, high-power tested and delivered by SLAC to FNAL for use in the NML SCRF facility. The first uses the VTO to allow the power to be adjusted to pairs of cavities. The power out of each VTO was split through the SLAC 3 dB H-hybrid with the idea that tests without isolators on each of the cavity inputs could be done. In this case, the reflected power from the two cavities goes to the load on the input side of the hybrid (such operation was subsequently shown to work reasonably well at STF, see Section 2.8.5). Additional components in the system include isolators, bends, loads, air-to-air windows, phase-shifters, directional couplers, and semi-flex guides to connect to the cavity-coupler boxes. Also a 5 MW load is included for the unused power that passes through the four VTOs. A second full-cryomodule system

followed with the VTO replaced by the VPD, providing remote control of the power division albeit still by pairs. It also substituted a T-waveguide for the H-hybrid to reduce cost (The ILC eventually decided the cavities would be feed individually, not in pairs, so the idea of eliminating the isolators was abandoned). Figure 2.61 shows a 2-cavity unit of each system on its support frame.

At KEK, two types of RF-power-distribution systems were built and tested, a RDR-style linear type and a *3 dB hybrid tournament* tree type, each of which power a 4-cavity cryomodule. These were used for the S1-Global test in 2011 [7] at the Superconducting Test Facility (STF). With the latter distribution method, the isolators connected to each superconducting cavity could be eliminated as discussed above. Some results of the tests are described in Section 2.8.5. A schematic drawing of the power-distribution system and a drawing of the layout are shown in Fig. 2.65.

Figure 2.65
STF Power-distribution system in the S1-Global test at KEK.

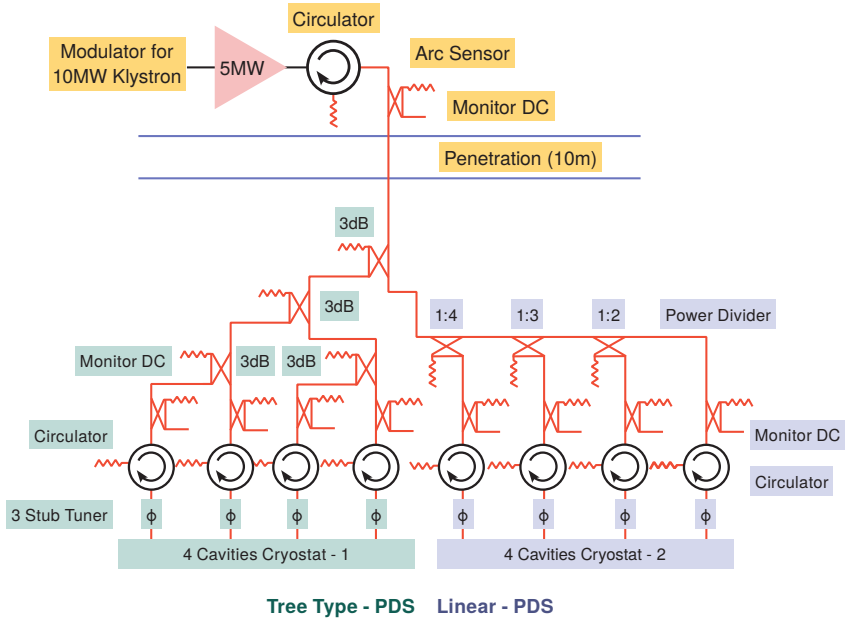

(a) Schematic

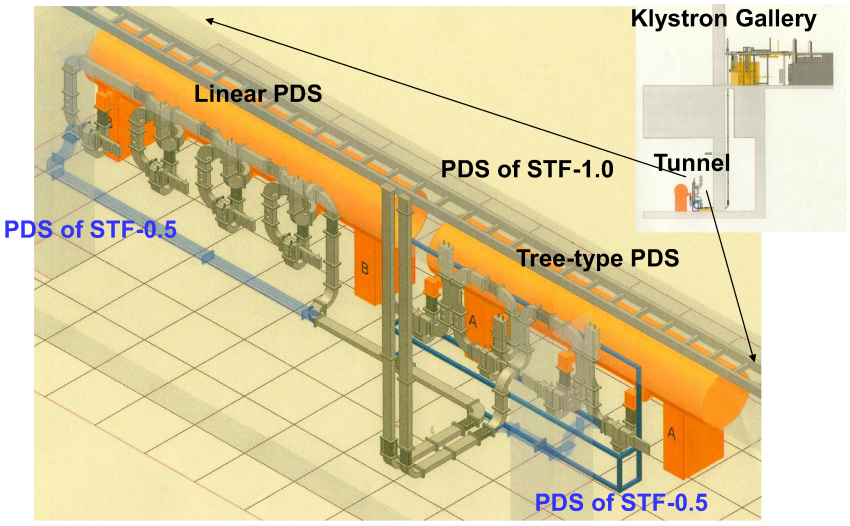

(b) Layout

2.8.5 R&D of the Distributed RF Scheme (DRFS)

A Distributed RF System (DRFS) suitable for a single-tunnel main linac has been designed and studied [50, 104]. The key idea was to produce lower-power, higher-reliability klystrons so availability would remain high given the limited access to the klystrons in a single-tunnel configuration. However, the klystron and modulator produce heat dissipation in the accelerator tunnel and protect the control devices from radiation damage.

For the DRFS design, an 800 kW klystron would power two cavities with the high-power upgrade and four cavities for the low-power baseline design. To reduce cost and save space, the possibility of eliminating the isolators was also considered. At KEK, the smallest functional unit of a DRFS device, including modulator and klystron, were manufactured and tested in the S1-Global experiment [7]. The results and the remaining R&D task for the DRFS klystron are described in the following.

The DRFS klystron is a modulated-anode-type klystron which has an output capability of 800 kW at an applied voltage of 67 kV, pulse width of 1.5 ms and a repetition rate of 5 Hz. Four DRFS klystrons were manufactured and two klystrons were successfully operated in the S1-Global experiment. Figure 2.66 and Fig. 2.67 show the performance of the DRFS klystron and a picture of the S1-Global operation, respectively. to achieve high availability, the DRFS klystron uses permanent-magnet focusing (Fig. 2.67b), which allowed for the elimination of the power supply and cooling system [113]. Ferrite material has been used for economic reasons; the test was carried out in the summer of 2012.

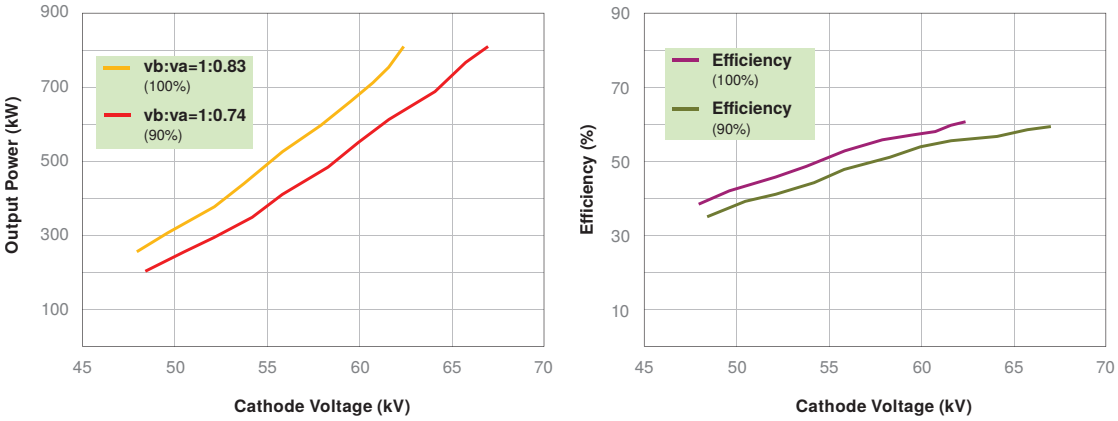

(a) Measured output power as a function of cathode voltage

(b) Measured efficiency as a function of cathode voltage

Figure 2.66. Performance of Toshiba DRFS Klystron powered by Marx Modulator

A prototype pulse modulator for the DRFS klystron has been manufactured at KEK, which consists of a DC power supply and a modulation-anode pulse modulator. Its function was tested in the S1-Global experiment. Since the prototype only supported a minimum set of functions, several components remain to be developed and tested. This includes development of a cost effective crowbar circuit and a gap switch, development of the sag-compensation circuit other than bouncer-type so that Marx-type circuits can be applied and development of a reliable HV relay to detach the klystron from the HV line in case of klystron failure. These developments are no longer pursued after the decision favouring another RF distribution scheme.

The power distribution scheme (PDS) of the DRFS is inherently simple. The power from the klystron is divided into two (two feed) or four (four feed) fractions. When the power load for cavities is paired (by selection) the expensive isolator can be eliminated. Reflection from the cavities and interference between the waveguide branches raises concerns for the LLRF feedback system in this case. Nonetheless the approach without isolators was tested and evaluated in the S1-Global experiment. A stable vector-sum operation was successfully established and the Q_L diagnostics at the cavity worked

Figure 2.67
Picture of Toshiba DRFS Klystron powered by Marx Modulator

(a) DRFS klystron in the S1-Global experiment

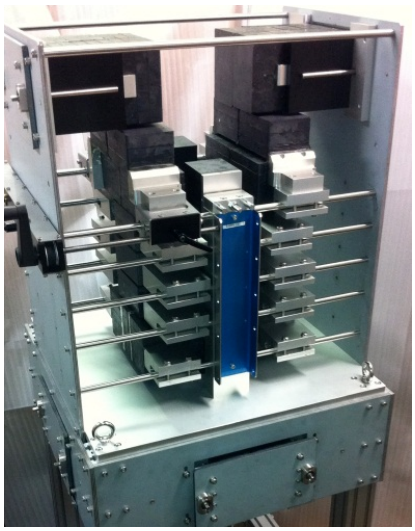

(b) Permanent magnet for beam focusing in the DRFS klystron.

well in the two cases of low reflection (VSWR $\sim$ 1.1) and large reflection (VSWR $\sim$ 3) under varying detuning. Figure 2.68 shows the characteristics of time vs. field gradient and Q_L diagnostics for operation without circulators.

Figure 2.68
Result for operation without a circulator in the S1-global test.

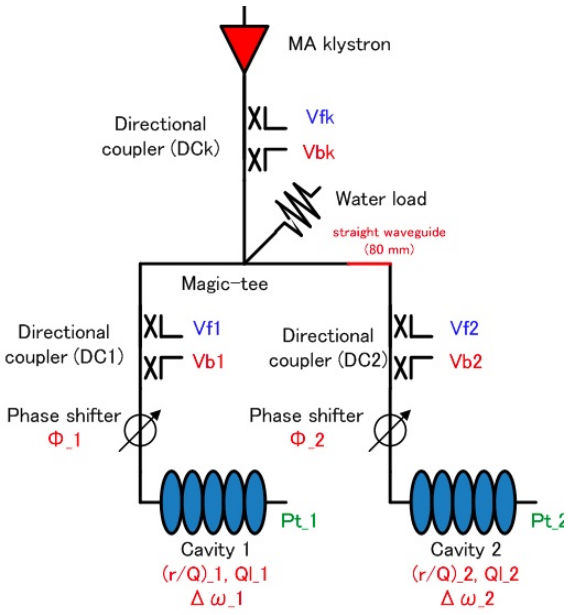

2.8.6 R&D of the Klystron Cluster RF Scheme (KCS)

In the wake of the post-RDR decision to eliminate the parallel utility tunnel that was to have housed the powering equipment, one of several single-tunnel solutions that emerged was the Klystron Cluster Scheme (KCS) [96], in which RF production is moved to the surface. Unlike in the RDR and current DKS option, where it is brought down as AC power, or the European XFEL, where it is brought down as DC power to underground klystrons, with KCS, the power for accelerating the beam is transported between the surface and the tunnel as RF. This approach follows the example of the SLAC linac, which served the only previous linear collider, the SLC. The differences arise both from having to accommodate a deep-bored (as opposed to cut-and-cover) tunnel and from the need to minimise surface impact over a much larger footprint. Thus the idea of clustering was adopted. Power from

groups of approximately 20-30 klystrons is combined into a single low-loss, over-moded waveguide and transported down to and along the tunnel to power approximately a kilometre of linac. At $\sim$ 38 m main linac unit intervals, partial power is siphoned from this main waveguide in 10 MW decrements, to be distributed to 26 cavities, as if from a local klystron.

2.8.6.1 Main Waveguide, Bends and Tap-offs

For low transmission loss and robustness against RF breakdown, an over-moded, 0.480 m-diameter circular waveguide (WC1890), operated in the TE_{01} mode, was chosen as the main high-power RF conduit. This azimuthally symmetric mode has the lowest loss and no electric fields terminating on the wall. Pressurisation with dry nitrogen further suppresses breakdown, so that peak powers of up to 300 MW might be transmitted. Minimising mode conversion requires millimetre-scale tolerances on radius, roundness and alignment, and straightness tolerances of half a degree. A flange joint or bellows is needed that can provide sufficient longitudinal flexibility to take up thermal expansion locally while maintaining concentricity and straightness.

Tapping partial RF power into and out from the circular TE_{01} mode transmission waveguide in a compact way, without breaking the internal symmetry, presented a special challenge. For this, a novel waveguide component was invented, the coaxial tap-off, or CTO [96]. In this device (see Fig. 2.69), a diameter step mixes TE_{01} with TE_{02}. Reintroduction of a wall at the original diameter divides the interior from a coaxial region. Because the two modes beat, the longitudinal distance between the step and the inner wall determines the power-split ratio, allowing the multiple couplings needed with minor design change. A small ridge at the input suffices to cancel any reflection. Power in the inner region continues on as TE_{01}; the tapped-off coaxial TE_{01} power in the shorted outer region is extracted through several apertures into a rectangular waveguide encircling it and thence through two radial WR650 ports in a wrap-around configuration [114].

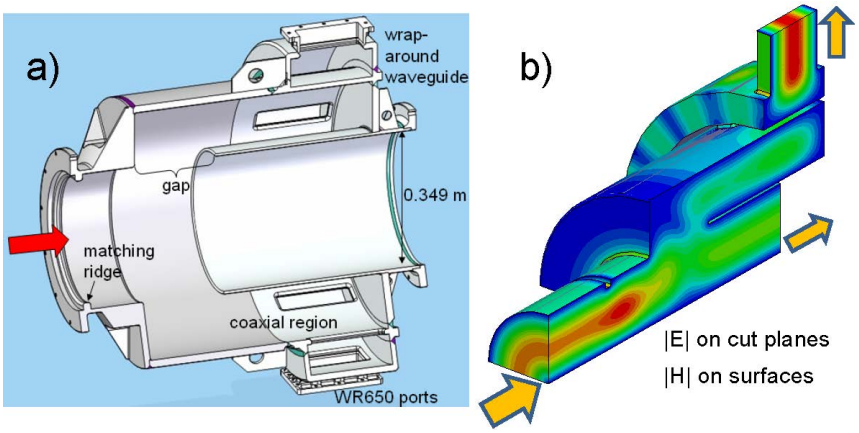

Figure 2.69 a) Cutaway and b) Simulated field patterns of a Coaxial Tap-Off (CTO), designed to extract (inject) fractional RF power from (into) a flowing TE_{01} wave in the circular KCS main waveguide.

To bring the RF down to the tunnel, bends are required. Bending in an over-moded waveguide is non-trivial, as geometrical changes tend to scatter power into parasitic modes. A special L-band TE_{01} bend, illustrated in Fig. 2.70 has been developed at SLAC. It includes two stepped transitions between a circular and an over-moded rectangular cross section, designed to map circular TE_{01} into a pure TE_{20} rectangular mode [115]; the actual bending is accomplished with a swept arc in the rectangular guide that restores the incoming mode after mixing with TE_{10}.

Both the bend and the CTO have 0.349 m diameter ports, somewhat smaller than the main waveguide. They interface with the latter through a simple matched double-step taper to 0.49 m.

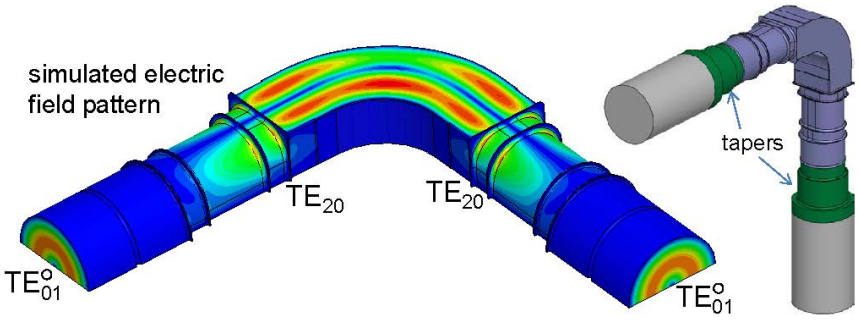

Figure 2.70
Overmoded bend for the circular TE_{01} mode KCS main waveguide. Mode-converting sections allow the actual bending to be done in the rectangular TE_{20} mode.

2.8.6.2 Experimental Program

A pair of 3 dB CTOs and step tapers were fabricated and a $\sim$ 10 m run of the KCS circular waveguide, in four sections, was constructed at SLAC. With proper depth shorting caps, the CTOs could be used as launchers for a successful transmission test using a Thales 5 MW klystron. Since a full-power transmission test is not feasible, comparable field levels were achieved by resonating the big pipe with one end blanked off and the shorting cap of the remaining CTO adjusted for near-critical coupling. Building up forward and backward waves to the 75 MW level gave peak field values equivalent to a single 300 MW wave.

Recently, a longer, 40 m run of WC1890 has been assembled (see Fig. 2.71) and a prototype of the TE_{01} bend has been built. The latter, unavoidably having high surface electric fields (2–3 MV/m), is the bottleneck of the whole scheme. Resonant testing was performed using a SLAC Marx Modulator and a Toshiba MBK. With the longer waveguide, more stored energy is available to test for damage from breakdowns. This system can be pressurised up to 210 kPa allowing the required pressurisation for tolerable break-down rate to be verified. After resonant testing of the pipe alone, the bend was installed at the end, and the combination tested. Breakdowns occurred during processing, but over 100 hours continuous operation without breakdown at field levels equivalent at the anti-nodes to over 250 MW travelling-wave has been observed. Testing will continue but the KCS main waveguide and components do appear to work as designed and to be capable of handling the ILC power levels.

Figure 2.71
Views of a CTO used as a launcher or coupler in high-power tests of KCS WC1890 main waveguide runs.

2.9 R&D towards Mass-production and Design for Manufacture

The ILC has commissioned studies at experienced industries in all three regions to understand the fabrication costs for the cryomodules and components in the quantities required for the ILC. The focus of these studies has been to create a more robust cost estimate for the TDR, so companies were asked to consider changes to production methods that could result in savings for the ILC. In addition to the commissioned studies, two industrialisation workshops were hosted, in conjunction with IPAC 2010 and SRF2011, where industry and laboratory experience was solicited and shared.

One of the important changes since the RDR has been the exploration of different production models: at the time of the RDR, a single-vendor model was used for the cost estimate. Although a final production model has not yet been chosen, more-distributed models dividing production of key components among multiple vendors and the possible roles of laboratories in the production model have been explored. Figure 2.72 shows one such model. The dashed circle in the figure indicates technical coordination links between regional laboratories, designated as 'hub-laboratories' in the model. The arrows in the figure highlight the central role world-wide industry has as 'build-to-print' manufacturors.

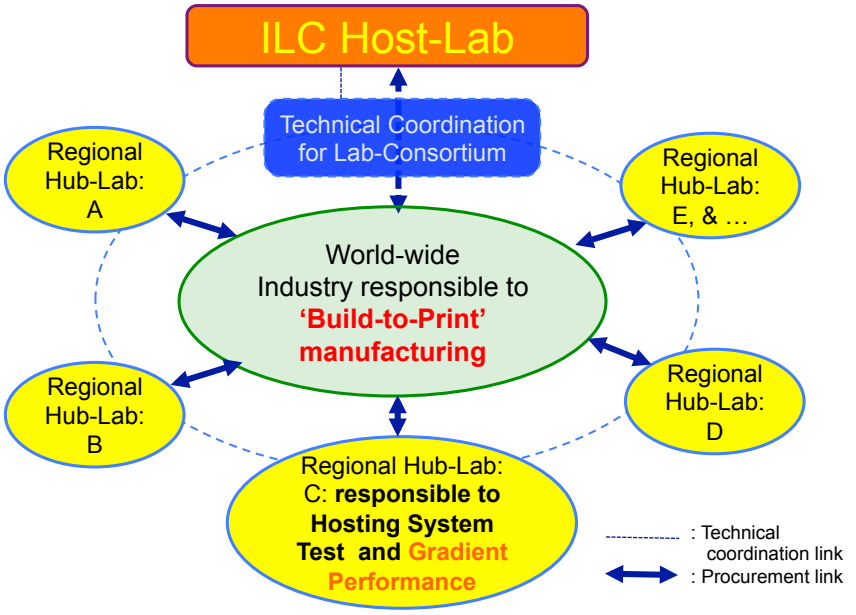

Figure 2.72 The industrialisation model.

2.9.1 R&D and Studies towards Cavity Industrialisation

The most direct source of information on the production of cavities in quantity will be the European XFEL production of 800 cavities, by two companies, over the course of 2 years. This is equivalent to about 5 % of the total required ILC production, and is the largest production of such cavities. This production and contractual experience will be invaluable.

To expand on this experience, and better understand the regional differences that might come into play during ILC production, three studies have been commissioned. In Europe, a study evaluating the needs and costs associated with the production of all 18,000 cavities, by a single vendor, over the course of 3 years, and the facility required for such a run, has been requested. Given the economies of scale, this study should present a best-case scenario for the cost per cavity. In the Americas, the study considered a 20 % production (3600 cavities) over the course of 6 years, and the plant associated with such numbers. Finally in Asia, a study considering full utilisation of the KEK pilot plant was requested, and resulted in a study considering 540 cavities per year. The last two scenarios

are consistent with a distributed model where 5 or 6 vendors worldwide share the production.

In addition to the baseline process studies, sensitivity and bottleneck analyses were included in the studies, on items like the assumed first- and second-pass yields, learning curves, the number of e-beam welding machines, and an extra study looking at alternative processing techniques.

Common threads through the studies include the role of the laboratories in providing test facilities and assuming risk in situations where industry does not have the expertise. Even for the smaller quantity studies, the use of a single supplier for a sub component, where existing expertise exists, is identified as a viable strategy, even if the larger components are assembled in a distributed manner. A distributed model may be more consistent with existing infrastructure and size of companies, and more robust and sustainable with respect to economic upsets, but still use sole sources for subcomponents.

2.9.2 R&D and Studies towards Cryomodule Industrialisation

As with the cavities, in the short term the most direct and applicable source of information for the cryomodule sub-components and assembly will be from the European XFEL, where the 100 cryomodules represent about 5 % of the 1950 similar devices for the ILC. The current experience is further limited by the low number of cryomodules built and tested worldwide to date, and that the majority of this work has been done in a laboratory setting rather than industry. Furthermore, when looking at subassemblies, such as tuners, the amount of cold mass, operational testing for some of the designs is limited. However the data at hand has been shared with companies familiar with cryomodule work. The LHC-dipole cryostat assembly provides a valuable benchmark, which has been utilised in the ILC studies. Figure 2.73 shows one such analysis where the volume of production is shown versus the number of variants required at the LHC.

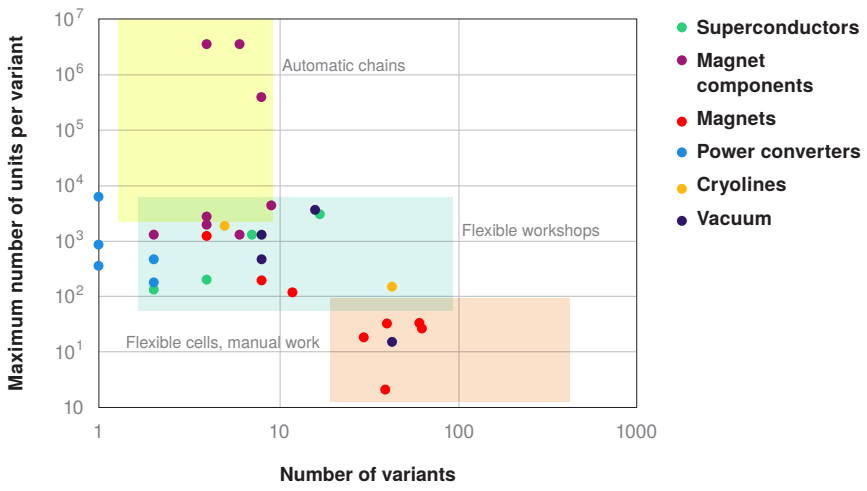

Figure 2.73 Units produced and variants required for major LHC components [116].

The commissioned studies can be separated into two types: one evaluating the costs of subcomponents in the cryomodule, the other looking at the labour and plant requirements for cryomdule assembly. As with the cavity, for these assembly studies all cold test facilities are assumed to be at the laboratories; subcomponents are fully qualified when delivered to the assembly facility and only incoming inspection is required.

In Europe, the assembly study covered full production of 1950 cryomodules over 4 years, or a subset of 650 (30 %) over the same timeframe; in the US, the study assumed 450 cryomodules over 6 years, consistent with the cavity production study; and in Japan the study looked at 390 (20 %), 950 (50 %), or 1950 (100 %) cryomodules over 6 years.

For parts and subcomponents, the studies looked at the needs consistent with the same quantities and durations listed above; parts costs were evaluated using current experience modified with learning curves to the quantities needed based on industrial best judgement. An additional specific study,

looking solely at the split quadrupole design, has been commissioned from Toshiba, who are an expert and experienced superconducting-magnet company and are currently assisting KEK in the re-assembly of a split quadrupole originally fabricated by Fermilab.

The guiding philosophy behind the cryomodule production model is that industry will be used whenever possible for component production. Final integration into cryomodules with involve both industry and the national labs. Cryomodule testing and shipping will take place in the hub laboratories, i.e. the regional laboratories that concentrate the regional efforts in component production in a particular region. LHC experience indicates that all high-technology components produced in industry will require engineering support from the national labs both during the initial set-up and pre-production phase as well as during the production cycle itself. It is likely that the ILC experience will be similar to the LHC in this regard.

Dressed cavities, couplers, tuners, quadrupoles, cryomodule vessels and other components will all be procured in volume from industry. Delivered cavities will be processed and cold-tested vertically for gradient performance at a hub laboratory. All cavity assemblies will be vertically cold tested. If necessary, cavity repair and a second-pass processing cycle will be performed at the hub lab. After cavity performance is certified, the final component integration into a complete cryomodule will be performed in or near the hub laboratory with industrial labour and laboratory oversight in a similar fashion to the LHC dipoles or the XFEL cryomodules. The final integration in or near a hub lab minimises the handling and transportation of the delicate cavity assemblies after processing and testing. The completed cryomodules will be cold tested at the hub laboratories. It is expected that all cryomodules in the pre-production phase will undergo cold testing; in full production mode only a fraction ($\approx 20\,\%$) will be cold tested before shipping. The overall scheme for cryomodule production is shown in Fig. 2.74.

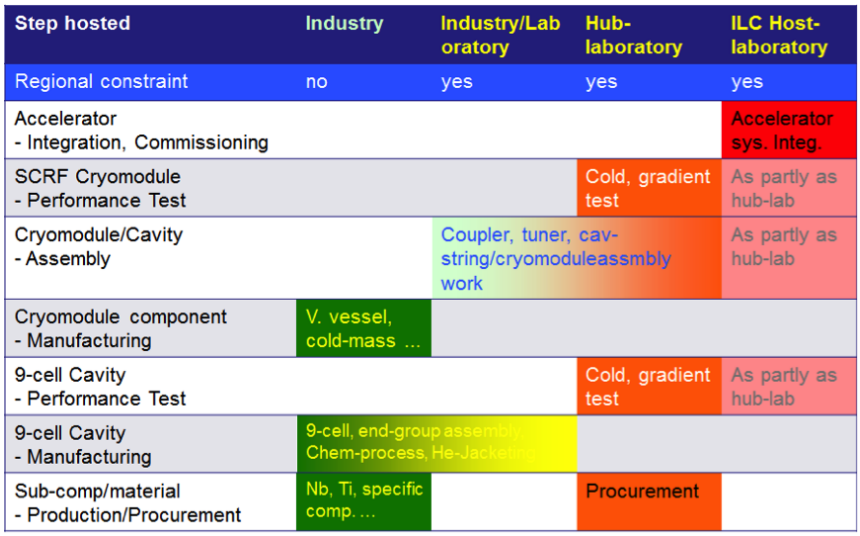

Figure 2.74 Scheme of manufacture for cavities and cryomodules.

Chapter 3
Beam Test Facilities

3.1 Overview

Beam Test Facilities are required for critical technical demonstrations, including accelerating gradient, beam dynamics, and precision beam handling. The scope of test-facility activity needed to mitigate critical technical risks was assessed during the development of the Reference Design with the intention of modifying the design in accordance with the results obtained. Purpose-built test facilities were then either constructed by collaborative teams or provided through adaptation of existing facilities. With two exceptions, high-gradient beam operation (SCRF – main linac) and beam-size tuning (BDS), these test facilities have met or exceeded goals established for the Technical Design.

Primary beam test facility goals are:

- demonstration of ILC linac performance and evaluation of realistic cavity performance with beam acceleration;
- demonstration of a number of cavities operated in an accelerator showing repeatable performance and providing an estimate of reliability;
- studies of instabilities, such as electron cloud, and mitigation techniques;
- demonstrations of the generation and handling of low-emittance beams using precision optics and stabilisation tools.

It is especially important that each region deploy a full superconducting linac system, including cryomodules, beam generation and handling, and RF power source and distribution systems, to integrate the accelerator technology and gain sufficient experience in that region. The strategy for accomplishing this depends on infrastructure limitations and schedule constraints at each of the test facilities, due in part to institutional commitments to non-ILC related projects. As shown in Table 3.1, the aggregate effort is evenly distributed among the three regions; for two of the regions, a separate, specialised beam facility has been built in addition to an SCRF linac facility.

Table 3.1
Table of Beam Test Facilities. Note that the Main Linac test facilities in USA and Japan will not be fully operational until after the Technical Design Phase.

	Test Facility	Purpose	Host lab
1	TESLA Test Facility(TTF)/ Free-Electron Laser Hamburg (FLASH)	Main Linac	DESY, Germany
2	SCRF Test Facility (STF) (2014)	Main Linac	KEK, Japan
3	New Muon Lab (2013)	Main Linac	FNAL, USA
4	Accelerator Test Facility (ATF)	Damping Ring	KEK, Japan
5	Cornell Test Accelerator	Damping Ring	Cornell, USA
6	Beam-Delivery Test Facility (ATF2)	Beam-Delivery System	KEK, Japan

Test facilities also serve to train scientific and engineering staff and regional industry. For example, ATF2, the final-focus test facility at KEK, was constructed through in-kind contributions and has been commissioned and operated by an international team of researchers. It is considered a possible model for a future ILC collaborative effort. A key component, present in both the test facility and the much larger-scale project, is good advance planning which takes into account the diverse and

complementary skills and resources of large accelerator laboratories and smaller university groups alike.

Beam tests done during the Technical Design Phase at other facilities are also important. For example, beam-coupling corrections applied at the Australian Synchrotron [117], have demonstrated beam emittance of 1.2 pm-rad, well below that needed for ILC.

3.2 FLASH 9 mA experiment

3.2.1 Introduction

The TESLA Test Facility (TTF) was constructed by the TESLA collaboration [118] to demonstrate that a linear collider based on superconducting accelerating cavities would be feasible and cost competitive with one based on conventional copper structures. Technical feasibility of ILC-type superconducting accelerating cavities was demonstrated in 2000 when an 800 microsecond-long 8-mA beam was accelerated through a single cryomodule to 168 MeV. The TTF was renamed FLASH (Free electron LASer in Hamburg) and became a user facility operating as a soft X-ray free-electron laser in 2005. The FLASH linac is a 1.25 GeV linac based on Tesla-type technology and operates 5000 hours per year on average. The '9-mA' program was proposed by the GDE in 2008 with the goals of demonstrating reliable operation of the TTF/FLASH linac with ILC-like bunch-trains and to characterise the limits of operation of gradient and RF power. Typical beam properties for FEL user operation (charge, number of bunches, average beam power) are far lower than those required for the 9mA studies. For DESY, however, these studies have been important for integration and operational issues associated with running long bunch trains and high bunch charge, both for FLASH itself and for the European XFEL (see Section 2.5).

The ILC main linac will accelerate a 5.8 mA (upgradeable to 9 mA) 726 microsecond beam pulse to 250 GeV with 0.1 % rms energy stability at a pulse-repetition rate of 5 Hz. The beam energy must be stabilised over two timescales: long-term pulse-to-pulse stability over minutes and hours; and energy stability within a bunch train.The ILC main linac also requires precision control of high-gradient SRF in the presence of heavy beam loading. Since gradient performance has the greatest cost impact, each cavity in the ILC will be set to a stable voltage near its gradient quench-limit. To leverage the most cost-effective performance, low-level RF controls are used to push the cavities to achieve the maximum practical gradient, expected to be within 5 % of the nominal maximum. Effects such as beam loss, beam turn-on, beam-current fluctuation, Lorentz-force detuning and errors in power input coupling should be properly managed and disturbances minimised in order to maintain stable operation. In addition, studies were made of the required high-level RF-power overhead needed for reliable operation.

The above scientific programme attracted strong interest and participation of low-level RF and machine experts from DESY and also internationally, from Argonne, Fermilab and KEK. The studies were performed over a total of about 5 separate week-long runs between September 2008 and September 2012.

Table 3.2 compares beam parameters for the 9 mA Studies with the ILC Main Linac design parameters, and those of the European XFEL.

Table 3.2 Parameters for the 9 mA Experiment in context

	units	TDR Baseline	TDR Upgrade	European XFEL	FLASH 9 mA Expt.
Number of bunches per pulse		1312	2625	3250	2400
Bunch repetition rate	MHz	1.8	2.73	5	3
Beam pulse length	μs	727	960	650	800
Bunch Charge	nC	1.9	3	1	3
Beam current	mA	5.8	9	5	9

3.2.2 FLASH Main Linac

The main elements of the FLASH linac are shown in Fig. 3.1 before and after the energy upgrade in 2009/2010, when the number of accelerating cavities was increased from 48 to 56, increasing the maximum operating energy to 1.25 GeV. The injector comprises a 5 MeV laser-driven photo-cathode RF gun and a two-stage bunch compressor. The RF system of the first-stage compressor has eight cavities in a single cryomodule (module ACC1), while that of the second bunch compressor has 16 cavities in two cryomodules (modules ACC2 and ACC3). The main linac comprises modules ACC4 onwards. Prior to 2010, the main linac comprised modules ACC4, ACC5, ACC6 (24 cavities), all fed from a single klystron and regulated using vector-sum control.

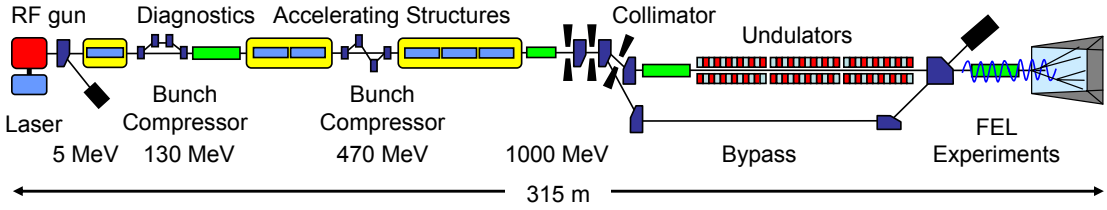

(a) 2008-2009 prior to energy upgrade

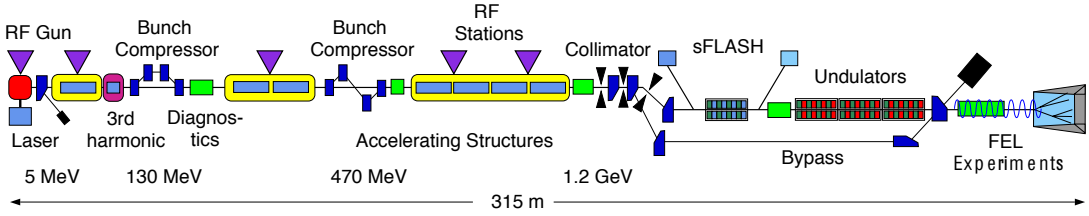

(b) 2010-2012, following upgrade to 1.25 GeV

Figure 3.1. Layout of the FLASH linac

The FLASH high-level RF systems are the basis of the HLRF system design for both the ILC and the European XFEL. The RF power is distributed from individual multi-beam klystrons of either 5 or 10 MW through a series of power-dividing elements to either one, two, or three groups of eight cavities. The relative power to each cryomodule (group of eight cavities) can be adjusted remotely. Pairs of adjacent cavities receive some fraction of the total RF power, with the power ratios having been set during fabrication based on measured quench limits of the cavities. These power-dividing ratios are not adjustable. Prior to 2010, the RF unit comprising the 24 cavities in ACC4,5,6 was of most interest for the 9 mA studies. In 2010, an additional cryomodule (ACC7) was added and the HLRF systems were reconfigured into two groups of 16 cavities each fed from it's own klystron (ACC4+5 and ACC6+7). Subsequent studies were focused on operation of ACC6 + 7. At the end of the linac, the beam is directed through a series of undulators for SASE FEL operation, or alternatively to a bypass line and then to the beam dump.

Figure 3.2
Measured cavity-gradient limits for the cavities in the FLASH Accelerator cryomodules for the 9 mA studies

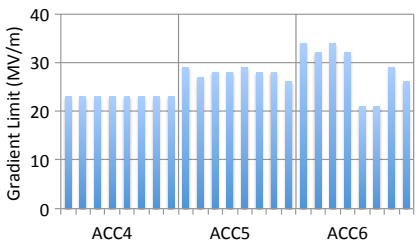

(a) Modules ACC4,5,6 (2008-2009)

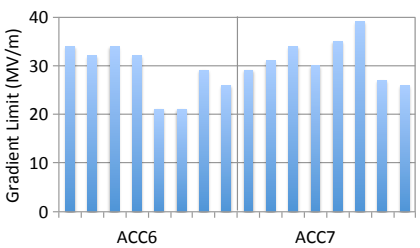

(b) Modules ACC6,7 (2010-2012)

The strong similarity of the ILC HLRF design to that at FLASH is a very important motivation for the 9 mA experiment. The most significant functional difference between the FLASH and ILC power distribution systems is the absence of remote adjustability of the power-divider ratios at FLASH, the impact of which will be discussed in Section 3.2.8.

Maximum operating gradients for the FLASH cavities for the two linac configurations are shown in Fig. 3.2.

3.2.3 Low-Level RF Control

DESY has been a pioneer in the field of digital LLRF control for pulsed superconducting linacs. The LLRF systems currently implemented at FLASH use the third generation of digital LLRF controllers developed by DESY ("Simcon-DSP"), and will shortly be upgraded to a fourth-generation system that has been developed with the European XFEL in mind. The main elements of the FLASH LLRF system are shown in Fig. 3.3 [119].

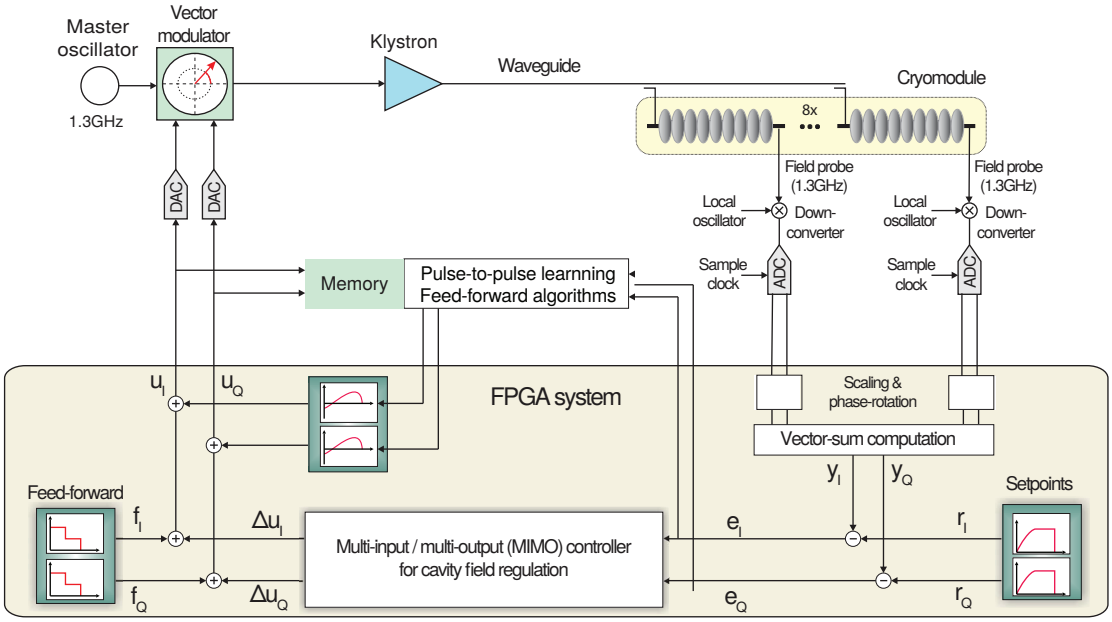

Figure 3.3. Block diagram of the FLASH digital LLRF control system [119]

The LLRF controller output to the klystron comprises two components, a feed-forward term to generate the cavity-field profile and handle the repetitive pulse-to- pulse artefacts while a dynamical intra-pulse feedback controller compensates for unpredictable pulse-to-pulse variations. A learning feedforward algorithm iteratively updates the shape of the feed-forward waveform in order to minimise the repetitive pulse-to-pulse errors and reduce the effort demanded of the feedback regulator.

Over the course of the 9 mA studies program, DESY has implemented many performance and functionality improvements on the LLRF systems: hardware and firmware upgrades and incremental development and refinement of high-level applications. Improvements in pulse-to-pulse jitter, intra-train regulation, repeatability, robustness, and long-term drift have all significantly improved over the course of the studies. Beam-based feedback has been incorporated into the RF systems of the two bunch compressors in order stabilise bunch-arrival time and bunch compression; beam-loading compensation is based on measured bunch charge. There have also been substantial benefits from the increasing degree of automation. FLASH FEL operations has also seen significant benefit from the improved performance of the LLRF systems.

3.2.4 FLASH Control System

The FLASH control system is implemented in DOOCS [120], which provides a powerful environment for control and monitoring of technical equipment and a framework for implementing integrated high-level applications. Hooks into the control system and data-acquisition system are provided for Matlab [121] and Octave [122], which are extensively used for developing high-level integrated applications.

Extensive use has also been made of the FLASH Data Acquisition System (DAQ), which provides access to several thousand signals that are pulse-to-pulse synchronous, including 1 MHz sample-synchronous and bunch-synchronous waveforms from the LLRF system and beam diagnostics [123]. The DAQ also serves to provide the data for pulse-to-pulse synchronous high-level applications, including computation of final beam energy from beam orbits and LLRF iterative learning feed-forward vector-sum control and piezo-tuner waveform optimisation for compensation of Lorentz-force detuning.

3.2.5 High-power long-pulse studies

The principal high-power long-pulse study goals were achieved during a two-week period in September 2009, having operated for several hours at 9 mA and pulse lengths of 500-600 µs (1500-1800 bunches). There were many additional hours of operation with 800 µs pulses (2400 bunches) and beam currents up to 6 mA. Figure 3.4 shows example energy profiles with the long bunch-trains at beam currents of 0.3 mA and 7.5 mA.

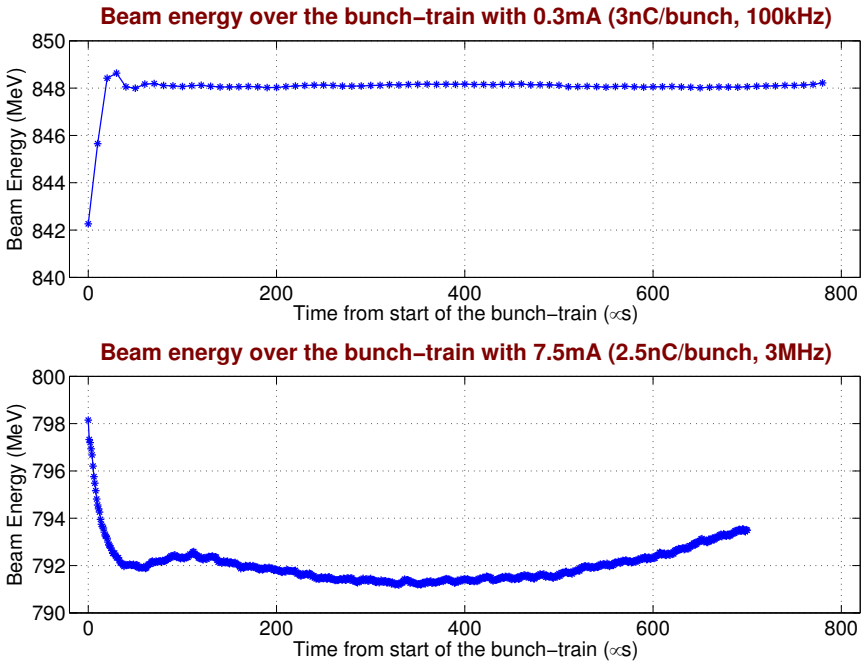

Figure 3.4 Linac energy profiles from 2009 study at 0.3 mA (top) and at 7.5 mA (bottom)

Operation at these high beam currents and long bunch trains required increasing the total charge per pulse by two orders of magnitude over typical FEL operation parameters. A significant side effect of this was the increased sensitive to changes in machine parameters that occur over periods of hundreds of microseconds, such as pulse-heating effects in RF components and drive-laser-beam transport that resulted in energy variations or orbit changes over the bunch train. An additional important consequence of the high total charge per pulse was that the per-bunch losses had to be very low in order to avoid reaching thresholds for integrated beam-loss per pulse.

A history of the number of bunches over the week of studies leading up to the 9 mA and full-length bunch trains operation during the September 2009 studies is shown in Fig. 3.5. Of particular note are the rapid recovery following a tunnel access on 19th September (less than one hour), followed by the

15-hr stable run at 3 mA with the full 800 µs bunch-train on 19 September before reconfiguring the laser for 3 MHz operation and ramp-up to 9 mA on 20th September.

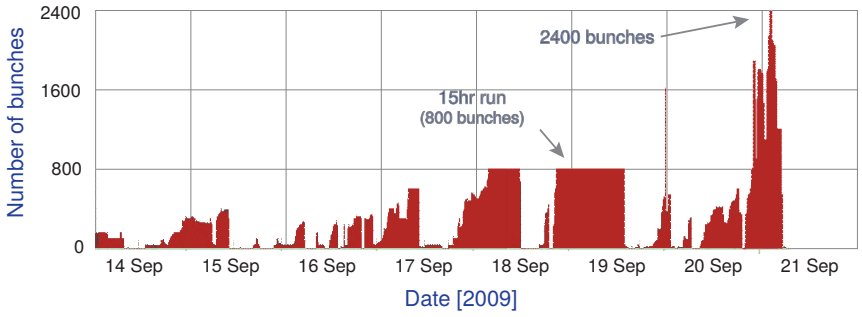

Figure 3.5 Number of bunches and bunch charge over 7 days of studies.

3.2.6 RF-power overhead studies

The ILC baseline design assumes that the main linac klystrons can be operated reliably within 10 % of their 10 MW maximum output, with some klystrons operating within 7 % of the maximum power. This has two consequences for RF control: there is limited power overhead available for vector-sum regulation; and the LLRF controller must contend with a power-dependent gain in the klystron as it approaches a saturation limit at the maximum output power. Figure 3.6 shows representative curves of the output power and gain at different anode voltages for the Toshiba 10 MW multi-beam klystron.

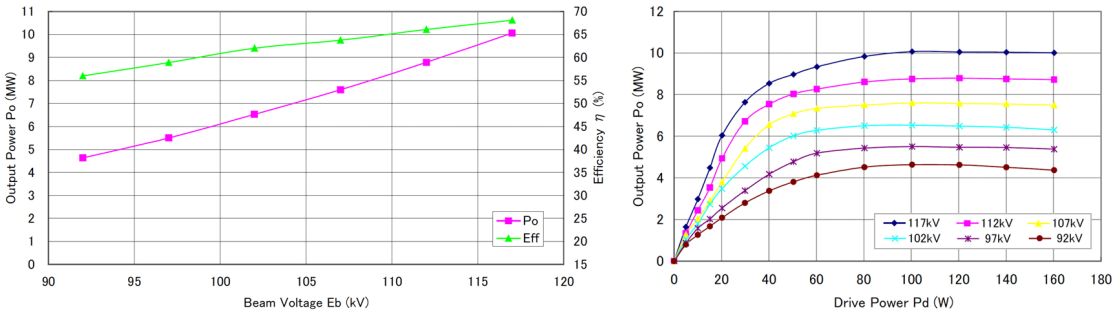

Figure 3.6. Representative RF power and gain curves for Toshiba multibeam klystron

Figure 3.7 Klystron gain curve and working point at 86.5 kV anode voltage

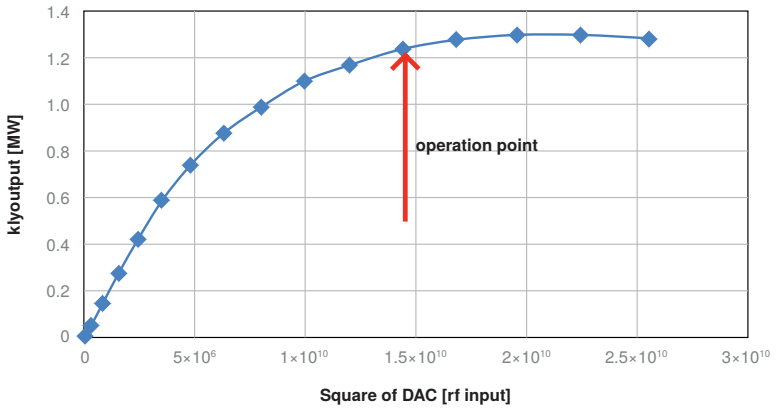

First tests of beam operation with klystrons running within a few percent of saturation were performed in February 2012. The studies was performed on the RF unit comprising ACC6/ACC7 with a beam current of 4.5 mA, which required approximately 1.2 MW of forward power from the klystron, which is nominally rated at 10 MW. The saturation point of the klystron was reduced to just above 1.2 MW by dropping the anode voltage. Figure 3.7 shows the measured klystron output power as a

function of drive at an anode voltage of 96.5 kV. It shows a factor five change in gain from the linear region to the operation point for the test and also that the output power starts to roll over if the klystron is driven too hard.

In order to observe the effects of klystron saturation during the beam pulse, a notch was introduced into the vector sum setpoint table. An example of the tracking response to the notch is shown in Fig. 3.8.

The effect of klystron saturation can be seen by comparing the speed of response on the vector sum at the start and end of the notch. The lower trace shows the negative- and positive-going blips in klystron forward power at the start and end of the notch as the LLRF controller attempts to make the vector sum follow. On the step up, the klystron output power demanded by the regulator is clipped by saturation, slowing the recovery time compared with the initial step down.

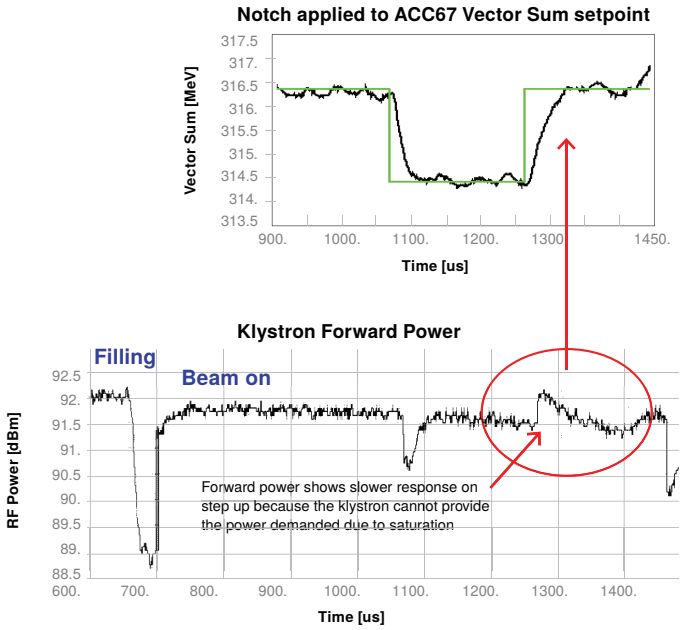

Figure 3.8
Klystron forward power and vector-sum response to a notch in the vector-sum setpoint

First beam tests with a klystron linearisation function were successfully performed in September 2012. This was implemented as a look-up table in the LLRF-controller output signal chain that has the inverse characteristic to the measured klystron saturation curves. Although the nonlinearity and saturation is a function of output power amplitude, linearisation tables must be applied to both amplitude and phase. Results from these first linearisation tests are shown in Fig. 3.9, where the input-output characteristics of the pre-amplifer/klystron drive chain are shown with and without linearisation.

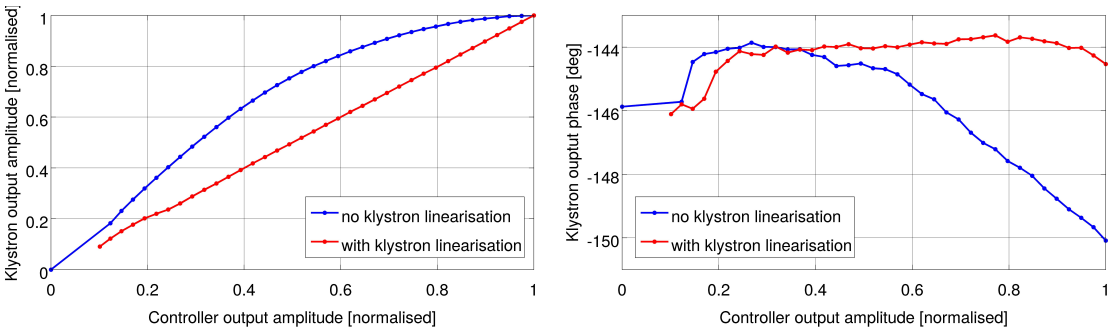

(a) Amplitude response

(b) Phase response

Figure 3.9. Klystron output as a function of LLRF Controller output with and without linearisation

3.2.7 Compensation Studies for Lorentz-force detuning

Lorentz forces cause the resonant frequency of the cavity to change linearly as a function of time over the RF pulse. At 35 MV/m, the change in detuning over the beam-on period can be 600 Hz or more. This Lorentz-force detuning must be compensated to the level of a few hertz in order to avoid an RF power penalty for driving a detuned cavity and to avoid cavity gradient deviations that otherwise could not be removed by the vector-sum controller.

Methods for compensation of Lorentz-force detuning at FLASH have been widely reported. A pulsed excitation is applied to the piezo tuners several milliseconds before the RF pulse in order to excite mechanical resonances of the cavity structures that apply forces to the cavity during the RF pulse that counteract the Lorentz forces. The excitation is in the form of a pulsed sinusoid where the amplitude, frequency, number of periods, start-time, and DC offset are adjusted in order to null the measured detuning profile during the beam-on period.

Observed mechanical modes are typically in the range of 200-400 Hz with damping times of tens of milliseconds. Figure 3.10 shows time-domain responses over 80 ms for the eight cavities in module ACC7.

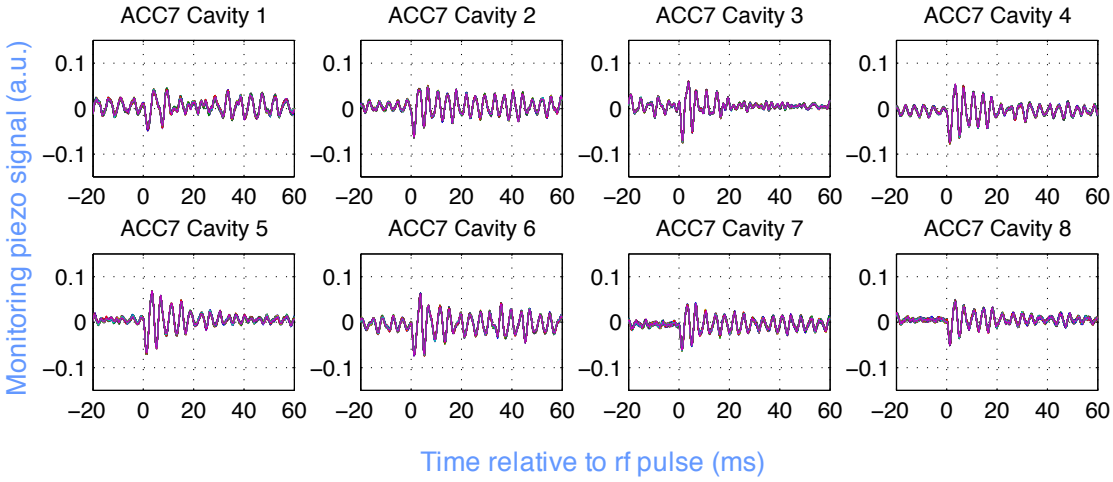

Figure 3.10. 'Monitoring' piezo signals from $-20\,\mathrm{ms}$ to $+60\,\mathrm{ms}$ relative to RF pulse showing cavity-to-cavity differences in damping times of the mechanical resonances.

The optimisation algorithm for the piezo tuner adjusted the amplitude, DC offset and start-time of the excitation in order to minimise the measured average ("static") detuning, change in detuning ("dynamic" detuning), and the curvature of the detuning profile over the pulse. Examples of detuning profiles showing the metrics and the result of the optimisation are illustrated in Fig. 3.11. Since each cavity operates at a different gradient, the excitation parameters must be optimised for each piezo tuner. Since the optimisation uses only the time period of the RF pulse, there is no cancellation of the actual mechanical motion, which typically takes several hundred milliseconds to decay (as was shown previously in Fig. 3.10).

The detuning profile used for piezo-tuner optimisation must be computed from the cavity probe and forward power waveforms. The computation must also take into account the beam-loading contribution to the total forward power.

Calibration of the forward power signal is complicated by the cross-contamination from the reflected power signal, and is performed by comparing forward and reflected power waveforms from knowledge that they must be equal at the start of the RF pulse, while the forward power must be zero after the RF pulse. For the studies, calibration was cross-checked by comparing the computed detuning with end-of-pulse measurements from scanning the RF-pulse length. The intra-pulse computation of detuning was also extended to include the beam-loading term. Figure 3.12 shows the computed

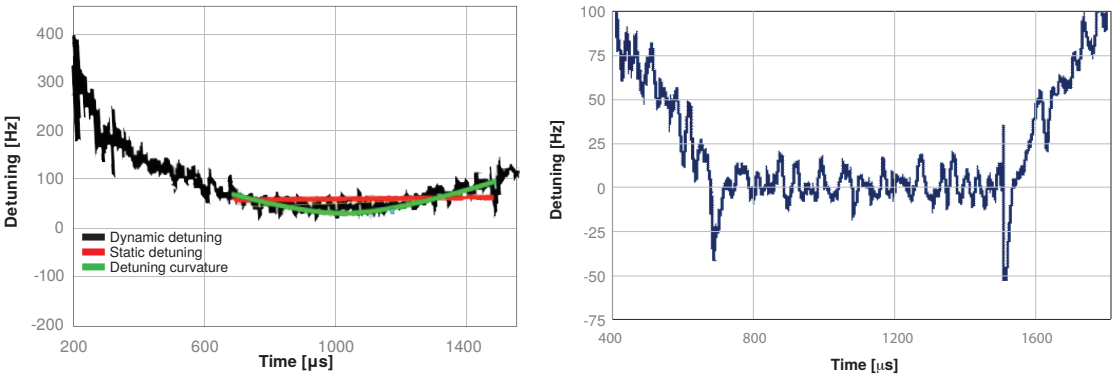

(a) Measures of detuning

(b) Residual detuning profile with compensation (0.3 Hz dynamic, -1.2 Hz static)

Figure 3.11. Definition of terms for detuning compensation algorithm and residual detuning for ACC6 Cavity #1

detuning with and without correction for the forward power from beam loading. Grecki *et al.* [124] contains further discussion of calibration and beam-loading issues with the detuning computations.

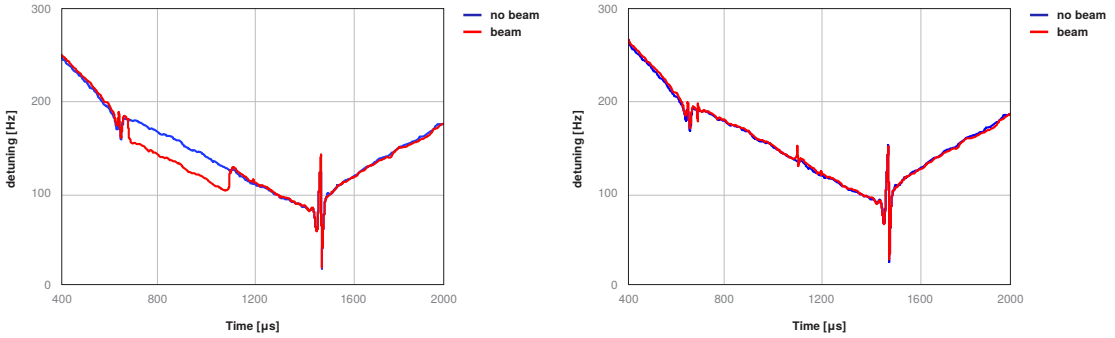

(a) No correction for beam loading

(b) With correction for beam loading

Figure 3.12. Comparison of computed detuning (red) with measurements from shortened pulses (blue) with and without beam loading

To date, piezo tuner studies have concentrated on minimising the measured detuning errors. In practice, however, the piezo tuners would also be used to make fine adjustments to the cavity-gradient profiles as part of the gradient-flattening algorithm. The principle benefit is that using the piezo tuners for fine adjustments avoids having to make frequent changes to the coupler motor positions.

3.2.8 Gradient Studies: Beam Operation close to Quench

To minimise the length of the tunnel, the main-linac design assumes that all cavities will operate close to their quench limits. Cavity strings are qualified at a nominal average of 33 MV/m with a spread from 26 MV/m to 38 MV/m, and will operate at 31.5 MV/m average. All cavities must operate within 1.5 MV/m of their quench limits. Any pulse-to-pulse gradient jitter or gradient changes along the bunch-train must be kept to a minimum in order to avoid squeezing this gradient margin even further. The primary sources of gradient changes along the bunch train are detuning (discussed in the previous section) and gradient tilts induced by beam loading.

Figure 3.13 shows examples of gradient tilts induced by beam loading from the September 2009 studies, which show that the tilts are proportional to beam current. These gradient tilts can be corrected if the individual cavity parameters (loaded Q and/or cavity forward power) are tailored to the respective cavity operating gradients and the nominal beam current. To achieve this, such that the voltage in a cavity remains constant at a specified gradient in the presence of beam loading, the

forward power and loaded Q must simultaneously satisfy two constraints:

- the cavity must have reached the specified gradient at the end of the cavity fill time;
- the RF power fed to the cavity during the beam-on period must exactly balance the power being removed from the cavity by the beam.

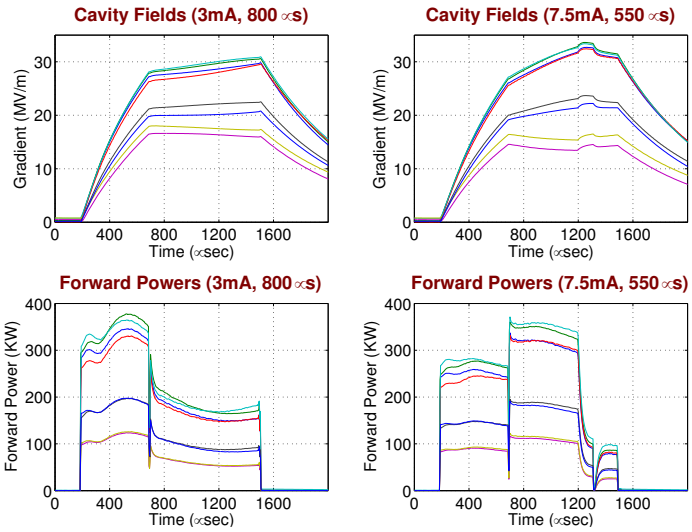

Figure 3.13
Gradient tilts from beam loading at 3 mA and 7.5 mA (Sept 2009)

Where there are multiple cavities fed from a single klystron, the above two constraints must be satisfied simultaneously for all cavities with the added constraint of a common fill-time. Provided the individual cavity loaded Qs and forward power ratios can be independent adjusted, a set of loaded Qs and power ratios can always be found that achieves flat gradients on all cavities simultaneously. However, if the power ratios are not adjustable, as is the case at FLASH, the only adjustments are the loaded Qs, the total forward power, and the common fill time. Solutions can still be found, but only over a restricted range of beam currents and operating gradients. The greater the spread in cavity operating gradients, the more restrictive is the range of beam currents and operating gradients over which solutions can be found. This is illustrated in Fig. 3.14, which shows the spread of loaded Q expanding exponentially with beam current to the point where there are no longer any valid solutions. The two outlier curves correspond to the two lowest-gradient cavities. Without those cavities, the spread of required QIs would be significantly less and solutions could be found over a wider range of currents.

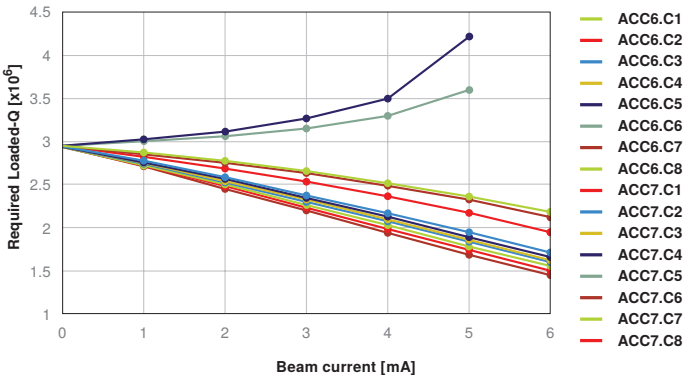

Figure 3.14
Calculated sets of loaded Qs that achieve flat gradients as a function of beam current, showning the divergence in the maximum-to-minimum loaded Qs as the beam current or the spread in gradients increases

The method of establishing flat gradients using both adjustable power ratios and loaded Qs has been referred to as 'Pk/QI control.' For the FLASH studies, where only the loaded Qs are adjustable, the term 'Pseudo-Pk/QI control' has been used. This method has been successfully applied for a range of operating conditions and beam currents up to 5 mA. Because of the limitation the range of currents and gradients where there were solutions, most of the studies were performed with the

two lowest gradient cavities were completely detuned in order effectively to remove them from the system. An automated iterative optimisation algorithm is described in Section 3.2.12. The approach to finding the optimum set of loaded Qs that produced flat gradients was to start with values that were determined analytically and then manually optimise the values iteratively using a model-based cavity simulator. The quality of the solution was evaluated by sweeping the beam current above and below the nominal value and observing the tilts. For each cavity, there will be one particular beam current at which the gradient is flat, as shown in Fig. 3.15a.

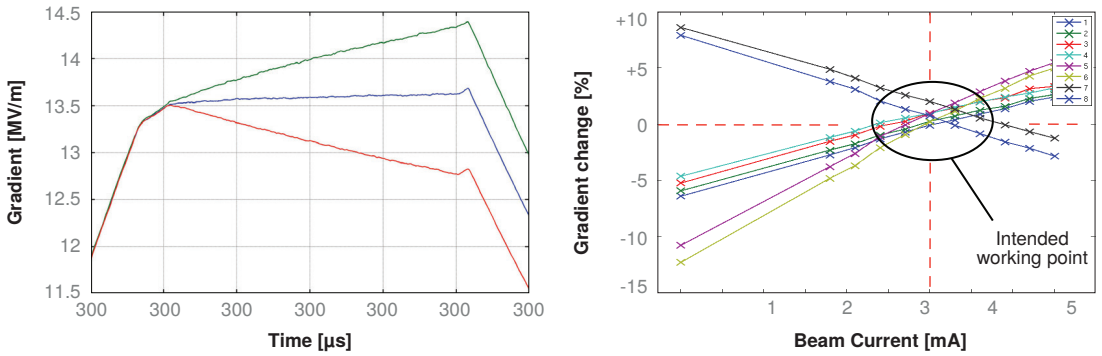

(a) Gradient profiles for one cavity at 1.8 mA, 3 mA, and 4.5 mA

(b) Gradient tilts as a function of beam current for all cavities

Figure 3.15. Evaluation of loaded-Q optimisation by scanning the beam current around the 3 mA nominal working point

Plotting the gradient tilts as a function of beam current for all the cavities will yield a straight line that goes through zero at a particular beam current. Shown in Fig. 3.15b are results of such a beam-current scan for all cavities where the loaded Qs have been set up for flat gradients at 3 mA beam current. Since not all cavities have zero tilts at the same beam current, the quality of the solution is judged by the spread in tilts at the nominal 3 mA.

3.2.9 Ramp-up to Full Beam Power and Maximum Gradients

An important operational issue associated with the beam-loading-induced tilts is how to avoid causing large gradient excursions when ramping from a cold start to nominal beam current and full pulse length. One approach would be to start at the nominal bunch charge and a short beam pulse. The loaded Qs (and power dividers if available) would be optimised to achieve flat gradients with the short beam pulse before increasing the pulse length. Given that the loaded-Q optimisation should be independent of the beam-pulse length, if the cavity gradients are flat for a short pulse, they should remain flat if the length of the bunch-train is increased. This approach was tested during the gradient flattening studies with 4 mA beam current; the results are shown in Fig. 3.16. The loaded Qs were initially optimised for flat gradients with a 400 µs beam pulse. The pulse length was then increased, first to 600 µs and then to 800 µs. The gradients did indeed remain flat, with changes in the loaded Qs being necessary to keep the gradients flat over the longer beam pulse.

In this experiment, the full RF pulse length was retained throughout in order to observe the gradient tilts after the end of the beam pulse. The large tilts occurred after the beam turned off because the loaded Qs were optimised for 4 mA and not for zero current. Clearly, if the gradients were close to quench, then the large tilts after the beam-on period would cause cavities to quench. Two options for avoiding the quenches have been tested: first, the RF pulse as well as the beam pulse can be shortened; secondly, gradient limiters can be used to prevent the gradients from reaching quench. This latter approach is discussed in Section 3.2.10.

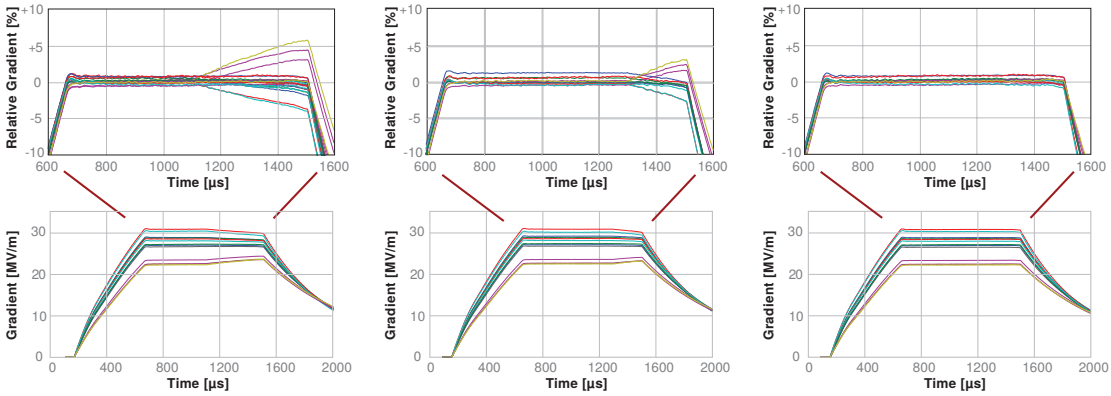

(a) 400 µs beam pulse **(b)** 600 µs beam pulse **(c)** 800 µs beam pulse

Figure 3.16. Cavity gradients during ramp-up of beam pulse length. Each cavity loaded Q was optimised for flat gradients during the beam-on period with 400 µs pulses (left); when the pulse length was extended to 600 µs (centre) and then to 800 µs (right), the gradients became flat for the full duration of the beam pulse without needing further loaded Q adjustments.

3.2.10 Management of Operational Gradient Limits

Suitable quench-protection mechanisms will be an essential requirement for routine operation close to cavity gradient limits. The prevention of quench events that require a long cryoplant recovery cycle and machine downtime is of primary importance. It is also vital to avoid false triggers from quench-detection mechanisms that are either too sensitive or have poor discrimination of quench signatures from other transient conditions.

Although this study is in its early days, two detection methods have been pursued: early detection of the onset of a quench by looking for a sudden drop in the loaded Q; and preemptive detection of a potential quench condition from a real-time comparison of cavity gradients with gradient-alarm thresholds based on knowledge of the quench limits. This latter method relies on there being consistent and repeatable quench limits.

A sudden drop in loaded Q is detected from the decay-time of the cavity field at the end of the RF pulse, where a sudden large drop in the loaded Q from pulse to pulse indicates that the cavity had started to quench during the pulse. The basic algorithm worked successfully when operating parameters were stable but is vulnerable to false triggers when parameters change, for example shortening the RF pulse or beam pulse, or when the loaded Qs are being changed by the gradient-flattening algorithm.

In the case of the gradient-alarm levels, each cavity field is continually compared with a predefined alarm threshold, allowing action to be taken before a quench begins. The RF pulse is terminated if any one of the cavities in the vector sum reaches its threshold. The most recent studies have used two gradient-alarm thresholds for each cavity. The upper threshold acts as a 'hard limiter,' turning off the RF pulse if any cavity exceeds its respective alarm threshold. The second threshold, set somewhat lower, is used as a 'pre-limiter', where instead of turning off the RF pulse, the vector-sum setpoint is dynamically reduced until all cavity gradients are again below their respective limiter thresholds. The original setpoint table is restored for the following pulse. The action of the pre-limiter is shown in Fig. 3.17.

The benefit of this pre-limiter is that it can keep all gradients below defined thresholds, pre-emptively avoid a quench without having to terminate the RF pulse. This makes it possible for beam operation at gradients right up to the pre-limiter thresholds and is particularly beneficial during machine tuning when frequent early pulse terminations could otherwise change the machine working point from changes in pulse-heating effects.

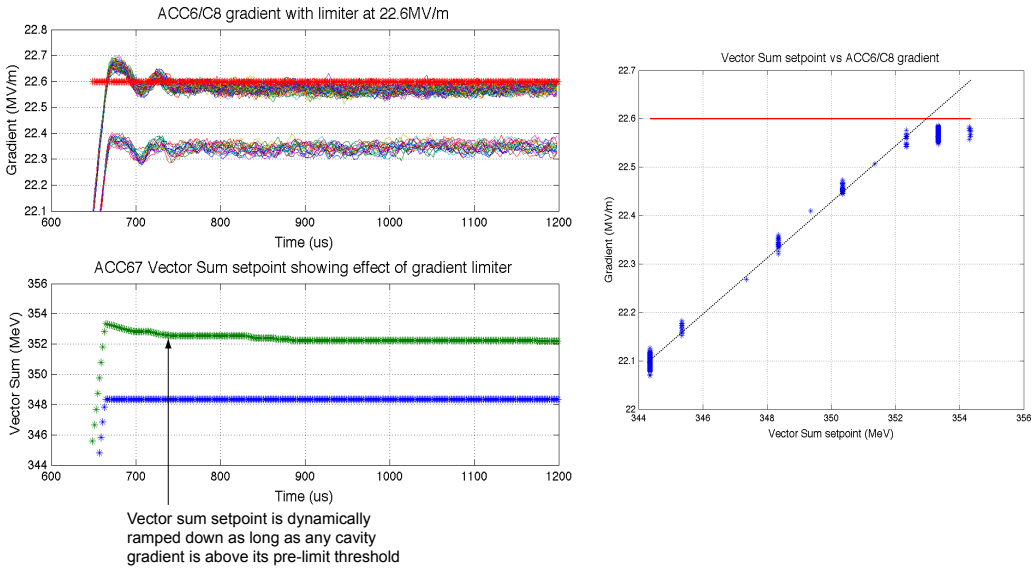

Figure 3.17. Cavity-gradient 'pre-limiter' action: dynamic ramping down of the vector-sum setpoint to keep the gradient below the defined threshold (left); clamping action on the vector sum (right)

3.2.11 Energy Stability

Requirements for energy stability encompass pulse-to-pulse energy jitter, intra-pulse jitter from bunch to bunch, and the mean energy profile over the bunch train, all of which have been monitored routinely throughout the FLASH studies. Examples of energy profiles from the high-current study were shown previously in Fig. 3.4.

Between 2009 and 2011, upgrades to the low-level RF systems, largely motivated by FLASH FEL user requirements, have significantly improved the energy stability, especially in the pulse-to-pulse jitter. These improvements are illustrated in Fig. 3.18, which overlay energy profiles from many pulses from the 2009 and 2011 studies. While the energy stability achieved in 2009 was about at ILC requirements, energy stability in 2011 is now significantly better than ILC requirements for both the main linac and bunch compressors. Representative long-term stability over a three-hour period during the 2011 studies is shown in Fig. 3.19.

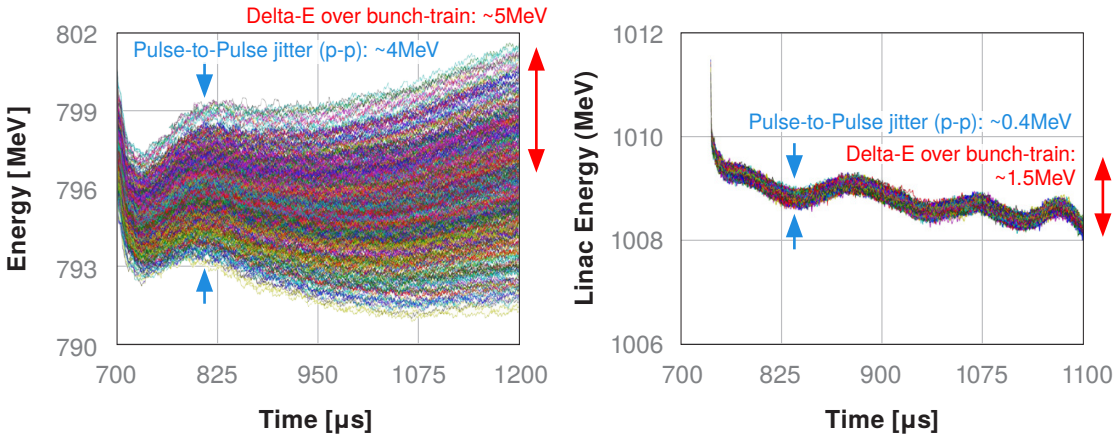

Figure 3.18. Comparison of pulse-to-pulse (left) and intra-pulse (right) energy stability between 2009 and 2011 4.5 mA

Beside stabilisation of the cavity vector sum, low-level RF controllers have been upgraded to make use of beam-based measurements in order to improve the pulse-to-pulse repeatability and

Figure 3.19
Pulse-to-pulse energy stability over a three-hour period with 4.5 mA and 400 µs bunch trains (from 2011 studies)

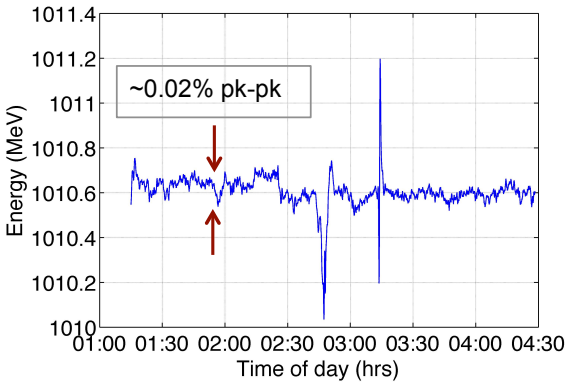

to compensate for pulse-to-pulse jitter. All LLRF systems now compensate beam loading using bunch-to-bunch charge measurements. Additionally, the amplitude and phase of the RF systems upstream of the bunch compressors are dynamically regulated in order to stabilise the downstream bunch-to-bunch energy and compression angle. This compensates for arrival-time jitter at the start of the bunch-train and any slewing over the length of the train. Figure 3.20 shows the pulse-to-pulse arrival-time jitter as a function of bunch-number. Using bunch-to-bunch feedback, the arrival-time jitter at the start of the bunch-train was attenuated by a factor five by the tenth bunch. Similar beam-based feedback that operates on the damping ring output kicker is planned for the ILC RTML turn-around.

Figure 3.20
Arrival jitter at end of the linac with beam-based LLRF feedback [119]

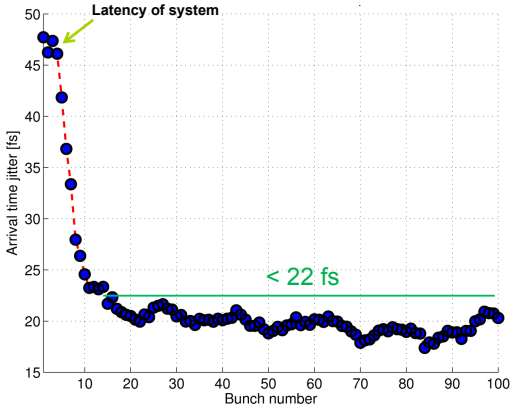

3.2.12 Automation

The level of automation of FLASH operations has increased significantly over the course of the 9 mA studies program, with much of the focus being on automating LLRF operations:

- use of state machines to automate procedures such as linac startup, recovery following interlock trips, and restoring standard setup files [125];
- feedback control using high level applications implemented in DOOCS servers [120]: examples include orbit feedback [126], cavity resonance control using piezo tuners [127], pulse-to-pulse iterative learning feedforward for klystron forward power [119].

Automation has also been developed specifically for the 9 mA studies, including the loaded Q optimisation for establishing and maintaining flat gradients and tracking changes in beam current to allow ramp-up of the machine energy and beam current [128].

Automation developed at FLASH will provide important lessons and a starting point for automating XFEL operations. Similarly, the ILC will benefit significantly from lessons learnt in automating XFEL.

3.2.13 Conclusions

The principle goals of the 9 mA Experiment at FLASH were to establish beam operation at ILC-like parameters and to study operation of an ILC-like RF unit at the limits of gradient and klystron power. These goals have been largely achieved, as summarised in Table 3.3.

Table 3.3
Results of high-power beam studies

Metric	Goal	Achieved
Pulse length & current	800 µs and 9 mA	▪ 800 µs pulses and current up to 6 mA ▪ 9 mA current and pulse lengths up to 600 µs
Charge per pulse	7200 nC	▪ 5400 nC (600 µs, 9 mA)
Average power	36 kW (7200 nC, 5 Hz, 1 GeV)	▪ 22 kW (5400 nC, 5 Hz, 800 MeV)
Operating gradients with beam loading	31.5 MV/m nominal average	▪ Several cavities above 30 MV/m ▪ 13 cavities totalling 380 MV/m with 13 cavities
Gradient flatness	2 % $\Delta V/V$ (800 µs, 5.8 mA)	▪ $<$ 0.3 % $\Delta V/V$ (800 µs, 4.5 mA) (800 µs, 9 mA) ▪ Automated the cavity-gradient flattening algorithm
Gradient margin	All cavities operating within 3 % of quench	▪ Some cavities within $\sim$ 5 % of quench (800 µs, 4.5 mA) ▪ First tests of operations strategies for gradients close to quench
Energy Stability	$<$ 0.1 % rms at 250 GeV	▪ $<$ 0.15 % p-p (400 µs pulses $<$ 0.02 % rms 5 Hz)
RF power overhead	Stable operation at ILC design parameters	▪ First tests of operation within 5 % of klystron saturation with 800 µs pulse lengths and 4 mA ▪ First tests of klystron linearisation close to saturation
Linac operations	▪ 15 hrs continuous running with 3 mA and 800 µs pulses ▪ Several hours operation close to 9 mA with bunch trains of 500-600 µs ▪ Energy deviations within long bunch trains: less than 0.5 % pulse-pulse at 7 mA ▪ Energy jitter pulse-to-pulse with long bunch trains: $\sim$ 0.13 % rms. at 7 mA ▪ Recovery to 2400 bunches and 4.5 mA on the first pulse after a beam-inhibiting cryo event	

No fundamental technology issues with operating a superconducting linac at the ILC Technical Design baseline parameters were encountered. The operation of FLASH has also benefitted from the 9 mA experiment, most particularly with regard to providing stable routine operation with long beam pulses for FEL users. There remains, however, much to be learnt at FLASH. The European XFEL currently under construction offers an even greater opportunity for gaining invaluable experience and lessons with constructing, commissioning, and operating a large-scale superconducting high-power linac and for developing necessary tools and techniques.

3.3 STF beam test facility at KEK

3.3.1 Introduction

The STF facility at KEK has been designed from the outset eventually to house a test accelerator consisting of two ILC cryomodules, accelerating ILC-like beam from a laser-driven photocathode RF gun. Figure 3.21 shows the envisaged layout. A staged approach has been adopted in developing this test accelerator:

- for STF phase 1 (STF-1, 2007–2011), the facility was used as a module RF test set-up for the early STF-1 cryomodules and for the S1-Global programme; (Section 2.6).
- In 2011–2012, in part in preparation for the STF-2 beam test accelerator shown in Fig. 3.21, a separate project called "Quantum-Beam Accelerator" [129] was installed and tested. Primarily designed as a demonstration for a compact X-ray source using Inverse Compton backscattering of laser photons, the laser-driven photocathode RF gun and two-cavity capture cryomodule which provided the electron beam are the first stage of STF-2. The X-ray-generation experiment was performed in October 2012, after which the X-Ray-generation beam line and Compton laser system was decommissioned and replaced with the first ILC eight-cavity cryomodule in preparation for the STF Phase-2 ILC beam test facility.

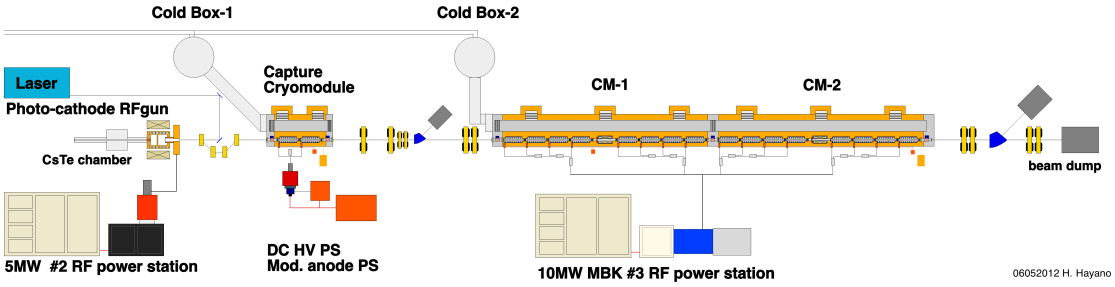

Figure 3.21. The STF Phase-2 accelerator, which will be constructed in the STF tunnel.

3.3.2 Quantum-Beam Accelerator as an injector for STF-2

Figure 3.22
The Quantum-Beam Accelerator. From the left to right, Cs_2Te photocathode preparation chamber, 1.3 GHz normal conducting RF gun, injection beam line, capture cryomodule with DRFS klystron power system, the focusing beam line, and beam dump.

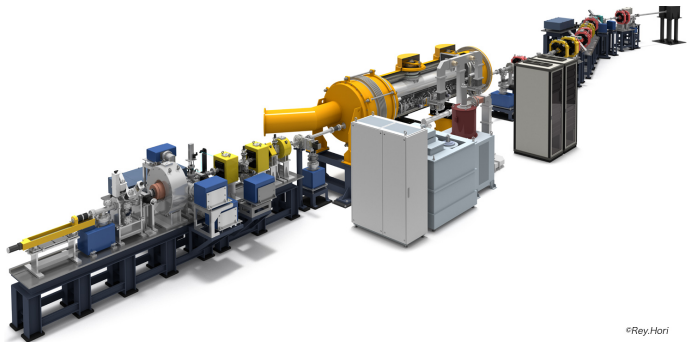

The Quantum-Beam accelerator is illustrated in Fig. 3.22; a photograph is shown in Fig. 3.23. The design parameters for the Quantum-Beam Accelerator and the STF phase-2 accelerator are listed in Table 3.4. The main difference in the electron beam requirements is the bunch spacing and bunch charge. The Quantum-Beam accelerator uses 162.5 MHz bunch-repetition frequency (6.15 ns spacing) with 62 pC/bunch, resulting in a peak pulse current of 10 mA. By comparison, the STF phase-2 accelerator requires a 2.708 MHz bunch rate (369.27 ns spacing) with 3.2 nC bunches, corresponding to a peak current of 8.7 mA (the ILC beam parameters), which will require a different RF gun laser system. STF-2 also requires a lower beam energy after the two-cavity capture accelerator of 21.5 MeV compared to 40 MeV for the Quantum-Beam Accelerator.

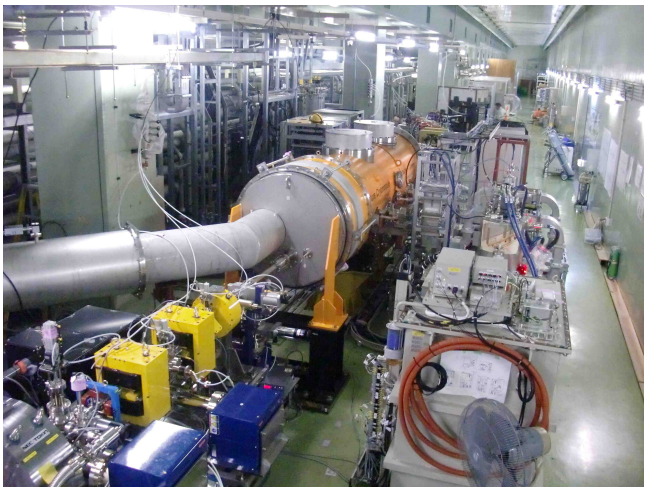

Figure 3.23
The injector for the STF-2 accelerator (Quantum Beam Accelerator), showing the 1.3 GHz normal-conducting RF gun, injection beam line, and SCRF capture cryomodule.

Table 3.4
Parameters for the Quantum-Beam Accelerator compared to those for the STF-2 injector

		Quantum Beam Accelerator	STF-2 Accelerator
Pulse length	ms	1.0	0.9
Repetition rate	Hz	5	5
Bunch spacing	ns	6.15	329.27
Bunch frequency	MHz	162.5	2.708
Bunches/pulse		162.500	2.437
Bunch charge	pC	62	3.200
Total charge /pulse	nC	10.000	7.798
Beam current	mA	10.0	8.7
Bunch length (laser FWHM)	ps	12	10
Max. beam energy	MeV	40.0	21.5
Beam power	kW	2.0	0.8

Before installation in the capture cryomodule, the two nine-cell cavities were tested and successfully reached gradients of up to 40 MV/m and 32 MV/m respectively. After installation in the cryomodule, the two cavities were connected to the 800 kW DRFS klystron power system Section 2.8.5. RF-gun commissioning began in February 2012, and acceleration of the ∼1 ms beam train was successfully achieved by June 2012.

3.3.2.1 Photocathode RF-gun commissioning

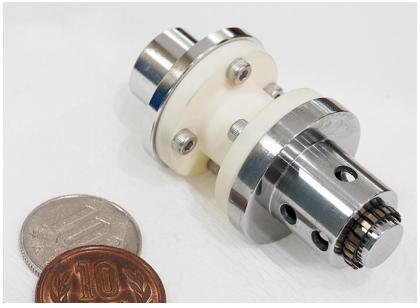

Figure 3.24
Photograph of the Molybdenum photocathode block. The head is thermally insulated by the ceramic interface to avoid the heat flow during surface heat cleaning. The heater is embedded in the blockhead. The Inconel crown contactor is used for the RF current contact between the block and the cavity endplate.

The design of the normal-conducting 1.3 GHz photocathode RF gun used was originally developed by DESY for FLASH and the European XFEL [130]. The Gun cavity was fabricated by FNAL and has a design peak field at the cathode of 50 MV/m at 4.5 MW RF power. To generate the long multi-bunch beam, a Cs_2Te photocathode is employed, which is prepared by evaporating a thin film on to a Molybdenum cathode block under vacuum. The Molybdenum cathode block is shown in Fig. 3.24. A special preparation chamber has been designed, allowing direct transfer of the cathode to the gun cavity under vacuum. In the preparation chamber, the surface of the Molybdenum plug is first baked to remove any impurities, followed by tellurium and caesium evaporation. To date,

a quantum efficiency (QE) of 7 % has been achieved. After an ethanol treatment followed by RF processing, the observed dark current was 247 µA with 46.7 MV/m (4 MW input power) for the bare Molybdenum surface cathode, and 688 µA with the Cs_2Te coating.

The drive laser for the cathode consists of a 162.5 MHz CW oscillator, Pockels cell, two-stage optical-burst amplifier and wavelength converter. The oscillator generates 1064 nm infrared pulses with 12 ps (FWHM) pulse width. The Pockels cell cuts out a pulse train of 1 ms with 5 Hz repetition from the CW oscillator output. The burst amplifiers boost the energy up to 10 µJ per pulse. The pulse train is converted to the 4th harmonic (266 nm) of the fundamental mode by LBO and BBO crystals. Figure 3.25 shows the 1 ms beam pulse successfully extracted by the gun in March 2012. The RF power was approximately 2.6 MW, and the cathode field gradient was approximately 37.5 MV/m, with 162,450 bunches at $\sim$ 30 pC per bunch.

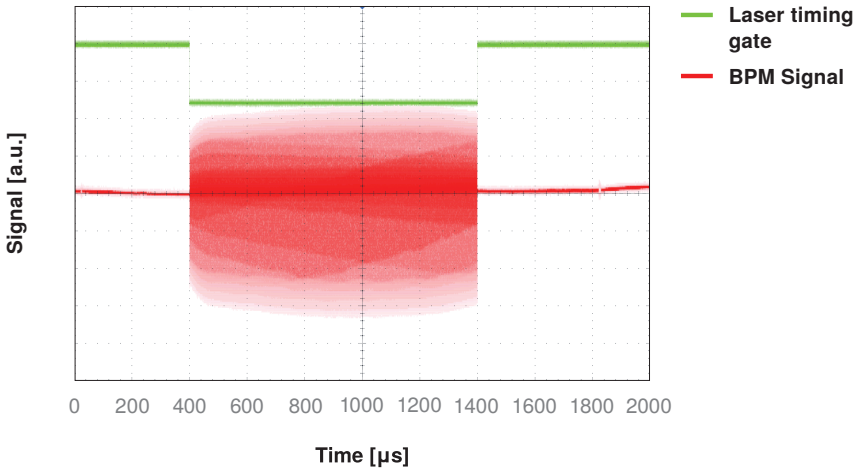

Figure 3.25
Plot of the 1 ms bunch train extracted from the photocathode RF gun. The lower (red) trace is the signal of the BPM; the upper (green) trace is the gate signal for the extracted laser pulse.

3.3.2.2 Capture-accelerator commissioning

The capture-cryomodule cool-down and adjustment of the superconducting cavities was started in April 2012. Both cavities were operated at 20 MV/m. For the initial commissioning, a short pulse of 28 bunches at 41 pC per bunch was used (5 Hz repetition rate). After successful commissioning of the digital feedback amplitude and phase control for both the RF gun cavity and superconducting cavities, a 1 ms-long beam train was successfully accelerated up to 40 MeV, with 15 pC bunches — 25 % of the target intensity — as shown in Fig. 3.26.

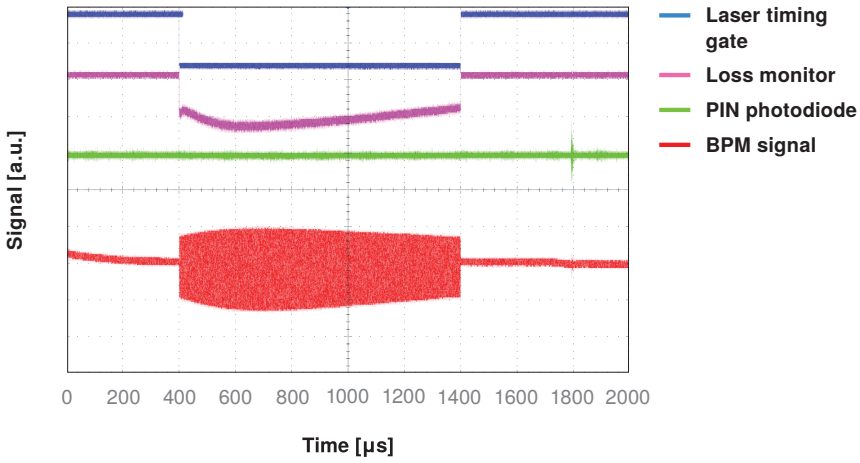

Figure 3.26
Plots showing 1 ms bunch train after acceleration to 40 MeV. The upper (blue) trace is the gate signal for the extracted laser pulse, the second (magenta) trace is the signal from the loss monitor, the third (green) trace is from the PIN photodiode signal used to measure beam loss at the Inverse Compton interaction point, and the lowest (red) trace is the signal from the bpm

3.3.3 The STF-2 accelerator

The STF-2 accelerator will consist of several ILC-type cryomodules. An existing laser capable of producing the required 1 ms pulse at 2.7 MHz (2437 bunches) will be used to drive the RF gun. The existing two-cavity capture-cryomodule will be used to accelerate the beam to 20 MeV before injection into the main ILC-type cryomodule accelerator. The first phase-2 cryomodule (CM-1) will consist of eight cavities, with a same-weight mock-up of an SC quadrupole installed at the centre of module. The quadrupole mock-up will also contain a BPM. Four cavities will have the slide-jack tuner mounted at the mid-point of the cavities (helium vessel), while the other four will have the tuner located at the end of the helium tank. The tuner motor will be placed outside the cryomodule vessel. The expected beam energy at the exit of CM-1 is 272 MeV. By November 2012, nine cavities have already been fabricated, and nearly all have completed their initial vertical test and have achieved gradients of 35 MV/m. The detail design and fabrication of CM-1 should be completed by the beginning of 2014. The originally foreseen second module (CM-2) is still under discussion. The RF power for the two ILC cryomodules (a total of 16 cavities) will be provided by a single 10 MW multi-beam klystron (Part II Section 3.6.3) driven by a Marx modulator (Part II Section 3.6.2). Beam operation of the STF-2 accelerator is planned for early 2015.

3.4 Fermilab Cryomodule 1 Test

3.4.1 Introduction/Goals

Fermilab's Cryomodule 1 (CM-1) is a Tesla Type III+ 8-cavity Superconducting RF module (Fig. 3.27). It came to Fermilab as a 'kit' from the DESY laboratory. CM-1 was assembled at Fermilab by its technical staff with assistance from colleagues from DESY and LASA/INFN, Milano. The goal of installing and operating CM-1 at NML was for Fermilab to gain expertise in assembling and operating a complete ILC-type Cryomodule as well as to demonstrate its capability. Successful cooldown and RF powering of all cavities simultaneously was the milestone for successful operation. Once installed, CM-1 was operated for fifteen months, ending in early March 2012. Concurrently with bringing CM-1 into operation, all necessary subsystems including cryogenics, high- and low-level RF, vacuum, protection systems, controls, safety systems etc., had to be commissioned and integrated. This operating period was invaluable both in terms of gaining experience in commissioning and operating an SCRF system but also in identifying improvements for future cryomodules.

Figure 3.27
Cryomodule 1 installed for operation at Fermilab's NML building. The waveguide distribution system, which feeds RF power to all 8 cavities simultaneously, is in the foreground.

3.4.2 Commissioning & Testing Protocol

CM-1 commissioning and testing approximately followed the standard protocol developed worldwide for bringing cryomodules into full operation. The steps include:

- RF cable calibration;
- technical sensor/interlock check;
- RF/waveguide check;
- warm coupler conditioning (off resonance);
- cooldown to 2 K;
- frequency spectra measurements;
- cavity tuning to nominal cold frequency (1300.00 MHz) via motorised slow tuner;
- $\mathrm{Q_L}$ adjustment (to 3×10^6 per ILC specification);
- RF system calibrations;
- cold coupler conditioning (on resonance);
- performance evaluation including:
  - maximum gradient;
  - dynamic heat load ($\mathrm{Q_0}$ vs. $\mathrm{E_{ACC}}$);
  - dark current and field emission (X-rays vs. $\mathrm{E_{ACC}}$).
- full cryomodule powering and evaluation.

As these steps were completed, additional measurements were made particularly with the LLRF and resonance control systems. Time was also made available to conduct a series of 'long pulse' 9 ms pulse-length studies on the two best cavities. As the end of the planned period of operation drew near, an additional step, namely thermally cycling CM-1 to room temperature and back to 2 K, was undertaken to determine its effect on cavity performance and provide data on longer-term operation.

3.4.3 Cold-Coupler Conditioning and Performance

CM-1 was installed in its final position and aligned in January of 2010 and final RF, cryogenics and vacuum connections were made thereafter. Since this was the first cryomodule of this type to be operated in this facility, commissioning entailed both the module itself as well as the RF, controls, protection system, vacuum, cryogenics, etc.

Warm off-resonance conditioning was performed with one cavity at a time connected to the output of the 5 MW klystron; it took anywhere from two weeks (for the first cavity) to four days to complete. Off resonance implies that the input RF was fully reflected back towards the load and no RF was directed into the cavity. The decrease in time was due to growing familiarity with the systems. The conditioning itself entailed applying successively higher amounts of RF power in successively longer pulse widths beginning with 20 µs to a maximum of the full 1.3 ms pulse. The peak power was as high as 1.1 MW for short pulses (20 µs – 400 µs) and 600 kW for 800 and 1300 µs pulse widths. An automated sequence was implemented which controlled the power and pulse width in a prescribed manner but responded to faults sensed by instrumentation monitoring excessive arcing, field emission, coupler temperature, and vacuum activity. In most cases, field emission coupled with vacuum activity from one of the three FEP sensors was the limiting factor in conditioning.

Once all eight couplers were conditioned, final vacuum work was completed leading to permission and initiation of cool down to 2 K. The module was cooled from room temperature to 4 K in slightly more than 2 days. The final cool-down to 2 K (23 Torr) required 2-1/2 hours. The CM-1 module first

reached operating temperature on 22 November 2010. The 1.3 GHz cryomodule design requires that its individual circuits be cooled at predetermined rates in order to limit thermal stresses. One such circuit is the helium-gas return pipe (GRP) which is a 300 mm pipe that acts as the rigid support (strong back) from which all of the cavities are suspended. Based on a computer simulation of the cryomodule cool-down and operating experience with similar design modules at DESY, the maximum vertical gradient along this circuit is limited to less than 15 K. The longitudinal gradient is to be maintained at 50 K or less and lastly the overall cool-down rate is to be 10 K per hour or less over the range of temperatures from approximately 300 K to 100 K. The thermal shield circuits have identical longitudinal cool-down-rate constraints.

Continuing with the sequence of commissioning steps, each cavity was then powered on resonance to complete coupler conditioning and determine cavity performance limitations. Again each cavity was powered singly. All cavities were characterised by June 11, 2011. Individual performance characteristics and limiting factors are summarised in Table 3.5. Cavities are numbered sequentially from the upstream end of the cryomodule (where upstream is defined as the end closest to the photo-injector gun), i.e. low-energy front end.

Table 3.5
CM-1 individual cavity performance characteristics.

Cavity	Peak Eacc (MV/m)	Estimated maximum Q_0 (E09)	Limitation/Comments
1/Z89	20.2	11	'soft' quench/heat load
2/AC75	22.5	12	Quench
3/AC73	23.2	0.43	'soft' quench/heat load
4/Z106	24*	2.3	*RF-limited
5/Z107	28.2	39	Quench
6/Z98	24.5	5.1	Quench
7/Z91	22.3	4.7	'soft' quench/heat load
8/S33	25	18	Resonant frequency at 1300.240 MHz; tuner motor malfunction

Three cavities exhibited unexpectedly high heat loads as evidenced by cryogenic activity – change in liquid level followed by an increase in system pressure, indicating heating and a drop in the Loaded Q (Q_L) at relatively low gradient, $<$20 MV/m. Significant field emission did not accompany this behaviour. It was found that the onset of the Q drop could be delayed by shortening the flat-top pulse length from the nominal 620 µs to 100 s. No source of this excessive heating has been definitely identified. Such behaviour has been observed elsewhere, most recently on a cavity under test at Fermilab's Horizontal Test Stand (HTS). With CM-1 now removed and disassembly started, plans are being made to disassemble the cavity string and re-evaluate these sub-performing components one at a time in the HTS facility. Reprocessing will be performed if deemed necessary. Additionally the 'slow' tuner on cavity #8 ceased functioning after approximately 20 minutes of cold operation leaving the cavity +240 kHz from the nominal 1.3 GHz resonant frequency. 'On-resonance' tests for this cavity were possible by adjusting the LLRF master oscillator, but this precluded inclusion of Cavity #8 in full module tests.

Comparison of individual cavity performance in CM-1 with that of previous tests is of interest. Figure 3.28 compares the peak gradient of each cavity to the values determined in vertical and horizontal tests at DESY. Table 3.6 provides a numerical comparison. A degradation of gradient of order 15 % or less is noted, perhaps not too surprising, considering that the cavities were vented to atmosphere and pumped back down a few times while at Fermilab. Differences in system calibration could also introduce disagreement in values.

Measurements of Q_0 were made on all cavities by measuring the static and dynamic heat load at discrete power levels. While maintaining each cavity at a fixed gradient for one hour the helium mass flow as well as incoming and outgoing temperatures and pressures were recorded. From this, a

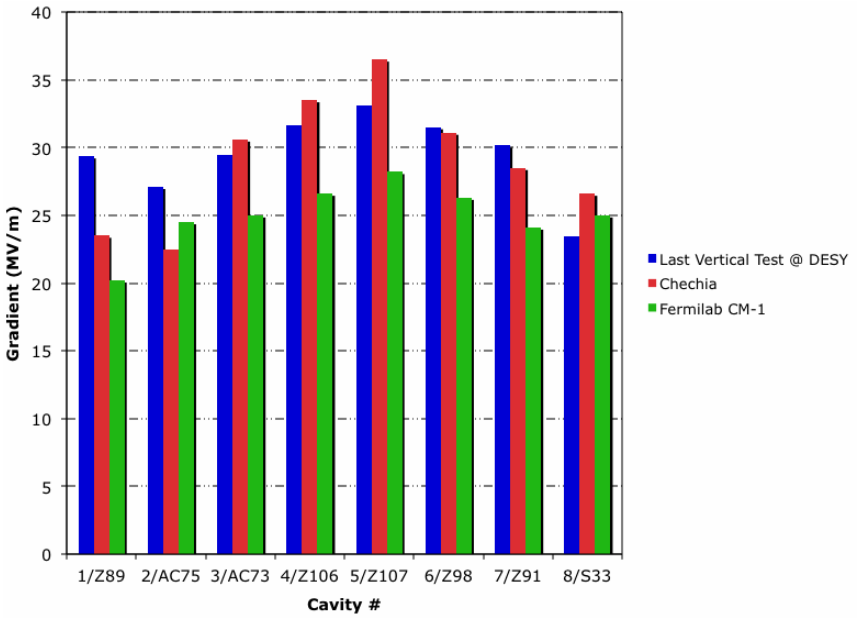

Figure 3.28
Comparison of cavity peak gradients – DESY single cavity vertical test results (blue), horizontal test results (Chechia) (red), and the complete CM-1 at Fermilab (green).

Table 3.6
Numerical comparison of CM-1 individual cavity performance

	Cavity								Avg.	Sum
	1/ Z89	2/ AC75	3/ AC73	4/ Z106	5/ Z107	6/ Z98	7/ Z91	8/ S33		
Last Vertical Test at DESY	29.36	27.10	29.49	31.65	33.07	31.51	30.16	23.44	29.47	235.78
Chechia	23.5	22.5	30.6	33.5	36.5	31.1	28.5	26.6	29.1	232.8
Fermilab CM-1 Final	20.2	24.5	25	26.6	28.2	26.3	24.1	25	24.99	199.9
Fermilab/ Vertical ratio	.688	.904	.848	.840	.853	.835	.799	1.07	.848	.848
Fermilab/ Chechia ratio	.860	1.09	.817	.794	.773	.846	.846	.940	.859	.859

dynamic heat load and thus Q_0 could be determined. The static heat load was measured before and after a powered run. Dynamic heat-load measurements were also made during operation of the entire cryomodule. Figure 3.29 shows a summary of Q_0 vs E for all cavities powered simultaneously. The static heat load was of order 22 W, consistent with independent measurements.

Following completion of single-cavity testing on 11 June 2011, the waveguide distribution system provided by SLAC, which allows for independent amplitude and phase control of adjacent pairs of cavities, was installed. Variable Tap Offs (VTO's) were set based upon the gradient limits identified during cavity characterisation.

Full-module testing was initiated on 6 July 2011 and largely continued until the end of the year. The bulk of the time spent powering the entire module was devoted to low-level RF (LLRF) optimisation, refining the Lorentz-force detuning compensation system and trying to understand the source of the 'soft quenching' cavities. Operation was largely reliable and there were periods of overnight operation. CM-1 ran for as many as 65.5 hours continuously at moderate gradient, average 16.5 MV/m per cavity, without a trip. Figure 3.30 shows seven cavities operating at the same frequency being powered simultaneously. The variation in peak gradient was due to individual cavity limitations and the resulting setting of the VTO's. Pairs of cavities were thus operating at similar gradients.

Development work on the low-level RF system was a constant throughout the running period. By the end of the run it was possible to control the RF amplitude and phase over 50 pulses to a RMS magnitude error of 2.5×10^{-4} and RMS error of 0.005°.

Significant time was also spent refining adaptive Lorentz-force detuning compensation. Gradients

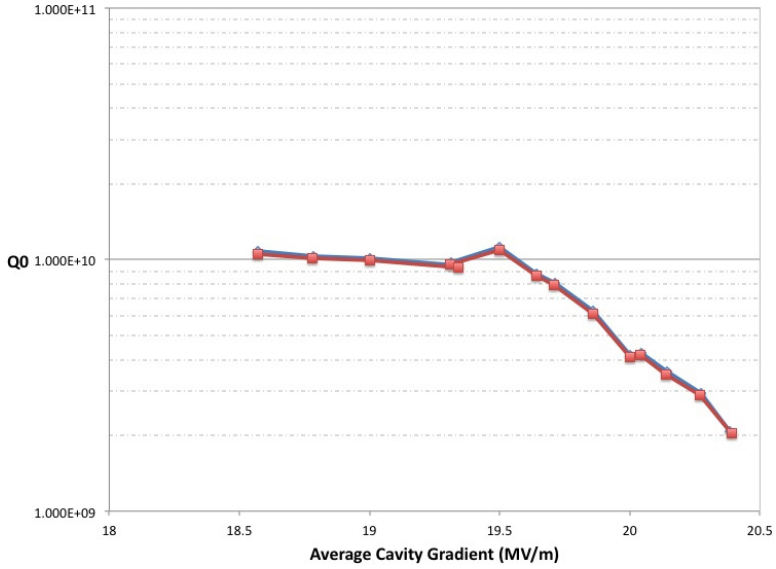

Figure 3.29
Q_0 vs E_{Acc} for CM-1 cavities

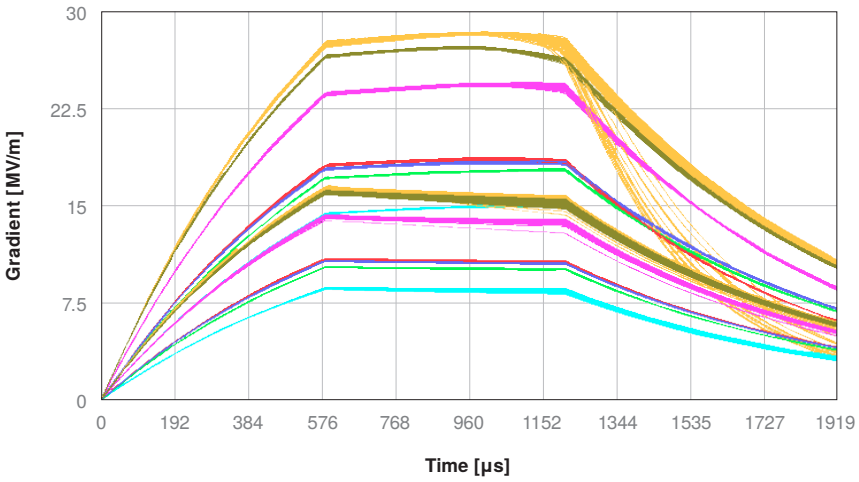

Figure 3.30
Transmitted power waveforms of all cavities pulsing at the nominal conditions: 5 Hz, 1.3 ms pulse length (580 μs fill, 620 μs flattop) with LLRF in closed loop and LFDC disabled just below the stable operating point. Some quenching by the highest-performing cavity and indications of Lorentz-force detuning can be observed.

in the cavities ranged between approximately 8 and 27 MV/m. Without compensation, the highest gradient cavities would detune by up to 400 Hz during the flattop. With adaptive compensation on, the detuning was negligible in all the cavities except for Cavity 1, which detuned by approximately 10 Hz during the RF pulse.

Even for cavities operating at the highest gradients, Lorentz-force detuning could be compensated using relatively modest voltages of $\sim \pm 20$ V to drive the piezo tuner. The waveforms do not exhibit fast transients that could potentially damage the piezo tuners. Figure 3.31 shows a screen capture of the resonance-control system during normal CM1 operation with the adaptive compensation on.

Once all planned tests were completed, the cryomodule was thermally cycled to room temperature and back to 2 K to determine if such action might have an effect on cavity performance. Warm-up proceeded uneventfully, however upon reaching 132 K during cooldown, vacuum activity was observed in the insulating vacuum space, the magnitude of which automatically closed the gate valves between the module and the feed and end cans. A nitrogen peak was observed. Upon opening the upstream insulating vacuum space, a leaking feedthrough for a nitrogen-line temperature sensor was identified as the source of the leak. The feedthrough was replaced with a blank and an alternate surface-mount sensor installed. Cooldown proceeded and operation resumed. Although this was an unfortunate occurrence, it did prove to be a valuable experience in terms of learning how to identify the location of leaks remotely and make in situ repairs, as well as assess vulnerabilities in types of thermometry. Upon the resumption of cold operation only minor changes in operating performance were noted

although some multi-pactoring was observed as some cavities approached their peak values. This was rapidly processed away.

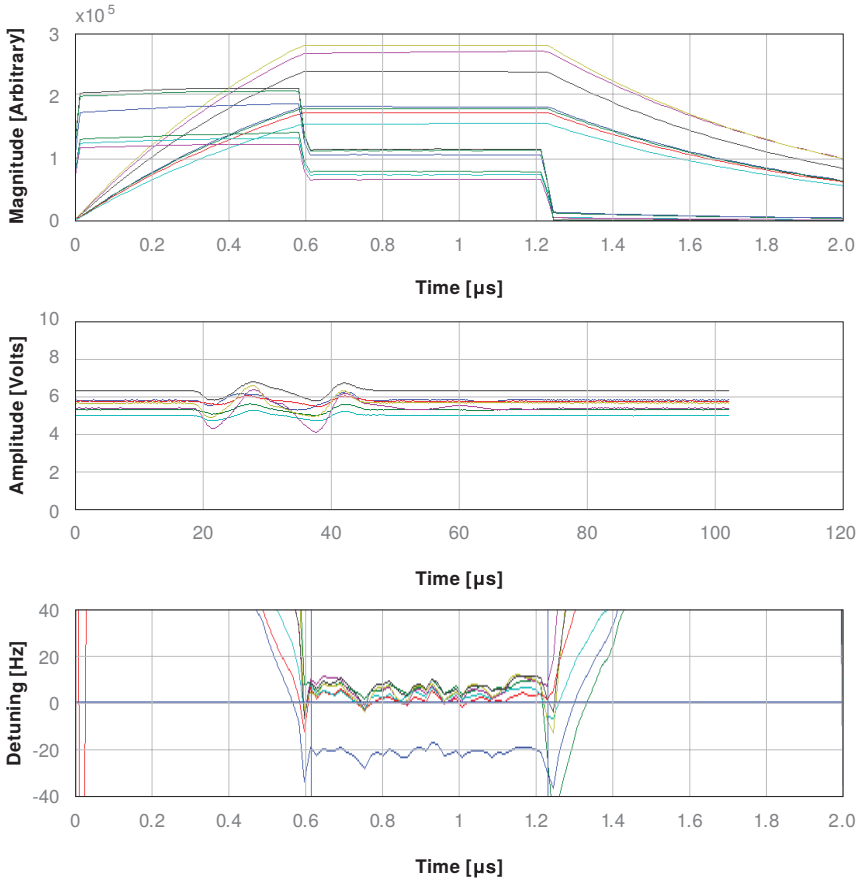

Figure 3.31
CM1 resonance-control online display during adaptive feed-forward compensation. The top section shows the magnitude of the RF waveforms of the cavities; the middle action shows the piezo monitor waveform; the 10 V full vertical scale of the piezo monitor signal corresponds to a piezo drive of 200 V. The bottom section shows the cavity detuning calculated from the RF waveforms.

3.4.4 Ancillary Systems and Findings

All of the necessary subsystems for operating and protecting the cryomodule performed largely as expected. The protection system appropriately limited power or triggered system shutdowns as conditions warranted. The cryogenics plant suffered only minor interruptions, usually due to external factors.

Diagnostics were in place to monitor field emission as well as the presence of dark current emanating from the cavities. These proved to be measurable, but not limiting factors in performance.

3.4.5 9-millisecond-Pulse Tests

Once the Cryomodule was well characterised, a 'long pulse' study was carried out in support of an R&D program for a proposed continuous-wave SRF accelerator at Fermilab. This effort, a proof or principle, entailed operating the two best performing cavities at a pulse length of up to 9 ms and determining the LLRF and resonance-control capabilities at various input powers and QL values. Planned operating parameters were:

- RF power limitations: 80 kW; 100 kW, 120 kW per two cavities;
- external Q_L: 3×10^6; 6×10^6; 1×10^7;
- gradient: 15 MV/m; 20 MV/m; 25 MV/m;
- 9 ms pulse width.

This study proved to be a good first-pass test. Lorentz-force detuning (LFD) Compensation at the nominal parameters Q=1×10^7 and 25 MV/m was demonstrated. The LLRF feedback worked

with phase stability good to $\pm$ 4°. The total range of detuning was of order $\pm$10 Hz peak-to-peak with comparable contribution from microphonics and residual LFD. The residual LFD's shape of detuning was repeatable from pulse to pulse with major harmonics $\sim$ 1 kHz. It is expected that LFD compensation can be improved by cancelling out this component. The measured microphonics level was in range 2-4 Hz, similar to what was measured for short 1 ms pulses. Although the behaviour of cavities #5 and #6 were different, the results of LFD compensation were comparable.

Areas requiring further work were uncovered. Input power limitation for the low Q case ($\sim 3 \times 10^6$) limited the peak gradients to < 20 MV/m. The system also proved to be highly sensitive under dynamic conditions. Nearly constant attention was required to maintain stable operation, especially when adjusting the power. Spontaneous quenching resulted from power adjustments without also adjusting LLRF system gains.

3.4.6 Future Prospects

The CM-1 module is the first of a series of cryomodules planned to be installed and tested at Fermilab. The second cryomodule is also a TTC Type III+, containing cavities that all achieved gradients of 35 MV/m when tested vertically and 31.5 MV/m when 'dressed' and tested at Fermilab's Horizontal Test Stand. Cooldown and first operation of this cryomodule, designed to meet ILC gradient specifications, is expected in late 2012. Most components are in hand and some assembly at Fermilab has begun on a third cryomodule, which will be a high-gradient TTC Type-IV cryomodule.

3.4.7 Summary

The CM-1 cryomodule was the first to be assembled at Fermilab, and as such was also the first cryomodule tested at the recently constructed New Muon Lab (NML) facility. The overall goal of demonstrating facility operations and cryomodule test capability was achieved successfully. The CM-1 module was operated stably near the peak achievable gradients with both LLRF feedback and LFDC enabled for an extended time. RF amplitude and phase were controlled within specification and detuning was successfully compensated over the full gradient range. Valuable experience was gained in both the commissioning and control of multi-cavity SCRF modules. A problem associated with a tuner prevented one cavity from operating on-resonance. A thermal cycle resulted in a vacuum leak in a feedthru. After repair and resuming cold operation the cryomodule showed only minor operating changes.

The next cryomodule, CM-2, is under fabrication and will be a complete ILC design with cavities that all reached the GDE gradient goals. Testing is anticipated in 2013.

3.5 CesrTA and Electron-cloud R&D

3.5.1 Introduction to the Electron-cloud R&D Program

One of the principal R&D issues for the positron damping ring of the ILC is to ensure that the build-up of the electron cloud (EC)) in the vacuum chambers can be kept below the levels at which EC-induced emittance growth and beam instabilities occur. During Phase I (2008-2010) of the ILC Technical Design Phase (TDP), a focused effort to study methods of suppressing the EC as well as measuring its impact on ultra-low emittance beams was undertaken at the Cornell Electron-Positron Storage Ring Test Accelerator (CesrTA). In addition, a complementary R&D program has continued at various laboratories around the world to develop better techniques to mitigate the build-up of the electron cloud. Section 3.5.2 describes the research effort that has been carried out at Cornell University by the CesrTA collaboration [131, 132], while Section 3.5.3 describes the work that has taken place at other laboratories around the world. As part of this coordinated global programme, a major emphasis has been placed on developing and benchmarking simulation tools as well as measurement techniques.

In order to incorporate the research results into the ILC damping ring (DR) design, an ECLOUD Working Group was formed whose main objective has been to provide recommendations on the EC mitigation techniques to apply to the DR design based on the results of the R&D programme [133, 134]. A dedicated Working Group meeting [135] was held during the ECLOUD10 Workshop [136], with a significant level of participation by experts attending the workshop. The recommendations, which have since been implemented in the ILC DR vacuum-system conceptual design [137], are summarised in Section 3.5.4.

3.5.2 The CesrTA R&D Programme

The CesrTA research programme was approved in late 2007 to carry out electron-cloud R&D in support of the ILC technical design. The first dedicated experiments using the Cornell Electron-Positron Storage Ring (CESR) began in March 2008 at the conclusion of 28 years of colliding beam operations for the CLEO experiment [138]. Two principal goals were specified for the programme. The first was to characterise the build-up of the electron cloud in each of the key magnetic-field regions of the accelerator, particularly in the dipoles and wigglers, and to study the most effective methods of suppressing it in each of these regions. This required the design and installation of detectors to study the local build-up of the cloud in each of these environments as well as a supporting simulation programme to fully characterise and understand the results. The second goal was to study the impact of the electron cloud on ultra-low-emittance beams. The ILC damping-ring design targets a geometric vertical emittance of 2 pm rad; no positron ring has yet been operated in this emittance regime. By benchmarking electron-cloud instability and emittance-growth simulations in a regime closer to that specified for the damping ring, confidence in projections of the final damping-ring performance could be significantly improved. This in turn helped to determine how much further R&D was required to achieve the necessary design specifications. In order to carry out these measurements, CESR had to be reconfigured as a damping ring and upgraded with the necessary beam instrumentation for low-emittance optics correction and characterisation of the resulting beams.

3.5.2.1 Conversion of CESR to a Damping-Ring Test-Accelerator Configuration

Modification of CESR into a damping-ring configuration involved three main thrusts:

1. Relocation of six of the twelve CESR-c damping wigglers [139, 140], to the L0 straight section in CESR to enable ultra-low-emittance CesrTA operation [138];

2. Upgraded beam instrumentation to achieve and characterise ultra-low-emittance beams, including deployment of a system for high-resolution beam-position monitoring [141] and X-ray beam-size monitors for both positron and electron beams [142];

3. Addition of vacuum-system diagnostics for characterisation of local electron-cloud growth in a range of vacuum chambers, including retarding-field analysers [143, 144], transverse-electric-wave transmission hardware [145] and shielded pickups for time-resolved measurements [146].

Table 3.7 shows the CesrTA lattice parameters for operation at 2 GeV and 5 GeV. At 2 GeV, $\sim 90\,\%$ of the synchrotron-radiation power is provided by the twelve damping wigglers and a horizontal design emittance of 2.6 nm rad is obtained [147]. During Phase I of the CesrTA programme, a vertical-emittance target of less than 20 pm rad (ten times the ILC damping-ring vertical-emittance target) was specified. A key element of the R&D programme has been the flexibility of CESR operation. CESR allows operation between 1.8 and 5.3 GeV with both positron and electron beams. The ability to operate over a wide range of energies, bunch spacings and bunch intensities has enabled systematic studies of primary photoelectron and secondary electron contributions to electron-cloud build-up in the vacuum chambers, which are not feasible at any other facility.

Table 3.7
2 GeV and 5 GeV lattice parameters for CesrTA.

Parameter	Symbol	Unit	2 GeV	5 GeV
Energy	E_{beam}	GeV	2.085	5.0
Number of wigglers			12	6
Wiggler peak field		T	1.9	1.9
Horizontal tune	Q_{x}		14.57	
Vertical tune	Q_{y}		9.6	
Longitudinal tune	Q_{z}		0.075	0.043
RF voltage	V_{RF}	MV	8.1	8
Horizontal emittance	ϵ_{x}	nm rad	2.6	35
Damping time constant	$\tau_{\mathrm{x,y}}$	ms	57	20
Momentum compaction	α_{p}		6.76×10^{-3}	6.23×10^{-3}
Bunch length	σ_{l}	mm	9.2	15.6
Relative energy spread	σ_{E}/E	%	0.81	0.93
Bunch spacing	t_{b}	ns	≥ 4, steps of 2	

A novel element of the CesrTA upgrade has been the development of a high-resolution X-ray beam-size monitor capable of single-pass measurements of each bunch in a train. Figure 3.32 shows one of the indium-gallium-arsenide detectors wire-bonded to its circuit board along with a single-pass fit of data acquired using pinhole imaging with a 1 mA bunch. In addition to pinhole imaging, coded aperture and Fresnel-zone-plate optics have also been installed in both the positron and electron beam lines. These detectors are the principal tools for verifying the vertical beam size in the ultra-low-emittance machine optics.

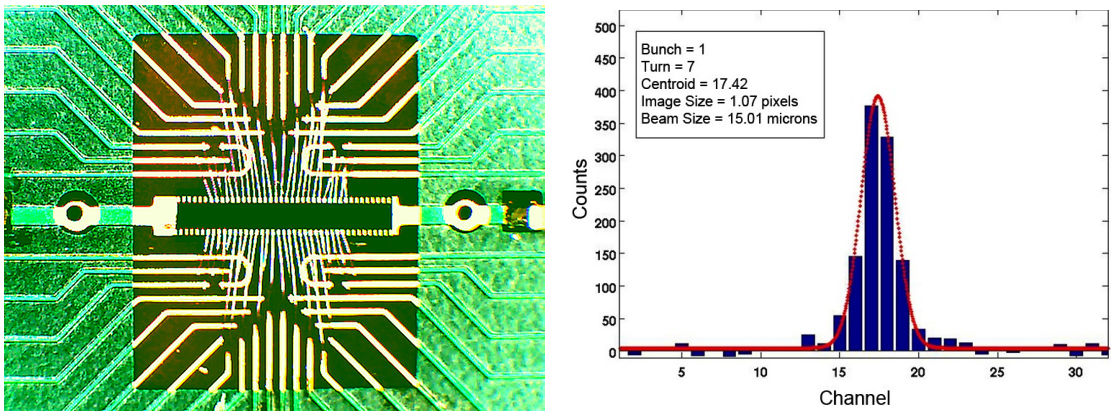

(a) **(b)**

Figure 3.32. (a) An X-ray beam-size monitor detector, an indium-gallium-arsenide diode array, mounted on its circuit board. Each detector has 32 diodes of 400 µm width and 50 µm pitch. (b) A single-turn fit to data acquired from a bunch with 0.8×10^{10} particles (at 2.1 GeV beam energy) using a heavy-metal slit as the X-ray imaging optic.

Figure 3.33 shows the layout of the CESR L0 straight section after installation of the wiggler string. This region is one of four dedicated CesrTA electron-cloud experimental areas. It is equipped with extensive diagnostics to study the growth and mitigation of the electron cloud in wigglers. A second electron-cloud experimental region was installed on the opposite side of CESR in the L3 straight section. Figure 3.34 shows the layout of the L3 region. It supports four electron-cloud experiments: a large-bore quadrupole housing a test chamber; the Positron Electron Project (PEP) II chicane for dipole-chamber tests, which was relocated from SLAC after the early termination of PEP II operations; a drift-chamber test section currently configured for testing titanium-zirconium-vanadium (TiZrV) non-evaporable getter (NEG) test chambers; and an in-situ secondary-electron-yield measurement station, which supports studies of the processing rates and equilibrium properties of secondary-electron yield of various technical surfaces. In addition to the L0 and L3 experimental regions, two arc sections were configured for flexible installation of experimental drift chambers to study the performance of various mitigations in the photon environment of the CESR arcs.

3840511-040

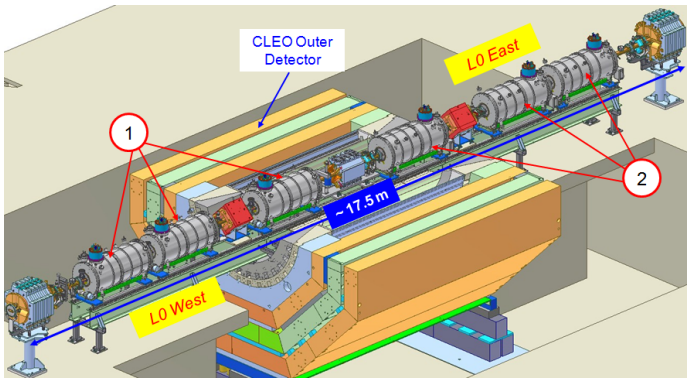

Figure 3.33
Layout of the CESR L0 wiggler straight and electron cloud experimental region with a cutaway view of the CLEO detector. Six superconducting CESR-c type wigglers are deployed in the straight, which is configured for zero dispersion operation. Wigglers labeled (1) are downstream wigglers, with respect to the positron beam direction, which are instrumented with retarding field analyzers. Wigglers labeled (2) are unmodified CESR-c type units. The straight section includes extensive vacuum diagnostics: retarding field analysers, residual gas analyser, and transverse electric wave measurement hardware.

3840511-043

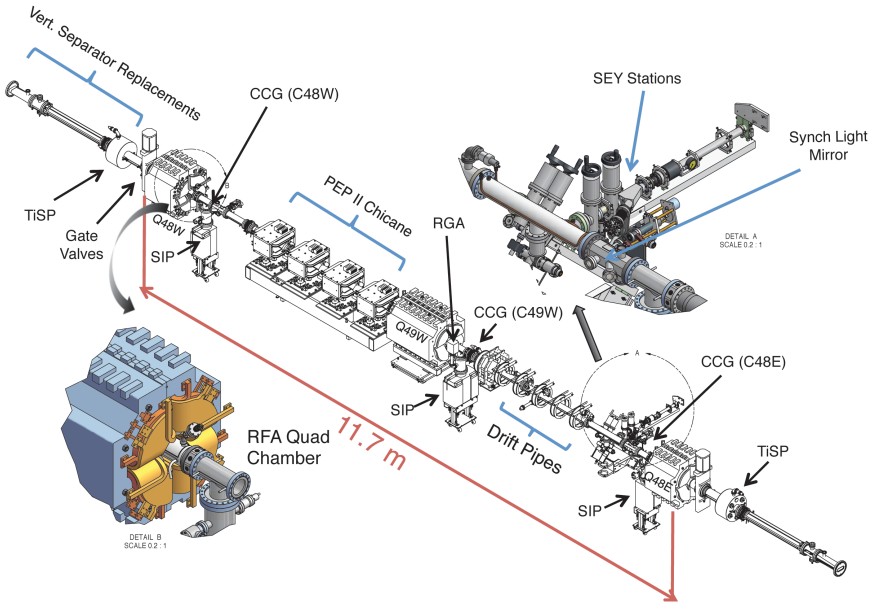

Figure 3.34
Layout of the CESR L3 straight and electron-cloud experimental region. Tests of electron-cloud mitigations in drift, dipole and quadrupole chambers are possible in this region. Additionally, an in-situ secondary-electron-yield station is also installed, which allows characterisation of the rate of processing and properties of equilibrium secondary-electron yield of various vacuum-system technical surfaces.

3.5.2.2 Electron-Cloud Build-up and Mitigation Studies

Retarding-field analysers deployed at approximately 30 locations around CESR have enabled the detailed study of local cloud build-up in a variety of vacuum chambers under a range of experimental conditions [148, 149]. The analysers provide a time-averaged current readout at each location. The majority of deployed retarding-field analysers utilise a segmented design to provide geometric information about the cloud build-up around the azimuth of the vacuum chamber. Analyser data taken in vacuum chambers fabricated with cloud-mitigation measures provide the foundation for comparison of the efficacy of different methods of electron-cloud mitigation. An active effort continues to model this analyser data in order to constrain experimentally the secondary-electron-yield and photoelectron-yield parameters of the vacuum chambers treated with mitigations in an operating accelerator environment [149–153]. In addition to the retarding-field analyser studies, transverse-electric-wave transmission methods [154–157] are also being used to characterise the build-up around the ring; a significant simulation effort is underway to take full advantage of these results [158–161]. A final method to study local cloud build-up is shielded pickup measurements [162–165], which are providing additional constraints on the vacuum-chamber surface parameters for the chambers in which they are installed. Table 3.8 summarises the range of chamber surfaces and mitigation methods that were prepared for testing during Phase I of the CesrTA R&D programme.

Figure 3.35 shows a comparison of the performance of various chamber surfaces in a dipole field along with a plot of the evolution of the transverse distribution of the electron cloud that develops

Table 3.8
Vacuum chambers fabricated for testing during the CesrTA R&D programme. Mitigation studies have been conducted in drift, dipole, quadrupole, and wiggler magnetic-field regions. Checks indicate chambers for which data has been acquired. CU stands for Cornell University.

Mitigation	Drift	Quad	Dip	Wig	Contributing Institutions
Al	X	X	X		CU, SLAC
Cu	X			X	CU, KEK, LBNL, SLAC
TiN on Al	X	X	X		CU, SLAC
TiN on Cu	X			X	CU, KEK, LBNL, SLAC
C on Al	X				CERN, CU
Diamond-like C on Al	X				CU, KEK
NEG on SS	X				CU
Solenoid Windings	X				CU
Fins w/TiN on Al	X				CU, SLAC
Triangular Grooves:					
On Cu				X	CU, KEK, LBNL, SLAC
With TiN on Al			X		CU, SLAC
With TiN on Cu				X	CU, KEK, LBNL, SLAC
Clearing Electrode				X	CU, KEK, LBNL, SLAC

in the dipole chamber as a function of the beam current. While coating with a material with low secondary-electron yield, such as titanium nitride, significantly reduces the growth of the cloud in this environment, the use of a grooved surface with titanium-nitride coating is clearly superior.

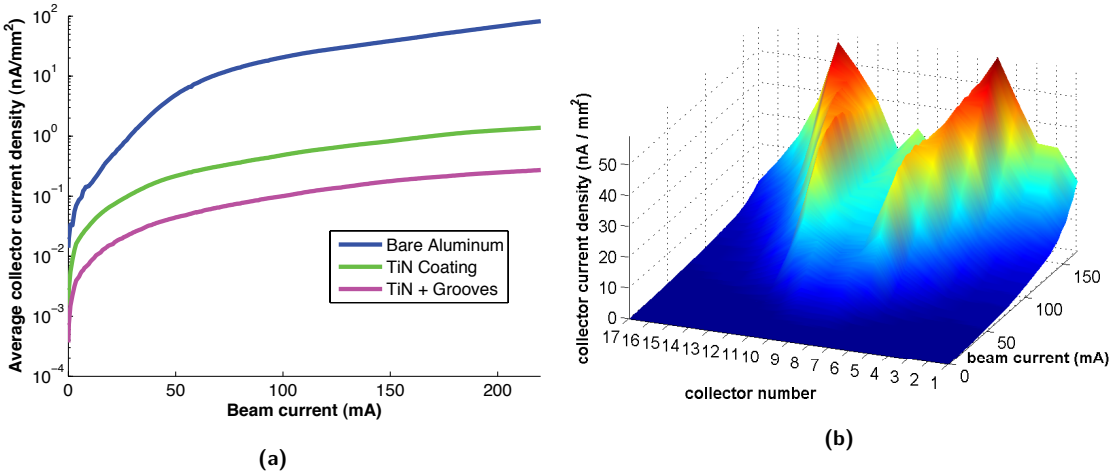

Figure 3.35. (a) The measured retarding field analyser current in a dipole versus beam current with a 20-bunch positron train for a bare aluminium surface, titanium nitride-coated surface and a grooved surface with titanium nitride coating. The efficacy of the grooved surface for suppressing the electron cloud is clearly evident. (b) The transverse shape of the electron cloud signal in the dipole retarding-field analyser (aluminium chamber surface) as a function of beam current.

Figure 3.36 shows two of the mitigation methods that have been tested in the CesrTA high-field damping wigglers: triangular grooves and a clearing electrode. The clearing electrode is a very thin structure developed at KEK [166] that offers very good thermal contact with the vacuum chamber and minimal impact on the chamber aperture (see also Section 3.5.3). A bare copper surface and a titanium-nitride-coated copper surface have also been tested. Figure 3.37a shows a comparison of the electron-cloud growth as a function of beam current with each of these surfaces. The data indicate that the best cloud suppression in the wiggler region is obtained with the clearing electrode. Figure 3.37b shows the transverse distribution of the cloud present in the vertical field region of the wiggler (copper surface) as a function of the retarding grid voltage, which probes the energy spectrum of the electron cloud.

Studies of the electron-cloud build-up in drift and quadrupole regions have also yielded important results. Drift measurements have been used to compare the performance of various coatings. A new coating of significant interest is amorphous carbon developed at CERN [167] for use in the Super Proton Synchrotron (SPS). Tests at CesrTA have afforded the opportunity to study the performance of this coating in the presence of synchrotron radiation. Initial studies show that the electron-cloud

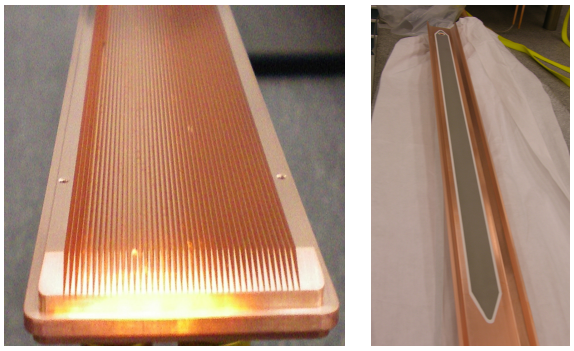

Figure 3.36
(a) A grooved copper insert with 21.8° triangular grooves having 1 mm pitch for testing in a CesrTA wiggler. (b) A thin clearing electrode applied with a thermal-spray method to the bottom half of another CesrTA experimental wiggler chamber.

(a) **(b)**

mitigation performance of carbon is quite comparable to that of titanium nitride and that its vacuum performance is quite reasonable in an environment with significant photon flux. Continued testing will provide information about the long-term durability of this very promising coating. Vacuum chambers in quadrupole magnetic fields can show quite significant cloud build-up. Concerns about long-term trapping of the cloud in quadrupole fields [168] require that cloud mitigation be incorporated into the ILC damping-ring quadrupole vacuum chambers. Tests in CesrTA have demonstrated the effectiveness of titanium-nitride coating in this region.

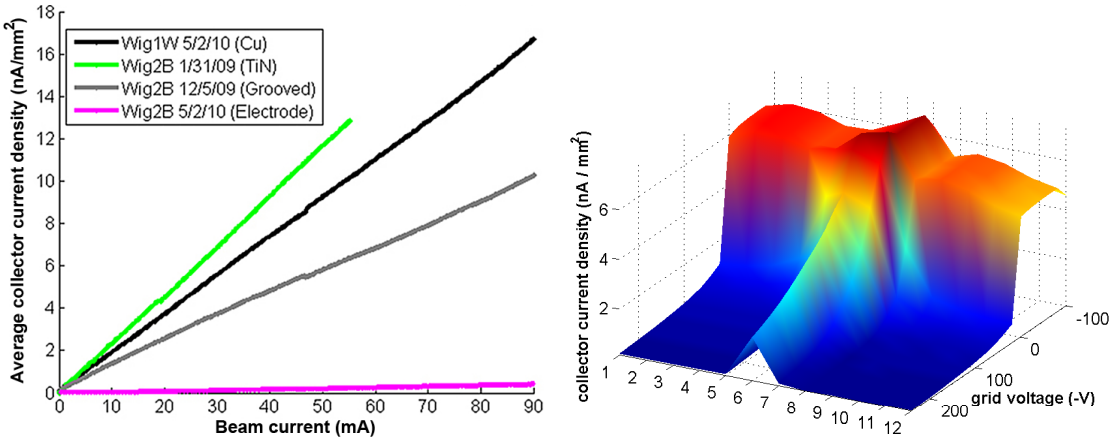

(a) **(b)**

Figure 3.37. (a) The measured retarding-field analyser current in a wiggler versus beam current with a 20-bunch positron train for a bare copper surface, a titanium-nitride-coated copper surface, a grooved copper surface and a clearing electrode. The efficacy of the clearing electrode for suppressing the electron cloud is clearly evident. (b) The transverse shape of the electron-cloud signal in the wiggler retarding-field analyser as a function of retarding voltage.

3.5.2.3 Studies of Electron-cloud-induced Beam Dynamics at Low Emittance

The CesrTA low-emittance tuning effort provides the basis for studying the emittance-diluting effects of the electron cloud in a regime approaching that of the ILC damping rings. As of early 2010, the low-emittance tuning programme had resulted in reliable operation at or below the CesrTA Phase I vertical emittance of 20 pm rad [169] for both single- and multi-bunch operation as confirmed by X-ray beam-size-monitor measurements of the vertical beam size [170]. As of the end of 2010, vertical emittances less than 10 pm-rad had been achieved.

A number of beam-dynamics studies have been conducted in order fully to characterise the impact of the electron cloud on beams in CESR. As the electron cloud builds up along a bunch train, the focusing effect of the cloud on the beam causes the natural frequency of oscillation of each bunch (i.e. the horizontal and vertical betatron tunes) to shift with respect to the preceding bunch.

Measurements of this electron-cloud-induced coherent tune shift [171–173] for trains of electron and positron bunches, as well as for witness bunches at various positions behind a leading train, have provided an important probe of the integrated effect of the cloud around the ring. Systematic measurements over a wide range of beam conditions (varying beam energy, emittance, bunch current, bunch spacing and train lengths) have been used to validate electron-cloud models more thoroughly. An important feature of these measurements has been the need to model accurately the photon transport, reflection and absorption around the ring in order to describe the data adequately. This has led to the implementation of a new ring photon propagation package, SYNRAD3D [174], which has most recently been applied to the design of the ILC damping-ring vacuum system and has resulted in important refinements of that design [137].

A principal deliverable of the CesrTA programme is the characterisation of instability thresholds and emittance-diluting effects in the regime of ultra-low vertical emittance [175–179]. Figure 3.38 shows the observed beam-motion spectrum for each bunch along a train obtained in these conditions. As described in the preceding paragraph, the development of the horizontal and vertical tune lines, denoted by F_h and F_v, along the bunch train provides information about the electron-cloud density experienced by each bunch. For a positron train, the attractive force of the bunch pinches the cloud into the bunch and can lead to the development of an oscillation of the bunch tail with respect to the head. This head-tail instability is expected to induce characteristic sidebands in the bunch-motion spectrum. In Fig. 3.38, the onset of the spectral lines denoted by $F_v \pm F_s$ part way along the bunch train indicate where the cloud density build-up has become sufficient for the onset of the instability.

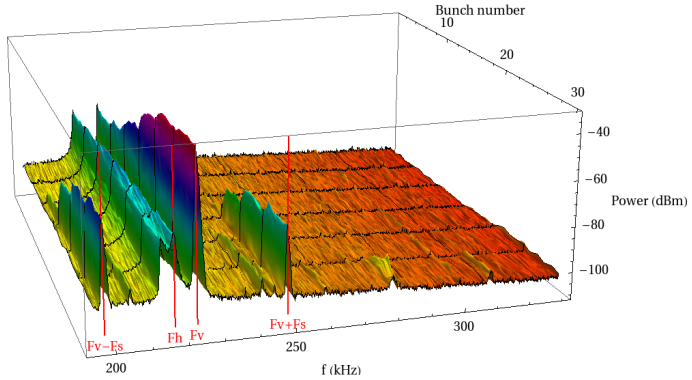

Figure 3.38
Bunch-by-bunch power spectrum for a positron train with a nominal bunch current of 0.75 mA/bunch. The horizontal (Fh) and vertical (Fv) tunes are clearly visible for all bunches. The onset of the sidebands labelled as $F_v \pm F_s$ are consistent with the onset of a head-tail instability around bunch number 15 in the train.

A second observable associated with this instability is a growth in the vertical beam size as measured along the train. Figure 3.39 shows bunch-by-bunch beam-size development along bunch trains with three different intensities. As the bunch currents are increased, the bunch number in the train at which beam-size blow-up occurs moves earlier in the train due to the more rapid build-up of the electron cloud. By studying both the spectral and beam-size information as a function of various parameters (bunch intensity, vertical emittance, bunch spacing, chromaticity, feedback conditions, and beam energy) and comparing with simulation [180–183] the simulations in a regime approaching that of the ILC damping ring have been validated, ensuring that the projections of the expected performance of the positron damping ring are accurate.

Analytical estimates of the head-tail instability thresholds, following the calculations described in [184,185], have been made for CesrTA as well as for the ILC damping ring [8]. Table 3.9 summarises the key parameters and instability thresholds, based on the parameters given in Table 3.10. The observed instability thresholds observed in CesrTA low-emittance experimental conditions are in good agreement with these calculations when the EC density near the beam is determined by tune-shift measurements along the train. This applies both to the appearance of synchrobetatron side-bands in the tune measurements as well as rapid beam-size growth as observed with the xBSM. The good agreement between data and experiment provides confidence in estimates for the ILC DR.

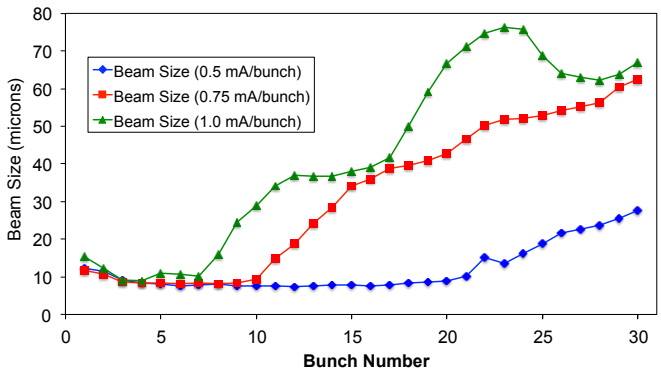

Figure 3.39
Bunch-by-bunch beam sizes based on turn-by-turn fits for each bunch for 30 bunch trains of varying current (0.8, 1.2, and 1.6×10^{10} particles/bunch). As the bunch currents are increased, the point in the train at which the electron cloud density is high enough to cause emittance and beam-size growth moves to earlier points in the train.

There is some evidence in the beam-size data that there may be sub-threshold emittance growth before the full onset of the head-tail instability. In the CesrTA data, such effects can occur at EC densities which are a few times smaller than the calculated instability thresholds. This suggests that some additional margin may be required in our estimates of the safe EC densities for stable operation of a damping ring and argues for an aggressive approach to the choice of EC mitigation techniques. This is consistent with the recommendations described in Section 3.5.4. Work continues on the simulations and measurements required to clarify this issue.

Table 3.9
Analytic estimate of the fast head-tail instability threshold for CesrTA and the ILC damping ring.

	CesrTA (2 GeV)	CesrTA (5 GeV)	ILC DR
Bunch Population N_+ ($\times$ 10^{10})	2	2	2
Bunch Spacing ℓ_{sp} (ns)	4	4	6
Average Vertical Beta Function β_y (m)	16	16	24
Electron Frequency $\omega_e/2\pi$ (GHz)	35	11	111
Phase Angle χ	8.9	3.7	14.0
Threshold Density $\rho_{e,th}$ ($\times 10^{12}$ m^{-3})	0.82	3.22	0.23
Tune Shift at Threshold $\Delta\nu_{x+y}$ ($\times$ 10^{-3})	9	14	5

Table 3.10
Parameters of CesrTA and the ILC damping ring used for instability threshold estimates.

	CesrTA (2 GeV)	CesrTA (5 GeV)	ILC DR
Circumference L (m)	768	768	3245
Energy E (GeV)	2.1	5.0	5.0
Bunch Population N_+ ($\times$ 10^{10})	2	2	2
Emittance ε_x (nm)	2.6	40	0.45
Momentum Compaction α ($\times$ 10^{-4})	67.6	62.0	3.3
RMS Bunch Length σ_z (mm)	12.2	15.7	6
RMS Energy Spread σ_E/E ($\times$ 10^{-3})	0.80	0.94	1.09
Horizontal Betatron Tune ν_x	14.57	14.57	47.37
Vertical Betatron Tune ν_y	9.62	9.62	28.18
Synchrotron Tune ν_s	0.055	0.0454	0.031
Damping Time $\tau_{x,y}$ (ms)	56.4	19.5	24

3.5.2.4 CesrTA Inputs to the ILC DR Technical Design

The results from the first three years (Phase I) of the CesrTA R&D programme have been incorporated into the design of the ILC damping-ring vacuum chamber [137]; the findings of the programme are documented in the CesrTA Phase I Report [8]. In particular, the observed efficacy of grooved chamber surfaces in the dipoles as well as that of the clearing electrode in the high-field wigglers provide confidence that practical electron-cloud mitigation measures can be prepared for the arc and wiggler straight regions of the ILC positron damping ring. The importance of cloud mitigation in the damping-ring quadrupole chambers has also been demonstrated. New coating technologies to suppress the secondary-electron yield show great promise. However, there is still the issue of studying the long-term performance and durability of these coatings. This will be a subject of study during Phase II of the CesrTA programme. Perhaps most importantly, the flexibility of CESR operations has enabled a

systematic programme of electron-cloud build-up and electron-cloud-induced beam-dynamics studies. By benchmarking physics models and simulations against these studies, confidence in being able to make valid projections of the expected ILC positron-damping performance has been significantly enhanced.

3.5.3 Electron-cloud R&D at Other Laboratories

During 2007 and 2008 in the Positron Low Energy Ring of the PEP II accelerator, a magnetic chicane and special vacuum chambers were installed to study electron-cloud effects in an accelerator beamline [186, 187]. A special chamber was used to monitor the secondary-electron yield of titanium-nitride and NEG coatings, copper, stainless steel and aluminium under the effect of electron and photon conditioning in situ in the beam line. A drastic reduction of the secondary-electron yield to approximately 0.95 for titanium nitride and a still-high value for aluminium of greater than 2.0 after exposure in the accelerator beam line was measured. Other vacuum-chamber materials including NEG-coated samples were also measured. In magnetic-field-free regions, chambers were installed with rectangular groove profiles meant to reduce the secondary-electron generation at the surface. The electron signals in the grooved chambers, when compared to signals in smooth chambers, were significantly reduced. Two important results in dipoles were reported from the electron-cloud chicane tests : 1) the titanium nitride coating reduces the cloud density by several orders of magnitude with respect to a bare aluminium surface; and 2) a new resonance phenomenon has been observed that results in the modulation of the electron wall flux, and hence, presumably, of the electron-cloud density. After the PEP II shutdown the magnetic chicane and the test chambers were installed in the CesrTA ring (see Section 3.5.2.1) to continue the cloud-mitigation studies.

Tests of coated chambers, grooves and clearing electrodes have been carried out at KEK in order to mitigate the electron-cloud instability in an intense positron ring [166, 188, 189]. Aiming for application in a dipole-type magnetic field, various shapes of triangular grooved surfaces have been studied. In a laboratory, the secondary-electron yields of small test pieces were measured using an electron beam in the absence of magnetic fields. The grooved surfaces clearly had low secondary-electron yield compared to flat surfaces of the same materials. The grooves with sharper vertices had smaller secondary electron yield. A test chamber installed in a wiggler magnet of the KEKB positron ring was used to investigate the efficacy of the grooved surface in a strong magnetic field. In the chamber, a remarkable reduction in the electron density around the beam orbit was observed compared to the case of a flat surface with titanium-nitride coating.

An electron-clearing electrode with an ultra-thin structure has been developed. The electrode was tested with a positron beam in KEKB. A drastic reduction in the electron density around the beam was demonstrated in a wiggler magnet with a dipole-type magnetic field of 0.78 T. No discharge or extra heating of the electrodes and feedthroughs was observed after using the latest connection structure. The same type of electrode was also successfully tested in a CesrTA wiggler (see Section 3.5.2.1). The clearing electrode has also been applied to a copper beam-pipe with antechambers in preparation for its application in the wiggler section of Super-KEKB. Simulations indicate a small impedance for the thin structure of this electrode design.

At the INFN Frascati National Laboratories in Italy, clearing electrodes to mitigate the electron-cloud instability have been installed in all the dipole and wiggler chambers of the DAΦNE positron ring, covering approximately 16 % of the circumference [190]. The electrodes have proven very effective in combatting the electron cloud and minimising its impact on the positron beam dynamics [191].

At CERN, carbon thin films have been applied to the liners in the electron-cloud monitors and to vacuum chambers of three dipole magnets in the SPS [167]. The electron cloud is completely suppressed for LHC-type beams in the liners even after three months of air venting, and no performance

deterioration is observed after one year of SPS operation. Following the positive preliminary results obtained at the SPS it was decided to test these types of coatings in an environment with high synchrotron radiation in a lepton machine at CesrTA (see Section 3.5.2.1).

3.5.4 Recommendations for Electron-cloud Mitigation

A working group has been set up to evaluate the electron-cloud effect and instability issues for the ILC positron damping ring and to recommend mitigation solutions. The collaborating institutions are Argonne National Laboratory, CERN, Cornell University, INFN, KEK, Lawrence Berkeley National Laboratory and SLAC. The first task of the working group was to compare the electron-cloud effect for two different damping-ring designs with 6.4 km and 3.2 km circumferences, respectively, and to investigate the feasibility of the shorter damping ring with respect to the electron-cloud build-up and related beam instabilities. The working group compared the instability thresholds and the electron-cloud formation assuming 6 ns bunch spacing in both configurations, that is, in the same beam current. Both ring configurations were found to exhibit very similar performance. The risk associated with the adoption of the 3.2 km damping-ring design, while maintaining the same bunch spacing, was deemed low and the 3.2 km ring was found to be an acceptable baseline design choice [134].

Table 3.11 Summary of the *Recommendations for Electron-Cloud Mitigation* for the ILC positron damping ring.

Field Region	Mitigation Recommendation		Alternatives for Further Study
	Primary	*Secondary*	
Drift†	TiN Coating	Solenoid Windings	NEG Coating
Dipole	Triangular Grooves with TiN Coating	Antechambers for synchrotron radiation power loads and photoelectron control	R&D into the use of clearing electrodes
Quad†	TiN Coating		R&D into the use of clearing electrodes or grooves with TiN coating
Wiggler	Clearing Electrode	Antechambers for synchrotron radiation power loads and photoelectron control	Grooves with TiN coating

† Where drift and quadrupole chambers are in arc or wiggler straight regions of the machine, the chambers will incorporate features of those sections, antechambers for power loads and photoelectron control.

The mitigation recommendations for the ILC damping rings were prepared during a meeting of the working group at Cornell University on 13 October 2010 as a satellite meeting to the ECLOUD10 Workshop. The input from the workshop participants was included in the evaluation. The results of the evaluation were presented at the IWLC10 Workshop at CERN [192], and the recommendations are summarised in Table 3.11 [193]. It should be noted that the choices of mitigation methods in Table 3.11 are nearly identical to the choices that have been made for the construction of the SuperKEKB [194] vacuum system. Thus operation of the SuperKEKB positron ring will serve as a crucial performance test that will further improve understanding of the anticipated performance of the ILC DR.

3.5.5 CesrTA Phase II Plans

Specification of the electron-cloud mitigation, magnet alignment tolerances, emittance-tuning procedure, and beam instrumentation for the damping ring is to a large extent based on the CesrTA findings. There remain, however, a number of outstanding questions regarding beam physics peculiar to low-emittance rings that CesrTA is well equipped to address. In particular, as regards growth of the electron cloud, while global measurements of cloud lifetime with tune-shift data, as well as local measurements with shielded pickups, suggest that the cloud decays on a timescale of hundreds of nanoseconds, there is a hint of a long-lived cloud with lifetime of many microseconds, possibly trapped in quadrupole and/or wiggler fields. With respect to beam-cloud dynamics, whereas emitttance

growth due to the electron cloud as well as cloud-induced head-tail instability has been observed, the former by direct measurement of beam size and the latter from the turn-by-turn bunch-position spectra, it must yet to be determined to what extent the two phenomena are related. The CesrTA team is developing both new instrumentation and computational tools to explore these and other aspects of electron-cloud physics.

As ever smaller emittance and higher charge density are achieved, the sensitivity to single particle as well as collective effects that can limit vertical emittance will be enhanced. Investigation of intra-beam scattering at CesrTA takes advantage of the instrumentation that allows simultaneous measurement of horizontal, vertical, and longitudinal bunch dimensions. Initial results show reasonable agreement with theory, but with some remaining discrepancies. Discriminating emittance blow-up due to intra-beam scattering from other collective effects will require more extensive study, including measurement of the current dependence of equilibrium emittance at different beam energies, and complementary measurements with both positron and electron beams. CesrTA is an excellent laboratory for investigating ion effects in electron beams, and in particular the fast ion instability in bunch trains in the ultra-low vertical-emittance regime. The same tools used to explore electron-cloud effects with positron beams are suitable for investigation of ion effects with electron beams.

Finally the work to collect RFA and SPU data during operation of CESR as an x-ray source for CHESS will be continued. Analysis of the data will inform models of electron-cloud growth and questions of the durability of mitigations and the long-term effects of beam processing.

3.6 ATF2 Final-Focus Experiment

3.6.1 Introduction

The challenge of colliding nanometre-sized beams at the interaction point (IP) involves three distinct issues:

- creating small emittance beams;
- preserving the emittance during acceleration and transport, and finally;
- focusing the beams to nanometers before colliding them.

Table 3.12
Main design parameters for ATF2 compared to ILC. The ATF2 37 nm (at the IP) includes residual effects from uncorrected higher-order optical aberrations.

Parameter		Unit	ATF2	ILC
Beam energy	E	GeV	1.3	250
Effective focal length	L^*	m	1	3.5 - 4.5
Horizontal emittance	ϵ_x	nm	2	1.0 (damping ring)
Vertical emittance	ϵ_y	pm	12	2 (damping ring)
Horizontal IP β function	β_x^*	mm	4	21
Vertical IP β function	β_y^*	mm	0.1	0.4
Horizontal IP dispersion divergence	η_x'		0.14	0.0094
Relative energy spread	σ_E	%	~ 0.1	~ 0.1
Vertical chromaticity	ξ_y		$\sim 10^4$	$\sim 10^4$
RMS horizontal beam size	σ_x^*	µm	2.8	0.655
RMS vertical beam size	σ_y^*	nm	37	5.7

The Accelerator Test Facility (ATF) at KEK is a prototype damping ring to deal with the first issue and has succeeded in obtaining the emittances that almost satisfy ILC requirements [195, 196]. ATF is now used as an injector for the ATF2 final-focus test beam line, which was constructed in 2008 to study the third issue. ATF2 is a follow-up to the Final-Focus Test Beam (FFTB) experiment at SLAC [197], but with different beam-line optics based on a scheme of local chromaticity correction [198]. The beam line is shorter than that originally tested at FFTB and promises better performance and greater extendibility to higher energies. As with FFTB, the value of β_y^* and hence the vertical beam size at the optical focal point are chosen to have a similar demagnification and yield a similar chromaticity as in the ILC final focus. The primary goals for ATF2 are [199, 200]:

1. achieving a 37 nm vertical beam size at the IP;

2. stabilising the beam at that point at the nanometer level.

The main parameters of ATF2 are given in Table 3.12 together with the corresponding values for the ILC.

The layout of the ATF/ATF2 facility and the design optical functions of the ATF2 beam line are displayed in Fig. 3.40 and Fig. 3.41 , respectively. The optics is a scaled-down version of the ILC design.

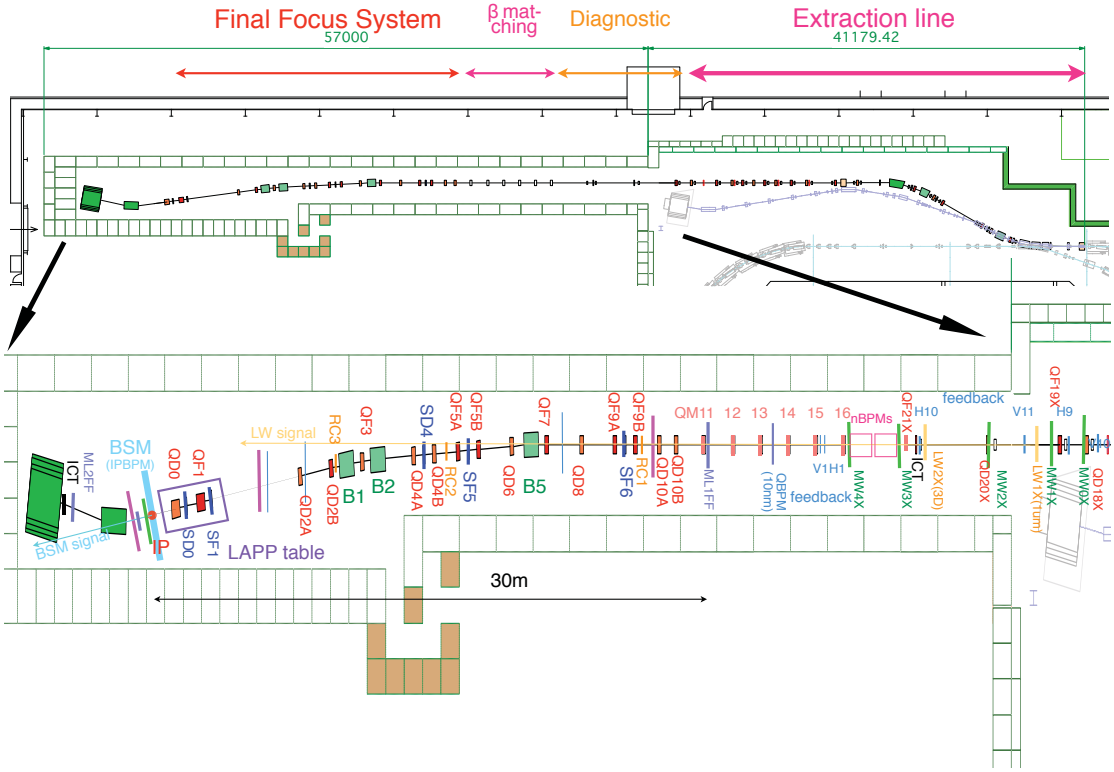

Figure 3.40. Top: the ATF2 beam line. Bottom: an enlargement of the final focus system.

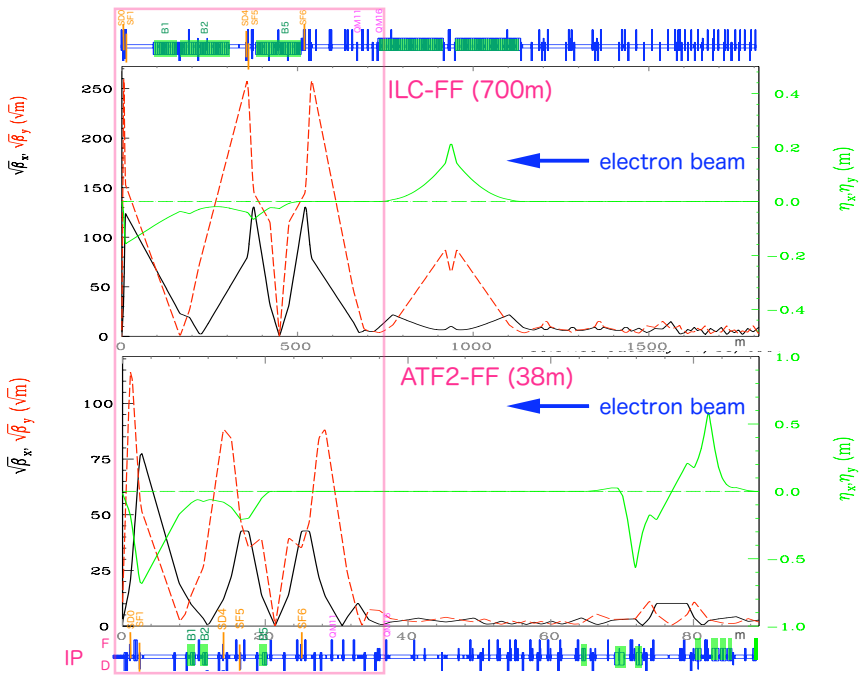

Figure 3.41
Top: Optics of the ILC beam-delivery system from the exit of the main linac on the right to the interaction point on the left. Bottom: ATF2 optics from the ATF damping-ring extraction point on the right to the interaction point on the left.

3.6.2 Status of ATF2 Systems

3.6.2.1 Magnets and Magnet Mover

Figure 3.42
View looking downstream along the final focus section of the ATF2 beamline.

The ATF2 beam line extends over about 90 meters from the beam extraction point in the ATF DR to the IP (see Fig. 3.40 and Fig. 3.42). Many quadrupoles and some dipoles were fabricated for ATF2, while others were reused from the old ATF extraction beam line and from the Final Focus Test Beam (FFTB) at SLAC [197]. Among the latter were the two quadrupole and two sextupole magnets composing the strong-focusing final-doublet (FD) system just before the IP. The apertures of the FD quadrupole magnets needed to be increased to accommodate the larger β function values at these magnets in the ATF2 optics design.

Anticipating gradual movements of supports and magnets due to thermal variations or slow ground motion, twenty quadrupole and five sextupole magnets in the final focus were mounted on remote-controlled three-axis movers recycled from the FFTB experiment. The movers have a precision of 1–2 µm for transverse motion (horizontal and vertical), and 3–5 µrad for rotations about the beam axis.

Overall alignment precisions of 0.1 mm (displacement) and 0.1 mrad (rotations) have been achieved using conventional alignment/metrology techniques. The final alignment of the magnets is achieved via beam-based alignment (BBA) techniques.

3.6.2.2 Final Doublet (FD)

The FD is composed of two quadrupole and two sextupole magnets (QD0, QF1, SD0, SF1 in Fig. 3.40). These magnets must be supported in a way that ensures their vertical vibration amplitude relative to the IP is smaller than 7 nm rms above 0.1 Hz, in order to limit effects on the measured beam size at the IP to less than 5 %. Below 0.1 Hz, beam-based feedback methods can be used (1/10th of the beam repetition rate of 1 Hz). A rigid support was chosen since the coherence length at ATF2 (about 4 m in this frequency range) exceeds the distance between the FD and IP, which strongly suppresses their relative motion. Vibration measurements with the table fixed to the floor and with all magnets and movers installed were performed in the laboratory for prior validation, including checking for potential effects from cooling water flowing in the magnets. Additional measurements after final installation of the FD confirmed that the residual motions of the magnets relative to the IP were within tolerance. The whole FD system is shown in Fig. 3.43 .

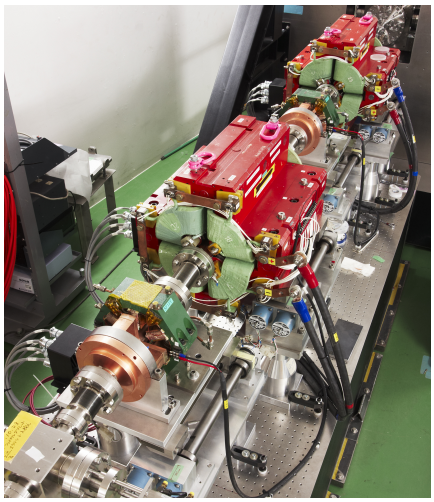

Figure 3.43
View of the final doublet installed on its rigid mechanical support system.

3.6.2.3 Cavity Beam-position Monitors

The ATF2 beam line is instrumented with 32 C-band (6.5 GHz) and four S-band (2.8 GHz) high-resolution cavity beam-position monitors (BPM). There are also four C-band and one S-band reference cavities to monitor beam charge and beam arrival phase. In the diagnostics and final-focus sections, every quadrupole and sextupole magnet is instrumented with a cavity BPM. The FD magnets use S-band BPMs, while the remaining quadupoles are equipped with C-band BPMs. The usable measurement range of the cavity BPMs was found to exceed the mechanical range of quadrupole movers ($\pm$1.5 mm). A resolution of 200–400 nm for the C-band BPMs has been demonstrated [201].

3.6.2.4 IP Beam-size Monitor (IPBSM)

Measuring transverse beam sizes of tens of nanometers at the IP requires specialised beam instrumentation, in particular a beam-size monitor based on laser interferometry (IPBSM, also referred to as a Shintake monitor [202]). The IPBSM is based on inverse Compton scattering between the electron beam and a laser interference fringe pattern. For the ATF2 beam energy, the energy of the generated gamma rays is typically rather low compared to that of bremsstrahlung photons, emitted when beam-tail electrons interact with apertures and start showering, which are the main detector background. In the monitor designed for ATF2, the signal is separated from this high-energy background by analysing the longitudinal shower profile measured with a multilayered detector located a few meters after the IP, downstream of a dipole magnet. The laser wavelength used is 532 nm, the 2nd harmonic of the Nd:YAG laser, which provides a suitable fringe pitch to measure the target vertical size of 37 nm. The monitor is designed to have three measurement modes by changing the crossing angle between the overlapping lasers, which give sensitives to beam sizes of 5000-350 nm (2-8 deg. mode), 100-350 nm (30 deg. mode), and 20-100 nm (174 deg. mode). In addition, a single "laser-wire" mode can be used for horizontal beam-size measurements [203].

The method to set up the electron and laser beams correctly was developed experimentally during early commissioning using diagnostics and instrumentation available for both electron and laser beams. It consists of five main steps: (i) carefully tuning the electron beam trajectory to reduce backgrounds; (ii) aligning the photon detector onto the electron beam axis at the IP; (iii) checking the synchronisation of both beams; (iv) scanning the laser beam horizontally to overlap its waist with that of the electron beam; and (v) scanning the two laser beams longitudinally across the electron beam to maximize the modulation.

3.6.2.5 Other Beam-line Instrumentation

The instrumentation from the old ATF extraction line – strip line BPMs, Integrated Current Transformers (ICTs), optical transition radiation (OTR), screen profile monitors, and wire scanners – is reused in the reconfigured beam line. There are five wire scanners with tungsten and carbon wires of 10 and 7 μm diameter, respectively, located in the diagnostic section upstream of the final-focus section (see Fig. 3.40). They are used to measure the horizontal and vertical beam emittances after extraction from the DR. An additional wire scanner is installed just downstream of the IP for beam-size tuning and has tungsten and carbon wires of 10 μm and 5 μm diameter, respectively. Screen monitors are located right after the extraction, in the middle of the beam line, and before and after the FD. An optical-fibre beam-loss monitor is installed all along the beam line to localise and quantify beam losses in a relative sense. Four OTR monitors close to the wire scanners with an improved resolution of 2 μm has been installed in the extraction line. They permit the measurement of the beam sizes as well as a fast emittance measurement, with high statistics giving a low error and a good understanding of the emittance jitter.

3.6.3 Tuning Status Towards Achievement of Goal 1

3.6.3.1 Summary of ATF2 Commissioning and IP Tuning Activities

The commissioning of ATF2 began in December 2008. During 2009, the various hardware diagnostic systems were commissioned whilst the beam line was commissioned with a relaxed optics configuration (10mm vertical beta function at the IP). The relaxed optics configuration was intended to allow for simplified checkout of the linear optics as the reduced chromaticity of the FFS at this level of focusing did not require the chromaticity compensation sextupoles to be switched on [204, 205]. It also provided a small-enough beam (∼1 μm vertical IP size) to commission the 2–8 degree modes of the IPBSM.

During 2010, a more aggressive optics (1 mm vertical IP beta function) was used, the FFS sextupoles were turned on on and the beam size tuned below 1 μm for the first time, with a smallest recorded spot size as measured by the IPBSM of 310 nm.

In the autumn runs of 2010 and at the start of 2011, the nominal vertical focusing optics was used, whilst keeping the horizontal beta function at 2.5 times the nominal design for reasons explained below.

The tuning work towards obtaining the nominal vertical IP spot size was expected to start during the spring of 2011. However, due to a fire in the modulator supplying power to the klystron generating RF for the gun, the program was delayed. The ATF was then damaged in the great Eastern Japan earthquake (M9.0), March 11 in 2011.

The ATF conventional facilities and accelerator systems were repaired during the summer and autumn of 2011, with the resumption of beam operations through ATF2 in the winter period. During the winter and spring periods of 2012, different optics configurations were applied while gaining experience on tuning the beam size and measuring in the 30-degree mode of operation of the IPBSM. The decision was made to relax the horizontal beta function at the IP to ten times that of the initial design (to 40 mm). This reduced the observed backgrounds in the IPBSM detectors and was also considered a prudent measure to lower the horizontal beam sizes throughout the FFS in order to reduce as much as possible the sensitivity to undesired multipole components in the FFS magnets. As the backgrounds detected in the IPBSM detectors were gradually reduced through alignment and beam-pipe enlargement activities, the vertical beta function at the IP was reduced, in a staged fashion, down to the design 0.1 mm. The IPBSM was ultimately found to function well in the 30-degree mode of operation with these settings. During the operation period February through June 2012, the beam was frequently tuned down to the 200nm level and below. Through careful online monitoring of both

beam conditions and internal conditions of the IPBSM itself, these beam sizes could be maintained.

It was realised that, in order to achieve the beam sizes of Goal 1, a tuning program that runs continuously over periods of many days, perhaps weeks, was required. During the April - June beam operation periods in 2012, a student training program was set up, involving post-graduate-level students and postdocs from the collaborating institutions across the world that make up ATF2. The aim of this program was to produce a core team of people capable of maintaining operational efficiency of ATF whilst progressing the ATF2 tuning program.

Thus, during the November and December operations periods, i.e. the last four weeks, ATF2 ran continuously in "ATF2 tuning mode". The 174-degree mode of operation of the IPBSM was successfully commissioned. At the end of the runs, the beam was tuned down to about 70nm as shown in Fig. 3.44, where the 70nm beam size could be maintained for about 7 hours at least. It is an achievement of important milestone towards full verification of the local chromaticity correction scheme at the ILC final focus system. However, it could be performed only at very low beam intensity of $1 \sim 2 \times 10^9$/bunch. We suspected the wakefield effect at the large beta function region at the final focus system for the major cause. We will prepare the mitigation plan to achieve the 37nm beam size in coming runs.

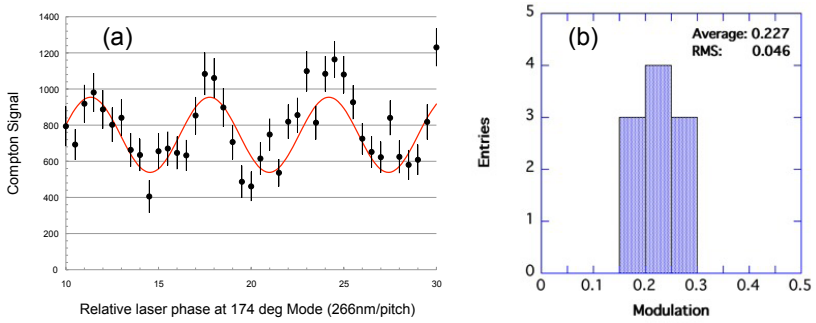

Figure 3.44
(a) The best modulation (M) measured to date by the IPBSM beam-size monitor with the 174° crossing angle, M=0.28±0.3, taken in December 2012. The measurement corresponds to a beam size of 68±3 (statistical) nm. (b) Histogram of modulations measured 10 times at the 174 degree mode, 21 December 2012. The average beam size corresponds to 73nm with an RMS of 5nm.

3.6.3.2 Software for Optics Analysis and Re-Design

Due to the non-linear nature of the FFS optics, multi macro-particle tracking software has been used to test the performance of the optics, to develop beam-tuning algorithms and to test their robustness under realistic error conditions. This has been done independently with multiple codes, which provides a useful cross-check of the methods used and the tracking software in the different codes themselves. Codes used for these studies are Lucretia, SAD [206], MADX (MAPCLASS) [207] and PLACET [208].

3.6.3.3 Optics Preparation and Beam-dynamics Simulation

In addition to the original FFS tuning procedure developed for ILC, three different analyses environments were constructed based on MADX, SAD and Lucretia. These are able to re-match the FFS optics and study effects of errors using tracking through the model lattice together with the inclusion of all envisaged error sources.

One such error source was discovered after construction was complete: the higher-order multipolar components of many of the quadrupole and dipole magnets in the EXT and FFS were large enough to generate aberrations at the IP which noticeably increase the expected vertical spot size. Measurements of the normal and skew multipole components of these magnets were made at IHEP, KEK and at SLAC and inserted into the models. It was found that multipole components up to octupole, and in

the case of the final doublet, up to 12-pole were important. To try and recover the beam size closer to the design goal, a study was performed to try and re-match the optics to mitigate the effects induced by the measured multipoles. The result of this process is shown in Fig. 3.45. By increasing the horizontal beta function at the IP by 2.5–10 mm, and thus reducing the horizontal beam size in the QF1FF aperture and other sensitive apertures, the effect of the various skew multipoles was somewhat mitigated.

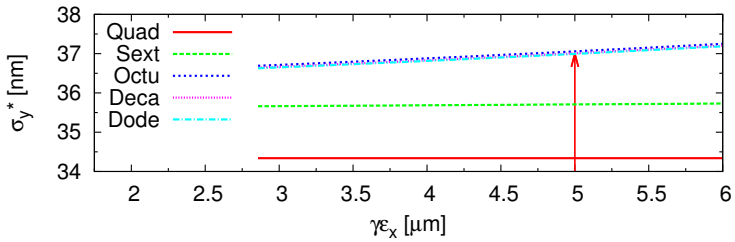

Figure 3.45
Re-tuned IP vertical beam-spot size as a function of input horizontal emittance, with 2.5 times nominal IP horizontal beta function. Each curve corresponds to different maximum multipoles included in the simulation.

Due to the sampling of more of the skew multipole fields at larger horizontal beam sizes at the high beta points, the vertical beam size scales noticeably with horizontal emittance. The normal horizontal emittance achieved is about 5 μm rad (normalised), but has been measured to be lower at lower bunch charge due to collective effects in the damping ring.

This retuning method has been repeated for the different operational optics used as discussed in Section 3.6.3.1. The results have also been cross-checked using MADX, Lucretia and SAD.

In addition to the retuning procedure described above, it has been shown that, through the addition of four skew-sextupole magnets into the FFS, the tolerances to the sextupole multipolar errors in some of the FFS magnets are considerably relaxed. One such skew-sextupole magnet has already been installed in the beam line, resulting in some effect on beam size. Three more were installed over the summer 2012 shutdown period. This arrows "multi knobs" to be formed, allowing these particular aberrations to be tuned out. In addition, the QF1FF was replaced with a PEP-II LER quadrupole magnet with negligibly small 12 pole component just before the continuos runs for last 4 weeks. This replacement is expected to recover the horizontal beta function to the design value at IP.

After generating the desired lattice as discussed above, the expected performance of the accelerator in the presence of all expected error conditions (e.g. survey alignment tolerances, magnet field strength errors, BPM errors, ground motion, beam size measurement errors etc) has been simulated using a Monte Carlo approach in which 100 random distributions of error conditions were generated and the full tuning procedure applied to each seed. The mean and spread in the final results represents the best guess of the expected performance of the machine and an uncertainty estimate in the results based on the level of knowledge of the expected error sources. These simulations also provide the basis for developing and testing different tuning algorithms and techniques. The simulations show the initial beam sizes are expected to be of the order of about 0.5–3 μm and can be tuned down to within 20 % above the nominal beam size in about 12 steps. At each step, the range of dominant aberrations at the IP (up to third order) are examined. The most common aberration at each step is then targeted across all Monte Carlo seeds. This forms the basis for the tuning procedure to be applied to the real accelerator. Further iteration of the tuning knobs produces a final beam-spot size within about 10 % above the design goal after several hours of tuning. This simulation has been performed additionally in MADX and PLACET with similar results.

3.6.3.4 Beam-tuning Procedure

The required procedures to tune the ATF2 beam are briefly outlined below. Not covered here is the process by which the beam is accelerated, transported into the ATF damping ring and the damping ring itself tuned (COD, dispersion and coupling). This is typically done once before a set of ATF2 tuning attempts, and occasionally during ATF2 tuning if the damping-ring conditions change, for example, due to a change in the ring circumference caused by temperature variations.

A notable problem that has presented itself since initial commissioning of the ATF2 is prompt emittance growth during damping-ring extraction. It is assumed that high-order magnetic fields experienced by the beam as it passes close to kicker and septa devices cause emittance growth via coupling effects as the beam is extracted. This manifests itself as a higher emittance as measured by the OTR system in the EXT than that measured in the damping ring. This effect has been observed to be highly sensitive to the extracted beam orbit, and has led to extracted emittances that vary from one operation period to the next. Typically the emittance is 2 nm $\times$ 12 pm in the DR and 2-3 nm $\times$ 20-30 pm in the EXT after coupling correction. Figure 3.46 shows vertical emittances measured at the DR and EXT in 2011 and 2012.

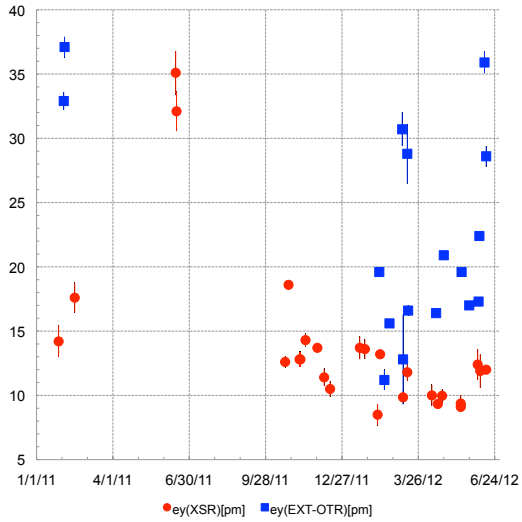

Figure 3.46
Vertical emittances measured by the X-ray synchrotron-radiation monitor(XSR) in the damping ring (red circles) and the optical transition-radiation monitor system (EXT-OTR) in the extraction line (blue squares), in 2011 and 2012.

Usually, beam tuning starts from steering the beam upstream of the extraction line. Next, the BPM readouts are aligned to the field centres of the quadrupole magnets by a "quad-shunting" procedure whereby the beam is steered through the magnet in question at various offsets at different quadrupole activation strengths. Then, orbit feedbacks are applied to maintain the "golden" beam orbit at both DR and EXT/FFS. It is especially critical to maintain the desired orbit through the FFS sextupole magnets to reduce drift in the beam size at the IP during tuning.

Horizontal and vertical dispersions are corrected by pairs of normal/skew quadrupole magnets at dispersive locations. The residual vertical dispersion coming from the damping ring can be corrected by rotation of QD0. Coupling is primarily corrected by four skew-quadrupole magnets in the EXT. One phase of coupling ($< x'y >$ at the IP phase) generated at the FFS would be corrected by the IP $< x'y >$knobs based on five sextupole magnets at the FFS.

The principal aberrations present at the IP are expected to be $< x'y >$ coupling, vertical waist shift and vertical dispersion. To cancel these, orthogonal knobs have been developed based on the five FFS sextupole magnets, which are deliberately offset to generate the required correction terms at the IP. Also, so-called non-linear knobs have been developed in order to correct high-order terms, predominantly T322, T326 and T324.

Figure 3.47 shows the simulation results of the tuning process (upper and lower one-sigma bounds

from 100 Monte Carlo seeds) and the results from ATF2 tuning shifts.

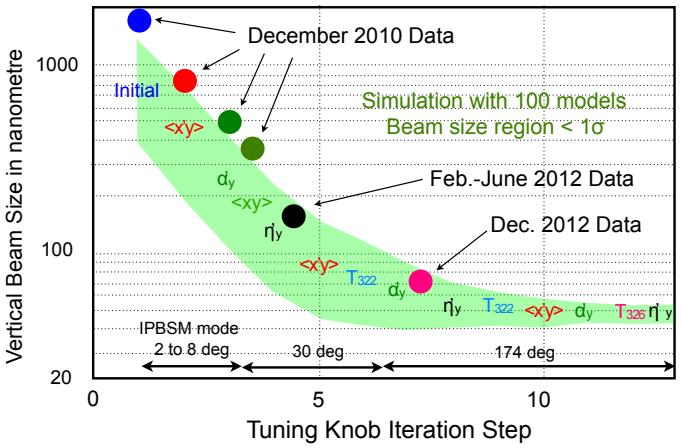

Figure 3.47
IP vertical beam-size tuning: experimental results and simulation. Shown are the data points from 2010 & 2012, the ±1-sigma curves from the Monte Carlo model; the tuning steps are indicated in text. The required operation modes of the IPBSM are also indicated for each relevant section of the plot.

3.6.4 Stability

The second goal of ATF2 is to achieve nanometer-level stability. Several R&D activities are currently being actively pursued:

- feedback on a nanosecond time scale (FONT);
- nanometer resolution IP-BPM [209];
- fast nanosecond-rise-time kicker [210];
- cavity BPM optimised to monitor angular variations of the beam near the IP with high accuracy;
- development of robust laser-wire diagnostics [211].

The most recent FONT results are shown in Fig. 3.48, where measurement of the beam offset at the first of a three-bunch train is used to correct the subsequent two bunches. Bunch separation is 151.2 ns. The data clearly indicates a reduction of the beam jitter by a factor of 5 from the first to the second bunch. The achieved 2.1 µm rms scales to 2.6 nm at the IP, given the demagnification of the optics.

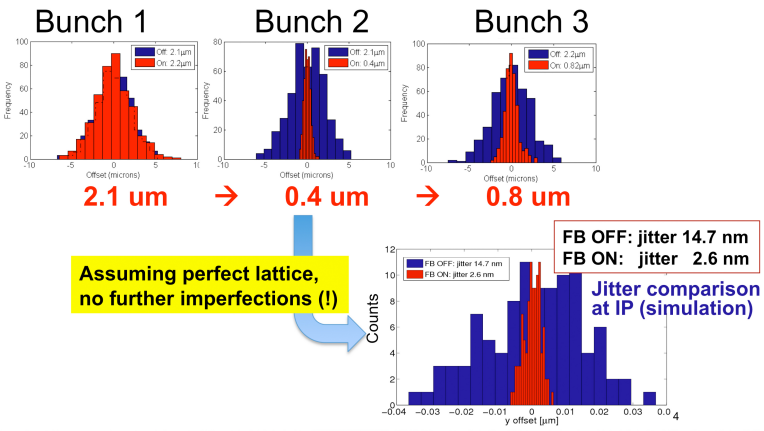

Figure 3.48
Recent results of FONT, the intra-train fast feedback. The three plots above are experimental results, while the bottom one is a simulated one to demonstrate the nanometer stabilisation at the IP assuming a perfect lattice for the final-focus beam line [212].

3.6.4.1 Post TDR and Future prospects

Post TDR, there will be a concerted effort to achieve the goal of 37 nm vertical beam size in parallel with studies related to achieving the stability goals.

Plans to upgrade the performance of ATF2 on the time scale of a few years, after the main goals of ATF2 have been achieved, are also under consideration. In particular, optical configurations with ultralow β^* values (2–4 times smaller than the current nominal in the horizontal and vertical planes), relevant to both the CLIC design and to some of the alternative ILC beam-parameter sets, are actively under study. An R&D program to develop a tuneable permanent magnet suitable for the FD is pursued in parallel, with an initial goal to construct a prototype for beam testing in the upstream part of the ATF2 beam line.

Chapter 4
Accelerator Systems R&D

4.1 Overview

In the R&D phase, work on accelerator systems has concentrated on alleviating technical rather than cost risk, since the cost of specific accelerator-system components is small compared to the costs associated with the main linac; however, the failure or sub-optimal operation of many accelerator components can prevent running of the ILC or severely limit its performance. The electron source photo-cathode gun, positron-source undulator, target and capture system, damping-ring kicker magnet system, and beam-delivery dumps are examples of such systems; work on these systems is described here. For much of this work, a strong collaborative team of experts that included both GDE members and collaborators on unrelated projects was an important factor in their success.

Technical risk is judged by assessing the state of the art for a given component against expected performance criteria. The strategy to mitigate technical risk in a long-term project development and construction cycle must balance potential gain against the time and resources to achieve it. The development of new ideas and beam tests of full systems have the longest lead times and should hereford be given priority.

The photo-cathode gun laser and in-vacuum high-voltage DC gun are the most critical electron-source components so these were chosen for study during the Technical Design Phase. Studies of the basic physical properties of the semiconductor photo-cathode itself were deemed successful and mature enough not to require further work. As is typical with the accelerator systems discussed here, the goal of work on the laser and the gun was focused on applying specialised high-technology solutions in an innovative manner to extend significantly the performance of off-the-shelf products. Wavelength tuneability and high average-power performance are a concern for the laser and the GDE teams are working to apply cryogenic technology to the lasing medium. Extending DC high-voltage capability without increasing field emission or dark current is the main concern for the gun. It is well known that beam quality will improve as the voltage is increased but this has to be balanced against the photo-cathode poisoning caused by excessive dark current.

The positron-source component studies are the most important effort related to accelerator systems because of the high level of integration required and the difficulty of performing a full-power system test. It is important to note that because the rate of positron creation is well beyond that achieved in existing facilities, an Alternate Configuration based on a normal-conducting linac with a high repetition rate is under active study. Both are described in this chapter. Furthermore, baseline performance goals include an option to provide 50 to 60 % positron polarisation, a performance characteristic also unmatched at any existing facility.

The undulator-based scheme has been adopted for the baseline design because the photon beam requires a thinner target and therefore dissipates less energy than an electron beam and because it provides polarised positrons. The use of a circularly polarised photon beam produced by the passage of high-energy electrons through a helical undulator to create polarised positrons is a well

understood process that was demonstrated early in the ILC design phase [213]. The achievable positron polarisation depends critically on the collimation scheme used to separate the core forward–directed gamma rays from the surrounding halo. Key R&D topics of concern here are the helical undulator and the collimator. Collimator design studies are presented in this chapter.

The undulator field period and characteristic strength 'K' determine both the incoming electron-beam threshold energy required to produce the positrons and the total undulator length needed. Two full-scale baseline prototype superconducting undulators were constructed and successfully tested during the design phase; results are reported here. The greatest overall flexibility for the collider physics program is provided with low minimum threshold energy which in turn corresponds to a small undulator period; development is focused on reducing the period from 11.5 to below 10 mm. The baseline design threshold energy is 150 GeV.

Power deposition in the positron target during the 730 microsecond-long train must be smeared out to avoid damage. Simulation work has identified average-power deposition, 'shock-wave' stress, thermal stress and eddy-current heating (from interaction with an externally applied axial magnetic field), as the most important concerns. It has not been practical during the design phase to test the power-handling capability of the 14 mm-thick titanium target. With the baseline 1 m diameter target rotating with a speed of 100 m/s at the rim, the incident beam energy is spread along a 75 mm long by 1.4 mm (rms) wide stripe. Additional target heating, of almost equivalent amplitude to the average beam heating, is caused by eddy currents. Applying a high-vacuum seal to the rotating shaft and providing cooling water through the target rim are the support-engineering tasks of greatest concern. Reports on studies of these topics using a full-scale test model are included here.

Two key elements of the capture section that follows the target are the high-field tapered solenoid, located 2 mm from the target rim, and the normal-conducting RF accelerator section. Design and prototyping of the high-field tapered solenoid, also referred to as an 'optical matching device' (OMD), and the high-current pulse modulator to power it is underway. The design uses a stack of single-turn flux-concentrating disks that are transformer-coupled to large – diameter 10- to 25-turn coils. Design studies of other kinds of OMD, such as a liquid-lithium lens, have also been done. A full power normal-conducting RF accelerator capture section has been built and fully tested.

R&D on an alternate positron production scheme based on a smaller peak-power incident beam on target is underway and is also reported in this chapter. A short, high-power, high-repetition-rate normal-conducting linac reduces concerns over thermo-acoustic shock-wave damage to the target. A state-of-the-art conventional fixed target can be used, removing the need for a system rotating at high speed.

The most serious performance concern raised for the damping ring is the potential impact of electron-cloud instabilities, notably in the positron damping ring. These instabilities have been studied extensively at the purpose-built test facility 'CesrTA,' the results of which are reported in Section 3.5. The technological aspects of the mitigation strategies, including vacuum-chamber electrodes and coatings, are also covered in that chapter.

The damping ring, as the source of low-emittance beams, and the beam-delivery system, as the demagnification section, must both be tested to validate the expected performance of beam-line components and tuning-strategy convergence. This topic is covered in Section 3.6.

The primary technical concern for the damping rings is the injection and extraction ultra-fast pulse kicker system. Roughly 40 pulser-kicker pairs are required for injection and extraction of the beam bunches from the damping ring. The ring minimum inter-bunch spacing, (and ultimately therefore the size of the ring) is determined by the pulse rise and fall time of these devices. A two-pair system has been built and tested successfully using the ATF.

The primary R&D goals for the BDS are associated with the beam demagnification and stability

tests at the ATF2. However, there are several other key R&D programmes not directly related to this. The GDE team is pursuing design and prototyping of the ILC superconducting final doublet, with most of the relevant ILC features reproduced. This prototype is not intended for a beam test but rather for laboratory studies with various instruments. A second focus is the engineering design work associated with the machine-detector interface, in support of the detector push-pull option. Finally, simulation work on the main beam dump has been done [214].

4.2 Polarised electron source

The R&D for the ILC polarised electron source has been focused on two aspects: first, to build a prototype of the source laser system and to use the laser system to generate an electron beam with ILC beam parameters (Section 4.2.1); secondly, R&D on the electron gun itself, the goal being to achieve the ILC specification for a gun voltage of 200 kV while maintaining a low dark current to ensure a long cathode lifetime. This development has been done at the Jefferson Laboratory's injector facility. Both the prototype of the ILC source laser and the high-voltage gun have been demonstrated.

4.2.1 Beam Parameters

The key beam parameters for the electron source are listed in Table 4.1.

Table 4.1
Electron Source system parameters.

Parameter	Symbol	Value	Units
Electrons per bunch (at gun exit)	N_-	3×10^{10}	
Electrons per bunch (at DR injection)	N_-	2×10^{10}	
Number of bunches	n_b	1312	
Bunch repetition rate	f_b	1.8	MHz
Bunch-train repetition rate	f_{rep}	5	Hz
FW Bunch length at source	Δt	1	ns
Peak current in bunch at source	I_{avg}	3.2	A
Energy stability	σ_E/E	<5	% rms
Polarisation	P_e	80 (min)	%
Photocathode Quantum Efficiency	QE	0.5	%
Drive laser wavelength	λ	790±20 (tunable)	nm
Single-bunch laser energy	u_b	5	μJ

4.2.2 System Description

Results from previous photocathode R&D projects have demonstrated that materials are available that can provide the ILC beam charge and polarisation. The ILC source will use a strained gallium-arsenide phosphide (GaAsP) highly doped photocathode. Figure 4.1 illustrates the performance of such a cathode. With bunch spacing of ∼500 ns, the surface-charge limit is not expected to be an issue. The optimum doping level remains to be determined. The prototype laser system could be used to help clarify this issue.

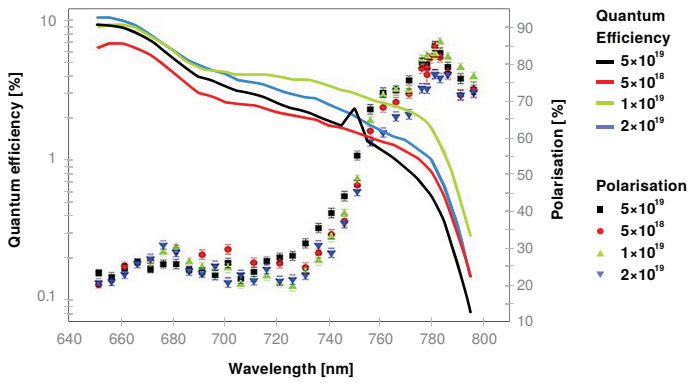

Figure 4.1
Performance of strained layers of GaAsP photocathodes at different doping levels.

4.2.2.1 Laser system development

A laser system has been developed for the ILC polarised injector that is capable of generating the ILC bunch train. This system was developed in the US by Kapteyn-Murnane Laboratories (KM Labs) of Boulder, Colorado.

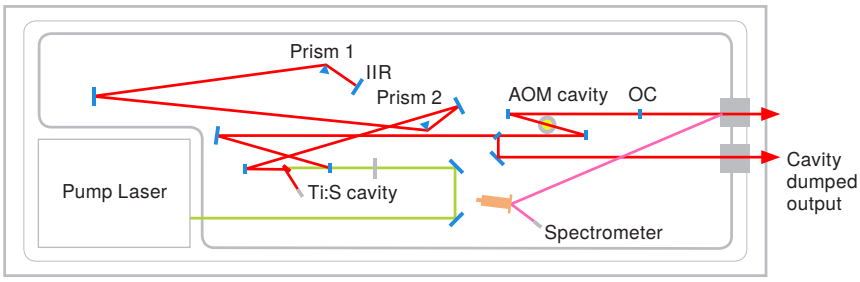

Figure 4.2 Optical layout of the KM Labs mode-locked cavity dumped ps oscillator

The laser wavelength must match the band gap of the cathode material. For GaAsP, a wavelength of approximately 790 nm is necessary. The laser system must provide the time structure of the ILC pulse train. One basic component of this laser system is the mode-locked oscillator that operates at a harmonic frequency of the micro-bunch repetition rate, which can be locked to an external reference frequency (see Fig. 4.2). A regenerative amplifier is used to amplify the pulse train (see Fig. 4.3). A key component of this amplifier is the cryogenic cell containing a titanium-sapphire crystal. Cryogenic technology allows large pump power and efficient amplification, minimising the effects of thermal lensing in the amplifying medium. The micro-bunch structure (1.8 MHz pulse train) is formed in the oscillator using a cavity-dumping acousto-optic modulator. The macro-bunch structure (5 to 10 Hz) is generated by electro-optical switching of the amplified beam. The KM Labs laser was successfully demonstrated in November 2010 at the KM Labs facilities. Due the design constraints and limited amplifier pump power, the laser output was limited to 1.5 MHz with pulse energies of ∼3 µJ. These laser systems are presently being installed at the SLAC ILC Injector Test Facility with stronger pump lasers. The prototype laser performance at SLAC is expected to exceed 5 µJ per pulse at 1.5 MHz.

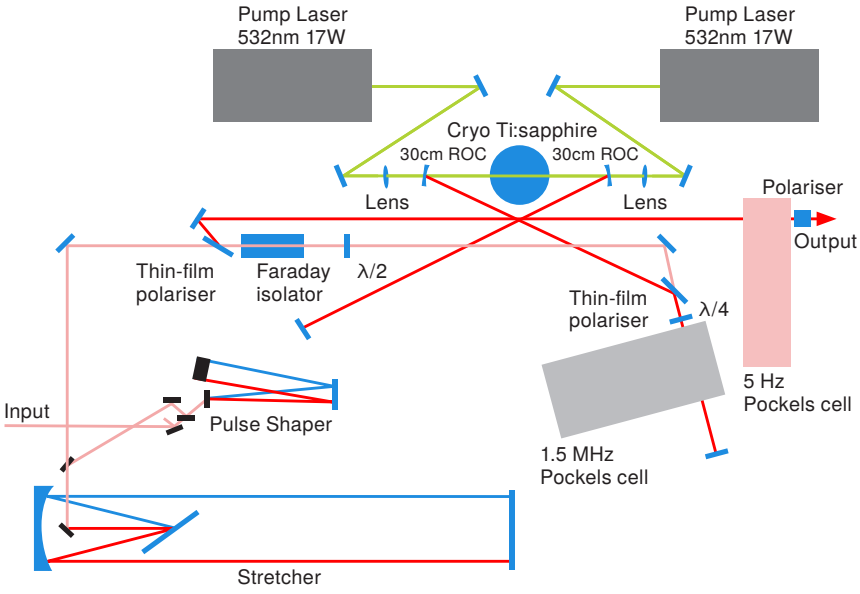

Figure 4.3 Optical layout of the KM Labs pulse stretcher, pulse shaper, and regenerative amplifier systems

4.2.2.2 Direct-current gun

The main goal of R&D towards a direct-current gun for polarised-electron generation is to increase the high-voltage capability while maintaining or reducing the dark current. A higher voltage is desirable to reduce the space-charge forces that the electrons experience at low energy before further acceleration. The reduction of space-charge forces is desirable to lower the transverse and longitudinal emittances of the generated electron bunches. A low dark current is necessary to maintain the negative electron-affinity properties of the photocathode, thereby increasing the lifetime of the electron source. The most important issue is to reduce field emission within the gun, which is the fundamental source of dark current.

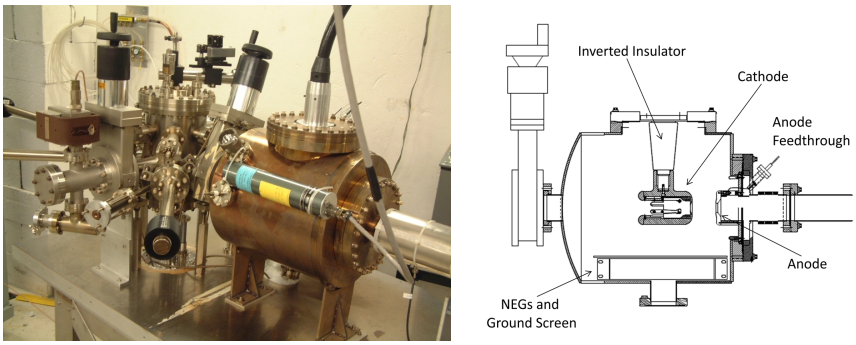

Figure 4.4
The chamber of the 200 kV DC high voltage photogun (a) and its schematic view (b).

A 200 kV DC high voltage photogun (Fig. 4.4) was constructed at Jefferson Lab using a compact inverted insulator (Fig. 4.5) and with a vacuum load-lock that supports relatively quick photocathode replacement [215]. The photogun employs a cathode electrode manufactured from large grain niobium that was demonstrated to reach higher voltages and field strengths compared to stainless steel electrodes that were prepared using traditional diamond-paste polishing. This photogun has undergone extensive testing, demonstrating reliable beam delivery from strained-superlattice GaAs/GaAsP photocathodes at average current up to 4 mA. A second load-locked photogun with an inverted insulator was constructed for CEBAF [216]. It employs a stainless steel cathode electrode biased at 130 kV. It has operated reliably for over two years, delivering more than 200 µA average beam current for month-long periods without interruption and with electron beam polarization $> 85\,\%$.

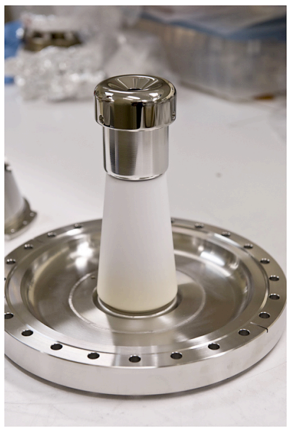

Figure 4.5
Compact inverted insulator with test electrode used to evaluate electrode materials, polishing techniques and inert gas processing.

High voltage processing in the presence of inert gas (He and Kr) was demonstrated to significantly improve the performance of stainless steel and niobium cathode electrodes, eliminating field emission (< 10 pA) at voltages to 225 kV and field strengths > 18 MV/m [217] (see Fig. 4.6).

The vacuum chambers and many internal components were baked at 400 °C prior to final construction which served to reduce the outgassing rate by a factor of ∼20 and resulted in the lowest

observed static vacuum of all the Jefferson Lab photoguns to date. The pressure registered by a Leybold extractor gauge was 2×10^{-12} Torr (nitrogen equivalent), which is very close to the X-ray limit of the gauge.

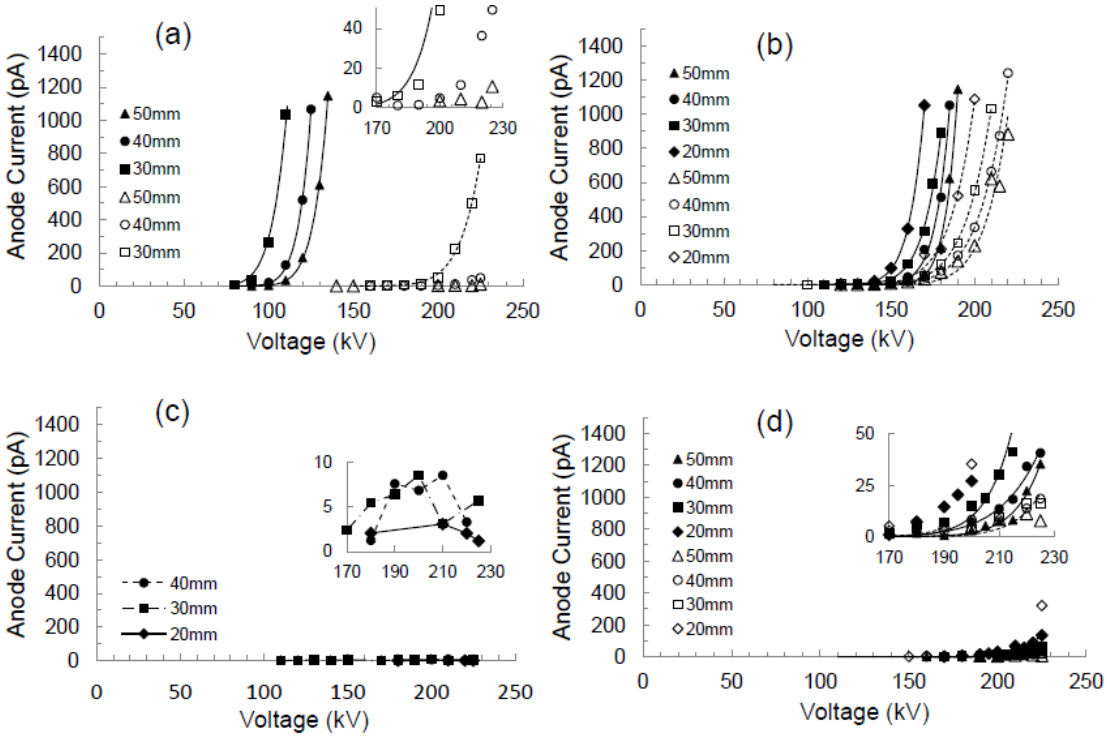

Figure 4.6. Results from a field emission test stand. Field emission current versus bias voltage and anode/cathode gap spacing for (a) DPP stainless steel, (b) fine-grain Nb, (c) large-grain Nb and d) single-crystal Nb. Each plot shows field emission behavior before (solid symbols) and after (open symbols) krypton processing, except for large-grain Nb which did not require krypton processing. Insets show an enhanced view of the low current data points. For all cases except large-grain Nb, the lines between data points represent Fowler-Nordheim fits.

4.3 Positron Source

4.3.1 Overview

The ILC Positron Source generates the positron beam for the ILC. To produce the positrons, the beam from the electron main linac passes through a long helical undulator to generate a multi-MeV photon beam which hits a thin metal target to generate showers of electrons and positrons. This system pushes the state of the art in many areas and there has been substantial R&D on several critical items including the undulator, positron-conversion target, optical-matching device, photon collimator, normal-conducting accelerating structures, radiation shielding and remote handling. There has also been work on the alternative conventional positron source and beam-line lattice design.

4.3.2 Undulator

At the time of the *Reference Design Report* (RDR), short superconducting helical-undulator prototypes using niobium-titanium superconductors had been successfully fabricated and tested by groups at Rutherford Appleton Laboratory (RAL) in the UK and at Cornell University [218, 219] in the US. This gave confidence that the undulator period and field strength selected for the ILC were feasible. Since that time the RAL group has successfully fabricated two identical long undulators, each 1.75 m in length, which have been magnetically tested and proven easily to achieve the field strength required. In fact, both exceeded the magnetic field specification by more than 30 % [220]. The quench training for the two magnets is shown in Fig. 4.7.

Figure 4.7
Quench history of the 2 of 1.8 m prototype superconducting helical undulator

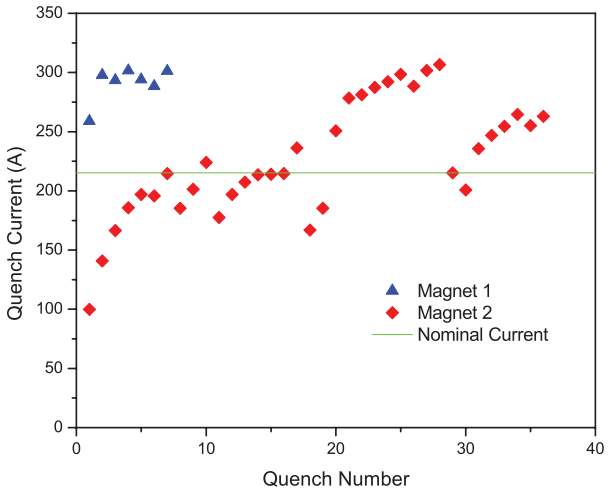

In addition the subsequent analysis of the magnetic field results by staff at Daresbury Laboratory in the UK has shown that both undulators have a very high field quality, certainly more than sufficient to provide the intense source of photons that is required. The RAL team has since incorporated both of these undulators into a single 4 m-long cryogenic module (which operates at -269 °C) of the design required by the ILC, and has proven that both undulators can be powered simultaneously at the field levels required [221]. A photo of the complete undulator cryomodule is shown in Fig. 4.8. In the future it would be valuable to test the module in an electron beam to measure the properties of the light generated by the undulators. The parameters of this undulator are given in Table 4.2.

Figure 4.8
The 4-m prototype superconducting helical undulator under test at Rutherford Appleton Laboratory.

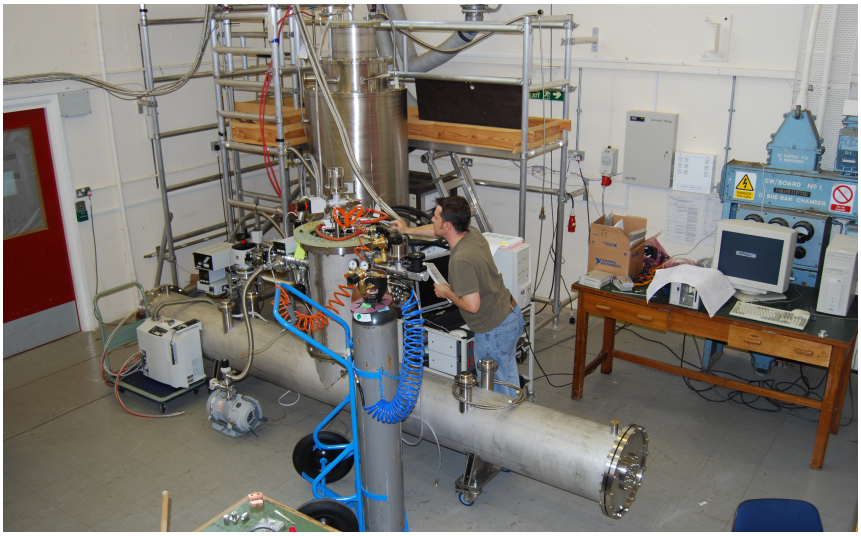

Table 4.2
Parameters of ILC undulator [222].

Undulator Type	helical
Undulator Period	11.5 mm
Undulator Strength, K	0.92
Field on-axis	0.86 T
Beam Aperture (diameter)	5.85 mm
Winding Bore	6.35 mm

The Daresbury/RAL team is now investigating the use of a more advanced superconducting material, niobium tin, which should produce even higher field strengths. This would make an even shorter-period undulator, which could generate the required positron yield at lower electron drive-beam energies. Currently the team is winding short prototypes to gain experience with this technically more challenging material and also to allow a direct comparison with the other prototypes built using niobium titanium [223]. Simulations of an undulator with niobium-tin conductor predict that a higher

field on axis is possible than with niobium titanium. The increased field could allow the period to be reduced to around 10 mm whilst maintaining a K value of 0.92, which could reduce the active undulator length by 10 %.

4.3.3 Conversion target

The conversion target is a 1-m-diameter wheel of titanium alloy that rotates at 100 m/s at the rim. To increase the positron-capture efficiency, the target rim passes through a strong magnetic field. Unfortunately, this then induces unwanted eddy currents in the wheel, causing the wheel to heat up. The level of heating that can be tolerated limits the usable magnetic field. Several groups have tried to model the eddy-current heating but inconsistent results were obtained from the different simulation codes used [224–226]. Consequently a full-scale prototype target was built at the Cockcroft Institute in the UK to benchmark the simulation codes. The target wheel was fabricated from the required titanium alloy and was rotated over a range of rim velocities in a strong magnetic field (Fig. 4.9a). The results of this unique experiment have accurately quantified the eddy-current effects and have confirmed which simulations were correct [227]. Furthermore, the experiment has proven that the magnetic-field level assumed by the positron-source design at the target wheel is feasible, with the eddy-current heating being easily tolerated.

Figure 4.9
Rotating target.

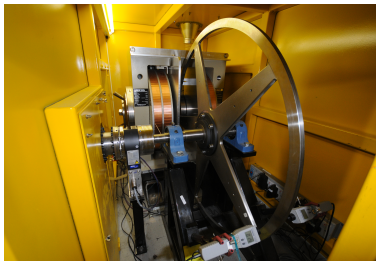

(a) Prototype setup for eddy current tests at Daresbury Lab.

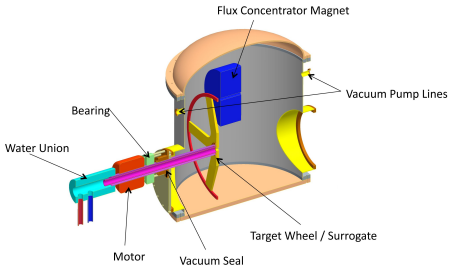

(b) Schematic of the engineering design.

The target wheel also has to operate inside a vacuum chamber while the motor is in air. This means that a rotating vacuum seal is required that is capable of operating at high velocity, near a magnet and in a high radiation environment – quite a demanding challenge. The team has identified a commercial vacuum seal that appears suitable for ILC conditions. Tests of the long-term performance of the seal were performed at Lawrence Livermore National Laboratory (LLNL) in the US.

Initially, an equivalent load to the target was rotated in a vacuum at the design 2000 RPM. The performance of the seal was evaluated by monitoring the vacuum level within the chamber along with the torque, vibration and temperature of the shaft. The ongoing vacuum test looks promising although these seals have occasional pressure spikes. A differential pumping solution will be required to mitigate the effect of this feature of the ferrofluidic seal. The temperature of the ferrofluid at these speeds is near the manufacturer's limit using standard seal designs. Seals with improved cooling characteristics will be needed for the final design. The full-size target wheel used at the Cockcroft Institute is available at LLNL, and can be installed for testing under vacuum. The engineering design concept for this test is shown in Fig. 4.9b.

Another issue is the effect of the shockwave on the target as a consequence of being struck by the intense pulses of gamma photons generated by the undulator [227]. Concerns were raised over possible material damage to the target itself on a shot-by-shot basis. Simulations with a numerical code at LLNL suggested that the effect is not significant. This has since been confirmed with a detailed analytical study, carried out at Durham University in the UK [228], and at DESY and Hamburg University [226].

4.3.4 Optical Matching Device

The flux concentrator is the pulsed magnet that generates the strong magnetic field close to the target wheel in order to enhance the positron yield. Many of these have been used successfully in the past but the parameters of the ILC are more technically challenging. A detailed R&D study has been initiated at LLNL to confirm the feasibility of the proposed magnet and later to build a suitable prototype to demonstrate the design performance.

The team has now completed the design [229] which operates at room temperature using a water-cooled coil and disk (see Fig. 4.10). In this design, the device sits in vacuum; all power and cooling connections move to the rim; the coils are kapton wound, hollow copper and water cooled; the plates are OFHC copper with water cooling pipes soldered in; there is only metal in the high-radiation areas; plates and coils are stacked and bolted together. With the help of a pulse-forming network, the flux-concentrator B field has a much better flat top than the previous design (see Fig. 4.10b).

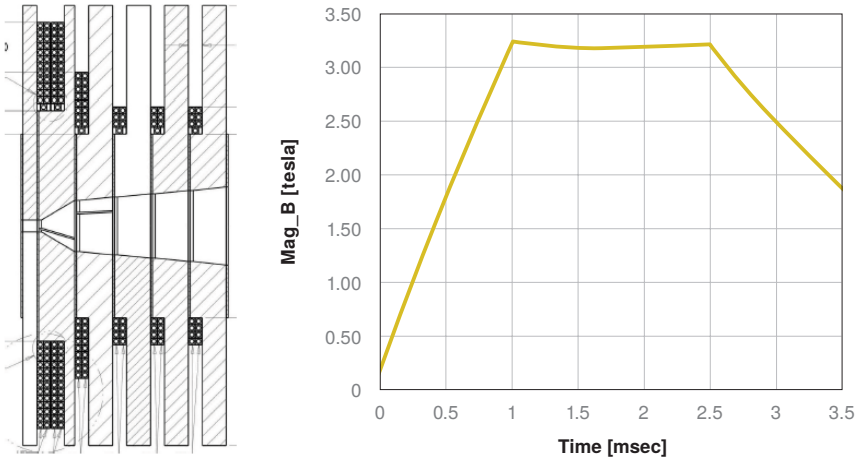

(a) (b)

Figure 4.10
(a) Drawing of new room-temperature flux concentrator; (b) the designed B field pulse of the flux concentrator

4.3.5 Photon collimator

The positron-beam polarisation of $\sim 30\,\%$ can be increased to 50–60 % with a photon collimator upstream of the target. This reduces the number of photons, requiring compensation by a longer active undulator (a length up to 231 m is to be reserved). The collimator must withstand a large heat load as well as the deposition of a huge peak energy density [230]. Table 1 summarises the basic requirements for the photon collimator depending on the centre-of-mass energy and the undulator parameters based on a positron yield of $Y = 1.5\ \mathrm{e}^+/\mathrm{e}^-$.

Table 4.3
Basic requirements for the photon collimator at the positron source and resulting degree of positron polarisation. The number of bunches is 1312 with a bunch population of 2×10^{10} positrons; the positron yield is $Y = 1.5\ \mathrm{e}^+/\mathrm{e}^-$ for the smallest aperture of the final collimator [222]

Parameter	Unit					L upgrade
Centre-of-mass energy	GeV	200-250	350	500	500	500
Drive-electron-beam energy	GeV	150	175	250	250	250
Undulator K value				0.92		
Undulator period	cm			1.15		
Positron polarisation	%	55	59	50	59	50
Collimator-iris radius	mm	2.0	1.4	1.0	0.7	1.0
Active undulator length	m	231	196	70	144	70
Photon beam power	kW	98.5	113.8	83	173	166
Power absorbed in collimator	kW	48.1	68.7	43.4	121	86.8
Power absorbed in collimator	%	48.8	60.4	52.3	70.1	52.3

The collimator parameters, in particular the radius of the collimator iris, are coupled to the drive-beam energy. Hence, instead of a universal collimator for the whole centre-of-mass-energy range, a multi-stage collimator design with decreasing iris is used. Each stage is constructed from the same materials but has different lengths to absorb the part of the photon beam with lower polarisation.

The first and longest section of the collimator is made of pyrolytic Carbon. This is followed by layers of materials with increasing Z, Titanium, Iron and Tungsten, which stop the shower and reduce the intensity of the absorbed photon beam after the final collimator to less than 0.1 % . Each section must be long enough to reduce the power to a value which can be handled by the next section. Conical bores in the Carbon and Titanium parts ensure a smooth heat-load distribution over a large region. The average heat load as well as the peak values of the energy deposition (PEDD) in the material are below the recommended stress limits. The collimators are water cooled; the pipes are embedded in a copper layer which encloses the carbon, titanium and iron parts.

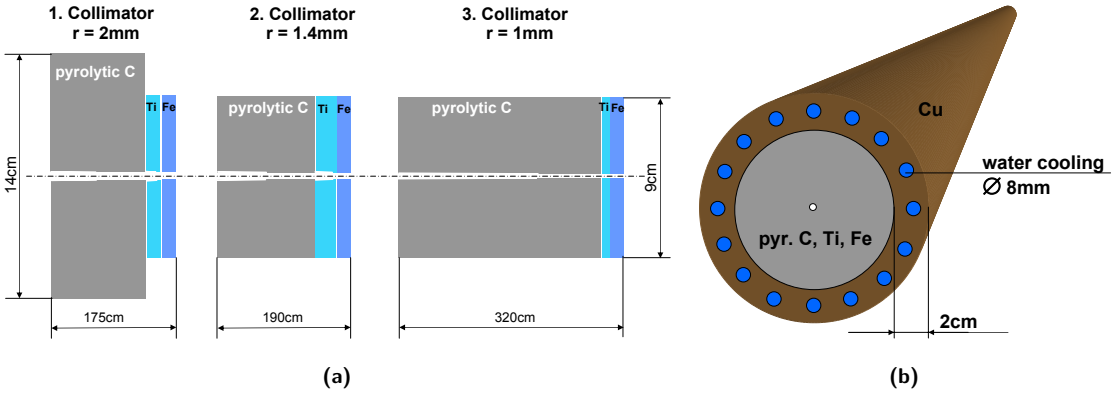

Figure 4.11. Basic layout of the multi-stage photon collimator at the positron source: (a) longitudinal section; (b) three-dimensional CAD model showing copper lading and water-cooling channels.

A sketch of the collimator layout is shown in Fig. 4.11. Each collimator stage can be moved onto or off the beamline. The maximum energy deposition and the average heat load in the collimator materials is summarised in Table 4.4. For the luminosity upgrade at 500 GeV, the values given in the last column have to be doubled.

Table 4.4. The peak power densities deposited in the components of the first ($(r = 2\,\mathrm{mm}$), second ($r = 1.4\,\mathrm{mm}$) and third ($r = 1\,\mathrm{mm}$) collimator stage for different centre-of-mass energies and the corresponding degrees of polarisation. The number of bunches is 1312 with a bunch population of 2×10^{10} positrons; the positron yield is 1.5 $\mathrm{e}^+/\mathrm{e}^-$ for the smallest aperture of the final collimator. Note the 10 Hz mode is used for 200-250 GeV case.

Parameter	Unit						
Centre-of-mass energy E_{cm}	GeV	$200-250$	350		500		
Drive-electron-beam energy	GeV	150	175		250		
collimator stages		1.	1.	2.	1.	2.	3.
iris radius r	mm	2	2	1.4	2	1.4	1
e^+ polarisation	%	55	59		50		
max. energy density in							
pyrolytic C	J/g	176.5	143.9	183	36.1	73.0	81.7
Titan	J/g	16.4	18.4	21.6	5.8	30.0	12.9
Iron	J/g	12.8	12.8	13.3	5.1	11.1	9.5
total power deposition in							
pyrolytic C	kW	44.8	36.3	25.9	7.9	12.9	17.9
Titan	kW	0.8	0.8	0.9	0.2	0.6	0.2
Iron	kW	0.2	0.3	0.2	0.1	0.1	0.1
Copper (cooling)	kW	2.3	1.9	2.4	0.4	1.2	1.8

The dimensions of the collimator stages, the average heat load in the sections and the corresponding cooling power are given in Table 4.5. The outer diameter is 20–30 cm. Due to radiation activation, remote handling will be required.

Table 4.5. Dimensions of the photon collimator parts. [222]

	1st collimator			2nd collimator			3rd collimator		
iris radius r	2 mm			1.4 mm			1 mm		
	length [cm]	out. radius [cm]	weight [kg]	length [cm]	out. radius [cm]	weight [kg]	length [cm]	out. radius [cm]	weight [kg]
pyr. C	135	7.0	72.7	140	4.5	31.2	290	4.5	64.6
Titan	20	4.5	13.8	30	4.5	8.6	10	4.5	2.9
Iron	20	4.5	24.2	20	4.5	10	20	4.5	10
active length	175			190			320		

4.3.6 Prototyping of normal-conducting RF accelerating structures and RF breakdown Study

Due to the extremely high energy deposition from positrons, electrons, photons and neutrons behind the positron target, the 1.3 GHz pre-accelerator has to use normal conducting structures up to an energy of 400 MeV. Major challenges are achieving adequate cooling with the high RF and heating from particle loss, and sustaining high accelerator gradients during millisecond-long pulses in a strong magnetic field. The positron-capture section contains both standing-wave (SW) and traveling-wave (TW) L-band accelerator structures. Detail about the parameters of these standing wave and travelling wave L-band accelerator structures can be found in Part II Section 5.5.4.

A half-length (5-cell) prototype standing-wave (SW) cavity was built at SLAC to verify that the gradient of 15 MV/m in 1.0 ms pulses can be achieved stably and without significant detuning from the RF heat load of 4 kW per cell. The cavity cross section is shown in Fig. 4.12. Figure 4.13a is a plot of the cold-test measurement of the mode frequencies (dots); the solid line is the fitted dispersion curve. The unloaded Q of the cavity is ∼29000 and the operating frequency (at π phase advance) is 1299.7 MHz. The time constant of this critically coupled cavity (0.5 Q_o/ω) is 1.8 µs.

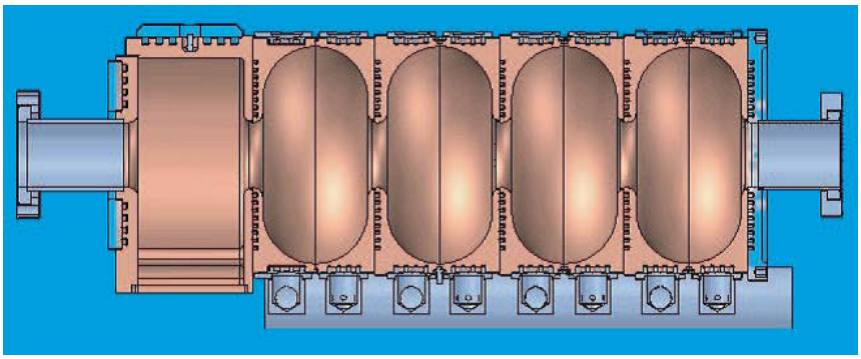

Figure 4.12
Cross section of 5-cell standing-wave cavity with cooling channels

The cavity has been rf processed at the π mode for about 530 h and it has incurred about 6200 breakdowns. The gradient goal of 15 MV/m with 1 ms pulses has been achieved. Figure 4.13b shows the breakdown-rate history during processing. For these data, the pulse repetition rate was 5 Hz except for 1 ms pulses where it was lowered to 1 Hz to reduce the detuning as the reflected power was causing waveguide breakdowns (the source of these breakdowns has since been eliminated and 5 Hz operation is expected to be possible in the future). The cooling system was designed to have about 25 % reflected power when the cavity was turned on 'cold' which then dropped to zero in steady state with full RF power dissipation (20 kW at 15 MV/m). In this way, a cavity temperature control system is not needed (at least for testing). However, the flow rate that was achieved (due to a limited supply of temperature-regulated water) was 86 gpm compared to the 140 gpm desired, which increased the cavity temperature by about 50 % (to 0.13 °C per kW dissipated). Also, the detuning of -2.7 kHz/kW was about 25 % larger than expected from simulations using the actual temperature rise and led to an overall reflection of about 50 % when cold with the appropriate choice of RF frequency to minimise the reflection at full power in steady state.

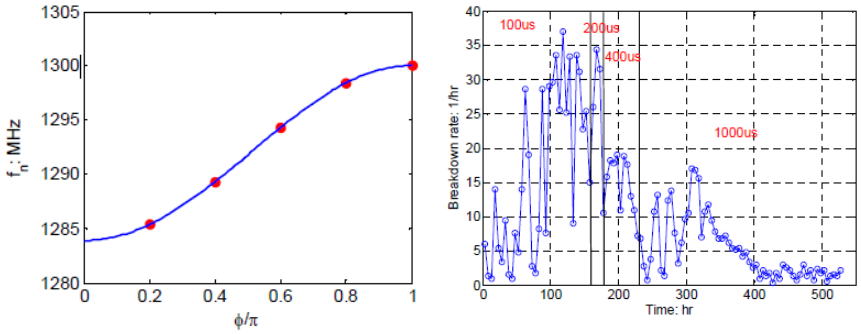

(a) **(b)**

Figure 4.13
(a) The 5 cell standing wave linac dispersion curve. (b) Breakdown-rate history of the cavity with different pulse length.

After hundreds of hours of conditioning, the breakdown rate was measured as a function of unloaded gradient (G), as shown in Fig. 4.13b. A G^{21} dependence was found, which is less steep than the G^{32} dependence recently observed for a CERN-designed, low a/λ, TW, X-band (11.4 GHz) structure. However, the gradient exponent is within the 20–30 range measured for NLC/GLC X-band prototype structures and close to the 19.5 value measured for the FNAL 805 MHz injector linac cavities.

4.3.7 Performance simulation

The parameters for source subsystems and the determination of the source performance can only be quantified using complex simulations. These simulations quite often require the combination of several sophisticated computer codes. The primary performance figure of merit is the yield, defined as the number of positrons captured in the acceptance of the damping ring per electron passing through the undulator. (Ideally a yield of 1 is required, but the design goal is set at 1.5 to allow a 50 % safety factor.) The second figure of merit is the polarisation of the captured positrons, which depends on additional parameters such as the collimation aperture of the photon beam before the target.

As shown in Fig. 4.14 and in Part II Fig. 5.3, for a given undulator and positron-capturing system, the performance of the positron source strongly depends on the energy of the main electron beam. At higher energy, the undulator B field is re-optimised to restore the polarisation to 30 %. The final parameters are listed in Part II Table 5.2. Performance simulation studies have also been done to determine the target energy deposition and the impact of the undulator on the electron-beam parameters [231–233].

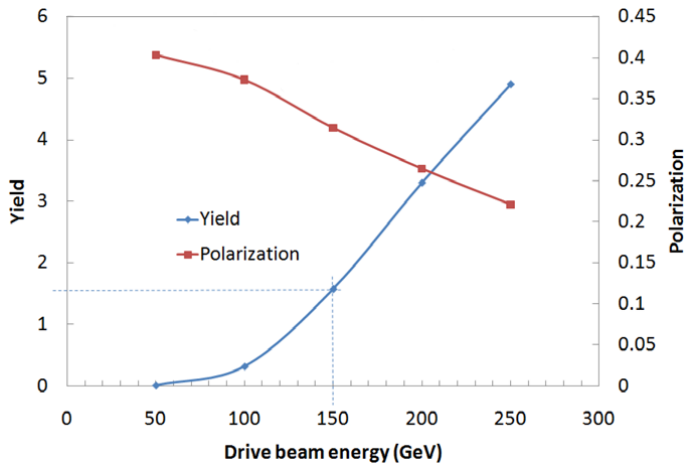

Figure 4.14
Simulation results of positron source yield and polarization for 231 m RDR undulator with QWT as OMD.

4.3.8 Lattice design

The layout of the ILC positron source beam line is shown in Part II Fig. 5.2 and the optics functions are shown in Part II Fig. 5.6. The lattice downstream of the separation chicane and through the transport line is the same as in the RDR. The quad settings of the FODO transport lattice have been re-optimised to minimise emittance growth and maximise transmission. The booster Linac lattice has been redesigned around the real geometry of cryomodules. The Linac-to-Ring lattice has also been redesigned to adapt to the central-region integration [234].

4.3.9 Spin flipper

The positron source based on a helical undulator provides a beam with a net polarization; its direction is defined by the helical winding of the undulator. Since the helicity of the positrons must be reversible as fast as that of the electrons, a spin flipper [235] complements the spin rotator system located in the PLTR line. The principle of the spin rotator and flipper system is shown in Fig. 4.15.

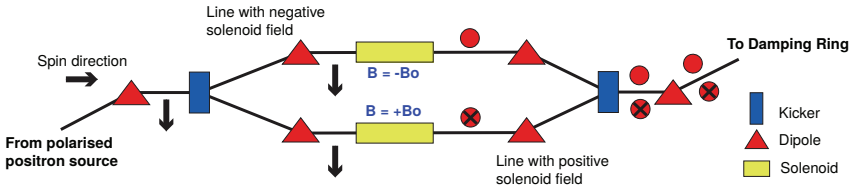

Figure 4.15 Schematic layout of positron transport to Damping Ring with spin rotator section

The beam is kicked into one of two identical parallel transport lines to rotate the spin in either the up or down vertical direction. Horizontal bends rotate the spin by $3 \times 90°$ from the longitudinal to the transverse horizontal direction. In each of the two symmetric branches a 5 m long solenoid with an integrated field of 26.2 Tm aligns the spins parallel or anti-parallel to the B field in the damping ring. Both lines are merged using horizontal bends and matched to the PLTR lattice. The length of the splitter section is approximately 26 m. Since the position of the solenoids is shifted along the straight section a horizontal offset of 0.54 m for each branch is obtained.

4.3.10 Remote handling and radiation shielding

The target will be highly activated after one year of operation. The RAL group produced a conceptual design of the target remote-handling system. Recent calculations confirmed the results from the RAL studies and showed that, with the nominal 150 kW photon beam, after 5000 hours of operation and 1 week of shutdown, the equivalent dose rate at 1 m from the target wheel will be approximately 170 mSv/h. Concrete shielding 0.8 m thick around the target is thought to be sufficient fully to contain the radiation associated with the beam and with the subsequently activated materials. Additional shielding may be needed upstream and downstream of the target and around the beam dump. Figure 4.16 shows the calculation results for the target activation and required shielding.

A remote-handling system is used to replace the target, OMD and 1.3 m NC RF cavities. To minimise the time required to exchange the target, the whole target system is designed into a plug with the top shielding. Inflatable seals for the vacuum enclosure form the interfaces of the target plug with the two beam lines. The targets will be removed and replaced vertically by an overhead crane, the disconnection and reconnection of the target being done locally. The used target is placed into a shielding cask for storage until the radiation has decayed to a safe level. Figure 4.17 shows the conceptual design of such a system.

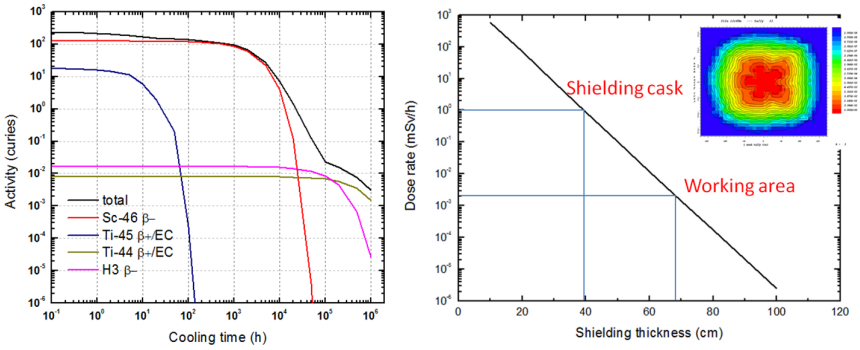

Figure 4.16
Shielding calculation for used target

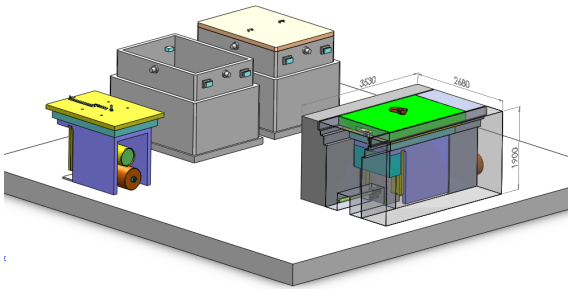

Figure 4.17
General layout concept for used-target remote handling.

4.3.11 Alternative source

As described above, the baseline design adopts a novel concept of positron generation, i.e. the undulator-based scheme. Although it can satisfy necessary requirements for the ILC positron source, some components, in particular the rotating target and the flux concentrator, are still under development for the final design. In view of this, two alternative positron sources are being investigated. First is the conventional positron source [236], which makes use of a few GeV electron beam on a thick target to produce positrons. This has been studied as a backup scheme for the baseline. The disadvantage is that it cannot create a polarised positron beam. The second option is a laser-Compton-based polarised-positron source as a possible future advanced scheme [237]. Both of these alternatives have an advantage that the positron source is independent of the electron beam to be used for collision. This would eliminate the complexity of operation, the need for an auxiliary source, the need for 10 Hz operation, and the constraint on the beam-line length.

4.3.11.1 Conventional source

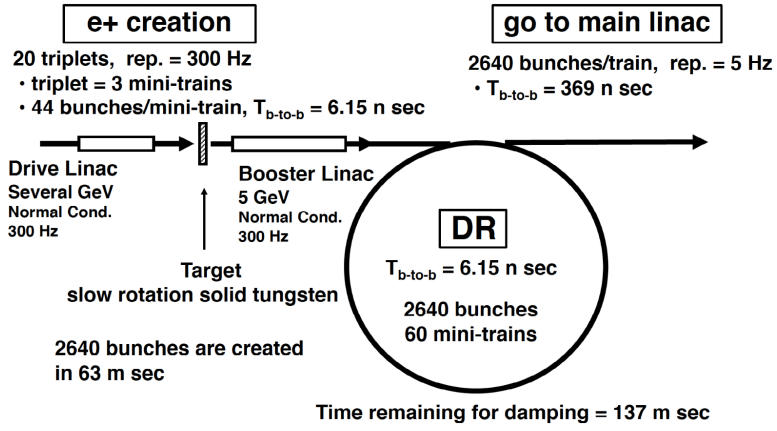

Figure 4.18
Schematic view of the 300 Hz positron generation scheme. The repetition rate of the drive linac and the booster linac is 300 Hz, whereas the repetition rate of the main linac is 5 Hz.

Though the concept of the electron-driven positron source is well known, ILC requires a new regime of the thermal and shockwave parameters in the target. The current design avoids these problems by stretching the pulse length of a bunch train. The schematic view of the 300 Hz scheme

is shown in Fig. 4.18. (The parameters for 2640 bunches per pulse are given, which are close to those at full power.)

The repetition rate of the ILC main linac is 5 Hz, giving an interval of 200 ms between two pulses, which is adequate for pulse stretching. We employ a normal conducting 300 Hz electron linac to create positrons. The pulse-to-pulse separation of the linac is 3.3 ms. Each pulse of the linac creates about 130 bunches, so 20 linac pulses create about 2600 bunches of positron in about 63 ms. This means 137 ms is left for the damping in the damping ring.

In the linac, a bunch-to-bunch separation of 6.15 ns is chosen, which is identical to that in the damping ring. To match the mini-train beam structure in the damping ring, one RF pulse of the linac accelerates three mini-trains with inter-mini-train gaps. This package of three mini-trains is called a triplet. Each mini-train contains 44 bunches. With 6.15 ns bunch-to-bunch separation and 44 bunches per mini-train, the length of a mini-train is 264 ns. Since a triplet contains three mini-trains, it consists of 132 bunches, thereby requiring 20 triplets to form 2640 bunches. There are gaps of about 100 ns between the mini-trains in a triplet. They are necessary for suppressing the instability caused by electron clouds in the damping ring.

In addition to employing 300 Hz generation, it is important to optimise the drive beam and target parameters to reduce target thermal issues. An intense simulation study concluded that a single production target made of tungsten alloy can be employed in the conventional source if appropriate parameters are used. The typical choice of the drive-beam parameters are: bunch charge of 3.2 nC, energy of 6 GeV, and R.M.S. spot size on the target of 4 mm. With these drive-beam parameters, the optimal target thickness is 14 mm. The slow rotation (tangential speed 0.5-1 m/s) is enough to deal with the thermal load. This is much slower than that of the undulator-based positron source.

Downstream of the target is a positron-capture system consisting of an Adiabatic Matching Device (AMD) and an L-band RF-section. A flux concentrator forms the AMD. The required pulse length of the flux concentrator is about 1 μs, which is the length of the triplet. This length is similar to that of existing flux concentrators. Moreover, the pulse length is short enough to use a high accelerating gradient in the RF section. After exiting the capture section, the positron energy is boosted to 5 GeV in a 300 Hz normal-conducting linac. Then a kicker with a pulse length of about 1 μs and repetition rate 300 Hz is employed to inject triplets of positrons into the DR.

4.3.11.2 Compton Sources

A disadvantage of the conventional scheme is that it cannot provide polarised positrons. To overcome this problem an upgrade to a polarised source in a later stage is considered by making use of the inverse-Compton scattering between electrons and a laser. Three possible schemes are under investigation: Ring-Compton; ERL-Compton; and Linac-Compton. The first two are similar: both use a 1-2 GeV electron beam, 1 micron laser light, and high-finesse laser stacking cavities in multiple laser-electron collision points. Both assume stacking of generated positrons in a storage ring. The Linac-Compton is rather different. It uses a 5-6 GeV electron beam and CO_2 laser light. Regenerating amplification in low-finesse laser cavities are assumed at the collision points. Positron stacking is not assumed.

The Compton source must match the 300 Hz normal-conducting linac for a smooth upgrade from non-polarised to a highly polarised positron source. Linac-Compton will smoothly upgrade the conventional source. The 6 GeV 300 Hz drive linac of the conventional scheme is reused. At the end of the linac, Compton IPs are placed, followed by the positron-production target. The 5 GeV booster linac is also reused. On the other hand, the Ring- and ERL-Compton will need relatively large modification of the system. What must be added are: a storage ring or an ERL as the electron driver for the Compton scattering; a low-energy storage ring for positron stacking; a long pulse linac

(most probably superconducting) between positron production and the stacking ring. Figure 4.19 shows a typical schematic view of the Ring- and ERL-Compton scheme as upgrade options from the conventional source.

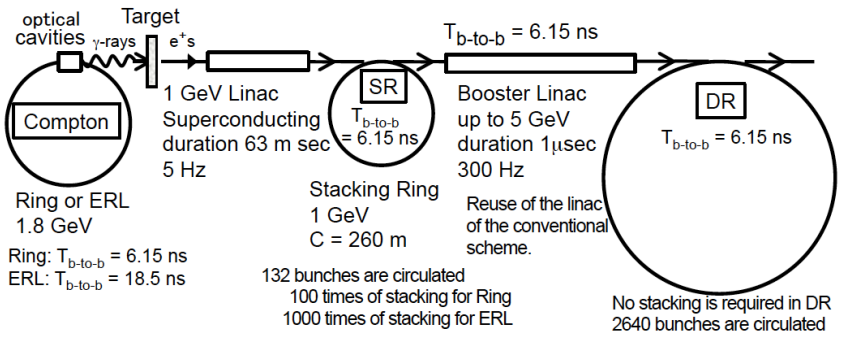

Figure 4.19
The conceptual design of Ring-Compton and ERL-Compton for the future upgrade from the 300 Hz conventional positron source.

Several critical issues remain with the Compton scheme.

For the Linac-Compton scheme, reliable CO_2 laser technology with a regenerating laser cavity and the heavy beam-loading compensation scheme of the linac are essential. For the Ring- and ERL-Compton schemes there are many common issues to be addressed. Firstly, a high-finesse laser-light stacking cavity is necessary. Both schemes assume a cavity with the enhancement factor 10^4, while the currently achieved value is 1200. Further improvement of the feedback system is needed to achieve this goal. Secondly, the large stored power in the optical cavity is also an issue. It raises heat and destruction issues for the cavity mirrors. To deal with the issue of the laser-light power, it is necessary to develop very good mirror-coating with the surface loss less than 1 ppm. A larger laser spot size on the mirror is also required to deal with the high power. It requires a longer cavity (longer mirror-to-mirror distance). The length of the current optical 4-mirror cavity is 0.42 m (round-trip path length 1.64 m). Development cavities with twice the lenght is now under way at KEK. Reduction of the crossing angle is also one of the critical R&D issues. It significantly increases the luminosity of laser-electron collision. A longer cavity makes a smaller crossing angle possible. Head-on collision is optimal for luminosity production. A test of head-on collision with two bending magnets upstream and downstream of the Compton collision point is under way at KEK. If head-on collisions are employed, the generated gamma-rays pass through the downstream mirror. Studies of possible mirror damage by the gamma-rays is necessary. Employing a crab-crossing is another way to obtain head-on collisions. A detailed feasibility study will be necessary. In the ERL-Compton scheme, the effect of finite crossing angle is much smaller than that in the Ring-Compton scheme because a bunch length significantly shorter than that in the storage ring can be achieved.

The positron stacking in a storage ring is another challenge of the Ring- and ERL-Compton schemes. The simulation studies performed at CERN showed that a positron-stacking efficiency around 95 % can be achieved. This is significant progress but a still-higher efficiency is necessary to avoid radiation activation of the stacking ring.

4.4 Damping ring

The ILC R&D programme identified the key areas for work during the Technical Design Phase:

- developing methods to suppress the electron cloud instability
- demonstration of operation at ultra-low vertical emittance (vertical emittance of 2 pm)
- demonstration of fast injection/extraction kickers performance.

Two dedicated test facilities were identified for this effort: CesrTA at Cornell University and ATF at KEK. Both programmes have been carried out by large collaborations, with contributors from institutions worldwide working on simulation, experiment and design.

4.4.1 Electron-cloud mitigation

The R&D effort on electron-cloud mitigation involves the large international collaboration participating in the CesrTA programme plus the effort that is in progress at other laboratories.

Results of the damping ring R&D program are described in Section 3.5 on the CesrTA programme.

4.4.2 Ultra-low-emittance operation

The demonstration of ultra-low emittance was carried out in the framework of the CesrTA and ATF collaborations, but important results have also come from the synchrotron-light-source community.

4.4.2.1 Diagnostics for low-emittance beams at ATF

The ATF damping ring achieved a vertical emittance as low as 4 pm before the publication of the RDR and has supported a wide range of important research for many years: low-emittance tuning and intra-beam scattering studies, studies of the fast-ion effect and fast-kicker tests. Currently, the main focus of activity at the damping ring is the production of an extracted beam with the required characteristics for the ATF2 programme (see Section 3.6) and the development and test of diagnostics for low-emittance beams. Instrumentation development includes laser wire, optical transition radiation, optical diffraction radiation, and a high-resolution X-ray monitor [196, 238, 239].

4.4.2.2 Diagnostics and tuning algorithms at CesrTA

The low-emittance-tuning effort provides the foundation for studies of the emittance-dilution effects of the electron cloud in a regime approaching that of the ILC damping rings. The vertical-emittance goal for the initial phase of the CesrTA programme is less than 20 pm. Low-emittance-tuning efforts have focused on the systematic elimination of optical and alignment errors that are the sources of vertical-emittance degradation [169]. Techniques have been developed to eliminate systematic errors in the beam-position monitors, measuring gain variation among the four button electrodes on each beam-position monitor, and to centre the monitors with respect to the adjacent quadrupole. Work has also been carried out to optimise the sextupole design, thus minimising sources of emittance coupling. During the most recent experimental run, this effort resulted in measurements of the vertical emittance consistent with having achieved the target vertical emittance of 20 pm in both single-bunch and multi-bunch operations.

An X-ray beam size monitor has been developed and successfully demonstrated at CesrTA. It is able to measure both integrated and single-bunch turn-by-turn beam sizes at positions for monitoring the progress of the low-emittance tuning of the machine and for beam dynamics related to instabilities driven by the electron cloud [170, 176].

4.4.2.3 Demonstration of vertical emittance below 2 pm at synchrotron light sources

A step forward in the demonstration of very low vertical emittance has been achieved at some synchrotron light sources, which operate low-emittance storage rings with characteristics very similar to the ILC damping ring and have developed alignment procedures, machine modelling, tuning algorithms, and orbit stabilisation for coupling correction and low-vertical-emittance tuning [240]. In particular, the Diamond Light Source in the UK, the Swiss Light Source and the Australian Synchrotron storage ring have achieved betatron-coupling correction down to 0.1 % and vertical emittances below 2 pm [241–243]. Significant progress has been made in the development of diagnostic systems for the measurement of such small vertical emittances [244–246]. Two low-emittance-ring workshops, LER10, at CERN in January 2010 and LOWϵRING 2011, in Crete in October 2011, were organised by the joint ILC-CLIC working group on damping rings. They were very successful in strengthening the collaboration within the two teams designing the damping rings and with the rest of the low-emittance-rings community, including synchrotron-light sources and B factories.

4.4.3 Performance of fast injection/extraction kickers

4.4.3.1 ILC-like multi-bunch extraction at ATF

The injection/extraction kickers act as the bunch-by-bunch beam manipulator to compress and decompress the bunch spacing into and from the damping ring. The kickers require high-repetition rate, 3 MHz, and very fast rise and fall times of the kicker field: 6 ns for the nominal configuration and 3 ns for the proposed luminosity upgrade. The tolerance on horizontal beam jitter of the extracted beam is approximately 10 % of the beam size, which requires the relative stability of the extraction kicker amplitude to be below 7×10^{-4}.

A rise and fall time of 3 ns has been already demonstrated in the ATF using a 30 cm-long strip-line kicker together with a semiconductor source of high-voltage pulses [247]. The time response of the strip-line kicker was observed by measuring the resulting betatron-oscillation amplitude of the stored electron beam.

An ILC-type beam-extraction experiment using two strip-line kickers has been carried out at ATF [248]. The length of the strip lines is 60 cm and the gaps of the two electrodes are 9 mm and 11 mm. Two pairs of pulsers with a peak amplitude of 10 kV, a rise time of 1.5 ns and a repetition rate of 3.3 MHz are used to drive the strip lines. The strip-line kicker system produced a 3 mrad total kick angle for the 1.3 GeV beam. The rise time of the kick field is less than 5 ns.

The multi-bunch beam stored in the damping ring with 5.6 ns bunch separation was successfully extracted with 308 ns bunch spacing in the extraction line (see Fig. 4.20). No deterioration of the extracted vertical beam size was observed (as measured with the laser wire). The resynchronisation circuit used for precise timing adjustment worked stably. The relative angle jitter of the single-bunch beam extraction was 3.5×10^{-4} rms, which is better than the requirements for ILC damping-ring extraction. For multi-bunch beam extraction a trigger timing circuit is needed to compensate the time drift of the pulser. Very recently, 30-bunch extraction with an rms angle jitter 10^{-3} has been achieved. This value can be further reduced by precise tuning of the timing system or by using a feed-forward system.

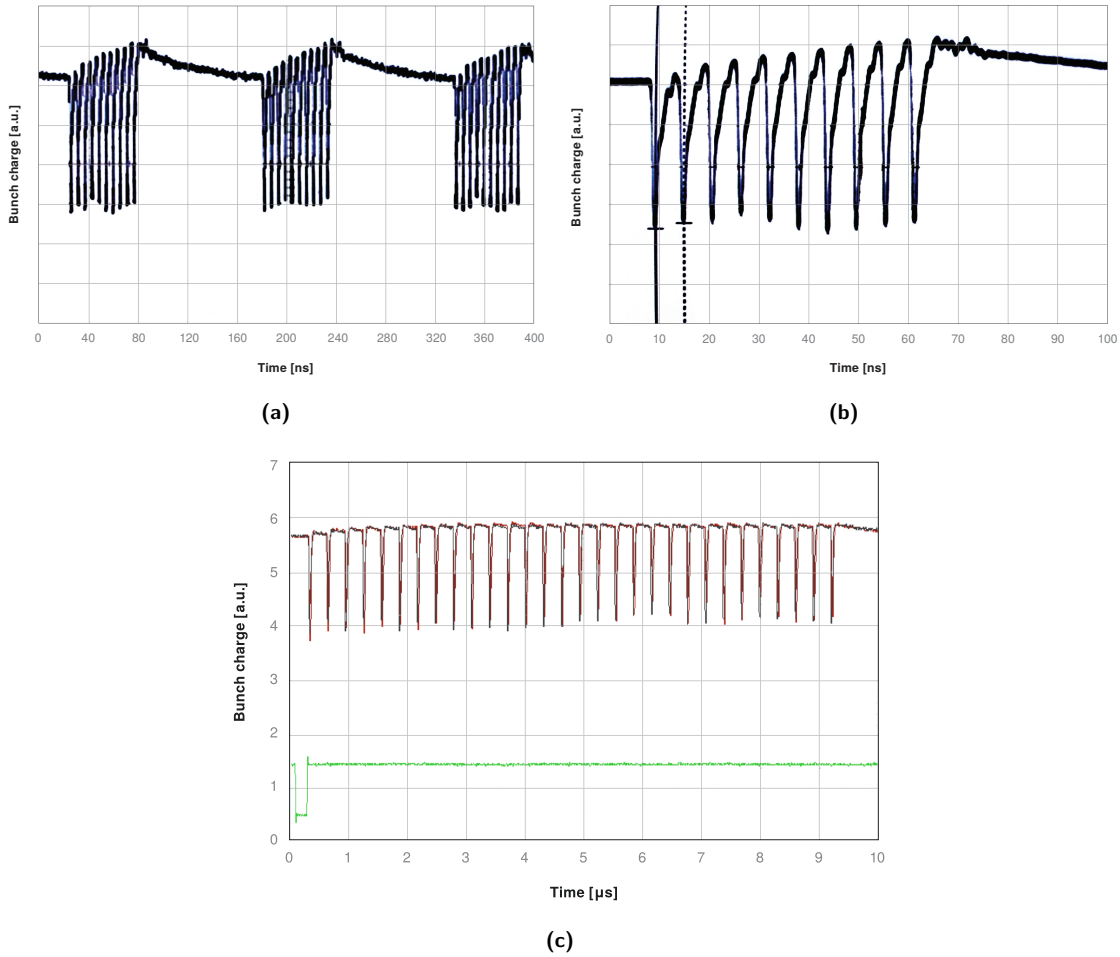

Figure 4.20. Bunch current monitor signals from the ATF damping ring and damping ring extraction line: (a) 3 trains of 10 bunches with 5.6 ns spacing stored in the damping ring; (b) close-up of one train in (a); (c) 1 train of 30 bunches with 308 ns spacing in the extraction line.

4.4.3.2 Strip-line-kicker design at DAΦNE

The design of the new, fast strip-line kickers for the injection upgrade of DAΦNE is based on strip-line tapering to obtain a device with low beam impedance and an excellent uniformity of the deflecting field in the transverse plane (see Fig. 4.21) [249]. These characteristics are essential also for the ILC damping ring; the experience gained with the new DAΦNE injection system will be applied to the design of the ILC damping-ring injection system. The rise and fall times of the kickers are all less than 6 ns, corresponding to the ILC damping-ring requirement for the nominal configuration.

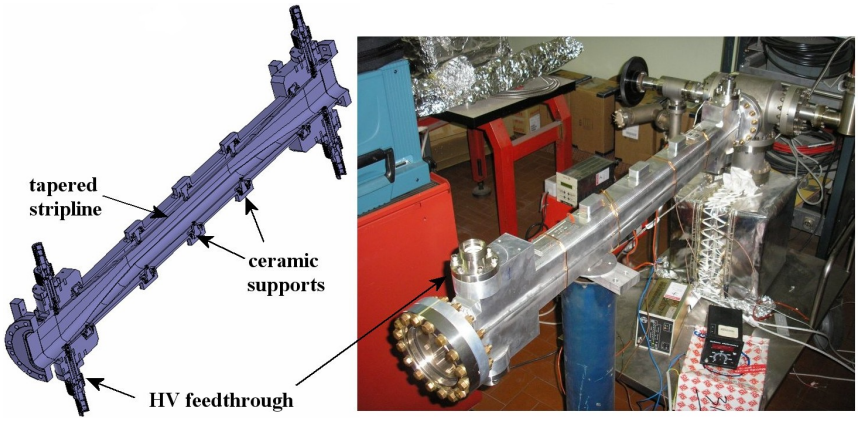

Figure 4.21
DAΦNE strip-line kicker.

The coupling impedance measurements and simulations have pointed out the absence of trapped higher-order modes in the longitudinal and horizontal planes when at least two ports are loaded by 50 W [250]. In the vertical plane, only four trapped higher-order modes were found. The instability growth rates of these resonances (in the worst case) were well below the damping rates provided by the DAΦNE feedback systems. After installing the injection system, no instability effects due to the kickers were observed and the DAΦNE broadband impedance arising from this and other vacuum-chamber modifications made at the same time was reduced by about 50 % [251].

4.4.3.3 SLAC pulser modulator

At SLAC, two related paths to meet the ILC kicker driver requirements were studied: a transmission-line adder topology, which combines the output of an array of ultra-fast MOSFET switches and a drift step-recovery diode (DSRD) approach.

For the adder topology, an ultra-fast hybrid MOSFET/driver, recently developed at SLAC, has achieved 1.2 ns switching of 33 A at 1000 V with a single power MOSFET die [252]. A transmission-line adder has been designed based on the ultra-fast hybrid MOSFET/driver switching module. The initial test demonstrated that the adder can combine pulses with 1.4 ns switching time without any degradation [253]. An improved switching module (Fig. 4.22) has been tested in 6 MHz burst operation [254].

Figure 4.22
Photo of improved HSM the insert shows the reverse side.

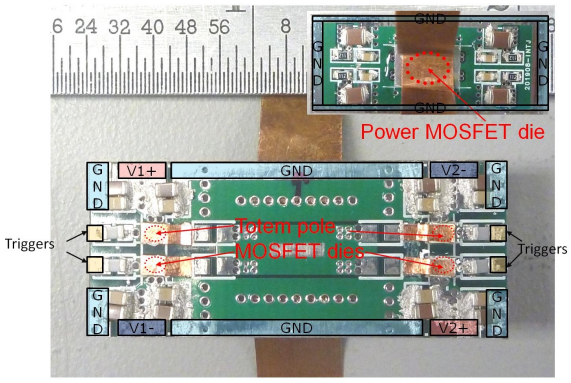

For the DSRD programme, development of a fully capable DSRD kicker driver is proceeding well, with excellent results obtained from the first commercially produced DSRDs, and from a refined circuit for the MOSFET driver [255]. A prototype with a 4 ns pulse length (as required for ATF) and 3 MHz pulse train has been demonstrated (see Fig. 4.23). A recent success was to eliminate the post pulse, which is unacceptable for the ILC kicker driver since it affects the bunches adjacent to the kicked bunch [256].

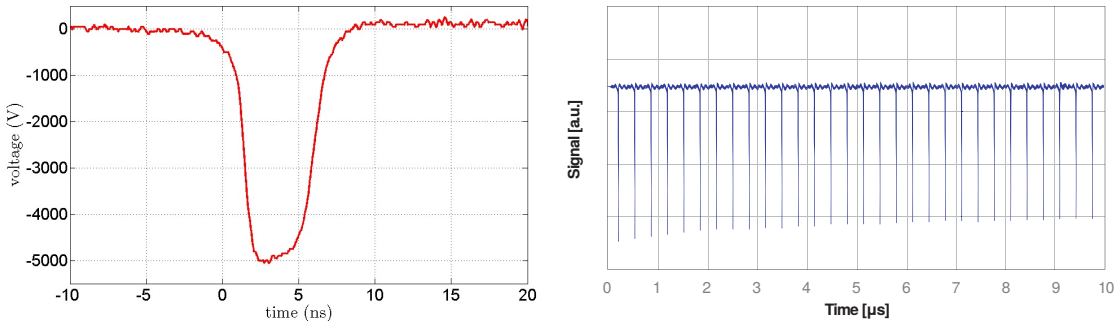

Figure 4.23. DSRD-based driver output; single pulse detail, 3 MHz 30-pulse pulse-train [256].

Figure 4.24a shows the output voltage of a kicker pulser (FPG10-3000KN, built by FID GmbH)

and tested at ATF [210]. Figure 4.24b shows the time dependence of the estimated kick field when applied to the KEK-ATF 60 cm strip line. In the ATF experiment, two 60 cm strip lines were installed to extract single bunches from trains of ten bunches circulating in the damping ring. The bunch spacing was 5.6 ns. The measured angle jitter of the extracted beam in the KEK-ATF experiment is 3.5×10^{-4} of the kick angle.

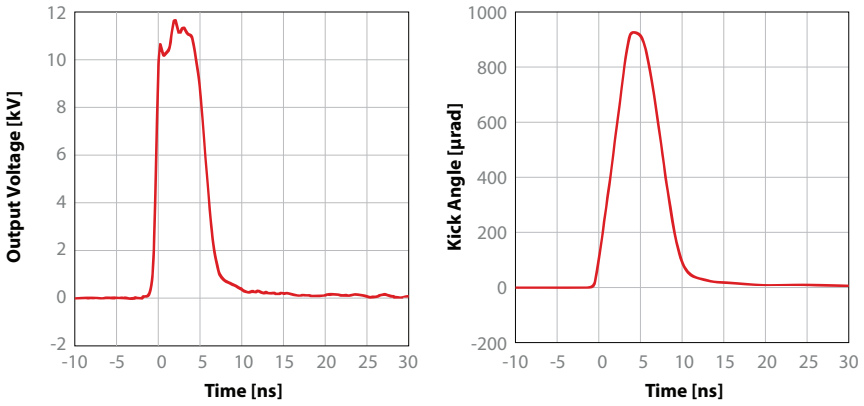

(a) (b)

Figure 4.24
(a) Pulse waveform of the FID pulser; and (b) estimated kick obtained using the 60 cm stripline kicker in the KEK-ATF beamline.

4.5 Beam Delivery System and MDI

4.5.1 Introduction

The beam-delivery system and the interface between the accelerator and detectors near the IP constitute some of the foremost challenges to be faced at any linear collider. This is a direct consequence of the extremely small beam size required for a "one-pass" collider to attain a luminosity competitive with that of a storage ring in order to observe the rare physics processes of interest. In many areas, the requirements of the ILC are beyond the current state of the art. This section describes the R&D carried out in several of these areas: the design of the final-focus magnets, including both superconducting and permanent-magnet options; maintaining the stability of the beams so that luminosity during collisions in maximised using a fast intra-train feedback system based on digital processing; the design of a high-accuracy but relatively rapid "push-pull" system that can exchange two massive particle-physics detectors with a minimal loss of luminosity; and a precise and rapid alignment system to ensure that all parts of the detector are aligned both internally and with respect to the final-focus machine elements.

4.5.2 Cold QD0 Design

The ILC IR final-focus (FF) magnets must satisfy many conflicting requirements; before the start of QD0 Prototype R&D work it was not clear that construction of such magnets would be feasible. The ILC FF system brings the incoming e^+e^- beams to nanometre-scale focus with optical demagnifications much greater than previously attempted but at the same time it must catch and refocus the disrupted outgoing beams with sufficient aperture to avoid particle loss and generation of detector backgrounds. The FF has strong quadrupoles with close side-by-side spacing, sextupole magnets to correct for higher-order chromatic effects and octupole magnets to reduce halo-particle backgrounds. The need for precision energy scans and low-energy running for detector calibration demands tuneable magnets making a compact superconducting system advantageous. The presence of strong detector-solenoid fields overlapping the magnets closest to the IP precludes magnetic yokes and requires incorporation of an active shield to reduce the unwanted external field at the extraction beam line.

The Prototype R&D programme investigated producing the FF magnets using BNL direct-wind magnet-production technology. This involves building up a multilayer coil structure with epoxy

impregnation that is then fibre-compression wrapped and cured. The resulting structure handles large magnetic Lorentz forces on the coil without the need for external clamping collars. Warm field-harmonic measurements that are used to control harmonic errors are made between winding different coil layers.

Initially, short prototype quadrupole and sextupole test coils were wound and tested. These coils exceeded ILC operational requirements by reaching the conductor short-sample limit in the presence of deliberately enhanced solenoidal background fields. Subsequently an opposite-polarity outer-quadrupole coil was added outside the main quadrupole so as to demonstrate active shielding via external field cancellation. Studies showed that it is important to rotationally align the main and cancellation coils in order to achieve the best performance; with proper adjustment the external field was dramatically reduced, with only a small impact on the overall QD0 operating margin.

In parallel, prototype full-length coils suitable for FF operation were produced. A major challenge in winding the full-length coil is that the aspect ratio (20 mm ID, 3.5 m length) of the coil support tube results in droop in the middle under a combination of its own weight and pressure applied to the tube during winding. This droop causes systematic conductor mis-positioning and modulation of the coil pattern, which lead to the generation of unwanted field harmonics. However, based on earlier work, small, consistent, support-tube offset modulations can be compensated via software-based corrections during coil winding. Rolling tube supports, that move along with the coil-winding head and reduce local support-tube deflection, were hence implemented.

Despite these measurers, field harmonic variations symptomatic of significant residual tube-offset motion were observed. Unfortunately stiffening the rolling support structure increased the risk of damaging a coil already wound and, more problematically, was found to increase positioning hysteresis that in turn made software compensation even more challenging. The moving support scheme was hence abandoned in favour of a simple fixed central-tube support that was precisely aligned via a laser system with the rest of the coil-winding mechanical structure.

The above approach requires that the quadrupole coil must be split into two parts. This has the advantage that it is possible to energise the coil closer to the IP more strongly at low beam energy, while reducing the gradient in the subcoil further from the IP. This causes the effective focusing centre to be closer to the IP at low energy, and can be used to improve the FF optical performance.

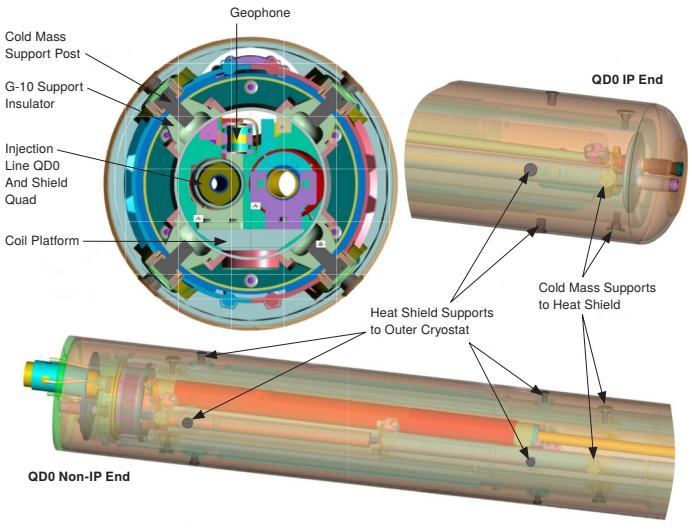

Figure 4.25
QD0 cryostat

Another fundamental component of the R&D programme was to develop practical solutions for installing and operating FF magnets located inside two different particle detectors. The MDI issues are especially challenging in light of the requirement for rapid push-pull swapping of the detectors. The conclusion is that each experiment should carry its own customised pair of QD0 and

cryogenic-feed cryostats. Each detector must hence interface with a pair of fixed QF1 and service cryostats that remain in place to define the IR beam-line axis. The QD0 cryostats must accommodate the incoming and extraction beam-line magnetic elements with different L^* and have customised features to facilitate their installation and alignment, as well as compatibility with detector access and maintenance. A QD0 cryostat is shown in Fig. 4.25.

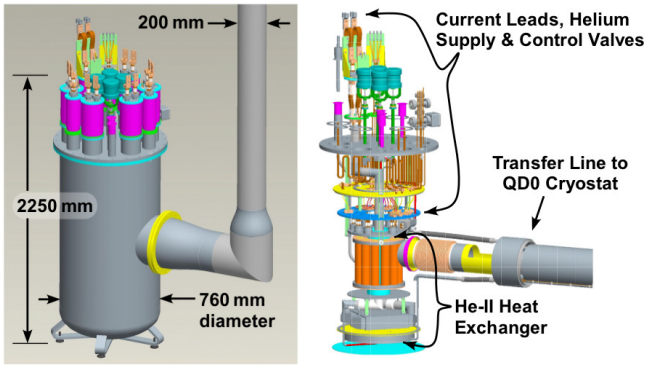

Figure 4.26
QD0 service cryostat

The FF magnets are designed to operate using pressurised superfluid He-II in order to avoid cryogens flowing through a long transfer supply line and the magnet cryostat structure. The interface point for the He-II supply heat exchanger and the magnet current power leads is the service cryostat shown in Fig. 4.26. Together, the service cryostat and cryogenic transfer line comprise an intricate system that should be made as stable as possible against vibration during operation. In order to explore the challenges inherent in such a system fully, the QD0 magnet cryostat is being fabricated to accept the full-length prototype coils. This system should be horizontally tested while connected via a transfer line to an ILC-style service cryostat that is also under construction. The partially assembled QD0 helium-containment vessel with its alignment supports is shown in Fig. 4.27a and the start of assembly of the service cryostat is shown in Fig. 4.27b. The QD0 prototype is designed to be compatible with vibration stability measurement via a laser doppler vibrometer system, as well as some internal accelerometers and external geophones. A conceptual design has also been developed for a stabilised pickup-coil system that could be inserted into the QD0 bore in an attempt to measure changes in the magnetic-field centre directly. Such a stabilised probe is also very useful for direct measurement of the field-centre stability of the SuperKEKB IR quadrupole magnets; its planned deployment there will gain valuable experience of direct relevance to ILC.

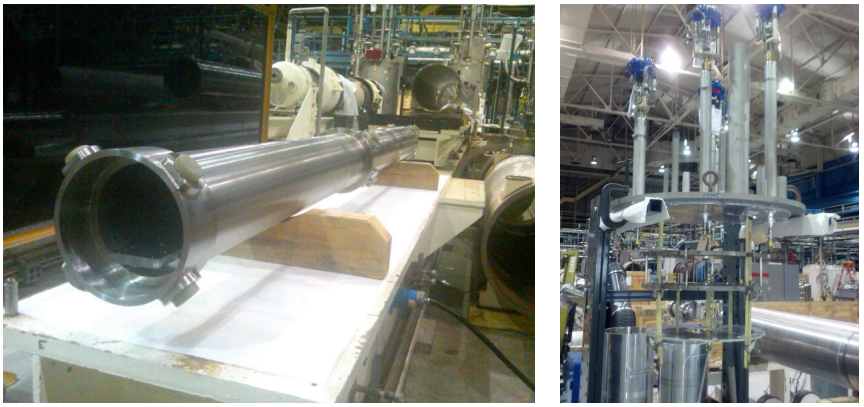

(a) **(b)**

Figure 4.27
(a) Partially assembled QD0 helium-containment vessel with alignment supports; (b) the start of assembly of the service cryostat.

4.5.3 Permanent QD0 design

4.5.3.1 Magnet Design and Test

Permanent-magnet quadrupoles (PMQ) [257–260] have been under study as an alternative technology for the final-focus magnets in a linear collider since 2002. Since the system is passive, there is no risk of introducing jitter via a cryogenic plant. However, demagnetisation is a concern, although a rough estimate shows that continuous operation for 10 years at the ILC may cause about 1 % demagnetisation on NEOMAX 32EH. Magnets made from SmCo are more durable against radiation but has lower magnetic strength.

An adjustable-strength PMQ, which is divided into five rotatable rings, is shown in Fig. 4.28. The rotation angles $\pm ø/2$ of the PMQ rings at even positions are opposite in sign compared to those at odd positions. By choosing a proper length for each magnet ring, the skew component can be eliminated up to the 5th order of rotation angle. A model magnet unit was fabricated with five magnet rings that have lengths of 20, 55, 70, 55, 20 mm, respectively. The total length is about 24 cm. Each magnet is divided into 20 pieces azimuthally and radially. The outer diameters of the magnet rings are 100 mm (without the magnet holder ring). The inner diameters are set at 55 mm for beam test at ATF2. Since the beam energy of ATF2 is about 0.5 % of that of the ILC, the gradient required is smaller. This 24 cm-length unit has nearly the same focusing strength as the currently used QD0 electromagnet in ATF2. Before the assembly of the magnet unit, the five rings have to be adjusted individually [261–263].

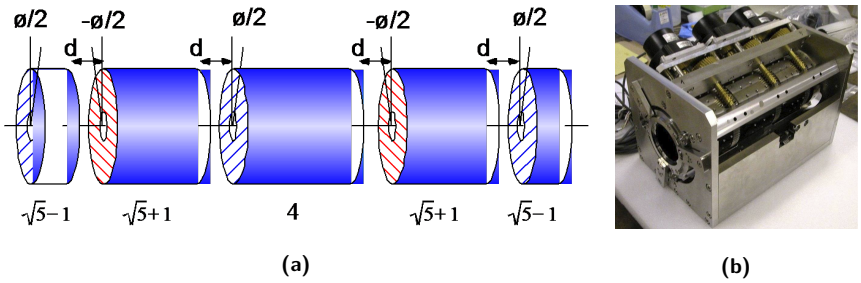

Figure 4.28
(a) Schematic view of the five-ring singlet; (b) the fabricated model.

Assuming a field gradient of 140 T/m and using 12 units of the five-ring-singlets, the total length becomes about 3 m. Using this design for QD0, a preliminary fine-tuning simulation was carried out with matching requirement for Twiss parameters: $\alpha_x = \alpha_y = 0$, $\beta_x = 0.021$ m, $\beta_y = 400$ µm, $\eta_x = 0$ at IP, starting with the ILC deck "ilc2006b.ilcbds1" (14 mrad version). The final rotation angle ø of the PMQ is 6.58°. Off-momentum matching was performed by re-optimising the K2 of the sextupoles by looking at the beam size at the IP [264]. The coupling between x and y was well suppressed and the final beam sizes at the IP are $\sigma_x/\sigma_y = 656/\ 544$ nm for $\gamma_{ex}/\gamma_{ey} = 9.2 \times 10^{-6}$ m$/\ 3.4 \times 10^{-8}$ m and $\sigma\delta = 6 \times 10^{-4}$. Further optimisation will improve these results. A rough sketch of the closest optical components is shown in Fig. 4.29. The QDEX1 and SD0 magnets can be also fabricated using permanent magnets.

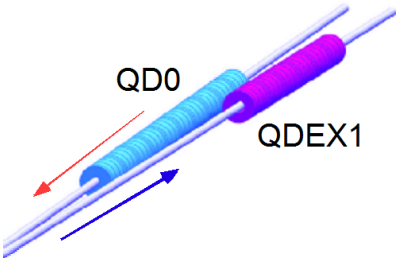

Figure 4.29
Rough sketch of QD0 and QDEX1.

An evaluation test of the fabricated five-ring-singlet model was successfully carried out at ATF2 to obtain practical experience in handling this new device [265].

4.5.3.2 Anti-solenoid for Permanent QD0

Since the system has to be located close to the IP where stray magnetic field from the detector solenoid exists and the permanent magnet should not be immersed in a high magnetic field, the stray field has to be reduced. Figure 4.30 shows the partially passive hybrid anti-solenoid, where the major part of the magnetic field is cancelled by the anti-solenoid coil [266]. The residual magnetic field can be easily shielded by the iron shield pipe as long as it is not saturated. This passive scheme makes the adjustment of the anti-solenoid current less critical. The outward thrust force on the solenoid coil and inward force on the iron shield can be balanced. While the force may be cancelled out in normal operation, it should have enough mechanical strength to hold the structure against an emergency case such as a fault on the power supply of the anti-solenoid coil.

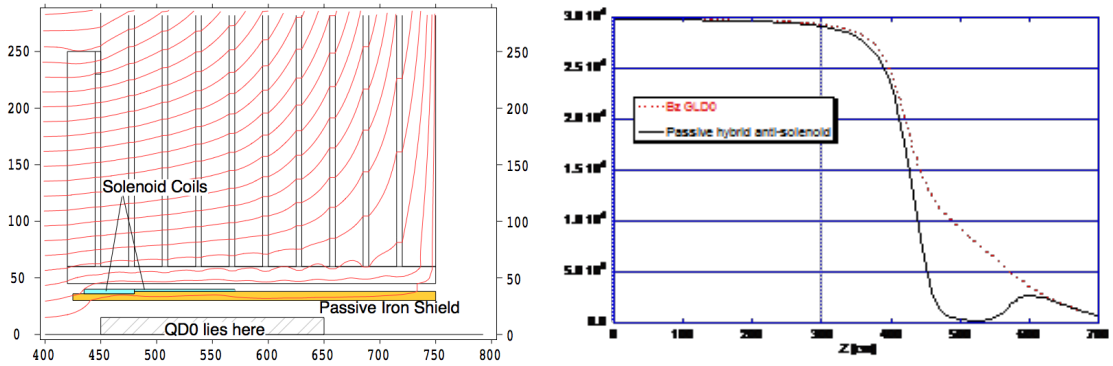

(a) **(b)**

Figure 4.30. (a) Partially passive hybrid anti-solenoid. The blue boxes denote the anti-solenoid coils wound on the passive iron magnetic-shield pipe and the QD0 lies in the hatched box area; (b) the stray field is well suppressed.

4.5.3.3 External Stray Field of PMQ

Assuming an L^* of 4.5 m, the distance between the in-coming and out-going beam is 63 mm at L^* from the IP and the bore diameter required for the outgoing beam would be 25 mm. The external stray field at the outgoing beam, which is located from $x = 50$ mm to 75 mm (see Fig. 4.31), is less than 10 G. Figure 4.32 shows the measured stray field on a horizontal line 10 cm from the beam axis. The distribution changes with the strength adjustment. An iron case as the PMQ holder will reduce the field by a factor of one hundred. The external magnetic field from the detector solenoid has to be dealt with when soft magnetic material is used; the iron case should be made of laminated iron with small enough packing factor to have less longitudinal permeability.

Figure 4.31
PMQ and outgoing beam.

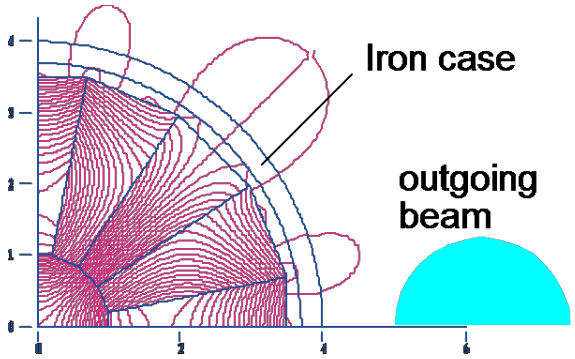

Figure 4.32
Measured external stray field.

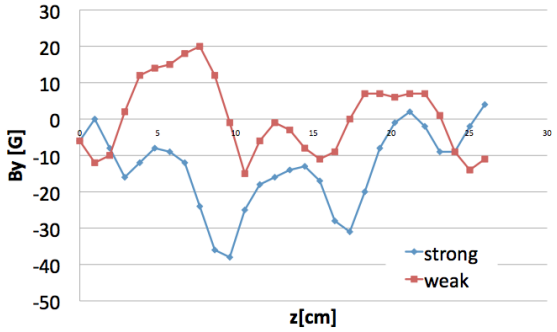

4.5.4 Intra-train Feedback System

A schematic of the IP intra-train beam-based feedback is shown in Fig. 4.33. Critical issues for the feedback performance include the latency of the system, as this affects the number of corrections that can be made within the duration of the bunch train, and the feedback algorithm.

Figure 4.33
Schematic of IP intra-train feedback system. The deflection of the outgoing beam is registered in a BPM and a correcting kick applied to the incoming other beam.

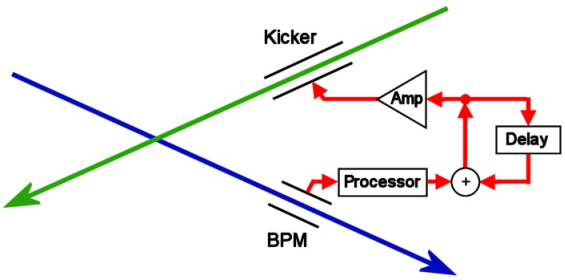

A prototype system has been designed and tested on the extraction line of the KEK Accelerator Test Facility (ATF). The FONT5 intra-train feedback system aims to stabilise the beam orbit by correcting both the position and angle jitter in the vertical plane on bunch-to-bunch time scales, providing micron-level stability at the entrance to the ATF2 final-focus system. The system comprises three stripline beam-position monitors (BPMs) and two stripline kickers, custom low-latency analogue front-end BPM processors, a custom FPGA-based digital processing board with fast ADCs, and custom kicker-drive amplifiers.

A schematic of the prototype of the FONT5 feedback system and the experimental configuration in the upgraded ATF extraction beamline, ATF2, is shown in Fig. 4.34. Two stripline BPMs (P2, P3) are used to provide vertical-beam-position inputs to the feedback. Two stripline kickers (K1, K2) are used to provide fast vertical beam corrections. A third stripline BPM (P1) is used to witness the incoming beam conditions. Upstream dipole corrector magnets (not shown) can be used to steer the beam so as to introduce a controllable vertical position offset in the BPMs. Each BPM signal is initially processed in a front-end analogue signal processor. The analogue output is then sampled, digitised and processed in the digital feedback board. Analogue output correction signals are sent to a fast amplifier that drives each kicker.

The ATF can be operated to provide an extracted train that comprises up to 3 bunches separated by an interval that is selectable in the range 140–300 ns. This provides a short ILC-like train which can be used for controlled feedback system tests. FONT5 has been designed as a bunch-by-bunch feedback with a latency goal of around 140 ns, meeting the ILC specification of c. 150 ns bunch spacing. This allows measurement of the first bunch position and correction of both the second and third ATF bunches.

The front-end BPM signal processor [267] utilises the top and bottom (y) stripline BPM signals, added with a resistive coupler and subtracted using a hybrid, to form a sum and difference signal

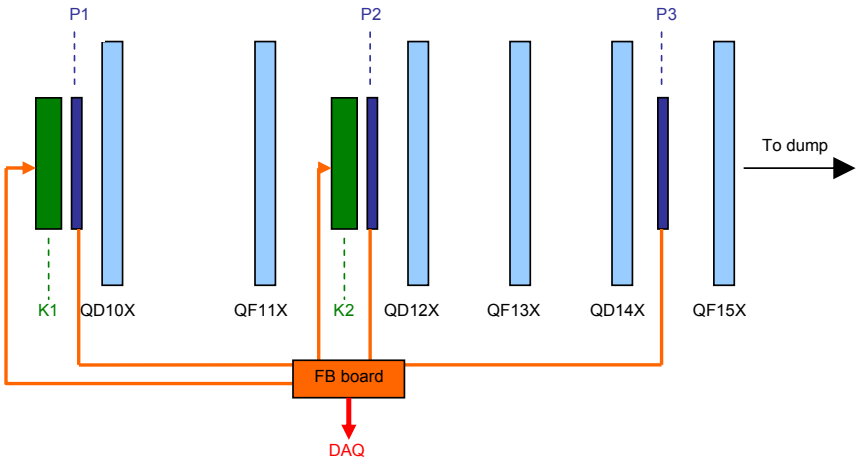

Figure 4.34
Schematic of FONT5 at the ATF2 extraction beam line showing the relative locations of the kickers, BPMs and the elements of the feedback system.

respectively. The resulting signals were band-pass filtered and down-mixed with a 714 MHz local oscillator signal which was phase-locked to the beam. The resulting baseband signals are low-pass filtered. The hybrid, filters and mixer were selected to have latencies of the order of a few nanoseconds to yield a total processor latency of 10 ns [268, 269].

The custom digital feedback processor board is shown in Fig. 4.35. There are 9 analogue input channels in which digitisation is performed using ADCs with a maximum conversion rate of 400 MS/s and 2 analogue output channels formed using DACs, which can be clocked at up to 210 MHz. The digital signal processing is based on a Xilinx Virtex5 FPGA [270]. The FPGA is clocked with a 357 MHz source derived from the ATF master oscillator and hence locked to the beam. The ADCs are also clocked at 357 MHz. The analogue BPM processor output signals are sampled on peak to provide the input signals to the feedback. The gain stage is implemented via a lookup table stored in FPGA RAM, alongside the reciprocal of the sum signal for beam charge normalisation. The delay loop is implemented as an accumulator in the FPGA. The output is converted back to analogue and used as input to the driver amplifier. A pre-beam trigger signal is used to enable the amplifier drive output from the digital board.

Figure 4.35
FONT5 digital feedback board.

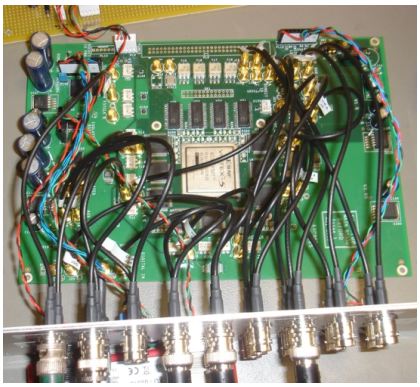

The driver amplifier was manufactured by TMD Technologies [271] and provides ± 30 A of drive current into the kicker. The risetime is 35 ns from the time of the input signal to reach 90 % of peak output. The output-pulse length was specified to be up to 10 µs. The latencies were measured to be 133 ns (P2-K1) and 130 ns (P3-K2).

An example of the feedback performance is given in Fig. 4.36a and Fig. 4.36b, which show the RMS vertical beam position (the 'jitter') of bunch 2 measured at P2 and P3, respectively. With the feedback off, the incoming jitter was measured to be 3.42 µm at P2 and 3.21 µm at P3. With the feedback on, the measured jitter was 0.64 µm and 1.04 µm, respectively, representing correction

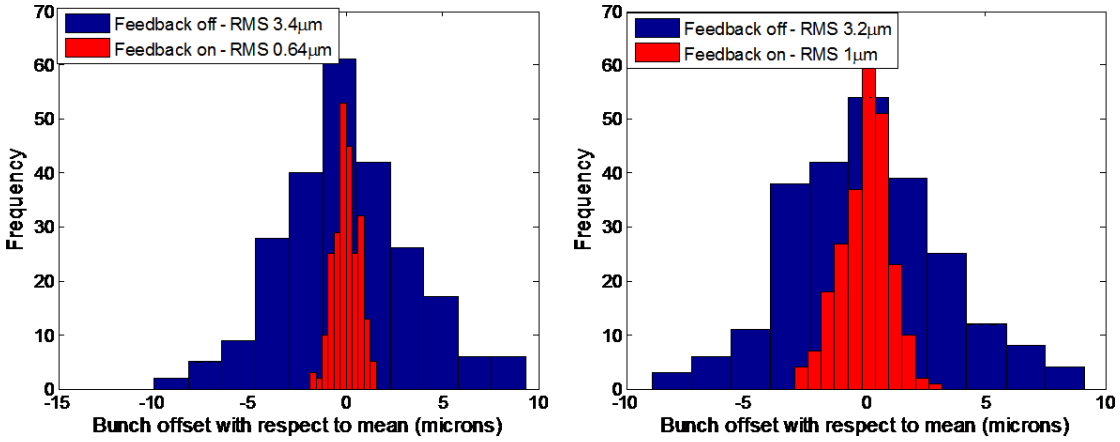

Figure 4.36. (a) Distribution of vertical beam position for bunch 2 at P2, without (blue) and with (red) feedback. (b) Distribution of vertical beam position for bunch 2 at P3, without (blue) and with (red) feedback.

factors of approximately 5 and 3 respectively.

The expected performance of the feedback can be calculated from the measured incoming jitter and knowledge of the bunch 1 – bunch 2 correlations. These correlations were measured to be 98 % and 97 % at P2 and P3, respectively. Using:

$$\sigma_1'^2 = \sigma_1^2 + \sigma_2^2 - 2\sigma_1\sigma_2\rho_{12} \geq 2\sigma_r^2$$

it follows that one expects corrected beam jitters of 0.64 μm and 0.83 μm for bunch 2 at P2 and P3 respectively, in very good agreement with the measured values. The coupled-loop feedback is operating at close to the optimal performance given the degree of correlation between the two bunches.

This measured performance of the system was input into a beam-transport simulation [272] of the ATF2 beam line and the expected vertical beam position downstream of the FONT5 system was evaluated and compared with measurements. In the absence of additional jitter sources and lattice imperfections the performance is equivalent to stabilising the beam at the ATF2 IP to below the 10 nm level [272].

4.5.5 Push-pull system

The most efficient architectural scheme for the push-pull operation is to have both detectors installed on individual reinforced-concrete platforms (see Fig. 4.37). A detailed report describes the outcome of a platform design study, which has been carried out together with an external contractor [273] based on the following assumptions:

- Maximum Detector Weight: 15 000 tons
- Movement duration: 5 hours
- Speed : $>$ 1 mm/s
- Number of movements: 10/year
- Limit of acceleration: $0.1g$
- Maintenance allowances On Beam: 2 m
- Maintenance allowances Off Beam: 6 m
- Positioning relative to beam: $\pm$ 1 mm

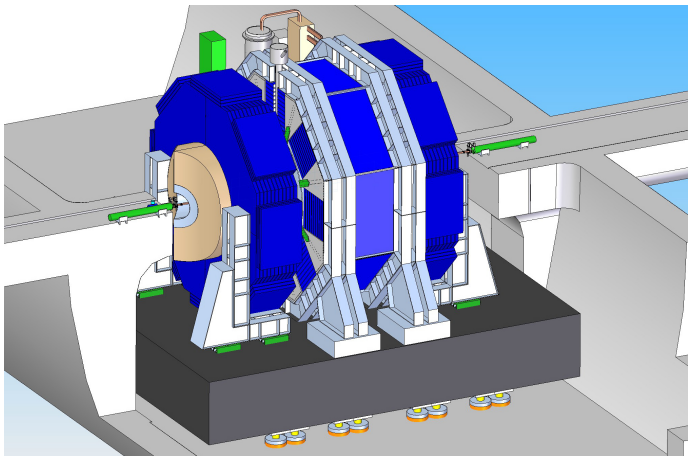

Figure 4.37
Illustration of detector on motion platform.

There are three essential results. First, a geological analysis indicates that special attention must be given to the design of the cavern invert, i.e. the floor where the platform motion system acts, to limit the deformations. Secondly, a reinforced-concrete platform with a maximum deformation < 1 mm under the detector-support points must have an approximate thickness of 2.5 m with a weight of ~ 3000 t. The contact point between the platform and the floor must be carefully located under the respective contact points of the detector with the platform. Finally, two motion systems were considered, air-pads and rollers. Both can be engineered to meet the requirements with a guiding system on the floor. Fifty air pads with 370 tons capacity (maximum capacity available on the market) will be required. Only eighteen rollers of 1 ktons will be required. Air pads will need a lighter moving system because the friction factor is only 1 % while for the roller it is estimated to 3-5 %. In both case a propulsion system based on gripper jacks is possible

A detailed analysis of the propagation of the ground and technical noise has been carried out [274, 275] to check if the push-pull scheme adopted is compatible with the stability requirements. The basic results show that, with a combined transfer function of the detector plus the platform, the ground vibration propagation at QD0 is $< 50\,\mathrm{nm}$, well under the maximum budget allowed. The relative displacements of the QD0, for different ground models, is also very low (see Fig. 4.38) [275].

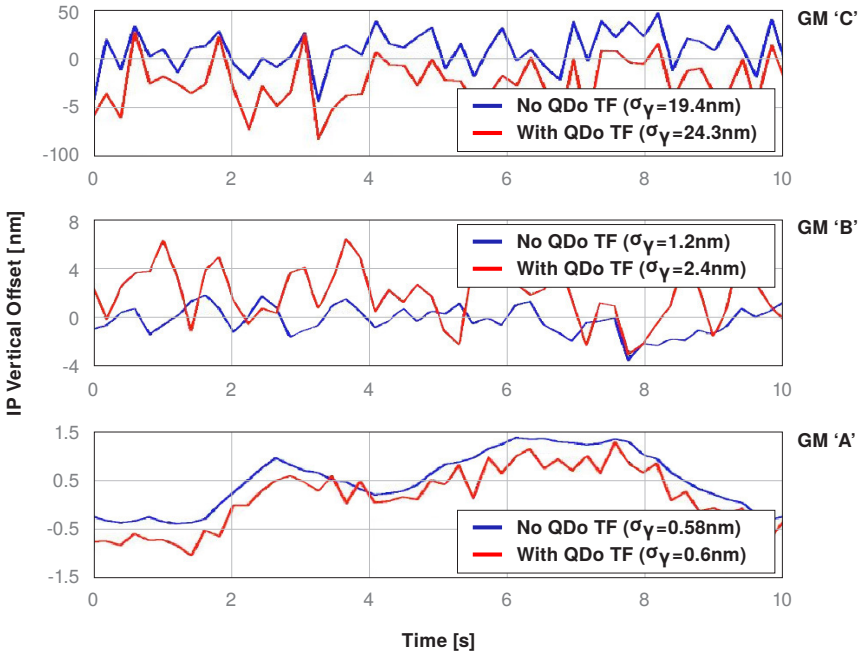

Figure 4.38
Vertical offset of the electron and positron beams at the IP for ground-motion models A, B and C, with and without the QD0 transfer function included.

A more refined model developed by Collette *et al.* (see Fig. 4.39) [276] shows that the technical noise developed by the detector is not harmful for the stability of a QD0 supported from the endcap.

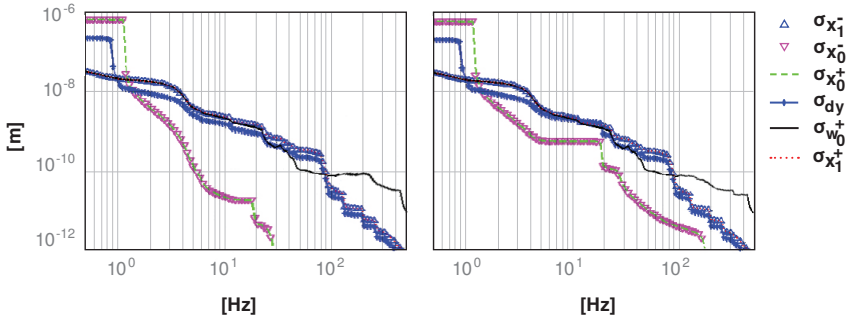

Figure 4.39 Induced vibrations (r.m.s.) vs. frequency on QF1(×0) and QD0 (×1) with (right) and without (left) technical noise [276].

4.5.6 Alignment systems

The IR detector push-pull configuration places severe demands on the alignment system both for the final-focus magnets and for the tracking subdetectors of the SiD and ILD detectors. Rapid realignment of the quadrupoles will be essential to minimise the downtime for colliding-beam running. In addition, the unprecedented momentum and impact-parameter resolutions envisioned for the charged-particle trackers also argue for prompt and precise *a priori* alignment, without the need to rely on the accumulation of millions of charged particles in the detectors. Hence it is desirable to establish an integrated alignment system for the final-focus magnets and the tracking subdetectors that can: 1) measure and correct magnet misalignments that interfere with establishing colliding beams; and 2) measure any global tracker-distortion parameters that degrade tracking performance (e.g. translation, rotation, twist, sag).

An attractive solution is offered by Frequency Scanned Interferometry (FSI), an alignment method pioneered and implemented by the Oxford group for the ATLAS Experiment [277, 278]. In FSI a geodetic grid of points attached to the object to be aligned and to nearby bedrock is used to measure positions, rotations and distortions of detector and accelerator elements. The points in the grid are optically linked via a network of laser beams, using optical fibres for beam launch and collection. Small beam splitters and retroreflectors define interferometers for which a scanning of laser frequency over a known range defines absolute distance measurements to sub-micron precision. The beam lines (between beam splitters and retroreflectors) can be thought of as optical "trusses," where degrees of freedom that would be made most rigid by a corresponding mechanical truss network are those most constrained by the FSI measurements. Conversely, degrees of freedom with the greatest remaining "play" are least constrained by measurement.

Focusing here on the needs for quadrupole alignment, the preliminary design requirements for *a priori* alignment for QD0 before attempting to establish beam collisions are 50 µm in x and y, 20 mrad in roll, and 20 µrad in pitch and yaw [279]. Simulations [280] indicate that these tolerances can easily be met, in principle, by a small network of 4 beam launchers mounted on the front face of the QF1 cryostat, each of which sends two beams to two similarly situated retroreflectors on the back end of the QD0 cryostat. Much better performance can be achieved, however, by placing (in addition) beam launchers on inner sections of the detector with retroreflectors on the QD0 front ends, provided a complete grid network that spans the IP is installed. More simulation work is needed, incorporating detailed detector line-of-sight constraints, to establish a design for the spanning task.

On the instrumental side, there has been recent R&D specific to an FSI system for SiD quadrupole and silicon-tracker alignment [281, 282]. This work, carried out on a bench at the University of Michigan, has used a multi-channel, dual-laser system to ensure robustness against systematic errors due to environmental disturbances, such as from unstable temperatures and turbulent air. Two lasers

are injected and scanned over the same wavelength range but in opposite directions and with optical choppers creating alternating beam injections (a technique pioneered by the Oxford ATLAS group).

A number of significant technical complications had to be overcome in implementing the dual-laser system. The most important were: the reduction by half of the light seen by the interferometer photodiode from each chopped beam; the reduction of useful Fabry-Perot transmission peaks; and the difficulty in handling "edge effects" at chopped-beam transitions. All of these lead to increased statistical uncertainties in FSI distance determinations, despite the decrease in systematic uncertainties. With refinement of the beam-chopping method and with improved analysis software, however, these hurdles were overcome. As a result, precisions better than 200 nm have been achieved for distances up to 40 cm under highly unfavourable conditions, using the dual-laser scanning technique. These early single-channel studies used relatively large, commercial retroreflectors and commercial clamps for the beam launchers. More recent work has focused on expanding to a multi-channel system, in addition to developing small, customised retroreflectors and beam launchers.

A six-channel system has now been commissioned on a bench, allowing for successful sub-micron reconstruction of 3-dimensional retroreflector translations of O(mm), with independent sub-micron confirmation of translations in 2 dimensions and O(micron) confirmation in the 3rd dimension, based on a precision, multi-axis translation stage. At the moment, the dynamic range for successful reconstruction is limited to ± 3 mm, with an eventual goal of ± 1 cm.

Although material burden of FSI components is not a critical consideration in alignment of quadrupole magnets, that burden is important for the use of FSI in the inner tracking system, where multiple scattering and photon conversions degrade detector performance. Hence there have also been recent studies using much smaller (but still commercial) retroreflectors which perform nearly as well as the larger units used previously.

In addition, customised plastic cartridges have been fabricated that allow easier mounting of launch/return fibres and beam splitters, with some flexibility in defining the relative displacement and tilt of the beam splitter with respect to the launch and return fibres. These cartridges have given comparable performance to the previous clamp system.

Significant R&D remains to be done in the context of an integrated alignment system for the quadrupole magnets and tracker. Specific tasks include:

- full miniaturisation of FSI components, using lightweight materials;
- establish a detailed conceptual design for an integrated grid of FSI beams connecting the magnets and tracker to bedrock on both sides of the interaction region;
- move from current visible to infrared laser wavelengths, from which significant cost reductions may be gained by using mass-produced modulated infrared lasers and beam components, because of the prevalence of infrared devices, including scannable lasers, in the telecommunications industry;
- build a large-scale mock-up of an inner-tracker barrel layer attached to mock quadrupole magnets, to test "bootstraping" the alignment to the required precision over tens of metres, using the ends of the IR as anchors, without interfering with the hermeticity or performance of the detector.

4.6 Beam dynamics (simulations)

4.6.1 Overview

The luminosity performance of the ILC will be affected by many issues ranging from space-charge effects at the electron gun to instabilities in the damping rings to timing errors at the IP. This section addresses issues associated with the emittance preservation from the damping-ring extraction to the IP which is referred to as the Low Emittance Transport (LET). Other accelerator physics issues are addressed in the respective subsystem descriptions.

Static and dynamic imperfections in the LET impact the luminosity performance: examples are the survey errors of beam-line components and ground motion. Preserving the ultra-small emittances requires component-alignment tolerances far beyond that which can be achieved by traditional mechanical and optical alignment techniques, hence the use of beam-based alignment and tuning techniques are essential in obtaining the design luminosity. The corresponding sensitivity to ground motion and vibration mandates the use of continuous trajectory-correction feedback systems in maintaining that luminosity. The necessary procedures and specifications of the required hardware and assessment of the potential luminosity degradations are described here.

Estimation of the luminosity performance, both the static (peak luminosity) and dynamic (integrated luminosity) behaviour of the machine in realistic conditions relies on complex simulations. The performance of the ILC has been simulated for a variety of errors and procedures. Design performance was achieved in essentially all of these studies. There are no major obstacles that would prevent the ILC from reaching design performance.

4.6.2 Sources of Luminosity Degradation

The performance of the real machine is degraded by errors in both component alignment and field quality. For example, misaligned magnets result in beam-trajectory errors which cause emittance growth via chromatic effects (dispersion) or impedance effects (wakefields). The primary sources of emittance degradation considered are:

- dispersion - the anomalous kicks from misaligned quadrupoles, coupled with the non-zero energy spread of the beam, cause dispersive emittance growth;
- cavity tilts - the transverse component of the accelerating field causes a transverse kick on the beam, which, coupled with the non-zero energy spread of the beam, causes dispersive emittance growth;
- $x - y$ coupling - rotated quadrupoles and vertically misaligned sextupoles (for example) couple some fraction of the large horizontal emittance into the small vertical emittance leading to beam-emittance growth;.
- single-bunch wakefields - an off-axis bunch in a cavity or beam pipe generates a dipole wakefield, causing a transverse deflection of the tail of the bunch with respect to the head; the wakefields are relatively weak for the SCRF accelerating cavities, and the cavity-alignment tolerances correspondingly loose;
- multi-bunch wakefields (higher-order modes) - leading bunches kick trailing bunches, which can lead to individual bunches in a train being on different trajectories.

4.6.3 Impact of Static Imperfections

4.6.3.1 Beam-Based Alignment and Tuning

The beam emittance at damping ring extraction is $\gamma\epsilon_{\mathrm{x}} = 8\,\mu\mathrm{m}$ and $\gamma\epsilon_{\mathrm{y}} = 20\,\mathrm{nm}$. In a perfect machine, the emittance would be essentially the same at the interaction point. To allow for imperfections, the ILC parameters specify a target emittance at the IP of $\gamma\epsilon_{\mathrm{x}} = 10\,\mu\mathrm{m}$ and $\gamma\epsilon_{\mathrm{y}} = 35\,\mathrm{nm}$. Depending on the actual misalignments, the machine performance can differ significantly. The goal for the alignment and tuning procedures is to ensure that the emittance growth is within the budget with a likelihood of at least 90 %.

Similar beam-based alignment and tuning procedures are applied in the different subsystems of the LET. First, the elements are aligned in the tunnel with high precision. When the beam is established, the corrector dipoles are used to zero the readings in the Beam Position Monitors (BPMs) (so-called one-to-one steering). Even with a very good installation accuracy, the final emittance will be significantly above the target. Achieving the emittance goal requires more complex beam-based alignment (BBA) to minimise the dispersive emittance growth (the dominant source of aberration).

All BBA algorithms attempt to steer the beam in a dispersion-free path through the centres of the quadrupoles, either by physically moving the magnets (remote magnet movers) or by using corrector dipoles close to the quadrupoles. The exact details of the algorithms and their relative merits differ. The three most studied methods are:

- dispersion-free steering (DFS) – beam trajectories are measured for different beam energies by changing acceleration upstream; the final trajectory minimises the difference, thereby minimising the dispersion;
- kick minimisation (KM) – the BPM offsets with respect to the associated quadrupole magnetic centres are measured by varying the quadrupole strength and monitoring the resulting downstream beam motion; this information is used in a second step to find a solution for the beam trajectory where the total kick from quadrupoles and correctors on the beam is minimised;
- ballistic alignment (BA) – a contiguous section of quadrupoles (and in the linac the RF) is switched off and the ballistic beam is used to determine the BPM offsets with respect to a straight line. The quadrupoles/RF are then restored, and the beam is steered to match the established straight line.

All BBA techniques rely on precise measurements from the BPMs to determine a near dispersive-free trajectory. The final performance of the algorithms is determined by the resolution of the monitors.

Once BBA is complete, a final beam-based tuning either minimises the beam emittance by direct measurement of the beam size (emittance) or maximises the luminosity. Closed-trajectory bumps or specially located and powered tuning magnets are used as orthogonal knobs to generate specific aberrations, such as dispersion or $x - y$ coupling. The knobs are tuned to minimise the emittance by cancelling the remaining aberrations in the beam.

4.6.3.2 RTML before the Bunch Compressor

The issue of static emittance growth from misalignments and errors has been studied in detail for the section of the RTML from the turnaround to the launch into the bunch compressor. The strong focusing, strong bending, strong solenoids, and large number of betatron wavelengths in this area can potentially lead to very serious growth in the vertical emittance, despite the relatively low energy spread of the beam extracted from the damping rings.

The tolerances used in the study for the warm solid-core iron-dominated magnets are listed in Table 4.6 and were similar to those found at the SLAC Final Focus Test Beam.

BPM is attached to a quadrupole magnet and its offset error with respect to the quadrupole-field centre is critically important for preserving low emittance. The accuracy is assumed to be 7 μm, which will be achieved by a technique called "quad shunting", where the strength of every quadrupole magnet is changed one by one and the downstream orbit is measured. (There should be no orbit change when the beam goes through the centre of the magnet.)

Table 4.6
Tolerance for RTML section up to the bunch compressors.

Error	RMS Value	Reference
Quadrupole Misalignment	150 μm	Design Line
BPM Misalignment	7 μm	Quad Center
Quadrupole Strength Error	0.25%	Design Value
Bend Strength Error	0.5%	Design Value
Quadrupole Rotation	300 μrad	Design
Bend Rotation	300 μrad	Design
BPM Resolution	1 μm	
Beam-size monitor	1 μm	

Dispersion Correction The preferred dispersion correction method was found to be a combination of Kick Minimization (KM) and dispersion knobs, the latter consisting of pairs of dedicated skew quadrupoles located in the turnaround, where there is non-zero horizontal dispersion. The two skew quads in a pair are separated by a $-I$ transform such that exciting the quads with equal-and-opposite strengths causes the resulting betatron coupling to cancel and the dispersion coupling to add. There are two such dispersion knobs in the turnaround, which allow correction of dispersion at each betatron phase. Simulations indicate that in the absence of measurement errors, the combination of KM and dispersion knobs (DK) can eliminate dispersion as a source of emittance growth in this part of the RTML. The principal remaining source of emittance dilution is betatron coupling, which typically contributes about 7 nm of emittance growth.

Coupling Correction The coupling-correction section consists of four skew quads phased appropriately to control all four betatron coupling parameters of the beam. The skew quads are used to minimise the vertical beam sizes as measured in the downstream emittance-measurement station. The correction system can eliminate the betatron coupling introduced by misalignments and errors in this section of the RTML, without measurement errors.

In addition to the studies described above, the emittance preservation issues in the long transfer line from the damping ring to the turnaround have been examined. Because of the weaker focusing, the alignment tolerances are much looser than in the turnaround area, and emittance preservation is relatively straightforward [283, 284].

Emittance growth in this section is expected to occur dominantly in the turnaround, assuming 1 μm BPM resolution. Simulations show the total emittance growth from the exit of the damping ring to the entrance of the bunch-compressor section is 5.4 nmon average and 9.9 nm at 90 % confidence level [285].

4.6.3.3 Bunch Compressors

The RF in the bunch compressor introduces an energy spread correlated to the longitudinal position in the bunch. The long bunch from the Damping Ring (6 mm) makes the beam particularly sensitive to cavity tilts in the bunch-compressor RF. The near-zero phase crossing of the bunch induces a strong transverse kick which is also correlated to the longitudinal location in the bunch (i.e. the bunch is crabbed), and therefore also strongly correlated to the induced energy spread. The resulting transverse kick-energy correlation can effectively be compensated using downstream dispersion knobs. Wakefield-driven head-tail correlations can also be compensated in the same way. As with other sections of the LET, the other primary source of emittance dilution is dispersion due to misaligned quadrupoles.

Transverse kicks due to the input coupler and HOM couplers of an accelerating cavity have been extensively studied [286]. The couplers induce asymmetries of the electromagnetic fields in the cavity, which cause transverse components of the accelerating field (coupler RF kick) and transverse wake field (coupler wake). The effects is included in the simulations.

Simulation studies with RMS random quadrupole offsets of 0.3 mm, cavity offsets of 0.3 mm and cavity pitch of 0.3 mrad indicate that combined DFS and DK will reduce the mean emittance dilution to 1.1 nm in average and 1.5 nm at 90 % confidence level [285].

4.6.3.4 Main Linac

Single-bunch emittance dilution in the main linac is dominated by chromatic (dispersive) effects and wakefield kicks arising from misaligned quadrupoles and cavities respectively. The $x - y$ coupling arising from quadrupole rotation errors also adds a small contribution to the vertical-emittance growth. The assumed installation errors are listed in Table 4.7. The tolerances for cavity offsets and quadrupole rolls can be achieved mechanically, but beam-based tuning is required for reducing the effects of the quadrupole and BPM offsets.

Table 4.7
Assumed installation errors in the main linac, and the emittance growth for each error assuming simple one-to-one steering. Note that with perfectly aligned BPMs, the one-to-one steering eliminates dispersive effects from quadrupole magnet offset and cavity tilt. With realistic BPM errors, the required emittance preservation can only be achieved using beam-based alignment of the magnets/BPMs.

Error	with respect to	value	$\Delta\gamma\epsilon_y$ [nm]
Cavity offset	module	300 µm	0.2
Cavity tilt	module	300 µrad	<0.1
BPM offset	module	300 µm	400
Quadrupole offset	module	300 µm	<0.1
Quadrupole roll	module	300 µrad	2.5
Module offset	perfect line	200 µm	150
Module tilt	perfect line	20 µrad	0.7

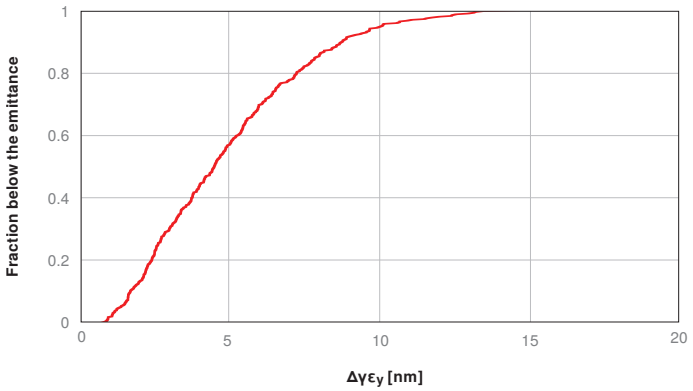

Figure 4.40
The fraction of simulated cases staying below the emittance-growth target for the main linac after Dispersion Free Steering.

The main linac follows the gravitational equipotential of the earth, and is therefore not laser-straight. This gentle bending in the vertical plane results in a small but non-negligible design dispersion which must be matched, and taken into consideration during beam-based alignment. A variant of dispersion-free steering, dispersion-matched steering (DMS), is used to attain the matched dispersion function along the lattice. This modified form of DFS requires well calibrated BPMs [287] to the level of 5 % with very stable readout. The method achieves the required performance in simulations [287–291]. An example simulation result is shown in Fig. 4.40. Additional tuning knobs to modify the dispersion at the beginning and end of the linac reduce the emittance growth still further [292]. Further improvement is possible with wakefield tuning knobs.

Studies of kick minimisation have shown similar performance as DMS [293, 294]. The ballistic alignment method has not been applied to the latest ILC lattice, however studies for TESLA showed that ballistic alignment and dispersion-free steering yielded comparable results (for a laser-straight machine) [295].

Multi-bunch wakefields (high-order modes, HOMs) with very high Q-values could lead to unacceptable multi-bunch emittance growth. Suppression of HOMs is achieved by random cavity detuning ($\sim 0.1\%$ spread in the HOM frequencies, expected from the manufacturing process), and by damping using HOM couplers. All the modes for the baseline cavity shape have been calculated and measured at FLASH. The resulting multi-bunch emittance growth due to cavity misalignment is expected to be below 0.5 nm. If the transverse wakefield modes are rotated due to fabrication errors, they can lead to a coupling of the horizontal and vertical planes, potentially increasing the vertical emittance [296]. This effect is mitigated by using a split-tune lattice in which the vertical and horizontal beam-oscillation wavelengths are different, thus avoiding resonant coupling.

Different codes have been compared in detail for the main linac [297], finding excellent agreement for both tracking and performance predictions for a specific beam-based alignment method. This cross-benchmarking increases confidence in the results of each individual code.

4.6.3.5 Undulator Section for Positron Production

At the end of the electron main linac, the beam passes through an undulator and emits hard photons for positron production. This insert has several potential consequences for emittance preservation:

- stronger focusing in the 1.2 km insert leads to additional dispersive emittance growth, which should be correctable using BBA methods;
- the undulator increases the energy spread of the beam, which increases the dispersive emittance growth in the downstream linac; this effect is estimated to be small;
- the narrow-bore vacuum chamber of the undulator is a potential source of transverse wakefields; the effect is expected to be small and can be corrected using precise alignment movers.

The total emittance growth in this insertion is estimated to be small compared to the overall emittance-growth budget.

Final beam energy will be changed as physics requires. Low-emittance preservation tends to be difficult for lower-energy operation, because of larger relative energy spread (dispersive effect) and relatively stronger transverse-wakefield effect. However, simulation studies for beam energies of 100 GeV and 250 GeV shows the difference of expected normalised emittance is smaller than 2 nm.

4.6.3.6 Beam-Delivery System (BDS)

Beam-based procedures have been developed to align and tune the BDS. First, all multipole (sextupoles and more) magnets are switched off and the quadrupoles and BPMs are aligned. Second the multipoles are switched on and aligned. Finally, tuning knobs are used to correct the different beam aberrations at the interaction point. Detailed simulations have been made assuming the realistic installation alignment errors and magnetic-field errors given in Table 4.8.

Table 4.8
Assumed imperfections in the BDS. The assumed magnet strength errors are very tight; it is expected that more realistic larger errors mainly lead to slower convergence of the procedures.

Error	with respect to	size
Quad, Sext, Oct x/y transverse alignment	perfect machine	200 µm
Quad, Sext, Oct x/y roll alignment	element axis	300 µrad
Initial BPM alignment	magnet center	30 µm
Strength Quads, Sexts, Octs	nominal	10^{-4}
Mover resolution (x/y)		50 nm
BPM resolutions (Quads)		1 µm
BPM resolutions (Sexts, Octs)		100 nm
Power supply resolution		14 bit
Luminosity measurement		1 %

Studies have been performed using the beam-beam interaction code GUINEA-PIG to give a realistic estimate of the luminosity, assuming the accuracy of luminosity measurement is 1 %. Important results of the beam-beam interaction studies has been crosschecked with the CAIN code.

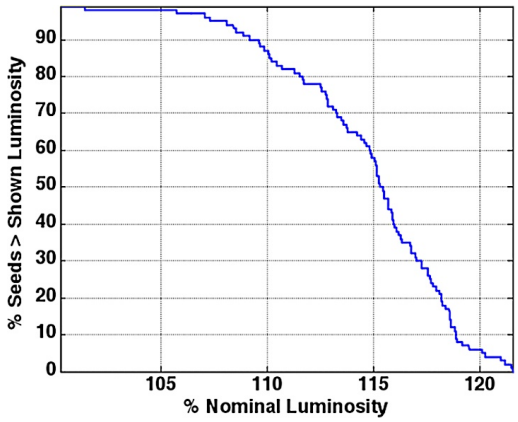

Figure 4.41
Results of simulation of the luminosity tuning in the beam-delivery system. The vertical axis indicates the ratio of the random seeds simulated that results in a relative luminosity greater than values in the horizontal axis [298].

Figure 4.41 shows an example of the BDS luminosity-tuning simulations for static errors. The vertical emittance at the entrance of BDS was assumed to be 34 nm, which assumes an emittance growth of 14 nm for the RTML and ML combined. The results show that for the given assumptions on static errors and input conditions, all seeds exceed the design luminosity after application of the beam-based tuning algorithms.

4.6.4 Dynamic Effects

The ILC relies on several different feedback systems to mitigate the impact of dynamic imperfections on the luminosity. These feedback systems act on different timescales. The long $\sim$ 1 ms pulse length and relatively large bunch spacing ($\sim$ 554 ns, $\sim$ 366 ns in update configuration) makes it possible to use bunch-to-bunch (or intra-train) feedbacks located at critical points. The most important is the beam-beam feedback at the interaction point that maintains the two beams in collision. Other feedback systems act from train to train (inter-train) at the 5 Hz pulse repetition rate of the machine. Over longer timescales (typically days or more), the beam may have to be invasively re-tuned.

Main dynamic error sources and their effects to orbit jitter and emittance growth in Main Linac are listed in Table 4.9.

Table 4.9
Dynamic errors and their effects in the main linac.

Error	assumed RMS amplitude	Orbit change	emittance growth
Quad offset change (vibration)	100 nm	1.5 σ	0.2 nm
Magnet-strength jitter	10^{-4}	1σ	0.1 nm
Cavity-tilt change	3 µrad	0.8σ	0.5 nm
Cavity-to-cavity strength change	1%	0.8σ	0.5 nm

Important sources of dynamic imperfections are ground motion and component vibration. The ground motion depends strongly on the site location. For the ILC-TRC study, three ground motion models were developed, all based on measurements at existing sites: Model A represents a very quiet site (deep tunnel at CERN); Model B a medium site (linac tunnel at SLAC); Model C a noisy site (shallow tunnel at DESY). A fourth model (K) was later developed based on measurements at KEK and is roughly equivalent to C. These models have been used in all subsequent simulations of the dynamic behaviour of the ILC.

Another possibly important source is cavity-to-cavity strength change within the $\sim 1\,\mathrm{ms}$ pulse, with mechanical cavity tilt (static alignment error). The effect leads to trajectory errors of individual bunches in a bunch train. While these trajectory errors (which are relatively slow over the 1 ms pulse) can easily be corrected with intra-train feedback at the end of the linac, the large variation in trajectories in the ML give rise to emittance growth. To suppress this effect, voltages in the individual cavities will be corrected to within 1 % over the pulse.

One possible issue is time-varying stray fields in the long transfer line of RTML which can

drive orbit oscillations. This orbit change can be cancelled downstream by the feed-forward system located across the turnaround, though this system cannot compensate possible emittance growth in the turnaround. Measurements at existing laboratories [297] indicate a reasonable estimate for the magnitude of time-dependent stray field is about 2 nT, which will not cause a problem. Even in the case that the stray fields turn out to be significant, adding an intra-pulse orbit-feedback system before the turnaround can eliminate the emittance growth of most of the bunches in a bunch train.

Tolerances of other dynamic errors are listed in Tables 4.10–4.11 and 4.12. None of these errors are expected to affect luminosity performance significantly.

Table 4.10
Other dynamic errors relevant to transverse motions.

Error	assumed RMS amplitude
Offset change (vibration) of warm magnet	10 nm
Strength change of warm magnet	1×10^{-5}
Strength change of cold magnet	1×10^{-4}

Table 4.11
Bunch-compressor RF dynamic errors, which induce 2 % luminosity loss.

Error	RMS amplitude	RMS phase
All klystron correlated change	0.5 %	0.32°
Klystron-to-klystron uncorrelated change	1.6 %	0.60°

Table 4.12
ML RF dynamic errors, which induce 0.07 % beam energy change.

Error	RMS amplitude	RMS phase
All klystron correlated change	0.07 %	0.35°
Klystron to klystron uncorrelated change	1.05 %	5.6°

4.6.4.1 Bunch-to-Bunch (Intra-Train) Feedback and Feedforward Systems

The damping-ring extraction kicker extracts each bunch individually. If this kicker does not fully achieve the required reproducibility, the beam will have bunch-to-bunch variations that cannot be removed by an intra-pulse feedback system (effective white noise). The feed-forward system in the RTML is designed to mitigate this effect. The position jitter of each bunch is measured before the turn-around and then corrected on that bunch after the turn-around.

Quadrupole vibration in the downstream bunch compressor and (predominantly) in the main linac will induce transverse beam jitter (coherent betatron oscillations). The tolerance on the amplitude of this jitter (and hence on the quadrupole vibration) from the main linac itself is relatively loose. Quadrupole vibration amplitudes of the order of 100 nm RMS lead to negligible pulse-to-pulse emittance growth. However the resulting oscillation (one- to two-sigma in the vertical plane) in the BDS could lead to significant emittance degradation from sources such as collimator wakefields. An intra-train feedback at the exit of the linac solves this problem. In addition, this feedback could correct any residual static HOM disturbance in the bunch train. If the main-linac quadrupole vibrations are significantly less than 100 nm (e.g. 30 nm RMS, as expected for a typical quiet site), then intra-train feedback at the exit of the linac may not be required.

Small relative offsets of the two colliding beams, in the range of nanometers, lead to significant luminosity loss. The offsets are particularly sensitive to transverse jitter of the quadrupoles of the final doublet. Fortunately, the strong beam-beam kick causes a large mutual deflection of the offset beams, which can be measured using BPMs just downstream of the final quadrupoles. The intra-train feedback system zeros the beam-beam kick by steering one (or both) beams using upstream fast kickers. The system typically brings the bunch trains into collision within several leading bunches (depending on the gain). The IP fast feedback and the long bunch train also affords the possibility to optimise the luminosity within a single train, using the fast pair monitor as a luminosity monitor [299].

4.6.4.2 Train-to-Train (5 Hz) Feedback

There are number of local feedbacks. At certain locations in the machine, a few correctors are used to steer the beam back through a few selected BPMs, thus keeping the trajectory locally fixed. These feedback systems can be used in a cascaded mode where each of the feedback anticipates the trajectory change due to the upstream feedback systems. Such a system was successfully implemented at SLC.

Since the system corrects only locally, a residual of the dynamic imperfections will remain, due to deterioration of the trajectory between the feedback locations. After longer times, this will require a complete re-steering of the machine back to the exact trajectory determined from the initial beam-based alignment (gold orbit).

There are other alternative options. One is to perform permanent re-steering with a very low gain; this method avoids the additional layer of steering but may be slower than local feedback. Another option is the use of a MICADO-type correction. In this procedure all BPMs are used to determine the beam orbit. A small number of the most effective correctors is identified after each measurement and these are used to correct the trajectory.

4.6.4.3 Luminosity Stabilisation

A complete and realistic simulation of the dynamic performance of the collider requires complex software models that can accurately model both the beam physics and the errors (e.g. ground motion and vibration). The problem is further complicated by the various time scales that must be considered, which span many orders of magnitude: performance of the fast intra-train feedbacks requires modelling of the detailed 10 MHz bunch train; fast mechanical vibrations at the Hz level need to be accurately modelled to test the performance of the pulse-to-pulse feedback systems; long-term slow drifts of accelerator components over many days must be studied to determine long-term stability and the mean time between invasive (re-)application of BBA. Ideally all these elements need to be integrated into a single simulation of the complete machine.

However, practically it is enough to have sets of various simulations focusing on individual aspects of the problem, with varying degrees of the feedback models. The results thus far give every indication that the ILC can achieve and maintain the desired performance.

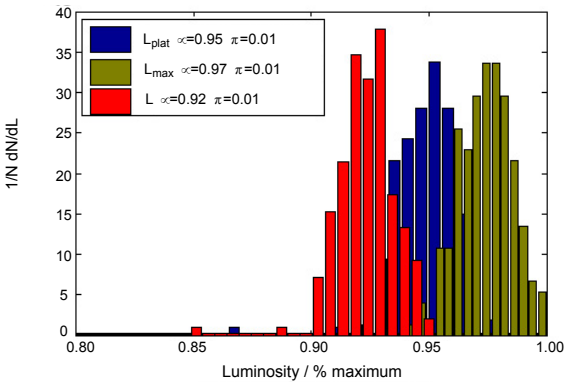

Figure 4.42
Example of integrated dynamic simulations, showing the performance of the beam-beam intra-train feedback system with realistic beams and beam jitter (simulated from the Main Linac and BDS). The histograms show performance over 100 seeds of random vibration motion: green - achieved luminosity for an infinitely fast beam-beam feedback and no bunch-to-bunch variations (3 % reduction from ideal); blue - performance including bunch-to-bunch variations (driven by long-range wakefields in the Main Linac); red - as blue but including a finite response time for the feedback (8 % reduction from ideal) [300, 301].

Extensive simulations have been made of the performance of the fast beam-beam (and other) intra-train feedback using a model of the main linac and BDS to generate realistic bunch trains [300, 301]. For realistic component vibration amplitudes, the results indicate that feedback can maintain the luminosity within a few percent of peak on a pulse-to-pulse timescale (5 Hz), as shown for example in Fig. 4.42. These results are in agreement with earlier studies [302, 303].

Drifts of components on the timescale of seconds to minutes have been studied [302, 303]. Simulations of 5 Hz operation with all ground-motion models, and assuming the beams are maintained

in collision by the fast IP feedback, indicate a slow degradation in luminosity. This can be mitigated by pulse-to-pulse feedback, especially in the BDS, where the tolerances are tightest. Noisy sites (model C) showed the most pronounced effect, and would place most demand on the slower feedback systems.

Longer-term stability has been studied, assuming a variety of configurations for the slower pulse-to-pulse feedbacks. Studies of the main linac [304] using local distributed feedback systems indicate that the time between re-steering ranges from a few hours to a few days for ground-motion models C and B respectively. After 10/200 days (models C/B), simple re-steering does not recover the emittance, at which point a complete re-tuning would be necessary.

Dynamic studies integrating the main linac and BDS, again based on distributed local pulse-to-pulse feedback systems (including one in the BDS) and incorporating many error sources and comparing all ground-motion models have been made [305]. It was shown that luminosity reduction in the noisy sites (models C and K) comes almost entirely from the BDS.

Other examples of such simulations of luminosity performances for models of ground motion and vibration are shown in Fig. 4.43. The primary effect is a beam-beam offset at collisions, which is quickly compensated by the intra-train feedback at the interaction point. The luminosity loss will not be serious even for the models C and K, which are much noisier than expected for possible ILC sites.

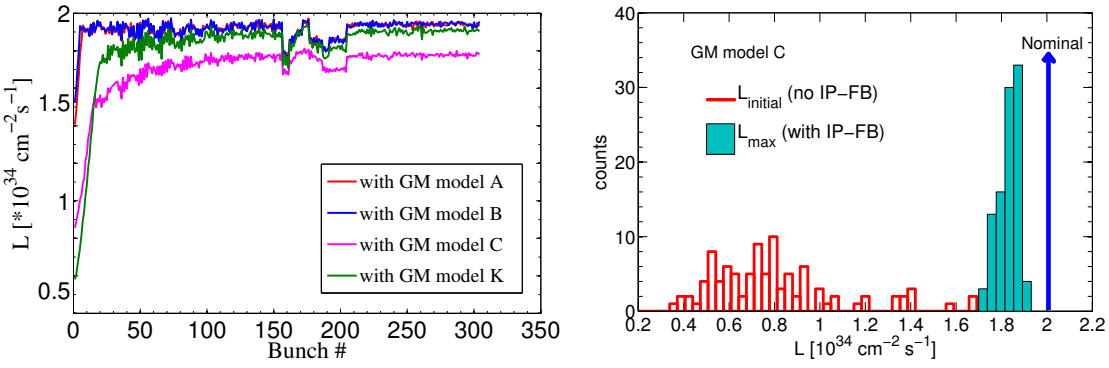

Figure 4.43. Time-dependent luminosity modelling in the beam-delivery system. (a): the luminosity is shown as a function of bunch number for the first 300 bunches of a pulse for various ground motion (vibration) models. The luminosity is quickly recovered by the beam-beam fast feedback. (b): a histogram of the results of 100 seeds, assuming model C, as referenced in the left graph, for the ground motion, with and without intra-pulse orbit feedback [298].

A key parameter is the maximum-allowed vibration of the Final Doublet (FD). This is primarily set by the limitations of the IP fast feedback, which becomes increasingly ineffective for larger beam-beam offsets. Figure 4.44 shows the luminosity as function of RMS offset of both final-doublet cryomodules. The allowed RMS FD offset tolerances is conservatively specified as 50 nm.

4.6.4.4 Requirements of Field-Ramping Speed of Main-Linac Components

The field strengths of the superconducting quadrupole and correction dipole magnets must be able to change at a sufficient speed to allow efficient commissioning and to adapt to the ground motion. The required speed of have of magnetic fields in the main linac has been roughly estimated as follows. [306]:

- Quadrupole magnet:

  0.001 T/m×m/s (0.003 %/s) for adjustment of optics with RF failure.

  0.01 T/m×m/s (0.03 %/s) for performing "quad shunting", beam-based alignment measurement, within a reasonable time.

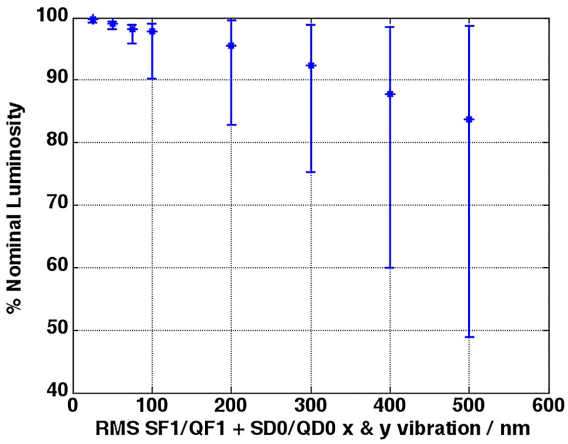

Figure 4.44
Simulated luminosity as a function of rms offset of both final-doublet cryomodules. Mean and standard deviation from tracking simulation are shown [298].

- Steering magnet:

  5×10^{-6} T×m/s (0.01 %) for following ground motion

  3×10^{-4} T×m/s (0.6 %/s) for orbit correction after a long shut down within a reasonable time end

For each type of magnets, the second number is the most stringent and should be adopted. These numbers are obtained assuming very pessimistic cases for the correction process under the ground-motion model C to safely define the specification of the magnets.

4.6.5 Optics for the Upgrade to 1 TeV

A possible scenario to upgrade ILC from the centre-of-mass energy 500 GeV to 1 TeV is described in Part II Section 12.4. Each main linac, from 15 GeV (after the bunch compressor) to 250 GeV in the baseline, will be extended to 500 GeV in the following way:

- the majority of the cryomodules of the 250 GeV linacs remain in place and become the final 225 GeV of the 500 GeV;
- the first section (from 15 GeV to 25 GeV) of the old linac will be moved to the upstream end of the new linac. This is because the magnets (quadrupole and correction dipole) in this section are shorter than others in order to avoid fields that are too low to be accurate;
- the newly constructed modules are inserted between these sections (25 GeV to 275 GeV).

The adoption of a FODO lattice in the entire new linac as in the old linac with the limited maximum strength of the quadrupole magnets, the beta-function and the vertical dispersion (induced by the beam line following the earth's curvature) would be large in the high-energy beam part of the linac. For a given lattice, the beta function is roughly proportional to the inverse of the magnet strength (normalised by the beam energy) and the dispersion to inverse square.

To preserve low emittance, DMS (Dispersion Matching Steering), in which the vertical dispersion at every BPM will be measured and adjusted to the designed non-zero value will be applied. This correction requires accurate measurement of dispersion, whose error will be proportional to the scale error of the BPMs and the designed dispersion. With large designed dispersion, the required accuracy of the BPM scale becomes too tight.

To keep the dispersion small along the main linac, a FOFODODO lattice will be used instead of a FODO lattice for the 250 GeV to 500 GeV section of the linac. In a curved linac, the typical vertical dispersion with a FOFODODO lattice is approximately half of that with FODO lattice. Simulations showed that emittance growth will be small enough in the whole linac if a FODO lattice is adopted from 15 GeV to 250 GeV and FOFODODO lattice from 250 GeV to 500 GeV [306].

Chapter 5
Conventional Facilities and Siting Studies

5.1 CFS design considerations

The Conventional Facilities and Siting Group used the Technical Design Phase to improve the maturity of the conventional design and respond to changes in the technical baseline criteria for the International Linear Collider Project. The maturity of the conventional design was influenced, in general, by two factors. First, more precise criteria were developed for the civil, mechanical and electrical design. Secondly, instead of the more generic approach taken for the design of the conventional facilities in the original reference design, regional conditions were taken into consideration and had a major impact on the design. The changes to the technical baseline were provided primarily through the Strawman Baseline 2009 (SB2009) analysis [104], which resulted in fundamental changes to the design of the conventional facilities. This chapter will describe these changes and also provide brief descriptions of the supporting consultant work and studies.

The overall maturity of the conventional facilities design was improved over the course of the TDP. Several value-engineering exercises were conducted. Optimisation of mechanical- and electrical-systems design, comparisons of tunneling techniques and configurations and more detailed criteria were pursued in all regions by the Conventional Facilities Group. This effort has provided better understanding of the impact of the design requirements and an overall increase in the level of detail. The local site conditions had a large influence on the conventional facilities design. This was especially the case with the two candidate sites in the Asian Region.

5.1.1 Central Region integration

In SB2009, the repositioning of the Electron Source and adjustments to the overall circumference, location and size of the Damping Ring contributed to a major revision for the central-region design and underground enclosures. Instead of encircling the Interaction Hall, the Damping Rings are now shifted to the side but with their centre still aligned with the interaction point. Moving the Positron Source to the end of the Main Linac reduced the length of transfer lines. The size of the tunnel for the Damping Rings was enlarged to allow for the possibility of accommodating three rings. Also the Electron and Positron Sources and transfer lines to and from the Damping Rings, the RTML and Beam-Delivery Systems are all co-located in the same enclosures, complicating issues of installation, life safety, personnel egress and equipment replacement. In addition, there are various improvements to the requirements and the design maturity of the Detector Hall.

5.1.2 Main Linac underground enclosures

Another major technical change, the development of different schemes for the High-Level RF system, introduced opportunities for adjustments to underground enclosures for the main linac. Two options for the High-Level RF system were considered: the Klystron Cluster system (KCS) and the Distributed Klystron system (DKS).

In the reference design, all sites used vertical shafts for access to the main-linac tunnel. The KCS system involved relocating all of the klystrons and supporting power-supply equipment to surface buildings at the vertical shafts. The microwave power is then transported to the cryomodules that make up the main linac through large-diameter waveguides that extend from the klystrons down the shaft and through the main-linac tunnel. The KCS approach provided the opportunity to eliminate the RDR service tunnel for the main linac since the klystrons and all supporting equipment are now located in surface buildings. This applies to both the Americas and European Sites. This single main-linac tunnel and shaft design was analysed by a Tunnel Configuration Study and a Tunnel Lining Study in the Americas Region as well as Life Safety studies in both the Americas and European Regions. The tunnel cross sections for the Americas and European regions are shown in Fig. 5.1 and Fig. 5.2, respectively.

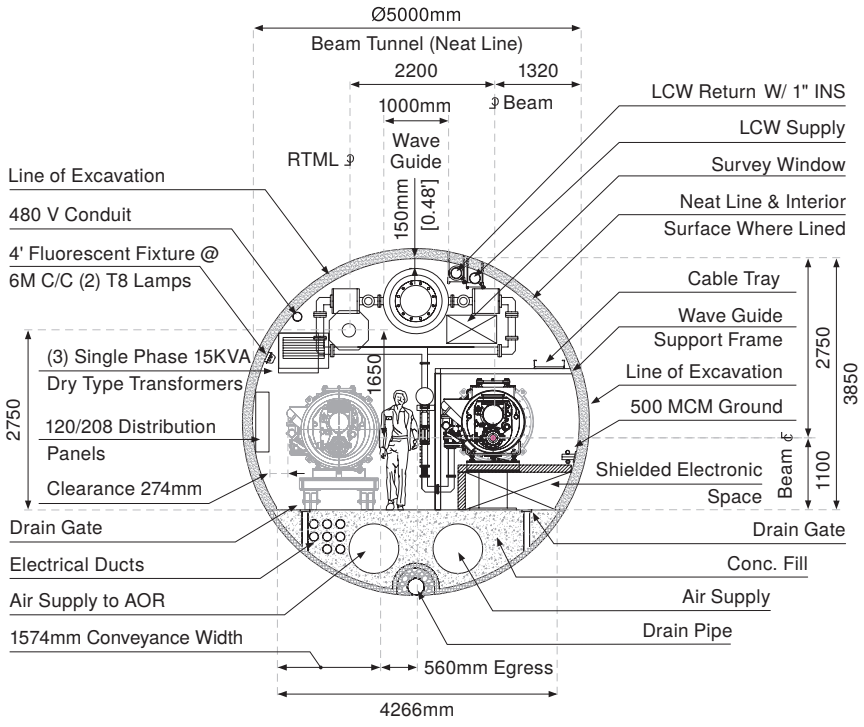

Figure 5.1
Americas Region tunnel Cross Section

For the Asian region, another solution was required. Two candidate sites were identified in mountainous regions of Japan, resulting in vertical shafts becoming less desirable. Horizontal access tunnels, with a slight downward incline, became the preferred solution for these sites. The lengthier horizontal tunnel access posed a problem for the KCS RF system. As the conventional design progressed in the Asian Region, different tunnel cross sections were studied. Eventually it was decided that, for the Japanese candidate sites, drilled tunnels using tunnel boring machines (TBMs) were not cost effective. As an alternative, the Asian CFS Group proposed the use of the New Austrian Tunnelling Method (NATM), which is basically a drill-and-blast method of construction, as a more cost-effective approach for construction of the underground enclosures. The cross section of the main-linac tunnel is larger than the circular cross sections of the Americas and European Regions that result from using a TBM. The larger tunnel illustrated in Fig. 5.3 is wide enough to be divided

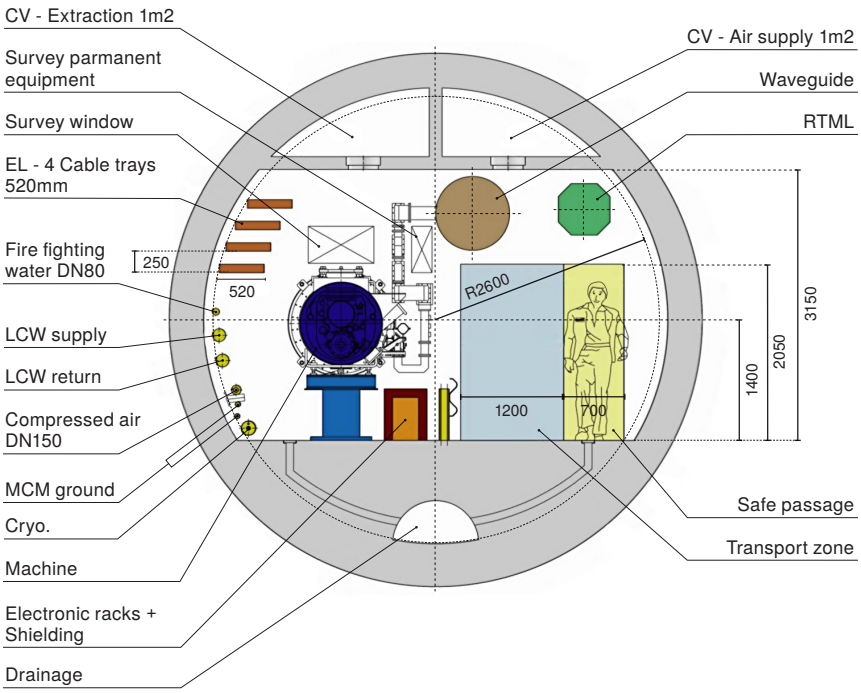

Figure 5.2
European Region tunnel Cross Section

into two compartments, making an alternative klystron system possible. One side will be used for the accelerator and the other for the DKS scheme, which is similar to the approach used in the ILC Reference Design. The DKS klystrons are shielded by the tunnel wall and can therefore be accessed while the beam is on. This solution works for both Asian candidate sites. The Civil design in the Asian region was also supported by a Tunnel Configuration Study and preliminary geotechnical investigation at both candidate sites.

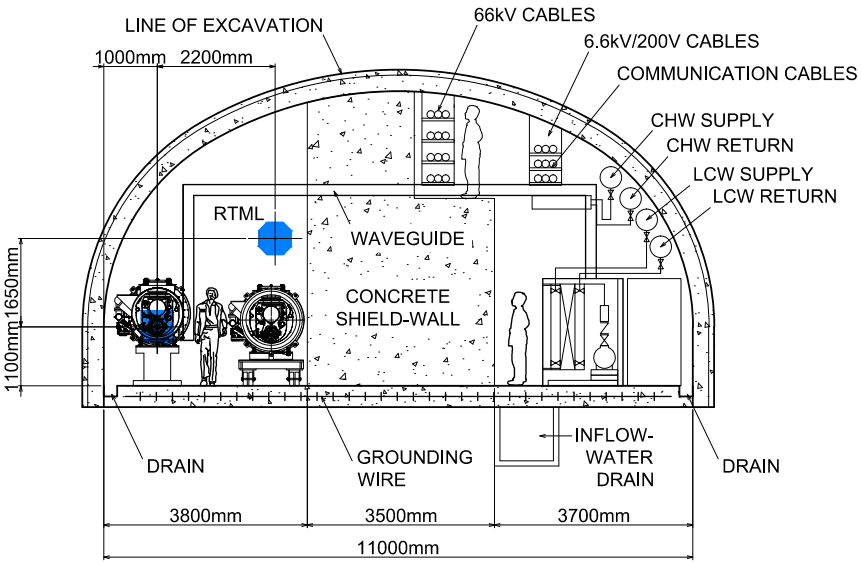

Figure 5.3
Asian Region tunnel Cross Section

5.1.3 Detector hall and detector assembly

The local site conditions also had a direct impact on the configuration of the Detector Hall and ultimately the assembly of the detectors themselves. In both the Americas and European Regions, large sections of the detectors are assembled in a surface assembly hall and lowered into the detector hall through a large diameter central shaft located directly over the eventual interaction point. Other vertical shafts are used to access the out-of-beam detector "garage" areas and for personnel access. In the Asian candidate sites, a single horizontal access tunnel provides the only access to the detector hall. Detector components must be assembled in small pieces and transported to the detector hall for final assembly. These regional differences, based on local conditions, have a significant effect on detector assembly and shaft/tunnel coordination strategies. In all regions, both detectors will be assembled on individual moveable platforms that will allow for movement to the interaction point. In the Americas Region, a consultant study was completed to provide design and movement alternatives for the detector platforms. In the European Region, a consultant study provided a 3-dimensional model to study the effects of the sample-site geology on detector hall construction.

5.1.4 Life-safety and egress

In all regions, life safety and egress solutions for local underground tunnel configurations were an important aspect of the technical design. The decision to eliminate the main-linac service tunnel and have only one main linac tunnel presented challenges for the Americas and European Region with respect to life safety and personnel egress. While the main-linac tunnel configuration in the Asian Region went through significant changes, the final solution produced a configuration very similar to the original twin-tunnel RDR scheme. Each regional solution for life safety and egress was shaped by local codes and regulations. It is important to note that the solutions described below are the direct result of extensive in-house analysis of regional requirements by the CFS Group, supported in part by independent consultant studies. Work to date has provided confidence that a single-tunnel solution can be constructed in all regions that will provide a safe working environment when personnel are underground performing machine installation and maintenance activities.

The Asian main-linac tunnel configuration for the two Japanese mountainous sites provides a single tunnel that is divided into two compartments separated by a concrete radiation shielding wall. This effectively creates two separate enclosures that can be used for egress. If a fire or other hazard occurs in one of the tunnels, the second tunnel can be isolated and used as the emergency escape route. The compartments are connected by labyrinths, spaced every 500 m, through the shielding wall. Each labyrinth is protected by fire doors to allow safe passage from the affected area to the other side of the tunnel for egress to the surface. At each horizontal access tunnel, a similar protected pathway is provided to the surface.

In the Americas Region, the main linac enclosure is a single tunnel. The prevailing codes require containment of those areas of the underground space that have the highest hazard potential by fire-rated walls and doors, so that the most likely hazardous areas are contained in the event of an emergency. Oil-filled electrical equipment, water pumps, motors and other utility equipment constitute the highest potential for fire. This equipment is located in the caverns at the base of the vertical access shafts located along the single main-linac tunnel enclosures. In the Americas Region solution, these local areas are isolated by fire-rated walls and doors, leaving the main linac (or damping ring) tunnel enclosure available for personnel access to the surface. Due to the overall length of the tunnels, it is required to have a fire-protected area of refuge at intervals of 1200 m along the length of the single tunnel to provide an intermediate safe area for injured personnel or to await emergency-response assistance.

In the European Region, the main-linac enclosure is also a single tunnel. However, local regulations

and previously established precedents with the LHC at CERN produced a very different life-safety solution that divides the single-tunnel enclosure for the main linac and damping ring into 500 m increments or "compartments" that are separated by fire walls and automatic fire doors that can isolate areas that are involved in a fire or other hazardous incident. Another important part of this approach is the requirement for the control of air flow in an emergency. A continuous duct for air supply and extraction, located at the tunnel crown, extends along the entire length of the tunnel. In the event of fire, dampers will close in the supply duct, preventing fresh air from contributing to the fire and stopping smoke from permeating beyond the area of the fire. In this way, the unaffected areas of the tunnel can be used for personnel egress to the surface and for emergency-response personnel to access the affected area.

5.1.5 Electrical and mechanical utilities

Another important part in the development of a mature design for the ILC conventional facilities is the optimisation of the design for the utility systems that support the accelerator operation. After the underground civil construction, the mechanical and electrical systems represent the second and third largest cost drivers in the conventional facilities cost. As design development progressed and local conditions contributed to different regional design solutions, the mechanical and electrical designs were also adapted to local conditions.

Another factor that contributed to progress in the mechanical and electrical design was the refinement of the mechanical and electrical criteria used to develop the designs. Early in the TD phase, the Americas CFS team completed a formal value-engineering review of the process water system. The value-engineering process involves the identification of major drivers of the design and identifying alternatives for evaluation and possible inclusion into the design to improve efficiency and reduce costs. One of the most important outcomes of the formal value-engineering review was the identification of specific extreme technical specifications that were complicating the design of the process water system. The CFS group worked with the various accelerator systems groups to relax some of the more stringent criteria of the identified specifications. In doing so a more uniform and simplified design was achieved and costs were reduced.

During the course of the TDP, the CFS group used a similar process to review all of the mechanical and electrical criteria provided by the various accelerator systems design teams. Improvements were identified in all areas and included into the formal mechanical- and electrical-design process in both the Americas and Asian Regions. This effort produced simplified designs and substantial cost savings. In each case the designs reflect the improved criteria and local conditions and were supported by independent consultant studies.

5.2 Descriptions of studies

The conventional facilities design for the TDR represents a much more complete effort in the Americas and Asian Regions. In all cases, the work represents significant improvement over the RDR design. The conventional facilities work to date provides a global approach to understanding the implications of site-specific design solutions and the relative cost for each of those solutions. The following is a listing of various consultant studies that were conducted in each of the three ILC Project Regions. These studies were conducted in the support of the work provided by the in-house Conventional facilities and Siting Group. They provide added depth and independent expertise for the overall Convention Facilities and Siting design effort.

5.2.1 Americas Region

5.2.1.1 ILC Tunnel Configuration Study

The purpose of this study [307] was to analyse various options for main-linac tunnel configuration for the Americas Region sample site. The original RDR deep twin-tunnel configuration was used as the baseline, alternative configurations were considered and cost estimates were provided. The alternatives were based on a single tunnel using the KCS system and investigated both deep-tunnel and near-surface solutions.

5.2.1.2 Tunnel Cross-Section Configuration Study

The purpose of the *Tunnel Cross-Section Configuration Study Technical Design Report* [308] was to evaluate tunnel-lining/ground-support systems; and systems to support equipment and utilities. Five tunnel-lining alternatives were compared to determine their relative cost and schedule. Supports for equipment and utilities were compared on the basis of cost. This study also compared a pre-cast concrete flooring system to a cast-in-place concrete floor.

5.2.1.3 Black and Veach: ILC Constructibility Study

The Constructability Study [309] reviewed the current method of construction considered for the Americas Region sample site including both tunnel boring and drill and blast methods for various parts of the underground enclosures, shaft construction and location, muck removal, disposal and alternatives for the finished tunnel lining. Other aspects of the construction process including community considerations, impact of construction noise and traffic were also considered.

5.2.1.4 Holabird and Root: Fermilab ILC Programming Study

The Surface Building study [310] developed a comprehensive plan for the size and arrangement for the surface buildings required for the Americas Region sample site using the KCS system. Plans were developed for the surface buildings required at both major and minor access shafts with respect to Klystron Service and Cryogenic Buildings.

5.2.1.5 Americas Region: Life-Safety/Fire-Protection Analysis for the ILC

The *Life-Safety/Fire-Protection Analysis* [311] determines life-safety requirements for the ILC single-tunnel designs for both the 30 m- and 100 m-depth designs. The analysis was prepared in accordance with the National Fire Protection Association (NFPA) 520-2005 Standard for Subterranean Spaces [312]. NFPA 205 categorizes underground facilities using two designations: "building" and "common space". Building portions of subterranean spaces are areas that are occupied. Common space portions are all other areas.

5.2.1.6 Americas Region: "Fire Egress Analysis for the ILC"

The *Fire and Egress Analysis for the International Linear Collider (ILC)* [313] provides a performance based analysis of the feasibility of the single-tunnel designs for the ILC from a life-safety standpoint. The basis for the analysis was the *Life-Safety/Fire-Protection Analysis* prepared by Hughes Associates, Inc., May 21, 2010 [311].

5.2.1.7 ILC Process Water and Air Treatment VE Cost Evaluation

The Value Engineering (VE) effort [314] was implemented with the intent of understanding the process water cost-driver elements and providing for a lower first-cost alternative solution for the process water and its impact on other systems. The effort was started with the VE session facilitated by the United States Army Corps of Engineers, which produced a number of potential VE lists for evaluation. The VE items selected were evaluated and the resulting report summarised the results of the assessments in terms of a matrix of cost savings versus impacts. Applicable elements from the study were incorporated into the current baseline design.

5.2.1.8 Mechanical Design and Cost Report

The Mechanical Design Study [315] provided the first comprehensive effort to develop a full design for the air-treatment equipment, piped utilities and process cooling water for the Americas Region sample site using the KCS scheme. Alternatives were evaluated and a cost-effective solution was developed.

5.2.1.9 Electrical Design and Cost Report

The Electrical Design Study [316] provided the first comprehensive effort to develop a full design for the electrical power and distribution for the Americas Region sample site using KCS. Alternatives were evaluated and a cost effective solution was developed.

5.2.2 Asian Region

5.2.2.1 AAA Report, "Investigating the Single Tunnel Proposal in a Japanese Mountainous Site"

The Advanced Accelerator Association Report [317] for tunnelling methods used for a mountain site was the first study completed for sites in the Asian Region. The study provided guidance for tunnel methods previously used for transportation tunnels in Japan's mountainous areas. It described primarily tunnel construction experience using tunnel-boring machines and methods used for dewatering tunnels in mountainous regions.

5.2.2.2 J-Power Asian Tunnel Configuration Study (FY2010)

Construction costs and schedules are studied in eight cases for different combinations of high-level RF systems, tunnel configurations and excavation methods including TBM and NATM [318].

5.2.2.3 J-Power Asian Tunnel Configuration Study (FY2011)

Case 8 in the FY2010 study was developed and revised [319]. A "Kamaboko" shape was selected for the Main Linac single-tunnel cross section and other tunnel and cavern designs were also updated.

5.2.2.4 J-Power Asian Detector-Hall Study

A structural design, construction costs and schedule were described [320]. An analysis for structural behavior for both detectors, ILD (14.700 t) and SiD (8.600 t) was shown.

5.2.2.5 Nikken-Sekkei Electrical and Mechanical Design Study

Electrical and Mechanical (process cooling-water system, piping system and air-ventilation system) designs were developed including an equipment layout in the underground caverns [321]. Construction cost estimates were also developed as part of this study.

5.2.2.6 Asian Region Fire Safety for ILC Single Tunnel

Fire safety was reviewed for various tunnel configurations including double- and single-tunnel configurations in Americas, Asian and European sample sites [322].

5.2.3 European Region

5.2.3.1 Site-Selection Criteria for European ILC Sites

The "Site Selection Criteria for European ILC Sites" [323] provided an overview of the site investigation work conducted in the European Region. Three sites, located at high energy physics laboratories, were considered as prospects for a European Region sample site and are described in this study. Sites included in the study were located at the DESY Laboratory in Hamburg, Germany, the JINR Laboratory in Dubna, Russia and the CERN Laboratory located near Geneva, Switzerland.

5.2.3.2 Siting Study for European ILC Sites

The "Siting Study for European ILC Sites" [324] described a set of selection criteria for possible sites in the European Region. A general description of the overall parameters and site requirements for the construction of the ILC project was provided. In addition, geological properties, environmental impact issues, and electrical and cooling requirements were also identified.

5.2.3.3 Dubna Site Investigation

This report [325] was developed using the information of the site specific geologic study that was conducted at the proposed ILC sample site near the JINR Laboratory in Dubna, Russia. Based on geologic information obtained, alternatives for the construction of the ILC tunnels and enclosures were considered.

5.2.3.4 Report on the Results of the Preliminary Geological Engineering Surveys Along the Proposed Route of the International Linear Collider (ILC) in the Taldom Area of the Moscow Region

In conjunction with the Joint Institute for Nuclear Research (JINR), the Russian Governmental Unitary Enterprise and the State Specialised Projecting Institute conducted a geological study of the proposed European Sample site near Dubna, Russia [326]. Overall geologic conditions were identified and along the proposed ILC alignment, vertical electric soundings were conducted that identified optimum locations for three soil-boring samples. This study was a preliminary investigation for a possible European sample site.

5.2.3.5 Linear Collider Interaction Region Design Studies. Review of Interaction Region Cavern Layout Design

This report [327] was completed in conjunction with the Americas Region. The purpose of the report was twofold. First, a computerised geotechnical model was developed using the ILC Interaction Region configuration and the criteria of the geology of the European sample site. This model provided an analysis of the anticipated movement to the interaction region due to the short-term and long-term effects of the excavation of the interaction region. Second, the study developed a solution for the platform and movement system to allow the two detectors planned for both the ILC and CLIC projects to move in and out of the interaction point in an alternating data-taking mode. Designs were provided for platforms for both detectors that met the criteria for both deflection and repositioning and alignment requirements during the "push-pull" operation of the two detectors.

5.2.3.6 Guidelines and Criteria for an Environmental Impact Assessment for the Linear Collider Project at CERN

The report [328] is a preliminary manual for an environmental-impact statement (EIA) which will have to be conducted for the linear collider project. It describes the process for conducting an EIA and the environmental impact criteria that will have to be evaluated for an environmental impact study.

Chapter 6
Post-TDR R&D

6.1 The R&D Program

The realisation of the ILC requires the global high-energy physics community to agree on the high priority of the project. During the time required to prepare recommendations and await government actions, a global ILC core accelerator and technology team must remain in being and continue development of the project in collaboration with the physics community. As it has in the past, ILC R&D will continue to benefit other projects having significant technical or design overlaps. The ILC project team will continue its partnership with those working on such projects, ensuring that new developments can modify the ILC design as appropriate.

The post-TDR program will have a different flavour than the GDE R&D efforts, which were primarily aimed at demonstrating project viability. The next phase will be more closely coupled to preparing for a possible construction project and thus will be more D than R. This work will cover any remaining technical elements needing further work, such as the positron target. Some effort will be made to simplify component designs to streamline industrial production. It is not expected that the baseline design presented in this document will change significantly, although a site specific design will require customisation of the baseline concept in certain systems.

A small cavity R&D program will be maintained with the goal of increasing the effective accelerating gradient aimed at 1 TeV operation (see Section 2.3.4). Cavity improvements are essentially independent of the cryostat design and as such can be adopted at almost any point in the program. Cavity gradient R&D is viewed as an independent effort from preparation for a construction project.

The main missions of the post-TDR R&D effort will be:

1. Accelerator Design and Integration (AD&I) (with physics and detector groups);

   The AD&I team will further develop the machine design, including:
   a) development of (potentially phased) options for running at other energies;
   b) incorporating new R&D results, and programmatic synergies;
   c) analysing specific siting choices.

2. coordination of R&D on improving the performance and reducing the cost of the superconducting main linac;

3. continuation of the industrialisation programme for mass production of key technical components, especially cavities and cryomodules.

As during the Technical Design Phase, the R&D Program for the ILC is a central focus for the community and will also produce any technical information requested by the contracting governments in order to proceed to approval of the project.

The post-TDR program will feature closer collaboration with the CLIC project under the new Linear Collider Collaboration (LCC). Many elements of the CLIC activities such as the beam-delivery system pose similar challenges.

6.2 Accelerator Design and Integration

6.2.1 Physics Requirements

The ILC baseline Technical Design satisfies criteria published by the ILC Steering Committee in the 'Parameters for the Linear Collider' document in 2003 (updated in 2006) [329, 330]. In the next few years the LHC will provide insight into some of the processes the ILC is intended to study, which may alter the physics requirements. The ILC design, because of the maturity and high performance of its underlying technology, will be able to satisfy the needs of a broad range of collider physics, in terms of energy reach, luminosity, polarisation and energy-scan flexibility.

The recent discovery at the LHC of a Higgs particle at 125 GeV is highly significant for the ILC. It provides a guaranteed physics program, ranging from precision measurements of Higgs branching ratios via ZH associated production, requiring a 250 GeV centre-of-mass energy, to measurements of ZHH (the Higgs self-coupling), which requires at least 500 GeV. This scenario suggests that a phased energy approach to a linear collider could be attractive. This dove-tails well with the possibility of a 1 TeV energy upgrade. This was specified in the ILCSC parameters document as a secondary goal of the TDP. The machine implications of energy scaling in a phased fashion both up and down from the 500 GeV baseline design will be the highest priority for the AD&I program after the TDP.

The scientific requirements dictated in the ILCSC parameters document include references to options beyond the baseline linear collider. These include operation at the Z-boson resonance, an electron-electron collider, operation at the WW threshold, and a polarised gamma-gamma collider. It appears unlikely that sufficient resources will be available to do significant work on any of these topics in the near future but should the physics program dictate, then AD&I priorities would change accordingly.

6.2.2 Programmatic Synergies

Few aspects of accelerator development have remained untouched by work done in the ILC programme in the last two decades. It is not surprising that this impact has been greatest on linac technology, as this is the primary cost-driver of the linear collider. However, further technological developments are to be expected from ongoing linear-accelerator projects, for example to provide high-intensity photon beams (XFEL) [6, 331, 332] or high-intensity proton beams (ESS [333, 334] and Project X [335]). Certainly, experience with large-scale production of SRF technology for the above projects will yield valuable lessons on how best to manufacture it for the ILC.

The impact of ILC R&D has also been large outside linac technology. Examples include control of collective effects (electron cloud), which has directly affected the B-factories Super KEK-B and Super B [336, 337] and implementation of precision optics, which has improved the performance of synchrotron-radiation sources. Both B factories have adopted electron-cloud mitigation schemes in their designs, and will provide valuable lessons for the ILC from the production, deployment and operation of this mitigation hardware. Precision optics, supported by multi-step correction sequences and ultra-high-resolution beam monitors, have been deployed at synchrotron-radiation sources, inspired by work on the linear-collider beam delivery. These developments have allowed these accelerators to produce beams with quantum-limited emittance [117]. The operation of these machines and the completion of new ones will deliver valuable experience with ultra-low-emittance tuning.

Other linear-collider beam-development work outside the ILC community is likely to yield information and experience valuable and relevant enough to be applied to the ILC design. Such work includes targetry, sources, feedback and low-emittance transport.

The knowledge gained from these developments must be understood and assimilated by the full AD&I team in order to translate it into improvements to the overall ILC design.

6.2.3 Site Studies

Studies of two specific ILC sites in Japan have started and will continue beyond the publication of the TDR. These possible sites have quite different characteristics from the sample sites considered during the preparation of the Reference Design (2007). They are in relatively remote hilly (or mountainous) locations; detailed ongoing dialog between the AD&I team and the site-study teams will be required to understand the implications. Planned site-development work includes geotechnical exploration and alignment optimisation. Both are intended to allow the tunnel and surface-building complex to be configured in the optimal, cost-effective manner in the rugged Japanese topography. While the deployment of ILC technology is largely site-independent, a few key systems, namely linac high-power RF and cryogenics, are not and these must be optimised together with their housing and support utilities. These SCRF linac subsystems are expensive and will require ongoing evaluation as site decisions proceed.

The topography of the sites suggests that the optimum location of utility equipment may be underground, since it may be cumbersome and intrusive to provide adequate surface facilities with appropriate easements. Underground location of high-power utilities, (power transformers, pumps, cryogen compressors etc.) has associated drawbacks that will require study by the AD&I team. Other sites that might be proposed will have specific characteristics that will require investigation.

6.3 Main-Linac Technical Components

The ILC Technical Design Phase has seen an unprecedented global technology transfer by the R&D teams who did pioneering work in the decade or so leading up to the ITRP choice of SCRF technology in 2004. In that decade, the TESLA Collaboration R&D on 1.3 GHz technology succeeded in reducing the cost per MeV by a large factor over the early 1990's state-of-the-art SCRF and demonstrated operation of a high-current pulsed SCRF linac. During the TDP, the ILC GDE established and deployed a reliable, industrial process for consistent production of 35 MV/m cavities worldwide. This critical step, implemented through the global GDE SCRF team, was the single most important action taken, enabling the community to move beyond an unreliable R&D fabrication process toward a mature technology suitable for a practical project plan. With mature infrastructure and industry and projects underway in each region, progress is expected to move at an increasing pace in the next few years. The role of the ILC team will be to coordinate and provide paths for communication between teams working on key aspects (gradient, Q0 and cost) of the technology.

6.3.1 Test Facilities – Superconducting Linac Technology

The most substantial and promising infrastructures built or under construction during the Technical Design Phase are the beam facilities: VUVFEL FLASH and XFEL (DESY), NML/ASTA (Fermilab) and STF (KEK).

Beam tests at FLASH were used to demonstrate main-linac parameters and show the effectiveness of the control schemes planned. The next step is to evaluate cost-performance trade-offs through the process of characterisation and analysis. There has not been enough time or resources to complete a main-linac technology value-engineering cycle using the new facilities. Given the R&D progress of the last few years, this effort is expected to be an important component of post–TDR work.

In Europe, the 20 GeV XFEL project is midway through construction and is expected to accelerate first beams in 2015 with almost 1000 TESLA-like cavities in operation. The scale of this production is a natural intermediate step between the recently completed technology transfer and the order-of-magnitude larger-scale production needed for ILC. Although the details are different, the XFEL beam-performance parameters, cavity and cryomodule-fabrication process overlap that foreseen for the ILC to an extent sufficient to allow experience to directly feed into the project.

In Asia, the STF and the Cavity Fabrication Facility at KEK uniquely provide in one location all the tools needed for significant advances in the standard production process, allowing studies and associated improvements of a sort not practical to explore in a construction project like the XFEL.

6.3.2 Cavity gradient

During the TDP, some 90 cavities were built for the purpose of demonstrating the ILC gradient. Of these, more than half were subjected to the defined standard process as described in Section 2.3.2, while the others were used for developing the process. Under the prioritised R&D guidance set by the ILC-GDE, the baseline cavity-processing recipe was fixed and improved in the so-called S0 study. The success of the study, (including the successful qualification of production and test infrastructures), has provided fresh insight into basic SCRF processes. With the ability to build high-performance cavities reliably, an R&D program aimed at higher gradients than in the baseline parameter set, based on new fabrication procedures, can be crafted. The techniques used reflect a sound understanding of the basic physics processes. These techniques will include studies of new welding technology, coating technology, new surface-preparation techniques and basic material parameters. Alternate cavity shapes will also be investigated.

6.3.3 Cryomodule

Around 10 cryomodules, three of which were assembled by teams outside Europe, were produced during the TDP. Many more will be made in the next three years as the roughly 100 cryomodules for the XFEL (DESY) are built and tested. In contrast to earlier cryomodule experience and to cavity-performance improvements, cryomodule performance suffers significantly from gradient degradation. It is presumed that this is associated with field emission due to contamination that happens during string assembly. Attention will be focused on this problem post-TDR, in each region.

6.3.4 Industrialisation

The pace of progress is evident in the fostering of cavity fabrication companies in each region. Four institutional cavity process-and-test facilities (one in Europe, two in the Americas and one in Asia), are actively providing ILC cavities fabricated by four companies (two in Europe, one in the Americas and one in Asia). This number will be roughly doubled soon after the TDP. Fully functional high-technology cavity-production capability in each region is mandatory for providing the ILC project with a strong global technology basis.

Up to now the industrialisation process has focused on cavity production. Post-TDR, the practicality of having cavities assemblies produced in industry will be examined. These assemblies, called dressed cavities, include a cavity together with its helium tank, 2-phase helium-supply line, the cold part of the high-power coupler, and the mount for the tuner. This step requires that dressed cavities can undergo the standard process and test cycle in a similar fashion to the bare cavities. Maximising the industrial content in a cryomodule will lead to cheaper and more reliable assembles.

6.4 Beam-Test Facilities

Beam tests at FLASH were used to demonstrate main-linac parameters and show the effectiveness of the control schemes planned. The next step is to evaluate cost-performance trade-offs through the process of characterisation and analysis. There has not been enough time or resources to complete a main-linac technology value-engineering cycle using the new facilities. Given the R&D progress of the last few years, this effort is expected to be an important component of post–TDR work.

Two large-scale beam-test facilities intended for the study of beam dynamics were built and commissioned during the TDP: the CESR Test Accelerator at Cornell [338] and the Accelerator Test Facility – BDS test 'ATF2' at KEK [204]. Both of these will remain active for ILC-related studies following the TDR. The CesrTA program in support of ILC is largely completed [8] and a smaller program will be targeted on small-emittance-beam techniques, but the work at ATF2 has been delayed by roughly a year due to damage caused by the Great East Japan Earthquake of 2011. The aim is to complete the ATF2 program.

The most noteworthy partnership in beam dynamics is with the CLIC Study. Although the two-beam CLIC linac design is quite different from the ILC superconducting linac, other aspects of the collider complex are very similar – in some cases almost identical. This includes for example, beam emittance, precision optics and collective effects.

6.4.1 Main Linac Technology - FLASH, XFEL, STF, NML

It is especially important that each region deploy a full superconducting-linac system, including cryomodules, beam generation and handling, and RF power source and distribution systems, to integrate the accelerator technology and gain sufficient experience in that region. NML at Fermilab and STF at KEK were conceived as ILC beam-test facilities for the Americas and Asian regions, respectively. During the Technical Design phase, both operated as single-cryomodule test facilities supported the S1 programme. Post TDR, both NML and STF should be upgraded with additional ILC-type cryomodules capable of ILC average gradients and subsequently be capable of accelerating ILC-like beams.

Continuing the programme of joint studies at FLASH will allow characterisation of operation at the limits of RF-power overhead and gradient margins to evaluate cost-performance and operability trade-offs. Experience at FLASH will be transferred to the European XFEL, which in turn will provide a wealth of experience for ILC.

6.4.2 Electron Cloud – Cesr Test Accelerator (CesrTA)

The next phase of the CesrTA program will involve an investigation of low-emittance beams. As is typical in precision storage rings, the low-emittance tuning procedure is limited by systematics associated with measurements of vertical dispersion. The CesrTA group is developing a beam-based technique for compensating for systematic errors in beam-position monitors. This, together with tools for measuring horizontal beam size, beam energy spread and bunch length, will allow the simultaneous measurement of vertical, horizontal and longitudinal phase space. This is essential to the study of emittance dilution.

Measurement and analysis of intra-beam scattering is an important component of the next phase of the CesrTA program. The instrumentation described above will provide a complete set of measurements of the equilibrium charge density. As that equilibrium has a strong beam-energy dependence, measurements over a range of energies will help to distinguish IBS from other emittance-diluting effects. Measurements with electron as well as positron beams will isolate contributions from ions and electron cloud.

CesrTA is also an excellent laboratory for investigating ion effects in electron beams, and in

particular the fast ion instability in bunch trains in the ultra-low vertical-emittance regime. The turn-by-turn spectra gathered with the high-bandwidth beam-position and vertical-beam-size monitors for each bunch in a train can provide signatures of ion-beam coupling and emittance dilution. Measurement of instability thresholds as a function of vacuum pressure, both for positrons as well as electrons, will be used to isolate the effects of ions from other collective phenomena.

6.4.3 Beam Delivery – Accelerator Test Facility (ATF / ATF2)

The challenge of colliding nanometre-sized beams at the interaction point involves three distinct issues:

- creating small emittance beams in the damping ring;
- preserving the emittance during acceleration and transport;
- focusing and stabilising the beams to nanometres before colliding them.

These three issues are being addressed at the Accelerator Test Facility (ATF/ATF2) at KEK. The prototype damping ring (ATF) is used as a beam injector for the final-focus test beam line, ATF2, built and commissioned during the TDP, but with different beam-line optics based on a scheme of local chromaticity correction [198]. The purpose of ATF2 is to demonstrate and characterise the performance of this scheme.

Regarding the first of the three issues highlighted above, R&D work needed to support the damping-ring design includes the development of the fast injection/extraction kicker system and the beam-optics tuning to achieve 2 pm-rad extracted-beam vertical emittance.

A vertical emittance of 2 pm-rad has been achieved in several light-source storage rings around the world. However, typical beam sizes in these rings are small enough to make verifying low-emittance performance difficult and these measurements were made using indirect methods [117]. Therefore, a key goal to measure directly an extracted-beam emittance of 2 pm-rad or less remains. This can only be done at the ATF, which is the only low-emittance storage ring with a properly instrumented extraction line. An important challenge is to transport the beam through the extraction kickers and septum magnets without causing emittance growth due to x-y coupling or wakefields.

The remaining two main goals of ATF2 are:

1. achieving the 37 nm vertical beam size of the ILC design;
2. stabilizing the beam at the nanometre level.

These goals were not achieved during the Technical Design Phase and work toward them is ongoing. Achieving the first goal requires the development and implementation of a variety of methods to validate the design optics in the presence of imperfections, in particular beam measurement and tuning techniques to cancel distortions of the beam phase space. For the second goal, aimed at characterising and improving beam-line stability, the collaboration pursues hardware developments of particular relevance to future linear colliders. These include long baseline ultra-high-precision laser-alignment schemes, low-latency high-precision beam feedback and iterative algorithms for beam-optics aberration tuning.

6.5 Remaining R&D at other facilities

6.5.1 Positron source

The ILC positron source must create positrons efficiently and reliably at a rate close to the existing state of the art. The R&D program during the TDP had a two-pronged aspect that included R&D on critical components for the baseline undulator-driven source and R&D on alternative source technologies that might be applied to an auxiliary source or, possibly, in different collider configurations.

Following the completion of the TDR, work will continue on target and pulsed-magnet flux-concentrator component testing for several years. Studies aimed toward superconducting undulators with shorter periods, perhaps using Nb3Sn conductor, are also underway and are expected to continue for several years.

The high-speed rotating-target mechanism and the tapered-solenoid flux-concentrator pulsed-magnet R&D studies include the construction of a fully functional test device capable of operating at nominal ILC parameters. Specifically, these tests will prove the performance of a high-vacuum rotary seal and a full-power flux concentrator.

6.5.2 Beam-Delivery System (BDS) and Machine-Detector Interface (MDI)

The primary BDS R&D goals, preserving beam emittance and focusing the beams to nanometres, are closely linked to the ATF2 Beam Test Facility program. In addition, specific studies for BDS technical components include the design and testing of the superconducting final-doublet focusing magnet and development of a design for the high-power beam dump [214]. The design and prototyping of a superconducting final doublet that includes the required specialised correction coils has been finished but laboratory testing remains to be done. The integrated design of the final doublet and detectors must also be completed.

Bibliography

[1] J. Brau *et al.* [ILC Collaboration], "International Linear Collider Reference Design Report Volume 1: Executive Summary," ICFA Beam Dyn. Newslett. **42** (2007) 7 [arXiv:0712.1950 [physics.acc-ph]].

[2] G. Aarons *et al.* [ILC Collaboration], "International Linear Collider Reference Design Report Volume 2: Physics at the ILC," arXiv:0709.1893 [hep-ph].

[3] N. Phinney, N. Toge and N. Walker, "International Linear Collider Reference Design Report Volume 3: Accelerator," arXiv:0712.2361 [physics.acc-ph].

[4] T. Behnke *et al.* [ILC Collaboration], "International Linear Collider Reference Design Report Volume 4: Detectors," arXiv:0712.2356 [physics.ins-det].

[5] "Executive summary of the International Technology Recommendation Panel", http://www.interactions.org/pdf/ITRPexec.pdf (2004).

[6] M. Altarelli *et al.*(eds.), "XFEL: The European X-Ray Free-Electron Laser. Technical design report," DESY-06-097 (2006).

[7] H. Hayano (ed.), "S1-Global final report," 2012, http://ilc.kek.jp/S1G/, EDMS ID: D00000001005135.

[8] M. A. Palmer *et al.* (eds.), "The CESR Test Accelerator Electron Cloud Research Program Phase I Report", 2012, https://wiki.lepp.cornell.edu/ilc/bin/view/Public/CesrTA/CesrTAPhaseIReport, EDMS ID: D00000001009305.

[9] B. Barish *et al.* [ILC Global Design Effort], "ILC research and development plan for the Technical Design Phase, Rel. 5," EDMS ID: D00000000813385 (2010).

[10] Jean-Eudes Augustin *et al.*[International Technology Recommendation Panel], "ITRP Recommendation," http://www.fnal.gov/directorate/icfa/recent_lc_activities_files/ITRP_Report_Final.pdf (2004).

[11] "TESLA: The superconducting electron positron linear collider with an integrated X-ray laser laboratory. Technical design report, Parts 1-6," DESY-2001-011 (2001).

[12] A. Yamamoto, "Global R&D effort for the ILC linac technology," *Proc. EPAC 08, Magazzini del Cotone, Italy, 2008, pp. 12-16 (MOYBGM01)*.

[13] A. Yamamoto, IEEE Trans. Appl. Supercond. **19** (2009) 1387–1393, DOI: 10.1109/TASC.2009.2018756.

[14] Y. Yamamoto *et al.*, "Summary of vertical tests for S1-Global project in KEK-STF," *Proc. IPAC'10, Kyoto, Japan, 2010, pp. p3368-3370 (WEPE012)*.

[15] Y. Yamamoto *et al.*, "Progress of high gradient performance in STF 9-cell cavities at KEK," *Proc. IPAC'12, New Orleans, LA, 2012, pp. 2233-2235 (WEPPC013)*.

[16] ILC HiGrade homepage, www.ilc-higrade.eu.

[17] J.Gao *et al.*, "IHEP 1.3 GHz SRF technology R&D status," *Proc. SRF 2011, Chicago, IL, 2011, pp. 87-89 (MOPO015)*.

[18] R. Geng, C. Crawford, H. Padamsee and A. Seaman, "Vertical electropolishing niobium cavities," *Proc. SRF 2005, Cornell, Ithaca, NY, 2005, pp. 459-463 (THP04)*.

[19] K. Saito *et al.*, *Proc. SRF'97, Abano Terme, Padua, Italy, 1997, Part. Accel.* **60** *(1998) 193-217 (SRF97D02)*.

[20] Y. Iwashita, Y. Tajima and H. Hayano, Phys. Rev. ST Accel. Beams **11** (2008) 093501, DOI: 10.1103/PhysRevSTAB.11.093501.

[21] R.L. Geng, T. Goodman, "A machine for high-resolution inspection of SRF cavities at Jefferson Lab," *Proc. SRF 2011, Chicago, IL, 2011, pp. 798-800 (THPO036)*.

[22] M. Wenskat *et al.*, "Image processing for characterization of superconducting RF cavities," *Proc. IPAC'12, New Orleans, LA, 2012, pp. 2218-2220 (WEPPC007)*.

[23] S. Berry *et al.*, "Topological analysis of samples and cavities: a new tool for morphologic inspection of quench site," *Proc. SRF 2003, Travemünde, Germany, 2003, pp. 591-595 (THP04)*.

[24] M. Ge *et al.*, Supercond. Sci. Technol. **24** (2011) 035002, DOI: 10.1088/0953-2048/24/3/035002.

[25] W. Singer *et al.*, Phys. Rev. ST Accel. Beams **14** (2011) 050702, DOI: 10.1103/PhysRevSTAB.14.050702.

[26] Jan-Hendrik Thie *et al.*, "Mechanical design of automatic cavity tuning machines," *Proc. SRF 2009, Berlin, Germany, 2009, pp. 797-800 (THPPO074)*.

[27] Jan-Hendrik Thie *et al.*, "Commissioning and upgrade of automatic cavity tuning machines for the European XFEL," *Proc. SRF 2011, Chicago, IL, 2011, pp. 495-500 (TUPO048)*.

[28] Z.A. Conway *et al.*, "Oscillating superleak transducers for quench detection in superconducting ILC cavities cooled with He-II," *Proc. LINAC 08, Victoria, BC, 2008, pp. 863-865 (THP036)*.

[29] Z.A. Conway *et al.*, "Defect location in superconducting cavities cooled with He-II using oscillating superleak transducers," *Proc. SRF 2009, Berlin, Germany, 2009, pp. 113-116 (TUOAAU05)*.

[30] J. Knobloch, "Advanced thermometry studies of superconducting RF cavities," Ph.D Thesis, Cornell University, (1997) [UMI-97-38186].

[31] Q. S. Shu *et al.*, "Experience in design, construction and application of a rotating T-R mapping system in superfluid He for TESLA 9-cell cavities," *Proc. SRF'95, Gif-sur-Yvette, 1995; Part. Accel.* **53** *(1996) 523-527 (SRF95C30)*.

[32] G. Ciovati *et al.*, "A 2-cell temperature mapping system for ILC cavities", Internal Report, JLAB-TN-08-012 (2008). http://tnweb.jlab.org/tn/2008/08-012.pdf.

[33] Y. Yamamoto *et al.*, "Cavity diagnostic system for the vertical test of the baseline SC cavity in KEK-STF," *Proc. SRF 2007, Beijing, China, 2007, pp. 464-468 (WEP13)*.

[34] M. Ge *et al.*, "Construction, evaluation, and application of a temperature map for multi-cell SRF cavities," *Proc. IPAC'12, New Orleans, LA, 2012, pp. 2369-2371 (WEPPC069)*.

[35] H. Sakai *et al.*, "Cavity diagnostics using rotating mapping system for 1.3 GHz ERL 9-cell superconducting cavity," *Proc. IPAC'10, Kyoto, Japan, 2010, pp. 2950-2952 (WEPEC028)*.

[36] M.P. Kelly, S.M. Gerbick, D.R. Olis and A.M. Rowe, "Surface Processing Facilities for Superconducting RF Cavities at ANL," *Proc. LINAC 08, Victoria, BC, 2008, pp. 839-841 (THP026)*.

[37] R. Carcagno *et al.*, "Commissioning and early operating experience with the Fermilab horizontal test facility," *Proc. SRF 2007, Beijing, China, 2007, pp. 469-471 (WEP14)*.

[38] C. Adolphsen *et al.*, "SLAC/FNAL TTF3 coupler assembly and processing experience," *Proc. SRF 2011, Chicago, IL, 2011, pp. 476-478 (TUPO042)*.

[39] C. Adolphsen *et al.*, "Coupler development and processing facility at SLAC," *Proc. PAC 09, Vancouver, BC, Canada, 2009, pp. 1020-1022 (WE5PFP019)*.

[40] B. Aune *et al.*, Phys. Rev. ST Accel. Beams **3** (2000) 092001 [arXiv:physics/0003011], DOI: 10.1103/PhysRevSTAB.3.092001.

[41] D. Reschke *et al.*, "Analysis of RF results of recent nine-cell cavities at DESY," *Proc. SRF 2009, Berlin, Germany, 2009, pp. 342-346 (TUPPO051)*.

[42] R. L. Geng *et al.*, "Progress of ILC high gradient SRF cavity R&D at Jefferson Lab," *Proc. IPAC 2011, San Sebastian, Spain, 2011, pp. 334-336 (MOPC111)*.

[43] R. L. Geng, G. V. Eremeev, H. Padamsee and V. D. Shemelin, "High gradient studies for ILC with single cell reentrant shape and elliptical shape cavities made of fine grain and large grain niobium," *Proc. PAC 07, Albuquerque, NM, 2007, pp. 2337-2339 (WEPMS006)*, DOI: 10.1109/PAC.2007.4441242.

[44] F. Furuta and K. Saito, "50 MV/m recipe for ICHIRO end groups with ethanol rinsing and wiping," *Proc. SRF 2009, Berlin, Germany, 2009, pp. 821-823 (THPPO084)*.

[45] S. Aderhold, "Optical inspection of SRF cavities at DESY," *Proc. SRF 2009, Berlin, Germany, 2009, pp. 286-288 (TUPPO035)*.

[46] R. L. Geng, G. Ciovati, A. C. Crawford, "Gradient limiting defects in 9-cell cavities EP processed and RF tested at Jefferson Lab," *Proc. SRF 2009, Berlin, Germany, 2009, pp. 370-374 (TUPPO059)*.

[47] K. Watanabe *et al.*, "Surface inspection on MHI-01 09 cavities," *Proc. IPAC'10, Kyoto, Japan, 2010, pp. 2962-2964 (WEPEC032)*.

[48] K. Watanabe *et al.*, "Repair techniques of superconducting cavity for improvement cavity performance at KEK-STF," *Proc. IPAC'10, Kyoto, Japan, 2010, pp. 2965-2967 (WEPEC033)*.

[49] C. A. Cooper and L. D. Cooley, "Mirror smooth superconducting RF cavities by mechanical polishing with minimal acid use," FERMILAB-PUB-11-032-TD (2011).

[50] E. Elsen *et al.*, "International Linear Collider (ILC): A technical progress report," ANL-11-09 (2011), ILC-REPORT-2011-030.

[51] R. L. Geng and A. C. Crawford, "Standard procedures of ILC high gradient cavity processing and handling at Jefferson Lab," *Proc. SRF 2011, Chicago, IL, 2011, pp. 391-393 (TUPO015)*.

[52] H. Diepers, O. Schmidt, H. Martens and F. S. Sun, Phys. Lett. A **37** (1971) 139-140, DOI: 10.1016/0375-9601(71)90095-8.

[53] K. Saito *et al.*, "R&D of superconducting cavities at KEK," *Proc. SRF'89, Tsukuba, 1989, pp. 635-694 (SRF89G18)*.

[54] A. C. Crawford and H. Padamsee, unpublished (2007).

[55] X. Zhao *et al.*, Phys. Rev. ST Accel. Beams **13** (2010) 124702, DOI: 10.1103/PhysRevSTAB.13.124702.

[56] B. van der Horst *et al.*, "Update on cavity preparation for high gradient superconducting multicell cavities at DESY," *Proc. SRF 2007, Beijing, China, 2007, pp. 196-199 (TUP30)*.

[57] J. Mammosser, "ILC cavity qualifications — Americas, " *Talk presented at the TTC meeting, April 6, 2007, Fermilab,* http://indico.desy.de/conferenceDisplay.py?confId=200, (2007).

[58] F. Furuta *et al.*, "High reliable surface treatment recipe of high gradient single cell SRF cavities at KEK," *Proc. SRF 2007, Beijing, China, 2007, pp. 125-131 (TUP10)*.

[59] R. L. Geng, "Progress on improving SC cavity performance for ILC," *Proc. PAC 09, Vancouver, BC, Canada, 2009, pp. 704-708 (TU3RAI03)*.

[60] T. Saeki *et al.*, "R&D for the post-EP processes of superconducting RF cavity," *Proc. SRF 2009, Berlin, Germany, 2009, pp. 824-828 (THPPO085)*.

[61] G. Eremeev, R. L. Geng, and A. D. Palczewski, "Probing the fundamental limit of niobium in high radio frequency fields by dual mode excitation in superconducting radio frequency cavities," *Proc. SRF 2011, Chicago, IL, 2011, pp. 746-749 (THPO017)*.

[62] J. Dai *et al.*, "Exploration of quench initiation due to intentional geometrical defects in a high magnetic field region of an SRF cavity," *Proc. SRF 2011, Chicago, IL, 2011, pp. 759-762 (THPO020)*.

[63] V. Shemelin and H. Padamsee, "Magnetic field enhancement at pits and bumps on the surface of superconducting cavities," Cornell report SRF-080903-04 (2008), http://www.lns.cornell.edu/public/SRF/2008/SRF080903-04/H_Enh_at_Pits_2.pdf.

[64] R. L. Geng *et al.*, "Gradient improvement by removal of identified local defects," *Proc. SRF 2011, Chicago, IL, 2011, pp. 436-438 (TUPO029)*.

[65] A. C. Crawford, Private communication (2011).

[66] M. Ge *et al.*, "Repair SRF cavities by re-melting surface effects via high power laser technique," *Proc. SRF 2011, Chicago, IL, 2011, pp. 740-744 (TUPO015)*.

[67] Cavity database, http://tesla.desy.de/oracle/ilc/DataBase/view.

[68] C. Ginsburg, "Cavity production yield statistics", 2012, EDMS ID: D00000001008325.

[69] C. A. Cooper *et al.*, "Centrifugal barrel polishing (CBP) of SRF cavities worldwide," *Proc. SRF 2011, Chicago, IL, 2011, pp. 571-5753 (WEIOA02)*.

[70] D. Reschke *et al.*, "Results on large grain nine-cell cavities at DESY: gradients up to 45 MV/m after electropolishing," *Proc. SRF 2011, Chicago, IL, 2011, pp. 490-494 (THPO046)*.

[71] R. L. Geng, A. K. Seaman, V. D. Shemelin and H. Padamsee, "World record accelerating gradient achieved in a superconducting niobium RF cavity," *Proc. PAC 05, Knoxville, TN, 2005, pp. 653-655 (ROAC009)*, DOI: 10.1109/PAC.2005.1590516.

[72] J. Sekutowicz *et al.*, "Design of a low loss SRF cavity for the ILC," *Proc. PAC 05, Knoxville, TN, 2005, pp. 3342-3344 (TPPT056)*, DOI: 10.1109/PAC.2005.1591465.

[73] Z. Li and C. Adolphsen "A new SRF cavity shape with minimized surface electric and magnetic fields for the ILC," *Proc. LINAC 08, Victoria, BC, 2008, pp. 867-869 (THP038)*.

[74] F. Furuta *et al.*, "Experimental comparison at KEK of high gradient performance of different single cell superconducting cavity designs," *Proc. EPAC 06, Edinburgh, Scotland, 2006, pp. 750-752 (MOPLS084)*.

[75] F. Furuta *et al.*, "High gradient results of ICHIRO 9-cell cavity in collaboration with KEK and Jlab," *Proc. SRF 2011, Chicago, IL, 2011, pp. 386-390 (THPO014)*.

[76] P. Kneisel, "Progress on large grain and single grain niobium-ingots and sheet and review of progress on large grain and single grain niobium cavities," *Proc. SRF 2007, Beijing, China, 2007, pp. 728-733 (TH102)*.

[77] F. Furuta, K. Saito and T. Konomi, AIP Conf. Proc. **1352** (2011) 169, DOI: 10.1063/1.3580643.

[78] J. Y. Zhai *et al.*, "IHEP 1.3 GHz low-loss large grain 9-cell cavity R&D for ILC," *Proc. SRF 2011, Chicago, IL, 2011, pp. 611-614 (WEIOB06)*.

[79] G. Ciovati, R. L. Geng, J. Mammosser and J. W. Saunders, IEEE Trans. Appl. Supercond. **21** (2011) 1914-1917, DOI: 10.1109/TASC.2010.2087305.

[80] R. L. Geng *et al.*, "Q_0 improvement of large-grain multi-cell cavities by using JLab's standard ILC EP processing," *Proc. SRF 2011, Chicago, IL, 2011, pp. 501-503 (TUPO049)*.

[81] W. Singer *et al.*, "Nine-cell Tesla shape cavities produced from hydroformed cells," *Poster at SRF2011, Chicago, IL (TUPO026) (2011),* http://adweb.desy.de/mpl/articles/TUPO026.pdf.

[82] W. Singer, private communication (2012).

[83] R. Crooks, "Fabrication of ILC cavities from axisymmetric RRR Nb tubes," Presentation at US Hydroforming Workshop, Sep. 1, 2010, Fermilab. https://indico.fnal.gov/materialDisplay.py?contribId=2&sessionId=0&materialId=slides&confId=3600.

[84] P. Kneisel, private communication (2012).

[85] W. Singer *et al.*, "Hydroforming of NbCu clad cavities at DESY," *Proc. SRF 2001, Tsukuba, 2001, pp. 467-470 (FA009)*.

[86] K. Saito *et al.*, "R&D of Nb/Cu clad seamless cavities at KEK," *Proc. SRF 2001, Tsukuba, 2001, pp. 523-530 (PT019)*.

[87] T. Higuchi *et al.*,"Investigation on barrel polishing for superconducting niobium cavities," *Proc. SRF'95, Gif-sur-Yvette, 1995; Part. Accel.* **53** *(1996) 723-727 (SRF95F34)*.

[88] T. Higuchi *et al.*, "Centrifugal barrel polishing of L-band niobium cavities," *Proc. SRF 2001, Tsukuba, 2001, pp. 431-432 (PR022)*.

[89] D. Kostin, W.-D. Moeller, A. Goessel, K. Jensch "Superconducting accelerating module tests at DESY," *Proc. SRF 2009, Berlin, Germany, 2009, pp. 180-184 (TUPPO005)*.

[90] E. Kako *et al.*, Phys. Rev. ST Accel. Beams **13** (2010) 041002, DOI: 10.1103/PhysRevSTAB.13.041002.

[91] N. Ohuchi *et al.*, "S1-Global collaborative efforts 8-cavity-cryomodule: 2 FNAL, 2 DESY and 4 KEK," *Proc. LINAC 10, Tsukuba, Japan, 2010, pp. 31-35 (MO302)*.

[92] N. Walker *et al.*, "Workshop on Linac Operation with Long Bunch Trains," DESY, Hamburg, 2011, https://indico.desy.de/conferenceDisplay.py?confId=3007.

[93] Y. Yamamoto *et al.*, "Observation and numerical calculation of Lorentz-detuning for the cryomodule test of STF baseline cavities at KEK-STF," *Proc. PAC 09, Vancouver, BC, Canada, 2009, pp. 999-1001 (TU5PFP075)*.

[94] W. Schappert and Y. Pischalnikov, "Adaptive compensation for Lorentz force detuning in superconducting RF cavities," *Proc. SRF 2011, Chicago, IL, 2011, pp. 940-942 (FRIOA01)*

[95] S. Michizono *et al.*, "Performance of LLRF system at S1-Global in KEK," *Proc. IPAC 2011, San Sebastian, Spain, 2011, pp. 451-453 (MOPC157)*.

[96] C. Nantista and C. Adolphsen, "Klystron Cluster Scheme for ILC high power RF distribution," SLAC-PUB-13696 (2009), *Proc. PAC 09, Vancouver, BC, Canada, 2009, pp. 2036-2038 (WE5PFP021)*.

[97] C. Pagani *et al.*, Adv. Cryogenic Eng. **43A** (1998) 87–97.

[98] D. Barni, C. Pagani and P. Pierini, "Towards the third generation of TTF cryomodule," TESLA-98-16, 1998.

[99] N. Ohuchi *et al.*, "Thermal performance of the S1-Global Cryomodule for ILC," *Proc. IPAC 2011, San Sebastian, Spain, 2011, pp. 2472-2474 (WEPO035)*.

[100] S. Barbanotti *et al.*, "Thermal and structural modeling of the TTF cryomodule cooldown and comparison with experimental data," *Proc. EPAC 08, Magazzini del Cotone, Italy, 2008, pp. 2494-2496 (WEPD038)*.

[101] X. L. Wang *et al.*, "Thermal performance analysis and measurements for the accelerator prototype modules of european XFEL," *Presented at the TESLA Technology Collaboration Meeting, IHEP, Bejing, China, 5-8 December, 2011*, http://indico.ihep.ac.cn/materialDisplay.py?contribId=25&sessionId=9&materialId=slides&confId=2240.

[102] V. S. Kashikhin *et al.*, IEEE Trans. Appl. Supercond. **22** (2012) 4002904 (Proc. MT-22), DOI: 10.1109/TASC.2011.2176297.

[103] N. Andreev *et al.*, IEEE Trans. Appl. Supercond. **23** (2013) 3500305, DOI: 10.1109/TASC.2012.2236135.

[104] M. Ross, N. Walker, A. Yamamoto *et al.*, "SB2009 proposal document," 2009, EDMS ID: D00000000900425.

[105] V. Katalev and S. Choroba, "Waveguide Distribution System for FLASH", Presentation at 6th CW and High Average Power RF Workshop (VWRF2010), Barcelona, May 4-7, 2010. http://indico.cern.ch/contributionDisplay.py?contribId=15&sessionId=10&confId=73280.

[106] S. Fukuda *et al.*, "Status of RF sources in Super-conducting RF Test Facility (STF) at KEK", *Proc. LINAC 08, Victoria, BC, 2008, pp. 909-911 (THP054)*.

[107] C. Burkhart *et al.*, "ILC Marx Modulator development program status," *Proc. LINAC 08, Victoria, BC, 2008, pp. 1015-1017 (THP097)*.

[108] K. Macken *et al.*, "A hierarchical control architecture for a PEBB-based ILC Marx modulator," *Proc. PPC'09, Washington, DC, 2009, pp. 826-831*, DOI: 10.1109/PPC.2009.5386259.

[109] D. Sprehn *et al.*, "Development of a 10 MW sheet beam klystron for the ILC," *Proc. PAC 09, Vancouver, BC, Canada, 2009, pp. 762-765 (TU4RAI02)*.

[110] K. L. F. Bane *et al.*, "Sheet Beam Klystron instability analysis," *Proc. PAC 09, Vancouver, BC, Canada, 2009, pp. 4728-4730 (FR5RFP082)*.

[111] C. D. Nantista *et al.*, "Planar waveguide hybrids for very high power RF", *Proc. PAC 99, New York, NY, 1999, pp. 1432-1434 (TUA153)*, DOI: 10.1109/PAC.1999.795572.

[112] C. D. Nantista and C. Adolphsen, "A variable directional coupler for an alternate ILC high-power RF distribution scheme," *Proc. LINAC 06, Knoxville, TN, 2006, pp. 643-645 (THP032)*.

[113] Y. Fuwa *et al.*, "Development of permanent magnet focusing system for klystrons", *Proc. LINAC 12, Tel-Aviv, Israel, Sep. 9-14, 2012.*.

[114] S. G. Tantawi, A. E. Vlieks, C. D. Nantista, and R. J. Loewen, IEEE Trans. Microwave Theor. Techn. **47** (1999) 2539-2546, DOI: 10.1109/22.809004.

[115] S.G. Tantawi N. M. Kroll and K. Fant, "RF components using over-moded rectangular waveguides for the Next Linear Collider multi-moded delay line RF distribution system," *Proc. PAC 99, New York, NY, 1999, pp. 1435-1437 (TUA154)*, DOI: 10.1109/PAC.1999.795573.

[116] P. Lebrun, "Industrial technology for unprecendented energy and luminosity: the Large Hadron Collider," *Proc. EPAC 04, Lucerne, Switzerland, 2004, pp. 6-10 (MOXBCH01)*.

[117] R. Dowd, M. Boland, G. LeBlanc and Y-R. E. Tan, Phys. Rev. ST Accel. Beams **14** (2011) 012804, DOI: 10.1103/PhysRevSTAB.14.012804.

[118] P. Castro [TESLA Collaboration], ICFA Beam Dyn. Newslett. **24** (2001) 20-34.

[119] C. Schmidt *et al.*, "Feedback strategies for bunch arrival time stabilisation at FLASH towards 10 fs," *Proc. FEL'11, Shanghai, China, 2011, pp. 531-534 (THPA26)*.

[120] DOOCS homepage, `http://doocs.desy.de`.

[121] Matlab homepage, `http://www.matlab.com`.

[122] Octave homepage, `http://www.gnu.org/software/octave/`.

[123] A. Agababyan *et al.*, "The data acquisition system (DAQ) of the FLASH facility," *Proc. ICALEPCS07, Knoxville, TN, 2007, pp. 564-566 (RPPA25)*.

[124] M. K. Grecki and S. Pfeiffer, "Resonance control of superconducting cavities at heavy beam loading conditions," *Proc. IPAC'12, New Orleans, LA, 2012, pp. 3467-3469 (THPPC077)*.

[125] O. Hensler, *et al.*, "Consolidating the FLASH LLRF system using DOOCS standard server and the FLASH DAQ," *Proc. PCaPAC 2010, Saskatoon, SK, Canada, 2010, pp. 55-57 (WEPL014)*.

[126] R. Kammering and J. Carwardine, "An orbit feedback for the free electron laser in Hamburg (FLASH)," *Proc. PCaPAC 2010, Saskatoon, SK, Canada, 2010, pp. 58-60 (WEPL015)*.

[127] M. K. Grecki *et al.*, "Compensation of Lorentz force detuning for SC Linacs (with Piezo tuners)," *Proc. EPAC 08, Magazzini del Cotone, Italy, 2008, pp. 862-864 (MOPP129)*.

[128] J. Branlard *et al.*, "LLRF automation for the 9 mA ILC tests at FLASH," *Proc. LINAC 12, Tel-Aviv, Israel, Sep. 9-14, 2012.*.

[129] Masao Kuriki *et al.*, Jap. J. Appl. Phys. **52** (2013) 056401, DOI: 10.7567/JJAP.52.056401.

[130] B. Dwersteg, K. Flöttmann, J. Sekutowicz and C. Stolzenburg, Nucl. Instrum. Meth. A **393** (1997) 93-95, DOI: 10.1016/S0168-9002(97)00434-8

[131] M. Palmer *et al.*, "Electron cloud at low emittance in CESRTA," *Proc. IPAC'10, Kyoto, Japan, 2010, pp. 1251-1255 (TUYMH02)*.

[132] The CesrTA Collaboration includes senior researchers from the following institutions: ANL, Australian Synchrotron, BNL, California Polytechnic State Univ., Carleton Univ., CERN, the Cockroft Institute, FNAL, INFN-LNF, KEK, LBNL, Purdue University, SLAC and Technion-Haifa.

[133] Electron cloud working group homepage, https://wiki.lepp.cornell.edu/ilc/bin/view/Public/DampingRings/WebHome#Working_Group_on_Electron_Cloud.

[134] M. T. F. Pivi *et al.*, "Recommendation for the feasibility of more compact LC damping rings," *Proc. IPAC'10, Kyoto, Japan, 2010, pp. 3578-3580 (WEPE097)*.

[135] ILC damping rings satellite meeting at ECLOUD'10, Ithaka, NY, 2010, http://www.lns.cornell.edu/Events/ECLOUD10/ILCDampingRingsSatelliteMeeting.html.

[136] ECLOUD'10, Ithaka, NY, 2010, http://www.lns.cornell.edu/Events/ECLOUD10/WebHome.html.

[137] J. Conway, Y. Li, and M. Palmer, "The conceptual design of a vacuum system for the ILC damping rings incorporating electron cloud mitigation techniques," *Proc. IPAC'12, New Orleans, LA, 2012, pp. 1960-1962 (TUPPR062)*.

[138] M. A.Palmer *et al.*, "The conversion and operation of the Cornell Electron Storage Ring as a Test Accelerator (CesrTA)," *Proc. PAC 09, Vancouver, BC, Canada, 2009, pp. 4200–4204 (FR1RAI02)*.

[139] Y. Li *et al.*, "CESRTA vacuum system modifications," *Proc. PAC 09, Vancouver, BC, Canada, 2009, pp. 357–359 (MO6RFP005)*.

[140] D. H. Rice, "CESR–c: A wiggler dominated collider," *Proc. PAC 07, Albuquerque, NM, 2007, pp. 48-52 (MOZBKI01)*, DOI: 10.1109/PAC.2007.4440337.

[141] M. Palmer *et al.*, "CESR beam position monitor system upgrade for CESRTA and CHESS operations," *Proc. IPAC'10, Kyoto, Japan, 2010, pp. 1191-1193 (MOPE089)*.

[142] J.P. Alexander *et al.*, "CESRTA X-Ray beam size monitor design," *Proc. PAC 09, Vancouver, BC, Canada, 2009, pp. 3503-3504 (TH5RFP026)*.

[143] M. A.Palmer *et al.*, "Design, implementation and first results of retarding field analyzers developed for the CESRTA program," *Proc. PAC 09, Vancouver, BC, Canada, 2009, pp. 3510-3512 (TH5RFP030)*.

[144] Y. Li *et al.*, "Design and implementation of CESRTA superconducting wiggler beampipes with thin retarding field analyzers," *Proc. PAC 09, Vancouver, BC, Canada, 2009, pp. 3507–3509 (TH5RFP029).*

[145] S. De Santis, J. Byrd, J. Sikora, M. Billing, "The TE wave transmission method for electron cloud measurements at Cesr-TA," *Proc. PAC 09, Vancouver, BC, Canada, 2009, pp. 3606–3608 (TH5RFP071).*

[146] M. Billing *et al.*, "Techniques for observation of beam dynamics in the presence of an electron cloud," *Proc. IPAC'10, Kyoto, Japan, 2010, pp. 1197–1199 (MOPE091).*

[147] D. L. Rubin, D. Sagan, J. P. Shanks, "CesrTA layout and optics," *Proc. PAC 09, Vancouver, BC, Canada, 2009, pp. 2551-2553 (WE6PFP103).*

[148] J. R. Calvey *et al.*, "CesrTA retarding field analyzer measurements in drifts, dipoles, quadrupoles and wigglers," *Proc. IPAC'10, Kyoto, Japan, 2010, pp. 1973–1975 (TUPD023).*

[149] J. R. Calvey *et al.*, "Electron cloud mitigation investigations at CesrTA," *To appear in Proc. ECLOUD'10, Cornell, Ithaca, NY, 2010 (slides).*

[150] J. Calvey *et al.*"CesrTA retarding field analyzer modeling results," *Proc. IPAC'10, Kyoto, Japan, 2010, pp. 1970-1972 (TUPD022).*

[151] J.R. Calvey *et al.*, "Methods for quantitative interpretation of retarding field analyzer data," *Proc. PAC 11, New York, NY, 2011, pp. 501-503 (MOP214).*

[152] J. R. Calvey, *et al.*, "Update on electron cloud mitigation studies at Cesr-TA," *Proc. IPAC 2011, San Sebastian, Spain, 2011, pp. 796-798 (MOPS083).*

[153] J. R. Calvey *et al.*, "Modeling and simulation of retarding field analyzers at CESRTA," *Proc. IPAC'12, New Orleans, LA, 2012, pp. 3138-3140 (WEPPR088).*

[154] S. De Santis *et al.*, Phys. Rev. ST Accel. Beams **13** (2010) 071002, DOI: 10.1103/PhysRevSTAB.13.071002.

[155] S. De Santis *et al.*, "TE wave measurements of the electron cloud in a dipole magnetic field," *Proc. PAC 11, New York, NY, 2011, pp. 531-533 (MOP228).*

[156] J. P. Sikora *et al.*, "Resonant TE Wave Measurements of Electron Cloud Densities at CesrTA," *Proc. IPAC 2011, San Sebastian, Spain, 2011, pp. 1434-1436 (TUPC170).*

[157] J. P. Sikora *et al.*, "Using TE wave resonances for the measurement of electron cloud density," *Proc. IPAC'12, New Orleans, LA, 2012, pp. 960-962 (MOPPR074).*

[158] G. Penn and J.-L. Vay, "Theoretical studies of TE-wave propagation as a diagnostic for electron cloud," *Proc. IPAC'10, Kyoto, Japan, 2010, pp. 1961–1963 (TUPD019).*

[159] K. Sonnad *et al.*, "Simulations using VORPAL on the effect of imperfections and nonuniformities in TE wave propagation through electron clouds," *To appear in Proc. ECLOUD'10, Cornell, Ithaca, NY, 2010 (slides).*

[160] S. Veitzer *et al.*, "Modeling electron cloud buildup and microwave diagnostics using VORPAL," *To appear in Proc. ECLOUD'10, Cornell, Ithaca, NY, 2010 (slides).*

[161] S. A. Veitzer, P. Stoltz, J. A. Crittenden and K. G. Sonnad, "3-dimensional modeling of electron clouds in non-uniform magnetic fields," *Proc. IPAC'12, New Orleans, LA, 2012, pp. 1059-1061 (TUOAA01)*.

[162] J.A. Crittenden *et al.*, "Electron cloud modeling results for time-resolved shielded pickup measurements at CesrTA," *Proc. PAC 11, New York, NY, 2011, pp. 1752-1754 (WEP195)*.

[163] L. E. Boon, J. A. Crittenden, K. C. Harkay and T. Ishibashi, "Application of the SYNRAD3D photon-tracking model to shielded pickup measurements of electron cloud buildup at CesrTA," *Proc. IPAC 2011, San Sebastian, Spain, 2011, pp. 2319-2321 (WEPC141)*.

[164] J. A. Crittenden *et al.*, "Recent developments in modeling time-resolved shielded-pickup measurements of electron cloud buildup at CESRTA," *Proc. IPAC 2011, San Sebastian, Spain, 2011, pp. 2313-2315 (WEPC135)*.

[165] J. A. Crittenden *et al.*, "Time-resolved shielded-pickup measurements and modeling of beam conditioning effects on electron cloud buildup at CesrTA," *Proc. IPAC'12, New Orleans, LA, 2012, pp. 1966-1968 (TUPPR064)*.

[166] Y. Suetsugu *et al.*, Nucl. Instrum. Meth. A **598** (2009) 372, DOI: 10.1016/j.nima.2008.08.154.

[167] C. Yin Vallgren *et al.*, "Amorphous carbon coatings for mitigation of electron cloud in the CERN SPS," *Proc. IPAC'10, Kyoto, Japan, 2010, pp. 2033-2035 (TUPD048)*.

[168] L. Wang, X. Huang and M. Pivi, "Electron trapping in wiggler and quadrupole magnets of CESRTA," *Proc. IPAC'10, Kyoto, Japan, 2010, pp. 1892-1894 (TUPEC077)*.

[169] J. Shanks, D. Rubin and D. Sagan, "CesrTA low emittance tuning," *Proc. IPAC'10, Kyoto, Japan, 2010, pp. 4620-4622 (THPE046)*.

[170] D. Peterson *et al.*,"CesrTA X-Ray beam size monitor operation," *Proc. IPAC'10, Kyoto, Japan, 2010, pp. 1194–1196 (MOPE090)*.

[171] J. A. Crittenden *et al.*, "Studies of the effects of electron cloud formation on beam dynamics at CesrTA," *Proc. PAC 09, Vancouver, BC, Canada, 2009, pp. 4631-4633 (FR5RFP044)*.

[172] J. Crittenden *et al.*, "progress in studies of electron-cloud-induced optics distortions at CesrTA," *Proc. IPAC'10, Kyoto, Japan, 2010, pp. 1976–1978 (TUPD024)*.

[173] D.L. Kreinick *et al.*, "Application of coherent tune shift measurements to the characterization of electron cloud growth," *Proc. PAC 11, New York, NY, 2011, pp. 1680-1682 (WEP108)*.

[174] G. F. Dugan *et al.*, "Synrad3D Photon Propagation and Scattering Simulation," *To appear in Proc. ECLOUD'10, Cornell, Ithaca, NY, 2010 (slides)*.

[175] G. F. Dugan *et al.*, "CesrTA EC-induced beam dynamics," *To appear in Proc. ECLOUD'10, Cornell, Ithaca, NY, 2010 (slides)*.

[176] J. Flanagan *et al.*, "Measurement of low-emittance beam with coded aperture X ray optics at CesrTA," *Proc. IPAC'10, Kyoto, Japan, 2010, pp. 966-968 (MOPE007)*.

[177] J. W. Flanagan *et al.*, "xBSM bunch-by-bunch measurements in EC conditions at CesrTA," *To appear in Proc. ECLOUD'10, Cornell, Ithaca, NY, 2010 (slides)*.

[178] M. G. Billing *et al.*, "Dependence of beam instabilities caused by electron clouds at CesrTA due to variations in chromaticity, bunch current and train length," *Proc. IPAC'12, New Orleans, LA, 2012, pp. 3135-3137 (WEPPR087)*.

[179] G. Dugan *et al.*, "Studies at CesrTA of electron-cloud-induced beam dynamics for future damping rings," *Proc. IPAC'12, New Orleans, LA, 2012, pp. 2081-2083 (WEYA02)*.

[180] K. Ohmi *et al.*, "Electron instability in low emittance rings, CesrTA and SuperKEKB," *To appear in Proc. ECLOUD'10, Cornell, Ithaca, NY, 2010 (slides)*.

[181] M. T. F. Pivi *et al.*, "ILC damping ring electron cloud R&D effort and single-bunch instability simulations using CMAD," *To appear in Proc. ECLOUD'10, Cornell, Ithaca, NY, 2010 (slides)*.

[182] K.G. Sonnad *et al.*, "Simulation of Electron Cloud Induced Instabilities and Emittance Growth for CesrTA," *Proc. PAC 11, New York, NY, 2011, pp. 1683-1685 (WEP109)*.

[183] K. G. Sonnad *et al.*, "Simulation of electron cloud beam dynamics for CesrTA," *Proc. IPAC 2011, San Sebastian, Spain, 2011, pp. 808-810 (MOPS088)*.

[184] H. Jin *et al.*, Jap. J. Appl. Phys. **50** (2011) 026401, DOI: 10.1143/JJAP.50.026401.

[185] K. Ohmi, F. Zimmermann and E. Perevedentsev, Phys. Rev. E **65** (2002) 016502, DOI: 10.1103/PhysRevE.65.016502.

[186] M. T. F. Pivi *et al.*, "Secondary electron yield measurements and groove chambers update tests in the PEP-II beam line," *Proc. EPAC 08, Magazzini del Cotone, Italy, 2008, pp. 691–693 (MOPP064)*.

[187] M. T. F. Pivi *et al.*, "A new chicane experiment in PEP-II to test mitigations of the electron cloud effect for linear colliders," *Proc. EPAC 08, Magazzini del Cotone, Italy, 2008, pp. 688–690 (MOPP063)*.

[188] Y. Suetsugu *et al.*, "Experimental studies on grooved surfaces to suppress secondary electron emission," *Proc. IPAC'10, Kyoto, Japan, 2010, pp. 2021-2023 (TUPD043)*.

[189] Y. Suetsugu *et al.*, "Beam tests of a clearing electrode for electron cloud mitigation at KEKB positron ring," *Proc. IPAC'10, Kyoto, Japan, 2010, pp. 2369-2371 (WEOAMH01)*.

[190] D. Alesini *et al.*, "Design and test of the clearing electrodes for e^- cloud mitigation in the e^+ DAΦNE ring," *Proc. IPAC'10, Kyoto, Japan, 2010, pp. 1515-1517 (TUPEB002)*.

[191] D. Alesini *et al.*, "Experimental measurements of e-cloud mitigation using clearing electrodes in the DAΦNE collider," *Proc. IPAC'12, New Orleans, LA, 2012, pp. 1107-1109 (TUOBC03)*.

[192] M. T. F. Pivi *et al.*[ILC DR working group], "Recommendations for the ILC DR EC mitigations," *Presented at the International Workshop on Linear Colliders IWLC, Geneva, Switzerland, 18-22 Oct, 2010.* http://ilcagenda.linearcollider.org/materialDisplay.py?contribId=544&sessionId=83&materialId=slides&confId=4507.

[193] M. T. F. Pivi *et al.*, "Recommendation for mitigations of the electron cloud instability in the ILC," *Proc. IPAC 2011, San Sebastian, Spain, 2011, pp. 1063–1065 (TUPC030)*.

[194] Y. Suetsugu *et al.*, J. Vac. Sci. Tech. A **30** (2012) 031602, DOI: 10.1116/1.3696683.

[195] K. Kubo *et al.* [ATF Collaboration], Phys. Rev. Lett. **88** (2002) 194801, DOI: 10.1103/PhysRevLett.88.194801.

[196] Y. Honda *et al.*, Phys. Rev. Lett. **92** (2004) 054802, DOI: 10.1103/PhysRevLett.92.054802.

[197] V. Balakin *et al.*, Phys. Rev. Lett. **74** (1995) 2479-2482, DOI: 10.1103/PhysRevLett.74.2479.

[198] P. Raimondi and A. Seryi, Phys. Rev. Lett. **86** (2001) 3779, DOI: 10.1103/PhysRevLett.86.3779.

[199] B. I. Grishanov *et al.* [ATF2 Collaboration], "ATF2 Proposal," KEK-REPORT-2005-2, SLAC-R-771 (2005), DOI: 10.2172/878752.

[200] B. I. Grishanov *et al.*, "ATF2 proposal. Vol. 2," arXiv:physics/0606194 (2006), DOI: 10.2172/876758.

[201] Y. I. Kim *et al.*, Phys. Rev. ST Accel. Beams **15** (2012) 042801, DOI: 10.1103/PhysRevSTAB.15.042801.

[202] T. Shintake, Nucl. Instrum. Meth. A **311** (1992) 453-464, DOI: 10.1016/0168-9002(92)90641-G.

[203] T. Suehara *et al.*, Nucl. Instrum. Meth. A **616** (2010) 1-8, DOI: 10.1016/j.nima.2010.02.065.

[204] P. Bambade *et al.*, Phys. Rev. ST Accel. Beams **13** (2010) 042801, [arXiv:1207.1334 [physics.acc-ph]], DOI: 10.1103/PhysRevSTAB.13.042801.

[205] S. Bai *et al.*, Phys. Rev. ST Accel. Beams **13** (2010) 092804, DOI: 10.1103/PhysRevSTAB.13.092804.

[206] K. Hirata, "An Introduction to SAD," *Proc. 2nd Advanced ICFA Beam Dynamics Workshop on Aperture-Related Limitations of the Performance and Beam Lifetime in Storage Rings, Lugano, Switzerland, 1988, pp. 62-68,* CERN-88-04 (1988).

[207] H. Grote and F. C. Iselin, "The MAD program (methodical accelerator design) version 8.4: User's reference manual," CERN-SL-90-13-AP-REV.2 (1990).

[208] D. Schulte, "PLACET: A program to simulate drive beams," *Proc. EPAC 2000, Vienna, Austria, 2000, pp. 1402-1404 (TUP7B05)* [CERN-PS-2000-028-AE]. See also the PLACET home page at `https://savannah.cern.ch/projects/placet/`.

[209] Y. Inoue *et al.*, Phys. Rev. ST Accel. Beams **11** (2008) 062801, DOI: 10.1103/PhysRevSTAB.11.062801.

[210] T. Naito *et al.* Phys. Rev. ST Accel. Beams **14** (2011) 051002, DOI: 10.1103/PhysRevSTAB.14.051002.

[211] S. T. Boogert *et al.*, Phys. Rev. ST Accel. Beams **13** (2010) 122801, DOI: 10.1103/PhysRevSTAB.13.122801.

[212] G.B. Christian *et al.*, "Latest performance results from the FONT5 intra-train position and angle feedback system at ATF2," *Proc. IPAC 2011, San Sebastian, Spain, 2011, pp. 520-522 (MOPO017).*

[213] G. Alexander *et al.*, "Observation of polarized positrons from an undulator-based source," Phys. Rev. Lett. **100** (2008) 210801, DOI: 10.1103/PhysRevLett.100.210801.

[214] Polepalle Satyamurthy *et al.*, Nucl. Instrum. Meth. A **679** (2012) 67-81, DOI: 10.1016/j.nima.2012.01.075.

[215] P. A. Adderley, *et al.*, "CEBAF 200 kV inverted electron gun," *Proc. IPAC 2011, San Sebastian, Spain, 2011, pp. 1501-1503 (WEODS3)*.

[216] P. A. Adderley *et al.*, Phys. Rev. ST Accel. Beams **13** (2010) 010101, DOI: 10.1103/PhysRevSTAB.13.010101.

[217] M. BastaniNejad *et al.*, Phys. Rev. ST Accel. Beams **15** (2012) 083502, DOI: 10.1103/PhysRevSTAB.15.083502.

[218] Y. Ivanyushenkov *et al.*, *Proc. PAC 07, Albuquerque, NM, 2007, pp. 2865-2867 (THPMN071)*, DOI: 10.1109/PAC.2007.4440602.

[219] A. Mikhailichenko, "ILC undulator based positron source, tests and simulations," *Proc. PAC 07, Albuquerque, NM, 2007, pp. 1974-1976 (WEZAB01)*, DOI: 10.1109/PAC.2007.4441330.

[220] E. Baynham *et al.*, "The Development of a superconducting undulator for the ILC positron source," *Proc. PAC 09, Vancouver, BC, Canada, 2009, pp. 1839-1843 (WE2RAI01)*.

[221] J. A. Clarke, "ILC e^- and e^+ sources overview," *Talk at IWLC 2010, Geneva, Switzerland, 2010,* slides: http://ilcagenda.linearcollider.org/materialDisplay.py?contribId=462&sessionId=77&materialId=slides&confId=4507.

[222] W. Gai *et al.*, "Positron source parameters," 2012, EDMS ID: D00000000943695.

[223] G. Ellwood, "Task 6: short period Nb3Sn superconducting helical undulator," *Talk at EUCARD-WP7-HFM collaboration meeting, Geneva, Switzerland, Nov. 2010,* slides: http://indico.cern.ch/materialDisplay.py?contribId=6&materialId=slides&confId=109166.

[224] S. P. Antipov, W. Gai, W. Liu and L. K. Spentzouris, "Simulations of the rotating positron target in the presence of OMD field," *Proc. PAC 07, Albuquerque, NM, 2007, pp. 2909-2911 (THPMN087)*, DOI: 10.1109/PAC.2007.4440617.

[225] L. J. Jenner *et al.*, "A study of mechanical and magnetic issues for a prototype positron source target," *Proc. EPAC 08, Magazzini del Cotone, Italy, 2008, pp. 715-717 (MOPP072)*.

[226] A. Ushakov *et al.*, "Polarized positrons for the ILC - update on simulations," *Proc. POSIPOL'11, Beijing, China, 2011,* arXiv:1202.0752 [physics.acc-ph], DOI: 10.1142/9789814401043_0004.

[227] I. Bailey *et al.*, "Eddy current studies from the undulator-based positron source target wheel prototype," *Proc. IPAC'10, Kyoto, Japan, 2010, pp. 4125-4127 (THPEC033)*.

[228] I.R. Bailey, "Overview of undulator-based sources for LC," *Talk at IWLC 2010, Geneva, Switzerland, 2010,* slides: http://ilcagenda.linearcollider.org/materialDisplay.py?contribId=485&sessionId=83&materialId=slides&confId=4507.

[229] J. Gronberg *et al.*, "Design and Prototyping of the ILC baseline target system," *Talk at KILC'12, Daegu, Korea, 2012,* slides: http://ilcagenda.linearcollider.org/materialDisplay.py?contribId=184&sessionId=32&materialId=slides&confId=5414.

[230] F. Staufenbiel *et al.*, "Heat load and stress studies for an design of the photon collimator for the ILC positron source," *Proc. POSIPOL'11, Beijing, China, 2011,* arXiv:1202.5987 [physics.acc-ph], DOI: 10.1142/9789814401043_0007.

[231] W. Liu and W. Gai, "Update on the ILC positron source study at ANL," *Proc. IPAC'10, Kyoto, Japan, 2010, pp. 4134-4136 (THPEC036)*.

[232] W. Liu, W. Gai, "Update on ILC positron source study at ANL," *Proc. IPAC'12, New Orleans, LA, 2012, pp. 1906-1908 (TUPPR040)*.

[233] A. Ushakov *et al.*, "Production of highly polarized positron beams," *Proc. IPAC 2011, San Sebastian, Spain, 2011, pp. 997-999 (TUPC006)*.

[234] W. Liu, W. Gai, "Update on ILC positron source start-to-end simulation," *Proc. IPAC'12, New Orleans, LA, 2012, pp. 1909-1911 (TUPPR041)*.

[235] L. I. Malysheva *et al.*, "The Design of spin-rotator with a possibility of helicity switching for polarized positron at the ILC," *Proc. IPAC'12, New Orleans, LA, 2012, pp. 1813-1815 (TUPPR003)*.

[236] T. Omori *et al.*, Nucl. Instrum. Meth. A **672** (2012) 52-56 [arXiv:1110.1450 [physics.acc-ph]], DOI: 10.1016/j.nima.2011.12.032.

[237] M. Kuriki *et al.*, AIP Conf. Proc. **980** (2008) 92-101, DOI: 10.1063/1.2888124.

[238] J. Urakawa, "Results from DR and instrumentation test facilities," *Proc. PAC 05, Knoxville, TN, 2005, pp. 305 (TOPE003)*, DOI: 10.1109/PAC.2005.1590420.

[239] P. Karataev *et al.*, Phys. Rev. Lett. **93** (2004) 244802, DOI: 10.1103/PhysRevLett.93.244802.

[240] R. Bartolini, "Performance and trends of storage ring light sources," *Proc. EPAC 08, Magazzini del Cotone, Italy, 2008, pp. 993-997 (TUXM02)*.

[241] R. Bartolini, "Light sources trends and common design issues with low emittance rings," *Talk at the Workshop on Low Emittance Rings 2010 (LER10), CERN, 2010*, `http://indico.cern.ch/contributionDisplay.py?contribId=92&confId=74380`.

[242] M. Böge *et al.*, "The Swiss Light Source a test-bed for damping ring optimization," *Proc. IPAC'10, Kyoto, Japan, 2010, pp. 3560-3562 (WEPE091)*.

[243] R. T. Dowd *et al.*, "Emittance coupling control at the Australian Synchrotron," *Proc. PAC 09, Vancouver, BC, Canada, 2009, pp. 3708-3710 (TH6PFP008)*.

[244] G. Rehm, "Recent development of diagnostics on 3rd generation light sources," *Proc. EPAC 08, Magazzini del Cotone, Italy, 2008, pp. 1016-1020 (TUZM01)*.

[245] C. Thomas, G. Rehm, I. Martin and R. Bartolini, Phys. Rev. ST Accel. Beams **13** (2010) 022805, DOI: 10.1103/PhysRevSTAB.13.022805.

[246] Å. Andersson *et al.*, Nucl. Instrum. Meth. A **591** (2008) 437-446, DOI: 10.1016/j.nima.2008.02.095.

[247] T. Naito *et al.*, Nucl. Instrum. Meth. A **571** (2007) 599, DOI: 10.1016/j.nima.2006.11.062.

[248] T. Naito *et al.*, "Multi-bunch beam extraction using strip-line kicker at KEK-ATF," *Proc. IPAC'10, Kyoto, Japan, 2010, pp. 2386-2388 (WEOBMH02)*.

[249] D. Alesini, S. Guiducci, F. Marcellini and P. Raimondi, "Design and tests of new fast kickers for the DAFNE collider and the ILC damping rings," *Proc. EPAC 06, Edinburgh, Scotland, 2006, pp. 1502-1504 (TUPLS009)*.

[250] F. Marcellini, D. Alesini, S. Guiducci and P. Raimondi, "Tests and operational experience with the DAΦNE stripline injection kicker," *Proc. PAC 09, Vancouver, BC, Canada, 2009, pp. 1739-1741 (TU6RFP082)*

[251] F. Marcellini *et al.*, "Coupling impedance of DAΦNE upgraded vacuum chamber," *Proc. EPAC 08, Magazzini del Cotone, Italy, 2008, pp. 1661-1663 (TUPP051)*.

[252] T. Tang and C. Burkhart, IEEE Trans. Dielectrics Elect. Insul. **16** (2009) 967-970 [SLAC-PUB-13269], DOI: 10.1109/TDEI.2009.5211841.

[253] T. Tang and C. Burkhart, "Development of an adder-topology ILC damping ring kicker modulator," *Proc. PAC 09, Vancouver, BC, Canada, 2009, pp. 1015-1017 (TU6RFP091)*.

[254] T. Tang and C. Burkhart, "Improved Hybrid MOSFET/driver Switching Module for pulsed power applications," *Proc. 18th IEEE International Pulsed Power Conference, Chicago, IL, 2011, pp. 1365-1368,* DOI: 10.1109/PPC.2011.6191616.

[255] F. O. Arntz, M. P. J. Gaudreau, A. Kardo-Sysoev, M. K. Kempkes and A. Krasnykh, "A kicker driver exploiting drift step recovery diodes for the International Linear Collider," *Proc. EPAC 08, Magazzini del Cotone, Italy, 2008, pp. 589-591 (MOPP017)*.

[256] A. Benwell *et al.*, "A 5 kV, 3 MHz solid-state modulator based on the DSRD switch for an ultra-fast beam kicker," *Proc. International Power Modulator and High Voltage Conference, San Diego, CA, 2012.*

[257] K. Halbach, IEEE Trans. Nucl. Sci. **26** (1979) 3882-3884, DOI: 10.1109/TNS.1979.4330638.

[258] K. Halbach, Nucl. Instrum. Meth. **169** (1980) 1-10, DOI: 10.1016/0029-554X(80)90094-4.

[259] K. Halbach, Nucl. Instrum. Meth. **187** (1981) 109-117, DOI: 10.1016/0029-554X(81)90477-8.

[260] K. Halbach, Nucl. Instrum. Meth. **198** (1982) 213-215, DOI: 10.1016/0167-5087(82)90258-7.

[261] T. Sugimoto *et al.*, "Continuously adjustable permanent magnet quadrupole for a final focus," *Proc. EPAC 08, Magazzini del Cotone, Italy, 2008, pp. 583-585 (MOPP015)*.

[262] T. Sugimoto *et al.*, "Development of the continuously adjustable permanent magnet quadrupole for ATF2," *Proc. LINAC 08, Victoria, BC, 2008, pp. 524-526 (TUP054)*.

[263] Yoshihisa Iwashita *et al.*, "Permanent magnet final focus doublet R&D for ILC at ATF2," *Proc. PAC 09, Vancouver, BC, Canada, 2009, pp. 187-189 (MO6PFP024)*.

[264] Yoshihisa Iwashita, "Permanent magnet final quadrupole," *Talk at International Linear Collider Workshop - LCWS 2007/ILC 2007, DESY, 2007.* http://ilcagenda.linearcollider.org/contributionDisplay.py?contribId=130&sessionId=97&confId=1296.

[265] Shotaro Ushijima *et al.*, "Preparation of adjustable permanent magnet quadrupole lens for beam test at ATF2," *Proc. LINAC 10, Tsukuba, Japan, 2010, pp. 305-307 (MOP105)*.

[266] Yoshihisa Iwashita, "Permanent magnet option for 14mr IR," *Talk at ILC Interaction Region Engineering Design Workshop IRENG'07, SLAC, 2007.* http://ilcagenda.linearcollider.org/contributionDisplay.py?contribId=69&sessionId=8&confId=2169.

[267] R. Apsimon *et al.*, "Development of a fast micron-resolution beam position monitor signal processor for linear collider beam-based feedback systems," *Proc. PAC 09, Vancouver, BC, Canada, 2009, pp. 4126-4128 (TH6REP074)*.

[268] P. Burrows *et al.*, "Design of the ILC prototype FONT4 digital intra-train beam-based feedback system," *Proc. EPAC 06, Edinburgh, Scotland, 2006, pp. 849-851 (MOPLS122)*.

[269] P. N. Burrows *et al.*, "The FONT4 ILC intra-train beam-based digital feedback system prototype," *Proc. PAC 07, Albuquerque, NM, 2007, pp. 416-418 (MOPAN108)*, DOI: 10.1109/PAC.2007.4440230.

[270] Xilinx Inc., "Virtex-5 FPGA device family," http://www.xilinx.com/products/virtex5/index.htm.

[271] TMD Technologies, http://www.tmdtechnologies.co.uk.

[272] J. Resta-López *et al.*, "Study of transverse pulse-to-pulse orbit jitter at the KEK Accelerator Test Facility 2 (ATF2)," *Proc. IPAC'12, New Orleans, LA, 2012, pp. 936-938 (MOPPR066)*.

[273] Ove Arup & Partners Ltd., "Review of interaction region cavern layout design," 2012, EDMS ID: D00000000983825.

[274] M. Oriunno, "Recent developments in planning the push-pull," *Talk at ALCPG11, Eugene, OR, 2011,* http://ilcagenda.linearcollider.org/contributionDisplay.py?contribId=138&sessionId=1&confId=4572.

[275] G. White, "Ground motion + vibration transfer function for final QD0/SD0 cryomodule system at ILC," *Talk at ALCPG11, Eugene, OR, 2011,* http://ilcagenda.linearcollider.org/getFile.py/access?contribId=316&sessionId=20&resId=1&materialId=slides&confId=4572.

[276] C. Collette, "Simplified models of ILD and SiD detectors: Simulations and scaled test bench," *Talk at LCWS'12, Arlington, TX, 2012,* http://ilcagenda.linearcollider.org/getFile.py/access?contribId=113&sessionId=24&resId=1&materialId=slides&confId=5468.

[277] A. F. Fox-Murphy, D. F. Howell, R. B. Nickerson and A. R. Weidberg, Nucl. Instrum. Meth. A **383** (1996) 229-237, DOI: 10.1016/S0168-9002(96)00617-1.

[278] S.M. Gibson *et al.*, "A novel method for ATLAS FSI alignment based on rapid, direct phase monitoring," ATLAS Report INDET-PROC-2010-037, 2010.

[279] B. Parker *et al.*, "Functional requirements on the design of the detectors and the interaction region of an e^+e^- Linear Collider with a push-pull arrangement of detectors," *Proc. PAC 09, Vancouver, BC, Canada, 2009, pp. 2679-2681 (WE6PFP078)*. (long version: ILC-NOTE-2009-050 (2009), EDMS ID: D00000000951395).

[280] K. Riles, "Update on FSI R&D for sid final focus magnet alignment," *Talk at LCWS 2011, Granada, Spain, 2011,* http://ilcagenda.linearcollider.org/materialDisplay.py?contribId=115&sessionId=10&materialId=slides&confId=5134.

[281] H.-J. Yang, J. Deibel, S. Nyberg and K. Riles, Appl. Opt. **44** (2005) 3937-3944. [arXiv:physics/0409110], DOI: 10.1364/AO.44.003937.

[282] H. -J. Yang and K. Riles, Nucl. Instrum. Meth. A **575** (2007) 395-401 [arXiv:physics/0609187 [physics.ins-det]], DOI: 10.1016/j.nima.2007.02.101.

[283] Kiyoshi Kubo, "Simulation of low emittance transport in long straight line of ILC RTML," ILC-NOTE-2007-008, ILC-ASIA-2006-06A (2006).

[284] Kiyoshi Kubo, "Rough estimation of effects of fast-changing stray field in long transport of RTML," ILC-NOTE-2007-007, ILC-ASIA-2006-05 (2006).

[285] A. Latina, "ILC RTML overview," *Talk at IWLC 2010, Geneva, Switzerland 2010,* http://ilcagenda.linearcollider.org/materialDisplay.py?contribId=330&sessionId=77&materialId=slides&confId=4507.

[286] A. Lunin, I. Gonin, N. Solyak and V. Yakovlev, "Final results on RF and wake kicks caused by the couplers for the ILC cavity," *Proc. IPAC'10, Kyoto, Japan, 2010, pp. 3431-3433 (WEPE034)*.

[287] P. Eliasson *et al.*, "Study of an ILC main linac that follows the earth curvature," *Proc. EPAC 06, Edinburgh, Scotland, 2006, pp. 786-788 (MOPLS096)*.

[288] N. Walker, "Emittance preservation in a possible ILC main linac which follows the earth's curvature," EUROTEV-REPORT-2005-017 (2005).

[289] Kirti Ranjan, "Emittance preservation for the curved ILC main linac," *Proc. LINAC 06, Knoxville, TN, 2006, pp. 192-194 (MOP064)*.

[290] Kiyoshi Kubo, "Beam dynamics in curved ILC linacs," ILC-ASIA-2005-23 (2005).

[291] Kiyoshi Kubo, "Beam dynamics in curved ILC linacs – 2," ILC-ASIA-2005-25 (2005).

[292] P. Eliasson and D. Schulte, "Dispersion free steering and emittance tuning bumps in the ILC," EUROTEV-REPORT-2005-021 (2005).

[293] Kiyoshi Kubo, "Alignment tolerances from single-bunch effect," ILC-ASIA-2005-18 (2005).

[294] Kiyoshi Kubo, "Tolerances of misalignment of quads and cavities of ILC Main Linacs," ILC-ASIA-2005-17 (2005).

[295] R. Brinkmann *et al.* (eds.), "TESLA: The superconducting electron positron linear collider with an integrated X-ray laser laboratory. Technical design report. Pt. 2: The accelerator," DESY-01-011 (2001).

[296] R. M. Jones and R. H. Miller, "Mitigation of emittance dilution due to transverse mode coupling in the L-band linacs of the ILC," *Proc. EPAC 06, Edinburgh, Scotland, 2006, pp. 843-845 (MOPLS120)*.

[297] J. Frisch, T. O. Raubenheimer and P. Tenenbaum, "Sensitivity to nano-Tesla scale stray magnetic fields," SLAC-TN-04-041, DOI: 10.2172/827018.

[298] G. White, "BDS BBA, tuning and beam dynamics," Talk at LET Beam Dynamics Workshop, SLAC, 11-13 Dec. 2007, http://ilcagenda.linearcollider.org/materialDisplay.py?contribId=20&sessionId=11&materialId=slides&confId=2364.

[299] O. Napoly and D. Schulte, "Luminosity monitor options for TESLA," CERN-OPEN-2000-135 (2000). *Proc. Linac 98, Chicago, IL, 1998, pp. 82-84 (MO4016)*.

[300] G. White, N. Walker and D. Schulte, "Multi-bunch simulations of the ILC for luminosity performance studies," *Proc. PAC 05, Knoxville, TN, 2005, pp. 1368-1370 (RPPP014)*, DOI: 10.1109/PAC.2005.1590764.

[301] G. R. White, G. R. White, D. Schulte and N. J. Walker, "Design and simulation of the ILC intra-train orbit and luminosity feedback systems," *Proc. EPAC 06, Edinburgh, Scotland, 2006, pp. 3041-3043 (THPCH104)*.

[302] D. Schulte, "An Update on the banana effect," CERN-AB-2003-009-ABP, CLIC-NOTE-560 (2003).

[303] G. A. Loew *et al.* [International Linear Collider Technical Review Committee,] "Second report," SLAC-R-0606 (2003).

[304] D. Schulte, "Dynamic Simulations using PLACET," *Talk given at the European LC Workshop, Jan. 8-11, 2007, Daresbury, UK.* http://ilcagenda.linearcollider.org/materialDisplay.py?contribId=41&sessionId=22&materialId=slides&confId=1265

[305] A. Seryi, L. Hendrickson and G. White, "Issues of stability and ground motion in ILC," SLAC-PUB-11661 (2006).

[306] K. Kubo and K. Yokoya, "Some comments from beam dynamics," *Talk at GDE Baseline Technical Review, KEK, 2012,* http://ilcagenda.linearcollider.org/materialDisplay.py?contribId=2&sessionId=1&materialId=slides&confId=5444.

[307] T. Lackowski and T. Lundin (Hanson Professional Services Inc.), "ILC tunnel configuration study," 2010, EDMS ID: D00000000974935 (restricted access).

[308] Tom Lakowski and Hanson Engineering, " ILC Americas region TDR, vol. 1, chapter 1: Tunnel cross section configuration study," 2012, EDMS ID: D00000000990585.

[309] Black & Veach, "ILC constructability study review report," 2012, EDMS ID: D00000000990555.

[310] Holabird & Root, "Fermilab ILC programming study (KCS surface building design)," 2010, EDMS ID: D00000000975805

[311] Hughes Associates Inc., "Life safety / fire protection analysis for the InternationalLinear Collider, single deep or near surface tunnel options," 2010, EDMS ID: D00000000899675.

[312] National Fire Protection Association (NFPA), "520-2005 Standard for Subterranean Spaces".

[313] Hughes Associates, Inc., "Fire and egress analysis for the ILC," 2011, EDMS ID: D00000000980055.

[314] Emil Huedem, "ILC process water and air treatment VE cost evaluation," 2008, EDMS ID: D00000000899835.

[315] R. Wielgos and Parsons, "ILC Americas region TDR, vol. 1, chapter 3: Mechanical design and cost report," 2012, EDMS ID: D00000000979905.

[316] T. Lackowski and Parsons, "ILC Americas region TDR, vol. 1, chapter 2: Electrical design and cost report," 2012, EDMS ID: D00000000979935.

[317] AAA Technology Study Group and Facilities Working Group, "Investigating the single tunnel proposal in a Japanese mountainous site," 2010, EDMS ID: D00000000994455.

[318] J-Power, "Study on a construction project of underground structures for the ILC," 2010, EDMS ID: D00000000996045 (in Japanese, restricted) and EDMS ID: D00000000996085 (English version, restricted).

[319] J-Power, "Study on configuration plans of underground structures for the future accelerator," 2011, EDMS ID: D00000000996085 (in Japanese, restricted).

[320] J-Power, "Study on structures of a detector hall for the future accelerator," 2012, EDMS ID: D00000000996115 (in Japanese, restricted).

[321] Nikken-Sekkei "Electrical and mechanical design study," 2012, EDMS ID: D00000000996145 (in Japanese, restricted).

[322] Masami Tanaka, "Asian region fire safety for ILC single tunnel," 2009, EDMS ID: D00000000899575.

[323] W. Bialowons and J. A. Osborne, "Site Selection Criteria for European ILC Sites," ILC-Hi-Grade-Report-2010-003-1, 2010, EDMS ID: D00000000994535

[324] W. Bialowons and J. A. Osborne, "Siting Study for European ILC Sites," ILC-Hi-Grade-Report-2010-004-1, 2010, EDMS ID: D00000000994485.

[325] Yulian Budagov *et al.*, "Dubna site investigation," 2010, EDMS ID: D00000000928865

[326] A. V. Kurnaev *et al.*, "Report on the Results of the Preliminary Geological Engineering Surveys Along the Proposed Route of the International Linear Collider (ILC) in the Taldom Area of the Moscow Region," 2008, EDMS ID: D00000000994635.

[327] ARUP, "Linear Collider interaction region design studies. Review of interaction region cavern layout design," 2012, EDMS ID: D00000000983825.

[328] C. S. Waaijer, "Guidelines and criteria for an environmental impact assessment for the linear collider project at CERN," 2011, EDMS ID: D00000000996465.

[329] R. D. Heuer *et al.*, "Parameters for the Linear Collider," 2003, EDMS ID: D00000000948165

[330] R. D. Heuer *et al.*, "Parameters for the Linear Collider, Update November 20, 2006," 2006, EDMS ID: D00000000948205.

[331] European XFEL homepage, http://www.xfel.eu/.

[332] J. N. Corlett *et al.*, "Next generation light source R&D and design studies at LBNL," *Proc. IPAC'12, New Orleans, LA, 2012, pp. 1762-1764 (TUPPP070)*.

[333] S. Peggs *et al.*, "Conceptual design of the ESS-SCANDINAVIA," *Proc. PAC 09, Vancouver, BC, Canada, 2009, pp. 1485-1487 (TU6PFP083)*.

[334] S.Peggs (ed.) *et al.*, "ESS conceptual design report," ESS-2012-001, 2012, http://ess-scandinavia.eu/ess-documents/589-cdr.

[335] P. N. Ostroumov *et al.*, "PXIE: Project X Injector Experiment," *Proc. IPAC'12, New Orleans, LA, 2012, pp. 3874 (THPPP058)*.

[336] Z. Doležal, PoS HQL **2010** (2010) 079, http://pos.sissa.it/archive/conferences/128/079/HQL%202010_079.pdf.

[337] W. Wittmer *et al.*, "Status of the Super-B factory Design," arXiv:1110.2167 [physics.acc-ph] (2011).

[338] M.G. Billing, G.F. Dugan, M.A. Palmer and D.L. Rubin [CESRTA Collaboration], "An update on the CESR Test Accelerator research program," ICFA Beam Dyn. Newslett. **54** (2011) 32-47.

List of Signatories

The following list of signatories represents a comprehensive list of those people who have contributed to the R&D and design work, for both the accelerator and the detectors, which is summarised in this report. The list also includes those people who wish to indicate their support for the next phases of the worldwide ILC effort.

It should be noted that inclusion in this list does not indicate any formal commitment by the signatories. It does not indicate commitment to the specific detector designs presented, nor exclusive support for ILC over other collider programs.

A. Abada[171], T. Abe[24], T. Abe[236], J. M. Abernathy[379], H. Abramowicz[265], A. Abusleme[231], S. Aderhold[47], O. Adeyemi[333], E. Adli[357,251], C. Adloff[164], C. Adolphsen[251], K. Afanaciev[209], M. Aguilar[31], S. Ahmad[93], A. Ahmed[382], H. Aihara[375], R. Ainsworth[237,139], S. Airi[154], M. Aizatskyi[208], T. Akagi[73], M. Akemoto[71], A. Akeroyd[367], J. Alabau-Gonzalvo[108], C. Albajar[46], J. E. Albert[379], C. Albertus[281], J. Alcaraz Maestre[31], D. Alesini[174], B. Alessandro[128], G. Alexander[265], J. P. Alexander[43], A. Alhaidari[243], N. Alipour Tehrani[33], B. C. Allanach[323], O. Alonso[311], J. Alwall[210], J. W. Amann[251], Y. Amhis[167], M. S. Amjad[167], B. Ananthanarayan[83], A. Andreazza[386,122], N. Andreev[58], L. Andricek[186], M. Anduze[172], D. Angal-Kalinin[258], N. Anh Ky[106,394], K. A. Aniol[18], K. I. Aoki[148], M. Aoki[148], H. Aoyagi[137], S. Aoyama[250], S. J. Aplin[47], R. B. Appleby[343,40], J. Arafune[96], Y. Arai[71], S. Araki[71], L. Arazi[404], A. Arbey[50], D. Ariza[47], T. Arkan[58], N. D. Arnold[7], D. Arogancia[194], F. Arteche[113], A. Aryshev[71], S. Asai[375], T. Asaka[137], T. Asaka[212], E. Asakawa[220], M. Asano[333], F. B. Asiri[58], D. Asner[225], M. Asorey[286], D. Attié[21], J. E. Augustin[169], D. B. Augustine[58], C. S. Aulakh[226], E. Avetisyan[47], V. Ayvazyan[47], N. Azaryan[142], F. Azfar[358], T. Azuma[246], O. Bachynska[47], H. Baer[355], J. Bagger[141], A. Baghdasaryan[407], S. Bai[102], Y. Bai[384], I. Bailey[40,176], V. Balagura[172,107], R. D. Ball[329], C. Baltay[405], K. Bamba[198], P. S. Bambade[167], Y. Ban[9], E. Banas[268], H. Band[384], K. Bane[251], M. Barbi[362], V. Barger[384], B. Barish[17,65], T. Barklow[251], R. J. Barlow[392], M. Barone[58,65], I. Bars[368], S. Barsuk[167], P. Bartalini[210], R. Bartoldus[251], R. Bates[332], M. Battaglia[322,33], J. Baudot[94], M. Baylac[170], P. Bechtle[295], U. Becker[185,33], M. Beckmann[47], F. Bedeschi[126], C. F. Bedoya[31], S. Behari[58], O. Behnke[47], T. Behnke[47], G. Belanger[165], S. Belforte[129], I. Belikov[94], K. Belkadhi[172], A. Bellerive[19], C. Belver Aguilar[108], A. Belyaev[367,259], D. Benchekroun[184], M. Beneke[57], M. Benoit[33], A. Benot-Morell[33,108], S. Bentvelsen[213], L. Benucci[331], J. Berenguer[31], T. Bergauer[224], S. Berge[138], E. Berger[7], J. Berger[251], C. M. U. Berggren[47], Z. Bern[318], J. Bernabeu[108], N. Bernal[295], G. Bernardi[169], W. Bernreuther[235], M. Bertucci[119], M. Besancon[21], M. Bessner[47], A. Besson[94,306], D. R. Bett[358,140], A. J. Bevan[234], A. Bhardwaj[326], A. Bharucha[333], G. Bhattacharyya[241], B. Bhattacherjee[150], B. Bhuyan[86], M. E. Biagini[174], L. Bian[102], F. Bianchi[128], O. Biebel[182], T. R. Bieler[190], C. Biino[128], B. Bilki[7,337], S. S. Biswal[221], V. Blackmore[358,140], J. J. Blaising[164], N. Blaskovic Kraljevic[358,140], G. Blazey[217], I. Bloch[48], J. Bluemlein[48], B. Bobchenko[107], T. Boccali[126], J. R. Bogart[251], V. Boisvert[237], M. Bonesini[121], R. Boni[174], J. Bonnard[168], G. Bonneaud[169], S. T. Boogert[237,139], L. Boon[233,7],

G. Boorman[237,139], E. Boos[180], M. Boronat[108], K. Borras[47], L. Bortko[48], F. Borzumati[272], M. Bosman[294], A. Bosotti[119], F. J. Botella[108], S. Bou Habib[401], P. Boucaud[171], J. Boudagov[142], G. Boudoul[89], V. Boudry[172], D. Boumediene[168], C. Bourgeois[167], A. Boveia[52], A. Brachmann[251], J. Bracinik[315], J. Branlard[47,58], B. Brau[346], J. E. Brau[356], R. Breedon[320], M. Breidenbach[251], A. Breskin[404], S. Bressler[404], V. Breton[168], H. Breuker[33], C. Brezina[295], C. Briegel[58], J. C. Brient[172], T. M. Bristow[329], D. Britton[332], I. C. Brock[295], S. J. Brodsky[251], F. Broggi[119], G. Brooijmans[42], J. Brooke[316], E. Brost[356], T. E. Browder[334], E. Brücken[69], G. Buchalla[182], P. Buchholz[301], W. Buchmuller[47], P. Bueno[111], V. Buescher[138], K. Buesser[47], E. Bulyak[208], D. L. Burke[251], C. Burkhart[251], P. N. Burrows[358,140], G. Burt[40], E. Busato[168], L. Butkowski[47], S. Cabrera[108], E. Cabruja[32], M. Caccia[389,122], Y. Cai[251], S. S. Caiazza[47,333], O. Cakir[6], P. Calabria[89], C. Calancha[71], G. Calderini[169], A. Calderon Tazon[110], S. Callier[93], L. Calligaris[47], D. Calvet[168], E. Calvo Alamillo[31], A. Campbell[47], G. I. E. Cancelo[58], J. Cao[102], L. Caponetto[89], R. Carcagno[58], M. Cardaci[201], C. Carloganu[168], S. Caron[97,213], C. A. Carrillo Montoya[123], K. Carvalho Akiba[291], J. Carwardine[7], R. Casanova Mohr[311], M. V. Castillo Gimenez[108], N. Castro[175], A. Cattai[33], M. Cavalli-Sforza[294], D. G. Cerdeno[111], L. Cerrito[234], G. Chachamis[108], M. Chadeeva[107], J. S. Chai[260], D. Chakraborty[217], M. Champion[254], C. P. Chang[201], A. Chao[251], Y. Chao[210], J. Charles[28], M. Charles[358], B. E. Chase[58], U. Chattopadhyay[81], J. Chauveau[169], M. Chefdeville[164], R. Chehab[89], A. Chen[201], C. H. Chen[203], J. Chen[102], J. W. Chen[210], K. F. Chen[210], M. Chen[330,102], S. Chen[199], Y. Chen[1], Y. Chen[102], J. Cheng[102], T. P. Cheng[351], B. Cheon[66], M. Chera[47], Y. Chi[102], P. Chiappetta[28], M. Chiba[276], T. Chikamatsu[193], I. H. Chiu[210,210], G. C. Cho[220], V. Chobanova[186], J. B. Choi[36,36], K. Choi[157], S. Y. Choi[37], W. Choi[375,248], Y. I. Choi[260], S. Choroba[47], D. Choudhury[326], D. Chowdhury[83], G. Christian[358,140], M. Church[58], J. Chyla[105], W. Cichalewski[263,47], R. Cimino[174], D. Cinca[337], J. Clark[58], J. Clarke[258,40], G. Claus[94], E. Clement[316,259], C. Clerc[172], J. Cline[187], C. Coca[206], T. Cohen[251], P. Colas[21], A. Colijn[213], N. Colino[31], C. Collard[94], C. Colledani[94], N. Collomb[258], J. Collot[170], C. Combaret[89], B. Constance[33], C. A. Cooper[58], W. E. Cooper[58], G. Corcella[174], E. Cormier[29], R. Cornat[172], P. Cornebise[167], F. Cornet[281], G. Corrado[123], F. Corriveau[187], J. Cortes[286], E. Cortina Gil[303], S. Costa[308], F. Couchot[167], F. Couderc[21], L. Cousin[94], R. Cowan[185], W. Craddock[251], A. C. Crawford[58], J. A. Crittenden[43], J. Cuevas[283], D. Cuisy[167], F. Cullinan[237], B. Cure[33], E. Currás Rivera[110], D. Cussans[316], J. Cvach[105], M. Czakon[235], K. Czuba[401], H. Czyz[365], J. D'Hondt[399], W. Da Silva[169], O. Dadoun[167], M. Dahiya[327], J. Dai[102], C. Dallapiccola[346], C. Damerell[259], M. Danilov[107], D. Dannheim[33], N. Dascenzo[47,238], S. Dasu[384], A. K. Datta[67], T. S. Datta[115], P. Dauncey[80], T. Davenne[259], J. David[169], M. Davier[167], W. De Boer[90], S. De Cecco[169], S. De Curtis[120], N. De Groot[97,213], P. De Jong[213], S. De Jong[97,213], C. De La Taille[93], G. De Lentdecker[307], S. De Santis[177], J. B. De Vivie De Regie[167], A. Deandrea[89], P. P. Dechant[49], D. Decotigny[172], K. Dehmelt[257], J. P. Delahaye[251,33], N. Delerue[167], O. Delferriere[21], F. Deliot[21], G. Della Ricca[388], P. A. Delsart[170], M. Demarteau[7], D. Demin[142], R. Dermisek[87], F. Derue[169], K. Desch[295], S. Descotes-Genon[171], A. Deshpande[252], A. Dexter[40], A. Dey[81], S. Dhawan[405], N. Dhingra[226], V. Di Benedetto[58,123], B. Di Girolamo[33], M. A. Diaz[231], A. Dieguez[311], M. Diehl[47], R. Diener[47], S. Dildick[331], M. O. Dima[206], P. Dinaucourt[167,93], M. S. Dixit[19], T. Dixit[252], L. Dixon[251], A. Djouadi[171], S. Doebert[33], M. Dohlus[47], Z. Dolezal[34], H. Dong[102], L. Dong[102], A. Dorokhov[94], A. Dosil[112], A. Dovbnya[208], T. Doyle[332], G. Doziere[94], M. Dragicevic[224], A. Drago[174], A. J. Dragt[345], Z. Drasal[34], I. Dremin[179], V. Drugakov[209], J. Duarte Campderros[110], F. Duarte Ramos[33], A. Dubey[272], A. Dudarev[142], E. Dudas[171,171], L. Dudko[180], C. Duerig[47], G. Dugan[43], W. Dulinski[94], F. Dulucq[93], L. Dumitru[206], P. J. Dunne[80], A. Duperrin[27], M. Düren[147], D. Dzahini[170], H. Eberl[224], G. Eckerlin[47], P. Eckert[297], N. R. Eddy[58],

W. Ehrenfeld[295], G. Eigen[314], S. Eisenhardt[329], L. Eklund[332], L. Elementi[58], U. Ellwanger[171], E. Elsen[47], I. Emeliantchik[209], L. Emery[7], K. Enami[71], K. Endo[71], M. Endo[375], J. Engels[47], C. Englert[49], S. Eno[345], A. Enomoto[71], S. Enomoto[197], F. Eozenou[21], R. Erbacher[320], G. Eremeev[269], J. Erler[287], R. Escribano[294], D. Esperante Pereira[108], D. Espriu[311], E. Etzion[265,33], S. Eucker[47], A. Evdokimov[336,107], E. Ezura[71], B. Faatz[47], G. Faisel[201], L. Fano[125], A. Faraggi[340], A. Fasso[251], A. Faus-Golfe[108], L. Favart[307], N. Feege[257], J. L. Feng[321], T. Ferber[47], J. Ferguson[33], J. Fernández[283], P. Fernández Martínez[108], E. Fernandez[294,293], M. Fernandez Garcia[110], J. L. Fernandez-Hernando[130], P. Fernandez-Martinez[32], J. Fernandez-Melgarejo[33], A. Ferrer[108], F. Ferri[21], S. Fichet[117], T. Fifield[347], L. Filkov[179], F. Filthaut[97,213], A. Finch[176], H. E. Fisk[58], T. Fiutowski[2], H. Flaecher[316], J. W. Flanagan[71], I. Fleck[301], M. Fleischer[47], C. Fleta[32], J. Fleury[93], D. Flores[32], M. Foley[58], M. Fontannaz[171], K. Foraz[33], N. Fornengo[128], F. Forti[126,391], B. Foster[47,140], M. C. Fouz[31], P. H. Frampton[353], K. Francis[7], S. Frank[224], A. Freitas[361], A. Frey[64], R. Frey[356], M. Friedl[224], C. Friedrich[48], M. Frigerio[163], T. Frisson[167], M. Frotin[172], R. Frühwirth[224], R. Fuchi[378], E. Fuchs[47], K. Fujii[71], J. Fujimoto[71], H. Fuke[134], B. Fuks[94,33], M. Fukuda[71], S. Fukuda[71], K. Furukawa[71], T. Furuya[71], T. Fusayasu[195], J. Fuster[108], N. Fuster[108], Y. Fuwa[95,159], A. Gaddi[33], K. Gadow[47], F. Gaede[47], R. Gaglione[164], S. Galeotti[126], C. Gallagher[356], A. A. Gallas Torreira[112], L. Gallin-Martel[170], A. Gallo[174], D. Gamba[140,33], D. Gamba[128], J. Gao[102], Y. Gao[24], P. H. Garbincius[58], F. Garcia[69], C. Garcia Canal[288], J. E. Garcia Navarro[108], P. Garcia-Abia[31], J. J. Garcia-Garrigos[108], L. Garcia-Tabares[31], C. García[108], J. V. García Esteve[286], I. García García[108], S. K. Garg[408], L. Garrido[311], E. Garutti[333], T. Garvey[167,261], M. Gastal[33], F. Gastaldi[172], C. Gatto[58,123], N. Gaur[326], D. Gavela Pérez[31], P. Gay[168], M. B. Gay Ducati[109], L. Ge[251], R. Ge[102], A. Geiser[47], A. Gektin[100], A. Gellrich[47], M. H. Genest[170], R. L. Geng[269], S. Gentile[387,127], A. Gerbershagen[33,358], R. Gerig[7], S. German[111], H. Gerwig[33], S. Ghazaryan[47], P. Ghislain[169], D. K. Ghosh[81], S. Ghosh[115], S. Giagu[387,127], L. Gibbons[43], S. Gibson[139,33], V. Gilewsky[143], A. Gillespie[328], F. Gilman[20], B. Gimeno Martínez[108], D. M. Gingrich[312,279], C. M. Ginsburg[58], D. Girard[164], J. Giraud[170], G. F. Giudice[33], L. Gladilin[180], P. Gladkikh[208], C. J. Glasman[343,40], R. Glattauer[224], N. Glover[49], J. Gluza[365], K. Gnidzinska[263], R. Godbole[83], S. Godfrey[19], F. Goertz[54], M. Goffe[94], N. Gogitidze[179,47], J. Goldstein[316], B. Golob[144,341], G. Gomez[110], V. Goncalves[290], R. J. Gonsalves[256], I. González[283], S. González De La Hoz[108], F. J. González Sánchez[110], G. Gonzalez Parra[294], S. Gopalakrishna[103], I. Gorelov[352], D. Goswami[86], S. Goswami[229], T. Goto[71], K. Gotow[398], P. Göttlicher[47], M. Götze[385], A. Goudelis[165], P. Goudket[258], S. Gowdy[33], O. A. Grachov[309], N. A. Graf[251], M. Graham[251], A. Gramolin[15], R. Granier De Cassagnac[172], P. Grannis[257], P. Gras[21], M. Grecki[47], T. Greenshaw[339], D. Greenwood[181], C. Grefe[33], M. Grefe[111], I. M. Gregor[47], D. Grellscheid[49], G. Grenier[89], M. Grimes[316], C. Grimm[58], O. Grimm[53], B. Grinyov[100], B. Gripaios[323], K. Grizzard[141], A. Grohsjean[47], C. Grojean[294,33], J. Gronberg[178], D. Grondin[170], S. Groote[370], P. Gros[240], M. Grunewald[310], B. Grzadkowski[382], J. Gu[102], M. Guchait[262], S. Guiducci[174], E. Guliyev[172], J. Gunion[320], C. Günter[47], C. Gwilliam[339], N. Haba[75], H. Haber[322], M. Hachimine[197], Y. Haddad[172], L. Hagge[47], M. Hagihara[378], K. Hagiwara[71,158], J. Haley[216], G. Haller[251], J. Haller[333], K. Hamaguchi[375], R. Hamatsu[276], G. Hamel De Monchenault[21], L. L. Hammond[58], P. Hamnett[47], L. Han[364], T. Han[361], K. Hanagaki[223], J. D. Hansen[211], K. Hansen[47], P. H. Hansen[211], X. Q. Hao[70], K. Hara[71], K. Hara[378], T. Hara[71], D. Harada[83], K. Harada[161], K. Harder[259], T. Harion[297], R. V. Harlander[385], E. Harms[58], M. Harrison[13], O. Hartbrich[47,385], A. Hartin[47], T. Hartmann[300], J. Harz[47], S. Hasegawa[197], T. Hasegawa[71], Y. Hasegawa[248], M. Hashimoto[38], T. Hashimoto[62], C. Hast[251], S. Hatakeyama[135], J. M. Hauptman[118], M. Hauschild[33], M. Havranek[105], C. Hawkes[315], T. Hayakawa[197], H. Hayano[71], K. Hayasaka[198], M. Hazumi[71,253], H. J. He[24], C. Hearty[317,104], H. F. Heath[316],

T. Hebbeker[235], M. Heck[90], V. Hedberg[183], D. Hedin[217], S. M. Heindl[90], S. Heinemeyer[110], I. Heinze[47], A. Hektor[205], S. Henrot-Versille[167], O. Hensler[47], A. Heo[23], J. Herbert[258], G. Herdoiza[138], B. Hermberg[47], J. J. Hernández-Rey[108], M. J. Herrero[111], B. Herrmann[165], A. Hervé[384], J. Hewett[251], S. Hidalgo[32], B. Hidding[333,318], N. Higashi[375], N. Higashi[71], T. Higo[71], E. Higón Rodríguez[108], T. Higuchi[150], M. Hildreth[354], C. T. Hill[58], S. Hillert[295], S. Hillier[315], T. Himel[251], A. Himmi[94], S. Himori[272], Z. Hioki[374], B. Hippolyte[94], T. Hiraki[159], K. Hirano[136], S. Hirano[197], K. Hirata[71], T. Hirose[276], M. Hirsch[108], J. Hisano[197], P. M. Ho[210], A. Hoang[302], A. Hocker[58], A. Hoecker[33], M. Hoeferkamp[352], M. Hoffmann[47], W. Hollik[186], K. Homma[72], Y. Homma[154], S. Honda[378], T. Honda[71], Y. Honda[71], N. T. Hong Van[106], K. Honkavaara[47], T. Honma[71], T. Hori[236], T. Horiguchi[272], Y. Horii[197], A. Horio[196], R. Hosaka[377], Y. Hoshi[271], H. Hoshino[197], K. Hosoyama[71], J. Y. Hostachy[170], G. W. Hou[210], M. Hou[102], A. Hoummada[184], M. S. Hronek[58], T. Hu[102], C. Hu-Guo[94], M. Huang[24], T. Huang[102], E. Huedem[58], F. Hügging[295], J. L. Hugon[330], C. Hugonie[173], K. Huitu[335], P. Q. Hung[380], C. Hunt[80], U. Husemann[90], G. Hussain[24], D. Hutchcroft[339], Y. Hyakutake[79], J. C. Ianigro[89], L. E. Ibanez[111], M. Ibe[96], M. Idzik[2], H. Igarashi[78], Y. Igarashi[71], K. Igi[236], A. Ignatenko[209], O. Igonkina[213], T. Iijima[198,197], M. Iinuma[73], Y. Iiyama[20], H. Ikeda[134], K. Ikeda[71], K. Ikematsu[301], J. I. Illana[281], V. A. Ilyin[207,180], A. Imhof[333], T. Inagaki[236], T. Inagaki[197], K. Inami[197], S. Inayoshi[248], K. Inoue[161], A. Irles[108], S. Isagawa[71], N. Ishibashi[378], A. Ishida[375], K. Ishida[212], N. Ishihara[71], S. Ishihara[77], K. Ishii[71], A. Ishikawa[272], K. Ishikawa[375], K. I. Ishikawa[72], K. Ishikawa[75], T. Ishikawa[71], M. Ishitsuka[275], K. Ishiwata[17], G. Isidori[174], A. Ismail[251], S. Iso[71], T. Isogai[197], C. Issever[358], K. Itagaki[272], T. Itahashi[223], A. Ito[275], F. Ito[378], S. Ito[272], R. Itoh[71], E. Itou[71], M. I. Ivanyan[26], G. Iwai[71], S. Iwamoto[375], T. Iwamoto[116], H. Iwasaki[71], M. Iwasaki[71], Y. Iwashita[95], S. Iwata[71], S. Iwata[276], T. Izubuchi[13,236], Y. Izumiya[272], S. Jablonski[401], F. Jackson[258], J. A. Jacob[316], M. Jacquet[167], P. Jain[40], P. Jaiswal[59], W. Jalmuzna[263], E. Janas[401], R. Jaramillo Echeverría[110], J. Jaros[251], D. Jatkar[67], D. Jeans[375], R. Jedziniak[58], M. J. Jenkins[176,40], K. Jensch[47], C. P. Jessop[354], T. Jezynski[47], M. Jimbo[35], S. Jin[102], O. Jinnouchi[275], M. D. Joergensen[211], A. S. Johnson[251], S. Jolly[309], D. T. Jones[340], J. Jones[258,40], R. M. Jones[343,40], L. Jönsson[183], N. Joshi[237], C. K. Jung[257,150], N. Juntong[343,40], A. Juste[88,294], W. Kaabi[167], M. Kadastik[205], M. Kado[167,33], K. Kadota[197], E. Kajfasz[27], R. Kajikawa[197], Y. Kajiura[197], M. Kakizaki[377], E. Kako[71], H. Kakuhata[377], H. Kakuno[276], A. Kalinin[258], J. Kalinowski[382], G. E. Kalmus[259], K. Kamada[47], J. Kaminski[295], T. Kamitani[71], Y. Kamiya[116], Y. Kamiya[71], R. Kammering[47], T. Kamon[266], J. I. Kamoshita[60], T. Kanai[275], S. Kananov[265], K. Kanaya[378], M. Kaneda[33], T. Kaneko[71,253], S. Kanemura[377], K. Kaneta[75], W. Kang[102], D. Kanjilal[115], K. Kannike[205], F. Kapusta[169], D. Kar[332], P. Karataev[237,139], P. E. Karchin[403], D. Karlen[379,279], S. Karstensen[47], Y. Karyotakis[164], M. Kasemann[47], V. S. Kashikhin[58], S. Kashiwagi[273], A. Kataev[98], V. Katalev[48], Y. Kataoka[116], N. Katayama[150], R. Katayama[375], E. Kato[272], K. Kato[155], S. Kato[71], Y. Kato[153], T. Katoh[71], A. Kaukher[47], S. Kawabata[71], S. I. Kawada[73], K. Kawagoe[161], M. Kawai[71], T. Kawamoto[116], H. Kawamura[71], M. Kawamura[71], Y. Kawamura[248], S. Kawasaki[71], T. Kawasaki[212], H. Kay[47], S. Kazama[375], L. Keegan[111], J. Kehayias[150], L. Keller[251], M. A. Kemp[251], J. J. Kempster[237], C. Kenney[251], I. Kenyon[315], R. Kephart[58], J. Kerby[7], K. Kershaw[33], J. Kersten[333], K. Kezzar[151], V. G. Khachatryan[26], M. A. Khan[23], S. A. Khan[242], Y. Khoulaki[184], V. Khoze[49], H. Kichimi[71], R. Kieffer[33], C. Kiesling[186], M. Kikuchi[377], Y. Kikuta[71], M. Killenberg[47], C. S. Kim[408], D. W. Kim[63], D. Kim[23], E. J. Kim[36,36], E. S. Kim[23], G. Kim[23], H. S. Kim[23], H. D. Kim[245], J. Kim[63], S. H. Kim[378], S. K. Kim[245], S. G. Kim[87], Y. I. Kim[358,140], Y. Kimura[71], R. E. Kirby[251], F. Kircher[21], Y. Kishimoto[96], L. Kisslinger[20], T. Kitahara[375], R. Kitano[272], Y. Kiyo[146,71], C. Kleinwort[47], W. Klempt[33], P. M. Kluit[213], V. Klyukhin[180,33], M. Knecht[28], J. L. Kneur[163], B. A. Kniehl[333], K. Ko[251], P. Ko[158], D. Kobayashi[275], M. Kobayashi[71], N. Kobayashi[71],

T. Kobayashi[116], M. Koch[295], P. Kodys[34], U. Koetz[47], E. N. Koffeman[213], M. Kohda[210], S. Koike[71], Y. Kojima[71], K. Kolodziej[365], Y. Kolomensky[319,177], S. Komamiya[375], T. Kon[244], P. Konar[229], Y. Kondou[71], D. Kong[23], K. Kong[338], O. C. Kong[201], T. Konno[275,275], V. Korbel[47], J. G. Körner[138], S. Korpar[344,144], S. R. Koscielniak[279], D. Kostin[47], K. Kotera[248], W. Kotlarski[382], J. Kotula[268], E. Kou[167], V. Kovalenko[333], S. V. H. Kox[170], K. Koyama[75], M. Krämer[235], S. Kraml[170], M. Krammer[224], M. W. Krasny[169], F. Krauss[49], T. Krautscheid[295], M. Krawczyk[382], K. Krempetz[58], P. Križan[341,144], B. E. Krikler[80], A. Kronfeld[58], K. Kruchinin[237,139], D. Krücker[47], K. Krüger[47], B. Krupa[268], Y. P. Kuang[24], K. Kubo[71], T. Kubo[71], T. Kubota[347], T. Kubota[275], Y. Kubyshin[298,180], V. Kuchler[58], I. M. Kudla[202], D. Kuehn[47], J. H. Kuehn[92], C. Kuhn[94], S. Kulis[2], S. Kulkarni[170], A. Kumar[10], S. Kumar[86], T. Kumita[276], A. Kundu[16], Y. Kuno[223], C. M. Kuo[201], M. Kurachi[198], A. Kuramoto[253], M. Kurata[375], Y. Kurihara[71], M. Kuriki[73,71], T. Kurimoto[377], S. Kuroda[71], K. Kurokawa[71], S. I. Kurokawa[71], H. Kuwabara[276], M. Kuze[275], J. Kvasnicka[105], P. Kvasnicka[34], Y. Kwon[408], L. Labun[210], C. Lacasta[108], T. Lackowski[58], D. Lacour[169], V. Lacuesta[108], R. Lafaye[164], G. Lafferty[343], B. Laforge[169], I. Laktineh[89], R. L. Lander[320], K. Landsteiner[111], S. Laplace[169], K. J. Larsen[213], R. S. Larsen[251], T. Lastovicka[105], J. I. Latorre[311], S. Laurien[333], L. Lavergne[169], S. Lavignac[22], R. E. Laxdal[279], A. C. Le Bihan[94], F. R. Le Diberder[167], A. Le-Yaouanc[171], A. Lebedev[13], P. Lebrun[33], T. Lecompte[7], T. Leddig[300], F. Ledroit[170], B. Lee[25], K. Lee[158], M. Lee[177], S. H. Lee[260], S. W. Lee[267], Y. H. Lee[210], J. Leibfritz[58], K. Lekomtsev[71], L. Lellouch[28], M. Lemke[47], F. R. Lenkszus[7], A. Lenz[49,33], O. Leroy[27], C. Lester[323], L. Levchuk[208], J. Leveque[164], E. Levichev[15], A. Levy[265], I. Levy[265], J. R. Lewandowski[251], B. Li[24], C. Li[364], C. Li[102], D. Li[102], H. Li[380], L. Li[195], L. Li[247], L. Li[364], S. Li[102], W. Li[102], X. Li[102], Y. Li[24], Y. Li[24], Y. Li[24], Z. Li[251], Z. Li[102], J. J. Liau[210], V. Libov[47], L. Lilje[47], J. G. Lima[217], C. J. D. Lin[204], C. M. Lin[154], C. Y. Lin[201], H. Lin[102], H. H. Lin[210], F. L. Linde[213], R. A. Lineros[108], L. Linssen[33], R. Lipton[58], M. Lisovyi[47], B. List[47], J. List[47], B. Liu[24], J. Liu[364], R. Liu[102], S. Liu[167], S. Liu[247], W. Liu[7], Y. Liu[102], Y. Liu[337,58], Z. Liu[361], Z. Liu[102], Z. Liu[102], A. Lleres[170], N. S. Lockyer[279,317], W. Lohmann[48,12], E. Lohrmann[333], T. Lohse[76], F. Long[102], D. Lontkovskyi[47], M. A. Lopez Virto[110], X. Lou[102,372], A. Lounis[167], M. Lozano Fantoba[32], J. Lozano-Bahilo[281], C. Lu[232], R. S. Lu[210], S. Lu[47], A. Lucotte[170], F. Ludwig[47], S. Lukic[396], O. Lukina[180], N. Lumb[89], B. Lundberg[183], A. Lunin[58], M. Lupberger[295], B. Lutz[47], P. Lutz[21], T. Lux[294], K. Lv[102], M. Lyablin[142], A. Lyapin[237,139], J. Lykken[58], A. T. Lytle[262], L. Ma[258], Q. Ma[102], R. Ma[312], X. Ma[102], F. Machefert[167], N. Machida[377], J. Maeda[276], Y. Maeda[159], K. Maeshima[58], F. Magniette[172], N. Mahajan[229], F. Mahmoudi[168,33], S. H. Mai[201], C. Maiano[119], H. Mainaud Durand[33], S. Majewski[356], S. K. Majhi[81], N. Majumdar[241], G. Majumder[262], I. Makarenko[47], V. Makarenko[209], A. Maki[71], Y. Makida[71], D. Makowski[263], B. Malaescu[169], J. Malcles[21], U. Mallik[337], S. Malvezzi[121], O. B. Malyshev[258,40], Y. Mambrini[171], A. Manabe[71], G. Mancinelli[27], S. K. Mandal[150], S. Mandry[309,186], S. Manen[168], R. Mankel[47], S. Manly[363], S. Mannai[303], Y. Maravin[149], G. Marchiori[169], M. Marcisovsky[105,45], J. Marco[110], D. Marfatia[338], J. Marin[31], E. Marin Lacoma[251], C. Marinas[295], T. W. Markiewicz[251], O. Markin[107], J. Marshall[323], S. Martí-García[108], A. D. Martin[49], V. J. Martin[329], G. Martin-Chassard[93], T. Martinez De Alvaro[31], C. Martinez Rivero[110], F. Martinez-Vidal[108], H. U. Martyn[235,47], T. Maruyama[251], A. Masaike[159], T. Mashimo[116], T. Masubuchi[116], T. Masuda[159], M. Masuzawa[71], Z. Mateusz[401], A. Matheisen[47], H. Mathez[89], J. Matias[293], H. Matis[177], T. Matsubara[276], T. Matsuda[71], T. Matsui[377], S. Matsumoto[161], S. Matsumoto[150], Y. Matsumoto[220], H. Matsunaga[71], T. Matsushita[154], T. S. Mattison[317], V. A. Matveev[142], U. Mavric[47], G. Mavromanolakis[33], K. Mawatari[399], S. J. Maxfield[339], K. Mazumdar[262], A. Mazzacane[58,123], R. L. Mccarthy[257], D. J. Mccormick[251], J. Mccormick[251], K. T. Mcdonald[232], R. Mcduffee[324], P. Mcintosh[258], B. Mckee[251], M. Medinnis[47], S. Mehlhase[211], T. Mehrling[47,333],

A. Mehta[339], B. Mele[127], R. E. Meller[43], I. A. Melzer-Pellmann[47], L. Men[102], G. Mendiratta[83], Z. Meng[316], M. H. Merk[213,400], M. Merkin[180], A. Merlos[32], L. Merminga[279], A. B. Meyer[47], A. Meyer[235], N. Meyners[47], Z. Mi[102], P. Michelato[119], S. Michizono[71], S. Mihara[71], A. Mikhailichenko[43], D. J. Miller[309], C. Milstene[403], Y. Mimura[210], D. Minic[398], L. Mirabito[89], S. Mishima[387], T. Misumi[13], W. A. Mitaroff[224], T. Mitsuhashi[71], S. Mitsuru[71], K. Miuchi[154], K. Miyabayashi[200], A. Miyamoto[71], H. Miyata[212], Y. Miyazaki[161], T. Miyoshi[71], R. Mizuk[107], K. Mizuno[3], U. Mjörnmark[183], J. Mnich[47], G. Moeller[47], W. D. Moeller[47], K. Moenig[48], K. C. Moffeit[251], P. Mohanmurthy[269], G. Mohanty[262], L. Monaco[119], S. Mondal[81], C. Monini[170], H. Monjushiro[71], G. Montagna[359,124], S. Monteil[168], G. Montoro[298], I. Montvay[47], F. Moortgat[53], G. Moortgat-Pick[333,47], P. Mora De Freitas[172], C. Mora Herrera[30], G. Moreau[171], F. Morel[94], A. Morelos-Pineda[280], M. Moreno Llacer[108], S. Moretti[367,259], V. Morgunov[47,107], T. Mori[71], T. Mori[272], T. Mori[116], Y. Morita[71], S. Moriyama[96,150], L. Moroni[121], Y. Morozumi[71], H. G. Moser[186], A. Moszczynski[268], K. Motohashi[275], T. Moulik[249], G. Moultaka[163], D. Moya Martin[110], S. K. Mtingwa[215], G. S. Muanza[27], M. Mühlleitner[91], A. Mukherjee[85], S. Mukhopadhyay[241], M. Mulders[33], D. Muller[251], F. Müller[47], T. Müller[90], V. S. Mummidi[83], A. Münnich[47], C. Munoz[111], F. J. Muñoz Sánchez[110], H. Murayama[375,319], R. Murphy[7], G. Musat[172], A. Mussgiller[47], R. Muto[71], T. Nabeshima[377], K. Nagai[71], K. Nagai[378], S. Nagaitsev[58], T. Nagamine[272], K. Nagano[71], K. Nagao[71], Y. Nagashima[223], S. C. Nahn[185], P. Naik[316], D. Naito[159], T. Naito[71], H. Nakai[71], K. Nakai[71,223], Y. Nakai[161], Y. Nakajima[177], E. Nakamura[71], H. Nakamura[71], I. Nakamura[71], S. Nakamura[159], S. Nakamura[71], T. Nakamura[116], K. Nakanishi[71], E. Nakano[222], H. Nakano[212], H. Nakano[272], Y. Namito[71], W. Namkung[230], H. Nanjo[159], C. D. Nantista[251], O. Napoly[21], Y. Nara[4], T. Narazaki[272], S. Narita[131], U. Nauenberg[324], T. Naumann[48], S. Naumann-Emme[47], J. Navarro[108], A. Navitski[47], H. Neal[251], K. Negishi[272], K. Neichi[270], C. A. Nelson[255], T. K. Nelson[251], S. Nemecek[105], M. Neubert[138], R. Neuhaus[218], L. J. Nevay[237], D. M. Newbold[316,259], O. Nezhevenko[58], F. Nguyen[175], M. Nguyen[172], M. N. Nguyen[251], T. T. Nguyen[106], R. B. Nickerson[358], O. Nicrosini[124], C. Niebuhr[47], J. Niehoff[58], M. Niemack[43], U. Nierste[92], H. Niinomi[159], I. Nikolic[169], H. P. Nilles[295], S. Nishida[71], H. Nishiguchi[71], K. Nishiwaki[67], O. Nitoh[277], L. Niu[24], R. Noble[251], M. Noji[71], M. Nojiri[71,150], S. Nojiri[197,198], D. Nölle[47], A. Nomerotski[358], M. Nomura[135], T. Nomura[201], Y. Nomura[319,177], C. Nonaka[198], J. Noonan[7], E. Norbeck[337], Y. Nosochkov[251], D. Notz[47], O. Novgorodova[48,12], A. Novokhatski[251], J. A. Nowak[349], M. Nozaki[71], K. Ocalan[192], J. Ocariz[169], S. Oda[161], A. Ogata[71], T. Ogawa[248], T. Ogura[248], A. Oh[343], S. K. Oh[156], Y. Oh[23], K. Ohkuma[61], T. Ohl[145], Y. Ohnishi[71], K. Ohta[189], M. Ohta[71,253], S. Ohta[71,253], N. Ohuchi[71], K. Oishi[161], R. Okada[71], Y. Okada[71,253], T. Okamura[71], H. Okawa[13], T. Okugi[71], T. Okui[59], K. I. Okumura[161], Y. Okumura[52,58], L. Okun[107], H. Okuno[236], C. Oleari[390], C. Oliver[31], B. Olivier[186], S. L. Olsen[245], M. Omet[253,71], T. Omori[71], Y. Onel[337], H. Ono[214], Y. Ono[272], D. Onoprienko[251], Y. Onuki[116,150], P. Onyisi[371], T. Oogoe[71], Y. Ookouchi[159], W. Ootani[116], M. Oreglia[52], M. Oriunno[251], M. C. Orlandea[206], J. Orloff[168], M. Oroku[375,71], R. S. Orr[376], J. Osborne[33], A. Oskarsson[183], P. Osland[314], A. Osorio Oliveros[282], L. Österman[183], H. Otono[223], M. Owen[343], Y. Oyama[71], A. Oyanguren[108], K. Ozawa[71,375], J. P. Ozelis[58,191], D. Ozerov[47], G. Pásztor[304,99], H. Padamsee[43], C. Padilla[294], C. Pagani[119,386], R. Page[316], R. Pain[169], S. Paktinat Mehdiabadi[101], A. D. Palczewski[269], S. Palestini[33], F. Palla[126], M. Palmer[58], F. Palomo Pinto[285], W. Pan[102], G. Pancheri[174], M. Pandurovic[396], O. Panella[125], A. Pankov[227], Y. Papaphilippou[33], R. Paparella[119], A. Paramonov[7], E. K. Park[75], H. Park[23], S. I. Park[23], S. Park[260], S. Park[373], W. Park[23], A. Parker[323], B. Parker[13], C. Parkes[343], V. Parma[33], Z. Parsa[13], R. Partridge[251], S. Pastor[108], E. Paterson[251], M. Patra[83], J. R. Patterson[43], M. Paulini[20], N. Paver[129], S. Pavy-Bernard[167],

B. Pawlik[268], A. Pérez Vega-Leal[285], B. Pearson[355], J. S. Pedersen[211], A. Pedicini[397], S. Pedraza López[108], G. Pei[102], S. Pei[102], G. Pellegrini[32], A. Pellegrino[213], S. Penaranda[286], H. Peng[364], X. Peng[102], M. Perelstein[43], E. Perez[112], M. A. Perez-Garcia[284,114], M. Perez-Victoria[281], S. Peris[293], D. Perret-Gallix[164], H. Perrey[47], T. M. Perry[384], M. E. Peskin[251], P. Petagna[33], R. Y. Peters[64,47], T. C. Petersen[211], D. P. Peterson[43], T. Peterson[58], E. Petrakou[210], A. A. Petrov[403], A. Petrukhin[89,107], S. Pfeiffer[47], H. Pham[94], K. H. Phan[395,71], N. Phinney[251], F. Piccinini[124], A. Pich[108], R. Pichai[85], J. Piedra[283], J. Piekarski[401], A. Pierce[348], P. Pierini[119], N. Pietsch[333,47], A. Pineda[293], J. Pinfold[312,152], A. Piotrowski[263], Y. Pischalnikov[58], R. Pittau[281], M. Pivi[251], W. Placzek[132], T. Plehn[296], M. A. Pleier[13], M. Poelker[269], L. Poggioli[167], I. Pogorelsky[13], V. Poireau[164], M. E. Pol[30], I. Polak[105], F. Polci[169], M. Polikarpov[107], T. Poll[316,259], M. W. Poole[258,40], W. Porod[145], F. C. Porter[17], S. Porto[333], J. Portolés[108], R. Pöschl[167], S. Poss[33], C. T. Potter[356], P. Poulose[86], K. T. Pozniak[401], V. Prahl[47], R. Prepost[384], C. Prescott[251], D. Price[87], T. Price[315], P. S. Prieto[58], D. Protopopescu[332], D. Przyborowski[2], K. Przygoda[263], H. Przysiezniak[164], F. Ptochos[325], J. Puerta-Pelayo[31], C. Pulvermacher[90], M. Purohit[366], Q. Qin[102], F. Qiu[102], H. Qu[102], A. Quadt[64], G. Quast[90], D. Quirion[32], M. Quiros[88], J. Rademacker[316], R. Rahmat[350], S. Rai[67], M. Raidal[205], S. Rakshit[84], M. Ramilli[333], F. Rarbi[170], P. Ratoff[176], T. Raubenheimer[251], M. Rauch[91], L. Raux[93], G. Raven[400,213], P. Razis[325], V. Re[124], S. Redford[33], C. E. Reece[269], I. Reichel[177], A. Reichold[358,140], P. Reimer[105], M. Reinecke[47], A. Rekalo[100], J. Repond[7], J. Resta-Lopez[108], J. Reuter[47], J. T. Rhee[156], P. M. Ribeiro Cipriano[47], A. Ribon[33], G. Ricciardi[292,123], F. Richard[167], E. Richter-Was[132], G. Riddone[33], S. Riemann[48], T. Riemann[48], M. Rijssenbeek[257], K. Riles[348], C. Rimbault[167], R. Rimmer[269], S. D. Rindani[229], A. Ringwald[47], L. Rinolfi[33], I. Ripp-Baudot[94], I. Riu[294], T. G. Rizzo[251], P. Robbe[167], J. Roberts[140,33], A. Robson[332], G. Rodrigo[108], P. Rodriguez[251], P. Rodriguez Perez[112], K. Rolbiecki[111], P. Roloff[33], R. S. Romaniuk[401], E. Romero Adam[108], A. Ronzhin[58], L. Roos[169], E. Ros[108], A. Rosca[47], C. Rosemann[47], J. Rosiek[382], M. C. Ross[251], R. Rossmanith[90], S. Roth[235], J. Rouënè[167], A. Rowe[58], P. Rowson[251], A. Roy[115], L. Royer[168], P. Royole-Degieux[93], C. Royon[21], A. Rozanov[27], M. Ruan[172], D. L. Rubin[43], I. Rubinskiy[47], R. Rückl[145], R. Ruiz[361], R. Ruiz De Austri[108], P. Ruiz Valls[108], P. Ruiz-Femenía[108], A. Ruiz-Jimeno[110], R. Ruland[251], V. Rusinov[107], J. J. Russell[251], I. Rutkowski[401], V. Rybnikov[47], A. Ryd[43], A. Sabio Vera[111], B. Sabirov[142], J. J. Saborido Silva[112], H. F. W. Sadrozinski[322], T. Saeki[71], B. Safarzadeh[101], P. Saha[305], H. Sahoo[7], A. Sailer[33], N. Saito[71], T. Saito[272], T. Sakaguchi[13], H. Sakai[71], K. Sakai[71], K. Sakaue[402], K. Sakurai[47], R. Salerno[172], J. Salfeld-Nebgen[47], J. Salt[108], L. Sanchez[31], M. A. Sanchis Lozano[108], J. Sandweiss[405], A. Santa[377], A. Santagata[286], A. Santamaria[108], P. Santorelli[292], T. Sanuki[272], A. A. Sapronov[142], M. Sasaki[96], H. Sato[248], N. Sato[71], Y. Sato[272], M. Satoh[71], E. Sauvan[164], V. Saveliev[238,47], A. Savoy-Navarro[166,126], M. Sawabe[71], R. Sawada[116], H. Sawamura[402], L. Sawyer[181], O. Schäfer[300,47], R. Schäfer[47], J. Schaffran[47], T. Schalk[322,251], R. D. Schamberger[257], J. Scheirich[34], G. Schierholz[47], F. P. Schilling[90], F. Schirra[89], F. Schlander[47], H. Schlarb[47], D. Schlatter[33], P. Schleper[333], J. L. Schlereth[7], R. D. Schlueter[177], C. Schmidt[47], U. Schneekloth[47], S. Schnetzer[239], T. Schoerner-Sadenius[47], M. Schram[225], H. J. Schreiber[48], S. Schreiber[47], K. P. Schüler[47], D. Schulte[33], H. C. Schultz-Coulon[297], M. Schumacher[5], S. Schumann[64], B. A. Schumm[322], M. H. Schune[167], S. Schuwalow[333,48], C. Schwanda[224], C. Schwanenberger[343], F. Schwartzkopff[295], D. J. Scott[258,58], F. Sefkow[47,33], A. Segui[286], N. Seguin-Moreau[93], S. Seidel[352], Y. Seiya[222], J. Sekaric[338], K. Seki[197], S. Sekmen[33], S. Seletskiy[13], S. Sen[337], E. Senaha[158], K. Senyo[406], S. Senyukov[94], I. Serenkova[227], D. A. Sergatskov[58], H. Sert[47,333], D. Sertore[119], A. Seryi[358,140], O. Seto[74], R. Settles[186], P. Sha[102], S. Shahid[301], A. Sharma[33], G. Shelkov[142], W. Shen[297], J. C. Sheppard[251], M. Sher[41], C. Shi[102], H. Shi[102], T. Shidara[71], W. Shields[237,139], M. Shimada[71], H. Shimizu[71], Y. Shimizu[272],

M. Shimojima[195], S. Shimojima[276], T. Shindou[155], N. Shinoda[272], Y. Shinzaki[272], M. Shioden[78,71], I. Shipsey[233], S. Shirabe[161], M. J. Shirakata[71], T. Shirakata[71], G. Shirkov[142], T. Shishido[71], T. Shishido[71], J. G. Shiu[210], R. Shivpuri[326], R. Shrock[257], T. Shuji[71], N. Shumeiko[209], B. Shuve[228,188], P. Sicho[105], A. M. Siddiqui[133], P. Sievers[33], D. Sikora[401], D. A. Sil[86], F. Simon[186], N. B. Sinev[356], W. Singer[47], X. Singer[47], B. K. Singh[10], R. K. Singh[82], N. Sinha[103], R. Sinha[103], K. Sinram[47], T. Sinthuprasith[14], P. Skubic[355], R. Sliwa[167], I. Smiljanic[396], J. R. Smith[373,7], J. C. Smith[251,43], S. R. Smith[251], J. Smolík[105,45], J. Snuverink[237,139], B. Sobloher[47], J. Sola[311], C. Soldner[186,57], S. Soldner-Rembold[343], D. Son[23], H. S. Song[260], N. Sonmez[51], A. Sopczak[44], D. E. Soper[356], P. Spagnolo[126], S. Spannagel[47], M. Spannowsky[49], A. Sparkes[329], C. M. Spencer[251], H. Spiesberger[138], M. Spira[261], M. Stahlhofen[47], M. Stanescu-Bellu[48], M. Stanitzki[47], S. Stapnes[33], P. Starovoitov[209], F. Staufenbiel[48], L. Steder[47], M. Steder[47], A. Steen[89], G. Steinbrueck[333], M. Steinhauser[92], F. Stephan[48], W. Stephen[237], S. Stevenson[358], I. Stewart[185], D. Stöckinger[264], H. Stoeck[369], M. Strauss[355], S. Striganov[58], D. M. Strom[356], R. Stromhagen[47], J. Strube[33], A. Strumia[205], G. Stupakov[251], N. Styles[47], D. Su[251], F. Su[102], S. Su[313], J. Suarez Gonzalez[209], Y. Sudo[161], T. Suehara[116], F. Suekane[274], Y. Suetsugu[71], R. Sugahara[71], A. Sugamoto[220], H. Sugawara[71], Y. Sugimoto[71], A. Sugiyama[240], H. Sugiyama[377], M. K. Sullivan[251], Y. Sumino[272], T. Sumiyoshi[276,71], H. Sun[102], M. Sun[20], X. Sun[170], Y. Sun[102], Y. Susaki[197], T. Suwada[71], A. Suzuki[71], S. Suzuki[240], Y. Suzuki[71], Y. Suzuki[73], Z. Suzuki[272], K. Swientek[2], C. Swinson[13], Z. M. Szalata[251], B. Szczepanski[47], M. Szelezniak[94], J. Szewinski[202], A. Sznajder[289], L. Szymanowski[202], H. Tabassam[329], K. Tackmann[47], M. Taira[71], H. Tajima[197,251], F. Takahashi[272], R. Takahashi[71], R. Takahashi[75], T. Takahashi[73], Y. Takahashi[197], K. Takata[71], F. Takayama[160], Y. Takayasu[75], H. Takeda[154], S. Takeda[71], T. Takeshita[248], A. Taketani[236], Y. Takeuchi[378], T. Takimi[262], Y. Takubo[71], Y. Tamashevich[47], M. Tamsett[181], M. Tanabashi[198,197], T. Tanabe[116], G. Tanaka[161], M. M. Tanaka[71], M. Tanaka[223], R. Tanaka[73], H. Taniuchi[377], S. Tapprogge[138], E. Tarkovsky[107], M. A. Tartaglia[58], X. R. Tata[334], T. Tauchi[71], M. Tawada[71], G. Taylor[347], A. M. Teixeira[168], V. I. Telnov[15,219], P. Tenenbaum[251], E. Teodorescu[206], S. Terada[71], Y. Teramoto[222], H. Terao[200], A. Terashima[71], S. Terui[71], N. Terunuma[71], M. Terwort[47], M. Tesar[186], F. Teubert[33], T. Teubner[340], R. Teuscher[376], T. Theveneaux-Pelzer[168], D. Thienpont[93,172], J. Thom-Levy[43], M. Thomson[323], J. Tian[71], X. Tian[366], M. Tigner[43], J. Timmermans[213], V. Tisserand[164], M. Titov[21], S. Tjampens[164], K. Tobe[197], K. Tobioka[150,319], K. Toda[278], M. Toda[71], N. Toge[71], J. Tojo[161], K. Tokushuku[71], T. Toma[49], R. Tomas[33], T. Tomita[161], A. Tomiya[223], M. Tomoto[197,198], K. Toms[352], M. Tonini[47], F. Toral[31], E. Torrence[356], E. Torrente-Lujan[33], N. Toumbas[325], C. Touramanis[339], F. Toyoda[161], K. Toyomura[71], G. Trahern[55], T. H. Tran[172], W. Treberspurg[224], J. Trenado[311], M. Trimpl[58], S. Trincaz-Duvoid[169], M. Tripathi[320], W. Trischuk[376], M. Trodden[360], G. Trubnikov[142], H. C. Tsai[39], J. F. Tsai[210], K. H. Tsao[336], R. Tschirhart[58], E. Tsedenbaljir[210], S. Y. Tseng[201], T. Tsuboyama[71], A. Tsuchiya[250], K. Tsuchiya[71], T. Tsukamoto[71], K. Tsumura[197], S. Tsuno[71], T. Tsurugai[189], T. Tsuyuki[96], B. Tuchming[21], P. V. Tyagi[68,254], I. Tyapkin[142], M. Tytgat[331], K. Uchida[295], F. Uchiyama[71], Y. Uchiyama[116], S. Uehara[71], H. Ueno[161], K. Ueno[71], K. Ueno[71], K. Ueshima[274], Y. Uesugi[73], N. Ujiie[71], F. Ukegawa[378], N. Ukita[378], M. Ullán[32], H. Umeeda[72], K. Umemori[71], Y. Unno[66], S. Uozumi[23], J. Urakawa[71], A. M. Uranga[111], J. Urresti[32], A. Ushakov[333], I. Ushiki[272], Y. Ushiroda[71], A. V[83], P. Vázquez Regueiro[112], L. Vacavant[27], G. Valencia[118], L. Valery[168], I. Valin[94], J. W. Valle[108], C. Vallee[27], N. Van Bakel[213], H. Van Der Graaf[213], N. Van Der Kolk[167], E. Van Der Kraaij[33], B. Van Doren[338], B. Van Eijk[213], R. Van Kooten[87], W. T. Van Oers[279], D. Vanegas[108], P. Vanhoefer[186], P. Vankov[47], P. Varghese[58], A. Variola[167], R. Varma[85], G. Varner[334], G. Vasileiadis[162], A. Vauth[47], J. Velthuis[316], S. K. Vempati[83], V. Vento[108], M. Venturini[177], M. Verderi[172], P. Verdier[89], A. Verdugo[31],

A. Vicente[171], J. Vidal-Perona[108], H. L. R. Videau[172], I. Vila[110], X. Vilasis-Cardona[299], E. Vilella[311], A. Villamor[32], E. G. Villani[259], J. A. Villar[286], M. A. Villarejo Bermúdez[108], D. Vincent[169], P. Vincent[169], J. M. Virey[28], A. Vivoli[58], V. Vogel[47], R. Volkenborn[47], O. Volynets[47], F. Von Der Pahlen[110], E. Von Toerne[295], B. Vormwald[47], A. Voronin[180], M. Vos[108], J. H. Vossebeld[339], G. Vouters[164], Y. Voutsinas[94,47], V. Vrba[105,45], M. Vysotsky[107], D. Wackeroth[256], A. Wagner[47], C. E. Wagner[7,52], R. Wagner[7], S. R. Wagner[324], W. Wagner[385], J. Wagner-Kuhr[90], A. P. Waite[251], M. Wakayama[197], Y. Wakimoto[276], R. Walczak[358,140], R. Waldi[300], D. G. E. Walker[251], N. J. Walker[47], M. Walla[47], C. J. Wallace[49], S. Wallon[171,393], D. Walsh[328], S. Walston[178], W. A. T. Wan Abdullah[342], D. Wang[102], G. Wang[102], J. Wang[251], L. Wang[251], L. Wang[52], M. H. Wang[251], M. Z. Wang[210], Q. Wang[102], Y. Wang[102], Z. Wang[24], R. Wanke[138], C. Wanotayaroj[356], B. Ward[8], D. Ward[323], B. Warmbein[47], M. Washio[402], K. Watanabe[71], M. Watanabe[212], N. Watanabe[71], T. Watanabe[155], Y. Watanabe[71], S. Watanuki[272], Y. Watase[71], N. K. Watson[315], G. Watts[383], M. M. Weber[90], H. C. Weddig[47], H. Weerts[7], A. W. Weidemann[251], G. Weiglein[47], A. Weiler[47], S. Weinzierl[138], H. Weise[47], A. Welker[138], N. Welle[47], J. D. Wells[33,348], M. Wendt[58,33], M. Wenskat[47], H. Wenzel[58], N. Wermes[295], U. Werthenbach[301], W. Wester[58], L. Weuste[186,57], A. White[373], G. White[251], K. H. Wichmann[47], M. Wielers[183], R. Wielgos[58], W. Wierba[202], T. Wilksen[47], S. Willocq[346], F. F. Wilson[259], G. W. Wilson[338], P. B. Wilson[251], M. Wing[309], M. Winter[94], K. Wittenburg[47], P. Wittich[43], M. Wobisch[181], A. Wolski[339,40], M. D. Woodley[251], M. B. Woods[251], M. Worek[385], S. Worm[33,259], G. Wormser[167], D. Wright[178], Z. Wu[251], C. E. Wulz[224], S. Xella[211], G. Xia[40,343], L. Xia[7], A. Xiao[7], L. Xiao[251], M. Xiao[102], Q. Xiao[102], J. Xie[7], C. Xu[102], F. Xu[210], G. Xu[102], K. Yagyu[201], U. A. Yajnik[85], V. Yakimenko[251], S. Yamada[71,116], S. Yamada[71], Y. Yamada[272], Y. Yamada[402], A. Yamaguchi[274], D. Yamaguchi[275], M. Yamaguchi[272], S. Yamaguchi[272], Y. Yamaguchi[375], Y. Yamaguchi[75], A. Yamamoto[71,375], H. Yamamoto[272], K. Yamamoto[222], K. Yamamoto[118], M. Yamamoto[71], N. Yamamoto[197], N. Yamamoto[71], Y. Yamamoto[71], Y. Yamamoto[375], T. Yamamura[375], T. Yamanaka[116], S. Yamashita[116], T. Yamashita[3], Y. Yamashita[214], K. Yamauchi[197], M. Yamauchi[71], T. Yamazaki[375], Y. Yamazaki[154], J. Yan[375,71], W. Yan[364], C. Yanagisawa[257,11], H. Yang[247], J. Yang[56], U. K. Yang[245,343], Z. Yang[24], W. Yao[177], S. Yashiro[71], F. Yasuda[375], O. Yasuda[276], I. Yavin[188,228], E. Yazgan[331], H. Yokoya[377], K. Yokoya[71], H. Yokoyama[375], S. Yokoyama[275], R. Yonamine[71], H. Yoneyama[240], M. Yoshida[71], T. Yoshida[62], K. Yoshihara[116,33], S. Yoshihara[116,33], M. Yoshioka[71,272], T. Yoshioka[161], H. Yoshitama[73], C. C. Young[251], H. B. Yu[348], J. Yu[373], C. Z. Yuan[102], F. Yuasa[71], J. Yue[102], A. Zabi[172], W. Zabolotny[401], J. Zacek[34], I. Zagorodnov[47], J. Zalesak[105,58], A. F. Zarnecki[381], L. Zawiejski[268], M. Zeinali[101], C. Zeitnitz[385], L. Zembala[401], K. Zenker[47], D. Zeppenfeld[91], D. Zerwas[167], P. Zerwas[47], M. Zeyrek[192], A. Zghiche[164], J. Zhai[102], C. Zhang[102], J. Zhang[102], J. Zhang[7], Y. Zhang[24,33], Z. Zhang[167], F. Zhao[102], F. Zhao[102], T. Zhao[102], Y. Zhao[251], H. Zheng[102], Z. Zhengguo[364], L. Zhong[24], F. Zhou[251], X. Zhou[364,102], Z. Zhou[102], R. Y. Zhu[17], X. Zhu[24], X. Zhu[102], M. Zimmer[47], F. Zomer[167], T. Zoufal[47], R. Zwicky[329]

1 Academia Sinica - 128 Sec. 2, Institute of Physics, Academia Rd., Nankang, Taipei 11529, Taiwan, R.O.C.

2 AGH University of Science and Technology, Akademia Gorniczo-Hutnicza im. Stanislawa Staszica w Krakowie, Al. Mickiewicza 30 PL-30-059 Cracow, Poland

3 Aichi Medical University, Nagakute, Aichi, 480-1195, Japan

4 Akita International University, Yuwa, Akita City, 010-1292, Japan

5 Albert-Ludwigs Universität Freiburg, Physikalisches Institut, Hermann-Herder Str. 3, D-79104 Freiburg, Germany

6 Ankara Üniversitesi Fen Fakültesi, Fizik Bölümü, Dögol Caddesi, 06100 Tandoğan Ankara, Turkey

7 Argonne National Laboratory (ANL), 9700 S. Cass Avenue, Argonne, IL 60439, USA

8 Baylor University, Department of Physics, 101 Bagby Avenue, Waco, TX 76706, USA

9 Beijing University, Department of Physics, Beijing, China 100871

10 Benares Hindu University, Benares, Varanasi 221005, India

11 Borough of Manhattan Community College, The City University of New York, Department of Science, 199 Chambers Street, New York, NY 10007, USA

12 Brandenburg University of Technology, Postfach 101344, D-03013 Cottbus, Germany

13 Brookhaven National Laboratory (BNL), P.O.Box 5000, Upton, NY 11973-5000, USA

14 Brown University, Department of Physics, Box 1843, Providence, RI 02912, USA

15 Budker Institute for Nuclear Physics (BINP), 630090 Novosibirsk, Russia

16 Calcutta University, Department of Physics, 92 A.P.C. Road, Kolkata 700009, India

17 California Institute of Technology, Physics, Mathematics and Astronomy (PMA), 1200 East California Blvd, Pasadena, CA 91125, USA

18 California State University, Los Angeles, Dept. of Physics and Astronomy, 5151 State University Dr., Los Angeles, CA 90032, USA

19 Carleton University, Department of Physics, 1125 Colonel By Drive, Ottawa, Ontario, Canada K1S 5B6

20 Carnegie Mellon University, Department of Physics, Wean Hall 7235, Pittsburgh, PA 15213, USA

21 CEA Saclay, IRFU, F-91191 Gif-sur-Yvette, France

22 CEA Saclay, Service de Physique Théorique, CEA/DSM/SPhT, F-91191 Gif-sur-Yvette Cedex, France

23 Center for High Energy Physics (CHEP) / Kyungpook National University, 1370 Sankyuk-dong, Buk-gu, Daegu 702-701, Republic of Korea

24 Center for High Energy Physics (TUHEP), Tsinghua University, Beijing, China 100084

25 Center For Quantum Spacetime (CQUeST), Sogang University, 35 Baekbeom-ro, Mapo-gu, Seoul 121-742, Republic of Korea

26 Center for the Advancement of Natural Discoveries using Light Emission (CANDLE), Acharyan 31, 0040, Yerevan, Armenia

27 Centre de Physique des Particules de Marseille (CPPM), Aix-Marseille Université, CNRS/IN2P3, 163, Avenue de Luminy, Case 902, 13288 Marseille Cedex 09, France

28 Centre de Physique Theorique, CNRS - Luminy, Universiti d"Aix - Marseille II, Campus of Luminy, Case 907, 13288 Marseille Cedex 9, France

29 Centre Lasers Intenses et Applications (CELIA), Université Bordeaux 1 - CNRS - CEA, 351 Cours de la Libération, 33405 Talence Cedex, France

30 Centro Brasileiro de Pesquisas Físicas (CBPF), Rua Dr. Xavier Sigaud, n.150 22290-180, Urca - Rio de Janeiro, RJ, Brazil

31 Centro de Investigaciones Energéticas, Medioambientales y Tecnológicas, CIEMAT, Avenida Complutense 22, E-28040 Madrid, Spain

32 Centro Nacional de Microelectrónica (CNM), Instituto de Microelectrónica de Barcelona (IMB), Campus UAB, 08193 Cerdanyola del Vallès (Bellaterra), Barcelona, Spain

33 CERN, CH-1211 Genève 23, Switzerland

34 Charles University, Institute of Particle & Nuclear Physics, Faculty of Mathematics and Physics, V Holesovickach 2, CZ-18000 Prague 8, Czech Republic

35 Chiba University of Commerce, 1-3-1 Konodai, Ichikawa-shi, Chiba, 272-8512, Japan

36 Chonbuk National University, Division of Science Education, Jeonju 561-756, Republic of Korea

37 Chonbuk National University, Physics Department, Jeonju 561-756, Republic of Korea

38 Chubu University, 1200 Matsumoto-cho, Kasugai-shi, Aichi, 487-8501, Japan

39 Chung Yuan Christian University, Department of Physics, 200 Chung Pei Rd., Chung Li 32023 Taiwan, R.O.C

40 Cockcroft Institute, Daresbury, Warrington WA4 4AD, UK

41 College of William and Mary, Department of Physics, Williamsburg, VA, 23187, USA

42 Columbia University, Department of Physics, New York, NY 10027-6902, USA

43 Cornell University, Laboratory for Elementary-Particle Physics (LEPP), Ithaca, NY 14853, USA

44 Czech Technical University in Prague, Institute of Experimental and Applied Physics (IEAP), Horska 3a/22, 12800 Prague 2, Czech Republic

45 Czech Technical University, Faculty of Nuclear Science and Physical Engineering, Brehova 7, CZ-11519 Prague 1, Czech Republic

46 Departamento de Física Teórica, Facultad de Ciencias, Módulo 15 (antiguo C-XI) y Módulo 8, Universidad Autónoma de Madrid, Campus de Cantoblanco, 28049 Madrid, Spain

47 Deutsches Elektronen-Synchrotron DESY, A Research Centre of the Helmholtz Association, Notkestrasse 85, 22607 Hamburg, Germany (Hamburg site)

48 Deutsches Elektronen-Synchrotron DESY, A Research Centre of the Helmholtz Association, Platanenallee 6, 15738 Zeuthen, Germany (Zeuthen site)

49 Durham University, Department of Physics, Ogen Center for Fundamental Physics, South Rd., Durham DH1 3LE, UK

50 École Normale Supérieure de Lyon, 46 allée d'Italie, 69364 Lyon Cedex 07, France

51 Ege University, Department of Physics, Faculty of Science, 35100 Izmir, Turkey

52 Enrico Fermi Institute, University of Chicago, 5640 S. Ellis Avenue, RI-183, Chicago, IL 60637, USA
53 ETH Zürich, Institute for Particle Physics (IPP), Schafmattstrasse 20, CH-8093 Zürich, Switzerland
54 ETH Zürich, Institute for Theoretical Physics (ITP), Wolfgang-Pauli-Str. 27, Zürich, Switzerland
55 European Spallation Source ESS AB, Box 176, 221 00 Lund, Sweden
56 Ewha Womans University, 11-1 Daehyun-Dong, Seodaemun-Gu, Seoul, 120-750, Republic of Korea
57 Excellence Cluster Universe, Technische Universität München, Boltzmannstr. 2, 85748 Garching, Germany
58 Fermi National Accelerator Laboratory (FNAL), P.O.Box 500, Batavia, IL 60510-0500, USA
59 Florida State University, Department of Physics, 77 Chieftan Way, Tallahassee, FL 32306-4350, USA
60 Fujita Gakuen Health University, Department of Physics, Toyoake, Aichi 470-1192, Japan
61 Fukui University of Technology, 3-6-1 Gakuen, Fukui-shi, Fukui 910-8505, Japan
62 Fukui University, Department of Physics, 3-9-1 Bunkyo, Fukui-shi, Fukui 910-8507, Japan
63 Gangneung-Wonju National University, 210-702 Gangneung Daehangno, Gangneung City, Gangwon Province, Republic of Korea
64 Georg-August-Universität Göttingen, II. Physikalisches Institut, Friedrich-Hund-Platz 1, 37077 Göttingen, Germany
65 Global Design Effort
66 Hanyang University, Department of Physics, Seoul 133-791, Republic of Korea
67 Harish-Chandra Research Institute, Chhatnag Road, Jhusi, Allahabad 211019, India
68 Helmholtz-Zentrum Berlin für Materialien und Energie (HZB), Wilhelm-Conrad-Röntgen Campus, BESSY II, Albert-Einstein-Str. 15, 12489 Berlin, Germany
69 Helsinki Institute of Physics (HIP), P.O. Box 64, FIN-00014 University of Helsinki, Finland
70 Henan Normal University, College of Physics and Information Engineering, Xinxiang, China 453007
71 High Energy Accelerator Research Organization, KEK, 1-1 Oho, Tsukuba, Ibaraki 305-0801, Japan
72 Hiroshima University, Department of Physics, 1-3-1 Kagamiyama, Higashi-Hiroshima, Hiroshima 739-8526, Japan
73 Hiroshima University, Graduate School of Advanced Sciences of Matter, 1-3-1 Kagamiyama, Higashi-Hiroshima, Hiroshima 739-8530, Japan
74 Hokkai-Gakuen University, 4-1-40 Asahimachi, Toyohira-ku, Sapporo 062-8605, Japan
75 Hokkaido University, Department of Physics, Faculty of Science, Kita, Kita-ku, Sapporo-shi, Hokkaido 060-0810, Japan
76 Humboldt Universität zu Berlin, Fachbereich Physik, Institut für Elementarteilchenphysik, Newtonstr. 15, D-12489 Berlin, Germany
77 Hyogo University of Teacher Education, 942-1 Shimokume, Kato-city, Hyogo 673-1494, Japan
78 Ibaraki National College of Technology, 866 Nakane, Hitachinaka, Ibaraki 312-8508, Japan
79 Ibaraki University, College of Technology, Department of Physics, Nakanarusawa 4-12-1, Hitachi, Ibaraki 316-8511, Japan
80 Imperial College, Blackett Laboratory, Department of Physics, Prince Consort Road, London, SW7 2BW, UK
81 Indian Association for the Cultivation of Science, Department of Theoretical Physics and Centre for Theoretical Sciences, Kolkata 700032, India
82 Indian Institute of Science Education and Research (IISER) Kolkata, Department of Physical Sciences, Mohanpur Campus, PO Krishi Viswavidyalaya, Mohanpur 741252, Nadia, West Bengal, India
83 Indian Institute of Science, Centre for High Energy Physics, Bangalore 560012, Karnataka, India
84 Indian Institute of Technology Indore, IET Campus, M-Block, Institute of Engineering and Technology (IET), Devi Ahilya Vishwavidyalaya Campus, Khandwa Road, Indore - 452017, Madhya Pradesh, India
85 Indian Institute of Technology, Bombay, Powai, Mumbai 400076, India
86 Indian Institute of Technology, Guwahati, Guwahati, Assam 781039, India
87 Indiana University, Department of Physics, Swain Hall West 117, 727 E. 3rd St., Bloomington, IN 47405-7105, USA
88 Institucio Catalana de Recerca i Estudis, ICREA, Passeig Lluis Companys, 23, Barcelona 08010, Spain
89 Institut de Physique Nucléaire de Lyon (IPNL), Domaine scientifique de la Doua, Bâtiment Paul Dirac 4, rue Enrico Fermi, 69622 Villeurbanne, Cedex, France
90 Institut für Experimentelle Kernphysik, KIT,Universität Karlsruhe (TH), Wolfgang-Gaede-Str. 1, Postfach 6980, 76128 Karlsruhe, Germany
91 Institut für Theoretische Physik (ITP), Karlsruher Institut für Technologie (KIT), Fakultät für Physik, Postfach 6980, 76049 Karlsruhe, Germany
92 Institut für Theoretische Teilchenphysik, Campus Süd, Karlsruher Institut für Technologie (KIT), 76128 Karlsruhe, Germany
93 Institut National de Physique Nucleaire et de Physique des Particules, 3, Rue Michel- Ange, 75794 Paris Cedex 16, France
94 Institut Pluridisciplinaire Hubert Curien, 23 Rue du Loess - BP28, 67037 Strasbourg Cedex 2, France
95 Institute for Chemical Research, Kyoto University, Gokasho, Uji, Kyoto 611-0011, Japan
96 Institute for Cosmic Ray Research, University of Tokyo, 5-1-5 Kashiwa-no-Ha, Kashiwa, Chiba 277-8582, Japan
97 Institute for Mathematics, Astrophysics and Particle Physics (IMAPP), P.O. Box 9010, 6500 GL Nijmegen, Netherlands
98 Institute for Nuclear Research, Russian Academy of Sciences (INR RAS), 60-th October Anniversary Prospect 7a, 117312, Moscow, Russia
99 Institute for Particle and Nuclear Physics, Wigner Research Centre for Physics, Hungarian Academy of Sciences, P.O. Box 49, 1525 Budapest, Hungary
100 Institute for Scintillation Materials (ISMA), 60 Lenina Ave, 61001, Kharkiv, Ukraine
101 Institute for studies in fundamental sciences (IPM), Niavaran Square, P.O. Box 19395-5746, Tehran, Iran
102 Institute of High Energy Physics - IHEP, Chinese Academy of Sciences, P.O. Box 918, Beijing, China 100049
103 Institute of Mathematical Sciences, Taramani, C.I.T. Campus, Chennai 600113, India
104 Institute of Particle Physics, Canada

105 Institute of Physics, ASCR, Academy of Science of the Czech Republic, Division of Elementary Particle Physics, Na Slovance 2, CZ-18221 Prague 8, Czech Republic

106 Institute of Physics, Vietnam Academy of Science and Technology (VAST), 10 Dao-Tan, Ba-Dinh, Hanoi 10000, Vietnam

107 Institute of Theoretical and Experimetal Physics, B. Cheremushkinskawa, 25, RU-117259, Moscow, Russia

108 Instituto de Fisica Corpuscular (IFIC), Centro Mixto CSIC-UVEG, Edificio Investigacion Paterna, Apartado 22085, 46071 Valencia, Spain

109 Instituto de Física da Universidade Federal do Rio Grande do Sul (UFRGS), Av. Bento Gonçalves 9500, Caixa Postal 15051, CEP 91501-970, Porto Alegre, RS, Brazil

110 Instituto de Fisica de Cantabria, (IFCA, CSIC-UC), Facultad de Ciencias, Avda. Los Castros s/n, 39005 Santander, Spain

111 Instituto de Física Teórica UAM/CSIC, C/ Nicolás Cabrera 13-15, Universidad Autónoma de Madrid, Cantoblanco, 28049 Madrid, Spain

112 Instituto Galego de Fisica de Altas Enerxias (IGFAE,USC) Facultad de Fisica, Campus Sur E-15782 Santiago de Compostela, Spain

113 Instituto Tecnológico de Aragón (ITA), C/ María de Luna 7-8, 50018 Zaragoza, Spain

114 Instituto Universitario de Física Fundamental y Matemáticas de la Universidad de Salamanca (IUFFyM), Casas del Parque, 37008 Salamanca, Spain

115 Inter-University Accelerator Centre, Aruna Asaf Ali Marg, Post Box 10502, New Delhi 110067, India

116 International Center for Elementary Particle Physics, University of Tokyo, Hongo 7-3-1, Bunkyo District, Tokyo 113-0033, Japan

117 International Institute of Physics, Federal University of Rio Grande do Norte, Av. Odilon Gomes de Lima, 1722 - Capim Macio - 59078-400 - Natal-RN, Brazil

118 Iowa State University, Department of Physics, High Energy Physics Group, Ames, IA 50011, USA

119 Istituto Nazionale di Fisica Nucleare (INFN), Laboratorio LASA, Via Fratelli Cervi 201, 20090 Segrate, Italy

120 Istituto Nazionale di Fisica Nucleare (INFN), Sezione di Firenze, Via G. Sansone 1, I-50019 Sesto Fiorentino (Firenze), Italy

121 Istituto Nazionale di Fisica Nucleare (INFN), Sezione di Milano Bicocca, Piazza della Scienza 3, I-20126 Milano, Italy

122 Istituto Nazionale di Fisica Nucleare (INFN), Sezione di Milano, Via Celoria 16, I-20133 Milano, Italy

123 Istituto Nazionale di Fisica Nucleare (INFN), Sezione di Napoli, Complesso Universitá di Monte Sant'Angelo,via, I-80126 Naples, Italy

124 Istituto Nazionale di Fisica Nucleare (INFN), Sezione di Pavia, Via Bassi 6, I-27100 Pavia, Italy

125 Istituto Nazionale di Fisica Nucleare (INFN), Sezione di Perugia, Via A. Pascoli, 06123 Perugia, Italy

126 Istituto Nazionale di Fisica Nucleare (INFN), Sezione di Pisa, Edificio C - Polo Fibonacci Largo B. Pontecorvo, 3, I-56127 Pisa, Italy

127 Istituto Nazionale di Fisica Nucleare (INFN), Sezione di Roma, c/o Dipartimento di Fisica - Università degli Studi di Roma "La Sapienza", P.le Aldo Moro 2, I-00185 Roma, Italy

128 Istituto Nazionale di Fisica Nucleare (INFN), Sezione di Torino, c/o Universitá di Torino, facoltá di Fisica, via P Giuria 1, 10125 Torino, Italy

129 Istituto Nazionale di Fisica Nucleare (INFN), Sezione di Trieste, Padriciano 99, I-34012 Trieste (Padriciano), Italy

130 ITER Organization, Route de Vinon-sur-Verdon, 13115 St. Paul-lez-Durance, France

131 Iwate University, 4-3-5 Ueda, Morioka, Iwate, 020-8551, Japan

132 Jagiellonian University, Institute of Physics, Ul. Reymonta 4, PL-30-059 Cracow, Poland

133 Jamia Millia Islamia, Department of Physics, Jamia Nagar, New Delhi 110025, India

134 Japan Aerospace Exploration Agency, Sagamihara Campus, 3-1-1 Yoshinodai, Sagamihara, Kanagawa 220-8510 , Japan

135 Japan Atomic Energy Agency, 4-49 Muramatsu, Tokai-mura, Naka-gun, Ibaraki 319-1184, Japan

136 Japan Atomic Energy Agency, Tokai Research and Development Center, 2-4 Shirane Shirakata, Tokai-mura, Naka-gun, Ibaraki 319-1195, Japan

137 Japan Synchrotron Radiation Research Institute (JASRI), 1-1-1, Kouto, Sayo-cho, Sayo-gun, Hyogo 679-5198, Japan

138 Johannes Gutenberg Universität Mainz, Institut für Physik, 55099 Mainz, Germany

139 John Adams Institute for Accelerator Science at Royal Holloway University of London, Egham Hill, Egham, Surrey TW20 0EX, UK

140 John Adams Institute for Accelerator Science at University of Oxford, Denys Wilkinson Building, Keble Road, Oxford OX1 3RH, UK

141 Johns Hopkins University - Henry A. Rowland Department of Physics & Astronomy 3701 San Martin Drive, Baltimore, Maryland (MD) 21218, USA

142 Joint Institute for Nuclear Research (JINR), Joliot-Curie 6, 141980, Dubna, Moscow Region, Russia

143 Joint Institute for Power and Nuclear Research "Sosny" at National Academy of Sciences of Belarus, 99 Academician A.K.Krasin Str., Minsk BY-220109, Belarus

144 Jozef Stefan Institute, Jamova cesta 39, 1000 Ljubljana, Slovenia

145 Julius-Maximilians-Universität Würzburg, Fakultät für Physik und Astronomie, Am Hubland, 97074 Würzburg, Germany

146 Juntendo University, School of Medicine, Dept. of Physics, Hiraga-gakuendai 1-1, Inzai-shi, Chiba 270-1695, Japan

147 Justus-Liebig-Universität Gießen, II. Physikalisches Institut, Heinrich-Buff-Ring 16, 35392 Gießen, Germany

148 Kanazawa University, Institute for Theoretical Physics (KITP), School of Mathematics and Physics, College of Science and Engineering, Kakuma-machi, Kanazawa city, Ishikawa 920-1192, Japan

149 Kansas State University, Department of Physics, 116 Cardwell Hall, Manhattan, KS 66506, USA

150 Kavli Institute for the Physics and Mathematics of the Universe (Kavli IPMU), University of Tokyo, 5-1-5 Kashiwanoha, Kashiwa, 277-8583, Japan

151 King Saud University (KSU), Dept. of Physics, P.O. Box 2454, Riyadh 11451, Saudi Arabia

152 King's College London - Department of physics, Strand, London WC2R 2LS, London, UK

153 Kinki University, Department of Physics, 3-4-1 Kowakae, Higashi-Osaka, Osaka 577-8502, Japan

154 Kobe University, Department of Physics, 1-1 Rokkodai-cho, Nada-ku, Kobe, Hyogo 657-8501, Japan

155 Kogakuin University, Department of Physics, Shinjuku Campus, 1-24-2 Nishi-Shinjuku, Shinjuku-ku, Tokyo 163-8677, Japan

156 Konkuk University, 93-1 Mojin-dong, Kwanglin-gu, Seoul 143-701, Republic of Korea

157 Korea Advanced Institute of Science & Technology, Department of Physics, 373-1 Kusong-dong, Yusong-gu, Taejon 305-701, Republic of Korea

158 Korea Institute for Advanced Study (KIAS), School of Physics, 207-43 Cheongryangri-dong, Dongdaemun-gu, Seoul 130-012, Republic of Korea

159 Kyoto University, Department of Physics, Kitashirakawa-Oiwakecho, Sakyo-ku, Kyoto 606-8502, Japan

160 Kyoto University, Yukawa Institute for Theoretical Physics, Kitashirakawa-Oiwakecho, Sakyo-Ku, Kyoto 606-8502, Japan

161 Kyushu University, Department of Physics, 6-10-1 Hakozaki, Higashi-ku, Fukuoka 812-8581, Japan

162 L.P.T.A., UMR 5207 CNRS-UM2, Université Montpellier II, Case Courrier 070, Bât. 13, place Eugène Bataillon, 34095 Montpellier Cedex 5, France

163 Laboratoire Charles Coulomb UMR 5221 CNRS-UM2, Université Montpellier 2, Place Eugène Bataillon - CC069, 34095 Montpellier Cedex 5, France

164 Laboratoire d'Annecy-le-Vieux de Physique des Particules (LAPP) , Université de Savoie, CNRS/IN2P3, 9 Chemin de Bellevue, BP 110, F-74941 Annecy-Le-Vieux Cedex, France

165 Laboratoire d'Annecy-le-Vieux de Physique Theorique (LAPTH), Chemin de Bellevue, BP 110, F-74941 Annecy-le-Vieux Cedex, France

166 Laboratoire d'AstroParticules et Cosmologie (APC), Université Paris Diderot-Paris 7 - CNRS/IN2P3, Bâtiment Condorcet, Case 7020, 75205 Paris Cedex 13, France

167 Laboratoire de l'Accélérateur Linéaire (LAL), Université Paris-Sud 11, Bâtiment 200, 91898 Orsay, France

168 Laboratoire de Physique Corpusculaire de Clermont-Ferrand (LPC), Université Blaise Pascal, I.N.2.P.3./C.N.R.S., 24 avenue des Landais, 63177 Aubière Cedex, France

169 Laboratoire de Physique Nucléaire et des Hautes Energies (LPNHE), UPMC, UPD, IN2P3/CNRS, 4 Place Jussieu, 75005, Paris Cedex 05, France

170 Laboratoire de Physique Subatomique et de Cosmologie (LPSC), Université Joseph Fourier (Grenoble 1), CNRS/IN2P3, Institut Polytechnique de Grenoble, 53 rue des Martyrs, F-38026 Grenoble Cedex, France

171 Laboratoire de Physique Theorique, Université de Paris-Sud XI, Batiment 210, F-91405 Orsay Cedex, France

172 Laboratoire Leprince-Ringuet (LLR), École polytechnique – CNRS/IN2P3, Route de Saclay, F-91128 Palaiseau Cedex, France

173 Laboratoire Univers et Particules de Montpellier (LUPM) - UMR5299, Université de Montpellier II, Place Eugène Bataillon - Case courrier 72, 34095 Montpellier Cedex 05, France

174 Laboratori Nazionali di Frascati, via E. Fermi, 40, C.P. 13, I-00044 Frascati, Italy

175 Laboratório de Instrumentação e Física Experimental de Partículas (LIP LISBOA), Av. Elias Garcia 14 - 1°, 1000-149 Lisbon, Portugal

176 Lancaster University, Physics Department, Lancaster LA1 4YB, UK

177 Lawrence Berkeley National Laboratory (LBNL), 1 Cyclotron Rd, Berkeley, CA 94720, USA

178 Lawrence Livermore National Laboratory (LLNL), Livermore, CA 94551, USA

179 Lebedev Physical Institute, Leninsky Prospect 53, RU-117924 Moscow, Russia

180 Lomonosov Moscow State University, Skobeltsyn Institute of Nuclear Physics (MSU SINP), 1(2), Leninskie gory, GSP-1, Moscow 119991, Russia

181 Louisiana Tech University, Department of Physics, Ruston, LA 71272, USA

182 Ludwig-Maximilians-Universität München, Fakultät für Physik, Am Coulombwall 1, D - 85748 Garching, Germany

183 Lunds Universitet, Fysiska Institutionen, Avdelningen för Experimentell Högenergifysik, Box 118, 221 00 Lund, Sweden

184 L'Université Hassan II, Aïn Chock, "Réseau Universitaire de Physique des Hautes Energies" (RUPHE), Département de Physique, Faculté des Sciences Aïn Chock, B.P 5366 Maarif, Casablanca 20100, Morocco

185 Massachusetts Institute of Technology (MIT), Laboratory for Nuclear Science, 77 Massachusetts Avenue, Cambridge, MA 02139, USA

186 Max-Planck-Institut für Physik (Werner-Heisenberg-Institut), Föhringer Ring 6, 80805 München, Germany

187 McGill University, Department of Physics, Ernest Rutherford Physics Bldg., 3600 University Street, Montreal, Quebec, H3A 2T8 Canada

188 McMaster University, Department of Physics & Astronomy, 1280 Main Street West, Hamilton, ON, L8S 4M1, Canada

189 Meiji Gakuin University, Department of Physics, 2-37 Shirokanedai 1-chome, Minato-ku, Tokyo 244-8539, Japan

190 Michigan State University, Department of Chemical Engineering & Materials Science, 2527 Engineering Building East Lansing, MI 48824-1226, USA

191 Michigan State University, Department of Physics and Astronomy, East Lansing, MI 48824, USA

192 Middle East Technical University, Department of Physics, TR-06531 Ankara, Turkey

193 Miyagi Gakuin Women's University, Faculty of Liberal Arts, 9-1-1 Sakuragaoka, Aoba District, Sendai, Miyagi 981-8557, Japan

194 MSU-Iligan Institute of Technology, Department of Physics, Andres Bonifacio Avenue, 9200 Iligan City, Phillipines

195 Nagasaki Institute of Applied Science, 536 Abamachi, Nagasaki-Shi, Nagasaki 851-0193, Japan

196 Nagoya University, Department of Materials Science and Engineering, Furo-cho, Chikusa-ku, Nagoya, 464-8603, Japan

197 Nagoya University, Department of Physics, School of Science, Furo-cho, Chikusa-ku, Nagoya, Aichi 464-8602, Japan

198 Nagoya University, Kobayashi-Maskawa Institute for the Origin of Particles and the Universe (KMI), Furo-cho, Chikusa-ku, Nagoya Aichi 464-8602, Japan

199 Nanjing University, Department of Physics, Nanjing, China 210093

200 Nara Women's University, High Energy Physics Group, Kitauoya-Nishimachi, Nara 630-8506, Japan

201 National Central University, High Energy Group, Department of Physics, Chung-li, Taiwan 32001, R.O.C

202 National Centre of Nuclear Research (NCBJ), ul. Andrzeja Soltana 7, 05-400 Otwock-Swierk, Poland

203 National Cheng Kung University, Physics Department, 1 Ta-Hsueh Road, Tainan, Taiwan 70101, R.O.C

204 National Chiao-Tung University, Institute of Physics, 1001 Ta Hsueh Rd, Hsinchu, Taiwan 300, R.O.C.

205 National Institute of Chemical Physics and Biophysics (NICPB), Ravala pst 10, 10143 Tallinn, Estonia

206 National Institute of Physics and Nuclear Engineering "Horia Hulubei" (IFIN-HH), Str. Reactorului no.30, P.O. Box MG-6, R-76900 Bucharest - Magurele, Romania

207 National Research Centre "Kurchatov Institute", 1 Akademika Kurchatova pl., Moscow, 123182, Russia

208 National Science Center - Kharkov Institute of Physics and Technology (NSC KIPT), Akademicheskaya St. 1, Kharkov, 61108, Ukraine

209 National Scientific & Educational Centre of Particle & High Energy Physics (NCPHEP), Belarusian State University, M.Bogdanovich street 153, 220040 Minsk, Belarus

210 National Taiwan University, Physics Department, Taipei, Taiwan 106, R.O.C

211 Niels Bohr Institute (NBI), University of Copenhagen, Blegdamsvej 17, DK-2100 Copenhagen, Denmark

212 Niigata University, Department of Physics, Ikarashi, Niigata 950-218, Japan

213 Nikhef, National Institute for Subatomic Physics, P.O. Box 41882, 1009 DB Amsterdam, Netherlands

214 Nippon Dental University School of Life Dentistry at Niigata, 1-8 Hamaura-cho, Chuo-ku, Niigata 951-1500, Japan

215 North Carolina A&T State University, 1601 E. Market Street, Greensboro, NC 27411, USA

216 Northeastern University, Physics Department, 360 Huntington Ave, 111 Dana Research Center, Boston, MA 02115, USA

217 Northern Illinois University, Department of Physics, DeKalb, Illinois 60115-2825, USA

218 Northwestern University, Department of Physics and Astronomy, 2145 Sheridan Road., Evanston, IL 60208, USA

219 Novosibirsk State University (NGU), Department of Physics, Pirogov st. 2, 630090 Novosibirsk, Russia

220 Ochanomizu University, Department of Physics, Faculty of Science, 1-1 Otsuka 2, Bunkyo-ku, Tokyo 112-8610, Japan

221 Orissa University of Agriculture & Technology, Bhubaneswar 751003, Orissa, India

222 Osaka City University, Department of Physics, Faculty of Science, 3-3-138 Sugimoto, Sumiyoshi-ku, Osaka 558-8585, Japan

223 Osaka University, Department of Physics, 1-1 Machikaneyama, Toyonaka, Osaka 560-0043, Japan

224 Österreichische Akademie der Wissenschaften, Institut für Hochenergiephysik, Nikolsdorfergasse 18, A-1050 Vienna, Austria

225 Pacific Northwest National Laboratory, (PNNL), PO Box 999, Richland, WA 99352, USA

226 Panjab University, Chandigarh 160014, India

227 Pavel Sukhoi Gomel State Technical University, ICTP Affiliated Centre & Laboratory for Physical Studies, October Avenue, 48, 246746, Gomel, Belarus

228 Perimeter Institute for Theoretical Physics, 31 Caroline Street North, Waterloo, Ontario N2L 2Y5, Canada

229 Physical Research Laboratory, Navrangpura, Ahmedabad 380 009, Gujarat, India

230 Pohang Accelerator Laboratory (PAL), San-31 Hyoja-dong, Nam-gu, Pohang, Gyeongbuk 790-784, Republic of Korea

231 Pontificia Universidad Católica de Chile, Avda. Libertador Bernardo OHiggins 340, Santiago, Chile

232 Princeton University, Department of Physics, P.O. Box 708, Princeton, NJ 08542-0708, USA

233 Purdue University, Department of Physics, West Lafayette, IN 47907, USA

234 Queen Mary, University of London, Mile End Road, London, E1 4NS, United Kingdom

235 Rheinisch-Westfälische Technische Hochschule (RWTH), Physikalisches Institut, Physikzentrum, Otto-Blumenthal-Straße, 52056 Aachen

236 RIKEN, 2-1 Hirosawa, Wako, Saitama 351-0198, Japan

237 Royal Holloway, University of London (RHUL), Department of Physics, Egham, Surrey TW20 0EX, UK

238 Russian Academy of Science, Keldysh Institute of Applied Mathematics, Muiskaya pl. 4, 125047 Moscow, Russia

239 Rutgers, The State University of New Jersey, Department of Physics & Astronomy, 136 Frelinghuysen Rd, Piscataway, NJ 08854, USA

240 Saga University, Department of Physics, 1 Honjo-machi, Saga-shi, Saga 840-8502, Japan

241 Saha Institute of Nuclear Physics, 1/AF Bidhan Nagar, Kolkata 700064, India

242 Salalah College of Technology (SCOT), Engineering Department, Post Box No. 608, Postal Code 211, Salalah, Sultanate of Oman

243 Saudi Center for Theoretical Physics, King Fahd University of Petroleum and Minerals (KFUPM), Dhahran 31261, Saudi Arabia

244 Seikei University, Faculty of Science and Technology, 3-3-1 Kichijoji-Kitamachi, Musashino-shi, Tokyo 180-8633, Japan

245 Seoul National University, San 56-1, Shinrim-dong, Kwanak-gu, Seoul 151-742, Republic of Korea

246 Setsunan University, Institute for Fundamental Sciences, 17-8 Ikeda Nakamachi, Neyagawa, Osaka, 572-8508, Japan

247 Shanghai Jiao Tong University, Department of Physics, 800 Dongchuan Road, Shanghai, China 200240

248 Shinshu University, 3-1-1, Asahi, Matsumoto, Nagano 390-8621, Japan

249 Shiv Nadar University, Village Chithera, Tehsil Dadri, District Gautam Budh Nagar, 203207 Uttar Pradesh, India

250 Shizuoka University, Department of Physics, 836 Ohya, Suruga-ku, Shizuoka 422-8529, Japan

251 SLAC National Accelerator Laboratory, 2575 Sand Hill Road, Menlo Park, CA 94025, USA

252 Society for Applied Microwave Electronics Engineering and Research (SAMEER), I.I.T. Campus, Powai, Post Box 8448, Mumbai 400076, India

253 Sokendai, The Graduate University for Advanced Studies, Shonan Village, Hayama, Kanagawa 240-0193, Japan

254 Spallation Neutron Source (SNS), Oak Ridge National Laboratory (ORNL), P.O. Box 2008 MS-6477, Oak Ridge, TN 37831-6477, USA

255 State University of New York at Binghamton, Department of Physics, PO Box 6016, Binghamton, NY 13902, USA

256 State University of New York at Buffalo, Department of Physics & Astronomy, 239 Franczak Hall, Buffalo, NY 14260, USA

257 State University of New York at Stony Brook, Department of Physics and Astronomy, Stony Brook, NY 11794-3800, USA

258 STFC Daresbury Laboratory, Daresbury, Warrington, Cheshire WA4 4AD, UK

259 STFC Rutherford Appleton Laboratory, Chilton, Didcot, Oxon OX11 0QX, UK

260 Sungkyunkwan University (SKKU), Natural Science Campus 300, Physics Research Division, Chunchun-dong, Jangan-gu, Suwon, Kyunggi-do 440-746, Republic of Korea

261 Swiss Light Source (SLS), Paul Scherrer Institut (PSI), PSI West, CH-5232 Villigen PSI, Switzerland

262 Tata Institute of Fundamental Research, School of Natural Sciences, Homi Bhabha Rd., Mumbai 400005, India

263 Technical University of Lodz, Department of Microelectronics and Computer Science, al. Politechniki 11, 90-924 Lodz, Poland

264 Technische Universität Dresden, Institut für Kern- und Teilchenphysik, D-01069 Dresden, Germany

265 Tel-Aviv University, School of Physics and Astronomy, Ramat Aviv, Tel Aviv 69978, Israel

266 Texas A&M University, Physics Department, College Station, 77843-4242 TX, USA

267 Texas Tech University, Department of Physics, Campus Box 41051, Lubbock, TX 79409-1051, USA

268 The Henryk Niewodniczanski Institute of Nuclear Physics, Polish Academy of Sciences (IFJ PAN), ul. Radzikowskiego 152, PL-31342 Cracow, Poland

269 Thomas Jefferson National Accelerator Facility (TJNAF), 12000 Jefferson Avenue, Newport News, VA 23606, USA

270 Tohoku Gakuin University, Department of Business Administration, 1-3-1 Tsuchitoi, Aoba-ku Sendai, Miyagi 980-8511, Japan

271 Tohoku Gakuin University, Faculty of Technology, 1-13-1 Chuo, Tagajo, Miyagi 985-8537, Japan

272 Tohoku University, Department of Physics, Aoba District, Sendai, Miyagi 980-8578, Japan

273 Tohoku University, Research Center for Electron Photon Science, Taihaku District, Sendai, Miyagi 982-0826, Japan

274 Tohoku University, Research Center for Neutrino Science, Aoba District, Sendai, Miyagi 980-8578, Japan

275 Tokyo Institute of Technology, Department of Physics, 2-12-1 O-Okayama, Meguro, Tokyo 152-8551, Japan

276 Tokyo Metropolitan University, Faculty of Science and Engineering, Department of Physics, 1-1 Minami-Osawa, Hachioji-shi, Tokyo 192-0397, Japan

277 Tokyo University of Agriculture Technology, Department of Applied Physics, Naka-machi, Koganei, Tokyo 183-8488, Japan

278 Toyama Prefectural University, Department of Mathematical Physics, 5180 Kurokawa Imizu-shi, Toyama, 939-0398, Japan

279 TRIUMF, 4004 Wesbrook Mall, Vancouver, BC V6T 2A3, Canada

280 Universidad Autónoma de San Luis Potosí, Alvaro Obregon 64, Col. Centro, San Luis Potosí, S.L.P. 78000, México

281 Universidad de Granada, Departamento de Física Teórica y del Cosmos, Campus de Fuentenueva, E-18071 Granada, Spain

282 Universidad de los Andes, Faculty of Science, Department of Physics, Carrera 1 18A-10, Bloque Ip. Bogotá, Colombia

283 Universidad de Oviedo, Departamento de Física, Campus de Llamaquique. C/ Calvo Sotelo, s/n 33005 Oviedo, Spain

284 Universidad de Salamanca, Departamento de Física Fundamental, Plaza de la Merced, s/n., 37008 Salamanca, Spain

285 Universidad de Sevilla, Escuela Técnica Superior de Ingeniería, Departamento Ingeniería Electrónica, Camino de los Descubrimientos s/n, 41092 Sevilla, Spain

286 Universidad de Zaragoza - Departamento de Física Teórica, Pedro Cerbuna 12, E-50009 Zaragoza, Spain

287 Universidad Nacional Autónoma de México, Instituto de Física, Circuito de la Investigación Cientifica s/n, Ciudad Universitaria, CP 04510 México D.F., Mexico

288 Universidad Nacional de La Plata, Departamento de Física, Facultad de Ciencias Exactas, C.C. N 67, 1900 La Plata, Argentina

289 Universidade do Estado do Rio de Janeiro (UERJ), Rio de Janeiro, RJ - Brasil 20550-900, Brazil

290 Universidade Federal de Pelotas, Instituto de Física e Matemática, Campus Universitário, Caixa Postal 354, 96010-900 Pelotas, RS, Brazil

291 Universidade Federal do Rio de Janeiro (UFRJ), Instituto de Física, Av. Athos da Silveira Ramos 149, Centro de Tecnologia - Bloco A, Cidade Universitária, Ilha do Fundão, Rio de Janeiro, RJ, Brazil

292 Universitá degli Studi di Napoli "Federico II", Dipartimento di Fisica, Via Cintia, 80126 Napoli, Italy

293 Universitat Autònoma de Barcelona, Departament de Física, Edifici C, 08193 Bellaterra, Barcelona, Spain

294 Universitat Autònoma de Barcelona, Institut de Fisica d'Altes Energies (IFAE), Campus UAB, Edifici Cn, E-08193 Bellaterra, Barcelona, Spain

295 Universität Bonn, Physikalisches Institut, Nußallee 12, 53115 Bonn, Germany

296 Universität Heidelberg, Institut für Theoretische Physik, Philosophenweg 16, 69120 Heidelberg, Germany

297 Universität Heidelberg, Kirchhoff-Institut für Physik, Im Neuenheimer Feld 227, 69120 Heidelberg, Germany

298 Universitat Politècnica de Catalunya, Institut de Tècniques Energètiques, Campus Diagonal Sud, Edifici PC (Pavelló C). Av. Diagonal, 647 08028 Barcelona, Spain

299 Universitat Ramon Llull, La Salle, C/ Quatre Camins 2, 08022 Barcelona, Spain

300 Universität Rostock, 18051 Rostock, Germany

301 Universität Siegen, Naturwissenschaftlich-Technische Fakultät, Department Physik, Emmy Noether Campus, Walter-Flex-Str.3, 57068 Siegen, Germany

302 Universität Wien - Theoretische Physik Boltzmanngasse 5, A-1090 Vienna, Austria

303 Université catholique de Louvain, Centre for Cosmology, Particle Physics and Phenomenology (CP3), Institute of Mathematics and Physics, 2 Chemin du Cyclotron, 1348 Louvain-la-Neuve, Belgium

304 Université de Genève, Section de Physique, 24, quai E. Ansermet, 1211 Genève 4, Switzerland

305 Université de Montréal, Département de Physique, Groupe de Physique des Particules, C.P. 6128, Succ. Centre-ville, Montréal, Qc H3C 3J7, Canada

306 Université de Strasbourg, UFR de Sciences Physiques, 3-5 Rue de l'Université, F-67084 Strasbourg Cedex, France

307 Université Libre de Bruxelles, Boulevard du Triomphe, 1050 Bruxelles, Belgium

308 Universittà di Catania, Dipartimento di Fisica e Astronomia, Via Santa Sofia 64, 95123 Catania, Italy

309 University College London (UCL), High Energy Physics Group, Physics and Astronomy Department, Gower Street, London WC1E 6BT, UK

310 University College, National University of Ireland (Dublin), Department of Experimental Physics, Science Buildings, Belfield, Dublin 4, Ireland

311 University de Barcelona, Facultat de Física, Av. Diagonal, 647, Barcelona 08028, Spain

312 University of Alberta - Faculty of Science, Department of Physics, 4-181 CCIS, Edmonton AB T6G 2E1, Canada

313 University of Arizona, Department of Physics, 1118 E. Fourth Street, PO Box 210081, Tucson, AZ 85721, USA

314 University of Bergen, Institute of Physics, Allegaten 55, N-5007 Bergen, Norway

315 University of Birmingham, School of Physics and Astronomy, Particle Physics Group, Edgbaston, Birmingham B15 2TT, UK

316 University of Bristol, H. H. Wills Physics Lab, Tyndall Ave., Bristol BS8 1TL, UK

317 University of British Columbia, Department of Physics and Astronomy, 6224 Agricultural Rd., Vancouver, BC V6T 1Z1, Canada

318 University of California (UCLA), Los Angleles, CA 90095, US

319 University of California Berkeley, Department of Physics, 366 Le Conte Hall, #7300, Berkeley, CA 94720, USA

320 University of California Davis, Department of Physics, One Shields Avenue, Davis, CA 95616-8677, USA

321 University of California Irvine, Department of Physics and Astronomy, High Energy Group, 4129 Frederick Reines Hall, Irvine, CA 92697-4575 USA

322 University of California Santa Cruz, Institute for Particle Physics, 1156 High Street, Santa Cruz, CA 95064, USA

323 University of Cambridge, Cavendish Laboratory, J J Thomson Avenue, Cambridge CB3 0HE, UK

324 University of Colorado at Boulder, Department of Physics, 390 UCB, University of Colorado, Boulder, CO 80309-0390, USA

325 University of Cyprus, Department of Physics, P.O.Box 20537, 1678 Nicosia, Cyprus

326 University of Delhi, Department of Physics and Astrophysics, Delhi 110007, India

327 University of Delhi, S.G.T.B. Khalsa College, Delhi 110007, India

328 University of Dundee, Department of Physics, Nethergate, Dundee, DD1 4HN, Scotland, UK

329 University of Edinburgh, School of Physics, James Clerk Maxwell Building, The King's Buildings, Mayfield Road, Edinburgh EH9 3JZ, UK

330 University of Florida, Department of Physics, Gainesville, FL 32611, USA

331 University of Ghent, Department of Subatomic and Radiation Physics, Proeftuinstraat 86, 9000 Gent, Belgium

332 University of Glasgow, SUPA, School of Physics & Astronomy, University Avenue, Glasgow G12 8QQ, Scotland, UK

333 University of Hamburg, Physics Department, Luruper Chaussee 149, 22761 Hamburg, Germany

334 University of Hawaii, Department of Physics and Astronomy, HEP, 2505 Correa Rd., WAT 232, Honolulu, HI 96822-2219, USA

335 University of Helsinki, Department of Physical Sciences, P.O. Box 64 (Vaino Auerin katu 11), FIN-00014, Helsinki, Finland

336 University of Illinois at Chicago, Department Of Physics, 845 W Taylor St., Chicago IL 60607, USA

337 University of Iowa, Department of Physics and Astronomy, 203 Van Allen Hall, Iowa City, IA 52242-1479, USA

338 University of Kansas, Department of Physics and Astronomy, Malott Hall, 1251 Wescoe Hall Drive, Room 1082, Lawrence, KS 66045-7582, USA

339 University of Liverpool, Department of Physics, Oliver Lodge Lab, Oxford St., Liverpool L69 7ZE, UK

340 University of Liverpool, Division of Theoretical Physics, Department of Mathematical Sciences, Chadwick Building, Liverpool L69 3BX, UK

341 University of Ljubljana, Faculty of Mathematics and Physics, Jadranska ulica 19, 1000 Ljubljana, Slovenia

342 University of Malaya, Faculty of Science, Department of Physics, 50603 Kuala Lumpur, Malaysia

343 University of Manchester, School of Physics and Astronomy, Schuster Lab, Manchester M13 9PL, UK

344 University of Maribor, Faculty of Chemistry and Chemical Engineering (FKKT), Smetanova ulica 17, 2000 Maribor, Slovenia

345 University of Maryland, Department of Physics and Astronomy, Physics Building (Bldg. 082), College Park, MD 20742, USA

346 University of Massachusetts - Amherst, Department of Physics, 1126 Lederle Graduate Research Tower (LGRT), Amherst, MA 01003-9337, USA

347 University of Melbourne, School of Physics, Victoria 3010, Australia

348 University of Michigan, Department of Physics, 500 E. University Ave., Ann Arbor, MI 48109-1120, USA

349 University of Minnesota, 148 Tate Laboratory Of Physics, 116 Church St. S.E., Minneapolis, MN 55455, USA

350 University of Mississippi, Department of Physics and Astronomy, 108 Lewis Hall, PO Box 1848, Oxford, Mississippi 38677-1848, USA

351 University of Missouri – St. Louis, Department of Physics and Astronomy, 503 Benton Hall One University Blvd., St. Louis Mo 63121, USA

352 University of New Mexico, New Mexico Center for Particle Physics, Department of Physics and Astronomy, 800 Yale Boulevard N.E., Albuquerque, NM 87131, USA

353 University of North Carolina at Chapel Hill, Department of Physics and Astronomy, Phillips Hall, CB #3255, 120 E. Cameron Ave., Chapel Hill, NC 27599-3255, USA

354 University of Notre Dame, Department of Physics, 225 Nieuwland Science Hall, Notre Dame, IN 46556, USA

355 University of Oklahoma, Department of Physics and Astronomy, Norman, OK 73071, USA

356 University of Oregon, Department of Physics, 1371 E. 13th Ave., Eugene, OR 97403, USA

357 University of Oslo, Department of Physics, P.O box 1048, Blindern, 0316 Oslo, Norway

358 University of Oxford, Particle Physics Department, Denys Wilkinson Bldg., Keble Road, Oxford OX1 3RH England, UK

359 University of Pavia, Department of Physics, via Bassi 6, I-27100 Pavia, Italy

360 University of Pennsylvania, Department of Physics and Astronomy, 209 South 33rd Street, Philadelphia, PA 19104-6396, USA

361 University of Pittsburgh, Department of Physics and Astronomy, 100 Allen Hall, 3941 O'Hara St, Pittsburgh PA 15260, USA

362 University of Regina, Department of Physics, Regina, Saskatchewan, S4S 0A2 Canada

363 University of Rochester, Department of Physics and Astronomy, Bausch & Lomb Hall, P.O. Box 270171, 600 Wilson Boulevard, Rochester, NY 14627-0171 USA
364 University of Science and Technology of China, Department of Modern Physics (DMP), Jin Zhai Road 96, Hefei, China 230026
365 University of Silesia, Institute of Physics, Ul. Uniwersytecka 4, PL-40007 Katowice, Poland
366 University of South Carolina, Department of Physics and Astronomy, 712 Main Street, Columbia, SC 29208, USA
367 University of Southampton, School of Physics and Astronomy, Highfield, Southampton S017 1BJ, England, UK
368 University of Southern California, Department of Physics & Astronomy, 3620 McClintock Ave., SGM 408, Los Angeles, CA 90089-0484, USA
369 University of Sydney, Falkiner High Energy Physics Group, School of Physics, A28, Sydney, NSW 2006, Australia
370 University of Tartu, Institute of Physics, Riia 142, 51014 Tartu, Estonia
371 University of Texas at Austin, Department of Physics, 1 University Station C1600, Austin, Texas 78712, USA
372 University of Texas at Dallas, Department of Physics, 800 West Campbell Road, Richardson, Texas 75080, USA
373 University of Texas, Center for Accelerator Science and Technology, Arlington, TX 76019, USA
374 University of Tokushima, Institute of Theoretical Physics, Tokushima-shi 770-8502, Japan
375 University of Tokyo, Department of Physics, 7-3-1 Hongo, Bunkyo District, Tokyo 113-0033, Japan
376 University of Toronto, Department of Physics, 60 St. George St., Toronto M5S 1A7, Ontario, Canada
377 University of Toyama, Department of Physics, 3190 Gofuku, Toyama 930-8555, Japan
378 University of Tsukuba, Faculty of Pure and Applied Sciences, 1-1-1 Ten'nodai, Tsukuba, Ibaraki 305-8571, Japan
379 University of Victoria, Department of Physics and Astronomy, P.O.Box 3055 Stn Csc, Victoria, BC V8W 3P6, Canada
380 University of Virginia, Department of Physics, 382 McCormick Rd., PO Box 400714, Charlottesville, VA
381 University of Warsaw, Institute of Experimental Physics, Ul. Hoza 69, PL-00 681 Warsaw, Poland
382 University of Warsaw, Institute of Theoretical Physics, Ul. Hoza 69, PL-00 681 Warsaw, Poland
383 University of Washington, Department of Physics, PO Box 351560, Seattle, WA 98195-1560, USA
384 University of Wisconsin, Physics Department, Madison, WI 53706-1390, USA
385 University of Wuppertal, Gaußstraße 20, D-42119 Wuppertal, Germany
386 Università degli Studi di Milano, Dipartimento di Fisica, Via Celoria 16, 20133 Milano, Italy
387 Università degli Studi di Roma "La Sapienza", Dipartimento di Fisica, Piazzale Aldo Moro 5, 00185 Roma, Italy
388 Università degli Studi di Trieste, Dipartimento di Fisica, via A. Valerio 2, I-34127 Trieste, Italy
389 Università dell'Insubria in Como, Dipartimento di Scienze CC.FF.MM., via Vallegio 11, I-22100 Como, Italy
390 Università di Milano-Bicocca, Dipartimento di Fisica"G. Occhialin", Piazza della Scienza 3, 20126 Milano, Italy
391 Università di Pisa, Departimento di Fisica "Enrico Fermi", Largo Bruno Pontecorvo 3, I-56127 Pisa, Italy
392 Universiy of Huddersfield, International Institute for Accelerator Applications, Queensgate Campus, Huddersfield HD1 3DH, UK
393 UPMC Univ. Paris 06, Faculté de Physique (UFR 925), 4 Place Jussieu, 75252 Paris Cedex 05, France
394 Vietnam National University, Laboratory of High Energy Physics and Cosmology, Faculty of Physics, College of Science, 334 Nguyen Trai, Hanoi, Vietnam
395 Vietnam National University, University of Natural Sciences, 227 Nguyen Van Cu street, District 5, Ho Chi Minh City, Vietnam
396 VINCA Institute of Nuclear Sciences, Laboratory of Physics, PO Box 522, YU-11001 Belgrade, Serbia
397 Virginia Commonwealth University, Department of Physics, P.O. Box 842000, 701 W. Grace St.,Richmond, VA. 23284-2000, USA
398 Virginia Polytechnic Institute and State University, Physics Department, Blacksburg, VA 2406, USA
399 Vrije Universiteit Brussel, Pleinlaan 2, 1050 Brussels, Belgium
400 Vrije Universiteit, Department of Physics, Faculty of Sciences, De Boelelaan 1081, 1081 HV Amsterdam, Netherlands
401 Warsaw University of Technology, The Faculty of Electronics and Information Technology, ul. Nowowiejska 15-19, 00-665 Warsaw, Poland
402 Waseda University, Advanced Research Institute for Science and Engineering, Shinjuku, Tokyo 169-8555, Japan
403 Wayne State University, Department of Physics, Detroit, MI 48202, USA
404 Weizmann Institute of Science, Department of Particle Physics, P.O. Box 26, Rehovot 76100, Israel
405 Yale University, Department of Physics, New Haven, CT 06520, USA
406 Yamagata University, 1-4-12 Kojirakawa-cho, Yamagata-shi, Yamagata, 990-8560, Japan
407 Yerevan Physics Institute, 2 Alikhanyan Brothers St., Yerevan 375036, Armenia
408 Yonsei University, Department of Physics, 134 Sinchon-dong, Sudaemoon-gu, Seoul 120-749, Republic of Korea

ISSUED BY • • • • • • • • • ilc international linear collider

WWW.LINEARCOLLIDER.ORG

ISBN 978-3-935702-76-8

Argonne National Laboratory: ANL-HEP-TR-13-20
Brookhaven National Laboratory: BNL-100603-2013-IR
CEA/irfu: IRFU-13-59
CERN: CERN-ATS-2013-037
Cockcroft Institute: Cockcroft-13-10
Cornell University: CLNS 13/2085
DESY: DESY 13-062
Fermilab: FERMILAB TM-2554
IHEP: IHEP-AC-ILC-2013-001
ILC report: ILC-REPORT-2013-040
INFN: INFN-13-04/LNF
JAI: JAI-2013-001
JINR: JINR E9-2013-35
JLab: JLAB-R-2013-01
KEK: KEK Report 2013-1
KNU: KNU/CHEP-ILC-2013-1
LLNL: LLNL-TR-635539
SLAC: SLAC-R-1004
ILC HiGrade: ILC-HiGrade-Report-2013-003

THE INTERNATIONAL LINEAR COLLIDER

Technical Design Report | Volume 3.II: Accelerator Baseline Design

The International Linear Collider

Technical Design Report

2013

Volume 1: Executive Summary

Volume 2: Physics

Volume 3: Accelerator

Part I: R&D in the Technical Design Phase

Volume 3: Accelerator

Part II: Baseline Design

Volume 4: Detectors

Volume 3

Accelerator

Part II

Baseline Design

Editors

Chris Adolphsen, Maura Barone, Barry Barish, Karsten Buesser,
Phil Burrows, John Carwardine (Editorial Board Chair), Jeffrey Clark,
Hélène Mainaud Durand, Gerry Dugan, Eckhard Elsen, Atsuto Enomoto,
Brian Foster, Shigeki Fukuda, Wei Gai, Martin Gastal, Rongli Geng,
Camille Ginsburg, Susanna Guiducci, Mike Harrison, Hitoshi Hayano,
Keith Kershaw, Kiyoshi Kubo, Vic Kuchler, Benno List, Wanming Liu,
Shinichiro Michizono, Christopher Nantista, John Osborne, Mark Palmer,
James McEwan Paterson, Thomas Peterson, Nan Phinney, Paolo Pierini,
Marc Ross, David Rubin, Andrei Seryi, John Sheppard, Nikolay Solyak,
Steinar Stapnes, Toshiaki Tauchi, Nobu Toge, Nicholas Walker,
Akira Yamamoto, Kaoru Yokoya

Acknowledgements

We acknowledge the support of BMWF, Austria; MinObr, Belarus; FNRS and FWO, Belgium; NSERC, Canada; NSFC, China; MPO CR and VSC CR, Czech Republic; Commission of the European Communities; HIP, Finland; IN2P3/CNRS, CEA-DSM/IRFU, France; BMBF, DFG, Helmholtz Association, MPG and AvH Foundation, Germany; DAE and DST, India; ISF, Israel; INFN, Italy; MEXT and JSPS, Japan; CRI(MST) and MOST/KOSEF, Korea; FOM and NWO, The Netherlands; NFR, Norway; MNSW, Poland; ANCS, Romania; MES of Russia and ROSATOM, Russian Federation; MON, Serbia and Montenegro; MSSR, Slovakia; MICINN-MINECO and CPAN, Spain; SRC, Sweden; STFC, United Kingdom; DOE and NSF, United States of America.

Contents

Common preamble to Parts I and II 1

1. Introduction 3

2. General Parameters, Layout and Systems Overview 7
2.1. Introduction . . . 7
2.2. Top-Level Parameters . . . 8
2.2.1. Physics related machine parameters for 200–500 GeV centre-of-mass running 8
2.2.2. Special considerations for running at low centre-of-mass energy . . . 9
2.3. Accelerator Layout and Design . . . 10
2.3.1. Superconducting RF Main Linacs . . . 10
2.3.2. Electron Source . . . 13
2.3.3. Positron Source . . . 14
2.3.4. Damping Rings . . . 14
2.3.5. Ring to Main Linac . . . 16
2.3.6. Beam-Delivery System . . . 16
2.4. Site Dependent Designs . . . 18
2.4.1. Flat-topography site-dependent design (Americas and European sample sites) 19
2.4.2. Mountainous-topography site-dependent design (Asian sample sites) . . . 20
2.5. Luminosity and Energy Upgrade Options . . . 22

3. Main Linac and SCRF Technology 23
3.1. Overview of the ILC Main Linacs . . . 23
3.1.1. Introduction . . . 23
3.1.2. Linac layout . . . 24
3.1.3. Accelerator Physics . . . 26
3.1.4. Operation . . . 28
3.1.5. Linac Systems . . . 29
3.2. Cavity production specifications . . . 30
3.2.1. Cavity Design . . . 30
3.2.2. Cavity fabrication and surface processing . . . 31
3.3. Cavity integration . . . 34
3.3.1. Fundamental-mode power coupler . . . 35
3.3.2. Frequency tuner . . . 37
3.3.3. HOM couplers . . . 38
3.3.4. Helium tank and its interface . . . 39
3.3.5. Plug-compatible design . . . 40
3.4. Cryomodule design including quadrupoles . . . 41
3.4.1. Overview . . . 41

3.4.2. Cryomodule technical description . . . 42
3.4.3. Cryomodule testing . . . 49
3.4.4. Shipping of cryomodules between regions . . . 51
3.5. Cryogenic cooling scheme . . . 52
3.5.1. Cryogenic cooling scheme for the main linacs . . . 53
3.5.2. Heat loads and cryogenic-plant power . . . 54
3.5.3. Helium inventory . . . 55
3.5.4. Pressure code compliance . . . 56
3.6. RF power source . . . 56
3.6.1. Overview . . . 56
3.6.2. Modulator . . . 57
3.6.3. 10 MW Multi-Beam Klystron (MBK) . . . 59
3.6.4. Local power-distribution system . . . 61
3.6.5. RF power requirements . . . 63
3.7. Low-level RF (LLRF) control concept . . . 65
3.7.1. Overview of Low-level RF control requirements . . . 65
3.7.2. Vector-sum control of cavity fields . . . 65
3.7.3. Operation at the limits . . . 67
3.7.4. Individual cavity control . . . 67
3.7.5. LLRF operations . . . 68
3.7.6. LLRF system implementation . . . 68
3.8. Main-linac layout for a mountainous topography . . . 69
3.8.1. Introduction . . . 69
3.8.2. Linac layout and cryogenic segmentation . . . 69
3.8.3. The DKS high-power distribution System . . . 71
3.8.4. LLRF control for DKS . . . 72
3.9. Main-linac layout for a flat topography . . . 73
3.9.1. Introduction . . . 73
3.9.2. Linac layout and cryogenic segmentation . . . 73
3.9.3. The KCS high-power distribution system . . . 75
3.9.4. LLRF control for KCS . . . 77

4. Electron source **81**
4.1. Overview . . . 81
4.2. Beam Parameters . . . 81
4.3. System Description . . . 82
4.3.1. Photocathodes for Polarized Beams . . . 82
4.3.2. Polarized Electron Gun . . . 83
4.3.3. ILC Source Laser System . . . 83
4.3.4. Bunching and Pre-Acceleration . . . 85
4.3.5. Chicane, Emittance Measurement and Matching Sections . . . 85
4.3.6. The 5 GeV Superconducting Pre-Acceleration (Booster) Linac . . . 85
4.3.7. Linac to Damping Ring Beamline and Main e^- Source Beam Dump . . . 85
4.4. Accelerator Physics Issues . . . 86
4.4.1. DC Gun and Bunchers . . . 86
4.4.2. The 5 GeV Booster Linac and Linac to Damping Ring Line (eLTR) . . . 86
4.5. Accelerator Components . . . 88
4.5.1. Table of Parts Count . . . 88

5. Positron source **89**
5.1. Introduction . . . 89
5.2. Beam parameters . . . 89
5.3. System description . . . 90
5.3.1. Photon production . . . 92
5.3.2. Positron production & capture . . . 93
5.3.3. Positron transport . . . 93
5.3.4. 5 GeV SC Booster Linac . . . 93
5.3.5. Linac to Damping-Ring Beam Line . . . 94
5.4. Optics parameters . . . 94
5.5. Accelerator components . . . 95
5.5.1. Undulator . . . 95
5.5.2. Target . . . 96
5.5.3. Optical matching device . . . 97
5.5.4. Normal-conducting RF accelerator system . . . 97
5.5.5. Magnets . . . 98
5.5.6. Diagnostics . . . 98
5.5.7. Electron & photon beam dumps . . . 99

6. Damping Rings **101**
6.1. Introduction . . . 101
6.2. Top-level parameters and configuration . . . 101
6.3. Lattice description . . . 104
6.4. Beam Dynamics . . . 105
6.4.1. Emittance Tuning . . . 105
6.4.2. Dynamic aperture . . . 106
6.4.3. Collective Effects . . . 107
6.4.4. Electron Cloud . . . 107
6.4.5. Fast Ion Instability . . . 109
6.5. Vacuum System . . . 111
6.6. RF systems . . . 113
6.6.1. Baseline . . . 113
6.6.2. 10 Hz operation . . . 114
6.6.3. Luminosity upgrade . . . 114
6.7. Magnets and Power Supplies . . . 115
6.7.1. Superconducting Wigglers . . . 115
6.7.2. Conventional Magnets . . . 115
6.7.3. Power Supply System . . . 116
6.8. Instrumentation and Feedback Systems . . . 116
6.8.1. Diagnostics and Instrumentation . . . 116
6.8.2. Fast Feedback systems . . . 116
6.9. Injection and Extraction systems . . . 117

7. Ring to Main Linac **119**
7.1. Overview . . . 119
7.2. Beam Parameters . . . 119
7.3. System Description . . . 120
7.3.1. Layout . . . 120

7.3.2. Geometry Match . . . 121
7.3.3. Sub-systems . . . 121
7.3.4. Collimation and diagnostics . . . 125
7.3.5. Tuning, Correction, and Operations . . . 126
7.4. Accelerator Physics Issues . . . 128
7.4.1. Incoherent (ISR) and Coherent (CSR) Synchrotron Radiation . . . 128
7.4.2. Stray Fields . . . 128
7.4.3. Beam-Ion Instabilities . . . 128
7.4.4. Static Misalignments . . . 128
7.4.5. RF Phase and Amplitude Jitter . . . 129
7.4.6. Halo Formation from Scattering . . . 130
7.4.7. Space-Charge effects . . . 130
7.4.8. Wake field in SRF cavities and collimators . . . 130
7.4.9. Emittance preservation . . . 130
7.5. Accelerator Components . . . 131
7.5.1. Magnets, Pulsed elements . . . 131
7.5.2. Vacuum Systems . . . 131
7.5.3. Cryogenics . . . 132
7.5.4. Service tunnels and Alcoves . . . 132

8. Beam Delivery System and Machine Detector Interface 133
8.1. Introduction . . . 133
8.2. Parameters and System Overview . . . 133
8.3. Lattice description . . . 136
8.3.1. Diagnostics, Tune-up dump, Machine Protection . . . 136
8.3.2. Collimation System . . . 137
8.3.3. Final focus . . . 138
8.3.4. Extraction line . . . 139
8.3.5. Beam dynamics and emittance growth . . . 141
8.4. Interaction-Region Layout and Machine-Detector Interface . . . 141
8.4.1. Requirements and boundary conditions . . . 141
8.4.2. The push-pull system . . . 141
8.4.3. Final focus . . . 142
8.4.4. Experimental-area layout and infrastructure . . . 144
8.4.5. Shielding . . . 145
8.4.6. Detector services . . . 146
8.5. Magnets and power supplies . . . 147
8.5.1. Tail-Folding Octupoles . . . 147
8.6. Vacuum system . . . 147
8.6.1. Wakes in vacuum system . . . 147
8.6.2. Beam-gas scattering . . . 148
8.6.3. Vacuum-system design . . . 148
8.7. Instrumentation and feedback systems . . . 148
8.7.1. Feedback systems and Stability . . . 148
8.7.2. Energy, Luminosity and polarization measurements . . . 149
8.7.3. Diagnostic and Correction devices . . . 151
8.8. Beam dumps and Collimators . . . 152
8.8.1. Main Dumps . . . 152

8.8.2. Collimators . . . 153
8.9. Crab cavity system . . . 154
8.10. Accelerator Components . . . 155

9. Global Accelerator Control Systems 157
9.1. Overview . . . 157
9.2. Requirements and Technical Challenges . . . 157
9.2.1. Scalability . . . 157
9.2.2. High Availability . . . 157
9.2.3. Support extensive automation and beam-based feedback . . . 158
9.2.4. Synchronous Control-System Operation . . . 158
9.2.5. Precision RF-Phase-Reference Distribution . . . 158
9.2.6. Standards and Standardisation, Quality Assurance . . . 158
9.2.7. Requirements on Technical Equipment . . . 158
9.2.8. Diagnostic Interlock Layer . . . 159
9.3. Impact of Requirements on the Control-System Model . . . 159
9.4. Control System Model . . . 160
9.4.1. Functional Model . . . 160
9.4.2. Physical Model . . . 162
9.4.3. Pulse-to-Pulse (5 Hz) Feedback Architecture . . . 163
9.5. Remote Access – Remote Control . . . 164
9.6. Timing and RF-Phase Reference . . . 164
9.6.1. RF-Phase-Reference Generator . . . 164
9.6.2. Timing and RF-Phase-Reference Distribution . . . 164
9.6.3. Timing and Sequence Generator . . . 165
9.7. Beam-based Feedback . . . 165
9.7.1. Architecture for Intra-Bunch Feedback Systems . . . 166
9.7.2. Hardware Implementation . . . 166

10. Availability, Commissioning and Operations 167
10.1. Overview . . . 167
10.2. Availability . . . 167
10.2.1. Importance of Availability . . . 167
10.2.2. Methodology . . . 168
10.2.3. Availability Studies . . . 168
10.3. Bunch Timing and Path-length Considerations . . . 169
10.4. Commissioning . . . 169
10.4.1. Phased Commissioning . . . 169
10.5. Radiation shielding and Personnel Protection System zones . . . 170
10.5.1. Summary of Regions' Radiation Requirements . . . 170
10.5.2. Summary of the Radiation Safety Design for the Main Linac . . . 170
10.5.3. PPS Zones . . . 171
10.5.4. Shielding between PPS Zones . . . 172
10.6. Machine-Protection System . . . 172
10.6.1. Overview . . . 172
10.6.2. Single-Pulse Damage . . . 172
10.6.3. Average Beam-Loss-Limiting System . . . 173
10.6.4. Abort Kickers and Dumps . . . 173

10.6.5. Restart Ramp Sequence . . . 174
10.6.6. Fault-Analysis Recorder System . . . 174
10.6.7. Rapidly Changing Fields . . . 174
10.6.8. Sequencing System Depending on Machine State . . . 175
10.6.9. Protection Collimators . . . 175
10.7. Operability . . . 175
10.7.1. Feedback systems . . . 175

11. Conventional Facilities and Siting **177**
11.1. Introduction . . . 177
11.2. Overall Layout and Common Design Criteria . . . 178
11.3. General site requirements . . . 179
11.4. Asian region (Mountain topography) . . . 179
11.4.1. Siting studies . . . 179
11.4.2. Civil construction . . . 181
11.4.3. Mechanical services . . . 186
11.4.4. Electrical . . . 189
11.4.5. Life safety and egress . . . 191
11.5. European region (Flat topography) . . . 192
11.5.1. Siting studies . . . 192
11.5.2. Civil construction . . . 196
11.5.3. Mechanical . . . 200
11.5.4. Electrical . . . 200
11.5.5. Life safety and egress . . . 200
11.6. Americas region (Flat topography) . . . 201
11.6.1. Siting studies . . . 201
11.6.2. Civil construction . . . 203
11.6.3. Mechanical . . . 206
11.6.4. Electrical . . . 210
11.6.5. Life safety and egress . . . 213
11.7. Handling equipment . . . 214
11.7.1. Introduction . . . 214
11.7.2. Transport operations . . . 215
11.7.3. Installed handling equipment . . . 215
11.7.4. Mobile handling equipment . . . 217
11.8. Alignment and survey . . . 218
11.8.1. Calibration Facility . . . 219
11.8.2. Geodesy and Networks . . . 219
11.8.3. Civil Engineering Phase . . . 219
11.8.4. Fiducialisation . . . 219
11.8.5. Installation and Alignment . . . 220
11.8.6. Information Systems . . . 220
11.9. Installation . . . 221
11.9.1. Scope . . . 221
11.9.2. Methodology . . . 221
11.9.3. Model of Main-Linac Installation . . . 222

12. Possible upgrade and staging options **225**
12.1. Introduction . . . 225
12.2. Parameters . . . 226
12.2.1. Luminosity upgrade . . . 226
12.2.2. Energy upgrade . . . 227
12.3. Scope of the luminosity upgrade . . . 227
12.3.1. Main linacs . . . 227
12.3.2. Damping Rings . . . 229
12.3.3. Electron and positron sources . . . 229
12.3.4. RTML (bunch compressors) . . . 230
12.3.5. Beam Delivery System . . . 230
12.4. Scope of energy upgrade to 1 TeV centre-of-mass energy . . . 230
12.4.1. Positron source . . . 232
12.4.2. RTML . . . 233
12.4.3. Beam Delivery System (BDS) . . . 233
12.4.4. AC Power requirements . . . 233
12.5. A Light Higgs Factory (250 GeV centre-of-mass) as a possible first-stage. . . . 234
12.6. Photon Collider Option . . . 235
12.7. Summary . . . 236

13. Project Implementation Planning **237**

14. Construction schedule **241**
14.1. Introduction . . . 241
14.2. Scope and assumptions . . . 241
14.3. Constructing the accelerator complex . . . 243
14.3.1. Civil engineering . . . 244
14.3.2. Conventional facilities installation . . . 245
14.3.3. Accelerator-Components Installation . . . 246
14.3.4. High-tech Mass-Production Plans . . . 246
14.4. Commissioning the ILC . . . 247
14.4.1. Early Commissioning (BDS, part of ML, DR, and PLTR) . . . 247
14.4.2. Global commissioning . . . 248
14.5. Detectors . . . 249

15. ILC TDR Value Estimate **253**
15.1. Introduction . . . 253
15.1.1. Overview . . . 253
15.1.2. Inflation Indices . . . 255
15.2. Goals . . . 256
15.3. Scope . . . 256
15.4. Methodology . . . 257
15.4.1. Definition of Value Estimating . . . 257
15.4.2. Definition of the ILCU for the TDR . . . 257
15.5. Cost Guidelines and Learning Curves . . . 260
15.5.1. General guidelines . . . 260
15.5.2. Specific Guidelines . . . 261
15.5.3. Learning curves . . . 262

15.6. Development and Format of the Estimate . . . 263
15.6.1. Estimate Development . . . 263
15.6.2. Format of the Estimate . . . 263
15.7. Cost Basis . . . 263
15.7.1. Cavities and Cryomodules . . . 263
15.7.2. L-band High-Level RF Systems . . . 268
15.7.3. Conventional Facilities (CFS) . . . 272
15.7.4. Installation . . . 277
15.7.5. Cryogenic Systems . . . 278
15.7.6. Magnet and Magnet Power-Supply Systems . . . 279
15.7.7. Vacuum Systems . . . 280
15.7.8. Instrumentation . . . 280
15.7.9. Dumps and Collimators . . . 281
15.7.10. Integrated Controls and Low-Level RF (LLRF) . . . 281
15.7.11. Computing Infrastructure . . . 282
15.7.12. Other High-Level RF . . . 282
15.7.13. Accelerator-Area-specific cost bases . . . 282
15.7.14. Management and Administration . . . 283
15.7.15. Summary . . . 284
15.8. Value and Labour Estimates for the Construction of the ILC . . . 285
15.8.1. Escalation and re-statement of the RDR . . . 285
15.8.2. Value Estimate for the TDR . . . 285
15.8.3. Explicit Labour Estimate for the TDR . . . 287
15.8.4. Site Dependence of the Value and Labour Estimates . . . 288
15.9. Cost Uncertainties, Confidence Levels and Cost Premiums . . . 289
15.9.1. General Methodology . . . 289
15.9.2. Median Estimates and Cost Premiums for Groups of Cost Elements . . . 290
15.9.3. Methodology for Assigning Cost Premiums for TDR Cost Elements . . . 291
15.9.4. Overall Cost Premiums for the TDR Value Estimate . . . 291
15.9.5. Overall Cost Premiums for the TDR Labour Estimate . . . 291
15.10. Value and Labour Time Profiles . . . 292
15.11. Value and Labour Estimates for Operations . . . 293
15.12. Value and Labour Estimates for Upgrade and Staging Options . . . 294
15.12.1. Value and Labour Estimate for Luminosity Upgrade . . . 294
15.12.2. Value Estimate and Labour Estimate for 1 TeV Energy Upgrade . . . 295
15.12.3. Value and Labour Estimates for a Light Higgs Factory as a First-Stage Option 297
15.12.4. Summary . . . 298

A. Evolution of the ILC design in the Technical Design Phase 299
A.1. The goals of the Technical Design Phase . . . 299
A.2. Approach to cost constraint and re-baselining the ILC . . . 301
A.3. Proposed top-level design modifications and their impact . . . 303

Bibliography 307

List of Signatories 323

Common preamble to Parts I and II

The International Linear Collider (ILC) is a linear electron-positron collider based on 1.3 GHz superconducting radio-frequency (SCRF) accelerating technology. It is designed to reach 200-500 GeV (extendable to 1 TeV) centre-of-mass energy with high luminosity. The design is the result of over twenty years of linear collider R&D, beginning in earnest with the construction and operation of the SLC at SLAC. This was followed by extensive development work on warm X-band solutions (NLC/JLC) and the pioneering work by the TESLA collaboration in the 1990s on superconducting L-band RF. In 2004, the International Technology Review Panel, set up by the International Committee for Future Accelerators, ICFA, selected superconducting technology for ILC construction. The Global Design Effort (GDE) was set up by ICFA in 2005 to coordinate the development of this technology as a worldwide international collaboration. Drawing on the resources of over 300 national laboratories, universities and institutes worldwide, the GDE produced the ILC *Reference Design Report* (RDR) [1–4] in August 2007. The report describes a conceptual design for the ILC and gives an estimated cost and the required personnel from collaborating institutions.

The work done by the GDE during the RDR phase identified many high-risk challenges that required R&D, which have subsequently been the focus of the worldwide activity during the Technical Design Phase. This phase has achieved a significant increase in the achievable gradient of SCRF cavities through a much better understanding of the factors that affect it. This improved understanding has permitted the industrialisation of the superconducting RF technology to more than one company in all three regions, achieving the TDP goal of 90 % of industrially produced cavities reaching an accelerating gradient of 31.5 MV/m. A further consequence is an improved costing and construction schedule than was possible in the RDR. Other important R&D milestones have included the detailed understanding of the effects of, and effective mitigation strategies for, the "electron-cloud" effects that tend to deteriorate the quality of the positron beam, particularly in the ILC damping rings. The achievement of the R&D goals of the TDR has culminated in the publication of this report, which represents the completion of the GDE's mandate; as such, it forms a detailed solution to the technical implementation of the ILC, requiring only engineering design related to a site-specific solution to allow the start of construction.

Volume 3 (Accelerator) of the *Technical Design Report* is divided into two separate parts reflecting the GDE's primary goals during the Technical Design Phase period (2007–2012):

Part I: R&D in the Technical Design Phase summarises the programmes and primary results of the risk-mitigating worldwide R&D including industrialisation activities.

Part II: Baseline Design provides a comprehensive summary of the reference layout, parameters and technical design of the accelerator, including an updated cost and construction schedule estimate.

The R&D results and studies of cost-effective solutions for the collider presented in Part I directly support the design presented in Part II, which is structured as a technical reference.

Chapter 1
Introduction

This reference report contains the technical specifications and design for an International Linear Collider that is based on mature technology and is relatively low risk. The heart of the accelerator consists of two approximately 11-km long SCRF main linacs, based on the technology developed by the TESLA collaboration and proposed in 2001 for the TESLA linear collider [5]. The updated design reflects the significant worldwide developments in this technology, with the establishment of R&D infrastructure as well as a significant industrial base in the Americas, Asia and Europe. The global high-gradient SCRF R&D driven by the GDE has succeeded in routinely establishing the required 35 MV/m average performance, with every indication that this could be exceeded in future years. Integrated systems tests at the TTF2/FLASH accelerator in DESY, Hamburg have demonstrated many of the design and performance parameters for the ILC, and this currently unique facility will soon be joined by similar test accelerators in both KEK, Japan, and Fermilab, USA.

The design evolution since the original RDR reflects the results of this R&D, a re-evaluation of cost-performance trade-offs, and a more detailed considerations of site-specific cost-optimum design options. Beyond the fundamental R&D, the on-going industrialisation of the technology has enabled the GDE to provide realistic industrial studies for globally mass-producing the approximately 18,000 SCRF nine-cell cavities required and assembling them into 1750 cryomodules. These studies have resulted in a relatively robust and defensible cost estimate, as well as clear concepts as to how the machine could be constructed as an international project based predominantly on in-kind contributions, complete with a realistic construction and installation schedule. The system designs and associated cost estimates reported here are considered sufficiently complete to form a sound basis for a "Proposal to Construct" soon after an International ILC Organisation has been formalised and a specific site has been selected.

Extensive studies of the physics potential of the ILC have taken place over many years [2, 6]. They have explored the complementarity of the ILC with the Large Hadron Collider (LHC) as well as the unique discovery potential of the ILC. The identification of a Higgs boson at the LHC [7–10] validates these studies of Standard Model physics at the ILC, not only with regard to the Higgs but also top physics and precisions studies. The lack to date of any signal for physics beyond the Standard Model gives no explicit motivation to go to energies higher than the 500 GeV of the first stage of the ILC while placing a premium on the flexibility of the ILC to be upgraded to energies up to and beyond 1 TeV. In addition, the precision studies possible at the ILC may well give indications of new physics at much higher energies.

The ILC design detailed in this volume can achieve the performance during the first years of operation that fullfil the physics potential of the ILC as detailed by the above process. These design criteria are:

- A continuous centre-of-mass energy range between 200 GeV and 500 GeV
- A peak luminosity of approximately 2×10^{34} cm^{-2} s^{-1} at 500 GeV centre-of-mass

- 80 % electron polarisation at the Interaction Point (IP)
- A relative energy stability and precision of $\leq$0.1%
- An option for 50 to 60 % positron polarisation

In addition the machine must be upgradeable to a centre-of-mass energy of 1 TeV, which at a minimum implies a site that can be expanded from 30 to 50 km in length. The ILC design documented here guarantees a rich, varied and flexible physics program to complement that of the Large Hadron Collider (LHC).

The parameters, the basic layout of the machine and the design of most of the technical subsystems represent a single generic solution, independent of considerations of possible site constraints. In particular, the design of the main linac technical systems (cavities, cryomodules, klystrons and modulators etc.) are independent of the final location of the machine. In addition, the design of the other accelerator systems (damping rings, electron and positron sources, beam delivery system) are also 'generic'. However, the optimum systems design and the dependence of choice of site – in particular the solutions for the main SCRF linac RF-power distribution and the Conventional Facilities and Siting (CFS) – have been addressed during the technical design phase. As a result, two variants of Civil and Technical design are elaborated in this report:

Flat topography refers to a site-specific design where relatively flat surface areas are readily available for equipment and service buildings, with access being provided to the underground accelerator tunnels via vertical shafts. The LHC is an example of such a topography, and both the European and Americas regional sample sites (CERN and FNAL respectively) are based on this design variant;

Mountainous topography refers to a site-specific design more suited to a steeply sloping surface environment where available space for 'surface buildings' is at a premium. In this case, the majority of equipment is housed underground, and access is provided by horizontal (or gently sloping) access tunnels. The Asian sample sites in Japan are based on this design variant.

In both cases, a significant difference in underground geology and local experience has also strongly influenced the choice of underground tunnel solutions. The two site-dependent variants are further differentiated by the approach adopted in supplying the RF power for the superconducting linacs: one predominantly surface based (Klystron Cluster Scheme, or KCS), and thus more suited to the flat-topography variant; and one a more traditional Distributed Klystron Scheme (DKS) suitable for underground implementation in the mountainous-region design. Each approach has significant differences in the criteria and requirements for the conventional facilities and civil engineering. They provide mature solutions which provide the flexibility to allow the ILC to be adapted relatively quickly to any emerging potential host site.

Despite the major differences of the two site variants, the core requirements, accelerator layout and technologies remain the same. Figure 1.1 describes the structure of the design work presented in the remainder of this report.

The ILC has from the outset been set up as a large science project with international governance from design through construction to operation. There have been several regional studies of the pros and cons of different approaches to the governance of large international science projects and the ILC GDE independently studied the issues and produced a Project Implementation Planning document [11]. This is summarised in Chapter 13. The issues discussed include funding models with both common funds and in-kind contributions from international partners, and the unique and extensive responsibilities of the host region or nation.

The remainder of this report – TDR Part II: ILC Baseline Design – provides a comprehensive description of the complete current baseline technical design and cost of the ILC, including the

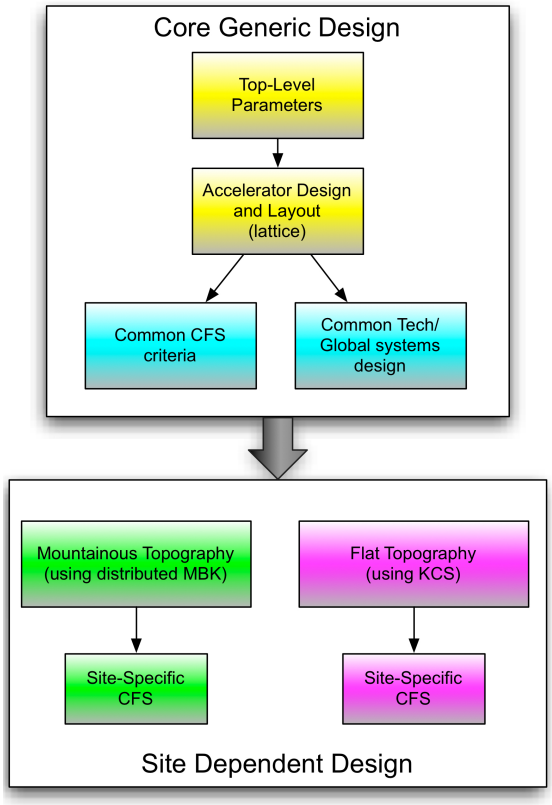

Figure 1.1
Approach to the site-specific design variants for the ILC.

site dependent variants. An overview of the design is given in Section 2.1. In brief, the 500 GeV centre-of-mass energy ILC has a footprint of ∼31 km. At its heart are two 11 km long linacs based on superconducting RF niobium cavities running at 1.3 GHz, operating at an average gradient of 31.5 MV/m and with a pulse length of 1.6 ms. The linacs are designed to accelerate beams of electrons and positrons to energies up to 500 GeV and collide them at energies up to 1 TeV. The electron and positron beams themselves are produced in different ways: the electron beams are obtained from a polarised source; positrons are produced via pair-conversion of high-energy photons produced in an undulator, which means that polarised positrons are more difficult to produce and are thus a design option. The high luminosity required to fulfil the ILC's ambitious physics programme can only be obtained if both electron and positron beams are "cooled" significantly, compressing their phase space at 5 GeV via damping rings with a circumference of 3.2 km. This low emittance is maintained by a beam-transport system followed by a two-stage compressor which produces bunch trains consisting of 1312 bunches in a train of length ∼500 ns at a repetition rate of 5 Hz on entry to the accelerating linacs. After acceleration, the beams are brought into collision by 2.25 km long beam-delivery systems, which bring the two beams into collision with a 14 mrad crossing angle and with the optimum parameters to maximise the produced luminosity.

Further detailed technical documentation is available in the ILC Technical Design Documentation EDMS system (http://ilc-edms.desy.de) or directly from http://www.linearcollider.org/ILC/GDE/technical-design-documentation, and are referenced in this report where appropriate. For details of the Technical Design Phase R&D programme, see TDR Part I.

Chapter 2
General Parameters, Layout and Systems Overview

2.1 Introduction

This chapter is intended to provide an introductory overview of the ILC machine design, its top-level parameters and sub-system functionality, in preparation for the more detailed descriptions in the remaining chapters of the report. Figure 2.1 shows a schematic view of the overall layout of the ILC, indicating the location of the major sub-systems:

- a polarised electron source based on a photocathode DC gun;
- an undulator-based positron source, driven by a the high-energy main electron beam;
- 5 GeV electron and positron damping rings (DR) with a circumference of 3.2 km, housed in a common tunnel at the centre of the ILC complex;
- beam transport from the damping rings to the main linacs, including acceleration to 15 GeV followed by a two-stage bunch compressor system prior to injection into the main linac;
- two 11 km long main linacs, utilising 1.3 GHz SCRF cavities, operating at an average gradient of 31.5 MV/m, with a pulse length of 1.6 ms;
- a $2\times$2.25 km-long beam-delivery system, which brings the two beams into collision with a 14 mrad crossing angle, at a single interaction point which can be shared by two detectors (push-pull).

The total footprint is $\sim$31 km. The electron source, positron source (including a low-powered auxiliary source), and the electron and positron damping rings are centrally located around the interaction region (IR) in the *central region*. The damping ring complex is laterally displaced by a sufficient distance so as not to interfere with the detector hall, and is connected to the main accelerator housing via transfer tunnels. The electron and positron sources themselves are housed in the same (main accelerator) tunnels as the beam-delivery systems, to reduce the overall cost and scope of the underground construction of the central region.

In the remainder of this chapter, Sections 2.2 and 2.3 provide an overview of the top-level parameters and the common accelerator description. Section 2.4 provides an introduction to the two site-dependent solutions, mostly pertaining to conventional facilities and siting. Finally, Section 2.5 briefly introduces the scope of the optional luminosity and energy upgrades.

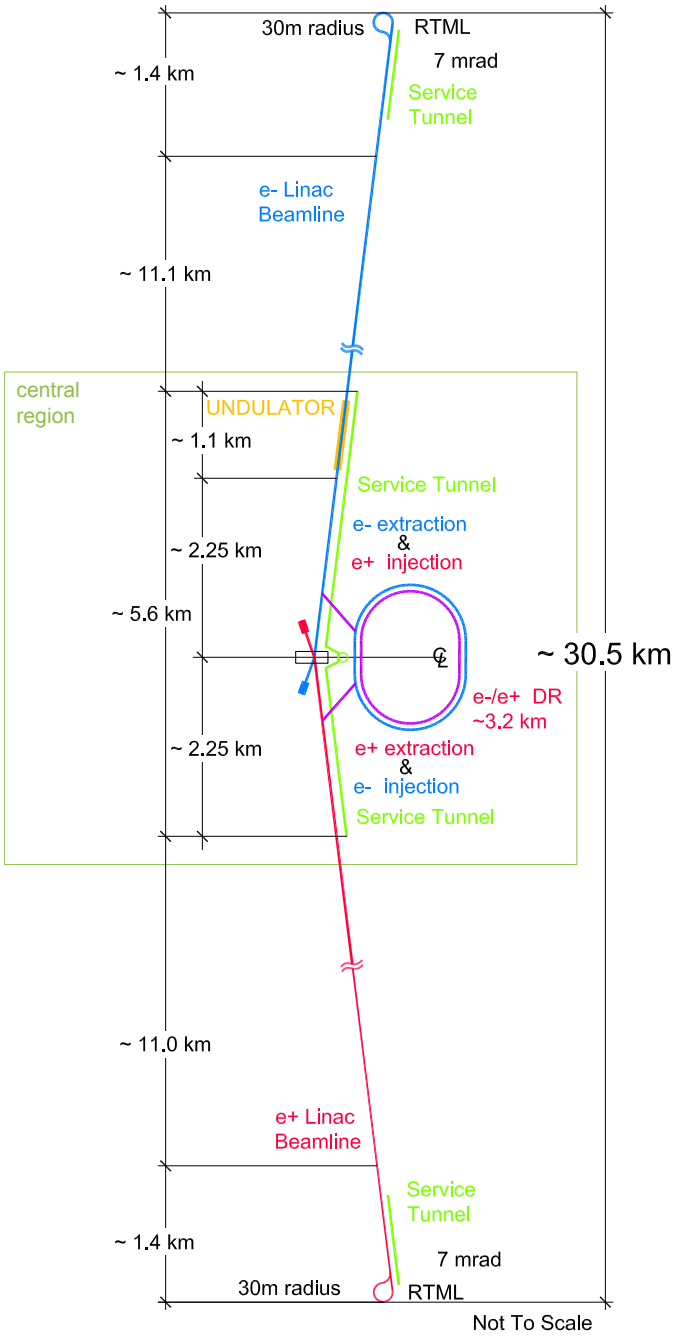

Figure 2.1
Schematic layout of the ILC complex for 500 GeV CM.

2.2 Top-Level Parameters

2.2.1 Physics related machine parameters for 200–500 GeV centre-of-mass running

The top-level parameters for the baseline operational range of centre-of-mass energies from 200 to 500 GeV have been optimised to provide the maximum attainable physics performance with a relatively low risk and minimum cost. Table 2.1 shows the primary parameters for 200, 250, 350 and 500 GeV centre-of-mass operation.

The choice of parameters represent trade-offs between the constraints imposed by the various accelerator sub-systems:

- For the damping rings, bunch charge, bunch spacing and the total number of bunches are limited by various instability thresholds. The most important is the electron cloud in the positron ring; other factors include realistically achievable injection and extraction kicker pulse rise-times and the desire to minimise the circumference of the rings and thereby the cost.

Table 2.1. Summary table of the 200–500 GeV baseline parameters for the ILC. The reported luminosity numbers are results of simulation [12]

Centre-of-mass energy	E_{CM}	GeV	200	230	250	350	500
Luminosity pulse repetition rate		Hz	5	5	5	5	5
Positron production mode			10 Hz	10 Hz	10 Hz	nom.	nom.
Estimated AC power	P_{AC}	MW	114	119	122	121	163
Bunch population	N	$\times 10^{10}$	2	2	2	2	2
Number of bunches	n_b		1312	1312	1312	1312	1312
Linac bunch interval	Δt_b	ns	554	554	554	554	554
RMS bunch length	σ_z	µm	300	300	300	300	300
Normalized horizontal emittance at IP	$\gamma\epsilon_x$	µm	10	10	10	10	10
Normalized vertical emittance at IP	$\gamma\epsilon_y$	nm	35	35	35	35	35
Horizontal beta function at IP	β_x^*	mm	16	14	13	16	11
Vertical beta function at IP	β_y^*	mm	0.34	0.38	0.41	0.34	0.48
RMS horizontal beam size at IP	σ_x^*	nm	904	789	729	684	474
RMS vertical beam size at IP	σ_y^*	nm	7.8	7.7	7.7	5.9	5.9
Vertical disruption parameter	D_y		24.3	24.5	24.5	24.3	24.6
Fractional RMS energy loss to beamstrahlung	δ_{BS}	%	0.65	0.83	0.97	1.9	4.5
Luminosity	L	$\times 10^{34}$ cm^{-2} s^{-1}	0.56	0.67	0.75	1.0	1.8
Fraction of L in top 1% E_{CM}	$L_{0.01}$	%	91	89	87	77	58
Electron polarisation	P_-	%	80	80	80	80	80
Positron polarisation	P_+	%	30	30	30	30	30
Electron relative energy spread at IP	$\Delta p/p$	%	0.20	0.19	0.19	0.16	0.13
Positron relative energy spread at IP	$\Delta p/p$	%	0.19	0.17	0.15	0.10	0.07

- The maximum length of the beam pulse is constrained by the decision to limit the length of the Main Linac RF pulse to the $\sim$ 1.6 ms now routinely achieved in the available 1.3 GHz 10 MW multi-beam klystrons and modulators. The beam current is further constrained by the need to minimise the required number of klystrons (peak power), as well as from consideration of high-order modes (cryogenic load and beam dynamics). Dynamic cryogenic load (refrigeration) is also a cost driver, and limits the repetition rate of the machine.
- Both the electron and positron sources set constraints on the achievable beam-pulse parameters. For the laser-driven photo-cathode polarised electron source, the limits are set by the laser; for the undulator-based positron source, the limits are set by consideration of power deposition in the photon target. The beam-pulse length is further constrained by the achievable performance of the warm RF capture sections (both sources).
- At the interaction points, single bunch parameters are limited by the strong beam-beam effects and a desire to control both beam-beam backgrounds and the kink instability.

Finally, a careful reevaluation of the cost-performance balance has resulted in a choice of parameters which are considered relatively low risk and cost effective. All the primary cost related parameters have been either directly demonstrated, or represent justifiable extrapolations from the current state of the art.

2.2.2 Special considerations for running at low centre-of-mass energy

While the maximum energy performance requirement dictates many of the key parameters and the overall geometry and cost of the machine, attention needs to be given to providing sufficient luminosity at the lower centre-of-mass-energy range, and in particular <300 GeV. Two issues limit the possible performance at these lower energies:

- positron production from the undulator-based source is significantly degraded for electron beam energy below 150 GeV;
- the beam divergence at the interaction point is nominally constrained by the collimation depth, which results in a γ^2 scaling of the luminosity, rather than the traditionally assumed γ-scaling.

The solution adopted for the current baseline for the positron source is to have an additional electron pulse at 150 GeV energy to make positrons. This additional pulse would be interleaved with

the nominal 5 Hz luminosity production pulse. This so-called 10 Hz operation mode leads to several design criteria for the baseline:

- Both electron and positron damping rings must now damp the beam in 100 ms instead of the nominal 200 ms. This requires additional wigglers and RF in the ring.
- The positron damping ring is 'empty' for 100 ms, after which the current is ramped up in ∼1 ms (and similarly ramped down during extraction). Dealing with transient beam loading requires an additional RF power overhead (approximately 15%).
- All the linacs for the electron machine (capture RF, 5 GeV booster linac, bunch compressors and main linac) must run at 10 Hz.
- The positron production pulse (150 GeV beam) must be safely extracted after the source undulator and dumped, requiring an additional pulsed magnet and extraction beamline system.
- A pulsed-magnet steering system is required upstream of the source undulator (downstream of the main electron linac) to compensate for the difference in trajectory between the 150 GeV positron production and <150 GeV luminosity pulses.

The 10 Hz mode is made cost effective by the fact the total RF power and cryoload for the main (electron) linac does not exceed the 500 GeV case when the beam energy (and therefore the main linac gradient) is reduced below 150 GeV. For the electron bunch compressor and source linacs, the AC power requirement effectively doubles for the 10 Hz operation mode. The 10 Hz mode also drives the design criteria and power requirements for the damping rings.

To mitigate the beam-divergence constraint at the IP, a shorter FD arrangement is used for $E_{\mathrm{cm}} \leq 300\,\mathrm{GeV}$, which increases the collimation depth and hence the IP beam divergence (by up to 30 % in the horizontal plane). The FD will be implemented in a modular design to accommodate both high- and low-energy running configurations, thus avoiding the need to exchange the magnet cryostat.

There are no issues with running the main SCRF linacs at reduced gradient in order to produce lower centre-of-mass energy. The lower average gradient results in a shorter fill time and overall higher RF-to-beam power efficiency. Simulations of the beam dynamics have indicated no significant additional degradation of vertical emittance.

2.3 Accelerator Layout and Design

2.3.1 Superconducting RF Main Linacs

The ILC Main Linacs accelerate the beams from 15 GeV (after acceleration in the upstream bunch compressors) to a maximum energy of 250 GeV. Beam acceleration in each linac is provided by approximately 7,400 ∼1 m-long superconducting niobium cavities consisting of nine elliptical cells (see Fig. 2.2) operating at 2 K, assembled into ∼850 cryomodules. The average gradient of the cavities is 31.5 MV/m (for 500 GeV centre-of-mass beam energy), with a corresponding $Q_0 \geq 10^{10}$. A random cavity-to-cavity gradient spread of ±20% is assumed to accommodate expected mass-production variations in the maximum achievable gradient.

For an average of 31.5 MV/m operation with the nominal beam current of 5.8 mA, the optimal matched $Q_L \approx 5.4 \times 10^6$. This corresponds to a cavity fill time of 925 µs, which, together with the nominal beam pulse of 727 µs, requires a total RF pulse length of 1.65 ms.

As well as the adjustable high-power coupler, the cavity package includes the cavity mechanical tuner, which is integrated into the titanium helium vessel of the cavity. In addition to a slow mechanical tuner (used for initial tuning and slow drift compensation), a fast piezo-driven tuner is also included to dynamically compensate Lorentz-force detuning during the RF pulse.

Figure 2.2
A 1.3 GHz superconducting nine-cell niobium cavity.

The Main Linacs are constructed almost entirely from the two standard variants of ILC cryomodule, both 12.65 m long: a Type A module with nine 1.3 GHz nine-cell cavities; and Type B with eight nine-cell cavities and one superconducting quadrupole package located at the centre of the module. The Main Linac has a FODO lattice structure, with a quadrupole (Type B module) every third cryomodule.

The cryomodule design is a modification of the Type-3 version (Fig. 2.3) developed and used at DESY in the TTF2/FLASH accelerator, and also being used for the 100 cryomodules currently being produced by industry for the European X-Ray FEL (XFEL), also based at DESY. Within the cryomodules, a 300 mm-diameter helium-gas return pipe serves as a strongback to support the nine cavities and other beam-line components in the case of the Type-A module. For the Type-B module, the central cavity package is replaced by a superconducting quadrupole package that includes the quadrupole itself, a cavity BPM, and superconducting horizontal and vertical corrector dipole magnets. The quadrupoles establish the main-linac magnetic lattice, which is a weak-focusing FODO optics with an average beta function of ∼80 m. Every cryomodule also contains a 300 mm-long higher-order-mode beam-absorber assembly that removes energy through the 40-80 K cooling system from beam-induced higher-order modes above the cavity-cutoff frequency.

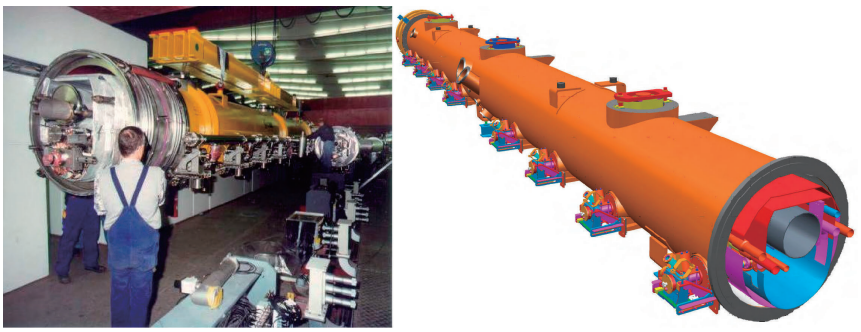

Figure 2.3
SCRF cryomodule. Left: a type-III module being installed at DESY's FLASH facility. Right: the ILC type-IV module.

To operate the cavities at 2 K, they are immersed in a saturated He II bath, and helium gas-cooled shields intercept thermal radiation and thermal conduction at 5–8 K and at 40–80 K. The estimated static and dynamic cryogenic heat loads per cryomodule at 2 K are approximately 1.7 W and 9.8 W, respectively. Liquid helium for the main linacs and the bunch-compressor RF is supplied from a total of 10–12 large cryogenic plants, each of which has an installed equivalent cooling power of ∼20 kW at 4.5 K. The plants are located in pairs approximately every 5 km along the linacs, with each plant cooling ∼2.5 km of contiguous linac. The main linacs follow the Earth's average curvature to simplify the liquid-helium transport.

The RF power is provided by 10 MW multibeam klystrons (MBK), each driven by a 120 kV Marx modulator. The 10 MW MBK is now a well established technology having achieved the ILC specifications and has several vendors worldwide (Fig. 2.4). The 120 kV Marx-modulator prototypes (Fig. 2.5) have achieved the required specifications and are now undergoing design for manufacture and cost.

Figure 2.4
Examples of industry produced 10 MW Multibeam Klystrons.

While the RF power source remains fundamentally the same, two cost-effective design variants for transporting the RF microwave power to the accelerator are considered in the baseline:

Figure 2.5
Prototype 120 kV Marx modulator.

- A more traditional Distributed Klystron Scheme (DKS), where a klystron is used to drive 39 cavities. The klystrons and modulators are distributed along the entire length of the SCRF linacs, in the same tunnel but shielded from the accelerator itself;
- A novel Klystron Cluster Scheme (KCS – see Fig. 2.6), where all the klystrons are located in 'clusters' in surface buildings located periodically along the linacs. The power from a single cluster of 19 klystrons (∼190 MW) is combined into an over-moded waveguide, which then transports the power down into the tunnel and along an approximately 1 km section of linac. For every three cryomodules, a Coaxial Tap Off (CTO) extracts ∼6.7 MW of power to a local power-distribution system feeding 26 cavities.

The advantages of KCS are primarily in transferring a large fraction of the heat load to the surface where it can be more cost-effectively removed, at the same time as reducing the required underground volume. The disadvantages are the need for additional surface buildings and shafts (one every 2 km of linac), and additional losses in the long waveguide distribution systems. In addition, significant R&D is still required compared to the mature and tested distributed system. Nonetheless, the estimated cost savings associated with KCS make it an attractive solution which has been adopted

for the Main Linacs in the flat-topography design variant.

The need for the extensive surface infrastructure does not make KCS a cost-effective solution for the mountainous topography, for which DKS has been adopted.

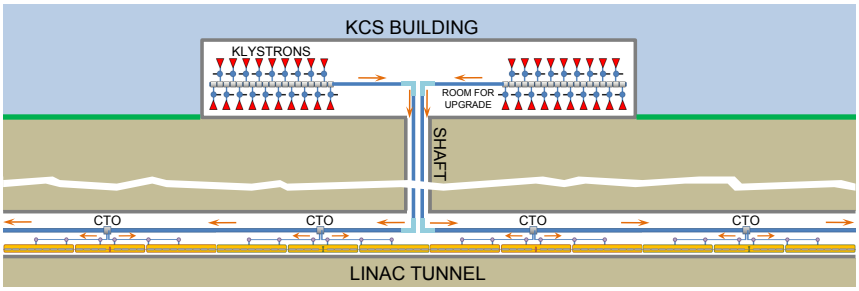

Figure 2.6
The Klystron Cluster Scheme (KCS).

For both KCS and DKS, the local power-distribution systems are essentially identical, other than the number of cavities being driven. A key requirement is the ability to tune remotely both the phase and forward power to each individual cavity, thereby supporting the $\pm 20\%$ gradient spread in the accelerator, and thereby maximising the average available gradient.

2.3.2 Electron Source

The polarised electron source is located in the central-region accelerator tunnel together with the positron Beam Delivery System. The beam is produced by a laser illuminating a strained GaAs photocathode in a DC gun, providing the bunch train with 90 % polarisation. Two independent laser and gun systems provide redundancy. Normal-conducting structures are used for bunching and pre-acceleration to 76 MeV, after which the beam is accelerated to 5 GeV in a superconducting linac using 21 standard ILC cryomodules. Before injection into the damping ring, superconducting solenoids rotate the spin vector into the vertical, and a separate superconducting RF structure is used for energy compression. The layout of the polarised electron source is shown in Fig. 2.7.

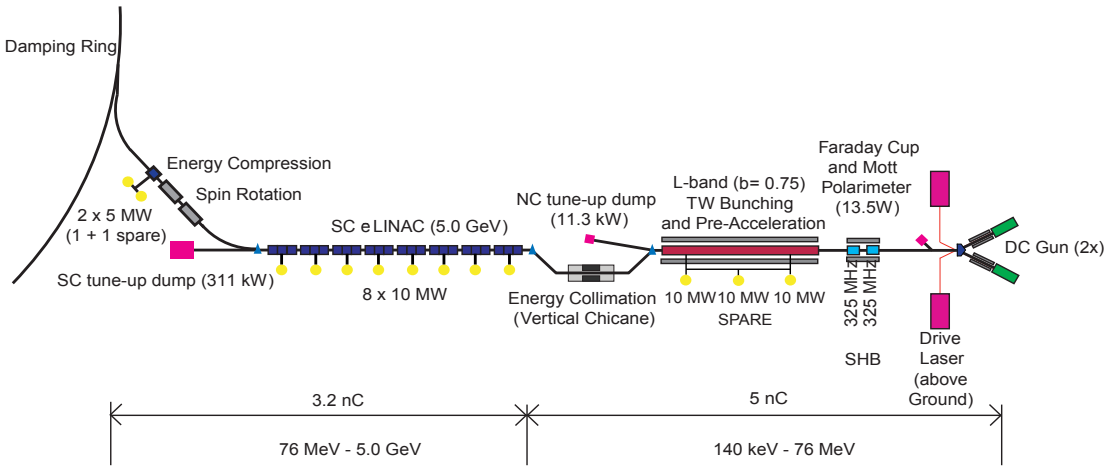

Figure 2.7. Schematic View of the Polarised Electron Source.

2.3.3 Positron Source

The major elements of the ILC positron source are shown in Fig. 2.8. The source uses photoproduction to generate positrons. After acceleration in the main linac, the primary electron beam is transported through a 147 m superconducting helical undulator which generates photons with energies from ∼10 MeV up to ∼ 30 MeV depending on the electron beam energy. The electron beam is then separated from the photon beam and displaced horizontally by approximately 2 m using a low-emittance chicane. The photons from the undulator are directed onto a rotating 0.4 radiation-length Ti-alloy target ∼ 500 meters downstream, producing a beam of electron and positron pairs. This beam is then matched using an optical-matching device (a pulsed flux concentrator) into a normal conducting (NC) L-band RF and solenoidal-focusing capture system and accelerated to 125 MeV. The electrons and remaining photons are separated from the positrons and dumped. The positrons are accelerated to 400 MeV in a NC L-band linac with solenoidal focusing. The beam is then accelerated to 5 GeV using superconducting L-band RF. Before injection into the damping ring, superconducting solenoids rotate the spin vector into the vertical, and a separate superconducting RF structure is used for energy compression.

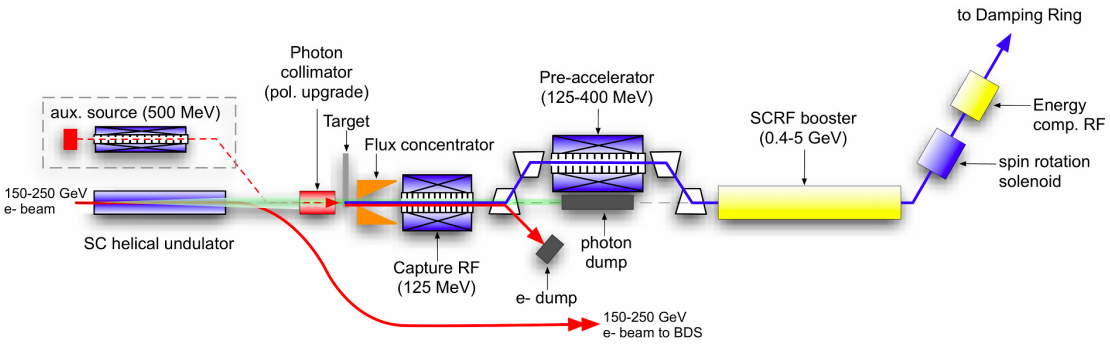

Figure 2.8. Overall Layout of the Positron Source.

The baseline design provides a polarisation of 30 %. Space for a ∼ 220 m undulator has been reserved for an eventual upgrade to 60 % polarisation, which would also require a photon collimator upstream of the target.

To allow commissioning and tuning of the positron and downstream systems when the high-energy electron beam is not available, a low-intensity auxiliary positron source is provided. This is effectively a conventional positron source, which uses a 500 MeV warm linac to provide an electron beam which is directed onto the photon target, providing a few percent of the nominal positron current.

To accommodate 10 Hz operation, a separate pulsed extraction line is required immediately after the undulator, to transport the 150 GeV electron-beam positron-production pulse to the high-power tune-up dump, located downstream in the Beam Delivery System.

The target and capture sections are high-radiation areas which require appropriate shielding and remote-handling facilities.

2.3.4 Damping Rings

The damping rings must accept e^- and e^+ beams with large transverse and longitudinal emittances and damp them (by five orders of magnitude for the positron vertical emittance) to the low-emittance beam required for luminosity production, within the 200 ms between machine pulses (100 ms for 10 Hz mode). In addition, they must compress on injection and decompress on extraction the ∼1 ms beam pulse by roughly a factor of 90 to fit into the ring circumference of 3.2 km.

The baseline design consists of one electron and one positron ring operating at a beam energy of 5 GeV. Both rings are housed in a single tunnel with one ring positioned directly above the other.

Space is foreseen in the tunnel for a third ring (second positron ring) as a possible upgrade. The damping ring complex is located in the central region, horizontally offset from the interaction region by approximately 100 m to avoid the detector hall. Two transfer tunnels connect the damping ring tunnel to the electron and positron main accelerator tunnels respectively (see Fig. 2.9).

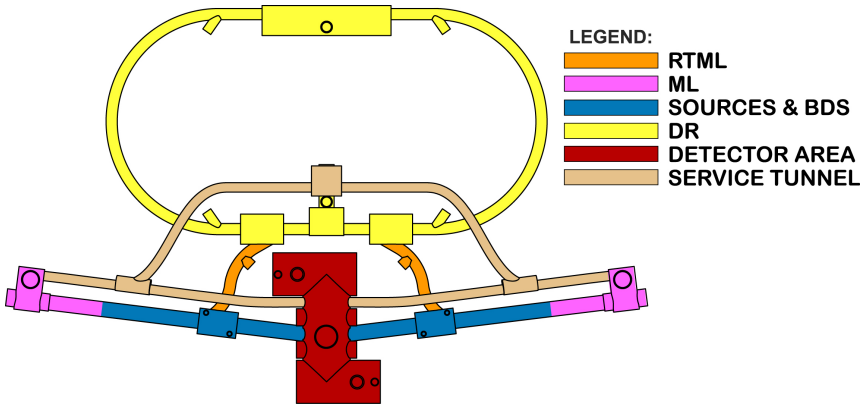

Figure 2.9
Damping ring location in the central region

The damping-ring lattice follows the race-track design shown schematically in Fig. 2.10. The two arc sections are constructed from 75 Theoretical Minimum Emittance (TME) cells. One of the two 712 m-long straight sections accommodates the RF cavities, damping wigglers, and a variable path length to accommodate changes in phase (phase trombone), while the other contains the injection and extraction systems, and a circumference-adjustment chicane.

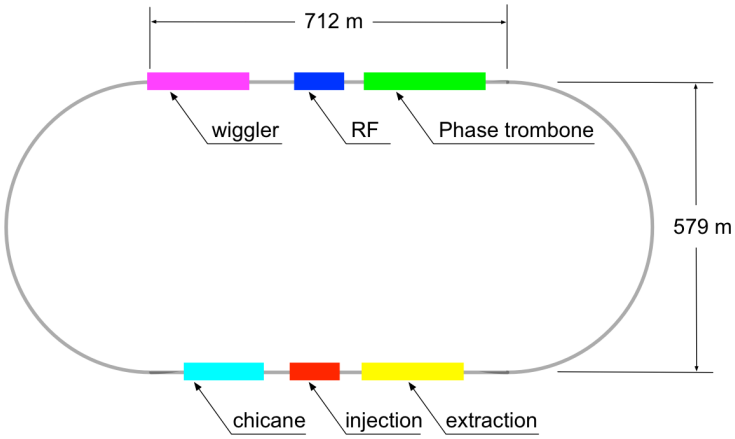

Figure 2.10
Schematic of the damping-ring layout.

Approximately 113 m of superferric wigglers (54 units $\times$2.1 m) are used in each damping ring. The wigglers operate at 4.5 K, with a peak field requirement of 2.16 T (positron ring 10 Hz mode).

The superconducting RF system is operated in continuous wave (CW) mode at 650 MHz, and provides a maximum of 20 MV for each ring, again specified for the positron ring in 10 Hz mode (nominal 5 Hz operation requires 14 MV for both electron and positron). The frequency is chosen to be half the linac RF frequency to maximise the flexibility for different bunch patterns. The single-cell cavities operate at 4.5 K and are housed in twelve 3.5 m-long cryomodules. The RF section of the lattice can accommodated up to 16 cavities, of which 12 are assumed to be installed for the baseline.

The momentum compaction of the lattice is relatively large, which helps to maintain single bunch stability, but requires a relatively high RF voltage to achieve the design RMS bunch length (6 mm). The dynamic aperture of the lattice is sufficient to allow the large-emittance injected beam to be captured with minimal loss.

The electron-cloud effect in the positron damping ring, which can cause instability, tune spread, and emittance growth, has been seen in a number of other rings and is relatively well understood. Extensive R&D and simulations (Part I Section 3.5) indicate that it can be controlled by proper

surface treatment and design of the vacuum chamber to suppress secondary emission, and by the use of solenoids and clearing electrodes to suppress the buildup of the cloud. A full specification of mitigation techniques based on the R&D results is included in the baseline and cost estimate.

Mitigation of the fast ion instability in the electron damping ring is achieved by limiting the pressure in the ring to below 1 nTorr, and by the use of short gaps in the ring fill pattern.

For the baseline parameters, the bunch spacing within trains is approximately 8 ns which sets the limit for the rise and fall time for the injection and extraction kicker systems. (For the luminosity upgrade this number reduces to ∼4 ns.) Short stripline kicker structures can achieve this, and extensive R&D on the pulser has demonstrated several technologies that can meet the specifications (Part I Section 4.4).

2.3.5 Ring to Main Linac

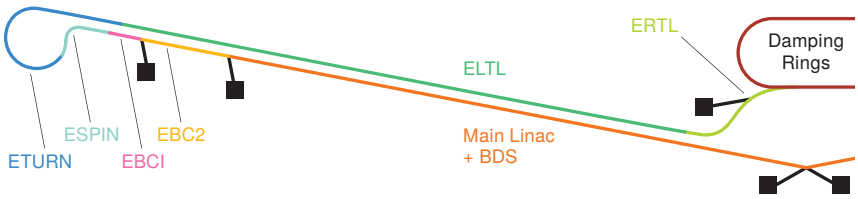

Figure 2.11 Schematic of the electron RTML (the positron system is a mirror image, with labels prefixed with 'P'). See text for explanation of the subsystems.

The electron and positron Ring to Main Linac (RTML) systems are the longest contiguous beamlines in the ILC. The layout of the RTML is identical for both electrons and positrons, and is shown in Fig. 2.11. The RTML consists of the following subsystems, representing the various functions that it must perform:

- a ∼ 15 km long 5 GeV transport line (ELTL);
- betatron- and energy-collimation systems (in ERTL);
- a 180° turn-around, which enables feed-forward beam stabilisation (ETURN);
- spin rotators to orient the beam polarisation to the desired direction (ESPIN);
- a two-stage bunch compressor to compress the beam bunch length from several millimetres to a few hundred microns, as required at the IP (EBC1 and EBC2).

The two-stage bunch compressor includes acceleration from 5 GeV to 15 GeV in order to limit the increase in fractional energy spread associated with bunch compression. The acceleration is provided by sections of SCRF main-linac technology. A primary challenge for the RTML systems is the preservation of the emittance extracted from the damping rings; the combination of the long uncompressed bunch from the damping ring and large energy spread (after compression) make the tuning and tolerances particular demanding. However, tuning techniques developed from detailed simulations have demonstrated acceptable emittance growth.

In addition to the beam-dynamics challenges, an RMS phase jitter of $\leq 0.24^\circ$ between the electron and positron bunch-compressor RF systems is specified to limit bunch arrival-time jitter at the interaction point to an acceptable level. Beam-based feedback systems integrated into the bunch-compressor low-level RF system should be able to limit the phase jitter to this level.

2.3.6 Beam-Delivery System

The ILC Beam-Delivery System (BDS) is responsible for transporting the e^+e^- beams from the exit of the high-energy linacs, focusing them to the sizes required to meet the ILC luminosity goals, bringing them into collision, and then transporting the spent beams to the main beam dumps. In addition, the BDS must perform several other critical functions:

- characterise the incoming (transverse) beam phase space and match it into the final focus;

- remove any large-amplitude particles (beam-halo) from the linac to minimize background in the detectors;
- measure and monitor the key physics parameters such as energy and polarisation before and after the collisions.

The layout of the beam-delivery system is shown in Fig. 2.12. There is a single collision point with a 14 mrad total crossing angle. The 14 mrad geometry provides space for separate extraction lines but requires crab cavities to rotate the bunches in the horizontal plane for effective head-on collisions. There are two detectors in a common interaction region (IR) hall in a so-called "push-pull" configuration.

The geometry of the BDS has been designed to accommodate the 1 TeV centre-of-mass-energy upgrade, in particular to minimise the emittance growth due to synchrotron radiation to a few percent at these beam energies. The baseline lattice uses fewer magnets (predominantly dipoles) for the lower-energy operation.

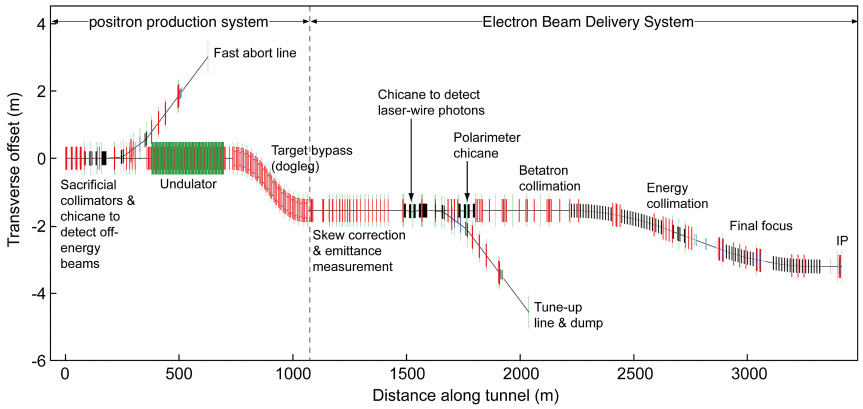

Figure 2.12 BDS lattice layout, showing the major sub-systems. Shown is the electron BDS, which starts at the vertical dotted line. (Also shown is the positron system upstream of the electron BDS). The positron BDS is a mirror image.

The main subsystems of the BDS are (beam direction):

- a section containing emittance measurement and matching (correction) sections, trajectory feedback, polarimetry and energy diagnostics;
- a collimation section which removes beam-halo particles that would otherwise generate unacceptable background in the detector, and also contains magnetised iron shielding to deflect and/or absorb muons generated in the collimation process;
- the final focus (FF), which uses strong compact superconducting quadrupoles to focus the beam at the IP, with sextupoles providing local chromaticity correction;
- the interaction region, containing the experimental detectors. The final-focus quadrupoles closest to the IP are integrated into the detector to facilitate detector "push-pull";
- the extraction line, which has a large enough bandwidth to transport the heavily disrupted beam cleanly to a high-powered water-cooled dump. The extraction line also contains important polarisation and energy diagnostics.

The beam-delivery optics provides demagnification factors of typically several hundreds in the beam size, resulting in very large beta functions (several thousand kilometres) at critical locations, leading to the tightest alignment tolerances in the entire machine. In addition, careful correction of the strong chromaticity and geometric aberrations requires a delicate balance of higher-order optical terms. The tight tolerances on magnet motion (down to tens of nanometres), makes continuous trajectory correction and the use of fast beam-based feedback systems mandatory. Furthermore, several critical components (e.g. the final focusing doublet) may well require mechanical stabilisation. Beam-based alignment and beam phase-space tuning algorithms are necessary to adjust and tune

the optical aberrations that would otherwise significantly degrade the luminosity. The ability to tune the beams to the required levels relies extensively on remote precision mechanical adjustment of the magnets, as well as precision diagnostics. Many of the techniques and required instrumentation are being successfully developed in the ATF2 programme (Part I Section 3.6).

The tight tolerance on the relative uncorrelated phase jitter between the electron and positron superconducting crab-cavity systems requires timing precisions at the level of tens of femtoseconds. Although this tolerance is tight, it is comparable to that achieved at modern linac-driven FELs.

Control of machine-generated backgrounds is performed by careful optics control and tuning of an extensive collimation system, as well as by the use of non-linear elements ("tail-folding" octupoles). The design of the collimation system carefully considers wakefield effects at small apertures; this requires careful electromagnetic design of the mechanical collimators themselves, as well as precision control of the beam motion using fast trajectory-correction (feedback).

The main beam dumps, which use a high-pressure high-velocity water design, represent a major installation. Since the dumps will be significantly activated during operation, they are designed and rated for the full average beam power at 1 TeV of 14 MW, in order to avoid having to replace them for the energy upgrade.

2.4 Site Dependent Designs

Conventional Facilities and Siting (CFS) is the designation for all aspects of the design relating to civil engineering, power distribution, water cooling and air conditioning systems. The CFS and the main-linac SCRF technology represent the two largest elements of the total project cost. The CFS design and costs can be broken down into three main areas:

1. Civil construction, including underground and surface structures, shafts and access tunnels;
2. Electrical systems (AC power distribution etc.);
3. Mechanical systems (water cooling and air handling etc.).

The CFS solutions and associated cost are developed based on the requirements defined by the accelerator layout and parameters briefly discussed in the previous sections. In order to minimise (optimise) the total CFS cost it is necessary to understand how it depends on the accelerator design, and if necessary re-evaluate and iterate the design approach. Reduction of the scope of the underground civil construction (for example) was considered a primary design goal during the Technical Design Phase, which resulted in significant modifications to the accelerator design and parameter space. In addition, the criteria for the electrical and mechanical systems, as well as the rationale and approach to access shafts and tunnels, have been scrutinised to reduce costs.

While the accelerator-systems layout and requirements are the primary driver for the CFS design, the solutions are heavily influenced by regional considerations of site topography and geology, as well as local legislation (such as safety requirements). Geology will determine the most cost-effective approach to tunnelling method, while topography can influence the surface structures and lengths and depths of access tunnels or shafts. All of these factors can shift the balance of the cost-optimisation and influence the accelerator design. As a result, the final machine construction will be strongly influenced by the choice of site.

In the absence of a definitive site for the ILC, it was necessary to evaluate, as far as possible, different sites with different characteristics. To this end, several sample sites have been developed:

- The Americas sample site lies in Northern Illinois near Fermilab. The site provides a range of locations to position the ILC in a north-south orientation. The site chosen has approximately one-quarter of the machine on the Fermilab site. The surface is primarily flat. The long tunnels are bored in a contiguous Dolomite rock stratum ("Galena Platteville"), at a typical depth of 30–100 m below the surface;

- For the Asian sites, two possible ILC candidate sites have been identified: Kitakami in the Tohoku district in northern Japan; and Sefuri in the Kyushu district in the south. Both potential sites provide a uniform terrain located along a mountain range, with a tunnel depth ranging from 40–600 m. The chosen geology is uniform granite highly suited to modern tunneling methods (e.g. New Austrian Tunneling Method (NATM));
- The European site is located at CERN, Geneva, Switzerland, and runs parallel to the Jura mountain range, close to the CERN site. The majority of the machine is located in the 'Molasse' (a local impermeable sedimentary rock), at a typical depth of 100–150 m.

The Americas and European sample sites are relatively similar and are examples of 'flat topography' sites. Both these sites use the Klystron Cluster Scheme for the RF power distribution. The geology lends itself well to the use of Tunnel Boring Machines (TBM) which provide a round tunnel cross section.

The Japanese sites are examples of mountainous topology, where available space for surface infrastructure is severely limited, requiring most of the accelerator infrastructure to be housed underground. The most cost-effective solution in this geology and topology is NATM. The Japanese sites use the Distributed Klystron Scheme.

In the following two sections, the site-dependent designs will be briefly described, with a focus on the main-linac accelerator tunnel, the central region and detector hall.

2.4.1 Flat-topography site-dependent design (Americas and European sample sites)

Figure 2.13 shows an artist's rendition of the civil construction layout for the flat-topography site. The shafts leading to surface installations (not shown) are clearly indicated. The KCS RF system requires an additional 3 shafts (per side).

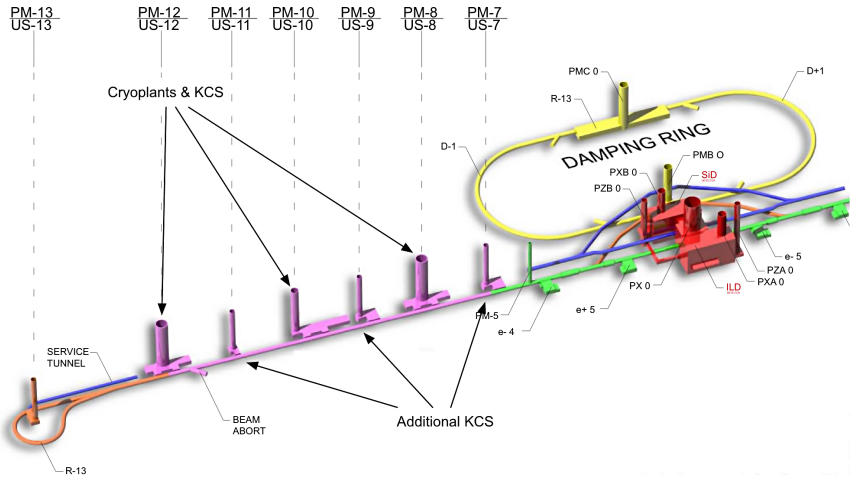

Figure 2.13 Artist's impression of the International Linear Collider (not to scale). Shown is the electron side of the machine and the central region. The layout shows the CFS solution for the flat topography, which utilises vertical shafts for access, and includes additional shafts for the KCS RF power distribution.

As the klystrons and modulators are housed on the surface, the single main-linac tunnel (main accelerator tunnel) can have a relatively small diameter. Figure 2.14 shows the cross-section of the tunnel.

For the bunch-compressor RF (RTML) and the central region (containing the source linacs as well as several parallel beam lines), a separate underground service tunnel is provided, which is connected to the main accelerator tunnel via penetrations. (The RF in these regions uses DKS rather than KCS, and the service tunnel is used to house the klystrons and modulators.)

The design of the detector hall (Fig. 2.15) accommodates the two detectors in a push-pull detector arrangement. The requirements for the hall and access shafts are primarily driven by the concepts of on-surface construction (similar to CMS at LHC), and the need to have sufficient access to the detectors while in the parked (i.e. off-beam) position. The large 18 m-diameter shaft located

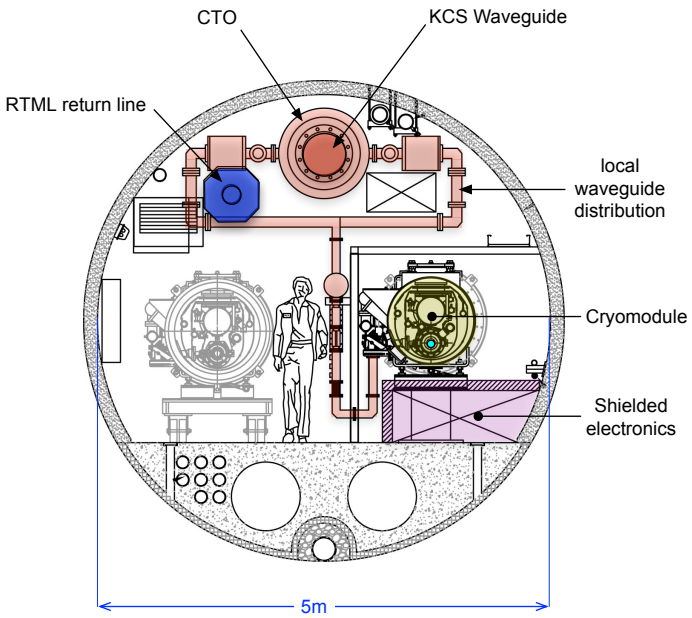

Figure 2.14
Cross section of the main linac tunnel for the flat-topography variant, using KCS.

directly over the interaction point serves as the primary access for lowering large parts of both detectors into the underground hall.

The overall power loads for the entire machine, including mechanical (water cooling), is strongly influenced by the main-linac configuration and in particular the possibility of having a large fraction of the heat load from the RF power source and cryogenics on the surface, allowing more cost-effective solutions.

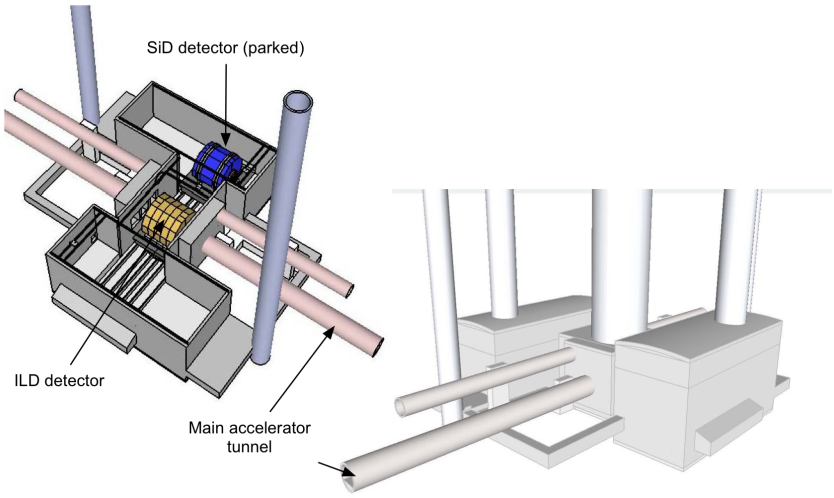

Figure 2.15
Two views of the design for the detector hall for the flat-topography site variant.

2.4.2 Mountainous-topography site-dependent design (Asian sample sites)

For the mountainous topography proposed for the two Japanese sample sites, the accelerator infrastructure must be predominantly housed in underground caverns. In addition, access is provided via gently sloping horizontal access tunnels. For the uniform hard granite geology, a single wide-tunnel solution constructed with NATM is the most cost-effect solution. In order to house both the accelerator (cryomodules) and the distributed RF power sources and associated electronics, an 11-m wide dome-shaped tunnel will be excavated. The tunnel is wide enough to accommodate a concrete shielding wall between the accelerator itself and the RF power systems, effectively providing a cost-effective twin-tunnel solution. Figure 2.16 shows a perspective view of a section of tunnel.

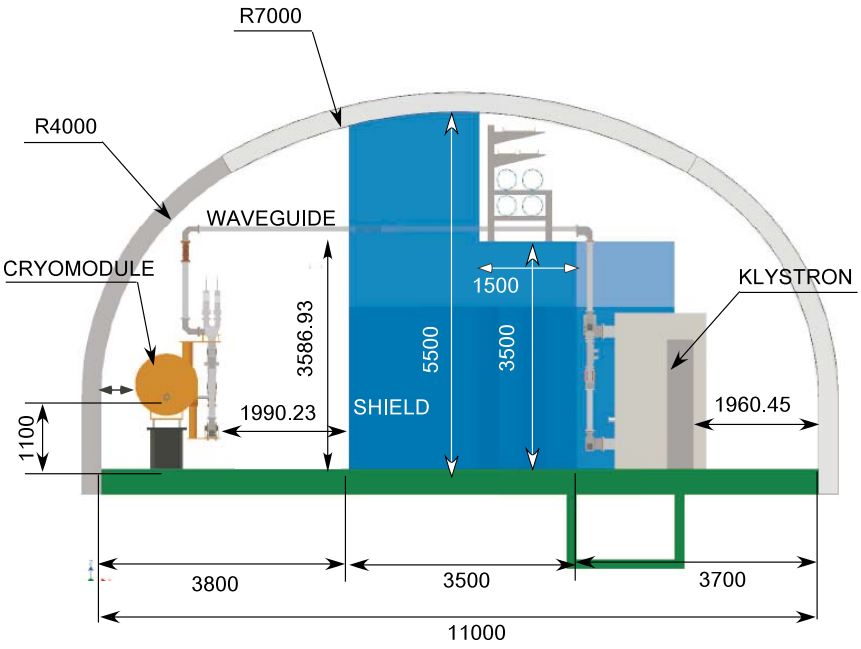

Figure 2.16
Cross section of the mountainous-topography tunnel (so-called 'Kamaboko').

The cryoplants and associated cooling and power systems are housed in caverns adjacent to the main accelerator tunnel (Fig. 2.17). The single wide-tunnel structure runs the entire length of the accelerator, and therefore removes the need for a separate service tunnel in the RTML (bunch compressor) and centra

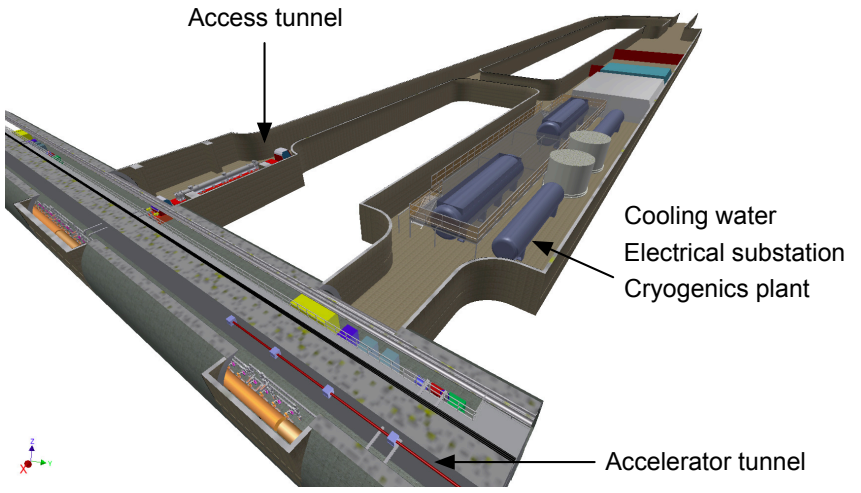

Figure 2.17
Perspective view of the underground cavern arrangement for the cryogenic plants, power and cooling systems.

Unlike the flat-topography site designs which utilise the KCS system, the mountainous-topography solution has all the primary heat loads located underground, and those associated with the RF power sources are distributed along the entire length of the linacs. This influences the design approach to mechanical and electrical systems, resulting in a different optimised solution from the flat-topography sites.

The need for horizontal access in the mountainous topography also strongly influences the design of the detector hall (Fig. 2.18). A CMS-like surface assembly is not considered cost-effective in this situation, and instead the underground hall is designed to accommodate underground *in situ* assembly. The single wide-access tunnel also serves the damping-ring installation.

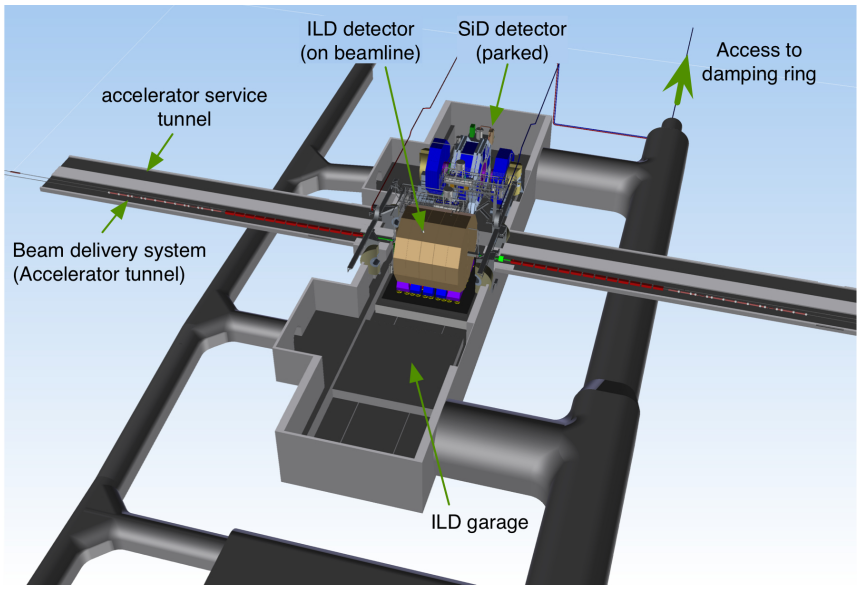

Figure 2.18
Perspective view of the underground detector hall for the mountainous topography, showing the two detectors and service tunnels.

2.5 Luminosity and Energy Upgrade Options

The technical design, cost estimate and construction schedule reported in this report have been optimised for the 500 GeV baseline scenario. Although considered in significantly less detail, two upgrade scenarios are foreseen:

- A luminosity upgrade (up to a factor of two), which is accomplished by doubling the number of bunches per beam pulse (doubling the beam power). This requires increasing the number of klystrons and modulators by approximately 50 %. The baseline design also foresees the possibility of constructing a second positron damping ring in the same tunnel, should electron-cloud effects require. All other accelerator systems are already rated for the higher beam power. Basic (minimum) provisions for the required conventional facilities are included in the baseline design to support the luminosity upgrade, although upgrades to the cooling systems will be required;
- An increase in the centre-of-mass energy up to 1 TeV by increasing the length of the SCRF main linacs. This requires a relocation of the bunch compressors and 180-degree turn-around, as well as an extension of the long return line from the damping rings to the turnaround and the extension of the main linacs. The latter upgrade is assumed to be based on a forward-looking SCRF technology compatible with the existing installation (RF pulse length etc.), but likely to have higher-performance specifications both in gradient and quality factor. The overall site-footprint requirement for the 1 TeV machine is approximately 50 km, with a site power requirement of approximately 300 MW. In order to minimise the impact on the existing machine during the upgrade construction, the baseline BDS geometry and high-power beam dumps are already to be compatible with 1 TeV operation.

Chapter 12 deals with both the luminosity and centre-of-mass energy upgrades in more detail.

Chapter 3
Main Linac and SCRF Technology

3.1 Overview of the ILC Main Linacs

3.1.1 Introduction

The two main linacs accelerate the electron and positron beams from their injected energy of 15 GeV to their final collision energy of between 100 GeV and 250 GeV, over a combined length of 22 km. The linacs utilise superconducting technology, consisting of approximately 16,000 L-band (1.3 GHz) nine-cell standing-wave niobium cavities operating at an average gradient of 31.5 MV/m in a 2 K superfluid-helium bath, integrated into ∼1,700 12 m-long cryomodules. The choice of operating frequency is a balance between the higher cost of larger, lower-frequency cavities and the increased cost at higher frequency associated with the lower sustainable gradient from the increased surface resistivity. The optimum frequency is in the region of ∼1.5 GHz, but during the early R&D on the technology, 1.3 GHz was chosen due to the commercial availability of high-power klystrons at that frequency [13].

The choice of accelerating gradient is the largest single cost-driver; it defines the required number of cavities and tunnel lengths of the Main Linacs. An average accelerating gradient of 31.5 MV/m is required for 500 GeV centre-of-mass-energy operation. However, the main linac systems — and in particular the RF power systems — are specified to accommodate up to a ± 20% spread in individual cavity performance. The gradient achieved in the low-power vertical test (mass production acceptance test) is specified ∼ 10% higher (35 MV/m) to allow for operational gradient overhead for low-level RF (LLRF) controls, as well as some degradation during cryomodule installation (few MV/m).

The TESLA elliptical cavity has been chosen for the ILC baseline design due to its maturity and the experience accumulated over the past decade and a half. In particular, approximately 800 TESLA cavities are currently under production for the European XFEL.

The design average acceleration gradient (31.5 MV/m) and qualify factor ($Q_0 = 10^{10}$ — see Section 3.2) has been achieved and exceeded in many cavities, several of which accelerate beam in the TTF/FLASH facility at DESY, Hamburg (see Part I Section 3.2). Mass production of high-performance cavities by industry has progressed significantly in recent years, giving confidence that the required parameters can be achieved (see Part I Section 2.3).

The cryomodule is similar in design to that developed by the TESLA collaboration, of which over ten examples have been constructed, six of which are operational at TTF/FLASH. For the ILC, two types of modules are foreseen, one integrating nine cavities (Type-A), and one integrating eight cavities, with a superconducting quadrupole package located at the centre of the string (Type-B). Both modules are designed to have the identical length of 12.652 m.

3.1.2 Linac layout

Table 3.1 provides an overview of the parameters and component counts for the ILC main linacs. The linacs are constructed from a near-contiguous string of cryomodules, interrupted only by the segmentation of the cryogenic strings (see below). The linacs are housed in underground tunnels which generally follow the curvature of the earth, primarily to simplify the flow of the two-phase helium at 2 K. The electron linac has an additional nine cryomodules to provide the $\sim$ 2.6 GeV needed to compensate the energy loss in the undulator-based positron source (Chapter 5). In addition both electron and positron linacs have $\sim$ 1.5 % energy-overhead to increase availability.

Table 3.1
Summary of key numbers for the SCRF Main Linacs for 500 GeV centre-of-mass-energy operation. Where parameters for positron and electron linacs differ, the electron parameters are given in parenthesis.

Cavity (nine-cell TESLA elliptical shape)		
Average accelerating gradient	31.5	MV/m
Quality factor Q_0	10^{10}	
Effective length	1.038	m
R/Q	1036	Ω
Accepted operational gradient spread	$\pm$20%	
Cryomodule		
Total slot length	12.652	m
Type A	9 cavities	
Type B	8 cavities	1 SC quad package
ML unit (half FODO cell) (Type A - Type B - Type A)	282 (285)	units
Total component counts		
Cryomodule Type A	564 (570)	
Cryomodule Type B	282 (285)	
Nine-cell cavities	7332 (7410)	
SC quadrupole package	282 (285)	
Total linac length – flat top.	11027 (11141)	m
Total linac length – mountain top.	11072 (11188)	m
Effective average accelerating gradient	21.3	MV/m
RF requirements (for average gradient)		
Beam current	5.8	mA
beam (peak) power per cavity	190	kW
Matched loaded Q (Q_L)	5.4×10^6	
Cavity fill time	924	µs
Beam pulse length	727	µs
Total RF pulse length	1650	µs
RF–beam power efficiency	44%	

Either 26 or 39 adjacent cavities are effectively driven by a common RF power source as indicated in Fig. 3.1. The local power distribution system provides flexibility in adjusting the forward power to each cavity, necessary in dealing with the expected spread in individual cavity gradient performance (see Section 3.6.4). The RF power is provided by 10-MW multi-beam klystrons driven by a solid-state Marx modulator (see Section 3.6.3 and Section 3.6.2 respectively).

Two possible schemes (flat and mountain topography respectively) have been developed during the Technical Design Phase for the layout of the tunnels, and in particular the approach to delivering RF power to the local distribution system and ultimately the cavities.

For a *mountainous topography*, such as the candidate sites in Japan, the more standard Distributed Klystron Scheme (DKS) would be used in a 11 m-wide, "kamaboko-shaped" tunnel whose interior is divided into two corridors by a thick (2.0 m to 3.5 m) concrete wall. The cryomodules occupy one side of the tunnel while the RF systems including modulators, klystrons, power supplies, and instrumentation racks, are located on the other side. This arrangement permits access to the RF equipment for maintenance, repair, or replacement during beam operation, and limits radiation exposure to most of the electronics (except for equipment placed in or near the cryomodules). For a *flat topography*, a novel Klystron Cluster Scheme (KCS) is envisioned, with all RF-generating

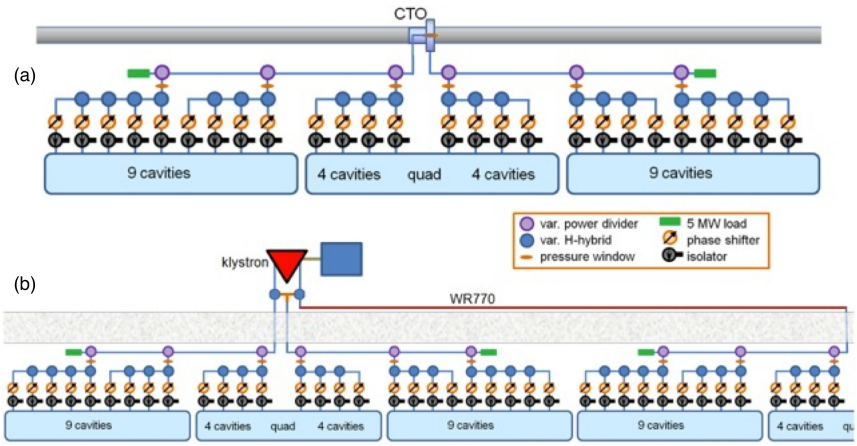

Figure 3.1
Schematic of the Local Power Distribution System (LPDS) which delivers RF power to 13 accelerating cavities in the main linacs; (a) and (b) show the KCS and DKS options respectively.

equipment located in surface facilities where the klystron power is combined (up to 300 MW) and transferred through overmoded circular waveguides to the linac tunnel below. The tunnel, which is about 5 m in diameter, mainly contains the cryomodules and waveguides with some electronics (e.g. quadrupole-magnet power supplies, LLRF monitoring and control electronics) that is housed in radiation-shielded, 2 m-wide racks under the cryomodules.

The tunnels are assumed to be deep underground (∼100 m) and connected to the surface through vertical shafts (flat topography) or sloped access routes (mountainous topography). The number, location and size of these shafts or access-ways is determined by the maximum length of a cryogenic unit (and maximum available size of a cryoplant, see below), and, in the case of KCS, the maximum distance over which the RF power can be realistically transported via the large overmoded circular waveguide (Section 3.9.3).

The cryogenic segmentation of the main linacs is organised as:

- an **ML unit** which consists of three cryomodules in a Type A – Type B – Type A arrangement (26 cavities and 1 quadrupole package);
- a **cryo string**, which consists of 4 ML units (long string with 12 cryomodules) or 3 ML units (short string with 9 cryomodules), followed by a 2.5 m cold-box;
- A **cryo unit** comprising of between 10 to 16 cryo strings, with the final cold-box being replaced by an 2.5 m service box.

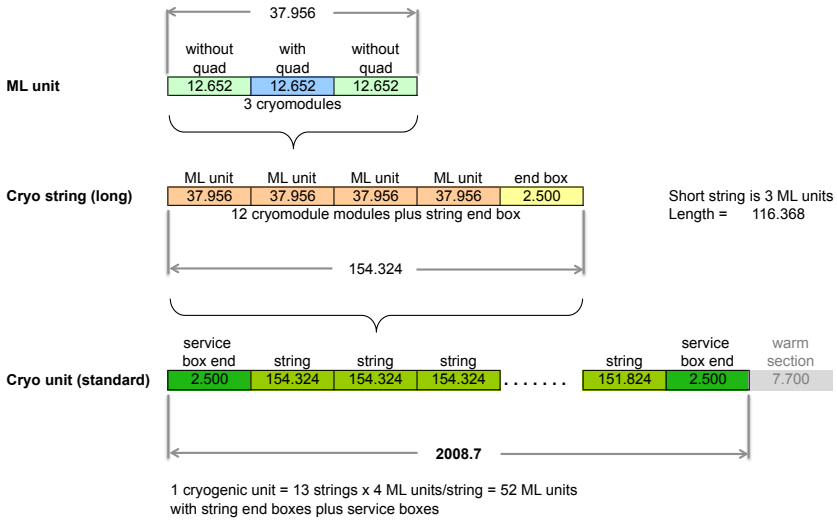

Figure 3.2
Basic cryogenic segmentation in the main linacs. Note that the length of the cryo units varies depending on the number of strings. (All lengths given in metres.)

Figure 3.2 shows an example configuration for a single cryo unit based on 13 long cryo strings. The maximum length for a cryo unit is approximately 2.5 km, and is set by consideration of the largest

practical cryoplant size (approximately 4 MW, comparable to those running at LHC). This includes a 40 % overcapacity to account for pre-cooling from room temperature, variation in cooling water temperature, and operational overhead. (About half of the AC power consumed in the cryoplants is used to remove the RF energy dissipated in the 2 K cavities.) Two cryoplants are typically located together, with one plant feeding an upstream cryo unit and the other a downstream cryo unit. This results in a typical spacing of cryo plant installations (vertical shafts or access ways) of approximately 5 km. The most upstream cryoplant also provides cooling for the accelerator sections for the bunch compressors in the RTMLs (Chapter 7). The exact linac segmentation and number of cryoplants differs for the two site-dependent variants considered, although the number of cryomodules in the linacs are the same. In particular, five cryoplants are envisaged for the mountainous topography, while for the flat topography the total load is distributed over six plants. These differences are driven by the approach to the RF power distribution for each site variant. Section 3.8 and Section 3.9 provide details of the main linac segmentation for the flat and mountainous topographies respectively.

Each cryo unit is separated by a short ∼7.7 m warm section that includes vacuum-system components and a 'laser wire' to measure beam size.

At the exit of main linacs there is a section of warm beamline which acts as the matching interface to the downstream systems. This section of beamline provides:

- matching and machine-protection collimation for the transition between the relatively large apertures in the main linac, to the smaller ones in the downstream (warm) systems (most notably the positron-source undulator located at the exit of the electron linac);
- beam-trajectory correction using a fast intra-train feedback/feedforward system, which should reduce pulse-to-pulse jitter to approximately 10 percent of the vertical beam height. The fast kickers will also be used to correct repetitive bunch-to-bunch variation possibly arising from long-range wake fields. On the electron linac side, in addition to the fast feedback correction, a 10 Hz pulsed magnet system is required to adjust the 150 GeV positron production beam during 10 Hz operation at low energy operation (see Section 3.1.4).

Table 3.2 summarises the combined power consumption of the Main Linacs. Of this power, 9.9 MW goes into the beams and the corresponding wall-plug to beam power efficiency is 9.6 %.

Table 3.2
Main Linac AC power consumption for both site-dependent variants. Details can be found in Chapter 11

System	Flat Topography AC power (MW)	Mountain Topography AC power (MW)
Modulators	58.1	52.1
Other RF system and controls	5.8	5.5
Conventional facilities	13.3	16.4
Cryogenics	32.0	32.0
Total	109.2	106.1

3.1.3 Accelerator Physics

Table 3.3 lists the basic beam parameters for the main linacs. The main-linac lattice uses FODO optics, with a quad spacing of 37.96 m, corresponding to one quad per three cryomodules (ML unit). Each quadrupole magnet is accompanied by horizontal and vertical dipole correctors and a cavity BPM which operates at 1.3 GHz. The lattice functions are not perfectly regular due to the interruptions imposed by the cryogenic system, but do not change systematically along the linac so the focusing strength is independent of beam energy. Figure 3.3 shows the lattice for the last cryo-unit of the main linac. The average lattice beta function is approximately 80 m and 90 m in the horizontal and vertical planes respectively. The mean phase advance per cell is 75° in the horizontal plane and 60° in the vertical plane. The small vertical bending required to follow the Earth's curvature is provided by vertical correctors near the quadrupole locations, and gives rise to $\sim 1\,\mathrm{mm}$ of vertical dispersion

Table 3.3
Nominal Linac Beam Parameters for 500 GeV CMS operation.

Parameter	Value	Unit
Initial beam energy	15	GeV
Final (max.) beam energy	250	GeV
Particles per bunch	2.0×10^{10}	
Beam current	5.8	mA
Bunch spacing	554	ns
Bunch train length	727	μs
Number of bunches	1312	
Pulse repetition rate	5	Hz
Initial $\gamma\epsilon_x$	8.4	μm
Final $\gamma\epsilon_x$[†]	9.4	μm
Initial $\gamma\epsilon_y$	24	nm
Final $\gamma\epsilon_y$[†]	30	nm
σ_z	0.3	mm
Final σ_E/E[†]	0.07	%
Bunch phase relative to RF crest	5	degrees ahead

[†] at exit of linac

(peak). Dispersion matching and suppression at the beginning and end of the linac are achieved by supplying additional excitation to small numbers of correctors in "dispersion-bump" configurations.

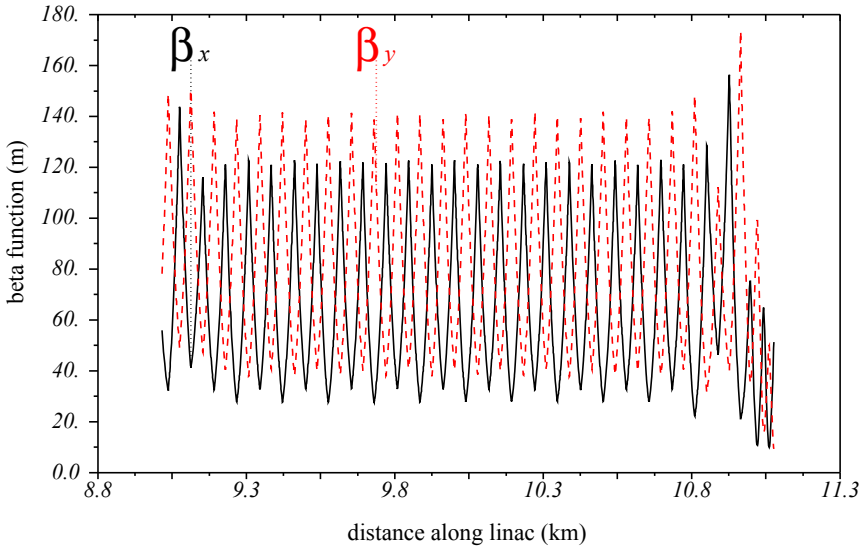

Figure 3.3
Example lattice functions for the main linac. The plot shows the beta functions for the last cryo-unit of the linac. (The warm post-linac collimation system is also included.)

The beam emittance at the damping ring extraction is $\gamma\epsilon_x = 8\,\mu\mathrm{m}$ and $\gamma\epsilon_y = 20\,\mathrm{nm}$. The biggest challenge is in keeping the small vertical emittance from being degraded during the beam transport to the beam interaction point (IP). This cannot be done perfectly, and the ILC parameters specify a target emittance at the IP of $\gamma\epsilon_x = 10\,\mu\mathrm{m}$ and $\gamma\epsilon_y = 35\,\mathrm{nm}$. An emittance growth budget has been set at $\Delta\epsilon_y \leq 10\,\mathrm{nm}$ for the total of the RTML and the main linac. The goal for the alignment and tuning procedures is to ensure that the emittance growth is within the budget.

To limit the emittance dilution, the position and orientation of the beamline elements are set fairly precisely during installation (Table 3.4), and beam-based alignment methods are then used to adjust the corrector magnet strengths to establish an orbit that minimises the beam emittance growth. The task is made easier by the fact that the long-range (bunch-to-bunch) wakefields are weak and the initial bunch trajectories are very similar, so minimising the emittance growth of one bunch will do it for all. As discussed above, any slow variation of the relative trajectories of the bunches along the trains will be removed after the linacs using a fast-kicker-based feedback system. The relatively weak single-bunch longitudinal wakefield can be compensated a small off-crest phase (5 degree at 31.5 MV/m).

To suppress any resonate buildup of the wakefields and their effect on the beam, a higher-order-mode (HOM) damping system has been carefully designed into the cavities and the HOM frequencies

are effectively detuned cavity-to-cavity at the 10^{-3} level as a result of geometric differences within the fabrication tolerances. Such fabrication variations can also lead to diagonal polarisation of the dipole modes instead of horizontal and vertical polarisation. The difference in horizontal and vertical betatron phase advance noted above prevents such x-y coupling from causing orbit jitter to couple between the horizontal and vertical planes. The high-impedance HOMs for TESLA cavities have been calculated and experimentally verified at TTF/FLASH at DESY, Hamburg [14]. A table of the HOMS and their r/Q values can be found in [13].

Table 3.4
Installation alignment errors (rms) of the linac beamline elements. BPM specifications are also included.

Error	with respect to	value	
Cavity offset	module	300	μm
Cavity tilt	module	300	μrad
BPM offset	module	300	μm
BPM resolution		5	μm
BPM calibration		≤10	%
Quadrupole offset	module	300	μm
Quadrupole roll	module	300	μrad
Module offset	beamline reference	200	μm
Module tilt	beamline reference	20	μrad

The assumed installation errors are listed in Table 3.4. Cavities and Quadrupole magnets are inaccessible once installed into the cryomodules, and need to be mounted and carefully aligned during assembly that allows for thermal contractions of the support system during the cryostat cool down. Results of stretched-wire measurements in cryomodules (see Part I Section 2.6) have demonstrated that the specifications can be reproducibly met over several thermal cycles [15]. After installation in the tunnel, the offsets of the quadrupole and BPM are ultimately established by beam-based techniques at the micron level (i.e. the quadrupole centres are shifted with corrector magnets and the BPM offsets are determined with a quadrupole-shunting technique). The bunch-emittance dilution is dominated by chromatic (dispersive) effects and wakefield kicks arising from misaligned quadrupole magnets and cavities respectively. Emittance growth from these perturbations is mainly corrected through local or quasi-local steering algorithms such as Ballistic Alignment (BA), Kick Minimisation (KM), or Dispersion Free Steering (DFS), with additional correction achieved through local orbit distortions, which produce offsetting amounts of dispersion at a given phase ('dispersion bumps'). A more complete description of the emittance-dilution mechanisms and the steering algorithms be can found in Part I Section 4.6.

A BPM with horizontal and vertical readout and micron-level single-bunch resolution is located adjacent to each quadrupole magnet. For beam-size monitoring, a single laser wire is located in each of the warm sections between main linac cryogenics units (about every 2.5 km). Upstream quadrupole magnets are varied to make local measurements of the beam emittances at these points.

3.1.4 Operation

Fast trajectory control is implemented in the warm regions upstream and downstream of the Main Linacs but not within the linacs themselves, as the trajectory jitter generated by magnetic and RF field variations is expected to be small (see Part I Section 4.6). Likewise, beam energy and energy spread are only measured upstream and downstream of the Main Linacs, and there are no beam-abort systems or energy collimation chicanes along the linacs. The Machine Protection System will only allow beam into the RTML if the trajectory is within a defined phase space, and if the RF phases in the RTML and Main Linac cavities are within a prescribed range prior to the beam extraction from the damping rings (during the approximately 800 μs fill time for the RF). The limiting apertures in the cryomodules are the 70 mm diameter cavity irises.

The linac length (number of cryomodules) includes a 1.5% energy overhead for 250 GeV operation. This overhead can compensate for failed cavities or RF systems. (See Section 10.2 for more details.)

The required beam energy is first 'coarsely' adjusted by setting the required RF power and cavity Q_{ext}, and 'finely' adjusted by cross-phasing RF units near the end of the linacs. For operation at low beam energy (low gradient), the modulator voltage and RF pulse length would be reduced to save energy.

As noted in Section 2.2.2 for operation below 250 GeV beam energy, the electron linac will be operated at 10 Hz to provide alternatively a 150 GeV beam for positron production, followed by a $\leq 125\,\mathrm{GeV}$ beam for luminosity production. (The positron linac only runs at the nominal 5 Hz.) For this reason, all linac RF devices are specified at 10 Hz, although at reduce peak power requirements (approximately one-half of that required at 250 GeV beam-energy operation). Furthermore, at the reduced gradient there is already sufficient RF and cryogenic AC power installed to run the linac at the higher repetition rate. (This is helped by the fact that the RF fill time is reduced by approximately one-half, and thus shortens the RF pulse; this has the effect of increasing both the RF-to-beam power efficiency, as well as reducing still further the dynamic cryogenic load.) Transport of the two different beam energies in 10 Hz mode has been simulated (see Part I Section 4.6). The main linac will be tuned to preserve the low emittance of the luminosity production pulse (lower energy); the emittance of the higher-energy positron-production pulse is not critical, and the simulations have shown that the trajectory offset at the exit of the linac is typically a few millimetres — well within the aperture of the linac. However, this offset will require adjustment to bring the beam on-axis of the source undulator, which requires a 10 Hz pulsed magnet system in the warm section immediately downstream of the electron linac.

3.1.5 Linac Systems

The remaining sections of this chapter describe in detail the main components of the Main Linacs, starting from the SC cavities and working outward through the cryomodule, high power RF systems and finally to the low-level RF (LLRF) controls:

Section 3.2 Cavity performance and production specifications covers the cavity design, performance specifications, and baseline industrial production process, including the required surface preparation to achieve the required high-performance.

Section 3.3 Cavity integration discusses the complete cavity package and how it is assembled, including the high-power RF coupler, HOM couplers, helium tank and mechanical frequency tuner.

Section 3.4 Cryomodule design including quadrupole and cryogenic systems describes the mechanical design of the 12.7 m long cryomodules, which comprise the vacuum vessel and the items within, including cavities, thermal shielding, cryogenic feed and return lines, beamline absorber and a quad 'package,' consisting of a quadrupole magnet, horizontal and vertical corrector magnets and an RF BPM. Estimates of the cryogenic heat loads are also presented.

Section 3.5 Cryogenic cooling system describes the layout of the cryogenic plants and required plant capacities.

Section 3.6 RF power source presents the common components of the RF system for the KCS and DKS systems, i.e. the 120 kV Marx Modulators and the 10 MW Multiple Beam Klystrons (MBKs) that they power. Also, the local RF distribution system that divides up the feed power to the cavities in the tunnel is described.

Section 3.7 Low-level RF-control concept covers the design and operational aspects of the low-level RF system (LLRF) that is required to stabilise the vector sum of cavity voltages to within less than 1 % across the beam pulse. This includes the more 'global' control via closed-loop

feedback on the klystrons, as well as local (per cavity) compensation of Lorentz-force frequency detuning using piezo-electric controllers.

Section 3.8 Main linac layout for a mountain topography discusses those design features specific to the mountain topography site-specific design, and in particular the linac layout and DKS.

Section 3.9 Main linac layout for a flat topography discusses those design features specific to the flat topography site-specific design, and in particular the linac layout and KCS.

3.2 Cavity production specifications

3.2.1 Cavity Design

Figure 3.4 shows schematics of a baseline 9-cell superconducting cavity and the assembly with liquid-helium (LHe) tank. Table 3.5 summarises the main design parameters of the cavity.

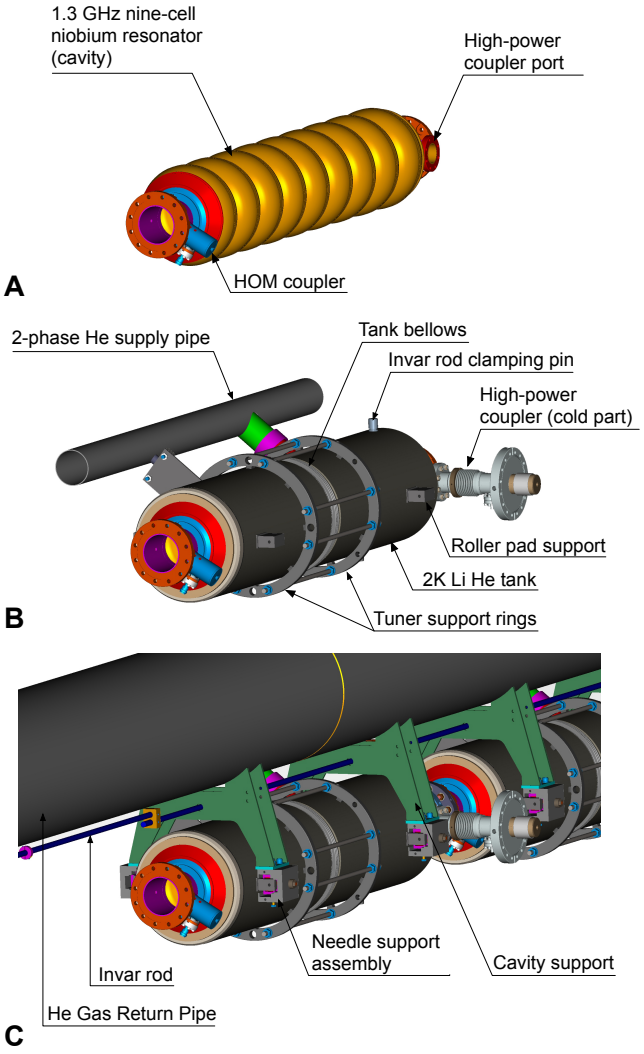

Figure 3.4
The baseline cavity package and string assembly: (A) the nine cell cavity (resonator); (B) the "dressed" cavity, showing the helium tank, 2-phase helium supply, high-power coupler (cold part) and the mount for the cavity tuner; (C) cavity package mounted into the cavity string and cryomodule. (Note the "blade" cavity tuner is not shown.)

Table 3.5
Cavity parameters for the SCRF cavities.

Parameter	Value
Type of accelerating structure	Standing wave
Accelerating mode	TM_{010}, π mode
Type of cavity-cell shape	Tesla (or Tesla-like)
Fundamental frequency	1.300 GHz
Operation:	
– Average gradient (range allowed)	31.5 MV/m ($\pm$20%)
– Quality factor (at 31.5 MV/m)	$\geq 1 \times 10^{10}$)
Qualification:	
– Average gradient (range allowed)	35.0 MV/m ($\pm$20%)
– Quality factor (at 35 MV/m)	$\geq 0.8 \times 10^{10}$
– Acceptable radiation (at 35 MV/m)	$\leq 10^{-2}$mGy/min[†]
Active length	1038.5 mm
Total length (beam flanges, face-to-face)	1247.4 mm
Input-coupler pitch distance, including inter-connection	1326.7 mm
Number of cells	9
Cell-to-cell coupling	1.87%
Iris aperture diameter (inner/end cell)	70/78 mm
Equator inner diameter	$\sim$210 mm
R/Q	1036 Ω
E_{peak}/E_{acc}	2.0
B_{peak}/E_{acc}	4.26 mT/(MV/m)
Tunable range	$\pm$300 kHz
$\Delta f/\Delta L$	315 kHz/mm
Number of HOM couplers	2
Q_{ext} for high-impedance HOM	$< 1.0 \times 10^5$
Nb material for cavity (incl. HOM coupler and beam pipe):	
- RRR	$\geq$300
- Mechanical yield strength (annealed)	≥ 39 MPa
Material for helium tank	Nb-Ti Alloy
Max design pressure (high-pressure safety code)	0.2 MPa
Max hydraulic-test pressure	0.3 MPa

[†] Example number taken from [16] — see text for more details

3.2.2 Cavity fabrication and surface processing

The fabrication process of ILC superconducting cavities and their surface treatment have substantially matured during the Technical Design Phase. The R&D leading to these procedures — as well as a more detailed discussion of the steps involved — can be found in Part I Section 2.3. The procedure is summarised in Table 3.6.

There are two key issues concerning the mechanical fabrication of the cavities for the ILC. The first is the quality assurance of the niobium materials. The second is the process quality control of electron-beam welding. The sheet and bulk niobium which are supplied by vendors must be scanned for detecting and avoiding materials with defects[1]; once accepted, they have to be the protected from mechanical damages and dust throughout the manufacturing process. Defective materials can become limit the performance of completed cavies. Impurities introduced into the welds and in the heat-affected zones next to welds will also limit the gradient performance. Weld joints must have smooth beads without surface irregularities and without sharp edges on locations where the weld puddle meets the bulk material. A defect on the equator weld will in general result in a local enhancement of the magnetic field. A single such defect can cause a quench, leading to a degradation of gradient performance. Current production experience suggests some 10–20% of cavities produced could suffer from this problem, and therefore procedures for repairing the cavity surface has been developed (see Part I Section 2.2.7). For ILC mass-production rates, however, it is expected that — after some initial ramp-up period — the electron-beam welding process will be improved to significantly reduce the number of such defects, to a level of $<$10%.

[1] During ILC mass production, it is conceivable that such scanning will be at a reduced rate for QC only, once the production has been established.

Table 3.6. Summary of steps required to fabricate a nine-cell cavity.

Steps	Reference parameters	Notes:
9-cell cavity fabrication:		
- Raw material preparation	Nb sheet: $t = 2.8\,\mathrm{mm}$, $RRR \geq 300$	Acceptance with sheet inspection including visual and non-destructive defect inspection.
- Component fabrication		Using press, machining, and electron-beam welding (EBW).
- Assembly of 9-cell cavity		Using EBW
- Inner-surface inspection		Using optical inspection method†.
Inner-surface treatment:		
- Light etching with BCP	5–20 µm	(Optional: EP, 5–20 µm)
- Heavy EP	100–120 µm	∼24 µm/hour at $30\,^{\circ}\mathrm{C} \leq T \leq 35\,^{\circ}\mathrm{C}$
- Post-heavy-EP cleaning		
- Out-gasing	800 °C, ≥2 hours	
- RF tuning		Using tuning machine and non-contacting bead-pull method*.
- Light EP	20–30 µm	∼12 µm/hour at $20\,^{\circ}\mathrm{C} \leq T \leq 30\,^{\circ}\mathrm{C}$.
- Ethanol or detergent rising	∼1 hour	
- First HPR rinsing	6 hours, 3 passes	Purity level of water: Resistivity 18 MΩ cm.
- First clean-room assembly		
- Final HPR rinsing	6 hours, 3 passes	
- Final assembly		In class 10 clean-room.
- Leak check		Sensitivity: $\leq 2 \times 10^{-10}\,\mathrm{Pa\,m^3\,s^{-1}}$.
- In-situ baking	∼48 hours at ∼120 °C	
Assembly of LHe tank:		
- Pre-assembly & check-out		Check-out of tank components. Validation of hermeticity and mechanical sturdiness under over-pressurised conditions from safety standpoint.
- Assembly of LHe tank		Assembly with 9-cell cavity part, using EB or TIG welding
- HPC inspection	1.5 (or 1.25)×2 bar	Differential. Depending on HPC in region.
- Leak-check		Sensitivity: $\leq 1 \times 10^{-9}\,\mathrm{Pa\,m^3\,s^{-1}}$.
- General inspection		Dimensions etc.
Cavity RF performance test:		
- Cool-down		Cool-down time: several hours
- Q_0 vs. gradient		π and pass-band mode, including radiation monitoring.
Post-performance test assembly and check:		
- coupler and HOM assembly		Including leak-check.
- tuner assembly		Including functioning test.
- General inspection		As an acceptance test for cavity-string assembly.

Terms:
RRR: residual resistance ratio
EBW: electron-beam welding
BCP: buffered chemical polishing
EP: electro-polishing
HPR: high-pressure (pure water) rinsing
TIG: tungsten inert-gas welding

† Dedicated tooling/facility provided by laboratories.

The surface-preparation steps have developed over many years into the established recipe outlined above. The details can be found in Part I Section 2.3. In summary, the process steps are designed to:

1. remove material damage incurred during the fabrication process or handling by using chemical procedures;
2. remove the chemical residues left over from the material removal steps;
3. remove hydrogen in the bulk niobium which has been captured during the chemical procedures in step 1;
4. remove any particulate contamination which entered during the cleaning and assembly steps; and
5. close up the cavity to form a hermetically sealed structure.

Figure 3.5 provides an overview of the cavity production process, and in particular the approach to testing. A key issue for mass production is achieving the required performance yield ($> 90\%$) in a cost-effective manner. The current approach — based on existing R&D experience discussed in Part I Section 2.3 — is to allow specific steps to be iterated in the production process. The first test in this respect is an optical inspection (Part I Section 2.2.2) of the cavity directly after fabrication, but before any surface treatment. This inspection is intended to identify candidate surface defects as described

above, which may limit the cavity performance to below 20 MV/m. These cavities (an estimated 10% or less after the production process has matured) would be removed from the production line and mechanically repaired using the techniques described in Part I Section 2.2.7. A second optical inspection is made after initial surface treatment (bulk electro-polishing, 800° heat treatment, followed by mechanical RF tuning), to identify weld defects that may have been uncovered by the removal of 150 µm niobium during bulk electro-polishing (an estimated few percent of the total production). The cavities then undergo the final surface preparation steps and the high-Q RF antenna, two HOM couplers and the helium tank are mounted. The final performance (acceptance) test is a low-powered RF test in a vertical cryostat at 2 K (so-called vertical test), where the cavity ultimate performance is measured (maximum acceptable gradient, quality factor, field emission etc.)[2]. Based on the current status of the R&D, it is expected that some fraction of cavities ($\leq$20%) will be limited to $<$28 MV/m and will require some remedial action, the exact nature of which depends on the mode of failure. If the cavity gradient is limited by field emission (excessive X-rays), then it is highly likely that only an additional high-pressure rinse (6 hours) will suffice, a process which is relatively straightforward. A limitation due to a breakdown (i.e. quench) will require an additional light electro-polishing step ($\sim 25\,\mu\mathrm{m}$), which is more process intensive, and requires the removal (at least) of HOM couplers and high-Q RF antenna, which must then be re-mounted after the surface treatment. It is anticipated that the removal of the helium tank can be avoided for this second-pass treatment. Irrespective of which procedure is followed, the cavity must then undergo a second vertical test. Although ultimately cavities with a gradient performance $\geq$28 MV/m will be accepted, this represents only the lower limit of the assumed gradient spread ($28\,\mathrm{MV/m} \leq G \leq 42\,\mathrm{MV/m}$). Therefore all cavities that fail to make 35 MV/m on the first-pass test undergo a second cycle (either HPR or light EP). On the second-pass test, cavities achieving the minimum required 28 MV/m are accepted for cryomodule assembly, as indicated in Fig. 3.5. Although a third-pass is feasible, it is not considered necessary and is not included in the cost

The acceptance criteria for gradient and quality factor have been well established and standardised during the technical design phase. The measurement and acceptable levels of X-rays generated in the vertical test (an indication of field emission) remains the least well-defined quantity. Methods and standards that can be unambiguously applied to test infrastructures around the world requires additional R&D. Table 3.5 quotes a radiation value for qualification of $\leq 10^{-2}\mathrm{mGy/min}$ at 35 MV/m, a number based in the current European XFEL experience [16]. However this number is particular to the DESY vertical test set-up, and cannot be universally adopted by other test infrastructures. Definition of such practical standards is especially important when the anticipated globally-distributed nature of the cavity manufacturing and testing is considered.

It is expected that the mechanical fabrication and surface preparation will be performed by industry. However, the final RF test will be performed by a collaborating laboratory or institute, which will host the required cryogenic and RF test infrastructure and personnel. The second-pass process steps could alternatively be dealt with locally by the lab hosting the test facility (as is the case for the European XFEL), or returned to industry.

[2] The decision to assemble the tank and HOM couplers before the vertical test is driven by mass production considerations, and follows the same approach taken for the cavity production for the European XFEL project.

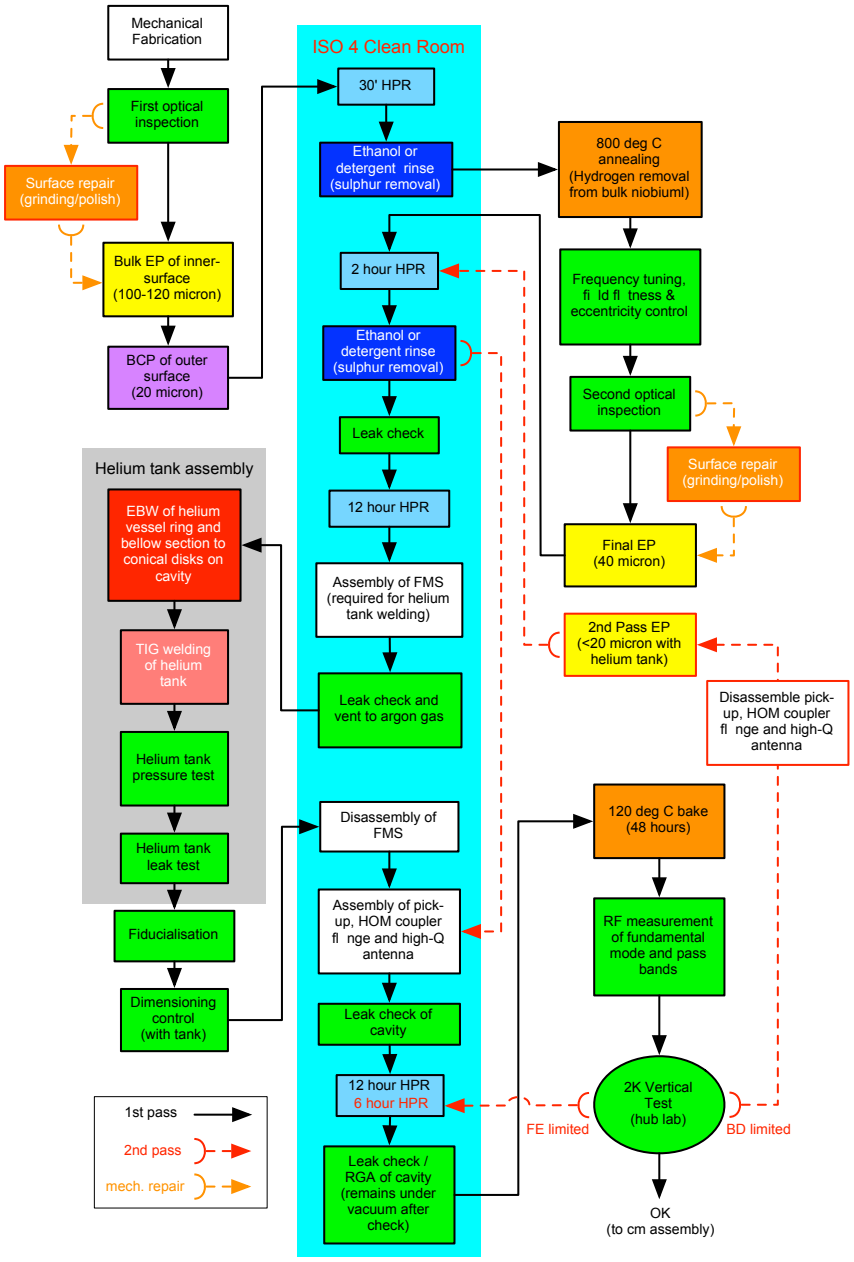

Figure 3.5
Flow chart showing the various steps involved in the surface treatment of high-gradient cavities. The 'first pass' (black arrows) is based on the process currently being used by XFEL and is slightly different from the steps presented in Table 3.6. Red arrows indicate possible 'second pass' procedures for a cavity which fails either optical inspection or the final 2 K vertical performance test. Note that the second-pass EP is assumed to be made with the helium tank still attached.

3.3 Cavity integration

The most important part of the cryomodule is the cavity package, which is an integrated system consisting of a 9-cell cavity, contained within a titanium-alloy helium tank connected to a helium supply pipe, a fundamental-mode power coupler, a frequency tuner, and a magnetic shield (see Fig. 3.4 A and B). The design of the ILC cavity system is based on the original TESLA design used in TTF/FLASH and currently being produced in industry for the European XFEL project. The ILC cavity package consists of the following:

- a nine-cell niobium resonator (cavity), complete with two HOM couplers and RF antenna, flanges etc.;
- a titanium-alloy helium tank (cryostat), split with a bellows to support the mechanical tuner;
- the mechanical tuner itself (so-called blade tuner), mounted on the two halves of the helium tank;
- a high-power fundamental-mode RF coupler;

- a magnetic shield which surrounds the cavity and is installed inside of the helium tank.

The cavity and its manufacture are discussed in the previous section (Section 3.2). The remainder of this section will describe the baseline high-power coupler, frequency tuner, helium tank and HOM couplers.

3.3.1 Fundamental-mode power coupler

The 'TTF-III' input coupler was originally developed for TESLA [17], [18], and has since been modified by a collaboration of LAL and DESY for use in the European XFEL [19]. Due to the maturity of the design and extensive experience with this coupler, it has been adopted as the baseline design of the fundamental power coupler for the ILC. The main specifications of this input coupler are listed in Table 3.7.

Table 3.7
Main specifications of the input coupler. The parameters represent the approximate maximum expected values during operation, including possible upgrades.

Parameter	Specifications
Frequency	1.3 GHz
Operation pulse width	1.65 ms
Operation Repetition rate	5 Hz / 10 Hz
Maximum beam current	8.8 mA
Accelerating gradient of cavity	31.5 MV/m ± 20%
Required RF power in operation	∼ 400 kW
Range of external Q value	(1.0 ∼ 10.0) $\times 10^6$ (tunable)
RF process in cryomodule	> 1200 kW for ≤ 400 μs pulse width > 500 kW for > 400 μs pulse width
RF process with reflection mode in test stand.	> 600 kW for 1.6 ms pulse width
RF process time	< 50 hours in warm state < 20 hours in cold state
Approximate heat loads	< 0.01 mW (2K static) 0.07 W (5K static) 0.6 W (40K static) < 0.02 W (2K dynamic) 0.12 W (5K dynamic) 1.6 W (40K dynamic)
Number of windows	2
Bias voltage capability	Required

The coupler is a complex device assembled from roughly 130 parts. As with the cavities, the couplers must be assembled in very clean environments.

3.3.1.1 Mechanical design

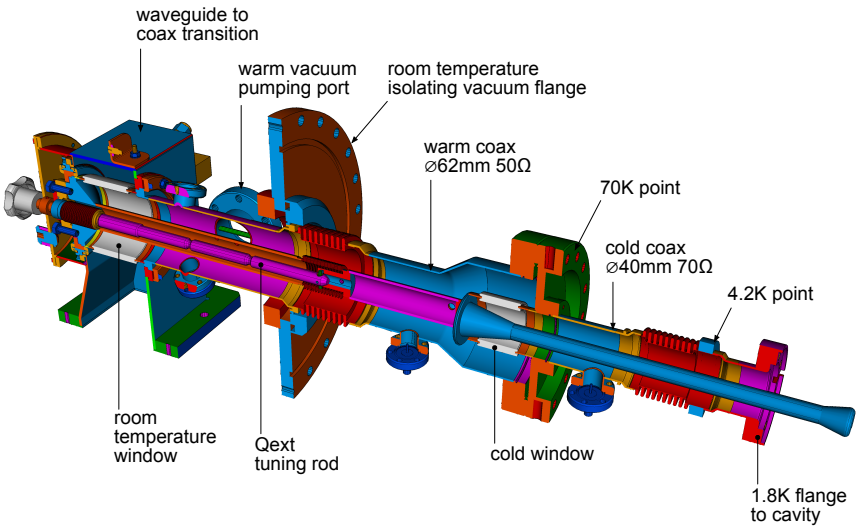

Figure 3.6
Schematic drawing of TTF-III (XFEL) input coupler.

A 3-dimensional sectioned schematic of the coupler assembly is shown in Fig. 3.6. The coupler is separated into a warm and cold part as shown, the latter of which is mounted into the cavity

at 2 K. RF power is brought in via a rectangular waveguide (WR650) into the "door-knob" mode converter at the warm transitionapproximate max . The RF power then propagates through a coaxial transmission line into the cavity beam pipe via the antenna (at 2 K). Both the warm and cold parts have a ceramic RF window, which protects and separates the cavity vacuum and the vacuum inside the warm coupler part. (The cold part shares the same vacuum with the cavity.) Both RF windows are cylindrical ceramic pieces made of Al_2O_3, the vacuum surfaces of which are coated with a few nanometers thickness of titanium-nitride in order to prevent multipacting. The two bellows (warm and cold) in the outer conductor allow a $\pm$ 10 mm adjustment of the antenna penetration into the cavity beam pipe to change the coupling to the cavity, providing a range of Q_{ext} of 1–10 $\times$ 10^6. The antenna position (Q_{ext}) is adjusted via a tuning rod housed in the central conductor, and driven by a remote actuator at the end of the warm transition.

The outer conductor is made of thin stainless steel whose inner surface has a 10 µm thick copper plating. The required thickness of the copper plaiting is a trade-off balance between providing enough electrical skin depth to prevent penetration of the RF into the stainless-steel outer conductor, thus minimising ohmic losses, and achieving a thermal balance between heat conduction from the warm end of the coupler (static load) while providing cooling for the RF losses (dynamic load).

Each input coupler is equipped with three electron-current pick-up probes for monitoring discharges inside the coupler. Provision is made to DC-bias the inner conductor to suppress the onset of multipacting. The warm coupler vacuum is maintained by a separate vacuum pumping system at a pressure of $< 10^{-8}$ mbar.

3.3.1.2 Initial coupler processing (acceptance testing) and final assembly

After receipt from industry and before assembly into the cavity, the input couplers undergo warm RF conditioning, which also forms part of the coupler acceptance testing. Coupler test facilities will likely be located at collaborating institutes, such as the one for the European XFEL at LAL, Orsay. The coupler test facility requires clean room facilities for the handling and cleaning the coupler parts, pumping and baking systems, and high-power RF systems for processing of the couplers.

The approach to the coupling processing, including clean-room assembly of the parts and subsequent cleaning and in-situ bake-out, is the result of extensive R&D at LAL for the European XFEL [20], which has resulted in a significant reduction in the time required to condition the couplers (now approximately 20 hours). Figure 3.7 shows the steps in preparing the coupler for the warm RF processing. First, the interior of coaxial parts and window ceramics of both the warm and cold parts of the couplers are inspected and cleaned in a clean-room environment, after which they are assembled together. A pair of couplers are then installed in a special rectangular waveguide system for RF processing. The typical conditioning procedure is to raise the RF power and pulse width in steps from near zero to predetermined maximums, avoiding out-gassing in excess of a prescribed vacuum trip level ($\sim 2 \times 10^{-7}$ mbar). The RF pulse width starts from 20 µs, and is then increased to 50, 100, 200, 400, 800, 1300, and 1500 µs. The entire procedure is automated.

Once successfully processed, the couplers are disassembled in a clean room to avoid any contamination of their interior surfaces, and then sealed and transported to a cryomodule assembly facility. Here, the cold and warm parts are separated and the cold part of the coupler mounted into the cavity in a class-10 clean room during the cavity string assembly. The warm part of the coupler is installed only after the complete string and cold mass have been installed into the cryomodule vacuum vessel. Final assembly of the warm couple part is made in a clean environment provided by mobile clean-room cabins.

After installation of the complete coupler into the cryomodule, further light conditioning is required at both room temperature and 2 K. This processing is performed either as part of the

Figure 3.7
Flow chart of the input coupler process and test.

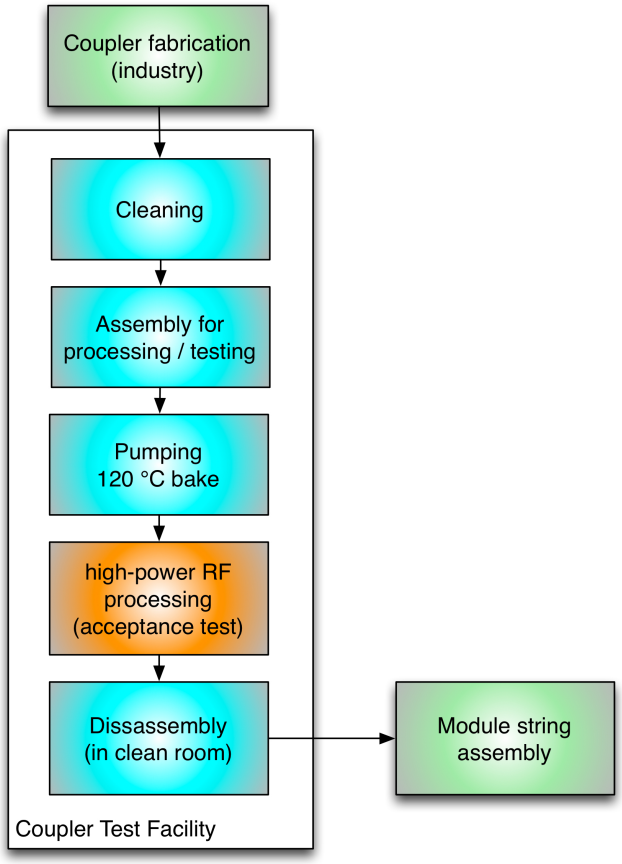

cryomodule tests, or in-situ after installation in the accelerator tunnel (see Section 3.4.3).

3.3.2 Frequency tuner

The mechanical cavity tuner is required to provide two functions:

- a slow mechanically adjustment of the frequency of the cavity and bring it on resonance (static tuning);
- a fast 'pulsed' adjustment using a piezo system to dynamically compensate Lorentz-force detuning during the RF pulse.

Specifications for the frequency tuner system is summarised in Table 3.8. The "Blade Tuner" design [21–24], which has been developed by INFN Milano-LASA as a coaxial and light tuning solution for TESLA-type cavities, has been adopted for the ILC baseline.

Figure 3.8
Schematic of the blade tuner.

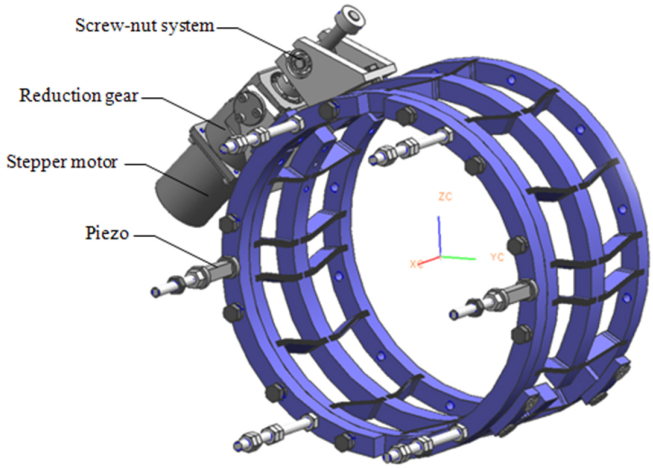

Table 3.8
Main specifications of the frequency tuner.

Tuner	Parameter	Specifications
Slow tuner		
	Tuning range	$>$ 600 kHz
	Hysteresis	$<$ 10 µm
	Motor characteristics	Step motor, power-off holding, magnetically shielded
	Motor location	Inside 5K shield, accessible from outside
	Magnetic shield	$<$ 20mG
	Heat load by motor	$<$ 50 mW at 2 K
	Motor lifetime	$> 20 \times 10^6$ steps
Fast tuner		
	Tuning range	$>$1KHz at 2 K
	LFD residuals	$<$ 50 Hz at 31.5 MV/m flat-top
	Actuator	Piezo actuator, located inside 5K shield, Two actuators for redundancy
	Heat load by actuator	$<$ 50 mW at 2 K
	Magnetic shield	$<$ 20mG
	Actuator lifetime	$> 10^{10}$ pulses

Figure 3.8 shows the tuner. The azimuthal movement of the central ring is converted into the required longitudinal cavity strain without backlash via the elastic blades. The tuner mechanics as well as the blades are made of titanium, which provides both mechanical strength and a small thermal expansion coefficient. The slow tuning action is generated by a stepper motor operating at 5 K, coupled via a mechanical reduction gear, to rotate a threaded shaft which moves the central ring azimuthally. A CuBe threaded shaft is used as a screw-nut system. Fast tuning action is driven by two piezoelectric ceramic actuators mounted symmetrically on either side of the cavity as shown in Fig. 3.8, which efficiently allows the transfer of their stroke to the helium tank, in series with the slow mechanical tuner. The coaxial tuner is installed on a mid location of the helium tank that is split in two halves by a bellow. This arrangement allows for simplification of end-cone regions of the cavity which need to accommodate fundamental mode and HOM couplers.

The blade-tuner and in particular the piezo actuators need to be under compression to operate. This is achieved by applying an initial pre-load using a calibrated cavity tensioning, which provides an initial frequency de-tuning and the correct amount of compression for the tuner.

The tuner mechanics, motor, gearbox and piezo actuators must be designed for high reliability, since a failure of the tuner mechanism will seriously hinder the optimal operation of that cavity, and in general these devices are not easily accessible once installed into the cryomodule. Possible solutions which could allow limited access to (for example) the motor and gearbox are being considered, but require much more detailed investigation of the impact on the cryomodule design. It should be noted that the tuners for the European XFEL can only accessed by removing and disassembling the module; the concept adopted here is the use of pre-testing for the components at cryogenic temperatures and careful design of the mechanical systems, such that a lifetime of $>$20 years can be expected. Once operational, the European XFEL will provide important experience on the reliability of such imbedded tuner systems. Part I Section 2.4 provides more detailed discussion on tuner designs and options.

3.3.3 HOM couplers

The higher-frequency eigenmodes in the cavity excited by the intense beam bunches must be damped to avoid multibunch instabilities and beam breakup. This is accomplished by extracting the stored energy via higher-order mode (HOM) couplers mounted on the both sides of the beam pipe of the 9-cell cavity [13, p. II-42]. The design of the HOM coupler is shown in Fig. 3.9. The superconducting pickup antenna is well cooled and insensitive to γ radiation and electron bombardment. A tuneable 1.3 GHz notch filter suppresses power extraction from the accelerating mode. The $Q_{\rm ext}$ for the high-impedance modes should be reduced to $< 10^5$ [13, p. II-55].

A TE121 'trapped mode' which is concentrated in the centre cells and has a low amplitude in

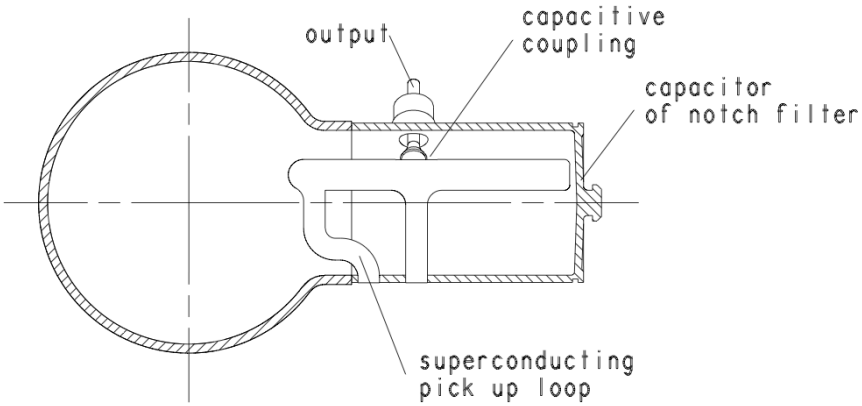

Figure 3.9
Cross section of the higher-order mode (HOM) coupler.

the end cells is damped by an asymmetric shaping of the end half cells. By using this asymmetric end half cells, one can enhance the field amplitude of the TE121 mode in one end cell, while preserving the field homogeneity of the fundamental mode and the good HOM coupling to the untrapped modes TE111, TM110 and TM011.

The two polarisation states of dipole modes in principle require two orthogonal HOM couplers at each side of the cavity. The optimum angle between the two couplers is 110°, with both couplers being installed at 35° to the horizontal, as shown in Fig. 3.10. Each HOM antenna plane is rotated 30° in its cylinder axis from the perpendicular plane of the beam pipe. The parts of the HOM antenna loops which project into beam pipe are positioned close to the end cells. Beam dynamics studies of the asymmetry arrangement of HOM coupler antenna together with RF field asymmetry of the input coupler antenna on the beam axis [25] have shown that the resulting effects on both the beam emittance and centroid are negligible.

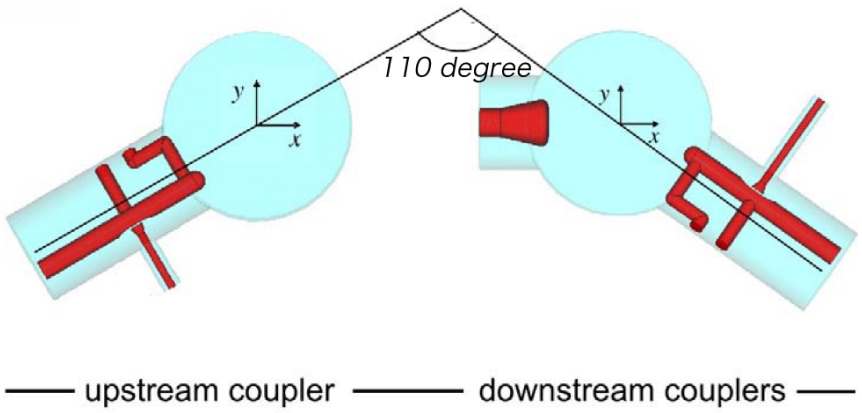

Figure 3.10
Orientations of the upstream HOM coupler (left) and the downstream HOM and main power couplers (right).

3.3.4 Helium tank and its interface

3.3.4.1 Helium tank

The design of the heliumtank for the ILC cavity package consists of a cylinder connected to a 2-phase-helium supply pipe, both of which are constructed from titanium (see Fig. 3.4 B).

Each helium tank has two pairs of "roller pad supports" made of titanium alloy, and welded at the horizontal mid-plane of the tank. The supports are used to hang the cavity from the cavity-support arms which extend underneath the gas return pipe (Fig. 3.4 C). The tank also has a clamping pin to connect it to the invar rod that runs the entire length of the cryomodule. The clamp (and the invar rod) prevents the cavities from moving longitudinally during cool down and warm up, keeping the locations of the high-power couplers fixed with respect to the outside of the cryostat. The roller-pad supports are mounted in slide bearings and adjuster bolts (needle support assembly), which allows

contraction and expansion of the helium-gas return pipe, to which the cavity-support arms are fixed.

The helium tank has to accommodate the tuner system as discussed in Section 3.3.2. For this purpose the tank has a thin titanium cylindrical bellows located at its centre. On both sides of the bellows, two flanges are welded for installation of the blade tuner.

The 2-phase-helium pipe has a short branch made of another pipe with the same diameter which is welded to an adaptor hole provided on the helium tank. The 2-phase-helium pipes of neighbouring cavities have their lengths chosen such that they can be readily welded to each other via bellows when they are assembled into a cryomodule.

3.3.4.2 Magnetic shield

The superconducting cavities have to be shielded from external magnetic fields to achieve their maximum performance. The cryoperm shield must cover the entire cavity including the end groups (down to the cavity beam pipe).The current philosophy for ILC is that the cryoperm shield will be placed inside the helium jacket, which is expected to simplify the design of the shield itself. The European XFEL design has the magnetic shield external to the tank, and is installed during the cryomodule assembly. It is expected that the cost of installing an internal shield (during cavity production) is less than the cost of assembling the external shield during module assembly. Furthermore, this simplifies some of the issues concerning the design of an external shield which is compatible with a mid-mounted tuner. There is currently no final design for a suitable shield which can be inserted inside the helium tank. Some experience at KEK with an internal cylindrical shield have demonstrated feasibility. The current TESLA design requires re-design to accommodate such a concept. Once a suitable mechanical solution is found, the effectiveness of the shield will need to be determined by measurement of the cavity quality factor at 2 K. Although this requires further engineering and prototyping, it is expected that cost-effective solutions can be found.

3.3.4.3 Flanges and seals

All the cavity flanges are made of Nb-Ti alloy and use a hexagonal ring seal made of aluminium alloy (Al-Mg-Si) for vacuum sealing. Flanges are required for the two beam pipes, input coupler port, fundamental power pick-up port, and two HOM pick-up ports. The surfaces of the flanges which meet the seal should be machined and polished to a very smooth surface finish. The edges of the hexagonal seal which meet the flange surface need to be sharp and firm.

3.3.5 Plug-compatible design

In order to allow various designs for sub-components to work together in the same cryomodule, a set of interface definitions have been internationally agreed upon [26]. To date, the interface definitions cover: the cavity (Section 3.2); fundamental-mode coupler (Section 3.3.1); mechanical tuner and helium tank (Section 3.3.2 and Section 3.3.4, respectively).

3.3.5.1 Cavity resonator

The boundary and the interfaces for the cavity are defined as shown in Fig. 3.11. The length of a cavity as measured from the surface of the two beam-port flanges is 1247 mm. The beam-port flanges are DN78, and a DN40 flange is used for the input coupler.

3.3.5.2 Helium tank

The interfaces of the helium tank are defined by the four roller-pad supports and two ends of the 2-phase-helium supply pipe as shown in Fig. 3.12. The end finish of the 2-phase-helium supply pipe has to have a weld-ready finish for connection of the titanium bellows. The roller-pad supports have to have smooth surfaces, compatible with the needle-support assembly.

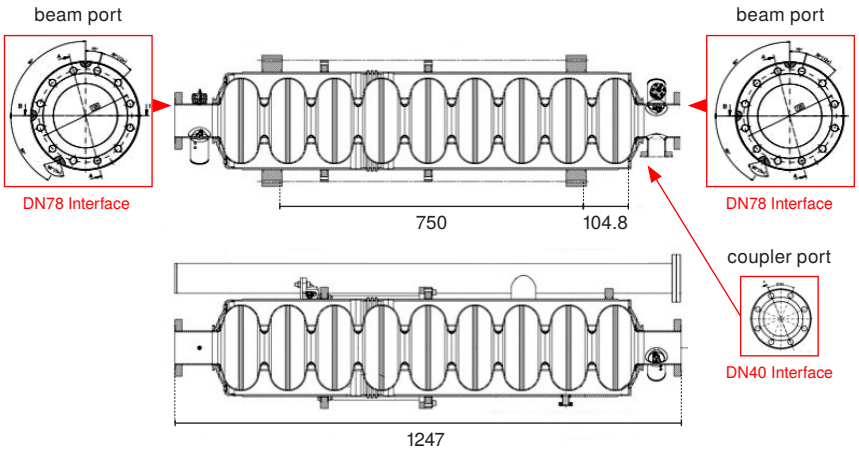

Figure 3.11
Interface definition of the cavity.

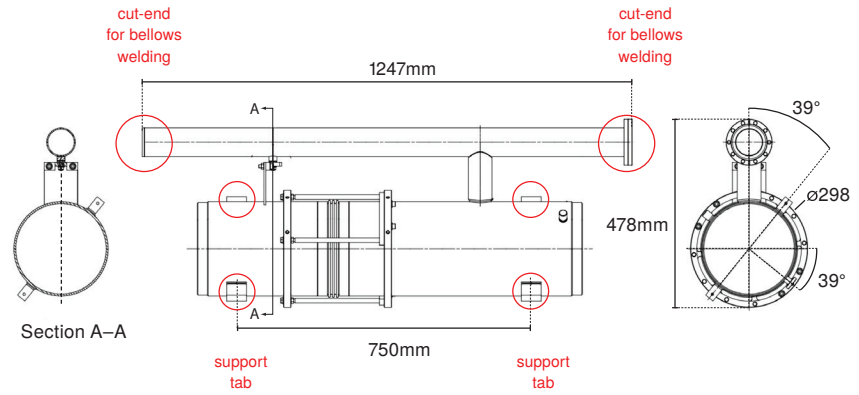

Figure 3.12
Interface definition of the helium jacket.

3.3.5.3 Fundamental-mode input coupler

The interfaces of the input coupler are defined by the cavity coupler port, cryomodule coupler port and the rectangular waveguide port, as shown in Fig. 3.13. The cavity coupler port is a DN40 interface flange which uses aluminium-made hexagonal sealing. The cryomodule coupler port is a flange with an outer diameter of 260 mm which uses a DN200 O-ring seal.

3.4 Cryomodule design including quadrupoles

3.4.1 Overview

Cryomodules are the modular building blocks of the ILC superconducting main linacs, and need to fulfil the following main functions:

1. provide mechanical support for beamline elements such as cavities and focussing elements;
2. facilitate achievement of the necessary alignment tolerance and stability according to beam dynamics specifications;
3. create and maintain in an efficient way the cold environment needed for the cavity and magnet operation.

The cryomodules represent the major heat loads at LHe temperatures, and therefore play an important role in the overall cryogenic system optimisation (See Section 3.5).

The highly-integrated design concept for the cryogenic systems leading to a high filling factor and reduced overall cost has been introduced in Section 3.1. In particular the concept of the use of single large cryoplants to cool kilometre-long *cryo-units* (similar to the LHC). Shorter *cryo-strings* are required to achieve segmentation of the insulating vacuum and of the two-phase-helium line.

Each of the 12.652 m-long cryomodules contains either nine cavities (Type A), or eight cavities and one superconducting quadrupole package (including horizontal and vertical dipole correctors and

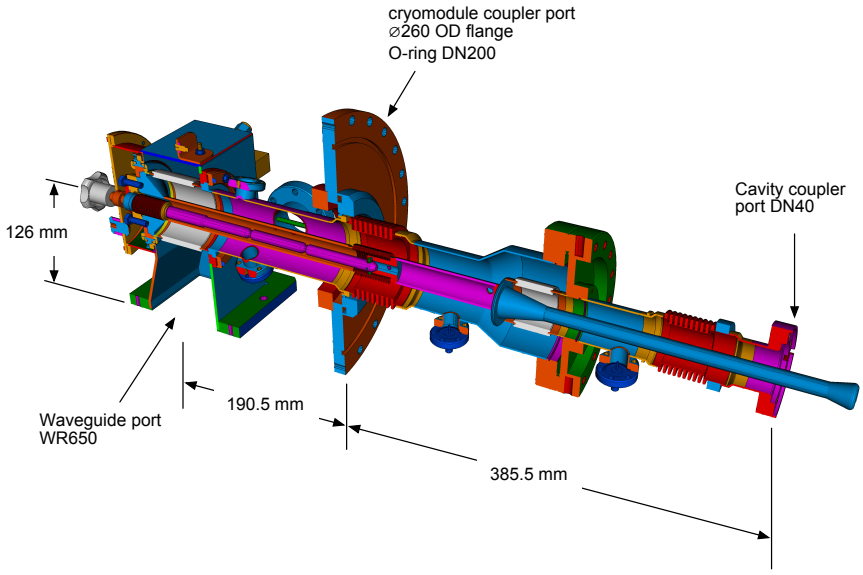

Figure 3.13 Interface definition of the input coupler.

a BPM) located at the centre of the cryomodule (Type B). The cavities and quadrupole package are integrated into the cryomodules along with their supporting structures, thermal shields and insulation, and all of the associated cryogenic piping required for the coolant flow distribution along a cryogenic unit without the need for additional external cryogenic distribution lines.

All the 14,742 1.3 GHz cavities in the ILC main linacs are grouped into 1,701 cryomodules (1,134 Type A, and 567 Type B). Another 152 cryomodules are located in the e^+ and e^- sources and RTML bunch compressors. Most of these are either the standard Type A or Type B cryomodules, although the sources contain a few with special configurations of cavities and quadrupoles.

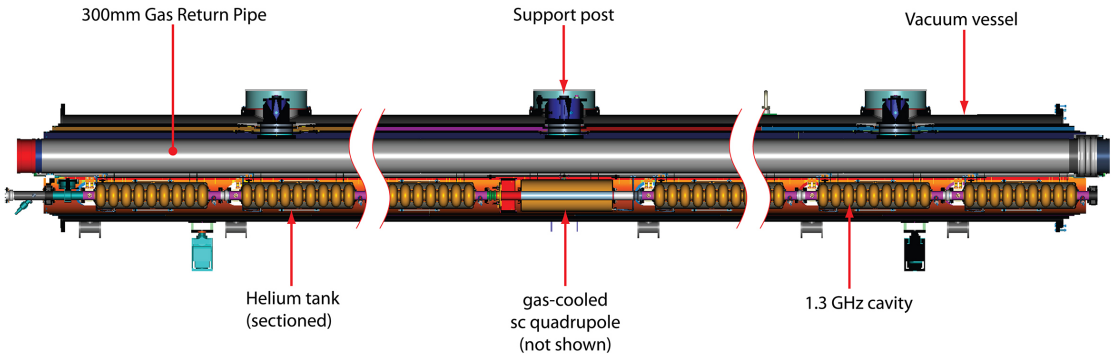

Figure 3.14. Longitudinal View of a Type IV Cryomodule (Type B), with eight cavities and a central quadrupole.

3.4.2 Cryomodule technical description

Figure 3.14 shows a longitudinal sectioned view of the Type-IV cryomodule (Type B). The design is a modification of the type developed and used in the TESLA Test Facility (TTF) at DESY, with three separate vacuum envelopes (beam vacuum, isolation vacuum and power-coupler vacuum) [27]. The cavity spacing within the cryomodule is $(6 - 1/4)\lambda_0 = 1.327$ m.

Copper-coated flanged bellows are located between beamline components to allow differential thermal contractions. Fundamental-mode couplers (described in Section 3.3.1) provide the RF power to the cavities, and are connected to ports on the vacuum vessel on one side and to the cavity coupler ports on the opposite side. RF cables bring the signals from the field pickup and the HOM antennas (See Section 3.3.3) to the LLRF control system outside the cryomodule for the control of the cavity field amplitude and phase and to extract HOM power from the 2 K level. Manually operated valves

required by the clean-room assembly terminate the beam pipe at both module ends. The valves are fitted with simple RF shields.

The decision to place the quadrupole package in the middle of the cryomodule (as in the Type IV design) allows the definition of a standard interconnection interface for all main-linac cryomodules, irrespective of their sub-type, simplifying the tunnel assembly procedures for module connections.

3.4.2.1 The cryomodule cross section

Figure 3.15 shows a cross section of the Type IV ILC Cryomodule derived from the TTF-III design [13, 28]. The largest component of the transverse cross section is the 300 mm-diameter helium-gas return pipe (GRP) which acts as the structural backbone for supporting the string of beamline elements and allows recovery of the mass flow of He vapours at a negligible pressure drop along the cryo-strings, to preserve temperature stability.

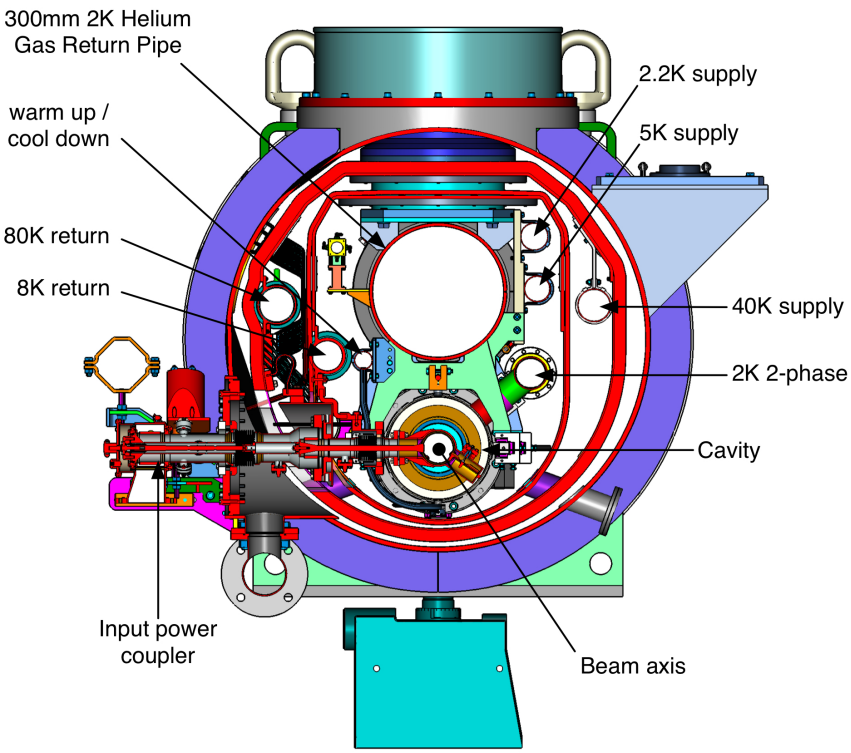

Figure 3.15 Representative cryomodule cross section

The GRP is supported from the top by three composite posts with small thermal conduction from the room-temperature environment. The posts are connected to adjustable suspension brackets resting on large flanges placed on the upper part of the vacuum vessel. This suspension scheme allows the correct alignment of the axis of the cavities and quadrupole magnets independently of the flange position, without requiring expensive precision machining of these vacuum-vessel components. The centre post is fixed to the vacuum vessel, while the two remaining posts are laterally adjustable and can slide on the flanges to allow the GRP longitudinal contraction/expansion with respect to the vacuum vessel during thermal cycling. Each post consists of a fibreglass pipe terminated by two shrink-fit stainless-steel flanges. Two additional shrink-fit aluminium flanges are provided to allow intermediate heat flow intercept connections to the 5–8 K and 40–80 K thermal shields; the exact location of these flanges has been optimised to minimise heat leakage [29].

3.4.2.2 Transverse / longitudinal cavity positioning and alignment

The cavities and magnet are supported from the GRP by means of stainless-steel brackets holding the four titanium pads on the helium tanks via a longitudinal sliding mechanism, which also provides adjusting screws and pushers for alignment in the transverse (vertical-horizontal) planes. During the module assembly, while the GRP is suspended on the assembly jig before insertion into the vacuum vessel, the beamline components are aligned and the alignment information is first transferred to references points on the GRP, and later transferred to reference points of the vessel for the cryomodule alignment, in order to achieve the installation alignment errors given in Table 3.4 (Section 3.1.3). All TTF cryomodules have been equipped with stretched-wire sensors to monitor the cold-mass displacement and positional reproducibility between cool downs [15] to qualify the alignment procedure, which will be used for the European XFEL.

A mechanical, coaxial (blade) and a piezo-electric tuner are mounted on the cavity vessels.

During cool down, the two ends of the ∼12 m-long GRP move by up to 18 mm toward the centre of the module. The cavity sliding support allows the cavity position to completely decouple from the large GRP contraction induced by the cool down, and avoids large stresses acting on the cavities due to differential shrinkage. To maintain the longitudinal position of the cavity-coupler flange within 1 mm from the coupler port on the warm vacuum vessel—in order to limit large coupler movements occurring with differential contraction—each cavity is clamped to a long invar rod, which is in turn longitudinally anchored at the neutral fixed point of the GRP at the centre post.

The beam-pipe interconnection between the cryomodules consists of a 0.38 m-long section between the end valves that incorporates a HOM absorber (similar to the XFEL design [30]), a bellows, and a vacuum pumping port; the latter is connected to a flange in the vacuum vessel every ninth cryomodule.

3.4.2.3 Thermal radiation shields

The cryostat includes two aluminium thermal-radiation shields operating in the temperature range of 5–8 K and 40–80 K, respectively [31]. The use of a double thermal-radiation shielding reduces the radiative thermal load at 2 K to a negligible amount. Each shield is constructed from a stiff upper part, and multiple lower sections (according to the number of the cold active components, e.g. cavities, magnets). The upper part is supported by the intermediate flanges on the fibreglass posts, constrained at the centre post but slides on the two lateral posts to which they are still thermally connected. The 'finger-welding' technique [31] is used both to connect each thermal shield to its properly shaped aluminium cooling pipe, and the lower-shield parts to the upper ones, by providing good thermal conduction without inducing high stresses on the structure.

Blankets of multi-layer insulation (MLI) are placed on the outside of the 5–8 K and the 40–80 K shields. The 5–8 K shield blanket is made of 10 layers of doubly aluminised mylar separated by insulating spacers while the 40–80 K blanket contains 30 layers. In addition, helium jackets for cavity and magnet packages, gas return pipe and 5–8 K pipes are wrapped with 5 layers of MLI as a mitigating provision to reduce heat transfer in the event of a vacuum failure.

3.4.2.4 The vacuum vessel

The cryostat outer vacuum vessel is constructed from carbon steel and has a standard outer diameter of 38″. Adjacent vacuum vessels are connected to each other by means of a flanged cylindrical sleeve with a bellows. Adjacent vessels have a flange-to-flange distance of 0.85 m, allowing sufficient space to perform the cryogenic connections between modules by means of automated orbital welders. In the event of accidental spills of liquid helium from the cavity vessels, a relief valve on the main-vessel body together with venting holes on the shields prevent excessive pressure build-up in the vacuum

vessel. Wires and cables from each module are extracted from the module using metallic sealed flanges with vacuum-tight connectors. The insulating-vacuum system is pumped during normal operation by permanent pump stations located at appropriate intervals. Additional pumping ports are available for movable pump stations, which are used for initial pump down, and in the event of a helium leak. The RF-power coupler needs an additional vacuum system on its room temperature side; this is provided by a common pump line for all couplers in a module, which is equipped with an ion getter and a titanium sublimation pump.

3.4.2.5 Cryogenic lines in the module

The following helium lines [32] are integrated into the cryomodules, as shown in Fig. 3.15.

- The 2 K supply line transfers pressurised single-phase helium through the cryomodule to the end of the cryogenic unit.
- The titanium 2 K two-phase supply line is connected to the cavity helium vessels. It supplies the cavities with liquid helium and returns cold gas to the 300 mm GRP at each module interconnection.
- The 2 K GRP returns the cold gas pumped off the saturated He II baths to the refrigeration plant. It is also a key structural component of the cryomodule
- The 5–8 K supply and return lines. The 5 K supply line is used to transfer the He gas to the end of the cryogenic unit. The 5–8 K return line directly cools the 5–8 K radiation shield and, through the shield, provides the heat-flow intercept for the main coupler and diagnostic cables, and the HOM absorber located in the module interconnection region.
- The 40–80 K supply and return lines. The 40 K supply line is used to transfer He gas to the cryogenic unit end and cools the high-temperature superconductor (HTS) current leads for the quadrupole and correction magnets. The 40–80 K return line directly cools the 40–80 K radiation shield and the HOM absorber and, through the shield, provides an additional heat-flow intercept for the main coupler and diagnostic cables.
- The warm-up/cool-down line connects to the bottom of each cavity helium vessel.

The helium vessels surrounding the cavities, the two-phase supply line and the GRP operate at low-pressure conditions (30 mbar, corresponding to 2 K) while all other cryogenic lines operate at a maximum pressure of 20 bar.

To provide sufficient cooling speed during cool down, the low-pressure lines around the cavities need to sustain a Maximum-Allowable Working Pressure (MAWP) of 2 bar differential, at room temperature. All components in the cryogenic system sustaining pressure conditions need to be assessed for pressure-code conformance [33], as discussed in Section 3.5.

The helium lines of adjacent modules are welded at the module interconnection regions. Only the vacuum flange incorporates a mechanical seal at the cryomodule interconnect. Thermal-shield lines are extruded aluminium with transition joints to stainless steel (similar to those used in the HERA magnets and in TTF and XFEL) at each interconnect, allowing the use of stainless-steel bellows. Similarly, the titanium two-phase line has transition joints to stainless steel in the interconnection region. The cryostat maintains the cavities and magnets at their operating temperature of 2 K.

3.4.2.6 Thermal design and module-heat-loss estimations

A low static heat load is an essential feature required of the cryostat design; the total heat load is dominated by the RF losses, and is thus principally determined by the cavity performance (and its spread). Table 3.9 lists the heat load assumed per cryomodule. The table reports the average values corresponding to one Main Linac unit (ML unit), i.e. three modules in a Type A – Type B – Type A configuration. The values reported here are based on the heat load of a 12-cavity cryomodule which has been calculated for the TESLA TDR [13], and refinement made on the basis of further assessments and static-load measurements obtained from S1-Global (Part I Section 2.7.1) and for the European XFEL prototypes. To scale to the ILC parameters, it is assumed that the gradient is 31.5 MV/m, the cavity Q_0 is 1×10^{10}, and the beam and RF parameters are those listed in Table 3.1 in Section 3.1. These values are used to define cryogenic heat loads and cryoplant parameters for the two variants of the cryogenic systems for the flat and mountainous topography respectively [34].

Table 3.9
Average heat loads per module in a ML unit, for the baseline parameter in Table 3.1. All values are in watts [27].

	2 K		5–8 K		40–80 K	
	Static	Dynamic	Static	Dynamic	Static	Dynamic
RF Load		8.02				
Radiation Load			1.41		32.49	
Supports	0.60		2.40		18.0	
Input coupler	0.17	0.41	1.73	3.06	16.47	41.78
HOM coupler (cables)	0.01	0.12	0.29	1.17	1.84	5.8
HOM absorber	0.14	0.01	3.13	0.36	-3.27	7.09
Beam tube bellows		0.39				
Current leads	0.28	0.28	0.47	0.47	4.13	4.13
HOM to structure		0.56				
Coax cable (4)	0.05					
Instrumentation taps	0.07					
Diagnostic cable			1.39		5.38	
Sum	1.32	9.79	10.82	5.05	75.04	58.80
Total	11.11		15.87		133.84	

Frequencies above the 1.3 GHz fundamental-mode operating frequency and below the beam-pipe cutoff are extracted by input- and HOM-couplers (in order to avoid additional power deposition at cold temperatures), but higher-frequency fields will propagate along the structure and be reflected at normal and superconducting surfaces. In order to reduce the losses at normal conducting surfaces at 2 K and 4 K, the cryomodule includes a special HOM absorber that operates at 70 K, where the cooling efficiency is much higher. The absorber basically consists of a pipe of absorbing material mounted in a cavity-like shielding, and integrated into the connection between two modules. As the inner surface area of this absorber (about 280 cm^2) is small compared to that of all the normal conductors in one cryomodule, the absorber has to absorb a significant part of all the RF power incident upon it. In field propagation studies, which assume a gas-like behaviour for photons, it has been shown that an absorber with a reflectivity below 50 % is sufficient [35, 36]. Theoretical and experimental studies indicate that the required absorption can be obtained with ceramics like MACOR or with artificial dielectrics. Figure 3.16 shows the design for the design implemented for the European XFEL, which has been successfully tested at FLASH [37]. The results show very good agreement with the theoretical predictions.

It is worth noting here that a substantial effort has been performed during the Technical Design Phase for the S1-Global module and for the European XFEL Project in the consolidation and benchmarking of the static heat-load assessments, as reported in Part I Section 2.7. The S1-Global measurements show a very good consistency with heat-load estimations when all conduction paths and heat-transfer mechanisms are taken properly into account in the budget, indicating that the module design is well understood and proven [38]. Values for the static loads in Table 3.9 are consistent with the experience gained during the Technical Design phase; the low estimates for static losses reflect

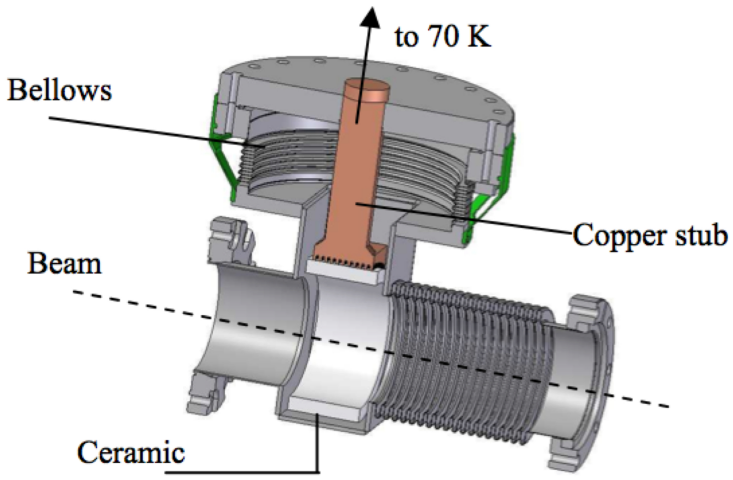

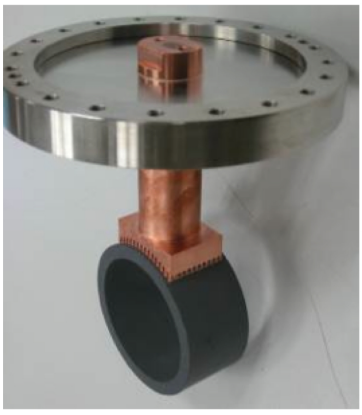

Figure 3.16
The design (top) and photographs (bottom left and right) of the HOM absorber for the European XFEL [37].

the assumption of the reduced diagnostic instrumentation foreseen for the ILC modules with respect to R&D activities such as the S1-Global module tests.

The experience reported with the European XFEL prototypes has highlighted the importance of the assembly procedures in achieving nominal loads, and "training" effects for the most sensitive 2 K environment [39] (Part I Fig. 2.50).

As a final remark on thermal loads, it must be noted from Table 3.9 that dynamic loads induced by RF are dominant in the 2 K region, and are intrinsically influenced by the spread of cavity performances (Q_0 values) and operating point (gradient setting). Much less experience and data is available on dynamic loads, and uncertainty factors need to be taken into account (see Section 3.5).

3.4.2.7 Quadrupole/Corrector/BPM Package

The baseline design for the ILC quadrupole/corrector/BPM package makes use of the conduction-cooled splittable quadrupole [40, 41] developed by FNAL and KEK (Part I Section 2.7). Figure 3.17 shows the magnet assembly; specifications are given in Table 3.10.

A key specification is the magnetic-centre stability of $< 5\,\mu m$ for a 20 % change in field strength, which is driven by beam-dynamics requirements (beam-based alignment). Because of superconductor magnetisation effects (cross coupling) between combined quadrupole and dipole coils [42, 43], the quadrupole and dipole correctors are separated.

The split-quadrupole is installed outside of the clean room around a beam pipe, thus decreasing possible contamination of the cavity RF surfaces, and greatly simplifying the string-assembly operation in the clean room.

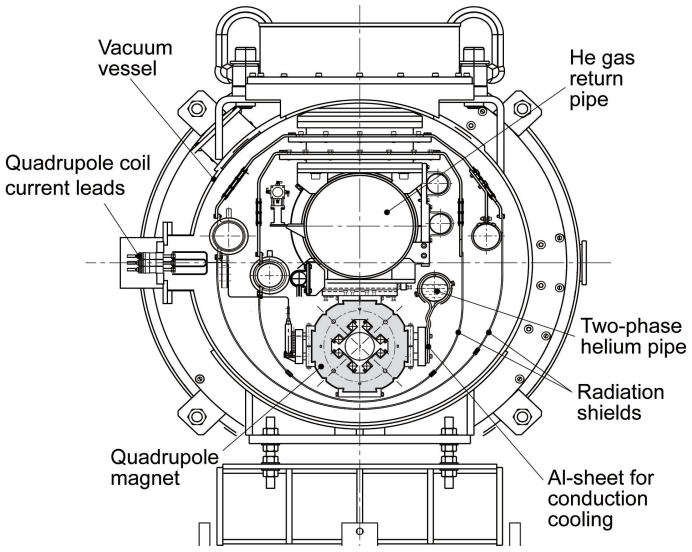

Figure 3.17
Cross section of a Type-B cryomodule showing the arrangement of the conduction-cooled split-yoke superconducting quadrupole.

Table 3.10
Splittable quadrupole magnet specifications and parameters.

Parameter	Value	Unit
Peak gradient	54	T/m
Peak integrated gradient	36	T
Field non-linearity at 5 mm radius	0.05	%
Dipole trim coils integrated strength	0.075	Tm
Aperture	78	mm
Pole-to-pole distance	90	mm
Magnetic stability (20 % field change)	< 5	μm
Peak operating quadrupole current	100	A
Magnet total length	680	mm
SC wire diameter	0.5	mm
NbTi filament size (vendor value)	3.7	μm
Cu:SC volume ratio	1.5	
Superconductor Critical current (5 T and 4.2 K)	200	A
Coil maximum field at 100 A current	3.3	T
Magnetic field stored energy	40	kJ
Quadrupole inductance	3.9	H
Quadrupole coil number of turns/pole	900	
Yoke outer diameter	280	mm

An important feature that must be addressed with the final engineering design is the package fiducialisation and subsequent transfer of these features to reproducible, external cryomodule fiducials to assure the correct alignment of the package with respect to the cryomodule string.

The accelerator lattice[3] (Section 3.1.3) has approximately constant focusing and FoDo cell length from 5 GeV up to the full beam energy of 250 GeV —a factor of 25 in beam rigidity. Hence it is not possible to use the identical effective magnet length for all magnets along the accelerator, since the lower-energy quadrupoles would then need to be run at fields (currents) which are too low to provide stable and reproducible performance. Two families of quadrupoles are considered sufficient to resolve this problem: above the nominal 25 GeV point, the long (high integrated field) magnet described above will work adequately. Below 25 GeV a shorter version will be used.

The L-band re-entrant BPM for the main linac is designed to effectively pick up the dipole TM110 mode through four symmetrically arranged waveguides. The dipole-mode frequency of 2.04 GHz is selected to avoid the 1.3 GHz and higher harmonics dark-current signals, and to avoid the cavity HOM frequencies. The re-entrant cavity is chosen for its compact size, and its compatibility with the 78 mm inner diameter of beam pipe. Four waveguides with loop pickups give more than 28 dB isolation from the common-mode excitation. The design L-band re-entrant BPM structure are shown in Fig. 3.18. A prototype model (Fig. 3.19) has been fabricated and tested with beam, and demonstrated a position resolution of 0.3 μm [44].

[3] including the RTML bunch compressors and Main Linac.

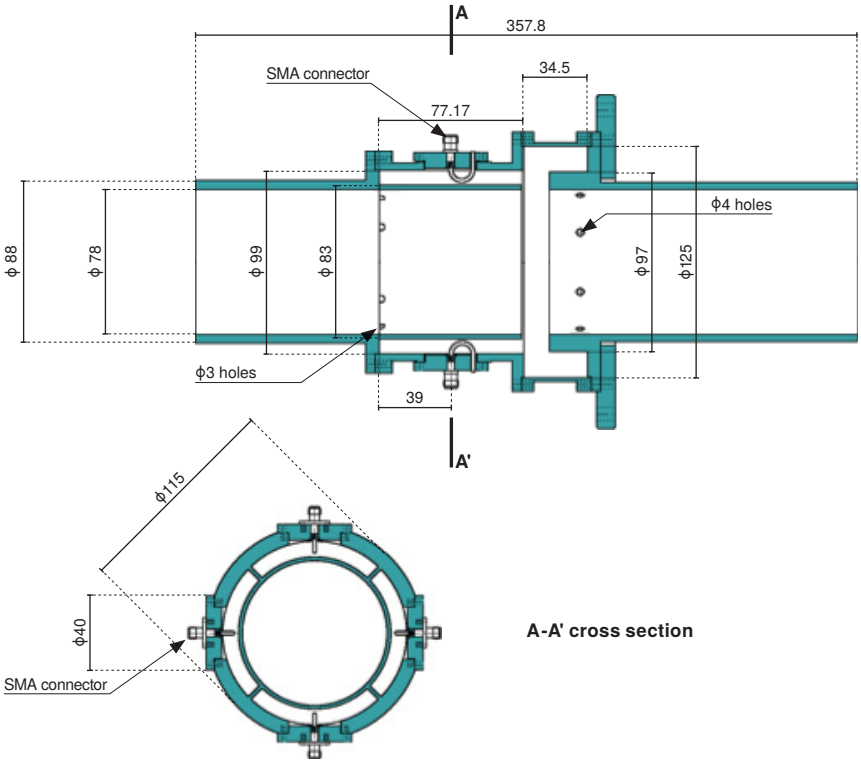

Figure 3.18
Schematic of the cold 2.04 GHz re-entrant cavity BPM.

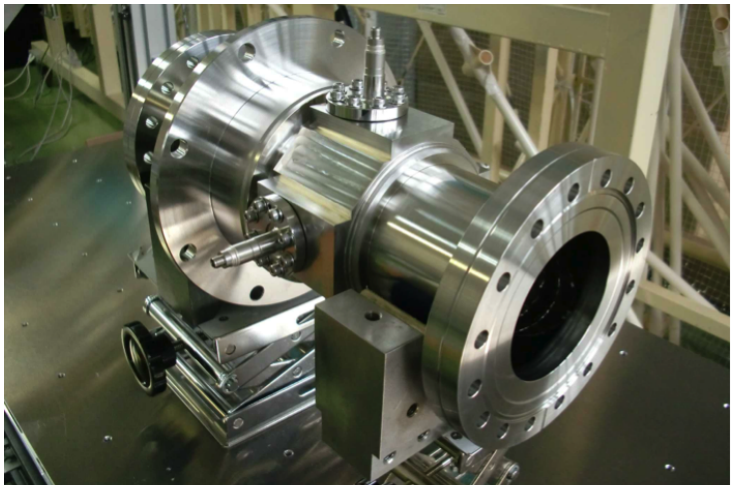

Figure 3.19
A photograph of the vacuum-tight prototype for the 2.04 GHz re-entrant cavity BPM.

3.4.3 Cryomodule testing

Before installation in the ML tunnel, assembled accelerator cryomodules will be qualified through sampled testing. The qualification includes checking mechanical fit, measuring cryogenic performance, and testing cavity systems at full power up to full voltage capability. A sampled-testing strategy is effective because 100 % of all key individual components, (including cavities, cavity auxiliaries, quadrupoles, instrumentation and cryogenic subsystems), will be fully tested before assembly of the cryomodules, as described in Section 3.3. The random sample cryomodule testing program will be phased in during the ramp-up stage of cryomodule production, during which a greater fraction of cryomodules will be tested, such that a total of one third of the full main-linac cryomodule complement will be tested before installation. All cryomodules will be tested during ramp up at the beginning of production, in order to qualify the production lines; the fraction to be tested will be reduced as the production rate is increased.

The project plan, (see Section 13), calls for an 8 to 10 year construction, installation and commissioning schedule so the peak cryomodule production rate required to produce the total of

1853 cryomodules is 15 per week, roughly 15 times the European XFEL cryomodule production rate (see Part I Section 2.5) During the mass-production cycle, cryomodule-test facilities will require large cryogenic and high-power RF infrastructure. It is expected that these facilities will be hosted and run by collaborating institutes in all three regions, possibly together with a cryomodule-assembly infrastructure. While it is desirable to co-locate the assembly and test facilities, this may prove intractable, and so it is necessary to consider the need to transport the modules (Section 3.4.4). This is the case for the European XFEL, where the cryomodule assembly is hosted at CEA Saclay, Paris, France, while the cavity- and cryomodule-test facilities is located at DESY, Hamburg, Germany.

Figure 3.20 shows the layout of the European cryomodule test facility. Three independent concrete test bunkers, located in the center of the figure, are used to test an average of one cryomodule per week. The test procedure to be followed during the ILC main-linac construction project will largely follow that of the European XFEL and is expected to take fifteen days, including interconnect, warm processing, cool down, high power cold test, warm up, and disconnect. The tests themselves take 8 to 10 days, not including tests and qualification of the local power distribution. At present, cryomodule testing has been done at CERN, DESY, KEK, JLab, and Fermilab and it is reasonable to consider the use of the infrastructures at these collaborating institutes for the purpose of the ILC project, thereby avoiding the delay and cost of building new test facilities.

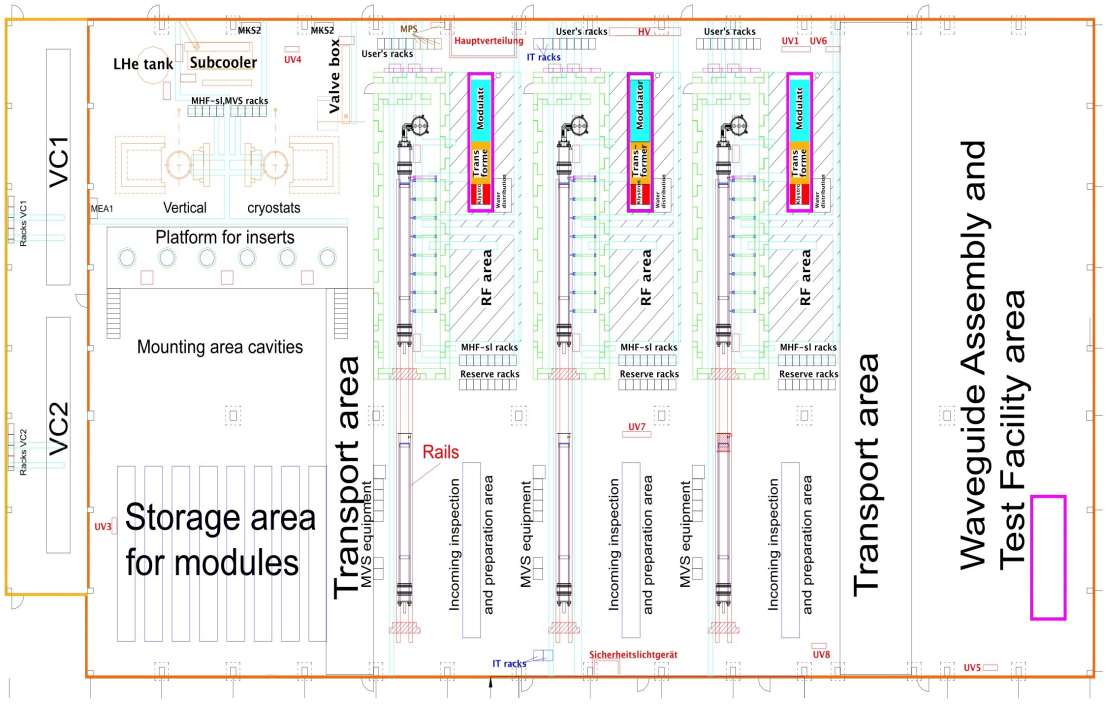

Figure 3.20. European XFEL cryomodule test facility Accelerator Module Test Facility, (AMTF), at DESY.

It is expected that a minimum of 15 cryomodule-test stands similar to those in the AMTF must be collectively made available through ILC collaborating institutes to satisfy the aggregate test rate requirement of five per week.

Figure 3.21 illustrates the test steps for cryomodules, starting with equipment hookup. The cryomodule is then placed inside a concrete-shielded test bay and connected to the various vacuum systems (cavity, coupler and insulation vacuum), cryogenic lines and RF wave-guide system. After pumping down the vacuum and performing necessary leak checks, warm RF processing of input couplers is done. The cryomodule is then cooled down to 2 K, and the RF characteristics of each of cavity are measured by feeding low-power RF through a coaxial-to-rectangular waveguide converter. The parameters of the couplers and waveguides are optimised in this condition, before starting

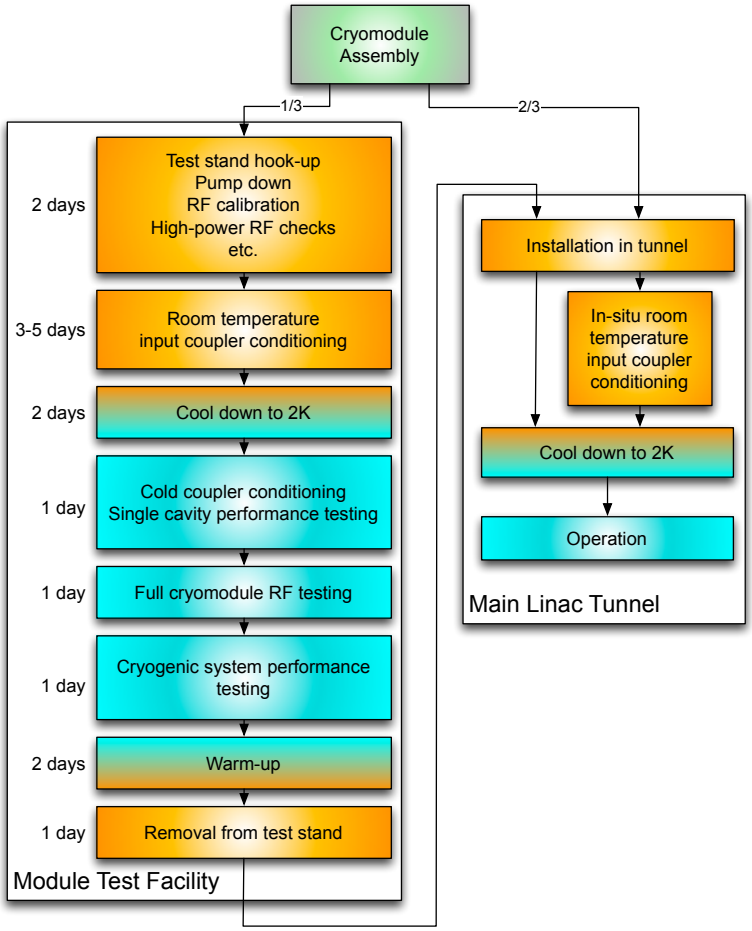

Figure 3.21
Flow chart of the cryomodule test. There are two test and processing streams, one third of the cryomodules are tested in the Module Test Facility and the other two thirds will be processed in situ after installation in the tunnel.

high-power RF processing of the couplers, followed by a suite of tests of the cavities and cavity auxiliaries, (including tuner mechanism, piezo tuner, cold coupler and $Q_{\rm ext}$ tuner), at full gradient.

Validation of the cryomodule is done by confirming that all the cavities will be able to provide the specified field gradient of 31.5 MV/m $\pm$ 20 %, with acceptable dark current (field emission), after installation in the accelerator. After completing the tests, the cryomodule is warmed up with the tuner tension released.

Figure 3.21 also shows the test and processing procedures to be done following installation in the main-linac tunnel. The remaining two thirds of the cryomodules, those that were not tested in the test facility, are connected to the local power distribution system for coupler conditioning.

3.4.4 Shipping of cryomodules between regions

To date, there is limited experience on the shipping of completed cryomodules across the main regions of the ILC collaboration. FNAL shipped the complete ACC39[4] module for FLASH by air transport to DESY (see Fig. 3.22), where the module has been successfully tested up to its specification [45] .

By the end of 2015, the European XFEL will have gained the experience of transporting by road 100 complete modules from the string and module assembly facility at CEA/Saclay to the AMTF testing area at DESY [46], providing a useful statistical sample of data. Figure 3.23 shows an XFEL prototype cryomodule in its transport frame. It is essential that this XFEL experience be incorporated in the development of a reliable method for overseas transport of complete ILC modules.

[4] A special short module derived from the TTF design for the 3.9 GHz cavities

Figure 3.22
The ACC39 in its transport box upon arrival in DESY.

Figure 3.23
An European XFEL prototype cryomodule in its transport frame. The module is supported on vibration dampers [46]

3.5 Cryogenic cooling scheme

Of the total of 1853 SCRF cryomodules in the ILC, the 1701 Main Linac SCRF cryomodules (92 %) comprise the largest cryogenic cooling load and therefore dominate the design of the cryogenic systems. The 102 cryomodules (6 %) in the bunch compressors (RTML see Chapter 7) are considered extensions to the Main Linacs for the purposes of the cryogenic layout. For this reason, the cryogenic system is described in this chapter.

Figure 3.24 illustrates the cryogenic-system arrangement for ILC, which clearly shows the concept of long 2–2.5 km contiguous cryo-units, cooled by a single large 2 K cryoplant. There are detailed differences in the two site-dependent design variants under consideration, primarily driven by the choice of the RF-power scheme. The most important difference is the choice of a total of 10 cryoplants for the mountainous topography variant (using DKS), and 12 cryoplants for the flat topography (using KCS), as illustrated in Fig. 3.24. The total cryogenic load is however the same, but is distributed

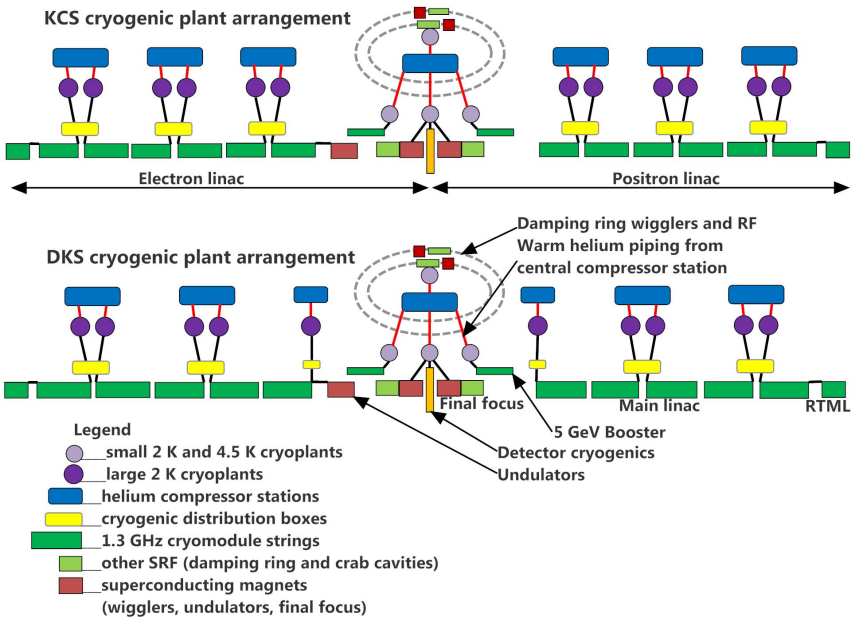

Figure 3.24
The overall layout concept for the cryogenic systems for both flat (KCS) and mountain (DKS) topography.

differently between the plants for the two schemes.

The most upstream cryoplants in either variant also provide cooling for the 102 cryomodules in the RTML bunch compressors. The remaining loads for the systems are cooled by separate dedicated plants in the central region as shown.

3.5.1 Cryogenic cooling scheme for the main linacs

Saturated He II cools RF cavities at 2 K, and helium-gas-cooled shields intercept thermal radiation and thermal conduction at 5–8 K and at 40–80 K. A two-phase line (liquid-helium supply and concurrent vapour return) connects to each helium vessel and connects to the major gas return header once per module. A small diameter warm-up/cool-down line connects the bottoms of the helium vessels. (see Section 3.4 for more details.)

A sub-cooled helium supply line connects to the two-phase line via a Joule-Thomson valve once per cryo-string (9 modules or 12 modules for a short and long string respectively — see Fig. 3.2 in Section 3.1). The 5 K and 40 K heat intercepts and radiation screens are cooled in series through an entire cryogenic unit of up to 2.5 km in length. For the 2 K-cooling of the RF cavities, a parallel architecture is implemented providing parallel cooling of cryo-strings resulting in operational flexibility. Consequently, each cryo-unit is subdivided into about 13 to 21 cryo-strings, each of which corresponds to either 116 m or 154 m-long elementary blocks of the cryogenic refrigeration system, for short and long cryo-strings respectively.

Figure 3.25 shows the cooling scheme of a cryo-string, which contains 12 cryomodules (long string). The cavities are immersed in baths of saturated superfluid helium, gravity filled from a2 K two-phase header. Saturated superfluid helium flows along the two-phase header, which has phase separators located at both ends; the first phase separator is used to stabilise the saturated liquid produced during the final expansion. The second phase separator is used to recover the excess of liquid, which is vaporised by a heater. At the interconnection of each cryomodule, the two-phase header is connected to the pumping return line.

The division of the Main Linac into cryogenic units is driven by various plant size limits and a practical size for the low-pressure return pipe. A cryogenic plant of 25 kW equivalent 4.5 K capacity is a practical limit due to industrial production for heat-exchanger sizes and over-the-road shipping size restrictions. Cryomodule piping pressure drops also start to become rather large with more than

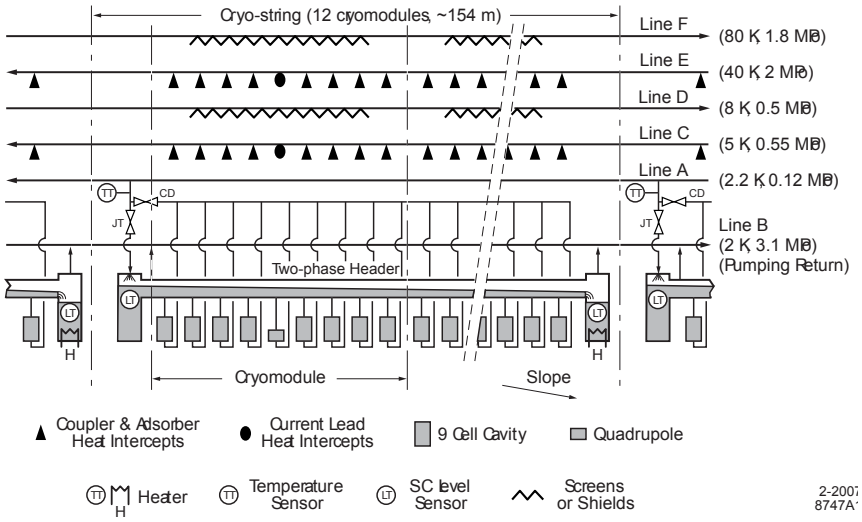

Figure 3.25
Cooling scheme of a cryo-string.

2.5 km distances. Practical plant size and gas-return header pressure drop limits are reached with 189 modules in a 21 short-string cryogenic unit, 2.5 km long.

3.5.2 Heat loads and cryogenic-plant power

Table 3.11 shows the predicted heat loads and resulting cryogenic plant sizes for main-linac cryo-units comprised of 13 long cryo-strings for the KCS layout (a total of 156 cryomodules) and for 21 short cryo-strings for the DKS layout (a total of 189 cryomodules). The resulting cryogenic plant capacities are equivalent to 15.4 kW at 4.5 K for the KCS layout and 19.0 kW at 4.5 K for the DKS (mountainous) layout. Both sizes are well within the range of typical large helium cryogenic plant capacities.

Table 3.11. Main-linac heat loads and cryogenic plant size [34]. Where there is a site dependence, the values for the flat / mountain topographies are quoted respectively. (The primary difference is in the choice the number of cryo-plants, specifically 6 and 5 plants for flat and mountainous topographies respectively.)

		40–80 K	5–8 K	2 K
Predicted module static heat load	(W/module)	75.04	10.82	1.32
Predicted module dynamic heat load	(W/module)	58.80	5.05	9.79
Number of cryomodules per cryogenic unit		156 / 189	156 / 189	156 / 189
Non-module heat load per cryo unit	(kW)	0.7 / 1.1	0.14 / 0.22	0.14 / 0.22
Total predicted heat per cryogenic unit	(kW)	21.58 / 26.40	2.61 / 3.22	1.87 / 2.32
Efficiency (fraction Carnot)		0.28	0.24	0.22
Efficiency in Watts/Watt	(W/W)	16.45	197.94	702.98
Overall net cryogenic capacity multiplier		1.54	1.54	1.54
Heat load per cryogenic unit including multiplier	(kW)	33.23 / 40.65	4.03 / 4.96	2.88 / 3.57
Installed power	(kW)	547/669	797/981	2028 / 2511
Installed 4.5 K equiv	(kW)	2.50 / 3.05	3.64 / 4.48	9.26 / 11.47
Percent of total power at each level		0.16	0.24	0.60
Total operating power for one cryo unit based on predicted heat (MW)			2.63 / 3.24	
Total installed power for one cryo unit (MW)			3.37 / 4.16	
Total installed 4.5 K equivalent power for one cryo unit (kW)			15.40 / 19.01	

The table lists an "overall net cryogenic capacity multiplier", which is a multiplier of the estimated heat loads. This factor accounts for cryogenic plant overcapacity required for control, off-design operation, seasonal temperature variations (which affect compressor operation), and uncertainty in static and dynamic heat loads at the various temperature levels. Note also that cryogenic plant efficiency is assumed to be 28 % at the 40 to 80 K level and 24 % at the 5 to 8 K temperature level. The efficiency at 2 K is only 20%, however, due to the additional inefficiencies associated with producing refrigeration below 4.2 K. All of these efficiencies are in accordance with recent industrial conceptual design estimates.

Table 3.12 summarises the required capacities of the cryogenic plants for the different area

systems, including the two configurations under study for the Main Linacs. Total installed power for all the cryogenic systems is about 44 to 46 MW (depending on KCS or DKS configuration), with an expected typical operating power of 34 to 35 MW.

Table 3.12. ILC cryogenic plant sizes (also includes sources, damping rings and beam delivery section for completeness) [47].

Area	# of Plants	Installed Plant Size (each) (MW)	Total Installed Power (MW)	Operating Power (each) (MW)	Total Operating Power (MW)
Main Linac + RTML flat/mntn	12 / 10	3.37 / 4.16	40.44 / 41.60	2.63 / 3.24	31.56 / 32.40
Positron Source	1	0.65	0.65	0.35	0.35
Electron Source	1	0.70	0.70	0.48	0.48
Damping Rings	1	1.45	1.45	1.13	1.13
BDS	1	0.41	0.41	0.33	0.33
Experiments	1	1.00	1.00	0.70	0.70
Total	17 / 15		44.65 / 45.81		34.55 / 35.39

3.5.3 Helium inventory

As illustrated in Fig. 3.26, most of the helium inventory consists of the liquid helium which bathes the RF cavities in the helium vessels. The total helium inventory in ILC will be roughly 63 % of that of the LHC at CERN, about 630 000 liquid litres, or about 82 metric tons (see Table 3.13).

Figure 3.26
Helium mass in a module.

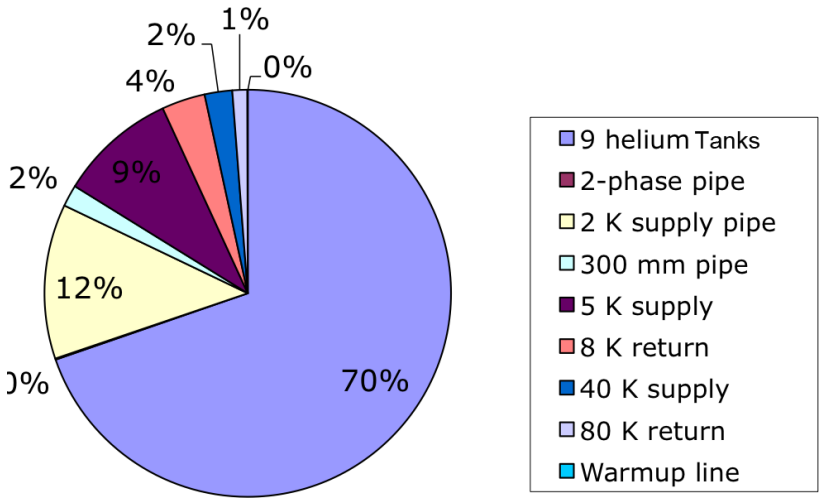

Table 3.13
Main Linac helium inventory [48].

Volumes	modules	Helium (liquid liters equivalent)	Tevatron Equiv.	LHC Equiv.
One module	1	346		
String (flat)	12	4153	0.07	
String (mountainous)	9	3115	0.05	
Cryogenic unit (flat)	156	54 000	0.9	0.054
Cryogenic unit (mountainous)	189	65 400	1.1	0.065
ILC Main Linacs	1825	632 000	10.5	0.63

3.5.4 Pressure code compliance

The niobium RF cavities limit the maximum allowable pressures at the 2 K level of the cryogenic system. In North America, Europe, and Asia, the titanium helium tanks which surround niobium RF cavities, and part or all of the RF cavity itself, fall under the scope of the local and national pressure vessel rules [33]. Thus, while used for its superconducting properties, niobium must be treated as a material for pressure vessels. Problems with the certification of pressure vessels constructed partially or completely of niobium arise due to the fact that niobium and titanium are not listed as acceptable vessel materials in pressure vessel codes. Considerable effort has been expended in all three regions to gain compliance with pressure vessel codes and permission from authorities to operate ILC-style cryomodules, which contain these exceptional pressure vessels.

Partly due to the constraints of pressure code compliance, and partly to avoid detuning of the RF cavities by high-pressure helium, the cavity helium vessels and associated low-pressure piping (30 mbar corresponding to 2 K), have a Maximum Allowable Working Pressure (MAWP) of 2 bar differential. A higher MAWP for liquid-helium temperature conditions may be established, if necessary, to accommodate pressures during emergency venting with loss of vacuum. Other piping such as the 2 K helium-supply pipe and thermal-shield lines will be rated for 20 bar differential pressure.

Details regarding methods to achieve compliance with pressure codes and permission to operate low-temperature containers made from niobium and titanium will depend on the legal requirements of the regions involved. Documentation and required testing pressures and procedures are not uniform around the world. Testing in one region and operation in another may invoke multiple sets of rules. Laboratories involved in ILC cryomodule development have established methods to satisfy local codes and demonstrate the safety of these systems, sometimes including special arrangements with local authorities for these exceptional vessels. Careful consideration and agreements between all the involved regional authorities will be required for the distributed mass production, testing and finally operation of the cryomodules.

3.6 RF power source

3.6.1 Overview

The centrepiece of the RF-power system is the 10 MW multibeam klystron (MBK). With the power required by each cavity including a certain overhead for power loss in the waveguides and allowance for tuning, the MBK provides enough peak power in the pulse to drive up to 39 cavities under the nominal beam-loading conditions (see Table 3.14).

Table 3.14
Main parameters relevant to the RF power that is required for one 9-cell cavity. The RF-power numbers are intended to give an indication of the power required; they represent the ideal match conditions, and do not include overheads for controls, waveguide losses or the expected spread in operating gradients.

Parameter	Unit	Value for baseline
RF Frequency	GHz	1.3
Beam current in the pulse	mA	5.8
Accelerating gradient	MV/m	31.5
Cavity length	m	1.038
Q_L (matched)		5.5×10^6
RF Voltage	MV	32.7
Beam phase	deg	5
RF pulse length	ms	1.65
Beam width	ms	0.72
Filling time	ms	0.93
Repetition rate	Hz	5
RF power into cavity	kW	188
RF for 26 cavities	MW	4.9
RF for 39 cavities	MW	7.4

The two site variants (flat and mountainous topography) differ significantly in how the MBK power is supplied to the cavities in the tunnel.

For the mountainous topography, such as the sites considered in Japan, a Distributed Klystron System (DKS) approach is taken where the klystrons are distributed along the main linac tunnel, with each klystron connected directly to 39 cavities (4.5 cryomodules). In this case the tunnel will have a wide flat-bottomed cross section shape referred to as "kamaboko"[5]. The tunnel is divided along its length by a thick concrete radiation shield into two parallel corridors – one for cryomodules and the beamline, the other for klystrons, DC power supplies and control hardware.

For the flat topography, the novel Klystron Cluster Scheme (KCS) is the preferred solution, where all the MBKs, modulators and associated DC power supplies are installed in "clusters" located on the surface. The combined power (∼200 MW) from from the klystrons in a cluster is transported down into and along the accelerator tunnel via a large over-moded circular waveguide.

This section describes those aspects of the components of the RF-power system and Low-level RF (LLRF) control that are common to both flat and mountainous topography site-dependent designs. Details specific to DKS and KCS are given in Section 3.8 and Section 3.9 respectively.

3.6.2 Modulator

A Marx-type modulator is used to generate the flat, high-voltage pulses required by the 10 MW klystron. The maximum output-power requirements for the modulator are 120 kV, 140 A, 1.65 ms pulses at a 5 Hz repetition rate. (For 10 Hz mode, the modulators need to provide approximately half the maximum peak power.) Table 3.15 lists the specifications for the modulator, required to drive a klystron producing a peak output power of 10 MW with a microperveance of 3.38 and an efficiency of 65 %.

Table 3.15
Parameter specifications for the klystron modulators of the main linacs of ILC.

Parameter	Unit	Specification
Output voltage	kV	120
Output current	A	140
Pulse width	ms	1.65
Pulse repetition frequency	Hz	5 (10)
Max. average power	kW	139
Output pulse flat-top	%	± 0.5
Pulse-to-pulse voltage fluctuation	%	± 0.5
Energy deposited into klystron during a gun spark	J	< 20

The Marx modulator uses solid-state switches to charge capacitors in parallel during the interval between output pulses. During the output pulse, the capacitors are discharged in series to generate a high-voltage output with a magnitude of the charging voltage times the number of stages. With this topology, low-voltage components can be used to produce a high-voltage output without requiring an output transformer. There are several ways to produce a flat output pulse. One method is to integrate a "buck converter" in series with each cell, which uses a closed-loop correction scheme to produce a square output pulse for each cell. A diagram of a Marx modulator and the circuit of one simple Marx cell are shown in Fig. 3.27.

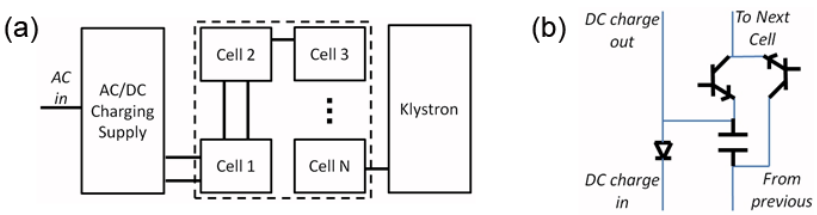

Figure 3.27
(a) Simple block diagram of a Marx modulator and (b) simple single cell circuit.

There are several advantageous characteristics of the Marx topology. The modular design simplifies fabrication and allows redundant hardware to be implemented. Solid-state switching is intrinsically long-life, and in conjunction with redundant hardware, a high-availability architecture is

[5] A Japanese fish cake which resembles the tunnel cross section.

possible. Modularity reduces the spares inventory and simplifies maintenance, thereby reducing the mean time to repair. Due to the absence of a high-voltage output transformer, short rise and fall times are possible, further increasing efficiency [54].

Multiple R&D programs have been pursued to develop and demonstrate the efficacy of a Marx-topology modulator to drive the klystron. The requirements and many technical advantages are discussed in Part I, Section 2.8. Figure 3.28 shows three prototypes, one built by Diversified technologies and one developed at SLAC, which have demonstrated the technical feasibility of the modulator, as well as providing a cost basis.

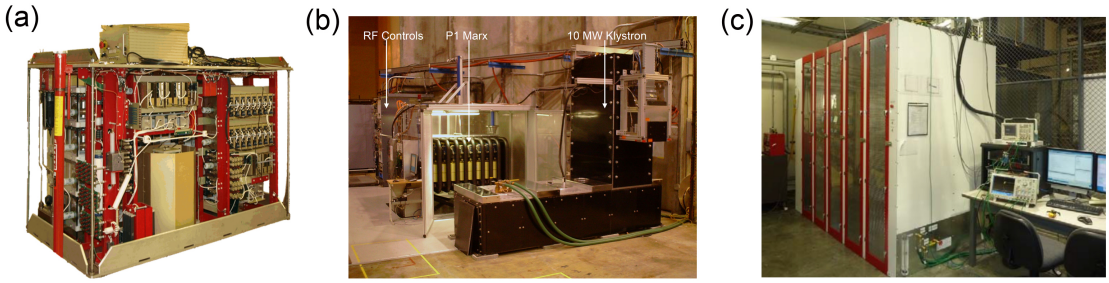

Figure 3.28. (a) DTI Marx modulator, (b) SLAC P1 Marx modulator and (c) SLAC P2 Marx.

The SLAC P2 Marx is an embodiment of the Marx concept which has many advanced features. It contains thirty-two identical cells, with $N + 2$ redundancy. Pulse-top flatness at the $\pm$ 0.05% level has been demonstrated with operation into a water load. A full-pulse waveform of this Marx and the flatness are shown in Fig. 3.29. The flat pulse is generated using a closed-loop regulation scheme which feeds forward on both the voltages of the individual cells as well as the overall output voltage. In addition, the cells are phase shifted to stagger the ripple of each individual cell with respect to others, which results in a net cancellation, achieving an overall low modulator ripple.

The energy in the rise and fall time of the pulse is dissipated in the klystron collector. Very fast rise and fall times of less than 15 µs were obtained with the water load, approximately 0.5 % of the total energy output from the Marx, corresponding to a very high efficiency.

The AC/DC charging power-supply technology has a low technical risk, but its performance is important in achieving a cost-effective and efficient RF system. A survey of available technologies indicates that a conversion efficiency of 95 % is realisable, which is assumed in the heat loads presented in Table 3.16.

Table 3.16
Power efficiencies and heat loads of Marx modulators assuming 10 µs rise and fall times.

Parameter	Unit	Specification
SLAC P2 Marx DC to pulse flattop efficiency	%	95 ± 1
Assumed charging supply AC to DC efficiency	%	95
Usable power delivered to klystron	kW	138.6
Power delivered to collector during pulse rise and fall	kW	0.5
Power dissipated to air inside of modulator enclosure	kW	7.1
Power dissipated in the DC chargers	kW	7.4

Additional characteristics of the SLAC P2 Marx include the use of air insulation and cooling rather than oil. At the marginal expense of compactness, air insulation simplifies maintenance, reduces hazardous-waste containment issues, and simplifies component compatibility. Waste heat is transferred from the modulator via an air-to-water heat exchanger.

The SLAC P2 Marx also utilises an intelligent control system with embedded diagnostic and prognostic systems. These can be used to monitor cell activity in real time and to anticipate the onset of components' end-of-life phase. Twelve 12-bit, 1 MS/s ADC are used within each cell to monitor voltage, current, and temperature values of interest. These are used in the closed-loop regulation

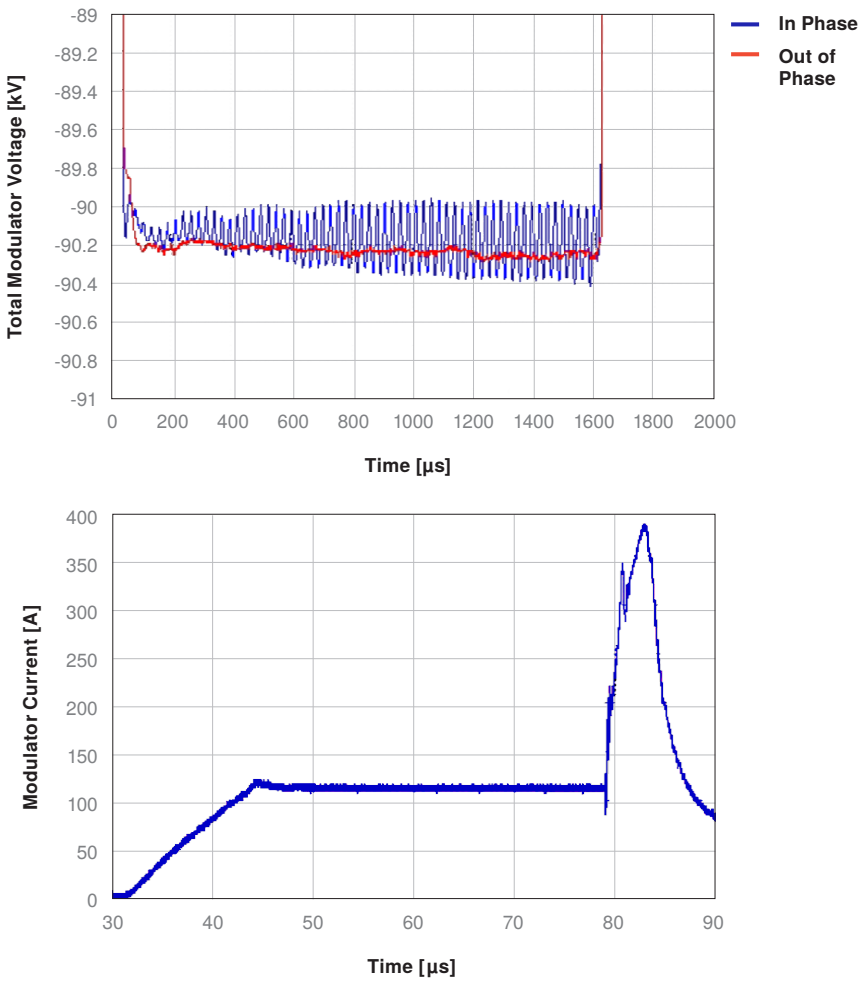

Figure 3.29
Top: flatness of the Marx modulator pulse flat-top. Bottom: measured modulator current pulse before and after an arc.

scheme and also can be used to troubleshoot the cells in-situ.

Fault susceptibility is another important characteristic. It is necessary not only to prevent damage to the modulator, but also to protect the klystron in the event of a gun arc. The Marx satisfies these requirements. The bottom plot of Fig. 3.29 shows the current waveform from an arc generated in a self-break spark gap that closely simulates a klystron fault. It shows that the IGBT opened with a 0.5 μs delay after sensing the arc, suppressing the energy deposited to less than 10 J, satisfying the requirement for klystron protection. In addition, if a main IGBT fails in the Marx during a gun spark event, the charge IGBT in the cell closes. In this way, the energy within the cell is contained in the cell and is not transferred to the klystron.

The majority of the capabilities of the P2 Marx have been demonstrated. However, to adequately characterise the mean time before failure and the mean time to repair, an extended testing and qualification period is necessary.

3.6.3 10 MW Multi-Beam Klystron (MBK)

The RF power to drive the accelerating cavities at the ILC is provided by 10 MW L-band klystrons, whose baseline design is based on a multi-beam scheme. The current baseline multi-beam klystron (MBK) splits the electron current into six beams of low perveance. This arrangement allows a reduction in the beam voltage while weakening the space-charge effect, the net result of which is an improved power efficiency with a lower-voltage modulator. Table 3.17 gives the main parameters for the MBK.

The design effort for the 10 MW-class MBKs began around the time of the TESLA conceptual design and has evolved through the European XFEL project. Vertically mounted prototypes were

Table 3.17
Parameters for the 10 MW multi-beam klystron

Parameter	Specification
Frequency	1.3 GHz
Peak power output	10 MW
RF pulse width	1.65 ms
Repetition rate	5.0 (10) Hz
Average power output (5 Hz)	82.5 kW
Efficiency	65 %
Saturated gain	$>$ 47 dB
Instantaneous 1 dB BW	$>$ 3 MHz
Cathode voltage	$>$ 120 kV
Cathode current	$<$ 140 A
Filament voltage	9 V
Filament current	50 A
Power asymmetry (between two output windows)	$<$ 1 %
Lifetime	$>$ 40,000 hours

initially developed by a few electron-tube manufacturers and successfully achieved the 10 MW goal. They were followed by horizontally mounted MBKs, whose construction is compatible with implementation at the European XFEL and ILC. The horizontal MBKs have successfully demonstrated the same RF-power performance as the vertical models. DESY, KEK and SLAC have all procured and operated these MBKs, evaluated their performance and obtained satisfactory results.

The current MBK designs are now relatively mature. All vendors have provided suitable solutions for both the resonant cavities within the klystron body and the internal beam focusing. Figure 3.30 shows photographs of two L-band MBKs from two different vendors (Thales and Toshiba). Typical performance data is shown in Fig. 3.31.

Figure 3.30
Thales TH1801 (left) and the horizontally mounted Toshiba E3736.

A crucial aspect for operations of the ILC linacs is the lifetime of the klystrons. The MTBF for the ILC klystrons is specified at $\geq$40,000 hours. The lifetime for linear beam tubes is dominated by the durability of the cathode. With cathode loading as low as 2 A/cm^2 achieved by some vendors, the expected (theoretical) lifetime is in excess of 50,000 hours. However, operational experience is required in order to estimate the true lifetime. Lifetime tests are planned, and the $\sim$30 MBKs required for the European XFEL will also provide significant data.

The manufacturability of MBKs is an important issue, since the ILC requires nearly 500 tubes to be prepared within a period of 5 to 7 years. The investment in RF test and processing infrastructure by industry is likely to be cost prohibitive for production at this scale. A more cost-effective model would be for collaborating institutes ("hub laboratories") to host such facilities and to either provide the personnel directly, or make the test infrastructure available to industry (klystron vendors) to use for conditioning and testing.

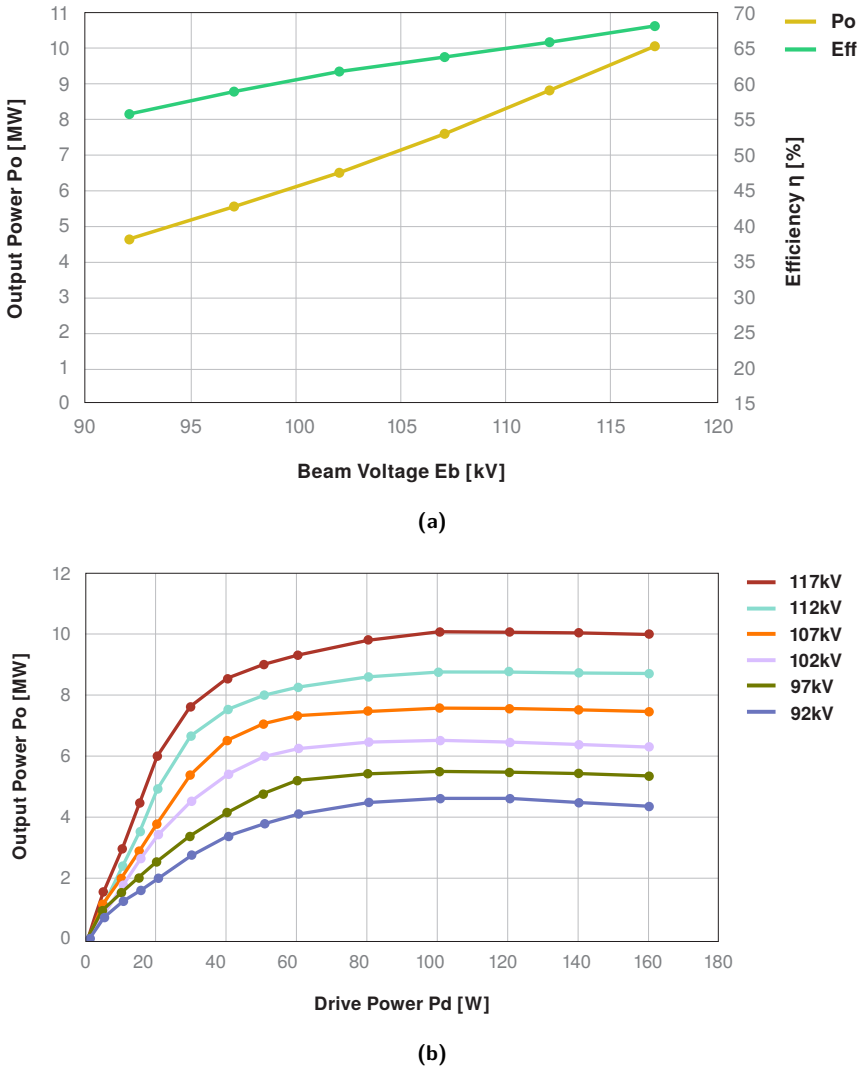

Figure 3.31 Measured performance data of Toshiba klystron, showing (top) output power and efficiency as functions of beam voltage and (bottom) gain characteristics.

3.6.4 Local power-distribution system

The arrangement and installation of waveguides near the cryomodules is the same in both cases for KCS and DKS, and is commonly referred to as the Local Power-Distribution System (LPDS). The design of the LPDS must provide:

- a cost-effective solution to distributing the RF power to the cavities with minimum RF loss;
- flexibility to remotely and independently adjust the power delivered to each individual cavity to allow for the expected $\pm$ 20% spread in gradient performance.

Furthermore it is desirable to keep as far as possible a common design between DKS and KCS, and in the case of DKS, provide a relatively straightforward reconfiguration to 26 cavities per klystron required for the luminosity upgrade (Section 12.3).

Figure 3.32 shows schematics of distribution of RF power onto cavities in the cryomodules, and a detailed list of components can be found in [49]. Each LPDS drives 13 cavities, and is capable of handling and distributing up to 5 MW of input power. For the KCS (Fig. 3.32(a)), two such LPDS distribute the RF power from one Coaxial Tap-Off (CTO) connected to the high-power overmoded waveguide to 26 cavities (one ML unit). For DKS, three LPDS feeds are used to drive a total of 39 cavities (one and a half ML units) from one single 10 MW klystron (Fig. 3.32(b)). Every third ML unit is thus without a klystron and is fed from the two adjacent ML units.

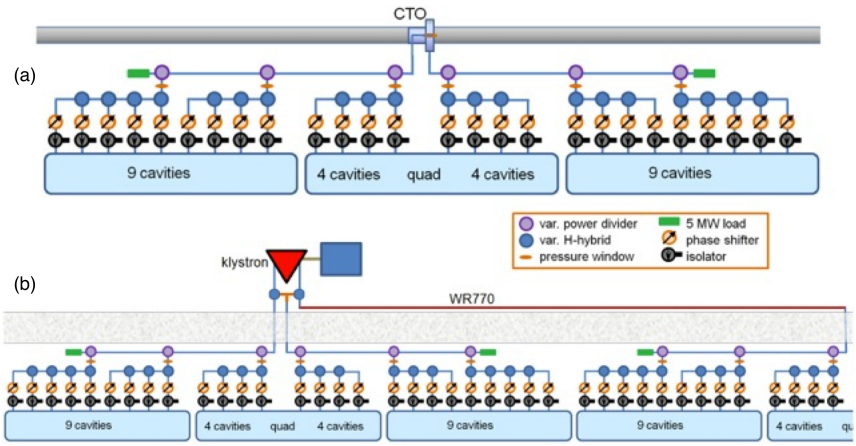

Figure 3.32 Schematic of the local power-distribution-system (LPDS) that delivers RF power to accelerator cavities in the main linacs. (a) shows the case of the KCS option, and (b) shows the case of the DKS option. In both cases, cavities are feed in groups of 13. (Reproduced from Fig. 3.1 in Section 3.1.)

The LPDS distributes the power from a klystron (DKS) or CTO feed (KCS) to the cavities as shown in Fig. 3.32. This is accomplished in 13 cavity groups, one of which is illustrated in Fig. 3.33. The same input power goes to each group of thirteen cavities, with the exception of the third arm for the DKS arrangement (see Section 3.9.3), but the power to each cavity differs due to the variation of up to $\pm$ 20% in gradient performance.

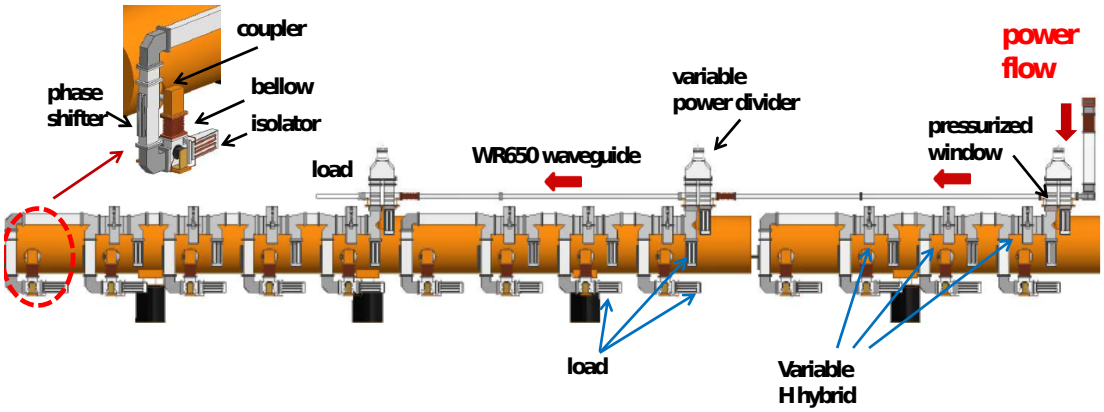

Figure 3.33. CAD model of a 13-cavity local power-distribution system (LPDS)

Two types of remotely-controllable variable power-splitters are used to customise the power sent to the cavities. As indicated in Fig. 3.32, three variable power dividers (VPDs) initially split the power into three lines, each feeding either four or five cavities. Any remaining power after the third VPD is dumped in a high-power load. The VPDs are pressurised to one bar N_2, and ceramic RF windows handle the pressure differential to the non-pressurised waveguides. The power division within each set is achieved using variable H-hybrids, and the cavity after the last split uses all the remaining power.

In each cavity feed line is a remotely-controllable phase shifter followed by a ferrite-based isolator (circulator with load). The latter prevents the power that is either reflected or discharged from the cavity from re-entering the waveguide system. RF pickups in the input and load ports of the isolators provide the low-level RF control system with information on the forward and reflected cavity power levels. Finally, a flexible rectangular bellows connects the waveguide to the warm end of the cavity input coupler.

A schematic of the VPD and photograph of the U-bend phase-shifter are shown in Fig. 3.34. The design of the U-bend phase-shifter features an inner waveguide which can be moved like a trombone by an external actuator. The VPD forms a 4-port device, and when one port is loaded it allows full range adjustment of power division between the forward waveguide and the downward extraction waveguide. By moving the phase shifters in opposite directions, the phases of the outputs can be

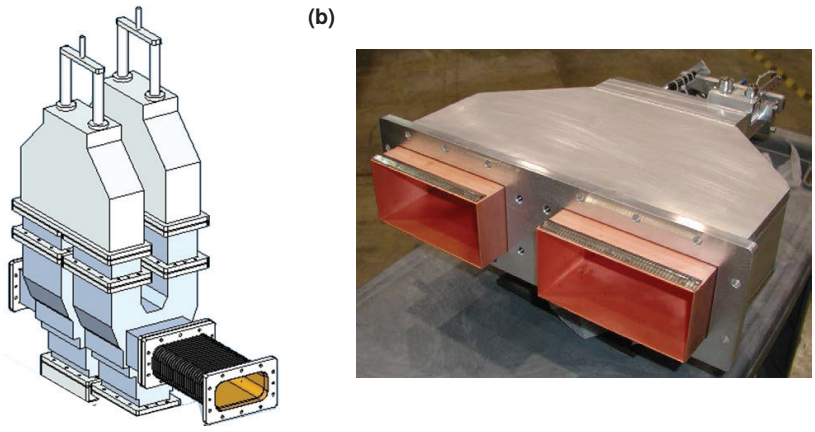

Figure 3.34 Schematic of a Variable Power Divider (VPD), comprising two folded magic-T's and two U-bend phase-shifters (left). b) Photograph of a U-bend phase-shifter (Finger-stock provides the contact with the mating waveguide).

held fixed, allowing a pure amplitude control.

Shown in Fig. 3.35 is the original design geometry for the variable H-hybrid, its electromagnetic-field patterns, and an in-line variant that simplifies daisy-chaining for use in the LPDS. This geometry formed the basis of the design for the devices in the 13-cavity LPDS shown previously in Fig. 3.33. The interior of the 4-port hybrid accommodates two electromagnetic-field modes whose relative phase-lengths can be changed by transversally moving the "pontoon-shaped" conductors, resulting in a change in the power division. Any residual phase-change is compensated using the upstream phase-shifter. Although the devices themselves do not allow the power ratios to be adjusted over the full range, the achievable power ratios can deviate significantly from the nominal ratios of 1/5, 1/4, 1/3 and 1/2.

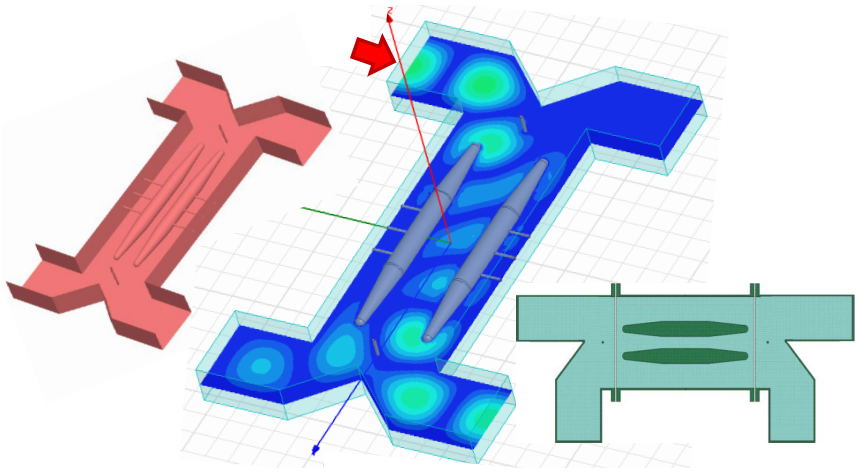

Figure 3.35 Illustrations of a variable H-hybrid: original design geometry (left); electromagnetic-field patterns (center); in-line variant used in the LPDS (right).

3.6.5 RF power requirements

In order to estimate the total number of klystrons required, it is necessary to take into account all the expected RF losses along the entire power distribution system to the cavity. A further inefficiency can be attributed to the random spread in cavity-gradient performance, since in general it is not possible to perfectly match all the cavities connected to the same power source, since the RF pulse and hence the fill time must be the same for all cavities [51]. This results in reflected power from most cavities. Finally, some small fraction of klystron power is required for LLRF control.

While estimation of the distribution-system losses and control overhead is relatively straightforward, estimation of the impact of the gradient spread can only be described in a statistical sense, since it is currently assumed that sorting the cavities with respect to performance is unlikely during mass production and installation into the cryomodules, resulting in an effectively random cavity distribution

in the linac. The approach adopted here is to use Monte Carlo techniques by running many random seeds, and taking the 95 % percentile limit of the power required [53].

Table 3.18 traces the RF-power budget from the cavities back to the klystrons for both DKS and KCS. The random cavity gradients are responsible for the first increase in the table. Some post-installation adjustment of the high-level power division (fine-tuning or changing CTO's and hybrids) is assumed in order to limit this to a few percent. The first number (extra beam power) reflects the statistical fluctuation of the total voltage of the cavities driven by the single source (the source must be able to accommodate the highest voltage, at least at the 95% level). The next effect (reflection) is due to the mismatch of the individual cavities arising from the constant fill time as mentioned above. This represents a real operational power that is dumped in the loads. Folded into this number is about 0.8 % to support the required 5° beam phase with respect to the RF crest. A 7 % overhead (5 % usable) is allotted for LLRF manipulation, and 8 % for average losses in the components of the waveguide circuit that provides local distribution of the power along the cryomodules.

Table 3.18 RF power budgets for KCS and DKS local power distribution systems

		KCS		**DKS**
Cavity and Local Power Distribution		(kW)		(kW)
Mean beam power per cavity		*189.18*		*189.18*
Extra beam power for ± 20% gradient spread	2.90 %	194.67	5.30 %	199.21
s.s. reflection for ± 20% gradient spread	6.00 %	206.35	6.00 %	211.16
Required LLRF overhead	7.00 %	220.8	7.00%	225.95
Local PDS average losses	8.00 %	240	8.00 %	245.59
Multiply by number of cavities fed as a unit	26	6239.9	39	9578.1
Required local PDS RF input power		*6239.9*		*9578.1*
Power Combining & Transport (DKS)				(MW)
RF power to local PDS				*9.578*
Combining/splitting and shielding penetrations			1.10 %	9.6847
WR770 run loss/3			1.40 %	9.8222
Required power from klystron (DKS)				*9.822*
Power Combining & Transport (KCS)		(MW)		
RF power to ML Unit		*6.2399*		
Multiply by number of ML Units per KCS	26 (25)	162.24 (156)		
KCS main waveguide loss	5.0 % (4.7)	170.78 (163.69)		
Shaft and bends loss	1.80 %	173.91 (166.69)		
CTO string and upgrade WC1375 run loss	1.50 %	176.55 (169.23)		
Klystron waveguide into CTO	5.60 %	187.03 (186.74)		
Divide by number of klystrons	19 (18)	9.8436 (9.9594)		
Required power from each klystron (KCS)		*9.844 (9.959)*		

Beyond the LPDS, the accounting diverges for the two options. DKS has additional losses in the WR650 shielding penetrations and dividing/combining components, as well as in the WR770 waveguide run supplying power for half an ML Unit to the vacant klystron position. The higher losses for KCS reflect the much longer waveguide system required to transport the RF power down from the surface cluster. The estimate includes the average loss along the main circular waveguide in the tunnel (assumed to be copper plated) to each CTO, the loss in the bends and shaft waveguide, and the loss along the surface main waveguide and combining CTO string. The latter includes a circular WC1375 waveguide which runs past an area where additional klystrons can be installed for the luminosity upgrade (Section 12). Finally, there is loss budgeted for the waveguide connections from the klystron output ports in the outer region of the CTO. A major contributor here is the 5 MW isolators required to protect the klystron from the reflected power it could see from a failed combining circuit (up to 10 MW). With all these effects taken into account, the final required RF power per klystron is within the specified 10 MW, albeit with relatively little overhead.

3.7 Low-level RF (LLRF) control concept

3.7.1 Overview of Low-level RF control requirements

The primary function of the main linac and RTML LLRF systems is to control the phase and amplitude of the klystron forward power so that the required cavity fields are reached at the end of the fill time and then remain stable for the duration of the beam pulse. Since many cavities are fed from each individual klystron (or cluster in the case of KCS), the LLRF system regulates the vector sum of all the cavity fields controlled by that klystron (or cluster).

LLRF performance requirements are derived from beam-dynamics considerations of energy stability, luminosity loss, and emittance growth (see Part 1 Section 4.6). RF phase and amplitude jitter tolerances for the bunch compressors and main linacs are given in Tables 3.19 and 3.20, respectively. Beam dynamics considerations of emittance growth also require that voltages in the individual cavities will be corrected to within a few percent over the duration of the pulse.

Table 3.19
Bunch Compressor RF dynamic errors, which induce 2 % luminosity loss.

Error	RMS amplitude	RMS phase
All klystron correlated change	0.5 %	0.32°
Klystron to klystron uncorrelated change	1.6 %	0.60°

Table 3.20
ML RF dynamic errors, which induce 0.07 % beam energy change.

Error	RMS amplitude	RMS phase
All klystron correlated change	0.07 %	0.35°
Klystron to klystron uncorrelated change	1.05 %	5.6°

3.7.2 Vector-sum control of cavity fields

The LLRF system design is based on the digital controller implemented at FLASH and that will be used on the European XFEL [55]. Similar systems have also been implemented at STF at KEK [56] and NML at Fermilab [57]. The main functional elements are illustrated in Fig. 3.36.

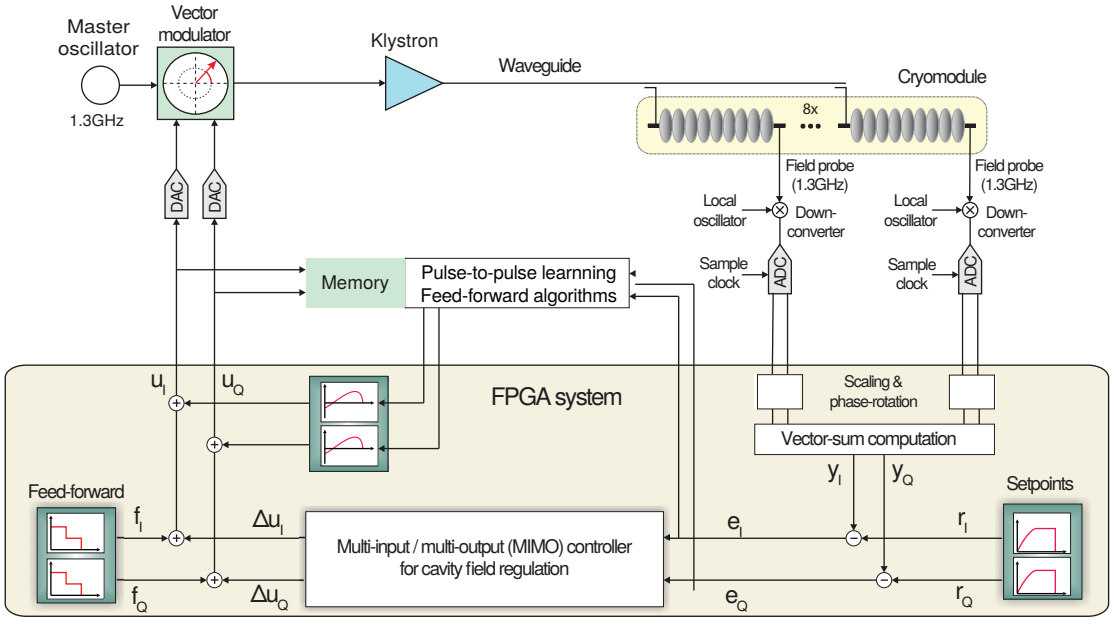

Figure 3.36. Functional block diagram of the digital LLRF control system at FLASH (for clarity, only one cryomodule is shown)

The signals from the cavity field probe and forward and reflected RF power arrive at the LLRF electronics as raw 1.3 GHz RF signals, where they are down-converted to an intermediate frequency (IF) and subsequently acquired by fast ADCs. Phase information is preserved by separating the

data-stream from the ADCs into in-phase and quadrature terms for processing by the FPGA-based digital LLRF control functions.

The drive signal to the klystron comes from the vector-sum regulator, and comprises two terms: a feed-forward term that is determined a-priori using knowledge of the required cavity-field profile and the expected beam-current profile; and a correction term that is generated dynamically by the feedback regulator based the measured error in cavity-field vector sum that is computed from the partial vector sums from the local LLRF controllers. The resulting controller output is up-converted via a vector modulator that varies the amplitude and phase of the 1.3 GHz master oscillator reference signal that drives the klystron.

3.7.2.1 Learning feed-forward controller

Due to the very low-bandwidth of the superconducting cavities and delays in the closed-loop system, dynamical feedback alone is not sufficient to completely suppress high-frequency distortions or to achieve zero steady-state errors. However, effects that are directly correlated with the 5 Hz pulse structure and that are repeatable from pulse to pulse can be pre-emptively compensated using feed-forward, leaving smaller residual and non-repetitive disturbances to be compensated using the closed-loop feedback regulator. A learning feed-forward system is used to iteratively adjust the shape of the feed-forward waveform in order to compensate for repetitive pulse-to-pulse errors, leaving the intra-pulse feedback system to attenuate pulse-to-pulse jitter and intra-pulse fluctuations. With knowledge about field imperfections in previous pulses, the residual control errors can be minimised. Optimisation of the learning feed-forward system is performed by a model-based learning feed-forward algorithm.

3.7.2.2 Beam loading compensation

The forward power during the fill time is a function of the required cavity fields, while the flat-top power is a function of both the cavity fields and the beam current. With the exception of the ideally matched case (no reflected power), the required forward power during the beam-on period is not the same as that required during the fill time. Since the beam current is assumed to be known a priori from the Damping Ring instrumentation, the LLRF system can pre-emptively step the forward power to the appropriate level immediately before the arrival of the first bunch. This is illustrated in Fig. 3.37, which shows the klystron forward power for operation over a range of beam currents around the nominal design value. Without this feed-forward pre-programming of the RF power, there would be a transient perturbation on the cavity fields as the LLRF feedback system dynamically corrected the forward power.

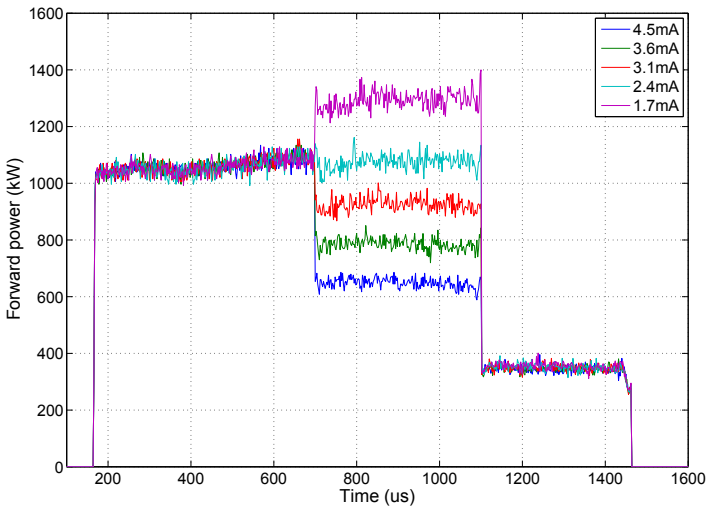

Figure 3.37
Klystron forward power for a range of beam currents, measured at FLASH. In this example, the beam-on time extends from 700μs to 1100μs. The power level from 1100μs to the end of the pulse corresponds to the zero beam-loading condition.

3.7.2.3 Intra-pulse dynamical feedback regulator

The feedback regulator operates dynamically within the RF pulse, and its primary function is to attenuate uncorrelated pulse-to-pulse and intra-pulse jitter. The feedback regulator also corrects any residual short-term repetitive errors while the learning feed-forward system adapts to new steady-state conditions or attempts to follow fast-changing pulse-to-pulse drift.

The feedback regulator uses a multi-variable, second-order controller whose coefficients are automatically tuned by model-based controller methods. A more detailed description of the FLASH LLRF system algorithms can be found in [55]. It is worth noting that the FLASH LLRF system makes extensive use of intra-pulse beam-based feedback for additional regulation, specifically bunch arrival time, compression, charge, and energy. Such extensive use of beam-based feedback is not possible in the ILC Main Linac due to the limited availability of intermediate diagnostics, but could be implemented in the bunch compressors, where the required tolerances on regulation are more demanding. Measurement of the final energy of the beam at the exit of the linac will be used to provide a global feedback adjustment.

3.7.3 Operation at the limits

Unique and challenging constraints on the main-linac LLRF systems come from the limited operating margins when the linac is operating at maximum operating energy and beam current, specifically

- all cavities must run reliably at up to 95 % of their gradient limits in order to reach the linac design energy of 250 GeV;
- the ± 20 % spread in the above limits;
- klystrons will run at up to 95 % of the maximum available forward power. In this region, the klystron gain and phase characteristics are highly non-linear as the klystron output asymptotically approaches saturation.

Studies under these limiting conditions have been performed during the beam tests at the DESY FLASH linac. Details of these studies are described in Part I Section 3.2.

3.7.4 Individual cavity control

While the vector-sum controller regulates the net sum (or equivalently the average) of the cavity fields, it does not constrain fields in individual cavities, which may be varying over the beam pulse even if vector-sum is flat. Establishing the optimum setup for individual cavities is achieved through several high-level LLRF applications that have remote control of individual cavity fast and slow tuners and input coupling (Q_{ext}), and the fraction of total klystron power to each cavity (P_k). The two most important cavity-level high-level functions are compensating Lorentz-force detuning and establishing flat gradients in the presence of beam loading, discussed below.

3.7.4.1 Lorentz-force detuning compensation

When there is RF field in the cavity, the cavity walls experience electrostatic and magnetic forces that act to distort the cavity shape and shift the resonant frequency of the cavity. The magnitude of the detuning (Δf) due to these Lorentz forces is proportional to the square of the field in the cavity (E_{acc}). Since the cavity and its support structure form a mechanical system with mass, resonant frequencies and damping times are slow relative to the 2 ms RF pulse. Resonant frequencies are typically 200-400 Hz with time-constants of tens of milliseconds. The detuning effect over the RF pulse does not occur instantaneously, but instead increases over the duration of the pulse. At 31.5 MV/m, Lorentz forces cause a detuning change of several hundred hertz over the length of the beam-on period.

This detuning must be compensated in order to avoid the significant increase in forward RF power (and the associated higher electric fields at the input coupler) that would otherwise be needed to overcome the reflected power from the detuned cavity. Compensation of the Lorentz-force detuning is accomplished using the fast piezo actuators that are integral to the cavity tuning mechanism (Section 3.3.2). The piezo tuners are driven with a feed-forward waveform to counteract the detuning as it changes over the duration of the pulse. Two different approaches have been successfully demonstrated to determine an appropriate drive waveform for the piezo tuners [58, 59]. Both methods use the piezo tuners to preemptively put the cavity structure into motion before the RF pulse in such a way as to cancel the effect of the Lorentz forces. The methods rely on indirect observations of the cavity detuning inferred from the measured forward- and reflected-power waveforms.

3.7.4.2 Control of cavity gradient flatness

Several strategies have been proposed for optimising the coupling (Q_{ext}) and forward power (P_k) for each cavity along with the common fill time [51, 52], the goal being to minimise the total klystron power as well as the gradient excursions ("tilts") of the individual cavities. The optimal values of P_k and Q_{ext} for each cavity are dependent on the respective operating gradient and on the beam current. Automated adjustment of the Q_{ext} of the individual cavities to achieve "flat" gradients to well within the required few percent has been successfully demonstrated in FLASH (see Part I, Section 3.2.8).

3.7.5 LLRF operations

Besides cavity vector sum control, the LLRF controller performs important control, protection and operations functions for the accelerating cavities.

3.7.5.1 Exception handling

The LLRF system must detect and react to off-normal conditions that could be potentially damaging or could result in machine downtime. Depending on the severity of the condition, the LLRF could either temporarily turn down the klystron output, turn off the RF drive until the next pulse, or turn off the RF drive and wait for operator intervention. All three approaches have been implemented in FLASH and are under study.

3.7.5.2 Automation

It will be essential to automate operation of the main-linac LLRF systems because of the impracticability of manually performing the necessary operational functions on a very large number of technical systems. Examples of automation that are already routinely in operation or are under development at FLASH include: startup and shutdown of the RF systems; cavity resonance control, including compensation of Lorenz forces; vector-sum calibration; quench detection; learning feedforward for the vector sum controller; drift compensation; and loaded-Q optimisation for flat gradients.

3.7.6 LLRF system implementation

LLRF system implementation requires high-performance analog RF front-end electronics for conditioning and digitising RF signals and custom real-time algorithms running on high-performance FPGA-based digital processors. Details of the physical implementation (numbers of cavities and signal channels, numbers and locations of electronics racks, cable plant, etc.) are highly dependent on the layout and architecture of the main-linac RF power systems. Implementation of the LLRF systems for KCS and DKS are therefore covered in the site-specific sections of this chapter, in Section 3.9.4 and Section 3.8.4 respectively.

3.8 Main-linac layout for a mountainous topography

3.8.1 Introduction

This chapter describes the features of the Main Linacs that are unique to the mountainous topography site-dependent design, which utilises the Distributed Klystron Scheme (DKS) for RF distribution. In mountainous regions — such as those sites being discussed in Japan (Section 11.4) — the accelerator is orientated along the side of a valley, and access is provided via near-horizontal access ways. The lack of flat terrain requires that nearly all the equipment including the cryoplants be located in underground caverns. As noted in previous sections, DKS has the RF sources evenly distributed along the linac, and housed in the same tunnel. The modulators and klystrons (Section 3.6.2 and Section 3.6.3 respectively) are separated from the high-radiation environment of the accelerator by a concrete wall up to 3.5 m thick. The RF power from each 10 MW klystron directly feeds 39 cavities (1-1/2 ML units) via the local power distribution system described in Section 3.6.4.

3.8.2 Linac layout and cryogenic segmentation

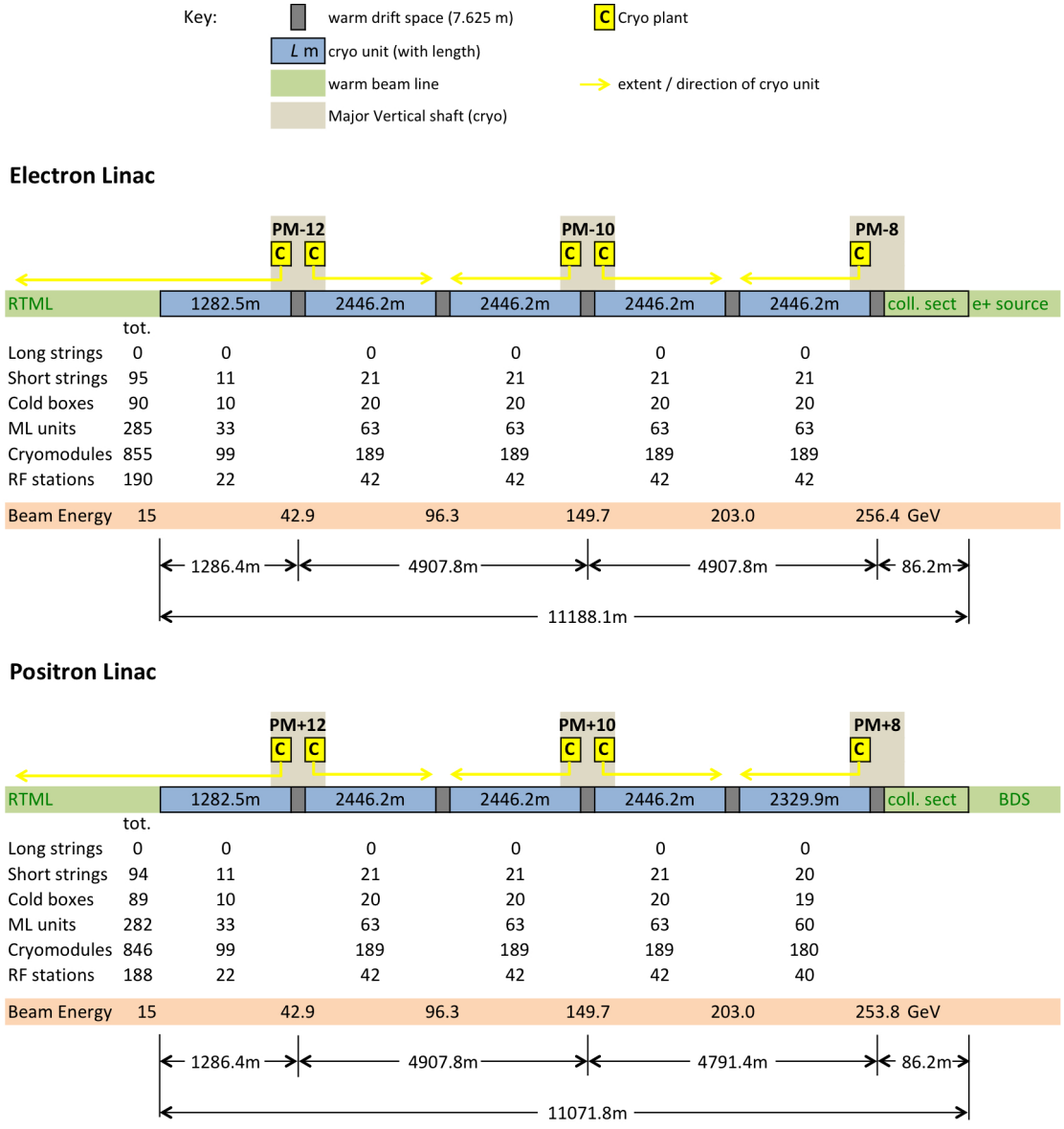

Figure 3.38. Schematic layout of the electron (top) and positron (bottom) main linacs for the mountainous topography site-dependent design, using DKS. The primary layout of the shaft arrangements are shown, along with the cryogenic segmentation. Distributions and totals (left-most column) of major linac sub-systems are given.

The main-linac layout is schematically shown in Fig. 3.38. The cryogenic cooling for each linac (and RTML bunch compressors, see Section 3.5) is provided by a total of five large cryoplants space approximately SI5km apart. The cryogenic plants are located underground and are accessible through long horizontal shafts as shown in Fig. 3.39. The cryogenic segmentation is constructed entirely from 'short cryostrings' (9 cryomodules or 2 ML units), as opposed to the more economical long strings (12 cryomodules). This is to accommodate a single design for the local power-distribution system (LPDS, see below). While use of short strings adds cold boxes and a small length increase to the linacs, this is offset by the benefits of having a single LPDS system (both in terms of manufacture and easier installation)

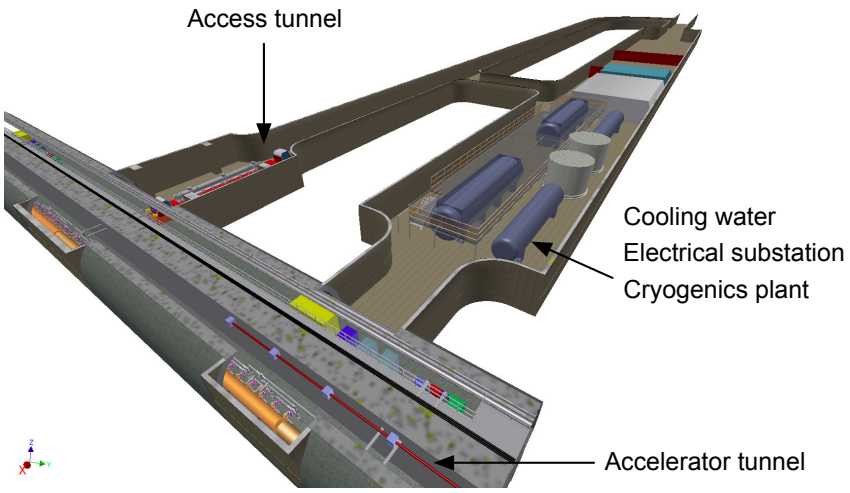

Figure 3.39
3D rendering of a cryo cavern and horizontal access way. For more details see Section 11.4.2.

The so-called 'Kamoboko' tunnel cross section is shown in Fig. 3.40. As noted above, this layout provides housing for the klystrons, modulators, electronics and related support infrastructure which is shielded from the radiation environment of the linac. The central-wall shielding is sufficient to permit personnel access to the service area during operations. RF power is brought in waveguides from the klystrons to the linac corridor through penetrations in the wall, which include a jog to prevent line-of-sight radiation. The shape of the tunnel is particularly suited for construction in the mountainous geology found in Japan (for more details see Section 11.4).

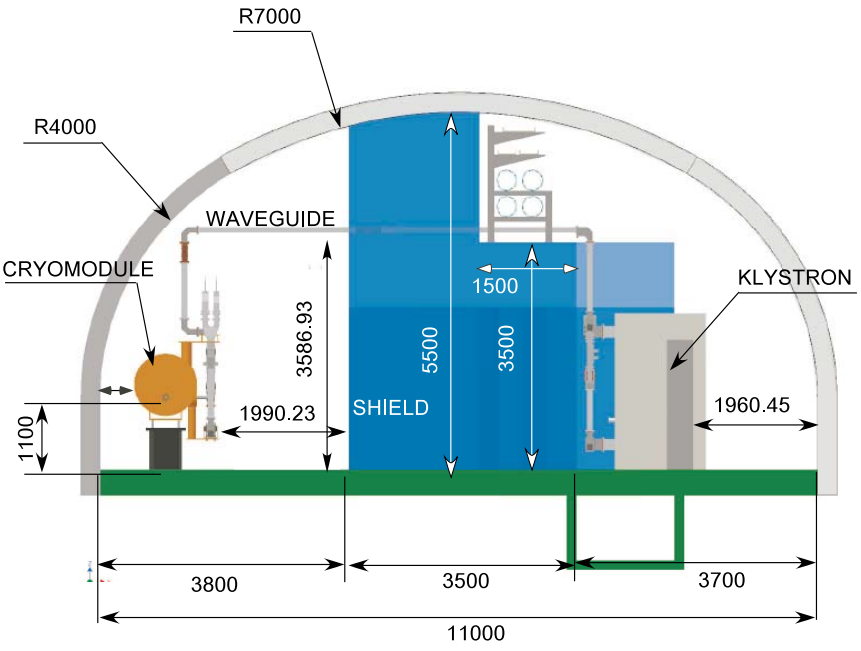

Figure 3.40
Cross section of the main-linac tunnel cross section for the mountainous topography site-dependent design.

3.8.3 The DKS high-power distribution System

Each unit of the RF system consists of a stand-alone RF source that powers 4 1/2 cryomodules (1-1/2 ML units), containing a total of 39 cavities — the maximum that can be realistically driven by a single 10 MW klystron (see Section 3.6.5).

There are a total of 378 RF sources, each comprising of a high-voltage Marx modulator, a 10 MW klystron, and a power-division waveguide circuit that feeds into the local power-distribution system (LPDS) as described in Section 3.6.

Figure 3.41 shows a schematic of a single DKS unit. The asymmetric layout (which is alternately reflected in each subsequent DKS unit) facilitates a relatively straightforward way to add the additional klystrons required for the luminosity upgrade (Section 12.3).

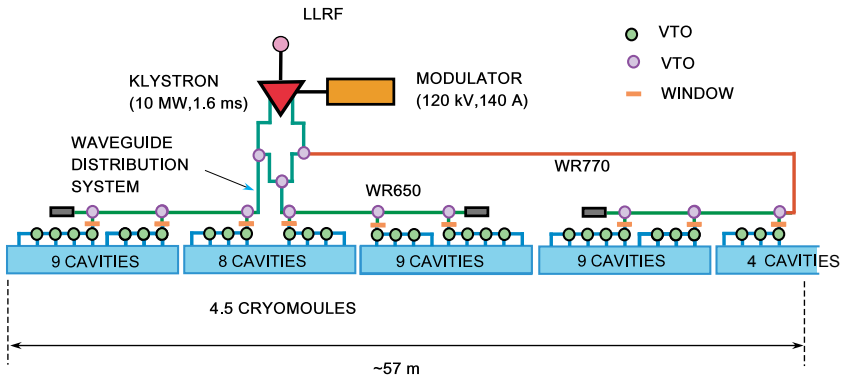

Figure 3.41
Schematic layout of a DKS RF unit, showing a single klystron driving 39 cavities (1-1/2 ML units).

A unique feature of the DKS approach is the klystron power-division circuit, i.e. the waveguide system connecting the klystron to the local power-distribution system. Three basic LPDS units (13 cavities, see Section 3.6.4) are fed from the two klystron outputs. Power from each output port is first split with a roughly 2:1 ratio through an H-type hybrid. The lower-power outputs from the hybrids are then combined through a T-type hybrid. Two of the resulting three feeds are fed locally through the shield wall; the third runs along the corridor to the location where an upgrade klystron would be situated, and then through one of the shield-wall penetrations prepared for that upgrade klystron. For this 34 m run, the waveguide size is stepped up from WR650 to WR770 to reduce transmission losses. The splitting and combining circuit and the waveguide layout are illustrated in Fig. 3.42.

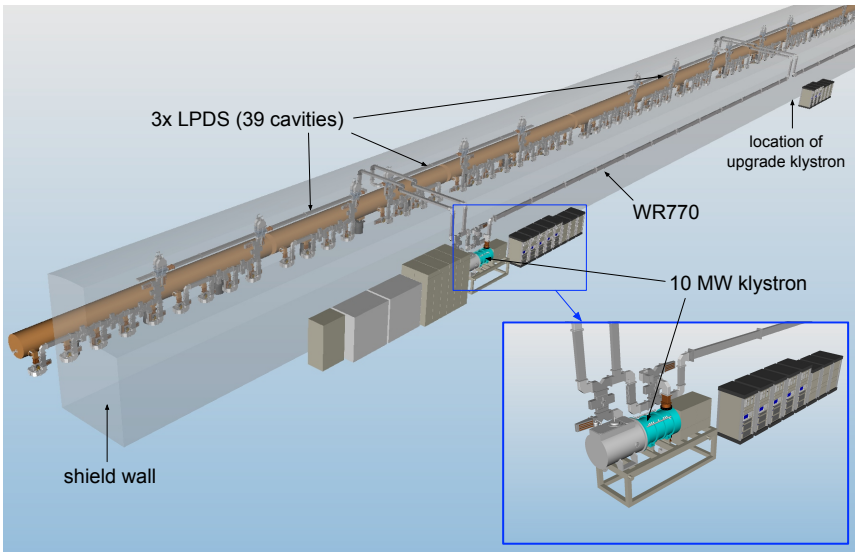

Figure 3.42
The DKS arrangement in the main-linac tunnel for the mountainous topography. One DKS unit (39 cavities) is shown.

3.8.4 LLRF control for DKS

LLRF requirements and design concepts were described in Section 3.7. This section describes the LLRF-system implementation specific for the DKS main-linac configuration.

The DKS layout and scale are very similar that planned for the European XFEL, which uses single 10 MW klystrons to drive groups 32 cavities. Originally proposed for TESLA, this configuration has been the subject of extensive R&D, and in particular there is many years of FEL operations experience from FLASH, as well as the more dedicated studies with ILC-like beams (see Part I Section 3.2).

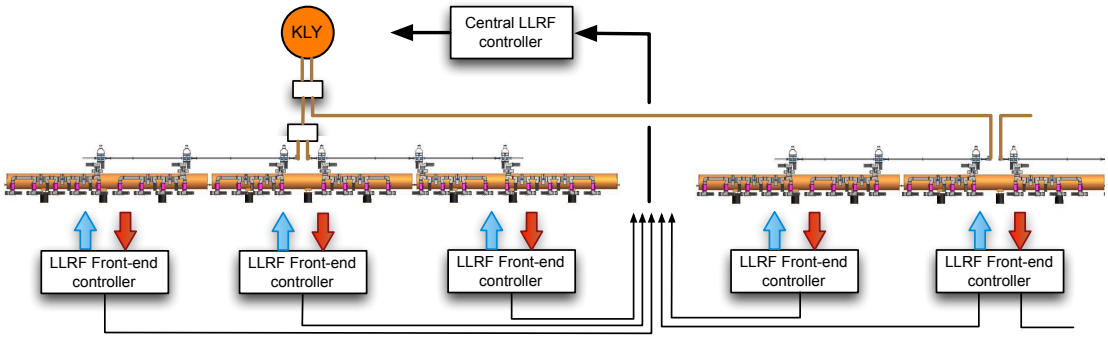

Figure 3.43. Implementation block diagram for the DKS LLRF system

An implementation block diagram for the DKS is shown in Fig. 3.43. Front-end LLRF controllers contain the analog interfaces, downconverters and digitisers for the field probe, forward and reflected RF power signals from each cavity. They also provide the control and monitoring interfaces to the cavity mechanical tuners, piezo tuners, cavity input coupler, and RF power dividers on the LPDS Fig. 3.1.

Each front-end controller computes in real-time a partial cavity-field vector sum for its respective cryomodules and sends it to the master LLRF controller over dedicated synchronous data links and fast Ethernet. The master controller, located close to the klystron, performs the vector-sum regulation, exception handling, and overall system coordination. The master controller communicates with the ILC global control system and with high-level applications such as linac energy and energy-profile management.

In addition to computing partial vector sums, the front-end controllers implement the algorithms and control functions associated with individual cavities or cryomodules (see Section 3.7.4).

The relatively short distances (few tens of metres) between cryomodules and klystron mean that cable delays can be kept short and control-loop delays short enough that the LLRF controller can respond almost from bunch to bunch. This allows, for example, fast compensation of jitter at the beginning of the bunch trains.

While Fig. 3.43 shows the front-end controllers located inside the beam enclosure close to each cryomodule, the split-tunnel arrangement of the Kamaboko tunnel offers the possibility of locating the front-end controllers either inside the beam enclosure next to the cryomodule or in the service corridor adjacent to the respective cryomodule. The latter approach has two important benefits: first, sensitive electronics are kept out of the high-radiation environment; second, electronics racks are accessible for service or repair without having to open up the beam enclosure. These benefits must be traded against longer RF-signal cables that must run through the penetrations in the beam enclosure shield wall. A final decision on the locations of electronics crates and cable penetrations will be made during the detailed design phase.

3.9 Main-linac layout for a flat topography

3.9.1 Introduction

This section describes the primary features of the Main Linacs that are specific to the flat-topography site-dependent design including the use of the Klystron Cluster Scheme (KCS) for the RF power distribution, and the corresponding impact on CFS, cryogenic segmentation and number of cryo plants, as well as the low-level RF control system (LLRF).

As already noted, KCS represents a novel approach to transporting the RF power into the accelerator tunnel. The klystrons and modulators are installed on the surface in 22 groups or 'clusters' (11 per linac). Each cluster contains 18 or 19 klystrons, the combined RF power of which (180–190 MW) is transported via a large 0.48 m-diameter overmoded cylindrical waveguide, first down a vertical shaft into the accelerator tunnel, and then along approximately 1 km of linac, where it drives ∼600 cavities (Fig. 3.44). At every ML unit (26 cavities, or every ∼ 38 m), about 7 MW of power is taped-off from the main KCS waveguide via a specially developed Coaxial Tap-Off (CTO). The CTO is connected directly to the local power-distribution system of the associated ML unit (Section 3.6.4).

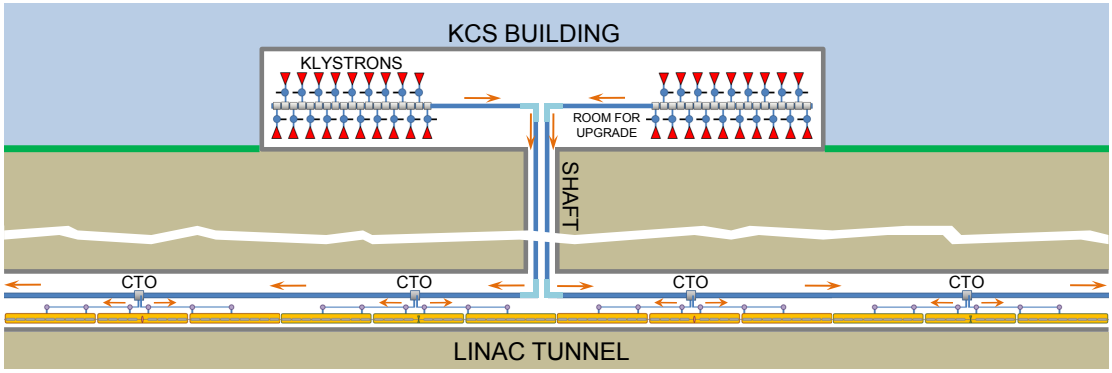

Figure 3.44. Schematic illustration (not to scale) of the klystron cluster scheme (KCS) for providing RF power to the main linacs. The upstream and downstream waveguides each extend roughly a kilometre.

The primary advantage of KCS is the removal of the RF power generation and all associated head loads from the underground accelerator tunnel, thus reducing the required tunnel volume, while at the same time easing the requirements on the air and water cooling systems, both of which result in a reduced cost. This must be countered by the need for additional shafts and surface buildings as well as additional waveguide systems and klystron overhead to compensate the additional associated losses. Technical issues with transporting such a high power in a single waveguide and associated components have been the subject of R&D during the Technical Design Phase (See Part I Section 2.8.6), and significant progress has been made in demonstrating individual components. Although further R&D is required, the results so far have proven sufficiently promising to justify adopting the approach for the flat-topography site-dependent baseline.

3.9.2 Linac layout and cryogenic segmentation

The most immediate and obvious impact of KCS is on the civil engineering and the need for additional shafts, as shown in Fig. 3.45. Without the need to house the modulators and klystrons underground, a single 5 m-diameter tunnel can be used as shown in Fig. 3.46, suitable for construction with a tunnel boring machine.

Figure 3.47 schematically shows the main-linac configuration, indicating both the KCS configuration and the cryogenic segmentation of the cryomodules and cryoplants. Along each main linac are 6 shafts and KCS buildings containing 11 KCS systems. All but the last building for each linac house two systems, one feeding upstream and one feeding downstream. All but five systems

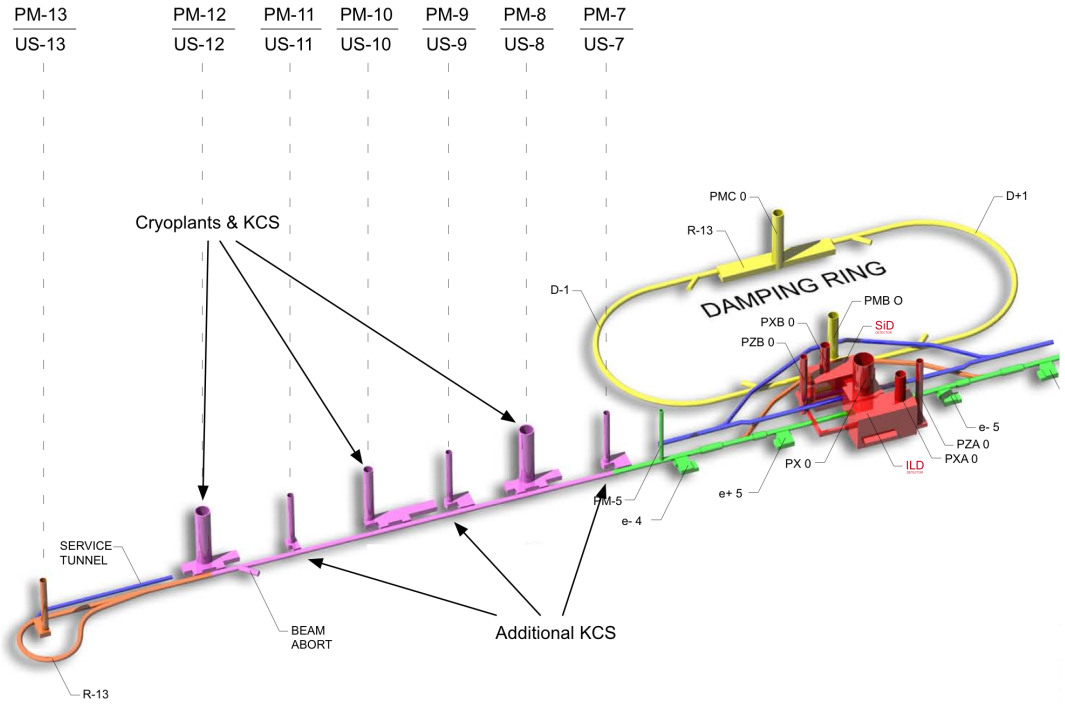

Figure 3.45. Schematic illustration (not to scale) of the layout for the flat-topography site-dependent design. The additional shafts required by KCS are indicated.

Figure 3.46
Sketch of the cross section of the Main-Linac tunnel for the flat-topography site-dependent design. The KCS cylindrical overmoded waveguide runs along the top of the tunnel as indicated.

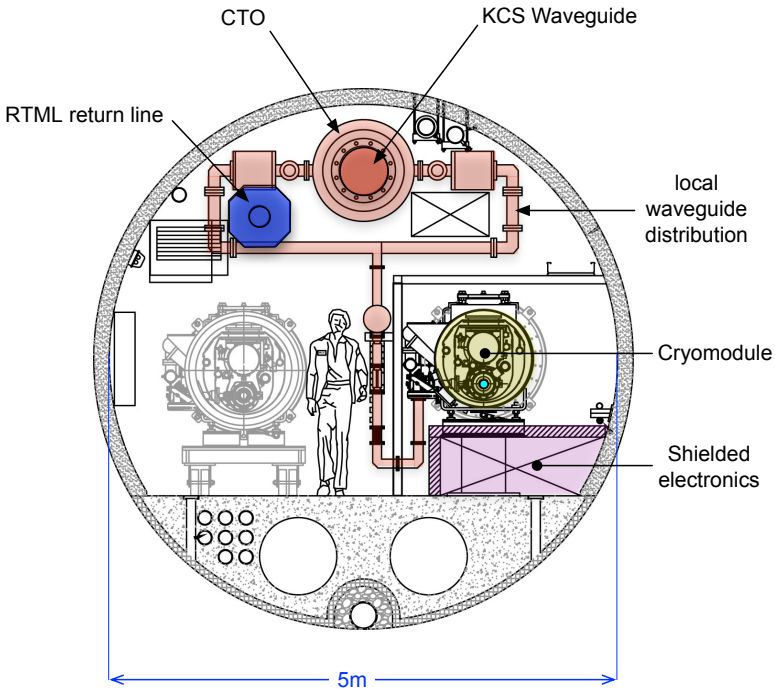

power 26 ML Units ($26 \times 26 = 676$ cavities). The last KCS in the electron linac (11th) and the 7th through 10th in the positron linac power 25 ML Units (650 cavities), as indicated in Fig. 3.47. This non-symmetric situation is due to the three additional ML units in the electron linac, required to provide the additional 2.6 GeV to drive the positron-source undulator (Chapter 5).

The total cryogenic load of each linac (see Section 3.5) is cooled by six cryoplants located at the major shafts (PM$\pm$8, PM$\pm$10 and PM$\pm$12 in Fig. 3.47), shared with the six klystron clusters at those locations. Although in principle five $\sim$4 MW plants are sufficient, the use of six plants provides

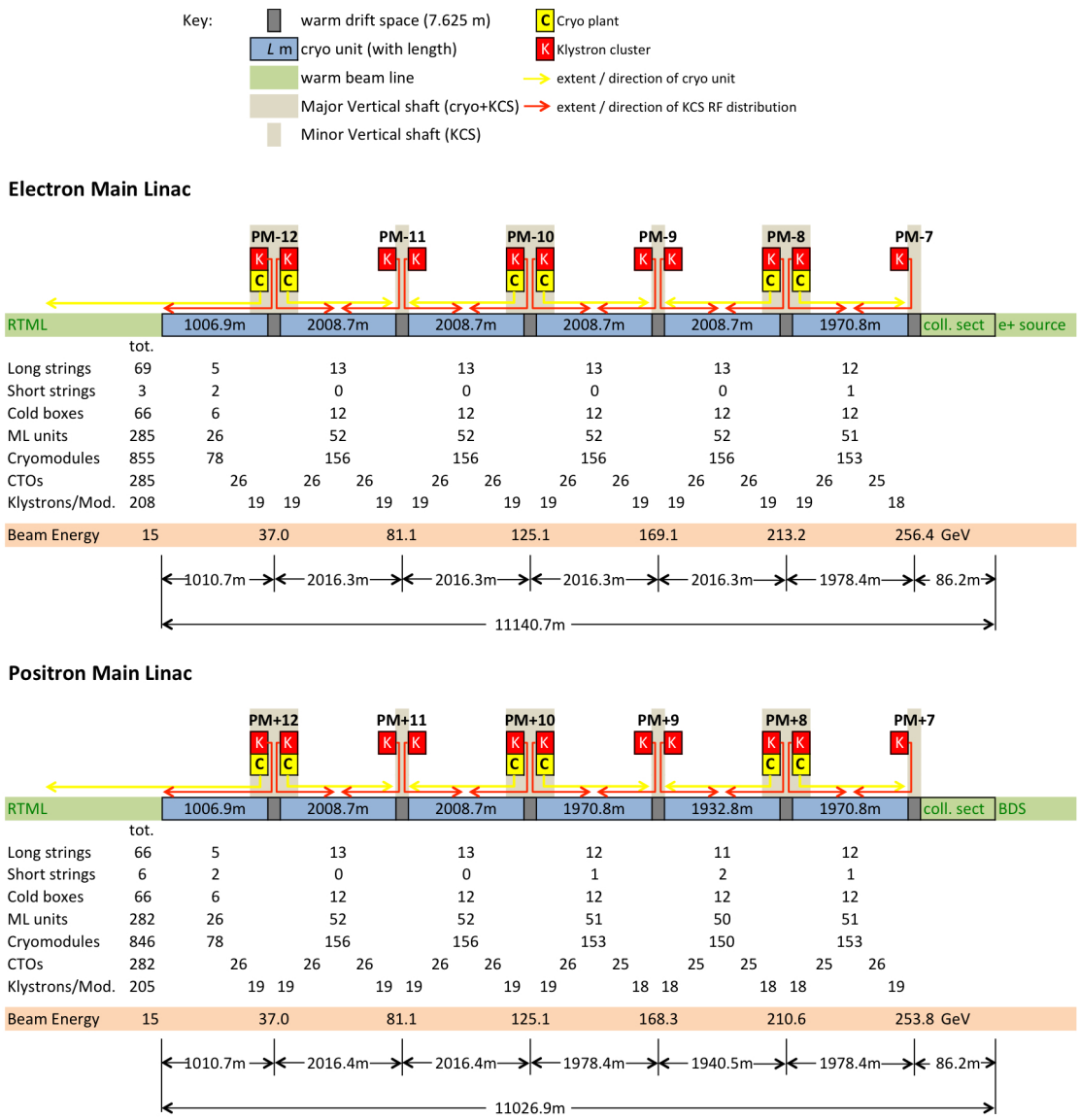

Figure 3.47. Schematic layout of the electron (top) and positron (bottom) main linacs for the flat-topography site-dependent design using KCS. The primary layout of the shaft arrangements are shown, along with the cryoplant and KCS segmentation. Distributions and totals (left-most column) of major linac sub-systems are indicated. The choice of six cryo plants is driven in part by compatibility with the KCS RF distribution.

an optimum use of the shaft spacing required by KCS (i.e. approximately 2.5 km), constrained by the maximum practical length of the main KCS waveguide.

3.9.3 The KCS high-power distribution system

Both for high-power handling and for minimal-loss transport over large distances, an overmoded circular waveguide operated in the TE_{01} mode is the preferred RF conduit. It has no surface electric field, and its attenuation constant, at sufficient radius, becomes the lowest. For the main KCS waveguide, a 0.480 m-diameter (WC1890) aluminium pipe is used, pressurised to 2 bar above atmosphere to suppress breakdown. With copper plating for improved surface conductivity, it presents a theoretical attenuation loss of 0.383 dB/km (∼8.44%/km). Because it is overmoded, the tolerances on the circular cross-section of this waveguide and its straightness must be kept fairly tight to avoid buildup of parasitic RF modes. In particular, the circular waveguide is specified to be round to ±0.5 mm (which has been met for the 80 m of bored circular waveguide that has been built). Also, the concentricity of the mating sections for the circular waveguide has a similar tolerance, which is

met by using the outer flange surface as a reference. The overall straightness of each KCS waveguide segment should be maintained within a degree or so from beginning to end to limit conversion to the degenerate TM_{11} mode.

The design of the CTO is illustrated in Fig. 3.48. A gap in the inner wall, where the diameter steps above the TE_{02} cutoff, couples a fraction of the power into a surrounding coaxial waveguide. At the termination of the latter, this flowing power is coupled through a set of openings in its outer wall into a wrap-around waveguide and finally through two radial rectangular WR650 ports. As the KCS power is gradually depleted, each successive CTO requires a different coupling. This is achieved via changes in the gap length and matching ridge. With a properly spaced end short, the final CTO becomes a full extractor. Ceramic block windows on the CTO rectangular ports isolate the pressure envelope of the KCS main waveguide. A short, double-stepped taper is used before and after the CTO to match the main KCS 0.48 m circular waveguide to the 0.35 m diameter CTO ports.

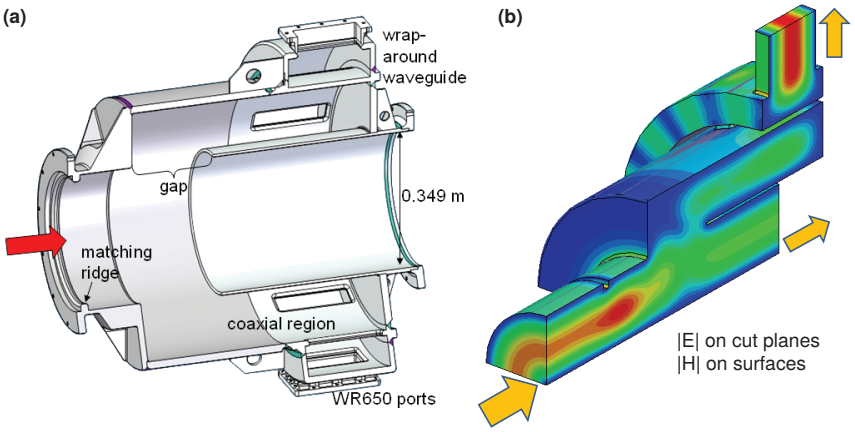

Figure 3.48
a) cutaway and b) simulated field patterns of a Coaxial Tap-Off (CTO), designed to extract (inject) fractional RF power from (into) a flowing TE_{01} wave in the circular KCS main waveguide. Many different couplings, controlled by gap width, are required; shown is a 3 dB design.

The same kind of waveguide circuit is used in reverse for combining power in the surface KCS buildings of the 18 or 19 klystrons in each cluster, with the CTO's spaced much more closely and no step tapers until the end. For their power to combine effectively in the passive circuit, the klystrons must all be run at the proper power with the proper relative phases. If power from a single 10 MW source drops out, a similar amount of power will be directed out from its CTO back toward that klystron. Thus a 5 MW isolator is required on each of the klystron outputs. For compactness, power can be fed alternately from klystrons arrayed on either side of the combining network.

Bringing the combined KCS RF power from the surface down to and along the tunnel requires navigating two or three 90° bends. Bending in overmoded waveguide is non-trivial, as modes tend to be coupled. A TE_{01} mode L-band bend, shown in Fig. 3.49, has been designed for this purpose. With ports the same diameter as the CTO's, it consists of a pair of mode converters to a single-polarization TE_{20} mode in a rectangular cross-section on either side of a sweep bend designed to preserve the latter [50]. Tapers to WC1890 are used to minimise losses in the shafts and in any other significant runs.

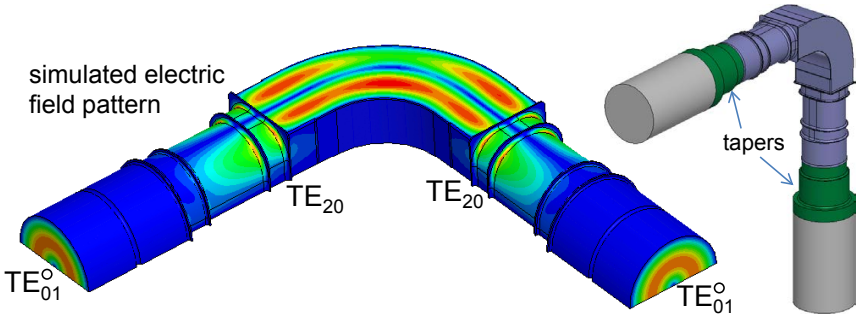

Figure 3.49
Overmoded bend for the circular TE_{01} mode KCS main waveguide. Mode converting sections allow the actual bending to be done in the rectangular TE_{20} mode. WC1375 ports connect to WC1890 through step-tapers.

Given that each KCS involves a large network of waveguide that includes 18 or 19 combiners and 25 or 26 tap-offs, the RF match of the CTOs and other components (bends and tapers) has to be very good to avoid significant losses. The power losses for KCS listed in Table 3.18 assumes the RF matches, especially those for the CTOs, are very good, and that the klystron RF amplitudes/phases can be precisely controlled to achieve optimal combining (e.g. by minimising reflections back to the klystrons). For the CTOs, this will likely require adding features that allow fine tuning of the match during cold-test setup.

From a circuit standpoint, the RF power the KCS pipe is back-terminated through the klystron isolators and forward-terminated through the cavity isolators, so misdirected power (e.g. from a breakdown) will be readily absorbed. Since the klystrons are isolated, they can be safety turned off when others are running, and as with DKS, the pressurised variable power dividers in the LPDS can be used to zero the power that goes to groups of 4-5 cavities if needed. From a safety standpoint, there are windows on the CTO ports to isolate the N_2 so the entire KCS pipe is not vented if there is a vent in the klystron feed lines or in one of the LPDS's.

3.9.4 LLRF control for KCS

The principle mechanisms of regulating the vector sum field of many cavities driven from a single RF source apply equally to the KCS configuration as to the RDR, FLASH, and XFEL layouts, and to that of the DKS. However, as will be explained, the unique features of the KCS layout apply some important additional constraints and functional requirements on the LLRF control system. resulting from the unique features very large number of cavities, long distances and correspondingly long cable delays, tapped RF power distribution and the use of a cluster of klystrons as the RF source.

At first glance, the implementation block diagram for KCS LLRF system in Fig. 3.50) is very similar to that of the RDR and the DKS system described in Section 3.8.4. Front-end LLRF controllers contain the analog interfaces, downconverters and digitisers for the field probe, forward and reflected RF power signals from each cavity. They also provide the control and monitoring interfaces to the cavity mechanical tuners, piezo tuners, cavity input coupler, and RF power dividers on the Local Power Distribution System (see figure Fig. 3.1 power dividers, and cavity input couplers). The front-end electronics are located in a radiation-shielded and temperature-regulated rack under each cryomodule.

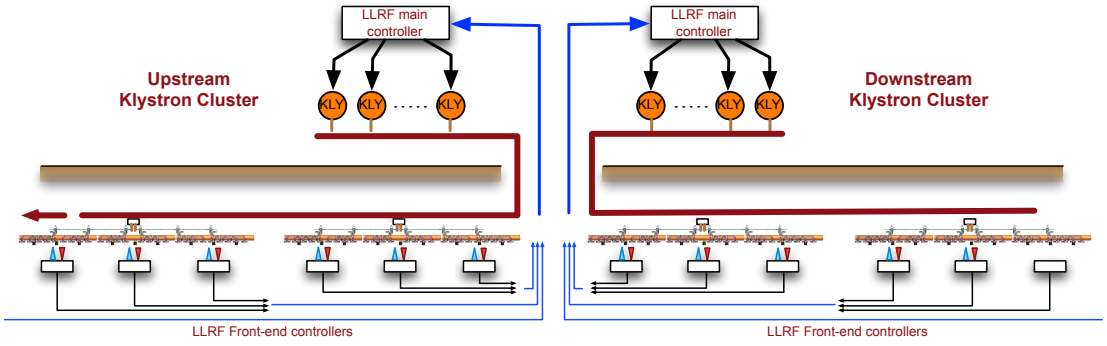

Figure 3.50. Implementation block diagram for the DKS LLRF system

Each front-end controller computes in real time a partial cavity field vector sum (i.e. the sum for those cavities in the cryomodule), and sends it to the master LLRF controller located in the surface building for the associated klystron cluster. This is done over dedicated synchronous data links and fast Ethernet. The master controller, located close to the klystrons, performs the full vector-sum addition, klystron drive waveform generation including feedback and feedforward corrections, exception handling, and overall system coordination. The master controller communicates with the ILC global control system and with high-level applications such as linac energy, energy profile management and

beam current feedforward (i.e. RF waveform corrections based on the measured current profile in the associated damping ring prior to the pulse).

In addition to computing partial vector sums, the front-end controllers implement the algorithms and control functions associated with individual cavities or crymodules such as the motor control of the power dividers, phase shifters and couplers (see Section 3.7.4).

3.9.4.1 Vector-sum regulation

The very long distance between the klystron cluster and the furthest cryomodule results in a delay of more than 4 µs from the time a change is made to the RF forward power to the time the change is seen by the furthest cavity and it then takes a further 4 µs for the change on the cavity field probe to be detected by the front-end controller and sent back to the LLRF main controller. This 8 µs total round-trip delay reduces closed-loop stability margins by ∼3 degrees per 1 kHz, reducing the maximum gain and bandwidth. Transport delays of the beam itself also play a role in the regulator dynamics and are different for the upstream and downstream clusters depending whether the RF power is traveling in the same direction of the opposite direction as the beam. Conversely, transport delays with respect to the closest cryomodules are less than a microsecond, and hence have no significant impact on regulator stability margins.

This range of transport delays over the cavity string results in a rather complex timing relationship between the beam, RF power, and RF signals, and these must be taken into account in the design of the vector-sum controller. A MIMO (multi-input/multi-output) optimal regulator design approach, where each partial vector sum is treated as a separate input, is likely to yield a regulator performance (gain-bandwidth) that is significantly better than would be achieved if the closed-loop performance were entirely dictated by the longest transport delays.

The impact of the reduced regulator performance depends largely on the environmental conditions around the main linacs (ground vibration, power line disturbances, microphonics induced by the flow of cryogenic fluids, etc.). Provided the environment is quiet, then the reduced jitter attenuation will still be sufficient to keep the cavity field stability within specification. Should it prove necessary, fast regulation of the total linac energy could be achieved by configuring a few of the cryomodules at the high energy end of the linacs in the RDR of DKS layout and use them to provide faster fine-tuning of the linac final energy.

3.9.4.2 Cavity-level algorithms

At the cavity and cryomodule level, there is an additional dimension to control of the local power distribution system, which in the case of KCS includes resistive loads to allow some of the power from the CTO to be diverted from the cavities, effectively giving some fine tuning of the total RF power to the sum of all cavities in the three-cryomodule cavity string. This allows fine tuning of the RF power that is fed to the 26 cavities in that local string

3.9.4.3 RF power source control

At the klystron cluster level, additional supervisor control functions are required to monitor and balance the RF power amongst all the klystrons. The total klystron power will be regulated in both the phase and amplitude, the latter which can be achieved by varying only the relative phase between banks of klystrons. There may also be a slow feedback loop on each klystron to optimise the match to the upstream power by minimising the reflected power to the klystron when trying to achieve the maximum beam energy.

At the local power distribution level, the input forward power is determined by the power ratio of the Coaxial Tap-off. An additional control knob on the local power distribution system allows the

total power to the 26-cavity string to be fine-tuned by diverting some of the power from the CTO to a separate RF load.

3.9.4.4 Klystron cluster LLRF system tests

While it is impractical to build a dedicated linac facility for testing the KCS, it may be possible to test LLRF control algorithms for the klystron cluster at the European XFEL, which has a similar number of cavities over similar distances as a klystron cluster in the TDR baseline design. The large-scale vector-sum control could be emulated by adding a 'supervisory' LLRF controller that communicates with the XFEL LLRF systems.

Chapter 4
Electron source

4.1 Overview

The ILC polarized electron source must produce the required train of polarized electron bunches and transport them to the Damping Ring. The nominal train is 1312 bunches of 2.0×10^{10} electrons at 5 Hz with polarization greater than 80 %. For low energy ILC operation ($E \leq$150 GeV /beam), the source is required to run at 10 Hz. The beam is produced by a laser illuminating a photocathode in a DC gun. Two independent laser and gun systems provide redundancy. Normal-conducting structures are used for bunching and pre-acceleration to 76 MeV, after which the beam is accelerated to 5 GeV in a superconducting linac. Before injection into the damping ring, superconducting solenoids rotate the spin vector into the vertical, and a separate superconducting RF structure is used for energy compression.

The SLC polarized electron source already meets the requirements for polarization, charge and lifetime. The primary challenge for the ILC source is the long bunch train, which demands a laser system beyond that used at any existing accelerator, and normal conducting structures which can handle high RF power. R&D prototypes have demonstrated the feasibility of both of these systems [60, 61].

4.2 Beam Parameters

The key beam parameters for the electron source are listed in Table 4.1.

Table 4.1
Electron Source system parameters.

Parameter	Symbol	Value	Units
Electrons per bunch (at gun exit)	N_-	$3{\times}10^{10}$	Number
Electrons per bunch (at DR injection)	N_-	$2{\times}10^{10}$	Number
Number of bunches	n_b	1312	Number
Bunch repetition rate	f_b	1.8	MHz
Bunch train repetition rate	f_{rep}	5 (10)	Hz
FW Bunch length at source	Δt	1	ns
Peak current in bunch at source	I_{avg}	3.2	A
Energy stability	σ_E/E	$<$5	% rms
Polarization	P_e	80 (min)	%
Photocathode Quantum Efficiency	QE	0.5	%
Drive laser wavelength	λ	790$\pm$20 (tunable)	nm
Single bunch laser energy	u_b	5	µJ

4.3 System Description

Figure 4.1 depicts schematically the layout of the polarized electron source. The key beam parameters are listed in Table 4.1. Two independent laser systems are located in a surface building. The light is transported down an evacuated light pipe to the DC guns. The beam from either gun is deflected on line by a magnet system which includes a spectrometer, and it then passes through the normal-conducting subharmonic bunchers, travelling wave bunchers and pre-accelerating sections. This is followed by the 5 GeV superconducting linac. The SC linac has 8 10MW klystrons each feeding 3 cryomodules, giving 24 cryomodules, 21 required and 3 spares. The Linac-to-Ring transfer line that brings the beam to the damping rings provides spin rotation and energy compression.

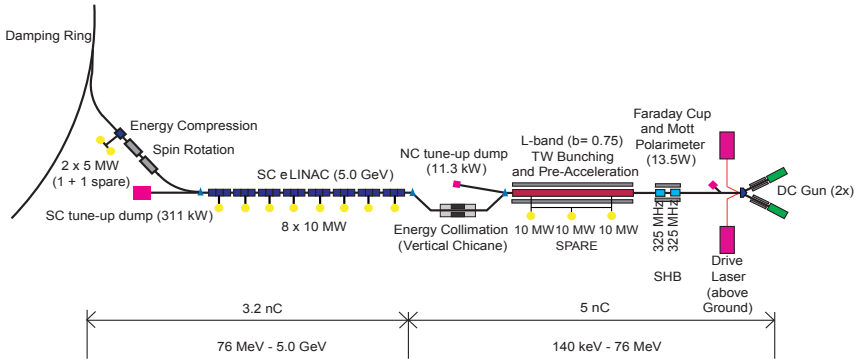

Figure 4.1 Schematic view of the polarized Electron Source.

4.3.1 Photocathodes for Polarized Beams

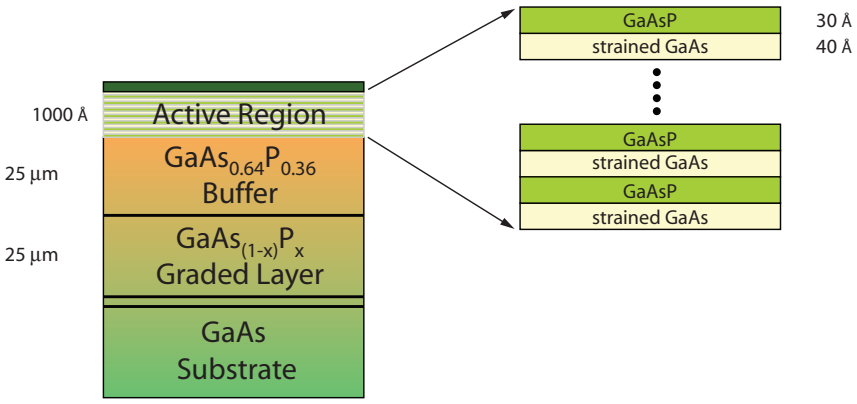

Figure 4.2 Structure of a strained GaAs/GaAsP superlattice photocathode for polarized electrons.

Photocathode materials have been the subject of intense R&D efforts for more than 20 years. The most promising candidates for the ILC polarized electron source are strained GaAs/GaAsP superlattice structures (see Fig. 4.2). GaAs/GaAsP superlattice photocathodes routinely yield at least 85 % polarization with a maximum QE of ∼1 % (routinely 0.3 to 0.5 %) [62–64]. The present cathodes consist of very thin quantum-well layers (GaAs) alternating with lattice-mismatched barrier layers (GaAsP). Each layer of the superlattice (typically 4 nm) is considerably thinner than the critical thickness (∼10 nm) for the onset of strain relaxation, while the transport efficiency for electrons in the conduction band can still be high [65]. The structures are p-doped using a high-gradient doping technique, consisting of a thin (10 nm), very highly doped ($5 \times 10^{19}\mathrm{cm}^{-3}$) surface layer with a lower density doping ($5 \times 10^{17}\mathrm{cm}^{-3}$) in the remaining active layer(s). A high-surface doping density is necessary to achieve high QE while reducing the surface-charge-limit problem [66, 67]. A lower doping density is used to maximize the polarization [68]. With bunch spacing of ∼500 ns, the surface-charge-limit problem for the ILC is not expected to be a major issue. The optimum doping level remains to be determined. An alternative under study is the InAlGaAs/GaAs strained superlattice

with minimum conduction band offset where a peak polarization of 91 % has been observed [69]. Research continues on various cleaning and surface-preparation techniques. Atomic hydrogen cleaning (AHC) is a well-known technique for removing oxides and carbon-related contaminants at relatively low temperatures [70].

4.3.2 Polarized Electron Gun

The ILC polarized electron gun is a DC gun producing a 200 keV electron beam based on the design developed at Jefferson Laboratory [71, 72]. Photocathodes for polarized electron production are not viable in an RF gun vacuum environment. DC gun technology for polarized sources has evolved considerably since the SLC [73, 74]. The ILC gun is optimized for a peak current, limited by space charge, of 4.5-5 A (4.5-5 nC/1 ns). This provides overhead to compensate for losses that occur primarily through the bunching system. The gun power-supply provides a cathode bias of 200 kV. An ultrahigh vacuum system with a total pressure $\leq 10^{-10}$ Pa (excluding H_2) is required to maintain the negative electron affinity (NEA) of the cathode. During HV operation the electric field on the cathode surface must be kept below 9 MV/m to ensure low dark current ($< 25\,\mathrm{nC}$). Excessive dark current leads to field emission resulting in molecular desorption from nearby surfaces. This process leads to deterioration of the gun vacuum and is destructive to the cathode's NEA surface.

The gun has an integrated cathode preparation and activation chamber and load-lock system. The activation chamber is attached to the gun and both volumes are maintained under high vacuum. The preparation chamber allows the option of local cathode cleaning and activation as well as storage of spare cathodes. Cathodes may be rapidly exchanged between the gun and preparation chamber. Cesiator channels in the preparation chamber are located behind the retractable photocathode. This eliminates the deposition of cesium on electrode surfaces, thereby reducing the dark current of the gun. The load-lock consists of a small rapidly pumped vacuum chamber for transferring cathodes from an external atmospheric source into or out of the preparation chamber without affecting the latter's vacuum.

The gun area is equipped with a Mott polarimeter to measure polarization and a Faraday cup to measure the charge. Several Residual Gas Analyzers (RGAs) characterise the vacuum near the gun. Other special diagnostics for the DC gun include measurement of the quantum efficiency of the cathode (using a cw diode laser integrated into the gun) and a nano-ammeter for dark-current monitoring.

The dominant source of intensity variations and timing jitter is the laser system. A secondary source for intensity variations is the gun power supply and beam dynamics influenced by space charge forces within the gun and the low-energy sections of the injector.

4.3.3 ILC Source Laser System

The conceptual layout schematic of the laser system is depicted in Fig. 4.3. To match the bandgap energy of GaAs photocathodes, the wavelength of the laser system must be 790 nm and provide tunability ($\pm$20 nm) to optimise conditions for a specific photocathode. Therefore, the laser system is based on Ti:sapphire technology.

A 1.8 MHz pulse train is generated by a cavity-dumped mode-locked oscillator. After diffractive pulse stretching to 1 ns and temporal pulse shaping, the bunch train is amplified using a multi-pass Ti:sapphire amplifier. The amplifier crystal must be cryogenically cooled to facilitate power dissipation and minimize instabilities caused by thermal lensing induced by the high-power amplifier pump [75]. A cw frequency-doubled Nd:YAG (or similar such as Nd:Vanadate) diode-pumped solid state (DPSS) laser provides the pump power for the Ti:sapphire amplifier. Additional amplification can be supplied by one or multiple flashlamp-pumped Ti:sapphire stages. Final laser pulse energy and helicity control

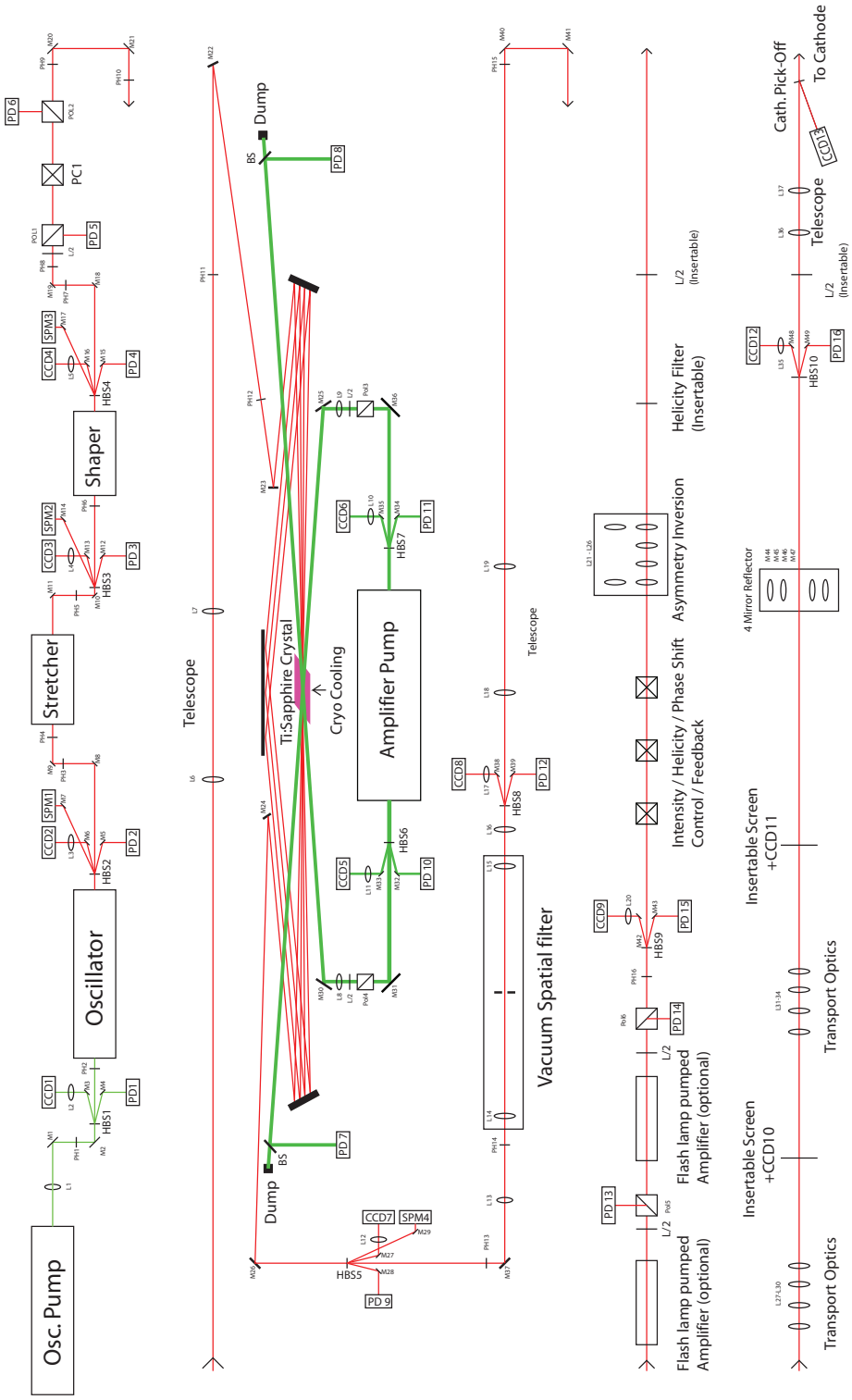

Figure 4.3. Schematic view of source drive laser system.

is achieved via electro-optical techniques (Pockels cells, polarizers, and waveplates). This system is also used as a feedback device to compensate for the QE decay of the photocathode between cesiations, to remove slow intensity drifts of laser and/or electron beam, and to maintain the circular polarisation state of the laser beam. Various optical techniques are used to cancel systematic effects caused by an asymmetric laser-beam profile or effects associated with the sign of the helicity of the laser light.

4.3.4 Bunching and Pre-Acceleration

The bunching system compresses the 1 ns micro-bunches generated by the gun down to ∼20 ps FWHM. It includes two subharmonic bunchers (SHB) and a 5 cell travelling wave β =0.75 L-band buncher. Two SHB cavities both operate at 325 MHz. Together they compress the bunch to ∼200 ps FWHM. The L-band bunching system is a modification of the TESLA Test Facility [76] design with a travelling-wave buncher to maximize capture efficiency. The buncher has 5 cells with β =0.75 and a gradient of 5.5 MV/m and compresses the bunch to 20 ps FWHM. The buncher and the first few cells of the following travelling wave pre-accelerator are immersed in a 7×10^{-2}T solenoidal field to focus the beam. Two 50 cell β =1 normal conducting (NC) TW accelerating sections at a gradient of 8.5 MV/m increase the beam energy to 76 MeV. These structures must withstand very high RF power for the duration of the very long pulse but they are identical to those being developed for the positron source. Further details of the bunching system are summarised elsewhere [77].

4.3.5 Chicane, Emittance Measurement and Matching Sections

Immediately downstream of the NC pre-acceleration, a vertical chicane provides energy collimation before injection into the SC booster linac. The chicane consists of four bending magnets and several 90° FODO cells. The initial dipole at the chicane entrance can be used as a spectrometer magnet (see Fig. 4.1). A short beam line leads to a diagnostic section that includes a spectrometer screen. The injector beam emittance is measured by conventional wire scanners downstream of the chicane. Two matching sections connect the chicane and emittance measurement station to the downstream SC booster linac.

4.3.6 The 5 GeV Superconducting Pre-Acceleration (Booster) Linac

Twenty-one standard ILC-type SC cryomodules accelerate the beam to 5 GeV and FODO cells integrated into the cryomodules transversely focus the beam. An additional string of three cryomodules is added to provide redundancy (total of 24 cryomodules). The booster linac consists of two sections. In the first section, the e^- beam is accelerated from 76 MeV to 1.7 GeV in cryomodules with one quadrupole per module. In the second section, the e^- beam is accelerated to the final 5 GeV in cryomodules with one quadrupole every other module.

4.3.7 Linac to Damping Ring Beamline and Main e^- Source Beam Dump

The Linac To Ring (LTR) beam line transports the beam to the injection point of the damping ring and performs spin rotation and energy compression. The 5 GeV longitudinally polarized electron beam is first bent through an arc. At 5 GeV, the spin component in the plane normal to the magnetic field precesses 90° in that plane for every n × 7.9° (n: odd integer) of rotation of momentum vector. An axial solenoid field integral of 26.2 T-m rotates the spin direction into the vertical [78]. A 5 GeV tune-up beam dump is installed near the LTR. To dump the 5 GeV beam, the first bend of the LTR is turned off, and the dump bend downstream energized. The dump drift is ∼ 12 m long.

4.4 Accelerator Physics Issues

Simulations indicate that >95% of the electrons produced by the DC gun are captured within the 6-D damping ring acceptance: $\gamma(A_x+A_y)$ ≤0.07 m and ΔE×Δz ≤(±3.75 MeV)×(±3.5 cm). The starting beam diameter at the gun is 2 cm, which is focused to a few mm diameter before it is injected into the DR. Calculations in the low-energy regions of the injector (≤ 76 MeV) include space-charge effects and use PARMELA [79]. The beam propagation through the superconducting booster linac and LTR beam line has been optimized using MAD [80] and tracked by the ELEGANT code [81].

4.4.1 DC Gun and Bunchers

The DC gun [72] creates a 200 keV electron beam with a bunch charge of 4.5-5 nC with a bunch length of 1 ns and an unnormalized transverse edge emittance at the gun exit of 70 mm-mrad. To minimize longitudinal growth of the bunch, it is desirable to locate the first subharmonic buncher (SHB) as close to the gun as possible. However, the beam lines needed to combine both guns require a distance of ∼1-1.5 m between gun and first SHB. The SHBs capture 92 % of the electrons generated at the gun. The beam parameters after the preaccelerator at 76 MeV (see Section 4.3.4) are summarized in Table 4.2. A plot of the beam envelope from gun up through the bunching system is given in Fig. 4.4.

Table 4.2
76 MeV beam parameters after NC bunching and pre-acceleration.

Parameters	β = 0.75 TW Buncher Design
Initial charge	4.5 - 5 nC
Transmitted charge	92 %
Phase extension FWHM	9 deg L-band
Energy spread FWHM	<100 keV
Normalized rms emittance	70 μm rad

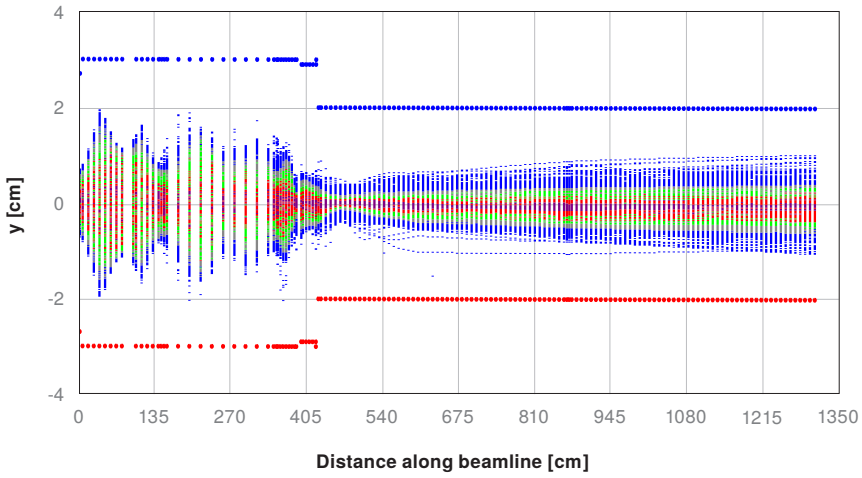

Figure 4.4
Beam envelope along the 76 MeV injector.

4.4.2 The 5 GeV Booster Linac and Linac to Damping Ring Line (eLTR)

The optics of the superconducting booster linac are shown in Fig. 4.5.

At the dump window, the beam size σ_x/σ_y is 0.72 cm/1.4 cm and 13.9 cm/1.4 cm for 0 % and $\pm 10\,\%$ energy spread, respectively. These beam sizes are within the dump window specifications. At the profile monitor before the beam dump location, the dispersion dominates the beam size and thus the dump also serves as an energy spectrometer with 0.1 % resolution.

The arc of the eLTR is designed to rotate the spin vector by 90 degrees from longitudinal into a horizontal position before injection into the damping ring and to provide the R_{56} necessary for energy compression. For every 90° of spin rotation, an arc angle of 7.9° is required. The initial LTR arc bending angle is 3 $\times 7.9° = 23.8°$. The R_{56} is adjustable (-0.75 ±0.40 m). The arc is followed by a SC solenoid and a standard SCRF cryomodule. A 8.3-m-long superconducting solenoid with 3.16 T

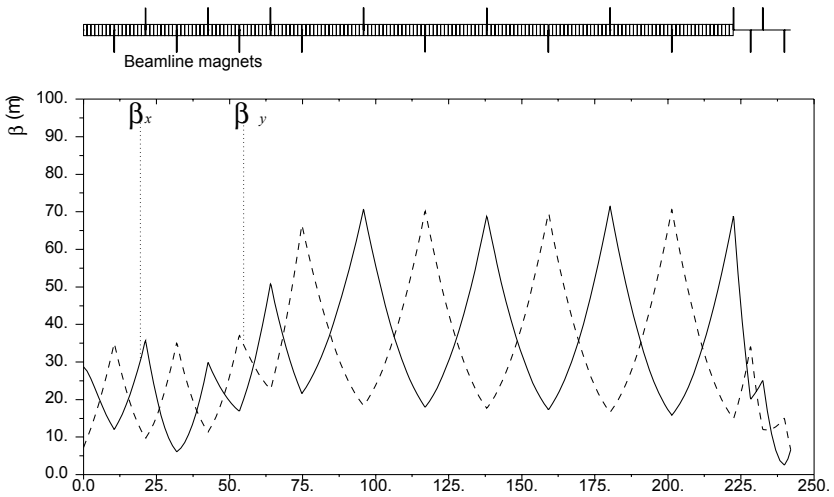

Figure 4.5
Optics of the SC electron booster linac.

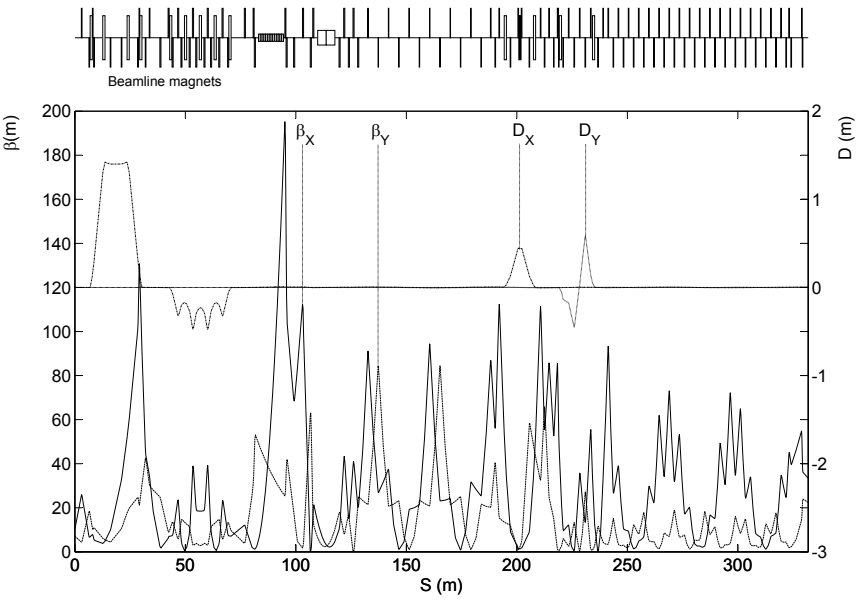

Figure 4.6
Optics of the LTR.

solenoid rotates the horizontal spin vector into the vertical. After the bunch is decompressed by the arc, an RF voltage of 225 MV provided by a 12.3 m-long 9-cavity superconducting linac, rotates the electrons in longitudinal phase space to match the longitudinal DR acceptance. The LTR includes approximately 200 m of additional transport and an optical transformer to match the Twiss parameters at the DR injection line [82]. There are three PPS stoppers each 1 m long in the LTR arc. Two FODO cells upstream of the LTR arc have laser-wire emittance-measurement stations. The optics of the LTR system are shown in Fig. 4.6.

4.5 Accelerator Components

4.5.1 Table of Parts Count

Table 4.3 lists the major components of the ILC electron source and Table 4.4 the lengths of the various electron source beamlines.

Table 4.3
Total number of components for the polarized electron source.

Magnets		Instrumentation		RF	
Bends	27	BPMs	100	325 MHz SHB Cavities	2
Quads (NC)	158	Wirescanners	4	5 Cell L-band buncher	1
Quads (SC)	16	Laserwires	1	L-band TW structures	2
Solenoids(NC)	12	BLMs	5	1.3 GHz cryomodules	24
Solenoids(SC)	2	OTRs	2	L-band klystrons/modulators	13
Correctors(SC)	32	Phase monitors	2		

Table 4.4
System lengths for the e^- source beamlines.

Beam Line Section	Length
Gun area	7 m
NC beam lines	14 m
Chicane + emittance station	54 m
SC beam lines	245 m
eLTR	332 m
Dumplines	12 m
Total beam line length	664 m
Total tunnel length	680 m

Chapter 5
Positron source

5.1 Introduction

The ILC Positron Source generates the positron beam. The production scheme uses the electron main linac beam passing through a long helical undulator to generate a multi-MeV photon drive beam which then impinges onto a thin metal target to generate positrons in electromagnetic showers. The positrons are captured, accelerated, separated from the shower constituents and unused drive-beam photons and transported to the Damping Rings. The baseline design is for 30 % polarised positrons. There are spin rotators before injection into the damping rings to preserve the polarisation and there is also sufficient beamline space to allow for an upgrade to a polarisation of $\sim 60\,\%$ [83].

The positron source performs several critical functions:

- generation of a high-power multi-MeV photon production beam. This requires suitable short-period, high-K-value helical undulators;
- production of the positron bunches in a metal target that can reliably deal with the beam power and radioactive environment induced by the production process. This requires high-power target systems;
- capture, acceleration and transport of the positron bunch to the Damping Rings with minimal beam loss. This requires high-gradient normal-conducting RF and special magnets to capture the positrons efficiently. The long transport lines also require large aperture magnets to transport efficiently the positron beams which have large transverse emittance.

The Positron Source also has sufficient instrumentation, diagnostics and feedback (feedforward) systems to ensure optimal operation.

5.2 Beam parameters

The key parameters of the Positron Source are given in Table 5.1 [84].

The source produces 2×10^{10} positrons per bunch at the IP with the nominal ILC bunch structure and pulse repetition rate. It is designed with a 50 % overhead and can deliver up to 3×10^{10} at injection into the 0.075 mrad transverse dynamic aperture of the damping ring. The main electron linac beam has an energy that varies between 100 and 250 GeV and passes through $\sim$ 150 m of helical undulator, with a 1.15 cm period and a K value of 0.92. At 150 GeV, the first harmonic cut-off of the photon drive beam is 10.1 MeV and the beam power is $\sim$63 kW. Approximately 4.4 kW of this power is deposited in the target in $\sim$ 1 mm rms. A windowless moving target is required to handle the high beam power and heat deposition.

The Positron Source undulator is long enough to provide adequate yield for any electron beam energy over 150 GeV. For lower energy operation, the electron complex operates at a 10 Hz repetition rate with 5 Hz of 150 GeV electrons used to produce positrons and 5 Hz of electrons at the desired energy for collisions.

Table 5.1
Nominal Positron Source Parameters

Parameter	Symbol	Value	Units
Positrons per bunch at IP	n_b	2×10^{10}	number
Bunches per pulse	N_b	1312	number
Pulse Repetition Rate	f_{rep}	5	Hz
Positron Energy (DR injection)	E_0	5	GeV
DR Dynamic Aperture	$\gamma(A_x + A_y)$	<0.07	m rad
DR Energy Acceptance	Δ	0.75	%
DR Longitudinal Acceptance	A_l	3.4 x 37.5	cm-MeV
Electron Drive Beam Energy†	E_e	150/175/250	GeV
Undulator Period	λ	1.15	cm
Undulator Strength‡	K	0.92/0.75/0.45	-
Undulator Type	-	Helical	-
Undulator Length	L_u	147	m
Photon Energy (1st harm cutoff)	E_{c10}	10.1/16.2/42.8	MeV
Photon Beam Power	P_γ	63.1/54.7/41.7	kW
Target Material	-	Ti-6%Al-4%V	-
Target Thickness	L_t	0.4 / 1.4	r.l. / cm
Target Absorption	-	7	%
Incident Spot Size on Target	σ_i	1.4/1.2/0.8	mm, rms
Positron Polarisation	P	31/30/29	%

† For centre-of-mass energy below 300 GeV, the machine operates in 10 Hz mode where a 5 Hz 150 GeV beam with parameters as shown in the table is a dedicated drive beam positron source.
‡ K is lowered for beam energies above 150 GeV to bring the polarisation back to 30 % without adding a photon collimator before the target.

5.3 System description

The layout of the electron side of the ILC is shown in Fig. 5.1, including the relative position of the major systems of the positron source. Figure 5.2 is a schematic of the positron source beamlines with dimension indicated, split into two sections [85]. The upper section shows the beamlines from the end of electron main linac to the end of the 400 MeV positron pre-accelerator. The lower section shows the beamlines from the end of the pre-accelerator to the end of the positron-source beamline or the beginning of the damping ring.

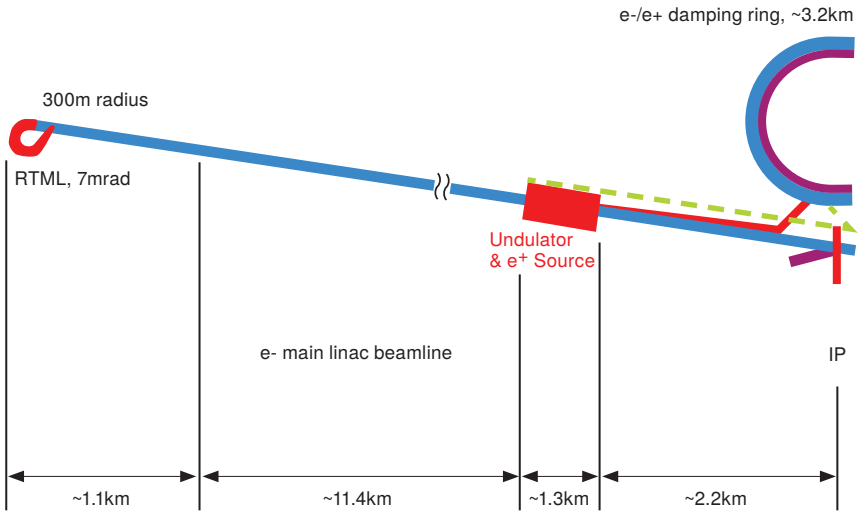

Figure 5.1
Layout of Positron system relative to the ILC

The electron beam from the main linac passes through the undulator and a dogleg before continuing to the IP for collisions. These beamlines are labeled as EUPM, EUND and EDOGL in Fig. 5.2. For lower energy operations (CM=200 GeV, 230 GeV and 250 GeV), a dedicated 5 Hz 150 GeV drive beam, alternating with the lower energy beam for physics, is used for positron production. After passing through the EUND beamline to generate photons, this 150 GeV drive beam is then sent to a beam dump in the beamline EPUNDDL.

The photon beam produced by the electron beam drifts through the section UPT and strikes a 1.4 cm thick Ti-alloy target to produce an electromagnetic shower of positrons and electrons. The

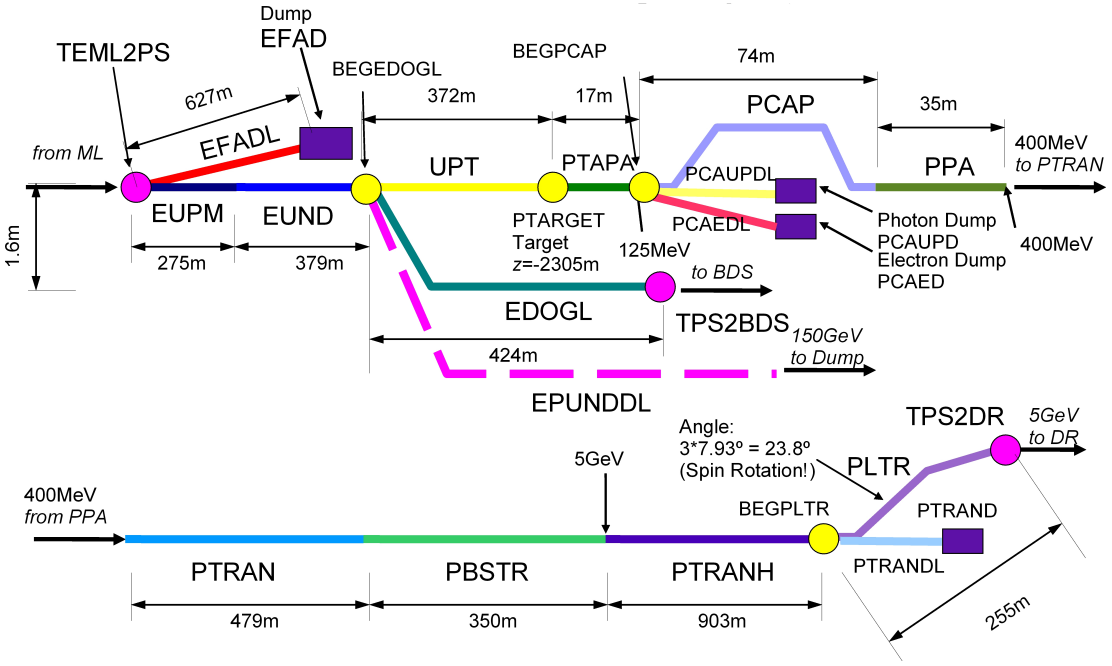

Figure 5.2. Positron Source beamlines cartoon

positrons are then captured within optical matching device (OMD) and then matched into a capture system (labeled PTAPA) consisting of normal conducting (NC) L-band RF cavities and surrounding solenoid. The positron beam is accelerated to 125 MeV before entering the chicane where the positrons, electrons and photons are separated, into beamlines PCAP, PCAPEDL and PCAUPDL respectively. Both electrons and photons are dumped. After the chicane, the positron beam is further accelerated to 400 MeV using a NC L-band RF system with solenoidal focusing (labelled beamline PPA).

The 400 MeV positron beam is transported for approximately 479 m in beamline PTRAN (400 MeV) to a booster linac (PBSTR) where the beams are further accelerated to 5 GeV using SC L-band RF. Before injection into the damping ring, the beam is transported 903 m in PTRANH before passing through a beamline section (PLTR) that carries out spin rotation and energy compression in order to maximise injection acceptance. Finally, the beam is injected into the positron damping ring at point TPS2DR.

Figure 5.3 shows how the performance of the positron source (yield and polarisation) strongly depends on the main electron-beam energy for the given undulator parameters (K, λ_u). At higher electron-beam energy, the undulator B field is re-optimized to restore the polarisation to 30 %. The final undulator parameters for a yield of 1.5 at 350 and 500 GeV energy are listed in Table 5.2.

One additional part of the positron-source system is the Auxiliary Source [86]. The current auxiliary source scheme generates a single-bunch low-intensity ($\sim$ 1 % of nominal beam intensity) positron beam which is intended for commissioning. This source uses 500 MeV electron drive beam from a conventional S-band electron accelerator impinging on the same production target as the normal beam to produce positrons which then pass through the capture, acceleration and transport beamlines sections, and subsequently injected into the damping ring. The 500 MeV S-band electron injector has 8 SLAC-type 3 m-long accelerator structures [87] and a microwave photo cathode gun. The KAS is less than 40 m long and is installed along-side the 370 m long undulator photon transport line. The electron injector is powered by 4 S-band RF stations, each with a 100 MW modulator, a 50 MW klystron and a SLED cavity [88].

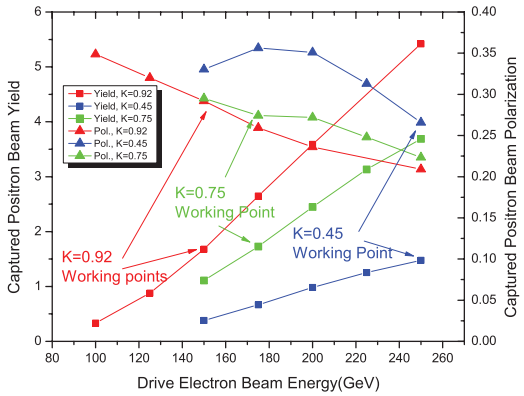

Figure 5.3
Simulation results of positron source yield and polarisation as a function of drive-beam energy for 147 m long undulator and λ_u=1.15 cm using a flux concentrator as OMD.

Table 5.2
Parameters for 350 GeV CM and 500 GeV CM.

Parameter	units	350 GeV	500 GeV
Electron beam energy (e^+ prod.)	GeV	178	253
Bunches per pulse	N	1312	1312
Photon energy (first harmonic)	MeV	16.2	42.8
Photon openning angle ($=1/\gamma$)	μrad	2.9	2
Undulator length	m	147	147
Required undulator field	T	0.698	0.42
undulator period length	cm	1.15	1.15
undulator K		0.75	0.45
Electron energy loss in undulator	GeV	2.6	2
Induced energy spread (assume 0% initial)	%	0.122	0.084
Emittance growth	nm	-0.55	-0.31
Average photon power on target	kW	54.7	41.7
Incident photon energy per bunch	J	8.1	6
Energy deposition per bunch (e^+ prod.)	J	0.59	0.31
Relative energy deposition in target	%	7.20%	5%
Photon rms spot size on target	mm	1.2	0.8
Peak energy density in target	J/ cm^3	295.3	304.3
	J/ g	65.6	67.5
Pol. of Captured Positron beam	%	30	30[†]

[†] Flux concentrator needs to operate at a stronger field.

5.3.1 Photon production

Production of an adequate number of positrons requires that the photons hitting the target have both sufficient intensity and high-enough energies to produce ∼1–100 MeV electron-positron pairs that can escape from the target to be captured. In general this means photon energies of at least 10 MeV. The total number of positrons produced must be suffient to allow for losses between the target and the IP.

A helical undulator generates twice the synchrotron radiation power per period than the equivalent (same maximum field) planar undulator, reducing the length required to produce the same number of positrons. Another benefit is that the helical undulator generates circularly polarised photons which in turn generate longitudinally polarised positrons. For the baseline undulator system with a 150 GeV drive beam, the photons produce enough captured positrons but the resulting polarisation is only $\sim 30\,\%$. To achieve higher positron polarisation requires a longer undulator to produce an excess of photons. That allows photons with the wrong polarisation state to be absorbed by photon collimator and still leave adequate photon yield on the target. A polarisation of 60 % can be achieved with an additional 73.5 m long undulator.

The undulator is installed at the end of the electron main linac as shown in Fig. 5.1. Above 150 GeV, the electron beam used in the final collisions at the IP is used as the drive beam, passing through the undulator to generate the required photons. At lower beam energy, the positron yield is too low and a dedicated 150 GeV drive beam is interleaved with the electron beam used in the IP collisions.

5.3.2 Positron production & capture

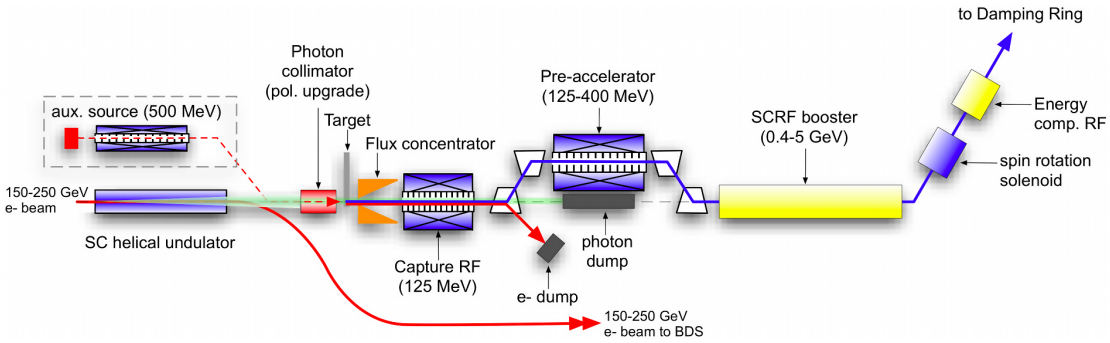

Figure 5.4. Schematic layout of Positron Source. Beamline sections are defined in Section 5.3.

Figure 5.4 shows the schematic layout for the positron-beam production, capture and transport to the damping rings. The photon beam generated from the helical undulator is incident on the rim of a rotating titanium target (see Section 5.5.2) with 0.4 radiation-lengths thickness. The incident photon beam has transverse size of $\sim$1 mm rms and electron and positron emerging from the downstream side of the target are captured in a 0.07 mrad transverse dynamic aperture. The target is followed by a tapered magnet called the Optical Matching Device (OMD) (see Section 5.5.3) which has a field starting from $<$0.5 T at the target and then quickly ramped to over 3 T in $\sim$2 cm, and then decays to 0.5 T over 14 cm. This OMD has wide energy acceptance and is used to match the beam phase-space out of the target into the capture L-band RF cavities (TAP). The capture RF cavities are placed directly after the OMD to accelerate the positron beam to 125 MeV. The accelerating RF cavities have an average gradient of 9 MV/m and are located inside 0.5 T solenoids which provide beam focusing.

The target and equipment immediately downstream will become highly activated. A remote-handling system is used to replace the target, OMD and 1.3 m NC RF cavities. The remote handling system is described in detail in Part I Section 4.3.10.

5.3.3 Positron transport

After capture, positrons are separated from electrons and photons in the dipole magnet at the entrance of an achromatic chicane which horizontally deflects the positrons by 1.5 m. The chicane includes collimators to remove positrons with large incoming angles and energy far from the nominal value.

The pre-accelerator immediately downstream of the chicane accelerates the positron beam from 125 MeV to 400 MeV. The normal-conducting L-band RF structures are immersed in a constant solenoid field of 0.5 T. The accelerating gradient is $\sim$ 8 MV/m and the total length is 34.6 m. The transport line is 480 m long and transfers the 400 MeV positron beam to the positron booster linac.

5.3.4 5 GeV SC Booster Linac

It accelerates the beam from 400 MeV to 5 GeV using SC L-band RF modules. There are three sections with a periodic FODO lattice. The first low-energy section which accelerates up to 1083 MeV contains four cryomodules with six 9-cell cavities and six quadrupoles. The quadrupole field strength $(\partial \mathrm{B}/\partial \mathrm{x}) \times \mathrm{L}$ varies from 0.8-2.4 T. The second section up to 2507 MeV uses six standard ILC-type cryomodules, each containing eight 9-cell cavities and two quadrupoles. The quad strength ranges from 0.6-1.4 T. The last section up to 5 GeV has twelve standard ILC-type cryomodules, each with eight 9-cell cavities and one quadrupole. The quadrupole field strength ranges from 0.8-1.7 T.

5.3.5 Linac to Damping-Ring Beam Line

The linac to damping-ring (LTR) system from the booster linac to the DR injection line has two main functions: to rotate the polarisation into the vertical plane, and to compress the energy spread to match the DR longitudinal acceptance.

The polarisation is preserved through transport and acceleration. The polarisation must be rotated into the vertical plane to preserve the polarisation in the DR. The spin-rotation system contains bending magnets and solenoids, changing the spin of positrons first from the longitudinal to the horizontal plane and then from horizontal to vertical. To produce $n \cdot 90^\circ$ of spin rotation (n is an odd integer) from the longitudinal to horizontal plane at 5 GeV, a total bending angle $\theta_{bend} = n \cdot 7.929^\circ$ is required. To rotate the spin by 90° from the horizontal to vertical plane at 5 GeV energy requires a solenoid magnetic-field integral of 26.2 T m. This is achieved with an 8.3 m-long superconducting solenoid with 3.16 T field.

The energy compression uses a combination of booster-linac RF phase, a chicane at the beginning of the LTR and RF voltage. The chicane has a transverse offset of 1.5 m and a nominal R56 of -0.75 m. The first arc of the LTR has a bending angle of $3 \times 7.929^\circ = 23.787^\circ$ to rotate the spin by 90°. After the first arc, an RF voltage of 225 MV is provided by a 9-cavity ILC cryomodule with no quads. This compresses the positron energy to match into the DR. The rest of the LTR system includes: a section with an additional 9.626° horizontal bending, a vertical dogleg to raise the elevation up by 1.65 m, another vertical dogleg to lower the elevation back to 0.35 m and a FODO lattice to transport the beam into a matching section into the DR injection line. Its geometry is shown in Fig. 5.5.

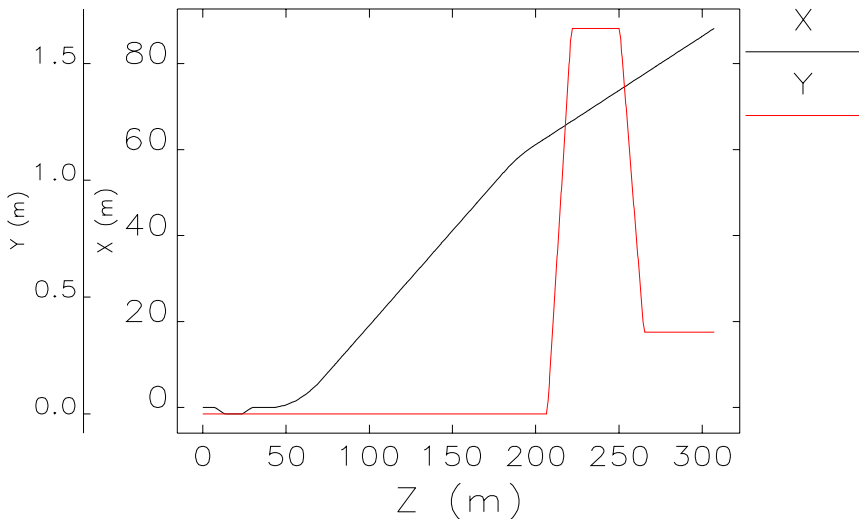

Figure 5.5 Geometry of LTR beamline. The LTR beamline starts at $z = 0$.

5.4 Optics parameters

The optics of the positron-source system starting from the capture section to the DR injection is shown in Fig. 5.6. The lattice is optimized to have maximum transmission and minimum emittance growth.

Multi-particle tracking has been performed from the target to the DR injection, using Elegant [89] to track the large angular divergence and long tails at low energy. Energy compression is required before injection into the DR to accommodate more positron beam within the 6-D acceptance in the DR equal to $A_x + A_y \leq 0.07\,\mathrm{m}$ and $\Delta E \times \Delta x \leq (\pm 3.75\,\mathrm{MeV}) \times (\pm 3.5\,\mathrm{cm})$.

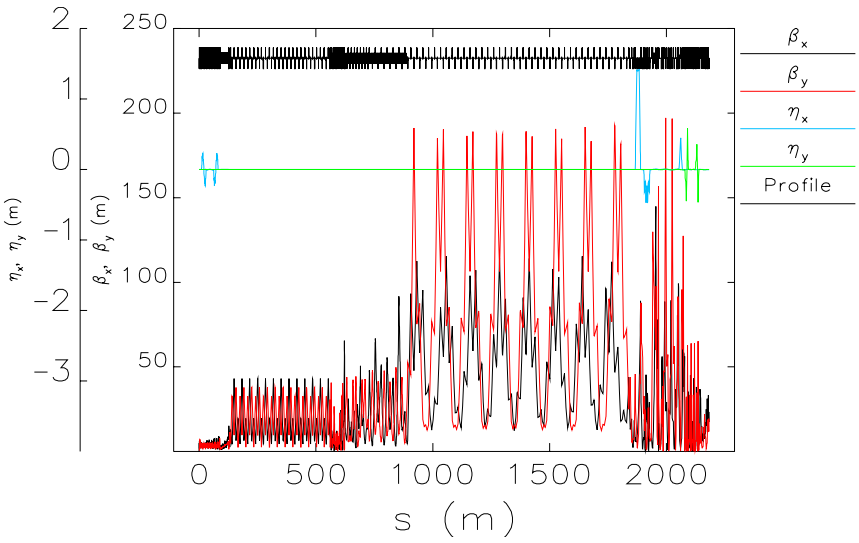

Figure 5.6
Optics of positron source

5.5 Accelerator components

5.5.1 Undulator

The undulator uses superconducting technology to achieve high field with a short period. Two interleaved helical windings of NbTi spaced half a period apart generate the transverse helical field. The large length of the undulator requires that it be built in modular units. Each 4 m-long cryomodule contains two separate undulators with an active undulator length of ~ 3.5 m [90]. The present baseline parameters are given in Table 5.3.

Table 5.3
Helical undulator parameters

Parameter	Value
Period (mm)	11.5
K	0.92
Field on Axis (T)	0.86
Beam aperture (mm)	5.85
First Harmonic Energy (MeV)	10.1
Nominal Drive Beam Energy(GeV)	150

The undulator vacuum chamber is made of copper and operates at a temperature of 4.2 K. Copper is selected for its high conductivity which alleviates resistive wall effects. Estimates for a 150 μm-long Gaussian bunch containing 1×10^{10} electrons (a more demanding case than the ILC nominal parameters of 300 μm and 2×10^{10} particles per bunch), interacting with a 200 m-long copper vessel with internal aperture of 5.6 mm, indicate that the resistive wall effect would increase the RMS energy spread from the nominal value of 0.05 % to 0.0505 %. Another advantage of using copper is that excellent surface quality is readily achievable in copper vessels. A pessimistic wakefield model has suggested that for a measured surface roughness (RA value) of < 100 nm, the electron energy spread would only increase from 0.05 % to $< 0.051\,\%$. The resistive-wall wakefield could potentially cause emittance growth, but numerical simulations have shown that there is no effect until the transverse kick strength is >5000 times the nominal value [91, 92].

The material between the superconducting windings is soft magnetic iron which serves as an outer yoke to increase the field and to provide additional support. Each cryomodule contains a liquid-helium bath; zero liquid boil off is achieved through the use of in-situ cryocoolers.

Since the electron vacuum vessel is at cryogenic temperatures, each module effectively acts as a long cryopump. Roughing pumps are installed in room temperature sections between cryomodules (approximately every 12 m) but achieving UHV conditions relies on cryopumping. The baseline pressure target of 10^{-8} mbar is set to avoid fast-ion instability problems. Vacuum calculations indicate that the

cryopumping is adequate provided that the number of photons with energy >10 eV striking the vessel surface is kept sufficiently low. Extensive calculations of the undulator photon output down to these very low energies have been carried out. These indicate that low-power photon absorbers [93] should be placed approximately every 12 m to provide an adequate shadowing of the cold vessel surfaces. These absorbers are in room temperature sections.

The electron-beam transport through the complete undulator system is based on a simple FODO arrangement with quadrupole spacing of $\sim$ 12 m (in the room temperature sections). There are electron beam-position monitors at every quadrupole and two small horizontal and vertical corrector magnets per cryomodule. Simple electron-beam transport calculations have shown that excellent relative alignment between the quadrupoles and neighboring BPMs is required. In this simple model, quadrupole to BPM misalignment of $\sim$ 5 µm leads to an emittance growth of $\sim$2%. It is important to note however that this is not due to the undulator but to the effect of the quadrupoles and is therefore a general problem for the ILC beam transport. Dispersion-free steering-correction algorithms will be required, similar to those used for the Main Linacs (see Part I Section 4.6).

5.5.2 Target

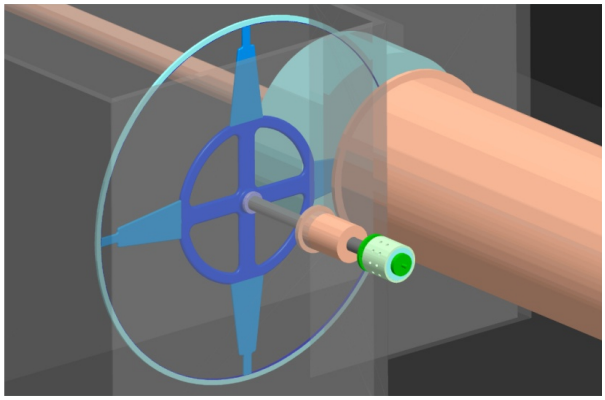

Figure 5.7
Overall target layout.

The positron-production target is a rotating wheel made of titanium alloy (Ti6Al4V). The photon beam from the undulator is incident on the rim of the spinning wheel. The diameter of the wheel is 1 m and the thickness is 0.4 radiation lengths (1.4 cm). During operation the outer edge of the rim moves at 100 m/s. The combination of wheel size and speed offsets radiation damage, heating and the shock-stress in the wheel from the $\sim$ 300 kW photon beam. A picture of the conceptual target layout is shown in Fig. 5.7. The motor is mounted on a single shaft, with a rotating water union to allow cooling water to be fed into the wheel. The beam power is too high to allow a vacuum window downstream of the target. The target wheels sit in a vacuum enclosure at 10^{-8} Torr (needed for NC RF operation), which requires vacuum seals for access to the vacuum chamber. The rotating shaft penetrates the enclosure using one vacuum passthrough. The optical matching device (OMD – see Section 5.5.3), is mounted on the target assembly, and operates at room temperature. The motor driving the target wheel is designed to overcome forces due to eddy currents induced in the wheel by the OMD.

The target-wheel assembly is designed for an operational life of two years. In the event that the target fails during a run, the assembly can be replaced by a new assembly in less than a day using a vertically removable target remote-handling scheme [94].

A series of sensors provides information on the target behavior. An infrared camera tracks temperatures on the wheel, to allow for quick shutdown in case of a cooling failure. Flowmeters monitor cooling water flow in and out of the wheel (to check for leaks), and thermocouples check ingoing and outgoing flow temperature. There is a torque sensor on the shaft, and vibration sensors

on the wheel to monitor mechanical behavior. Finally, the wheel's rotational speed is monitored.

R&D on the target — and in particular on the rotating vacuum seal — remains on-going, and progress is reported in Part I Section 4.3. While the vacuum specification of the seal has been demonstrated, its lifetime and reliability require further R&D.

5.5.3 Optical matching device

The OMD generates a solenoidal magnetic field which peaks in strength at 3.2 T close to the target and falls off to 0.5 T to match the solenoidal field at the entrance of the capture section. The OMD increases the capture efficiency by a factor of 2. The OMD is a normal-conducting pulsed flux concentrator designed and prototyped by LLNL.

The magnetic field of the OMD interacts with the spinning metal of the target to create Eddy currents. The target design must take into account this drag force which produces an increased average heat load, requires a stronger drive motor and possibly causes 5 Hz resonance effects.

5.5.4 Normal-conducting RF accelerator system

Due to the extremely high energy deposition from positrons, electrons, photons and neutrons behind the positron-production target, the 1.3 GHz pre-accelerator uses normal conducting structures up to an energy of 400 MeV. Major challenges are achieving adequate cooling with the high RF and particle-loss heating, and sustaining high accelerating gradients during millisecond-long pulses in a strong magnetic field. The current design contains both standing-wave (SW) and travelling-wave (TW) L-band accelerator structures. The capture region has two 1.27 m SW accelerator sections at 15 MV/m and three 4.3 m TW accelerator sections with 8.5 MV/m accelerating gradient. The electrons are then accelerated from 125–400 MeV in the pre-accelerator region, which contains eight 4.3 m TW sections at 8.5 MV/m accelerating gradient. All accelerator sections are surrounded with 0.5 T solenoids. Figure 5.8 shows the schematic layout [61].

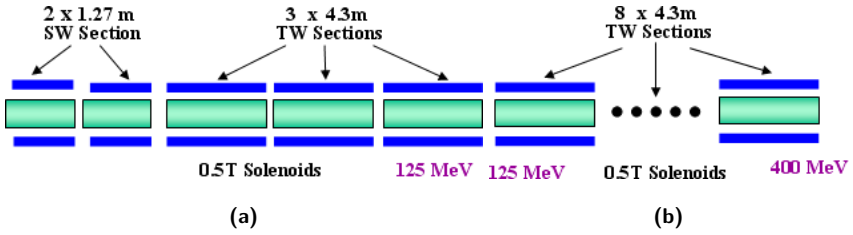

Figure 5.8 Layout of the capture region (a) and pre-accelerator region (b).

5.5.4.1 Standing wave accelerator structure for positron capture

The high-gradient (15 MV/m) positron-capture sections are simple π mode 11 cell SW accelerator structures. The benefits are an effective cooling system, high shunt impedance with larger aperture (60 mm), low RF pulse heating, simplicity and cost efficiency. The mode and amplitude stability under various cooling conditions have been theoretically verified for this type of structure. Figure 5.9 shows a section view of the SW structure; Table 5.4 gives the important RF parameters.

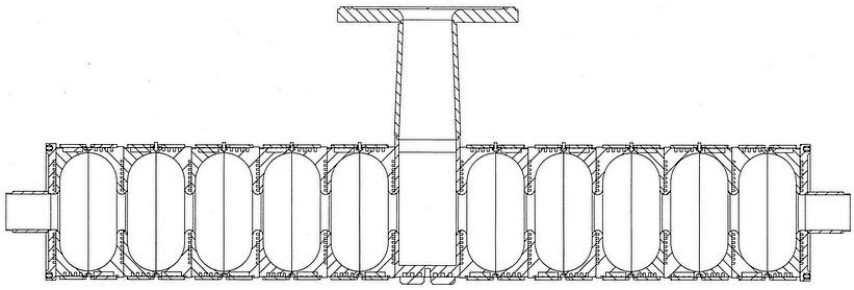

Figure 5.9 11–cell SW Structure.

Table 5.4
Parameters of SW structure.

Structure Type	Simple π Mode
Cell Number	11
Aperture 2a	60 mm
Q	29700
Shunt impedance r	34.3 MΩ/m
E0 (8.6 MW input)	15.2 MV/m

5.5.4.2 Travelling wave accelerator structure for pre-accelerator region

All TW sections are 4.3 m long, $3\pi/4$-mode constant-gradient accelerator structures. The "phase advance per cell" was chosen to optimize the RF efficiency for this large-aperture structure. The benefits are a low pulse heating, easy installation for long solenoids, no need to use circulators for RF reflection protection, apparent simplicity and cost efficiency. Table 5.5 gives the important RF parameters.

Table 5.5
Parameters of TW structure.

Structure Type	TW $3\pi/4$ Mode
Cell Number	50
Aperture 2a	46 mm
Attenuation τ	0.98
Q	24842 – 21676
Group velocity Vg/c	0.62% – 0.14%
Shunt impedance r	48.60 – 39.45 MΩ/m
Filling time $\mathrm{T_f}$	5.3 μs
Power Dissipation	8.2 kW/m
$\mathrm{E_0}$ (10 MW input)	8.5 MV/m

5.5.4.3 RF systems

Each of these accelerator sections has an individual RF station powered by a 1300 MHz, peak-power 10 MW pulsed klystron. The RF station consists of modulator, RF windows, phase shifters, RF loads, directional couplers and low-level RF system. For the SW structures, RF circulators are needed for reflection protection of the power klystrons.

5.5.5 Magnets

The positron-source magnet system has 157 dipoles, 509 quadrupoles and 253 corrector magnets. The large magnet count is a result of the long beamlines connecting the various segments of the source. The magnet designs themselves are quite straightforward. In addition, are used large-aperture DC solenoids, surrounding the L-band capture RF elements, to focus the positrons at low energies. These magnets are normal conducting to withstand the beam loss in the target area. There are also two SC solenoids for spin rotation in the PLTR. The three types of solenoids and their parameters are shown in Table 5.6.

Table 5.6
Solenoid Parameters

Item	Length (m)	ID (cm)	Field Range (kG)	Field, nominal (kG)	N (#)
Short Solenoid	1.3	36	4-8	5	4
Long Solenoid	4.3	31	4-8	5	23
SC Solenoid	2.5	6	52.4	52.4	2

5.5.6 Diagnostics

The Positron source has the normal complement of beamline instrumentation to measure orbit, emittance, charge and energy spread. Specialised diagnostics are designed into systems that are unique to the positron source, e.g. target. The largest channel count comes from the BPM system and the long beamlines. Performance specifications for the diagnostics are in most cases more relaxed than the Main Linac or RTML.

5.5.7 Electron & photon beam dumps

There are 9 beam dumps, 16 variable-aperture collimators, 1 fixed-aperture collimator and 5 stoppers with burn-through monitors in the positron-source system. Three of the beam dumps must absorb sufficiently large beam power that they require designs with water in the path of the beam. The plumbing required to cool and treat the resulting radioactive water dominates the cost of the dump and collimator technical system in this area of the ILC.

There is a tune-up dump upstream of the undulator (downstream of the Main Linac). It is assumed that this dump is only used with a shortened bunch train (100 bunches) at nominal beam parameters and 5 Hz. At the maximum electron-beam energy of 250 GeV, the tune-up dump must absorb 400 kW. This dump also serves as the abort dump for up to a full train of electrons (1.35 MJ) to protect the undulator. The dump is a 40 cm diameter by 250 cm long stainless-steel vessel filled with 10 mm- diameter aluminum balls through which flows approximately 114 liters per minute of water; it is backed by a short length of solid copper cooled on its periphery by water. Personal access needs to be shielded from the dump by 10 cm of steel and 40 cm of concrete. A service cavern is required to house a heat exchanger, pumps and a system to extract and safely dispose of hydrogen and tritium from the water.

A second dump, technically identical is required for tuning the 5 GeV positrons before injection into the damping ring.

The most challenging dump in the positron-production system is the one that absorbs non-interacting undulator photons from the positron-production target. This dump must absorb 300 kW continuously (2×10^{17} photons/sec of 10 MeV average energy produced with a 3 μrad angular spread.) The primary absorber in this case must be water, contained in a vessel with a thin window. Calculations have shown that, at the nominal distance of 500 m from the middle of the undulator to the positron target and the nominal distance of 150 m from the target to the dump, the power density on a 1 mm Ti window is 0.5 kW/cm^2 and the resultant temperature rise after the passage of one bunch train is 425 °C; in the core of the beam, the rise in the water temperature would be 190 °C. The dump is a compact (10 cm diameter by 100 cm long) pressurized (12 bar) water vessel with a Ti window, with a radioactive-water processing system.

The remaining dumps and collimators in the positron system are all based on peripherally cooled solid-metal construction, with the cooling water supplied directly from the accelerator low-conductivity water (LCW) system.

Chapter 6
Damping Rings

6.1 Introduction

The ILC damping rings include one electron and one positron ring, each 3.2 km long, operating at a beam energy of 5 GeV. The two rings are housed in a single tunnel in the central region of the site, with one ring positioned directly above the other. The damping rings must perform three critical functions:

- accept e^- and e^+ beams with large transverse and longitudinal emittances and produce the low-emittance beams required for high-luminosity production;
- damp incoming beam jitter (transverse and longitudinal) and provide highly stable beams for downstream systems;
- Delay bunches from the source to allow feed-forward systems to compensate for pulse-to-pulse variations in parameters such as the bunch charge.

The damping ring system includes the injection and extraction systems, which themselves include sections of transport lines matching to the sources (upstream of the damping rings) and the RTML system (downstream of the damping rings).

This chapter first discusses the parameters and configuration of the damping rings before describing the lattice and various instabilities, most notably the electron-cloud effect, that can affect the beam parameters. The vacuum and RF systems are described, followed by the magnet systems and finally injection and extraction.

6.2 Top-level parameters and configuration

The nominal parameters of injected and extracted beams for both the electron and positron damping rings in the baseline configuration are listed in Table 6.1.

Table 6.1
Nominal parameters of injected and extracted beams for the baseline configuration.

Parameter	Electron Beam	Positron Beam
Train repetition rate [Hz]	5.0	
Main Linac Bunch separation [ns]	554	
Nom. # bunches per train	1312	
Nom. bunch population	2×10^{10}	
Required acceptance[†]		
Norm. betatron amplitude $(a_\mathrm{x} + a_\mathrm{y})_\mathrm{max}$ [m rad]	0.07	
Long. emittance $(\Delta E/E \times \Delta l)_\mathrm{max}$ [% × mm]	0.75×33	
Extraction Parameters:		
Norm. horizontal emittance $\gamma\epsilon_\mathrm{x}$ [μm rad]	5.5	
Norm. vertical emittance $\gamma\epsilon_\mathrm{x}$ [nm rad]	20	
RMS relative energy spread σ_p/p [%]	0.11	
RMS Bunch length σ_z [mm]	6	
Max. allowed transfer jitter $[\sigma_\mathrm{x,y}]$	0.1	

[†] specified for the positron damping ring

The configuration of the damping rings is constrained by the timing scheme of the main linac [95]. In particular, each damping ring must be capable of storing a full bunch train (1312 bunches) and reducing the emittances to the required level within the 200 ms (100 ms in the 10 Hz mode) interval between machine pulses. In addition, the relatively large bunch separation in the main linacs means that the damping rings must be capable of injecting and extracting individual bunches without affecting the emittance or stability of the remaining stored bunches. The exact circumference has been chosen to provide adequate flexibility in the fill pattern allowing different timing configurations in the linac. The bunch trains are separated by gaps to mitigate the fast ion instability in the electron ring.

The superconducting RF system is operated at 650 MHz which is exactly half the linac frequency. To achieve the short damping times necessary to reduce the emittance (by roughly six orders of magnitude in the case of the positron vertical emittance) within the allowed 200 ms interval, superconducting wigglers of total length roughly 100 m are used in each damping ring.

The layout [96] of the damping ring is a racetrack, with long straights [97] to accommodate damping wigglers, RF cavities, phase trombone, injection, extraction, and circumference-adjusting chicane as shown in Fig. 6.1.

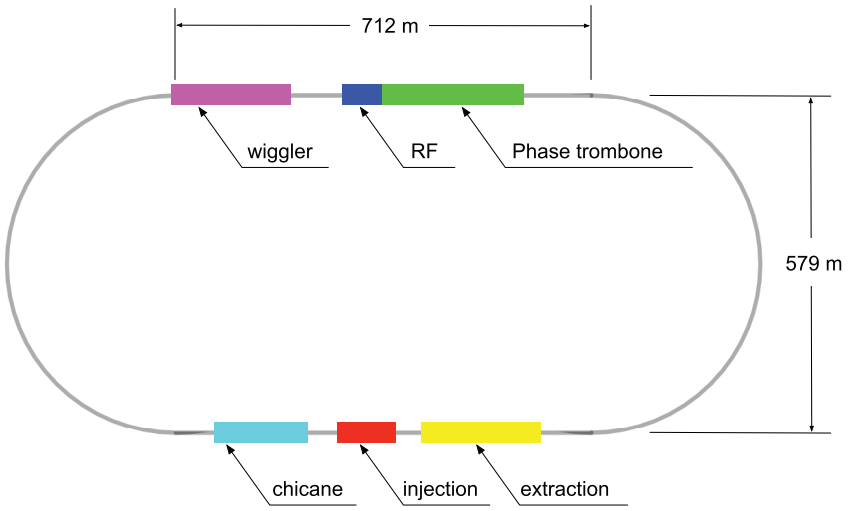

Figure 6.1
Damping-ring layout: the circumference is 3238.7 m; the length of each straight is 710.2 m.

Damping-ring parameters for three ILC operating modes, corresponding to four distinct configurations, have been developed. Two of these operating modes utilize a 5 Hz repetition rate: the low-power baseline with 1312 bunches in each ring; and the high-luminosity upgrade with 2625 bunches. The third operating mode is at 10 Hz and has distinct configurations for the operation of the positron and electron rings. The parameters of these operating modes are summarized in Table 6.2 based on the current version of the DR baseline lattice.

In the 10 Hz operating configuration, the electron linac is operated with alternating pulses, a high-energy pulse for positron production followed by a low energy pulse for collisions. Each damping ring has a pulsed time profile with beam injection/extraction times of 1 ms. In the positron ring, full beam current is stored for 100 ms and then extracted, leaving the ring empty for 100 ms before the next injection cycle. A shorter damping time is necessary to achieve the same extracted vertical emittance in half the nominal storage time.

For the high-luminosity upgrade, twice the number of bunches need to be stored in the DR with 3.1 ns bunch spacing. The doubling of the current in the rings poses a particular concern for the positron DR due to the effects of the electron-cloud instability. In the event that the electron-cloud mitigations that have been recommended [99] are insufficient to achieve the required performance for this configuration, allowance had been made for the installation of a second positron ring in the same

Table 6.2
Damping ring lattice parameters for 5 Hz *Low Power* (baseline) and *High Luminosity* (upgrade) operating modes and 10 Hz repetition rate (baseline) operation [98].

Parameter	5 Hz Mode		10 Hz Mode	
	Low Power	High Lumi	Positrons	Electrons
Circumference [km]	3.238		3.238	
Number of bunches	1312	2625	1312	
Particles per bunch [$\times 10^{10}$]]	2	2	2	
Maximum beam current [mA]	389	779	389	
Transverse damping time τ_x, τ_y [ms]	23.95		12.86	17.5
Longitudinal damping time τ_z [ms]	12.0		6.4	8.7
Bunch length σ_z [mm]	6.02		6.02	6.01
Energy spread σ_E/E [%]	0.11		0.137	0.12
Momentum compaction factor α_p [$\times 10^{-4}$]	3.3		3.3	
Normalized horizontal emittance $\gamma\epsilon_x$[μm]	5.7		6.4	5.6
Horizontal chromaticity ξ_x	−51.3		−50.9	−51.3
Vertical chromaticity ξ_y	−43.3		−44.1	−43.3
Wiggler Field [T]	1.51		2.16	1.81
Number of Wigglers	54		54	
Energy loss/turn [MeV]	4.5		8.4	6.19
RF Specifications:				
Frequency [MHz]	650		650	
Number of cavities	10†	12	12	
Total voltage [MV]	14.0		22.0	17.9
Voltage per cavity [MV]	1.40	1.17	1.83	1.49
RF synchronous phase [°]	18.5		21.9	20.3
Power per RF coupler [kW]‡	176	294	272	200

† The baseline RF deployment for positrons is 12 cavities to support 5 and 10 Hz modes.
‡ Power/coupler computed as (Max. Current) × (E loss/turn)/(No. cavities).

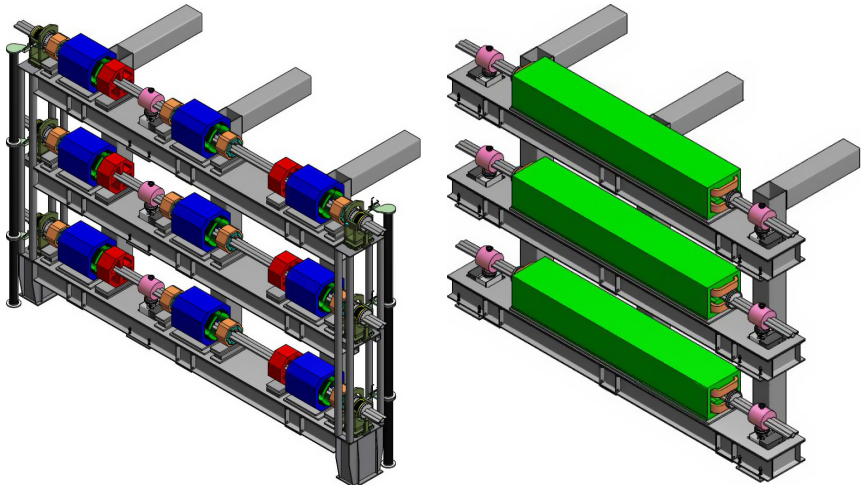

(a) **(b)**

Figure 6.2
Damping-ring arc magnet layout with positron ring at the bottom and electron ring directly above. A second positron ring would be placed above the electron ring if required: (a) quadrupole section layout and (b) dipole section layout.

tunnel. In this scenario, the two positron rings would both operate with the baseline parameters. The third ring would be placed above the electron ring as indicated in Fig. 6.2a and Fig. 6.2b.

The superconducting damping wigglers [100] are based on the CESR-c design, with 14 poles and 30 cm period. The peak field of the 54 1.875 m long wigglers is 1.51 T for a 24 ms damping time in the 5 Hz mode and 2.16 T for a 13 ms damping time for 10 Hz operation. The horizontal emittance is near 0.5 nm rad over the range of relevant wiggler fields. There are 10 single-cell 650 MHz superconducting cavities in the baseline configuration. For 5 Hz operation, 8 of these cavities can provide a total of 14 MV for a 6 mm bunch length, even in the event of a single klystron failure. For 10 Hz operation, the number of cavities is increased to 12 and the accelerating voltage to 22 MV for the same 6 mm bunch length. A phase trombone provides for adjustment of betatron tune and a chicane for small variations of the circumference.

6.3 Lattice description

Each arc in the DR consists of 75 cells [101], each with one focusing and two defocusing quadrupoles placed symmetrically about a single 3 m bend. Focusing and defocusing sextupoles are located adjacent to the corresponding quadrupoles. Each cell contains one vertical, one horizontal, and one skew quad corrector as well as two beam-position monitors adjacent to the defocusing sextupoles, as shown in Fig. 6.3. Dispersion suppressors, at the ends of the arc, match the finite dispersion in the arcs to zero dispersion in the straights. The dispersion suppressor beam line includes two dipole bending magnets and seven quadrupoles. There is a skew quad corrector at each of the two dipoles.

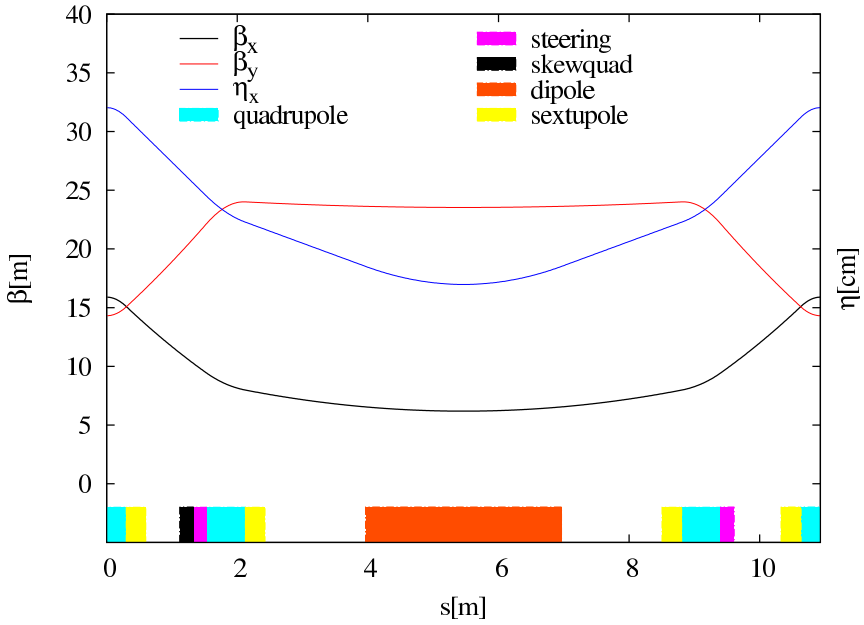

Figure 6.3
Arc cell. The cell boundaries are at the midpoint of the focusing quadrupole. Each cell contains a vertical and horizontal dipole corrector, a skew quad corrector in each cell, and two beam position monitors adjacent to the defocusing sextupoles.

Acceptable values of the momentum compaction are bounded from below by the single-bunch instability threshold, and from above by the RF voltage required to achieve the requisite 6 mm bunch length. In practice, the dynamic aperture shrinks as the focusing strength is increased to reduce momentum compaction. The design has nonlinear aperture adequate to accept the entire phase space of the injected positrons, and consistent with the specified horizontal emittance. The resulting momentum compaction is 3.3×10^{-4}. The TME-style arc cell gives somewhat better dynamic aperture than the FODO cell tuned to give comparable emittance and with the same 3 m dipole.

The RF-Wiggler straight provides space for 12 RF cavities at 650 MHz (as well as open space for up to 4 additional cavities) and 54 wigglers (with open space for 6 more). The phase trombone is also located in this straight.

The phase trombone consists of five cells, each constructed from six equally spaced, alternating-gradient quadrupoles. The overall length of the phase trombone is 339 m. The range of the phase trombone is a full betatron wavelength in both horizontal and vertical. There is a single-skew quadrupole corrector in each of the five cells.

The machine circumference is adjusted by varying the field of the chicane dipoles. A 4.4 mm increase in path length is accompanied by an increase in horizontal emittance of about 3 %.

There are horizontal and vertical dipole correctors and a beam-position monitor adjacent to each quadrupole in the straights. The lattice functions for the ring are shown in Fig. 6.4.

The injection is located upstream of the centre of the long injection/extraction straight, and the extraction downstream of the centre as shown in Fig. 6.1.

The injection line grazes the outside of a quadrupole, and is deflected horizontally by a pair of septum bend magnets so the trajectory passes inside the aperture of the next quadrupole. This

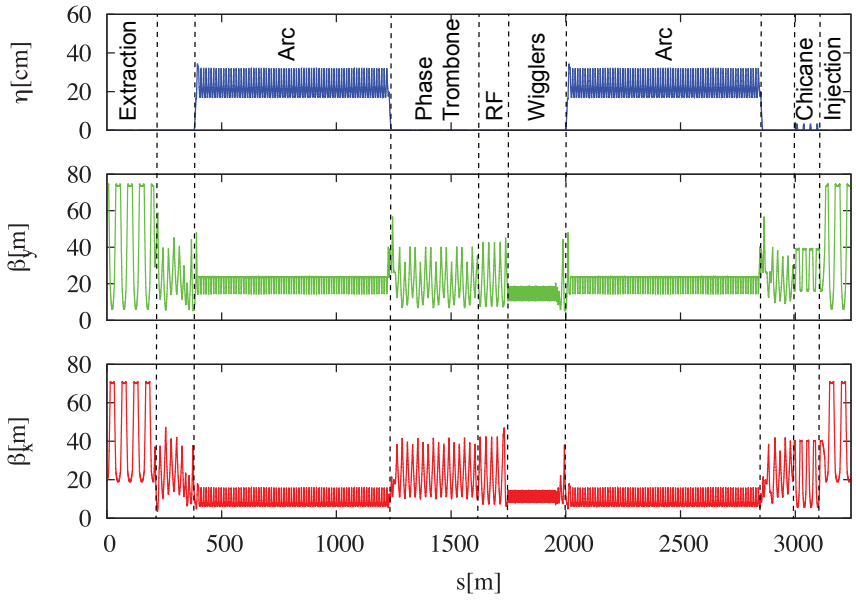

Figure 6.4
Damping ring lattice functions with the major functional sections (injection, extraction arcs, RF, wigglers, circumference chicane, and phase trombone) labelled.

horizontally defocusing quadrupole makes the trajectory nearly parallel to the stored orbit. At 90° of betatron phase downstream from the septa, where the injection trajectory crosses the stored orbit, a set of kickers deflects the single injected bunch onto the stored orbit.

Extraction is accomplished with a similar set of kickers that deflects a single damped bunch horizontally. A horizontally defocusing quadrupole increases the deflection and at 90° of betatron phase downstream of the kickers, the bunch passes through the bending fields of a pair of septum magnets. These deflect the trajectory further horizontally, so it passes outside of the next focusing quadrupole and into the extraction-line optics. The stored orbit is located in the nominally field-free region of the septum magnets and is not significantly affected.

6.4 Beam Dynamics

6.4.1 Emittance Tuning

An emittance-tuning procedure based on that developed at CESRTA [102] has been used to compensate for misalignments and field errors in the DR design. The procedure has three basic steps:

1. Measure and correct the closed orbit errors using all BPMs and all dipole correctors;
2. Measure betatron phase and coupling by resonant excitation and correct errors, using all quadrupoles and skew-quadrupole correctors;
3. Repeat measurement of orbit and coupling, and measure dispersion by resonant excitation of the synchrotron motion, and then fit simultaneously using vertical dipole correctors and skew quadrupoles.

The tuning algorithm depends for its effectiveness on the accuracy of the beam-position monitors. The BPM specification is given in Table 6.3. The alignment tolerances are given in Table 6.3, as are the multipole errors measured at SLAC for the SPEAR and PEPII dipoles, quadrupoles and sextupoles [103]. The results of the emittance-tuning procedure for 100 lattices with a randomly chosen Gaussian distribution of multipole and alignment errors are summarised in Fig. 6.5a and Fig. 6.5b. The tuning procedure consistently achieves the specified geometric vertical emittance of 2 pm rad.

Table 6.3
BPM and magnet alignment tolerances.

Parameter	RMS
BPM Differential resolution†	2 μm
BPM Absolute resolution	100 μm
BPM Tilt	10 mrad
BPM differential button gain	1%
Quad & Sextupole Offset (H&V)	50 μm
Quadrupole Tilt	100 μrad
Dipole Roll	100 μrad
Wiggler vertical Offset	200 μm
Wiggler - Roll	200 μrad

† Reproducibility of single pass measurement

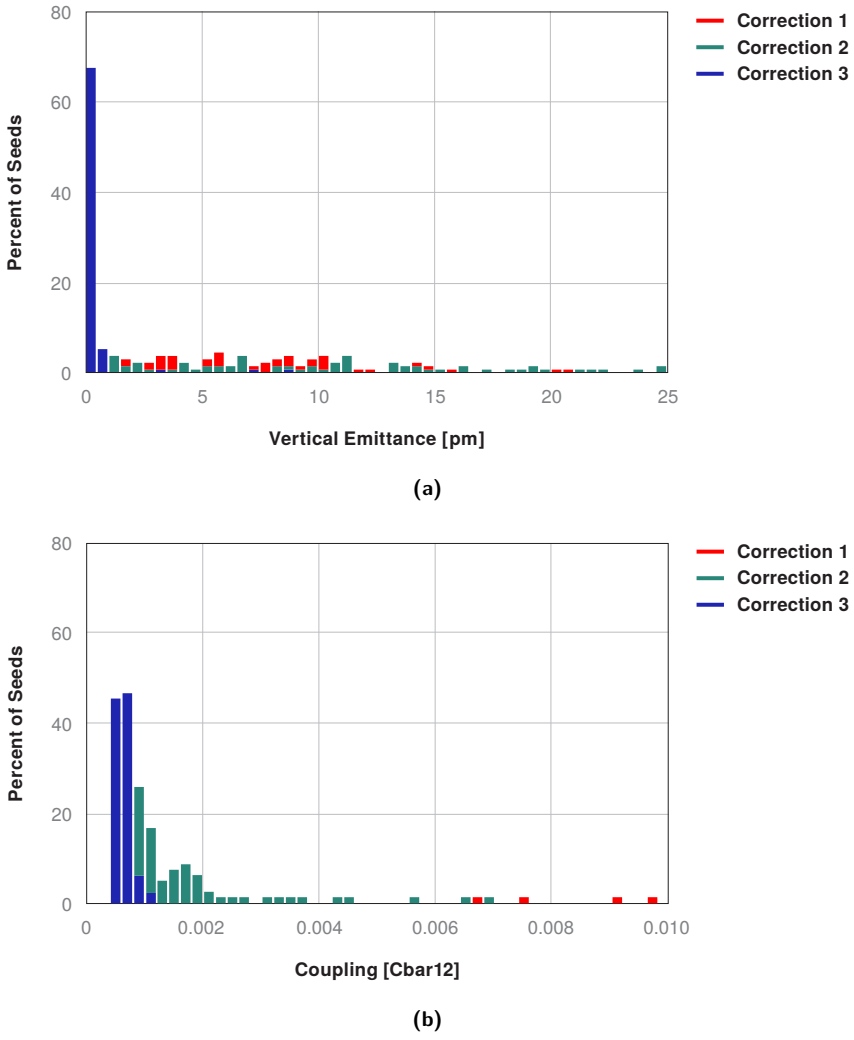

Figure 6.5
Histogram of the (a) vertical emittance and (b) rms coupling ($\overline{C}_{12}$) at the conclusion of each step in the low-emittance tuning procedure for 100 lattice files with randomly chosen misalignments and multipole errors.

6.4.2 Dynamic aperture

The specification for the phase space distribution of the injected positron bunch is an amplitude of $A_x + A_y \leq 0.07$ m rad (normalized) and an energy spread of $\Delta E/E \leq 0.75\%$. The dynamic aperture for a lattice with the specified misalignments and multipole errors, and wiggler nonlinearities including those due to end effects and finite pole width, is shown in Fig. 6.6. In order to evaluate the effect of the wiggler nonlinearities on dynamic aperture, the wiggler field is computed with a finite-element code (Vector Fields), and fit to an analytic form as a Fourier expansion that automatically satisfies Maxwell's equations. A symplectic tracking algorithm ensures that the phase space is not distorted by numerical noise. None of the injected particles are lost in these simulations.

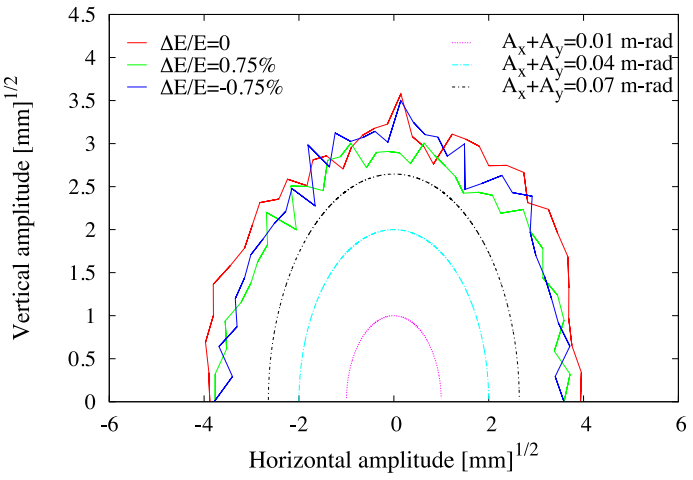

Figure 6.6
Dynamic aperture including multipoles, wiggler nonlinearities and magnet misalignments. Defined as the largest stable amplitude after tracking 1000 turns.

6.4.3 Collective Effects

The many collective effects that may affect beam quality in the damping rings were examined during the original baseline configuration studies [104]. These include impedance-driven instabilities, intrabeam scattering, space-charge effects, electron cloud effects in the positron ring and ion effects in the electron ring. The beam's Touschek lifetime is expected to be much longer than the nominal 200 ms spent in the DR, however, obtaining suitable lifetimes for commissioning and tuning will be important. The largest sources of emittance dilution were found to be the Electron Cloud (EC) instability in the positron DR and the Fast Ion Instability (FII) in the electron DR.

6.4.4 Electron Cloud

Electron Cloud (EC) induced instabilities and emittance growth are critical issues for the positron damping ring. The electron cloud develops quickly as photons striking the vacuum chamber wall knock out photoelectrons that are then accelerated by the beam, gain energy, and strike the chamber again, producing secondary electrons. The peak secondary electron yield (SEY) of typical vacuum chamber materials is >1, even after surface treatment, leading to electron amplification of the cascade. Once the cloud is present, coupling between the electrons and the circulating beam can cause a single-bunch (head-tail) instability and incoherent tune spreads that may lead to increased emittance, beam oscillations, or even beam losses. The threshold electron cloud density, beyond which there is emittance growth and the onset of instabilities, has been determined using measurements at CesrTA and calculations with the simulation code CMAD. The electron density is computed with codes that simulate cloud growth for various bunch configurations and vacuum chamber geometries and surface properties.

The build-up of the EC in the DR vacuum chambers has been modeled using the EC mitigations specified by the ILC Electron Cloud Working Group [99] (see Table 6.4). The simulations employ the vacuum system conceptual design described in Section 6.5.

Table 6.4
EC mitigations specified for the positron DR.

Magnetic Region	Primary Mitigation	Secondary Mitigation
Drift	TiN Coating	Solenoid Windings
Dipole	Grooves with TiN Coating	Antechamber
Wiggler	Clearing Electrodes	Antechamber
Quadrupole	TiN Coating	—

6.4.4.1 Photon Transport Model

The distribution of absorption sites for synchrotron radiation photon around the ring can be used to predict the sources of the photoelectrons which seed the electron cloud. This distribution has been computed for the DR lattice using a newly developed photon-tracking simulation code, Synrad3D [105]. This code computes the synchrotron-radiation photons per electron generated by a beam circulating in the magnetic lattice, and simulates in three dimensions the propagation of the photons as they scatter off, or are absorbed by, the vacuum chamber. The design vacuum-chamber geometry (see Section 6.5), including details such as antechambers and photon stops, is used in the calculation. Both specular and diffuse photon scattering are included in the simulation. For the scattering calculation, the surface material is approximated as aluminum with a thin carbon coating, and the surface parameters are representative of a typical technical vacuum chamber, namely an rms roughness of ∼100 nm and a correlation length of ∼5000 nm.

6.4.4.2 EC Buildup

The EC buildup in each of the principal magnetic field regions of the damping ring has been modeled. In the dipole field regions, the modeling code POSINST [106] was employed. Simulations with both POSINST and ECLOUD [107] were carried out in the quadrupole, sextupole and drift regions. The CLOUDLAND [108] package was used for simulations in the wiggler region.

Simulations of the EC buildup in the dipole chambers were based on:

- SEY model parameters for a TiN surface based on the most recent data obtained at CesrTA;
- Photon distributions around the vacuum chambers based on Synrad3d modeling of the ILC DR vacuum system;
- A quantum efficiency of 0.05, independent of photon energy and incident angle.

The SEY model corresponding to the above-mentioned fits yields a peak SEY value of 0.94 at an incident electron energy of 296 eV. In addition to this, the simulations have also been run with the SEY set to 0 (meaning that any electron hitting the chamber walls gets absorbed with unit probability) in order to isolate the contribution to the EC density N_e from photoemission. The cloud densities in the dipoles are expected to be between these two limits since the simulation does not directly model the reduction in the effective SEY from having grooved top and bottom chamber surfaces.

Cloud densities averaged over the full vacuum chamber as well as those averaged over a $20\sigma_\mathrm{x} \times 20\sigma_\mathrm{y}$ elliptical cross-sectional area were calculated. The modelling statistical uncertainties are at the level of less than 30 %.

Simulations of the EC buildup in the quadrupoles and sextupoles in the arc and wiggler regions and in the drift regions of the wiggler sections for the DR lattice utilized the same photoelectron and SEY model parameters as were used for the dipole region. Representative field strengths of 10 T/m (70 $\mathrm{T/m^2}$)were used for the quadrupoles (sextupoles). Trapping effects were evident in the beam-pipe-averaged cloud densities, which had not yet reached equilibrium during the eight trains simulated, but since the trapping does not occur in the beam region, the 20σ densities prior to the passage of each bunch were stable after just a couple of trains.

The simulations for the field-free regions were repeated with a solenoidal magnetic field of 40 G, as recommended during the ECLOUD10 workshop [99]. Such a field was shown to reduce the cloud buildup in the beam region to negligible levels.

Table 6.5 shows the 20σ EC density estimates obtained from the above simulations.

The EC buildup in the wiggler is simulated using the CLOUDLAND code [109]. The ring length occupied by wigglers is 118 m. The simulation assumes a peak SEY of 1.2 for the copper surface of a wiggler chamber. The energy at the peak SEY is 250 eV. The photon flux used in the simulation is

Table 6.5
POSINST and ECLOUD modelling results for the 20σ density estimates, N_e (10^{11} m^{-3}), just prior to each bunch passage with the baseline lattice.

	Field-free	Field Free w/solenoid	Dipole	Quad	Sext
Arc Region	2.5	0	0.4	1.6	1.35
Wiggler Region	40	0		12	

0.198 photon/m/positron with a uniform azimuth distribution. The quantum efficiency is 0.1 and the beam size $\sigma_x/\sigma_y = 80\mu/5.5\mu$. The peak wiggler field for the simulation is set to 2.1 T. The beam chamber of the wiggler section includes an antechamber with 1 cm vertical aperture. A round chamber with diameter of 46 mm is used, which is a good approximation since most electrons accumulate near the horizontal centre due to multipacting. The CLOUDLAND calculation shows that a beam with bunch population of 2×10^{10} and bunch spacing of 6 ns can excite strong multiplication near the horizontal centre. The peak electron density seen by the last bunch along the bunch train is about $1.2 \times 10^{13}\mathrm{m}^{-3}$. However, the wiggler vacuum design includes clearing electrodes. Application of a modest positive voltage (of a few hundred volts) has been shown to reduce the electron density near the beam by more than three orders of magnitude, ie, to levels well below those at which beam instabilities are expected to develop.

6.4.4.3 EC Instability

The above estimates of cloud density place an upper limit on the ring-averaged density of about $4 \times 10^{10}\mathrm{m}^{-3}$, about a factor of three below the expected single bunch instability threshold [110]. Thus operation in the baseline configuration is expected to have negligible emittance dilution from the EC. This operating margin should also minimize the possibility of any adverse impacts from sub-threshold emittance growth on the positron beam. For the high-luminosity upgrade, a second positron ring may be added if insufficient operating margin remains with a single ring.

6.4.5 Fast Ion Instability

A significant concern for the electron damping ring is the fast ion instability (FII). In contrast to the more familiar ion-trapping effect, where ions oscillate stably for long periods in the potential well of the stored beam, the fast ion instability is associated with ions created in the beam path by interaction with the circulating beam during a single turn. Ions created at the head of the bunch train move slowly, and remain in the beam path, influencing the motion of subsequent bunches. The resultant ion-induced beam instabilities and tune shifts are critical issues due to the ultra-low vertical emittance. A low base vacuum pressure at the 1×10^{-7}Pa level is essential to reduce the number of ions formed. To mitigate bunch motion, there are also bunch-by-bunch feedback systems with a damping time of ≈0.1 ms.

To reduce further the core ion density, short gaps are introduced into the electron-beam bunch train by omitting a number of successive bunches. The use of such *mini-gaps* in the train significantly mitigates the FII by reducing the core ion density and by inducing tune variation along the train. The bunch patterns selected for the DR provide these mini-gaps for any of the proposed main-linac train structures.

The dependence of FII growth rates on gaps in the bunch trains is evident in simulations. Two sets of simulations have been carried out to study this effect in the DR. The simplest meaningful simulation is based on a weak strong model. The circulating bunch is represented as a single macro particle, and is sensitive only to centroid dipole motion. The ion cloud consists of multiple macro particles, that are free to move transversely in the vacuum chamber. This method can be used to characterise the growth of the vertical oscillation amplitude [111].

For a pressure of 1×10^{-7}Pa with CO as the only gas species, and a single long train of 1312 bunches, with 2×10^{10} particles/bunch and $4\lambda_{\mathrm{RF}}$ bunch spacing, the vertical amplitude versus turn

is shown in Fig. 6.7a. The oscillation amplitude is greater than the beam size in only 6 turns.

If the 1312 bunches are distributed into 41 trains of 32 bunches, with a train gap of $43\lambda_{\mathrm{RF}}$, then the growth time is 26 turns as shown in Fig. 6.7b.

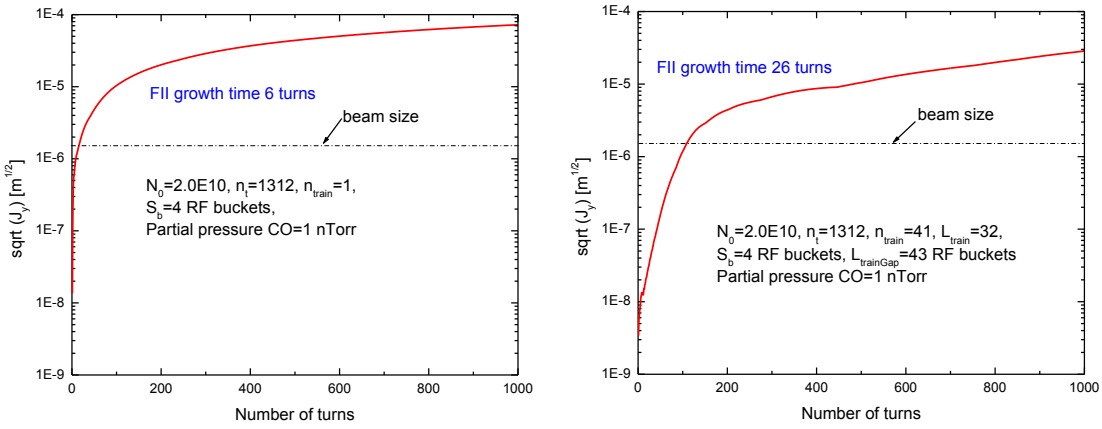

(a) **(b)**

Figure 6.7. Simulated vertical amplitude vs number of turns for (a) 1312 bunches in a single train at 1×10^{-7}Pa CO and (b) for 41 trains of 32 bunches.

A second simulation [112] has been carried out using vacuum parameters based on those observed at SPEAR3 (0.5×10^{-7} Pa pressure with a composition of: 48 % H_2 , 5 % CH_4, 16 % H_2O, 14 % CO, and 17 % CO_2). The inclusion of multiple gas species is expected to contribute some Landau damping due to the spread in ion frequencies. A uniform pressure along the ring is assumed and the bunch patterns used in the baseline DR configuration as well as in the high-luminosity upgrade were explored. The electron bunch was divided into roughly 11 slices to allow for the possibility of a more complex single-bunch instability than the simple dipole motion in the simulation described above [113]. The code has been benchmarked with a SPEAR3 experiment [114] where there is a good agreement.

Modeling of two possible bunch patterns in the DR gives the fastest exponential growth times of 56 turns and 84 turns (see Table 6.1) during operation in the baseline configuration and 37 turns for the high-luminosity configuration. Figure 6.8 shows the unstable modes within the first of these bunch patterns. A broad-band spectrum is exhibited.

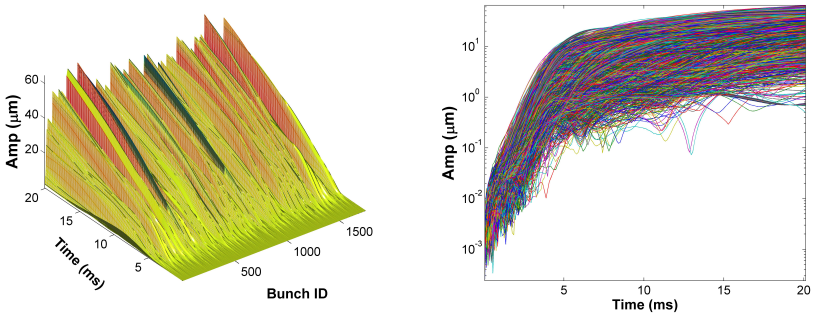

(a) **(b)**

Figure 6.8 Simulated vertical amplitude versus time for the bunch pattern with the shortest growth time. The different lines in the plots correspond to individual bunches. The vertical instability growth time is 56 turns. Note (b) uses a logarithmic scale.

The dependence on pressure and bunch spacing in the two simulations is consistent and growth rates are comparable. The radiation damping time is approximately 2000 turns so feedback is essential to stabilize the beam-ion interaction. Experience at KEK-B and DAΦNE suggests that feedback systems with damping times of order 20 turns, which can suppress the FII, are practical [115].

6.5 Vacuum System

The vacuum system conceptual design incorporates EC-mitigation techniques enumerated in Table 6.4, and targets the vacuum performance required to suppress the FII in the electron ring as described in Section 6.4.5. The present conceptual design [116] draws on previous design work [117–119] and incorporates inputs from the lattice designers, magnet engineers, and electron-cloud-dynamics simulation group.

Dipole chambers, shown in Fig. 6.9a, incorporate three EC mitigation techniques: antechambers with radially sloped outside walls are used to minimize scattered photons entering the main beam aperture; a titanium nitride (TiN) coating is applied to the inside surface of the chamber to reduce secondary electron yield (SEY); and grooves on the top and bottom of the vacuum chamber further reduce the number of secondary electrons that enter the central region of the vacuum chamber near the beam [109]. The inside of the antechamber contains non-evaporable Getter (NEG) strips to provide distributed pumping. Explosion bonded transition pieces are used on the ends of the chambers to allow the use of stainless steel flanges.

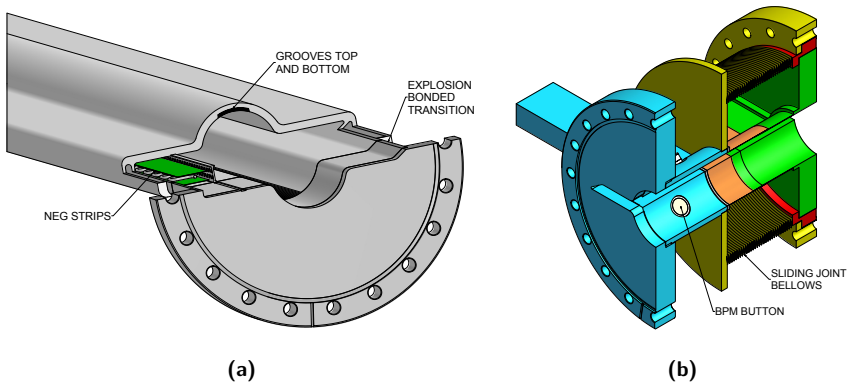

Figure 6.9
(a) Dipole Chamber with grooved top and bottom surfaces, radially inside antechamber with NEG strips, and radially outside antechamber with sloped wall. (b) BPM and sliding joint assembly. [116].

The remainder of an arc cell consists of two short drift chambers on either side of the dipole, and one chamber extending through three quadrupoles, four sextupoles, and three corrector magnets. These chambers have the same profiles and TiN coating as the dipole chamber, but without the grooves on top and bottom. BPM assemblies as shown in Fig. 6.9b are located at each end of the chamber extending through the quadrupoles.

The wiggler-region vacuum chambers shown in Fig. 6.10a are made from copper to provide good thermal conductivity in this high-power region. The copper also minimizes the rate of scattered photons that escape the vacuum chamber to deposit energy into the cold mass and coils of the superconducting wigglers. The wigglers are grouped in pairs and a single vacuum chamber runs through two wigglers as well as the quadrupole magnet between them. The long vacuum chamber traversing each wiggler pair has a 46 mm beam aperture and 20 mm tall antechambers, including in the quadrupole. The choice of 20 mm-tall antechambers was based on photon-tracking simulation results in Synrad3D [109]. NEG Strips are recessed into the upper wall of the antechambers to act as distributed pumping and are shielded from beam-induced heating by means of a perforated aluminum strip. Most synchrotron radiation (SR) passes through the wiggler antechambers and is trapped in the photon stops located at the end of each cell. A tungsten clearing electrode is deposited via thermal spray on the bottom of the chamber as the primary EC mitigation technique [120, 121].

The other drift and quadrupole chambers in the wiggler section are copper chambers with TiN coating. They also have a 46 mm aperture and incorporate 20 mm tall antechambers to match the wiggler chambers and minimize impedance issues. The design is based on those previously specified for an earlier lattice variant [117, 118]. These chambers have gradually sloping, grooved antechambers are shown in Fig. 6.10b to dilute power density striking the photon stop. The gap between the sloping

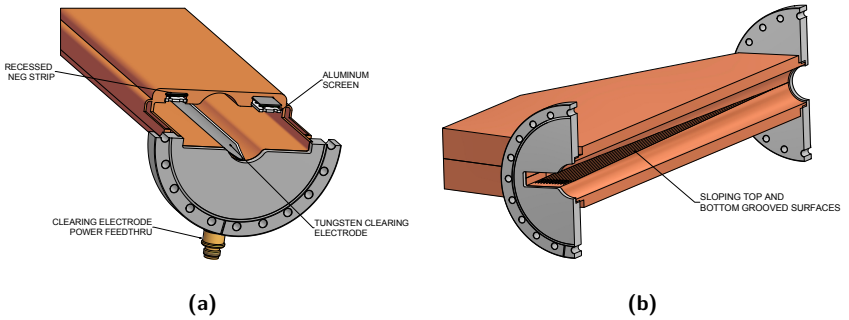

Figure 6.10
(a) Wiggler vacuum chamber with clearing electrode and 20 mm tall antechambers with recessed NEG strips. (b) Wiggler section photon stop showing sloping and grooved photon-absorbing walls [116].

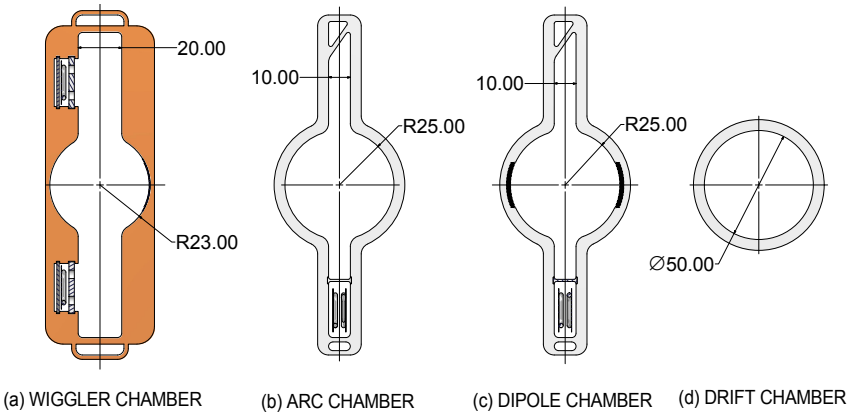

Figure 6.11
Side-by-side comparison of ILC DR vacuum chamber profiles. Dimensions are in millimeters [116].

surfaces opens to antechambers pumped with an ion pump and Titanium sublimation pumps through ducts. An additional photon stop is required at the first bending magnet of the arc after the wiggler straight to intercept the forward SR component.

The remaining straight sections have simple round aluminum vacuum chambers with 50 mm aperture and TiN coating as shown Fig. 6.11. Aluminum-stainless-steel explosion-bonded transitions on the ends allow welding to stainless steel flanges. At the ends of the straight drift sections, tapered chambers match to the sections with antechambers.

Solenoid windings cover all accessible drift sections throughout the DRs to further reduce the number of secondary electrons approaching the beam axis.

Beam-position monitors (BPMs) are located near the majority of quadrupoles in the DR. There are no BPMs near the quadrupole trapped between the wiggler pairs due to lack of space, nor is there a BPM near the centre quadrupole in each arc cell. The BPM near the central quad in the arc cell is omitted because simulations indicate that, with the support and alignment scheme of the arc cell magnets, one BPM at the beginning and end of the magnet girder is sufficient [122]. The BPM blocks are paired with a sliding joint on one side as shown in Fig. 6.9b to allow them and the chamber they are connected to through the quadrupole to float. This maintains the absolute position of the BPM as steady as possible and allows movement of the BPM to be monitored. The sliding joint also allows for expansion and contraction of the surrounding vacuum chambers.

A sufficient number of ultra-high vacuum pumps, both localized (lumped) and distributed, are installed in the vacuum system to maintain the required average gas pressure ($\sim 10^{-9}$ torr) at the design beam current. The installed pumping system has enough pumping speed and capacity to allow vacuum system conditioning in a reasonably short duration during the initial accelerator commissioning, and after installation of new vacuum components for upgrades and/or repairs. Typical pumps are sputter-ion pumps (noble-diode style), non-evaporable Getters (NEGs) and titanium sublimation pumps (TiSPs). As illustrated for the dipole and wiggler chambers, NEG strips are inserted into the ante-chambers to provide distributed pumping. The final design must provide adequate pumping speed and capacity to handle the SR-induced gas load. Lumped ion pumps are installed periodically,

with a typical spacing of 5 m. These ion pumps assist initial pump down and beam conditioning of the DR vacuum chambers, and handle any non-Getterable gases (such as CH4 and trace Ar) in the vacuum system.

The vacuum system is divided into sectors by RF-shielded gate valves to facilitate staged installation, upgrades, maintenance, and repairs. A typical length for each vacuum sector is 50 m. Cold-cathode ion gauges (CCGs) are installed periodically throughout the vacuum system to monitor performance and for trouble shooting. Each vacuum sector is equipped with at least one residual gas analyzer (RGA). Numerous thermocouples monitor local temperatures of vacuum components. Monitoring and interlock functions are integrated into the central control system.

6.6 RF systems

The damping-ring RF frequency of 650 MHz has a simple relationship with the main linac RF (1.3 GHz) to accommodate varying bunch patterns. While high-power 650 MHz RF sources are not commercially available, several klystron manufacturers can develop them by modifying 500 MHz klystrons of equivalent power level. Similarly, the RF cavity units can be designed by scaling from existing 500 MHz superconducting module designs currently in operation at CESR, KEK, [123–125] and elsewhere. New designs are required for the input coupler because the power handling capability must be kept at a level of about 300 kW CW, as well as for the HOM dampers and cryostats. The parameters presented in Table 6.6 are scaled from the 500 MHz units developed by industry and being operated in various laboratories. The RF-cryomodules are 3.5 m in length and 1.5 m in diameter.

Table 6.6
RF system parameters for the 3 different operating configurations [98].

Parameter	Unit	Nominal 5 Hz	10 Hz mode e^+ ring	Luminosity upgrade
Frequency	MHz		650	
Total RF voltage	MV	14	22	14
Overvoltage factor		2.94	2.49	2.94
Active cavity length	m		0.23	
R/Q	Ω		89	
Q_0 at operating gradient	10^9	1	0.6	1
Number of cavities/ring		10	12	12
Cavity RF voltage	MV	1.4	1.83	1.17
Cavity average gradient	MV/m	6.1	8.0	5.1
Beam power per cavity	kW	185.5	287	309
Input coupler $Q_{\rm ext}$			68×10^3	
Cavity tuning		stationary	fixed	stationary
RF reflected power	%	8.0	11.4	2.6
HOM Power	%		5	
Total RF power	MW	2.00	3.83	3.80
Number of klystrons/ring		5	6	6
Klystron peak power (10% overhead)	kW	441	703	698
Operating temperature	K		4.5	
RF cryogenic losses per cavity	W	15	50	15
Number of SC modules per ring		10	12	12
Static cryo losses at 4.5 K	W		30	
Total cryo losses per ring	W	450	960	540

6.6.1 Baseline

For the nominal baseline configuration, a beam current of 0.4 A is stored in 1312 bunches. The value of the RF voltage is chosen in order to achieve a 6 mm bunch length. The beam power and the total RF voltage for each ring is shared among 10 superconducting cavities in 5 RF stations. The 10 modules ensure adequate energy and beam-power margin in case of an RF-station fault, and permit continued operation at full performance with the 8 remaining units by increasing their RF output power. The cavities of the faulty station can still contribute to the bunch longitudinal focusing in this case, being passively excited by the 650 MHz spectral harmonic of beam current. The stations are

located in the RF straight section, roughly 100 m long, upstream of the wigglers. The section has space for up to 16 cavities. Waveguides connect pairs of cavities to klystrons housed in a centrally located alcove which has access shafts to the surface. Each distribution system has magic-tees for power splitting and circulators for protecting the klystron against reflected power.

The possibility to add 2nd harmonic cavities in order to increase the flexibility of the system and reduce the cost for the nominal baseline configuration has been considered. This would require a new design to adapt the cells of the 1.3 GHz cavities as 2nd harmonic cavities. The beam is powered only through the fundamental cavities and the harmonic cavities are used to control the bunch length, allowing the same bunch length with less fundamental voltage or a shorter bunch with the same voltage.

6.6.2 10 Hz operation

For the positron damping ring in the 10 Hz operating mode the radiated energy is doubled to achieve the required shorter damping time. As shown in Table 6.6, this requires twice the beam power and two more RF cavities. In this configuration the damping ring has a pulsed time profile with beam injection/extraction times of 1 ms. Full beam current is stored for 100 ms and then extracted, the ring is then empty for the next 100 ms before the next injection cycle. This is a concern for the operation of the superconducting cavities whose tuning actuators have limited speed and excursion, so that it is quite difficult to follow, in real time, the rapidly changing beam-loading conditions. The simplest approach to overcome this difficulty requires keeping the cavities tuned at a certain fixed resonant frequency. The RF system can be optimized for this operating mode [126]. The main RF parameters for the positron ring are listed in Table 6.6. It is assumed that both rings will be operated identically in the 10 Hz mode, keeping the cavities tuned at a fixed resonant frequency. The only difference between the electron and positron ring is that the damping time required for the electrons is longer and the power required for the RF system is lower: 10 cavities assure adequate beam power.

6.6.3 Luminosity upgrade

For the luminosity upgrade there are 2625 bunches per main linac pulse, corresponding to a 0.8 A damping-ring current. The beam power required for the RF system is doubled with respect to nominal and 12 RF cavities are needed in order to keep the power per cavity at a level of about 300 kW. The parameters are listed in Table 6.6.

As with the baseline operation, in case of the failure of one klystron the system can be retuned to exploit the two unpowered cavities as passive, beam-excited devices, providing the same RF gradient across the bunch. The power to restore the beam losses will be provided by the ten active cavities. To guarantee a sufficient power margin to operate in the various configurations, including with a klystron fault, the maximum klystron power is 0.8 MW CW.

6.7 Magnets and Power Supplies

6.7.1 Superconducting Wigglers

The superferric wiggler design [100] provides the necessary operating flexibility over the range of peak fields required for the various DR operating modes, while maintaining the requisite field quality. Table 6.7 compares the parameters of the CESR-c wiggler, the ILC RDR wiggler and the recent redesign necessitated by the 10 Hz operating mode. The ten central poles of the magnet, each of 15 cm length, utilize coils of 660-turns carrying 93 kA. The poles at each end taper successively to 3/4- and 1/2-length as was used in the CESR-c design. The end poles have been simplified, omitting trim coils used to tune the second integral. Instead, the number of turns in the end pole coil has been adjusted to limit residual horizontal orbit displacement for 5 GeV electrons incident on axis to about 50 µm. There are 158 turns in the end-pole coils in this design. Each wiggler is powered by an individual AC-to-DC power supply.

Table 6.7
Superferric Wiggler Comparison

Parameter	Unit	CESR-c	ILC RDR	ILC TDR
Peak Field	T	2.10	1.67	2.16
No. Poles		8	14	14
Length	m	1.3	2.5	1.875
Period	m	0.40	0.40	0.30
Pole Width	cm	23.8	23.8	23.8
Pole Gap	cm	7.6	7.6	7.6
$\Delta B/B\|_{x=10\,\mathrm{mm}}$	%	0.0077	0.0077	0.06
Coil Current	A	141	112	141
Beam Energy	GeV	1.5–2.5	5	5

The superconducting damping wigglers are 4.5 K devices with static heat loads of 2 W/m or less, based on CESR-c experience [100]. To avoid a significant dynamic heat load, care must be taken to minimize the scattered synchrotron radiation that reaches the cold mass. The wigglers are co-located in the RF/Wiggler straight with the superconducting RF cavities in order to concentrate the cryogenic infrastructure.

6.7.2 Conventional Magnets

The damping ring has conventional electromagnets for the dipole, quadrupole, sextupole, and corrector magnets. This technology choice offers flexibility for tuning and optimizing the rings as well as for adjusting the operating beam energy by a few percent around the nominal value of 5 GeV. Magnet counts are shown in Table 6.8. Table 6.9 gives the key magnet parameters and maximum higher-order harmonic content specifications.

Table 6.8
Magnet types and counts for a single ILC Damping Ring using the baseline lattice. These counts do not include magnets, kickers, and septa associated with the damping ring abort beam dump located in the RTML (see Chapter 7). Wiggler magnets are superconducting, all others are normal conducting. In the engineering style designation, which is of the form *MxxLyyy*, *M* indicates the magnet type, *xx* indicates the bore diameter in millimetres, and *yyy* indicates the physical length in millimetres [127].

Magnet	Type	Eng. Style	Qty	Power Method
Dipoles:	Corrector	D60L250	304	Individual
	Chicane	D60L940	28	String
	Disp. Supp.	D60L1940	10	String
	Arc	D60L2940	150	String
Quadrupoles:	Arc	Q60L480	482	Individual
	Straight	Q60L700	121	Individual
	Wig/Inj/Ext	Q85L309	50	Individual
	Wiggler	Q85L600	30	Individual
Skew Quads	Corrector	Q60L250	158	Individual
Sextupoles	—	SX60L250	600	Individual
Wigglers	—	WG76L2100	54	Individual
Kickers	Inj/Ext	Striplines	42	Individual
Thin Pulsed Septa	Inj/Ext	—	2	Individual
Thick Pulsed Septa	Inj/Ext	—	2	Individual

Table 6.9
Target field tolerances used for error simulations at a reference radius of 30 mm for damping-ring magnets. For the wigglers, the field quality is specified by the observed roll-off for a horizontal displacement from the beam axis by the indicated distance. The maximum KL-value specifies the nominal strength of the strongest magnet of each magnet type.

Type	Unit	Max Field Max KL	Error
Dipoles	mrad	41	2×10^{-4}
Quadrupoles	m^{-1}	0.35	2×10^{-4}
Sextupoles	m^{-2}	1.23	2×10^{-4}
H correctors	mrad	2	5×10^{-3}
V correctors	mrad	2	5×10^{-3}
Skew quads	m^{-1}	0.03	3×10^{-3}
Wigglers		–	3×10^{-3}

6.7.3 Power Supply System

All quadrupoles, sextupoles, wigglers and corrector magnets (dipole, skew quadrupole, and possibly other multipoles) have individual power supplies. Individual control of the quadrupole and sextupole magnets significantly enhances the ability to tune and locally correct the machine optics in a ring with very aggressive operating parameters. Individual power supplies for the wigglers offer simplified control in the event of a magnet quench by eliminating the power system coupling between magnets. Alcoves used by the power system are located at the junctions between each straight and the arcs. Because of the long distances between individually powered magnets and the alcoves, the power supply system uses bulk supplies located in the main alcoves that power a master "bus" from which DC-to-DC converters supply power to individual magnets. This design minimizes cable heat loads in the ring and provides for an efficient distribution of power. For the arc dipole magnets, one-half of each arc is powered as a string from the nearest alcove. The pulsed power supplies for the stripline kickers require short cable runs to preserve the necessary timing synchronization, and are housed in small secondary alcoves near each group of kickers.

6.8 Instrumentation and Feedback Systems

6.8.1 Diagnostics and Instrumentation

The principal ring instrumentation required consists of systems whose performance is fairly standard for light sources or which has been demonstrated as part of the R&D program. This complement includes the following:

1. beam position monitors with turn by turn capability and precision as in Table 6.3;
2. "tune tracker" that tracks three normal modes of a single bunch and drives the bunch at those tunes via feedback kickers or equivalent;
3. visible and/or x-ray synchrotron light monitors for measuring transverse bunch dimensions and streak camera for bunch length
4. toroid current monitor and bunch-bunch current monitor;
5. Beam-loss monitors (based on ion chambers, photomultiplier and scintillator).

6.8.2 Fast Feedback systems

With over a thousand bunches circulating in the ring, wakefields induced in vacuum chamber components can give rise to coupled-bunch instabilities that cause bunch jitter and/or emittance growth. To combat this, the rings have fast bunch-by-bunch feedback systems in all three oscillation planes (longitudinal, horizontal and vertical) [128, 129]. Modern commercial FPGAs (Field Programmable Gate Arrays), with many digital signal processor units on a single chip, can easily manage the requirements of the feedback systems in terms of speed and number of bunches. The bandwidth of the fast feedback system must be at least f_{RF} (that is, 650 MHz in the DR). This means that every block of the system must have the capability to manage the full bandwidth except for the power

section (amplifiers and kickers), where half bandwidth is sufficient. The main elements of each system are the analog front end, the digital processing unit, the analog back end, amplifiers and kicker(s).

The pickups can be 4-button monitors (two or three for each ring) with at least full bandwidth and dynamic range of the order $\sim$90 dB. The analog front ends are capable of extracting the oscillation signals from the monitors in each of the three planes (L, H, V) and giving them to the digital sections with a swing in the range of $\sim$0.5 V (typical of many analog-to-digital converters).

To minimize the quantization noise and have an adequate dynamic range, the digital units are based on a 14- or 16-bit signal processing system. The processing must compute the correction signal for all buckets (including the empty ones) to decouple the feedback behavior from the fill pattern. This means that all feedback systems have the capability to process, in real time, 7,022 input/output channels, although the real bunches are in, at most, 2,625 buckets. The digital unit sampling frequency is 650 MHz. A real-time FIR (finite impulse response) filter (with $\geq$50 taps, corresponding to an individual memory for each bunch of $\geq$50 acquisitions) provides the correction signal in terms of synchrotron or betatron phase advance using only one pickup for each system. The feedback setup is designed to be easily configurable using software tools. A down-sampling feature is also needed to manage very low-frequency oscillations.

The analog back-end systems adapt the output correction signals to the power section. The longitudinal kicker (an over-damped c cavity) works with a centre frequency between 800 and 2000 MHz, whereas the transverse kickers (striplines) operate at baseband (from 10 kHz up to half the bandwidth of the fast feedback system). Each power section has four 250 W amplifiers (1 kW total), with the bandwidth required by the kicker.

6.9 Injection and Extraction systems

The bunch separation in the main linacs is much longer than in the damping rings, so individual bunches must be injected and extracted without affecting the emittance or stability of the remaining stored bunches. For this to be the case, the kicker field must be negligible for any stored bunch upstream or downstream of the injected or extracted bunch, requiring that the effective kicker pulse width be less than twice the bunch spacing.

Individual bunch injection and extraction is accomplished in the horizontal plane using a fast kicker with rise/fall time $\sim$3 ns. The injection septum and injection kicker are separated by a horizontal phase advance of $\pi/2$ (as are the extraction septum and extraction kicker) and inserted in long drifts with low phase advance and high horizontal beta function, $\sim$70 m. If the DR is filled with 1312 bunches separated by 4 DR RF buckets in a train, the extraction kicker pulses with a repetition rate of up to 1.8 MHz (3 MHz is needed for the luminosity upgrade, 2625 bunches) to provide the specified uniform bunch spacing in the extraction line. The injection and extraction are performed simultaneously to reduce variations in beam loading, but the injection kicker starts to pulse a few turns after the beginning of the extraction. Thus, injected bunches fill the gaps vacated by extracted bunches in the same order as the bunches were extracted.

The kicker modules are 50 Ω stripline structures inside the vacuum pipe, each 30 cm long with a 30 mm gap. The required kick angle to extract the damped low emittance ($\sim$0.5 nm rad) bunch is $\sim$0.6 mrad and nearly twice that for the large ($\sim 7 \times 10^{-6}$ mrad) injected bunch. Based on experience with ultrafast pulsers at the KEK-ATF, the design provides $\pm$10 kV pulses on opposite electrodes. Thus a total complement of 42 kickers is required to handle injection and extraction for each ring. This corresponds to 84 high voltage pulsed power supplies.

The 30 cm stripline gives a 2 ns contribution to the kicker pulse width, leaving less than 10 ns for the electrical pulse width at the nominal ring bunch spacing of 6 ns. The kickers pulse about every 554 ns during the linac pulse of about 1 ms. For the high luminosity parameters, the ring

bunch spacing is 3 ns, requiring an electrical pulse width of less than 4 ns and a pulse about every 366 ns. The tolerance on horizontal beam jitter of the extracted beam is 0.1—0.2σ, which requires the extraction kicker amplitude stability to be less than 5–10 $\times$ 10^{-4}. A similar tolerance applies to the kicker amplitude for bunches before and after the target bunch.

The septum magnets are modeled after the Argonne APS injection septa. The thin (2 mm) septum magnet has a 0.73 T field, and the thick (30 mm) septum magnet has a 1.08 T field. Each magnet has an effective length of 1 m. Both magnets are pulsed once per linac cycle to reduce power dissipation, with eddy currents in the septum shielding the circulating beam. A half-sine pulse of about 10 ms width is used, and post-regulation is required to produce a 1 ms plateau flat to 10^{-4}.

Chapter 7
Ring to Main Linac

7.1 Overview

The ILC Ring to Main Linac (RTML) is responsible for transporting and matching the beam from the Damping Ring to the entrance of the Main Linac. The RTML must perform several critical functions:

- transport of the electron and positron beams from the damping rings, at the center of the ILC accelerator complex, to the upstream ends of their respective linacs ("geometry matching");
- collimation of the beam halo generated in the damping ring to $\leq 10^{-5}$, based on SLC experience;
- rotation of the spin polarisation vector from the vertical to any arbitrary angle required at the IP;
- compression of the long Damping-Ring bunch length by a factor of 20–30 to provide the short bunches required by the Main Linac and the IP.

In addition, the RTML must provide sufficient instrumentation, diagnostics and feedback/feedforward systems to preserve and tune the beam quality.

This chapter is organised as follows. The first two sections define the beam parameters and give a detailed description of the operation of the differing parts of the system. Important beam dynamics considerations relevant to the operation of the system are discussed in Section 7.4. The final section gives a manifest and definition of the various elements required to construct the system.

7.2 Beam Parameters

The key beam parameters of the RTML are listed in Table 7.1. Parameters are shown for the different operation modes, namely the low-energy 5/10 Hz configuration, nominal 5 Hz and luminosity upgrade.

Table 7.1
Basic beam parameters for the RTML.

Parameter	Unit	Nominal e^-/e^+	Low energy e^-/e^+
Repetition rate	Hz	5	5/10
Initial energy	GeV	5.0	5.0
Initial energy spread	%	0.11	0.12/0.137
Initial norm. hor. emit.	μm	5.5	5.9/6.0
Initial norm. ver. emit.	nm	19.6/20.0	20.1/20.9
Initial hor. beam jit.	$\sigma_{x,y}$	0.1	0.1
Initial bunch length	mm	6.0	6.0
Final bunch length	mm	0.3	0.3
Final energy	GeV	15.0	15.0
Final energy spread	%	1.5	1.5
Final hor. beam jitter	$\sigma_{x,y}$	0.1	0.1
Norm. hor. emit. budget	μm	0.9	0.9
Norm. ver. emit. budget	nm	6.5	6.5

7.3 System Description

7.3.1 Layout

Figure 7.1 depicts schematically the general layout of the ILC with emphasis on the various sub-beamlines and components of the RTML relative to Damping Rings, Main Linacs and Beam Delivery System (BDS). The RTML includes the short transfer line from the Damping Ring (DR) extraction to the main tunnel and the long low-emittance transport from the DR. This is followed by a 180° turn-around, the spin-rotation and the two-stage bunch-compression sections. The beamlines upstream of the turn-around are collectively known as the "upstream RTML," while those from the turn-around to the start of the main linac are collectively known as the "downstream RTML". In order to accommodate the different damping-ring elevations and linac lengths, the electron and positron RTMLs have minor differences in their short transport sections, but are otherwise identical. The Twiss functions along the positron RTML are shown in Fig. 7.2. The electron RTML is almost identical and is not shown here.

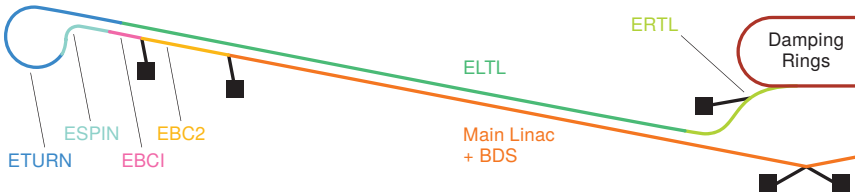

Figure 7.1 Schematic of the RTML, indicating the various functions described in the text.

Each of the key functions of the RTML listed in Section 7.1 is supported by several of the sub–beamlines shown in Fig. 7.1.

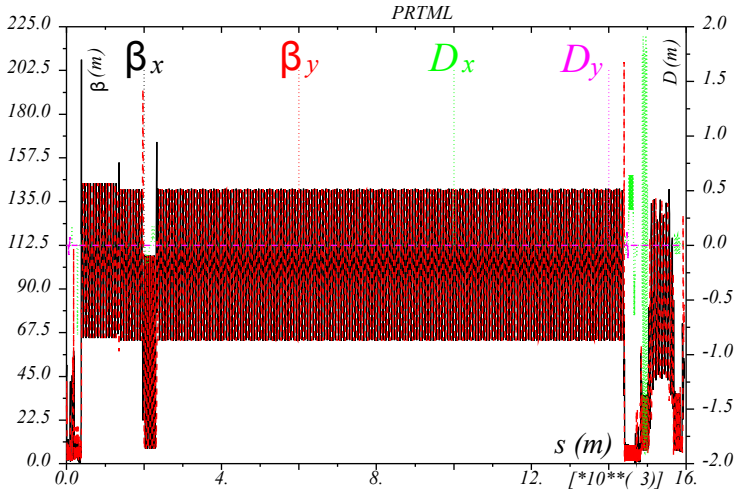

Figure 7.2 Twiss functions of the positron RTML.

The name abbreviations used for RTML sub-beamlines are the following:

- ERTL (PRTL) for the Electron (Positron) "Ring-To-Line" beamline from the damping ring to main tunnel, including Dump Lines (EC_DL);
- ELTL (PLTL) for Electron (Positron) "Long-Transfer-Line" or "Return Line";
- ETURN (PTURN) for Electron (Positron) TURN-around beamline;
- ESPIN (PSPIN) for Electron (Positron) SPIN-rotation system;
- EBC1 (PBC1) and EBC2 (PBC2) for the first and second stage of the Electron (Positron) Bunch Compressor, including their Dump Lines BC1_DL and BC2_DL.

7.3.2 Geometry Match

The RTML geometry and design is largely determined by the requirements of other areas, for example the length of the linac and its required curvature in the vertical plane, the positioning of the Damping Rings and their diameter, etc. The exact coordinates and angles of the connection points between Damping Rings and RTML and RTML and BDS/Main Linac are specified [130, 131]. Following extraction from the Damping Rings, the beams follow the lines ERTL and PRTL located in the Central Region tunnel and are injected into the long transfer line, parallel to the axis of the Main Linac. The PRTL contains a vertical dogleg which brings the positron beam from the height of the positron Damping Ring to the height of the PLTL in the main tunnel. The ELTL and PLTL (Return Lines) have an Earth-curved geometry along the Main Linac and a straight-line geometry elsewhere, except for areas near the connection to the Main Linac and BDS, where the beam geometry is adjusted using horizontal doglegs. In addition, small vertical and horizontal doglegs at the upstream end of the Turn-around change the beam elevation from the ceiling of the linac tunnel to the nominal linac elevation, and adjust the horizontal position between the ELTL (PLTL) line axis and the main linac axis.

7.3.3 Sub-systems

This subsection describes the functionality and specification of the subsystems of the RTML, starting from the damping ring and working out to the turn-arounds and then back towards the Interaction Point, as shown in Fig. 7.1.

7.3.3.1 Extraction from the DR (ERTL/PRTL)

Figure 7.3a shows a plot of survey data for the PRTL line using the global Cartesian coordinate system x, y, z with origin at the interaction point. In order to specify a complicated geometry, the ERTL and PRTL lines have been divided onto four logical sub-lines: horizontally straight section B containing a vertical dogleg, horizontal arc C, straight section D, and horizontal arc E. (Section A is the extraction line from the Damping ring.) Section B of PRTL consists of a matching section followed by regular FODO cells and a vertical dogleg to change the elevation of the positron beam. This plot shows circles for the given coordinates of the connection points between the sections along with solid-lines from the beamline survey. The nominal values of the coordinate displacements x, y, z and angles the corresponding spherical coordinates Θ, Φ, Ψ for the connection points are given [131]. The ERTL is identical to the PRTL except for an extra vertical dogleg.

For the Luminosity Upgrade configuration, there are 2 positron Damping Rings and two vertical doglegs instead of one. They merge the two positron beams coming from lower and upper Damping Rings into a single beamline (see Fig. 7.4).

The Twiss functions of the PRTL are shown in Fig. 7.3b where the boundaries of sections B, C, D and E are marked by blue lines.

7.3.3.2 Return Line (ELTL/PLTL)

The ELTL and PLTL lines follow the earth's curvature in the Main Linac tunnel and have straight line geometry in other locations except near the positron production where there is a horizontal dogleg. The first section of each line contains a system of skew quadrupoles for coupling correction, a beam diagnostics section with 4 laser wires, a magnetic chicane for emittance measurements, and a collimation section to remove beam halo. Since the first part of the ELTL and PLTL share the BDS tunnel, a horizontal dogleg must be inserted at the junction between the BDS and Main Linac [132], corresponding to the dogleg after the undulator, to follow the geometry of the main beam line in this area. The positron source is located at the end of the electron linac where it joins the BDS; and the

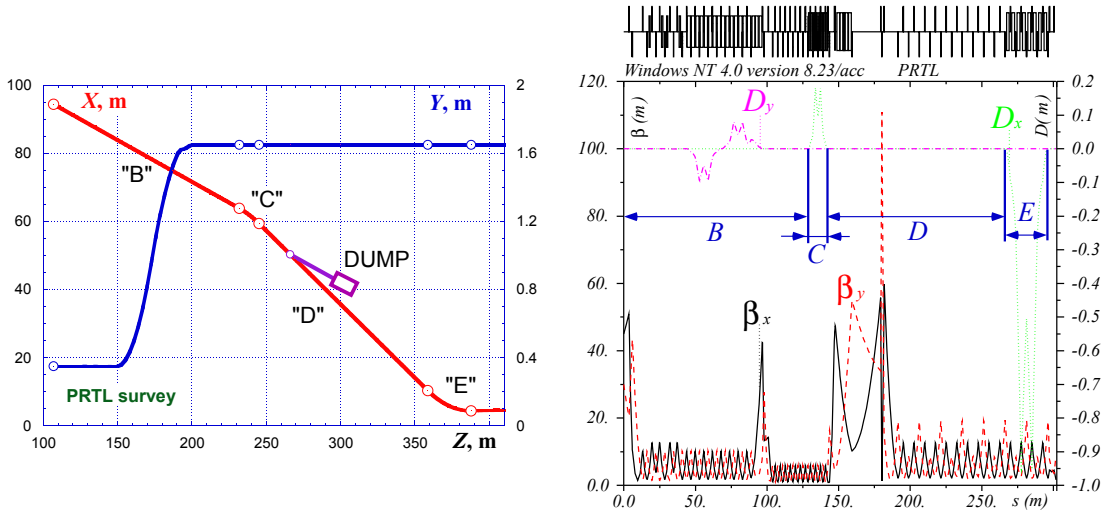

(a) Survey plot for PRTL **(b)** PRTL lines

Figure 7.3. Survey plot (left) and Twiss functions (right) for PRTL line.

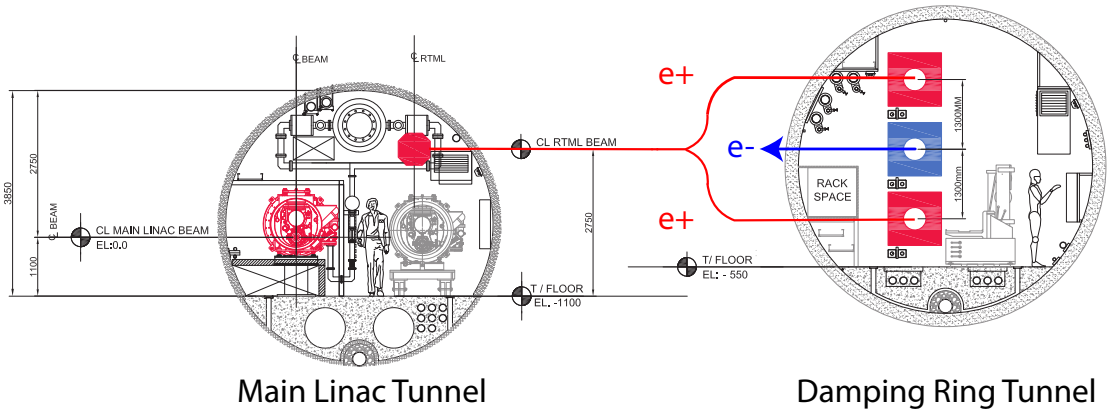

Figure 7.4. Layout of the vertical Doglegs in PRTL.

electron beam performs a dogleg around the positron target. The ELTL follows the same path in the opposite direction (see Fig. 7.5). Because of the high radiation at the positron target, no nearby beamlines has magnets in that section of beamline. The PLTL line also includes a dogleg at the junction between the Main Linac and the BDS, but without the complication of the positron target and radiation.

Because the Main Linac tunnel follows the curvature of the Earth, the ELTL and PLTL have vertical correctors at each quadrupole of the FODO system in the Main Linac tunnel. Each of these correctors gives the beam the vertical kick necessary for the beam to follow the curvature of the Earth. These correctors also generate a small dispersion that is propagated periodically along the FODO system cells. To match this vertical dispersion to the straight sections, there are an additional 4 vertical correctors before and after the curved sections.

7.3.3.3 Turn-around

As well as changing the direction of the beams, the turn-around copes with a change in elevation and a change in horizontal offset to get from the return line location at the top of the tunnel to the main linac orientation. The Turn-around accomplishes this change in geometry as follows:

- The Turn-around is achieved by 29 cells with 108°/108° phase advance per cell; there are 18 "forward" arc cells, 3 "reverse" arc cells, and 8 cells for matching or suppressing dispersion.

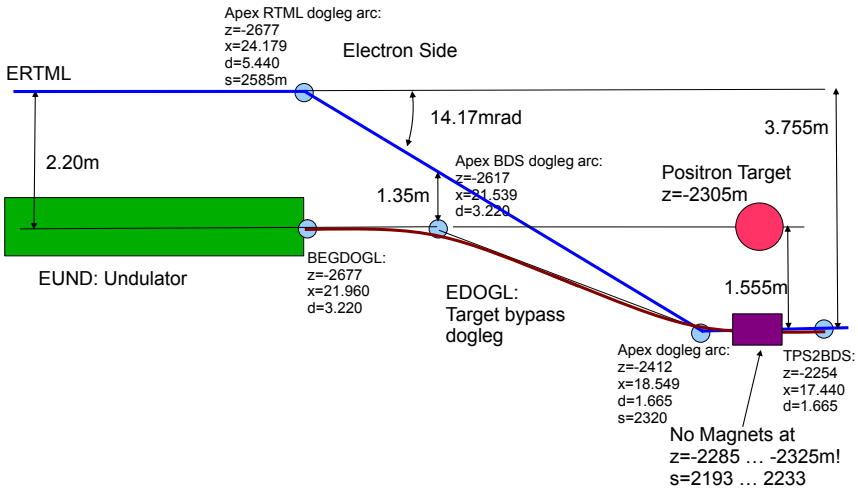

Figure 7.5
Layout of the horizontal dogleg on the electron side of the RTML.

This is a total of 180° minus the 7.9° needed in the Spin Rotator, and also includes most of the needed horizontal offset;

- upstream of the turnaround is a vertical dogleg which produces the 1.65 m offset in 8 cells of 90°/90° phase advance;
- upstream of the vertical dogleg is a horizontal dogleg which produces a small horizontal offset in 8 cells of 90°/90° phase advance.

The radius of the arc is about 30 m. This is a compromise between the cost, which implies a short Turn-around, and the emittance growth, which implies relatively small pole-tip fields in the bending magnets. The dispersion is corrected entirely by adjusting the strengths of the quadrupoles in the vertical dogleg and in the main Turn-around arc. The Turn-around also includes a feedforward correction system, which corrects residual bunch-by-bunch orbit errors from the DR extraction. The BPMs for the feedforward correction are near the end of the Return Line, separated by 2 cells (for 90 degree coverage). The time delay of the beam through the turn-around is 600 ns, which is adequate for applying corrections. The R_{56} of the turn-around is 2.37 m.

7.3.3.4 Spin Rotation

The beam polarisation is vertical in the damping rings; this polarisation is transported with negligible loss or precession to the end of the Turn-around. Before entering the linac, the spin orientation should be set to any direction required by the experiments. This is accomplished for both the electrons and positrons by a spin-rotation system composed of a pair of 5 T superconducting solenoids, followed by an arc with a net 7.9° bend angle, followed by another pair of solenoids. The spin direction is selected by adjusting the excitation in the solenoid pairs. In order to rotate the spin without introducing undesirable $x - y$ coupling, the solenoid-based rotators each use a pair of identical superconducting solenoids separated by a quadrupole lattice which introduces a $+I$ transformation in the horizontal plane and a $-I$ transformation in the vertical plane [133], the net effect of which is to cancel the cross-plane coupling.

7.3.3.5 Bunch Compression

There is a two-stage bunch-compression system in order to achieve the required factor of 20 [134]. Compared with a single-stage compression [135], the 2-stage compressor reduces the energy spread of the beam throughout the RTML and allows more flexibility to reduce the bunch length below 0.3 mm for the Energy Upgrade configuration. Table 7.2 summarises the important parameters for both the first stage (BC1) and second stage (BC2) of the Bunch Compressor.

Table 7.2
Key parameters for the two-stage bunch compressor in the nominal and low-energy configurations, assuming compression to 0.3 mm RMS final bunch length.

Parameter	Unit	BC1	
		Nominal e^-/e^+	Low Energy e^-/e^+
Repetition rate	Hz	5	10/5
Initial energy	GeV	5.0	5.0/5.0
Initial energy spread	%	0.11	0.12/0.137
Initial bunch length	mm	6.0	6.0
RF voltage	MV	465	465
RF phase	°	−115	−115
Wiggler R_{56}	mm	−372	−372
Final energy	GeV	4.8	4.8
Final energy spread	%	1.42	1.42
Final bunch length	mm	0.9	0.9
Parameter	**Unit**	**BC2**	
		e^-/e^+	e^-/e^+
RF voltage	GV	11	11
RF phase	°	−24	−25.3
Wiggler R_{56}	mm	−55	−55
Final energy	GeV	14.9	14.8/14.6
Final energy spread	%	1.12	1.17/1.24
Final bunch length	mm	0.3	0.3

The two-stage bunch compressor also allows some flexibility to balance longitudinal and transverse tolerances by adjustment of the wiggler magnet strengths, RF voltages, and RF phases. The nominal compressor configurations ease tolerances on damping-ring extraction phase, damping-ring bunch length, and bunch-compressor phase stability, at the expense of tightening the tolerances on the transverse alignment of accelerator components. Alternate configurations are possible that loosen transverse alignment tolerances but tighten the longitudinal (i.e. phase) tolerances.

The linacs in both compressor stages use standard SCRF cryomodules and an RF power-unit configuration similar to that of the Main Linac (i.e. one klystron driving three cryomodules). The first-stage compressor has a single RF unit, with 8 cavities and one quadrupole in each of its 3 cryomodules; the second-stage compressor uses 16 RF units which are identical to the main-linac configuration (i.e. 26 cavities and 1 quad per 3 cryomodules). The stronger focusing in the first stage is necessary to mitigate the higher wakefields and cavity-tilt effects resulting from the longer bunch length in the compressors.

Each bunch compressor stage includes a 150 m lattice of wiggler magnets which provides the required momentum compaction.

Figure 7.6 shows the longitudinal phase space after compression from 6 mm to 0.3 mm RMS length.

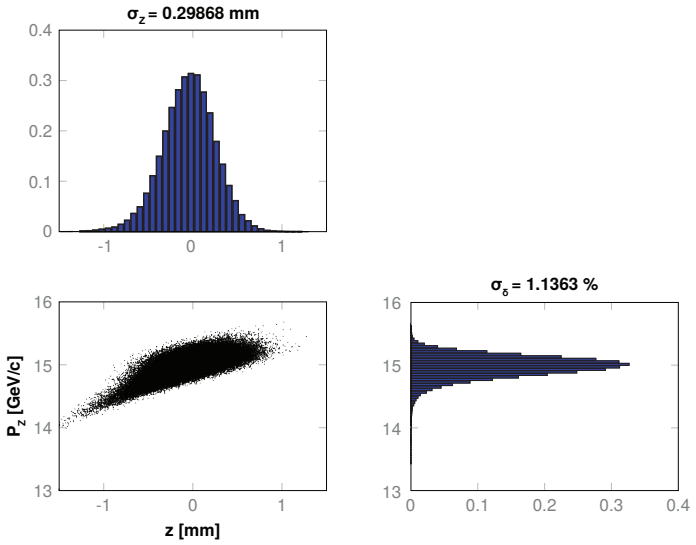

Figure 7.6
Longitudinal phase space of the compressed bunch.

7.3.4 Collimation and diagnostics

The betatron collimation section is downstream of the Central Region, at the beginning of the Return Line. It consists of two sets of thin spoiler and thick absorber pairs, placed 90° apart in betatron phase. This is sufficient to reduce the halo density by 3-4 orders of magnitude. The thin spoilers are needed to protect the absorbers from a direct hit from an errant beam [136]. There are additional collimators for energy collimation in the Turn-around and in the wigglers of the Bunch Compressor. There are both adjustable-jaw collimators with a rectangular aperture, and fixed-aperture collimators with a cylindrical geometry.

7.3.4.1 Adjustable-Aperture Collimators

All of the adjustable-aperture, rectangular collimators (RCOLs) are of the same design: two jaws in the same plane (x or y), with a 0.6 RL titanium "spoiler" and no water cooling. The amount of collimated halo is about 0.1 % of the beam power of 220 kW, corresponding to 220 W; since the energy deposited in the titanium is a small fraction of the total halo power, water cooling is not required. The nominal betatron collimation depth is $10\sigma_x$ and $60\sigma_y$. Each RTML has two x and two y betatron spoilers, for a total of eight adjustable spoilers for betatron collimation. Each RTML also has 6 sets of adjustable spoilers for longitudinal collimation: two in the horizontal dogleg portion of the turn-around; two in the BC1 wiggler; and two in the BC2 wiggler. The number of two-jaw, single-plane adjustable collimators in each RTML is 10, giving 20 in total.

7.3.4.2 Fixed-Aperture Collimators

There are 28 fixed-aperture collimators with circular geometry (ECOLs): 8 circular collimators in each collimation section before the Return Line, 2 in each turn-around (in the horizontal dogleg), 2 in each BC1, and 2 in each BC2. The collimators in the Return Lines and turn-arounds have 6.5 mm half-gaps, the ones in BC1 have 30 mm half-gaps, and the ones in BC2 have 5 mm half-gaps. The circular collimators absorb the beam power which is scattered from the adjustable-aperture spoilers. To accomplish this, they are 20 RL lengths thick. These collimators are water cooled, and can handle a CW power of about 200 W. The circular collimators are "shadowed" by the spoilers, so that for a particle or bunch to hit a circular collimator it is generally necessary that the particle or bunch pass through a spoiler first. Table 7.3 gives the type, number and location of the collimators in the RTML.

Table 7.3
Type, number and location of collimators in RTML.

Type	Aperture X×Y mm^2	Budget W	Cooling	Location	Number
Rectangular	3.43×10	$\ll$ 220	—	ELTL/PLTL	4
Rectangular	10×1	$\ll$ 220	—	ELTL/PLTL	4
Circular	6.5	200 (CW)	water	ELTL/PLTL	16
Rectangular	1×10	$\ll$ 220	—	ETURN/PTURN	4
Circular	6.5	200 (CW)	water	ETURN/PTURN	4
Rectangular	18×20	$\ll$ 220	—	EBC1/PBC1	4
Circular	30	200 (CW)	water	EBC1/PBC1	4
Rectangular	4×10	$\ll$ 220	—	EBC2/PBC2	4
Circular	5	200 (CW)	water	EBC2/PBC2	4

7.3.4.3 Diagnostics

At the entrance to each Return Line before the collimation section, there is a skew quadrupole system for coupling correction, a beam-diagnostics section with multiple laser-wire stations and a magnetic chicane for emittance measurements. The lattices for these sections are taken from the RDR design rematched into the new line [137].

Figure 7.7 shows the layout of the electron RTML with the location of collimators and diagnostic sections. The positron side is identical.

Figure 7.7
Location of collimator and diagnostic sections in the RTML.

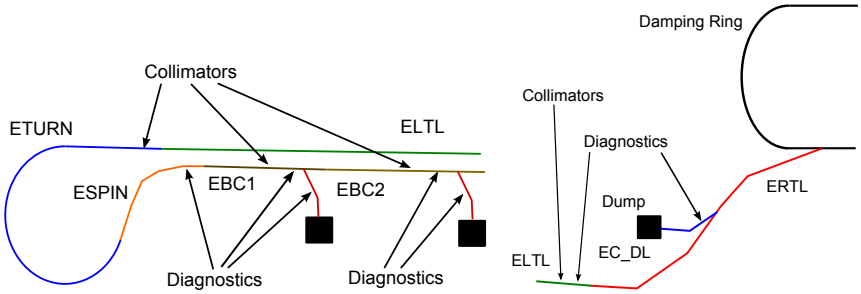

(a) ELTL, ETURN, ESPIN, EBC1 and EBC2 lines. **(b)** ERTL and ELTL lines.

7.3.5 Tuning, Correction, and Operations

The diagnostic, correction, and operational requirements of the RTML have been carefully integrated into the design of the entire beamline and are described in detail below.

7.3.5.1 Global Dispersion Correction

The Arc, the BC1 wiggler, and the BC2 wiggler contain normal and skew quads in regions of horizontal dispersion which are used to tune any residual dispersion due to misalignments and errors. The quads are arranged in pairs, with an optical $-I$ transform between the two quads in a pair; this permits tuning of the dispersion without introducing any betatron coupling or beta beats. The dispersions in the turn-around is adjusted by tuning normal quads in the horizontal and vertical doglegs at the upstream end of the turn-around.

7.3.5.2 Global Coupling Correction

There are two decoupling regions: the first is immediately downstream of the Arc, and the second is immediately downstream of the Spin Rotator. Each decoupling region contains 4 orthonormal skew quads in regions of zero dispersion, which allow complete and independent control of the 4 betatron coupling terms. The first station is conceptually intended to correct the coupling introduced by the damping-ring extraction system, while the second corrects coupling generated by errors in the spin-rotation system, as well as the remaining betatron coupling from small rotation errors on the RTML quads.

7.3.5.3 Emittance Measurements

There are three emittance measurement stations: the first is between the first decoupling section and the first collimation section, the second is between the second decoupling station and the bunch compressor, and the third is between the bunch compressor and the linac. Each of these stations contains 4 laser-wire scanners embedded in a FODO lattice with 45° betatron phase; each station can therefore measure the projected x and y emittances of the beam. The first station can be used to tune the Arc dispersion and the skew quads in the first decoupler; the second station can be used to tune the Turn-around dispersion and the skew quads in the second decoupler; the third station can be used to tune the dispersion correction in the Bunch Compressor wigglers. Although none of the systems have the capability to measure normal-mode emittances and coupling parameters directly, the optics of the first two stations are compatible with a later upgrade if needed.

7.3.5.4 Beam-Position Monitors

There are cavity-type beam-position monitors (BPMs) with horizontal and vertical readout at each quadrupole, with additional units close to the laser wires, at high-dispersion regions in the Bunch-Compressor wigglers, and at other critical locations. The BPMs in the room-temperature sections of the RTML almost all operate in the 6 GHz frequency band ("C-band"), while the BPMs in the cryomodules and at a handful of other locations use the 1 GHz frequency band ("L-band"). At the nominal bunch charge of 3.2 nC, these BPMs can achieve sub-micron single-bunch resolution. The standard RTML BPM requires high precision and stability of the BPM's offset with respect to the device's mechanical centre; a few of the BPMs have other requirements, such as high bandwidth or low latency.

7.3.5.5 Longitudinal Diagnostics

Each stage of the Bunch Compressor contains arrival-time (phase) monitors, beam position monitors at dispersive locations, X-ray synchrotron-light monitors, and two types of bunch-length monitors (a passive device based on measuring the RF spectrum of the bunch, and an active device based on transverse deflecting cavities [138]). The active bunch-length monitor can also measure the correlation between energy and longitudinal position within a bunch.

7.3.5.6 Feedback and Feedforward

The RTML is not expected to require any intra-train trajectory feedback systems, although there are a number of train-to-train (5 Hz) trajectory feedbacks. In addition, the beam energy at BC1 and BC2 is controlled by a 5 Hz feedback, as is the electron-positron path-length difference through their respective bunch compressors (see Section 7.4). There is also a trajectory feed-forward that uses BPMs at the end of the Return line to make bunch-by-bunch orbit measurements, which are fed forward to a set of fast correctors downstream of the Turn-around. The speed-of-light travel time between these two points is about 600 ns, and the actual distance between them is on the order of a few tens of meters; the resulting delay of the beam relative to the propagated signal is more than adequate for a digital low-latency orbit correction system [139].

7.3.5.7 Machine Protection

Intermediate Extraction Points: There are 3 locations where the beam in the RTML may be directed to a beam dump: upstream of the first collimation section, downstream of BC1, and downstream of BC2 [140]. At each of these locations, there are both pulsed kickers and pulsed bends for beam extraction. The kickers are used when an intra-train extraction is required, for example during a machine protection fault, while the bends are used to send entire trains to their beam dumps. The pulsed bends can also be energized by DC power supplies if a long period of continual dump running is foreseen. All 3 dumps are capable of absorbing 220 kW of beam power. This implies that the first 2 dumps, which are at 5 GeV, can absorb the full beam power, while the third dump, at 15 GeV, can absorb only about 1/3 of the nominal beam power. Full trains can be run to this dump at reduced repetition rate, or short trains at full rate.

7.4 Accelerator Physics Issues

A number of beam dynamics issues were considered in the design and specifications of the RTML.

7.4.1 Incoherent (ISR) and Coherent (CSR) Synchrotron Radiation

Current estimates indicate that the horizontal emittance growth from ISR is around 90 nm (1.1 %) in the Arc, 380 nm (4.8 %) in the Turn-around, and 430 nm (5.4 %) in the Bunch Compressor in its nominal configuration. Vertical emittance growth from ISR in the vertical dogleg is negligible.

Studies of the ILC Bunch Compressor indicate that there are no important effects of coherent synchrotron radiation, primarily because the longitudinal emittance of the beam extracted from the damping ring is so large [141].

7.4.2 Stray Fields

Studies have found that fields at the level of 2.0 nT can lead to beam jitter at the level of $0.2\sigma_y$ [142]. This is considered acceptable since the orbit feed-forward corrects most of this beam motion. Measurements [143] indicate that 2 nT is a reasonable estimate for the stray-field magnitude in the ILC. Emittance-growth considerations also place limits on the acceptable stray fields, but these are significantly higher.

7.4.3 Beam-Ion Instabilities

Because of its length and its weak focusing, the electron Return line has potential issues with ion instabilities. To limit these to acceptable levels, the base pressure in the Return line must be smaller than 2 µPa [144].

7.4.4 Static Misalignments

The main issues for emittance growth are: betatron coupling introduced by the Spin Rotator or by rotated quads; dispersion introduced by rotated bends, rotated quads in dispersive regions, or misaligned components; wakefields from misaligned RF cavities; and time-varying transverse kicks from pitched RF cavities.

Studies of emittance growth and control in the region from the start of the Turn-around to the end of the second emittance region have shown that a combination of beam steering, global dispersion correction, and global decoupling can reduce emittance growth from magnetostatic sources to negligible levels, subject to the resolution limits of the measurements performed by the laser wires [145, 146]. Although the upstream RTML is much longer than the downstream RTML, its focusing is relatively weak and as a result its alignment tolerances are actually looser. Studies have shown that the same tuning techniques can be used in the upstream RTML with the desired

effectiveness [147]. The tolerances for RF cavity misalignment in the RTML are large (0.5 mm RMS would be acceptable) because the number of cavities is small and the wakefields are relatively weak [148]. Although in principle the RF pitch effect is difficult to manage, in practice it leads to a position-energy correlation which can be addressed by the Bunch Compressor global dispersion correction [149]. A full and complete set of tuning simulations have not yet been performed, but it is expected that the baseline design for the RTML can satisfy the emittance preservation requirements. Table 7.4 summarises the alignment errors estimated for the RTML components.

Table 7.4
Standard local alignment error in RTML.

Error	Unit	Cold Sections	Warm Sections
Quad. offset	μm	300	150
Quad. roll	μrad	300	300
RF cavity offset	μm	300	—
RF cavity tilt	μrad	300	—
BPM offset	μm	300	100 (w.r.t. magnet)
CM offset	μm	200	—
CM pitch	μrad	20	—
Bend offset	μm	—	300
Bend. roll	μrad	—	300

7.4.5 RF Phase and Amplitude Jitter

Phase and amplitude errors in the bunch compressor RF lead to energy and timing jitter at the IP, the latter directly resulting in a loss of luminosity. Table 7.5 shows the RMS tolerances required to limit the integrated luminosity loss to 2 %, and to limit growth in IP energy spread to 10 % of the nominal energy spread [150].

Table 7.5
Key tolerances for the two-stage bunch compressor.

Parameter	Arrival Time	Energy Spread
Correlated BC phase errors	0.24°	0.35°
Uncorrelated BC phase errors	0.48°	0.59°
Correlated BC amplitude errors	0.5 %	1.8 %
Uncorrelated BC amplitude errors	1.6 %	2.8 %

The tightest tolerance which influences the arrival time is the relative phase of the RF systems on the two sides: in the nominal configuration, a phase jitter of the electron and positron RF systems of 0.24° RMS, relative to a common master oscillator, results in 2 % luminosity loss. The tight tolerances are met through a three-level system:

- Over short time scales, such as 1 second, the low-level RF system is required to keep the two RF systems phase-locked to the level of 0.24° of 1.3 GHz;
- Over longer time periods, the arrival times of the two beams are directly measured at the IP and a feedback loop adjusts the low-level RF system to synchronize the beams. This system is required to compensate for drifts in the low-level RF phase-locking system which occur over time scales long compared to a second;
- Over a period of many minutes to a few hours, the arrival time of one beam is "dithered" with respect to the arrival time of the other beam, and the relative offset which maximizes the luminosity is determined. This offset is used as a new set-point for the IP arrival-time feedback loop, and serves to eliminate drifts which arise over time scales long compared to a minute.

7.4.6 Halo Formation from Scattering

Halo formation is dominated by Coulomb scattering from the nuclei of residual gas atoms, and it is estimated that 10^{-5} Pa base pressure in the downstream RTML will cause approximately 9×10^{-7} of the beam population to enter the halo [151]. A similar calculation was performed for the upstream RTML, which indicates that 2×10^{-6} Pa base pressure causes approximately 2×10^{-6} of the beam population to enter the halo. This is well below the requirement of 10^{-5}.

7.4.7 Space-Charge effects

In the long, low-energy, low-emittance transfer line from the damping ring to the bunch compressor, the incoherent space-charge tune shift is on the order of 0.15 in the vertical, the impact of which will be the subject of further studies.

7.4.8 Wake field in SRF cavities and collimators

Assuming collimation of the beam extracted from the damping ring at $10\sigma_x$, $60\sigma_y$, and $\pm 1.5\,\%$ ($10\sigma_\delta$) in momentum, the worst-case jitter amplification for untapered, "razor-blade" spoilers is expected to be around 10 % in x, around 75 % in y, and the contribution to x jitter from energy jitter is expected to be negligible [152, 153]. The vertical jitter amplification figure can be brought to an acceptable level by the use of spoilers with modest longitudinal tapers. The other collimator wakefield "figures of merit" are acceptable even assuming untapered spoilers.

7.4.9 Emittance preservation

Preservation of the vertical emittance in the RTML is a challenging task, which cannot be achieved without dedicated beam-based alignment algorithms. Simulations have studied one-to-one correction, kick minimisation, dispersion bumps and coupling-correction algorithms to achieve small emittance growth in the entire RTML, excluding the Bunch compressor. The results are shown in Fig. 7.8. After corrections, the growth of normalised emittance is 5.3 nm rms (9.94 nm for 90 % of seeds). In the two-stage bunch compressor the biggest effect comes from cavity misalignments, tilts and asymmetries from the geometry of the main power and HOM couplers. In addition to the other BBA algorithms, the simulations applied a "girder optimisaton" (or tilting of cryomodules) algorithm to minimize emittance growth to 1.09 nm rms (1.48 for 90 % of seeds).

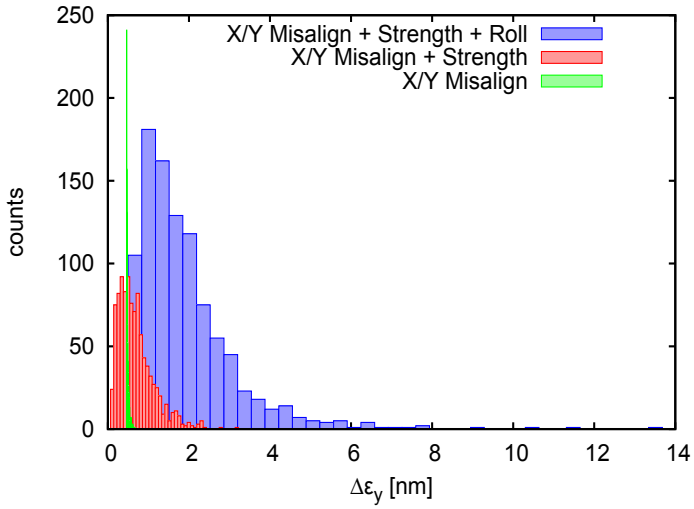

Figure 7.8
Histogram of the final emittance growth for 1000 seeds in RTML, excluding BC.

7.5 Accelerator Components

7.5.1 Magnets, Pulsed elements

Table 7.6 shows the total number of components of each type in each RTML. The number of quadrupoles, dipole correctors, and BPMs is larger in the electron RTML than in the positron RTML due to the longer electron Return line; for these 3 component classes, the different totals for each side are shown. Detailed information about the magnet families used in the RTML can be found elsewhere [154]. Each quadrupole and dipole has its own power supply, while other magnets are generally powered in series with one power supply supporting many magnets [155]. The cost estimate for the S-band dipole-mode structures was developed based on recent experience with accelerator-structure construction at IHEP.

Table 7.6
Total number of components in each RTML. Where 2 totals are shown, the larger number refers to the longer electron-side RTML, the smaller number refers to the shorter positron-side RTML.

Magnets		Instrumentation		RF	
Bends	336/356	BPMs	782/752	Cavities	440
Quads	825/793	Wires	12	Cryo-Mod.	51
Dipoles	1229/1157	BLMs†	2	RF sources	17
Kickers	18	OTRs	5	S-band struct.	2
Septa	14	Φ monitors	5	S-band sources	2
Pulsed bends	3	Xray SLMs‡	1		
Extr. bends	12	Rect. Coll.	10		
Rasters	6	Circ. Coll.	14		
Solenoids	4				

† Bunch Length Monitor
‡ Synchrotron Light Monitor

Table 7.7 shows the system lengths for the RTML beamlines.

Table 7.7
System lengths for each RTML beamline. The larger number refers to the longer electron-side RTML, the smaller number refers to the shorter positron-side RTML.

Beamline	Length
ERTL/PRTL	302 m
ELTL/PLTL	15 302 /14 109 m
ETURN/PTURN	275 m
ESPIN/PSPIN	123 m
EBC1/PBC1	231 m
EBC2/PBC2	908 m
Dumplines (E/P)	182 m
Total	17 323 /16 130 m
Total excluding dumplines	17 141 /15 948 m
Footprint	30 456 m

7.5.2 Vacuum Systems

The base-pressure requirement for the downstream RTML is set by limiting the generation of beam halo to tolerable levels, while in the upstream RTML it is set by the necessity of avoiding beam-ion instabilities. As described in Section 7.4, the base pressure requirement for the downstream RTML is 10 µPa, while in the upstream RTML it is 2 µPa. Both upstream and downstream RTML vacuum systems are stainless steel with 2 cm OD; the upstream RTML vacuum system is installed with heaters to allow *in situ* baking, while the downstream RTML vacuum system is not. The bending sections of the turn-around and bunch compressors are not expected to need photon stops or other sophisticated vacuum systems, as the average beam current is low, and the fractional power loss of the beam in the bending regions is already small to limit emittance growth from ISR.

7.5.3 Cryogenics

Each RTML includes 51 cryomodules in the RF system of BC1 and BC2 and 4 superconducting solenoids in the Spin Rotator. Solenoids are cooled by a local cryocooler system operating at 4.2 K. The cryocooler requires only a small volume of liquid helium which is recondensed in the system. The RTML cryomodules are the same as used in the Main Linac. Liquid helium at 2 K needed for cryomodule cooling is transported from the ML area by a transfer line.

7.5.4 Service tunnels and Alcoves

In the area of the two-stage Bunch Compressor, there is a service tunnel that runs parallel to the beam tunnel. All of the power supplies, RF sources, and rack-mounted instrumentation and controls equipment needed for the bunch compressor are installed in the service tunnel. This configuration allows repairs and maintenance to be performed while minimizing disruption to the accelerator itself.

Chapter 8
Beam Delivery System and Machine Detector Interface

8.1 Introduction

The ILC Beam Delivery System (BDS) is responsible for transporting the e^+/e^- beams from the exit of the high-energy linacs, focusing them to the sizes required to meet the ILC luminosity goals (σ_x^* =474 nm, σ_y^* =5.9 nm in the nominal parameters, see Section 2.2), bringing them into collision, and then transporting the spent beams to the main beam dumps. In addition, the BDS must perform several critical functions:

- measure the linac beam and match it into the final focus;
- protect the beamline and detector against mis-steered beams from the main linacs[1];
- remove any large amplitude particles (beam-halo) from the linac to minimize background in the detectors;
- measure and monitor the key physics parameters such as energy and polarization before and after the collisions.

The BDS must provide sufficient instrumentation, diagnostics and feedback systems to achieve these goals.

8.2 Parameters and System Overview

Tables 8.1 and 8.2 show the key BDS parameters.

Table 8.1
Key parameters of the BDS [12]. The range of L^*, the distance from the final quadrupole to the IP, corresponds to values considered for the existing SiD and ILD detector concepts.

Parameter	Value	Unit
Length (start to IP distance) per side	2254	m
Length of main (tune-up) extraction line	300 (467)	m
Max. Energy/beam (with more magnets)	250 (500)	GeV
Distance from IP to first quad, L^*, for SiD / ILD	3.51 / 4.5	m
Crossing angle at the IP	14	mrad
Normalized emittance $\gamma\epsilon_x$ / $\gamma\epsilon_y$	10 000 / 35	nm
Nominal bunch length, σ_z	300	μm
Preferred entrance train to train jitter	<0.2–0.5	σ_y
Preferred entrance bunch to bunch jitter	< 0.1	σ_y
Typical nominal collimation aperture, x/y	6-10 / 30-60	beam sigma
Vacuum pressure level, near/far from IP	0.1 / 5	μPa

[1] This applies to the positron side of the BDS; on the electron side the protective fast abort extraction is located upstream of the positron source undulatory section.

Table 8.2. Energy-dependent parameters of the Beam Delivery System [84].

		Center-of-mass energy, $E_{\rm cm}$ (GeV)							
		Baseline				Upgrades			
Parameter		200	250	350	500	500	1000 (A1)	1000 (B1b)	Unit
Nominal bunch population	N	2.0	2.0	2.0	2.0	2.0	1.74	1.74	$\times 10^{10}$
Pulse frequency	$f_{\rm rep}$	5	5	5	5	5	4	4	Hz
Bunches per pulse	$N_{\rm bunch}$	1312	1312	1312	1312	2625	2450	2450	
Nominal horizontal beam size at IP	$\sigma_{\rm x}^*$	904	729	684	474	474	481	335	nm
Nominal vertical beam size at IP	$\sigma_{\rm y}^*$	7.8	7.7	5.9	5.9	5.9	2.8	2.7	nm
Nominal bunch length at IP	$\sigma_{\rm z}^*$	0.3	0.3	0.3	0.3	0.3	0.250	0.225	mm
Energy spread at IP, $\rm e^-$	$\delta E/E$	0.206	0.190	0.158	0.124	0.124	0.083	0.085	%
Energy spread at IP, $\rm e^+$	$\delta E/E$	0.190	0.152	0.100	0.070	0.070	0.043	0.047	%
Horizontal beam divergence at IP	$\theta_{\rm x}^*$	57	56	43	43	43	21	30	μrad
Vertical beam divergence at IP	$\theta_{\rm y}^*$	23	19	17	12	12	11	12	μrad
Horizontal beta-function at IP	$\beta_{\rm x}^*$	16	13	16	11	11	22.6	11	mm
Vertical beta-function at IP	$\beta_{\rm y}^*$	0.34	0.41	0.34	0.48	0.48	0.25	0.23	mm
Horizontal disruption parameter	$D_{\rm x}$	0.2	0.3	0.2	0.3	0.3	0.1	0.2	
Vertical disruption parameter	$D_{\rm y}$	24.3	24.5	24.3	24.6	24.6	18.7	25.1	
Energy of single pulse	$E_{\rm pulse}$	420	526	736	1051	2103	3409	3409	kJ
Average beam power per beam	$P_{\rm ave}$	2.1	2.6	3.7	5.3	10.5	13.6	13.6	MW
Geometric luminosity	$L_{\rm geom}$	0.30	0.37	0.52	0.75	1.50	1.77	2.64	$\times 10^{34}\,{\rm cm}^{-2}\,{\rm s}^{-1}$
– with enhancement factor		0.50	0.68	0.88	1.47	2.94	2.71	4.32	$\times 10^{34}\,{\rm cm}^{-2}\,{\rm s}^{-1}$
Beamstrahlung parameter (av.)	$\Upsilon_{\rm ave}$	0.013	0.020	0.030	0.062	0.062	0.127	0.203	
Beamstrahlung parameter (max.)	$\Upsilon_{\rm max}$	0.031	0.048	0.072	0.146	0.146	0.305	0.483	
Simulated luminosity (incl. waist shift)	L	0.56	0.75	1.0	1.8	3.6	3.6	4.9	$\times 10^{34}\,{\rm cm}^{-2}\,{\rm s}^{-1}$
Luminosity fraction within 1 %	$L_{1\%}/L$	91	87	77	58	58	59	45	%
Energy loss from BS	$\delta E_{\rm BS}$	0.65	0.97	1.9	4.5	4.5	5.6	10.5	%
$\rm e^+e^-$ pairs per bunch crossing	$n_{\rm pairs}$	45	62	94	139	139	201	383	$\times 10^3$
Pair energy per B.C.	$E_{\rm pairs}$	25	47	115	344	344	1338	3441	TeV

On the electron side, the BDS starts at the end of the target bypass dogleg of the positron source; on the positron side, it begins at the exit of the machine-protection system of the positron main linac [131]. The main subsystems of the beam delivery are [156]: the fast extraction and tuneup beam line; the betatron and energy collimation; the final focus; the interaction region; and the extraction line. A diagnostic section to determine the beam properties is located at the end of the main linacs. The layout of the beam delivery system is shown in Fig. 8.1. The BDS is designed for 500 GeV centre-of-mass energy but can be upgraded to 1 TeV with additional magnets.

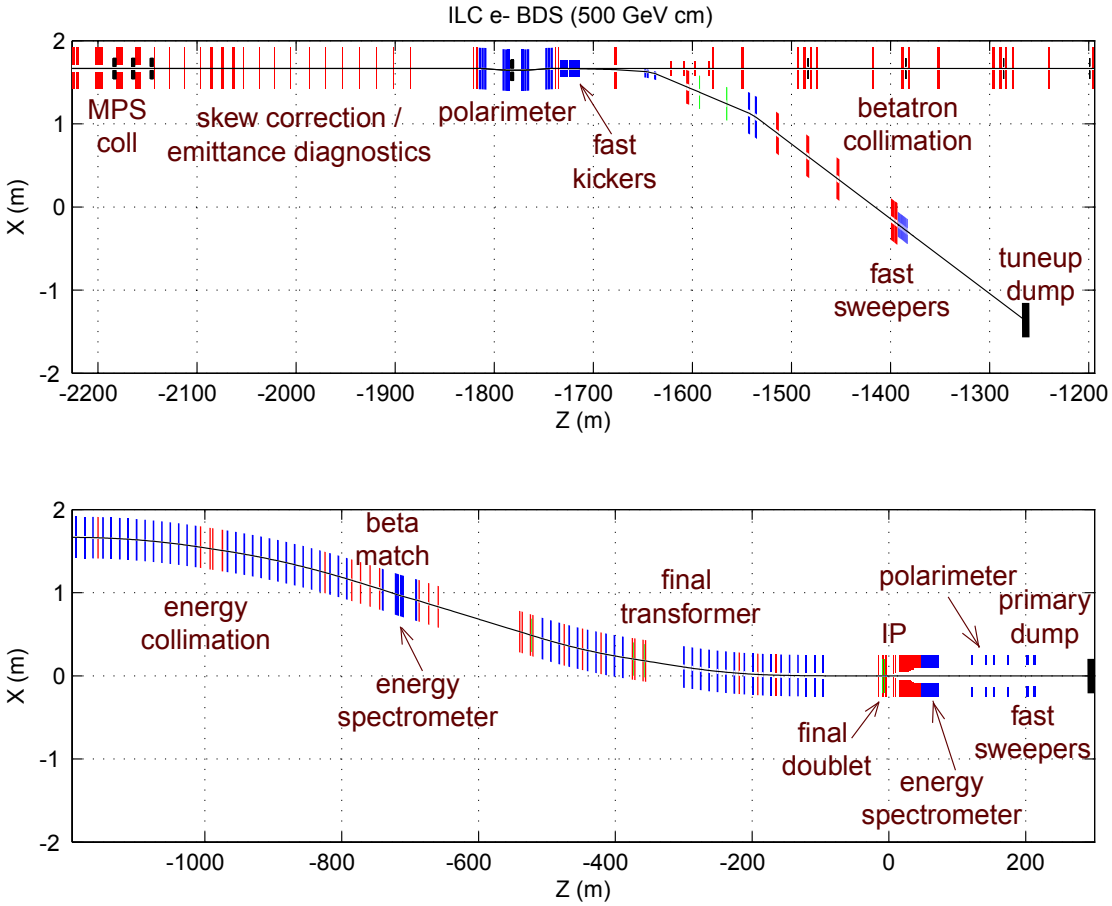

Figure 8.1. BDS layout showing functional subsystems, starting from the linac exit; X – horizontal position of elements, Z – distance measured from the IP.

There is a single collision point with a 14 mrad beam-crossing angle. To support future energy upgrades the beam-delivery systems are in line with the linacs and the linacs are also oriented at a 14 mrad angle. The 14 mrad geometry provides space for separate extraction lines and requires crab cavities to rotate the bunches into the horizontal for head-on collisions. There are two detectors in a common IR hall which alternately occupy the single collision point, in a so-called "push-pull" configuration. This approach, which is significantly more challenging for detector assembly and operation than a configuration with two separate interaction regions, has been chosen for economic reasons.

8.3 Lattice description

The BDS lattice [157] starts 2254 m away from the Interaction Point; on the electron side, the BDS follows the target bypass section of the positron source, while on the positron side it starts after the Machine Protection and Collimation section of the Main Linac [131].

8.3.1 Diagnostics, Tune-up dump, Machine Protection

The initial part of the BDS, from the end of the main linac to the start of the collimation system, is responsible for measuring and correcting the properties of the beam before it enters the Collimation and Final-Focus systems. In addition, errant beams must be detected here and safely extracted in order to protect the downstream systems. Starting at the exit of the main linac, the system includes the skew-correction section, emittance-diagnostic section, polarimeter with energy diagnostics, fast-extraction/tuning system and beta-matching section.

8.3.1.1 Skew Correction

The skew correction section contains 4 orthonormal skew quadrupoles which provide complete and independent control of the 4 betatron-coupling parameters. This scheme allows correction of any arbitrary linearised coupled beam.

8.3.1.2 Emittance Diagnostics

The emittance diagnostic section contains 4 laser wires which are capable of measuring horizontal and vertical RMS beam sizes down to 1 µm. The wire scanners are separated by 45° in betatron phase to allow a complete measurement of 2D transverse phase space and determination of the projected horizontal and vertical emittances.

8.3.1.3 Polarimeter and Energy Diagnostics

A magnetic chicane used for Compton polarimetry and auxiliary beam-energy measurement is situated after the emittance-diagnostic section, directly after the branch-off of the tune-up extraction line [158]. At the center of the chicane is the interaction point for Compton scattering and two BPMs to monitor relative beam-energy changes and the angle. The length of the chicane is set to limit horizontal emittance growth due to synchrotron radiation to less than 1 % with a 500 GeV beam. The detector for the Compton-scattered electrons is placed behind the last chicane magnet.

8.3.1.4 Tune-up and Emergency Extraction System

The pulsed extraction system is used to extract beams in the event of an intra-train Machine Protection System (MPS) alarm. It is also used at any time when beams are not desired in the collimation, final-focus, or IR areas, for example during commissioning of the main linacs. The extraction system includes both fast kickers which can rise to full strength in the 300 ns between bunches, and pulsed bends which can rise to full strength in the 200 ms between trains. These are followed by a transfer line with ±10 % momentum acceptance which transports the beam to a full-beam-power water-filled dump. There is a 125 m drift which allows the beam size to grow to an area of $2\pi\text{mm}^2$ at the dump. A set of rastering kickers sweep the beam in a 6 cm-radius circle on the dump window. By using the nearby and upstream BPMs in the polarimeter chicane and emittance sections, it is possible to limit the number of errant bunches which pass into the collimation system to 1–2.

8.3.2 Collimation System

Particles in the beam halo produce backgrounds in the detector and must be removed in the BDS collimation system. One of the design requirements for the ILC BDS is that no particles are lost in the last several hundred meters of beam line before the IP. Another requirement is that all synchrotron radiation passes cleanly through the IP to the extraction line. The BDS collimation must remove any particles in the beam halo that do not satisfy these criteria. These requirements define a system where the collimators have very narrow gaps and the system is designed to address the resulting machine protection, survivability and issues related to beam-emittance dilution.

The collimation system has a betatron-collimation section followed by energy collimators. The downstream energy collimators help to remove particles whose energy has been degraded that originate in the betatron-collimation section but are not absorbed there. The betatron-collimation system has two spoiler/absorber x/y pairs located at high-beta points, providing single-stage collimation at each of the final doublet (FD) and IP betatron phases. The energy-collimation section has a single spoiler located at the central high-dispersion point (1530 µm/%). Dedicated studies [159] show that two additional quadrupoles between the collimators may be beneficial to tune the phase advance between the collimators and the interaction point. All spoilers and absorbers have adjustable gaps. Protection collimators (PC) are located throughout the system to provide local protection of components and additional absorption of scattered halo particles.

The spoilers are 0.5–1 X_0 (radiation length) thick, the absorbers are 30 X_0, and the protection collimators are 45 X_0. The betatron spoilers as well as the energy spoiler are "survivable", i.e. they can withstand a hit of two errant bunches of 250 GeV/beam, matching the emergency-extraction design goal. With 500 GeV beam, they would survive only one bunch, and would therefore require more effective MPS or the use of a collimator pre-radiator.

The collimation apertures required are approximately $\sim$6–9σ_{x} in the x plane and $\sim$40–60σ_{y} in the y plane. These correspond to typical half-gaps of the betatron spoiler of $\sim$1 mm in the x plane and $\sim$0.5 mm in the y plane.

8.3.2.1 Beam Energy Measurement

Following the energy-collimation section is another magnetic chicane for the beam-energy spectrometer. The chicane consists of four dipoles which introduce a fixed dispersion of $\eta = 5$ mm at the centre. Its length is chosen to limit horizontal emittance growth due to synchrotron radiation to less than 1 % with a 500 GeV beam. Before, after and at the centre of the chicane, the beam line is instrumented with cavity BPMs mounted on translation systems. When operating the spectrometer with a fixed dispersion over the whole energy range, a BPM resolution of 0.5 µm is required.

8.3.2.2 Muon suppression

Electromagnetic showers created by primary beam particles in the collimators produce penetrating muons that can easily reach the collider hall [161]. The muon flux through the detector is reduced by a 5 m-long magnetised iron shield 330 m upstream of the collision point that fills the cross-sectional area of the tunnel and extends 0.6 m beyond the ID of the tunnel, as shown in Fig. 8.2 [162]. The shield has a magnetic field of 1.5 T, with opposite polarities in the left and right halves of the shield such that the field at the beam line is zero. The shield also provides radiation protection for the collider hall during access periods when beam is present in the linac.

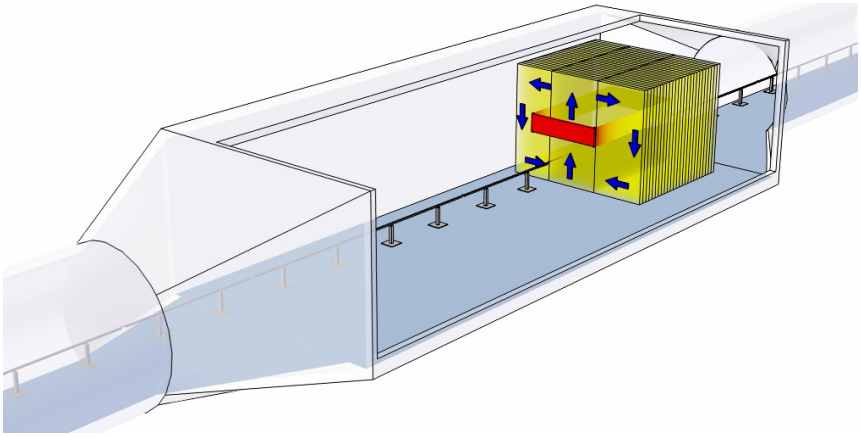

Figure 8.2
Schematic of the 5 m-long magnetised muon shield installed in a tunnel vault which is configured to accommodate a possible upgrade to a 19 m-long shield. The coil is shown in red, and blue arrows indicate the direction of the magnetic field in the iron.

8.3.2.3 Halo-power handling

The power-handling capacity of the collimation system is set by two factors: the ability of the collimators to absorb the incident beam power and the ability of the muon-suppression system to reduce the muon flux through the detector. In the baseline design, the muon-suppression system presents the more restrictive limitation, setting a tolerance of $1 - 2 \times 10^{-5}$ on the fraction of the beam collimated in the BDS. With these losses and the 5 m wall, the number of muons reaching the collider hall would be a few muons per 150 bunches (a reduction by more than a factor of 100). Since the actual beam-halo conditions are somewhat uncertain, the BDS includes caverns large enough to increase the muon shield from 5 m to 19 m and to add an additional 9 m shield downstream. Filling all of these caverns with magnetized muon shields would increase the muon suppression capacity of the system to 1×10^{-3} of the beam. The primary beam spoilers and absorbers are water cooled and capable of absorbing 1×10^{-3} of the beam continuously.

8.3.2.4 Tail-folding octupoles

The final focus includes two superconducting octupole doublets [163]. These doublets use nonlinear focusing to reduce the amplitude of beam-halo particles while leaving the beam core untouched [164]. This "tail-folding" would permit larger collimation amplitudes, which in turn would dramatically reduce the amount of beam power intercepted and the wakefields. In the interest of conservatism, the collimation system design described above does not take this tail folding into account in the selection of apertures and other parameters.

8.3.3 Final focus

The role of the final-focus (FF) system is to demagnify the beam to the required size (∼474 nm horizontal and ∼5.9 nm vertical) at the IP. The FF optics creates a large and almost parallel beam at the entrance to the final doublet (FD) of strong quadrupoles. Since particles of different energies have different focal points, even a relatively small energy spread of ∼0.1 % significantly dilutes the beam size, unless adequate corrections are applied. The design of the FF is thus mainly driven by the need to cancel the chromaticity of the FD. The ILC FF has local chromaticity correction [165] using sextupoles next to the final doublets. A bend upstream generates dispersion across the FD, which is required for the sextupoles to cancel the chromaticity. The dispersion at the IP is zero and the angular dispersion is about $\eta'_x \sim 0.009$, i.e. small enough that it does not significantly increase the beam divergence. Half of the total horizontal chromaticity of the whole final focus is generated upstream of the bend in order for the sextupoles to cancel the chromaticity and the second-order dispersion simultaneously [166].

The horizontal and the vertical sextupoles are interleaved in this design, so they generate third-

order geometric aberrations. Additional upstream sextupoles in proper phase with the FD sextupoles partially cancel the third-order aberrations. The residual higher-order aberrations can be minimised further with octupoles and decapoles. The final-focus optics is shown in Fig. 8.3.

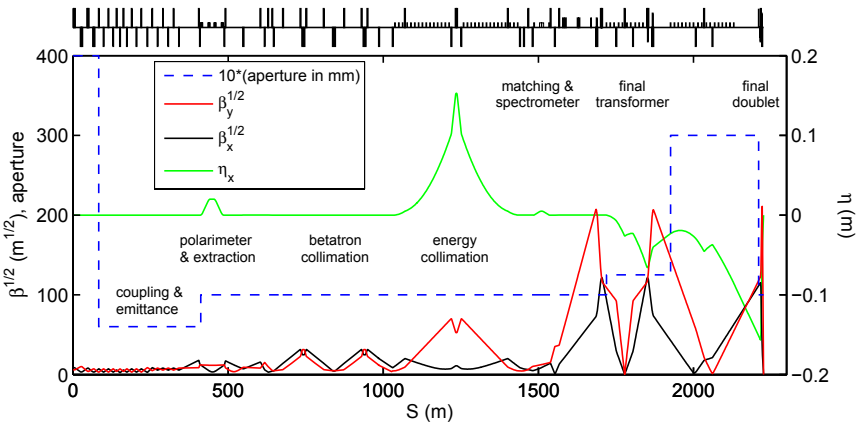

Figure 8.3
BDS optics, subsystems and vacuum chamber aperture; S is the distance measured from the entrance.

Synchrotron radiation from the bending magnets causes emittance dilution, so it is important to maximize the bending radius, especially at higher energies. The FF includes bending magnets for 500 GeV centre-of-mass energy and space for additional bending magnets that are necessary at higher energies. At 500 GeV, every fifth bending magnet is installed, leading to an emittance dilution of 0.5 %; at 1 TeV, with all bending magnets implemented, the figure is 1 %.

In addition to the final-doublet and chromaticity-correction magnets, the final focus includes: an energy spectrometer (see Section 8.7.2.1); additional absorbers for the small number of halo particles that escape the collimation section; tail-folding octupoles (see Section 8.3.2); the crab cavities (see Section 8.9); and additional collimators for machine protection or synchrotron-radiation masking of the detector.

8.3.4 Extraction line

The ILC extraction line [167,168] has to transport the beams from the IP to the dump with acceptable beam losses, while providing dedicated optics for beam diagnostics. After collision, the beam has a large angular divergence and a huge energy spread with very low-energy tails. It is also accompanied by a high-power beamstrahlung photon beam and other secondary particles. The extraction line must therefore have a very large geometric and energy acceptance to minimise beam loss.

The optics of the ILC extraction line is shown in Fig. 8.4. The extraction line can transport particles with momentum offsets of up to 60 % to the dump. There is no net bending in the extraction line, which allows the charged-particle dump to also act as a dump for beamstrahlung photons with angles of up to 0.75 mrad.

The first quadrupole is a superconducting magnet 5.5 m from the IP, as shown in Fig. 8.7. The second quadrupole is also superconducting, with a warm section between their cryostats. The downstream magnets are normal conducting, with a drift space to accommodate the crab cavity in the adjacent beamline. The quadrupoles are followed by two diagnostic vertical chicanes for the energy spectrometer and Compton polarimeter, with a secondary focal point in the centre of the latter. The horizontal angular amplification (R_{22}) from the IP to the Compton IP is set to -0.5 so that the measured Compton polarisation is close to the luminosity weighted polarisation at the IP. The lowest-energy particles are removed by a vertical collimator in the middle of the energy chicane. A large chromatic acceptance is achieved through the soft D-F-D-F quadruplet system and careful optimization of the quadrupole strengths and apertures. The two SC quadrupoles are compatible with up to 250 GeV beam energy, and the warm quadrupoles and the chicane bends with up to 500 GeV.

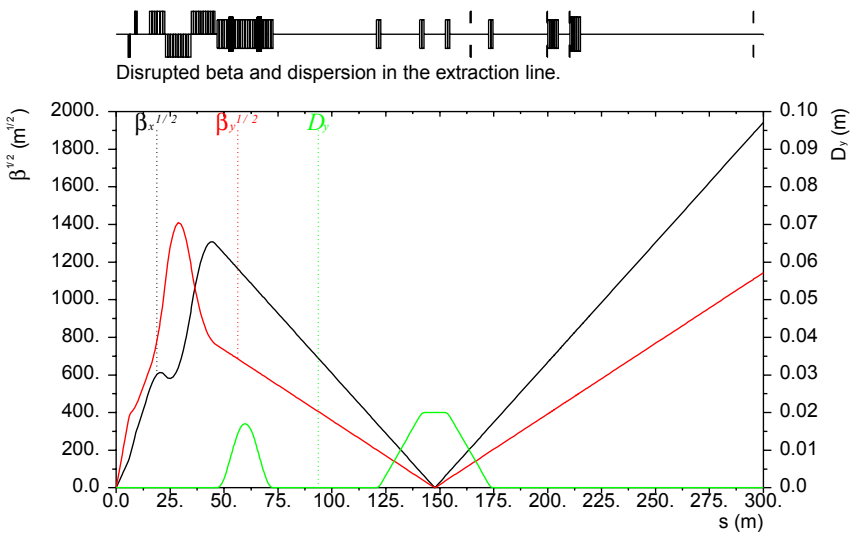

Figure 8.4
Disrupted β-functions and dispersion in the extraction line for the nominal 250 GeV beam.

The diagnostic section is followed by a 100 m-long drift to allow adequate transverse separation (>3.5 m) between the dump and the incoming line. It also allows the beam size to expand enough to protect the dump window from the small undisrupted beam. A set of rastering kickers sweep the beam in a 3 cm circle on the window to avoid boiling the water in the dump vessel. They are protected by three collimators in the 100 m drift that remove particles that would hit outside the 15 cm-radius dump window.

Extraction beam loss has been simulated for realistic 250 GeV GUINEA-PIG beam distributions [169], with and without beam offset at the IP. No primary particles are lost in the SC quadrupoles, and all particles above 40 % of the nominal beam energy are transmitted cleanly through the extraction magnets. The total primary loss on the warm quadrupoles and bends is a few Watts, while the loss on the protection collimators is a few kW for the nominal beam parameters. Figure 8.5 shows that even for an extreme set of parameters, with very high beamstrahlung energy loss, the radiation deposition in the magnet region is manageable.

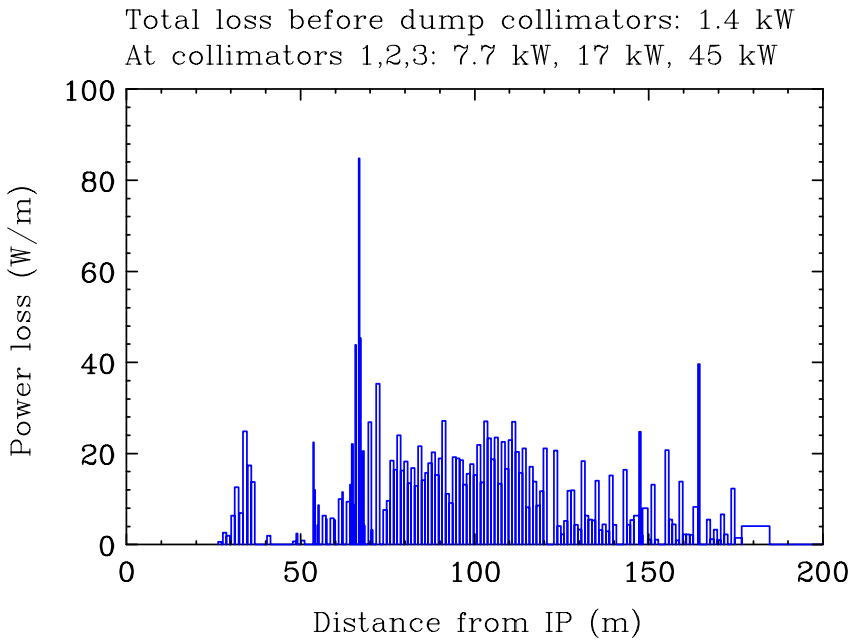

Figure 8.5
Power loss density in the magnet region for disrupted beam at 250 GeV, for high-luminosity operation.

8.3.5 Beam dynamics and emittance growth

Wakefield calculations for the BDS spoilers and absorbers give IP jitter amplification factors [153] of $\mathcal{A}_{\rm x}$ =0.14 and $\mathcal{A}_{\rm y}$ =1.05 for an assumed collimation depth of $9\sigma_x$ and $65\sigma_y$ in the horizontal and vertical planes respectively. Estimated as $\delta\varepsilon/\varepsilon = (0.4\, n_{\rm jitter}\, \mathcal{A})^2$, these parameters give an emittance dilutions of 0.08 % and 4.4 % in the x and y planes respectively, assuming a $0.5\,\sigma$ incoming beam jitter. The current ILC collimation depth is still being re-evaluated and is likely to be smaller, in particular for lower centre-of-mass energy operations. A more stringent requirement on the pulse-to-pulse jitter of $0.2\sigma_y$ will likely be required at the entrance of the BDS (specifically at the collimators), but this should be achievable using the fast intra-train feedback system located at the exit of the linac. Energy jitter at the collimators also amplifies the horizontal jitter at the IP. An energy jitter of 1 % produces a horizontal emittance growth of 2.2 %.

8.4 Interaction-Region Layout and Machine-Detector Interface

8.4.1 Requirements and boundary conditions

The ILC is configured to have two detectors that share one interaction point with only one detector in data-taking position at a time, so-called "push-pull" operation mode. The time spent to roll detectors in and out needs to be as short as possible to maximise the time available for data taking.

The need for high efficiency sets specific requirements and challenges for many detector and machine systems, in particular the IR magnets, the cryogenics, the alignment system, the beamline shielding, the detector design, and the overall integration. The minimal functional requirements and interface specifications for the push-pull IR have been successfully developed and published [170]. This constrains all further IR design on both the detectors and machine. The developments lead to a detailed design of the technical systems and the experimental area layout that follow detailed engineering specifications [171].

8.4.2 The push-pull system

The detector motion and support system is designed to ensure reliable push-pull operation, allowing a hundred moves over the life of the experiment, while preserving the internal alignment of the detector's internal components and ensuring accuracy of detector positioning. The motion system preserves the structural integrity of the collider-hall floor and walls. Moreover, the motion and support system must be compatible with the vibration stability requirements of the detector, which are at the level of tens of nanometers. In regions with seismic activity, the system must also be compatible with earthquake-safety standards.

The detectors are placed on platforms that preserve the detector alignment and distribute the load evenly onto the floor (see Fig. 8.6). The platform also carries some of the detector services like electronic racks. Cables and supply lines are routed to the platform in flexible cable chains that move in trenches underneath the platform itself. In combination with a simple indexing mechanism, the platform with the detector can be positioned quickly within the required precision of 1 mm with respect to the beam axis.

An engineering study on a possible platform design has concluded that the flexure of the platform and the distortion of the cavern invert would total less than $\pm$2 mm [172]. Two different types of transport systems are under study for the platform, air pads and Hilman rollers. In both cases, the platforms are jacked onto the transport system to allow for the movement of a slightly undulating surface. The platform with the detector can be positioned within approximately six hours. In parking or beam position, the platforms are lowered onto permanent supports. Trenches in the hall floor for the cable chains also provide access to the platform undercarriage for maintenance.

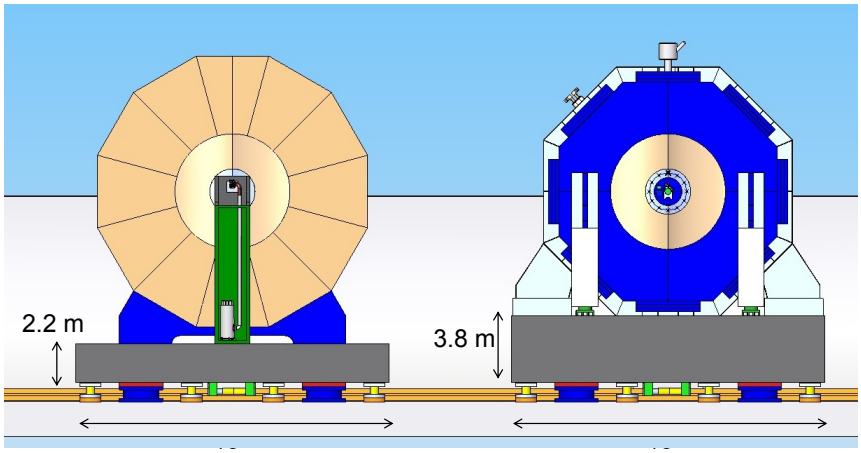

Figure 8.6
Platform support concept for the push-pull system. Left - ILD; right - SiD

8.4.2.1 SiD in a push-pull configuration

As the half-height of SiD is 1.7 m less than that of ILD, an extra thick support platform is required. With the magnetic field on and the endcap doors sucked into the central barrel, SiD is very stiff. The last quadrupole lens package, QD0, rests on a 5 d.o.f. magnetically insensitive mover system which in turn rests on cylindrical cutouts in the doors which are only marginally larger than the diameter of the QD0 cryostat. This design emphasises maximal hermeticity and rapid push-pull detector exchange. The forward-calorimeter package (LumiCal, BeamCal and masking) is logically a cantilevered extension of the QD0 cryostat. An alignment system based on Frequency Scanning Interferometry (FSI) aligns the opposing QD0/FCAL packages to the tunnel-mounted QF1 cryostats that complete the final doublet telescope and ensure precision positioning of the LumiCal with respect to the IP. The same FSI system guarantees vertex- and tracking-detector alignment after each push-pull operation without the need to reacquire beam-based alignment data. This design requires that all mechanical systems mounted on the detector be vibration free. The IP vacuum is assumed to be achievable via QD0 cryo-pumping without external or NEG pumps.

8.4.2.2 ILD in a push-pull configuration

The ILD detector is somewhat larger than SiD and is also designed to be assembled from slices in a similar way to the CMS detector at LHC. The detector placement on the platform preserves detector alignment and distributes the load evenly onto the floor. The platform also carries some of the detector services like electronic racks. The ILD slices have their own motion system based on air pads and grease pads. In the parking position, the detector can be opened for maintenance by moving the yoke slices on air pads from the platform. The QD0 magnets of ILD are supported by an external pillar that couples the magnet directly to the platform floor. In the barrel of the detector, the QD0 magnets are stabilised by a tie-rod system. This arrangement allows the detector end caps to open to some extent without removing the quadrupoles. An FSI system ensures the alignment of the quadrupoles to each other and to the beam line that is defined by the stationary QF1 magnets.

8.4.3 Final focus

The ILC final focus uses independently adjustable compact superconducting magnets for the incoming and extraction beam lines. The adjustability is needed to accommodate beam-energy changes and the separate beam line allows optics suitable for post-IP beam diagnostics. The BNL direct-wind technology is used to produce closely spaced coil layers of superconducting multi-strand cable. The design is extremely compact and the coils are almost touching inside shared cold-mass volumes. Cooling is provided by superfluid helium at 2 K.

To facilitate "push-pull" at a shared IP, the superconducting final-focus magnets are arranged into two groups so that they can be housed in two separate cryostats as shown in Figure 8.7, separated by only warm components and vacuum valves. The first cryostat grouping in Fig. 8.7 moves with the detector during switchover, while the second remains fixed on the beam line.

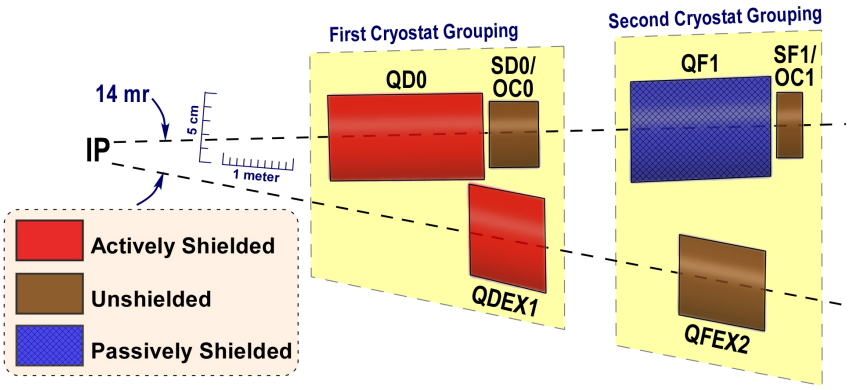

Figure 8.7
Schematic layout of magnets in the IR.

Figure 8.8 shows the engineering model of the magnets that are in the detector-mounted cryostat: the QD0 quadrupole; the sextupole package; and the extraction line quadrupole. In the current design, the QD0 magnet is split into two coils. This allows for higher flexibility in running at lower energies.

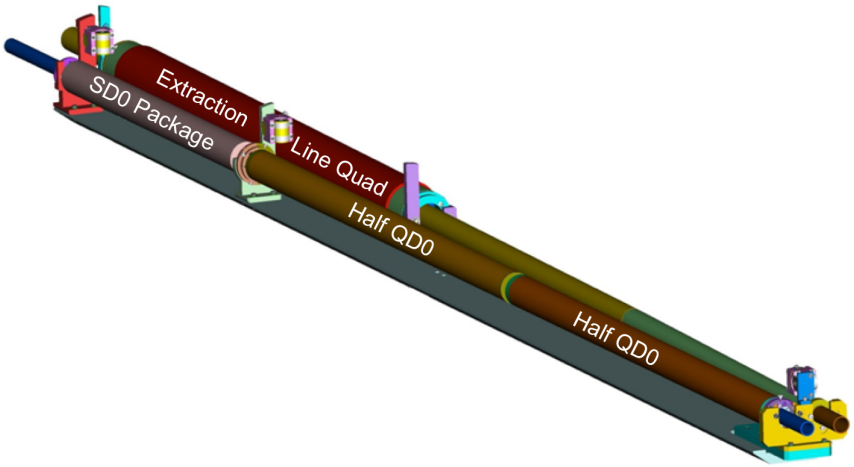

Figure 8.8
Engineering model of the detector-mounted final-focus magnets [173]. The QD0 magnet is split into two coils to allow for energy flexibility.

The technology of the superconducting final-focus magnets has been demonstrated by a series of short prototype multi-pole coils. The schematic layout of magnets in the IR is shown in Fig. 8.7. The quadrupoles closest to the IP are actually inside the detector solenoidal field and therefore cannot have magnetic-flux-return yokes; at the closest coil spacing, the magnetic cross talk between the two beam lines is controlled by using actively shielded coil configurations and by use of local correction coils, dipole, skew dipole and skew quadrupole or skew sextupole, as appropriate.

An additional optical element is required in the IR to compensate the effects of the detector's solenoidal field interacting with the accelerator IR magnets. The so-called large-aperture Detector Integrated Dipole (DID) [175] reduces detector backgrounds at high beam energies, while minimising orbit deflections at low energies.

The vertical position of the centre of the incoming-beam-line quadrupole field must be stable to order of 50 nm, in order to stay within the capture range of the intra-train-collision feedback (see Section 8.7.1 and references [170, 176]). This requirement is well beyond experience at existing accelerators and is being addressed in a world-wide R&D program.

8.4.4 Experimental-area layout and infrastructure

The design layout of the experimental areas – at the surface and underground – needs to fulfil the requirements of both detectors and the machine while at the same time minimising the cost. As the boundary conditions for flat topography sites and for mountain sites for the ILC are very different, two different solutions have been developed.

8.4.4.1 Flat topography sites

At the flat topography ILC sites, e.g. in the US or in Europe, the access to the detector cavern is provided by vertical shafts of $\approx 100\,\mathrm{m}$ length. The detectors are pre-assembled and tested in large sections in surface buildings, similar to what was done for CMS. Only late in the construction phase, about one year before the machine start-up, can the detector parts be lowered via a large shaft of 18 m diameter into the cavern. This procedure decouples to a large extent the time lines of the civil construction and the machine and detector installation work. In addition, the space in the underground cavern is minimised as no lengthy detector-installation procedures need to be done there.

Figure 8.9 shows the layout for these sites. The hall floor layout follows a z-shape that allows for two maintenance positions where detector parts could be moved away from the push-pull platform. The platforms run along the straight section of the hall, perpendicular to the beam line. Access is provided by a set of five vertical shafts. The largest, with 18 m diameter, is only used in the installation phase of both detectors. It is located directly over the IP, so that the heavy detector parts with masses of up to 3500 t can be lowered directly onto the respective platforms. Two shafts of 8 m and 10 m diameter are located in the maintenance parts of the hall. They provide independent access to each maintenance region so that one detector can always take data undisturbed at the beam position. These shafts allow transport of material for maintenance and upgrades and contain service lines (power, data, cooling, etc.) into the hall. Two small 6 m additional shafts are needed for personnel transport and safety egress.

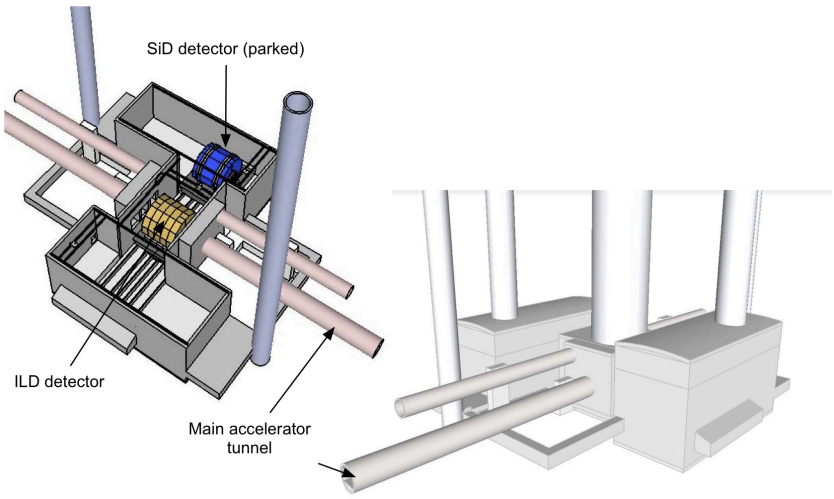

Figure 8.9
Layout of the detector cavern for the American region.

8.4.4.2 Mountainous sites

At the mountainous sites that are under study in Japan, no vertical access will be possible to the detector cavern. All material and personnel needs to be brought into the hall via an access tunnel of $\approx 1\,\mathrm{km}$ length that may have a slope of up to 10 %. The diameter of this tunnel and the capacity of the transport system limits the masses and sizes of the detector parts that can be brought into the hall. This forbids the application of the CMS-type detector-assembly scheme as described above.

A modified scheme is needed, where most of the detector assembly is done inside the underground cavern. The largest parts that cannot be assembled in situ are the superconducting coils of the detector solenoids. They define the diameter of the access tunnel to be $\approx 11\,\mathrm{m}$.

Figure 8.10 shows the underground cavern for the Japanese sites. The access tunnel on the right extends beyond the cavern to the central ILC region with the damping rings. The larger entrance into the hall is used for ILD, the slightly smaller rear entrance for SiD. The SiD coil is smaller and fits into the tapered tunnel that passes underneath the ILC beam line. The main cavern has alcoves that extend the parking positions of the detectors to allow the unslicing and maintenance operations. The assembly phase of the detectors in this arrangement takes much longer inside the cavern ($>3\,\mathrm{y}$ compared to $1\,\mathrm{y}$ in the flat topography case) and needs careful planning of the use of the underground space and the transport capacity in the access tunnel.

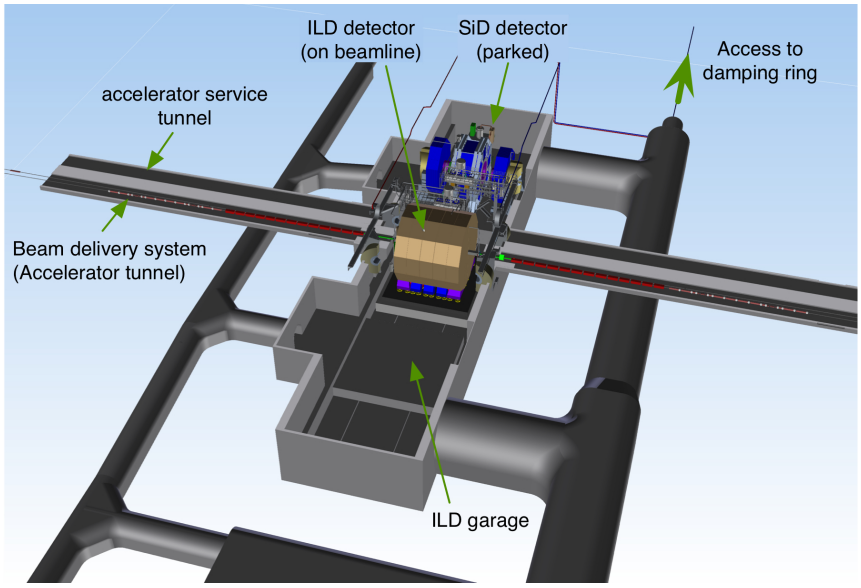

Figure 8.10
Layout of the detector cavern for mountainous sites.

8.4.5 Shielding

8.4.5.1 Radiation

The ILC detectors are self-shielding with respect to ionising radiation stemming from maximum-credible-beam-loss scenarios [177]. Additional shielding in the hall is necessary to fill the gap between the detector and the wall in the beam position. The design of this beam-line shielding needs to accommodate both detectors, SiD and ILD, which are significantly different in size. A common 'pac-man' design has been developed, where the movable shielding parts are attached to the wall of the detector hall and matched to interface pieces on the experiments (see Fig. 8.11).

8.4.5.2 Magnetic fields

The magnetic stray fields outside the iron return yokes of the detectors need to be small enough to cause no disturbance to the other detector during operation or maintenance. The magnetic-field limit has been set to $5\,\mathrm{mT}$ at a lateral distance of $15\,\mathrm{m}$ from the beam line [170]. This allows the use of standard iron-based tools at the other detector. The design of the detector return yokes has been verified in simulations for the design fringe fields.

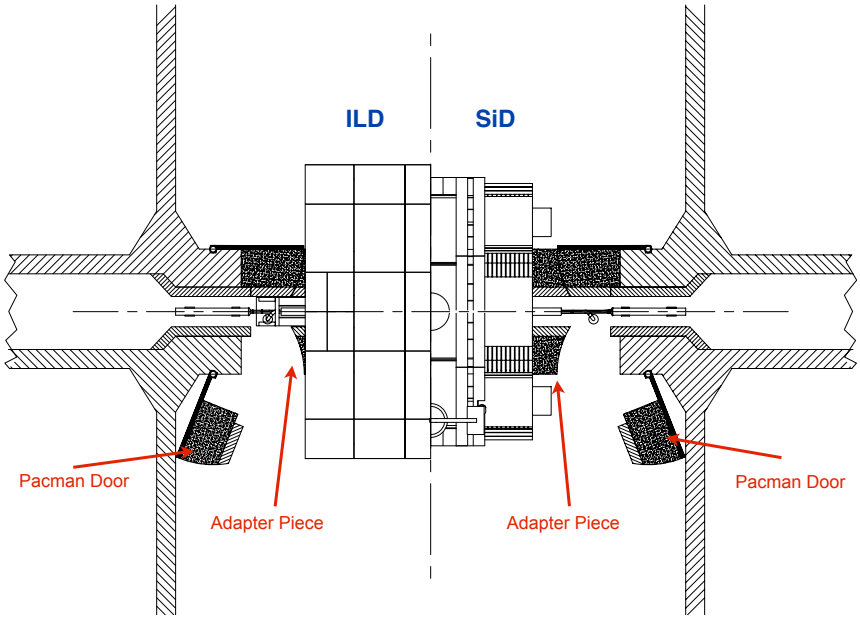

Figure 8.11
Design of the beamline shielding compatible with two detector of different size.

8.4.6 Detector services

Services are required for the operation and maintenance of both detectors, with different requirements on their proximity to the detector. Primary services are located on the surface above the experimental hall (in the flat-topography sites) or in nearby service caverns (in the mountainous sites). There are usually large and sometimes noisy facilities such as water chillers, high-voltage transformers, auxiliary power supplies, Helium storage and compressors and gas-storage systems. Secondary services are placed in the underground cavern in dedicated service areas. Examples are cooling-water distributions, power supplies, gas-mixture systems, power converters, and parts of the cryogenic system for the detectors. As the detectors are not disconnected during push-pull exchange, all supplies that go directly to the detector are run in flexible cable chains. The detectors carry on-board those services that need short connections, e.g. front-end electronics, patch panels, electronic containers.

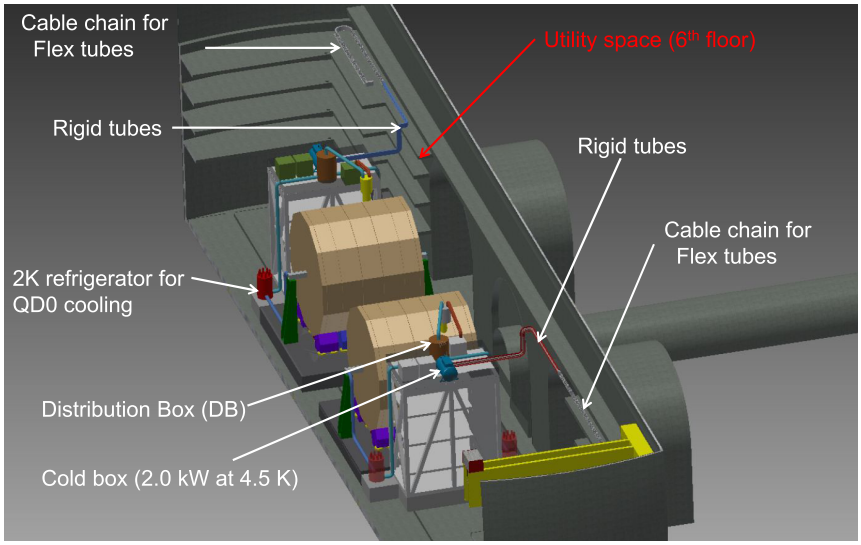

Figure 8.12
Common detector cryogenic system (study) with the cold boxes placed on service racks close to the detectors.

Cryogenic Helium for the superconducting solenoids and the QD0 magnets is supplied by a common system for both detectors. Two solutions are currently under study. In one, the liquid He is brought to the detectors via flexible cryogenic lines (see Fig. 8.12), and the cold boxes are in service areas at the cavern walls. The second solution places the cold boxes close to the detectors while

gaseous He is supplied via flexible lines to the detector platforms. In each case, a re-cooler is placed on the platform of each detector for the 2 K He supply of the QD0 magnets.

8.5 Magnets and power supplies

The BDS has a wide variety of different magnet requirements, and the most distinct magnet types (67) of any ILC area, even though there are only 636 magnets in total. Of these, 86 are superconducting magnets clustered into 4 cryostats close to the IP, as described in Section 8.4.3, and the tail-folding octupoles described below. There are 64 pulsed magnets: 5 types of abort kickers, sweepers and septa. These are used to extract the beams to a fast extraction/tuning dump and to sweep the extracted beam in a 3 cm circle on a dump window.

The remaining 474 magnets are conventional room-temperature magnets, mostly with low-carbon steel cores and water-cooled coils of hollow copper conductor. The bending magnets in the final focus have fields of less than 0.5 kG to minimize synchrotron radiation that would cause beam dilution; they use solid wire coils. The quadrupoles and sextupoles have straight-forward designs adequate for up to 500 GeV beam. The extraction-line magnets have large apertures, e.g. over 90 mm and up to 272 mm, to accommodate the disrupted beam and the photons emerging from the IP. These magnets must fit in alongside the incoming beamline.

The main technical issue with the BDS magnets is their positional stability. All the incoming beam line quadrupoles and sextupoles sit on 5 degree-of-freedom magnet movers with a smallest step size of 50 nm. Data on the relative position of each magnet with respect to the beam is provided by BPMs inserted in the magnet bores so that the magnets can be moved if necessary. The absolute field strength of the BDS magnets has a tight tolerance, requiring power supplies with stability of a few tens of ppm for the tightest tolerances, although most are looser. Magnet-temperature changes lead to strength and position variations so the ambient temperature in the tunnel must be controlled to a relative temperature of about 0.5 °C and the cooling water to within 0.1 °C.

8.5.1 Tail-Folding Octupoles

The tail-folding octupoles are the only superconducting magnets in the BDS (other than the FD and extraction quadrupoles) and have the smallest (14 mm ID) clear working aperture in order to reach the highest practical operating gradient. The magnets are energised via NbTi conductor cooled to 4.5 K. With such a small aperture, the beam pipe must have high conductivity to minimise the impact of wakefields. This can be achieved with a beam pipe at 4.5 K made of either aluminium or stainless-steel with a high-conductivity coating. Because these magnets are isolated in the BDS, being far from either the IP or the linac, cryocoolers are used to provide standalone cooling.

8.6 Vacuum system

While the aperture of the BDS vacuum chamber is defined by the sizes of the beam, its halo and other constraints, the design of the chambers and vacuum level are governed mainly by two effects: resistive and geometric wakes and the need to preserve the beam emittance; beam-gas scattering and minimisation of detector background.

8.6.1 Wakes in vacuum system

The resistive-wall (RW) wakefield of the BDS vacuum system and the geometric wakefield of the transitions in the beam pipe may cause emittance growth due to incoming (transverse) jitter or drift, or due to beam-pipe misalignment. In order to limit these effects to tolerable levels, the inner surface of the BDS vacuum chamber is coated with copper, the vacuum chambers are aligned with an RMS accuracy of $\sim 100\,\mu$m [178], and incoming beam jitter is limited to 0.5 σ_y train-to-train and 0.25 σ_y within a train, to limit the emittance growth to 1–2 %.

8.6.2 Beam-gas scattering

The specification for the pressure in the BDS beam pipe is driven by detector tolerance to beam-gas-scattering background. Studies have shown that electrons scattered within 200 m of the IP can strike the beam pipe within the detector and produce intolerable backgrounds, while electrons which scatter in the region from 200 to 800 m from the IP are much more likely to hit the protection collimator upstream of the final doublet and produce far less severe detector backgrounds [179]. Based on these studies, the vacuum in the BDS is specified to be 0.1 µPa within 200 m of the IP, 1 µPa from 200 m to 800 m from the IP, and 5 µPa more than 800 m from the IP.

In the extraction lines, the pressure is determined by backgrounds from beam-gas scattering in the Compton polarimeter located about 200 m from the IP. Here the signal rates are large enough that 5 µPa would contribute a negligible background in the detectors.

8.6.3 Vacuum-system design

The BDS vacuum is a standard UHV system. The main beam pipes are stainless steel, copper coated to reduce the impedance, with the option of an aluminum-alloy chamber. In locations where there is high synchrotron-radiation (SR) power ($\geq 10\,\mathrm{kW/m}$) (e.g. in the chicanes or septa regions), the beam pipe is copper with a water-cooled mask to intercept the photons. The beam pipes are cleaned and baked before installation. There is no *in situ* baking required except possibly for the long drift before the IP.

The required maximum pressure of 5 µPa (N_2/CO equivalent) can be achieved by standard ion pumps located at appropriate intervals. The beam pipe near the IP must have pressure below 0.1 µPa for background suppression, and may be baked *in situ* or NEG-coated.

8.7 Instrumentation and feedback systems

8.7.1 Feedback systems and Stability

Maintaining the stability of the BDS is an essential prerequisite to producing luminosity. Since the beams have RMS vertical sizes of roughly 6 nm at the IP, vertical offsets of about 1 nm will noticeably reduce the luminosity. In addition, especially for parameter sets with higher disruption, the beam-beam interaction is so strong that the luminosity is extremely sensitive to small variations in the longitudinal shape of the bunch caused by short-range wakefields. Finally, the size of the beam at the IP is sensitive to the orbit of the beam through the final-doublet quadrupoles, the sextupoles and other strong optical elements of the BDS. Care must be taken to minimise thermal and mechanical disturbances, by stabilising the air temperature to 0.5 °C and the cooling water to 0.1 °C, and by limiting high-frequency vibrations from local equipment to ~ 100 nm.

Beam-based orbit-feedback loops are used to maintain the size and position of the beam at the IP. All of the feedback loops use beam-position monitors with at least micron-level (and in some cases sub- micron) resolution to detect the beam position and dipole magnets or stripline kickers to deflect the beam. There are two basic forms of feedback in the BDS: train-by-train feedbacks, which operate at the 5 Hz repetition rate of the ILC, and intra-train feedbacks, which can apply a correction to the beam between bunches of a single train.

8.7.1.1 Train-by-train feedback

A train-by-train feedback with five correctors controls the orbit through the sextupoles in the horizontal and vertical planes, where the optical tolerances are tightest. Additional correctors throughout the BDS help reduce long-term beam-size growth. The orbit control feedback can maintain the required beam sizes at the IP over periods from a few hours to several days depending on details of the environment. On longer timescales, IP dispersion and coupling knobs need to be applied.

8.7.1.2 Intra-Train IP position and angle feedbacks

The intra-train feedbacks use the signals detected on early bunches in the train to correct the IP position and angle of subsequent bunches. The offset of the beams at the IP is determined by measuring the deflections from the beam-beam interaction; this interaction is so strong that nanometre-level offsets generate deflections of tens of microradians, and thus BPMs with micron-level resolution can be used to detect offsets at the level of a fraction of a nanometer. Corrections are applied with a stripline kicker located in the incoming beam line between SD0 and QF1. The angle of the beams at the IP is determined by measuring the beam positions at locations 90° out of phase with the IP; at these locations the beam is relatively large so micron resolution is sufficient to measure the beam position (and hence the IP angle) directly to a small fraction of its RMS size. A stripline kicker for the angle correction is located at the entrance to the final focus, causing a latency of about four bunch spacings.

The position-feedback BPM is located near the IP in a region where electromagnetic backgrounds or particle debris from the collisions are a concern. Results from simulations and from a test-beam experiment indicate that backgrounds are an order of magnitude too small to cause a problem [180].

8.7.1.3 Luminosity feedback

Because the luminosity may be extremely sensitive to bunch shape, the maximum luminosity may be achieved when the beams are slightly offset from one another vertically, or with a slight nonzero beam-beam deflection. After the IP position and angle feedbacks have converged, the luminosity feedback varies the position and angle of one beam with respect to the other in small steps to maximize the measured luminosity.

8.7.1.4 Hardware Implementation for intra-train feedbacks

High-bandwidth, low-latency ($\sim$ 5 ns) signal processors for stripline and button BPMs have been tested at the NLCTA, ATF [181] and ATF2 [182]. The feedback processor has been prototyped using fast state-of-the-art FPGAs. A complete system prototype has been demonstrated with a total latency of $\sim$ 140 ns [183].

8.7.2 Energy, Luminosity and polarization measurements

8.7.2.1 Energy measurements

Absolute beam-energy measurements are required by the ILC physics program to set the energy scale for particle masses. An absolute accuracy better than 200 ppm is required for the centre-of-mass energy, which implies a requirement of 100 ppm on determination of the absolute beam energy. The intra-train relative variation in bunch energies must be measured with a comparable resolution. Measurements of the disrupted energy spectrum downstream of the IP are also useful to provide direct information about the collision process. It is important that the energy spectrometers be able to make precision energy measurements between 45.6 GeV (Z-pole) and the highest ILC energy of 500 GeV. A precise measurement at Z-pole energies is of particular importance since it defines the absolute energy scale.

To achieve these requirements, there are two independent and complementary measurements for each beam [158]. About 700 m upstream of the IP, a spectrometer similar to the one employed at LEP-II [184] is capable of making high-precision bunch-to-bunch relative measurements in addition to measuring the absolute beam-energy scale. A four-magnet chicane in the energy-spectrometer region provides a point of dispersion which can be measured using triplets of high-precision RF BPMs. The nominal displacement of the beam is 5 mm and must be measured to a precision of 100 microns. Precision movers keep the beam nearly centred in the BPMs in order to achieve this accuracy.

About 55 m downstream from the IP is a synchrotron radiation spectrometer [185]. A three-magnet chicane in the extraction line, shown in Fig. 8.13, provides the necessary beam deflection, while the trajectory of the beam in the chicane is measured using synchrotron radiation produced in wiggler magnets imaged $\sim 70\,\mathrm{m}$ downstream at a secondary focus near the polarimeter chicane. The synchrotron light produced by the wigglers also comes to a vertical focus at this point, and position-sensitive detectors in this plane arrayed outside the beam pipe measure the vertical separation between bands of synchrotron radiation.

The energy spectrum of the beam after collision contains a long tail as a result of the beam-beam disruption in the collision process. This disrupted beam spectrum is not a direct measure of the collision energy spectrum, but it is produced by the same physical process, and direct observation of this disrupted tail serves as a useful diagnostic of the collision process. The position-sensitive detector in the spectrometer is designed to measure this beam-energy spectrum down to 50 % of the nominal beam energy.

8.7.2.2 Luminosity measurements

The ILC luminosity can be measured with a precision of 10^{-3} or better by measuring the Bhabha rate in the polar-angle region from 30–90 mrad. Two detectors are located just in front of the final doublets. The LumiCal covers the range from 30–90 mrad and the BeamCal covers the range from 5–30 mrad. At 500 GeV centre-of-mass energy, the expected rate in the LumiCal region is ~ 10 Bhabhas per bunch train, which is too low to permit its use as an intra-train diagnostic for tuning and feedback. At smaller polar angles of 5-30 mrad the rate or energy deposition of beamstrahlung $\mathrm{e^+e^-}$ pairs can be measured and provides a fast luminosity diagnostic. The expected rate in this region is 15 000 pairs (and 50 TeV energy deposition) per bunch crossing. Furthermore, the spatial distributions of pairs in this region can be used to determine beam-collision parameters such as transverse sizes and bunch lengths.

8.7.2.3 Polarisation measurements

Precise polarimetry with 0.25 % accuracy is needed to achieve the ILC physics goals [186]. Compton polarimeters [158] are located both $\sim$ 1800 m upstream of the IP, as shown in Fig. 8.1, and downstream of the IP, as shown in Fig. 8.13, to achieve the best accuracy for polarimetry and to aid in the alignment of the spin vector.

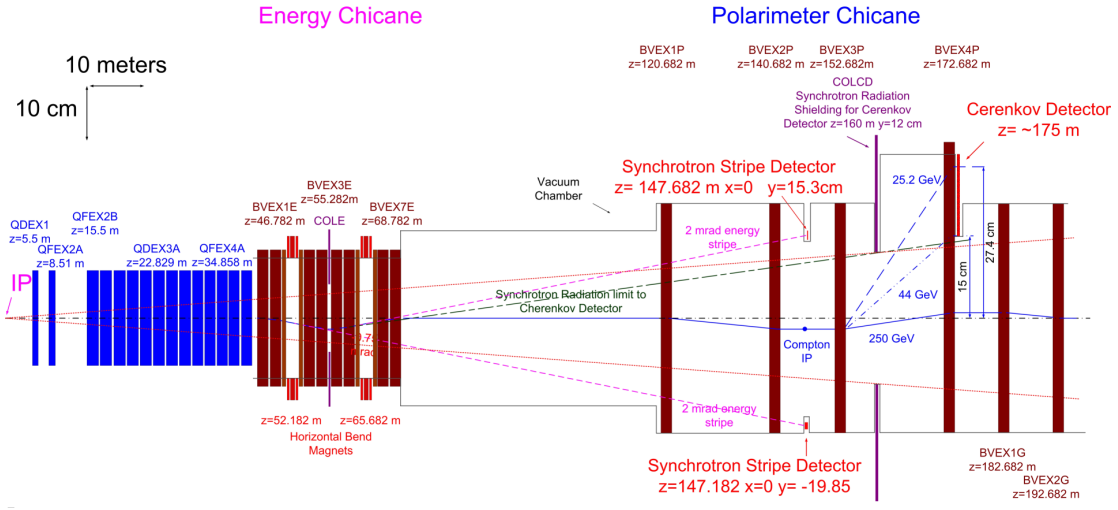

Figure 8.13. Schematics of energy and polarimeter chicanes in the 14 mrad extraction line, shown in a configuration with two additional bends at the end. Longitudinal distances are given from the IP. Also shown is the 0.75 mrad beam stay-clear from the IP.

The upstream polarimeter measures the undisturbed beam before collisions. It consists of a dedicated 4-bend horizontal chicane with the Laser-Compton IP in the middle and a detector for the Compton-scattered electrons at the end, as shown in Fig. 8.14. The length of the chicane is chosen such that the total emittance growth due to synchrotron radiation stays below 1%, even at the highest beam energy of 500 GeV. The relatively clean environment allows a laser system that measures every single bunch in the train and a large lever arm in analysing power for a multi-channel detector, which facilitates internal systematic checks. The good field region of the individual dipoles is wide enough to accommodate all beam energies from 500 GeV down to 45.6 GeV.

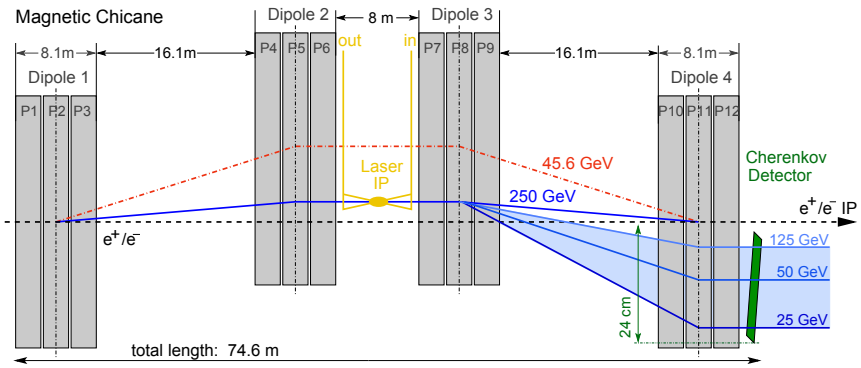

Figure 8.14 Schematics of upstream polarimeter chicane.

The downstream polarimeter measures the polarisation of the outgoing beam after collision. The estimated average depolarisation for colliding beams is 0.3 %, and for the outgoing beam 1 %. A schematic drawing of the extraction line is shown in Fig. 8.13. In the high background environment of the disrupted beam, the required high laser power allows measurement of only a few bunches out of each train. The chicane of the downstream polarimeter consists of six vertical bends to maximise the analysing power and to deflect the Compton-scattered electrons out of the synchrotron-radiation fan [187].

Both polarimeters are designed to meet the physics requirements at all energies from the Z pole to the full energy of the ILC.

8.7.3 Diagnostic and Correction devices

Each quadrupole, sextupole, and octupole magnet in the incoming BDS beam lines is placed on a 5 degree-of-freedom mover, and has an associated BPM. There are also several tens of correctors in the incoming beam lines for 5 Hz feedback, and in the extraction lines, where there are no movers. The BPMs in the incoming beam line are RF cavities, either S, C or L-band, depending on the beam line aperture. Long chains of bends or kickers have sparsely placed BPMs. BPMs in the extraction lines are button or strip-line design.

Additional instrumentation in the BDS includes a deflecting cavity to measure vertical-time correlation, ion-chamber and PMT loss monitors, transverse profile monitors for horizontal synchrotron light, OTR monitors, current monitors, pickup phase monitors, etc.

8.8 Beam dumps and Collimators

8.8.1 Main Dumps

The beam-delivery system contains two tune-up dumps and two main beam dumps. These four dumps are all designed for a peak beam power at nominal parameters of 18 MW at 500 GeV per beam, which is also adequate for the 14 MW beam power of the 1 TeV upgrade. The dumps consist of 1.8 m-diameter cylindrical stainless-steel high-pressure (10 bar) water vessels with a 30 cm diameter, 1 mm-thick Ti window and also include their shielding and associated water systems (Fig. 8.15). The design [188] is based on the SLAC 2.2 MW water dump [189, 190].

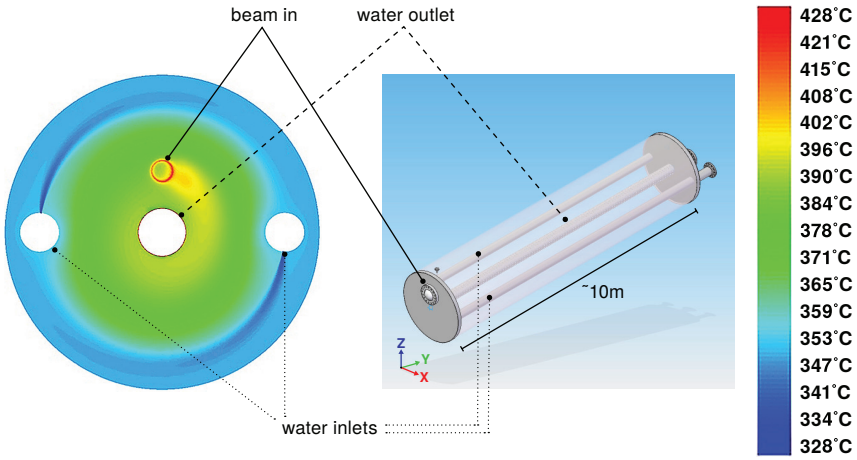

Figure 8.15 Temperature distribution at the shower maximum of the beam in the main 18 MW dump just after passage of the beam train (left). (The geometry of the dump is also shown on the right.) The colour bar shows temperature in kelvin; the maximum temperature is 155 °C [191].

The dumps absorb the energy of the electromagnetic shower cascade in 11 m ($30\,X_0$) of water. Each dump incorporates a beam-sweeping magnet system to move the charged beam spot in a circular arc of 6 cm radius during the passage of the 1 ms-long bunch train. Each dump operates at 10 bar pressure and also incorporates a vortex-flow system to keep the water moving across the beam. In normal operation with 500 GeV beam energy, the combination of the water velocity and the beam sweepers limits the water temperature rise during a bunch train to 155 °C [191]. The pressurisation raises the boiling temperature of the dump water; in the event of a failure of the sweeper, the dump can absorb up to 250 bunches without boiling the dump water.

The integrity of the dump window, the processing of the radiolytically evolved hydrogen and oxygen, and containment of the activated water are important issues for the full-power dumps. The dump service caverns include three-loop pump-driven 145 L/s heat-exchanger systems, devices to remotely exchange dump windows during periodic maintenance, catalytic H_2-O_2 recombiners, mixed-bed ion-exchange columns for filtering of ^{7}Be, and sufficient storage to house the volume of tritiated water during maintenance operations.

8.8.1.1 Ensuring the integrity of the dump and dump window

The main vessel is welded using low-carbon stainless steel (316L) and all welds are radiographed to ensure quality; the 10 bar radioactive-water cooling system is closed but communicates with the atmosphere via a small diameter tube from the gas space on top of the surge tank to avoid it being classified as a nuclear pressure vessel. Several materials are under consideration for use in the dump window: 316L stainless, Ti-6Al-4V, and Inconel (A601,718,X750). All of these materials have been extensively used in nuclear reactors; their mechanical properties, thermal properties, and reaction to radiation damage have been thoroughly studied. As described above, the bunches in each train are swept in a circle to reduce further the thermal stress and radiation damage to the dump windows; the windows also have additional water cooling from multiple water jets in a separate cooling loop from the main vessel. Each dump incorporates a remote-controlled mechanism for exchanging the highly

activated windows on a regular schedule driven by integrated specific dose, along with local temporary storage for all tritiated water. As a final backup to guarantee environmental safety in the event of a failure of the dump body or dump window, the dump enclosure is air tight and incorporates adequate sump volume and air drying capacity to prevent the release of tritiated water even in the case of catastrophic dump failure. Since a failure of the window could create a catastrophic water-to-vacuum leak with highly radioactive tritiated water, a pre-window, with peripheral and gas cooling, isolates the beamline vacuum system and provides secondary containment. Storage space for a damaged dump and a removable cavern wall are provided for dump replacement.

8.8.1.2 Mitigation of water-activation products

Activation products are primarily the result of photo-spallation on ^{16}O, primarily ^{15}O, ^{13}N, ^{11}C, ^{7}Be and ^{3}H (tritium). The first three radionuclides have short half lives and decay after $\sim$ 3 hours. The ^{7}Be is removed from the system by filtering it out in a mixed-bed ion-exchange column located in the dump-support cavern. Tritium, a $\sim$ 20 keV β emitter with a half life of 12.3 years, builds up in the water to some equilibrium level; the tritium is contained by the integrity of the dump system and the backup measures described in the preceding section.

8.8.1.3 Radiolysis and hydrogen and oxygen evolution

Hydrogen is produced via the reaction $H_2O \rightarrow H_2 + H_2O_2$ at the rate of 0.3 L/ MW s, or 5.4 L/s at 18 MW beam power. The lower explosive limit (LEL) of hydrogen in air is $\sim$ 4 %. Experience at SLAC [192] indicates that a catalyst consisting of a high-nickel stainless-steel ribbon coated with platinum and palladium, in the form of a 46 cm diameter 6.4 cm-thick mat, will reduce the H_2 concentration to 25 % of the LEL in one pass. Other types of higher-density catalyst are also available. The gases released in a surge tank are heated to 65 °C and are pumped through the catalyst, which does not need replacement or servicing.

8.8.1.4 Shielding and protection of site ground water

Assuming a dry rock site, as in the baseline configuration, 50 cm of iron and 150 cm of concrete shielding are needed between the dump and other areas of the tunnel enclosure to protect equipment from radiation damage. If the chosen site is not dry, the area surrounding the dump must be enveloped by an additional 2 m-thick envelope of concrete to prevent tritium production in the ground water.

8.8.2 Collimators

The beam-delivery system contains 32 variable-aperture collimators and 32 fixed aperture collimators. The devices with the smallest apertures are the 12 adjustable spoilers in the collimation system. To limit their impedance to acceptable levels, these 0.6–1.0 X_0 Ti spoilers have longitudinal Be tapers. Figure 8.16 shows a collimator design suitable for the ILC [160, 193].

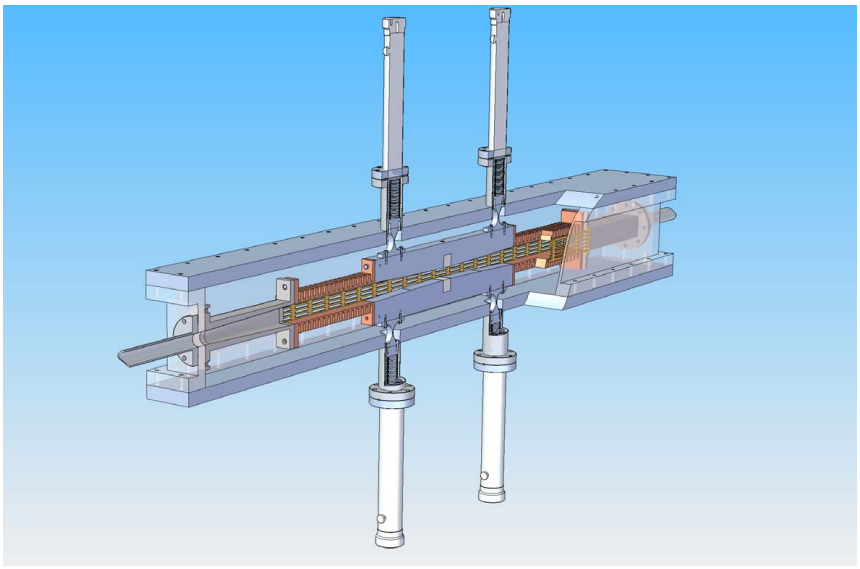

Figure 8.16
Tentative spoiler candidate design [160, 193].

8.9 Crab cavity system

Crab cavities are required to rotate the bunches from a 14 mrad crossing angle so they collide head on. Two 3.9 GHz SC 9-cell cavities in a 2–3 m long cryomodule are located 13.4 m from the IP. The cavities are based on the Fermilab design for a 3.9 GHz TM_{110} π-mode 13-cell cavity [194, 195]. The ILC has two 9-cell versions (see Fig. 8.17) of this design operated at 5 MV/m peak deflection. This provides enough rotation for a 500 GeV beam and 100 % redundancy for a 250 GeV beam [196, 197].

The most challenging specification of the crab-cavity system is on the uncorrelated phase jitter between the incoming positron and electron cavities which must be controlled to 61 fsec to maintain optimised collisions [199]. A proof-of-principle test of a 7-cell 1.5 GHz cavity at the JLab ERL facility [200] has achieved a 37 fsec level of control, demonstrating feasibility. The higher- and lower-order modes of the cavity must be damped effectively to limit unwanted vertical deflections at the IP, as must the vertical polarization of the main deflecting mode.

Couplers with lower Q_{ext} and greater power-handling capability are required to handle beam loading and LLRF feedback for off-axis beams. The crab cavity needs $\sim$ 3 kW per cavity for about 10 msec, with a Q_{ext} of $\sim 10^6$ [196–198, 201]. The crab cavity is placed in a cryostat with tuner, $x - y$ and roll adjustment which provides proper mechanical stability and microphonic rejection. The cryostat also accommodates the beam pipe of the extraction line which passes about 19 cm from the centre of the cavity axis.

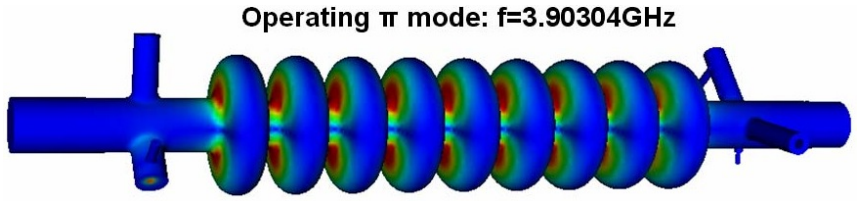

Figure 8.17
Field distribution for the operating mode of the 3.9 GHz crab cavity [198].

8.10 Accelerator Components

The total counts of the BDS accelerator components are summarized in Table 8.3.

Table 8.3 BDS components, total counts.

Magnets		Instrumentation		Dumps & Collimators	
Warm dipoles	190	BPMs C-band	262	Full power dumps	4
Warm quads	204	BPMs L-band	42	Insertable dumps	2
Warm sextupoles	10	BPMs S-band	14	Adjustable collim.	32
Warm octupoles	4	BPMs stripline/button	120	Fixed apert. collim.	32
SC quads	32	Laser wire	8	Stoppers	14
SC sextupoles	12	SR transv. profile imager	10		
SC octupoles	14	OTR screens	2	Vacuum	
Muon spoilers	2	Crab & deflection cavities	4	Pumps	3150
		Loss monit. (ion chamb., PMT)	110	Gauges	28
Warm correctors	64	Current monitors	10	Gate valves	30
SC correctors	36	Pick-up phase monitors	2	T-connections	10
Kickers/septa	64	Polarimeter lasers	3	Switches	30

Chapter 9
Global Accelerator Control Systems

9.1 Overview

Rapid advances in electronics and computing technology in recent decades have had a profound effect on the performance and implementation of accelerator control systems. These advances will continue through the time of ILC construction, when network and computing capabilities will far surpass that of equipment available today. Nevertheless, a machine of the scope of an ILC presents some unique control system challenges independent of technology, and it is important to set out functional requirements for the ILC control system.

This section discusses the control-system requirements for the ILC, and describes a functional and physical model for the system. In several places implementation details are described, but this has been done largely as a means to describe representative technologies, and in particular, to establish a costing model. Regardless of the final technology implementation, the control system model described in this chapter contains a number of architectural choices that are likely to survive.

9.2 Requirements and Technical Challenges

The broad-scope functional requirements of the ILC control system are largely similar to those of other modern accelerator control systems, including control and monitoring of accelerator technical systems, remote diagnostics, troubleshooting, data archiving, machine configuration, and timing and synchronisation. However, several features of the ILC accelerator push implementation beyond the present state of the art. These are described below.

9.2.1 Scalability

The ILC has an order of magnitude more technical system devices than other accelerators to date. The primary challenges of scalability in relation to existing accelerator control systems are the physical distances across the accelerator, the large number of components and number of network connections, and the implied network bandwidth. Real-time access to control-system parameters must be available throughout the site, and by remote access. These challenges are also present in the commercial domain, notably in telecommunication applications, and lessons learned there are almost certainly applicable to the ILC control system.

9.2.2 High Availability

Requirements for high availability drive many aspects of the ILC control system design and implementation. These requirements were derived from accelerator-wide availability simulations. The control system as a whole is allocated a 2500 hour MTBF and 5 hour MTTR (15 hours downtime per year). This translates to control system availability between 99% and 99.9% (2-nines and 3-nines). A detailed analysis of how control system availability relates to beam availability is complicated. However, a coarse analysis shows that if the control system comprises some 1200 controls shelves

(electronics crates), then each shelf must be capable of providing 99.999% (5-nines) availability. Such availability is routinely implemented in modern telecom switches and computer servers, but has not been a requirement of present accelerator control systems.

9.2.3 Support extensive automation and beam-based feedback

A very complex series of operations is required to produce the beams and deliver them to the collision point with the required emittance. The control system must provide functionality to automate this process. This includes both getting beam through the entire chain and also tune-up procedures to maximise the luminosity. Beam-based feedback loops are required to compensate for instabilities and time-dependent drifts in order to maintain stable performance. Inter-pulse feedback should be supported in the control-system architecture to minimise development of custom hardware and communication links. The automation architecture should have some built-in flexibility so procedures can easily be changed and feedback loops added or modified as needed. Automation and feedback procedures should incorporate online accelerator models where appropriate.

9.2.4 Synchronous Control-System Operation

The ILC is a pulsed machine operating at a nominal rate of 5 Hz. Sequences of timing events must be distributed throughout the complex to trigger various devices to get beam through the accelerator chain. These events are also used to trigger acquisition of beam instrumentation and other hardware diagnostic information so that all data across the machine can be properly correlated for each pulse.

9.2.5 Precision RF-Phase-Reference Distribution

The control system must generate and distribute RF phase references and timing fiducials with stability and precision consistent with the RF system requirements.

9.2.6 Standards and Standardisation, Quality Assurance

A critical aspect of implementing a high-availability control system is the use of consistent ("best") work practices and a level of quality assurance process that is unprecedented in the accelerator-controls environment. Additional technical solutions to high availability will rely on this foundation of work practices and quality-assurance processes. Commercial standards should be used wherever they can meet the requirements, for such things as hardware packaging and communication networks.

The control system must specify standard interfaces between internal components and to all other systems. This makes integration, testing, and software development easier and more reliable. Standard interfaces allow parts of the system to be more easily upgraded if required for either improved performance or to replace obsolete technologies.

9.2.7 Requirements on Technical Equipment

Technical equipment comprises field hardware such as power-supply controllers, vacuum equipment, beam instrumentation, and motion-control devices. These systems are the responsibility of the technical groups. However, they must interface to the control system in a coherent way to allow equipment to be accessed via a common interface for application programming, data archiving, and alarms. In order to meet the very stringent requirements for overall system reliability, as well as provide for more efficient R&D and long-term maintenance, standards must be applied to the technical equipment for packaging, field bus, communication protocol, cabling, and power distribution.

9.2.8 Diagnostic Interlock Layer

A Diagnostic Interlock Layer (DIL) complements normal self-protection mechanisms built into technical equipment. The DIL utilises information from diagnostic functions within the technical equipment to monitor the health of the equipment and identify anomalous behaviour indicative of impending problems. Where possible, corrective action is taken, such as pre-emptive load balancing with redundant spares, to avert or postpone the fault before internal protective mechanisms trip off the equipment.

9.3 Impact of Requirements on the Control-System Model

In order to meet the high-availability requirements of the ILC, a rigorous failure-mode analysis must be carried out in order to identify the significant contributors to control system downtime. Once identified, many well-known techniques can be brought to bear at different levels in the system, as well as system wide, and at different time scales (i.e. bunch-to-bunch, macro pulse, process control) to increase availability. The techniques begin with relatively straightforward, inexpensive practices that can have a substantial impact on availability. A careful evaluation and selection of individual components such as connectors, processors, and chassis are crucial. Administrative practices such as QA, agile development methodology, and strict configuration management must also be applied. Other techniques are much more complex and expensive, such as component redundancy with automatic detection and failover [202]. The control system must be based on new standards for next-generation instrumentation that:

1. are modular in both hardware and software for ease in repair and upgrade;
2. include inherent redundancy at internal module, module assembly, and system levels;
3. include modern high-speed, serial, inter-module communications with robust noise-immune protocols;
4. include highly intelligent diagnostics and board-management subsystems that can predict impending failure and invoke evasive strategies.

The Control System Model incorporates these principles through the selection of the front-end electronics packaging standard and component redundancy.

In addition to its intrinsic availability, the control system is responsible at the system level for adapting to failures in other technical systems. For example, the feedback system is responsible for reconfiguring a response matrix due to the loss of a corrector, or switching on a spare RF unit to replace a failed station.

Scalability requirements are met through a multi-tier hierarchy of network switches that allow for the flexible formation of virtual local area networks (VLANs) as necessary to segment network traffic. Control system name-servers and gateways are utilised extensively to minimise broadcast traffic and network connections. These software components manage the otherwise exponential growth of connections when many clients must communicate with many distributed control points.

Automation and flexible pulse-to-pulse feedback algorithms are implemented by a coordinated set of software services that work together through global coordination and distributed execution. The distributed execution is synchronised with the machine pulse rate via the timing event system which can produce software interrupts where needed. The network backbone accommodates the distribution of any sensor value to any feedback computation node. This distribution can be optimised to allow for efficient local as well as global feedback.

9.4 Control System Model

The model of the ILC control system is presented here from both functional and physical perspectives. This model has served as a basis for the cost estimate, as well as to document that the control-system requirements have been satisfied. Functionally, the control-system architecture is separated into three tiers, as shown in Fig. 9.1. Communication within and between these tiers is provided by a set of network functions. A physical realization, as applied to the Main Linac, is shown in Fig. 9.2. The remainder of the section describes the functional and physical models in more detail.

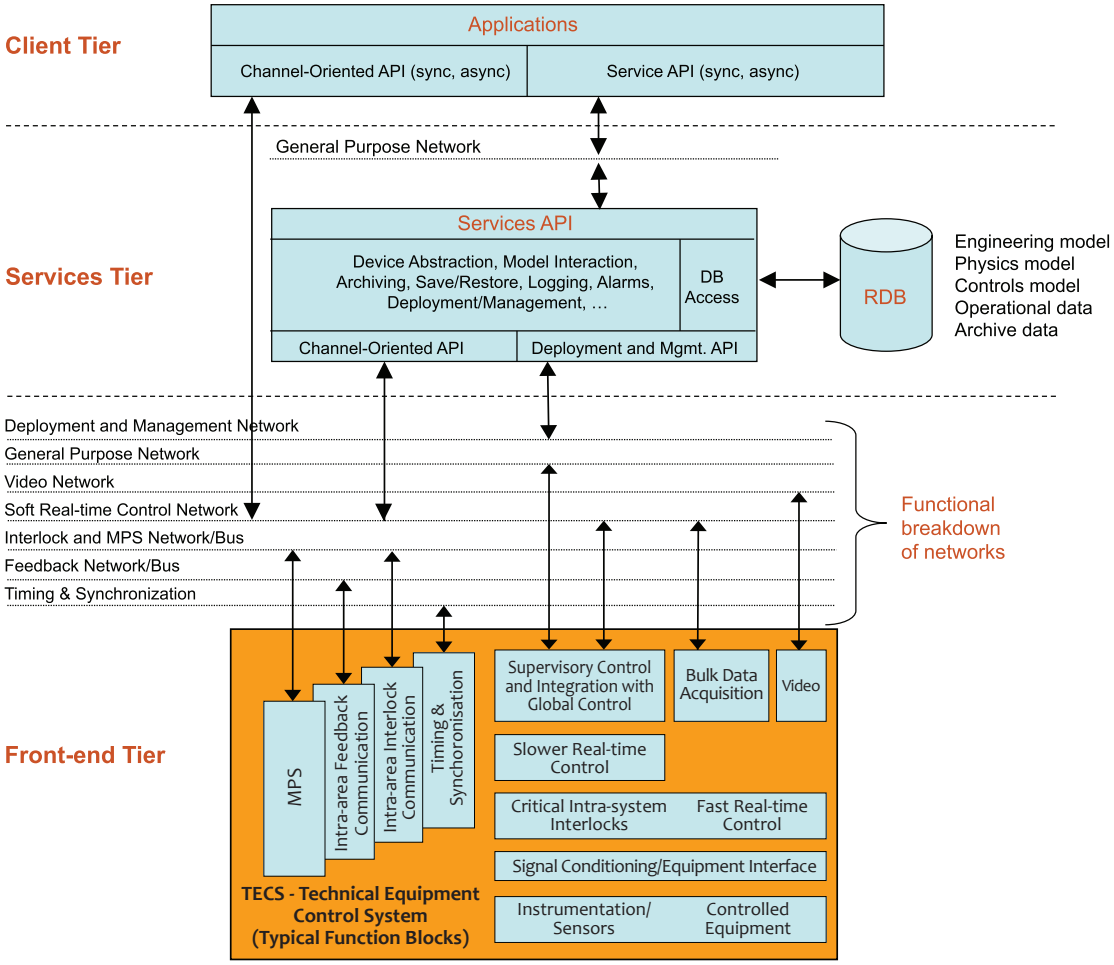

Figure 9.1. Control-system functional model.

9.4.1 Functional Model

The control-system model is functionally composed of three distinct tiers, as shown in Fig. 9.1. The 3-tier model includes a middle tier that implements significant portions of the logic functionality through software services that would otherwise reside in the client tier of a 2-tier system [203]. The three tiers are described in more detail below:

Client Tier: Provides applications with which people directly interact. Applications range from engineering-oriented control consoles to high-level physics control applications to system configuration-management applications. Engineer-oriented consoles are focused on the operation of the underlying accelerator equipment. High-level physics applications require a blend of services that combine data from the front-end tier and supporting data from the relational database in the context of high-level device abstractions (e.g. magnets, BPMs).

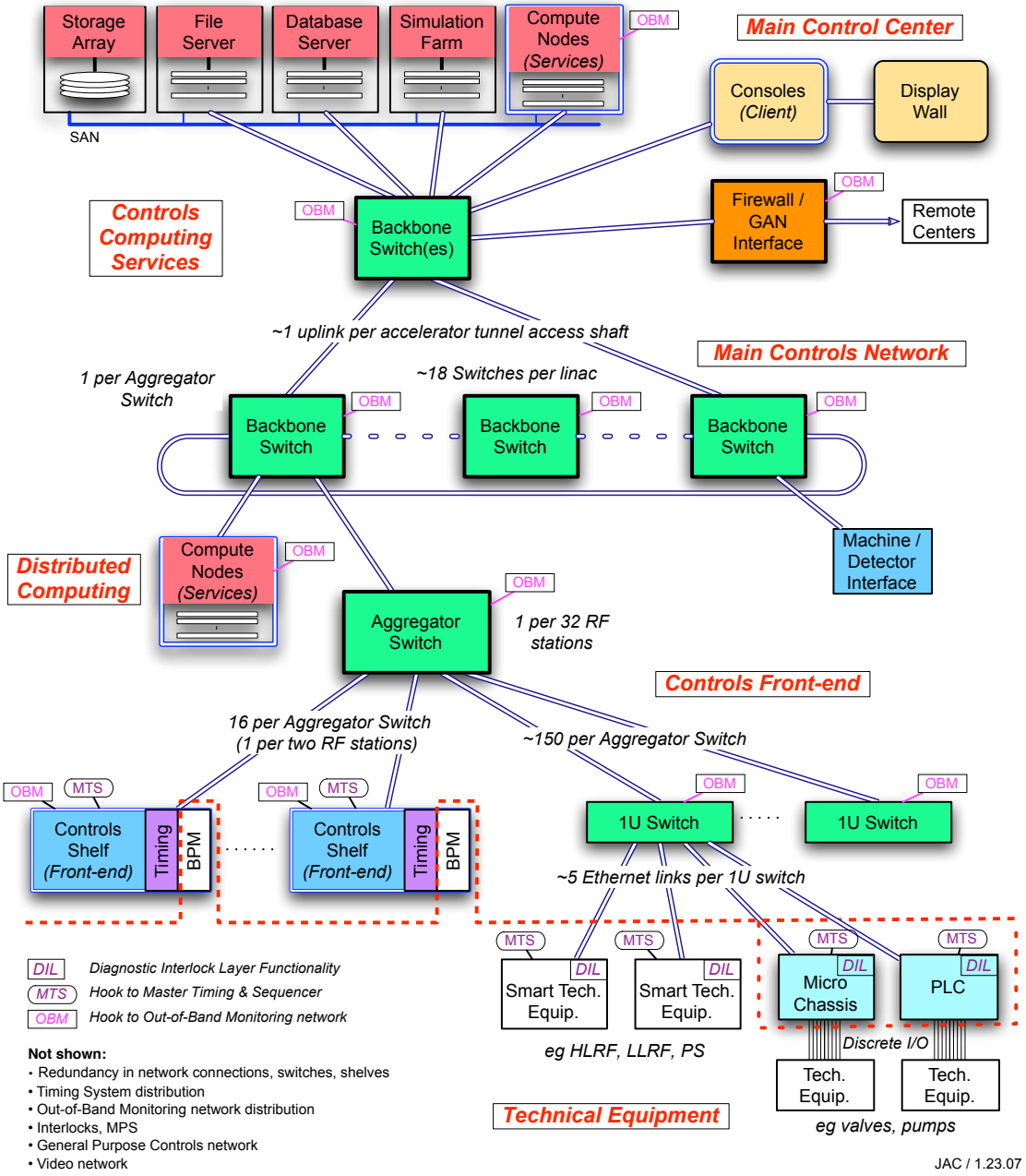

Figure 9.2. Control-system physical model.

Services Tier: Provides services that coordinate many activities while providing a well-defined set of public interfaces (non-graphical). Device abstractions such as magnets and BPMs that incorporate engineering, physics, and control models are represented in this tier. This makes it possible to relate high-level machine parameters with low-level equipment settings in a standard way. For example, a parameter save/restore service can prevent two clients from simultaneously attempting to restore a common subset of operational parameters. This centralisation of control provides many benefits in terms of coordination, conflict avoidance, security, and optimisation.

Front-end Tier: Provides access to the field I/O and underlying dedicated fast feedback systems. This tier is configured and managed by the services tier, but can run autonomously. For example, the services tier may configure a feedback loop in the front-end tier, but the loop itself runs without direct involvement. The primary abstraction in this tier is a channel, or process variable, roughly equivalent to a single I/O point.

9.4.2 Physical Model

The ILC control system must reliably interact with more than 100,000 technical system devices that could collectively amount to several million scalar and vector Process Variables (PVs) distributed across the many kilometres of beam lines and facilities at the ILC site. Information must be processed and distributed on a variety of timescales from microseconds to several seconds. The overall philosophy is to develop an architecture that can meet the requirements, while leveraging the cost savings and rapid evolutionary advancements of commercial off-the-shelf (COTS) components.

9.4.2.1 Main Control Centre

The accelerator control room contains consoles, servers, displays, and associated equipment to support operations of the ILC accelerator from a single location. Operators and technical staff run the accelerator and interact with technical equipment through Client Tier applications that run in the Main Control Centre.

9.4.2.2 Controls Computing Services

Conventional computing services dedicated to the control system include storage arrays, file servers, and compute nodes. A separate simulation farm is anticipated for offline control-system modelling and simulation, and for potentially performing model-reference comparisons to dynamically detect unusual conditions. Enterprise-grade relational databases act as a central repository for machine-oriented data such as physics parameters, device descriptions, control system settings, machine model, installed components, signal lists, and their relationships with one another.

9.4.2.3 Controls Networks and Distributed Computing

9.4.2.3.1 Main Controls Network Data collection, issuing and acting on setpoints, and pulse-to-pulse feedback algorithms are all synchronised to the pulse repetition rate. The controls network must therefore be designed to ensure adequate response and determinism to support this pulse-to-pulse synchronous operation, which in turn requires prescribing compliance criteria for any device attached to this network. Additionally, large data sources must be prudently managed to avoid network saturation.

For example, in the Main Linac, waveform capture from the LLRF systems is likely to dominate linac network traffic. Full-bandwidth raw waveforms from individual RF stations could be required for post-event analysis and therefore must be captured on every pulse. However, only summary data is required for archiving and performance verification. By grouping multiple RF stations together (notionally into groups of 32), full-bandwidth waveforms can be locally captured and temporarily stored, with only summary data sent on.

Dedicated compute nodes associated with each backbone network switch run localised control-system services for monitoring, data reduction, and implementing feedback algorithms.

9.4.2.3.2 Other Physical Networks To accommodate communication functions that are not compatible with the Main Controls Network, several other physical networks are envisioned, namely: a *General-purpose controls network* for general controls network access, including wireless access and controls network access to non-compliant devices; an *Out-of-band monitoring network*: to provide independent means to access and configure all Network switches and Controls Shelves; a *Video network* to distribute video data streams facility-wide. A *Technical Equipment Interlock Network* provides a means to distribute interlock signals. Functionally, this has similarities with the Machine Protection System described elsewhere. Technical equipment may report equipment or sensor status for use by other systems or utilise status information provided by other technical systems.

Based on initial assessments, commodity-computing equipment (e.g. 10-GB redundant Ethernet) is adequate to meet the requirements for all the networks.

9.4.2.4 Controls Front-end

The control-system model front-end comprises the following three main elements:

1U Switch: Aggregates the many Ethernet-controlled devices in a rack or neighbourhood of racks. Some of these devices speak the controls protocol natively, while others have proprietary protocols that must be interfaced to the control system. It is assumed these 1U switches reside in many of the technical equipment racks.

Controls Shelf: Consists of an electronics chassis, power supplies, shelf manager, backplane switch cards, CPUs, timing cards, and instrumentation cards (mainly BPMs). The Controls Shelf serves several purposes: (1) to host the protocol gateways, reverse gateways, and name servers to manage the connections required for clients to acquire controls data; (2) to run the core control system software for managing the various Ethernet device communication protocols, including managing any instrumentation (BPM) cards in the same shelf; (3) to perform data reduction, for example, so that full-bandwidth RF/BPM waveforms need not be sent northbound in the control system. The control-system physical model references the commercial standard AdvancedTCA (ATCA) for the Controls Shelves. This is a specification that has been developed for the telecommunications industry [204], and has applicability for the ILC control-system in part because of its high-availability feature set.

Aggregation Switch: Aggregates network connections from the 1U switches and Controls shelves and allows flexible formation of virtual local-area networks (VLANs) as needed.

9.4.2.5 Technical Equipment Interface

It has been common practice at accelerator facilities for the control system to accommodate a wide variety of interfaces and protocols, leaving the choice of interface largely up to the technical system groups. The large scale of the ILC accelerator facility means that following this same approach would almost certainly make the controls task unmanageable, so the approach must be to specify a limited number of interface options. For the purpose of the conceptual design and for the costing exercise, two interface standards were chosen: a Controls-shelf compliant electronics module for special sensor signals and specific beam-instrumentation applications such as BPM electronics; a controls compliant redundant network for all *smart* technical systems. While not explicitly part of the control-system model, it is assumed that discrete analog and digital I/O can be provided through micro-controller chassis or PLCs.

In addition to conventional interfaces for controls purposes, the control system provides functionality for remote configuration management of technical equipment for micro- controllers, PLCs, application-oriented FPGAs, etc.

9.4.3 Pulse-to-Pulse (5 Hz) Feedback Architecture

Many of the beam-based feedback algorithms required for ILC apply corrections at the relatively low machine pulse rate (nominally 5 Hz). This low correction rate and the distributed nature of many of the monitors and actuators make it desirable to use the integrated controls infrastructure for these feedback systems.

Using the integrated control-system architecture to implement the feedback algorithms offers many advantages, including:

- simpler implementation, since dedicated interfaces are not required for equipment involved in feedback loops;
- higher equipment reliability, since there are fewer components and interfaces;

- greater flexibility, since all equipment is inherently available for feedback control, rather than limited to predefined equipment;
- simplified addition of ad-hoc or un-anticipated feedback loops with the same inherent functionality and tools. This could significantly enhance the commissioning process and operation of the ILC.

Referring to Fig. 9.2, feedback algorithms are implemented as services running in both distributed and centralised compute nodes. Design and implementation of feedback algorithms is enhanced through high-level applications such as Matlab [205] integrated into the Services Tier shown in Fig. 9.1.

Implementing feedback at the machine pulse rate demands synchronous activity of all involved devices and places stringent compliance criteria on technical equipment, control system compute nodes, and the main controls network.

9.5 Remote Access – Remote Control

It is becoming commonplace for accelerator-based user facilities to provide means for technical experts to access remotely machine parameters for troubleshooting and machine-tuning purposes. This requirement for remote access is more critical for the ILC because of the likelihood that expert personnel are distributed worldwide.

9.6 Timing and RF-Phase Reference

Precision timing is needed throughout the machine to control RF phase and time-sampling beam instrumentation [206]. The timing system emulates the architecture of the control system, with a centrally located, dual-redundant source distributed via redundant fibre signals to all machine sector nodes for further local distribution. Timing is phase-locked to the RF system.

9.6.1 RF-Phase-Reference Generator

The RF-phase-reference generator is based on dual phase-locked frequency sources for redundancy. It includes fiducial generation (nominally at 5 Hz) and line lock. The macro-pulse fiducial is encoded on the distributed phase reference by a momentary phase shift of the reference signal. Failure of the primary frequency source can be detected and cause an automatic failover to the backup source.

9.6.2 Timing and RF-Phase-Reference Distribution

The phase reference is distributed via dual redundant active phase-stabilised links. Figure 9.3 shows an overview of dual redundant phase-reference transmission and local, intra-sector distribution.

The Phase Comparator unit detects failures in the primary phase-reference link and automatically fails over to the secondary link. Both the Phase Comparator unit and the Sector Timing Control units are fault tolerant. A local DRO or VCXO is phase-locked to the phase reference to develop a local reference with low phase noise for distribution within an RF sector of the main linac.

Figure 9.4 shows a block diagram of a single active phase-stabilised link. A portion of the optical signal is reflected at the receiving end. The phase of the reflected optical signal is compared with the phase of the frequency source. The resulting error signal controls the temperature of the shorter series section of fibre to compensate for environmentally induced phase shifts [207].

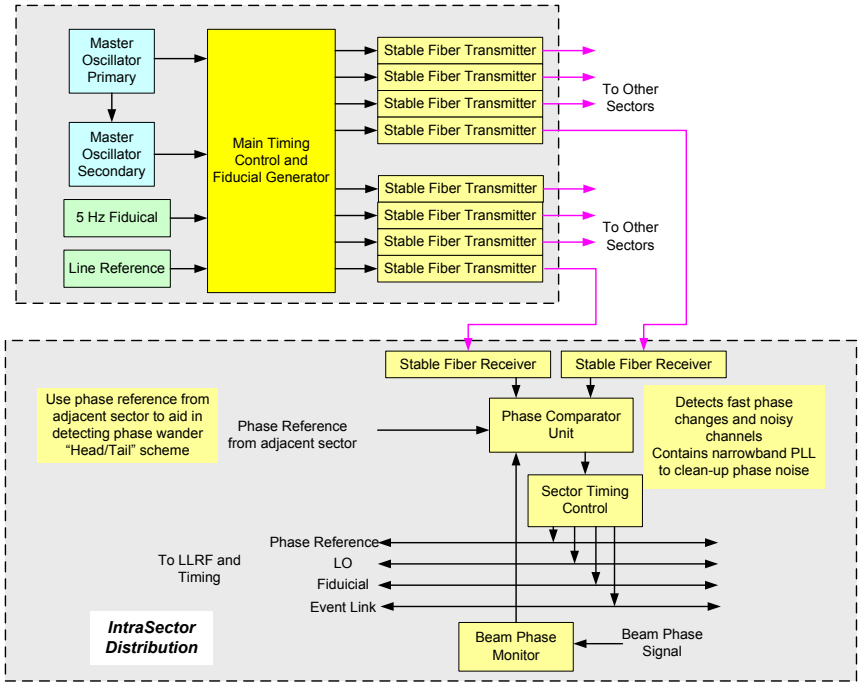

Figure 9.3
Timing-system overview showing redundant phase-reference distribution and local intra-sector timing distribution.

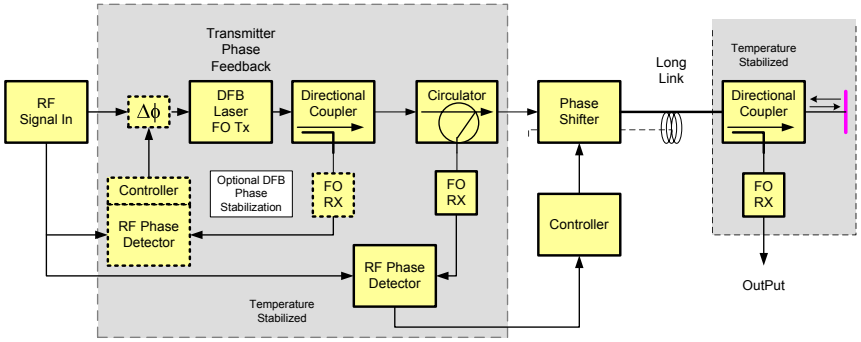

Figure 9.4
Phase stabilised reference link.

9.6.3 Timing and Sequence Generator

An event stream is distributed via dual redundant links in a star configuration. The system automatically fails over to the redundant link upon detection of a failure. The event system provides a means for generating global and local sequences, synchronising software processing to timing events, and generating synchronous time stamps.

9.7 Beam-based Feedback

Beam-based dynamical feedback control is essential for meeting the high performance and luminosity needs of the ILC. Feedback systems stabilise the electron and positron trajectories throughout the machine, correct for emittance variations, and provide measurement and correction of dispersion in the Main Linac. Two timescales of beam-based feedback are anticipated, namely pulse-to-pulse feedback at the 5 Hz nominal pulse-repetition rate, and intra-train feedback that operates within the bunch train.

9.7.1 Architecture for Intra-Bunch Feedback Systems

Unlike pulse-to-pulse feedback, which is implemented through the control system, dedicated systems are required for intra-bunch feedback. These must operate at the bunch rate of $\sim$3 MHz, and include the RTML turnaround trajectory feed-forward control and intra-bunch trajectory control at the IP. Orbit feedback in the damping ring is synchronised to the damping-ring revolution frequency.

Local input/output processors acquire beam position, cavity fields, beam current, and other local beam parameters at the full 3 MHz bunch rate and distribute that information through a fast synchronous network. Local interconnections with the low-level RF systems provide opportunities for local feedback loops at the full 3 MHz bunch rate. Dedicated processing crates provide both dedicated real-time bunch-to-bunch control, and dispersion-free steering, while additional uncommitted crates could provide spare capacity and flexibility.

9.7.2 Hardware Implementation

Most of the feedback-processing requirements described in this section, including dynamic orbit control in the damping ring can be met using commercial hardware. Custom hardware solutions are used in cases where low latency or unique capabilities are required, such as for the RTML turnaround trajectory feed-forward and the IP intra-bunch trajectory feedback. High-availability solutions are implemented as appropriate, using the same standards and approach as for other instrumentation and control-system equipment.

Chapter 10
Availability, Commissioning and Operations

10.1 Overview

The ILC is a complex machine with hundreds of thousands of components most of which must be tuned with exquisite precision to achieve the design luminosity. This high luminosity must be maintained routinely in order to deliver the required integrated luminosity. Great care must be taken at all stages of the design to ensure that the ILC can be commissioned rapidly and operate efficiently with minimal downtime. Some of the critical design issues are:

- high-availability components and redundancy to minimize downtime;
- ease of commissioning;
- separation of regions to allow beam in one region while another is in access;
- Machine Protection System (MPS) to prevent the beam from damaging the accelerator;
- ensuring automated rapid recovery;
- feedback systems and control procedures to maintain optimum performance.

Many of these issues are mentioned elsewhere but are presented here as an integrated package to emphasise their importance to the ILC and the need for a powerful state-of-the-art control system.

10.2 Availability

10.2.1 Importance of Availability

The important figure of merit for the ILC is not the peak luminosity but the integrated luminosity recorded by the experiments. The integrated luminosity of the accelerator is the average luminosity multiplied by the uptime of the accelerator. Having surveyed the uptime fraction (availability) of previous accelerators, a goal of 75 % availability has been chosen for the ILC. This is comparable to HEP accelerators whose average complexity is much less than that of the ILC. As such, it should be a challenging but achievable goal. This goal is made even more challenging by the fact that all ILC subsystems must be performing well to generate luminosity. In contrast, a storage ring has an injector complex that can be offline between fills without impacting performance. Because it has more components and all systems must be working all the time, attaining the target availability for the ILC requires higher-availability components and more redundancy than previous accelerator designs. High availability must be an essential part of the design from the very beginning. A methodology is in place to apportion the allowed downtime among various components and hence arrive at availability requirements for the components.

10.2.2 Methodology

A simulation has been developed that calculates accelerator availability based on a list of parts (e.g. magnet, klystron, power supply, water pump). Input includes the numbers of each component, an estimate of its mean time between failure (MTBF) and mean time to repair (MTTR), and a characterisation of the effect of its failure (e.g. loss of energy headroom, minor loss of luminosity, or ILC down). The simulation includes extra repair time for components in the accelerator tunnel (for radiation cool-down and to turn devices off and on), repair of accessible devices while the accelerator is running, repair of devices in parallel to overlap their downtimes, and extra time to recover the beam after repairs are completed. It also allows repairs to be made in one region of the ILC while beam is used for accelerator physics studies in an upstream region. The inputs to the simulation were varied to test different machine configurations and different MTBFs/MTTRs to develop a machine design that had a calculated downtime of 15 %. The ILC design goal is > 75 % uptime, but 10 % downtime was reserved as contingency for things that are missing from the simulation or for design errors. More details of the availability simulation model and its application to the ILC can be found in [3, 208].

10.2.3 Availability Studies

Simulations have been used to evaluate the impact of proposed design changes during the Technical Design Phase (TDP) [209]. The largest design change with impact on overall availability was going from a twin tunnel to a single tunnel for the two main linacs. This was part of the SB2009 change proposals. This is a rather complete analysis of the impact on alternate RF system designs which would be required to maintain a constant availability in a single tunnel design as a function of the installed energy overhead. The cases considered included KCS (Klystron Cluster System), DRFS (Distributed RF System with many smaller klystrons) along with a Central Region which contained the electron, positron sources, the DR's and the BDS which have second tunnel for support equipment that is accessible during beam running.

The results of a typical example simulation run giving the desired 15 % "downtime" are shown in Fig. 10.1 for a KCS with 4 % minimum overhead.

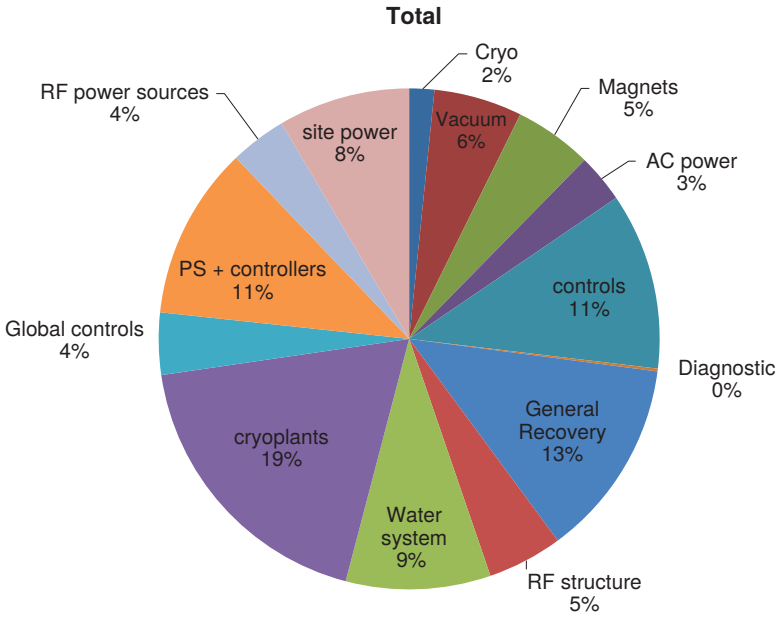

Figure 10.1
This figure shows the distribution of the downtime by area of the accelerator for a typical simulation run (KCS with 4% energy overhead). The downtime fractions shown are percent of the total downtime of about 15 %. So the actual downtime caused by the cryoplants is 19 % of 15 % = 2.8 %. 'General Recovery' is the excess, (beyond time nominally allotted), time spent recovering from scheduled maintenance days and is lumped because it cannot be directly attributed to a particular area [209].

The energy overhead varies with the actual operating energy and will be much larger as one operates the ILC below the installed energy capability but the downtime associated with the linac

does not get much lower than 1 % as there always remain some non-RF accelerator components, e.g. RTML systems, in the accelerator tunnel.

10.3 Bunch Timing and Path-length Considerations

In order to extract the bunches in the damping ring one by one and inject into the main linac, there are certain constraints to satisfy among the DR circumference, number of bunches, RF frequencies and bunch distances in the DR and main linac [95]. The present parameters satisfy these constraints and allow for a flexible choice of bunch patterns as required for best operating performance. In addition, there is another constraint due to the fact that the positrons are generated by electrons from the previous pulse. For the most flexible operation, it is highly desirable that the difference in path-length travelled by the positrons (from target, through DR, RTML, Linac and BDS to IP) and the electrons (from target location direct to IP) is an integer multiple of the DR circumference. Other solutions involving pulse-to-pulse variation of the timing of electron injection are possible but less flexible. Because of this constraint, the exact location of the injector complex and the layout of the transport lines is a subject that can be fixed only after the final component lengths and the site details are decided.

10.4 Commissioning

This section describes general ideas on commissioning. The actual implementation will evolve with the schedule for construction of the conventional facilities, the installation of services and technical components and the availability of access to regions of the accelerator. These schedules will be site dependent but a typical example is shown in Fig. 10.2.

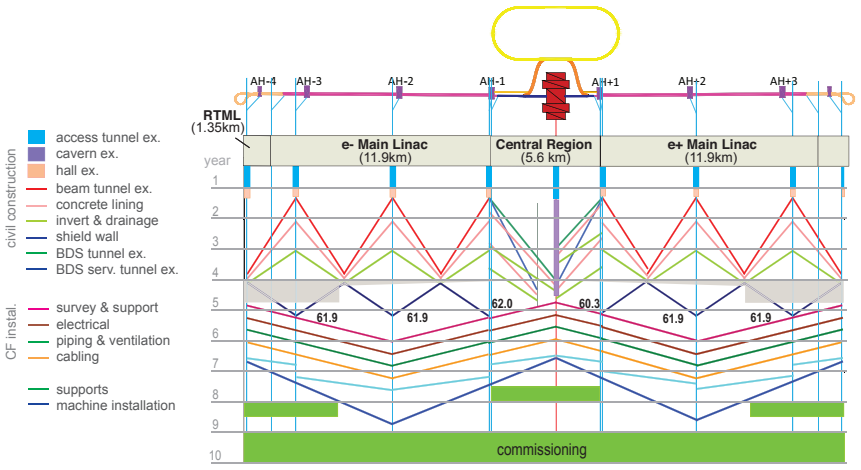

Figure 10.2
An example schedule which shows civil construction, installation of services and accelerator components followed by testing and beam commissioning of ILC systems (green bars).

10.4.1 Phased Commissioning

To minimize the time from completion of construction of the ILC to operation for high luminosity, it is desirable to complete upstream regions of the accelerator early. Commissioning can then start on these regions while construction continues downstream. This is called phased commissioning. In particular, it would be beneficial to complete the injectors and damping rings in time to allow one or two years of commissioning while construction of the linacs and BDS continues. The central region of the ILC includes the Interaction Region hall and facilities whose construction schedule, combined with the construction and commissioning of the detectors, is a critical path element to begin operation for physics. These drive the general scheduling philosophy of starting in the central region and progressing outwards in both directions along the two 11 km linacs.

A large amount of hardware validation and alignment and beam commissioning studies are necessary to produce low-emittance beams with good stability and availability. Consequently, it is

important to allocate a sufficient amount of commissioning time at an early stage. A major function of the DR commissioning period is to achieve the alignment of optical components and to establish a small beam emittance. In addition, there are issues related to beam intensity that need to be checked and high-intensity beams are needed for vacuum chamber scrubbing. The use of the damping rings obviously necessitates functional beam source systems. Since both DRs are in the same tunnel, a schedule optimization has to be done to determine if it is best to install both DRs at the same time or if the e^- ring should be installed and commissioned followed by the e^+ ring. The example construction schedule shown in Fig. 10.2 assumes that both rings are installed together and commissioned in parallel. The electron ring can be commissioned to full current with the standard electron source whereas the positron ring will use electrons from the auxiliary source or positrons produced by the auxiliary source on the target systems. The construction of the experiment is likely to consume the largest contiguous amount of time. It is recognized that construction of the underground detector hall is a major undertaking which cannot be completed until several years after groundbreaking of ILC. To mitigate the schedule impact, most of the sub-assemblies of ILC detector facilities are built on the surface and later installed into the hall in large pieces.

10.5 Radiation shielding and Personnel Protection System zones

To enable efficient operation and commissioning, the personnel protection system (PPS) is designed to allow personnel access in one region while beam is in another upstream region. As an example, the main-linac beam tunnel can be accessed while there is beam in the damping ring. Those parts of the accelerator accessible to people could have radiation levels that exceed the levels allowed for the public. Therefore, the radiation shielding and PPS zones described here are designed for radiation workers.

For the single main-linac tunnel design there is no service tunnel and therefore no need for detailed evaluation of radiation levels during the operation. The Japanese 'Kamaboko' design is an exception to this. The 'Kamaboko' tunnel design allows the main-linac tunnel to be divided into two regions, one for the main linac and the other for RF sources with utilities (service side). Personnel access to the service side during main-linac beam operation is crucial for long-term continuous operation of the main linac. Therefore, the separation wall thickness should be designed to allow such access.

10.5.1 Summary of Regions' Radiation Requirements

Maximum-allowable radiation levels for radiation and non-radiation workers in several scenarios have been examined and the most conservative case has been used for shielding calculations for non-site-specific design. This is referred to as the "maximum credible beam-loss condition" where all active limiting systems are off (system failure); radiation levels for radiation workers must be less than "250 μSv/hr" or "30 mSv/event". For the separation wall in the Japanese 'Kamaboko' main-linac tunnel, site-specific regulatory limits have been applied, i.e, radiation level for occupied area must be kept below "1 mSv/week" under normal operation condition. Radiation shielding and PPS devices must be designed to satisfy these criteria under the ILC operating beam loss scenarios.

10.5.2 Summary of the Radiation Safety Design for the Main Linac

Induced activity in air is estimated for 1 W/m continuous beam loss in the main-linac ventilation unit which is 5000 m long, between access tunnels. The ventilation system is designed to replace the entire air in the unit within 3 hours, therefore the air is irradiated with neutrons and photons for a maximum of 3 hours. The exhausted air from the main-linac tunnel passes through a vertical shaft. The induced activities were calculated based on Swanson's parameter with 1 W/m beam loss, 1 % fraction of deposited energy per beam loss and 2 m average path length of photons passing through the air. The nuclide, ^{3}H, ^{7}Be, ^{11}C, ^{13}N, ^{15}O, ^{38}Cl and ^{39}Cl, were obtained by this manner. In addition to these,

^{40}Ar production is estimated from thermal neutron flux in the section. The highest activation comes from 13N, 5.8×10^{-4} Bq/m^3, which is low in comparison with the airborne activation limit.

Induced activities in cooling water were estimated in the same way as for air. The amount of cooling water in the main-linac section is assumed to fill two 2-inch-diameter, 5000 m-long, water channels for each ventilation unit. The nuclides, ^{3}H, ^{7}Be, ^{11}C, ^{13}N, ^{15}O, are produced. Highest value is 162 Bq/m^3 for ^{15}O, but its short half-life means that this is unimportant.

The conclusion of the radiation-safety study for the main-linac tunnel is that the beam loss from normal operation with 1 W/m continuously produced is acceptable from the radiation-safety viewpoint. In actual operation, hardware systems and operation procedures to maintain beam losses at less than design value are quite important, as are tunnel design and installation. Radiation-safety design was performed for typical main-linac tunnel design concerning the tunnel separation wall, induced activities in air and cooling water assuming 1 W/m continuous beam loss.

The separation wall in the 'Kamaboko tunnel' design, should be designed considering the following items: the radiation level on the service side should be less than 1 mSv/week; the wall should have through holes every 20 m; and the tunnel should have horizontal emergency passage way every 500 m. An example of such a wall that satisfies these items has the following features: 3 m thickness for the normal section with ordinary concrete (2.3 g/cm^3); a 5 m-thick region of heavy concrete (3.0 g/cm^3) region with 8 m long non-modulator area for the emergency passageway; a reduced thickness part above 3 m from floor level.

10.5.3 PPS Zones

The personnel protection system (PPS) prevents people from being in the accelerator tunnel when the beam is on. A system of gates and interlocks turn off the beam before allowing access to the accelerator housing. Access to the service tunnel is not part of the PPS system. The ILC is divided into different regions (PPS zones) with tune-up dumps and shielding to allow beam in one region while there is access in another region. The PPS zones are the injectors, DR, main linac and BDS. Entrance gates for PPS zones are monitored and dump the beam when opened.

The ILC PPS zones are long and it would be burdensome to search the full region after each permitted access. To ameliorate this problem, they are divided into multiple search zones separated by fences with gates that are also monitored. The search zones are up to several hundred meters long. For example, in the linac a search zone is 500 m long and is separated by gates midway between each cross tunnel passageway or safety vault. Personnel access from a service area (service tunnel, shaft, detector hall etc.) to an accelerator area is controlled by PPS gates, as is the access from one accelerator region (PPS zone) to another accelerator region. Fences, doors, or moving shields are used for these gates and they have redundant gate-closed status switches for PPS monitoring. They are locked to prevent careless access but have an unlocking mechanism for emergencies. Information and communication systems are provided at the gates to show the operational status and allow communication between a person at the gate and an operator granting permission to go through the gate.

There are personnel-access passages between accelerator area and service area at the main linac, shafts, alcoves and the detector hall with PPS gates near each end. Since the passageways are used as emergency exits, heavy moving doors are avoided if possible. PPS gates between the accelerator areas and the service areas (including the access passageway) need to restrict the flow of activated air from the accelerator tunnel to the service area.

10.5.4 Shielding between PPS Zones

Shielding between PPS zones is designed to allow beam in the upstream zone while people are in the downstream zone. The upstream beam is deflected into a tune-up dump and there are triply redundant beam stoppers between the beam and the accessed region to ensure the beam does not enter the accessed region.

10.6 Machine-Protection System

The task of the machine-protection system, MPS, is to protect the machine components from being damaged by the beam when equipment failure or human error causes the beam to strike the vacuum envelope. The MPS design must take into account all types of failures that may occur and the damage they could produce.

10.6.1 Overview

Both the damage caused by a single bunch and the residual radiation or heating caused by small (fractional) losses of many bunches are important for MPS. The MPS consists of:

- a single bunch damage mitigation system;
- an system to limit the average beam loss;
- a series of abort kickers and dumps;
- a restart ramp sequence;
- a fault-analysis recorder system;
- a strategy for limiting the rate with which magnetic fields (and insertable device positions) can change;
- a sequencing system that provides for the appropriate level of protection depending on machine mode or state;
- a protection collimator system.

The systems listed must be tightly integrated in order to minimize time lost to aberrant beams and associated faults.

10.6.2 Single-Pulse Damage

Single-pulse damage is mitigated by systems that check the preparedness of the machine before the high-power beam passes. Single pulse damage control is only necessary downstream of the damping ring. Three basic subsystems are involved:

1. a beam-permit system that surveys all appropriate devices before damping-ring beam extraction begins and provides a permit signal if each device is in the proper state;
2. an abort system that stops the remaining bunches of a train if a bunch does not arrive at its intended destination;
3. spoilers upstream of devices (typically collimators) to expand the beam size enough that several incident bunches do not cause damage.

In addition, some exceptional devices (damping-ring RF and extraction kickers for example) have fast-monitoring systems and redundancy. Spoilers or sacrificial collimators are placed before the bunch compressors, in the undulator chicane, at the beginning of the BDS system and in the collimator section of the BDS. Locations with dispersion downstream of an accelerator section have spoilers to intercept off-energy beam caused by klystron faults or phase errors before the beam can hit a downstream collimator or beam pipe. The spoilers are designed to survive the number of incident

bunches that hit before the abort system can stop the beam. The use of a *pilot bunch* is also being kept as an option. A pilot bunch is one percent of nominal current and is spaced 10 μs ahead of the start of the nominal train. If it does not arrive at its intended destination, the beam abort system is triggered to prevent full-intensity bunches from hitting the spoiler.

Studies have shown that for many failure scenarios such as quadrupole errors or klystron phase errors, the beam is so defocused by the time it hits the linac aperture that it does not cause damage. For this reason, no spoilers or extra beam-abort kickers are included in the linac.

The beam-abort system uses BPMs and current detectors to monitor the beam trajectory and detect losses. On a bunch-by-bunch basis, the system checks for major steering errors or loss of beam. When a problem is detected, it inhibits extraction from the damping ring and fires all abort kickers upstream of the problem. The abort kickers cleanly extract the beam into dumps, protecting downstream beam lines. In the few milliseconds before the start of the pulse train, the beam-permit system checks the readiness of the modulators and kicker pulsers, and the settings of many magnets before allowing extraction of beam from the damping rings.

10.6.3 Average Beam-Loss-Limiting System

Average beam loss is limited, throughout the ILC, by using a combination of radiation, thermal, beam intensity and other special sensors. This system functions in a manner similar to other machines, such as SLC, LHC, SNS and Tevatron. If exposure limits are exceeded at some point during the passage of the train, damping ring extraction or source production (e^+/e^-) are stopped. For stability, it is important to keep as much of the machine as possible operating at a nominal power level. This is done by segmenting it into operational MPS regions. There are 7 of these regions, as noted in Table 10.1. Beam rate or train length can be limited in a downstream region while higher rate and train lengths are maintained in upstream regions. The maximum power-handling capabilities of the beam dumps, as shown in Table 10.1, vary with the location, beam energy and the operating requirements.

Table 10.1 Maximum power handling capabilities of the beam dumps.

E-1	SC Tune-up Dump	311 kW‡	E+1	SC Tune-up Dump	311 kW‡
E-2	EDRX Tune-up Dump	220 kW	E+2	PDRX Tune-up Dump	220 kW
E-3	RTML Tune-up Dump	220 kW	E+3	RTML Tune-up Dump	220 kW
E-4	BDS Tune-up Dump	14 MW	E+4	BDS Tune-up Dump	14 MW
E-5	Primary E- Dump	14 MW†	E+5	Primary E+ Dump	14 MW†
E-6	RTML Tune-up Dump	220 kW	E+6	RTML Tune-up Dump	220 kW
E-7	E- Fast Abort Dump	250 kW	E+7	E+ Target Dump	200 kW†

† Always ON
‡ 45 kW always ON

10.6.4 Abort Kickers and Dumps

Abort systems are needed to protect machine components from single-bunch damage. It is expected that a single-bunch impact on a vacuum chamber will leave a small hole, roughly the diameter of the beam. Each abort system uses a fast kicker to divert the beam onto a dump. The kicker rise time must be fast enough to produce a guaranteed displacement of more than the beampipe radius in an inter-bunch interval.

There are abort systems at the end of each linac, before the undulator entrance, and one at the entrance to the BDS on the positron linac.

There will be many meters of fast kickers needed at each dump and megawatts of peak power from pulsers. R&D will be needed to optimize the final system and ensure its reliability.

10.6.5 Restart Ramp Sequence

Actual running experience is needed to exactly define the restart ramp sequence. For that reason the sequencer must be flexible and programmable. Depending on the beam dynamics of the long trains, it may be advisable to program short trains into a restart sequence. There may also be single bunch, intensity dependent effects that require an intensity ramp. The system must be able to determine in advance if the beam loss expected at the next stage in the ramp sequence is acceptable. Given the number of stages and regions, the sequence controller must distribute its intentions so that all subsidiary controls can respond appropriately and data-acquisition systems are properly aligned. It may be necessary to have a pilot bunch mode with the nominal intensity but large emittance. The initial stages of the sequence can be used to produce 'diagnostic' pulses to be used during commissioning, setup and testing.

10.6.6 Fault-Analysis Recorder System

A post-mortem analysis capability is required that captures the state of the system at each trip. This must have enough information to allow the circumstances that led to the fault to be uncovered. Data to be recorded on each fault include: bunch-by-bunch trajectories, loss-monitor data, machine-component states (magnets, temperature, RF, insertable-device states), control system states (timing system, network status) and global system status (sequencer states, PPS, electrical, water and related sensors). The fault-analysis system must automatically sort this information to find what is relevant.

10.6.7 Rapidly Changing Fields

In addition to the above, there are critical devices whose fields (or positions) can change quickly, perhaps during the pulse, or (more likely) between pulses. These devices need 1) special controls protocols, 2) redundancy or 3) external stabilization and verification systems.

1. Depending on the state of the machine, there are programmed (perhaps at a very low level) ramp-rate limits that keep critical components from changing too quickly. For example, a dipole magnet is not allowed to change its kick by more than a small fraction of the aperture (few percent) between beam pulses during full power operation. This may have an impact on the speed of beam-based feedbacks. Some devices, such as collimators, are effectively frozen in position at the highest level of beam power. There may be several different modes, basically defined by beam power, that indicate different ramp-rate limits.

2. There are a few critical, high-power, high-speed devices (damping-ring kicker and RF, linac front-end RF, bunch-compressor RF and dump magnets) that need some level of redundancy or extra monitoring in order to reduce the consequence of failure. In the case of the extraction kicker, this is done by having a sequence of independent power supplies and stripline magnets that have minimal common-mode failure mechanisms.

3. There are several serious common-mode failures in the timing and phase distribution system that need specially engineered controls. This is necessary so that, for example, the bunch compressor or linac common phase cannot change drastically compared to some previously defined reference, even if commanded to do so by the controls, unless the system is in the benign beam-tune-up mode.

10.6.8 Sequencing System Depending on Machine State

The ILC is divided into segments delineated by beam stoppers and dump lines. There may be several of these in the injector system, two beam dumps in each RTML, and 2 (or 3) in the beam delivery and undulator system. In addition, the ring-extraction system effectively operates as a beam stopper assuming the beam can remain stored in the ring for an indefinite period. This part of the MPS assumes that the beam power in each of these segments can be different and reconfigures the protection systems noted above accordingly.

10.6.9 Protection Collimators

The entire ILC requires protection collimators and spoilers that effectively shadow critical components. These devices must be engineered to withstand innumerable single-pulse impacts.

10.7 Operability

To ensure high average luminosity it is important that the ILC have many features built in to make its operation mostly automatic and efficient. These features include:

- accurate, reliable, robust diagnostics;
- monitoring, recording, and flagging of out-of-tolerance readings of all parameters that can affect the beam, some of which must be checked milliseconds before each pulse train so beam can be aborted if there is a problem;
- beam-based feedback loops to keep the beam stable through disturbances like temperature changes and ground motion;
- automated procedures to perform beam-based alignment, steering, dispersion correction, etc.;
- automatic recovery from MPS trips starting with a low-intensity, high-emittance beam and gradually increasing to nominal beam parameters.

10.7.1 Feedback systems

Transporting the beam through the ILC while maintaining a small emittance requires a large number of feedback systems.

These feedback systems include measurements from various beam-position monitors, from laser wires scanning the beam profile and other diagnostics. The feedback loops must be carefully designed to be orthogonal and to maintain corrections that are within the device ranges. The feedback systems must avoid trying to compensate for large deviations of the beam due to component failure. It is hence necessary to use flexible setups for the control loops such as provided by MATLAB tools and analysis techniques (see Section 9.7).

Chapter 11
Conventional Facilities and Siting

11.1 Introduction

In the RDR, a generic CFS design was developed and used in each of three regional sample sites. This resulted in very similar overall layouts using a twin Main Linac (ML) tunnel configuration and common designs for supporting mechanical and electrical utility systems. The current design is tailored to accommodate local site conditions and incorporates the results of value engineering and tunnel configuration studies and detailed site-specific designs for conventional facilities and mechanical and electrical utility systems. For the Americas and European regions, a single ML tunnel constructed by tunnel-boring machines is preferred; for the Asian region, where both candidate sites are in mountainous regions and there is great experience with tunneling in mountainous regions, the drill-and-blast New Austrian Tunneling Method (NATM) is preferred. This means that a larger single tunnel is the preferred method of construction, since NATM can cost-effectively produce large tunnels. This larger tunnel can then be divided into two with a shielding wall to allow klystrons etc to be separated from the running accelerator. Another major development associated with these tunnel geometries is the introduction of the Klystron Cluster high-level RF system (KCS) for the Americas and European regions and the Distributed Klystron high level RF system (DKS) for the Asian region.

The designs that have been developed for the Americas and European regions are very similar. The Americas design has been based on the Fermilab site in northeastern Illinois. The European design has been developed for a site near the CERN Laboratory in Switzerland. A preliminary evaluation of a second site near the Joint Institute for Nuclear Research in Dubna, Russia has also been performed. In all cases a single ML tunnel is used with the KCS, which places all of the klystrons and related equipment in surface buildings at the tops of vertical shafts. From these klystron buildings, waveguides distribute the microwave power through the vertical shafts and ML tunnel.

Two candidate sites have been identified in the Asian region, both in mountainous areas of Japan. Access considerations preclude the use of vertical shafts so that inclined tunnels are used for access to the main tunnels and IR Hall. There are some surface buildings at the entrances to the access tunnels, but surface facilities are minimized to limit environmental impact. Detector construction and assembly methods are different between a mountain site and one with relatively uniform surface elevations. This alone has a direct impact on the integrated construction, installation and commissioning schedule and possibly overall project cost.

After a sketch of the overall layout of the ILC, (Fig. 11.1), and some other general considerations related to common design criteria and general site considerations, this chapter sets out the detailed conventional facility designs for first the Asian region and then the European and Americas regions. Finally, common issues of handling and the installation plan and estimate of effort required are discussed.

11.2 Overall Layout and Common Design Criteria

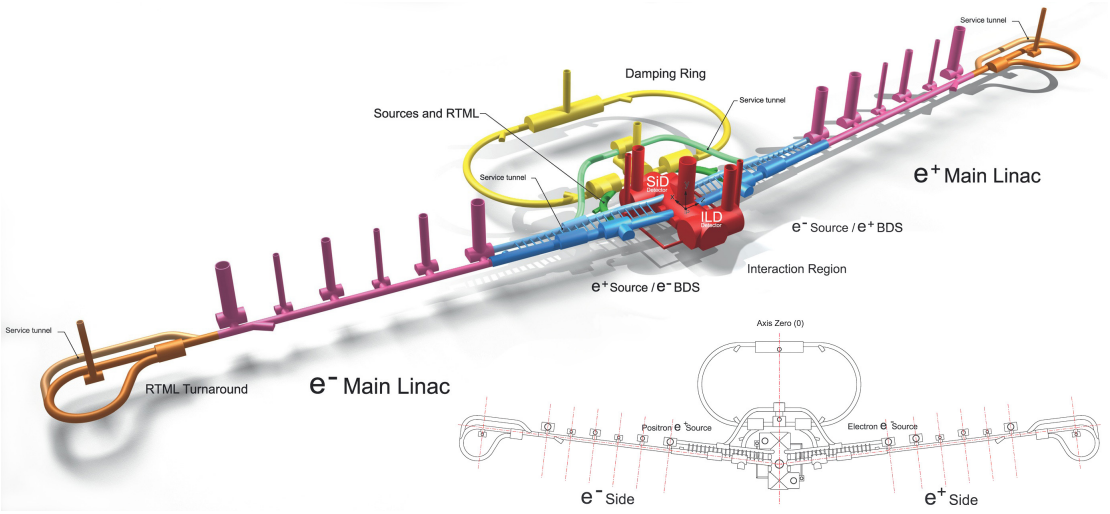

Figure 11.1. ILC tunnel schematic for KCS showing accelerator systems, IR hall and support tunnels.

The ML is housed in a single tunnel; in the Asian design this is a wide tunnel with parallel galleries, one containing the beamlines and one accessible by personnel. The ML beam tunnel also houses the RTML 5 GeV transport line supported from the ceiling and positioned towards the center of the tunnel. The DR has a single tunnel large enough to contain an electron ring, a positron ring and a possible future second positron ring.

The Central Region area, from the IR Hall to the ends of the MLs, has both a beam tunnel and a parallel service tunnel. The beam tunnel houses multiple beamlines including the e^- and e^+ sources, the BDS, the RTML and beam abort and dump lines. This region also includes the short segments that route beamlines to and from the DR. All tunnels have been sized for the respective equipment and its installation, transport and replacement, as well as personnel egress. The beam and service tunnels are widened as needed to maintain the same aisle width as in the ML.

The service and beam tunnels are separated by sufficient material to provide structural stability and radiation shielding for workers in the service tunnel while the accelerator is operating. Penetrations between tunnels have been sized and configured to provide the required radiation shielding, as have the V-shaped personnel passageways between the two tunnels.

The IR Hall is sized to support two detectors in a 'push-pull' configuration. Each detector garage area is connected to the beam tunnel, and to the egress elevator through a passageway.

The beamline configuration and the arrangement and operational requirements of the IR Hall and detectors are site invariant. Each detector will be constructed on a moveable platform which must have the capability to accurately move efficiently into and out of the interaction point. However the design and construction of the enclosures and tunnels that house the beamlines and related equipment must conform to local geological conditions.

While the KCS and DKS differ in configuration and equipment layout, the electrical power and cooling systems are very similar, though local conditions and climate will have a direct influence on their design.

11.3 General site requirements

The site must accommodate the initial 31 km overall length, as well as the upgrade to 50 km length, and the area adjacent to the IR for the DRs. Requirements for tunnel access, support equipment and surface buildings must be included.

Alignment and stability are very important for reliable accelerator operation. Even more critical is the stability of the IR floor. Two detectors , with respective weights of approximately 15 kt and 10 kt, will be supported on concrete platforms each weighing approximately 2 kt. The geology at any proposed site must be able to accommodate the detector movements and allow their repositioning without unsatisfactory deflection or settlement over time.

Electrical power requirements are substantial. Operation at 500 GeV (1 TeV) will require approximately 161 MW (285 MW) respectively. These requirements are almost certainly a significant addition to any existing local electrical-grid power capability. In addition a reliable and ample water source for process cooling will be needed.

Suitable access will be needed during both the construction phase, during which a great deal of excavated material will be removed, and the operational phase. Trucking routes and deposit locations will need to be identified. For the installation of components, shipping by road is likely to be the main delivery option and roads to the site must be able to accommodate both the length and weight requirements of the major components. Rail, air and/or seaport access may be required for specific components and convenient access to a major airport is essential for a fully international project.

11.4 Asian region (Mountain topography)

11.4.1 Siting studies

11.4.1.1 Location and properties of Asian sample sites

The Asian region currently has two candidate sites, both in Japan (Fig. 11.2), which were selected after several years of study:

- Kitakami site: located in Iwate prefecture (Tohoku district);
- Sefuri site: located in Fukuoka & Saga prefecture (Kyushu district).

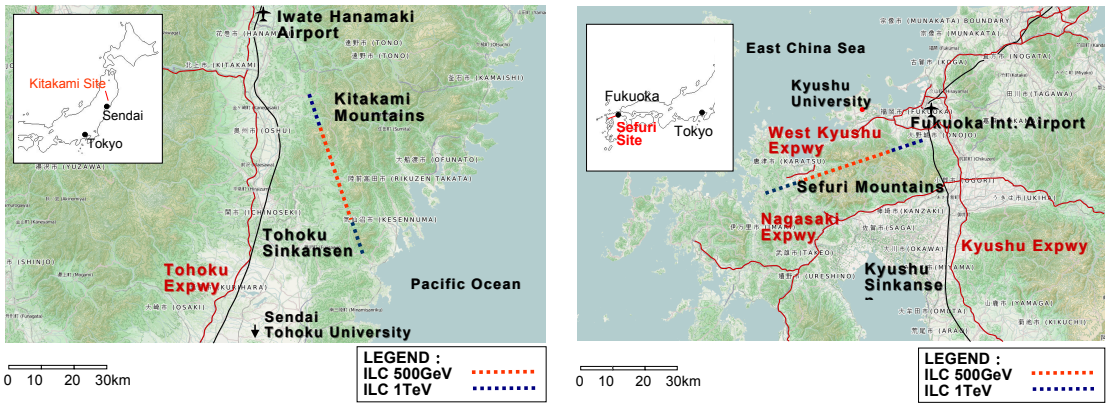

(a) **(b)**

Figure 11.2. Candidate sites in (a) Kitakami and (b) Sefuri.

They are favoured because of their geographical and geological characteristics, as well as the strong support of the local government and residents. The common geographical and geological features of the two sites include:

- although mountainous, the region is not particularly steep.

- location in bedrock suitable for construction of a 31 km accelerator tunnel and a large IR Hall cavern;
- potential to extend to 50 km tunnel length;
- small ground vibrations;
- no active faults near the tunnel so no danger of nearby earthquakes;
- no man-made vibration source nearby.

Additional favourable characteristics include a suitable climate, stable source of 300 MW electric power, adequate cooling water supply, possibility for adequate groundwater treatment, tunnel access capability, and suitable road access for construction and delivery vehicles.

11.4.1.2 Land features

Although the sites are located in mountainous regions largely covered by forest, the base of the mountains is more gently sloping terrain, sparsely populated with small clusters of houses and comparatively small-scale agriculture and dairy farms. Access to the underground tunnels would be located in this more accessible terrain. These areas would also serve as a base for construction, and provide access to the experimental facility after completion.

11.4.1.3 Climate

The Kitakami site has a slightly cold climate with a mean air temperature in the coldest (hottest) month of $-4.8\,^{\circ}$C ($+28.8\,^{\circ}$C) respectively. The mean annual rainfall is 1,318 mm. The Sefuri site has a mild climate with a mean air temperature in the coldest (hottest) month of $+3.0\,^{\circ}$C ($+32.1\,^{\circ}$C) respectively. The mean annual rainfall is 1,612 mm. In both sites, there is occasional light snowfall in January and February.

The Kitakami site is located in the Tohoku district which was hit by a massive earthquake in March 2011, although there was little damage at the site itself. The Sefuri site is located in the Kyushu district, which, although hit by typhoons every year, suffers little damage.

11.4.1.4 Geology and tunnel structures

The tunnels at both sites would be built in hard granite bedrock (Fig. 11.3). If the ML tunnel is extended to 50 km, one end would extend beyond the granite into sedimentary rock, which, however, would also provide a stable base for construction.

The ML tunnel is located at a depth of between 50 m and 400 m; access is through a sloped tunnel with a grade of no more than 10 %. The access tunnel for the IR Hall has a maximum grade of 7 %.

The ML tunnel has a 'Kamaboko' shape. Rock-bolt reinforcement is not usually required in stable granite, but may be required in wider sections. The tunnel interior is lined with concrete to provide waterproofing so that external groundwater can be processed by normal drainage. The access tunnels do not need to be waterproof and the interiors are of sprayed concrete. Rock anchor or bolt reinforcement is required for the IR Hall.

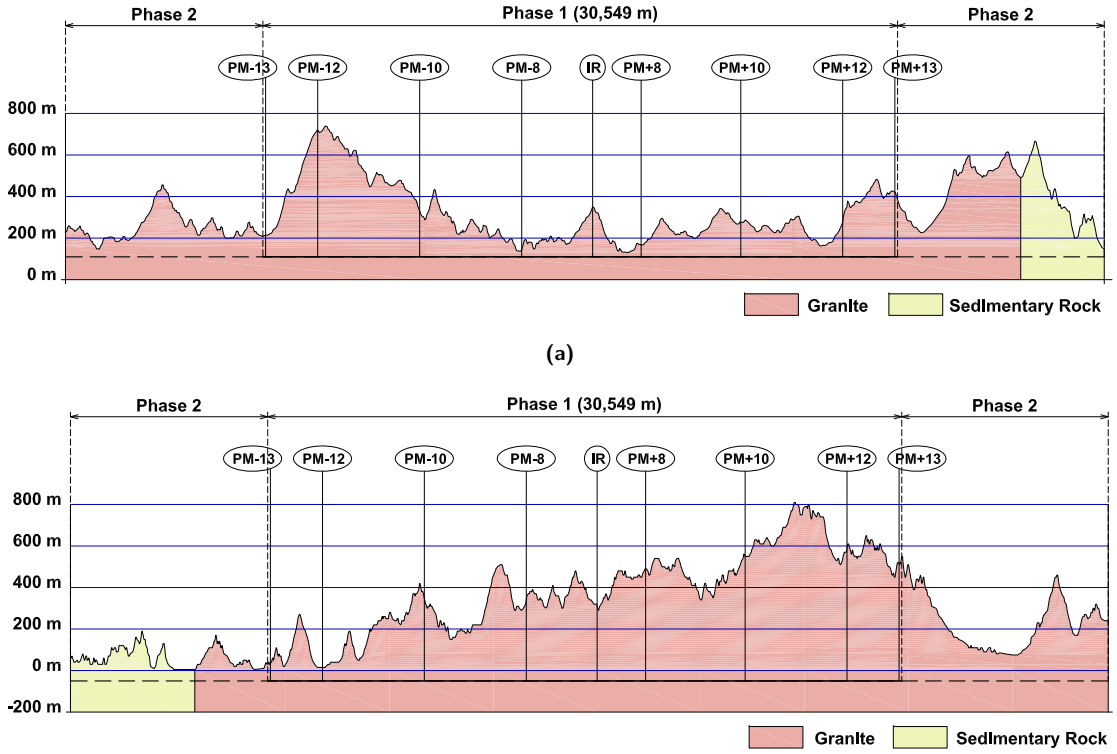

Figure 11.3. Elevation of the sites (a) Kitakami and (b) Sefuri. The 500 GeV baseline tunnel (phase 1) is shown, as well as the extent of the 1 TeV upgrade (phase 2). For Phase 1 the access tunnel spacing is shown.

11.4.1.5 Power Availability

Both sites have sufficient electric power to meet requirements. Kitakami has a 275 kV line and Sefuri a 345 kV line. Electric power stability should be adequate for accelerator operation.

11.4.1.6 Construction Methods

The ML tunnel is 11.0 m wide and 5.5 m high and is excavated using NATM. After construction it is divided into two parallel galleries by a central concrete wall The access tunnels are also excavated by NATM, except where they penetrate the 10 m to 20 m thick surface soil layer, where steel reinforcement is required. The IR Hall is excavated from the top down, starting from a top-heading tunnel connected to the access tunnel using a bench-cut construction method. As the excavation progresses it is reinforced by rock-bolts into the cavern wall.

11.4.2 Civil construction

Because the Japanese sites are deep underground, they have some unique requirements:

- the ML RF power is supplied via DKS with the RF sources in the service gallery;
- due to the capacity of the cryogenic plants, the underground structures are separated into seven zones, each with a maximum span of ± 2.5 km from the access point (Fig. 11.4);
- the sloped access tunnels dictate a particular design for the underground enclosures as well as a particular installation method;
- electrical, mechanical and cryogenic utilities are located in underground caverns.

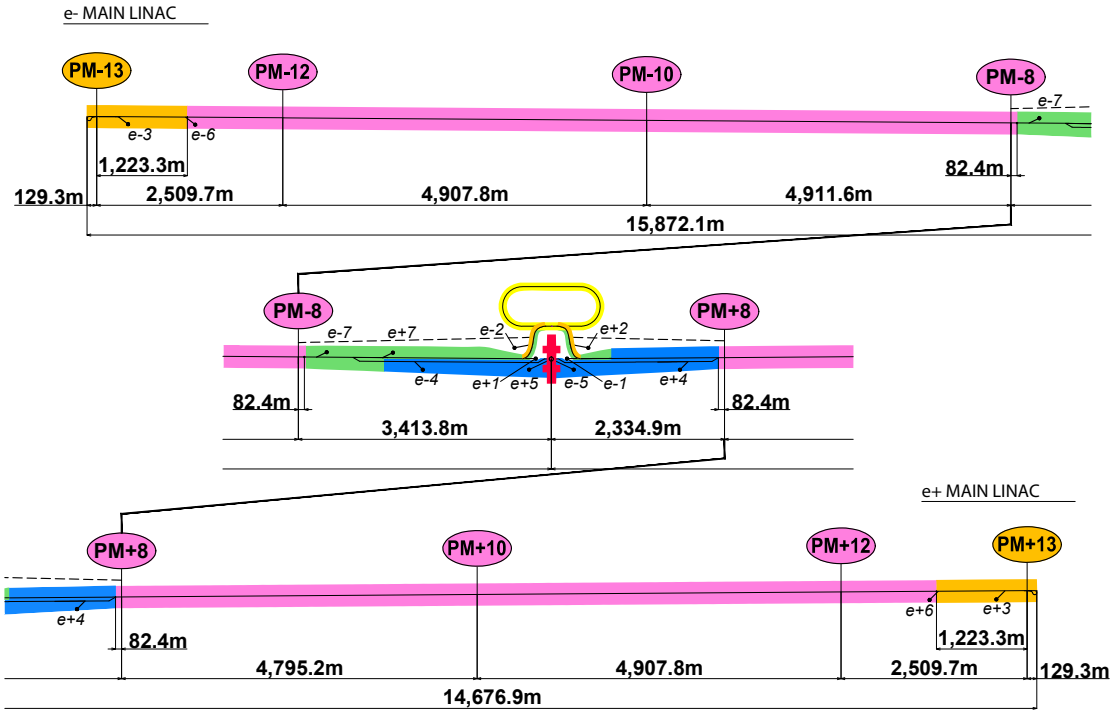

Figure 11.4. Asian region overall site layout.

11.4.2.1 Overall site layout

The overall site layout is shown in Fig. 11.4. Because of the cryogenic-string length, the ML, shown schematically in Fig. 11.5, is slightly longer with DKS than with KCS: the electron arm is 11,188 m, while the positron arm is 11,072 m. The number of access points is the minimum consistent with the cryogenic plant layout.

11.4.2.2 Underground enclosures

Tables 11.1, 11.2 and 11.3 show the extent of the required underground construction for the different accelerator systems. The features of the major underground enclosures are described below.

Table 11.1
Tunnel lengths and volumes

Accelerator section	Length(m)	Volume (m^3)
e^- source (beam)	368	17,757
e^- source (service)	223	4,881
e^+ source (beam)	1,678	67,364
e^+ source (service)	1,523	33,351
Damping Ring	3,239	120,352
RTML	3,305	200,237
Main Linac	22,425	1,395,754
BDS (beam)	3,847	184,019
BDS (service)	3,102	67,915
TOTAL	39,710	2,091,630

Table 11.2
Cavern summary and volumes. The six large Main Linac caverns house the helium compressors, cryogenic facilities, electrical substations, cooling-water systems, and plumbing systems.

Accelerator section	Qty	Volume (m^3)
e^- source	0	0
e^+ source	0	0
Damping Ring	4	21,151
RTML	2	15,522
Main Linac	6	293,687
BDS	0	0
IR	1	189,381
TOTAL	13	519,741

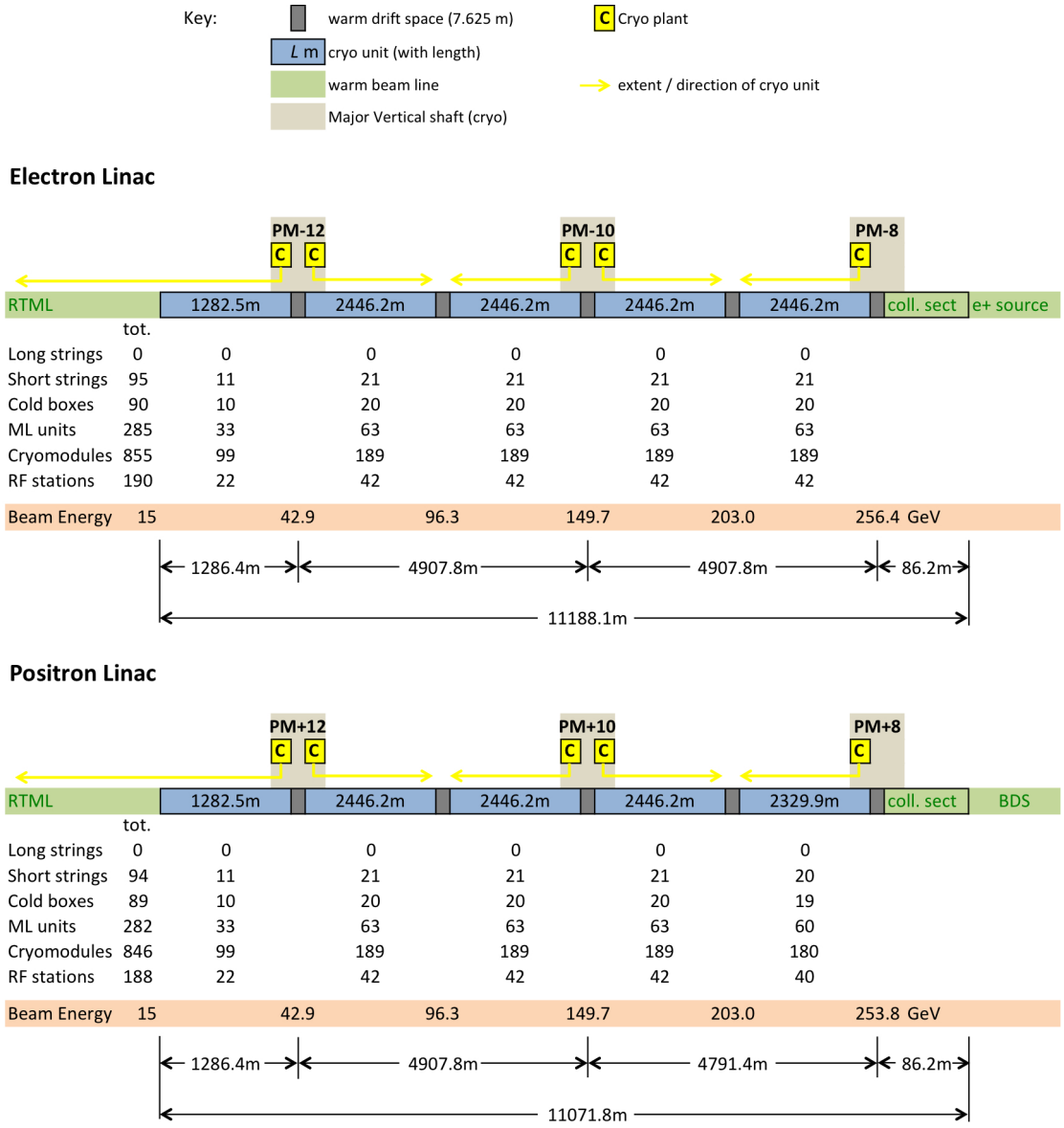

Figure 11.5. Main Linac schematic showing the cryostrings, cryogenic fluid control cold boxes, 3-cryomodule ML units, cryomodules and HLRF generation stations. The beams energy increases from the left side of the figure for both the electron and positron linac diagrams.

Table 11.3
Access tunnel lengths and volumes

Accelerator section	Qty	Volume (m^3)
e^- source	0	0
e^+ source	0	0
Damping Ring	1,320	88,335
RTML	2,000	117,186
Main Linac	6,000	351,558
BDS	0	0
IR	1,772	155,914
TOTAL	11,092	712,993

11.4.2.2.1 ML tunnel A comparison of various construction methods indicated that NATM would be the most cost effective for mountainous sites (see Part I Section 5.2.2.2) The slower excavation speed ($\sim 100\,\mathrm{m}$/month) is compensated by greater flexibility with short construction zones and more parallel excavation.

The cross-sectional layout of the ML tunnel with centre wall is shown in Fig. 11.6. Both beam and service gallery have functional zones for equipment installation, survey, conveyance, and human

egress. Water pipes are installed in the lower part of the tunnel and electric power lines are installed in shielded racks on the ceiling.

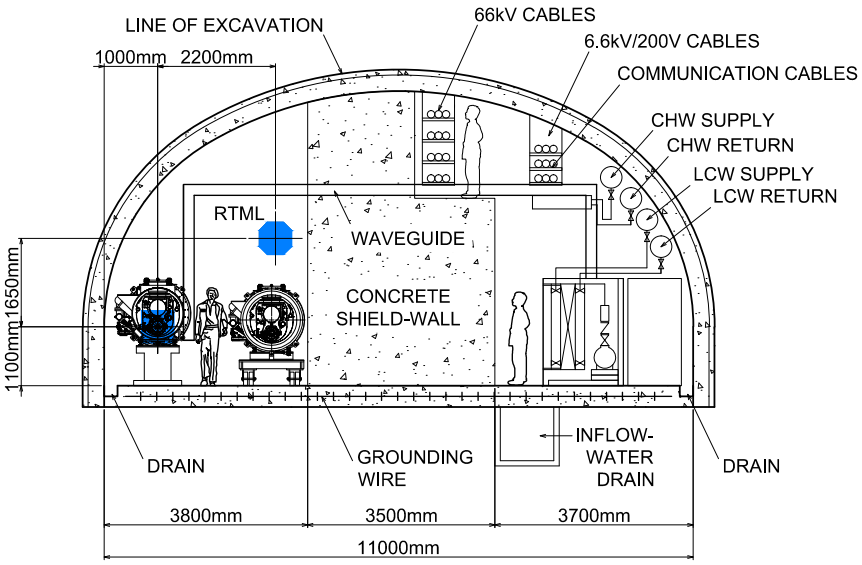

Figure 11.6
Equipment layout in the ML tunnel

At its base, the centre wall is 3.5 m thick to provide radiation shielding and the upper side thickness is 2.0 m. At intervals of 12 RF units, there is a connection passage between the beam and service galleries, which can be used for evacuation in case of emergency. At each connection, the centre wall thickness is increased by 2 m in the downbeam direction to provide more shielding. To allow efficient excavation, the tunnel height must be at least 5 m, based on the passage of standard excavation machines ($\sim$3.5 m high), plus the sliding-form for the concrete lining ($\sim$1 m thick), and the concrete liner itself 30 cm thick. The tunnel floor is 40 cm thick. The ML tunnel is nominally aligned along a geoid surface. A small slope of no more than $\pm$0.8 % is acceptable for the main-linac cryomodule and may be introduced to minimise total access-tunnel length for a given specific site.

Previous constructions have shown that grout can limit inflow to no better than $\sim$1 l/min/m at 100 m depth underground.The inflow water rate must be confirmed by geologic studies before construction, but any inflow beyond this will be completely isolated by the concrete liner and drained to a ditch that will be sized assuming the inflow water for 5 km is gathered to one access point.

11.4.2.2.2 Access halls (AH) An"access hall" at the Asian site (Fig. 11.7) corresponds functionally to a "shaft-base cavern" at the other sites. The six halls for the ML/RTML/BDS areas are located alongside the main underground tunnel (Fig. 11.3). They provide an entrance to the tunnel as well as a local center for electricity, air, cooling water, and liquid He infrastructure. Each AH includes:

- an electrical substation with two 30 MW 66 kV/6.6 kV transformers, an incoming panel, and a distribution panel for cryogenics, accelerator supplies, and service equipment;
- a mechanical station with the second-loop heat exchangers with pumps which isolate it from the first loop, which handles the water-pressure differential due to the depth;
- a liquid He cryogenic station with 4 K cold boxes with dewars, cold compressors, 2 K cold boxes, and He distribution system;
- a warm compressor whose location must take into account its vibration and noise impacts.

11.4.2.2.3 IR Hall The IR Hall (Fig. 11.8) consists of a main hall (142 m long by 25 m wide by 42 m high) that has enough space for assembly of the two detectors, as well as space for the operating detector that sits on the beamline. It also has several work areas on either side and a tunnel loop for egress. All of the central region beamline equipment, including the DR equipment, and the detector components are carried in through the IR Hall access tunnel.

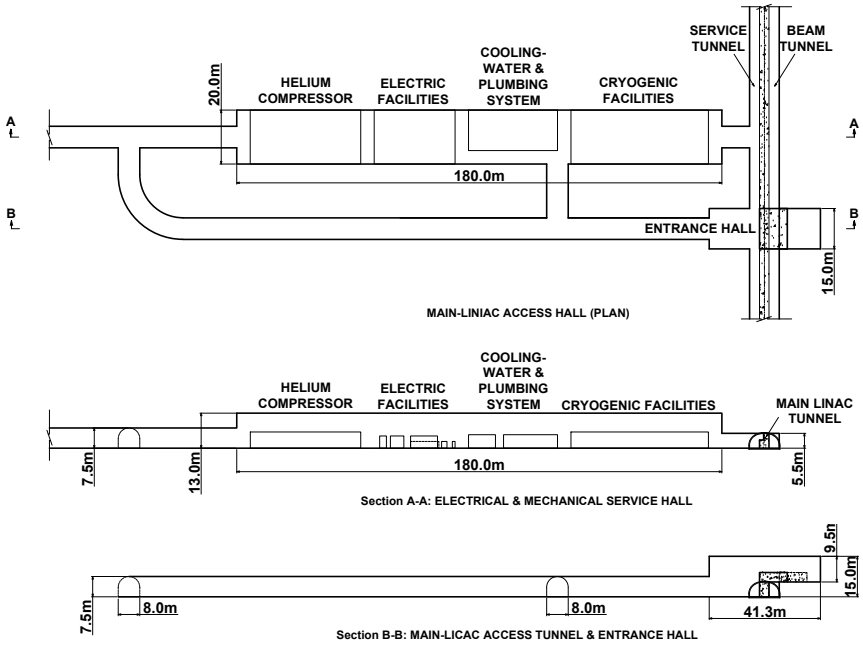

Figure 11.7
Typical Access Hall Plan and Elevation View

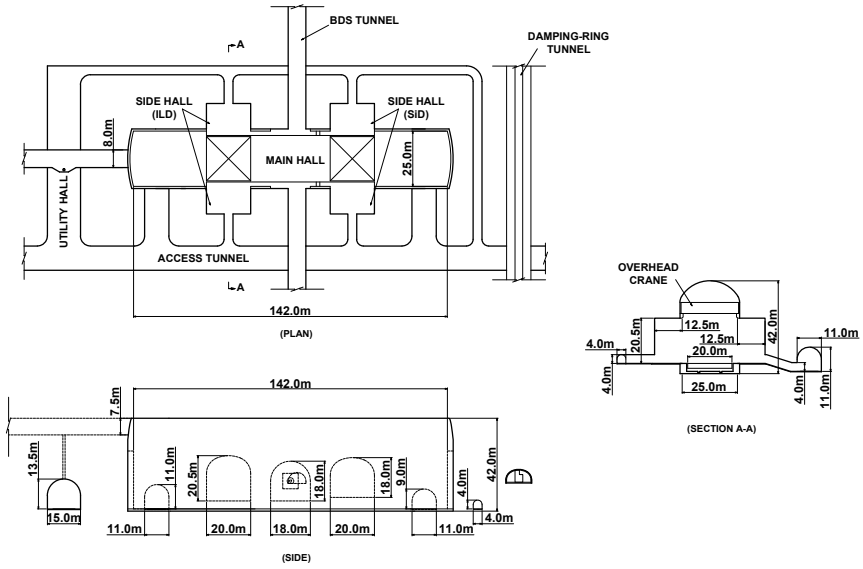

Figure 11.8
IR Hall

11.4.2.3 Access to Underground Areas

Inclined tunnels provide access to the underground facilities. There are 10 access tunnels; six for the main linacs, two for both ends of ILC, and two for the central region. A great advantage of access tunnels over vertical shafts is that vehicles can be used to transport people and equipment. A disadvantage is the long distances involved which affect the size of cooling/ventilation pipes and pumps; an alternative option is to use small-bore vertical shafts, which can be excavated by a boring machine.

The eight access tunnels at PM-13, -12, -10, -8, +8, +10, +12, +13 along the main linac and an access tunnel for the damping ring, have a vaulted section with an inner width of 8 m and height of 7.5 m (Fig. 11.9 left). The tunnel width is wide enough that two large trucks can pass each other and leave a human escape zone, and the height is sufficient to accommodate large pipes for cooling water and air ventilation. The IR Hall access tunnel (Fig. 11.9 right) is larger to allow transport of the detector solenoids from the detector assembly building on the surface. Its width is 11.0 m and its height is 11.0 m. A damping ring access tunnel is also constructed. Assuming the lengths of access tunnel, which will be known after a real site and the tunnel routes are fixed, to be 1 km in

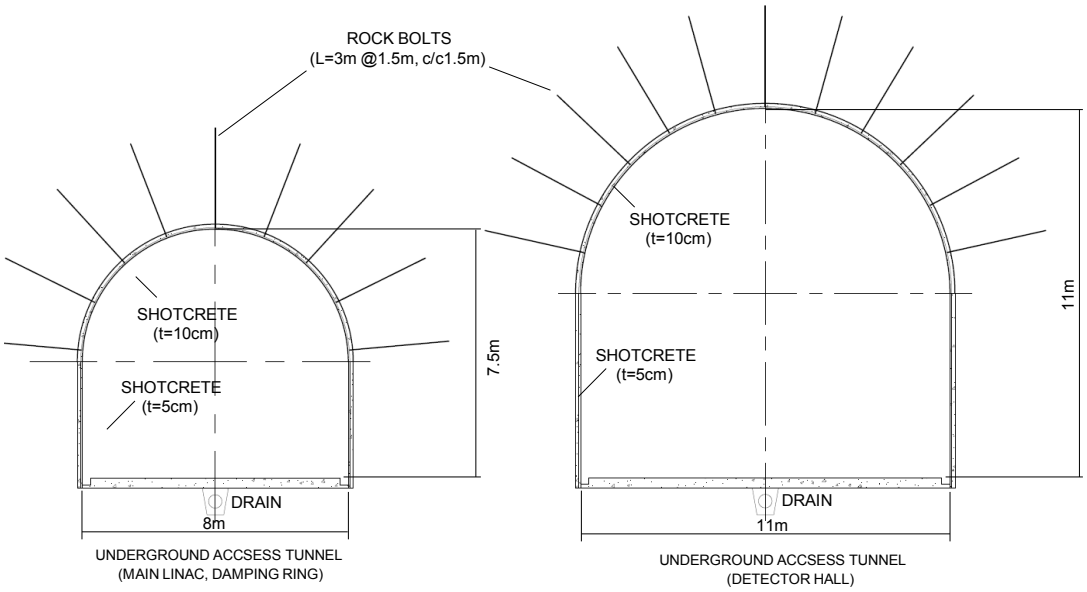

Figure 11.9. Underground access tunnels.

average, the total length and excavation volume of the ten access tunnels are 10 km and 643,000 m^3 respectively.

The surface entrances of the access tunnels are located near existing roads. The surface sites around the entrances support construction and are later utilised for facilities such as cooling towers. The tunnel excavation starts from the surface which is assumed to be soil or soft rock down to a depth of ∼20 m. The tunnel walls are reinforced by rock bolts and finished with sprayed concrete ("shotcrete") of ∼20 cm thick. The tunnel floor is 30 cm thick.

11.4.2.4 Surface facilities

In these mountainous sites, some facilities that would otherwise be on the surface must be located underground. Table 11.4 summarises the area of the surface facilities. Neither of the two sites is close to an existing accelerator facility so provision must be made for general purpose buildings, accounting for roughly half of the total in Table 11.4. The remaining surface facility area is roughly 60 % of that at the Americas site.

Table 11.4
Asian site surface facilities. The IR surface facilities include general purpose buildings.

Accelerator section	Qty	Area (m^2)
e^- source	0	–
e^+ source	0	–
Damping Ring	0	–
RTML	0	–
Main Linac	65	22,375
BDS	10	3,650
IR	28	65,250
TOTAL	103	91,275

11.4.3 Mechanical services

The main aspects of the mechanical design are:

The location and quantity of the ML heat loads (Table 11.5) are based on the DKS. ∼90 % of the heat load is cooled by processed water at a temperature of ∼34 °C. About 10 %of the heat loads such as air conditioning and racks are cooled by chilled water at ∼9 °C. Cryomodules are in a 9-cryomodule string and RF is fed by klystrons and modulators installed in the service gallery. As a staged approach, in the baseline one klystron feeds 4.5 modules located every 54 m. Later, for the

luminosity upgrade, more klystrons are added and each klystron feeds 3 modules located every 36 m. Chilled water is used to cool instrument racks and gallery air.

The cooling-water plants are located next to the cryogenic plants in the underground access halls. Heat is transferred through the access tunnels and released to the air by cooling towers on the surface near the access tunnel entrance. Cryogenic warm compressors are distributed in the underground access halls.

Table 11.5
Summary of DKS heat loads (MW) by Accelerator section. Heat loads generated by the utilities themselves (pumps, fan motors, and etc) are listed as 'Conventional'.

Accelerator section	load to LCW	load to Air	Conventional	Cryo (Water load)	Total
e^- sources	1.40	0.70	1.87	0.80	4.77
e^+ sources	5.82	0.64	2.27	0.59	9.32
DR	10.92	0.73	2.69	1.45	15.79
RTML	4.16	0.76	2.02	part of ML cryo	6.94
Main Linac	42.17	5.57	16.89	32.00	96.63
BDS	9.20	1.23	1.68	0.41	12.52
Dumps	14.00		1.12		15.12
IR	0.40	0.76	1.79	2.65	5.60
TOTALS	88.1	10.4	30.3	37.9	167

11.4.3.1 Processed water

The heat loads are distributed up to ±2.5 km from the nearest access hall. Considering both construction costs and operational safety, the cooling-water system is based on 3 loops (Fig. 11.10). The first loop includes surface cooling towers, pumps, and piping underground. The second loop provides processed cooling water out to ±2.5 km in both directions along the ML service gallery. The heat exchanger protects underground equipment against high water pressure from the surface. The third loop provides low conductivity water (LCW) to the local heat loads.

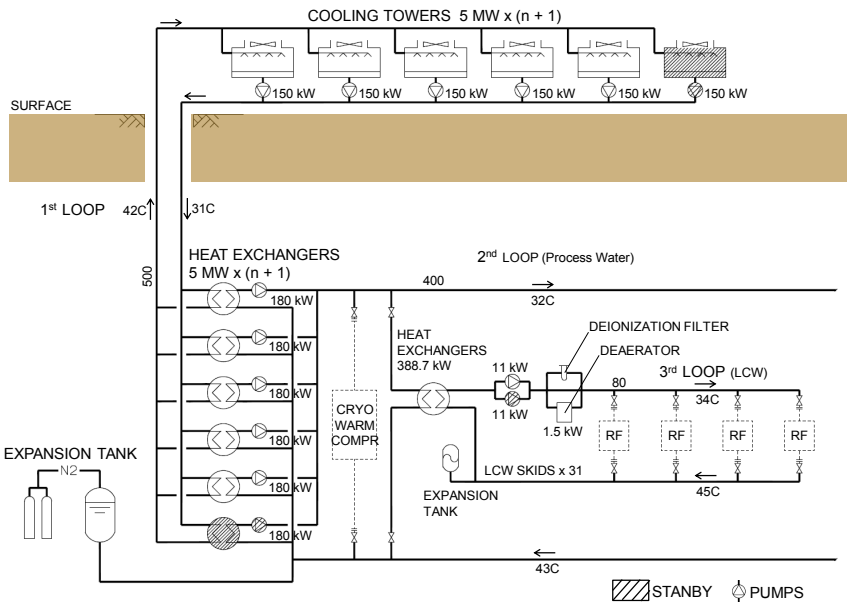

Figure 11.10
The cooling water system in access hall 2.

11.4.3.1.1 Cooling towers The cooling towers are open-water type because of the advantages of lower construction cost, smaller footprint, and lower noise. The evaporation rate of 600 m^3/h for cooling 200 MW of heat load can be compensated with water flowing into the tunnel, which would otherwise need to be disposed of. A group of cooling towers with one stand-by tower is located at each access tunnel entrance, supplying cooling water of 31 °C and returning water of 42 °C.

11.4.3.1.2 Underground cooling-water loops The second-loop water temperature is 32 °C in supply and 43 °C in return water. The second loop has also a group of heat exchangers and pumps with one

back-up. The third loop, which finally cools the accelerator technical equipment, needs to supply deoxygenated and demineralised water via stainless-steel pipes. It feeds four RF units using a compact cooling-water unit with heat exchanger, pump, de-aerator, and de-ionizer. The water temperature is 34 °C in supply and 45 °C in return.

11.4.3.1.3 Chilled-water system The chilled-water system (Fig. 11.11) is similar to the cooling - water system except it includes a refrigerator. Chilled water is produced by "Inverter-Turbo"-type refrigerators which have high efficiency and small CO_2 gas emission. The system configuration is also three loop. The third loop covers four RF units and the water temperature is 7 °C at the supply and 18 °C at the return.

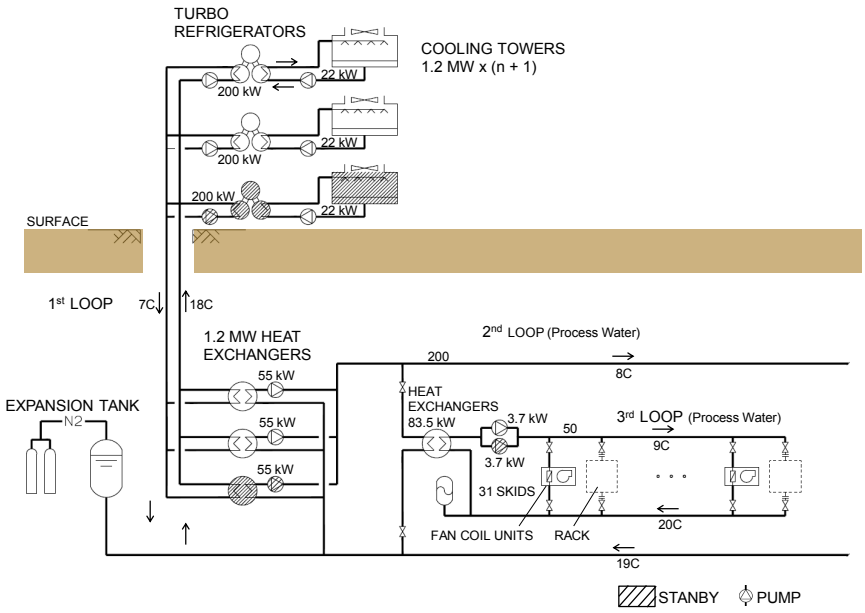

Figure 11.11
The chilled-water system (access hall 3).

11.4.3.2 Piped utilities

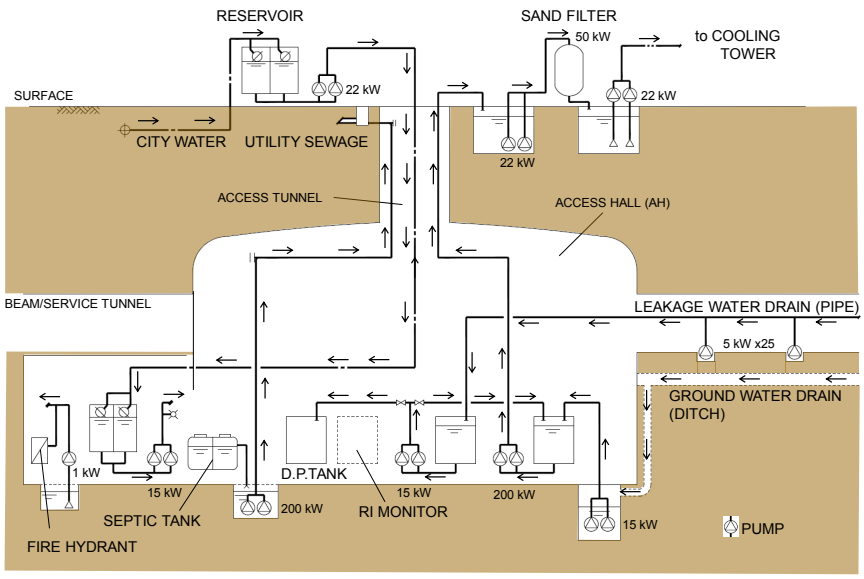

Figure 11.12
Piped utilities.

Figure 11.12 shows a flow chart of the piped utilities. The municipal water system is used for potable water. It is stored in tanks both on the surface and underground. Sewage water is processed and sent to a drain sewer on the surface.

The inflow water outside the thick tunnel lining is collected in a tank at each access hall. Water leaking into the tunnel is collected to pits located at intervals and pumped to the access hall tank. This water is monitored for activation, and if activated, stored in a holding tank. Otherwise, it is merged into the inflow water and pumped to the surface. Part of the water is sand-filtered and utilised for the cooling-tower makeup water.

11.4.3.3 Air treatment

Fresh ambient air is treated by air-conditioning equipment on the surface (Fig. 11.13). The air is cooled and dehumidified in the summer and heated in the winter, and supplied to the underground structures by large-bore ducts installed in the access tunnels. The air blows in the tunnel without ducts at a flow rate of ∼0.5 m/s. The tunnel temperature is 29 °C and the humidity is 35 %. The service tunnel is cooled by fan-coil units using chilled water. The air is exhausted to the surface. The atmospheric pressure is controlled by dampers in the ducts so that the pressure of the service tunnel is slightly higher than the beam tunnel. The exhaust duct is also the smoke exhaust in the case of fire. Helium leakage is vented through the small-bore survey shafts located every ∼2.5 km (Fig. 11.13).

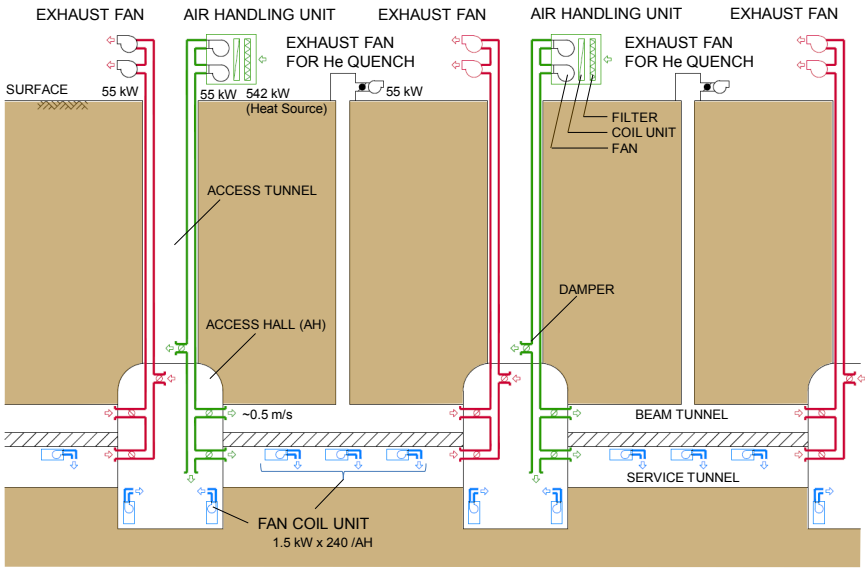

Figure 11.13 Main Linac tunnel ventilation scheme.

11.4.4 Electrical

This section describes the electrical power requirements for the ILC site. A summary of electrical power loads is given in Table 11.6.

Table 11.6 Estimated DKS power loads (MW) at 500 GeV centre-of-mass operation. 'Conventional' refers to power used for the utilities themselves. This includes water pumps and heating, ventilation and air conditioning, (HVAC). 'Emergency' power feeds utilities that must remain operational when main power is lost.

Accelerator section	RF Power	Racks	NC magnets	Cryo	Conventional		Total
					Normal	Emergency	
e^- sources	1.28	0.09	0.73	0.80	1.47	0.50	4.87
e^+ sources	1.39	0.09	4.94	0.59	1.83	0.48	9.32
DR	8.67		2.97	1.45	1.93	0.70	15.72
RTML	4.76	0.32	1.26		1.19	0.87	8.40
Main Linac	52.13	4.66	0.91	32.00	12.10	4.30	106.10
BDS			10.43	0.41	1.34	0.20	12.38
Dumps					0.00	1.21	1.21
IR			1.16	2.65	0.90	0.96	5.67
TOTALS	68.2	5.2	22.4	37.9	20.8	9.2	164

11.4.4.1 Electrical power distribution

The electrical power is distributed in three stages:

- the site electric power is stepped down from local-district high voltage (150-500 kV) to 66 kV in the main substation and distributed to the 6 access hall and the IR Hall substations;
- the 66 kV electricity is further stepped down to 6.6 kV at each substation and distributed inside the areas;
- the electric loads such as RF modulators and cryogenic warm compressors are powered directly at 6.6 kV and other local loads are fed at lower voltages stepped down in local substations distributed along the accelerator.

11.4.4.2 Main substation and 66 kV power distribution

A primary voltage of 275 kV was assumed for the site. The single-line diagram of the main substation is shown in Fig. 11.14. The primary-line configuration is a two-way system including a stand-by line. The power capacity is designed to be 300 MW and space is reserved for an additional 200 MW for the future 1 TeV upgrade.

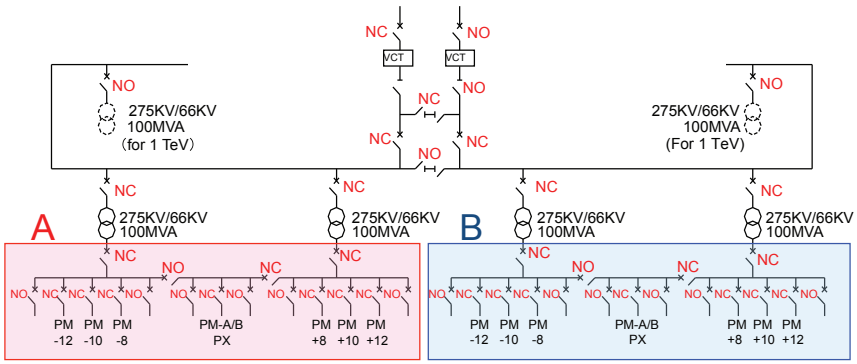

Figure 11.14
Single-line diagram for the main substation.

The main transformers have an n+1 redundancy scheme and use four banks of 100 MW transformers. The switching gears are gas insulation type. They are located in an outside yard of area $\sim$4000 m^2. The secondary voltage is 66 kV and the power is distributed through the BDS and ML service galleries and access halls with two pairs of three-phase cables.

11.4.4.3 Access hall substations

With a power range between 28 MW and 44 MW, two 30 MVA 66 kV/6.6 kV transformers are required at each substation, allowing more than a half of the operational power to be maintained in case of a transformer fault. There is one spare transformer at the main substation, with capacitors to improve power efficiency. The single-line diagram and the equipment layout in the hall are shown in Fig. 11.15.

11.4.4.4 Local substations

The local distribution board diagram is shown in Fig. 11.16. There are 6.6 kV boards for the modulators at an interval of every four RF units, and cryogenic compressors in the access halls. The local substations step down 6.6 kV to lower voltages at an interval of every four RF units.

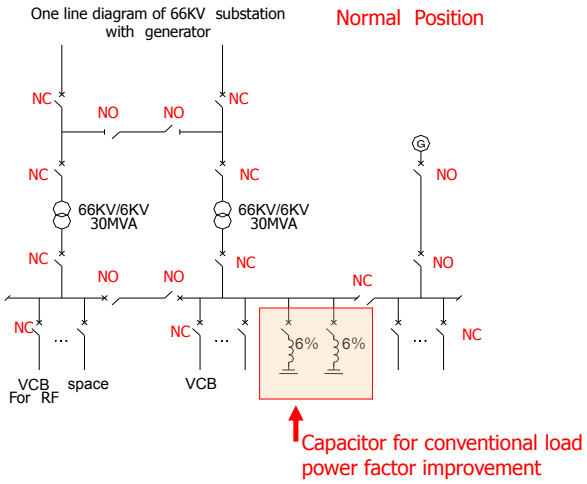

Figure 11.15
Access hall substation single-line diagram and the equipment layout.

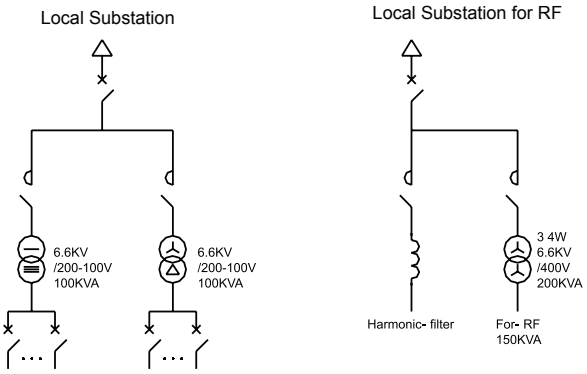

Figure 11.16
Local distribution panels.

11.4.4.5 Emergency and backup electrical power

There are emergency generators at each of the seven 66 kV substations. The emergency power generators are adequate for fire-fighting and to maintain minimal functioning of the building and the compressor for He-gas storage during an electricity outage. Each of seven diesel-engine generators installed at the surface yards supplies the underground 66 kV substation with ∼1 MVA power.

DC power supplies are used for the substation control system and emergency lights. They are installed in seven AHs and the IR Hall. Chargeable batteries are used for tunnel emergency lights, evacuation lights, and local substations. The equipment is a cubicle system and valve-regulated, sealed-cell lead-acid batteries are used.

To provide backup power for critical systems, UPSs are installed in each control room beside the substations. Technical equipment includes its own UPS where necessary.

11.4.5 Life safety and egress

11.4.5.1 Fire safety

There are no existing laws and design guidelines in Japan which specify safety and disaster prevention measures for deep underground tunnels. A special committee established by the Japan Society of Civil Engineers is currently reviewing the basic policy proposal on the disaster prevention design for the ILC underground facilities.

Of primary importance in an underground tunnel is safe refuge when a fire breaks out. However, the distance to the surface via an access hall can be as long as 5-6 km and a secondary evacuation route is required. This is provided by access passages located every 500 m along the ML that connect the two galleries so the other gallery can provide an escape route (see Section 10.5.3).

Evacuation from the tunnel to the surface is via the access hall and the access tunnel every 5 km. Even with rapid egress, it can take up to 1 hour to reach the surface. If a fire is detected, the

partition door and damper for the access passage will close automatically, and will prevent smoke reaching the escape route.

Each of the two galleries is separately ventilated from the access halls. There is no separate emergency smoke-control system. The main ventilation system switches to a smoke-exhaust function automatically in case of a fire.

There is no installed fire-extinguishing sprinkler system to avoid possible water damage to the accelerator machine and experimental equipment. The ML tunnel is equipped with the following standard emergency equipment:

- smoke detector and fire detector;
- fire alarm system;
- emergency lighting system;
- emergency illuminated exit signs;
- emergency exit guide lights;
- fire extinguishers.

11.4.5.2 Safety for Helium

Since there is a large quantity of liquid helium in the ML tunnel, oxygen deficiency monitoring is required throughout. When the oxygen concentration drops below an acceptable level, emergency measures are taken and an alarm sounds. The main ventilation system switches to emergency mode and the helium gas from the upper part of the tunnel is discharged outside by exhaust shafts in the access tunnels.

11.5 European region (Flat topography)

11.5.1 Siting studies

Two European sites were considered: the Geneva region (deep-site study), along the French-Swiss border and the Dubna region (shallow-site study) in Russia. The European design is based on the KCS RF concept developed by the Americas Region. This assumes that as much as possible of the technical equipment is housed on the surface in order to minimise the underground enclosure volumes.

11.5.1.1 Geneva region (deep site)

11.5.1.1.1 Location This site is set in the North-Western part of the Geneva region, near the CERN laboratory (Fig. 11.17). Since no real discussions with local authorities have taken place, this position is only indicative. The IR is fully located within existing CERN land at the Prevessin Campus. The new underground structures will mostly be constructed at a depth of 100-150 m in stable Molasse rocks in an area with moderate seismic activity.

All necessary infrastructure to accommodate the project is available in the Geneva area. This includes the possibility of accommodating specialists for the accelerator construction period, storage and assembly of equipment, and the provision of project-production support during manufacturing of the special-purpose equipment. Excellent transport and communication networks already exist.

11.5.1.1.2 Land Features The proposed location is within the Swiss midlands embedded between the high mountain chains of the Alps and the lower mountain chain of the Jura. CERN is situated at the foot of the Jura mountain chain in a plain slightly inclined towards Lake Geneva. The absolute altitude of the surface ranges from 430 m to 500 m with respect to sea level.

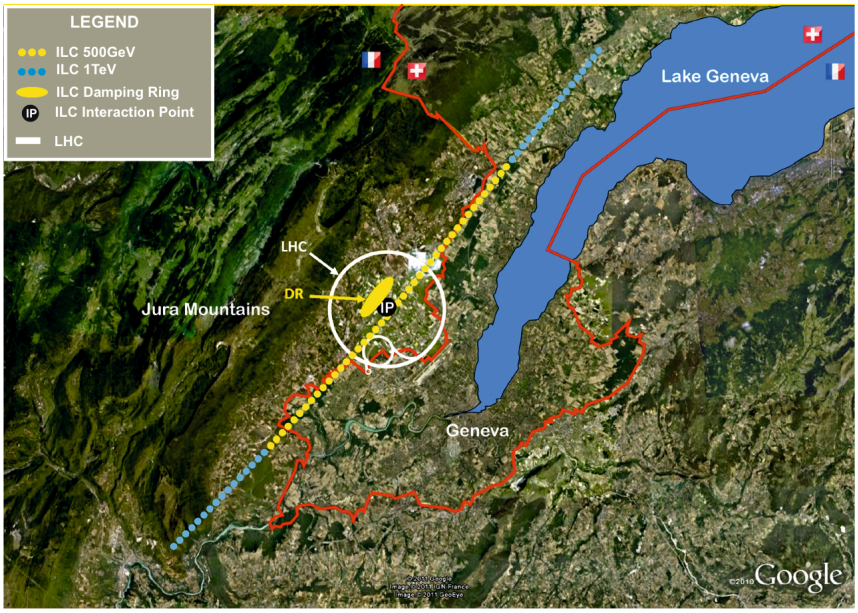

Figure 11.17 The potential location of ILC in the Geneva region.

11.5.1.1.3 Climate The climate of the Geneva region is temperate, with mild winters and warm summers. The mean annual air temperature is 9.6 °C, with a maximum temperature of 25.7 °C in July and a minimum temperature of −1.9 °C in January. The mean annual relative humidity is 75%. Precipitation is well-distributed throughout the year, with a mean annual precipitation of 954 mm. An average of 42.5 cm of snow falls in the period November to March.

11.5.1.1.4 Geology Most of the proposed path of the ILC is situated in the Geneva Basin, a sub-basin of the large North Alpine Foreland (or Molasse) Basin. Characterized as stable and impermeable, the Molasse rock is considered to be very suitable for underground constructions. A simplified geological profile of the region is shown in Fig. 11.18.

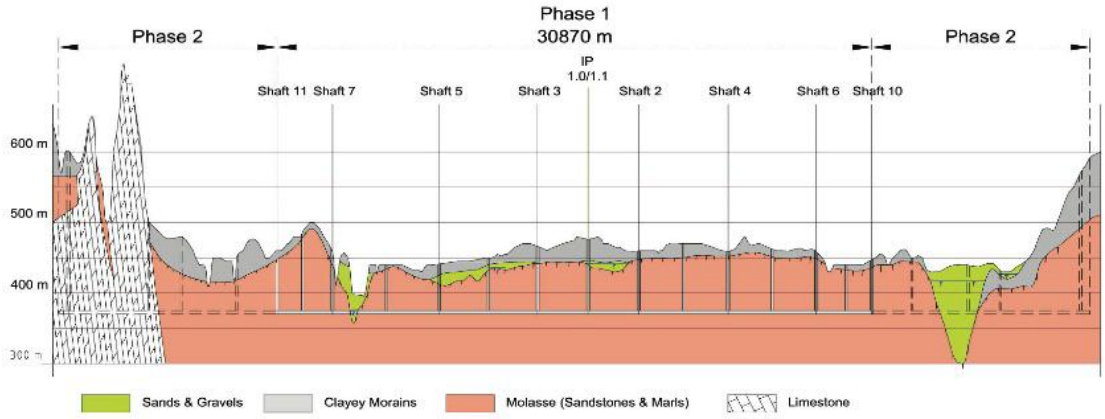

Figure 11.18. Simplified geological profile. ILC is mostly housed in the Molasse Rock.

11.5.1.1.5 Power Availability The CERN region has a very well developed electrical supply with a 400 kV line coming into the Prevessin Site on the French side of the campus and a 130 kV line arriving on the Meyrin Site on the Swiss side. The existing CERN networks carry electrical energy to major sub-stations via 66 kV and 18 kV underground links. Final loads are supplied at 18 kV, 3.3 kV or 400 V.

11.5.1.1.6 Construction Methods For the upper parts of the shafts, located in dry moraines up to 50 m depth, traditional excavation means are foreseen. Where water-bearing units are encountered the ground-freezing technique will be used to allow safe excavation of the shafts under dry conditions. This involves freezing the ground with a primary cooling circuit using ammonia and a secondary circuit

using brine at −23 °C, circulating in vertical tubes in pre-drilled holes at 1.5 m intervals. Besides creating dry conditions, the frozen ground acts as a retaining wall.

When the underlying rock (sandstone) is reached the shafts and caverns will be excavated using rock breakers and road headers. A temporary lining will be set in place using rock bolts, mesh and shotcrete, after which the walls and vaults will be sealed with waterproof membranes and covered with cast in-situ reinforced concrete.

The underground enclosures have diameters of 5.2 m, 6.0 m, 8.0 m and up to 12.0 m. For the Molasse rock, it is estimated that it is cheaper to excavate these tunnels using a TBM with 8.0 m diameter for the entire length of the BDS tunnels, with some local cavern enlargements using roadheaders in a second phase.

11.5.1.2 Dubna Region (shallow site)

11.5.1.2.1 Location The Dubna area provides a potential shallow tunnel site. The Joint Institute for Nuclear Research (JINR) is an International Intergovernmental Organization and has experience of organizing and realizing large-scale research projects based on international cooperation among scientific centers and industrial enterprises. Figure 11.19 shows the site location.

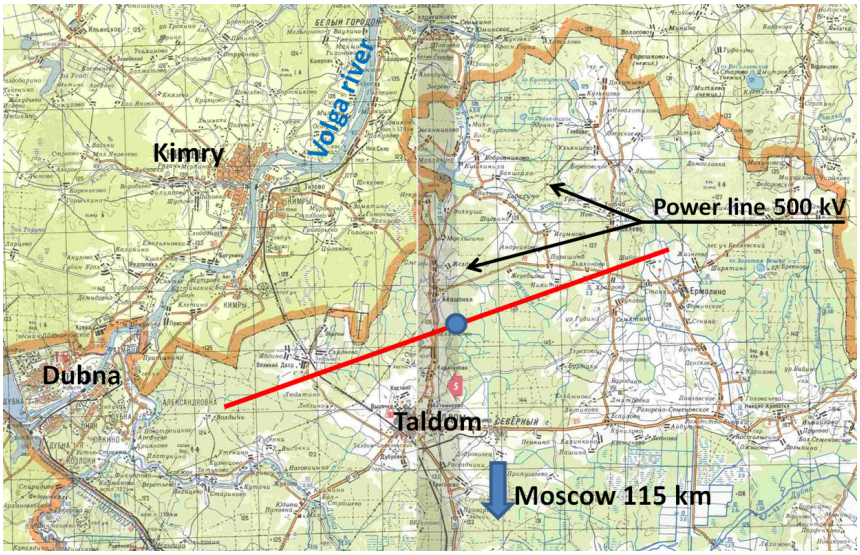

Figure 11.19 The proposed path of the accelerator construction (indicated as a red line) in the Dubna region

Due to the special economic zone established in Dubna in December 2005, preferential terms for the development and manufacturing of high technology products are provided. Furthermore, the prevalent legal conditions in the Dubna region provide the opportunity to acquire land free of charge, as has been the case for JINR, with the agreement of the Russian Federation government.

11.5.1.2.2 Land features The main feature of the proposed location is a flat topography, with an altitude ranging between 125 m and 135 m above sea level. The relief increases away from the site as the plain changes into smoothly sloping separate hills. The area is swampy with potential waterlogged conditions. During floods of the Dubna River, the groundwater level increases by up to between 0.6 m and 0.9 m, and a high percentage of the area is flooded. The territory is sparsely populated and practically free of industrial structures. The region around the accelerator path is mainly covered with forests containing small inclusions of agricultural land. The accelerator path traverses two small settlements and a railway with light traffic between Taldom and Kimry. Construction will not affect national parks or religious and historical monuments. Infrastructure and communication systems are in place.

11.5.1.2.3 Climate The region is characterized by a moderate continental climate with long and relatively cold winters and warm summers. The average annual air temperature is +3.10 °C, with a

maximum of +36.0 °C and a minimum of -43.0 °C. The average maximum air temperature of the hottest and coldest months is +22.7 °C, and -19.0 °C respectively. The average monthly relative air humidity in the region during the coldest and the hottest months is 84% and 57% respectively. The annual rainfall is 630 mm, of which 447 mm precipitates during the warm period (April-October) and 183 mm during the cold period (November-March). Snow cover typically starts in November, with an average snow depth of 30-40 cm in open places during the winter period.

11.5.1.2.4 Geology The site is situated within the Russian Plate, which is a part of the ancient East-European platform. The area is located in the southern part of a very gently sloping saucer-shaped structure, called the Moscovian syncline. The top layer consists of alluvial deposits, i.e. fine water-saturated sands with a varying thickness of 1 m to 5 m. These deposits cover the underlying semi-solid moraines of the Moscovian glaciation, which contains inclusions of detritus and igneous rocks. The thickness of the moraine deposits is between 30 m and 40 m. The moraines cover the fluvio-glacial saturated sands and loams of the Dnieper glaciation. Jurassic clays and carboniferous limestones are located at a depth of 50 m–60 m. The region has low seismic activity.

As the ILC is proposed to be placed in the moraines, at a depth of 20 m, an impermeable soil layer should be present under the tunnel to prevent water inflow from underlying water-bearing units (see Fig. 11.20). Overall, the available data show that the geological, hydrological and geotechnical conditions are favourable.

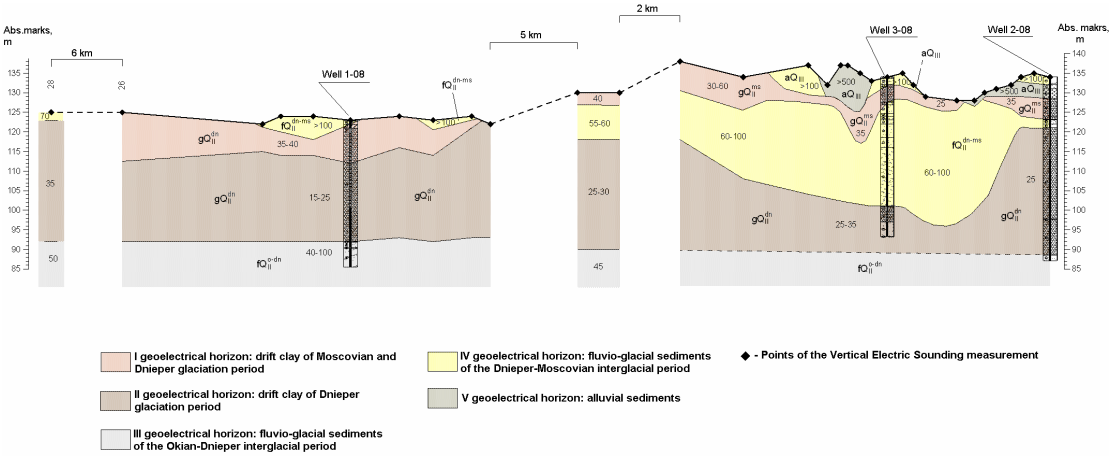

Figure 11.20. A geology study near Dubna

11.5.1.2.5 Power availability The northern part of the Moscow region, as well as the neighboring regions, has a developed electrical energy generation, transmission and distribution network. Two trunk transmission lines with voltages of 220 kV and 500 kV pass through the Dubna territory. The proposed ILC path is deliberately placed nearby and parallel to these power lines.

11.5.1.2.6 Construction methods A one-tunnel solution for the accelerator structures is possible at the Dubna site. A communication tunnel will be placed directly above the accelerator tunnel near the ground surface at a depth of 3 m-4 m. This tunnel is necessary for power supplies, RF power sources, data storage devices, electronic and control systems, etc. Near sub-surface buildings would be constructed by an open pit method and the tunnel could be constructed using TBMs, although 'cut and cover' construction techniques are possible over nearly the whole length.

11.5.2 Civil construction

The European design is developed to fit the local geological and environmental constraints of the Geneva area. Studies performed by external consultants [210–212] have been aimed at minimising the infrastructure costs, such as civil engineering, which are main cost-drivers of the project. This section describes the technical designs for the civil engineering for the 500 GeV baseline.

11.5.2.1 Overall site layout

Figure 11.21 shows a schematic layout of the civil engineering complex. Key characteristics of the ILC baseline layout are:

- tunnel footprint of approximately 31 km, positioned at 100-150 m depth;
- horizontal tunnel following a geoid surface;
- IR and injection complex fully located on the Prevessin Campus;
- ML housed within a single tunnel with an internal diameter of 5.2 m;
- two turn-around tunnels connected to the ML with a bending radius of 30 m in the horizontal plane;
- a service tunnel, linking the ML with the IR Hall and the DR;

  two additional RTML tunnels are planned for the central injector region, connecting the DR and the sources.
- two independent caverns for detector assembly and maintenance linked via a transfer tunnel;
- Shafts and surface installations approximately every 2 km along the ML.

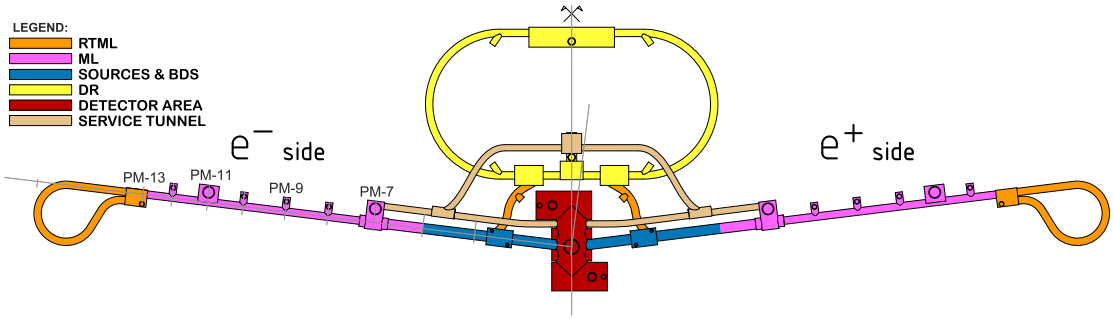

Figure 11.21. Schematic layout of the civil engineering complex

11.5.2.2 Underground Construction

Table 11.7, Table 11.8, and Table 11.9 summarize the European underground construction tunnels, caverns and access shafts, respectively. Of all the deep-tunnel sites studied, the soft 'molasse' sandstone near CERN is the most soft and weakest. For this reason, the cavern ceilings are dome-shaped leading to a larger overall excavation.

Table 11.7
Tunnel lengths and volumes by Accelerator section

Accelerator section	Length (m)	Volume (m^3)
e^- source (beam)	368	18,522
e^- source (service)	618	9,828
e^+ source (beam)	1,678	84,329
e^+ source (service)	2,203	35,038
Damping Ring	3,239	91,571
RTML (beam)	3,305	74,546
RTML (service)	1,955	31,090
Main Linac	22,168	470,782
BDS (beam)	3,847	193,379
BDS (service)	3,847	61,183
TOTAL	43,228	1,070,268

Table 11.8
Cavern summary and volumes

Accelerator section	Qty	Volume (m^3)
e^- source	1	2,029
e^+ source	1	6,715
Damping Ring	6	59,604
RTML	10	20,312
Main Linac	12	41,280
BDS	6	26,292
IR	5	127,100
TOTAL		283,332

Table 11.9
Shaft depths and volumes

Accelerator section	Depth (m)	Volume (m^3)
e^- source	100	0
e^+ source	100	0
Damping Ring	100	12,723
RTML	100	5,655
Main Linac	100	69,665
BDS	100	707
IR	100	39,584
TOTAL		128,334

11.5.2.3 ML tunnel

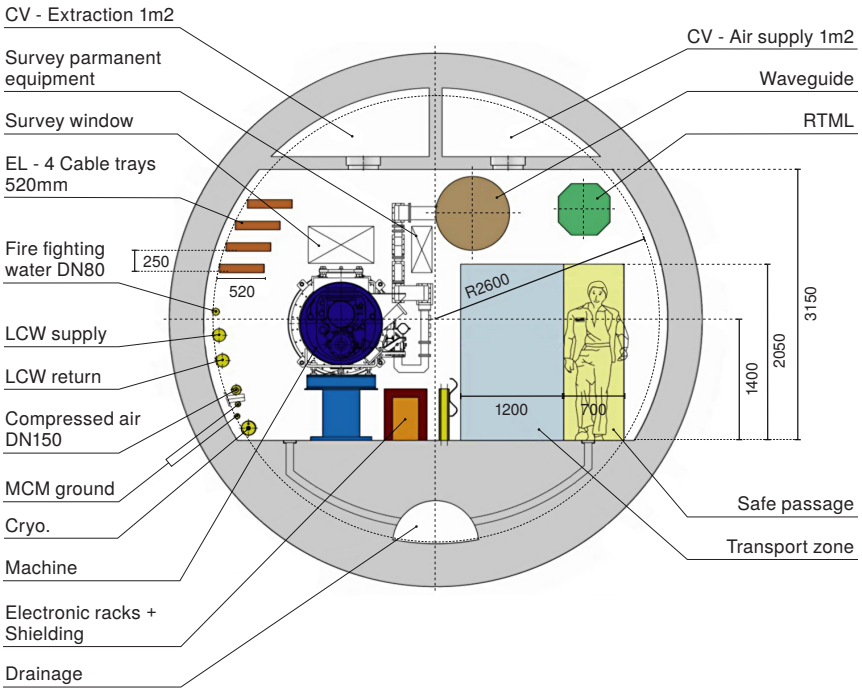

Figure 11.22
Typical tunnel cross section.

Figure 11.22 shows a typical cross section of the ML tunnel. The diameter has been optimized through 3D modelling of the accelerator and its services. The diameter is within the common range

of TBMs used for metro transportation tunnels; machinery and spare parts are easily found on the market.

A driving factor of the tunnel size is the ventilation concept, adopted mainly for safety reasons. This differs from the LHC, which has a longitudinal ventilation scheme. Cryo-modules are attached directly to the tunnel floor, which minimizes ground movement and allows for easy access.

11.5.2.4 Central injection region

The central injection complex (Fig. 11.23) consists of DRs, polarised electron and positron sources and the electron and positron 5 GeV SCRF injector linacs.

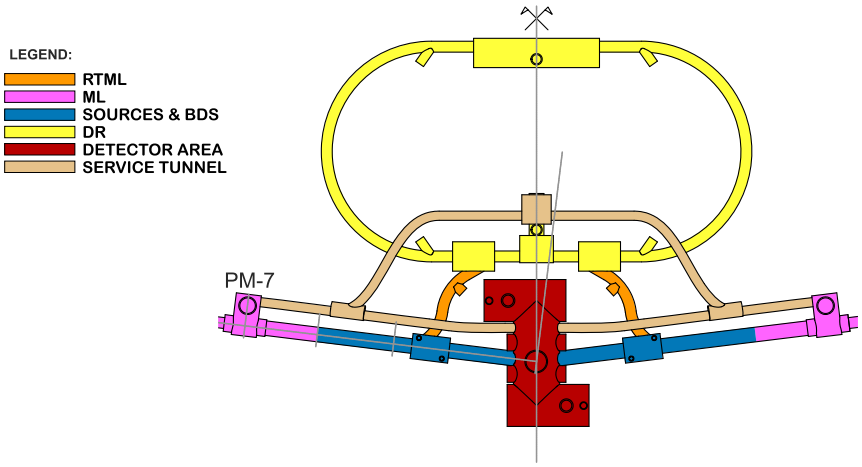

Figure 11.23
Model of the central injection region.

The DR complex is an approximately 3 km-long quasi-circular tunnel with an internal diameter of 6 m and containing 4 alcoves. There are two 9 m-diameter shafts, one in the middle of each long straight section. It is connected to the ML through two 250 m long RTML tunnels, the ELTR and PLTR transfer tunnels, with an internal diameter of 6 m. The electron and positron injector linacs are located in tunnels of 8 m internal diameter. The sources are housed in 7 m-diameter tunnels connected at their ends to the ML. A 4.5 m-diameter service tunnel passes over the DR and connects the Ring to the IR Hall and ML.

11.5.2.5 IR and BDS

The IR and BDS facilities are situated in the middle of the complex (Fig. 11.24). The IR Hall (Fig. 11.25) houses the two detectors in two 60 m caverns on either side of the interaction point, each of which has an 8 m-diameter vertical access shaft. Both detector caverns are connected to a sub-cavern, with a 6 m-diameter shaft. Escape tunnels connect each of the detector caverns with a safety shelter located in the other detector cavern. A survey gallery allows the alignment of magnets located in the beam tunnels on both sides of the IR.

Before being lowered underground, the detectors will be assembled and tested in a surface building. An 18 m-diameter shaft connects this surface building to the transfer cavern which in turn connects the two detector caverns. Travelling cranes will have to be installed to allow the assembly and servicing of the detectors. The surface building is equipped with a temporary 4000 t gantry crane and the transfer cavern is equipped with a 40 t crane.

The detector platform allows the sliding of each detector into on-beam position through a push-pull system. The geotechnical and structural behavior of the ground-detector complex interface was studied using existing local geological data and known geotechnical rock characteristics available at CERN. A 3D model was developed for understanding the stress conditions of the underground cavern complex at the IR. The analysis identified the in-situ stress development across the IR and has shown that the current orientation of the cavern alignment is preferred.

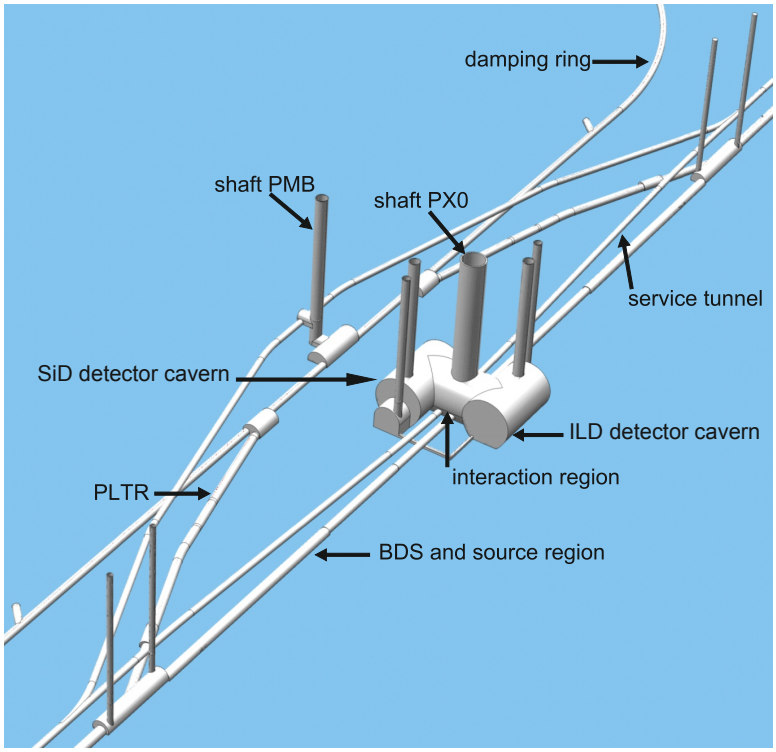

Figure 11.24
Model of the Central Injection Region.

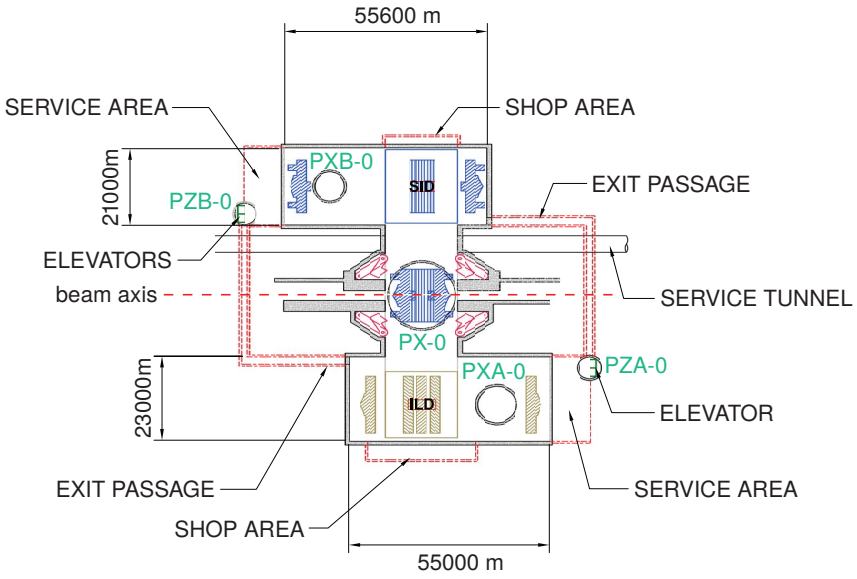

Figure 11.25
IR Hall plan view.

The BDS handles the incoming and outgoing beams in and out of the IR. It houses several beam dump caverns (e^- and e^+ tune-up dump, e^- and e^+ fast-abort dump, photon dump), positron-capture chicanes, target-bypass 'dog-leg' areas, undulator areas and service caverns for equipment storage. The beam-dump facilities are located at both sides of the IR in caverns accommodating water dump tanks at high pressure.

11.5.2.6 Surface facilities

Surface buildings are foreseen approximately every 2 km along the machine length in a rural environment with easy access for large vehicles. This includes equipment buildings, cooling towers and pump stations, cryo buildings, shaft-head buildings, storage areas, and assembly areas. As local workshops and technical offices are already in place at CERN, these are not considered. A large fraction of the buildings are expected to be located at the Prevessin Campus, near the IR.

Stations with klystron clusters and cryo-plants have to be located roughly every 4 km on the surface. Klystron clusters without cryo-plants are located approximately every 2 km. Hybrid installations are foreseen at the outer end of the tunnels, where a single klystron cluster powers the first 1.25 km of the ML [213].

11.5.3 Mechanical

The European mechanical design is based on the America's KCS mechanical design (see Section 11.6.3). However, a major difference between the two concepts lies in the ventilation systems, which for Europe consists of an overhead ventilation scheme in the main tunnel. This scheme has been adopted for CLIC, mainly due to fire safety constraints, and its design is readily applicable to the ILC complex. For further details, see the CLIC CDR [214].

11.5.4 Electrical

This is based on the Americas design, see Section 11.6.4.

11.5.5 Life safety and egress

11.5.5.1 Introduction

A detailed life-safety study has been conducted for CLIC. From a fire-safety point of view, the ILC single-tunnel complex is comparable with CLIC. Therefore the CLIC life safety and egress study can be applied to the ILC facility. For further details, see the CLIC CDR [215].

11.5.5.2 Fire Risk Assessments and scenarios

Detailed fire risk assessments and scenarios will have to be made for every specific area i.e. tunnels, experiment caverns, alcoves for equipment, linking galleries, once more information is available on the layouts and their interconnects through ventilation systems.

11.5.5.3 Fire Prevention strategy

Fire prevention measures at every possible level of functional design need to be implemented to ensure that large adverse events are only possible in the very unlikely event of multi-level safety barrier failure.

11.5.5.4 Fire Safety Measures

The tunnels can be split into compartments with solid doors and fire walls, with internal longitudinal passages. An example of such a firewall is shown in Fig. 11.26.

The action of splitting the facility into compartments needs to be accompanied by a coherent design of the ventilation and smoke-handling systems. The ventilation system in the tunnel should be capable of creating a lower pressure in the compartment affected by the fire and an over pressure in the areas at the sides, as shown in Fig. 11.27. The smoke-handling system should withstand the thermal impact of fire and ensure the continuity of its functioning to prevent smoke propagation from one compartment to another.

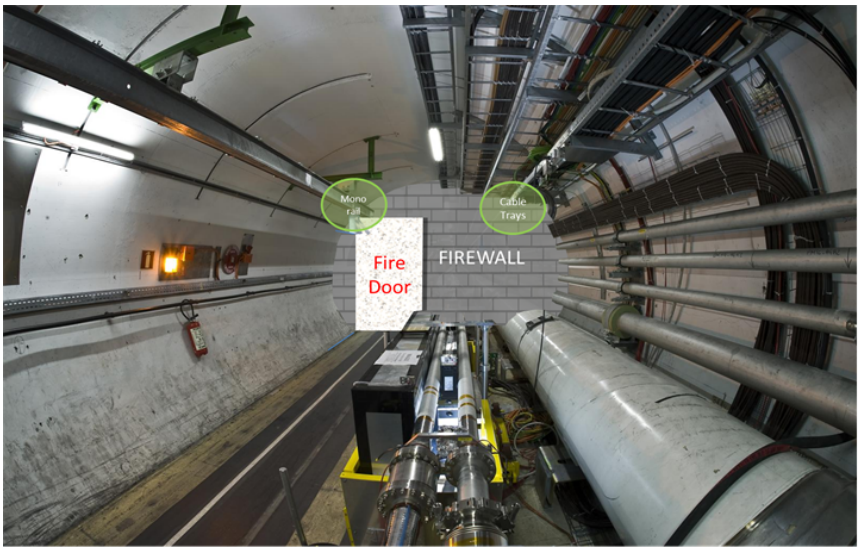

Figure 11.26 Conceptual representation of a tunnel firewall.

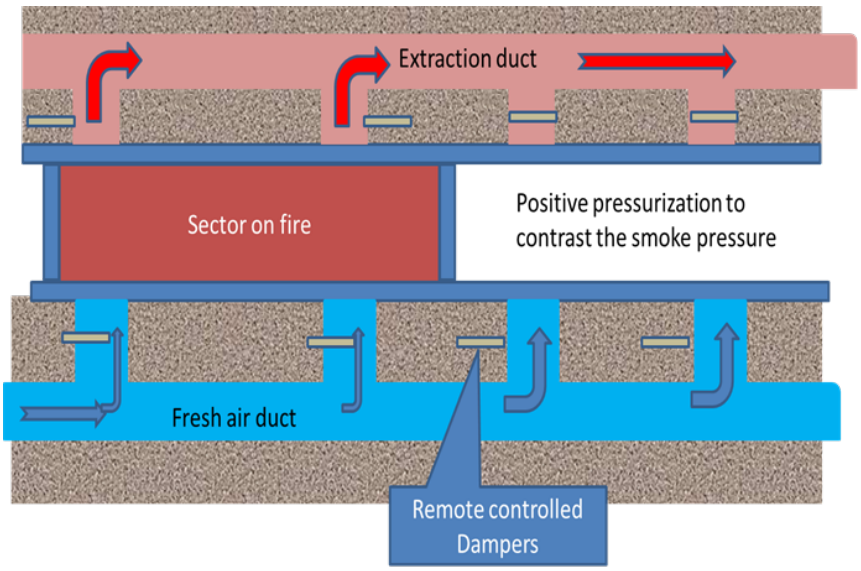

Figure 11.27 Schematic representation of the pressurization of a sector adjacent to the sector on fire

11.6 Americas region (Flat topography)

11.6.1 Siting studies

11.6.1.1 Location

The Americas sample site is in Northern Illinois, with a north-south orientation roughly centered on Fermilab. The central campus and IR are located on the Fermilab site, located approximately 35 miles west of downtown Chicago. The surrounding area has a medium population density supported by robust utilities and transportation infrastructure. While the routing requires the tunnel to pass below residential areas, the shafts can be located in non-residential areas.

11.6.1.2 Land Features

The surface of northern Illinois is primarily flat, with surface elevations ranging from 200 m to 275 m above sea level. Much of the eastern half of northern Illinois is developed with many commercial, residential and industrial complexes. The 2751 hectare (6800-acre) Fermilab site is also relatively flat with less than 15 m of fall from northwest to southeast.

11.6.1.3 Climate

The climate is typical of the Midwestern United States, with four distinct seasons. In summer, temperatures ordinarily reach between 26°C and 33°C and humidity is moderate. Yearly precipitation averages 920 mm. Winter temperatures average -2°C during the daytime, and -10°C at night. Temperatures can be expected to drop below -18°C for on average 15 days throughout the winter season.

11.6.1.4 Geology

Geologic information has been obtained from previous underground construction at Fermilab and in northeastern Illinois, and not from ILC-specific investigations. The tunnels are located in a dry, uniform and massive dolomitic limestone deposit (Fig. 11.28). An overlying layer of shale provides a hydrogeologic barrier between upper aquifers and the dolomite. These geologic conditions should provide a relatively dry tunnel, during both construction and operations, but it is expected that some grouting will be required.

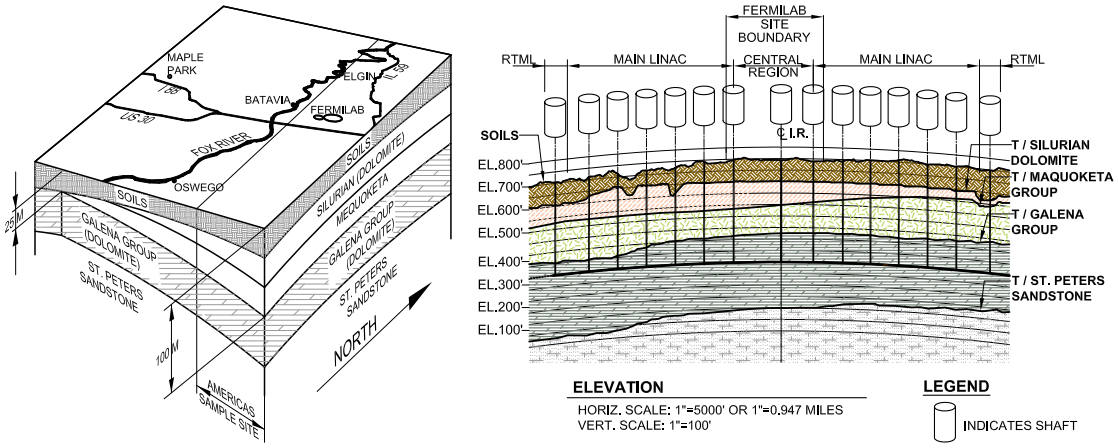

(a) North/South and East/West geology sections near the Americas sample site

(b) Geological profile of the Americas sample site showing the layers of hard limestone

Figure 11.28. Geology of the Americas sample site

11.6.1.5 Power Distribution System

The investor-owned utility, Commonwealth Edison Company, services the Northern Illinois area with a capacity of more than 22,000 MVA. This capacity is made available through both fossil fuel and nuclear power generating stations. The electrical transmission infrastructure in Northern Illinois is very strong. The local power grid is capable of tying to three other national power generating sources. Transmission lines with voltage at 365 kV currently serve Fermilab along the eastern boundary of the site.

11.6.1.6 Construction Methods

The tunnels are excavated with TBMs and lined with a cast concrete invert. Widened portions and caverns are excavated using drill and blast. Temporary supports are required for the largest spans, permanent support is provided by rock bolts. Shaft overburden is excavated using standard earth excavators and muck boxes, supported by ring beams and timber lagging, keyed into the underlying rock. Excavation through the limestone and shale to the final depth uses conventional drill and blast methods. Support is provided by resin encapsulated rockbolts and the shaft is reinforced and concrete lined.

11.6.2 Civil construction

11.6.2.1 Underground enclosures

Figure 11.29 shows the overall plan view.

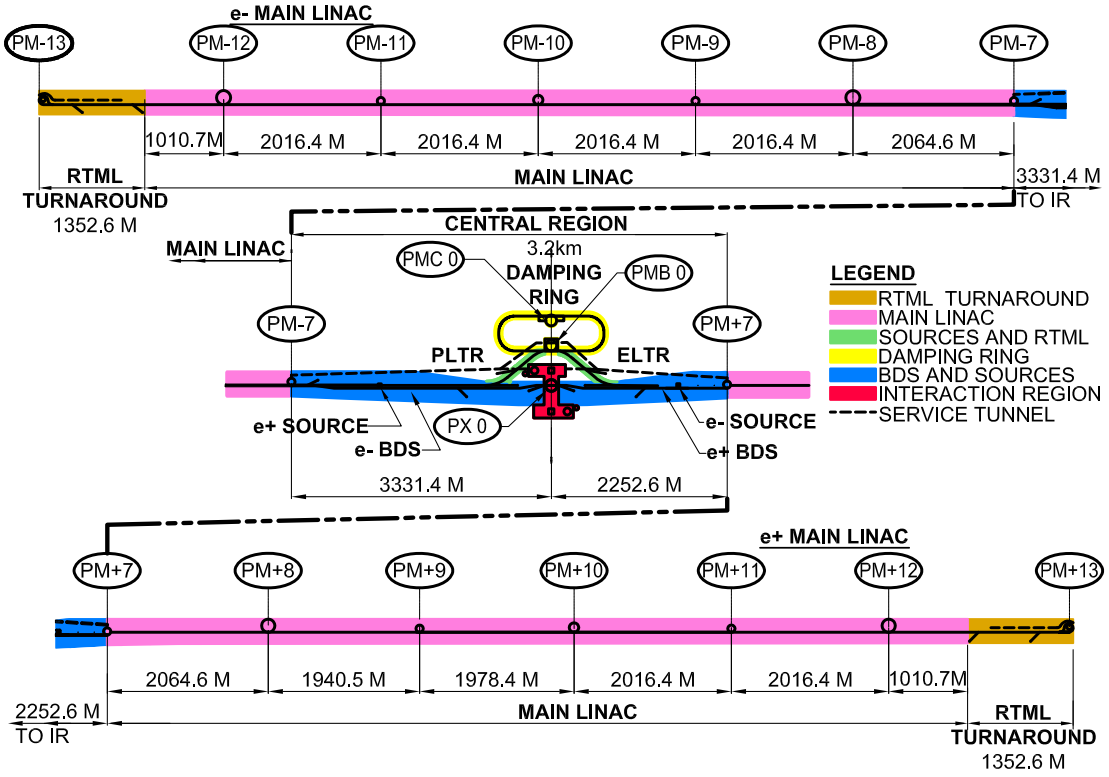

Figure 11.29. Americas tunnel layout. The colors reflect the Accelerator sections locations.

11.6.2.1.1 Tunnels The accelerator complex contains a combined total tunnel length of $\sim 44\,\mathrm{km}$, where the breakdown by accelerator section is listed in Table 11.10. Where two accelerator sections share the same tunnel segment, the length of tunnel is apportioned according to the fraction of the tunnel length occupied by each respective accelerator section. So for example, the ELTR and PLTR are divided equally between the Sources and RTML, while the tunnel between the end of the Main Linac and the IR Hall is apportioned 54 % to 46 % between the BDS and the e^+ source on the electron side and 90 % to 10 % between the BDS and e^- source on the positron side.

Table 11.10
Tunnel lengths and volumes by Accelerator section

Accelerator section	Length (m)	Volume (m^3)
e^- source (beam)	368	8,064
e^- source (service)	618	11,584
e^+ source (beam)	1,678	33,770
e^+ source (service)	2,203	36,922
Damping Ring	3,239	76,945
RTML (beam)	3,305	68,619
RTML (service)	1,955	31,090
Main Linac	22,168	435,264
BDS (beam)	3,847	141,440
BDS (service)	3,847	61,183
TOTAL	43,228	904,881

Figure 11.30 shows a typical cross-section through the ML tunnel. The cryomodule waveguides are located on the aisle side of the cryomodule and are fed from circular over-moded waveguide on the tunnel ceiling. The circular over-moded waveguide comes from the Klystron Service Building located at each of the ML Shafts. Space is reserved for survey lines of sight.

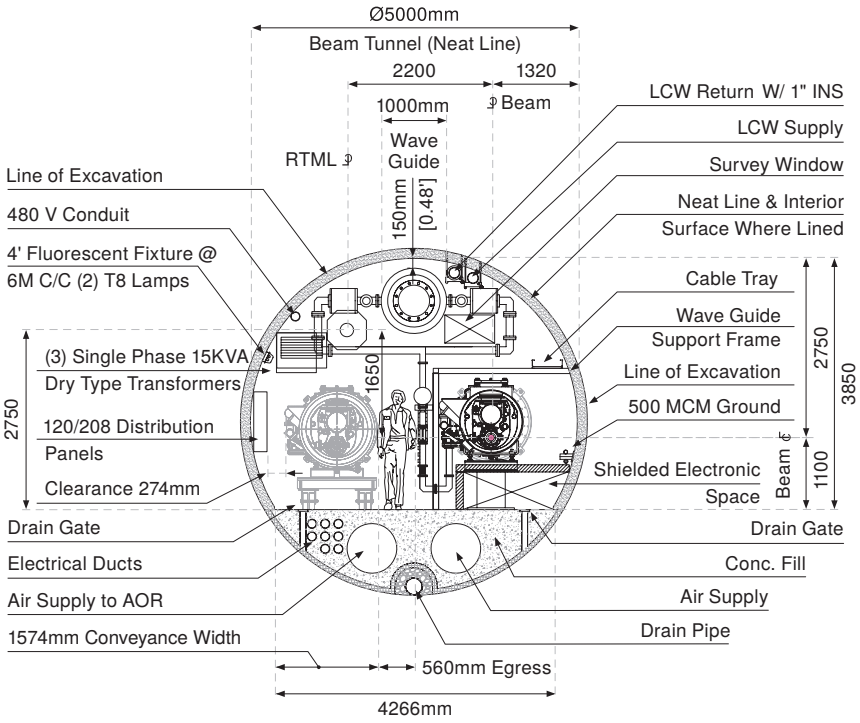

Figure 11.30
Typical ML tunnel cross section

11.6.2.1.2 Cost Allocation of Underground Tunnels between Area Systems The costs for the tunnel that are attributed to each of the area systems are based on the percentage of beam length for each Area System in a specific tunnel segment. As shown in Table 11.11, the ELTR and PLTR Beam and adjacent Service tunnels are divided equally between the Sources and RTML. The Beam and adjacent Service tunnels between the end of the Main Linac and the IR Hall are proportioned 54 % to the e^- BDS and 46 % to the e^+ source, on the electron side, and 90 % to the e+ BDS and 10 % to the e^- source, on the positron side. The RTML Turnarounds, Main Linacs and Damping Ring tunnel lengths are considered 100 % part of those Area Systems respectively. The RTML Service tunnel at the turnarounds is considered 100 % part of the RTML.

Table 11.11
Tunnel Cost Allocations

	Beam Tunnel	Adjacent Service Tunnels Americas and European Region	Adjacent Service Tunnels or Service side of Tunnel in Asian Region
RTML Turnarounds	100% RTML	100% RTML	100% RTML
Main Linacs	100% Main Linac	NA	100 Main Linac
End of -e Main Linac to IR Hall	54% e- BDS 46% e+Source	54% e- BDS 46% e+Source	54% e- BDS 46% e+Source
PLTR	50% RTML 50% e+ Source	50% RTML 50% e+ Source	50% RTML 50% e+ Source
Damping Ring	100% Damping Ring	NA	NA
ELTR	50% RTML 50% e- Source	50% RTML 50% e- Source	50% RTML 50% e- Source
End of +e Main Linac to IR Hall	90% e+ BDS 10% e- Source	90% e+ BDS 10% e- Source	90% e+ BDS 10% e- Source

11.6.2.1.3 IR Hall, caverns, and alcoves There are underground caverns and alcoves along the tunnels, in addition to the central IR Hall; the IR Hall is described in Section 11.5.2.5. Caverns are located at the base of each shaft, and alcoves provide safe havens in emergencies and also house equipment. The caverns and alcoves, summarised in Table 11.12 are sized for:

- the amount and nature of equipment to be housed: cryogenic, electrical, cooling and ventilation,

Table 11.12
Cavern summary and volumes

Accelerator section	Qty	Volume (m^3)
e^- source	0	-
e^+ source	1	324
Damping Ring	8	26,821
RTML	6	12,575
Main Linac	49	57,165
BDS	8	36,869
IR	1	135,703
TOTAL		269,458

water distribution, electronics, etc;

- connecting services between access shafts and tunnels;
- lowering, assembly, and commissioning of TBMs for the excavation work (at those caverns where excavation starts or ends).

The caverns have moveable steel-concrete shielding doors moving on air-pads or rails, which can be opened for equipment transfer into the beamline area.

11.6.2.2 Underground access

There are a total of 14 vertical shafts (Fig. 11.29): two 6 m-diameter shafts for the RTML, four 14 m-diameter major equipment shafts, two 9 m-diameter shafts and six smaller 6 m-diameter shafts for the ML, summarised in Table 11.13. The shafts allow movement of equipment and personnel, and provide accessways for services such as cooling water, potable water, compressed air, cryo-fluids, electrical supply, and controls. The over-moded waveguide also uses these shafts. Two shafts service the ML and Sources/BDS areas. There are two access shafts serving the DR tunnel. The 9 m-diameter shafts are situated at opposite sides of the DR at the midpoint of the straight sections. In the Central Region there are four 1.5 m-diameter shafts that supply utilities to the high-power-beam-abort caverns. The IR Hall has an 18 m-diameter shaft used for lowering major detector segments from the surface-assembly building. There are also two 8 m-diameter shafts for lowering smaller equipment into the hall, one for each detector, and two 6 m-diameter shafts for utilities and personnel egress.

Table 11.13
Shaft depths and volumes

Accelerator section	Depth (m)	Volume (m^3)
e^- source	125	0
e^+ source	125	0
Damping Ring	125	15,896
RTML	125	7,065
Main Linac	125	114,021
BDS	125	883
IR	125	54,950
TOTAL		192,815

11.6.2.3 Surface structures

The KCS RF feeds the ML at 2.5 km intervals. The ML surface infrastructure installations are spaced every 2.5 km at the heads of service shafts to the tunnel. The surface installations every 5.0 km also have cryogenic cooling plants (see Fig. 11.31). At the central region end of the ML, there are hybrid installations where a single Klystron cluster powers the last 1.25 km section.

The numbers and sizes of buildings associated with each accelerator section are listed in Table 11.14. The Americas proposed sample site centers the alignment of the ILC on the Fermilab site. Spaces normally required in a central campus such as office space, tech space, machine shops, storage, and cafeteria are considered to be existing on the Fermilab Site and suitable for the needs of the ILC project, and therefore not included in the table. Electrical power and other associated

infrastructure are also considered to be part of these existing buildings. Therefore no additional surface support facilities are included in the Americas Region TDR design.

Figure 11.31. Typical KCS surface facility layout

Table 11.14
Surface structures by Accelerator section

Accelerator section	Qty	Area (m^2)
e^- source	0	–
e^+ source	0	–
Damping Ring	3	5,294
RTML	2	1,410
Main Linac	18	60,200
BDS	0	–
IR	1	7,695
TOTAL	24	74,599

11.6.3 Mechanical

11.6.3.1 Processed water

Thermal heat loads were tabulated for each accelerator section. Design specifications were developed [216–225]. The ML accounts for about 60 % of the total load. Tables 11.15 and 11.16 show the distribution of heat loads by component (above and below ground) and accelerator sections.

Table 11.15. Main Linac KCS RF Heat Load (TDR Baseline Low Power)

			To Low Conductivity Water								to CHW	to AIR
	Q.ty	Average heat load (kW)	Heat load to LCW water (kW)	Max all. temp. (°C)	Supply temp. (°C)	Delta temp. (°C delta)	Water flow (l/min)	Max all. press. (bar)	Typical (wtr) press. drop (bar)	Accept. temp. variation (delta °C)	Racks heat load (kW)	Heat load to air (kW)
COMPONENTS IN THE SURFACE (listed per RF unit)												
RF components x (413)												
RF charging supply	413/ML	2.39	1.67		40	8.5	*2.84*	18	5	10	NA	0.72
Switching power supply	413/ML	5.5	3.3		35	6.25	7.6	13	5	10	NA	2.2
Filament transformer	413/ML	0.79	0.6	60	35	0.40	20		1	n/a	NA	0.2
Marx modulator	413/ML	4.96	3.0		35	2.14	20	10	5	n/a	NA	2.0
Klystrn scket tank / gun	413/ML	0.99	0.79	60	35	1.14	10	15	1	n/a	NA	0.2
Focusing coil (solenoid)	413/ML	1.68	1.6	80	55	2	10	15	1	n/a	NA	0.1
Klystron collector	413/ML	38.43	37.1	87	38[†]	14	37	15	0.3	n/a	NA	1.29
Klystron body & windows	413/ML	3.37	3.4	40	25 to 40	5	10	15	4.5	±2.5 °C	NA	
CTOs & combining loads/circulators	2/klstrn	11.71	9.36			6.04	22.28		*(80 psid)*			2.3
Relay racks (Instrument racks)		3.0	0	N/A	N/A	N/A		N/A	N/A	None	3	0.0
Subtotal surface heat load to LCW water			60.74	Total surface (heat to water and air)				69.82			3.0	9.1
COMPONENTS IN THE TUNNEL (listed per RF unit)												
RF components (x 567)												
RF pipe in shaft (shaft & bends)		1.89	1.70			10	*2.445*		*(80 psid)*			0.2
Relay racks (instrument racks)		5	5	N/A	N/A	N/A	N/A	N/A	N/A	None		0.0
Main tunnel wvgde & local wvgd		12.23	11.62			12	*13.9*		*(80 psid)*			0.6
Distribution end loads & Cavity reflection loads		31.80	31.3			20	*20.54*		*(80 psid)*	*±2.5°C*		0.5
Subtotal tunnel heat load to LCW water			49.62	Total tunnel (heat to water and air)				50.9				1.3

[†] (inlet temp 25 to 63)

Table 11.16 Summary of Heat Loads (MW) by Accelerator section. Heat loads generated by the utilities themselves (pumps, fan motors, and etc) are listed as 'Conventional'.

Acc. section	load to LCW	load to Air	Conventional	Cryo (Water Load)	Total
e^- sources	1.40	0.70	0.80	0.80	3.70
e^+ sources	5.82	0.64	1.51	0.59	8.56
DR	10.92	0.73	1.79	1.45	14.89
RTML	4.16	0.76	0.68	part of ML cryo	5.59
Main Linac	46.5	5.53	5.32	32.0	89.34
BDS	9.2	1.23	3.23	0.41	14.07
Major Dumps	14		0.05		14.05
IR	0.4	0.76	0.10	2.65	3.91
Total	92.4	10.4	13.5	37.9	154

There are two types of water-cooling system: the first uses a chiller to provide cool supply water (chilled water/LCW), and the second uses a cooling tower that provides somewhat warmer water (process water/LCW). The chilled water/LCW-type system is used in the DR, IR and Central Region (which includes e^+ source, e^- source, and BDS). This provides tight air-temperature stability in these areas. The ML, RTML and the Main Dump use the process/LCW water. Figures 11.32 and 11.33 show typical schematic diagrams of the process water and chilled-water support utility systems.

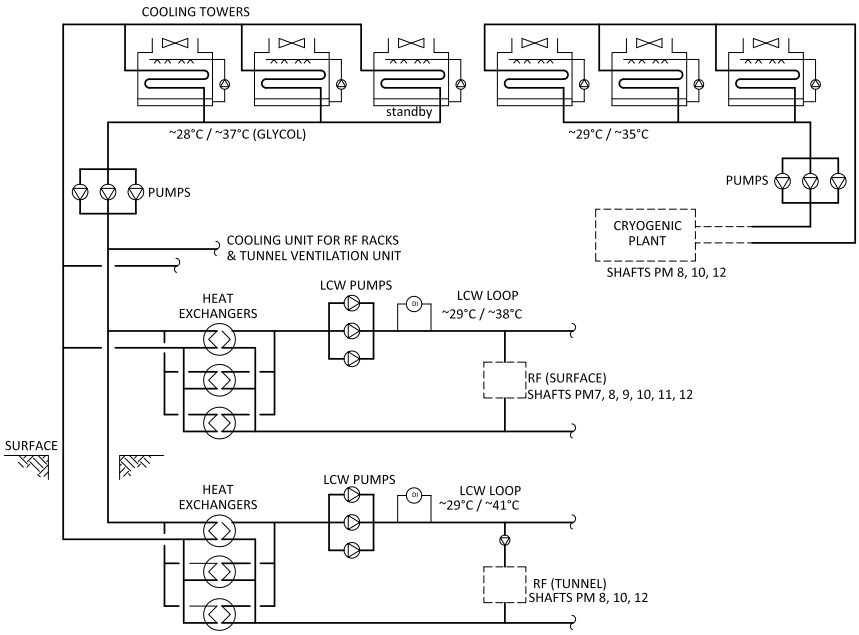

Figure 11.32 Typical process water schematic.

For both systems, the cooling tower type is a closed-circuit evaporative cooler, using closed-loop glycol water as is customary in cold climates. This type of tower conserves water and treatment chemicals as compared to an open tower system. All surface plants are provided with n+1 redundancy. The make-up water to the system is supplied from individual wells or municipal water supply at each surface plant.

For the ML and RTML process water/LCW system, cooling towers provide a maximum 28.3 °C cooling water supply to the LCW heat exchangers. The heat exchanger supplies about 29.4 °C LCW to the loads. About 60 % of the heat loads from the ML are located on the surface. The load-to-air component of the tunnel heat loads is minor and handled by the tunnel ventilation system. At the surface, the ML surface heat loads to air from the RF components are dissipated using ambient air-ventilation systems. The HLRF for the RTML is located in a short support tunnel adjacent to the accelerator and therefore requires fan coils for conditioning its relatively large heat load to air. The Main Dumps near the IR have a dedicated process water system.

For the DR, tunnel fan coils use a cooler 10 °C supply water to maintain a tunnel temperature closer to the mean temperature of the magnet loads and to provide for better air-temperature stability [226]. The rest of the loads in the damping ring and central region, such as magnets, power

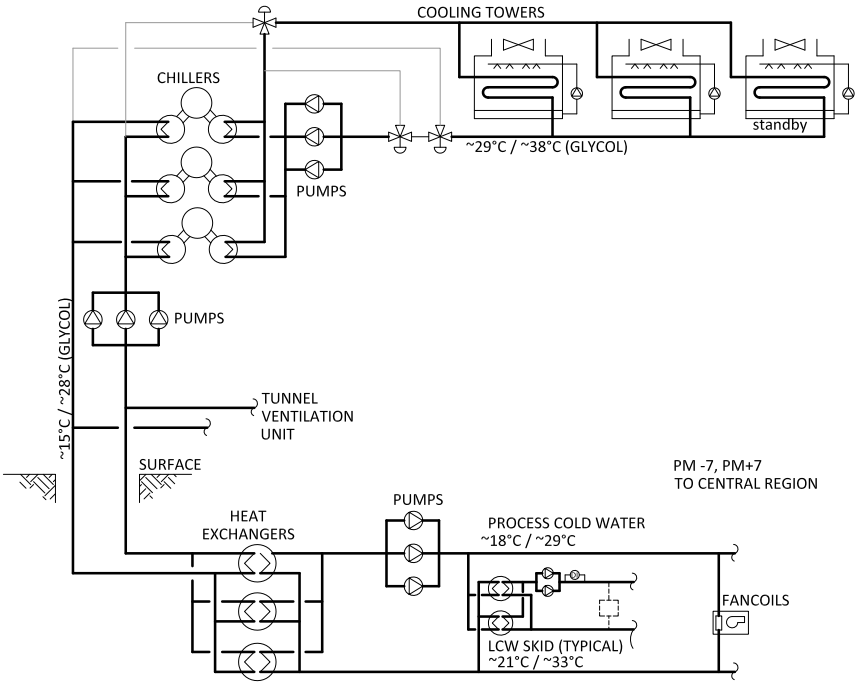

Figure 11.33
Chilled Water/LCW System at Central Region.

supplies, and RF, are provided with approximately 18 °C LCW supply. The chiller-system design includes a waterside economiser that would automatically provide free cooling using the cooling tower if the ambient conditions are adequate.

The main distribution of the cooling-water system follows the location of the shafts [227]. There are nineteen surface water plants, twelve for the ML and RTML, two for the central region, two for the IR, two for the DR, and one for the main dumps.

11.6.3.2 Piped utilities

Groundwater inflow and condensate drainage for all underground areas is estimated to be 21 $m^3/h/km$. The total number of duplex sump pumps required are 132 in the ML, 121 in the Central Region and IR, and 32 in the DR. Groundwater duplex lift pumps and collection tanks are provided at every major shaft location. Each groundwater lift station has three pumps, any of which can pump the entire inflow volume. Water discharge is piped up the shaft through separate and protected piping systems.

11.6.3.3 Air treatment

There are two ventilation systems, one for the Areas of Refuge (AOR) and the other for the general tunnel ventilation. Both systems have individual separate supply air ducts through the shafts from the surface ventilation units down to the cavern floor. They use the tunnel floor for further distribution along the length of the tunnel as well as into the AOR. Each unit is sized to 20% overcapacity to provide some redundancy in case one surface-unit fails. The general tunnel ventilation is conditioned to provide neutral temperature dehumidified air, while the AOR ventilation unit is non-conditioned raw outside air to be used only when the AOR is occupied. Return air from the general tunnel ventilation system is ducted up from the caverns to the surface units. In general the heat is removed from the tunnel areas by separate fan coils, except in the ML area where the heat load is minor and the tunnel ventilation is adequate. The tunnel ventilation provides 0.45 m/s air speed and an air change rate of approximately 2 per hour. The temperature in the tunnels is a maximum of 29 °C in the ML/RTML tunnel area and 29 °C in the central region, Damping Ring, IR, and service tunnels/caverns. Figure 11.34 shows a typical schematic diagram of the ventilation system.

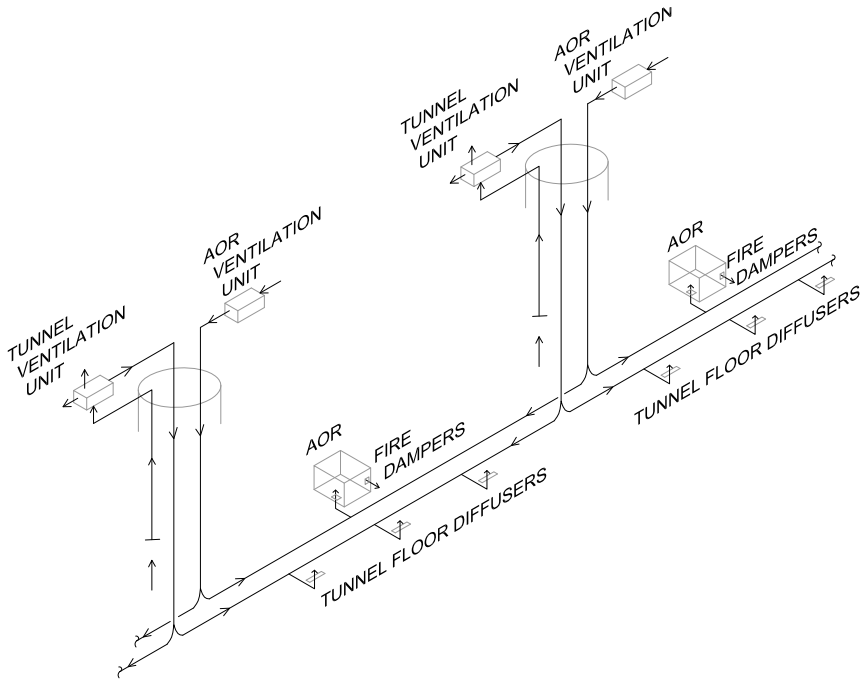

Figure 11.34
Typical ventilation scheme.

11.6.4 Electrical

Electrical load tables were compiled for each area and the systems designed. The ML has about 70 % of the total loads. The conventional loads are from the components associated with running support facilities for the experimental equipment and facilities, such as pumps, fans and other mechanical/electrical systems not provided by the experiment. The power-factor value used for equipment sizing is the actual expected, if given, or a 90 % for all other equipment. Table 11.17 shows a summary of the power loads distributed by component and Accelerator section.

Table 11.17
Summary of power loads (MW) by Accelerator section. 'Conventional' refers to power used for the utilities themselves. This includes water pumps and heating, ventilation and air conditioning, (HVAC). 'Emergency' power feeds utilities that must remain operational when main power is lost.

Accelerator section	RF Power	RF Racks	NC magnets & Power supplies	Cryo	Conventional		Total
					Normal load	Emergency load	
e^- source	1.28	0.09	0.73	0.80	1.02	0.16	4.08
e^+ source	1.39	0.09	4.94	0.59	2.19	0.35	9.56
Damping Ring	8.67		2.97	1.45	1.84	0.14	15.08
RTML	4.76	0.32	1.26	part of ML cryo	0.12	0.14	6.59
Main Linac	58.1	4.9	0.914	32	8.10	5.18	109.16
BDS			10.43	0.41	0.24	0.28	11.36
Dumps					1		1.00
IR			1.16	2.65	0.09	0.17	4.07
Total	74.2	5.4	22.4	37.9	14.6	6.4	161

The electrical power supply is divided into major systems by function:

- supply: 345 kV large overhead interconnect with the local Utility transmission grid;
- transmission: 69 kV and 34.5 kV main feeders serving local substations;
- medium voltage distribution: 34.5 kV distribution lines from local substations to service transformers distributed throughout the project;
- medium voltage standby power distribution: 4.16 kV distribution lines from generators to dedicated power transformers that serve standby loads;
- low voltage distribution: 480 and 208/120 V local distribution lines that directly serve loads;
- low voltage standby power distribution: 480 and 208/120 V local distribution lines that directly serve standby power loads.

11.6.4.1 Supply system

The Supply system consists of a 345 kV overhead line from the local utility grid to the central campus substation. The interconnect point with the local utility serves as the ownership demarcation point with a switching device and revenue metering. The local Utility has a switching device at this point to manage services to the project. All loads and losses beyond this point are included in the electrical power bill. Due to the large power requirements, the electrical system is designed to be independent and standalone from the local electrical utility infrastructure at the highest possible level.

The electrical power system for the project originates at the Central Campus Substation, which includes two 345 kV to 69 kV transformers and two 345 kV to 34.5 kV transformers. Each transformer serves a specific part of the project through switchgear. The 69 kV switchgear is outdoor rated, SF6 gas insulated switchgear (GIS) that enables a compact reliable installation at this voltage class. The 34.5 kV switchgear type is enclosed bus with vacuum circuit breakers that provide a compact reliable installation at this voltage class. Figure 11.35 illustrates the Central Campus Substation.

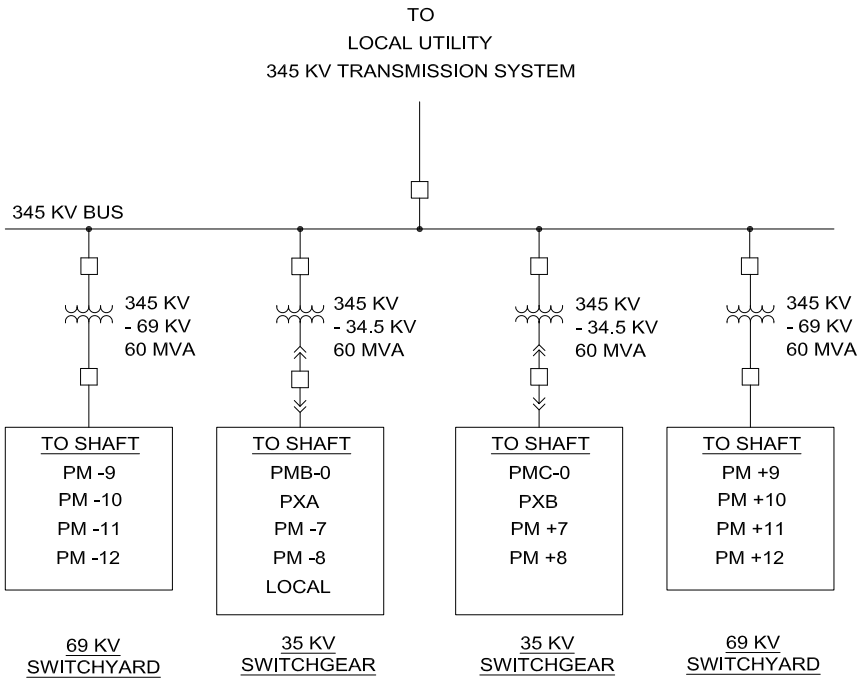

Figure 11.35
Electrical transmission system.

11.6.4.2 Transmission system

The 69 kV and 34.5 kV transmission system provides the required power to each local substation or switching station generally located at the top of each shaft. The system is a combination of substations, switching stations, 69 kV feeder lines and 34.5 kV feeder lines. The architecture of the system is a single-feed radial configuration extending from the central campus to the ends of the accelerator tunnels and the far side of the DR.

The 34.5 kV transmission feeders originating in the Central Substation serve the DR and near shafts, PM-7, PM+7, PM-8 and PM+8 local substations. The local Central Region loads are served directly from the substation switchgear while 34.5 kV feeders are routed through the tunnel to other shafts. The feeder that serves shafts PM-7 and PM-8 extends down the tunnel to shaft PM-7 where 34.5 kV switchgear provides service to local Medium-Voltage Distribution and a feed through to shaft PM-8 for local distribution. Similarly a feeder configuration is included for PM+7 and PM+8. The 34.5 kV transmission voltage to these locations enables direct Medium-Voltage Distribution through switchgear without the installation of local substation transformers at the DR, PM±7 and PM±8.

The 69 kV transmission feeders originating in the Central Substation serve the shafts PM±9 to the end of the tunnels. The 69 kV voltage level is used to minimize the number and size of conductors and conduits installed in the tunnel. The 69 kV feeders are extended from the Central Substation GIS to shafts PM+/-9 and PM±11. 69 kV to 34.5 kV substations are located at each of these shafts to provide local Medium Voltage Distribution and 34.5 kV feed to subsequent shafts, PM±10 and PM±12. No substation transformers are required at shafts PM±10 and PM±12.

11.6.4.3 Medium-Voltage Distribution system

The Medium-Voltage Distribution system provides power to each distribution transformer that serves a load in the tunnel or on the surface. The distribution feeder system is a radial configuration from the local substation switchgear to the distribution transformers. On the surface, transformers serve specific loads such as RF units, cryogenics or conventional facilities. In the tunnel, a distribution transformer is located in the base cavern to serve all conventional loads. The technical loads in the central region that include a service tunnel are served by a separate local transformer. Figure 11.36 illustrates a 34.5 kV distribution switchgear that serves both local loads and provides the origin of the transmission feeders to other shaft substations.

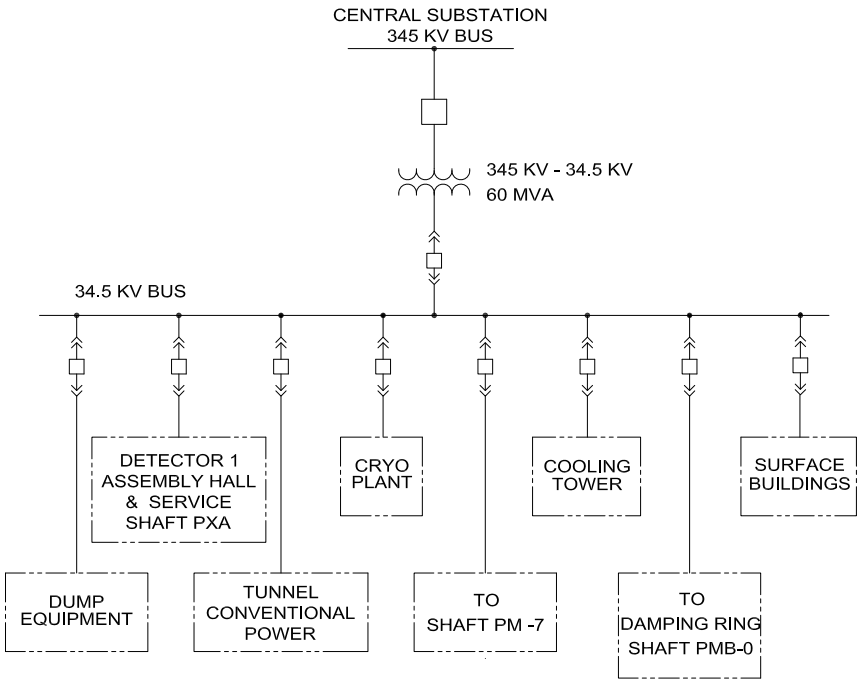

Figure 11.36
Central Region 35 kV Switchgear One-Line Diagram

11.6.4.4 Standby power

Standby power generation is provided at each shaft location to support life-safety facilities when normal power is not available. The standby power-distribution system automatically generates electricity for selected facilities when called upon using diesel generators. The generators are rated at 4.16 kV and sized for the load served. The 4.16 kV voltage is needed due to the length of the distribution feeders. On the surface and in the tunnel, a dedicated standby power transformer is provided to serve the standby power loads.

The electrical lines are installed in the underground tunnels and enclosures in conduits that are either in concrete-encased duct banks or embedded in the tunnel floor and routed up to the surface at each shaft. Cable installation and splicing is accommodated with vaults spaced at approximately 522 m along the length of the main tunnel.

11.6.5 Life safety and egress

The life-safety requirements and fire-protection systems for the single-tunnel design concept are based upon the National Fire Protection Association (NFPA) 520, Standard for Subterranean Spaces, 2005 Edition. In addition, Hughes Associates, Inc. was retained to assess the feasibility of the single-tunnel design by analysing different fire scenarios in the beam tunnel and damping ring. A fire analysis of the single-tunnel portions of the ILC installation was conducted using the Fire Dynamics Simulator (FDS) computational fluid-dynamics program developed by USA National Institute of Standards. Models of different fire sizes were constructed for the ML tunnel, base caverns, and DR. Anticipated combustible fuel loadings in the single tunnels were evaluated and it was determined that pool/spill fire scenarios involving transformer oil were the most demanding fire scenarios. Table 11.18 summarises fire-size limitations for various size tunnels based on spill area, rates and volumes.

Table 11.18
Summary of Tunnel Fire Modelling Results

Tunnel type	Tunnel diameter (m)	Limiting fire size (kW)	Confined spill area (m^2)	Continuous spill rate (l/min)	Unconfined spill volume (l)
Main Linac/	4.5	750	0.8	1.28	1.25
Straight	5.0	1,000	1.0	1.70	1.57
Damping Ring	5.5	1,100	1.1	1.87	1.69
	6.5	1,500	1.4	2.55	2.17
Base cavern	4.5	3,000	2.4	5.10	3.86
	5.0	4,000	3.0	6.81	4.95
	5.5	4,500	3.3	7.66	5.48
	6.5	6,000	3.6	10.21	7.08
Curved	4.5	2,500	2.0	4.25	3.31
Damping Ring	5.0	3,250	2.5	5.53	4.13
	5.5	4,000	3.0	6.81	4.95
	6.5	5,000	3.6	8.51	6.02

The findings support the single-tunnel concept and prove that the life-safety requirements and fire-protection system requirements of NFPA 520 will allow occupants in the single-tunnel portions to evacuate safely during a fire, provided that the maximum anticipated fire size in a tunnel can be restricted to the limiting fire sizes for each tunnel type and diameter established in the analysis. In addition, the analysis concluded that it is not necessary for ventilation systems in the tunnel to shut down during a fire event, provided air velocities supplied during the fire are less than 1 m/s.

11.6.5.1 Personnel egress

At the base of each ML access shaft is a cavern that contains oil-filled electrical equipment, water pumps, motors and other utility equipment. This equipment has the highest risk for fire. The prevailing codes require the containment of such areas through the use of fire-rated walls and doors. In addition, the elevators located in each shaft are also isolated by fire-rated walls and doors. Once these areas are properly isolated, the main linac (or DR) tunnel can be used for personnel travel to the shaft exit in the event of an emergency incident. Due to the overall tunnel length, it is also required to have a fire-protected AOR located at the midpoint between shafts to provide an intermediate safe area for injured personnel or to await emergency assistance. In areas where a service tunnel is located adjacent to the main tunnel, such as the RTML and BDS, crossover labyrinths are provided for passage between the two tunnels. These crossover labyrinths are located such that the travel distance to the crossover does not exceed 120 m from any point in either tunnel. The crossover labyrinths are separated by 2 h fire rated construction. The DR is an extension of the single portion of the tunnel and is provided with two vertical exits. These exits are separated from the common space by 2 h fire-rated construction. The following provisions for the required emergency fixtures are included:

- emergency lighting;

- illuminated exit signage;
- illuminated exist direction signs;
- a check in and check out system.

11.6.5.2 Fire suppression

Automatic sprinkler protection is required throughout the facility. It is a class I standpipe system with 2.5-inch fire department hose valves spaced approximately 100 m apart. Portable fire extinguishers are also provided.

11.6.5.3 Fire detection

Addressable fire detection and voice alarm is provided. Manual pull stations are spaced approximately 120 m apart. Smoke detection is provided at caverns and other sensitive areas. A voice/alarm system is capable of transmitting voice instructions from the fire command station located at the surface buildings. A two-way fire department communication system is provided and operated from the Fire Command Station. The two-way communication jacks are spaced 130 m apart.

11.7 Handling equipment

11.7.1 Introduction

This section covers the handling equipment used for on-site transport and installation of components. The on-site handling and transport operations start with unloading of components following delivery by their supplier to the site and finish when the components are installed in their final positions in the accelerator tunnels and service buildings.

ILC Handling equipment can be split into two main categories:

- "installed handling equipment" that is permanently installed in buildings or underground structures, such as cranes, elevators, hoists, and the external gantry used to lower experiment modules to the underground area;
- "mobile handling equipment" that can move between buildings or underground structures, such as road transport and handling equipment, industrial lift trucks, tractors and trailers,and custom-designed vehicles for transport and installation of equipment underground.

For the underground transport and installation of cryomodules and magnets, special equipment is needed so as to fit within the tunnel cross section, taking account of cost and installation timescale considerations. The mobile equipment used on the surface and in the tunnels is essentially the same for the Americas, European and Asian sites.

Equipment used to move detector components before lowering is not discussed in this section. The Americas and European handling equipment solutions that are based on the use of vertical access shafts are described. Inclined access tunnels are used in the Asian design. In this case, a fleet of goods and passenger vehicles is used for equipment and personnel transit between the surface and underground areas. The fleet is defined and operated to ensure adequate throughput as required by the installation schedule and also to ensure safe exit for personnel working underground in the event of fire or accident. Vehicles equipped with internal combustion engines are used for the inclined access tunnels; these are not suitable for use in the rest of the underground areas. To allow transfer of equipment from the inclined tunnel access vehicles to the tunnel transport and installation vehicles, junction caverns equipped with overhead travelling cranes provide the interface between the underground accelerator areas and the sloping access tunnels.

11.7.2 Transport operations

11.7.2.1 Initial delivery to site

Delivery of equipment to site is covered by the supply contracts for each item of equipment. This means delivery to assembly halls, storage areas or tunnel-access points as appropriate.

11.7.2.2 Surface transport and handling on and between sites

Surface transport operations include transfers inside and between buildings on the main laboratory site as well as transfers between the main laboratory site and the tunnel access points. These operations are carried out using a fleet of road transport vehicles. Vehicle unloading is carried out by industrial lift trucks or overhead travelling cranes.

11.7.2.3 Transfer between surface and underground via vertical access shafts

Lowering of equipment from the surface to the underground areas is carried out via vertical access shafts equipped with elevators and overhead travelling cranes. Shafts of different diameters are used along the length of the accelerator; four 14 m diameter shafts are available for lowering of cryomodules.

The surface buildings above the access shafts are equipped with overhead travelling cranes with sufficient lift heights to lower equipment to the caverns at the base of the shafts via handling openings reserved in the shaft cross section. In addition goods/personnel lifts allow personnel access and are also used to lower equipment. The cross section of a 9 m machine-access shaft with crane-handling opening and lift shaft (European site version) is shown in Fig. 11.37.

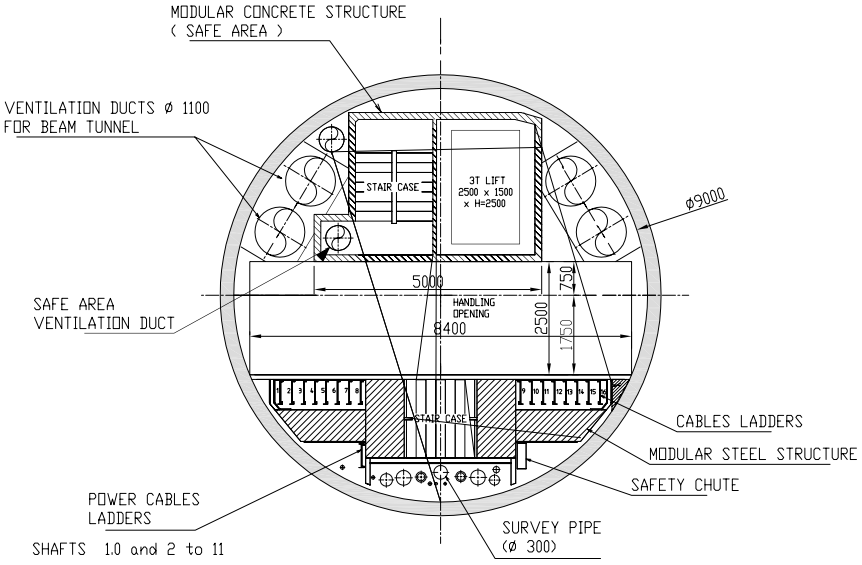

Figure 11.37
Cross section of access shaft

11.7.3 Installed handling equipment

11.7.3.1 Elevators

The elevators for the European scheme are listed in Table 11.19. The European scheme is based on one elevator per access shaft with an adjacent stairwell built into the concrete modules that are used to build up the elevator shaft. The Americas scheme is based on the use of twin elevators in the access shafts; the elevator shafts are separated by a fire-resistant wall.

Table 11.19 Elevators (European scheme)

Location		Area			
Shaft Diameter	Shaft/location	DR	RTML	Main Linac	Experiment
14m	PM-12, PM-8, PM+8, PM+12			4× 3 t	
9m	PM-10, PM+10			2× 3 t	
6m	PM-13, PM-11, PM-9, PM-7, PM+7, PM+9, PM+11, PM+13		2× 3 t	6× 3 t	
9m	PMB-0, PMC- 0	2× 3 t			
6m	PZB-0, PZA-0				2× 3 t
	Control room				2× 1.6 t
	Detector caverns				2× 1.6t

11.7.3.2 Cranes

11.7.3.2.1 Shaft transfer and underground area cranes For the Americas and European sites the transfer of heavy loads between the surface and the underground areas is carried out using overhead travelling cranes installed in the surface buildings above shafts. Cranes are used for handling of loads underground in the experimental detector caverns and interaction region as well as in the beam-dump and positron-source caverns. Table 11.20 lists the cranes and hoists.

Table 11.20. Cranes and hoists

	A1 e^- source	A2 e^+ source	A3 DR	A4 RTML	A5 Main Linac	A6 BDS	E Experiment
Surface Buildings							
Detector assembly							1× 4000 t+ 2× 20 t+ 2×400 t 40 t aux
Cooling Towers			2× 5 t		12× 5 t		1× 5 t
Cooling ventilation			2× 15 t		12× 15 t		1× 15 t
Shaft access			2× 20 t	2× 20 t	12× 20 t		
Cryo Compressors			1× 20 t		6× 20 t		1× 20 t
KlyCluster Building					12× 10 t		
Miscellaneous surface hoists			2× 5 t	2× 5 t	12× 5 t		4× 5 t
Underground Structures							
Detector Caverns							3× 40 t
Beam Dumps						4× 5 t	
Sources Facilities	1× 20 t						
Miscellaneous cavern hoists			2× 5 t	2× 5 t	12× 5 t	6× 5 t	6× 5 t

In addition to the cranes installed in surface buildings above access shafts, cranes are installed in the service buildings to carry out installation and maintenance of plant.

11.7.3.3 Hoists

Hoists are installed in surface buildings and underground areas for various installation and maintenance activities.

11.7.3.4 External gantry used to lower experiment modules to the underground area

An external gantry of 4000 t capacity is used to lower assembled detector modules from the surface to underground. This gantry is rented from an industrial supplier for the period scheduled for lowering the modules; the supply contract includes its assembly, operation then dismantling and removal from site.

11.7.4 Mobile handling equipment

11.7.4.1 Underground transport and handling

11.7.4.1.1 Schedule and space considerations Initially the full width of the accelerator tunnels are available for installation of services, allowing the use of standard industrial lift trucks, tractors and trailers. The available space for transport narrows once the beam-line equipment starts to be installed. For tunnel construction cost reasons the transport passage is kept to a minimum; this means that cryomodule transport vehicles, for instance, are not able to pass each other in the tunnel.

11.7.4.1.2 Cryomodules The space required for module transport and installation in the tunnel has a major influence on the cross section of the main linac tunnel. The large number of cryomodules to be transported and installed means that it is important to optimise the whole sequence of cryomodule transport to allow rapid transport and installation.

The design of the cryomodule transport vehicle design minimises the width of the reserved transport volume. It is capable of transport along the tunnel as well as transfer from the transport zone onto the support jacks. The vehicle (Fig. 11.38) is based on that used to install conventional magnets for the LHC. The vehicles are equipped with an automatic guidance system. The operator is required to ensure that the floor is clear of personnel and equipment. The vehicle can be configured for different loads and can therefore also be used for transport of other items.

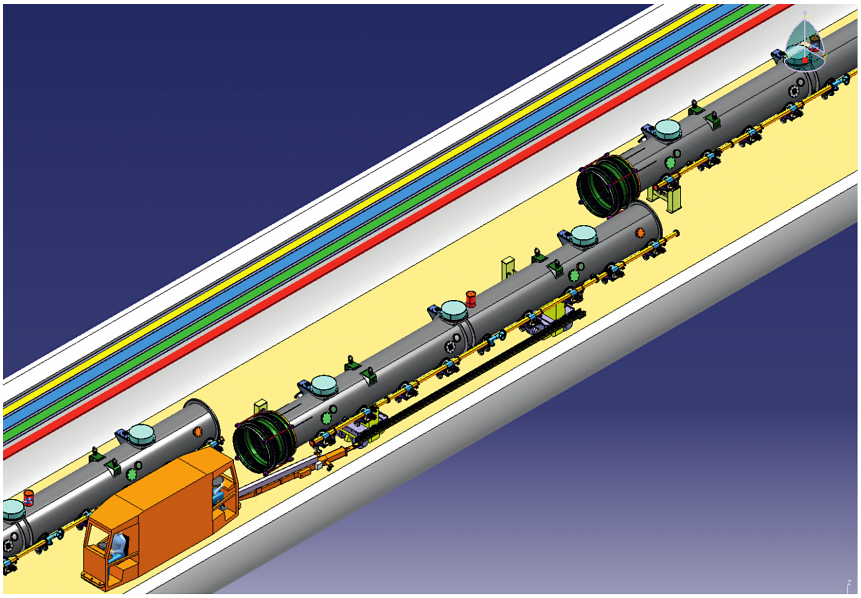

Figure 11.38 Cryomodule transport vehicle during transfer onto supports (Case shown is installation between two previously installed cryomodules)

Although module installation logistics aims for sequential installation, the installation process allows installation of cryomodules between two previously installed cryomodules in the event of supply delays or if sorting of modules is required. In addition the system is able to remove a previously installed cryomodule if major repairs are needed.

The interconnections between cryomodules are installed after the cryomodules have been positioned on their floor supports – this gives a clearance between modules of over 150 mm during their transfer onto their supports which allows rapid lateral transfer under manual control with minimum risk of damage to the adjacent cryomodule.

The cryomodule design includes lifting points and support points to allow the whole sequence of transport and handling operations. These are needed during the phases of module assembly, testing, storage, road transport to access points, lowering, tunnel transport and installation. The cryomodule design includes the transport restraints and special lifting beams used when handling fully assembled cryomodules during the installation process.

11.7.4.1.3 Magnets Specially designed vehicles (Fig. 11.39) are used for magnet transport along the tunnel followed by their installation. The use of vehicles combining transport, lifting and transfer avoids the need to transfer the load between different items of equipment and results in optimised installation times.

Figure 11.39
Special vehicle for magnet installation – shown in damping rings tunnel.

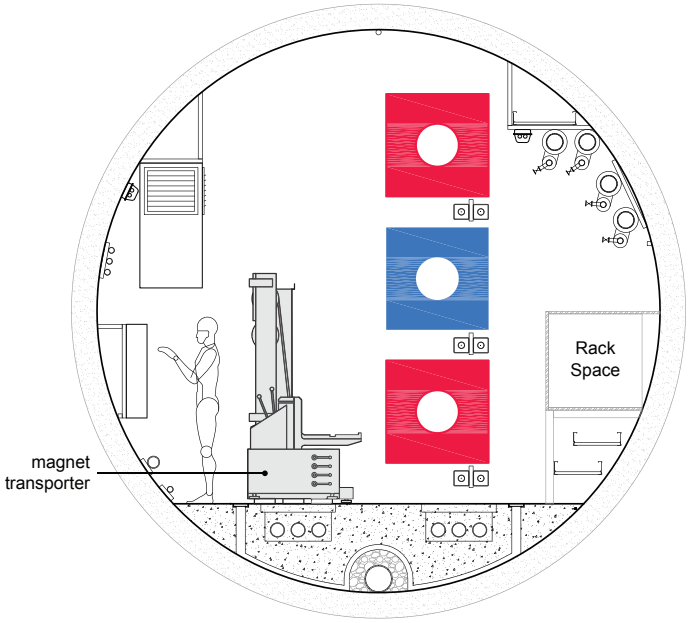

11.7.4.1.4 RF equipment RF equipment installation requires transport along the tunnel followed by precise positioning at a range of heights. The solution is to use an adaptation of the magnet transport and installation vehicle.

11.7.4.1.5 Other accelerator equipment Standard industrial handling equipment such as forklift trucks, electrical tractors and trailers are used to transport and install equipment other than cryomodules, magnets and RF in the tunnel. Where optimal this installation is carried out before cryomodule and magnet installation.

11.7.4.1.6 Personnel transport Personnel transport in the underground areas is by means of small electrical tractors or bicycles.

11.7.4.2 Surface transport and handling equipment

Standard road-going trucks and trailers are used for surface transport between sites. Standard industrial handling equipment such as forklift trucks, are used for material handling where it is not feasible to use overhead travelling cranes.

11.8 Alignment and survey

Survey and alignment covers a very broad spectrum of activities, starting from the conceptual design of the project, through the commissioning of the machines, to the end of operations. The cost estimate developed covers the work necessary until successful completion of the machine installation. It includes equipment needed for the tasks to be performed, and equipment for a dedicated calibration facility and workshops. It also includes the staff that undertake the field work, and the temporary manpower for the workshops. Full time, regular staff is considered to be mainly dedicated to organisational, management, quality control, and special alignment tasks. The cost estimate is mostly based on scaling the equivalent costs of the LHC to the ILC scope.

11.8.1 Calibration Facility

A 100 m long calibration facility is needed for the calibration of all the metrological instruments. The facility is housed in a climate controlled and stable building. Due to the range limit of current day commercial interferometers against which the instruments are to be compared the facility has been restricted to 100 m. A mechanical and an electronic workshop are also needed during the preparation phase and throughout the entire project. They are used for prototyping, calibration, and maintenance of the metrological instruments.

11.8.2 Geodesy and Networks

A geodetic reference frame is established for use across the whole site, together with appropriate projections for mapping and any local 3D reference frames appropriate for guaranteeing a coherent geometry between the different beam lines and other parts of the project. An equipotential surface in the form of a geoid model is also established and determined to the precision dictated by the most stringent alignment tolerances of the ILC. The geodetic reference frame consists of a reference network of approximately 80 monuments that cover the site. These monuments are measured at least twice, by multi-satellite GPS for horizontal coordinates, and by direct levelling for determining the elevations. The first determination is used for the infrastructure and civil engineering tasks. The second, and more precise determination, is used for the transfer of coordinates to the underground networks prior to the alignment of the beam components. A geodetic reference network is also installed in the tunnel and in the experimental cavern. For costing purposes it is assumed that the reference points in the tunnel are sealed in the floor and/or wall (depending on the tunnel construction) every 50 m. In the experimental cavern, the reference points are mostly wall brackets. The underground networks are connected to the surface by metrological measurements through vertical shafts or horizontal access ways. The distance between two consecutive shafts can exceed 2.5 km in some cases and some additional small diameter shafts may be required.

11.8.3 Civil Engineering Phase

The layout points which define the tunnel locations and shapes are calculated according to the beam lines in the local 3D reference frame. The tunnel axes are controlled as needed during the tunnel construction. All tunnels, including profiles, are measured in 3D using laser scanner techniques when the tunnels are completed. The same process is applied to the experiment cavern(s) and other underground structures. The buildings and surface infrastructure are also measured and the as-built coordinates are stored in a geographical information system (GIS).

11.8.4 Fiducialisation

Systematic geometrical measurements are performed on all beamline elements to be aligned prior to their installation in the tunnels. The alignment of elements installed on common girders or in cryomodules is first performed, and the fiducial targets used for the alignment in the tunnels are then installed on the girders (cryomodules) and all individually positioned elements. The positional relation between the external markers and the defining centrelines of the elements are then measured. For this report, an estimated 10,000 magnetic elements were assumed to need referencing. It is also assumed that most corrector magnets do not need fiducialisation. This number does not account for instrumentation, collimators, or other special beam elements.

11.8.5 Installation and Alignment

The trajectories of all the beamlines are defined in the local 3D reference frame which covers the entire site. The location of reference markers at the ends of each beam line element to be aligned are defined in this reference system, together with the roll angle giving a full 6 degrees of freedom description of element location and orientation. Likewise the position of all geodetic reference points is determined in this reference frame.

Prior to installation, the beamlines and the positions of the elements are marked out on the floors of the tunnels. These marks are used for installing the services, and the element supports. The supports of the elements are then aligned to their theoretical position to ensure that the elements can be aligned whilst remaining within the adjustment range of the supports.

After installation of services such as LCW and cable trays, the tunnels are scanned with a laser scanner. The point clouds are then processed, and the results inserted into a CAD model. A comparison with theoretical models is used by the integration team to help identify any non-conformity and prevent interference with the subsequent installation of components. The current requirements for the one sigma tolerances on the relative alignment of elements or assemblies are given in Table 11.21.

Table 11.21
Components and required alignment tolerances.

Area	(km)	Nb of beam	Error of misalignment on the fiducials (1σ)
e^- source	2.3	1	0.1 mm rms over 150 m
e^+ source	3.3	1	0.1 mm rms over 150 m
2 DRs	6.6	2	0.1 mm rms over 150 m
RTML	1.7	1	0.1 mm rms over 150 m
Main linac	23.9	1	0.2 mm rms over 600 m
BDS	6.5	1	0.02 mm rms over 200 m

The components are aligned in two steps:

- A first alignment is performed to allow connection of the vacuum pipes or interconnection of the various devices. This is done using the underground geodetic network as reference.
- After all major installation activities are complete in each beamline section, a final alignment, or so-called smoothing, is performed directly from component to component in order to guarantee their relative positions over long distances.

To reach and maintain the positioning tolerances of the final doublets in the BDS IR, a 150 m straight reference line is set up as close as possible to the beam components. This line, consisting of lasers or stretched wires and hydrostatic levels and allows for the geometrical connection between the beam lines and the detectors. The IR hall with movable detectors will require an extensive network with monuments and markers on the floors and walls, at several levels, for the use of laser trackers to develop and to maintain a 3D network which is coupled to the in-tunnel networks. This network will continue to evolve during the assembly of the detectors and into operation.

11.8.6 Information Systems

The theoretical positions of all the components to be aligned on the beam lines is managed in a dedicated database. This database is also used for managing all the geodetic and alignment measurements and the instrument calibrations. All measurement data are captured and stored electronically and subsequently transferred to the database. Pre-processing of the measurements are carried out in the database and then dedicated software for data analysis is used to calculate the best fit position of the elements and components. These results are also stored in the database where they can be accessed for further post-processing, analysis and presentation. A geographic information system (GIS) is set up for managing all location data.

11.9 Installation

11.9.1 Scope

This section covers activities required to prepare, coordinate, integrate, and execute a detailed plan for the installation of the ILC components, including the associated site-wide logistics. It includes all labor, materials and equipment required to receive, transport, situate, affix, accurately position, interconnect, integrate, and check out all components and hardware from a central storage or subassembly facility to its operational location within the beam and service tunnels as well as the surface service buildings where applicable. The premise is that the installation group receives fully tested assemblies certified for installation. Fabrication, assembly, component quality control and commissioning, as well as the basic utilities provided by conventional facilities, such as ventilation, air conditioning, fire prevention, high voltage electrical, chilled water and low-conductivity water distribution are described elsewhere.

11.9.2 Methodology

The installation WBS is broken down into two major categories, general installation and technical system installation. General installation includes all common activities and preparations and associated logistics. It is further broken down into logistics management, engineering support, equipment, vehicles, shipping and receiving, warehousing, and transportation. Technical system installation includes all efforts required for complete installation of the technical components underground, and in the surface buildings where applicable. General Installation is further broken down into logistics management, engineering support, equipment, vehicles, shipping-receiving, warehousing, and transportation. Technical System Installation covers the six machine areas, viz. electron sources, positron source, damping ring, RTML, main linac and beam delivery. Each element of the WBS for both general and technical systems is then extended two levels further and populated with required labor as well as incidental material and equipment costs. Table 11.22 shows the top-level Installation WBS.

Table 11.22
Top-Level WBS Installation.

WBS					Component
1	7	3	1		General installation
				1	Logistics management
				2	Engineering support
				3	Equipment
				4	Vehicles
				5	Shipping and receiving
				6	Warehousing
				7	Surface transport
1	7	3	2		Technical-system installation
				1	Electron source
				2	Positron source
				3	Damping Ring
				4	RTML
				5	Main Linac
				6	Beam Delivery

The installation estimates made for the RDR are used as a starting point. The scope of major changes impacting the installation work was identified and used to scale the RDR installation estimates accordingly.

General installation accounts for 18 % of the effort in Japan and 16 % at the US/CERN sites; the remaining effort is required for the accelerator systems.

Figure 11.40 indicates the split of effort among accelerator systems.

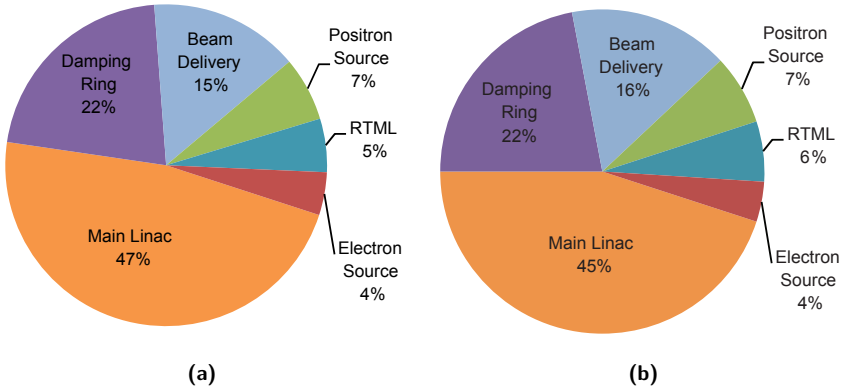

Figure 11.40
Relative labor effort for the various accelerator systems for (a) the Japan sites and (b) the US/CERN sites.

11.9.3 Model of Main-Linac Installation

The complete ILC main linac requires the installation of 1,840 Cryomodules, over 11,130 magnets and approximately 480 high-level RF stations. Since the main linac is a major cost driver, the installation of cryomodules and RF sources is modelled in detail.

The installation rate is one RF unit (Fig. 11.41) and associated services per day for each crew, which includes the following steps:

- tunnel preparation for installation;
- move, place, adjust and fix cryomodule supports;
- install, adjust, fix and prepare section of cryo and beam pipe connections;
- complete cryogenic and vacuum connections, leak check;
- cryomodule sleeve coupling connection.

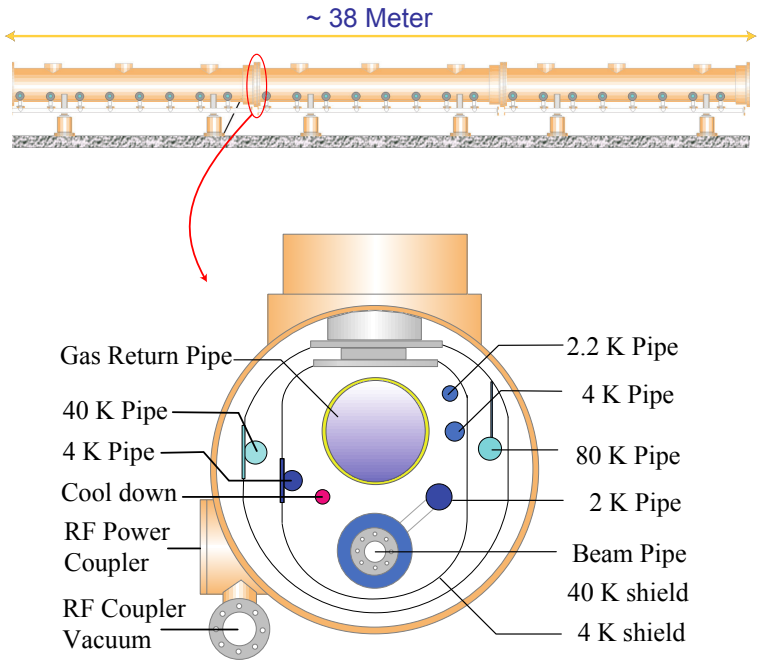

Figure 11.41
The installation of one of the Main Linac RF units. The cryomodule cross section indicates various pipe interconnects that need to be made.

Labor productivity is taken to be 75 %, or 6 hours per shift, given transport distances and handling difficulty. The model includes the number and size of the equipment pieces, distances to installation, speed of transportation and estimates of number of staff and hours for each task. To estimate the installation effort to assemble an entire RF unit, the Japan site using the DKS is used as a model. The entire RF unit includes Marx modulator, klystron, control racks, cable trays, control

cables and complex waveguides. The installation of one RF unit (three cryomodules) is estimated to take a total of 72 person-days.

11.9.3.1 Installation planning in underground segment

To create a cost effective, timely and safe installation plan, certain facility conditions are assumed to exist prior to the start of installation. Some examples include, but are not limited to, the availability of utilities, communication, above-ground warehousing and equipment staging areas. Once these and details of the technical components are known, a very general model, both in time and 3-D, can be developed. Figure 11.42 shows a schematic installation plan for the main linac. The 72-man crew is working in a (moving) 1 km section of the tunnels at the rate of one RF unit per day. Similar activities and crews will be working in other sections of the linac tunnels as they become available. This is also true for the central complex of injectors and damping ring.

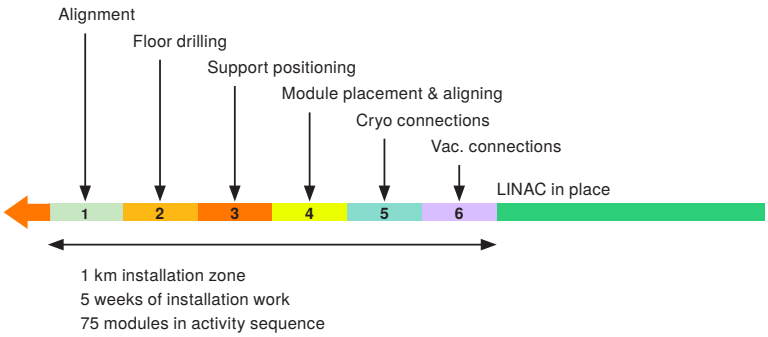

Figure 11.42
Installation Model for main-linac components in an underground segment.

This estimate assumes a 2-year installation schedule, a six-month period of ramp-up and on the job training, and 75 % efficiency. In-tunnel activities are concentrated on a day shift, with transport and staging on swing shift. Based on this multi-shift model, the total manpower to fit all the installation activities into the 2-year peak period comprises over 450 people on day shift and another 250 on swing shift in various parts of the tunnel. There are also about 100 people involved in surface logistics.

A detailed plan for installation of the ILC must await the choice of a site. However, an outline plan has been drawn up which is illustrated in Fig. 11.43. This shows the relative effort required to install each accelerator systems, including the main linac and is the basis for the costing of the ILC installation in Chapter 15.

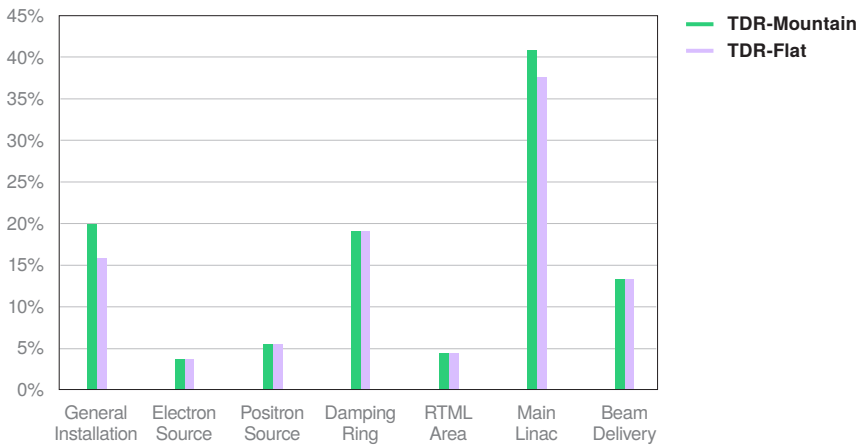

Figure 11.43
Relative effort required to install the accelerator system indicated on the x axis.

Chapter 12
Possible upgrade and staging options

12.1 Introduction

The physics performance requirements for the ILC [228] specify a continuous centre-of-mass energy range from 200 GeV to 500 GeV, with the possibility of an optional upgrade to a centre-of-mass energy of 1 TeV after some years of running. The GDE has focused on providing a mature and robust design and cost estimate for the 200–500 GeV baseline machine, which has been the subject of the previous chapters of this report. The design represents a solution that is cost-performance optimised for that energy range. This chapter presents scenarios for the energy upgrade to 1 TeV and a luminosity upgrade of the baseline 500 GeV machine by up to a factor of two. Furthermore, with the recent discovery of a Higgs boson by the LHC [7, 8] at approximately 125 GeV, a further scenario for a staged approach to the baseline machine is presented, starting at an initial centre-of-mass-energy range of 200–250 GeV.

The level of design detail of the staging and upgrade scenarios is significantly less mature then the baseline. In particular, the TeV upgrade parameters and associated conceptual design are a relatively simple and straightforward scaling of the baseline machine, based on forward-looking assumptions of higher achievable operational parameters for the SCRF technology of 45 MV/m average accelerating gradient with $Q_0 = 2 \times 10^{10}$; achieving these values requires further R&D beyond the baseline technology, but the extrapolation seems realistic. It is assumed that this R&D will continue in parallel to both construction and operation of the baseline machine, such that the extension to the main linacs required for the energy upgrade would benefit from the improved technology (see Part I Section 2.3.4). Both the luminosity upgrade and the low-energy staging are based on the existing technology and require no additional R&D. However, no attempt has been made at this time to study engineering and potential cost trade-offs. The initial 250 GeV stage ("Light Higgs Factory") in particular could well benefit for a re-evaluation of machine parameters that may lead to further cost-performance optimisation at that energy.

The remainder of this chapter deals with the top-level parameters for the staging and upgrade scenarios, and the implications for the machine sub-systems. For the TeV upgrade, an approach to construction that has the minimum impact on ILC operation is discussed. The two TeV upgrade parameter sets presented (so-called low and high Beamstrahlung) were arrived at after careful consideration of the physics impact after discussion with the physics and detector community. Rough cost estimates for the upgrades based on a direct scaling of the TDR baseline costs are provided in Section 15.8.

12.2 Parameters

Table 12.1 shows the main parameters for a possible first-stage 250 GeV centre-of-mass-energy machine, the 500 GeV luminosity upgrade, and two possible parameter sets for the TeV upgrade. In the remainder of this section, the parameter sets for the luminosity and TeV upgrade will be discussed. The parameters for the first-stage 250 GeV machine are identical to the baseline parameter set for that energy (see Section 2.2) with the exception of the AC power which will be discussed in Section 12.5.

Table 12.1. Primary parameters for a proposed 250 GeV centre-of-mass-energy first stage, the luminosity upgrade for the 500 GeV baseline machine, and the two parameter sets for the TeV upgrade: low Beamstrahlung (A) and high Beamstrahlung (B). The baseline 500 GeV parameters are included for reference.

				1st	L	TeV Upgrade	
			Baseline	Stage	Upgrade	A	B
Centre-of-mass energy	E_{CM}	GeV	500	250	500	1000	1000
Collision rate	f_{rep}	Hz	5	5	5	4	4
Electron linac rate	f_{linac}	Hz	5	10	5	4	4
Number of bunches	n_b		1312	1312	2625	2450	2450
Bunch population	N	$\times 10^{10}$	2.0	2.0	2.0	1.74	1.74
Bunch separation	Δt_b	ns	554	554	366	366	366
Pulse current	I_{beam}	mA	5.79	5.8	8.75	7.6	7.6
Average total beam power	P_{beam}	MW	10.5	5.9	21.0	27.2	27.2
Estimated AC power	P_{AC}	MW	163	129	204	300	300
RMS bunch length	σ_z	mm	0.3	0.3	0.3	0.250	0.225
Electron RMS energy spread	$\Delta p/p$	%	0.124	0.190	0.124	0.083	0.085
Positron RMS energy spread	$\Delta p/p$	%	0.070	0.152	0.070	0.043	0.047
Electron polarisation	P_-	%	80	80	80	80	80
Positron polarisation	P_+	%	30	30	30	20	20
Horizontal emittance	$\gamma\epsilon_x$	µm	10	10	10	10	10
Vertical emittance	$\gamma\epsilon_y$	nm	35	35	35	30	30
IP horizontal beta function	β_x^*	mm	11.0	13.0	11.0	22.6	11.0
IP vertical beta function (no TF)	β_y^*	mm	0.48	0.41	0.48	0.25	0.23
IP RMS horizontal beam size	σ_x^*	nm	474	729	474	481	335
IP RMS veritcal beam size (no TF)	σ_y^*	nm	5.9	7.7	5.9	2.8	2.7
Luminosity (inc. waist shift)	L	$\times 10^{34}$ cm^{-2}s^{-1}	1.8	0.75	3.6	3.6	4.9
Fraction of luminosity in top 1%	$L_{0.01}/L$		58.3%	87.1%	58.3%	59.2%	44.5%
Average energy loss	δ_{BS}		4.5%	0.97%	4.5%	5.6%	10.5%
Number of pairs per bunch crossing	N_{pairs}	$\times 10^3$	139.0	62.4	139.0	200.5	382.6
Total pair energy per bunch crossing	E_{pairs}	TeV	344.1	46.5	344.1	1338.0	3441.0

12.2.1 Luminosity upgrade

The luminosity upgrade is achieved by a straightforward doubling of the number of bunches per pulse from the baseline number of 1312 to 2625[1], resulting in a doubling of the average beam power and hence luminosity. All other single-bunch parameters are assumed unchanged from their original baseline values. The bunch spacing is reduced from 554 ns to 366 ns resulting in an increase in beam current from 5.8 mA to 8.8 mA. The beam pulse length increases from 714 µs to 961 µs. The choice of bunch spacing is consistent with both the damping ring harmonic number and the main linac RF pulse length (see Section 12.3).

[1] The number in the original 2007 *Reference Design Report* nominal parameter set.

12.2.2 Energy upgrade

The choice of beam parameters and ultimately the luminosity for the TeV energy upgrade is also based on a direct scaling from the baseline parameter set, but is more constrained by additional considerations from the higher energy and average beam power:

- the total AC power required by the upgraded machine should be kept below some realistic limit (assumed to be 300 MW);
- the beam current and pulse length should be compatible with the injectors, damping rings and main linac of the baseline design;
- the energy loss due to Beamstrahlung δ_{BS} ($\propto \frac{N^2}{\sigma_x^2 \sigma_z}$) should be kept low and the maximum pair-production angle ($\propto \sqrt{\frac{N}{\sigma_z}}$) constrained while maximizing the luminosity per bunch crossing.

The total AC power constraint requires the reduction of the repetition rate from 5 Hz to 4 Hz, while the need to keep the RF pulse length in the original main linac to approximately 1.6 ms and the choice of damping ring harmonic number constrains the number of bunches to 2450 (see Section 12.4).

The Beamstrahlung limits tend to be physics dependent, therefore two parameter sets were proposed to the physics and detector groups for study: a low Beamstrahlung parameter set with δ_{BS} ~5% and a luminosity of $3.6 \times 10^{34}\,\mathrm{cm}^{-2}\mathrm{s}^{-1}$ equal to the luminosity-upgrade value for the 500 GeV baseline, and a second, high-Beamstrahlung set with $\delta_{BS} \sim 10\%$ and a correspondingly higher luminosity of $\sim 4.9 \times 10^{34}\,\mathrm{cm}^{-2}\mathrm{s}^{-1}$. Both of these parameter sets are based on a reduced single-bunch charge ($\sim 1.7 \times 10^{10}$), shorter bunch lengths (250 µm and 225 µm for low and high δ_{BS} respectively) and an increased horizontal beam size to control the Beamstrahlung and pair-production angle, while the vertical beta-function at the interaction point (IP) is further reduced to increase the luminosity per bunch crossing [229]. The bunch lengths and IP beta-functions are within the range of the bunch compressor and final-focus systems respectively. It is relatively straightforward to adjust the machine parameters between these two Beamstrahlung parameter sets.

12.3 Scope of the luminosity upgrade

A doubling of the average beam power requires the installation of additional RF power (klystrons and modulators) for the main linacs, as well as significant modifications to the damping rings. The baseline designs for other sub-systems (electron and positron sources, bunch compressors, beam delivery and in particular the high-power dump systems) are already specified to cope with the higher beam power (larger number of bunches per pulse). The reduced bunch spacing in the main linac (366 ns) is consistent with the required bunch patterns in the damping rings with a harmonic number of 7044 [95], and a maximum RF pulse length of 1.65 ms.

The following sections briefly describe the impact and necessary modifications to each accelerator system.

12.3.1 Main linacs

The upgraded main linac parameters are given in Table 12.2. The doubling of the number of bunches per pulse (1312 to 2625) and the reduction of the bunch spacing (554 ns to 366 ns), results in a ~50 % increase in beam current (5.8 mA to 8.8 mA). The higher current reduces the matched external Q and thus the fill time by the same factor, resulting in an overall slight shortening of the RF pulse length, and an increase in the RF-beam power efficiency from 44 % to 61 %. Hence a doubling of the average beam power only requires an increase of approximate 44 % in the RF power source (number of klystrons), while the power dumped to the RF loads (reflected power) does not change.

The approach to adding the required additional klystrons, modulators, charging supplies and conventional facilities support differs significantly for the two site-dependent variants considered. For

Table 12.2
The main linac RF parameters for the luminosity upgrade (the baseline numbers are including for comparison).

		Baseline	L upgrade
Gradient	MV/m	31.5	31.5
Bunch spacing	ns	554	366
Bunch charge	nC	3.2	3.2
Bunches per pulse		1312	2625
Beam current	mA	5.8	8.8
Beam pulse length	μs	727	961
Q_{ext} (matched)	$\times 10^6$	5.5	3.6
Fill time	μs	927	613
RF pulse length	ms	1.65	1.57
RF to beam power eff.		44 %	61 %

the *flat topography* utilising the *Klystron Cluster Scheme* (KCS, see Section 3.9), the additional RF power sources are added to the surface clusters. Each of the 22 clusters requires an additional 10 klystrons and modulators, or an increase in the total number from 413 to 633. This can most easily be done by adding to the combining waveguide system at the downstream (high power) end, between it and the vertical shaft, if space is left (see Section 3.9). Power extracted by each Coaxial Tap-Off (CTO) along the linac then increases from ∼5.8 MW to ∼8.8 MW. All the RF power-distribution systems, including the main long high-power overmoded waveguide and CTO's, are already specified for the higher power and do not need upgrading. An advantage of the KCS approach is that the additional klystrons can be added adiabatically in parallel to operations, since minimal installation work is require in the accelerator tunnel itself. The majority of the additional water cooling (for the klystrons and modulators) is also primarily localised the surface buildings, making the upgrade relatively straightforward. (Note that there is in principle no additional load in the tunnel itself, with the exception of the water cooling associated with the waveguides.) With the *Distributed Klystron Scheme* (DKS, see Section 3.8) used for the *mountainous topography*, the additional klystrons and modulators must be installed in the tunnel and require modification of the local power distribution systems, since each klystron now drives 26 cavities as opposed to 39 in the baseline. Figure 12.1 shows the approach to upgrading the PDS.

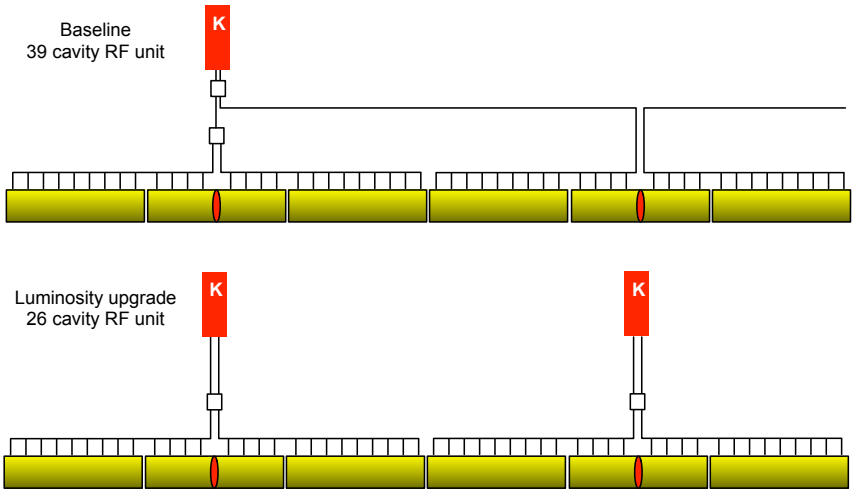

Figure 12.1
Scheme for adding klystrons for the luminosity upgrade for the Distributed Klystron Scheme (DKS).

Unlike KCS, the invasive nature of the installation work requires a shutdown during which all the additional RF power would need to be installed. This would also include the additional water cooling and AC power required, although pipe sizes are already specified for the additional load in the baseline, and would not need upgrading. In all other respects, the main linacs would not require modification. In particular, the ∼25 % increase in cryogenic load (dominated by losses from the high-power coupler and HOM losses due to the higher current) is within the baseline specification. All beam-position monitors (and other instrumentation) are compatible with the shorter bunch spacing. Beam dynamics issues (multibunch effects) are also acceptable, and the high-power couplers and

HOM couplers/absorbers are specified in the baseline for the higher beam currents (power).

12.3.2 Damping Rings

For the high-luminosity upgrade, twice the number of bunches need to be stored in the damping rings, requiring a 3.1 ns bunch spacing. The doubling of the current in the rings poses a particular concern for the positron ring due to the effects of the electron-cloud instability. In the event that the electron-cloud mitigations that have been recommended (see Section 6.5) are insufficient to achieve the required performance for this configuration, the baseline damping ring tunnel and associated underground vaults have been designed to allow the possibility of installing a second positron ring (three rings in total, see Fig. 12.2). The two positron rings would both operate with the baseline parameters (i.e. 1312 bunches per ring). Space has also been provided for the additional power supplies and klystrons in the respective caverns, and the injection and extraction lines (part of the positron RTML system) are designed to accommodate pulsed vertical separation/combination of the positron beam pulse into/from the two rings.

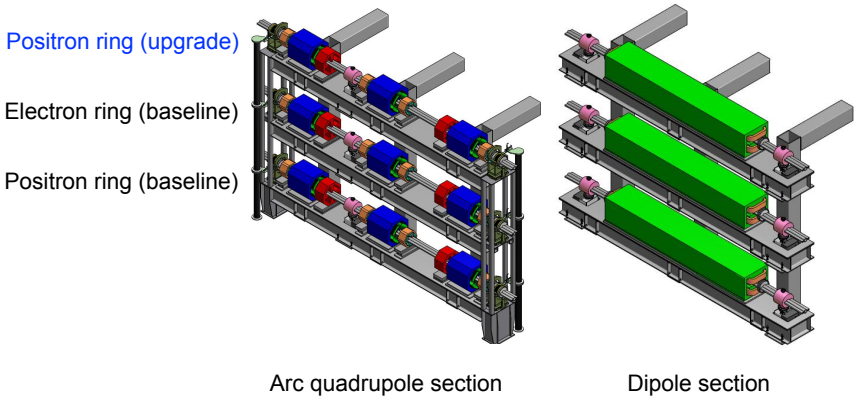

Figure 12.2 Damping ring configuration, showing the location of the (optional) positron ring for the luminosity upgrade.

For a single ring storing the complete 2625 bunches (corresponding to an average beam current of 0.78 mA and a 200 ms store time at 5 Hz operation), 12 RF cavities are required, supplying 294 kW per cavity to the beam (total of 3.53 MW). However, this is compatible with the power required by the 10 Hz baseline mode (1312 bunches, 0.39 mA). Running the 10 Hz mode with the higher beam current would in principle require a factor of two higher RF power, requiring a doubling of the number of cavities to 24 (since the power coupler is assumed to be limited to ∼300 kW). Currently there is space foreseen for an additional 4 cavities, giving a total of 16; thus the number of bunches would be limited to 1750 for low centre of mass running. Although provision is made for a second positron ring should the electron cloud effect at the higher number of bunches prove prohibitive, it is assumed that the electron ring will be able to run with the higher beam current. The principle beam instability issue is the fast ion instability (FII), which becomes more critical at the shorter bunch spacing. However, with the baseline pressure of 1 nTorr, simulations indicate that the FII will be manageable, although the faster growth rate will prove challenging for the multibunch feedback systems (see Section 6.4.5). The vacuum system and in particular the photon stops in the wigglers are all specified for the higher synchrotron-radiation load.

12.3.3 Electron and positron sources

The baseline designs for both the electron and positron sources are specified for the production of the higher number of bunches required for the upgrade (see Chapter 4 and Chapter 5 respectively). This includes the DC gun and CW laser systems for the electron source, the photon target for positron production, radiation shielding (positron source), power handling, and the room-temperature RF capture and pre-accelerator sections for both sources. The 5 GeV SCRF booster linac for the

positron source will require an additional three 10 MW klystrons and a minor reconfiguration of the power-distribution system. (The electron booster linac, due to its different configuration, has significant RF power margin and requires no additional klystrons for the upgrade.)

12.3.4 RTML (bunch compressors)

The RTML — and in particular the SCRF RF linac sections for the bunch compressors — are already compatible with the higher number of bunches (beam current). In particular the RF power configuration has enough overhead to accommodate the increased beam power.

12.3.5 Beam Delivery System

All systems in the BDS are specified for the higher beam power (shorter bunch spacing) and no additional modifications are required. In particular the factor of two higher average beam power is well within the specification of the main beam dumps, which are designed to handle the beam power associated with the TeV upgrade parameters.

12.4 Scope of energy upgrade to 1 TeV centre-of-mass energy

The upgrade of the beam energy will require extending the main SCRF linacs to provide the additional 250 GeV per beam. The beam current for the TeV upgrade (7.6 mA) is higher than the baseline parameter (5.8 mA) but less than that for the luminosity upgrade (8.8 mA), which assumes some level of the modifications outlined in Section 12.3. Assuming that the luminosity upgrade occurs first, then the injectors (sources and damping rings) will be reused unchanged. The bunch compressor sections will be relocated to the beginning of the extended linacs, as will the 180° turn-around of the RTML (see Section 7.3); the 5 GeV long-transfer line from the damping ring to the turn-around will also need be extended. The undulator-based positron source will remain located at the end of the electron main linac (central campus), but the undulator will need to be replaced with one more suited to the 500 GeV electron beam energy (see Section 12.4.1). The Beam Delivery System will require the installation of additional dipoles to provide the required higher integrated field strength.

The cost and schedule for the upgrade is completely dominated by the extension of the main linacs. One key cost-related consideration is the choice of the accelerating gradient. It is assumed that the current R&D into high-gradient SCRF will continue in parallel with construction and operation of the baseline machine — a period of more than a decade. With this in mind, both a higher gradient and quality factor are assumed for the upgrade linac technology. The actual choice of these parameters will clearly depend on the state-of-the-art at the time the upgrade is approved. However, for the purposes of this discussion, an average accelerating gradient of 45 MV/m with a $Q_0 = 2 \times 10^{10}$ will be assumed. Although significant R&D is required to achieve these ambitious parameters, they are considered realistic (see Part I, Section 2.3.4 and Chapter 6). Assuming that the unit cost of the higher-performance cavities (cryomodules) does not significantly change, the cost of the additional linacs would be reduced by approximately 20% over the baseline (based on the current TDR estimates).

Three scenarios for the upgrade are described in Table 12.3. Scenario A represents a straightforward doubling of the existing main-linac technology, based on the current gradient specifications of 31.5 MV/m average accelerating gradient. Scenario B assumes that the baseline linac is maintained as is (base), but that the additional linac (upgrade) is based on 45 MV/m technology. Finally, scenario C assumes the entire linac is replaced with the higher-gradient technology.

Scenario C would require a complete refurbishing and re-installation of the existing SCRF main linacs. For the linac hardware this is likely to be the most expensive option. However, it would require only an additional 6 km of linac tunnel (and one to two shafts or horizontal access ways) and associated conventional facilities support, and has the smallest overall footprint. Scenario B takes a

Table 12.3 Comparison of main linac upgrade scenarios (gradient). Approximate cavity numbers and linac lengths assume the same cavity length and packing fraction (64%) as the current baseline linac design.

		500 GeV	TeV Upgrade			
		Baseline	Scenario A	Scenario B		Scenario C
				upgrade	base	
Energy range	GeV	15–250	15–500	15–275	275–500	15–500
Gradient	MV/m	31.5	31.5	45	31.5	45
Num. of cavities		7400	15 280	8190	7090	10 700
				total cavities: 15280		
Linac length	km	12	25	9.5	11.5	17.5
				total length: 21.0		

more conservative approach, and assumes the maximum reuse of the existing baseline infrastructure. Approximately 9 km of additional tunnel (two to three vertical shafts/horizontal access ways) per linac are required (a total of an additional 18 km to the overall footprint). While not as space efficient as scenario C, the assumption of the higher gradient still reduces the overall footprint by 2×4 km as compared with a straightforward doubling of the baseline linacs (scenario A). Since scenario B is the less disruptive of the existing hardware, it also opens the possibility of significantly reducing interruption to physics running by allowing the construction and installation of the upgrade linac to occur in parallel with operations. Fig. 12.3 shows a possible scenario for parallel construction based on scenario B.

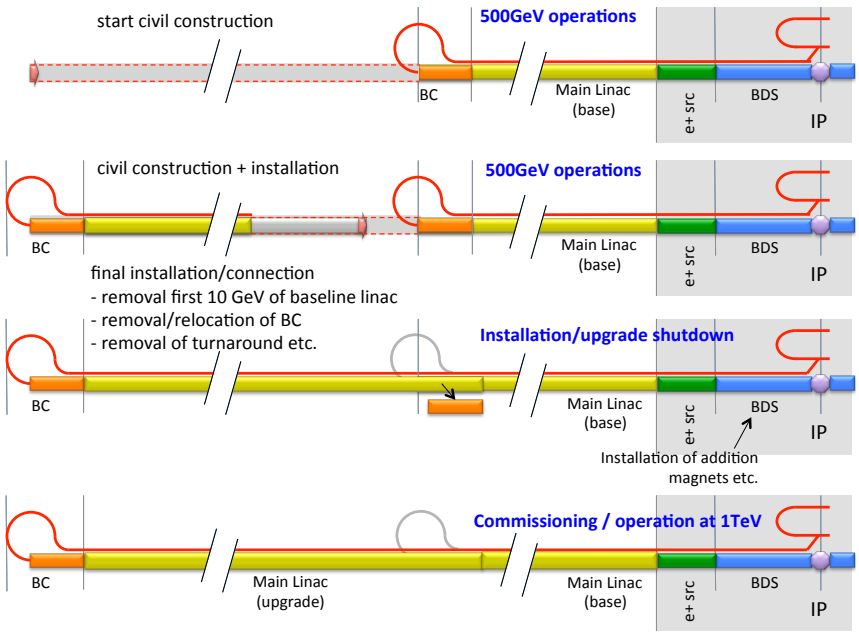

Figure 12.3 Parallel construction stages for the TeV upgrade (scenario B). Construction of the main linac (yellow) extensions occurs in parallel to 500 GeV operations, requiring a minimum interruption to make the final connections and necessary installation work in the RTML (orange), positron source (green) and BDS (blue). Note that the serial approach shown for the main linac extension construction is oversimplified, and sections of tunnel would likely be constructed and installed in parallel.

Making use of the existing baseline linac in this way has three key implications for the upgrade:

- The beam current and pulse length must be compatible with the existing RF installation and cryogenic cooling capacity.
- The existing linac lattice — which is initially designed to transport a beam energy from 15–250 GeV — must now transport a beam energy of 265 GeV to 500 GeV. This will require the replacement of the first 10 GeV of original linac, since these quadrupoles will not be capable of transporting the higher energy beam (265 GeV to 500 GeV as opposed to 15 GeV to 250 GeV). The remainder of the original linac will use a FoFoDoDo lattice as opposed to the baseline FoDo lattice, resulting in weaker focusing and larger beta functions. Simulations of the beam dynamics have indicated that the vertical-emittance growth can be contained within acceptable limits (see Part I Section 4.6).

- The higher-gradient technology is likely to be based on a cavity shape that has a higher impedance than the current baseline design, potentially resulting in higher wakefield effects that could impact the emittance growth and energy spread of the beam exiting the linacs.

The second and third bullet points would favour replacing the existing linac with the new higher-gradient technology, moving the existing cryomodules upstream. The new quadrupoles could be designed to accommodate the higher beam energy, and the effects of higher wakefields would be reduced. However, this scenario would require a much longer interruption to physics operation than that depicted in Fig. 12.3. For this reason, scenario B is currently seen as more attractive. The approximate numbers given in Table 12.3 for scenario B also assume that the upgrade linac with 45 MV/m will also be used to replace the first 10 GeV of the original baseline linac to provide the stronger quadrupoles (second bullet point). While clearly not the only scenario, this is likely to be the most straightforward and least time consuming. The thirty-five 31.5 MV/m cryomodules removed per linac could in principle be refurbished and used as spares. The principle parameters for the main-linac SCRF for scenario B are given in Table 12.4.

Table 12.4
Key main linac parameters for the TeV upgrade (scenario B) compared to the 500 GeV luminosity upgrade parameters. The relative dynamic cryoload gives the total estimated (scaled) dynamic cryogenic load for the linacs relative to the baseline linac.

		Baseline (L upgrade)	TeV upgrade upgrade	TeV upgrade base
Acceleration	GeV	15–250	15–275	275–500
Repetition rate	Hz	5	4	
Gradient	MV/m	31.5	45	31.5
Q_0	$\times 10^{10}$	1	2	1
Beam current	mA	8.8	7.6	
Beam pulse length	ms	0.96	0.90	
Fill time	ms	0.6	1.0	0.7
RF pulse length	ms	1.6	1.9	1.6
Rel. dyn. cryoload		1	1.2	0.8

The beam parameters are chosen to keep the RF pulse length for the baseline linac to ∼1.6 ms in accordance with the first bullet point above. In principle this particular constraint could be relaxed if new RF power sources were considered. The RF pulse length in the higher-gradient upgrade linac is ∼2 ms (longer fill time), which will require R&D for the upgrade linac klystron and modulator technology. Finally the lower repetition rate (4 Hz) and assumption of the higher Q_0 (2×10^{10}) compensate the average dynamic (RF and beam related) cryogenic losses per cavity for the higher gradient, as compared to the 500 GeV luminosity-upgrade parameters.

For the injector systems, it is assumed that the modifications for the luminosity upgrade described in Section 12.3 have been made. For the TeV upgrade parameters, the reduced bunch charge, number of bunches and repetition rate relax the requirements for the sources and damping rings. In particular no modification is in principle required for the electron source or damping rings, the latter of which benefits from the reduced repetition rate to achieve a longer damping time. However, modifications are required for the positron source, RTML and Beam Delivery Systems, which will be briefly described below, followed by a summary of the AC power requirements.

12.4.1 Positron source

The undulator-based positron source must be made compatible with an initial electron beam energy of 500 GeV. The solution is to replace the baseline helical undulator with one which is shorter and has a longer period and a lower field (Table 12.5). The upgrade undulator provides a photon beam similar enough to the baseline that the same target and capture arrangement can be used without modification [230]. One important consideration is the photon opening angle ($\sim 1/\gamma_e$) which is reduced by a factor of two for the higher beam energy; this makes photon collimation for polarisation more challenging. Currently a conservative estimate of 20 % polarization is considered feasible, but higher values could be possible provided a suitable solution for the smaller aperture photon collimation

Table 12.5
Helical undulator (and other) parameters for the TeV upgrade positron source, compared to the 500 GeV luminosity upgrade parameters. The critical target parameters (and yield) are kept the same for the higher-energy electron beam by replacing the helical undulator [230].

			500 GeV L upgrade	TeV upgrade
Electron beam energy		GeV	250	500
Positron pulse production rate		Hz	5.0	4.0
Bunch population	N	$\times 10^{10}$	2.0	1.7
Effective undulator length	L_{und}	m	147	132
Effective undulator field	B_{und}	T	0.4	0.2
Undulator period	λ_u	cm	1.2	4.3
Photon energy (1st harmonic)		MeV	42.8	27.6
Photon opening angle ($= 1/\gamma$)		μrad	2.0	1.0
Electron energy loss in undulator	ΔE_{und}	GeV	2.6	2.4
Average photon power		kW	79.3	65.5
Peak energy density in target		J/cm^{-3}	456	475

can be found [234]. The baseline design geometry of the target-bypass chicane for the high-energy electron beam already accommodates the 500 GeV beam transport (higher synchrotron radiation) with a few percent horizontal emittance growth [231], although additional dipole magnets will need to be installed.

12.4.2 RTML

The two-stage bunch-compressor system needs to be "moved" to the new upstream location. The scenario outlined in Fig. 12.3 assumes that a new two-stage compressor will be installed, together with a new turnaround and long transport line. During the shutdown for the final installation work, the baseline warm wiggler sections and cryomodules will be removed together with the first 10 GeV of the baseline Main Linac and replaced with the upgrade linac. The original turnaround would be disconnected and bypassed by the new long transfer line. It is likely that space between the original and upgrade linacs would also be used for additional diagnostics and dump systems, including an emergency extraction dump for machine protection, similar to the one at the exit of the linac (entrance to the BDS).

12.4.3 Beam Delivery System (BDS)

The BDS geometry (length and average bending radii) are already compatible with transporting a 500 GeV beam, with acceptable emittance growth generated by synchrotron radiation [230]. Additional dipoles are required (and associated power supplies and cooling) which will be installed in the drift spaces provided in the baseline lattice. The main high-power dumps are already specified for the higher average beam power, to avoid having to replace them for the upgrade (the dumps will be radioactive after several years of operation).

12.4.4 AC Power requirements

A comprehensive requirements analysis of the electrical power loads was made for the baseline design. A similar level of engineering analysis was not practicable for the upgrade scenarios presented here. Instead, an extrapolation of the top-level baseline loads (Chapter 11) has been made, based on simplistic scaling laws for main linacs. Table 12.6 gives the approximate loads for the TeV energy upgrade (scenario B). The estimated site power is ∼300 MW, compared to ∼160 MW for the baseline, and ∼210 MW for the luminosity upgrade.

Table 12.6
Rough estimate of the power requirements (in MW) for the 1 TeV upgrade (scenario B), based on extrapolation of the baseline design parameters using simple scaling laws [232].

	RF Power	RF Racks	NC Magnets	Cryo	Conventional load Normal	Conventional load Emergency	Total
e^- source	1.3	0.1	0.7	0.8	1.0	0.2	4.1
e^+ source	1.4	0.1	4.9	0.6	2.2	0.4	9.6
DR	12.8		4.5	1.5	2.6	0.1	21.5
RTML	7.2	0.3	2.1	2.0	0.1	0.1	11.8
ML (base)	59.2	7.4	0.9	28.3	7.8	5.2	108.8
ML (upgrade)	74.2	7.4	0.7	25.1	10.2	3.9	121.3
BDS			16.1	0.4	0.2	0.3	17.1
Dumps					1.0		1.0
IR			1.2	2.7	0.1	0.2	4.2
Total	156	15	31	61	25	10	300

12.5 A Light Higgs Factory (250 GeV centre-of-mass) as a possible first-stage.

Following the discovery of a Higgs boson with a mass of ∼125 GeV [7–10], it is useful to discuss an initial-stage project which would start with a centre-of-mass energy of 250 GeV, which could then be later upgraded to 350 GeV for top physics, and then still later to the full 500 GeV, or even directly to a higher energy should the physics case prove compelling.

A first stage 250 GeV centre-of-mass-energy machine would require the installation of approximately half the linacs of the 500 GeV baseline machine. There are two possible scenarios for the civil construction and conventional facilities:

1. Only the tunnel required for the 250 GeV machine is constructed and installed. The next energy stages would then require additional civil construction.

2. The complete tunnel and support shafts (access ways) for the 500 GeV machine is constructed at the beginning, and only half filled with linac, the remaining tunnel housing a beam transfer line to the central region. Staging the energy then simply requires additional linac and associated conventional facilities to be installed.

The first scenario is conceptual the same as that proposed for the 1 TeV upgrade, although half the scale. It is likely to represent the minimum cost for the initial phase machine. The second scenario requires greater investment for the initial phase (for the civil construction), but increasing the centre-of-mass energy then becomes relatively straightforward, and opens up the possibility for a more adiabatic approach to increasing the energy. A very rough scaled estimate suggests approximately 65% and 70% of the 500 GeV baseline cost (Section 15.8) for both scenarios respectively. Since a strong physics case exists for a staged approach up to (or slightly above) 500 GeV centre-of-mass energy, scenario 2 is the preferred option, and will be the focus of the remainder of this discussion. Extension beyond the baseline 500 GeV machine would then require additional civil construction, as already outline in Section 12.4.

The primary machine parameters (including luminosity) are assumed to be the same as those specified for the 500 GeV baseline machine at 250 GeV centre-of-mass energy (see Section 2.2) and are repeated in Table 12.1. This effectively means the injector systems (electron and positron sources, damping rings, bunch compressors) remain unchanged from the baseline. The beam-delivery system could in principle be further optimised for the lower-energy beam, but the overall geometry is still assumed to be consistent with the TeV energy upgrade. For positron production, the 10 Hz mode is currently assumed, again consistent with the approach adopted for the baseline machine (see Section 2.2.2). However, this has additional ramifications for the shorter (electron) linac now running at the full gradient (31.5 MV/m):

- The electron linac must be capable of accelerating the positron production pulse to the nominally required 150 GeV; this now requires an additional 25 GeV of electron linac than would otherwise be required for 250 GeV centre-of-mass-energy running.

- The 10 Hz operation of the electron linac will require a doubling (per unit length) of the average RF power, cryogenic cooling, and associated conventional facilities capacity as compared to the baseline 500 GeV machine.

Thus the electron main linac requires approximately 100% of both the average RF and cryogenic cooling power of the full 500 GeV centre-of-mass-energy baseline linac, while the positron linac would require approximately 50%. The overall scaling is approximately 80% of the AC power load of the baseline machine for the first-stage 250 GeV machine (∼129 MW) [232]. The need for the 10-Hz mode at 250 GeV centre-of-mass energy operation could be removed by increasing the length of the superconducting helical undulator from the baseline length of 147 m to approximately 250 m. The electron linac would now only require an additional 3.5 GeV to drive the undulator and only needs to run at 5 Hz. This would reduce the AC power to the ∼100 MW level. Another option is the possibility of an independent but unpolarised conventional positron source [233], but this requires further detailed design study, and the loss of polarised positrons should be discussed with the physics community.

The impact on the construction schedule remains to be studied in detail. However, the dominant schedule drivers are likely to be the central region, interaction region hall and the construction of the detectors themselves. While there will be some saving in the overall time required, it is unlikely to be more than 12-18 months based on the current baseline schedule (Chapter 14). The impact on the main-linac component production schedules requires study in order to ascertain the bests cost optimum scenario. If the schedule is indeed constrained by the central region and detectors, a lower production rate could be considered, which may have cost benefits. Furthermore the timescales considered before an upgrade to the second-stage energy would also influence the approach to manufacturing: if a more continuous adiabatic upgrade over several years is considered, this would favour extending the existing linac component manufacturing beyond the initial construction period, possibly at a reduced rate; if the first-stage physics programme requires several years, then it may be necessary or cost beneficial to shutdown and then re-start industrial manufacture. A more detailed study will require a better model for the staging from the physics perspective, as well as an assessment of the most cost-effective approach to dealing with the component manufacture over the longer time scales.

12.6 Photon Collider Option

The possibility of developing a gamma-gamma collider option from an e^+e^- or e^-e^- collider, has been extensively discussed over many years. The principle approach has always been to backscatter intense laser beams from the strongly focused charge particle beams close the IR, producing two focused and colliding gamma beams with energies close to that of the particle beams.

To obtain sufficient gamma-gamma luminosity, one requires very high-power lasers, with optical cavities to further enhance the photon intensity, and optical-path designs that can fit around the detectors with photon-bunch timing that matches a possible charged-particle timing pattern. R&D on suitable lasers and optical cavities is ongoing. [235, 236]

With the parameters which give adequate luminosity, the charged-particle beams are severely disrupted and a large crossing angle is required to cleanly extract the beams after collision. Studies suggest that a minimum crossing angle of 25 mrad is required (compared to 14 mrad in the e^+e^- baseline design) and to implement such a layout would require modification of the civil design of the IR hall and the horizontal displacement of the interaction point by a few meters [237].

Given future developments, in lasers and optical cavities and in physics from the LHC and the ILC, a gamma- gamma collider could be considered as a future option for the ILC.

12.7 Summary

This chapter has considered staged and upgrade options other than the 500 GeV baseline design described in relative detail in the previous chapters of report, and demonstrates the great flexibility in the design and options of the ILC machine. The baseline design already contains a minimum support for a straightforward luminosity upgrade by doubling the average beam power (increasing the average RF power by ∼50 %). Parameters and scope for a future upgrade to 1 TeV centre-of-mass energy have been presented, based on extending the main linacs with a minimum impact on the existing (baseline) machine. Construction of the extended machine could in principle go in parallel with physics running, with only a minimum interruption for connection of the baseline and upgrade linacs and subsequent machine commissioning. The physics parameters (luminosity) for the TeV upgrade represent a trade-off between the physics requirements of the beam-beam (limiting Beamstrahlung and pair-production angle), and a desire to cap the total AC power requirement to approximately 300 MW. Finally, a staged approach to the baseline machine, starting with a 250 GeV centre-of-mass energy first stage has been briefly outlined, where only half the baseline linac would be installed, but the full tunnel and associated civil engineering for the 500 GeV machine would be constructed.

None of these scenarios have been studied in detail, but they represent realistic scaling from the existing baseline design and can be considered as possible example approaches. Other scenarios can certainly be considered as the LHC physics results continue to become available and the physics case for the linear collider becomes further refined.

Chapter 13
Project Implementation Planning

In the early 2000s, several study reports [238, 239] were issued by American, Asian and European regional bodies representing the relevant high-energy physics communities on possible organisational structures for the project management of a linear collider (LC). The Consultative Group on High-Energy Physics of the Organisation for Economic Cooperation and Development (OECD) also issued a report [240] on their consensus, concurrently with these regional reports.

All these reports agreed that a high-energy electron-positron LC should be the next major facility on the roadmap of international high-energy physics, and that this project would require a hitherto unknown scale of global collaboration, calling for special attention by the world's research, administrative and political sectors. Together, these reports laid the foundations for an international organisation for the design and development stage of an LC, leading to establishment of the Global Design Effort (GDE) for the International Linear Collider (ILC). Following the International Committee for Future Accelerators (ICFA) decision to base the design of a global linear collider on superconducting radiofrequency (SCRF) technology, the GDE mandate of coordinating the worldwide R&D programme and developing a technical design for a 0.5 TeV linear collider was established. This mandate is completed with the publication of this TDR. Based on various physics studies, ICFA gave the GDE guidance on the accelerator performance to be achieved. In creating the baseline design presented in this report, close attention was also paid as to how best to implement such a global project in order to make it as realistic as possible. The results of these deliberations have been collected as a stand-alone document on Project Implementation Planning (PIP) [11]. In this chapter the guiding principles underlying the PIP are outlined and a brief synopsis of the contents of each section are provided.

It is clear that the international HEP community cannot usurp the role of government or officials in tackling the concomitant intergovernmental issues. Therefore, the PIP focusses on making statements from the standpoint of the primary executor of the research and on presenting the GDE's preferences from the scientific and technical viewpoints in order to inform the debate as much as possible.

Large-scale research undertakings cannot be realised without firm commitments by the nations/regions that undertake them. Moreover, when the scale of a research project goes beyond what can be readily sustained by a single nation/region, its guiding principles have also to expand. One such principle that needs to be underlined is "openness to the world". High-energy physics has been characteristically international in nature since its inception.

The opportunity for research in particle physics has been, and must be, equally open to all scientists in the field, as formulated in the ICFA guidelines. The ILC project is a novel and unique opportunity to realise internationalisation and cooperation in particle physics on a global scale with numerous positive implications for science, technology and education. This is perhaps one of the most important ways in which the ILC can be popularly perceived as making a valuable global contribution to society.

Several different organisational models are conceivable for managing the construction, commissioning and operation of the ILC. Irrespective of the specific details of such models, a clear legal status needs to be defined for an organisation to manage execution of the ILC project. The adequacy of that organisation and its management needs to be assessed from the standpoint of how its legal structure can address the following points effectively: as a scientific project, it is open to participation by any nation/region that is prepared to make a significant contribution; it is driven by in-kind contributions from multiple participants; solid accountability is ensured in both the scientific/technical and budget/financial aspects.

The organisation needs to be able to implement a mechanism that provides long-term stability in terms of maintaining the productivity and continuity of the project, together with the agility to address short-term problems in project execution, in both technical and financial contexts.

The ILC project will go through a number of evolutionary steps towards construction and operation. The early stage of the ILC organisation cannot be completely static because the participating countries/regions may or may not be able to negotiate the necessary approval processes simultaneously. Successful project execution requires a predictable budget with good stability. The ILC project, including construction, will have a life span of 20 years or longer.

The **governance** of a large international science project is a very complex endeavour. There are no precedents for a truly global project without a strong host laboratory. It is crucially important to determine how decisions are made on design and technical issues, who appoints key staff, and the responsibilities of the host when implementing such a project.

A study of other recent major science projects, including ALMA, XFEL, ITER and the LHC was carried out to inform the PIP. Lessons learned from these projects have helped to identify the key considerations for effective governance of the ILC. In developing the ILC *Technical Design Report* (TDR), the importance of defining the responsibilities of the host, having a well established and agreed-to scheme for in-kind contributions, an adequate common fund, etc. were all recognized as important issues. The conclusions and key recommendations of this study with respect to governance have been reported to FALC, ILCSC and publicly at ICHEP 2010. The key points are discussed in the section on governance.

Various **funding models** for a globally supported ILC have been considered in order to understand how it could be built, the responsibilities of the host, etc. Earlier models for the ILC were based on equal sharing among three regions of the world, the Americas, Asia and Europe. Such a model no longer seems viable; instead, a funding model similar to that used in both XFEL and ITER is recommended, namely a "share" system where the "major" partners should contribute a minimum, perhaps 10%, and others would join as members of regional consortia or by making particular contributions. The host nation would contribute a significantly larger share of the construction costs. Running and decommissioning costs need to also be considered and agreed at the time the project is funded.

The responsibilities and the authority of the **project management** and project team need to be determined in advance and must be sufficient to make the team effective. This central management team will be responsible for finalising the design, carrying configuration management, a formal change control process, making technical decisions, maintaining schedules and other responsibilities of project management.

Certain **host responsibilities** are crucial to the success of a global project. The host will need to provide a variety of services similar to those provided by CERN, a successful example of a multi-country large collaborative laboratory. In addition to the necessary contributions to the infrastructure, construction and operations, the host will be expected to achieve status for the ILC laboratory as an international organisation within its local legal system.

Siting is a major issue, from selecting the site to dealing with the configuration and site-dependent aspects of the design and implementation. Technical issues, such as seismic conditions, will need to be considered and a site-dependent design, taking the conditions of a particular site into consideration, will need to be developed by modifying the original generic design. Matters such as access, providing infrastructure, safety, etc. will need to be considered issue by issue in developing the site-dependent design to be implemented. The design will evolve from the configuration-controlled ILC design produced by the global design team; the site-dependent changes will be done through a formal change control process.

It is assumed that the majority of contributions from countries to the ILC will be in the form of **in-kind contributions**. This has the substantial advantage that most resources for the construction, other than civil construction, can be made within the collaborating countries. This is important for political reasons, as well as to build technical capacity within the collaborating countries. However, this scheme comes with major challenges in terms of managing the different deliverables, integrating them, maintaining schedules, dealing with unforeseen cost increases for specific items, etc.

The issues discussed above and options to solve them have been carefully studied. A **flexible** form of in-kind contribution, for example one employing a form of '*juste retour*', is preferable (i.e. each member state receives a guaranteed fraction of the industrial contracts in proportion to the value of their contribution). This gives the central management some flexibility to place the work where it will be the most effective while spreading the work and resources equitably. A very important additional lesson from projects which have in-kind contributions is that sufficient central resources must be made available to effectively coordinate and integrate the project through the central management.

An implementation topic unique for the ILC is **the industrialisation and mass production of the SCRF linear accelerator components**. A model for this production that involves multiple vendors worldwide and a globally distributed model based on the "hub laboratory" concept has been developed. Basically, the proposed cost-effective scheme will use industry for what they do best, large-scale manufacturing, and the participating high-energy laboratories for what they do best, integration and carrying the technical risk for performance.

The overall **project schedule** for ILC construction and commissioning has been analysed; it is dominated by the time to construct the conventional facilities as well as by the time required to construct, install and commission long-lead-time technical components such as the SCRF system. An 8 to 10 year construction, installation and commissioning schedule appears necessary.

Finally, the **future technical activities** that will help continue to advance the ILC towards construction have been analysed. Overall, the project implementation planning has served as an integrated element in developing a technical design for the ILC that can smoothly evolve into a final design and implementation plan for the ILC project once it is approved and funded.

One of the most important, problematic and difficult areas is the transition between the current LC organisation and a fully fledged ILC laboratory with an agreed site, specification and budget. In order to separate these considerations, which necessarily change with time, from the more general principles that pertain to a final organisation, only the structure of the final ILC laboratory is discussed in the PIP.

The subjects outlined above are best analysed assuming a specific roadmap. This is particularly important given the evolutionary nature of the ongoing R&D and the steps to follow when a laboratory organisation for the ILC is formed; some must be done in parallel, some in series, some in national and others in international contexts. Figure 13.1 shows a high-level overview of a possible roadmap towards realisation of the ILC.

One important consideration that should be noted is the separation of technical/scientific and political aspects. Without doubt, the final negotiations and decisions concerning the legal agreements,

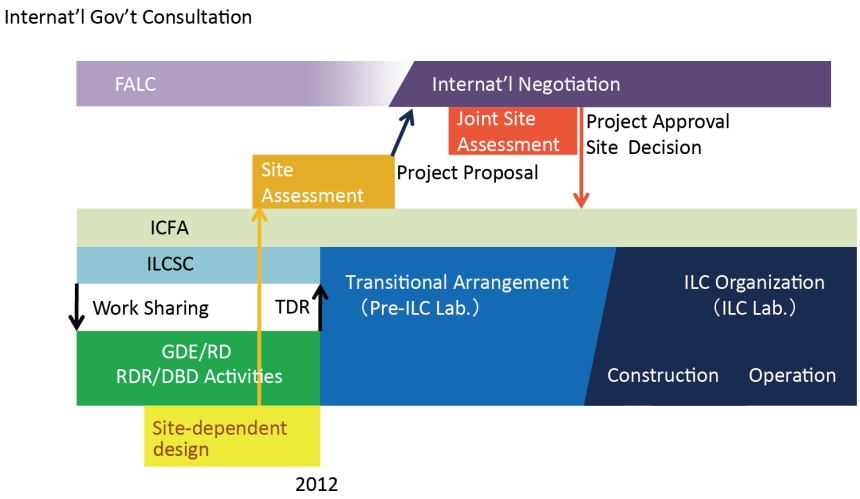

Figure 13.1
Possible roadmap towards realisation of the ILC

budget sharing and site selection for the ILC will have to be made by the appropriate government agencies of the interested nations/regions. On the other hand, the technical contexts and resultant boundary conditions or specifications for the project (such as the base performance parameters and/or the technical specifications for possible sites) should be dictated by the scientific requirements. It is thus important to identify where the responsibilities of scientists end, and where those of the government officers and statesmen begin.

In the area of government-level discussion regarding the ILC's future development, the Funding Agencies for Large Colliders (FALC) currently holds regular meetings. Once the project is ready to be formally proposed, a suitable forum to discuss the necessary arrangements should be formed.

Chapter 14
Construction schedule

14.1 Introduction

This chapter provides an overview of possible ILC construction schedules for the flat and mountain topography design variants. It updates the study published in the RDR and goes further to cover all major steps from construction to final commissioning. It provides a list of level-1 milestones (top level, a few for the whole project) that can be used to compare various scenarios and later to track project progress. All three sample regions (Europe, Americas and Asia) are considered.

Because of the assumed in-kind nature of the ILC project, this construction schedule should be regarded a target baseline schedule that can be used to plan the pace of various activities, the need for multiple shifts for particular activities, etc., rather than a solid schedule estimate. A more accurate schedule can only be developed after a specific site has been selected and the in-kind contributions to the project have been explicitly defined. *Component or system delivery schedules, with appropriate contingencies, will be an important part of negotiations and agreements between collaborators and the project management.*

14.2 Scope and assumptions

The scheduling exercise that is presented in this section focuses on three major steps: construction; installation; and commissioning. A first attempt is made at considering the constraints on the high-tech component mass-production schedule. Other important activities like the R&D programs or procurement processes are not included. The scope of this exercise is to show how the ILC, including the detectors, could be built and delivered for operation at the selected sample sites.

The origin of time considered in what follows is the start of construction work. The mobilisation of equipment and manpower referred to as "site set-up" is omitted. Taking the CERN LEP project as benchmark, this is an activity that can take up to 6 months. It includes building the personnel-support facilities (changing rooms, rest rooms, catering areas) throughout the building sites and the completion of the construction of access roads. Storage facilities required to launch the first steps of the construction, such as parking lots, warehouses, and tip yards, are also assumed to be available.

The acquisition of the land on which the ILC is to be built is also assumed to be complete. This is a step that can take a significant amount of time depending on the location chosen. It is affected by environmental studies, the final layout of the facility and the local context (density of population, accessibility, etc.). For the European sample site, this process will take at least a year.

In what follows, the focus is the critical path of the work sequence. At a later stage the remaining activities that can be carried out in parallel will need to be added. For monitoring purposes, it might be considered to develop an Earned Value Management tool to track the progress of all activities and not only the ones on the critical path. This was successfully used during the construction of the LHC at CERN.

The time estimates that are used in this scheduling exercise are the result of an assessment based

on past and on-going projects. The LHC, XFEL and CMS projects have been used most extensively as references. They are all recent and relevant scientific projects. A motorway built in Japan has also been used as it is located in a mountainous region and requires excavation techniques relevant to the ILC project.

Table 14.1 shows reference projects for those relevant areas where ILC time estimates are needed.

Table 14.1
ILC time estimates and reference projects

Activities	Shaft excavation	Tunneling	Cavern construction	Accelerator components installation	Detector installation	Accelerator commissioning	Cooling and ventilation installation	Electrics installation
LHC			×	×		×	×	×
CMS					×		×	
XFEL				×		×		
LEP	×	×						
JP motorway		×						

Progress rates depend heavily on the organisation of working time. In some cases, workers should be asked to work in shifts. In other cases, having too many workers in the same area is detrimental to efficient working conditions. When using valuable pieces of equipment that are energy and manpower intensive, a three-shift system is recommended. This is most particularly the case with Tunnel Boring Machines or TBMs. In this study, it is assumed that the progress rates stated for TBMs are for three shifts and can therefore not be speeded up. Table 14.2 sums up the progress rates that have been used for the main linac to reach the corresponding time estimates.

This study considers two types of topography. The flat topography (FT) applies to the sample sites located in European and Americas. The mountainous region (MR) applies to the sample site located in Asia.

Table 14.2
ILC time estimates and progress rates

Activity in Main Linac	Region	Progress rates (m/week)	For x shifts
Tunnelling using 8m ⌀TBM	FT	100	3
	MR	n/a	
Tunnelling using 5.2 m or 6 m ⌀TBM	FT	150	3
	MR	n/a	
Tunnelling using 6 m–8 m ⌀road header or 'Drill and Blast' (NATM)	FT	30	3
	MR (NATM)	20	3
Concreting, invert and tunnel finishing	FT	50	3
	MR	Concrete lining 25 Invert, drainage 45	3
Ventilation ceiling-ducts installation	FT (Europe only)	50	3
	MR	n/a	
Survey and set out of components supports	All	120	1
Electrics General Services	All	120	1
Piping and ventilation	All	120	1
Cabling	All	120	1
Installation of supports for machine components	All	250	1
Installation of machine components	All	100	1

The number of teams working in a given location is a parameter that can have great impact on the overall progress rate. It might appear tempting to inject more manpower in a particular activity. However, experience with the LHC has proven that this temptation should be resisted. Particularly for space-consuming activities, it is preferable to leave plenty of space for a team to work. When appropriate, this study looks at the impact of doubling the number of teams in action in a sector

(section of tunnel between two shafts). In addition to space management, it is important to also balance the benefits of injecting more resources against the required delivery date of a sector. For example, if the commissioning of a sector requires the availability of several facilities, the number of teams should be chosen in order to minimise the time spent waiting for the last facility to become available. This consideration was used when optimising the workflow.

Working time is another parameter that can have a significant impact on progress rates. In this study we assume that work will be carried out five days a week. No public holidays have been taken into account.

Fulfilling the commissioning objectives is a driving force behind this scheduling study. An attempt is made at describing how to go from an installed facility to an operational one, which requires consideration of not only accelerator facilities but also the detectors.

This study is based primarily on the latest ILC European and Asian layouts. At this stage, it is reasonable to assume that the Americas' layout will not introduce major changes in the schedule compared to the European one. The Asia ILC layout is significantly different from the European and American ones and required a specific study. The naming convention used to refer to the various parts of the accelerator is the one designed for the European region (see Fig. 14.1).

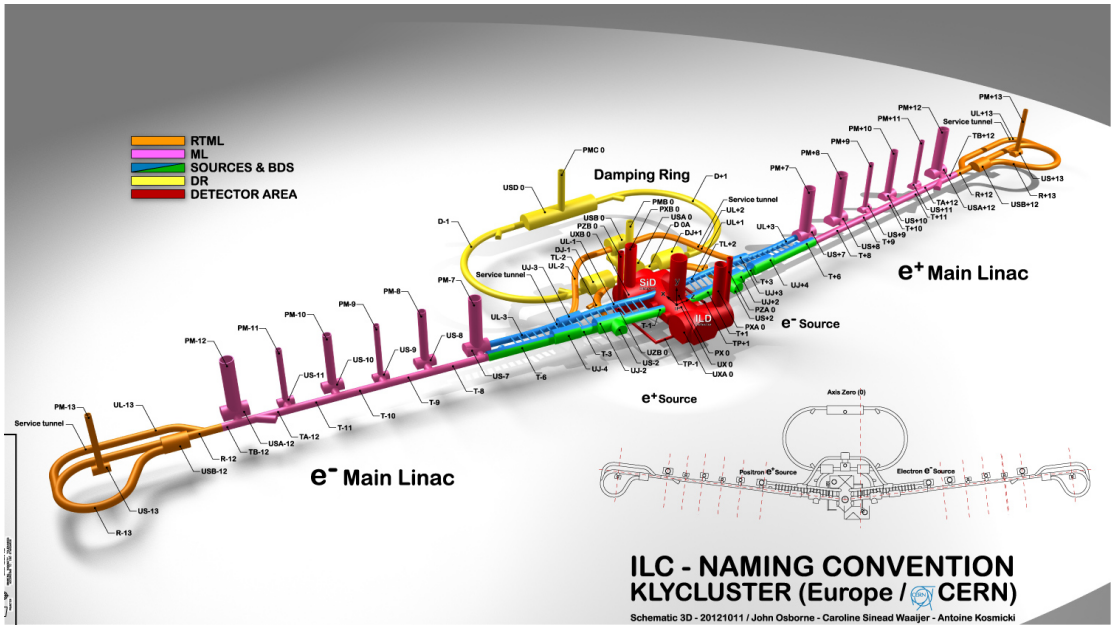

Figure 14.1. European ILC layout

The three following sections present the construction of the accelerator complex and high-tech mass-production plans, the commissioning plans and the detector installation and will refer to these figures.

14.3 Constructing the accelerator complex

The schedule of the three main phases involved in the delivery of the accelerator complex are discussed below: civil engineering; installation of common facilities; and accelerator component installation. A graphical representation for the complete construction and commissioning schedules for the flat and mountain topography design variants is given in Fig. 14.2 and Fig. 14.3, respectively. These figures will be referred to in the following sections.

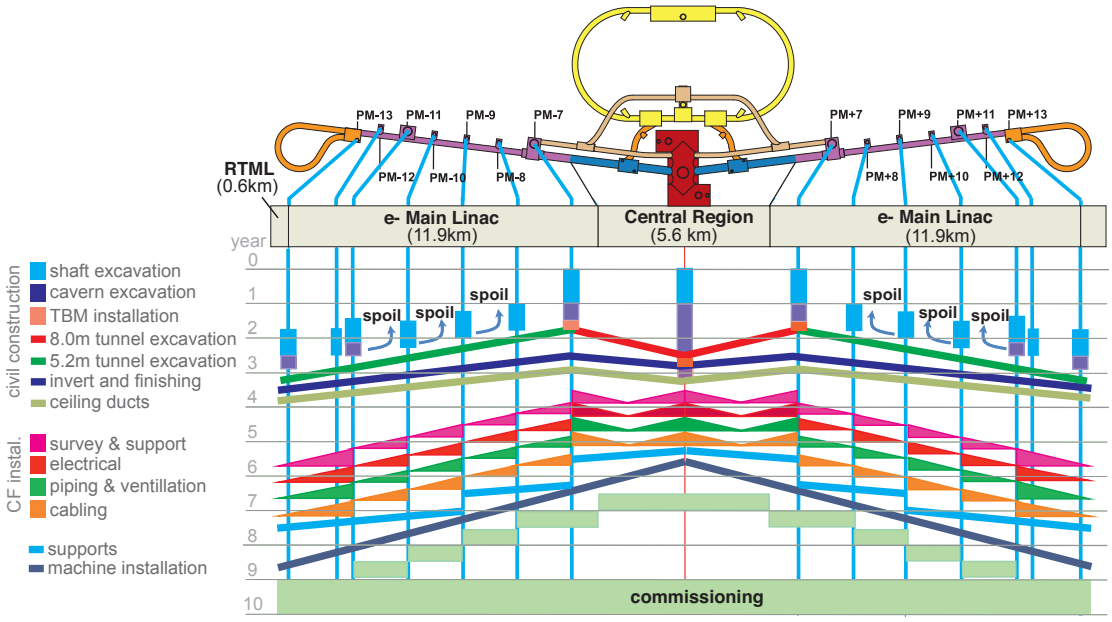

Figure 14.2. The construction and commissioning schedule for the flat topography design variant. Years after construction start are represented vertically, while construction progress along the machine footprint is indicated horizontally (not to scale). The vertical lines represent the locations of shafts.

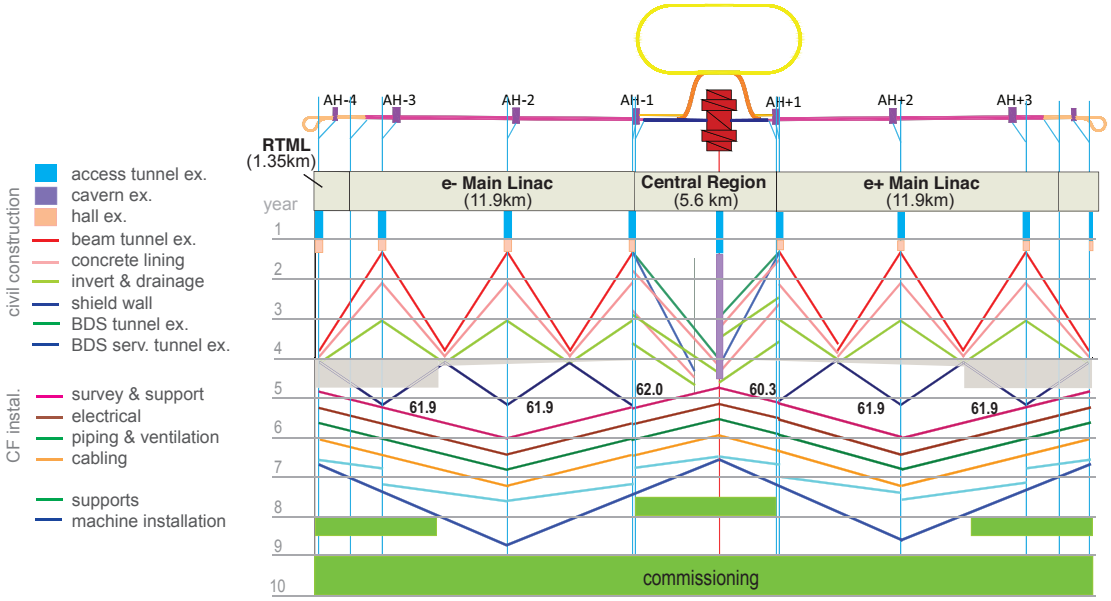

Figure 14.3. The construction and commissioning schedule for the mountain topography design variant. See Fig. 14.2 caption for details.

14.3.1 Civil engineering

14.3.1.1 Flat-Topography Sites

The ILC layouts that are being considered in this study are significantly different from the one presented in the RDR. The Main Linac and BDS consist of a single tunnel of varying diameter. For the FT sites, it was decided that using two types of TBMs with respective diameter of 8 m and 5.2 m would facilitate the construction. Figure 14.4 shows where each type of TBM is to be used.

The civil construction phase is expected to be complete in the first four years of of the construction schedule (Fig. 14.2 years 1–4). The first step in the civil engineering (CE) phase is to excavate the access shafts that will be used to launch the TBMs and start excavating the caverns in the interaction region. Experience from LHC implies one year is necessary to deliver a fully equipped shaft.

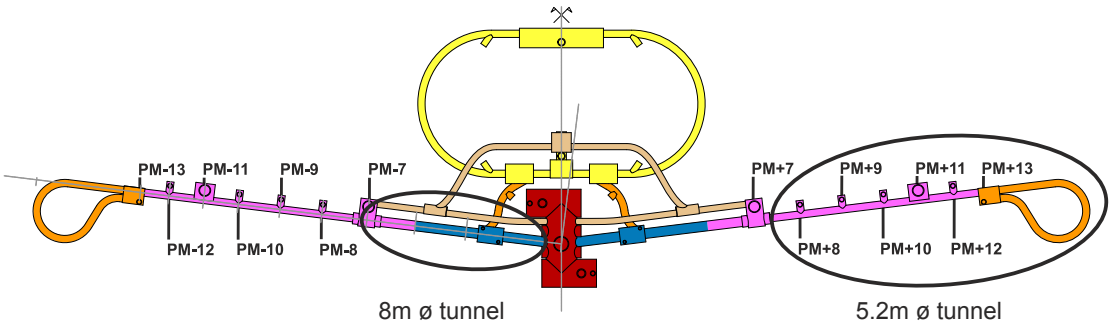

Figure 14.4. Choice of TBMs

Results of the ARUP/J Osborne studies [172] recommend minimising stress concentration on the interaction region by excavating and finishing the interaction cavern before tackling the tunnels and service caverns. This leads to the choice of PM7 as the location to launch the TBMs. By the time they reach the IR, the caverns will be excavated and finished.

Once a tunnel section is excavated, the next step is to build the invert and complete the finishing. The progress rate for these steps has been stated in Section 14.2. In the case of the European design, concrete ventilation ducts will be formed on the ceiling. A light-green line in Fig. 14.2 year 4 represents this activity.

14.3.1.2 Mountainous Region site

Years 1–5 of Fig. 14.3 shows the schedule for the civil-engineering phase of the construction schedule for the MR site. The MT site requires excavating horizontal access tunnels as opposed to shafts. Fourteen of these tunnels and the interaction cavern have to be excavated concurrently. Once a long enough section of an access tunnel is made available, the concrete lining activity should start. The next step consists in constructing the invert and drainage system. Finally, the shielding wall has to be erected inside the Main Linac tunnel. This activity will take a full year as the progress rate is 45 m/week.

At this stage. a first set of level-1 milestone can be extracted and are shown in (Table 14.3).

Table 14.3
The first set of level-1 milestones.

Milestone	Flat topography	Mountainous region
Civil Engineering work complete	Y4, Q4	Y5, Q1

14.3.2 Conventional facilities installation

This phase of the construction schedule studies the installation of the supporting infrastructure such as survey and setout supports for accelerator components, electrical general services (cable trays, cables, sockets), infrastructure for cooling and ventilation (pipes, ducts), and accelerator cables.

14.3.2.1 FT sites

Figure 14.2 years 4–7 shows the schedule for the conventional facilities installation. It has been chosen to exclude 2 activities of a different nature sharing the same tunnel section. The number of teams deployed has a significant impact on the completion date of this phase. In what follows it has been chosen to inject 4 teams in the BDS regions and only 2 in the main linac. This choice is justified by the progress rate of the subsequent activities.

14.3.2.2 MR site

The progress rates and the installation sequence for all the activities considered in this phase are the same as for the FT sites. However, due to the shielding-wall partition in the tunnel, it has been chosen to allow activities of different natures to unfold in the same location. (see Fig. 14.3 years 5–7.) A set of level-1 milestones for this phase is shown in Table 14.4.

Table 14.4
The second set of level-1 milestones.

Milestone	Flat topography	Mountainous region
Civil Engineering work complete	Y4, Q4	Y5, Q1
Common Facilities installed	Y7, Q3	Y8, Q2

14.3.3 Accelerator-Components Installation

This phase consists in first installing accelerator components and their supports. At that stage, the high-tech mass-manufacturing process has to provide the required components. In order to allow for an early commissioning exercise to take place, the schedule has been designed to install accelerator components in the Central Region first. The estimated progress rates are the same for the MR and FT sites.

14.3.3.1 FT sites

Based on experience at the LHC, only two teams are deployed for the installation of the accelerator components and their supports. The installation phase is shown in years 6–9 of Fig. 14.2.

14.3.3.2 MR site

For reasons already given in the previous section, four teams are deployed to install the accelerator components. The installation rates are the same as for the FT. However to reduce potential overcrowding and increase the productivity and efficiency, installation activities for the MT site will be spread over 3 shifts per day. The machine installation can be seen in years 7–9 in Fig. 14.3. The level-1 set of milestones for this phase are given in Table 14.5.

Table 14.5
The third set of level-1 milestones.

Milestone	Flat topography	Mountainous region
Civil Engineering work complete	Y4, Q4	Y5, Q1
Common Facilities installed	Y7, Q3	Y8, Q2
Accelerator ready for early commissioning (BDS and ML up to PM7/AH1)	Y7, Q2	Y8, Q2
ILC ready for full commissioning (whole accelerator available)	Y9, Q4	Y9, Q4

14.3.4 High-tech Mass-Production Plans

Figures 14.5 and 14.6 are a first attempt to match the manufacturing plans of the accelerator parts with the construction schedule. Each figure shows the mass-production plans in the background. The time window dedicated to installation of the accelerator components for the FT and MR is depicted by a coloured rectangle and has been superimposed. The resulting figures show the time constraints of both activities.

For both types of sample site it appears that the components will be ready on time to start the installation of the accelerator. The Asian-region schedule allows for a longer production time of the accelerator parts.

A more detailed study is needed to show how the production, storage and installation rates can be optimised.

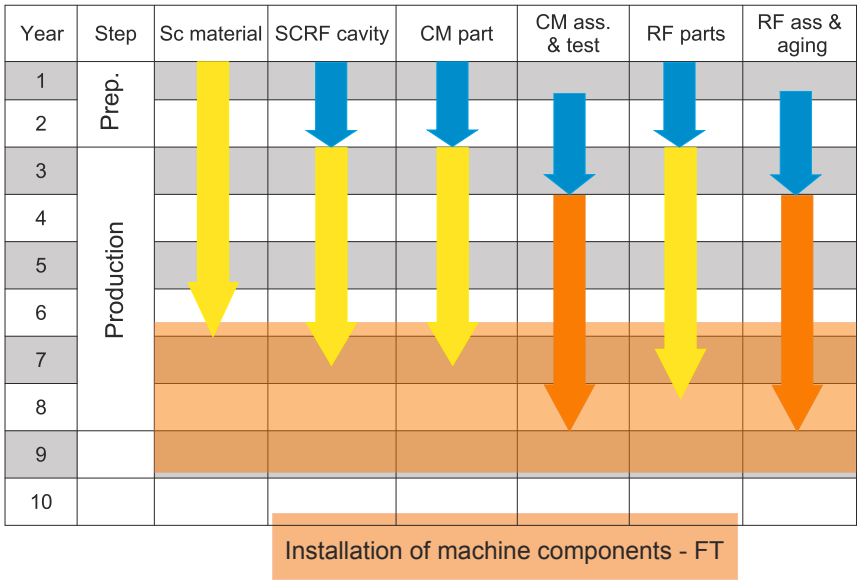

Figure 14.5
Production plans for FT.

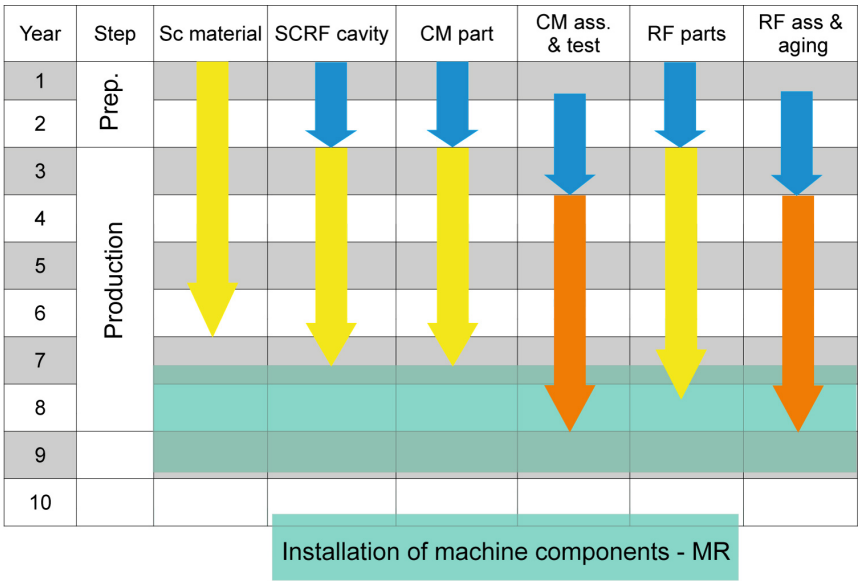

Figure 14.6
Production plans for MR.

14.4 Commissioning the ILC

14.4.1 Early Commissioning (BDS, part of ML, DR, and PLTR)

An early commissioning draft plan has been prepared for this study. The key objectives, together with their foreseen durations, are:

- test of the e^- injector system to 5 GeV and dump: 3 months;
- test of the e^+ source and systems to 5 GeV and dump utilising the auxiliary low current e^- source to produce e^+: 3 months;
- hardware commissioning of injection lines and both damping rings: 3 months;
- commission both rings with beams from injectors with extraction only into first dump in the PLTR (beam still in injection/extraction tunnels): 9 months.

This commissioning exercise requires the availability of the BDS and main linac up to PM7/AH1, the PLTR, and both Damping Rings. In what follows, only the FT sites are considered; a similar study can be carried out for the MR site.

It has been established that the BDS and necessary sections of the Main Linac will become available in Y7 Q2 for the FT sites. In order to assess the feasibility of the early commissioning plan,

a construction schedule of the DR and PLTR has been built.

The Damping Rings are houses in a 6 m diameter, 3259 m-long tunnel. It will be excavated using a road header at a rate of 150 m/week using 3 shifts a day. The PLTR consists in two 6-8 m diameter, 250 m long tunnels. These tunnels are to be excavated using road headers at a rate of 30 m/week using 3 shifts a day.

Table 14.6 shows the assumptions made for developing the DR and PLTR installation plan.

Table 14.6
Assumed progress rate for installation in the DR and PLTR tunnels.

Progress rate	DR (m/w)	PLTR (m/w)
Invert and finishing	250	250
Survey	120	120
Electrics	80	120
Piping and ventilation	80	120
Cabling	80	120
Supports	250	250
Accelerator components	50	100

The Gantt chart in Fig. 14.7 shows that the DR and PLTR should be ready for early commissioning by Y7 Q1. This means that by the time the BDS and ML become available for early commissioning, the DR and PLTR should also be ready. The commissioning exercise would then start by Y7 Q2.

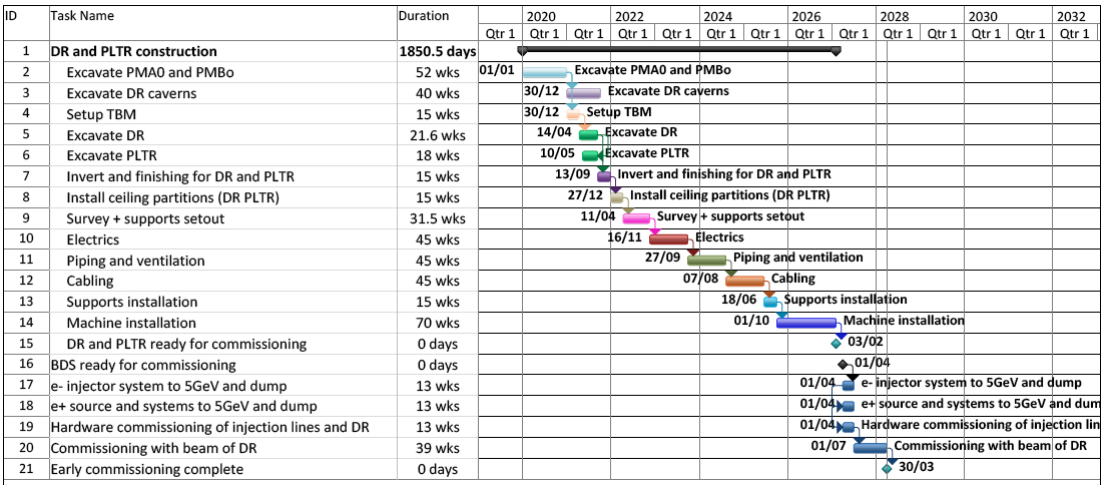

Figure 14.7. Draft schedule for delivery of DR and PLTR for commissioning

14.4.2 Global commissioning

It is challenging to assess how much time would be needed for the commissioning of the ILC. Based on experience at LHC, 6 months of pre-commissioning per sector would be necessary. In addition, 12 months would be needed to complete the final global commissioning.

Global commissioning is indicated in year 10 in Fig. 14.2 and Fig. 14.3 for flat and mountain topography sites respectively. Level-1 milestones for the commissioning phase are listed in Table 14.7.

Table 14.7
The fourth set of level-1 milestones.

Milestone	Flat topography	Mountainous region
Civil Engineering work complete	Y4, Q4	Y5, Q1
Common Facilities installed	Y7, Q3	Y8, Q2
Accelerator ready for early commissioning (BDS and ML up to PM7/AH1)	Y7, Q2	Y8, Q2
ILC ready for full commissioning (whole accelerator available)	Y9, Q4	Y9, Q4
ILC ready for physics programme	Y10, Q4	Y10, Q4

This study shows that it would be possible to build and commission the ILC in less than 10 years. This statement holds for both the FT and MR sites. The scheduling studies will continue so as to incorporate any new modifications to the designs and implications on the availability of resources.

14.5 Detectors

This study presents the basic structure of an ILC detector construction, underground installation and commissioning schedule. The scenario considered focuses on the ILD detector for a Flat Topography site. The applicable layout of the interaction region is shown in Fig. 14.8.

Figure 14.8
Layout of the interaction region in a Flat Topography site

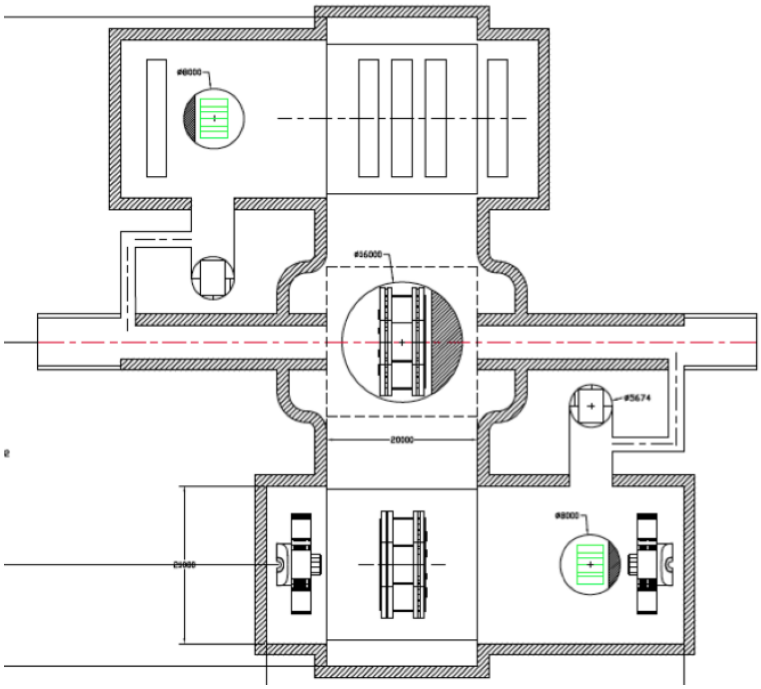

Using the CMS concept, the ILD detector is to be assembled in a surface hall before being lowered to the underground facilities. This allows work underground to proceed unaffected by the construction of the detector. In a first stage, two-thirds of the surface hall will be assembled and handed over to the detector-construction crew. At a later stage, the building will be completed to include the shaft linking the building to the underground facilities. The important milestones to extract from this scheduling study are the "Caverns ready for beneficial occupancy", "Detector ready to be lowered" and "Detector ready for commissioning with beam". The Gantt chart in Fig. 14.9 presents a preliminary schedule for the construction of the ILC interaction region.

	Task Name	Duration
1	ILC construction started	0 days
2	Excavate 2 shafts	12 mons
3	Construct of 2/3 of Surface Assembly Halls	12 mons
4	Excavate and finish Detector Caverns	24 mons
5	Assemble and commission Detectors	1280 days
6	Construct Surface Service Buildings	24 mons
7	Install Caverns Infrastructure	44 mons
8	Complete 1st Surface Assembly Hall	12 mons
9	Complete 2nd Surface Assembly Hall	12 mons
10	Install Crane for Heavy Lowering	4 mons
11	Detector Caverns ready for beneficial occupancy	0 days
12	Lower Detectors	150 days
13	Connect detectors to their services	11 mons
14	Commission Detectors & Push-Pull	12 mons
15	Ready for commissioning with beam	0 days

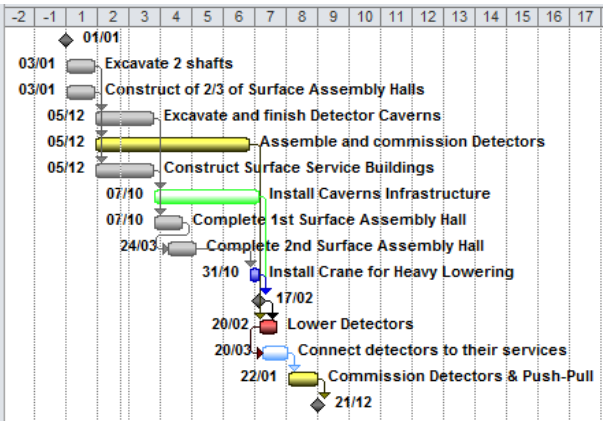

Figure 14.9. Flat Topography Interaction Region construction schedule

From this study, it appears that the caverns should become available for detector installation by Y7Q1.

Using this milestone, the Gantt chart in Fig. 14.10 originally produced by the ILD community has been modified. It shows the three phases of the detector activities:

- detector construction on the surface;
- lowering and installation in the underground cavern;
- commissioning without beam.

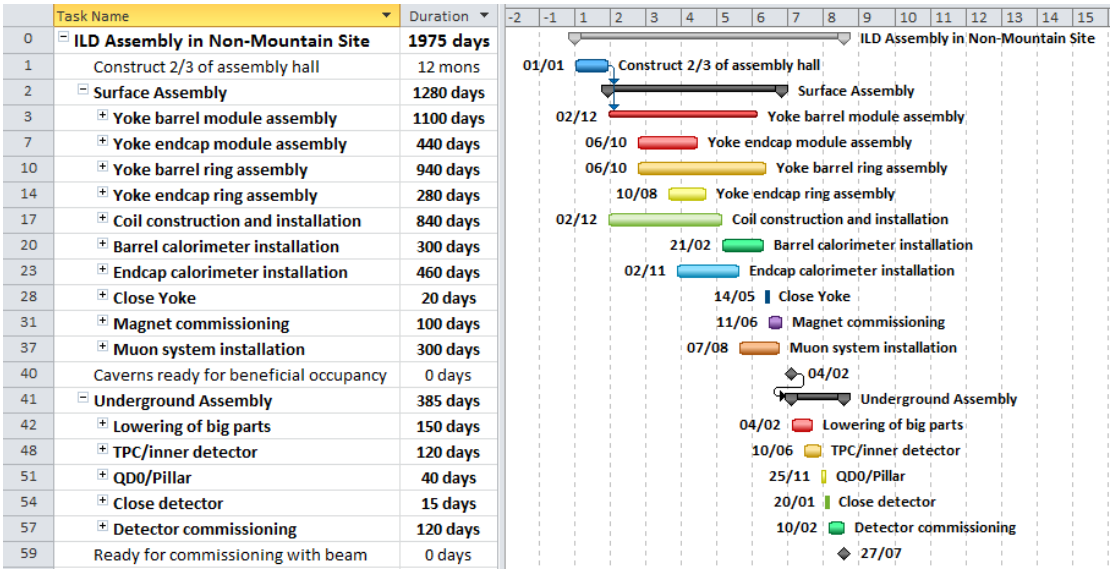

Figure 14.10. ILD construction schedule for Flat Topography sites

One conclusion of this study is that by the time the detector community is ready to start the detector-lowering phase (Y7Q1), the cavern will be available for beneficial occupancy. It also shows that by the end of year 8 the detector should be ready to be commissioned with beam. This means that the Push-Pull system should also be ready.

The commissioning of the detector together with the Push-Pull system should be seen as a separate exercise. This is reflected in Fig. 14.9 were the commissioning task lasts till Y8 Q4. The commissioning task in Fig. 14.10 only reflects the commissioning of the detector in parking position (finished by Y8Q3).

The detector readiness for beam should therefore coincide with the beginning of the accelerator final-commissioning phase. However, in order to decouple the commissioning of the accelerator from the commissioning of the detectors, it would be wise to plan the use of a temporary beam-pipe that would allow the beam to be circulated through the interaction region even if no detector can be put in beam position.

A final set of milestones can be extracted from the detector scheduling studies (see Table 14.8).

Table 14.8
The fifth set of level-1 milestones.

Milestone	Flat topography	Mountainous region
Civil Engineering work complete	Y4, Q4	Y5, Q1
Common Facilities installed	Y7, Q3	Y8, Q2
Accelerator ready for early commissioning (BDS and ML up to PM7/AH1)	Y7, Q2	Y8, Q2
ILC ready for full commissioning (whole accelerator available)	Y9, Q4	Y9, Q4
ILC ready for beam	Y10, Q4	Y10, Q4
Caverns ready for beneficial occupancy	Y7, Q1	
Detector ready to be lowered	Y7, Q1	
Detector ready for commissioning with beam	Y8, Q3	

The detector hall for the Mountain Topography layout differs significantly from that of the Flat Topography (see Fig. 14.11). Access to the hall is via horizontal access tunnels rather than shafts, which limits the size of the components that can be brought into the detector hall. Therefore much of the detectors will need to be constructed in the detector hall similar to the approach used for ATLAS at the LHC. Although not as detailed as the surface construction schedule for the Flat Topography site, preliminary studies have indicated that the underground detector assembly is feasible within the same overall time frame.

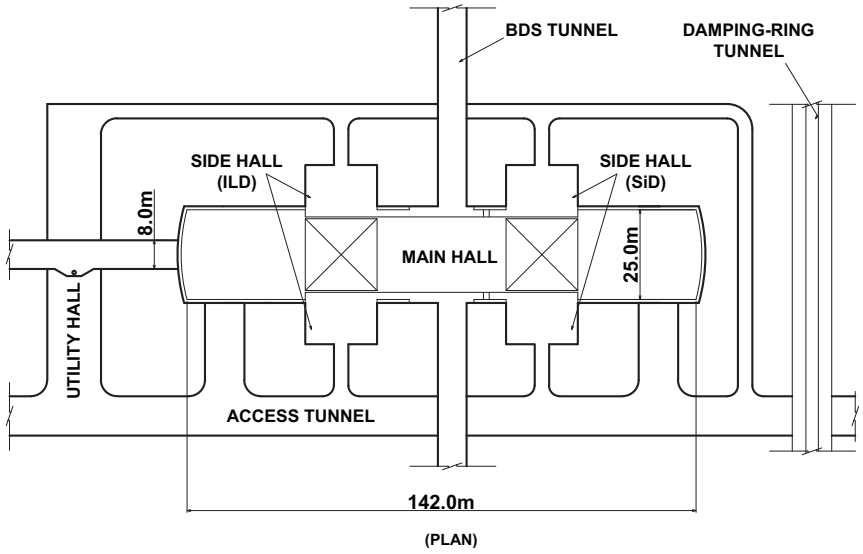

Figure 14.11
Layout of the interaction region in a MoutainTopography site

Chapter 15
ILC TDR Value Estimate

15.1 Introduction

This chapter presents a high-level summary of the International Linear Collider Technical Design Report (ILC TDR) Value estimate. The details of the costs and the cost basis are contained in the Engineering Document Management System (EDMS) technical-design documentation files, many of which are referenced in this chapter.

Throughout the chapter, the estimate will be referred to as a "Value" estimate. This is to emphasise that its scope is limited relative to cost estimates which may be developed based on region-specific guidelines or practices. The Value estimate omits a number of items (for example, pre-construction, contingency, escalation during project execution, commissioning with beam, etc.) that would be included in some region-specific cost estimates. The precise scope of the Value estimate will be presented in detail below.

15.1.1 Overview

This overview provides a brief summary of the contents of each section of this chapter.

15.1.1.1 Goals and scope

The ILC TDR Value estimate is for a machine of 500 GeV centre-of-mass energy, but includes some items rated for 1 TeV to enable a later energy upgrade. The scope is clearly defined by stating what is included, and what is excluded, in the estimate.

15.1.1.2 Methodology

As is appropriate for a project likely to be funded mainly by in-kind contributions, the Value-estimating methodology is used. The reference currency (the "ILCU") is the United States dollar (USD) as of January, 2012. In order to eliminate regional price distortions related to exchange rates, conversions from other currencies to ILCU are based on purchasing-power-parity (PPP) indices published by the Organisation for Economic Co-operation and Development (OECD). The motivations for, and issues related to, the use of PPP indices are discussed, and the PPP indices are compared graphically with exchange rates over the past 6 years.

15.1.1.3 Cost Guidelines and Learning Curves

One important general guideline is that at least two vendors are assumed for industrial procurements. Specific guidelines are defined for specialised cost elements, such as cavities, cryomodules, and conventional facilities. One important specific guideline is that the cavities and cryomodules are fabricated by industrial vendors based on build-to-print specifications. Performance is guaranteed through testing using labour and facilities provided by collaborating host laboratories. General considerations on the use of learning curves are presented in the final part of this section.

15.1.1.4 Development and Format of the Estimate

Approximately 75 % of the TDR estimate has a new cost basis; the remaining 25 % is taken from the RDR. The format in which the TDR estimate will be documented in EDMS is presented.

15.1.1.5 Cost Basis

For cavities and cryomodules, the cost bases selected for the TDR are described. Other sources of cost information, including those used for the International Linear Collider *Reference Design Report* [3] (RDR) estimate, are presented, and the reasons for selecting the TDR cost bases are explained. For L-band high-level RF systems, a similar discussion is provided. In this case, there are different bases for the flat- and mountainous-topography sites.

The cost bases for the major elements of the conventional facilities are presented. The civil-engineering cost bases for the three regional sites are discussed. Differences between the regional cost bases, resulting from site-specific factors, are explained. The cost bases for the conventional electrical, mechanical and safety systems for the Asian and Americas sites are also discussed. Finally, the cost bases for handling systems, and for survey and alignment are described.

Subsequently, the cost bases for the following technical or administrative areas are presented: installation, cryogenics, magnets and power supplies, vacuum, instrumentation, controls and computing infrastructure, other high-level RF systems, management and administration, and cost elements specific to some of the accelerator systems.

15.1.1.6 Value and Labour Estimates

To provide a reference for comparison, the RDR estimate is re-stated in terms of the 2012 ILCU, using the inflation indices presented in Section 15.1.2. The TDR Value estimate is then presented, broken down into subsystems. The total explicit Labour estimate, broken down by subsystem, is presented. The site dependences of the Value and Labour estimates are presented and discussed.

15.1.1.7 Cost Uncertainty

Uncertainty estimates have been made for each cost element in the TDR. The uncertainties are based on the design maturity of the item, the level of associated technical risk, the source and quality of the cost or Labour information, and the extent, if any, of scaling to large quantities. Tables of the cost-uncertainty parameters for the major Value elements in the TDR estimate are presented.

For each cost element, the fractional level of cost increase required to reach the 84 % confidence level was computed. This cost increase is called a "cost premium". The cost premiums were summed over groups of cost elements, to provide a conservative estimate of the overall cost premium required to reach the 84 % confidence level for that cost-element group. These summed cost premiums are presented graphically, broken down by system, and the overall cost premium for the total project is presented.

In a similar way, premiums on the Labour estimate are developed. Summed labour premiums, broken down by system, are also presented, and the overall Labour premium required to reach the 84 % confidence level on the Labour estimate is presented.

15.1.1.8 Value and Labour Time Profiles

Given the schedule described in Chapter 14, and the Value and Labour estimates given in Section 15.8, profiles describing the Value and Labour resources needed as a function of time have been developed. These profiles assume a flat funding profile for the major civil and technical procurements for each accelerator system, which is a crude assumption, but one which captures the essential features of the overall project resource requirements.

15.1.1.9 Value and Labour Estimates for Operations

A top-down estimate of projected operating costs is presented.

15.1.1.10 Value and Labour Estimates for Upgrade and Staging Options

This section estimates the Value and Labour changes associated with the upgrade and staging options described in Chapter 12 of the *Technical Design Report*.

15.1.2 Inflation Indices

Many of the cost bases used for the TDR are stated in currencies as of a date different from the TDR reference date (January, 2012). For example, any estimates taken from the RDR are generally stated in 2006 or 2007 currencies. All costs used in the TDR estimate have been escalated to the TDR reference date. The inflation index used depends on the cost element type (either "civil engineering", which refers to all civil engineering cost elements, or "machinery and equipment", which refers to all other cost elements), and on the region in which the estimate was made. The regional [1] inflation indices [241–247] are shown in Fig. 15.1. After escalation, costs were re-stated in ILCU, using PPP indices for currencies other than the USD, as discussed in Section 15.4.2.

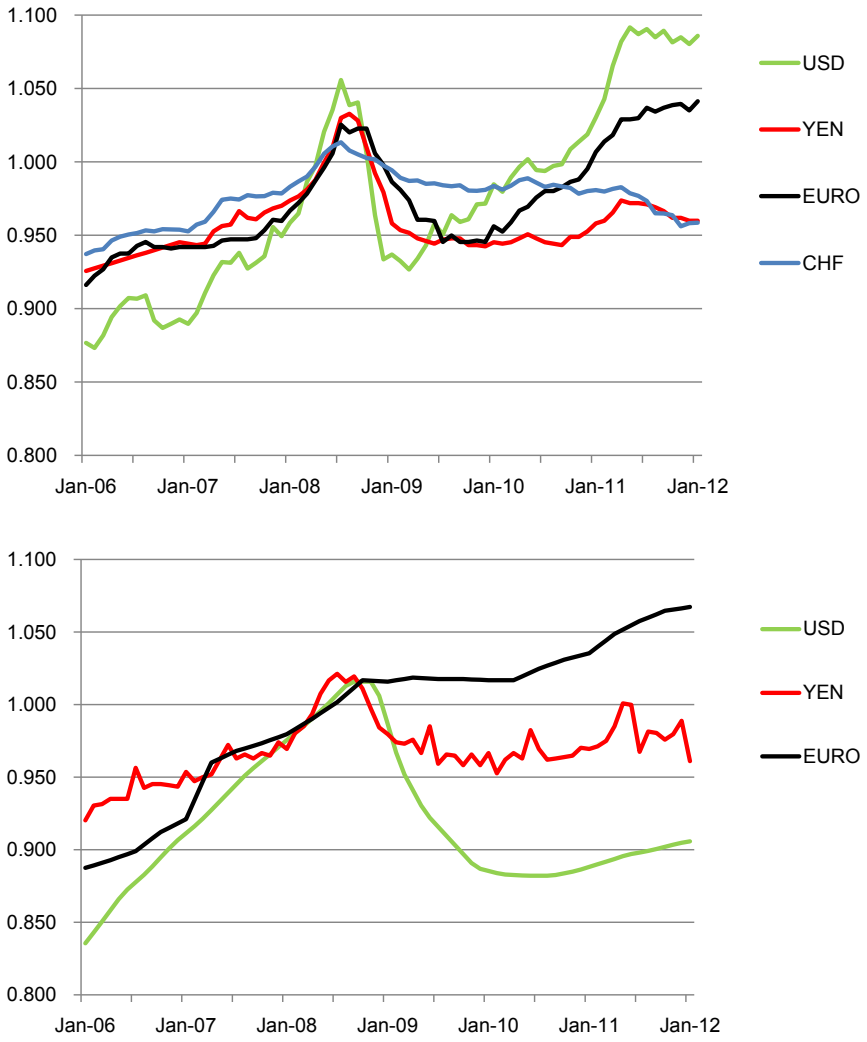

Figure 15.1 National inflation indices. Top: machinery and equipment; Bottom: civil engineering

[1] The inflation indices for the Euro were taken to be those of Germany, the dominant manufacturing economy which uses the Euro.

15.2 Goals

The ILC TDR Value estimate is a comprehensive and well-documented estimate of the resources required to build the ILC, as described in the *Technical Design Report*. The project is intended to be funded by a mixture of cash and in-kind contributions from a collaboration of countries or regions around the world. The ILC TDR Value estimate should:

1. allow funding agencies in nations that are considering in-kind contributions to the ILC project to assess the nature and scope of resources needed for the project;
2. provide detailed information on cost drivers and cost trade-offs which can be used in the pre-construction phase for further cost-optimisation of the project through value engineering and R&D.

15.3 Scope

The ILC TDR Value estimate is made for a machine of 500 GeV centre-of-mass energy, but it includes some items rated for 1 TeV, such as the beam dumps and the Beam Delivery tunnel, to enable a later energy upgrade. The estimate does not include the cost of the detectors. They are assumed to be funded by a separate agreement between the collaborating institutes, in the way the LEP and LHC detectors were built. The estimate does include civil engineering work for the detectors, e.g. assembly buildings, underground experimental halls, shafts, etc. Table 15.1 summarises the items that are included in, or excluded from, the estimate.

The estimate assumes a 9-year construction period (see Chapter 14). The estimate for a given item covers the cost from the day the project obtains funding until that item is installed, tested, and ready for commissioning. Commissioning in one area may overlap with construction elsewhere. The construction period covered by the Value estimate ends when the last component has been installed and tested, and the machine is ready for commissioning with beam.

Table 15.1
Summary of the items that are included in, or excluded from, the ILC TDR Value estimate.

Included	Excluded
Construction, installation, and hardware commissioning costs for a 500 GeV machine	Beam commissioning, operations, decommissioning
Tooling-up industry, final engineering designs and construction management	Engineering, design, or preparation activities that can be accomplished before construction starts, such as research & development, and prototype systems tests
Construction of all conventional facilities, including the tunnels, surface buildings, access shafts and other facilities	Pre-construction costs (e.g. architectural engineering, conceptual and construction drawings, component and system designs), surface land acquisition and underground easement acquisition costs
Construction of the detector-assembly building, underground experimental halls and detector-access shafts	Experimental detectors
Explicit labour, including that for management and administrative personnel.	Taxes, contingency and escalation
Costs for upgrading the machine to 1 TeV which would be very difficult to provide after construction of the 500 GeV machine (e.g., beam dumps, BDS length).	Additional costs due to potential overheads related to management of in-kind contributions

15.4 Methodology

15.4.1 Definition of Value Estimating

In order to achieve the first goal stated in Section 15.2, the ILC TDR Value estimate must be structured so that it can be useful to all potential collaborators. Each of these collaborators may have different currencies, and different traditions and conventions for planning and estimating the cost of large projects. In order to divide up these in-kind contributions equitably among the collaborators, a project estimate that is independent of any particular accounting system but compatible with all of them must be developed. The "value-estimating methodology" for stating this estimate has become the standard for such international projects. It was adopted by ITER (the International Thermonuclear Experimental Reactor project) and by the LHC (Large Hadron Collider) experiments, among others.

As expressed using the "value-estimating methodology", the ILC TDR Value estimate consists of two important parts:

- Value[2] (in terms of currency units) for items procured from vendors. The Value of a component is defined as the lowest reasonable estimate of the procurement cost of an item with the required specification and in the appropriate quantity, based on production costs in a major industrial nation. It is expressed in current-year currency units (not escalated to the years in which the funds are projected to be spent) and does not include R&D, pre- or post-construction, beam commissioning, operating costs, taxes or contingency. It is effectively the barest cost estimate that would be used by any of the funding agencies. Individual regions can then add to the base Value any other items usually included in their own estimating system;
- Labour[3] (in terms of person-hours). In this context, Labour is defined as "explicit" labour, which may be provided by the collaborating laboratories and institutions, or may be purchased from industrial firms. This to be distinguished from a company's "implicit" labour associated with the industrial production of components and contained (implicitly) within the purchase price. The implicit labour is included in the Value part of the estimate.

The ILC TDR Value estimate, stated in terms of Value and Labour, is the basis on which contributions may be apportioned among the collaborators. Each participant makes an agreement with the ILC project management to provide a certain amount of Value and Labour to the project, which may be in the form of in-kind component and service contributions. The ILC TDR Value estimate documents the specific project items associated with these Value and Labour contributions. The collaborators are then responsible for providing these contracted items, independently of what they may cost as measured by national accounting systems.

15.4.2 Definition of the ILCU for the TDR

One of the key elements of the Value-estimating methodology is the definition of a common currency unit (the "ILCU"), and the development of a consistent and reasonable procedure [248] for converting costs in national currencies into this unit.

15.4.2.1 Purchasing Power Parity

For the 2007 ILC *Reference Design Report* (RDR), the ILCU was defined to be equal to the USD as of January 1, 2007. Conversions from other regional currencies to ILCU were based on averages of currency exchange rates to the USD over the previous 5 years. Explicitly, the RDR ILCU was equal to 0.8333 Euro and 116.7 Yen.

A similar procedure for the TDR estimate is problematic, however. This is because, in general, and particularly in times of wide fluctuations in monetary supplies related to financial crises, exchange

[2] Value is capitalised in this document when it has the specific meaning described in this paragraph.
[3] Labour is capitalised in this document when it has the specific meaning described in this paragraph.

rates do not necessarily represent true comparative prices between items manufactured in different regions of the world. Exchange rates can be strongly influenced by the supply and demand for different currencies, and the supply and demand for currencies are influenced by factors such as capital flows between countries and currency speculation, rather than simply by the needs of international trade.

International economists have introduced the concept of "purchasing power parity" (PPP) to deal with this issue. Compiled through extensive surveys by the research arm of the Organisation for Economic Co-operation and Development (OECD) and Eurostat (the European Union's statistical agency), PPP indices [249] are price relatives derived from the ratio of the prices in national currencies of the same good or service in different countries.

15.4.2.2 Motivations for the Use of PPP Indices

There are two primary motivations for the use of PPP indices. The first motivation is related to the development of the estimate, while the second motivation is related to the use of the estimate.

First, in the development of an estimate of an item's Value, it is common to have Value estimates for the same item, from different regions, stated in different currencies. These estimates are developed in the region, and typically correspond to the prices of the items from fabricators in the region in which the estimate is made. The proper way to compare these costs, so as to arrive at the lowest reasonable cost (the Value of the item), is on the basis of PPP indices, which are specifically designed to compare prices of similar items across national boundaries, avoiding the distortions associated with the use of exchange rates.

Secondly, as discussed above, the ILC project is expected to be funded through in-kind contributions. Since the Value of each item is stated in terms of an ILCU based on PPP indices, regional collaborators, seeking to assess the local resource requirements for their in-kind contributions, can use the PPP indices to translate components of the Value estimate into an estimate of the local currency required to build those components in their region. This can be done in a way which is not dependent on volatile exchange rates, now or in the future. Note that the local currency estimate derived in this way is independent of the region and currency in which the original estimate was made.

15.4.2.3 Issues with the Use of PPP Indices

There are several issues related to the use of PPP indices:

1. **Cost-element-type dependence.** Similar to inflation indices, PPP indices depend on the type of cost element (e.g. consumer goods, food, technical equipment, etc.). This dependence has been recognized by the OECD and other organizations which compile PPP indices, and separate indices have been derived and published for different types of elements. The two types of cost elements that are important for the ILC are civil engineering and technical equipment and machinery. The accounting framework for the ILC estimate, which was designed to handle different inflation indices for these two types of cost element, can also handle different PPP indices for these types.

2. **Accuracy.** Since the Value estimate uses PPP indices for conversions of estimates other than those in USD, the accuracy of the estimate depends on the accuracy of these indices. The Eurostat-OECD price surveys used to determine the PPP indices are comprehensive and well documented. The PPP indices from these surveys are used by many international organisations throughout the world. For industrialised nations, estimates [250] of the standard errors for PPP indices are in the range of 5-8 %. These uncertainties are considerably smaller than price distortions which would be introduced by the use of exchange rate and are typically also smaller than the overall uncertainties associated with the local-currency Value estimates themselves.

3. **Extrapolations.** The most recent published PPP benchmark survey was in 2008 [251], and the results from the next one, made in 2011, will not be available until 2013[4]. Following OECD recommended practice, the current PPP index can be obtained by extrapolation from the 2008 PPP index, based on the relative national[5] rates of inflation [241–247] from 2008 to the present, for the two national currencies that are related by the index. Errors introduced by this extrapolation are expected to be $\sim 5\,\%$ [248]. Once the 2011 Eurostat-OECD PPP benchmarks become available, the Value estimate could easily be updated.

4. **Regional versus global procurements.** The Value of a component, translated into the local currency in a region using PPP indices, corresponds to the price of this component if it is made and purchased in that region using the local currency. If, as a result of exchange-rate fluctuations, the region happens to have an overvalued currency relative to some other region, it is possible that the price of the component could be lower, in local currency units, if the component were purchased from the other region. In this case, a regional collaborator could choose between regional production of the component (which could benefit regional industry) or procurement from another region (which would require less local currency). But the Value estimate, translated to local currency using PPP indices, always establishes the required local currency for the component.

15.4.2.4 ILCU Definition in terms of PPP Indices

For the TDR, the ILCU will be defined as equal to the USD on January 1, 2012. Conversions of estimates obtained in currencies other than USD to ILCU will be based on PPP indices (as of January 1, 2012) relating those currencies to the USD. The only exception to this rule is for the superconducting material for the cavities. There is only one supplier of RRR-niobium raw material in the world. Thus, it is appropriate to consider this cost element to be a commodity which must be purchased on the international market. In preparing the Value estimate, conversions from currencies other than USD to ILCU for this cost element have been based on exchange rates as of January, 2012. The PPP indices of four regional[6] currencies, relative to the USD, together with exchange rates, are shown in Fig. 15.2. Numerical values of the PPP indices and exchange rates for January, 2012, which are used in the Value estimate, are given in Table 15.2.

Table 15.2. Currency conversion factors between ILCU and national currencies (January, 2012). To convert a cost element from ILCU to the indicated currency, multiply by the factor appropriate for the type of cost element.

Cost element type	ILCU→USD	ILCU→Euro	ILCU→Yen	ILCU→CHF
Civil construction (PPP)	1	0.939	109.3	1.303
Machinery and equipment (PPP)	1	0.923	127.3	1.480
Superconducting material (EX)	1	0.776	76.9	0.939

[4] PPP indices for European Union nations are compiled annually [252] by Eurostat.
[5] The PPP and inflation indices for the Euro were taken to be those of Germany, the dominant manufacturing economy which uses the Euro.
[6] The PPP indices for the Euro were taken to be those of Germany, the dominant manufacturing economy which uses the Euro.

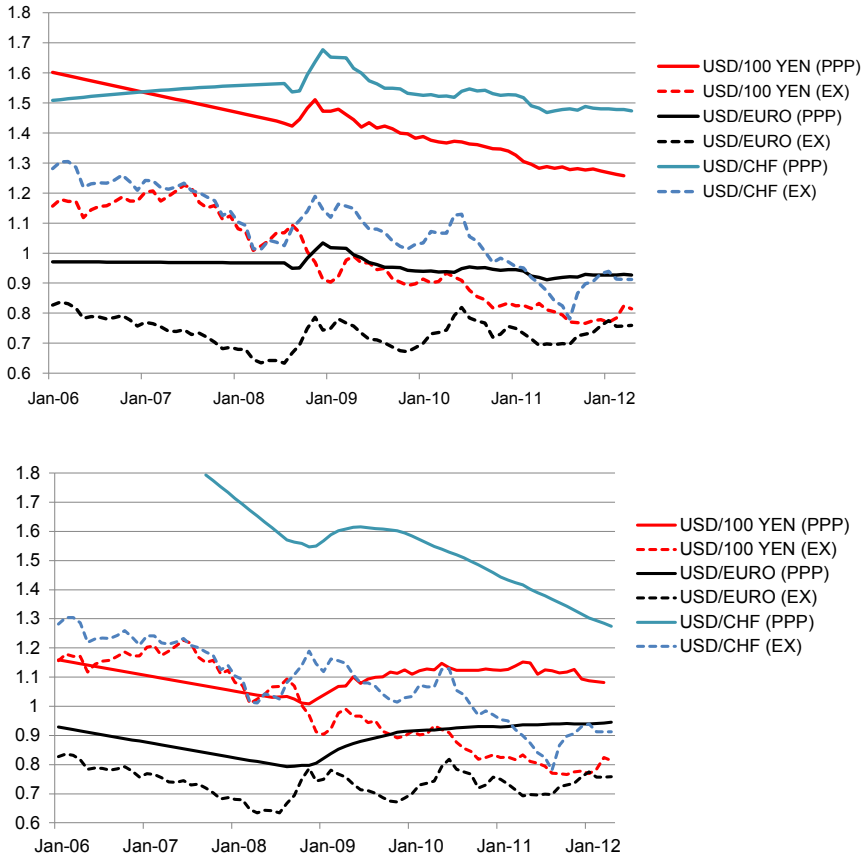

Figure 15.2
PPP indices and exchange rates. Top: machinery and equipment. Bottom: civil engineering. Indices between 2005 and 2008 are based on a linear interpolation between the 2005 [253] and 2008 [251] survey points. Indices after 2008 are extrapolated from the 2008 survey point, based on relative inflation rates. For the case of CHF, since a civil engineering inflation index is not readily available, the CHF civil engineering PPP index was based on scaling from the Euro PPP index, using the annual Eurostat PPP indices to relate the Euro and CHF PPP indices.

15.5 Cost Guidelines and Learning Curves

The specific cost guidelines used in preparing the Value estimate for the TDR were similar to those used for the RDR [254, 255].

15.5.1 General guidelines

The key elements of the general guidelines, which apply to all cost elements, are:

- the estimates for each cost element are median estimates. In other words, the estimate corresponds to the 50 % probability point in the cumulative cost-distribution curve. Thus, if a given item were to be offered independently for bid many times, taking the lowest world-wide bid each time, half of the lowest bids would be below the median estimate, and half above. Due to limited resources, no estimate was actually obtained by taking the median of a large number of bidding attempts. The TDR estimate for a given cost element was typically obtained by choosing from the available sources (such as vendor quotes, engineering estimates, or industrial studies) that estimate which was deemed to be the most reliable representative of a median lowest-bid;
- the specifications and quantities for each component or subsystem in the estimate correspond to the design documented in the TDR, which is intended to represent the optimal balance between technical performance, reliability, acquisition cost, and operating cost (over a 10 year lifetime);
- the Value estimate for a component or subsystem is the lowest world-wide vendor cost for the item, as determined by PPP, that is practical, feasible, and reasonable, for the required specification and quantity, with a procurement time consistent with the project schedule;

- in estimating the costs, at least two vendors were assumed for all industrial procurements for which the cost model has an explicit dependence on the number of items;
- the manufacturer's implicit labour for all fabrication activities, and for Engineering, Design, Inspection and Acceptance (EDIA), quality control, quality assurance and technical testing, is included in the item's Value;
- tooling, instrumentation and infrastructure necessary for the fabrication, acceptance and testing of the item or subsystem is included in the Value, if it does not exist or is not available at collaborating laboratories or other associated institutions; transportation costs are included;
- only those spares that are installed in the accelerator complex and are required for operational or reliability margins (as specified in the TDR) are included;
- explicit Labour (labour at the ILC, collaborating laboratories or other associated institutions, or labour purchased from an industrial vendor) includes, for example, final engineering design to prepare bid packages (after construction start), contract management, sustaining engineering, vendor liaison, inspection and acceptance tests, quality assurance, installation, system integration, alignment, and initial checkout (without beam). Commissioning with beam is not included. This Labour is estimated, separately from the item's Value, in person-hours. To convert person-years to person-hours, the number of hours per year was taken to be 1,700. Four classes of explicit manpower are included: engineer, scientist, technical staff, and administrative staff.

15.5.2 Specific Guidelines

In addition to the general guidelines, specific guidelines were applied to cavities and cryomodules, and to conventional facilities.

15.5.2.1 Cavities and Cryomodules

Cavity fabrication costs are based on a build-to-print specification to industrial vendors with minimum acceptance criteria, which must include vacuum leak testing, room-temperature RF tuning, high-pressure test, etc. but without a guarantee of accelerating-gradient performance. Superconducting material will be supplied by the project to the vendors.

All of the cavities will be vertically tested. Testing and quality assurance for the cavities and quadrupoles, and high-power processing of the couplers, is the responsibility of the project and its multi-region partner institutions; the effort is included in the explicit Labour estimate. Cryomodule fabrication and assembly is also based on a build-to-print specification to industrial vendors.

The overall performance of the cavities and cryomodules will be guaranteed by the project and its partner institutions. Approximately one third of the cryomodules will be fully tested. The required testing and QA effort is included in the explicit Labour estimate.

15.5.2.2 Conventional Facilities

There is one common machine design. The footprints for the sites have small geology-driven differences, such as shaft and hall locations, and minor differences in tunnel lengths. Nevertheless, the costs for many aspects of conventional facilities are site-specific and there are separate estimates for each sample site (one in each region: the Americas, Europe and Asia[7]). These are driven by real considerations, e.g. different geology and landscape, availability of electrical power and cooling water, etc. The cost of surface land and underground easements, and site-dependent costs due to local regulations, are not included.

[7] There are two Asian site candidates. The Asian TDR estimate corresponds to an average of the costs for these two sites.

The site-specific costs are combined into a single average conventional facilities (CFS) Value estimate for the TDR. The reasons for any major differences between the site-specific costs are discussed in Section 15.7.3.

15.5.3 Learning curves

Many of the cost bases used for the ILC TDR Value estimate correspond to smaller numbers of units that those required for the ILC. To account for expected economies of scale, when the cost basis explicitly corresponds to a much smaller number of units than required for the ILC, the unit Value estimate for ILC quantities has been obtained by applying a discount based on a (Crawford) learning curve [256].

In using learning curves to estimate quantity discounts, care must be used in the choice of the learning-curve slope. Table 15.3 [256, p. 180] shows the typical range of learning-curve slopes that have been found for various types of manufacturing processes or general categories of items. The components manufactured for the ILC generally correspond to mixtures of the first five lines in this table. Components for the ILC components would thus be expected to have learning curve slopes roughly in the range of 85-95%.

Table 15.3
Typical learning curve slopes [256, p. 180].

Manufacturing process or item	Range of learning curve slopes
Raw materials	93-96%
Repetitive electronics manufacturing	90-95%
Repetitive machining or punch-press operations	90-95%
Repetitive welding operations	90%
Purchased parts	85-88%
Repetitive clerical operations	75-85%
Construction operations	70-90%

The discount is a sensitive function of the slope, as shown in Fig. 15.3, which demonstrates that the discount varies by a factor of about 2 in going from a 95% slope to a 90% slope.

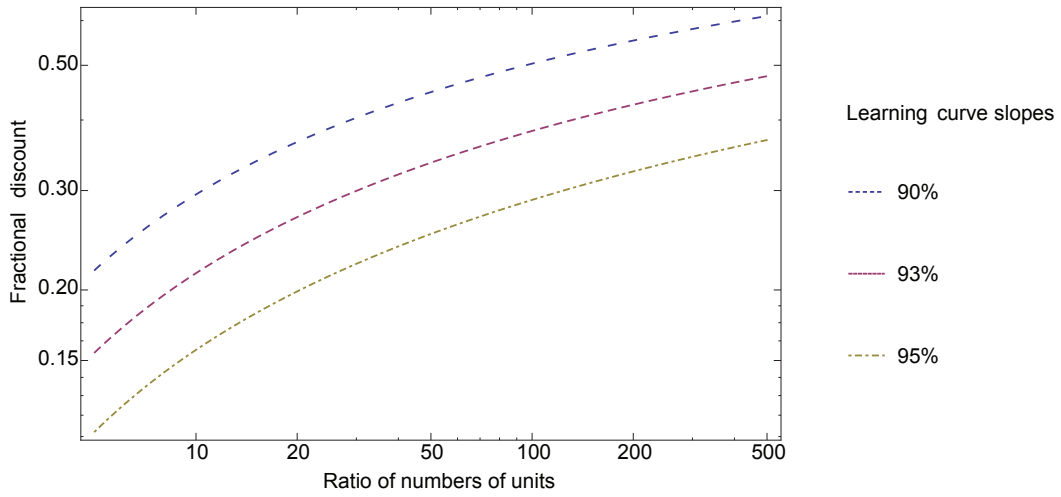

Figure 15.3. Discount versus the ratio of the number of units in the discounted estimate to that in the original estimate, for learning curves with 90%, 93%, and 95% slopes.

Without a specific manufacturing model for an ILC component, it is difficult to determine precisely what learning-curve slope should be used. Thus, when there is no specific manufacturing study (or vendor quote in the appropriate quantity) for a component, a conservative choice of a learning curve slope at the upper end of the expected range (95%) has been made. No saturation of the learning curve has been assumed.

For the L-band modulators, the engineering cost estimate does have a specific breakdown of labour and materials costs. Thus, for this component, a 90% learning curve for the labour cost and a 95% learning curve for the materials cost have been used.

No learning curves have been used when the component cost basis has explicitly accounted for the correct quantity of items required from a given vendor for the ILC. The most important examples of such components are the industrial studies for production of the cavity resonator and assembly of the cryomodule, and vendor quotes for the klystrons. For these cases, the extensively documented work explains precisely how the discount is obtained. The effective learning curves that can be derived from the explicit studies or the vendor quotes are in fact between 87% and 92%, illustrating the conservatism of the choice of a 95% slope.

15.6 Development and Format of the Estimate

15.6.1 Estimate Development

A complete Value estimate for the ILC was developed at the time of the *Reference Design Report* (2007). Subsequently, value engineering, design development, and component R&D have led to the evolution of a more cost-optimised machine design, and to more mature concepts for many of the components. For the TDR, new estimates for the conventional facilities, the superconducting cavities and their cryomodules, the L-band high-level RF systems, and the cryogenic facilities have been made. In addition, since the damping-ring design in the TDR is substantially changed from the RDR, major elements of the damping ring were re-estimated, as were significant portions of the positron source. Overall, the new estimates comprise about 75 % of the total cost of the project.

For the remaining approximately 25 % of the estimate, the estimated Value and explicit Labour per component unit were generally taken from those provided at the time of the RDR. Unit costs were escalated from the RDR estimate date to the TDR estimate date based on the regional escalation indices shown in Fig. 15.1, and converted to 2012 ILCU using the PPP indices shown in Fig. 15.2.

15.6.2 Format of the Estimate

The Value estimate has been formatted using the ILC Cost Estimating Tool (ICET). The tool is a series of Windows and Visual Basic scripts which allows the manipulation of custom Excel spreadsheets, called "Cost Estimating Modules (CEMs)", that contain the cost data and links to the cost-basis documents in EDMS. The ICET organises the CEM cost data into a WBS structure, where each cost element includes a description, basis of estimate, quantity required, materials and services estimate, explicit labour, and an uncertainty characterisation. ICET can be used to load the cost data into a database. Subsequently, a series of reports detailing and cross-cutting the estimate can be generated from the database. There are approximately 700 cost elements in the cost database for the TDR estimate.

15.7 Cost Basis

The bases of estimate for each major cost-element category are discussed in the following sections.

15.7.1 Cavities and Cryomodules

The cavities and cryomodules represent a substantial fraction (about 1/3) of the total ILC project Value. For the RDR, the Value estimate was based on the cost studies carried out for the TESLA TDR [13] more than 10 years ago. Since the publication of the RDR, there have been two developments which allow this TDR estimate to have a much more diverse and mature cost basis:

- substantial R&D has been carried out in all three regions, so that a more extensive world-wide experience base now exists, allowing industrial cost studies for cavity fabrication and cryomodule assembly to be carried out in all regions;

- extensive experience from procurements for the European XFEL (EXFEL) is available, which provides actual costs for all the key components of the ILC cavities and cryomodules, albeit for a smaller number of units than for the ILC.

Based on these industrial studies and the EXFEL experience, and following the cost guidelines outlined above, Value and Labour estimates have been developed for the cavities and cryomodules. A brief description of the cost basis of each subcomponent is given in the following subsections.

For almost all the elements of the cavities and cryomodules, the TDR estimates are substantially higher than those of the RDR. For the total cavity and cryomodule cost, the TDR estimate is about 1.7 times higher than the escalated RDR estimate. This difference arises from the much broader R&D and procurement experience base on which the TDR cost basis rests.

The essential elements of this broader experience base are:

- procurements of cavities and cryomodules made for the EXFEL project;
- industrial studies by qualified vendors focused on fabrication and processing of the cavity resonator;
- industrial studies by qualified vendors focused on assembly of the cryomodule.

To provide a clear picture of the relationship between these elements, the most important cost drivers for the cavity and cryomodule are listed in Table 15.4, and the TDR cost basis is listed. For most of the items, the TDR estimate is based on the EXFEL procurement, with a quantity discount (on the basis of a 95 % learning curve) associated with the increase in the number of items by a factor of 10. For the cavity resonator, the TDR estimate is based on detailed industrial studies performed by qualified cavity vendors. For the magnet package, the TDR estimate is based on a direct vendor quote. For the cryomodule assembly, the TDR estimate is based on a detailed industrial study, again performed by an experienced company.

For the sum of these major cost drivers for an 8-cavity cryomodule with quadrupole, the TDR estimate is about 72% of the actual EXFEL procurement cost; that is, a reduction of 28 %. About 16 % of the overall reduction is due to quantity discounts, based on a 95 % learning curve. The remaining 12% is primarily due to the cost reductions resulting from the industrial study.

Table 15.4
Cavity and cryomodule cost drivers: Summary of the TDR cost basis.

Item	TDR Cost Basis
Superconducting material	EXFEL procurement[†]
Cavity resonator	industrial study
Power coupler	EXFEL procurement[†]
Tuner	EXFEL procurement[†]
Helium vessel	EXFEL procurement[†]
Magnet package	vendor quote
Cryostat materials	EXFEL procurement[†]
Cryomodule assembly	industrial study

[†] discount based on a 95 % learning curve

More details about all the elements of the TDR cavity and cryomodule estimate are presented in the following sections.

15.7.1.1 Dressed and Qualified Cavity

15.7.1.1.1 Superconducting material Vendor quotes and recent procurements for the EXFEL and Fermilab Cryomodule 3 (CM3) were reviewed to establish the basis of estimate for the cavity superconducting material. The most reliable cost basis was judged to be the EXFEL procurement, since this was a true price obtained in the world-wide market for a substantial number of cavities. Thus, the TDR estimate is based on the cost of the EXFEL superconducting material. This cost includes material quality control.

About half of the high-purity superconducting material cost is for the niobium raw material; the remainder is smelting infrastructure ($\sim 25\,\%$) and smelting and rolling operations labour ($\sim 25\,\%$). A 95 % learning curve has been used to estimate the discount associated with the increase in the amount of superconducting material from the EXFEL quantity to that required for the ILC (assuming 2 vendors). The learning curve discount in this case is about 16 %.

To derive the total costs, a 90 % cavity production yield was assumed to determine the superconducting material required for the total number of ILC cavities (17,804).

15.7.1.1.2 Cavity resonator Cost information on fabrication and chemical processing of the cavity resonator is available from the EXFEL procurement, and from three industrial studies, one in each region.

The cost estimate was based on the industrial studies adjusted where needed to a nominal series production of both 9,000 and 18,000 cavities. The estimate assumed a 2.67-year series-production schedule, and includes the costs for an additional 3 year ramp-up period, which includes 1 year of pre-series cavity production. Ramp-down costs were also included, including a modest (10 %) infrastructure cost recovery. The unit costs for a total production of 9,000 cavities, approximately corresponding to a 2 vendor procurement for the ILC, were used.

The scope of work includes cavity fabrication and chemical processing, and welding of the cavity into the helium vessel. The total cost includes all manufacturing and labour for the total number of cavities, and infrastructure for two fabrication sites.

Where necessary, adjustments have been applied to the estimates presented in the industrial studies. An example is the late adoption in the ILC baseline an internal magnetic shield, the fabrication and integration of which was not included in the industrial studies. To account for the mounting of this shield, the cost of the additional labour was added The cost of material for the magnetic shield is accounted for separately below. It should be noted that these items have a relatively minor cost impact.

Since industrial studies were done for two different numbers of cavities, the average costs for these two cavity production numbers can be used to derive an effective learning curve slope. This slope is 87 % for the mechanical fabrication of the cavities, and 89 % for cavity chemical processing.

To compute the total costs, a 90 % overall cavity-fabrication and chemical-processing yield was assumed to determine the required number of ILC cavities to be fabricated (17,804). The cost of a second chemical processing for 20 % of the cavities (3,561) has been included.

15.7.1.1.3 Cavity qualification Materials and supplies (M&S) have been included for cavity qualification, based on an internal ILC cost study at Fermilab done in 2007 in connection with the development of the RDR.

This task is accounted for as explicit Labour. The labour estimate is also based on the Fermilab internal ILC cost study. The total labour and M&S costs cover qualification of the total number of processed cavities (21,365).

15.7.1.1.4 Power coupler Cost information on the high-power coupler is available from the procurements for Fermilab CM3 and EXFEL, and from a 2008 industrial study on cost-reduction options for an ILC cryomodule, made by a qualified experience vendor.

The TDR cost basis is derived from the EXFEL procurement, which is the most reliable in-quantity recent cost. To allow for economies of scale, a 95 % learning curve has been used to estimate the unit cost discount for ILC quantities. This discount is 16 %. The total cost covers the baseline number of couplers (16,024).

15.7.1.1.5 Coupler processing Materials and supplies costs have been included for coupler processing, based on the the same 2008 industrial study quoted above. This task is accounted for as explicit

Labour. The labour estimate is based on a scaling from EXFEL experience with coupler processing.

15.7.1.1.6 Tuner Cost information on the tuner is available from the procurements for Fermilab CM3 and EXFEL, and an industrial study conducted in 2012. The EXFEL costs are for a Saclay/DESY-style tuner, while the Fermilab CM3 and industrial study costs are for blade tuners. The costs include the mechanical parts, motor drives and piezoelectric devices.

The TDR baseline is the blade tuner, but no large quantity procurements of these tuners are available to provide a sound cost basis. Thus, the TDR cost basis is derived from the EXFEL cost, which is a reliable in-quantity recent procurement of an item similar to the TDR baseline design. To allow for economies of scale, a 95 % learning curve has been used to estimate the unit cost discount for ILC quantities. This discount is 16 %.

Post-TDR research and development will be required to develop either a shorter Saclay/EXFEL style tuner for the ILC, or a different design with an equivalent cost. The total cost covers the baseline number of tuners (16,024).

15.7.1.1.7 Helium vessel Cost information on the helium vessel is available from the procurements for Fermilab CM3 and EXFEL, and several industrial studies. The EXFEL costs are for a helium vessel matched to a Saclay/DESY style tuner, while the Fermilab CM3, and industrial study costs are for a helium vessel appropriate for a blade tuner.

The TDR baseline is the helium vessel appropriate for a blade tuner, but no large quantity procurements of these vessels are available to provide a sound cost basis. Thus, the TDR cost basis is derived from the EXFEL cost, which is a reliable in-quantity recent procurement of an item similar to the TDR baseline design. To allow for economies of scale, a 95 % learning curve has been used to estimate the unit cost discount for ILC quantities. This discount is 16 %.

Post-TDR tuner research and development will include development of a helium vessel appropriate for a blade tuner, with a cost equivalent to that of a vessel matched to the Saclay/DESY-style tuner. Since the vessel is carried with the cavity in vertical test, the total cost covers the number of fabricated cavities (17,804).

15.7.1.1.8 Cavity magnetic shield The cost basis for materials for this item is a vendor quote contained in recent industrial study. Since the shield is carried with the cavity in vertical test, the total cost covers the number of fabricated cavities (17,804).

15.7.1.1.9 Cavity shipping and handling The cost basis for this item is an internal ILC cost study done at Fermilab in 2007. The total cost covers the baseline number of processed cavities (21,365).

15.7.1.2 Quadrupole-Magnet Package

This item refers to the superconducting quadrupole and the correction dipole, together with their current leads and associated hardware. (The beam-position monitor is included in the Instrumentation estimate.)

Cost information on the magnet package corresponding to the RDR design is available from the procurements for Fermilab CM3 and EXFEL, qualified vendor industrial studies, and the Fermilab internal ILC cost study. Cost information on a magnet package corresponding to the conduction-cooled TDR design is available from a direct vendor quote based on fabrication of 300 or 600 units.

The vendor quote unit cost estimate for the conduction-cooled magnet (for 300 units) is used as the TDR cost basis since it corresponds to the TDR design and is a well-developed estimate. The total number of magnet packages required for the ILC is 673. The M&S costs for quadrupole qualification, and the associated explicit Labour, are also included. For these items, the cost basis is the Fermilab internal ILC cost study.

15.7.1.3 Cryomodule

15.7.1.3.1 Cryomodule EDIA Final engineering design, and sustaining engineering, for the cryomodule and all of its components, at the ILC or collaborating institutions, is included as cryomodule EDIA explicit Labour. The cost basis is an engineering estimate taken from the Fermilab internal ILC cost study.

15.7.1.3.2 Cryostat material This item refers to the materials which comprise the cryostat. Cost information for this item is available from the procurements for Fermilab CM3 and EXFEL, the Fermilab internal ILC cost study, qualified vendor industrial studies, as well as a direct vendor quote.

The TDR cost basis is derived from the EXFEL procurement, which is the most reliable in-quantity recent cost. The EXFEL procurement has been scaled up by 5 %, to account for the length difference between the EXFEL and ILC designs. To allow for economies of scale, a 95 % learning curve has been used to estimate the unit cost discount for ILC quantities. This discount is 15 %. The total cost covers the baseline number of cryomodules (1,855).

15.7.1.3.3 Cryomodule assembly Cost information for assembly of the cryostat is available from the procurements for the EXFEL, the Fermilab internal ILC cost study and qualified vendor industrial studies, for both 1950 and 650 cryomodules.

The cost basis for the TDR is based on detailed industrial studies for 650 cavities, corresponding to a 3-vendor procurement. The particular study was chosen because of its depth, detail, and comprehensive scope. The study assumed a 2.6-year ramp-up period, followed by 3.5 years of cryomodule production. The Value estimate includes all labour and infrastructure for three assembly sites. Ramp-up and ramp-down costs were included, but no cost recovery for infrastructure was assumed. Following the EXFEL procedure, the effort includes assembly of the coupler and tuner onto the helium vessel containing the cavity and magnetic shield, which is received after cavity qualification, followed by assembly of the cavity string with quadrupole, alignment, and completion of the vacuum-vessel assembly. Labour rates (a variable across different studies) have been harmonised where applicable.

Since estimates are available for two different numbers of cryomodules, the average unit costs for these two numbers of assembled cryomodules can be used to derive an effective learning-curve slope. This slope is 89 % for the total cryomodule assembly labour.

The total cost covers the baseline number of cryomodules (1855), plus an additional 5 % assumed to need re-work (see below, Section 15.7.1.3.6), for a total of 1948.

15.7.1.3.4 Cryomodule shipping and handling The cost basis for this item is an internal ILC cost study done at Fermilab in 2007. The total cost covers the baseline number of cryomodules, including rework (1,948).

15.7.1.3.5 Cryomodule qualification Materials and supplies have been included for cryomodule qualification, based on the Fermilab internal ILC cost study. In addition, the cost of electrical power for RF, cryogenics, and water for the test stands has been included, based on scaling from EXFEL experience.

This task is accounted for as explicit Labour. The Labour estimate is based on a scaling from EXFEL experience[8]. The number of cryomodules to be tested is based on the assumption that, at peak production rate, 33 % of the cryomodules will be tested before installation. An additional 5 % has been added for testing during the ramp-up period.

15.7.1.3.6 Cryomodule hardware commissioning in the tunnel enclosure Additional explicit Labour will be required to commission the cryomodules in the tunnel. This Labour covers the preparation

[8] It is assumed that all of the testing labour reported for the EXFEL is for cryomodule testing.

and conditioning of untested cryomodules. To account for cryomodule failures which occur either during testing or during hardware commissioning in the tunnel, an allowance for re-working 5 % of the cryomodules has been included in the Value element for the total cryomodule assembly. The unit cost of a rework has been assumed to be the same as the unit cost for assembly of a cryomodule.

15.7.1.4 Coupler Processing, and Cavity and Cryomodule Test Infrastructure

Coupler processing, cavity qualification, magnet testing and cryomodule qualification will be done in existing facilities supplied by international institutional collaborators.

The total test and processing facility costs have been estimated based on the Fermilab internal ILC cost study. The relative breakdown of the costs for each of the facilities is presented in Table 15.5.

The facilities are owned by the institutional collaborators and used by the project for the duration of the cavity and cryomodule production period, which is about 5 years. Maintenance and required upgrades to the facilities during this period are assumed to cost about 10 % per year. Thus, the cost to the project associated with this infrastructure has been taken to be equal to 50 % of the estimated total facility cost given in the Fermilab study.

Table 15.5
Processing and test infrastructure relative cost

Facility	Fraction of total cost of processing and test infrastructure
Cavity vertical test	26 %
Coupler processing	27 %
Magnet qualification	4 %
Cryomodule qualification	43 %

15.7.1.5 Cryomodule Vacuum System

This system includes the beam-line vacuum, the insulating vacuum for the cryomodule, and the coupler vacuum. The TDR unit-cost basis for the cryomodule vacuum system was taken from the RDR.

The RDR cost was based on a bottoms-up accounting of the parts associated with the vacuum-system hardware. The prices were based on price lists and vendor quotes, with some adjustments for quantity price reductions. Associated Labour (EDIA) is included.

15.7.1.6 Summary

The basis for the components of the estimates for cavities and cryomodules is summarised in Table 15.6 and Table 15.7.

15.7.2 L-band High-Level RF Systems

The principal components of the L-band high-level RF system are the multi-beam klystrons (MBKs), the modulators, and the RF distribution system.

The flat and mountainous topography sites described in the TDR require different designs for the high-level RF systems. These designs (called the Klystron Cluster System (KCS) for the flat sites, and the Distributed Klystron System (DKS) for the mountainous site) require different numbers of klystrons and modulators, and different RF-distribution systems. Consequently, a separate Value estimate was developed for each design.

Table 15.6
Value basis for cavities and cryomodules

Sub-component	Basis Type	Basis Source (Date)	Number of units
Superconducting material	Procurement[a]	EXFEL (2011)	17804[b]
Cavity fabrication	Industrial study	qualified vendor	17804[b]
Cavity chemical processing	Industrial study	qualified vendor	21365[c]
Cavity qualifications	Engineering estimate	FNAL (2007)	21365[c]
Power coupler	Procurement[a]	EXFEL (2011)	16024
Power coupler processing	Engineering estimate	qualified vendor	16024
Tuner	Procurement[a]	EXFEL (2011)	16024
Helium vessel	Procurement[a]	EXFEL (2011)	17804[b]
Magnetic shield	Vendor quote[d]	qualified vendor	17804[b]
Cavity shipping and handling	Engineering estimate	FNAL (2007)	21365[c]
Magnet system	Vendor quote	qualified vendor	673
Magnet qualification	Engineering estimate	FNAL (2007)	673
Cryostat materials	Procurement[e]	EXFEL (2011)	1855
Cryomodule assembly	Industrial study	qualified vendor	1948[f]
Cryomodule qualification	Engineering qualification	FNAL (2007)	711[g]
Cryomodule shipping and handling	Engineering estimate	FNAL (2007)	1948[f]
Cryomodule vacuum	Vendor quote	INFN (2007)	1855
Cavity fabrication and chemical procesing infrastructure	Industrial study	qualified vendor	2
Cryomodule assembly infrastructure	Industrial study	qualified vendor	3
Infrastructure for coupler processing, and for cavity and cryomodule test	Engineering[h] estimate	FNAL (2007)	≥ 3

[a] discounted by 16 %, based on a 95 % learning curve
[b] assuming 90 % overall yield
[c] assuming 80 % first pass yield
[d] discounted by 6 %, based on a 95 % learning curve
[e] discounted by 15 %, based on a 95 % learning curve
[f] assumes 5 % more than the baseline, to account for re-work
[g] assumes 38.3 % of CM's are tested
[h] cost for maintenance and upgrades of existing facilities at collaborating labs is taken as 50 % of the estimated facility cost

Table 15.7
Explicit Labour basis for cavities and cryomodules

Task	Basis Type	Basis Source (Date)	Number of units
Cavity qualification	Engineering estimate	FNAL internal cost study (2007)	21365[†]
Coupler processing	Lab experience	EXFEL (2011)	16024
Quadrupole qualification	Engineering estimate	FNAL internal cost study (2007)	673
Cryomodule EDIA	Engineering estimate	FNAL internal cost study (2007)	1855
Cryomodule qualification	Lab experience	EXFEL (2011)	711[‡]
Cryomodule hardware commissioning in the tunnel	Engineering estimate	GDE (2012)	1855
Cryomodule vacuum EDIA	Engineering estimate	RDR (estimate from INFN) (2007)	1855

[†] assuming 80 % first pass yield
[‡] assuming 38.3 % of CM's are tested

15.7.2.1 Klystron

15.7.2.1.1 Klystron Tube Cost information for the klystron is available from direct vendor quotes. The procurement costs for the klystrons acquired for the EXFEL project are also available.

For the TDR, the most current vendor quote has been chosen as the cost basis. The vendor gave quotes for two quantities of klystrons, one quantity lower than required for DKS, and one quantity higher than required for KCS. The two quotes allow the standard (Crawford) learning-curve parameters to be determined[9], which were used to estimate the unit costs corresponding to the number of klystrons to be procured (assuming two vendors) for the KCS and DKS configurations.

The quotes correspond to the procurement of fully processed klystrons. The full cost of labour at the vendor for the processing has been assumed, but the processing infrastructure costs given by the vendor have been discounted by 50 %. The infrastructure costs in the estimate are the costs of modulators and associated controls. However, the project will have access to modulators and controls which can be supplied to the vendor for the processing, substantially reducing the costs.

15.7.2.1.2 Klystron Accessories The vendor quotes correspond to a fully processed tube body, including the focusing magnet, mounting hardware, tube socket, and oil tank. However, there are additional costs associated with the solenoid, filament and ion-pump power supplies, the RF pre-driver, and related controls, software, and interlock systems. These additional costs are included in the TDR, with a unit cost basis taken from the RDR (after adjustment for quantity discounts).

15.7.2.2 Modulator

The baseline modulator for the TDR is a Marx modulator. Cost information for this device is available from vendor quotes and from an engineering estimate carried out at SLAC. The procurement costs for the modulators acquired for the EXFEL project are also available.[10]

Based on the extensive experience at SLAC in developing the Marx modulator, the cost basis for this item is the SLAC engineering estimate. This is a bottoms-up estimate of the material and fabrication costs. This cost is intended to be that of an industrially produced item, so the estimate uses industrial labour rates (derived from 2012 RSMeans[11] contractor labour rate tables) and includes a typical profit margin (15 %). The first article unit costs have been discounted using a 95 % learning curve for materials (which are 80 % of the total first article cost), and a 90 % learning curve for labour (the remaining 20 %). The number of units is based on a two-vendor procurement of the number of modulators needed for the ILC. The average quantity discount from the first article cost is about 31 %.

15.7.2.3 RF-distribution system

The RF-distribution system brings the high-level RF from the klystrons to the power couplers. For the KCS layout, the RF must be transported from the surface to the cryomodules in the tunnel, and then distributed locally to the power couplers. For the DKS layout, only the local power-distribution system is needed. For the KCS system, the components are (by cost) 68 % standard catalogue microwave components, and 32 % specialised devices (CTO's, loads, variable hybrids, and phase shifters).

The procurement costs for the RF-distribution system acquired for the EXFEL project are available. However, these costs cannot be used directly, since increased functionality[12] is needed in the TDR systems.

For both types of distribution system, the cost was estimated based on catalogue unit prices for the standard microwave components, and vendor quotes for the specialised devices. The prices were

[9] The effective learning curve slope for the klystron fabrication is 92%; for the processing labour, it is 87 %.
[10] Note that these devices do not use the Marx modulator technology.
[11] North America's leading supplier of construction cost information
[12] The increased functionality is needed to cope with the cavity gradient spread allowed by the TDR specifications.

developed jointly by the engineering teams at SLAC and KEK. The system costs in quantity were then estimated based on a discount derived from a 95 % learning curve, and assuming a two-vendor procurement for each component. The average quantity discount from the single-item unit prices is about 33 %.

The TDR-DKS unit costs are larger than those of the RDR, and larger than the EXFEL procurement costs, because of the increased functionality required by the TDR design requirements. The TDR-KCS unit costs are larger than those of the TDR-DKS because of the additional microwave hardware needed to bring RF from the klystron clusters on the surface to the cryomodules in the tunnel.

15.7.2.4 Supporting Infrastructure in the Tunnel

There are additional costs for the high-level RF system related to cabling, instrumentation, and electrical distribution. The unit Value estimate for these items has been taken from the RDR.[13]

15.7.2.5 High-level RF Explicit Labour

Final engineering design, and sustaining engineering, for the L-band high-level RF systems, is accounted for as explicit Labour. This includes documentation and supervision of bid packages for delivery of tested klystrons, modulators and distribution assemblies; support of factory testing, factory verification of testing, and acceptance to ship; on-site final assembly area development, supervision, and management; systems engineering and documentation for production and final assembly; engineering team development, support of final integration and equipment commissioning in tunnels; and sustaining engineering and technical maintenance of tested systems during commissioning.

The estimate is taken to be that developed for the RDR, but rescaled for the TDR, based on the ratio of M&S costs between the RDR and the TDR.

15.7.2.6 Summary

The basis for the components of the estimates for the high-level RF system is summarized in Table 15.8.

Table 15.8
Basis for high-level RF system

Sub-component	Basis Type	Basis Source (Date)	Number of units (DKS)	Number of units (KCS)
Klystrons	Vendor quote*	qualified vendor	426	461
Klystron auxiliary items	Engineering estimate	RDR (2007)	426	461
Modulators	Engineering estimate†	SLAC (2012)	426	461
KCS RF distribution	Catalog prices and vendor quotes‡	SLAC, KEK (2012)	0	567
Local RF distribution	Catalog prices and vendor quotes‡	SLAC, KEK (2012)	616	616
Explicit manpower	Engineering estimate	RDR (2007)		

* includes processing labour and 50 % of processing infrastructure
† discounted by 30 %, based on a 90 % (labour) and 95 % (materials) learning curve
‡ discounted by about 33 %, based on a 95 % learning curve

[13] The cost per RF unit has been assumed to be the same for KCS and DKS.

15.7.3 Conventional Facilities (CFS)

15.7.3.1 Introduction

The Value estimate for the ILC CFS has been developed internationally with teams in each of the three regions (Americas, Asia and Europe). These teams have worked closely together to optimise the CFS design, based on the requirements supplied by the Accelerator and Technical Systems. The three estimates have been formatted using the same detailed WBS structure up to level 5 of the WBS. At deeper levels, there are site-specific differences.

Information was drawn from consultant engineers, historical data from other accelerator or similar projects, industry-standard cost-estimating guides, and, where applicable, the scaling of costs from similar systems. In all cases, the estimates reflect a median value for the work based on the criteria provided to date.

The Americas estimate includes a small increase to represent typical cost growth from a design estimate to the "Final Construction Cost". It accounts for Americas-specific features, such as possible claims resulting from design immaturity. However, it does not correspond to contingency. There are no explicit factors for contingency contained in any of the CFS Value estimates.

For each category of the CFS estimate, costs associated with ongoing engineering and documentation are included in the category labeled "Engineering, study work and documentation". Part of this work is done through A&E firms, and this is included in the Value estimates described below. Additional work, which may be done at the ILC laboratory or collaborating institutions, is included as person-hours in the CFS component of the explicit Labour estimate.

15.7.3.2 Civil Engineering

Due to the differences in geology and topography at the different sites, separate Value estimates were developed for each of the three sites. These estimates were developed using the same criteria. The drawings for each site reflected necessary site-specific differences.

Costs for activities that take place prior to the construction start are explicitly not included in the estimate. Some examples of such costs are A&E Services before the start of construction, development costs for geotechnical and environmental investigation, land-acquisition costs, and costs incurred for compliance with local governmental statutes and regulations. These costs cannot be accurately identified until a specific site selection is made.

15.7.3.2.1 Underground construction All major elements of the civil engineering, such as tunnels, shafts, caverns, halls, etc. are included in the estimate. The costs have been estimated with the help of consultants, using information from similar projects and standard civil engineering practices. All temporary facilities needed for construction work, as well as the necessary site preparation before start of the work, are included in the Value estimate.

The local geology at the European site near CERN, consisting of stable Molasse rock, permits the creation of underground facilities using standard excavation methods. Tunnel-boring machines (TBM's) will be used to excavate beam tunnels with finished inside diameters varying from 5.2 m to 8 m. Shafts will be constructed using traditional excavation methods for the dry moraines (upper 50 m) and ground freezing techniques for the wet moraines. When the Molasse rock is reached, the shafts will be further excavated using rock breakers and roadheaders. These machines are also used for cavern excavation. No drilling and blasting is required for the European site.

The Americas site uses TBM's to excavate beam tunnels with finished inside diameters of 4.5 m and 5 m. At the Americas site, due to the local hard rock (Dolomite), shaft and cavern excavation requires drilling and blasting.

All Asian underground construction is carried out using drill and blast excavation, following the

New Austrian Tunneling Method (NATM).

The different excavation methods used at the three sites result in different unit costs, as discussed below.

15.7.3.2.2 Surface buildings The type, number and dimensions of the buildings include only those surface facilities required for construction, installation and operation of the project, taking into account the specifics of each of the three sample sites. For instance, for the Americas and European sites, additional infrastructure such as seminar rooms, guest houses, restaurants, administrative facilities, warehouses, etc. are assumed to be supplied by a nearby (host) laboratory, and are not included in the Value estimate. The Asian sample site does not have a nearby laboratory so that the Asian estimate does include such central campus facilities. It also includes 3 large warehouses to be used during installation.

For the areas where surface buildings are located (central campus, shaft positions), the following items have been included in the cost estimate:

- fences and gates;
- roads and car parks within fences and from fence to existing road network;
- pedestrian walkways;
- lighting for walkways and around buildings including buried electrical connections;
- all necessary drains along roads and car parks, including sumps, water treatment facilities and connections to existing mains;
- all needed water supply pipes, tanks and connections to existing water-supply networks;
- landscaping and planting of trees, bushes, seeding of grass as required;
- spoil dumps (where applicable) created close to the building areas, including landscaping.

15.7.3.2.3 Tunnel volumes and surface-building areas The total beam- and service-tunnel volumes, and the total surface-building areas, for each regional site, are shown in Table 15.9.

Table 15.9
Beam- and service-tunnel volumes, and surface-building areas.The Asian surface building total includes 3 warehouses, each with an area of 6,000 m^2.

Region	Tunnel Volume (m^3)	Cavern Volume (m^3)	IR Hall Volume (m^3)	Surface Building Area (m^2)
Americas	904,881	133,755	135,703	74,599
Europe	1,070,268	156,232	127,100	
Asia	2,091,630	330,360	189,381	109,275

15.7.3.2.4 Unit costs The CFS group established a set of similar definitions for underground construction unit costs. This ensured consistency across all three regions. Estimates for each unit cost were independently produced by experts and consultant engineering firms in each of the three regions. These unit costs, together with the civil-engineering design details specific to each site, were used to develop the site-specific civil-engineering costs.

Unit cost definitions For the European region, underground civil-engineering costs have been estimated for tunnels, shafts and caverns. Excavation is performed using TBM, rock breakers and roadheader machines. The unit prices for these elements include items shown in Table 15.10.

The unit costs for the Asian site always correspond to drill and blast excavation, and include both direct and indirect costs. The direct costs include blast excavation, transport of muck, sprayed concrete finish in the sloping access tunnels, rock bolts, inflow water treatment, a mold frame for lining, a concrete-lining finish in beam/service tunnels, floor concrete finish, survey, grouting (20 % of direct costs), and construction support. Indirect costs are 100 % of the direct costs. Site preparation costs (8 % of total costs) are contained in a separate WBS element.

Table 15.10
European civil-estimate unit costs. This table shows what is included in the civil engineering costs for the European estimate. The percentages given are of the "direct" costs, defined as the sum of all costs without a percentage after them.

Item	Tunnels	Shafts	Caverns
Manpower (no overhead)†	X	X	X
Excavation & deposit	X	X	X
Outer lining incudes:			
Bolts		X	X
Shotcrete with fibre		X	X
Ring gap/tolerance filling	X	X	X
Sealing		X	X
Inner lining includes:			
Hydroshield	X	X	X
Double-sided formwork		X	X
reinforcement	X	X	X
Ceiling			X
Finishing (floor)	X		
Special works includes			
Moraines		X	
Walls ceilings (10 %)			X
Drainage & dewatering (4 %)‡	X	X	X
Probes (2 %)‡	X	X	X
Auxiliary measures (15 %)‡	X	X	X
Installation $(25 - 35\,\%)$‡	X	X	X
Overhead ($\sim 16\,\%$)‡	X	X	X

† Manpower includes 4 shifts working 24 h/day, 7 days/week and 320 days/yr

‡ These percentages are different between the Americas and European regions

The Americas unit costs include the direct and indirect costs for the shaft, tunnels and cavern excavation. Unit costs have been developed from both parametric scaling of excavations in the Chicago and Milwaukee areas, and bottoms-up estimates for items for which the parametric data is not available. Shaft costs include soil rock interface grouting, earth retention for the overlaying soft-ground excavation and drill and blast excavation in the hard rock. Shafts costs also include feature grouting and concrete lining. Tunnel unit costs include the excavation and mucking of the hard rock, feature grouting, invert and lining concrete. Caverns and hall unit costs include the drill-and-blast excavation, mucking of spoils, feature grouting, invert slab and shotcrete lining. Rock bolts or rock dowels will be required for permanent rock support for the shafts, tunnels, caverns and halls.

Vertical shafts and horizontal sloping access tunnels For the same cross-sectional area, the unit costs for the horizontal sloping tunnels used for access in the Asian site are much lower than the vertical shaft unit costs used in the other regions. The vertical shafts are generally more expensive because of more expensive surface construction support, and the need for more excavation time per unit length (since, for example, transportation or movement of the excavation machine is limited).

The vertical-shaft unit cost is higher for the Americas than in Europe because the excavation methods used for the Americas site are more complex. For the Americas site, two different means and methods are required to excavate the softer overlaying soils and the harder rock below. The soils require an earth retention system with a grout curtain installed to control water inflow, and the harder rock requires drill and blast equipment. As noted above, in the European region, no drilling and blasting is required. In addition, underground potable water and sanitary sewers are not included in the civil unit costs in the European region. Furthermore, both regions use different overheads percentages. In the Americas region, having two different construction means and methods results in higher overhead costs.

Beam and service tunnels Tunneling units costs used for American and European estimates are based on the use of TBM's, while the Asian estimate is based on the NATM drill-and-blast technique. For the same cross-sectional area, the NATM costs in the Asian region are lower than the TBM costs in the other regions. Part of this difference is related to labour cost differences between the regions.

The unit cost for the large "Kamaboko" tunnel in the Asian site is about 50 % greater than for the smaller $\sim 5\,\mathrm{m}$ Main Linac tunnels in the Americas and European regions. The unit cost difference increases to more than a factor of 2, however, when the cost of the shield wall is included.

Caverns Cavern unit costs are generally lower for the European region than for the Americas, for the same reasons as for the shaft unit prices, namely a difference in excavation methods and overheads.

The Asian cavern unit costs are generally considerably lower than those at the American site, for the same cross section, despite the fact that both use drill and blast excavation method. Part of this difference is related to labour-cost differences between the two regions.

Halls The IR hall unit costs are lowest for the Asian region and highest for the Americas region. Unit hall prices are lower for the European region than for the Americas, for the same reasons as for the shaft and cavern unit prices, namely a difference in excavation methods and division of overhead percentages. One of the reasons for the lower Asian unit costs is related to regional labour-cost differences.

15.7.3.2.5 Total costs In general, the distribution of total costs among tunnels, shafts, caverns and halls for the American and European sites is similar, as expected given the similarity in their designs. The beam-tunneling unit costs are similar for the two regions, as is the total cost for beam tunnels. Although the European region has fewer caverns, the volumes are larger, so that, despite the lower cavern unit costs in Europe, the overall cavern prices for both regions are similar.

The total shaft costs are significantly higher in the Americas estimate. This is due in part to the higher vertical shaft unit costs for the Americas region. In addition, there is a difference in shaft bottom definition between the two regions. The European region delineates the length of a shaft from the surface to the top of the connecting cavern, while the Americas region defines the shaft length from the surface to the bottom of the connecting cavern. This makes the Americas shafts 30% longer than the European shafts (130 m versus 100 m, respectively).

Relative to the flat topography sites, the beam tunnels are a larger fraction of the total civil engineering cost for the Asian site, because of the larger cross section of the "Kamaboko" tunnel, and consequent higher unit costs. The horizontal sloping access tunnels are a smaller fraction of the total, due to low unit costs for horizontal access tunnel excavation. Similarly, although the cavern volumes are larger for the Asian site, the cavern-excavation unit costs are much lower, leading to an overall cavern cost similar to that of the flat topography sites.

Since it is a "greenfield" site, the costs for site development are higher for the Asian site than for the other sites. The "greenfield" Asian site also contains additional surface structures associated with the central lab, office buildings, user facilities, and warehouses. However, there are fewer service buildings required for the mountainous region site, so the overall surface structure costs are comparable to those of the flat topography sites, which are located close to existing labs.

15.7.3.3 Conventional Electrical Systems

Conventional electrical systems include high- and low-voltage equipment and power distribution networks, emergency power sources, and communications and power network monitoring equipment.

The machine designs for the flat and mountainous sites utilise different distribution systems for high-level RF and have different layout configurations for electrical systems. Consequently, separate Value estimates for the conventional electrical systems for the Americas and Asian sites

were developed by consultant engineering firms. These estimates, which were based on the RDR electrical requirements, were modified as needed and adjusted to correspond to the TDR design power requirement for each site.

The final Americas (Asian) electrical system Value estimate is based on a total nominal operational power requirement of 161 (164) MW.

The differences in the distribution of costs between the estimates for the two regions reflect the different equipment layouts (e.g. high-voltage distribution in tunnels or on the surface) and differences in system redundancies for the two types of sites. The details are documented in Chapter 11. Based on the design similarities between the flat topography sites, the Americas estimate for the conventional electrical systems was used for the European site.

15.7.3.4 Conventional Mechanical Systems

Conventional mechanical systems include HVAC equipment, piped utilities (sump systems and fire suppression systems), and primary and secondary process (cooling) water systems.

The different topographies of the flat and mountainous sites result in substantially different solutions and costs for conventional mechanical systems. Again, consultant engineering firms were used to develop Value estimates for the conventional mechanical systems for both the Americas and Asian sites. These estimates, which were based on the RDR cooling requirements, were modified as needed and adjusted to correspond to the TDR design power requirement for each site.

Part of the difference in conventional mechanical system costs between the Asian and the Americas sites is due to the different main-linac high-level-RF configurations (KCS for the Americas, versus DKS for Asia). The KCS configuration places the majority of the heat loads at the surface; these are less expensive to manage than the DKS heat loads, which are in the tunnel.

Another difference is due to the different cooling approaches used at the two sites. The Americas region utilises a single water system in the main linac, which is a single-process low-conductivity water (LCW) system serving the main-linac tunnel loads. The Asian site follows the RDR approach of having two systems (both process-LCW and chilled-water systems) serving the tunnel loads.

Finally, for the KCS configuration, water-cooling systems for surface cryo plants are simplified because of the close proximity of the plants to the cooling towers. For the DKS configuration, the cryogenic plants are in the underground caverns.

Since the conventional mechanical systems design is similar for the Americas and European sites, the Americas estimate has been used for the European site. An important difference between the two regions is the ventilation scheme adopted by CERN, which is chosen to be transversal, mainly to satisfy regional safety regulations and for temperature stabilisation. A costing study has been performed by CERN for the transversal ventilation system for the Compact Linear Collider at CERN (CLIC) machine, but not for the ILC machine. It is expected that the costs found in this CLIC study are higher than would be required for the ILC, due to the higher CLIC heat loads, and the tighter temperature stabilisation requirements. However, a realistic comparison is not possible at this stage due to the different machine designs.

15.7.3.5 Handling Equipment

Handling equipment estimates were made both for installed equipment such as overhead traveling cranes and elevators, and for mobile equipment such as the special vehicles used for installation in the tunnel. The mobile equipment estimates are included under Installation (Section 15.7.4). The estimate is based on the European site layout. It was used for the Asian site without modification. For the Americas site, the only change was an increase in the number of lifts in the shafts, which is required in the Americas design.

The handling-equipment Value estimates for installed equipment (overhead traveling cranes, elevators and hoists) are based on European-supplier cost information provided at the time of the RDR. The Value estimate for the rented gantry for detector lowering is extrapolated from contract costs for the rented gantry used to lower the LHC CMS experiment at CERN.

Manpower estimates for installed equipment cover the engineering activities such as finalisation of requirements, agreement of interfaces with other infrastructure groups, specification, tendering, contract management, installation organisation and supervision, commissioning and maintenance management during the installation period. The external contractor support is taken as 2 % of purchase costs. The internal manpower estimate is extrapolated from LHC experience, based on crane and elevator quantities, and then shared among the area systems in proportion to purchase costs.

15.7.3.6 Safety Equipment

Safety equipment includes primarily alarm systems. The estimate was made independently for the Americas and Asian sites, by experts at Fermilab and KEK, and was based on the regional-code requirements that dictate the requirements of the safety system. No detailed studies have been performed specifically for the European ILC site. For this reason, the Americas estimate was used for the European site.

15.7.3.7 Survey and Alignment

Survey and alignment covers a very broad spectrum of activities, starting from the conceptual design of the project, through the commissioning of the machines, to the end of operations. The Value estimate developed covers the work necessary until successful completion of the machine installation. It includes equipment needed for the tasks to be performed. However, it does not include equipment for a dedicated calibration facility and workshops. It does include the staff that undertake the field work, and the temporary manpower for the workshops. Full-time staff are considered to be mainly dedicated to organisational, management, quality control, and special alignment tasks.

The Value estimate is mostly based on scaling the equivalent costs of the LHC to the ILC scope. The estimate was made for the European site and was used for the Americas and Asian sites without modification.

15.7.4 Installation

The installation estimate developed for the RDR was revised for the TDR. Because of the differences in tunnel layout and RF-component placement between the flat and mountainous sites, two different installation estimates were prepared, one for each site. However, the cost basis and methodology for each estimate was essentially the same as that for the RDR. The major changes were in areas for which the TDR design differs substantially from that of the RDR (main linacs with the KCS HLRF configuration, and the damping rings).

The installation Value estimate is characterised almost exclusively as explicit Labour, with minimum costs for material-handling equipment. The reason for this is that part of the installation and system check-out labour at the ILC site could be contributed by the staff of the ILC laboratory, or of collaborating institutions or laboratories. The degree to which laboratory staff could contribute depends on the availability of the necessary skilled manpower and local labour regulations. Because of the size of the project, it is likely that many tasks like electrical and plumbing work will need to be outsourced to industry. Trade-offs and translations are likely between using in-house labour and external contracts. Since the details of these trade-offs are not known, the installation manpower has been accounted for entirely as explicit Labour. It is estimated that a minimum of 10 % of the installation task must be management and supervision by in-house manpower.

The Value estimate was based on scaled information from a variety of sources, including the actual manpower used for the installation of recent accelerator projects. The installation cost model used a work-breakdown structure (WBS) that listed all of the activities required for installation of the technical systems, including the management, planning, and engineering support. The WBS was broken down into two major level-of-effort categories: General Installation and Accelerator-Systems Installation. General Installation included all common activities and preparations and associated logistics on the surface. Accelerator-system Installation included all efforts required for complete installation of the components underground.

To populate the WBS, a comprehensive list of components was compiled and interfaces and boundaries with the technical systems carefully defined. The estimates for labour and equipment required to install the components came from a wide variety of sources. For conventional components, like beam pipes and magnets, the technical system leaders provided estimates, based on experience with other projects. Visits to CERN and DESY provided data on installation of cryomodules, LHC magnets and the CMS detector as well as the opportunity to observe actual installation procedures. RSMeans 2006 cost data was used in estimating total work-hours needed for installing equivalent size/weight equipment under similar conditions. Since the main linac is a major cost driver, the installation of cryomodules and RF sources was modelled in detail. For other systems where there was no appropriate experience base, the estimates were scaled from similar installation tasks based on an assessment of complexity.

The Value estimate for mobile equipment for installation was built up by identifying suitable technical solutions for cryomodule and RF installation with allowances for powering and guidance infrastructure. The number of convoys was estimated based on the time available for installation, distances, speeds and estimated times for loading and unloading. An estimate for ad-hoc solutions for load interfaces to allow installation of other equipment was added. The cost of the individual vehicles is based on European costs for similar equipment purchased by CERN. Manpower estimates for mobile-equipment engineering activities were included.

At the time of the RDR, the estimates were reviewed by experts and crosschecked. The estimates were also compared with individual estimates from other sources, and with the actual manpower used for the installation of recent accelerator projects. There was also a bottoms-up study for installation of the cryomodules for the main linac done by two separate engineering teams, with comparable results.

Scientists, engineers and administrators comprise approximately 15 % of the installation manpower; the remainder is technician manpower.

15.7.5 Cryogenic Systems

Due to the different topologies of the flat and mountainous sites, which necessitate a different cryogenic layout, a separate Value estimate was developed for each site. However, the same cost basis was used for each. It was assumed that there was no difference in cost due to the fact that the cryoplants must be installed in underground caverns in the mountainous site.

The cost-estimating relationship for a cryogenic plant is a non-linear parametric relation between cost and plant power. For cryogenic distribution systems, linear relations between cost and length were used. The parameters in these relations are based on experience in procurement of cryogenic plants and distribution equipment at Fermilab, CERN, DESY, and other laboratories.

For the main linac plants, the cost basis is the same as that used for the RDR. This basis was independently validated through a comparison with experience in cryogenic-plant procurements at Jefferson Lab in 2010.

For the smaller plants used by the injectors and the damping rings, the cost basis was derived from recent procurement costs of the plant at Fermilab's New Muon Laboratory.

The explicit Labour estimate is based on the experience of staffing levels for cryogenic systems at the Superconducting Super Collider (SSC).

15.7.6 Magnet and Magnet Power-Supply Systems

Except for the damping rings, the unit-cost basis for all magnets and their power supplies is the same as that used for the RDR. The component counts for each area system were updated based on the TDR design.

The unit Value estimates were based on conceptual designs for magnets, power systems, stands and movers, with additional assumptions about estimated costs of material and labour. Given time and resource limitations, detailed conceptual designs were developed for only a small number of the magnet styles. The majority of the estimates are engineering estimates based on existing designs with similar requirements. Standardised labour rates were determined from laboratory and industrial sources in the Americas region.

In order to determine the material costs, the weights of magnet and cable materials, primarily copper and iron, were estimated and summed, and based on world commodity prices obtained at the time of the RDR (2007). Similarly, prices were obtained at the time of the RDR for commercially available electronic components such as power supplies, FPGAs and PLCs, controllers and Ethernet interfaces. These prices were escalated to the TDR estimate date (January, 2012) based on escalation rates for manufactured items. While this procedure is generally reliable for typical manufactured items, it may have limited accuracy for items whose cost is dominated by volatile commodity prices.

At the time of the RDR, a design and a complete set of drawings was developed for a positron-source transfer-line quadrupole, and a request for quote sent to a number of magnet vendors. The vendor quotes obtained were in reasonable agreement with an internal estimate: the average agreed within a few percent of the internal estimate, with a spread of $\sim 25\,\%$.

For a few magnet systems, more detailed Value estimates were provided based on R&D prototypes already in progress at the time of the RDR (e.g. the Daresbury/Rutherford undulators); in a similar fashion, Brookhaven provided detailed Value estimates for the superconducting insertion magnets at the IR based on experience with similar magnet designs.

Estimates of Engineering, Design, Inspection and Acceptance (EDIA) labour costs were based upon reviews of recent large accelerator magnet and power-supply projects at SLAC and Fermilab, where the materials, fabrication and EDIA labour fractions are well known. The fractional distribution of EDIA among several types of labourers, which were estimated at the standardised labour rates, was assigned on the basis of project-management experience.

Because of the major changes made to the design of the damping rings, for the TDR, new magnet unit Value estimates were developed. A new distributed power-supply system was designed and its cost was estimated for the TDR. The Value estimates were produced by two of the same engineers involved with the RDR estimates. The same general description given above for the RDR applies to the new TDR damping-ring magnet and power-supply cost bases.

The engineering and fabrication experience for the CESR-c wigglers were used to provide reliable Value estimates for the ILC damping wigglers, taking proper account of the well-defined differences in specification. New estimates were made for the TDR, since the damping wiggler design was modified from that in the RDR.

Costs for the damping-ring kicker pulser were based on a commercially available pulser (a fast ionisation dynistor, or FID, device) that comes close to meeting the specifications for the damping-ring injection/extraction kickers; this cost dominates the total cost of the injection/extraction system. Other components, including the strip-line electrodes and the septa, are relatively conventional, and costs were based on similar existing devices. The unit Value estimates developed for the RDR were

taken for the TDR.

The costs of the main-linac quadrupoles and correctors are included with that of the cryomodules. The costs of the quadrupole power supplies are included here.

15.7.7 Vacuum Systems

Except for the damping rings, the unit-cost basis for all vacuum systems is the same as that used for the RDR. The component counts for each area system were updated based on the TDR design.

The main parts of the vacuum systems were obtained from quotations from vendors and from recent large-quantity procurements. "Consumables," such as flanges, gaskets, bolts and nuts, cables, etc, were either not included or were estimated for quantity discounts of catalog items.

For the damping rings, since the TDR vacuum system is considerably different from that specified for the RDR, new vacuum-system Value estimates were developed. These include the costs of the surface treatments and antechamber designs, which are required to mitigate the electron-cloud effect in the positron ring. The Value estimate is based on estimates made for the Super-KEKB positron ring, which has a very similar vacuum system. The cryomodule vacuum system cost is included with that of the cryomodules.

15.7.8 Instrumentation

The unit-cost basis for all instrumentation systems is the same as that used for the RDR. The component counts for each area system were were taken to be the same as in the RDR, except for the positron source[14], for which they were updated based on the TDR design. The cost of the BPM's in the cryomodules is included under Instrumentation.

For beam monitors the Instrumentation Value estimate covers:

- all pickup stations, as part of the vacuum system;
- scintillators, PMTs, laser systems, calibration systems;
- RF systems and infrastructure for the DMC-based bunch-length monitors;
- associated motors, switches, and mechanical set up;
- signal and control cables, connectors, patch cables, etc.;
- dedicated read-out electronics (analog & digital), control units, local timing electronics, calibration electronics, local software and firmware.

Except for special cases, e.g. certain feedback systems, data-acquisition infrastructure is covered by the control-system Value estimate.

For costing purposes, instrumentation was classified into 17 different *systems*. Core cost and manpower information was estimated for each individual component of an instrumentation system and its subcomponents, including the cost reductions due to volume and/or technology advances. No spares were included. Counts of control racks required for data acquisition were generated from the above data. Labour information (in person-years) was estimated separately for Prototyping, Testing and Installation. The Installation labour was then incorporated into the Installation estimate and not included in Instrumentation.

The cost for the S-band dipole-mode structures, used for bunch-length measurements, was developed specifically for the RTML. The RDR estimate, which was used for the TDR, was based on recent experience with accelerator construction at IHEP.

[14] The redesign of the damping rings should also result in some changes to the RDR Instrumentation estimate for this system, but these changes are expected to be small and were ignored.

15.7.9 Dumps and Collimators

The unit-cost basis for all dumps and collimators is the same as that used for the RDR. The component counts for each system were updated based on the TDR design.

The systems that put water into direct contact with the beam dominate the Value estimate of this technical system. For the main beam dumps, the Value estimate is based on industrial studies [257, 258] by two German companies expert in nuclear reactor technology. At the time of the RDR, their estimates were examined by the staff responsible for the ISIS neutron-spallation target and adjusted, for example, to add the costs of the remote-controlled window-replacement system and air drying systems. For the aluminium-ball dumps that do not operate at high pressure, the cost of the 2006 ISIS target-cooling system was used as the basis of estimate.

Items with peripheral cooling supplied by the tunnel LCW system have only mechanical design and construction costs. Whether for collimators or solid dumps, these costs are estimated based on the production costs of similar devices in use at SLAC.

15.7.10 Integrated Controls and Low-Level RF (LLRF)

The scope of the Integrated Controls and LLRF system includes:

- global control system hardware and software;
- central computers for the accelerator control system;
- control-system databases;
- control-system network infrastructure;
- control-system front-end electronics and cabling;
- LLRF electronics and cabling;
- Personnel-Protection-System and Machine-Protection-System logic; and
- 5-Hz-feedback infrastructure.

The unit-cost basis for all controls systems is the same as that used for the RDR. The component counts were taken to be the same as in the RDR[15]. An inherent assumption is that the control-system hardware model can be implemented largely using COTS equipment.

Manpower estimates were developed top down, using assumptions about the level of effort required to implement a control system for ILC, and, at the time of the RDR, were compared with levels of effort from recent accelerator projects. It is assumed that the ILC control-system software framework is founded on an existing framework, rather than developing a new framework from the ground up. Assumptions were made on the level of extra effort needed to implement high-availability control-system hardware and software.

Materials and Services Value estimates were derived from a bottom-up assessment of the controls requirements from each accelerator and technical system. Costs for computing infrastructure (servers, networking, storage) were based on current commodity-computing vendor prices, with an inherent assumption that technology advances will bring commodity computing to the level of performance required for the ILC by the time of project construction. Estimates for the distribution of the RF phase reference were developed from a reference design and vendor quotes. Estimates for ATCA front-end electronics were based on technically comparable components in other electronics platforms since, at the time of the RDR, equivalent components were not yet available (or at least not in quantity) for ATCA.

[15] This is not precisely correct, especially for the positron source and the damping rings, but the error in the TDR estimate resulting from this approximation is expected to be much less than the uncertainty in the estimate.

Costs of the ILC damping-ring fast-feedback systems were taken directly from comparable systems in existing machines. Power amplifiers dominate the cost of the fast-feedback systems. Amplifiers operating in the appropriate parameter regime are available commercially, and costs for these were obtained from an experienced manufacturer.

15.7.11 Computing Infrastructure

Computing infrastructure costs required to operate the facility were taken from the RDR estimate. They include business computing facilities and software, a core campus network with associated software, central computing services, a computer security system, and engineering software.

The IT infrastructure estimates were based on actual costs for building and running IT infrastructure at Fermilab, assuming that an ILC laboratory requires equivalent functionality at approximately the same scale.

15.7.12 Other High-Level RF

This item refers to all systems generating RF power except the L-band systems. Specifically, this includes the warm sub-harmonic bunching system in the electron source, the warm high-level RF systems in the positron source, and the 650 MHz RF systems in the damping rings.

For the sources, the unit costs for the RDR were based on engineering estimates from warm RF experts at SLAC. For the TDR, the same unit-cost basis is used. The total costs were adjusted based on the TDR design requirements and component counts.

For the damping rings, the RF system is CW and operates at 650 MHz, a different frequency from the RF systems used elsewhere in the ILC. The designs of high-power RF components, such as klystrons and circulators, were scaled from commercially available 500 MHz devices. Estimates from klystron manufacturers indicated that development costs would increase the total cost by roughly the cost of one additional unit at the standard catalogue price.

The TDR estimate for this system is based on the unit Value estimates developed for the RDR. The TDR estimate was derived from these unit costs using the RF component counts associated with the TDR design.

15.7.13 Accelerator-Area-specific cost bases

In the following subsections, the cost basis for items specific to an accelerator system are described. For all systems, the Labour estimate includes the EDIA resources required for the system-specific Value elements (if any), together with the staff required for overall accelerator system integration during project construction and hardware commissioning. Except where noted, all estimates are those made at the time of the RDR.

15.7.13.1 Electron Source

The costs for the following items were estimated specifically for the electron source: the laser systems, the polarised-electron guns, the sub-harmonic bunchers and the travelling-wave bunchers. The costs were engineering estimates made at SLAC at the time of the RDR based on experience with polarised electron sources.

15.7.13.2 Positron Source

The costs for the following items were estimated specifically for the positron source: the positron-production target and its housing, the optical-matching device, the standing-wave and travelling-wave warm accelerators, the auxiliary source, and the target remote-handling system. Except for the last two items, the estimates were taken from engineering estimates made at the time of the RDR by engineers at SLAC.

The estimate for the new TDR auxiliary source was developed at ANL. This is an engineering estimate, based on experience with electron sources at that laboratory. The engineering estimate for the target remote handling is also new for the TDR, and is based on experience with remote handling of similar systems at IHEP.

15.7.13.3 Damping Rings

The cost of the cavities and cryomodules for the CW 650-MHz system were estimated specifically for the damping ring. The TDR estimate is based on the unit Value estimates developed for the RDR by engineers from INFN. Manufacturing costs for the cavities and cryomodules were assumed to be the same as for commercial versions of 500 MHz systems developed at Cornell and KEKB, with increased engineering effort to account for the rescaling, or in some cases redesign, of the existing subcomponents. The TDR estimate was derived from these unit costs using the cryomodule-component counts associated with the TDR design. For the TDR, the EDIA estimate for the cavities and cryomodules was taken to be 10 % of the M&S costs.

15.7.14 Management and Administration

As for the RDR[16], the model for management and administration staff is based on 50 % of the actual staffing levels during the construction phase (March, 1992) of the Superconducting Super Collider (SSC), but without central computing staff, which are included in Computing Infrastructure. A detailed breakdown is given in Table 15.11.

Table 15.11 Composition of the management model at ILC. The numbers indicate the percentage of the total management and administration manpower associated with that function.

Unit	Percent of total	Responsibilities
Directorate	10	Director's Office, Planning, ES&H Oversight, Legal, External Affairs, Education, International Coordination, Technology Transfer
Management Division	4	Quality Assurance, ES&H
Laboratory Technical Services	42	Facilities Services, Engineering Support, Material and Logistical Services, Laboratory Fabrication Shops, Staff Services
Administrative Services	32	Personnel, Finance, Procurement, Minority Affairs
Project-Management Division	11	Management, Administrative, Project-Management Division Office

The total management manpower is estimated by taking the FTE count for eight years, and converting to hours using 1700 hrs/yr. The eight-year duration assumes a two-year linear staffing ramp-up at the start of the nine-year construction project, followed by seven years at full staffing levels.

It is the practice in some regions to apply general and administrative overheads to purchases and labour for projects. These overheads are applied as a multiplier on the underlying Labour and Value,

[16] The total FTE count is reduced slightly from the RDR estimate due to a correction to the SSC project management office staff.

and cover the costs of the behind-the-scenes support personnel. In this estimate, such personnel are explicitly enumerated as labour under Directorate, Management Division, Laboratory Technical Service, and Administrative Services in Table 15.11. Therefore, the overheads are included as additional explicit Labour, rather than as a multiplier on Value and technical Labour.

It should be noted that this model for management and administrative staff is based on a project which was centrally managed. The ILC project, with its strong in-kind-contribution character, may require additional management or administrative staffing located centrally or in collaborating regions. These additional resources, if any, are difficult to estimate without a specific in-kind model, and so have not been included in this estimate.

15.7.15 Summary

The cost bases for the Value and Labour estimates developed for the ILC TDR have been presented and discussed in the previous sections.

A breakdown of the Value estimate, by type of cost basis, is shown in Fig. 15.4. A breakdown of the Labour estimate, by type of cost basis, is shown in Fig. 15.5.

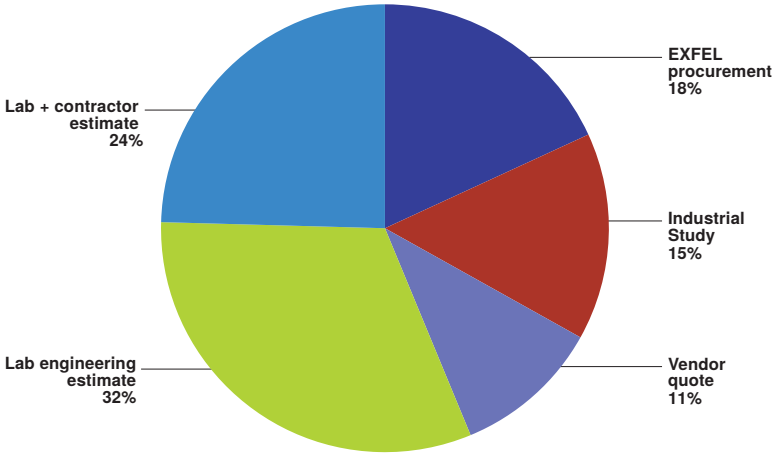

Figure 15.4
Breakdown of the ILC TDR Value estimate, by cost basis type

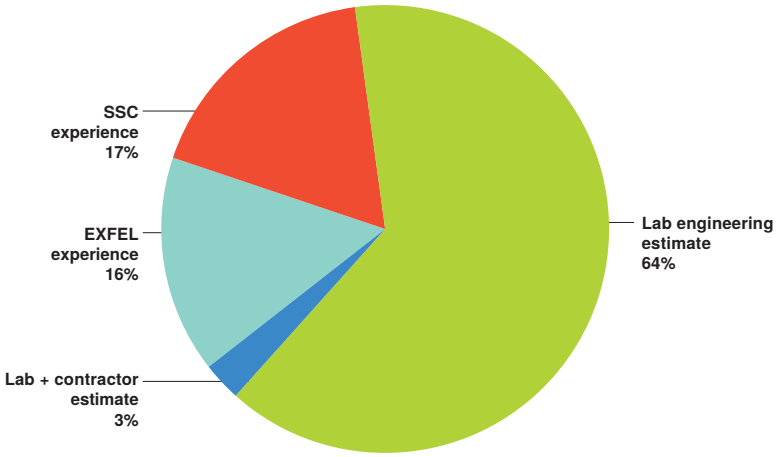

Figure 15.5
Breakdown of the ILC TDR Labour estimate, by cost basis type

15.8 Value and Labour Estimates for the Construction of the ILC

15.8.1 Escalation and re-statement of the RDR

As discussed in Section 15.4.2.4 above, the ILCU for the TDR is defined as equal to the USD on January 1, 2012. Conversions of estimates obtained in currencies other than USD to ILCU are based on PPP indices (as of January 1, 2012) relating those currencies to the USD, except for the cavity superconducting material, for which exchange rates are used. With this definition of the ILCU for the TDR, the RDR estimate can be re-stated in these units by escalating the elements of the RDR Value estimate from their original date to 2012, based on the regional escalation indices shown in Fig. 15.1, and converting to 2012 ILCU using the PPP indices shown in Fig. 15.2.

The resulting breakdown of the escalated RDR, in units of 2012 ILCU, is shown in Fig. 15.6. The cost breakdown categories are the same as those presented in Section 15.7. The total Value for the escalated RDR is 7,266 MILCU. This would be the TDR estimate if the TDR design and cost basis were identical to that of the RDR.

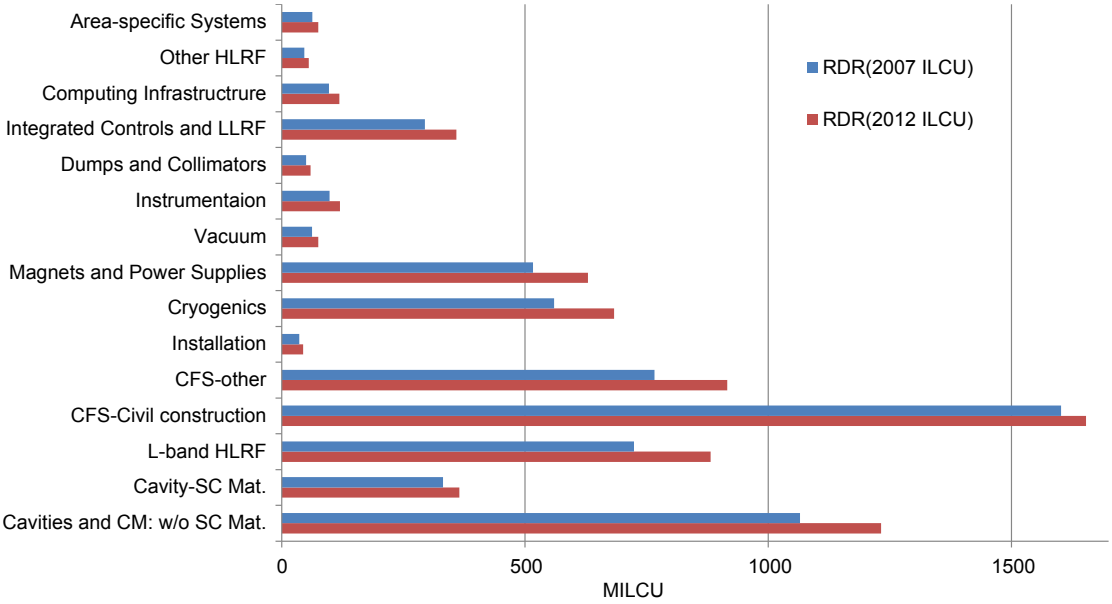

Figure 15.6. RDR Value escalation from 2007 to 2012. The total escalated RDR Value (red bars) is 7,266 (2012 MILCU). Also shown (blue bars) is the RDR stated in terms of an ILCU based on 2007 PPP indices. In these units, the RDR Value is 6,312 MILCU. The ratio between the RDR in 2012 ILCU (7,266) and in 2007 ILCU (6,312) is 1.15, which is the inflation rate (in USD, averaged over the project cost element types) over the period from 2007 to 2012.

15.8.2 Value Estimate for the TDR

The Value estimate for the cost of the ILC design as presented in this *Technical Design Report*, averaged over the three regional sites, is 7,780 MILCU. This may be compared with the escalated RDR estimate of 7,266 MILCU.

The cost optimisation of the machine design discussed in Section 15.6.1 resulted in a cost decrease of approximately 9% in the total project cost. The TDR estimate for the fabrication of cavities and cryomodules, which is based on extensive experience not available at the time of the RDR, increased relative to the RDR estimate by about 16% of the total project cost. The net overall effect (after correction for inflation) is a cost growth of approximately 7% from the RDR to the TDR.

The breakdown of the Value estimate for the TDR, in units of 2012 ILCU, is shown in Fig. 15.7. The cost breakdown categories are the same as those presented in Section 15.7. All estimates have been averaged over the three regional sites. For comparison, the escalated RDR is also shown. The

superconducting RF components, including their cryogenic systems and RF-power systems, represent about 76% of the estimate for all non-CFS components.

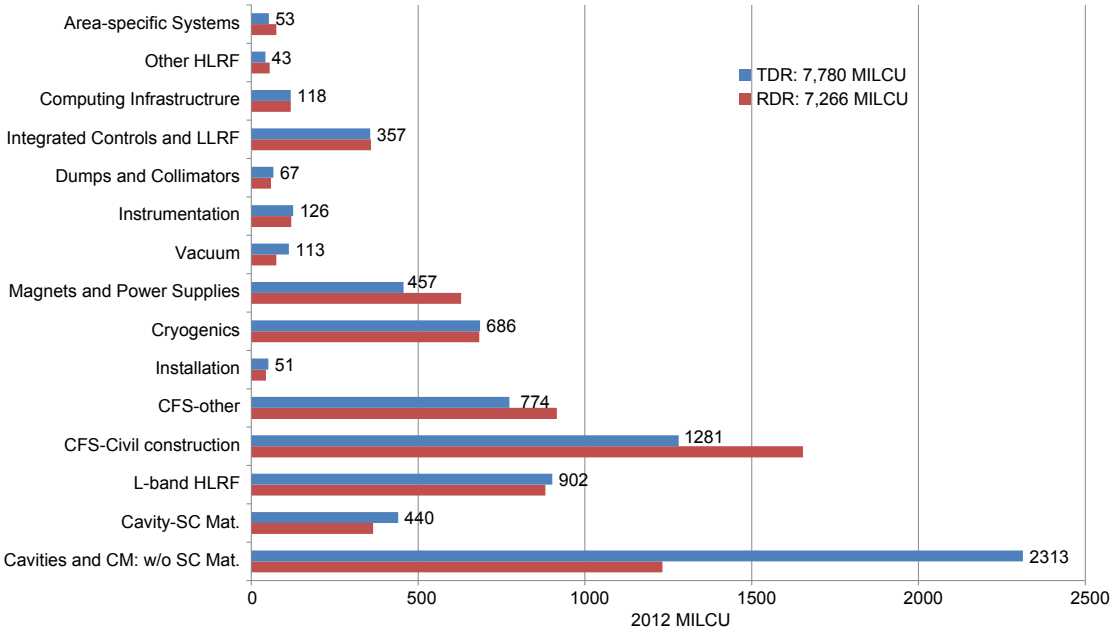

Figure 15.7. TDR Value estimate by technical system. Also shown for comparison is the escalated RDR. The numbers give the TDR estimate for each system in MILCU.

The Value estimates broken down by Area (Accelerator) System are shown separately for both the conventional facilities and the components in Fig. 15.8. The system labeled "Common" refers to infrastructure elements such as computing infrastructure, high-voltage transmission lines and main substation, common control system, general installation equipment, site-wide alignment monuments, temporary construction utilities, soil borings and site characterisation, safety systems and communications.

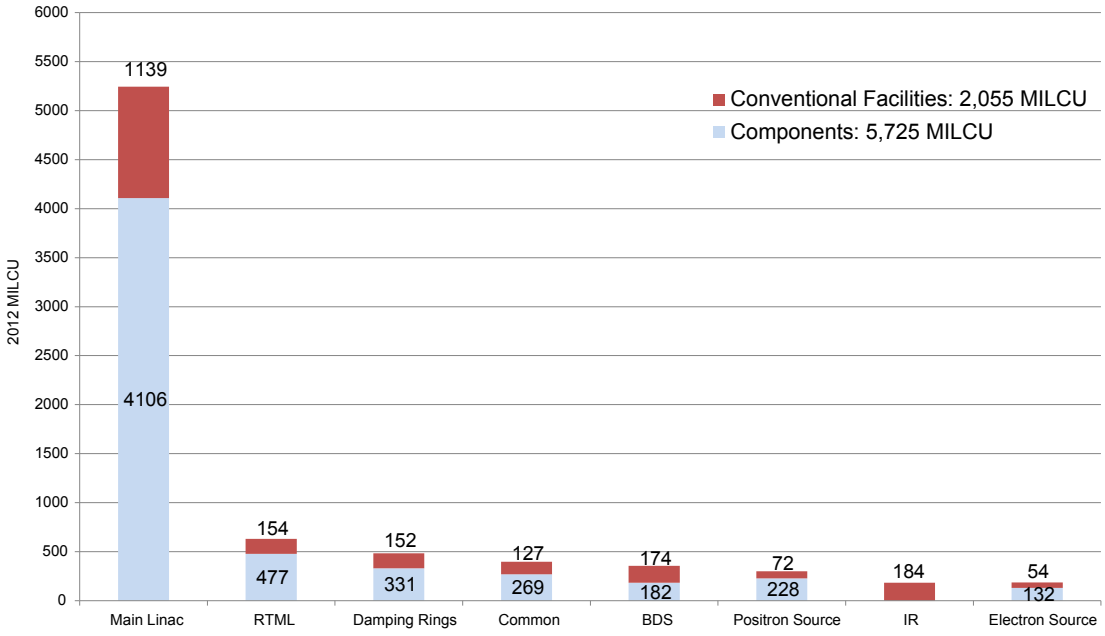

Figure 15.8. Distribution of the ILC value estimate by system and common infrastructure, in ILC Units. The numbers give the TDR estimate for each system in MILCU.

The component value estimates for each of the Accelerator Systems include their respective RF

sources and cryomodules, cryogenics, magnets and power supplies, vacuum system, beam stops and collimators, controls, low-level RF, instrumentation, installation, etc. The main linac comprises about 67% of the total project Value.

15.8.3 Explicit Labour Estimate for the TDR

The explicit Labour for the technical systems, and specific specialty items for Electron Source, Positron Source, Damping Rings, and Ring to Main Linac, includes the scientific, engineering, and technical staff needed to plan, execute, and manage those elements including specification, design, procurement oversight, vendor liaison, quality assurance, acceptance testing, integration, installation, and preliminary check-out of the installed systems.

The Labour estimate for the ILC design as presented in this Technical Design Report, averaged over the three regional sites, is 22,613 thousand person-hrs. This may be compared with the RDR estimate: 24,427 thousand person-hrs. The overall reduction of about 7% results partially from the cost optimization of the machine design discussed in Section 15.6.1, and partially from re-estimates of management and system-integration manpower.

The breakdown of the Labour estimate for the TDR, in units of thousand person-hrs, is shown in Fig. 15.9. The cost breakdown categories are the same as those presented in Section 15.7. All estimates have been averaged over the three regional sites. For comparison, the RDR is shown also. Installation is the largest fraction of explicit Labour, about 24%. Laboratory management and administration is the second largest fraction at about 18%, followed by L-band cavities and cryomodules at 16%.

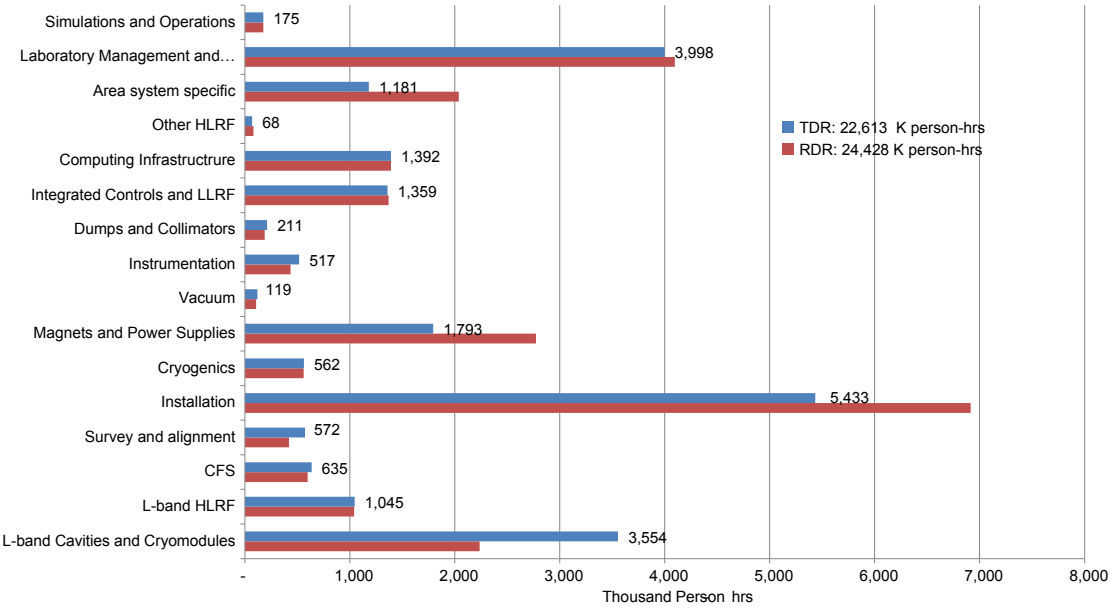

Figure 15.9. Explicit Labour, which may be supplied by collaborating laboratories or institutions, listed by technical system, and some Accelerator-specific systems. The numbers give the TDR estimate for each system in thousand person-hours. Also shown for comparison is the RDR.

The Labour estimates broken down by Area (Accelerator) System are shown separately for both the installation and all other labour elements in Fig. 15.10. The system labeled "Common" refers to computing infrastructure labour, laboratory management and administration, simulation and operations labour, and global elements of CFS, installation, and controls labour.

The component Labour estimates for each of the Accelerator Systems include system installation labour, EDIA for all accelerator components, and system integration staff. The main linac comprises about 37% of the total project Labour, followed by "Common" at 31%.

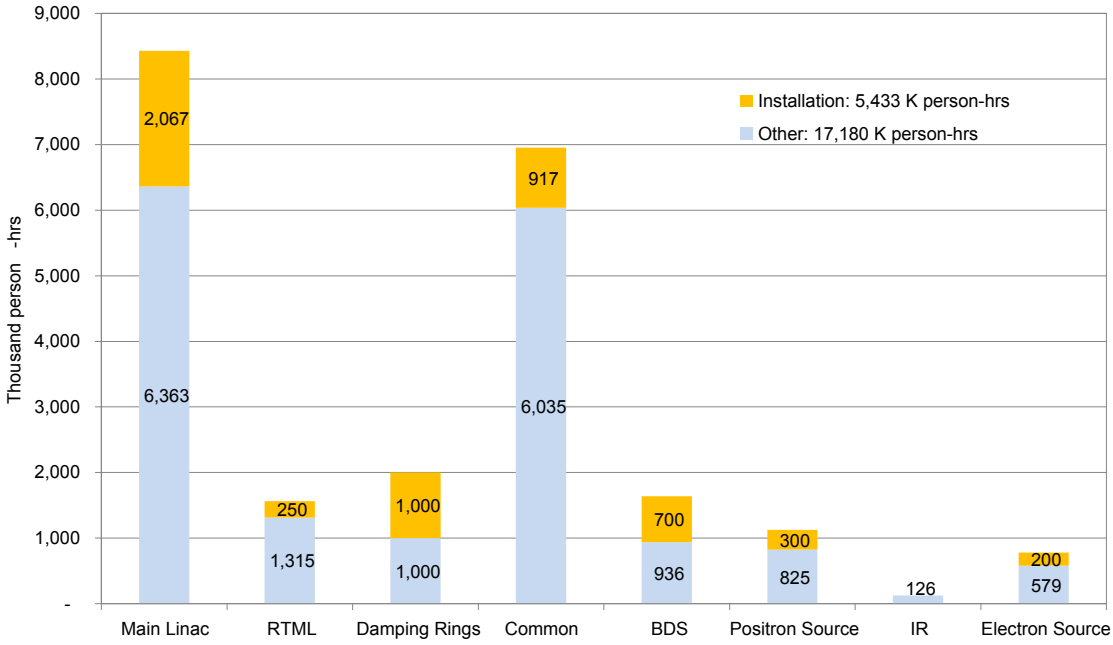

Figure 15.10. Distribution of the ILC Labour estimate by accelerator system. The numbers give the TDR estimate for each system in thousand person-hrs.

15.8.4 Site Dependence of the Value and Labour Estimates

The Value estimate may be broken down into two parts: the Value for site-specific costs, and the Value for shared parts. In one possible model for the division of responsibilities among the collaborating regions, the host region is expected to provide the site-specific parts, because of the size, complexity, and specific nature of these elements. The site-specific elements include all the civil engineering (tunnels, shafts, underground halls and caverns, surface buildings, and site development work); the primary high-voltage electrical-power equipment, main substations, medium-voltage distribution, and transmission lines; and the primary water-cooling towers, primary pumping stations, and piping. Responsibilities for the other parts of the conventional facilities: low-voltage electrical power distribution, emergency power, communications, HVAC, plumbing, fire suppression, secondary water-cooling systems, elevators, cranes, hoists, safety systems, and survey and alignment, could be shared between the host and non-host regions. All other technical components for the machine could, of course, also be shared between the host and non-host regions.

The Value estimates corresponding to this division of costs, for each regional site, are summarised in Table 15.12. The shared costs are higher for the flat topography sites because they require the more expensive KCS high-level RF-system configuration. The rms spread in the total costs among the three regional sites is 147 MILCU (1.9%).

Table 15.12
Possible division of Value for the 3 sample sites (2012 MILCU).

Region	Site-Specific	Shared	Total
Asia	1,756	6,226	7,982
Americas	1,413	6,310	7,723
Europe	1,330	6,304	7,634
Average	1,499	6,281	7,780

Similarly, the Labour estimate may be broken down into two parts: the Labour for site-specific parts, and the Labour for shared parts. The Labour for site-specific costs is the EDIA associated with the site-specific Value elements, together with Laboratory management and administration.

The Labour estimates corresponding to this division, for each regional site, are summarized in

Table 15.13. The rms spread in the total Labour among the three regional sites 1%.

Table 15.13
Possible division of Labour for the 3 sample sites (thousand person-hrs).

Region	Site-Specific	Shared	Total
Asia	4,536	18,356	22,892
Americas	4,272	18,096	22,368
Europe	4,496	18,084	22,580
Average	4,435	18,178	22,613

15.9 Cost Uncertainties, Confidence Levels and Cost Premiums

In this section, estimates of the uncertainties in the ILC TDR Value and Labour estimates are given. It is important to understand that these uncertainty estimates do not in general correspond to what is often referred to as contingency. Contingency is a broader term, and includes not only cost uncertainties but also, for example, allowances for missing items.

Cost risk is due to uncertainties or errors in the cost basis (e.g, procurement of a similar item, quantity discount from a single unit price, engineering estimate, etc.) on which the cost of a specific item is based. Technical risk is related to failure of a specific item to achieve the design performance, requiring a redesign which may result in schedule delays and increase the cost. Schedule risk is related to failure to supply a specific item on schedule, requiring delays which may increase the cost (typically by introducing inefficiencies and additional manpower requirements). Market risk is related to deviations in procurement costs from the estimate, due to changes in economic market conditions between when the estimate was made, and when the procurement is made.

The cost uncertainties estimated for the TDR only express the cost risk. They do not cover cost increases due to technical, schedule, or market risk, or to items that have been inadvertently omitted from the estimate. They also do not include allowances related to the potential cost and schedule risks associated with projects having large in-kind contribution components from several different regions of the world.

15.9.1 General Methodology

15.9.1.1 Confidence Level for the TDR Estimate

Cost estimation always involves some degree of uncertainty, which can be characterised by the width of the differential cost-distribution function. The cost of each element in the ILC TDR cost estimate corresponds to the median of the distribution: that is, it corresponds to the 50% probability point on the cumulative cost-distribution function. For simplicity, all cost distribution functions used in the ILC TDR estimate were taken to be symmetric Gaussian distributions. For such distributions, the median and the mean are identical.

The confidence level of an estimate is the probability that the actual cost of the item will be less than the estimate. Thus, the confidence level of each cost element in the ILC TDR cost estimate is 50%.

15.9.1.2 Cost-Element Uncertainty Characterisation

15.9.1.2.1 Development of Cost Uncertainties during the RDR.

Description of the uncertainties The uncertainty associated with each cost element depends on the nature, quality and maturity of the basis of estimate for that element. During the development of the RDR estimate, for each cost element, the estimator was required to evaluate the uncertainty. General guidelines were established to associate cost uncertainty with quality of the cost basis. These guidelines included the following elements:

- the maturity of the item's design (conceptual, preliminary, or detailed);

- the level of technical risk involved in the design and manufacture of the item;
- the impact of delays in this item on the project schedule (critical-path impact, non-critical-path impact, no schedule impact on any other item);
- the source of the cost information (engineering estimate based on minimal experience, engineering estimate based on extensive experience, vendor quote, industrial study, catalogue price);
- the extent, if any, of cost scaling to large quantities.

Using these guidelines, or by other means, the estimator identified the shape of the differential cost-distribution function for the cost element, choosing from three possible shapes: rectangular, Gaussian, or triangular. The estimator then characterized the upper(σ_U) and lower(σ_L) root-mean-square (rms) widths of the curve. The widths of the curves are measured from the mode (the cost corresponding to the maximum of the cost-distribution curve).

Cost premiums at the 84% confidence level From the differential cost-distribution function and the median estimate, the cost increase required to achieve a higher confidence level (84%) was computed for each element. In this section, this cost increase is called the "cost premium" (P). The premium is the cost that must be added to the median estimate (M) to obtain a "high-confidence estimate". Assuming that the cost distribution curve properly describes all sources of cost uncertainty for this element, the chance of the "high-confidence estimate" ($M + P$) being exceeded during project execution is 16%.

15.9.1.2.2 Treatment of cost uncertainties for the TDR. For the TDR, a simpler approach to the description of cost uncertainties has been adopted. This is based on the fact that the cost premium is the only information required from the cost distribution for the TDR.

For the TDR, only symmetric Gaussian distributions are used for all cost elements. To describe the uncertainty for such distributions, only one parameter is required: the rms width σ. Moreover, for such a distribution, the cost premium P at the 84% confidence level is simply equal to σ. A σ is determined for all cost elements that have a new estimate developed for the TDR, using guidelines similar to those developed for the RDR. For all other cost elements, σ is set equal to the cost premium computed from the original cost distribution given for the RDR. This procedure ensures that, for cost elements taken from the RDR, the cost premium in the TDR estimate is the same as that specified for the RDR estimate. The shapes of the distributions may be different in the TDR, since the normal distribution is used for all cost elements. However, since the cost premium is the only information required from the cost distribution for the TDR, the change in shape is of no consequence, as long as the premium is the same.

15.9.2 Median Estimates and Cost Premiums for Groups of Cost Elements

For any group of cost elements, the median estimates for all the cost elements in the group are summed to give the median estimate for the total cost of the group. This also applies to the total project cost. Thus, the confidence level of the total project cost stated in the ILC TDR cost estimate is taken to be 50%.

Similarly, for any group of cost elements, the cost premiums were summed over all the cost elements to approximate the cost premium on the total group cost. If the cost elements were completely uncorrelated, taking a summation in quadrature of the cost premiums would be approximately correct. However, the cost elements are correlated to some degree. In such a case, the use of a linear sum provides a relatively conservative estimate of the cost premium on the total group cost. For the group of all the cost elements, corresponding to the total project cost, the TDR estimate plus the total cost premium represents a "high-confidence estimate" with a confidence level of 84%.

15.9.3 Methodology for Assigning Cost Premiums for TDR Cost Elements

For cost elements whose estimates were newly developed for the TDR, a general methodology was developed to make an estimate of σ/M for a symmetric Gaussian (i.e. the relative cost premium). In this methodology, a "basic" (relative) premium was assigned, depending on the nature of the cost basis used for the cost element. To account for the uncertainty in the quantity discount used in the TDR estimate, an additional premium was added, equal to half of the quantity discount. Finally, to account for any additional sources of cost risk specific to a particular cost element, a "special" premium was added, if necessary. The total premium used for the cost element is the linear sum of the basic premium, half the quantity discount, and the special premium, if any.

15.9.4 Overall Cost Premiums for the TDR Value Estimate

Figure 15.11 shows the relative cost premiums for the TDR, broken down by the cost categories described in Section 15.7. For cavities and cryomodules, L-band high-level RF, conventional facilities, and installation, the cost premiums were developed using the methodology described in Section 15.9.3. For all other technical systems, the cost premiums are those developed during the RDR. The overall relative Value premium for the total ILC TDR Value estimate is 26%.

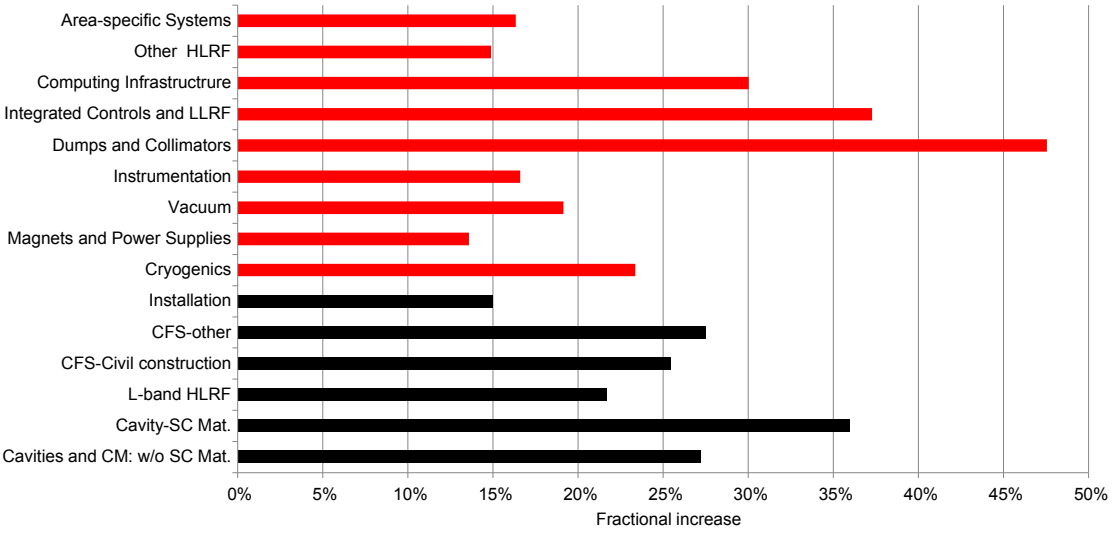

Figure 15.11. Relative Value premiums, broken down by subsystem, for the TDR.The red bars are taken from the RDR; the black bars correspond to premiums developed for the TDR.

15.9.5 Overall Cost Premiums for the TDR Labour Estimate

New estimates were made for installation labour, for cavity and cryomodule test and commissioning labour, for coupler processing labour, for conventional facilities labour (including survey and alignment), for management and administration labour, and for accelerator system-integration labour. The premiums for these cost elements were developed using the methodology described in Section 15.9.3. No special premiums were applied. For all other technical systems, the labour premiums are those developed during the RDR.

Figure 15.12 shows the relative Labour premiums for the TDR, broken down by the categories described in Section 15.7. The overall relative Labour premium for the total ILC TDR Labour estimate is 24%.

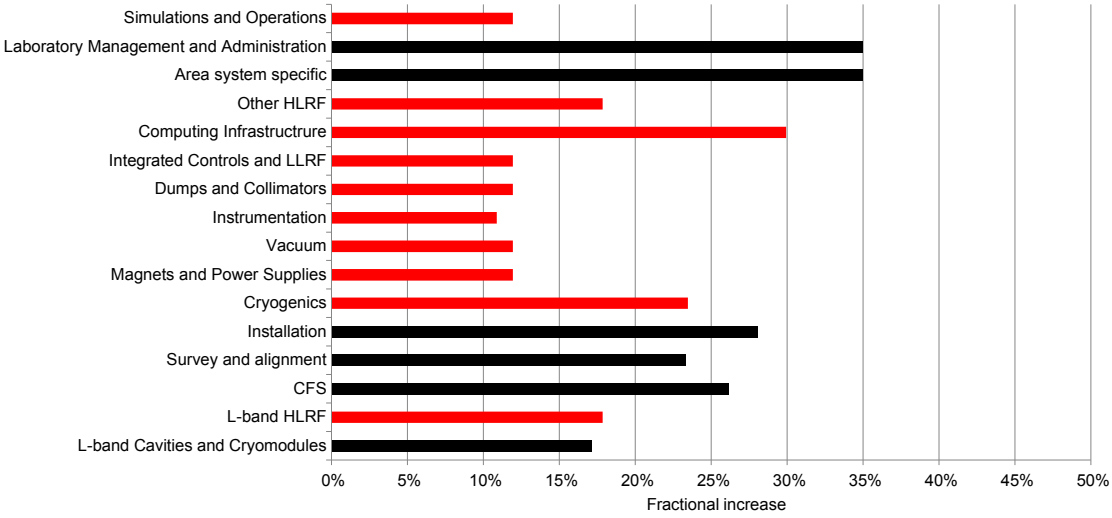

Figure 15.12. Relative Labour premiums, broken down by subsystem, for the TDR. The red bars are taken from the RDR; the black bars correspond to premiums developed for the TDR.

15.10 Value and Labour Time Profiles

Given the schedule described in Chapter 14, and the Value and Labour estimates given in Section 15.8, profiles describing the Value and Labour resources needed as a function of time can be developed. These profiles assume a flat funding profile for the major civil and technical procurements for each accelerator system, which is a crude assumption, but one which captures the essential features of the overall project-resource requirements.

The Value profile is shown in Fig. 15.13, broken down by technical system. The profile shows the front-loading of the civil construction effort, and the overall roughly six-year period for ramp-up and production of the cavities and cryomodules, which completes in year 7. The peak Value requirement is about 1,200 MILCU in years 4 and 5.

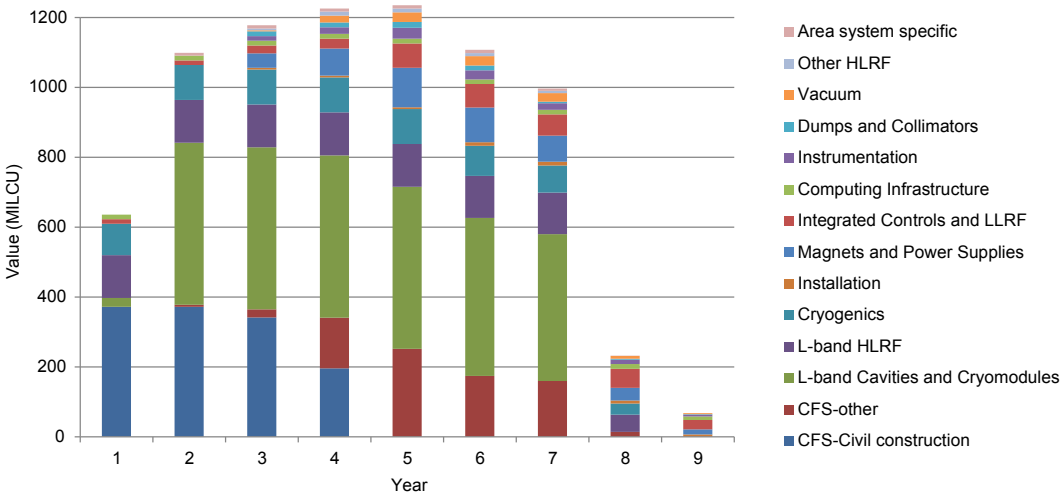

Figure 15.13. Value profile vs. project year. broken down by technical system.

The Labour profile (excluding installation) is shown in Fig. 15.14, broken down by technical system, while the installation Labour is shown in Fig. 15.15. The Labour profiles are in FTE, and assume 1700 person-hrs per year[17]. The back-loading of the installation profile is evident. The peak manpower requirements are about 1600 FTE in year 5 for all tasks except installation, and about

[17] 2000 person-hrs per year for installation.

950 FTE in year 7 for installation.

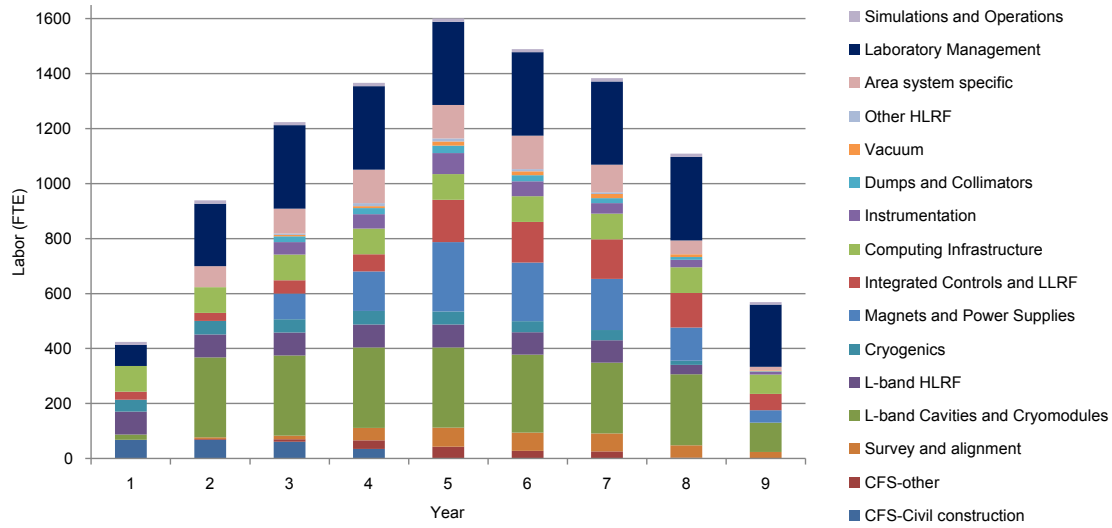

Figure 15.14. Profile for explicit Labour (excluding installation) vs. project year, broken down by technical system.

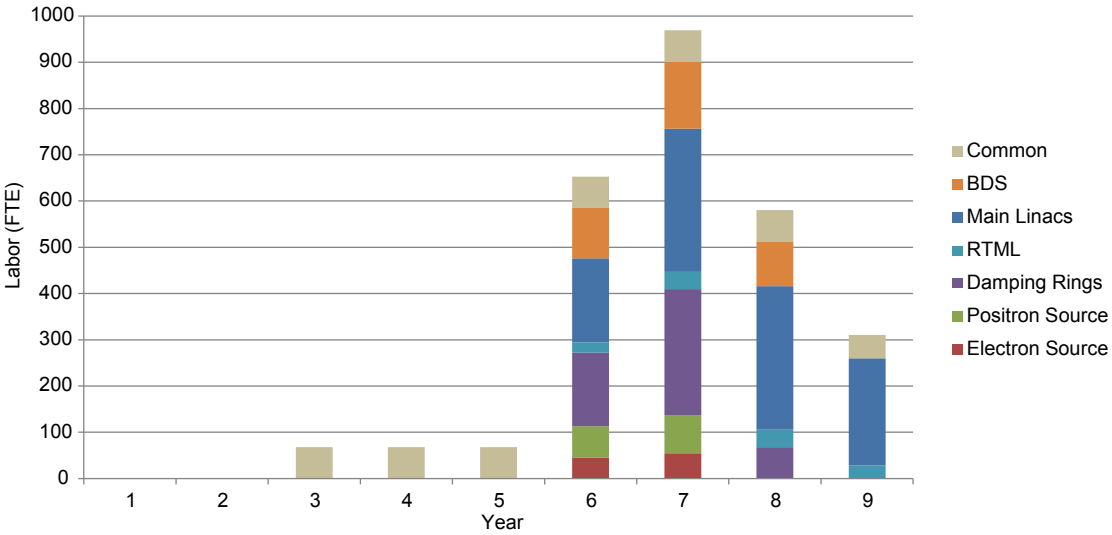

Figure 15.15. Profile for explicit installation Labour vs. project year

15.11 Value and Labour Estimates for Operations

Operating costs are not included in the estimate for the construction project, but a very preliminary estimate is given in this section. It is also to be noted that spare components (those stored in warehouses and not the installed redundant components), although fabricated along with the installed components, are assumed to be financed through operating funds, and are not considered part of the construction project.

Major factors in the Value estimate for operations include electrical power, maintenance and repairs, helium and nitrogen consumables, and components that have a limited life expectancy and need continuous replacement or refurbishment, like klystrons. The electric power costs and the cost for material and supplies during operation are estimated to lie in a range of 280 to 510 MILCU per year. The Value estimate for operations is taken to be the center of this range: 390 MILCU per year. The cost premium for this estimate is taken to be the standard deviation of the upper or lower estimate from the center, which gives a premium of about 40%.

The Labour estimate, corresponding to the continuing operations and administrative staff, is expected to be comparable to that at existing facilities (not including support of the scientific program). On this basis, the operations staff is estimated to be between 700 and 1000 FTE. Using the center of this range to set the Labour estimate, and the standard deviation of the upper or lower estimate from the center to set the premium, the Labour estimate for operations is 850 FTE, with a premium of about 25%.

Operating costs are anticipated to gradually increase over the fourth through ninth years of construction from zero up to the full level of long-term operations at the end of the 9 year construction phase.

15.12 Value and Labour Estimates for Upgrade and Staging Options

This section estimates the Value and Labour changes associated with the upgrade and staging options described in Chapter 12 of this *Technical Design Report*.

15.12.1 Value and Labour Estimate for Luminosity Upgrade

In Section 12.3, a luminosity upgrade for the 500 GeV baseline machine is discussed. The luminosity upgrade is accomplished by doubling the number of bunches, resulting in a doubling of the average beam power. Additional RF power sources (klystrons and modulators) are added to the main linacs, and an additional positron damping ring is installed in the damping ring enclosure.

15.12.1.1 Technical system scope, Value and Labour changes

15.12.1.1.1 L-band high-level RF systems In the main linacs, additional klystrons and modulators are added, and microwave power distribution systems must be modified. The technical scope changes differ for the flat and mountainous topography sites, due to their different RF power source configurations.

For the KCS configuration at the flat topography sites, an additional 10 klystrons and modulators are added at each of the 22 klystron clusters. The total number of klystrons and modulators thus increases by 220. In addition, some additional microwave hardware is required in the KCS power distribution system.

For the DKS configuration at the mountainous topography sites, the local PDS systems are reconfigured so that 26, rather than 39, cavities are driven by each klystron. This increases the required number of klystrons and modulators in the main linacs from the baseline number (378) to $378 \times 39/26 = 567$, which corresponds to an increase of 189 klystrons and modulators.

In addition to these changes in the main linacs, 3 more klystrons and modulators must be added to the 5 GeV booster in the positron source.

The Value estimates for the additional klystrons, modulators and associated microwave hardware have been made assuming the components are procured in the required numbers from 2 vendors. The unit costs have been adjusted for the number of procured components, using the same cost estimating relationship that was used for the baseline estimates. The Labour estimates were based on simple scaling with Value from the baseline Labour estimates.

15.12.1.1.2 Conventional facilities Conventional facilities support systems (electrical and mechanical) must be upgraded to handle the increased beam power in all accelerator systems, and the increased number of RF power sources in the main linacs. The Value estimates for the cost of these upgraded support systems are based on information developed for the Americas region conventional systems baseline estimate. The Labour estimates were based on simple scaling with Value from the baseline Labour estimates.

15.12.1.1.3 Damping rings Since the number of bunches is doubled, the bunch spacing in the damping rings is halved. To maintain the same bunch spacing for positrons[18], an additional positron damping ring is added, in the same tunnel as the baseline positron and electron rings.

Low-energy operation at 10 Hz with twice the beam current in the electron ring requires the addition of more RF cavities. The available space in the lattice permits 4 more cavities to be added.

The Value and Labour estimates for the new positron damping ring are based on simple scaling from the baseline damping rings estimate. The small additional cost of 4 more RF cavities in the electron damping ring has been included.

15.12.1.1.4 Common In addition to the items noted above, changes in the scope of Common elements of the associated technical systems (conventional facilities, installation, and control systems) are also included. This is based on a simple scaling with changes in the associated technical system Value or Labour. No changes in laboratory-wide Common Value or Labour elements, (i.e. computing infrastructure, laboratory management and administration, and simulation and operations) are included, as it is not clear how these elements would scale with the technical scope changes.

15.12.1.2 Summary of Value and Labour changes

The total Value change associated with the luminosity upgrade is 483 MILCU. This is about 6% of the 500 GeV baseline Value estimate. The total Labour change associated with the luminosity upgrade is 1,537 thousand person-hrs. This is about 7% of the 500 GeV baseline Labour estimate.

15.12.2 Value Estimate and Labour Estimate for 1 TeV Energy Upgrade

In Section 12.4, the upgrade of the baseline machine to 1 TeV center-of-mass is discussed. The beam current needed for the 1 TeV machine requires the luminosity upgrade discussed in Section 12.3. Consequently, in evaluating the Value and Labour changes for the 1 TeV upgrade, the technical scope, and corresponding Value and Labour estimates, have been taken to be that of the baseline with the luminosity upgrade.

The beam energy upgrade is accomplished by extending the main SCRF linacs to provide the additional 250 GeV beam energy. The main linac tunnels are lengthened to accommodate the additional SCRF hardware, new RTML turn-arounds and bunch compressor systems are constructed at the new low-energy ends of the main linacs, and the long 5 GeV transfer line is extended. The positron-production undulator is replaced with one suitable for 500 GeV beam energy, and additional dipoles are added in the BDS to provide the required higher integrated field strength.

Three possible scenarios for the re-configuration of the main linacs are presented:

- **Scenario A:** The linac extension is accomplished using the baseline SCRF technology, i.e. cavities with an average gradient of 31.5 MV/m.
- **Scenario B:** The linac extension is accomplished using improved SCRF technology, i.e. cavities with an average gradient of 45 MV/m.
- **Scenario C:** The entire main linac is removed and replaced with improved SCRF technology, i.e. cavities with an average gradient of 45 MV/m, with a length sufficient to provide a beam energy of 500 GeV.

[18] The minimum bunch spacing is determined by the electron cloud effect in the positron ring.

15.12.2.1 Technical system scope, Value and Labour changes

15.12.2.1.1 Main linacs The changes in the main linacs and associated civil construction depend on the scenario, as detailed in the following bullets:

- **Scenario A:** An additional 260 GeV of main linac is added. Since the baseline linac energy is 235 GeV, the addition is essentially the baseline scaled up in energy by 260/235=1.106. The gradient for the new linac is the same as for the baseline, so the additional tunnel and linac have a length scaled up by the same factor as the energy. The additional cryogenics load is 70% of the baseline.
- **Scenario B:** Again, an additional 260 GeV of main linac is added. The addition is essentially the baseline scaled up in energy by 1.106. However, since the average gradient for the new linac is 45 MV/m, the additional tunnel and linac have a length scaled up by $1.106 \times 31.5/45$=0.774. The additional cryogenics load is 60% of the baseline.
- **Scenario C:** In this case, as far as power sources, cryogenics, and conventional facilities support are concerned, an additional 260 GeV of main linac is again added. However, the cavities and cryomodules for the entire linac are replaced: this corresponds to adding 485 GeV of linac. The associated linac length scale factor relative to the baseline is $485/235 \times 31.5/45$=1.445. However, the scale factor for additional linac tunnel is 0.445. The additional cryogenics load is 50% of the baseline.

In estimating the Value changes for the cavities and cryomodules based on improved SCRF technology, the cost per unit length is taken to be the same as for the baseline SCRF technology. Note that the system Value or Labour is simply scaled with the change in associated technical scope, assuming that component unit costs do not change. In fact, the change in the numbers of components would result in unit cost changes, but this effect is neglected.

15.12.2.1.2 Other accelerator systems In addition to the linac changes, for all scenarios, the baseline RTML is essentially duplicated, and installed at the low energy end of the 1 TeV machine. Consequently, the Value and Labour for the baseline RTML is added, for all scenarios[19]. The Value of the baseline undulator is also added, to approximate the cost of the required new undulator. Finally, the Value of 10% of the baseline BDS magnets and power supplies is included, to approximate the costs of the new BDS components required for 1 TeV.

15.12.2.1.3 Common In addition to changes in the linacs and RTML, changes in the scope of Common elements of the associated technical systems (CFS, installation, and control systems) are also included. This based on a simple scaling with changes in the associated technical system Value or Labour. No changes in laboratory-wide Common Value or Labour elements are included, (i.e. computing infrastructure, laboratory management and administration, and simulation and operations), as it is not clear how these elements would scale with the technical scope changes.

15.12.2.2 Summary of Value and Labour changes

The total Value changes associated with scenario A, B and C are 6,706, 5,489 and 7,082 MILCU, respectively. These increases correspond to 81%, 66%, and 86%, respectively, of the 500 GeV Value estimate for the baseline with luminosity upgrade. The total Labour changes associated with scenario A, B and C are 11,988, 9,416 and 14,256 thousand person-hrs, respectively. These increases correspond to 50%, 42%, and 59%, respectively, of the 500 GeV baseline Labour estimate with luminosity upgrade.

[19] This is not quite correct, since some of the baseline RTML Value and Labour is associated with the beamlines from the damping rings to the long 5 GeV transfer line. The RTML contribution to the 1 TeV upgrade is thus slightly overestimated.

15.12.3 Value and Labour Estimates for a Light Higgs Factory as a First-Stage Option

In Section 12.5, a 250 GeV center-of-mass machine is discussed, which could be implemented as the first stage of a route to the baseline 500 GeV ILC. The first stage machine would require the installation of approximately half of the baseline linacs. Two possible scenarios are presented:

1. Only the tunnel and support shafts (access ways) required for the 250 GeV machine are constructed, and the linacs are installed in this tunnel.
2. The complete tunnel and support shafts (access ways) for the 500 GeV machine are constructed as part of the first stage, and the linacs are installed in the first half of each tunnel, followed by a beam transfer line to the central region.

The first scenario is conceptually the same as that proposed for the 1 TeV upgrade, although half the scale. It is likely to represent the minimum cost for the initial phase machine. The second scenario requires greater investment for the initial phase (for the civil construction), but increasing the centre-of-mass energy then becomes relatively straightforward, and opens up the possibility for a more adiabatic approach to increasing the energy.

15.12.3.1 Technical system scope, Value and Labour changes

For the first stage machine described in Section 12.5 of the TDR, the electron and positron sources, the damping rings, and the beam delivery systems, are identical to those of the baseline machine. Both scenarios require a 150 GeV electron linac operating at 10 Hz[20] (for positron production) and a 125 GeV positron linac. Scenario 1 also requires an RTML with a transfer line only about half the length of the baseline system, while scenario 2 requires essentially the baseline RTML.

15.12.3.1.1 Scenario 1 The technical scope reductions in this scenario are the removal of 100 GeV of electron linac (together with its tunnel), 125 GeV of positron linac (and tunnel), and the corresponding lengths of the RTML long transfer lines. The ratio of the electron linac removed to the total baseline linac is $100/470 = 0.212$. The ratio of the positron linac removed to the total baseline linac is $125/470 = 0.266$. The fraction of the RTML long transfer line removed is the sum: $0.212+0.266 = 0.479$.

In evaluating the Value and Labour changes associated with these technical scope reductions, the system Value or Labour are simply scaled with the change in associated technical scope, assuming that component unit costs do not change. In fact, the change in the numbers of components would result in unit cost changes, but this effect is neglected.

In addition to changes in the linacs and RTML, changes in the scope of Common elements of the associated technical systems (CFS, installation, and control systems) are also included. This based on a simple scaling with changes in the associated technical system Value or Labour. No changes in laboratory-wide Common Value or Labour elements, (i.e. computing infrastructure, laboratory management and administration, and simulation and operations) are included, as it is not clear how these elements would scale with the technical scope changes.

The total Value change associated with scenario 1 is -2,425 MILCU. This is about 31% of the 500 GeV baseline Value estimate. The total Labour change associated with scenario 1 is -4,583 thousand person-hrs. This is about 20% of the 500 GeV baseline Labour estimate.

15.12.3.1.2 Scenario 2 Relative to scenario 1, this scenario simply adds back the tunnels for 100 GeV of electron linac and 125 GeV of positron linac, and the corresponding lengths of the RTML long transfer lines. In addition, a beamline is required to transport the 125 or 150 GeV beam from the end

[20] The need for the 10-Hz mode could be removed by increasing the length of the superconducting helical undulator from the baseline length of 147 m to approximately 250 m. The electron linac would now only require an additional 3.5 GeV beyond 125 GeV to drive the undulator, and only needs to run at 5 Hz.

of the linac to the entry to the BDS. As a crude approximation, the cost of this beamline is taken to be the same as that of an equal length of 5 GeV RTML beamline.

The net Value change associated with scenario 2, relative to the baseline, is -1,934 MILCU. This is about 25% of the 500 GeV baseline Value estimate. The net Labour change associated with scenario 2, relative to the baseline, is -3,563 thousand person-hrs. This is about 16% of the 500 GeV baseline Labour estimate.

15.12.4 Summary

Relative to the baseline, the Value and Labour estimates for the options discussed in Chapter 12 of the TDR are plotted in Fig. 15.16 and Fig. 15.17.

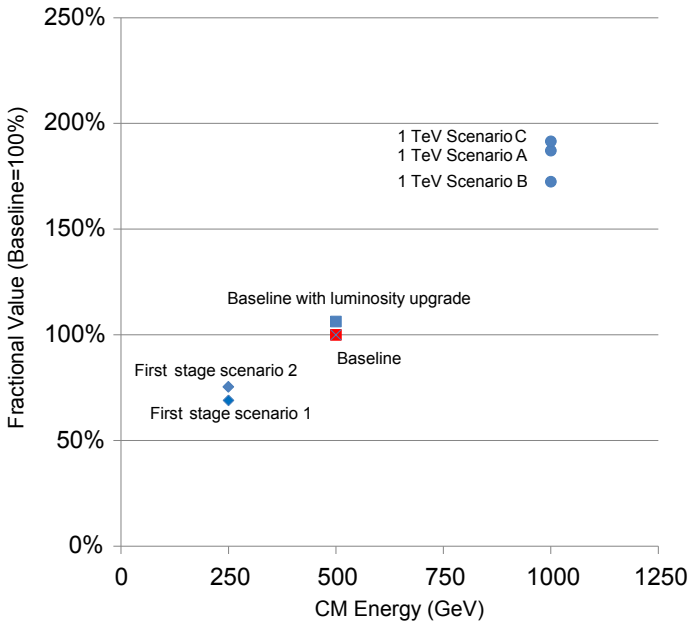

Figure 15.16
Relative Value estimates for upgrade and staging options.

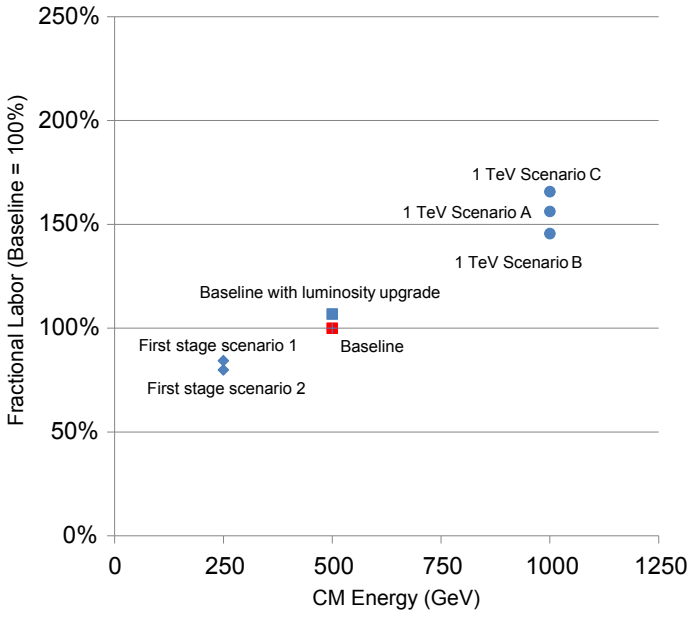

Figure 15.17
Relative Labour estimates for upgrade and staging options.

Appendix A
Evolution of the ILC design in the Technical Design Phase

A.1 The goals of the Technical Design Phase

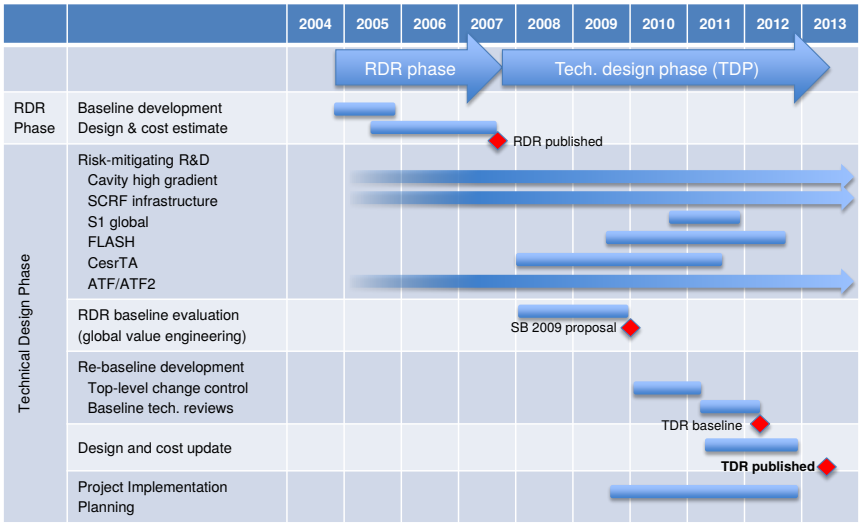

Figure A.1
Path to the ILC Technical Design Report, indicating the two distinct project phases of the Global Design Effort: the RDR phase, which focused on design and cost-estimate work for the GDE first major deliverable, the 2007 Reference Design Report; and the subsequent Technical Design Phase, which focused on risk-mitigating R&D and worldwide development of SCRF technology, and a re-evaluation of the RDR baseline and updated cost estimate.

The Technical Design (TD) phase of the ILC Global Design Effort (GDE) began after the publication of the ILC Reference Design Report (RDR) in 2007 [3]. The main objectives have been mitigation of the remaining identified high-risk issues associated with the RDR baseline design, and to further refine that design with a strong emphasis on cost optimisation. The primary GDE deliverables summarised in the TDR are:

- an updated technical description of the ILC Technical Design in sufficient detail to justify the associated VALUE estimate;
- results from critical R&D programmes and test facilities, which either demonstrate or support the choice of key parameters in the machine design;
- one or more models for a Project Implementation Planning (PIP), including scenarios for globally distributed mass-production of high-technology components as "in-kind" contributions;
- an updated and robust VALUE estimate and construction schedule consistent with the scope of the machine.

Figure A.1 shows the GDE's top-level phases, while Fig. A.2 shows how the R&D programmes together with the Accelerator Design and Integration (AD&I) activities factor into the TDR and also the PIP. The five themes identified (risk-mitigating R&D, of which SCRF R&D is a special case, AD&I cost and schedule and finally risk assessment) form an integrated approach to producing a mature and relative low-risk design for the ILC.

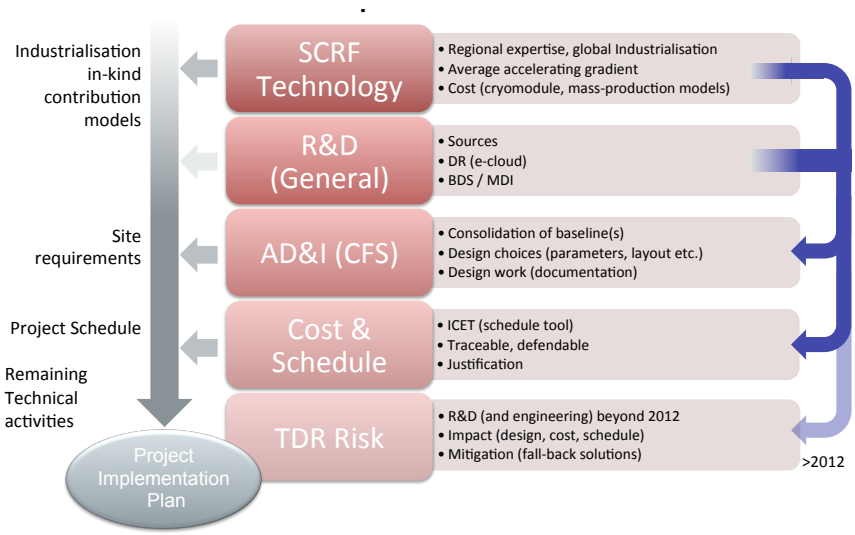

Figure A.2
The primary themes of the GDE's Technical Design Phase, and how they relate to the key deliverables of the Technical Design Report.

To coordinate the TD-Phase plans, the GDE implemented a monolithic project management structure shown in Fig. A.3. The project was divided into three main Technical Areas, each representing about one third of the total project cost: SCRF Technology; Conventional Facilities and Siting (CFS), together with global systems; and finally Accelerator Systems, which effectively covered the accelerator design of the sources, damping rings and beam-delivery system. Each Technical Area was managed by one of three project managers, who formed a central management team. Under each project manager, a number of Technical Area Groups were identified. The Technical Area project managers and Technical Area group leaders – together with integration and documentation technical support, formed the central ILC design group for the TD phase.

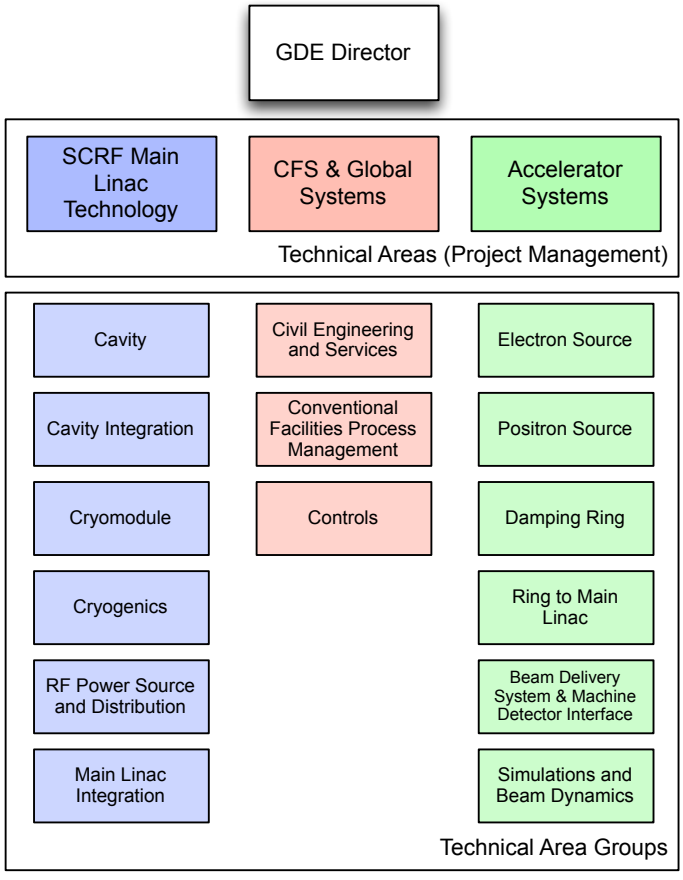

Figure A.3
The GDE project structure for the Technical Design phase.

A.2 Approach to cost constraint and re-baselining the ILC

The 2007 RDR published a value estimate of 6.7 Billion ILCU together with an estimated 14,200 person-years of institutional labour, for the construction costs of the machine. As part of the overall project risk mitigation, the need to constrain the total construction cost was mandated early on in the technical design phase. This resulted in an approach to the risk-mitigation R&D and in particular the AD&I activities which maintained a strong emphasis on cost impact. For the RDR, the cost of the SCRF technology included in the RDR was based entirely on the European estimates developed for the TESLA project and subsequently updated for the European XFEL, and assumed a single-vendor model. An important goal of the TD phase was to bring the SCRF capabilities of the Americas and Asian region, including industry, and to reconsider the single-vendor model in the light of possible global distribution of the manufacturing, as well as risk reduction. Similarly, the CFS costs – in particular for civil engineering – were consider a risk item as the constraints and issues arising from site-dependent designs became more apparent as they were developed during the TD phase.

With these potential cost risks in mind, a complete high-level cost-driven review of the RDR machine layout and design was undertaken early in the TD phase, in order to reduce the RDR cost and provide margin to hedge any component-level unit cost from the TD phase R&D programmes. The approach adopted to re-baselining was based on an assumption that the RDR design – although sound – was conservative in many of its design decisions, relatively immature from a detailed engineering standpoint, and was "performance-driven" as opposed to cost optimised. Conventional Facilities and Siting (CFS) was identified early on as a strong focus for design optimisation; in particular the reduction of underground civil construction, achieved by a critical re-evaluation of the criteria driven by the accelerator design assumptions. On analysis of the RDR costs drivers, it quickly became apparent that no major cost savings (i.e. tens of percent) where achievable without a change in project scope. Value engineering was expecting to provide savings on the order of $\sim 10\,\%$ total project cost, by consolidating many detailed design elements at the $< 1\,\%$ level. The engineering resources required for such detailed design work were not available to the GDE during the TD phase, and value engineering is now considered part of the post-TDR work, likely as part of a pre-construction project. With this in mind, a strategic decision was made to focus the limited design resources available on relatively high-level layout and design modifications, each of which could provide 1—2% cost savings (based on the RDR costs). The RDR design review or "global value engineering" as it later became known, was based on the following premises:

- **overall cost reduction** – Any opportunities for cost reduction should be taken, in so far as they do not unacceptably impact performance or increase technical risk;
- **improved cost balancing** – Cost margins created as part of the cost-reduction exercise can be made available for other subsystems which incur increased (estimated) construction costs.
- **improved understanding of system functionality** – Understanding how a given system's requirements and functionality impact cost forced a careful analysis of the system's strengths and vulnerabilities; this has a critical value on its own beyond cost-reduction;
- **more complete and robust design** – Revisiting many of the design and implementation details that were not completely covered during the RDR design phase.

The analysis and subsequent review resulted in six major design modifications reflecting an approximate 10 % reduction in the 2007 RDR cost estimate. The final proposed modifications were captured in the "straw-man baseline" SB2009 proposal report [209], submitted by the project management to the GDE Director. To achieve the global consensus of all stake-holders required, a formal process known as Top-Level Change Control was initiated, which was developed over a twelve-month period. A second phase of lower-level change control followed, consolidating more detailed

Table A.1. The ILC baseline re-evaluation process during the Technical Design Phase

Top Level Change Control: Baseline Assessment Workshops (BAW)				
BAW 1	7-8.10.2009	KEK	Choice of average accelerating gradient, including margins for installation and operation. RF power overhead for support of ±20% spread in cavity gradients, including design of power distribution system and impact on low-level RF control.	[259]
BAW 2	9-10.10.2009	KEK	Removal of Main Linac service tunnel (single-tunnel solutions) RF power generation and distribution for single tunnel solutions (Klystron Cluster scheme and Distributed RF Source scheme).	[260]
BAW 3	18-19.01.2010	SLAC	Relocation of the undulator-based positron source to the exit of the main electron linac (nominal 250 GeV beam energy), including integration into central region. Considerations for low centre-of-mass energy running (10 Hz operation mode).	[261]
BAW 4	20-21.01.2011	SLAC	Reduction of the number of bunches per pulse by 50 % (reduced beam power). Associated reduction of the damping ring circumference and main linac klystron and modulator count. Luminosity recoverted by stronger beam-beam interaction at the interaction point (stronger focusing in the final-focus system).	[262]
Baseline Technical Reviews (BTR)				
BTR 1	6-8.07.2011	INFN Frascati	Damping rings	[263]
BTR 2	24-27.10.2011	DESY	Electron source Positron source Ring to main linac (bunch compressor) Beam-delivery system and machine-detector interface	[264]
BTR 3	19-20.01.2012	KEK	Superconducting RF technology Main-linac layout	[265]
BTR 4	20-23.03.2012	CERN	Conventional facilities and siting: ▪ civil construction ▪ mechanical and electrical systems ▪ site variant designs ▪ schedule, installation and alignment ▪ detector hall	[266]

design decisions. Each phase of the design and evaluation process culminated in a focus workshop where a particular subset of the proposed design modifications underwent a final management-level review before a consensus decision was made. For the initial TLCC, a series of four Baseline Assessment Workshops (BAW) were held, each of which resulted in a written proposal to the GDE Director. These workshops focused on the primary high-level concepts outlined in the SB2009 proposal [209]. The second phase was a more comprehensive and detailed review of the entire machine layout, in order to consolidated and document the results of the TLCC decisions, as well as the many lower-level technical decisions that still required resolution. This phase was also accomplished by a series of focus workshops (Baseline Technical Reviews, BTR). Table A.1 summarises the workshops and their focus. The process successfully established the updated baseline for the TDR which is presented in Part II: *ILC Baseline Design*

A.3 Proposed top-level design modifications and their impact

The global value engineering process briefly outlined above culminated in six top-level modifications to the published 2007 Reference Design.

1. A Main Linac length consistent with an average accelerating gradient of 31.5 MV/m and maximum operational beam energy of 250 GeV, together with a RF distribution scheme which optimally supports a spread $\leq$20% of individual cavity gradients. This differs from the RDR assumption that all cavities operated at 31.5 MV/m. The inclusion of the operational gradient spread, allowing acceptance of cavities achieving as low as 28 MV/m in the vertical test, increases the effective yield seen in mass production and thus produces a cost benefit. It is assumed that the average 35 MV/m (vertical test) is maintained by cavities achieving $\geq$42 MV/m (vertical test), which has been demonstrated. Operation with a spread in cavity gradients requires a more complex RF distribution system, and places higher demands on the low-level RF control systems, as well as requiring an additional RF power overhead of approximately 6%, all of which adds cost. However the net cost benefit is considered to be positive.

2. The RDR main linac adopted a two-tunnel solution, where one tunnel housed the accelerator (beam tunnel), while the second service tunnel housed the klystrons, modulators and other support equipment. This solution was arrived at by initial considerations of life-safety egress requirements, as well as machine operational availability. In order to reduce significantly the scope and cost of the underground construction work, a single-tunnel solution was further evaluated, and was subsequently shown to be feasible both from the perspective of life safety and availability. The evaluation process highlighted the need for site specific rather than generic solutions, and resulted in two different approaches to the RF power distribution:

    a) A Klystron Cluster Scheme (KCS), which places 10 MW multi-beam klystrons (MBK) and modulators on the surface in "clusters" every two kilometres. The RF power from a cluster is combined into a single over-moded waveguide and transported as microwave power from the surface building into the tunnel, where it is then incrementally tapped-off to feed units of three cryomodules (26 SCRF cavities). This novel solution has many attractive features, but the cost savings are partially offset by the need for additional shafts and surface buildings, as well as additional klystrons to compensate the higher RF losses in the long waveguides. Significant R&D on the distribution system is also still required.

    b) Distributed RF Source scheme (DRFS), which installs many small 850 MW modulated anode klystrons and modulators in the single beam tunnel, in a high-availability configuration, with each klystron driving 4 cavities. This solution does not require the surface buildings needed by KCS and was considered more cost-effective for mountainous topographies, such as the proposed Japanese sites. This solution was later dropped in favour of the more cost-effective and established 2007 Reference Design concept using distributed 10 MW MBKs, after more detail considerations of tunnel-construction methods in mountainous geology showed that a single wide tunnel was both cost effective and provided the same functionality as the original twin-tunnel solution.

3. undulator-based positron source was relocated from the nominal (and fixed) 150 GeV point in the main electron linac to its exit (nominal 250 GeV). This effectively consolidated all the source infrastructure in the central region of the accelerator, as well as removing the need for a long transfer line from the source to the damping rings. Low centre-of-mass energy operation

($< 300\,\mathrm{GeV}$) now requires a second electron pulse to generate positrons in a 10 Hz operation mode, which also has implications for the damping rings (half the damping time).

4. A lower beam-power parameter set with the number of bunches per pulse reduced by a factor of two ($n_b = 1312$), as compared to the nominal RDR parameter set ($n_b = 2625$). The luminosity is approximately restored by a stronger beam-beam interaction, at the cost of tighter tolerances on the beam collision. The reduced beam power (beam current) allows significant cost savings by reducing the required number of klystrons and modulators by about 33%, as well as halving the circumference of the damping rings to 3.2 km. The possibility of restoring the full 2007 RDR parameters has been maintained in the baseline design as a potential future luminosity upgrade. In particular, the damping-ring tunnel can accommodate installation of a third damping ring (second positron ring) if the higher current in the single ring is limited by electron-cloud effects.
5. The new design of damping rings can provide a 6 mm bunch length as opposed to the 9 mm length reported in the RDR. This opened up the possibility to consider a single-stage bunch compressor with a compression ratio of 20, as compared to the RDR two-stage solution. Although a cheaper solution, during the formal change-control review process, the small savings were not considered substantial enough to merit the loss of tuning range and margin of the bunch length implied by the single-stage design. Consequently the TDR remains with the two-stage concept.
6. Further integration of the positron and electron sources into a common central-region beam tunnel, together with the Beam-Delivery System, resulting in an overall simplification of civil construction in the central region.

The result of the re-baselining has produced a machine design that is both more robust, generally lower risk and more cost effective than the 2007 Reference Design. The process by which the new baseline was established followed the GDE mandate to provide a global-consensus-driven design which included all stakeholders. In particular, items 3, 4 and 5 above had potential physics-scope impact, requiring studies by the physics and detector groups.

The complete design of the ILC encompasses a mechanical and geometric description of the planned facility, a description of its function suitable for simulations, a cost estimate and an implementation plan. The aim of Design Integration is to ensure that this overall design is complete, correct, and self-consistent. During the design-integration process, the separate design results from the various accelerator systems and the technical groups are brought together. During the Technical Design Phase II, the design integration focussed on the lattice as a central description of the overall accelerator layout. First, the individual lattices of the accelerator systems were fit together with the help of treaty points that had been negotiated and agreed upon by the lattice designers and integration team. Then, using simple 3D visualisations of the lattices, the lattice geometry was optimised in order to avoid collisions between beamlines, to ensure there was sufficient space for installation of the components, and to assess whether or not it would be possible to reduce tunnel cross sections by a suitable alignment of the beamlines.

In addition to this horizontal integration work across accelerator systems, the design was integrated vertically between different technical areas. The geometrically-integrated lattice was translated into coordinate sets that were communicated to the CFS group, who based the final tunnel layout on the lattice geometry. This ensures consistency between the accelerator and tunnel geometry as well as correctness and completeness (for instance with respect to space requirements of the various dump locations). Combining the 3D visualisation of the beamlines with a 3D tunnel design facilitates further planning and optimisation with regard to installation, accessibility and egress and life safety. Figure A.4 shows a particularly complex region around the branch off of the transfer tunnel, where

the beamline geometry was substantially altered in the integration process after the inspection of the 3D model of an earlier design. By sharing a common vision of the machine through 3D modelling, the involved parties can evaluate the design at an early stage and agree on necessary modifications, which may affect the tunnel layout, the lattice geometry, or both.

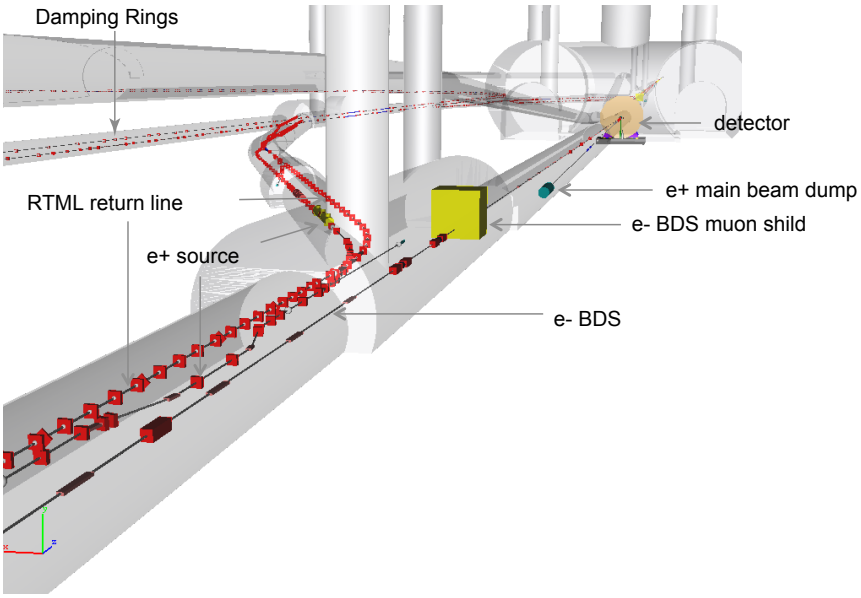

Figure A.4 Example for design integration: the region where the transfer-tunnel branches off from the electron main tunnel towards the damping rings is shown. The European tunnel is shown together with a visualisation of the electron RTML and BDS and the positron-source beamlines. The transfer-tunnel geometry was changed in the central-region integration process in order to avoid the region around the positron main dump and the electron BDS muon shield.

More detailed designs of individual components are also incorporated into the lattice as they become available.

In particular, dimensions of complex components such as cryomodules or space-requirements of special devices such as dumps, targets, or instrumentation can be incorporated into the lattice. By structuring the lattice such that it represents the physical dimensions of the components, and by capturing the correspondence between the components and their lattice representation, it is possible to extract accurate and up-to-date component counts from the lattice, which can be provided to the installation-planning team or to the cost estimate. The availability of automated procedures for the extraction of this information makes it possible to track the effect of design changes efficiently and propagate their consequences. Thus, a process has been introduced that allows a real-time view on the various facets of the overall design to be kept while the design evolves.

In summary, design integration is an inherently important task that is essential for a coherent execution of the project. A central design office that collects and provides design information in a uniform manner under quality control and develops, establishes, and coordinates the integration process is instrumental for a successful and efficient implementation of design integration.

Bibliography

[1] J. Brau *et al.* [ILC Collaboration], "International Linear Collider Reference Design Report Volume 1: Executive Summary," ICFA Beam Dyn. Newslett. **42** (2007) 7 [arXiv:0712.1950 [physics.acc-ph]].

[2] G. Aarons *et al.* [ILC Collaboration], "International Linear Collider Reference Design Report Volume 2: Physics at the ILC," arXiv:0709.1893 [hep-ph].

[3] N. Phinney, N. Toge and N. Walker, "International Linear Collider Reference Design Report Volume 3: Accelerator," arXiv:0712.2361 [physics.acc-ph].

[4] T. Behnke *et al.* [ILC Collaboration], "International Linear Collider Reference Design Report Volume 4: Detectors," arXiv:0712.2356 [physics.ins-det].

[5] R. Brinkmann *et al.* (eds.), "TESLA: The superconducting electron positron linear collider with an integrated X-ray laser laboratory. Technical design report. Pt. 2: The accelerator," DESY-01-011 (2001).

[6] R.-D.Heuer, D.Miller, F.Richard and P.M.Zerwas (eds.), "TESLA Technical Design Report Part III: Physics at an e^+e^- linear collider," DESY-2001-011C (2001), arXiv:hep-ph/0106315.

[7] G. Aad *et al.* [ATLAS Collaboration], Phys. Lett. B **716** (2012) 1-29 [arXiv:1207.7214 [hep-ex]], DOI: 10.1016/j.physletb.2012.08.020.

[8] S. Chatrchyan *et al.* [CMS Collaboration], Phys. Lett. B **716** (2012) 30-61 [arXiv:1207.7235 [hep-ex]] DOI: 10.1016/j.physletb.2012.08.021.

[9] The ATLAS Collaboration, "Combined coupling measurements of the Higgs-like boson with the ATLAS detector using up to 25 fb^{-1} of proton-proton collision data," ATLAS-CONF-2013-034 (2013).

[10] S. Chatrchyan *et al.* [CMS Collaboration], "Observation of a new boson with mass near 125GeV in pp collisions at $\sqrt{s} = 7$ and 8 TeV," arXiv:1303.4571 [hep-ex].

[11] "ILC Project Implementation Planning," 2011, EDMS ID: D00000000979545.

[12] "ILC Parameters," 2012, EDMS ID: D00000000925325.

[13] "TESLA: The superconducting electron positron linear collider with an integrated X-ray laser laboratory. Technical design report, Parts 1-6," DESY-2001-011 (2001).

[14] G. Devanz *et al.*, "HOM beam coupling measurements at the TESLA Test Facility (TTF)," *Proc. EPAC 2002, Paris, France., 2002, pp. 230-232 (WEAGB003)*.

[15] D. Giove, A. Bosotti, C. Pagani and G. Varisco, "A Wire Position Monitor (WPM) system to control the cold mass movements inside the TTF cryomodule," *Proc. PAC 97, Vancouver, BC, 1997, pp. 3657-3659 (7P067)*, DOI: 10.1109/PAC.1997.753375.

[16] D. Reschke *et al.*, "Analysis of RF results of recent nine-cell cavities at DESY," *Proc. SRF 2009, Berlin, Germany, 2009, pp. 342-346 (TUPPO051)*.

[17] W.-D. Moeller [TESLA Collaboration], "High power coupler for the TESLA Test Facility," *Proc. SRF'99, Santa Fe, NM, 1999, pp. 577-581 (THA010)*.

[18] B. Dwersteg *et al.*, "Tesla RF Power Couplers Development at DESY," *Proc. SRF 2001, Tsukuba, 2001, pp. 443-447 (PT001)*.

[19] M. Lacroix, F. Richard, L. Lukovac and W. Kaabi, "Coupler status," ILC-HiGrade-Report-2010-002-1 (2010).

[20] H. Jenhani, T. Garvey and A. Variola, Nucl. Instrum. Meth. A **595** (2008) 549-560. DOI: 10.1016/j.nima.2008.07.111

[21] A. Bosotti, C. Pagani and N. Panzeri, "Improved design of the ILC blade tuner for large scale production," *Proc. PAC 07, Albuquerque, NM, 2007, pp. 2089 (WEPMN020)*, DOI: 10.1109/PAC.2007.4441159.

[22] A. Bosotti *et al.*, "Full characterization of the Piezo blade tuner for superconducting RF cavities," *Proc. EPAC 08, Magazzini del Cotone, Italy, 2008, pp. 838-840 (MOPP120)*

[23] A. Bosotti, C. Pagani, N. Panzeri, and R. Paparella, "The coaxial blade tuner – final report and evaluation of operation," CARE-Report-2008-018-SRF (2008).

[24] C. Pagani, A. Bosotti and R. Paparella, "WP8 - blade tuner deliverable 8.2: report on blade tuner activity," ILC-HiGrade-Report-2010-001-1 (2010).

[25] D. Kruecker, I. Melzer-Pellmann, F. Poirier and N. J. Walker, "Simulation studies on coupler wakefield and RF kicks for the International Linear Collider with MERLIN," *Proc. EPAC 08, Magazzini del Cotone, Italy, 2008, pp. 1649-1651 (TUPP047)*.

[26] M. Ross, N. Walker and A. Yamamoto, "Plug compatibility," 2008, EDMS ID: D00000000865055.

[27] P. Pierini, B. List, "ILC cryomodule parameters," 2012, EDMS ID: D00000000973345.

[28] C. Pagani *et al.*, Adv. Cryogenic Eng. **43A** (1998) 87–97.

[29] T. H. Nicol, "TESLA test cell cryostat support post thermal and structural analysis," TESLA 94-12 (1994).

[30] N. Mildner, M. Dohlus, J. Sekutowicz and K. Zapfe, "A beam line HOM absorber for the european XFEL linac," *Proc. SRF 2005, Cornell, Ithaca, NY, 2005, pp. 593-595 (THP55)*.

[31] C. Pagani *et al.*, Adv. Cryogenic Eng. **43A** (1998) 307–314.

[32] K. Jensch, R. Lange, and B. Petersen, AIP Conf. Proc. **790** (Adv. Cryogenic Eng., **49A**) (2004) 371, DOI: 10.1063/1.1774705.

[33] T. Peterson *et al.*, AIP Conf. Proc. **1434** (Adv. Cryogenic Eng. **57**), (2012) 1575-1582, DOI: 10.1063/1.4707088.

[34] T. Peterson, "ILC cryogenic heat loads and cryoplant parameters," 2012, EDMS ID: D00000000994395.

[35] A. Jöstingmeier, M. Dohlus, M. Wendt and C. Cramer, "Theoretical and practical investigations concerning the design of a HOM broadband absorber for TESLA," DESY-TESLA-2000-10 (2000).

[36] A. Jöstingmeier, M. Dohlus and C. Cramer, "Photon diffusion model for TTF-2," DESY-TESLA-2000-11 (2000).

[37] J. Sekutowicz, A. Gössel, N. Mildner and M. Dohlus, "Beam tests of HOM absorber at FLASH," *Proc. IPAC'10, Kyoto, Japan, 2010, pp. 4092-4094 (THPEC022)*.

[38] N. Ohuchi *et al.*, "Thermal performance of the S1-Global Cryomodule for ILC," *Proc. IPAC 2011, San Sebastian, Spain, 2011, pp. 2472-2474 (WEPO035)*

[39] X.L. Wang *et al.*, "Thermal performance analysis and measurements for the accelerator prototype modules of european XFEL," *Presented at the TESLA Technology Collaboration Meeting, IHEP, Bejing, China, 5-8 December, 2011*, http://indico.ihep.ac.cn/materialDisplay.py?contribId=25&sessionId=9&materialId=slides&confId=2240.

[40] V. S. Kashikhin *et al.*, IEEE Trans. Appl. Supercond. **22** (2012) 4002904 (Proc. MT-22), DOI: 10.1109/TASC.2011.2176297.

[41] Nikolai Andreev *et al.*, IEEE Trans. Appl. Supercond. **23** (2013) 3500305, DOI: 10.1109/TASC.2012.2236135.

[42] V. S. Kashikhin *et al.*, IEEE Trans. Appl. Supercond. **18** (2008) 155-158 (Proc. MT-20), DOI: 10.1109/TASC.2008.921945.

[43] V. S. Kashikhin *et al.*, IEEE Trans. Appl. Supercond. **19** (2009) 1176-1181 (Proc. ASC 2008), DOI: 10.1109/TASC.2009.2017889.

[44] A. Heo, E. -S. Kim and H. Hayano, "Status of cold cavity beam position monitor for STF," *Proc. IPAC 2011, San Sebastian, Spain, 2011, pp. 1236-1238 (TUPC097)*.

[45] M. W. McGee, V. Vocean, C. Grimm and W. Schappert, "Transatlantic transport of Fermilab 3.9 GHz cryomodule for TTF/FLASH to DESY," *Proc. EPAC 08, Magazzini del Cotone, Italy, 2008, pp. 592-594 (MOPP022)*.

[46] S. Barbanotti *et al.*, "Monitoring the FLASH cryomodule transportation from DESY Hamburg to CEA Saclay: coupler contact, vacuum, acceleration and vibration analysis," *Proc. PAC 09, Vancouver, BC, Canada, 2009, pp. 1659-1661 (TU6RFP050)*.

[47] Tom Peterson, "ILC total cryogenics power," 2012, EDMS ID: D00000001005045.

[48] Tom Peterson, "ILC helium inventory," 2012, EDMS ID: D00000001004755.

[49] Shigeki Fukuda, "ILC Local Power Distribution System (LPDS) component list," 2012, EDMS ID: D00000000997235.

[50] C. Nantista, C. Adolphsen, and Faya Wang, "Waveguide component R&D for the ILC," *to appear in Proc. IPAC 2013, Shanghai, China, 2013 (WEPFI080)*.

[51] K. L. F. Bane, C. Adolphsen and C. Nantista, "RF distribution optimization in the main linacs of the ILC," *Proc. PAC 07, Albuquerque, NM, 2007, pp. 2424-2426 (WEPMS037)*, DOI: 10.1109/PAC.2007.4441271.

[52] J. Branlard *et al.* [Linear Collider Collaboration], "Optimal coupler and power setting for superconductive linear accelerators," *Proc. LINAC 08, Victoria, BC, 2008, pp. 1063-1065 (THP113)*.

[53] C. Nantista, "RF power budgets for KCS and DKS local power distribution systems," 2012, EDMS ID: D00000001007505.

[54] C. Burkhart *et al.*, "ILC Marx modulator development program status," *Proc. IPAC'10, Kyoto, Japan, 2010, pp. 3636-3638 (THOARA03)*.

[55] C. Schmidt *et al.*, "Feedback strategies for bunch arrival time stabilization at FLASH towards 10 fs," *Proc. FEL'11, Shanghai, China, 2011, pp. 531-534 (THPA26)*.

[56] S. Michizono *et al.*, "Performance of Digital LLRF System for STF in KEK," *Proc. LINAC 08, Victoria, BC, 2008, pp. 1048-1050 (THP108)*.

[57] E. Harms *et al.*, "RF test results from cryomodule 1 at the Fermilab SRF Beam Test Facility," *Proc. SRF 2011, Chicago, IL, 2011, pp. 79-82 (MOPO013)*.

[58] M. K. Greckiet *al.*, "Compensation of Lorentz force detuning for SC Linacs (with Piezo tuners)," *Proc. EPAC 08, Magazzini del Cotone, Italy, 2008, pp. 862-864 (MOPP129)*.

[59] R. Carcagno *et al.*, "First Fermilab results of SRF cavity Lorentz force detuning compensation using a Piezo tuner," *Proc. SRF 2007, Beijing, China, 2007, pp. 259-263 (TUP57)*.

[60] S. Backus and Kapteyn-Murnane Laboratories Inc., "Laser Systems Development for the International Linear Collider (ILC) Photoinjector," US DOE SBIR/STTR Grant DE-FG02-06ER84469 Final Report, February, 2011.

[61] J. W. Wang *et al.*, "Positron injector accelerator and RF system for the ILC," SLAC-PUB-12412 (2007), *Contributed to Asian Particle Accelerator Conference, APAC 2007, Indore, India, 2007.*

[62] T. Nishitani *et al.*, J. Appl. Phys. **97** (2005) 094907, DOI: 10.1063/1.1886888.

[63] T. Maruyama, Appl. Phys. Lett. **85** (2004) 2640-2642, DOI: 10.1063/1.1795358.

[64] T. Nakanishi *et al.*, Nucl. Instrum. Meth. A **455** (2000) 109-112, DOI: 10.1016/S0168-9002(00)00715-4.

[65] T. Saka *et al.*, Surf. Sci. **454-456** (2000) 1042-1045, DOI: 10.1016/S0039-6028(00)00096-0.

[66] K. Togawa *et al.*, Nucl. Instrum. Meth. A **414** (1998) 431-445, DOI: 10.1016/S0168-9002(98)00552-X.

[67] S. Tanaka *et al.*, J. Appl. Phys. **95** (2004) 551-556, DOI: 10.1063/1.1632548.

[68] Y. Kurihara *et al.*, Nucl. Instrum. Meth. A **313** (1992) 393-397, DOI: 10.1016/0168-9002(92)90816-M.

[69] Yu. A. Mamaev *et al.*, AIP Conf. Proc. **915** (2007) 1049-1054 [SLAC-PUB-12249], DOI: 10.1063/1.2750951.

[70] T. Maruyama *et al.*, Appl. Phys. Lett. **82** (2003) 4184-4186, DOI: 10.1063/1.1581981.

[71] P. A. Adderley *et al.*, Phys. Rev. ST Accel. Beams **13** (2010) 010101. DOI: 10.1103/PhysRevSTAB.13.010101

[72] P. Adderley *et al.*, "CEBAF 200 kV inverted electron gun," *Proc. PAC 11, New York, NY, 2011, pp. 1501-1503 (WEODS3)*.

[73] R. Alley *et al.*, Nucl. Instrum. Meth. A **365** (1995) 1-27, DOI: 10.1016/0168-9002(95)00450-5.

[74] C. K. Sinclair *et al.*, Phys. Rev. ST Accel. Beams **10** (2007) 023501, DOI: 10.1103/PhysRevSTAB.10.023501.

[75] Xiaoshi Zhang *et al.*, Optics Express **20** (2012) 7015-7021., DOI: 10.1364/OE.20.007015.

[76] A. Curtoni and M. Jablonka, "Study of the TESLA preaccelerator for the polarised beam," DESY-TESLA-2001-22 (2001), EDMS ID: D00000000967125.

[77] F. Zhou *et al.*, "Start-to-end transport design and multi-particle tracking for the ILC electron source," SLAC-PUB-12240 (2007), DOI: 10.2172/898870.

[78] K. Moffeit *et al.*, "Spin rotation schemes at the ILC for two interaction regions and positron polarization with both helicities," SLAC-TN-05-045 (2005), EDMS ID: D00000000950455.

[79] L. Young, "Parmela Manual," LA-UR-96-1835 (2001).

[80] MAD 8.51, http://mad8.web.cern.ch/mad8/.

[81] M. Borland, "Elegant: A flexible SDDS-compliant code for accelerator simulation," Technical Report No. LS-287, ANL (2000). DOI: 10.2172/761286.

[82] M. A. Palmer, "Targeted specifications for the DR-RTML and DR-Esource treaty points," 2011, EDMS ID: D00000000966225.

[83] J.A. Clarke *et al.*, "The design of the positron source for the International Linear Collider," *Proc. EPAC 08, Magazzini del Cotone, Italy, 2008, pp. 1915-1917 (WEOBG03)*.

[84] W. Gai *et al.*, "Positron source parameters," 2012, EDMS ID: D00000000943695.

[85] B. List, "Positron source beamline overview," 2012, EDMS ID: D00000000959325.

[86] W. Gai, "A 500 MeV S-band low cost electron beam," *Talk at KILC12, Daegu, Korea,* 2012, slides: http://ilcagenda.linearcollider.org/contributionDisplay.py?contribId=188&sessionId=32&confId=5414.

[87] R. B. Neal, (ed.), D. W. Dupen, H. A. Hogg and G. A. Loew, "The Stanford two mile accelerator," New York, NY (W.A. Benjamin) 1968, 1183pp, http://www.slac.stanford.edu/library/2MileAccelerator/2mile.htm.

[88] P. B. Wilson, "Sled: A method for doubling SLAC's energy," SLAC-TN-73-015 (1973).

[89] M. Borland, "ELEGANT: A Flexible SDDS-Compliant Code for Accelerator Simulation" Technical Report No. LS-287, ANL (2000), DOI: 10.2172/761286.

[90] Y. Ivanyushenkov *et al.*, "Development of a full scale superconducting undulator module for the ILC positron source," *Proc. PAC 07, Albuquerque, NM, 2007, pp. 2862-2864 (THPMN070)*, DOI: 10.1109/PAC.2007.4440601.

[91] D. Scott, "Longitudinal resistive wall wakefields for the ILC positron undulator vessel," EUROTeV-Report-2006-084 (2006).

[92] D. Scott and J. Jones, "Transverse resistive wall wakefields of the ILC positron undulator beam tube and their effects on an orbit dependant emittance growth," EUROTEV-REPORT-2007-007 (2007).

[93] A. Bungau *et al.*, "Design of the photon collimators for the ILC positron helical undulator," *Proc. EPAC 08, Magazzini del Cotone, Italy, 2008, pp. 649-651 (MOPP008)*.

[94] C. Li *et al.*, "ILC positron source remote handling system," 2012, EDMS ID: D00000001205623.

[95] B. List, "Harmonic number for the ILC damping rings," 2011, EDMS ID: D00000000960865.

[96] S.Guiducci *et al.*, "Updates to the International Linear Collider damping rings baseline design," *Proc. IPAC 2011, San Sebastian, Spain, 2011, pp. 32–34 (MOOCA03)*.

[97] A. Wolski, "ILC Damping Ring design studies at the Cockcroft Institute," ILC-NOTE-2010-057 (2010), EDMS ID: D00000000931755.

[98] M.A. Palmer and S. Guiducci, "Damping ring parameters," 2012, EDMS ID: D00000000960955.

[99] M. T. F. Pivi *et al.*, "Recommendation for mitigations of the electron cloud instability in the ILC," *Proc. IPAC 2011, San Sebastian, Spain, 2011, pp. 1063–1065 (TUPC030)*.

[100] J. A. Crittenden, M. A. Palmer, D. L. Rubin, "Wiggler magnet design development for the ILC damping rings," *Proc. IPAC'12, New Orleans, LA, 2012, pp. 1969-1971 (TUPPR065)*.

[101] D. Rubin, "DTC Lattice (DTC04)," 2012, EDMS ID: D00000000960185.

[102] J. P. Shanks *et al.*, "Status of low emittance tuning at CesrTA," *Proc. PAC 11, New York, NY, 2011, pp. 1540-1542 (WEP022)*.

[103] Y. Cai, "Measured multipole errors in PEP-II and SPEAR3 magnets," *presentation given at SLAC, June 14, 2005,* EDMS ID: D00000000997795.

[104] A. Wolski, J. Gao and S. Guiducci, "Configuration studies and recommendations for the ILC damping rings," ILC-NOTE-2009-051 (2006), DOI: 10.2172/882090.

[105] G. F. Dugan *et al.*, "Synrad3D photon propagation and scattering simulation," *To appear in Proc. ECLOUD'10, Cornell, Ithaca, NY, 2010 (slides)*.

[106] M. A. Furman and M. T. F. Pivi, Phys. Rev. ST Accel. Beams **5** (2002) 124404, DOI: 10.1103/PhysRevSTAB.5.124404.

[107] F. Zimmermann, G. Rumolo and K. Ohmi, ICFA Beam Dyn. Newslett. **33** (2004) 14.

[108] L. F. Wang *et al.*, Phys. Rev. ST Accel. Beams **5** (2002) 124402, DOI: 10.1103/PhysRevSTAB.5.124402.

[109] J. Crittenden *et al.*, "Investigation into electron cloud effects in the ILC damping ring design," *Proc. IPAC'12, New Orleans, LA, 2012, pp. 1963-1965 (TUPPR063)*.

[110] M.T.F. Pivi, *et al.*"Recommendation for the feasibility of more compact LC damping rings," *Proc. IPAC'10, Kyoto, Japan, 2010, pp. 3578–3580 (WEPE097)*.

[111] Guoxing Xia, "Ion instability study for the ILC 3 km damping ring," *Proc. PAC 11, New York, NY, 2011, pp. 1671–1673 (WEP103)*.

[112] L. Wang, "Optimization of the dynamic aperture for SPEAR3 low-emittance upgrade," *Proc. IPAC'12, New Orleans, LA, 2012, pp. 1380-1382 (TUPPC096)*.

[113] L. Wang, Y. Cai, T. O. Raubenheimer and H. Fukuma, Phys. Rev. ST Accel. Beams **14** (2011) 084401, DOI: 10.1103/PhysRevSTAB.14.084401.

[114] L. Wang *et al.*, "Observation of beam ion instability in SPEAR3," *Proc. IPAC 2011, San Sebastian, Spain, 2011, pp. 814-816 (MOPS090)*.

[115] H. Fukuma and L. Wang, "Ion Effects at SuperKEKB," Proc ECLOUD'07, 2007, SLAC-PUB-12757.

[116] J. Conway, Y. Li, and M. Palmer, "The conceptual design of a vacuum system for the ILC damping rings incorporating electron cloud mitigation techniques," *Proc. IPAC'12, New Orleans, LA, 2012, pp. 1960-1962 (TUPPR062)*.

[117] O. B. Malyshev *et al.*, "Mechanical and vacuum design of the wiggler section of the ILC damping rings," *Proc. IPAC'10, Kyoto, Japan, 2010, pp. 3563-3565 (WEPE092)*.

[118] O. Malyshev *et al.*, "SR Power Distribution along Wiggler Section of ILC DR," *Proc. IPAC'10, Kyoto, Japan, 2010, pp. 3569-3571 (WEPE094)*.

[119] M. Korostelev *et al.*, "Wake field simulations for the vacuum chamber transitions of the ILC damping ring," *Proc. PAC 09, Vancouver, BC, Canada, 2009, pp. 4619-4621 (FR5RFP040)*.

[120] Y. Suetsugu *et al.*, "Beam Tests of a clearing electrode for electron cloud mitigation at KEKB positron ring," *Proc. IPAC'10, Kyoto, Japan, 2010, pp. 2369-2371 (WEOAMH01)*.

[121] Y. Suetsugu *et al.*, Nucl. Instrum. Meth. A **598** (2009) 372, DOI: 10.1016/j.nima.2008.08.154.

[122] J. Shanks, D. L. Rubin, J. Crittenden and M.Palmer, "Characterization of single particle dynamics of the International Linear Collider damping ring lattice," *Proc. IPAC'12, New Orleans, LA, 2012, pp. 1972-1974 (TUPPR066)*.

[123] S. Belomestnykh *et al.*, "Operating experience with superconducting RF at CESR and overview of other SRF related activities at Cornell University," *Proc. SRF'99, Santa Fe, NM, 1999, pp. 24–30 (MOA006)*.

[124] K. Akai *et al.* Nucl. Instrum. Meth. A **499** (2003) 45, DOI: 10.1016/S0168-9002(02)01773-4.

[125] R. Boni, G. Cavallari: "RF System for the ILC Damping Rings," Technical Note ILC-LNF-001 (2006), EDMS ID: D00000000954405.

[126] A. Gallo, "Optimal Fixed Detuning of the Damping Ring Cavities for the ILC 10 Hz Operation," LC-NOTE-2011-060 (2011), EDMS ID: D00000000973035.

[127] C. Spencer, "Directive from magnet systems group for how to name ILC magnet types," 2006, EDMS ID: D00000000958895.

[128] A. Drago, "Fast Feedback System," ILC-LNF-002 (2006), EDMS ID: D00000000954285.

[129] A. Drago, "Trends in Fast Feedback R&D," arXiv:0806.1864 [physics.acc-ph], 2008, *Proc. 40th ICFA ABDW 2008, Novosibirsk, Russia, 2008, pp. 60-62 (TUACH12)*.

[130] M. Palmer, B. List, "ILC central region design optimization," 2011, EDMS ID: D00000000969765.

[131] B. List, "Main linac treaty points," 2012, EDMS ID: D00000000970685.

[132] B. List, "RTML doglegs," 2011, EDMS ID: D00000000969955.

[133] P. Emma, T. Raubenheimer and F. Zimmermann, "A Bunch compressor for the Next Linear Collider," *Proc. PAC 05, Knoxville, TN, 2005, pp. 704-706 (RPC03)*, DOI: 10.1109/PAC.1995.504764.

[134] S. Seletskiy, "Renovated two-stage bunch compressor for the International Linear Collider," *Proc. IPAC'12, New Orleans, LA, 2012, pp. 1801-1803 (TUPPP092)*.

[135] A. Latina and N. Solyak, "Single-stage bunch compressor for ILC-SB2009," *Proc. IPAC'10, Kyoto, Japan, 2010, pp. 4611-4613 (THPE042)*.

[136] C. Adophsen *et al.* [NLC Design Group], "Zeroth order design report for the Next Linear Collider," SLAC-R-474 (1996), pp. 573-575.

[137] N. Solyak, V. Kapin, A. Vivoli and S. Seletskiy, "New baseline design of the ILC RTML system," *Proc. IPAC'12, New Orleans, LA, 2012, pp. 1915-1917 (TUPPR043)*.

[138] R. Akre, L. Bentson, P. Emma and P. Krejcik, "Bunch length measurements using a transverse RF deflecting structure in the SLAC Linac," *Proc. EPAC 2002, Paris, France., 2002, pp. 1882-1884 (THPRI097)*, DOI: 10.2172/799088.

[139] P.N. Burrows *et al.*, "Tests of the FONT3 Linear Collider intra-train beam feedback system at the ATF," *Proc. PAC 05, Knoxville, TN, 2005, pp. 1359-1361 (RPPP013)*, DOI: 10.1109/PAC.2005.1590761.

[140] S. Seletskiy *et al.*, "Design of the ILC RTML extraction lines," SLAC-PUB-14638 (2008), *Proc. EPAC 08, Magazzini del Cotone, Italy, 2008, pp. 2752-2754 (WEPP102)*.

[141] J. Wu, private communication.

[142] K. Kubo, "Rough estimation of effects of fast-changing stray field in long transport of RTML," ILC-NOTE-2007-007, ILC-Asia-2006-05 (2006), EDMS ID: D00000000950615.

[143] J. Frisch, T. O. Raubenheimer, P. Tenenbaum, "Sensitivity to Nano-Tesla scale stray magnetic fields," SLAC-TN-04-041 (2004), DOI: 10.2172/827018.

[144] L. Wang, P. Tenenbaum, "Fast ion instability in the long transport line of RTML," ILC-NOTE-2007-005 (2007), EDMS ID: D00000000954435.

[145] J. Smith, "Coupling correction in the ILC Ring to Main Linac," ILC-NOTE-2007-006 (2007), EDMS ID: D00000000954475.

[146] P. Tenenbaum, "Application of kick minimization to the RTML 'Front End'," SLAC-TN-07-002 (2007), DOI: 10.2172/898865.

[147] K. Kubo, "Simulation of low emittance transport in long straight line of ILC RTML," ILC-NOTE-2007-008, ILC-Asia-2006-06A (2006), EDMS ID: D00000000954565.

[148] P. Tenenbaum, T. O. Raubenheimer, A. Wolski, "Multi-stage bunch compressors for the International Linear Collider," *Proc. PAC 05, Knoxville, TN, 2005, pp. 2357-2359 (RPPP034)*, DOI: 10.1109/PAC.2005.1591109.

[149] P. Tenenbaum, "Emittance correction in the 2006 ILC bunch compressor," SLAC-TN-07-004, ILC-NOTE-2007-003 (2007), DOI: 10.2172/900604.

[150] M. Church, "Analysis of phase and amplitude sensitivity for '300B' bunch compressor and linac," ILC-NOTE-2007-004 (2007), EDMS ID: D00000000954735.

[151] S. M. Seletskiy, "Thermal photon and residual gas scattering of the electrons in the ILC RTML," SLAC-TN-06-007 (2006), DOI: 10.2172/889674.

[152] P. Tenenbaum *et al.*, Phys. Rev. ST Accel. Beams **10** (2007) 034401, DOI: 10.1103/PhysRevSTAB.10.034401.

[153] P. Tenenbaum, "Collimator wakefield calculations for ILC-TRC report," SLAC-TN-03-038, LCC-0101 (2002), DOI: 10.2172/826490.

[154] A. Vivoli, N. Solyak, "ILC RTML magnets," 2012, EDMS ID: D00000001017485 (restricted).

[155] A. Vivoli, N. Solyak, "ILC RTML magnet power supply list," 2012, EDMS ID: D00000001017455 (restricted).

[156] B. List, "BDS beamline overview," 2012, EDMS ID: D00000000976355.

[157] J. Jones, D. Angal-Kalinin, Y. Nosochkov, "BDS Lattice BDS2012b," 2012, EDMS ID: D00000000972985.

[158] S. Boogert *et al.*, JINST **4** (2009) P10015 [arXiv:0904.0122 [physics.ins-det]], DOI: 10.1088/1748-0221/4/10/P10015.

[159] F. Jackson *et al.*, "Collimation optimisation in the beam delivery system of the International Linear Collider," *Proc. PAC 07, Albuquerque, NM, 2007, pp. 2871-2873 (THPMN073)*, DOI: 10.1109/PAC.2007.4440604.

[160] B. D. Fell *et al.*, "Mechanical design of collimators for the ILC," *Proc. EPAC 08, Magazzini del Cotone, Italy, 2008, pp. 2883-2885 (WEPP168)*.

[161] D. S. Denisov *et al.*, JINST **1** (2006) P12003 [arXiv:hep-ex/0608001], DOI: 10.1088/1748-0221/1/12/P12003

[162] A. I. Drozhdin *et al.*, "Suppression of muon backgrounds generated in the ILC beam delivery system," *Proc. PAC 07, Albuquerque, NM, 2007, pp. 2945-2947 (THPMN100)*, DOI: 10.2172/922037.

[163] B. Parker *et al.*, "The superconducting magnets of the ILC beam delivery system," SLAC-PUB-12832 (2007), *Proc. PAC 07, Albuquerque, NM, 2007, pp. 3196-3198 (THPMS091)*, DOI: 10.1109/PAC.2007.4440713.

[164] R. Brinkmann, P. Raimondi and A. Seryi, "Halo reduction by means of nonlinear optical elements in the NLC final focus system," *Proc. PAC 2001, Chicago, IL, 2001, pp. 3828-3830 (FPAH066)*, DOI: 10.1109/PAC.2001.988267.

[165] P. Raimondi and A. Seryi, Phys. Rev. Lett. **86** (2001) 3779, DOI: 10.1103/PhysRevLett.86.3779.

[166] A. Seryi, M. Woodley and P. Raimondi, "A recipe for linear collider final focus system design," *Proc. PAC 03, Portland, OR, 12-16 May 2003, pp. 2766-2768 (RPAP018)*, DOI: 10.1109/PAC.2003.1289261.

[167] Y. Nosochkov *et al.*, "ILC extraction line for 14 mrad crossing angle," SLAC-PUB-11591 (2005), *Presented at 36th ICFA Advanced Beam Dynamics Workshop (NANOBEAM 2005), Kyoto, Japan, 2005.*

[168] A. Ferrari and Y. Nosochkov, "Beam losses in the extraction line of a TeV e^+e^- linear collider with a 20 mrad crossing angle," EUROTEV-REPORT-2005-025 (2005), DOI: 10.2172/878350.

[169] D. Schulte, "Study of electromagnetic and hadronic background in the interaction region of the TESLA Collider," PhD thesis Univ. Hamburg (1996), TESLA-97-08.

[170] B. Parker *et al.*, "Functional requirements on the design of the detectors and the interaction region of an e^+e^- Linear Collider with a push-pull arrangement of detectors," *Proc. PAC 09, Vancouver, BC, Canada, 2009, pp. 2679-2681 (WE6PFP078)*.
Long version: ILC-NOTE-2009-050 (2009), EDMS ID: D00000000951395.

[171] T. Tauchi, "Engineering specifications for the ILC experimental hall," 2012, EDMS ID: D00000000983825.

[172] ARUP, "Review of interaction region cavern layout design," 2012, EDMS ID: D00000000967835.

[173] B. Parker, "CAD model of QD0 and QDEX1A assembly," 2012, EDMS ID: D00000001019413.

[174] Y. Nosochkov and A. Seryi, Phys. Rev. ST Accel. Beams **8** (2005) 021001, DOI: 10.1103/PhysRevSTAB.8.021001.

[175] B. Parker and A. Seryi, Phys. Rev. ST Accel. Beams **8** (2005) 041001, DOI: 10.1103/PhysRevSTAB.8.041001.

[176] G. R. White, N. J. Walker and D. Schulte, "Design and simulation of the ILC intra-train orbit and luminosity feedback systems," *Proc. EPAC 06, Edinburgh, Scotland, 2006, pp. 3041-3043 (THPCH104)*.

[177] T. Sanami, A. Fasso, M. Santana *et al.*, "IR hall dose rate estimates with detector concepts," SLAC RP-09-08, EDMS ID: D00000001001665.

[178] K. L. F. Bane and A. Seryi, *Proc. PAC 07, Albuquerque, NM, 2007, pp. 3088-3090 (THPMS039)*, DOI: 10.1109/PAC.2007.4440677.

[179] Lew Keller, "Beam-gas bremsstrahlung and Coulomb scattering in the ILC," *Presentation in ILC BDS Meeting, SLAC, December 4, 2006,* `http://ilcagenda.linearcollider.org/materialDisplay.py?contribId=2&materialId=slides&confId=1277`.

[180] G. Christian *et al.*, "The electromagnetic background environment for the interaction-point beam feedback system at the International Linear Collider," *Proc. EPAC 06, Edinburgh, Scotland, 2006, pp. 2997-2999 (THPCH089)*.

[181] P. Burrows *et al.*, "Performance of the FONT3 fast analogue intra-train beam-based feedback system at ATF," *Proc. EPAC 06, Edinburgh, Scotland, 2006, pp. 852-854 (MOPLS123)*.

[182] D.R. Bett *et al.*, "Latest performance results from the FONT5 intra-train beam position and angle feedback system at ATF2," *Proc. IPAC'12, New Orleans, LA, 2012, pp. 2864-2866 (WEPPP068)*.

[183] P. Burrows *et al.*, "Development of a fast, single-pass, micron-resolution beam position monitor signal processor: beam test results from ATF2," *Proc. IPAC'10, Kyoto, Japan, 2010, pp. 1152-1154 (MOPE074)*.

[184] R. Assmann *et al.*[LEP Energy Working Group Collaboration], Eur. Phys. J. C **39** (2005) 253-292, [arXiv:hep-ex/0410026], DOI: 10.1140/epjc/s2004-02108-8.

[185] E. Torrence, "Downstream synchrotron radiation stripe spectrometer status," Talk at the Workshop on Polarization and Energy Measurements at the ILC, Zeuthen, 2008, https://indico.desy.de/materialDisplay.py?contribId=18&sessionId=1&materialId=slides&confId=585.

[186] G. Moortgat-Pick *et al.*, Phys. Rept. **460** (2008) 131-243 [arXiv:hep-ph/0507011], DOI: j.physrep.2007.12.003.

[187] K. Moffeit *et al.*, "Proposal to modify the polarimeter chicane in the ILC 14 mrad extraction line," SLAC-PUB-12425 (2007), DOI: 10.2172/901838.

[188] W. Bialowons, M. Schmitz, M. Maslov and V. Sychev, "Concept of the high power $e^{\pm}$ beam dumps for TESLA," TESLA-2001-04.

[189] D. R. Walz, J. Jurow and E. L. Garwin, IEEE Trans. Nucl. Sci. **12** (1965) 867, DOI: 10.1109/TNS.1965.4323748

[190] D. R. Walz *et al.*, IEEE Trans. Nucl. Sci. **14** (1967) 923, DOI: 10.1109/TNS.1967.4324681.

[191] Polepalle Satyamurthy *et al.*, Nucl. Instrum. Meth. A **679** (2012) 67-81, DOI: 10.1016/j.nima.2012.01.075.

[192] D. R. Walz and E. J. Seppi, "Radiolysis and hydrogen evolution in the A–beam dump radioactive water system," SLAC-TN-67-029 (1967).

[193] S. Appleton, B. Fell, N. Collomb, "3D CAD model of an ILC collimator," 2008, EDMS ID: D00000001082993.

[194] J. D. Fuerst *et al.*, "An RF separated kaon beam from the main injector: superconducting aspects," FERMILAB-TM-2060 (1998). DOI: 10.2172/2210.

[195] M. McAshan and R. Wanzenberg, "RF design of a transverse mode cavity for kaon separation," FERMILAB-TM-2144 (2001).

[196] G. Burt *et al.*, "Crab cavities for linear colliders," *Proc. LINAC 08, Victoria, BC, 2008, pp. 830-832 (THP023)* [arXiv:0810.2880 [physics.acc-ph]].

[197] P. Ambattu *et al.*, "Development of crab cavity systems at the Cockcroft Institute," ICFA Beam Dyn. Newslett. **51** (2010) 48-60.

[198] C. Adolphsen *et al.*, "Design of the ILC crab cavity system," EUROTEV-REPORT-2007-010 (2007), DOI: 10.2172/915387.

[199] G. Burt, A. Dexter, P. Goudket, "Effect and tolerances of RF phase and amplitude errors in the ILC Crab Cavity," EUROTeV-REPORT-2006-098 (2006).

[200] Matthias Liepe, "Review on progress in RF control systems," *Presentation given at 12th International Workshop on RF Superconductivity (SRF 2005), Ithaka, NY, July 10–15, 2005 (THA08).* http://www.lepp.cornell.edu/public/SRF2005/talks/thursday/ThA08_talk_srf2005.pdf

[201] G. Burt *et al.*, "Power coupler for the ILC crab cavity," *Proc. PAC 07, Albuquerque, NM, 2007, pp. 2212-2214 (WEPMN079).* DOI: 10.2172/915126.

[202] E. Marcus and H. Stern., "Blueprints for high availability (2nd ed.)," Indianapolis, IN (Wiley), 2003.

[203] A. Götz, D. Schmidt and M. Clausen, "Middleware in accelerator and telescope control systems," *9th Int. Conf. Accelerator and Large Experimental Physics Control Systems (ICALEPCS 2003), Gyeongju, Korea, 2003, pp. 322-326 (WE202)*.

[204] R. W. Downing and R. S. Larsen, "High availability instrumentation packaging standards for the ILC and detectors," SLAC-PUB-12208 (2006).

[205] Matlab, http://www.mathworks.com/products/matlab/.

[206] R.S. Larsen, "Technical systems configurations – electrical; subsystem: instrumentation – timing," 2001, EDMS ID: D00000001006125.

[207] J. Frisch, D. Bernstein, D. Brown and E. Cisneros, "A High stability, low noise RF distribution system," *Proc. PAC 2001, Chicago, IL, 2001, pp. 816-818 (MPPH-023)*, DOI: 10.1109/PAC.2001.986485.

[208] T. Himel, J. Nelson, N. Phinney and M. Ross, "Availability and reliability issues for ILC," *Proc. PAC 07, Albuquerque, NM, 2007, pp. 1966-1969 (WEYAB02)*, DOI: 10.1109/PAC.2007.4441325.

[209] M. Ross, N. Walker, A. Yamamoto (eds.), "The SB2009 Proposal," 2009, EDMS ID: D00000000900425.

[210] Amberg Engineering AG., Trockenloostrasse 21, CH-8105 Regensdorf-Watt, Switzerland

[211] ARUP, 13 Fitzroy Street, London W1T 4BQ, United Kingdom

[212] Geotechnique Appliquee Deriaz S.A. (GADZ), Chemin des Vignes, 9, CH-1213 Petit-Lancy, Geneva, Switzerland

[213] Holabird and Root, "Fermilab ILC programming study (KCS surface building design)," 2010, EDMS ID: D00000000975805.

[214] M. Aicheler *et al.* (eds.), "A Multi-TeV Linear Collider based on CLIC Technology: CLIC Conceptual Design Report," CERN-2012-007, 2012, DOI: 10.5170/CERN-2012-007.

[215] F. Corsanego, "Compact Linear Collider: guidelines on reduction of fire hazards. Preliminary evaluation of fire safety aspects related to CLIC layout," CERN, 2007, EDMS ID: D00000000899715.

[216] ILC CFS team, "Electron source design criteria for CFS," 2012, EDMS ID: D00000000970195.

[217] ILC CFS team, "Positron source design criteria for CFS," 2012, EDMS ID: D00000000970225.

[218] ILC CFS team, "Damping ring design criteria for CFS," 2012, EDMS ID: D00000000960625.

[219] ILC CFS team, "Interaction region design criteria for CFS," 2012, EDMS ID: D00000000979405.

[220] ILC CFS team, "RTML design criteria for CFS," 2012, EDMS ID: D00000000960275.

[221] ILC CFS team, "Main linac KCS design criteria for CFS," 2012, EDMS ID: D000000009703555.

[222] ILC CFS team, "BDS design criteria for CFS," 2012, EDMS ID: D00000000970315.

[223] ILC CFS team, "ILC laser equipment enclosures design criteria for CFS," 2012, EDMS ID: D00000000974815.

[224] ILC CFS team, "ILC dumps design criteria for CFS," 2012, EDMS ID: D00000000974845.

[225] ILC CFS team, "Cryo info for CFS," 2012, EDMS ID: D00000000970445.

[226] Parsons Engineering Group, "Mechanical design report," 2012, EDMS ID: D00000000979905.

[227] CFS team, "Process water plants," 2012, EDMS ID: D00000000971215.

[228] R.-D. Heuer *et al.*, "Parameters for the Linear Collider (updated)", 2006, EDMS ID: D00000000829685.

[229] K. Yokoya, "Out-coming angle of incoherent pairs", 2012, EDMS ID: D00000000997435.

[230] Wei Gai *et al.*, "Positron source TeV upgrade report," 2012 (in preparation). See also "positron parameters," 2012, EDMS ID: D00000000943695.

[231] J. Jones and D. Angal-Kalinin, "Beam delivery system dogleg design and integration for the International Linear Collider", *Proc. IPAC'10, Kyoto, Japan, 2010, pp. 3422-3424 (WEPE031)*.

[232] N. Walker, "AC power estimate for TeV upgrade", 2012, EDMS ID: D00000000965055.

[233] T. Omori *et al.*, Nucl. Instrum. Meth. A **672** (2012) 52 [arXiv:1110.1450 [physics.acc-ph]], DOI: 10.1016/j.nima.2011.12.032.

[234] A. Ushakov *et al.*, "Positron source simulations for ILC 1TeV upgrade," arXiv:1301.1222 [physics.acc-ph].

[235] J. Gronberg, B. Suardt, "Photon collider laser work at LLNL," *Talk at TILC09, Tsukuba, Japan, 2009,* http://ilcagenda.linearcollider.org/getFile.py/access?contribId=175&sessionId=21&resId=0&materialId=slides&confId=3154.

[236] T. Takahashi, "Status of gamma ray generation at KEK-ATF," *Talk at LCWS 2012, Arlington, TX, 2012,* http://ilcagenda.linearcollider.org/getFile.py/access?contribId=197&sessionId=11&resId=1&materialId=slides&confId=5468.

[237] V.I. Telnov, "Photon colliders: summary", *Talk at LCWS 2012, Arlington, TX, 2012,* http://ilcagenda.linearcollider.org/getFile.py/access?contribId=302&sessionId=4&resId=1&materialId=slides&confId=5468.

[238] G. Kalmus *et al.* [European Linear Collider steering group], "Report of the sub-group on organisational matters," ECFA-2003-225, CERN, Geneva, (2004).

[239] S. Yamada *et al.* [JLC Globalisation Committee], "Report of the JLC Globalisation Committee," KEK, Japan, (2002). http://lcdev.kek.jp/GLCC/glcc_report.pdf.

[240] OECD Global Science Forum, "Report of the Consultative Group on High–Energy–Physics," Paris, France, (2002). http://www.oecd.org/document/18/0,3746,en_2649_34269_1949714_1_1_1_1,00.html.

[241] Turner Construction, "American construction inflation index (Turner Construction Index)," http://www.turnerconstruction.com/cost-index.

[242] OECD, "American non-construction inflation index (US Manufacturing Producer Price Index)," http://stats.oecd.org/Index.aspx?DataSetCode=MEI_PRICES_PPI.

[243] Statistisches Bundesamt (German Statistical Office), "German construction inflation index (non-residential buildings/industrial buildings)," https://www.destatis.de/EN/FactsFigures/Indicators/ShortTermIndicators/Prices/bpr110.html.

[244] Statistisches Bundesamt, (German Statistical Office) "German non-construction inflation index (index of producer prices of industrial products)," https://www.destatis.de/EN/FactsFigures/Indicators/ShortTermIndicators/Prices/pre110.html.

[245] OECD, "Swiss non-construction inflation index (Swiss Manufacturing Producer Price Index)," http://stats.oecd.org/Index.aspx?DataSetCode=MEI_PRICES_PPI.

[246] Japanese Ministry of Land, Infrastructure, Transport and Tourism, "Japanese construction inflation index (Construction Cost Deflator)," http://www.mlit.go.jp/toukeijouhou/chojou/stat-e.htm.

[247] The Statistics Bureau and the Director-General for Policy Planning of Japan, "Japanese non-construction inflation index (Manufacturing Industry Products)," http://www.stat.go.jp/data/getujidb/zuhyou/h01.xls.

[248] G. Dugan, "Purchasing Power Parity (PPP) and its possible use in the ILC TDR cost estimate," 2012, EDMS ID: D00000001001495 (restricted).

[249] Eurostat, "Eurostat-OECD methodological manual on Purchasing Power Parities," Luxembourg (Publications Office of the European Union) 2012, DOI: 10.2785/33942.

[250] A. Deaton, "Calibrating measurement uncertainty in purchasing power parity exchange rates," April, 2012 (to be published).

[251] OECD, "2008 PPP Benchmark results," http://stats.oecd.org/Index.aspx?DataSetCode=PPP2008.

[252] Eurostat, "Purchasing power parities (PPPs)," http://epp.eurostat.ec.europa.eu/portal/page/portal/purchasing_power_parities/data/database.

[253] OECD, "2005 PPP Benchmark results," http://stats.oecd.org/Index.aspx?DataSetCode=PPP2005.

[254] P. Garbincius, "RDR costing guidelines," 2006, EDMS ID: D00000000828835.

[255] P. Garbincius, "RDR cost estimating instructions & standards," 2006, EDMS ID: D00000000828875.

[256] R. D. Stewart, R. W. Wyskida and J. D. Johannes, "Cost estimator's reference manual (2nd ed.), Chapter 5: Learning Curves and Progress Functions," New York, NY (Wiley) 1995.

[257] B. Jahraus (Fichtner), "Projekt TESLA - Strahlabsorber Erstellung des Basiskonzepts, Endbericht," unpublished report, 2003, 114pp.

[258] Framatome ANP, "Projekt 18 MW-Beam Dump für TESLA," unpublished report, 2002, 78pp.

[259] M. Ross, N. Walker, A. Yamamoto, "TLCC-1 Proposal for average accelerating gradient", 2010, EDMS ID: D00000000927465; GDE Change Evaluation Panel, "CEP Decision on TLCC-1 Gradient and Gradient Spread", 2010, EDMS ID: D00000000930935; See also material on http://ilcagenda.linearcollider.org/conferenceDisplay.py?confId=4593.

[260] M. Ross, N. Walker, A. Yamamoto, "TLCC-2 Proposal for Main Linac Single Tunnel", 2010, EDMS ID: D00000000927405; "CEP Decision on TLCC-2 Single Tunnel for Main Linac", 2010, EDMS ID: D00000000931025; see also material on http://ilcagenda.linearcollider.org/conferenceDisplay.py?confId=4593.

[261] M. Ross, N. Walker, A. Yamamoto, "TLCC-3 Proposal for reduced beam parameter set", 2011, EDMS ID: D00000000940545; "CEP Decision on TLCC-3 reduced parameter set", 2011, EDMS ID: D00000000955215; see also material on http://ilcagenda.linearcollider.org/conferenceDisplay.py?confId=4612.

[262] M. Ross, N. Walker, A. Yamamoto, "TLCC-4 Proposal to re-locate the positron source", 2011, EDMS ID: D00000000940575; "CEP Decision on TLCC-4 Positron Source Relocation", EDMS ID: D00000000955255 (2011); see also material on http://ilcagenda.linearcollider.org/conferenceDisplay.py?confId=4612.

[263] M. Ross, N. Walker, A. Yamamoto, "DR BTR Close Out," 2011, EDMS ID: D00000000994145; see also material on http://ilcagenda.linearcollider.org/conferenceDisplay.py?confId=5183.

[264] N. Walker, M. Ross, A. Yamamoto, "Decisions and Action Items arising from the 2nd ILC Baseline Technical Review, DESY, 24.-27-10.2011," EDMS ID: D00000000992935 (2011); see also material on http://ilcagenda.linearcollider.org/conferenceDisplay.py?confId=5222.

[265] A. Yamamoto, M. Ross, N. Walker, "Summary of Decisions from Main-Linac and SCRF Baseline Technical Review (BTR), KEK, 19.-20.1.2012," 2012, EDMS ID: D00000000992975 (2012); see also material on http://ilcagenda.linearcollider.org/conferenceDisplay.py?confId=5444.

[266] M. Ross, N. Walker, A. Yamamoto, "Summary of Decisions from CFS Baseline Technical Review (BTR),CERN, 21.-23.3.2012," 2012, in preparation; see also material on http://indico.cern.ch/conferenceDisplay.py?confId=165201.

List of Signatories

The following list of signatories represents a comprehensive list of those people who have contributed to the R&D and design work, for both the accelerator and the detectors, which is summarised in this report. The list also includes those people who wish to indicate their support for the next phases of the worldwide ILC effort.

It should be noted that inclusion in this list does not indicate any formal commitment by the signatories. It does not indicate commitment to the specific detector designs presented, nor exclusive support for ILC over other collider programs.

A. Abada[171], T. Abe[24], T. Abe[236], J. M. Abernathy[379], H. Abramowicz[265], A. Abusleme[231], S. Aderhold[47], O. Adeyemi[333], E. Adli[357,251], C. Adloff[164], C. Adolphsen[251], K. Afanaciev[209], M. Aguilar[31], S. Ahmad[93], A. Ahmed[382], H. Aihara[375], R. Ainsworth[237,139], S. Airi[154], M. Aizatskyi[208], T. Akagi[73], M. Akemoto[71], A. Akeroyd[367], J. Alabau-Gonzalvo[108], C. Albajar[46], J. E. Albert[379], C. Albertus[281], J. Alcaraz Maestre[31], D. Alesini[174], B. Alessandro[128], G. Alexander[265], J. P. Alexander[43], A. Alhaidari[243], N. Alipour Tehrani[33], B. C. Allanach[323], O. Alonso[311], J. Alwall[210], J. W. Amann[251], Y. Amhis[167], M. S. Amjad[167], B. Ananthanarayan[83], A. Andreazza[386,122], N. Andreev[58], L. Andricek[186], M. Anduze[172], D. Angal-Kalinin[258], N. Anh Ky[106,394], K. A. Aniol[18], K. I. Aoki[148], M. Aoki[148], H. Aoyagi[137], S. Aoyama[250], S. J. Aplin[47], R. B. Appleby[343,40], J. Arafune[96], Y. Arai[71], S. Araki[71], L. Arazi[404], A. Arbey[50], D. Ariza[47], T. Arkan[58], N. D. Arnold[7], D. Arogancia[194], F. Arteche[113], A. Aryshev[71], S. Asai[375], T. Asaka[137], T. Asaka[212], E. Asakawa[220], M. Asano[333], F. B. Asiri[58], D. Asner[225], M. Asorey[286], D. Attié[21], J. E. Augustin[169], D. B. Augustine[58], C. S. Aulakh[226], E. Avetisyan[47], V. Ayvazyan[47], N. Azaryan[142], F. Azfar[358], T. Azuma[246], O. Bachynska[47], H. Baer[355], J. Bagger[141], A. Baghdasaryan[407], S. Bai[102], Y. Bai[384], I. Bailey[40,176], V. Balagura[172,107], R. D. Ball[329], C. Baltay[405], K. Bamba[198], P. S. Bambade[167], Y. Ban[9], E. Banas[268], H. Band[384], K. Bane[251], M. Barbi[362], V. Barger[384], B. Barish[17,65], T. Barklow[251], R. J. Barlow[392], M. Barone[58,65], I. Bars[368], S. Barsuk[167], P. Bartalini[210], R. Bartoldus[251], R. Bates[332], M. Battaglia[322,33], J. Baudot[94], M. Baylac[170], P. Bechtle[295], U. Becker[185,33], M. Beckmann[47], F. Bedeschi[126], C. F. Bedoya[31], S. Behari[58], O. Behnke[47], T. Behnke[47], G. Belanger[165], S. Belforte[129], I. Belikov[94], K. Belkadhi[172], A. Bellerive[19], C. Belver Aguilar[108], A. Belyaev[367,259], D. Benchekroun[184], M. Beneke[57], M. Benoit[33], A. Benot-Morell[33,108], S. Bentvelsen[213], L. Benucci[331], J. Berenguer[31], T. Bergauer[224], S. Berge[138], E. Berger[7], J. Berger[251], C. M. U. Berggren[47], Z. Bern[318], J. Bernabeu[108], N. Bernal[295], G. Bernardi[169], W. Bernreuther[235], M. Bertucci[119], M. Besancon[21], M. Bessner[47], A. Besson[94,306], D. R. Bett[358,140], A. J. Bevan[234], A. Bhardwaj[326], A. Bharucha[333], G. Bhattacharyya[241], B. Bhattacherjee[150], B. Bhuyan[86], M. E. Biagini[174], L. Bian[102], F. Bianchi[128], O. Biebel[182], T. R. Bieler[190], C. Biino[128], B. Bilki[7,337], S. S. Biswal[221], V. Blackmore[358,140], J. J. Blaising[164], N. Blaskovic Kraljevic[358,140], G. Blazey[217], I. Bloch[48], J. Bluemlein[48], B. Bobchenko[107], T. Boccali[126], J. R. Bogart[251], V. Boisvert[237], M. Bonesini[121], R. Boni[174], J. Bonnard[168], G. Bonneaud[169], S. T. Boogert[237,139], L. Boon[233,7],

G. Boorman[237,139], E. Boos[180], M. Boronat[108], K. Borras[47], L. Bortko[48], F. Borzumati[272], M. Bosman[294], A. Bosotti[119], F. J. Botella[108], S. Bou Habib[401], P. Boucaud[171], J. Boudagov[142], G. Boudoul[89], V. Boudry[172], D. Boumediene[168], C. Bourgeois[167], A. Boveia[52], A. Brachmann[251], J. Bracinik[315], J. Branlard[47,58], B. Brau[346], J. E. Brau[356], R. Breedon[320], M. Breidenbach[251], A. Breskin[404], S. Bressler[404], V. Breton[168], H. Breuker[33], C. Brezina[295], C. Briegel[58], J. C. Brient[172], T. M. Bristow[329], D. Britton[332], I. C. Brock[295], S. J. Brodsky[251], F. Broggi[119], G. Brooijmans[42], J. Brooke[316], E. Brost[356], T. E. Browder[334], E. Brücken[69], G. Buchalla[182], P. Buchholz[301], W. Buchmuller[47], P. Bueno[111], V. Buescher[138], K. Buesser[47], E. Bulyak[208], D. L. Burke[251], C. Burkhart[251], P. N. Burrows[358,140], G. Burt[40], E. Busato[168], L. Butkowski[47], S. Cabrera[108], E. Cabruja[32], M. Caccia[389,122], Y. Cai[251], S. S. Caiazza[47,333], O. Cakir[6], P. Calabria[89], C. Calancha[71], G. Calderini[169], A. Calderon Tazon[110], S. Callier[93], L. Calligaris[47], D. Calvet[168], E. Calvo Alamillo[31], A. Campbell[47], G. I. E. Cancelo[58], J. Cao[102], L. Caponetto[89], R. Carcagno[58], M. Cardaci[201], C. Carloganu[168], S. Caron[97,213], C. A. Carrillo Montoya[123], K. Carvalho Akiba[291], J. Carwardine[7], R. Casanova Mohr[311], M. V. Castillo Gimenez[108], N. Castro[175], A. Cattai[33], M. Cavalli-Sforza[294], D. G. Cerdeno[111], L. Cerrito[234], G. Chachamis[108], M. Chadeeva[107], J. S. Chai[260], D. Chakraborty[217], M. Champion[254], C. P. Chang[201], A. Chao[251], Y. Chao[210], J. Charles[28], M. Charles[358], B. E. Chase[58], U. Chattopadhyay[81], J. Chauveau[169], M. Chefdeville[164], R. Chehab[89], A. Chen[201], C. H. Chen[203], J. Chen[102], J. W. Chen[210], K. F. Chen[210], M. Chen[330,102], S. Chen[199], Y. Chen[1], Y. Chen[102], J. Cheng[102], T. P. Cheng[351], B. Cheon[66], M. Chera[47], Y. Chi[102], P. Chiappetta[28], M. Chiba[276], T. Chikamatsu[193], I. H. Chiu[210,210], G. C. Cho[220], V. Chobanova[186], J. B. Choi[36,36], K. Choi[157], S. Y. Choi[37], W. Choi[375,248], Y. I. Choi[260], S. Choroba[47], D. Choudhury[326], D. Chowdhury[83], G. Christian[358,140], M. Church[58], J. Chyla[105], W. Cichalewski[263,47], R. Cimino[174], D. Cinca[337], J. Clark[58], J. Clarke[258,40], G. Claus[94], E. Clement[316,259], C. Clerc[172], J. Cline[187], C. Coca[206], T. Cohen[251], P. Colas[21], A. Colijn[213], N. Colino[31], C. Collard[94], C. Colledani[94], N. Collomb[258], J. Collot[170], C. Combaret[89], B. Constance[33], C. A. Cooper[58], W. E. Cooper[58], G. Corcella[174], E. Cormier[29], R. Cornat[172], P. Cornebise[167], F. Cornet[281], G. Corrado[123], F. Corriveau[187], J. Cortes[286], E. Cortina Gil[303], S. Costa[308], F. Couchot[167], F. Couderc[21], L. Cousin[94], R. Cowan[185], W. Craddock[251], A. C. Crawford[58], J. A. Crittenden[43], J. Cuevas[283], D. Cuisy[167], F. Cullinan[237], B. Cure[33], E. Currás Rivera[110], D. Cussans[316], J. Cvach[105], M. Czakon[235], K. Czuba[401], H. Czyz[365], J. D'Hondt[399], W. Da Silva[169], O. Dadoun[167], M. Dahiya[327], J. Dai[102], C. Dallapiccola[346], C. Damerell[259], M. Danilov[107], D. Dannheim[33], N. Dascenzo[47,238], S. Dasu[384], A. K. Datta[67], T. S. Datta[115], P. Dauncey[80], T. Davenne[259], J. David[169], M. Davier[167], W. De Boer[90], S. De Cecco[169], S. De Curtis[120], N. De Groot[97,213], P. De Jong[213], S. De Jong[97,213], C. De La Taille[93], G. De Lentdecker[307], S. De Santis[177], J. B. De Vivie De Regie[167], A. Deandrea[89], P. P. Dechant[49], D. Decotigny[172], K. Dehmelt[257], J. P. Delahaye[251,33], N. Delerue[167], O. Delferriere[21], F. Deliot[21], G. Della Ricca[388], P. A. Delsart[170], M. Demarteau[7], D. Demin[142], R. Dermisek[87], F. Derue[169], K. Desch[295], S. Descotes-Genon[171], A. Deshpande[252], A. Dexter[40], A. Dey[81], S. Dhawan[405], N. Dhingra[226], V. Di Benedetto[58,123], B. Di Girolamo[33], M. A. Diaz[231], A. Dieguez[311], M. Diehl[47], R. Diener[47], S. Dildick[331], M. O. Dima[206], P. Dinaucourt[167,93], M. S. Dixit[19], T. Dixit[252], L. Dixon[251], A. Djouadi[171], S. Doebert[33], M. Dohlus[47], Z. Dolezal[34], H. Dong[102], L. Dong[102], A. Dorokhov[94], A. Dosil[112], A. Dovbnya[208], T. Doyle[332], G. Doziere[94], M. Dragicevic[224], A. Drago[174], A. J. Dragt[345], Z. Drasal[34], I. Dremin[179], V. Drugakov[209], J. Duarte Campderros[110], F. Duarte Ramos[33], A. Dubey[272], A. Dudarev[142], E. Dudas[171,171], L. Dudko[180], C. Duerig[47], G. Dugan[43], W. Dulinski[94], F. Dulucq[93], L. Dumitru[206], P. J. Dunne[80], A. Duperrin[27], M. Düren[147], D. Dzahini[170], H. Eberl[224], G. Eckerlin[47], P. Eckert[297], N. R. Eddy[58],

W. Ehrenfeld[295], G. Eigen[314], S. Eisenhardt[329], L. Eklund[332], L. Elementi[58], U. Ellwanger[171], E. Elsen[47], I. Emeliantchik[209], L. Emery[7], K. Enami[71], K. Endo[71], M. Endo[375], J. Engels[47], C. Englert[49], S. Eno[345], A. Enomoto[71], S. Enomoto[197], F. Eozenou[21], R. Erbacher[320], G. Eremeev[269], J. Erler[287], R. Escribano[294], D. Esperante Pereira[108], D. Espriu[311], E. Etzion[265,33], S. Eucker[47], A. Evdokimov[336,107], E. Ezura[71], B. Faatz[47], G. Faisel[201], L. Fano[125], A. Faraggi[340], A. Fasso[251], A. Faus-Golfe[108], L. Favart[307], N. Feege[257], J. L. Feng[321], T. Ferber[47], J. Ferguson[33], J. Fernández[283], P. Fernández Martínez[108], E. Fernandez[294,293], M. Fernandez Garcia[110], J. L. Fernandez-Hernando[130], P. Fernandez-Martinez[32], J. Fernandez-Melgarejo[33], A. Ferrer[108], F. Ferri[21], S. Fichet[117], T. Fifield[347], L. Filkov[179], F. Filthaut[97,213], A. Finch[176], H. E. Fisk[58], T. Fiutowski[2], H. Flaecher[316], J. W. Flanagan[71], I. Fleck[301], M. Fleischer[47], C. Fleta[32], J. Fleury[93], D. Flores[32], M. Foley[58], M. Fontannaz[171], K. Foraz[33], N. Fornengo[128], F. Forti[126,391], B. Foster[47,140], M. C. Fouz[31], P. H. Frampton[353], K. Francis[7], S. Frank[224], A. Freitas[361], A. Frey[64], R. Frey[356], M. Friedl[224], C. Friedrich[48], M. Frigerio[163], T. Frisson[167], M. Frotin[172], R. Frühwirth[224], R. Fuchi[378], E. Fuchs[47], K. Fujii[71], J. Fujimoto[71], H. Fuke[134], B. Fuks[94,33], M. Fukuda[71], S. Fukuda[71], K. Furukawa[71], T. Furuya[71], T. Fusayasu[195], J. Fuster[108], N. Fuster[108], Y. Fuwa[95,159], A. Gaddi[33], K. Gadow[47], F. Gaede[47], R. Gaglione[164], S. Galeotti[126], C. Gallagher[356], A. A. Gallas Torreira[112], L. Gallin-Martel[170], A. Gallo[174], D. Gamba[140,33], D. Gamba[128], J. Gao[102], Y. Gao[24], P. H. Garbincius[58], F. Garcia[69], C. Garcia Canal[288], J. E. Garcia Navarro[108], P. Garcia-Abia[31], J. J. Garcia-Garrigos[108], L. Garcia-Tabares[31], C. García[108], J. V. García Esteve[286], I. García García[108], S. K. Garg[408], L. Garrido[311], E. Garutti[333], T. Garvey[167,261], M. Gastal[33], F. Gastaldi[172], C. Gatto[58,123], N. Gaur[326], D. Gavela Pérez[31], P. Gay[168], M. B. Gay Ducati[109], L. Ge[251], R. Ge[102], A. Geiser[47], A. Gektin[100], A. Gellrich[47], M. H. Genest[170], R. L. Geng[269], S. Gentile[387,127], A. Gerbershagen[33,358], R. Gerig[7], S. German[111], H. Gerwig[33], S. Ghazaryan[47], P. Ghislain[169], D. K. Ghosh[81], S. Ghosh[115], S. Giagu[387,127], L. Gibbons[43], S. Gibson[139,33], V. Gilewsky[143], A. Gillespie[328], F. Gilman[20], B. Gimeno Martínez[108], D. M. Gingrich[312,279], C. M. Ginsburg[58], D. Girard[164], J. Giraud[170], G. F. Giudice[33], L. Gladilin[180], P. Gladkikh[208], C. J. Glasman[343,40], R. Glattauer[224], N. Glover[49], J. Gluza[365], K. Gnidzinska[263], R. Godbole[83], S. Godfrey[19], F. Goertz[54], M. Goffe[94], N. Gogitidze[179,47], J. Goldstein[316], B. Golob[144,341], G. Gomez[110], V. Goncalves[290], R. J. Gonsalves[256], I. González[283], S. González De La Hoz[108], F. J. González Sánchez[110], G. Gonzalez Parra[294], S. Gopalakrishna[103], I. Gorelov[352], D. Goswami[86], S. Goswami[229], T. Goto[71], K. Gotow[398], P. Göttlicher[47], M. Götze[385], A. Goudelis[165], P. Goudket[258], S. Gowdy[33], O. A. Grachov[309], N. A. Graf[251], M. Graham[251], A. Gramolin[15], R. Granier De Cassagnac[172], P. Grannis[257], P. Gras[21], M. Grecki[47], T. Greenshaw[339], D. Greenwood[181], C. Grefe[33], M. Grefe[111], I. M. Gregor[47], D. Grellscheid[49], G. Grenier[89], M. Grimes[316], C. Grimm[58], O. Grimm[53], B. Grinyov[100], B. Gripaios[323], K. Grizzard[141], A. Grohsjean[47], C. Grojean[294,33], J. Gronberg[178], D. Grondin[170], S. Groote[370], P. Gros[240], M. Grunewald[310], B. Grzadkowski[382], J. Gu[102], M. Guchait[262], S. Guiducci[174], E. Guliyev[172], J. Gunion[320], C. Günter[47], C. Gwilliam[339], N. Haba[75], H. Haber[322], M. Hachimine[197], Y. Haddad[172], L. Hagge[47], M. Hagihara[378], K. Hagiwara[71,158], J. Haley[216], G. Haller[251], J. Haller[333], K. Hamaguchi[375], R. Hamatsu[276], G. Hamel De Monchenault[21], L. L. Hammond[58], P. Hamnett[47], L. Han[364], T. Han[361], K. Hanagaki[223], J. D. Hansen[211], K. Hansen[47], P. H. Hansen[211], X. Q. Hao[70], K. Hara[71], K. Hara[378], T. Hara[71], D. Harada[83], K. Harada[161], K. Harder[259], T. Harion[297], R. V. Harlander[385], E. Harms[58], M. Harrison[13], O. Hartbrich[47,385], A. Hartin[47], T. Hartmann[300], J. Harz[47], S. Hasegawa[197], T. Hasegawa[71], Y. Hasegawa[248], M. Hashimoto[38], T. Hashimoto[62], C. Hast[251], S. Hatakeyama[135], J. M. Hauptman[118], M. Hauschild[33], M. Havranek[105], C. Hawkes[315], T. Hayakawa[197], H. Hayano[71], K. Hayasaka[198], M. Hazumi[71,253], H. J. He[24], C. Hearty[317,104], H. F. Heath[316],

T. Hebbeker[235], M. Heck[90], V. Hedberg[183], D. Hedin[217], S. M. Heindl[90], S. Heinemeyer[110], I. Heinze[47], A. Hektor[205], S. Henrot-Versille[167], O. Hensler[47], A. Heo[23], J. Herbert[258], G. Herdoiza[138], B. Hermberg[47], J. J. Hernández-Rey[108], M. J. Herrero[111], B. Herrmann[165], A. Hervé[384], J. Hewett[251], S. Hidalgo[32], B. Hidding[333,318], N. Higashi[375], N. Higashi[71], T. Higo[71], E. Higón Rodríguez[108], T. Higuchi[150], M. Hildreth[354], C. T. Hill[58], S. Hillert[295], S. Hillier[315], T. Himel[251], A. Himmi[94], S. Himori[272], Z. Hioki[374], B. Hippolyte[94], T. Hiraki[159], K. Hirano[136], S. Hirano[197], K. Hirata[71], T. Hirose[276], M. Hirsch[108], J. Hisano[197], P. M. Ho[210], A. Hoang[302], A. Hocker[58], A. Hoecker[33], M. Hoeferkamp[352], M. Hoffmann[47], W. Hollik[186], K. Homma[72], Y. Homma[154], S. Honda[378], T. Honda[71], Y. Honda[71], N. T. Hong Van[106], K. Honkavaara[47], T. Honma[71], T. Hori[236], T. Horiguchi[272], Y. Horii[197], A. Horio[196], R. Hosaka[377], Y. Hoshi[271], H. Hoshino[197], K. Hosoyama[71], J. Y. Hostachy[170], G. W. Hou[210], M. Hou[102], A. Hoummada[184], M. S. Hronek[58], T. Hu[102], C. Hu-Guo[94], M. Huang[24], T. Huang[102], E. Huedem[58], F. Hügging[295], J. L. Hugon[330], C. Hugonie[173], K. Huitu[335], P. Q. Hung[380], C. Hunt[80], U. Husemann[90], G. Hussain[24], D. Hutchcroft[339], Y. Hyakutake[79], J. C. Ianigro[89], L. E. Ibanez[111], M. Ibe[96], M. Idzik[2], H. Igarashi[78], Y. Igarashi[71], K. Igi[236], A. Ignatenko[209], O. Igonkina[213], T. Iijima[198,197], M. Iinuma[73], Y. Iiyama[20], H. Ikeda[134], K. Ikeda[71], K. Ikematsu[301], J. I. Illana[281], V. A. Ilyin[207,180], A. Imhof[333], T. Inagaki[236], T. Inagaki[197], K. Inami[197], S. Inayoshi[248], K. Inoue[161], A. Irles[108], S. Isagawa[71], N. Ishibashi[378], A. Ishida[375], K. Ishida[212], N. Ishihara[71], S. Ishihara[77], K. Ishii[71], A. Ishikawa[272], K. Ishikawa[375], K. I. Ishikawa[72], K. Ishikawa[75], T. Ishikawa[71], M. Ishitsuka[275], K. Ishiwata[17], G. Isidori[174], A. Ismail[251], S. Iso[71], T. Isogai[197], C. Issever[358], K. Itagaki[272], T. Itahashi[223], A. Ito[275], F. Ito[378], S. Ito[272], R. Itoh[71], E. Itou[71], M. I. Ivanyan[26], G. Iwai[71], S. Iwamoto[375], T. Iwamoto[116], H. Iwasaki[71], M. Iwasaki[71], Y. Iwashita[95], S. Iwata[71], S. Iwata[276], T. Izubuchi[13,236], Y. Izumiya[272], S. Jablonski[401], F. Jackson[258], J. A. Jacob[316], M. Jacquet[167], P. Jain[40], P. Jaiswal[59], W. Jalmuzna[263], E. Janas[401], R. Jaramillo Echeverría[110], J. Jaros[251], D. Jatkar[67], D. Jeans[375], R. Jedziniak[58], M. J. Jenkins[176,40], K. Jensch[47], C. P. Jessop[354], T. Jezynski[47], M. Jimbo[35], S. Jin[102], O. Jinnouchi[275], M. D. Joergensen[211], A. S. Johnson[251], S. Jolly[309], D. T. Jones[340], J. Jones[258,40], R. M. Jones[343,40], L. Jönsson[183], N. Joshi[237], C. K. Jung[257,150], N. Juntong[343,40], A. Juste[88,294], W. Kaabi[167], M. Kadastik[205], M. Kado[167,33], K. Kadota[197], E. Kajfasz[27], R. Kajikawa[197], Y. Kajiura[197], M. Kakizaki[377], E. Kako[71], H. Kakuhata[377], H. Kakuno[276], A. Kalinin[258], J. Kalinowski[382], G. E. Kalmus[259], K. Kamada[47], J. Kaminski[295], T. Kamitani[71], Y. Kamiya[116], Y. Kamiya[71], R. Kammering[47], T. Kamon[266], J. I. Kamoshita[60], T. Kanai[275], S. Kananov[265], K. Kanaya[378], M. Kaneda[33], T. Kaneko[71,253], S. Kanemura[377], K. Kaneta[75], W. Kang[102], D. Kanjilal[115], K. Kannike[205], F. Kapusta[169], D. Kar[332], P. Karataev[237,139], P. E. Karchin[403], D. Karlen[379,279], S. Karstensen[47], Y. Karyotakis[164], M. Kasemann[47], V. S. Kashikhin[58], S. Kashiwagi[273], A. Kataev[98], V. Katalev[48], Y. Kataoka[116], N. Katayama[150], R. Katayama[375], E. Kato[272], K. Kato[155], S. Kato[71], Y. Kato[153], T. Katoh[71], A. Kaukher[47], S. Kawabata[71], S. I. Kawada[73], K. Kawagoe[161], M. Kawai[71], T. Kawamoto[116], H. Kawamura[71], M. Kawamura[71], Y. Kawamura[248], S. Kawasaki[71], T. Kawasaki[212], H. Kay[47], S. Kazama[375], L. Keegan[111], J. Kehayias[150], L. Keller[251], M. A. Kemp[251], J. J. Kempster[237], C. Kenney[251], I. Kenyon[315], R. Kephart[58], J. Kerby[7], K. Kershaw[33], J. Kersten[333], K. Kezzar[151], V. G. Khachatryan[26], M. A. Khan[23], S. A. Khan[242], Y. Khoulaki[184], V. Khoze[49], H. Kichimi[71], R. Kieffer[33], C. Kiesling[186], M. Kikuchi[377], Y. Kikuta[71], M. Killenberg[47], C. S. Kim[408], D. W. Kim[63], D. Kim[23], E. J. Kim[36,36], E. S. Kim[23], G. Kim[23], H. S. Kim[23], H. D. Kim[245], J. Kim[63], S. H. Kim[378], S. K. Kim[245], S. G. Kim[87], Y. I. Kim[358,140], Y. Kimura[71], R. E. Kirby[251], F. Kircher[21], Y. Kishimoto[96], L. Kisslinger[20], T. Kitahara[375], R. Kitano[272], Y. Kiyo[146,71], C. Kleinwort[47], W. Klempt[33], P. M. Kluit[213], V. Klyukhin[180,33], M. Knecht[28], J. L. Kneur[163], B. A. Kniehl[333], K. Ko[251], P. Ko[158], D. Kobayashi[275], M. Kobayashi[71], N. Kobayashi[71],

T. Kobayashi[116], M. Koch[295], P. Kodys[34], U. Koetz[47], E. N. Koffeman[213], M. Kohda[210], S. Koike[71], Y. Kojima[71], K. Kolodziej[365], Y. Kolomensky[319,177], S. Komamiya[375], T. Kon[244], P. Konar[229], Y. Kondou[71], D. Kong[23], K. Kong[338], O. C. Kong[201], T. Konno[275,275], V. Korbel[47], J. G. Körner[138], S. Korpar[344,144], S. R. Koscielniak[279], D. Kostin[47], K. Kotera[248], W. Kotlarski[382], J. Kotula[268], E. Kou[167], V. Kovalenko[333], S. V. H. Kox[170], K. Koyama[75], M. Krämer[235], S. Kraml[170], M. Krammer[224], M. W. Krasny[169], F. Krauss[49], T. Krautscheid[295], M. Krawczyk[382], K. Krempetz[58], P. Križan[341,144], B. E. Krikler[80], A. Kronfeld[58], K. Kruchinin[237,139], D. Krücker[47], K. Krüger[47], B. Krupa[268], Y. P. Kuang[24], K. Kubo[71], T. Kubo[71], T. Kubota[347], T. Kubota[275], Y. Kubyshin[298,180], V. Kuchler[58], I. M. Kudla[202], D. Kuehn[47], J. H. Kuehn[92], C. Kuhn[94], S. Kulis[2], S. Kulkarni[170], A. Kumar[10], S. Kumar[86], T. Kumita[276], A. Kundu[16], Y. Kuno[223], C. M. Kuo[201], M. Kurachi[198], A. Kuramoto[253], M. Kurata[375], Y. Kurihara[71], M. Kuriki[73,71], T. Kurimoto[377], S. Kuroda[71], K. Kurokawa[71], S. I. Kurokawa[71], H. Kuwabara[276], M. Kuze[275], J. Kvasnicka[105], P. Kvasnicka[34], Y. Kwon[408], L. Labun[210], C. Lacasta[108], T. Lackowski[58], D. Lacour[169], V. Lacuesta[108], R. Lafaye[164], G. Lafferty[343], B. Laforge[169], I. Laktineh[89], R. L. Lander[320], K. Landsteiner[111], S. Laplace[169], K. J. Larsen[213], R. S. Larsen[251], T. Lastovicka[105], J. I. Latorre[311], S. Laurien[333], L. Lavergne[169], S. Lavignac[22], R. E. Laxdal[279], A. C. Le Bihan[94], F. R. Le Diberder[167], A. Le-Yaouanc[171], A. Lebedev[13], P. Lebrun[33], T. Lecompte[7], T. Leddig[300], F. Ledroit[170], B. Lee[25], K. Lee[158], M. Lee[177], S. H. Lee[260], S. W. Lee[267], Y. H. Lee[210], J. Leibfritz[58], K. Lekomtsev[71], L. Lellouch[28], M. Lemke[47], F. R. Lenkszus[7], A. Lenz[49,33], O. Leroy[27], C. Lester[323], L. Levchuk[208], J. Leveque[164], E. Levichev[15], A. Levy[265], I. Levy[265], J. R. Lewandowski[251], B. Li[24], C. Li[364], C. Li[102], D. Li[102], H. Li[380], L. Li[195], L. Li[247], L. Li[364], S. Li[102], W. Li[102], X. Li[102], Y. Li[24], Y. Li[24], Y. Li[24], Z. Li[251], Z. Li[102], J. J. Liau[210], V. Libov[47], L. Lilje[47], J. G. Lima[217], C. J. D. Lin[204], C. M. Lin[154], C. Y. Lin[201], H. Lin[102], H. H. Lin[210], F. L. Linde[213], R. A. Lineros[108], L. Linssen[33], R. Lipton[58], M. Lisovyi[47], B. List[47], J. List[47], B. Liu[24], J. Liu[364], R. Liu[102], S. Liu[167], S. Liu[247], W. Liu[7], Y. Liu[102], Y. Liu[337,58], Z. Liu[361], Z. Liu[102], Z. Liu[102], A. Lleres[170], N. S. Lockyer[279,317], W. Lohmann[48,12], E. Lohrmann[333], T. Lohse[76], F. Long[102], D. Lontkovskyi[47], M. A. Lopez Virto[110], X. Lou[102,372], A. Lounis[167], M. Lozano Fantoba[32], J. Lozano-Bahilo[281], C. Lu[232], R. S. Lu[210], S. Lu[47], A. Lucotte[170], F. Ludwig[47], S. Lukic[396], O. Lukina[180], N. Lumb[89], B. Lundberg[183], A. Lunin[58], M. Lupberger[295], B. Lutz[47], P. Lutz[21], T. Lux[294], K. Lv[102], M. Lyablin[142], A. Lyapin[237,139], J. Lykken[58], A. T. Lytle[262], L. Ma[258], Q. Ma[102], R. Ma[312], X. Ma[102], F. Machefert[167], N. Machida[377], J. Maeda[276], Y. Maeda[159], K. Maeshima[58], F. Magniette[172], N. Mahajan[229], F. Mahmoudi[168,33], S. H. Mai[201], C. Maiano[119], H. Mainaud Durand[33], S. Majewski[356], S. K. Majhi[81], N. Majumdar[241], G. Majumder[262], I. Makarenko[47], V. Makarenko[209], A. Maki[71], Y. Makida[71], D. Makowski[263], B. Malaescu[169], J. Malcles[21], U. Mallik[337], S. Malvezzi[121], O. B. Malyshev[258,40], Y. Mambrini[171], A. Manabe[71], G. Mancinelli[27], S. K. Mandal[150], S. Mandry[309,186], S. Manen[168], R. Mankel[47], S. Manly[363], S. Mannai[303], Y. Maravin[149], G. Marchiori[169], M. Marcisovsky[105,45], J. Marco[110], D. Marfatia[338], J. Marin[31], E. Marin Lacoma[251], C. Marinas[295], T. W. Markiewicz[251], O. Markin[107], J. Marshall[323], S. Martí-García[108], A. D. Martin[49], V. J. Martin[329], G. Martin-Chassard[93], T. Martinez De Alvaro[31], C. Martinez Rivero[110], F. Martinez-Vidal[108], H. U. Martyn[235,47], T. Maruyama[251], A. Masaike[159], T. Mashimo[116], T. Masubuchi[116], T. Masuda[159], M. Masuzawa[71], Z. Mateusz[401], A. Matheisen[47], H. Mathez[89], J. Matias[293], H. Matis[177], T. Matsubara[276], T. Matsuda[71], T. Matsui[377], S. Matsumoto[161], S. Matsumoto[150], Y. Matsumoto[220], H. Matsunaga[71], T. Matsushita[154], T. S. Mattison[317], V. A. Matveev[142], U. Mavric[47], G. Mavromanolakis[33], K. Mawatari[399], S. J. Maxfield[339], K. Mazumdar[262], A. Mazzacane[58,123], R. L. Mccarthy[257], D. J. Mccormick[251], J. Mccormick[251], K. T. Mcdonald[232], R. Mcduffee[324], P. Mcintosh[258], B. Mckee[251], M. Medinnis[47], S. Mehlhase[211], T. Mehrling[47,333],

A. Mehta[339], B. Mele[127], R. E. Meller[43], I. A. Melzer-Pellmann[47], L. Men[102], G. Mendiratta[83], Z. Meng[316], M. H. Merk[213,400], M. Merkin[180], A. Merlos[32], L. Merminga[279], A. B. Meyer[47], A. Meyer[235], N. Meyners[47], Z. Mi[102], P. Michelato[119], S. Michizono[71], S. Mihara[71], A. Mikhailichenko[43], D. J. Miller[309], C. Milstene[403], Y. Mimura[210], D. Minic[398], L. Mirabito[89], S. Mishima[387], T. Misumi[13], W. A. Mitaroff[224], T. Mitsuhashi[71], S. Mitsuru[71], K. Miuchi[154], K. Miyabayashi[200], A. Miyamoto[71], H. Miyata[212], Y. Miyazaki[161], T. Miyoshi[71], R. Mizuk[107], K. Mizuno[3], U. Mjörnmark[183], J. Mnich[47], G. Moeller[47], W. D. Moeller[47], K. Moenig[48], K. C. Moffeit[251], P. Mohanmurthy[269], G. Mohanty[262], L. Monaco[119], S. Mondal[81], C. Monini[170], H. Monjushiro[71], G. Montagna[359,124], S. Monteil[168], G. Montoro[298], I. Montvay[47], F. Moortgat[53], G. Moortgat-Pick[333,47], P. Mora De Freitas[172], C. Mora Herrera[30], G. Moreau[171], F. Morel[94], A. Morelos-Pineda[280], M. Moreno Llacer[108], S. Moretti[367,259], V. Morgunov[47,107], T. Mori[71], T. Mori[272], T. Mori[116], Y. Morita[71], S. Moriyama[96,150], L. Moroni[121], Y. Morozumi[71], H. G. Moser[186], A. Moszczynski[268], K. Motohashi[275], T. Moulik[249], G. Moultaka[163], D. Moya Martin[110], S. K. Mtingwa[215], G. S. Muanza[27], M. Mühlleitner[91], A. Mukherjee[85], S. Mukhopadhyay[241], M. Mulders[33], D. Muller[251], F. Müller[47], T. Müller[90], V. S. Mummidi[83], A. Münnich[47], C. Munoz[111], F. J. Muñoz Sánchez[110], H. Murayama[375,319], R. Murphy[7], G. Musat[172], A. Mussgiller[47], R. Muto[71], T. Nabeshima[377], K. Nagai[71], K. Nagai[378], S. Nagaitsev[58], T. Nagamine[272], K. Nagano[71], K. Nagao[71], Y. Nagashima[223], S. C. Nahn[185], P. Naik[316], D. Naito[159], T. Naito[71], H. Nakai[71], K. Nakai[71,223], Y. Nakai[161], Y. Nakajima[177], E. Nakamura[71], H. Nakamura[71], I. Nakamura[71], S. Nakamura[159], S. Nakamura[71], T. Nakamura[116], K. Nakanishi[71], E. Nakano[222], H. Nakano[212], H. Nakano[272], Y. Namito[71], W. Namkung[230], H. Nanjo[159], C. D. Nantista[251], O. Napoly[21], Y. Nara[4], T. Narazaki[272], S. Narita[131], U. Nauenberg[324], T. Naumann[48], S. Naumann-Emme[47], J. Navarro[108], A. Navitski[47], H. Neal[251], K. Negishi[272], K. Neichi[270], C. A. Nelson[255], T. K. Nelson[251], S. Nemecek[105], M. Neubert[138], R. Neuhaus[218], L. J. Nevay[237], D. M. Newbold[316,259], O. Nezhevenko[58], F. Nguyen[175], M. Nguyen[172], M. N. Nguyen[251], T. T. Nguyen[106], R. B. Nickerson[358], O. Nicrosini[124], C. Niebuhr[47], J. Niehoff[58], M. Niemack[43], U. Nierste[92], H. Niinomi[159], I. Nikolic[169], H. P. Nilles[295], S. Nishida[71], H. Nishiguchi[71], K. Nishiwaki[67], O. Nitoh[277], L. Niu[24], R. Noble[251], M. Noji[71], M. Nojiri[71,150], S. Nojiri[197,198], D. Nölle[47], A. Nomerotski[358], M. Nomura[135], T. Nomura[201], Y. Nomura[319,177], C. Nonaka[198], J. Noonan[7], E. Norbeck[337], Y. Nosochkov[251], D. Notz[47], O. Novgorodova[48,12], A. Novokhatski[251], J. A. Nowak[349], M. Nozaki[71], K. Ocalan[192], J. Ocariz[169], S. Oda[161], A. Ogata[71], T. Ogawa[248], T. Ogura[248], A. Oh[343], S. K. Oh[156], Y. Oh[23], K. Ohkuma[61], T. Ohl[145], Y. Ohnishi[71], K. Ohta[189], M. Ohta[71,253], S. Ohta[71,253], N. Ohuchi[71], K. Oishi[161], R. Okada[71], Y. Okada[71,253], T. Okamura[71], H. Okawa[13], T. Okugi[71], T. Okui[59], K. I. Okumura[161], Y. Okumura[52,58], L. Okun[107], H. Okuno[236], C. Oleari[390], C. Oliver[31], B. Olivier[186], S. L. Olsen[245], M. Omet[253,71], T. Omori[71], Y. Onel[337], H. Ono[214], Y. Ono[272], D. Onoprienko[251], Y. Onuki[116,150], P. Onyisi[371], T. Oogoe[71], Y. Ookouchi[159], W. Ootani[116], M. Oreglia[52], M. Oriunno[251], M. C. Orlandea[206], J. Orloff[168], M. Oroku[375,71], R. S. Orr[376], J. Osborne[33], A. Oskarsson[183], P. Osland[314], A. Osorio Oliveros[282], L. Österman[183], H. Otono[223], M. Owen[343], Y. Oyama[71], A. Oyanguren[108], K. Ozawa[71,375], J. P. Ozelis[58,191], D. Ozerov[47], G. Pásztor[304,99], H. Padamsee[43], C. Padilla[294], C. Pagani[119,386], R. Page[316], R. Pain[169], S. Paktinat Mehdiabadi[101], A. D. Palczewski[269], S. Palestini[33], F. Palla[126], M. Palmer[58], F. Palomo Pinto[285], W. Pan[102], G. Pancheri[174], M. Pandurovic[396], O. Panella[125], A. Pankov[227], Y. Papaphilippou[33], R. Paparella[119], A. Paramonov[7], E. K. Park[75], H. Park[23], S. I. Park[23], S. Park[260], S. Park[373], W. Park[23], A. Parker[323], B. Parker[13], C. Parkes[343], V. Parma[33], Z. Parsa[13], R. Partridge[251], S. Pastor[108], E. Paterson[251], M. Patra[83], J. R. Patterson[43], M. Paulini[20], N. Paver[129], S. Pavy-Bernard[167],

B. Pawlik[268], A. Pérez Vega-Leal[285], B. Pearson[355], J. S. Pedersen[211], A. Pedicini[397], S. Pedraza López[108], G. Pei[102], S. Pei[102], G. Pellegrini[32], A. Pellegrino[213], S. Penaranda[286], H. Peng[364], X. Peng[102], M. Perelstein[43], E. Perez[112], M. A. Perez-Garcia[284,114], M. Perez-Victoria[281], S. Peris[293], D. Perret-Gallix[164], H. Perrey[47], T. M. Perry[384], M. E. Peskin[251], P. Petagna[33], R. Y. Peters[64,47], T. C. Petersen[211], D. P. Peterson[43], T. Peterson[58], E. Petrakou[210], A. A. Petrov[403], A. Petrukhin[89,107], S. Pfeiffer[47], H. Pham[94], K. H. Phan[395,71], N. Phinney[251], F. Piccinini[124], A. Pich[108], R. Pichai[85], J. Piedra[283], J. Piekarski[401], A. Pierce[348], P. Pierini[119], N. Pietsch[333,47], A. Pineda[293], J. Pinfold[312,152], A. Piotrowski[263], Y. Pischalnikov[58], R. Pittau[281], M. Pivi[251], W. Placzek[132], T. Plehn[296], M. A. Pleier[13], M. Poelker[269], L. Poggioli[167], I. Pogorelsky[13], V. Poireau[164], M. E. Pol[30], I. Polak[105], F. Polci[169], M. Polikarpov[107], T. Poll[316,259], M. W. Poole[258,40], W. Porod[145], F. C. Porter[17], S. Porto[333], J. Portolés[108], R. Pöschl[167], S. Poss[33], C. T. Potter[356], P. Poulose[86], K. T. Pozniak[401], V. Prahl[47], R. Prepost[384], C. Prescott[251], D. Price[87], T. Price[315], P. S. Prieto[58], D. Protopopescu[332], D. Przyborowski[2], K. Przygoda[263], H. Przysiezniak[164], F. Ptochos[325], J. Puerta-Pelayo[31], C. Pulvermacher[90], M. Purohit[366], Q. Qin[102], F. Qiu[102], H. Qu[102], A. Quadt[64], G. Quast[90], D. Quirion[32], M. Quiros[88], J. Rademacker[316], R. Rahmat[350], S. Rai[67], M. Raidal[205], S. Rakshit[84], M. Ramilli[333], F. Rarbi[170], P. Ratoff[176], T. Raubenheimer[251], M. Rauch[91], L. Raux[93], G. Raven[400,213], P. Razis[325], V. Re[124], S. Redford[33], C. E. Reece[269], I. Reichel[177], A. Reichold[358,140], P. Reimer[105], M. Reinecke[47], A. Rekalo[100], J. Repond[7], J. Resta-Lopez[108], J. Reuter[47], J. T. Rhee[156], P. M. Ribeiro Cipriano[47], A. Ribon[33], G. Ricciardi[292,123], F. Richard[167], E. Richter-Was[132], G. Riddone[33], S. Riemann[48], T. Riemann[48], M. Rijssenbeek[257], K. Riles[348], C. Rimbault[167], R. Rimmer[269], S. D. Rindani[229], A. Ringwald[47], L. Rinolfi[33], I. Ripp-Baudot[94], I. Riu[294], T. G. Rizzo[251], P. Robbe[167], J. Roberts[140,33], A. Robson[332], G. Rodrigo[108], P. Rodriguez[251], P. Rodriguez Perez[112], K. Rolbiecki[111], P. Roloff[33], R. S. Romaniuk[401], E. Romero Adam[108], A. Ronzhin[58], L. Roos[169], E. Ros[108], A. Rosca[47], C. Rosemann[47], J. Rosiek[382], M. C. Ross[251], R. Rossmanith[90], S. Roth[235], J. Rouënè[167], A. Rowe[58], P. Rowson[251], A. Roy[115], L. Royer[168], P. Royole-Degieux[93], C. Royon[21], A. Rozanov[27], M. Ruan[172], D. L. Rubin[43], I. Rubinskiy[47], R. Rückl[145], R. Ruiz[361], R. Ruiz De Austri[108], P. Ruiz Valls[108], P. Ruiz-Femenía[108], A. Ruiz-Jimeno[110], R. Ruland[251], V. Rusinov[107], J. J. Russell[251], I. Rutkowski[401], V. Rybnikov[47], A. Ryd[43], A. Sabio Vera[111], B. Sabirov[142], J. J. Saborido Silva[112], H. F. W. Sadrozinski[322], T. Saeki[71], B. Safarzadeh[101], P. Saha[305], H. Sahoo[7], A. Sailer[33], N. Saito[71], T. Saito[272], T. Sakaguchi[13], H. Sakai[71], K. Sakai[71], K. Sakaue[402], K. Sakurai[47], R. Salerno[172], J. Salfeld-Nebgen[47], J. Salt[108], L. Sanchez[31], M. A. Sanchis Lozano[108], J. Sandweiss[405], A. Santa[377], A. Santagata[286], A. Santamaria[108], P. Santorelli[292], T. Sanuki[272], A. A. Sapronov[142], M. Sasaki[96], H. Sato[248], N. Sato[71], Y. Sato[272], M. Satoh[71], E. Sauvan[164], V. Saveliev[238,47], A. Savoy-Navarro[166,126], M. Sawabe[71], R. Sawada[116], H. Sawamura[402], L. Sawyer[181], O. Schäfer[300,47], R. Schäfer[47], J. Schaffran[47], T. Schalk[322,251], R. D. Schamberger[257], J. Scheirich[34], G. Schierholz[47], F. P. Schilling[90], F. Schirra[89], F. Schlander[47], H. Schlarb[47], D. Schlatter[33], P. Schleper[333], J. L. Schlereth[7], R. D. Schlueter[177], C. Schmidt[47], U. Schneekloth[47], S. Schnetzer[239], T. Schoerner-Sadenius[47], M. Schram[225], H. J. Schreiber[48], S. Schreiber[47], K. P. Schüler[47], D. Schulte[33], H. C. Schultz-Coulon[297], M. Schumacher[5], S. Schumann[64], B. A. Schumm[322], M. H. Schune[167], S. Schuwalow[333,48], C. Schwanda[224], C. Schwanenberger[343], F. Schwartzkopff[295], D. J. Scott[258,58], F. Sefkow[47,33], A. Segui[286], N. Seguin-Moreau[93], S. Seidel[352], Y. Seiya[222], J. Sekaric[338], K. Seki[197], S. Sekmen[33], S. Seletskiy[13], S. Sen[337], E. Senaha[158], K. Senyo[406], S. Senyukov[94], I. Serenkova[227], D. A. Sergatskov[58], H. Sert[47,333], D. Sertore[119], A. Seryi[358,140], O. Seto[74], R. Settles[186], P. Sha[102], S. Shahid[301], A. Sharma[33], G. Shelkov[142], W. Shen[297], J. C. Sheppard[251], M. Sher[41], C. Shi[102], H. Shi[102], T. Shidara[71], W. Shields[237,139], M. Shimada[71], H. Shimizu[71], Y. Shimizu[272],

M. Shimojima[195], S. Shimojima[276], T. Shindou[155], N. Shinoda[272], Y. Shinzaki[272], M. Shioden[78,71], I. Shipsey[233], S. Shirabe[161], M. J. Shirakata[71], T. Shirakata[71], G. Shirkov[142], T. Shishido[71], T. Shishido[71], J. G. Shiu[210], R. Shivpuri[326], R. Shrock[257], T. Shuji[71], N. Shumeiko[209], B. Shuve[228,188], P. Sicho[105], A. M. Siddiqui[133], P. Sievers[33], D. Sikora[401], D. A. Sil[86], F. Simon[186], N. B. Sinev[356], W. Singer[47], X. Singer[47], B. K. Singh[10], R. K. Singh[82], N. Sinha[103], R. Sinha[103], K. Sinram[47], T. Sinthuprasith[14], P. Skubic[355], R. Sliwa[167], I. Smiljanic[396], J. R. Smith[373,7], J. C. Smith[251,43], S. R. Smith[251], J. Smolík[105,45], J. Snuverink[237,139], B. Sobloher[47], J. Sola[311], C. Soldner[186,57], S. Soldner-Rembold[343], D. Son[23], H. S. Song[260], N. Sonmez[51], A. Sopczak[44], D. E. Soper[356], P. Spagnolo[126], S. Spannagel[47], M. Spannowsky[49], A. Sparkes[329], C. M. Spencer[251], H. Spiesberger[138], M. Spira[261], M. Stahlhofen[47], M. Stanescu-Bellu[48], M. Stanitzki[47], S. Stapnes[33], P. Starovoitov[209], F. Staufenbiel[48], L. Steder[47], M. Steder[47], A. Steen[89], G. Steinbrueck[333], M. Steinhauser[92], F. Stephan[48], W. Stephen[237], S. Stevenson[358], I. Stewart[185], D. Stöckinger[264], H. Stoeck[369], M. Strauss[355], S. Striganov[58], D. M. Strom[356], R. Stromhagen[47], J. Strube[33], A. Strumia[205], G. Stupakov[251], N. Styles[47], D. Su[251], F. Su[102], S. Su[313], J. Suarez Gonzalez[209], Y. Sudo[161], T. Suehara[116], F. Suekane[274], Y. Suetsugu[71], R. Sugahara[71], A. Sugamoto[220], H. Sugawara[71], Y. Sugimoto[71], A. Sugiyama[240], H. Sugiyama[377], M. K. Sullivan[251], Y. Sumino[272], T. Sumiyoshi[276,71], H. Sun[102], M. Sun[20], X. Sun[170], Y. Sun[102], Y. Susaki[197], T. Suwada[71], A. Suzuki[71], S. Suzuki[240], Y. Suzuki[71], Y. Suzuki[73], Z. Suzuki[272], K. Swientek[2], C. Swinson[13], Z. M. Szalata[251], B. Szczepanski[47], M. Szelezniak[94], J. Szewinski[202], A. Sznajder[289], L. Szymanowski[202], H. Tabassam[329], K. Tackmann[47], M. Taira[71], H. Tajima[197,251], F. Takahashi[272], R. Takahashi[71], R. Takahashi[75], T. Takahashi[73], Y. Takahashi[197], K. Takata[71], F. Takayama[160], Y. Takayasu[75], H. Takeda[154], S. Takeda[71], T. Takeshita[248], A. Taketani[236], Y. Takeuchi[378], T. Takimi[262], Y. Takubo[71], Y. Tamashevich[47], M. Tamsett[181], M. Tanabashi[198,197], T. Tanabe[116], G. Tanaka[161], M. M. Tanaka[71], M. Tanaka[223], R. Tanaka[73], H. Taniuchi[377], S. Tapprogge[138], E. Tarkovsky[107], M. A. Tartaglia[58], X. R. Tata[334], T. Tauchi[71], M. Tawada[71], G. Taylor[347], A. M. Teixeira[168], V. I. Telnov[15,219], P. Tenenbaum[251], E. Teodorescu[206], S. Terada[71], Y. Teramoto[222], H. Terao[200], A. Terashima[71], S. Terui[71], N. Terunuma[71], M. Terwort[47], M. Tesar[186], F. Teubert[33], T. Teubner[340], R. Teuscher[376], T. Theveneaux-Pelzer[168], D. Thienpont[93,172], J. Thom-Levy[43], M. Thomson[323], J. Tian[71], X. Tian[366], M. Tigner[43], J. Timmermans[213], V. Tisserand[164], M. Titov[21], S. Tjampens[164], K. Tobe[197], K. Tobioka[150,319], K. Toda[278], M. Toda[71], N. Toge[71], J. Tojo[161], K. Tokushuku[71], T. Toma[49], R. Tomas[33], T. Tomita[161], A. Tomiya[223], M. Tomoto[197,198], K. Toms[352], M. Tonini[47], F. Toral[31], E. Torrence[356], E. Torrente-Lujan[33], N. Toumbas[325], C. Touramanis[339], F. Toyoda[161], K. Toyomura[71], G. Trahern[55], T. H. Tran[172], W. Treberspurg[224], J. Trenado[311], M. Trimpl[58], S. Trincaz-Duvoid[169], M. Tripathi[320], W. Trischuk[376], M. Trodden[360], G. Trubnikov[142], H. C. Tsai[39], J. F. Tsai[210], K. H. Tsao[336], R. Tschirhart[58], E. Tsedenbaljir[210], S. Y. Tseng[201], T. Tsuboyama[71], A. Tsuchiya[250], K. Tsuchiya[71], T. Tsukamoto[71], K. Tsumura[197], S. Tsuno[71], T. Tsurugai[189], T. Tsuyuki[96], B. Tuchming[21], P. V. Tyagi[68,254], I. Tyapkin[142], M. Tytgat[331], K. Uchida[295], F. Uchiyama[71], Y. Uchiyama[116], S. Uehara[71], H. Ueno[161], K. Ueno[71], K. Ueno[71], K. Ueshima[274], Y. Uesugi[73], N. Ujiie[71], F. Ukegawa[378], N. Ukita[378], M. Ullán[32], H. Umeeda[72], K. Umemori[71], Y. Unno[66], S. Uozumi[23], J. Urakawa[71], A. M. Uranga[111], J. Urresti[32], A. Ushakov[333], I. Ushiki[272], Y. Ushiroda[71], A. V[83], P. Vázquez Regueiro[112], L. Vacavant[27], G. Valencia[118], L. Valery[168], I. Valin[94], J. W. Valle[108], C. Vallee[27], N. Van Bakel[213], H. Van Der Graaf[213], N. Van Der Kolk[167], E. Van Der Kraaij[33], B. Van Doren[338], B. Van Eijk[213], R. Van Kooten[87], W. T. Van Oers[279], D. Vanegas[108], P. Vanhoefer[186], P. Vankov[47], P. Varghese[58], A. Variola[167], R. Varma[85], G. Varner[334], G. Vasileiadis[162], A. Vauth[47], J. Velthuis[316], S. K. Vempati[83], V. Vento[108], M. Venturini[177], M. Verderi[172], P. Verdier[89], A. Verdugo[31],

A. Vicente[171], J. Vidal-Perona[108], H. L. R. Videau[172], I. Vila[110], X. Vilasis-Cardona[299], E. Vilella[311], A. Villamor[32], E. G. Villani[259], J. A. Villar[286], M. A. Villarejo Bermúdez[108], D. Vincent[169], P. Vincent[169], J. M. Virey[28], A. Vivoli[58], V. Vogel[47], R. Volkenborn[47], O. Volynets[47], F. Von Der Pahlen[110], E. Von Toerne[295], B. Vormwald[47], A. Voronin[180], M. Vos[108], J. H. Vossebeld[339], G. Vouters[164], Y. Voutsinas[94,47], V. Vrba[105,45], M. Vysotsky[107], D. Wackeroth[256], A. Wagner[47], C. E. Wagner[7,52], R. Wagner[7], S. R. Wagner[324], W. Wagner[385], J. Wagner-Kuhr[90], A. P. Waite[251], M. Wakayama[197], Y. Wakimoto[276], R. Walczak[358,140], R. Waldi[300], D. G. E. Walker[251], N. J. Walker[47], M. Walla[47], C. J. Wallace[49], S. Wallon[171,393], D. Walsh[328], S. Walston[178], W. A. T. Wan Abdullah[342], D. Wang[102], G. Wang[102], J. Wang[251], L. Wang[251], L. Wang[52], M. H. Wang[251], M. Z. Wang[210], Q. Wang[102], Y. Wang[102], Z. Wang[24], R. Wanke[138], C. Wanotayaroj[356], B. Ward[8], D. Ward[323], B. Warmbein[47], M. Washio[402], K. Watanabe[71], M. Watanabe[212], N. Watanabe[71], T. Watanabe[155], Y. Watanabe[71], S. Watanuki[272], Y. Watase[71], N. K. Watson[315], G. Watts[383], M. M. Weber[90], H. C. Weddig[47], H. Weerts[7], A. W. Weidemann[251], G. Weiglein[47], A. Weiler[47], S. Weinzierl[138], H. Weise[47], A. Welker[138], N. Welle[47], J. D. Wells[33,348], M. Wendt[58,33], M. Wenskat[47], H. Wenzel[58], N. Wermes[295], U. Werthenbach[301], W. Wester[58], L. Weuste[186,57], A. White[373], G. White[251], K. H. Wichmann[47], M. Wielers[183], R. Wielgos[58], W. Wierba[202], T. Wilksen[47], S. Willocq[346], F. F. Wilson[259], G. W. Wilson[338], P. B. Wilson[251], M. Wing[309], M. Winter[94], K. Wittenburg[47], P. Wittich[43], M. Wobisch[181], A. Wolski[339,40], M. D. Woodley[251], M. B. Woods[251], M. Worek[385], S. Worm[33,259], G. Wormser[167], D. Wright[178], Z. Wu[251], C. E. Wulz[224], S. Xella[211], G. Xia[40,343], L. Xia[7], A. Xiao[7], L. Xiao[251], M. Xiao[102], Q. Xiao[102], J. Xie[7], C. Xu[102], F. Xu[210], G. Xu[102], K. Yagyu[201], U. A. Yajnik[85], V. Yakimenko[251], S. Yamada[71,116], S. Yamada[71], Y. Yamada[272], Y. Yamada[402], A. Yamaguchi[274], D. Yamaguchi[275], M. Yamaguchi[272], S. Yamaguchi[272], Y. Yamaguchi[375], Y. Yamaguchi[75], A. Yamamoto[71,375], H. Yamamoto[272], K. Yamamoto[222], K. Yamamoto[118], M. Yamamoto[71], N. Yamamoto[197], N. Yamamoto[71], Y. Yamamoto[71], Y. Yamamoto[375], T. Yamamura[375], T. Yamanaka[116], S. Yamashita[116], T. Yamashita[3], Y. Yamashita[214], K. Yamauchi[197], M. Yamauchi[71], T. Yamazaki[375], Y. Yamazaki[154], J. Yan[375,71], W. Yan[364], C. Yanagisawa[257,11], H. Yang[247], J. Yang[56], U. K. Yang[245,343], Z. Yang[24], W. Yao[177], S. Yashiro[71], F. Yasuda[375], O. Yasuda[276], I. Yavin[188,228], E. Yazgan[331], H. Yokoya[377], K. Yokoya[71], H. Yokoyama[375], S. Yokoyama[275], R. Yonamine[71], H. Yoneyama[240], M. Yoshida[71], T. Yoshida[62], K. Yoshihara[116,33], S. Yoshihara[116,33], M. Yoshioka[71,272], T. Yoshioka[161], H. Yoshitama[73], C. C. Young[251], H. B. Yu[348], J. Yu[373], C. Z. Yuan[102], F. Yuasa[71], J. Yue[102], A. Zabi[172], W. Zabolotny[401], J. Zacek[34], I. Zagorodnov[47], J. Zalesak[105,58], A. F. Zarnecki[381], L. Zawiejski[268], M. Zeinali[101], C. Zeitnitz[385], L. Zembala[401], K. Zenker[47], D. Zeppenfeld[91], D. Zerwas[167], P. Zerwas[47], M. Zeyrek[192], A. Zghiche[164], J. Zhai[102], C. Zhang[102], J. Zhang[102], J. Zhang[7], Y. Zhang[24,33], Z. Zhang[167], F. Zhao[102], F. Zhao[102], T. Zhao[102], Y. Zhao[251], H. Zheng[102], Z. Zhengguo[364], L. Zhong[24], F. Zhou[251], X. Zhou[364,102], Z. Zhou[102], R. Y. Zhu[17], X. Zhu[24], X. Zhu[102], M. Zimmer[47], F. Zomer[167], T. Zoufal[47], R. Zwicky[329]

1 Academia Sinica - 128 Sec. 2, Institute of Physics, Academia Rd., Nankang, Taipei 11529, Taiwan, R.O.C.

2 AGH University of Science and Technology, Akademia Gorniczo-Hutnicza im. Stanislawa Staszica w Krakowie, Al. Mickiewicza 30 PL-30-059 Cracow, Poland

3 Aichi Medical University, Nagakute, Aichi, 480-1195, Japan

4 Akita International University, Yuwa, Akita City, 010-1292, Japan

5 Albert-Ludwigs Universität Freiburg, Physikalisches Institut, Hermann-Herder Str. 3, D-79104 Freiburg, Germany

6 Ankara Üniversitesi Fen Fakültesi, Fizik Bölümü, Dögol Caddesi, 06100 Tandoğan Ankara, Turkey

7 Argonne National Laboratory (ANL), 9700 S. Cass Avenue, Argonne, IL 60439, USA

8 Baylor University, Department of Physics, 101 Bagby Avenue, Waco, TX 76706, USA

9 Beijing University, Department of Physics, Beijing, China 100871

10 Benares Hindu University, Benares, Varanasi 221005, India

11 Borough of Manhattan Community College, The City University of New York, Department of Science, 199 Chambers Street, New York, NY 10007, USA

12 Brandenburg University of Technology, Postfach 101344, D-03013 Cottbus, Germany

13 Brookhaven National Laboratory (BNL), P.O.Box 5000, Upton, NY 11973-5000, USA

14 Brown University, Department of Physics, Box 1843, Providence, RI 02912, USA

15 Budker Institute for Nuclear Physics (BINP), 630090 Novosibirsk, Russia

16 Calcutta University, Department of Physics, 92 A.P.C. Road, Kolkata 700009, India

17 California Institute of Technology, Physics, Mathematics and Astronomy (PMA), 1200 East California Blvd, Pasadena, CA 91125, USA

18 California State University, Los Angeles, Dept. of Physics and Astronomy, 5151 State University Dr., Los Angeles, CA 90032, USA

19 Carleton University, Department of Physics, 1125 Colonel By Drive, Ottawa, Ontario, Canada K1S 5B6

20 Carnegie Mellon University, Department of Physics, Wean Hall 7235, Pittsburgh, PA 15213, USA

21 CEA Saclay, IRFU, F-91191 Gif-sur-Yvette, France

22 CEA Saclay, Service de Physique Théorique, CEA/DSM/SPhT, F-91191 Gif-sur-Yvette Cedex, France

23 Center for High Energy Physics (CHEP) / Kyungpook National University, 1370 Sankyuk-dong, Buk-gu, Daegu 702-701, Republic of Korea

24 Center for High Energy Physics (TUHEP), Tsinghua University, Beijing, China 100084

25 Center For Quantum Spacetime (CQUeST), Sogang University, 35 Baekbeom-ro, Mapo-gu, Seoul 121-742, Republic of Korea

26 Center for the Advancement of Natural Discoveries using Light Emission (CANDLE), Acharyan 31, 0040, Yerevan, Armenia

27 Centre de Physique des Particules de Marseille (CPPM), Aix-Marseille Université, CNRS/IN2P3, 163, Avenue de Luminy, Case 902, 13288 Marseille Cedex 09, France

28 Centre de Physique Theorique, CNRS - Luminy, Universiti d"Aix - Marseille II, Campus of Luminy, Case 907, 13288 Marseille Cedex 9, France

29 Centre Lasers Intenses et Applications (CELIA), Université Bordeaux 1 - CNRS - CEA, 351 Cours de la Libération, 33405 Talence Cedex, France

30 Centro Brasileiro de Pesquisas Físicas (CBPF), Rua Dr. Xavier Sigaud, n.150 22290-180, Urca - Rio de Janeiro, RJ, Brazil

31 Centro de Investigaciones Energéticas, Medioambientales y Tecnológicas, CIEMAT, Avenida Complutense 22, E-28040 Madrid, Spain

32 Centro Nacional de Microelectrónica (CNM), Instituto de Microelectrónica de Barcelona (IMB), Campus UAB, 08193 Cerdanyola del Vallès (Bellaterra), Barcelona, Spain

33 CERN, CH-1211 Genève 23, Switzerland

34 Charles University, Institute of Particle & Nuclear Physics, Faculty of Mathematics and Physics, V Holesovickach 2, CZ-18000 Prague 8, Czech Republic

35 Chiba University of Commerce, 1-3-1 Konodai, Ichikawa-shi, Chiba, 272-8512, Japan

36 Chonbuk National University, Division of Science Education, Jeonju 561-756, Republic of Korea

37 Chonbuk National University, Physics Department, Jeonju 561-756, Republic of Korea

38 Chubu University, 1200 Matsumoto-cho, Kasugai-shi, Aichi, 487-8501, Japan

39 Chung Yuan Christian University, Department of Physics, 200 Chung Pei Rd., Chung Li 32023 Taiwan, R.O.C

40 Cockcroft Institute, Daresbury, Warrington WA4 4AD, UK

41 College of William and Mary, Department of Physics, Williamsburg, VA, 23187, USA

42 Columbia University, Department of Physics, New York, NY 10027-6902, USA

43 Cornell University, Laboratory for Elementary-Particle Physics (LEPP), Ithaca, NY 14853, USA

44 Czech Technical University in Prague, Institute of Experimental and Applied Physics (IEAP), Horska 3a/22, 12800 Prague 2, Czech Republic

45 Czech Technical University, Faculty of Nuclear Science and Physical Engineering, Brehova 7, CZ-11519 Prague 1, Czech Republic

46 Departamento de Física Teórica, Facultad de Ciencias, Módulo 15 (antiguo C-XI) y Módulo 8, Universidad Autónoma de Madrid, Campus de Cantoblanco, 28049 Madrid, Spain

47 Deutsches Elektronen-Synchrotron DESY, A Research Centre of the Helmholtz Association, Notkestrasse 85, 22607 Hamburg, Germany (Hamburg site)

48 Deutsches Elektronen-Synchrotron DESY, A Research Centre of the Helmholtz Association, Platanenallee 6, 15738 Zeuthen, Germany (Zeuthen site)

49 Durham University, Department of Physics, Ogen Center for Fundamental Physics, South Rd., Durham DH1 3LE, UK

50 École Normale Supérieure de Lyon, 46 allée d'Italie, 69364 Lyon Cedex 07, France

51 Ege University, Department of Physics, Faculty of Science, 35100 Izmir, Turkey

52 Enrico Fermi Institute, University of Chicago, 5640 S. Ellis Avenue, RI-183, Chicago, IL 60637, USA
53 ETH Zürich, Institute for Particle Physics (IPP), Schafmattstrasse 20, CH-8093 Zürich, Switzerland
54 ETH Zürich, Institute for Theoretical Physics (ITP), Wolfgang-Pauli-Str. 27, Zürich, Switzerland
55 European Spallation Source ESS AB, Box 176, 221 00 Lund, Sweden
56 Ewha Womans University, 11-1 Daehyun-Dong, Seodaemun-Gu, Seoul, 120-750, Republic of Korea
57 Excellence Cluster Universe, Technische Universität München, Boltzmannstr. 2, 85748 Garching, Germany
58 Fermi National Accelerator Laboratory (FNAL), P.O.Box 500, Batavia, IL 60510-0500, USA
59 Florida State University, Department of Physics, 77 Chieftan Way, Tallahassee, FL 32306-4350, USA
60 Fujita Gakuen Health University, Department of Physics, Toyoake, Aichi 470-1192, Japan
61 Fukui University of Technology, 3-6-1 Gakuen, Fukui-shi, Fukui 910-8505, Japan
62 Fukui University, Department of Physics, 3-9-1 Bunkyo, Fukui-shi, Fukui 910-8507, Japan
63 Gangneung-Wonju National University, 210-702 Gangneung Daehangno, Gangneung City, Gangwon Province, Republic of Korea
64 Georg-August-Universität Göttingen, II. Physikalisches Institut, Friedrich-Hund-Platz 1, 37077 Göttingen, Germany
65 Global Design Effort
66 Hanyang University, Department of Physics, Seoul 133-791, Republic of Korea
67 Harish-Chandra Research Institute, Chhatnag Road, Jhusi, Allahabad 211019, India
68 Helmholtz-Zentrum Berlin für Materialien und Energie (HZB), Wilhelm-Conrad-Röntgen Campus, BESSY II, Albert-Einstein-Str. 15, 12489 Berlin, Germany
69 Helsinki Institute of Physics (HIP), P.O. Box 64, FIN-00014 University of Helsinki, Finland
70 Henan Normal University, College of Physics and Information Engineering, Xinxiang, China 453007
71 High Energy Accelerator Research Organization, KEK, 1-1 Oho, Tsukuba, Ibaraki 305-0801, Japan
72 Hiroshima University, Department of Physics, 1-3-1 Kagamiyama, Higashi-Hiroshima, Hiroshima 739-8526, Japan
73 Hiroshima University, Graduate School of Advanced Sciences of Matter, 1-3-1 Kagamiyama, Higashi-Hiroshima, Hiroshima 739-8530, Japan
74 Hokkai-Gakuen University, 4-1-40 Asahimachi, Toyohira-ku, Sapporo 062-8605, Japan
75 Hokkaido University, Department of Physics, Faculty of Science, Kita, Kita-ku, Sapporo-shi, Hokkaido 060-0810, Japan
76 Humboldt Universität zu Berlin, Fachbereich Physik, Institut für Elementarteilchenphysik, Newtonstr. 15, D-12489 Berlin, Germany
77 Hyogo University of Teacher Education, 942-1 Shimokume, Kato-city, Hyogo 673-1494, Japan
78 Ibaraki National College of Technology, 866 Nakane, Hitachinaka, Ibaraki 312-8508, Japan
79 Ibaraki University, College of Technology, Department of Physics, Nakanarusawa 4-12-1, Hitachi, Ibaraki 316-8511, Japan
80 Imperial College, Blackett Laboratory, Department of Physics, Prince Consort Road, London, SW7 2BW, UK
81 Indian Association for the Cultivation of Science, Department of Theoretical Physics and Centre for Theoretical Sciences, Kolkata 700032, India
82 Indian Institute of Science Education and Research (IISER) Kolkata, Department of Physical Sciences, Mohanpur Campus, PO Krishi Viswavidyalaya, Mohanpur 741252, Nadia, West Bengal, India
83 Indian Institute of Science, Centre for High Energy Physics, Bangalore 560012, Karnataka, India
84 Indian Institute of Technology Indore, IET Campus, M-Block, Institute of Engineering and Technology (IET), Devi Ahilya Vishwavidyalaya Campus, Khandwa Road, Indore - 452017, Madhya Pradesh, India
85 Indian Institute of Technology, Bombay, Powai, Mumbai 400076, India
86 Indian Institute of Technology, Guwahati, Guwahati, Assam 781039, India
87 Indiana University, Department of Physics, Swain Hall West 117, 727 E. 3rd St., Bloomington, IN 47405-7105, USA
88 Institucio Catalana de Recerca i Estudis, ICREA, Passeig Lluis Companys, 23, Barcelona 08010, Spain
89 Institut de Physique Nucléaire de Lyon (IPNL), Domaine scientifique de la Doua, Bâtiment Paul Dirac 4, rue Enrico Fermi, 69622 Villeurbanne, Cedex, France
90 Institut für Experimentelle Kernphysik, KIT,Universität Karlsruhe (TH), Wolfgang-Gaede-Str. 1, Postfach 6980, 76128 Karlsruhe, Germany
91 Institut für Theoretische Physik (ITP), Karlsruher Institut für Technologie (KIT), Fakultät für Physik, Postfach 6980, 76049 Karlsruhe, Germany
92 Institut für Theoretische Teilchenphysik, Campus Süd, Karlsruher Institut für Technologie (KIT), 76128 Karlsruhe, Germany
93 Institut National de Physique Nucleaire et de Physique des Particules, 3, Rue Michel- Ange, 75794 Paris Cedex 16, France
94 Institut Pluridisciplinaire Hubert Curien, 23 Rue du Loess - BP28, 67037 Strasbourg Cedex 2, France
95 Institute for Chemical Research, Kyoto University, Gokasho, Uji, Kyoto 611-0011, Japan
96 Institute for Cosmic Ray Research, University of Tokyo, 5-1-5 Kashiwa-no-Ha, Kashiwa, Chiba 277-8582, Japan
97 Institute for Mathematics, Astrophysics and Particle Physics (IMAPP), P.O. Box 9010, 6500 GL Nijmegen, Netherlands
98 Institute for Nuclear Research, Russian Academy of Sciences (INR RAS), 60-th October Anniversary Prospect 7a, 117312, Moscow, Russia
99 Institute for Particle and Nuclear Physics, Wigner Research Centre for Physics, Hungarian Academy of Sciences, P.O. Box 49, 1525 Budapest, Hungary
100 Institute for Scintillation Materials (ISMA), 60 Lenina Ave, 61001, Kharkiv, Ukraine
101 Institute for studies in fundamental sciences (IPM), Niavaran Square, P.O. Box 19395-5746, Tehran, Iran
102 Institute of High Energy Physics - IHEP, Chinese Academy of Sciences, P.O. Box 918, Beijing, China 100049
103 Institute of Mathematical Sciences, Taramani, C.I.T. Campus, Chennai 600113, India
104 Institute of Particle Physics, Canada

105 Institute of Physics, ASCR, Academy of Science of the Czech Republic, Division of Elementary Particle Physics, Na Slovance 2, CZ-18221 Prague 8, Czech Republic

106 Institute of Physics, Vietnam Academy of Science and Technology (VAST), 10 Dao-Tan, Ba-Dinh, Hanoi 10000, Vietnam

107 Institute of Theoretical and Experimetal Physics, B. Cheremushkinskawa, 25, RU-117259, Moscow, Russia

108 Instituto de Fisica Corpuscular (IFIC), Centro Mixto CSIC-UVEG, Edificio Investigacion Paterna, Apartado 22085, 46071 Valencia, Spain

109 Instituto de Física da Universidade Federal do Rio Grande do Sul (UFRGS), Av. Bento Gonçalves 9500, Caixa Postal 15051, CEP 91501-970, Porto Alegre, RS, Brazil

110 Instituto de Fisica de Cantabria, (IFCA, CSIC-UC), Facultad de Ciencias, Avda. Los Castros s/n, 39005 Santander, Spain

111 Instituto de Física Teórica UAM/CSIC, C/ Nicolás Cabrera 13-15, Universidad Autónoma de Madrid, Cantoblanco, 28049 Madrid, Spain

112 Instituto Galego de Fisica de Altas Enerxias (IGFAE,USC) Facultad de Fisica, Campus Sur E-15782 Santiago de Compostela, Spain

113 Instituto Tecnológico de Aragón (ITA), C/ María de Luna 7-8, 50018 Zaragoza, Spain

114 Instituto Universitario de Física Fundamental y Matemáticas de la Universidad de Salamanca (IUFFyM), Casas del Parque, 37008 Salamanca, Spain

115 Inter-University Accelerator Centre, Aruna Asaf Ali Marg, Post Box 10502, New Delhi 110067, India

116 International Center for Elementary Particle Physics, University of Tokyo, Hongo 7-3-1, Bunkyo District, Tokyo 113-0033, Japan

117 International Institute of Physics, Federal University of Rio Grande do Norte, Av. Odilon Gomes de Lima, 1722 - Capim Macio - 59078-400 - Natal-RN, Brazil

118 Iowa State University, Department of Physics, High Energy Physics Group, Ames, IA 50011, USA

119 Istituto Nazionale di Fisica Nucleare (INFN), Laboratorio LASA, Via Fratelli Cervi 201, 20090 Segrate, Italy

120 Istituto Nazionale di Fisica Nucleare (INFN), Sezione di Firenze, Via G. Sansone 1, I-50019 Sesto Fiorentino (Firenze), Italy

121 Istituto Nazionale di Fisica Nucleare (INFN), Sezione di Milano Bicocca, Piazza della Scienza 3, I-20126 Milano, Italy

122 Istituto Nazionale di Fisica Nucleare (INFN), Sezione di Milano, Via Celoria 16, I-20133 Milano, Italy

123 Istituto Nazionale di Fisica Nucleare (INFN), Sezione di Napoli, Complesso Universitá di Monte Sant'Angelo,via, I-80126 Naples, Italy

124 Istituto Nazionale di Fisica Nucleare (INFN), Sezione di Pavia, Via Bassi 6, I-27100 Pavia, Italy

125 Istituto Nazionale di Fisica Nucleare (INFN), Sezione di Perugia, Via A. Pascoli, 06123 Perugia, Italy

126 Istituto Nazionale di Fisica Nucleare (INFN), Sezione di Pisa, Edificio C - Polo Fibonacci Largo B. Pontecorvo, 3, I-56127 Pisa, Italy

127 Istituto Nazionale di Fisica Nucleare (INFN), Sezione di Roma, c/o Dipartimento di Fisica - Università degli Studi di Roma "La Sapienza", P.le Aldo Moro 2, I-00185 Roma, Italy

128 Istituto Nazionale di Fisica Nucleare (INFN), Sezione di Torino, c/o Universitá di Torino, facoltá di Fisica, via P Giuria 1, 10125 Torino, Italy

129 Istituto Nazionale di Fisica Nucleare (INFN), Sezione di Trieste, Padriciano 99, I-34012 Trieste (Padriciano), Italy

130 ITER Organization, Route de Vinon-sur-Verdon, 13115 St. Paul-lez-Durance, France

131 Iwate University, 4-3-5 Ueda, Morioka, Iwate, 020-8551, Japan

132 Jagiellonian University, Institute of Physics, Ul. Reymonta 4, PL-30-059 Cracow, Poland

133 Jamia Millia Islamia, Department of Physics, Jamia Nagar, New Delhi 110025, India

134 Japan Aerospace Exploration Agency, Sagamihara Campus, 3-1-1 Yoshinodai, Sagamihara, Kanagawa 220-8510 , Japan

135 Japan Atomic Energy Agency, 4-49 Muramatsu, Tokai-mura, Naka-gun, Ibaraki 319-1184, Japan

136 Japan Atomic Energy Agency, Tokai Research and Development Center, 2-4 Shirane Shirakata, Tokai-mura, Naka-gun, Ibaraki 319-1195, Japan

137 Japan Synchrotron Radiation Research Institute (JASRI), 1-1-1, Kouto, Sayo-cho, Sayo-gun, Hyogo 679-5198, Japan

138 Johannes Gutenberg Universität Mainz, Institut für Physik, 55099 Mainz, Germany

139 John Adams Institute for Accelerator Science at Royal Holloway University of London, Egham Hill, Egham, Surrey TW20 0EX, UK

140 John Adams Institute for Accelerator Science at University of Oxford, Denys Wilkinson Building, Keble Road, Oxford OX1 3RH, UK

141 Johns Hopkins University - Henry A. Rowland Department of Physics & Astronomy 3701 San Martin Drive, Baltimore, Maryland (MD) 21218, USA

142 Joint Institute for Nuclear Research (JINR), Joliot-Curie 6, 141980, Dubna, Moscow Region, Russia

143 Joint Institute for Power and Nuclear Research "Sosny" at National Academy of Sciences of Belarus, 99 Academician A.K.Krasin Str., Minsk BY-220109, Belarus

144 Jozef Stefan Institute, Jamova cesta 39, 1000 Ljubljana, Slovenia

145 Julius-Maximilians-Universität Würzburg, Fakultät für Physik und Astronomie, Am Hubland, 97074 Würzburg, Germany

146 Juntendo University, School of Medicine, Dept. of Physics, Hiraga-gakuendai 1-1, Inzai-shi, Chiba 270-1695, Japan

147 Justus-Liebig-Universität Gießen, II. Physikalisches Institut, Heinrich-Buff-Ring 16, 35392 Gießen, Germany

148 Kanazawa University, Institute for Theoretical Physics (KITP), School of Mathematics and Physics, College of Science and Engineering, Kakuma-machi, Kanazawa city, Ishikawa 920-1192, Japan

149 Kansas State University, Department of Physics, 116 Cardwell Hall, Manhattan, KS 66506, USA

150 Kavli Institute for the Physics and Mathematics of the Universe (Kavli IPMU), University of Tokyo, 5-1-5 Kashiwanoha, Kashiwa, 277-8583, Japan

151 King Saud University (KSU), Dept. of Physics, P.O. Box 2454, Riyadh 11451, Saudi Arabia

152 King's College London - Department of physics, Strand, London WC2R 2LS, London, UK

153 Kinki University, Department of Physics, 3-4-1 Kowakae, Higashi-Osaka, Osaka 577-8502, Japan

154 Kobe University, Department of Physics, 1-1 Rokkodai-cho, Nada-ku, Kobe, Hyogo 657-8501, Japan

155 Kogakuin University, Department of Physics, Shinjuku Campus, 1-24-2 Nishi-Shinjuku, Shinjuku-ku, Tokyo 163-8677, Japan

156 Konkuk University, 93-1 Mojin-dong, Kwanglin-gu, Seoul 143-701, Republic of Korea

157 Korea Advanced Institute of Science & Technology, Department of Physics, 373-1 Kusong-dong, Yusong-gu, Taejon 305-701, Republic of Korea

158 Korea Institute for Advanced Study (KIAS), School of Physics, 207-43 Cheongryangri-dong, Dongdaemun-gu, Seoul 130-012, Republic of Korea

159 Kyoto University, Department of Physics, Kitashirakawa-Oiwakecho, Sakyo-ku, Kyoto 606-8502, Japan

160 Kyoto University, Yukawa Institute for Theoretical Physics, Kitashirakawa-Oiwakecho, Sakyo-Ku, Kyoto 606-8502, Japan

161 Kyushu University, Department of Physics, 6-10-1 Hakozaki, Higashi-ku, Fukuoka 812-8581, Japan

162 L.P.T.A., UMR 5207 CNRS-UM2, Université Montpellier II, Case Courrier 070, Bât. 13, place Eugène Bataillon, 34095 Montpellier Cedex 5, France

163 Laboratoire Charles Coulomb UMR 5221 CNRS-UM2, Université Montpellier 2, Place Eugène Bataillon - CC069, 34095 Montpellier Cedex 5, France

164 Laboratoire d'Annecy-le-Vieux de Physique des Particules (LAPP) , Université de Savoie, CNRS/IN2P3, 9 Chemin de Bellevue, BP 110, F-74941 Annecy-Le-Vieux Cedex, France

165 Laboratoire d'Annecy-le-Vieux de Physique Theorique (LAPTH), Chemin de Bellevue, BP 110, F-74941 Annecy-le-Vieux Cedex, France

166 Laboratoire d'AstroParticules et Cosmologie (APC), Université Paris Diderot-Paris 7 - CNRS/IN2P3, Bâtiment Condorcet, Case 7020, 75205 Paris Cedex 13, France

167 Laboratoire de l'Accélérateur Linéaire (LAL), Université Paris-Sud 11, Bâtiment 200, 91898 Orsay, France

168 Laboratoire de Physique Corpusculaire de Clermont-Ferrand (LPC), Université Blaise Pascal, I.N.2.P.3./C.N.R.S., 24 avenue des Landais, 63177 Aubière Cedex, France

169 Laboratoire de Physique Nucléaire et des Hautes Energies (LPNHE), UPMC, UPD, IN2P3/CNRS, 4 Place Jussieu, 75005, Paris Cedex 05, France

170 Laboratoire de Physique Subatomique et de Cosmologie (LPSC), Université Joseph Fourier (Grenoble 1), CNRS/IN2P3, Institut Polytechnique de Grenoble, 53 rue des Martyrs, F-38026 Grenoble Cedex, France

171 Laboratoire de Physique Theorique, Université de Paris-Sud XI, Batiment 210, F-91405 Orsay Cedex, France

172 Laboratoire Leprince-Ringuet (LLR), École polytechnique – CNRS/IN2P3, Route de Saclay, F-91128 Palaiseau Cedex, France

173 Laboratoire Univers et Particules de Montpellier (LUPM) - UMR5299, Université de Montpellier II, Place Eugène Bataillon - Case courrier 72, 34095 Montpellier Cedex 05, France

174 Laboratori Nazionali di Frascati, via E. Fermi, 40, C.P. 13, I-00044 Frascati, Italy

175 Laboratório de Instrumentação e Física Experimental de Partículas (LIP LISBOA), Av. Elias Garcia 14 - 1°, 1000-149 Lisbon, Portugal

176 Lancaster University, Physics Department, Lancaster LA1 4YB, UK

177 Lawrence Berkeley National Laboratory (LBNL), 1 Cyclotron Rd, Berkeley, CA 94720, USA

178 Lawrence Livermore National Laboratory (LLNL), Livermore, CA 94551, USA

179 Lebedev Physical Institute, Leninsky Prospect 53, RU-117924 Moscow, Russia

180 Lomonosov Moscow State University, Skobeltsyn Institute of Nuclear Physics (MSU SINP), 1(2), Leninskie gory, GSP-1, Moscow 119991, Russia

181 Louisiana Tech University, Department of Physics, Ruston, LA 71272, USA

182 Ludwig-Maximilians-Universität München, Fakultät für Physik, Am Coulombwall 1, D - 85748 Garching, Germany

183 Lunds Universitet, Fysiska Institutionen, Avdelningen för Experimentell Högenergifysik, Box 118, 221 00 Lund, Sweden

184 L'Université Hassan II, Aïn Chock, "Réseau Universitaire de Physique des Hautes Energies" (RUPHE), Département de Physique, Faculté des Sciences Aïn Chock, B.P 5366 Maarif, Casablanca 20100, Morocco

185 Massachusetts Institute of Technology (MIT), Laboratory for Nuclear Science, 77 Massachusetts Avenue, Cambridge, MA 02139, USA

186 Max-Planck-Institut für Physik (Werner-Heisenberg-Institut), Föhringer Ring 6, 80805 München, Germany

187 McGill University, Department of Physics, Ernest Rutherford Physics Bldg., 3600 University Street, Montreal, Quebec, H3A 2T8 Canada

188 McMaster University, Department of Physics & Astronomy, 1280 Main Street West, Hamilton, ON, L8S 4M1, Canada

189 Meiji Gakuin University, Department of Physics, 2-37 Shirokanedai 1-chome, Minato-ku, Tokyo 244-8539, Japan

190 Michigan State University, Department of Chemical Engineering & Materials Science, 2527 Engineering Building East Lansing, MI 48824-1226, USA

191 Michigan State University, Department of Physics and Astronomy, East Lansing, MI 48824, USA

192 Middle East Technical University, Department of Physics, TR-06531 Ankara, Turkey

193 Miyagi Gakuin Women's University, Faculty of Liberal Arts, 9-1-1 Sakuragaoka, Aoba District, Sendai, Miyagi 981-8557, Japan

194 MSU-Iligan Institute of Technology, Department of Physics, Andres Bonifacio Avenue, 9200 Iligan City, Phillipines

195 Nagasaki Institute of Applied Science, 536 Abamachi, Nagasaki-Shi, Nagasaki 851-0193, Japan

196 Nagoya University, Department of Materials Science and Engineering, Furo-cho, Chikusa-ku, Nagoya, 464-8603, Japan

197 Nagoya University, Department of Physics, School of Science, Furo-cho, Chikusa-ku, Nagoya, Aichi 464-8602, Japan

198 Nagoya University, Kobayashi-Maskawa Institute for the Origin of Particles and the Universe (KMI), Furo-cho, Chikusa-ku, Nagoya Aichi 464-8602, Japan

199 Nanjing University, Department of Physics, Nanjing, China 210093

200 Nara Women's University, High Energy Physics Group, Kitauoya-Nishimachi, Nara 630-8506, Japan

201 National Central University, High Energy Group, Department of Physics, Chung-li, Taiwan 32001, R.O.C

202 National Centre of Nuclear Research (NCBJ), ul. Andrzeja Soltana 7, 05-400 Otwock-Swierk, Poland

203 National Cheng Kung University, Physics Department, 1 Ta-Hsueh Road, Tainan, Taiwan 70101, R.O.C

204 National Chiao-Tung University, Institute of Physics, 1001 Ta Hsueh Rd, Hsinchu, Taiwan 300, R.O.C.

205 National Institute of Chemical Physics and Biophysics (NICPB), Ravala pst 10, 10143 Tallinn, Estonia

206 National Institute of Physics and Nuclear Engineering "Horia Hulubei" (IFIN-HH), Str. Reactorului no.30, P.O. Box MG-6, R-76900 Bucharest - Magurele, Romania

207 National Research Centre "Kurchatov Institute", 1 Akademika Kurchatova pl., Moscow, 123182, Russia

208 National Science Center - Kharkov Institute of Physics and Technology (NSC KIPT), Akademicheskaya St. 1, Kharkov, 61108, Ukraine

209 National Scientific & Educational Centre of Particle & High Energy Physics (NCPHEP), Belarusian State University, M.Bogdanovich street 153, 220040 Minsk, Belarus

210 National Taiwan University, Physics Department, Taipei, Taiwan 106, R.O.C

211 Niels Bohr Institute (NBI), University of Copenhagen, Blegdamsvej 17, DK-2100 Copenhagen, Denmark

212 Niigata University, Department of Physics, Ikarashi, Niigata 950-218, Japan

213 Nikhef, National Institute for Subatomic Physics, P.O. Box 41882, 1009 DB Amsterdam, Netherlands

214 Nippon Dental University School of Life Dentistry at Niigata, 1-8 Hamaura-cho, Chuo-ku, Niigata 951-1500, Japan

215 North Carolina A&T State University, 1601 E. Market Street, Greensboro, NC 27411, USA

216 Northeastern University, Physics Department, 360 Huntington Ave, 111 Dana Research Center, Boston, MA 02115, USA

217 Northern Illinois University, Department of Physics, DeKalb, Illinois 60115-2825, USA

218 Northwestern University, Department of Physics and Astronomy, 2145 Sheridan Road., Evanston, IL 60208, USA

219 Novosibirsk State University (NGU), Department of Physics, Pirogov st. 2, 630090 Novosibirsk, Russia

220 Ochanomizu University, Department of Physics, Faculty of Science, 1-1 Otsuka 2, Bunkyo-ku, Tokyo 112-8610, Japan

221 Orissa University of Agriculture & Technology, Bhubaneswar 751003, Orissa, India

222 Osaka City University, Department of Physics, Faculty of Science, 3-3-138 Sugimoto, Sumiyoshi-ku, Osaka 558-8585, Japan

223 Osaka University, Department of Physics, 1-1 Machikaneyama, Toyonaka, Osaka 560-0043, Japan

224 Österreichische Akademie der Wissenschaften, Institut für Hochenergiephysik, Nikolsdorfergasse 18, A-1050 Vienna, Austria

225 Pacific Northwest National Laboratory, (PNNL), PO Box 999, Richland, WA 99352, USA

226 Panjab University, Chandigarh 160014, India

227 Pavel Sukhoi Gomel State Technical University, ICTP Affiliated Centre & Laboratory for Physical Studies, October Avenue, 48, 246746, Gomel, Belarus

228 Perimeter Institute for Theoretical Physics, 31 Caroline Street North, Waterloo, Ontario N2L 2Y5, Canada

229 Physical Research Laboratory, Navrangpura, Ahmedabad 380 009, Gujarat, India

230 Pohang Accelerator Laboratory (PAL), San-31 Hyoja-dong, Nam-gu, Pohang, Gyeongbuk 790-784, Republic of Korea

231 Pontificia Universidad Católica de Chile, Avda. Libertador Bernardo OHiggins 340, Santiago, Chile

232 Princeton University, Department of Physics, P.O. Box 708, Princeton, NJ 08542-0708, USA

233 Purdue University, Department of Physics, West Lafayette, IN 47907, USA

234 Queen Mary, University of London, Mile End Road, London, E1 4NS, United Kingdom

235 Rheinisch-Westfälische Technische Hochschule (RWTH), Physikalisches Institut, Physikzentrum, Otto-Blumenthal-Straße, 52056 Aachen

236 RIKEN, 2-1 Hirosawa, Wako, Saitama 351-0198, Japan

237 Royal Holloway, University of London (RHUL), Department of Physics, Egham, Surrey TW20 0EX, UK

238 Russian Academy of Science, Keldysh Institute of Applied Mathematics, Muiskaya pl. 4, 125047 Moscow, Russia

239 Rutgers, The State University of New Jersey, Department of Physics & Astronomy, 136 Frelinghuysen Rd, Piscataway, NJ 08854, USA

240 Saga University, Department of Physics, 1 Honjo-machi, Saga-shi, Saga 840-8502, Japan

241 Saha Institute of Nuclear Physics, 1/AF Bidhan Nagar, Kolkata 700064, India

242 Salalah College of Technology (SCOT), Engineering Department, Post Box No. 608, Postal Code 211, Salalah, Sultanate of Oman

243 Saudi Center for Theoretical Physics, King Fahd University of Petroleum and Minerals (KFUPM), Dhahran 31261, Saudi Arabia

244 Seikei University, Faculty of Science and Technology, 3-3-1 Kichijoji-Kitamachi, Musashino-shi, Tokyo 180-8633, Japan

245 Seoul National University, San 56-1, Shinrim-dong, Kwanak-gu, Seoul 151-742, Republic of Korea

246 Setsunan University, Institute for Fundamental Sciences, 17-8 Ikeda Nakamachi, Neyagawa, Osaka, 572-8508, Japan

247 Shanghai Jiao Tong University, Department of Physics, 800 Dongchuan Road, Shanghai, China 200240

248 Shinshu University, 3-1-1, Asahi, Matsumoto, Nagano 390-8621, Japan

249 Shiv Nadar University, Village Chithera, Tehsil Dadri, District Gautam Budh Nagar, 203207 Uttar Pradesh, India

250 Shizuoka University, Department of Physics, 836 Ohya, Suruga-ku, Shizuoka 422-8529, Japan

251 SLAC National Accelerator Laboratory, 2575 Sand Hill Road, Menlo Park, CA 94025, USA

252 Society for Applied Microwave Electronics Engineering and Research (SAMEER), I.I.T. Campus, Powai, Post Box 8448, Mumbai 400076, India

253 Sokendai, The Graduate University for Advanced Studies, Shonan Village, Hayama, Kanagawa 240-0193, Japan

254 Spallation Neutron Source (SNS), Oak Ridge National Laboratory (ORNL), P.O. Box 2008 MS-6477, Oak Ridge, TN 37831-6477, USA

255 State University of New York at Binghamton, Department of Physics, PO Box 6016, Binghamton, NY 13902, USA

256 State University of New York at Buffalo, Department of Physics & Astronomy, 239 Franczak Hall, Buffalo, NY 14260, USA

257 State University of New York at Stony Brook, Department of Physics and Astronomy, Stony Brook, NY 11794-3800, USA

258 STFC Daresbury Laboratory, Daresbury, Warrington, Cheshire WA4 4AD, UK

259 STFC Rutherford Appleton Laboratory, Chilton, Didcot, Oxon OX11 0QX, UK

260 Sungkyunkwan University (SKKU), Natural Science Campus 300, Physics Research Division, Chunchun-dong, Jangan-gu, Suwon, Kyunggi-do 440-746, Republic of Korea

261 Swiss Light Source (SLS), Paul Scherrer Institut (PSI), PSI West, CH-5232 Villigen PSI, Switzerland

262 Tata Institute of Fundamental Research, School of Natural Sciences, Homi Bhabha Rd., Mumbai 400005, India

263 Technical University of Lodz, Department of Microelectronics and Computer Science, al. Politechniki 11, 90-924 Lodz, Poland

264 Technische Universität Dresden, Institut für Kern- und Teilchenphysik, D-01069 Dresden, Germany

265 Tel-Aviv University, School of Physics and Astronomy, Ramat Aviv, Tel Aviv 69978, Israel

266 Texas A&M University, Physics Department, College Station, 77843-4242 TX, USA

267 Texas Tech University, Department of Physics, Campus Box 41051, Lubbock, TX 79409-1051, USA

268 The Henryk Niewodniczanski Institute of Nuclear Physics, Polish Academy of Sciences (IFJ PAN), ul. Radzikowskiego 152, PL-31342 Cracow, Poland

269 Thomas Jefferson National Accelerator Facility (TJNAF), 12000 Jefferson Avenue, Newport News, VA 23606, USA

270 Tohoku Gakuin University, Department of Business Administration, 1-3-1 Tsuchitoi, Aoba-ku Sendai, Miyagi 980-8511, Japan

271 Tohoku Gakuin University, Faculty of Technology, 1-13-1 Chuo, Tagajo, Miyagi 985-8537, Japan

272 Tohoku University, Department of Physics, Aoba District, Sendai, Miyagi 980-8578, Japan

273 Tohoku University, Research Center for Electron Photon Science, Taihaku District, Sendai, Miyagi 982-0826, Japan

274 Tohoku University, Research Center for Neutrino Science, Aoba District, Sendai, Miyagi 980-8578, Japan

275 Tokyo Institute of Technology, Department of Physics, 2-12-1 O-Okayama, Meguro, Tokyo 152-8551, Japan

276 Tokyo Metropolitan University, Faculty of Science and Engineering, Department of Physics, 1-1 Minami-Osawa, Hachioji-shi, Tokyo 192-0397, Japan

277 Tokyo University of Agriculture Technology, Department of Applied Physics, Naka-machi, Koganei, Tokyo 183-8488, Japan

278 Toyama Prefectural University, Department of Mathematical Physics, 5180 Kurokawa Imizu-shi, Toyama, 939-0398, Japan

279 TRIUMF, 4004 Wesbrook Mall, Vancouver, BC V6T 2A3, Canada

280 Universidad Autónoma de San Luis Potosí, Alvaro Obregon 64, Col. Centro, San Luis Potosí, S.L.P. 78000, México

281 Universidad de Granada, Departamento de Física Teórica y del Cosmos, Campus de Fuentenueva, E-18071 Granada, Spain

282 Universidad de los Andes, Faculty of Science, Department of Physics, Carrera 1 18A-10, Bloque Ip. Bogotá, Colombia

283 Universidad de Oviedo, Departamento de Física, Campus de Llamaquique. C/ Calvo Sotelo, s/n 33005 Oviedo, Spain

284 Universidad de Salamanca, Departamento de Física Fundamental, Plaza de la Merced, s/n., 37008 Salamanca, Spain

285 Universidad de Sevilla, Escuela Técnica Superior de Ingeniería, Departamento Ingeniería Electrónica, Camino de los Descubrimientos s/n, 41092 Sevilla, Spain

286 Universidad de Zaragoza - Departamento de Física Teórica, Pedro Cerbuna 12, E-50009 Zaragoza, Spain

287 Universidad Nacional Autónoma de México, Instituto de Física, Circuito de la Investigación Cientifica s/n, Ciudad Universitaria, CP 04510 México D.F., Mexico

288 Universidad Nacional de La Plata, Departamento de Física, Facultad de Ciencias Exactas, C.C. N 67, 1900 La Plata, Argentina

289 Universidade do Estado do Rio de Janeiro (UERJ), Rio de Janeiro, RJ - Brasil 20550-900, Brazil

290 Universidade Federal de Pelotas, Instituto de Física e Matemática, Campus Universitário, Caixa Postal 354, 96010-900 Pelotas, RS, Brazil

291 Universidade Federal do Rio de Janeiro (UFRJ), Instituto de Física, Av. Athos da Silveira Ramos 149, Centro de Tecnologia - Bloco A, Cidade Universitária, Ilha do Fundão, Rio de Janeiro, RJ, Brazil

292 Universitá degli Studi di Napoli "Federico II", Dipartimento di Fisica, Via Cintia, 80126 Napoli, Italy

293 Universitat Autònoma de Barcelona, Departament de Física, Edifici C, 08193 Bellaterra, Barcelona, Spain

294 Universitat Autònoma de Barcelona, Institut de Fisica d'Altes Energies (IFAE), Campus UAB, Edifici Cn, E-08193 Bellaterra, Barcelona, Spain

295 Universität Bonn, Physikalisches Institut, Nußallee 12, 53115 Bonn, Germany

296 Universität Heidelberg, Institut für Theoretische Physik, Philosophenweg 16, 69120 Heidelberg, Germany

297 Universität Heidelberg, Kirchhoff-Institut für Physik, Im Neuenheimer Feld 227, 69120 Heidelberg, Germany

298 Universitat Politècnica de Catalunya, Institut de Tècniques Energètiques, Campus Diagonal Sud, Edifici PC (Pavelló C). Av. Diagonal, 647 08028 Barcelona, Spain

299 Universitat Ramon Llull, La Salle, C/ Quatre Camins 2, 08022 Barcelona, Spain

300 Universität Rostock, 18051 Rostock, Germany

301 Universität Siegen, Naturwissenschaftlich-Technische Fakultät, Department Physik, Emmy Noether Campus, Walter-Flex-Str.3, 57068 Siegen, Germany

302 Universität Wien - Theoretische Physik Boltzmanngasse 5, A-1090 Vienna, Austria

303 Université catholique de Louvain, Centre for Cosmology, Particle Physics and Phenomenology (CP3), Institute of Mathematics and Physics, 2 Chemin du Cyclotron, 1348 Louvain-la-Neuve, Belgium

304 Université de Genève, Section de Physique, 24, quai E. Ansermet, 1211 Genève 4, Switzerland

305 Université de Montréal, Département de Physique, Groupe de Physique des Particules, C.P. 6128, Succ. Centre-ville, Montréal, Qc H3C 3J7, Canada

306 Université de Strasbourg, UFR de Sciences Physiques, 3-5 Rue de l'Université, F-67084 Strasbourg Cedex, France

307 Université Libre de Bruxelles, Boulevard du Triomphe, 1050 Bruxelles, Belgium

308 Universittà di Catania, Dipartimento di Fisica e Astronomia, Via Santa Sofia 64, 95123 Catania, Italy

309 University College London (UCL), High Energy Physics Group, Physics and Astronomy Department, Gower Street, London WC1E 6BT, UK

310 University College, National University of Ireland (Dublin), Department of Experimental Physics, Science Buildings, Belfield, Dublin 4, Ireland

311 University de Barcelona, Facultat de Física, Av. Diagonal, 647, Barcelona 08028, Spain

312 University of Alberta - Faculty of Science, Department of Physics, 4-181 CCIS, Edmonton AB T6G 2E1, Canada

313 University of Arizona, Department of Physics, 1118 E. Fourth Street, PO Box 210081, Tucson, AZ 85721, USA

314 University of Bergen, Institute of Physics, Allegaten 55, N-5007 Bergen, Norway

315 University of Birmingham, School of Physics and Astronomy, Particle Physics Group, Edgbaston, Birmingham B15 2TT, UK

316 University of Bristol, H. H. Wills Physics Lab, Tyndall Ave., Bristol BS8 1TL, UK

317 University of British Columbia, Department of Physics and Astronomy, 6224 Agricultural Rd., Vancouver, BC V6T 1Z1, Canada

318 University of California (UCLA), Los Angleles, CA 90095, US

319 University of California Berkeley, Department of Physics, 366 Le Conte Hall, #7300, Berkeley, CA 94720, USA

320 University of California Davis, Department of Physics, One Shields Avenue, Davis, CA 95616-8677, USA

321 University of California Irvine, Department of Physics and Astronomy, High Energy Group, 4129 Frederick Reines Hall, Irvine, CA 92697-4575 USA

322 University of California Santa Cruz, Institute for Particle Physics, 1156 High Street, Santa Cruz, CA 95064, USA

323 University of Cambridge, Cavendish Laboratory, J J Thomson Avenue, Cambridge CB3 0HE, UK

324 University of Colorado at Boulder, Department of Physics, 390 UCB, University of Colorado, Boulder, CO 80309-0390, USA

325 University of Cyprus, Department of Physics, P.O.Box 20537, 1678 Nicosia, Cyprus

326 University of Delhi, Department of Physics and Astrophysics, Delhi 110007, India

327 University of Delhi, S.G.T.B. Khalsa College, Delhi 110007, India

328 University of Dundee, Department of Physics, Nethergate, Dundee, DD1 4HN, Scotland, UK

329 University of Edinburgh, School of Physics, James Clerk Maxwell Building, The King's Buildings, Mayfield Road, Edinburgh EH9 3JZ, UK

330 University of Florida, Department of Physics, Gainesville, FL 32611, USA

331 University of Ghent, Department of Subatomic and Radiation Physics, Proeftuinstraat 86, 9000 Gent, Belgium

332 University of Glasgow, SUPA, School of Physics & Astronomy, University Avenue, Glasgow G12 8QQ, Scotland, UK

333 University of Hamburg, Physics Department, Luruper Chaussee 149, 22761 Hamburg, Germany

334 University of Hawaii, Department of Physics and Astronomy, HEP, 2505 Correa Rd., WAT 232, Honolulu, HI 96822-2219, USA

335 University of Helsinki, Department of Physical Sciences, P.O. Box 64 (Vaino Auerin katu 11), FIN-00014, Helsinki, Finland

336 University of Illinois at Chicago, Department Of Physics, 845 W Taylor St., Chicago IL 60607, USA

337 University of Iowa, Department of Physics and Astronomy, 203 Van Allen Hall, Iowa City, IA 52242-1479, USA

338 University of Kansas, Department of Physics and Astronomy, Malott Hall, 1251 Wescoe Hall Drive, Room 1082, Lawrence, KS 66045-7582, USA

339 University of Liverpool, Department of Physics, Oliver Lodge Lab, Oxford St., Liverpool L69 7ZE, UK

340 University of Liverpool, Division of Theoretical Physics, Department of Mathematical Sciences, Chadwick Building, Liverpool L69 3BX, UK

341 University of Ljubljana, Faculty of Mathematics and Physics, Jadranska ulica 19, 1000 Ljubljana, Slovenia

342 University of Malaya, Faculty of Science, Department of Physics, 50603 Kuala Lumpur, Malaysia

343 University of Manchester, School of Physics and Astronomy, Schuster Lab, Manchester M13 9PL, UK

344 University of Maribor, Faculty of Chemistry and Chemical Engineering (FKKT), Smetanova ulica 17, 2000 Maribor, Slovenia

345 University of Maryland, Department of Physics and Astronomy, Physics Building (Bldg. 082), College Park, MD 20742, USA

346 University of Massachusetts - Amherst, Department of Physics, 1126 Lederle Graduate Research Tower (LGRT), Amherst, MA 01003-9337, USA

347 University of Melbourne, School of Physics, Victoria 3010, Australia

348 University of Michigan, Department of Physics, 500 E. University Ave., Ann Arbor, MI 48109-1120, USA

349 University of Minnesota, 148 Tate Laboratory Of Physics, 116 Church St. S.E., Minneapolis, MN 55455, USA

350 University of Mississippi, Department of Physics and Astronomy, 108 Lewis Hall, PO Box 1848, Oxford, Mississippi 38677-1848, USA

351 University of Missouri – St. Louis, Department of Physics and Astronomy, 503 Benton Hall One University Blvd., St. Louis Mo 63121, USA

352 University of New Mexico, New Mexico Center for Particle Physics, Department of Physics and Astronomy, 800 Yale Boulevard N.E., Albuquerque, NM 87131, USA

353 University of North Carolina at Chapel Hill, Department of Physics and Astronomy, Phillips Hall, CB #3255, 120 E. Cameron Ave., Chapel Hill, NC 27599-3255, USA

354 University of Notre Dame, Department of Physics, 225 Nieuwland Science Hall, Notre Dame, IN 46556, USA

355 University of Oklahoma, Department of Physics and Astronomy, Norman, OK 73071, USA

356 University of Oregon, Department of Physics, 1371 E. 13th Ave., Eugene, OR 97403, USA

357 University of Oslo, Department of Physics, P.O box 1048, Blindern, 0316 Oslo, Norway

358 University of Oxford, Particle Physics Department, Denys Wilkinson Bldg., Keble Road, Oxford OX1 3RH England, UK

359 University of Pavia, Department of Physics, via Bassi 6, I-27100 Pavia, Italy

360 University of Pennsylvania, Department of Physics and Astronomy, 209 South 33rd Street, Philadelphia, PA 19104-6396, USA

361 University of Pittsburgh, Department of Physics and Astronomy, 100 Allen Hall, 3941 O'Hara St, Pittsburgh PA 15260, USA

362 University of Regina, Department of Physics, Regina, Saskatchewan, S4S 0A2 Canada

363 University of Rochester, Department of Physics and Astronomy, Bausch & Lomb Hall, P.O. Box 270171, 600 Wilson Boulevard, Rochester, NY 14627-0171 USA
364 University of Science and Technology of China, Department of Modern Physics (DMP), Jin Zhai Road 96, Hefei, China 230026
365 University of Silesia, Institute of Physics, Ul. Uniwersytecka 4, PL-40007 Katowice, Poland
366 University of South Carolina, Department of Physics and Astronomy, 712 Main Street, Columbia, SC 29208, USA
367 University of Southampton, School of Physics and Astronomy, Highfield, Southampton S017 1BJ, England, UK
368 University of Southern California, Department of Physics & Astronomy, 3620 McClintock Ave., SGM 408, Los Angeles, CA 90089-0484, USA
369 University of Sydney, Falkiner High Energy Physics Group, School of Physics, A28, Sydney, NSW 2006, Australia
370 University of Tartu, Institute of Physics, Riia 142, 51014 Tartu, Estonia
371 University of Texas at Austin, Department of Physics, 1 University Station C1600, Austin, Texas 78712, USA
372 University of Texas at Dallas, Department of Physics, 800 West Campbell Road, Richardson, Texas 75080, USA
373 University of Texas, Center for Accelerator Science and Technology, Arlington, TX 76019, USA
374 University of Tokushima, Institute of Theoretical Physics, Tokushima-shi 770-8502, Japan
375 University of Tokyo, Department of Physics, 7-3-1 Hongo, Bunkyo District, Tokyo 113-0033, Japan
376 University of Toronto, Department of Physics, 60 St. George St., Toronto M5S 1A7, Ontario, Canada
377 University of Toyama, Department of Physics, 3190 Gofuku, Toyama 930-8555, Japan
378 University of Tsukuba, Faculty of Pure and Applied Sciences, 1-1-1 Ten'nodai, Tsukuba, Ibaraki 305-8571, Japan
379 University of Victoria, Department of Physics and Astronomy, P.O.Box 3055 Stn Csc, Victoria, BC V8W 3P6, Canada
380 University of Virginia, Department of Physics, 382 McCormick Rd., PO Box 400714, Charlottesville, VA
381 University of Warsaw, Institute of Experimental Physics, Ul. Hoza 69, PL-00 681 Warsaw, Poland
382 University of Warsaw, Institute of Theoretical Physics, Ul. Hoza 69, PL-00 681 Warsaw, Poland
383 University of Washington, Department of Physics, PO Box 351560, Seattle, WA 98195-1560, USA
384 University of Wisconsin, Physics Department, Madison, WI 53706-1390, USA
385 University of Wuppertal, Gaußstraße 20, D-42119 Wuppertal, Germany
386 Università degli Studi di Milano, Dipartimento di Fisica, Via Celoria 16, 20133 Milano, Italy
387 Università degli Studi di Roma "La Sapienza", Dipartimento di Fisica, Piazzale Aldo Moro 5, 00185 Roma, Italy
388 Università degli Studi di Trieste, Dipartimento di Fisica, via A. Valerio 2, I-34127 Trieste, Italy
389 Università dell'Insubria in Como, Dipartimento di Scienze CC.FF.MM., via Vallegio 11, I-22100 Como, Italy
390 Università di Milano-Bicocca, Dipartimento di Fisica"G. Occhialin", Piazza della Scienza 3, 20126 Milano, Italy
391 Università di Pisa, Departimento di Fisica "Enrico Fermi", Largo Bruno Pontecorvo 3, I-56127 Pisa, Italy
392 Universiy of Huddersfield, International Institute for Accelerator Applications, Queensgate Campus, Huddersfield HD1 3DH, UK
393 UPMC Univ. Paris 06, Faculté de Physique (UFR 925), 4 Place Jussieu, 75252 Paris Cedex 05, France
394 Vietnam National University, Laboratory of High Energy Physics and Cosmology, Faculty of Physics, College of Science, 334 Nguyen Trai, Hanoi, Vietnam
395 Vietnam National University, University of Natural Sciences, 227 Nguyen Van Cu street, District 5, Ho Chi Minh City, Vietnam
396 VINCA Institute of Nuclear Sciences, Laboratory of Physics, PO Box 522, YU-11001 Belgrade, Serbia
397 Virginia Commonwealth University, Department of Physics, P.O. Box 842000, 701 W. Grace St.,Richmond, VA. 23284-2000, USA
398 Virginia Polytechnic Institute and State University, Physics Department, Blacksburg, VA 2406, USA
399 Vrije Universiteit Brussel, Pleinlaan 2, 1050 Brussels, Belgium
400 Vrije Universiteit, Department of Physics, Faculty of Sciences, De Boelelaan 1081, 1081 HV Amsterdam, Netherlands
401 Warsaw University of Technology, The Faculty of Electronics and Information Technology, ul. Nowowiejska 15-19, 00-665 Warsaw, Poland
402 Waseda University, Advanced Research Institute for Science and Engineering, Shinjuku, Tokyo 169-8555, Japan
403 Wayne State University, Department of Physics, Detroit, MI 48202, USA
404 Weizmann Institute of Science, Department of Particle Physics, P.O. Box 26, Rehovot 76100, Israel
405 Yale University, Department of Physics, New Haven, CT 06520, USA
406 Yamagata University, 1-4-12 Kojirakawa-cho, Yamagata-shi, Yamagata, 990-8560, Japan
407 Yerevan Physics Institute, 2 Alikhanyan Brothers St., Yerevan 375036, Armenia
408 Yonsei University, Department of Physics, 134 Sinchon-dong, Sudaemoon-gu, Seoul 120-749, Republic of Korea

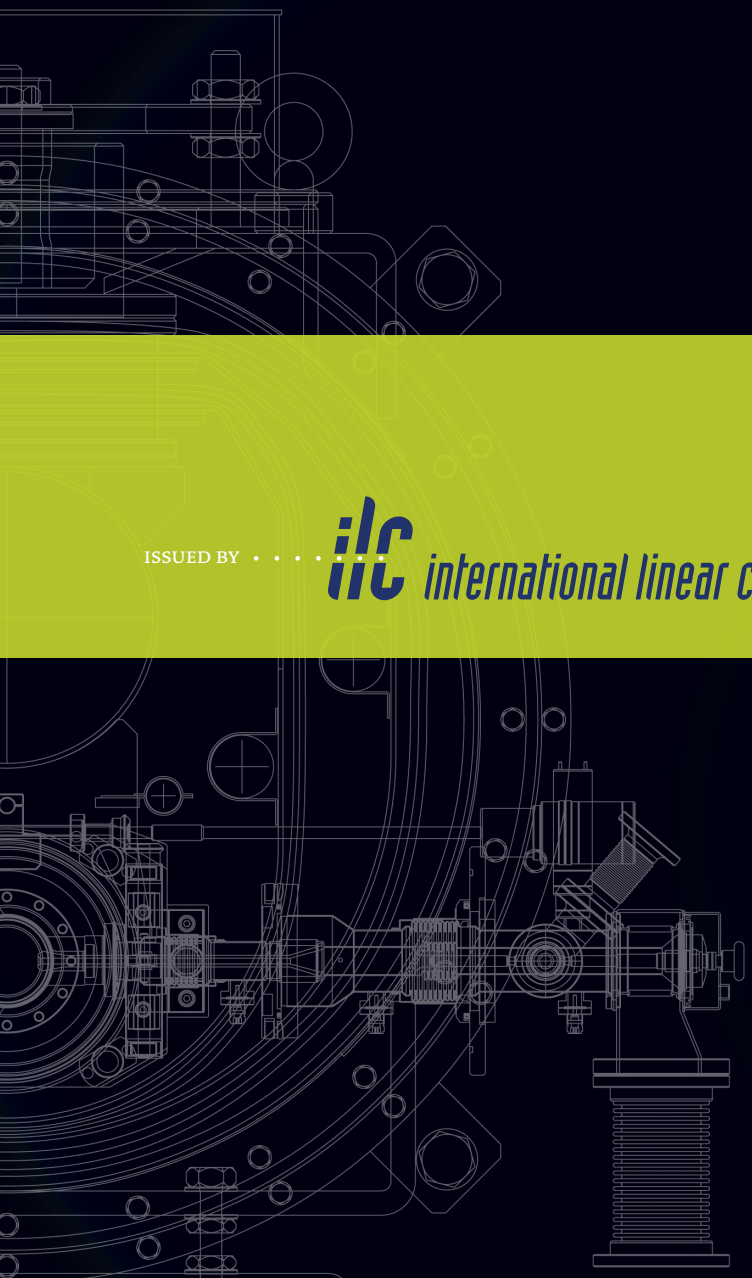

ISSUED BY • • • • • • • • ilc international linear collider

WWW.LINEARCOLLIDER.ORG

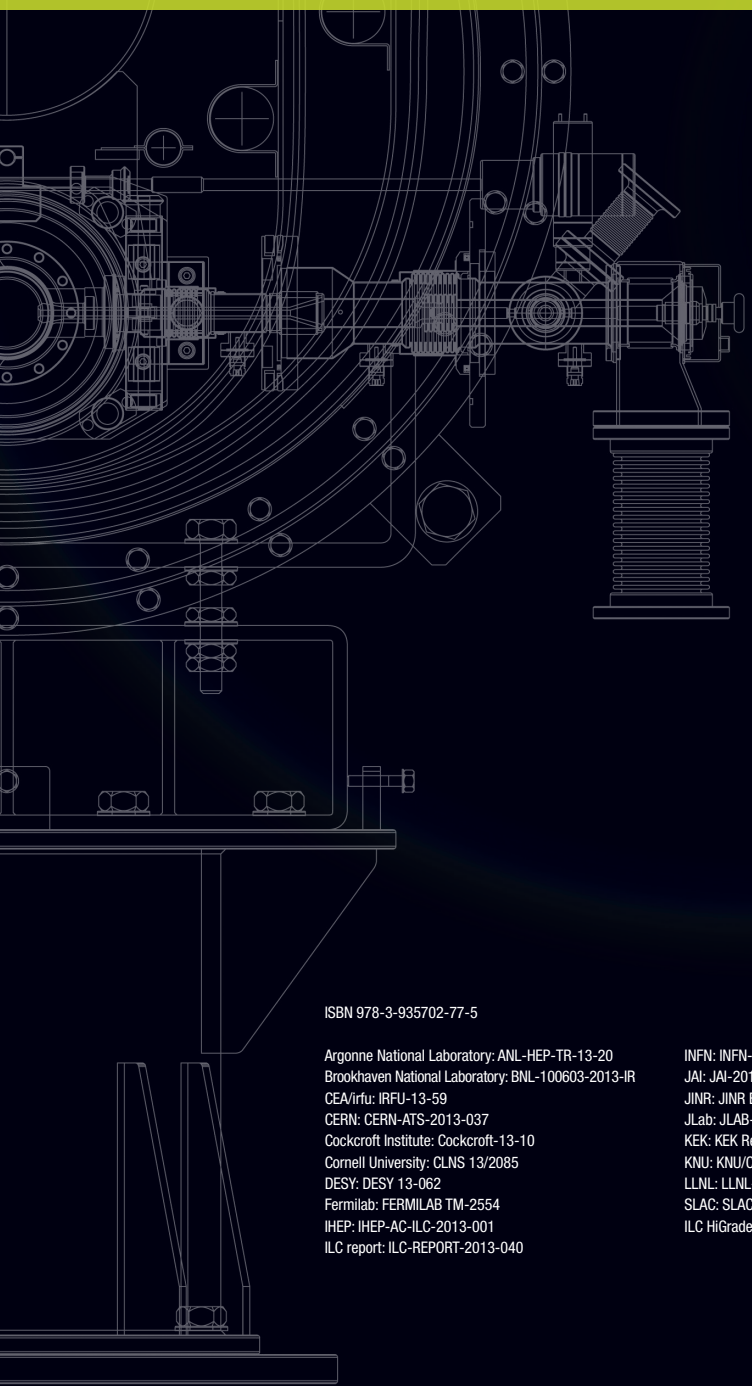

ISBN 978-3-935702-77-5

Argonne National Laboratory: ANL-HEP-TR-13-20
Brookhaven National Laboratory: BNL-100603-2013-IR
CEA/irfu: IRFU-13-59
CERN: CERN-ATS-2013-037
Cockcroft Institute: Cockcroft-13-10
Cornell University: CLNS 13/2085
DESY: DESY 13-062
Fermilab: FERMILAB TM-2554
IHEP: IHEP-AC-ILC-2013-001
ILC report: ILC-REPORT-2013-040
INFN: INFN-13-04/LNF
JAI: JAI-2013-001
JINR: JINR E9-2013-35
JLab: JLAB-R-2013-01
KEK: KEK Report 2013-1
KNU: KNU/CHEP-ILC-2013-1
LLNL: LLNL-TR-635539
SLAC: SLAC-R-1004
ILC HiGrade: ILC-HiGrade-Report-2013-003

THE INTERNATIONAL LINEAR COLLIDER

Technical Design Report | Volume 4: Detectors

The International Linear Collider

Technical Design Report

2013

Volume 1: Executive Summary

Volume 2: Physics

Volume 3: Accelerator

Part I: R&D in the Technical Design Phase

Volume 3: Accelerator

Part II: Baseline Design

Volume 4: Detectors

Volume 4

Detectors

Editors

Ties Behnke, James E. Brau, Philip Burrows, Juan Fuster, Michael Peskin,
Marcel Stanitzki, Yasuhiro Sugimoto, Sakue Yamada, Hitoshi Yamamoto

Acknowledgements

We acknowledge the support of BMWF, Austria; MinObr, Belarus; FNRS and FWO, Belgium; NSERC, Canada; NSFC, China; MPO CR and VSC CR, Czech Republic; Commission of the European Communities; HIP, Finland; IN2P3/CNRS, CEA-DSM/IRFU, France; BMBF, DFG, Helmholtz Association, MPG and AvH Foundation, Germany; DAE and DST, India; ISF, Israel; INFN, Italy; MEXT and JSPS, Japan; CRI(MST) and MOST/KOSEF, Korea; FOM and NWO, The Netherlands; NFR, Norway; MNSW, Poland; ANCS, Romania; MES of Russia and ROSATOM, Russian Federation; MON, Serbia and Montenegro; MSSR, Slovakia; MICINN-MINECO and CPAN, Spain; SRC, Sweden; STFC, United Kingdom; DOE and NSF, United States of America.

Contents

Introduction to the Detailed Baseline Design report **1**

I Detectors at the ILC:
Challenges, Coordination and R&D 3

1 The physics and detector challenges of the ILC **5**
1.1 Physics program of the International Linear Collider . . . 5
1.1.1 Physics goals of the ILC . . . 5
1.1.2 Energy and beam polarisation of the ILC . . . 7
1.2 Experimentation at the ILC . . . 9
1.3 Detector challenges and performance requirements . . . 9
1.3.1 Machine backgrounds . . . 11
1.3.2 Beam Instrumentation . . . 12
1.3.3 Two detectors . . . 13
1.4 Physics benchmarks studies . . . 13
1.4.1 Definition of the first set of benchmark processes (250, 500 GeV) for the LOI 14
1.4.2 Definition of the second set of benchmark processes (1 TeV) for the DBD . . 15
1.5 The Physics and Detector Study of the International Linear Collider . . . 15
1.5.1 Call for LOIs . . . 16
1.5.2 The management formation . . . 16
1.5.3 Organisation of detector activity . . . 16
1.5.4 The LOIs and their validation . . . 17
1.5.5 Work for the detailed baseline designs . . . 18
1.5.6 The common task groups . . . 18
1.5.7 Other working groups . . . 19
1.6 The World Wide Study . . . 20

2 Description of Common Tasks and Common Issues **21**
2.1 ILC Detector Research and Development . . . 21
2.1.1 Overview of the overall detector strategies . . . 22
2.1.2 Vertex Detector Technologies . . . 23
2.1.3 Tracking Detector . . . 25
2.1.4 Calorimetry . . . 26
2.1.5 Forward Calorimetry . . . 30
2.1.6 Beam Tests . . . 31
2.2 Common simulation and software tools . . . 32
2.2.1 Common generator samples . . . 32

2.2.2 Common simulation and reconstruction tools . . . 36
2.2.3 Summary of benchmark studies . . . 38
2.3 Machine Detector Interface . . . 39
2.3.1 The push-pull concept . . . 39
2.3.2 Detector motion system . . . 39
2.3.3 Shielding . . . 40
2.3.4 Detector installation schemes and timelines . . . 41
2.3.5 Experimental area layout . . . 42
2.3.6 Detector services . . . 43
2.4 Beam Instrumentation . . . 44
2.4.1 Beam Energy Measurements . . . 44
2.4.2 Polarisation Measurements . . . 46
2.4.3 Luminosity weighted averages and correlations . . . 48
2.5 Common Engineering Tools . . . 48
2.6 Detector Costing Methodology . . . 49

II SiD Detailed Baseline Design 51

SiD Introduction **55**

1 SiD Concept Overview **57**
1.1 SiD Philosophy . . . 57
1.2 Silicon-based Tracking . . . 58
1.2.1 Vertex detector . . . 58
1.2.2 Main tracker . . . 60
1.3 Main calorimeters . . . 60
1.4 Forward calorimeters . . . 61
1.5 Magnet Coil . . . 61
1.6 Muon System . . . 62
1.7 The Machine-Detector Interface . . . 62

2 SiD Vertex Detector **63**
2.1 Introduction . . . 63
2.1.1 Vertex detector requirements . . . 63
2.2 Baseline Design . . . 64
2.2.1 Sensor Technology . . . 64
2.3 3D-Based Module Design . . . 65
2.3.1 Active Edge Devices . . . 65
2.3.2 Barrel Sensor Interconnect to Readout . . . 66
2.3.3 Sensor tiling for disks . . . 67
2.4 Support structures and Integration . . . 67
2.4.1 Power delivery . . . 68
2.4.2 Cooling . . . 69
2.4.3 Cabling . . . 70
2.5 R&D Status . . . 70
2.5.1 Chronopixel . . . 70
2.5.2 VIP 3D Chip . . . 71
2.5.3 Thinned hybrid detector with high-density interconnect . . . 71

2.5.4 Active Edge Tiles . . . 71
2.5.5 Critical R&D . . . 71
2.6 Summary . . . 72

3 SiD Main Tracker 73
3.1 Introduction . . . 73
3.2 Baseline Design . . . 73
3.3 Baseline Design . . . 74
3.3.1 Barrels . . . 75
3.3.2 Disks . . . 76
3.3.3 Barrel and disk Integration . . . 76
3.4 Critical R&D . . . 77
3.5 Performance . . . 79
3.5.1 Tracking Efficiency . . . 79
3.5.2 Fake Rates . . . 81
3.5.3 Tracking Resolution . . . 81
3.6 Alignment . . . 82
3.6.1 Alignment Methods . . . 84
3.6.2 Push-Pull Considerations . . . 85

4 SiD Calorimetry 87
4.1 Introduction . . . 87
4.2 Electromagnetic Calorimeter . . . 87
4.2.1 Introduction . . . 87
4.2.2 Global ECAL Design . . . 88
4.2.3 Baseline Technology . . . 90
4.2.4 MAPS option . . . 92
4.2.5 Calibration and alignment . . . 94
4.3 Hadronic Calorimeter . . . 94
4.3.1 HCAL requirements . . . 94
4.3.2 Description of the DHCAL concept . . . 94
4.3.3 Global HCAL mechanical design . . . 95
4.3.4 Baseline technology . . . 95
4.3.5 DHCAL prototype performance . . . 100
4.3.6 R&D towards technical feasibility and optimisation . . . 102
4.3.7 Calibration of a Digital Hadron Calorimeter . . . 103
4.3.8 Alternative technologies . . . 105
4.4 Summary . . . 109

5 SiD Muon System 111
5.1 Backgrounds . . . 112
5.2 Detector design . . . 112
5.2.1 Scintillating strips . . . 113
5.2.2 Resistive Plate Chambers . . . 115

6 SiD Superconducting Magnet System 117
6.1 Introduction . . . 117
6.1.1 List of subsystems . . . 117
6.1.2 Design Philosophy . . . 117

6.2 Magnetic Field and Forces . . . 118
6.2.1 Requirements and Design . . . 118
6.2.2 Calculations . . . 119
6.3 Mechanical Engineering . . . 119
6.3.1 Solenoid Coil Production . . . 119
6.3.2 Integration of DID to solenoid . . . 119
6.3.3 Thermal shield, cooling tubes, current leads and standpipe . . . 120
6.3.4 Stress Analysis . . . 120
6.3.5 Vacuum Shell Design . . . 121
6.3.6 Assembly procedure . . . 121
6.4 Cryogenics . . . 122
6.5 Conductor . . . 123
6.5.1 Solenoid baseline conductor (CMS) . . . 123
6.5.2 Modified CMS Conductor Choices . . . 123
6.5.3 DID conductor . . . 123
6.6 Electrical . . . 124
6.6.1 Magnet Safety . . . 124
6.6.2 Power Supply, Dump Resistor and Dump Switch . . . 124

7 SiD Engineering, Integration and the Machine Detector Interface 125
7.1 Introduction . . . 125
7.2 IR Hall Layout Requirements and SiD Assembly . . . 125
7.2.1 Vertical Access (Europe and Americas sites) . . . 126
7.2.2 Horizontal Access (Japan sites) . . . 128
7.2.3 Detector Access for Repairs . . . 128
7.3 Detector Exchange Via a Sliding Platform . . . 129
7.3.1 Introduction . . . 129
7.3.2 Platform . . . 129
7.3.3 Vibration analysis and Luminosity Preservation . . . 129
7.3.4 Push Pull Detector Exchange Process and Time Estimate . . . 130
7.4 Beampipe and Forward Region Design . . . 130
7.4.1 Introduction to the Near Beamline Design . . . 130
7.4.2 Beampipe . . . 130
7.4.3 LumiCal, BeamCal, Mask and QD0 Support and Alignment . . . 130
7.4.4 Vacuum System and Performance . . . 131
7.4.5 Feedback and BPMs . . . 131
7.4.6 Frequency Scanning Interferometric (FSI) Alignment of QD0 and QF1 . . . 132

8 SiD Forward Systems 133
8.1 Forward Detector . . . 133
8.1.1 Design criteria . . . 133
8.1.2 Baseline Design . . . 134
8.1.3 Forward Systems Development Work . . . 135

9 SiD Electronics and DAQ 139
9.1 ASIC developments . . . 139
9.1.1 KPiX . . . 139
9.2 On-Detector Electronics . . . 140

9.3 Off-Detector Electronics . . . 140
9.4 Overview of Electronics Channels and Expected Data Rates . . . 142

10 SiD Simulation and Reconstruction 143
10.1 Overview of the Simulation and Reconstruction Software . . . 143
10.2 The SiD DBD Production . . . 143
10.3 Simulating the SiD Detector Geometry . . . 144
10.3.1 The SIDLOI3 Model . . . 144
10.4 Simulation of the full Detector Response . . . 145
10.4.1 Silicon Pixel and Strip Hit Digitisation . . . 145
10.4.2 Simulation of the Calorimeter Response . . . 145
10.4.3 Clustering . . . 146
10.5 Properties of Machine-Induced Background . . . 146
10.6 Detector Performance . . . 147
10.6.1 Particle Identification: Photon, Electron and Muon ID . . . 147
10.6.2 Jet Flavour Tagging: Efficiency and Purity . . . 148
10.6.3 Energy and Mass Resolution . . . 149
10.7 Summary . . . 150

11 SiD Benchmarking 151
11.1 Summary of the LOI Results . . . 151
11.2 DBD Benchmark Reactions . . . 154
11.2.1 Event Generation . . . 154
11.2.2 Analysis Tools . . . 155
11.2.3 Measurement of the top Yukawa coupling . . . 156
11.2.4 Higgs branching fractions . . . 158
11.2.5 Measurement of beam polarisation using WW pairs . . . 163
11.2.6 Top quark cross-section and forward-backward asymmetry . . . 167
11.3 Additional Benchmarks . . . 169
11.3.1 Measurement of scalar tau leptons . . . 169
11.4 Benchmarking Summary . . . 171

12 SiD Costs 173
12.1 Introduction . . . 173
12.2 Parametric cost model . . . 173
12.3 Results . . . 175
12.4 Parameter Dependencies . . . 177

13 SiD Summary 179
13.1 The Status of the SiD Detector Concept . . . 179
13.2 Further Development of the SiD Detector Concept . . . 179
13.3 SiD and the New Global Linear Collider Organisation . . . 180

III ILD Detailed Baseline Design 181

1 ILD: Executive Summary 185
1.1 ILD philosophy and challenges . . . 186
1.2 ILD layout and performance . . . 187

2 ILD Tracking System **191**
2.1 ILD vertex system . . . 191
2.1.1 Baseline design . . . 192
2.1.2 Pixel technologies and readout electronics . . . 192
2.1.3 Ladder design . . . 196
2.1.4 Cooling system . . . 197
2.1.5 Detector mechanics . . . 198
2.1.6 Future prospects . . . 198
2.2 The ILD silicon tracking system . . . 199
2.2.1 The central silicon: SIT, SET, and ETD . . . 200
2.2.2 Forward silicon tracking . . . 204
2.3 The ILD TPC system . . . 209
2.3.1 Design of the TPC . . . 209
2.3.2 Calibration and internal alignment of the TPC . . . 215
2.3.3 Status of R&D for the ILD TPC . . . 215

3 ILD Calorimeter System **217**
3.1 Calorimeter overview . . . 217
3.1.1 The challenges of high granularity . . . 218
3.1.2 Beam tests . . . 218
3.2 The electromagnetic calorimeter system . . . 219
3.2.1 Detector implementation . . . 220
3.2.2 Detector optimisation . . . 223
3.2.3 Test beam validation . . . 226
3.2.4 Calibration and alignment . . . 228
3.2.5 Future directions . . . 229
3.3 The Hadronic calorimeter system . . . 230
3.3.1 Detector optimisation . . . 231
3.3.2 Detector implementation . . . 232
3.3.3 Test beam results . . . 235
3.3.4 Technical validation . . . 238
3.3.5 Calibration and alignment . . . 239
3.3.6 Future R&D . . . 239
3.4 Particle flow performance of the ILD calorimeter system . . . 240
3.5 Forward calorimetry . . . 240
3.5.1 Mechanical concept . . . 241
3.5.2 LumiCal . . . 241
3.5.3 BeamCal . . . 242
3.5.4 ASIC developments . . . 243
3.5.5 Beam tests . . . 244
3.5.6 Summary and future plans . . . 244

4 ILD Outer Detector **245**
4.1 The ILD muon system/ tail catcher . . . 245
4.1.1 Muon system layout . . . 246
4.1.2 Technologies . . . 246
4.1.3 Performance . . . 247

4.2 The ILD coil and yoke system . . . 248
4.2.1 Magnet design . . . 249
4.2.2 Solenoid design . . . 250
4.2.3 Anti-DID design . . . 251
4.2.4 Assembly of the solenoid . . . 251
4.2.5 Ancillaries . . . 251
4.2.6 Final tests and field mapping . . . 252
4.2.7 Iron yoke design . . . 252
4.2.8 Barrel yoke design . . . 252
4.2.9 End-cap yoke design . . . 253
4.2.10 Yoke assembly . . . 254

5 The ILD Detector System 255
5.1 ILD integration . . . 255
5.1.1 Mechanical concept . . . 255
5.1.2 Detector assembly . . . 259
5.1.3 Service paths and interfaces . . . 260
5.1.4 General Safety Issues . . . 261
5.1.5 ILD modelling . . . 262
5.2 ILD alignment and calibration . . . 263
5.2.1 Alignment of the tracking system . . . 263
5.2.2 Calorimeter calibration . . . 265
5.3 ILD data acquisition and computing . . . 269
5.3.1 DAQ structure . . . 271
5.3.2 Data processing . . . 273
5.3.3 Outlook and R&D . . . 273
5.4 ILD software and tools . . . 274
5.4.1 Detector models in Mokka . . . 274
5.4.2 Marlin: Reconstruction and analysis system . . . 275
5.4.3 Monte Carlo productions . . . 277
5.5 ILD - machine-detector interface and experimental area . . . 278
5.5.1 ILD push-pull issues . . . 278
5.5.2 Final focus magnets . . . 278
5.5.3 Beam pipe and interaction region . . . 279
5.5.4 Experimental area for flat surface ILC sites . . . 280
5.5.5 Experimental area for mountainous ILC sites . . . 281
5.5.6 Machine induced backgrounds . . . 281

6 ILD Performance 283
6.1 ILD performance . . . 283
6.1.1 Software for performance studies . . . 283
6.1.2 ILD tracking performance . . . 284
6.1.3 ILD particle flow performance . . . 286
6.1.4 Flavour tagging performance . . . 287
6.1.5 Comparison of detector models . . . 288
6.2 ILD physics performance at 250 and 500 GeV . . . 288
6.2.1 Higgs recoil mass reconstruction . . . 288
6.2.2 Tau reconstruction . . . 290

6.2.3 Strong EWSB . . . 290
6.3 ILD benchmarking . . . 291
6.3.1 Common reconstruction tools . . . 292
6.3.2 $\mathrm{e^+e^-} \to \nu\bar{\nu}\mathrm{h}$ . . . 293
6.3.3 $e^+e^- \to W^+W^-$ . . . 296
6.3.4 $e^+e^- \to t\bar{t}h$ . . . 297
6.3.5 $e^+e^- \to t\bar{t}$ at $E_{CMS} = 500$ GeV . . . 298
6.3.6 Other physics processes . . . 299

7 ILD Costs **303**
7.1 Methodology of costing . . . 303
7.2 ILD work breakdown structure . . . 304
7.3 ILD cost evaluation . . . 305
7.3.1 Vertex detector . . . 305
7.3.2 Silicon tracking . . . 305
7.3.3 Time Projection Chamber . . . 305
7.3.4 Calorimeter System . . . 306
7.3.5 Magnet . . . 307
7.3.6 Muon system . . . 309
7.3.7 Cost summary . . . 309
7.4 Detector cost dependencies . . . 310
7.4.1 Scaling with the field . . . 310
7.4.2 Scaling the detector size . . . 310
7.4.3 Changing the ECAL . . . 310
7.4.4 Scaling the hadronic cell size . . . 311
7.5 Conclusion . . . 311

8 ILD Summary **313**

IV Summary and Future Plans 315

V Appendices 319

Bibliography **323**

SiD Bibliography **325**

ILD Bibliography **333**

List of Signatories **347**

Introduction to the Detailed Baseline Design report

For the past five years, the global physics and detector community of linear collider physicists has continued to advance the physics studies and detector developments toward the International Linear Collider (ILC). This report presents the outcome of this recent large and successful phase in four individual parts. In Part I, an outline of the physics motivation is presented first, in Chapter 1, drawn from the detailed physics volume [1] accompanying this volume. With the recent discovery at the LHC of a boson with Higgs Boson-like properties this physics program initially emphasises studies of this particle. The physics summary makes a more general note of the open questions in particle physics and the potential role of the ILC in addressing these questions. Why is Nature asymmetric? What is the nature of dark matter? Why do baryons dominate anti-baryons in the universe? These are the questions that define the frontier of particle physics and the TeV scale holds the potential to provide illumination on each of them, with the Higgs Boson likely playing an essential role.

Following the physics summary, Chapter 1 contains the detector performance requirements and the main challenges for detectors in realising this level of performance. Each detector capability has high performance level goals set by physics needs. The vertex sensors provide excellent flavour tagging. The trackers target precise recoiling mass measurements in the Higgs-strahlung process. Calorimetry must separate di-jet decays of the W and Z. The precision expected of the ILC detectors is unprecedented and specific detector benchmark reactions have been defined to demonstrate this precision can be achieved. Two detectors are planned for the ILC and the motivation for this is explained. With this in mind, two specific detector concepts with complementary designs have been developed and studied. While significant progress has been reached in developing these detector designs and the technical validation through R&D, significant work is still needed to bring the technical designs to a similar state of maturity and construction readiness as the collider.

Following this overview of physics and detectors, Chapter 1 concludes with a description of the process that has guided the global effort through Letters of Intent (LOIs), to the validation of two detector concept groups, leading finally to completion of the Detailed Baseline Designs of SiD and ILD presented later in this report.

The two detector groups have worked together successfully on many common aspects of the ILC. Chapter 2 presents some details of the common efforts, including detector R&D, software tool development and generator sample production, machine detector interface, beam instrumentation, engineering tools, and detector costing.

ILC detector R&D goals have been addressed by many collaborations formed to address the diverse needs. Many of these collaborations contribute to both detector concepts. The vertex detector R&D aims to develop the fine pitched, low mass sensor demanded by the ILC physics goals. Several sensor technologies are under development, applying the monolithic active pixel sensor (MAPS) approach. Fine Pixel Charge Coupled Devices are also being developed. Mechanical design, a critical aspect of achieving the performance goals, is also being pursued. Silicon tracking and Time Projection

Chamber (TPC) R&D have been carried out to support the two complementary approaches for tracking of SiD and ILD. Many options for calorimetry have received R&D effort. Silicon-tungsten as well as scintillator strips with silicon photodiodes are the approaches being developed for the ECAL of the detectors. The Hadron Calorimeter options which have been developed include glass RPCs and Scintillator pads, as well as a number of other technologies that are described. The development of particle flow analysis (PFA) has been a central consideration and a guide for the calorimeter R&D. Forward calorimetry has been a specialised subject with dedicated R&D.

The two detector groups have developed independent software frameworks, but they have cooperated on many tools and projects. For example, the generator samples for physics studies have been produced jointly. A common event data model, LCIO, has been adopted. PandoraPFA and LCFIPlus have been applied by both detector concept groups.

Work on the machine detector interface (MDI) has been an area of close collaboration between the two detector concept groups, as well as with the GDE machine physicists. This includes work on push-pull, detector shielding, installation, and collider hall designs.

An effort has been made to develop and apply common engineering tools, including an engineering data management system. Likewise, common considerations have been made in estimating the costs of each of the detector designs.

Parts II and III present the details of each of the detector concept studies, SiD and ILD. Since submitting the Letters of Intent in 2009, both detectors designs have been updated. Their subsystem technologies have benefited from substantial R&D. Some engineering studies have been possible. The reconstruction software and simulation models have improved and been applied to the specified benchmark reactions.

SiD is a compact, cost-constrained detector made possible by silicon tracking in a 5 Tesla magnetic field produced by a superconducting solenoid. Silicon detectors enable time-stamping on single bunch crossings to provide robust performance. The ILD concept evolved from two similar concepts: GLD and LDC. The ILD design results in a large detector optimised for resolution and track separation, with flexibility for operation at energies up to the TeV range. The ILD tracker is a Time Projection Chamber (TPC) providing continuous tracking for excellent pattern recognition and dE/dx capability. ILD employs a large, 3.5 Tesla superconducting solenoid. Both detector designs employ low-mass high-resolution vertex detectors, highly granular calorimeters optimised for particle flow analysis and operate with a triggerless readout. The designs have been developed in concert with the design of a push-pull system and adequate experimental hall space, as well as a realistic installation scheme. Both are self shielding in order to allow occupancy in the collider hall by one detector group while the other is accumulating collider beam interactions. Results of the simulation studies by each detector concept group of the benchmark reactions are presented in Parts II (SiD) and III (ILD).

Finally, this report ends with a brief concluding statement and a comment on future directions in Part IV. The detectors presented here are mature concepts, backed by detailed R&D studies, with very limited engineering considerations so far. It is time for increased emphasis on engineering, further optimisation, while R&D studies continue to advance the detector technologies.

Volume 4

Detectors

Part I

Detectors at the ILC:

Challenges, Coordination and R&D

Chapter 1
The physics and detector challenges of the ILC

This initial chapter introduces the background for the ILC physics and detector efforts of the past five years. First, the physics motivation is outlined, highlighting the precision measurements of the Higgs Boson candidate that was recently discovered at the LHC. Next, the detector challenges and performance requirements are described, including machine backgrounds, beam instrumentation, and the motivation for two detectors, as well as the benchmark processes defined to demonstrate detector performance. The chapter ends with a description of the process that guided the ILC physics and detector work to its current state of maturity.

1.1 Physics program of the International Linear Collider

In the Physics Volume of this report, we have described the goals of the experimental program of the ILC in full detail. In this section, we review those goals and the experimental program that they call for.

1.1.1 Physics goals of the ILC

Among the great mysteries of elementary particle physics, there are three that are likely to be solved by new information from experiments at the TeV energy scale. These concern the three areas in which the Standard Model of particle physics is incomplete as the theory of nature: First, though the Standard Model incorporates a simple phenomenological model of spontaneous symmetry breaking through its Higgs field, the Standard Model gives no understanding of this symmetry breaking. It does not provide a mechanism for the phenomenon or even predict the mass scale at which it occurs. Second, the Standard Model does not provide a particle to describe the "dark matter" that makes up 80% of the mass in the universe. Third, the Standard Model does not provide a mechanism to generate the baryon-antibaryon asymmetry of the universe.

The discovery by the ATLAS and CMS experiments of the "Higgs-like particle" near 125 GeV—and the exclusion of the possibility that the Higgs boson could be at higher mass—gives us a direct path by which experiments can clarify the origin of the symmetry breaking of the electroweak interactions. It has long been appreciated that an electron-positron collider operating in the centre-of-mass energy range of 250 GeV to 1 TeV would be an ideal instrument for the precision study of the Higgs boson. The discovery of the new particle now allows us to map out a specific program of experiments. This program accesses all of the Higgs boson production reactions shown in Figure I-1.1.

The Higgs boson program of the ILC begins at the energy of 250 GeV, near the peak of the cross section for $e^+e^- \to Zh$. The presence of a Z boson at the energy appropriate to recoil tags the Higgs boson events. This allows direct measurement of the Higgs boson branching ratios. The ILC detectors can identify and separate the various predicted Higgs decays, including the two-jet hadronic

decays to $b\bar{b}$, $c\bar{c}$, and gg. The Z tag also allows the ILC experiments to measure the branching ratio to invisible modes, and also to unexpected models with exotic long-lived particles. Measurement of the peak in the Z recoil energy also gives a precise determination of the Higgs boson mass.

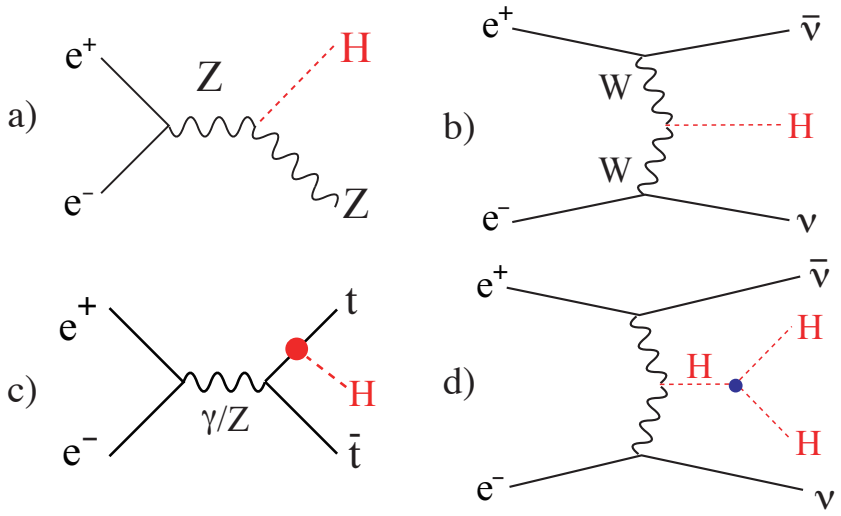

Figure I-1.1 Representative Feynman diagrams for the major Higgs production processes at the ILC: (a) $e^+e^- \to Zh$; (b) $e^+e^- \to \nu\bar{\nu}h$; (c) $e^+e^- \to t\bar{t}h$; (d) $e^+e^- \to \nu\bar{\nu}hh$.

At higher energy, the WW fusion process of Higgs production, $e^+e^- \to \nu\bar{\nu}h$, turns on. Measurement of this process at the full ILC energy of 500 GeV gives a model-independent precision measurement of the total Higgs boson width. Experiments at 500 GeV also allow first measurements of the Higgs boson coupling to $t\bar{t}$ and of the Higgs boson self-coupling. At a centre-of-mass energy of 1000 GeV, all of the Higgs boson production reactions are fully accessible and the Higgs boson branching ratios can be studied with even higher precision.

A complete review of the Higgs boson program of the ILC, with numerical estimates of the experimental capabilities and comparison to the expectations for the LHC, can be found the Physics Volume of the ILC Technical Design Report [1] (Chapter 2).

Models that repair the incompleteness of the Standard Model and give dynamical explanations for electroweak symmetry breaking necessarily contain additional particles beyond the Higgs boson. These might be the particles of an extended Higgs boson sector, or exotic partners of the quarks, leptons, and gauge bosons. For many of these particles, there are strong arguments that their masses lie in the ILC energy range. New particles beyond the Standard Model have not yet been discovered at the LHC, but there is still great opportunity to discover such particles when the LHC operates at 14 TeV. The discovery of new strongly interacting particles with TeV masses by the LHC could well point to additional new particles with only electroweak interactions that lie in the ILC energy range.

The discussion in the Physics Volume of the ILC Technical Design Report [1] reviews the current picture of new physics models, incorporating what we have learned from the LHC measurements at 7 and 8 TeV, and surveys the opportunities that these models offer for the ILC experiments. For any new particle in the ILC energy range, the ILC provides a rich program to clarify its properties. The ILC experiments will be able to measure the masses with high precision, determine the electroweak quantum numbers and measure any associated mixing angles, and measure the decay branching ratios in a model-independent way.

In models in which the Higgs boson is composite or a part of a complex new sector, the interactions that lead to the light Higgs boson must also leave their imprint on the Standard Model particles, especially on the top quark and the W and Z bosons that couple to it most strongly. The ILC experiments offer powerful capabilities to measure the electroweak couplings of the quarks, leptons, and gauge bosons. The estimates of the precision expected for probes of electroweak couplings and

Table I-1.1 Major physics processes to be studied at the ILC, together with the lowest centre-of-mass energy at which they can be studied. Shown are the reaction, the process to be studied, and a key indicating which polarisation scenario would bemost advantageous. For more information see the text.

Energy	Reaction	Physics Goal	Pol.
91 GeV	$e^+e^- \to Z$	ultra-precision electroweak	*A*
160 GeV	$e^+e^- \to WW$	ultra-precision W mass	*H*
250 GeV	$e^+e^- \to Zh$	precision Higgs couplings	*H*
	$e^+e^- \to t\bar{t}$	top quark mass and couplings	*A*
350–400 GeV	$e^+e^- \to WW$	precision W couplings	*H*
	$e^+e^- \to \nu\bar{\nu}h$	precision Higgs couplings	*L*
	$e^+e^- \to f\bar{f}$	precision search for Z'	*A*
	$e^+e^- \to t\bar{t}h$	Higgs coupling to top	*H*
500 GeV	$e^+e^- \to Zhh$	Higgs self-coupling	*H*
	$e^+e^- \to \tilde{\chi}\tilde{\chi}$	search for supersymmetry	*B*
	$e^+e^- \to AH, H^+H^-$	search for extended Higgs states	*B*
	$e^+e^- \to \nu\bar{\nu}hh$	Higgs self-coupling	*L*
	$e^+e^- \to \nu\bar{\nu}VV$	composite Higgs sector	*L*
700–1000 GeV	$e^+e^- \to \nu\bar{\nu}t\bar{t}$	composite Higgs and top	*L*
	$e^+e^- \to \tilde{t}\tilde{t}^*$	search for supersymmetry	*B*

discussions of the importance of these measurements to the more general question of the origin of electroweak symmetry breaking are given in in Ref. [1] (Chapters 3,4 and 5). They will supersede the precision of the existing data and enable the study of new physics at energy scales beyond the centre-of-mass energy of the ILC.

Many models of dark matter give as its origin a new stable particle with its mass in the hundred-GeV range. For such models, it would be ideal to collect experimental measurements of the properties of the particle and use these to predict the cosmic density, for comparison to astrophysical observations. A number of examples of models of new physics in which the ILC measurements are sufficiently detailed to make this comparison possible are also shown in Ref. [1] (Chapters 7 and 8).

Models of baryogenesis based on new physics at the TeV scale require new parameters of CP violation in a Higgs boson sector that is necessarily extended beyond that of the Standard Model. Experimental tests of these models require detailed studies of these new Higgs particles. The capabilities of the ILC experiments of carrying out these measurements is described in Ref. [1] (Chapters 6 and 8).

The ILC thus offers a rich experimental program that addresses the most important open issues in elementary particle physics.

1.1.2 Energy and beam polarisation of the ILC

The discussion above of the ILC program on the Higgs boson emphasised the ability of the ILC to run at any energy within its range that might give the greatest physics potential. This is a unique advantage of a linear collider. The accelerator can run with only minor modifications at any energy below its design energy, with instantaneous luminosity roughly proportional to the energy. If higher energy is needed, it is only necessary to make the main linac longer. There are limits, of course, but the ILC is designed to run effectively over a very broad range in energy.

The flexibility of the ILC in energy is described in Table I-1.1, which summarizes the most important reactions that will be studied by the ILC experiments at a range of its possible energy settings. The Higgs boson reactions described in the previous section come into play in an orderly way as the energy of the collider is increased.

The last column of Table I-1.1 describes the importance of polarization in the ILC program. Another important advantage of a linear collider is that it preserves the polarization of an electron or positron beam during the acceleration process. Polarization has central importance in electroweak physics above the Z. At these high energies at which the ILC operates, it becomes obvious that the left- and right-handed spinning electrons are different elementary particles with distinct electroweak quantum numbers. In particular, the left- and right-handed electrons couple differently to the $SU(2)$ and $U(1)$ components of the Standard Model gauge group, so the different polarized reactions access different slices of the electroweak interaction. This increases the power of the ILC in several different respects.

In explanations to follow, $P(-)$ and $P(+)$ are the polarizations for the e^- and e^+ beams, with, for example, $P(-) = -1$ corresponding to 100% left-handed polarization.

H- At the minimum, polarization can be used to enhance the event rate. In e^+e^- annihilation, an electron annihilates a positron of the opposite helicity. The ILC offers beam polarization both for electrons and for positrons. Thus, it is possible to tune the electron and positron polarization to be opposite ($e^-_L e^+_R$ or $e^-_R e^+_L$), enhancing the probability of an annihilation. The increase in the effective luminosity is

$$\mathcal{L}/\mathcal{L}_0 = 1 - P(-)P(+) \ , \tag{I-1.1}$$

giving $\mathcal{L}/\mathcal{L}_0 = 1.24$ for $\mp$80% e^-, $\pm$30% e^+ polarisation.

A- At the Z resonance, in the precision measurement of the electroweak couplings of the top quark, and in precision measurement of $e^+e^- \to f\bar{f}$, the beam polarisation asymmetry is itself an observable containing crucial physics information. The effective polarisation for annihilation reactions is enhanced by the presence of positron polarisation,

$$P_{eff} = \frac{P(-) - P(+)}{1 - P(-)P(+)} \ . \tag{I-1.2}$$

giving $P_{eff} = 89\%$ for $\mp$80% e^-, $\pm$30% e^+ polarisation.

L- Certain Standard Model processes, especially at high energy, occur dominantly from the $e^-_L e^+_R$ polarisation state. Polarising to this state enhances the rates for such processes by

$$\mathcal{L}/\mathcal{L}_0 = (1 - P(-))(1 + P(+)) \ , \tag{I-1.3}$$

or $\mathcal{L}/\mathcal{L}_0 = 2.34$ for -80% e^-, $+30\%$ e^+ polarisation.

B- Conversely, new physics searches at high energy benefit from suppression of the $e^-_L e^+_R$ state to suppress Standard Model backgrounds from WW production and WW fusion processes.

The flexibility of the ILC in the choice of energy and polarisation is exploited in the physics analyses described in the Physics Volume and in the benchmarking analyses presented in this volume. It is a very important advantage of the ILC design that the precise energy and polarisation settings can be chosen year by year in response to ILC discoveries and complementary information from the LHC program.

1.2 Experimentation at the ILC

The arguments in the previous sections show that the ILC is highly motivated on theoretical grounds. But there is another justification for the ILC from a different point of view. The ILC experiments will be carried out with the most precise detectors ever built for general studies of particle interactions at high energy. They will give us an unprecedented view of the dynamics of the Standard Model. These capabilities will drive the detailed study of the Higgs boson and of any other particles that appear in the ILC energy range.

The ILC detectors will improve on the detectors built for LEP and for LHC in the precision of their tracking and calorimetry.

The ILC beams provide an environment so benign that it is possible to design detectors with minimal material in the tracking volume. The angular coverage of the tracking will be enhanced compared to the LEP experiments. The calorimetry will make use of the strategy of particle flow to reduce the uncertainty in calorimetric di-jet mass measurements by a factor of two over what has been achieved at LEP and LHC. These improvements are driven by physics requirements, to obtain the Higgs boson mass at the highest precision, and to discriminate the W and Z bosons in the hadronic decays. They will also bring improvements to event reconstruction in many other aspects of QCD and electroweak measurements.

The ILC detectors will feature pixel vertex detectors that give unprecedented capability to tag displaced vertices from b, c, and τ decays. At a hadron collider, the large rates of QCD events make it difficult to exclude light quarks without sacrificing tagging efficiency.

Finally, the set of physical observables available in e^+e^- annihilation at high energy is intrinsically richer as cross sections and beam polarisation asymmetries contain independent essential pieces of information on the electroweak couplings of the particles under study. In addition, particles with masses above the Z mass have order-1 spin asymmetries in their weak decays. The full structure of these decays can be studied by the detailed event reconstructions available at the ILC.

All of these capabilities can be brought to bear, in particular, in the precision study of the Higgs boson. We have argued above the that study of this particle will be the next major exploration in elementary particle physics, the most direct route that we have now to answering the great questions of the TeV energy scale. The ILC experiments will reveal the Higgs boson in high-precision, low-background observations that encompass all of the major couplings of this particle. It is these experiments that will truly bring the Higgs boson to light.

1.3 Detector challenges and performance requirements

The ILC detectors face new challenges that require significant advances in collider detector performance. The physics goals described in the previous section drive this exceptional performance. The machine environment is benign by LHC standards, enabling designs and technologies that are unthinkable at the LHC. However, the ILC environment poses its own set of background issues that must be overcome. The payoff will be physics studies with unprecedented precision.

The ILC provides a broad spectrum of physics opportunities, which the detector must be prepared to address. These include Higgs Factory, Giga-Z, Top Yukawa couplings, di-boson production, SUSY, and other new physics often motivated by alternative models. Each of these creates its own particular set of requirements. In general, the detectors have been designed to cover the requirements for all such possibilities, over the full range of energy operations. The initial machine is planned for a capability of up to 500 GeV, with energy variability down to 200 GeV, and special running at the Z-pole as well. The upgrade of the energy would bring the operation up to 1 TeV.

The physics opportunities place a premium on high resolution jet energy reconstruction and di-jet mass performance. Consequently, calorimetry must advance beyond current state of the art, and

Particle Flow Algorithm (PFA) calorimetry has been developed to meet this challenge. This technique of energy reconstruction makes use of the fact that many of the energy deposits in the calorimeter (on average about 65% of jet energies) are generated by charged tracks, which are very well measured by the tracker. Separation of such deposits from those generated in the calorimeter by neutral particles (photons and neutral hadrons) results in a much better energy measurement of jets. A calorimeter that can isolate and measure separately each individual particle contribution results in an optimal precision when the neutral energy measured in the calorimeter is combined with the charged energy measured in the tracker. The dominant limit comes from confusion within the calorimeter between the individual particle contributions. This motivates the high granularity of the electromagnetic and hadron calorimeters. New detector technologies and new reconstruction algorithms enable the needed precision of 3 to 4 percent for 100 GeV jets, set by the requirement to separate W and Z di-jet final states to be reached.

The requirements on charged track momentum resolution are driven by Higgs studies, particularly through the Higgs-strahlung process, where the recoiling Higgs is reconstructed from the associated Z boson decaying into a lepton pair. In order to realise this extremely high accuracy, the ILC R&D program has been developing high field magnets and high precision/low mass trackers. The requirement set by the recoiling Higgs reconstruction of $\Delta p/p^2$ of 5×10^{-5} (GeV/c)$^{-1}$ has been achieved.

Flavour tagging, as well as quark charge tagging, will be available at an unprecedented level of performance as a result of the development of a new generation of vertex detectors. New sensor designs have been developed to address the modest, but challenging, ILC backgrounds. The soft beamstrahlung pairs create high occupancies that demand fast readouts, requiring extra power. These factors must be accommodated with very low mass detectors and supports. This is a significant challenge. However, the low duty cycle of the ILC permits power pulsing, which reduces the heat load and the need for cooling.

Muon systems are required for identification, as the inner tracker provides adequate tracking precision for muon momentum measurements. The iron flux return for the detector magnetic field supplies the material needed to identify muons, and also leads to a self-shielded detector.

Significant soft e^+e^- pairs are produced at the interaction point from the beam collision induced beamstrahlung (see machine backgrounds below); the interaction region layout has been designed to guide these charged background particles out of the detector. Optimally, the direction of the magnetic field along the beamline must be directed parallel to the outgoing beam, which passes through the detector off-axis to the main solenoid field direction. This optimal configuration can be achieved through the superposition of the conventional solenoidal field from the detector with a dipole field, produced by adding some dedicated dipole windings to the detector solenoid. Such a so-called Detector Integrated Dipole (DID) becomes effective once the crossing-angle increases beyond a few mrad. For historical reasons, this configuration with the field aligned with the outgoing beam is called anti-DID.

The very forward calorimetry must contend with high backgrounds primarily from the soft e^+e^- pairs that are guided through the detector. These high radiation loads with bunch crossings every few hundred nanoseconds complicate the very forward calorimeter designs. The high energy singly-produced electrons and positrons buried in the large number of pairs must be detected.

Table I-1.2 summarises several selected benchmark physics processes and fundamental measurements that make particular demands on one subsystem or another, and set the primary requirements for detector performance.

Time stamping to an individual bunch train is important for reducing the overlap of events. Two-photon events contribute a particularly strong source of such backgrounds, increasing with

centre-of-mass energy. The ILC time structure with its fraction of a per cent duty cycle (1 millisecond bunch trains at 5 Hz) makes power pulsing a possible and desirable feature for many of the detector subsystems, significantly reducing heat load. Nevertheless, powering the readout electronics of each subsystem, such as the front-end readout chip of the silicon tracker, is a challenge. The readout chips require high current at low voltage with large conductor mass. In order to reduce this mass, power delivery based on serial power or capacitive DC-DC conversion is being studied. In addition, the pulsed power system must deliver quiescent currents.

Table I-1.2. Detector performance needed for key ILC physics measurements.

Physics Process	Measured Quantity	Critical System	Physical Magnitude	Required Performance
Zhh $Zh \to q\bar{q}b\bar{b}$ $Zh \to ZWW^*$ $\nu\bar{\nu}W^+W^-$	Triple Higgs coupling Higgs mass $B(h \to WW^*)$ $\sigma(e^+e^- \to \nu\bar{\nu}W^+W^-)$	Tracker and Calorimeter	Jet Energy Resolution $\Delta E/E$	3% to 4%
$Zh \to \ell^+\ell^- X$ $\mu^+\mu^-(\gamma)$ $Zh + h\nu\overline{\nu} \to \mu^+\mu^- X$	Higgs recoil mass Luminosity weighted E_{cm} BR($h \to \mu^+\mu^-$)	μ detector Tracker	Charged particle Momentum Resolution $\Delta p_t/p_t^2$	$5 \times 10^{-5}(GeV/c)^{-1}$
$Zh, h \to b\bar{b}, c\bar{c}, b\bar{b}, gg$	Higgs branching fractions b-quark charge asymmetry	Vertex	Impact parameter	$5\mu m \oplus$ $10\mu m/p(\mathrm{GeV/c})\sin^{3/2}\theta$
SUSY, eg. $\tilde{\mu}$ decay	$\tilde{\mu}$ mass	Tracker Calorimeter μ detector	Momentum Resolution Hermeticity	

1.3.1 Machine backgrounds

While benign by LHC standards, for optimal performance of the detectors backgrounds must be carefully studied. A variety of processes create beam induced backgrounds in the detectors [202]. The main sources are:

Beamstrahlung

The passage of the two tightly focused beams near each other results in

- disrupted beam;
- photons, radiated into a very narrow cone in the forward direction, where those striking components result in significant backgrounds;
- electron-positron pairs, radiated into the forward direction and steered by the collective field of the opposing beam and the central magnetic field of the detector solenoid.

Synchrotron Radiation

The non-Gaussian tail of each beam passing through, but off axis, the final focusing elements of the beam delivery system near the interaction point generates synchrotron radiation entering the detector.

Muons

The non-Gaussian tail of each beam interacts with collimators defining the aperture of the beam line, generating muons, which are transported through the tunnel to the detector.

Neutrons

Interactions producing neutrons may arise from:

- Beamstrahlung induced e^+e^- pairs which strike beam line components;
- Disrupted beam particles which strike beam line components;
- Backscatter of neutrons from primary beams and beamstrahlung which strike beam dumps.

Hadrons and muon

Electron - Positron pairs created by $\gamma\gamma$ interactions.

Each source has its own character.

Pair Background

Large numbers of e^+e^- pairs created at the interaction point primarily follow the outgoing beams, with the detector solenoid controlling their motion. Some are produced with large enough transverse momenta to enter detector components. Also, the pairs create secondary particles by interacting with detector or collider components. These secondary particles can enter the detector and are another important background source.

Photon Background

The beam-beam interaction at the IP also produces a large number of photons, mostly radiated in the forward direction. While carrying a large amount of energy, they mostly leave with the outgoing beam. However, like the pairs, some generate secondary particles when interacting with forward components, and represent another important source of background.

Synchrotron Radiation Background

Synchrotron radiation photons produced in wakefield-induced beam scattering in the upstream machine elements represent another potential source. An optimised collimation system can control this source.

Beam Halo Muon Background

Muons are produced upstream of the detector when the beam halo interacts with collimators, generating high energy electromagnetic showers. Many muons can be created, and are then relatively easily transported to the detector, generating spurious horizontal tracks.

Summary of Backgrounds

The background sources have been investigated in various studies. For example, the beam-beam interaction and pair generation, radiative Bhabhas, disrupted beams and beamstrahlung photons for the 500 GeV ILC were studied with GUINEAPIG [333]. Also, the $\gamma\gamma$ hadronic cross section was approximated in the Peskin-Barklow scheme [2]. Based on these studies densities of particles which will reach the different sun-detectors have been estimated. Table I-1.3 summarises these estimates.

Table I-1.3 Background sources for the nominal 500 GeV beam parameters.

Source	#particles per bunch	$< \mathrm{E} >$ (GeV)
Disrupted primary beam	2×10^{10}	244
Bremstrahlung photons	2.5×10^{10}	244
e^+e^- pairs from beam-beam interactions	75k	2.5
Radiative Bhabhas	320k	195
$\gamma\gamma \rightarrow$ hadrons/muons	0.5 events/1.3 events	–

1.3.2 Beam Instrumentation

Precise knowledge of beam parameters is critical to the ILC physics program. Luminosity, beam energy, and polarisation are measured by instrumentation close to the main detectors, which are described in more detail in Chapter 2.

Luminosity measurement: Accurate knowledge of the luminosity is required, both the energy-integrated luminosity, as well as the luminosity as a function of energy, dL/dE. Low-angle Bhabha scattering detected by dedicated calorimeters can provide the necessary precision for the integrated luminosity. Acollinearity and energy measurements of Bhabha events in the polar angle region from 120-400 mrad can be used to extract dL/dE.

Beam energy measurement: Beam energy measurements with an accuracy of (100-200) parts per million are needed for the determination of particle masses, including m_{top} and m_{Higgs}. Energy measurements both upstream and downstream of the collision point are foreseen by two different techniques to provide redundancy and reliability of the results.

Polarisation measurements:. Precise measurements of parity-violating asymmetries require polarisation measurements with a precision of 0.25% or better. High statistics Giga-Z running requires polarimetry at the 0.1% level. The primary polarisation measurement comes from dedicated Compton polarimeters detecting the backscattered electrons and positrons. The best accuracy is achieved by implementing polarimeters both upstream and downstream of the IR.

1.3.3 Two detectors

The scientific productivity of collider facilities, such as the Tevatron, LEP, HERA, and the LHC, has benefited from independent operation of multiple experiments. This leads to operation of detectors with complementary strengths, cross-checking and confirmation of results, reliability, insurance against mishaps, competition between collaborations, as well as increased number of involved scientific personnel, all contributing to enhanced scientific success. Such complementary efforts benefit from independent software systems and differing philosophies and methodologies. There are numerous historical examples where this complementarity was essential, such as the inability of UA2 to confirm the mistaken claim for top quark discovery by UA1. Therefore, the ILC has been designed to enable two experimental detectors to share one interaction region.

Through the process described elsewhere in this report, two detector designs have been developed with complementary features. These detectors are described in detail in the following section, where first SiD is described followed by ILD. Both experiments are designed to achieve the ILC precision measurements and searches for new physics.

SiD is a compact, cost-constrained detector made possible with a 5 Tesla magnetic field and silicon tracking. Silicon enables time-stamping on single bunch crossings to provide robust performance. The highly granular calorimeter is optimised for particle flow analysis.

The ILD design results in a large detector optimised for good energy and momentum resolution, with flexibility for operation at energies up to the TeV range. It employs a highly granular calorimeter, with minimal material between the interaction point and the calorimeter. The tracker is a Time Projection Chamber (TPC) providing continuous tracking for excellent pattern recognition and dE/dx capability.

Each detector can be alternately be moved to the beam line to operate with collisions by way of the push-pull system. The push-pull system is designed with the detectors and associated infrastructure arranged to enable quick movement of each detector into and out of the interaction region. The details of this have been studied, and resulted in specific layouts. The alignment of detectors must be re-established after each movement, and procedures are being developed for this.

Figure I-1.2 shows the display of two simulated events showing two different configurations as they will be seen by the two detectors.

1.4 Physics benchmarks studies

Benchmark reaction processes have been defined for the detector groups to assess the performance level of each detector. A set was first produced for the detector Letters of Intent (LOIs) [3], and later a few additional processes were added for the Detailed Baseline Design efforts. Benchmark studies can demonstrate the performance of the overall detector concept, as well as quantify the physics reach of the experiment.

The LOI benchmarks [3] were designed to measure and demonstrate the performance of the overall detector concept at energies up to 500 GeV. The benchmarks specified for the DBD were defined to assess the detector performance up to 1 TeV.

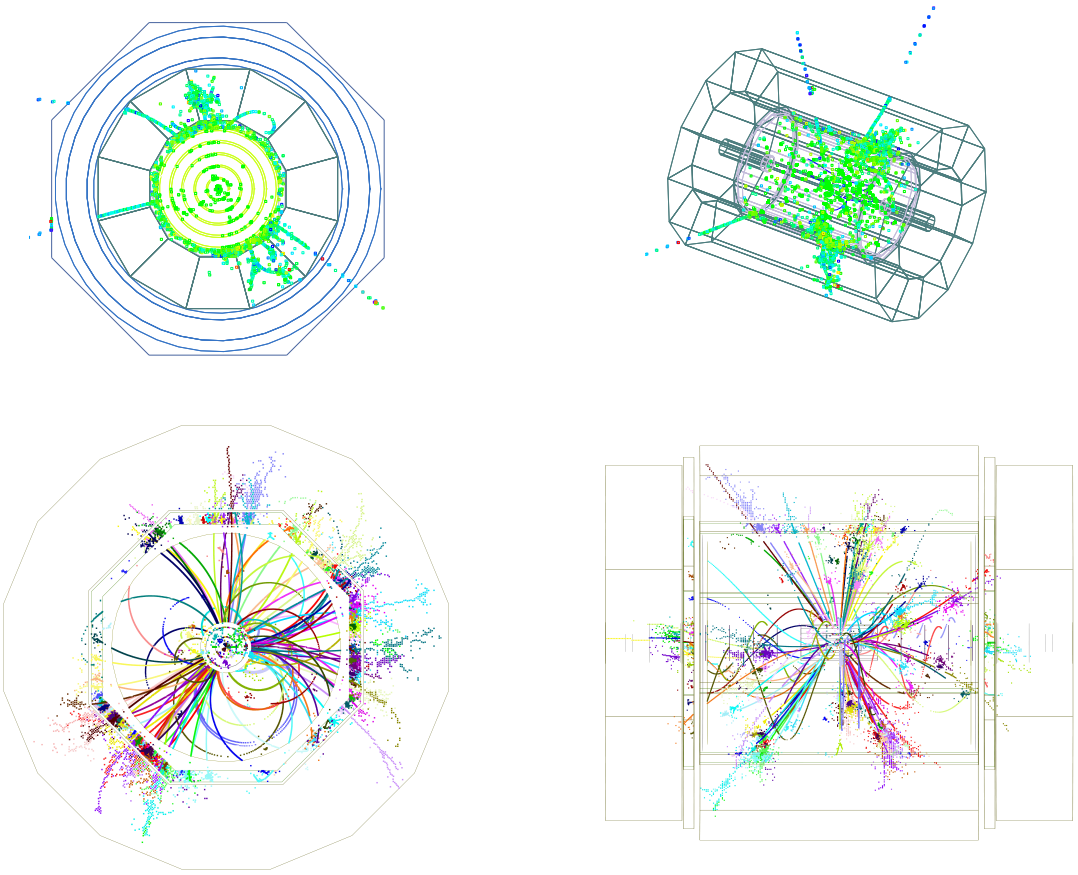

Figure I-1.2. Two event displays for: (up) $e^+e^- \to Zh; Z \to \mu^+\mu^-; h \to b\bar{b}$ at 250 GeV from SiD and (down) $e^+e^- \to t\bar{t}h; t\bar{t} \to 6q; h \to b\bar{b}$ from ILD at 1 TeV.

1.4.1 Definition of the first set of benchmark processes (250, 500 GeV) for the LOI

The first set of benchmark reactions was defined for the LOI [3]. For each reaction, the performance for both 250 fb^{-1} for $\sqrt{s}$ = 250 GeV and 500 fb^{-1} for 500 GeV was requested.

1. $e^+e^- \to Zh$, $Z \to e^+e^-$ or $\mu^+\mu^-, h \to X$ (M_h = 120 GeV, $\sqrt{s}$ = 250 GeV), measuring the Higgs mass and the cross section. These processes test: a.- momentum resolution, b.- material distribution in the detector, in particular in the tracker, and c.- photon ID;

2. $e^+e^- \to Zh$, $h \to c\bar{c}$ and $\mu^+\mu^-$, $Z \to \nu\overline{\nu}$ (M_h = 120 GeV, $\sqrt{s}$ = 250 GeV), measuring the BR($h \to c\bar{c}$) and the BR($h \to \mu^+\mu^-$). These final states check: a.- heavy flavour tagging, secondary vertex reconstruction, b.- multi jet final state, c-tagging in jets, uds anti-tagging (particle ID), and c.- anti-tagging by studying the $h \to gg$ channel;

3. $e^+e^- \to Zh$, $h \to c\bar{c}$, $Z \to q\overline{q}$ (M_h = 120 GeV, $\sqrt{s}$ = 250 GeV), measuring BR($h \to c\bar{c}$). In addition to the charm tagging, this final state tests the confusion resolution capability;

4. $e^+e^- \to \tau^+\tau^-$ ($\sqrt{s}$ = 500 GeV), measuring efficiency and purity, as well as cross section, forward-backward asymmetry (A_{FB}) and P_τ (τ polarisation). These channels test: a.- tau reconstruction, aspects of particle flow, b.- π^0 reconstruction, and c.- tracking of very close-by tracks;

5. $e^+e^- \to t\bar{t}$, $t \to bW^+$, $W^+ \to q\overline{q'}$ (M_{top} = 175 GeV, $\sqrt{s}$ = 500 GeV), measuring cross section, forward-backward asymmetry (A_{FB}), and m_{top}. This tests the following: a.- multi jet final states, dense jet environment, b.- particle flow, c.- b-tagging inside a jet, d.- lepton

tagging in hadronic events (b-ID), and e.- tracking in a high multiplicity environment;

6. $e^+e^- \to \chi^+\chi^-$ / $\chi_0^2\ \chi_0^2$ ($\sqrt{s}$ = 500 GeV), for SUSY parameter point 5 of Table 1 of [4], measuring cross section and masses.These channels test the following: a.- particle flow (WW, ZZ separation), and b.- multi-jet final states.

The above reactions represent a minimum number of physics processes that were studied for the LOI and in fact they are far from all physics studies envisioned but are representative tests of the detector capabilities. The next reactions are of very high importance for the physics reach of the ILC project. However they were considered less relevant to the optimisation of the detector parameters, or had overlap with other reactions included in the list above. These are:

1. $e^+e^- \to Zhh$, While this reaction is very challenging for the particle flow performance, it has a very small cross-section, and as such not well suited for a detector study or optimisation. However, it is a very important physics goal;
2. secondary vertex reconstruction and quark charge measurement. This reaction is very important for the optimisation of the vertex detector. It relies on very sophisticated vertexing tools to be fully implemented;
3. low mass difference between SUSY states (low ΔM SUSY). This tests the detector in the very forward direction, including the electron veto capability in the extreme forward region.

1.4.2 Definition of the second set of benchmark processes (1 TeV) for the DBD

A supplementary set of processes was defined for the DBD. Motivated by the important open questions regarding the scaling of the detector performance to the higher energy of 1 TeV, a few reactions were chosen based on their usefulness in studying this.

These processes were to be carried out with event samples of 1 ab^{-1}. The electron and positron polarisation was assumed to be consistent with the estimate from the GDE for 1 TeV, close to 80% and 20%, respectively The sample should be equally divided between the configurations (-/+) and (+/-) [5].

1. $e^+e^- \to \nu\bar{\nu}h$ at $\sqrt{s}$ = 1 TeV, where h is a Standard Model Higgs boson of mass 125 GeV, in the final states $h \to \mu^+\mu^-$, $b\bar{b}$, $c\bar{c}$, gg, WW*. The goal is to measure the cross section times branching ratio for these reactions;
2. $e^+e^- \to W^+W^-$ at $\sqrt{s}$ = 1 TeV, considering both hadronic and leptonic (e, μ) decays of the W. The goal is to use the value of the forward W pair production cross section to measure in situ the effective left-handed polarisation $(1 - P_{e^-})(1 + P_{e^+})/4$ for each of two polarisation configurations;
3. $e^+e^- \to t\bar{t}h$ at $\sqrt{s}$ = 1 TeV, where h is a Standard Model Higgs boson of mass 125 GeV, in the final state $h \to b\bar{b}$. The reaction involves final states with eight jets and final states with six jets, one lepton, and missing energy. The goal is to measure the top Yukawa coupling.

1.5 The Physics and Detector Study of the International Linear Collider

The physics and detector studies matured from a Letter-of-Intent (LOI) process started in 2007. As the plan to develop a technical design for the ILC unfolded, the ILC Steering Committee (ILCSC) [6] recognised the importance of defining detailed detector concepts so that they could be considered in the design of the ILC, addressing issues of the interaction region and demonstrating the feasibility and the capability of pursuing physics at ILC, and they initiated the LOI process. The framework and various milestones of the process are described briefly in this introduction. More details can be found in the Interim Report [7].

1.5.1 Call for LOIs

In October 2007, the ILCSC announced a call for Letters of Intent to produce reference designs for two detectors for the ILC [8]. When the GDE published the ILC Reference Design Report in summer 2007, there were four detector concepts in its detector volume. The call for LOIs was intended to lead the community to form two capable groups that would develop their concepts to a technically advanced stage and produce detailed baseline designs at the same time as the GDE's accelerator Technical Design Report. The submitted LOIs were reviewed by an advisory body called the International Detector Advisory Group (IDAG). In order to conduct the LOI procedure, the ILCSC appointed Sakue Yamada as Research Director, who was to set up a management structure and to recruit the IDAG members.

1.5.2 The management formation

With consultation and agreement of the ILCSC and the steering body of each region, the Research Director invited the three co-chairs of the World Wide Study (WWS) [9, 10] to join the management team as the regional contacts. This management structure ensured good communication with the detector community during the tenure of the Research Director, a period of continued R&D and preparation for realization of the ILC.

Jim Brau from North America, Francois Richard from Europe and Hitoshi Yamamoto from Asia joined the management by January 2008. Later, from February 2011, Juan Fuster took over the role of the European regional contact.

The IDAG was formed with the approval of ILCSC as listed in Table I-1.4.

Table I-1.4
Members of the international detector advisory group, IDAG

Exp. & Det.	Michael Danilov	ITEP
	Michel Davier (Chair)	LAL/Paris Sud
	Paul Grannis	Stony Brook
	Dan Green	FNAL
	Dean Karlen	Victoria
	Sun-Kee Kim	SNU
	Tomio Kobayashi	Tokyo
	Weiguo Li	IHEP
	Richard Nickerson	Oxford
	Sandro Palestini	CERN
Phenomenology	Rohini Godbole	IIS
	Christophe Grojean	CEA-Irfu/CERN
	JoAnne Hewett	SLAC
Accelerator	Eckhard Elsen	DESY
	Tom Himel	SLAC
	Nobu Toge	KEK

1.5.3 Organisation of detector activity

The organisation of the detector activity is illustrated in Figure I-1.3. It has a decision making body, various working bodies, links to the outer community for necessary cooperation and a central management. Much of the detector R&D and physics simulation was carried within the concept groups, which cooperate with various R&D collaborations. Each group designed a detector system following its concept and carried out the R&D work outlined in its LOI. In this process it was thought that cooperation among the separate concept groups would be important.

There were certain tasks like the push-pull studies that could be pursued only with close cooperation among the concept groups and with the accelerator's beam delivery system team. Also, sharing of commonly needed tasks was encouraged in order to optimise the outcomes. In order to facilitate such cooperation and communication among the concept groups, there were common task groups (CTG) consisting of members from all the concept groups and, where necessary, members

Figure I-1.3
ILC detector management organisation

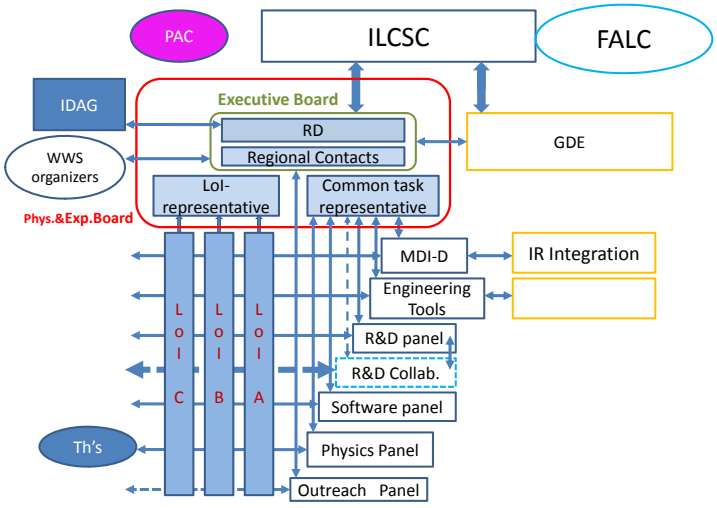

from the wider detector R&D and/or theory communities.

Three LOI groups were identified by a call for Expression of Interest (EOI) announced in February 2008. They were ILD (International Large Detector), SiD (Silicon Detector) and Fourth. The Physics and Experiment Board (PEB) is the decision-making body, which started out with representatives of the LOI groups and the management members.

The five common task groups were set up by end of May 2008; the machine-detector interface (MDI) group, engineering tools group, detector R&D group, software group and physics group. The MDI group established a link to the beam delivery system group of the GDE and had to start immediately. For the detector R&D common task group, several horizontal R&D collaborations, such as calorimetry or tracking, were asked to send representatives to maintain good communication. The physics common task group included additional theory members. The PEB became filled by Summer 2008 with the conveners of the common task groups.

1.5.4 The LOIs and their validation

The Letters of Intent were submitted from the ILD, SiD and Fourth groups by the due date, March 2009 [11, 12, 13]. They were examined by the IDAG in detail. Following multiple interviews with the concept groups IDAG made its recommendations for validation in August 2009. The conclusion that ILD and SiD should be validated was presented by the RD to the ILCSC and was approved. During the ALCPG workshop in Albuquerque, USA, in September 2009, the IDAG examination and validation were reported by the chair [14].

The validation was a clearly defined milestone and the validated groups were authorised to proceeed toward the final goal, the completion of the detailed base line designs of their detector concepts. The organisation of the detector activity was modified accordingly.

IDAG monitored further the activities of the validated groups and also the activity of the common task groups. ILCSC extended the mandate of the IDAG, keeping the same membership, through to the end of the DBD process.

1.5.5 Work for the detailed baseline designs

The validated groups prepared detailed plans with milestones for key items to reach the final goal. In order to guide this, the RD directorate and the IDAG agreed on nine crucial items to be included in the planning such as; completion of R&D for critical detector components for their feasibility proof, defining a detailed baseline design of the detector system, completing basic integration of the baseline design accounting for insensitive zones, setting up a realistic model of the detector for physics simulation, completion of studies of a push-pull scheme and integration into the interaction region, making physics simulations for the new set of benchmark reactions at 1 TeV, and improving the cost estimate.

The plan of each group was produced by October 2011 with a caveat that it was made under the assumption that necessary resources would become available in due course. It was agreed that all the efforts be made in order to satisfy the minimum requirement for each item. This was achieved as is described in this report. An indispensable element for the success of the project is the close cooperation between the two groups under the consensus that limited resources need to be shared efficiently wherever possible. Also, in some area of the studies cooperation with the CLIC detector group was helpful.

IDAG monitored the progress regularly twice a year, during the LC workshops and gave timely suggestions for improvement. At the meeting in April 2012, IDAG reviewed the outlined contents of DBD prior to drafting, and finally it reviewed the entire draft in October, 2012.

1.5.6 The common task groups

The common task groups aimed to solve issues which are common to the both concept groups. Each of the five common task groups had specific roles. The members were provided from the both concept groups and, where appropriate, also from the wider communities or detector R&D collaborations. Each CTG was represented in the Physics and Experiment Board. They made substantial achievements as described in the next chapter. Here a brief introduction is given for each common task group.

Machine Detector Interface group This group worked on all the matters related to the interplay of the detector with the accelerator. It had a close link to the accelerator colleagues working on the beam delivery system and the experimental hall design. One of its important objectives was a push-pull mechanism for the two detectors which allows quick and stable operation both for the detectors and the collider. The group contributed much in the discussions with the accelerator team on the design of the beam parameters, as well.

The members are: Karsten Buesser (convener), Phillip Burrows (deputy), Alain Hervé, Thomas Markiewicz, Marco Oriunno and Toshiaki Tauchi.

Engineering Tool Group This group worked to find a common engineering design tool, which could used by the two groups, and also with the accelerator team. Once a scheme was defined, the group tried to make it familiar to the both groups. This effort was very effective though given the limited resources available.

The members are: Catherine Clerc (convener), Alain Herve, Kurt Krempetz, Thomas Markiewicz, Marco Oriunno (deputy), and Hiroshi Yamaoka.

Detector R&D group The group facilitated various ways to promote detector R&D studies. It made a contact point to the various horizontal R&D collaborations, which are independent bodies but play crucial roles for developing the ILC detector components. In order to keep good communication with these collaborations, major R&D collaborations sent representatives to this group. One of the outcomes was a survey of the spin-off technologies that emerged from the ILC R&D activities.

The members are:Dhiman Chakraborty, Marcel Demarteau (convener), John Hauptman, Ronald

Lipton, Wolfgang Lohmann (deputy), Burkhard Schmidt, Aurore Savoy-Navarro, Felix Sefkow, Tohru Takeshita, Jan Timmermans, Andrew White, Marc Winter.

Software Group This group worked to prepare necessary simulation tools and to produce common event samples for the benchmark studies. Due to the limited human resources, sharing tasks for the new benchmark simulation was crucial. The group coordinated this in an effective way. It also had close contact with the CLIC simulation team.

The members are: Frank Gaede, Norman Graf (deputy), Tony Johnson, Akiya Miyamoto (convener).

Physics Group This group began its work to understand the physics issues associated with the case for the ILC and the priorities of its experimental program. The group was made of representatives of the concept groups, plus a number of interested theorists. The group also carried out various physics studied requested by the management. This group tracked the progress of the LHC experiments to investigate their implications to the ILC program. Most recently this group organised the writing of the Physics volume of this report.

The members are: Tim Barklow, Stewart Boogert, Seong Youl Choi, Klaus Desch, Keisuke Fujii(deputy), Youannning Gao, Heather Logan, Klaus Moenig, Andrei Nomerotski, Michael Peskin(convener), Aurore Savoy-Navarro, Georg Weiglein(deputy), Jae Yu.

1.5.7 Other working groups

In addition to the original five common task groups, more working groups were created subsequently to solve specific tasks in a relatively short period.

A typical case is the SB2009 working group, which was organised soon after the ALCPG workshop, 2009 in Albuquerque, to study the effects of the proposed SB2009 accelerator parameters on experiments. The members include representatives of the concept groups, related Common Task Groups (MDI, Software and Physics), and some theorists, and was convened by James Brau of the management. This group made a contact point with the accelerator team to communicate systematically and organise necessary works like simulations using the given beam parameters. It continued further to discuss with the accelerator group on the beam parameters for the simulation of benchmarks at 1 TeV. Details of its activity are described in the Interim Report[7].

There was a working group for the new benchmarks to be added for the DBD. It was led by the physics common task group and worked with the representatives of the two groups and the software common task group. It made a report on the list of priority- and work-sharing for each possible physics channel as introduced in the previous section.

We had a common costing working group to coordinate costing methodology between the two groups. The group also learned from the accelerator costing how to handle the inflation or the changes of currency exchange rates. More details of the group are presented in the next chapter.

The CLIC-ILC joint working group was initiated in early 2010 following the discussions of the ILCSC. It surveyed ongoing cooperation and looked for further synergies between the two linear collider detector activities. Before this working group was formed, there had already been much grass root cooperation since 2008. The cooperation has become more intensive since CLIC deployed the two ILC concepts for its detectors. There was an overlap of the members who prepare both CLIC Conceptual Design Report and the ILC DBD. More description can be found in the Interim Report [7].

1.6 The World Wide Study

The World Wide Study of Physics and Detectors for Future Linear e^+e^- Colliders (WWS) was organised in 1998 to give voice to the community of physicists interested in the realisation of the linear collider. The WWS OC (organising committee) is a broadly representative formal committee selected by each region from the WWS members. Since its formation in 1998, the WWS, mostly represented by the WWS OC, initially served a number of roles:

- voice the views of the global linear collider physics community,
- formulate the physics justification for the linear collider and promote its case in the broader physics community,
- coordinate the work of the three regional linear collider studies,
- organise the program for the series of linear collider workshops (LCWS),
- serve as a physics and detectors subcommittee of the ILCSC.

The WWS has remained independent from any other organisation, with no official role in any project based organisation of the linear collider effort (GDE, Research Directorate, CLIC study group etc.). When the ILC Research Directorate was created in 2007 under the leadership of Sakue Yamada, many of the WWS ILC specific studies were integrated into the ILC Research Directorate and the role of the WWS narrowed somewhat. Nevertheless, many of the roles outlined above remained for the WWS.

The WWS represents a broad community of physicists interested in the physics and detectors of a linear collider. All linear collider options are addressed and promoted; the WWS provides a forum for the open comparison among possible directions. In particular, it provides the principal forum in which theorists and experimentalists discuss and elaborate the linear collider. It engages and motivates theorists to do studies critical to developing and explaining the scientific case for the linear collider. Additionally, the WWS gives a voice to the diverse set of universities and research institutes that must be mobilised in support of the linear collider. It also connects to the broader particle physics community that is not currently directly involved in the linear collider activities. Finally, it speaks with an independent voice, on issues of physics requirements, organisation, and other relevant issues, always with positive motivation.

The WWS has been a valuable resource to the overall effort, being drawn on when needed to provide additional services beyond those explicitly outlined above, such as providing the membership for the parameters committee that established the requirements for the ILC design and initiating the development of detector concepts which paved the way to the development of detector LoIs and detailed baseline designs presented in this report.

Chapter 2
Description of Common Tasks and Common Issues

In this chapter the common tasks and issues of the two detector concepts are presented. They are the outputs of common efforts between the two concept groups with a wider community as well as with the accelerator team. The joint approach was necessary and effective to share loads under limited resources for various common goals and also to contact the BDS and CFS teams of the accelerator group in a well coordinated manner. Those works were carried out mostly through the common task groups, which were organised for this purpose from the very beginning. For the detector R&D programs various cooperative relations were formed with many R&D collaborations. While each detector group collaborated with R&D collaborations depending on its detector component, there was also regular contact with major R&D collaborations through the detector R&D common task group in order to facilitate better communication. All these efforts were indispensable for the presented accomplishment of the two detector groups.

While each group will describe specific items relevant to the concept in its chapter, the most common items or very similar items are described in this section. Covered topics are common detector R&D, common simulation and software tools, machine-detector interface issues including the push-pull scheme, common engineering tools, beam instrumentation for the energy and polarisation measurements and detector costing methodology.

2.1 ILC Detector Research and Development

Because of the well-defined initial state, an electron-positron collider offers the possibility to carry out measurements with an unprecedented level of precision. To realise this exceedingly high level of measurement accuracy, stringent requirements are placed on the performance of the detectors. In some cases, this calls for innovative detector designs employing new detector technologies. Novel analysis techniques are also proposed. For example, the particle flow reconstruction introduced at LEP [15] has been developed to new levels of performance by addressing the challenges posed for the detectors. The operational conditions of the machine allow for a unique way to operate the detectors which, if demonstrated to be feasible, would provide significant advantages. This chapter first introduces some concepts common to both detectors. This is followed by a description of the research and development projects that are necessitated by the physics and as such are shared by the proposed experiments. Detector concept specific R&D is discussed in the respective chapters of the SiD and ILD sections in this report. It should be noted that the potential merits of this research and development work reaches far beyond the ILC for most efforts.

2.1.1 Overview of the overall detector strategies

Many of the interesting physics processes at the ILC will be characterised by multi-jet final states. The reconstruction of the invariant masses of two or more jets will provide a powerful tool for event reconstruction and event identification. The physics at the ILC requires a clean separation of the hadronic decays of the W- and Z-boson. An invariant mass resolution comparable to the gauge boson widths, i.e. $\sigma_m/m = 2.7\% \approx \Gamma_{\mathrm{W}}/\mathrm{m_W} \approx \Gamma_{\mathrm{Z}}/\mathrm{m_Z}$, leads to an effective separation of better than 3 σ in the mass peaks of the hadronic decays of the vector bosons. To achieve this unprecedented mass resolution, the ILC detectors have adopted the particle flow approach by combining calorimetry and tracking. In contrast to a purely calorimetric measurement, particle flow calorimetry requires the reconstruction of the four-vectors of all visible particles in an event. The jet energy reconstruction then proceeds as follows. First, the energy deposits in the calorimeter are identified. The momenta of all charged particles are then measured in the tracking detectors. The energy deposits in the calorimeter are then associated with the charged particle tracks. To reconstruct the jet energy, the measurement of the momentum in the tracker is used rather than the measurement of the energy in the calorimeter since the tracker has superior resolution and the energy deposits in the calorimeter associated with the tracks are removed. Only the energy measurements for photons and neutral hadrons are obtained from the calorimeters. In this manner, the poor hadronic energy resolution affects only about 10% of the energy in the jet and a jet energy resolution of about $0.19/\sqrt{\mathrm{E(GeV)}}$ would be ideally obtained. In practice, this level of performance cannot be achieved as it is impossible to perfectly associate all energy deposits with the correct particles. For example, if part of a charged hadron shower is identified as a separate cluster, the energy is associated with a neutron and effectively double-counted as it is already accounted for by the track momentum. Similarly, when a photon and hadronic particle are close together, hits originating from one could be assigned to the other and not be accounted for. These effects are called "confusion" and represent the limiting factor in particle flow calorimetry. The concept of particle flow calorimetry relies crucially on the ability to correctly assign calorimeter energy deposits to the correct reconstructed particle. This in turn drives the calorimeters to be highly granular, both longitudinally as well as transversely, a trademark of the ILC calorimeters. For ILC detectors, jet energy reconstruction has evolved into a very complex pattern recognition problem.

Those requirements have spurred the development of new technologies for calorimetry. Figure I-2.1 shows the "technology tree" of all technologies being pursued by the CALICE LC calorimetry collaboration for both electromagnetic as well as hadronic calorimeters. As an absorber medium, both tungsten and iron are being studied with both analogue and digital readout. A plethora of active media are being studied ranging from scintillators with novel SiPM readout, silicon based monolithic active pixel sensors (MAPS) to gaseous detectors such as Resistive Plate Chambers (RPCs) and Micromegas. Granularity of the readout can range from 3x3 cm^2 pixel size to 50x50 $\mu\mathrm{m}^2$ for the MAPS-based electromagnetic calorimeter.

ILC detectors must have complementary properties operating as a single unit therefore an excellent tracking performance goes hand-in-hand with the concept of particle flow calorimetry. The tracking technologies being considered are either silicon- or gaseous-based. For the former, silicon strip technology is being considered but also highly pixelated silicon sensors are an option. A Time Projection Chamber (TPC) is the detector being considered for gaseous based tracking in which ionisation generated by a traversing charged particle will drift towards the endplate where the signal is amplified and processed. The Micromegas, GEM and CMOS technology are being studied within the Linear Collider TPC collaboration.

An important physics goal at the ILC is the identification of hadronic jets originating from heavy quarks. This is best achieved by a topological reconstruction of the displaced vertex structure and the kinematics associated with their decays. The ability to reconstruct the sequence of primary, secondary

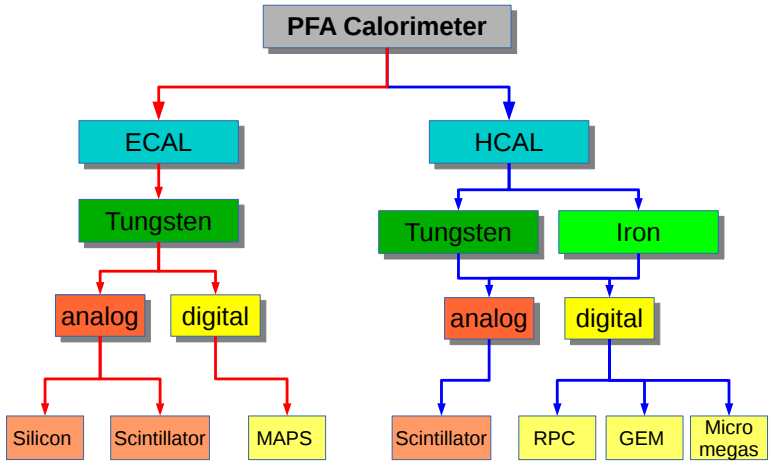

Figure I-2.1
Tree of electromagnetic calorimeter technologies -ECAL- (left) and hadron calorimeter technologies -HCAL- (right).

and tertiary vertices depends on the impact parameter resolution and the track reconstruction capability. These in turn are related to the single point resolution of the sensors, the location of the first measurement, and the overall occupancy in the detector. To meet the ILC requirements this leads to fine pitch, low-mass pixel vertex detectors as close to the interaction point as possible. The material budget desired is about 0.1% X_0 per layer for the vertex detector and less than 1% X_0 per layer for a silicon tracker. For a TPC the material budget is accumulated in the end plates and a material budget of 30% X_0 per endplate is the goal. The ILC concept detectors have not decided on a baseline technology for the vertex detector and all technology options are considered common and are described in more detail in the next section.

To achieve an ultra low-mass detector configuration, a unique feature of the ILC machine is exploited. The ILC time structure results in collisions of bunches at the interaction point every 308 ns. Bunch trains consisting of 2820 bunches in each beam pass through the interaction point five times per second. Consequently, the bunch trains are about one millisecond long, separated by about 199 milliseconds. The detector can thus be put in a quiescent state for 199 out of 200 milliseconds at the machine repetition rate of 5 Hz, since there are no interactions during this period. This is referred to as "power-pulsing". Allowing for transient times, to turn the detector "on and off" and starve the system of power, power-pulsing could lead to an overall reduction in power consumption of nearly a factor of hundred. This feature is employed by both detector concepts. One of the most significant benefits of power-pulsing is that the vertex and tracking detector does not need active cooling. This significantly lowers the overall mass budget for these detectors, which is crucial for obtaining the required resolutions. It is expected that a heat load of about 20W for the barrel vertex detector can be removed using forced convection with dry air.

The feasibility of power-pulsing has already been demonstrated for several technologies. System tests at full magnetic field strengths and an evaluation of the mechanical stability under pulsed power still need to be performed. Test are being planned by both detector concepts of detectors with balanced load lines in high magnetic fields to measure the detector alignment stability.

2.1.2 Vertex Detector Technologies

Within the ILC many different pixel sensor technologies are being studied. Integration of the sensing node with front-end signal processing circuitry in a single unit is a key characteristic shared by many efforts. The aim is to go to very small pixel size for superior impact parameter resolution and minimisation of pattern recognition ambiguities, ultra-thin detectors to minimise the material budget and low power to eliminate the need for active cooling. The Monolithic Active Pixel Sensor (MAPS) technology implements a high density matrix of pixels with signal processing circuitry on the same

substrate as the sensitive volume. The DEPFET technology implements a single active element within the active pixel. The CMOS Pixel Sensor (CPS) technology is able to integrate a full front-end signal processing chain with correlated double sampling in each pixel. In the 3D and Silicon-On-Insulator (SOI) technology the sensing and processing functionalities are separated in different layers. In the SOI technology, the sensing is provided by a high-resistive substrate connected through an insulating layer with the processing layer. In the 3D technology each function is fully separated in different wafers, processed independently, which are then bonded together. All of these technologies have the capability of delivering sensors less than 75 μm thick with better than 5 μm hit resolution and low power consumption.

Fine Pixel Charged Coupled Devices (FPCCDs) allow for particularly small pixels, 5×5 μm^2, which results in a sub-micron spatial resolution and excellent two-track separation capability. The fine segmentation also mitigates occupancy issues and thus allows for integration over numerous bunch-crossings. The CCDs have to be operated at cryogenic temperatures and the detector would need to be installed in a light foam cryostat. Prototype devices have been made and sub-micron position resolution has been achieved. The FPCCD instantaneous power consumption is moderate and a slow signal processing in between consecutive bunch trains can be envisaged.

The DEPFET concept integrates a p-MOS transistor in each pixel on the fully depleted, detector-grade bulk silicon [16]. Electrons, produced in the bulk through ionising radiation are collected in the internal gate and modulate the transistor current. Their low input capacitance ensures low noise operation and makes them suitable for a broad range of applications from collider detectors to X-ray astronomy. Even though the first formulation of the concept goes back to the 1980s, it took nearly two decades before progress in silicon processing capabilities at HEP institutes and industry allowed it to be possible to turn the idea into a complete detector concept. A DEPFET sensor generally is a 700×250 matrix of 50×50 μm^2 pixels. Auxiliary readout is integrated on the edge of the sensor, which allows thinning to 50 μm in the sensitive region, using an etching technique, retaining a frame which ensures the stiffness of the mechanical module. The sensors are read out in "rolling shutter"mode with a frame rate of 50 kHz. Many prototype devices were produced and tested to demonstrate the viability of the concept and to establish DEPFETs as a mature technology for vertex detectors [17].

A considerable effort is going into the development of MAPS detectors, notably the CMOS Pixel Sensors (CPS). Matrices with 1152×576 pixels, with 18.4 μm pitch with a column parallel read-out architecture with amplification and correlated double sampling inside each pixel have been demonstrated [18]. A spatial resolution approaching 3 μm has been achieved with binary charge encoding. The current architectures are being extended to address the critical ILC specifications. The Chronopixel sensor is a monolithic CMOS pixel sensor, which has the capability to record the time of each hit with sufficient precision to assign each hit to a specific bunch crossing of the collider. This reduces the backgrounds due to integration over many beam crossings to a virtually negligible level. Two prototype devices were built to date with a pixel size of 50×50 μm^2 in a 180 nm process. The design for the final device calls for a pixel size of 15×15 to 20×20 μm^2, which requires a 45 nm technology which is impractical for prototypes. Progress with the prototype devices is very good and indicate good signal to noise performance, reasonable power consumption, good circuit flexibility and adequate charge collection in the epitaxial layer in the presence of sophisticated front-end electronics.

In microelectronics, 3D technology refers to the stacking of multiple thin layers of circuitry with vertical interconnections between them. This area is developing rapidly as a way of increasing circuit density without the major retooling and investment needed for smaller feature size.The enabling technologies for 3D are wafer thinning, aligning and bonding, and the formation of Through-Silicon Vias (TSVs). Although the increased circuit density provided by multi-layer circuits is in itself an important application for High Energy Physics, it is the increased range of processing and interconnection options

that the technology provides that has the most potential. Using these technologies arrays of chips can be bonded to sensors and electronics to form essentially monolithic arrays of sensors with no dead space between chips and with interconnections taken from the back rather than the edge of the IC. The Vertically Integrated Pixel (VIP) chip was conceived as a demonstration readout chip for the ILC vertex detector. The first version of the chip (VIP2a) was a three-tier device produced at MIT Lincoln Laboratory using a fully depleted SOI process [19]. A major success was that all of the interconnections between the circuit layers worked. A second iteration, the VIP2b was fabricated in the 3D process developed by Tezzaron/Global Foundries. This process uses a bulk 130 nm CMOS process with modifications to allow the top copper metal layer to be used for face-to-face wafer bonding, and to include vias that extend 6 μm into the bulk material. Initial testing of the 2D parts show excellent analog performance. Tests of the full functionality of the 3D chips are underway.

Active edge sensors are an outgrowth of work done to develop 3D sensors, which provide good charge collection combined with radiation hardness and yields sensors that are active over its full area. Combination of active edge technology with 3D integration can provide a technique for tiling complex shaped areas with fully active sensor arrays with no dead regions.

The development of vertex detector technologies within the framework of the ILC is a poster child for technology spin-off to other areas of the field and synergy with other scientific disciplines [20]. The DEPFET technology has been adopted by the BELLE-II collaboration at the KEK b-factory as the baseline design for their vertex detector; the MAPS sensors are developed for the STAR experiment and the next generation of sensors are being considered for the ALICE Inner Tracker System upgrade. The 3D technology is a candidate technology for the LHC tracker upgrades. Because of the extensive R&D carried out under the ILC umbrella, these projects had a mature technology available to be taken to the detector stage. Other applications of the DEPFET concept are X-ray imaging in space experiments and at the XFEL X-ray light source at DESY.

Most of the technologies discussed are making excellent progress toward the development of a high-performing pixel detector for the ILC. There are remaining challenges to be met in the areas of material budget, power and pixel size, but steady progress is being made. Moreover, these efforts benefit greatly from the fast-paced developments in the semi-conductor industry.

2.1.3 Tracking Detector

The two ILC concept detectors have a complementary approach to tracking. The ILD detector employs a hybrid tracking system consisting of a large-volume gaseous TPC tracking detector surrounded by silicon tracking layers. The SiD detector is based on silicon technology only. Since silicon is the only technology common to both detectors, some key common development aspects for silicon will be described here. The R&D on the TPC is fully described in the ILD section.

Tracking detectors have grown tremendously in size over the last generations of experiments. As observed with the evolution of vertex detector technologies, also here there is a trend toward integration. Both experiments propose hybrid-less silicon sensors. These sensors have integrated pitch adapters to route traces to a single readout ASIC mounted directly on the sensor. Power and clock signals are provided directly to the ASIC on the sensor. This research is closely related to the development of silicon tracking sensors themselves. Given the large areas involved, various strip layouts are being studied to improve the pattern recognition while simultaneously limiting the number of readout channels. Thinner sensors are being studied that meet the required signal to noise ratio for the expected radiation dose.

Since large areas are to be covered, special emphasis is placed on efficient mechanical designs that provide modularity for ease of construction, minimise the material budget and provide sufficient space points to allow efficient pattern recognition especially in the forward and backward regions. Modules

are arranged in self-supporting, light and robust structures which not only serve as support structures but also provide for cooling, cabling, services and alignment. As already mentioned, the alignment and stability issues are particularly important for the ILC where the modules are power-pulsed.

Traditional detector designs with a short central solenoid are not well suited for precision measurements in the forward and backward regions and designs for collider experiments were always a compromise favouring precision in the central region. Maintaining good tracking performance over a large polar angle range is a challenge for a number of reasons: The momentum resolution is degraded by the much smaller lever arm perpendicular to the magnetic field. Likewise, the vertexing capabilities are degraded by the large distance between the first measurement and the interaction point. Furthermore, the pattern recognition in the forward region must cope with low momentum particles "looping" through the detector, and background levels at the ILC increase rapidly with decreasing radius. Innovative solutions are required, that would benefit the community at large, to improve the performance of forward tracking systems. Sensor research geared towards fully active low-mass sensors, integrated front-end electronics, greater granularity and light-weight support structures with optimised tiling schemes may prove to be a most promising approach to overcome some of the limitations inherent in traditional forward tracking systems.

2.1.4 Calorimetry

The ILD and SiD detector concepts are both based on the particle flow algorithm (PFA) approach. For the electromagnetic and hadronic calorimeters, the ECAL and HCAL respectively, this requires unprecedented granularity to resolve the topologies, and a compact design, in order to keep showers as confined as possible. Over the past years, those demands have spurred the development of new technologies for calorimetry, like the use of silicon diode arrays for large scale detectors, novel high-gain low-cost photo-sensors (SiPMs), 2D-segmented Resistive Plate Chambers (RPCs), or Micro-Pattern Gas amplification Detectors (MPGD). All of them rely crucially on highly integrated low power mixed circuit Application Specific Integrated Circuits (ASICs).

The principal role of the ECAL is to identify photons and measure their energy. For the particle flow jet reconstruction, but also for hadronic τ decays, the capability to separate photons from each other and from near-by hadrons is of primary importance. The large difference between electromagnetic radiation length and nuclear interaction length is thus one of the reasons for the choice of tungsten as absorber material, the other being its small Molière radius. Silicon pad diodes lead to the highest possible compactness (and effective Molière radius) and exhibit excellent stability of calibration. Scintillating strips with silicon photo-detector readout provide a similar effective segmentation and offer a less costly, but also somewhat less compact, option. Both technologies could be combined in order to reach a cost performance optimum.

The role of the HCAL is to separate the deposits of charged and neutral hadrons and to precisely measure the energy of the neutrals. Their contribution to the jet energy, around 10% on average, fluctuates widely from event to event, and the accuracy of the measurement is the dominant contribution to the particle flow resolution for jet energies up to about 100 GeV. For higher energies, the performance is dominated by confusion, and both topological pattern recognition and energy information are important for correct track cluster assignment. Stainless Steel has been chosen both for mechanical and calorimetric reasons. Due to its rigidity, a self-supporting structure without auxiliary supports (dead regions) can be realised. Moreover, in contrast to heavier materials, iron with its moderate ratio of hadronic interaction length ($\lambda_I = 17$ cm) to electromagnetic radiation length ($X_0 = 1.8$ cm) allows a fine longitudinal sampling in terms of X_0 with a reasonable number of layers in a given total hadronic absorption length, thus keeping the detector volume and readout channel count small. This fine sampling is beneficial both for the measurement of the sizeable electromagnetic

energy part in hadronic showers as for the topological resolution of shower substructure, needed for particle separation and weighting. For the HCAL read-out, two options have been developed: one is based on scintillator tiles with silicon photo-sensors and analogue read-out electronics, and the other is based on gaseous devices with one or two-bit, so-called semi-digital readout but finer transverse segmentation. The relative merits of the more detailed energy or spatial information of either option for the particle flow reconstruction are the subject of the ongoing studies. The main gaseous technology pursued is glass resistive plate chambers (RPCs), but structures based on GEMs or Micromegas are being considered as alternatives. The latter both provide a better correlation of the charge signal with deposited energy, but are less advanced in the realisation of large area detectors.

A broad R&D effort has been carried out to test these technologies and validate the simulations and the PFA performance predictions. This involved test beam campaigns with large installations, and due to their high granularity, set world records in terms of their channel count, exceeding that of the largest LHC calorimeter systems. This was made possible by maximising the use of common infrastructure such as mechanical devices, ASIC architectures and DAQ systems, and working within a common software and analysis framework that facilitates combination and comparison of test beam data. Most of this effort was organised within the CALICE collaboration which currently involves 350 members from 57 participating institutes worldwide. In addition R&D towards a highly compact silicon tungsten ECAL was performed by the SiD collaboration, as well as first studies towards a 3D segmented total absorption calorimeter with dual readout.

The development of calorimeter prototypes was roughly organised in two steps, which in practice overlapped. Physics prototypes provide a proof-of-principle of the viability of a given technology in terms of construction, operation and performance. In addition they are used to collect the large data sets which are invaluable for testing shower simulation programs, and for the development of PFAs with real data.

In a second step, technological prototypes address issues of scaling, integration and cost optimisation. They are required for each technology, but many large-area and multi-layer issues can already be addressed with so-called demonstrators, that is, modules with the adequate functionality but not completely instrumented, or at real scale and hence limited in terms of full system tests. These are not yet pre-production prototypes, and many of the issues addressed are still generic for each particular concept.

In 2011 CALICE reached a major milestone and completed a seven year series of test beam campaigns with physics prototypes of all major ECAL and HCAL technologies. About 400 million physics events have been recorded at CERN and Fermilab, and have been stored on the grid for analysis. In the meantime demonstrators are under intensive tests for all options, and physics data taking of the first full-size technological prototype has started in 2012. This has been very timely, enabling a description of the detectors together with the ILC technical design report. Not all efforts, however, have progressed at the same speed, and several beam tests are still being carried out and the data has not been fully analysed yet. It is already very clear that the test beam campaigns have provided the community with an unprecedented data sample revealing hadronic showers in exquisite detail which will form the basis for an in-depth evaluation in the near future.

A highlight among the rich amount of test beam results is the application of a PFA to beam test data [21]. Two displaced showers measured in CALICE prototypes of an analogue hadron and an electromagnetic calorimeter were mapped into the ILD detector geometry and subsequently processed by the Pandora particle flow algorithm for event reconstruction. Figure I-2.2 shows the probability to recover the energy of a 10 GeV neutral hadron within three sigma of the detector resolution as a function of the distance to a 10 GeV and 30 GeV charged pion, compared with simulations using different physics lists in Geant4. The good agreement of data and simulations, in particular for the

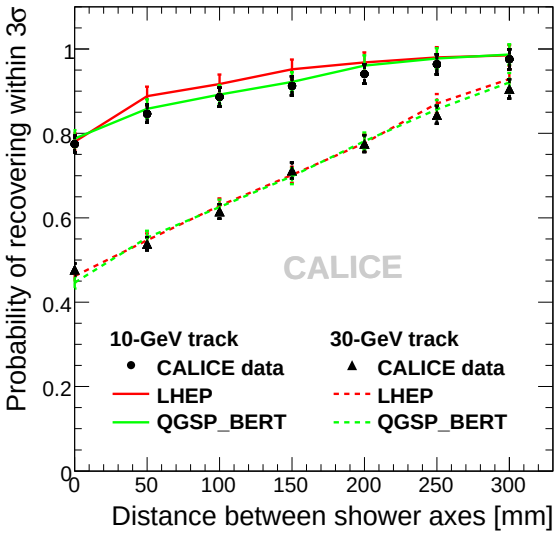

Figure I-2.2
Probability to recover the energy of a 10 GeV neutral hadron within three sigma of the detector resolution as a function of the distance from a 10 GeV (circles and continuous lines) and 30 GeV (triangles and dashed lines) charged hadron, respectively. Events are generated by mapping showers in the CALICE SiW ECAL, and AHCAL, into the ILD calorimeter system, and by reconstructing with PandoraPFA.

QGSP-BERT physics list, underlines the reliability of full detector simulations in predicting the particle flow performance of the detector system. QGSP-BERT simulations apply the Quark Gluon String (QGS) model for high energy interactions of protons, neutrons, pions, kaons and nuclei. The high energy interactions create exited nuclei, which are passed to the precompound (P) model, which models the nuclear de-excitation. For primary protons, neutrons, pions and kaons below about 10 GeV Bertini cascades are used. The Bertini model produces more secondary neutrons and protons than the low energy parametrised model and clearly gives good agreement with the experimental data.

Similar studies will also be done using data taken with a digital HCAL (DHCAL) prototype tested in the same beam line and absorber structure with and without the ECAL in front. The prototype is instrumented with glass RPCs and has the front-end electronics embedded in the active layers to read its nearly 500,000 channels and provides the first possibility of an in-depth exploration of the digital approach to hadron calorimetry. Its superior imaging capabilities mark another highlight of ILC targeted calorimeter R&D and is illustrated in Figure I-2.3. Studies towards calibration and quantitative comparisons with simulations for the DHCAL are ongoing.

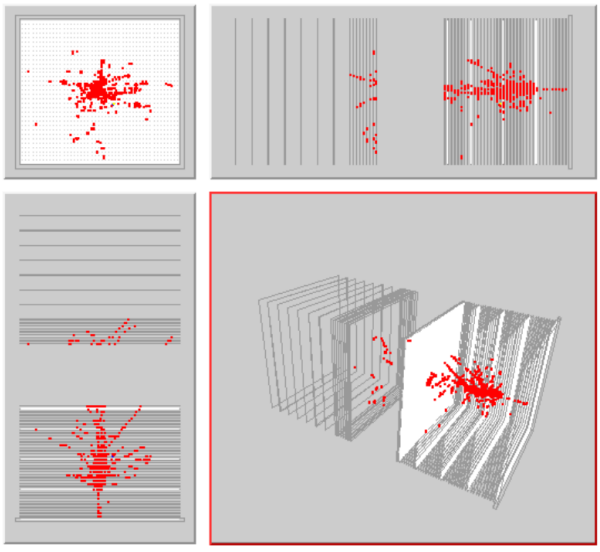

Figure I-2.3
Event display showing the interaction of a 10 GeV pion in the CALICE DHCAL with RPC read-out.

The optimisation of PFAs and the prediction of their performance relies on a realistic and detailed description of the propagation of hadronic showers in the calorimeters. It is one of the primary goals of the CALICE test beam campaigns to use the unprecedented granularity of the prototypes for

detailed tests of the simulation models implemented in Geant4. Figure I-2.4 shows, as an example, the comparison of the average longitudinal shower profile for pions interacting in the SiW ECAL with a prediction using the QGSP-BERT physics list. The decomposition in terms of particles actually depositing energy is also shown. It shows that the detailed measurements provide specific information for the refinement of the models.

As a further example, the multiplicity of charged track segments reconstructed within hadronic showers is plotted as a function of the incoming particle energy and compared with model predictions. The agreement is not perfect, but still remarkable, given the level of detail probed, and far better than earlier versions of the simulation. This illustrates the progress towards the development of truly realistic Monte Carlo hadron shower simulations. The most recent simulations match the data within typically 5% , which qualifies them as a reliable tool for detector optimisation. This indicates that there has been significant progress with respect to the state of the art at the time when, for example, the LHC detectors were designed, and reflects the refinements based on the LHC calorimeter test beam series. The ILC-based calorimeter test beam data will provide the next step in providing more accurate simulations.

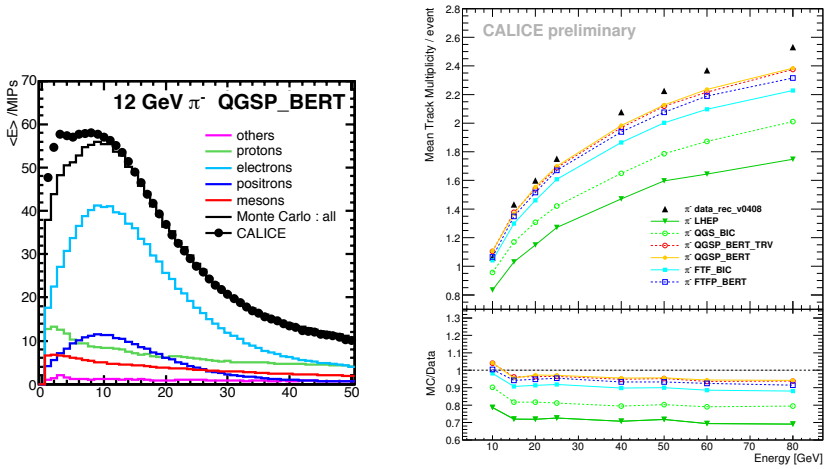

Figure I-2.4
Comparison of CALICE test beam data with simulations: longitudinal shower profile in the silicon tungsten ECAL, charged track multiplicity in the scintillator steel analogue HCAL.

A major achievement of the test beam results is that it demonstrated the viability of new technologies. Silicon pad diodes and scintillator tiles have shown a performance in terms of energy and topology resolution which quantitatively agree with simulations, and for scintillator strips and RPCs preliminary results indicate the same. The silicon pads benefit enormously from the intrinsic stability offered by this technology as demonstrated by the operation and analysis of a 10,000 channel calorimeter system. Scalable engineering solutions have recently been developed, with which highly compact structures can be realised for a collider detector, and first demonstrators have been exposed to beam. Within SiD, the KPiX chip, a 1024 channel mixed circuit ASIC which forms the heart of an ambitious ultra-compact silicon tungsten ECAL with direct hybrid-less chip-to-wafer bonding, has been developed and successfully tested.

The CALICE AHCAL was the first device that used the novel SiPM technology on a large scale, and its robustness and reliability has in the meantime encouraged other experiments, e.g. T2K, CMS and BELLE-II, to apply it in their detector upgrades. Correction procedures for intrinsic non-linearities and temperature sensitivities of the SiPMs were developed and successfully demonstrated.

Glass RPCs have for the first time been equipped with 2D segmented pad read-out and applied to calorimetry. The granularity of 1 cm^2 required the electronics to be embedded right from the first prototype. The 500,000 channel prototype has been operated stably at Fermilab and CERN

and delivered first results. A second prototype with power-pulsed electronics has taken data in 2012. Power-cycling is one of the key strategies to minimise heat dissipation and cooling. The desire for more compact structures seemed to be contrary to these two goals, but it was demonstrated during the beam tests not to affect the performance.

Gas Electron Multipliers (GEMs) and Micromegas have demonstrated in tests with a few modules that they provide the necessary imaging capability, including low noise rates, and that they can be operated stably, as shown in tests deploying the small chamber configurations produced so far.

The data taking and analysis of the recorded data is far from complete and must continue, providing the basis for a full evaluation of the strengths and weaknesses of each technology for the application in a particle flow based detector.

In order to fully demonstrate integrated solutions, including a stable operation with on-detector zero-suppression, the second generation demonstrator units must be extended to systems large enough to record showers. In addition, there are still open issues at the system level, concerning power distribution, cooling, services and interfaces to be addressed with these second generation prototypes. The results so far, however, have clearly demonstrated that a particle flow calorimeter can be built, and deliver the predicted performance. Continued R&D is needed to complete the full program.

2.1.5 Forward Calorimetry

Special calorimeters are foreseen for the very forward regions of the ILC detectors. First, there is the so-called LumiCal to measure the luminosity with a precision of better than 10^{-3} using Bhabha scattering as reference process, $e^+e^- \to e^+e^-(\gamma)$. Then there is the BeamCal, positioned adjacent to the beampipe, to provide a bunch-by-bunch luminosity estimate and a determination of the beam parameters [22]. A third calorimeter, GamCal, about 100 m downstream of the detector, will assist in beam-tuning. A pair monitor positioned just in front of the BeamCal, which has a fast feedback system to the accelerator, will also be used for beam-tuning. These forward detectors, common to both experiments, have to withstand relatively high occupancies, requiring special front-end electronics and data transfer systems.

Monte Carlo simulations have been carried out to optimise the design of the forward region. In all calorimeters a robust electron and photon shower measurement is essential, making a small Molière radius preferable. Compact cylindrical sandwich calorimeters using tungsten absorber rings interspersed with finely radially segmented silicon or GaAs sensor planes are found to match the requirements. The LumiCal is used to measure precisely the polar angle of scattered electrons and positrons. It must be centred around the outgoing beam, with a precision requirements of 10 μm for the inner diameter of the acceptance radius and about 100 μm for the position with respect to the beam-line.

Due to the high occupancy created by the beamstrahlung and the two-photon processes, both calorimeters need a fast readout. Furthermore, the lower polar angle range of the BeamCal is exposed to a large flux of electrons, approaching one MGy per year. Hence, radiation hard sensors are needed.

A prototype of a silicon sensor for LumiCal is shown in Figure I-2.5 (left). They were manufactured by Hamamatsu using n-type silicon. The thickness is 350 μm and the strip pitch is 1.8 mm.

A possible sensor for the BeamCal is a high Ohmic GaAs sensor, shown in Figure I-2.5 (right) produced using the Liquid Encapsulated Czochralski method doped with a shallow donor and compensated with Cr as a deep acceptor. Sensors with several doping concentrations were exposed to a low energy high intensity electron beam up to a dose of 1 MGy. The leakage current per pad increased slightly with dose but was still at the level of 100 nA at room temperature. The charge collection efficiency is reduced at constant voltage by a factor of 10, but can be partially recovered by increasing the operation voltage. The challenge of BeamCal is to provide sensors that are radiation hard up to

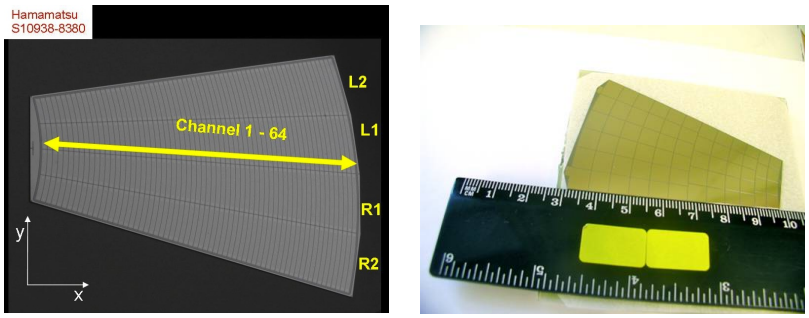

Figure I-2.5 Prototypes sensors for LumiCal (left) and BeamCal (right).

10 MGy of dose per year, a specification not unique to the ILC. Studies are being carried out in close collaboration with other experiments that also need very radiation hard sensors.

The pair monitor consists of one layer of silicon pixel sensors just in front of BeamCal to measure the distribution of the number of beamstrahlung pairs. GamCal is supposed to detect the photons from beamstrahlung for fast beam diagnostics.

Dedicated front-end and ADC ASICs have been designed in the 350 and 180 nm CMOS technology for the BeamCal and LumiCal. Dual gain charge sensitive amplifiers allow operation in calibration and standard data taking modes. The high amplification mode allows to measure the depositions of minimum ionising particles. Hence muons can be used from the beam halo or from annihilations for the calibration and sensor alignment studies. The low amplification mode will be used for the measurement of electromagnetic showers. Short shaping and conversion times allow readout or storage after each bunch crossing. The ASIC to be used for the BeamCal has in addition a fast analog adder to provide a fast feedback signal for beam tuning. In a test beam signal-to-noise ratios of better than 20 are measured for minimum ionising particles both for LumiCal and BeamCal sensors.

A critical aspect for the forward detectors is their very stringent alignment requirements. A novel laser position monitoring system has been designed, built and successfully tested to monitor the position of the two calorimeters with respect to the beam-pipe and the distance between them.

2.1.6 Beam Tests

A particularly important aspect of common detector development is the execution of beam tests. Beam tests have always played a critical role in the design and construction of new detectors. With the increase in sophistication of the experiments for high energy colliders, the importance of these tests has grown. Common beam instrumentation available for all detector development projects has proven to be extremely beneficial. Many benefits can be derived from the use of the same beam line instrumentation. Common instrumentation brings familiarity and provides for a larger user base that contributes towards further developing the peripheral instrumentation and software needed. Common instrumentation will also eliminate a source of uncertainty in the comparison of data between different technologies in the same beam line.

Within the ILC framework the EUDET project [23], aimed at providing infrastructures for research and development of novel detector technologies for the ILC, has been very successful. The main joint research activity was developing and improving test beam infrastructures in particular the commissioning of a high resolution pixel beam telescope.

A telescope consisting of six reference planes equipped with 18.4 μm pitch CMOS pixel sensors, called Mimosa26 developed by Strasbourg IPHC [18], was constructed. The Mimosa26 sensor is a fully digital sensor with binary readout. The sensors were thinned to 50 μm and a hit position resolution of better than 3 μm was achieved with a readout rate at the kHz level.

The excellent resolution, readout rate and data acquisition integration capabilities made the

telescope a primary test beam tool for many groups. The commercial readout allowed easy cloning and by now four copies are running in addition to the original EUDET telescope. The user groups have extended far beyond the original ILC detector R&D groups and now include several LHC groups. Within the new European detector infrastructure project the test beam telescope will be further extended in terms of cooling infrastructure, read-out speed and precision. In order to provide a system optimised for the different requirements by the user community a combination of various pixel technologies is foreseen.

The EUDET program also provided the community with a large bore, high field superconducting solenoid for the studies of various micro-pattern gas detector technologies. This enabled the initiation of combined modular test beam campaigns. The word combined here refers to a beam test of various sub-detectors in one beam line at the same time. The term "modular" refers to the ability to exchange sub-detectors and replace them with one of different technology. Such test beam campaigns address the integrated nature of the ILC detectors, where the overall performance of the detector is determined by a critical, subtle interplay in performance of the subdetectors. Over the last years beam tests were carried out as collaborative efforts, not only within a horizontal R&D collaboration, but also between various ILC detector development groups. All ILC detector development projects have benefited tremendously from the creation of this common infrastructure. The advantages are self-evident and it behoves the community at large to further encourage and strengthen common infrastructure for combined test beams. Some crucial tests such as power-pulsing in a high magnetic field have not been carried out due to the limited availability of such infrastructure.

2.2 Common simulation and software tools

Software tools are the basis of detector benchmarkings. While the detector concept groups ILD and SID have developed their own independent software frameworks, they have also collaborated in developing a number of common software tools. Such tools include event generator programs and samples, event data models, file formats, and event reconstruction tools. These common tools and the summary of detector benchmark studies are presented in the following subsections.

2.2.1 Common generator samples

As the machine parameters and selected benchmark processes are common between the concepts, it was decided to perform benchmark studies based on the same event generator samples as a common effort between ILD and SiD. It was also decided that a system should be set up so that the effort could be shared between different sites. To this end, the event generation program, Whizard [24], was selected for the generation of events with up to 6-fermion final states and Physsim [25] for $t\bar{t}h$ and relevant background processes with more than 6-fermion and the common generator samples have been generated as follows.

2.2.1.1 Overview of event generation

The generation framework based on Whizard was originally developed at SLAC for the LOI. Certain short comings of the LOI framework were remedied. By using the full CKM-matrix - rather than just it's diagonal elements - generating events with rare quark flavour combinations became possible. The treatment of τ polarisation, which for the LOI was only done for some particularly important cases ($e^+e^- \to \tau^+\tau^-$ and $e^+e^- \to \tilde{\tau}^+\tilde{\tau}^-$), was generalised to be applied to all τ modes. Finally, certain useful information (spin and colour-flow, energies of the initial particles) from the generator was output with the generated events, and hence made available for use in the physics analysis.

The requirement that the generated events should be usable both for ILD and SiD, and should be producible at different sites, implied that a set of well defined event-generator conditions must be documented. This would then enable the event-generation conditions to be propagated down the event

processing stream, independently of the details of the implementation of the stream. The requirement was accomplished by demanding that each generation job should provide a set of meta-data describing the generated data.

GuineaPig [26] was used to simulate the beam-beam effects, based on a set of beam parameters defined by the GDE [27]. Such effects influence both the energy spectrum of the interacting initial particles, and the composition of the beams, notably how large the photon component is. The output from the GuineaPig simulation was used to create the needed spectra, which were then passed on to the event-generators.

The produced events were stored in STDHEP format [28], in files of a maximal size of 500 MB. At the end of a generation job, these files were uploaded to the grid, from where any user with a valid ILC grid-certificate could access them. In addition to the data-files themselves, the meta-data and the log-files are kept on the grid. Further details such as the various steering-files controlling any generation jobs were made available for inspection on the web [29]. In the case of Whizard, the integration grids - which are produced by evaluating the phase-space of the process, and subsequently used to efficiently generate un-weighted events - are also available for download on the web.

The source-code of the generators used, together with auxiliary programs needed (Pythia for fragmentation, Tauola for polarised tau-decays, STDHEP for the output, and Cernlib), with the beam-spectrum files for various machine configurations, and with installation procedures are maintained in an SVN repository, housed at CERN [30].

2.2.1.2 Event generation by Whizard

The Whizard Monte Carlo was used for the generation of all $2 \to n$ processes, $n = 2, 3, 4, 5, 6$, where n is the number final state fermions, and the two initial state particles are e^+e^-, $e^+\gamma$, γe^-, or $\gamma\gamma$. It was also used for the generation of $e^+e^- \to f\bar{f}h$. Whizard provides a lowest order calculation of each $2 \to n$ sub-process, and simulates multiple photon radiation from the initial state electron and positron in the leading-logarithmic approximation. The luminosity weighted energy spectra of the initial state electron and positron including intrinsic machine energy spread and beamstrahlung effects can be supplied by the user through Fortran90 user interface subroutines. The spectra could be two dimensional to include a correlation between two beams. For sub-processes with γ's in the initial state, Whizard provides a simulation of nearly real Weizsäcker-Williams photons, while the energy spectra and overall normalisation of beamstrahlung photons is supplied by the user.

The two dimensional luminosity weighted e^+e^- energy spectra and beamstrahlung $\gamma\gamma$ energy spectra were calculated using the GuineaPig program [26]. GuineaPig output consisting of several million pairs of e^+e^- or $\gamma\gamma$ energies were processed by a program that created Monte Carlo integration grid files. These grid files are read in by the Whizard user interface subroutines. They faithfully reproduce the underlying correlated two dimensional GuineaPig distributions, and can be used to generate large numbers of independent initial state e^+e^- or $\gamma\gamma$ pairs. The $e^-\gamma$ and γe^+ spectra were simulated using the one-dimensional $e^\pm$ and γ distributions, and so correlations were not included for these initial states.

Final state QCD and QED showering of all final state quarks, and QED showers of final state muons and taus are simulated using the Pythia Monte Carlo program [31]. Pythia is also used for fragmentation and particle decay. Final state showering from electrons is normally switched off because Pythia does not use the correct showering Q^2 for most final state electron configurations.

The Higgs mass is set to 2 TeV unless the Higgs boson is a final state particle. When the Higgs is a final state particle its mass is set to 125 GeV, its branching fractions are set to the recommendations of the LHC Handbook on Higgs cross sections [32], and the decay is simulated using Pythia.

Gluon splitting is simulated using the the parton showering algorithm of Pythia, while amplitudes

with a gluon propagator are switched off in the simulation of the $2 \to n$ sub-processes. This is the normal method for generating events in e^+e^- collisions. Interference between QCD and electroweak amplitudes is not simulated in this arrangement, but is thought to be a 10% effect at most [33]. At some point in the future amplitudes with gluon propagators will be included in the $2 \to n$ sub-process simulation along with the matching algorithms that are needed to prevent double counting with QCD parton showering. However, this effort could not be completed in time for the DBD benchmarking studies.

2.2.1.3 Event generation by Physsim

The study of the $t\bar{t}h$ benchmark process required generations of processes involving 8 or more fermion final states. Generations of such processes were not easy for Whizard, because very long CPU times were required to reach reasonable precisions of phase space integration due to the many channels involved. Therefore, the event generation of these processes were made by Physsim [25], which was used previous study on $t\bar{t}h$ coupling at 500 GeV [34].

Physsim calculates helicity amplitudes by Helas [35] and phase space integration and event generation are performed by the Bases/Spring package [36]. The processes generated by Physsim were, (1) $e^+e^- \to t\bar{t}h \to 6f + h$, (2) $e^+e^- \to t\bar{t}Z \to 6f + f\bar{f}$, and (3) $e^+e^- \to t\bar{t}g^* \to 6f + b\bar{b}$. Here $6f$ denotes 6 fermions decayed from $t\bar{t}$ system. The resonance effect in the $t\bar{t}$ system was not included. The decay of Higgs and the hadronisation of quarks were performed by Pythia with the same parameters as Whizard events, the $6f$ system and the remainder being hadronised independently. The colour flow effect between $6f$ and $b\bar{b}$ system in the process (3) was neglected. The algorithm to generate the initial state radiation, the hadronisation parameters and the version of Tauola used were same as those used for Whizard events in order to have the same event property as those generated by Whizard. The Feynman diagrams in the case of the $t\bar{t}h$ process is shown in I-2.6.

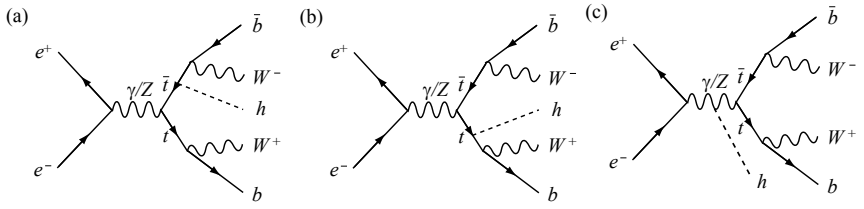

Figure I-2.6 Feynman diagrams for the $e^+e^- \to t\bar{t}h$ process.

The events were generated separately depending on the initial beam helicity and the decay mode of $t\bar{t}$, either 6 quarks, 4 quarks plus lepton and neutrino, or 2 quarks ($b\bar{b}$), 2 leptons and 2 neutrinos. The $t\bar{t}h$ process was further divided by the decay mode of Higgs to $b\bar{b}$ or the rest.

2.2.1.4 Hadronisation tuning

In the event-generation done for the LOI, hadronisation was done with the default settings of Pythia. However, it has been shown by the LEP collaborations that these setting do not describe the observations at LEP in all aspects.

Table I-2.1 Predicted average numbers of various particle species in e^+e^- collisions at 92 GeV, for default Pythia settings or OPAL settings compared to LEP data

	Standard tune	OPAL tune	LEP combined data
All charged	20.6246	20.5685	20.9400 ± 0.1900
π^0	9.6814	9.8866	9.3800 ± 0.4500
π	17.1178	17.5467	17.0500 ± 0.4300
K	2.2879	2.1108	2.3600 ± 0.1100
p	1.2190	0.9110	0.9750 ± 0.0870
n	1.1661	0.8664	-
K^0_S	1.1168	1.0150	1.0040 ± 0.0150
K^0_L	1.1057	1.0164	-

In particular, the data indicates that the amounts of neutral, long-lived hadrons are over-estimated by Pythia. This has a direct influence on the expected jet-energy resolution, since more neutral hadrons in a jet implies higher risk for confusion-errors. Even in the absence of confusion, a higher neutral hadronic component deteriorates the jet- energy resolution, simply because neutral hadronic energy is the component measured with least precision.

The LEP collaborations were contacted, and asked to provide their best estimates of how to tune Pythia to the data. For technical reasons, the tunings provided by OPAL was chosen. Table I-2.1 shows a comparison between LEP data [37, 38], default Pythia and OPAL-tuned Pythia for particle multiplicities for a few selected particle species. Of particular importance are the numbers for protons and K^0_S, as these serve as proxies for the amount of neutrons and K^0_L, respectively, ie. for the amount of long-lived neutral hadrons expected. It is clearly seen that the default Pythia settings significantly over-estimate these particles - by about 15% - and hence the amount of neutral hadronic energy. Table I-2.2 shows the difference between the two settings at ILC energies. It can be observed that the difference has become even larger than at 92 GeV: Pythia with default settings predict about 25% more neutral hadrons than what the OPAL tune does

Table I-2.2 Predicted average numbers of various particle species in $e^+e^- \to q\bar{q}$ $(q = uds)$ collisions at 500 GeV, for default Pythia settings or OPAL settings.

	Standard tune	OPAL tune
All charged	37.4267	37.4975
π^0	17.2502	17.7834
π	31.1060	32.3830
K	3.7395	3.2706
p	2.5812	1.8439
n	2.5109	1.7778
K^0_S	1.8006	1.6120
K^0_L	1.8069	1.6119

2.2.1.5 Generator samples

A generated *process* is defined by an initial state and a final state. For the initial state this includes the polarisation of the incoming particles, as well as their nature. For the final state, it is defined by a combination of quarks and/or leptons, possibly in conjunction with one or more photons.

Processes were grouped into a physics oriented classification in order to reduce a number of processes. For example, The 4-fermion processes were classified as ZZ, WW, or mixed WW and ZZ, according to the intermediate particles involved in the diagrams. The pure ZZ class would typically contain processes with only one flavour present in the final state (e.g., $u\bar{u}u\bar{u}$), while the pure WW class would contain more than 2 flavours (e.g., $u\bar{d}s\bar{c}$). The mixed class would be cases where both ZZ and WW diagrams could contribute, e.g.. $u\bar{d}\bar{u}d$. The processes with contributions from single-boson production were treated separately. In addition, there was a sub-division between full hadronic, semi-leptonic and fully leptonic final-states. This scheme reduced the several hundreds of unique channels for the 2- and 4-fermion samples to a few tens. Processes other than 2- and 4-fermion were also classified similarly.

This grouping of processes was implemented using two features in Whizard: particle aliases and process-grouping. Aliasing gives the possibility to assign aliases to groups of particles, which are then treated as a single entity. For instance, aliases were defined for up-type quarks (u and c) and down-type quarks (d, s and b). Process-grouping, on the other hand, groups individual processes together at the event-generation stage, so that a random mix of the selected processes are generated with the correct relative fractions.

The generated samples are summarised in Table I-2.3. In the table, f is a quark, lepton, or an alias particle; γ's in the initial state are due to beamstrahlung or initial state radiation. For each

Table I-2.3
Summary of the common generator samples.

event-type	process
1f	$e^{\pm}\gamma \to \gamma e$
2f	$e^+e^- \to f\bar{f}$
3f	$e^{\pm}\gamma \to (e \text{ or } \nu) + 2f$
4f	$e^+e^- \to 4f$
5f	$e^{\pm}\gamma \to (e \text{ or } \nu) + 4f$
6f	$e^+e^- \to 6f$
aa_2f	$\gamma\gamma \to 2f$
aa_4f	$\gamma\gamma \to 4f$
aa_minijet	$\gamma\gamma \to$ hadron mini-jets
aa_lowpt	$\gamma\gamma \to$ low $\mathrm{p_t}$ hadrons
eepairs	beam induced low $\mathrm{p_t}$ $e^{\pm}$ pairs
higgs	$e^+e^- \to f\bar{f}h$
tt$h$	$e^+e^- \to t\bar{t}h, t\bar{t}Z,$ and $t\bar{t}g^*(g^* \to b\bar{b})$

combinations of $e^{\pm}$ beam polarisation, samples of 1 ab^{-1} were generated separately with fully polarised beams, except for a few exceptions; $e^+e^- \to e^+e^-$ process was generated as $e^+e^- \to e^+e^-\gamma$ with a kinematical cut on e^+e^- invariant mass, opening angle and acoliniarity for WW benchmark studies; The $t\bar{t}h$ and relevant 8-fermion samples include about 50k events which correspond to at least 8 ab^{-1}. The low p_t e^+e^- background events were generated by GuineaPig. The $\gamma\gamma \to$ mini-jets hadron events were generated by Pythia implemented in the Whizard framework using the same lumi-spectrum as other generators. Low p_t, high cross section, minimum bias $\gamma\gamma \to$ hadron events were generated based on the cross section model by M.Peskin [39] using either a phase space particle production model or the Pythia model for $\gamma\gamma \to$ hadrons, depending on whether the $\gamma\gamma$ centre of mass energy was less than or greater than 10 GeV.

These samples were generated without beam crossing angle, spread of interaction points, nor background overlay. These effects were taken into account at detector simulations or event reconstructions.

2.2.2 Common simulation and reconstruction tools

Besides the common generator tools and samples described above, both concepts have based their detailed simulation applications on the Geant4 [40] tool kit and share a common event data model and file format which is provided by LCIO [41]. At the reconstruction stage the pattern recognition and track fitting tasks are performed independently, whereas for the particle flow algorithm, the vertex finding and flavour tagging again common tools are used: PandoraPFA [42] and LCFIPlus [43] respectively. In the following we describe the common tools that have been developed in the context of the Linear Collider activities in more detail.

2.2.2.1 LCIO

The LCIO software package provides a common *Event Data Model* (EDM) and persistency solution for Linear Collider detector R&D. The development of LCIO started in 2003 and provides implementations in *C++, Java* and *Fortran* the languages used at the time. Using a common EDM and file format is a key requirement for easy sharing of software tools and algorithms across detector concepts and working groups.

In Figure I-2.7 the hierarchical EDM of LCIO is shown. It has been recently extended and improved as a preparation for the DBD. In particular the *Track* class has been extended to hold a number of *TrackStates* for the same set of *TrackerHits*, typically at the *Interaction Point*(IP), the first and last hit and at the entry point to the calorimeter. New classes for one dimensional measurements from Si-Strip detectors have been added in order to allow for an increased level of realism with respect to the LOI [44].

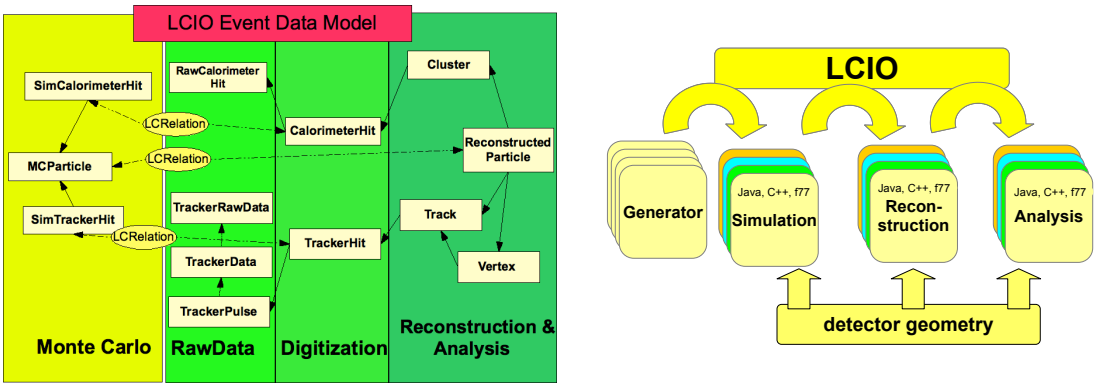

Figure I-2.7. Left: Schematic overview of the hierarchical event data model (EDM) of LCIO. Right: The common EDM and persistency scheme allow to exchange software tools even when they are written in different frameworks and languages.

2.2.2.2 PandoraPFA

PandoraPFA is an implementation of the *particle flow algorithm (PFA)*, which originally has been developed in the Marlin [45] framework for LC-like detectors. In a recent redesign of the framework it has been turned into a standalone library with interfaces to external software through well defined *Application Programming Interfaces* and essentially no external dependencies. Figure I-2.8 shows

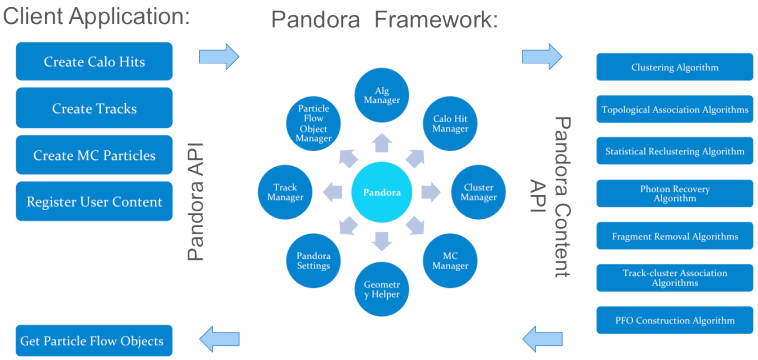

Figure I-2.8 Schematic overview of the structure of the PandoraPFA algorithm showing the separation between the Client Application, the framework and the algorithms.

the layout of the new PandoraPFA tool kit. Both detector concepts have written client applications that interface the input data collections from LCIO, augmented with the corresponding geometry information of the detectors, to PandoraPFA and convert the output into the final collection of *ReconstructedParticles*, used for analysis. The actual algorithm will be described in the ILD and SiD specific sections.

2.2.2.3 LCFIPlus

The LCFIVertex [46] software package had been developed for vertexing, flavour tagging and vertex charge reconstruction with an ILC vertex detector. It was originally developed for Z-pole physics and designed to find the vertex and tag the flavour of a jet, thus its algorithm is applied after reconstruction of a jet in an event. LCFIPlus [43] is a new Marlin package targeted for multi-jet events. In this package, vertices in an event are reconstructed before jet reconstruction so as to use found vertex information for jet reconstruction. The flavour tagging is made with the help of TMVA (*Toolkit for Multivariate Data Analysis with ROOT*). In addition to the standard variables, user specific variables for tagging can be easily introduced depending on the needs for the analysis. LCFIPlus is used by both detector concepts. The actual algorithms will be described in the ILD and

SiD specific sections.

2.2.3 Summary of benchmark studies

The ILD and SiD detector concept groups made detector benchmark studies using the common generator samples described in the previous sub-section. While the details of software tools and analysis procedures are presented in the ILD and SiD chapters, a summary of them is presented in Table I-2.4. Note that the numbers quoted are indicative of the precisions achieved in full simulation studies from ILD and SiD.

The benchmark studies have been performed to investigate the physics capability of proposed detectors selecting a few numbers of channels. The implications of these estimates for the study of a 125 GeV/c^2 Higgs boson and ILC physics case are described in the physics volume.

Table I-2.4. Summary table of results from the benchmarking studies. In the luminosity column, the electron beam polarisation for eL (eR) is -80% (+80%) and the positron beam polarisation is +20%(-20%) at 1000 GeV and +30%(-30%) at other energies. For the earlier studies at 250 GeV, the Higgs boson mass was taken to be 120 GeV and the default Pythia 6.412 branching ratios were assumed. For the more recent studies at 1 TeV, the Higgs boson mass was taken to be 125 GeV and the branching ratios of ref.[32] were used.

$\sqrt{s}$ (GeV)	L (ab^{-1}) eL/eR	Channel ($e^+e^- \to$)	Observable	Precision	Comment
250	0.25/0	$Zh, Z \to e^+e^-/\mu^+\mu^-$	$\Delta\sigma/\sigma$	2.5 %	model indep.
			Δm_h	32 MeV	analysis
		$Zh, h \to b\bar{b}$	$\Delta(\sigma Br)/(\sigma Br)$	1.0%	
		$Zh, h \to c\bar{c}$		7.3%	
		$Zh, h \to gg$		8.9%	
		$Zh, h \to \mu^+\mu^-$		89%	
500	0.25/0.25	$t\bar{t} \to 6\text{-}jet$	$\Delta\sigma/\sigma$	0.5%	
			Δm_t	40 MeV	
			ΔA_{FB}	0.011	
		$\tau^+\tau^-$	ΔA_{FB}	0.21%†, 0.24%‡	†eL, ‡eR
			$\Delta\langle P_\tau\rangle$	1%(stat)$\oplus$0.6%(stat)	
	0.5/0	$\tilde{\chi}_1^+\tilde{\chi}_1^-$ & $\tilde{\chi}_2^0\tilde{\chi}_2^0$ $\to WW/ZZ + \not{E}$	$\Delta\sigma/\sigma(\tilde{\chi}_1^+\tilde{\chi}_1^-)$	0.6%	template fitting
			$\Delta\sigma/\sigma(\tilde{\chi}_2^0\tilde{\chi}_2^0)$	2.1%	
		$\to 4\text{-}jet + \not{E}$	$\Delta m(\tilde{\chi}_1^\pm)$	2.4 GeV	2 parameter fit
			$\Delta m(\tilde{\chi}_2^0)$	0.9 GeV	
			$\Delta m(\tilde{\chi}_0^0)$	0.8 GeV	
		$\tilde{\mu}_L^+\tilde{\mu}_L^- \to \mu^+\mu^- + \not{E}$	$\Delta\sigma/\sigma$	2.5%	
			$\Delta m(\tilde{\mu}_L)$	0.5 GeV	
		$\tilde{\tau}_1^+\tilde{\tau}_1^- \to \tau^+\tau^- + \not{E}$	$\Delta m(\tilde{\tau}_1)$	0.1 GeV $\oplus 1.3\sigma_{LSP}$	
	2/0	Zhh	$\Delta\lambda/\lambda$	44%	
1000	1/0	$\nu\bar{\nu}h, h \to b\bar{b}$	$\Delta(\sigma Br)/(\sigma Br)$	0.47 %	
		$\nu\bar{\nu}h, h \to c\bar{c}$		7.6 %	
		$\nu\bar{\nu}h, h \to gg$		3.1 %	
		$\nu\bar{\nu}h, h \to WW^*$		3.3 %	
		$\nu\bar{\nu}h, h \to \mu^+\mu^-$		32 %	
	0.5/0.5	$t\bar{t}h$	$\Delta(\sigma Br)/(\sigma Br)$	8.7%	8 jets $\oplus$ 6 jets
		W^+W^-	$\Delta\lvert P_{e^-}\rvert$	0.16%	full angle analysis
			$\Delta\lvert P_{e^+}\rvert$	0.23%	
			$\Delta P_{e^-}(L)_{\text{eff}}$	0.11%†, 0.036%‡	†eL, ‡eR
	2/0	$\nu\bar{\nu}hh$	$\Delta\lambda/\lambda$	18%	

2.3 Machine Detector Interface

The Machine-Detector Interface (MDI) at the ILC covers all aspects that are of common concern to both detectors and to the machine. This usually covers topics like beam induced backgrounds, integration of the machine and detector elements in the Interaction Region (IR) as well as physics related beam instrumentation issues (e.g. polarisation and energy measurements). This section deals with those MDI topics that are of common concern to both detectors and that are not specific to the respective implementation of the IR: common assembly procedures, experimental area layouts, the push-pull system. Detector concept specific MDI topics are discussed in the respective chapters of the SiD and ILD sections in this report.

2.3.1 The push-pull concept

The ILC design foresees to have two detectors that share one interaction region in a push-pull operation scheme. In that scheme, one detector would take data, while the other one is waiting in the close-by maintenance position. At regular intervals, the data-taking detector is pushed laterally out of the interaction region, while the other detector is being pulled in. As the data taking intervals for each experiment should be short enough to avoid a potential discovery by one detector alone, the transition time for the exchange of the detectors needs to be short, i.e. in the order of one day, to keep the total integrated luminosity at the ILC high.

A time efficient implementation of the push-pull model of operation sets specific requirements and challenges for many detector and machine systems, in particular the IR magnets, the cryogenics, the alignment system, the beam line shielding, the detector design, and the overall integration. The minimal functional requirements and interface specifications for the push-pull IR have been successfully developed and published [47], to which all further IR design work on both the detectors and machine sides are constrained. The developments lead to a detailed design of the technical systems and the experimental area layout that follow detailed engineering specifications [48].

2.3.2 Detector motion system

The detector motion and support system has to be designed to ensure reliable push-pull operation allowing a hundred moves over the life of the experiment, while preserving internal alignment of the detectors internal components and ensuring accuracy of detector positioning. The motion system must be designed to preserve structural integrity of the collider hall floor and walls. Moreover, the motion and support system must be compatible with the tens of nanometre level vibration stability of the detector. In seismic regions the system must also be compatible with earthquake safety standards.

The detectors will be placed on platforms that preserve the detector alignment and will distribute the load evenly onto the floor (c.f. Figure I-2.9) The platform will carry also some of the detector services like electronic racks. Cables and supply lines will be routed to the platform in flexible cable chains that move in trenches underneath the platform itself.

An engineering study on a possible platform design has concluded that the flexure of the platform and the distortion of the cavern invert would sum to less than ± 2 mm [49]. Two different types of transport systems are under study for the platform, air pads and high capacity rollers. In both cases, the platforms would be jacked onto the transport system to allow for the movement of a slightly undulated surface. In combination with a simple positive indexing mechanism, the platform with the detector can be positioned quickly within the required precision of 1 mm with respect to the beam axis. In parking or beam position, the platforms will be lowered on permanent supports. Trenches in the hall floor are needed for cable chains and for access to the platform undercarriage in case of maintenance.

Figure I-2.9
Platform support concept for the push-pull system. Left - ILD; right - SiD

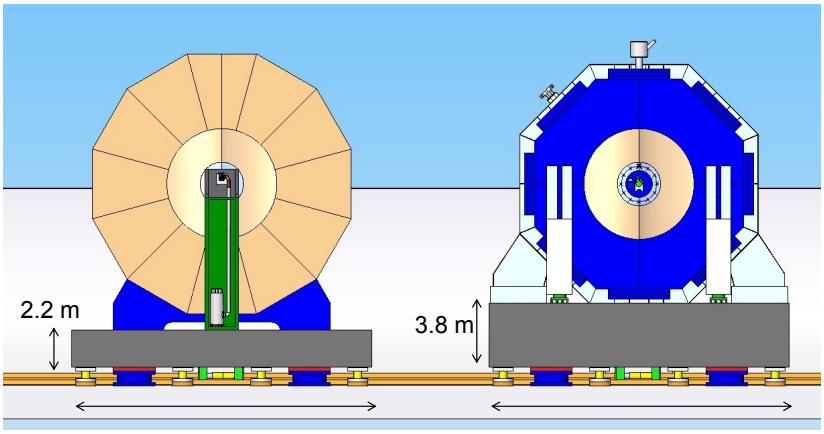

2.3.3 Shielding

2.3.3.1 Radiation

The ILC detectors are self-shielding with respect to ionising radiation that stems from maximum credible beam loss scenarios [50]. Additional shielding in the hall is necessary to fill the gap between the detector and the wall in the beam position. The design of this beam line shielding needs to accommodate both detectors, SiD and ILD, that are of significant size differences.

A common 'pac-man' design has been developed, where the movable shielding parts are attached to the wall of the detector hall - respectively to the tunnel stubs of the collider - and match to interface pieces that are borne by the experiments (c.f. Figure I-2.10).

Figure I-2.10
Design of the beam line shielding compatible with two detectors of different sizes.

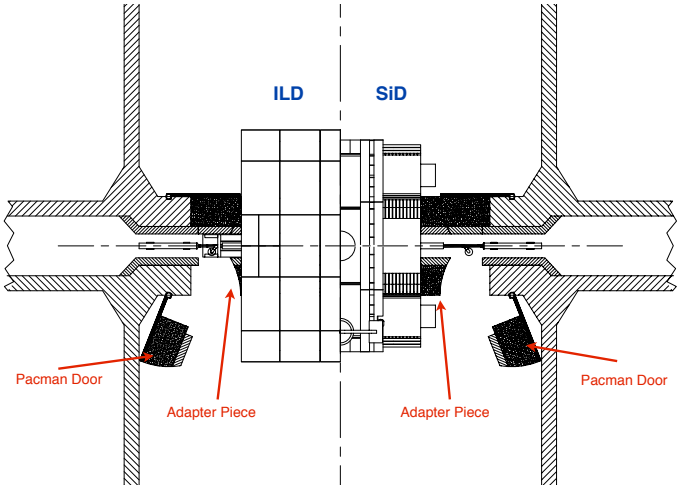

2.3.3.2 Magnetic fields

The magnetic stray fields outside the iron return yokes of the detectors need to be small enough to not disturb the other detector during operation or maintenance. A limit for the magnetic fields has been set to 5 mT at a lateral distance of 15 m from the beam line [141]. This allows the use of standard iron-based tools at the other detector. The design of the detector return yokes has been tested carefully for the fringe fields in simulations.

2.3.4 Detector installation schemes and timelines

The installation schemes of the detectors and the layout of the experimental areas on surface and underground depend on the geographical situation of the possible ILC sites. While the European and American sample sites assume a flat surface area, the Asian sample sites in Japan are located in the mountains where the requirements for the conventional facilities and buildings are different.

2.3.4.1 Flat surface ILC sites

In ILC sites with a flat surface, it is foreseen to have the underground experimental halls connected vertically with shafts to the surface area. In these conditions, the ILC detectors follow the assembly scheme that has been adopted by the CMS experiment at the LHC. The detectors will be pre-assembled, cabled and tested as much as possible in surface assembly buildings. The underground excavations and installations are thus done in parallel at the same time. Therefore the time schedule for the detector assembly, the civil construction, and the machine installation are mostly decoupled. Rather late in the construction period, about 1-2 years before the first beam is in the machine, the large detector parts will be lowered into the underground cavern through a large vertical shaft. The diameter of the shaft and the capacity of the temporary gantry crane for this procedure is defined by the largest detector part. This will be the central iron yoke ring of ILD with the mounted solenoid coil and installed barrel calorimeters. The big detector parts for both, ILD and SiD, can be loaded directly onto the respective platform. The final installation and commissioning of the detectors should then be performed in the maintenance areas of the underground cavern. Figure I-2.11 (top) shows a generic timeline for installation of the detectors in the flat surface sites.

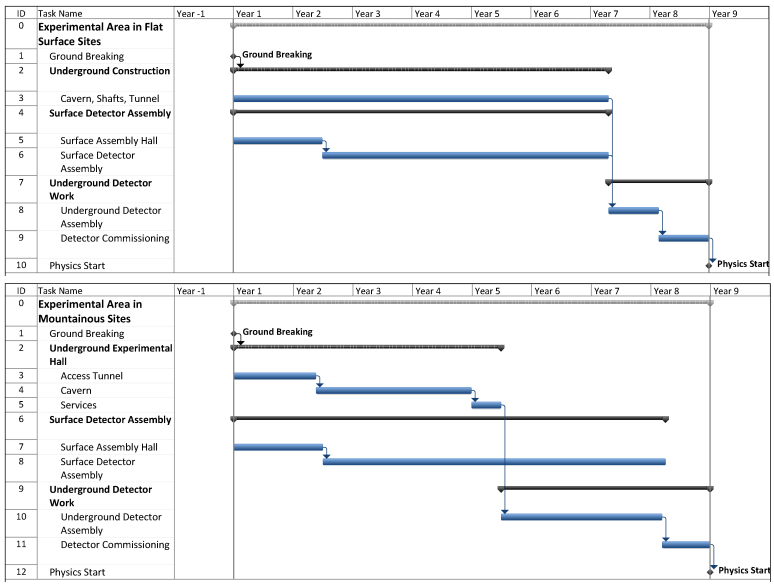

Figure I-2.11
Generic detector assembly time lines for flat surface (top) and mountainous (bottom) ILC sites.

2.3.4.2 Mountainous ILC sites

The ILC sites that are under study in Japan are in mountain regions. Therefore it is not possible to have vertical access shafts of ≈100 m length into the underground caverns. Instead, access will be provided by means of a horizontal access tunnel of ≈1 km length. The diameter of this tunnel will be given by the largest parts that need to be delivered into the experimental cavern in one piece. This would be the coil of the ILD detector solenoid that has a diameter of ≈9 m so the tunnel diameter would be in the order of 11 m. The transport system in the tunnel limits the mass of the parts to a maximum of ≈400 t.

Due to this boundary conditions, a modified detector installation scheme needs to be followed. In that case, still most parts of the detector would be pre-assembled and tested in the surface areas. However, more assembly work needs to be done underground. As for example the big yoke rings of ILD could not be transported through the tunnel, the assembly of the iron yoke needs to be done in the underground cavern. Also the installation of the solenoid and the calorimeters needs to be done in situ. Additional underground space and working time is needed in the mountain site cases of the ILC. Figure I-2.11 (bottom) shows a generic timeline for the installation of the detectors in the mountain sites. The timelines for the detector assemblies, the civil construction and the machine installation are interwoven.

2.3.5 Experimental area layout

The experimental area layouts for the different ILC sites need to fulfil the boundary conditions that are given by the installation schemes of the detectors, the needs for a safe and efficient running of the machine and both detectors in push-pull mode, and need to allow for efficient maintenance of the technical installations.

2.3.5.1 Flat surface ILC sites

Figure I-2.12 shows the conceptual design of the underground experimental cavern for the flat surface ILC sites. The hall layout follows a Z-shape where the platforms transport the detectors perpendicular to the beam line. Each detector has a parking cavern where the detector could be opened for service and maintenance. One big 18 m diameter shaft enters the hall directly over the interaction point (IP). This shaft will be used for the initial assembly of both detectors. The large pre-assembled parts can be loaded directly onto the platforms. Two service shafts in the maintenance caverns will be used for services and for access in maintenance periods of one detector while the other one is taking data on the IP. Two smaller elevator shafts are foreseen for people and material transport as well as for safety egress.

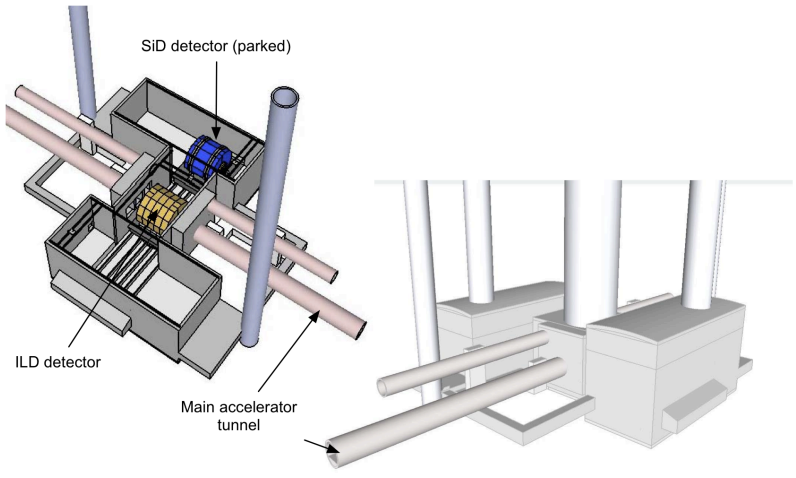

Figure I-2.12
SiD and ILD in the experimental hall for the American (flat surface) ILC site.

2.3.5.2 Mountainous ILC sites

The conceptual design of the experimental cavern for the mountainous ILC sites is shown in Figure I-2.13. The push-pull system will be very similar to the one in the flat surface case. Alcoves in the cavern enlarge the parking positions of the detectors to allow for the lateral opening and servicing of the detector parts. The access tunnel enters the hall twice, at the ILD and at the SiD side, to minimise the interference during the detector installation phase. The tunnel passes underneath the ILC beam line tunnel and extends towards the central region where the damping rings are located.

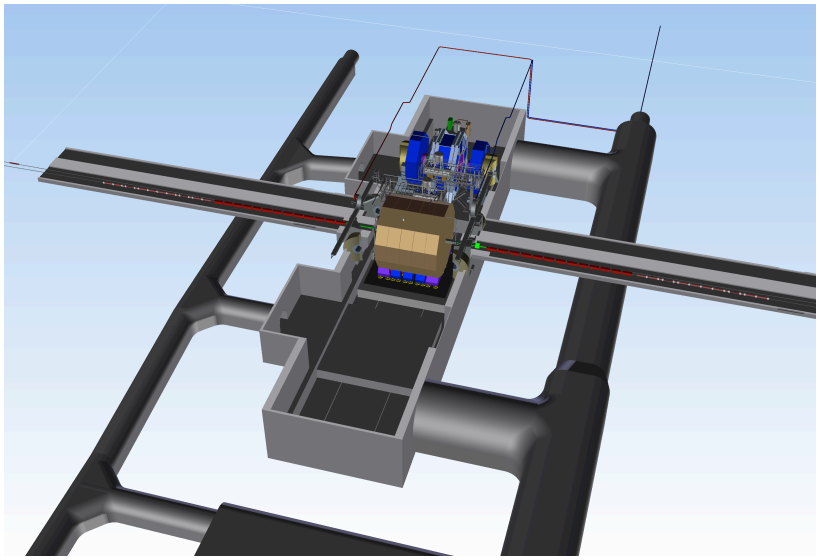

Figure I-2.13
The experimental hall for mountainous ILC sites.

2.3.6 Detector services

A number of service and supply equipments needs to be established for the running and the maintenance of both detectors. The arrangement of the services depends on the technical requirements and can be sorted according to their proximity to the detector. Primary services should be located on the surface above the experimental hall (in the flat-surface sites) or in close-by service caverns (in the mountain site cases). They comprise of usually large and sometimes noisy facilities like water chillers, high voltage transformers, auxiliary power supplies, helium storage and compressors, and gas storage systems. Secondary services will be placed into the underground cavern in dedicated service areas. Examples are cooling water distributions, power supplies, gas mixture systems, power converters, and parts of the cryogenic system for the detectors. As the detectors will not be disconnected during the push-pull operations, all supplies that go directly to the detector will be run in flexible cable chains. The detectors will carry those services on-board that need to stay close, e.g. front-end electronics, patch panels, electronic containers.

Cryogenic helium for the superconducting solenoids and the QD0 magnets is foreseen to be supplied by a common system for both detectors. Two solutions are currently under study. In one, the liquid He is brought to the detectors via flexible cryogenic lines (c.f. Figure I-2.14). In that case, the cold boxes would be placed at service areas at the cavern walls. The second solution would place the cold boxes close to the detectors while gaseous He is supplied via flexible lines to the detector platforms. In each case, a re-cooler is placed on the platform of each detector for the 2K He supply of the QD0 magnets.

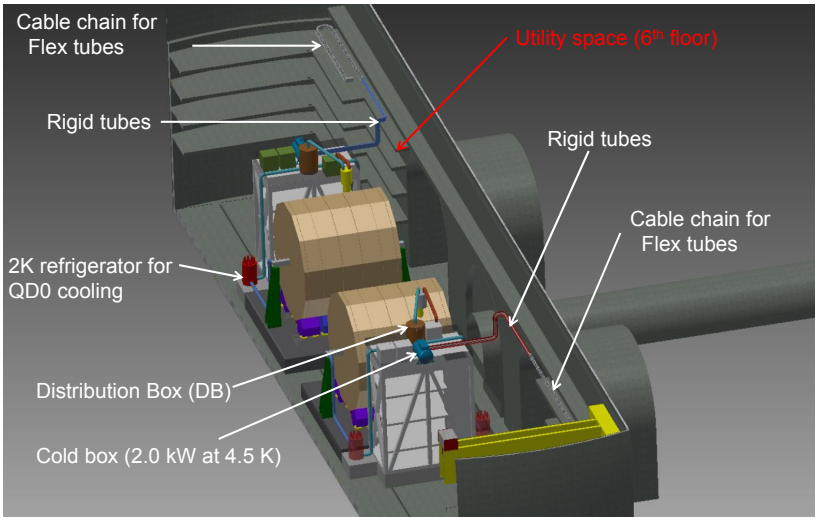

Figure I-2.14
Common detector cryogenic system (study) with the cold boxes placed on service racks close to the detectors.

2.4 Beam Instrumentation

This section discusses the beam energy and polarisation measurement for the ILC. Since they are of crucial importance for the analysis of the e^+e^- collision data, these devices are typically designed and operated by the detector collaborations. Located in the Beam Delivery System far away from the central detectors, they are shared between the two experiments and their cost is included in the accelerator costing. Additional information on these systems can be found in the ILC TDR and in [51].

2.4.1 Beam Energy Measurements

The ILC TDR design foresees redundant beam-based measurements of the incoming beam energy, capable of achieving a 10^{-4} accuracy, and of the energy spectrum of the disrupted beam after collisions. The measurements will be available in real time as a diagnostic tool to machine operators and will provide the basis for the determination of the luminosity-weighted centre-of-mass energy for physics analyses. Physics reference channels, such as a final state muon pair at the known Z^0 mass, are then foreseen to provide valuable cross checks of the collision scale, but only long after the data has been recorded.

2.4.1.1 Upstream Energy Spectrometer

An energy spectrometer acts as a beam position monitor (BPM). It is located about 700 m upstream of the interaction point, just after the energy collimation system. This spectrometer consists of four dipoles which introduce a fixed displacement of about 5 mm at the centre. Before, after and at the centre the beam line is instrumented with two or more cavity BPMs mounted on translation systems (so that the cavities can always be operated at their electromagnetic centre), shown in Figure I-2.15.

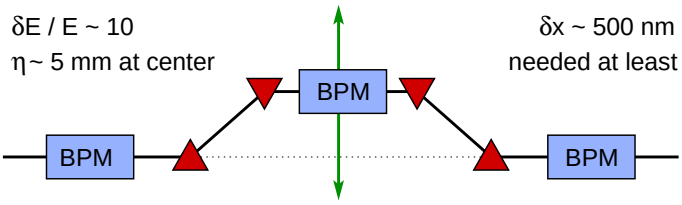

Figure I-2.15
Schematic for the upstream energy spectrometer using beam position monitors.

With the four magnet chicane system, systematics effects produced by the magnets can be investigated, such as hysteresis and residual fields. The four magnet chicane also allows the spectrometer to be operated at different field strengths without disturbing the rest of the machine. It is important that the energy spectrometer be able to make precision energy measurements between 45.6 GeV

(Z-pole) and the highest ILC energy of 1 TeV. A precise measurement at Z-pole energies is of special importance since it defines the absolute energy scale. When operating the spectrometer with a fixed dispersion over the whole energy range, a BPM resolution of 0.5 μm is required.

A prototype test setup for such an energy spectrometer was commissioned in 2006 and 2007 in the T-474 experiment in the End Station A beamline at SLAC. The setup involved four dipole magnets and high-precision RF cavity BPMs in front, behind and in between the magnets. ESA test beams operated at 10 Hz with a bunch charge of $1.6 \cdot 10^{10}$ electrons, a bunch length of 500 μm and an energy spread of 0.15%, i.e. with properties similar to ILC expectations. measurements normalised to the 5 mm dispersion (same dispersion as for the present ILC baseline energy spectrometer). The system turned out to be stable at the micron level over the course of one hour. When combining all the BPM stations to measure the precision of the orbit over the whole ESA-chicane beamline, a resolution of 0.8 μm in x and 1.2 μm in y was achieved [52]. This translates to a relative energy resolution of $5.5 \cdot 10^{-4}$ [53].

This result can be improved further by employing more precise BPMs. At high energies, the energy resolution is directly limited by the BPM resolution. Due to the fixed dispersion design, the running at lower energies, especially at the Z-pole, requires the chicane magnets to be operated at low fields, where the magnetic field measurement may not be accurate enough. A BPM resolution of 20 nm would allow the chicane dipoles to be run at the same magnetic field for both the Z-pole and highest energy operation. This type of single shot accuracy has recently been demonstrated with the cavity BPM system at ATF2 [54].

2.4.1.2 Extraction Line Energy Spectrometer

The ILC Extraction-Line Spectrometer (XLS) design [55] is largely motivated by the experience of the Wire Imaging Synchrotron Radiation Detector (WISRD) at the SLC [56]. The WISRD measured the distance between two synchrotron stripes created by horizontal bend magnets which surrounded a precisely-measured dipole that provided a vertical bend proportional to the beam energy. The WISRD achieved a precision of $\Delta E_b/E_b \sim 2 \cdot 10^{-4}$ (200 ppm), where the limiting systematic errors were due to relative component alignment and magnetic field mapping.

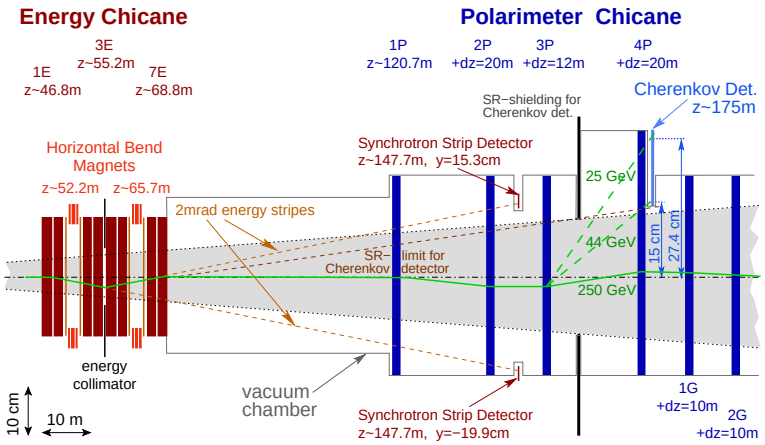

Figure I-2.16 Schematic of the ILC extraction line diagnostics for the energy spectrometer and the Compton polarimeter.

The analysing dipole for the XLS is provided by a vertical chicane just after the capture quad section of the extraction line, about 55 m downstream of the interaction point (see Figure I-2.16). The chicane provides a ± 2 mrad vertical bend to the beam and in both legs of the chicane horizontal wiggler magnets are used to produce the synchrotron light needed to measure the beam trajectory. The optics in the extraction line is designed to produce a secondary focus about 150 m downstream of the IP, which coincides with the centre of the polarimeter chicane and the Compton interaction point. The synchrotron light produced by the wigglers will also come to a vertical focus at this

point, and position-sensitive detectors in this plane arrayed outside the beampipe will measure the vertical separation between the synchrotron stripes. With a total bend angle of 4 mrad, and a flight distance of nearly 100 m, the synchrotron stripes will have a vertical separation of 400 mm, which must be measured to a precision of 40 μm to achieve the target accuracy of 10^{-4}. In addition to the transverse separation of the synchrotron stripes, the integrated bending field of the analysing dipole also needs to be measured and monitored to a comparable precision of 10^{-4}. The distance from the analysing chicane to the detectors needs to only be known to a modest accuracy of 1 cm. For the XLS spectrometer, it has been proposed to use an array of radiation-hard 100 μm quartz fibres. These fibres do not detect the synchrotron light directly, but rather detect Cherenkov radiation from secondary electrons produced when the hard photons interact with material near the detector. At ILC beam energies, the critical energy for the synchrotron radiation produced in the XLS wigglers is several tens of MeV, well above the pair-production threshold, and copious numbers of relativistic electrons can be produced with a thin radiator in front of the fibre array. The leading candidates for reading out these fibres are multi-anode PMs from Hamamatsu, similar in design to those used in scintillating fibre calorimeters. The advantage of this scheme over wires (as used in the SLC energy spectrometer) is to produce a reliable, passive, radiation-hard detector which does not suffer from cross talk or RF pickup, and still allows for easy gain adjustment and a large dynamic range. A more traditional wire-based detector could also be considered instead of (or in addition to) the quartz fibre detector. The energy spectrum of the beam after collision contains a long tail as a result of the beam-beam disruption in the collision process. This disrupted beam spectrum is not a direct measure of the collision energy spectrum, but it is produced by the same physical process, and direct observation of this disrupted tail will serve as a useful diagnostic for the collision process. The position-sensitive detector in the XLS is designed to measure this beam energy spectrum down to 50% of the nominal beam energy. Near the peak, for a beam energy of $E_b = 250$ GeV, each 100-micron fibre spans an energy interval of 125 MeV. Given a typical beam energy width of 0.2%, this means the natural width of the beam energy will be distributed across at least a handful of fibres, which will allow the centroid to be determined with a precision better than the fibre pitch, and some information about the beam energy width can be extracted as well.

2.4.2 Polarisation Measurements

The ILC TDR design foresees redundant beam-based measurements of the incoming beam polarisation and of the polarisation of the disrupted beam after collisions. The measurements will be available in real time as a diagnostic tool to machine operators and will provide the basis for the determination of the luminosity-weighted polarisation for physics analyses. Physics reference channels, such as W pair production, are then foreseen to provide valuable cross checks of the luminosity-weighted polarisation scale, but only long after the data has been recorded. The systems have been designed to reach a final precision of 10^{-3} on the luminosity-weighted polarisation.

2.4.2.1 Upstream Polarimeter

The upstream Compton polarimeter is located at the beginning of the Beam Delivery System, upstream of the tuneup dump 1800 m before the e^+e^- IP. In this position it benefits from clean beam conditions and very low backgrounds. The upstream polarimeter configuration is shown in Figure I-2.17. It will provide fast and precise measurements of the polarisation before collisions. The beam direction at the Compton IP in both the vertical and horizontal must be the same as that at the IP within a tolerance of ~ 50 μrad. The parameters for the upstream chicane and Cherenkov detector [57] were chosen such that the entire Cherenkov spectrum can be measured for all beam energies while still keeping the Cherenkov detector at a clearance of 2 cm with respect to the beam pipe.

The upstream polarimeter can be equipped with a laser similar to one used at the TTF/Flash source in operation at DESY. It can have the same pulse structure as the electron beam allowing measurements of every bunch. This permits fast recognition of polarisation variations within each bunch train as well as time-dependent effects that vary train-by-train. The statistical precision of the polarisation measurement is estimated to be 3% for any two bunches with opposite helicity, leading to an average precision of 1% for each bunch position in the train after the passage of only 20 trains (4 seconds). The average over two entire trains with opposite helicity will have a statistical error of $\Delta P/P = 0.1\%$.

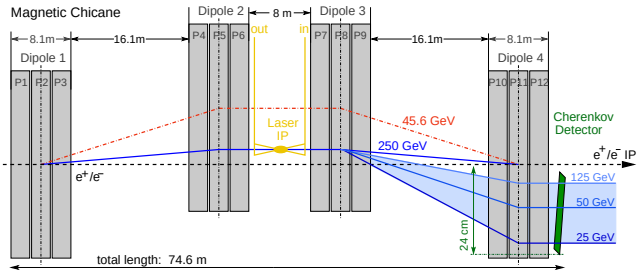

Figure I-2.17 Schematic of the upstream polarimeter chicane.

2.4.2.2 Downstream Polarimeter

The downstream polarimeter, shown in Figure I-2.16, is located 150 m downstream of the IP in the extraction line and on axis with the IP and IR magnets. It can measure the beam polarisation both with and without collisions, thereby testing the calculated depolarisation due to collisions and the spin tracking. The downstream polarimeter chicane further accommodates a detector for the downstream energy spectrometer and provides magnetic elements for the GAMCAL system.

In order for the downstream Cherenkov detector to avoid the synchrotron radiation fan from the e^+e^- IP (extending about 15 cm from the beam pipe, see Figure I-2.16), the downstream dipole magnets are larger and have much higher fields. In addition, magnets 3P and 4P are operated at higher fields (compared to magnets 1P and 2P) in order to bend the scattered electrons further from the main beam axis. Therefore, two additional magnets (1G and 2G) are needed to bring the main beam back to its original trajectory.

The laser for the downstream polarimeter requires high pulse energies to overcome the substantially larger backgrounds in the extraction line. Three 5 Hz laser systems will be used to generate Compton collisions for three out of 2800 bunches in a train. Each laser is an all solid-state diode-pumped Nd:YAG, with a fundamental wavelength of 1064 nm that will be frequency-doubled to 532 nm. Each laser will sample one particular bunch in a train for a time interval of a few seconds to a minute, then select a new bunch for the next time interval, and so on in a pre-determined pattern. The Compton statistics are high with more than 1000 Compton-scattered electrons per bunch in a detector channel at the Compton edge. With this design, a statistical uncertainty of less than 1% per minute can be achieved for each of the measured bunches. This is dominated by fluctuations in Compton luminosity due to beam jitter and laser targeting jitter and to possible background fluctuations.

Background studies have been carried out for disrupted beam losses and for the influence of synchrotron radiation (SR). There are no significant beam losses for the nominal RDR ILC parameter set and beam losses still look acceptable for the nominal TDR beam parameters based on the low power option of the RDR. An SR collimator protects the Compton detector and no significant SR backgrounds are expected.

2.4.3 Luminosity weighted averages and correlations

There is a strong complementarity between beam-based instrumentation and physics reference reactions which are sensitive to collision energy and beam polarisation. While beam-based measurements generally provide higher statistics and more immediate feedback, physics reactions naturally provide a luminosity-weighted sampling of conditions over long time scales. In general, both pieces of information are necessary to achieve the physics goals of the ILC, and it is expected that a mixture of beam-based and physics reference reactions will be used to determine the collision energy spectrum and the beam polarisation values. One such reference reaction, namely the determination of the luminosity weighted long-term average of the beam polarisation for W^+W^- production, has been chosen for benchmarking the ILD and SiD performance.

Even without the necessity of instrumentation to provide fast feedback for operations, beam-based instrumentation also provides crucial information to measure and constrain possible correlations between the collision energy, luminosity, and beam polarisation which are typically impossible to measure with the available statistics in physics reference reactions. Correlations between these parameters can arise due to long-term drifts in the machine, bunch-to-bunch variations along the bunch train, and even due to beam-beam interactions in the highly disrupted collision process.

One concrete example is the luminosity as a function of energy used at various steps in a threshold scan to measure the top quark mass. In addition to the luminosity-weighted average collision energy at each scan point, it is also necessary to know the shape of the luminosity spectrum at each point in detail, which includes any correlations between beam energy jitter and delivered luminosity. To achieve a relative accuracy of $\mathcal{O}(10^{-4})$ on the top quark mass, these correlations must be understood and controlled to a degree which requires detailed beam instrumentation to be able to measure these correlations directly. Similar arguments can be made for understanding beam polarisation, where direct correlations with energy and luminosity can arise due to the large spin precession of highly relativistic electrons in magnetic fields. Being able to correlate changes in the polarisation alignment due to final-focus orbit drifts with delivered luminosity or collision energy, for instance, may be an important systematic for high-precision measurements.

2.5 Common Engineering Tools

The design and integration of the ILD and SID detectors, together with the push-pull requirements asking for an unprecedented amount of infrastructures shared by the two experiments, call for common engineering tools enabling a consistent sharing of engineering documents like interfaces, radiation and magnetic field maps and specifications of CFS equipments.

ILC-EDMS (Engineering Data Management System) is a fully web based system which has the features answering these needs. It is promoted by the GDE and supported and operated at DESY ([58, 59, 60, 61] and links).

Among other key features, it will allow the international community to collaboratively design components using evolving CAD models and view the results using visualisation tools (see Figure I-2.18

All the data stored on EDMS have well defined life-cycle managed by the owner and shared with the relevant distribution lists. Documents can be kept as temporary, released or obsolete along the evolution of the project life.

The organisation of the ILC EDMS for detectors implies an efficient and logical description of the projects under a WBS (Work Breakdown Structure), defined under the responsibility of each concept group.

As a result, the ILC-EDMS include by now a level devoted to detectors, subdivided in one sub-level per detector, and specific workspace to manage the interaction between detectors and the civil engineering of the ILC facility. This node already contains some material for studies of the

mechanism of push-pull, and the dimensioning of the hall and services. (see Figure I-2.19.)

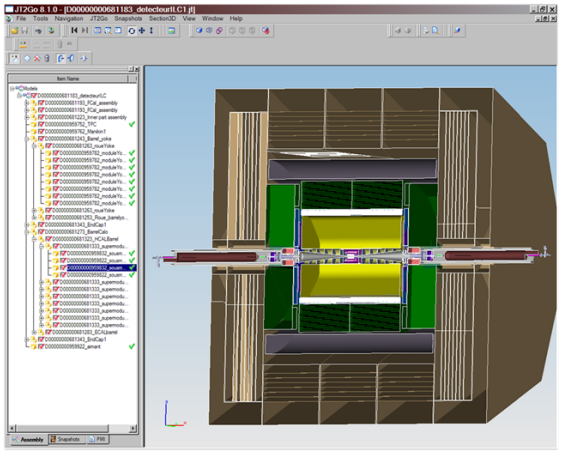

Figure I-2.18
Cross-sectional view of the ILD detector using the EDMS visualisation tool.

The detector top node in ILC-EDMS and the details for the two detectors SID and ILD is ready to operate. It will become an important and major tool for the future of the ILC detectors as a collaborative and management tool. It is already organised to efficiently follow the two detectors projects among each step of their life. The use of this EDMS provides the selection, definition and tracking of the mandatory documentation but the management of this documentation is a major issue and needs to be established [62].

2.6 Detector Costing Methodology

Costing is a key element of detector design and will become crucial for the detector approval and its construction. The performance of a detector, in general, is correlated with the cost, which normally will be bound by the resources. Thus, together with the technical aspects, realistic costing needs to be considered in the design work although the present designs are not meant for commitment for construction as announced by ILCSC in the call of LOIs.

The validated groups seriously worked on the cost estimation of their designed detectors. There are several difficulties, however, in the study which limit the precision and maturity of the cost estimation. First, it is still unknown when the detectors will be built. The prices of some raw materials vary with time and depending on the world economy. The variation may exceed the range of over-all inflation rate. Also technological advance or mass production could reduce the cost in a favourable direction. These make the long range extrapolation of the cost difficult. Second, there is another complexity for costing in that the detectors will be built by large international collaborations where the funding schemes and the costing methods are different among the participating institutions. Here also arises the question of currency exchange rates, which change often unstably, in estimating the total cost in one particular currency. The number of participating institutions and their counties

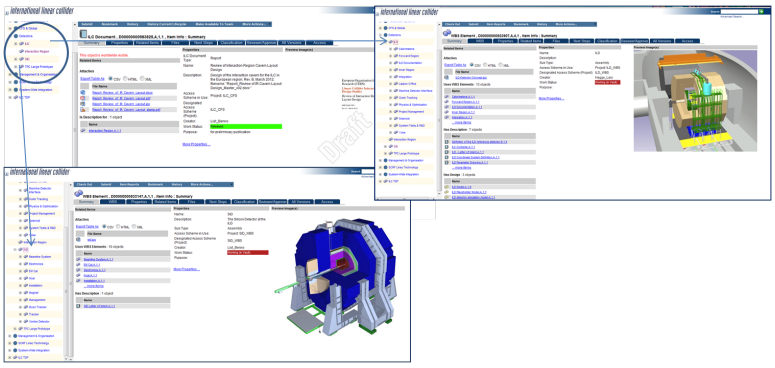

Figure I-2.19
The detector top node in the ILC-EDMS and the details for the two detectors SID and ILD

will be very many, exceeding those of accelerator participation, and the unstable exchange rates requires careful handling in producing an total cost estimation, while in practice they will not cause a serious problem at the time of construction because most components will be provided by in-kind contribution. The HEP community has rich experience for building large collider detectors in big international collaborations handling these matters smoothly.

Both detector concepts made their best effort for costing under such circumstances. We also made an effort to make the costing method comparable between the two groups. However, there remain some differences between the groups on top of the above mentioned uncertainties. For the same reasons, the detector cost estimates should be compared with that of the accelerator with a caution. While we tried to present the detector costs in a similar way, they are less matured and the funding scheme will be different.

A common costing working group was formed for a close communication between the groups. The working group invited an adviser member from the accelerator team to deploy a consistent methodology to handle some of the issues, e.g. handling the exchange rate variations. One member from each detector group served in the CLIC detector costing, too. This was effective to coordinate indirectly between the costings of ILC detectors and CLIC detectors.

The group agreed about a few guidelines for the costing method and its presentation to be compatible as much as possible so that the delivered costs can be approximately compared even though the exact costing methods are not the same:

1. the detector cost will be provided in the unit of 2012 ILCU like the accelerator cost. Those component costs which were estimated in the past are converted to the 2012 cost by taking the appropriate inflation rate;
2. some costs of raw materials are fixed between the groups. While the items are not many, these cover a fair part of the total cost. They include tungsten for the calorimeter, two types of steel for the yoke, and the Si detector sensors. These raw material costs were used first for the CLIC detectors in the CLIC CDR;
3. the material cost and manpower cost are listed separately. The man power cost does not include in-house labour of participating Institutions;
4. where contingency needs to be indicated explicitly, it is listed separately. This depends on the country and SiD group followed this line;
5. the platform to be used for push-pull system is costed as a CFS component and is not included in the detector cost;
6. the electric power and the cooling water are assumed to be delivered in the experimental hall;
7. where currency exchange rates are needed, purchase power parity of different currencies of OECD is used as is done for the accelerator costing.

The groups have discussed costing of the large solenoids in some detail. While the both groups referred to the CMS magnet, the assumed construction models were different mainly depending on the past experiences. Nevertheless, each group understands how the other group estimates its magnet cost, and the given numbers look consistent.

Although the physics aims are similar, each group had its own design philosophy which lead to different designs of the detectors. For example there are different selection of the components, operation parameters and their sizes. In the costing section of each group, the subdivisions of the components is left free but the listed categorisation of the component costs are very similar allowing each item to be compared. Where differences are seen, the reason can be understood.

Volume 4

Detectors

Part II

SiD Detailed Baseline Design

SiD Editors

Main Editors
P.N. Burrows, L. Linssen, M. Oreglia, M. Stanitzki, A. White

Vertex Detector
W. Cooper, R Lipton

Silicon Tracking
W. Cooper, M. Demarteau, T. Nelson

Calorimetry
R. Frey, A. White, L. Xia

Muon System
H. Band, G. Fisk

Superconducting Magnet System
W. Craddock, M. Oriunno

Engineering, Integration and the Machine Detector Interface
P. Burrows, T. Markiewicz

Forward Systems
T. Maruyama, B. Schumm

Electronics and DAQ
M. Breidenbach, G. Haller, M. Stanitzki

Simulation and Reconstruction
N. Graf, J. Strube

Benchmarking
D. Asner, T. Barklow, P. Roloff

Costs
M. Breidenbach

SiD Introduction

The next generation of collider detectors, to study electroweak symmetry breaking and potential discoveries beyond the Standard Model, will demand a high level of precision in the measurement of physics processes. SiD was conceived as a fully integrated, unified design with the basic features of compactness, silicon-based tracking, fine-grained calorimetry and a high central magnetic field. Building on extensive experience with previous detectors, and exploiting major advances in sensors, materials, and electronics, this design has been developed for experiments at a future linear collider.

SiD is the result of many years of creative design by physicists and engineers, backed up by a substantial body of past and ongoing detector research and development. While each component has benefitted from continual development, the SiD design integrates these components into a complete system for excellent measurements of jet energies, based on the Particle Flow Algorithm (PFA) approach, as well as of charged leptons, photons and missing energy. The use of robust silicon vertexing and tracking makes SiD applicable to lepton colliders spanning a wide energy range, from a Higgs factory to multi-TeV machines. SiD has been designed in a cost-conscious manner, with the compact design that minimises the volumes of high-performing, high-value, components. The restriction on dimensions is offset by the relatively high central magnetic field from a superconducting solenoid.

This Detailed Baseline Design builds on the results presented in our earlier Letter of Intent [63]. We present an overview of the SiD Concept, its design philosophy, and the approach to the development of each component. We present detailed discussions of each of the SiD subsystems, an overview of the full GEANT4 description of SiD, the status of the tracking and calorimeter reconstruction algorithms, studies of subsystem performance based on these tools, results of physics benchmark analyses, an estimate of the cost of the detector, and an assessment of the research and development needed to provide the technical basis for an optimised SiD design. While detector and physics studies continue, we regard this document as a substantive starting point for the development of a full Technical Design Report.

Chapter 1
SiD Concept Overview

1.1 SiD Philosophy

SiD [63] is a general-purpose detector designed to perform precision measurements at a Linear Collider. It satisfies the challenging detector requirements that are described in the Common Section. SiD is based on the PFA paradigm, an algorithm by which the reconstruction of both charged and neutral particles is accomplished by an optimised combination of tracking and calorimetry. The net result is a significantly more precise jet energy measurement that results in a di-jet mass resolution good enough to distinguish between W and Z hadronic decays.

SiD (Figures II-1.1, II-1.2) is a compact detector based on a powerful silicon pixel vertex detector, silicon tracking, silicon-tungsten electromagnetic calorimetry (ECAL) and highly segmented hadronic calorimetry (HCAL). SiD also incorporates a high-field solenoid, iron flux return, and a muon identification system. The use of silicon sensors in the vertex, tracking and calorimetry enables a unique integrated tracking system ideally suited to particle flow.

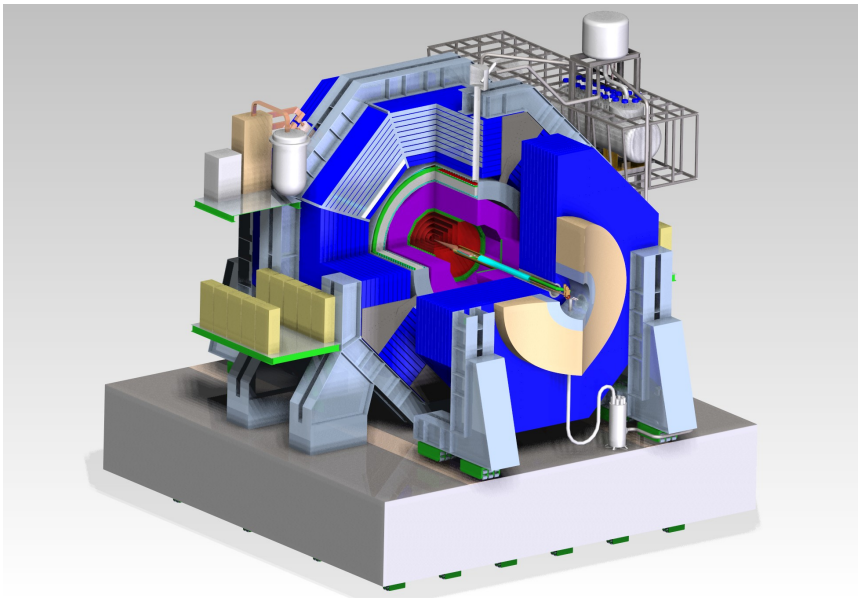

Figure II-1.1
SiD on its platform, showing tracking (red), ECAL (green), HCAL (violet) and flux return (blue).

The choice of silicon detectors for tracking and vertexing ensures that SiD is robust with respect to beam backgrounds or beam loss, provides superior charged particle momentum resolution, and eliminates out-of-time tracks and backgrounds. The main tracking detector and calorimeters are "live" only during each single bunch crossing, so beam-related backgrounds and low-p_{T} backgrounds from $\gamma\gamma$ processes will be reduced to the minimum possible levels. The SiD calorimetry is optimised for excellent jet energy measurement using the PFA technique. The complete tracking and calorimeter systems are contained within a superconducting solenoid, which has a 5 T field strength, enabling the overall compact design. The coil is located within a layered iron structure that returns the magnetic

flux and is instrumented to allow the identification of muons.

All aspects of SiD are the result of intensive and leading-edge research aimed at achieving performance at unprecedented levels. At the same time, the design represents a balance between cost and physics performance. The key parameters of the SiD design are listed in Table II-1.1.

Table II-1.1 Key parameters of the baseline SiD design. (All dimension are given in cm).

SiD Barrel	Technology	Inner radius	Outer radius	z extent
Vertex detector	Silicon pixels	1.4	6.0	$\pm$ 6.25
Tracker	Silicon strips	21.7	122.1	$\pm$ 152.2
ECAL	Silicon pixels-W	126.5	140.9	$\pm$ 176.5
HCAL	RPC-steel	141.7	249.3	$\pm$ 301.8
Solenoid	5 Tesla SC	259.1	339.2	$\pm$ 298.3
Flux return	Scintillator-steel	340.2	604.2	$\pm$ 303.3
SiD Endcap	**Technology**	**Inner z**	**Outer z**	**Outer radius**
Vertex detector	Silicon pixels	7.3	83.4	16.6
Tracker	Silicon strips	77.0	164.3	125.5
ECAL	Silicon pixel-W	165.7	180.0	125.0
HCAL	RPC-steel	180.5	302.8	140.2
Flux return	Scintillator/steel	303.3	567.3	604.2
LumiCal	Silicon-W	155.7	170.0	20.0
BeamCal	Semiconductor-W	277.5	300.7	13.5

1.2 Silicon-based Tracking

The tracking system is a key element of the ILC detector concepts. The particle flow algorithm requires excellent tracking with superb efficiency and two-particle separation. The requirements for precision measurements, in particular in the Higgs sector, place high demands on the momentum resolution at the level of $\delta(1/p_{\mathrm{T}}) \sim 2 - 5 \times 10^{-5}/\mathrm{GeV}/c$.

Highly efficient charged particle tracking is achieved using the pixel detector and main tracker to recognise and measure prompt tracks, in conjunction with the ECAL, which can identify short track stubs in its first few layers to catch tracks arising from secondary decays of long-lived particles. With the choice of a 5 T solenoidal magnetic field, in part chosen to control the $\mathrm{e^+e^-}$ pair background, the design allows for a compact tracker design.

1.2.1 Vertex detector

To unravel the underlying physics mechanisms of new observed processes, the identification of heavy flavours will play a critical role. One of the main tools for heavy flavour identification is the vertex detector. The physics goals dictate an unprecedented spatial three-dimensional point resolution and a very low material budget to minimise multiple Coulomb scattering. The running conditions at the ILC impose the readout speed and radiation tolerance. These requirements are normally in tension. High granularity and fast readout compete with each other and tend to increase the power dissipation. Increased power dissipation in turn leads to an increased material budget. The challenges on the vertex detector are considerable and significant R&D is being carried out on both the development of the sensors and the mechanical support.

The SiD vertex detector uses a barrel and disk layout. The barrel section consists of five silicon pixel layers with a pixel size of $20 \times 20\ \mu\mathrm{m}^2$. The forward and backward regions each have four silicon pixel disks. In addition, there are three silicon pixel disks at a larger distance from the interaction point to provide uniform coverage for the transition region between the vertex detector and the outer tracker. This configuration provides for very good hermeticity with uniform coverage and guarantees excellent charged-track pattern recognition capability and impact parameter resolution over the full solid angle. This enhances the capability of the integrated tracking system and, in conjunction with

Figure II-1.2
SiD quadrant view.

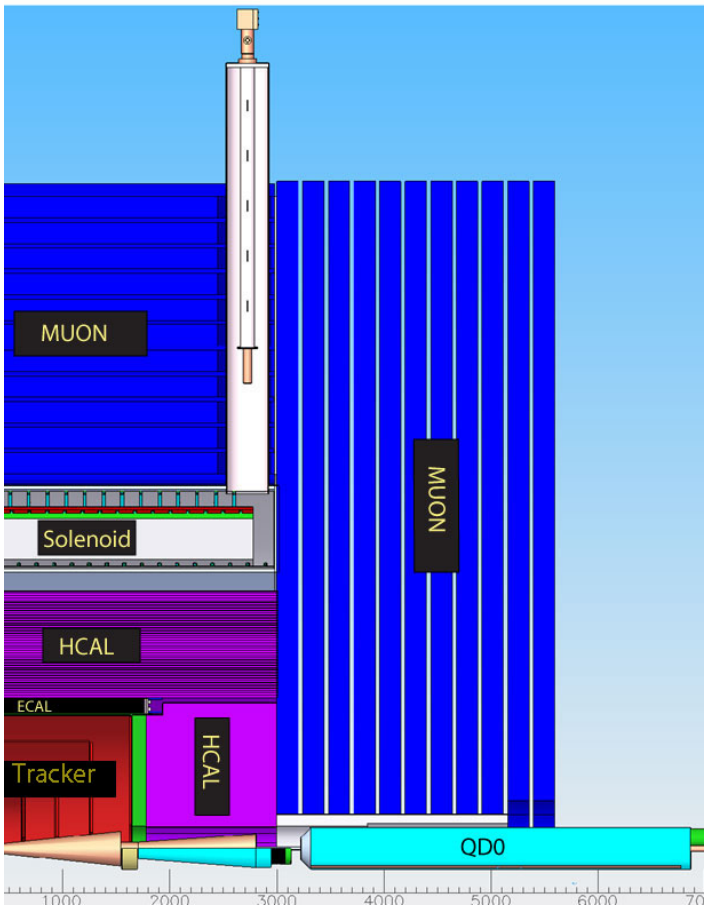

the high magnetic field, makes for a very compact system, thereby minimising the size and costs of the calorimetry.

To provide for a very robust track-finding performance the baseline choice for the vertex detector is a sensor technology that provides time-stamping of each hit with sufficient precision to assign it to a particular bunch crossing. This significantly suppresses backgrounds.

Several technologies are being developed. One of them is a CMOS-based monolithic pixel sensor called Chronopixel. The main goal for the design is a pixel size of about $10 \times 10\ \mu\mathrm{m}^2$ with 99% charged-particle efficiency. Prototype devices have demonstrated that the concept works; what should be a fully functional chip is presently under test. More challenging is the 3D vertical integrated silicon technology, for which a full demonstration is also close.

Minimising the support material is critical to the development of a high-performance vertex detector. Different groups are studying an array of low-mass materials such as reticulated foams and silicon-carbide materials. An alternative approach that is being pursued very actively is the embedding of thinned, active sensors in ultra low-mass media. This line of R&D explores thinning active silicon devices to such a thickness that the silicon becomes flexible. The devices can then be embedded in, for example, Kapton structures, providing extreme versatility in designing and constructing a vertex detector.

Power delivery must be accomplished without exceeding the material budget and over heating the detector. The vertex detector design relies on power pulsing during bunch trains to minimise heating and uses forced air for cooling.

1.2.2 Main tracker

The main tracker technology of choice is silicon strip sensors arrayed in five nested cylinders in the central region and four disks following a conical surface with an angle of 5 degrees with respect to the normal to the beamline in each of the end regions. The geometry of the endcaps minimises the material budget to enhance forward tracking. The detectors are single-sided silicon sensors, approximately 10 $\times$ 10 cm^2 with a readout pitch of 50 μm. The endcaps utilise two sensors bonded back-to-back for small angle stereo measurements. With an outer cylinder radius of 1.25 m and a 5 T field, the charged track momentum resolution will be better than $\delta(1/p_{\mathrm{T}}) = 5 \times 10^{-5}/(\mathrm{GeV}/c)$ for high momentum tracks with coverage down to polar angles of 10 degrees.

The all-silicon tracking approach has been extensively tested using full Monte-Carlo simulations including full beam backgrounds. Besides having an excellent momentum resolution it provides robust pattern recognition even in the presence of backgrounds and has a real safety margin, if the machine backgrounds will be worse than expected.

1.3 Main calorimeters

The SiD baseline design incorporates the elements needed to successfully implement the PFA approach. This imposes a number of basic requirements on the calorimetry. The central calorimeter system must be contained within the solenoid in order to reliably associate tracks to energy deposits. The electromagnetic and hadronic sections must have imaging capabilities that allow both efficient track-following and correct assignment of energy clusters to tracks. These requirements imply that the calorimeters must be finely segmented both longitudinally and transversely. In order to ensure that no significant amount of energy can escape detection, the calorimetry must extend down to small angles with respect to the beampipe and must be sufficiently deep to prevent significant energy leakage. Since the average penetration depth of a hadronic shower grows with its energy, the calorimeter system must be designed for the highest-energy collisions envisaged.

In order to ease detector construction the calorimeter mechanical design consists of a series of modules of manageable size and weight. The boundaries between modules are kept as small as possible to prevent significant non-instrumented regions. The detectors are designed to have excellent long-term stability and reliability, since access during the data-taking period will be extremely limited, if not impossible.

The combined ECAL and HCAL systems consist of a central barrel part and two endcaps, nested inside the barrel. The entire barrel system is contained within the volume of the cylindrical superconducting solenoid.

The electromagnetic calorimeter has silicon active layers between tungsten absorber layers. The active layers use 5$\times$5 mm^2 silicon pixels, which provide excellent spatial resolution. The structure has 30 layers in total, the first 20 layers having a thinner absorber than the last ten layers. This configuration is a compromise between cost, electromagnetic shower radius, sampling frequency, and shower containment. The total depth of the electromagnetic calorimeter is 26 radiation lengths (X_0) and one nuclear interaction length.

The hadronic calorimeter has a depth of 4.5 nuclear interaction lengths, consisting of alternating steel plates and active layers. The baseline choice for the active layers is the glass resistive plate chamber, which has been extensively evaluated in testbeam campaigns at Fermilab and CERN. Two other technologies (GEM, and Micromegas) are currently being prototyped and evaluated as potential options for SiD.

1.4 Forward calorimeters

Two special calorimeters are foreseen in the very forward region: LumiCal for precise measurement, and BeamCal for fast estimation, of the luminosity. LumiCal and BeamCal are compact cylindrical electromagnetic calorimeters centred on the outgoing beam. They are based on 30 layers' depth of semiconductor-tungsten technology. BeamCal is placed just in front of the final focus quadrupole and LumiCal is aligned with the electromagnetic calorimeter endcap. LumiCal uses silicon sensor readout. It is a precision device with challenging requirements on the mechanics and position control. BeamCal is exposed to a large flux of low-energy electron-positron pairs originating from beamstrahlung. These depositions, useful for a bunch-by-bunch luminosity estimate and the determination of beam parameters, require radiation hard sensors. The detectors in the very forward region have to tackle relatively high occupancies, requiring dedicated front-end electronics.

The challenge for BeamCal is to find sensors that will tolerate about one MGy of dose per year. So far polycrystalline chemical vapour deposition (CVD) diamond sensors of area 1 cm^2 and larger sectors of GaAs pad sensors have been studied. Since large-area CVD diamond sensors are extremely expensive, they may be used for only the innermost part of BeamCal. At larger radii GaAs sensors appear to be a promising option. Sensor samples produced using the liquid encapsulated Czochralski method have been studied in a high-intensity electron beam.

For SiD, the main activities are the study of these radiation-hard sensors, development of the first version of the so-called Bean readout chip, and the simulation of BeamCal tagging for physics studies. SiD coordinates these activities with the FCAL R&D Collaboration.

1.5 Magnet Coil

The SiD superconducting solenoid is based on the CMS solenoid design philosophy and construction techniques, using a slightly modified CMS conductor as its baseline design. Superconducting strand count in the coextruded Rutherford cable was increased from 32 to 40 to accommodate the higher 5 T central field.

Many iron flux return configurations have been simulated in two dimensions so as to reduce the fringe field. An Opera 3D calculation with the Detector Integrated Dipole (DID) coil has been completed. Calculations of magnetic field with a 3D ANSYS program are in progress. These will have the capability to calculate forces and stress on the DID as well as run transient cases to check the viability of using the DID as a quench propagator for the solenoid. Field and force calculations with an iron endcap HCAL were studied. The field homogeneity improvement was found to be insufficient to pursue this option.

Conceptual DID construction and assembly methods have been studied. The solenoid electrical power system, including a water-cooled dump resistor and grounding, was established. Significant work has been expended on examining different conductor stabiliser options and conductor fabrication methods. This work is pursued as a cost- and time-saving effort for solenoid construction.

1.6 Muon System

The flux-return yoke is instrumented with position sensitive detectors to serve as both a muon filter and a tail catcher. The total area to be instrumented is very significant - several thousand square meters. Technologies that lend themselves to low-cost large-area detectors are therefore under investigation. Particles arriving at the muon system have seen large amounts of material in the calorimeters and encounter significant multiple scattering inside the iron. Spatial resolution of a few centimetres is therefore sufficient. Occupancies are low, so strip detectors are possible. The SiD baseline design uses scintillator technology, with RPCs as an alternative. The scintillator technology uses extruded scintillator readout with wavelength shifting fibre and SiPMs, and has been successfully demonstrated. Simulation studies have shown that nine or more layers of sensitive detectors yield adequate energy measurements and good muon-detection efficiency and purity.

1.7 The Machine-Detector Interface

The push-pull system for the two detectors was only conceptual at the time of LoI publication, but since then the engineering design has progressed significantly. A time-efficient implementation of the push-pull model of operation sets specific requirements and challenges for many detector and machine systems, in particular the interaction region (IR) magnets, the cryogenics, the alignment system, the beamline shielding, the detector design and the overall integration. The minimal functional requirements and interface specifications for the push-pull IR have been successfully developed and published [64, 65], to which all further IR design work on both the detectors and machine sides are constrained.

Chapter 2
SiD Vertex Detector

2.1 Introduction

The SiD vertex detector consists of a central barrel section with five silicon pixel layers and forward and backward disk regions, each with four silicon pixel disks. Three silicon pixel disks at large z provide uniform coverage for the transition region between the vertex detector and the silicon micro-strip based outer tracker. The barrel layers and disks are arranged to provide good hermeticity to $\cos(\theta) \approx 0.984$ and to guarantee good pattern recognition capability for charged tracking and excellent impact parameter resolution over the whole solid angle.

2.1.1 Vertex detector requirements

The physics goals of the ILC, particularly the need to separate bottom and charm vertices, drive the need for a very precise, light vertex detector. The time structure and low radiation background in the ILC provides an environment which allows us to consider very light, low power detector structures. The bunch structure, with a 1 ms long bunch train at 5 Hz, enables power pulsing of the electronics, providing a power saving of a factor of 50-100 for front-end analog power. Low power allows gas-based cooling, saving mass in cooling channels and associated structures. The vertex detector for SiD is designed to meet the following goals:

- Hit resolution better then 5 $\mu\mathrm{m}$ in the barrel
- Less than 0.3% radiation length per layer
- Average power less than 130 $\mu\mathrm{W/mm}^2$ in the barrel
- Single bunch time resolution.

These requirements then drive the design of the vertex system. The 5 $\mu\mathrm{m}$ resolution implies a pixel size of 17 $\mu\mathrm{m}$, larger if charge sharing is used to improve the resolution. Some CMOS MAPS devices, which collect charge by diffusion rather than drift, can utilise larger pixels because diffusion naturally spreads the charge.

The small radiation length per layer is driven by the need for precise three dimensional vertex resolution for heavy quark decays. This resolution has a direct effect on the efficiency for b and c hadron identification. For a device with less than 0.3% radiation length per layer air cooling appears to be the only viable low-mass sensor cooling technique. Gas cooling places a limit on the average power based on the heat which can be removed by laminar flow of the cooling gas. We combine this with an effective duty factor of 50-100 to calculate the maximum average power in the barrel.

Timing resolution affects the number of overlapping events that occur when the detector is read out. Here there is a tradeoff between speed and front-end signal-to-noise and power. Fortunately, the low capacitance and high signal-to-noise ratio of a finely pixelated sensor allows for acceptable power dissipation for single-crossing ($\approx$ 300-700 ns) time resolution. Therefore our baseline design assumes single-crossing time-resolution.

2.2 Baseline Design

Given the significantly extended physics reach that can be achieved with superb vertex reconstruction – primary, secondary and tertiary – the vertex detector for SiD is proposed to be an all-silicon structure in a barrel-disk geometry. Side views of the vertex detector are shown in Figures II-2.1 and II-2.2.

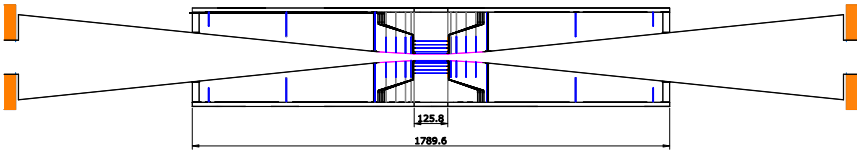

Figure II-2.1 Layout of the vertex and forward tracking region, including carbon-fibre support and forward cone. Dimensions are in mm

The geometry parameters of the vertex detectors are summarised in Table II-2.1. The five barrel sensor layers are arranged at radii ranging from 14 to 60 mm. The vertex detector also has four disk layers supported by carbon-fibre support disks at z positions ranging from about 72 to 172 mm. The innermost disk covers radii from 14 mm out to 71 mm. Forward tracking continues beyond the vertex detector proper with three additional small pixel disks, extending in z from about 207 to 832 mm. The vertex barrel and inner endcaps have $\approx 20 \times 20$ μm pixels. The pixel size increases to $\approx 50 \times 50$ μm^2 for the forward tracker disks. The total area of the vertex barrels is 1.63×10^5 mm^2 and is 0.59×10^5 mm^2 for each set of 4 inner pixel disks and 1.96×10^5 mm^2 for each set of 3 forward pixel disks. The simulation described in the following chapters assumes 0.1% radiation length per layer excluding cables and 20×20 μm pixels for the forward tracker disks.

Table II-2.1 The geometry parameters of the SiD vertex detector (Barrel, Disks and Forward Disks). Units are mm.

Barrel	R	z_{max}	
Layer 1	14	63	
Layer 2	22	63	
Layer 3	35	63	
Layer 4	48	63	
Layer 5	60	63	
Disk	R_{inner}	R_{outer}	z_{center}
Disk 1	14	71	72
Disk 2	16	71	92
Disk 3	18	71	123
Disk 4	20	71	172
Forward Disk	R_{inner}	R_{outer}	z_{center}
Disk 1	28	166	207
Disk 2	76	166	541
Disk 3	117	166	832

2.2.1 Sensor Technology

There are a number of possible choices of sensor technology for the vertex detector, including 3D integrated sensors and readout chips [66], Silicon-on-insulator (SOI) [67], Monolithic Active Pixels (MAPS) [68, 69], hybrid pixels [70, 71], and DEPFETs [72].

All of these technologies have the capability of delivering sensors less than 75 μm thick with 5 μm hit resolution and low power consumption. They are also changing rapidly with advances in microelectronics. The vertex detector is physically small and SiD is designed to make insertion and removal of the vertex detector straightforward. These factors motivate postponing a decision on the details of sensor technology for the SiD vertex detector to a date as late as possible in the final design process. In this document we have chosen 3D technology to provide a definite reference for the detector design. Other choices would differ in details of the mechanical and electronic design of the vertex detector but would not affect the overall design philosophy. To achieve minimum mass in the barrel ladders we are exploring an all-silicon assembly as the baseline. Alternatives include foam-based

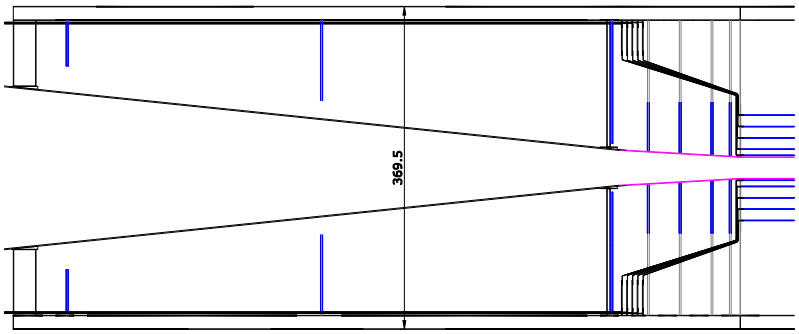

Figure II-2.2
R-z view of the vertex detector and its support structure. Cable routes are also shown with DC-DC converters located on the support structure near the end of the first set of pixel disks. Dimensions are in mm.

ladders as explored in the PLUME collaboration [73], and carbon-fibre supports as prototyped at Fermilab.

2.3 3D-Based Module Design

In microelectronics, 3D technology refers to the stacking of multiple layers of circuitry with vertical interconnections between them. This area is developing rapidly as a way of increasing circuit density without the major re-tooling and investment needed for smaller feature sizes. The enabling technologies for 3D are wafer thinning, wafer bonding, and the formation of Through-Silicon Vias (TSVs). Although the increased circuit density provided by multi-layer circuits is in itself an important application for High Energy Physics, it is the increased range of processing and interconnection options provided by technology that offers the largest potential [74]. Using these technologies arrays of chips can be bonded to sensors and electronics to form essentially monolithic arrays of sensors with no dead space between chips and with interconnections taken from the back rather than the edge of the IC. Chip-to wafer technologies such as Direct Oxide Bonding (DBI) from Ziptronix [75] also promise lower cost and much finer pitch (4 μm has been utilised for the Fermilab wafers) than conventional bump bonding. Heterogeneous layers of different technologies can be combined in a 3D stack to optimise overall sensor performance.

Combining 3D with active edge processing can result in fully active tiles which can be used to populate detector arrays in a variety of geometries with small dead regions. This is especially important for the forward disks where tiling will allow full coverage with minimal dead area.

2.3.1 Active Edge Devices

Active edge sensors are an outgrowth of work done to develop 3D silicon sensors, which provide good charge collection combined with radiation hardness. The technique utilises a deep reactive ion etch of silicon to create a nearly vertical trench with smooth edges. The high quality of the trench wall avoids charge generation normally associated with saw-cut edges [76]. The trenches are filled with doped polycrystalline silicon. Combination of active edge technology with 3D integration can provide a technique for tiling sensor arrays with low mass and high yield. Readout wafers are oxide bonded to sensor wafers with active edge processing. The resulting stack is thinned to expose the Through-Silicon-Vias and the handle wafer is removed by grinding and etching. This results in active tiles with coarse pitch bump-bond connections for readout. Using such tiles, large-area pixelated modules with complex shapes can be assembled with known good integrated sensor/readout dies and with large-pitch backside bump-bond interconnects. All fine-pitch bonds to the sensor are made using wafer-to-wafer oxide bonding. This is particularly useful for the pixel disks, where we want to populate an $\approx$18 cm radius disk with IC reticule ($\approx 2.5 \times 2.5$ cm^2) sized objects.

2.3.2 Barrel Sensor Interconnect to Readout

Any complex, pixelated device will require integration of sensors with readout chips whose size is limited by the reticle area of the CMOS process. There are several choices if we wish to fabricate a 12 cm long ladder. A "stitching" process modifies the reticules to allow reticule to reticule connections on the wafer, by double exposing an overlap region to form connections. The yield of the stitched array is the product of the individual yields. Active tiles can be bonded to a thin substrate which provides power and signal routing. There is a mass penalty associated with the backing structure. A third process, which we have chosen as the baseline, uses sensor wafers bonded to matched 3D wafers. The resulting stack is thinned and the readout and power connections are fabricated on the top aluminium layer of the readout IC layer. This results in minimum mass ladders with no additional material needed for support.

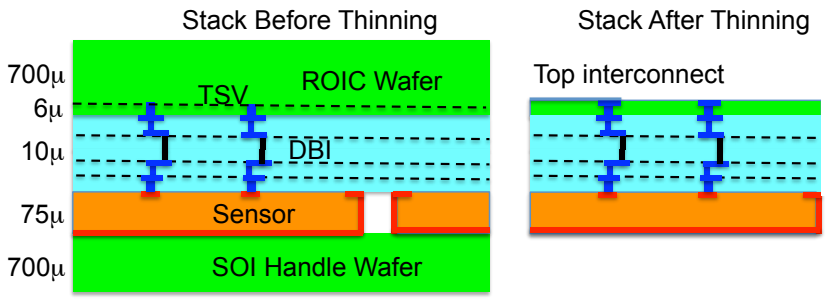

Figure II-2.3 Wafer stack structure before and after thinning and singulation.

Our design includes a number of features which have been or are being demonstrated, but full ladders have not yet been assembled. The design is based on active-edge SOI sensors bonded to readout chips with Through-Silicon-Vias [77]. Similar results can be obtained with SOI sensors utilising the handle wafer as a sensor, or MAPS-type designs.

A possible process would include:

1. Fabricate sensor wafer as an SOI stack with a 50 μm thick sensor bonded to a thick handle which will be removed after processing. Trenches are etched in the perimeter of sensors to provide the active edge.
2. Fabricate ReadOut Integrated Circuit (ROIC) Through-Silicon-Vias wafers with reticule pitch matched to the sensors.
3. Oxide bond ROICs to sensors with seed metal routing to match a smaller ROIC pixel pitch at the edges. This allows for the regions near the edges of reticules to be used for test structures and alignment.
4. Thin the stack to expose the Through-Silicon-Vias. Pattern the top layer to provide bussing to all power and readout connections. Form bump bond pads near the edges.
5. Etch the regions at the sensor periphery to singular the individual sensors.
6. Backgrind and etch the wafer to remove the handle.

Figure II-2.3 shows the wafer stack structure before and after thinning and singulation. This process is very similar to work currently being done at VTT and Ziptronix to demonstrate active-edge tile fabrication. The only significant difference for SiD would be the thickness of the sensor (50 vs. 200 μm) and bonding of multiple reticules to a single sensor. Alternatives, such as carbon-fibre or foam supports would simplify the process at some expense in mass.

2.3.3 Sensor tiling for disks

The ROIC/sensor bonding process for the four forward pixel disks is similar to that used for the barrel ladders except that single reticules are bonded and singulated. Each tile has a set of bump bonds distributed on the back side for power and readout interconnect. The tiles are bump bonded to a carbon-fibre backing plate co-cured with a Kapton circuit which provides routing to external connections. The four different inner radii of the disks would require four different reticule layouts. A optimised final design might utilise identical disks to minimise the varieties of layouts.

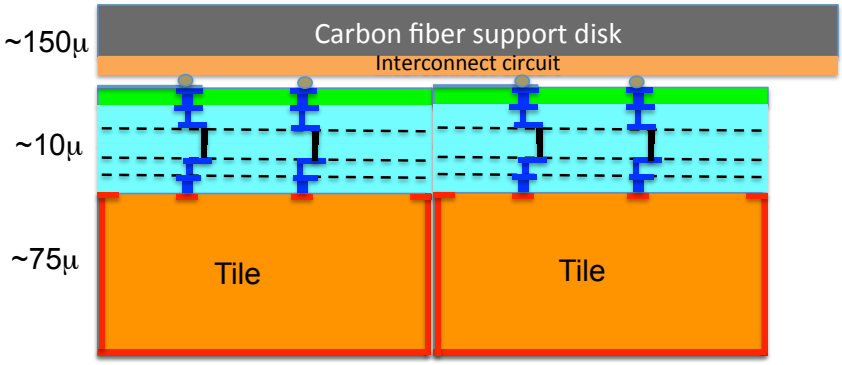

Figure II-2.4 Tiled structure used for the disk layers utilising a carbon-fibre backing disk.

A similar layout can be used for the forward pixel disks at large z. Figure II-2.5 shows a possible tiling which utilises only two reticule types. In this design the outer disk would use two rows of tiles, the middle would use four and the inner would use six. The active edge technique has the additional advantage that edges are formed by etching rather then saw cutting, so the trapezoid shapes can be fabricated easily.

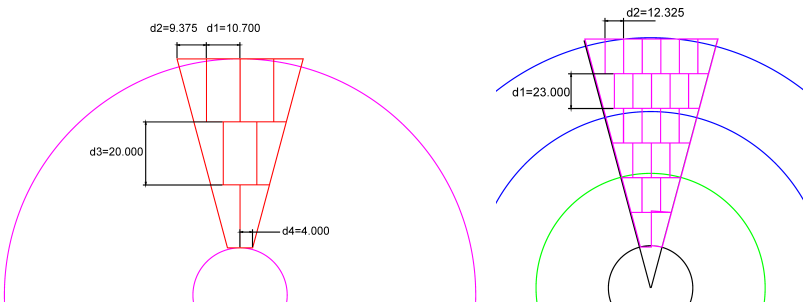

Figure II-2.5 Design of the reticule-based tiling for the innermost pixel disk (left) and for the disks at large z (right) with inner radii of 28 (black), 76 (green) and 117 (blue) mm and an outer radius of 166 mm.

2.4 Support structures and Integration

The vertex subsystem is supported by a double-walled carbon-fibre cylinder (Figure II-2.6) which serves multiple functions. In addition to supporting the vertex detector barrels and disks the cylinder stiffens the beampipe in the vertex region, serves as a cooling gas transport and manifold, and provides locations to mount cables and power converters.

To allow assembly about the beampipe and later servicing, the vertex detector is split at the level of the horizontal plane into top and bottom sub-assemblies. To accommodate the sensor geometry, the split line is offset between the right and left hemisphere. Once mated, the two sub-assemblies are supported from the beam pipe and stiffen the portion of the beampipe passing through them.

To prevent bending of the small-radius portion of the beampipe and ensure good stability of the vertex detector position, the outer vertex detector support cylinder is coupled to the beampipe at four longitudinal locations: $\pm$ 21.4 and $\pm$ 88.2 cm. The support cylinder is separated into top and bottom halves, as are all vertex detector structures. Inner and outer support cylinder walls are 0.26 mm thick. They are made from four plies of high-modulus carbon-fibre resin pre-preg. Wall separation is 15 mm.

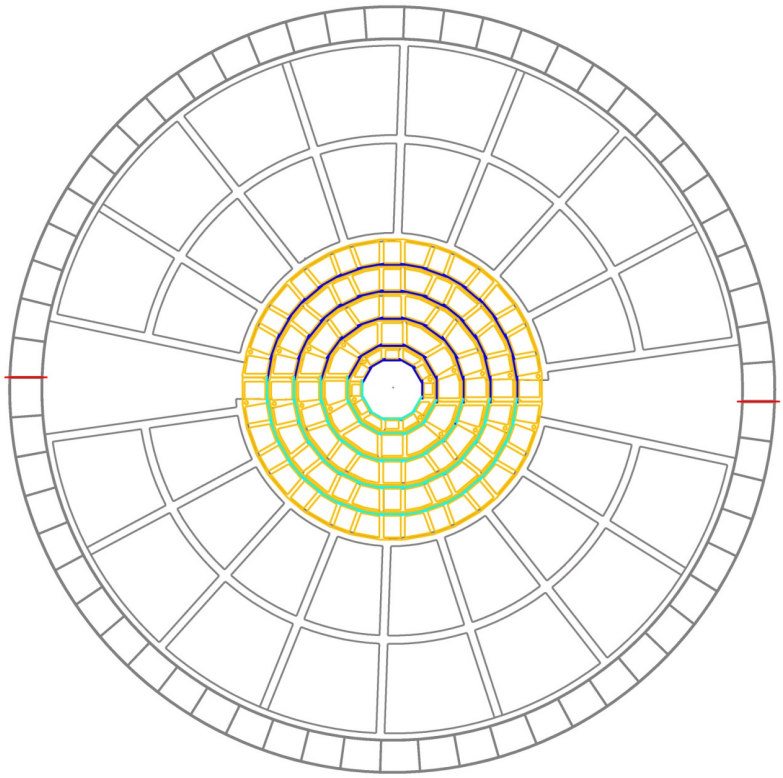

Figure II-2.6
End view of the vertex support cylinder showing ribs and cooling gas passages, internal stiffening web structures, and the barrel vertex detector. Top and bottom sections of the barrel are shown in blue and green.

During silicon tracker servicing the vertex detector and beampipe remain fixed while the outer silicon tracker rolls longitudinally. To allow for that motion and to permit the outer silicon tracker elements to be at the lowest possible radius, the outer radius of the vertex detector, including its support structures, has been limited to 18.5 cm. Additional space for any additional thermal insulation which might be needed, has been foreseen. To maximise the physics potential, the inner radius of vertex detector elements has been chosen to be as small as possible, while still being consistent with beam-related backgrounds and the beampipe profile. In the barrel region, the minimum radius to a sensor surface is 1.4 cm, governed by the beam backgrounds.

2.4.1 Power delivery

2.4.1.1 Readout Considerations

The vertex detector readout is illustrated using the scheme with in-pixel storage of analog information and digital time stamps used both in the 3D-VIP or the Chronopixel chip [78]. In this scheme analog and digital information is stored within a pixel during the bunch train and read out between bunch trains. The pixel complexity is minimised by storing the address information on the periphery of the chip. Table II-2.2 summarises the power consumption of this readout scheme. Electrical connections of about one meter from the ladders to optical links installed on the support tube have been assumed. Assuming 32 bits are used per hit and 100 pF interconnect capacitance at 1.5 V, the local readout consumes 0.24 W of average power. If each of the 108 ladders is independently driven using a 200 MHz clock, the inner layers would dominate the readout time at 75 ms/ladder. The bit rate from the entire vertex detector is about 2 Gbit/s.

We base our estimates on the VIP chip, which utilises 6 μA per 24×24 μm^2 pixel in steady-state operation. An effective duty factor of 80 for power pulsing leads to an average power of $\approx$120 μW/mm^2. The average power in the vertex barrel is then 19.1 W. A similar calculation yields an average power of 1.37 W/disk.

Table II-2.2
Readout rates for the vertex detector.

Layer	Ladders	hits/crossing	bits/train	Readout time (s)	Readout Power (W)	Analog Power (W)
1	12	2000	1.8×10^8	7.5×10^{-2}	0.10	1.7
2	12	1200	1.1×10^8	4.5×10^{-2}	0.06	2.5
3	20	800	7.2×10^7	1.8×10^{-2}	0.04	3.7
4	28	450	4.1×10^7	7.2×10^{-3}	0.02	5.0
5	36	400	3.6×10^7	5.0×10^{-3}	0.02	6.2

2.4.1.2 Pulsed Power and DC-DC conversion

The stringent power dissipation requirements for the vertex detector can be met by delivering power to the front-end electronics only when it is actually needed. The time structure of the ILC beam, with ≈1 ms bunch trains followed by ≈199 ms gaps, allows for power pulsing. Analog and digital circuits can be turned on and off selectively, taking into account capacitive rise and fall times of individual sub-circuits as well as the time to handle the actual data load. Bias levels, however, need to be maintained at all times.

Although the average power in the vertex detector is low, the instantaneous current during the bunch train can be quite high, especially in view of the low supply voltages in modern CMOS technologies. This results in either unacceptable voltage drops in the cables or the use of high cable masses to reduce resistance. To solve this problem, which is also a significant issue for the ATLAS and CMS detector upgrades, we plan to place DC-DC converters in the vicinity of the vertex detector. Moreover, adequate voltage regulation will be implemented in the power supply chain to avoid voltage spikes due to power pulsing. The design includes low-mass flex cables which are routed from the vertex barrel and disk modules to a location at the inner wall of the support cylinder

The powering of the SiD readout chips was studied with a one-step DC-DC buck converter providing the required voltage and current. Input to the converter is 12 V for an output of 1.2 V using an air core inductor. Test boards were constructed operating at 1 MHz with several different commercial DC-DC converter chips. Tests with ATLAS tracker silicon strip detectors [79, 80] indicated that the electrical noise is primarily electrostatic and can be shielded by a 20 μm Al foil. To further reduce the mass, higher frequency operation of the inductor and the buck converter is required. The portable platform industry (smartphones, tablets, etc) currently uses DC-DC converters operating up to 6 MHz, while 20 MHz converters are in the R&D stage.

2.4.2 Cooling

Cooling in the SiD vertex detector is based on forced convection with dry air. The flow for barrel cooling is assumed to be from one barrel end to the other. For a study of the heat dissipation and cooling, the average power dissipated in a sensor was taken to be131 $\mu W/mm^2$. That corresponds to a total power of 20 W for the five barrel layers. These numbers presume power pulsing. Power is assumed to be distributed uniformly over the sensor active surface and both sensor surfaces participate in heat removal. The supply air temperature was taken to be -15 ^{0}C. For a given sensor, heat transferred inward through the carbon-fibre support was taken to be proportional to the surface contact between the sensor and carbon fibre. Thermal impedance through silicon, epoxy, and carbon-fibre laminate has been included, but turns out not to be very significant. The remaining heat was assumed to be transferred outward into the layer to layer gap. For flow and heat transfer calculations, the gap between barrel layers was taken to be 1 mm less than the nominal layer spacing and laminar flow was assumed.

In the gap between the innermost layer and the beam tube, flow is likely to be lower and temperature higher, once supply and return distribution patterns of air flow have been taken into account. Higher flow rate clearly improves the uniformity of sensor temperatures and reduces the

difference between the sensor temperature and the cooling air. All flow rates which have been considered lead to temperature variations which should be acceptable for dimensional stability, which is crucial for high-precision vertexing. The time-dependent effects of power cycling remain to be investigated. Those depend on the thermal mass in the barrel and the details of the power cycling. The outer support cylinder of the vertex detector offers a natural thermal enclosure. Details of end openings in barrel membranes remain to be included. Those openings provide a mechanism for adjusting relative flow between barrel layers. A membrane between the outermost barrel layer and the vertex support cylinder will ensure that flow does not excessively bypass the barrel-to-barrel gaps. Similar calculations have been made to understand disk cooling. Those calculations are based on barrel results with a Reynold's number of 1800 (barrel flow = 20 g/s). Heat removal calculations for the first four disks at each end of the barrel assume the same power per unit area as the pixel sensors of the barrel. The result is a total power of 16.9 W for all eight disks and an air flow of 16.4 g/s.

We propose to deliver air via the outer support cylinder. To allow that, the two walls of the cylinder are separated by radially-oriented ribs running along the full cylinder length. The calculations assume ribs at 60 azimuths. Openings, each approximately 12.2 mm $\times$ 15 mm, at 18 z-locations in the inner cylinder wall distribute the flow to the various disk locations and to the barrel. At each azimuth, the cell through which flow passes was approximated by a rectangle of height 15 mm and width 18.2 mm. The wall thickness was assumed to be 0.26 mm for both cylinders and for all ribs.

The results gave a Reynold's number of 3105 in the portion of the cell which sees full flow, indicating turbulent flow. Since a portion of the flow exits the cell at each opening, the Reynold's number drops to 1725 at approximately z = 51.9 cm (a short distance inboard of the two outermost disks). While entrance effects may remain, the flow should gradually become laminar after that point. Supply and return connections to the outside world remain to be fully evaluated. With eight connections per end, each represented by a 20 mm $\times$ 40 mm rectangular passage, the Reynold's number is 12900 and flow is turbulent.

2.4.3 Cabling

We plan to utilise low-mass strip line cables based on aluminium conductor for signal communication and power distribution from the sensors to the DC-DC converter region. The inner ends of the cables will be wire bonded directly to the sensor ladders. In the DC-DC converter region signals will be converted to optical fibres. Power will be brought into the vertex region at ≈ 12 V by aluminium cables which make the transition to copper outside the tracker volume. Varying Lorentz forces due to pulsing of the power are a particular concern. This is minimised by utilising balanced supply and return lines and twisted wires where appropriate. We will utilise a three-layer strip-line design with centre supply and outer return traces to minimise forces on the cables [81]. Tests of mechanical forces and vibration are planned utilising KPiX chips and a 7 T magnet available at Yale. The pulsed power frequency, 5 Hz, is significantly below the resonance frequency expected for major support structures.

2.5 R&D Status

2.5.1 Chronopixel

We have developed a design, in collaboration with SARNOFF Research Labs, for the Chronopixel devices that satisfy the ILC requirements [78]. The design of the ultimate device requires high resistivity silicon (5 kΩ-cm) with a 15 μm thick epilayer and pixels of 10 $\times$ 10 to 15 $\times$ 15 μm which will require to use 45 nm technology. The 45 nm technology is currently too expensive for prototyping, so we foresee a series of prototypes that approach the ultimate design. The first prototype has been designed, fabricated and extensively tested. The second prototype has recently been fabricated and the testing of these devices is just getting started.

2.5.2 VIP 3D Chip

The Vertically Integrated Pixel (VIP) ASIC was conceived of as a demonstration readout chip for the ILC vertex detector [82]. The Lincoln Laboratory process has the advantage of very well-established wafer bonding and thinning, but the fully depleted SOI process is not well suited for analog applications and has larger feature size than advanced commercial processes. The final Fermilab designed ASIC (VIP2a) using this process was received and tested late in 2009. The analog front end of VIP2a, which was laid out using design rules modified at Fermilab based on failings of the earlier prototypes, worked well, as did all of the interconnections between circuit layers.

A second iteration, the VIP2b was fabricated in the 3D process developed by Tezzaron/Global Foundries. This process uses a bulk 0.13 μm CMOS IC process with modifications to allow the top copper metal layer to be used for face-to-face wafer bonding, and to include vias that extend 6 μm into the bulk material. After wafer bonding, one of a pair of wafers was back thinned to expose the deep vias, and metal pads deposited that are suitable for wire bonding or for further wafer bonding. We now have chips with successful 3D bonds between tiers. Initial testing of the 2D parts show excellent analog performance. Tests of the full functionality of the 3D chips are underway.

2.5.3 Thinned hybrid detector with high-density interconnect

An alternative option for a low-mass vertex detector combines thinned high-functionality readout ASICs with thin high-resistivity sensors, assembled using advanced low-mass interconnect technologies. For the ASIC the 65 nm deep sub-micron technology was successfully assessed, through the design and production of relevant pixel readout sub-circuits [83]. Subsequently a fully functional test chip has been designed in 65 nm technology. It comprises 64×64 pixels of 25×25 μm size providing time-of-arrival and time-over-threshold functionality [84]. The ASIC foresees individual power pulsing of its analog and digital circuits. It has been submitted for production at the end of 2012. Development has been initiated towards low-mass fine-pitch flip-chip interconnect based on copper pillars. Module assembly is foreseen to make use of Through Silicon Vias (TSV) to carry interface signals to the backside of the pixel chip. This will offer 4-side buttable pixel chips, enabling the assembly of large-area pixel detectors with minimal dead space between individual pixel tiles. The TSV technology has meanwhile been applied successfully on Medipix3 chips manufactured using a 130 nm process [85].

2.5.4 Active Edge Tiles

Active tiles are central to the conceptual design of the forward disks. A program to demonstrate these devices is underway in collaboration with Fermilab, SLAC, and Cornell University. Sensors of 200 μm thickness are being fabricated on SOI wafers by VTT and planar dummy top wafers with tungsten contacts are being fabricated by Cornell. The two will be wafer-bonded by Ziptronix and this stack will be singulated and thinned by SLAC. We expect the VTT wafer to be complete by the end of 2012.

2.5.5 Critical R&D

By the conclusion of the current round of R&D, we expect to have demonstrated the basic sensor and IC technologies needed for SiD. The next logical step would be to develop a full sized ladder for the barrels and a wedge segment for the disks. We need to build prototype support structures, including the double walled outer cylinder and barrel and disk supports. We also would need to demonstrate the integration of ladders and wedges into barrels and disks, initially with one live and several dummy sensors. Finally, a full-sized prototype with heating elements would allow us to study air cooling and confirm flow and temperature calculations.

Studies of power delivery and cabling are critical. We would like to demonstrate a low-mass cabling system, including aluminium conductors, DC-DC conversion, and optical interconnects in the context of a full sized mechanical prototype. Again, many of the individual technologies have been demonstrated by the LHC experiments, the RHIC projects, or in ILC detector R&D, but a complete system has yet to be demonstrated.

2.6 Summary

The basic concepts in the SiD Vertex detector, low-mass mechanical designs, the split cylinder support structures, and the barrel/disk geometry are essentially unchanged from the SiD LOI. However, more detailed designs for cabling, power conversion, sensor technology, and mechanical supports and cooling are included in this report. Most of these components are, or will soon be, ready for the module prototype phase. At that point decisions would need to be made on tradeoffs such as the lower mass, but more challenging, all-silicon design vs a design which has carbon-fibre or foam supports and, ultimately, sensor technology.

Chapter 3
SiD Main Tracker

3.1 Introduction

The ILC physics goals impose performance requirements on the tracking system that exceed those met by any previous system. These are summarised in Table II-3.2. In particular, the need for excellent momentum resolution over a broad p_{T} spectrum creates significant design challenges. For high-p_{T} tracks superior position resolution and mechanical stability are required while for low- p_{T} tracks, an aggressive material budget is critical. Meanwhile, the need for high efficiency over a wide range of momenta and large solid angle motivates an integrated approach to tracking: the vertex detector, main tracker and calorimeter are designed to work in concert to achieve these goals robustly but with a narrow margin of extra layers that result in unnecessary material.

3.2 Baseline Design

The main tracker is a large all-silicon detector filling the space between the vertex detector and the electromagnetic calorimeter. It comprises five cylindrical barrel layers, with the four outer layers closed at the ends by conical, annular disks, as shown in Figure II-3.1.

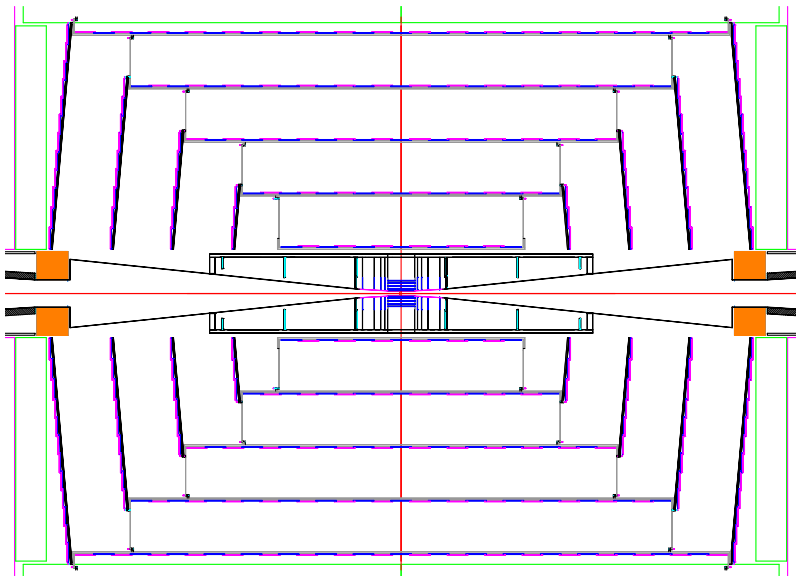

Figure II-3.1
$r-z$ view of the vertex detector and outer tracker.

In the baseline design the barrels are tiled with modules hosting a single silicon micro-strip sensor for axial-only measurement, while the disks are tiled with modules having a stereo pair of silicon micro-strip sensors. These cylinders are nested, connected by annular rings at the ends of each, to create a single unit supported from the ends of the electromagnetic calorimeter (ECAL). The design of the outer tracker is summarised in Table II-3.1 and more details of the design may be found in [63].

The coverage of the complete tracking system is shown in Figure II-3.2 as a function of the polar angle. At least six hits are measured for all tracks with a polar angle down to about 8°. For polar

Table II-3.1
The layout of the main tracker.

Barrel Region	R (cm)	Length of sensor coverage (cm)	Number of modules in ϕ	Number of modules in z
Barrel 1	21.95	111.6	20	13
Barrel 2	46.95	147.3	38	17
Barrel 3	71.95	200.1	58	23
Barrel 4	96.95	251.8	80	29
Barrel 5	121.95	304.5	102	35
Disk Region	**z_{inner} (cm)**	**R_{inner} (cm)**	**R_{outer} (cm)**	**Number of modules per end**
Disk 1	78.89	20.89	49.80	96
Disk 2	107.50	20.89	75.14	238
Disk 3	135.55	20.89	100.31	438
Disk 4	164.09	20.89	125.36	662

angles above 13° ten layers or more are traversed. The goals of the ILC physics program impose performance requirements on the tracking that exceed those met by any previous system and are summarised in Table II-3.2.

Figure II-3.2
The coverage of the SiD tracking system as a function of the polar angle θ.

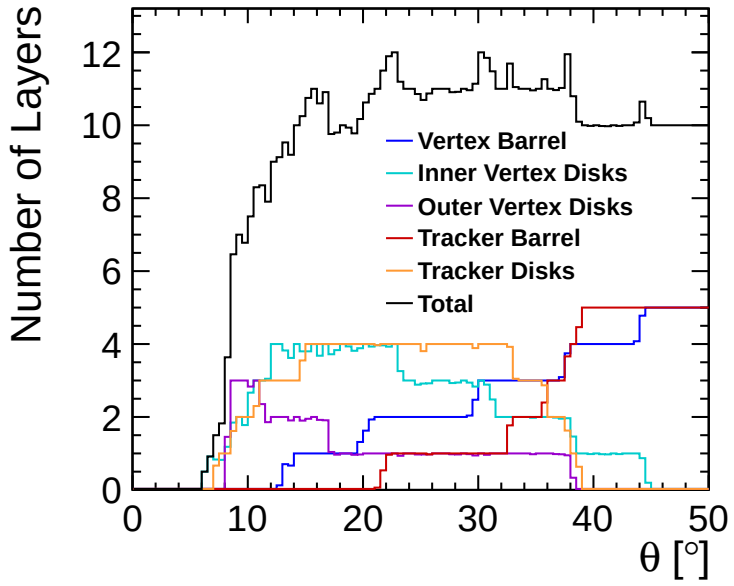

3.3 Baseline Design

The baseline design uses relatively conventional technologies to achieve the performance goals with low risk and minimal cost. The sensors are single-sided micro-strips. The barrel and disk supports, as well as the module supports, are composites of carbon fibre and low-density Rohacell 31 [86] foam. Low-mass hardware is fabricated in polyether ether ketone (PEEK).

There are, however, some key elements where novel solutions are required. The sensors, like those for the ECAL, employ a double-metal layer to route signals to bump-bonding arrays for readout by the KPiX ASIC [87, 88, 89]. As with the ECAL, traces on the second metal layer of the sensor connect power and signal lines on the KPiX chip to a readout cable that is also bump bonded to the face of the sensor. This arrangement eliminates the material and assembly complexity of hybrid circuit boards to host the readout electronics. The low power dissipation of KPiX makes gas cooling feasible, reducing further the required material. However, since KPiX achieves low power consumption through power pulsing with a duty cycle of approximately 1%, the instantaneous currents required to power the tracker are still large and requires a significant mass of conductor.

Table II-3.2 Performance goals for the main tracker.

Parameter	Design Goal
coverage	hermetic above $\theta \sim 10^{\circ}$
momentum resolution $\delta(1/p_{\mathrm{T}})$	$\sim 2 - 5 \times 10^{-5}/\mathrm{GeV}/c$
material budget	$\sim 0.10 - 0.15\mathrm{X}_0$ in central region
	$\sim 0.20 - 0.25\mathrm{X}_0$ in endcap region
hit efficiency	$> 99\%$
background tolerance	Full efficiency at $10\times$ expected occupancy

Concentrator boards located on the support rings at the ends of each barrel host DC-DC converters to transform high-voltage, low-current input power into low-voltage, high-current power for the modules, thus minimising the conductor and cross-sectional area required to deliver power into the boards from outside the tracking volume.

3.3.1 Barrels

A set of five cylindrical layers provides tracking coverage in the central portion of the detector. Each cylinder is formed from a sandwich of carbon fibre and Rohacell cured as a single unit, similar to those used in the DØ CFT and the ATLAS SCT [90]. The inherent rigidity of the cylinders allows for holes to be cut where allowed by module mounting locations to further reduce the average material experienced by passing particles without significantly compromising rigidity. However, it should be noted that such measures to reduce the material in the barrel and disk supports are not included in the current simulation or material estimates shown here. The outer surface of each cylinder is populated with PEEK mounting clips for the modules that allow the insertion and extraction of individual modules without the use of tools, facilitating module replacement without complete disassembly of the tracker. The normal to each module is tilted with respect to the radial direction to allow for overlap between modules that are adjacent in ϕ and partially compensate for the Lorentz direction. Adjacent modules in z alternate between inner and outer mounting positions to provide longitudinal overlaps. Excluding overlaps, the material presented by a single barrel layer is approximately 0.9% X_0 for tracks at normal incidence.

The modules themselves comprise a single sensor, read out via two bump-bonded KPiX ASICs and a short polyimide cable supported by a composite support frame. A picture of a prototype sensor and cable is shown in Figure II-3.4. The sensors are single-sided, poly-biased, AC-coupled, micro-strip sensors fabricated on 300 $\mu\mathrm{m}$ thick, p+ on n bulk, high resistivity silicon. The nominal sensor (readout) pitch is 25 (50) $\mu\mathrm{m}$, with the intermediate strips capacitively coupled to the readout strips to improve single hit resolution. The KPiX chips bonded to the surface of the sensor, described more fully in Chapter 4, store time-stamped hits from the tracker exactly as for the ECAL sensors, for readout between bunch trains. Traces on the second metal layer of the sensor connect power and signal lines on the KPiX chip to a short readout cable, or pigtail, that is also bump-bonded to the face of the sensor. These copper-on-polyimide cables have tabs that provide bias voltage to the edges of the sensors and have micro-connectors that mate to the extension cables running along the surface of the cylinder to the concentrator boards located at each end. Great care has been taken to model the conductor required for each cable run and the stacks of cables required for each layer to arrive at realistic material estimates.

The back side of the sensor is glued to the face of a module support frame that comprises a pair of carbon composite sheets sandwiched around a thin sheet of Rohacell 31 [86]. This frame is approximately 50% void to reduce material and is passivated to isolate the carbon fibre from the high voltage on the rear of the sensor. A set of three spheres around the periphery of each frame provide a three-point kinematic mount to the mounting clips on the outer surface of the barrel cylinder. A small handle on each module provides a strain relief for the pigtail as it leaves the module and safe

handling during assembly and installation.

3.3.2 Disks

The outer four barrel cylinders are partially closed at each end by slightly conical, annular disks that extend the coverage to the forward regions. These disks are fabricated using a carbon fibre and Rohacell 31 sandwich similar to that of the barrel cylinders. As with the barrel cylinders, the outer surfaces of the endcap disks are covered by a set of PEEK mounting clips that hold the disk modules. Adjacent modules in ϕ alternate between inner and outer mounting positions to provide overlap. The modules, mounted normal to the z axis, step along the five degree slope of the cone to provide radial overlap. Excluding overlaps, the material budget for a single disk layer is approximately 1.3% X_0 for tracks at normal incidence.

The endcap modules are similar to those for the barrels, but have sensors on both sides of the module frames to provide a stereo measurement. The sensors on each side are identical trapezoids with strips parallel to one edge, and are technologically identical to those used in the barrel. A smaller sensor is used for small-radius portions of the disk, while a larger sensor is used in the larger-radius regions. As in the barrel, short pigtail cables bonded directly to the sensors connect to extension cables that transmit power from, and data, to concentrator boards mounted at the outer radius of each disk. The layout of the outer disk is shown in Figure II-3.3.

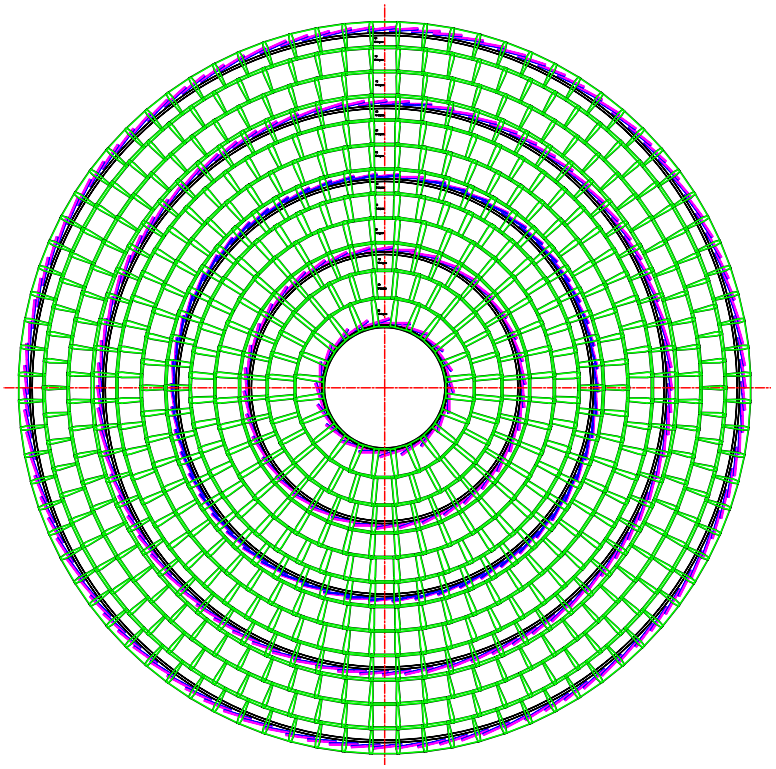

Figure II-3.3
Rφ projection view of the main tracker barrels (red) and disks (green).

3.3.3 Barrel and disk Integration

The barrel cylinders are nested, one inside the other, with spoked annular rings at the ends of each cylinder supporting it from the inside surface of the next cylinder outward. The outermost cylinder is mounted to the inside surface of the ECAL barrel. The disks that close the ends of the barrels mount to the inside circumference of these same rings, extending beyond the barrel radii to provide overlap between the barrels and disks. On the outer faces of these support rings are the concentrator boards that connect to individual modules. Each board hosts charge storage and DC-DC conversion to provide pulsed power to at least ten sensors, as well as distribution of clock and control signals, and electrical

to optical conversion of output signals to concentrate the data. With high-voltage low-current power and optical transmission of data, the cable cross-section needed to service the concentrator boards for the entire detector is minimised, thereby improving the hermeticity at the barrel-disk transitions. In order to spread out the material of the concentrator boards and support rings, the barrel-disk transitions of the different layers are non-projective. The impact of the concentrator boards on the material budget can be seen in Section 10.3..

3.4 Critical R&D

The main tracker embraces conventional technologies where possible to minimise the risks and costs of the system and minimise the R&D necessary to bring it into production. However, there are several key areas where exploring new technologies, targeted at addressing specific performance limitations, is critical to meeting the performance goals. These technologies focus on minimising the tracker material necessary for good resolution for low-momentum particles while maintaining the mechanical stability. The key R&D projects involve the sensor readout, data transmission, power, cooling and the mechanical stability of the system.

Key to minimising the material in the tracker is the KPiX readout. Development of KPiX and the critical elements of the readout chain are of great importance, including bump bonding KPiX to sensors, development of sensors and cables, and development of the complete DAQ chain. Because the tracker is technologically identical to the ECAL in all of these respects, KPiX R&D for the tracker is undertaken together with that for the ECAL and is largely described in Chapter 4. However, with a very different set of requirements, the implementation for the tracker still differs in some respects that motivate tracker-specific R&D. This R&D has focused first on producing prototypes of a barrel module; that is the simplest module needed and solutions developed apply directly to the key issues for the disk modules.

With the requirement of full efficiency for minimum ionising particles and excellent single-hit precision, a signal-to-noise ratio in excess of 20 is required. This, in turn, sets the requirement for the noise performance of KPiX and necessitates sensors with very low readout capacitances and resistances. Prototype sensors (Figure II-3.4) were fabricated by the Hamamatsu Photonics Corporation and meet the noise performance requirements. Successive generations of KPiX chips have undergone improvements in noise performance and are now able to meet the goal, although testing of a fully assembled module will be required to verify the as-built noise performance. Assembly of a full module has been awaiting recently developed interconnect techniques for first ECAL prototypes, as described in Chapter 4.

The cable for the tracker differs somewhat from that required for the ECAL. It must have the lowest possible mass and the best possible noise performance, while servicing two KPiX chips simultaneously. A prototype cable that meets all of the requirements for the tracker has been produced (Figure II-3.4).

To speed development, this prototype cable was planned to be glued and then wire bonded to the sensor, rather than bump-bonded as called for in the design. However, a processing deficiency in the prototype sensors makes them susceptible to damage during wire bonding of the readout cable. The design and fabrication of a cable for bump bonding attachment, as successfully demonstrated in the ECAL, is under way. It will enable assembly and test of full prototype modules with the KPiX chips and sensors already in hand.

The other keys to the tracker design are low-mass support and cooling. While the module support frames are quite conventional, the techniques being considered for mounting these frames to the support cylinders and disks are somewhat novel and it is important to verify the details of these designs with prototypes before considering large-scale production. Testing with basic prototypes is

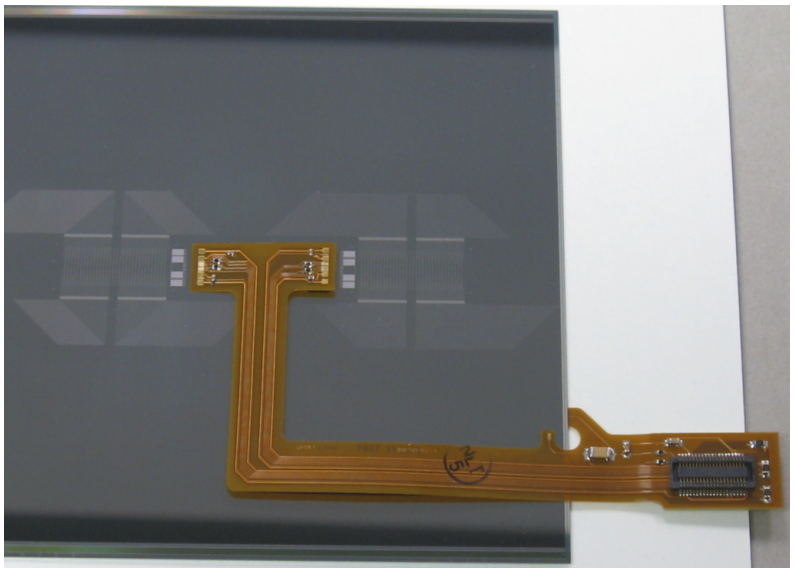

Figure II-3.4
Prototypes of the barrel sensor and its pigtail cable shown together as they would be assembled. The bump bonding arrays for the KPiX chips and the double-metal fan outs can be seen on either side of the cable. The tab at the edge provides bias to the sensor.

being pursued so as to allow the design to evolve quickly. With a working prototype in hand, and using standard design guidelines, it should be possible to ensure success with a high degree of confidence. However, the final step of ensuring that these parts can be mass-produced will be expensive and must await further resources.

Use of gas cooling depends principally on meeting the power consumption goals with KPiX, which has already been achieved [63]. The requirements for other cooling loads, such as those from the concentrator boards, can already be met with commercially available components. With gas velocities of approximately 1 cm/s, the impact on mechanical stability is negligible compared with other low-mass, gas-cooled silicon detectors being assembled for other experiments [91]. However, the requirement for hermetic coverage severely restricts gas flow in some parts of the detector, and further study is required to engineer the cooling system.

The main issue for the mechanical stability is Lorentz forces on the various elements of the tracker due to power-pulsing in the 5-Tesla magnetic field. In the barrel, conductors are largely parallel to the field, but the opposite is true in the disks. Development of cables with closely paired supply and return lines is a priority, and incorporation of this requirement into the next pigtail prototype is planned. Tests of modules inside a small-bore MRI magnet are being considered that would allow for collection of critical data on these effects. The rigidity of support structures should place any resonances well above the 5 Hz excitation frequency, but the design of the detector must take into account any harmonics.

Charge storage and high-voltage, low-current supply to the concentrator boards greatly reduce Lorentz effects on the supply of power from the outside, but present their own R&D challenges. Storing enough energy on the concentrator boards to provide power for the duration of a complete bunchtrain has become much more feasible due to industrial advances in high energy density capacitors. In fact, it appears likely that charge storage using a capacitor on each module may soon be feasible, which would all but eliminate Lorentz forces. Meanwhile, R&D into DC-DC conversion for the supply of future detectors has become an active field in recent years, with some work focused specifically on the needs of the ILC experiments [92, 93].

Efforts are ongoing that would significantly improve the performance of the outer tracker beyond that of the baseline design. One such effort considers the use of resistive charge sharing to determine the position of hits along strips to the precision of a few mm [63]. While instrumentation of both ends of each strip doubles the readout and the material budgets, cost, powering, and cooling constraints do not obviously exclude this option. Another topic of active investigation is whether the tracker could

be built using monolithic active pixel sensors (MAPS). While this would clearly result in improved tracking performance, none of the technologies being investigated for the vertex detector can be convincingly scaled in power and cost to provide a solution for the outer tracker in the near future.

3.5 Performance

The tracking performance of the SIDLOI3 geometry has been studied using full event simulation and realistic event reconstruction of single-muon as well as di-jet events. In the reconstruction of each di-jet event a realistic number of hits from incoherent pairs and hadronic beam backgrounds are overlaid [94], corresponding to one bunch crossing at 1 TeV. This assumes that the time resolution of the tracking detectors is sufficient to separate hits from different bunch crossings..

The digitisation of the simulated tracker hits in the silicon detectors is performed using the SiSim package [95]. Diffusion of the deposited charge in the silicon is taken into account. A nearest-neighbour algorithm is used to identify the clusters which are input to the track finding. The seed tracker algorithm is used for the track finding and track fitting. This algorithm uses a strategy-based approach, where several sets of combinations of three layers define the possible seed layers for the track finding.

For the studies presented here "inside-out" tracking strategies are used. The two innermost vertex detector layers are excluded from seeding to mitigate the impact of the large number of hits from beam backgrounds on the track reconstruction time. Similarly, choosing as small a χ^2 cut-off as possible in rejecting track candidates without compromising the track finding efficiency is essential in the presence of high-occupancy events.

In general a minimum of seven hits are required to define a track. In the barrel region this requirement is reduced to six hits to increase the track-finding efficiency for central low-momentum tracks. A secondary tracking algorithm using calorimeter stubs as seeds can be used to find those tracks with fewer hits from in-flight decays [96]. This algorithm is not used in the performance studies presented here.

3.5.1 Tracking Efficiency

The track-finding efficiency is defined as the fraction of the successfully reconstructed findable particles. The true match of the reconstructed track is determined by the majority of contributed hits. The findable particles are defined as those charged particles originating from within $\pm$5 cm of the IP and travelling at least 5 cm. Any additional cuts are noted in the corresponding figures. In case of multiple interactions, only particles from the signal event are considered for the Track-finding efficiency. Due to the small total number of hits, falsely assigned hits have a significant impact on the reconstructed track parameters. Thus, an additional quality cut is introduced and only tracks with a maximum of one falsely assigned hit are counted as successfully reconstructed.

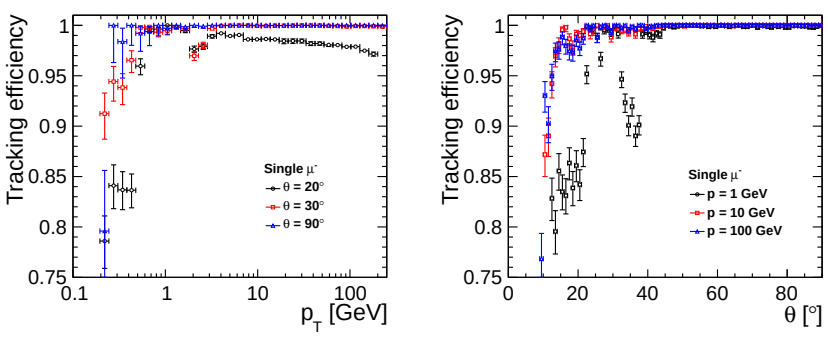

Figure II-3.5
Tracking efficiency for single muon events in SIDLOI3 as function of the transverse momentum (left) and the polar angle (right).

For single muons the dependence of the track-finding efficiency on transverse momentum, p_{T}, and polar angle, θ, is shown in Figure II-3.5. The efficiency is nearly 100% for all tracks with a polar angle larger than 15° and a transverse momentum larger than 1 GeV. The efficiency for tracks below 15° deteriorates towards the detector acceptance of about 10°, where it drops sharply. Requiring a minimum of seven hits reduces the efficiency for 1 GeV tracks in the region between 35° and 40° by about 10%. More central tracks are found efficiently for momenta as low as 0.2 GeV. Low-momentum tracks at polar angles below 25° suffer from an inefficiency of about 15% due to the higher material budget.

The track-finding efficiency has also been studied in di-jet decays of a Z' boson with mass of 1 TeV. The average tracking efficiency in these events, including beam induced backgrounds, is approximately 98%. The efficiency is almost constant for most polar angles and transverse momenta (Figure II-3.6). Similar to the performance for single-muon events there is a slightly reduced track finding efficiency for low-momentum tracks at a polar angle of around 40° and for very forward tracks of all momenta. In addition there is a drop in the efficiency for high-momentum forward tracks. These are typically in the centre of the jet and thus suffer most from confusion due to ghost hits in the stereo strip detectors.

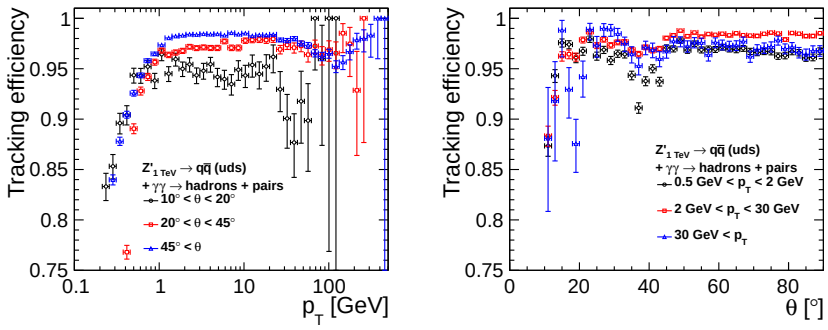

Figure II-3.6
Tracking efficiency in di-jet decays of a Z' particle with a mass of 1 TeV in SIDLOI3 as a function of the transverse momentum (left) and the polar angle (right) of the corresponding particle. Incoherent pairs and $\gamma\gamma \rightarrow$ hadrons events corresponding to 1 bunch crossing are included.

In general the track-finding efficiency is limited by the total number of hits created by the corresponding particle and the local hit density (Figure II-3.7). The efficiency for particles within the acceptance that reach the calorimeters and thus necessarily pass through at least 10 layers is about 99%. The efficiency in dense jets is limited by the silicon micro-strip sizes. Particles which have any other hit closer than 100 μm, which corresponds to twice the pitch of the readout in the strip detectors, have a reduced efficiency. For more isolated particles the efficiency is higher than 98%.

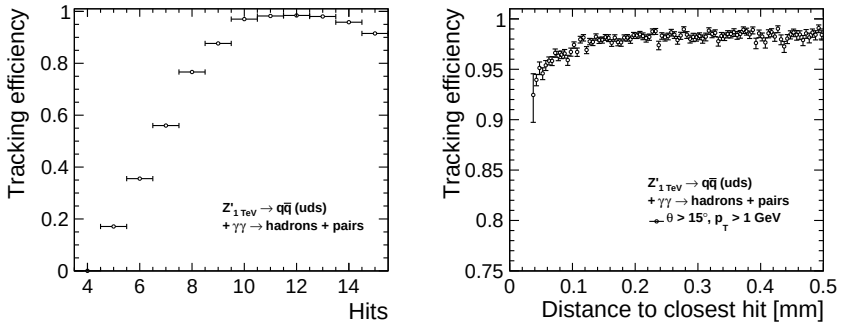

Figure II-3.7
Tracking efficiency in di-jet decays of a Z' particle with a mass of 1 TeV in SIDLOI3 as a function of the number of hits produced by the charged particle (left) and the distance to the closest hit from a different particle (right). Incoherent pairs and $\gamma\gamma \rightarrow$ hadrons events corresponding to 1 bunch crossing are included.

3.5.2 Fake Rates

As mentioned above, the low number of tracking layers requires a very tight track purity definition. All reconstructed tracks with more than one falsely assigned hit are counted as fakes. This fake rate is shown in Figure II-3.8 for tracks in di-jet events including beam-induced backgrounds. Unlike the definition of tracking efficiency, these rates include tracks reconstructed from background particles. The fake rate is between 1% and 3%. High-momentum tracks are more likely to have more than one false hit assigned, since they are necessarily in the centre of a jet and suffer from higher local hit densities. The fake rate for tracks below 40° is lower by one order of magnitude than tracks in the central region. All tracker hits in the forward region have 3D information, which is not the case for the barrel strip detectors.

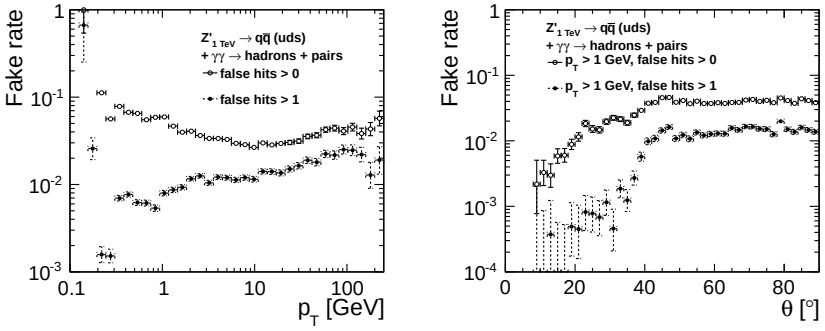

Figure II-3.8
Fraction of reconstructed tracks with spurious hits in di-jet decays of a particle with a mass of 1 TeV in SIDLOI3 as a function of the transverse momentum (left) and the polar angle (right) of the reconstructed track. Incoherent pairs and $\gamma\gamma \rightarrow$ hadrons events corresponding to 1 bunch crossing are included.

3.5.3 Tracking Resolution

The normalised transverse momentum resolution achieved in the SIDLOI3 geometry is shown in Figure II-3.9 for single-muon events. The data points show the width of a Gaussian fit to the $\delta(p_\mathrm{T})/p_\mathrm{T}^2$ distribution of the corresponding reconstructed tracks. The dashed line represents a fit to the canonical parametrisation of the transverse momentum resolution:

$$\sigma(p_\mathrm{T})/p_\mathrm{T}^2 = a \oplus \frac{b}{p \sin\theta}. \qquad \text{(II-3.1)}$$

Despite the ambitious material budget, the multiple scattering term given by b dominates the momentum resolution for tracks up to 100-200 GeV. Whereas the momentum resolution for very forward tracks is limited by the short lever arm in the transverse projection, a momentum resolution of $\sigma(p_\mathrm{T})/p_\mathrm{T}^2 < 10^{-4}$ GeV^{-1} is achieved for high-momentum tracks at polar angles larger than 30°. Central tracks exceed a resolution of $\sigma(p_\mathrm{T})/p_\mathrm{T}^2 < 2 \times 10^{-5}$ GeV^{-1}.

The resolution on the transverse impact parameter, d_0, as well as the longitudinal impact parameter, z_0, is shown in Figure II-3.10. The d_0 resolution is better than a few μm for central tracks with a momentum exceeding a few GeV. For 1 GeV muons the d_0 resolution drops to about 10 μm for central tracks. In the forward region the resolution degrades by up to one order of magnitude at the acceptance limit of $\theta \approx 10^\circ$. The z_0 resolution has a stronger dependence on the polar angle and, while similar to the d_0 resolution in the central region, it is about one order of magnitude worse for very forward tracks. In addition, the z_0 resolution for central tracks is limited by the lever arm of the straight line fit. In the current algorithm the strip hits in the barrel region are excluded from the straight line fit which results in a very short lever arm for central tracks. More details about the tracking performance can be found in [97].

Overall the silicon tracker shows excellent performance. Tracking efficiencies in excess of 99% are demonstrated over most of the momentum and acceptance range. An asymptotic momentum

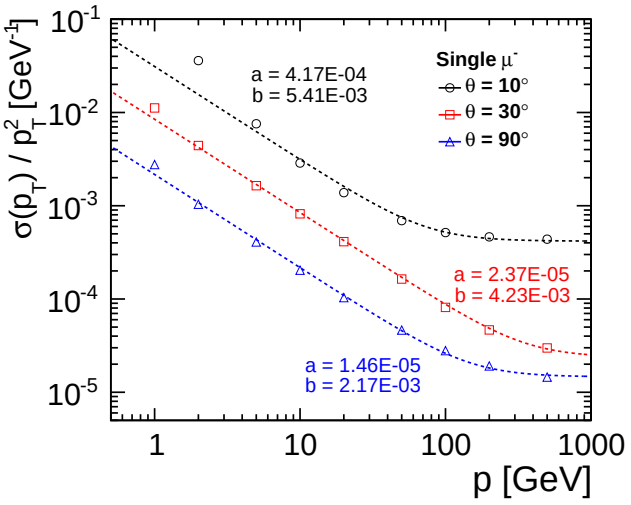

Figure II-3.9
Normalised transverse momentum resolution for single-muon events in SIDLOI3 as function of momentum. The dashed lines indicate a fit to the parametrisation given in Equation II-3.1.

resolution of 1.46 $\cdot 10^{-5}$ and transverse impact parameter resolution better than 2 μm has been obtained. Even though the SiD tracker is very "thin" the studies show that the material budget still imposes limitations and a further reduction in mass would be beneficial. It is expected that some of the performance features can be mitigated through a further optimisation of the overall detector design. The physics results presented later are based on the tracking performance described here.

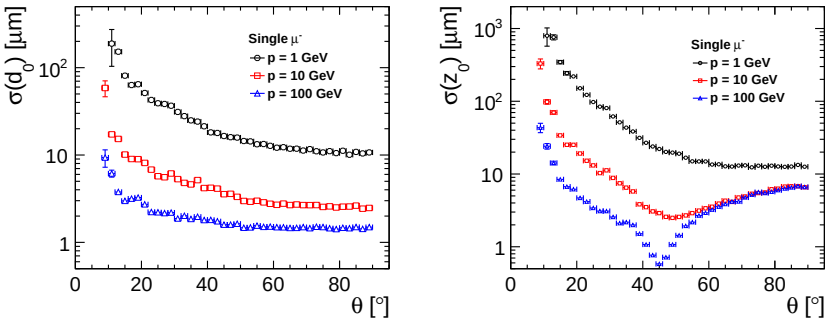

Figure II-3.10
Impact parameter resolution $\sigma(d_0)$ (left) and $\sigma(z_0)$ (right) for single muon events in SIDLOI3 as function of the polar angle θ.

3.6 Alignment

The alignment strategy for the SiD main tracker, vertex detector, and beam-pipe assemblies is based on:

1. a small number of robust, rigid elements;
2. precise positioning of smaller components during fabrication and assembly;
3. real-time monitoring of alignment changes, including during push-pull moves; and
4. track-based alignment for final precision.

It is expected to achieve ≈20 μm relative precision among outer tracker sensor modules in different layers after fabrication and assembly in the full detector. The final precision of a few μm is attained for individual sensor modules from track-based alignment, with real-time Frequency Scanned Interferometry (FSI) and laser-track monitoring providing both a bridge from the coarse to the fine alignment and a set of global corrections for time dependent structure motion and deformation [98].

The support structures for the vertex detector and main tracker have been designed to minimise distortions and maintain alignment. For the outer tracker, the double-walled support cylinders, concave disk support, and nested assembly with annular rings and kinematic mounts are intended

to lead to a robust structure which can be treated as a single unit. Kinematic support from the central calorimetry is intended to minimise distortions of that structure under geometry changes of the calorimeters. For the vertex detector, double-walled support half cylinders are intended to preserve good internal alignment. Since the support structures deflect under beampipe loads, substantial R&D including measurements of prototypes will be necessary to confirm that this design will perform well.

Tracker alignment is expected to begin during fabrication and assembly. Sensor alignment within each main tracker module will be measured with respect to fiducials and mounting features of the module. Modules will be solidly anchored with stable relative position to stiff support cylinders and support disks, which are based upon carbon fibre laminate material. This material provides good thermal stability and should result in rigidity that is about 50 times higher than that of the CMS tracker. Predicted deflections of the support structures under gravity are below 10 $\mu\mathrm{m}$. Modules will be installed in groups with internal alignment of a group controlled to about 10 $\mu\mathrm{m}$. Reference features on each barrel and disk will allow the positions of each group of modules to be known with respect to the reference features to about 10 $\mu\mathrm{m}$. Hence the position and orientation of a given sensor should be known to approximately $10 \times \sqrt{3} = 17$ $\mu\mathrm{m}$. A large coordinate measuring machine (CMM) or equivalent laser-based equipment will be needed to achieve this accuracy.

Frequency scanned laser interferometry during assembly offers the potential for still better knowledge of alignment than the values above [99]. Moreover, tracker sensor modules slightly overlap within layers (and hence are tilted), which provides valuable linking of sensors within layers for track-based alignment.

We plan to use ball and cone mounts to mate barrels and disks with one another. This type of mount provides a reproducibility of 3 $\mu\mathrm{m}$. Again, a large CMM or laser-based equipment will be used to measure reference features on each object with a precision of about 10 $\mu\mathrm{m}$. This implies the precision to which individual sensors are known of $\approx$20 $\mu\mathrm{m}$, although individual groups of sensors will be known relative to one another with slightly better precision. Kinematic mounts will be used to support the outermost tracker barrel from the interior of ECAL. Support via kinematic mounts from some other portion of the detector has also been considered. All other outer tracker elements are then supported either directly or indirectly from the outermost barrel. If the kinematic mounts are designed correctly, push-pull operations may affect the absolute position of the main tracker, but should not affect its internal alignment.

The vertex detector is supported independently of the outer tracker. Outer support half-cylinders locate all vertex detector elements relative to one another. Relative alignment of elements within either top or bottom support cylinder is likely to be better than half-cylinder to half-cylinder alignment, which suggests that the two half-cylinders and detector elements they support may need to be treated as independent objects. The tracker would then be treated as three pieces: the outer tracker (including all barrel layers and disks), the upper half of the vertex detector, and the lower half of the vertex detector.

Alignment of the three pieces relative to one another will be monitored via FSI. A combination of frequency scanned interferometry and "laser-track" monitoring of relative sensor positions will monitor the internal alignment of the main tracker. After assembly, during data taking, and during push-pull operations, the FSI system will be run nearly continuously, providing "real time" measurement of global tracker distortions and of vibration amplitudes and frequencies (up to the Nyquist frequency of the FSI DAQ sampling). This type of monitoring may not be feasible for internal alignment of the two vertex detector halves due to constraints on the material budget.

A deformation monitoring system based on optical fibre sensing techniques is also under consideration [100]. Strain Optical Fibre Sensors (OFS) would be embedded in the carbon fibre supporting structures or/and sensor modules. The OFS would provide real-time strain information during the

production, assembly, operation and push-pull operation of the instrumented tracker structures. From a detector integration point of view, using this kind of distributed monitoring requires only the embedding of 120 μm diameter optical fibres in the carbon fibre composite; this means that it can be also considered as a suitable technology for the vertex detector.

3.6.1 Alignment Methods

The FSI system incorporates multiple interferometers fed by optical fibres from the same laser sources, where the laser frequency is scanned and fringes counted, to obtain a set of absolute lengths. This alignment method was pioneered by the Oxford group on the ATLAS experiment [98, 101, 102]. By defining $\mathcal{O}(100)$ "lines of sight" in the tracker system for absolute distance measurements, we will over-constrain the locations of fiducial points in space, allowing global distortions of the carbon-fibre support structure layers (translation, rotation, twist, bending, stretching, etc.) to be determined to the required precision. The real-time FSI measurements should allow for relevant time-dependent corrections to be applied when carrying out the final step of track-based alignment of individual silicon modules [99, 103].

With a test apparatus, the state of the art in precision DC distance measurements over distance scales of a meter under laboratory-controlled conditions has been reached and extended. Precisions better than 100 nm have been attained using a single tunable laser when environmental conditions are carefully controlled. Precisions under uncontrolled conditions (e.g., air currents, temperature fluctuations) were, however, an order of magnitude worse with the single laser measurements.

Hence for the tracker a dual-laser FSI system is foreseen that employs optical choppers to alternate the beams introduced to the interferometer by the optical fibres. By using lasers that scan over the same wavelength range but in opposite directions during the same short time interval, major systematic uncertainties can be eliminated. Bench tests have achieved a precision of 200 nm under highly unfavourable conditions using the dual-laser scanning technique [104].

A separate real-time alignment method with different systematic uncertainties will be provided by a "laser-track" system in which selected sensor modules are penetrated by laser beams to mimic infinite-momentum tracks. This method exploits the fact that silicon sensors have a weak absorption of infrared (IR) light. Consecutive layers of silicon sensors are traversed by IR laser beams.

The same sophisticated alignment algorithms as employed for track alignment with real particles can then be applied with arbitrarily high statistics to achieve relative alignment between modules to better than a few microns. This method employs the tracking sensors themselves, with only a minor modification to make them highly transparent to infrared light. A window with a diameter of few millimetres in the aluminium metallisation on the back of the sensor allows the IR beam to pass through. Since IR light produces a measurable signal in the silicon bulk, there is no need for any extra readout electronics. This alignment method has been implemented by both the AMS and CMS experiments [105, 106, 107].

The sensing element of the OFS monitor is a Fibre Bragg Grating (FBG) sensor operated as an optical strain gauge [100]. FBG sensors have many enhanced features with respect to traditional electrical strain gauges: no need for power or readout cabling, long term stability, immunity to electromagnetic fields and high voltage, as well as extreme temperature and radiation resistance. Concerning its application in tracker systems, one of the most important properties is its light weight since the actual FBG is "written" in a short section, only a few mm in length, of an optical fibre with a 125 μm diameter. Multiplexing capabilities with many distributed FBG sensors on the same optical fibre are available; this technology also allows for long-range sensing, placing the readout unit well outside of the detector. The FBG sensor would be embedded in the carbon fibre structures supporting the modules and the module mechanics itself. The system is expected to reach local deformation

sensitivities better than 1 μm strain. The OFS monitor will provide very fast information on full structure deformations during the push-pull operations.

The final alignment of individual sensor modules will be track-based, using accumulated statistics from many detected tracks and constrained fitting to determine local position and orientation corrections for each module. The time to accumulate sufficient statistics for alignment of each individual module is expected, however, to be long enough to require continuous monitoring of global structure motions and deformations via the FSI and laser-track systems and to warrant robust, stable mechanical structures, as discussed above. Although six parameters are needed to describe a rigid module's position and orientation, the most critical parameter for microstrip planes is the offset of the module from nominal along the direction normal to the microstrips and in the module plane, since this is the coordinate measured most precisely by the strips. Expected translations in the orthogonal directions should have a negligible effect on tracking. Rotations of module planes about an axis parallel to the strips can lead to small biases in coordinate reconstruction, while rotation about an axis in the module plane and perpendicular to the strips should have negligible effects. To determine systematic offsets in the measured coordinate to a precision that is an order of magnitude smaller than the hit resolution requires $\mathcal{O}(100)$ tracks per module, assuming systematic variations in hit reconstruction for different strips in the same module are negligible. The sensor modules receiving the least number of tracks, i.e. $\cos(\theta) = 0$, outer barrel layer, are expected to be penetrated by $\mathcal{O}(10^4)$ tracks per month, making track-based alignment feasible for each separate data-taking epoch between push-pull moves. The fact that a large number of tracks produced will be back-to-back in the $x - y$ plane with approximately equal p_{T} values should enable more powerful constrained-fit determination of module offsets.

3.6.2 Push-Pull Considerations

Six rigid-body degrees of freedom are anticipated for main tracker alignment after a move of the detector: two transverse positions per end, an azimuth, and a z-position. Measurement data will be collected to monitor additional degrees of freedom corresponding to shape distortions which are expected to be quite small (twist, bending and stretching). The data will also be used to monitor long- and short-term instabilities of the rigid-body degrees of freedom. Twelve degrees of freedom are anticipated for the vertex detector alignment after a move: two transverse positions per barrel end, two transverse positions per support cylinder end, one azimuth per support cylinder end, and one z-position per support cylinder end. An additional four degrees of freedom (two transverse positions of the beampipe near each LumiCal) will be considered in estimates of support structure distortions.

During detector moves; alignment of the beampipe, the ends of the main tracker, and LumiCAL and BeamCAL will be monitored nearly continuously relative to the central calorimeter via frequency scanned interferometry. At the end of motion; alignment of the beampipe, LumiCAL and BeamCAL, and final quadrupoles will be adjusted relative to the main tracker and central calorimeter. The vertex detector is mounted from the beampipe and follows its motion. No adjustments to the position of the outer tracker are anticipated. Tune-up of beam position will be performed at low intensity while monitoring vertex detector and outer tracker backgrounds. The time required depends upon accelerator procedures.

During each move the FSI system will be operational and taking data continuously. At least six types of measurements are anticipated. The transverse and longitudinal positions of the ends of each outer tracker barrel layer at approximately eight azimuths will be measured. Also the transverse positions of each barrel layer for at least eight azimuths and additional z-locations along the layer will be determined as will be the overall length of each barrel layer for at least eight azimuths. The transverse and longitudinal positions of each disk near its outer periphery for at least eight azimuths

will be evaluated as well as the beampipe transverse positions just inboard of each LumiCal location. Furthermore, the transverse and longitudinal positions of each vertex detector support cylinder at each end at approximately four azimuths will be assessed. Alarms will be set for any motion measured outside of what is expected. Consequently, electrical power will need to be maintained continuously for the laser system, and the optical bench will need to move with the detector. In addition, we envision measuring the strain of the structure during the move through the OFS method. Again, alarms would be set for measured values outside the expected range. Laser-track monitoring is also planned for a subset of the sensor modules. The OFS deformation monitoring system can be also operated continuously.

In summary, with the methodology described above, we expect to achieve a precision of 3 $\mu\mathrm{m}$ or better on main tracker transverse coordinate offsets (barrels and disks) for an assumed hit precision of 7 $\mu\mathrm{m}$ before and after a detector move. For the vertex detector, which is more demanding given an expected single hit resolution for two coordinates of better than 3 $\mu\mathrm{m}$, the goal is a relative alignment precision of 1 $\mu\mathrm{m}$ for coordinates transverse to the track.

Chapter 4
SiD Calorimetry

4.1 Introduction

The SiD baseline design uses a Particle Flow Algorithm (PFA) approach to Calorimetry. PFAs have been successfully applied to existing detectors, such as CDF, ZEUS, and CMS and have resulted in significant improvements of the jet energy resolution compared to methods based on calorimetric measurement alone. None of these detectors were originally designed with the application of PFAs in mind. The SiD design on the other hand considers a PFA approach necessary to reach the goal of obtaining a measurement uncertainty on the jet energy resolution of the order of 3% or better for jet energies above 100 GeV. SiD is therefore optimised for the PFA approach and the major challenge imposed on the calorimeter is the association of energy deposits with either charged or neutral particles impinging on the calorimeter. This results in several requirements on the its design:

- To minimise the lateral shower size of electromagnetic clusters the Molière radius of the ECAL must be minimised. This promotes efficient separation of electrons and charged hadron tracks.
- Both ECAL and HCAL must have imaging capabilities which allow assignment of energy cluster deposits to charged or neutral particles. This implies that the readout of both calorimeters needs to be finely segmented transversely and longitudinally.
- The calorimeters need to be inside the solenoid to be able to do track to cluster association; otherwise, energy deposited in the coil is lost and associating energy deposits in the calorimeter with incident tracks becomes problematic.
- The gap between the tracker and the ECAL should be minimised.
- The calorimeter needs to be extendable to small angles to ensure hermeticity, and be deep enough to contain hadronic showers.

Following is a description of the baseline designs and options for the ECAL and the HCAL. Also included are brief descriptions of alternative calorimeter technologies being considered by SiD.

4.2 Electromagnetic Calorimeter

4.2.1 Introduction

The major challenge imposed on the calorimeter by the application of PFAs is the association of individual particles with their energy depositions in the calorimeters. For the ECAL, this implies that electromagnetic showers be confined to small volumes in order to avoid overlaps. Effective shower pattern recognition is possible if the segmentation of readout elements is small compared to the showers. This level of transverse segmentation then also facilitates the separability of the electromagnetic showers from charged particle tracks due to un-interacted charged hadrons (and muons). The longitudinal segmentation is chosen not only to achieve the required electromagnetic energy resolution, but also to provide discrimination between electromagnetic showers and those hadrons which interact (typically deeper) in the ≈ 1 interaction length of the ECAL. Finally, there

should be a sufficient number of longitudinal readout layers to provide charged particle tracking in the ECAL. This is important not only for the PFA algorithms, but also to aid the tracking detectors, especially for tracks which do not originate from the IP.

The ECAL described in this section according to the qualitative description above is expected to have capabilites including:

- Measurement of beam-energy electrons and positrons (and photons) from (radiative) Bhabha scattering. This is sensitive to contact terms and the angular distribution provides important information on electroweak couplings, for example in interference terms between Z, γ, and a new Z'. Precise Bhabha acollinearity distributions provides a key piece of the measurement of the luminosity spectrum [108], which is crucial for correct measurement of sharp threshold features in the annihilation cross section.
- electrons from $Q \to Q' e \nu$ (where Q = heavy quark).
- adequate electromagnetic energy resolution; the anticipated $\sim 0.17/\sqrt{E} \oplus 1\%$ is sufficient for this component in the PFA.

The imaging ECAL can also provide these more challenging measurements abilities compared to previous ECALs. These have already been demonstrated in simulation and in the PFA-based reconstruction:

- PFA reconstruction of photons in jets with high (95%) efficiency
- PFA tracking of charged particles in jets
- ECAL-assisted tracking (especially for decays of long-lived particles)
- π^0 reconstruction in τ decays. This is a crucial for identification of τ final states which are important for measuring τ polarisation, P_τ.

Some other possibilities have not yet been fully demonstrated in simulation, but are under study and will be further studied:

- π^0 reconstruction in jets - this allows improvement of the EM component of jet energy [109]
- photon vertexing - the impact parameter resolution for photons of ~ 1 cm would be important for identifying decays where photons are the only visible decay products, such as predicted from some gauge-mediated SUSY-breaking models

In the following, we provide a description of the baseline ECAL. We then discuss the R&D program, including recent progress.

4.2.2 Global ECAL Design

A sampling ECAL provides adequate energy resolution for the ILC physics, as discussed above. Because of its small radiation length and Molière radius, as well as its mechanical suitability, we have chosen tungsten absorber/radiator. Due to practical considerations for ease of production of large plates and machining, the tungsten will be a (non-magnetic) alloy. This currently chosen alloy includes 93% W with radiation length 3.9 mm and Molière radius 9.7 mm. An additional benefit of tungsten is that it has a relatively large interaction length, which helps to ameliorate confusion between electromagnetic and hadron showers in the ECAL.

The longitudinal structure we have chosen has 30 total layers. The first 20 layers each have 2.50 mm tungsten thickness and 1.25 mm readout gap. The last 10 layers each have 5.00 mm tungsten plus the same 1.25 mm readout gap. This configuration is a compromise between cost, shower radius, sampling frequency, and shower containment. The cost is roughly proportional to the silicon area, hence the total number of layers. We chose finer sampling for the first half of the total depth, where it has the most influence on electromagnetic resolution for showers of typical energy. However, as discussed below, an increase in sampling with fixed readout gaps has a detrimental effect

on the shower radius. The total depth is 26 X_0, providing reasonable containment for high energy showers. Simulations in EGS4 and GEANT4 have shown the energy resolution $\Delta E/E$ for electrons or photons to be well described by $0.17/\sqrt{E} \oplus 1\%$.

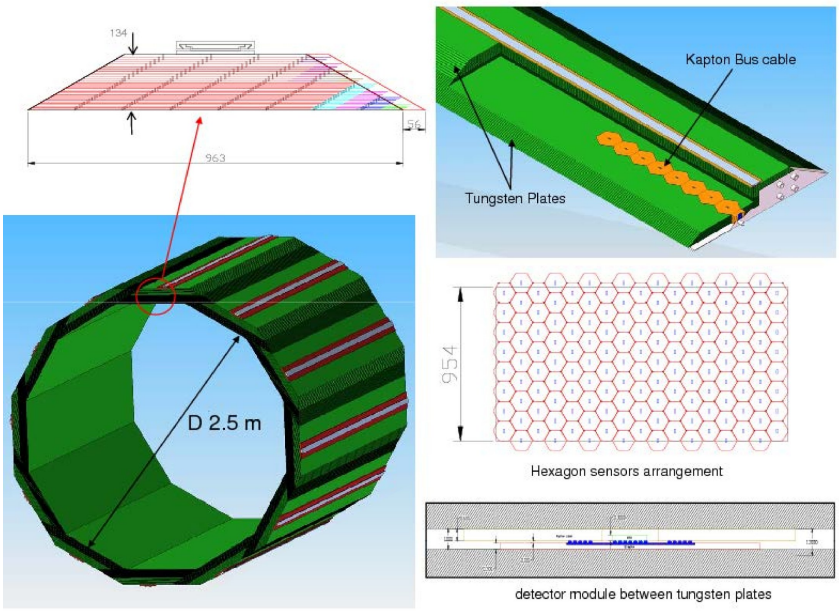

Figure II-4.1
Overall mechanical layout of the ECAL.

Silicon detectors are readily segmented. In the baseline design we have chosen (see description below), there is little penalty for segmenting the silicon sensors much more finely than typical shower radii. (The MAPS option takes this to the extreme.) As discussed above, the scale for this is set by the shower size, which we wish to be as small as feasible. A useful figure of merit for this is the Molière radius, which is 9 mm for pure tungsten. Since showers will spread in the material between tungsten layers, it is crucial to keep the readout gaps as small as possible. We can scale the shower radii by a simple factor to provide a figure of merit. In our case, this factor is $(2.50 + 1.25)/2.50 = 1.50$ for the crucial first 20 layers. We can then define the effective Molière radius, $\mathcal{R}$, as the Molière radius of the radiator multiplied by this factor. In our case, this is about 14 mm. A crucial driving force in our design has been to provide as small a $\mathcal{R}$ as feasible, along with a transverse segmentation of the readout which is well below $\mathcal{R}$.

Table II-4.1 summarises the basic ECAL parameters. Figure II-4.1 shows the overall mechanical structure of the ECAL barrel, including detectors layout (for the baseline option) and readout gap.

Table II-4.1
Nominal parameters of the silicon-tungsten ECAL for SiD.

inner radius of ECAL barrel	1.27 m
maximum z of barrel	1.76 m
longitudinal profile	20 layers $\times$ 0.64 X_0
	10 layers $\times$ 1.30 X_0
EM energy resolution	$0.17/\sqrt{E} \oplus 1\%$
readout gap	1.25 mm (or less)
effective Molière radius ($\mathcal{R}$)	14 mm

Referring to Figure II-4.1, the construction of a barrel "wedge" module is carried out as follows. Because tungsten plates are only available with a maximum size of 1×1 m^2, the wedge assembly is done by interconnecting the plates with a screw-and-insert network, which transfers the load from the bottom of the stack to the rail. The design is self-supporting and it does not require additional material to provide the required stiffness. The assembly procedure for a single wedge is sequential with the sensors permanently captured in the gap between tungsten plates, which are specified to have high planarity, achieved at the vendor site by grinding. This specification has been verified on a batch

of 15×15 cm^2 plates procured for the beam test module (see Section 4.2.3.2), which have planarity tolerances of ± 10 µm, and have been confirmed by interviewing several tungsten vendors/producers. Because of the trapezoidal cross-section of the wedge, the assembly sequence is bottom up, with the wider plate at the base. The first layer of tungsten will be laid down on a jig tool to set the basic tolerances of the stack. Spacing inserts are placed at the locations of the cutouts at the sensor edges (see Figure II-4.2), followed by the sensors with flex cables.

The control of the gap tolerances relies on the flatness of the tungsten plate and on the spacers, which are individually quality-checked by metrology. The positioning tolerances of the sensor modules in the plane rely on the QC of spacers too, but also on the flex-cable, which will have mounting pads which mate with the inserts. The assembly of the sensors on the flex-cable will be done on a precision jig, which will guarantee the repeatability of the assigned tolerances. The second layer of tungsten will be overlaid on the sensors, once mechanical and electrical connection are tested. This process is repeated 30 times along the stack, which is the number of the active layers of a single wedge module. The last plate on the top has rails, which will allow the insertion and the support from the HCAL. Prior to insertion, each individual wedge will be equipped with a cold plate for thermal management, running along z on one side of the wedge. The boxes on the two opposite sides at $\pm z$ contain the data concentrator electronics, which completes the assembly

4.2.3 Baseline Technology

In the baseline design, the ECAL readout layers are tiled by large, commercially feasible silicon sensors (presently from 15 cm wafers). The sensors are segmented into hexagonal pixels which are individually read out over the full range of charge depositions. The complete electronics for the pixels is contained in a single chip (the KPiX ASIC) which is bump bonded to the wafer. We take advantage of the low beam-crossing duty cycle (10^{-3}) to reduce the heat load using power pulsing, thus allowing passive thermal management within the ECAL modules. The realisation of this technology has been the subject of an intensive, ongoing R&D program.

The main parameters associated with the baseline technology choice are given in Table II-4.2. Some details of the design and R&D results are given below. Further details can be found in the references [110, 111].

Table II-4.2
Parameters of baseline silicon-tungsten ECAL and the MAPS option.

	Baseline	MAPS option
pixel size	13 mm^2	50× 50 µm
readout gap	1.25 mm	similar
	(incl. 0.32 mm thick Si sensors)	
effective Molière radius	14 mm	14 mm
pixels per silicon sensor	1024	$1 \cdot 10^6$
channels per KPiX chip	1024	-
dynamic range	~ 0.1 to 2500 MIPs	1 MIP
heat load	20 mW per sensor	20 mW per sensor

Figure II-4.2 shows a sensor with 1024 pixels. Not shown in the drawing are the signal traces, part of the second layer metallisation of the sensors, which connect the pixels to a bump-bonding pad at the centre of the sensor for input to the KPiX readout chip. The pixels are DC-coupled to the KPiX, thus only two metallisation layers are required for the sensors. The pixels near the bump-bonding array at the centre are split to reduce capacitance from the large number of signal traces near the sensor centre. The electronic noise due to the resistance and capacitance of the traces has been minimised within the allowed trace parameters. The cutouts at the corners of the sensor are to accommodate mechanical stand-offs which support the gaps between the tungsten layers.

The lower-right image of Figure II-4.1 depicts a cross-sectional view of the readout gap in the vicinity of the centre of the sensor. The silicon sensor is about 320 µm thick. The KPiX is bump-bonded to the silicon sensor at an array of bump pads which are part of the second metallisation

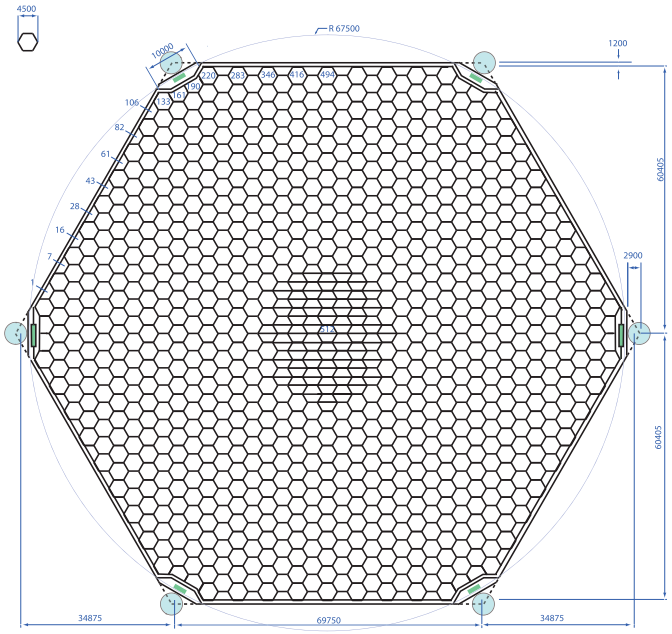

Figure II-4.2
Drawing of a silicon sensor for the ECAL. The sensors are segmented into 1024 13 mm^2 pixels.

layer from sensor fabrication. This is a 32 $\times$ 32 array of bump bond pads. Polyimide (Kapton) flex cables connect near the centre of the sensors. The cables bring power and control signals into the KPiX chip and bring out the single digital output line for the 1024 channels.

Thermal management is a crucial feature of this design. Our requirement is to hold the average power dissipation per wafer to less than 40 mW. This will allow the heat to be extracted purely passively, providing a highly compact and simple design, less subject to destructive failures. The ILC bunch structure allows for power pulsing. A factor 80-100 reduction in power consumption is obtained by switching off the most power hungry elements of the KPiX chip, e.g. the analog front end, for most of the interval between the bunch trains. The design of the KPiX chip yields an average power below 20 mW when power pulsing is applied. While we do not foresee the need for cosmic ray data, the power pulsing eliminates this possibility.

After several interactions with the R&D, in early 2012 a full 1024-channel KPiX was successfully bump-bonded to a sensor by IZM Company. Following this, a Kapton cable was successfully bump-bonded to the sensor assembly at UC Davis. The cable bonding uses a lower temperature solder than that used for the KPiX bonding. Figure II-4.3 shows the fully bonded assembly.

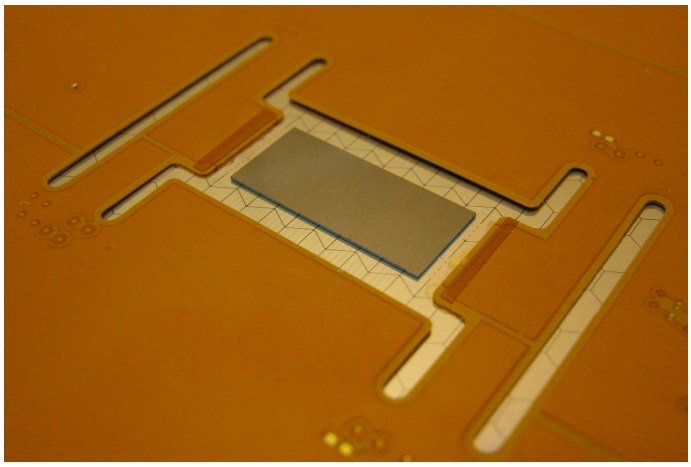

Figure II-4.3
Photograph of the central region of a sensor. The KPiX chip is bump-bonded to the sensor and is visible through the central cutout of the Kapton cable. The slots in the Kapton allow for differential thermal expansion.

4.2.3.1 Bonded sensor results

Initial bench tests of the bonded sensor of Figure II-4.3 have been carried out and the results are quite promising. A cosmic ray telescope was used to trigger KPiX and the charge of the pixel having the maximum charge was entered in the distributions shown in Figure II-4.4. The red distribution resulted when the ECAL sensor was placed within the telescope acceptance, while the blue distribution resulted when the sensor was outside the telescope acceptance. A Landau distribution (black) is fit to the red signal. The peak of the signal at about 4 fC is consistent with our expectation for MIPs passing through the fully-depleted 320 μm thick sensors.

With the highly integrated design we have chosen, a potential worry is crosstalk between channels. Figure II-4.4 indicates no evidence for crosstalk in any other channel when a large 500 fC signal is injected. The noise distribution is nicely fit by a Gaussian with RMS 0.2 fC. This is to be compared with the 4 fC MIP signal. This noise level exceeds our requirements for the ECAL.

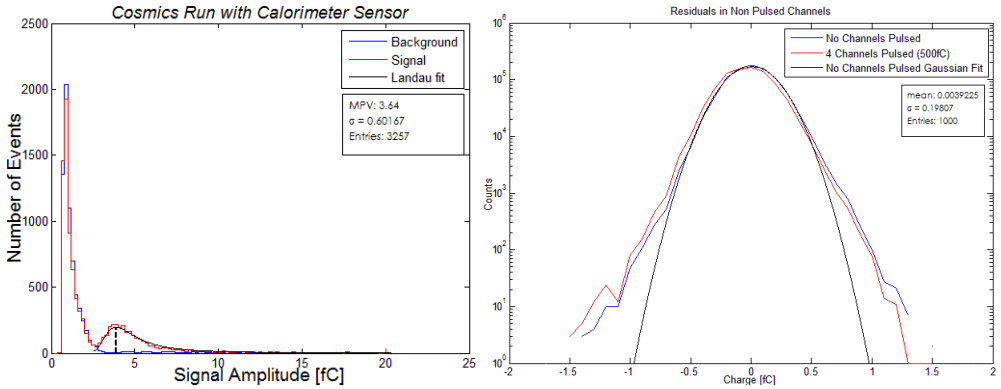

Figure II-4.4. Distribution of charge depositions in bonded sensor for cosmic ray triggered events (left). The MIP peak is clearly visible above the noise peak. Crosstalk test of bonded sensor (right). The charge distributions for all non-pulsed pixels are compared for a large pulse injection (red) and no pulse injection (blue). Also shown is a Gaussian fit with RMS 0.2 fC.

4.2.3.2 Prototype Module and Test Beam

Given the positive initial results of the first bonded sensors, we are moving forward with our plans to build a full-depth test module. This is shown in Figure II-4.5. The test stack is to have a width of one sensor, easily sufficient to contain electromagnetic showers. The longitudinal structure closely matches that of the SiD ECAL. The main difference is that we will have 1.5 mm readout gaps for the test stack, rather than the nominal 1.25 mm gaps of the SiD design, in order to allow clearance for sensor assemblies to be slid in or out of the stack.

Since the operation of KPiX has been optimised for the bunch timing structure of the ILC, the optimal test facility would be a linear collider having a similar timing structure. Fortunately, SLAC is presently restoring a test beam capability at End Station A. We expect to have the sensors for the test module prepared and first data from this facility in 2013.

4.2.4 MAPS option

The Monolithic Active Pixel Sensor option [112] uses 50 $\times$50 μm^2 silicon pixels as readout material. The main difference here is the usage of digital electromagnetic calorimetry where the ECAL is operated as a shower particle counter. The simulated performance [113] is illustrated in Figure II-4.6 where the potential advantages are clearly visible. These sensors could be manufactured in a commercial mixed-mode CMOS process using standard 300 mm wafers. This is an industrial and widely available process, so pricing for these wafers should be very competitive. We have also incorporated the usage

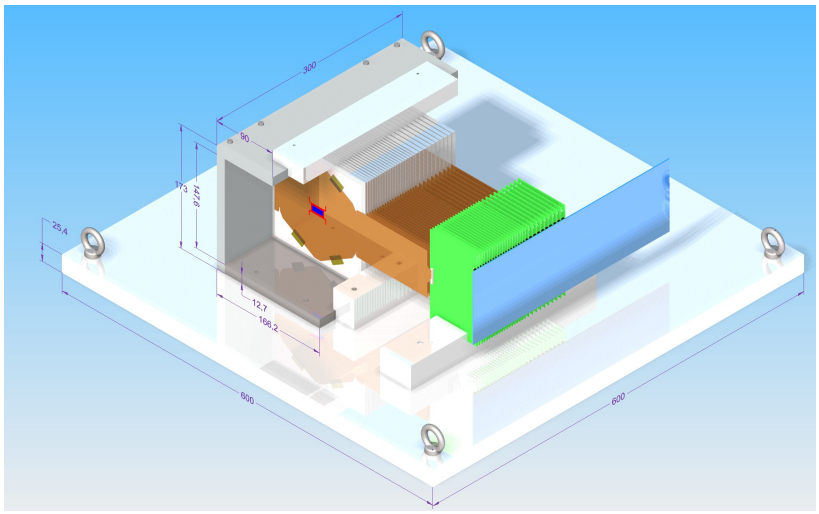

Figure II-4.5 Schematic of test module to be tested in a beam. The module has a width of one sensor and a depth of 30 layers. The Kapton cables attached to each sensor feed concentrator boards, which in turn are connected to a mother board.

of deep p-well implants and high resistivity epitaxial layers in this design, which was used to be rather non-standard for CMOS processes previously. This allows to include full CMOS functionality in a MAPS pixel, which has been possible before.

Three first-generation sensors for digital electromagnetic calorimetry, TPAC 1.0, 1.1 and 1.2 [113, 114] have been manufactured and tested. They consists of 168×168 pixels with the required size of 50×50 μm. The TPAC 1.2 will be described in more detail. It uses a the pre-Shaper architecture and consists of a charge preamplifier, a CR-RC shaper which generates a shaped signal pulse proportional to the amount of charge collected and a two-stage comparator which triggers the hit-flag. The sensor supports single-bunch time stamping with up to 13 bits. Each pixel has a 6 bit trim to compensate for pedestal variations and each pixel can be masked off individually. A bank of forty-two pixels shares nineteen memory buffers to store the hits during the bunch train. The sensor also supports power-pulsing already and is able to power off its front-end in the quiet time between bunch trains.

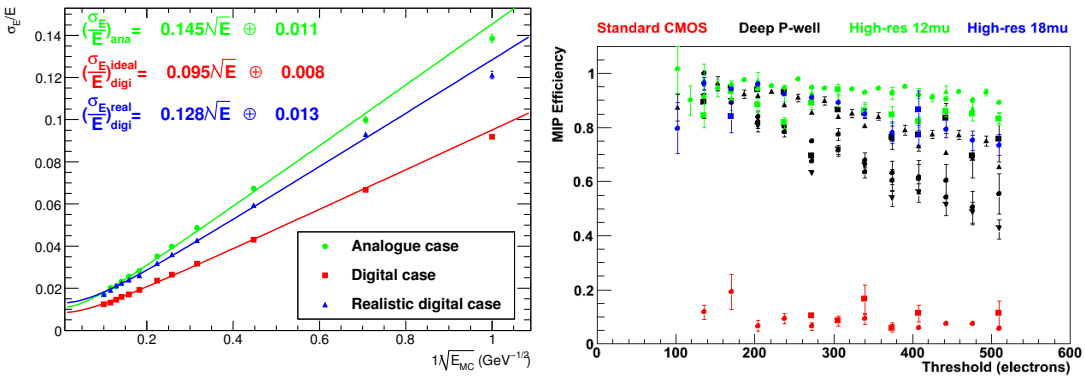

Figure II-4.6. Left: The energy resolution as a function of the incident energy for single electrons for both analog and digital readout using a GEANT4 simulation. The realistic digital cases includes effects of saturation and charge sharing, leading to a degradation of 35% [113]. Right: The MIP detection efficiency as a function of the comparator threshold for different process variants of TPAC 1.2 [114, 115]; no deep p-well implant (standard CMOS), deep p-well implant and high-resistivity epitaxial layer (all 12 μm) and 18 μm high-resistivity layer

All sensors have been tested using sources and lasers [112, 113, 114, 115]. The TPAC 1.2 sensor was tested in test beams at CERN and DESY using a stack of six TPAC sensors. The minimum ionising particle efficiency was found by using the outer four TPAC planes to perform the track finding and then deriving the MIP detection efficiency of the two inner planes [114, 115]. This was done for a range of threshold values (see Figure II-4.6). The version without a deep p-well (using plain CMOS)

shows a very low MIP efficiency. Including the deep p-well then increases the detection efficiency to around 80-85%. The addition of the high-resistivity epitaxial layer then makes TPAC close to a 100% efficient for minimum ionising particles.

The MAPS option is designed to fit in the same mechanical structure as the baseline option and we foresee a sensor size of 5 $\times$ 5 cm^2 (baseline) for a final system. As the active sensor area is less than 20 μm thick, it does allow back-thinning of the wafers down to 100 μm or less. The main parameters for the MAPS option are summarised in Table II-4.2.

4.2.5 Calibration and alignment

Silicon detectors are inherently insensitive to gain variations with time and should not have significant inter-pixel gain differences. Pixel to pixel gain differences in the electronic readout are calibrated by dedicated calibration circuitry within the KPiX chip. Perhaps the main calibration issue will be sensor to sensor gain differences. These are not expected to be large, but we are investigating different options for this calibration.

Alignment within ECAL modules and between modules should not be difficult to control with careful fabrication. Alignment to the inner detectors can be sufficiently established using charged particle tracks.

4.3 Hadronic Calorimeter

4.3.1 HCAL requirements

Within the PFA paradigm the role of the hadron calorimeter is to allow identification of the energy deposits from charged particles, and to measure the energy associated with neutral hadronic particles, such as neutrons and $K_L^0 s$. In this approach the challenge is to unambiguously identify energy deposits in the calorimeter as belonging to charged particles (and therefore to be ignored) or to neutral particles (and therefore to be measured). As a consequence, the optimal application of PFAs requires calorimeters with the finest possible segmentation of the readout. Further requirements imposed by the application of PFAs on the hadron calorimeter include:

- Operation in a (strong) magnetic field;
- Limitations on the thickness of the active element (to keep the coil radius as small as possible);
- Manageable accidental noise rate (to keep the confusion term manageable).

In general, the active elements need to satisfy standard performance criteria, such as reliability, stability, a certain rate capability and be affordable.

4.3.2 Description of the DHCAL concept

The PFA-based HCAL is a sandwich of absorber plates and instrumented gaps with active detector elements. The active detector element has very finely segmented readout pads, with 1$\times$1 cm^2 size, for the entire HCAL volume. Each readout pad is read out individually, so the readout channel density is approximately 4$\times$10^5/m^3. For the entire SiD HCAL, with 10^2m^3 total volume, the total number of channels will be 4$\times$10^7 which is one of the biggest challenges for the HCAL system. On the other hand, simulation suggests that, for a calorimeter with cell sizes as small as 1$\times$1 cm^2, a simple hit counting is already a good energy measurement for hadrons. As a result, the readout of each channel can be greatly simplified and just record 'hit' or 'no hit' according to a single threshold (equivalent to a '1-bit' ADC). A hadron calorimeter with such simplified readout is called a Digital Hadron Calorimeter (DHCAL). In a DHCAL, each readout channel is used to register a 'hit', instead of measure energy deposition, as in traditional HCAL. In this context, gas detectors (such as RPC, GEM and Micromegas) become excellent candidates for the active element of a DHCAL. The SiD baseline design uses a DHCAL with RPC as the active element.

4.3.3 Global HCAL mechanical design

The SiD HCAL is located inside the magnet and surrounds the electromagnetic calorimeter, the latter being fixed to it. The HCAL internal and external radii are respectively: R_{int}=1417 mm and R_{ext}=2493 mm. The overall length is 6036 mm, centred on the interaction point.

The HCAL is divided into twelve identical azimuthal modules, as illustrated in Figure II-4.7. Each module has a trapezoidal shape and covers the whole longitudinal length. The chambers are inserted in the calorimeter along the Z-direction from both ends and can eventually be removed without taking out the absorber structure from the magnet. Special care of the detector layout has been taken into account to avoid a crack at θ=90°.

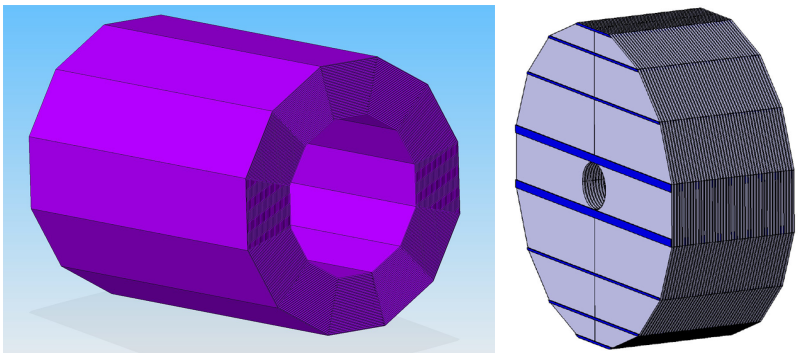

Figure II-4.7
Cross-section of the HCAL barrel (left) and face and top views of the HCAL endcap (right).

The absorber plates are supported by several stringers fixed radially on both sides of the modules. Stringers of two consecutive modules are staggered in order to maximise the active detector area. Although the space between two consecutive modules is not instrumented, it is however filled by the absorber material. The barrel will be fixed on the magnet at 3 and 9 o'clock or 5 and 7 o'clock. Each endcap forms a plug that is inserted into an end of the barrel calorimeter. The layer structure of the end cap calorimeters is the same as for the barrel. Figure II-4.7 shows a view of one endcap.

4.3.4 Baseline technology

In the baseline design, the active element of the SiD DHCAL uses Resistive Plate Chambers (RPCs). RPC fulfils all the above mentioned requirements for a PFA DHCAL. For the standard two-glass plate design [116], a position resolution of a few hundred μm is typical and so a segmentation of the readout into pads of 1 $\times$ 1 cm^2 or smaller is technically meaningful. The design can be tuned to minimise the thickness. With two glass plates a layer thickness smaller than 8 mm appears achievable. If using the 1-glass design [116] an overall thickness of 1 mm less is conceivable. The noise rate for RPCs is in general extremely low, with values below 1 Hz/cm^2 for MIP detection efficiencies exceeding 90% [117].

RPCs with glass plates as resistive plates are reliable and operate stably. Long term tests showed no changes in performance [117]. The rate capability of RPCs is well understood [118] and is adequate for most of the solid angle of a colliding beam detector. In the forward region, where the rates are in general higher, RPCs using resistive plates with lower bulk resistivity or other high rate gas detectors might be required.

4.3.4.1 RPC chamber designs

Resistive Plate Chambers (RPCs) are gaseous detectors primarily in use for the large muon systems of colliding beam detectors. The detectors feature a gas volume defined by two resistive plates, typically Bakelite or glass.

The outer surface of the plates is coated with a layer of resistive paint to which a high voltage is applied. Depending on the high voltage setting of the chamber, charged particles crossing the gas gap initiate a streamer or an avalanche. These in turn induce signals on the readout strips or pads located on the outside of the plates.

Various chamber designs have been investigated [116] for the SiD DHCAL. Of these two are considered particularly promising: a two-glass and an one-glass plate design. Schematics of the two chamber designs are shown in Figure II-4.8. The thickness of the glass plates is 1.1 mm and the gas gap is maintained with fishing lines with a diameter of 1.2 mm. The overall thickness of the chambers, including layers of Mylar for high voltage protection but excluding readout board, is approximately 3.7 mm and 2.6 mm, respectively. The two-glass design is the current baseline, however, due to its attractive features, the one-glass design is being actively developed.

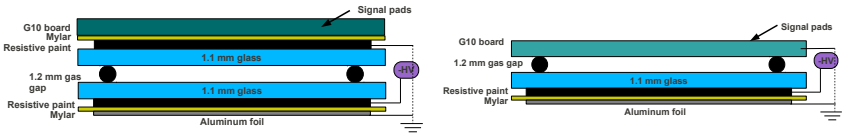

Figure II-4.8 Schematic of the RPC design with two glass plates (left) and one glass plate (right). Not to scale.

4.3.4.2 Readout

The electronic readout system needs to be optimised for the readout of tens of millions of readout channels envisaged for the SiD hadron calorimeter operating at the future International Linear collider. Due to the high channel count, a front end ASIC and several layers of data concentration are considered necessary. In the R&D phase, a readout system was developed and constructed for the DHCAL prototype which handles nearly 500,000 readout channels. Even though the system was optimised for test beam operation and did not address all requirements for a realistic SiD DHCAL system, it achieved the very first embedded front-end readout for a calorimeter system and serves as a milestone towards the final engineering design.

A block diagram of the prototype DHCAL readout system is shown in Figure II-4.9. The electronics is divided into two parts: The "on-detector" electronics processes charge signals from the detector, collects data for transmission out, and acts as the interface for slow controls. The "back-end" electronics receives and processes the streams of data from the front-end electronics, and in turn passes it to the Data Acquisition (DAQ) system. It also has an interface to the timing and trigger systems.

A custom integrated circuit (ASIC) has been developed for the front-end. The ASIC chip, called DCAL performs, in addition to ancillary control functions, all of the front-end processing, including signal amplification, discrimination/comparison against threshold, recording the time of the hit, temporary storage of data, and data read out. It services 64 detector channels with a choice of two programmable gain ranges ($\sim$10 fC and $\sim$100 fC sensitivity.)

The chips reside on front-end printed circuit boards that are embedded in the DHCAL active layer. There are 24 chips on a front-end board, servicing 1,536 channels. An FPGA based data concentrator (DCON) resides on the edge of the front-end board which collects data from the 24 DCAL chips and serves as the first level of data concentration. The DCON's send their data to the data collectors (DCOL's) through serial links. The DCOL's are located in VME crates and serves as

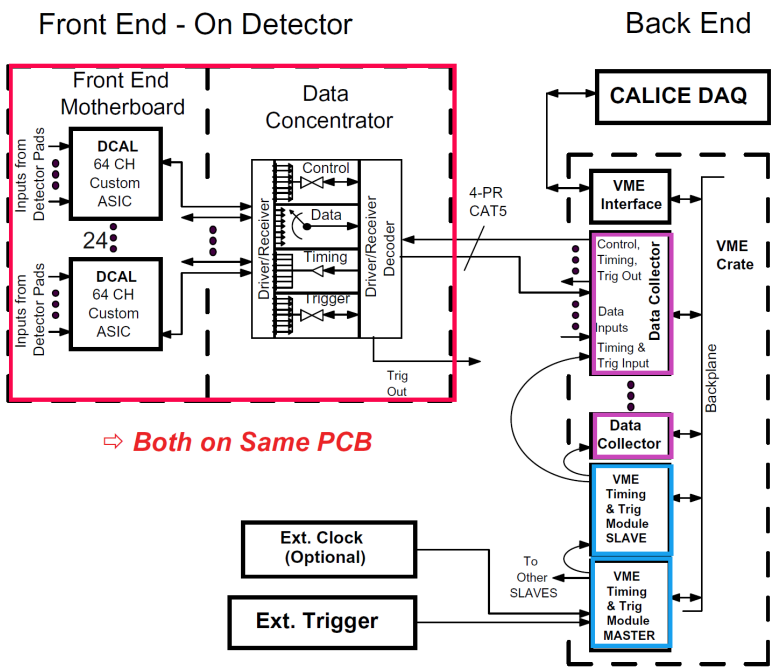

Figure II-4.9
Block diagram of the readout system of the DHCAL prototype.

the second level of data concentration. Each DCOL receives data from 12 DCON's and store the data into a large buffer for DAQ program to read via VME bus.

The system runs in two modes: triggered mode and triggerless (or self-triggered) mode. The first was designed for test beam runs with an external trigger. The second mode was designed for noise measurement, but was also found to be extremely useful in monitoring the RPC condition, collecting cosmic ray data for calibration and capturing all particles in a spill at a test beam.

The readout system for the DHCAL prototype is proven to be very reliable and has extremely low error rate. The front-end has very low noise. For all practical purposes, the noise coming from the front-end electronics can be safely ignored. As previously mentioned, the readout system for the DHCAL prototype did not address all requirements for a real DHCAL system in a colliding beam experiment. Further R&D is needed for the final readout design. There are two possibilities:

- Continue the development based on the success of the current DHCAL prototype readout system and focus on reducing power consumption, improving data transmission routing and optimising readout board thickness;
- Adopting KPiX readout for the DHCAL. The R&D needs to start from small scale chamber test and have several system level prototyping. This approach will be a longer development, however, it has the potential benefit of having a more uniform readout across the entire SiD detector;

4.3.4.3 Active layer design

In the baseline design, the barrel modules have a trapezoidal cross section. There are 40 layers in each module, each layer is 28 mm thick, consists of a 20 mm thick steel absorber and a 8 mm active layer for the RPC and its front-end readout. The innermost layer has a size of 740 mm $\times$ 6036 mm, and the outermost layer has a size of 1350 mm $\times$ 6036 mm.

Within each active layer, there are six RPCs that cover the entire area. Each RPC has a width 10 mm shorter than the full width of the layer. Along the beam direction, there are two different lengths for the RPCs: five at 966 mm and one at 1206 mm. With a 3 mm frame, the RPCs will have an active length of 960 mm or 1200 mm, which accommodates 96 or 120 readout pads of 1 $\times$ 1 cm^2 size. The six RPCs forms a row within a layer with the long RPC at the end. Neighbouring layers

have the long RPC at alternating ends so that the dead areas between the RPCs are not lined up in all layers. The smallest RPC unit has a size of 730 mm $\times$ 966 mm, while the largest RPC has a size of 1340 mm $\times$ 1200 mm, which is still within comfortable range for RPC construction and handling.

The RPC sizes exceed the size of a reasonable PCB board, so each RPC will be read out by several boards that have 1 $\times$ 1 cm^2 pads on the RPC side and front-end components on the other side. The basic dimension of the readout board is 32$\times$32 cm^2. The short RPC needs exactly three readout boards along its length, and the long RPC needs three standard boards and a 32$\times$24 cm^2 board to fill the whole length. Several special boards, that are 32 cm or 24 cm long and have different widths, are needed to fill the entire width of the RPCs in different layers. Boards that are in the same row along beam direction are chained together using flex cables and are read out from both ends of the module.

The baseline design uses a two-glass RPC design, which has a thickness of 3.7 mm, including insulation material. The readout board has a total thickness of 3.8 mm, including the height of surface mount components. The total thickness of the active elements adds up to 7.5 mm, which leaves 0.5 mm tolerance to slide the RPC and the readout boards in and out of the 8 mm gap between the absorbers.

The RPCs run with negative high voltage. The high voltage side of the RPC faces the inner absorber, and the readout is on the ground side of the RPC and is close to the outer absorber. The RPCs leave 5 mm space along both sides of the gap which allow two 1/8" gas tubes and one thin high voltage cable to run into the gap along each side. They supply gas and high voltage to the two inner RPCs on the same half of the module, and the end RPC is directly accessible from the end of the module.

The endcap modules have a similar active layer design, except that all RPC's have direct access form the end of the modules which make gas and high voltage connections significantly easier.

4.3.4.4 Results of prototype testing

The development of a hadron calorimeter based on the RPC technology progressed in several stages: a) Studies of various RPC designs, b) Construction and testing of a small scale calorimeter prototype, the Vertical Slice Test (VST), c) Construction of the DHCAL prototype, d) Testing of the DHCAL prototype in the Fermilab and CERN test beams. In the following we briefly report on the main results obtained in these stages.

RPC tests We choose to operate the RPCs in a saturated avalanche mode with an typical high voltage setting around 6.3 kV. The working gas has three components: Freon R134A (94.5%), isobutane (5.0%) and sulphur-hexafluoride (0.5%).

The size of the signal charges, the MIP detection efficiency and the pad multiplicity (as function of operating conditions) were measured with both cosmic rays and beam muons. As an example, Figure II-4.10 shows the pad multiplicity versus MIP detection efficiency [119]. Note the constant pad multiplicity at 1.1, independent of efficiency, for the one-glass design.

The RPCs in the Vertical Slice Test were also exposed to 120 GeV protons at various beam intensities to study their rate capability. The results show no loss of the MIP detection efficiency for rates below 100 Hz/cm^2. For higher rates, the efficiency drops exponentially in time (with a time constant depending on the beam intensity) until reaching a constant level.

The RPCs being tested have been operated continuously for over 18 months. Within the time period of these studies there was no evidence of long-term aging effects.

DHCAL prototype and TCMT The DHCAL prototype constitutes the first large scale hadron calorimeter with digital readout and embedded front-end electronics. It also utilised, for the first

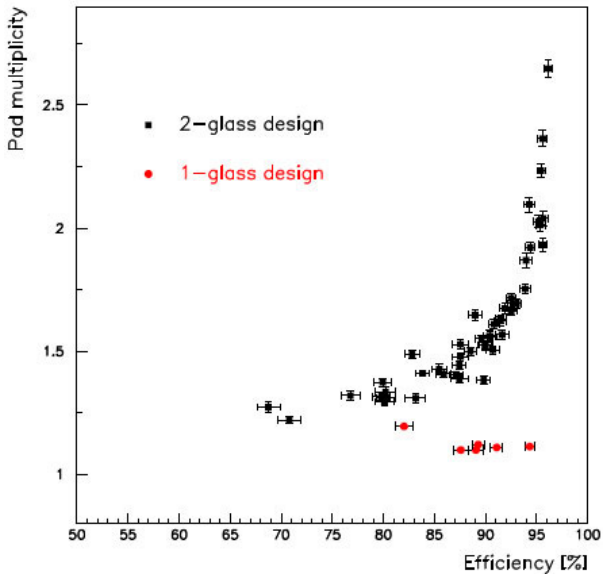

Figure II-4.10
Pad multiplicity versus MIP detection efficiency for 2-glass RPC and 1-glass RPC, measured with muon beam.

time, a pad-readout together with RPCs. The design of the DHCAL was based on preliminary work done with the Vertical Slice Test.

The DHCAL prototype consists of two parts: a 38-layer structure with 17.5 mm thick steel absorber plates and a 14-layer structure with eight 2.54 cm thick steel plates followed by six 10.0 cm thick steel plates. The former is commonly referred to as the DHCAL, or the Main Stack, and the latter is called the Tail Catcher and Muon Tracker (TCMT). These absorber structures were equipped with RPCs as active elements. Each layer measured approximately 1×1 m^2 and was inserted between neighbouring steel absorber plates. The Main Structure rested on a movable stage, which offered horizontal and vertical movements in addition to the possibility of rotating the entire stack. Figure II-4.11 shows photographs of the Main Structure and the TCMT.

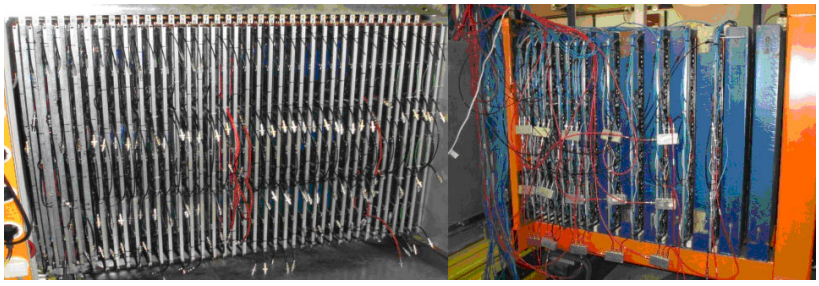

Figure II-4.11
Left: the DHCAL main stack (before cabling), right: the TCMT.

Each layer consists of three RPCs, each with an area of 32×96 cm^2 and stacked vertically on top of each other to create a 1×1 m^2 active area. Each RPC in turn is read out with two front-end boards, which covered the entire gas volume of the chambers. The three chambers and their boards are contained in a cassette structure providing the mechanical protection during transportation and installation.

The construction of the DHCAL prototype and TCMT started in fall 2008 and finished in early 2011.

DHCAL prototype test beam campaigns The DHCAL was tested extensively in the Fermilab test beam in various configurations: with the Scintillator Tail Catcher, with the Tail catcher equipped with RPCs, with or without the CALICE Silicon-Tungsten ECAL in front, and also with minimal absorber material between layers. In total, 9.4 million triggers were collected from muon beam and 14.4 million triggers are collected from secondary beam. Figure II-4.12 shows some events recorded by the DHCAL prototype and TCMT during the test beam campaigns.

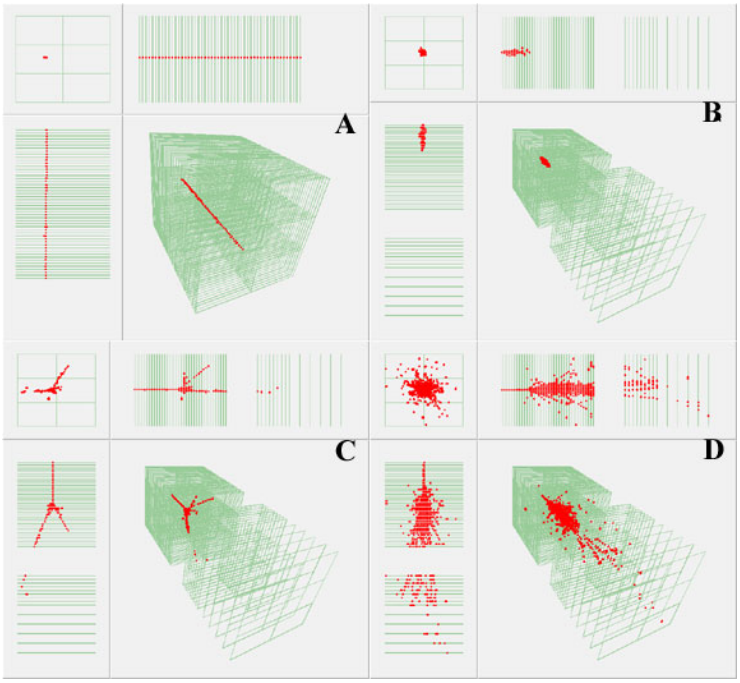

Figure II-4.12 Events recorded by DHCAL prototype at the Fermilab test beam. A: a muon track; B: 8 GeV positron shower; C: 8 GeV pion shower; D: 120 GeV proton shower.

In Spring 2012 the DHCAL layers were transported to CERN and were inserted into a Tungsten absorber structure with 39 layers and a Steel tail catcher with 15 layers. Tests at both the Proton-Synchrotron and the Super-Proton-Synchrotron have been carried out. So far, 5 million muon events and 22 million secondary beam events have been collected.

4.3.5 DHCAL prototype performance

To first order the energy E of an incident particle is reconstructed as being proportional to the number N of pads hits. However, a non-vanishing noise rate and variations in the chamber efficiencies and average pad multiplicities need to be corrected for, such that the energy of an incident particle is reconstructed as

$$E = \alpha_{sample} \times (\sum_{i=0}^{n} N_i \cdot \frac{\varepsilon_0}{\varepsilon_i} \cdot \frac{\mu_0}{\mu_i} - N_{noise}) \quad \text{(II-4.1)}$$

where the sum runs over all layers of the detector, α_{sample} is the sampling fraction which may depend on particle energy, ε_0 and μ_0 are the average MIP detection efficiency and the average pad multiplicity of the detector, ε_i and μ_i are the MIP detection efficiency and average pad multiplicity of layer i and N_{noise} is the average contribution from noise. All these calibration parameters are carefully measured and monitored over time during the test beam campaigns for the DHCAL prototype. The DHCAL response for positrons and pions are measured at different beam momenta, and data analysis is still on-going. We show preliminary results for the DHCAL noise measurement, muon calibration, positron response and pion response.

4.3.5.1 Noise measurement

The accidental noise rate was measured both with random triggers and with trigger-less acquisitions. Confirming our measurement with the Vertical Slice Test, the rate was found to be low, but to depend on the temperature of the stack and the ambient air pressure. For a given event, the accidental noise rate adds on average 0.01 to 0.1 hits in the entire DHCAL prototype, where one hit corresponds to about 60 MeV.

4.3.5.2 Muon calibration

At Fermilab, muons traversing the DHCAL were collected using the 32 GeV secondary beam, a 3 m long iron absorber and a trigger based on the coincidence of a pair of 1×1 m^2 Scintillator paddles located upstream and downstream of the detector.

Muon events were used to measure the local response of RPCs (efficiency and average pad multiplicity) in the DHCAL and TCMT. As an example, Figure II-4.13 (left) shows the MIP detection efficiency ε_i, the average pad multiplicity μ_i and the so-called calibration factors, $c_i=(\varepsilon_i\mu_i)/(\varepsilon_0\mu_0)$, as measured with two different techniques (tracks and track segments) versus layer number.

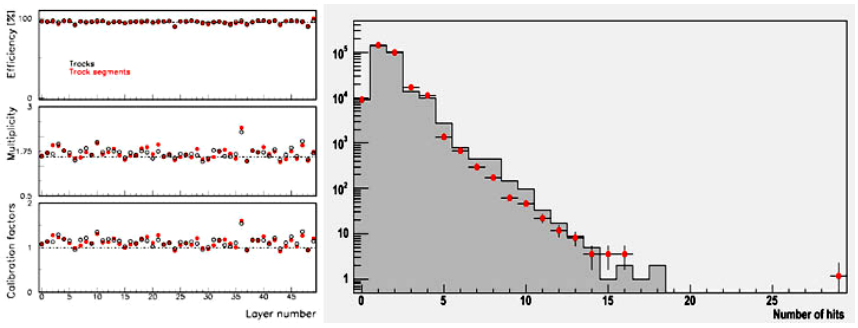

Figure II-4.13
Left: MIP detection efficiency, average pad multiplicity and calibration factors as function of layer number, as measured with both tracks and track segments; Right: response of a detector layer to muons averaged over the entire DHCAL with the histogram (data points) showing data (simulation).

The average response in clean regions of the stack, i.e. away from borders and fishing lines, was measured and is being used to tune the Monte Carlo simulation of the RPC response. Figure II-4.13 (right) shows a comparison of the measured and simulated RPC response.

4.3.5.3 Positron response

Secondary beam particles were collected at momentum points covering the range of 1 to 60 GeV at the Fermilab test beam. Data with the primary 120 GeV proton beam were also collected. The trigger (provided by the coincidence of two 19 × 19 cm^2 scintillator paddles positioned upstream of the DHCAL) accepted positrons and hadrons indiscriminately. The particles were later identified offline based on the information from the Cerenkov counters and shower shape.

The mean response of the DHCAL (before calibration) to identified positrons is shown in Figure II-4.14 (left). The response is fit with the nonlinear function $N=a+bE^m$. The fit describes the data well and is in accordance with the predictions in the VST results of positron showers [120]. In order to measure the electromagnetic energy resolution of the DHCAL the positron response need to be corrected for non-linearity. Figure II-4.14 (right) shows the electromagnetic energy resolution for both uncorrected and corrected values.

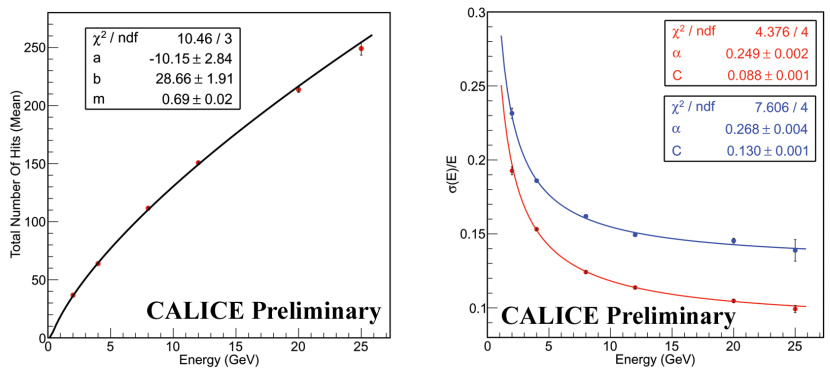

Figure II-4.14
Left: Mean response of DHCAL to positrons; Right: Non-linearity corrected (blue) and uncorrected (red) electromagnetic energy resolution for DHCAL.

4.3.5.4 Pion response

The mean response of the DHCAL (before calibration) to pions is shown in Figure II-4.15 (left). The response is linear up to 25 GeV, and at 32 GeV, the response deviates from linear behaviour due to RPC response fluctuation and possible saturation effect. Therefore, 32 GeV data point is not included in the linear fit (N=aE where N is the total number of hits and E is the beam energy). Figure II-4.14 (right) shows the hadronic energy resolution of the DHCAL with the current particle identification algorithms. The fits represent the data well and for the longitudinally contained pions -that have no hits in the last two layers- a stochastic term of approximately 55% and a constant term of 7.5% is achieved. The measurements are within 1-2% of predictions based on the simulation of the large-size DHCAL prototype using the VST results [121].

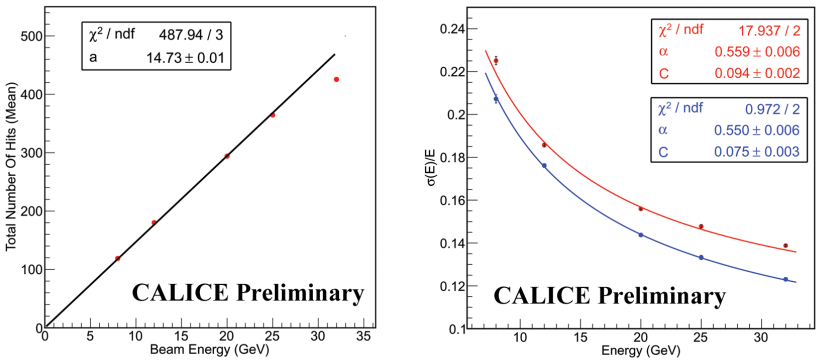

Figure II-4.15
Left: Mean response of DHCAL to pions; Right: hadronic energy resolution of DHCAL for all identified pions (red) and the longitudinally contained pions (blue).

With the data analysis still in a preliminary state, there are nevertheless a few conclusions to be drawn regarding an RPC-based digital hadron calorimeter:

- The RPC technology appears to satisfy the requirements of the active media of a highly segmented calorimeter.
- The dark rate in the DHCAL is very low and corresponds to a negligible amount of energy added to a single event.
- The response to positrons is as expected and consistent with predictions based on the VST [120]. As expected the response to positrons is non-linear, due to saturation effects introduced by the finite size of the readout pads.
- The response to pions is as expected and consistent with predictions based on the VST [121]. The response appears to be linear up to about 30 GeV.
- Using Tungsten absorbers instead of Steel plates leads to a reduced number of hits, by about 30%. To extend the range of the linear response beyond 20 GeV, a finer segmentation of the readout is required. It is conceivable that the application of software compensation techniques, which utilise the density of hits, is able to restore the linearity and improve the resolution at these higher particle energies.

4.3.6 R&D towards technical feasibility and optimisation

The DHCAL prototype was designed for proof of principle, R&D in several areas are still critical to demonstrate the technical feasibility and achieve design optimisation:

- The front-end of the DHCAL readout need to have significantly reduced power consumption, in order to avoid active cooling. Low power ASIC design techniques and power pulsing scheme are being considered to reduce the power dissipation by a factor of ∼100.

- The digital part of the readout system need to be optimised for better data concentration and reduced number of data connections without sacrificing reliability. Several ideas, including token ring passing and wireless data link, are being considered.
- A novel 1-glass RPC design is being developed, which features distinct advantages, such as an average pad multiplicity close to unity, a thinner chamber, a higher rate capability and a generous insensitivity to the surface resistivity of the resistive paint. The feasibility of larger chambers based on this design needs to be established.
- The high rate RPC could be a nice solution for the forward region of the DHCAL. The group is currently collaborating with several other institutes in developing low resistivity glass and Bakelite material for high rate RPC.
- The group is pursuing the development of a realistic design of a DHCAL module. Several configurations are being considered.
- A high voltage distribution system is being developed which is capable of turning onoff, adjust voltage value, and monitoring the current of individual chambers from a single high voltage input source.
- In order to operate a large DHCAL system at a future colliding beam experiment, a gas recirculation system is needed for both cost and environmental considerations. Initial development has started.

4.3.7 Calibration of a Digital Hadron Calorimeter

The event record for the DHCAL will contain a list of hits and their location. The energy of a hadron E_h will be reconstructed as described in formula II-4.1. In a running experiment, one needs to determine α_{sample}, ε_0, μ_0, and constantly monitor ε_i, μ_i and N_{noise}.

4.3.7.1 Sampling fraction and energy scale

The sampling fraction α_{sample} for charged hadrons can be measured by placing detector modules into a pion test beam of varying energies, which can also determine the energy dependence. The test beam data can also be used to validate a simulation procedure to reproduce the response of the modules to charged pions. The response of the modules to neutral hadrons will be simulated and the sampling term for neutral hadrons will be determined.

The overall energy scale of the jets reconstructed at the ILC will be cross checked using di-jet events and reconstructed W and Z boson masses. At $\sqrt{s} = 500$ GeV with an integrated luminosity of 1 fb^{-1}/day we expect to collect 2,800 (1,900) di-jet ($\mathrm{W}^+\mathrm{W}^-$) events/day. With enough statistics the dependence of the reconstructed jet energy on the electro-magnetic fraction of a jet or the fraction of neutral hadrons in a jet can be studied.

4.3.7.2 Monitoring of individual RPC's

Under fixed operating conditions (high voltage and threshold setting) the performance of RPCs depends on the ambient temperature, the atmospheric pressure and, for completeness, the gas flow. The last item only impacts the noise rate and the pad multiplicity. However, above a minimum gas flow these are seen to be constant and do not depend on variations of the flow. The performance of the RPCs does not depend on the ambient air humidity.

The dependence on the environmental conditions can be parameterised [117] as

$$\Delta\varepsilon = [-0.06 \cdot \Delta p(100Pa) + 0.3 \cdot \Delta T(^0C)]\%$$

$$\Delta\mu = [-0.25 \cdot \Delta p(100Pa) + 2.0 \cdot \Delta T(^0C)]\%$$

In the following we assume that the changes in performance are uniform within an entire chamber. Two methods will be employed to monitor the chamber's performance: one utilising track segments in events from ILC collisions and the other utilising cosmic rays.

- Track segment monitoring

  Imaging calorimeters offer the possibility to reconstruct individual track segments within hadronic showers [119] or in $e^+e^- \to \mu^+\mu^-$ events. Such track segments can be used to monitor the MIP detection efficiency ε_i and the pad multiplicity μ_i of individual RPC's during the data taking period.

  It is estimated that a 3% measurement is achievable, either using track segment method or muon tracks, within approximately 5 days of running.

- Cosmic ray monitoring

  Cosmic rays are an ideal tool to monitor the performance of the chambers. With a crude estimate of the underground muon flux, horizontal chambers with an area of 2 m^2 obtain 1000 measurements per minute. The rate in vertical chambers will be reduced by say one order of magnitude. Nevertheless, the required precision of 3% can be obtained in less than one hour. However, if the front-end power is pulsed, this will lead to a reduction in duty cycle of up to a factor of 200. In this case, time estimate needs to be increased to approximately 1 week. Further studies are needed to understand the cooling needs of the DHCAL and to define the optimal duty factor, taking into account the need for monitoring the performance of the RPCs.

In long-term studies of prototype RPCs, the efficiency and pad multiplicity were seen to vary by $\pm 0.9\%$ and $\pm 5\%$, respectively. Applying corrections for the environmental conditions (i.e. ambient temperature and air pressure) based on the above mentioned equations reduces these variations to $\pm 0.8\%$ and $\pm 3\%$.

Based on detailed simulations of the response of RPCs the effect of uncertainties in the calibration on the measurement of single particle energies was estimated. The studies showed that, for instance, for 10 GeV π^+ the energy resolution degrades by approximately by 1%, if the entire module's response is smeared by a Gaussian distribution with a sigma of 3%. This is the worst case scenario, where the responses of all layers in a given module are 100% correlated. If, on the other hand, all individual layers in a module fluctuate independently say by a Gaussian distribution with a sigma of 3%, the effect on the energy resolution is negligible.

4.3.7.3 Measurement of the noise rate

The background rate can be measured utilising the self-triggered mode of the front-end readout. Measurements on the prototype chambers typically showed a background rate of 0.1 - 0.2 Hz/cm^2 at room temperature. As an example Figure II-4.16 shows the noise rate as function of high voltage setting for the same threshold as in the test beam.

Assuming a gate width of 200 ns and a total of 5 $\times 10^7$ readout channels, the expected noise rate at the ILC will be about 2 hits/event in the entire DHCAL. Assuming a calibration of 13.6 hits/GeV, as obtained in recent simulations of the DHCAL, the noise contribution corresponds in average to around 150 MeV/event and can be ignored for all practical purposes.

Beam related background rates, due to neutrons for instance, will be measured using bunch-crossing events and algorithms for separating energy deposits from e^+e^- collisions and from beam backgrounds.

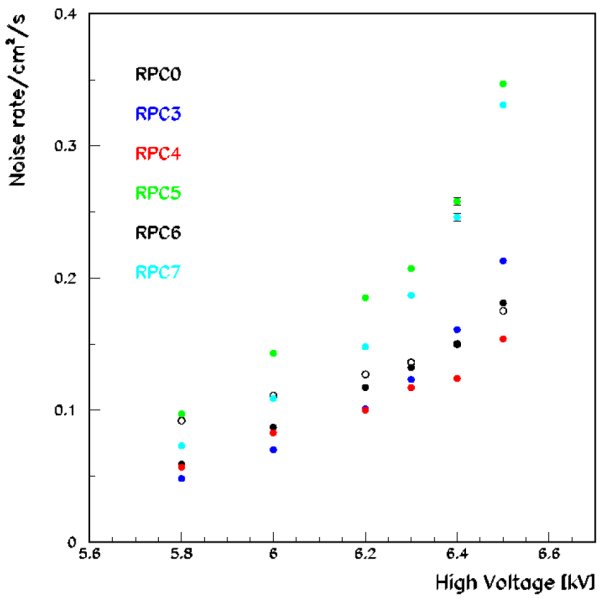

Figure II-4.16
Noise rate as function of high voltage for six different chambers. The threshold was set at the default value of 110 counts. The default high voltage setting was 6.2 kV.

4.3.8 Alternative technologies

A number of viable alternative approaches to PFA-based hadronic calorimetry are also considered by SiD. Two, GEM and Micromegas, use advanced micro-pattern gas detector technologies benefitting from participation in the RD51 collaboration. A third approach uses small scintillator tiles readout by silicon photomultipliers. As for the baseline RPC approach, all these alternatives are the subject of development within the CALICE collaboration.

4.3.8.1 GEM

We have also been developing a digital hadronic calorimeter (DHCAL) using GEM as the sensitive gap detector technology. GEM detectors can provide flexible configurations which allow small anode pads for high granularity. It is robust and fast with only a few nano-second rise time, and has a short recovery time which allows a higher rate capability than other detectors. It operates at a relatively low voltage across the amplification layer, and can provide high gain using a simple gas ($ArCO_2$), which protects the detector from long term degradation issues, and is stable. The ionisation signal from charged tracks passing through the drift section of the active layer is amplified using a double GEM layer structure. The amplified charge is collected at the anode layer with pads at zero volts. The GEM design allows a high degree of flexibility with, for instance, possibilities for micro-strips for precision tracking layer(s) and variable pad sizes and shapes. Figure II-4.17 depicts how the double GEM approach can be incorporated into a DHCAL scheme.

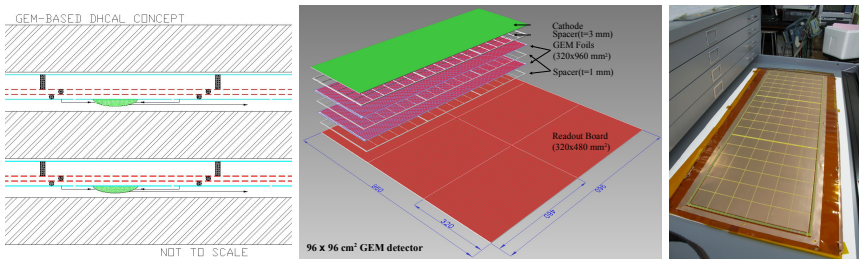

Figure II-4.17
Left: GEM DHCAL Concept. Centre: Drawing of the large-area GEM chamber. Right: Large-area GEM chamber under construction.

A number of double GEM chambers have been built and tested with cosmic rays, sources, and test beam. Stable operation has been achieved with 390 V across each GEM foil, leading to a gain of 11,000. The resulting typical MIP signal size is 40-50 fC, well above the noise level from the readout KPiX chip from SLAC.

The next step in developing the GEM approach to digital hadron calorimetry is the construction of a number of 1 m $\times$ 1 m layers for exposure as part of a 1 m^3 test beam stack. 1 m x 33 cm foils developed with CERN are being used to assemble double-GEM prototypes of the same size. Following this, a number of 1 m $\times$ 1 m layers will be assembled. Figure II-4.17 shows a schematic view of one of the 1 m $\times$ 33 cm layers under construction.

Single thick-GEMs [122] are also considered as an alternative to the double-GEM structure discussed above. A thick-GEM consists of a single circuit board about 0.5 mm thick and having holes of 200-400 μm in diameter. An advantage of thick-GEMs is a possible reduction in overall DHCAL active layer thickness and easier handling and construction compared with regular thin foils.

4.3.8.2 Micromegas

Introduction Digital calorimeters proposed for ILC or CLIC are expected to suffer from saturation due to the high particle multiplicity in the core of the showers. The resulting loss of linearity and resolution can in principle be mitigated if more than one threshold is used. A necessary condition for this approach to work is the proportionality between cell signals and the number of traversing particles. On average, this condition is met in Micro Pattern Gas Detectors like GEM and Micromegas because they are free of space charge effects.

Micromegas is a fast, position sensitive Micro Pattern Gas Detector operating in the proportional mode [123]. It functions in simple gas mixtures (*e.g.* Ar/CO_2) and at low fields and voltages (< 500 V) and is thus extremely radiation hard. It is an alternative to RPCs that offers lower hit multiplicity and proportional signals well suited for a semi-digital readout. On the other hand, Micromegas suffers from discharges but efficient protections exist.

Micromegas chambers developed for the active part of a semi-digital HCAL (SDHCAL) consist of a commercially available 20 μm thick woven mesh which separates the gas volume in a 3 mm drift gap and a 128 μm amplification gap (so-called Bulk). Micromegas of 32 $\times$48 cm^2 acting as signal generating and processing units have been designed and fabricated. They were used to construct three chambers of 1 m^2 size which are described below.

Mechanical layout and assembly The 1 m^2 chamber features 9216 readout channels (1 $\times$1 cm^2 anode pads) and consists of six Printed Circuit Boards (PCB) of 32 $\times$48 cm^2 placed in the same gas chamber. Front-end chips and spark protection circuits are first soldered on the PCBs. Then a mesh is laminated on the opposite pad side of each PCB to obtain an Active Sensor Unit (ASU). Having 6 meshes instead of a single larger one decreases proportionally the energy that is released in the front-end electronics circuitry during a spark (Figure II-4.18).

Small spacers (1 mm wide, 3 mm high) are inserted between ASUs and support the cathode cover, defining precisely the drift gap. Plastic frames are closing the chamber sides, leaving openings for two gas pipes and flexible cables. The chamber is eventually equipped with readout boards and a patch panel for voltage distribution. The total thickness amounts to 9 mm which includes 2 mm for the steel cathode cover (part of the absorber), 3 mm of drift gap and 4 mm for PCB and ASICs. With this mechanical design, less than 2% of inactive area is achieved.

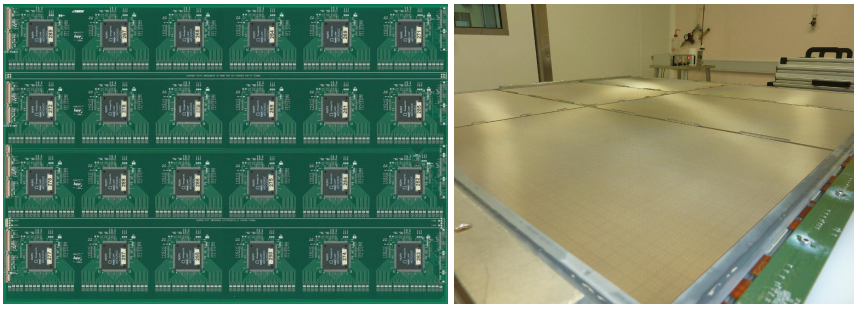

Figure II-4.18 *One Active Sensor Unit (ASIC side) and the 1 m^2 prototype during assembly.*

Performance to MIPs The response to minimum ionising particles (MIPs) was studied in a 150 GeV muon beam at CERN/SPS. The 1 m^2 chamber was flushed with a non-flammable mixture of $Ar/CF_4/iC_4H_{10}$ 95/3/2, the mesh voltages were varied between 300-420 V (gas gain G of 100-8000). A profile of the beam recorded in internal trigger mode is shown in Figure II-4.18 (left) and indicates that the noise level can be kept low and uniform.

The strong dependence of the detection efficiency on the applied voltage is shown in Figure II-4.18 (centre). Thanks to the very low readout threshold (1-2 fC), a gas gain as low as 10^3 (at 365 V) is sufficient to detect MIPs with an efficiency larger than 95%. Upon full exposure of two chambers, detailed efficiency maps over 8 $\times$8 cm^2 regions were produced revealing an efficiency of (96 $\pm$ 2)% (Figure II-4.18 (right)). Such a little variation indicates a good control of the chamber dimensions (gas gaps) as well as of the electronics parameters (gains, thresholds).

A benefit of Micromegas w.r.t. other gas detector technologies is the limited spatial extension of the avalanche signals. As a result of the little transverse diffusion experienced by the electrons in the gas (100-150 μm RMS), the hit multiplicity is below 1.15 up to 390 V ($G = 3000$). At higher gains, neighbouring pads become sensitive to single electrons, increasing the multiplicity to 1.35 at 420 V ($G = 8000$). There is however no reason to work in that regime as high MIP efficiency is reached at lower gains ($G = 1000$).

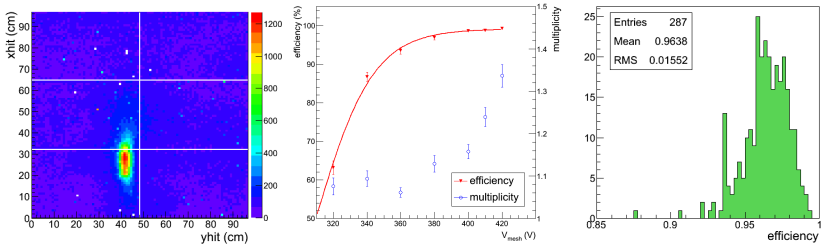

Figure II-4.19
Muon beam profile using internal trigger mode (left) efficiency and pad multiplicity.

Performance to pions The response of the chamber to hadronic showers was studied with pions using first a 20 cm long block of iron (1 λ_I) upstream of the chamber. Later, two chambers were inserted inside the Fe/GRPC SDHCAL in the last two layers, behind 5 λ_I.

Directing a 150 GeV pion beam at the iron block, the distribution of the number of hits in the chamber was measured at mesh voltages of 325, 350 and 375 V (G of about 350, 800 and 1700). The number of hit distributions, shown in Figure II-4.20 (left), exhibit a peak at $N_{hit} = 1$ and a long tail from penetrating and showering pions respectively. The distributions at 350 and 375 V yield different efficiency to penetrating pions but remarkably, have a similar tail. Accordingly, a gas gain as low as 800 is sufficient to image most of the shower. Such a low working gas gain greatly improves the stability of the detector.

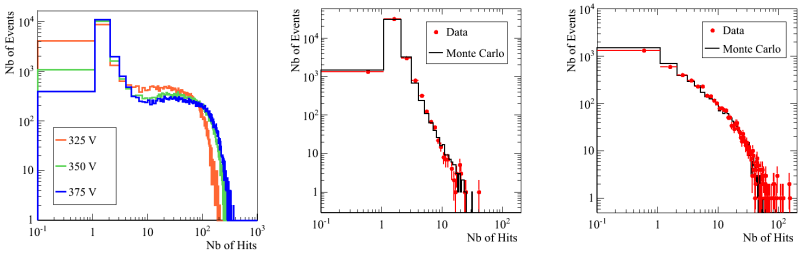

Figure II-4.20
Hit distribution from 150 GeV pions traversing a 20 cm thick iron block at various mesh voltages (left). Hit distributions from 100 GeV muons (centre) and pions (right) at layer 48 of the CALICE Fe/GRPC SDHCAL.

A good understanding of the detector is being achieved by comparing test beam data to Monte Carlo predictions. Preliminary results are presented in Figure II-4.20 (right) which shows the distribution after 5 λ_I of Fe for 100 GeV pions. The readout threshold was tuned so as to reproduce

the efficiency to muons (Figure II-4.20 (centre)). A satisfactory agreement is obtained for muons and pions meaning that the simulation is reliable. It should be stressed that no noise was introduced in the simulation, therefore, data are essentially free of noise.

4.3.8.3 Scintillators

The CALICE Collaboration has been pursuing the design and prototyping of a fine granularity scintillator-based hadron calorimeter. This option capitalises on the marriage of proven detection techniques with novel photodetector devices. The main challenge for a scintillator-based calorimeter is the architecture and cost of converting light, from a large number of channels, to electrical signal. Studies demonstrate that small tiles (4-9 cm^2) interfaced to Silicon Photomultipliers (SiPMs)/Multi Pixel Photon Counter (MPPC) photodetectors [124], [125] offer an elegant solution. SiPM/MPPCs are multi-pixel photo-diodes operating in the limited Geiger mode. They have distinct advantage over conventional photomultipliers due to their small size, low operating voltages and insensitivity to magnetic fields. The *in situ* use of these photodetectors opens the doors to integration of the full readout chain to an extent that makes a high channel count scintillator calorimeter entirely plausible. Also, in large quantities the devices are expected to cost a dollar per channel making the construction of a full-scale detector instrumented with these photo-diodes financially feasible.

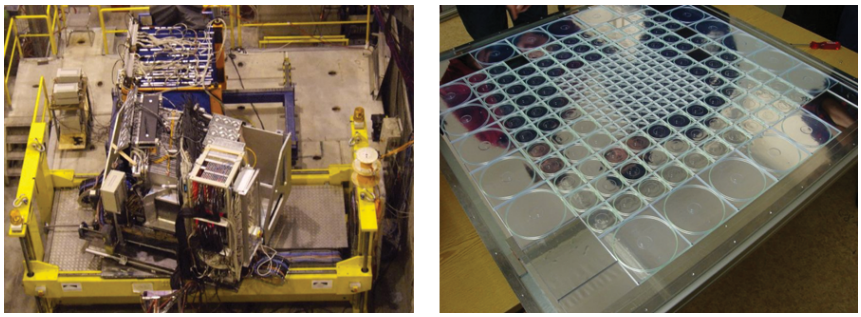

Figure II-4.21 CALICE test beam setup at CERN (left) and an active layer of the scintillator-SiPM prototype (right)

A $\sim$ 1 m^3 size scintillator-SiPM prototype [126] has been designed, constructed and exposed to a test beam during the 2006-2009 period at CERN and Fermilab (see Figure II-4.21). The active layers have subsequently been embedded in a tungsten stack which has collected data in the 2010-2011 period. Over numerous run periods the technology has proven to be versatile and robust, millions of electron, pion and proton events in the 2-180 GeV range were written to disk. Ongoing analysis of the data collected, has gone a long way in establishing the scintillator-SiPM option as a calorimeter technology (see Figure II-4.22), benchmarking hadron shower simulations [127] and testing the particle-flow paradigm using hadrons from real data [128].

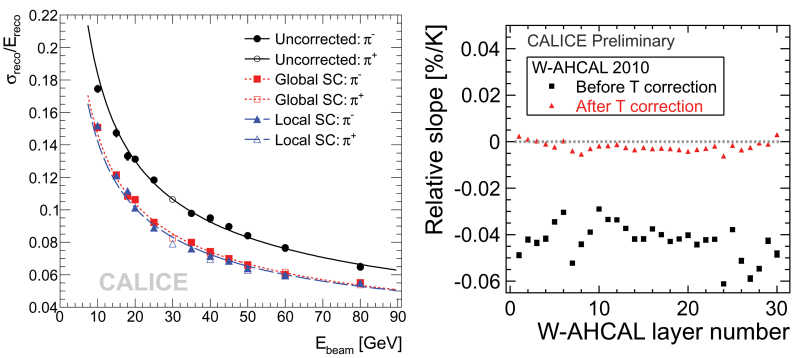

Figure II-4.22 Single pion resolution using simple energy sum and software compensation techniques (left) and slope of the SiPM response temperature dependence for AHCAL layers without and with temperature correction (right)

The focus of the current and future R&D effort is to demonstrate the scalability of this technology taking into account the stringent constraints on the power consumption and mechanical compactness

through the development of an Integrated Readout Layer (IRL). In general for the IRL, it is proposed to have a printed circuit board (HCAL Base Unit or HBU) inside the detector which will support the scintillator tiles, connect to the silicon photodetectors and carry the necessary front-end electronics and signal/bias traces (see Figure II-4.23). This can however be achieved in a number of ways and a number of promising complementary approaches (e.g.fibre vs. direct or fibreless coupling of SiPMs to the tiles) have been developed in a coordinated fashion such that they can be characterised in a common electronics environment. This next generation front-end electronics carried aboard the HBUs is capable of self-triggering, precise time stamping, channel-by-channel bias control and a built-in LED calibration system. Commissioning of these readout slabs is at an advanced stage and is expected to expand into exposure in electron and hadron test beams in the near future.

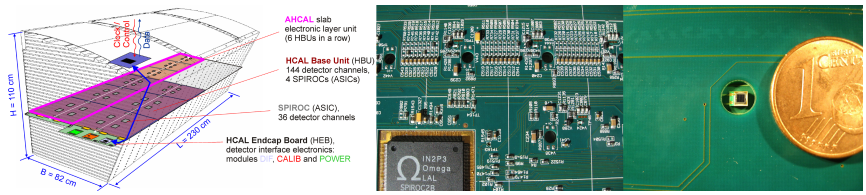

Figure II-4.23 Conceptual design of a barrel wedge instrumented with IRL planes (left), a HBU prototype (centre) with a MPPC surface-mounted on it (right).

4.4 Summary

We have a silicon-tungsten electromagnetic calorimeter design that can satisfy the PFA requirements. We have developed a first-level mechanical design and have all the components and processes in place to construct and test a full-depth prototype. The technologies for PFA-based hadron calorimetry have seen significant development and testing since the submission of the SiD LOI. The construction of the cubic metre HCAL stack in the baseline RPC technology has provided much practical experience and confidence towards producing a full detector in this technology. The test beam data, providing unprecedented detail on hadronic showers, have shown that this is indeed a very promising technology, in the PFA context, for the SiD detector. We have also benefitted from the development of several alternative technologies.

Chapter 5
SiD Muon System

The SiD muon system is designed to identify muons from the interaction point with high efficiency and to reject almost all hadrons (primarily pions and kaons). The muon detectors will be installed in the gaps between steel layers of the solenoid flux return. The required position and rate capabilities of the detectors are modest and can be met by several different detector technologies. The baseline design uses double layers of extruded scintillator strips read out by silicon photomultipliers (SiPMs). Resistive plate chambers (RPCs) are also under consideration as an alternative design.

The SiD muon selection will combine information from the central tracker, calorimeter, and muon detectors to construct 3-dimensional tracks through the entire detector for each muon candidate. Candidates will be required to penetrate a number of interaction lengths consistent with the muon momentum. In addition, the observed number and position of hits along the fitted track length can be used to further discriminate against hadrons. The first layers of the muon system may also be useful as a tail-catcher for the hadronic calorimeter.

Muon systems characteristically cover large areas and are difficult to access or replace. Reliability and low cost are major requirements. Over 2.4 m of steel thickness will be required for the solenoid flux return, providing > 13 nuclear interaction lengths to filter hadrons emerging from the hadron calorimeter and solenoid. Since the central tracker will measure the muon candidate momentum with high precision, the muon system only needs sufficient position resolution to unambiguously match calorimeter tracks with muon tracks. Present studies indicate that a resolution of ≈ 2 cm is adequate. This can be achieved by two orthogonal layers of 4 cm wide extruded scintillators or RPC pickup strips.

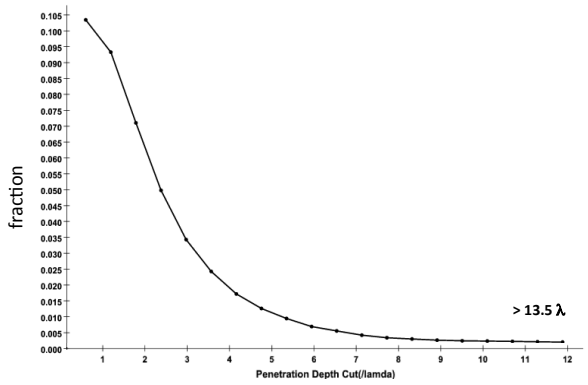

Figure II-5.1 Misidentification of pions as a function of the depth of the last hit muon layer.

Full optimisation of the muon system design has not been completed. The total steel thickness is set by the solenoid flux return requirements. To check that the present design is thick enough we studied the misidentification rate of pions between 10 GeV and 50 GeV as a function of the depth in the flux return. As shown in Figure II-5.1, requiring that the track makes hits in some of the outer layers is sufficient to reduce the pion misidentification rate to 0.25%, consistent with the expected

level of pion to muon decays. The present design, shown in Figure II-5.2 has ten layers in the barrel section and nine layers in each endcap. This provides a comfortable level of redundancy (≥ 6 layers) even in the region between the barrel and endcap. The optimum number of detector layers to cover the muon identification and tail catching functions was also studied for the CLIC case [129], where nine layers were found to be sufficient.

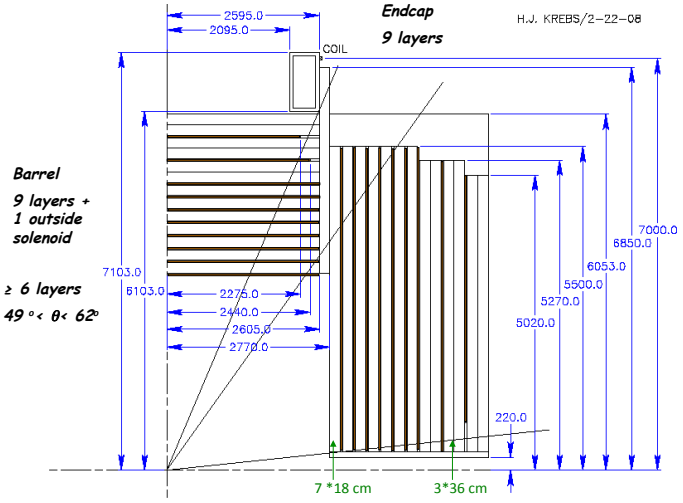

Figure II-5.2 Quarter section view of the SiD steel flux return.

5.1 Backgrounds

Backgrounds in the muon system are expected to come primarily from beam losses upstream of the detector. The muon system is shielded from backgrounds generated at the collision point or along the internal beam lines by the calorimeters, which are greater than five absorption lengths thick. Therefore only penetrating backgrounds, such as high-energy muons or neutrons, affect the barrel muon detectors. Calculations [130] of the expected background from muons produced by collimators near the detector hall predict a rate of 0.8 muons/cm^2 per pulse train (1 ms) without muon spoilers, which is reduced to 3×10^{-3}/cm^2 per pulse train with the addition of muon spoilers. Physics backgrounds from two-photon processes producing hadrons or muon pairs significantly increase the expected signal rate in the endcap detectors near the beamline. At a radius of 22 cm the expected rate from hadrons and muons above 2 GeV is ≤ 0.04/cm^2 per pulse train. The endcap detectors can also be hit by electromagnetic shower debris from local beam losses and may require additional shielding

5.2 Detector design

The muon system will start outside of the highly segmented electromagnetic and hadronic calorimeters and the 5 T solenoid cryostat at a radius of 3.3 m. In the design shown in Figure II-5.2 the barrel flux return is divided into seven layers of 18 cm steel and three layers of 36 cm steel in an octagonal barrel geometry. Endcaps of seven 18 cm thick steel octagons plus three 36 cm octagons will cap both ends of the barrel. The muon detectors will be inserted in the 4 cm gaps between the plates. In the barrel a detector layer is also inserted between the solenoid and the first steel plate. The size of the first barrel layer within each octant is approximately 2.9 m by 5.5 m, while the last layer is 4.7 m by 5.5 m. The total detector area needed in the barrel is $\approx$ 1600 m^2.

The endcap design is shown in Figure II-5.3 (left). Each octagonal layer is made from three steel plates bolted together. The spacers between layers are staggered as seen in Figure II-5.3 (right) to reduce projective cracks in the muon detection. The endcap detectors are subdivided by the spacers into rectangular or trapezoidal modules $\approx$ 1.8 m by 5.5 m. Each endcap has a total detector area of $\approx$ 1000 m^2.

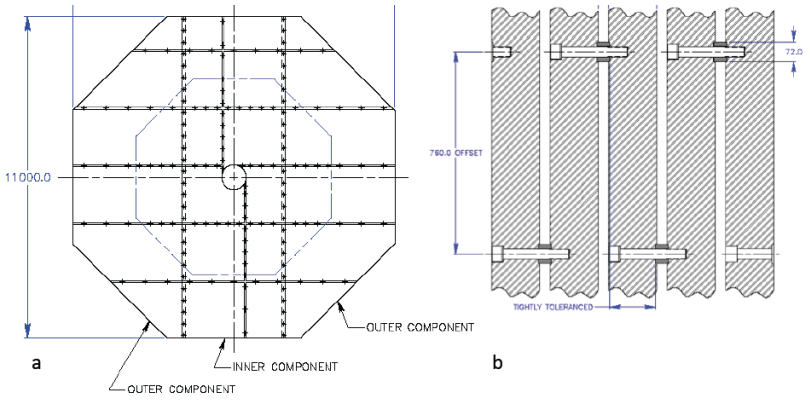

Figure II-5.3
(left) Each layer of the endcap flux return is made of three vertical steel pieces bolted together. (right) Horizontal spacers separating the steel layers are offset by 0.7 m in alternate layers to avoid projective cracks.

5.2.1 Scintillating strips

Extruded scintillating strips have been used in MINOS [131] and T2K [132] and are planned for $\mu 2e$ [133] and SuperB [134]. Wavelength shifting fibre is run down the centre of each strip. A TiO_2 reflective coating is co-extruded on the outside of the scintillator. The fibres extend out of the strips by ~ 1 cm and are readout by SiPMs

The baseline muon detector employs 1 cm thick by 4.1 cm wide scintillating strips, arranged in back-to-back twin-planes with perpendicular strips as shown in Figure II-5.4 (left). In the barrel strips in one plane are parallel to the beam direction (z-strips), while those in the adjacent plane are orthogonal (r, ϕ strips). These layers are glued together with aluminium sheets to form a rigid module. The aluminium sheets provide support while optically isolating the two layers. In the endcap, Figure II-5.4 (right), the gaps between the steel layers are broken up by rows of horizontal spacers. The vertical strips are short (≈ 1.8 m) while the horizontal strips are ≈ 5.5 m long.

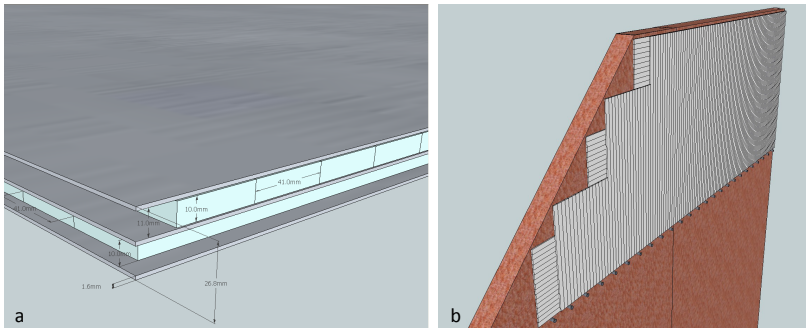

Figure II-5.4
(left) Each gap in the barrel flux return is filled by two orthogonal planes of scintillating strips glued to three aluminium sheets to form a rigid rectangular sandwich. (right) The endcap modules are ≈ 1.8m high to slide between the spacers separating the endcap steel layers.

Particles emerging from e^+e^- collisions at the interaction region create optical pulses via dE/dx when traversing the scintillator strips placed in the gaps of the barrel and endcap Fe return yokes. A fraction of the light is captured in a 1.2 mm diameter wave-length shifting (WLS) fibre located in a groove that runs along the length of the scintillator bar. The light travels through the WLS over 2 m to 5 m distance before reaching the input face of a Si photo-diode (SiPM) matrix, where it triggers an avalanche in one of the few-hundred micron-sized individual photo-diodes cells whose outputs are ganged together through individual output resistors to a common output. In our tests of candidate SiPMs for muon detection we have focused on devices with ≈700 cells with $40\ \mu m \times 40\ \mu m$ size fitting inside a 1.2 mm diameter circle [135]. As the cells in the Si matrix have good uniformity with similar areas and Si thicknesses, the summed avalanche signal output of the ganged cells is proportional to the number of cells hit. Therefore the devices can be calibrated adequately by using the individual photoelectron peaks in the summed signal of the SiPM. The calibration procedure makes use of peaks with one or two photoelectrons, as well as noise peaks. Signals from individual SiPMs are then sent on to receivers and collected for further digital processing.

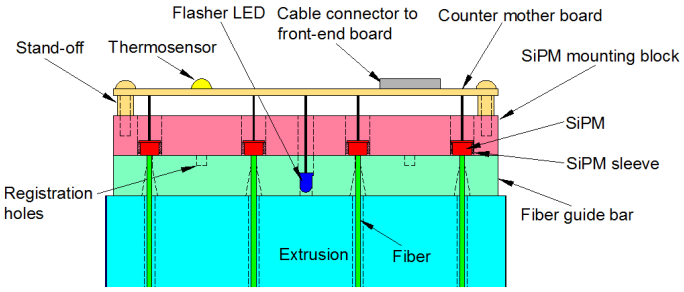

Figure II-5.5
SiPMs are positioned at the end of each fibre by a SiPM mounting block and fibre guide.

There are 7,451 axial barrel channels where both ends of the fibres are read for the barrel strips, making 14,902 readout channels. There are 10,810 (r, ϕ) scintillator strips that add 10,810 single ended readout channels to make the barrel (B) channel count 25,712. The reason for not reading out both ends of the (r,ϕ) strips is that there are more and consequently shorter WLS fibres (less occupancy) and less attenuation in these barrel channels. All the outer periphery ends of the Forward/Backward (F/B) channels are read (no double-ended readout). The F/B strip-scintillator planes add a 21,620 scintillator strips (21,620 channels of readout and electronics) to make a total of 25,712 central and 21,620 F/B in back-to-back quadrants for a total of 47,332 channels. The sum of WLS fibre and scintillator totals $\approx$ 164 km ($\approx$ 86 km for the ten barrel planes and $\approx$ 78 km for the nine endcap planes).

Recently the University of Virginia HEP group have developed small molded plastic parts that capture the detector end of the WLS fibre and accurately position it relative to the centre of the SiPM which has 600 Si pixels contained inside a circular area of 1.2 mm diameter. With this kind of connection of the polished signal fibre to the photodetector it should be possible to locate the readout devices on a separate long plastic or fibreglass strip that accepts the WLS ends for a plane or half plane of detectors as drawn in Figure II-5.5. A prototype strip/SiPM combination was tested in Fermilab Test Beam Experiment T995. Two 3.6 m long strips were connected by fibre to make an effective 7.2 m long strip. SiPMs were glued on both ends of the fibre. Beam was scanned along the length of the strip to study pulse height as a function of the distance from the SiPM. As seen in Figure II-5.6 the number of photoelectrons can be easily counted on either end of the strip even if the beam is placed near one end. The pedestal was quite small and stable. Requiring two or more photoelectrons eliminates nearly all of the noise signals.

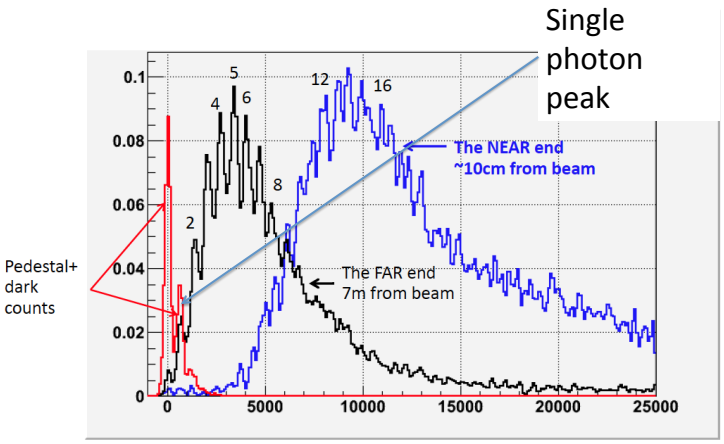

Figure II-5.6
Test beam data of two strips coupled by fibre to simulate a single long strip. Pulse height from the top strip (blue) and the bottom strip (black) are shown. The beam is 10 cm from the end of the top strip.

In Figure II-5.7 multiple beam positions in two different prototype strips were used to measure the attenuation of the light signal with fibre/strip length. The data can be modelled by the sum of two exponential fall-offs. Near the sensor, the attenuation length is $\sim$ 2.9 m. At 7 m from the sensor, the attenuation length is $\approx$ 6.5 m. Since the longest strips in SiD are less than six meters long the minimum expected pulse height is > 5 photoelectrons. With a threshold of two photoelectrons the

scintillating strips with SiPM readout are very efficient.

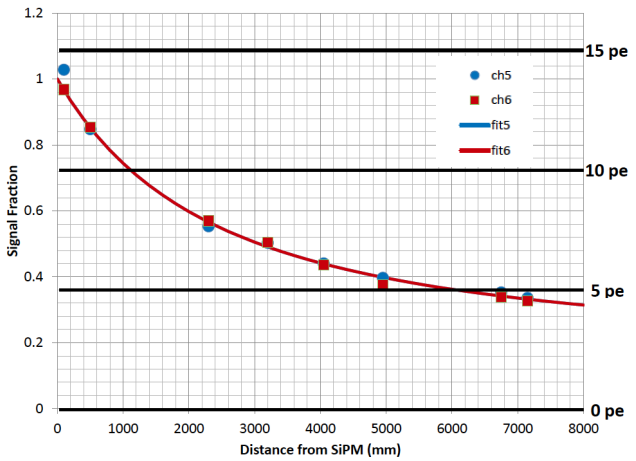

Figure II-5.7
The fraction of the total light collected by the SiPM as a function of the beam position along the strip for two different strips (ch 5 and 6).

5.2.2 Resistive Plate Chambers

Many large RPC systems have been built within the last ten years and understanding their performance will provide strong guidance for an SiD design. Several types of RPC construction have been used in high energy experiments. RPCs with Bakelite cathodes and anodes, initially reported in [136], found application in BaBar, CMS, ATLAS and a variety of cosmic ray and neutrino experiments. RPCs are inexpensive to build and can be easily constructed in a variety of shapes and sizes. There are, however, a few concerns about the use of RPCs in future experiments. RPCs use fluorocarbon gases which are regulated as greenhouse warming gases and require nontrivial gas delivery systems adding to operational costs. Further restrictions on the use of fluorocarbon gases are possible in the future. RPCs have also had reliability problems (BaBar was forced to replace its original RPCs and Belle had startup problems). However, significant progress has been made in understanding RPC aging mechanisms. The current ATLAS [137] and CMS [138] detectors, which run in avalanche mode, have shown good stability even at the high background rates expected at the LHC. The second generation BaBar RPCs [139] and the Belle RPCs preformed reliably at the low signal rates ($< 0.2\text{Hz/cm}^2$) expected for SiD detectors. RPCs are a viable detector alternative for the muon system, particularly if the RPC option is chosen for the hadron calorimeter. Bakelite was chosen for the RPCs because for the foreseen plate thickness of 2 mm, glass is significantly heavier than Bakelite and more brittle. Given the large-area chambers needed for the muon system, a Bakelite RPC system is most likely easier to construct and install, hence a conservative choice was made.

A RPC design for the muon detector planes would utilise two layers of single gap RPC HV chambers (1×2 m) with orthogonal readout strips on either side assembled into modules of the required size to fill each slot in the octagonal barrel or endcap. The chamber size would be varied so that joints between chambers do not align in the top and bottom layer. If the single gap RPC efficiency is 90%, then an average module efficiency of 93% can be achieved.

Close integration of the RPCs and front-end and digitisation electronics is necessary to minimise cabling and costs since the expected channel counts for the SiD detector are high (nearly one million for the muon system). One possible low cost solution that has been investigated is to adapt the KPiX chip, presently being developed for use in the SiD electromagnetic calorimeter, for use with RPCs. An RPC/KPiX interface board was designed and built to provide ribbon cable connections to a 64-channel KPiX chip (v7). The RPC strip signal is AC coupled to the KPiX input through a 5 nF blocking capacitor and a 2-stage diode protection network. Each strip is also tied to signal ground via a resistor external to the interface board.

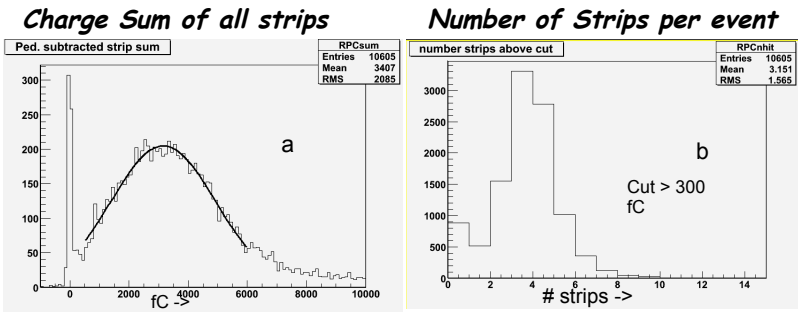

Figure II-5.8
(left) Sum of the pulse heights in 13 RPC strips readout by a 64-channel KPiX chip (v7). The peak position of 3 pC and efficiency of $> 90\%$ are consistent with previous studies of avalanche mode RPCs. (right) The number of strips with a signal height above 300 fC per track.

A small (0.5 m $\times$ 0.5 m) test RPC with 13 strips was connected to the interface board by a 0.5 m cable. The chamber was operated at 9300 V in avalanche mode using a premix gas with composition of 75.5% Freon 134a, 19.4% Argon, 4.5% isobutane, and 0.5% SF6. The chamber efficiency had been previously measured to be $\approx 90\%$ using BaBar electronics. The signal sum of the 13 RPC strips on the HV ground side (positive signal) is shown in Figure II-5.8 (left). The sharp spike near zero is due to cosmic ray tracks that either missed the test RPC or to RPC inefficiency. The signal peak is centred at 3.8 pC with a width of 2.2 pC. The signal height is consistent with, but larger than, avalanche RPC signals measured by other groups ($\approx$ 1 pC), which used avalanche gases with no Argon component. The avalanche gas contains 19.4% Argon and is expected to have a higher gas gain. The charge distribution in the RPC pickup strips was also studied. For each trigger, the strip with the maximum charge has typically less than half of the total charge in the event. The strip multiplicity was measured as a function of the discrimination threshold. With a threshold of 300 fC, about 92% of the cosmic triggers have one or more strips hit and the average strip multiplicity is 3.1, more than twice that observed with BaBar electronics. Although a good proof of principle, these tests show that further characterisation and optimisation of the interface board between the RPC and chip is needed

Chapter 6
SiD Superconducting Magnet System

6.1 Introduction

6.1.1 List of subsystems

The magnet subsystem consists of its own following subsystems:

1. A 6.8 m outside diameter $\times$ 6 m long 5 T superconducting solenoid with a separated iron plate flux return that is integral with the muon tracking system.
2. A superconducting 600 G Detector Integrated Dipole (DID) integrated with the solenoid.
3. A power supply, a DC contactor, a pressurised water cooled dump resistor, and a conventional mechanical dump switch that move with the detector.
4. A 1.5 kW helium liquefier and 5000 litre LHe storage dewar that supply 4.5 K LHe to both the solenoid and to a pair of 2 K cold boxes for each of the superconducting focusing magnets (QD0).
5. Interconnecting cold, warm, and vacuum plumbing lines including those to QD0, mounted directly on the detector.
6. Controls and instrumentation for the magnets and helium liquefier.

The shared resource ILC helium compressor system and the two superconducting QD0 focusing magnets with the internal design of their 2 K distribution boxes are not part of this subsection.

6.1.2 Design Philosophy

The superconducting solenoid is an expensive and technically challenging component. Its design is based on the successful 4 T CERN CMS superconducting solenoid, and thus a direct comparison is warranted in Table II-6.1 [140]. High purity aluminium superconductor stabilisation with indirect LHe cooling will be used. The CMS individual self supporting winding turn design philosophy is used for SiD, becoming even more important due to the higher 5 T field and the increased radial softness of six layers versus four layers. Figure II-6.1 shows a 3D cut-out with the principal elements of the SiD magnet.

The SiD solenoid has a stored energy per unit of cold mass of 12 kJ/kg, which is only slightly larger than the CMS value. The value of 12 kJ/kg is close to the upper bound at which such a large aluminium dominated magnet can be operated in a fail safe manner, in case the quench detection or energy extraction circuit were to fail. Upon such a failure, the average magnet temperature would reach 130 K. Engineering studies of the SiD solenoid indicate that the total volume of aluminium stabiliser/structure cannot be reduced by much with respect to the present baseline design.

Table II-6.1
SiD and CMS Superconducting Coil Comparison

Quantity	SiD	CMS	Units
Central Field	5.0	4.0	T
Stored Energy	1.59	2.69	GJ
Stored Energy Per Unit Cold Mass	12	11.6	kJ/kg
Operating Current	17.724	19.2	kA
Inductance	9.9	14.2	H
Fast Discharge Voltage to Ground	300	300	V
Number of Layers	6	4	
Total Number of Turns	1459	2168	
Peak Field on Superconductor	5.75	4.6	T
Number of CMS superconductor strands	40	32	
% of Short Sample	32	33	
Temperature Stability Margin	1.6	1.8	K
Total Cold Mass of Solenoid	130	220	tonne
Number of Winding Modules	2	5	
R_{min} Cryostat	2.591	2.97	m
R_{min} Coil	2.731	3.18	m
R_{max} Coil	3.112	3.49	m
R_{max} Cryostat	3.392	3.78	m
Z_{max} Cryostat	$\pm$ 3.033	$\pm$ 6.5	m
Z_{max} Coil	$\pm$ 2.793	$\pm$ 6.2	m
Operating Temperature	4.5	4.5	K
Cooling Method	Forced flow	Thermosiphon	

6.2 Magnetic Field and Forces

6.2.1 Requirements and Design

The SiD magnet system requires a 5 T central field, an alternating 600 G field along the axis from the DID, and a fringe field of less than 100 G at a metre distance from the outer iron surface [141]. An economic solution to the fringe field requirement has not yet been found. Two iron plates placed around the barrel and overlapping the doors with a combined thickness of 14 cm drops the 1 meter fringe field to 300 G. The 100 G at one meter is certainly achievable with the addition of sufficient iron and air gaps. Some components such as the expansion turbines inside the helium liquefier will most likely require additional local iron shielding.

Figure II-6.1
Magnet section showing its principal elements.

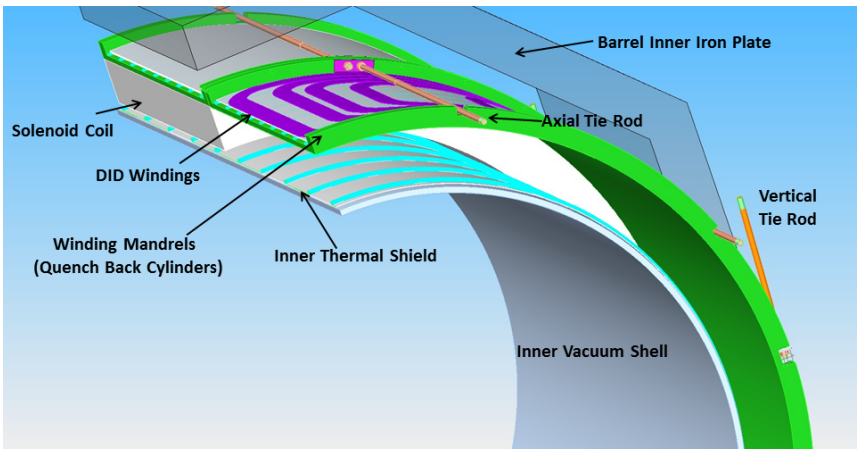

Eleven 20 cm thick iron plates with 4 cm gaps form both the barrel and end wall portions of the flux return. There is also a 5 cm gap between the barrel and endcap that is partially filled with barrel iron connecting plates. These connecting plates are also part of the solenoid axial restraint system. The iron plates of the endcaps are held together with an iron cylinder on the inner diameter and top plates on the outer diameter.

6.2.2 Calculations

The results of two- and three-dimensional ANSYS magnetic field calculations of the magnet are shown in Figure II-6.2. The 3D ANSYS model also includes the DID, barrel/endcap iron gap details, and the cryogenic chimney and current lead penetration details. The DID coil position was calculated using OPERA 3D and custom codes. The ANSYS 3D model uses an edge element formulation and has seven million elements [142]. Advances in computation give a significant advantage to the SiD design as compared to prior CMS design work. The magnetic axial spring constant was found to be constant from 1 cm to 20 cm coil displacement. The axial magnetic force is maximum at full current; there is no iron saturation effect. An iron HCAL endcap was studied and rejected due to minimal improvement in field and field uniformity versus increased cost and complexity [143].

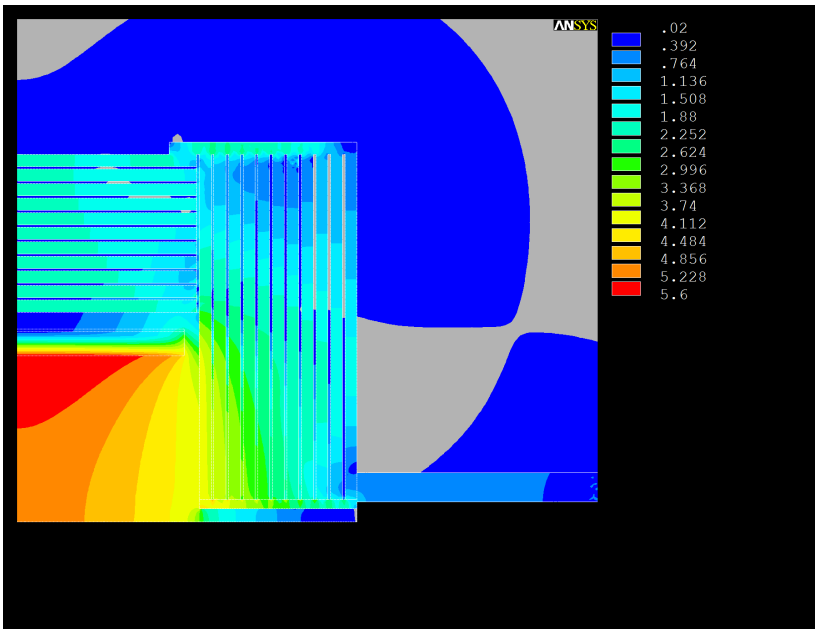

Figure II-6.2
:2D Axisymmetric showing B_{max}. Only a small portion of the air is displayed. The gray/blue boundary is the 200 G line.

6.3 Mechanical Engineering

6.3.1 Solenoid Coil Production

The superconductor will be internally wound into two precision aluminium 5083-H321 mandrels using CMS winding procedures, including epoxy vacuum impregnation and mandrel joining techniques, and conductor splicing methods. The CMS coil winding experience will significantly reduce the SiD time and expense of winding line setup and commissioning. Coil winding and vacuum impregnation will take place at the vendors facility. The magnet will be shipped as two separate coils of 65 tonne each.

6.3.2 Integration of DID to solenoid

The Detector Integrated Dipole (DID) is mounted directly on top of the solenoid cooling tubes. The four separate 600 kA turn winding packages are sandwiched between a lower 3 mm Al sheet and an upper 5 mm Al sheet. Each package consists of five coils all electrically connected in series creating either a DID or anti-DID field. The coil packages are mounted directly on top of the solenoid LHe cooling loops by metal screws attached to the solenoid winding mandrel. Twenty two solenoid splices rest on top of the upper DID Al sheet and are supported by direct connection to the solenoid winding mandrel at the centre of the four DID winding packages. Conduction through the DID and direct physical connection through the DID centres establish cooling for the solenoid splices. All DID splices except for the two connections to the DID current leads are made in the space between the two aluminium sheets.

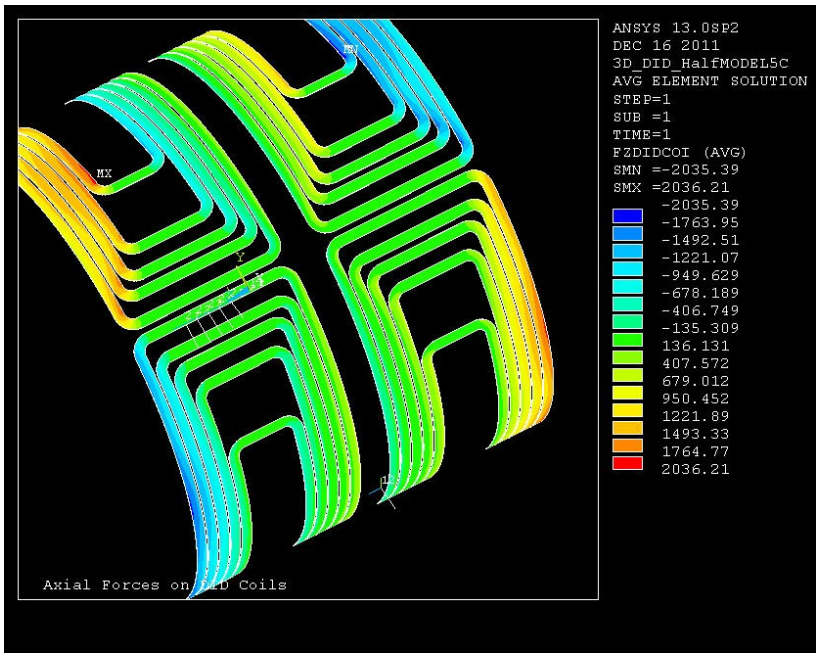

Figure II-6.3
DID coils showing axial forces; Only half of the coils are shown

6.3.3 Thermal shield, cooling tubes, current leads and standpipe

Both the inner and outer thermal shields are directly mounted on the inner and outer vacuum shells with Ti 15-3-3-3 studs and small diameter fibreglass epoxy tubes. The shields are fixed at the midplane and contract symmetrically from both ends. The shields are made from aluminium alloy with appropriate high resistance joints to reduce eddy current forces during solenoid fast discharge. Baseline design for shield and coil cooling loops is square aluminium tubing welded to the aluminium shells with transition to round stainless steel tubing. All stainless steel or bimetallic tubing that is generally more leak tight is an option to be studied. Some of these details are depicted in Figure II-6.1.

The cryostat, $\approx$ 60 K thermal shield, current leads, tie rods, and instrumentation will all be designed using standard cryogenic techniques. Current leads will be very similar to the CMS current leads. Two separate iron penetrations will be used, a 70 cm $\times$ 40 cm chimney for the current leads and 36 cm diameter chimney for the cryogenic plumbing. Vacuum pump down will take place through both chimneys.

6.3.4 Stress Analysis

ANSYS studies compared SiD and CMS solenoid stresses, deflections and forces. All stresses are evaluated after cool down and energisation. For this comparison the CMS conductor was used in the SiD analysis with results given in Table II-6.2. Note that all stress and deflections are very similar for the two coils.

Table II-6.2
Mechanical Comparison of the SiD and CMS Solenoid coils

Quantity	SiD	CMS
Von Mises Stress in High Purity Aluminium (MPa)	22.4	22
Von Mises Stress in Structural Aluminium (MPa)	165	145
Von Mises Stress in Rutherford Cable (MPa)	132	128
Maximum Radial Displacement (mm)	5.9	5
Maximum Axial Displacement	2.9	3.5
Maximum Shear Stress on Insulation (MPa)	22.6	21
Radial Decentering Force (kN/cm)	280	80
Axial Decentering Force (kN/cm)	1870	850

Cold mass tie rods will be segmented into three different systems based on direction (axial, vertical and radial) just as they were with CMS and BaBar. They will be manufactured from age

hardened Inconel 718. Radial and vertical loads will be carried to the cryostat outer wall. Axial loads will be carried to the cryostat end plates. In all cases, the tie rod systems are substantially stiffer than the magnetic spring constant.

6.3.5 Vacuum Shell Design

The 304 stainless steel vacuum shells will be built according to the ASME (American Society of Mechanical Engineers) pressure vessel code design rules, but the cryostat will not be a coded vessel. Inner shell, outer shell and both end flanges are all 50 mm thick. In addition to the magnet weight and magnetic force loads, a detector weight of 450 tonnes, vacuum load and gravity self weight are imposed on the vacuum shell. The detector weight is carried by two linear rails on the inner shell. The total weight is transferred on two linear rails on the outer shell to the magnet iron. The solenoid axial decentering forces are transferred to the barrel/endcap spacer plates.

The linear and non-linear vacuum buckling ANSYS analysis has been completed and the primary stress results are summarised in Table II-6.3. Local peak stresses are much higher especially for the magnetic axial decentering case. These peak stress values and maximum primary stress values can easily be reduced to ASME Section VIII Div. 2 allowables by small additions of local reinforcing. The outer end plates will need radial rib reinforcing which is compatible with the detector cable routing. The ASME allowable stress is 138 MPa. A non-linear analysis gives a 0.62 MPa (6 atm.) vacuum buckling load [144].

Table II-6.3 Cryostat vacuum shell maximal stress and deflection

Load	Stress (MPa)	Deflection (mm)	Location of Max Stress
Axial Magnetic	125	1.5	Axial Support Pad
Detector Mass	45	2.3	Inner Vacuum Shell
Cold Mass + Radial Magnetic	23	0.44	Vertical Tie Rod Support Pad
Vacuum	7.5	0.17	Outer Shell
Gravity on Shell	Small	0.11	Both Shells
All Loads Combined	**190**	**3.5**	**Vacuum Shell End Plate**

6.3.6 Assembly procedure

1. The coil mandrels are precision machined with welding of seamless end rings and cooling loops. The cooling loops are extensively leak tested.
2. The solenoid modules are wound with each layer in alternating direction.
3. The four DID coil modules are wound on a 3 mm thick Al sheet that is mounted onto a machined cylinder. The internal coil to coil splices for each of the four modules are completed. A 5 mm sheet is attached to the outer diameter of the DID coils.
4. The DID coils are vacuum impregnated. This is a higher temperature resin than the solenoid resin.
5. The DID coils are mechanically attached on top of the solenoid cooling loops with screws to the solenoid mandrel.
6. The Solenoid modules with attached DID coils are vacuum impregnated.
7. The two mating ends of the solenoid modules are precision machined.
8. The solenoid modules are stacked vertically and joined above ground at the detector site.
9. All 24 solenoid splices are completed above the DID. All DID module to module splices are completed
10. The axial tie rods are attached to the solenoid.

11. The inner and outer thermal shields are mounted to inner and outer vacuum shells.
12. The inner and outer vacuum shells are placed on the solenoid.
13. The vertical and radial tie rods are attached to the outer vacuum shell.
14. All internal plumbing and electrical connections are completed along with the mounting of the thermal shield end plates. Piping extends a short distance past the chimney opening. The solenoid lead ends and DID lead ends extend through the vacuum shell current lead opening and are wrapped in a loop.
15. Top and bottom vacuum end plates are welded.
16. All tie rods are tightened.
17. The completed magnet assembly is rotated horizontal on a shaft parallel to the ground using the overhead crane and two pulling cables.
18. The magnet is moved to the detector cavern and lowered vertically into the bottom half of the magnet iron.
19. The current leads and cryogenic chimney pipe assemblies are completed and welded.

6.4 Cryogenics

A helium refrigerator/liquefier of approximately 1.5 kW of 4.5 K refrigeration is located on the detector near the top. This choice means that the liquefier high pressure helium and compressor suction return lines must be flexible for push-pull operations. The QD0 2 K vacuum pumping lines must also be flexible. The liquefier supplies both forced flow 4.5 K saturated LHe and 40 to 80 K helium for the thermal shield and support rod thermal intercepts. The liquefier is a custom built commercial product whose detailed design and construction will be carried out by industry as part of the complete cryo plant procurement.

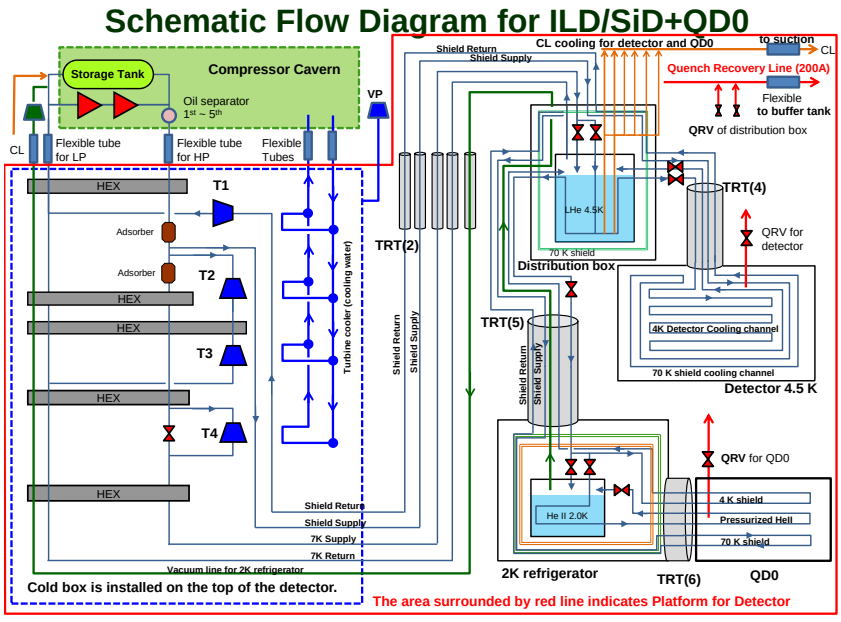

Figure II-6.4
Cryogenic Flow Schematic

A 5000 litre LHe storage dewar is stationed next to the refrigerator liquefier. It serves as a pressure buffer for forced flow operation and as a LHe supply reservoir during liquefier down times. This technique was used successfully for a decade of running BaBar.

The detector valve box near the top of the detector is used to minimise flexible connections between detector and refrigerator. It also serves as the distribution point for supply of LHe to the

two superconducting QD0 final focusing magnets 2 K cold boxes that are fixed on the detector. Figure II-6.4 is a flow diagram of the SiD cryogenic system.

6.5 Conductor

6.5.1 Solenoid baseline conductor (CMS)

A slightly modified CMS conductor is the SiD baseline design. The CMS conductor is fabricated by ebeam welding structural aluminium to the coextruded high purity Al/superconducting cable insert. A superconductor stability margin similar to CMS will be used requiring that the Rutherford cable be increased in size from 32 to 40 strands. In comparison to CMS, operating current as a % of critical current based on magnet peak field and temperature, improves from 33% to 32% for SiD.

However, the SiD conductor thermal margin will decrease from 1.8 K to 1.6 K. All magnet ANSYS finite element stress analysis to date has been with this conductor with overall dimensions of 21.6 mm $\times$ 64 mm.

6.5.2 Modified CMS Conductor Choices

Many other conductor designs are possible. One possibility is replacement of the high purity aluminium with an Al-0.1%Ni alloy that is stronger but still has good conductivity. This material was used for the ATLAS Central Solenoid conductor. Coextrusion tests of this alloy are currently being pursued by CERN [145]. Many other dilute aluminium alloys (e.g. scandium or binary elements) that form small intermetallic precipitates are possible but largely unexplored. Still other high purity reinforcement such as the standard TiB_2 grain refiner or carbon nanotubes are possibilities. Replacement of the structural aluminium with internal stainless steel rope would simplify conductor manufacture if a different method of coextrusion such as the ConKlad process could be industrialised for this size.

The ANSYS coupled transient electromagnetic and thermal diffusion model was used to evaluate conductor stability. With large size high purity aluminium stabilised superconducting conductors, current is slow to diffuse into the high purity aluminium during a temperature excursion reducing conductor stability. ANSYS results show that equivalent conductor stability is achieved when both types of CMS aluminium are replaced with a single aluminium that has one third the electrical and one third the thermal conductivity of the high purity aluminium.

6.5.3 DID conductor

The dipole coils are to be wound from a high purity aluminium and a CMS single superconducting strand co-extrusion. Two layers of 75 turns of 2.5 mm $\times$ 1.8 mm superconductor per winding are proposed. There will be 0.5 mm of fibreglass cloth between each turn and each layer. 800 A at 30% of I_{critical} is the operating point. The stored energy for an independently powered DID is in the range of 240 kJ. When coupled to the solenoidal field, the stored energy increases by $\approx$ 8 MJ. Because the stored energy is so small, the volume fraction of high purity aluminium to superconductor needed for safe energy extraction during a quench has been reduced from the CMS 12.4 to a ratio of 2.5. Forces on each of the four coils are rather large in sum but spread somewhat uniformly and are manageable (4100 kN radial and 7800 kN axial).

6.6 Electrical

6.6.1 Magnet Safety

The lower stored energy and inductance of the SiD magnet compared to the CMS case make it easier to protect in case of a quench. A conservative 300 V to centred tapped ground is chosen. Experimental tests and computer simulations show that the CMS quench propagation velocity around one complete turn is faster than the turn to turn quench propagation through the insulation. Because we have chosen the same conductor size and insulation thickness as CMS, with very similar electrical and thermal properties, peak temperatures will be less than the 80 K at CMS with dump resistor, but equal to the 130 K at CMS in case of a dump breaker failure. Both SiD and CMS safety rely on the winding mandrel serving as a quench back cylinder spreading the quench over the outer layer and absorbing some of the stored energy. Fast discharge of the DID as a solenoid quench propagator to reduce winding peak temperature and stress is a reasonable option. However, the detailed transient 3D ANSYS calculations remain to be done.

6.6.2 Power Supply, Dump Resistor and Dump Switch

The power supply, contactor, dump resistor and dump switch are attached on the side of the detector near the top. These three components are arranged to minimise the 18 kA bus lines. Power supply, DC contactor and mechanical dump switch are standard design components procured from outside vendors. The DC contactor allows for normal slow mode discharge and fast discharge. The power supply operates in only one quadrant, positive current and positive voltage. Therefore, more robust free wheeling diodes can be employed instead of the thyristors used at CMS and which permitted voltage control ramp down. The SiD magnet does not have a current reversal switch. The dump switch is a conventional commercially purchased double pole mechanical breaker with arc chutes. Both the positive and negative legs are mechanically ganged together ensuring that they open at the same time. The breaker and controls are housed in a steel box 2.6 m $\times$ 0.9 m $\times$ 1.5 m (high). The power supply is a standard water cooled power supply tailored to low inductance operation. Overall dimensions of this unit are 3.7 m $\times$ 1.0 m $\times$ 2.0 m (high).

A novel compact pressurised water cooled dump resistor will be used instead of a very large air cooled dump resistor such as the type used for CMS and other large superconducting magnets. An ASME coded vessel holding 3100 litre of water will rise to a conservative design value of 150 C at 0.48 MPa assuming the worse case of all 1.56 GJ deposited as sensible heat in the water of the resistor [146, 147]. Correct dimensioning of the stainless steel resistor element ensures that boiling heat transfer is only a third of the peak nucleate boiling flux at the metal/water interface. A 1.50 m diameter $\times$ 3.5 m tall cylindrical tank could be used. Internal connections will provide for both fast dump and normal slow dump modes. A centre tap grounding wire is attached to the electrical centre of the resistor.

Chapter 7
SiD Engineering, Integration and the Machine Detector Interface

7.1 Introduction

The ILC Reference Design Report (RDR) [148] was based on a site presumed to run ∼100 m below a topographically flat landscape. It specified the civil engineering parameters of a shared underground interaction region (IR) Hall accessed by two shafts symmetrically located around the beam line. More recently:

- A set of functional requirements for the design of the detectors and the IR was defined [141].
- The SiD and ILD detector concepts were validated.
- A platform similar to the CMS shaft plug was agreed to be the means of effecting the push-pull exchange of the detectors.
- A new cavern layout was designed featuring one shared 18 m diameter central shaft directly over the interaction point, serviced by a 4000 tonne gantry crane, separate assembly areas accessible to the sliding platform and separate garage areas for major detector component replacement, each serviced by an 8 m equipment shaft and a 5.6 m personnel elevator shaft. See Figure II-7.1.
- The possibility has arisen that the ILC would be built in a mountainous site where the IR would be accessed by a tunnel of limited diameter of length of order 1 km.

These features are described in more detail in the first part of this Volume (see 2.3) and in Volume 2 (Accelerator) of this TDR [149].

7.2 IR Hall Layout Requirements and SiD Assembly

The main subcomponents of SiD are its central barrel and its two endcaps. The majority of the SiD mass results from the flux return iron. The iron will be shipped to the ILC site from an industrial production facility in the form of sub-modules suitably sized (∼100 tonne) for road transportation. The solenoid coil will likewise be wound industrially and transported in sections, probably two, amenable to transport.

We expect the VXD, Tracker, ECAL, HCAL and muon system modules to be built at collaborating labs and universities and transported to the ILC site for final assembly. Table II-7.1 lists the masses and sizes of the SiD elements that determine the crane capacity and shaft size for installation.

Table II-7.1
List of SiD element masses and sizes. For each barrel component the size given is the outer diameter × length (z), and for each endcap component it is length × outer diameter.

Name	Mass (10^3 kg)	# Subcomponents	Mass (10^3 kg)	Size (m×m)
Barrel	4160			
ECAL	60	12	5.0	2.8 × 3.5
HCAL	367	12	31.7	5 × 5.9
Tracker	3	1	3	2.5 × 3.3
Coil	180	2	90	6.8 × 5.9
Magnet Yoke	3360	8	420	12 × 5.9
Yoke Arch Supports	150	2	75	12 × 1
Peripherals	40			
Each of Two Endcaps	2450			
ECAL	10	1	10	0.15 × 2.5
HCAL	23	1	23	1.2 × 2.8
Muon System	30			2.6 × 12
MDI Components	10			
Endcap Steel Plates	2200	11	200	0.2 × 12
Endcap Leg Supports	140	2	70	2.6 × 6
Infrastructure	37			

7.2.1 Vertical Access (Europe and Americas sites)

Figure II-7.1 shows the layout of the IR Hall. This allows the 3 m thick SiD push-pull platform to be positioned directly under the gantry crane.

The service caverns allow for storage of the endcaps and unimpeded access to the barrel region for the initial installation or replacement of detector subcomponents. Access to the service caverns is through an 8 m diameter shaft serviced by a 40 tonne crane.

The vertical access assembly presumes that the SiD magnet, comprising the superconducting coil, iron barrel yoke and iron endcaps, will be pre-assembled and tested in an assembly hall above ground. Any detector subcomponents, notably the HCAL and ECAL, that are ready in time can be installed and tested above ground. Then SiD's three main subcomponents, the majority of the barrel and the two endcaps, will each be lowered as units onto the platform below.

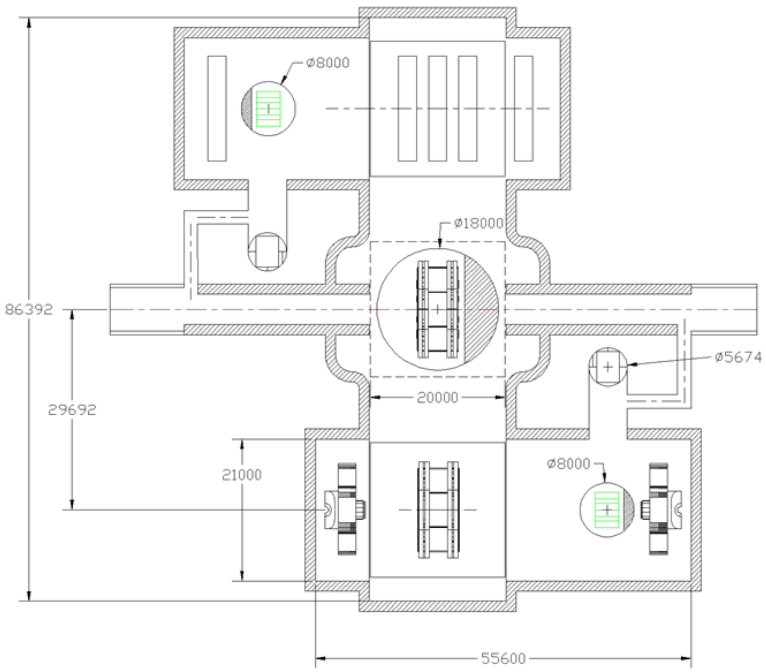

Figure II-7.1
Layout of the IR Hall for vertical access, showing installation shafts and push-pull platforms.

The basic requirements for the assembly hall above ground are:

- A devoted crane with a minimum of 215 tonne main hook capacity, set by the largest subcomponent weight. The ILD and SiD cranes should roll on the same bridgework so that

they can be used in tandem if the need arises.

- A steel reinforced concrete platform, upon which SiD will be assembled, which is structurally robust when supported on three sides as it slides over the 18 m diameter main access shaft to deliver the SiD barrel and endcaps to the gantry crane.
- A circa 4000 tonne capacity gantry that can lower the roughly 15 m $\times$ 5 m $\times$ 6 m 3500 tonne instrumented SiD Barrel and the two 11 m $\times$ 14 m $\times$ 6 m 2500 tonne endcaps onto the push-pull platform in the IR Hall.

It is foreseen that the surface assembly hall is aligned with its long axis parallel to the beam line. The construction platform will move in this direction as well. Its width is 20 m, approximately the width of the building, while the length will be large enough to comfortably house the barrel and the endcaps when open. The platform surface will be at floor grade and thus run in a track. The endcaps will move across the platform-floor junction on the rollers when required to mate with the barrel.

The SiD barrel, once lowered, will remain stationary on its platform. The endcaps, which must be routinely opened to service the detector, will move on a system of rollers guided by hardened rails. The current plan is to lower the endcaps first and to put them in their service caverns to await mating with the barrel. Once the barrel and endcaps have been lowered the main shaft and gantry crane are no longer needed.

The above-ground assembly sequence for a vertical access site can also be used for a horizontal access subterranean site. In the latter case the individual subcomponents are separately transported through an access tunnel of limited diameter to the IR Hall, where a 215 tonne bridge crane suffices for installation. In either case a plausible assembly sequence is:

- Assemble the two endcap leg supports on top of the platform.
- Transport each of the eleven 200 tonne endcap plates in three industrially manufactured segments to the crane and assemble into 11 m x 11 m octagonal plates. Mount each on the support legs and make plate to plate connections.
- Install muon chambers from the sides into each gap, and the endcap HCAL and ECAL to the innermost face.
- Assemble detector mounted PACMAN shielding on the endcaps.
- Once endcaps are completed move them to their alcoves.
- Assemble lower halves of barrel arch supports.
- Assemble industrially manufactured $\sim$100 tonne barrel steel stacked plate segments into sixteen $\sim$210 tonne half-wedges and use the crane to assemble the five lower barrel wedges, forming a cradle open at the top.
- Assemble the solenoid coil segments and DID coils into their cryostat and test at low current. Lift coil with fixture and thread into the cradle.
- Finish the remaining three barrel wedges, install muon system and finish with shear plates at each wedge-to-wedge junction.
- Thread solenoid with an assembly beam and mount the HCAL assembly spider onto it. Load each of the twelve 32 tonne HCAL wedges onto the spider and push into barrel on rollers.
- Repeat HCAL sequence with the much lighter ECAL.
- Thread in Tracker and VXD units when available.

The QD0 assembly (QD0, masks, FCAL) will need to be installed below ground. The platform will transport the endcaps to the alcove area, whence the assembly will be loaded from the rear.

7.2.2 Horizontal Access (Japan sites)

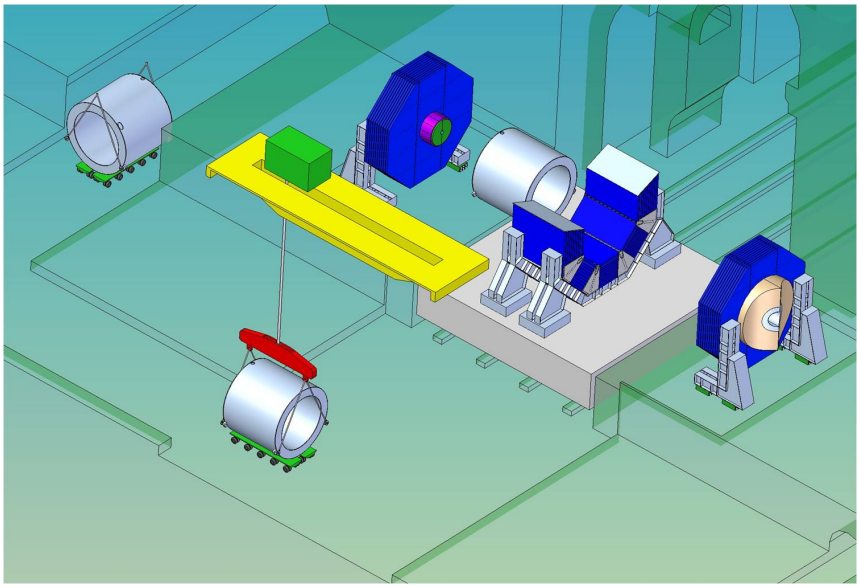

Figure II-7.2
Transporting the largest detector element, the SiD solenoid, through the 11 m diameter access tunnel to the assembly area where the 215 tonne crane can lift it and place it within the SiD barrel.

The barrel and endcap installation procedures outlined above are directly applicable. One need only plan for the lengthier procedure of loading the heavy sub-elements onto the tunnel transport carts and their delivery to the IR Hall assembly area. The Japan site design specifies an 11 m diameter tunnel, which is sufficient to transport the largest element of SiD, its solenoid. Figure II-7.2 shows the SiD solenoid being transported around the final right-angle bend to the IR Hall where it is lifted by the 215 tonne crane and placed in the cradle formed by the lower elements of the SiD barrel yoke. Clearly, if the ILC schedule permits below-ground assembly of the detectors for the vertical access site, the diameter of the access shaft could be reduced from 18 m to 11 m.

7.2.3 Detector Access for Repairs

The upper part of Figure II-7.3 shows SiD with one of its endcaps opened by 2 m, sufficient to expose the FCAL region and the Tracker. This is the basic configuration for quick repair opportunities that may occur while SiD is on the beamline. In the lower part of Figure II-7.3 the endcap has been opened by 2.8 m, the maximum possible for SiD without having to disconnect the QD0 cryostat.

In this figure, the Tracker has been slid to one side to expose the VXD, a manoeuvre that would require the use of some portion of the tracker installation tooling. As such, it would probably be scheduled for a time when SiD is off the beamline. Repairs more major than replacement of a VXD module, such as replacement of the Tracker, barrel ECAL or barrel HCAL, will take place off the beamline.

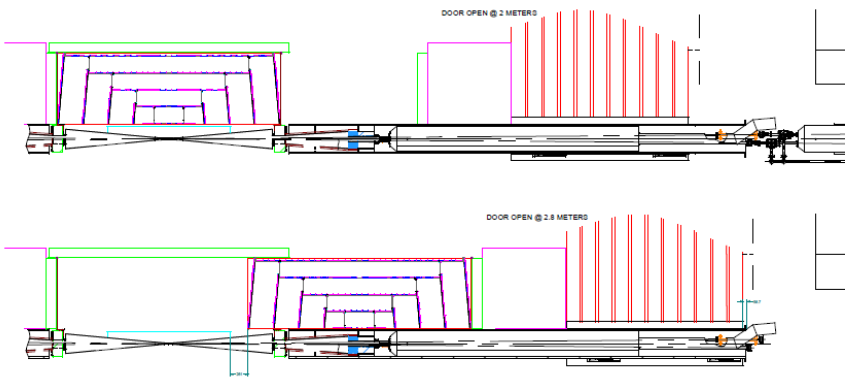

Figure II-7.3
Upper: SiD with one of its endcaps opened by 2 m, sufficient to expose the FCAL region and the Silicon Tracker. Lower: the endcap has been opened by the maximum 2.8 m and the tracker has been slid to one side to expose the VXD for repair or replacement.

7.3 Detector Exchange Via a Sliding Platform

7.3.1 Introduction

Among the challenges to be addressed in the push-pull operation are the reproducibility of tight alignment to the beam at the ± 1 mm level; the time requested to complete the swap cycle must be as low as reasonably achievable since it will reduce the integrated luminosity; umbilicals are needed to keep the detector connected to the DAQ and services such as cryogenics.

7.3.2 Platform

These requirements have been addressed by developing the concept of a reinforced concrete platform 20×20 m^2 in area and 3.8 m tall, with a total mass of $\sim$4500 tonne. To compensate for the different detector heights the SiD platform is thicker than that of ILD. Assuming the total SiD mass to be 9000 tonne, preliminary calculations have shown [150] that the maximum static deformation achievable is less than 1mm at the locations where the detector is supported by the platform. The construction will be very similar to the concrete slab designed for the CMS detector [151].

The movement system is designed for $\sim$14,000 tonne total mass of detector and platform. Two options are under consideration, air pads and Hillman rollers, each with hydraulic jacks above. For the air pads the expected friction is 1% and the total force required for the horizontal motion is 140 tonne. Assuming a maximum load capacity of 350 tonne for a single air pad, SiD will require the installation of 40 units under the platform. For the rollers the friction will be $\sim$3% and the force required for the horizontal motion will be $\sim$420 tonne, while only 14 units with 1000 tonne load capacity will be required. In both cases, the floor will need to be hardened with steel to prevent wear that would spoil the alignment performance.

A reliable linear guiding system built in the floor is also essential for air pads as well as for rollers. The force required in both cases for the horizontal motion can be comfortably provided by a set of hydraulic climbing jacks. Another set of hydraulic jacks will be placed at the beamline location of the platform to correct the final transverse alignment, if needed.

7.3.3 Vibration analysis and Luminosity Preservation

A structural dynamic model of the QD0 supported from SiD, including the platform, has been developed to calculate the free modes as well as the transfer function between the ground and the doublet. Using different ground vibration models available in the literature, that correspond to different accelerator sites, a maximum r.m.s. QD0 displacement of 20 nm has been calculated, more than a factor two below the maximum allowed. A campaign of experimental measurements of vibrations has been carried out to validate some key features of the model: the simulation of the reinforced concrete platform and correlation measurements between distant locations in the detector hall of CMS at CERN and SLD at SLAC. The reinforced concrete slab of CMS has been instrumented with geophones in various locations and the data have been used to benchmark a finite element model of the platform [152].

Good agreement between experimental data and simulation has been found with an internal damping ratio of 6.5%, somewhat higher than the values recommended for similar materials. The difference can be explained by the soil deformation and the presence of wheels, both of which were not included in the model. The measurements done at CMS and SLD have shown a good correlation at low frequencies between points at the two extreme sides of the cavern, i.e. the location of the final focus system [153].

7.3.4 Push Pull Detector Exchange Process and Time Estimate

The sequence of push-pull operations should allow a fast detector interchange to minimise loss of beamtime; realistically it should not take more than a few days. Defining as $t = 0$ the time when the beams have been dumped and the interlocks are released to allow the access of the technical personnel, the key steps are the opening of the PACMAN shielding, the breaking of the vacuum between the QD0 and the QF1, a reasonably fast horizontal movement from the IP to the garage position with an easy and reliable alignment system. The cryogenic system will stay on during the push-pull, with the umbilical able to accommodate the ∼30 m movement requested. Figure II-7.4 summarises the sequence of steps and the minimum required time for the push-pull operation.

Figure II-7.4 Summary chart of push-pull operational steps.

Task	Duration (hour)	8-hour shift	8-hour shift	8-hour shift	8-hour shift
Secure ILC beams	1				
Ramp magnets down	3				
Open beamline shielding	1				
Disconnect beamlines	2				
Checkout detector transport system	2				
Transport detector over 20 m	2				
Transport other detector onto beamline	2				
Connect beamline	2				
Close beamline shileding	1				
Check crude detector alignment and adjust	2				
Ramp magnets up	3				
Perform safety checks before beams	1				
Start beam-based alignment	10				

7.4 Beampipe and Forward Region Design

7.4.1 Introduction to the Near Beamline Design

The SiD near-beamline design minimises the radial space required for the support and alignment of the final quadrupole lens QD0 to limit any loss of tracking and calorimeter acceptance. In the SiD design the silicon tracker slides over the QD0 support to expose the vertex detector for servicing (see Figure II-7.3).

7.4.2 Beampipe

The beampipe through the central portion of the vertex detector has been taken to be all-beryllium. Within the barrel region of the vertex detector, the beryllium beampipe forms a straight cylinder with inner radius of 1.2 cm and a wall thickness of 0.04 cm. At z = ±6.25 cm, a transition is made to a conical beampipe with a wall thickness of 0.07 cm. The half angle of the cone is 3.266°. Transitions from beryllium to stainless steel are made beyond the four inner vertex disks, at approximately z = ±20.5 cm. The initial stainless steel wall thickness is 0.107 cm; it increases to 0.15 cm at approximately z = ±120 cm. The half angle of the stainless steel cone is 5.329°. The inner profile of the beampipe is dictated by the need to avoid the envelope of e^+e^- pairs from beamstrahlung.

7.4.3 LumiCal, BeamCal, Mask and QD0 Support and Alignment

The QD0 support tube (Figure II-7.5) is extended toward the IP to support the 220 kg LumiCal, the 507 kg 3 cm thick conical tungsten mask, the lightweight 13 cm thick 25 cm diameter borated polyethylene neutron absorber and the 136 kg BeamCal. The low-z end of the support tube will be split along its centreline so that it can be opened to install the mask, absorber and BeamCal. The LumiCal will be bolted to the front end of the tube and be positioned so that it hangs 10 cm in front of the endcap ECAL when the detector is closed. While this choice complicates the vertex detector support system, it minimises any loss of acceptance between the LumiCal and the ECAL endcap. The loading of the support tube results in a deflection of 100 μm when the detector is closed, growing to 2.2 mm when the endcap is opened the nominal 2 m required to service the detector when on

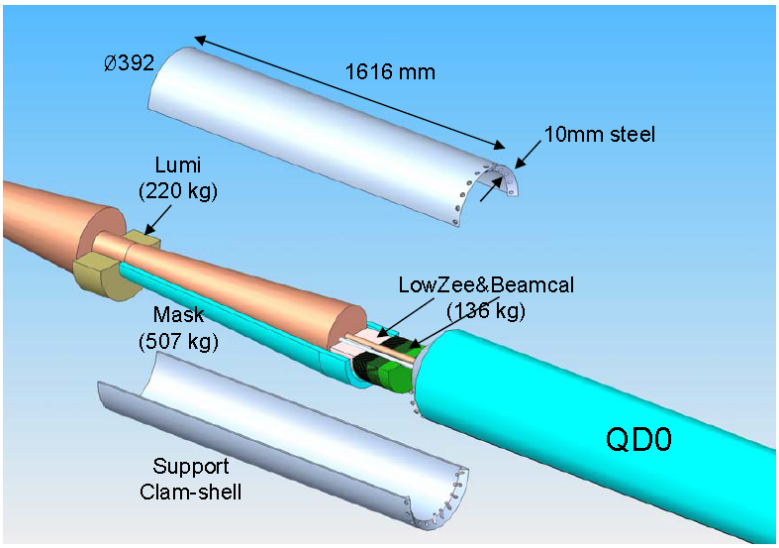

Figure II-7.5 Detail of the LumiCal, mask and BeamCal which must be supported by the QD0 support tube and alignment system.

beamline, and 6 mm when the endcap is opened the maximum 2.8 mm allowed by the location of QF1 and the obstruction of the cryo-transfer line joining QD0 to its local 2 K refrigerator. A wedge mover system will need to act in conjunction with the endcap opening mechanism to keep the front end of the LumiCal fixed in space.

The beampipe through BeamCal terminates in a commercial flange. The conversion of the common beampipe to separate incoming and outgoing beampipe takes place in the 215 mm space between the back of BeamCal and the front face of the QD0 cryostat at 3.283 m from the IP.

7.4.4 Vacuum System and Performance

The vacuum requirements for the final focus and interaction region lengths of the beampipe have been specified [154] as 10 nTorr from 200-800 m from the IP, 1 nTorr in the region from 200 m up to the QD0 quadrupole and "much looser" than 1 nTorr between the QD0 cryostats. The region between QD0 and QF1 is evacuated to < 10 nTorr by the pumping action of the two cryostats and the 100 l/s ion pump on each beam line in front of QF1. Achieving 1 nTorr upbeam of QF1 will be a challenge. With a 20 mm diameter stainless beampipe and 50 l/s ion pumps every 2 m, the average pressure is 23 nTorr. Likely, either distributed pumping (antechamber, pumpscreens or NEG coatings) and/or larger diameter beampipes with bakeout facilities will be required to meet the 1 nTorr tolerance.

7.4.5 Feedback and BPMs

The intratrain feedback system is based on that described in the RDR [148]. A prototype system has been developed and tested with beam at ATF [155]. The parameters of the BPM and kicker required for ILC have been specified [156]. By combining a ground motion model with a set of transfer functions describing the vibrational effect of the magnet support system, in this case the SiD platform and detector, the reduction of luminosity loss can be studied [157, 158].

The left side of Figure II-7.6 shows the fractional loss of nominal luminosity as a function of the rms jitter of the opposing SD0/QD0 magnet systems when they are supported from SiD and the SF1/QF1 magnets are, like all the other magnets in the final focus, assumed to be rigidly attached to the ground. The feedback system limits the luminosity loss to 2% (4%) of the nominal value for rms motions up to 50 nm (200 nm), ∼10 (∼40) times the vertical spot size of beam at the IP.

The right side of Figure II-7.6 shows the contribution of mechanical jitter to the total jitter in the case where the ground motion model is that of the noisiest site studied (DESY near Hamburg). Even in this extreme case, the feedback system would limit luminosity loss to 2% with up to 17 nm of

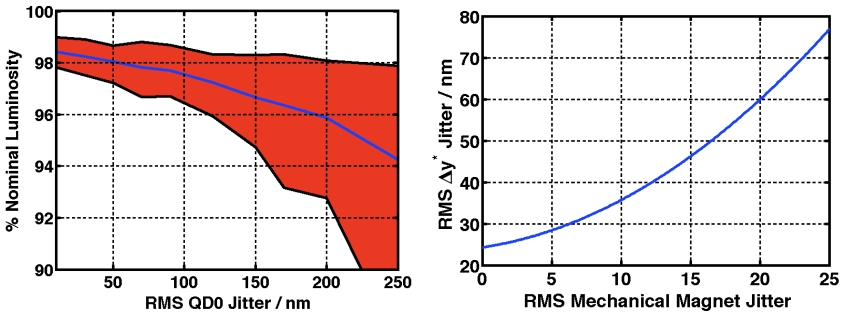

Figure II-7.6
The fractional loss of nominal luminosity as a function of the rms x and y vibration of the SF1/QF1 and SD0/QD0 magnet systems (left). Contribution of mechanical jitter to overall vibration budget (right)

additional mechanical jitter, coming from, for example, vibrations induced by the liquefier or flow of liquid helium. A modelling program to ensure that the ground to magnet transfer function is correct is ongoing [159].

7.4.6 Frequency Scanning Interferometric (FSI) Alignment of QD0 and QF1

The FSI system incorporates multiple interferometers fed by optical fibres from the same laser sources, where the laser frequency is scanned and fringes counted, to obtain a set of absolute lengths [101, 103, 160].

To monitor the position of the QD0 cryostat to the required accuracy [141] of 50 μm in x, y, and 20 μrad in roll, pitch and yaw a network of "optical trusses" between beam launchers at known positions and reflectors placed on the QD0 cryostat is needed. Simulations [161], conservatively assuming 500 nm length accuracy, indicate that a network of four beam launchers placed on the front face of the QF1 cryostat, each of which sends a split beam to two of four similarly situated reflectors on the back end of the QD0 cryostat, and a similar network tying the inner edge of the innermost HCAL endcap to the front end of the QD0 cryostat, can achieve an precision of $\sim$1 μm in x and y and $\sim$1 μrad in all axis rotations. Schemes that can tie this network across the IP are important to develop.

Chapter 8
SiD Forward Systems

8.1 Forward Detector

The forward region is defined as polar angles $|\cos\theta| > 0.99$ ($\theta < 140$ mrad), which is the angular region forward of the coverage of the SiD Endcap ECAL. The angular coverage is completed by two detectors, the Luminosity Calorimeter (LumiCal) and the Beam Calorimeter (BeamCal). As discussed in more detail below, the LumiCal is an annular calorimeter located approximately 1.6 m from the interaction point (IP), subtending angles between 40 mrad and 90 mrad. The BeamCal, the most forward of all the SiD subsystems, lies at a distance of approximately 2.8 m from the IP, subtending angles between 3 mrad and 40 mrad.

The instrumentation goals in this region are:

- Measurement of the integrated luminosity using small-angle Bhabha scattering (LumiCal) to an accuracy better than 10^{-3};
- Instantaneous luminosity measurement using beamstrahlung pairs (BeamCal);
- Extension of the calorimeter hermeticity into the small angles for physics searches (LumiCal and BeamCal);
- Provide a two-photon veto for new particle searches (BeamCal);
- Possible contribution to the determination of the luminosity spectrum by measuring the acolinearity angle of Bhabha scattering (LumiCal).

The detector challenges include good energy resolution, radiation hardness, interfacing with the final focus elements, high occupancy rate requiring special readout, and performing the physics measurements in the presence of the very high background in the forward direction (see Chapter 11.3.1).

8.1.1 Design criteria

8.1.1.1 LumiCal Physics Requirements

The number of Bhabha events per bunch crossing for a detector with minimum and maximum polar angle coverage θ_{min} and θ_{max} (in mrad) is:

$$N = 0.5\mathrm{pb}\frac{\mathrm{L}}{\mathrm{R}}\int_{\theta_{\mathrm{min}}}^{\theta_{\mathrm{max}}}\frac{\mathrm{dcos}\theta}{\sin^4\theta/2} \sim 6\times10^{-6}\left(\frac{1}{\theta^2_{\mathrm{min}}}-\frac{1}{\theta^2_{\mathrm{max}}}\right)$$

for $\sqrt{s}$ =0.5 TeV, L=$2\times10^{34}\mathrm{cm}^{-2}\mathrm{s}^{-1}$, and bunch crossing rate R=$1.4\times10^4\mathrm{s}^{-1}$. Our goal is to measure the luminosity normalisation with an accuracy of several 10^{-4} for $\sqrt{s}$ =0.5 TeV. To do this one needs $\approx 10^8$ events collected over $\approx 10^7$ s, or about ten events per second. One can then calculate the absolute luminosity with $\approx 10\%$ statistical error every several minutes during the run. With a bunch crossing rate of $1.4\times10^4\mathrm{s}^{-1}$, we need $> 10^{-3}$ events per bunch crossing. To achieve this statistical accuracy, we start the fiducial region for the precision luminosity measurement well away

from the beamstrahlung pair edge at θ=20 mrad, with a fiducial region beginning at θ_{min}=46 mrad, which gives $\approx 2 \times 10^{-3}$ events per bunch crossing.

8.1.1.2 Luminosity precision and detector alignment

Since the Bhabha cross section is $\sigma \sim 1/\theta^3$, the luminosity precision can be expressed as

$$\frac{\Delta L}{L} = \frac{2\Delta\theta}{\theta_{min}},$$

where $\Delta\theta$ is a systematic error (bias) in polar angle measurement and $\theta_{min} = 46$ mrad is the minimum polar angle of the fiducial region. Because of the steep angular dependence, the precision of the minimum polar angle measurement determines the luminosity precision. To reach the luminosity precision goal of 10^{-3}, the polar angle must be measured with a precision $\Delta\theta < 0.02$ mrad and the radial positions of the sensors must be controlled within 30 μm relative to the IP.

8.1.1.3 Monitoring the Instantaneous Luminosity with BeamCal

The colliding electron and positron bunches at the ILC generate large Lorentz forces, which cause radiation of gammas called beamstrahlung. Under the ILC Nominal beam parameters at $\sqrt{s} =$ 0.5 TeV, approximately 75k of the beamstrahlung photons convert into e^+e^- pairs. Since the number of pairs is directly proportional to the beam overlap, the instantaneous luminosity can be monitored to ≈10% per beam crossing by detecting pairs in the BeamCal.

8.1.1.4 Dynamic range and MIP sensitivity

While minimum ionising particles (MIP) deposit 93 keV in a 320 μm-thick Si layer, a 250 GeV electron can deposit up to 160 MeV or 1700 MIP equivalents in a single cell near shower maximum. If we want a 100% MIP sensitivity, the S/N ratio for MIP should be greater than 10, and the dynamic range of the electronics needs to be at least 17,000. This dynamic range can be achieved by using a 10-bit ADC with two gain settings.

8.1.1.5 Radiation hardness

The beamstrahlung pairs will hit the BeamCal, depositing 10 TeV of energy every bunch crossing. Sensor electronics could be damaged by the energy deposition, and sensor displacement damage could be caused by the resulting neutrons. The radiation dose varies significantly with radius, and a maximum dose of up to 100 MRad/year is expected near the beampipe. The main source of neutrons is from secondary photons in the energy range 5-30 MeV, which excite the giant nuclear dipole resonance, with subsequent de-excitation via the evaporation of neutrons. The neutron flux is approximately $5 \times 10^{13} \mathrm{n/cm^2}$ per year.

8.1.2 Baseline Design

The layout of the forward region is illustrated in Figure II-8.1. The LumiCal covers the polar angles from 40 mrad to 90 mrad, and the BeamCal from 3 mrad to 40 mrad.

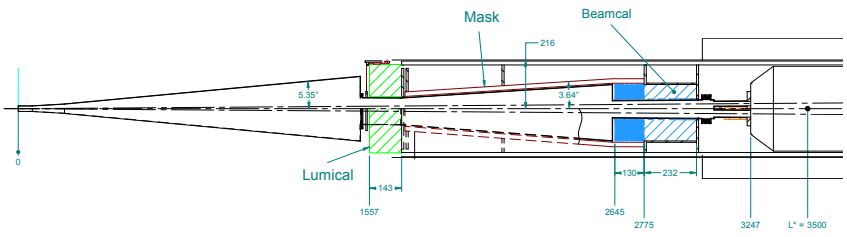

Figure II-8.1 The SiD forward region.

The LumiCal consists of two cylindrical C-shaped modules surrounding the beampipe. The inner radius is 6 cm centred on the outgoing beam line with a horizontal offset of $\Delta x = 1.1$ cm (158 cm $\times$ 0.007). The inner radius is dictated by the requirement that no detector intercepts the intense beamstrahlung pairs, which are confined within 4 cm radius by the 5 Tesla solenoid field.

The longitudinal structure follows the ECAL design, consisting of 30 alternating layers of tungsten and silicon. The first 20 layers of tungsten each have a thickness equivalent to 2.5 mm (or 5/7 radiation length) of pure tungsten. The last 10 layers have twice this thickness, making a total depth of about 29 radiation length. The sensor is segmented with a $R - \phi$ geometry; a fine radial segmentation with 2.5 mm pitch is used to reach the luminosity precision goal of 10^{-3}. The azimuthal division is 36 with each sensor covering 10 degrees. Table II-8.1 summarises the LumiCal parameters as well as those for the BeamCal, the description of which follows.

Table II-8.1 Forward Calorimeter Parameters

Parameter	LumiCal	BeamCal
z Extent	155.7 – 170.0 cm	277.5 – 300.7 cm
Inner radius	6.0 cm	2.0 cm
Outer Radius	20.0 cm	13.5 cm
Instrumented	42 – 110 mrad	5 – 45 mrad
Fiducial	46 – 86 mrad	—
Tungsten thickness	2.5/5.0 mm (20/10 layers)	2.5 mm
Sensor thickness	320 μm	320 μm
Radial division	2.5 mm	5.0 mm (2.5 mm $R > 7.5$ cm)
Azimuthal division	36 segments	5.0 mm

The BeamCal consists of two cylindrical C-shaped modules split in half horizontally to accommodate the incoming and outgoing beam lines. The inner radius is 2 cm, centred on the outgoing beam line, and the outer radius is 13.5 cm. A second hole, of radius approximately 1 cm and displaced from the centre by approximately 5 cm, allows for the incoming beam line. The longitudinal structure consists of 50 alternating layers of tungsten and silicon. The tungsten thickness is 2.5 mm, making a total depth of 36 radiation lengths.

The inner region, at a radius of $R < 7.5$ cm, has a high signal rate from beamstrahlung pairs. The segmentation in this region is approximately $5\mathrm{mm} \times 5\mathrm{mm}$, which is roughly one half of the Molière radius. This segmentation is optimised so that tell-tale electrons or positrons from two-photon processes can be detected in the high beamstrahlung pair background. The outer region $R > 7.5$ cm is treated as a "far LumiCal" and has the same geometrical segmentation as the LumiCal.

Currently two electronic readout chips are being developed. The KPiX chip with 1024 channels is designed primarily for the ECAL. The chip has four hits per bunch train to be stored for each channel. The FCAL chip with 64 channels is designed to handle the 100% occupancy in the BeamCal. The chip has 2820 buffer space so that a complete bunch train can be stored.

Although the LumiCal occupancy is not 100%, the LumiCal region smaller than about 10 cm will have more than four hits per bunch train. Therefore, the LumiCal is foreseen to use the FCAL chip in the inner region and the KPiX chip in the outer region.

8.1.3 Forward Systems Development Work

In this section we present the recent developments on the forward systems that have been carried out in the framework of the SiD collaboration. These developments are a component of the overall R&D effort for linear collider forward systems.

Table II-8.2
BeamCal instrumentation ASIC specifications summary. Note that these prototype chip specifications are based on a now-outdated version of machine parameters; the next prototype will address the change.

Input rate	3.25 MHz during 0.87 ms, repeated every 200 ms
Channels per ASIC	32
Occupancy	100%
Resolution	10 bits for individual channels, 8 bits for fast feedback
Modes of operation	Standard data taking (SDT), Detector Calibration (DCal)
Input signals	37 pC in SDT, 0.74 pC in DCal
Input capacitance	40 pF (20-pF detectors and 20-pF wires)
Additional feature	Low-latency (1 μs) output
Additional feature	Internal pulser for electronics calibration
Radiation tolerance	1 Mrad (SiO_2) total ionising dose
Power consumption	2.19 mW per channel
Total ASIC count	2,836

8.1.3.1 FCAL Electronics Development

The initial set of specifications for the BeamCal instrumentation ASIC is listed in Table II-8.2.

The Bean (BeamCal Instrumentation IC) prototype is a custom IC designed in a 180-nm CMOS process as a proof-of-concept to fulfil the BeamCal instrumentation specifications. The Bean block diagram, shown in Figure II-8.2, depicts the three channels of the prototype ASIC, as well as the adder that combines the outputs of all channels to provide a fast feedback signal. Each channel has a dual-gain charge amplifier, a precharger and calibration circuit, a filter, connecting buffers, and a dedicated analog-to-digital converter (ADC). The filter is only necessary in the calibration mode of operation (DCal mode), since in the standard data taking mode (SDT) the charge amplifier bandwidth is sufficient for filtering purposes. Future revisions of the Bean will be designed for a new set of machine specifications and will include additional channels, improved features, and a digital memory array.

Circuit description The charge amplifier was designed around a single-ended folded cascode amplifier with capacitive feedback. The feedback network has two selectable capacitors to implement the two gains for the SDT and DCal modes of operation. The feedback network also has a reset transistor that discharges the feedback capacitance in order to reset the charge amplifier between pulses, and a slow reset-release circuit that opens the reset transistor gradually in order to reduce the noise due to split doublets.

The charge amplifier and a dummy baseline generator are connected to the fully-differential ADC when in SDT mode, or to the fully-differential filter when in DCal mode, through level-shifting buffers. The filter is a switched-capacitor integrator that effectively reduces series noise by averaging eight samples of the charge amplifier output in the analog domain.

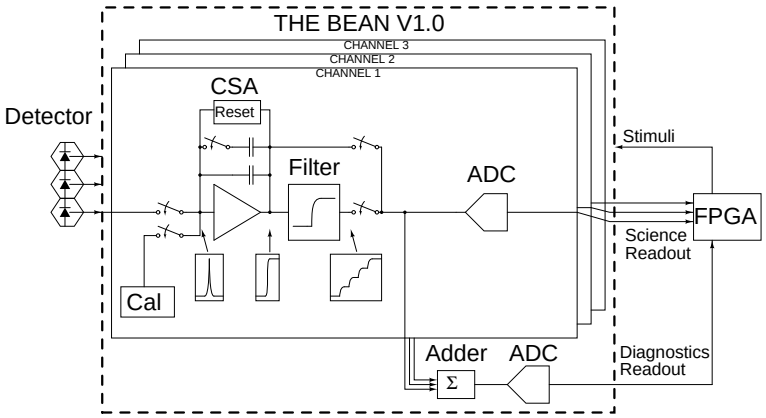

Figure II-8.2
The simplified block diagram of the Bean ASIC.

In order to provide the low-latency output[1] that combines the outputs of all channels in the chip, an analog adder is used. The adder operates in the sampled-data domain using switched capacitors,

[1] The low-latency output will be used for beam tuning and diagnostics.

and can be easily scaled to include more channels. Both the signal and the adder output are digitised using a custom 10-bit successive approximation register (SAR) ADC. The converter samples the differential input voltage and, using an internal digital-to-analog converter (DAC), produces a voltage that tries to match the input voltage. Using a binary search algorithm for the internal DAC output voltage, on each conversion step the ADC produces the next significant bit of the digital output, starting from the most significant bit. The full conversion takes less than 250 ns to complete. The Bean die (Figure II-8.3) measures $2.4\,\mathrm{mm} \times 2.4\,\mathrm{mm}$. The channel pitch is $360\,\mu\mathrm{m}$ and includes generous power buses; four 1.8-V power supplies are required by the chip.

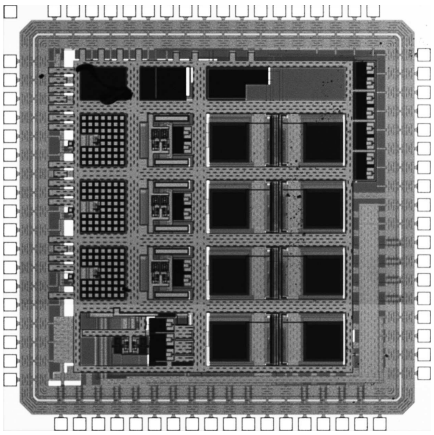

Figure II-8.3
The Bean microphotograph.

Test results The Bean ASIC was tested for linearity, crosstalk gain, adder operation and gain, bandwidth, weighting function, and noise. The chip linearity meets the specifications, with less than 1% nonlinearity mainly due to the charge amplifier finite open-loop gain. The ADC nonlinearity contribution is negligible, except for a few missing codes due to the inductance in the reference lines. This problem will be fixed in future revisions of the chip. Figure II-8.4 shows the channel integral nonlinearity (INL) and differential nonlinearity (DNL) for the SDT mode.

The crosstalk, for either mode of operation, was measured to be less than 1.7%, and it is mostly due to indirect channel-to-channel coupling. The gain from each channel to the adder output was measured. Since there are three channels, the gain from each channel should be 0.33. The measured gains range from 0.329 to 0.345, well within the expectations. The adder digital output is available in less than $1\,\mu\mathrm{s}$ from the pulse injection at the chip input. This low latency in providing the chip output is compatible with the fast feedback requirement specifications.

A 'chip bandwidth' test was performed to quantify the residual effect of an input pulse at the output measured in subsequent cycles. If the residual effect on subsequent cycles is null, then the chip can operate at the maximum speed without piling up data from different cycles. The bandwidth measurement was done by injecting a large input at a certain cycle, and measuring the output for that cycle and subsequent cycles. The test results show no evidence of memory effect in either mode of operation, which allows to operate the chip for 100% occupancy.

From the chip weighting function and from the amplifier input-referred noise power spectral density and the detector leakage current, it is possible to compute the chip signal-to-noise ratio. The weighting functions were obtained through SPICE simulations, and then measured using the test setup described earlier. The measured weighting functions match the expectations, supporting the use of switched-capacitor filters.

The chip noise was measured in LSB units by using the histogram method. The capacitance at the chip input, mostly due to the test PCB, is higher than the expected input capacitance from the specifications, and consequently the noise measured is higher. In order to obtain fair measurements, noise was then estimated from the measured noise, scaling it down according to the ratio between

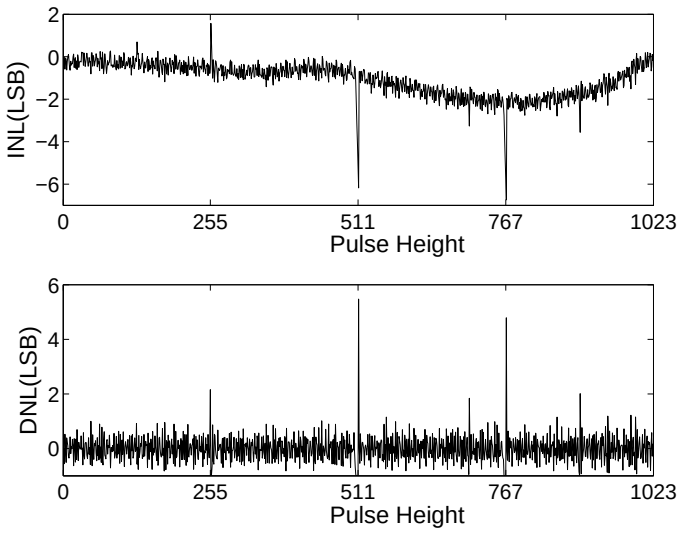

Figure II-8.4
The Bean integrated (INL) and differential (DNL) non-linearity in the standard data-taking (SDT) mode.

actual and specified input capacitance. The noise estimation is 0.6 LSB in the SDT mode, and 1.41 LSB in the DCal mode. Most of the noise in the DCal mode is due to a design flaw in the filter amplifier, and will be fixed in future revisions of the chip.

8.1.3.2 Electromagnetic Radiation Damage Studies

The expected integrated dose of 100 MRad per year of electromagnetically-induced radiation poses a challenge to the design of the BeamCal. Standard n-bulk silicon diode sensors are not thought to be capable of withstanding such a dose without degrading to unacceptable levels of charge collection efficiency.

Prior studies [162] suggest substantially greater electromagnetic radiation tolerance for p-bulk sensors. However, particularly for p-type sensors for which damage from electromagnetic irradiation may be minimised, damage may be dominated by the hadronic component of the electromagnetic shower. Thus, a radiation-damage study of various silicon-sensor technologies is getting underway. This study will explore the charge-collection efficiency of both n- and p-type float-zone and magnetic Czochralski sensors exposed to electromagnetic showers radiation as well as that from a beam of pure electromagnetic particles, so that the two potential sources of radiation damage can be separated. GEANT4 simulations suggest a shower-maximum exposure rate of

$$1\ \mathrm{MRad} \simeq \frac{0.8}{I_{beam}(\mathrm{nA}) \cdot E_{beam}(\mathrm{GeV})} \mathrm{hours}$$

Even for a low-intensity beam, such as that of the SLAC ESTB testbeam facility, a four-hour run will expose a sample sensor to 100 MRad. An initial campaign of electromagnetic radiation damage studies is proposed for early 2013; if successful, the setup will be offered as a facility for the study of radiation hardness for other sensor technologies provided by the FCAL collaboration.

Chapter 9
SiD Electronics and DAQ

SiD has a coherent approach to its electronics architecture that is intended to satisfy the requirements of all subsystems. It is closely tied to the unique ILC timing structure with a long bunch train with 1 ms duration and then a period of 199 ms quiet time. The SiD electronics is designed to cope with up to 8192 bunches per train and a bunch spacing as small as 300 ns; this can easily satisfy the current ILC requirements of up to 2625 bunches per train and a bunch spacing of 344 ns [163]. A simplified block diagram of the SiD data-acquisition from the front-end electronics to the online-farm and storage system is shown in Figure II-9.1.

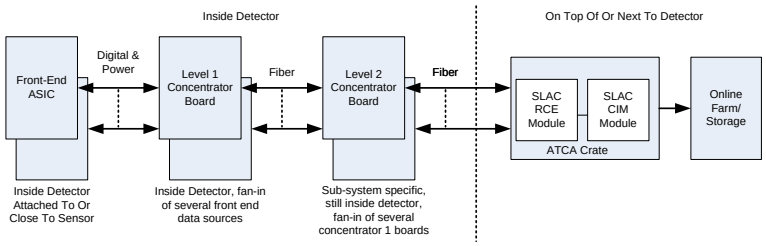

Figure II-9.1 Simplified block-diagram of the SiD detector control and readout chain using the ATCA RCE and CIM modules (defined later in this chapter).

9.1 ASIC developments

All subsystems with the exception of the Vertex detector (for which the sensor technology has not been selected yet) and the BeamCal (which has approximately unit occupancy) are foreseen to be read out by variants of KPiX as the front-end Application-Specific Integrated Circuit (ASIC). For the BeamCal the Bean ASIC has been developed to address its specific requirements, see Section 8.1.3.1.

9.1.1 KPiX

KPiX [87, 88] is a multi-channel system-on-chip for self-triggered detection and processing of low-level charge signals. Figure II-9.2 shows a simplified block diagram of the KPiX, processing signals from 1024 input channels. The low level charge signal at the input is processed by the charge amplifier in two ranges with an automatic range switching controlled by the range threshold discriminator. The built-in calibration covers the full dynamic range of up to 10 pC. Leakage compensation is available for DC-coupled detectors and either internal or external trigger options can be selected.

Up to four sets of signals for each channel can be stored in one acquisition cycle corresponding to one ILC bunch train. The timestamp is stored using a 13-bit-deep counter, while the signal amplitude is first stored as a voltage on a capacitor before its subsequent digitisation using a Wilkinson-type ADC with 13-bit resolution. At the end of the acquisition and digitisation cycle nine words of digital information are available for each of the 1024 cells of the KPiX chip. The data are then read out serially from the KPiX before the next acquisition cycle starts. The power consumption for each

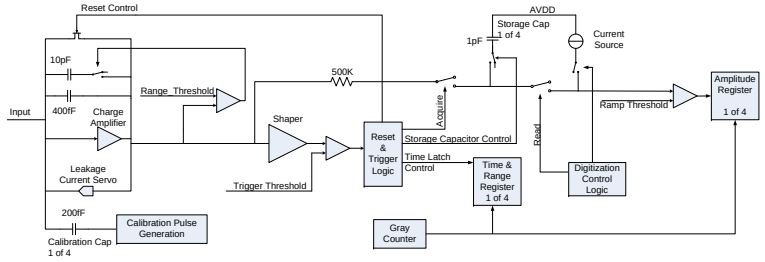

Figure II-9.2
Simplified block diagram of one KPiX channel.

individual channel is less than 20 μW. The latest version of KPiX has been manufactured using a 250 nm mixed-mode CMOS process and is currently being tested [88].

Table II-9.1 lists the currently foreseen number of KPiX ASICs for each subsystem. Main Tracker, ECAL, and HCAL use the 1024-channel version of the KPiX while the Muon subsystem uses a 64-channel KPiX version.

Table II-9.1
Approximate count of KPiX ASICs for each subsystem.

Sub-System	KPiX Count	Channels/KPiX
Main Tracker	27464	1024
ECAL	102573	1024
HCAL	35071	1024
Muons	8839	64
Total	173947	

9.2 On-Detector Electronics

As illustrated in Figure II-9.1, several front-end ASICs (KPiX, Bean or Vertex ASICs) are connected to a Level-1 Concentrator (L1C) board using LVDS. The main functions of the L1C board are to fan out incoming signals and commands to the front-end modules and to bundle data from the front-end modules for transmission to the Level 2 Concentrator (L2C) boards. Additionally it can perform zero-suppression and sorting of the incoming event data. For example, for the ECAL Barrel 96 1024-channel KPiX chips would be served by eight front-end cables with twelve KPiX per L1C board, yielding a total of 821 L1C boards and 52 L2C boards (80000 KPiX, 96 per L1C board; 16 L1C boards for each L2C board). Figure II-9.3 shows a block diagram of the L1C board.

The Level 1 Concentrator boards are in turn connected via 3-Gbit/s fibres to the Level-2 Concentrator boards. Besides distributing signals to/from the L1C boards, the L2C boards merge and sort the data-streams of the incoming event data before transmission to the off-detector processor boards. Depending on the sub-system, the L2C boards are either located inside the detector or immediately outside. E.g. for the ECAL Barrel there are 52 L2C boards inside the detector volume.

9.3 Off-Detector Electronics

The L2C boards are connected via fibres to ATCA crates either on or next to the detector. ATCA (Advanced Telecommunications Computing Architecture) is the next generation communication equipment currently used by the telecommunication industry. It incorporates the latest trends in high-speed interconnect, processors and improved reliability, availability, and serviceability. Instead of parallel bus back-planes like VME, it uses high-speed serial communication and advanced switch technology within and between modules, redundant power, plus monitoring functions. For SiD the usage of 10 Gbit/s Ethernet is foreseen as the serial protocol.

Two custom ATCA boards, the Reconfigurable Cluster Element (RCE) Module and the Cluster Interconnect Module (CIM) were designed previously. Based on those two modules, a second generation RCE was built, as shown in Figure II-9.4 which combines the switch interconnect function of the

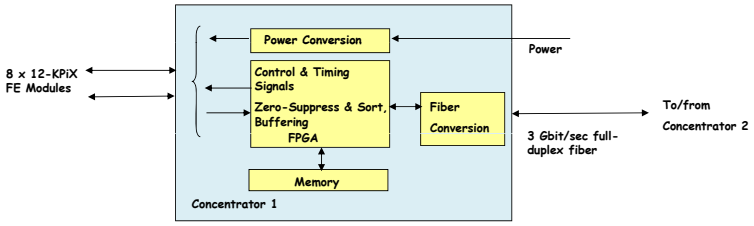

Figure II-9.3 Block Diagram of the Level 1 Concentrator Board.

CIM onto the RCE itself. A 96-port 10 Gbit/s Ethernet ASIC is placed on the RCE, providing communication between all the RCE modules in a crate and to destinations external to the crate with data rates up to 10 Gbit/s. The RCE modules connect via the backplane to the Rear Transition Modules (RTM) which interface via 48 3-Gbit/s fibre links to the sub-system L2C boards. The main ATCA board can hold up to five daughter-cards (shown in Figure II-9.4) each with a Virtex FPGA with two embedded PowerPC processors, four Gbytes of DDR3 memory, 8 Gbytes/sec cpu-data memory interface, four 10-Gbit/s Ethernet event data interfaces, and an open-source RTEMS (Real-Time Executive for Multiprocessor Systems) realtime operating system [164]. One ATCA crate can host up to 14 RCE boards, providing connections to $48 \times 14 = 672$ 3-Gbit/s fibre links into the detector for 2 Tbit/s IO.

The maximum available data transfer rate is up to 520 Gbit/s, while the estimate for the complete SiD is approximately 320 Gbit/s including a factor of two safety margin. In principle, a partially loaded ATCA crate could serve the complete detector. However for partitioning reasons, the ability to run each of the subsystems completely independently during commissioning is highly desirable, and therefore a crate for each subsystem is planned.

The data are further sorted on an event-by-event basis in the ATCA system and then sent to the online processing system for potential further data reduction. Whether further data reduction is required is not determined yet, and the data may directly be forwarded to the offline system. Note that the event data are zero-suppressed in the sub-systems without the need for a global trigger system. All data produced in the front-ends above a programmable threshold is subsequently read out. For diagnostics and debugging, the DAQ includes the ability to assert calibration strobe and trigger signals, transmitted to the front-ends via the L2C and L1C boards using the fibres shown in Figure II-9.1.

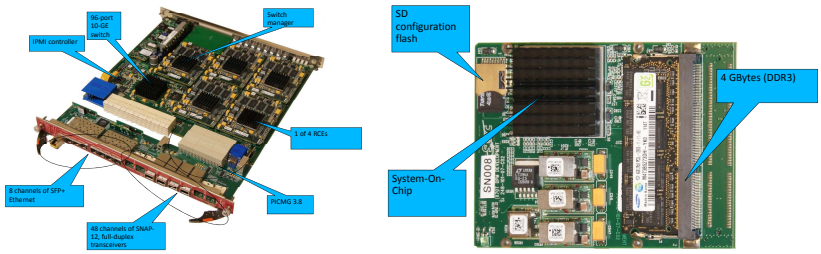

Figure II-9.4 ATCA Reconfigurable Cluster Element (left) and RCE daughter module (right)

Power conversion circuits on the L2C and L1C boards supply the power to the front-ends, starting with 48 V or higher voltages from off-detector supplies and then using DC-DC converters. Alternatively, serial powering architectures are also under consideration. The power supplies will be located in several racks on, or next to, the detector. Environmental and health monitoring circuits are also included on the concentrator boards. In addition there may be additional monitoring boards in the detector, connected to RCE fibre interfaces. In addition there are crates of monitoring modules mounted in several racks on or next to the detector.

9.4 Overview of Electronics Channels and Expected Data Rates

Table II-9.2 provides a global overview of the electronic channel counts for SiD. For each subdetector the detector granularity, as currently used in the SIDLOI3 simulation model, and the approximate number of readout channels are listed. Preliminary studies have been carried out to estimate the average and maximum cell occupancies to be expected for a full bunch train at the ILC at 1 TeV [165]. The number of bits per hit provides a first estimate, and is based on a simplified approximation for individual hits with full on-detector zero-suppression and without on-detector clustering. It foresees some bits for addressing. The estimated data volume per bunch train is also listed. The beam parameters at 1 TeV presume 476 ns bunch separation and 2450 bunches per train. In the vertex and main tracker regions, it was found that the occupancy from $\gamma\gamma \to \mathrm{hadrons}$ events is typically more than one order of magnitude below the occupancy from incoherent pairs. The occupancies in the vertex detector and main tracker have therefore been calculated using incoherent pairs only. Average cluster sizes of 3.1 and 2.6 have been assumed for the pixel and strip detectors respectively.

Uncertainties in the simulation of the production rates and in the detector response have been estimated. As a result, safety factors of two for the background rates from $\gamma\gamma \to \mathrm{hadrons}$ and five for the ones from incoherent pairs have been included. The occupancy studies have used a uniform 5 T solenoid field along the z-direction. The use of a more realistic field map including anti-DID will alter the results for incoherent pairs in the most inner detector regions up to a few ten percent.

The simulations at 1 TeV show that expected occupancies in the first layers of Lumical are well above 400% over the full surface. Contrary to the 500 GeV case, it is therefore assumed that the Bean chip will be used throughout BeamCal and Lumical for 1 TeV running. The full 2820 Bean buffer depth is assumed to be read out for each cell and for each bunch train.

Table II-9.2 Overview of readout details for the various subdetectors. Occupancies and data volumes are for a full bunch train at 1 TeV and include beam-induced background as well as charge sharing between pixels/strips. Safety factors of five and two have been applied to the rates of incoherent pairs and $\gamma\gamma \to \mathrm{hadrons}$ respectively. BeamCal and Lumical are expected to be using the Bean chip with a buffer depth of 2820.

	cell size (mm^2)	number of channels (10^6)	av. to max. occ. (%)	approx. # bits per hit (bit)	data volume (Mbyte)
VXD barrel	0.02×0.02	408	8 - 60	32	130
VXD disks inner	0.02×0.02	295	4 - 70	32	50
VXD disks outer	0.05×0.05	980	0.5 - 20	32	20
Main tracker barrel	0.05×100	16	33 - 300	32	20
Main tracker disks	0.05×100	11	4 - 500	32	2
ECAL barrel	3.5×3.5	72	2 - 45	40	7
ECAL endcap	3.5×3.5	22	33 - 2300	40	36
HCAL barrel	10×10	30	0.07 - 200	40	0.1
HCAL endcap	10×10	5	96 - 3600	40	24
LumiCal	2.5×var.	0.061	≫100	16	340
BeamCal	2.5(5.0)×var.	0.076	≫100	16	430

Including safety factors, the average hit occupancies in the muon barrel system amount to $7.5{\cdot}10^6/\mathrm{cm}^2$ per train, with a maximum of $0.08/\mathrm{cm}^2$ at the transition region to the endcap, due to particles passing through the HCAL barrel-endcap gap. To determine muon endcap occupancies the simulation model would need to be extended. Currently the model does not contain all material in the very forward region, such as QDO support tubes, which will shield backscattered particles. Overall the data from the muon system will have a very small impact on the data volume.The table shows that the occupancies can exceed 100% in several detector regions. The KPiX chip presently provides fast buffering of up to four hits per channel. The KPiX design can be adapted to contain a larger buffer depth if deemed required for high-occupancy regions.

Chapter 10
SiD Simulation and Reconstruction

10.1 Overview of the Simulation and Reconstruction Software

A large fraction of the software for the generation, simulation and reconstruction is shared between the ILD and SiD detector concepts (see 2.2). The generated events are simulated in the SiD detector by SLIC [166], a program encapsulating the functionality of the GEANT4 [167] tool kit, but providing the ability to define all aspects of the detector at runtime. The output information consists of primary charge deposition in the sensitive detectors providing the primary information regarding the energy deposition, hit position, time and Monte Carlo particle causing the energy deposition. At this level each of the physics events at 1 TeV is merged with a simulated event containing the equivalent of one bunch crossing of incoherent pair interactions. Additionally, hits and particles from $\gamma\gamma \rightarrow \text{hadrons}$ events are merged with each physics event. The number of $\gamma\gamma \rightarrow \text{hadrons}$ events follows a Poisson distribution with a mean of 4.1 (1.7) per bunch crossing at 1 TeV (500 GeV). Events produced for the 500 GeV study are not merged with incoherent pairs background.

The energy deposits in the active material of the detectors are then digitised into simulated hits using the `org.lcsim` reconstruction framework [168]. A more detailed description of the digitisation is given in Section 10.4. Pattern recognition and track fitting is the task of the SeedTracker algorithm, which has been used successfully in the benchmarking of SiD detector variants at a 500 GeV ILC [63] as well as at a 3 TeV CLIC [129]. The algorithms of the PANDORAPFA package [169] are responsible for the calorimetric reconstruction and the creation of particle flow objects (PFOs). In a first step, muons are identified, their hits removed from the calorimeters, and the remaining hits are clustered using a cone clustering algorithm. Charged particles are created through the positive match of a track with a cluster, where consistency of the measured energies is ensured through iterative re-clustering. The remaining clusters are assigned to neutral PFOs. A more detailed description of the particle identification is given in Section 10.6.1.

Vertices from secondary interactions are found by the LCFIPlus [170] flavour tagging package. The found vertices are then used in the jet clustering, which is described in more detail in Section 11.2.2.1.

10.2 The SiD DBD Production

The detector response simulation and event reconstruction was performed on the Worldwide LHC Computing Grid (WLCG) and the Open Science Grid (OSG). The ILCDIRAC [171, 172] tool was used for the full chain of bookkeeping, handling of meta data, automated job submission and monitoring. The jobs were submitted under the common ILC Virtual Organisation. Figure II-10.1 shows a distribution of the computing time used by country. Major contributors were CERN, various Grid sites in the UK (primarily RAL and Manchester), IN2P3 in France and Open Science Grid resources at FNAL and PNNL.

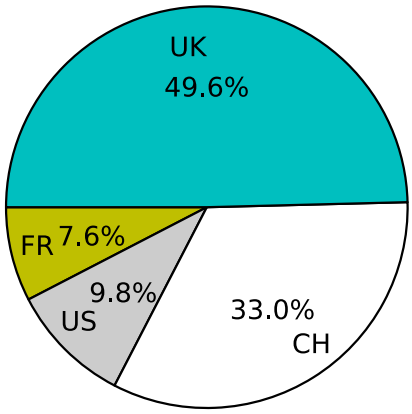

Figure II-10.1
CPU time used in the DIRAC mass production by country

10.3 Simulating the SiD Detector Geometry

10.3.1 The sidloi3 Model

The SIDLOI3 detector model reflects the design of SiD, as described in this document, with the Silicon-Tungsten ECAL and the RPC HCAL as the baseline. All of the tracker elements are modelled as planar silicon wafers with accompanying support structures. The geometry of the services (power and readout) is simplified, but reflects the gross amount and general distribution of the materials. The calorimeters are modelled as polygonal staves in the barrel region or planes in the endcaps, with interleaved readouts. For the complete details of the model as implemented in GEANT4 see [173].

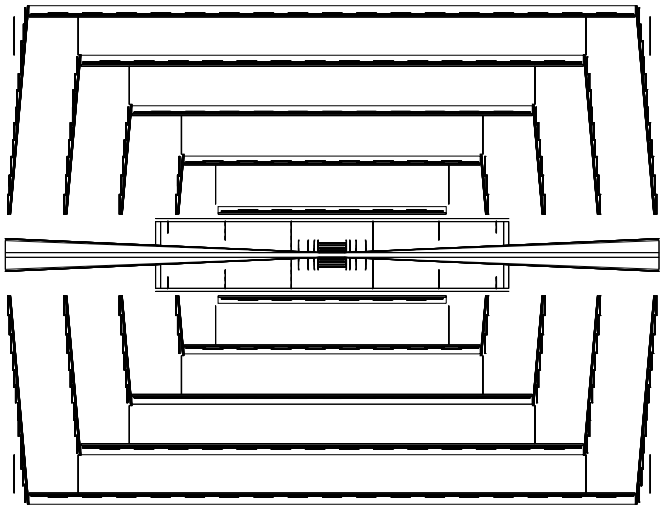

Figure II-10.2
R-z view of the tracking system as implemented in SIDLOI3 model. Some support and readout structures have been hidden to improve the visibility of the sensors.

A cross-section of the tracking detector is shown in Figure II-10.2. This is to be compared with Figure II-3.3 showing an engineering elevation view of the tracking system. An orthographic cutaway view of the central tracker as implemented in the SIDLOI3 model is shown in Figure II-10.3 (left). An orthographic cutaway view of the complete detector as implemented in the SIDLOI3 model is shown in Figure II-10.3 (right). The electromagnetic barrel calorimeter is modelled as a dodecagonal tube with overlapping staves. The hadron calorimeter barrel is composed of twelve symmetric staves. Finally, the octagonal layout of the magnetic flux return yoke, with its eleven layers of muon detection instrumentation is clearly visible.

Figure II-10.4 (left) shows the cumulative hadronic interaction lengths of the SiD detector elements as a function of the polar angle θ, including the self-shielding provided by the thick mantle of

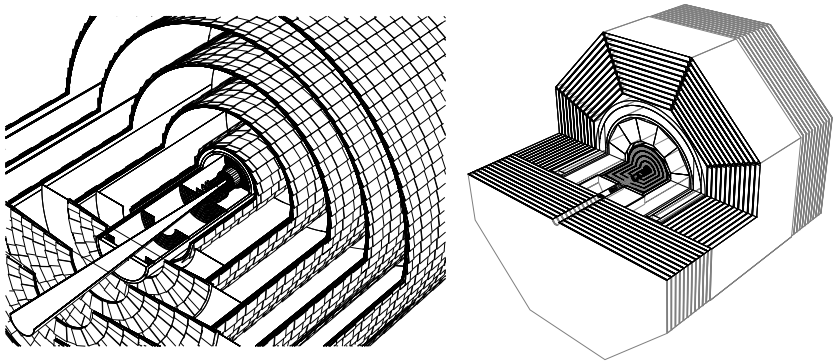

Figure II-10.3
Cutaway view of the tracking system as implemented in SIDLOI3 (left) and the complete detector (right). Some support and readout structures have been hidden to improve the visibility of the sensors (left) and the calorimeters.

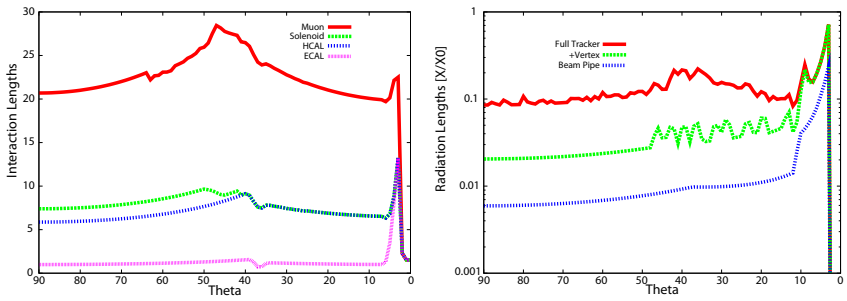

Figure II-10.4
The nuclear interaction lengths of SIDLOI3 (left) and the radiation lengths of SIDLOI3 tracking system (right) as a function of the polar angle θ.

the flux-return steel, while Figure II-10.4 (right) displays cumulative material (expressed as a fraction of X_0) of the tracking region.

10.4 Simulation of the full Detector Response

The hits which are recorded and written out from the full Monte Carlo simulation contain the primary charge deposition. To simulate the response of a realistic, physical detector, this information needs to be converted to information which represents the electronic readout that would be collected from the detector. We refer to this process as hit digitisation.

10.4.1 Silicon Pixel and Strip Hit Digitisation

The silicon-based tracking detectors are precision devices with very high intrinsic spatial resolution. In order to realistically model their response, the effects of charge drift and diffusion in the silicon, as well as effects of pulse shaping and electronic noise need to be implemented in the simulation. The charge deposition for silicon strip detectors is simulated using an algorithm based on the CDF silicon sensor simulation. An extension of this model to pixels is used to model the response of the vertex detector elements.

10.4.2 Simulation of the Calorimeter Response

Calorimeters are designed to measure the energy of incident particles by inducing them to shower in the detector and to record the deposited energy. Because of the vast number of secondary particles produced when an incident particle showers, and because precise details of these secondary particles are unimportant to the energy measurement, we do not by default record primary charge depositions for each of them. Instead, we define volume elements in which we sum up the total amount of deposited energy, and record the earliest time of deposition from each separate incident particle. The energy in the ECAL is reconstructed by multiplying the energy deposited in the sensitive readout layers with sampling fractions, while in the digital HCAL, the energy is obtained from the number of cells with an energy deposition multiplied by a sampling fraction. These sampling fractions are determined from the response of SIDLOI3 to single muons, photons and K^0_L, respectively, at a variety of energies.

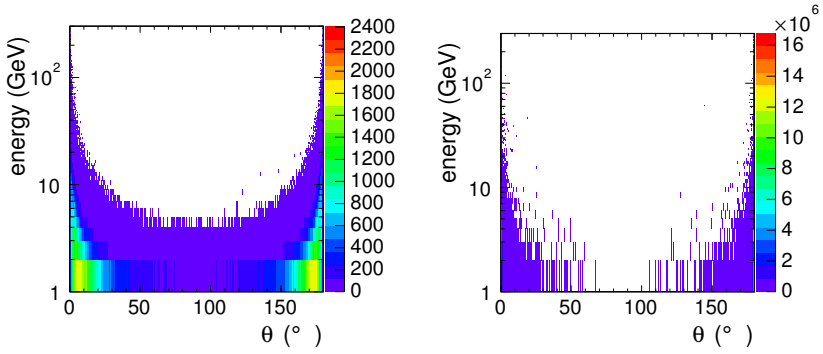

Figure II-10.5
Kinematic properties of the machine-induced backgrounds from $\gamma\gamma \to \mathrm{hadrons}$ processes (left) and from incoherent pairs (right) at 1 TeV.

10.4.3 Clustering

The association of nearby strips, pixels or volume elements into a single hit is referred to as clustering. The signal sharing across readout elements can lead to improvements in the measurement precision and is therefore a crucial step in the reconstruction. The silicon strip and pixel signals are clustered using a nearest neighbour algorithm. Lookup tables are used to achieve approximately linear scaling of clustering time. Settable parameters are provided for noise, readout and clustering thresholds. Tracker hits are then created from these clusters. The position measurements (1D for strips, 2D for pixels) are derived from the energy-weighted centroids of the clusters, and the uncertainties are provided on a cluster-by-cluster basis. These hits are the input for the track finding. The algorithms used by PandoraPFA to cluster energy depositions in the calorimeters are described in more detail elsewhere [174].

10.5 Properties of Machine-Induced Background

Beamstrahlung processes in the ILC machine operated at 1 TeV result in a large rate of $\mathrm{e^+e^-}$ pairs at low transverse momenta that are predominantly produced in the forward region. These processes result in higher occupancies in the inner layers of the vertex detector and in the forward detectors. The main source of processes with higher transverse momentum are multiple $\gamma\gamma \to \mathrm{hadrons}$ events per bunch crossing.

The event samples for the compulsory DBD benchmarks are described in detail in Section 11. They were mixed with machine-induced background on an event-by-event basis. Samples at 1 TeV were mixed with an average of 4.1 $\gamma\gamma \to \mathrm{hadrons}$ events for each physics event and the 500 GeV processes were mixed with an average of 1.7 $\gamma\gamma \to \mathrm{hadrons}$ events. In addition, the 1 TeV samples include the detector response to an average of 450,000 low-momentum incoherent $\mathrm{e^+e^-}$ pairs. These processes follow a Gaussian distribution with a width of 225 $\mu\mathrm{m}$ in z to account for the finite size of the ILC bunches. The physics process from the primary $\mathrm{e^+e^-}$ interaction was produced at $z = 0$.

The backgrounds were simulated in a separate step and merged with the primary physics process before the digitisation step outlined above. In order to keep the file size to a manageable level, particles that do not leave primary charge depositions in the sensitive detectors were dropped. The tool for the merging of the processes [94] has been developed for and tested in the CLIC CDR benchmarking analyses.

Figure II-10.5 shows two-dimensional distributions of the energy versus the polar angle of simulated particles produced in $\gamma\gamma \to \mathrm{hadrons}$ processes (left) and from incoherent $\mathrm{e^+e^-}$ pair production (right) at 1 TeV. While particles from incoherent pairs are predominantly in the forward region, particles from $\gamma\gamma \to \mathrm{hadrons}$ processes have significant energy also in the central region and reach the barrel calorimeters.

10.6 Detector Performance

10.6.1 Particle Identification: Photon, Electron and Muon ID

Particle identification (particle ID), and in particular lepton identification will be central to many physics studies at the ILC. Muons are identified and all of their hits removed before the calorimeter hits are clustered. The track-cluster agreement is optimised using various re-clustering strategies, which are guided by identifying the cluster as belonging to an electromagnetic or a hadronic interaction.

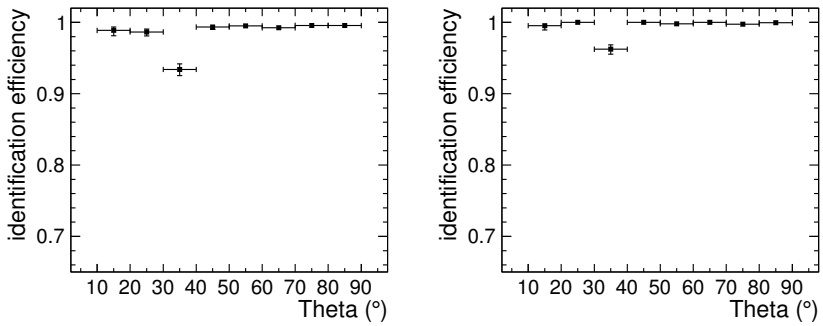

Figure II-10.6
Particle identification efficiency for 10 GeV photons (left) and 100 GeV photons (right) as a function of the angle θ.

The particle identification has been evaluated on samples of single photons, electrons, muons and pions of 10 GeV and 100 GeV, respectively (see Figures II-10.6, II-10.7 and II-10.8). In these plots, the reconstructed particle is required to have the same type as the generated particle, and for electrons and pions a loose energy cut of five times the resolution of the EM calorimeter above or below the energy of the generated particle is applied.

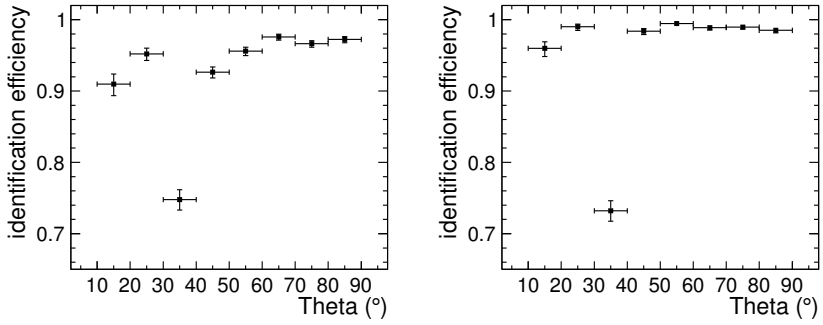

Figure II-10.7
Particle identification efficiency for 10 GeV electrons (left) and 100 GeV electrons (right) as a function of the angle θ.

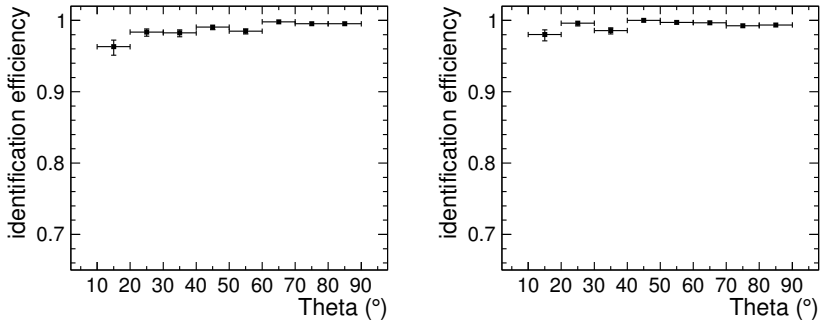

Figure II-10.8
Particle identification efficiency for 10 GeV muons (left) and 100 GeV muons (right) as a function of the angle θ.

The default for neutral particles is the neutron hypothesis, while charged particles are assigned the pion hypothesis by default. The muon identification efficiency is above 95% for values of the polar angle $10^\circ < \theta < 170^\circ$. The photon identification efficiency is above 99% over the same angular range, except for an inefficiency in the transition region between calorimeter barrel and endcap, which

results in a dip in the bin $30^\circ < \theta < 40^\circ$. That same region results also in a dip of the electron efficiency, which is otherwise over 90% for 10 GeV electrons and above 98% for 100 GeV electrons.

The performance of the reconstruction as shown here has not been optimised for particle identification efficiency, but rather for jet energy resolution. We expect that a significant improvement can be achieved - particularly in the transition region between calorimeter barrel and endcap - with dedicated particle identification algorithms that are optimised for performance with the SiD digital HCAL.

10.6.2 Jet Flavour Tagging: Efficiency and Purity

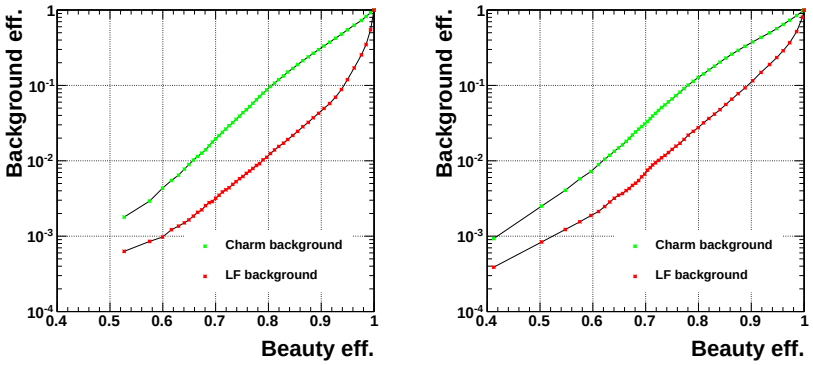

Figure II-10.9 Mis-identification efficiency of light quark jets (red points) and charm jets (green points) as beauty jets versus beauty identification efficiency in di-jets at $\sqrt{s} = 91$ GeV. The performance is shown without (left) and with background from $\gamma\gamma \to$ hadrons events and incoherent pairs (right).

(a) without $\gamma\gamma \to$ hadrons **(b)** with $\gamma\gamma \to$ hadrons

The ability to tag bottom and charm decays with high purity is a crucial aspect in the design of the vertex detector. Figure II-10.9 shows the b-tagging efficiency of a light quark sample (red curve) or a charm quark sample (green curve) versus the b-tagging efficiency of a bottom quark sample. The neural networks have been trained on a sample of di-jets at $\sqrt{s} = 91$ GeV and tested on a statistically independent sample.

10.6.2.1 Vertex Resolution

One of the most important variables in jet flavour tagging networks is the decay length of the secondary vertices. The vertex resolution of the SiD vertex detector has been assessed in the context of the analysis of the top Yukawa coupling and in a sample of Z decays to light quarks at $\sqrt{s} = 91$ GeV. Figure II-10.10 (left) shows the position of the reconstructed primary vertex in events containing two isolated leptons and four b quarks. The physics interaction has been generated at the position (0, 0, 0), and the beam spot constraint has been turned off for the purpose of this study.

Figure II-10.10 (right) shows the resolution of the primary vertex position versus the number of tracks originating from the primary interaction.

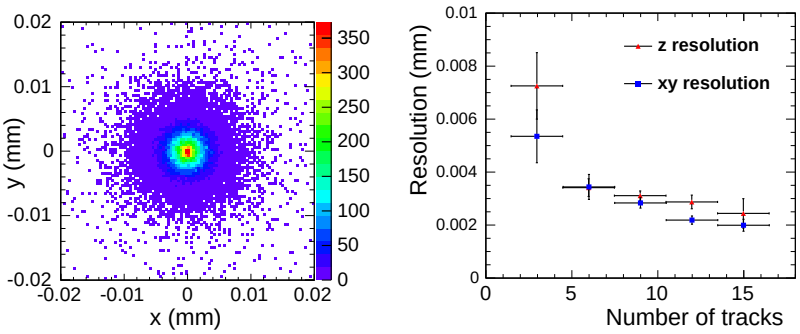

Figure II-10.10 Position of the reconstructed primary vertex (left) and resolution of the primary vertex position as a function of the number of tracks originating from that vertex (right).

10.6.3 Energy and Mass Resolution

The design of the SiD detector concept has been optimised for jet energy resolution using the particle flow approach. This puts stringent requirements on the interplay of the various subdetectors and has led to the choice of calorimeters with a high degree of segmentation and transverse granularity. In addition, sophisticated reconstruction algorithms are necessary to obtain a jet energy resolution that allows to separate W and Z decays.

Figure II-10.11 (left) shows the PFA jet energy resolution without the effects from jet finding or background. To avoid a bias from possible tails, the rms90 value is computed to describe the energy or mass resolution of a particle flow algorithm. It is defined as the standard deviation of the distribution in the smallest range that contains 90% of the events. The events consist of Z' bosons of different masses decaying at rest to a pair of light quark jets. In these events the jet energy resolution is computed as the event energy resolution times $\sqrt{2}$, and the jet energy is half of $\sqrt{s}$ of the process.

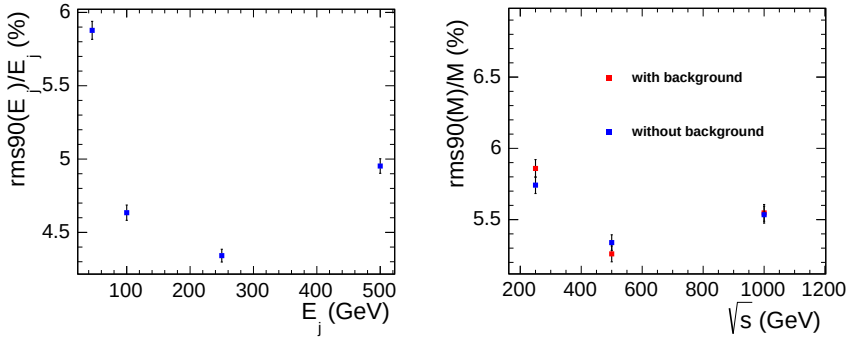

Figure II-10.11
Left: Energy resolution of reconstructed Z' events of different masses decaying at rest to a pair of light quark jets. Right: Mass resolution of reconstructed ZZ events with and without the backgrounds at different values of $\sqrt{s}$. In these events, one Z boson decays invisibly and the other to a pair of jets.

Figure II-10.11 (right) shows the mass resolution of reconstructed Z bosons in $\mathrm{e^+e^-} \to \mathrm{ZZ}$ events at different collision energies, where one Z decays to neutrinos, the other to two light quarks that give rise to two jets. The events have been clustered into two jets using the k_t algorithm as implemented in the FastJet [175] package. The jets are combined to form a Z boson.

The value at each point in Figure II-10.11 (right) is computed as rms90(M)/M and given in per cent. The error bars indicate the error of the rms90 value of the distribution at each point. The addition of background from $\gamma\gamma \to \mathrm{hadrons}$ events and incoherent pairs results in only a minor change in resolution in these events. The difference can be explained by the additional background energy in the reconstructed jets balancing the small reconstruction bias towards lower energies in events without background.

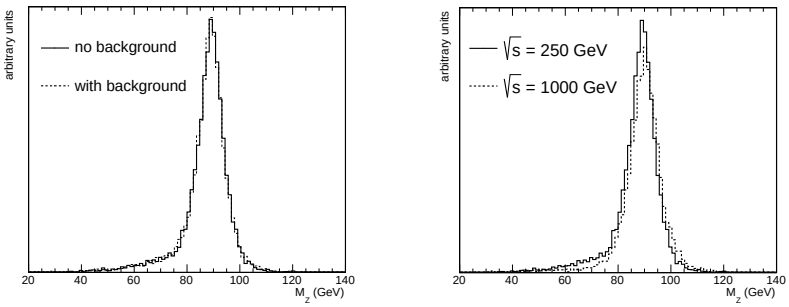

Figure II-10.12
Comparison of the distributions of the reconstructed Z mass in ZZ events at $\sqrt{s}$ =250 GeV with and without background (left) and at two different values of $\sqrt{s}$ without background (right). In these events one Z decays invisibly and the other to a pair of jets.

Figure II-10.12 (left) shows a comparison of the distributions of the reconstructed Z mass in ZZ events simulated with and without background at $\sqrt{s}$ =250 GeV. The effect of the background on the reconstructed mass at these energies is partially mitigated by the jet clustering. Figure II-10.12

(right) shows a comparison of the distributions of of the reconstructed Z mass in ZZ events at $\sqrt{s}$ =250 GeV and $\sqrt{s}$ =1 TeV without background. It is expected that the relative shift of 1 GeV in the distributions can be reduced with improved calibration and calorimetric reconstruction.

10.7 Summary

The production of events for the benchmarking analyses described in Chapter 11 includes generation of a comprehensive set of Standard Model processes taking into account the ILC beam spectrum, full GEANT4 detector simulation, generation, simulation and mixing of machine-induced background processes with the signal samples and PFA-based reconstruction of the mixed events.

To evaluate the performance of the SIDLOI3 detector concept and the reconstruction software as relevant for the DBD analyses kinematic properties of the machine-induced backgrounds, vertex reconstruction and flavour tagging, and performance of the particle flow algorithms have been studied in detail. While some critical work items have been identified in this process, the overall performance of the simulated detector and the simulation and reconstruction software as described in this section is adequate to carry out the DBD benchmarking analyses.

Chapter 11
SiD Benchmarking

Results of detailed simulation studies of the SiD detector are discussed in this chapter. First a short review of the studies performed for the SiD LOI is given. Several additional benchmark reactions were studied for the DBD. The generation of the events and common analysis tools used for several benchmark analyses are described briefly. Three new benchmark studies were performed at a centre-of-mass energy of 1 TeV. One of the LOI studies was repeated using the DBD version of the detector simulation and event reconstruction. In addition, the production of scalar tau leptons was investigated to illustrate the importance of the BeamCal detector.

11.1 Summary of the LOI Results

For the SiD LOI [63] several physics performance studies have been conducted to quantify the physics performance of the SiD detector concept. These studies were also used to broaden and emphasise the physics case of the ILC. From a list of physics benchmark reactions [176] six reactions were compulsory for the LOI submission. Three of the benchmark studies were conducted at a centre-of-mass energy of 250 GeV using a dataset of 250 fb^{-1}:

- $\mathrm{e^+e^-} \to \mathrm{e^+e^-h},\ \mu^+\mu^-\mathrm{h}$;
- $\mathrm{e^+e^-} \to \mathrm{hZ},\ \mathrm{h} \to \mathrm{c\bar{c}},\ \mathrm{Z} \to \nu\bar{\nu}, \mathrm{q\bar{q}}$;
- $\mathrm{e^+e^-} \to \mathrm{hZ},\ \mathrm{h} \to \mu^+\mu^-,\ \mathrm{Z} \to \nu\bar{\nu}, \mathrm{q\bar{q}}$.

The remaining analyses were performed assuming $\sqrt{s}$ =500 GeV and using a dataset of 500 fb^{-1}:

- $\mathrm{e^+e^-} \to \tau^+\tau^-$;
- $\mathrm{e^+e^-} \to \mathrm{t\bar{t}} \to 6$ jets;
- $\mathrm{e^+e^-} \to \tilde{\chi}_1^+\tilde{\chi}_1^-,\ \tilde{\chi}_2^0\tilde{\chi}_2^0$ assuming "Point 5" as defined in [176].

In addition to these compulsory LOI benchmark reactions SiD has also investigated the the $\mathrm{e^+e^-} \to \tilde{\mathrm{b}}\tilde{\mathrm{b}},\ \tilde{\mathrm{b}} \to \mathrm{b}\tilde{\chi}_1^0$ process [177]. For all the LOI analyses, the SM Higgs mass was set to 120 GeV and the top quark mass was set to 174 GeV. In the following, a short summary of the results from the individual benchmark analyses will be given. All results from the LOI are summarised in Table II-11.17 as well. Compared to the DBD, the detector simulation for the LOI [63] was less detailed. In contrast to the DBD studies, beam-induced backgrounds were not considered for the LOI analyses.

For the analyses at $\sqrt{s} = 250$ GeV a dataset of 250 fb^{-1} was used assuming a polarisation set of 80% right-handed e^- and 30% left-handed e^+. This polarisation parameter set is referred to as "80eR" in this section. Additional signal samples with 80% left-handed e^- and 30% right-handed e^+ ("80eL") have also been investigated.

One of the key measurements is the model-independent measurement of the Higgs mass and production cross-section using the process $\mathrm{e^+e^-} \to \mathrm{hZ},\ \mathrm{Z} \to \mathrm{e^+e^-},\ \mu^+\mu^-,\ \mathrm{h} \to \mathrm{anything}$. The recoil mass against the Z can be measured very accurately using the leptonic Z decays.

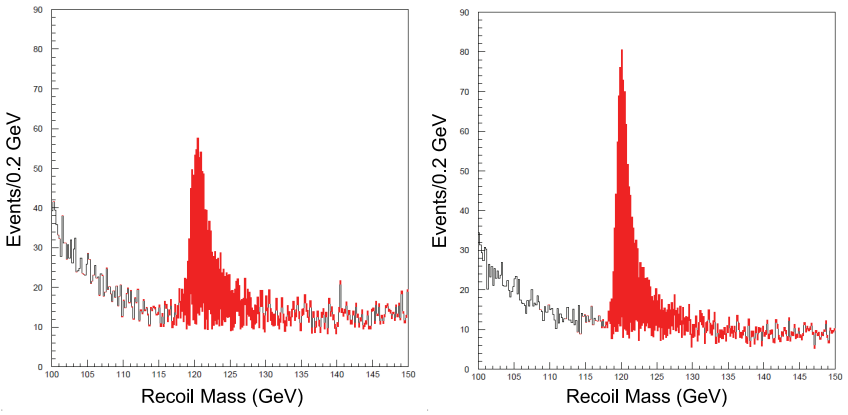

Figure II-11.1
Recoil mass distributions following selection cuts for e^+e^-h (left) and $\mu^+\mu^-h$ (right) assuming 250 fb^{-1} luminosity with 80eR initial state polarisation at $\sqrt{s} = 250$ GeV. The signal in red is added to the background in white.

The distributions for the recoil measurements in both the e^+e^-h and $\mu^+\mu^-h$ channels are shown in Figure II-11.1. Main background sources include mainly di-boson production (W^+W^-, ZZ). The amount of W^+W^- background can be greatly reduced by running exclusively with the 80eR configuration. A summary of the results of both leptonic Z modes and using both 80eR and 80eL is given in Table II-11.1.

Table II-11.1
Summary of Higgs mass and hZ cross-section results for different channels and the different luminosity assumptions at $\sqrt{s} = 250$ GeV. The error includes the measurement statistical error and the systematic error due to the finite statistics of the Monte Carlo training sample.

80eR (fb^{-1})	80eL (fb^{-1})	Channel	ΔM_h (GeV)	$\Delta\sigma_{hZ}/\sigma_{hZ}$
250	0	e^+e^-h	0.078	0.041
250	0	$\mu^+\mu^-h$	0.046	0.037
250	0	$e^+e^-h + \mu^+\mu^-h$	0.040	0.027
0	250	e^+e^-h	0.066	0.067
0	250	$\mu^+\mu^-h$	0.037	0.057
0	250	$e^+e^-h + \mu^+\mu^-h$	0.032	0.043

Measuring the branching ratios of the Higgs boson is of vital importance to distinguish the SM Higgs boson from possible alternative scenarios. For the LOI the decays of the Higgs into $c\bar{c}$ and $\mu^+\mu^-$ have been studied at $\sqrt{s} = 250$ GeV using the Higgsstrahlung process, where the Z decayed either in $q\bar{q}$ or $\nu\bar{\nu}$. The identification of the $h \to c\bar{c}$ decay mode took advantage of the excellent c-tagging capabilities of SiD (see [63]) and employed neural networks to separate the $c\bar{c}$ signal from the overwhelming $h \to b\bar{b}$ background. For the $c\bar{c}$ branching ratio, the finally achieved accuracies are 11% ($Z \to \nu\bar{\nu}$) and 6% ($Z \to q\bar{q}$), respectively.

For the rare Higgs decay into $\mu^+\mu^-$ the challenge is to extract the signal out of an overwhelming Standard Model background of mainly four-fermion events. While for the $Z \to \nu\bar{\nu}$ decay mode, it has been proven quite difficult to extract the signal, the LOI analysis has demonstrated sensitivity in the hadronic channel, selecting 7.6 signal events over a background event of 39.3 events with a signal selection efficiency of 62%. This yields a measurement of the cross-section for the process $e^+e^- \to hZ,\ h \to \mu^+\mu^-$ with a precision of 89%.

For the analyses at $\sqrt{s} = 500$ GeV a dataset of 500 fb^{-1} was used with 80eR polarisation unless explicitly stated otherwise.

The first analysis using the 500 GeV dataset studies the process $e^+e^- \to \tau^+\tau^-$ and aims to measure the τ polarisation with high precision. The measurement of the τ polarisation allows a search for multi-TeV Z' resonances. Tightly collimated jets with only a few tracks must be reconstructed to identify the underlying charged hadron and π^0 constituents. Therefore additional reconstruction algorithms were applied in a second pass of the reconstruction, which were dedicated for identifying τ decays. This leads to τ samples with purities of 85% or larger. To measure the mean τ polarisation over all τ production angles, $< P_\tau >$, the optimal observable technique [178, 179] is used. For this study two datasets with an integrated luminosity of 250 fb^{-1} each were used, one with 80eR

polarisation and one with 80eL polarisation. The true $< P_\tau >$ values are given by 0.528 (80eR) and -0.625 (80eL), respectively.

The results obtained for the measured polarisation are $< P_\tau >= 0.501 \pm 0.010\ (\mathrm{stat.}) \pm 0.006\ (\mathrm{syst.})$ (80eR) and $< P_\tau >= -0.611 \pm 0.009\ (\mathrm{stat.}) \pm 0.005\ (\mathrm{syst.})$ (80eL).

The second benchmark analysis investigates top quark pair production at $\sqrt{s} = 500$ GeV, where both top quarks decay hadronically. The goal is to measure the cross-section, the top-quark mass and the forward-backward asymmetry (A^t_{FB}). Events are selected by requiring two b-tagged jets and the events being compatible with a six-jet configuration. The mass is then reconstructed applying a constrained kinematic fit to all pre-selected events and selecting only candidate events with a good fit probability. The top mass and cross-section is then extracted using a fit to the mass peak (see Figure II-11.2). This yields a top-quark mass of 173.918±0.053 GeV and a cross-section of 284.1±1.4 fb.

The forward-backward asymmetry measurement provides a window to new physics at the terascale [180]. A key tool for this analysis is the usage of the reconstructed vertex and jet charges. In this analysis both A^b_{FB} and A^t_{FB} are measured, yielding A^b_{FB}=0.293 ± 0.008 and A^t_{FB}=0.356 ± 0.008 assuming an integrated luminosity of 250 fb^{-1} with 80eR polarisation and 250 fb^{-1} of integrated luminosity with 80eL polarisation [181].

The last compulsory benchmark at $\sqrt{s}$ =500 GeV was a measurement of the masses of charginos and neutralinos in the processes $\mathrm{e^+e^-} \to \tilde{\chi}^+_1\tilde{\chi}^-_1 \to \mathrm{W^+W^-}\tilde{\chi}^0_1\tilde{\chi}^0_1$ and $\mathrm{e^+e^-} \to \tilde{\chi}^0_2\tilde{\chi}^0_2 \to \mathrm{ZZ}\tilde{\chi}^0_1\tilde{\chi}^0_1$. The analysis focused on the final states with four jets and missing energy and thereby focused on measuring the gaugino masses using di-jet final states from the two gauge bosons. The four reconstructed jets were then paired using a χ^2 fit maximising the compatibility with the two di-jet pairs having equal masses. This then also allows separating the $\tilde{\chi}^+_1\tilde{\chi}^-_1$ from the $\tilde{\chi}^0_2\tilde{\chi}^0_2$ process by using the obtained di-jet resolutions (see Figure II-11.2).

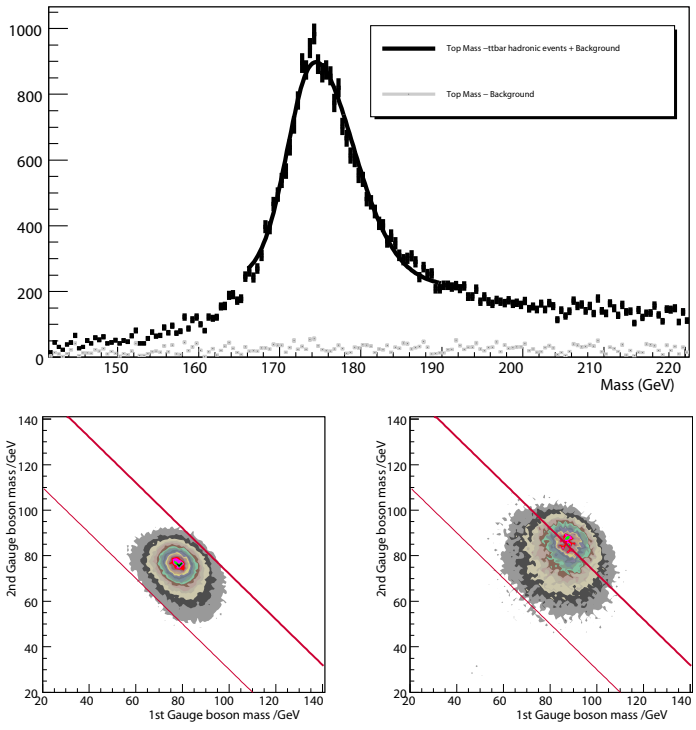

Figure II-11.2 Top analysis: Distribution of the top invariant mass after kinematic fitting (top). Chargino/neutralino analysis: The reconstructed boson masses from the four jets, selecting chargino events with a pure chargino signal (bottom left); and a pure neutralino signal (bottom right). The region between the two straight lines indicates the allowed chargino selection window.

The masses of the gauginos were then derived using a template fit to the energy distributions of the reconstructed bosons. For the $\tilde{\chi}^\pm_1$ and $\tilde{\chi}^0_1$ masses from the $\mathrm{e^+e^-} \to \tilde{\chi}^+_1\tilde{\chi}^-_1 \to \mathrm{W^+W^-}\tilde{\chi}^0_1\tilde{\chi}^0_1$ process the resulting mass uncertainties are 450 MeV and 160 MeV. Using the reaction $\mathrm{e^+e^-} \to \tilde{\chi}^0_2\tilde{\chi}^0_2 \to \mathrm{ZZ}\tilde{\chi}^0_1\tilde{\chi}^0_1$, uncertainties of 490 MeV and 280 MeV are obtained for the $\tilde{\chi}^0_2$ and $\tilde{\chi}^0_1$ masses, respectively, which

are larger due to the smaller cross-section for $e^+e^- \to \tilde{\chi}_2^0\tilde{\chi}_2^0$ and the lower sample purity.

In addition to these six compulsory benchmarks, SiD also looked into the $e^+e^- \to \tilde{b}\tilde{b},\ \tilde{b} \to b\tilde{\chi}_1^0$ process at $\sqrt{s} = 500$ GeV in scenarios where the sbottom is the next-to-lightest supersymmetric particle (NLSP) [182]. It has been shown, that SiD has sensitivity for this scenario up to sbottom masses close to the kinematic limit [177].

11.2 DBD Benchmark Reactions

For the DBD three additional benchmarks at $\sqrt{s} = 1$ TeV have been defined [183] using a Higgs mass of 125 GeV and a data sample of 1 ab^{-1}. For half of this data sample 80% right-handed electron polarisation and 20% left-handed positron polarisation were assumed. 80% left-handed electron polarisation and 20% right-handed positron polarisation were assumed for the other half of the integrated luminosity.

The first benchmark is the process $e^+e^- \to t\bar{t}h$, where the Higgs decays into $b\bar{b}$. The final states include eight jets (all-hadronic) and six jets, a lepton and missing energy (semi-leptonic). The aim is to measure the top Yukawa-coupling.

The second benchmark is a measurement of the Standard Model Higgs boson branching ratios into $b\bar{b}$, $c\bar{c}$, W^+W^-, gg and $\mu^+\mu^-$ using the $e^+e^- \to \nu_e\bar{\nu}_e h$ production process.

The last benchmark is a measurement of the forward $e^+e^- \to W^+W^-$ pair cross-section considering both hadronic and leptonic decays of the W^+W^- pairs. The goal is to measure in situ the effective left-handed polarisation $(1-P_{e^-})(1+P_{e^+})/4$ for each of the two polarisation configurations.

Additionally, one benchmark from the LOI was repeated using the DBD detector layout and the updated simulation and reconstruction software. The $e^+e^- \to t\bar{t}$ process at $\sqrt{s} = 500$ GeV was chosen for this purpose.

The DBD benchmark results presented in this chapter correspond to our present level of understanding and can be refined further. This holds in particular for the measurement of the Higgs to $c\bar{c}$ decay, where possibilities for further improvement of the analysis have already been identified.

11.2.1 Event Generation

11.2.1.1 Monte Carlo event generators

The event generation was carried out in common for SiD and ILD. The WHIZARD Monte Carlo event generator was used for the generation of all $2 \to n$ processes, $n = 2...6$, where n is the number final state fermions (e, μ, τ, u, d, s, c, b), and the two initial state particles are e^+e^-, $e^+\gamma$, $e^-\gamma$, or $\gamma\gamma$. The $t\bar{t}h$ signal process and the eight fermion backgrounds were generated using the PHYSSIM Monte Carlo program. All event samples were generated with 100% polarisation for the initial state electron and positron. The Higgs branching ratios listed in [184] were assumed for the event generation. A complete review of the event generation process is given in the chapter on common tasks and issues.

11.2.1.2 Generated signal and background samples

Events from files with different 100% initial state polarisations and possibly different final states were combined at generator level to form "mixed files" with 80% electron and 20% (30%) positron polarisation for $\sqrt{s} = 1000$ (500) GeV. Only these mixed files were used as input to the full simulation and reconstruction in SiD. All mixed files are summarised in Table II-11.2.

Separate mixed background files were generated for the eight-fermion final states and for the dominant $\nu\bar{\nu}h$ backgrounds, while everything else was combined together in the "all other SM processes" sample. The composition of the events in the "all other SM processes" sample is shown in Table II-11.3.

All Monte Carlo samples were processed using the full simulation of the SIDLOI3 detector. Beam-induced backgrounds from $\gamma\gamma \to$ hadrons interactions and incoherent e^+e^- pairs were mixed

Table II-11.2 Overview of the mixed samples used as input for the full detector simulation and reconstruction.

Process	$\sqrt{s}$ (GeV)	N_{Events} (10^6)	$\mathcal{L}$ (ab^{-1})
$\mathrm{t\bar{t}h}$	1000	0.4	52
$\mathrm{t\bar{t}}Z$, $\mathrm{t\bar{t}}g^*$	1000	0.4	15
$\mathrm{t\bar{t}}$	1000	1.0	2.0
$\nu\bar{\nu}\mathrm{h}$, $\mathrm{h} \to \mathrm{b\bar{b}}$, $\mathrm{c\bar{c}}$, WW^*, gg	1000	3.1	7.4
$\nu\bar{\nu}\mathrm{h}$, $\mathrm{h} \to \mu^+\mu^-$	1000	0.5	6400
$\mathrm{e}\nu\mathrm{W}$, eeZ, $\nu\nu\mathrm{Z} \to \mathrm{e}\nu\mathrm{qq}$, eeqq, $\nu\nu\mathrm{qq}$	1000	4.0	0.034
eeZ, $\nu\nu\mathrm{Z}$, $\mathrm{W^+W^-} \to \mathrm{ee}\mu\mu$, $\nu\nu\mu\mu$	1000	1.0	0.004
$\mathrm{W^+W^-}$	1000	6.0	2.0
all other SM processes	1000	6.0	$1 \cdot 10^5 - 1.0$
$\mathrm{t\bar{t}}$	500	2.0	1.0 for each m_{top}
$\mathrm{t\bar{t}}$ background SM processes	500	2.0	varies
TOTAL		26	

Table II-11.3 Contents of the "all other SM processes" mixed sample at $\sqrt{s} = 1$ TeV. The weights of the individual processes were calculated assuming an integrated luminosity of $1\ \mathrm{ab}^{-1}$ for each of the two polarisations.

Process	$\mathcal{L}$ (ab^{-1}) per pol.	$N_{Events}(10^5)$ P($\mathrm{e}^-/\mathrm{e}^+$) $= -0.8/+0.2$	$N_{Events}(10^5)$ P($\mathrm{e}^-/\mathrm{e}^+$) $= +0.8/-0.2$	Weight
$\mathrm{e}\gamma \to \mathrm{e}\gamma$	$4 \cdot 10^{-5}$	0.5	0.5	$2.5 \cdot 10^{+4}$
$\mathrm{e^+e^-} \to 2f, 4f$	0.034	3.7	2.0	29
$\mathrm{e}\gamma \to 3f$	0.003	3.5	3.1	330
$\mathrm{e}\gamma \to 5f$	0.25	3.1	2.1	4
$\mathrm{e^+e^-} \to 6f$	1.0	1.8	0.6	1
$\gamma\gamma \to 2f$	0.001	5.7	5.7	7700
$\gamma\gamma \to 4f$	0.083	2.5	2.5	12
$\gamma\gamma \to$ minijets:				
$4 < p_\mathrm{T} < 40$ GeV	0.012	9.2	9.2	$80 - 9000$
$p_\mathrm{T} > 40$ GeV	0.105	2.3	2.3	12

with the physics events for all event samples. More details on the detector simulation and on the properties of the machine-induced backgrounds are given in Chapter 10.

11.2.2 Analysis Tools

In the following, the software tools common to more than one of the DBD detector benchmark analyses are described.

11.2.2.1 Jet finding

To reconstruct jets in hadronic final states, the Durham algorithm as implemented in LCFIPlus or the k_t algorithm from the FastJet [185, 186] package were used. Especially for the reconstruction of jets in the forward direction, where the contribution from beam-related backgrounds is larger, the k_t algorithm developed for hadron collisions is more suitable. This has already been demonstrated for the CLIC CDR [129]. More details and the parameters used for the jet finding are given in the descriptions of the individual analyses.

11.2.2.2 Multivariate analysis tools

The traditional approach in high energy physics to separate a signal from backgrounds is based on a set of fixed cuts. However, for complex final states and large backgrounds this method is often not optimal. Hence multivariate analysis techniques like artificial neutral networks or boosted decision trees (BDTs) are commonly used today. The implementations of these models in the TMVA [187] software package were used for the benchmark analyses described in the following unless explicitly stated otherwise.

11.2.3 Measurement of the top Yukawa coupling

The measurement of the cross-section for the process $e^+e^- \to t\bar{t}h$ using two different final states is described in the following [188]. The Feynman diagrams for this process are shown in Figure II-11.3. Here h is a Standard Model Higgs boson of mass 125 GeV. The diagram shown on the left represents the dominant contribution to the cross-section.

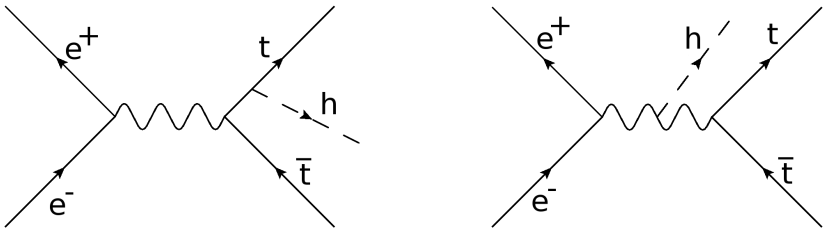

Figure II-11.3 Diagrams for $t\bar{t}h$ production in e^+e^- collisions.

Hence the measurement of the $t\bar{t}h$ cross-section at the ILC allows a direct extraction of the top Yukawa coupling, y_t, with good precision. The contribution to the cross-section from Higgs radiation off the intermediate Z boson represents a small correction which needs to be taken into account in the extraction of y_t from the measured cross-section. In the analysis presented here, the Higgs decay $h \to b\bar{b}$ is considered.

Two final states are investigated in the following:

- **8 jets:** In this case both W bosons decay hadronically. Hence this final state contains eight jets out of which four originate from b-quark decays.
- **6 jets:** Here one W boson decays hadronically and the other W boson decays leptonically. The final state contains four b-jets, two further jets, an isolated lepton and missing energy. Only electrons and muons are considered as isolated leptons in the final state.

This study requires jet clustering in complex hadronic final states, missing energy reconstruction, flavour-tagging and reconstruction and identification of high energy leptons. Hence it represents a comprehensive check of the complete analysis chain and overall detector performance.

Table II-11.4 Production cross-sections times branching ratios or production cross-sections for the signals and for the considered backgrounds. All samples were generated assuming a Standard Model Higgs mass of 125 GeV. The numbers for "other $t\bar{t}h$" processes in this table do not include either of the signal final states (see text). The $t\bar{t}Z$ and $t\bar{t}g^*$ samples do not contain events where both top quarks decay leptonically. The $t\bar{t}$ samples contain all possible decays of both top quarks.

Type	Final state	P(e^-)	P(e^+)	Cross-section [× BR] (fb)
Signal	$t\bar{t}h$ (8 jets)	-80%	+20%	0.87
Signal	$t\bar{t}h$ (8 jets)	+80%	-20%	0.44
Signal	$t\bar{t}h$ (6 jets)	-80%	+20%	0.84
Signal	$t\bar{t}h$ (6 jets)	+80%	-20%	0.42
Background	other $t\bar{t}h$	-80%	+20%	1.59
Background	other $t\bar{t}h$	+80%	-20%	0.80
Background	$t\bar{t}Z$	-80%	+20%	6.92
Background	$t\bar{t}Z$	+80%	-20%	2.61
Background	$t\bar{t}g^* \to t\bar{t}b\bar{b}$	-80%	+20%	1.72
Background	$t\bar{t}g^* \to t\bar{t}b\bar{b}$	+80%	-20%	0.86
Background	$t\bar{t}$	-80%	+20%	449
Background	$t\bar{t}$	+80%	-20%	170

An overview of the cross-sections for the signal final states as well as for the considered backgrounds is shown in Table II-11.4. For the measurement in the final state with six jets all other $t\bar{t}h$ events, i.e. all events where both top quarks decay leptonically or hadronically, or events where the Higgs boson does not decay into $b\bar{b}$, are treated as background. For the eight jets final state events where at least one top quark decays leptonically or where the Higgs boson does not decay into $b\bar{b}$ are considered as background.

11.2.3.1 Event reconstruction

As a first step of the event reconstruction chain, isolated leptons are searched for. The particle flow objects (PFOs) identified as muons or electrons are excluded from the jet reconstruction procedure. Only PFOs in the range $20^\circ < \theta < 160^\circ$ are considered in the following, because the particles originating from the signal processes are located in the central part of the detector while the beam-related backgrounds peak in the forward direction. The Durham jet clustering algorithm is used in the exclusive mode with six or eight jets. A b-tag value is obtained for each jet.

To form W, top and Higgs candidates from the reconstructed jets, the following function is minimised for the final state with eight jets:

$$\frac{(M_{12}-M_{\mathrm{W}})^2}{\sigma_{\mathrm{W}}^2}+\frac{(M_{123}-M_{\mathrm{t}})^2}{\sigma_{\mathrm{t}}^2}+\frac{(M_{45}-M_{\mathrm{W}})^2}{\sigma_{\mathrm{W}}^2}+\frac{(M_{456}-M_{\mathrm{t}})^2}{\sigma_{\mathrm{t}}^2}+\frac{(M_{78}-M_{\mathrm{h}})^2}{\sigma_{\mathrm{h}}^2}, \quad \text{(II-11.1)}$$

where M_{12} and M_{45} are the invariant masses of the jet pairs used to reconstructed the W candidates, M_{123} and M_{456} are the invariant masses of the three jets used to reconstruct the top candidates and M_{78} is the invariant mass of the jet pair used to reconstruct the Higgs candidate. M_{W}, M_t and M_{h} are the nominal W, top and Higgs masses. The resolutions σ_{W}, σ_{t} and σ_{h} were obtained from reconstructed jet combinations matched to W, top and Higgs particles at generator level. The corresponding function minimised for the six jets final state is given by:

$$\frac{(M_{12}-M_{\mathrm{W}})^2}{\sigma_{\mathrm{W}}^2}+\frac{(M_{123}-M_{\mathrm{t}})^2}{\sigma_{\mathrm{t}}^2}+\frac{(M_{45}-M_{\mathrm{h}})^2}{\sigma_{\mathrm{h}}^2}. \quad \text{(II-11.2)}$$

11.2.3.2 Event selection

Events were selected using boosted decision trees as implemented in TMVA (see Section 11.2.2.2). The BDTs were trained separately for the eight and six jet final states.

The following input variables were used:

- the four highest b-tag values;
- the event thrust;
- a transition value from the Durham algorithm. For the six jet final state $Y_{6\to5}$ is used while $Y_{8\to7}$ is used for the eight jet final state;
- the number of reconstructed PFOs in the range $20^\circ < \theta < 160^\circ$;
- the number of identified isolated electrons or muons;
- the missing transverse momentum calculated from the reconstructed jets;
- the total visible energy defined as the scalar sum of all jet energies;
- the masses M_{12}, M_{123} and M_{45} as defined above.

For the eight jet final state two additional variables are included:

- M_{456} and M_{78} as defined above.

The output values of the BDTs for the signals and the different backgrounds are shown in Figure II-11.4 for both final states. To select events, cuts on the BDT output values are applied. The cuts were optimised by maximising the signal significance given by: $\frac{S}{\sqrt{S+B}}$, where S is the number of signal events and B is the number of background events. As an example, the reconstructed top and Higgs masses in six jet events after the cut on the BDT output are shown in Figure II-11.5. The selection efficiencies for signal events are 42% and 54% for the six and eight jet final states, respectively.

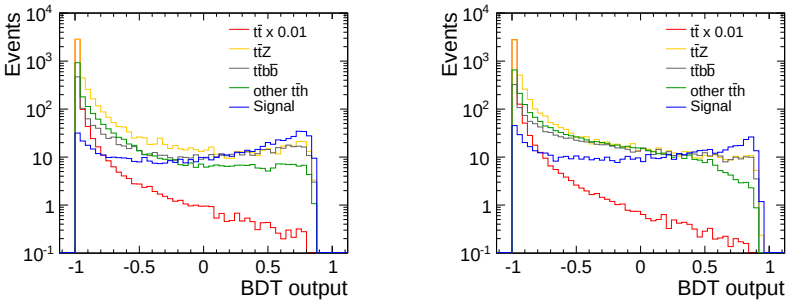

Figure II-11.4 Output distributions of the BDTs for the eight (left) and six (right) jet final states. The signals are shown in blue while the backgrounds are shown in different colours. The distribution for $\mathrm{t\bar{t}}$ was scaled by a factor 0.01.

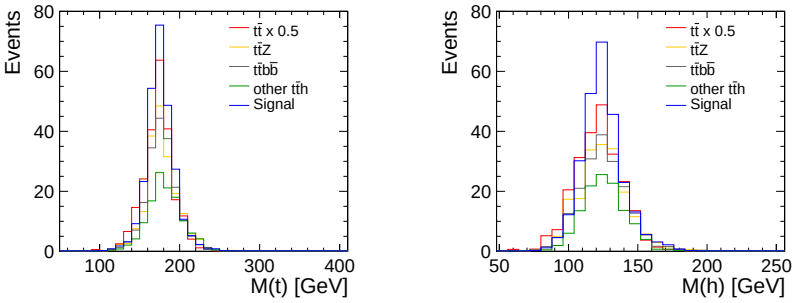

Figure II-11.5 Reconstructed top (left) and Higgs (right) masses for selected (BDT output $>$ 0.1978) six jet events. The signal is shown in blue while the backgrounds are shown in different colours. The distribution for $\mathrm{t\bar{t}}$ was scaled by a factor 0.5.

11.2.3.3 Results on the cross-section and top Yukawa coupling

The cross-section can be directly obtained from the number of background-subtracted signal events after the event selection. Assuming an integrated luminosity of 1 ab^{-1}, the cross-section can be measured with a statistical accuracy of 11.5% using the eight jet final state and with a statistical accuracy of 13.2% for the six jet final state. As a cross check, the analysis was repeated preselecting events with one isolated lepton for the six jet final state and events without isolated leptons for the eight jet final state. The differences in precision compared to the nominal analysis are negligible.

To extract the top Yukawa coupling from the measured cross-sections, signal Monte Carlo samples with different values of the top Yukawa coupling were generated. The dependence of the cross-section on the value of the coupling was fitted using a quadratic function. The following relation was found: $\frac{\Delta y_t}{y_t} = 0.52 \cdot \frac{\Delta\sigma}{\sigma}$. The factor between the cross-section uncertainty and the coupling uncertainty differs from 0.5 due to the contribution from Higgsstrahlung to the $\mathrm{t\bar{t}h}$ production cross-section. The uncertainties of the measured cross-sections translate to precisions on the top Yukawa coupling of 6.0% and 6.9% from the eight and six jet final states, respectively.

If both measurements are combined, the top Yukawa coupling can be extracted with a statistical accuracy of 4.5%. For 1 ab^{-1} of data with only P(e^-) = -80%, P(e^+) = +20% polarisation, this number would improve to 4.0%. The precision for the six jets final state could be improved further if τ-leptons were included in the reconstruction.

11.2.4 Higgs branching fractions

Here the process to be studied is $\mathrm{e^+e^-} \to \nu_\mathrm{e}\bar{\nu}_\mathrm{e}\mathrm{h}$ at $\sqrt{s}$ =1 TeV, where h is a SM Higgs boson of mass 125 GeV. The $\nu_\mathrm{e}\bar{\nu}_\mathrm{e}\mathrm{h}$ final state occurs in the WW fusion (see Figure II-11.6) and Higgsstrahlung processes. This benchmark study provides a test of jet energy resolution, missing energy reconstruction, flavour-tagging, and reconstruction and identification of electrons and muons in the forward region.

The cross-section times branching ratio for the Standard Model Higgs boson decays into $\mathrm{b\bar{b}}$, $\mathrm{c\bar{c}}$, $\mathrm{W^+W^-}$, gg and $\mu^+\mu^-$ has been measured using the $\mathrm{e^+e^-} \to \nu_\mathrm{e}\bar{\nu}_\mathrm{e}\mathrm{h}$ production process. We focus on the WW fusion process which dominates at high energies since the cross-section grows as $\log(s)$. The datasets used for this analysis are shown in Table II-11.5.

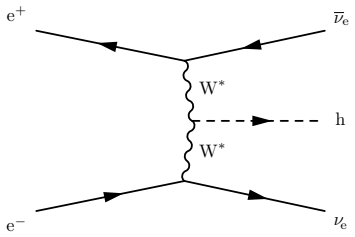

Figure II-11.6
Higgs production through the WW fusion process. Unlike the Higgsstrahlung interaction, the WW fusion interaction has a cross-section that grows as $\log(s)$ which results in making it the dominant interaction at $\sqrt{s}$ =1 TeV.

Table II-11.5
Simulated data samples used for the $\nu_e\bar{\nu}_e h$ analysis.

Process	$P(e^-)/P(e^+)$	N_{Events}
Higgs	-80%/+20%	1,544,378
	+80%/-20%	1,544,398
$evW + eeZ + vvZ$ semileptonic	-80%/+20%	6,570,292
	+80%/-20%	5,080,159
All other SM background mix	-80%/+20%	3,232,672
	+80%/-20%	2,814,719

The analysis of the Higgs boson decays to $b\bar{b}$, $c\bar{c}$, W^+W^- and gg are described first (see Section 11.2.4.1), followed by a section dedicated to $\mu^+\mu^-$ (see Section 11.2.4.4).

11.2.4.1 Event reconstruction for $h \to b\bar{b}, c\bar{c}, W^+W^-, gg$

To reconstruct events in the decay topology consistent with the two particle Higgs decays with no other visible event activity in the WW fusion interactions, events are clustered into two jets using the exclusive k_t algorithm. This algorithm clusters particles apparently from beam activity into a beam jet thus avoiding introduction of those particles into the rest of the analysis.

Figure II-11.7
Visible mass distributions for the backgrounds and $\nu_e\bar{\nu}_e h$ events for the various Higgs decay modes.

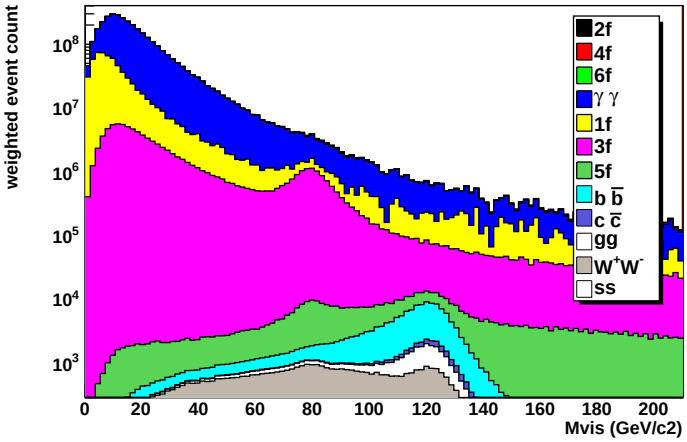

The jet clustering size parameter used for the exclusive k_t algorithm was chosen to be 1.5 based on the visible mass resolutions. The visible mass distributions for the backgrounds and the $\nu_e\bar{\nu}_e h$ decay modes are shown in Figure II-11.7. From this figure one can see the poor reconstruction of the $h \to W^+W^-$ events. To address this, the PFO objects are used from the jets obtained when using the k_t algorithm with a jet size parameter, R, of 0.7 and clustering into six jets. This was found to improve the rejection of beam particles.

The flavour-tagging is used as implemented in the LCFIPlus package which uses boosted decision trees on vertexing quantities to determine b-tag and c-tag probabilities for bottom and charm jets respectively. It is trained using samples of two-jet events from $Z \to b\bar{b}, c\bar{c}$ and $q\bar{q}$ at $\sqrt{s} = 250$ GeV and the tagging is accordingly applied to all signal and background samples.

11.2.4.2 Event Selection for $h \to b\bar{b}, c\bar{c}, W^+W^-, gg$

Events are preselected based on the Higgs decay mode being studied using the criteria shown in Table II-11.6.

Table II-11.6 Overview of the preselections for the different Higgs decay modes. The cuts as well as the efficiencies for signal and background events are shown.

Higgs decay	Preselection cuts	Signal eff.	Background eff.
$h \to b\bar{b}$	$50 < p_{vis}^T < 250$ GeV $100 < E_{vis} < 400$ GeV $110 < M_{vis} < 140$ GeV $\lvert\cos(\theta_{jet})\rvert < 0.90$ $N_{tracks} > 15$ b-tag$_{1,2} > 0.2$	21.6%	1.3×10^{-6}
$h \to c\bar{c}$	$50 < p_{vis}^T < 250$ GeV $150 < E_{vis} < 400$ GeV $115 < M_{vis} < 135$ GeV $\lvert\cos(\theta_{jet})\rvert < 0.95$ $10 < N_{tracks} < 50$ b-tag$_{1,2} < 0.8$	12.2%	1.3×10^{-6}
$h \to gg$	$50 < p_{vis}^T < 250$ GeV $150 < E_{vis} < 400$ GeV $100 < M_{vis} < 140$ GeV $\lvert\cos(\theta_{jet})\rvert < 0.90$ $N_{tracks} > 20$ b-tag$_{1,2} < 0.8$ $M_{jet,2} > 20$ GeV	16.1%	4.8×10^{-6}
$h \to W^+W^-$	$50 < p_{vis}^T < 250$ GeV $150 < E_{vis} < 400$ GeV $100 < M_{vis} < 140$ GeV $\lvert\cos(\theta_{jet})\rvert < 0.90$ $N_{tracks} > 15$ b-tag$1, 2 < 0.8$ $M_{jet,2} > 40$ GeV	7.5%	7.4×10^{-6}

After the preselection, Fisher discriminants, as implemented in TMVA, are then used to maximise the significance ($S/\sqrt{S+B}$) of the selection. They are trained using 10% of the signal and background events and done separately for the different polarisations and integrated luminosities. The cuts on the Fisher discriminant which maximise the significance for each decay mode are used to obtain the final results. The input variables for Fisher discriminants are given by:

- the b-tag and c-tag values of both jets;
- the masses and energies of both jets;
- the number of reconstructed PFOs;
- the number of high-momentum isolated electrons;
- the visible energy, mass and transverse momentum;
- the cosines of the polar angles of both jets;
- the angle between both jets in the plane perpendicular to the beam axis.
- the c-tag value divided by the sum of the b-tag and c-tag values for each jet (for $h \to c\bar{c}$ only)

The probability distributions for example Higgs decay modes are shown in Figure II-11.8. Plots showing the efficiency and significance curves vs. cuts on the Fisher discriminant output are shown in Figure II-11.9.

The composition of the samples of events passing all selections of the analysis are shown in Table II-11.7 for the polarisation P(e^-) = -80%, P(e^+) = +20% and an integrated luminosity of 500 fb^{-1}.

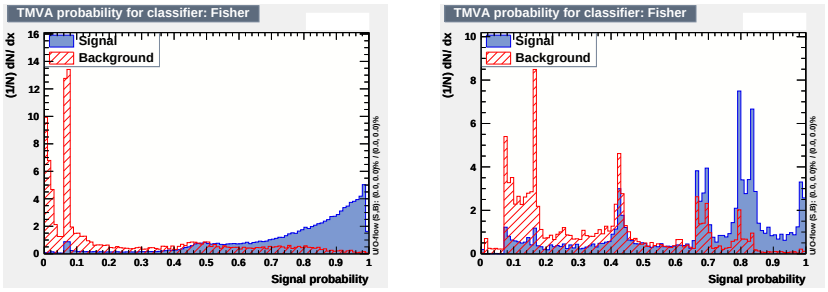

Figure II-11.8
Probability distributions for selecting Higgs boson decays to $b\bar{b}$ (left) and $c\bar{c}$ (right) from the Fisher Discriminant.

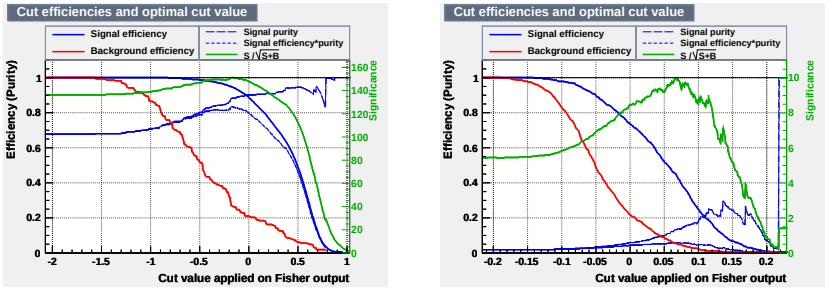

Figure II-11.9
Efficiency and significance curves vs. cuts on the MVA Fisher discriminant output for the $h \to b\bar{b}$ (left) and $c\bar{c}$ selections (right).

The visible mass distribution for the $h \to b\bar{b}$ selected events with the visible mass preselection cut removed is shown in Figure II-11.10 for an integrated luminosity of 500 fb^{-1} and the P(e^-) = -80%, P(e^+) = +20% polarisation.

Table II-11.7
Composition of the events passing all analysis selections for each of the four Higgs decay mode studied in this analysis for the polarisations P(e^-) = -80%, P(e^+) = +20% and integrated luminosity of 500 fb^{-1}.

	$h \to b\bar{b}$ (%)	$h \to c\bar{c}$ (%)	$h \to gg$ (%)	$h \to W^+W^-$ (%)
$e^+e^- \to 2$ fermions	0.14	0.40	0.14	0.00
$e^+e^- \to 4$ fermions	6.41	22.3	19.6	20.0
$e^+e^- \to 6$ fermions	0.23	2.30	2.38	2.64
$\gamma\gamma \to X$	1.19	8.11	11.0	11.9
$\gamma e^+ \to X$	3.03	15.3	18.1	19.3
$e^-\gamma \to X$	3.80	23.5	28.5	28.3
$h \to b\bar{b}$	83.7	7.00	0.36	0.96
$h \to c\bar{c}$	0.28	12.6	0.45	0.65
$h \to gg$	0.50	1.42	15.2	2.81
$h \to WW^*$	0.17	6.03	3.8	12.3

11.2.4.3 Results for $h \to b\bar{b}, c\bar{c}, W^+W^-, gg$

The uncertainties on the cross sections times Higgs branching fractions, $\Delta(\sigma \times BR)$, are determined from the numbers of signal and background events passing each selection. The uncertainties for both polarisation configurations assuming an integrated luminosity of 500 fb^{-1} and for P(e^-) = -80%, P(e^+) = +20% polarisation for an integrated luminosity of 1 ab^{-1} at $\sqrt{s}$ =1 TeV are shown in Table II-11.8. For 1 ab^{-1} of integrated luminosity the precision for the $b\bar{b}$ final state is about 0.5%. For the W^+W^- and gg final states precisions of about 3% can be reached while the $c\bar{c}$ decay can currently be reconstructed with a precision of 7.6%. Given the results from the detector's flavour tagging performance studies, it is felt that ongoing efforts to refine the analysis of $h \to c\bar{c}$ will certainly lead to significant improvements in the error on $\sigma \times BR(h \to c\bar{c})$.

In Table II-11.9 the results obtained when not including the backgrounds from $\gamma\gamma$ interactions or with five fermion final states are shown to illustrate the impact of these contributions. The precision for the $c\bar{c}$ decay improves by 20% while all other Higgs decays are only marginally affected. Such backgrounds can be reduced in practice by optimising the forward detector design to minimise the incoherent e^+e^- pair background, and through the inclusion of the Detector Integrated Dipole.

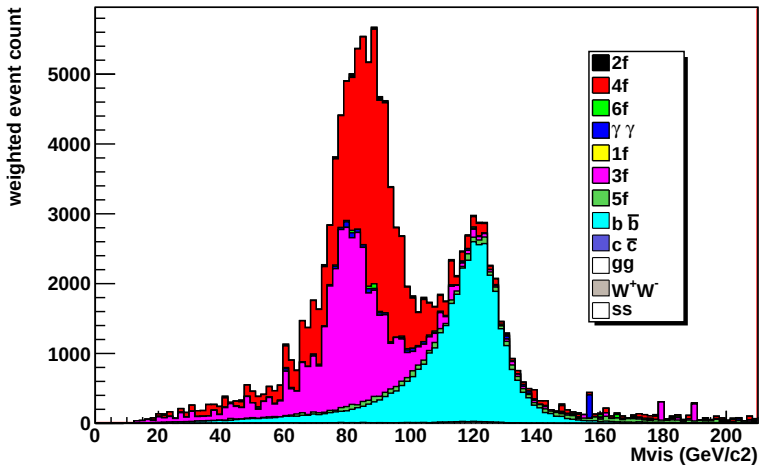

Figure II-11.10
The visible mass distribution for the $h \to b\bar{b}$ selected events without the visible mass preselection cut for 500 fb^{-1} and the $P(e^-)$ = -80%, $P(e^+)$ = +20% polarisation configuration.

Table II-11.8
Relative uncertainties on the Higgs $\sigma \times BR$ expected at $\sqrt{s}$ =1 TeV using the SiD detector with integrated luminosities of 500 fb^{-1} and 1 ab^{-1} and polarisation sets $P(e^-)$ = -80%, $P(e^+)$ = +20% and $P(e^-)$ = +80%, $P(e^+)$ = -20%.

	$\mathcal{L}$ = 500 fb^{-1}		$\mathcal{L}$ = 1 ab^{-1}
	$P(e^-)$ = -80%, $P(e^+)$ = +20%	$P(e^-)$ = +80%, $P(e^+)$ = -20%	$P(e^-)$ = -80%, $P(e^+)$ = +20%
$h \to b\bar{b}$	0.0067	0.046	0.0047
$h \to c\bar{c}$	0.108	0.843	0.076
$h \to gg$	0.044	0.294	0.031
$h \to W^+W^-$	0.047	0.346	0.033

11.2.4.4 Event selection and results for $h \to \mu^+\mu^-$

Higgs boson decays to $\mu^+\mu^-$ are selected by requiring that there be two and only two muons in the event, that they have opposite charge, that the sum of their energies be less than 400 GeV, that the closest distance of approach of each muon to the primary event vertex be less than 7 microns in the plane transverse to the beam direction, and that the sum of the transverse momenta of the two muons be greater than 100 GeV.

In addition, the total missing energy in the event must be greater than 450 GeV, the total missing transverse momentum must be greater than 55 GeV, the number of charged particle flow objects with energy greater than 15 GeV must be less than 4, and there must not be any electrons with energy greater than 15 GeV. The muon pair invariant mass distribution following these cuts is shown for signal and background in Figure II-11.11.

The cross section times branching ratio is measured by counting the number of events with $\mu^+\mu^-$ mass in the range $124 < M_{\mu^+\mu^-} < 126$ GeV. The number of events for signal and background in this mass window is shown in Table II-11.10. For background processes the number of events in the mass window $124 < M_{\mu^+\mu^-} < 126$ GeV is calculated under the assumption that the $\mu^+\mu^-$ mass distribution is flat in the range $115 < M_{\mu^+\mu^-} < 145$ GeV. The error on the cross section times branching ratio for $h \to \mu^+\mu^-$ under different assumptions for background and luminosity is summarised in Table II-11.11.

Table II-11.9
Relative uncertainties on the Higgs $\sigma \times BR$ expected at $\sqrt{s}$ =1 TeV using the SiD detector with integrated luminosities of 500 fb^{-1} and 1 ab^{-1} and polarisation sets $P(e^-)$ = -80%, $P(e^+)$ = +20% and $P(e^-)$ = +80%, $P(e^+)$ = -20% with the five fermion and $\gamma\gamma$ backgrounds removed.

	$\mathcal{L}$ = 500 fb^{-1}		$\mathcal{L}$ = 1 ab^{-1}
	$P(e^-)$ = -80%, $P(e^+)$ = +20%	$P(e^-)$ = +80%, $P(e^+)$ = -20%	$P(e^-)$ = -80%, $P(e^+)$ = +20%
$h \to b\bar{b}$	0.0065	0.026	0.0046
$h \to c\bar{c}$	0.100	0.733	0.071
$h \to gg$	0.040	0.234	0.028
$h \to W^+W^-$	0.042	0.260	0.030

Figure II-11.11
Muon pair mass for $\mathrm{h} \to \mu^+\mu^-$ (left) and for all Standard Model background (right) following all cuts. The plots are normalised to 1 ab^{-1} luminosity.

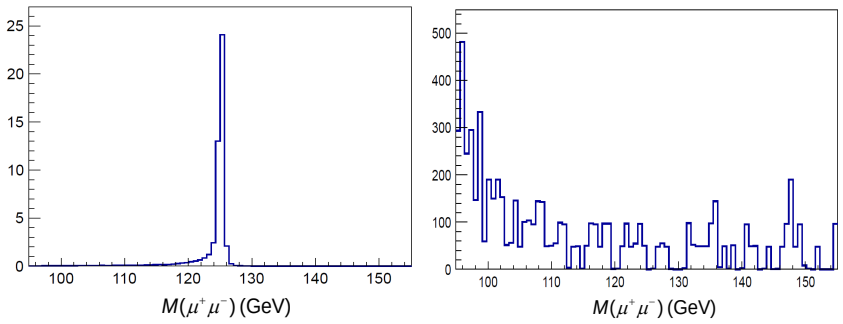

Table II-11.10
Number of events passing all cuts with $124 < M_{\mu^+\mu^-} < 126$ GeV for 500 fb^{-1} luminosity. The error from Monte Carlo statistics is indicated. The number of events for $e^-\gamma$ processes includes events from the γe^+ charge conjugate process.

Process	N_{Events}
$\mathrm{e^+e^-} \to \nu_\mathrm{e}\bar{\nu}_\mathrm{e}\mathrm{h} \to \nu_e\bar{\nu}_e\mu^+\mu^-$	20.0 ± 0.1
$\mathrm{e^+e^-} \to \nu_e\bar{\nu}_e\mu^+\mu^-$	17.4 ± 5.3
$\mathrm{e^+e^-} \to \nu_\mu\bar{\nu}_\mu\mu^+\mu^-$	7.9 ± 3.5
$\mathrm{e^+e^-} \to \nu_\tau\bar{\nu}_\tau\mu^+\mu^-$	1.6 ± 1.6
$\mathrm{e^+e^-} \to t\bar{t} \to b\bar{b}\nu_\mu\bar{\nu}_\mu\mu^+\mu^-$	0.8 ± 0.2
$\mathrm{e^+e^-} \to \nu_\tau\bar{\nu}_\mu\tau^+\mu^-$	0.2 ± 0.1
$\gamma\gamma \to \nu_\mu\bar{\nu}_\mu\mu^+\mu^-$	29.3 ± 6.7
$e^-\gamma \to e^-\nu_\mu\bar{\nu}_\mu\mu^+\mu^-$	4.8 ± 2.7
$e^-\gamma \to \nu_e\nu_\mu\bar{\nu}_\mu\mu^-\mu^+\mu^-$	1.6 ± 1.6
$e^-\gamma \to \nu_e\bar{\nu}_\mu\mu^-\mu^+\mu^-$	0.2 ± 0.2
$\mathrm{e^+e^-} \to q\bar{q}\nu_\mu\bar{\nu}_\mu\mu^+\mu^-, q \neq b$	0.2 ± 0.1

11.2.5 Measurement of beam polarisation using $\mathrm{W^+W^-}$ pairs

The baseline ILC design at $\sqrt{s}$ =1 TeV includes longitudinal electron and positron beam polarisations of 80% and 20% respectively. Polarimeters upstream and downstream of the collision point measure the average beam polarisation before and after collision, but cannot provide an estimate of the luminosity weighted beam polarisation without complex modelling of the beam collision process. Physics processes that are sensitive to beam polarisation, however, can directly measure the luminosity weighted beam polarisation.

The process $\mathrm{e^+e^-} \to \mathrm{W^+W^-}$ is very sensitive to beam polarisation. It is dominated by t-channel neutrino exchange in the forward region, where only left-handed electrons and right-handed positrons contribute, and continues to exhibit polarisation dependence in the central and backward regions through s-channel diagrams. The production of $\mathrm{W^+W^-}$ in the forward region has the advantage of high statistics and negligible sensitivity to new physics.

The primary objective of this benchmark is the measurement of the effective left- and right-handed polarisations

$$P_{\mathrm{e^-}}(L)_{\mathrm{eff}} = \frac{(1-P_{\mathrm{e^-}})(1+P_{\mathrm{e^+}})}{4}\,, \qquad P_{\mathrm{e^-}}(R)_{\mathrm{eff}} = \frac{(1+P_{\mathrm{e^-}})(1-P_{\mathrm{e^+}})}{4}$$

Table II-11.11
Cross section times branching ratio resolution for $\mathrm{h} \to \mu^+\mu^-$ under different luminosity and background assumptions. The Monte Carlo statistical error for each entry in the table is shown.

Background Processes	L (fb^{-1})	$N_{\mathrm{background}}$	N_{signal}	$\frac{\Delta(\sigma\times BR)}{\sigma\times BR}$
$\mathrm{e^+e^-} \to f\bar{f}$, $f\bar{f}f\bar{f}$, $t\bar{t}$ only	500	28.0 ± 6.5	20.0 ± 0.1	0.35 ± 0.02
	1000	56.0 ± 13.0	40.0 ± 0.2	0.24 ± 0.02
all background	500	64.1 ± 9.9	20.0 ± 0.1	0.46 ± 0.03
	1000	128.2 ± 19.8	40.0 ± 0.2	0.32 ± 0.02

through a measurement of the W production and decay angles Θ and θ in $e^+e^- \to W^+W^- \to q\bar{q}q\bar{q}$, $q\bar{q}l^-\bar{\nu}$ at $\sqrt{s}$ =1 TeV in the forward region with $0.8 < \cos\Theta$. This measurement is made independently for two different configurations, $(P_{e^-}, P_{e^+}) = (-0.8, 0.2)$, $(+0.8, -0.2)$ assuming 500 fb^{-1} integrated luminosity for each configuration. This benchmark study provides a test of jet reconstruction of boosted W bosons in forward regions, jet energy resolution, differential luminosity measurement, and reconstruction and identification of leptons in the forward region.

Once $P_{e^-}(L)_{\rm eff}$ and $P_{e^-}(R)_{\rm eff}$ have been measured the actual electron and positron polarisations P_{e^-} and P_{e^+} can be extracted using the relations

$$P_{e^-} = b - a \pm \sqrt{(b-a)^2 - 2(a+b) + 1}$$
$$P_{e^+} = P_{e^-} - 2(b-a) \ .$$

where $a = P_{e^-}(L)_{\rm eff}$ and $b = P_{e^-}(R)_{\rm eff}$. The sign ambiguity is resolved using knowledge of the signs of the beam polarisations.

The production angle Θ is defined to be the polar angle of the W^- in the W^+W^- rest frame. No attempt is made to measure the charges of the hadronically decaying W's in the fully hadronic topology $W^+W^- \to q\bar{q}q\bar{q}$, and so $|\cos\Theta|$ is used in this case. The charge of the decay lepton determines the charge of the W for the semileptonic topology $e^+e^- \to W^+W^- \to q\bar{q}l^-\bar{\nu}$.

For the semileptonic topology the decay angle θ is defined to be the polar angle of the fermion in the W^- rest frame ($W^- \to l^-\bar{\nu}$) or the antifermion in the W^+ rest frame ($W^+ \to l^+\nu$). For the fully hadronic topology $|\cos\theta|$ is used where θ is the polar angle of either of the two jets in the W^- rest frame. The effective right handed polarisation $P_{e^-}(R)_{\rm eff}$ is measured rather poorly in the forward region $0.8 < \cos\Theta$ due to the dominance of the polarisation configuration with left-handed electrons and right handed positrons. Therefore the effective polarisation parameters $P_{e^-}(L)_{\rm eff}$ and $P_{e^-}(R)_{\rm eff}$ are also measured using the entire solid angle $-1 < \cos\Theta < 1$, with the caveat that the result is only valid for Standard Model W^+W^- production. Only the semileptonic topology is used for measuring the polarisation outside the forward region.

Finally, it can also be assumed that the magnitudes of the beam polarisations do not change as the signs of the polarisations are changed. In this case data from the two polarisation configurations $(P_{e^-}, P_{e^+}) = (-0.8, 0.2)$, $(+0.8, -0.2)$ can be combined in order to measure $|P_{e^+}|$and $|P_{e^-}|$. The measured parameters $P_{e^-}(L)_{\rm eff}$ and $P_{e^-}(R)_{\rm eff}$ are replaced by

$$\alpha = \frac{(1+|P_{e^-}|)(1+|P_{e^+}|)}{4} \ , \qquad \beta = \frac{(1-|P_{e^-}|)(1-|P_{e^+}|)}{4}$$

and the absolute polarisation values are given by

$$|P_{e^-}| = \alpha - \beta \pm \sqrt{(\alpha-\beta)^2 - 2(\alpha-\beta) + 1}$$
$$|P_{e^+}| = 2(\alpha-\beta) - P_{e^-} \quad .$$

11.2.5.1 Event reconstruction

Particle Flow Objects (PFOs) were used as input to the analysis. Isolated electrons, muons and photons must be identified to separate W pairs from background processes and to classify a W^+W^- event as semileptonic or fully hadronic. The algorithm to identify isolated objects loops through electrons, muons and photons with $p_T > 25$ GeV, removes them one at a time from the PFO list, and performs the inclusive k_t jet algorithm with R=0.7 on the modified PFO list.

For each inclusive jet with $E_{\rm jet}/E_{\rm lepton} > 2E_{\rm lepton}$ the variable $\rho = 2E_{\rm lepton}(1 - \cos\theta_{\rm jet-lepton})$ is calculated where $\theta_{\rm jet-lepton}$ is the angle between the lepton and the jet. If the minimum value of ρ over

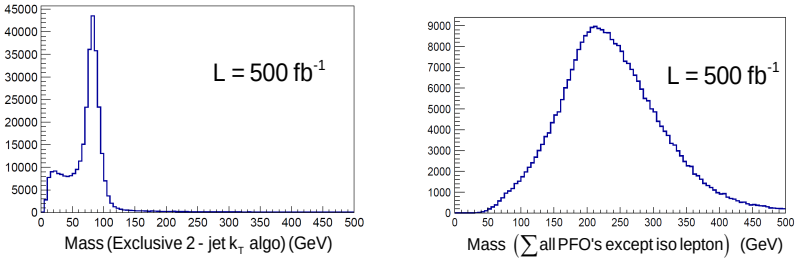

Figure II-11.12 Mass of the hadronically decaying W in semileptonic $\mathrm{W^+W^-}$ events using the two jets from the exclusive k_t jet algorithm (left) and using all PFO objects other than the isolated charged lepton (right). The broad and displaced mass distribution on the right results from including PFO objects arising from background processes.

all jets is greater than 2 then the object is said to be isolated. Further event reconstruction depends on whether an event contains one or zero isolated objects. If an event contains zero isolated electron, muons and photons, then the 4-jet exclusive k_t jet algorithm with R=0.7 is applied to the PFO list. The three jet pair combinations are considered, and the one that minimises $(M_{12}-M_{\mathrm{W}})^2+(M_{34}-M_{\mathrm{W}})^2$ is chosen to represent the $\mathrm{W^+W^-}$ in the fully hadronic mode. The exclusive mode of the k_t jet algorithm is used because it discards beam jets and returns only central jets. In this way the $\gamma\gamma \to \mathrm{hadrons}$ background is minimised [129].

If an event contains one isolated electron or muon and no other isolated object then the lepton is removed from the PFO list and the 2-jet exclusive k_t jet algorithm with R=0.7 is performed using the modified PFO list. The di-jet system returned by the k_t jet algorithm represents the hadronically decaying W in the semileptonic $\mathrm{W^+W^-}$ topology. The neutrino from the leptonically decaying W is reconstructed assuming that the $\mathrm{W^+W^-}$ is produced back-to-back: $\vec{p}_\nu = -(\vec{p}_{\mathrm{lepton}} + \vec{p}_{\mathrm{2jet}})$.

11.2.5.2 Event selection

Semileptonic $\mathrm{W^+W^-}$ events are selected by requiring that there be exactly one isolated electron or muon, that the total number of PFO's in the hadronically decaying W (the two jets returned by the two-jet exclusive k_t jet algorithm) be greater than 12, that the mass of the hadronically decaying W be greater than 60 GeV and less than 100 GeV, that the mass of the leptonically decaying W be less than 250 GeV, and that the energy of the hadronically decaying W be greater than 300 GeV. The cut on mass of the leptonically decaying W is required to remove $\gamma e^- \to \nu W^-$ events. Such events can provide interesting polarisation information, but are considered beyond the scope of this benchmark.

The reconstructed mass of the hadronically decaying W in semileptonic events is shown in Figure II-11.12 along with the mass obtained by summing together all PFO objects with the exception of the charged lepton. The effectiveness of the 2-jet exclusive k_t jet algorithm in removing $\gamma\gamma \to \mathrm{hadrons}$ is clear. The number of signal and background events following these cuts is summarised in Table II-11.12.

Table II-11.12 Number of events passing semileptonic $\mathrm{W^+W^-}$ cuts for 500 $\mathrm{fb^{-1}}$ luminosity.

Type	Solid Angle	P($\mathrm{e^-}$)	P($\mathrm{e^+}$)	N_{Events}
Signal	$0.8 < \cos\Theta < 1.0$	-80%	+20%	204031
Signal	$-1 < \cos\Theta < 0.8$	-80%	+20%	58912
Signal	$0.8 < \cos\Theta < 1.0$	+80%	-20%	16090
Signal	$-1 < \cos\Theta < 0.8$	+80%	-20%	5315
Background	$0.8 < \cos\Theta < 1.0$	-80%	+20%	7994
Background	$-1 < \cos\Theta < 0.8$	-80%	+20%	7053
Background	$0.8 < \cos\Theta < 1.0$	+80%	-20%	5173
Background	$-1 < \cos\Theta < 0.8$	+80%	-20%	4962

Fully hadronic $\mathrm{W^+W^-}$ events are selected by requiring that there be no isolated electron, muon or photon, that the total number of PFO's in the two hadronically decaying W's (the four jets returned by the four-jet exclusive k_t jet algorithm) be greater than 28, that the mass of each of the

hadronically decaying W's be greater than 55 GeV and less than 105 GeV, and that the sum of the energies of the two hadronically decaying W be greater than 600 GeV. The number of signal and background events following these cuts is summarised in Table II-11.13.

Table II-11.13 Number of events passing fully hadronic W^+W^- cuts for 500 fb^{-1} luminosity.

Type	Solid Angle	P(e^-)	P(e^+)	N_{Events}
Signal	$0.8 < \|\cos\Theta\| < 1.0$	-80%	+20%	296813
Signal	$0.8 < \|\cos\Theta\| < 1.0$	+80%	-20%	22967
Background	$0.8 < \|\cos\Theta\| < 1.0$	-80%	+20%	31764
Background	$0.8 < \|\cos\Theta\| < 1.0$	+80%	-20%	12548

11.2.5.3 Beam Polarisation Measurements

The effective polarisation parameters $P_{e^-}(L)_{\rm eff}$ and $P_{e^-}(R)_{\rm eff}$ are extracted by counting events in bins of $(\cos\Theta, \cos\theta)$ and fitting for $P_{e^-}(L)_{\rm eff}$ and $P_{e^-}(R)_{\rm eff}$ with a linear least squares fit:

$$\chi^2 = \sum_i \frac{(N_i - (a\mu_i + b\nu_i)L)^2}{N_i}$$

where N_i is the number of events in bin i, L is the integrated luminosity

$$\mu_i = \int d\vec{x}_i d\vec{x'} \eta(\vec{x'}) \Omega(\vec{x}_i, \vec{x'}) \frac{d\sigma_{LR}}{d\vec{x'}}$$
$$\nu_i = \int d\vec{x}_i d\vec{x'} \eta(\vec{x'}) \Omega(\vec{x}_i, \vec{x'}) \frac{d\sigma_{RL}}{d\vec{x'}}$$

$\eta(\vec{x})$ is the detection efficiency, $\Omega(\vec{x}_i, \vec{x'})$ is the resolution function, and $d\sigma_{LR}/d\vec{x}$ and $d\sigma_{RL}/d\vec{x}$ are the true differential cross-sections for 100% polarised beams for signal *and* background. The background must be included in this way since it in general has a polarisation dependence.

There is no need to separately calculate $\eta(\vec{x})$ and $\Omega(\vec{x}_i, \vec{x'})$ since the parameters μ_i and ν_i are linearly related to the bin contents of a $(\cos\Theta, \cos\theta)$ histogram of fully simulated Monte Carlo events. Let M_{ki} be the number of events in bin i from a Monte Carlo sample produced with effective beam polarisations a_k and b_k and luminosity L_k. The SiD Monte Carlo samples were produced with $(P_{e^-}, P_{e^+}) = (-0.8, +0.2)$ $(k = 1)$ and $(P_{e^-}, P_{e^+}) = (+0.8, -0.2)$ $(k = 2)$. The parameters μ_i and ν_i are then given by

$$\mu_i = \frac{1}{a_1 b_2 - a_2 b_1}\left[b_2 \frac{M_{1i}}{L_1} - b_1 \frac{M_{2i}}{L_2}\right], \qquad \nu_i = \frac{1}{a_1 b_2 - a_2 b_1}\left[-a_2 \frac{M_{1i}}{L_1} + a_1 \frac{M_{2i}}{L_2}\right].$$

Ten divisions each are used for $\cos\Theta$ and $\cos\theta$ so that 100 bins are defined for each of the two event topologies, semileptonic and fully hadronic. A total of 200 bins are then used for the least squares fit of the effective polarisations $P_{e^-}(L)_{\rm eff}$ and $P_{e^-}(R)_{\rm eff}$ or α and β. The errors on the effective polarisations are displayed in Table II-11.14 along with the errors on the actual polarisations P_{e^-} and P_{e^+}.

Table II-11.14 Polarisation errors assuming 500 fb^{-1} luminosity for each initial state polarisation configuration.

$\cos\Theta$ range	P_{e^-}, P_{e^+}	$\Delta P_{e^-}(L)_{\rm eff}$	$\Delta P_{e^-}(R)_{\rm eff}$	ΔP_{e^-}	ΔP_{e^+}
$0.8 < \cos\Theta < 1$	-0.8,+0.2	0.0011	0.022	0.13	0.087
$0.8 < \cos\Theta < 1$	+0.8,-0.2	0.00036	0.0096	0.0050	0.024
$-1 < \cos\Theta < 1$	-0.8,+0.2	0.0011	0.0104	0.062	0.041
$-1 < \cos\Theta < 1$	+0.8,-0.2	0.00036	0.0077	0.0045	0.020
$\cos\Theta$ range	P_{e^-}, P_{e^+}	$\Delta\alpha$	$\Delta\beta$	$\Delta\|P_{e^-}\|$	$\Delta\|P_{e^+}\|$
$-1 < \cos\Theta < 1$	sum	0.0010	0.00032	0.0020	0.0029

11.2.6 Top quark cross-section and forward-backward asymmetry

11.2.6.1 Introduction

The top quark is the heaviest elementary particle known. The explanation for its large mass may come from beyond the Standard Model physics [189, 190]. Generally, models predict that due to its large mass, the top quark couples strongly to the particle(s) that generate the spontaneous symmetry breaking of the electroweak interaction. As such, it is important to measure the characteristics of the top quark with high precision.

In this analysis, we investigate the determination of the cross-section and the forward-backward asymmetries for both the b and $\overline{\mathrm{b}}$ quarks and t and $\bar{\mathrm{t}}$ quarks using the fully hadronic $\mathrm{t\bar{t}}$ decay mode ($\mathrm{e^+e^-} \to \mathrm{t\bar{t}} \to \mathrm{b\bar{b}q\bar{q}q\bar{q}}$). The forward-backward asymmetry is defined in Equation II-11.3.

$$A_{FB} = \frac{\sigma(\theta < 90^o) - \sigma(\theta > 90^o)}{\sigma(\theta < 90^o) + \sigma(\theta > 90^o)} \tag{II-11.3}$$

where $\sigma(\theta < 90^o)$ is the cross-section of the events in which the b or t quark has a polar angle of less than 90° in the centre-of-mass frame of reference.

11.2.6.2 Event Selection

The event selection presented in this study is closely based on an earlier study [181]. We require that jets be composed of at least two reconstructed particles in order to reject semi-leptonic $\mathrm{t\bar{t}}$ decays and other SM backgrounds. The total energy originating from the six jets is required to be greater than 400 GeV in order to suppress events with leptons and neutrinos. We also require that each event has a particle and track multiplicity greater than 80 and 30, respectively.

The next step of the event selection is to identify the two b-jets in the signal event, which is achieved by using the LCFIPlus package [170]. The importance of correctly identifying the b-jets is twofold: to reduce the SM background and to reduce the number of combinations required to reconstruct the full signal event. As such, we require that the jet with the highest b-tag value be greater than 0.9 and the jet with the second highest b-tag value be greater than 0.4. Once the b-jets are identified, the remaining jets are assumed to be associated with the W boson hadronic decays. The top quark mass is determined using a kinematic fitting approach with constraints listed in Table II-11.15. The combination with the smallest χ^2 is selected as the proper event configuration. The results from the kinematic fitting algorithm are presented in Figure II-11.13. Finally, we require that the reconstructed mass of the top quark candidates is between 150 GeV and 200 GeV, yielding a final signal efficiency of $27.3 \pm 0.1\%$. The signal efficiency was determined by using the Monte Carlo truth information to identify the $\mathrm{e^+e^-} \to \mathrm{t\bar{t}} \to \mathrm{b\bar{b}q\bar{q}q\bar{q}}$ decay chain within the generic ($\mathrm{e^+e^-} \to \mathrm{b\bar{b}}\ 4f$).

Table II-11.15
The kinematic constraints used in the $\mathrm{t\bar{t}}$ analysis.

$m(\mathrm{top}_1)$	=	$m(\mathrm{top}_2)$
$m(W_1)$	=	80.4 GeV
$m(W_2)$	=	80.4 GeV
$m(b_1)$	=	5.8 GeV
$m(b_2)$	=	5.8 GeV
E_{tot}	=	$\sqrt{s}$
$\vec{p}_{tot}$	=	0

After the event selection, the cross-section for $\mathrm{e^+e^-} \to \mathrm{t\bar{t}} \to \mathrm{b\bar{b}q\bar{q}q\bar{q}}$ was calculated using Equation II-11.4.

$$\sigma = \frac{N_{tot} - N_{bkg}}{\epsilon_{sig} \int \mathcal{L} dt} \tag{II-11.4}$$

Here N_{tot} is the number of total events that survive all selection cuts, N_{bkg} is the estimated background events after the selection cuts,

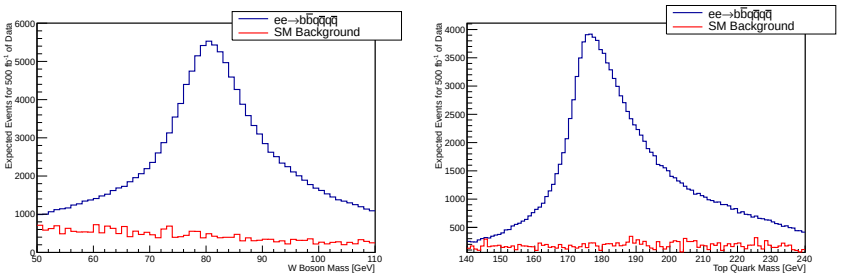

Figure II-11.13
Mass distribution of the W boson candidates (left) and top quark candidates (right).

ϵ_{sig} is the signal efficiency, and $\int \mathcal{L}dt$ is the integrated luminosity. The statistical uncertainty on the cross-section, assuming 500 fb^{-1} of integrated data, was calculated to be approximately 0.47% and 0.69% for the P(e^-) = +0.8, P(e^+) = -0.3 and P(e^-) = -0.8, P(e^+) = +0.3 polarisation configuration, respectively.

11.2.6.3 Forward-Backward Asymmetry

In order to determine the forward-backward asymmetry, the charges of the bottom and top quarks must be determined. Based on the previous studies [181], the vertex charge and the jet charge are the two variables that are used in determining the quark charge. The vertex charge is determined by calculating a momentum weighted charge using the tracks associated to the secondary vertex within the identified b-jet, as defined in Equation II-11.5.

$$Q = \frac{\sum_j p_j^k Q_j}{\sum_j p_j^k} \tag{II-11.5}$$

Here p_j^k and Q_j are the momentum and the charge of the j-th track and $k = 0.3$ is a power weight. Similarly, the jet charge is also calculated using Equation II-11.5, however, it is determined by using all the tracks associated to a b-jet. These two variables are combined to provide a single discriminate variable, C, as defined in Equation II-11.6.

$$C = \frac{1-r}{1+r}; \qquad r = \prod_i \frac{f_i^{\bar{b}}(x_i)}{f_i^b(x_i)} \tag{II-11.6}$$

Here $f_i^b(x_i)$ and $f_i^{\bar{b}}(x_i)$ is the probability density function for variable x_i for the b and $\bar{b}$ quarks, respectively.

The calculation of A_{FB} for the top quarks can be performed by using the effective charge of the b-quark jets from Equation II-11.6 and the angle θ of the reconstructed top quark. The corrected number of top quarks in each hemisphere is calculated using Equation II-11.7.

$$N_b = (N_{tot} - N_{bkg}) \cdot \epsilon_p \cdot \epsilon_{sig} \tag{II-11.7}$$

Here, N_{tot} is the total number of events, N_{bkg} is the background events, ϵ_p is the purity, and ϵ_{sig} is the signal efficiency. The purity and signal efficiency was determined by using the Monte Carlo truth information to identify the $\mathrm{e}^+\mathrm{e}^- \to \mathrm{t\bar{t}} \to \mathrm{b\bar{b}q\bar{q}q\bar{q}}$ decay chain within the generic ($\mathrm{e}^+\mathrm{e}^- \to \mathrm{b\bar{b}}\ 4f$). Finally, we require that the product of the two effective charges is negative. As a result, the expected statistical uncertainty of the top quark forward-backward asymmetry, assuming 500 fb^{-1} of integrated data, is approximately 2% and 2.5% for the P(e^-) = +0.8, P(e^+) = -0.3 and P(e^-) = -0.8, P(e^+) = +0.3 polarisation configuration, respectively. These numbers agree with the MC input value and previous studies [181].

11.2.6.4 Conclusion

The achievable cross-section resolution for the top quark at the ILC in the $e^+e^- \to t\bar{t} \to b\bar{b}q\bar{q}q\bar{q}$ channel is less than 1% for a total luminosity of 500 fb^{-1}. Additionally, in the case of both polarised beam configurations the achievable resolution for the top quark asymmetries is approximately 2%.

11.3 Additional Benchmarks

To illustrate the importance of the BeamCal, an additional benchmark study was performed.

11.3.1 Measurement of scalar tau leptons

One of the processes whose detection is very difficult at the LHC but easier at the ILC is $\tilde{\tau}$ production [191]. In this benchmark, the $\tilde{\tau}^{\pm}$ production and decay has been studied [192] at $\sqrt{s} = 500$ GeV for the kinematically accessible benchmark points B', C', D', G', and I' as proposed in [193]. At these points, the LSP is the $\tilde{\chi}_1^0$, and the NLSP is the $\tilde{\tau}^{\pm}$, with the masses shown in Table II-11.16. Having similar masses, the two particles are a candidate for the co-annihilation mechanism that can explain the WMAP relic dark-matter density. It is therefore important to identify and measure the mass of the NLSP, as well as the LSP. Several studies of the $\tilde{\tau}^{\pm}$ at the ILC have already been made. These include an analysis at D' [194], an analysis at SPS1a' [195], and a much broader analysis covering many parameter points [196].

Table II-11.16
SUSY Particle Masses (GeV) for the kinematically accessible benchmark points at $\sqrt{s} = 500$ GeV [193].

Model	B'	C'	D'	G'	I'
$\tilde{\tau}^-$	110.6	170.6	223.9	158.6	144.6
$\tilde{\chi}_1^0$	96.5	161.0	216.4	150.9	140.8

At the benchmark points analysed here, the $\tilde{\tau}^{\pm}$ has only one decay channel: $\tilde{\tau}^{\pm} \to \tau^{\pm}\tilde{\chi}_1^0$. The production of τ leptons via the two-photon process $e^+e^- \to e^+\gamma^*e^-\gamma^* \to e^+e^-\tau^+\tau^-$ is by far the most significant background process, and the BeamCal is an essential detector to veto two-photon events by detecting high energy scattered e^+e^- beam particles. Figure II-11.14 shows the detection efficiency as a function of radius in the BeamCal for 5, 15, 30, 50, 100, and 150 GeV electrons. As the beamstrahlung energy has a strong radial and azimuthal dependence, the detection efficiency is calculated as a function of the distance from the outgoing beam axis at three azimuthal angles (0, 90, and 180 degrees). The inefficiency between 30 and 50 mm at $\phi = 180°$ is due to the incoming beam hole. Since the beamstrahlung background energy is the highest at $\phi \approx 90°$ (and $270°$), the detection efficiency is lower in this angular region. The efficiency to detect electrons with energy above 150 GeV is almost 100% up to 8 mrad from the beam axis.

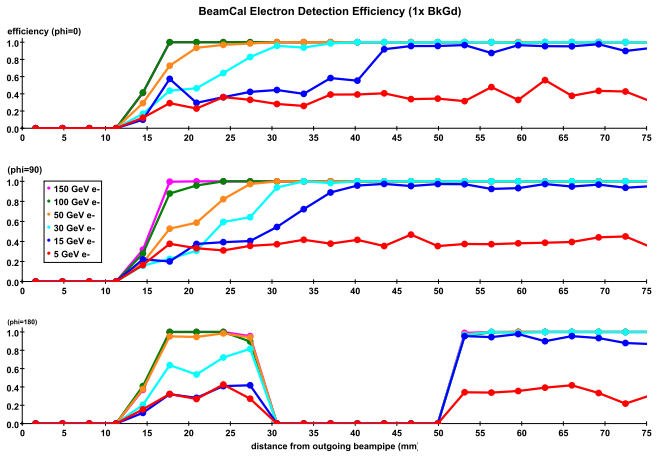

Figure II-11.14
The BeamCal detection efficiency of electrons, at various energies and angles, as a function of distance from the outgoing beam.

Events are grouped based on their vectorially combined transverse momentum, and it is expected that the SUSY events will often have higher vectorially combined momentum due to the momentum carried away by the $\tilde{\chi}_1^0$. Detection of the $\tilde{\tau}^{\pm}$ by these methods relies on a significant mass difference between the $\tilde{\tau}^{\pm}$ and the $\tilde{\chi}_1^0$. If the mass difference between the $\tilde{\tau}^{\pm}$ and $\tilde{\chi}_1^0$ is not large enough, the visible τs will not have sufficient scalar momentum to be visible above the two-photon process (even if the visible products have a preferred direction). For this reason a cut is made on the acoplanarity of the two jets in the plane perpendicular to the beampipe. The requirements that the mass of each jet is less than 1.8 GeV and the number of charged particles in each jet is either one or three, serve to select $\tau^{\pm}$ events and eliminate other processes such as $\mathrm{hZ} \rightarrow$ hadrons.

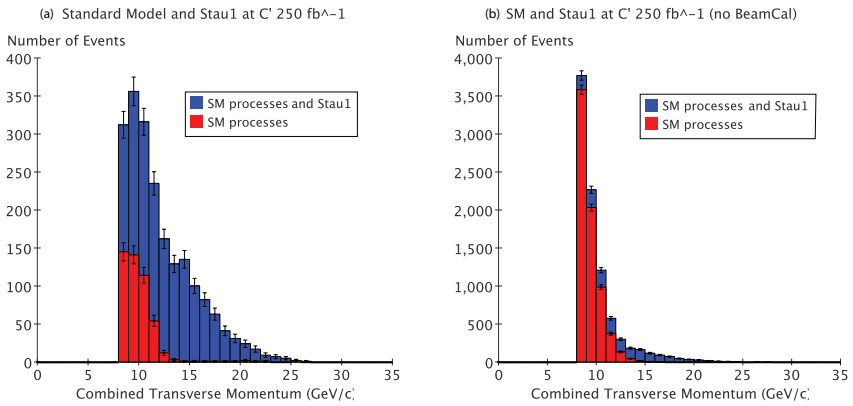

Figure II-11.15 Fill event p_{T} distribution with (left) and without (right) the BeamCal veto at the benchmark point C'.

Figure II-11.15 shows the transverse momentum of combined SM and $\tilde{\tau}^{\pm}$ events (blue) and the SM backgrounds (red) at the benchmark point C' using a data sample based on an integrated luminosity of 250 fb^{-1} at $\sqrt{s} = 500$ GeV. Figure II-11.15 (left) shows the distribution when the BeamCal is used to veto SM backgrounds, while Figure II-11.15 (right) shows the distribution without the veto. A significant excess of $\tilde{\tau}^{\pm}$ signal is observable over SM backgrounds only when the BeamCal is used as a veto. The mass difference between $\tilde{\tau}^{\pm}$ and $\tilde{\chi}_1^0$ is 9.6 GeV at the benchmark point C', and it is possible to measure the $\tilde{\tau}^{\pm}$ mass with a 1 GeV uncertainty.

Figure II-11.16 shows the transverse momentum of combined SM and $\tilde{\tau}^{\pm}$ events (blue) and the SM backgrounds (red) at the benchmark point I' using a data sample based on an integrated luminosity of 250 fb^{-1} at $\sqrt{s} = 500$ GeV. Figure II-11.16 (left) shows the distribution when the BeamCal is used to veto SM backgrounds, while Figure II-11.16 (right) shows when the BeamCal is not used. Although the $\tilde{\tau}^{\pm}$ signal can be enhanced when the BeamCal is used for a veto, the mass difference between the $\tilde{\tau}^{\pm}$ and the $\tilde{\chi}_1^0$ is only 3.8 GeV at this benchmark point I' and the signal is not very visible even after applying the BeamCal veto.

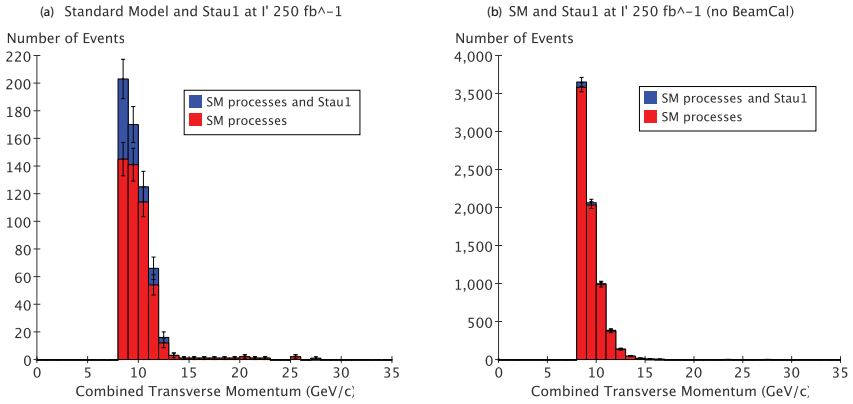

Figure II-11.16 p_{T} distribution with BeamCal veto (left) and without (right) at the benchmark point I')

Table II-11.17. Summary of the SiD benchmarking results. The LOI Higgs results were obtained assuming a polarisation of P(e^-) = +80%, P(e^+) = -30% while the the total luminosity was equally divided between P(e^-) = $\mp$80%, P(e^+) = $\pm$30% for the LOI $t\bar{t}$ and $\tau^+\tau^-$ results. The $t\bar{t}h$ and W^+W^- results assume P(e^-) = -80%, P(e^+) = +20% for half of the integrated luminosity and P(e^-) = +80%, P(e^+) = -20% for the other half. For the $\nu_e\bar{\nu}_e h$ studies only P(e^-) = -80%, P(e^+) = +20% was considered. The DBD $t\bar{t}$ analysis assumes both P(e^-) = $\mp$80%, P(e^+) = $\pm$30%.

Process $e^+e^- \to$	$\sqrt{s}$ (GeV)	$\mathcal{L}$ (fb^{-1})	SiD	Meas. Quant.	Unit	Result
$e^+e^-h/\mu^+\mu^-h$	250	250	LOI	m_H	GeV	$\pm$ 0.04
				σ	%	$\pm$ 2.7
$hZ^0 \to c\bar{c}q\bar{q}$	250	250	LOI	BR	%	$\pm$ 6.0
$hZ^0 \to c\bar{c}\nu\bar{\nu}$	250	250	LOI	BR	%	$\pm$ 11.0
$hZ^0 \to \mu^+\mu^- q\bar{q}$	250	250	LOI	σ	%	89.1
$\tau^+\tau^-$	500	500	LOI	$A^\tau{}_{FB}$	-	$\pm$ 0.0021/0.0024
				$< P_\tau >$	%	$\pm$ 1.7/2.3
$t\bar{t} \to 6$ jets	500	500	LOI	m_{top}	GeV	173.92 $\pm$ 0.05
				σ	%	0.49
				$A^t{}_{FB}$	-	$\pm$ 0.008
$\tilde{\chi}^0_2\tilde{\chi}^0_2 \to \tilde{\chi}^0_1\tilde{\chi}^0_1 Z^0Z^0$	500	500	LOI	$m_{\tilde{\chi}^0_1}$	GeV	$\pm$ 0.16
$\tilde{\chi}^0_2\tilde{\chi}^0_2 \to \tilde{\chi}^0_1\tilde{\chi}^0_1 Z^0Z^0$	500	500	LOI	$m_{\tilde{\chi}^+_1}$	GeV	$\pm$ 0.45
$\tilde{\chi}^+_1\tilde{\chi}^-_1 \to \tilde{\chi}^0_1\tilde{\chi}^0_1 W^+W^-$	500	500	LOI	$m_{\tilde{\chi}^0_1}$	GeV	$\pm$ 0.28
$\tilde{\chi}^+_1\tilde{\chi}^-_1 \to \tilde{\chi}^0_1\tilde{\chi}^0_1 W^+W^-$	500	500	LOI	$m_{\tilde{\chi}^0_2}$	GeV	$\pm$ 0.49
$t\bar{t}h$ (6 jets)	1000	1000	DBD	σ	%	$\pm$ 13.2
$t\bar{t}h$ (8 jets)	1000	1000	DBD	σ	%	$\pm$ 11.5
$t\bar{t}h$ (combined)	1000	1000	DBD	σ	%	$\pm$ 8.7
$\nu_e\bar{\nu}_e h; h \to WW^*$	1000	1000	DBD	$\sigma \times$ BR	%	$\pm$ 3.3
$\nu_e\bar{\nu}_e h; h \to gg$	1000	1000	DBD	$\sigma \times$ BR	%	$\pm$ 3.1
$\nu_e\bar{\nu}_e h; h \to c\bar{c}$	1000	1000	DBD	$\sigma \times$ BR	%	$\pm$ 7.6
$\nu_e\bar{\nu}_e h; h \to b\bar{b}$	1000	1000	DBD	$\sigma \times$ BR	%	$\pm$ 0.47
$\nu_e\bar{\nu}_e h; h \to \mu^+\mu^-$	1000	1000	DBD	$\sigma \times$ BR	%	$\pm$ 32
W^+W^-	1000	1000	DBD	$P_{e^-}(L)_{\rm eff}$	%	$\pm$ 0.20/0.90
W^+W^-	1000	1000	DBD	$\lvert P_{e^-}\rvert$	%	$\pm$ 0.25
W^+W^-	1000	1000	DBD	$\lvert P_{e^+}\rvert$	%	$\pm$ 1.45
$t\bar{t} \to 6$ jets	500	500	DBD	σ	%	$\pm$ 0.47/0.69
				$A^t{}_{FB}$	%	$\pm$ 2.0/2.5

Similarly, good signal-to-noise was achieved by the application of the BeamCal veto for the benchmark points B', C', and G', where the mass difference between $\tilde{\tau}^\pm$ and $\tilde{\chi}^0_1$ is about 10 GeV, while the $\tilde{\tau}^\pm$ signal was not strong enough for mass measurements for the benchmark points D' and I', where the mass difference is about 5 GeV.

11.4 Benchmarking Summary

A large set of benchmarks have been conducted with the SiD detector using both simulations of the LOI and the more detailed DBD detector variants. They illustrate the detector performance of the SiD concept for centre-of-mass energies in the range from 250 GeV up to 1 TeV. All results obtained have been summarised in Table II-11.17.

Chapter 12
SiD Costs

12.1 Introduction

The SiD cost estimate is a construction cost estimate; it does not include R&D, commissioning, operating costs, or physicist salaries.

The SiD design process has continuously monitored costs using a parametric cost model. This tool has been essential for the ongoing detector optimisation process. At various stages, detector parameters (e.g. dimensions or masses) have been transferred to a Work Breakdown Structure where it is more convenient to describe a subsystem to arbitrary levels of detail. Here we describe this method of costing for the DBD version of SiD.

Table II-12.1
Unit Costs agreed to by SiD, ILD, and CLIC [197].

	agreed unit cost (US-$)	agreed error margin (US-$)
Tungsten for HCAL	105/kg	45/kg
Tungsten for ECAL	180/kg	75/ kg
Steel for Yoke	1000/t	300/t
Stainless Steel for HCAL	4500/t	1000/t
Silicon Detector	6 / cm^2	2 / cm^2

The SiD baseline for the DBD has been changed from RPC's to scintillator bars for the muon system (see Chapter 5), which is also included in the costing model.

At the time of the LOI, the cost optimisation of the global SiD design was studied by using a parametric model of PFA based jet energy resolution and the parametric cost tools described here. The tracker radius, B field, and HCAL depth were varied holding the jet energy resolution fixed at 3.78% for 180 GeV jets. The cost optimal point was quite near the baseline SiD parameters of R = 1.25 m, B = 5 T, and HCAL $\lambda_I = 4.5$. This work has not been repeated.

12.2 Parametric cost model

The parametric model of the detector is a large set of Excel spreadsheets that first maintain a self consistent model of SiD. It is straightforward to vary parameters ranging from the most basic, such as the tracker radius and aspect ratio, to parameters such as the number of tracking layers, the number and thickness of HCAL layers, and calorimeter radiator material. The tracking layers and disks are adjusted to fit the allocated space.The calorimeter inner radii and minimal z coordinate are adjusted for the tracker size, and thicknesses are set parametrically. The solenoid model is adjusted for its radius and field, and the flux return is adjusted to roughly contain the return flux.

For each system, the cost driving component count, such as tungsten plate, silicon detectors, and readout chips for the ECAL, are calculated. The model has tables for material costs and estimates both M&S and labour costs that are associated with the actual scale of SiD.

Costs that are approximately fixed, for example, engineering, fixturing, or solenoid He plants, are imported from the separate Work Breakdown Structure program. Finally, a set of macros calculate the costs of SiD as parameters are varied. The cost process also develops a Work Breakdown

Table II-12.2
Summary of Costs per Subsystem.

	M&S Base (M US-$)	M&S Contingency (M US-$)	Engineering (MY)	Technical (MY)	Admin (MY)
Beamline Systems	3.7	1.4	4.0	10.0	
VXD	2.8	2.0	8.0	13.2	
Tracker	18.5	7.0	24.0	53.2	
ECAL	104.8	47.1	13.0	288.0	
HCAL	51.2	23.6	13.0	28.1	
Muon System	8.3	3.0	5.0	22.1	
Electronics	4.9	1.6	44.1	41.7	
Magnet	115.7	39.7	28.3	11.8	
Installation	4.1	1.1	4.5	46.0	
Management	0.9	0.2	42.0	18.0	30.0
	314.9	126.7	186.0	532.1	30.0

Structure using the SLAC program WBS. WBS facilitates the description of the costs as a hierarchical breakdown with increasing levels of detail. Separate tables describe cost estimates for purchased M&S and labour. These tables include contingencies for each item, and these contingencies are propagated by WBS. The M&S costs are estimated in 2008 US-$ except for those items described in Table II-12.1.

Labour is estimated in man-hours or man-years as convenient. The WBS had about 50 labour types, but they are condensed to engineering, technical, and clerical for this estimate. The statement of base M&S and labour in man-years by the three categories results in a cost which we believe is comparable to that used by the ILC machine, and is referred to here as the ILC cost.

Contingency is estimated for each quantity to estimate the uncertainties in the costs of the detector components. However, we do not use the ILC value system for these estimates. Items which are commodities, such as detector iron, have had costs swinging wildly over the last few years. While there is agreement on a set of important unit costs, those quantities also have "error margins". SiD, ILD, and CLIC have worked together to reach agreed values for some unit costs as shown in Table II-12.1.

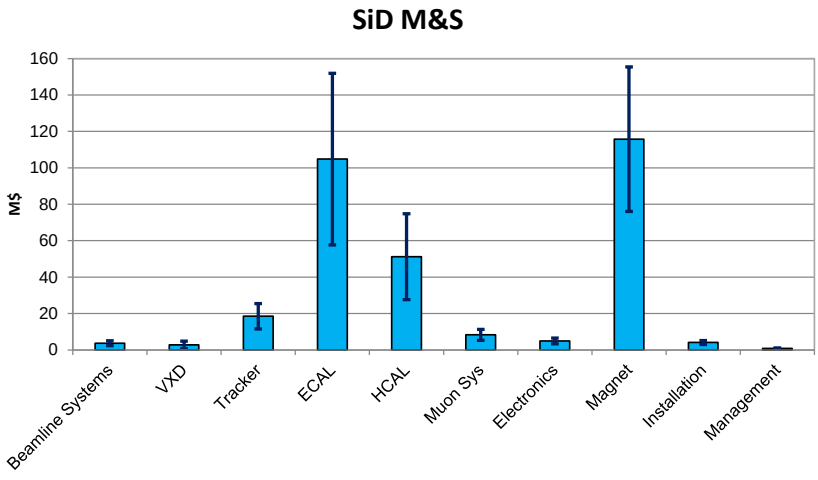

Figure II-12.1
Subsystem M&S Costs in million US-$, the error bars show the contingency per subsystem.

There are a substantial set of interfaces in the interaction region hall. For the purpose of this estimate, the following has been assumed:

- The hall itself, with finished surfaces, lighting, and HVAC are provided by the machine.
- Utilities, including 480 VAC power, LCW, compressed air, and Internet connections are provided.
- An external He compressor system with piping to the hall is provided. The refrigeration and associated piping is an SiD cost.
- All surface buildings, gantry cranes, and hall cranes are provided by the machine.

- Data storage systems and offline computing are provided by others.
- SiD will be assembled and will travel on a suitable platform for push-pull. This platform and its motion and alignment systems will be provided by the machine.
- QD0's and their 2K systems are provided by the machine. The beampipe is an SiD cost.

12.3 Results

The subsystem level summary is shown in Table II-12.2, the M&S costs are plotted in Figure II-12.1, and the labour costs are shown in Figure II-12.2. The costs are dominated by the Magnet and the ECAL. The magnet has roughly equal costs for the superconducting coil and the iron. The ECAL is dominated by the silicon detectors.

The cost estimate has several important "commodity" items whose costs have recently been fluctuating significantly. For SiD, these include most metals and processed silicon detectors. Table II-12.3 illustrated the cost sensitivity to these prices by indicating the unit cost used in the estimate and the effect on the SiD M&S cost of doubling the unit cost.

Figure II-12.2
Subsystem Labour

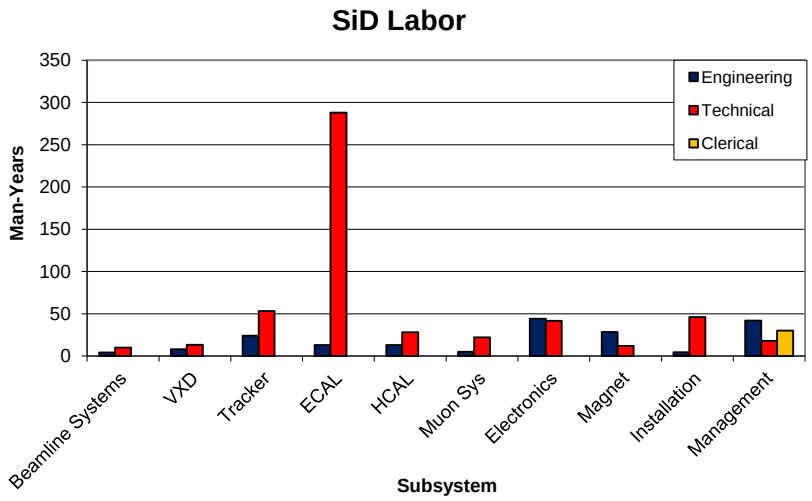

The superconducting coil cost is difficult to estimate, because there is little data and experience with coils of this size and field. An attempt was made to extract the CMS coil cost, and it is believed to be US-$ 48M for cold mass and vacuum tank.

Table II-12.3
Sensitivity to selected unit costs. The table shows the effect on the total M&S cost if the selected unit cost were to double.

Material	Base Cost (US-$)	Delta Cost (M US-$)	Fractional Delta (%)
Magnet Iron	6.00 /kg	48	16
Silicon Sensors	6.00 /cm^2	79	26
Tungsten ECAL	180 /kg	14	5
Stainless	4.5 /kg	2	1
HCAL Detector	12K /m^2	42	14

A Japanese industrial estimate for the SiD coil was obtained, and it was approximately the same as CMS, but for a coil with roughly half the stored energy. Cost functions linear in the stored energy and with a 0.66 exponential dependence have been studied.

SiD has taken a conservative approach and for the parametric study has used a linear model fit to the BaBar coil at the low end and the industrial estimate at the high end. The result for the current SiD design is US-$ 55M, higher than the CMS cost, but inflation and currency exchange variations have been ignored. SiD is doing R&D on advanced conductor design, and there is some reason to expect the coil cost estimate to decrease.

Table II-12.4
Components of the US accounting style estimate.

	M&S (M US-$)	Labour (M US-$)	Totals (M US-$)
Base	315	81	396
Contingency	127	18	144
Total	442	99	540
Indirect rates	0.06	0.20	
Indirects	26	20	46
Totals w/ indirects	468	119	587
Total in FY2016 M$	2008		586.7
Start Year	2016		
Construction Duration	6 years		
Inflation	3.5%/a		
Factor	1.460		
Total Escalation			269.9
Total			856.6

The SiD cost in ILC value units is US-$ 315M for M&S, 186 MY engineering, 532 MY technical, and 30 MY administrative labour. The estimated M&S contingency, reflecting uncertainty in unit costs and some estimate of the maturity of this study, is US-$ 127M.

The cost in US accounting, assuming a construction start in 2016 and 3.5% per year inflation and US National Laboratory labour rates, is US-$ 857M. The components of the US accounting calculation are indicated below in

Table II-12.4.

Figure II-12.3
Dependence of the SiD M&S base cost on the thickness of the HCAL

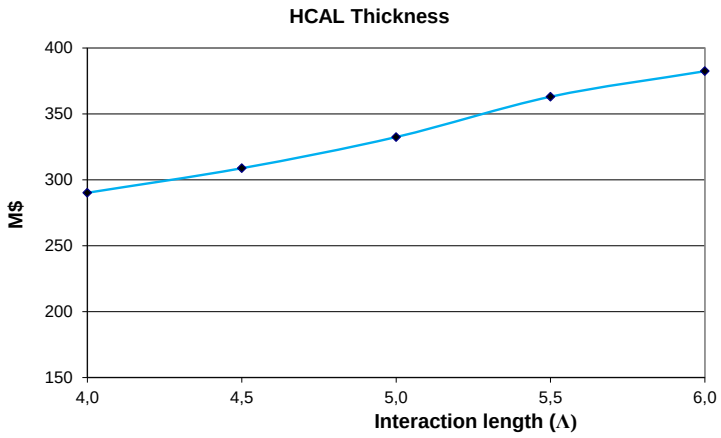

Figure II-12.4
Dependence of the SiD M&S base cost on the Solenoid Field

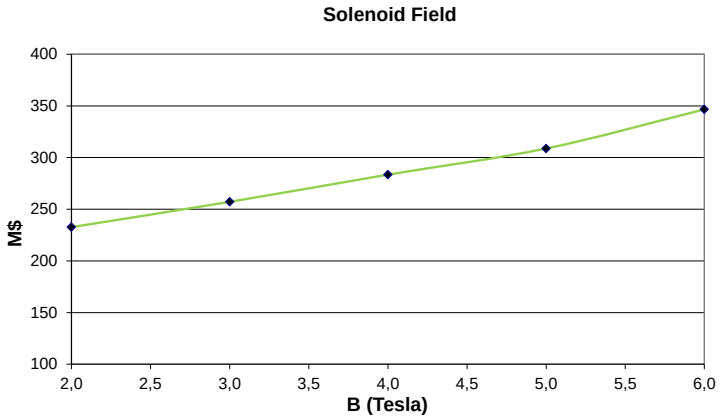

12.4 Parameter Dependencies

The parametric fitter enables studies of the SiD cost against the major parameters of the detector. Figure II-12.3 shows the dependence on the HCAL thickness, Figure II-12.4 on the central value of the magnetic field, and Figure II-12.5 on the tracker radius. In all case the cost is M&S base cost; contingency and labour are not included.

SiD has also examined using higher density absorber material in terms of their cost impact, especially by reducing the diameter of the coil. In this exercise, the number of layers and λ_I has been keep constant. It has been found, that moving from an all-steel HCAL to an all-tungsten HCAL would increase the total cost of SiD by about US-$ 26M.

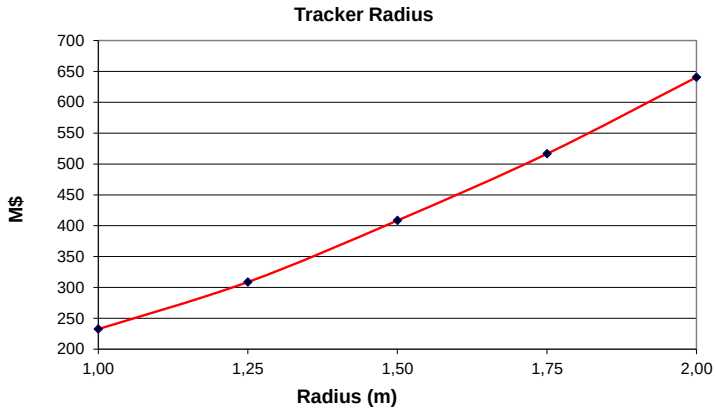

Figure II-12.5
Dependence of the SiD M&S base cost on the Tracker barrel radius

In adapting a configuration used in CLIC_SiD [129] where the transition of barrel and endcap has been optimised for cost and by using tungsten only for the barrel, the cost increase goes down to US-$ 15M. So in terms of cost optimisation, moving to a tungsten HCAL is not beneficial for SiD.

Chapter 13
SiD Summary

13.1 The Status of the SiD Detector Concept

We have presented a Detailed Baseline Design for the SiD Detector Concept for experiments at the future International Linear Collider. Our design is mature and delivers the required detector and physics performance as demonstrated so far by our simulations and benchmark physics studies.

The design of SiD represents a significant advance over the current generation of collider detectors. The baseline choices for the SiD subsystems represent our current selections in terms of level of successful R&D, measured and or simulated performance characteristics, dimensional practicality, and cost. We will continue to develop alternative technology options where they show promise for enhanced performance. The detector design presented here has been aimed specifically at a 500 GeV or 1 TeV ILC. A modified SiD design, aimed at CLIC energies up to 3 TeV, has already been described in the CLIC Conceptual Design Report (CDR) [129].

13.2 Further Development of the SiD Detector Concept

As a detector concept we strongly believe that, while technologies and/or their implementations may evolve over time, SiD will remain an excellent tool for exploration of physics at the International Linear Collider or CLIC.

There are several aspects to this from the detector, physics, organisational, and resource perspectives. We therefore propose to further study and develop the SiD design as new information emerges in the Higgs and possibly other new physics areas. There are areas of detector R&D that must be further developed and completed, followed by studies of specific implementations in a full technical design.

In parallel, while a limited number of physics processes have been studied for this DBD, there are other processes that should be addressed in continued studies. The sum of all these detector and physics activities points towards a lively and sustained effort on SiD as a well identified concept moving forward into the next phase of linear collider development. We therefore see SiD as a vital element of the future program and a major component of the Physics and Detectors section of the new Linear Collider Organisation.

SiD has evolved from the Letter-of-Intent stage as a largely U.S.- based activity to a more global concept with increased contributions from outside the Americas. Our aim is to expand to an even more global level of participation, and we will pursue this vigorously within the new organisation.

13.3 SiD and the New Global Linear Collider Organisation

The members of the SiD Detector Concept look forward to working with the new global Linear Collider Organisation. We view the new organisation as a framework within which we can advance our concept towards a full technical detector design for the ILC, and, working with our CLIC colleagues, for CLIC also. We strongly support the efforts of our Japanese colleagues to construct the ILC and will actively work to promote this project.

Organisationally, we support the creation of a group having broad representation from the concept groups and R&D collaborations to advance the physics and detector case for a linear collider. We believe that, when the time is right for the linear collider to move towards realisation, having well identified detector concepts with a substantial participation from all regions within the global organisation, will significantly benefit discussion of the funding agency contributions to the project as a whole.

Volume 4

Detectors

Part III

ILD Detailed Baseline Design

ILD Editors

Main Editors:
T. Behnke, D. Karlen, Y. Sugimoto, H. Videau, H. Yamamoto

Tracking System:
T. Matsuda, A. Ruiz-Jimeno, A. Savoy Navarro, R. Settles, Y. Sugimoto, I. Vila, M. Vos, M. Winter

Calorimer System:
H. Abramowicz, J.C. Brient, M. Fouz, D. Jeans, I. Laktineh, W. Lohmann, R. Poeschl, F. Sefkow, F. Simon, T. Takeshita

Outer Detector System:
M. Danilov, K. Elsener, F. Kircher, V. Saveliev, U. Schneekloth

Data Acquisition:
V. Boudry

Machine Detector Interface:
K. Buesser, T. Tauchi

Integration:
K. Buesser, C. Clerc, T.Tauchi

Alignment:
M. Fernández, F. Sefkow

Software:
F. Gaede, A. Miyamoto

Performance:
M. Berggren, A. Miyamoto, T. Tanabe, M. Thomson

Costing:
C. Clerc, H. Videau

Chapter 1
ILD: Executive Summary

The **I**nternational **L**arge **D**etector (ILD) is a concept for a detector at the International Linear Collider, ILC [198]. In a slightly modified version, it has also been proposed for the CLIC linear collider [199].

The ILD detector concept has been optimised with a clear view on precision. In recent years the concept of particle flow has been shown to deliver the best possible overall event reconstruction. Particle flow implies that all particles in an event, charged and neutral, are individually reconstructed. This requirement has a large impact on the design of the detector, and has played a central role in the optimisation of the system. Superb tracking capabilities and outstanding detection of secondary vertices are other important aspects. Care has been taken to design a hermetic detector, both in terms of solid-angle coverage, but also in terms of avoiding cracks and non-uniformities in response. The overall detector system has undergone a vigorous optimisation procedure based on extensive simulation studies both of the performance of the subsystems, and on studies of the physics reach of the detector. Simulations are accompanied by an extensive testing program of components and prototypes in laboratory and test-beam experiments.

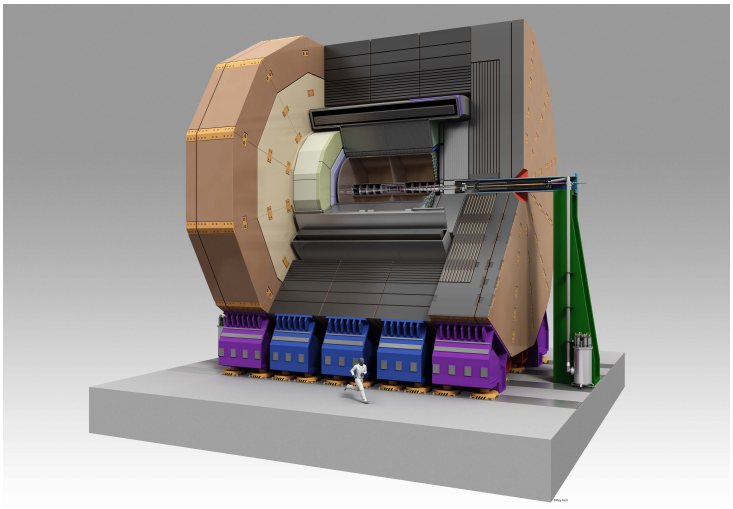

Figure III-1.1
View of the ILD detector concept.

The ILD detector concept has been described in a number of documents in the past. Most recently the letter of intent [198] gave a fairly in depth description of the ILD concept. The ILD concept is based on the earlier GLD and LDC detector concepts [200, 201, 202]. Since the publication of the letter of intent, major progress has been made in the maturity of the technologies proposed for ILD, and their integration into a coherent detector concept.

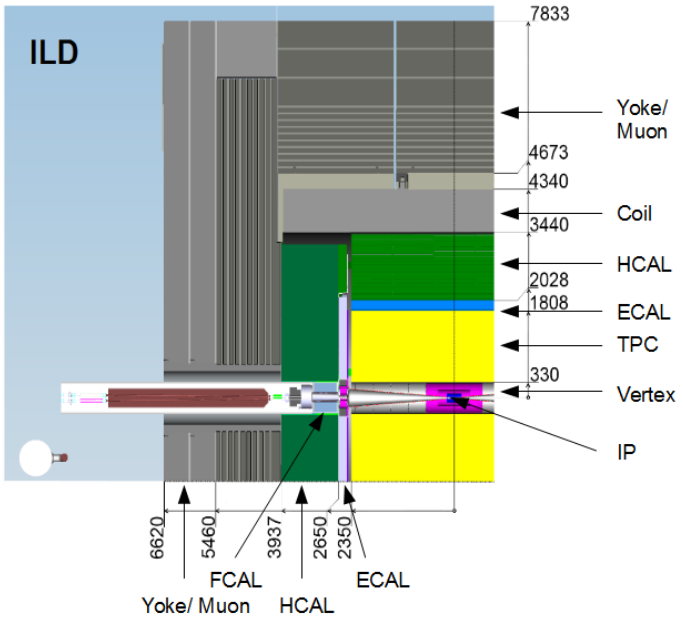

Figure III-1.2
Quadrant view of the ILD detector concept. The interaction point is in the lower right corner of the picture. Dimensions are in mm.

1.1 ILD philosophy and challenges

The particle flow paradigm translates into a detector design which stresses the topological reconstruction of events. A direct consequence of this is the need for a detector system which can separate efficiently charged and neutral particles, even inside jets. This emphazises the spatial resolution for all detector systems. A highly granular calorimeter system is combined with a central tracker which stresses redundancy and efficiency. The whole system is immersed in a strong magnetic field of 3.5 T. In addition, efficient reconstruction of secondary vertices and very good momentum resolution for charged particles are essential for an ILC detector. An artistic view of the detector is shown in Figure III-1.1, a vew of a quarter of the detector is seen in Figure III-1.2.

The interaction region of the ILC is designed to host two detectors, which can be moved in and out of the beam position with a "push-pull" scheme. The mechanical design of ILD and the overall integration of subdetectors takes these operational constraints into account.

The ILC is designed to investigate the mechanism of electroweak symmetry breaking. It will allow the study of the newly found higgs-like particle at 126 GeV. It will search for and explore new physics at energy scales up to 1 TeV. In addition, the collider will provide a wealth of information on standard model (SM) physics, for example top physics, heavy flavour physics, and physics of the Z and W bosons, as discussed earlier in this document. A typical event ($t\bar{t}$ at 500 GeV) is shown in Figure III-1.3. The requirements for a detector are, therefore, that multi-jet final states, typical for many physics channels, can be reconstructed with high accuracy. The jet energy resolution should be sufficiently good that the hadronic decays of the W and Z can be separated. This translates into a jet energy resolution of $\sigma_E/E \sim 3-4\%$ (equivalent to $30\%/\sqrt{E}$ at $100\,\mathrm{GeV}$). Secondary vertices which are relevant for many studies involving heavy flavours should be reconstructable with good efficiency and purity. Highly efficient tracking is needed with large solid-angle coverage.

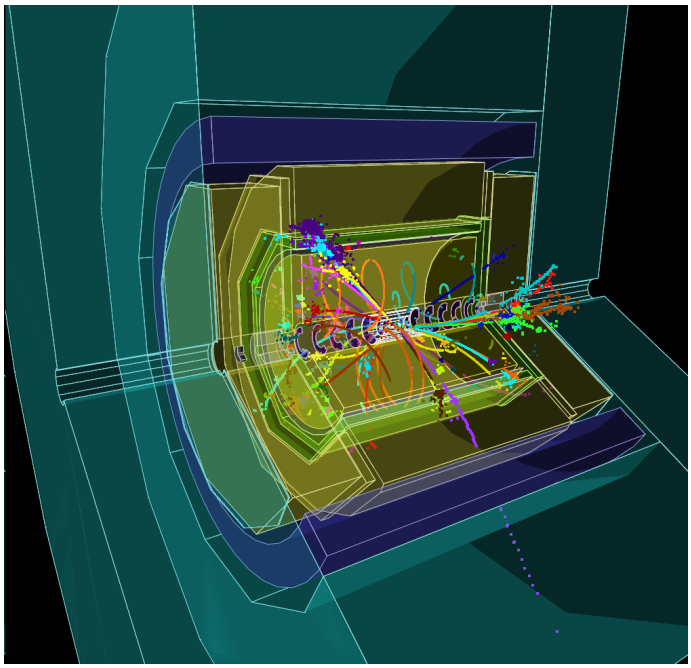

Figure III-1.3
Three-dimensional view of a typical multi jet final state at the ILC (500 GeV $t\bar{t}$ event with multi-hadronic final state). The picture was generated by the detailed detector simulation of the ILD detector.

1.2 ILD layout and performance

The ILD concept has been designed as a multi-purpose detector. A high precision vertex detector is followed by a hybrid tracking layout, realised as a combination of silicon tracking with a time projection chamber, and a calorimeter system. The complete system is located inside the large solenoid. On the outside of the coil, the iron return yoke is instrumented as a muon system and as a tail catcher calorimeter.

The vertex detector is realised as a multi-layer pixel-vertex detector (VTX), with three super-layers each comprising two layers, or a 5 layer geometry. In either case the detector has a pure barrel geometry. To minimise the occupancy from background hits, the first super-layer is only half as long as the outer two. Whilst the underlying detector technology has not yet been decided, the VTX is optimised for point resolution and minimum material thickness.

A system of silicon strip and pixel detectors surrounds the VTX detector. In the barrel, two layers of silicon strip detectors (SIT) are arranged to bridge the gap between the VTX and the TPC. In the forward region, a system of two silicon-pixel disks and five silicon-strip disks (FTD) provides low angle tracking coverage.

A distinct feature of ILD is a large volume time projection chamber (TPC) with up to 224 points per track. The TPC is optimised for 3-dimensional point resolution and minimum material in the field cage and in the end-plate. It also allows $\mathrm{d}E/\mathrm{d}x$ based particle identification.

Outside the TPC a system of Si-strip detectors, one behind the end-plate of the TPC (ETD) and one in between the TPC and the ECAL (SET), provide additional high precision space points which improve the tracking performance and provide additional redundancy in the regions between the main tracking volume and the calorimeters.

A highly segmented electromagnetic calorimeter (ECAL) provides up to 30 samples in depth and small transverse cell size, split into a barrel and an end cap system. For the absorber Tungsten has been chosen, for the sensitive area silicon diodes or scintillator strips are considered.

This is followed by a highly segmented hadronic calorimeter (HCAL) with up to 48 longitudinal samples and small transverse cell size. Two options are considered, both based on a Steel-absorber structure. One option uses scintillator tiles of $3 \times 3\,\mathrm{cm}^2$, which are read out with an analogue system. The second uses a gas-based readout which allows a $1 \times 1\,\mathrm{cm}^2$ cell geometry with a binary or

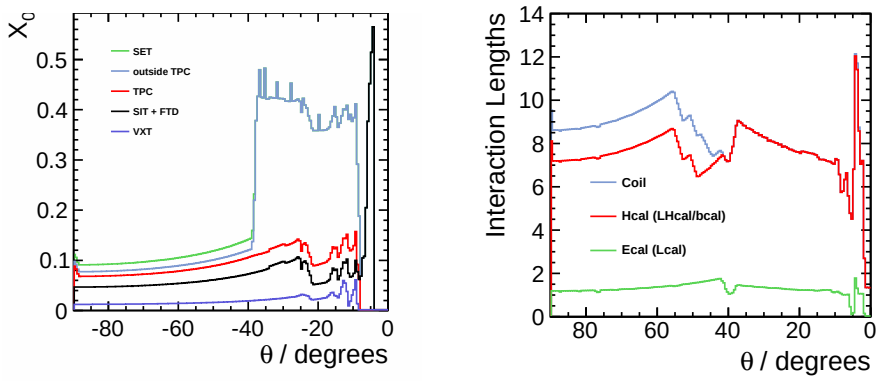

Figure III-1.4
Left: Average total radiation length of the material in the tracking detectors as a function of polar angle. Right: Total interaction length in the detector, up to the end of the calorimeter system, and including the coil of the detector.

semi-digital readout of each cell.

At very forward angles, below the coverage provided by the ECAL and the HCAL, a system of high precision and radiation hard calorimetric detectors (LumiCAL, BeamCAL, LHCAL) is foreseen. These extend the calorimetric coverage to almost 4π, measure the luminosity, and monitor the quality of the colliding beams.

A large volume superconducting coil surrounds the calorimeters, creating an axial B-field of nominally 3.5 Tesla.

An iron yoke, instrumented with scintillator strips or resistive plate chambers (RPCs), returns the magnetic flux of the solenoid, and, at the same time, serves as a muon filter, muon detector and tail catcher calorimeter.

To maximise the sensitivity of the detector to the physics at the ILC, the detector will be operated in a continuous readout mode, without a traditional hardware based trigger.

Precision physics at the ILC requires that the beam parameters are known with great accuracy. The beam energy and the beam polarization will be measured in small dedicated systems, which are shared by the two detectors present in the interaction region.

The ILD detector has been designed and optimised as a detector which can be used in a push-pull configuration, as described in section 5.5.

The main parameters of the ILD detector are summarised in Table III-1.1 and table III-1.2.

The performance of the ILD concept has been extensively studied using a detailed GEANT4 based simulation model and sophisticated reconstruction tools. Backgrounds have been taken into account to the best of current knowledge. A key characteristics of the detector is the amount of material in the detector. Particle flow requires a thin tracker, to minimise interactions before the calorimeters, and thick calorimeters, to fully absorb the showers. Figure III-1.4 (left) shows the material in the detector in radiation lengths, until the entry of the calorimeter. The right plot shows

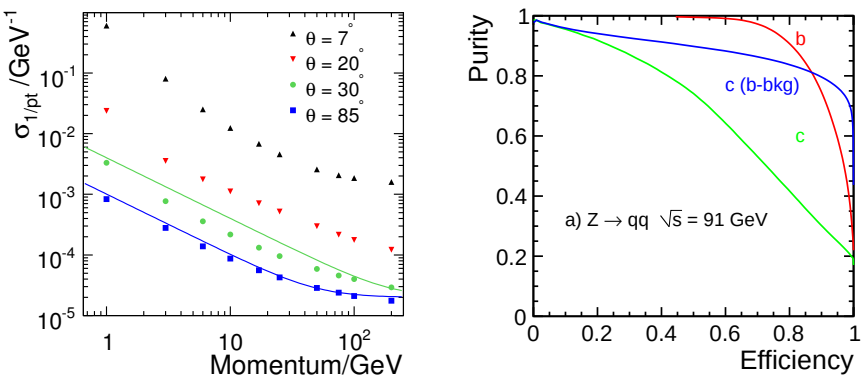

Figure III-1.5
Left: Momentum resolution as a function of the transverse momentum of particles, for tracks with different polar angles. Also shown is the theoretical expectation. Right: Flavour tagging performance for $Z \to q\bar{q}$ samples at different energies.

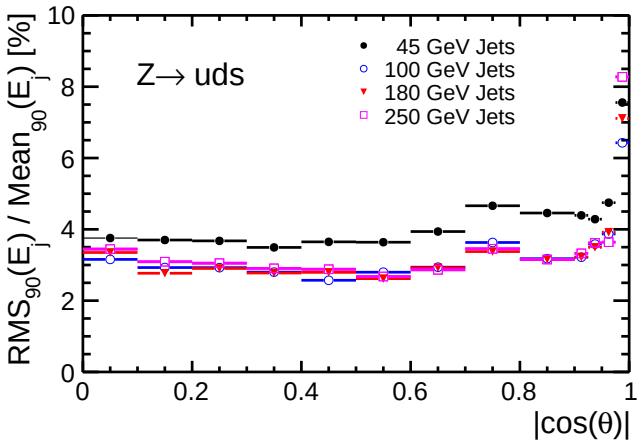

Figure III-1.6
Fractional jet energy resolution plotted against $|\cos\theta|$ where theta is the polar angle of the thrust axis of the event.

Table III-1.1. List of the main parameters of the ILD detector for the barrel part.

Barrel system						
System	R(in)	R(out) [mm]	z	comments		
VTX	16	60	125	3 double layers layer 1: $\sigma < 3\mu m$	Silicon pixel sensors, layer 2: $\sigma < 6\mu m$	 layer 3-6 $\sigma < 4\mu m$
Silicon						
- SIT	153	300	644	2 silicon strip layers	$\sigma = 7\mu m$	
- SET	1811		2300	2 silicon strip layers	$\sigma = 7\mu m$	
- TPC	330	1808	2350	MPGD readout	1×6mm^2 pads	$\sigma = 60\mu m$ at zero drift
ECAL	1843	2028	2350	W absorber	SiECAL	30 Silicon sensor layers, 5×5 mm^2 cells
					ScECAL	30 Scintillator layers, 5×45 mm^2 strips
HCAL	2058	3410	2350	Fe absorber	AHCAL	48 Scintillator layers, 3×3cm^2 cells, analogue
					SDHCAL	48 Gas RPC layers, 1×1 cm^2 cells, semi-digital
Coil	3440	4400	3950	3.5 T field	2λ	
Muon	4450	7755	2800	14 scintillator layers		

the total interaction length including the calorimeter system.

The performance of the tracking system can be summarised by its combined momentum resolution, shown in Figure III-1.5 (left). A resolution of $\sigma_{1/p_T} = 2 \times 10^{-5}$ GeV^{-1} has been achieved for high momenta. For many physics studies the tagging of long lived particles is of key importance. Several layers of pixel detectors close to the IP allow the reconstruction of displaced vertices, as shown in Figure III-1.5 (right).

Calorimeter system and tracking system together enter into the particle flow performance. The performance of the ILD detector for different energies and as a function of the polar angle is shown in Figure III-1.6.

The few plots shown in this executive summary illustrate the anticipated performance of the detector and illustrate the potential for precision measurements with the ILD detector. More details

Table III-1.2. List of the main parameters of the ILD detector for the end cap part.

End cap system						
System	z(min)	z(max) [mm]	r(min), r(max)	comments		
FTD	220	371		2 pixel disks 5 strip disks	$\sigma = 2 - 6\mu m$ $\sigma = 7\mu m$	
ETD	2420	2445	419-1822	2 silicon strip layers	$\sigma = 7\mu m$	
ECAL	2450	2635		W-absorber	SiECAL ScECAL	Si readout layers Scintillator layers
HCAL	2650	3937	335-3190	Fe absorber	AHCAL SDHCAL	48 Scintillator layers 3×3cm^2 cells, analogue 48 gas RPC layers 1×1cm^2 cells, semi-digital
BeamCal	3595	3715	20-150	W absorber	30 GaAs readout layers	
Lumical	2500	2634	76-280	W absorber	30 Silicon layers	
LHCAL	2680	3205	93-331	W absorber		
Muon	2560		300-7755	12 scintillator layers		

on the performance may be found in section 6.1 of this document.

In this document the design of ILD is presented. Intense R&D has taken place over the last decade to develop the necessary technologies. This work has typically happened within dedicated R&D collaborations, which are independent but maintain very close connections to ILD. All technologies selected by ILD for one of its subsystems have been proven experimentally to meet the performance goals, or to come very close. In some cases ILD presents more than one technology for a given sub-detector. At this moment no attempt has been made by the ILD group to down-select or limit the number of different technologies. The concept group wants to remain open and flexible to be prepared to select the most modern and most powerful technology once it is necessary. However a distinction is made between options and alternatives: while options have undergone an extensive R&D program and have passed critical proof-of-concept tests, alternatives are potentially interesting and promising technologies which have not matured to a similar level at the time of writing this document.

Chapter 2
ILD Tracking System

Key features of the ILD detector are a very powerful and redundant tracking systems, consisting of a high precision large volume time projection chamber, surrounded by a complete Silicon based vertexing and tracking system, all contained, together with a highly granular calorimeter system, inside a 3.5 T strong solenoidal field.

2.1 ILD vertex system

The identification of heavy (charm and bottom) quarks and tau leptons is essential for the ILC physics programme. The reconstruction of decay vertices of short lived particles, such as D or B mesons, deserves therefore much attention and requires a particularly light and precise vertex detector. The vertices are tracked back by reconstructing the trajectory of the short lived particles decay products. This is achieved through the very precise measurement of the charged particles' track parameters in the vicinity of the interaction point, which are then combined with those of the other tracking detectors to reconstruct vertices. The performance of a vertex detection system may be expressed by the resolution on the impact parameter of charged particles. The main performance goal of the ILD vertexing system resumes in a resolution on the track impact parameter of $\sigma_b \ < \ 5 \ \oplus \ 10/p \sin^{3/2}\theta \ \mu$m. In order to reach such a high performance level, the ILD vertex detector should comply with the following specifications:

- A spatial resolution near the IP better than 3 μm ;
- A material budget below 0.15% X_0/layer;
- A first layer located at a radius of ~ 1.6 cm;
- A pixel occupancy not exceeding a few %.

The power consumption should be low enough to minimise the material budget of the cooling system inside the detector sensitive volume. Power savings may be obtained by exploiting the beam time structure and power pulse the sensors equipping the detector. Alternatively, the signals may be integrated over the complete bunch train and read out in-between consecutive trains at very low frequency and thus very low power.

The required radiation tolerance follows entirely from the beam related background (i.e. beamstrahlung) (see section 5.5.6), which is expected to affect predominantly the innermost layer. The requirements for the total ionising dose and the fluence amount respectively to about 1 kGy and 10^{11} n_{eq}/cm^2 per annum. These values assume that neutrons backscattered from the beam dump are shielded well enough to add a minor contribution to the overall radiation load.

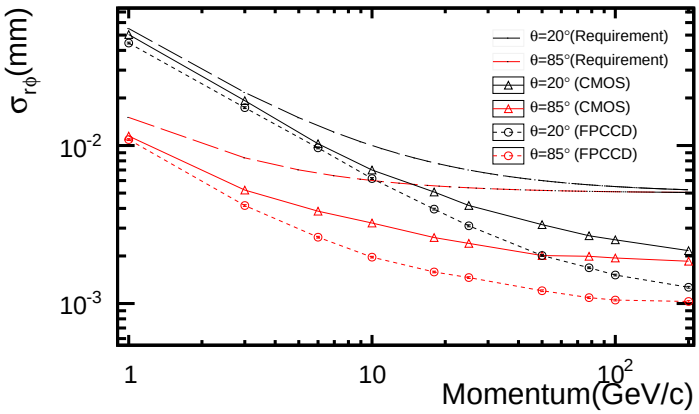

Figure III-2.1
Impact parameter resolution of the ILD vertex detector for two different particle production angles (20° and 85°), assuming the baseline point resolution given in Table III-2.1 for the CMOS option (solid line), and the FPCCD option (dotted line). The curves with long dashes show the performance goal.

2.1.1 Baseline design

The baseline design of the ILD vertex detector consists of three, nearly cylindrical, concentric layers of double-sided ladders. Each ladder is equipped with pixel sensors on both sides, $\sim$ 2 mm apart, resulting in six measured impact positions for each charged particle traversing the detector. The radii covered by the detector range from 16 mm to 60 mm. The material budget of each ladder amounts to $\sim 0.3\%\ X_0$, equivalent to $0.15\%\ X_0$/layer.

An alternative geometry is also considered, based on five equally spaced single-sided layers, with radii ranging from 15 to 60 mm.

The current layout of the proposed vertex detector is summarised in Table III-2.1. It is based on extensive simulation and technical studies. The parameters are considered conservative.

Table III-2.1
Vertex detector parameters. The spatial resolution and readout times are for the CMOS option described in section 2.1.2.1.

	R (mm)	$\lvert z\rvert$ (mm)	$\lvert\cos\theta\rvert$	σ (μm)	Readout time (μs)
Layer 1	16	62.5	0.97	2.8	50
Layer 2	18	62.5	0.96	6	10
Layer 3	37	125	0.96	4	100
Layer 4	39	125	0.95	4	100
Layer 5	58	125	0.91	4	100
Layer 6	60	125	0.9	4	100

The impact parameter resolution following from the single point resolutions provided in the table is displayed in Figure III-2.1 as a function of the particle momentum, showing that the ambitious impact parameter resolution is achievable.

2.1.2 Pixel technologies and readout electronics

Currently three sensor technology options are actively developed for the ILD vertex detector. They have been shown to have the potential of meeting the detector requirements or to come close to them. Those technological options are CMOS Pixel Sensors (CPS) [203, 204, 205, 206], Fine Pixel CCD (FPCCD) sensors [207, 208, 209, 210], and Depleted Field Effect Transistor (DEPFET) sensors [211, 212, 213]. The development and optimisation of each technology is closely associated to a specific readout architecture. For CPS and DEPFETs a power pulsed readout is under study and offers attractive advantages. For the FPCCD, the very large number of pixels calls for a slow (low power) readout, which must be performed in between bunch trains.

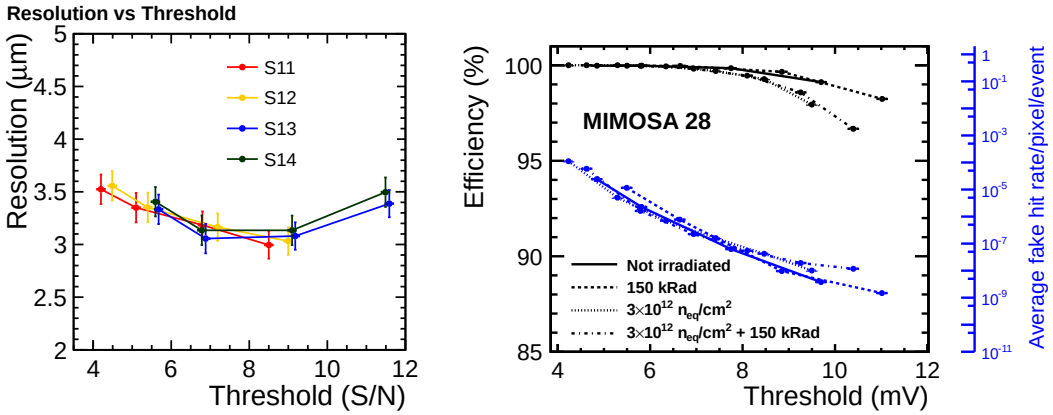

Figure III-2.2. Left: Single point resolution measured with a 18.4 μm pitch as a function of the discriminator threshold (the colours refer to different in-pixel circuits). Right: Measured variations of the minimum ionising particle (m.i.p.) detection efficiency and fake hit rate (fraction of pixel noise fluctuations above threshold) of the STAR sensor as a function of the discriminator threshold, before and after irradiation (150 kRad, 3×10^{12} n_{eq}/cm^2) at a coolant temperature of $30°C$.

2.1.2.1 CMOS pixel sensors

CMOS pixel sensors (CPS) use as a sensitive volume the 10-20 μm thin, high-resistivity epitaxial layer deposited on low resistivity substrates of commercial CMOS processed chips, which makes them particularly well suited for a low-mass detector. A high density sensing node lattice is implemented on the layer, allowing for high spatial resolution. Moreover, the full signal processing circuitry may be integrated on the same substrate as the sensitive volume, which makes CPS flexible and cost effective.

Developments over the last couple of years have shown that these genuine features can be combined into a single, full scale device, fabricated by industry, which complies with the vertex detector specifications. The proof of principle was achieved with the MIMOSA-26 sensor, initially developed for the beam telescope of the European Union (EU) funded project EUDET [203].

The sensor architecture is based on a column parallel read-out with amplification and correlated double sampling inside each pixel. The chip features 1152 columns of 576, 18.4 μm pitch, pixels. Each column is terminated with a precision discriminator and is read out in a rolling shutter mode at a frequency of 5 MHz (200 ns/row). Due to charge sharing, the spatial resolution obtained is close to 3 μm (see left of Figure III-2.2) despite the single bit charge encoding.

The MIMOSA-26 architecture was extended to a sensor (MIMOSA-28) [204] adapted to the (air cooled) vertex detector (PXL) of the STAR experiment at BNL [205], foreseen to start data taking in 2013. Its current assembly and upcoming operation provide valuable experience for the vertex detector at ILD. The sensor minimum ionising particle (m.i.p.) detection performances measured at $30°C$ are displayed in Figure III-2.2 (right), before and after irradiation with loads well above the annual values expected at the ILC ($\lesssim 100$ kRad, $< 10^{11}$ n_{eq}/cm^2), showing the adequacy of the CPS radiation tolerance up to high temperatures.

CPS complying with the vertex detector specifications were derived from MIMOSA-26, with modified spatial resolution and read-out times, and adapted to different requirements for distinct layers.

For the inner layer, which accounts only for $\sim 10\%$ of the detector active surface, the sensors are optimised for single point resolution and short read-out time, relaxing the power consumption constraints. The conflict between high granularity and fast read-out is resolved by equipping the innermost ladders with two different types of sensors, one achieving the required spatial resolution and one providing a fast time stamp.

The high precision sensors mounted on one side of a ladder, feature square pixels with ~ 17 μm

pitch and provide a spatial resolution < 3 μm. The frame read-out time is 50 μs, which may lead to a relatively high occupancy if the beam related background happens to be a few times higher than expected from simulations. The fast sensors are installed on the other side of the ladder. They feature rectangular pixels (e.g. 17×85 μm^2), which result in five times less pixels per column and therefore in a 10 μs time resolution, at the expense of an increased spatial resolution of ~ 6 μm.

The combination of a very precise sensor with a much faster one in a geometry which provides a tight correlation between the two allows to achieve a spatial resolution of < 3 μm and a timing resolution of $\lesssim 10$ μs (see left of Figure III-2.5), from the first layer alone. This is expected to strongly suppress the perturbation of the track reconstruction due to beam related background, even if its rate is well above simulated values.

The design of these sensors is ready and has been partially validated. Further improvements might consist in integrating a low power discriminator for each pixel [206]. It reduces the read-out time to < 5 μs and the pixel array power consumption by at least 30%. This approach, which is also followed for the ALICE-ITS upgrade, is expected to be mature within 2-3 years.

The sensors for the outer layers have to cover a much larger area, but see significantly lower occupancies. Therefore their design has been optimised to minimise the power consumption. Pixels of 34×34 μm^2 are used, organised in columns terminated with 4-bit ADCs. They achieve a spatial resolution of ~ 4 μm, at a read-out time of 100 μs. A prototype composed of 64×64 pixels is currently being tested.

The instantaneous power consumption of the full detector was evaluated to be < 600 W. Assuming power cycling with a conservative duty cycle value of 2% (i.e. 5 ms long periods of power dissipation encompassing the 1 ms long bunch trains), the average power dissipation is about 10 W, an amount expected to comply with air cooling.

2.1.2.2 Fine Pixel CCD

The use of FPCCD sensors allows for particularly small pixels (~ 5 μm pitch), which results in a sub-micron spatial resolution and an excellent two-track separation capability. It allows simultaneously to mitigate the occupancy generated by the beam related background even when integrating the signal over many bunch-crossings.

The sensitive volume is a ~ 15 μm-thick epitaxial layer. It is fully depleted, resulting in a limited charge spread, which is essential to keep the number of hit pixels per hit small. The pixel occupancy is therefore expected to remain affordable even if accumulating the signals over a full bunch train without time stamping. The FPCCD instantaneous power consumption being moderate, a slow signal processing in-between consecutive bunch trains can be envisioned.

FPCCD may also be advantageous in case of intense beam-induced RF noise, to which they are intrinsically insensitive. Moreover their readout circumvents potential difficulties associated to power cycling (see section 2.1.6).

For the inner two layers, where the hit density due to pair-background is particularly high, 5 μm pitch pixels will be used, while 10 μm pitch pixels will be used for the outer four layers. As shown in Figure III-2.1, in which a single point resolution equivalent to the pixel size divided by $\sqrt{12}$ is assumed for FPCCD, a significant improvement in impact parameter resolution is achieved w.r.t. the baseline performance, reflecting the outstanding spatial resolution of the two inner layers.

The sensitive area of each FPCCD sensor is divided into 16 areas. The horizontal registers which are embedded in the sensitive area run parallel to the detector axis, and the readout nodes are located at one end of the chip. The outputs from the sensor are connected to read-out ASICs on the ladder. The read-out ASIC consists of amplifiers, low-pass filters, correlated double samplers (CDS), and analog-to-digital converters. FPCCD sensors are operated at $\sim -40°$C in order to suppress the effect

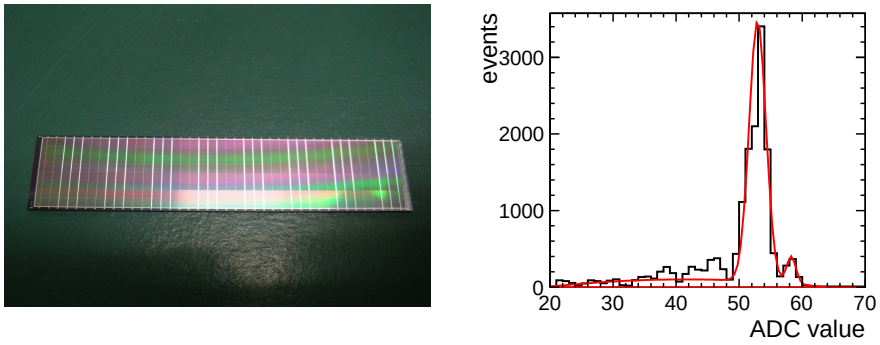

Figure III-2.3
Full size FPCCD prototype (left) and response to a $^{55}\mathrm{Fe}$ source (right).

of radiation damage. Each ladder has a few tens of centimetre-long pig-tail Kapton flat cables which are connected to junction circuits outside of the cryostat using micro-connectors (see section 2.1.5). The junction circuits, which include clock drivers, data suppression circuits, optical fibre drivers, etc., are surrounding the beam pipe. The total power consumption inside the cryostat is expected to be about 35 W.

Prototypes of FPCCD sensors and ASICs have been made and tested. Figure III-2.3 shows a full size prototype sensor and the response of a prototype sensor (coupled to its ASIC) to a $^{55}\mathrm{Fe}$ X-Ray source.

2.1.2.3 DEPFET sensors

In the DEPFET [211, 212, 213] active pixel detector concept a field effect transistor is incorporated into each pixel of a detector-grade silicon sensor. A voltage applied over the thickness of the detector depletes the sensor of free charge carriers and ensures rapid and efficient collection of the signal on a deep implant underneath the field effect transistor. As the collected charge modulates the source-drain current, a first amplification of the signal takes place inside the pixel, that is crucial to achieve an excellent signal/noise (S/N) ratio for a thin detector.

Columns of pixels that stretch across the length of the ladder are read out by two auxiliary ASICs: the DCD [214, 215] that digitises the signal and DHP, located at both ladder ends. Both ASICs could eventually be merged. Rows of pixels are read out in a rolling shutter mode. They are addressed by an ASIC known as the SWITCHER [215], that is located on a narrow balcony on the sensor periphery. At any time during operation, only one single row of pixels is active, keeping the power consumption within the strict ILD budget.

An international collaboration [216] pursues the development of the DEPFET concept for use in the vertex detectors of future collider experiments (Belle-II, LC). Over the decade 2002-2012, realistic prototype sensors have been produced and submitted to exhaustive tests with radioactive sources and particles from beams at CERN and DESY [217, 218]. The successful production of sensors with 20×20 μm^2 pixels demonstrates the feasibility of the process. Sensors produced in the most recent run with a thickness of 50 μm are found to be fully functional electrically. The response of such thin sensors to 120 GeV pions is compared to the prediction of H. Bichsel [219] in Figure III-2.4.

The internal gain of the field-effect-transistors extracted from such measurements is found to lie in the $g_q = 300$-600 pA$/e^-$ range, depending on design variations [220], sufficient to provide a S/N value of up to 40 for a 50 μm thick sensor.

Row read-out times of $\sim$ 80 ns have been obtained in the operation of a DEPFET sensor with the DCDv2 read-out ASIC. The R&D goal for the vertex detector is to improve the row read-out time to $\sim$ 40 ns, thus achieving a frame read-out time of 50 μs and 100 μs for the innermost and outer layers respectively. Further improvements in the read-out speed can be obtained by reading more rows in parallel (two rows are assumed for the LC estimate above, in the Belle-II design four rows are

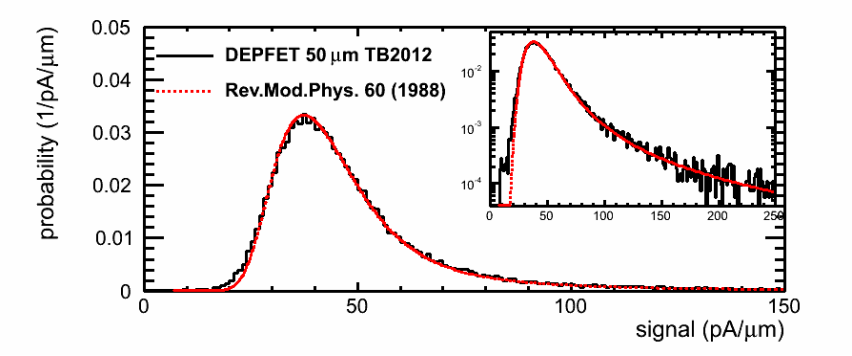

Figure III-2.4
The response of a 50 μm thick DEPFET sensor to 120 GeV pions. The prediction of H. Bichsel [219] is compared to the measurements, the most probable value being left free to vary.

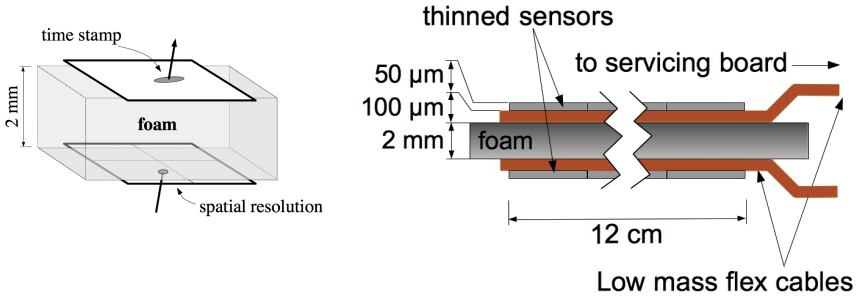

Figure III-2.5
Left: Illustration of the double-sided ladder concept based on a high-resolution sensor on one side and a fast sensor on the other side. Right: Schematic cross-section of the double-sided ladder developed within the PLUME project.

read out simultaneously), and by increasing the length of the pixels towards the end of the ladder.

2.1.2.4 Other sensor technologies

Development of pixel detectors is a very active and fast moving area. A number of alternative technologies are under study by groups around the world, which could feature the required high granularity and low material budget. Very few of them, however, are under active development for ILD, and none have reached a degree of maturity comparable to that of the technologies described above. It is not excluded, however, that the developments undertaken for the high energy run of the ILC (see 2.1.6) will promote an alternative technology to those described earlier. This remark may in particular apply to high-resistivity substrate CMOS sensors and to multi-tier 3D pixel sensors.

2.1.3 Ladder design

The vertex detector ladders must comply with a particularly tight material budget reflecting the ambitious impact parameter resolution goals. Excellent mechanical properties are required, in particular when power pulsing is foreseen. Three options are currently under study, each related to one of the three pixel technologies introduced earlier. Two of them address the baseline design, using double-sided ladders, while the third one focusses on the alternative geometry using single-sided ladders.

The double-sided ladder design has a structure of a rigid foam core sandwiched by thin (~ 50 μm) silicon pixel sensors. Low density silicon carbide (SiC) and carbon foams (RVC) are considered for the core material. The number of ladders of each layer is 10, 11, and 17 for the first, second, and third layer, respectively. The width of a ladder is 11 mm in the innermost layer, and 22 mm in the outer two layers.

The hits generated by a traversing particle can be used to reconstruct a mini-vector with potential benefits in terms of resolution, alignment and reconstruction of shallow angle tracks. Moreover, as stated earlier, it allows mitigating the conflict between granularity and read-out time.

The double-sided ladder concept envisaged for CPS consists of two sensor layers mounted on a flex cable and separated by a $\sim$ 2 mm thick support layer made of very low density (few per-cent) SiC foam, as illustrated on the right of Figure III-2.5.

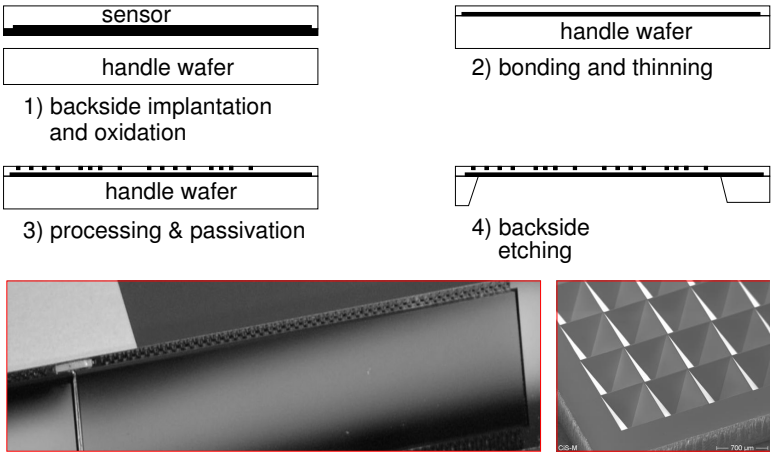

Figure III-2.6 Illustration of the most important steps in the creation of a thin all-silicon ladder (see text). A photograph of an all-silicon ladder and a scanning electron microscope image of a detail of the support structure are also shown.

The concept is developed within the PLUME collaboration [221]. It uses 50 μm thin MIMOSA-26 sensors, but can be extended to other technologies, and may actually combine different technologies. The first complete prototype, featuring 0.6% X_0 total material budget, was fabricated and validated with a 100 GeV particle beam. Currently, a lighter prototype, featuring only 0.35% X_0, is under construction and foreseen to be tested with beam particles in 2013.

An alternative approach is investigated with the FPCCD sensors, which relies on Reticulated Vitreous Carbon foam (RVC) for the core material, with a density of 3-5% of the graphite density. RVC is somewhat less rigid than SiC foam but is expected to be sufficient because of the rigidity provided by the $\sim$ 6.5 cm long FPCCD sensor slabs.

The single-sided, silicon-only, ladder design is pursued by the DEPFET collaboration. A fully self-supporting silicon ladder is being developed, that requires no external support structure over the full length of the ladder. The use of a single material reduces mechanical stress due to mismatching of thermal coefficients. Auxiliary detector components and power and signal lines are integrated onto an additional metal layer on the sensor, thus strongly reducing the material for this high-density interconnection on the ladder.

The process [222, 223] is schematically depicted in Figure III-2.6: (1) backside implants and oxidation of the sensor wafer; (2) bonding of the sensor and handle wafer and thinning of the former; (3) front-side processing and passivation; (4) photolithographic thinning of the handle wafer, leaving support structures around the edges. The sensor wafer is ground to a thickness of 50-75 μm. The remaining material from the handle wafer forms a support structures. The resulting self-supporting ladder has excellent mechanical properties and represents a minimal material budget. The thermo-mechanical performance of a realistic detector mock-up with thin DEPFET ladders has been characterised in the presence of a forced air flow [224, 225].

The detailed ladder design for the Belle-II vertex detector envisages 0.21% X_0/layer within the acceptance of the ladder [226]. This value may still be reduced for ILD by further thinning of the active material, that is one of the dominant contributions. Further reduction of the Silicon support frame may finally allow achieving the ILD goal of $\sim$ 0.15% X_0/layer.

2.1.4 Cooling system

Two different cooling options are considered, depending on the sensor technology.

For the CPS and DEPFET options cooling strategies which generate a minimal amount of material inside the fiducial volume, if any, are being studied. Those may be air flow cooling similar to the one used for the STAR-PXL [205] or cool nitrogen gas cooling.

For the FPCCD sensor option, in which more than 30 W is consumed inside the cryostat, two-phase CO_2 cooling may be used. Because of its large cooling power, typically $\sim$ 300 J/g, a thin

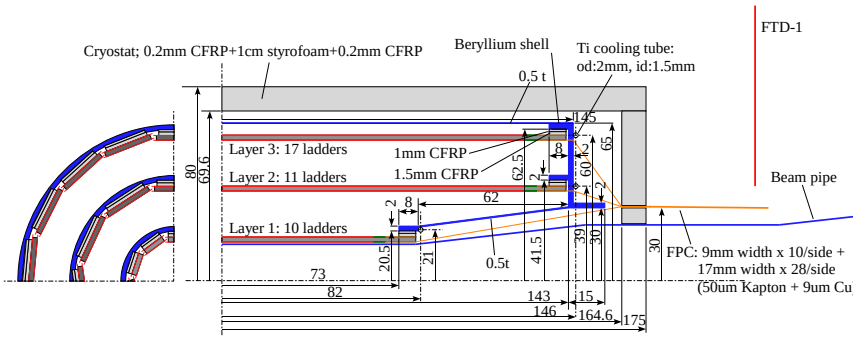

Figure III-2.7
Mechanical support structure of ILD vertex detector

(OD $\sim$ 2 mm) cooling tube may be sufficient. It may be attached at the detector end plate. The increase of the material budget due to the titanium cooling tube on the end plate is only 0.3% X_0 if averaged over the end plate. The main heat source of a FPCCD based vertex detector (CCD on-chip amplifier and read-out ASIC) is located near the ladder ends and the end plate, so that the heat is expected to be rather easily removed. The cooling temperature is -40 °C. In order to prevent condensation on the cooling tube, and to avoid occupying space with a heat insulator around the tube, the inner support tube supporting the vertex detector and the inner silicon tracker should be filled with dry air.

2.1.5 Detector mechanics

The vertex detector mechanical design implemented in the full simulation model is shown in Figure III-2.7. It is similar to the SLD vertex detector. The ladders are supported by a 2 mm thick beryllium end plate and a 0.5 mm-thick beryllium outer shell. The strength of this beryllium structure has been calculated with a finite element analysis, which showed that the largest deformation under 9.8 N compression along the beam lines is less than 2 μm. The whole detector is contained in a cryostat made of 1 cm thick styrofoam (though only mandatory for FPCCD sensors). The material budget of the cryostat including 50 μm CFRP sheets on both sides is only 0.1% X_0.

The vertex detector is supported by the beam pipe, the latter being supported by the inner support tube. The vertex detector is thus integrated as a part of the ILD'inner silicon trackers' inside the inner support tube.

The alignment of the vertex detector will be performed in two major steps. In the assembly phase, micrometrical pre-alignment will be performed by optical survey. After installation, a precise beam-based alignment will be achieved. The latter may proceed through two phases. The first one will consist in aligning the ladders composing a layer, using the few hundred micrometers wide overlapping bands of neighbouring ladders. The second phase will allow making the global detector alignment.

2.1.6 Future prospects

The vertex detector is relatively easy to upgrade or replace. The evolution of sensor technologies and performance can therefore be exploited quite efficiently, in particular to comply with the manyfold increase of the beam related background expected at a collision of $\sim$ 1 TeV. It should therefore not be an issue to introduce new sensors featuring much shorter readout times than those foreseen for the first years of data taking.

Despite the achievements described above, the detector is still premature in various aspects, and requires therefore substantial R&D.

The overall detector mechanical design is among the least advanced components. More detailed design studies, including the assembly procedure and important thermal aspects (e.g. power cycling in the experimental magnetic field) are necessary. Manufacturing real scale mechanical prototypes will be an important step of the development.

The CPS foreseen for the outer layers, equipped with ADCs, still need two years of development. For the 1 TeV run, a fast sensor achieving $\lesssim 2\ \mu s$ read-out time is under development, based on in-pixel signal discrimination and two-row simultaneous read-out. It addresses the ALICE-ITS and CBM-MVD applications and may therefore be ready for the 500 GeV run. Once the sensor development is finalised, multi-reticule sensors will be fabricated using industrial stitching, which may be used in order to suppress dead areas and improve the ladder stiffness.

The main R&D activities addressing system integration aspects focus on finalising the present double-sided ladder prototype featuring 0.35% X_0. The next generation of prototypes will follow, to tighten the material budget below 0.3% X_0.

Power cycling studies of the ladders will also be performed within the AIDA [227] project, which offers also a framework for high precision alignment studies. Finally, the integration of CPS, similar to those developed for ILD, in the STAR, ALICE, and CBM experiments is expected to generate substantial progress in most system integration aspects.

For FPCCD sensors, the radiation immunity has to be proven and the electronics downstream of the read-out ASIC needs to be developed (in particular the data suppression circuitry given the huge amount of pixels). Software developments are also needed in order to achieve efficient track finding in the presence of a large number of background hits.

For the DEPFET option, complete system integration aspects are being addressed at the occasion of the Belle-II vertex detector construction. Concerning the sensors, R&D is performed to further improve their read-out speed, motivated by the innermost vertex detector layers requirements. A more aggressive design of the all-Silicon ladder is also being investigated to meet the ILD goal of 0.15% X_0/layer.

R&D is also performed to develop sensors fast enough to provide bunch tagging, which may allow coming closer to the IP in order to improve the reconstruction of low momentum tracks, and will naturally be best suited to the highest energy running. VDSM CMOS processes using high-resistivity, fully depleted, substrates are being studied for this purpose, as well as 3D CPS exploiting industrial stacking techniques to interconnect multi-tier sensors at the pixel level.

2.2 The ILD silicon tracking system

The silicon part of the ILD tracking system is made of four components: two barrel components, the Silicon Inner Tracker (SIT) and the Silicon External Tracker (SET), one end cap component behind the endplate of the TPC (ETD), and the forward tracker (FTD). They form the Silicon Envelope [228]. The overall layout of the system is shown in Figure III-2.8.

The barrel silicon parts SIT and SET provide precise space points before and after the TPC; this improves the overall momentum resolution, helps in linking the VTX detector with the TPC, and in extrapolating from the TPC to the calorimeter. The coverage of the TPC with silicon tracking is completed by the ETD, located within the gap separating the TPC and the end-cap calorimeter. Together these systems help in calibrating the overall tracking system, in particular the TPC. The good timing resolution of the silicon detectors relative to the time between bunches in the ILC together with the high spatial precision helps in time-stamping tracks and assigning them to a given bunch within an ILC bunch train.

In the very forward region, where the TPC does not provide any coverage, a system of seven silicon disks (pixel and strips) ensures efficient and precise tracking down to very small angles. Good forward coverage is particularly important for the ILC since at $\sqrt{s} \geq 350$ GeV the relative weight of t-channel exchange processes and high-multiplicity ($2 \to 4$ and $2 \to 6$) processes increases. In a large fraction of collisions some of the outgoing particles are emitted at very small polar angle. Compared to previous experiments at e^+e^- colliders, the instrumentation of the forward region of the tracking

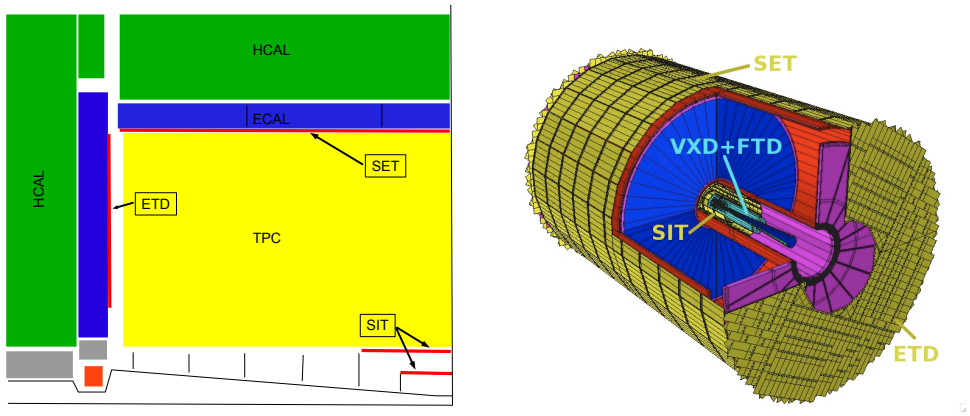

Figure III-2.8. Left: a quadrant view of the ILD silicon envelope system made of four components, SIT, SET, FTD, and ETD as included in MOKKA full simulation. Right: a 3D detailed GEANT 4 simulation description of the silicon system as sketched in the quadrant view on the left.

thus becomes important [229].

A special challenge to all silicon systems is the design of lightweight, thin systems that can be operated at minimum power to avoid the need for intricate cooling systems. This requires careful management of the materials for the detector support. Power consumption is minimised by power pulsing. This requirement leads to a synchronised power distribution that has to deal with large pulsed currents, which must not generate any electromagnetic interference phenomena or transients altering the front-end electronics performance during the active period. Highly integrated readout electronics moves significant processing power close to the detector, and thus reduces the number of cables needed to exit from the system. An advanced scheme is pursued to minimise the material needed to bring the necessary power to the detector. Powering schemes like DC-DC conversion or the use of super-capacitors mounted on the detector are being investigated.

The silicon tracking system of ILD has been developed by the SiLC collaboration. Detailed descriptions of the wide ranging R&D activities can be found in [230, 231, 232, 233].

2.2.1 The central silicon: SIT, SET, and ETD

The central silicon components SIT, SET, and ETD are realised with layers made each of two single-sided strip layers tilted by a small angle with respect to each other; this is also called 'false' double-sided layers. SIT includes two such layers and SET one; together they thus provide three precise space points for central tracks, the ETD adds one precise point to tracks going into the end-cap. The main parameters of the system are given in Table III-2.2.

A central design feature of the silicon envelope detectors is that the same sensor type is used throughout the system. This minimises the complexity of this large system, and will help to minimise the costs. Similarly the same mechanical design for the basic detector unit, the ladder, is used throughout. It is based on modern silicon detector technology, deep sub-micron (DSM) CMOS technology for the front-end (FE) electronics with a new on-detector electronics connection and new material technology for the support structure. Special challenges for ILD are a significant reduction in material compared to the most recent examples of large scale silicon detectors (e.g. currently running LHC detectors), operating at very low power, and reaching excellent point resolution and calibration.

The SIT is positioned in the radial gap between the vertex detector and the TPC. Its role is to improve the linking efficiency between the vertex detector and the TPC; it improves the momentum

Table III-2.2
Main parameters of the central silicon systems SIT, SET, and ETD.

SIT (baseline = false double-sided Si microstrips)					
Geometry			Characteristics		Material
R [mm]	Z [mm]	cos θ	Resolution R-ϕ [μm]	Time [ns]	X_0 [%]
153	368	0.910	R: σ=7.0	307.7 (153.8)	0.65
300	644	0.902	z: σ=50.0	σ=80.0	0.65
SET (baseline = false double-sided Si microstrips)					
Geometry			Characteristics		Material
R [mm]	Z [mm]	cos θ	Resolution R-ϕ [μm]	Time [ns]	X_0 [%]
1811	2350	0.789	R: σ=7.0	307.7 (153.8)	0.65
ETD (baseline = single-sided Si micro-strips)					
Geometry			Characteristics		Material
R [mm]	Z [mm]	cos θ	Resolution R-ϕ [μm]		X_0 [%]
419.3-1822.7	2420	0.985-0.799	x: σ=7.0		0.65

resolution and the reconstruction of low p_T charged particles and improves the reconstruction of long lived stable particles. The SET is located in the barrel part between the TPC and the central barrel electromagnetic calorimeter (ECAL). The SET gives an entry point to the ECAL after the TPC field cage. It acts as the outermost silicon layer in the central barrel and also improves the overall momentum resolution. The SIT and SET, in addition to improving momentum resolution, provide time-stamping information; by combining the hits from these silicon detectors (especially the SET) with the TPC hits, a very precise time stamping is possible as explained in details in section 4.1.2.5. These two central silicon components may serve in monitoring the distortion of the TPC and for the alignment of the overall tracking.

The ETD is positioned between the TPC end plate and the end cap calorimeter system. The ETD provides an entry point for the calorimeter and improves the momentum resolution for charged tracks with a reduced path in the TPC. Moreover it helps reducing the effect of the material of the TPC end-plate (currently estimated to be 15% X_0). It thus might improve the matching efficiency between the TPC tracks and the shower clusters in the EM calorimeter. It also contributes to extending the lever arm and angular coverage of the overall tracking system at large angle. Both the ETD and the FTD ensure the full tracking hermeticity.

An intense R&D program is carried out to further develop the sensors and the overall detector concept. This work is in many areas done in close collaboration with groups from the LHC, as many of the requirements and technologies are similar.

2.2.1.1 The basic silicon sensor

The microstrip sensors that will equip the SIT, SET, and ETD components are the basic element of the silicon system architecture. The baseline sensor has an area of 10×10 cm^2, with 50 μm pitch, 200 μm thick silicon, edgeless (i.e. with a non-active edge decreased from a few 100 μm to a few tens of μm), and an integrated pitch adapter (IPA) in order to directly connect strips with the front-end nd ASIC channels. This design allows the construction of a detector without overlapping sensors, significantly simplifying the construction and minimising the material.

The sensor is undergoing a vigorous R&D program to identify the most appropriate technology and layout. A special effort is made to find more than one vendor to produce these sensors.

Reducing the non-active edge of the sensors is an important step towards reducing the material budget and simplifying the detector mechanical construction. Edgeless sensors allow building large area seamlessly tiled detector matrices and thus getting flat tracking areas without excess of material in the overlapping region between two silicon tiles, the tiles being made of one or several unique size strip sensors. Prototype sensors have been developed and successfully tested.

The integration of the pitch adapter into the basic silicon sensor is another important step towards simplification of the sensors. This would allow the direct connection of the front-end with

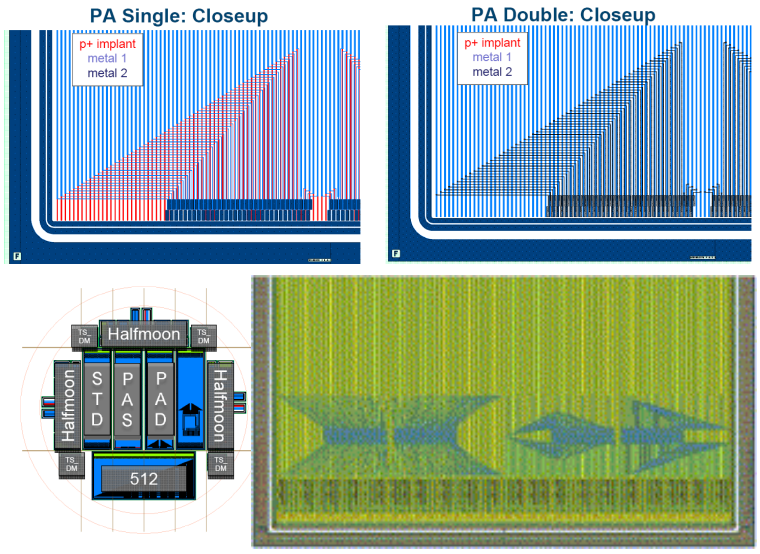

Figure III-2.9
Picture of a silicon test-structure developed to test the integrated pitch adapter technology.

the sensor chip. This technology has been pioneered by the ILC community through the SiLC collaboration [232, 234, 235], and has been adopted and further developed especially by the CMS upgrade program. Recently, progress has been achieved by including Integrated Pitch Adapter (IPA) prototypes in the test structures of the silicon sensors (see Figure III-2.9). The LHC groups are testing various IPA schemes and are studying the impact on the crosstalk, noise, and other sensor characteristics. This is indeed a very important step ahead and makes it feasible to have IPA fabricated by industry.

Another innovative packaging technology based on 3D-packaging using Through Silicon Vias (TSV) is currently under development in close collaboration with industry [236]. The technology has not reached the maturity needed to be included as a baseline but may well be in the future.

2.2.1.2 Front-end electronics

The front-end will be based on a custom designed ASIC realised in deep sub-micron CMOS technology. It will provide the analogue to digital conversion, and a high degree of digital processing capabilities, to minimise the data volume which needs to be transferred out of the detector. The chip will be developed with low-noise, low-power consumption in mind, and will be capable of power pulsing. To arrive at a compact design, new interconnection technologies will be explored, like bump bonding or 3D vertical interconnects.

Over the past years a prototype version of such a chip, the SiTRK ASIC, has been developed in the SiLC collaboration. It pioneered this aspect by introducing high-level data processing already at the front-end thanks to an early digitisation stage [237]. It was developed in 130 nm CMOS technology and each of its components was successfully tested. It includes an analogue pipeline, low noise operational amplifier, and an 8-bit Wilkinson ADC, together with the required control circuitry [238]. The next iteration of this chip will move to the commercial 65 nm technology.

2.2.1.3 Powering schemes and thermal management

A key element of the powering scheme for the silicon detectors is the use of pulsed powering. A significant part of the front-end ASIC is switched off in-between ILC bunch trains, thus reducing on average the power consumption by close to two orders of magnitude. In the development of the ASIC for silicon tracking the power pulsing capability has been taken into account.

Most of the power consumption and thus also the heat load will be concentrated in the ASICs at the ends of the ladders. A design of a cooling strategy based on forced cooled gas flow should be possible. Special care has to be taken to avoid the introduction of unwanted oscillations due to the gas flow. The complete inner tracking volume will need to be flooded with dry air to avoid condensation.

A significant reduction in the amount of material needed for the low voltage power cables can be achieved by either a DC-DC powering scheme, or by the use of super-capacitors mounted close to the front-ends. This technology is also used by the LHC experiment upgrades. First tests with ILD readout systems have delivered promising results.

2.2.1.4 Mechanical design and integration

The silicon tracking system poses several challenges for the mechanical design. It should introduce a low amount of dead material, be fairly simple and modular, but at the same time stable also during external manipulations of the detector. During detector push-pull operations it should maintain its position so that a new calibration can be done quickly and efficiently. The proposed mechanical design tries to address these issues.

The inner silicon detectors are supported from a central tube inside the inner radius of the TPC. This tube is hung on either side on the TPC endplates. SIT and FTD are both connected to this tube. A challenge is the development of a lightweight but stiff structure. Given the high degree of precision required for the inner detectors it might be needed to suspend this inner tube from the TPC using remote-controlled movers. This has not yet been studied in detail, but such movers might be needed to return the system back to a good initial alignment after a push-pull operation.

Studies are under way to investigate how well different functions can be integrated into the support structure. Cooling systems, calibration systems, and possibly even cabling can become an integral part of the support system, and thus in addition to providing the needed functionality, also help in minimising the overall material. Progress in materials will also be utilised to arrive at optimised structures. An example of such an 'intelligent' system is the one proposed for the Super-B support structure [239].

Within the silicon tracker two options are studied. One uses staves, the other one is based on super-modules. Both are built with Carbonfibre Reinforced Plastic (CFRP) material [240]. These are self-supporting light, but robust, structures assembled and inserted in the corresponding barrel layers. At the very end of the detector edge, an independent part hosts the module services, the cooling, and signal cabling connections. Because of its location at the detector ends, this strategic part can be replaced rather easily.

The preferred solution for the cable routing of the SIT component is that the cables run along the inner radius of the TPC, because it reduces the amount of material around the beam pipe and in front of the FTD as well. The cabling for the SET is less critical, and will run directly inside the calorimeter inner radius in z to the end of the silicon tracker, and follow the central cabling routes from there.

2.2.1.5 Calibration and alignment

The hybrid tracking system as proposed for ILD has a number of special considerations.

1. Alignment of the SIT and SET with respect to the TPC;
2. Alignment of the ETD with the FTD and/ or the TPC, but the precision required in the ETD case is not the same as for the other Si tracking components;
3. Quick-and-precise re-installation and positioning of these components after push-pull operation.

A particular challenge for the central silicon system is the precise alignment of components separated by large distances like the SIT and the SET. In principle a system of laser beams can be used to register these systems relative to each other, with sufficient precision. There is, to date, no detailed design which could be integrated with the overall ILD layout. However no fundamental problems are anticipated.

The silicon trackers are mechanically stable devices that will help to improve the absolute alignment of the overall tracking system, and of ILD as a whole. This alignment is sensitive in particular to temperature fluctuations, which will need to be understood to the 2 μm level. These alignment systematics will be very different from those for the TPC. The TPC is sensitive to ambient temperature and to atmospheric pressure variations, to non-homogeneities in electric and magnetic fields, etc. In particular the electric drift field in the TPC may depend on space charge transient effects due to variations in the machine induced backgrounds. The SIT and SET give an independent and effective means to monitor accurately such effects with real data. Experience at LEP has shown that this capability gives an invaluable redundancy during data analysis, and a unique mean to disentangle and understand anomalous behaviour. It is a necessary complement to the unique pattern recognition capabilities of the TPC.

The experience gained on LHC silicon tracking systems shows that, once the mechanical alignment is achieved with the precision of about 100 μm, the commissioning with cosmic rays allows a remarkably precise alignment. Data with colliding beams will then be used to further improve the alignment.

2.2.1.6 Future R&D perspectives

Silicon tracking is a field which is developing very rapidly. The need of the LHC experiments to make major upgrades to their silicon based tracker within the next few years is driving innovation in the field. Many developments in the area of sensors, readout and mechanical construction are expected in the near future.

The baseline solutions for constructing the silicon envelope components of the ILD detector concept are well established. Beyond baseline R&D activities are pursued in parallel on new sensor technologies, new associated front-ends, and higher-level signal processing. Solutions with much higher granularity are being investigated including a full silicon pixel tracker [241], or a modest version of this proposal, where only part of the silicon envelope is made with pixels. Depending on when the ILC will be built, the silicon envelope tracking components might evolve in design and technology.

2.2.2 Forward silicon tracking

The forward tracking in the ILD concept contains seven tracking disks installed between the beam pipe and the inner field cage of the TPC. The first two are realised as pixel detectors to cope with the expected high occupancies in this area, the remaining five are strip detectors. The layout is given in detail in Table III-2.3. Their precise space points with a large lever arm are crucial to maintain good momentum resolution in the forward region.

The detection of charged particles emitted in the forward and backward directions faces a number of significant challenges. The magnetic field becomes less and less useful in bending charged tracks in the forward region, thus making a precise momentum determination difficult. In addition forward

Table III-2.3
Layout of the Forward Tracking Disks. The quoted single hit resolution for the pixel disk depends on its technological implementation which has also an effect on the material budget.

FTD (baseline: pixels for two inner disks, microstrips for the rest)				
	Geometry		Characteristics	Material
R [mm]	Z [mm]	cos θ	Resolution R-ϕ [μm]	RL [%]
39-164	220	0.985-0.802		0.25-0.5
49.6-164	371.3	0.991-0.914	σ=3-6	0.25-0.5
70.1-308	644.9	0.994-0.902		0.65
100.3-309	1046.1	0.994-0.959		0.65
130.4-309	1447.3	0.995-0.998	σ=7.0	0.65
160.5-309	1848.5	0.996-0.986		0.65
190.5-309	2250	0.996-0.990		0.65

going jets are not opened up by the field as much as they are in the barrel, resulting in significantly larger occupancies. Finally, the disk are very close to the beam axis and are thus prone to high backgrounds from the interaction region.

2.2.2.1 Detector optimisation

The main challenge for the forward tracker is to deliver good momentum resolution in this difficult environment. The momentum resolution scales approximately with the inverse of the B-field component orthogonal to the direction of movement of the charged particle, with the inverse of the square of the track length being measured, and with the inverse of the number of hits. Thus in the forward direction with the effective B-field approaching zero as the particle travels along the beam pipe, high precision measurements using a large lever arm are needed.

The parameters are highly constrained by the overall detector layout (and cost). Additional measurement layers would improve the momentum resolution for very high momentum tracks, but the extra material considerably reduces the reconstruction precision for the abundant low momentum tracks.

To achieve the best momentum measurement within the constraints described above, the FTD is instrumented with those detectors that yield the most precise $r\phi$-measurement within the tight material budget. Micro-strip detectors have proven to be capable of resolutions of several microns with minimum channel and power density. The orthogonal radial measurement is only relevant in the pattern recognition stage and little is gained by improving the radial resolution beyond the several hundred microns that is readily obtained with pairs of micro-strip detectors under a small stereo angle.

The extrapolation of the trajectories of charged particles emitted at very shallow angle to the interaction point is crucial for flavour tagging of very forward jets. The optimal segmentation and placement has been studied in the context of the CLIC study [242].

To achieve a precise measurement of the longitudinal impact parameter the radial segmentation of the innermost disks is crucial. An optimisation of the vertexing performance for very shallow tracks requires a first precise measurement at minimal distance from the interaction point. Even a small amount of material before the first measurement severely degrades the measurement. The best performance in this respect is obtained by minimising the gap between the z-position corresponding to the end-of-stave of the vertex detector and that of the innermost disk. Services of the vertex detector barrel must avoid as much as possible the line of sight between the interaction point and the innermost disk.

2.2.2.2 Pixel disk implementation

Due to their higher occupancy, the first two disks are implemented using highly granular pixel detectors. As in section 2.1, three technologies are under consideration: CPS, CCD and DEPFET.

For the CMOS based technology (CPS) each of the two stations closest to the interaction point (IP) (FTD1 and FTD2) would be equipped with 50 μm thin CPS sensors on their front and back sides, thus providing four high resolution space points per track traversing the end-cap. Each station

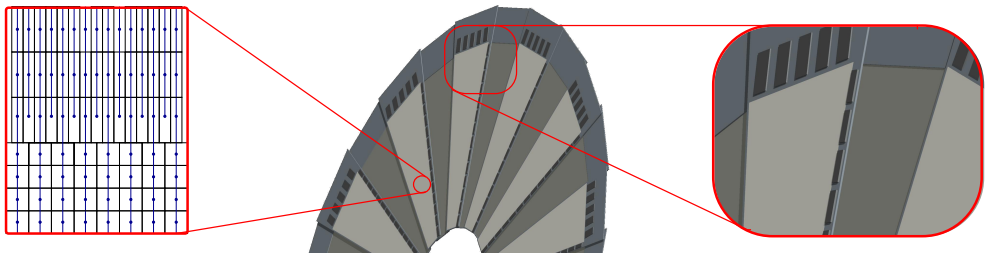

Figure III-2.10. A half-disk for the FTD in the DEPFET petal concept. The rightmost zoom image shows a detail of the end-of-petal area that houses the read-out electronics and the balcony with the steering chips. The leftmost image shows the region at $R = 8$ cm where both the column width and the R-dimension of the pixels changes.

side is composed of 16, slightly overlapping, petals featuring a structure similar to the one of the double-sided ladders equipping the vertex detector. With a mechanical support including a 2 mm thick, low density, SiC foam layer, the total material budget of a station is expected to be $\sim 0.5\%$ X_0, averaged over the azimuthal angle.

The petals are equipped with four sensors, which intercept different 3 cm wide radius ranges. Each sensor is equipped with the same number of pixels, so that the size of the pixels increases with increasing radius. Each sensor type is thus composed of an active area of 480 $\times$ 1152 pixels. The dimensions of the pixels vary from 26 $\times$ 29 $\mu\mathrm{m}^2$ for the innermost sensor to 26 $\times$ 67 $\mu\mathrm{m}^2$ for the outermost one. The single point resolution varies accordingly from $\lesssim$ 6 to 9 $\mu\mathrm{m}$, depending on the sensor.

The CPS architecture reproduces the one used for the vertex detector, based on a continuous read-out in rolling shutter mode allowing efficient power saving. The sensitive area is subdivided in columns of 480 pixels read out continuously and in parallel. Within each column, the pixels are read out in pairs to accelerate the read-out, resulting in a frame read-out time of $\lesssim$ 50 $\mu\mathrm{s}$. Each column ends with a discriminator, whose outputs are processed through a sparsification circuitry integrated in the sensor periphery.

Each petal dissipates nearly 10 W, resulting in a total instantaneous power dissipation of $\sim$ 600 W per end-cap. Assuming a powering duty cycle of $\lesssim$ 2 %, the average power dissipation per end-cap is in the order of 10 W, compatible with air flow cooling.

Industrial stitching may allow combining several of the four chips composing a petal in one single silicon slab, for the benefit of material budget, system integration and alignment. This possibility remains however to be assessed in view of the fabrication yield and handling issues.

Fine pixel CCDs (FPCCDs) can be used as sensors for FTD1 and FTD2. Each disk is divided into sectors and each sector is covered by one trapezoidal FPCCD sensor. FPCCD sensors can be as thin as 50 μm and the material budget can be $0.15\%X_0$ per layer including the support structure. Electrical connection (clock input and signal output) is made at the outer edge of the sensors using Kapton flexible cables.

From the consideration of beam background and pixel occupancy, a pixel size of 10 μm can be used with the signal accumulation in one train and read out between trains. Spatial resolution better than 3 μm is expected with this pixel size. The total number of readout channels is 1400/disk and the power dissipation is 21 W/disk (15 mW/ch) including on-chip source followers and the front-end ASICs.

The DEPFET-based all silicon ladder concept is adapted to the geometry of the Forward Tracking Disks, as shown in Figure III-2.10. The solution is optimised to yield excellent $r - \phi$ resolution of

3-5 μm, with narrow read-out columns oriented radially. The read-out electronics is located at the end-of-petal area on the upper rim of the petal. The steering chips are located on the balcony that is visible in the zoom image. The active area of the petal is divided in two sections that meet at $R = 8$ cm. A zoom image is shown in the leftmost panel of Figure III-2.10. In each of these the column pitch fans out gradually from 25 μm to 50 μm with increasing radial distance to the beam line. Along the column direction (i.e. radially) three pixel dimensions are moreover used: 25 μm in the innermost region, 50 μm for $6 < R < 8$ cm and 100 μm for $R > 8$ cm. The increased granularity at small radius ensures good vertexing performance for very shallow tracks that leave no hits on the barrel vertex detector and helps to cope with the strongly increasing background levels towards the smallest R values.

The material budget of this arrangement is comparable to that of the barrel vertex detector based on the same all silicon concept (0.15% X_0/layer). The power consumption per unit area is slightly less due to the slightly smaller column density, allowing for cooling through a forced air flow.

2.2.2.3 Strip disk implementation

In the following paragraphs the key design aspects of the microstrip-based FTD disks are briefly presented.

Given the relatively low hit occupancy expected for the disks three to seven, the detector technology based on AC coupled p-on-n fine-pitch microstrip silicon sensors is proposed as the detector baseline. Two sensors will be glued on opposite sides of the same petal frame with a stereo angle configuration allowing for a two dimensional determination of the particle's impact point on the petal; furthermore, for minimising the multiple scattering, the sensors will be manufactured on wafers 200 μm thick and a second metal layer will be used to fan-in the signals into the FEE input pads, avoiding the material burden introduced by an external pitch adaptor.

As an option beyond the above introduced baseline, with somewhat reduced material budget, real double-side microstrip sensors are being considered. Similar sensors have been already employed successfully [243].

The strip FTD requires around 4000 front-end readout chips with 256 channels and a 50 μm pitch. The FE readout chip will have the typical architecture used for Si-strip readout in high energy physics experiments [244], adapted to the particular conditions of the experiment and the sensors. A channel composed of preamplifier and shaper followed by analogue pipelines, sparsification and analogue to digital conversion stages and simple slow control and processing digital electronics is planned. Special care has to be taken to maintain an acceptable ratio between noise and power consumption. A limit of 700 μW per channel and a figure of noise of 400 e^- for a detector capacitance of 20 pF with 2 μs shaping time are established as specifications. Power reduction techniques, including switching off analogue modules during defined periods, and the use of a deep-submicron technology are essential to manage the constrains. Prototypes of the constituent modules, the main channel and several multichannel chips are being planned [245].

The outer FTD disks are segmented in 16 petals mounted in two half rings manufactured in composite material. The petal consists in a trapezoidal shaped frame made of monolithic high modulus carbon fibre material laminate (M55J) while the ring is designed as a sandwich structure with two skins of high modulus carbon fibre laminate with a foam or honeycomb core. The petals must have a good face finishing (planarity) allowing for the proper gluing of the sensors. Four sensors will be glued in each petal, two per petal face (false double-sided sensor). The electronic hybrids will be located on the frame edge. Adjacent petals are staged along the z coordinate allowing for a petal's edge overlapping along the azimuthal coordinate (φ).

2.2.2.4 Power distribution system

With the current design one disk of the FTD strip system will use less than 200 W of power during electronics-on time, or less than 40 W on average. This estimate has been computed taking into account the front-end and power distribution electronics dissipation; a conservative effective duty cycle of 20% has been assumed. For the complete strip detector less than 400 W of power needs to be dissipated [246].

Two different power distribution system topologies are under study for the FTD sub-detector. One is based on DC-DC power converters; the other is based on super-capacitors and low voltage regulators. DC-DC based power distribution system has been the preferred option for the latest generation of HEP experiments; however, this topology presents some limitations due to stability and EMI issues [247] that have to be analysed in detail.

A supercapacitor-based power distribution system has been selected as an alternative option to power up the strip FTD system [248]. The FTD will be powered remotely by a current source that supplies low current to the periphery of each disk. At that location a set of super-capacitors will supply the high peak current to the periphery of each petal, where LV regulators stabilise the voltage at the input of each hybrid electronics. The most important element of this option are the super-capacitors. Supercapacitors for power applications are emerging devices [249]. The high power density of these capacitors makes them a very suitable solution for the characteristics required for a power pulsing system. The use of this type of device is new for HEP experiments but not for industrial applications. Key issues which need to be studied are to understand the radiation hardness of these devices, and to optimise the number of power cycles before failure.

At the modest heat loads of the of strip-based FTD disks, about 6-9 mW/cm^2, an air-forced cooling system seems a feasible and reliable solution. Cooling implementations have been studied which include air conducts in the CFRP supporting cylinder for blowing cool air into the detector, and extract the heated air. The actual challenge for this cooling system is to probe its validity to extract the heat dissipated by the two inner pixelated disks which have a much higher heat load. Finite element simulations are being carried out to optimise the layout and get a first estimate of the required air flow and temperature. Moreover, the mechanical instabilities introduced by the blowing air should be studied in dedicated mockups.

2.2.2.5 Integration and System Aspects

The FTD system is to be installed inside the boundaries defined by the beam pipe outer radius and the inner surface of the support cylinder which encloses all the inner volume delimited by the TPC inner radius. All the FTD disks are supported by this cylinder. The vertex detector and the SIT are directly supported from the beam pipe, which is turn is hung from the support cylinder through the third disk of the FTD. To comply with this extra requirement, the FTD ring three will be reinforced.

For each petal a dimensional metrology measurement of predefined fiducial marks will be carried out at each step of the assembly procedure, including the final mounting of the eight petals in its corresponding half supporting ring. During system assembly, the lower half ring will be mounted directly on the lower half of the inner support cylinder. After the installation of all the lower half rings, VTX, SIT, and beam pipe, the upper half ring will be connected to the already mounted lower half ring. Finally, the upper part of the support cylinder will complete the assembly of the FTD systems inside the support cylinder envelope. The fully equipped support cylinder will then be finally inserted as a whole into the inner volume bounded by the TPC inner radius.

Structural (deformation and displacements) and environmental (temperature and humidity) real-time monitoring of the FTD supporting structure is instrumental to achieve the design accuracy under the major detector movements required by the push-pull operating mode. Structural monitoring

should be focused on the monitoring of those overall deformation modes called 'weak modes' to which the conventional track-based off-line alignment algorithms are blind. As monitoring technology in-fibre Bragg grating sensors (FBG) will be used [250]; FBG sensors have become a very attractive solution for strain and temperature monitoring in hostile or hazardous environments. In particular, their small weight, size and intrinsic immunity to EMI combined with the absence of electrical signals and cables have recently encouraged the use of FBG sensors in high energy physics experiments [251, 252]. Moreover, FBG sensors can be embedded in composite materials, allowing the fabrication of the so-called smart structures where the actual sensors are just part of the CFRP laminate, allowing for a straight forward integration into the supporting structure with a negligible interference from the point of view of the material budget. This is the technological solution adopted for the real-time monitoring of the FTD supporting structure [253].

A careful electrical grounding design is necessary to preserve the performance of the front-end electronics. For this reason, it will be necessary to develop an electromagnetic compatibility (EMC) plan [254] that systematically approaches the grounding design and quantifies the immunity/ emission of the electronic systems to integrate safely the FTD system. The EMC plan comprises two basic steps; grounding topology definition and EMC test.

2.3 The ILD TPC system

The central tracker of ILD is a Time Projection Chamber (TPC). A TPC tracker in a linear collider experiment offers several advantages. Tracks can be measured with a large number of three-dimensional (r, ϕ, z) space points. The point resolution, σ_{point}, and double-hit resolution, which are moderate when compared to silicon detectors, are compensated by continuous tracking. The TPC presents a minimum amount of material as required for the best calorimeter and PFA performance. A low material budget also minimises the effects due to the $\simeq 10^3$ beamstrahlung photons per bunch-crossing which traverse the barrel region [255]. Topological time-stamping in conjunction with inner silicon detectors is an important tool that is explained in section 6.1.2.5. To obtain good momentum resolution and to suppress backgrounds, the detector will be situated in a strong magnetic field of 3.5 T. Under this condition a point resolution of better than 100 μm for the complete drift and a double hit resolution of < 2 mm are possible.

Continuous tracking facilitates the reconstruction of non-pointing tracks which are significant for the particle-flow measurement and for the reconstruction of physics signatures in many scenarios. The TPC yields particle identification via the specific energy loss dE/dx which is valuable for many physics analyses.

Over the past years systematic R&D work to develop the design of a high-resolution TPC for a linear collider detector has been pursued in the context of the LCTPC collaboration [227, 256, 257, 258].

2.3.1 Design of the TPC

The main parameters for the TPC are summarised in Table III-2.4. The overall dimensions of the ILD detector and the TPC have been optimised to obtain the best physics performance, as described in the ILD Letter of Intent (LOI) [198]. The design goal has been to maintain a very low material budget and to achieve the required single and double-point resolution. The mechanical structure of the TPC consists of an endplate, where the readout of the amplified signals takes place using custom-designed electronics, and a fieldcage, made from advanced composite materials. Two options for the gas amplification systems are Micromegas [259] and Gas Electron Multipliers (GEM) [260]. At present either option would use pads of size $\approx 1 \times\ 6\ \text{mm}^2$, resulting in about 10^6 pads per endplate. An alternative technology of a pixelated readout with much smaller pitch is being investigated [261].

The readout endplate (Figure III-2.11) is a concentric assembly of modules. The modules

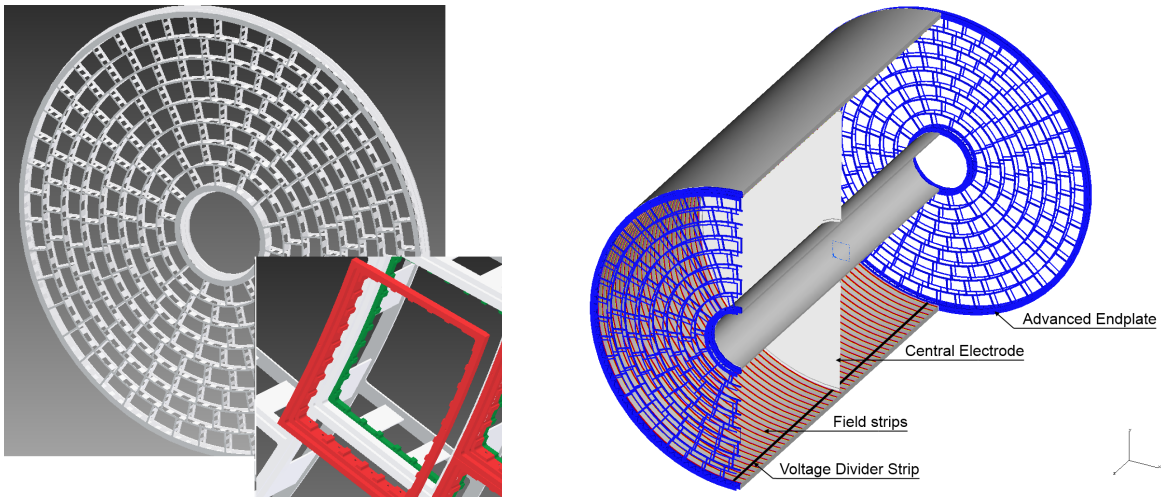

Figure III-2.11. Left: Drawing of the proposed end-plate for the TPC. In the insert a backframe which is supporting the actual readout module, is shown. Right: Conceptual sketch of the TPC system showing the main parts of the TPC (not to scale).

Table III-2.4 Performance and design parameters for the TPC with standard electronics and pad readout.

Parameter	
Geometrical parameters	r_{in} r_{out} z 329 mm 1808 mm $\pm$ 2350 mm
Solid angle coverage	up to $\cos\theta \simeq 0.98$ (10 pad rows)
TPC material budget	$\simeq 0.05$ X_0 including outer fieldcage in r < 0.25 X_0 for readout endcaps in z
Number of pads/timebuckets	$\simeq$ 1-2 $\times$ 10^6/1000 per endcap
Pad pitch/ no.padrows	$\simeq 1\times$ 6 mm^2 for 220 padrows
σ_{point} in $r\phi$	$\simeq$ 60 μm for zero drift, $<$ 100 μm overall
σ_{point} in rz	$\simeq 0.4 - 1.4$ mm (for zero – full drift)
2-hit resolution in $r\phi$	$\simeq 2$ mm
2-hit resolution in rz	$\simeq 6$ mm
dE/dx resolution	$\simeq 5$ %
Momentum resolution at B=3.5 T	$\delta(1/p_t) \simeq 10^{-4}$/GeV/c (TPC only)

are self-contained and integrate the gas amplification, readout electronics, supply voltages, and cooling [262].

2.3.1.1 Gas amplification system

The gas amplification system for a pad-based TPC will be either GEM or Micromegas (see [263] and [264] for examples of results using small prototypes). It has been demonstrated that both amplification technologies combined with pad readout can be built as modules which cover large areas with little dead space.

The use of Multi-Wire Proportional Chamber (MWPC) technology has been ruled out [264], because it does not meet the ambitious performance goals.

Two or three GEM foils are stacked together to achieve sufficient charge amplification. For a GEM readout the transverse diffusion within the GEM stack itself is enough to spread the charge over

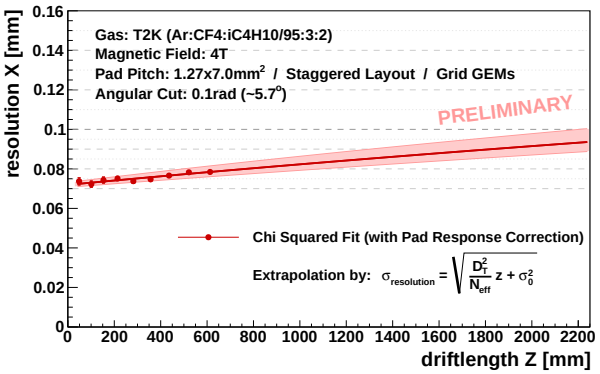

Figure III-2.12
Measured point resolution using data taken with a triple GEM stack at a magnetic field of 4 T, recorded in a small TPC prototype with T2K gas.

several 1 mm wide pads, which enables a good point reconstruction.

Micromegas have enough amplification in a single structure, but the spatial extent of the signals is very small on the readout plane. In order to spread the charge signal out over several pads, Micromegas use a resistive coating on the anode surface with resistivity of order 2 to 3 MΩ per square [258] [265].

The properties of the gas determine the drift velocity and the diffusion constant [266]. The parameters are chosen to minimise the diffusion in the transverse and longitudinal directions, to preserve an intrinsically excellent resolution.

For a drift length of more than 2 m and a high field of 3.5 T, the so-called T2K gas mixture (Ar-CF4(3%)-isobutane(2%) [267]) is a promising candidate, as was demonstrated using a small prototype chamber [268] and equipped with Grid GEMs [269, 270]. Data taken with that chamber are presented in Figure III-2.12: the single point resolution versus the drift length as measured in a 4 T magnetic field. The length of the chamber was 600 mm, and the extrapolation (error indicated by pink shaded area [271]) to full drift for the ILD TPC agrees with the goal of a resolution of better than 100 μm, as predicted by simulation [198].

2.3.1.2 Endplate

The modules are integrated on an endplate (Figure III-2.11) which closes the TPC gas volume and supports the modules. It is important that he endplate is designed to have low mass, while retaining the required mechanical and thermal stability [262].

The material of the endplate in front of the endcap calorimeter can potentially disturb the particle flow performance. In recent studies [258, 272, 273] the particle flow performance was evaluated using the PandoraPFA program [274] and the full ILD simulation for a range of endplate thicknesses X_0. Increasing from 15% to 60% X_0 degrades the jet energy resolution from 4.2% to 4.8% for 45 GeV jets and 3.2% to 3.3% for 100 GeV jets (and about the same for 250 GeV jets). From this a material budget of up to $25\%X_0$ for the endplate seems acceptable.

A prototype for a low mass endplate has been designed and built for use with the Large Prototype (LP) TPC. It meets the requirements for the ILD TPC [262]. It is based on a thinned aluminium structure stabilised by a system of adjustable struts (Figure III-2.13 left). Finite element methods, which were validated by measurements, show that this system provides adequate stability and precision (an example is pictured in Figure III-2.13 right). The current design of the endplate foresees 240 modules of approximately 17×21 cm^2, as they are used in the large prototype. Depending on the final choice of technology the size will be optimised.

2.3.1.3 Readout module

Each readout module consists of the gas amplification system (GEM or Micromegas), the pad plane, the readout electronics, and cooling.

A design issue for the multi-GEM systems is the provision of a support system that keeps the GEM surfaces both flat and parallel without introducing dead space or adding too much material to the detector. Several options have been developed and successfully operated [258]. With a recently demonstrated system [269, 270] based on ceramic spacers, good flatness and mechanical stability could be demonstrated while introducing only about 2% of dead space.

The Micromegas system with one stage amplification has a fine wire mesh mounted in front of the readout pad plane. A system of small pillars maintains a constant distance between the mesh and the pad plane. This system has been shown to operate very reliably over long periods. The pillars introduce a dead area of a few %.

2.3.1.4 Readout electronics

Small pads of 1×6 mm^2 area require that the electronics per channel does not exceed this footprint; the most modern readout system for a TPC, the AFTER system developed for the T2K experiment [275], has a footprint per channel of about three times this area. A picture of Micromegas-based modules mounted on the LP is seen in Figure III-2.14 left and an event in figure III-2.14 right, taken during a testbeam run at DESY [276]. They demonstrate that, for this technology and a pad size of between $2.7 - 3.2 \times 6.1$ mm^2, a solution exists which fits inside the current module boundaries.

Efforts are underway to develop more compact, fast, low noise, and power pulsed systems [277, 278]. The fundamental layout consists of a charge sensitive preamplifier, a fast ADC, and a digital signal processing unit which is used to analyse the data online, find pulses, determine time and charge, and, where applicable, reduce the total amount of data.

The power management relies critically on the ability of the system to use power pulsing. Power pulsing has been demonstrated for the S-ALTRO16 system [278]. Even with power pulsing, however, an active cooling of the endplates will be needed, for which two-phase CO_2 cooling is planned. The power-pulsing goal is to reduce the power consumption to less than 100 W/m^2 (1 kW per endplate).

An alternative readout concept relies on the coupling of a gas amplification system and a pixelated silicon chip [261]. The Timepix chip, derived from the Medipix family of chips, has been used in a series of proof-of-principle experiments. The pixel sizes are about 50×50 μm and thus are small compared to the contribution from diffusion. The Timepix chip allows both time and charge to be measured per pixel, providing potentially a very detailed view of the charge pattern on the end plate. Challenges of this system are the large number of pixels, the readout speed, and the robust and safe integration of the silicon pixel chip with the gas amplification system. For the moment this system is considered to be an interesting variant to the more traditional pad-based readout systems, but is not

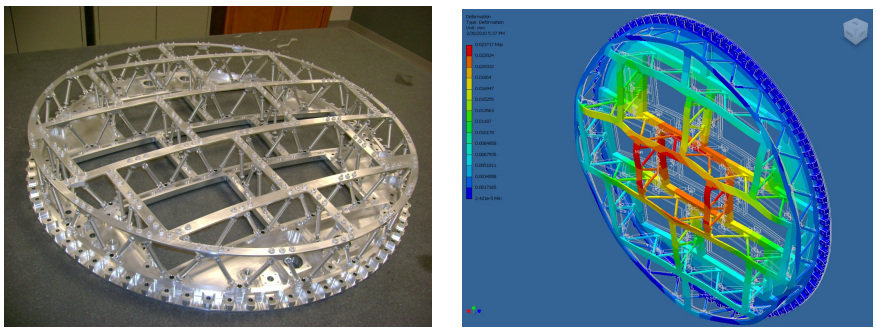

Figure III-2.13
Left: A low mass endplate for the LP. Right: Study of deflection of the LP endplate due to a load on the central module: load = 100 N, deflection = 23 μm.

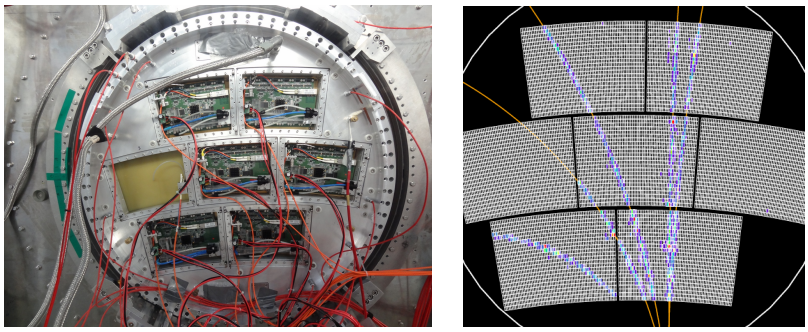

Figure III-2.14
Left: Six micromegas modules (with resistive anode) mounted on the endplate of the large prototype, equipped with highly integrated electronics. Right: An event recorded using a micromegas equipped readout at teh DESY testbeam facility.

yet far enough advanced to be proposed as an alternative to the baseline.

2.3.1.5 Fieldcage

The inner and the outer fieldcages will be built using composite materials [279]. A core made of honeycomb is covered on the inside and outside with a layer of glass-fibre reinforced epoxy. On the drift-volume side of the inner and outer cylinders, Kapton sheets with metallised potential strips provide insulation and field-shaping electrodes. The potential of the strips is defined by a resistive divider mounted inside the gas volume. Mirror strips on the back of the Kapton sheets shield the field against the grounds on the outside of the TPC, where each cylinder will be covered with grounding sheets.

The conceptual design of the fieldcage has been tested and demonstrated with the LP [279]. Based on this a prototype a material budget of 1% X_0 for the inner and 3% X_0 for the outer fieldcage seems to be feasible. The fieldcage will provide a homogeneous electric field. Simulations show that field distortions due to the electrical properties of the field cage alone should stay below 50 μm [280]. Designs exist for the transition from the fieldcage to the endcap, which will add only minimal material in the corner region. Experience from the large prototype shows that the mechanical tolerances of the system, in particular the parallelism of the cathode and the endcap, are difficult to achieve. A careful survey of the cathode and the endcap is mandatory to measure possible deviations so that they can be corrected later on. The design of the central cathode membrane is less well developed. At the moment a thin membrane is stretched between a light-weight inner and an outer ring, at $z = 0$, similar to the central cathode design of the ALICE TPC [281].

2.3.1.6 Support structure

The TPC support structure will be non-magnetic, have a low thermal expansion coefficient, be robust in all directions (x,y,z), maintain accuracy and stability over long time periods, absorb vibrations, and provide a position accuracy of 100 μm or better.

In the present design the TPC endplates are suspended from the solenoid. A number of spokes run radially along the faces of the calorimeter to the TPC endplates (Figure III-2.11 right). With the total mass of the TPC estimated to be around 2 t, the weight is not a problem. A mechanism must be developed which prevents the TPC to move in the longitudinal direction to ensure that the system is not damaged in case of earthquakes and simplifies the recovery of the alignment of the TPC after a push-pull cycle. In the present design, supports using double-T beams made of lightweight carbon, carbon fibre reinforced composite (CFRP) or by a system of flat CFRP ribbons are being studied. The ribbon system needs less space in the endcap-barrel transition region, but requires an additional fixation of the TPC in longitudinal direction.

The TPC fieldcage will support the inner and outer silicon trackers. While there are no conceptual issues, this additional load on the fieldcage might require a stiffer system and more material than anticipated.

Figure III-2.15. (Left) Effects of the ion disks on the electrons inside the TPC volume. The effects without (top half of the figure) and with (botton half of the figure) are compared. (Right) Expected distortions in $r - \phi$ as simulated for a disk of charge located inside the TPC drift volume at different z-values, for a range of radii. For more details see the text.

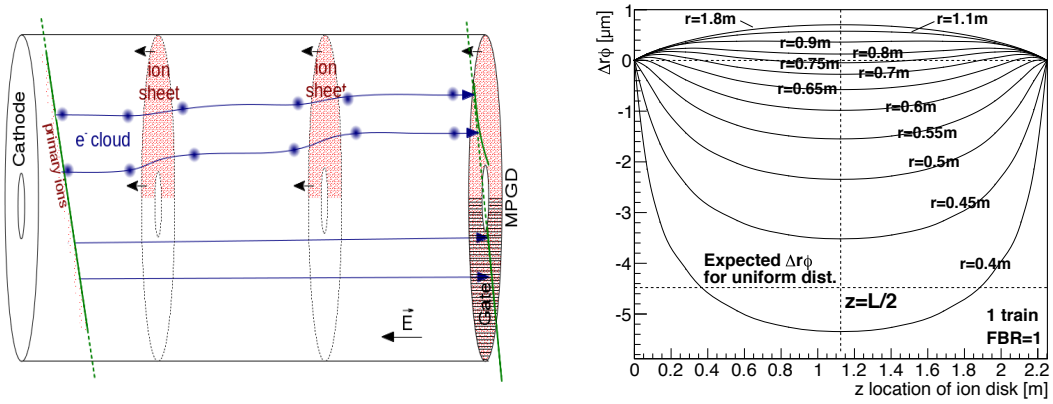

2.3.1.7 System performance

The design of the TPC system has been studied extensively to understand its impact on the overall performance. The electric field is covered in section 2.3.1.5. The main distortions in the TPC will originate from the magnetic field, which will need to be measured with high precision, as described in section 2.3.2.

Another source of deviations is the accumulation of charge inside the TPC drift volume. Studies and detailed simulations have been performed to understand the impact of ions on detector performance which were produced during the primary ionisation and during the amplification phase [282, 283]. The requirement of continuous operation during an ILC bunch train implies that no gating of primary ions will be possible during a bunch train.

The studies [282, 283] at a 500 GeV ILC have shown that the effects of primary ions are manageable and that effects from ions between a gate and the amplification region are negligible. Distortions arising from the so-called 'ion discs' due to the secondary-ion backflow into the drift region from the micro pattern gas detector (MPGD) gas-amplification region can result inup to 60 μm of transverse displacement of the drifting electrons. The ion discs arise because the TPC is active during the 1 ms bunch train followed by a 199 ms pause, while the backflow ions from the amplification region take about 1 s to drift out of the TPC. An ion gate can eliminate the discs by gating before the ions can enter the drift region, as seen in Figure III-2.15. In the upper half of this sketch of a TPC the drift of electrons in the TPC volume in the presence of ion feedback is shown. In the lower half the same situation but this time with an ion gating grip, is illustrated. [282, 283]. The track near the cathode gives rise to electron clouds that drift to the anode. The track registered by the MPGD at the anode in the x, y plane is indicated by solid lines, distorted (above) and undistorted (below). Present gas candidates are compatible with there being 3 discs in the chamber (without gating) and with a feedback ratio (the product of gas amplification and intrinsic ion suppression by the MPGD) of about 3; a distortion of $\approx$ 60 μm would occur without gating, at the inner fieldcage. The right plot shows the results from a simulation, for a single ion disk. Shown is the expected distortion as a function of the disk position in z, and at different radial positions within the TPC. The charge assumed for the disk is that from the normal operation. To obtain the total distortion this needs to be multiplied by the number of trains over which the TPC integrates (3) and the ratio between primary and secondary ions (1:3). With a maximum distortion of $6.4\mu m$ as seen in the plot, this results in a total distortion of around $60\mu m$, as quoted above. While it is in theory possible to

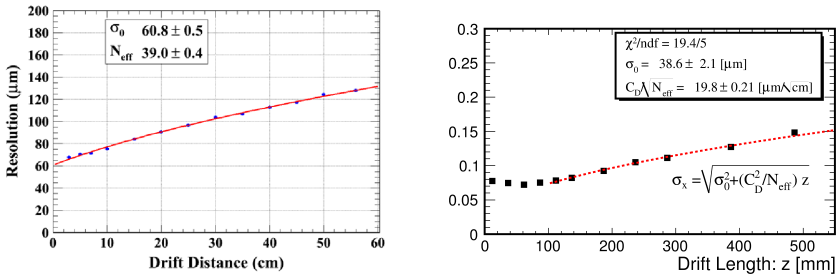

Figure III-2.16 Preliminary results from the large prototype running at 1 Tesla magnetic field, for (left) a micromegas readout [258] and (right) a GEM based readout [276]

correct for these distortions, it is planned to include an ion gate [284] into the design of all MPGD options; prototype gates have been manufactured.

2.3.2 Calibration and internal alignment of the TPC

As described in the LOI [198], achieving a momentum resolution an order of magnitude better than collider detectors to date will require significant effort. The systematics of the internal alignment of the TPC must be well understood to guarantee its performance. Redundant tools [285, 286] for solving this issue are Z peak running, laser system (described below), a good B-field map, possibly complemented by a matrix of Hall-plates/ NMR-probes outside the TPC, and use of the SIT and SET-layers inside the inner fieldcage and outside the outer fieldcage. In general based on experience at LEP, about 10 pb^{-1} of data at the Z peak during commissioning could be sufficient for the alignment of the different subdetectors, and typically 1 pb^{-1} during the year may be needed depending on the background and operation of the linear collider (e.g., after push-pull operations). For detector calibration, the accelerator is requested to deliver about $10^{32}/\mathrm{cm}^2/\mathrm{s}$ at the Z peak.

For alignment purposes a laser system is foreseen and may be integrated into the fieldcage [281, 287]. The laser system could either be used to create calibration tracks inside the drift volume, or to illuminate calibration spots on the cathode. Electrons will be released from these spots via the photo effect. These electrons then drift into the drift volume at well defined places and at well defined times, under the influence of all field components along its path. Such a system is being tested at the LP [258], and is being used at the T2K experiment [275, 288].

2.3.3 Status of R&D for the ILD TPC

To date at the LP, the GEM and Micromegas-based readout systems have been tested, both equipped with either pad-based or pixelated readout. GEM-equipped LP endplates have been tested with two and three modules. Figure III-2.16 shows preliminary resolution results from earlier [258] and recent [276] LP running. For both technologies the basic system goals have been reached.

The pixel-based readout scheme for a TPC [261] has so far only been used with small systems with up to eight readout chips. It has been shown to work with both GEM-based and Micromegas-based systems. Missing is the proof that large area readouts can be realised in this technology.

In addition to the issues described above, the following tasks are important:

- continue electron beam tests to perfect correction and alignment procedures;
- future tests for momentum resolution, for two-track resolution, and for performance in a jet environment;
- further reduction of the pad size is a topic for the far future.

Chapter 3
ILD Calorimeter System

Particle flow as a basis for event reconstruction has striking and far-reaching consequences in the design of the detector. This is particularly true for the calorimeter system. Particle flow implies that each particle be reconstructed individually in the detector. This requires unprecedented granularity for the electromagnetic and hadronic calorimeters, ECAL, HCAL and FCAL. To determine the properties of the particles precisely the system should be thick and hermetic, to minimise energy leackage. For a realistic detector a compact calorimeter design is favorable [289]. The imaging capabilities are thus emphasised more than the intrinsic single particle energy resolution, although the latter is still an important ingredient to the particle flow performance for jets [274].

3.1 Calorimeter overview

The calorimeter system for ILD consists of a nearly cylindrical barrel system and two large end caps. At very small angles dedicated calorimeter systems provide hermeticity and sensitity to measure the luminosity and monitor beam parameters.

The barrel and end cap calorimeter is divided in depth into an electromagnetic and hadronic section. The principal role of the ECAL is to identify photons and measure their energy. The capability to separate photons from each other and from near-by particles is of prime importance. The ECAL forms the first section for hadron showers and, with its fine segmentation, makes important contributions to the hadron hadron separation. The HCAL is optimized to measure neutral hadrons well and thus has to provide the topological resolution power for separating them from the showers of the much more abundant charged hadrons which must be matched with tracks.

In the very forward region, three systems, LumiCal, BeamCal and LHCAL, are proposed. These system serve as luminosity monitor (LCAL) and beamstrahlungsmonitor (BeamCal), and they close the coverage down to very small angles, also for neutral hadrons (LHCAL).

The transverse and longitudinal segmentation of both calorimeters has been optimised based on detailed simulation and test beam data. It has been shown that the granularity must be of the order of X_0 in all three dimensions. This implies that a sampling calorimeter is the best option for both ECAL and HCAL. For the ECAL the most compact design can be realised with tungsten as absorber material. For the HCAL iron is chosen as this allows an excellent energy resolution for hadrons at manageable granularity.

For the ECAL, silicon pad diodes lead to the highest possible compactness (and effective Molière radius) and exhibit excellent stability of calibration. As an option scintillating strips with silicon photo-sensor readout are studied, which provide a similar effective segmentation. The two technologies can be combined in order to reach a cost-performance optimum.

For the hadronic calorimeter, two options have been developed: one based on scintillator tiles with silicon photo-sensors and analogue read-out electronics, and one based on gaseous devices with two-bit, so-called semi-digital readout but finer transverse segmentation. The main development

for gaseous readout planes uses glass resistive plate chambers (RPCs), but structures based on micromegas are being considered as alternatives. For the HCAL barrel, two different geometrical concepts of routing the read-out are being proposed, independently of the read-out technology.

3.1.1 The challenges of high granularity

The ILD calorimeter system will have about 10^8 channels in total. Handling such a large number of channels presents a significant challenge. A compact and hermetic design can only be realised if the readout system is as much as possible integrated into the sensitive layers. Special care needs to be taken to minimise the power consumption of the readout. The ILD concept has adopted a scheme to power pulse the detector in between bunch trains, which will be an important ingredient of the power management strategy of the calorimeter as well. The large number of channels will also impact the calibration strategies for the detector. In particular in view of the anticipated push-pull operation a fast and efficient calibration will be needed.

The main challenges of the calorimeter system are the development of optimised and cost effective sensor systems, the design of a low power integrated readout electronics, the development of an effective thermal management and calibration strategy, and a mechanical concept which combines large stability with minimal dead zones.

A central component to the design is the readout electronics. Is is based for all calorimeter systems on a family of custom developed ASICs which are derived from a common base system. The main features are

- Auto trigger and zero-suppression to reduce the data volume;
- Fully digital output;
- Power-pulsing capability to reduce the power dissipation by a factor 100 down to values of about $25\,\mu\mathrm{W/channel}$.

The ASIC family is based on a track and hold scheme with a pre-amplifier shaper sequence allowing for low noise and large dynamic range, and integrating analogue storage pipelines and digitisation. Slow control parameters ensure various configurations and therefore versatility with respect to sensor properties. The large number of channels requires minimising the data lines and the power. The digital readout integrated in the ASICs is therefore common to all the calorimeters. It has been designed to be daisy chained using a token ring mode, without any external components.

The following ASICs have been developed and are used for the different systems:

- HaRDROC [290] to read out the RPCs of the Semi-Digital Hadronic Calorimeter (SDHCAL).
- MICROROC [291] to readout the micromegas alternative of the SDHCAL.
- SPIROC [292] to readout the silicon photomultipliers, SiPM, of the analogue hadron calorimeter and of the electromagnetic calorimeter based on scintillators.
- SKIROC [293] to readout the Si pin diodes of the silicon tungsten electromagnetic calorimeter.

A generic data acquisition system has been developed which is used to read out all different systems [294]. This DAQ includes many features which are proposed for a full DAQ for the ILD detector, but is also suitable for use at a test beam setup.

3.1.2 Beam tests

A key role in the development of a calorimeter suitable for particle flow is played by extensive test beam experiments. A large international effort has been ongoing for a number of years, within the CALICE collaboration, to organise common test beam experiments for the different technologies considered. Given the complexity and the scale of the setups common infrastructure such as mechanical devices, readout systems, data acquisition and software were essential to successfully organise this effort. CALICE has been able to expose all major technologies to test beams and collect large amounts of data. Power pulsing has been demonstrated by the SDHCAL beam test which supports the approach

for all proposed technologies. It has also been verified that interactions of shower particles do not affect the stable operation of the embedded ASICs [295].

Detailed comparisons have been made between the test beam data and different simulation models. With recent results it is possible to match the simulation and data within typically 5% [296, 297, 298], sufficiently good to reliably model the performance of the detector. In the future further analysis of the data and more test beam campaigns will be needed to continually improve the understanding of data and simulation.

3.2 The electromagnetic calorimeter system

The particle flow paradigm has a large impact on the design of the electromagnetic calorimeter system. A key requirement is the capability of the system to separate overlapping showers from each other. A calorimeter for particle flow thus needs to be able to do pattern recognition in the shower. The electromagnetic section has a number of tasks to fulfill. It should be able to reconstruct photons in the presence of close-by particles. It should be able to reconstruct the detailed properties of the shower, such as shower shape, starting point and energy to distinguish early starting electromagnetic showers from hadronic ones. It should be noted that about half of the hadronic showers start inside the electromagnetic calorimeter. Thus an excellent three-dimensional granularity of the device is of utmost importance.

Earlier studies [198] have shown that the separation and reconstruction continues to improve, even with pixel size smaller than the Molière Radius. The study was done with square pixels between 1 mm and 2 cm size. For ILD a pixel size of $5\times5\,\mathrm{mm}^2$ has been chosen.

In order to have a better separation of close-by showers in the calorimeter, a system with a small Molière radius is advantageous. Further help in the separation between electromagnetic and hadronic showers can come from a large ratio between interaction length and radiation length. A small radiation length will move the start of the electromagnetic shower earlier in the calorimeter, while a large interaction length will reduce the fraction of hadronic showers starting in the ECAL.

The particle flow approach requires that the calorimeters are placed inside the magnetic coil, see Sec. 1.2. This has a major impact on the layout of the detector, and on the cost. Therefore, a compact calorimeter is preferred in order to minimise the overall physical thickness, which in turn reduces the size of the coil. For the ECAL tungsten is a good choice for the radiator as it is dense, and has a large ratio of interaction length to radiation length. The final system layout is a compromise between performance and cost. The energy resolution scales with $\sqrt{T}$, where T is the individual absorber plate thickness, while the cost scales linearly with the surface area of the readout layers. For ILD a solution with 30 readout layers and a thickness of the ECAL of $24\,\mathrm{X}_0$ has been chosen as the baseline. The optimisation of the layout is ongoing.

For a chosen pad size of $5\times5\,\mathrm{mm}^2$ silicon pin diodes are a good choice. They can cover large areas, are reliable and simple to operate, allow for a thin readout layer and can operate in the 3.5 T strong central magnetic field. While the very thin silicon layers offer excellent performance for the tracking capabilities of the calorimeter, the energy resolution is somewhat degraded. Here a less compact device, with a thicker readout layer, will show better performance.

As an alternative option a sensitive layer based on scintillator strips could be used. With scintillators individual tiles of size $5\times5\,\mathrm{mm}^2$ are difficult to realise. By using strips of $5\times45\,\mathrm{mm}^2$arranged in alternative directions an effective granularity approaching $5\times5\,\mathrm{mm}^2$ can be achieved. However, the reconstruction becomes more complicated, in particular in dense jets.

An alternative to silicon could be micromegas chambers. This technology however is significantly less advanced than either the silicon or the scintillator option.

In the following sections the detailed design of the ECAL will be presented. In addition industrial

aspects will be addressed, with variables such as numbers of producers, time of production, etc..

The requirements on granularity, compactness and particle separation lead to the choice of a sampling calorimeter with tungsten (radiation length $\mathrm{X}_0 = 3.5$ mm, Moliere Radius $\mathrm{R}_\mathrm{M} = 9$ mm and interaction length $=$ 99 mm) as absorber material. This allows for a compact design with a depth of roughly 24 X_0 within 20 cm and, compared to e.g. lead, a better separation of electromagnetic showers generated by near-by particles. To achieve an adequate energy resolution, the ECAL is longitudinally segmented into 30 layers, possibly with varying tungsten thicknesses. In order to optimise the pattern recognition performance, the active layers (either silicon diodes or scintillator) are segmented into cells with a lateral size of 5 mm.

3.2.1 Detector implementation

Figure III-3.1 shows the position of the electromagnetic calorimeter in the ILD detector, the trapezoidal form of the modules and how it is envisaged to be interfaced mechanically with the hadron calorimeter.

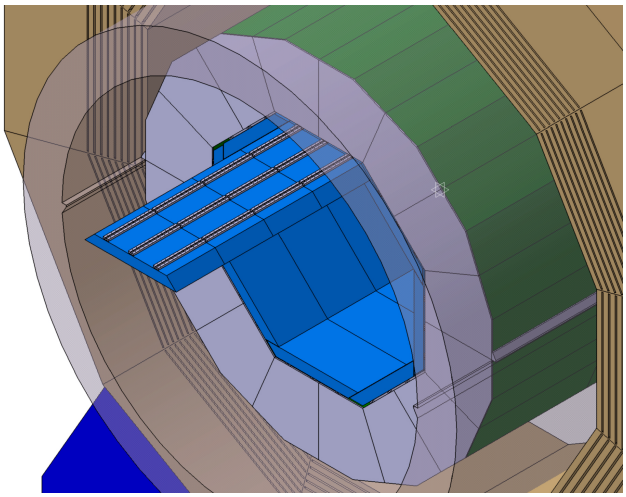

Figure III-3.1 The electromagnetic calorimeter (in blue) within the ILD Detector.

After several years of successful operation of small so called *physics prototypes* the focus of the work turns to the realisation of *technological prototypes*, see e.g. [299]. These prototypes address the engineering challenges which come along with the realisation of highly granular calorimeters.

3.2.1.1 Alveolar structure and general integration issues

The mechanical structure consists of a carbon reinforced epoxy (CRP) composite structure, which supports every second tungsten absorber plate. The carbon fibre structure ensures that the tungsten plates are at a well defined distance, and provide the overall mechanical integrity of the system (the so-called alveolar structure). Into the space between two tungsten plates another tungsten plate is inserted, which supports on both sides the active elements, the readout structure and necessary services. This results in a very compact structure with minimal dead space. The mechanical structure is equally well suited for both proposed technologies. Figure III-3.2 shows a prototype which is 3/5 of the size of a final structure for the barrel. For the end-cap region alveolar layers of up to 2.5 m length have been fabricated. While in the barrel the shape of all alveolar structures is the same, three different shapes of alveolar structures are needed in the end-caps. Recent studies revealed that in the end-caps considerable forces are exerted onto the thin carbon fibre walls, which enclose the alveolar structure. This issue has to be addressed in the coming R&D phase.

Figure III-3.3 shows a cross section through a calorimeter layer for the electromagnetic calorimeter with silicon (SiECAL), and one layer for the electromagnetic calorimeter with scintillator (ScECAL). The two readout layers of the SiECAL will be mounted on two sides of a tungsten slab, which is

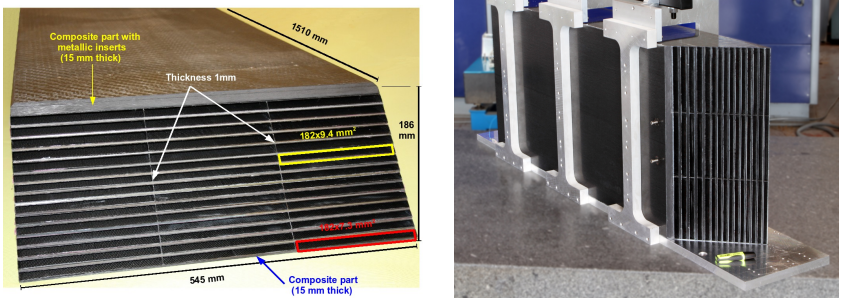

Figure III-3.2
Left: Front view with dimensions on the alveolar structure which houses the sensitive parts of the electromagnetic calorimeter prototype. Right: Side view on the completed structure and its mechanical protection.

inserted into the alveoli of the mechanical stricture. The insertion process has been successfully implemented for the physics prototype with short layers and has in addition been demonstrated with layers of up to 1.3 m length for a mechanical demonstrator of the technological prototype. In case of the ScECAL one side of the tungsten board will be equipped with scintillating strips for the x direction and the other side with strips for the y direction.

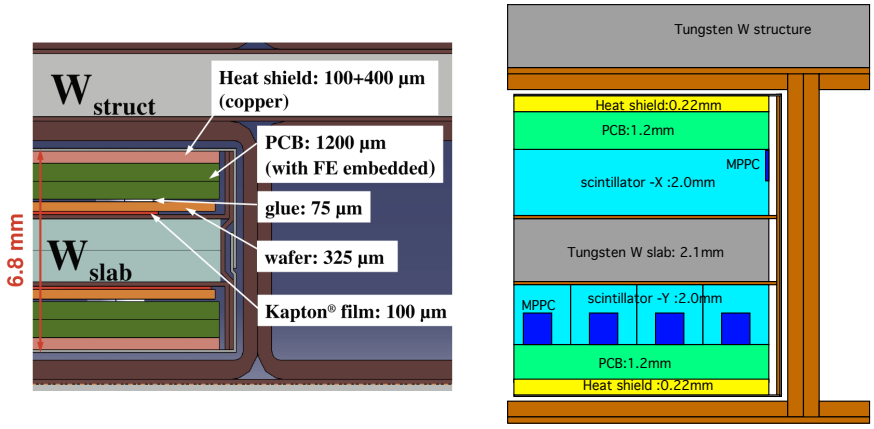

Figure III-3.3
Cross sections through electromagnetic calorimeter layers for the silicon option (left) and for the scintillator option (right).

A notable difference between the two options is the thickness of the active sensors. While silicon wafers can be produced easily with a thickness of a few 100 microns, the scintillator thickness needs to be at least 1 mm. This is due to the size of the photo-sensor MPPC and number of photons detected by this sensor.

3.2.1.2 Silicon wafers:

An example of a silicon wafer matrix as employed in the current R&D phase is shown in Fig. III-3.5. Silicon allows for a thin and easily segmented readout detection system suited for high granularity. The proposed technology is shown to deliver an excellent signal to noise ratio, which will allow to detect also small energy deposits, thus facilitating the two particle separation. The R&D goal for the S/N ratio is 10:1 at 1 MIP level.

The wafers are composed of silicon with a typical resistivity of $5\,\mathrm{k}\Omega\cdot\mathrm{cm}$. To achieve full depletion, the bias voltage to be applied to the wafers is between 100 V and 200 V. While the manufacturing of these wafers is a well known technique, a key challenge is to produce these wafers at a low cost in order to reduce the cost since a surface of about $3000\,\mathrm{m}^2$ will be needed for ILD. Contacts and discussions with industry are being developed.

The measurements with the physics prototype revealed cross talk between the guard ring which surrounds the silicon wafers and neighbouring silicon pads resulting in so-called square events, the frequency of which increased with the energy of primary electrons [300]. Currently an R&D effort is

under way to understand this problem and to optimise the system. These "square events" however show a very distinct signature so that during the offline reconstruction they could be removed. The final performance of the system was shown to be essentially unchanged by this cross-talk effect.

3.2.1.3 Scintillator strips

Optimal particle flow performance requires a cell size of about $5 \times 5\text{mm}^2$. The ScECAL has a strip width of 5 mm, while the length of the strip may depend on the performance of the details of the Particle Flow Algorithm. Current results indicate that 45 mm long strips are sufficient. Good hermeticity is also relevant for the calorimeter, which inspired a design in which the photosensor is embedded into the strip resulting in a dead area of 1.9% of the total surface. In order to reduce the passive area different ideas to extract the scintillation light at the bottom of the scintillator are under study.

3.2.1.4 Front-end electronics

Figure III-3.4 shows the performance of the SKIROC circuit. The curve shows the threshold of the 50% trigger efficiency as a function of the injected charge, in units of MIPs. The signal over noise ratio is about ten, which meets the goal.

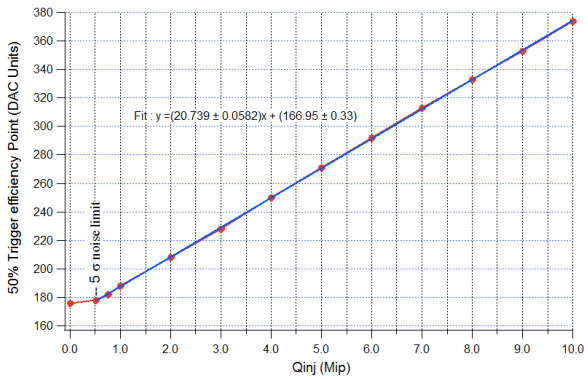

Figure III-3.4 Validation of the SKIROC circuit; shown is the threshold for 50% trigger efficiency as a function of the injected charge, in units of MIPs.

The front-end electronics has to be integrated into the calorimeter layers as illustrated in Figure III-3.3. This is a major challenge for the construction of the calorimeter. In the current design the room available for the readout circuits (ASICs) and the interface boards between the ASICs and the sensitive material is about 1.2 mm. Figure III-3.5 shows a picture of four ASICs bonded onto a PCB. The PCB is a very thin multi-layer board. PCBs for 16 ASICs are now available and will be equipped soon with ASICs. It should be noted that one of the major challenges to be solved in the near future is the planarity of the PCB. This issue is currently addressed in collaboration with industrial partners as well as by revising the entire assembly process of the detector. For protection purposes the ASICs will be encapsulated. For this encapsulation standard industrial processes can be applied.

3.2.1.5 Module assembly and cooling system:

A calorimeter layer will have a length of up to 1.5 m in the barrel and up to 2.5 m in the end-caps and will be composed of several units which carry the sensitive devices as well as the front end electronics. Great care is taken in the development of the technique to interconnect the individual units. The signal transfer along the slab to the interconnection pad must be very reliable and at the same time should not exert mechanical or thermal stress e.g. to the silicon wafers which are very close to the interconnection pads. Good progress has been made in the past years and a viable solution is currently applied to the first layers of the technological prototype of the SiECAL. The sensitive ensemble is then to be inserted into the alveolar structure which houses the calorimeter layers. The integration

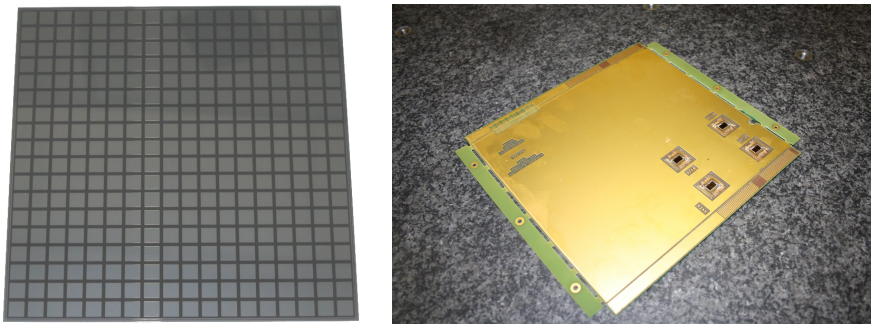

Figure III-3.5
Left: Example of a silicon wafer matrix as studied for the large scale prototype. Right: The wafers are mounted onto interface boards, PCB. The photo shows a PCB for the CALICE SiECAL prototype with wire bonded readout ASICs.

cradles are under development and a first integration test with a demonstrator has been successfully conducted.

For this demonstrator a leak-less water system for cooling has been developed [301]. A heat exchanger will be coupled to a copper drain at the outer part of the ECAL layers. The FPGAs mounted at the end of the modules are a major source of heat and are directly connected to the cooling pipes. Thin copper plates will ensure heat evacuation of residual heat from the inner parts of the detector layers. Earlier studies for SiECAL have shown that the temperature gradient along an ECAL layer is about 6° C in the detector end-caps and only 2.2^o C in the barrel region. Due to this comparatively small temperature gradient the concept of applying cooling only at the detector ends seems possible. The cooling pipes routed from outside the detector to the ECAL module will be passed in the 3 cm wide radial space between the HCAL and the ECAL.

3.2.1.6 Signal and power cable routing:

The gap between the electromagnetic and hadronic calorimeter is also used for the power and signal cables. Low voltage of about 5 V is needed for the front-end electronics while high voltage between 200 V or 50 V is needed to saturate the silicon wafers or to operate the silicon photomultipliers. Although no detailed concept exists today it is likely that the power will be brought close to a detector module and then fanned out to the individual layers. The data coming from the detector layers will be concentrated in a device on top of the module and routed out via one cable per module. This cable can also be used to transmit slow control and configuration commands to the individual detector elements. The challenge is to reduce the number of cables to an absolute minimum. In the ideal case signal propagation and power delivery would share the same cable.

3.2.2 Detector optimisation

The main parameters of the ECAL to be optimised are the inner radius of the detector, its thickness (in X_0), the number of detection layers, and the segmentation within the layers. These parameters determine the detector performance as well as its cost. A full cost-performance optimisation has not yet been performed, however several aspects required to perform such an optimization have been studied. The cost of the detector option with silicon sensors scales mainly with the surface area of the wafers, while the cost of the scintillator option scales with the number of channels. Many aspects of the optimization are, at least to first order, independent of the particular technological solution.

The inner radius of the ECAL is chosen to be relatively large, allowing particles within a hadronic jet to spread, thereby increasing particle separation in the calorimeters. An optimization of the inner radius and the magnetic field has been performed in the context of the Letter of Intent [198], where the jet energy resolution was found to scale approximately as $\sigma_E/E \sim R^{-1}B^{-0.3}$. The inner radius of the ECAL is strongly correlated with the outer radius of the TPC. The actual outer radius of the TPC has an effect on the momentum resolution of the tracking system. This dependence on the

variation in momentum resolution is however relatively weak.

3.2.2.1 Optimization of the silicon-only ECAL option

It has been shown in the ILD LOI and validated in beam test studies (see section 3.2.3 and [302]) that the silicon diodes are perfectly suited to meet the precision requirements of an ECAL at a future linear collider. The cost of such a high precision system has been estimated based on current best knowledge and careful extrapolations, and is presented in chapter 7. Several options are under study to understand the scaling of costs and to find ways to optimise the cost-performance ratio.

In the baseline model, the ECAL consists of 30 silicon (Si) and 29 tungsten (W) layers. Some details of the design are given in Table III-3.1. Five alternative ECAL models (26, 20, 16, 12 and 10 layers) have been studied. Their parameters are also summarised in Table III-3.1. Other configuration parameters such as the total tungsten thickness, a $1:2$ ratio of W thickness between inner and outer absorber layers, carbon fibre, cooling layers, Si thickness etc. remain the same for the six models.

Table III-3.1 ECAL models with different numbers of layers, $N_{lay.}$ and layer thicknesses, d, corresponding to different layer sets.

$N_{lay.}$	10		16		20		26		30	
W layers	6	3	10	5	13	6	17	8	20	9
d [mm]	6.7	13.3	4.0	8.0	3.2	6.3	2.4	4.8	2.1	4.2

The detector performance is studied using the example of the jet energy resolution measured as rms_{90} of the jet invariant mass distribution. The jets are reconstructed by the PandoraPFA algorithm [274] using $Z \to q\bar{q}$ events generated at $\sqrt{s} = 91$, 200, 360 and 500 GeV. Defined in [198], the rms_{90} is the root-mean-squared deviation from the mean of the jet invariant mass distribution, in the region around the mean, which contains 90% of the reconstructed events. To avoid the barrel/end-cap overlap region, a cut on the polar angle of the generated $q\bar{q}$ system of $|\cos\theta_{q\bar{q}}| < 0.7$ is applied.

The results in Figure III-3.6 and Table III-3.2 show the relative jet energy resolution for a single jet. A degradation of 10% in jet-energy resolution is observed going from 30 to 20 layers for events at 91 GeV, a smaller deterioration for higher energies. Going below 20 layers, the resolution starts to degrade significantly, though again less so at higher energies.

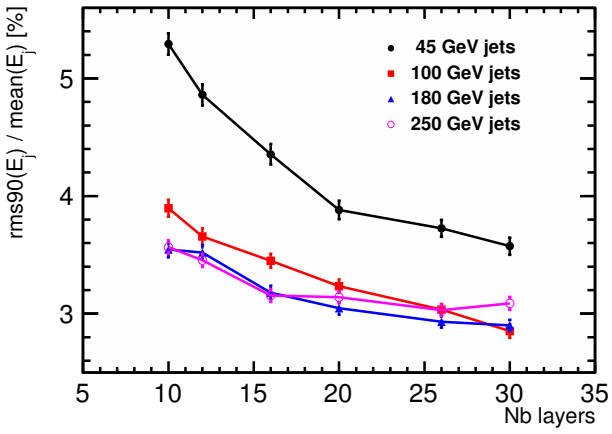

Figure III-3.6 Dependence of the relative jet energy resolution (rms_{90}/E_j) for single jets on the number of ECAL layers for events with $|\cos\theta_{q\bar{q}}| < 0.7$, for the SiECAL option. The resolutions are shown for $e^+e^- \to Z \to u\bar{u}, d\bar{d}, s\bar{s}$ events at $\sqrt{s} = 91$, 200, 360 and 500 GeV.

Table III-3.2
Jet energy resolution for $Z \to uds$ events with $|\cos\theta_{q\bar{q}}| < 0.7$ expressed as rms_{90}/E_j for SiECALs with different number of layers.

Jet energy	10 layers	16 layers	20 layers	26 layers	30 layers
45 GeV	5.3 ± 0.1	4.4 ± 0.1	3.9 ± 0.1	3.7 ± 0.1	3.6 ± 0.1
100 GeV	3.9 ± 0.1	3.5 ± 0.1	3.2 ± 0.1	3.0 ± 0.1	2.9 ± 0.1
180 GeV	3.6 ± 0.1	3.2 ± 0.1	3.1 ± 0.1	2.9 ± 0.1	2.9 ± 0.1
250 GeV	3.6 ± 0.1	3.2 ± 0.1	3.1 ± 0.1	3.0 ± 0.1	3.1 ± 0.1

3.2.2.2 Optimzation of the scintillator strip ECAL option

Two-jet events at 200 GeV centre of mass energy have been simulated with a scintillator-based ECAL and different strip lengths, and have been analysed using PandoraPFA. The jet energy resolution achieved as a function of different strip lengths is shown in Figure III-3.7. To resolve the ambiguities introduced by crossing strips of 5 mm width and different length a strip splitting algorithm (SSA) [303] has been developed, which is run in addition to PandoraPFA. For the purpose of this particular analysis, the strip thickness was set to the same as the SiECAL sensor thickness (0.5 mm). Results with and without the use of SSA are shown. At least for this type of event, no strong deterioration with increasing the strip length is found after applying SSA. A strip length of 45 mm is chosen for the baseline.

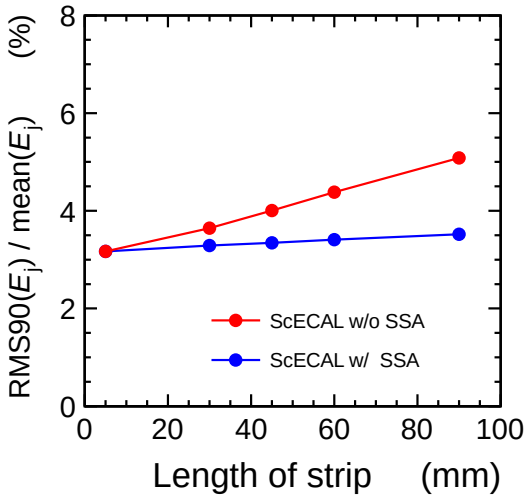

Figure III-3.7
Jet energy resolution for $e^+e^- \to Z \to u\bar{u}, d\bar{d}, s\bar{s}$ event at 200 GeV centre of mass energy as a function of strip length, for the ScECAL option, shown without (red) and with (blue) the strip splitting algorithm.

3.2.2.3 The hybrid ECAL option

Another option could be a mixture of silicon layers and scintillator-strip layers (Hybrid ECAL). Such an design, restricting the use of silicon sensors to the more critical areas of the detector (up to around the position of the maximum of electromagnetic showers), may be more cost-effective than a silicon-only ECAL. A number of configurations were studied, all using the same 27 layer tungsten absorber structure, the first 20 layers with a thickness of 2.1 mm, the remaining 7 of 3.5 mm. Note that this is a slightly different structure to the default ECAL, so results cannot be directly compared.

Different arrangements of the sensitive layers were studied. The inner layers were instrumented with silicon sensors and the outer layers with scintillator, with the following arrangements: (20 silicon + 8 scintillator); (14 silicon + 14 scintillator); and (8 silicon + 20 scintillator). Models with scintillator-only and silicon-only readout were also studied. The thickness of the sensitive detectors was 0.5 mm for silicon and 2.0 mm for scintillator. Note that the total thicknesses of these ECAL models are different, models with more scintillator layers having a larger thickness.

Events were reconstructed using the standard reconstruction chain, including PandoraPFA including the strip splitting algorithm. The jet energy resolution in $e^+e^- \to q\bar{q}(q = uds)$ events generated at centre of mass energies of 91, 200, 360, and 500 GeV was measured for each of these

ECAL models. Figure III-3.8 shows this jet energy resolution as a function of the fraction of ECAL layers which are scintillator, for each of the jet samples. For 45 GeV jets, the jet energy resolution does not degrade with increasing scintillator layers. At higher energies, degradation in performance is seen for an increasing number of scintillator layers, particularly when the scintillator fraction is above 50%.

Figure III-3.8
Jet energy resolution in $q\bar{q}(q = uds)$ events at different centre of mass energies, using a hybrid ECAL with silicon (Si) and scintillator (Sc) layers. The jet energy resolution is shown as a function of the fraction of scintillator layers in the ECAL, (Sc/(Sc+Si)). The total number of ECAL layers (Sc+Si) is 28.

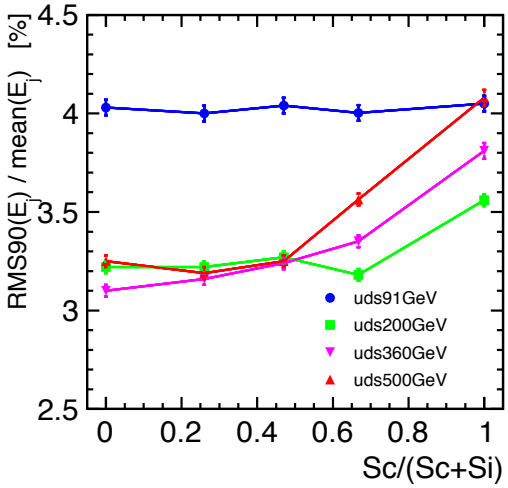

3.2.3 Test beam validation

Within the framework of the CALICE collaboration physics and technological prototypes for both options of the electromagnetic calorimeters have been built and tested in beam tests since 2004. They were exposed to a wide variety of particle beams (electrons/ positrons, pions, protons and muons) over a wide range of momenta, between 2 and 180 GeV.

3.2.3.1 SiECAL test beam validation

The CALICE SiECAL group has designed and built a so-called "physics prototype" [304], shown in Figure III-3.9, whose aim was to demonstrate the ability of this ECAL to meet the performance requirements. It had an active area of $18 \times 18\,\mathrm{cm}^2$ and 30 sampling layers. The active sensors had a granularity of $1 \times 1\,\mathrm{cm}^2$, giving a total of nearly 10k readout channels. These data have been used to calibrate the detector, to measure its performance, and to tune and validate the simulation of the SiECAL and particle interactions within it. Since these tests have been carried out over a number of

Figure III-3.9
(Left) the SiECAL physics prototype. (Right) linearity of the energy response, as measured in both real data and simulation [296].

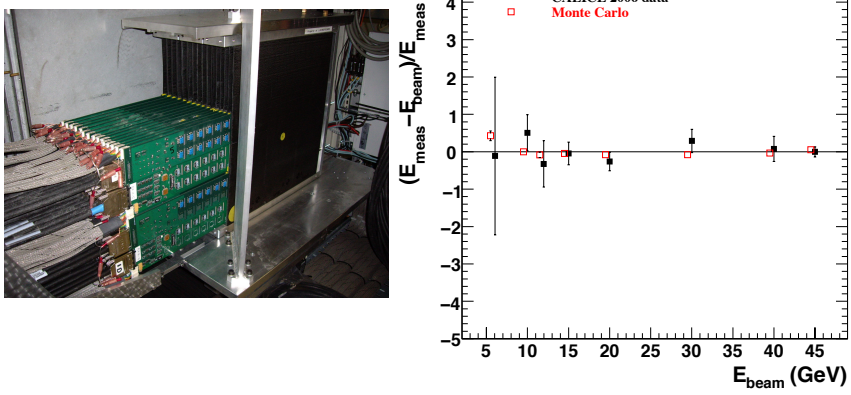

years, they have also given important information about the long term stability of the detectors and associated systems.

The SiECAL physics prototype has been successfully and stably operated over a period of five years. No major systematic problems were identified with the concept of this detector or with its technical design. The detector could be operated reliably and will minimal intervention also for lobger periods of time. The signal-over-noise ratio in the physics prototype was measured to be 7.5:1 [304]. This value was confirmed over the years. First measurements with the technological prototype show similar of even better performance.

The response of the detector to electrons is presented in [296]. The energy response is found to be linear to within 1% in the energy range between 1 and 45 GeV, as shown in Figure III-3.9. The energy resolution for electrons was measured to be $16.6/\sqrt{E(\mathrm{GeV})} \oplus 1.1\%$. Both the energy response and the longitudinal shower profiles of electron showers are well described in the simulation, as is the effective Molière radius. The results are compatible with the values assumed for the full detector simulation of the ILD detector as indicated above.

The data collected with hadron beams have been used to constrain the models for hadronic showers implemented in GEANT4, with the FTFB_BERT physics list giving the best description of the data [305, 306]. Analysis of overlaid "MIP"-like and EM shower events shows that the efficiency to distinguish them (in the ECAL alone) begins to decrease at a separation of 3 cm, to a minimum of around 50% for overlapping particles [307].

The position resolution of the physics prototype was found to be about 0.6 mm for electrons with energy above 20 GeV. The angular resolution is found to be $(106 \pm 2)/\sqrt{E} \oplus (4 \pm 1)\,\mathrm{mrad}$ along the x direction and $(100 \pm 2)/\sqrt{E} \oplus (14 \pm 1)\,\mathrm{mrad}$ along the y direction [308]. The differences between the two directions can be explained by the different arrangement of the detector layers in x and y direction.

In the coming years the technological prototype will be progressively equipped. The finer granularity will allow for a more precise tomography of hadronic showers. Currently, data recorded with first layers are analysed for the electromagnetic response of the new prototype.

3.2.3.2 ScECAL test beam validation

A physics prototype of the scintillator ECAL has been built and exposed to test beam. The prototype consists of 30 active layers, each of which includes 72 scintillator strips readout by photosensors. The minimum detecting unit has a 45 mm long and 10 mm wide plastic scintillator and a MPPC (Multi Pixel Photon Counter) semiconductor photosensor packaged in a 4.2 $\times$ 3.0 $\times$ 1.3 mm^3 housing. There is an one mm hole for a wave length shifting fibre to absorb the scintillation light generated by the charged particles and guide it to the end where the MPPC is located. The thickness of the unit is 3 mm [309].

The basic performance of the calorimeter has been tested in a hadron beam at Fermilab. The linearity of the system is shown in Figure III-3.10(left), the energy resolution is shown in figure III-3.10(right). The results include a temperature correction calibrated using data for an temperature range between 19 to 28°C. The deviation from a linear behaviour is determined to be less than 2% and the energy resolution is found to be $12.9/\sqrt{E\mathrm{GeV}} \oplus 1.2\%$ for 2 - 32 GeV electron beams [310].

A first layer of the technological prototype has been constructed and tested at DESY in autumn 2012. This layer combines absorber material, scintillator and read out electronics. The layer is equipped with 144 scintillator strips each 5 mm wide and MPPCs. MIP like signals have been observed. The efficiency and S/N ratio will be studied with these data. The power pulsing mode will be tested in 2013.

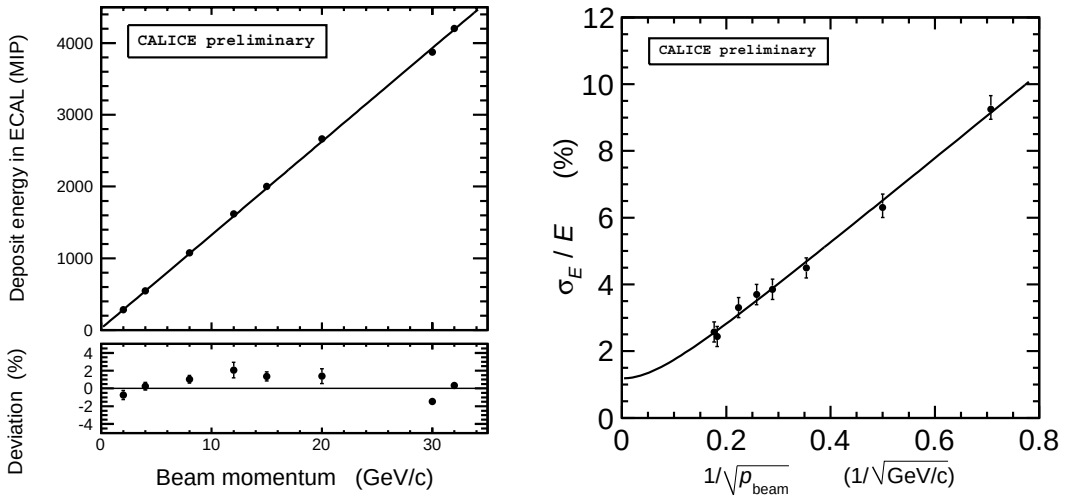

Figure III-3.10. Left: Response curve for the physics prototype of the ScECAL prototype vs. beam energy, with the deviation from a linear behaviour shown in the bottom part of the plot. The linearity is better than 2%. Right: Measured energy resolution of the physics prototype of the ScECAL prototype after temperature correction, for electrons in the energy range between 2 and 32 GeV. [310]

Figure III-3.11 Left: Correlation between calibration constants obtained on a cosmics test bench and in beam test. Right: Comparison between calibration constants obtained in two different data taking periods in 2006. Results are taken from [304].

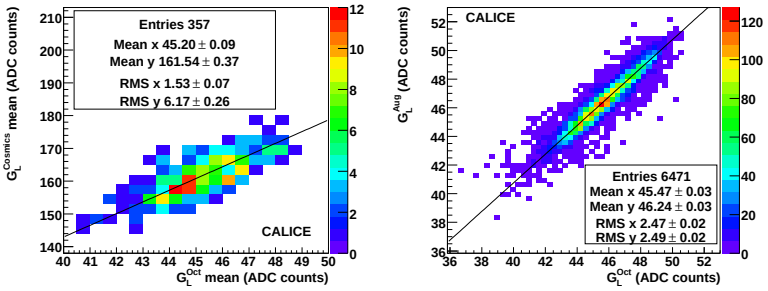

3.2.4 Calibration and alignment

As shown above the energy resolution of the electromagnetic calorimeters is of order $15\%/\sqrt{E}$. Therefore a calibration procedure at the percent level seems to be sufficient. In the following the experience from beam test campaigns and the resulting projection to a full calorimeter system will be outlined for the two options of the electromagnetic calorimeter.

3.2.4.1 SiECAL calibration

The calibration factors were stable over long time periods to the % level, where the variations are mainly due to different experimental conditions (e.g. cable length) at the beam test sites. The calibration constants showed no influence from external factors like temperature. The correlation of calibration constants obtained for different periods of data taking 2006 are published in [304] (see Figure III-3.11). In [311, 312] it is shown that the correlation coefficient is 83.8% between the calibration constants obtained at FNAL in 2008 and at CERN in 2006. Considering that many operations like mounting, un-mounting, and shipping occurred between 2006 and 2008, this high correlation coefficient demonstrates the stability with time of the SiECAL prototype. The same level of correlation exists between calibration constants derived for the beam tests in 2008 and 2011 at FNAL.

The test beam experience gives confidence that the calibration can be well controlled for a full SiECAL. In this case all detector modules will have to be scanned by a muon beam in a test beam

experiment prior to the installation. This operation would take several months but it should be possible to complete this in time for the start of detector operation. Afterwards it should be possible to monitor the calibration constants with muons. An alternative are charged pions which pass through the detector as a MIP or track segments of secondaries after a hadronic interaction. For the latter no study exists for the electromagnetic calorimeter so far but the studies performed for the analogue hadronic calorimeter give confidence that the monitoring of the calibration constants is feasible using this method.

The detailed alignment procedure has not been worked out. However, given the position resolution of about 1 mm, see section 3.2.3, the alignment of the detector has to be precise to about 100 μm. This value should be easily achievable with electron and muon tracks measured in the TPC and other tracking detectors, provided that these are correctly aligned.

3.2.4.2 ScECAL calibration

There are more than 10 million channels of small scintillator strip units in this calorimeter option. The stability of the light output has to be controlled and monitored. Three calibration schemes are under investigation.

In the first system light from an LED is guided with a clear optical fibre to the strips and coupled into the strip through notches in the fibre. This system will be used to monitor the stability of the system. Experience from test beams show that this is possible to within a few %. The other systems use particles from the beam halo or pions within a jet that traverse the scintillators. These particles behave as minimum ionising particles for the scintillator strips. The arrival of these particles is synchronous with the beam and thus the calibration schemes can be applied in power pulsing mode. For this dedicated track finding methods have been developed. Simulation studies show that with the proposed segmentation 50 hits/cell/day will be recorded using muons from a dedicated run of the accelerator at the Z-pole. Therefore a couple of days of running at the Z pole will be sufficient for calibration. The in situ calibration can also be done using beam-halo muons. They are distributed isotropically over the tunnel diameter. Their density is estimated to be about 4.1 muons/cm^2/s [313] without a muon spoiler. The energies are high enough to pass through the detector. Hence they can be used for the MIP calibration of the calorimeter endcap. With the current accelerator parameters and tunnel design about 500 seconds are needed to collect enough halo muons in each cell. However it should be noted that this procedure depends critically on the beam line design. For example, if muon spoilers are introduced to suppress the halo-muon flux the rate can easily go down by 2 orders of magnitude.

3.2.5 Future directions

CALICE has completed a series of full-size proof-of-principle tests with physics prototypes of both silicon and scintillator ECAL technologies. Large data sets have been collected and demonstrate the performance at ILD. The emphasis in the more realistic second generation technological prototypes is shifted towards a demonstration of the feasibility of a compact integrated detector design fulfilling the ambitious demands on compactness and hermeticity. Operational challenges not yet addressed with prototypes are the power-pulsed front-end electronics and the on-detector zero suppression in auto-triggered mode, which requires continuous and precise on-line controls of thresholds. Beam campaigns with technological prototypes started in 2012, with the focus rather on calibration and stability than on shower physics, and will continue for a couple of years. The campaigns, together with the design studies given in this document, will make it possible to construct an EM calorimeter system for a real ILC detector.

Until actual construction of the detector many aspects of the system will be continued to see

improvements as a result of further R&D. Some of the issues to be addressed are:

- silicon technology: sensor guard rings, AC coupling, chip bonding, PCB thickness;
- scintillator technology: developments of MPPC with more pixels and photon readout system;
- further hybrid simulation study;
- development of mass production and mass test system of sensor;
- alternative sensor technologies: e.g. MAPS;
- further studies of power pulsing;
- possible reduced scope (for cost reasons): reduced layers, radius. Estimate of cost scaling.

3.3 The Hadronic calorimeter system

The role of the HCAL is to separate the deposits of charged and neutral hadrons and to precisely measure the energy of the neutrals. Their contribution to the jet energy, around 10% on average, fluctuates over a wide range from event to event, and the accuracy of the measurement is the dominant contribution to the particle flow resolution for jet energies up to about 100 GeV. For higher energies, the performance is dominated by confusion, and both topological pattern recognition and energy information are important for correct track cluster assignment.

The HCAL is conceived as a sampling calorimeter with steel absorber and scintillator tiles (analogue HCAL) or gaseous devices (semi-digital HCAL) as active medium. Due to the rigidity of stainless steel, a self-supporting structure without auxiliary supports (dead regions) can be realised. Moreover, in contrast to heavier materials, iron with its moderate ratio of hadronic interaction length ($\lambda_I = 17$ cm) to electromagnetic radiation length ($X_0 = 1.8$ cm) allows a fine longitudinal sampling in terms of X_0 with a reasonable number of layers in a given total hadronic absorption length, thus keeping the detector volume and readout channel count at an acceptable level. This fine sampling is beneficial both for the measurement of the sizeable electromagnetic energy part in hadronic showers and for the topological resolution of shower substructure, needed for particle separation and weighting. Two baseline technology options have been developed, the scintillator-tile based AHCAL and the Glass Resistive Plate Chamber (GRPC) based SDHCAL.

With the advent of novel, multi-pixel Geiger mode silicon photo-diodes, so-called SiPMs, high granularities as required for a particle flow detector can be realised with the well-established and robust scintillator technology at reasonable cost. The scintillator tiles provide both energy and position measurement and thus allow to optimise amplitude and spatial resolution together. They exhibit a very homogenous response and with 3 mm thickness allow for a compact design with high MIP efficiency for tracking inside showers and calibration purposes. The transverse segmentation suggested by simulations is about 3×3 cm^2 and leads to a number of read-out channels an order of magnitude smaller than in the digital case with 1×1 cm^2 cells. The CALICE AHCAL [314] was the first device that used the novel SiPM technology on a large scale, and its robustness and reliability has encouraged other experiments, e.g. T2K, CMS and Belle, to apply it in their detector upgrades.

Gaseous detectors are good candidates for the active layers of a sampling calorimeter of high granularity. In addition to their excellent efficiency, gaseous detectors provide very good homogeneity. Another important advantage of the gaseous detectors is the possibility to have very fine segmentation. Indeed the segmentation is to a large extent driven by the electronics readout granularity used to read them. The thickness of gaseous detectors is also of importance for an ILD hadronic calorimeter to be placed inside the magnetic field. Highly efficient gaseous detectors can be built with a thickness of less than 3 mm. Other gaseous detectors such as micromegas and GEMs could also be alternatives to GRPC once the technology of producing large areas of such detectors cost effectively becomes available.

For the barrel calorimeter, two different absorber geometries are being proposed. The first version is separated longitudinally into 2 rings and azimuthally into 16 modules. The signal readout is guided

along the z axis towards the barrel/ end-cap gap. Alternatively, the 2nd version is segmented into 5 rings in z and 8 modules in azimuth. The signals are guided towards the outer perimeter in a similar way as in the ECAL. The main advantage of the first is the accessibility of the module level electronics and connections for maintenance and repair. On the other hand, the second provides superior rigidity and less deformation in the transverse plane. In principle, both geometries can be combined with all proposed technologies. However, the detailed engineering is presently being worked out for scintillator in the first, and for gaseous readout in the second approach.

3.3.1 Detector optimisation

3.3.1.1 AHCAL design optimisation

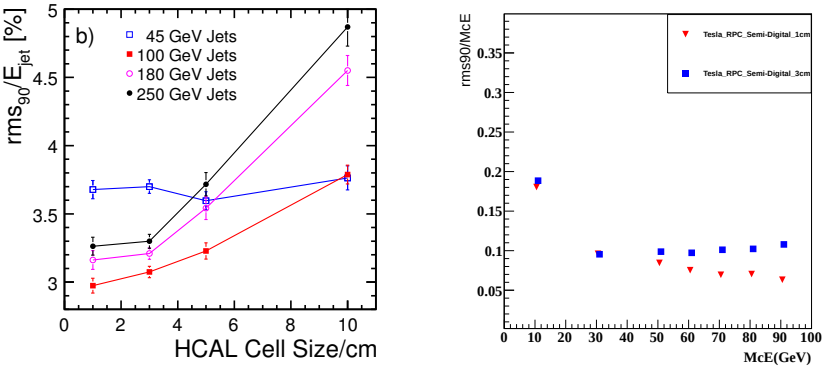

Figure III-3.12 Optimization of the hadron calorimeter cell sizes. Left: Particle flow jet energy resolution as a function of the AHCAL cell size. Right: Single K_0 energy resolution for particles showering in the SDHCAL for two different cell sizes.

The parameters of the AHCAL have been optimised using full detector simulations with particle flow reconstruction, comparing the performance for different design parameters. Of particular relevance are the thickness of the calorimeter and the cell size. The former strongly influences the energy resolution at higher jet energies due to potential leakage out of the back of the detector, while also driving the size of the solenoid, and the latter is crucial for the two-particle separation but also affects the overall system cost and complexity due to the impact on the channel count.

Figure III-3.12 *left* shows the particle flow performance as a function of the lateral segmentation of the AHCAL readout layers. It is apparent that going below a size of 3×3 cm^2 does not provide substantial advantages, while larger cells lead to reduced performance, resulting in the choice of 3×3 cm^2 for the size of the AHCAL scintillator tiles. With the same studies, the depth of the calorimeter was optimized. In order to not reduce the performance at 1 TeV, where typical jet energies are up to 250 GeV, a depth of 48 layers, corresponding to 6 λ_I was chosen.

3.3.1.2 SDHCAL design optimisation

The fine granularity of the hadronic calorimeter is an important asset to provide an excellent tracking capability needed for PFA but this is not the only element in favor of high granularity in the case of the SDHCAL. The energy measurement performance of the SDHCAL depends essentially on its capability to account for the particles produced within the hadronic shower. It is then necessary to find the best cell size which allows one to account for the many tracks produced in the hadronic shower. The first optimization studies indicated that a few mm cell size is the one which leads to the best energy resolution using a simple binary readout. However, this leads to a huge number of electronics channels (more than 200 million) making the technical realization of such a detector extremely complicated. In order to reduce this number without deteriorating the physics performance a compromise was found. It consists of choosing larger cell size while going from a simple binary to a three-threshold electronics (2 bit) readout. The role of the different thresholds is to help separating among one, few and many particles crossing the same cell. A detailed study using a full ILD detector

model with 48 active layers and 6 λ_I shows that a 1 cm size cell achieves better precision than a one of 3 cm size, as shown in figure III-3.12 right. This is the option that was selected for the SDHCAL base line.

3.3.2 Detector implementation

The first version of the mechanical design for the calorimeter barrel is based on two rings with 16 modules each. One module has a weight of almost 20 tons, which is manageable with standard installation techniques. The modules are constructed independently of the active layers, which can be inserted before or after installation of the modules. There are 48 absorber plates, 16 mm thick each, held together by 5 mm thick side panels in the rz planes; no additional spacers are foreseen. The active layers will contribute 4 mm of steel to each absorption layer, and require 5.5 mm for instrumentation (3 mm thick scintillator plus readout and calibration devices). The structure has been extensively simulated using finite element methods, including the integration of the heavy ECAL structure. Maximum deformations are found to be less than 3 mm, if the barrel structure is supported by two rails in the cryostat.

Presently the boundaries between modules are pointing in φ and in z. Variants with non-pointing boundaries have been validated in finite element calculations as well, but are disfavoured to ease the mechanical construction. The pointing geometry does not degrade the performance as long as the cracks between modules are filled with absorber material, and if the active instrumentation extends up to the boundary within tolerances, which is the case in the present scintillator layer design.

This mechanical concept has been fully developed, with horizontal and vertical prototypes successfully assembled and tested (see Figure III-3.13.) The measurements done on the horizontal prototype demonstrate that the required tolerances (flatness better than 1 mm over the full area of about 2 m x 1 m) and mechanical stability can be achieved with realistic stainless steel structures using roller-levelled plates. This avoids a cost-intensive machining of the delivered rolled steel sheets. In addition a mechanical design for the end caps has been completed and is also shown in Figure III-3.13.

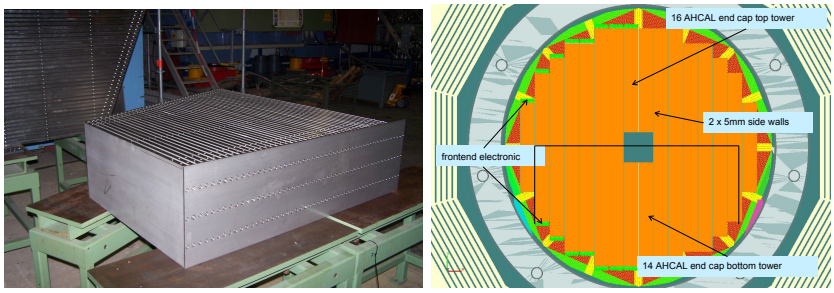

Figure III-3.13 Left: the mechanical prototype for the first version of the barrel structure. Right: mechanical design of the HCAL endcap.

The second mechanical structure is a self-supporting mechanical structure called the V structure. The structure has been designed to eliminate the projective holes and cracks so none of the particles produced close to the detector centre could escape detection. The V structure has additional advantages. It eliminates in principle the space between the barrel and the Endcaps avoiding the shower deformation which results not only because of this space but also of the different cables and services needed in CMS-like mechanical structures. In this structure the different services such as the gas tubes, data collection and electric cables of both the barrel and the Endcaps are taken out from the outer radius side. Detailed studies have shown that the deformation of this structure is extremely low and its robustness was verified experimentally with the SDHCAL technological prototype built with a self-supporting structure following the design of the V structure.

3.3.2.1 AHCAL readout technology and implementation

The arrangement of the active layers with internal and external electronics components is sketched in Figure III-3.14. The layer consists, from bottom to top, of a 0.5 mm thick steel support plate covered with reflector foil, the scintillator tiles (3 mm), the printed circuit board with electronics components (2 mm), covered with reflector foil from underneath, and a polymide foil for insulation. The PCB

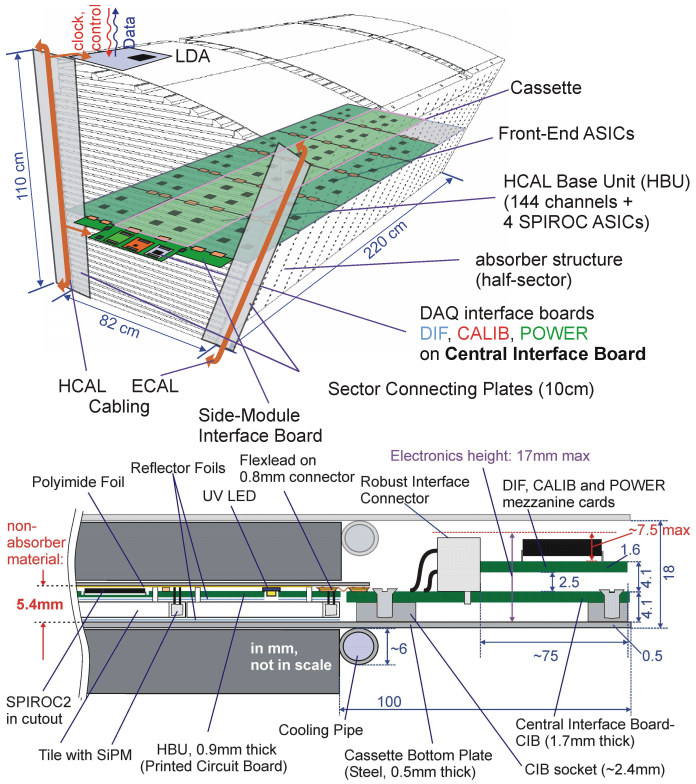

Figure III-3.14 Arrangement of AHCAL layers with electronic components (left), cross section of an active layer (right).

carries the SPIROC readout ASICs, introduced in section 3.1.1, and auxiliary components as well as a LED based optical calibration system. Interfaces for data acquisition, clock and control, for power distribution and for calibration system steering are accessible at the end face. Since the ASICs are operated in power-pulsed mode, no cooling is needed inside the detector volume.

The PCB is subdivided into units (HCAL base units, HBUs) of smaller size, manageable for automated mounting and soldering techniques. The standard unit is 12 by 12 tiles, 36×36 cm^2 , so six units are aligned along z to fill a half barrel. In order to accommodate the variation in layer width with increasing radius, 4 different HBUs, 8 to 12 tiles wide, are needed. At the layer edges, tiles with smaller size, e.g. 2×3 cm^2, are placed such that the width of the uninstrumented region near the sector boundary is on average 2.5 mm, but never larger than 5 mm. The electronics at the end face will require cooling, mainly due to the use of FPGAs in the DIF (Detector InterFace board introduced in section 3.1.1). The boards will extend 5 to 10 cm in z, but occupy only a fraction of the full width in φ, thus leaving space for ECAL and main tracker services as well as for the TPC support along radial directions.

Figure III-3.15 shows the details of the scintillator tiles, with a thickness of 3 mm and embedded wavelength shifting fiber which couples the light to an embedded SiPM. This new design is based on the experience with the physics prototype, and has been adapted for easier manufacturing. In extensive laboratory and beam tests, the tiles together with the SiPMs have been proven to deliver the expected performance in terms of signal yield and uniformity.

Figure III-3.15
The AHCAL scintillator tiles with embedded SiPMs, mounted on the readout PCB.

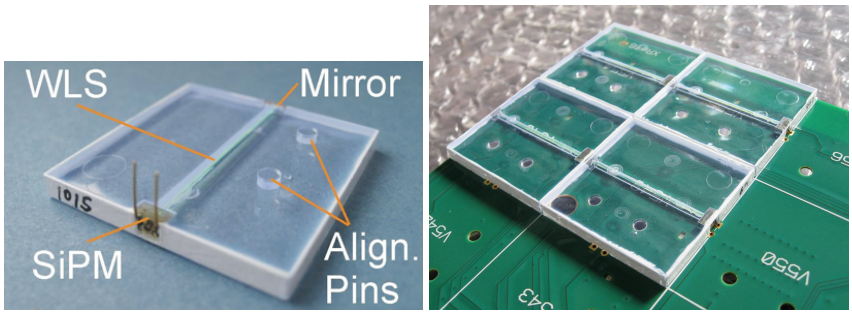

3.3.2.2 SDHCAL readout technology and implementation

The basic unit of the SDHCAL is a cassette that contains the active layer. The cassettes whose walls are made of 2.5 mm thick stainless steel are inserted into the mechanical structure. The structure itself is made of 1.5 cm thick plates of the same material. The cassette walls together with the structure plates play the role of the absorber. In total 2 cm of stainless steel is separating two active layers. The active layer itself is composed of a GRPC detector and its embedded readout electronics. The former is made of two glass plates. The anode plate has a thickness of 0.7 mm, the cathode plate of 1.1 mm. The two plates are separated by 1.2 mm space which is maintained constant by a special spacers (see Figure III-3.16). The distance and the size of these spacers were optimized to eliminate dead zones in the detector while providing an uniform electric field between the two plates. The two glass plates are covered on their outer side by a conductive painting. A high voltage is applied to these layers to create an electric field between the plates. The gap between the two plates is filled with a gas mixture of TFE(93%), CO2 (5%) , SF6(2%). The first gas provides the primary electrons when ionized by a charged particle (8 electrons/mm) while the second and the third are photon and electron quencher respectively. Their role is to limit the size of the avalanche that follows the creation of primary electrons. Gas tightness is provided by a frame made of robust insulating material. The frame is 3 mm wide resulting in a the dead area of less than 1.3%. A gas distribution system was developed. It allows to renew the gas content of the chamber in an efficient way taking into consideration the fact that gas inlets and outlets are to be on one side of the chamber. The system is designed to reduce the gas consumption. This and the recycling progress achieved by the RPC-gas group at CERN are important elements to reduce the cost of the gas consumption.

Figure III-3.16
Cross sectional drawing of the GRPC used in the SDHCAL.

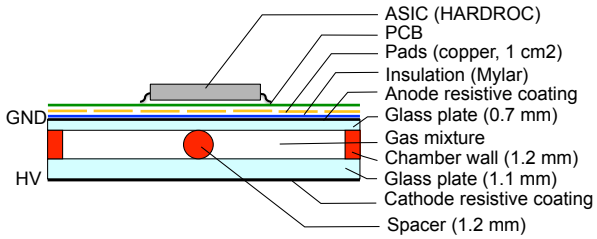

The avalanche signal created between the two glas plates is read out inductivly by a pad plane. A very thin (0.8 mm), 8-layer printed circuit board (PCB) has been designed. One side of the PCB hosts the readout ASICs called HARDROC. The other side carries the signal pick-up pads with a pad area of 1 cm^2. The PCB is designed to connect the ASICs to each other (DAISY chain). The PCB size chosen for the technological prototype was 33×50 cm^2. To read out large GRPC the PCB were conceived to be connected to each other using tiny connectors which are capable to transmit the signal as well as the different electric powers from one PCB to another. For the technological prototype boards of 1 m^2 were constructed by connecting four PCBs to form so-called slabs (see Figure III-3.17). Each slab is then connected to the data acquisition through a detector interface

board (DIF) which hosts an FPGA responsible for the communication with the 48 ASICs of one slab. Three slabs were soldered together in an appropriate way to ensure the same grounding for the three of them and to have a flat surface on the pads side. The boards are then fixed on the top cover of the cassette acquiring in this way a better rigidity. This is then fixed on the cassette that contains the GRPC. The total active layer thickness is less than 6 mm. The total thickness of one cassette is less than 11 mm.

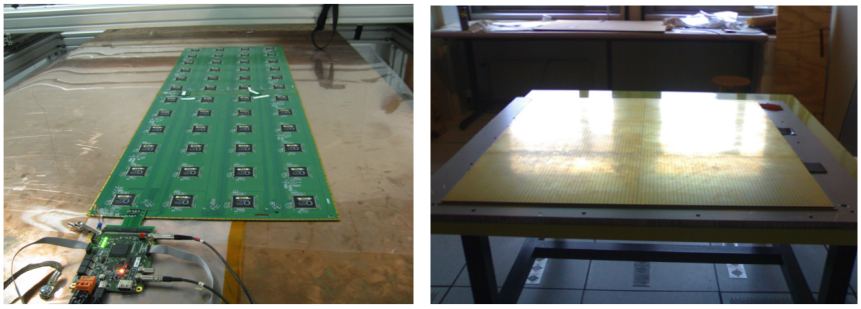

Figure III-3.17
An electronic slab made of two boards hosting each 24 ASIC and connected with a tiny connector. The interface DAQ board(DIF) is also shown (left) and the final 1 m^2 board.

3.3.3 Test beam results

3.3.3.1 AHCAL test beam results and operational experience

From the extensive CALICE test beam program, in which the AHCAL physics prototype [314] modules were used from 2006 until 2011, a wealth of results on detector performance, simulation validation and operational experience are available. The long-term operation of the AHCAL physics prototype, together with a large number of assembly and disassembly procedures, often coupled with long-distance shipping of the detector, has provided substantial information of the stability and reliability of the AHCAL technology. The number of observed non-working channels is very moderate at roughly 2%, most of which are due to broken solder points at the connection of the SiPMs to the PCB leading to the front-end electronics that were caused by deformations of the board during detector movements [314].

The linearity and the energy resolution – a key performance parameter even for a particle flow detector — of the AHCAL have been studied using pion beam at different energies [315]. In Figure III-3.18(left) the reconstructed single particle energy is shown as a function of the beam energy. The deviations from a linear response are within $\pm 1\%$. The uncorrected energy resolution is shown in Figure III-3.18(right). In addition the energy resolution after applying a software compensation technique is shown. The AHCAL has an e/π ratio of approximately 1.2. The compensation algorithm makes use of the fact that electromagnetic sub-showers have different spatial characteristics compared to purely hadronic energy deposits. Using the high granularity of the calorimeter fluctuations between the electromagnetic and hadronic component of the shower can be corrected on an event by event basis. This improves the resolution by close to 20%, reaching a stochastic term of 45%.

In the analysis, events from different data taking periods with operating temperatures ranging between 15 and 25 ^{o}C were combined. The overall good performance is demonstrate that a reliable temperature corrections can be applied. It shows that the temperature sensitivity of the photon sensor does not limit intrinsically the performance.

Electromagnetic showers are used to validate the simulation of the detector as well as to assess possible intrinsic performance limits. Both the linearity of the response and the energy resolution for electrons are very well reproduced by simulations once saturation effects of the photon sensor are taken into account in the event reconstruction [316]. Since the simulations do not include a modeling of response non-uniformities and gaps between tiles, this good agreement demonstrates that the

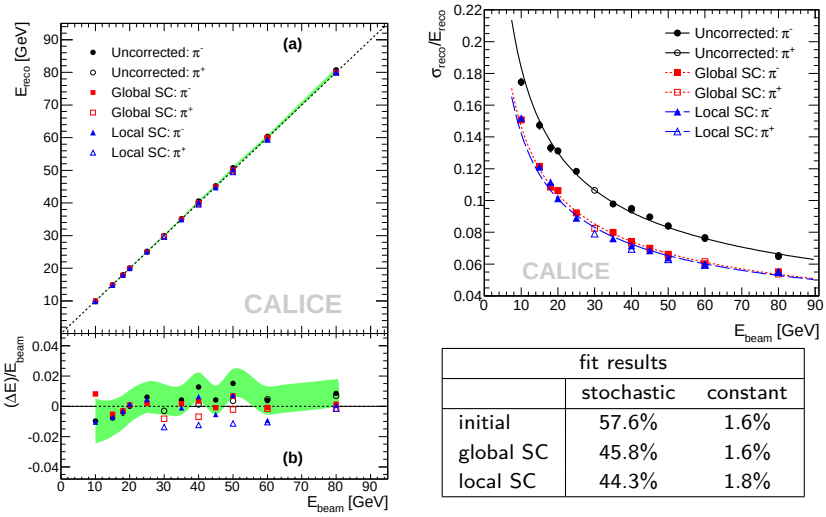

fit results		
	stochastic	constant
initial	57.6%	1.6%
global SC	45.8%	1.6%
local SC	44.3%	1.8%

Figure III-3.18
Reconstructed energy (left) and energy resolution (right) of the AHCAL for pion showers starting in the first five calorimeter layers. Shown are results obtained with a simple energy sum and with a local and a global software compensation (SC) technique, respectively. The green band indicates the systematic error of the calibration, and is shown around the results with with initial energy reconstruction. Figure taken from [315].

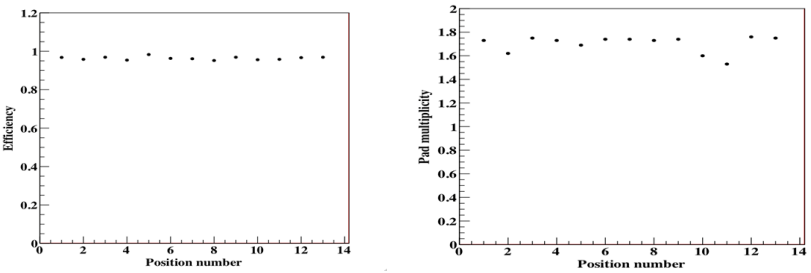

Figure III-3.19
Efficiency (left) and multiplicity (right) measured for different points of the SDHCAL prototype cassette. The measurement points include the critical area where readout boards join, and where potentially areas of lower efficiency are introduced.

non-uniformities present in the detector do not affect the electromagnetic performance, and thus are irrelevant for the performance for hadrons.

Beyond this evaluation of the performance of an imaging analogue scintillator HCAL, the high granularity of the detector has also been used for detailed investigations of the substructure of hadronic showers to study the realism of various Geant4 shower models. These studies include the measurement of shower profiles [317] and of secondary high-energy particle production within hadronic showers, accessible via minimum-ionizing tracks identified within the showers [318]. While older Geant4 physics lists often disagree with data, state-of-the-art physics lists are in general able to provide a good description of the measurements. Overall, these results give additional confidence in the realism of the AHCAL simulation in full detector performance predictions for ILD.

3.3.3.2 SDHCAL test beam results and operational experience

A technological prototype for the SDHCAL was built. The mechanical structure of this prototype is constructed using 1.5 cm thick stainless steel plates. The flatness of the plates was measured using a laser-based interferometer system and was found to be better than 500 μm. This result guarantees that for the V structure proposed for the SDHCAL, a tolerance of less than 1 mm is achievable. This mechanical structure can host up to 50 cassettes described above.

The first cassettes were extensively tested using a cosmic-ray test bench and particle beam at CERN. Both the efficiency and the multiplicity of the GRPC cassettes were studied. These studies (see Figure III-3.19) showed high efficiency and good homogeneity and validated the cassette concept.

In addition a single cassette was tested in a magnetic field of 3 Tesla (H2 line at CERN) applying the power-pulsed mode [319]. The results indicated clearly that the use of the power-pulsed mode in such a magnetic field is possible. The behavior of the detector (efficiency, multiplicity etc.) was

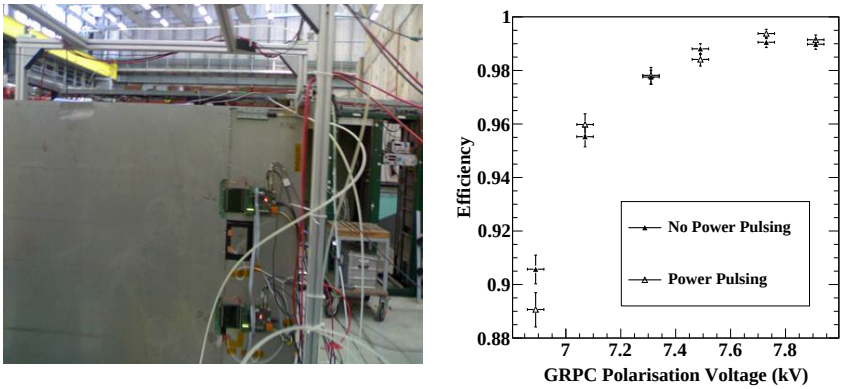

Figure III-3.20
(left) Photograph of a prototype cassette of the SDHCAL. (right) Efficiency of the SDHCAL module measured with the power-pulsing in a 3-Tesla magnetic field at CERN.

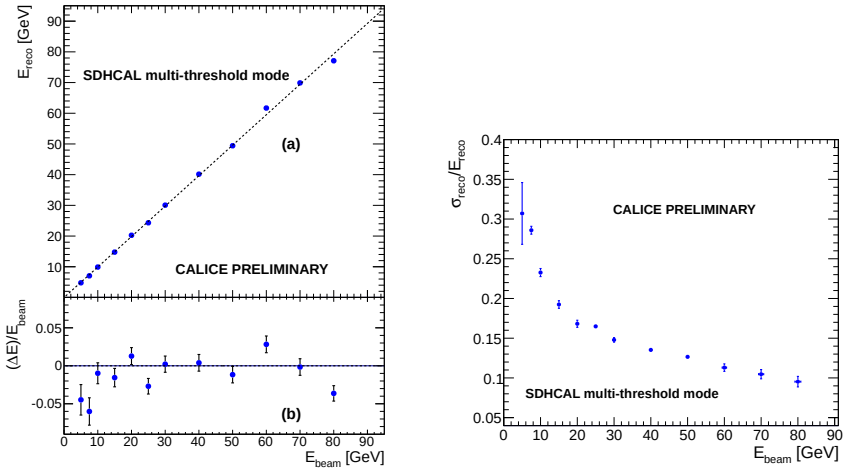

Figure III-3.21
Reconstructed energy linearity (left) and energy resolution (right) for Pions using a weighted sum of the three-threshold number of hits and with no data correction, for the SDHCAL prototype [320].

found to be similar to those obtained in the absence of both the magnetic field and the power-pulsed mode (see Figure III-3.20).

The prototype construction lasted less than 6 months. A commissioning test at CERN in 2011 allowed to understand the behavior of the complete system.

In April 2012 the prototype was exposed to pion, muon and electron beam at both the PS and the SPS at CERN. The power-pulsed mode was applied to all electronic channels of the prototype using the beam time structure (0.3 ms on-time duration for the PS beam and 9 s for the SPS beam every 45 s). A basic water-based cooling system was used to control the temperature particularly in the case of the SPS where the power consumption reduction is only 5 (to be compared with a factor of more than 100 in the ILC case). Data were collected continuously in a triggerless mode. The DAQ stops when the memory of one ASIC is full. Data are then transferred to a storage station and then the acquisition starts again.

Preliminary results [320] obtained from this short test beam confirm the excellent results of the binary-readout DHCAL physics prototype which uses the same active medium (GRPC) (DHCAL). The SDHCAL prototype results obtained with a minimum data treatment (no corrections) show clearly that excellent linearity and good resolution could be achieved on large energy scale as can be seen in Figure III-3.21. In future analyses the data from the tests will be used to study thoroughly the hadronic showers topology and to improve the energy resolution by, among others, separating the electromagnetic and the hadronic contribution as was done in the case of the AHCAL option. The separation between close-by showers is expected to benefit from the high granularity on the one hand and from the very low noise of the detector (< 1 Hz/cm^2) on the other hand.

3.3.4 Technical validation

3.3.4.1 AHCAL technical validation

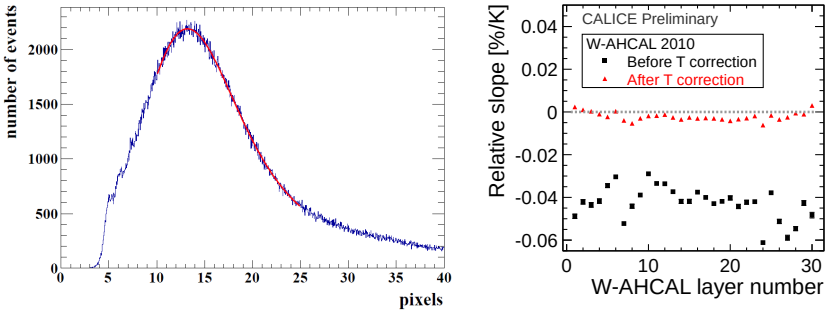

Figure III-3.22
(Left) Response of a sensitive layer of the AHCAL technical prototype to 2 GeV electrons.(Right) Layer wise distribution of the relative response variation per degree change in temperature for minimum-ionizing particles with (red) and without (black) temperature correction [298].

To scale the technology of the analogue HCAL up to a full collider detector, particular care has been taken to minimize dead space and to maximize the depth of the calorimeter inside of the magnetic coil. The new generation of front-end electronics, based on the SPIROC2 ASIC, have been fully designed, with first boards successfully taking data in beam. These HCAL base units (HBU) each take 144 scintillator tiles, 3 mm thick with embedded wave length shifting (WLS) fiber and improved SiPMs. These SiPMs have considerably reduced noise rates compared to those installed in the physics prototype, resulting in a significant reduction of the noise occupancy. The relative impact of the thinner tiles (3 mm thick compared to the previously used 5 mm thick strip) on the energy resolution was simulated to be 2–7%. The scintillator tiles and electronics perform as expected, with the response to minimum ionizing particle shown in figure III-3.22 (left), giving a light yield of approximately 15 photo-electrons/ MIP. The electronics also provides the capabilities for self-triggering and precise time-stamping with a resolution of approximately 300 ps. The ASICs have channel by channel voltage control, and an LED calibration system is interfaced into the read-out boards .

In addition to the use of scintillator tiles with embedded WLS fibers, directly coupled scintillators are being considered for the AHCAL. Two designs have been established [321, 322], with the second one directly compatible with the current HBU design. For these scintillator tiles, promising first results with a molding procedure compatible with mass production have been achieved, demonstrating that large scale production of the required tiles is possible.

3.3.4.2 SDHCAL technical validation

The quality of data obtained during three weeks of data taking validates the SDHCAL concept as proposed in the LOI. This is especially encouraging since no gain correction was applied to the electronics channels to equalize their response. However a gain correction mode is elaborated and tested during the test beam. It will be applied in the future to assess the effect of such correction on the energy resolution.

Another important aspect is the full success of the power-pulsing mode applied to the more than 460000 channels of this prototype. The performance of the 48 cassettes during the whole test beam period remained stable and identical to that observed for single cassettes operated with a permanent powering. Power-pulsing is used to reduce the power consumption, which also significantly reduces the heat load and thus the temperature variations of the GRPC chambers. This largely simplifies the high voltage system.

3.3.5 Calibration and alignment

Key issues, such as the capability to fully calibrate the HCAL detector with minimum-ionizing particles and the ability to reliably correct the temperature dependence of the response of the photo-sensors for temperature variations far outside of the range expected in ILD have already been demonstrated with the physics prototype. The performance of the temperature correction is illustrated in figure III-3.22 (right) for minimum-ionizing particles recorded in the AHCAL [298]. The capability of the SiPM to detect single photons is used in addition to internally calibrate the gain of the system [323].

3.3.6 Future R&D

3.3.6.1 AHCAL future R&D

The large data sets taken with the AHCAL physics prototype hold the potential for further analysis, in particular in the area of detailed validation of GEANT4 hadronic shower models. A particularly interesting field has recently been opened here with the addition of data taken with tungsten absorbers.

The R&D plans for the analogue HCAL mainly go into the direction of fully demonstrating the concepts for a real detector, further improving the production and performance of components and exploiting the capabilities of the new electronics in test beams. The time scale of the R&D, in particular involving larger prototypes, will be driven by the available funding.

In the November 2012 test beam at CERN, one HCAL layer with 4 HBUs has been successfully tested with hadrons. The data will allow to further expand the investigations of the time structure of hadronic showers in steel and tungsten begun by earlier studies at CERN. A laboratory test of one full readout slab consisting of 6 HBUs is foreseen in the existing mechanical prototype with absorber layers of the same size as in the ILD HCAL barrel. Beyond 2012, the construction of a vertical stack with a minimum of 10 to 12 HBUs is planned. This stack will use the existing wedge-shaped mechanical prototype of a barrel module as absorber. This structure will be tested in electron beams at DESY in 2013. It is planned to be expanded to a full hadronic system for tests at CERN in 2014 or beyond.

On the basic technological front, new types of photo-sensors are being explored, in close cooperation with developers in research and industry. The goal is to push the limits in dynamic range, noise and device uniformity. The electronics and integration concept is versatile enough to accommodate advances on the sensor and tile side, integrate them into existing test structures and combine different types in the same beam tests. In this way, sensor technology and system integration can be optimised together.

3.3.6.2 SDHCAL future R&D

Large GRPC of 1 m^2 were developed and built for the technological prototype. However, larger GRPC are needed in the future DHCAL with the largest one being 290×91 cm^2. These large chambers with gas inlet and outlet on one side need a dedicated study to guarantee a uniform gas gap everywhere, independent of the mounting angle of the plate. It is also necessary to ensure an efficient gas distribution as it was done for the 1 m^2 chambers. The readout of such chambers needs to be as efficient as the one of the technological prototype. An upgrade of the readout ASIC is under way. The new ASIC will be directly addressable and can be easily bypassed in case of failure. Although no major difficulties are expected the R&D needed to validate the feasibility of the SDHCAL with the V mechanical structure will start soon. In addition it is needed to improve the interface boards (DIF) for the control of the ASICs synchronization and data transfer. Indeed, the space left between the active layer of one module and the cryostat is only 5 cm. This means that the DIF components should be optimized to cope with the volume availability.

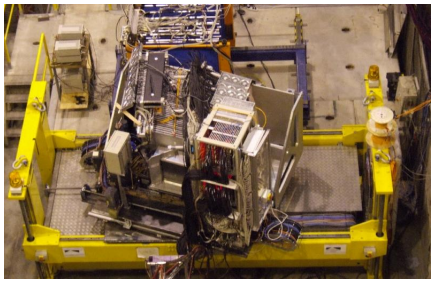

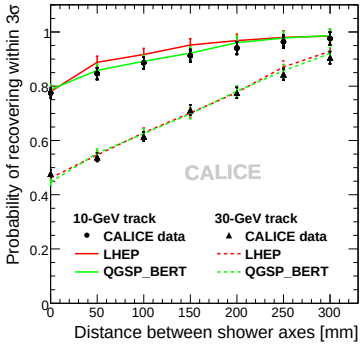

Figure III-3.23
Left: CALICE test beam set-up at CERN. Right: Probability to recover the energy of a 10 GeV neutral hadron within three sigma of the detector resolution as a function of the distance from a 10 GeV and 30 GeV charged hadron, respectively, using the Pandora PFA for test beam showers mapped into the ILD detector [302].

3.4 Particle flow performance of the ILD calorimeter system

Based on data taken with the physics prototypes of the SiECAL and the AHCAL the particle flow performance of the ILD calorimeter concept has been studied [302]. Two displaced showers measured in CALICE prototypes of an analogue hadron and an electromagnetic calorimeter were mapped into the ILD detector geometry and processed by the Pandora particle flow algorithm for event reconstruction. Figure III-3.23 (left) shows the setup used. The right part of this figure shows the probability to recover the energy of a 10 GeV neutral hadron within three sigma of the detector resolution as a function of the distance to a 10 GeV and 30 GeV charged pion, compared with simulations using different physics lists in GEANT4. The good agreement of data and simulations, in particular for the QGSP_BERT physics list, underlines the reliability of full detector simulations in predicting the particle flow performance of the detector system.

3.5 Forward calorimetry

Two special calorimeters are foreseen in the very forward regions of the detector [324], denoted hereafter as LumiCal and BeamCal. LumiCal will measure the luminosity with a precision of better than 10^{-3} at 500 GeV centre-of-mass energy[1], and BeamCal will perform a bunch-by-bunch estimate of the luminosity and, supplemented by a pair monitor, assist beam tuning when included in a fast feedback system [325]. Both calorimeters extend the detector coverage to low polar angles, important e.g. for new particle searches with missing energy signature [326]. The additional low angle hadron calorimeter LHCAL extends the coverage of the hadron calorimeter to the polar angle range of LumiCal. A sketch of the design is shown in Figure III-3.24.

LumiCal is positioned in a circular hole of the end-cap electromagnetic calorimeter ECAL. BeamCal is placed just in front of the final focus quadrupole. LumiCal covers polar angles between 31 and 77 mrad and BeamCal between 5 and 40 mrad.

Due to the high occupancy originating from beamstrahlung and two-photon processes, both calorimeters need a fast readout. In addition, the lower polar angle range of BeamCal is exposed to a large flux of low energy electrons, resulting in radiation depositions up to one MGy per year. Hence, radiation hard sensors are needed.

[1] At 1 TeV centre-of-mass energy this requirement is relaxed to 3×10^{-3} due to the expected lower statistics of the relevant physics processes.

3.5.1 Mechanical concept

Monte Carlo simulations have been performed to optimise the design. In both calorimeters a robust electron and photon shower measurement is essential, making a small Molière radius preferable. Compact, cylindrical sandwich calorimeters using tungsten absorber disks of one radiation length thickness, interspersed with finely segmented silicon (LumiCal) or GaAs (BeamCal) sensor planes, as sketched in Figure III-3.24, are found to match the requirements [324]. For the innermost part of BeamCal, adjacent to the beam-pipes, also Chemical Vapour Deposition (CVD) diamond sensors are considered. Since LumiCal is used to measure precisely the polar angle of scattered electrons[2], it must be centred around the outgoing beam.

Both calorimeters consist of two half-cylinders. The tungsten absorber disks are embedded in a mechanical frame stabilised by steel rods. Finite element calculations were done for the support structure to ensure the necessary precision and stability. The sensors are fixed on the tungsten half-disks and connected via a flexible PCB to the front-end readout. The gap between the absorber disks is minimised to about 1 mm to achieve the smallest possible Molière radius.

The distance between the two calorimeters of LumiCal and the position of the beam with respect to the calorimeter axis must be known to about 1 mm and 500 μm, respectively. A laser based position monitoring system has been developed [327] to control the position of LumiCal e.g. with respect to QD0 with the necessary precision.

3.5.2 LumiCal

Bhabha scattering will be used as the gauge process for the luminosity measurement. The cross section can be calculated precisely from theory [328], and the luminosity, L, is obtained as $\mathrm{L} = \mathrm{N_B}/\sigma_\mathrm{B}$, where σ_B is the integral of the differential cross section over the considered polar angle range, and $\mathrm{N_B}$ the number of counted events in the same range. Bhabha scattering events were generated using the BHWIDE generator [329]. Electromagnetic showers were simulated and reconstructed using the standard ILD software tools. The sensor pad size was chosen to obtain sufficient polar angle resolution and to keep the polar angle measurement bias small for fully contained electron showers [324]. The energy resolution is $\sigma_\mathrm{E}/\mathrm{E} = \mathrm{a_{res}}/\sqrt{\mathrm{E_{beam}\ (GeV)}}$, where E and σ_E are, respectively, the central value and the standard deviation of the distribution of the energy deposited in the sensors for a beam of electrons with energy $\mathrm{E_{beam}}$ and $\mathrm{a_{res}} = (0.21 \pm 0.02)\ \sqrt{\mathrm{GeV}}$, as shown in Figure III-3.25. From the energy depositions in the pads for the passage of minimum ionising particles and for showers of

[2] 'Electrons' is used here to describe equally electrons and positrons originating from Bhabha scattering.

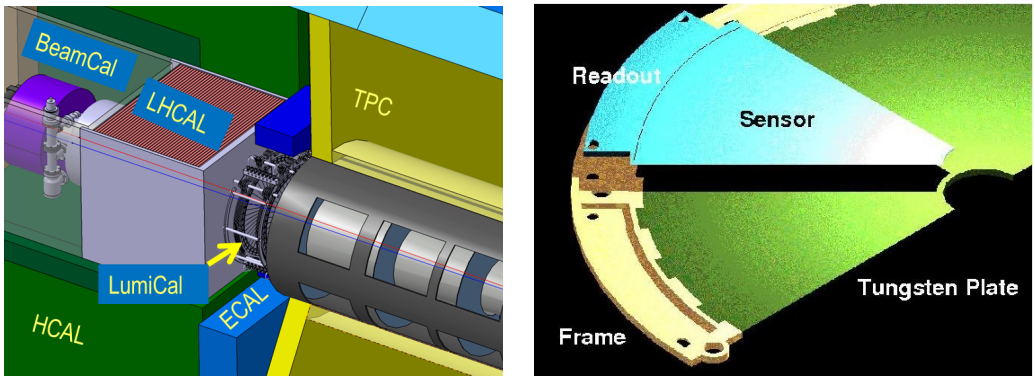

Figure III-3.24. Left: The very forward region of the ILD detector. LumiCal, BeamCal and LHCAL are carried by the support tube for the final focusing quadrupole QD0 and the beam-pipe. TPC denotes the central track chamber, ECAL the electromagnetic and HCAL the hadron calorimeter. Right: A half layer of an absorber disk with a sensor sector and front-end electronics.

250 GeV electrons [330], the distribution of the charge deposited in a single pad, Q_{pad}, was estimated to range between $4 < Q_{pad} < 6000$ fC. Signal digitisation with a 10-bit ADC preserves the energy measurement.

Prototypes of LumiCal sensors have been designed and manufactured by Hamamatsu Photonics. Their shape is a ring segment of 30°. The thickness of the n-type silicon bulk is 0.320 mm. The pitch of the concentric p^+ pads is 1.8 mm and the gap between two pads is 0.1 mm. The bias voltage for full depletion ranges between 39 and 45 V, and the leakage currents per pad are below 5 nA. Pad capacitances between 8 pF for the smallest pads and 25 pF for the largest pads were measured [331].

3.5.3 BeamCal

BeamCal will be hit after each bunch-crossing by a large amount of beamstrahlung pairs. For the current ILC beam-parameter set [332], beamstrahlung pairs were generated with the GUINEA-PIG program [333]. Inside the ILD detector an anti-DID field [334] was assumed. The energy deposited in the sensors of BeamCal per bunch crossing allow a bunch-by-bunch luminosity estimate and the determination of beam parameters with a precision of better than 10% [325]. Applying a shower-finding algorithm, single high energy electrons, as illustrated in Figure III-3.25. can be detected with high efficiency even at low polar angles.

The signals expected on the pads range up to 40 pC. Digitising with a 10-bit ADC has no impact on the performance of the calorimeter [335]. The dose and the neutron fluence in the sensors after one year of operation with nominal beam parameters are estimated for a sensor layer at the depths of the shower maximum to be about 1 MGy and 0.4×10^{12} neutrons per mm^2 and year, respectively, near the beam-pipe.

CVD diamond sensors were obtained from Element6 and IAP Freiburg. Large area GaAs sensors, as shown in Figure III-3.26, were produced by means of the Liquid Encapsulated Czochralski method, doped by a shallow donor (Sn or Te), and then compensated with Chromium. This results in a semi-insulating GaAs material with a resistivity of about 10^7 Ωm.

Sensors were exposed to a 10 MeV electron beam at the S-DALINAC accelerator [336]. The diamond sensors were found to keep good performance under irradiation of up to 7 MGy [337]. The GaAs shows a significant drop in charge collection efficiency as shown in Figure III-3.26, but even

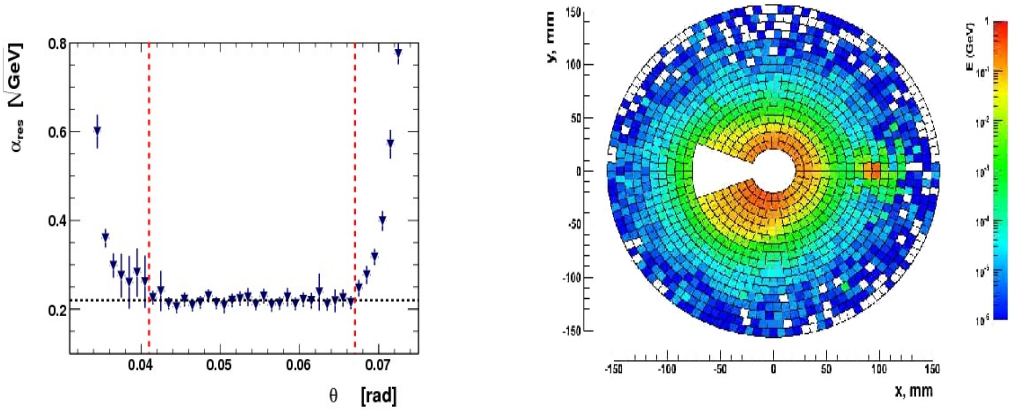

Figure III-3.25. Left: The energy resolution, a_{res}, for electrons as a function of the polar angle, covering the range of LumiCal. Right: The distribution of the energy deposited by beamstrahlung pairs after one bunch crossing in the sensors of BeamCal at a depth of 5 radiation lengths. Superimposed is the deposition of a single high energy electron, seen as red spot on the right side.

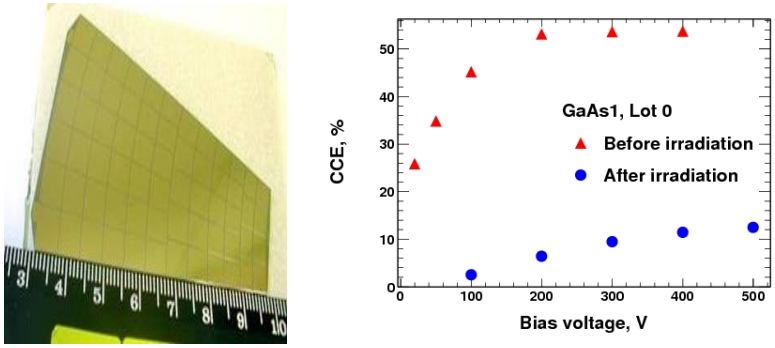

Figure III-3.26
Left: A prototype of a GaAs sensor sector for BeamCal with pads of about 30 mm^2 area. Right: The charge collection efficiency (CCE) as a function of the applied voltage for a GaAs sensor before and after irradiation.

after irradiation with 1.2 MGy a signal from a MIP is still visible [338].

3.5.4 ASIC developments

The readout comprises a physics mode and a calibration mode. In the physics mode signals from electromagnetic showers are recorded. In the calibration mode smaller signals from relativistic muons, considered here as minimum ionising particles, must be detected to be used for alignment and calibration. Signals from the subsequent bunch crossings, separated in time by about 300 ns, must be resolved. To reduce power dissipation switching off the power between bunch trains is implemented. An architecture [339, 340] comprising a charge sensitive amplifier and a shaper was chosen for the LumiCal ASIC. A variable gain in both the charge amplifier and the shaper is implemented by a mode switch. The peaking time of the shaper output signal is 60 ns. ASICs, containing 8 front–end channels, were designed and fabricated in 0.35 μm CMOS technology. A micrograph of the prototype, glued and bonded on the PCB, is shown Figure III-3.27. Measurements of the performance are published elsewhere [341]. A dedicated low power, small area, multichannel ADC is designed and produced. It comprises eight 10-bit power and frequency (up to 24 MS/s) scalable pipeline ADCs and the

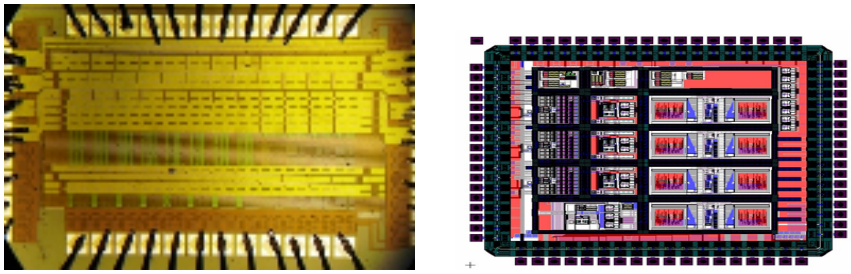

Figure III-3.27
Left: Micrograph of the front–end ASIC. Right: Micrograph of the Bean ASIC.

necessary auxiliary components. The active size of the ASIC is $3.17\ \mathrm{mm} \times 2.59\ \mathrm{mm}$. Eight ADC channels are placed in parallel with 200 μm pitch and are followed by the serialiser and LVDS pads, while the analog and digital peripheral circuits are on the ASIC sides. Measurements of the static and dynamic parameters, power scaling, and cross-talk are performed and published elsewhere [342].

The Bean (BeamCal Instrumentation IC), shown in Figure III-3.27, is designed and produced in a 180-nm CMOS process. Each channel has a dual-gain charge amplifier, a filter, and a successive approximation register ADC. Groups of channels can be put into an adder that combines the outputs and provide a fast feedback signal which will be used for beam tuning and diagnostics. Two different gains can be selected for physics and calibration modes of operation. Both the signal and the adder output are digitised using a custom 10-bit successive approximation register ADC. The full conversion takes less than 250 ns, the adder output is available in less than 1 μs. Tests with prototype chips have confirmed the performance [343].

3.5.5 Beam tests

Prototypes of sensor planes assembled with FE and ADC ASICs, as shown in Figure III-3.28, were built using LumiCal and BeamCal sensors [344]. The detector plane prototypes were installed in

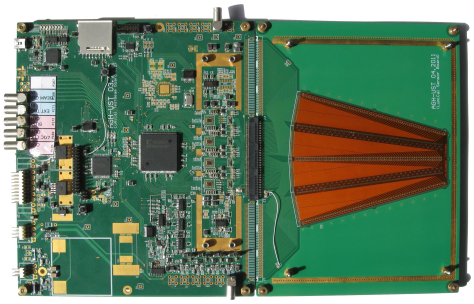

Figure III-3.28
Photograph of LumiCal readout module with sensor connected.

an electron beam and the trajectories of beam particles were measured by four planes of a silicon strip telescope. The front-end electronics outputs were sampled synchronously with the beam clock, a mode to be used at the ILC. Data were taken for different pads and also for regions covering

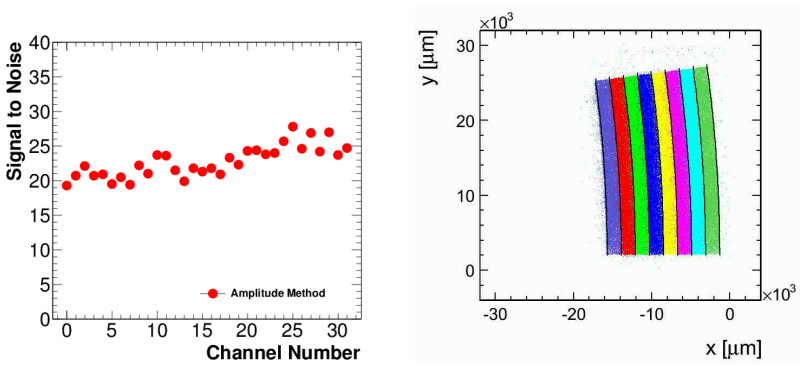

Figure III-3.29
Left: The signal-to-noise ratio of all read-out channels before calibration. Right: Distribution of the predicted impact points on pads with a colour coded signal.

pad boundaries. Signal-to-noise ratios of better than 20 are measured for beam particles both for LumiCal and BeamCal sensors, as illustrated in Figure III-3.29. The impact point on the sensor is reconstructed from the telescope information. Using a colour code for the signals on the pads the structure of the sensor becomes nicely visible, as also seen in Figure III-3.29. The sensor response was found to be uniform over the pad area and to drop by about 10% in the area between pads.

3.5.6 Summary and future plans

The design of the forward calorimeters for ILD has been optimised for a precise luminosity measurement, and to assist beam tuning to optimise the accelerator operation. Dedicated sensors and ASICs have been produced and tested. A fully assembled sensor plane segment was studied in the beam. The functionality was demonstrated with excellent performance. A concept has been developed how these detectors can be integrated into the ILD detector. In the future, studies of a calorimeter prototype are needed to fully establish the design of the system. A new generation of ASICs for LumiCal using 130 nm CMOS technology is under development to reduce power dissipation and space for the on board electronics. The Bean-ASIC will be extended to a multi-channel version with a digital memory array on chip. Also effort will be invested in the development of a beamstrahlung photon calorimeter, GamCal, important for beam diagnostics [325].

Chapter 4
ILD Outer Detector

4.1 The ILD muon system/ tail catcher

A stable, highly efficient muon identification system with excellent hadron rejection is an important requirement to meet the physics goals of the ILD detector. The ILD muon system provides a number of measurement stations outside the solenoid coil, which supplement the measurements taken with the calorimeter system and the tracker. It is used to identify the muons and to act as a tail catcher, to recover energy which is leaking out of the back of the calorimeter. However, the barrel part location behind the coil limits its role to fairly high momentum particles.

The muon system/ tail catcher instruments the iron return yoke in the barrel and in the forward region. The yoke barrel part is equipped with one sensitive layer in front of the iron yoke, 10 layers spaced 14 cm apart, followed by three sensitive layers spaced by 60 cm apart. The forward part of the yoke is equipped with 10 layers spaced by 14 cm, followed by two sensitive layers spaced by 60 cm. The overall layout of the muon system/ tail catcher is shown in Figure III-4.1.

Two main options are investigated for the sensitive layers, scintillator strips equipped with wavelength shifting fibres and read out with silicon photomultipliers (SiPM), or resistive plate chambers (RPC). The main parameters of the system are summarised in Table III-4.1.

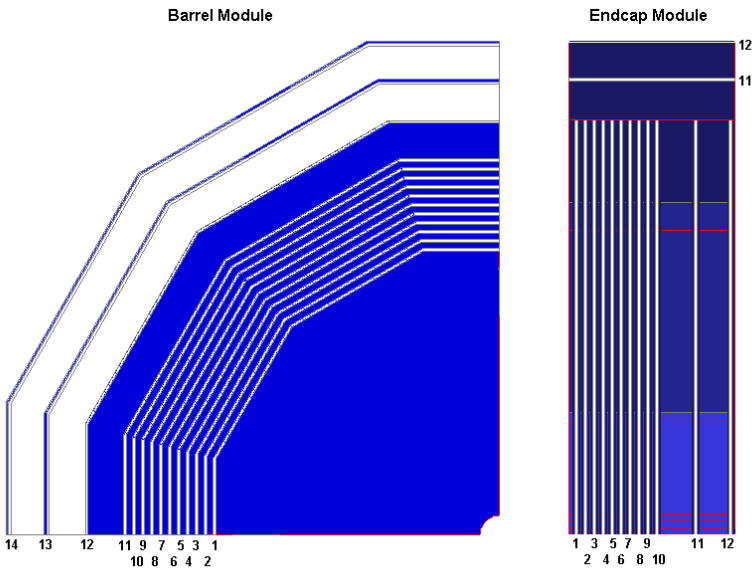

Figure III-4.1
Sensitive Layers of ILD Muon System/Tail Catcher

Table III-4.1
Table of parameters of the ILD muon system.

Modules:	Barrel: 3	Endcap: 2
Rmin, Rmax, length [mm]	4450, 7760, 2800	300, 7760, 2560
No. of sens. layers	14	12
Scintillation strips:	total 125000	
thickness, width, length [mm]	10, 30, 2800	

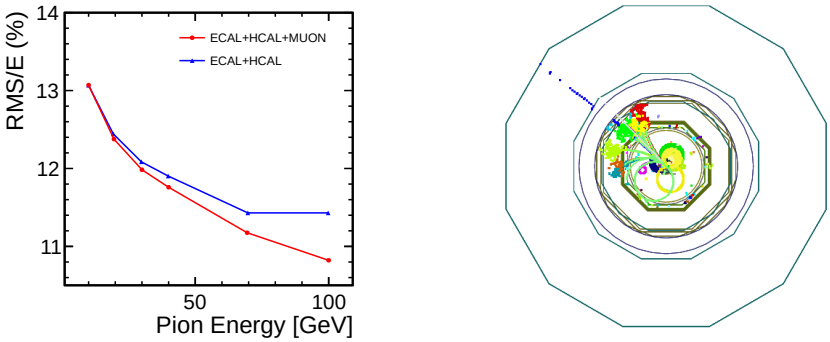

Figure III-4.2
Left: Energy resolution of pions without and with tail catcher. Right: Event display of the 50 GeV b-jet with muon track in muon system.

4.1.1 Muon system layout

The requirement that the muon system/tail catcher serves both as a muon identifier and as a tail catcher impacts its design. The first section of the system provides ten relatively closely spaced layers, to act as a calorimeter. Mechanical constraints limit the iron thickness between readout stations to be at least 10 cm. At the rear of the muon system the distance between stations in much increased, since they only need to act as a muon tracker. Three layers in the barrel, two in the endcap are spaced 60 cm apart [345].

The potential improvement of the jet energy resolution with a perfect tail catcher, as estimated from simulation, is shown in Figure III-4.2 (left). The fact that the coil adds about two interaction lengths of material in front of the muon system limits the effect of the tail catcher. To maximise its impact a sensitive layer is placed in front of the iron yoke, directly behind the coil and the first 10 layers are spaced more closely to improve the calorimetric performance of the system.

With the anticipated point resolution of about 1 cm and the current design, the achievable momentum resolution for muons is limited by multiple scattering up to momenta of 7 GeV. However in particular for muons inside jets the addition of the information from the muon system/tail catcher can significantly improve the purity of the muon sample, as shown in Figure III-4.2 (right).

4.1.2 Technologies

The main option for the sensitive layers will use extruded scintillation strips with a thickness of 7-10 mm and a width of 25-30 mm. A 1 mm wide extruded groove running along the center of the strip will take a commercially available wave length shifting (WLS) fibre. The scintillator strips will be covered on the outside by a layer of TiO_2, that is co-extruded alongside the scintillator during the extrusion process. The maximal length of strips required for ILD is 270 cm. The technology was successfully tested in ITEP [346].

The signals will be readout from both sides of the strips by silicon photo multipliers, coupled to the wave length shifting (WLS) fibres. Reading out both sides of a strip offers the possibility to define the position of the hits along the strip, which will help in reducing the fake rate in the muon system.

Fig. III-4.3 (left) shows the design of the scintillator strip. The right picture presents the signal (number of photons) of the scintillation strip with WLS and SiPM readout from both sides.

Resistive plate chambers (RPC) are considered as alternative sensitive layers. Main features are

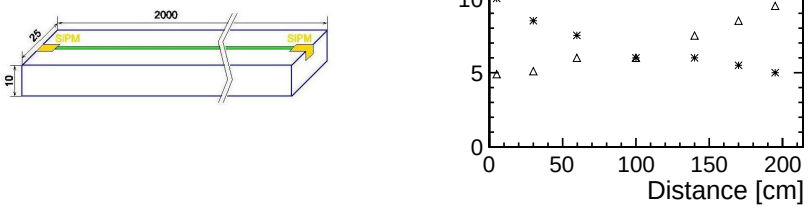

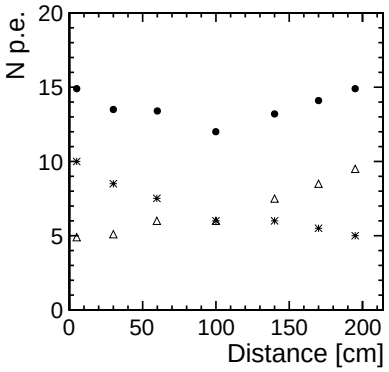

Figure III-4.3
Left: Technology of muon system sensitive elements: schematic view of scintillator strip with SiPM readout. Right: Signal from both sides of the 2 m length scintillator strip with WLS and SiPM readout.

excellent granularity up to 1×1 cm^2 pads and one threshold (1-bit) digital readout. Several types of RPCs have been successfully constructed and tested in the HEP community and within the ILC R&D program [347].

4.1.3 Performance

The performance of muon system and tail catcher was studied with the full ILD Monte Carlo simulation and reconstruction chain. In the model the sensitive elements are implemented as square tiles of 30 x 30 mm^2 and a thickness of 10 mm, with SiPM readout, similar to the AHCAL tiles. This is a simplification compared to the proposed system, which will reduce significantly the fake-rate problem present in a readout with long strips.

4.1.3.1 Muon Identification

One of the main tasks of the muon system/tail catcher is the identification of isolated muons. The main source for wrongly identified muons are pions. A number of scenarios have been identified how this can happen:

- pions can decay into emitting a muon, which is then detected in the muon system;
- pions may pass the calorimeter system without interaction ('sail through') and are detected in the muon system;
- particles from the shower in the calorimeter may pass to the muon system and are detected there.

The muon identification for single particles is based on the analysis of the hits in the sensitive stereo layers of the muon system in coincidence with a region of interest defined as a cone extrapolated along the direction of the track measured in the tracking system and calorimeter system. The angle of the cone is defined as a function of the multiple scattering angle.

Figure III-4.4 left shows the efficiency of the muon identification and the contamination with pions as a function of the energy of the particles. The colour of the lines corresponds to the layers of the muon system which are used for the muon identification: blue are the first 10 layers, green are more widely spaced layers. In jets the muon is accompanied by hadronic background in the same region of interest. Study of the identification of muons in jets and the contamination by hadrons was performed using semileptonic decays of b-quarks. The results are shown in Figure III-4.4 (right). The blue lines correspond to the identification of muons in the first 11 layers of the barrel part, normalised to 5 GeV muons inside jet. The green lines represents data recorded beyond layer 11, normalised to 7 GeV muons due to the fact that low energetic muons do not reach this layers. The results show that an identification efficiency of more than 97% can be reached for energies higher than 7 GeV, with a hadronic contamination at the few percent level.

The muon identification power at low energies, below 4 GeV, is affected by dead material in front of the muon system and by the deflecting of particles in the magnetic field, which do not allow the particles to reach the sensitive layers of the muon system. The muon identification at low energy is possible using the highly granular structure of the ILD calorimeter system which allows the identification of muons as minimum ionising particles (mip) like tracks in the calorimeter system.

4.1.3.2 Muon system as tail catcher

The first layers of the muon system serve as a tail catcher, measuring the energy which leaks through the end of the calorimeter system. Figure III-4.5 shows the effect of an ideal tail catcher (no dead material between the calorimeter and the tail catcher) and the realistic scenario at ILD, with two interaction lengths of material in front of the tail catcher, as a function of the total depth of the calorimeter system. For 6 λ, the value for the ILD calorimeter system, a roughly 10% improvement is possible with the tail catcher [348].

A prototype of the muon system/tail catcher was successfully tested during the 2007-2012 CALICE test beam campaign with ECAL and analogue HCAL. A tail catcher was placed behind the HCAL instrumented with scintillator strips and readout with SiPMs [348]. Results from the tests show that the proposed system delivers the anticipated performance and thus validates the technology needed to built a muon system for ILD.

4.2 The ILD coil and yoke system

The ILD detector design asks for a nominal 3.5 T and maximum 4 T solenoidal central field in a warm aperture of 6.88 m in diameter and 7.35 m in length. In addition, in order to suppress background from incoherent pairs from beamstrahlung, an anti-DID (Detector-Integrated-Dipole) is needed. In order to achieve high precision tracking with the TPC, accurate field mapping after construction is requested.

The iron yoke will be instrumented to be used for the detection of muons and for measuring showers escaping the hadron calorimeter (tail catcher). In addition, the yoke serves as the main mechanical structure of the ILD detector and, combined with the calorimeters, should make the detector self-shielding in terms of radiation protection. To allow work in the vicinity of the detector while its magnet is powered, the fringe field should be less than 50 G at 15 m from the IP, in the radial direction.

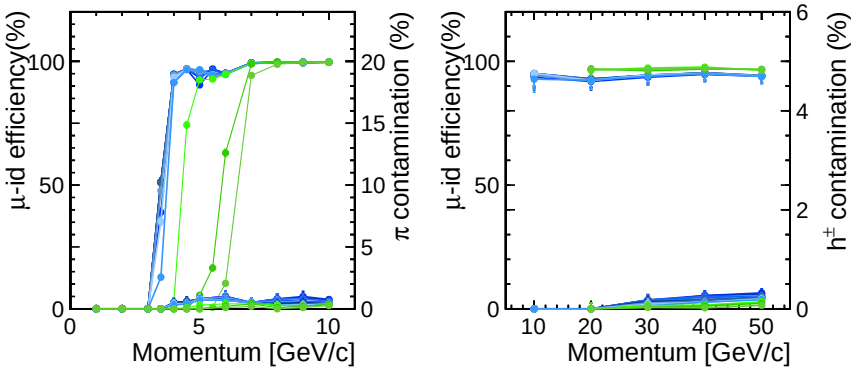

Figure III-4.4 Simulated muon efficiencies and contamination, left: muon efficiency and contamination as function of energy for single particles, right: muon efficiency and hadron contamination as function of energy for b-jet.

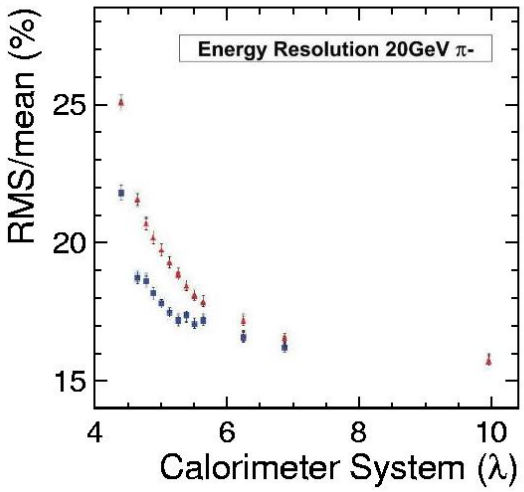

Figure III-4.5
Muon system as tail catcher: comparison of energy resolution of a calorimeter system with a tail catcher without a coil separating the two, in blue, with a system including a simulated coil (about 2 λ of dead material) in front of the tail catcher, in red, for 20 GeV πs.

4.2.1 Magnet design

The ILD magnet design is very similar to the CMS one, except for its geometrical dimensions, and the presence of the anti-DID. Consequently, many technical solutions successfully used for CMS [349] are proposed for ILD. The magnet consists of three main parts:

- the superconducting solenoid coil, made of three modules, mechanically and electrically connected. With its thermal shields, it makes up the cold mass, supported inside the vacuum tank by several sets of tie-rods;
- the anti-DID, located on the outer radius of the main solenoid, the dipolar magnetic field of which enables to reduce the beam background in the vertex and tracking volume;
- the iron yoke, consisting of the barrel yoke and the two end-cap yokes, of dodecagonal shape. The yokes are laminated to house muon detectors.

A detailed description of the conceptual design of the ILD magnet system is given in [350]. The main parameters and characteristics are summarised in this section. A schematic cross section of the magnet is given in Figure III-4.6. The main geometrical parameters of the ILD magnet are summarised in Table III-4.2.

Table III-4.2. ILD magnet main parameters

Cryostat inner radius [mm]	3440	Barrel yoke outer radius [mm]	7755
Cryostat outer radius [mm]	4400	Yoke overall length [mm]	13240
Cryostat length [mm]	7810	Barrel weight [t]	6900
Cold mass weight [t]	168	End cap weight [t]	6500
Barrel yoke inner radius [mm]	4595	Total yoke weight [t]	13400

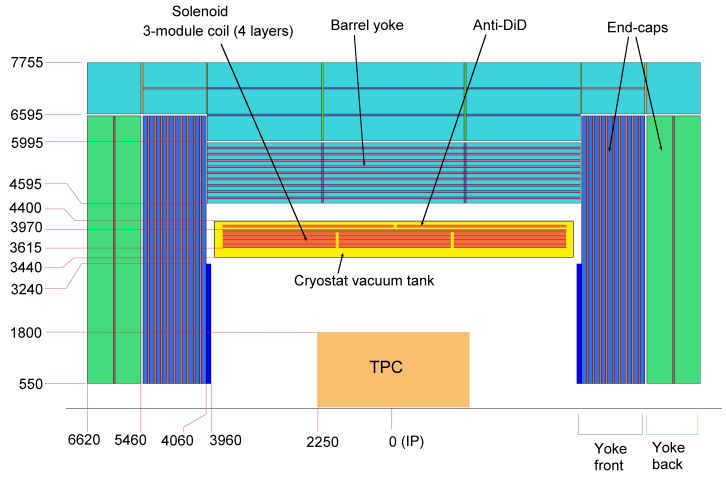

Figure III-4.6
ILD magnet cross section, dimensions are in mm (half upper part, cylindrical symmetry)

4.2.2 Solenoid design

The ILD solenoid main parameters are given in Table III-4.3. The 7.35 m length of the ILD coil enables to make it in three modules, each 2.45 m long. The reasons of this choice of three modules, rather than two or one, are linked to the fabrication of the external mandrel, to winding and impregnation as well as to transport and handling. Moreover, this enables to have shorter unit lengths of conductor, of about 2.6 km, and to join the units in known positions and in low field regions, on the outer radius of the solenoid. Each module consists of four layers, with 105 turns per layer.

Table III-4.3
ILD solenoid main parameters

Design maximum solenoid central field [T]	4.0	Nominal current [kA]	22.5
Maximum field on conductor [T]	4.77	Total ampere-turns solenoid [MAt]	27.65
Field integral [T*m]	32.65	Inductance [H]	9.26
Coil inner radius [mm]	3615	Stored energy [GJ]	2.27
Coil outer radius [mm]	3970	Stored energy per unit of cold mass [kJ/kg]	13.5
Coil length [mm]	7350		

The conductor design uses a superconducting cable, electrically stabilised and mechanically reinforced. The temperature safety margin is around 1.93 K, assuming a maximum operating temperature in the coil of 4.5 K.

The winding will be done inside the coil mandrel, using the inner winding technique, similarly to CMS [351]. This Al-alloy mandrel, about 50 mm thick, has several important other roles, as it will also be used as a mechanical support, a path for the indirect cooling of the coil (done with cooling tubes where liquid helium circulates welded on the outer radius of the mandrel), and a quench back tube (induced currents in this mandrel in case of quench or fast discharge enable a uniform quench of the coil and a limited radial temperature gradient). The anti-DID and the tie rods supporting the whole cold mass will be attached to the mandrel. The cold mass will be indirectly cooled by saturated liquid helium at 4.5 K, circulating in a thermosiphon mode.

The coil protection in case of quench uses an external dump circuit. With a dump voltage of 500 V, the maximum temperature within the coil does not exceed 82 K.

4.2.3 Anti-DID design

The magnetic dipole field B_x generated by the anti-DID should reach 0.035 T at z=3 m from the IP, and should extend up to z=5 m. The anti-DID coil is formed with two dipoles centred on the beam axis with their magnetic field in opposite direction. The anti-DiD design parameters are given in Table III-4.4. Details of the design can be found in [350].

Table III-4.4. ILD anti-DID main parameters

Design dipole central field on beam axis [T]	0.035	Nominal current [A]	1075
Position of max dipole field in z [m]	3	Maximum field on conductor [T]	2.0
Anti-DID total length in z [mm]	6820	Anti-DID inner radius [mm]	4160

The anti-DID is located within the same cryostat as the main solenoid, and benefits from the cryogenics of the main coil. The preferred superconductor is NbTi to tolerate some deformation of the winding pack but other superconductors (like Nb_3Sn and MgB_2) will be evaluated at a more advance stage of the design.

The manufacturing of the four poles constituting the anti-DID is independent from the main solenoid. It is proposed to do the winding inside a coil casing, similarly to the ATLAS barrel toroids [352]. The winding procedure and tooling will be validated with a winding test using a dummy conductor.

4.2.4 Assembly of the solenoid

The proposed assembly of the solenoid is similar to CMS [353]. The three modules of the main solenoid will be assembled on the ILC experimental site in a surface hall. They will be stacked vertically for the mechanical coupling. After the completion of the solenoid assembly, the anti-DID poles will be fixed on the main solenoid in the same vertical position, and all their connections (mechanical, electrical and cryogenic) done.

After the installation of the thermal screens in vertical position, the cold mass is swivelled to the horizontal position on its supporting platform, and brought to the position where it can be inserted into the outer cylinder of the vacuum tank which is fixed in cantilever to the central yoke barrel.

4.2.5 Ancillaries

The classical power circuit will consist of a two-quadrant converter (25 kA, $\pm$20 V), a dump resistance allowing both fast and slow discharges, and redundant current breakers. A superconducting high critical temperature (HTS) link is the preferred option for the flexible power lines. The current leads will be built as well with HTS superconductor. The anti-DID will have its own power circuit with similar characteristics as the one described for the main coil, connected through the same chimney across the yoke as the solenoid.

The magnet control and safety systems consist of (a) controls for all operation phases, (b) a system to safely discharge the energy of the magnet and (c) redundant quench detectors (QDs) on coil modules, anti-DiD poles and on the superconducting busbars connected to the HTS power lines.

A common refrigerator will be used to cool down the main solenoid and the anti-DID. It is also able to extract the dynamic losses during the various magnet ramps or discharges. An estimate for the cryogenic losses is 400 W at 4.5 K.

4.2.6 Final tests and field mapping

A full test of the magnet at its nominal current is mandatory before the inner detectors are installed. A complete field map of the magnet, to an accuracy of about 1 G in an overall field of 4 T, i.e. with a relative accuracy of around 2 10^{-5}, is needed. Possibilities to reach such a measurement accuracy could be to use a differential method, or to aim for a very large number of measurement points during the field mapping.

4.2.7 Iron yoke design

The yoke has several functions. It provides the flux return of the solenoidal field and reduces the outside stray fields to an acceptable level. It is instrumented with detectors for muon identification and tail catching of hadronic showers. In addition, the yoke is the main mechanical structure of the detector. The ability for access and work in the interaction region (IR) hall during beam operation requires the detector to be self-shielding. The design allows for a fast opening in order to get access to the inner detector components.

For the inner part of the yoke a fine segmentation of the iron was chosen, 10 layers of 100 mm thick plates with 40 mm gaps for detectors to be inserted for good muon reconstruction, rejection of hadron background and good performance of the tail catcher (see section 4.1). This segmentation is in particular useful for the tail catcher, whereas a similar performance of the muon system could be achieved by arranging the detectors in groups of layers. In addition to the inner fine segmentation, some 560 mm steel plates are added on the outer part mainly to reduce the stray field.

During beam operation the IR hall has to be accessible due to the push-pull concept. Since all activities in a high magnetic field are very cumbersome and potentially dangerous, a field limit of 50 G at 15 m radial distance from the beam line was agreed upon [354]. Two- and three-dimensional FEM field calculations were done using the CST EM Studio program, varying the thickness and geometry of the iron in the barrel and end-caps until the goal of less than 50 G at 15 m radial distance was achieved. This was obtained with three 560 mm thick steel plates in the barrel and two 560 mm plates in each end-cap in addition to the ten 100 mm thick inner layers. This results in a total thickness of the iron of 2.68 m in the barrel and 2.12 m in the end-caps, respectively. In order to obtain the desired limit, all gaps between the steel plates on the outer radius have to be closed with iron. The only exception are the gaps between the barrel rings and between barrel and end-caps. This space will be needed for cables, cooling pipes and other services.

It should be noted, that the field calculations assume no additional magnetic material outside the yoke and that the results are at the limit of the accuracy of the FEM calculations.

The strong magnetic field, maximum of 4 T, introduces large magnetic forces on the end-caps, which were calculated using different FEM programs (CST EM Studio and ANSYS). The largest force, an inward pulling force in the z-direction of about 180 MN, acts on each end-cap, which has to be taken into account in the mechanical design.

4.2.8 Barrel yoke design

The solenoid with the central subdetectors is supported by the central barrel ring, the only stationary part around the interaction point. Both outer rings can be moved independently along the z-direction to allow access to muon chambers and services. A dodecagonal shape was chosen in order to reduce the weight and size of the sections. The twelve segments come in two slightly different sizes to avoid segment edges pointing towards the beam line. The average weight of a segment is about 190 t. Fig. III-4.7 gives an overview of the design.

The 10 plates of an inner segment and the three outer plates are welded together with 30 x 40 mm spacers between the plates along the segment edges. Segments are then bolted together

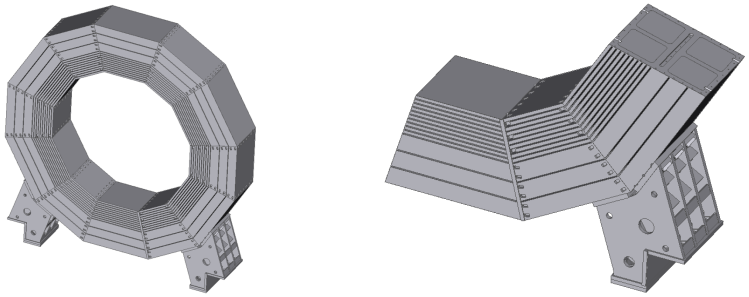

Figure III-4.7
The yoke barrel design: general view of one barrel ring (left) and detailed view of a sector with one supporting foot (right)

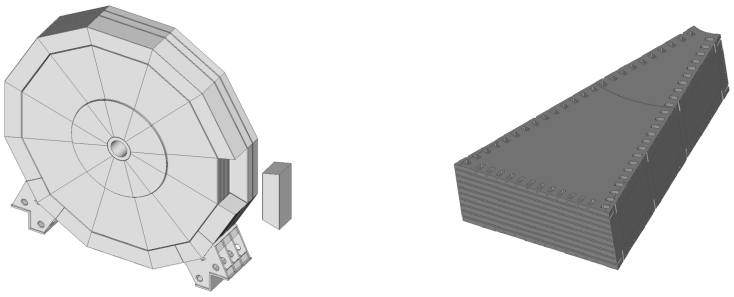

Figure III-4.8
The yoke end-cap design: overview (left) and detailed view of one sector (right)

on all sides using M36 bolts. (bigger on outside). Shear keys between the segments prevent radial displacement, whereas shear pins on the inner and outer edges are used to prevent movements along the z-direction.

The fully assembled barrel ring is a very stiff structure. The maximum vertical deformation of an outer ring is 1.6 mm, which is due to the gravitational load. At the very end of the coil there is a radial magnetic field component acting on the inner plate of the outer ring, which introduces a force of about 1.3 MN. This leeds to a 1.5 mm radial deformation of the plate.

Each barrel ring has a mass of about 2300 t, including the support feed. The central barrel ring has to carry an additional weight of almost 1000 t, the mass the cryostat with the coil, barrel calorimeters and central tracking detectors. For the calculation of deformation and stress the cryostat was approximated by a single 50 mm thick steel cylinder attached to the barrel at 12 points. The additional gravitational load was introduced by increasing the density of the cylinder. The maximum vertical deformation is 4 mm.

4.2.9 End-cap yoke design

The design of the end-cap is more challenging compared to the barrel due to the large magnetic forces, about 180 MN acting in the z-direction. Several geometries were considered. A design with radial supports instead of horizontal supports was chosen due to the larger second moment of area, better transfer of force to the barrel, symmetric iron distribution and a minimum of dead material. This design minimises the end-cap deformation and stress. An overview of the design as shown in Fig. III-4.8 The end-cap is made out of twelve wedge-shaped segments, extending from the inner hole to the outside of the yoke, consisting of 10 inner 100 mm thick plates, and two outer plates 560 mm thick. In addition, a 100 mm thick steel plate was introduced to improve the self-shielding of the detector.

Similar to the barrel, the 10 plates of an inner segment are welded together with spacers along the segment edges. Thus forming rigid structures, with the spacers acting as supports. Segments are then bolted together on the front and back sides using M36 bolts. A central cylindrical support tube of 1.0 m (1.2 m) inner (outer) diameter is bolted to the individual inner and outer plates, making a rigid connection of the inner and outer parts.

The maximum deformation of the end-cap due to the magnetic force of 180 MN is about 3 mm.

The force are transmitted to the barrel through z-stops the resulting stress is less than 200 MPa. The total weight of one end-cap is about 3250 t.

4.2.10 Yoke assembly

After a full trial assembly at the manufacturer, the barrel end-cap segments with a maximum weight of 200 and 90 t, respectively, are transported to the experimental site. In case of vertical access shaft, the assembly of the barrel rings and end-caps is done in the surface building above the IR region. Complete barrel rings and the end-caps are then lowered into the IR hall, similar to the CMS assembly.

The design does not have to be changed for a mountain site with horizontal access tunnels. Barrel and end-cap segments have to be transported into the IR hall, where the rings and end-caps are then assembled. This requires more work and time spent in the IR hall and requires a 250 t crane in the IR hall.

Chapter 5
The ILD Detector System

A central part of the activities of the ILD group has been the integration of the different sub-systems into a coherent detector, and the coordination between the detector and the machine. In this section a coherent integration scheme is presented, with a first realistic estimate about space and extra material this requires. Also described are systems which concern the complete detector as overall calibration scenarios, data acquisition, and central software and tools. The chapter closes with a description of the assembly procedure which is planned for ILD, and a discussion of the impact the different sites discussed for ILC will have on this procedure.

5.1 ILD integration

The integration of the different sub-detectors into a coherent and functioning ILD detector concept is an important aspect of the ILD work. Not only the mechanical integration, but also the coordination of the services, cabling, cooling strategies, thermal stabilisation and alignment of the various sub-detectors is an on-going task, which evolves with the better knowledge about the respective detector technologies. Moreover, the envisaged push-pull scenario at the ILC imposes additional requirements.

5.1.1 Mechanical concept

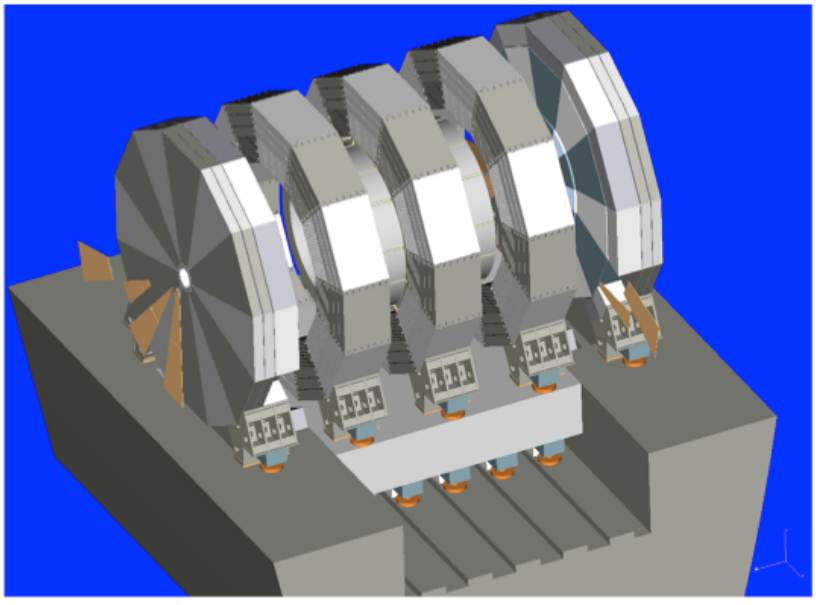

Figure III-5.1
The mechanical design of ILD.

The mechanical design of the ILD detector is shown in figures III-5.1 and III-1.1. The major components are the five parts of the iron return yoke: three barrel rings and two endcaps. The central barrel ring carries the cryostat with the solenoid coil in which the barrel calorimeters are installed. The TPC and the outer silicon envelope detectors are also suspended from the cryostat using tie rods. The

endcap calorimeters are supported by the endcap yoke sections which can be moved independently from the barrel sections. The beam pipe, the vertex detector and the other inner silicon detectors are supported from a structure of carbon fibre reinforced plastic (CFRP), which hangs at the flanges of the TPC field cage. The whole structure can be aligned with respect to the beam axis using actuators and a laser alignment system. The final focus quadrupole (QD0) magnets are mounted independently of the yoke endcaps in a support structure that carries the magnets and the forward calorimeters. This structure is supported from a pillar outside of the detector and is suspended from the solenoid cryostat using tie rods. The QD0 magnets are also monitored by an alignment system and can be moved using actuators.

5.1.1.1 Yoke and magnet

The mechanical design of the return yoke and the solenoid is described in section 4.2. The central barrel yoke ring supports the detector magnet solenoid. The magnet cryostat has been designed to carry the load of all central detectors, i.e. barrel calorimeters, TPC, inner tracking. The cryostat itself is bolted to 24 double-brackets that are welded to the inner support structure of the yoke barrel. Figure III-5.2 shows how the outer cryostat shell is fixed to the barrel yoke (left) and the simulated deformation of the cryostat under its own load and the load of the barrel calorimeters (right). Under the assumption that the loads are distributed evenly over the cryostat flanges, maximum deformations of less than 1.3 mm are expected. Simulations for a more realistic support system, where the barrel calorimeters are supported by rails in the cryostat, yield maximum deformations of $\approx$ 2.5 mm. Details of the magnet cryostat integration are described in [355].

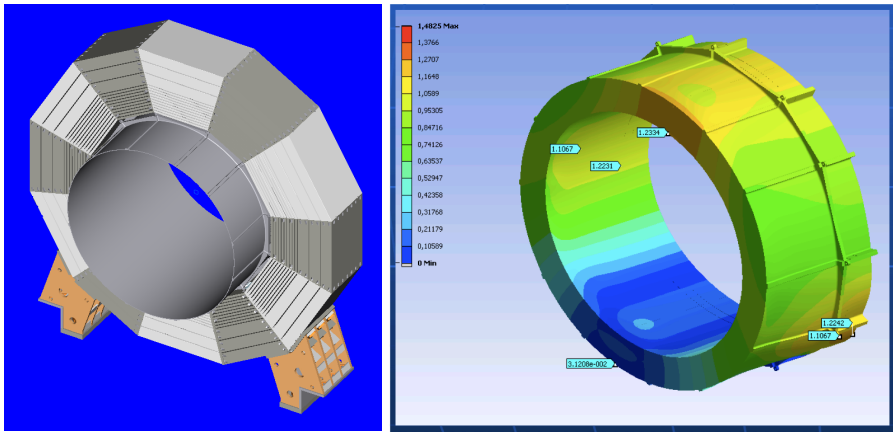

Figure III-5.2 Integration of the solenoid cryostat and the central yoke ring (left). FEM simulation of the cryostat deformations under its own mass and the mass of the barrel detectors (right).

5.1.1.2 Hadronic barrel calorimeters

The hadronic barrel calorimeters are installed in the cryostat of the detector solenoid. The calorimeter modules are assembled in rings and are supported inside the cryostat. Two different mechanical absorber structures are under investigation. The structure of the analogue hadronic calorimeter (AHCAL) is shown in Figure III-5.3, the structure of the semi-digital hadronic calorimeters (SDHCAL) is shown in Figure III-5.4. Two rings of eight AHCAL modules form the barrel that is installed in the cryostat. All services for the modules are accessible from the open ends of the barrel. In the SDHCAL case, the barrel consist of five rings that are assembled from eight wedge-shaped modules each. The services for the calorimeter run in this case on the outside of the barrel. In both cases, the barrels are supported from rails in the cryostat. The mass of the HCAL steel absorber structures is of the order of 600 t. The expected distortions are in the order of a few millimetres.

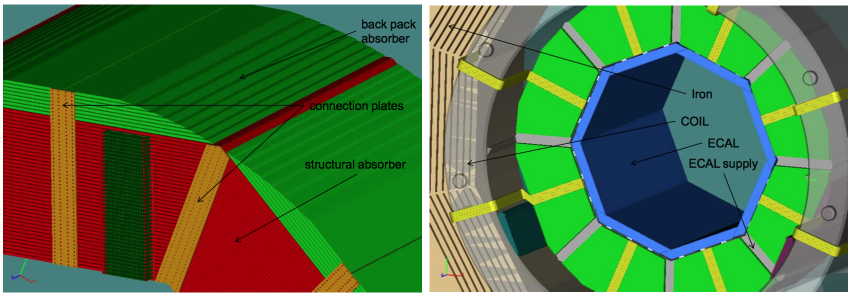

Figure III-5.3
Integration of the AHCAL structures into the cryostat.

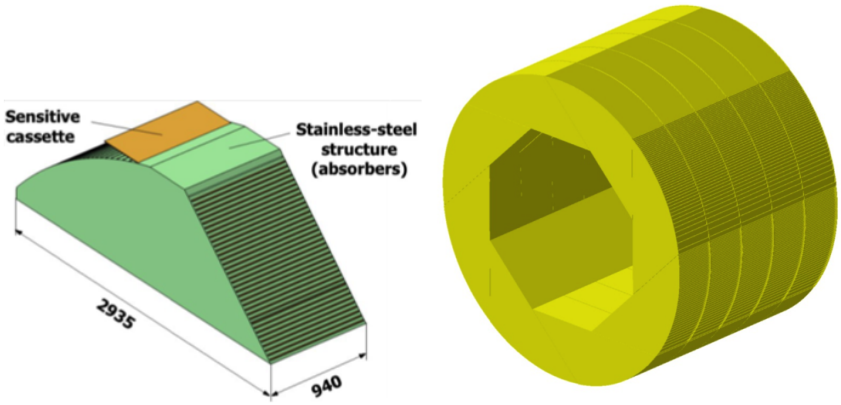

Figure III-5.4
Integration of the SDHCAL structures.

5.1.1.3 Electromagnetic barrel calorimeters

The electromagnetic calorimeter (ECAL) modules are supported by rails from the HCAL barrel modules. Figure III-5.5 shows the installation procedure of the ECAL modules. An external cradle that holds a rotatable support cage will be used during the installation phase.

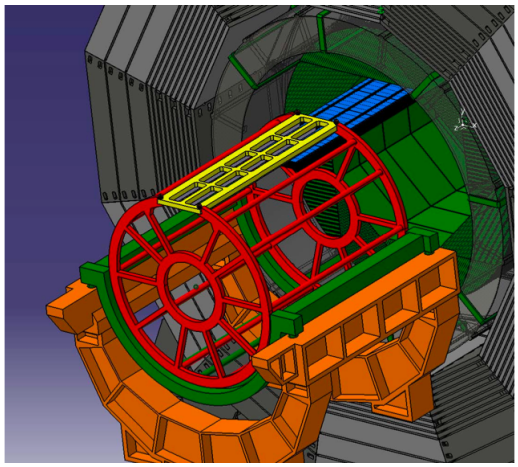

Figure III-5.5
ECAL installation.

5.1.1.4 Endcap calorimeters

The endcap calorimeters are supported from the endcap iron yoke. Figure III-5.6 shows the endcap assembly where the ECAL and HCAL endcap detectors are supported from the iron yoke endcap. The support for the HCAL endcap from the yoke needs to balance the bending of the iron yoke in the strong magnetic field (c.f. section 4.2).

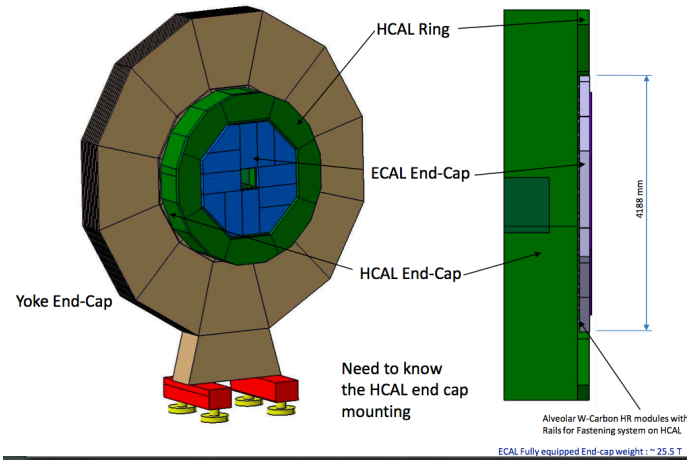

Figure III-5.6
The endcap detectors of the HCAL and the ECAL are supported by the yoke endcap.

5.1.1.5 TPC

The Time Projection Chamber (TPC) will be supported from the solenoid cryostat by a system of either double-T beams from lightweight CFRP or by a system of flat CFRP ribbons. Both systems will run along the front face of the HCAL barrel (see Figure III-5.7). The ribbon system needs less space in the endcap-barrel transition region, but requires an additional fixation of the TPC in longitudinal direction. A U-bracket with a spring based suspension would fix the TPC w.r.t. the ECAL barrel calorimeter.

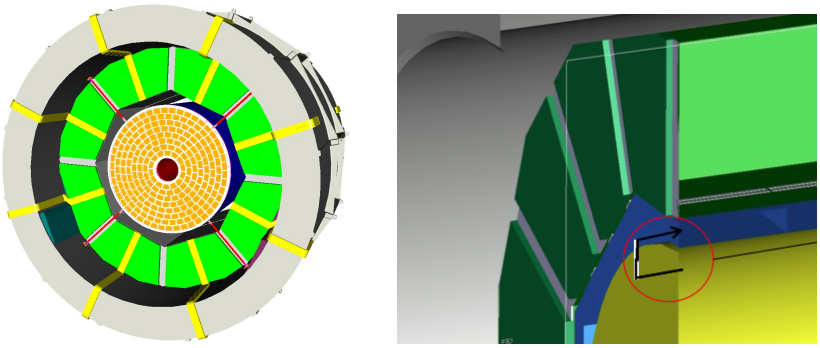

Figure III-5.7
TPC support from the cryostat.

5.1.1.6 Inner tracking system

The inner tracking system consists of the Silicon Inner Tracker (SIT), the Forward Tracking Disks (FTD) and the Vertex Detector (VTX). These detectors will be mounted together with the Beryllium beam pipe in the Inner Support Structure (ISS), as indicated in Figure III-5.8. The ISS consists of a CRFP tube that is fixed to the end plates of the TPC. This support system needs to be remotely adjustable to allow for alignment of the inner trackers and the beam pipe after a push-pull operation. As the push-pull system will align the overall ILD detector axis only to ± 1 mm, a re-adjustment of the beam pipe might be necessary to keep the stay-clear margin between the beam pipe and the cone of background radiation at safe levels. Details of the inner detector system are described in [356].

5.1.1.7 Forward region

The forward detectors (c.f. section 3.5) LumiCal, BeamCal and LHCal are supported by the same structure that supports also the QD0 magnet (c.f. section 5.5.2). A support tube with a square cross section extends from the external pillar and is suspended from the coil cryostat with a tie-rod system. The support structure is a double-tube structure where the inner tube supports the QD0 magnet and the outer tube supports the forward detectors. This decouples the heavy masses of the calorimeters

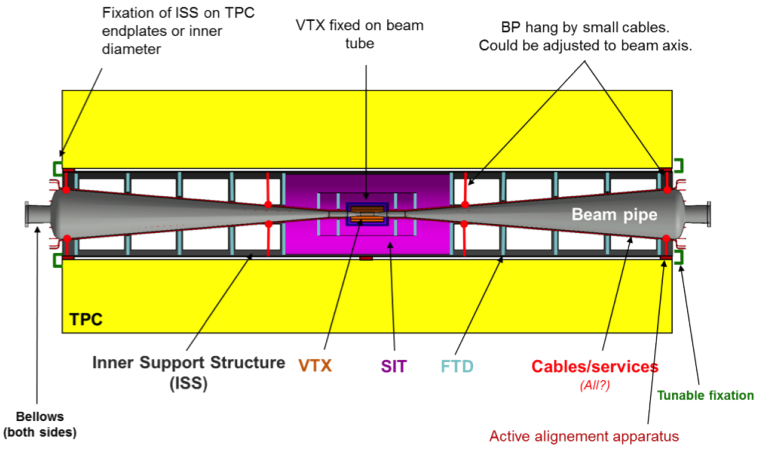

Figure III-5.8
Top: support of the inner tracking detectors. Bottom: schematic representation of the cable distribution along the beam pipe (from IP to the position of TPC endplate).

from the QD0 and eases the alignment procedures of the final focus magnets. A detailed view of the forward region is shown in Figure III-3.24.

5.1.2 Detector assembly

5.1.2.1 Non-mountain sites

The main assemblies of ILD are the five rings of the iron yoke, three in the barrel part and two end caps. The assembly scenario will be similar to the CMS experiment at the LHC:

The detector will be pre-assembled and tested in a surface building. The large sub-assemblies will then be lowered into the experimental hall through a large vertical access shaft. The dimensions of the shaft and of the (temporary) crane for these operations are given by the masses and dimensions of the biggest assembly piece. In the case of ILD this would be the central yoke ring, which carries the solenoid coil. The size and mass of this biggest piece drive the requirements for the central shaft diameter (18 m) and the capacity of the hoist crane (3500 t).

The five yoke rings are mounted on air pads and can therefore be moved easily within the underground experimental hall. In the beam position and during the push-pull movement, the detector is mounted on the transport platform. In the maintenance position, the detector can be opened and the yoke rings can move independently away from the platform. Figure III-5.9 shows the detector opened for maintenance, in the beam position and in the maintenance area. The hall layout needs to foresee enough space in the maintenance position to allow the complete opening of the detector rings. Access to the inner detector parts and, in the maintenance area, the removal of large detector components (e.g. the time projection chamber) needs to be possible.

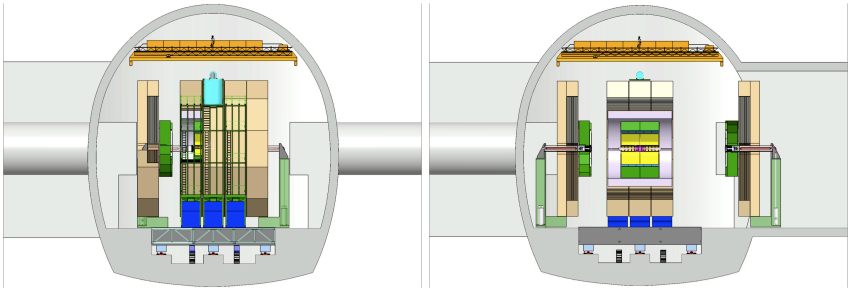

Figure III-5.9
ILD detector opened on the beam line (left) and in the maintenance area (right) [198].

5.1.2.2 Mountain sites

Possible ILC sites in Japan are different to the other reference sites as they are situated in mountainous regions where a vertical access to the experimental hall might not be possible. Instead, horizontal tunnels of $\approx$ 1 km length will serve as access ways into the underground experimental area. As the tunnel diameters and the transport capacities are limited for technical and economic reasons, a modified assembly scheme for the ILD detector is applied for these sites: In these cases, it is foreseen to also pre-assemble most detector parts on the surface. However, the yoke rings are too big and heavy and can only be assembled in the underground hall. The yoke would be transported in segments into the hall where enough space for the yoke assembly and the necessary tools need to be provided. The largest part of the ILD detector, which should not be divided and therefore needs to be transported in one piece, is the superconducting solenoid coil. Its outer diameter of $\approx$ 8.7 m puts stringent limits on the diameter of the access tunnel.

The detector assembly procedures in mountain sites are part of an on-going optimisation process that needs to balance the requirement for space - linked to the time needed for the detector assembly - and the cost of the underground caverns.

5.1.3 Service paths and interfaces

A number of services (cables, cooling, gases) are needed for the operation of the ILD detector. The understanding of the needs and the analysis of their distribution inside the detector are major issues of the integration and mechanical design studies. Figure III-5.10 shows the main service paths

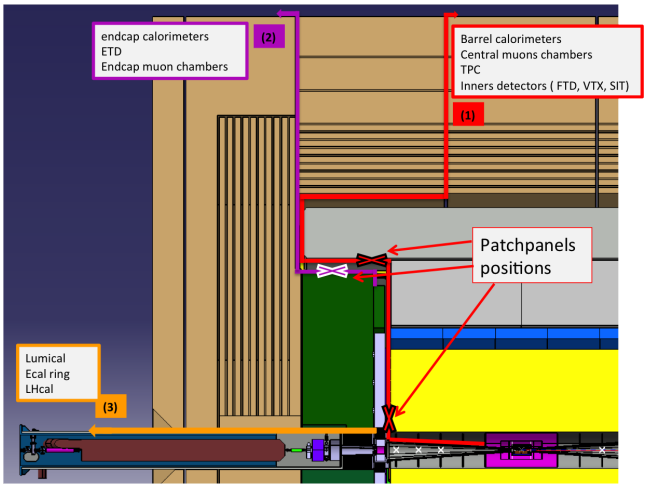

Figure III-5.10
Illustration of the main service paths in the ILD detector.

within the ILD detector. The routing of services is foreseen as follows:

1. All the services of the barrel detectors will be routed outwards via the endcap/barrel gaps, then along the outer radius of the coil, and finally between the central yoke rings. The assembly procedures of the inner detectors (SIT, FTD, VTX) and the volume of cables associated to each, imply that all the inner detector services will follow the same way.
2. The endcap detector services will run in the same gap, up to the coil outer diameter and will then be fixed on the return yoke endcap.
3. The forward components (forward calorimeters, QD0 magnets, support structures) will be built as one unit, and the required services will be distributed along the QD0 support structure.

The locations of the cable patch panels are under study, taking into account:

- assembly and maintenance procedures;
- the power distribution considerations as power convertor positions need to be chosen to limit the voltage loss in the cables;
- optimisation of the overall volume of services;

- material budget and impact on physics performance.

The requirements for both service lines and patch panels define the space that needs to be reserved in the detector for gaps. The geometry of these gaps is a major issue to be optimised as these gaps are dead zones in the detector. In addition to the space that is needed for services, additional dead zones are needed for construction tolerances, mechanical deformation of detector parts under loads (gravitational and magnetic), space needed for integration and assembly, alignment tools. etc..

Each sub-detector group has begun to define the amount of cables they foresee for power distribution and signal transmission as well as the power consumption. The later is particularly critical as it is needed to define the cooling method and the distribution of fluids. Currently, the amount of cables for the barrel calorimeters and the TPC is estimated to be small with respect to the numbers of channels in these sub-detectors, less than 3000 cables per side of the detector. For the inners part (SIT, FTD, VTX) up to 600 cables per side might be needed. This represents an average are of about 2000 cm^2 occupied by cables and piping at the radius of the HCAL. Figure III-5.11 shows the cable paths and their occupancies in the gap between barrel and endcap detectors.

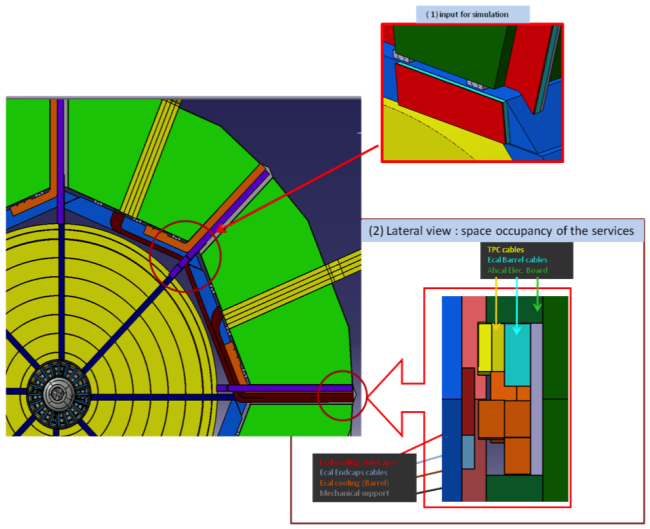

Figure III-5.11
Front view of the barrel calorimeters (green/blue), TPC (yellow), inner part and of their associated services. (1) The volume occupied by cables and services in each way-out has been translated into equivalent thickness of conductor and insulator to be implemented in the simulation model. (2) Lateral view of one way-out, with representation of the space needed per sub-detectors services.

The inner detector layout is very challenging as the amount of cables from the inner silicon detectors (VTX, FTD, SIT) represent dead material immediately around the beam pipe and may become a source of background. It is presently estimated to be some few percent of X_0 at some positions of the beam pipe. In addition a mass of some few kg of material needs to be supported by the light structure of the beam pipe. Specific R&D on the definition of the cables according to the nature of the conductor and the optimisation of the insulator is mandatory in order to minimise the effects of the services on the physics performance of the detector. A schematic view of the cable routing in the inner detector is shown in Figure III-5.8.

5.1.4 General Safety Issues

The final ILD installation needs to follow the applicable safety rules, given by the collaborative aspect of the project and requested by the site retained. Some general rules have been established to allow the co-existance of the two detectors, ILD and SiD, in one underground experimental hall (c.f. section 2.3). Other safety aspects need to be respected in the integration scheme for ILD. Among others, this covers:

- Mixing of flammable gases will be done in protected areas and only non-flammable mixtures will be sent to the experimental cavern;
- Fire prevention will be an important feature of the integrated design - a particular worry is to prevent fire from propagating inside the vaccum vessel of the coil, e.g. caused by the explosion

of a super-capacitor;

- General protection against earthquakes will be developed, to protect the ILD detector during assembly, maintenance and operation.

5.1.5 ILD modelling

Three different types of models are being used for the design of the ILD detector. While engnieering and placeholder models are needed for the mechanical design of the detector, physics simulation models are used to study the detector performance:

- Placeholder models are used for global integration purposes. They describe the boundaries and volumes of the sub-elements and enable fast integration, checks for conflicts and compliance of the interfacing components. They also include reserved space that is needed for assembly purposes and tolerances. Different technology options for sub-detectors need to fit into the global sub-detector placeholder to enable and check plug compatibility;
- Detailed engineering models of the sub-detectors form the basis of the construction. They define how to assemble a component from parts and provide exact geometry and material description. Detailed models exist for each sub-detector option and are the basis of the cost evaluations;
- Physics simulation models are used in the Monte-Carlo simulations of the detector performance. They describe the segmentation, shape, and physics behaviour of the active and passive components.

While the placeholder and the detailed engineering models are usually derived from CAD systems, the ILD physics model is part of the Geant4 based full detector simulation MOKKA. Figure III-5.12 shows, for the example of the ECAL barrel detector, the three model types.

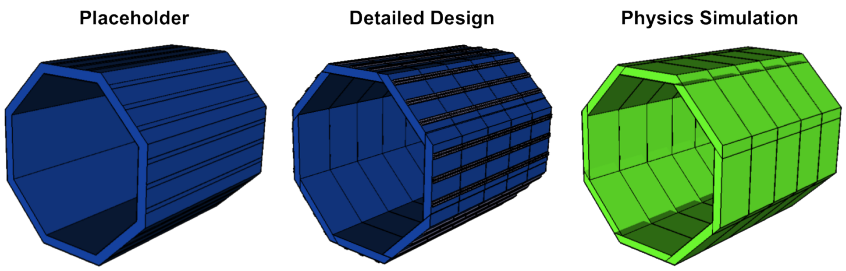

Figure III-5.12 Different models describe the ILD detector (this example: the ECAL barrel).

While the CAD models (placeholders and engineering) are by default stored in the ILC Engineering Data Management System (ILC-EDMS) [357], a process has been set up to convert the geometric information from the MOKKA model into a 3D format that allows comparison with the engineering models using the design analysis tools. Figure III-5.13 shows an overlay of the simulation and the engineering model of the ECAL barrel. Differences and overlaps are colour-coded so that the compatibility of the models can be checked quickly.

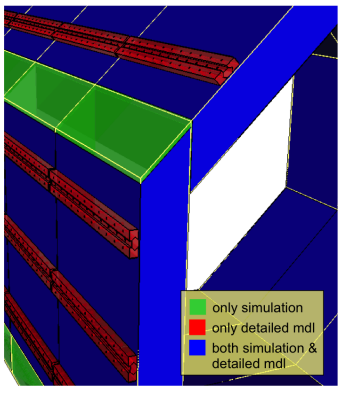

Figure III-5.13 Geometry comparison of the simulation and the detailed engineering model of the ECAL barrel detector. The blue parts are in both models, while the red ones are only in the engineering model (labelled "mdl") and the green ones are only in the Geant4 description.

5.2 ILD alignment and calibration

5.2.1 Alignment of the tracking system

Achieving one order of magnitude improvement on momentum resolution over state of the art detectors imposes stringent requirements on the performance of the tracking devices and on the stability of their support structures. The list of structural properties needed for mechanical supports is long: low mass material, stiff and lightweight, stable to electric and magnetic fields, robust against temperature and humidity gradients. The particular conditions at the ILC add two new sources of instability: power pulsing of the electronics and push-pull operation. Power pulsing induces temperature changes around front-end electronics and vibrations that can be propagated as oscillation modes to higher order structures. Opening and closing of the detectors, and moving detectors between maintenance and on-beam position will demand a quick re-alignment of the full experiment.

The quest for spatial precision spans the life time of the detector. During construction, accurate positioning of individual active elements is granted by tight assembly tolerances and then measured using Coordinate Measuring Machines (CMM). Elements are arranged together into higher order structures (modules, supermodules and sub-detectors). Once the full sub-detector is assembled, global measurements of its degrees of freedom are obtained by standard survey techniques. During operation, hardware alignment systems can monitor internal stability of sub-detectors and even movements of sub-detectors with respect to each other. The ultimate micrometer-level geometrical description of the experiment is achieved by means of exhaustive but time consuming track alignment algorithms. Tracks have very little sensitivity to deformations of the support structures that make χ^2 invariant, the so-called weak modes. Some of these will be measured using an innovative monitoring of structural stability in ILD: Fiber optical sensors laid inside the support structures are sensitive to changes that induce strain in the fiber and, therefore, deformations of the supports can be recorded and taken into account in the analysis.

5.2.1.1 Silicon sensor hardware alignment system

The internal hardware alignment of the Si-microstrip tracker uses infrared (IR) laser tracks to align consecutive layers of Si detectors. This system exploits the partial absorption/transmission of Si to infrared light, generating signals in consecutive sensors that are measurable by the readout electronics. The aluminum back-metallization of the sensor is removed locally to allow downstream propagation of the IR light, using the so-called alignment passages. The transmittance to IR light is maximized using the top and bottom passivation layers as an anti-reflection coating. IR optimized sensors produced at CNM-IMB (Barcelona, Spain) showed maximum transmittance values of 50% (30% increase with respect to untreated sensors) for sensors of 50 μm pitch.

The IR laser system uses optical fibers and collimators inside the tracker volume while the corresponding laser heads remain outside. It provides quick reconstruction ($<$ 1 min) of the positions of the measured modules with a relative resolution (between consecutive measurements) of 10 μm. Therefore, it can monitor shifts and rotations on a short time scale. It does not, however, distinguish global movements of the monitored structure from global movements of the laser beams.

5.2.1.2 Structural and environmental monitors using fiber optical sensors

A fiber Bragg grating (FBG) is a type of distributed Bragg reflector embedded in a short segment of optical fiber that reflects particular wavelengths of light and transmits all others. Any strain (temperature, pressure, vibration etc.) at the grating will cause a shift and magnitude change of the reflections. This change allows for very accurate measurements of the magnitude of strain.

Distributed sensing is achieved by recording gratings for different wavelengths in the same fiber. Deformation, displacement, temperature, humidity etc. can then be sampled at different locations

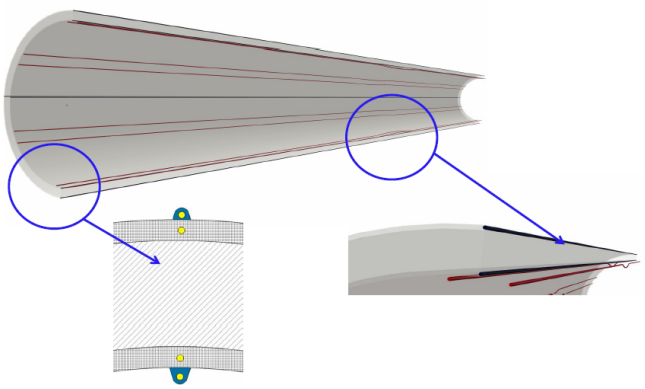

Figure III-5.14
Embedding of fibers along the tracker support structure for structural monitoring of distortion, temperature, humidity, etc..

along the fiber. The light transmitted in the fiber is immune to electromagnetic disturbances, does not dissipate power and works in a wide range of temperatures. Due to the negligible loss of light in the fiber, all readout electronics for this system will be placed outside of the experiment.

In ILD, fiber optical sensors will be embedded in carbon fiber reinforced plates. The measured deformation will help to determine the shape of the support structure, measure its displacements with respect to locking points, and calculate temperature distribution and gradients. In particular, these smart support structures will be able to detect and diagnose weak modes. Figure III-5.14 shows a cylindrical support structure with fibers inserted near the inner and outer boundaries. From the difference in traction and compression from top and bottom fibers, the shape of the structure can be obtained.

5.2.1.3 Track-based Alignment

Individual tracking sensors have an excellent intrinsic spatial resolution. During construction, the position of sensors inside each module can be measured with a precision of $\sim$5 μm. Modules are then assembled into higher order structures, positioned and surveyed with uncertainties in the range of 200-500 μm. Hardware alignment procedures reduce this uncertainty to a level of about 100 μm, such that tracks can be reconstructed by software alignment algorithms. Track alignment takes the task of reducing alignment uncertainties below the intrinsic sensor resolution. To reach the required precision reliably the track based alignment must include the constraints from construction, survey and hardware alignment (laser system and fiber Bragg system) into the global alignment procedure. This will dramatically reduce the number of degrees of freedom and speed up alignment after push-pull.

Typically, the alignment sample is composed of a mixture of collision data and tracks from cosmics and beam halo. These tracks are useful as they allow to relate different parts of the detector (upper and lower half, both end-caps). Tracks with known momentum are extremely valuable, both as a means to determine some of the weakly constrained alignment parameters and as a monitoring tool to validate the alignment. This role has traditionally been played by tracks from resonances with a well-known mass (Z, J/Ψ and Υ resonances).

The alignment precision should be such that the momentum resolution of the tracker is degraded by less than 5%, which leads to alignment constraints of $\sim$2 μm for the vertex detector, $\sim$4 μm for the inner silicon tracking, $\sim$ 6 μm for the outer silicon tracking and $\sim$ 20μm for the TPC.

5.2.1.4 Pixel alignment

The pixel system will be aligned in two steps. Within each layer, alignment will be achieved using hadronic tracks crossing the overlap region between ladders (a few thousands per day at nominal beam parameters). Across different layers and with respect to the rest of the detector, tracks from muon pairs at the Z-pole (estimated several thousands in a day) will be used.

5.2.1.5 Alignment of the silicon strip tracking system

The total number of degrees of freedom of the ILD tracker is of the order of 10^5. The time required to accumulate sufficient tracks to resolve all of them will be of the order of months, comparable to the push-pull period.

After a push-pull operation the goal of ILD is to obtain a quick re-alignment. If the relative sensor positions inside a module are known to 5 μm precision (from construction data) the number of degrees of freedom will be reduced by a factor 2-10, depending on the sub-detector. Another sizeable reduction will be obtained if the internal degrees of freedom of the subsystems (ladders and rings, cylinders and disks) are stable over time. This requires a careful design of the mechanical support of the detector. Relative movements of these rigid bodies can be monitored using the laser alignment system and the embedded fiber optical sensors. In total, 26 degrees of freedom will be present if only the sub-detectors need to be re-aligned against each other.

5.2.1.6 Alignment after Push-Pull

Push-pull of the full detector between the interaction point and the garage position and opening and closing of the experiment for maintenance are evident sources of misalignment. To facilitate maintenance and accessibility to different detector regions, a modular detector design will allow to open the detector by pulling it on a combined system of air and grease pads. A system able to control the relative distance from bulky elements to delicate objects like the beam pipe has been implemented in the CMS experiment with a distance measuring system, using about 200 sensors (contact and non-contact distance meters) to accomplish this task. This system will ensure precise and safe handling and overall repositioning of the experiment. Internal alignment of each sub-detector has to be obtained using hardware alignment and cosmics in the maintenance area.

A special task is the alignment of the final focus magnets (QD0). An optical alignment system based on RASNIK sensors has been proposed for CLIC [358]. The alignment requirements at CLIC are about 5-10 times more stringent than at the ILC. An adaptation of this system to ILD is under investigation.

5.2.2 Calorimeter calibration

This section discusses general calibration issues for particle flow calorimeters. Aspects specific to each technology are summarised in the subsystem sections. The discussion is limited here to the single particle energy calibration; corrections at jet level are part of the particle flow reconstruction and need to take tracking information on an event-by-event basis into account.

Calibration as a general term is used for several aspects of the calorimeter reconstruction. For the channel-to-channel normalisation we use the term equalisation, to be distinguished from the corrections of time-dependent effects, induced for example by temperature or pressure variations. Tracing such variations is called monitoring. Establishing an absolute scale in units of GeV is again a separate task, and different scales, electromagnetic, hadronic or weighted scales need to be distinguished. If applied at particle level, they may depend on the clustering definition. Other corrections, like for dead materials, may be applied at particle level, too.

A common feature of all particle flow calorimeter technologies is their relative insensitivity to any sort of stochastic calibration or alignment uncertainty. The large number of cells required for the topological resolution is an asset rather than a burden, since the precision with which these effects need to be known scale with $\sqrt{N}$, where N is the number of channels.

In contrast, coherent systematic effects must be corrected with higher precision, depending on the fraction of the detector affected. If it is the entire calorimeter, the precision required is given by the constant term aimed at, about 1% for the ECAL and 2-3% for the HCAL. The challenge of

the high granularity is that time-dependent corrections cannot be applied at cell level, and cell-wise corrections require stability over time to reach statistical precision. On the other hand, since every cell is individually read out, one is free to form averages over space or time according to the specific problem, but finding the optimal averaging procedure and identifying the leading effects is often an involved analysis and intimately related to understanding the detector and its systematics. The procedures needed in practice can only be developed from real data. Such studies form an important part of the test beam data analysis, and they are also the reason why the next generation of prototypes must undergo beam tests at system level again to obtain realistic performance figures.

5.2.2.1 Calibration scheme

The calibration of the electromagnetic and hadronic response of the calorimeter proceeds in the following general steps:

1. Test bench characterization of sensor parameters at cell level
2. Inter-calibration of the electronic response of all individual cells using muon test beams, and conversion to the MIP scale
3. Verification of the electromagnetic scale and linearity using electron beams impinging directly on the detector modules
4. Determination of the hadronic response using hadron test beams
5. Determination of combined ECAL and HCAL hadronic response, including weighting procedures
6. Verification of dead material corrections at inter-module connections using hadron test beams
7. In-situ validation and monitoring using kinematic constraints, tracker information and track segments in hadronic showers

5.2.2.2 Channel equalisation

On the test bench, one measures parameters like, for example, gain, efficiency, dependence on operating conditions, and the non-linear response function of the photo-sensors. Also time-consuming threshold scans can be done to equalise zero-suppression DACs at the input stage of the front end electronics to compensate for channel-to-channel gain variations. Measurements are done at different production stages, for example before and after integration into the scintillator tiles. Already for the beam tests this was done for ECAL and HCAL prototypes using semi-automatic procedures, and studies are underway to automatise this further.

The inter-calibration with muon beams must be done for all cells and all detector layers. Thanks to the modular design, this can be done with the bare active layers before insertion into the absorber, or with the assembled modules. In the CERN test beam 12 hours were needed for the AHCAL to acquire sufficient statistics on a stack with a square meter front face and 38 layers. This would translate into about two months for the entire ILC detector, or less, if more layers are aligned after each other in the beam. Likewise, the analysis of the calibration data and the fits to the pulse height spectra can be massively parallelised.

For the silicon ECAL with its excellent stability and linearity, only one electronic conversion factor per channel is needed. For scintillator options, due to the non-linearity of the photo-sensors, two inter-calibration constants per channel are required, the MIP and the single photon response. For gaseous detectors, the response is proportional to the product of efficiency and pad multiplicity which are also determined with muon beams (for the three thresholds).

5.2.2.3 Energy scales

The response to electromagnetic showers on the MIP scale can be uniquely predicted by simulations and verified in test beams with known energy. The electromagnetic (em) scale is thus related to the MIP scale by a simple conversion factor MIP, or hit per GeV. In practice, the usefulness of the em scale depends on the linear range for electrons. While for the silicon ECAL, no significant non-linearities were found, the scintillator detectors start to deviate at the 2% level around 50 GeV.

The hadronic response for the AHCAL shows small deviations from linearity (less than 2% up to 80 GeV), mainly due to the non-compensating features of the structure ($e/\pi \sim 1.19$) [315] and to leakage. It can be predicted by simulations and was verified with test beam data. For the gaseous calorimeters, the hit multiplicity noticeably deviates from a linear behaviour for energies above 30 GeV.

In the semi-digital option, (2 bits per cell), weighted combinations of the hit multiplicity for each threshold are used. With this procedure, a linearity at the percent level was achieved up to 80 GeV. The combined ECAL and HCAL measurement requires the application of weighting factors in any case. Making use of the fine granularity, or even of resolved shower sub-structure, allows to significantly improve the resolution. The weighted energy scale depends on the applied algorithm.

Additional corrections will be necessary to account for uninstrumented regions or additional material from support structures, electronics and service lines, at the ECAL-HCAL transition and at inter-module boundaries. This must be extracted from simulations which need to be benchmarked in test beams with realistical ECAL and HCAL prototypes combined.

Apart from the inter-calibration, which must be done for every individual active detector element, we assume that all studies addressing the absolute em and weighted scalers can be done with single representative sample structures. One such sample structure should be immersed into a magnetic field to verify the modeling of magnetic effects.

5.2.2.4 Monitoring techniques

The above calibration scheme needs to be complemented by monitoring techniques in order to take time-dependent variations into account when the test beam based calibrations are applied to collider data. The general approach is that if the MIP scale - or the MIP hit multiplicity - is maintained and under control, all derived scales are stabilised as well.

Test beam experience has demonstrated that the MIP scale of the silicon-based ECAL is intrinsically stable. Variations of the MIP scale of scintillation detectors are mainly due to changes of the electronic response of the photo-sensor, induced by changed thermal conditions, whereas the hit multiplicity of gaseous detectors mainly varies as a consequence of temperature or pressure-induced gain variations.

Apart from slow-control recording of bias voltages, temperatures and pressures, the monitoring is based on mostly innovative techniques, namely in-situ MIP calibration using track segments in hadron showers, and, for photo-detectors, auto-calibration of the photo-sensor gain using LED light. This can be extracted from the spacing between peaks in the pulse-height spectrum attributed to small, discrete numbers of registered photo-electrons, and does not require LED light stability.

In principle it is also possible to adjust the voltage in order to compensate the temperature variation, and use the gain to watch the stability. This will be tried with the second generation prototypes now under construction. The use of radioactive sources is not necessary according to present understanding.

Changes in the amplification of the read-out chain were checked independently and found to be much smaller than those of the sensors. We therefore do not discuss them further here; they are absorbed in the other corrections. The pedestals of the read-out electronics are regularly monitored using random trigger events; this also detects and monitors dead or noisy channels.

5.2.2.5 In-situ calibration

The absolute calibration of the ECAL can be verified and adjusted by comparison with the tracker or using electrons and photons kinematically constrained like Bhabha's or return to the Z. This does not require any running at the Z peak.

Due to the underground location, the orientation of the detector layers, the power pulsing, and due to the high granularity, cosmic rays might not be sufficient for monitoring the MIP scale in-situ. However, thanks to the excellent imaging capabilities of the calorimeters, MIP-like track segments can be identified in hadronic showers and used for calibration purposes. This has been demonstrated using the CALICE AHCAL test beam data, and the potential for in-situ calibration of the ILD detector was studied in simulations - for details see [318]. Although typically two tracks are found in each shower which are used for the calibration of 20 cells, it is even at the Z resonance not possible to obtain a channel-by-channel calibration within realistic running times. However, the method is well suited for the determination of average corrections for a sub-section of the detector, e.g. a layer in a module.

At the Z pole, 1 pb^{-1} is sufficient to provide at least 1000 identified tracks per layer module out to AHCAL layer 20, while 20 pb^{-1} are necessary to reach out to the last AHCAL layer, layer 48. For the last layers in the calorimeter, also $Z^0 \rightarrow \mu^+\mu^-$ events contribute significantly to the overall statistics, reducing the required integrated luminosity to 10 pb^{-1}.

At 500 GeV, significantly larger integrated luminosities are necessary to achieve the same precision due to the much lower cross section. Less than 2 fb^{-1} will allow for a 3% calibration for each layer-module out to layer 20, so even at full energy running a monitoring of the calibration on the layer-module level will be possible. Also here, muons contribute to the calibration of the last layers in the detector.

Similar luminosity are expected to be necessary for the semi-digital gaseous detectors, the decreased statistics due to small cells (by a factor of 9), being compensated by the binomial statistics governing the efficicency determination (with a average 95%) and the relative uniformity of the sensors. The relative weights of the hit population above the 3 thresholds can be monitored from Z Z channels with one of the Z decaying into hadronic channels; charged hadronic with energy measured in the tracker can also be used to control the previous population ratios for different energies. For reference, the possibilities with cosmic muons were also studied. At the surface, the rate of cosmic muons with energies above 10 GeV (necessary to ensure penetration through the complete detector) is approximately 20 Hz/m^2. Taking the duty cycle of the electronics of 0.5% into account, the detectable muon rate reduces to 0.1 Hz/m^2. The area of one layer module is around 2.5 m^2, so for horizontal calorimeter layers about 70 minutes would be sufficient to acquire 1000 tracks. In underground locations, this needed time will increase with increasing depth. For non-horizontal layers, in particular also in the endcaps, the needed time is significantly higher, and in deep underground, this will presumably be prohibitive. However, also cosmic muons will be a valuable calibration and monitoring tool for parts of the detector. For the endcaps, there is the additional possibility of using muons from the beam halo. Their rate depends strongly on the shielding of the detector, but is expected to be between 100 Hz/m^2 and 10 kHz/m^2 at full energy. The fact that these muons arrive in time with the beam, and thus don't suffer an effective rate reduction due to power pulsing, make them well suited for the calibration of the end-cap calorimeter. Even a cell-by-cell calibration using these muons might be possible.

5.2.2.6 Required accuracy

Using fully detailed simulations of the ILD detector and reconstruction based on the Pandora particle flow algorithm, we have modeled different scenarios of statistically independent as well as coherent mis-calibration effects, affecting the entire HCAL or parts (module layers) of it. Purely statistical variations, like those arising from calibration errors or random aging effects, hardly affect the energy resolution at all. However, they may degrade the in-situ MIP calibration capability. From this, a moderate requirement of the inter-calibration stability to be ensured by hardware design of $\pm 10\%$ is derived.

Coherent effects which could for example arise from uncorrected temperature variation induced changes of the response are potentially more harmful, as they directly show up in the constant term, if they affect the entire detector. However, these are easy to detect, and even a 5% variation only mildly propagates into the jet energy resolution. Systematic effects shifting sub-sections like layers are unnoticeable unless they exceed about 15%, comfortably in range of the in-situ calibration method accuracies.

We have demonstrated the validity of these simulation based estimates by treating our AHCAL test beam experiment like a collider detector, using cell-by-cell inter-calibrations only from data taking at a different site, under different conditions and after having it exposed to disassembly, transport and re-assembly influences. Applying only in-situ monitoring techniques, we re-established the scale and reproduced the resolution. Imperfections absent in any simulation showed up, but were successfully compensated.

5.2.2.7 Conclusion on calibration

All in all, we conclude that the high granularity and channel count is a blessing rather than a curse. On one hand, due to the law-of-large-numbers suppression of statistical effects, the requirements on individual cell precision are very relaxed. Coherent effects, on the other hand, can be studied with any desired combination of channels, be it layers, longitudinal sections, electronics units or according to any other supposed hypothesis of systematic effects. The high degree of redundancy and the full information for each channel provide maximum freedom, without having to rely on intrinsic homogeneity as in the case of internal, in-transparent optical or analog summing in less finely segmented readout. Testing the second generation prototypes under beam conditions will be an important step towards working out the procedures for the full detector in detail and demonstrate their performance.

5.3 ILD data acquisition and computing

The DAQ system for the ILD concept has to fulfill the needs of a high luminosity, high precision experiment without compromising on rare or yet unknown physics processes. Although the average collision rate of the order of a few kHz is small compared to the LHC, peak rates within a bunch train will reach several MHz due to the bunched operation. In addition, the ILC physics goals require higher precision than has ever been achieved in a colliding beam experiment. This increased precision is to a large extent achieved through increased granularity and thus leads to a substantially bigger number of readout channels than that used in previous detectors

Taking advantage of the bunch train operation at the ILC, event building without a central trigger, followed by a software-based event selection was proposed in [359] and has been adopted for ILD. This will assure the needed flexibility and will be able to cope with the expected complexity of the physics and detector data without compromising on efficiency or performance. The only foreseeable drawback from bunched operation is the reduction of cosmics event recording and their use for calibration and alignment.

The LHC experiments have up to 10^8 front-end readout channels and a maximum event building rate of 100 kHz, moving data with up to 300 GB/s (with an average throughput of $\lesssim 200\,\mathrm{GB/s}$ required [360, 361, 362]). The proposed ILD DAQ system will be less demanding in terms of data throughput but the number of readout channels is likely to be a factor of 10 or more larger. The computing requirements for event processing at the ILC, in terms of storage and CPU, are also going to be less demanding than those of the LHC experiments. The details of the DAQ and computing system depend to a large extent on the developments in microprocessors and electronics and the final design of the different sub-detector electronic components. Therefore the DAQ and computing system presented here has to be rather conceptual, highlighting some key points to be addressed in the coming years.

In contrast to past and recent colliders such as HERA, Tevatron or LHC, which have a continuous rate of equidistant bunch crossings, the ILC has a pulsed operation mode. The nominal parameter set [332] of the ILC at 500 GeV (1 TeV) with

- 1312 bunch crossings in a train about 1 ms long,
- 366 ns between bunch crossings inside a bunch train and
- a bunch train repetition rate of 5 Hz

results in a burst of collisions at a rate of 2.7 MHz over $\lesssim 1\,\mathrm{ms}$ followed by 199 ms without any interaction. The overall collision rate of 13 kHz is significantly smaller than the event building rate at the LHC experiments

The very large number of readout channels for ILD will require signal processing and data compression already at the detector electronics level as well as high bandwidth for the event building network to cope with the data.

The traditionally deployed front-end electronics (VFE), will have to be fully integrated in the detectors. This is achievable by dedicated Readout-Chips (ROC) that are able to treat a large number of channels (~ 100) and perform amplification, auto-triggering, time-stamping, signal (and eventually time) digitisation and local storage. A local zero-suppression is mandatory as only a very small fraction of the channels are hit. It can be achieved ROC by ROC or channel by channel, the optimum depending on the occupancy per ROC.

The data volume will be dominated by machine background, mainly from pair production from beam-beam interactions, as described in section 5.5.6. The rate of hadronic e^+e^- events at design luminosity is expected to be of the order of 0.1 per bunch train and will contribute less then 1 % to the data recorded.

The particle flow analysis approach requires, as much as possible, to follow all particles individually through the detector. At the electronics level, this implies the capacity to be able to trigger with a high level of efficiency on a mip signal. If this seems obvious for trackers, it is more challenging for calorimeter systems, as the noise level will have to be kept at a low level.

The memory size that is needed for a given ROC depends on the expected machine background rate in its position in the detector, the internal noise which is expected to be uniform and the actual physics rates.

A large security margin should be kept since a "RAM full" event implies a local loss of information and, depending on the reconstruction procedure, either a loss of luminosity or modification of the calibration. Although the very high number of channels allows for software restoration of information, the tracking of individual, unavailable cells will add complexity to the reconstruction.

Table III-5.1 lists for the major ILD detector components and options the number of channels, occupancy, noise frequency and the expected data volume per train.

Table III-5.1
Data Volume in MB per bunch train for the major ILD detector components, for nominal ILC operation at 500 GeV.
The noise frequency reflects the noise rate taken during an acquisition;
The occupancy is the fraction of occupied channel during one Bunch crossing.
$*$ Numbers to be updated.
$**$ Raw output; after online treatment, a maximum of 5% of this data should be kept on tape.

Sub-detector	Channels $[10^6]$	Beam induced [Hits/BX]	Noise [Hits/BX]	Data volume per train [MB]
VTX (CPS)	300	1700	1.2	< 100
VTX (FPCCD)	4200	1700	1200	135
TPC	2	216	2000	12
FTD	1	260	0.3	2
SIT	1	11	0.3	6
SET	5	1		1
ETD	4			7
SiECAL	100	444	29	3
ScECAL	10	44	40	
AHCAL	8	18000	640	1
SDHCAL	70	28000	70	
MUON	0.1		8	≤ 1
LumiCal	0.2			4
BeamCal	0.04			126**

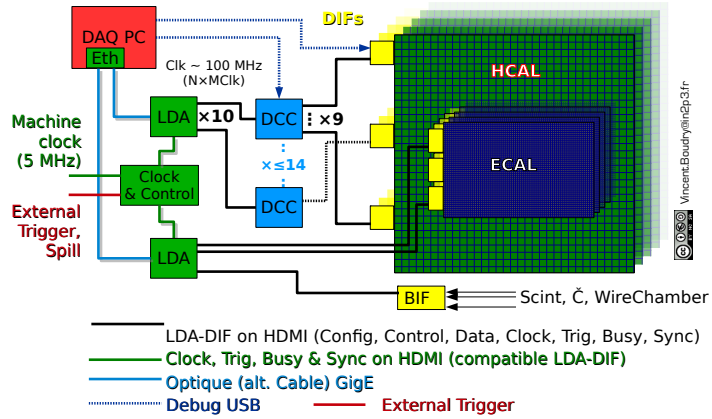

Figure III-5.15
General layout of the calorimeters DAQ system.

5.3.1 DAQ structure

The general layout of the proposed DAQ system for calorimeters is shown in Figure III-5.15. It is representative of the general structure of the complete system, including the tracking detectors: one or several PCB's equipped with ROC's (up to a few hundred for the calorimeters) are interfaced to the DAQ by specific front-end boards; these ensure the control of the ROC, dispatching and collection of the signals, the readout sequencing and mode of operation. The FE boards are linked with single cables to concentrator boards (LDA's) which ensure the separation of data (in and out) based on standard protocols from the DAQ specific fast signals (clock, busy, spill). The fast signals are handled by dedicated cards to ensure synchronous operation of the complete detector. The size of the boards and the location of functions on each board is still subject of intense R&D.

5.3.1.1 Front-end electronics:

The front-end electronics on the sub-detector or sensor level has to be detector specific; it will digitise and store the data of ~2600 bunch crossings.

In contrast to the central DAQ system, the front-end readout electronics for the different sub-detector prototype designs has started, with the realisation of technological prototypes (AHCAL, SDHCAL, SiECAL, TPC, FCAL, Silicon Trackers and VTX) taking into account realistic engineering as well as detector performance tests. Several approaches are underway for the calorimeters, TPC, silicon trackers and vertex detectors. Common to all the designs is a highly integrated front-end electronics

with signal shaping, amplifying, digitising, hit detection, data storage and highly multiplexed data transfer to reduce the number of cables. Some designs foresee data processing such as noise detection or cluster finding already at this stage to further reduce cables.

For a highly granular detector like the ILD with the resulting large channel counts both the material budget as well as the power consumption are areas of concern. Minimising the number of cables by data processing and multiplexing already on the sensor level is required as well as high density electronics with low power consumption. A common approach to reduce the power consumption is to turn the front-end electronics off in the gaps between bunch trains. First systems have been designed and built with this power pulsing capability. For a recent overview of such a system see [363].

The VFE chip will be powered a few 10μs before the arrival of a spill. Recent studies [319, 363] have shown that this preparation time is enough to get the stability of the amplifier and the ADC threshold to a level of one percent. The data is stored locally in the VFE chips. The pipeline length has to be adapted to data flux plus expected noise to avoid saturation of the local memory. Online procedures are of prime importance to control noisy cells. One noisy cell will effectively blind the entire region corresponding to all cells that are covered by its ROC.

Fast, hence online, correction procedures are mandatory to either suppress the noisy channels or correct their gain. Given the number of channels, the overall gains and mask configurations might change rather often, and the possibility of time evolving calibration parameters should be studied carefully as well as the failure rate of electronics and the stability of detectors w.r.t. the noise level.

5.3.1.2 Middle level DAQ:

The middle level includes all the intermediate cards dispatched in the detector. It will have to be designed to use standard tools as much as possible and be fault tolerant, in particular by the use of signal path redundancy.

Standard protocols for data exchange should be used in order to profit from the development of commercial products. The usage of distribution networks [361] in the first running phase of the LHC has fulfilled all requirements.

The xTCA (ATCA modified for acquisition) is likely to become the new standard for DAQ in the coming years. Its use in current and upcoming experiments (PANDA, LHC detector upgrade) should be followed closely.

Since machine parameters and beam conditions such as the beam energy or the polarisation will be a vital input for the high precision physics analyses, they should be stored together with the data. The time structure and data volume are similar, hence a common DAQ and data storage model is envisaged.

In addition, the ILD will be operated in a truly international collaboration, with partners all over the world. Similarly to the global accelerator network (GAN), a global detector network (GDN) is proposed to operate the ILD detector remotely from the participating institutes. First experience with (not so) small set-up was gained with the CALICE remote control room at DESY during test beams at CERN and FNAL. For large setups the experience from the CMS remote operation centres at CERN, FNAL and DESY will be taken into account. The design of the DAQ and control system should have remote operation features built in from the start.

5.3.2 Data processing

The details of the DAQ and computing system depend to a large extent on the developments in microprocessors and electronics and the final design of the different sub-detector electronic components. The key points that will have to be addressed in the coming years are highlighted below.

The reconstructed events are written to the storage systems in an object oriented data format that is suited for further analysis with appropriate pointers into the raw data file containing the bunch train data. LCIO [364] provides a first version of such an event data and is in use for several test beam efforts and for the offline analyses within ILD.

5.3.2.1 Event building and prompt reconstruction

The purpose of the online event processing will mainly be event classification, calibration, alignment and data quality monitoring. Although no event rejection is foreseen, a scheme of event finders may be used to identify "bunches of interest" which could then be used for the physics analysis or for fast analysis streams.

Event building and prompt reconstruction will be performed on the *Online Filter Farm* – a sufficiently large farm of processing units near the detector, connected to the front-end electronics via the Common Event Building Network. The raw data of a complete bunch train is kept in the raw data file after compression. This is essential as many detectors will integrate over several bunch crossings or even the full bunch train. The event reconstruction will be an iterative process where in a first step a preliminary reconstruction will be done on the data from every sub-detector. Bunches of interest are then identified by exploiting correlations in time and space between the data from all sub-detectors. After calibration and alignment finally a full event reconstruction is performed on the event data.

An event filter mechanism run at prompt reconstruction will provide the necessary meta data for fast event selection at the physics analysis level. One processor per Bunch Train Event building of all data from the bunch train will be done in a single processing unit. Hence all data of the complete train will be available for the event processing without further data transfer which is essential since many detectors will integrate over several bunch crossings.

Each processing unit of the Online Filter Farm will process the data of one complete bunch train at a time.

5.3.2.2 Offline computing

The further offline data processing will exploit a Grid infrastructure for distributed computing using a multi-tier like approach following closely what is done for the LHC-experiments [365, 366]. The offline computing tasks such as the production of more condensed files with derived physics quantities (DST/AOD), Monte Carlo simulations and re-processing of the data will be distributed to the various tiers of the ILC-computing Grid. Setting up a data Grid and suitable data catalogues will allow the physicists to efficiently access the data needed for their analyses.

5.3.3 Outlook and R&D

Key elements of the DAQ systems have to be defined to guide the R&D of the sub-detector front-end electronics especially when entering the technical prototype stage. The effort started in the European FP6 project EUDET program is pursued in the FP7 project AIDA, with emphasis on the integration of the various DAQ systems (Pixel EUDAQ, CALICE, FCAL, Silicon trackers) for common test beams by 2014-15. These tests will serve as a first test-stand for an ILD data acquisition system. Large bandwidth systems such as xTCA are also being evaluated, e.g. for the TPC.

Due to the timescales involved and the rapid changing computing and network market, a decision on the DAQ hardware will be made as late as possible to profit from the developments in this area. A

performance enhancement by a factor of 20 is expected in bandwidth, storage and processing in the coming 10 years.

5.4 ILD software and tools

The ILD detector concept uses the iLCSoft software framework which provides the core tools LCIO [364], Gear [367], Mokka [368] and Marlin [369] as well as reconstruction and analysis tools for LC detector R&D. The framework, which has already been used for a massive Monte Carlo production for ILD's Letter Of Intent [198], has since been extended and improved with the focus on enabling a more realistic simulation and reconstruction of physics events in the ILD detector.

LCIO provides a hierarchical event data model and persistency and is used by all detector concepts for linear colliders, providing a basis for common software developments and the exchange of algorithms and tools. A recent major release of LCIO (2.0) comprises many new features, the most important of which are:

- direct access to runs and events in a file allowing for efficient overlay of background events;
- introduction of 1D and 2D TrackerHit classes enabling a more detailed description of Si-strip and pixel detectors;
- extension of the Track class to hold many TrackStates per track: typically one at the IP, the first and last hit and at the face of the calorimeter are stored;
- introduction of a ROOT [370] dictionary to facilitate analysis of LCIO data;
- a number of extensions to the Event Data Model.

Gear provides an API for querying the detector geometry and material distribution at the reconstruction stage, including a detailed description of the measurement surfaces of tracking detectors including their sensitive and insensitive materials.

The Geant4 [371] based full simulation application Mokka's handling of the generator information has been enhanced with respect to the treatment of long lived and exotic particles and their decay vertices. The description of the ILD sub-detectors has been made more realistic by introducing gaps, imperfections as well as support and service materials.

Marlin is the C++ application framework that is used for further processing of the simulated detector response and is based on LCIO and Gear. Marlin contains a plug-in mechanism that supports the modular development of user software packages. The per-module and global configuration of the application is performed via an XML steering file with optional overwrite through command line arguments. A logging mechanism ensures that the actual configuration is stored for future reference and reproducibility.

5.4.1 Detector models in Mokka

All ILD sub-detectors in Mokka have been implemented including a significant amount of engineering detail such as mechanical support structures, electronics and cabling as well as dead material and cracks. Some sub-detectors, for which this level of realism had not been reached at the time of the LOI, have been completely re-written for this report.

Where possible, sub-detectors have been implemented in a way that is agnostic to the actual readout technology, for others different implementations exist. The following three Mokka models have been created for comparison of the different technology options with Monte Carlo simulations:

- **ILD_o1_v05:** ILD model with analogue HCAL and Si-ECAL
- **ILD_o2_v05:** ILD model with semi-digital HCAL and Si-ECAL
- **ILD_o3_v05:** ILD model with analogue HCAL and Scintillator-Strip-ECAL

Figure III-5.16 shows a 3D view of one of these simulation models. The simulation models comprise the following sub-detectors:

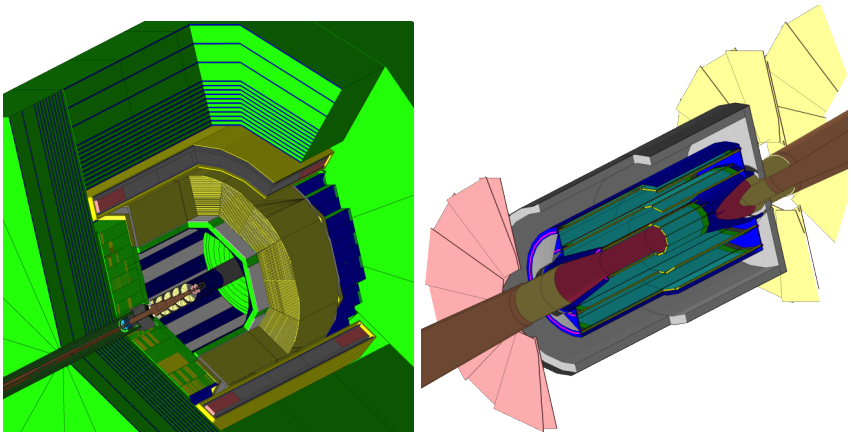

Figure III-5.16
The ILD simulation model. *Left:* 3D view of the ILD simulation model ILD_o1_v05, from inside to outside: VTX, SIT, TPC, SET, ECAL, HCAL, Coil, Yoke and in the forward direction: FTD, LumiCal, LHCal, BeamCal. *Right:* Blowup of the inner tracking detectors in the simulation model.

- **VTX:** detailed description of the sensitive and support part of the ladders in the three double layers including a surrounding cryostat;
- **SIT/SET:** Si-Strip detectors with planar ladders of sensitive and realistically averaged support material;
- **FTD:** Si-Pixel and Si-Strip disc detectors, built from sensitive Si-petals on a space frame support structure – a realistic estimate of the material budget from power and readout cables for the inner tracking detectors VTX, SIT and FTD has been averaged into an Al cylinder running just inside the TPC field cage and a cone just around the beam pipe in order to correctly account for the effect of multiple scattering;
- **TPC:** cylindrical volume filled with correct gas mixture, surrounded by a realistic field cage and a conservatively estimated back plane comprised of material for the space frame structure, electronics and cooling pipes;
- **ECAL:** detailed description of the alveolar layer structure with W as absorber material and a readout part that is either based on Si-wafers with $5 \times 5\ mm^2$ cell size or on $5 \times 45\ mm^2$ scintillator strips – gaps between modules are properly modeled;
- **HCAL:** realistic models for the analogue and semi-digital HCAL options with a different layout of the absorber and readout structure; the gaps and electronics are properly modeled in both cases; Birk's law is taken into account for the analogue case;
- **Muon:** the iron Yoke has been instrumented with scintillator based active layers. At the moment tiles with $3 \times 3\ cm^2$ granularity are used, for muon detection and serving as a tail catcher for the HCAL; this is different than the detector baseline which uses 3 cm wide and 1 m long strips;
- **LumiCal, LHCal, BeamCal:** the forward calorimeters are also modeled realistically with their corresponding sandwich structure consisting of W absorbers and Si (LumiCal, LHCal) and diamond (BeamCal) readout, respectively.

5.4.2 Marlin: Reconstruction and analysis system

More than 20 million events have been fully simulated with the Mokka detector models described above and then reconstructed with the following Marlin modules :

5.4.2.1 Digitisation

The digitisation of hits in the tracking detectors is performed by a parameterisation of the point resolution as established by the R&D groups and shown in Table III-5.2. In the case of the Si-Strip detectors in SIT/SET and FTD, 1D TrackerHits are created at the digitisation stage and then combined into 3D space points that are used for pattern recognition in order to correctly account for ghost hits. Calorimeter hits are scaled with a calibration factor according to the sampling fraction, where in the case of the semi-digital HCAL effects of cross talk between neighboring cells are included.

Table III-5.2. Effective point resolution as used in the digitisation of the tracking detectors' response.

Detector			Point Resolution
VTX	$\sigma_{r\phi,z}$	=	2.8μm (layer 1)
	$\sigma_{r\phi,z}$	=	6.0μm (layer 2)
	$\sigma_{r\phi,z}$	=	4.0μm (layers 3-6)
SIT	σ_{α_z}	=	7.0μm
	α_z	=	$\pm 7.0^\circ$ (angle with z-axis)
SET	σ_{α_z}	=	7.0μm
	α_z	=	$\pm 7.0^\circ$ (angle with z-axis)
FTD	σ_r	=	3.0μm
Pixel	$\sigma_{r_\perp}$	=	3.0μm
FTD	σ_{α_r}	=	7.0μm
Strip	α_r	=	$\pm 5.0^\circ$ (angle with radial direction)
TPC	$\sigma^2_{r\phi}$	=	$(50^2 + 900^2 \sin^2\phi + \left((25^2/22) \times (4T/B)^2 \sin\theta\right) (z/\mathrm{cm}))\,\mu\mathrm{m}^2$
	σ^2_z	=	$(400^2 + 80^2 \times (z/\mathrm{cm}))\,\mu\mathrm{m}^2$
	where ϕ and θ are the azimuthal and polar angle of the track direction		

5.4.2.2 Track reconstruction

The reconstruction of charged particles is done with a set of new C++ packages recently added to iLCSoft: Kaltest, IMarlinTrK, Clupatra and FwdTracking, replacing the previously used FORTRAN tracking code that dated back to LEP. Clupatra is a TPC pattern recognition algorithm that combines topological clustering methods for seed finding with Kalman Filter based extrapolations for picking up hits. Optionally the hit search can be extended inwards to include the Si-tracking detectors. FwdTracking [372] is a newly developed pattern recognition for the FTD that is based on cellular automatons and hopfield networks. The IMarlinTrK package provides the interface to the track fitter based on a Kalman Filter implemented using KalTest [373]. SiliconTracking is a package for standalone tracking in VTX, SIT/SET and FTD. FullLDCTracking finally combines the track segments from all sub-detectors into a consistent final list of tracks which is then used as input to particle flow.

5.4.2.3 Particle flow

PandoraPFANew [274] is an implementation of the *particle flow algorithm (PFA)*, which recently has been re-written to be detector and framework independent. MarlinPandora is a Marlin package that converts the calorimeter hit and track objects from LCIO objects into corresponding data structures used in PandoraPFA, augmented with relevant information from the detector geometry and with suitable track quality cuts applied. The resulting list of particle flow objects is then converted back into a list of ReconstructedParticles which is used for further analysis. PandoraPFANew uses sophisticated clustering algorithms and track-cluster matching as an initial step. The application of re-clustering methods, based on cluster energy to track momentum comparisons, is crucial to eventually achieve the optimal jet energy resolution based on single particle reconstruction.

5.4.2.4 Vertex finding and jet flavour tagging

LCFIVertex [374] is a package for vertex finding, based on the ZVTop algorithm and for jet flavour tagging using Artificial Neural Networks (ANNs). LCFIPlus is a new package that provides improved flavour tagging, introducing additional input variables and replacing the ANNs with Mutli Variate Analysis techniques, as well as a new jet clustering algorithm [375]. The secondary vertex finding is run centrally as part of the standard reconstruction, whereas jet finding and flavour tagging are run by the users, individually tuned according to the specific needs of their physics analysis.

5.4.2.5 Background overlay

The main source of background are hits from e^+e^- pairs, resulting in considerable hit densities, predominantly in the VTX detector (see section 5.5.6). While these hits pose a non-trivial problem to the pattern recognition, eventually the effect of ghost tracks can be reduced very efficiently by requiring hits in the SIT which provides an exact time stamp per bunch crossing [198]. Thus pair background is not overlayed for the Monte Carlo events analysed here, with the exception of the BeamCal, where an averaged energy weighted hit density from pair background is taken into account in reconstruction.

The other source of background are multi-peripheral $\gamma\gamma \to$ hadrons events. These give raise to much lower occupancies – on average one expects 1.7 (4.1) low multiplicity events per bunch crossing at nominal beam conditions for 500 GeV (1 TeV). As these events of course result in real tracks and clusters, fully simulated $\gamma\gamma \to$ hadrons events are overlaid statistically before the reconstruction. As these events come from a different vertex than the physics event, their z-position is smeared with a spread of $\sigma_{vertex,z} = 300\mu\mathrm{m}\ (225\mu\mathrm{m})$ at 500 GeV (1TeV) reflecting the resulting difference of the z-position of the vertices of independent events originating from a Gaussian beam profile.

5.4.3 Monte Carlo productions

Around 20 million Monte Carlo events (see Table III-5.3) have been produced on the Grid with the help of a newly developed production system: GridProd. It is based on a MySQL data base and a set of python scripts with a web interface, that provides an up-to-date view of the requested and already processed events. It allows to query the file catalog based on a set of meta-data tags, such as center of mass energy, process name and type.

Table III-5.3 Number of Monte Carlo Events produced for the DBD.

Process	E_{CMS}	Detector model	Events $[10^6]$
$e^+e^- \to \nu\nu h$			0.3
$e^+e^- \to t\bar{t}h$			0.04
$e^+e^- \to W^+W^-$	1 TeV	ILD_o1_v05	1.4
SM background (2-8 fermion)			11.4
$e^+e^- \to t\bar{t}h$	1TeV	ILD_o2_v05	0.04
$e^+e^- \to t\bar{t}$	500 GeV	ILD_o1_v05	0.8
SM background (2-8 fermion)			6.8
total			20.9

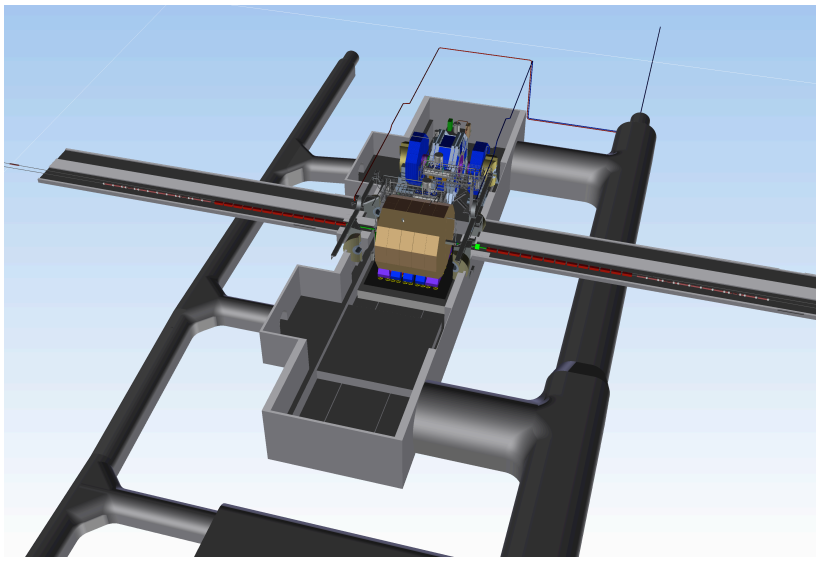

Figure III-5.17 The push-pull system at the ILC: ILD (front) and SiD (back) in the experimental hall (example of a mountainous ILC site.

5.5 ILD - machine-detector interface and experimental area

This section deals with the ILD specific issues of the Machine-Detector Interface and the experimental areas [376].

5.5.1 ILD push-pull issues

The ILC push-pull system is described in section 2.3. Adapting this system to the ILD detector is a challenge, taking into account the dimensions and masses of the detector on the on hand and the required precision on the other hand. Figure III-5.17 shows a design of a detector hall with the push-pull system.

The ILD detector is somewhat larger than SiD and is designed to be assembled from slices in a similar way as the CMS detector. The detector placement on the push-pull platform preserves detector alignment and distributes the load evenly onto the floor. The platform will carry also some of the detector services like electronic racks. The ILD yoke slices each have their own motion system that is based on air pads and grease pads. In the parking position, the detector can be opened for maintenance by moving the yoke slices on air pads from the platform.

5.5.2 Final focus magnets

The interaction region of ILD is designed to fulfil at the same time the requirements from the ILC machine as well as the needs of the detector. As the allowed focal length range of the inner final focus quadrupoles (QD0) for ILC (3.5 m $\leq L^* \leq 4.5$ m) is smaller than the detector size, the QD0 magnet of the final lens needs to be supported by the detector itself. As a consequence, SiD and ILD will have their own pair of QD0 magnets that move together with the respective detector during push-pull operations. In contrast, the QF1 magnets of the final lenses with a focal length of $L^* = 9.5$ m are not supported by the detectors and stay on the beam line during detector movements. A set of vacuum valves between the QD0 and the QF1 magnets defines the break point for the push-pull operations. The biggest concerns for the QD0 support system are the alignment and the protection against ground motion vibrations. The limit on vibrations is given at 50 nm above 1 Hz [354].

Due to these tight requirements, the support of the magnets in the detector is of special importance. ILD has chosen a design where the magnets are supported from pillars that are standing directly on the transport platform (see Figure III-5.18). In the detector, the magnets are supported by a system of tie rods from the cryostat of the solenoid coil. This design de-couples the detector end caps from the QD0 magnets and allows a limited opening of the end caps also in the beam position,

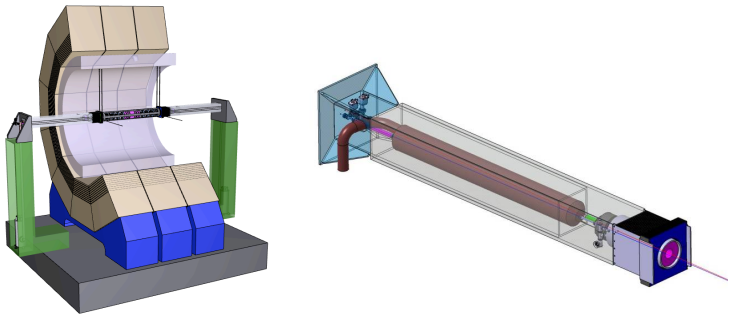

Figure III-5.18
Left: support system of the QD0 magnets in ILD; the inner parts of the detector and the end caps are not shown [198]. Right: double-tube support structure for the QD0 magnet and the forward calorimeters.

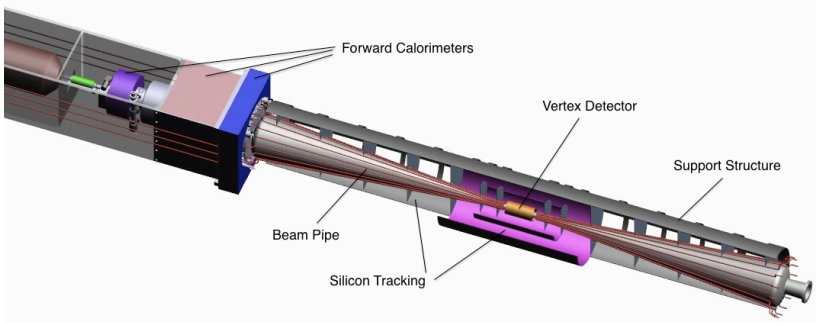

Figure III-5.19
The interaction region of ILD.

without the need to break the machine vacuum (see Figure III-5.9). In addition, the QD0 magnets are coupled via the pillar directly to the platform and limit in that way the number of other vibration sources. Simulations taking into account realistic ground motion spectra for different sample sites have been done to understand the vibration amplification in the QD0 support system [377]. These studies show that, with the exception of very noisy sites, the requirements for the QD0 magnets are fulfilled with large safety margins. Even if the additional amplification characteristics of the platform (c.f. [378]) are taken into account, the total integrated vibration amplitudes are expected to be in the order of less than 10 nm for frequencies above 1 Hz.

The proper alignment of the QD0 magnets with respect to the axis that is defined by the QF1 quadrupoles is also of crucial importance. While the alignment accuracy of the detector axis after the movement into the beamline is moderate (horizontal: $\pm$ 1 mm and $\pm$ 100 μrad), the requirements for the initial alignment of the quadrupoles are much tighter: $\pm$ 50 μm and $\pm$ 20 μrad. An alignment system that comprises an independent mover system for the magnets and frequency scanning interferometers is part of the detector design.

5.5.3 Beam pipe and interaction region

The central interaction region of ILD comprises the beam pipe, the surrounding silicon detectors, the forward calorimeters and the interface to the QD0 magnets (see Figure III-5.19).

The most delicate component of this region is the very light beam pipe made from Beryllium, that is surrounded by the vertex detector and the intermediate silicon tracking devices. A carbon fibre reinforced cylindrical structure will form the mechanical support for these elements. This tube is attached to the inner field cage of the surrounding time projection chamber (not shown in the figure). As the horizontal alignment tolerance of the detector axis after push-pull operations is $\pm$1 mm, an adjustment system is needed to eventually re-align the tube structure with the beam pipe and the inner tracking detectors. This is especially important to keep the stay-clear distances to the tracks of the beam induced background particles within the beam pipe.

The beam pipe opens conically away from the interaction point to allow enough space for the beam induced background, most importantly the electron-positron pairs from beamstrahlung. The shape of the beam pipe results in a rather large volume that needs to be kept evacuated by means of

vacuum pumps that are on both sides 3.3 m away from the interaction point. Simulations show that the vacuum requirements for the ILC can be met with this configuration [198].

The forward calorimeters are discussed in detail in section 3.5.

5.5.4 Experimental area for flat surface ILC sites

The design of the underground experimental cavern for the non-mountainous sites follows a z-shape floor layout. The common interaction point is in the middle of the hall, the detectors move in and out of the beam position on their transport platforms. Alcoves in the maintenance positions allow for lateral space that is needed to open the detectors. Figure III-5.20 shows the layout in the parking position for ILD. The detector is shown in fully opened position that allows for the removal of the large detector parts. The biggest element that might need to be removed from the detector (though not in routine maintenance periods) is the superconducting solenoid. Enough space is foreseen to manoeuvre the parts of the detector in the hall and bring them safely to the vertical access shafts. In addition, space for the detector services (c.f. section 2.3) is available in this design.

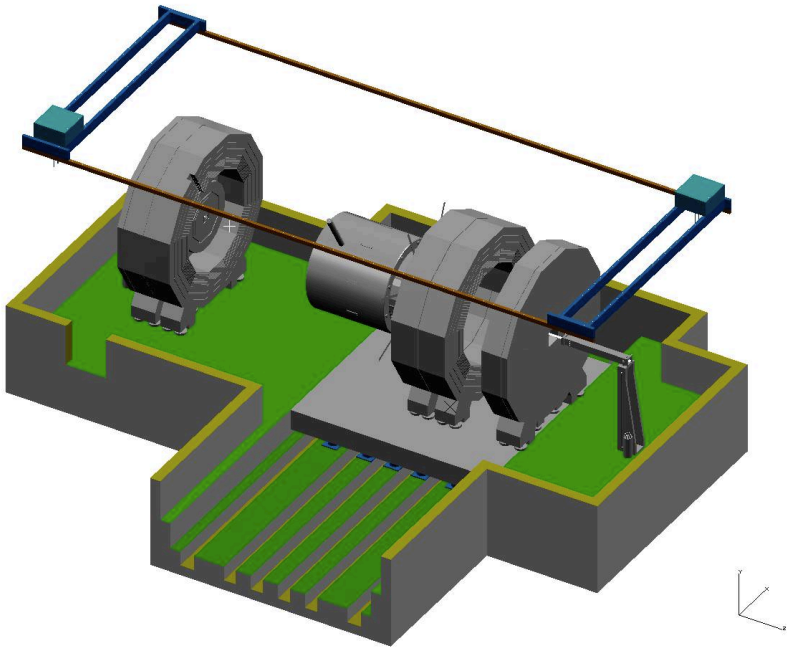

Figure III-5.20
Conceptual design of the underground facilities for ILD. The detector is opened in the maintenance position, the crane coverage is shown [379].

Access to the underground cavern is enabled via five vertical shafts. One central big shaft is located directly above the interaction point with a diameter of 18 m. This shaft would be used during the assembly of both detectors where the big parts are pre-assembled on the surface and then lowered through the big shaft directly onto the respective transport platform. Two smaller diameter shafts (8 m for SiD and 10 m for ILD) are needed in the maintenance positions to allow access from the surface while one detector is at the beam position and blocks the access to the big shaft. Two additional smaller shafts of $\approx$5 m diameter are foreseen for elevators and services.

As the yoke rings will be moved on air pads within the hall, the crane covering the maintenance area needs to have a modest capacity of preferably 2 $\times$ 40 t. However, a temporary hoist with a capacity of up to 3500 t is needed on the surface over the main access shaft to lower the big detector parts during the primary assembly.

5.5.5 Experimental area for mountainous ILC sites

The design of the underground facilities for the mountainous ILC sites is discussed in section 2.3. The current design has been optimised to the needs of ILD as well. Figure III-5.21 shows the space that is needed to open ILD for maintenance in the parking position. Alcoves in the hall provide enough lateral space to move the endcaps away from the platform. Large detector parts, e.g. the beam pipe or the QD0 magnets, can be removed in that area.

Figure III-5.21
Opening ILD in the maintenance alcove of the mountain site hall.

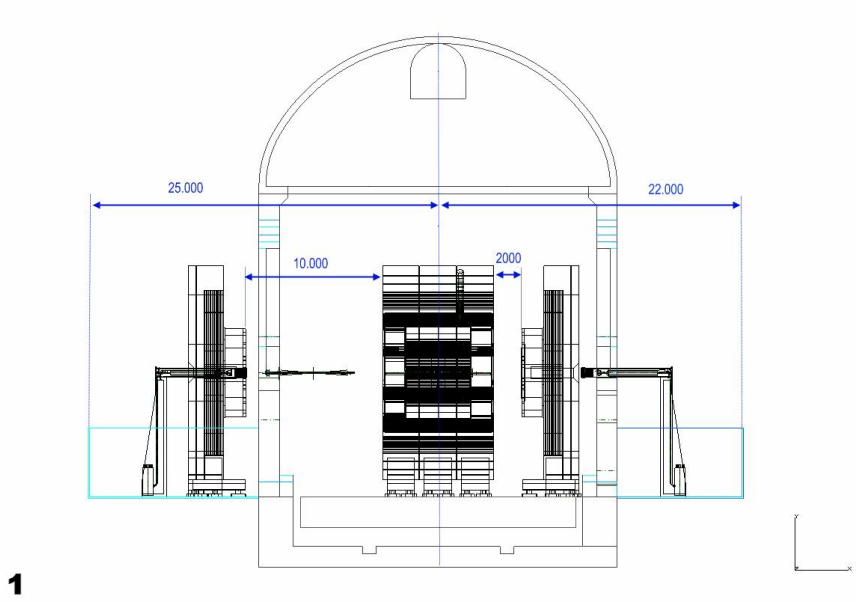

5.5.6 Machine induced backgrounds

Machine-induced backgrounds have been studied in detail for the ILD detector [198, 255] and have recently been updated for the latest machine parameter sets at 500 GeV and 1000 GeV collision energies [380]. The main relevant background stems from e^+e^- pairs from beamstrahlung which are produced in the highly charged environment of the beam-beam interaction. The background levels found are well below the critical limit for most sub-detectors. The sub-detector most sensitive to beam-related backgrounds is the vertex detector, which features an inner radius value dictated by the maximum affordable beamstrahlung hit rate.

Table III-5.4 summarises the expected background levels in the ILD sub-detectors for the nominal ILC beam parameter sets at 500 and 1000 GeV cms energy. The background occupancies have been simulated with the ILD full detector simulation with the nominal detector geometries and 3.5 T magnetic field in the solenoid that is overlaid with an 'anti-DID' dipole component [334]. The double-layer option has been chosen for the vertex detector in these simulations.

5.5.6.1 Background uncertainties

As the vertex detector is most critical with respect to beam induced backgrounds, detailed studies have been performed to understand the impact of different detector geometries and simulation parameters like the choice of range cut parameters in Geant4. The number of hits on the vertex detector change up to 30% when changing parameters in the simulation, which indicates the magnitude of the uncertainties for these simulation results. Another study of the uncertainties of the background simulations has been done in [255]. From these studies and using a rather conservatice approach a safety factor for backgrounds between 5 and 10 is used in ILD.

Table III-5.4. Pair induced backgrounds in the subdetectors for nominal 500 GeV and 1 TeV collision energy beam parameters [380]. The numbers for the ECAL and the HCAL are summed over barrel and endcaps. For the vertex detecor, the double-layer option has been chosen for this simulation. The TPC hits are the digitised hits that would be written to the data acquisition system. The errors represent the RMS of the hit number fluctuations of ≈ 100 bunch crossing (BX) simulations.

Sub-detector	Units	Layer	500 GeV	1000 GeV
VTX-DL	hits/cm^2/BX	1	6.320 ± 1.763	11.774 ± 0.992
		2	4.009 ± 1.176	7.479 ± 0.747
		3	0.250 ± 0.109	0.431 ± 0.128
		4	0.212 ± 0.094	0.360 ± 0.108
		5	0.048 ± 0.031	0.091 ± 0.044
		6	0.041 ± 0.026	0.082 ± 0.042
SIT	hits/cm^2/BX	1	0.0009 ± 0.0013	0.0016 ± 0.0016
		2	0.0002 ± 0.0003	0.0004 ± 0.0005
FTD	hits/cm^2/BX	1	0.072 ± 0.024	0.145 ± 0.024
		2	0.046 ± 0.017	0.102 ± 0.016
		3	0.025 ± 0.009	0.070 ± 0.009
		4	0.016 ± 0.005	0.046 ± 0.007
		5	0.011 ± 0.004	0.034 ± 0.005
		6	0.007 ± 0.004	0.024 ± 0.006
		7	0.006 ± 0.003	0.022 ± 0.006
SET	hits/BX	1	0.196 ± 0.924	0.588 ± 2.406
		2	0.239 ± 1.036	0.670 ± 2.616
TPC	hits/BX	-	216 ± 302	465 ± 356
ECAL	hits/BX	-	444 ± 118	1487 ± 166
HCAL	hits/BX	-	18049 ± 729	54507 ± 923

Chapter 6
ILD Performance

The performance of the ILD detector has been studied in detail both in terms of technical performance criteria, and in terms of selected physics processes. In this chapter the system performance of the ILD detector is discussed. Then a series of different physics studies done using full Monte Carlo at different center of mass energies from 250 to 1000 GeV are presented. These analyses have not been selected to demonstrate the physics reach of the ILC facility, but rather to stress the detector and its performance. For completness results from earlier studies done in the context of the letter of intent, with a slightly different detector model, are also summarised.

6.1 ILD performance

The overall performance of ILD is established using a detailed GEANT4 model [368] and full reconstruction of the simulated events. Using full simulation and a realistic reconstruction ensures that the performance is as realistic as possible and takes into account the detailed knowledge on detector mechanics, dead areas, and non-perfect response.

6.1.1 Software for performance studies

Three distinct detector models have been implemented in the Mokka GEANT4 detector simulation program. The only differences are in the technology choices for the ECAL and HCAL. The first model (ILD_o1_v5) simulates a SiW ECAL and a scintillator tile analogue HCAL, the second (ILD_o2_v5) simulates a SiW ECAL and semi-digital RPC-based HCAL, and the final model (ILD_o3_v5) includes a scintillator strip ECAL and the analogue tile scintillator HCAL. The different detector models are treated equally and provide a demonstration of the performance of the different technology options within ILD. Because of the relative maturity of the reconstruction software, the majority of the physics studies are performed using the SiW ECAL, which assumes a 5×5 mm^2 transverse cell size, and the steel-scintillator HCAL option with $3 \times 3\,$cm^2 tiles; unless otherwise stated, the detector model used in the performance studies is ILD_o1_v05

The level of detail included in the detector simulation represents a significant step forward compared to the ILD LoI. Most of the sub-detectors in the ILD models have been implemented with a significant amount of engineering detail such as mechanical support structures, electronics and cabling as well as dead material and cracks. The material budget associated with the support structures and services are based on the best current estimates from the detector R&D groups. In addition, the material associated with the delivery of power and cooling to the sub-detectors have been implemented in the simulation so as to provide a reasonable description of the mean material budget. The improvements in the simulation are crucial for a realistic demonstration of particle flow and tracking performance. A description of the detector parameters and the reconstruction software can be found in Section 5.4.

All events are reconstructed based on a sophisticated reconstruction chain, including using a

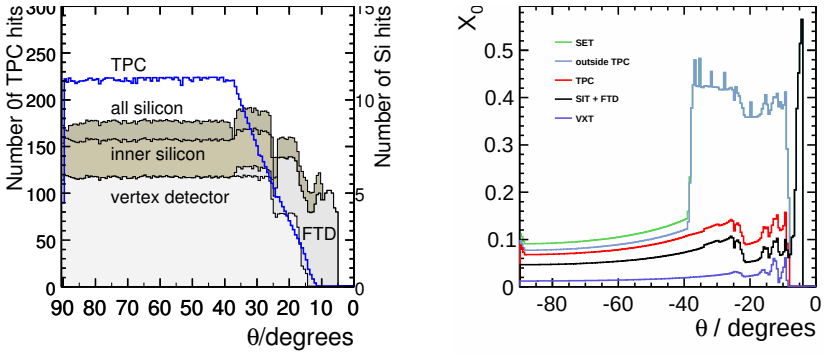

Figure III-6.1
(Left) Average number of hits for simulated charged particle tracks as a function of polar angle. (Right) Average total radiation length of the material in the tracking detectors as a function of polar angle.

Kalman-filter based track reconstruction, MarlinTrk, the PandoraPFA particle flow algorithm and the LCFIPlus flavour tagging package.

6.1.2 ILD tracking performance

ILD tracking is designed around three subsystems capable of standalone tracking: VTX, FTD and the TPC. These are augmented by three auxiliary tracking systems, the SIT, SET and ETD, which provide additional high resolution measurement points. The momentum resolution goal [381] is

$$\sigma_{1/p_T} \approx 2 \times 10^{-5}\ \text{GeV}^{-1}.$$

This level of performance ensures that the model-independent selection of the higgsstrahlung events from the recoil against leptonic $Z \to \mu^+\mu^-$ decays is dominated by beam energy spread rather than the detector resolution. The performance goal for the impact parameter resolution is

$$\sigma_{r\phi} = 5\ \mu\text{m} \oplus \frac{10}{p(\text{GeV})\sin^{3/2}\theta}\ \mu\text{m}. \qquad \text{(III-6.1)}$$

Meeting this gaol is crucial for the flavour tagging performance, and in particular the efficient separation of charm and bottom quark decays of the higgs boson.

6.1.2.1 Coverage and material budget

Figure III-6.1a shows, as a function of polar angle, θ, the average number of reconstructed hits associated with simulated 100 GeV muons. The TPC provides full coverage down to $\theta = 37°$. Beyond this the number of measurement points decreases. The last measurement point provided by the TPC corresponds to $\theta \approx 10°$. The central inner tracking system, consisting of the six layer VTX and the two layer SIT, provides eight precise measurements down to $\theta = 26°$. The innermost and middle double layer of the VTX extend the coverage down to $\theta \sim 16°$. The FTD provides up to a maximum of five measurement points for tracks at small polar angles. The SET and ETD provide a single high precision measurement point with large lever arm outside of the TPC volume down to a $\theta \sim 10°$. The different tracking system contributions to the detector material budget, including support structures, is shown in Figure III-6.1b. The spikes at small polar angles correspond to the support structures, electronics and cabling in the around the TPC endcap region. The bump at around $90°$ for the TPC corresponds to the central cathode membrane. Compared to the letter of intent the material has overall increased slightly due to the more detailed and realistic simulation, except for the TPC endplate where it has grown by close to 50%. This is explained in more detail in the TPC section 2.3.

6.1.2.2 Tracking efficiency

With over 200 contiguous readout layers, pattern recognition and track reconstruction in a TPC is relatively straightforward, even in an environment with a large number of background hits. In addition, the standalone tracking capability of the VTX enables the reconstruction of low transverse momentum tracks which do not reach the TPC. Hermetic tracking down to low angles is important at the ILC [229] and the FTD coverage enables tracks to be reconstructed to polar angles below $\theta = 7°$.

Figure III-6.2 shows, as a function of momentum and polar angle, the track reconstruction efficiency in simulated (high multiplicity) $t\bar{t} \rightarrow$ 6 jet events at $\sqrt{s}$ =500 GeV and 1 TeV respectively. Efficiencies are plotted with respect to MC tracks that stem from a region of 10 cm around the IP with $p_t > 100$ MeV and $cos(\theta) < 0.99$, excluding decays in flight and requiring at least 90 % purity. For the combined tracking system, the track reconstruction efficiency is on average 99.7 % for tracks with momenta greater than 1 GeV across the entire polar angle range, and it is larger than 99.8 % for $cos(\theta) < 0.95$.

The effects of background from coherent pair background and from multi-peripheral $\gamma\gamma \rightarrow$ hadrons events are taken into account by overlaying the corresponding number of events. For the pair background the correct number of bunch crossings resulting form the foreseen readout times are overlayed.

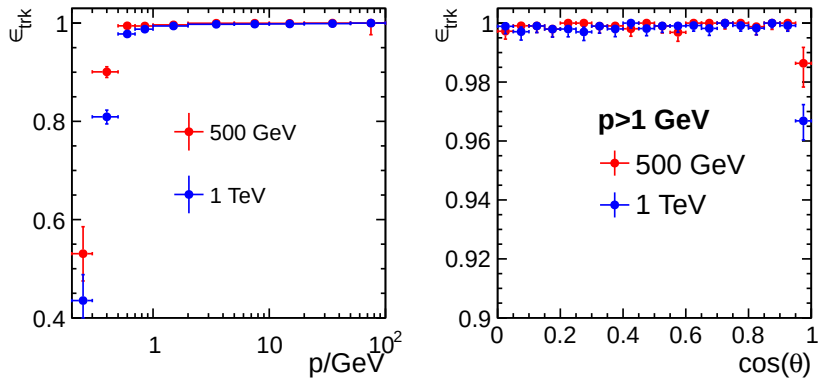

Figure III-6.2
Tracking Efficiency for $t\bar{t} \rightarrow$ 6 jets at 500GeV and 1 TeV plotted against (left) momentum and (right) $\cos\theta$.

6.1.2.3 Momentum resolution for the overall tracking system

The momentum resolution with the ILD simulation and full reconstruction is shown in Figure III-6.3a. The study was performed using muons generated at fixed polar angles of $\theta = 7°, 20°, 30°$ and $85°$, and the momentum was varied over the range $1 - 200$ GeV. For two polar angles, this is compared to the expected parametric form of, $\sigma_{1/p_T} = a \oplus b/(p_T \sin\theta)$, with $a = 2 \times 10^{-5}$ GeV^{-1} and $b = 1 \times 10^{-3}$. As can be seen, at a polar angle of $85°$, the required momentum resolution is attainable over the full momentum range from 1 GeV upwards. This remains true over the full length of the barrel region of the detector, where the TPC in conjunction with the SET is able to provide the longest possible radial lever arm for the track fit. For high momentum tracks, the asymptotic value of the momentum resolution is $\sigma_{1/p_T} = 2 \times 10^{-5}$ GeV^{-1}. At $\theta = 30°$, the SET no longer contributes, the effective lever-arm of the tracking system is reduced by 25 %. Nevertheless, the momentum resolution is still within the required level of performance. In the very forward region, the momentum resolution is inevitably worse due to the relatively small angle between the B-field and the track momentum.

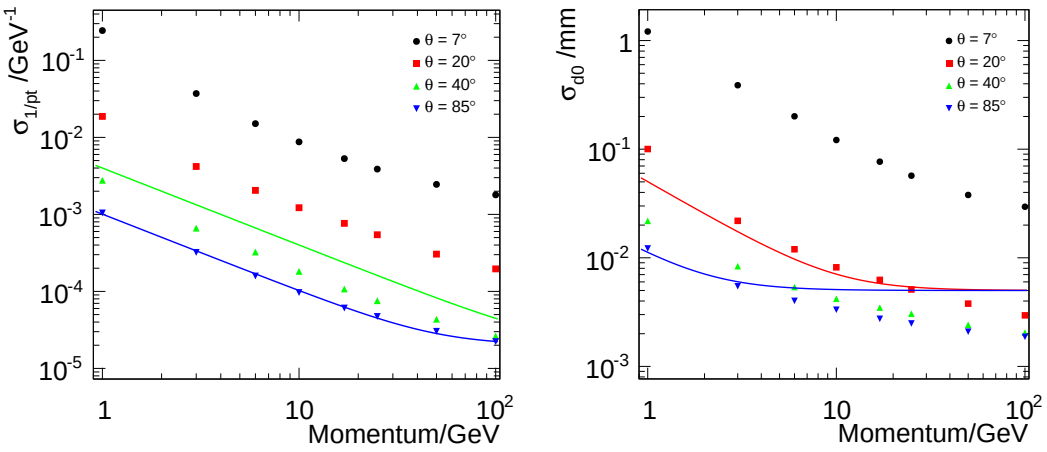

Figure III-6.3. (Left) Transverse momentum resolution for single muon events as a function of the transverse momentum for different polar angles. The lines show $\sigma_{1/p_T} = 2 \times 10^{-5} \oplus 1 \times 10^{-3}/(p_T \sin\theta)$ for $\theta = 30°$ (green) and $\theta = 85°$ (blue). (Right) Impact parameter resolution for single muon events as a function of the transverse momentum for different polar angles. The lines show $\sigma_{r\phi} = 5\ \mu\text{m} \oplus \frac{10}{p(\text{GeV})\sin^{3/2}\theta}\ \mu\text{m}$ for $\theta = 20°$ (red) and $\theta = 85°$ (blue).

6.1.2.4 Impact parameter resolution

Figure III-6.3b shows $r\phi$ impact parameter resolution as a function of the transverse track momentum. The required performance is achieved down to a track momentum of 1 GeV, whilst it is exceeded for high momentum tracks where the asymptotic resolution is 2 μm. The rz impact parameter resolution (not shown) is better than $\sim 10\,\mu$m down to momenta of 3 GeV and reaches an asymptotic value of $< 5\,\mu$m for the whole barrel region. Because of the relatively large distance of the innermost FTD disk to the interaction point, the impact parameter resolution degrades for very shallow tracks, $\theta < 15°$. The impact parameter resolution here assumes perfect alignment of the tracking systems.

6.1.2.5 Topological time-stamping

The hybrid tracking concept, combining a TPC with silicon tracking devices, is quite powerful also in terms of time-stamping performance. Since the TPC drifts the tracks while the silicon pixels are fixed in space, the silicon can act as an external z detector (T_0 device). Drifting TPC tracks are well-measured in $r\phi$ and angle; extrapolating a TPC track to match related silicon hits establishes where the track was in the z direction. An detailed description of this technique for a TPC and a similar one for a standard drift chamber is found in [382]. The time-stamping in ILD is found to be precise to $\simeq 2$ ns (to be compared to $\simeq 300$ ns between BXs at the ILC) so that the bunch crossing which produced the track (the T0) can be uniquely identified. Cosmic background tracks can be eliminated with this tool. It is also viable in the CLIC environment [383].

6.1.3 ILD particle flow performance

Many important physics channels at the ILC will consist of final states with at least six fermions, setting a "typical" energy scale for ILC jets as approximately 85 GeV and 170 GeV at $\sqrt{s} = 500$ GeV and $\sqrt{s}$ =1 TeV respectively. Meeting the performance goal of a jet energy resolution of $< 3.5\,\%$ ensures an efficient separation of hadronic decays from W, Z and H bosons. The current performance of the PandoraPFA algorithm applied to ILD Monte Carlo simulated data is summarised in Table III-6.1.

The observed jet energy resolution (rms_{90}) is not described by the expression $\sigma_E/E = \alpha/\sqrt{E/\text{GeV}}$. This is not surprising, as the particle density increases it becomes harder to cor-

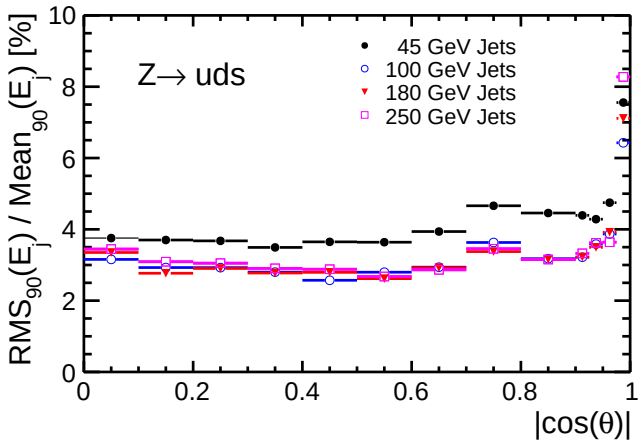

Figure III-6.4
Fractional jet energy resolution plotted against $|\cos\theta|$ where theta is the thrust axis of the event.

rectly associate the calorimetric energy deposits to the particles and the confusion term increases. The single jet energy resolution is also listed. The jet energy resolution (rms_{90}) is better than 3.7 % for jets of energy greater than 40 GeV. The resolutions quoted in terms of rms_{90} should be multiplied by a factor of approximately 1.1 to obtain an equivalent Gaussian analysing power[274]. Despite, the inclusion of dead material in the Monte Carlo simulation, the resolutions achieved are between 2 % and 7 % better than for the previous detector model described in [198]. In part this reflects a number of improvements to the particle flow reconstruction software. Nevertheless, it can be concluded that the additional dead material associated with services does not significantly degrade the jet energy resolution.

Figure III-6.4 shows the jet energy resolution for $\mathrm{Z} \rightarrow$uds events plotted against the cosine of the polar angle of the generated $\mathrm{q\bar{q}}$ pair, $\cos\theta_{\mathrm{q\bar{q}}}$, for four different values of $\sqrt{s}$. Due to the calorimetric coverage in the forward region, the jet energy resolution remains good down to $\theta = 13^\circ$ $(\cos\theta = 0.975)$.

6.1.4 Flavour tagging performance

Identification of b-quark and c-quark jets plays an important role within the ILC physics programme. The vertex detector design and the impact parameter resolution are of particular importance for flavour tagging. The LCFIPlus flavour tagging software uses boosted decision trees to discriminate b jets from udsc jets (b-tag), c jets from udsb jets (c-tag), and c jets from b jets (bc-tag).

The flavour tagging performance [384] of ILD was previously studied for the two vertex detector geometries considered, three double-sided ladders (VTX-DL) and five single-sided (VTX-SL) ladders. No significant differences in the input variables for the multivariate analysis were seen. Here results are presented only for the double-layer layout. The flavour tagging performance is studied using simulated and fully reconstructed samples for $\mathrm{Z} \rightarrow q\bar{q}$ reactions, shown in Figure III-6.5a, and

Table III-6.1. Jet energy resolution for $\mathrm{Z} \rightarrow$uds events with $|\cos\theta_{\mathrm{q\bar{q}}}| < 0.7$, expressed as, rms_{90} for the di-jet energy distribution, the effective constant α in $\mathrm{rms}_{90}/E = \alpha(E_{jj})/\sqrt{E_{jj}/\mathrm{GeV}}$, and the fractional jet energy resolution for a single jets, σ_{E_j}/E_j. The jet energy resolution is calculated from rms_{90}.

Jet Energy	rms_{90}	$\mathrm{rms}_{90}/\sqrt{E_{jj}/\mathrm{GeV}}$	σ_{E_j}/E_j
45 GeV	2.4 GeV	24.7 %	(3.66 ± 0.05) %
100 GeV	4.0 GeV	28.3 %	(2.83 ± 0.04) %
180 GeV	7.3 GeV	38.5 %	(2.86 ± 0.04) %
250 GeV	10.4 GeV	46.6 %	(2.95 ± 0.04) %

$ZZZ \to q\bar{q}q\bar{q}q\bar{q}$ reactions, shown in Figure III-6.5b. The latter process is forced to decay into the same quark pairs for all three Z decays. The $\gamma\gamma \to \mathrm{hadrons}$ backgrounds are not overlaid for this study. The boosted decision trees are retrained for the different energies and different final states. A slight performance degradation is seen by increasing the jet energy. The performance also degrades by increasing the number of jets in the final state, which can be attributed to reconstruction effects in busy environments.

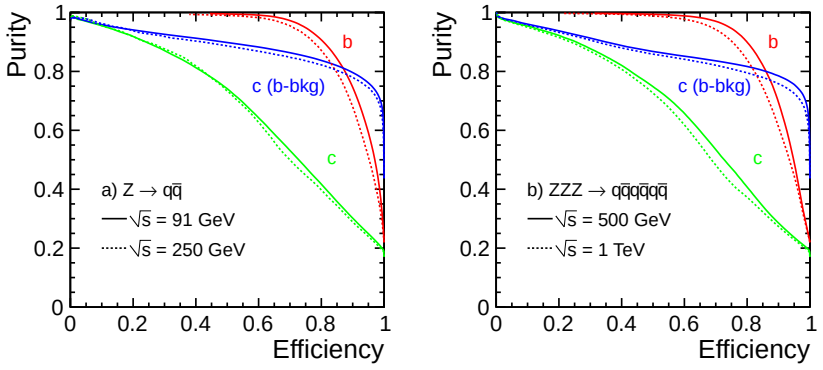

Figure III-6.5
Flavour tagging performance plots for (a) $Z \to q\bar{q}$ samples at $\sqrt{s} = 91\,\mathrm{GeV}$ and 250 GeV, and (b) $ZZZ \to q\bar{q}q\bar{q}q\bar{q}$ samples at $\sqrt{s} = 500\,\mathrm{GeV}$ and 1 TeV.

6.1.5 Comparison of detector models

To compare the AHCAL and SDHCAL options, the $e^+e^- \to t\bar{t}h$ benchmark signal samples were simulated and fully reconstructed using dedicated detector models (ILD_o1_v05 and ILD_o2_v05, respectively) and reconstruction software for each option, and analyzed as described in Sec. 6.3.4. It was found that the there were no significant differences in the mass resolutions of the top and higgs candidates.

6.2 ILD physics performance at 250 and 500 GeV

In this section the performance of ILD is described for $\sqrt{s} = 250\,\mathrm{GeV}$ and $\sqrt{s} = 500\,\mathrm{GeV}$. More details may be found in [198]. The results are summarised in Table III-6.2. These measurements demonstrate the excellent performance of the ILD detector for many different final states. In this chapter three topics are reviewed in more detail, which stress in particular the detector performance.

6.2.1 Higgs recoil mass reconstruction

The precise determination of the properties of the higgs boson is one of the main goals of the ILC. In particular, the model independent determination of the higgs boson branching ratios is central to the physics goals of the ILC. Here the measurement of the $\mathrm{e^+e^-} \to h\mathrm{Z}$ cross section from the recoil mass distribution in $Zh \to \mathrm{e^+e^-}X$ and $Zh \to \mu^+\mu^-X$ events, determines the absolute $g_{h\mathrm{ZZ}}$ coupling. In $Zh \to \mu^+\mu^-X$ events the recoil mass resolution is determined by the beam-energy spread and the muon momentum resolution, whereas for $Zh \to \mathrm{e^+e^-}X$ events Bremsstrahlung and final-state radiation (FSR) dominate. The reconstructed recoil mass distributions for simulated events is shown in Figure III-6.6. Measurement precisions on the $h\mathrm{Z}$ production cross section of 3.6 % and 4.3 % were obtained from the respective $\mu^+\mu^-$ and $\mathrm{e^+e^-}(n\gamma)$ final states. In the $\mu^+\mu^-$ final state, the resolution is limited by the beam energy spread rather than by the momentum resolution of the detector.

Table III-6.2. A summary of the main physics benchmark measurements presented in the ILD LOI and [385].

$\sqrt{s}$	Observable	Precision	Comments
250 GeV	$\sigma(e^+e^- \to Zh)$	± 0.30 fb (2.5 %)	Model Independent
	m_h	32 MeV	Model Independent
	m_h	27 MeV	Model Dependent
250 GeV	$Br(h \to b\bar{b})$	2.7 %	includes 2.5 %
	$Br(h \to c\bar{c})$	7.3 %	from
	$Br(h \to gg)$	8.9 %	$\sigma(e^+e^- \to Zh)$
500 GeV	$\sigma(e^+e^- \to \tau^+\tau^-)$	0.29 %	$\theta_{\tau^+\tau^-} > 178^\circ$
	A_{FB}	± 0.0025	$\theta_{\tau^+\tau^-} > 178^\circ$
	P_τ	± 0.007	exclucing $\tau \to a_1\nu$
500 GeV	$\sigma(e^+e^- \to \tilde{\chi}_1^+\tilde{\chi}_1^-)$	0.6 %	
	$\sigma(e^+e^- \to \tilde{\chi}_2^0\tilde{\chi}_2^0)$	2.1 %	
	$m(\tilde{\chi}_1^\pm)$	2.4 GeV	from kin. edges
	$m(\tilde{\chi}_2^0)$	0.9 GeV	from kin. edges
	$m(\tilde{\chi}_1^0)$	0.8 GeV	from kin. edges
500 GeV	$\sigma(e^+e^- \to t\bar{t})$	0.4 %	$(bq\bar{q})$ $(\bar{b}q\bar{q})$ only
	m_t	40 MeV	fully-hadronic only
	m_t	30 MeV	+ semi-leptonic
	Γ_t	27 MeV	fully-hadronic only
	Γ_t	22 MeV	+ semi-leptonic
	A_{FB}^t	± 0.0079	fully-hadronic only
500 GeV	$\sigma(e^+e^- \to \tilde{\mu}_L^+\tilde{\mu}_L^-)$	2.5 %	
	$m(\tilde{\mu}_L)$	0.5 GeV	
500 GeV	$m(\tilde{\tau}_1)$	$0.1\,\text{GeV} \oplus 1.3\sigma_{\text{LSP}}$	SPS1a'
1 TeV	α_4	$-1.4 < \alpha_4 < 1.1$	SPS1a'
	α_5	$-0.9 < \alpha_5 < +0.8$	WW Scattering

6.2.2 Tau reconstruction

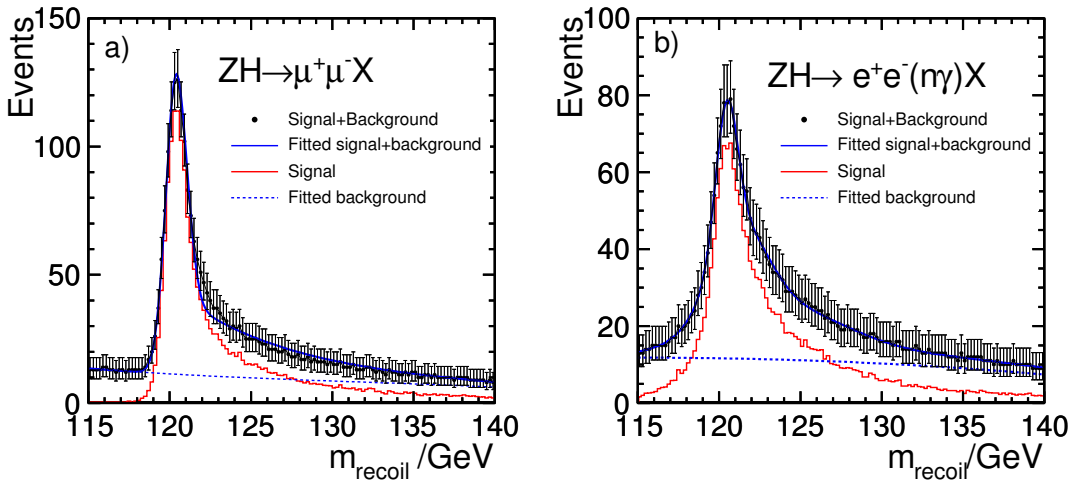

Figure III-6.6. Results of the model independent analysis of the Higgs-strahlung process $e^+e^- \to hZ$ in which a) $Z \to \mu^+\mu^-$ and b) $Z \to e^+e^-$ (including the reconstruction of bremsstrahlung and FSR photons). The results are shown are for the $P(e^+, e^-) = (+30\,\%, -80\,\%)$ beam polarisation.

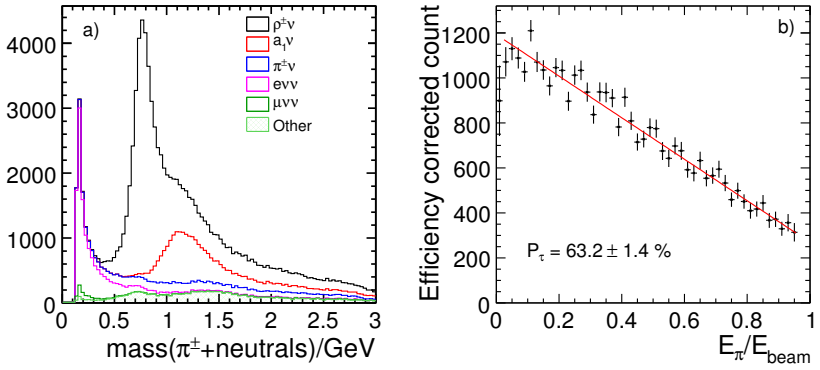

Figure III-6.7
a) The invariant mass distribution for selected 1-prong tau-candidates and b) The efficiency corrected reconstructed pion energy distribution for selected $\tau \to \pi\nu$ candidates.

The higgs recoil mass analysis provides a clear demonstration of excellent tracking performance of the ILD detector concept. The reconstruction of $\tau^+\tau^-$ events at $\sqrt{s} = 500$ GeV provides a challenging test of the detector performance in terms of separating nearby tracks and photons. The reconstruction of the tau final states enables the mean tau polarisation P_τ to be determined. For the tau polarisation measurement, the $\tau \to \pi\nu$ and $\tau \to \rho\nu$ decays have the highest sensitivity. The separation of the 1-prong decay modes relies on lepton identification and the ability to separate the neutral energy deposits from π^0 decays from the hadronic shower. The invariant mass distribution for 1-prong events is shown in Figure III-6.7a.

A neural network approach based on nine input variables is used to identify the tau decays modes. The variables include: the total energy of the identified photons, the invariant mass of the track and all identified photons (Figure III-6.7a); and electron and muon particle identification variables based on calorimetric information and track momentum.

Table III-6.3
Purity and efficiency of the main tau decay mode selections.

Mode	Efficiency	Purity
$e\nu\nu$	98.9 %	98.9 %
$\mu\nu\nu$	98.8 %	99.3 %
$\pi\nu$	96.0 %	89.5 %
$\rho\nu$	91.6 %	88.6 %
$a_1\nu$ (1-prong)	67.5 %	73.4 %
$a_1\nu$ (3-prong)	91.1 %	88.9 %

Table III-6.3 shows the efficiency and purity achieved for the six main tau decay modes. The selection efficiency is calculated with respect to the sample of $\tau^+\tau^-$ after the requirement that the two tau candidates are almost back-to-back. The purity only includes the contamination from other $\tau^+\tau^-$ decays. The high granularity and the large detector radius of ILD results in excellent separation.

6.2.3 Strong EWSB

If strong electroweak symmetry breaking (EWSB) is realised in nature, the study of the WW-scattering processes is particularly important. At the ILC, the $\mathrm{W^+W^-} \to \mathrm{W^+W^-}$ and $\mathrm{W^+W^-} \to \mathrm{ZZ}$ vertices can be probed via the processes $\mathrm{e^+e^-} \to \nu_e\bar{\nu}_e\mathrm{q\bar{q}q\bar{q}}$ where the final state di-jet masses are from the decays of two W-bosons or two Z-bosons. Separating the two processes through the reconstruction of the di-jet masses provides a test of the jet energy resolution of the ILD detector. Strong EWSB can be described by an effective Lagrangian approach in which there are two anomalous quartic gauge couplings, α_4 and α_5 which are identically zero in the SM. Figure III-6.8 shows, for $\nu_e\bar{\nu}_e\mathrm{WW}$ and $\nu_e\bar{\nu}_e\mathrm{ZZ}$ events at $\sqrt{s} = 1$ TeV, a) the reconstructed di-jet mass distribution, and b) the distribution of average reconstructed mass, $(m_{ij} + m_{kl})/2.0$. Clear separation between the W and Z peaks is

obtained, demonstrating that the ILD jet energy resolution is sufficient to separate the hadronic decays of gauge bosons.

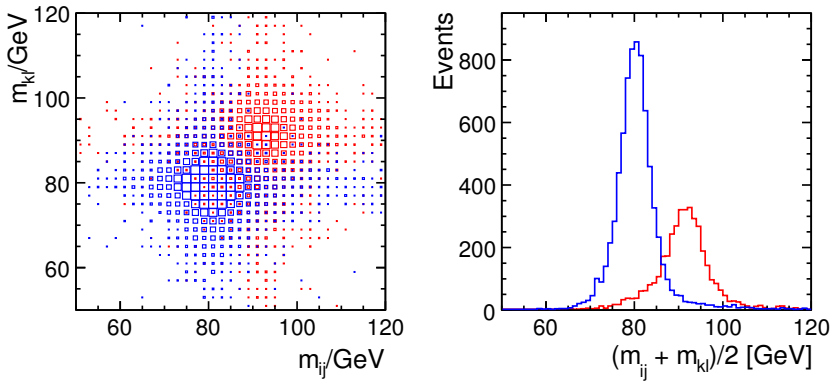

Figure III-6.8
a) The reconstructed di-jet mass distributions for the best jet-pairing in selected $\nu_e\bar{\nu}_e$WW (blue) and $\nu_e\bar{\nu}_e$ZZ (red) events at $\sqrt{s} = 1\,TeV$. b) Distributions of the average reconstructed di-jet mass, $(m_{ij} + m^B_{kl})/2.0$, for the best jet-pairing for $\nu_e\bar{\nu}_e$WW (blue) and $\nu_e\bar{\nu}_e$ZZ (red) events.

6.3 ILD benchmarking

In chapter 1.4, the list of benchmark reactions is described which have been studied by the detector groups (for more detail see [386]). The result of the analyses of these benchmarks are briefly presented in this section. The generation of both signal, physics background, and machine background was done as a common effort between ILD and SiD and is described in detail in chapter 2.2. The detector simulation software and detector model used are described in chapter 5.4. Events for the analyses were generated and simulated with the detailed GEANT4 based ILD model, and centrally reconstructed. The PandoraPFA and LCFIPlus algorithms (described in chapter 2.2) were used.

The first three benchmark processes presented are at $\sqrt{s}$=1 TeV. They were chosen partly to demonstrate the capability of the detectors under the conditions of the ILC operating at 1 TeV, partly to exploit the opportunities that this higher energy would bring. More specifically:

$e^+e^- \to \nu\bar{\nu}h$ is intended to test the detector capabilities in simple topologies.

$e^+e^- \to W^+W^-$ is complementing the first benchmark by topologies with jets at higher energies and at lower angles.

$e^+e^- \to t\bar{t}h$ is intended to demonstrate the capability of the detector to disentangle very complicated final states.

These processes were studied assuming an integrated luminosity (L) of 1 ab^{-1}, and with polarised beams. Using the convention that $\mathcal{P}_{p^-,p^+}$ denotes a configuration of $p-\%$ degree of polarisation for the electrons, $p+\%$ for the positrons, the full sample was evenly divided in two samples with $\mathcal{P}_{-80,+20}$ and $\mathcal{P}_{+80,-20}$. The full sample is referred to as the full DBD sample in the following, while the two sub-samples are called the DBD $\mathcal{P}_{-80,+20}$ and $\mathcal{P}_{+80,-20}$ samples.

The last of the benchmark processes was the analysis of $e^+e^- \to t\bar{t}$ at $\sqrt{s}$ = 500 GeV. The integrated luminosity was assumed to be 500 fb^{-1}, evenly divided in a $\mathcal{P}_{-80,+30}$ sample and a $\mathcal{P}_{+80,-30}$ one. This particular reaction was chosen to compare the current more detailed ILD model to the one used in earlier studies to understand the impact the improved simulation model has on the physics reach.

6.3.1 Common reconstruction tools

6.3.1.1 Isolated lepton finding

In several analyses the task is to identify an isolated lepton within a jet. The strategy proposed in [387] is to force the jet clustering algorithm to form a given number of jets, e.g. four in the case of semi-leptonic $\mathrm{t\bar{t}}$ decays. The searched lepton has distinct features with respect to other particles in the jet. A lepton is called "isolated" if it is either the particle with the highest momentum (the "leading" particle) in the jet or if it has a large transverse momentum with respect to the jet axis. The two variables x_T and z are defined to take these two configurations into account:

$$x_T = \frac{p_{T,\mathrm{lepton}}}{m_{\mathrm{jet}}}$$

where $p_{T,\mathrm{lepton}}$ is the transverse momentum of the identified lepton with respect to its jet axis and m_{jet} is the mass of the jet ($m^2 = E^2 - \mathbf{p}^2$), and

$$z = \frac{E_{\mathrm{lepton}}}{E_{\mathrm{jet}}},$$

which corresponds to the fraction of jet-energy from the lepton. The distribution for leptons in semi-leptonic and fully hadronic $\mathrm{t\bar{t}}$ events can be seen in Figure III-6.9, left. The fraction z is restricted to values smaller than 1. The variable x_T must be less than $1/2$ which is the kinematic limit of a jet taken at rest where the lepton and the other particles are almost back-to-back and share the same energy $m_{jet}/2$.

6.3.1.2 Jet clustering

At lepton colliders, exclusive jet algorithms – in which every particle is assigned to a jet – have been favoured. An example of this algoritm-type is the Durham algorithm [388]. However, at the ILC such algorithms work poorly: while it is still true that all particles from the main interaction can be assigned to jets in a unique fashion, and that this interaction does not contain an "underlying event", the large cross section for $\gamma\gamma \to \mathrm{hadrons}$ implies that most interesting events will be accompanied by several unrelated $\gamma\gamma \to \mathrm{hadrons}$ events ("pile-up events") in the same bunch crossing. Exclusive jet algorithms will inevitably include particles from the pile-up events into the jets.

This problem was studied at CLIC, where the pile-up conditions are much more challenging than at ILC [199]. It was concluded that the use of inclusive algorithms, developed for hadron colliders, was well-suited to mitigate this problem. The algorithm used was the k_t algorithm [389], as implemented in the FASTJET package[390]. In the k_t algorithm, the measure of distance between two objects i and j (particles or proto-jets) is $d_{ij} = \min(p_{Ti}^2, p_{Tj}^2)[\Delta_{\eta ij}^2 + \Delta_{\phi ij}^2]/R^2$. In each iteration, d_{ij} is calculated for all ij. The smallest of all d_{ij} ($=d_{min}$) is compared with the smallest p_{Tk}^2 ($=p_{T,min}^2$) of all objects k. If $p_{T,min}^2 < d_{min}$ the corresponding object k is removed from the event. In the opposite case, the corresponding objects i and j are merged. The procedure is then repeated until an end condition is fulfilled, which might be that only N_{jet} objects still are left to consider, or that the lowest measure in the iteration was above a pre-defined limit. As the polar distance is measured in pseudo-rapidity (η), rather than polar angle, particles close to the beam axis - where η tends to $\pm\infty$ - are less likely to be considered close enough to be merged, and are more likely to be removed as particles not belonging to any jet. Hence, the algorithm will remove low p_T, low polar angle particles - typical for pile-up events - from the jets. By choosing appropriate values of the parameters R and N_{jet}, an optimal performance can be found. This optimum will in general not be the same for different benchmark reactions, due to the differences in number of expected jets, amount of invisible energy, or the angular distributions of the signal reaction.

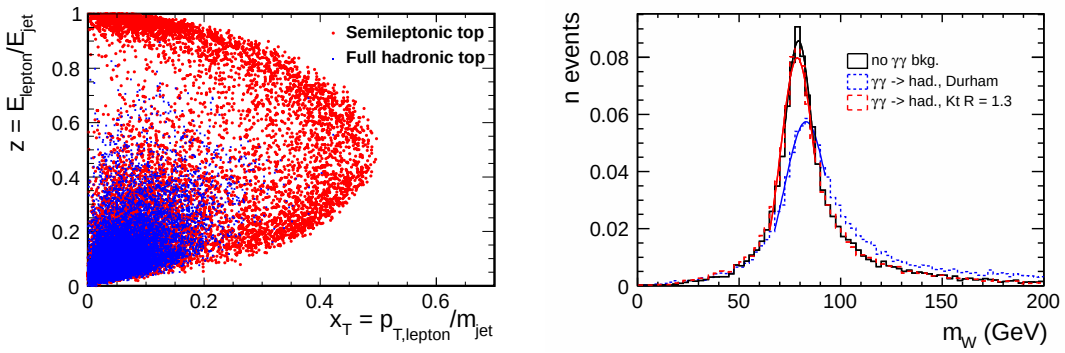

Figure III-6.9. Left: Distribution of variables x_T and z used to identify isolated leptons in semi-leptonic (red) and full hadronic (blue) top events. Right: Reconstructed di-jet mass distribution in $e^+e^- \to \mathrm{WW} \to \ell\nu qq$. Black solid: Durham algorithm, no pile-up; Blue dotted: Durham algorithm, with pile-up; Red dashed : k_t algorithm, with pile-up.

In Figure III-6.9 (right) these features are demonstrated. The figure shows the di-jet mass distribution for the $\mathrm{WW} \to \ell\nu qq$ reaction. The isolated lepton was removed before each jet algorithm was applied. It can be clearly seen that the result without pile-up is almost restored.

6.3.2 $\mathrm{e^+e^-} \to \nu\bar{\nu}\mathrm{h}$

At $\sqrt{s} = 1$ TeV, the Higgs boson is mainly produced via the WW-fusion process ($\mathrm{e^+e^-} \to \nu_e\bar{\nu}_e h$), with a cross section exceeding the maximum cross section close to threshold (at around 250 GeV), where production is dominated by the Higgs-strahlung ($\mathrm{e^+e^-} \to \mathrm{Z}h$) process, as shown in Figure III-6.10.

For this analysis [391, 392], Higgs boson production and decay were fully simulated, as was relevant background processes. In the simulation, the SM Higgs boson BRs for m_h= 125 GeV were used, see table III-6.4. The aim of the study is to determine to which accuracy the cross section weighted branching ratios (σ·BR) can be determined from the data for the decay modes $\mathrm{b\bar{b}}$, $\mathrm{c\bar{c}}$, gg, $\mathrm{WW^*}$, and $\mu^+\mu^-$.

Table III-6.4
Higgs branching ratios, from [184].

Mode	$\mathrm{b\bar{b}}$	$\mathrm{c\bar{c}}$	gg	$\mathrm{WW^*}$	$\mu^+\mu^-$	$\tau^+\tau^-$	$\mathrm{ZZ^*}$	$\gamma\gamma$	$\mathrm{Z}\gamma$
BR (%)	57.8	2.7	8.6	21.6	0.02	6.4	2.7	0.23	0.16

Figure III-6.10
Higgs production cross section as a function of $\sqrt{s}$ for $\mathcal{P}_{-80,+20}$.

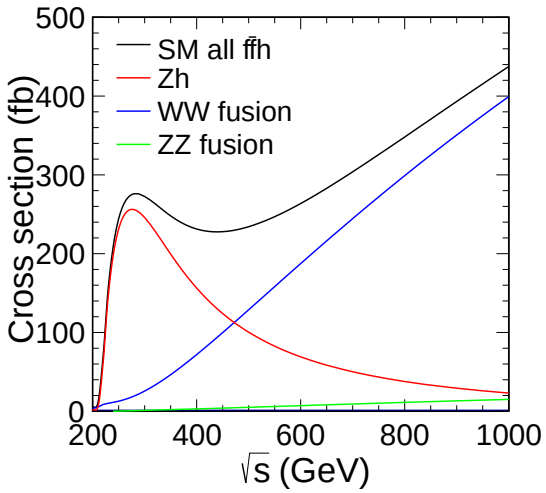

In the hadronic decay channels of the Higgs, the final state forms two jets and flavour tagging performance is crucial to measure the BRs. In the $h \to \mathrm{WW^*}$ channel, only the fully hadronic decay

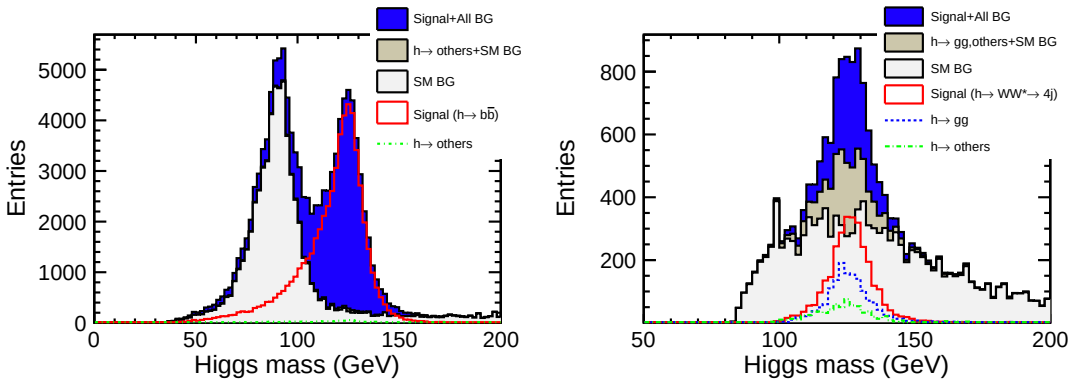

Figure III-6.11. Left:Reconstructed $h \to \mathrm{b\bar{b}}$ di-jet mass distribution after the b-tagging selection. Right: Reconstructed Higgs mass distribution in $h \to \mathrm{WW^*}$ fully hadronic decay channel. Both figures correspond to the DBD $\mathcal{P}_{-80,+20}$ sample.

mode, $h \to \mathrm{WW^*} \to \mathrm{q\bar{q}q\bar{q}}$, was considered. At $\sqrt{s} = 1$ TeV, higher instantaneous luminosity is expected than at 250 or 500 GeV. This, together with the rising Higgs production cross section, implies that one can accumulate observable amounts of $h \to \mu^+\mu^-$ events (σ·BR$= 0.089$ fb for $\mathcal{P}_{-80,+20}$).

In the $\boldsymbol{h \to \mathrm{b\bar{b}}, \mathrm{c\bar{c}}}$ **, and** $\boldsymbol{gg}$ **channels**, the events have in common that they contain two jets with a di-jet mass consistent with the Higgs mass and that they have large missing energy due to the neutrinos. Flavour tagging is crucial to distinguish the decay channels.

Jets were reconstructed by first employing the k_t jet clustering algorithm with $R = 1.1$ and $N_{jet} = 2$ to remove particles from pile-up events, and then the Durham algorithm on the remaining particles. In order to reduce the background, it was required that the visible energy and longitudinal momentum should be small, while the transverse momentum should be high. Cuts based on the total particle-multiplicity and the polar angle of the jets were applied to reduce the 2-fermion background. Finally, the Higgs candidate events for flavour tagging were selected by requiring the mass of the di-jet to be in $[110,\ 150]$ GeV. The efficiency to select $h \to \mathrm{b\bar{b}}$, $\mathrm{c\bar{c}}$ and gg at this stage were 35.0%, 37.3% and 35.9%, respectively, while the major background was the $\nu\bar{\nu}q\bar{q}$ (non-Higgs) final state.

A flavour tagging template fitting was performed to extract σ·BR for the different channels. The flavour templates of $h \to \mathrm{b\bar{b}}$, $\mathrm{c\bar{c}}$, gg, and backgrounds were obtained from the flavour tagging boosted-decision tree output of LCFIPlus. Figure III-6.11 (left) shows the reconstructed $h \to \mathrm{b\bar{b}}$ di-jet mass distribution after applying a b-tagging cut for the DBD $\mathcal{P}_{-80,+20}$ sample. By repeating the template fit 5000 times on distributions generated by a toy Monte Carlo, the measurement expected accuracies on σ·BR could be evaluated.

In the fully hadronic $\boldsymbol{h \to \mathrm{WW^*}}$ **channel**, the expected final state is four jets consistent with $\mathrm{WW^*}$, with total mass consistent with the Higgs mass, while having large missing energy and missing transverse momentum. Background from pile-up events was removed by employing the k_t jet clustering algorithm with $R = 0.9$ and $N_{jet} = 4$. The remaining particles were forced to into a four-jet configuration using the Durham algorithm. From the reconstructed four jets, the jet pairing yielding the di-jet mass closest to m_{W} was assumed to be the W. The other di-jet should have a mass between 15 and 60 GeV. In the jet clustering, it was demanded that the Durham algorithm should show a preference for the four-jet configuration. Subsequently, pre-selections similar to those of the two-jet channel were applied. In this channel, $h \to \mathrm{b\bar{b}}$ could be a major background, therefore the b-likeness from LCFIPlus was required to be low.

The distribution of the reconstructed Higgs mass in the $h \to \mathrm{WW^*}$ hadronic decay channel is shown in Figure III-6.11 (right) for the DBD $\mathcal{P}_{-80,+20}$ sample. Signal selection efficiency of $h \to \mathrm{WW^*}$ was 12.4% and remaining major backgrounds are 4-fermions ($e^+e^- \to \nu\bar{\nu}q\bar{q}$), 3-fermions

($e\gamma \to \nu q\bar{q}$) and other decay channels of the Higgs. The relative measurement error on σ·BR was evaluated by $\frac{\sqrt{N_s+N_{BG}}}{N_s}$, where $N_s(N_{BG})$ is the number of signal (background) events in the signal region.

The $h \to \mu^+\mu^-$ **channel**, due to its very low branching-ratio was only studied in the DBD $\mathcal{P}_{-80,+20}$ sample where the Higgs production cross section is larger. The main backgrounds are $e^-e^+ \to \nu\bar{\nu}\mu^-\mu^+$ and $\gamma\gamma \to \nu\bar{\nu}\ell^-\ell^+$. Events with two reconstructed high momentum isolated tracks were selected, provided that the two tracks were identified as muons. The invariant mass of the di-muon system was required to be between 95 and 155 GeV, and its energy to be lower than 400 GeV. Fully leptonic events were selected by requiring low multiplicity and high missing energy. The di-τ background was reduced by requiring that the significance of the impact parameters should be small. The signal efficiency at this pre-selection stage was found to be 81.1 %. Further cuts on missing energy and transverse momentum, the minimum angle to the beam-axis of the muons and on energy detected in the very forward calorimeter were applied. The final signal efficiency after all cuts was 37.0 %.

Figure III-6.12 shows the reconstructed di-muon mass of $h \to \mu^+\mu^-$. After the final selection was applied, the resulting invariant mass distributions for the background and the signal were fitted individually. Those fits were used to generate mass-distributions for 5000 pseudo-experiments, assuming L = 500 or 1000 fb^{-1} with $\mathcal{P}_{-80,+20}$. The signal and background was fitted to each of the pseudo-experiments, and the distribution of the fit-results was used to evaluate the statistical accuracy of σ·BR.

The statistical uncertainties for all studied decay-modes are summarised in Table III-6.5 separately for the $\mathcal{P}_{-80,+20}$ and $\mathcal{P}_{+80,-20}$ DBD samples. In addition, the obtainable precisions assuming the full 1 ab^{-1} sample was collected with $\mathcal{P}_{-80,+20}$ are given.

Table III-6.5
Summary of the accuracies of $(\sigma \cdot Br)$ at $\sqrt{s} = 1$ TeV. The shown values correspond to statistical errors only.

L	500 fb^{-1}		1 ab^{-1}
Beam polarisation	$\mathcal{P}_{-80,+20}$	$\mathcal{P}_{+80,-20}$	$\mathcal{P}_{-80,+20}$
$\Delta\sigma\mathrm{BR}/\sigma\mathrm{BR}(\mathrm{h} \to \mathrm{b\bar{b}})$	0.54%	2.1%	0.39%
$\Delta\sigma\mathrm{BR}/\sigma\mathrm{BR}(\mathrm{h} \to \mathrm{c\bar{c}})$	5.7%	36.8%	3.9%
$\Delta\sigma\mathrm{BR}/\sigma\mathrm{BR}(\mathrm{h} \to \mathrm{gg})$	3.9%	25.7%	2.8%
$\Delta\sigma\mathrm{BR}/\sigma\mathrm{BR}(\mathrm{h} \to \mathrm{WW^* \to 4j})$	3.6%	23.7%	2.5%
$\Delta\sigma\mathrm{BR}/\sigma\mathrm{BR}(\mathrm{h} \to \mu^+\mu^-)$	41%	-	31%

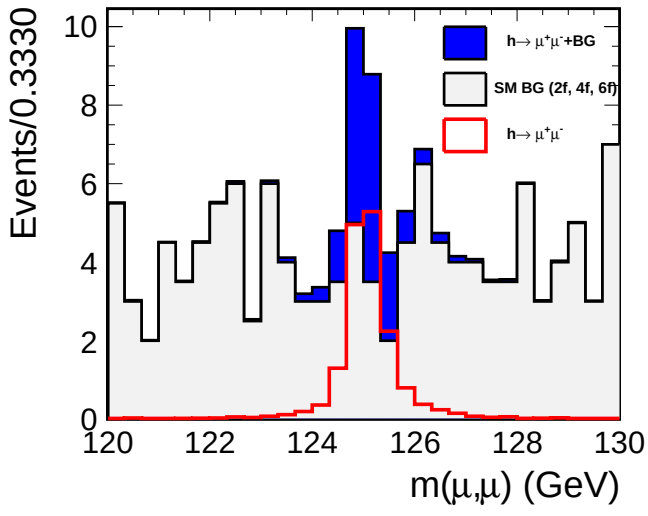

Figure III-6.12
Reconstructed di-muon mass distribution of $h \to \mu^+\mu^-$ in the DBD $\mathcal{P}_{-80,+20}$ sample.

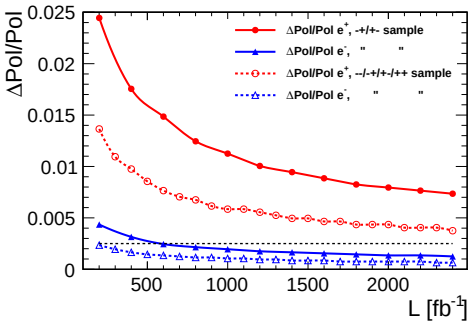

Figure III-6.13
Relative error of the polarisation measured from the study of the WW scattering cross section. The different curves correspond to different beam polarisations (see legend). The black dashed line indicates the error from the direct measurement of the polarisation using the polarimeters.

6.3.3 $e^+e^- \to W^+W^-$

The use of beam polarisation is very beneficial for the physics programme at the ILC. Many examples from the Standard Model as well as beyond the Standard Model [393] demonstrate that having simultaneously polarised electron and positron beams will be very useful for the discovery of new particles, analysing signals in a model independent manner or resolving precisely the underlying model.

At the ILC operated at $\sqrt{s}$=1 TeV, the expected nominal beam-polarisations are $\mathcal{P}_{\pm 80,\mp 20}$. For both beams, the polarisation measurement will be done with Compton polarimetry (see 2.4), with an expected precision of 0.25%. This can limit the usefulness of the beam polarisation: For instance, in the measurement of the Triple Gauge Couplings (TGCs) of the W, the uncertainty due to a 0.25% error on the beam polarisation is of a similar size as the expected statistical error.

To get a higher precision in the polarisation measurement it is necessary to use annihilation data. The benchmark WW process is ideally suited for this purpose due to its high cross section and to the pure left(right) handedness of the $\mathrm{W}^{-(+)}$ couplings to fermions. In the method used here, information on the angular distribution of the production angle $\cos\theta_{\mathrm{W}}$ of the W^- with respect to the direction of the incoming electron beam is exploited. Even though this method would profit from having data at the $++$ and $--$ helicity combinations, it does not depend crucially on the existence of such samples, in contrast to the well-known Blondel scheme [394, 395].

To estimate the possible precision of a polarisation measurement using W-pair production a detailed study has been done and is described in [396, 397]. Only semi-leptonic WW events were used in this analysis, since they allow to unambiguously determine the charge of the W bosons. Semileptonic decays of the W bosons were selected using the isolated lepton-finder. The k_T algorithm with R=1.3 and $N_{jet} = 2$, applied to all particles except the isolated lepton, was used to reject particles from pile-up events. Cuts on number of reconstructed particles, missing mass, missing energy and missing transverse momentum were used to further reduce background. Finally, a 2C kinematic fit was performed, with - apart from energy and momentum conservation - the constraint that the two reconstructed bosons should have equal mass. In order to perform the fit, it was necessary to remove $\mathrm{W}^+\mathrm{W}^- \to \tau\nu qq$ events, which was done by cutting on the discriminant τ_{disc}, described in [398]. Events where the fitted mass was between 40 and 120 GeV were accepted for further analysis. The efficiency to select $\mathrm{e}^+\mathrm{e}^- \to \mathrm{W}^+\mathrm{W}^- \to \mu(e)\nu qq$ was 36%, yielding a sample with 82% purity.

Templates of the $\cos\theta_{\mathrm{W}}$ distributions were created for different polarisations and the data was fitted to the templates in order to determine the polarisation. It was found that the uncertainty on the electron (positron) beam polarisation would be 0.0016 (0.0023) using the DBD sample. The correspondig fractional uncertainties are 0.0019 and 0.0113, respectively. How the relative precission depends on integrated luminosity is shown by the solid curves in Figure III-6.13.

As mentioned above, the method profits from having samples with the beams having the same-sign polarisation. If the same L of 1 ab^{-1} is divided between $\mathcal{P}_{-80,+20}$, $\mathcal{P}_{-80,-20}$, $\mathcal{P}_{+80,+20}$ and $\mathcal{P}_{+80,-20}$ in the proportions 4:1:1:4, the uncertainty of the electron (positron) beam polarisation was

found to be further reduced to 0.00084 (0.0012), yielding a relative uncertaitny of 0.0011 (0.0060). The integrated luminosity dependence is shown by the dashed curves in Figure III-6.13.

It should be pointed out that the precision of the angular fit method does not depend on assuming that the TGCs have their SM values. Indeed, in [399], it was shown that simultaneously fitting the polarisation and the TGCs is possible, and that changes greater than 0.02% to the polarisation stemming from TGC contributions could be disentangled from the beam-polarisation in the angular fit method.

6.3.4 $e^+e^- \to t\bar{t}h$

The precision measurement of the top–higgs Yuwaka coupling ($g_{t\bar{t}h}$) is an important benchmark for the ILC, in particular to assess the capabilities of the detectors to analyse complicated event topologies.

This study [400] investigates the semi-leptonic and fully hadronic decay modes of the $t\bar{t}$ system with the higgs boson decaying via the $b\bar{b}$ mode. The semi-leptonic decay mode leads to a signal of six jets, an isolated lepton and missing energy. The fully hadronic decay mode results in a signal of eight jets. Both decay modes include four b jets. The signal was reconstructed by locating isolated leptons in the event. The number of isolated leptons was used to divide the analysis samples into the semi-leptonic and hadronic decay modes to ensure no overlap. In the semi-leptonic sample, the number of isolated leptons is required to be exactly one; this isolated lepton candidate was then set aside whilst forcing the rest of the event into six jets. In the hadronic sample, the number of isolated leptons was required to be zero; these events were then forced into eight jets. Particles from the $\gamma\gamma \to hadrons$ events were discarded by using the k_t algorithm with R=1.2. The subsequent jet–finding and flavour–tagging procedures were performed using LCFIPlus. The top quarks were reconstructed using a b jet plus a W boson, where each W boson was formed either from two jets not tagged as b jets or, in the case of the semi-leptonic sample, from the isolated lepton and missing momentum. The Higgs was reconstructed using the two remaining b jets. The optimal combination of jets in the event was chosen so that the top and Higgs candidates have the most consistent mass.

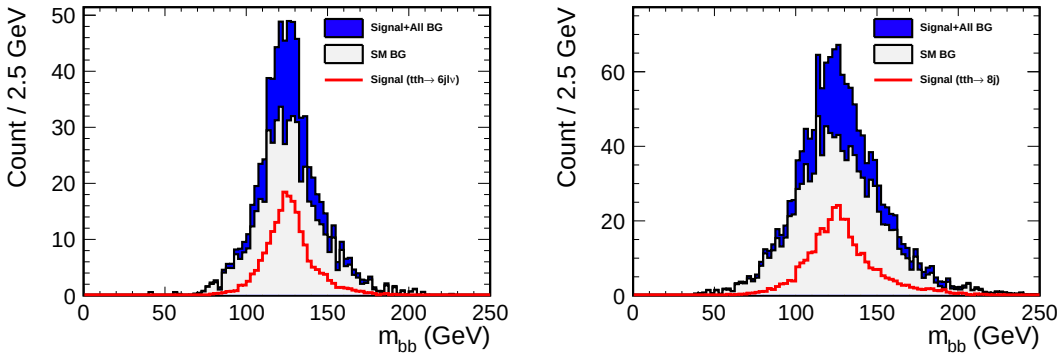

Figure III-6.14. Reconstructed h mass for the optimal jet combination of events passed the isolated lepton and Boosted Decision Tree cuts. Left: Semi-leptonic channel. Right: Fully hadronic channel. Both figures show the full DBD sample.

The main backgrounds to this process are $t\bar{t}b\bar{b}$ and $t\bar{t}Z$ as these can easily mimic the signal, and $t\bar{t}$ due to the huge relative cross section compared to the signal. The backgrounds were reduced by a multivariate analysis technique employing boosted decision trees [401] and the results were cross checked by a cut-based analysis. The input variables include the total visible energy and number of particles in the event, the b-likeness of the jets, event shape variables such as the thrust and those from the jet-clustering algorithm, the reconstructed masses of the top, W and higgs candidates and their consistency, and the helicity angle of the Higgs decay. The final discriminant was optimised to

yield the maximum statistical significance. At this point, the efficiency of selecting $\mathrm{t\bar{t}}h$ events was 50.0% with a purity of the selected sample of 29.1%. The reconstructed di-jet masses for the pair most likely to be the h are shown in Figure III-6.14 for the two channels separately.

Using the full DBD sample, the statistical precision of $g_{\mathrm{t\bar{t}}h}$ was found to be 6.9% for the semi-leptonic mode and 5.4% for the hadronic mode. The combined statistical precision was found to be

$$\left(\frac{\Delta g_{\mathrm{t\bar{t}}h}}{g_{\mathrm{t\bar{t}}h}}\right) = 4.3\%$$

.

The quoted error is statistical only. It is expected that the theoretical uncertainties on background cross sections and higgs branching ratios will be at the sub-percent level at the time the 1 TeV phase of the ILC starts. Also the relevant machine parameters – luminosity, energy and polarisation – are expected to be controlled to a similar precision. Therefore, the main systematic uncertainty is expected to be the estimate of signal and background efficiencies. These uncertainties could, for instance, be evaluated from the data itself: the theoretically well-understood $\mathrm{t\bar{t}Z}$ channel is quite similar to the $\mathrm{t\bar{t}}h$ channel, and can serve as a proxy to determine the signal efficiency; similarly, the $\mathrm{t\bar{t}}$ background could be estimated by selecting events with similar topology as the signal, but with very low probabilities that there are more then two b jets. The best procedure to follow is currently under study.

6.3.5 $e^+e^- \to t\bar{t}$ at E_{CMS} = 500 GeV

The ILC provides an ideal environment to measure the couplings at the $\mathrm{t\bar{t}Z}$ and $\mathrm{t\bar{t}}\gamma$ vertex. The produced $\mathrm{t}(\bar{\mathrm{t}})$ quark decays almost exclusively into a bW pair. The b quark hadronises giving rise to a jet, while the W can either decay hadronically into light quarks, which turn into jets, or leptonically into a charged lepton and a neutrino. The semi-leptonic process is defined to be case where one W decays hadronically while the other one decays leptonically.

Analyses of both the semi-leptonic and the fully hadronic mode have been done[402]. The latter is the benchmark reaction from the LOI, and is presented in this section, while the former is discussed in Section 6.3.6.2.

6.3.5.1 Analysis of the fully hadronic decay

The top quark forward-backward asymmetry, $A_{\mathrm{FB}}^{\mathrm{t}}$, provides an important test of the SM. In the fully-hadronic channel the t and $\bar{\mathrm{t}}$ can be identified by tagging the $\mathrm{b}/\bar{\mathrm{b}}$ from the charge of the secondary vertex from charged b-hadron decays. This measurement provides a test of the vertex reconstruction capability of ILD.

The six-jet final state is reconstructed using the Durham jet finder, and the jets subsequently are analysed with LCFIPlus to assign b-tag values. The two jets with the highest b-tag are considered to be the jets from the b quarks, while events for which one of the b-tag values is smaller than 0.3 were rejected. The two W bosons were reconstructed from the remaining four jets. For each possible combination of W bosons and b-quarks, a χ^2 was formed comparing the reconstructed mass, energy and b-quark momentum with the expected values. The combination yielding the best χ^2 was selected. Events where the best χ^2 was too large, the di-jet mass of either W-candidate was far from m_{W}, or tri-jet mass of either t-candidate was far from m_{t} were rejected. For each of the two identified b-jets, the charge of the secondary vertices were reconstructed. Events with like-sign combinations were rejected as were events with two neutral secondary vertices. The efficiency to select fully hadronic $\mathrm{t\bar{t}}$ events was 13 %. Of the selected events, 60 % had the correctly identified top quark charge. Figure III-6.15 shows the distribution of the cosine of the reconstructed polar angle of the tagged top-quark, showing a clear forward-backward asymmetry. The relative numbers of events

in the forward and backward hemispheres, accounting for the charge identification/mis-identification probabilities, were used to determine $A^{\mathrm{t}}_{\mathrm{FB}} = 0.34$ for a left handed polarised electron beam and $A^{\mathrm{t}}_{\mathrm{FB}} = 0.44$ for a right handed polarised one. The errors of these quantities, corrected for the statistics expected at $\mathcal{P}_{-80,+30}$ and $\mathcal{P}_{+80,-30}$ beam polarisation, are 3.0% and 3.2%, respectively. The statistical and systematic errors have been added in quadrature; however the statistical ones largely dominates.

The measured asymmetry for left-handed electron beam polarisation, $A^{\mathrm{t}}_{\mathrm{FB}} = 0.344 \pm 0.011$, agrees well with the result presented in the LOI: $A^{\mathrm{t}}_{\mathrm{FB}} = 0.334 \pm 0.008$, taking into account that the LOI analysis was assuming twice the integrated luminosity. Further improvement of the result can be expected in the future since the charge determination is not yet optimised in the new LCFIPlus package.

6.3.6 Other physics processes

In this section, we present studies of physics channels that are not benchmarks, but nevertheless depend on the details of detector hardware, software and analysis and potentially might have changed substantially with respect to the LOI.

Many new analyses have indeed been performed since the LOI, and are presented in [403]. What is presented here are only those done with the updated event generator, with all backgrounds taken into account and with the full detector simulation model.

A new analysis of Higgs self-coupling was done and is presented in this section. It contains both a new analysis at $\sqrt{s} = 500$ GeV, and also an extended study what an ILC operating at 1 TeV would bring to our knowledge of the properties of the Higgs.

The $\mathrm{t\bar{t}}$ channel has been studied beyond the benchmark-measurement of A^{t}_{FB} from fully hadronic decays. The more precise measurement that can be done in the semi-leptonic channel has been carried out.

6.3.6.1 Higgs self-coupling.

The ILC running at 500 GeV and 1 TeV offers the opportunity to measure the Higgs trilinear self-coupling, which is very difficult to do at LHC if the Higgs mass is around 125 GeV [404, 405, 406, 407, 408]. It would be the first non-trivial test of the Higgs potential, crucial to understand the nature of Higgs' mechanism and the spontaneous breaking of electroweak symmetry. Many physics models beyond the Standard Model have been studied that show significant deviations of the Higgs self-coupling [409, 410, 411, 412, 413, 414, 415, 416, 417, 418, 419, 420, 421, 422]. Depending on

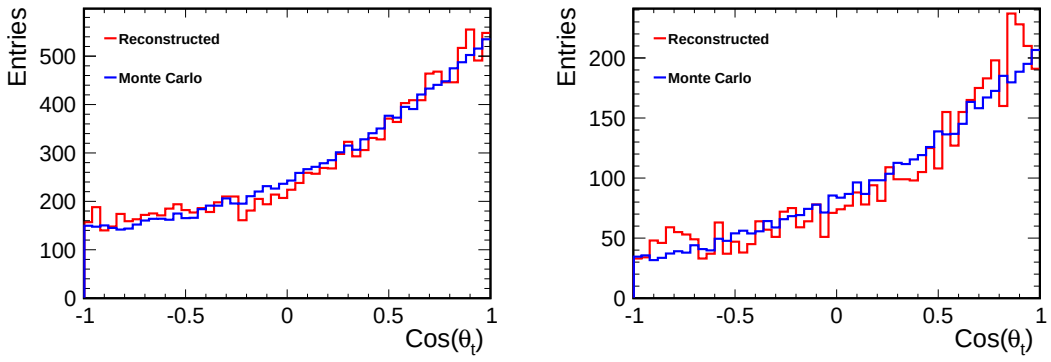

Figure III-6.15. Distribution of the true (blue curve) and reconstructed (red curve) polar angles of the identified top quark in fully-hadronic $\mathrm{t\bar{t}}$ events. The expected contributions from events with the wrong charge have been subtracted from the observed distribution. Left plot: $\mathcal{P}_{-100,+100}$; right plot: $\mathcal{P}_{+100,-100}$. Both plots assume $L = 250$ fb^{-1}.

the model, the deviations could be as large as 100%, but also as low as 10%. It is a great challenge to measure the Higgs self-coupling at the ILC, and it has been investigated by many groups over the years [423, 424, 425, 426, 427, 428, 429].

At ILC, the measurement of the trilinear Higgs self-coupling can be carried out through two leading processes shown in the Figure III-6.16: the Higgs-strahlung process $e^+e^- \to Zhh$ and the WW fusion process $e^+e^- \to \nu\bar{\nu}hh$ [430, 431, 432, 433, 434]. cross sections of these two processes are also shown in Figure III-6.16. The $e^+e^- \to Zhh$ process has its maximum cross section at around $\sqrt{s} = 500$ GeV and the WW fusion process becomes important at around $\sqrt{s} = 1$ TeV.

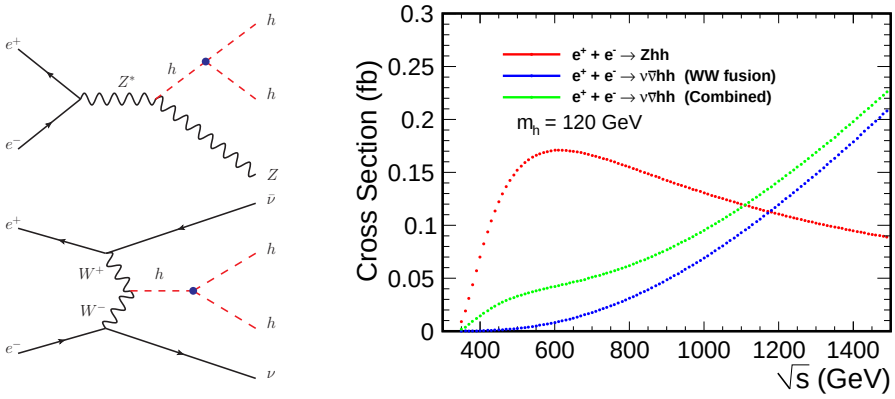

Figure III-6.16. Left: The Feynman diagrams involving the trilinear Higgs self-coupling for the two processes: $e^+e^- \to Zhh$ (top) and $e^+e^- \to \nu\bar{\nu}hh$ (bottom); Right: Cross section for these two processes as a function of $\sqrt{s}$ for m_h=120 GeV. The blue dotted line shows the cross section for $e^+e^- \to \nu\bar{\nu}hh$ from the WW fusion process alone, while the green dotted line shows the sum of the WW fusion contribution and the contribution from $e^+e^- \to Zhh \to \nu\bar{\nu}hh$.

In the absence of interfering diagrams, the relative uncertainty of the coupling of a given diagram is half the relative uncertainty of the measured cross section. However, in both the Higgs-strahlung and the WW fusion processes, there exist Feynman diagrams which have the same final state but that are not related to the Higgs self-coupling. These diagrams largely degrade the sensitivity of Higgs self-coupling to the cross section: For $e^+e^- \to Zhh$ at 500 GeV, the relation becomes $\delta\lambda/\lambda = 1.8\,\delta\sigma/\sigma$, while for $e^+e^- \to \nu\bar{\nu}hh$ at 1 TeV, it becomes $\delta\lambda/\lambda = 0.85\,\delta\sigma/\sigma$. This is illustrated in the Figure III-6.17 were the relation between σ and and λ is shown for the two cases. Recently, a weighting method has been developed [435]. It gives events where the observed invariant mass of the two Higgses is in the region where the self-coupling process is more important a higher weight and events in a region depleted of the self-coupling process a lower one. As can be seen comparing the slopes of the red and blue curves in Figure III-6.17, this method enhances the sensitivity of Higgs self-coupling, so that the factors become 1.66 and 0.76, respectively.

Figure III-6.17 The sensitivity of the Higgs self-coupling for the two processes: $e^+e^- \to Zhh$ (left) and $e^+e^- \to \nu\bar{\nu}hh$ (right). The red ones are without weighting and the blue ones are with the optimal weighting described in the reference [435].

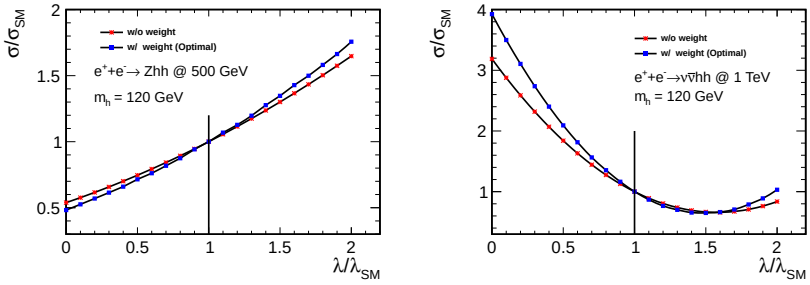

Based on the full detector simulation of ILD (see sect. 5.4), a new analysis of $e^+e^- \to Zhh$ at 500 GeV was performed considering all the decay modes of Z ($\ell^+\ell^-$, $\nu\bar{\nu}$, and $q\bar{q}$) and with both

Higgses decaying to $\mathrm{b\bar{b}}$. The analysis strategy is fully described in [436] and in [437]. Even with $\mathcal{P}_{-80,+30}$, the cross section of the signal process is still very small, $\sim$ 0.22 fb, so L= 2 ab^{-1} is assumed. The remaining numbers of signal and background events are summarised in Table III-6.6 for different search modes. The study shows that by combining all the modes with a likelihood ratio test, the expected $\mathrm{Z}hh$ excess significance is 5.0 σ and the cross section of $\mathrm{e^+e^-} \to \mathrm{Z}hh$ can be measured to the accuracy of 27%, corresponding to the precision of Higgs self-coupling of 44% [438], applying the weighting method in reference [435].

Table III-6.6. The numbers of the remaining signal and background events in each search mode of the $\mathrm{Z}hh$ analysis based on the full detector simulation at 500 GeV, with $\mathcal{P}_{-80,+30}$. The last two columns are $\mathrm{Z}hh$ excess significance (i) and cross section measurement significance (ii). The $\mathrm{q\bar{q}}hh$ mode is separated to two categories: (a) $\mathrm{b\bar{b}}hh$ dominant, (b) light $\mathrm{q\bar{q}}hh$ dominant.

Search Mode	Signal	Background	Significance (i)	Significance (ii)
$\mathrm{q\bar{q}}hh$ (a)	13.6	30.7	2.2σ	2.0σ
$\mathrm{q\bar{q}}hh$ (b)	18.8	90.6	1.9σ	1.8σ
$\nu\bar{\nu}hh$	8.5	7.9	2.5σ	2.1σ
$\mathrm{e^+e^-}hh$	3.7	4.3	1.5σ	1.1σ
$\mu^+\mu^-hh$	4.5	6.0	1.5σ	1.2σ

At 1 TeV, one expects a clearer signal, due to the larger contribution of WW fusion process, which has lower background, and has lower amount of interference from other double-Higgs diagrams compared to the Higgs-strahlung process. The process $\mathrm{e^+e^-} \to \nu\bar{\nu}hh$ at 1 TeV was studied with both Higgses decaying to $\mathrm{b\bar{b}}$. An initial study was based on the fast simulation framework SGV [439]. The analysis followed a strategy quite similar to the analysis at 500 GeV, and showed that indeed a precision on the Higgs self-coupling of $\sim$ 17 % is achievable with L = 2 ab^{-1} and $\mathcal{P}_{-80,+20}$[435]. Using the same strategy, a preliminary analysis using fully simulated ILD events confirms these results: It was found that 35.7 signal events were expected, with a background of 33.7 events. This yields expected uncertainties $\delta\sigma/\sigma$ = 23 % and $\delta\lambda/\lambda$ = 18 %, ie. a 5σ observation of Higgs self-coupling. It is also found that the statistical significance of the double-Higgs production excess is expected to be 7.2σ.

6.3.6.2 Further $\mathrm{t\bar{t}}$ studies

In the semi-leptonic mode, $\mathrm{t\bar{t}} \to (\mathrm{bW})(\mathrm{bW}) \to (\mathrm{bqq'})(\mathrm{b}\ell\nu)$, the charged lepton allows the determination of the W charge, and hence to separate t and $\bar{\mathrm{t}}$. At the same time, the hadronically decaying t allows to determine the direction of the t or $\bar{\mathrm{t}}$.

The isolated decay lepton was identified, and it was found that the decay lepton could be identified with an efficiency of 85%. The b jets among the remaining four jets were identified as those with the highest value of the b-tag from LCFIPlus, while the two remaining jets were associated with the W. The b jet to combine with the two jets from the W to form the t system was decided by the choice giving the total 3-jet mass closest to m_{t}. It has to be noted however that the final state gives rise to ambiguities in the correct association of the b quarks to the W bosons, see [440] for an explanation. These ambiguities affect mainly the reconstruction in case of a left handed electron beam. The ambiguities can be nearly eliminated by requiring a high quality of the event reconstruction. The control of the ambiguities however requires an excellent detector performance and event reconstruction. The signal selection efficiency was 27.6% in case of a left handed electron beam and 56.5% in case of a right handed electron beam The resulting spectrum of the polar angle of the t quark is shown in Figure III-6.18 (left). From this spectrum, one could determine forward-backward asymmetry: $A_{\mathrm{FB}}^{\mathrm{t}} = 0.36$ for a left handed polarised electron beam and $A_{\mathrm{FB}}^{\mathrm{t}} = 0.41$ for a right handed polarised electron beam. The statistical precision on these quantities is 1.7% and 1.3%, respectively.

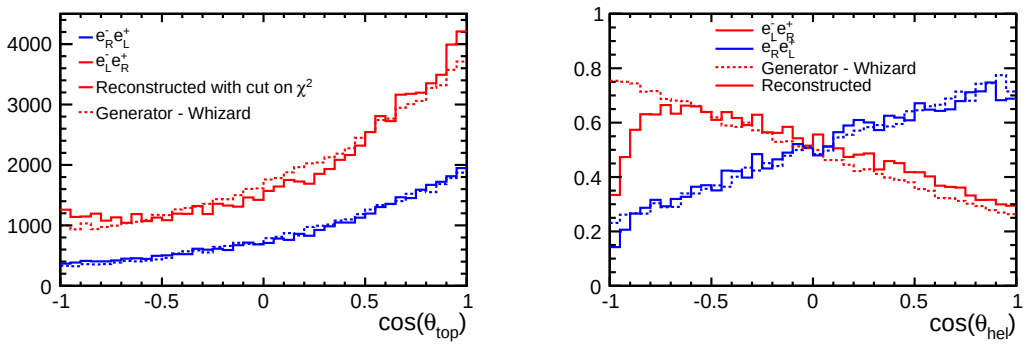

Figure III-6.18. Left: Reconstruction of the direction of the t quark for two different beam polarisations. The plot shown is an update of the one presented in [440]. Note that the figure does not include background, however, it is known from the studies in [387] that the background is negligible. Right: Generated and reconstructed distribution of the helicity angle $\cos\theta_{hel}$.

Measurements using optimised observables are investigated in [441]. These observables are the top pair production cross section for left and right-handed polarised beams and the fraction of right-handed (t_R) and left handed top quarks (t_L). Following [442], the fraction of t_L and t_R can be determined with the slope of the helicity asymmetry (λ_t). In the top quark rest frame the distribution of the polar angle θ_{hel} of a decay lepton is

$$\frac{1}{\Gamma}\frac{d\Gamma}{d\cos\theta_{hel}} = \frac{1+\lambda_\mathrm{t}\cos\theta_{hel}}{2}$$

where λ_t varies between $+1$ and -1 depending on the fraction of t_R and t_L. The observable $\cos\theta_{hel}$ can easily be measured at the ILC, and is less sensitive to ambiguities in the event reconstruction than eg. A^t_FB. The slope of the differential cross section wrt. $\cos\theta_{hel}$ directly measures λ_t, and hence the net polarisation of a top quark sample. The result of a full simulation study is shown in Figure III-6.18 (right), where it can be seen that parton-level spectrum is only slightly distorted by hadronisation and detector effects. The remaining discrepancies in case of left handed electron beams can be explained by reconstruction inefficiencies for low energetic final state leptons. By fitting the slopes in the interval $-0.6 < \cos\theta_{hel} < 0,9$, the helicity asymmetry could be determined: $\lambda_\mathrm{t} = -0.48$ (left-hand polarised electron beam) and $\lambda_\mathrm{t} = +0.51$ (right-hand polarised electron beam). The errors of these quantities are 3.3% and 3.7%, respectively. Statistical and systematic contributions have been added in quadrature. Note that for λ_t and A^t_FB, the dominant systematic error is expected to come from the ambiguities discussed above. The role of theory errors will have to be evaluated in the future.

Chapter 7
ILD Costs

In this chapter an estimate of the cost of the ILD detector concept is presented. The costs shown are essentially the construction costs. Person-power needed has not been studied with the same level of detail, and only a very rough estimate is presented in section 7.3.7. The costing is an evolution of the one presented in the letter of intent for ILD [198] but has been significantly further developed and detailed. A major difference is that many of the costs are now based on experience gained with actual prototypes. The basis of the costing form the work breakdown structures for the different sub-detectors (WBS) which have been developed to include the materials, the fabrication process, the assembly and the commissioning. In this chapter abbreviated versions of the WBS are shown, to describe the main cost components.

What has been costed is the baseline ILD detector including the different options. Where costs of the different options are very different a mean price and a range is quoted. In the second part of the chapter the scaling of the main component is discussed, to provide the material for a cost - performance optimization. It can be expected that many of the costs quoted will change significantly once serious industrialisation studies are undertaken.

7.1 Methodology of costing

The method used by ILD is based on the methodology developed for the accelerator parts of the TDR, and is very similar to the one which was used for the RDR [443]. An attempt has been made to use for major components unit costs common with SiD and CLIC [444] detectors, as shown in Table III-7.1.

Table III-7.1 Unit costs agreed to by SiD, ILD, and CLIC [444].

	agreed unit cost [ILCU]	agreed error margin [ILCU]
Tungsten for HCAL	105/kg	45/kg
Tungsten for ECAL	180/kg	75/ kg
Steel for Yoke (raw material)	1000/t	300/t
Stainless Steel for HCAL	4500/t	1000/t
Silicon Detector	6/cm^2	3/cm^2

It should be noted that these common costs can only serve as a guideline, as the detailed costs depend on many factors. The ILD estimate has started from the costs in the table, and has adjusted them if needed to take into account specific ILD circumstances. A particularly important example is the cost for the silicon sensor. For the ECAL a careful study with industry has revealed scope for significant savings, as will be discussed below, considering the very special application in the ECAL. This has been taken into account.

It is obvious that the costs quoted have a large uncertainty. In particular raw material costs - which for some part like e.g. the yoke are quite important - vary widely and might change significantly with time.

A major difference compared to the previous cost estimate is that many numbers are based on actual prototyping work. From this work a detailed description of the fabrication and assembly sequences including tests and tooling is known, which can be extrapolated to the full detector, and a first approximation of the item prices are available, in some instances with quantities still far from the final numbers needed but nevertheless significant (for example 400k channels for the sDHCAL). Where possible, estimates of the testing and commissioning costs are included.

An engineering study of the integration of the ILD detector has been done, as it is documented in chapter 5.1. Proper integration will also require tools and special setups which have been wherever possible included in the estimate. It should be noted that these costs might be very site-dependent.

Costs for the ILD detector estimated in different currencies are converted into ILCU using the Purchase Power Parity (PPP) system. The conversion factor is based on the actual costs of a defined set of items, rather than the currency conversion rate at some point in time. For the purpose of this document the PPP rates shown in Table III-7.2 have been used.

Table III-7.2
Conversion rate based on purchase power parity used in the cost estimate.

currency	Dollar	Euro	Yen
ILCU	1	0.9732	127.3

The results should nevertheless be treated with care. In some cases where the cost estimates are based on concrete offers, or have been obtained based on previous experiments, the input numbers might already include implicit currency conversions. Wherever possible or known, these effects have been unfolded, to obtain consistent results.

No attempt was made to guess the impact of future escalation. Contingencies are currently not taken explicitly into account, but some estimates based on real fabrications include them implicitly, for example for the coil. Spares were accounted for only for construction, not for maintenance. No R&D costs are included, except in some cases costs for industrialisation. No maintenance and operations costs has been estimated.

7.2 ILD work breakdown structure

A condensed WBS for the different sub-systems can be found in the following section together with comments and remarks on the way costs were determined. The following items were estimated for the sub-systems:

- the procurements of materials including costs for testing,
- the procurements of the sensors including costs for testing,
- the procurements of the front-end electronics,
- the cost of needed assembly and the needed tooling,
- the cost of the local data-acquisition,
- some estimate of the transportation costs, though this is very imprecise given that the location of the experiment is not yet known,
- the costs for assembly on site, including costs for tooling,
- the costs for services.

7.3 ILD cost evaluation

The different sub-detectors for ILD have reached different levels of maturity, which is clearly reflected in the cost estimate. Not in all cases extensive production and industrialisation studies have been done, nor are for all system tooling costs etc well known. However for the most expensive parts of ILD, in particular the calorimeter and the yoke, such studies are available at least at a preliminary level.

The building of prototypes has often provided a starting value for the procurements, though of course for smaller numbers than what will eventually be needed. Thus scaling factors have been applied to reduce the actually quoted prices, after discussions with suppliers, which reflect the current best knowledge about costs at the time of ordering large quantities.

To provide the cost of operations and related tooling, an estimate of the fabrication is needed. Again the prototype construction provides valuable input to this.

The descriptions accompanying each sub-detector should provide enough detail to the reader to understand the limits of the relevant cost estimate. A summary table at the end will put all this into a global perspective.

7.3.1 Vertex detector

The vertex detector exists in 3 versions. They differ essentially by the sensors and the read-out electronics. The cost of the mechanical installation and services has been taken to be identical. It is based on the cost of the STAR vertex detector, which is constructed using the same technology as proposed for the ILD CMOS option.

For the CMOS version the sensor price comes from the STAR experiment and the electronics from the Mimosa prototypes, for the FPCCD the information comes from prototypes, and for the DEPFET version it comes from the Belle II experiment. For the different options the cost vary between 3.2 MILCU and 4.2 MILCU. The value used for the ILD cost estimate is 3.4 MILCU.

7.3.2 Silicon tracking

The silicon tracking contains four disks with pixels, close to the vertex detector, 12 forward disks with strips, two cylinders of strip detectors of the SIT and the outer tracking, all made with the same strip technology. Experience from the LHC experiments has played an important role in the cost estimate. The cost of the readout ASICS is based on current 130 nm technology; after the conversion to the new 65 nm technology these costs might change. The cost for the inner Silicon system (SIT and FTD) together is estimates to be 2.3 MILCU, for the outer Silicon susyem (SET and ETD) 21 MILCU.

7.3.3 Time Projection Chamber

The estimate of the TPC price comes largely from the prices found in the construction of the STAR and ALICE TPCs. It has been updated for inflation but does not contain any added contingency. The cost of the field cage includes the experience from the construction of the large prototype, which was built in industry, using technology similar to the one to be used for a full scale field cage. A significant part of the TPC cost will be in the readout electronics, estimated to be around 30% of the total cost. The field cage - the iner cylinder, the outer cylinder, and the endplates, will account for around 20% of the cost, the rest being in tooling, anciliary systems and control systems. The total cost of the detector is estimated to be 35.9 MILCU.

7.3.4 Calorimeter System

The calorimeter system is a major part of the ILD detector, and one of the largest single cost items. In Table III-7.3 costs for major components are shown, with their current (prototype) costs, and the anticipated costs for the full detector construction. The cost of the tungsten used is based on the agreed value but translated back into the original currency (EUR) and the re-converted into ILCU using the PPP scheme.

Table III-7.3 Expected prices for major components in the calorimeters, see text for further comments. Except where explicitly stated all current costs are based on actual costs of components procured for the prototypes.

Material	Cost [ILCU]	System	Comment
Tungsten	123/kg	SiECAL, ScECAL, AHCAL, FCAL	quote from manufacturer (130 EUR/kg)
Stainless Steel	5/kg	AHCAL, SDHCAL	processing costs to be added (1-4 EUR/ kg)
Si sensors	3/cm^2	SiECAL	based on extrapolation of current quotation of 5 EUR/ cm^2
SiPM	1/pc	ScECAL, AHCAL, muon	based on manufacturer extrapolation, current price 7-10 EUR/piece
ASIC	0.22-0.25/ch	SiECAL, ScECAL, AHCAL	current price 0.5 EUR/ch
ASIC	0.1/ch	SDHCAL	current price of 0.18 EUR/ch
PCB	7900/m^2	SiECAL	prototype
PCB	2600/m^2	ScECAL	extrapolated from prototype price of 10800/m^2
PCB	1800/m^2	SDHCAL, AHCAL	for AHCAL extrapolated from prototype price of 10800/m^2

For the Silicon Tungsten ECAL a very complete and careful study has been performed to build and understand the WBS. Studies with industry have been undertaken to understand the costs of the major components: Tungsten plates, silicon sensors, and readout boards. The costing table for the electromagnetic calorimeter is shown in Table III-7.4. It should be noted however that this represents a snapshot, and that significant room for further optimization of these costs exist.

Table III-7.4 Cost table of the electromagnetic calorimeter.

SiECAL		ScECAL	
Item	Cost [kILCU]	Item	Cost [kILCU]
Tungsten	16310	Tungsten + carbon parts	18500
Carbon fiber structure	2130	Module realisation	1700
Silicon sensors	75000	Scintillators	1030
Readout ASIC	16500	Photo Detectors	10200
Readout Board	21000	Readout ASIC	2500
Materials	1300	Readout Board	25000
Cables, connectors	2220	Readout System	6200
Tooling	9300	Cables, connectors	1000
Assembly	13500	Power supplies	4100
Integration	500	Tooling	3800
Sum SiECAL	157760	Sum ScECAL	74000

A major cost item for the SiECAL is the cost of the silicon wafers. The quoted number corresponds

to a cost of 3 ILCU/cm^2. This estimate is based on a current cost of $5-6$ ILCU /cm^2 in 2011. Since then careful studies have resulted in a much increased production efficiency, which led to a reduction of this price by about a factor of 2, to 3 ILCU/cm^2. This price can be so low because the structures for the SiECAl are comparativly simple, and the requirements on the rate of dead pixels and the acceptable leakage current can be relaxed compared to other silicon based detectors. A further reduction of the price is not excluded.

For the Scintillator based option of the electromagnetic calorimeter the silicon based photon detectors are a major expense. Quotes have been obtained from industrial suppliers for the large number of detectors needed for the complete system. Current small scale production runs result in prices per detector of around 10 EUR, but it seems realistic to expect that a reduction to a level of 1 EUR/ channel can be realised. The assembly procedures for the scintillator ECAL are not yet as well understood as for the Si based ECAL. At the moment no estimate of the assembly cost for the scintillator planes is included in the cost estimate.

Figure III-7.1
Beginning of the full silicon tungsten electromagnetic calorimeter WBS.

3		2.1	Electromagnetic Calorimeter								
4		2.1.1	General procurement (Barrel + endcaps?)								
5	1		2.1.1.1	Mechanical structures							
6	2			2.1.1.1.1	W						
7	3					barrel					
8	4						Material		90.3	ton			Industry Several supplier
9	5						Dimensional inspection		24000	plates	3D measurement system	HOME/Industry
10	6					endcaps						
11	7						Material		42	ton			IndustrySeveral suppliers
12	8						Dimensional inspection		12000	plates	3D measurement system	HOME/Industry
13	9			2.1.1.1.2	Carbon fibers prepeg							
14	10					K (H structure)			8600	m^2			Industry
15	11					3K (Modules)			19000	m^2			Industry
16	12					Carbon plates(modules) 12 K						
17	13						Th. :2mm	BARREL	40	plates			Industry
18	14						Th. :15 mm	BARREL	40	plates			Industry
19	15						Th. :2mm	ENDCAPS	24	m^2			Industry
20	16						Th. :15 mm	Endcaps	24	m^2			Industry
21	17			2.1.1.1.3	Metal inserts				1728	inserts			Industry
22	18			2.1.1.1.4	Rails				80	rails			Industry
23	19		2.1.1.2	Detector								
24	20			2.1.1.2.1	Wafers		processed		308800				Industry several suppliers
25	21			2.1.1.2.2	ASIC				1235200				Industry
26	22			2.1.1.2.3	PCB				75500				Industry
27	23			2.1.1.2.4	Boards							
28	24					DC/DC converters			400			
29	25					Data Concentrator			440			
30	26					GDCC			140			
31	27			2.1.1.2.5	other elect. Components							
32	28					Active						
33	29					passive						

The hadronic calorimeter has been costed in both options, the analogue(AHCAL) and the semi-digital option (SDHCAL). The main cost items for both versions are shown in Table III-7.5. For both AHCAL and SDHCAL significant prototypes have been built, which provide important information for the cost estimate. For the AHCAL the same cost of 1 ILCU/ piece is used for the SiPM as for the ScECAL version discussed above. More detailed work has been done for both options for the barrel part of the calorimeter. The cost of the end-caps has been estimated based on the sensitive area and the total system weight. A significant part of the cost is the readout boards, which are for both options complex large multi layer printed circuit boards. The quoted prices are based on several independent quotes and on actual experience with the prototypes.

In the very forward region two small calorimeter systems close the coverage, LumiCal, BeamCal. LumiCal and BeamCal have been carefully studied and costed. A major cost item are the sensors, which are based on silicon and diamond technology. In total a cost of 8.05 MILCU is estimated. Note that ILD discusses the possibilty to add a third system in the forward direction, LHCAL, for which however no detailed design and thus no cost estimate exists at the moment.

7.3.5 Magnet

The magnet system has three major components, the coil, the iron return yoke, and the ancillaries. For the coil, CMS has been used as a "prototype", the complete actual CMS fabrication chart has been revisited for ILD, taking into account the change in dimensions, the variations in technology and assembly, and the cost escalation since the building of CMS. The cost of the ancillaries is also derived directly from CMS.

For the yoke, the weight has been estimated and the agreed upon price for machined and assembled iron (see Table III-7.1) has been used. The estimate is based on a fairly detailed engineering

Table III-7.5
Cost breakdown for the two HCAL options AHCAL and SDHCAL.

AHCAL		SDHCAL	
Item	Cost [kILCU]	Item	Cost [kILCU]
Absorber	5200	Absorber	6500
Module production	3400	Module mechanics	2300
Cassettes	2100		
Scintillators	1500	RPC incl cassettes	6800
Reflective Foil	1200		
Photo sensors	7700		
ASIC	1800	ASIC	6600
Readout Board	13200	Readout Board	13000
Readout	2300	Readout	2000
Cabling, connections	1000	Elec Integration	1600
HV/ LV supplies	1000	Services incl. HV/ LV	200
Cooling system	1000	Cooling System	1000
		Gas System	900
Tooling, testing	500	Testing	200
Assembly, installation	2800	Assembly, tooling	3900
DAQ	200		incl.
Sum AHCAL	44900	Sum SDHCAL	44800

model, including assembly procedures. The yoke iron is a large item of the total cost. This is driven not by requirements from physics but results from the request to control the stray field outside of the ILD detector to a level of 50 G at 15 m distance from the detector [354].

The cost of the coil is based on the information from CMS obtained from CERN. Since this information is given in CHF, most of the components however are sourced in the EUR area, the cost estimate has been converted into EUR based on a sensible currency exchange rate of 1.5, before translated into ILCU using the PPP scheme.

Table III-7.6
Cost table of the coil and the iron yoke.

Item	Cost [kILCU]	Item	Cost [kILCU]
Coil		**Yoke**	
Conductor and winding	12900	Steel, including machining	80400
Internal Cryogenics	1000	Support	1700
Suspension system	560	Moving System	3500
tooling, assembly	10000	Assembly	6700
Qualification, testing	1100	Survey	500
Ancillaries			
Cryogenics, vacuum	6800	Integration	933
Electrical installation	1700	Field Mapping	560
Control and Safety system	350	Engineering	2200
Sum	131000		

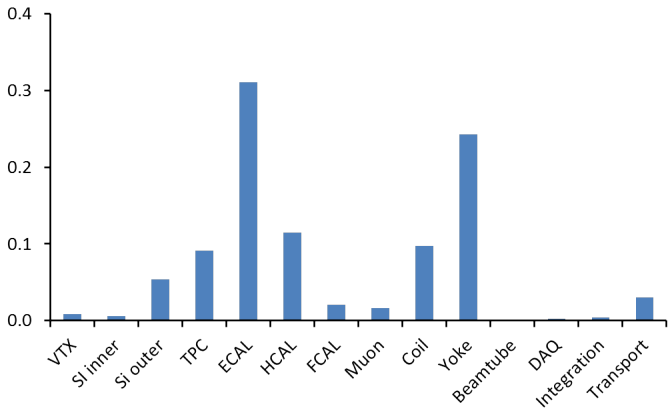

Figure III-7.2
Summary plot of the relative contribution by the different sub-components to the total cost of the ILD detector.

7.3.6 Muon system

The muon system being made of scintillator read out with SiPM like the AHCAL, the costs have been derived from there. It corresponds mostly to the procurements of materials without assembly and tooling. The cost is dominated by the costs if the sensor system. In total 6.5 MILCU is estimated.

7.3.7 Cost summary

The total cost of the ILD detector is summarised in Table III-7.7. The distribution of the costs among the different systems is shown in Figure III-7.2.

Table III-7.7
Summary table of the cost estimate of the ILD detector. Depending on the options used the cost range is between 336 Mio ILCU and 421 Mio ILCU.

System	Option	Cost [MILCU]	Mean Cost [MILCU]
Vertex			3.4
Silicon tracking	inner	2.3	2.3
Silicon tracking	outer	21.0	21.0
TPC		35.9	35.9
ECAL			116.9
	SiECAL	157.7	
	ScECAL	74.0	
HCAL			44.9
	AHCAL	44.9	
	SDHCAL	44.8	
FCAL		8.1	8.1
Muon		6.5	6.5
Coil, incl anciliaries		38.0	38.0
Yoke		95.0	95.0
Beamtube		0.5	0.5
Global DAQ		1.1	1.1
Integration		1.5	1.5
Global Transportation		12.0	12.0
Sum ILD			391.8

The cost driving items are the yoke, and the calorimeter system. The cost for the integration is an estimate of the scenario described in section 5.1, and might vary significantly with different scenarios. It includes the extra cost for the large platform (see chapter 5.5.1) on which the detectors moves, as well as the extra costs of the cryogenics needed to allow a cold move of the detector. The offline computing represents a significant cost. Owing to the continued large advances in computing technology, we have estimated this at 20% of the equivalent cost for a LHC detector.

A first estimate of the person-power needed has been done. For each calorimeter it is estimate to be around 200 MY, for the coil, 500 MY. From this the total person-power needed is extrapolated to

be around 1400 MY. The average cost per MY has been taken to be 93 kILCU including overheads. This value is typical for the mix of qualifications needed for a sophisticated project like the ILD. The estimate only includes the person-power needed to build the detector, and does not include needs to finish the R&D or work out a detailed design of the detector. The person-power is then estimated 130 MILCU.

The study has been carried out assuming that the detector is in a push-pull configuration. Most of the sub-system costs are only marginally affected by this assumption, with the exception of the yoke cost and the integration costs, as discussed above. It has been estimated that without these requirements the total cost of the detector might be reduced by some 10%.

7.4 Detector cost dependencies

The ILD detector as presented in this document has been strongly driven by the physics requirements. At this moment no complete cost - performance optimisation has taken place. With the information known now and available based on real prototyping experience such an overall optimisation can be performed. In this section the dependence of the main cost items on input assumptions are discussed.

The parameters which have been considered for possible scalings are the following:

- a characteristic transverse size of the detector chosen as the inner radius of the ECAL barrel;
- a characteristic longitudinal size of the detector chosen as the length of the ECAL barrel or TPC;
- the number of samples for the ECAL (for a given number of radiation lengths);
- the calorimeter cell sizes.

The study was done under the assumption that the technologies remain the same. This then results in typical cost changes below 25% of the system cost. More significant cost changes imply changes in the technologies.

7.4.1 Scaling with the field

The nominal magnetic field is 3.5 T, but the magnet is designed to withstand 4 T. Reducing the field below 3.5 T might offer some cost savings, but also results in a loss of the physics potential of the detector, inparticular its upgradability to higher energies. ILD therefore does not consider this option of de-scoping.

7.4.2 Scaling the detector size

The dimensions of the detector parts inside the TPC are dictated by considerations of background and assembly procedures. They are not very relevant for costing. Most relevant for the costing is the inner radius of the coil, and the inner radius of the calorimeter system. Another important consideration is the length of the TPC, as this drives the length of the calorimeter system and the coil and the Yoke.

The cost scaling has been studied under two scenarios: the aspect ratio of the detector remains constant, with corresponding correlated changes of radius and length, or the radius alone is changed. In Figure III-7.3 the cost impact when only changing the outer radius of the TPC is shown, on the left are the effects on sub-components, on the right the global effect is shown.

7.4.3 Changing the ECAL

The scaling of the number of ECAL readout layers has been done under the assumption that the total number of radiation lengths in the ECAL is kept constant. The area of sensitive medium and the number of readout channels then scale proportional to the number of samplings. On the other hand as the total amount of radiator does not change, the thickness of the absorber plates changes and the cost for manufacturing the plates varies. Reducing the number of samples will reduce the overall thickness of the ECAL even when the total amount of absorber material stays constant. For

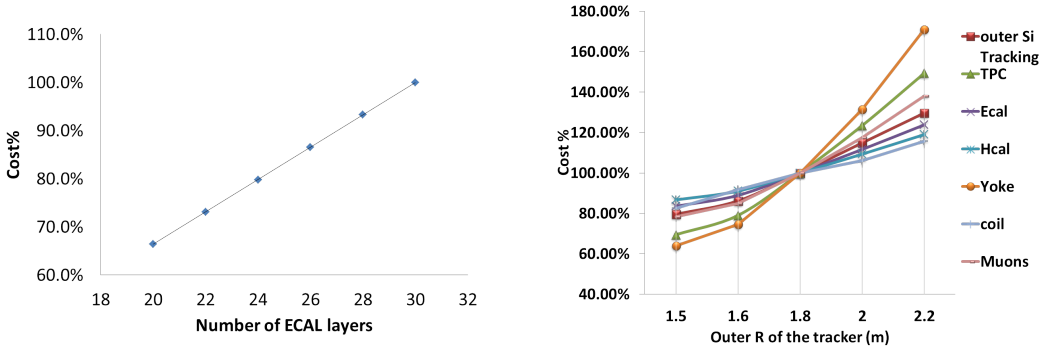

Figure III-7.3. Left: Dependence of the SiECAL cost on the number of sensitive layers. (right) Scaling of the cost of the ILD dector if the transverse size is changed, split into relative cost changes for the different sub-detectors.

example, going from 30 to 20 samples will reduce the radial thickness by 20 mm. This space in turn can be used to reduce the constraints on the sensitive part in particular on the PCB. All this together makes the scaling essentially proportional to the area and then to the sampling.

The cell sizes of the electromagnetic calorimeter cannot be easily reduced any further with the current technological solution. To go below, a new design, may be a totally different approach will be needed. Increasing the cell sizes within the same technology will have only a minor impact on the cost, as the cost roughly scales with the area of silicon, not so much the number of readout channels. There is some effect due to a different cost of the printed circuit boards and other ancillary equipment. We estimate that reducing the number of cells by an order of magnitude reduces the cost of the ECAL by less than 10%, or 3% of the total detector cost. The impact on the cost for the scintillator version may be larger but it is unlikely that scaling up the size in this version would be considered.

7.4.4 Scaling the hadronic cell size

For the hadronic calorimeter changing the cell sizes will result in a changed number of FE chips, calibration devices etc. We estimate that a reduction of the number of readout channels by an order of magnitude reduces the cost of the digital HCAL by about 20%, of the analogue HCAL by about 10%. This has to be balanced with a significant performance loss.

7.5 Conclusion

The cost of the ILD detector has been estimated to be about 400 MILCU. It includes the material to build the detector, but does not include cost escalation and contingencies. Person-power is with few exceptions not included. The dependence of the cost on the main detector parameters has been studied, and effects of order 10% or less per item on the total detector cost have been found. To illustrate the possibilities, a cost reduction of 20% can be reached by reducing the inner radius of the ECAL to 150 cm, without changing the length. The quoted cost of the ILD detector is comparable to the total cost of the large LHC detectors.

Chapter 8
ILD Summary

The ILD detector concept as presented in this document has been developed over a number of years. It is the result of the work of a large group of people from around the world. The design has matured over the last few years to a point where a realistic proposal for a detector has been made. The concept has undergone a careful optimization and validation using detailed simulation studies.

A key difference between this document and the Letter of Intent, published in 2009, is that essentially all technologies proposed as part of the ILD concept have been experimentally validated. ILD has worked very closely with R&D groups on different topics to proposed, develop and validate technologies. As elaborated in this document, significant progress has been achieved in many areas, and the ILD concept is technologically now on a very sound basis.

The evaluation of the anticipated performance of the ILD concept has been done using full and detailed simulation. Great care has been taken to include to the best of the current knowledge imperfections in the detectors, dead zones, dead material and the like. With this the level of realism in the simulation was significantly increased. In key areas - for example the particle flow performance - some key experiments have been done which demonstrate that the simulation indeed correctly describes the data. Thus not only the realism but also the reliability of the ILD simulation could be improved and demonstrated.

In the progress of the experimental validation of the different technologies significant prototypes of the main detector components have been designed and built. This is in particular the case for the calorimeters and key parts of the tracker. In doing so not only the performance of these components was studied but also significant experience was gained on the cost of these modules. Some of these prototypes included many 10s of thousands of channels thus approaching a level where true mass production of components is needed. The experience gained in this process entered into the way a cost estimate of the final detector has been developed. Nevertheless caution is advised when interpreting these numbers, as many of the cost factors are difficult to extrapolate many years into the future, and thus the final price is subject to significant uncertainties.

It has been the policy of the ILD concept group to propose a detector which is technically feasible, and which includes only minimal extrapolations from current levels of technology. In many cases more than one technology meets these requirements and are proposed as options for different subsystems. The ILD concept group intentionally does not want to take technological decisions at this stage, at a time where the ILC project is still not approved, to not block the way for more modern technologies yet to come, or to support future improvements of current technologies. While this makes the definition of a baseline ILD detector at this moment difficult, it keeps the options for ILD open to either improve performance even further, or to reduce cost.

Once the ILC project becomes reality ILD is prepared to rather quickly initiate a process to finalise a technology selection. Based on the large body of experience and a well functioning cooperation with the major R&D groups this selection should be driven by the scientific needs of the project, and

the realities of funding as they exist at the time of the decision taking.

Until then the ILD concept group intends to continue to improve the detector design, push further on the development of technologies, and study the integration of the different subdetectors into one coherent detector.

Volume 4

Detectors

Part IV

Summary and Future Plans

On July 4, 2012, the ATLAS and CMS Collaborations announced the discovery of a particle resulting from the search at the LHC for the Standard Model Higgs Boson. This newly discovered boson has a mass of 125-126 GeV and the early measurements, albeit of limited precision, are consistent with the Standard Model Higgs Boson. The clearest evidence comes from the gamma-gamma and Z-Z channels; after the 2012 data is fully analysed the nature will be better known. The discovery immediately increases the relevance and interest in the ILC, since the ILC offers precision measurements of the new boson's properties when operating near the Higgs-strahlung threshold, between 215 and 250 GeV.

In addition to the important studies of this new Higgs Boson candidate an ILC capable of also operating at the top threshold at 350 GeV provides crucial precision in the study of top quark properties. ILC top quark measurements would far surpass the precision of those of the LHC. Among the top measurements the ILC would make is the precise top mass at threshold, of relevance to the interest in the question of vacuum stability. The ILC and the ILC detectors have been designed specifically to exploit this opportunity and they are now ready to do so.

Over the past few years many studies have been conducted toward the realisation of an experimental program at the International Linear Collider (ILC). These have ranged from phenomenological studies on the physics potential of the ILC to the pre-engineering designs of detectors. Beginning with a call for Letters of Intent (LOIs) in 2007, a large global community has marshalled resources and effort to achieve significant progress, which is described in the preceding parts.

The physics requirements for the ILC detectors are demanding. Two detector design groups, ILD and SiD, have independently developed concepts based on complementary strategies and technologies. They have demonstrated the capability to realise the unprecedented resolutions in impact parameter, charged particle momentum, and jet energies demanded by the ILC physics program. Advances in the state of the art of detector technology operating in the clean environment offered by the electron-positron collisions make these capabilities possible. Both detector designs employ calorimetry based on the particle flow algorithm (PFA), with full detector information utilised to reconstruct quark jets. The two detector designs adopt different approaches to achieve excellent PFA performance: SiD chooses a compact design enabling finer granularity of calorimeters in a cost-constrained environment, while ILD chooses to enable larger particle separation with a larger detector.

The two detector concepts have been studied through detailed and realistic simulation codes. While collaborating closely with theorists, the capabilities of the ILC detectors to study many physics topics have been evaluated using these simulation tools. The results of these studies are summarised in the physics and detector sections, clearly demonstrating that the detector designs can realise the physics potential of the ILC.

The detector R&Ds have been conducted by international collaborative groups, working closely with the detector design teams to formulate the two detector designs. In some cases, these detector R&D groups extend their applications beyond the ILC, e.g. to CLIC and the B-factory upgrade. In particular, close collaborations exist between the ILC and CLIC detector efforts both in hardware and

software. These collaborations allowed effective use of limited resources.

The detector groups also have worked in close collaboration with the GDE accelerator team, especially on MDI issues and in guiding the choice of machine parameters to ensure good physics performance for the ILC. The ILC Research Directorate has fostered and coordinated these collaborations, such as with the design of the push-pull system and the SB2009 working group. The design of the push-pull system required closely cooperation of the relevant detector and accelerator experts. The SB2009 common task group worked closely with the accelerator team to optimise ILC machine parameters for lowered cost and power consumption while protecting the physics performance.

The details contained here are meant to provide a reference on the progress that has been achieved, working in parallel with the GDE's effort toward a TDR on the collider. It should be a valuable resource for future project planning, demonstrating that efforts can move forward with confidence that the designs can successfully pursue the important physics goals of the ILC.

When the ILC project is realised, these detectors can be built with the technologies that have been developed and described in this document. Their performances have been verified with realistic and detailed detector configurations. However, engineering design for construction remains to be done. The call for LOIs did not require commitment of detector concept groups to actually build the detectors. Even though many advances have been achieved, the detector designs are still mostly conceptual. As the project approaches reality, detailed engineering designs will be needed and, once it is possible, these must be adapted to the selected site.

While optimisation possibilities remain, calling for future R&D efforts, the maturity of the detector R&D justifies increased engineering studies at this point. Each subsystem of each detector design can be further optimised for performance and cost through such engineering studies. In any case, significant work remains to bring the technical designs to the level of construction readiness of the collider.

An era in the preparation for the ILC has passed. The 2012 discovery of a Higgs Boson candidate at the LHC makes the project even more compelling. The detector R&D and detector design efforts have reached a significant level of maturity. Everyone involved wants the ILC to be realised in the near term so its scientific program can commence with studies of the 125-126 GeV Higgs-like boson.

Volume 4

Detectors

Part V

Appendices

Bibliography

[1] H. Baer *et al.*, "ILC, Technical Design Report - Volume 1, Physics at the International Linear Collider".

[2] P. Chen, T. Barklow, and M. E. Peskin, "Beamstrahlung and minijet background from gamma gamma collisions in linear colliders" *Conf.Proc.* **C930426** (1993) 590–595. SLAC-REPRINT-1993-031.

[3] **WWS Software Panel**, T. Behnke, N. Graf, and A. Miyamoto, "Benchmark reactions for the ILC LoI". http://ilcdoc.linearcollider.org/record/14681/files/Benchmark_Reactions_for_the_ILC_LOI.pdf. ILC-MEMO-2008-001.

[4] M. Battaglia, T. Barklow, M. Peskin, Y. Okada, and P. Zerwas, "Physics Benchmarks for the ILC detectors".

[5] **ILC PEB Benchmarks Task Force**, T. Barklow, M. Berggren, K. Fujii, N. Graf, A. Miyamoto, M. Peskin, F. Richard, and G. Weiglein, "Detector Benchmarking for the 2012 DBD".

[6] **The International Linear Collider Steering Committee**. http://www.fnal.gov/directorate/icfa/International_ILCSC.html.

[7] **ILC physics and detector**, "International linear collider physics and detectors, *2011 status report*" *ISBN 978-3-935702-61-4* , ILC-REPORT-2011-033, CERN-LCD-Note-2011-038, DESY 2011-190, FERMILAB-FN-0936-PPD, KEK Report 2011-5, LAL 11-246, SLAC-R-973.

[8] **ILC, call for Letter of Intend**. http://ilcdoc.linearcollider.org/record/15684/files/CallForLOI.pdf.

[9] **The World Wide Study**. http://physics.uoregon.edu/~lc/wwstudy/.

[10] **The ILC Research Directorate for physics and detectors**. http://www.linearcollider.org/physics-detectors.

[11] **LoI of the ILD group**. http://ilcild.org/documents/ild-letter-of-intent/LOI%20Feb2010.pdf/.

[12] **LoI of the SiD group**. http://silicondetector.org/download/attachments/46176132/SilicondetectorLetterOfIntent.pdf/.

[13] **LOI of the Fourth group**. http://www.4thconcept.org/4LoI.pdf.

[14] **IDAG detector concept validation**. http://ilcdoc.linearcollider.org/record/23970/files/IDAGreport090816.pdf.

[15] **ALEPH Collaboration**, D. Buskulic *et al.*, "Performance of the ALEPH detector at LEP" *Nucl.Instrum.Meth.* **A360** (1995) 481–506.

[16] K. Lutz *Nucl. Instr.Meth* **A253** (1987) 365–377.

[17] T. Abe *et al.*, "Belle ii technical design report" *arXiv:1011.0352* (2010) .

[18] C. Hu-Guo *et al. Nucl. Instrum. Meth* **A623** (2010) 480.

[19] D. Deptuch *et al. IEEE Trans.Nucl.Sci.* **57** (2010) 880–890 ; 2178–2186.

[20] **Detector R&D Common Task Group**, D. Chakraborty *et al.*, "Ilc detector r&d: Its impact".

[21] **CALICE collaboration** *JINST* **6** (2011) 7005.

[22] H. Abramowicz *et al.*, "Forward instrumentation for ilc detectors" *JINST* **5** (2010) 12002.

[23] F. E. report, "Detector Research and Development towards the International Linear Collider. Integrating Activity implemented as Integrated Infrastructure Initiative".

[24] J. R. W. Kilian, T. Ohl, "Simulating Multi-Particle Processes at LHC and ILC" *Eur. Phys. J.* **C71** (2011) 1742.

[25] "PHYSSIM".

[26] D. Schulte, "Study of electromagnetic and hadronic background in the interaction region of the TESLA Collider". DESY-TESLA-97-08.

[27] GDE, "Top Level ILC Machine Parameter Tables". http://ilc-edmsdirect.desy.de/ilc-edmsdirect/item.jsp?edmsid=D00000000925325.

[28] P. L. Lynn Garren, "StdHep 5.06.01 - Monte Carlo Standarization at FNAL". http://cepa.fnal.gov/psm/stdhep/.

[29] http://ilcsoft.desy.de/dbd/generated.

[30] "lcgentools". https://svnweb.cern.ch/trac/lcgentools.

[31] S. M. T. Sjostrand and P. Skands, "Pythia 6.4, physics and manual" *JHEP* **05** (2006) 28. http://home.thep.lu.se/~torbjorn/Pythia.html.

[32] **LHC Higgs Cross Section Working Group**, O.Brein *et al.*, "Handbook of LHC Higgs cross sections". http://arxiv.org/abs/1101.0593v3.

[33] M. Peskin, "Communication at LCWS11, Granada". http://www.ugr.es/~lcws11/.

[34] R. Yonamine, K. Ikematsu, T. Tanabe, K. Fujii, Y. Kiyo, Y. Sumino, and H. Yokoya, "Measuring the top Yukawa coupling at the ILC at $\sqrt{s} = 500$ GeV" *Phys. Rev. D* **84** (Jul, 2011) 014033.

[35] H. Murayama, I. Watanabe, and K. Hagiwara, "HELAS". KEK Report No. 91-11, 1992.

[36] S. Kawabata *Comput. Phys. Commun* **41** (1986) 127.

[37] A. Bohrer, "Inclusive particle production in hadronic decays of the Z boson at LEP I" *Phys. Rep.* **291** (1997) 107–117.

[38] **ALEPH collaboration**, R. Barete *et al.*, "Studies of Quantum Chromodynamics with the ALEPH detector" *Phys. Rep.* **294** (1998) 1–165.

[39] P. Chen, T. L. Barklow, and M. E. Peskin, "Hadron production in gamma gamma collisions as a background for e+ e- linear colliders" *Phys.Rev.* **D49** (1994) 3209–3227, arXiv:hep-ph/9305247 [hep-ph].

[40] **GEANT4 Collaboration**, S. Agostinelli *et al.*, "GEANT4: A simulation toolkit" *Nucl. Instrum. Meth.* **A506** (2003) 250–303.

[41] F. Gaede, T. Behnke, N. Graf, and T. Johnson, "LCIO: A persistency framework for linear collider simulation studies" *Proceedings of CHEP 03, La Jolla, California, 24-28 Mar 2003, TUKT001* (2003) , arXiv:physics/0306114.

[42] M. A. Thomson, "Particle Flow Calorimetry and the PandoraPFA Algorithm" *Nucl. Instrum. Meth.* **A611** (2009) 25–46.

[43] T. Suehara, "The LCFIPlus package: ". http://ilcagenda.linearcollider.org/getFile.py/access?contribId=183&sessionId=12&resId=1&materialId=slides&confId=5468.

[44] **ILD concept group**, *Letter of Intent of the Large International Detector, ILD*. DESY, 2009.

[45] F. Gaede, "Marlin and LCCD: Software tools for the ILC" *Nucl. Instrum. Meth.* **A559** (2006) 177–180.

[46] **LCFI**, . D. Bailey *et al.*, "The LCFIVertex package: vertexing, flavour tagging and vertex charge

reconstruction with an ILC vertex detector" *Nucl. Instrum. Meth.* **A610** (2009) 573–589, arXiv:0908.3019 [physics.ins-det].

[47] B. Parker, A. Mikhailichenko, K. Buesser, J. Hauptman, T. Tauchi, *et al.*, "Functional Requirements on the Design of the Detectors and the Interaction Region of an e+ e- Linear Collider with a Push-Pull Arrangement of Detectors" SLAC-PUB-13657, ILC-NOTE-2009-050.

[48] T. Tauchi, "Engineering Specifications for the ILC Experimental Hall". ILC EDMS D*983825.

[49] ARUP, "Review of Interaction Region Cavern Layout Design". ILC EDMS D*967835.

[50] T. Sanami, A. Fasso, M. Santana, L. Keller, A. Seryi, *et al.*, "IR hall dose rate estimates with detector concepts" SLAC RP-09-08.

[51] S. Boogert *et al.*, "Polarimeters and energy spectrometers for the ilc beam delivery system" *JINST* **4** (2009) P10015, arXiv:0904.0122 [physics.ins-det].

[52] M. Slater *Nucl. Instrum. Meth.* **A592** (2008) 201–217.

[53] M. Lyapin *et al.*, "Results from a prototype chicane-based energy spectrometer for a linear collider" *JINST* **6** (2011) P02002, arXiv:1011.0337 [physics.acc-ph].

[54] Y. Kim *et al.*, "Cavity beam position monitor system for the accelerator test facility 2" *Phys. Rev. ST Accel. Beams* **15** (2012) 042801.

[55] E. Torrence, "Downstream synchrotron radiation stripe spectrometer status". Presentation at the Workshop on Polarization and Energy Measurements at the ILC.

[56] F. Rouse *et al.*, "Measuring the mass and width of the z^0: The status of the energy spectrometers". SLAC-PUB-4977.

[57] C. Bartels *et al.*, "Design and construction of a cherenkov detector for compton polarimetry at the ilc" *JINST* **7** (2012) P01019, arXiv:1011.6314 [physics.ins-det].

[58] J. Buerger *et al.*, "DESY and ILC EDMS : Engineering Data Management for large scientific projects".

[59] N. Bergel *et al.*, "3D CAD Collaboration at European XFEL and ILC".

[60] B. List *et al.*, "Organizing the ILC Technical Design Documentation".

[61] J. Dammann *et al.*, "Making engineering data available at the European XFEL".

[62] **ILC EDMS Support team (ilc-edms-support@desy.de)**. https://ilc-edms.desy.es.

SiD Bibliography

[63] Aihara, H., (Ed.) and Burrows, P., (Ed.) and Oreglia, M., (Ed.) and others, "SiD Letter of Intent" arXiv:0911.0006 [physics.ins-det]. arXiv:0911.0006, SLAC-R-944.

[64] MDI Common Task Group, "MDI CTG Agreement Granada 2011 to use Platform for Push-Pull".

[65] MDI Common Task Group and ILC CFS Group, "MDI CTG and CFS Agreement Granada 2011 for Layout of Vertical Access IR Hall".

[66] G. Deptuch, M. Demarteau, J. Hoff, F. Khalid, R. Lipton, *et al.*, "Vertically integrated pixel readout chip for high energy physics".

[67] Y. Onuki, H. Katsurayama, Y. Ono, H. Yamamoto, Y. Arai, *et al.*, "SOI detector developments" *PoS* **VERTEX2011** (2011) 043.

[68] M. Winter, J. Baudot, A. Besson, G. Claus, A. Dorokhov, *et al.*, "Development of CMOS Pixel Sensors fully adapted to the ILD Vertex Detector Requirements" arXiv:1203.3750 [physics.ins-det].

[69] L. Gaioni, M. Manghisoni, L. Ratti, V. Re, and G. Traversi, "A 3D deep n-well CMOS MAPS for the ILC vertex detector" *Nucl.Instrum.Meth.* **A617** (2010) 324–326.

[70] M. Benoit, "Vertex Detectors for future Linear Colliders" 2012. CERN LCD-OPEN-2012-013.

[71] D. Dannheim, "Vertex-Detector R&D for CLIC" 2012. CERN LCD-OPEN-2012-014.

[72] **DEPFET Collaboration**, S. Rummel and L. Andricek, "The DEPFET active pixel sensor for vertexing at ILC and Super KEKB" *Nucl.Instrum.Meth.* **A623** (2010) 189–191.

[73] **PLUME Collaboration**, A. Nomerotski *et al.*, "PLUME collaboration: Ultra-light ladders for linear collider vertex detector" *Nucl.Instrum.Meth.* **A650** (2011) 208–212.

[74] R. Lipton, "3D detector and electronics integration technologies: Applications to ILC, SLHC, and beyond" *Nucl.Instrum.Meth.* **A636** (2011) S160–S163.

[75] P. Enquist, G. Fountain, C. Petteway, A. Hollingsworth, and H. Grady, "Low Cost of Ownership scalable copper Direct Bond Interconnect 3D IC technology for three dimensional integrated circuit applications" *3D System Integration* (2009) .

[76] C. Kenney, J. Segal, E. Westbrook, S. Parker, J. Hasi, *et al.*, "Active-edge planar radiation sensors" *Nucl.Instrum.Meth.* **A565** (2006) 272–277.

[77] R. Lipton *et al.*, "Combining the Two 3Ds" *submitted to Jinst.* (2012) .

[78] C. Baltay, W. Emmet, D. Rabinowitz, J. Brau, N. Sinev, *et al.*, "Chronopixel Vertex Detectors for Future Linear Colliders" arXiv:1109.2811 [physics.ins-det].

[79] A. Affolder, B. Allongue, G. Blanchot, F. Faccio, C. Fuentes, *et al.*, "DC-DC converters with reduced mass for trackers at the HL-LHC" *JINST* **6** (2011) C11035.

[80] C. Fuentes, B. Allongue, G. Blanchot, F. Faccio, S. Michelis, *et al.*, "Optimization of DC-DC converters for improved electromagnetic compatibility with high energy physics front-end electronics" *IEEE Trans.Nucl.Sci.* **58** (2011) 2024–2031.

[81] W. E. Cooper, "Vertex Detector Cable Considerations" *FERMILAB-CONF-09-047-E* (2009) , arXiv:0902.3023 [physics.ins-det].

[82] **ASIC Development Group Collaboration**, G. Deptuch *et al.*, "A vertically integrated pixel readout device for the Vertex Detector at the International Linear Collider" *IEEE Trans.Nucl.Sci.* **57** (2010) 880–890.

[83] P. Valerio *et al.*, "Evaluation of 65 nm technology for CLIC pixel front-end" 2011. CERN LCD-Note-2011-022.

[84] P. Valerio, "Design of the 65 nm CLICpix demonstrator chip" 2012. CERN LCD-Note-2012-018.

[85] T. Tick and M. Campbell, "Tsv processing of medipix3 wafers by cea-leti: a progress report" *Journal of Instrumentation* **6** (2011) no. 11, C11018. http://stacks.iop.org/1748-0221/6/i=11/a=C11018.

[86] ROHACELL IG/IG-F Product Information,http://www.rohacell.com/sites/dc/Downloadcenter/Evonik/Product/ROHACELL/product-information/ROHACELL IG_IG-F Product Information.pdf.

[87] D. Freytag, R. Herbst, J. Brau, M. Breidenbach, R. Frey, *et al.*, "KPiX, An Array of Self Triggered Charge Sensitive Cells Generating Digital Time and Amplitude Information".

[88] D. Freytag, R. Herbst, J. Brau, M. Breidenbach, R. Frey, *et al.*, " KPiX: a 1024 Channel Readout ASIC for the ILC" *IEEE Nuclear Science Symposium and Medical Imaging Conference* . Accepted for presentation.

[89] C. Neher, R. Lander, A. Moskaleva, J. Pasner, M. Tripathi, *et al.*, "Further Developments in Gold-stud Bump Bonding" *JINST* **7** (2012) C02005, arXiv:1112.1037 [physics.ins-det].

[90] **ATLAS Collaboration**, "ATLAS inner detector: Technical design report. Vol. 1".

[91] **STAR Collaboration**, C. C. et al., "A Heavy Flavor Tracker for STAR" 2006.

[92] S. Dhiwan, "Powering Delivery to KPiX Chips" 2010. http://shaktipower.sites.yale.edu/sites/default/files/Powering_KPiX_Chips_SiD_Workshop_111410_0.pdf.

[93] S. Dhiwan, "Testing of Cables for KPiX Pulse Load" 2011. http://shaktipower.sites.yale.edu/sites/default/files/Testing_Cables_KPiX_Pulse_Load_ALCPG11.pdf.

[94] C. Grefe, "OverlayDriver: An event mixing tool for org.lcsim" 2011.

[95] C. Grefe, *Detector Optimization Studies and Light Higgs Decay into Muons at CLIC*. PhD thesis, 2012. to appear.

[96] D. Onoprienko and E. von Toerne, "Calorimeter Assisted Tracking Algorithm for SiD".

[97] C. Grefe, "Tracking Performance in sidloi3" 2012.

[98] A. Fox-Murphy, D. Howell, R. Nickerson, and A. Weidberg, "Frequency scanned interferometry (FSI): The basis of a survey system for ATLAS using fast automated remote interferometry" *Nucl.Instrum.Meth.* **A383** (1996) 229–237.

[99] H.-J. Yang, J. Deibel, S. Nyberg, and K. Riles, "High-precision absolute distance and vibration measurement using frequency scanned interferometry" *Appl.Opt.* **44** (2005) , arXiv:physics/0409110 [physics].

[100] D. Moya and I. Vila, "Structural and environmental monitoring of tracker and vertex systems using Fiber Optic Sensors" arXiv:1203.0109 [physics.ins-det].

[101] P. Coe, D. Howell, and R. Nickerson, "Frequency scanning interferometry in ATLAS: Remote,

multiple, simultaneous and precise distance measurements in a hostile environment" *Measur.Sci.Tech.* **15** (2004) 2175–2187.

[102] S. Gibson, P. Coe, A. Mitra, D. Howell, and R. Nickerson, "Coordinate measurement in 2-d and 3-d geometries using frequency scanning interferometry" *Optics and Lasers in Engineering* **43** (2005) no. 7, 815 – 831. http://www.sciencedirect.com/science/article/pii/S0143816604001691. Fringe Analysis special interest group (FASIG).

[103] H.-J. Yang and K. Riles, "High-precision absolute distance measurement using dual-laser frequency scanned interferometry under realistic conditions" *Nucl.Instrum.Meth.* **A575** (2007) 395–401, arXiv:physics/0609187 [physics.ins-det].

[104] H.-J. Yang, S. Nyberg, and K. Riles, "Frequency Scanned Interferometry for ILC Tracker Alignment" *eConf* **C050318** (2005) 0816.

[105] W. Wallraff, V. Vetterle, and J. Vandenhirtz, "The AMS Infrared Tracker Alignment System - from STS91 to Iss"*Advanced Technology - Particle Physics* (Nov., 2002) 149–153.

[106] B. Wittmer, *The Laser Alignment System for the CMS Silicon Microstrip Tracker*. PhD thesis, 2001.

[107] B. Wittmer, R. Adolphi, M. Henke, A. Ostaptchouk, M. Thomas, *et al.*, "The laser alignment system for the CMS silicon microstrip tracker" *Nucl.Instrum.Meth.* **A581** (2007) 351–355.

[108] S. T. Boogert and D. J. Miller, "Questions about the measurement of the e+ e- luminosity spectrum at a future linear collider" arXiv:hep-ex/0211021 [hep-ex].

[109] G. Wilson, "http://ilcagenda.linearcollider.org/conferenceDisplay.py?confId=1556" 2007. ALCPG, Chicago.

[110] Frey, R. et al., "Design considerations for a silicon-tungsten electromagnetic calorimeter for a linear collider detector" in *Proc. 10th International Conference on Calorimetry in High Energy Physics*, p. 304. World Scientific, 2002.

[111] D. Strom, "Review of the Calorimeter R&D program, DESY" 2007. http://ilcagenda.linearcollider.org/sessionDisplay.py?sessionId=38&slotId=22&confId=1296#20070531.

[112] J. Ballin, J. Crooks, P. Dauncey, B. Levin, M. Lynch, *et al.*, "A MAPS-based readout for a tera-pixel electromagnetic calorimeter at the ILC" *Nucl.Phys.Proc.Suppl.* **197** (2009) 342–345.

[113] J. Ballin, P. Dauncey, A.-M. Magnan, M. Noy, Y. Mikami, *et al.*, "A Digital ECAL based on MAPS" arXiv:0901.4457 [physics.ins-det].

[114] **SPiDeR Collaboration**, M. Stanitzki, "Advanced monolithic active pixel sensors for tracking, vertexing and calorimetry with full CMOS capability" *Nucl.Instrum.Meth.* **A650** (2011) 178–183.

[115] **SPiDeR Collaboration**, P. Dauncey, "Performance of CMOS sensors for a digital electromagnetic calorimeter" *PoS* **ICHEP2010** (2010) 502.

[116] G. Drake, J. Repond, D. G. Underwood, and L. Xia, "Resistive Plate Chambers for hadron calorimetry: Tests with analog readout" *Nucl.Instrum.Meth.* **A578** (2007) 88–97.

[117] B. Bilki, J. Butler, E. May, G. Mavromanolakis, E. Norbeck, *et al.*, "Environmental Dependence of the Performance of Resistive Plate Chambers" *JINST* **5** (2010) P02007, arXiv:0911.1351 [physics.ins-det].

[118] B. Bilki, J. Butler, E. May, G. Mavromanolakis, E. Norbeck, *et al.*, "Measurement of the Rate Capability of Resistive Plate Chambers" *JINST* **4** (2009) P06003, arXiv:0901.4371 [physics.ins-det].

[119] B. Bilki, J. Butler, T. Cundiff, G. Drake, W. Haberichter, *et al.*, "Calibration of a digital hadron calorimeter with muons" *JINST* **3** (2008) P05001, arXiv:0802.3398 [physics.ins-det].

[120] B. Bilki, J. Butler, E. May, G. Mavromanolakis, E. Norbeck, *et al.*, "Measurement of Positron Showers with a Digital Hadron Calorimeter" *JINST* **4** (2009) P04006, arXiv:0902.1699 [physics.ins-det].

[121] B. Bilki, J. Butler, G. Mavromanolakis, E. May, E. Norbeck, *et al.*, "Hadron Showers in a Digital Hadron Calorimeter" *JINST* **4** (2009) P10008, arXiv:0908.4236 [physics.ins-det].

[122] R. Chechik, A. Breskin, C. Shalem, and D. Mormann, "Thick GEM-like hole multipliers: Properties and possible applications" *Nucl.Instrum.Meth.* **A535** (2004) 303–308, arXiv:physics/0404119 [physics].

[123] Y. Giomataris, P. Rebourgeard, J. Robert, and G. Charpak, "MICROMEGAS: A High granularity position sensitive gaseous detector for high particle flux environments" *Nucl.Instrum.Meth.* **A376** (1996) 29–35.

[124] P. Buzhan, B. Dolgoshein, L. Filatov, A. Ilyin, V. Kantserov, *et al.*, "Silicon photomultiplier and its possible applications" *Nucl.Instrum.Meth.* **A504** (2003) 48–52.

[125] Hamamatsu Photonics, "Technical Note".

[126] **CALICE collaboration**, C. Adloff *et al.*, "Construction and Commissioning of the CALICE Analog Hadron Calorimeter Prototype" *JINST* **5** (2010) P05004, arXiv:1003.2662 [physics.ins-det].

[127] CALICE Analysis Notes, https://twiki.cern.ch/twiki/bin/view/CALICE/CaliceAnalysisNotes.

[128] **CALICE Collaboration**, C. Adloff *et al.*, "Tests of a particle flow algorithm with CALICE test beam data" *JINST* **6** (2011) P07005, arXiv:1105.3417 [physics.ins-det].

[129] L. Linssen, A. Miyamoto, M. Stanitzki, and H. Weerts, "Physics and Detectors at CLIC: CLIC Conceptual Design Report" arXiv:1202.5940 [physics.ins-det].

[130] A. Drozhdin, N. Mokhov, N. Nakao, S. Striganov, and L. Keller, "Suppression of muon backgrounds generated in the ILC beam delivery system" *Conf.Proc.* **C070625** (2007) 2945.

[131] Minos Collaboration, D. G. Michael, P. Adamson, T. Alexopoulos, W. W. M. Allison, G. J. Alner, K. Anderson, C. Andreopoulos, M. Andrews, R. Andrews, and et al., "The magnetized steel and scintillator calorimeters of the MINOS experiment"*Nuclear Instruments and Methods in Physics Research A* **596** (Nov., 2008) 190–228, arXiv:0805.3170 [physics.ins-det].

[132] Adloff and et al., "Construction and performance of a silicon photomultiplier/extruded scintillator tail-catcher and muon-tracker"*Journal of Instrumentation* **7** (Apr., 2012) 4015, arXiv:1201.1653 [physics.ins-det].

[133] **Mu2e Collaboration**, R. Carey *et al.*, "Proposal to search for μ-N $\rightarrow e$-N with a single event sensitivity below 10^{-16}".

[134] **SuperB Collaboration**, M. Bona *et al.*, "SuperB: A High-Luminosity Asymmetric e+ e- Super Flavor Factory. Conceptual Design Report" arXiv:0709.0451 [hep-ex].

[135] P. Rubinov, "Studies of pulse shape in SiPMs" *TiPP 2011* . .

[136] R. Santonico and R. Cardarelli, "DEVELOPMENT OF RESISTIVE PLATE COUNTERS" *Nucl.Instrum.Meth.* **187** (1981) 377–380.

[137] A. Barashkov, G. Glonti, A. Gongadze, M. Gostkin, A. Guskov, *et al.*, "Common support and integration of the BMS/BMF type MDT/RPC chambers of the muon spectrometer of the ATLAS experiment".

[138] **CMS Collaboration**, S. Chatrchyan *et al.*, "Performance Study of the CMS Barrel Resistive Plate Chambers with Cosmic Rays" *JINST* **5** (2010) T03017, arXiv:0911.4045 [physics.ins-det].

[139] H. Band, J. Hollar, P. Tan, F. Anulli, R. Baldini, *et al.*, "Performance and aging studies of BaBar resistive plate chambers" *Nucl.Phys.Proc.Suppl.* **158** (2006) 139–142.

[140] CMS, "CMS Coil Parameter Book, Ver. F, 5/03/01".

[141] B. Parker, A. Mikhailichenko, K. Buesser, J. Hauptman, T. Tauchi, *et al.*, "Functional Requirements on the Design of the Detectors and the Interaction Region of an e+ e- Linear Collider with a Push-Pull Arrangement of Detectors".

[142] W. Craddock, "Magnet DBD Status" *SiD Workshop, SLAC, January 2013* . 2013-01-17.

[143] W. Craddock, "SiD Magnetic Field Studies" *LCWS 2010,Beijing, China* . 2010-03-29.

[144] W. Craddock, "SiD Vacuum Shell Analysis" *ALCPG 2011, Eugene,OR , March 2011* .

[145] S. A. E. Langeslag, B. Cure, S. Sgobba, D. A., and H. H. J. ten Kate, "Characterization of large size co-extruded al-ni stabilized nb-ti superconducting cable for future detector magnets" 2012. CERN LCD-OPEN-2012-016.

[146] W. Craddock, "Compact pressurized water cooled dump resistor for the SiD superconducting solenoid" 2009. Presentation given at the LCD Magnet workshop held at CERN during CLIC09.

[147] A. Gaddi and R. F. Duarte, "Design of a compact dump resistor system for LCD magnet" 2010. CERN LCD-Note-2010-003.

[148] Brau, James, (ed.) and Okada, Yasuhiro, (ed.) and Walker, Nicholas J., (ed.) and Djouadi, Abdelhak, (ed.) and Lykken, Joseph, (ed.) and others, "International Linear Collider reference design report. 1: Executive summary. 2: Physics at the ILC. 3: Accelerator. 4: Detectors".

[149] B. Barish *et al.*, "ILC Technical Design Report".

[150] ARUP, "ARUP Final Report: Task 2". http://ilcdoc.linearcollider.org/record/33917.

[151] **CMS Collaboration**, G. Acquistapace *et al.*, "CMS, the magnet project: Technical design report".

[152] CERN Vibration Team, "CERN EDMS 1099646".

[153] K. Bertsche, "CERN EDMS 1027459".

[154] T. Keller L., Markiewicz and T. Maruyama, "Beam-Gas Interactions in the ILC Beam Delivery System" *ILC-Note-2007-016* .

[155] R. Apsimon *et al.*, "The FONT5 prototype ILC intra-train beam feedback system at ATF2" *Proceedings of the Particle Accelerator Conference, New York* (2011) .

[156] S. Smith, "SiD Intratrain Feedback BPM and Kicker Design".

[157] G. White, D. Schulte, and N. Walker, "Design and simulation of the ILC intra-train orbit and luminosity feedback systems" *Conf.Proc.* **C060626** (2006) 3041–3043.

[158] G. White, "Beam-Beam Feedback, ALCPG11, Eugene, OR, 2011".

[159] D. T. C. Collette, S. Janssens, "Control strategies for the final focus of future linear particle collider" *Nucl.Instrum.Meth.* **A684** (2012) 7–17.

[160] Y. Han, A. Reichold, C. Perry, and R. Bingham, "Frequency Scanning Fibre Interferometer for Absolute Distance Measurements Over a Large Target Area" *eConf* **C06092511** (2006) WEPO09.

[161] K. Riles, "Update on FSI R&D for SiD Final Focus Magnet Alignment" *LCWS 2011,Granada, Spain* . 2011-09-28.

[162] G. Summers, E. Burke, P. Shapiro, S. Messenger, and R. Walters, "Damage correlations in

semiconductors exposed to gamma, electron and proton radiations" *Nuclear Science, IEEE Transactions on* **40** (dec, 1993) 1372 –1379.

[163] N. Walker *et al.*, "ILC Machine Parameter Tables". ILC-EDMS-925325.

[164] RTEMS Homepage,http://www.rtems.com/.

[165] C. Grefe, "Occupancies from Beam-Related Backgrounds in SiD for the DBD". SiD Workshop January 2013,https://ilcagenda.linearcollider.org/getFile.py/access?contribId=40&resId=0&materialId=slides&confId=5950.

[166] Simulator for the Linear Collider (SLIC),http://www.lcsim.org/software/slic/,.

[167] S. Agostinelli *et al.*, "Geant4 – a simulation toolkit" *Nucl. Instrum. Methods Phys. Res. A* **506** (July, 2003) 250–303. http://www.sciencedirect.com/science/article/B6TJM-48TJFY8-5/2/23ea98096ce11c1be446850c04cfa498.

[168] Linear Collider simulations,http://lcsim.org/software/lcsim/1.18/,.

[169] M. A. Thomson, "Particle Flow Calorimetry and the PandoraPFA Algorithm" *Nucl. Instrum. Methods* **A611** (2009) 25–40. arXiv:0907.3577.

[170] LCFIPlus, https://confluence.slac.stanford.edu/display/ilc/LCFIPlus.

[171] A. Casajus, K. Ciba, V. Fernandez, R. Graciani, V. Hamar, V. Mendez, S. Poss, M. Sapunov, F. Stagni, ATsaregorodtsev, and M. Ubeda, "Status of the dirac project" *Journal of Physics: Conference Series* **396** (2012) no. 3, 032107. http://stacks.iop.org/1742-6596/396/i=3/a=032107.

[172] ILCDIRAC Homepage,https://twiki.cern.ch/twiki/bin/view/CLIC/DiracUsage.

[173] The sidloi3 detector description, http://www.lcsim.org/detectors/sidloi3.html.

[174] J. Marshall, A. Munnich, and M. Thomson, "Performance of Particle Flow Calorimetry at CLIC" arXiv:1209.4039 [physics.ins-det].

[175] M. Cacciari and G. P. Salam, "Dispelling the N^3 myth for the k_t jet-finder" *Phys. Lett.* **B641** (2006) 57–61. hep-ph/0512210.

[176] M. Battaglia, T. Barklow, M. E. Peskin, Y. Okada, S. Yamashita, *et al.*, "Physics benchmarks for the ILC detectors" *eConf* **C050318** (2005) 1602, arXiv:hep-ex/0603010 [hep-ex].

[177] A. Belyaev, T. Lastovicka, A. Nomerotski, and G. Lastovicka-Medin, "Discovering Bottom Squark Co-annihilation at ILC" *Phys.Rev.* **D81** (2010) 035011, arXiv:0912.2411 [hep-ph].

[178] M. Davier, L. Duflot, F. Le Diberder, and A. Rouge, "The Optimal method for the measurement of tau polarization" *Phys.Lett.* **B306** (1993) 411–417.

[179] L. Duflot, "New method of measuring tau polarization. Application to the tau $\to$ a1 tau-neutrino channel in the ALEPH experiment".

[180] E. Boos, M. Dubinin, M. Sachwitz, and H. Schreiber, "Probe of the W t b coupling in t anti-t pair production at linear colliders" *Eur.Phys.J.* **C16** (2000) 269–278, arXiv:hep-ph/0001048 [hep-ph].

[181] E. Devetak, A. Nomerotski, and M. Peskin, "Top quark anomalous couplings at the International Linear Collider" *Phys.Rev.* **D84** (2011) 034029, arXiv:1005.1756 [hep-ex].

[182] S. Profumo, "Neutralino dark matter, b tau Yukawa unification and nonuniversal sfermion masses" *Phys.Rev.* **D68** (2003) 015006, arXiv:hep-ph/0304071 [hep-ph].

[183] **ILC PEB Benchmarks Task Force**, T. Barklow, M. Berggren, K. Fujii, N. Graf, A. Miyamoto, M. Peskin, F. Richard, and G. Weiglein, "Detector benchmarking for the 2012 dbd".

[184] **LHC Higgs Cross Section Working Group**, S. Dittmaier, C. Mariotti, G. Passarino, R. Tanaka, *et al.*, "Handbook of LHC Higgs Cross Sections: 1. Inclusive Observables"

arXiv:1101.0593 [hep-ph].

[185] M. Cacciari, G. P. Salam, and G. Soyez, "FastJet User Manual" *Eur.Phys.J.* **C72** (2012) 1896, arXiv:1111.6097 [hep-ph].

[186] M. Cacciari and G. P. Salam, "Dispelling the N^3 myth for the k_t jet-finder" *Phys.Lett.* **B641** (2006) 57–61, arXiv:hep-ph/0512210 [hep-ph].

[187] A. Hoecker, P. Speckmayer, J. Stelzer, J. Therhaag, E. von Toerne, and H. Voss, "TMVA: Toolkit for Multivariate Data Analysis" *PoS* **ACAT** (2007) 040, arXiv:physics/0703039.

[188] P. Roloff and J. Strube, "Measurement of the top Yukawa coupling at a 1 TeV International Linear Collider using the SiD detector" 2013.

[189] R. S. Chivukula, S. B. Selipsky, and E. H. Simmons, "Nonoblique effects in the Z b anti-b vertex from ETC dynamics" *Phys.Rev.Lett.* **69** (1992) 575–577, arXiv:hep-ph/9204214 [hep-ph].

[190] R. Chivukula, E. H. Simmons, and J. Terning, "A Heavy top quark and the Z b anti-b vertex in noncommuting extended technicolor" *Phys.Lett.* **B331** (1994) 383–389, arXiv:hep-ph/9404209 [hep-ph].

[191] M. Peskin, "Will these be supersymmetry at the ILC? Presented at the workshop: Implications of LHC Results for TeV-scale Physics, July 2012".

[192] A. Jenkins *et al.*, "Signal Analysis of the Stau at the ILC".

[193] M. Battaglia, A. De Roeck, J. R. Ellis, F. Gianotti, K. Olive, *et al.*, "Updated post - WMAP benchmarks for supersymmetry" *Eur.Phys.J.* **C33** (2004) 273–296, arXiv:hep-ph/0306219 [hep-ph].

[194] C. Long, "Undergraduate Honors Thesis, Department of Physics, High Energy Physics Group, University of Colorado at Boulder, August 2010" Master's thesis.

[195] P. Bechtle, M. Berggren, J. List, P. Schade, and O. Stempel, "Prospects for the study of the $\tilde{\tau}$-system in SPS1a' at the ILC" *Phys.Rev.* **D82** (2010) 055016, arXiv:0908.0876 [hep-ex].

[196] C. F. Berger, J. S. Gainer, J. L. Hewett, and T. G. Rizzo, "Supersymmetry Without Prejudice" *JHEP* **0902** (2009) 023, arXiv:0812.0980 [hep-ph].

[197] M. Breidenbach *et al.*, "CLIC Detector Costing" 2012. CERN LCD-Note-2012-005.

ILD Bibliography

[198] **ILD Concept Group**, T. Abe *et al.*, "The International Large Detector: Letter of Intent" arXiv:1006.3396 [hep-ex]. FERMILAB-LOI-2010-03, FERMILAB-PUB-09-682-E, DESY-2009-87, KEK-REPORT-2009-6.

[199] L. Linssen, A. Miyamoto, M. Stanitzki, and H. Weerts, eds., *Physics and Detectors at CLIC: CLIC Conceptual Design Report*. 2012. arXiv:1202.5940 [physics.ins-det]. CERN-2012-003, ANL-HEP-TR-12-01, DESY-12-008, KEK-REPORT-2011-7.

[200] **GLD Concept Study Group**, K. Abe *et al.*, "GLD Detector Outline Document: Version 1.2" arXiv:physics/0607154 [physics].

[201] **LDC Working Group**, D. Kisielewska *et al.*, "Detector Outline Document for the Large Detector Concept". http://ilcild.org/documents/misc-doc/ldc/outlinedoc/view.

[202] **ILC Global Design Effort and World Wide Study**, T. Behnke, C. Damerell, J. Jaros, and A. Miyamoto, eds., *ILC Reference Design Report Volume 4 - Detectors*. 2007. arXiv:0712.2356 [physics.ins-det]. ILC-REPORT-2007-001.

[203] C. Hu-Guo, J. Baudot, G. Bertolone, A. Besson, A. Brogna, *et al.*, "First reticule size MAPS with digital output and integrated zero suppression for the EUDET-JRA1 beam telescope" *Nucl.Instrum.Meth.* **A623** (2010) 480–482.

[204] I. Valin, C. Hu-Guo, J. Baudot, G. Bertolone, A. Besson, *et al.*, "A reticle size CMOS pixel sensor dedicated to the STAR HFT" *JINST* **7** (2012) C01102.

[205] L. Greiner, E. Anderssen, H. Matis, H. Ritter, J. Schambach, *et al.*, "A MAPS based vertex detector for the STAR experiment at RHIC" *Nucl.Instrum.Meth.* **A650** (2011) 68–72.

[206] Y. Fu, "A vertically integrated 3D CMOS Monolithic Active Pixel Sensors with fast digital readout slides". Presented at the Workshop on Vertically Integrated Pixel Sensors (VIPS 2010), Pavia, Italy, 22-24 April 2010.

[207] Y. Sugimoto, "Fine Pixel CCD Option for the ILC Vertex Detector" *eConf* **C050318** (2005) 0804. LCWS-2005-0804.

[208] A. Miyamoto *et al.*, "FPCCD vertex detector R&D for ILC". http://www-jlc.kek.jp/subg/vtx/pub/FPCCD_Rev.pdf. Internal Note.

[209] Y. Sugimoto, H. Ikeda, A. Miyamoto, T. Nagamine, Y. Takubo, *et al.*, "R and D status of FPCCD VTX" arXiv:0902.2067 [physics.ins-det].

[210] Y. Sugimoto, H. Ikeda, D. Kamai, E. Kato, A. Miyamoto, *et al.*, "R&D Status of FPCCD Vertex Detector for ILD" arXiv:1202.5832 [physics.ins-det].

[211] **DEPFET Collaboration**, O. Alonso *et al.*, "DEPFET active pixel detectors for a future linear e^+e^- collider" arXiv:1212.2160 [physics.ins-det]. accepted for publication by IEEE Trans. Nucl. Sc.

[212] M. Vos, J. Fuster, C. Lacasta, C. Marinas, A. Dieguez, *et al.*, "DEPFET active pixel detectors" *PoS* **VERTEX2009** (2009) 015.

[213] J. Velthuis, R. Kohrs, M. Mathes, A. Raspereza, L. Reuen, *et al.*, "DEPFET, a monolithic

active pixel sensor for the ILC" *Nucl.Instrum.Meth.* **A579** (2007) 685–689.

[214] I. Peric, T. Armbruster, M. Koch, C. Kreidl, and P. Fischer, "DCD: The multi-channel current-mode ADC chip for the readout of DEPFET pixel detectors" *IEEE Trans.Nucl.Sci.* **57** (2010) 743–753.

[215] I. Peric *et al.*, "DCDB and SWITCHERB, the Readout ASICs for Belle II DEPFET Pixel Detector" *IEEE Nuclear Science Symposium Conference Record* **N31-5** (2011) 1536–1539.

[216] **DEPFET collaboration**. http://www.depfet.org/.

[217] L. Andricek, J. Caride, Z. Dolezal, Z. Drasal, S. Esch, *et al.*, "Intrinsic resolutions of DEPFET detector prototypes measured at beam tests" *Nucl.Instrum.Meth.* **A638** (2011) 24–32.

[218] J. Velthuis, Z. Drasal, D. Scheirich, Z. Dolezal, P. Kodys, *et al.*, "A DEPFET based beam telescope with submicron precision capability" *IEEE Trans.Nucl.Sci.* **55** (2008) 662–666.

[219] H. Bichsel, "Straggling in thin silicon detectors" *Rev.Mod.Phys.* **60** (1988) 663–699.

[220] **Belle II Collaboration**, T. Abe *et al.*, "Belle II Technical Design Report" arXiv:1011.0352 [physics.ins-det]. KEK-REPORT-2010-1.

[221] **PLUME Collaboration**, A. Nomerotski *et al.*, "PLUME collaboration: Ultra-light ladders for linear collider vertex detector" *Nucl.Instrum.Meth.* **A650** (2011) 208–212.

[222] L. Andricek, G. Lutz, R. H. Richter, and M. Reiche, "Processing of ultra-thin silicon sensors for future e+ e- linear collider experiments" *IEEE Trans.Nucl.Sci.* **51** (2004) 1117–1120.

[223] P. Fischer, L. Andricek, S. Herrmann, M. Karagounis, R. Kohrs, *et al.*, "Progress towards a large area, thin DEPFET detector module" *Nucl.Instrum.Meth.* **A582** (2007) 843–848.

[224] A. Oyanguren, "Air cooling for Vertex Detectors" arXiv:1202.6239 [physics.ins-det].

[225] C. M. Marinas Pardo, "DEPFET: A silicon pixel detector for future colliders. Fundamentals, characterization and performance". CERN-THESIS-2011-101.

[226] "The PXD Whitebook". ild-vxd.tex ild:dbd:VTXdepfet:whitebook.

[227] **AIDA**, "Advanced european infrastructures for detectors ad accelerators". http://aida.web.cern.ch.

[228] J. Augustin *et al.*, "A Silicon Envelope for the TPC". LC-DET-2003-013.

[229] J. Fuster, S. Heinemeyer, C. Lacasta, C. Marinas, A. Ruiz Jimeno, *et al.*, "Forward tracking at the next e+ e- collider. Part I. The Physics case" *JINST* **4** (2009) P08002, arXiv:0905.2038 [hep-ex].

[230] A. Savoy-Navarro, "Large Area Silicon Tracking: New Perspectives" 1203.0736 [hep-ex]. and references therein.

[231] A. Savoy-Navarro, "SiLC R&D New Outcomes and Results". http://ilcagenda.linearcollider.org/conferenceOtherViews.py?view=standard&confId=4507. IWLC2012.

[232] **SiLC Collaboration**, T. Blass *et al.*, "SiLC: Silicon tracking for the Linear Collider" 0903.4361 [physics.ins-det]. Proposal of the SiLC R&D Collaboration to the R&D ILCSC Panel, Feb. 2008 at BILWC-2008.

[233] W. Chen *et al.*, "SiLC: Silicon tracking for the Linear Collider". http://www.desy.de/f/prc/html/session-html/session-index.htm. Proposal of the SiLC R&D Collaboration to the PRC-DESY in May 2003 and addendum in October 2003; and status reports of the SiLC R&D Collaboration to the PRC in 2005, 2008 and references therein.

[234] T. Bergauer *et al.* http://www.eudet.org/e26/e28/. EUDET-Memo-2009-18.

[235] K.-H. Hoffmann, "Campaign to identify the future MCMS tracker baseline" *Nucl.Instrum* **A658** (2011) 30–35. and references therein.

[236] R. Patti, "3D IC Overview". http://nepp.nasa.gov/workshops/etw2012/talks/Tuesday/T01_Patti_Tezzaron_3D_IC_Overview.pdf. Third Annual Electronics Technology Workshop of NEPP, 2011.

[237] T. Pham *et al. Nucl.Instrum.Meth.* **A623** (2010) 498–500.

[238] A. Lazhar, "Conception d'un convertisseur Analogique/Numerique pour un systeme de traitement du signal d'un trajectometre Silicium pour Physique des Particules". Master Diploma Report, INSA and Ecole Centrale de Lyon.

[239] F. Bosi, "Light Prototype Support Using Micro-channel Technology as High Efficiency for Silicon Pixel Cooling" *Nucl.Instrum.Meth.* **A650** (2011) 213–217.

[240] P. Allport, "The ATLAS Tracker Upgrade". http://conference.ippp.dur.ac.uk/conferenceDisplay.py?confId=314.

[241] C. Damerell and K. Stefanov, "The Silicon pixel tracker: beginning of a revolution?" *PoS VERTEX 2011* (2011) 021.

[242] D. Dannheim and M. Vos, "Simulation studies for the layout of the vertex and tracking regions of the CLIC detectors". http://cds.cern.ch/record/1443503/files/LCD-2011-031.pdf. LCD-Note-2011-031.

[243] S. Straulino, O. Adriani, L. Bonechi, M. Bongi, S. Bottai, *et al.*, "Spatial resolution of double-sided silicon microstrip detectors for the pamela apparatus" *Nucl.Instrum.Meth.* **A556** (2006) 100–114, arXiv:hep-ex/0510012 [hep-ex].

[244] H.-G. Moser, "Silicon detector systems in high energy physics" *Prog.Part.Nucl.Phys.* **63** (2009) 186–237.

[245] A. Dieguez *et al.*, "Design of a FE ASIC in TSMC-65nm for Si tracking at the ILC". PREL-LC-DET-2012-005.

[246] F. Arteche *et al.*, "Powering requirements and constraints of the microstrip-FTD detector at the Linear Collider". http://ilcagenda.linearcollider.org/contributionDisplay.py?contribId=4&sessionId=4&confId=5010.

[247] F. Arteche *et al.*, "EMI Filter Design and Stability Assessment of DC Voltage Distribution based on Switching Converters" in *LEB 2001 7th Workshop on Electronics for LHC Experiments Proceedings*. 2001.

[248] F. Arteche *et al.*, "Base line design of FTD sub-detector power distribution system for ILD". http://www-flc.desy.de/lcnotes/notes/LC-REP-2012-074.pdf. LC-REP-2012-072.

[249] R. Nelms *et al.*, "Using a Debye Polarization Cell to Predict Double-Layer Capacitor Performance" *IEEE Transactions on Industry Applications* **37** (2001) 4–9.

[250] A. D. Jersey *et al.*, "Fiber Gratings Sensors" *Journal of Lightwave Technology* **15** (1997) 22.

[251] E. Curras *et al.*, "Influence of the Fiber Coating Type on the Strain Response of Proton-Irradiated Fiber Bragg Gratings" *Nuclear Science, IEEE Transactions on* **59** (2012) 937–942.

[252] M. Consales *et al.*, "Fiber optic humidity sensors for high-energy physics applications at CERN" *Sensors and Actuators B* **159** (2011) 66–74.

[253] D. Moya *et al.*, "FBG sensor based self-monitoring support structures for trackers". http://www-flc.desy.de/lcnotes/notes/LC-REP-2012-075.pdf. LC-REP-2012-075.

[254] F. Arteche *et al.*, "Electromagnetic Compatibility plan for CMS experiment at CERN" in *Proceedings 15th International Zurich Symposium and Technical Exhibition on EMC*. 2003.

[255] A. Vogel, "Beam-induced backgrounds in detectors at the ILC". PhD Thesis, University of Hamburg, DESY-THESIS-2008-036.

[256] **LCTPC Collaboration**. http://www.lctpc.org.

[257] **EUDET**, "Detector R&D towards the International Linear Collider". www.eudet.org.

[258] **LCTPC Collaboration**, "Report to the DESY PRC 2010". http://www-flc.desy.de/lcnotes/notes/LC-DET-2012-067.pdf. ILC NOTE 2012-063, LC-DET-2012-067.

[259] Y. Giomataris, P. Rebourgeard, J. P. Robert, and G. Charpak, "MICROMEGAS: A high-granularity position-sensitive gaseous detector for high particle-flux environments" *Nucl.Instrum.Meth.* **A376** (1996) 29–35.

[260] F. Sauli, "GEM: A new concept for electron amplification in gas detectors" *Nucl.Instrum.Meth.* **A386** (1997) 531–534.

[261] J. Kaminski, "Status of European Pixel Modules (LCTPC collaboration meeting presentation).". http://ilcagenda.linearcollider.org/getFile.py/access?contribId=18&sessionId=9&resId=0&materialId=slides&confId=5504.

[262] D. Peterson, "Development of a Low-Material TPC Endplate for ILD". http://www-flc.desy.de/lcnotes/notes/LC-DET-2012-072.pdf. LC-DET-2012-072.

[263] D. Arogancia *et al.*, "Study in a beam test of the resolution of a Micromegas TPC with standard readout pads" *Nucl.Instrum.Meth.* **A602** (2009) 403.

[264] K. Ackermann *et al.*, "Results from a TPC Prototype for the Linear Collider Tracker with the MWPC and GEM Endplate Technologies". http://www-flc.desy.de/lcnotes. LC-DET-2012-066.

[265] M. Dixit *et al.*, "Position sensing from charge dispersion in micro-pattern gas detectors with a resistive anode" *Nucl.Instrum.Meth.* **A518** (2004) 721.

[266] A. Ishikawa *et al.*, "Gas-Property Study at Saga U.". http://www-hep.phys.saga-u.ac.jp/ILC-TPC/gas/index.html.

[267] M. Kobayashi *et al.*, "Cosmic ray tests of a GEM-based TPC prototype operated in Ar-CF4-isobutane gas mixtures" *Nucl.Instrum.Meth.* **A641** (2011) 37–47, arXiv:1008.5068v2.

[268] T. Lux, "Studies for a Time Projection Chamber for the Internationnal Linear Collider and Measurement of Beauty Cross Section in Deep Inelastic Scattering at HERA". PhD Thesis, University of Hamburg, DESY-THESIS-2005-019.

[269] L. Hallermann, "Analysis of GEM Properties and Development of a GEM Support Structure for the ILD Time Projection Chamber". http://www-library.desy.de/cgi-bin/showprep.pl?desy-thesis-10-015. DESY-THESIS-2010-015.

[270] T.Behnke *et al.*, "A Novel Self-supporting GEM-based Amplification Structure for a Time Projection Chamber at the ILC" arXiv:1211.4382v1.

[271] R. Diener. Private Communication on the analysis of the Grid GEM data.

[272] M. Thomson and S. Aplin, "TPC Endcap X_0 Study (All results in [258])".

[273] S. Aplin, "Study of the TPC Endcap Mechanical Thickness (All results in [258])".

[274] M. Thomson, "Particle Flow Calorimetry and the PandoraPFA Algorithm" *Nucl.Instrum.Meth.* **A611** (2009) 25–40, arXiv:0907.3577 [physics.ins-det]. CU-HEP-09-11.

[275] N. Abgrall *et al.*, "Time Projection Chambers for the T2K Near Detectors" arXiv:1012.0865.

[276] http://www.lctpc.org/e201346/e201361/. Testbeam runs 2012.

[277] V. Hedberg *et al.*, "Development of the Readout System for a TPC at the Future Linear Collider". http://www-flc.desy.de/lcnotes/notes/LC-DET-2012-080.pdf.

LC-DET-2012-080.

[278] P. Aspell, M. De Gaspari, *et al.*, "Super-Altro 16: a Front-End System on Chip for DSP Based Readout of Gaseous Detectors". http://www-flc.desy.de/lcnotes. LC-DET-2012-077.

[279] T. Behnke *et al.*, "A Lightweight Field Cage for a Large TPC Prototype for the ILC" *JINST* **5** (2010) P10011, arXiv:1006.3220v1.

[280] P. Schade, "Correction Methods for TPC Operation in Inhomogeneous Magnetic Fields". http://www-flc.desy.de/lcnotes. LC-DET-2010-001.

[281] **ALICE Collaboration**, G. Dellacasa *et al.*, "ALICE: Technical design report of the time projection chamber". CERN-OPEN-2000-183, CERN-LHCC-2000-001.

[282] D. Arai, "Ion Problem Report (LCTPC Workpackage Meeting # 145).". http://ilcagenda.linearcollider.org/getFile.py/access?subContId=1&contribId=3&resId=0&materialId=slides&confId=5522.

[283] K. Fujii, "Positive Ion Effects (LCTPC collaboration meeting presentation).". http://ilcagenda.linearcollider.org/getFile.py/access?contribId=3&sessionId=8&resId=0&materialId=slides&confId=5504.

[284] **LCTPC Japan Collaboration**, "Considerations for an ion gate for LCTPC". http://www-flc.desy.de/lcnotes/notes/LC-DET-2012-079.pdf. LC-DET-2012-079.

[285] R. Settles and W. Wiedenmann, "The Linear Collider TPC: Revised Magnetic-field Requirements". http://www-flc.desy.de/lcnotes/notes/LC-DET-2008-002.pdf. LC-DET-2008-002.

[286] R. Settles, "LCTPC and the Magnetic Field for ILD: Update 2010". http://www-flc.desy.de/lcnotes/notes/LC-DET-2011-002.pdf. LC-DET-2011-002.

[287] **STAR Collaboration**, "STAR TPC". http://www.star.bnl.gov/.

[288] D. Karlen, "LCTPC collaboration meeting presentation". http://ilcagenda.linearcollider.org/getFile.py/access?contribId=0&sessionId=8&resId=0&materialId=slides&confId=5504.

[289] J. Brient and H. Videau, "The calorimetry at the future e^+e^- linear collider" *eConf* (2001) no. C010630, E3047, arxiv:hep-ex/0202004v1.

[290] F. Dulucq *et al.*, "HARDROC: Readout chip for CALICE/EUDET Digital Hadronic Calorimeter" *Nuclear Science Symposium Conference Record (NSS/MIC)* (2010) 1678–1683.

[291] C. Adloff, J. Blaha, M. Chefdeville, A. Dalmaz, C. Drancourt, *et al.*, "MICROROC: MICRO-mesh gaseous structure Read-Out Chip" *JINST* **7** (2012) C01029.

[292] L. Raux *et al.*, "SPIROC (SiPM Integrated Read-Out Chip): Dedicated very front-end electronics for an ILC prototype hadronic calorimeter with SiPM read-out" *JINST* **6** (2011) C01098.

[293] S. Callier *et al.*, "SKIROC2, front-end chip designed to readout the Electromagnetic CALorimeter at the ILC" *JINST* **6** (2011) C12040.

[294] M. Goodrick, L. Hommels, R. Shaw, D. Ward, D. Bailey, M. Kelly, V. Boisvert, B. Green, M. Green, A. Misiejuk, *et al.*, "Development of a modular and scalable data acquisition system for calorimeters at a linear collider" *JINST* **6** (2011) no. 10, P10011.

[295] **CALICE Collaboration**, C. Adloff *et al.*, "Effects of high-energy particle showers on the embedded front-end electronics of an electromagnetic calorimeter for a future lepton collider" *Nucl.Instrum.Meth.* **A654** (2011) 97, arXiv:1102.3454 [physics.ins-det].

[296] **CALICE Collaboration**, C. Adloff *et al.*, "Response of the CALICE Si-W Electromagnetic Calorimeter Physics Prototype to Electrons" *Nucl.Instrum.Meth.* **A608** (2009) 372,

arXiv:0811.2354 [physics.ins-det].

[297] **CALICE Collaboration**, J. Apostolakis *et al.*, "Validation of GEANT4 hadronic models using CALICE data". http://www.eudet.org/e26/e28/e86887/e109012/EUDET-Memo-2010-15.pdf. EUDET-Memo-2010-15.

[298] **CALICE Collaboration**, A. Lucaci-Timoce *et al.*, "Shower development of particles with momenta from 1 to 10 GeV in the CALICE Scintillator-Tungsten HCAL". https://twiki.cern.ch/twiki/pub/CALICE/CaliceAnalysisNotes/CAN-036.pdf. CALICE Analysis Note CAN-036.

[299] M. Anduze *et al.*, "JRA3 Electromagnetic Calorimeter Technical Design Report". http://www.eudet.org/e26/e26/e27/e43691/eudet-report-09-01.pdf. EUDET-Report-2009-01.

[300] R. Cornat, "Design of a SiW electromagnetic calorimeter for the International Linear Collider and study of cross talk in silicon sensors" *Nuclear Science Symposium Conference Record. NSS'08 IEEE* (2008) .

[301] P. Sicho *et al.*, "A large scale prototype for a SiW electromagnetic calorimeter for a future linear collider - EUDET Module". EUDET-Memo-2010-17.

[302] **CALICE Collaboration**, C. Adloff *et al.*, "Tests of a particle flow algorithm with CALICE test beam data" *JINST* **6** (2011) P07005, arXiv:1105.3417 [physics.ins-det].

[303] K. Kotera, "Scintillator ECAL reconstruction". https://ilcagenda.linearcollider.org/getFile.py/access?contribId=169&sessionId=22&resId=0&materialId=slides&confId=5414.

[304] **CALICE Collaboration**, J. Repond *et al.*, "Design and Electronics Commissioning of the Physics Prototype of a Si-W Electromagnetic Calorimeter for the International Linear Collider" *JINST* **3** (2008) P08001, arXiv:0805.4833 [physics.ins-det].

[305] **CALICE Collaboration**, C. Adloff *et al.*, "Study of the interactions of pions in the CALICE silicon-tungsten calorimeter prototype" *JINST* **5** (2010) P05007, arXiv:1004.4996 [physics.ins-det].

[306] **CALICE Collaboration**, P. Doublet *et al.*, "Interactions of hadrons in the CALICE SiW ECAL prototype" arXiv:1203.1240v2 [physics.ins-det]. CALICE Analysis Note CAN-025.

[307] **CALICE Collaboration**, F. Fehr *et al.*, "Tracking with the CALICE Si-W electromagnetic calorimeter prototype using the Hough transform". CALICE Analysis Note CAN-023a.

[308] **CALICE Collaboration**, M. Faucci-Gianelli, "Position and Angular Resolution of the SiW Ecal Prototype". CALICE Analysis Note CAN-017.

[309] **CALICE Collaboration**, K. Kotera *et al.*, "First Stage Analyis of the Energy Response and Resolution of the Scintillator ECAL in the Beam Test at FNAL, 2008". https://twiki.cern.ch/twiki/pub/CALICE/CaliceAnalysisNotes/CAN-016.pdf. CALICE Analysis Note CAN-016.

[310] **CALICE Collaboration**, "Update of the Analysis of the Test Beam Experiment of the CALICE ScECAL Physics Prototype". CALICE Analysis Note CAN-016b.

[311] H. Li, *Higgs Recoil Mass and Cross-Section Analysis at ILC and Calibration of the CALICE SiW ECAL Prototype*. PhD thesis, Université Paris XI, 2009. http://tel.archives-ouvertes.fr/docs/00/43/04/32/PDF/Li.pdf.

[312] J. Rouëné, "MIP Calibration of the Physics Prototype of the Silicon Tungsten Electromagnetic Calorimeter for the International Linear Collider". http://ilcagenda.linearcollider.org/getFile.py/access?contribId=

1&sessionId=15&resId=0&materialId=slides&confId=5213. CALICE Collaboration Meeting Heidelberg 2011.

[313] A. Drozhdin *et al.*, "Suppression of muon backgrounds generated in the ilc beam delivery system" *SLAC-PUB-12741* (2007) . http://www.slac.stanford.edu/cgi-wrap/getdoc/slac-pub-12741.pdf.

[314] **CALICE Collaboration**, C. Adloff *et al.*, "Construction and Commissioning of the CALICE Analogue Hadron Calorimeter Prototype" *JINST* **5** (2010) P05004, arXiv:1003.2662 [physics.ins-det]. DESY-10-032.

[315] **CALICE Collaboration**, C. Adloff *et al.*, "Hadronic energy resolution of a highly granular scintillator-steel hadron calorimeter using software compensation techniques" *JINST* **7** (2012) P09017, arXiv:1207.4210 [physics.ins-det]. MPP-2012-116.

[316] **CALICE Collaboration**, C. Adloff *et al.*, "Electromagnetic response of a highly granular hadronic calorimeter" *JINST* **6** (2011) P04003, arXiv:1012.4343 [physics.ins-det]. DESY-10-241.

[317] **CALICE Collaboration**, "Pion Showers in the CALICE AHCAL". CALICE Analysis Note CAN-026.

[318] **CALICE Collaboration**, "Identification of Track Segments in Hadronic Showers in the Analog Hadron Calorimeter - Algorithm and Comparisons to Simulations". CALICE Analysis Note CAN-022.

[319] L. Caponetto *et al.*, "First test of a power-pulsed electronics system on a GRPC detector in a 3-Tesla magnetic field" *JINST* **7** (2012) P04009, arxiv:1111.5630v1 [physics.ins-det].

[320] **CALICE Collaboration**, "First results of the CALICE SDHCAL Technological Prototype". CALICE Analysis Note CAN-037.

[321] G. Blazey, D. Chakraborty, A. Dyshkant, K. Francis, D. Hedin, *et al.*, "Directly coupled tiles as elements of a scintillator calorimeter with MPPC readout" *Nucl.Instrum.Meth.* **A605** (2009) 277–281. FERMILAB-PUB-09-585-E.

[322] F. Simon and C. Soldner, "Uniformity Studies of Scintillator Tiles directly coupled to SiPMs for Imaging Calorimetry" *Nucl.Instrum.Meth.* **A620** (2010) 196–201, arXiv:1001.4665 [physics.ins-det]. MPP-2010-10.

[323] **CALICE Collaboration**, "First T3B Results - Initial Study of the Time of First Hit in a Scintillator-Tungsten HCAL". CALICE Analysis Note CAN-033.

[324] H. Abramowicz, A. Abusleme, K. Afanaciev, J. Aguilar, P. Ambalathankandy, *et al.*, "Forward Instrumentation for ILC Detectors" *JINST* **5** (2010) P12002, arXiv:1009.2433 [physics.ins-det]. DESY-10-142.

[325] C. Grah and A. Sapronov, "Beam parameter determination using beamstrahlung photons and incoherent pairs" *JINST* **3** (2008) P10004.

[326] P. Bambade, V. Drugakov, and W. Lohmann, "The Impact of BeamCal performance at different ILC beam parameters and crossing angles on stau searches" *Pramana* **69** (2007) 1123–1128, arXiv:physics/0610145 [physics]. LAL-06-145.

[327] W. Daniluk *et al.*, "Laser Alignment System for LumiCal". http://www.eudet.org/e26/e26/e27/e826/EUDET_report_05.pdf. EUDET-Report-2008-05.

[328] M. Czakon, J. Gluza, and T. Riemann, "The Planar four-point master integrals for massive two-loop Bhabha scattering" *Nucl.Phys.* **B751** (2006) 1–17, arXiv:hep-ph/0604101 [hep-ph]. DESY-06-021, WUE-ITP-2006-004, SFB-CPP-06-17.

[329] S. Jadach, W. Placzek, and B. Ward, "BHWIDE 1.00: O(alpha) YFS exponentiated Monte

Carlo for Bhabha scattering at wide angles for LEP-1 / SLC and LEP-2" *Phys.Lett.* **B390** (1997) 298–308, arXiv:hep-ph/9608412 [hep-ph].

[330] H. Abramowicz *et al.*, "Revised requirements on the readout of the luminosity calorimeter ". http://www.eudet.org/e26/e28/e615/eudet_memo_2008_08.pdf. EUDET-Memo-2008-08.

[331] J. Blocki *et al.*, "Silicon Sensors Prototype for LumiCal Calorimeter". EUDET-Memo-2009-07.

[332] N. Walker, "Machine Parameters for the ILC TDR Baseline". http://ilc-edmsdirect.desy.de/ilc-edmsdirect/item.jsp?edmsid=D00000000925325. EDMS-ID: D*925325.

[333] D. Schulte, "Study of Electromagnetic and Hadronic Background in the Interaction Region of the TESLA Collider". TESLA-97-08.

[334] A. Seryi, T. Maruyama, and B. Parker, "IR Optimization, DID and anti-DID". SLAC-PUB-11662.

[335] E. Kuznetsova, "Design studies and sensor tests for the beam calorimeter of the ILC detector". DESY-THESIS-2007-010.

[336] http://www.ikp.tu-darmstadt.de/beschleuniger_1/S-DALINAC.de.jsp. S-DALINAC: Superconducting DArmstadt LInear ACcelerator.

[337] C. Grah, K. Afanaciev, I. Emeliantchik, U. Harder, H. Henschel, *et al.*, "Polycrystalline CVD diamonds for the beam calorimeter of the ILC" *IEEE Trans.Nucl.Sci.* **56** (2009) 462–467.

[338] K. Afanaciev *et al.*, "Investigation of the Radiation Hardness of GaAs Sensors in an Electron Beam". submitted to JINST.

[339] R. Boie, A. Hrisoho, and P. Rehak, "Signal shaping and tail cancellation for gas proportional detectors at high counting rates" *IEEE Trans.Nucl.Sci.* **28** (1981) 603–609.

[340] E. Gatti and P. Manfredi, "Processing the signals from solid state detectors in elementary particle physics" *Riv.Nuovo Cim.* **9N1** (1986) 1–146.

[341] M. Idzik, S. Kulis, and D. Przyborowski, "Development of front-end electronics for the luminosity detector at ILC" *Nucl.Instrum.Meth.* **A608** (2009) 169–174.

[342] M. Idzik *et al.*, "A 10-bit multichannel digitizer ASIC for detectors in particle physics experiments" *IEEE Trans.Nucl.Sci.* **59** (2012) 294–302. FCAL.tex ild:bib:lumi-adc.

[343] A. Abusleme, A. Dragone, G. Haller, and B. A. Wooley, "BeamCal Instrumentation IC: Design, implementation, and test results" *IEEE Trans.Nucl.Sci.* **59** (2012) 589–596.

[344] S. Kulis, A. Matoga, M. Idzik, K. Swientek, T. Fiutowski, *et al.*, "A general purpose multichannel readout system for radiation detectors" *JINST* **7** (2012) T01004.

[345] V. D'Ascenso, N. Saveliev, "Mathematical modeling and Study of the ILD Muon System/Tail Catcher". http://www-flc.desy.de/lcnotes. LC-DET-2012- xxx.

[346] V. Balagura, M. Danilov, *et al.*, "Study of scintillator strip with wavelength shifting fiber and silicon photomultiplier" *Nucl.Instrum.Meth.* **A564** (2006) 590–596, arXiv:physics/0504194 [physics.ins-det].

[347] J. Repond, "Overview of the DHCAL Project" arXiv:1005.0412 [physics.ins-det].

[348] C. Adloff *et al.*, "Construction and performance of a silicon photomultiplier/extruded scintillator tail-catcher and muon tracker" *JINST* **7** (2012) 4015, arXiv:1201.1653 [physics.ins-det].

[349] F. Kircher *et al.*, "CMS Coil Design and Assembly" *IEEE Trans.Appl.Superconductivity* **12** (2002) no. 1, 395–398.

[350] F. Kircher, U. Schneekloth, *et al.*, "Conceptual Design of the ILD Detector Magnet System".

LC-DET-2012-081.

[351] P. Fabbricatore *et al.*, "The Manufacture of Modules for CMS Coil" *IEEE Trans.Appl.Superconductivity* **16** (2006) no. 2, 512–516.

[352] J. Rey *et al.*, "Cold Mass Integration of the ATLAS Barrel Toroid Magnets at CERN" *IEEE Trans.Appl.Superconductivity* **16** (2006) no. 2, 553–556.

[353] B. Levesy *et al.*, "CMS Solenoid Assembly" *IEEE Trans.Appl.Superconductivity* **16** (2006) no. 2, 517–520.

[354] B. Parker, A. Mikhailichenko, K. Buesser, J. Hauptman, T. Tauchi, *et al.*, "Functional Requirements on the Design of the Detectors and the Interaction Region of an e+ e- Linear Collider with a Push-Pull Arrangement of Detectors". SLAC-PUB-13657, ILC-NOTE-2009-050.

[355] R. Stromhagen, "Note on the integration of the cryostat into the central barrel - ILD detector". http://edmsdirect.desy.de/edmsdirect/file.jsp?edmsid=D00000001010065,A,1,1. EDMS ID: D*1010065.

[356] C. Bourgeois and A. Gonnin, "Integration of inner detector region". http://edmsdirect.desy.de/edmsdirect/file.jsp?edmsid=D00000001003815,A,1,1. EDMS-ID: D*1003815,A,1,1.

[357] ilc-edms.desy.de. ILC Engineering Data Management System ILC-EDMS.

[358] **CLIC MDI Working Group**, L. Gatignon, "CLIC MDI Overview" arXiv:1202.6511 [physics.acc-ph].

[359] T. Behnke, S. Bertolucci, R. Heuer, and R. Settles, eds., *TESLA: The superconducting electron positron linear collider with an integrated X-ray laser laboratory. Technical design report. Pt. 4: A detector for TESLA*. 2001. DESY-01-011, DESY-2001-011, DESY-01-011D, DESY-2001-011D, DESY-TESLA-2001-23, DESY-TESLA-FEL-2001-05, ECFA-2001-209.

[360] P. Sphicas, ed., *CMS: The TriDAS project. Technical design report, Vol. 2: Data acquisition and high-level trigger*. 2002. CERN-LHCC.

[361] A. Oh, "The CMS DAQ and run control system" *J.Phys.Conf.Ser.* **110** (2008) 092020.

[362] S. Gameiro, G. Crone, R. Ferrari, D. Francis, B. Gorini, M. Gruwe, M. Joos, G. Lehmann, L. Mapelli, A. Misiejuk, *et al.*, "The rod crate daq software framework of the atlas data acquisition system" *Nuclear Science, IEEE Transactions on* **53** (2006) no. 3, 907–911.

[363] R. Cornat, "Acquisition system and detector interface for power pulsed detectors" vol. 37, pp. 1791 – 1798. 2012. http://www.sciencedirect.com/science/article/pii/S1875389212018913. Proceedings of the 2nd International Conference on Technology and Instrumentation in Particle Physics (TIPP 2011).

[364] F. Gaede, T. Behnke, N. Graf, and T. Johnson, "LCIO: A Persistency framework for linear collider simulation studies" *eConf* **C0303241** (2003) TUKT001, arXiv:physics/0306114 [physics]. SLAC-PUB-9992, CHEP-2003-TUKT001.

[365] **ATLAS Collaboration**, G. Duckeck *et al.*, eds., *ATLAS computing: Technical design report*. 2005. CERN-LHCC-2005-022, ATLAS-TRD-017.

[366] **CMS Collaboration**, "CMS: The computing project. Technical design report". CERN-LHCC-2005-023.

[367] "GEAR - a geometry description toolkit for ILC reconstruction software". http://ilcsoft.desy.de/portal/software_packages/gear.

[368] P. Mora de Freitas and H. Videau, "Detector simulation with MOKKA / GEANT4: Present

and future". LC-TOOL-2003-010.

[369] F. Gaede, "Marlin and LCCD: Software tools for the ILC" *Nucl.Instrum.Meth.* **A559** (2006) 177–180.

[370] R. Brun and F. Rademakers, "ROOT: An object oriented data analysis framework" *Nucl.Instrum.Meth.* **A389** (1997) 81–86.

[371] **GEANT4**, S. Agostinelli *et al.*, "GEANT4: A Simulation toolkit" *Nucl.Instrum.Meth.* **A506** (2003) 250–303. SLAC-PUB-9350, FERMILAB-PUB-03-339.

[372] R. Glattauer, R. Frühwirth, J. Lettenbichler, and W. Mitaroff, "Forward Tracking in the ILD Detector" arXiv:1202.2761 [physics.data-an].

[373] K. Fujii, "KalTest: A ROOT-based Kalman Filter Package". http://www-jlc.kek.jp/subg/offl/kaltest/.

[374] **LCFI Collaboration**, D. Bailey *et al.*, "The LCFIVertex package: vertexing, flavour tagging and vertex charge reconstruction with an ILC vertex detector" *Nucl.Instrum.Meth.* **A610** (2009) 573–589, arXiv:0908.3019 [physics.ins-det].

[375] T. Suehara, T. Tanabe, and S. Yamashita, "Improved jet clustering algorithm with vertex information for multi-bottom final states" arXiv:1110.5785 [hep-ex].

[376] K. Buesser, "ILD Machine-Detector Interface and Experimental Hall Issues" arXiv:1201.5807 [physics.ins-det].

[377] H. Yamaoka, "ILD Vibration Studies". Presented at LCWS10 and ILC10, Beijing, China, 2010.

[378] M. Oriunno, "Planning the Push-pull". Presented at ALCPG'11, Eugene, OR, USA, 2011.

[379] K. Sinram *et al.*, "ILD Experimental Hall Design". http://ilcagenda.linearcollider.org/materialDisplay.py?contribId=7&sessionId=3&materialId=slides&confId=5399. SiD/ILD Engineering and Detector Interface Working Meeting, SLAC, 2011.

[380] E. Avetisyan, "Study of the anti-DID Magnetic Field Effects on the Beam-induced Pair Backgrounds in ILD". http://www-flc.desy.de/lcnotes/notes/LC-REP-2013-002.pdf. LC-REP-2013-002.

[381] T. Barklow, "Physics Impact of Detector Performance". http://www-conf.slac.stanford.edu/lcws05/program/talks/18mar2005.ppt. Presentation for LCWS05.

[382] K. Fujii, "Time Stamping: CDC/TPC Comparison Studies. (NB: "CDC" was the central drift chamber for the detector in the early days of JLC/NLC.)". http://www-jlc.kek.jp/jlc/sites/default/files/groups/tpc/talks/T0.CDCvsTPC.pdf.

[383] M. Killenberg, "Time Stamping of TPC Tracks in the CLIC_ILD Detector". https://edms.cern.ch/file/1158960/1/tpc_time_stamping.pdf. LCD-NOTE-2011-030.

[384] R. Walsh *et al.*, "Flavour tagging optimisation studies at ILD". http://ilcild.org/documents/ild-letter-of-intent/ild-loi-material/flavour_tagging.pdf/view.

[385] H. Ono and A. Miyamoto, "Evaluation of measurement accuracies of the higgs boson branching fractions in the International Linear Collider" arXiv:1207.0300 [hep-ex].

[386] T. Barklow, M. Berggren, K. Fujii, N. Graf, A. Miyamoto, M. Peskin, F. Richard, and G. Weiglein, "Detector benchmarking for the 2012 DBD". ILC-NOTE-2011-059.

[387] P. Doublet, *Hadrons in a highly granular SiW ECAL - Top quark production at the ILC*. PhD thesis, Laboratoire d'Accélérateur Linéaire and Université Paris Sud - Paris XI, 2011. http://tel.archives-ouvertes.fr/tel-00657967.

[388] S. Catani, Y. L. Dokshitzer, M. Olsson, G. Turnock, and B. Webber, "New clustering algorithm for multi - jet cross-sections in e+ e- annihilation" *Phys.Lett.* **B269** (1991) 432–438.

[389] S. D. Ellis and D. E. Soper, "Successive combination jet algorithm for hadron collisions" *Phys.Rev.* **D48** (1993) 3160–3166, arXiv:hep-ph/9305266 [hep-ph].

[390] M. Cacciari and G. P. Salam, "Dispelling the N^3 myth for the k_t jet-finder" *Phys.Lett.* **B641** (2006) 57–61, arXiv:hep-ph/0512210 [hep-ph].

[391] H. Ono, "Higgs branching ratio study for DBD detector benchmarking in ILD". http://www-flc.desy.de/lcnotes/notes/LC-REP-2013-005.pdf. LC-REP-2013-005.

[392] C. Calancha, "Study of $H \to \mu^+\mu^-$ at $\sqrt{s} = 1$ TeV at the ILC". http://www-flc.desy.de/lcnotes/notes/LC-REP-2013-006.pdf. LC-REP-2013-006.

[393] G. Moortgat-Pick, T. Abe, G. Alexander, B. Ananthanarayan, A. Babich, *et al.*, "The Role of polarized positrons and electrons in revealing fundamental interactions at the linear collider" *Phys.Rept.* **460** (2008) 131–243, arXiv:hep-ph/0507011 [hep-ph].

[394] A. Blondel, "A scheme to measure the polarization asymmetry at the Z pole in LEP" *Phys.Lett.* **B202** (1988) 145.

[395] K. Moenig, "The use of positron polarization for precision measurements". LC-PHSM-2000-59-TESLA.

[396] P. Bechtle, W. Ehrenfeld, and I. Marchesini, "Measurement of the beam polarization at the ILC using the WW production". LC-DET-2009-009.

[397] A. Rosca, "Measurement of the beam polarisation at the ILC using the WW annihilation data". http://www-flc.desy.de/lcnotes/notes/LC-REP-2013-009.pdf. LC-REP-2013-009.

[398] I. Marchesini, "Triple gauge couplings and polarization at the ILC and leakage in a highly granular calorimeter".

[399] W. Menges, "A study of charged current triple gauge couplings at TESLA". LC-PHSM-2001-022.

[400] T. Price, N. Watson, T. Tanabe, and V. Martin, "Measurement of the top Yukawa coupling at $\sqrt{s} = 1$ TeV using the ILD detector". http://www-flc.desy.de/lcnotes/notes/LC-REP-2013-004.pdf. LC-REP-2013-004.

[401] A. Hoecker, P. Speckmayer, J. Stelzer, J. Therhaag, E. von Toerne, and H. Voss, "TMVA: Toolkit for Multivariate Data Analysis" *PoS* **ACAT** (2007) 040, arXiv:physics/0703039.

[402] M. Amjad, T. Frisson, R. Pöschl, F. Richard, and J. Rouëné, "Forward backward asymmetry in $e^+e^- \to t\bar{t}$ at $\sqrt{s} = 500$ GeV for fully hadronic decays of the $t\bar{t}$ pair". http://www-flc.desy.de/lcnotes/notes/LC-REP-2013-008.pdf. LC-REP-2013-008.

[403] H. Baer *et al.*, "Physics at the International Linear Collider". http://lcsim.org/papers/DBDPhysics.pdf. to be published in the ILC Detailed Baseline Design Report.

[404] F. Gianotti, M. Mangano, T. Virdee, S. Abdullin, G. Azuelos, *et al.*, "Physics potential and experimental challenges of the LHC luminosity upgrade" *Eur.Phys.J.* **C39** (2005) 293–333, arXiv:hep-ph/0204087 [hep-ph].

[405] U. Baur, T. Plehn, and D. L. Rainwater, "Measuring the higgs boson self coupling at the LHC and finite top mass matrix elements" *Phys.Rev.Lett.* **89** (2002) 151801, arXiv:hep-ph/0206024 [hep-ph].

[406] U. Baur, T. Plehn, and D. L. Rainwater, "Determining the higgs boson selfcoupling at hadron colliders" *Phys.Rev.* **D67** (2003) 033003, arXiv:hep-ph/0211224 [hep-ph].

[407] U. Baur, T. Plehn, and D. L. Rainwater, "Probing the higgs selfcoupling at hadron colliders

using rare decays" *Phys.Rev.* **D69** (2004) 053004, arXiv:hep-ph/0310056 [hep-ph].

[408] U. Baur, T. Plehn, and D. L. Rainwater, "Examining the higgs boson potential at lepton and hadron colliders: A Comparative analysis" *Phys.Rev.* **D68** (2003) 033001, arXiv:hep-ph/0304015 [hep-ph].

[409] S. Kanemura, S. Kiyoura, Y. Okada, E. Senaha, and C. Yuan, "New physics effect on the higgs selfcoupling" *Phys.Lett.* **B558** (2003) 157–164, arXiv:hep-ph/0211308 [hep-ph].

[410] S. Kanemura, Y. Okada, E. Senaha, and C.-P. Yuan, "Higgs coupling constants as a probe of new physics" *Phys.Rev.* **D70** (2004) 115002, arXiv:hep-ph/0408364 [hep-ph].

[411] E. Asakawa, D. Harada, S. Kanemura, Y. Okada, and K. Tsumura, "Higgs boson pair production in new physics models at hadron, lepton, and photon colliders" *Phys.Rev.* **D82** (2010) 115002, arXiv:1009.4670 [hep-ph].

[412] A. Djouadi, W. Kilian, M. Muhlleitner, and P. Zerwas, "Testing higgs selfcouplings at e+ e- linear colliders" *Eur.Phys.J.* **C10** (1999) 27–43, arXiv:hep-ph/9903229 [hep-ph].

[413] C. Grojean, G. Servant, and J. D. Wells, "First-order electroweak phase transition in the standard model with a low cutoff" *Phys.Rev.* **D71** (2005) 036001, arXiv:hep-ph/0407019 [hep-ph].

[414] S. Kanemura, Y. Okada, and E. Senaha, "Electroweak baryogenesis and quantum corrections to the triple higgs boson coupling" *Phys.Lett.* **B606** (2005) 361–366, arXiv:hep-ph/0411354 [hep-ph].

[415] S. Ham and S. Oh, "Electroweak phase transition and higgs self-couplings in the two-higgs-doublet model" arXiv:hep-ph/0502116 [hep-ph].

[416] M. Aoki, S. Kanemura, and O. Seto, "Neutrino mass, Dark Matter and Baryon Asymmetry via TeV-Scale Physics without Fine-Tuning" *Phys.Rev.Lett.* **102** (2009) 051805, arXiv:0807.0361 [hep-ph].

[417] M. Aoki, S. Kanemura, and O. Seto, "A Model of TeV Scale Physics for Neutrino Mass, Dark Matter and Baryon Asymmetry and its Phenomenology" *Phys.Rev.* **D80** (2009) 033007, arXiv:0904.3829 [hep-ph].

[418] A. Noble and M. Perelstein, "Higgs self-coupling as a probe of electroweak phase transition" *Phys.Rev.* **D78** (2008) 063518, arXiv:0711.3018 [hep-ph].

[419] A. G. Cohen, D. Kaplan, and A. Nelson, "Progress in electroweak baryogenesis" *Ann.Rev.Nucl.Part.Sci.* **43** (1993) 27–70, arXiv:hep-ph/9302210 [hep-ph].

[420] M. Quiros, "Field theory at finite temperature and phase transitions" *Helv.Phys.Acta* **67** (1994) 451–583.

[421] V. Rubakov and M. Shaposhnikov, "Electroweak baryon number nonconservation in the early universe and in high-energy collisions" *Usp.Fiz.Nauk* **166** (1996) 493–537, arXiv:hep-ph/9603208 [hep-ph].

[422] G. D. Kribs, T. Plehn, M. Spannowsky, and T. M. Tait, "Four generations and higgs physics" *Phys.Rev.* **D76** (2007) 075016, arXiv:0706.3718 [hep-ph].

[423] C. Castanier, P. Gay, P. Lutz, and J. Orloff, "Higgs self coupling measurement in e+ e- collisions at center-of-mass energy of 500-GeV" arXiv:hep-ex/0101028 [hep-ex].

[424] T. Barklow, "Higgs self-coupling measurement". http://ilcagenda.linearcollider.org/getFile.py/access?contribId=154&sessionId=71&resId=1&materialId=slides&confId=1296. Presentation for LCWS07.

[425] M. F. Giannelli, "Sensitivity to the higgs Self-coupling Using the ZHH Channel"

arXiv:0901.4895 [hep-ex].

[426] Y. Takubo, "Analysis of higgs Self-coupling with ZHH at ILC" arXiv:0907.0524 [hep-ph].

[427] Y. Takubo, "Analysis of ZHH in the 4-jet mode" arXiv:0901.3598 [hep-ph].

[428] J. Tian, K. Fujii, and Y. Gao, "Study of higgs Self-coupling at ILC" arXiv:1008.0921 [hep-ex].

[429] S. Yamashita, "A study of higgs self-coupling measurement at about 1 TeV". http://indico.cern.ch/getFile.py/access?contribId=s3t15&sessionId=4&resId=0&materialId=0&confId=a04172. Presentation for LCWS04.

[430] G. Gounaris, D. Schildknecht, and F. Renard, "Test of higgs boson nature in e+ e – H H Z" *Phys.Lett.* **B83** (1979) 191.

[431] A. Djouadi, H. Haber, and P. Zerwas, "Multiple production of MSSM neutral higgs bosons at high-energy e+ e- colliders" *Phys.Lett.* **B375** (1996) 203–212, arXiv:hep-ph/9602234 [hep-ph].

[432] V. Ilyin, A. Pukhov, Y. Kurihara, Y. Shimizu, and T. Kaneko, "Probing the H**3 vertex in e+ e-, gamma e and gamma gamma collisions for light and intermediate higgs bosons" *Phys.Rev.* **D54** (1996) 6717–6727, arXiv:hep-ph/9506326 [hep-ph].

[433] V. D. Barger and T. Han, "Double higgs boson production via W W fusion in TeV e+ e- collisions" *Mod.Phys.Lett.* **A5** (1990) 667–674.

[434] F. Boudjema and E. Chopin, "Double higgs production at the linear colliders and the probing of the higgs selfcoupling" *Z.Phys.* **C73** (1996) 85–110, arXiv:hep-ph/9507396 [hep-ph].

[435] J. Tian and K. Fujii, "Update on the higgs self-coupling measurement". http://ilcphys.kek.jp/meeting/physics/archives/2012-09-08/zhh120908_tianjp.pdf. The 27th General Physics Meeting of the ILC Physics Subgroup .

[436] J. Tian, "Study of higgs Self-coupling at ILC". Ph.D. Thesis (2011.6).

[437] J. Tian, "Study of higgs self-coupling at the ILC based on the full detector simulation at $\sqrt{s} =$ 500 GeV and $\sqrt{s} = 1$ TeV". http://www-flc.desy.de/lcnotes/notes/LC-REP-2013-003.pdf. LC-REP-2013-003.

[438] J. Tian *et al.*, "Updates on the higgs self coupling measurement". http://ilcphys.kek.jp/meeting/physics/archives/2012-06-09/zhh120609_tianjp.pdf. The 26th General Physics Meeting of the ILC Physics Subgroup .

[439] M. Berggren, "SGV 3.0 - a fast detector simulation" arXiv:1203.0217 [physics.ins-det]. https://svnsrv.desy.de/websvn/wsvn/General.sgv?

[440] P. Doublet *et al.*, "Determination of Top-quark Asymmetries at the ILC" arxiv:1202.6659v1 [hep-ex].

[441] M. Amjad, T. Frisson, I. Garcia, R. Pöschl, E. Ros, F. Richard, J. Rouëné, and M. Vos, "A precise determination of top quark electroweak couplings at the ILC operating at $\sqrt{s} = 500$ GeV ". http://www-flc.desy.de/lcnotes/notes/LC-REP-2013-007.pdf. LC-REP-2013-007.

[442] E. Barger *et al.*, "The Top Quark Production Asymmetries $\mathrm{A}_{\mathrm{FB}}^{\mathrm{t}}$ and $\mathrm{A}_{\mathrm{FB}}^{\ell}$" *Phys.Rev.Lett.* (2012) no. 108, , arxiv:1201.1790 [hep-ph].

[443] **ILC Global Design Effort and World Wide Study**, N. Phinney, N. Toge, and N. Walker, eds., *ILC Reference Design Report Volume 3 - Accelerator*. 2007. arXiv:0712.2361 [physics.acc-ph]. ILC-REPORT-2007-001.

[444] "CLIC detector costing". LCD-Note-2012-005.

List of Signatories

The following list of signatories represents a comprehensive list of those people who have contributed to the R&D and design work, for both the accelerator and the detectors, which is summarised in this report. The list also includes those people who wish to indicate their support for the next phases of the worldwide ILC effort.

It should be noted that inclusion in this list does not indicate any formal commitment by the signatories. It does not indicate commitment to the specific detector designs presented, nor exclusive support for ILC over other collider programs.

A. Abada[171], T. Abe[24], T. Abe[236], J. M. Abernathy[379], H. Abramowicz[265], A. Abusleme[231], S. Aderhold[47], O. Adeyemi[333], E. Adli[357,251], C. Adloff[164], C. Adolphsen[251], K. Afanaciev[209], M. Aguilar[31], S. Ahmad[93], A. Ahmed[382], H. Aihara[375], R. Ainsworth[237,139], S. Airi[154], M. Aizatskyi[208], T. Akagi[73], M. Akemoto[71], A. Akeroyd[367], J. Alabau-Gonzalvo[108], C. Albajar[46], J. E. Albert[379], C. Albertus[281], J. Alcaraz Maestre[31], D. Alesini[174], B. Alessandro[128], G. Alexander[265], J. P. Alexander[43], A. Alhaidari[243], N. Alipour Tehrani[33], B. C. Allanach[323], O. Alonso[311], J. Alwall[210], J. W. Amann[251], Y. Amhis[167], M. S. Amjad[167], B. Ananthanarayan[83], A. Andreazza[386,122], N. Andreev[58], L. Andricek[186], M. Anduze[172], D. Angal-Kalinin[258], N. Anh Ky[106,394], K. A. Aniol[18], K. I. Aoki[148], M. Aoki[148], H. Aoyagi[137], S. Aoyama[250], S. J. Aplin[47], R. B. Appleby[343,40], J. Arafune[96], Y. Arai[71], S. Araki[71], L. Arazi[404], A. Arbey[50], D. Ariza[47], T. Arkan[58], N. D. Arnold[7], D. Arogancia[194], F. Arteche[113], A. Aryshev[71], S. Asai[375], T. Asaka[137], T. Asaka[212], E. Asakawa[220], M. Asano[333], F. B. Asiri[58], D. Asner[225], M. Asorey[286], D. Attié[21], J. E. Augustin[169], D. B. Augustine[58], C. S. Aulakh[226], E. Avetisyan[47], V. Ayvazyan[47], N. Azaryan[142], F. Azfar[358], T. Azuma[246], O. Bachynska[47], H. Baer[355], J. Bagger[141], A. Baghdasaryan[407], S. Bai[102], Y. Bai[384], I. Bailey[40,176], V. Balagura[172,107], R. D. Ball[329], C. Baltay[405], K. Bamba[198], P. S. Bambade[167], Y. Ban[9], E. Banas[268], H. Band[384], K. Bane[251], M. Barbi[362], V. Barger[384], B. Barish[17,65], T. Barklow[251], R. J. Barlow[392], M. Barone[58,65], I. Bars[368], S. Barsuk[167], P. Bartalini[210], R. Bartoldus[251], R. Bates[332], M. Battaglia[322,33], J. Baudot[94], M. Baylac[170], P. Bechtle[295], U. Becker[185,33], M. Beckmann[47], F. Bedeschi[126], C. F. Bedoya[31], S. Behari[58], O. Behnke[47], T. Behnke[47], G. Belanger[165], S. Belforte[129], I. Belikov[94], K. Belkadhi[172], A. Bellerive[19], C. Belver Aguilar[108], A. Belyaev[367,259], D. Benchekroun[184], M. Beneke[57], M. Benoit[33], A. Benot-Morell[33,108], S. Bentvelsen[213], L. Benucci[331], J. Berenguer[31], T. Bergauer[224], S. Berge[138], E. Berger[7], J. Berger[251], C. M. U. Berggren[47], Z. Bern[318], J. Bernabeu[108], N. Bernal[295], G. Bernardi[169], W. Bernreuther[235], M. Bertucci[119], M. Besancon[21], M. Bessner[47], A. Besson[94,306], D. R. Bett[358,140], A. J. Bevan[234], A. Bhardwaj[326], A. Bharucha[333], G. Bhattacharyya[241], B. Bhattacherjee[150], B. Bhuyan[86], M. E. Biagini[174], L. Bian[102], F. Bianchi[128], O. Biebel[182], T. R. Bieler[190], C. Biino[128], B. Bilki[7,337], S. S. Biswal[221], V. Blackmore[358,140], J. J. Blaising[164], N. Blaskovic Kraljevic[358,140], G. Blazey[217], I. Bloch[48], J. Bluemlein[48], B. Bobchenko[107], T. Boccali[126], J. R. Bogart[251], V. Boisvert[237], M. Bonesini[121], R. Boni[174], J. Bonnard[168], G. Bonneaud[169], S. T. Boogert[237,139], L. Boon[233,7],

G. Boorman[237,139], E. Boos[180], M. Boronat[108], K. Borras[47], L. Bortko[48], F. Borzumati[272], M. Bosman[294], A. Bosotti[119], F. J. Botella[108], S. Bou Habib[401], P. Boucaud[171], J. Boudagov[142], G. Boudoul[89], V. Boudry[172], D. Boumediene[168], C. Bourgeois[167], A. Boveia[52], A. Brachmann[251], J. Bracinik[315], J. Branlard[47,58], B. Brau[346], J. E. Brau[356], R. Breedon[320], M. Breidenbach[251], A. Breskin[404], S. Bressler[404], V. Breton[168], H. Breuker[33], C. Brezina[295], C. Briegel[58], J. C. Brient[172], T. M. Bristow[329], D. Britton[332], I. C. Brock[295], S. J. Brodsky[251], F. Broggi[119], G. Brooijmans[42], J. Brooke[316], E. Brost[356], T. E. Browder[334], E. Brücken[69], G. Buchalla[182], P. Buchholz[301], W. Buchmuller[47], P. Bueno[111], V. Buescher[138], K. Buesser[47], E. Bulyak[208], D. L. Burke[251], C. Burkhart[251], P. N. Burrows[358,140], G. Burt[40], E. Busato[168], L. Butkowski[47], S. Cabrera[108], E. Cabruja[32], M. Caccia[389,122], Y. Cai[251], S. S. Caiazza[47,333], O. Cakir[6], P. Calabria[89], C. Calancha[71], G. Calderini[169], A. Calderon Tazon[110], S. Callier[93], L. Calligaris[47], D. Calvet[168], E. Calvo Alamillo[31], A. Campbell[47], G. I. E. Cancelo[58], J. Cao[102], L. Caponetto[89], R. Carcagno[58], M. Cardaci[201], C. Carloganu[168], S. Caron[97,213], C. A. Carrillo Montoya[123], K. Carvalho Akiba[291], J. Carwardine[7], R. Casanova Mohr[311], M. V. Castillo Gimenez[108], N. Castro[175], A. Cattai[33], M. Cavalli-Sforza[294], D. G. Cerdeno[111], L. Cerrito[234], G. Chachamis[108], M. Chadeeva[107], J. S. Chai[260], D. Chakraborty[217], M. Champion[254], C. P. Chang[201], A. Chao[251], Y. Chao[210], J. Charles[28], M. Charles[358], B. E. Chase[58], U. Chattopadhyay[81], J. Chauveau[169], M. Chefdeville[164], R. Chehab[89], A. Chen[201], C. H. Chen[203], J. Chen[102], J. W. Chen[210], K. F. Chen[210], M. Chen[330,102], S. Chen[199], Y. Chen[1], Y. Chen[102], J. Cheng[102], T. P. Cheng[351], B. Cheon[66], M. Chera[47], Y. Chi[102], P. Chiappetta[28], M. Chiba[276], T. Chikamatsu[193], I. H. Chiu[210,210], G. C. Cho[220], V. Chobanova[186], J. B. Choi[36,36], K. Choi[157], S. Y. Choi[37], W. Choi[375,248], Y. I. Choi[260], S. Choroba[47], D. Choudhury[326], D. Chowdhury[83], G. Christian[358,140], M. Church[58], J. Chyla[105], W. Cichalewski[263,47], R. Cimino[174], D. Cinca[337], J. Clark[58], J. Clarke[258,40], G. Claus[94], E. Clement[316,259], C. Clerc[172], J. Cline[187], C. Coca[206], T. Cohen[251], P. Colas[21], A. Colijn[213], N. Colino[31], C. Collard[94], C. Colledani[94], N. Collomb[258], J. Collot[170], C. Combaret[89], B. Constance[33], C. A. Cooper[58], W. E. Cooper[58], G. Corcella[174], E. Cormier[29], R. Cornat[172], P. Cornebise[167], F. Cornet[281], G. Corrado[123], F. Corriveau[187], J. Cortes[286], E. Cortina Gil[303], S. Costa[308], F. Couchot[167], F. Couderc[21], L. Cousin[94], R. Cowan[185], W. Craddock[251], A. C. Crawford[58], J. A. Crittenden[43], J. Cuevas[283], D. Cuisy[167], F. Cullinan[237], B. Cure[33], E. Currás Rivera[110], D. Cussans[316], J. Cvach[105], M. Czakon[235], K. Czuba[401], H. Czyz[365], J. D'Hondt[399], W. Da Silva[169], O. Dadoun[167], M. Dahiya[327], J. Dai[102], C. Dallapiccola[346], C. Damerell[259], M. Danilov[107], D. Dannheim[33], N. Dascenzo[47,238], S. Dasu[384], A. K. Datta[67], T. S. Datta[115], P. Dauncey[80], T. Davenne[259], J. David[169], M. Davier[167], W. De Boer[90], S. De Cecco[169], S. De Curtis[120], N. De Groot[97,213], P. De Jong[213], S. De Jong[97,213], C. De La Taille[93], G. De Lentdecker[307], S. De Santis[177], J. B. De Vivie De Regie[167], A. Deandrea[89], P. P. Dechant[49], D. Decotigny[172], K. Dehmelt[257], J. P. Delahaye[251,33], N. Delerue[167], O. Delferriere[21], F. Deliot[21], G. Della Ricca[388], P. A. Delsart[170], M. Demarteau[7], D. Demin[142], R. Dermisek[87], F. Derue[169], K. Desch[295], S. Descotes-Genon[171], A. Deshpande[252], A. Dexter[40], A. Dey[81], S. Dhawan[405], N. Dhingra[226], V. Di Benedetto[58,123], B. Di Girolamo[33], M. A. Diaz[231], A. Dieguez[311], M. Diehl[47], R. Diener[47], S. Dildick[331], M. O. Dima[206], P. Dinaucourt[167,93], M. S. Dixit[19], T. Dixit[252], L. Dixon[251], A. Djouadi[171], S. Doebert[33], M. Dohlus[47], Z. Dolezal[34], H. Dong[102], L. Dong[102], A. Dorokhov[94], A. Dosil[112], A. Dovbnya[208], T. Doyle[332], G. Doziere[94], M. Dragicevic[224], A. Drago[174], A. J. Dragt[345], Z. Drasal[34], I. Dremin[179], V. Drugakov[209], J. Duarte Campderros[110], F. Duarte Ramos[33], A. Dubey[272], A. Dudarev[142], E. Dudas[171,171], L. Dudko[180], C. Duerig[47], G. Dugan[43], W. Dulinski[94], F. Dulucq[93], L. Dumitru[206], P. J. Dunne[80], A. Duperrin[27], M. Düren[147], D. Dzahini[170], H. Eberl[224], G. Eckerlin[47], P. Eckert[297], N. R. Eddy[58],

W. Ehrenfeld[295], G. Eigen[314], S. Eisenhardt[329], L. Eklund[332], L. Elementi[58], U. Ellwanger[171], E. Elsen[47], I. Emeliantchik[209], L. Emery[7], K. Enami[71], K. Endo[71], M. Endo[375], J. Engels[47], C. Englert[49], S. Eno[345], A. Enomoto[71], S. Enomoto[197], F. Eozenou[21], R. Erbacher[320], G. Eremeev[269], J. Erler[287], R. Escribano[294], D. Esperante Pereira[108], D. Espriu[311], E. Etzion[265,33], S. Eucker[47], A. Evdokimov[336,107], E. Ezura[71], B. Faatz[47], G. Faisel[201], L. Fano[125], A. Faraggi[340], A. Fasso[251], A. Faus-Golfe[108], L. Favart[307], N. Feege[257], J. L. Feng[321], T. Ferber[47], J. Ferguson[33], J. Fernández[283], P. Fernández Martínez[108], E. Fernandez[294,293], M. Fernandez Garcia[110], J. L. Fernandez-Hernando[130], P. Fernandez-Martinez[32], J. Fernandez-Melgarejo[33], A. Ferrer[108], F. Ferri[21], S. Fichet[117], T. Fifield[347], L. Filkov[179], F. Filthaut[97,213], A. Finch[176], H. E. Fisk[58], T. Fiutowski[2], H. Flaecher[316], J. W. Flanagan[71], I. Fleck[301], M. Fleischer[47], C. Fleta[32], J. Fleury[93], D. Flores[32], M. Foley[58], M. Fontannaz[171], K. Foraz[33], N. Fornengo[128], F. Forti[126,391], B. Foster[47,140], M. C. Fouz[31], P. H. Frampton[353], K. Francis[7], S. Frank[224], A. Freitas[361], A. Frey[64], R. Frey[356], M. Friedl[224], C. Friedrich[48], M. Frigerio[163], T. Frisson[167], M. Frotin[172], R. Frühwirth[224], R. Fuchi[378], E. Fuchs[47], K. Fujii[71], J. Fujimoto[71], H. Fuke[134], B. Fuks[94,33], M. Fukuda[71], S. Fukuda[71], K. Furukawa[71], T. Furuya[71], T. Fusayasu[195], J. Fuster[108], N. Fuster[108], Y. Fuwa[95,159], A. Gaddi[33], K. Gadow[47], F. Gaede[47], R. Gaglione[164], S. Galeotti[126], C. Gallagher[356], A. A. Gallas Torreira[112], L. Gallin-Martel[170], A. Gallo[174], D. Gamba[140,33], D. Gamba[128], J. Gao[102], Y. Gao[24], P. H. Garbincius[58], F. Garcia[69], C. Garcia Canal[288], J. E. Garcia Navarro[108], P. Garcia-Abia[31], J. J. Garcia-Garrigos[108], L. Garcia-Tabares[31], C. García[108], J. V. García Esteve[286], I. García García[108], S. K. Garg[408], L. Garrido[311], E. Garutti[333], T. Garvey[167,261], M. Gastal[33], F. Gastaldi[172], C. Gatto[58,123], N. Gaur[326], D. Gavela Pérez[31], P. Gay[168], M. B. Gay Ducati[109], L. Ge[251], R. Ge[102], A. Geiser[47], A. Gektin[100], A. Gellrich[47], M. H. Genest[170], R. L. Geng[269], S. Gentile[387,127], A. Gerbershagen[33,358], R. Gerig[7], S. German[111], H. Gerwig[33], S. Ghazaryan[47], P. Ghislain[169], D. K. Ghosh[81], S. Ghosh[115], S. Giagu[387,127], L. Gibbons[43], S. Gibson[139,33], V. Gilewsky[143], A. Gillespie[328], F. Gilman[20], B. Gimeno Martínez[108], D. M. Gingrich[312,279], C. M. Ginsburg[58], D. Girard[164], J. Giraud[170], G. F. Giudice[33], L. Gladilin[180], P. Gladkikh[208], C. J. Glasman[343,40], R. Glattauer[224], N. Glover[49], J. Gluza[365], K. Gnidzinska[263], R. Godbole[83], S. Godfrey[19], F. Goertz[54], M. Goffe[94], N. Gogitidze[179,47], J. Goldstein[316], B. Golob[144,341], G. Gomez[110], V. Goncalves[290], R. J. Gonsalves[256], I. González[283], S. González De La Hoz[108], F. J. González Sánchez[110], G. Gonzalez Parra[294], S. Gopalakrishna[103], I. Gorelov[352], D. Goswami[86], S. Goswami[229], T. Goto[71], K. Gotow[398], P. Göttlicher[47], M. Götze[385], A. Goudelis[165], P. Goudket[258], S. Gowdy[33], O. A. Grachov[309], N. A. Graf[251], M. Graham[251], A. Gramolin[15], R. Granier De Cassagnac[172], P. Grannis[257], P. Gras[21], M. Grecki[47], T. Greenshaw[339], D. Greenwood[181], C. Grefe[33], M. Grefe[111], I. M. Gregor[47], D. Grellscheid[49], G. Grenier[89], M. Grimes[316], C. Grimm[58], O. Grimm[53], B. Grinyov[100], B. Gripaios[323], K. Grizzard[141], A. Grohsjean[47], C. Grojean[294,33], J. Gronberg[178], D. Grondin[170], S. Groote[370], P. Gros[240], M. Grunewald[310], B. Grzadkowski[382], J. Gu[102], M. Guchait[262], S. Guiducci[174], E. Guliyev[172], J. Gunion[320], C. Günter[47], C. Gwilliam[339], N. Haba[75], H. Haber[322], M. Hachimine[197], Y. Haddad[172], L. Hagge[47], M. Hagihara[378], K. Hagiwara[71,158], J. Haley[216], G. Haller[251], J. Haller[333], K. Hamaguchi[375], R. Hamatsu[276], G. Hamel De Monchenault[21], L. L. Hammond[58], P. Hamnett[47], L. Han[364], T. Han[361], K. Hanagaki[223], J. D. Hansen[211], K. Hansen[47], P. H. Hansen[211], X. Q. Hao[70], K. Hara[71], K. Hara[378], T. Hara[71], D. Harada[83], K. Harada[161], K. Harder[259], T. Harion[297], R. V. Harlander[385], E. Harms[58], M. Harrison[13], O. Hartbrich[47,385], A. Hartin[47], T. Hartmann[300], J. Harz[47], S. Hasegawa[197], T. Hasegawa[71], Y. Hasegawa[248], M. Hashimoto[38], T. Hashimoto[62], C. Hast[251], S. Hatakeyama[135], J. M. Hauptman[118], M. Hauschild[33], M. Havranek[105], C. Hawkes[315], T. Hayakawa[197], H. Hayano[71], K. Hayasaka[198], M. Hazumi[71,253], H. J. He[24],

C. Hearty[317,104], H. F. Heath[316], T. Hebbeker[235], M. Heck[90], V. Hedberg[183], D. Hedin[217], S. M. Heindl[90], S. Heinemeyer[110], I. Heinze[47], A. Hektor[205], S. Henrot-Versille[167], O. Hensler[47], A. Heo[23], J. Herbert[258], G. Herdoiza[138], B. Hermberg[47], J. J. Hernández-Rey[108], M. J. Herrero[111], B. Herrmann[165], A. Hervé[384], J. Hewett[251], S. Hidalgo[32], B. Hidding[333,318], N. Higashi[375], N. Higashi[71], T. Higo[71], E. Higón Rodríguez[108], T. Higuchi[150], M. Hildreth[354], C. T. Hill[58], S. Hillert[295], S. Hillier[315], T. Himel[251], A. Himmi[94], S. Himori[272], Z. Hioki[374], B. Hippolyte[94], T. Hiraki[159], K. Hirano[136], S. Hirano[197], K. Hirata[71], T. Hirose[276], M. Hirsch[108], J. Hisano[197], P. M. Ho[210], A. Hoang[302], A. Hocker[58], A. Hoecker[33], M. Hoeferkamp[352], M. Hoffmann[47], W. Hollik[186], K. Homma[72], Y. Homma[154], S. Honda[378], T. Honda[71], Y. Honda[71], N. T. Hong Van[106], K. Honkavaara[47], T. Honma[71], T. Hori[236], T. Horiguchi[272], Y. Horii[197], A. Horio[196], R. Hosaka[377], Y. Hoshi[271], H. Hoshino[197], K. Hosoyama[71], J. Y. Hostachy[170], G. W. Hou[210], M. Hou[102], A. Hoummada[184], M. S. Hronek[58], T. Hu[102], C. Hu-Guo[94], M. Huang[24], T. Huang[102], E. Huedem[58], F. Hügging[295], J. L. Hugon[330], C. Hugonie[173], K. Huitu[335], P. Q. Hung[380], C. Hunt[80], U. Husemann[90], G. Hussain[24], D. Hutchcroft[339], Y. Hyakutake[79], J. C. Ianigro[89], L. E. Ibanez[111], M. Ibe[96], M. Idzik[2], H. Igarashi[78], Y. Igarashi[71], K. Igi[236], A. Ignatenko[209], O. Igonkina[213], T. Iijima[198,197], M. Iinuma[73], Y. Iiyama[20], H. Ikeda[134], K. Ikeda[71], K. Ikematsu[301], J. I. Illana[281], V. A. Ilyin[207,180], A. Imhof[333], T. Inagaki[236], T. Inagaki[197], K. Inami[197], S. Inayoshi[248], K. Inoue[161], A. Irles[108], S. Isagawa[71], N. Ishibashi[378], A. Ishida[375], K. Ishida[212], N. Ishihara[71], S. Ishihara[77], K. Ishii[71], A. Ishikawa[272], K. Ishikawa[375], K. I. Ishikawa[72], K. Ishikawa[75], T. Ishikawa[71], M. Ishitsuka[275], K. Ishiwata[17], G. Isidori[174], A. Ismail[251], S. Iso[71], T. Isogai[197], C. Issever[358], K. Itagaki[272], T. Itahashi[223], A. Ito[275], F. Ito[378], S. Ito[272], R. Itoh[71], E. Itou[71], M. I. Ivanyan[26], G. Iwai[71], S. Iwamoto[375], T. Iwamoto[116], H. Iwasaki[71], M. Iwasaki[71], Y. Iwashita[95], S. Iwata[71], S. Iwata[276], T. Izubuchi[13,236], Y. Izumiya[272], S. Jablonski[401], F. Jackson[258], J. A. Jacob[316], M. Jacquet[167], P. Jain[40], P. Jaiswal[59], W. Jalmuzna[263], E. Janas[401], R. Jaramillo Echeverría[110], J. Jaros[251], D. Jatkar[67], D. Jeans[375], R. Jedziniak[58], M. J. Jenkins[176,40], K. Jensch[47], C. P. Jessop[354], T. Jezynski[47], M. Jimbo[35], S. Jin[102], O. Jinnouchi[275], M. D. Joergensen[211], A. S. Johnson[251], S. Jolly[309], D. T. Jones[340], J. Jones[258,40], R. M. Jones[343,40], L. Jönsson[183], N. Joshi[237], C. K. Jung[257,150], N. Juntong[343,40], A. Juste[88,294], W. Kaabi[167], M. Kadastik[205], M. Kado[167,33], K. Kadota[197], E. Kajfasz[27], R. Kajikawa[197], Y. Kajiura[197], M. Kakizaki[377], E. Kako[71], H. Kakuhata[377], H. Kakuno[276], A. Kalinin[258], J. Kalinowski[382], G. E. Kalmus[259], K. Kamada[47], J. Kaminski[295], T. Kamitani[71], Y. Kamiya[116], Y. Kamiya[71], R. Kammering[47], T. Kamon[266], J. I. Kamoshita[60], T. Kanai[275], S. Kananov[265], K. Kanaya[378], M. Kaneda[33], T. Kaneko[71,253], S. Kanemura[377], K. Kaneta[75], W. Kang[102], D. Kanjilal[115], K. Kannike[205], F. Kapusta[169], D. Kar[332], P. Karataev[237,139], P. E. Karchin[403], D. Karlen[379,279], S. Karstensen[47], Y. Karyotakis[164], M. Kasemann[47], V. S. Kashikhin[58], S. Kashiwagi[273], A. Kataev[98], V. Katalev[48], Y. Kataoka[116], N. Katayama[150], R. Katayama[375], E. Kato[272], K. Kato[155], S. Kato[71], Y. Kato[153], T. Katoh[71], A. Kaukher[47], S. Kawabata[71], S. I. Kawada[73], K. Kawagoe[161], M. Kawai[71], T. Kawamoto[116], H. Kawamura[71], M. Kawamura[71], Y. Kawamura[248], S. Kawasaki[71], T. Kawasaki[212], H. Kay[47], S. Kazama[375], L. Keegan[111], J. Kehayias[150], L. Keller[251], M. A. Kemp[251], J. J. Kempster[237], C. Kenney[251], I. Kenyon[315], R. Kephart[58], J. Kerby[7], K. Kershaw[33], J. Kersten[333], K. Kezzar[151], V. G. Khachatryan[26], M. A. Khan[23], S. A. Khan[242], Y. Khoulaki[184], V. Khoze[49], H. Kichimi[71], R. Kieffer[33], C. Kiesling[186], M. Kikuchi[377], Y. Kikuta[71], M. Killenberg[47], C. S. Kim[408], D. W. Kim[63], D. Kim[23], E. J. Kim[36,36], E. S. Kim[23], G. Kim[23], H. S. Kim[23], H. D. Kim[245], J. Kim[63], S. H. Kim[378], S. K. Kim[245], S. G. Kim[87], Y. I. Kim[358,140], Y. Kimura[71], R. E. Kirby[251], F. Kircher[21], Y. Kishimoto[96], L. Kisslinger[20], T. Kitahara[375], R. Kitano[272], Y. Kiyo[146,71], C. Kleinwort[47], W. Klempt[33], P. M. Kluit[213], V. Klyukhin[180,33], M. Knecht[28], J. L. Kneur[163],

B. A. Kniehl[333], K. Ko[251], P. Ko[158], D. Kobayashi[275], M. Kobayashi[71], N. Kobayashi[71], T. Kobayashi[116], M. Koch[295], P. Kodys[34], U. Koetz[47], E. N. Koffeman[213], M. Kohda[210], S. Koike[71], Y. Kojima[71], K. Kolodziej[365], Y. Kolomensky[319,177], S. Komamiya[375], T. Kon[244], P. Konar[229], Y. Kondou[71], D. Kong[23], K. Kong[338], O. C. Kong[201], T. Konno[275,275], V. Korbel[47], J. G. Körner[138], S. Korpar[344,144], S. R. Koscielniak[279], D. Kostin[47], K. Kotera[248], W. Kotlarski[382], J. Kotula[268], E. Kou[167], V. Kovalenko[333], S. V. H. Kox[170], K. Koyama[75], M. Krämer[235], S. Kraml[170], M. Krammer[224], M. W. Krasny[169], F. Krauss[49], T. Krautscheid[295], M. Krawczyk[382], K. Krempetz[58], P. Križan[341,144], B. E. Krikler[80], A. Kronfeld[58], K. Kruchinin[237,139], D. Krücker[47], K. Krüger[47], B. Krupa[268], Y. P. Kuang[24], K. Kubo[71], T. Kubo[71], T. Kubota[347], T. Kubota[275], Y. Kubyshin[298,180], V. Kuchler[58], I. M. Kudla[202], D. Kuehn[47], J. H. Kuehn[92], C. Kuhn[94], S. Kulis[2], S. Kulkarni[170], A. Kumar[10], S. Kumar[86], T. Kumita[276], A. Kundu[16], Y. Kuno[223], C. M. Kuo[201], M. Kurachi[198], A. Kuramoto[253], M. Kurata[375], Y. Kurihara[71], M. Kuriki[73,71], T. Kurimoto[377], S. Kuroda[71], K. Kurokawa[71], S. I. Kurokawa[71], H. Kuwabara[276], M. Kuze[275], J. Kvasnicka[105], P. Kvasnicka[34], Y. Kwon[408], L. Labun[210], C. Lacasta[108], T. Lackowski[58], D. Lacour[169], V. Lacuesta[108], R. Lafaye[164], G. Lafferty[343], B. Laforge[169], I. Laktineh[89], R. L. Lander[320], K. Landsteiner[111], S. Laplace[169], K. J. Larsen[213], R. S. Larsen[251], T. Lastovicka[105], J. I. Latorre[311], S. Laurien[333], L. Lavergne[169], S. Lavignac[22], R. E. Laxdal[279], A. C. Le Bihan[94], F. R. Le Diberder[167], A. Le-Yaouanc[171], A. Lebedev[13], P. Lebrun[33], T. Lecompte[7], T. Leddig[300], F. Ledroit[170], B. Lee[25], K. Lee[158], M. Lee[177], S. H. Lee[260], S. W. Lee[267], Y. H. Lee[210], J. Leibfritz[58], K. Lekomtsev[71], L. Lellouch[28], M. Lemke[47], F. R. Lenkszus[7], A. Lenz[49,33], O. Leroy[27], C. Lester[323], L. Levchuk[208], J. Leveque[164], E. Levichev[15], A. Levy[265], I. Levy[265], J. R. Lewandowski[251], B. Li[24], C. Li[364], C. Li[102], D. Li[102], H. Li[380], L. Li[195], L. Li[247], L. Li[364], S. Li[102], W. Li[102], X. Li[102], Y. Li[24], Y. Li[24], Y. Li[24], Z. Li[251], Z. Li[102], J. J. Liau[210], V. Libov[47], L. Lilje[47], J. G. Lima[217], C. J. D. Lin[204], C. M. Lin[154], C. Y. Lin[201], H. Lin[102], H. H. Lin[210], F. L. Linde[213], R. A. Lineros[108], L. Linssen[33], R. Lipton[58], M. Lisovyi[47], B. List[47], J. List[47], B. Liu[24], J. Liu[364], R. Liu[102], S. Liu[167], S. Liu[247], W. Liu[7], Y. Liu[102], Y. Liu[337,58], Z. Liu[361], Z. Liu[102], Z. Liu[102], A. Lleres[170], N. S. Lockyer[279,317], W. Lohmann[48,12], E. Lohrmann[333], T. Lohse[76], F. Long[102], D. Lontkovskyi[47], M. A. Lopez Virto[110], X. Lou[102,372], A. Lounis[167], M. Lozano Fantoba[32], J. Lozano-Bahilo[281], C. Lu[232], R. S. Lu[210], S. Lu[47], A. Lucotte[170], F. Ludwig[47], S. Lukic[396], O. Lukina[180], N. Lumb[89], B. Lundberg[183], A. Lunin[58], M. Lupberger[295], B. Lutz[47], P. Lutz[21], T. Lux[294], K. Lv[102], M. Lyablin[142], A. Lyapin[237,139], J. Lykken[58], A. T. Lytle[262], L. Ma[258], Q. Ma[102], R. Ma[312], X. Ma[102], F. Machefert[167], N. Machida[377], J. Maeda[276], Y. Maeda[159], K. Maeshima[58], F. Magniette[172], N. Mahajan[229], F. Mahmoudi[168,33], S. H. Mai[201], C. Maiano[119], H. Mainaud Durand[33], S. Majewski[356], S. K. Majhi[81], N. Majumdar[241], G. Majumder[262], I. Makarenko[47], V. Makarenko[209], A. Maki[71], Y. Makida[71], D. Makowski[263], B. Malaescu[169], J. Malcles[21], U. Mallik[337], S. Malvezzi[121], O. B. Malyshev[258,40], Y. Mambrini[171], A. Manabe[71], G. Mancinelli[27], S. K. Mandal[150], S. Mandry[309,186], S. Manen[168], R. Mankel[47], S. Manly[363], S. Mannai[303], Y. Maravin[149], G. Marchiori[169], M. Marcisovsky[105,45], J. Marco[110], D. Marfatia[338], J. Marin[31], E. Marin Lacoma[251], C. Marinas[295], T. W. Markiewicz[251], O. Markin[107], J. Marshall[323], S. Martí-García[108], A. D. Martin[49], V. J. Martin[329], G. Martin-Chassard[93], T. Martinez De Alvaro[31], C. Martinez Rivero[110], F. Martinez-Vidal[108], H. U. Martyn[235,47], T. Maruyama[251], A. Masaike[159], T. Mashimo[116], T. Masubuchi[116], T. Masuda[159], M. Masuzawa[71], Z. Mateusz[401], A. Matheisen[47], H. Mathez[89], J. Matias[293], H. Matis[177], T. Matsubara[276], T. Matsuda[71], T. Matsui[377], S. Matsumoto[161], S. Matsumoto[150], Y. Matsumoto[220], H. Matsunaga[71], T. Matsushita[154], T. S. Mattison[317], V. A. Matveev[142], U. Mavric[47], G. Mavromanolakis[33], K. Mawatari[399], S. J. Maxfield[339], K. Mazumdar[262],

A. Mazzacane[58,123], R. L. Mccarthy[257], D. J. Mccormick[251], J. Mccormick[251], K. T. Mcdonald[232], R. Mcduffee[324], P. Mcintosh[258], B. Mckee[251], M. Medinnis[47], S. Mehlhase[211], T. Mehrling[47,333], A. Mehta[339], B. Mele[127], R. E. Meller[43], I. A. Melzer-Pellmann[47], L. Men[102], G. Mendiratta[83], Z. Meng[316], M. H. Merk[213,400], M. Merkin[180], A. Merlos[32], L. Merminga[279], A. B. Meyer[47], A. Meyer[235], N. Meyners[47], Z. Mi[102], P. Michelato[119], S. Michizono[71], S. Mihara[71], A. Mikhailichenko[43], D. J. Miller[309], C. Milstene[403], Y. Mimura[210], D. Minic[398], L. Mirabito[89], S. Mishima[387], T. Misumi[13], W. A. Mitaroff[224], T. Mitsuhashi[71], S. Mitsuru[71], K. Miuchi[154], K. Miyabayashi[200], A. Miyamoto[71], H. Miyata[212], Y. Miyazaki[161], T. Miyoshi[71], R. Mizuk[107], K. Mizuno[3], U. Mjörnmark[183], J. Mnich[47], G. Moeller[47], W. D. Moeller[47], K. Moenig[48], K. C. Moffeit[251], P. Mohanmurthy[269], G. Mohanty[262], L. Monaco[119], S. Mondal[81], C. Monini[170], H. Monjushiro[71], G. Montagna[359,124], S. Monteil[168], G. Montoro[298], I. Montvay[47], F. Moortgat[53], G. Moortgat-Pick[333,47], P. Mora De Freitas[172], C. Mora Herrera[30], G. Moreau[171], F. Morel[94], A. Morelos-Pineda[280], M. Moreno Llacer[108], S. Moretti[367,259], V. Morgunov[47,107], T. Mori[71], T. Mori[272], T. Mori[116], Y. Morita[71], S. Moriyama[96,150], L. Moroni[121], Y. Morozumi[71], H. G. Moser[186], A. Moszczynski[268], K. Motohashi[275], T. Moulik[249], G. Moultaka[163], D. Moya Martin[110], S. K. Mtingwa[215], G. S. Muanza[27], M. Mühlleitner[91], A. Mukherjee[85], S. Mukhopadhyay[241], M. Mulders[33], D. Muller[251], F. Müller[47], T. Müller[90], V. S. Mummidi[83], A. Münnich[47], C. Munoz[111], F. J. Muñoz Sánchez[110], H. Murayama[375,319], R. Murphy[7], G. Musat[172], A. Mussgiller[47], R. Muto[71], T. Nabeshima[377], K. Nagai[71], K. Nagai[378], S. Nagaitsev[58], T. Nagamine[272], K. Nagano[71], K. Nagao[71], Y. Nagashima[223], S. C. Nahn[185], P. Naik[316], D. Naito[159], T. Naito[71], H. Nakai[71], K. Nakai[71,223], Y. Nakai[161], Y. Nakajima[177], E. Nakamura[71], H. Nakamura[71], I. Nakamura[71], S. Nakamura[159], S. Nakamura[71], T. Nakamura[116], K. Nakanishi[71], E. Nakano[222], H. Nakano[212], H. Nakano[272], Y. Namito[71], W. Namkung[230], H. Nanjo[159], C. D. Nantista[251], O. Napoly[21], Y. Nara[4], T. Narazaki[272], S. Narita[131], U. Nauenberg[324], T. Naumann[48], S. Naumann-Emme[47], J. Navarro[108], A. Navitski[47], H. Neal[251], K. Negishi[272], K. Neichi[270], C. A. Nelson[255], T. K. Nelson[251], S. Nemecek[105], M. Neubert[138], R. Neuhaus[218], L. J. Nevay[237], D. M. Newbold[316,259], O. Nezhevenko[58], F. Nguyen[175], M. Nguyen[172], M. N. Nguyen[251], T. T. Nguyen[106], R. B. Nickerson[358], O. Nicrosini[124], C. Niebuhr[47], J. Niehoff[58], M. Niemack[43], U. Nierste[92], H. Niinomi[159], I. Nikolic[169], H. P. Nilles[295], S. Nishida[71], H. Nishiguchi[71], K. Nishiwaki[67], O. Nitoh[277], L. Niu[24], R. Noble[251], M. Noji[71], M. Nojiri[71,150], S. Nojiri[197,198], D. Nölle[47], A. Nomerotski[358], M. Nomura[135], T. Nomura[201], Y. Nomura[319,177], C. Nonaka[198], J. Noonan[7], E. Norbeck[337], Y. Nosochkov[251], D. Notz[47], O. Novgorodova[48,12], A. Novokhatski[251], J. A. Nowak[349], M. Nozaki[71], K. Ocalan[192], J. Ocariz[169], S. Oda[161], A. Ogata[71], T. Ogawa[248], T. Ogura[248], A. Oh[343], S. K. Oh[156], Y. Oh[23], K. Ohkuma[61], T. Ohl[145], Y. Ohnishi[71], K. Ohta[189], M. Ohta[71,253], S. Ohta[71,253], N. Ohuchi[71], K. Oishi[161], R. Okada[71], Y. Okada[71,253], T. Okamura[71], H. Okawa[13], T. Okugi[71], T. Okui[59], K. I. Okumura[161], Y. Okumura[52,58], L. Okun[107], H. Okuno[236], C. Oleari[390], C. Oliver[31], B. Olivier[186], S. L. Olsen[245], M. Omet[253,71], T. Omori[71], Y. Onel[337], H. Ono[214], Y. Ono[272], D. Onoprienko[251], Y. Onuki[116,150], P. Onyisi[371], T. Oogoe[71], Y. Ookouchi[159], W. Ootani[116], M. Oreglia[52], M. Oriunno[251], M. C. Orlandea[206], J. Orloff[168], M. Oroku[375,71], R. S. Orr[376], J. Osborne[33], A. Oskarsson[183], P. Osland[314], A. Osorio Oliveros[282], L. Österman[183], H. Otono[223], M. Owen[343], Y. Oyama[71], A. Oyanguren[108], K. Ozawa[71,375], J. P. Ozelis[58,191], D. Ozerov[47], G. Pásztor[304,99], H. Padamsee[43], C. Padilla[294], C. Pagani[119,386], R. Page[316], R. Pain[169], S. Paktinat Mehdiabadi[101], A. D. Palczewski[269], S. Palestini[33], F. Palla[126], M. Palmer[58], F. Palomo Pinto[285], W. Pan[102], G. Pancheri[174], M. Pandurovic[396], O. Panella[125], A. Pankov[227], Y. Papaphilippou[33], R. Paparella[119], A. Paramonov[7], E. K. Park[75], H. Park[23], S. I. Park[23], S. Park[260], S. Park[373], W. Park[23],

A. Parker[323], B. Parker[13], C. Parkes[343], V. Parma[33], Z. Parsa[13], R. Partridge[251], S. Pastor[108], E. Paterson[251], M. Patra[83], J. R. Patterson[43], M. Paulini[20], N. Paver[129], S. Pavy-Bernard[167], B. Pawlik[268], A. Pérez Vega-Leal[285], B. Pearson[355], J. S. Pedersen[211], A. Pedicini[397], S. Pedraza López[108], G. Pei[102], S. Pei[102], G. Pellegrini[32], A. Pellegrino[213], S. Penaranda[286], H. Peng[364], X. Peng[102], M. Perelstein[43], E. Perez[112], M. A. Perez-Garcia[284,114], M. Perez-Victoria[281], S. Peris[293], D. Perret-Gallix[164], H. Perrey[47], T. M. Perry[384], M. E. Peskin[251], P. Petagna[33], R. Y. Peters[64,47], T. C. Petersen[211], D. P. Peterson[43], T. Peterson[58], E. Petrakou[210], A. A. Petrov[403], A. Petrukhin[89,107], S. Pfeiffer[47], H. Pham[94], K. H. Phan[395,71], N. Phinney[251], F. Piccinini[124], A. Pich[108], R. Pichai[85], J. Piedra[283], J. Piekarski[401], A. Pierce[348], P. Pierini[119], N. Pietsch[333,47], A. Pineda[293], J. Pinfold[312,152], A. Piotrowski[263], Y. Pischalnikov[58], R. Pittau[281], M. Pivi[251], W. Placzek[132], T. Plehn[296], M. A. Pleier[13], M. Poelker[269], L. Poggioli[167], I. Pogorelsky[13], V. Poireau[164], M. E. Pol[30], I. Polak[105], F. Polci[169], M. Polikarpov[107], T. Poll[316,259], M. W. Poole[258,40], W. Porod[145], F. C. Porter[17], S. Porto[333], J. Portolés[108], R. Pöschl[167], S. Poss[33], C. T. Potter[356], P. Poulose[86], K. T. Pozniak[401], V. Prahl[47], R. Prepost[384], C. Prescott[251], D. Price[87], T. Price[315], P. S. Prieto[58], D. Protopopescu[332], D. Przyborowski[2], K. Przygoda[263], H. Przysiezniak[164], F. Ptochos[325], J. Puerta-Pelayo[31], C. Pulvermacher[90], M. Purohit[366], Q. Qin[102], F. Qiu[102], H. Qu[102], A. Quadt[64], G. Quast[90], D. Quirion[32], M. Quiros[88], J. Rademacker[316], R. Rahmat[350], S. Rai[67], M. Raidal[205], S. Rakshit[84], M. Ramilli[333], F. Rarbi[170], P. Ratoff[176], T. Raubenheimer[251], M. Rauch[91], L. Raux[93], G. Raven[400,213], P. Razis[325], V. Re[124], S. Redford[33], C. E. Reece[269], I. Reichel[177], A. Reichold[358,140], P. Reimer[105], M. Reinecke[47], A. Rekalo[100], J. Repond[7], J. Resta-Lopez[108], J. Reuter[47], J. T. Rhee[156], P. M. Ribeiro Cipriano[47], A. Ribon[33], G. Ricciardi[292,123], F. Richard[167], E. Richter-Was[132], G. Riddone[33], S. Riemann[48], T. Riemann[48], M. Rijssenbeek[257], K. Riles[348], C. Rimbault[167], R. Rimmer[269], S. D. Rindani[229], A. Ringwald[47], L. Rinolfi[33], I. Ripp-Baudot[94], I. Riu[294], T. G. Rizzo[251], P. Robbe[167], J. Roberts[140,33], A. Robson[332], G. Rodrigo[108], P. Rodriguez[251], P. Rodriguez Perez[112], K. Rolbiecki[111], P. Roloff[33], R. S. Romaniuk[401], E. Romero Adam[108], A. Ronzhin[58], L. Roos[169], E. Ros[108], A. Rosca[47], C. Rosemann[47], J. Rosiek[382], M. C. Ross[251], R. Rossmanith[90], S. Roth[235], J. Rouënè[167], A. Rowe[58], P. Rowson[251], A. Roy[115], L. Royer[168], P. Royole-Degieux[93], C. Royon[21], A. Rozanov[27], M. Ruan[172], D. L. Rubin[43], I. Rubinskiy[47], R. Rückl[145], R. Ruiz[361], R. Ruiz De Austri[108], P. Ruiz Valls[108], P. Ruiz-Femenía[108], A. Ruiz-Jimeno[110], R. Ruland[251], V. Rusinov[107], J. J. Russell[251], I. Rutkowski[401], V. Rybnikov[47], A. Ryd[43], A. Sabio Vera[111], B. Sabirov[142], J. J. Saborido Silva[112], H. F. W. Sadrozinski[322], T. Saeki[71], B. Safarzadeh[101], P. Saha[305], H. Sahoo[7], A. Sailer[33], N. Saito[71], T. Saito[272], T. Sakaguchi[13], H. Sakai[71], K. Sakai[71], K. Sakaue[402], K. Sakurai[47], R. Salerno[172], J. Salfeld-Nebgen[47], J. Salt[108], L. Sanchez[31], M. A. Sanchis Lozano[108], J. Sandweiss[405], A. Santa[377], A. Santagata[286], A. Santamaria[108], P. Santorelli[292], T. Sanuki[272], A. A. Sapronov[142], M. Sasaki[96], H. Sato[248], N. Sato[71], Y. Sato[272], M. Satoh[71], E. Sauvan[164], V. Saveliev[238,47], A. Savoy-Navarro[166,126], M. Sawabe[71], R. Sawada[116], H. Sawamura[402], L. Sawyer[181], O. Schäfer[300,47], R. Schäfer[47], J. Schaffran[47], T. Schalk[322,251], R. D. Schamberger[257], J. Scheirich[34], G. Schierholz[47], F. P. Schilling[90], F. Schirra[89], F. Schlander[47], H. Schlarb[47], D. Schlatter[33], P. Schleper[333], J. L. Schlereth[7], R. D. Schlueter[177], C. Schmidt[47], U. Schneekloth[47], S. Schnetzer[239], T. Schoerner-Sadenius[47], M. Schram[225], H. J. Schreiber[48], S. Schreiber[47], K. P. Schüler[47], D. Schulte[33], H. C. Schultz-Coulon[297], M. Schumacher[5], S. Schumann[64], B. A. Schumm[322], M. H. Schune[167], S. Schuwalow[333,48], C. Schwanda[224], C. Schwanenberger[343], F. Schwartzkopff[295], D. J. Scott[258,58], F. Sefkow[47,33], A. Segui[286], N. Seguin-Moreau[93], S. Seidel[352], Y. Seiya[222], J. Sekaric[338], K. Seki[197], S. Sekmen[33], S. Seletskiy[13], S. Sen[337], E. Senaha[158], K. Senyo[406], S. Senyukov[94], I. Serenkova[227],

D. A. Sergatskov[58], H. Sert[47,333], D. Sertore[119], A. Seryi[358,140], O. Seto[74], R. Settles[186], P. Sha[102], S. Shahid[301], A. Sharma[33], G. Shelkov[142], W. Shen[297], J. C. Sheppard[251], M. Sher[41], C. Shi[102], H. Shi[102], T. Shidara[71], W. Shields[237,139], M. Shimada[71], H. Shimizu[71], Y. Shimizu[272], M. Shimojima[195], S. Shimojima[276], T. Shindou[155], N. Shinoda[272], Y. Shinzaki[272], M. Shioden[78,71], I. Shipsey[233], S. Shirabe[161], M. J. Shirakata[71], T. Shirakata[71], G. Shirkov[142], T. Shishido[71], T. Shishido[71], J. G. Shiu[210], R. Shivpuri[326], R. Shrock[257], T. Shuji[71], N. Shumeiko[209], B. Shuve[228,188], P. Sicho[105], A. M. Siddiqui[133], P. Sievers[33], D. Sikora[401], D. A. Sil[86], F. Simon[186], N. B. Sinev[356], W. Singer[47], X. Singer[47], B. K. Singh[10], R. K. Singh[82], N. Sinha[103], R. Sinha[103], K. Sinram[47], T. Sinthuprasith[14], P. Skubic[355], R. Sliwa[167], I. Smiljanic[396], J. R. Smith[373,7], J. C. Smith[251,43], S. R. Smith[251], J. Smolík[105,45], J. Snuverink[237,139], B. Sobloher[47], J. Sola[311], C. Soldner[186,57], S. Soldner-Rembold[343], D. Son[23], H. S. Song[260], N. Sonmez[51], A. Sopczak[44], D. E. Soper[356], P. Spagnolo[126], S. Spannagel[47], M. Spannowsky[49], A. Sparkes[329], C. M. Spencer[251], H. Spiesberger[138], M. Spira[261], M. Stahlhofen[47], M. Stanescu-Bellu[48], M. Stanitzki[47], S. Stapnes[33], P. Starovoitov[209], F. Staufenbiel[48], L. Steder[47], M. Steder[47], A. Steen[89], G. Steinbrueck[333], M. Steinhauser[92], F. Stephan[48], W. Stephen[237], S. Stevenson[358], I. Stewart[185], D. Stöckinger[264], H. Stoeck[369], M. Strauss[355], S. Striganov[58], D. M. Strom[356], R. Stromhagen[47], J. Strube[33], A. Strumia[205], G. Stupakov[251], N. Styles[47], D. Su[251], F. Su[102], S. Su[313], J. Suarez Gonzalez[209], Y. Sudo[161], T. Suehara[116], F. Suekane[274], Y. Suetsugu[71], R. Sugahara[71], A. Sugamoto[220], H. Sugawara[71], Y. Sugimoto[71], A. Sugiyama[240], H. Sugiyama[377], M. K. Sullivan[251], Y. Sumino[272], T. Sumiyoshi[276,71], H. Sun[102], M. Sun[20], X. Sun[170], Y. Sun[102], Y. Susaki[197], T. Suwada[71], A. Suzuki[71], S. Suzuki[240], Y. Suzuki[71], Y. Suzuki[73], Z. Suzuki[272], K. Swientek[2], C. Swinson[13], Z. M. Szalata[251], B. Szczepanski[47], M. Szelezniak[94], J. Szewinski[202], A. Sznajder[289], L. Szymanowski[202], H. Tabassam[329], K. Tackmann[47], M. Taira[71], H. Tajima[197,251], F. Takahashi[272], R. Takahashi[71], R. Takahashi[75], T. Takahashi[73], Y. Takahashi[197], K. Takata[71], F. Takayama[160], Y. Takayasu[75], H. Takeda[154], S. Takeda[71], T. Takeshita[248], A. Taketani[236], Y. Takeuchi[378], T. Takimi[262], Y. Takubo[71], Y. Tamashevich[47], M. Tamsett[181], M. Tanabashi[198,197], T. Tanabe[116], G. Tanaka[161], M. M. Tanaka[71], M. Tanaka[223], R. Tanaka[73], H. Taniuchi[377], S. Tapprogge[138], E. Tarkovsky[107], M. A. Tartaglia[58], X. R. Tata[334], T. Tauchi[71], M. Tawada[71], G. Taylor[347], A. M. Teixeira[168], V. I. Telnov[15,219], P. Tenenbaum[251], E. Teodorescu[206], S. Terada[71], Y. Teramoto[222], H. Terao[200], A. Terashima[71], S. Terui[71], N. Terunuma[71], M. Terwort[47], M. Tesar[186], F. Teubert[33], T. Teubner[340], R. Teuscher[376], T. Theveneaux-Pelzer[168], D. Thienpont[93,172], J. Thom-Levy[43], M. Thomson[323], J. Tian[71], X. Tian[366], M. Tigner[43], J. Timmermans[213], V. Tisserand[164], M. Titov[21], S. Tjampens[164], K. Tobe[197], K. Tobioka[150,319], K. Toda[278], M. Toda[71], N. Toge[71], J. Tojo[161], K. Tokushuku[71], T. Toma[49], R. Tomas[33], T. Tomita[161], A. Tomiya[223], M. Tomoto[197,198], K. Toms[352], M. Tonini[47], F. Toral[31], E. Torrence[356], E. Torrente-Lujan[33], N. Toumbas[325], C. Touramanis[339], F. Toyoda[161], K. Toyomura[71], G. Trahern[55], T. H. Tran[172], W. Treberspurg[224], J. Trenado[311], M. Trimpl[58], S. Trincaz-Duvoid[169], M. Tripathi[320], W. Trischuk[376], M. Trodden[360], G. Trubnikov[142], H. C. Tsai[39], J. F. Tsai[210], K. H. Tsao[336], R. Tschirhart[58], E. Tsedenbaljir[210], S. Y. Tseng[201], T. Tsuboyama[71], A. Tsuchiya[250], K. Tsuchiya[71], T. Tsukamoto[71], K. Tsumura[197], S. Tsuno[71], T. Tsurugai[189], T. Tsuyuki[96], B. Tuchming[21], P. V. Tyagi[68,254], I. Tyapkin[142], M. Tytgat[331], K. Uchida[295], F. Uchiyama[71], Y. Uchiyama[116], S. Uehara[71], H. Ueno[161], K. Ueno[71], K. Ueno[71], K. Ueshima[274], Y. Uesugi[73], N. Ujiie[71], F. Ukegawa[378], N. Ukita[378], M. Ullán[32], H. Umeeda[72], K. Umemori[71], Y. Unno[66], S. Uozumi[23], J. Urakawa[71], A. M. Uranga[111], J. Urresti[32], A. Ushakov[333], I. Ushiki[272], Y. Ushiroda[71], A. V[83], P. Vázquez Regueiro[112], L. Vacavant[27], G. Valencia[118], L. Valery[168], I. Valin[94], J. W. Valle[108], C. Vallee[27], N. Van Bakel[213], H. Van Der Graaf[213], N. Van Der Kolk[167],

E. Van Der Kraaij[33], B. Van Doren[338], B. Van Eijk[213], R. Van Kooten[87], W. T. Van Oers[279], D. Vanegas[108], P. Vanhoefer[186], P. Vankov[47], P. Varghese[58], A. Variola[167], R. Varma[85], G. Varner[334], G. Vasileiadis[162], A. Vauth[47], J. Velthuis[316], S. K. Vempati[83], V. Vento[108], M. Venturini[177], M. Verderi[172], P. Verdier[89], A. Verdugo[31], A. Vicente[171], J. Vidal-Perona[108], H. L. R. Videau[172], I. Vila[110], X. Vilasis-Cardona[299], E. Vilella[311], A. Villamor[32], E. G. Villani[259], J. A. Villar[286], M. A. Villarejo Bermúdez[108], D. Vincent[169], P. Vincent[169], J. M. Virey[28], A. Vivoli[58], V. Vogel[47], R. Volkenborn[47], O. Volynets[47], F. Von Der Pahlen[110], E. Von Toerne[295], B. Vormwald[47], A. Voronin[180], M. Vos[108], J. H. Vossebeld[339], G. Vouters[164], Y. Voutsinas[94,47], V. Vrba[105,45], M. Vysotsky[107], D. Wackeroth[256], A. Wagner[47], C. E. Wagner[7,52], R. Wagner[7], S. R. Wagner[324], W. Wagner[385], J. Wagner-Kuhr[90], A. P. Waite[251], M. Wakayama[197], Y. Wakimoto[276], R. Walczak[358,140], R. Waldi[300], D. G. E. Walker[251], N. J. Walker[47], M. Walla[47], C. J. Wallace[49], S. Wallon[171,393], D. Walsh[328], S. Walston[178], W. A. T. Wan Abdullah[342], D. Wang[102], G. Wang[102], J. Wang[251], L. Wang[251], L. Wang[52], M. H. Wang[251], M. Z. Wang[210], Q. Wang[102], Y. Wang[102], Z. Wang[24], R. Wanke[138], C. Wanotayaroj[356], B. Ward[8], D. Ward[323], B. Warmbein[47], M. Washio[402], K. Watanabe[71], M. Watanabe[212], N. Watanabe[71], T. Watanabe[155], Y. Watanabe[71], S. Watanuki[272], Y. Watase[71], N. K. Watson[315], G. Watts[383], M. M. Weber[90], H. C. Weddig[47], H. Weerts[7], A. W. Weidemann[251], G. Weiglein[47], A. Weiler[47], S. Weinzierl[138], H. Weise[47], A. Welker[138], N. Welle[47], J. D. Wells[33,348], M. Wendt[58,33], M. Wenskat[47], H. Wenzel[58], N. Wermes[295], U. Werthenbach[301], W. Wester[58], L. Weuste[186,57], A. White[373], G. White[251], K. H. Wichmann[47], M. Wielers[183], R. Wielgos[58], W. Wierba[202], T. Wilksen[47], S. Willocq[346], F. F. Wilson[259], G. W. Wilson[338], P. B. Wilson[251], M. Wing[309], M. Winter[94], K. Wittenburg[47], P. Wittich[43], M. Wobisch[181], A. Wolski[339,40], M. D. Woodley[251], M. B. Woods[251], M. Worek[385], S. Worm[33,259], G. Wormser[167], D. Wright[178], Z. Wu[251], C. E. Wulz[224], S. Xella[211], G. Xia[40,343], L. Xia[7], A. Xiao[7], L. Xiao[251], M. Xiao[102], Q. Xiao[102], J. Xie[7], C. Xu[102], F. Xu[210], G. Xu[102], K. Yagyu[201], U. A. Yajnik[85], V. Yakimenko[251], S. Yamada[71,116], S. Yamada[71], Y. Yamada[272], Y. Yamada[402], A. Yamaguchi[274], D. Yamaguchi[275], M. Yamaguchi[272], S. Yamaguchi[272], Y. Yamaguchi[375], Y. Yamaguchi[75], A. Yamamoto[71,375], H. Yamamoto[272], K. Yamamoto[222], K. Yamamoto[118], M. Yamamoto[71], N. Yamamoto[197], N. Yamamoto[71], Y. Yamamoto[71], Y. Yamamoto[375], T. Yamamura[375], T. Yamanaka[116], S. Yamashita[116], T. Yamashita[3], Y. Yamashita[214], K. Yamauchi[197], M. Yamauchi[71], T. Yamazaki[375], Y. Yamazaki[154], J. Yan[375,71], W. Yan[364], C. Yanagisawa[257,11], H. Yang[247], J. Yang[56], U. K. Yang[245,343], Z. Yang[24], W. Yao[177], S. Yashiro[71], F. Yasuda[375], O. Yasuda[276], I. Yavin[188,228], E. Yazgan[331], H. Yokoya[377], K. Yokoya[71], H. Yokoyama[375], S. Yokoyama[275], R. Yonamine[71], H. Yoneyama[240], M. Yoshida[71], T. Yoshida[62], K. Yoshihara[116,33], S. Yoshihara[116,33], M. Yoshioka[71,272], T. Yoshioka[161], H. Yoshitama[73], C. C. Young[251], H. B. Yu[348], J. Yu[373], C. Z. Yuan[102], F. Yuasa[71], J. Yue[102], A. Zabi[172], W. Zabolotny[401], J. Zacek[34], I. Zagorodnov[47], J. Zalesak[105,58], A. F. Zarnecki[381], L. Zawiejski[268], M. Zeinali[101], C. Zeitnitz[385], L. Zembala[401], K. Zenker[47], D. Zeppenfeld[91], D. Zerwas[167], P. Zerwas[47], M. Zeyrek[192], A. Zghiche[164], J. Zhai[102], C. Zhang[102], J. Zhang[102], J. Zhang[7], Y. Zhang[24,33], Z. Zhang[167], F. Zhao[102], F. Zhao[102], T. Zhao[102], Y. Zhao[251], H. Zheng[102], Z. Zhengguo[364], L. Zhong[24], F. Zhou[251], X. Zhou[364,102], Z. Zhou[102], R. Y. Zhu[17], X. Zhu[24], X. Zhu[102], M. Zimmer[47], F. Zomer[167], T. Zoufal[47], R. Zwicky[329]

1 Academia Sinica - 128 Sec. 2, Institute of Physics, Academia Rd., Nankang, Taipei 11529, Taiwan, R.O.C.

2 AGH University of Science and Technology, Akademia Gorniczo-Hutnicza im. Stanislawa Staszica w Krakowie, Al. Mickiewicza 30 PL-30-059 Cracow, Poland

3 Aichi Medical University, Nagakute, Aichi, 480-1195, Japan

4 Akita International University, Yuwa, Akita City, 010-1292, Japan

5 Albert-Ludwigs Universität Freiburg, Physikalisches Institut, Hermann-Herder Str. 3, D-79104 Freiburg, Germany

6 Ankara Üniversitesi Fen Fakültesi, Fizik Bölümü, Dögol Caddesi, 06100 Tandoğan Ankara, Turkey

7 Argonne National Laboratory (ANL), 9700 S. Cass Avenue, Argonne, IL 60439, USA

8 Baylor University, Department of Physics, 101 Bagby Avenue, Waco, TX 76706, USA

9 Beijing University, Department of Physics, Beijing, China 100871

10 Benares Hindu University, Benares, Varanasi 221005, India

11 Borough of Manhattan Community College, The City University of New York, Department of Science, 199 Chambers Street, New York, NY 10007, USA

12 Brandenburg University of Technology, Postfach 101344, D-03013 Cottbus, Germany

13 Brookhaven National Laboratory (BNL), P.O.Box 5000, Upton, NY 11973-5000, USA

14 Brown University, Department of Physics, Box 1843, Providence, RI 02912, USA

15 Budker Institute for Nuclear Physics (BINP), 630090 Novosibirsk, Russia

16 Calcutta University, Department of Physics, 92 A.P.C. Road, Kolkata 700009, India

17 California Institute of Technology, Physics, Mathematics and Astronomy (PMA), 1200 East California Blvd, Pasadena, CA 91125, USA

18 California State University, Los Angeles, Dept. of Physics and Astronomy, 5151 State University Dr., Los Angeles, CA 90032, USA

19 Carleton University, Department of Physics, 1125 Colonel By Drive, Ottawa, Ontario, Canada K1S 5B6

20 Carnegie Mellon University, Department of Physics, Wean Hall 7235, Pittsburgh, PA 15213, USA

21 CEA Saclay, IRFU, F-91191 Gif-sur-Yvette, France

22 CEA Saclay, Service de Physique Théorique, CEA/DSM/SPhT, F-91191 Gif-sur-Yvette Cedex, France

23 Center for High Energy Physics (CHEP) / Kyungpook National University, 1370 Sankyuk-dong, Buk-gu, Daegu 702-701, Republic of Korea

24 Center for High Energy Physics (TUHEP), Tsinghua University, Beijing, China 100084

25 Center For Quantum Spacetime (CQUeST), Sogang University, 35 Baekbeom-ro, Mapo-gu, Seoul 121-742, Republic of Korea

26 Center for the Advancement of Natural Discoveries using Light Emission (CANDLE), Acharyan 31, 0040, Yerevan, Armenia

27 Centre de Physique des Particules de Marseille (CPPM), Aix-Marseille Université, CNRS/IN2P3, 163, Avenue de Luminy, Case 902, 13288 Marseille Cedex 09, France

28 Centre de Physique Theorique, CNRS - Luminy, Universiti d"Aix - Marseille II, Campus of Luminy, Case 907, 13288 Marseille Cedex 9, France

29 Centre Lasers Intenses et Applications (CELIA), Université Bordeaux 1 - CNRS - CEA, 351 Cours de la Libération, 33405 Talence Cedex, France

30 Centro Brasileiro de Pesquisas Físicas (CBPF), Rua Dr. Xavier Sigaud, n.150 22290-180, Urca - Rio de Janeiro, RJ, Brazil

31 Centro de Investigaciones Energéticas, Medioambientales y Tecnológicas, CIEMAT, Avenida Complutense 22, E-28040 Madrid, Spain

32 Centro Nacional de Microelectrónica (CNM), Instituto de Microelectrónica de Barcelona (IMB), Campus UAB, 08193 Cerdanyola del Vallès (Bellaterra), Barcelona, Spain

33 CERN, CH-1211 Genève 23, Switzerland

34 Charles University, Institute of Particle & Nuclear Physics, Faculty of Mathematics and Physics, V Holesovickach 2, CZ-18000 Prague 8, Czech Republic

35 Chiba University of Commerce, 1-3-1 Konodai, Ichikawa-shi, Chiba, 272-8512, Japan

36 Chonbuk National University, Division of Science Education, Jeonju 561-756, Republic of Korea

37 Chonbuk National University, Physics Department, Jeonju 561-756, Republic of Korea

38 Chubu University, 1200 Matsumoto-cho, Kasugai-shi, Aichi, 487-8501, Japan

39 Chung Yuan Christian University, Department of Physics, 200 Chung Pei Rd., Chung Li 32023 Taiwan, R.O.C

40 Cockcroft Institute, Daresbury, Warrington WA4 4AD, UK

41 College of William and Mary, Department of Physics, Williamsburg, VA, 23187, USA

42 Columbia University, Department of Physics, New York, NY 10027-6902, USA

43 Cornell University, Laboratory for Elementary-Particle Physics (LEPP), Ithaca, NY 14853, USA

44 Czech Technical University in Prague, Institute of Experimental and Applied Physics (IEAP), Horska 3a/22, 12800 Prague 2, Czech Republic

45 Czech Technical University, Faculty of Nuclear Science and Physical Engineering, Brehova 7, CZ-11519 Prague 1, Czech Republic

46 Departamento de Física Teórica, Facultad de Ciencias, Módulo 15 (antiguo C-XI) y Módulo 8, Universidad Autónoma de Madrid, Campus de Cantoblanco, 28049 Madrid, Spain

47 Deutsches Elektronen-Synchrotron DESY, A Research Centre of the Helmholtz Association, Notkestrasse 85, 22607 Hamburg, Germany (Hamburg site)

48 Deutsches Elektronen-Synchrotron DESY, A Research Centre of the Helmholtz Association, Platanenallee 6, 15738 Zeuthen, Germany (Zeuthen site)

49 Durham University, Department of Physics, Ogen Center for Fundamental Physics, South Rd., Durham DH1 3LE, UK

50 École Normale Supérieure de Lyon, 46 allée d'Italie, 69364 Lyon Cedex 07, France

51 Ege University, Department of Physics, Faculty of Science, 35100 Izmir, Turkey

52 Enrico Fermi Institute, University of Chicago, 5640 S. Ellis Avenue, RI-183, Chicago, IL 60637, USA

53 ETH Zürich, Institute for Particle Physics (IPP), Schafmattstrasse 20, CH-8093 Zürich, Switzerland

54 ETH Zürich, Institute for Theoretical Physics (ITP), Wolfgang-Pauli-Str. 27, Zürich, Switzerland

55 European Spallation Source ESS AB, Box 176, 221 00 Lund, Sweden

56 Ewha Womans University, 11-1 Daehyun-Dong, Seodaemun-Gu, Seoul, 120-750, Republic of Korea

57 Excellence Cluster Universe, Technische Universität München, Boltzmannstr. 2, 85748 Garching, Germany

58 Fermi National Accelerator Laboratory (FNAL), P.O.Box 500, Batavia, IL 60510-0500, USA

59 Florida State University, Department of Physics, 77 Chieftan Way, Tallahassee, FL 32306-4350, USA

60 Fujita Gakuen Health University, Department of Physics, Toyoake, Aichi 470-1192, Japan

61 Fukui University of Technology, 3-6-1 Gakuen, Fukui-shi, Fukui 910-8505, Japan

62 Fukui University, Department of Physics, 3-9-1 Bunkyo, Fukui-shi, Fukui 910-8507, Japan

63 Gangneung-Wonju National University, 210-702 Gangneung Daehangno, Gangneung City, Gangwon Province, Republic of Korea

64 Georg-August-Universität Göttingen, II. Physikalisches Institut, Friedrich-Hund-Platz 1, 37077 Göttingen, Germany

65 Global Design Effort

66 Hanyang University, Department of Physics, Seoul 133-791, Republic of Korea

67 Harish-Chandra Research Institute, Chhatnag Road, Jhusi, Allahabad 211019, India

68 Helmholtz-Zentrum Berlin für Materialien und Energie (HZB), Wilhelm-Conrad-Röntgen Campus, BESSY II, Albert-Einstein-Str. 15, 12489 Berlin, Germany

69 Helsinki Institute of Physics (HIP), P.O. Box 64, FIN-00014 University of Helsinki, Finland

70 Henan Normal University, College of Physics and Information Engineering, Xinxiang, China 453007

71 High Energy Accelerator Research Organization, KEK, 1-1 Oho, Tsukuba, Ibaraki 305-0801, Japan

72 Hiroshima University, Department of Physics, 1-3-1 Kagamiyama, Higashi-Hiroshima, Hiroshima 739-8526, Japan

73 Hiroshima University, Graduate School of Advanced Sciences of Matter, 1-3-1 Kagamiyama, Higashi-Hiroshima, Hiroshima 739-8530, Japan

74 Hokkai-Gakuen University, 4-1-40 Asahimachi, Toyohira-ku, Sapporo 062-8605, Japan

75 Hokkaido University, Department of Physics, Faculty of Science, Kita, Kita-ku, Sapporo-shi, Hokkaido 060-0810, Japan

76 Humboldt Universität zu Berlin, Fachbereich Physik, Institut für Elementarteilchenphysik, Newtonstr. 15, D-12489 Berlin, Germany

77 Hyogo University of Teacher Education, 942-1 Shimokume, Kato-city, Hyogo 673-1494, Japan

78 Ibaraki National College of Technology, 866 Nakane, Hitachinaka, Ibaraki 312-8508, Japan

79 Ibaraki University, College of Technology, Department of Physics, Nakanarusawa 4-12-1, Hitachi, Ibaraki 316-8511, Japan

80 Imperial College, Blackett Laboratory, Department of Physics, Prince Consort Road, London, SW7 2BW, UK

81 Indian Association for the Cultivation of Science, Department of Theoretical Physics and Centre for Theoretical Sciences, Kolkata 700032, India

82 Indian Institute of Science Education and Research (IISER) Kolkata, Department of Physical Sciences, Mohanpur Campus, PO Krishi Viswavidyalaya, Mohanpur 741252, Nadia, West Bengal, India

83 Indian Institute of Science, Centre for High Energy Physics, Bangalore 560012, Karnataka, India

84 Indian Institute of Technology Indore, IET Campus, M-Block, Institute of Engineering and Technology (IET), Devi Ahilya Vishwavidyalaya Campus, Khandwa Road, Indore - 452017, Madhya Pradesh, India

85 Indian Institute of Technology, Bombay, Powai, Mumbai 400076, India

86 Indian Institute of Technology, Guwahati, Guwahati, Assam 781039, India

87 Indiana University, Department of Physics, Swain Hall West 117, 727 E. 3rd St., Bloomington, IN 47405-7105, USA

88 Institucio Catalana de Recerca i Estudis, ICREA, Passeig Lluis Companys, 23, Barcelona 08010, Spain

89 Institut de Physique Nucléaire de Lyon (IPNL), Domaine scientifique de la Doua, Bâtiment Paul Dirac 4, rue Enrico Fermi, 69622 Villeurbanne, Cedex, France

90 Institut für Experimentelle Kernphysik, KIT,Universität Karlsruhe (TH), Wolfgang-Gaede-Str. 1, Postfach 6980, 76128 Karlsruhe, Germany

91 Institut für Theoretische Physik (ITP), Karlsruher Institut für Technologie (KIT), Fakultät für Physik, Postfach 6980, 76049 Karlsruhe, Germany

92 Institut für Theoretische Teilchenphysik, Campus Süd, Karlsruher Institut für Technologie (KIT), 76128 Karlsruhe, Germany

93 Institut National de Physique Nucleaire et de Physique des Particules, 3, Rue Michel- Ange, 75794 Paris Cedex 16, France

94 Institut Pluridisciplinaire Hubert Curien, 23 Rue du Loess - BP28, 67037 Strasbourg Cedex 2, France

95 Institute for Chemical Research, Kyoto University, Gokasho, Uji, Kyoto 611-0011, Japan

96 Institute for Cosmic Ray Research, University of Tokyo, 5-1-5 Kashiwa-no-Ha, Kashiwa, Chiba 277-8582, Japan

97 Institute for Mathematics, Astrophysics and Particle Physics (IMAPP), P.O. Box 9010, 6500 GL Nijmegen, Netherlands

98 Institute for Nuclear Research, Russian Academy of Sciences (INR RAS), 60-th October Anniversary Prospect 7a, 117312, Moscow, Russia

99 Institute for Particle and Nuclear Physics, Wigner Research Centre for Physics, Hungarian Academy of Sciences, P.O. Box 49, 1525 Budapest, Hungary

100 Institute for Scintillation Materials (ISMA), 60 Lenina Ave, 61001, Kharkiv, Ukraine

101 Institute for studies in fundamental sciences (IPM), Niavaran Square, P.O. Box 19395-5746, Tehran, Iran

102 Institute of High Energy Physics - IHEP, Chinese Academy of Sciences, P.O. Box 918, Beijing, China 100049

103 Institute of Mathematical Sciences, Taramani, C.I.T. Campus, Chennai 600113, India

104 Institute of Particle Physics, Canada

105 Institute of Physics, ASCR, Academy of Science of the Czech Republic, Division of Elementary Particle Physics, Na Slovance 2, CZ-18221 Prague 8, Czech Republic

106 Institute of Physics, Vietnam Academy of Science and Technology (VAST), 10 Dao-Tan, Ba-Dinh, Hanoi 10000, Vietnam

107 Institute of Theoretical and Experimetal Physics, B. Cheremushkinskawa, 25, RU-117259, Moscow, Russia

108 Instituto de Fisica Corpuscular (IFIC), Centro Mixto CSIC-UVEG, Edificio Investigacion Paterna, Apartado 22085, 46071 Valencia, Spain

109 Instituto de Física da Universidade Federal do Rio Grande do Sul (UFRGS), Av. Bento Gonçalves 9500, Caixa Postal 15051, CEP 91501-970, Porto Alegre, RS, Brazil

110 Instituto de Fisica de Cantabria, (IFCA, CSIC-UC), Facultad de Ciencias, Avda. Los Castros s/n, 39005 Santander, Spain

111 Instituto de Física Teórica UAM/CSIC, C/ Nicolás Cabrera 13-15, Universidad Autónoma de Madrid, Cantoblanco, 28049 Madrid, Spain

112 Instituto Galego de Fisica de Altas Enerxias (IGFAE,USC) Facultad de Fisica, Campus Sur E-15782 Santiago de Compostela, Spain

113 Instituto Tecnológico de Aragón (ITA), C/ María de Luna 7-8, 50018 Zaragoza, Spain

114 Instituto Universitario de Física Fundamental y Matemáticas de la Universidad de Salamanca (IUFFyM), Casas del Parque, 37008 Salamanca, Spain

115 Inter-University Accelerator Centre, Aruna Asaf Ali Marg, Post Box 10502, New Delhi 110067, India

116 International Center for Elementary Particle Physics, University of Tokyo, Hongo 7-3-1, Bunkyo District, Tokyo 113-0033, Japan

117 International Institute of Physics, Federal University of Rio Grande do Norte, Av. Odilon Gomes de Lima, 1722 - Capim Macio - 59078-400 - Natal-RN, Brazil

118 Iowa State University, Department of Physics, High Energy Physics Group, Ames, IA 50011, USA

119 Istituto Nazionale di Fisica Nucleare (INFN), Laboratorio LASA, Via Fratelli Cervi 201, 20090 Segrate, Italy

120 Istituto Nazionale di Fisica Nucleare (INFN), Sezione di Firenze, Via G. Sansone 1, I-50019 Sesto Fiorentino (Firenze), Italy

121 Istituto Nazionale di Fisica Nucleare (INFN), Sezione di Milano Bicocca, Piazza della Scienza 3, I-20126 Milano, Italy

122 Istituto Nazionale di Fisica Nucleare (INFN), Sezione di Milano, Via Celoria 16, I-20133 Milano, Italy

123 Istituto Nazionale di Fisica Nucleare (INFN), Sezione di Napoli, Complesso Universitá di Monte Sant'Angelo,via, I-80126 Naples, Italy

124 Istituto Nazionale di Fisica Nucleare (INFN), Sezione di Pavia, Via Bassi 6, I-27100 Pavia, Italy

125 Istituto Nazionale di Fisica Nucleare (INFN), Sezione di Perugia, Via A. Pascoli, 06123 Perugia, Italy

126 Istituto Nazionale di Fisica Nucleare (INFN), Sezione di Pisa, Edificio C - Polo Fibonacci Largo B. Pontecorvo, 3, I-56127 Pisa, Italy

127 Istituto Nazionale di Fisica Nucleare (INFN), Sezione di Roma, c/o Dipartimento di Fisica - Università degli Studi di Roma "La Sapienza", P.le Aldo Moro 2, I-00185 Roma, Italy

128 Istituto Nazionale di Fisica Nucleare (INFN), Sezione di Torino, c/o Universitá di Torino, facoltá di Fisica, via P Giuria 1, 10125 Torino, Italy

129 Istituto Nazionale di Fisica Nucleare (INFN), Sezione di Trieste, Padriciano 99, I-34012 Trieste (Padriciano), Italy

130 ITER Organization, Route de Vinon-sur-Verdon, 13115 St. Paul-lez-Durance, France

131 Iwate University, 4-3-5 Ueda, Morioka, Iwate, 020-8551, Japan

132 Jagiellonian University, Institute of Physics, Ul. Reymonta 4, PL-30-059 Cracow, Poland

133 Jamia Millia Islamia, Department of Physics, Jamia Nagar, New Delhi 110025, India

134 Japan Aerospace Exploration Agency, Sagamihara Campus, 3-1-1 Yoshinodai, Sagamihara, Kanagawa 220-8510 , Japan

135 Japan Atomic Energy Agency, 4-49 Muramatsu, Tokai-mura, Naka-gun, Ibaraki 319-1184, Japan

136 Japan Atomic Energy Agency, Tokai Research and Development Center, 2-4 Shirane Shirakata, Tokai-mura, Naka-gun, Ibaraki 319-1195, Japan

137 Japan Synchrotron Radiation Research Institute (JASRI), 1-1-1, Kouto, Sayo-cho, Sayo-gun, Hyogo 679-5198, Japan

138 Johannes Gutenberg Universität Mainz, Institut für Physik, 55099 Mainz, Germany

139 John Adams Institute for Accelerator Science at Royal Holloway University of London, Egham Hill, Egham, Surrey TW20 0EX, UK

140 John Adams Institute for Accelerator Science at University of Oxford, Denys Wilkinson Building, Keble Road, Oxford OX1 3RH, UK

141 Johns Hopkins University - Henry A. Rowland Department of Physics & Astronomy 3701 San Martin Drive, Baltimore, Maryland (MD) 21218, USA

142 Joint Institute for Nuclear Research (JINR), Joliot-Curie 6, 141980, Dubna, Moscow Region, Russia

143 Joint Institute for Power and Nuclear Research "Sosny" at National Academy of Sciences of Belarus, 99 Academician A.K.Krasin Str., Minsk BY-220109, Belarus

144 Jozef Stefan Institute, Jamova cesta 39, 1000 Ljubljana, Slovenia

145 Julius-Maximilians-Universität Würzburg, Fakultät für Physik und Astronomie, Am Hubland, 97074 Würzburg, Germany

146 Juntendo University, School of Medicine, Dept. of Physics, Hiraga-gakuendai 1-1, Inzai-shi, Chiba 270-1695, Japan

147 Justus-Liebig-Universität Gießen, II. Physikalisches Institut, Heinrich-Buff-Ring 16, 35392 Gießen, Germany

148 Kanazawa University, Institute for Theoretical Physics (KITP), School of Mathematics and Physics, College of Science and Engineering, Kakuma-machi, Kanazawa city, Ishikawa 920-1192, Japan

149 Kansas State University, Department of Physics, 116 Cardwell Hall, Manhattan, KS 66506, USA

150 Kavli Institute for the Physics and Mathematics of the Universe (Kavli IPMU), University of Tokyo, 5-1-5 Kashiwanoha, Kashiwa, 277-8583, Japan

151 King Saud University (KSU), Dept. of Physics, P.O. Box 2454, Riyadh 11451, Saudi Arabia

152 King's College London - Department of physics, Strand, London WC2R 2LS, London, UK

153 Kinki University, Department of Physics, 3-4-1 Kowakae, Higashi-Osaka, Osaka 577-8502, Japan

154 Kobe University, Department of Physics, 1-1 Rokkodai-cho, Nada-ku, Kobe, Hyogo 657-8501, Japan

155 Kogakuin University, Department of Physics, Shinjuku Campus, 1-24-2 Nishi-Shinjuku, Shinjuku-ku, Tokyo 163-8677, Japan

156 Konkuk University, 93-1 Mojin-dong, Kwanglin-gu, Seoul 143-701, Republic of Korea

157 Korea Advanced Institute of Science & Technology, Department of Physics, 373-1 Kusong-dong, Yusong-gu, Taejon 305-701, Republic of Korea

158 Korea Institute for Advanced Study (KIAS), School of Physics, 207-43 Cheongryangri-dong, Dongdaemun-gu, Seoul 130-012, Republic of Korea

159 Kyoto University, Department of Physics, Kitashirakawa-Oiwakecho, Sakyo-ku, Kyoto 606-8502, Japan

160 Kyoto University, Yukawa Institute for Theoretical Physics, Kitashirakawa-Oiwakecho, Sakyo-Ku, Kyoto 606-8502, Japan

161 Kyushu University, Department of Physics, 6-10-1 Hakozaki, Higashi-ku, Fukuoka 812-8581, Japan

162 L.P.T.A., UMR 5207 CNRS-UM2, Université Montpellier II, Case Courrier 070, Bât. 13, place Eugène Bataillon, 34095 Montpellier Cedex 5, France

163 Laboratoire Charles Coulomb UMR 5221 CNRS-UM2, Université Montpellier 2, Place Eugène Bataillon - CC069, 34095 Montpellier Cedex 5, France

164 Laboratoire d'Annecy-le-Vieux de Physique des Particules (LAPP) , Université de Savoie, CNRS/IN2P3, 9 Chemin de Bellevue, BP 110, F-74941 Annecy-Le-Vieux Cedex, France

165 Laboratoire d'Annecy-le-Vieux de Physique Theorique (LAPTH), Chemin de Bellevue, BP 110, F-74941 Annecy-le-Vieux Cedex, France

166 Laboratoire d'AstroParticules et Cosmologie (APC), Université Paris Diderot-Paris 7 - CNRS/IN2P3, Bâtiment Condorcet, Case 7020, 75205 Paris Cedex 13, France

167 Laboratoire de l'Accélérateur Linéaire (LAL), Université Paris-Sud 11, Bâtiment 200, 91898 Orsay, France

168 Laboratoire de Physique Corpusculaire de Clermont-Ferrand (LPC), Université Blaise Pascal, I.N.2.P.3./C.N.R.S., 24 avenue des Landais, 63177 Aubière Cedex, France

169 Laboratoire de Physique Nucléaire et des Hautes Energies (LPNHE), UPMC, UPD, IN2P3/CNRS, 4 Place Jussieu, 75005, Paris Cedex 05, France

170 Laboratoire de Physique Subatomique et de Cosmologie (LPSC), Université Joseph Fourier (Grenoble 1), CNRS/IN2P3, Institut Polytechnique de Grenoble, 53 rue des Martyrs, F-38026 Grenoble Cedex, France

171 Laboratoire de Physique Theorique, Université de Paris-Sud XI, Batiment 210, F-91405 Orsay Cedex, France

172 Laboratoire Leprince-Ringuet (LLR), École polytechnique – CNRS/IN2P3, Route de Saclay, F-91128 Palaiseau Cedex, France

173 Laboratoire Univers et Particules de Montpellier (LUPM) - UMR5299, Université de Montpellier II, Place Eugène Bataillon - Case courrier 72, 34095 Montpellier Cedex 05, France

174 Laboratori Nazionali di Frascati, via E. Fermi, 40, C.P. 13, I-00044 Frascati, Italy

175 Laboratório de Instrumentação e Física Experimental de Partículas (LIP LISBOA), Av. Elias Garcia 14 - 1°, 1000-149 Lisbon, Portugal

176 Lancaster University, Physics Department, Lancaster LA1 4YB, UK

177 Lawrence Berkeley National Laboratory (LBNL), 1 Cyclotron Rd, Berkeley, CA 94720, USA

178 Lawrence Livermore National Laboratory (LLNL), Livermore, CA 94551, USA

179 Lebedev Physical Institute, Leninsky Prospect 53, RU-117924 Moscow, Russia

180 Lomonosov Moscow State University, Skobeltsyn Institute of Nuclear Physics (MSU SINP), 1(2), Leninskie gory, GSP-1, Moscow 119991, Russia

181 Louisiana Tech University, Department of Physics, Ruston, LA 71272, USA

182 Ludwig-Maximilians-Universität München, Fakultät für Physik, Am Coulombwall 1, D - 85748 Garching, Germany

183 Lunds Universitet, Fysiska Institutionen, Avdelningen för Experimentell Högenergifysik, Box 118, 221 00 Lund, Sweden

184 L'Université Hassan II, Aïn Chock, "Réseau Universitaire de Physique des Hautes Energies" (RUPHE), Département de Physique, Faculté des Sciences Aïn Chock, B.P 5366 Maarif, Casablanca 20100, Morocco

185 Massachusetts Institute of Technology (MIT), Laboratory for Nuclear Science, 77 Massachusetts Avenue, Cambridge, MA 02139, USA

186 Max-Planck-Institut für Physik (Werner-Heisenberg-Institut), Föhringer Ring 6, 80805 München, Germany

187 McGill University, Department of Physics, Ernest Rutherford Physics Bldg., 3600 University Street, Montreal, Quebec, H3A 2T8 Canada

188 McMaster University, Department of Physics & Astronomy, 1280 Main Street West, Hamilton, ON, L8S 4M1, Canada

189 Meiji Gakuin University, Department of Physics, 2-37 Shirokanedai 1-chome, Minato-ku, Tokyo 244-8539, Japan

190 Michigan State University, Department of Chemical Engineering & Materials Science, 2527 Engineering Building East Lansing, MI 48824-1226, USA

191 Michigan State University, Department of Physics and Astronomy, East Lansing, MI 48824, USA

192 Middle East Technical University, Department of Physics, TR-06531 Ankara, Turkey

193 Miyagi Gakuin Women's University, Faculty of Liberal Arts, 9-1-1 Sakuragaoka, Aoba District, Sendai, Miyagi 981-8557, Japan

194 MSU-Iligan Institute of Technology, Department of Physics, Andres Bonifacio Avenue, 9200 Iligan City, Phillipines

195 Nagasaki Institute of Applied Science, 536 Abamachi, Nagasaki-Shi, Nagasaki 851-0193, Japan

196 Nagoya University, Department of Materials Science and Engineering, Furo-cho, Chikusa-ku, Nagoya, 464-8603, Japan

197 Nagoya University, Department of Physics, School of Science, Furo-cho, Chikusa-ku, Nagoya, Aichi 464-8602, Japan

198 Nagoya University, Kobayashi-Maskawa Institute for the Origin of Particles and the Universe (KMI), Furo-cho, Chikusa-ku, Nagoya Aichi 464-8602, Japan

199 Nanjing University, Department of Physics, Nanjing, China 210093

200 Nara Women's University, High Energy Physics Group, Kitauoya-Nishimachi, Nara 630-8506, Japan

201 National Central University, High Energy Group, Department of Physics, Chung-li, Taiwan 32001, R.O.C

202 National Centre of Nuclear Research (NCBJ), ul. Andrzeja Soltana 7, 05-400 Otwock-Swierk, Poland

203 National Cheng Kung University, Physics Department, 1 Ta-Hsueh Road, Tainan, Taiwan 70101, R.O.C

204 National Chiao-Tung University, Institute of Physics, 1001 Ta Hsueh Rd, Hsinchu, Taiwan 300, R.O.C.

205 National Institute of Chemical Physics and Biophysics (NICPB), Ravala pst 10, 10143 Tallinn, Estonia

206 National Institute of Physics and Nuclear Engineering "Horia Hulubei" (IFIN-HH), Str. Reactorului no.30, P.O. Box MG-6, R-76900 Bucharest - Magurele, Romania

207 National Research Centre "Kurchatov Institute", 1 Akademika Kurchatova pl., Moscow, 123182, Russia

208 National Science Center - Kharkov Institute of Physics and Technology (NSC KIPT), Akademicheskaya St. 1, Kharkov, 61108, Ukraine

209 National Scientific & Educational Centre of Particle & High Energy Physics (NCPHEP), Belarusian State University, M.Bogdanovich street 153, 220040 Minsk, Belarus

210 National Taiwan University, Physics Department, Taipei, Taiwan 106, R.O.C

211 Niels Bohr Institute (NBI), University of Copenhagen, Blegdamsvej 17, DK-2100 Copenhagen, Denmark

212 Niigata University, Department of Physics, Ikarashi, Niigata 950-218, Japan

213 Nikhef, National Institute for Subatomic Physics, P.O. Box 41882, 1009 DB Amsterdam, Netherlands

214 Nippon Dental University School of Life Dentistry at Niigata, 1-8 Hamaura-cho, Chuo-ku, Niigata 951-1500, Japan

215 North Carolina A&T State University, 1601 E. Market Street, Greensboro, NC 27411, USA

216 Northeastern University, Physics Department, 360 Huntington Ave, 111 Dana Research Center, Boston, MA 02115, USA

217 Northern Illinois University, Department of Physics, DeKalb, Illinois 60115-2825, USA

218 Northwestern University, Department of Physics and Astronomy, 2145 Sheridan Road., Evanston, IL 60208, USA

219 Novosibirsk State University (NGU), Department of Physics, Pirogov st. 2, 630090 Novosibirsk, Russia

220 Ochanomizu University, Department of Physics, Faculty of Science, 1-1 Otsuka 2, Bunkyo-ku, Tokyo 112-8610, Japan

221 Orissa University of Agriculture & Technology, Bhubaneswar 751003, Orissa, India

222 Osaka City University, Department of Physics, Faculty of Science, 3-3-138 Sugimoto, Sumiyoshi-ku, Osaka 558-8585, Japan

223 Osaka University, Department of Physics, 1-1 Machikaneyama, Toyonaka, Osaka 560-0043, Japan

224 Österreichische Akademie der Wissenschaften, Institut für Hochenergiephysik, Nikolsdorfergasse 18, A-1050 Vienna, Austria

225 Pacific Northwest National Laboratory, (PNNL), PO Box 999, Richland, WA 99352, USA

226 Panjab University, Chandigarh 160014, India

227 Pavel Sukhoi Gomel State Technical University, ICTP Affiliated Centre & Laboratory for Physical Studies, October Avenue, 48, 246746, Gomel, Belarus

228 Perimeter Institute for Theoretical Physics, 31 Caroline Street North, Waterloo, Ontario N2L 2Y5, Canada

229 Physical Research Laboratory, Navrangpura, Ahmedabad 380 009, Gujarat, India

230 Pohang Accelerator Laboratory (PAL), San-31 Hyoja-dong, Nam-gu, Pohang, Gyeongbuk 790-784, Republic of Korea

231 Pontificia Universidad Católica de Chile, Avda. Libertador Bernardo OHiggins 340, Santiago, Chile

232 Princeton University, Department of Physics, P.O. Box 708, Princeton, NJ 08542-0708, USA

233 Purdue University, Department of Physics, West Lafayette, IN 47907, USA

234 Queen Mary, University of London, Mile End Road, London, E1 4NS, United Kingdom

235 Rheinisch-Westfälische Technische Hochschule (RWTH), Physikalisches Institut, Physikzentrum, Otto-Blumenthal-Straße, 52056 Aachen

236 RIKEN, 2-1 Hirosawa, Wako, Saitama 351-0198, Japan

237 Royal Holloway, University of London (RHUL), Department of Physics, Egham, Surrey TW20 0EX, UK

238 Russian Academy of Science, Keldysh Institute of Applied Mathematics, Muiskaya pl. 4, 125047 Moscow, Russia

239 Rutgers, The State University of New Jersey, Department of Physics & Astronomy, 136 Frelinghuysen Rd, Piscataway, NJ 08854, USA

240 Saga University, Department of Physics, 1 Honjo-machi, Saga-shi, Saga 840-8502, Japan

241 Saha Institute of Nuclear Physics, 1/AF Bidhan Nagar, Kolkata 700064, India

242 Salalah College of Technology (SCOT), Engineering Department, Post Box No. 608, Postal Code 211, Salalah, Sultanate of Oman

243 Saudi Center for Theoretical Physics, King Fahd University of Petroleum and Minerals (KFUPM), Dhahran 31261, Saudi Arabia

244 Seikei University, Faculty of Science and Technology, 3-3-1 Kichijoji-Kitamachi, Musashino-shi, Tokyo 180-8633, Japan

245 Seoul National University, San 56-1, Shinrim-dong, Kwanak-gu, Seoul 151-742, Republic of Korea

246 Setsunan University, Institute for Fundamental Sciences, 17-8 Ikeda Nakamachi, Neyagawa, Osaka, 572-8508, Japan

247 Shanghai Jiao Tong University, Department of Physics, 800 Dongchuan Road, Shanghai, China 200240

248 Shinshu University, 3-1-1, Asahi, Matsumoto, Nagano 390-8621, Japan

249 Shiv Nadar University, Village Chithera, Tehsil Dadri, District Gautam Budh Nagar, 203207 Uttar Pradesh, India

250 Shizuoka University, Department of Physics, 836 Ohya, Suruga-ku, Shizuoka 422-8529, Japan

251 SLAC National Accelerator Laboratory, 2575 Sand Hill Road, Menlo Park, CA 94025, USA

252 Society for Applied Microwave Electronics Engineering and Research (SAMEER), I.I.T. Campus, Powai, Post Box 8448, Mumbai 400076, India

253 Sokendai, The Graduate University for Advanced Studies, Shonan Village, Hayama, Kanagawa 240-0193, Japan

254 Spallation Neutron Source (SNS), Oak Ridge National Laboratory (ORNL), P.O. Box 2008 MS-6477, Oak Ridge, TN 37831-6477, USA

255 State University of New York at Binghamton, Department of Physics, PO Box 6016, Binghamton, NY 13902, USA

256 State University of New York at Buffalo, Department of Physics & Astronomy, 239 Franczak Hall, Buffalo, NY 14260, USA

257 State University of New York at Stony Brook, Department of Physics and Astronomy, Stony Brook, NY 11794-3800, USA

258 STFC Daresbury Laboratory, Daresbury, Warrington, Cheshire WA4 4AD, UK

259 STFC Rutherford Appleton Laboratory, Chilton, Didcot, Oxon OX11 0QX, UK

260 Sungkyunkwan University (SKKU), Natural Science Campus 300, Physics Research Division, Chunchun-dong, Jangan-gu, Suwon, Kyunggi-do 440-746, Republic of Korea

261 Swiss Light Source (SLS), Paul Scherrer Institut (PSI), PSI West, CH-5232 Villigen PSI, Switzerland

262 Tata Institute of Fundamental Research, School of Natural Sciences, Homi Bhabha Rd., Mumbai 400005, India

263 Technical University of Lodz, Department of Microelectronics and Computer Science, al. Politechniki 11, 90-924 Lodz, Poland

264 Technische Universität Dresden, Institut für Kern- und Teilchenphysik, D-01069 Dresden, Germany

265 Tel-Aviv University, School of Physics and Astronomy, Ramat Aviv, Tel Aviv 69978, Israel

266 Texas A&M University, Physics Department, College Station, 77843-4242 TX, USA

267 Texas Tech University, Department of Physics, Campus Box 41051, Lubbock, TX 79409-1051, USA

268 The Henryk Niewodniczanski Institute of Nuclear Physics, Polish Academy of Sciences (IFJ PAN), ul. Radzikowskiego 152, PL-31342 Cracow, Poland

269 Thomas Jefferson National Accelerator Facility (TJNAF), 12000 Jefferson Avenue, Newport News, VA 23606, USA

270 Tohoku Gakuin University, Department of Business Administration, 1-3-1 Tsuchitoi, Aoba-ku Sendai, Miyagi 980-8511, Japan

271 Tohoku Gakuin University, Faculty of Technology, 1-13-1 Chuo, Tagajo, Miyagi 985-8537, Japan

272 Tohoku University, Department of Physics, Aoba District, Sendai, Miyagi 980-8578, Japan

273 Tohoku University, Research Center for Electron Photon Science, Taihaku District, Sendai, Miyagi 982-0826, Japan

274 Tohoku University, Research Center for Neutrino Science, Aoba District, Sendai, Miyagi 980-8578, Japan

275 Tokyo Institute of Technology, Department of Physics, 2-12-1 O-Okayama, Meguro, Tokyo 152-8551, Japan

276 Tokyo Metropolitan University, Faculty of Science and Engineering, Department of Physics, 1-1 Minami-Osawa, Hachioji-shi, Tokyo 192-0397, Japan

277 Tokyo University of Agriculture Technology, Department of Applied Physics, Naka-machi, Koganei, Tokyo 183-8488, Japan

278 Toyama Prefectural University, Department of Mathematical Physics, 5180 Kurokawa Imizu-shi, Toyama, 939-0398, Japan

279 TRIUMF, 4004 Wesbrook Mall, Vancouver, BC V6T 2A3, Canada

280 Universidad Autónoma de San Luis Potosí, Alvaro Obregon 64, Col. Centro, San Luis Potosí, S.L.P. 78000, México

281 Universidad de Granada, Departamento de Física Teórica y del Cosmos, Campus de Fuentenueva, E-18071 Granada, Spain

282 Universidad de los Andes, Faculty of Science, Department of Physics, Carrera 1 18A-10, Bloque Ip. Bogotá, Colombia

283 Universidad de Oviedo, Departamento de Física, Campus de Llamaquique. C/ Calvo Sotelo, s/n 33005 Oviedo, Spain

284 Universidad de Salamanca, Departamento de Física Fundamental, Plaza de la Merced, s/n., 37008 Salamanca, Spain

285 Universidad de Sevilla, Escuela Técnica Superior de Ingeniería, Departamento Ingeniería Electrónica, Camino de los Descubrimientos s/n, 41092 Sevilla, Spain

286 Universidad de Zaragoza - Departamento de Física Teórica, Pedro Cerbuna 12, E-50009 Zaragoza, Spain

287 Universidad Nacional Autónoma de México, Instituto de Física, Circuito de la Investigación Cientifica s/n, Ciudad Universitaria, CP 04510 México D.F., Mexico

288 Universidad Nacional de La Plata, Departamento de Física, Facultad de Ciencias Exactas, C.C. N 67, 1900 La Plata, Argentina

289 Universidade do Estado do Rio de Janeiro (UERJ), Rio de Janeiro, RJ - Brasil 20550-900, Brazil

290 Universidade Federal de Pelotas, Instituto de Física e Matemática, Campus Universitário, Caixa Postal 354, 96010-900 Pelotas, RS, Brazil

291 Universidade Federal do Rio de Janeiro (UFRJ), Instituto de Física, Av. Athos da Silveira Ramos 149, Centro de Tecnologia - Bloco A, Cidade Universitária, Ilha do Fundão, Rio de Janeiro, RJ, Brazil

292 Universitá degli Studi di Napoli "Federico II", Dipartimento di Fisica, Via Cintia, 80126 Napoli, Italy

293 Universitat Autònoma de Barcelona, Departament de Física, Edifici C, 08193 Bellaterra, Barcelona, Spain

294 Universitat Autònoma de Barcelona, Institut de Fisica d'Altes Energies (IFAE), Campus UAB, Edifici Cn, E-08193 Bellaterra, Barcelona, Spain

295 Universität Bonn, Physikalisches Institut, Nußallee 12, 53115 Bonn, Germany

296 Universität Heidelberg, Institut für Theoretische Physik, Philosophenweg 16, 69120 Heidelberg, Germany

297 Universität Heidelberg, Kirchhoff-Institut für Physik, Im Neuenheimer Feld 227, 69120 Heidelberg, Germany

298 Universitat Politècnica de Catalunya, Institut de Tècniques Energètiques, Campus Diagonal Sud, Edifici PC (Pavelló C). Av. Diagonal, 647 08028 Barcelona, Spain

299 Universitat Ramon Llull, La Salle, C/ Quatre Camins 2, 08022 Barcelona, Spain

300 Universität Rostock, 18051 Rostock, Germany

301 Universität Siegen, Naturwissenschaftlich-Technische Fakultät, Department Physik, Emmy Noether Campus, Walter-Flex-Str.3, 57068 Siegen, Germany

302 Universität Wien - Theoretische Physik Boltzmanngasse 5, A-1090 Vienna, Austria

303 Université catholique de Louvain, Centre for Cosmology, Particle Physics and Phenomenology (CP3), Institute of Mathematics and Physics, 2 Chemin du Cyclotron, 1348 Louvain-la-Neuve, Belgium

304 Université de Genève, Section de Physique, 24, quai E. Ansermet, 1211 Genève 4, Switzerland

305 Université de Montréal, Département de Physique, Groupe de Physique des Particules, C.P. 6128, Succ. Centre-ville, Montréal, Qc H3C 3J7, Canada

306 Université de Strasbourg, UFR de Sciences Physiques, 3-5 Rue de l'Université, F-67084 Strasbourg Cedex, France

307 Université Libre de Bruxelles, Boulevard du Triomphe, 1050 Bruxelles, Belgium

308 Universittà di Catania, Dipartimento di Fisica e Astronomia, Via Santa Sofia 64, 95123 Catania, Italy

309 University College London (UCL), High Energy Physics Group, Physics and Astronomy Department, Gower Street, London WC1E 6BT, UK

310 University College, National University of Ireland (Dublin), Department of Experimental Physics, Science Buildings, Belfield, Dublin 4, Ireland

311 University de Barcelona, Facultat de Física, Av. Diagonal, 647, Barcelona 08028, Spain

312 University of Alberta - Faculty of Science, Department of Physics, 4-181 CCIS, Edmonton AB T6G 2E1, Canada

313 University of Arizona, Department of Physics, 1118 E. Fourth Street, PO Box 210081, Tucson, AZ 85721, USA

314 University of Bergen, Institute of Physics, Allegaten 55, N-5007 Bergen, Norway

315 University of Birmingham, School of Physics and Astronomy, Particle Physics Group, Edgbaston, Birmingham B15 2TT, UK

316 University of Bristol, H. H. Wills Physics Lab, Tyndall Ave., Bristol BS8 1TL, UK

317 University of British Columbia, Department of Physics and Astronomy, 6224 Agricultural Rd., Vancouver, BC V6T 1Z1, Canada

318 University of California (UCLA), Los Angeleles, CA 90095, US

319 University of California Berkeley, Department of Physics, 366 Le Conte Hall, #7300, Berkeley, CA 94720, USA

320 University of California Davis, Department of Physics, One Shields Avenue, Davis, CA 95616-8677, USA

321 University of California Irvine, Department of Physics and Astronomy, High Energy Group, 4129 Frederick Reines Hall, Irvine, CA 92697-4575 USA

322 University of California Santa Cruz, Institute for Particle Physics, 1156 High Street, Santa Cruz, CA 95064, USA

323 University of Cambridge, Cavendish Laboratory, J J Thomson Avenue, Cambridge CB3 0HE, UK

324 University of Colorado at Boulder, Department of Physics, 390 UCB, University of Colorado, Boulder, CO 80309-0390, USA

325 University of Cyprus, Department of Physics, P.O.Box 20537, 1678 Nicosia, Cyprus

326 University of Delhi, Department of Physics and Astrophysics, Delhi 110007, India

327 University of Delhi, S.G.T.B. Khalsa College, Delhi 110007, India

328 University of Dundee, Department of Physics, Nethergate, Dundee, DD1 4HN, Scotland, UK

329 University of Edinburgh, School of Physics, James Clerk Maxwell Building, The King's Buildings, Mayfield Road, Edinburgh EH9 3JZ, UK

330 University of Florida, Department of Physics, Gainesville, FL 32611, USA

331 University of Ghent, Department of Subatomic and Radiation Physics, Proeftuinstraat 86, 9000 Gent, Belgium

332 University of Glasgow, SUPA, School of Physics & Astronomy, University Avenue, Glasgow G12 8QQ, Scotland, UK

333 University of Hamburg, Physics Department, Luruper Chaussee 149, 22761 Hamburg, Germany

334 University of Hawaii, Department of Physics and Astronomy, HEP, 2505 Correa Rd., WAT 232, Honolulu, HI 96822-2219, USA

335 University of Helsinki, Department of Physical Sciences, P.O. Box 64 (Vaino Auerin katu 11), FIN-00014, Helsinki, Finland

336 University of Illinois at Chicago, Department Of Physics, 845 W Taylor St., Chicago IL 60607, USA

337 University of Iowa, Department of Physics and Astronomy, 203 Van Allen Hall, Iowa City, IA 52242-1479, USA

338 University of Kansas, Department of Physics and Astronomy, Malott Hall, 1251 Wescoe Hall Drive, Room 1082, Lawrence, KS 66045-7582, USA

339 University of Liverpool, Department of Physics, Oliver Lodge Lab, Oxford St., Liverpool L69 7ZE, UK

340 University of Liverpool, Division of Theoretical Physics, Department of Mathematical Sciences, Chadwick Building, Liverpool L69 3BX, UK

341 University of Ljubljana, Faculty of Mathematics and Physics, Jadranska ulica 19, 1000 Ljubljana, Slovenia

342 University of Malaya, Faculty of Science, Department of Physics, 50603 Kuala Lumpur, Malaysia

343 University of Manchester, School of Physics and Astronomy, Schuster Lab, Manchester M13 9PL, UK

344 University of Maribor, Faculty of Chemistry and Chemical Engineering (FKKT), Smetanova ulica 17, 2000 Maribor, Slovenia

345 University of Maryland, Department of Physics and Astronomy, Physics Building (Bldg. 082), College Park, MD 20742, USA

346 University of Massachusetts - Amherst, Department of Physics, 1126 Lederle Graduate Research Tower (LGRT), Amherst, MA 01003-9337, USA

347 University of Melbourne, School of Physics, Victoria 3010, Australia

348 University of Michigan, Department of Physics, 500 E. University Ave., Ann Arbor, MI 48109-1120, USA

349 University of Minnesota, 148 Tate Laboratory Of Physics, 116 Church St. S.E., Minneapolis, MN 55455, USA

350 University of Mississippi, Department of Physics and Astronomy, 108 Lewis Hall, PO Box 1848, Oxford, Mississippi 38677-1848, USA

351 University of Missouri – St. Louis, Department of Physics and Astronomy, 503 Benton Hall One University Blvd., St. Louis Mo 63121, USA

352 University of New Mexico, New Mexico Center for Particle Physics, Department of Physics and Astronomy, 800 Yale Boulevard N.E., Albuquerque, NM 87131, USA

353 University of North Carolina at Chapel Hill, Department of Physics and Astronomy, Phillips Hall, CB #3255, 120 E. Cameron Ave., Chapel Hill, NC 27599-3255, USA

354 University of Notre Dame, Department of Physics, 225 Nieuwland Science Hall, Notre Dame, IN 46556, USA

355 University of Oklahoma, Department of Physics and Astronomy, Norman, OK 73071, USA

356 University of Oregon, Department of Physics, 1371 E. 13th Ave., Eugene, OR 97403, USA

357 University of Oslo, Department of Physics, P.O box 1048, Blindern, 0316 Oslo, Norway

358 University of Oxford, Particle Physics Department, Denys Wilkinson Bldg., Keble Road, Oxford OX1 3RH England, UK

359 University of Pavia, Department of Physics, via Bassi 6, I-27100 Pavia, Italy

360 University of Pennsylvania, Department of Physics and Astronomy, 209 South 33rd Street, Philadelphia, PA 19104-6396, USA

361 University of Pittsburgh, Department of Physics and Astronomy, 100 Allen Hall, 3941 O'Hara St, Pittsburgh PA 15260, USA

362 University of Regina, Department of Physics, Regina, Saskatchewan, S4S 0A2 Canada

363 University of Rochester, Department of Physics and Astronomy, Bausch & Lomb Hall, P.O. Box 270171, 600 Wilson Boulevard, Rochester, NY 14627-0171 USA

364 University of Science and Technology of China, Department of Modern Physics (DMP), Jin Zhai Road 96, Hefei, China 230026

365 University of Silesia, Institute of Physics, Ul. Uniwersytecka 4, PL-40007 Katowice, Poland

366 University of South Carolina, Department of Physics and Astronomy, 712 Main Street, Columbia, SC 29208, USA

367 University of Southampton, School of Physics and Astronomy, Highfield, Southampton S017 1BJ, England, UK

368 University of Southern California, Department of Physics & Astronomy, 3620 McClintock Ave., SGM 408, Los Angeles, CA 90089-0484, USA

369 University of Sydney, Falkiner High Energy Physics Group, School of Physics, A28, Sydney, NSW 2006, Australia

370 University of Tartu, Institute of Physics, Riia 142, 51014 Tartu, Estonia

371 University of Texas at Austin, Department of Physics, 1 University Station C1600, Austin, Texas 78712, USA

372 University of Texas at Dallas, Department of Physics, 800 West Campbell Road, Richardson, Texas 75080, USA

373 University of Texas, Center for Accelerator Science and Technology, Arlington, TX 76019, USA
374 University of Tokushima, Institute of Theoretical Physics, Tokushima-shi 770-8502, Japan
375 University of Tokyo, Department of Physics, 7-3-1 Hongo, Bunkyo District, Tokyo 113-0033, Japan
376 University of Toronto, Department of Physics, 60 St. George St., Toronto M5S 1A7, Ontario, Canada
377 University of Toyama, Department of Physics, 3190 Gofuku, Toyama 930-8555, Japan
378 University of Tsukuba, Faculty of Pure and Applied Sciences, 1-1-1 Ten'nodai, Tsukuba, Ibaraki 305-8571, Japan
379 University of Victoria, Department of Physics and Astronomy, P.O.Box 3055 Stn Csc, Victoria, BC V8W 3P6, Canada
380 University of Virginia, Department of Physics, 382 McCormick Rd., PO Box 400714, Charlottesville, VA
381 University of Warsaw, Institute of Experimental Physics, Ul. Hoza 69, PL-00 681 Warsaw, Poland
382 University of Warsaw, Institute of Theoretical Physics, Ul. Hoza 69, PL-00 681 Warsaw, Poland
383 University of Washington, Department of Physics, PO Box 351560, Seattle, WA 98195-1560, USA
384 University of Wisconsin, Physics Department, Madison, WI 53706-1390, USA
385 University of Wuppertal, Gaußstraße 20, D-42119 Wuppertal, Germany
386 Università degli Studi di Milano, Dipartimento di Fisica, Via Celoria 16, 20133 Milano, Italy
387 Università degli Studi di Roma "La Sapienza", Dipartimento di Fisica, Piazzale Aldo Moro 5, 00185 Roma, Italy
388 Università degli Studi di Trieste, Dipartimento di Fisica, via A. Valerio 2, I-34127 Trieste, Italy
389 Università dell'Insubria in Como, Dipartimento di Scienze CC.FF.MM., via Vallegio 11, I-22100 Como, Italy
390 Università di Milano-Bicocca, Dipartimento di Fisica"G. Occhialin", Piazza della Scienza 3, 20126 Milano, Italy
391 Università di Pisa, Departimento di Fisica "Enrico Fermi", Largo Bruno Pontecorvo 3, I-56127 Pisa, Italy
392 Universiy of Huddersfield, International Institute for Accelerator Applications, Queensgate Campus, Huddersfield HD1 3DH, UK
393 UPMC Univ. Paris 06, Faculté de Physique (UFR 925), 4 Place Jussieu, 75252 Paris Cedex 05, France
394 Vietnam National University, Laboratory of High Energy Physics and Cosmology, Faculty of Physics, College of Science, 334 Nguyen Trai, Hanoi, Vietnam
395 Vietnam National University, University of Natural Sciences, 227 Nguyen Van Cu street, District 5, Ho Chi Minh City, Vietnam
396 VINCA Institute of Nuclear Sciences, Laboratory of Physics, PO Box 522, YU-11001 Belgrade, Serbia
397 Virginia Commonwealth University, Department of Physics, P.O. Box 842000, 701 W. Grace St.,Richmond, VA. 23284-2000, USA
398 Virginia Polytechnic Institute and State University, Physics Department, Blacksburg, VA 2406, USA
399 Vrije Universiteit Brussel, Pleinlaan 2, 1050 Brussels, Belgium
400 Vrije Universiteit, Department of Physics, Faculty of Sciences, De Boelelaan 1081, 1081 HV Amsterdam, Netherlands
401 Warsaw University of Technology, The Faculty of Electronics and Information Technology, ul. Nowowiejska 15-19, 00-665 Warsaw, Poland
402 Waseda University, Advanced Research Institute for Science and Engineering, Shinjuku, Tokyo 169-8555, Japan
403 Wayne State University, Department of Physics, Detroit, MI 48202, USA
404 Weizmann Institute of Science, Department of Particle Physics, P.O. Box 26, Rehovot 76100, Israel
405 Yale University, Department of Physics, New Haven, CT 06520, USA
406 Yamagata University, 1-4-12 Kojirakawa-cho, Yamagata-shi, Yamagata, 990-8560, Japan
407 Yerevan Physics Institute, 2 Alikhanyan Brothers St., Yerevan 375036, Armenia
408 Yonsei University, Department of Physics, 134 Sinchon-dong, Sudaemoon-gu, Seoul 120-749, Republic of Korea

ISSUED BY • • • • • • • • ilc international linear collider

WWW.LINEARCOLLIDER.ORG

ISBN 978-3-935702-78-2

Argonne National Laboratory: ANL-HEP-TR-13-20
Brookhaven National Laboratory: BNL-100603-2013-IR
CEA/irfu: IRFU-13-59
CERN: CERN-ATS-2013-037
Cockcroft Institute: Cockcroft-13-10
Cornell University: CLNS 13/2085
DESY: DESY 13-062
Fermilab: FERMILAB TM-2554
IHEP: IHEP-AC-ILC-2013-001
ILC report: ILC-REPORT-2013-040
INFN: INFN-13-04/LNF
JAI: JAI-2013-001
JINR: JINR E9-2013-35
JLab: JLAB-R-2013-01
KEK: KEK Report 2013-1
KNU: KNU/CHEP-ILC-2013-1
LLNL: LLNL-TR-635539
SLAC: SLAC-R-1004
ILC HiGrade: ILC-HiGrade-Report-2013-003

THE INTERNATIONAL LINEAR COLLIDER

From Design to Reality

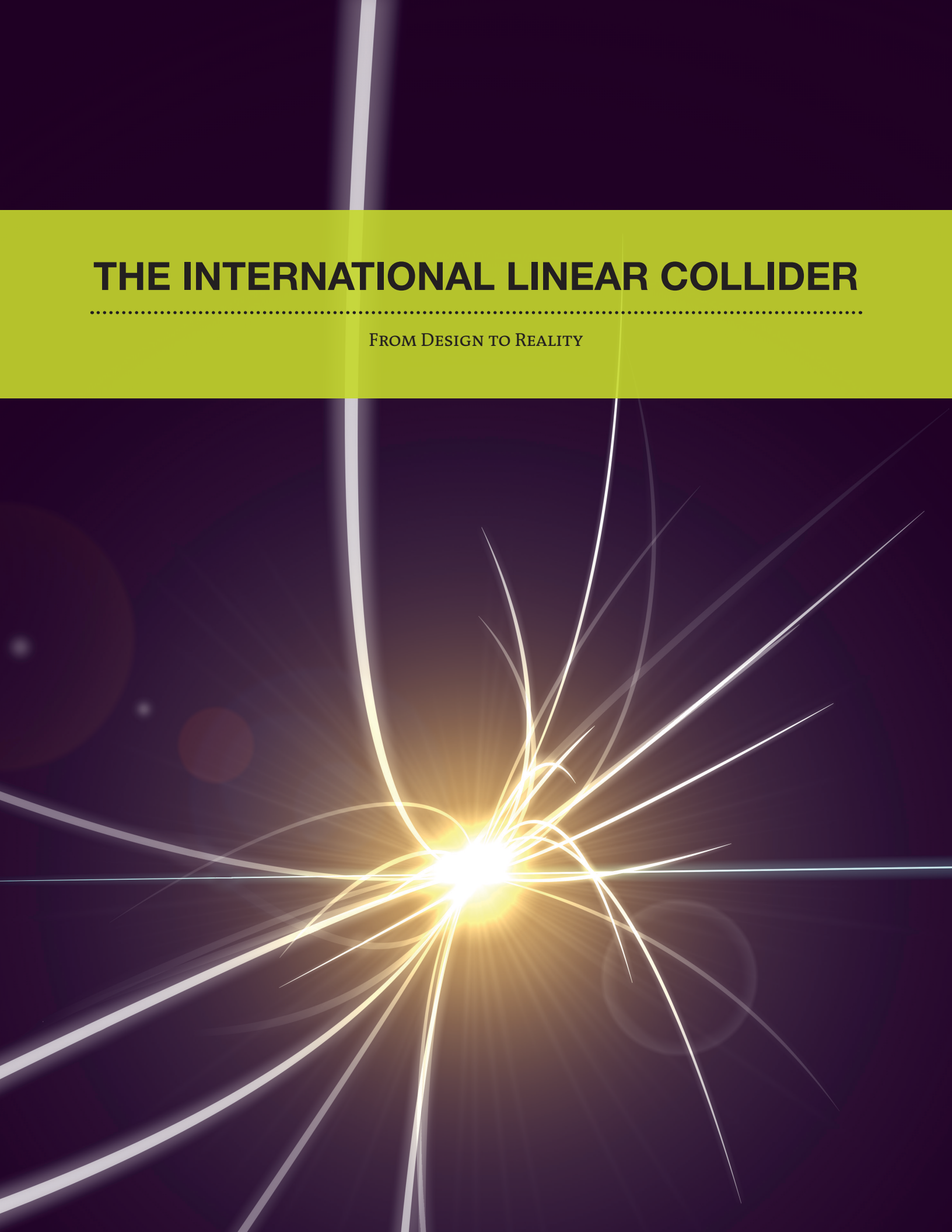

Image: form one

FOREWORD:
WINDOW TO THE TERASCALE

Particle accelerators have been the primary tool of particle physics for over 60 years. They have enabled great advances and discoveries, the latest being the discovery of the Higgs boson at the Large Hadron Collider at CERN. Using complementary approaches of colliding protons on protons as a broad-band discovery device and colliding electrons on positrons as a precision probe of the physics, we have uncovered the basic constituents of matter and fundamental symmetries in nature. The International Linear Collider is the next advance in accelerators and will be the complementary electron-positron collider for the Large Hadron Collider. The ILC will enable precision studies of the underlying physics of the Higgs, a completely new kind of particle responsible for the creation of mass in nature.

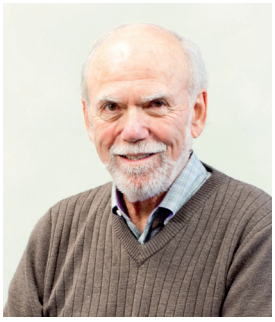

Among the earliest particle accelerators were cyclotrons, which were followed by larger and larger particle accelerators and colliders that brought us at each step to higher energies and new discoveries of physics at very short distances. Now, the development of a linear collider represents yet another major step in our ability to accelerate very light particles, like electrons and positrons, and pave the way to new insights into how our world works. The technologies for a linear collider have been developed through an ambitious global R&D programme and are now, with the publication of the ILC Technical Design Report, ready to be employed in the next particle accelerator. We are technically prepared to build a complementary electron-positron collider to the Large Hadron Collider. Japan is seriously considering offering to host the ILC for the global collaboration, siting it in the mountains of Japan. They propose to begin with a Higgs Factory and extend it to higher energies in the future. This possibility is now being considered both within Japan and by the worldwide community. We look forward to taking the next step in the adventure that is the ILC.

Barry C. Barish

June 2013

THE INTERNATIONAL LINEAR COLLIDER – FROM DESIGN TO REALITY
EDITORIAL COMMITTEE

Philip Burrows
University of Oxford

John Carwardine
Argonne National Laboratory

Marcel Demarteau
Argonne National Laboratory

Brian Foster
DESY and University of Hamburg

Keisuke Fujii
KEK

Michael Harrison
Brookhaven National Laboratory

Nicholas Walker
DESY

Kirk Yamamoto
KEK

Linear Collider Communicators:
Pan Qian, Perrine Royole-Degieux, Rika Takahashi, Barbara Warmbein

This brochure represents Volume 5 of the ILC's *Technical Design Report*. It summarises the content of the four TDR volumes for a non-expert audience. For more information go to www.linearcollider.org

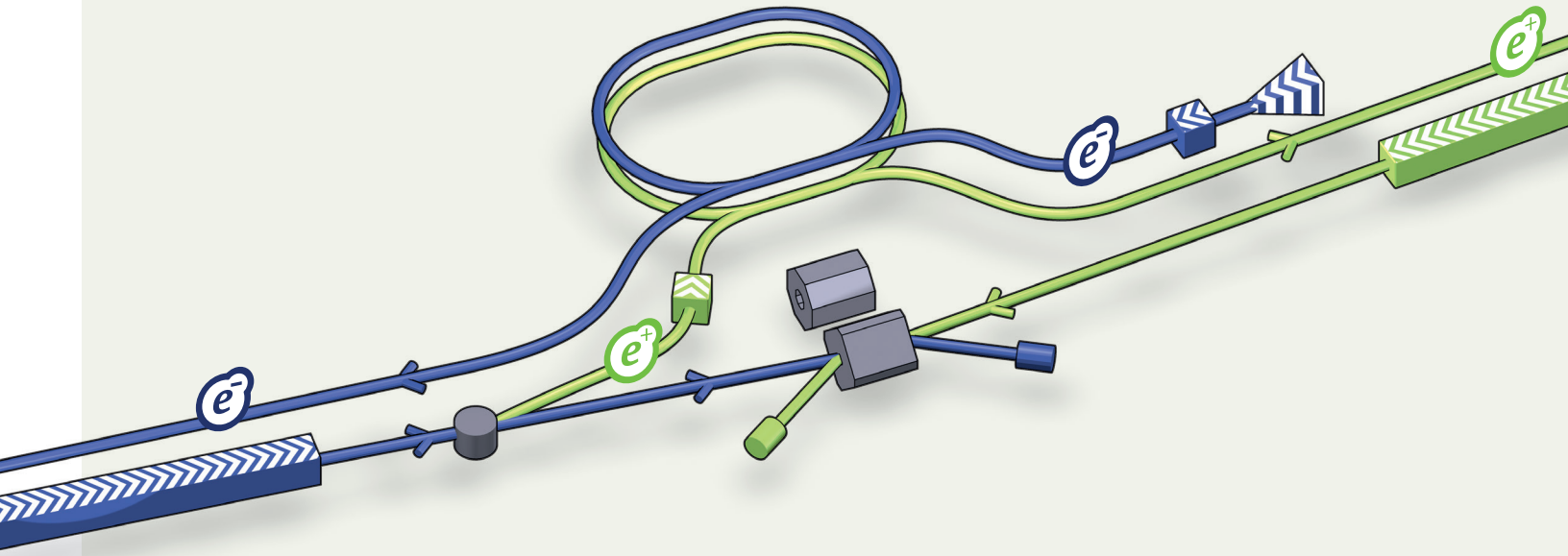

CONTENTS

3 FOREWORD: WINDOW TO THE TERASCALE

01 6 THE SCIENCE BEHIND THE NEW COLLIDER

7 The LHC has discovered the Higgs – what does that mean?
8 What is the Standard Model?
10 What is the Higgs and Higgs mechanism?
13 How will the ILC investigate the Higgs and other phenomena precisely?
15 How far can the Standard Model go?
15 What are dark matter and dark energy?
16 How is the ILC complementary to the ILC?
16 What is supersymmetry? And how can the ILC study it?
17 What are extra dimensions?
19 The ILC – shaping the future of particle physics

02 20 TECHNOLOGIES BEHIND THE NEW COLLIDER

21 The ILC travel guide
22 Source
23 Damping ring
24 Ring to main linac and bunch compression
24 Main linac
26 Positron source
27 Final focus
28 Interaction point and detectors

03 30 THE ORGANISATION WITHOUT BOUNDARIES

31 The project that goes beyond boundaries
32 The project that attracts people
32 The project that nurtures the next generation
33 The project that pushes technology and other sciences
34 The project that has economic impact as its home

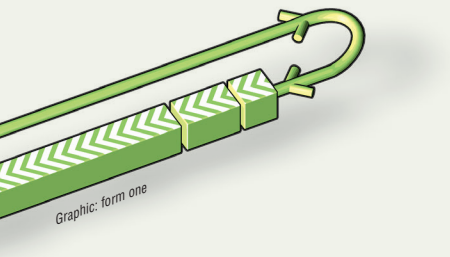

Graphic: form one

01 | THE SCIENCE BEHIND THE NEW COLLIDER

Image: CERN

THE LHC HAS DISCOVERED THE HIGGS – WHAT DOES THAT MEAN?

July 4th in 2012 is destined to be a special day in the history of humankind. On that day, physicists working with the world's largest scientific facility, the Large Hadron Collider (LHC), at the European particle physics laboratory CERN, in Switzerland, announced that they have discovered a particle that looks a lot like the long-sought Higgs boson – the final missing piece in the Standard Model that describes fundamental particles and forces. The Higgs boson is the key to the explanation of how all the other fundamental particles get their masses. A few months later, this particle was confirmed to be a Higgs particle.

Discovering this new particle at the LHC is a triumph. After two successful years of operation at the LHC, the next step in our understanding of the Universe has been revealed. Now that the scientists have found a Higgs boson, many more years of follow-up research will be needed to verify its full identity. For a particle to be exactly the Higgs as originally conceived, all of its properties must be measured with great accuracy; a tough job indeed.

The energy of the Higgs particle recently discovered at CERN is well within the range of the ILC. It is too soon to know exactly what additional information will be uncovered from the LHC experiments, but even without this information the potential for exploiting Higgs physics at the ILC is enormous. At the ILC, Higgs particles will be created in electron-positron collisions and their properties measured: e.g. mass, the strength of their interactions with all other elementary particles with unprecedented precision and without assumptions. Will the Higgs properties be as predicted by the Standard Model? Or will it be just the first of a family? Will nature be more complicated than a single "minimal" Higgs boson? The precision of the measurements that can be made at the ILC allow us to estimate at what energy new particles may appear. There is agreement in the high-energy physics community that a linear collider like the ILC is the ideal facility to make these vital measurements.

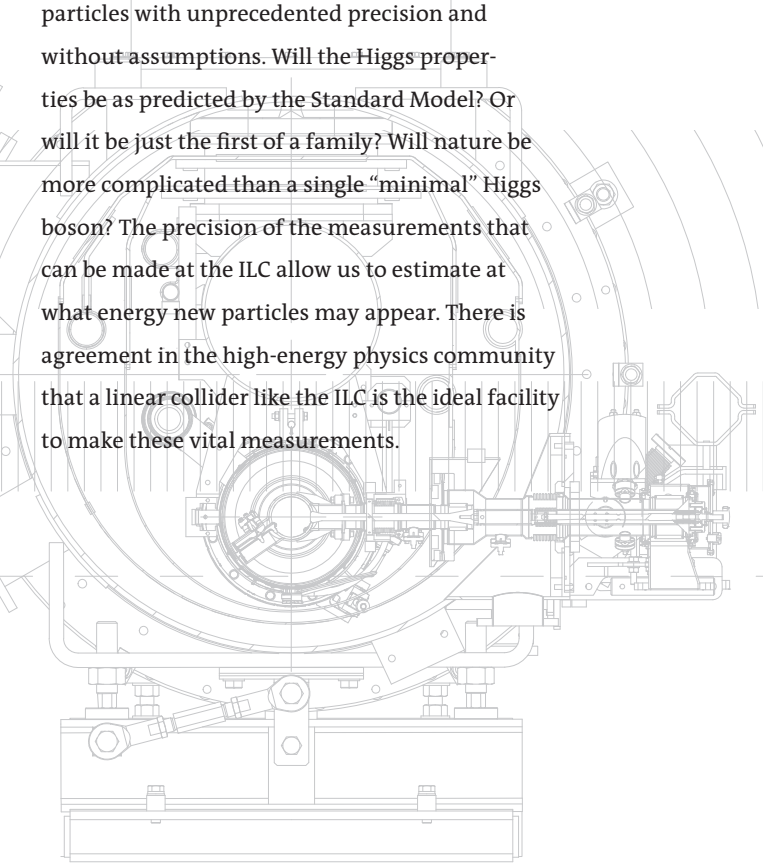

WHAT IS THE STANDARD MODEL?

The Standard Model of particle physics is a theory that describes the known particles that are the constituents of matter and three of the four known fundamental interactions between them. These interactions, or forces, are the electro-magnetic force (which we experience every day when we turn on the light, the TV, use wireless communication etc), the strong force (which holds quarks together inside the protons and neutrons in the atomic nucleus, thereby forming the plethora of elements, from helium to iron to uranium, that make up our world) and the weak force (which is responsible for the Sun shining, without which life on Earth would be impossible, as well as for many radioactive decays).

The Standard Model works extremely well, but we know that it cannot be the complete theory if for no other reason than that it is incomplete; it does not incorporate gravity. It describes beautifully the ordinary matter of which we, and the entire visible universe, are made. It does not describe the invisible 95% of the universe that we know to be there, but which has thus far evaded detection. The Standard Model has nevertheless been tested to exquisite precision over a wide range of energies. It must therefore be a good approximation to a final, unified, theory.

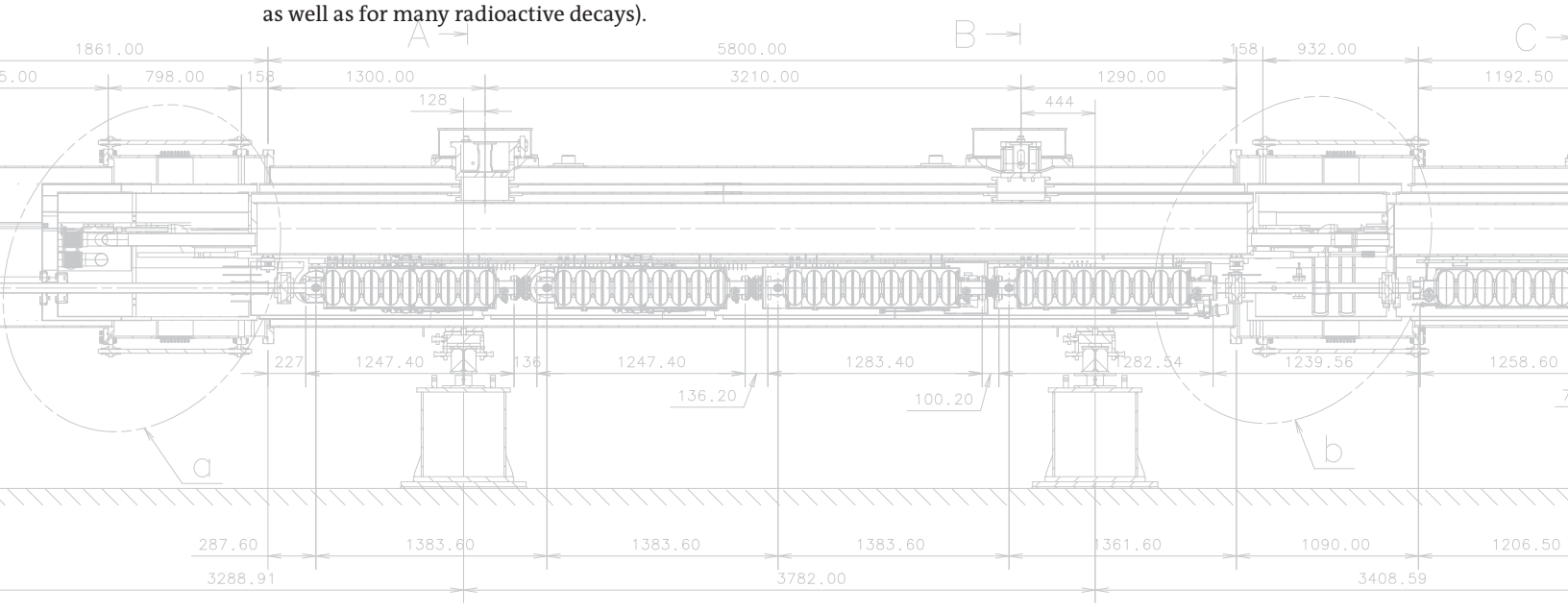

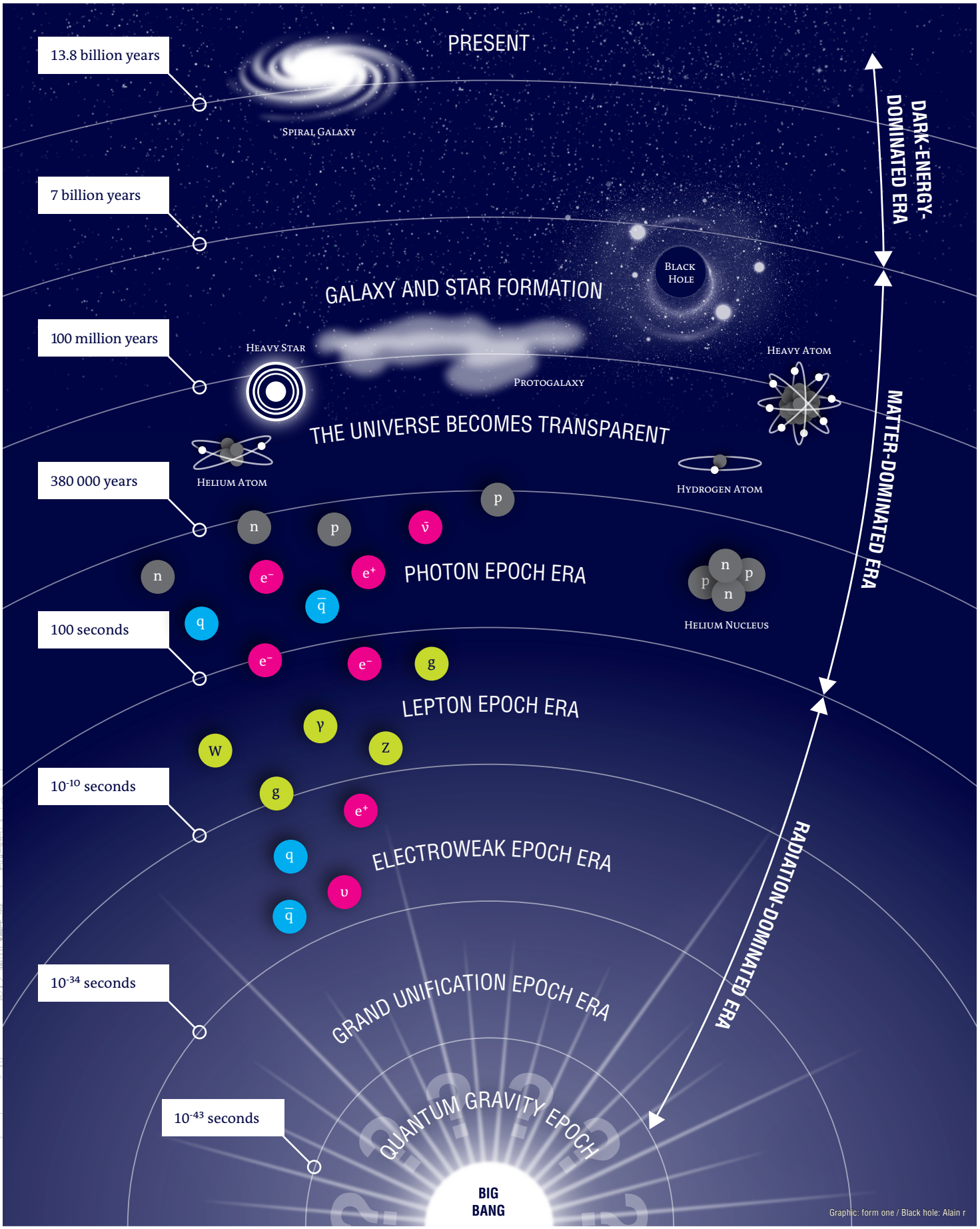
13.8 billion years
PRESENT
Spiral Galaxy
7 billion years
GALAXY AND STAR FORMATION
Black Hole
100 million years
Heavy Star
Protogalaxy
Heavy Atom
THE UNIVERSE BECOMES TRANSPARENT
Helium Atom
Hydrogen Atom
380 000 years
PHOTON EPOCH ERA
Helium Nucleus
100 seconds
LEPTON EPOCH ERA
10-10 seconds
ELECTROWEAK EPOCH ERA
10-34 seconds
GRAND UNIFICATION EPOCH ERA
10-43 seconds
QUANTUM GRAVITY EPOCH
BIG BANG
DARK-ENERGY-DOMINATED ERA
MATTER-DOMINATED ERA
RADIATION-DOMINATED ERA
Graphic: form one / Black hole: Alain r

WHAT IS THE HIGGS AND HIGGS MECHANISM?

The Standard Model successfully describes all of the elementary particles we know to exist and how they interact with one another. But one piece is missing. The Standard Model cannot yet answer one basic question: why do most of these elementary particles have mass?

Theoretical physicists Robert Brout, François Englert, Peter Higgs, Gerald Guralnik, Carl Hagen and Tom Kibble proposed a mechanism that would explain how particles get their mass. This mechanism postulates a medium that exists everywhere in space. Particles gain mass by interacting with this medium, or "field". Peter Higgs pointed out that the mechanism required the existence of a particle unseen until now, which we now call the Higgs boson after its inventor. The Higgs mechanism predicts the Higgs boson to be a fundamental scalar, meaning a spinless particle. No other fundamental spinless particles exist in nature. Its spinless nature allows the Higgs to condense and fill the vacuum much like steam condenses to form the sea. The Higgs discovery raises a variety of new questions on the supposed nature of this boson and opens up a very important area of research.

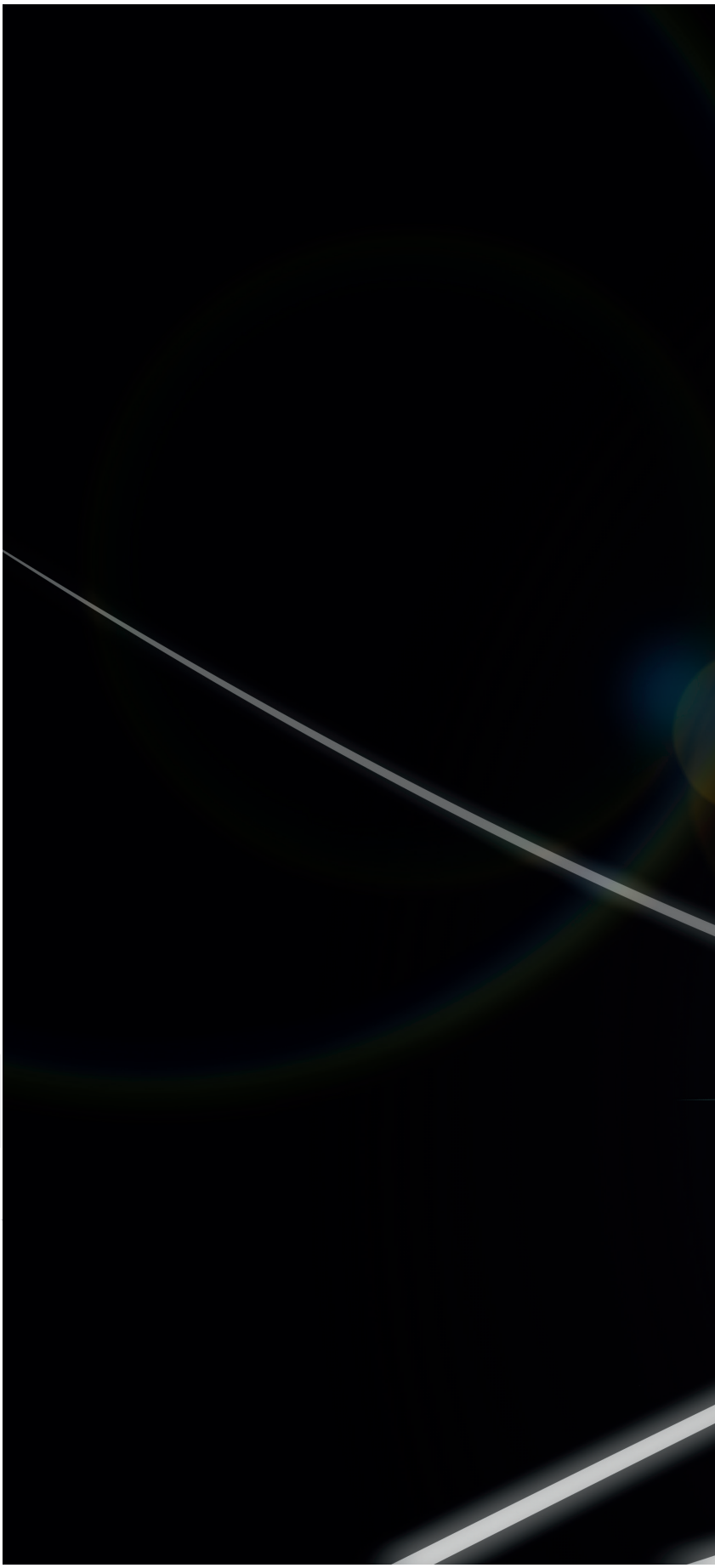

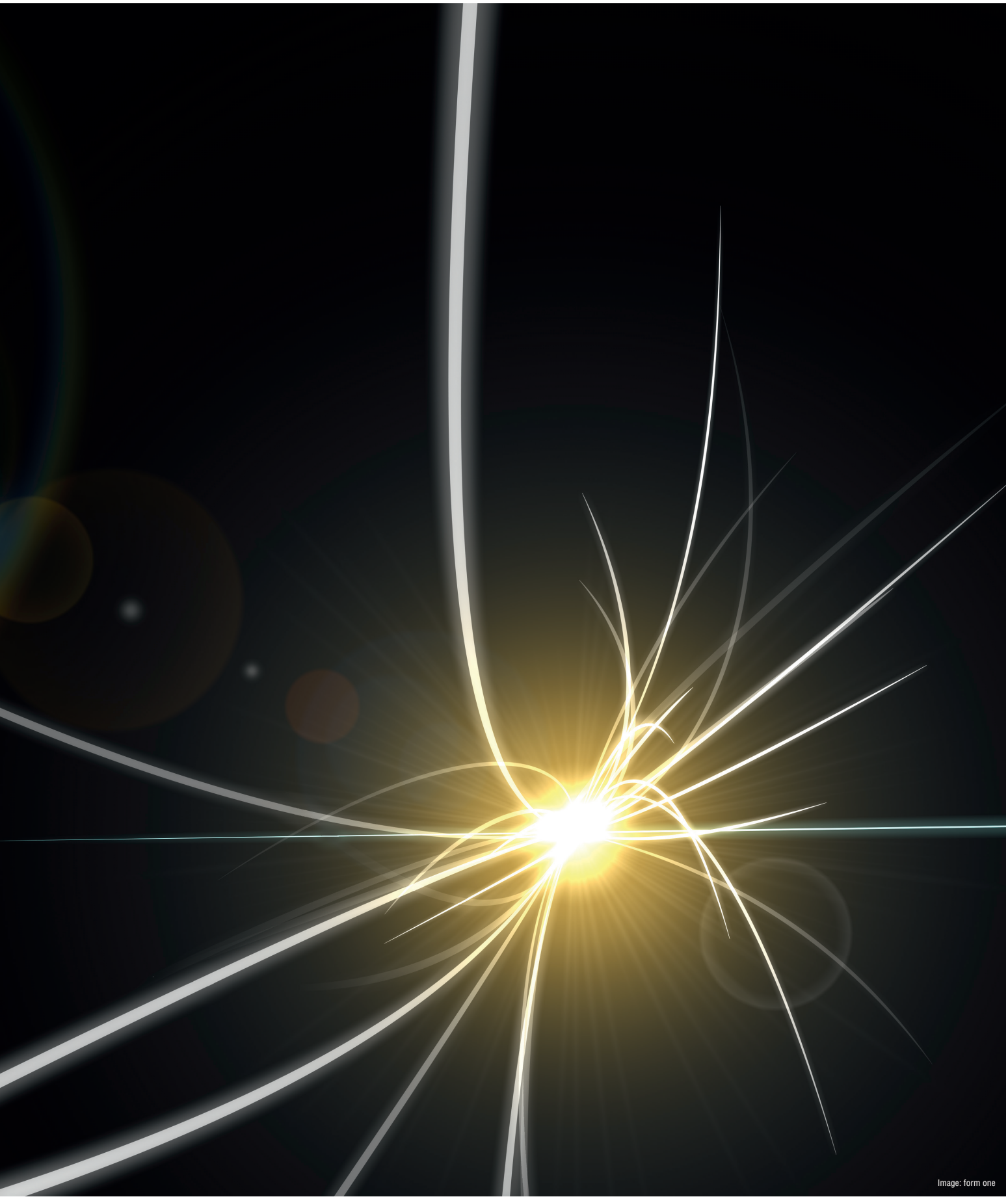

Image: form one

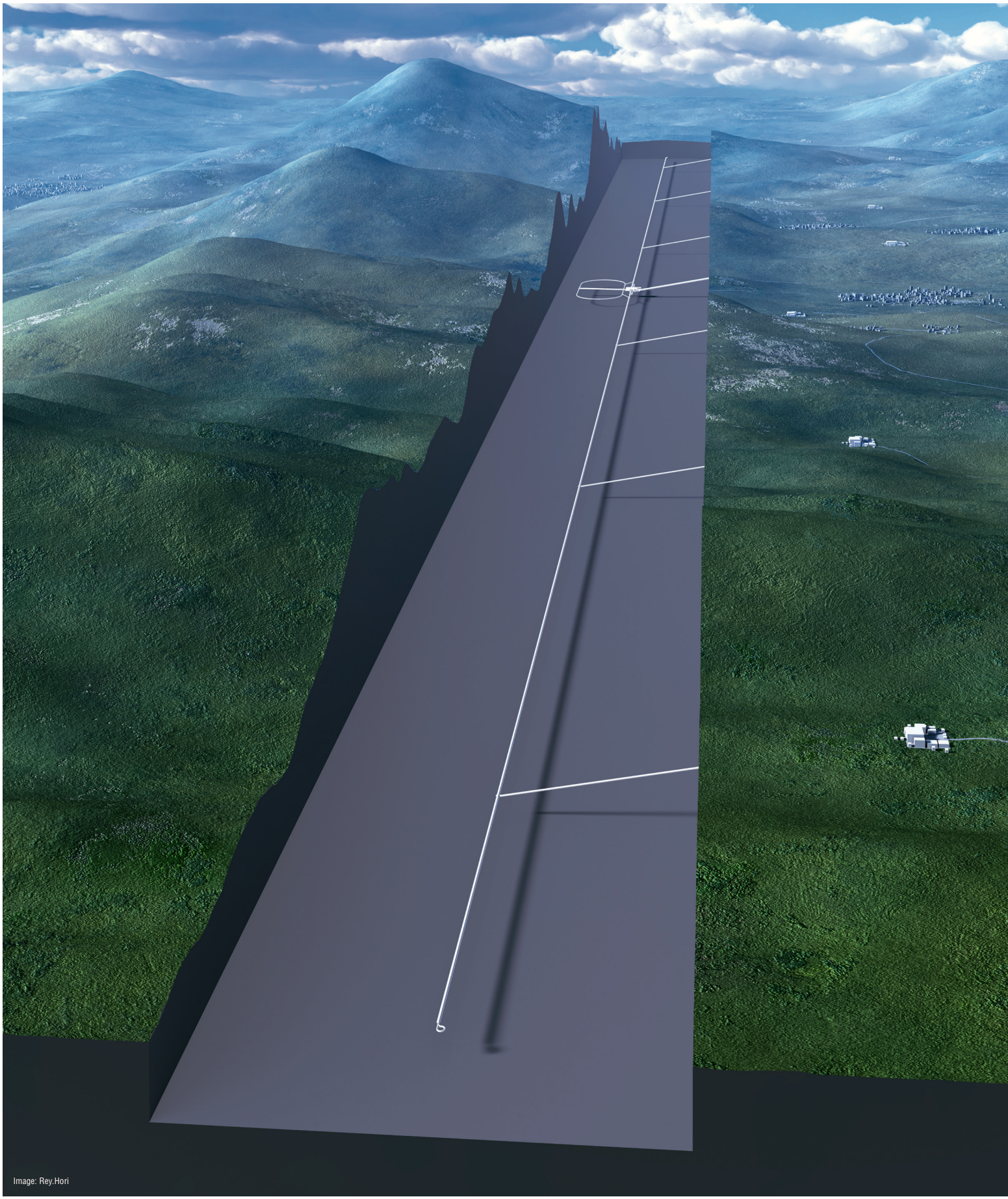

Image: Rey.Hori

HOW WILL THE ILC INVESTIGATE THE HIGGS AND OTHER PHENOMENA PRECISELY?

The ILC is complementary to the LHC's proton-proton collisions. The LHC, a circular proton-proton synchrotron, operates at the highest energies any particle accelerator has ever achieved. The International Linear Collider will explore the same phenomena using a different approach. By colliding electrons with positrons, the ILC would allow us to home in with exquisite precision on the new landscape that the LHC will reveal. It will expand on the discoveries made by the LHC and investigate new laws of nature.

Apart from its spinless property, the Higgs boson's coupling strength to other particles is its second unique feature, which is ultimately responsible for generating these particles' masses. Measuring the strength with which the Higgs boson interacts with particles having different masses will investigate whether the predicted relative strengths are correct. The many precisely measured Higgs events at the ILC will produce quantitative measurements of the different coupling strengths that will enable us to distinguish among possible different types of Higgs bosons.

Another unique feature of the Higgs boson is its coupling to itself. The Standard Model precisely describes how the Higgs boson couples to other particles, including itself. With its precision, the ILC enables an accurate measurement of the Higgs' self-coupling and determines its potential, confirming or disproving in a completely model-independent way whether it is the Standard-Model Higgs boson.

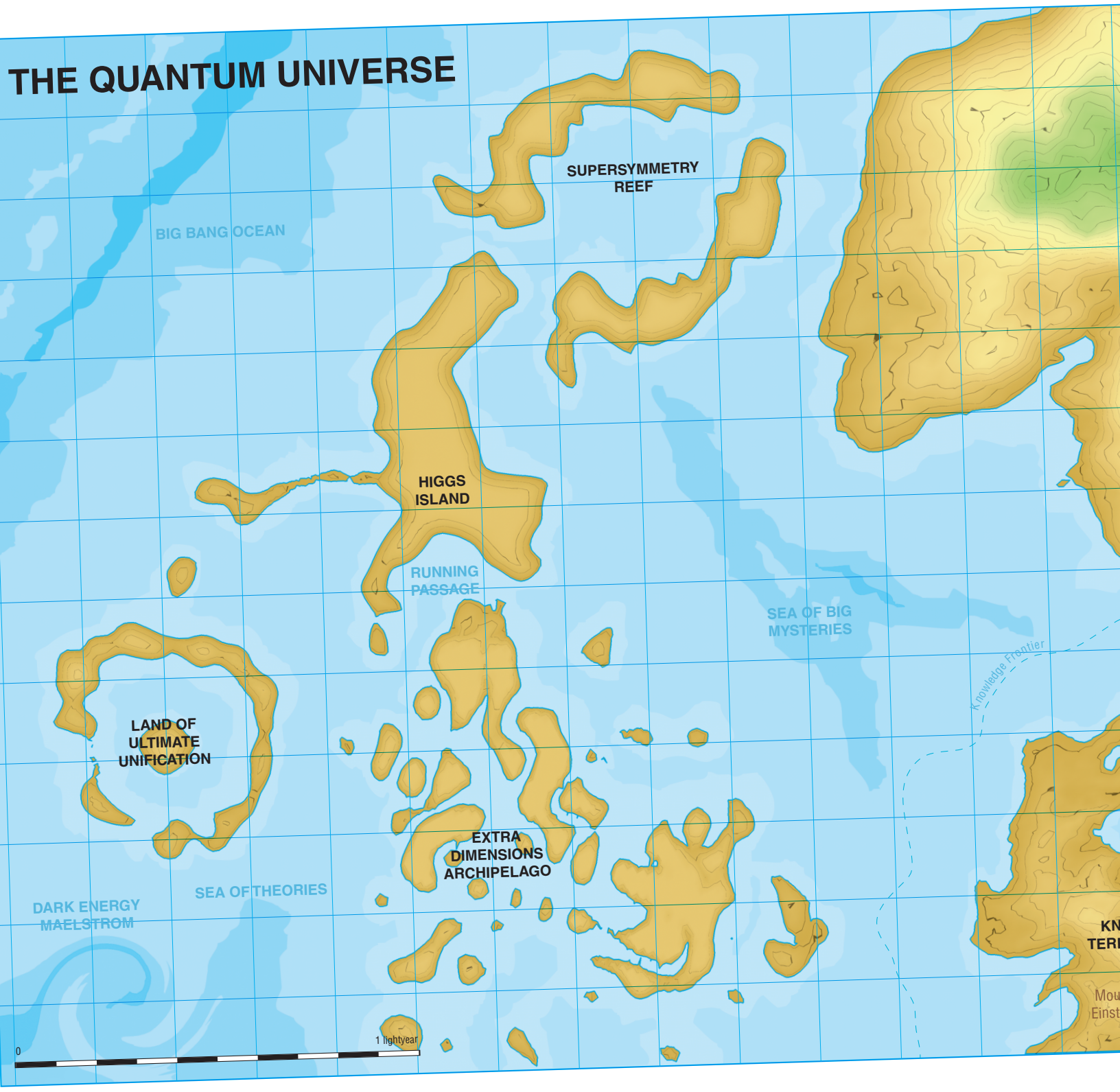

Graphic: form one

HOW FAR CAN THE STANDARD MODEL GO?

If the LHC does not find anything that hints at a deviation from the Standard Model, scientists would have to test the energy scale up to which the Standard Model can be valid. One way to do this is to check the stability of the theory. This is determined by values of the Higgs mass and the mass of the top quark. Whether the theory – its "vacuum stability", as it is called – is absolutely stable or not depends critically on the precise value of the top mass. The ILC can measure the mass to unprecedented precision and decide the fate of the Standard Model.

WHAT ARE DARK MATTER AND DARK ENERGY?

Most of the matter in the universe is dark. Without dark matter, galaxies and stars would not have formed and life would not exist. It holds the universe together. What is it?

It is only in the last 10 to 15 years that scientists have made substantial progress in understanding the properties of dark matter, mostly by establishing what it is not. Recent observations of the effect of dark matter on the structure of the universe have shown that it is unlike any form of matter that we have discovered or measured in the laboratory. At the same time, new theories have emerged that may tell us what dark matter actually is.

Searches for candidate dark matter particles are underway at present-day colliders. If these particles have masses at the TeV scale, they will surely be discovered at the LHC. However, verifying that these new particles are indeed related to dark matter will require a linear collider to characterise their properties. The International Linear Collider can measure their mass, spin and parity with extremely high precision. These results will permit calculation of the present-day cosmic abundance of dark matter and comparison to cosmological observations. If the values agree, it will be a great triumph for both particle physics and cosmology and will extend the understanding of the evolution of the universe after the big bang.

HOW IS THE ILC COMPLEMENTARY TO THE LHC?

The LHC and the ILC provide very different conditions to produce and allow us to study particles. High-energy interactions of protons at the LHC proceed via the interactions of the constituents of protons, the quarks and gluons; the ILC will study collisions of electrons and positrons. As electrons and positrons are elementary particles and have no known internal structure, linear-collider experiments are able to study simpler, more elementary processes without the complicated "background" present at the LHC and hence achieve a higher level of precision. The LHC is already operating, so it gives us the chance to discover new particles and to study properties of the known particles today. The linear collider, with its higher level of precision, will add qualitatively new knowledge. It has the potential to reveal new details and possibly particles that are invisible to the LHC experiments.

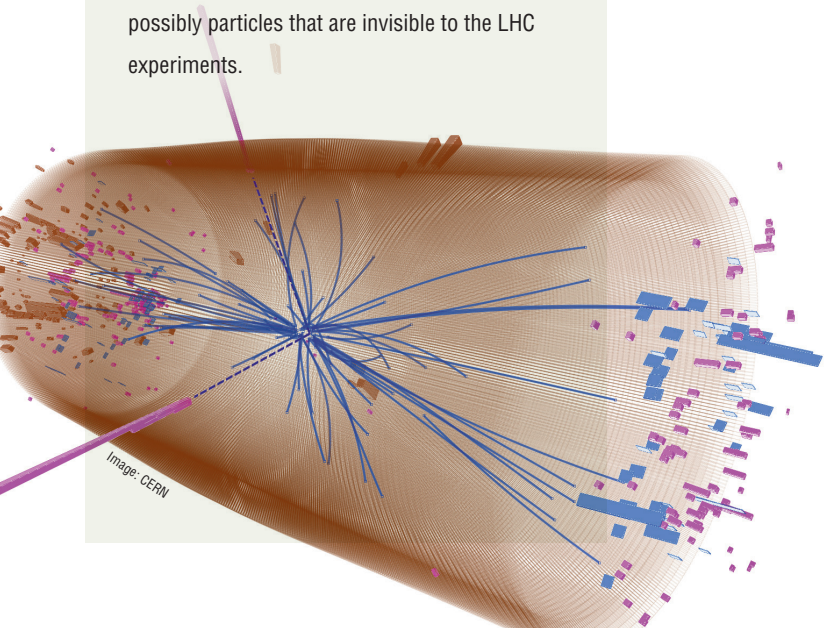

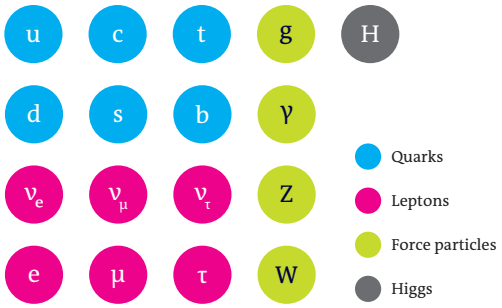

WHAT IS SUPERSYMMETRY? AND HOW CAN THE ILC STUDY IT?

The theory of supersymmetry says that all known particles have heavier superpartners, new particles that bring a new dimension to the subatomic world. The lightest superpartner is a likely candidate to be dark matter, and could thus also explain the structure of the cosmos.

A linear collider would be best suited for producing the lighter superpartners. Linear-collider experiments could focus on one type of superpartner at a time, measuring their properties precisely enough to detect the symmetry of supersymmetry, and to reveal the supersymmetric nature of dark matter. In this way, physicists could discover how supersymmetry shapes both the inner workings and the grand designs of the universe. Designed with great accuracy and precision, the ILC becomes the perfect machine to conduct the search for dark-matter particles with unprecedented precision; we have good reasons to anticipate other exciting discoveries along the way.

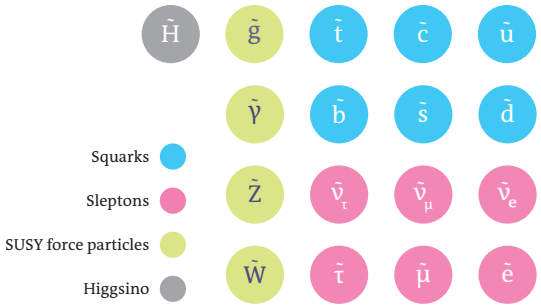

WHAT ARE EXTRA DIMENSIONS?

Many theories, such as Superstrings, that try to unify gravity with the other forces require the Universe to have additional dimensions to those of space and time that are familiar to us. Such theories attach additional spatial dimensions to each point in space. The extra dimensions must be very tiny or otherwise hidden from view since none of our experiments have so far given any evidence that they exist. Matter might be made of particles that already live in extra dimensions and feel their effects. A particle moving in an extra dimension would have extra energy, making it look like a heavier version of itself. Measurement of the mass and other properties of these travelers would show what the additional dimensions look like.

If new dimensions exist at the Terascale, then the LHC should discover them; experiments will look for high-energy collisions in which particles literally disappear into an extra dimension. The ILC would be able to reveal the detailed structure of these extra dimensions and their associated particles and might detect signs for others that cannot be seen by the LHC.

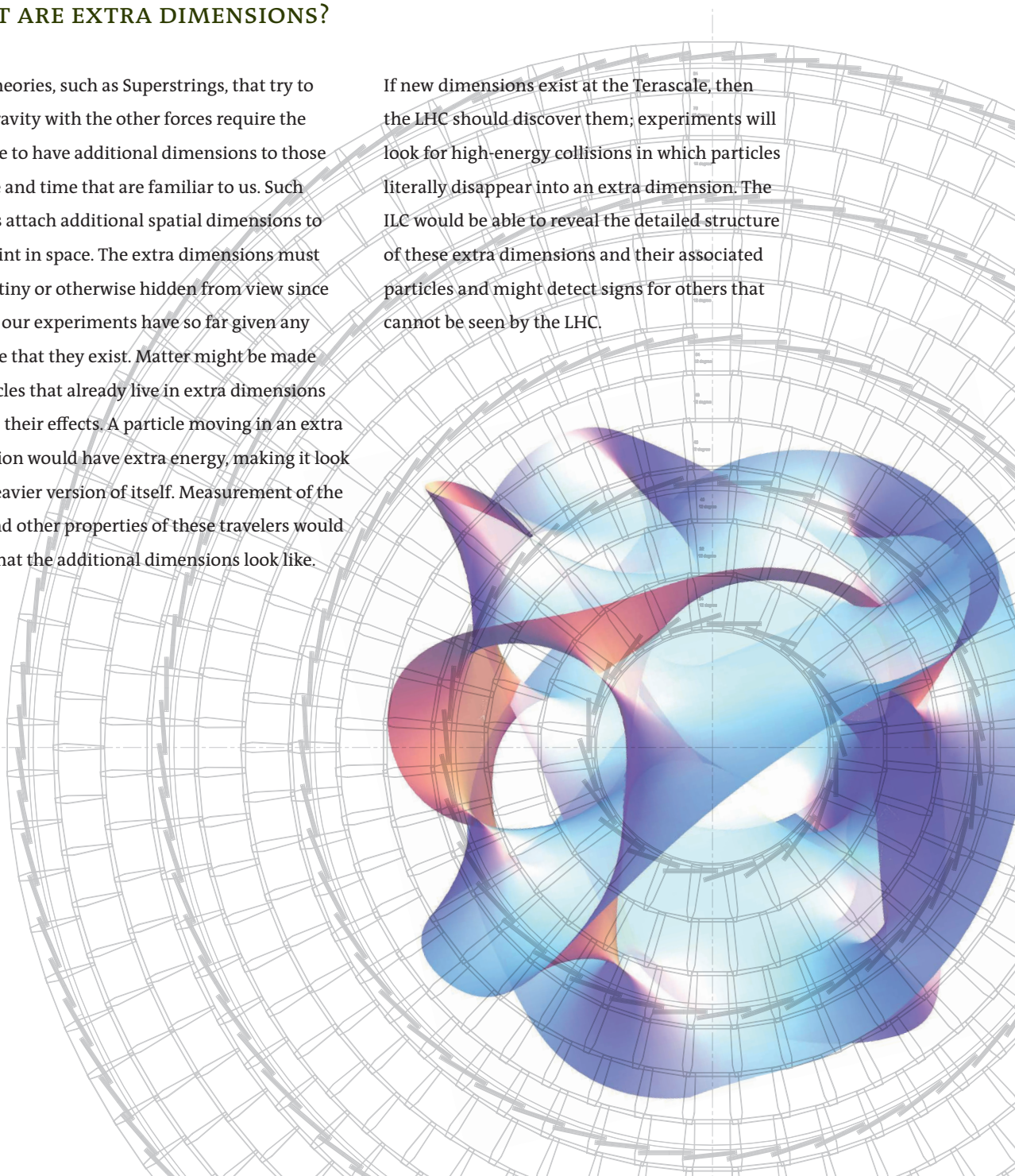

"NEW DIRECTIONS IN SCIENCE ARE LAUNCHED BY NEW TOOLS MUCH MORE OFTEN THAN BY NEW CONCEPTS. THE EFFECT OF A CONCEPT-DRIVEN REVOLUTION IS TO EXPLAIN OLD THINGS IN NEW WAYS. THE EFFECT OF A TOOL-DRIVEN REVOLUTION IS TO DISCOVER NEW THINGS THAT HAVE TO BE EXPLAINED." FREEMAN DYSON, Imagined Worlds

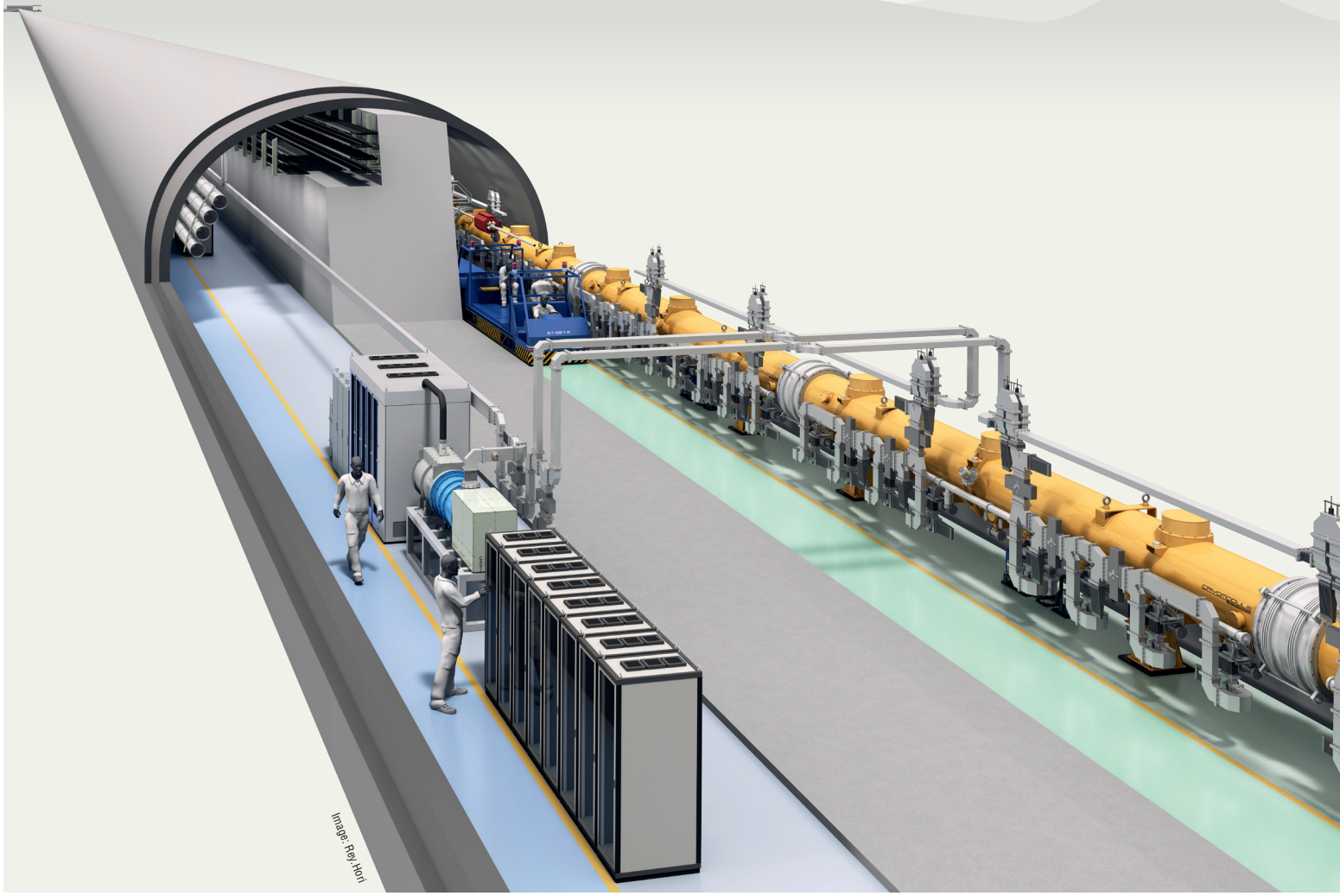

Image: Rey Hori

THE ILC – SHAPING THE FUTURE OF PARTICLE PHYSICS

With the discovery of a Higgs boson, the ILC has a guaranteed, rich physics program to explore. If the new particle is truly a spinless fundamental particle, it is the only such particle that we know about. It adds a completely new dimension to our understanding of the fabric of space-time. The ILC and its detectors are precision instruments allowing the properties of the Higgs boson to be studied with laserlike focus. The impact of the ILC, however, reaches far beyond the Higgs. With its variable center of mass energy, it can, as future measurements might require, carry out a programme of ultra-precise electroweak measurements of the Z-boson, study the top quark in great depth and study the self-coupling of the Higgs boson at its highest centre-of-mass energy. Furthermore, it can make measurements which do not rely on any theoretical assumptions, thereby investigating the internal consistency of new theories. The ILC will be a tool of unprecedented versatility. As Freeman Dyson once said, “New directions in science are launched by new tools much more often than by new concepts. The effect of a concept-driven revolution is to explain old things in new ways. The effect of a tool-driven revolution is to discover new things that have to be explained”. The ILC is such a tool!

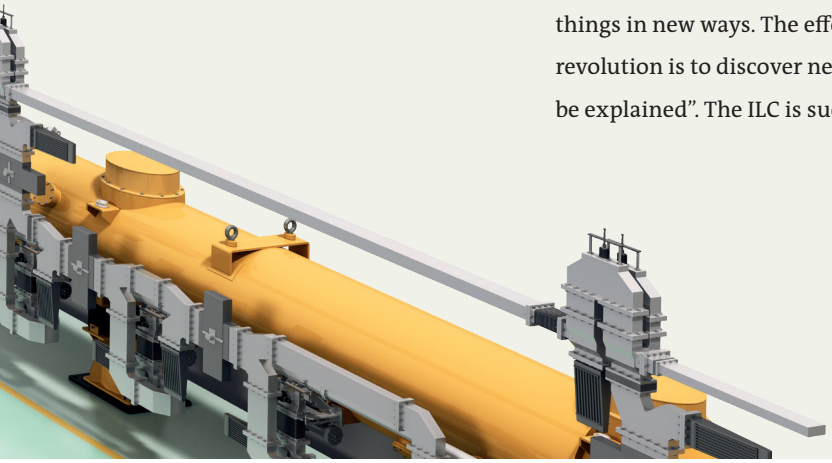

02 | TECHNOLOGIES BEHIND THE NEW COLLIDER

Image: DESY/CEA

THE ILC TRAVEL GUIDE:

follow the particles on their trip through the accelerator and discover ingenious technologies along the way

At the height of operation, bunches of electrons and their antiparticles (positrons) will collide roughly 7,000 times per second at a total collision energy of 500 GeV, creating a surge of new particles that are tracked and registered in the ILC's detectors. Each bunch will contain 20 billion electrons or positrons – this means a very high rate of collisions. This high "luminosity", when combined with the very precise interaction of two point-like colliding particles that annihilate each other, will allow the ILC to deliver a wealth of data to scientists that will allow the properties of particles, such as the recently discovered Higgs boson, to be measured precisely. It could also shed light on new areas of physics such as dark matter.

How will it work? How do the particles get from one end of the accelerator to the collision point at the centre, and what happens to them on their way? Here's your travel guide.

0

START HERE

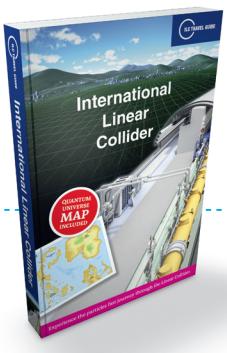

Image: DESY

WHY IS THE LINEAR COLLIDER LINEAR?

When an electric charge follows a curved track, it emits X-rays and loses energy. The higher its energy, the more energy it loses. The energy loss also depends on the mass of the particle and is much more severe for electrons and positrons than for the LHC's protons. The solution to reach high energies is to eliminate the curves, hence to build a "linear" collider.

WHAT IS A GEV?

An electronvolt, eV, is the basic unit of energy or mass used in particle physics. It refers to the amount of energy a single electron gains when it is accelerated across an electric potential difference of one volt. One eV is extremely small, and units of a million electronvolts, MeV, or a billion electronvolts, GeV, are more common. The latest generation of energy-frontier particle accelerators, such as the LHC, reaches up to several trillion electronvolts, or TeV.

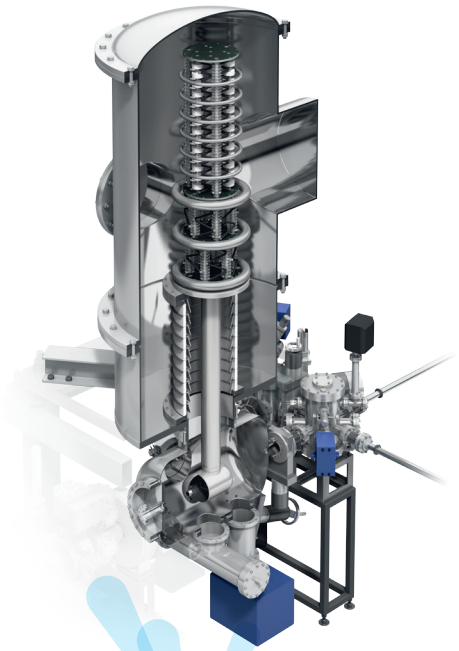

1

SOURCE

Electrons are produced in the electron source. An intense laser beam shines onto a semiconductor cathode and knocks out billions of electrons. Electric and magnetic fields gather the electrons together and accelerate them to an initial energy of 5 GeV.

2
DAMPING RING

Their next port of call is the damping ring. The density of the particles in the bunch generated by the source is far too low, and the particles need to be packed into a much small volume – or damped – to reach the high ILC performance requirements. This is done in a closed storage ring accelerator similar to many synchrotron light sources around the world. Indeed it is the same "synchrotron light" that the particles radiate as they go around the ring that causes them to pack together more tightly. But the ILC pushes this technology still further, demanding that the entire damping process happen in a fraction of a second before the bunches are extracted and sent on the next stage of their journey to the collision point. This requires some impressive technologies to make the particles radiate as fast as possible. No easy feat, but experiments at test accelerators have shown that these requirements can be met. Experts from the fields of light sources and high-energy-physics accelerators have worked together to create a design of a high-performance damping ring that will be up to the ILC job. One kind of special magnet, the so-called wiggler, sends the particle bunches on a serpentine course, causing them to shed some of their energy, which makes them more uniform within the bunch and thus reduces its size. Other technologies for the vacuum system needed to deal with the very high number of particles in the rings have also been the subject of intense study over the last several years. There are two damping rings of three-kilometre circumference installed inside one tunnel – one for electrons, the other for positrons. When the electron or positron bunches leave their respective damping ring they will have gone around the rings about 20,000 times and become very compact and dense – but not quite dense enough. The bunches are still too long and need to be "compressed", but that's the next part of the story.

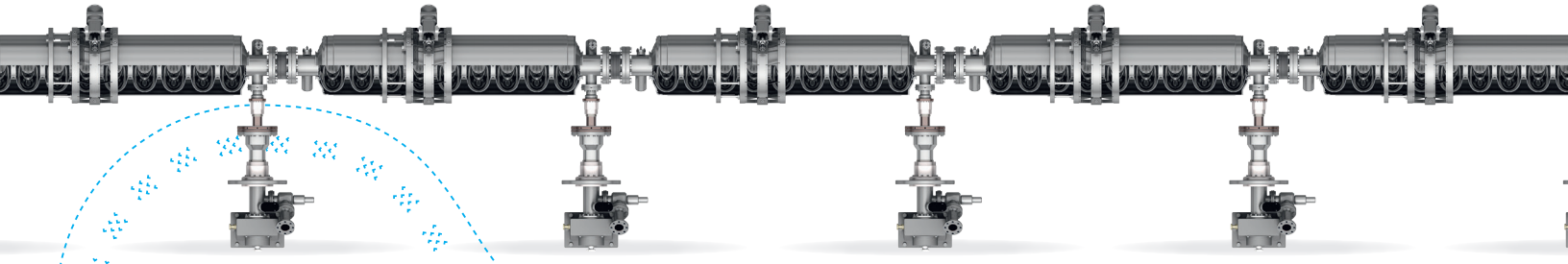

3 RING TO MAIN LINAC & BUNCH COMPRESSION

The neatly packaged and tiny – but still too long – electron and positron bunches are extracted from their respective damping rings and transported in opposite directions some 15 kilometres before being turned 180 degrees in a gentle arc of magnets, ready for the race back to the collision point. Before that all-important sprint through the main accelerator, the bunch length is compressed from 6 mm down to just 0.3 mm, using special sections of the same accelerator technology used in the main linacs, together with some special magnets. While doing this compression, the bunches undergo their first acceleration from 5 to 15 GeV. Now the ultra-compact bunches are ready to be accelerated to the collision energy.

4 MAIN LINAC

Now comes the fast part. Up until this point, the electrons and positrons have been accelerated to a modest 15 GeV. The energy they need to reach at the collision point, however, is 250 GeV (or even twice that at a possible later phase of the ILC). At these energies, scientists hope they can see, and study in detail, the physics phenomena that have been out of reach or only been glimpsed at by other colliders.

Superconducting microwave cavities are the key to reaching this energy. The more accelerating voltage they can apply to the electrons and positrons, the shorter the accelerator can be (which can reduce the cost quite substantially). The cavities' core quality is their acceleration gradient – the higher the gradient, the bigger the boost they can give to the particles. Gradients are however limited by the quality of the inner surface of the cavities, which must have an ultra-clean mirror-like finish as perfect as possible.

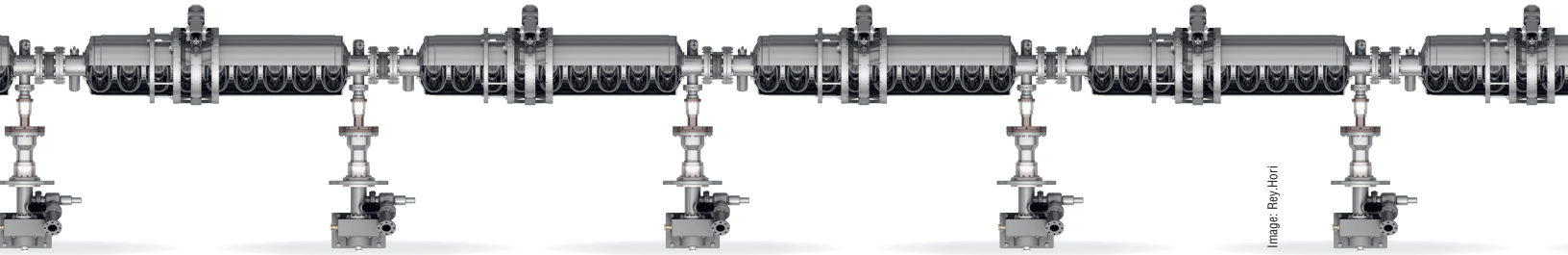

Image: Rey Hori

Several decades of research on superconducting cavities have resulted in a recipe for fabrication and surface treatment that can produce cavities with a gradient exceeding the average 35 Megavolts per metre required for the ILC. Despite this state-of-the-art performance, the two linacs still need to each be 12 kilometres long in order to accelerate the particle bunches to 250 GeV. Operating at -271 degrees Centigrade, the ILC's main linacs will also require one of the world's largest liquid-helium refrigeration plants like the one in operation at the LHC.

The electrons and positrons zoom through the cavities, carried along by the force of electromagnetism. An oscillating electric field inside the cavity at the frequency of radio waves – which is where the name of the acceleration technology comes from: superconducting radio-frequency acceleration – push the particles from cavity to cavity. For a beam energy of 250 GeV, they will pass through 8,000 cavities, or a total of 16,000 cavities for both accelerators.

The production of these cavities and their surrounding equipment has been one of the greatest challenges in the R&D work for the ILC. Accelerator and particle physicists from institutes all over the world have worked together with industry from different countries to work out the best way to produce reliable as well as affordable cavities and their cryomodules, the containing structures within which they operate. The production of accelerator parts like cavities and cryomodules will be done by industry, almost certainly different companies in different regions of the world, whose products then have to fit together to ultra-high precision.

Once accelerated through the main linacs, the positrons are ready for the final leg of the journey to collisions. However, the electrons have one additional job to do before colliding. We have omitted to say where the positrons come from – they are in fact produced by the electron beam!

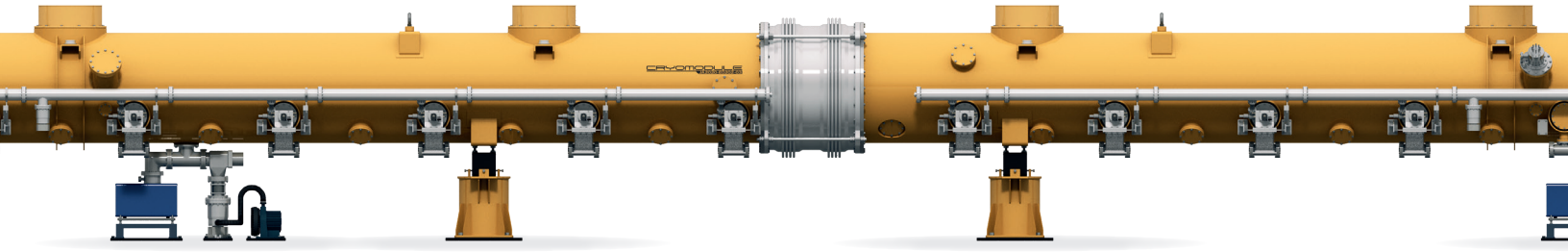

5 POSITRON SOURCE

While it is relative straightforward to rip electrons out of a semiconductor with a laser beam, making positrons presents an altogether bigger challenge. This is because, unlike their matter counterparts the electrons, positrons do not actually exist naturally in our universe. They have to be made.

The way the ILC will do this is by using the 250 GeV electron beam on its way to the collision point. The high-energy electrons will pass through a special magnet called a helical undulator, which is 200 metres long. Just as in the damping rings, the electrons will be made to radiate light in this magnet – indeed it is exactly the same phenomenon.

The difference is in the energy: the 250 GeV electron beam in the positron source's helical undulator generates high-energy gamma rays in a very narrow cone. These gamma rays slam into a thin titanium-alloy target, knocking loose a shower of electrons and positrons. The accelerator sections downstream then collect the positrons and throw away the electrons. The positrons are then bunched, accelerated to 5 GeV and injected into the positron damping ring in much the same way as the electrons.

In the meantime, the 250 GeV electron beam is gently bent away from the gamma ray cone and around the metal target before it proceeds on its way to meet the positrons generated on the previous machine pulse at the collision point.

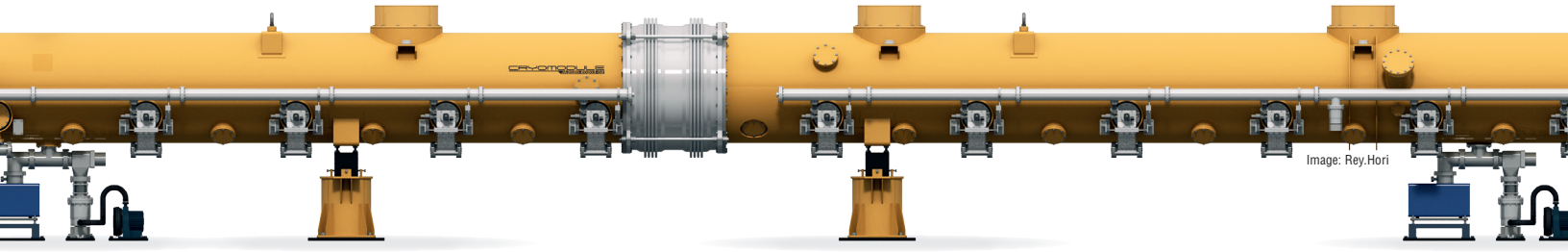

6 FINAL FOCUS

When electrons and positrons have each reached their collision energy of 250 GeV, the beams get one last massage before they enter the hall where it all happens: the interaction point around which the detector sits ready to record the collisions.

In the last two kilometres, instead of running through accelerating cavities the beams pass a series of specially designed and arranged magnets that ultimately focus them down to a height of just a few nanometres at the collision point. The “final focus” system can be thought of as a sort of microscope in reverse, where the beams are demagnified – instead of magnified – by a factor of about 300. Rather than using glass lenses as in an optical microscope, special arrangements of magnets are used to produce the focusing “lenses”.

The tiny beams need to be collided with an accuracy of a fraction of their size, so less than a nanometre! At this level, great care has to be taken to deal with vibration and other tiny fluctuations in magnetic and electric fields that can easily cause the bunches to wobble as they pass through the accelerator and final focus. Ultra-fast diagnostics systems analyse the shape and position of the bunches and tell the magnets how to correct them to optimise the collisions: without such fast “feedback systems”, the beams would simply miss each other. Using a purpose-built final-focus test beamline in Japan, an international collaboration has developed the controls and instrumentation needed to achieve these challenging parameters.

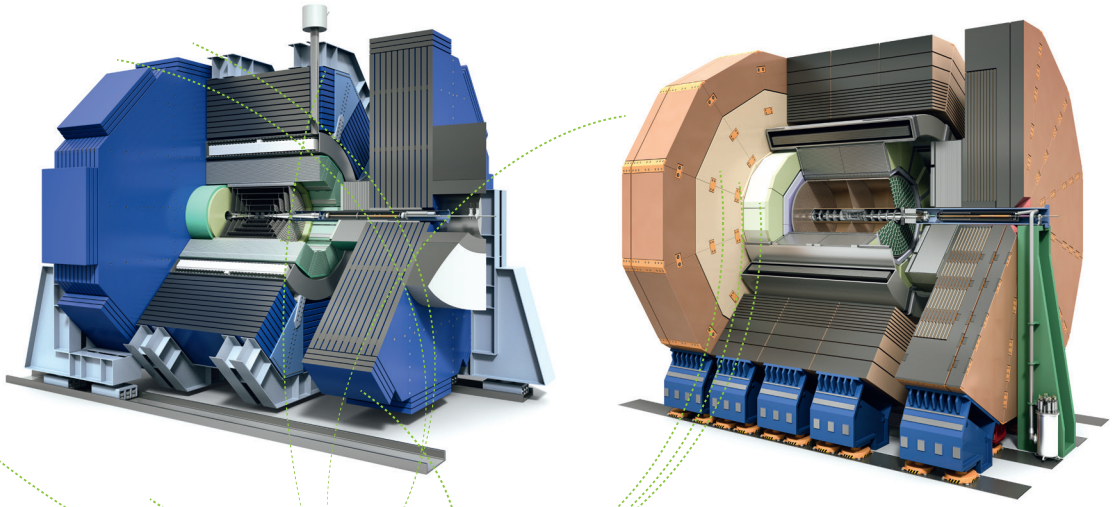

7

INTERACTION POINT AND DETECTORS

After all the squeezing, acceleration and focussing, the particles can finally hurtle towards their final destination: the collision between electron and its antiparticle, the positron. At full operation there are a potential 1.3 x 10^{14} (that's 130 trillion) electron-positron collisions per second, crammed into the tiny interaction area of just 6x500 nm^2 – or just 0.000000003 mm^2. Despite these impressive numbers, only a tiny fraction of the electrons and positrons actually collide. The higher the density of the particles at the interaction point, the greater the probability that some will collide: one reason why so much effort is made to produce tiny intense beams at the collision point.

When they do collide, electrons and positrons annihilate in a burst of energy, creating an array of new particles that fly out from the collision point. It's these new particles, their interactions, lifetime, and energy that the detectors will study.

Arranged in concentric cylinders of subdetectors with different technologies and tasks, these detectors are awe-inspiring in speed and precision (and in physical volume). Years of research and development have already produced mature technologies and concepts which will be required for the unprecedented precision of the measurements that need to be made. This R&D will go on until the very last minute to get even better, faster results more cost-effectively. The way the detectors will take data is unique, too. Two detectors will be built as one has to verify the results of the other before physicists can claim to have made a discovery. In order to avoid building a second, very costly, final-focus system, the ILC scientists invented the push-pull system: while one detector is installed in the interaction point and takes data, the other is in servicing position. After some time they swap position, being moved on two gigantic platforms that ensures the stability of even the tiniest part within the huge detector.

WHAT ARE THE POSSIBLE STAGES OF CONSTRUCTION?

The current design foresees an ILC with a maximum operating energy of 500 GeV centre-of-mass energy, i.e. 250 GeV per beam, which could be raised to one TeV at a later stage by making the linacs longer. The ILC could also be built as a so-called Higgs factory: at half the original design energy, requiring just half of the linacs, it could mass-produce and study the new particle found at the LHC in great detail. Such a scenario should be considered as a first phase of the larger machine.

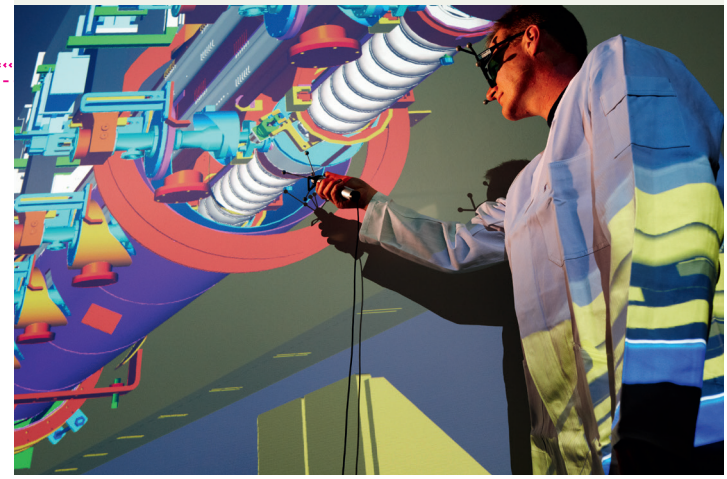

HOW MUCH WILL IT COST?

For the Technical Design Report, the GDE has produced a “value estimate”. Value estimates are a common form of costing large international projects that are usually constructed using mainly in-kind contributions from participating nations.
The value estimate for the construction of the ILC in the Technical Design Report is 7.8 billion ILCU together with 23 million person hours (approximately 13,000 person years) of additional labour (ILCU stands for ILC value Unit. One ILCU is 1 US Dollar in January 2012. The relation of the ILCU to a currency other than the US Dollar is determined by purchasing power parity indices published by the Organization for Economic Co-operation and Development.). This estimate is averaged over three regional sample sites and represents the construction cost of a 500 GeV linear collider as described in the cost chapter of the Technical Design Report.
The variance among the three regional site estimates is about 2%. The value estimate has an uncertainty of 25%. A more accurate estimate can be calculated when a host site is identified and the international project governance and in-kind contributions are agreed upon.

WHAT IS SUPERCONDUCTIVITY AND SUPERCONDUCTING RF?

Some metals become superconducting when they are cooled down to very low temperatures, which means that they lose all electrical resistance and can conduct electricity in an ultra-efficient way. Superconducting radio-frequency cavities are at the heart of the technology in the International Linear Collider. The ILC will use a voltage generator to fill a hollow structure called a cavity with an electromagnetic field. Made out of pure niobium, the cavities will be chilled to 2 Kelvin, near absolute zero temperature, at which point niobium is a superconductor and the cavities have almost no electrical resistance. Inside the cavities, the voltage of the field oscillates with a certain frequency – a radio frequency. Charged particles feel the force of the electric field and accelerate. String enough of these cavities together, and you will have a particle accelerator.

03 | THE ORGANISATION WITHOUT BOUNDARIES

Image: Fermilab

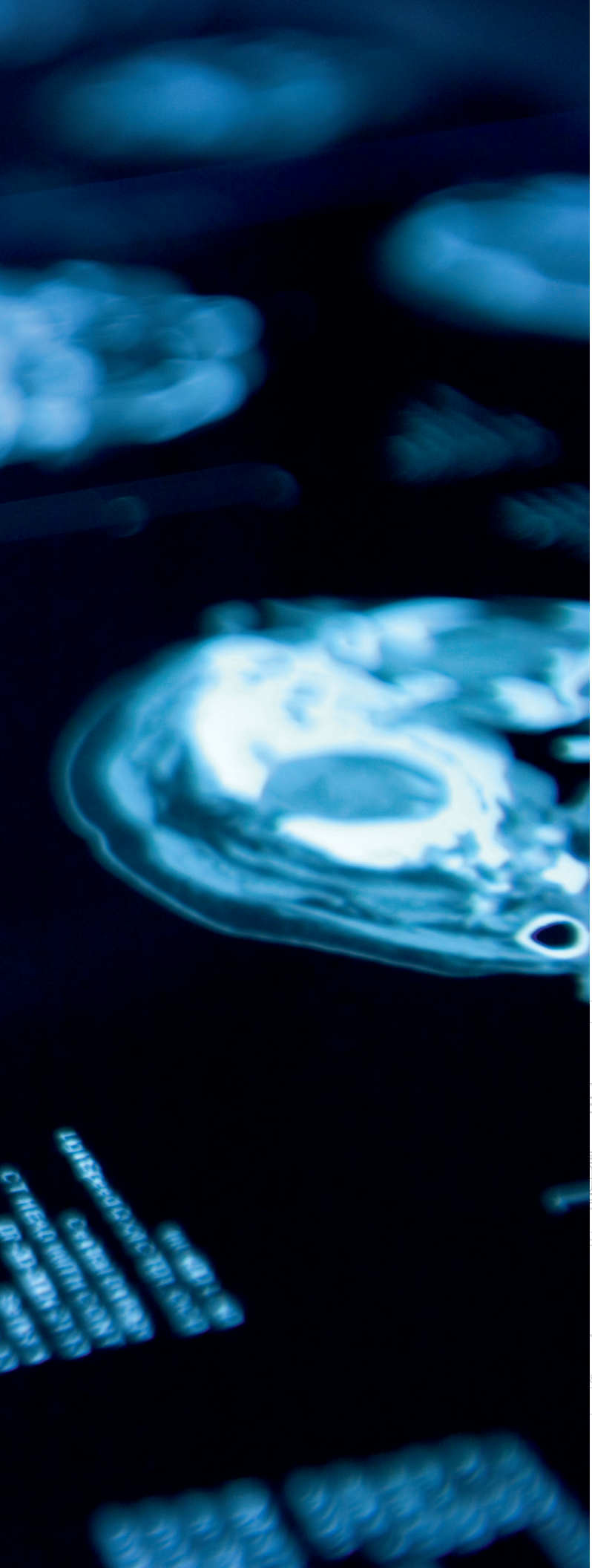

THE PROJECT THAT GOES BEYOND BOUNDARIES

The International Linear Collider will be one of the world's largest and most sophisticated scientific endeavours.

Planning, designing, funding, building and operating the ILC will require true global participation. The ILC can be realised only as a collaboration between many people in many fields: engineers, business persons, scientists, students, local officials and residents.

The ILC is the culmination of an assembly of all kinds of cutting-edge technologies and expertise. We can expect the breakthroughs led by ILC R&D to have huge impact on our society, both technologically and economically, which goes far beyond the pure science results of particle physics.

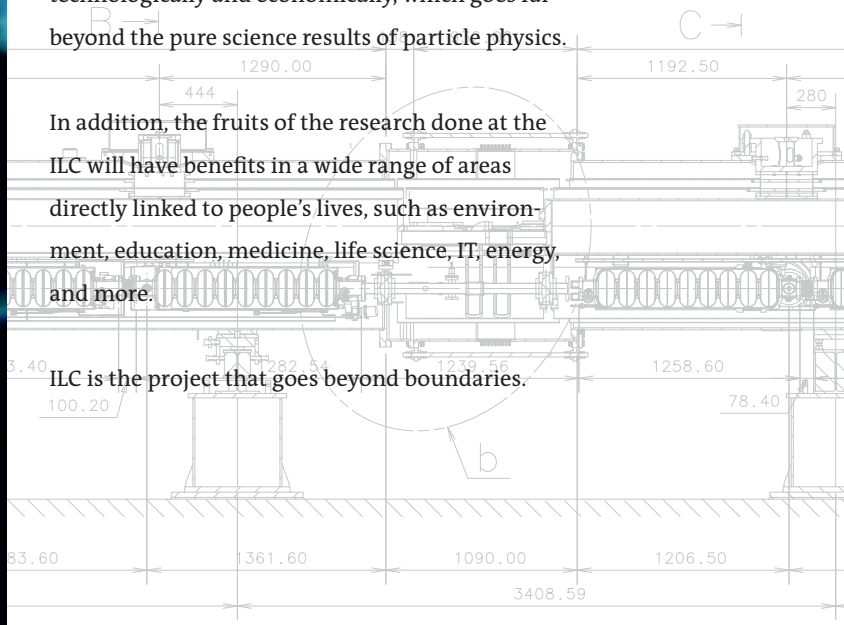

In addition, the fruits of the research done at the ILC will have benefits in a wide range of areas directly linked to people's lives, such as environment, education, medicine, life science, IT, energy, and more.

ILC is the project that goes beyond boundaries.

Image: DESY

THE PROJECT THAT ATTRACTS PEOPLE

Particle physics inspires. Particle physicists are on a quest to solve the universal questions – the mysteries of the universe – by studying fundamental laws of nature. They are working together across time zones, borders and languages. This cooperation across the world produced the World-Wide Web; the ILC may catalyze other groundbreaking technologies.

The ILC will provide a melting pot of the world's wisdom, attracting some of the best minds in science and technology. These great minds will continue to advance technology and yield many applications in science and industry.

The ILC will also attract people who wish to fulfill their intellectual curiosity, and to share the excitement of the science.

THE PROJECT THAT NURTURES THE NEXT GENERATION

Today at laboratories and universities around the world, several hundred students, under the guidance of senior scientists and engineers, are already contributing to the ILC. The international nature of particle physics provides younger generations with a working environment in which the experience and knowledge of different cultures are harnessed towards a common goal.

The ILC allows us to train future generations of scientists and engineers. But the ILC is not an island; ILC scientists come from other projects and work on other projects in parallel. Also, more than half of the students who obtain their PhD in particle physics go on to work for high-tech industry, financial institutions, and information technology companies. There is high demand for their talents because of their broad array of skills, as well as their physics knowledge. This benefits all of us.

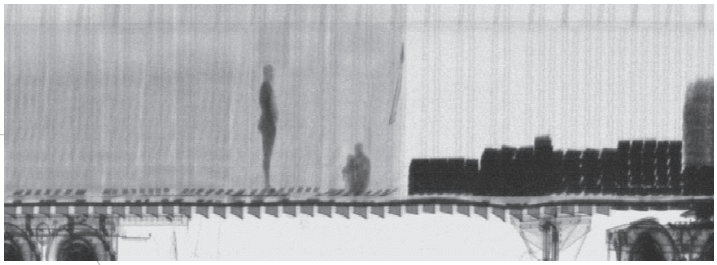

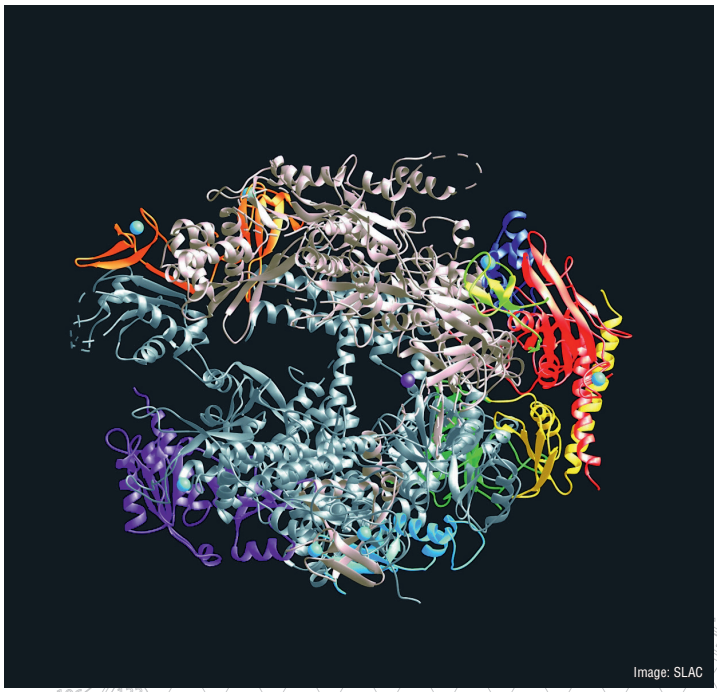

Image: SLAC

THE PROJECT THAT PUSHES TECHNOLOGY AND OTHER SCIENCES

The first *Free-Electron Lasers* (FELs) now being built or in operation in the US, Japan and Germany are direct consequences of linear-collider research. Light sources like these FELs have brought important advances in many sciences over the past decades, leading to many applications in materials science, drugs research and even the arts. Superconducting technology should also advance work on *Energy Recovery Linacs* (ERLs), permitting substantial savings in size and cost. The ILC technology can also be applied to the acceleration of protons and nuclei, which can lead to a wide range of studies on biological properties.

The ILC detectors must deliver exquisite precision. A hallmark of the ILC detectors is their fine granularity. These detectors are 3-D imaging devices that enable unprecedented study of the physics processes. Imaging calorimeters developed for the ILC, for example, are already being used in the development of proton-computed tomography for the treatment of cancer. This is just one of the societal "spin-offs" that the ILC detector development can already point to.

Fundamental research in particle physics is done to advance the boundaries of our knowledge of the Universe, not with the aim to serve other sciences or technologies. However, the track record shows that numerous applications in materials science, nuclear science, chemistry, structural biology and environmental science have already taken place. Many of these will have direct applications on everyday life.

THE PROJECT THAT HAS ECONOMIC IMPACT AS ITS HOME

Particle physics has been the source of many innovations. Many of those – medical diagnostics and therapy and the World Wide Web are two striking examples – have changed the way we live and do our business. History tells us that a tool for the future, such as the ILC, should be the source of yet more technological breakthroughs.

Independent experts have estimated that the social and economic impact of hosting this highly visible and prestigious facility will be great. Thousands of jobs will be created locally to directly and indirectly support the construction of the ILC and then its research programs, and there will be many other benefits from having a large world-famous science facility in the area.

The campus that will grow around the ILC site will be a future home for scientists, engineers, students and their families from around the world. The campus – which can become a science city – needs to fulfil the needs of people from different cultures, such as education, medical and social services, and leisure pursuits and amusements. Those needs will definitely create significant impact on the ILC construction region and beyond, both economically and culturally.

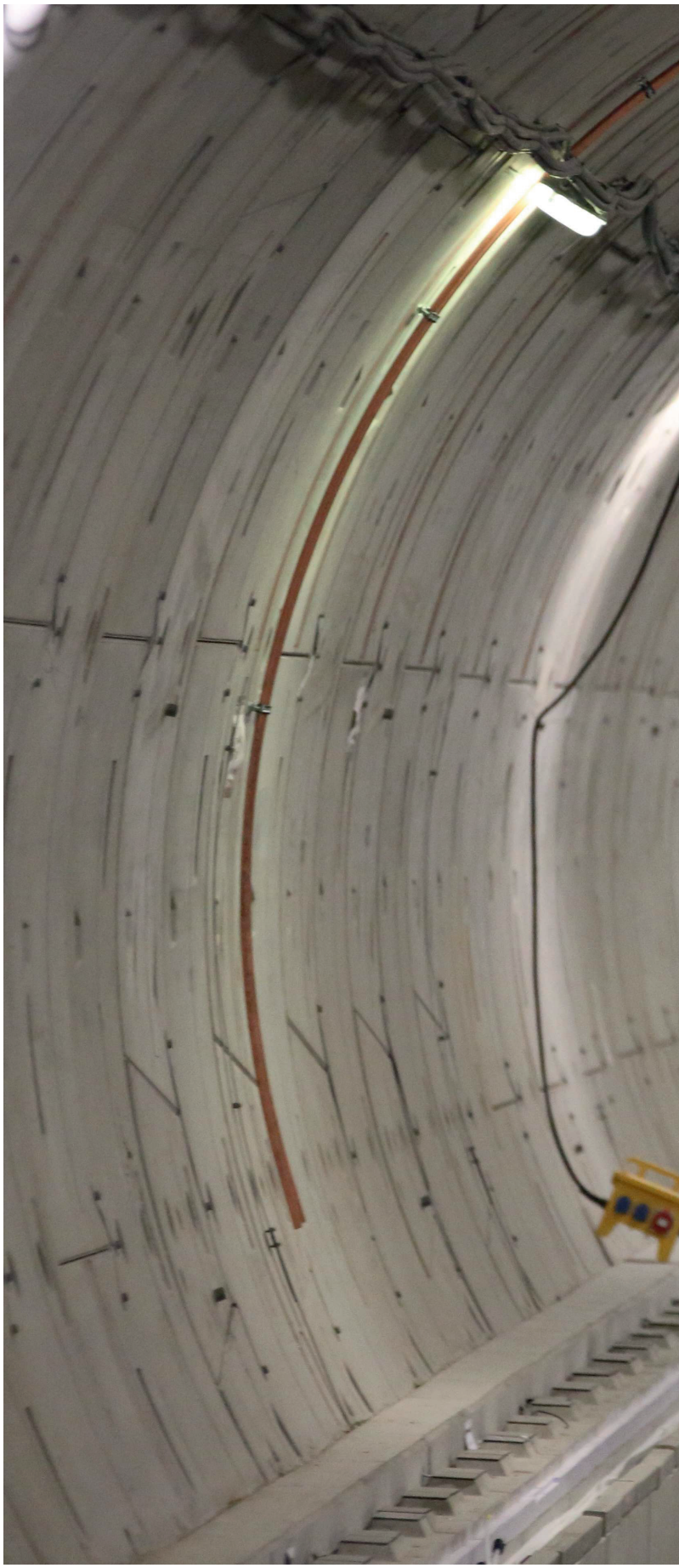

Image: DESY

brochure layout: www.form-one.de

ISSUED BY • • • • • • • • • ilc international linear collider

WWW.LINEARCOLLIDER.ORG

ISBN 978-3-935702-79-9

Argonne National Laboratory: ANL-HEP-TR-13-20
Brookhaven National Laboratory: BNL-100603-2013-IR
CEA/irfu: IRFU-13-59
CERN: CERN-ATS-2013-037
Cockcroft Institute: Cockcroft-13-10
Cornell University: CLNS 13/2085
DESY: DESY 13-062
Fermilab: FERMILAB TM-2554
IHEP: IHEP-AC-ILC-2013-001
ILC report: ILC-REPORT-2013-040
INFN: INFN-13-04/LNF
JAI: JAI-2013-001
JINR: JINR E9-2013-35
JLab: JLAB-R-2013-01
KEK: KEK Report 2013-1
KNU: KNU/CHEP-ILC-2013-1
LLNL: LLNL-TR-635539
SLAC: SLAC-R-1004
ILC HiGrade: ILC-HiGrade-Report-2013-003